NASA/CP—2000-210470

Proceedings of the Fifth Microgravity Fluid Physics and Transport Phenomena Conference

December 2000

The NASA STI Program Office . . . in Profile

Since its founding, NASA has been dedicated to the advancement of aeronautics and space science. The NASA Scientific and Technical Information (STI) Program Office plays a key part in helping NASA maintain this important role.

The NASA STI Program Office is operated by Langley Research Center, the Lead Center for NASA's scientific and technical information. The NASA STI Program Office provides access to the NASA STI Database, the largest collection of aeronautical and space science STI in the world. The Program Office is also NASA's institutional mechanism for disseminating the results of its research and development activities. These results are published by NASA in the NASA STI Report Series, which includes the following report types:

- TECHNICAL PUBLICATION. Reports of completed research or a major significant phase of research that present the results of NASA programs and include extensive data or theoretical analysis. Includes compilations of significant scientific and technical data and information deemed to be of continuing reference value. NASA's counterpart of peer-reviewed formal professional papers but has less stringent limitations on manuscript length and extent of graphic presentations.

- TECHNICAL MEMORANDUM. Scientific and technical findings that are preliminary or of specialized interest, e.g., quick release reports, working papers, and bibliographies that contain minimal annotation. Does not contain extensive analysis.

- CONTRACTOR REPORT. Scientific and technical findings by NASA-sponsored contractors and grantees.

- CONFERENCE PUBLICATION. Collected papers from scientific and technical conferences, symposia, seminars, or other meetings sponsored or cosponsored by NASA.

- SPECIAL PUBLICATION. Scientific, technical, or historical information from NASA programs, projects, and missions, often concerned with subjects having substantial public interest.

- TECHNICAL TRANSLATION. English-language translations of foreign scientific and technical material pertinent to NASA's mission.

Specialized services that complement the STI Program Office's diverse offerings include creating custom thesauri, building customized data bases, organizing and publishing research results . . . even providing videos.

For more information about the NASA STI Program Office, see the following:

- Access the NASA STI Program Home Page at *http://www.sti.nasa.gov*

- E-mail your question via the Internet to help@sti.nasa.gov

- Fax your question to the NASA Access Help Desk at 301–621–0134

- Telephone the NASA Access Help Desk at 301–621–0390

- Write to:
  NASA Access Help Desk
  NASA Center for AeroSpace Information
  7121 Standard Drive
  Hanover, MD 21076

NASA/CP—2000-210470

Proceedings of the Fifth Microgravity Fluid Physics and Transport Phenomena Conference

Proceedings of a conference sponsored by the
NASA Glenn Research Center
and held at the Sheraton City Centre, Cleveland, Ohio
August 9–11, 2000

National Aeronautics and
Space Administration

Glenn Research Center

December 2000

Available from

NASA Center for Aerospace Information
7121 Standard Drive
Hanover, MD 21076
Price Code: A99

National Technical Information Service
5285 Port Royal Road
Springfield, VA 22100
Price Code: A99

Available electronically at http://gltrs.grc.nasa.gov/GLTRS

Table of Contents

Wednesday, August 9, 2000

Friday, August 11, 2000

Fifth Microgravity Fluids Physics and Transport Phenomena Conference
Detailed Program

Wednesday, August 9, 2000

Registration	7:30-8:30 AM
Opening Plenary Speakers: (Ballroom)	
Plenary Chair Mr. Jack Salzman, Chief, Microgravity Science Division, GRC	
Welcome Mr. Gerald J. Barna, Acting Deputy Director, NASA GRC	8:30-8:40 AM
Microgravity Sciences Program Overview Dr. Eugene H. Trinh, Director for Microgravity Research Division, NASA HQ	8:40-9:10 AM
NASA Research Announcement Dr. Gerald Pitalo, Fluids Enterprise Scientist, Microgravity Research Division, NASA HQ	9:10-9:30 AM
Fluid Physics/Transport Phenomena Research Thrusts Prof. G. P. Neitzel, Georgia Institute of Technology, DWG Chair	9:30-9:50 AM
International AO Dr. Bradley Carpenter, Lead Enterprise Scientist, Microgravity Research Division, NASA HQ	9:50-10:10 AM
Break	10:10-10:30 AM
Research for Design and Industrial Outreach Dr. Simon Ostrach, Director, NCMR	10:30-11:15 AM
Keynote Speaker:	
Microgravity Research in Support of Technologies for the Human Exploration And Development of Space and Planetary Bodies Prof. Raymond Viskanta, Purdue University	11:15-12:00 AM
Lunch (free time)	12:00-1:30 PM
Session 1A: Multiphase Flow and Phase Change I (West Ballroom)	
Session Chair G. Tryggvason, University of Michigan	
Pressure-Radiation Forces on Vapor Bubbles A. Prosperetti, Johns Hopkins University	1:30-1:50 PM

Experimental Investigation of Pool Boiling Heat Transfer Enhancement in Microgravity in the Presence of Electric Fields — 1:50-2:10 PM
C. Herman, Johns Hopkins University

Saturated Pool Boiling Heat Transfer Mechanisms — 2:10-2:30 PM
J. Kim, University of Maryland

Wetting and Partially Wetting Fluid Profiles in a Constrained Vapor Bubble Heat Exchanger — 2:30-2:50 PM
P. Wayner, Jr., Rensselear Polytechnic Institute

A Mechanistic Study of Nucleate Boiling Heat Transfer Under Microgravity Conditions — 2:50-3:10 PM
V.K. Dhir, University of California, Los Angeles

Session 1 B: Complex Fluids I (Dolder-Hassler)

Session Chair
H. Aref, University of Illinois

Physics of Hard Spheres Experiment: Microscopy of Colloidal Particles — 1:30-1:50 PM
P. Chaikin, Princeton University

Physics of Colloids in Space — 1:50-2:10 PM
D. Weitz, Harvard University

Colloidal Assembly in Entropically Driven, Low-Volume-Fraction Binary Particle Suspensions — 2:10-2:30 PM
A. Yodh, University of Pennsylvania

Micromechanics and Dynamics in Magnetorheological Suspensions — 2:30-2:50 PM
A. Gast, Stanford University

Freely Suspended Smectic Filaments and the Structure of the B7 Phase of MHOBOW — 2:50-3:10 PM
N. Clark, University of Colorado

Session 1 C: Interfacial Phenomena I (East Ballroom)

Session Chair
S. Davis, Northwestern University

Thermocapillary-Induced Phase Separation with Coalescence — 1:30-1:50 PM
R. Davis, University of Colorado

Fluid Dynamics and Solidification of Molten Solder Droplets Impacting on a Substrate in Microgravity — 1:50-2:10 PM
C. Megaridis, University of Illinois at Chicago

Fluid Flow in a Rotating Circular Cylinder — 2:10-2:30 PM
M. Perlin, University of Michigan

An Interferometric Investigation of Contact Line Dynamics in Spreading Polymer Melts and Solutions
G. McKinley, MIT — 2:30-2:50 PM

Coalescence and Non-Hydrodynamic Forces Across Thin Films Between Two Fluid Interfaces
L.G. Leal, University of California, Santa Barbara — 2:50-3:10 PM

Break — 3:10-3:40 PM

Session 2 A: Multiphase Flow and Phase Change II (West Ballroom)

Session Chair
A. Prosperetti, Johns Hopkins University

Modeling of Transport Processes in a Solid Oxide Electrolyzer Generating Oxygen
K. Sridhar, University of Arizona — 3:40-4:00 PM

Production and Removal of Gas Bubbles in Microgravity
H. Oguz, Johns Hopkins University — 4:00-4:20 PM

Using Surfactants to Control Bubble Coalescence in Nucleate Pool Boiling
K. Stebe, Johns Hopkins University — 4:20-4:40 PM

The Physics of Boiling at Burnout
T. Theofanous, University of California, Santa Barbara — 4:40-5:00 PM

Marangoni Effects on Near-Bubble Microscale Transport During Boiling of Binary Fluid Mixtures
V. Carey, University of California, Berkeley — 5:00-5:20 PM

Thermal Control and Enhancement of Heat Transport Capacity of Two-Phase Loops with Electrohydrodynamic Conduction Pumping
J. Seyed-Yagoobi, Texas A&M — 5:20-5:40 PM

Session 2 B: Flow of Granular Media I (Dolder-Hassler)

Session Chair
D. Durian, University of California, Los Angeles

Slide Conveying of Granular Materials-Thinking Out of the Glovebox
J. Goddard, University of California-San Diego — 3:40-4:00 PM

Shaken Granular Systems and the Effects of Gravity
R. Behringer, Duke University — 4:00-4:20 PM

Particle Segregation in Collisional Shearing Flows
J. Jenkins, Cornell University — 4:20-4:40 PM

Studies of Gas - Particle Interactions in a Microgravity Flow Cell — 4:40-5:00 PM
M. Louge, Cornell University

Electrostatics of Granular Material (EGM): Space Station Experiment — 5:00-5:20 PM
J. Marshall, SETI Institute NASA Ames

Assessment of Constitutive and Stability Behavior of Sands Under Plane Strain Condition — 5:20-5:40 PM
S. Sture, University of Colorado

Session 2 C: Dynamics and Instabilities I (East Ballroom)

Session Chair
I. Alexander, NCMR/Case Western Reserve University

Thermal Field Imaging Using Ultrasound — 3:40-4:00 PM
D. Andereck, Ohio State University

Stability of Thermocapillary Return Flows Under Vertical Gravity Modulation — 4:00-4:20 PM
G. Homsy, Stanford University

Molecular Dynamics Fluid-Solid Systems — 4:20-4:40 PM
J. Koplik, City College of New York

Diffusing Light Photography of Containerless Ripple Turbulence — 4:40-5:00 PM
S. Putterman, University of California, Los Angeles

Weakly Nonlinear Description of Parametric Instabilities in Vibrating Flows — 5:00-5:20 PM
E. Knobloch, University of California, Berkeley

Instabilities and Spatio-Temporal Chaos of Hexagonal Convection Patterns in the Presence of Rotation — 5:20-5:40 PM
H. Riecke, Northwestern University

Free Time — 5:40 PM on

Thursday, August 10, 2000 (Ballroom)

Plenary Chair
Dr. Iwan Alexander, Fluids Chief Scientist, NCMR/Case Western Reserve University

Theme Speaker:

"An Integrated Exploration Strategy" — 8:00-8:45AM
Mr. Michael Conley, Deputy Manager, Advanced Development Office,
NASA Lyndon B. Johnson Space Center

Keynote Speakers:

"The Interaction of Convection and Solidification" Prof. Stephen Davis, Northwestern University	8:45-9:30 AM
"Macromolecular Influences on Liquid Flow in Narrow Channels: The Role of Boundary Conditions for Adsorption" Prof. Matthew Tirrell, University of California, Santa Barbara	9:30-10:15 AM
Break	10:15-10:40 AM

Session 3A: Multiphase Flow and Phase Change III (West Ballroom)

Session Chair
V. Dhir, University of California, Los Angeles

Computations of Boiling in Microgravity G. Tryggvason, University of Michigan	10:40-11:00 AM
Numerical Simulation of Three Dimensional Bubble Growth and Detachment in a Microgravity Shear Flow S. Banerjee, University of California, Santa Barbara	11:00-11:20 AM
Three-Dimensional Oscillations of Inviscid Drops Induced by Surface Tension C. Pozrikidis, University of California, San Diego	11:20-11:40 AM
Scaling of Multiphase Flow Regimes and Interfacial Behavior at Microgravity C. Crowley, Creare, Inc.	11:40-12:00 PM
Development of a Magnetic Resonance Imaging Technique for Measuring Emulsion Coalescence R. Powell, University of California, Davis	12:00-12:20 PM

Session 3B: Complex Fluids II (Dolder-Hassler)

Session Chair
J. Goddard, University of California-San Diego

Gas & Liquid Transport Inside Aqueous Foams D. Durian, University of California, Los Angeles	10:40-11:00 AM
Foam Evolution: Experiments and Simulations H. Aref, University of Illinois	11:00-11:20 AM
Linear Viscoelastic Response of a Concentrated Emulsion M. Loewenberg, Yale University	11:20-11:40 AM
Dusty Plasma Dynamics Near Surfaces in Space J. Colwell, University of Colorado, Boulder	11:40-12:00 PM

Rheology of Foam Near the Order-Disorder Phase Transition 12:00-12:20 PM
R. Holt, Boston University

Session 3 C: Interfacial Phenomena II (East Ballroom)

Session Chair
R. Davis, University of Colorado

Micro-Fluid Dynamics in an Evaporating Sessile Droplet 10:40-11:00 AM
R. Larson, University of Michigan

Inertial Effects on the Hydrodynamics of Moving Contact Lines 11:00-11:20 AM
S. Garoff, Carnegie Mellon University

Liquid Bridge Stabilization with Acoustic Radiation and Maxwell Stress 11:20-11:40 AM
P. Marston, Washington State University

The Effect of Convection on Morphological Instability 11:40-12:00 PM
S. Davis, Northwestern University

The Dynamics of Miscible Interfaces: A Space Flight Experiment 12:20-12:20 PM
T. Maxworthy, University of Southern California

Lunch –free time 12:30-2:00 PM

Exposition Session (Ballroom) 2:00-5:00 PM

Longitudinal and Transverse Waves in Coulomb Crystals Formed in a Dusty Plasma
A. Bhattacharjee, University of Iowa

Diffusive Coarsening of Liquid Foams in Microgravity
J. Glazier, University of Notre Dame

Phase-Shifting Liquid Crystal Point-Diffraction Interferometry
D. Griffin, NASA Glenn Research Center

DSD-A Particle Simulation Code for Modeling Dusty Plasmas
G. Joyce, Plasma Physics Division

Aggregation and Gelation of Anisometric Colloidal Particles: Preliminary Results and Research Plan
M. Solomon, University of Michigan

Gelation Kinetics in Aerosols
C. Sorensen, Kansas State University

Novel Optical Diagnostic Techniques for Studying Particle Deposition Upon Large Cylinders in a Sheared Suspension
M. Yoda, Georgia Institute of Technology

(Exposition Session Continued)

Effect of Pressure on Microstructure of $C_{12}E_5$/n-Octane-in-D_2O Microemulsions
M. Paulaitis, Johns Hopkins University

Non-Equilibrium Particle Configuration in Sedimentation
P. Tong, Oklahoma State University

Dynamics of Grain Boundaries in 2D Colloids
Q.-H. Wei, University of Pittsburgh

Photonic Crystals Based on Self-Assembly of Colloidal Particles
D. Weitz, Harvard University

Gravitational Effects on Flow Instability and Transition in Low Density Jets
A. Agrawal, University of Oklahoma

Lattice-Boltzmann Methods for Multiphase Flows in Microgravity Environments
R. Chella, Florida State University

Resonance Effects in a Horizontal Double-Diffusive Layer Under Gravity Modulation
C. Chen, The University of Arizona

Separation of Carbon Monoxide and Carbon Dioxide for Mars ISRU-Concepts
M. LeVan, Vanderbilt University

Rivulet Dynamics with Variable Gravity and Wind Shear
J. Marshall, University of Iowa

Periodic Flow and Its Effect on the Mass Transfer of a Species
R. Narayanan. University of Florida

Instability and Breakup of Gas Jets Injected in Coflowing Liquids
R. Parthasarathy, The University of Oklahoma

Fluid Physics and Macromolecular Crystal Growth in Microgravity
M. Pusey, NASA Marshall Space Flight Center

Electrohydrodynamic Flows in Electrochemical Systems
D. Saville, Princeton University

Competing Harmonic and Subharmonic Instabilities and Parametrically Excited Surface Wave Patterns
M. Silber, Northwestern University

Dynamics and Stability of Liquid Bridges
I. Alexander, NCMR/Case Western Reserve University

Droplet Formation by Vortex Rings
L. Bernal, University of Michigan

(Exposition Session Continued)

Thermophoretic Force Measurements on Single Spherical and Nonspherical Particles
E.J. Davis, University of Washington

Capillary Instabilities in the Microgravity Environment
J. Grotberg, University of Michigan

Experiments on the Richtmyer-Meshkov Instability of Incompressible Fluids
J. Jacobs, The University of Arizona

Absolute and Convective Instability and Splitting of a Liquid Jet at Microgravity
S. Lin, Clarkson University

A Compact Laser Velocity Strain and Vorticity Probe for Microgravity Research
M. Otugen, Polytechnic University

Decoupling the Roles of Inertia and Gravity on Particle Dispersion
C. Rogers, Tufts University

Ground Based Studies of Thermocapillary Flows in Levitated Laser-Heated Drops
S. Sadhal, University of Southern California

Stability of Shapes Held by Surface Tension and Subjected to Flow
P. Steen, Cornell University

Instability of Miscible Interfaces
R. Balasubramaniam, The National Center for Microgravity Research

Low Velocity Impact Experiments in Microgravity
J. Colwell, University of Colorado

Surface Collisions Involving Particles and Moisture (SCIP'M)
R. Davis, University of Colorado

Stereo Imaging Velocimetry of Mixing Driven by Buoyancy Induced Flow Fields
W. Duval, NASA Glenn Research Center

Granular Material Flows with Interstitial Fluid Effects
M. Hunt, California Institute of Technology

Sheet Flows, Avalanches, and Dune Migration on Earth and Mars
J. Jenkins, Cornell University

Turbulent Coagulation of Aerosol Particles
D. Koch, Cornell University

Microscopic Flow Visualization in Demixing Fluids During Polymeric Membrane Formation in Low-G
W. Krantz, University of Cincinnati

(Exposition Session Continued)

Microgravity Driven Instabilities in Gas-Fluidized Beds
A. Ladd, University of Florida

The Dynamics of Particulate Deposition and Resuspension Processes at Moderate to High Reynolds Numbers
E. Meiburg, University of California at Santa Barbara

Studies of Wet Granular Media
P. Schiffer, University of Notre Dame

Superfluid Contact Line Dynamics
P. Taborek, University of California, Irvine

Splashing Droplets
R. Vander Wal, The National Center for Microgravity Research

Capillary Flow in Interior Corners
M. Weislogel, TDA Research Inc.

Driven Two-Dimensional Turbulence
X. Wu, University of Pittsburgh

Taylor Cones on Thin Flowing Films
S. Bankoff, Northwestern University

Dynamics and Arrest by Freezing of a Molten Contact Line Advancing Over a Cold Substrate
A. Sonin, Massachusetts Institute of Technology

Stability and Heat Transfer Characteristics of Condensate Fluid Layers in Reduced Gravity
J. Hermanson, Worcester Polytechnic Institute

Two Phase Flow in Multi-Channels – Liquid Holdup and Capillary Flow
F. Issacci, Honeywell Aerospace

Buoyancy-Driven Instabilities in Single-Bubble Sonoluminescence
T. Matula, University of Washington

A Study of Bubble and Slug Gas-Liquid Flow in a Microgravity Environment
J. McQuillen, NASA Glenn Research Center

Investigation of Critical Heat Flux in Reduced Gravity Using Photomicrographic Techniques
I. Mudawar, Purdue University

Computational Modeling of the Effect of Secondary Forces on the Phase Distribution in Dispersed Multiphase Channel Flows
G. Tryggvason, University of Michigan

Heat Transfer Performances of Pool Boiling on Metal-Graphite Composite Surfaces
N. Zhang, NASA Glenn Research Center

(Exposition Session Continued)

Thermocapillary Migration of Bubbles
V. Arpaci, University of Michigan

Determination of the Accommodation Coefficient Using Vapor-Gas Bubble Dynamics in an Acoustic Field
N. Gumerov, Dynaflow, Inc.

Gas-Evolving Effect on Mass Transfer in Rotating Electrochemical Cells Under Microgravity
Y. Kamotani, Case Western Reserve University

Industrial Processes Influenced by Gravity
Y. Kamotani, Case Western Reserve University

Bubble Formation on a Wall in Cross-Flowing Liquid and Surrounding Fluid Motion, With and Without Heating
Y. Kamotani, Case Western Reserve University

Bubble Dynamics on a Heated Surface
M. Kassemi, The National Center for Microgravity Research

The Investigation of the Effects of Gravity on Single Bubble Sonoluminescence
P. Marston, Washington State University

Atomization Processes in Fluid-Fluid Flows: Prediction of the Frequency of the Precursor Solitary Waves
M. McCready, University of Notre Dame

Recent Development in the Studies of Annular Two-Phase Flow at Microgravity
K. Rezkallah, University of Saskatchewan

Free time 5:00-6:00 PM

Dinner and Speaker (begins at 6:00 P.M.) 6:00-10:00 PM
Windows on the River (shuttle service provided)
Presiding: Dr. Simon Ostrach, Director, NCMR
Guest Speaker: Dr. Kathie Olsen, Chief Scientist, NASA HQ

Friday, August 11, 2000 (Ballroom)

Plenary Chair
Prof. Paul Neitzel, Georgia Institute of Technology, DWG Chair

Keynote Speakers:

"Virtual Surfaces Using Fluidic Actuators" 8:00-8:45 AM
Prof. Ari Glezer, Georgia Institute of Technology

"Microgravity Effects on Cardiovascular Flow and Transport" 8:45-9:30 AM
Prof. John Tarbell, Pennsylvania State University

Theme Speaker:

Dr. Donald Henninger, Deputy Project Manager, Advanced Life 9:30-10:15 AM
Support Program, NASA JSC

Break 10:15-10:45 AM

Session 4 A: Multiphase Flow and Phase Change IV (West Ballroom)

Session Chair
C. Herman, Johns Hopkins University

Fluid Dynamics of Bubbly Liquids 10:45-11:05 AM
A. Sangani, Syracuse University

Sonoluminescence in Space: The Critical Role of Buoyancy in Stability and 11:05-11:25 AM
Emission Mechanisms
R. Holt, Boston University

Attenuation of Gas Turbulence by a Nearly Stationary Dispersion of Solid Particles 11:25-11:45 AM
J.Eaton, Stanford University

Thermocapillary Flow and Aggregation of Bubbles on a Solid Wall 11:45-12:05 PM
P. Sides, Carnegie Mellon University

Transition from Pool to Flow Boiling-The Effect of Reduced Gravity 12:05-12:25 PM
V. Dhir, University of California, Los Angeles

Session 4 B: Complex Fluids III (Dolder-Hassler)

Session Chair
A. Gast, Stanford University

Inertial Effects in Suspension Dynamics 10:45-11:05 AM
J. Brady, California Institute of Technology

Plasma Dust Crystallization 11:05-11:25 AM
J. Goree, University of Iowa

Characterization of Acousto-Electric Cluster and Array Levitation and its 11:25-11:45 AM
Application to Evaporation
R. Apfel, Yale University

Particle Segregation in a Flowing Suspension Subject to High-Gradient Strong Electric Fields A. Acrivos, City College of New York	11:45-12:05 PM
Engineering Novel Biocolloid Suspensions D. Hammer, University of Pennsylvania	12:05-12:25 PM

Session 4C: Dynamics and Instabilities II (East Ballroom)

Session Chair
Y. Kamotani, Case Western Reserve University

Non-Coalescence in Microgravity: Science and Technology G. Neitzel, Georgia Institute of Technology	10:45-11:05AM
Critical Velocities in Open Capillary Flow M. Dreyer and H. Rath, Center for Applied Space Technology and Microgravity (ZARM), University of Bremen	11:05-11:25 AM
Geophysical Flow Experiments in Rotating Spherical Capacitors J. Hegseth, University of New Orleans	11:25-11:45 AM
The Evolution of Tensile Stresses in Uniaxial Elongational Flows of Dilute Polymer Solutions Subjected to a Known Preshear History G. McKinley, MIT	11:45-12:05 PM
Acoustic Study of Critical Phenomena in Microgravity M. Moldover, NIST	12:05-12:25 PM
Lunch and Speaker Sheraton City Centre Hotel (West Ballroom) Guest Speakers: Mr. Robert Corban Fluid and Combustion Facility Deputy Project Manager NASA Glenn Research Center "Fluid Physics Research on the International Space Station" Professor John Goree University of Iowa "International Microgravity Plasma Facility (IMPF)"	12:45-2:00 PM
Forum for Emerging Research Themes (East Ballroom)	2:00-4:00 PM
Adjourn	4:00 PM

PREFACE AND ACKNOWLEDGMENTS

The Fifth Microgravity Fluid Physics and Transport Phenomena Conference provides us the opportunity to view the current scope of the microgravity Fluid Physics and Transport Phenomena Program and conjecture about its future. The program currently has a total of 100 ground-based and 20 candidate flight principal investigators. A look at the collection of abstracts in this document clearly shows both the high quality and the breadth of the ongoing research program. One can easily notice many established world-class scientists as well as investigators who are early in their career poised to achieve that stature. We hope that many of the participants in this conference will perceive microgravity fluid physics as an exciting and rewarding area of research and choose to participate in the upcoming NASA Research Announcement expected to be released in Fall of 2000.

The microgravity program under the leadership of its new director, Dr. Eugene Trinh, is poised for some changes. Although the utilization of the International Space Station (ISS) and development of facilities and hardware to achieve that will continue to be the centerpiece of the program, the research to be conducted on it as well as in the ground-based program is likely to see a shift in emphasis. Dr. Trinh indicates that the first goal of the Microgravity Research Program is the development of a fundamental scientific base for human and robotic forays into outer space. The second goal is the utilization of the unique space environment for basic and applied scientific knowledge, both to fulfill innate curiosity and to improve the human condition on Earth. As the Agency moves to tap the potential of the emerging disciplines of nanotechnology and biologically inspired technologies, the Microgravity Research Program plans to play a significant role by promoting research in these areas. Cross-disciplinary research is another theme that program is emphasizing.

Two elements of the International Space Station (ISS) are already on the orbit and the next major phase of the assembly is about to begin in earnest this year. ISS provides the microgravity research community with a tremendous opportunity to conduct long-duration microgravity experiments, which can be controlled and operated from their own laboratory. Frequent planned shuttle trips will provide opportunities to conduct many more experiments than were previously possible. NASA Glenn Research Center is in the process of designing a Fluids and Combustion Facility (FCF) to be located in the US Laboratory Module of the ISS that will accommodate multiple users with a broad range of fluid physics and transport phenomena experiments and enable these experiments to be conducted in a cost effective manner. Physics of Colloids in Space (PCS) our first major experiment is to be launched in April of 2001. Launch of the Fluids and Combustion facility in 2004 will begin the full utilization of ISS by the discipline.

NASA had asked the National Research Council (NRC) to undertake an assessment of scientific and related technological issues facing NASA's Human Exploration and Development of Space endeavor. An NRC committee Chaired by Prof. Raymond Viskanta (Purdue University) recommended the following areas of high priority research on fundamental phenomena/processes:

- Surface and Interfacial Phenomena
- Multiphase Flow and Heat Transfer
- Multiphase Systems Dynamics
- Fire Phenomena
- Granular Mechanics

As one might have expected, most of these high priority areas fit well within the fluid physics and transport phenomena discipline. They bear a strong resemblance to the performance goals previously developed by the Microgravity Research Program that are listed below:

1. Advance the state of knowledge sufficiently to allow development of reliable and efficient heat transfer technologies for space and extraterrestrial operations.
2. Advance the state of knowledge sufficiently to allow development of effective fluid management technology for space and extraterrestrial and industrial applications.
3. Establish the knowledge base required to design chemical process systems for exploration missions.
4. Advance the state of knowledge sufficiently to enable dust control technologies and bulk material handling for extraterrestrial habitats and/or in situ resource utilization.

Like the Microgravity Research Program, this conference has undergone a number of changes and innovations. In consultation with the Fluid Physics and Transport Phenomena Discipline Working Group chaired by Professor Paul Neitzel, we decided to abandon the production of proceedings with the full-length papers on a CD ROM and elected to go with a virtual proceedings of the presentation charts on the World Wide Web at the website http://www.ncmr.org/events/fluids2000.html. In this regard we acknowledge the support of our principal investigators who have provided us timely inputs of their charts and abstracts and accommodated our format requirements. This cooperation was critical in implementing this and is very much appreciated.

The Discipline Working Group has provided the much-needed guidance in planning the content and the format of this conference. Their advice and guidance were essential for the success of this conference.

This conference has been organized and hosted by the National Center for Microgravity Research on Fluids and Combustion under the leadership of its Director, Professor Simon Ostrach. I would like to acknowledge the extensive efforts of Ms. Christine Gorecki and other members of the Center in planning, organizing, and hosting the conference and in preparing the proceedings and Conference materials. Sincere appreciation is offered to the authors for providing the abstracts and presentation charts in a timely manner and to the members of the Microgravity Fluids Physics Branch of NASA Glenn Research Center for their many contributions.

Finally I would like to express my gratitude to all of the Conference participants for their contributions to the success of this Conference.

Dr. Bhim S. Singh
Fluid Physics Discipline Lead Scientist
Mail Stop 500–102
NASA Glenn Research Center
21000 Brookpark Road
Cleveland, Ohio 44135
Phone: 216–433–5396
Fax: 216–433–8660
E-mail: bhim.s.singh@grc.nasa.gov

This conference was made possible by the efforts of many people. We acknowledge the contributions of the following individuals:

Fluid Physics and Transport Phenomena Discipline Working Group:
G. Paul Neitzel (chair), Georgia Institute of Technology
Bhim Singh (vice-chair), NASA Glenn Research Center
Iwan Alexander, Case Western Reserve/National Center for Microgravity Research
Sanjoy Banerjee, University of California-Santa Barbara
Bradley Carpenter, NASA Headquarters
Stephen Davis, Northwestern University
Donald Gaver, Tulane University
Joe Goddard, University of California, San Diego
Joel Koplik, City College of the City University of New York
Gerald Pitalo, NASA Headquarters
Matthew Tirrell, University of California Santa Barbara
David Weitz, Harvard University

Session Chairs
Plenary Sessions:

Jack Salzman, Chief, Microgravity Science Division, NASA Glenn Research Center
Iwan Alexander, Case Western Reserve University, NCMR
G. Paul Neitzel, Georgia Institute of Technology
Simon Ostrach, Case Western Reserve University, NCMR

Parallel Sessions (In Session Order):

Gretar Tryggvason, University of Michigan
Hasan Aref, University of Illinois
Stephen Davis, Northwestern University
Andrea Prosperetti, Johns Hopkins University
Douglas J. Durian, University of California, Los Angeles
Iwan Alexander, Case Western Reserve University, NCMR
V.K. Dhir, University of California, Los Angeles
Joe Goddard, University of California, San Diego
Robert Davis, University of Colorado
Cila Herman, Johns Hopkins University
Alice Gast, Stanford University
Yasu Kamotani, Case Western Reserve University

National Center for Microgravity Research on Fluids and Combustion:

Simon Ostrach, Director
Thomas Labus, Deputy Director
Iwan Alexander, Fluids Senior Scientist
Christine Gorecki, Conference Coordinator

Conference Team:

Christine Gorecki
Beatrix Norton
Jennifer Wells
Ann Heyward
Sandra Jones
Iwan Alexander
Norman Weinberg
William Yanis
Sandra Reynolds

The Logistics and Technical Information Division and its support service contractors, particularly Kristen Easton, Patricia Webb, and Gayle DiBiasio.

August 9, 2000
Opening Plenary Speaker

Microgravity Sciences Program Overview

Dr. Eugene Trinh
NASA Headquarters
Director for Microgravity Research Division

NASA/CP—2000-210470

Fifth Microgravity Fluid Physics and Transport Phenomena Conference
Cleveland, Ohio, August 9-11, 2000

Physical Sciences Research in Microgravity

E.H. Trinh
NASA Headquarters
Code UG

Outline

- NASA Program Organization
- Physical Sciences Research in Space - Biology Connection
- Fluid Physics Program Dual Thrust - Integrating Function
- Immediate and Future Plans

NASA/CP—2000-210470

Physical Sciences Research Division Goals

- To carry out cutting-edge, peer-reviewed, and multi-disciplinary basic research enabled by the space environment to address NASA's goal of advancing and communicating knowledge
- To develop a rigorous cross-disciplinary scientific capability bridging physical sciences and biology to address NASA's human and robotic space exploration goals
- To establish the ISS facilities into a unique on-orbit science laboratory addressing targeted scientific and technological issues of high significance
- To enhance the knowledge base impacting Earth-based technological and industrial applications

NASA/CP—2000-210470

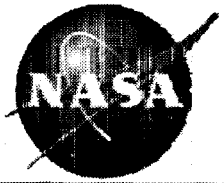

Proposed Organization

Division of Physical Sciences in Space*

- Fundamental Research
  - Fundamental Physics
  - Materials Science
  - Fluid Physics
  - Combustion Science
  - Exploration Research
- Biomolecular Physics
  - Atomic and Molecular Processes in Biosystems
  - Biological Sensing Phenomena
  - Cellular Components Assembling Mechanisms
- Biotechnology & Earth-based Application
  - Cellular Biotechnology
  - Macromolecular Biotechnology
  - Earth-based Applications
- Manage Division Education & Outreach, Unique Facilities Utilization, Internat'l Science and CSC Research Collaborations

Cross-disciplinary Science and Technology Working Group
Commercial Space Centers

***Research and technology development from TRL 1 - 3**

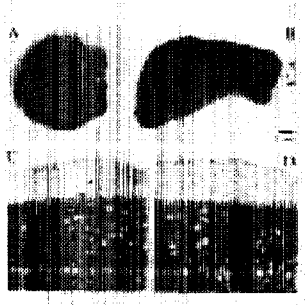

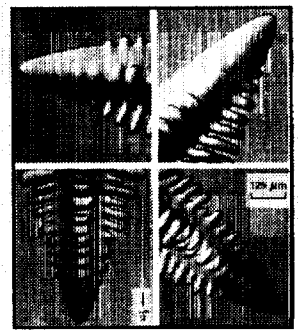

Goal-oriented basic and applied research

Fundamental research enabled by the microgravity environment

Basic research targeting human space exploration goals

Microgravity research in support of Earth-based applications

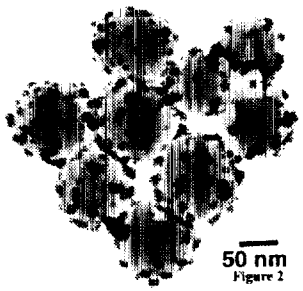

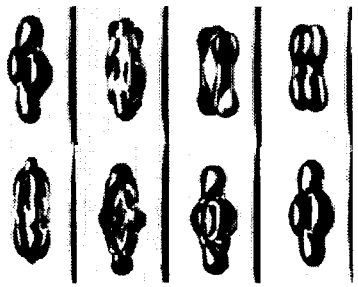

- The Microgravity fundamental research carried out in Code U (Office of Fundamental Research) involves a substantial multi-disciplinary scientific community

- This peer-reviewed research is laying the groundwork for the development of enabling technologies for future human exploration

- This research is complementary to the technology development efforts carried out in both Code R (Office of Aerospace Technology) and Code M (Office of Space Flight): The Knowledge generated by basic research in code U can be transferred to Codes R and M for the development of Capabilities, and finally to Code M for integration of Products into systems and platforms.

NASA/CP—2000-210470

Physical Sciences and Microgravity: Fundamental and Applied Research

Fundamental Research

Atomic Physics/Laser Cooling

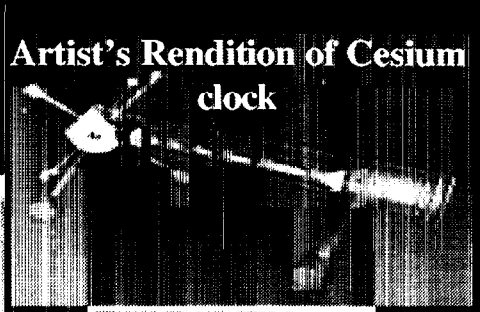

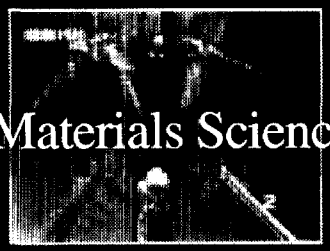

Materials Science

Fundamental Fluid Physics

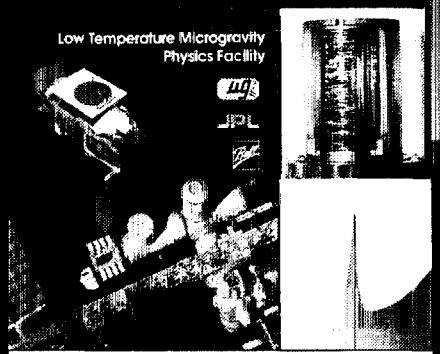

Low Temperature and Condensed Matter Physics

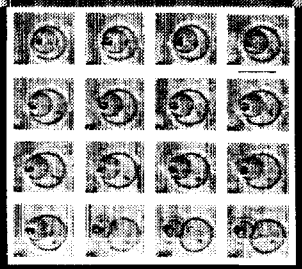

Biological Physics

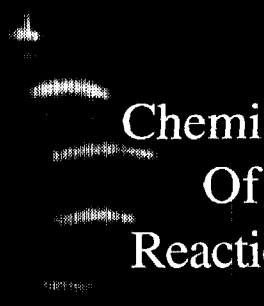

Chemistry Of Reactions

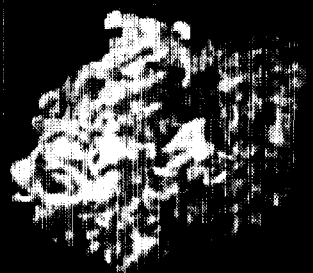

Structural Biology

Applied Research:

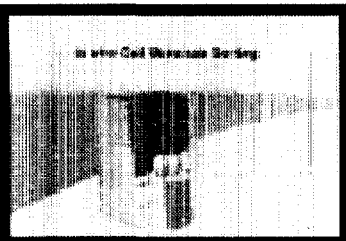

Biomolecular Physics & Chemistry

Fluid Flows and Management

Cellular Biotechnology

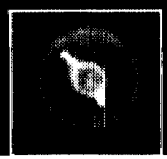

Micro-G Fire Safety

Microgravity Fluid Physics PIs Currently in the Program

NRA	Flight Definition/Flight	Ground-based
Prior	1	-
91	3	-
94	9	<71
96	6	33
98	14	61
Total Current	14	<165
00	16**	50**

**Planned

Fluid Physics Program Dual Thrust:

- Peer-reviewed research based on scientific value and exploiting advantages of the microgravity environment
- Peer-reviewed research based on engineering applications and relevant to human space exploration endeavor

The second component will be strengthened with a rigorous research program coordinated with other NASA enterprises

NASA/CP—2000-210470

NASA/CP—2000-210470

Fluid Physics Relevance to NASA Biology Program:

- Fluid Physics is " The Foundation for all other Microgravity science Disciplines"

This statement must be validated by implementing an Integrating function across the physical sciences disciplines as well as across the entire the biological sciences relevant to the Code U program

Example in current research program: S. Garoff's *Micro-Scale Hydrodynamics near Moving Contact Lines*

NASA/CP—2000-210470

Microscale Hydrodynamics Near Moving Contact Lines (μSCALE)

Objective:

To understand the wetting of solids by fluids.

Payoff:

Value and Benefit: A correct understanding of wetting physics would have a significant impact on:

- **The design and optimization of coating processes, including rapid coating of optical fibers, and durable coatings on metals.**
- **Materials for oil recovery processes.**
- **The design of MEMS and BIOMEMS devices.**
- **Design of processes for preparation of pharmaceuticals.**

Contact Line Hydrodynamics (f2)

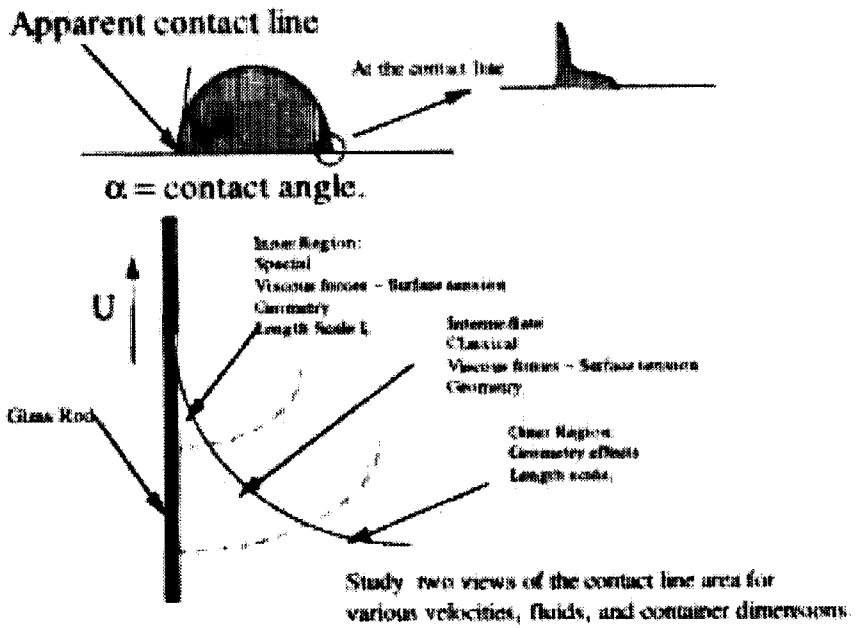

PI: **Steve Garoff**
Carnegie Mellon University

PS: **David Jacqmin**
NASA Glenn Research Center

PM: **Amy Jankovsky**
NASA Glenn Research Center

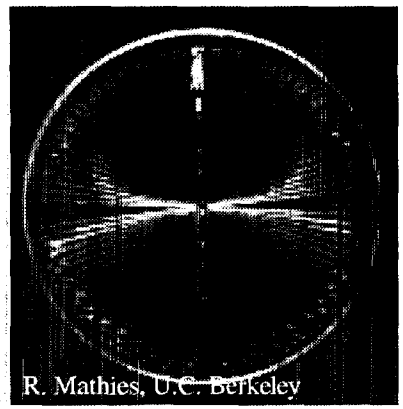

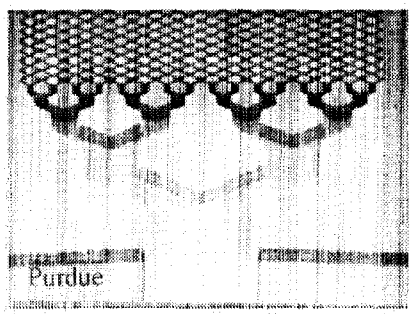

Microfluidic devices for fundamental biology investigations in space

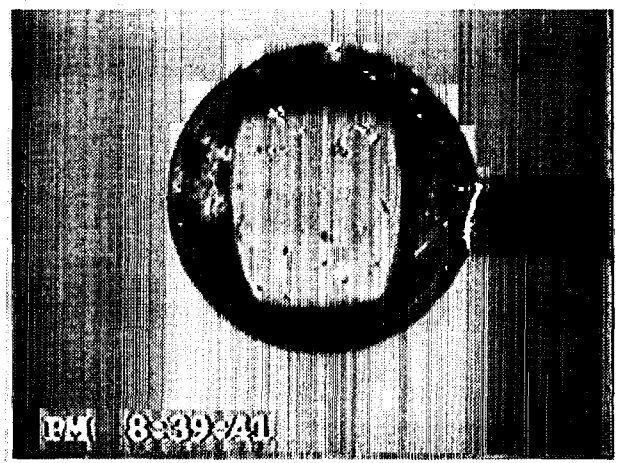

Liquid Management in μG

Interface Dynamics in multiphase flows and heat transfer systems

Immediate and Future Plans

- Establish and sustain an engineering-oriented research program coordinated with NASA's Offices of Space Flight and of Aerospace Technology
- Define a discipline roadmap to implement an integrating function across the physical and biological sciences
- Create a vigorous research program with a mix of "high risk" research combined with rigorous, detailed oriented tasks to strengthen its status within NASA, and to advocate for growth

NASA/CP—2000-210470

August 9, 2000
Keynote Speaker

Microgravity Research in Support of Technologies for the Human Exploration and Development of Space and Planetary Bodies

Prof. Raymond Viskanta
Purdue University

NASA/CP—2000-210470

MICROGRAVITY RESEARCH IN SUPPORT OF TECHNOLOGIES FOR THE HUMAN EXPLORATION AND DEVELOPMENT OF SPACE AND PLANETARY BODIES

Dr. Raymond Viskanta
Purdue University
Past Chair, Committee on Microgravity Research
National Research Council

Fifth Microgravity Fluid Physics and Transport Phenomena Conference

August 9, 2000

NASA/CP—2000-210470

Committee on Microgravity Research
(Membership through June 30, 2000)

RAYMOND VISKANTA, Purdue University, *Chair*
ROBERT A. ALTENKIRCH, Mississippi State University
ROBERT L. ASH, Old Dominion University
ROBERT J. BAYUZICK, Vanderbilt University
CHARLES W. CARTER, JR., University of North Carolina at Chapel Hill
GRETCHEN DARLINGTON,* Baylor College of Medicine
RICHARD T. LAHEY, JR., Rensselaer Polytechnic Institute
RALPH A. LOGAN, AT&T Bell Laboratories (retired)
FRANKLIN K. MOORE, Cornell University
WILLIAM W. MULLINS, Carnegie Mellon University (emeritus)
ROSALIA N. SCRIPA,* University of Alabama at Birmingham
FORMAN A. WILLIAMS, University of California at San Diego

SANDRA J. GRAHAM, National Research Council, *Study Director*

***Former member.**

History

Study requested by MSAD in 1996 in response to reorganization of NASA and placement of microgravity in HEDS enterprise

Phase I report (published 1997)

- a preliminary report
- considered broad categories of HEDS technologies
- assessed current microgravity research for potential to contribute to HEDS
- provided programmatic recommendations regarding MRD's role in HEDS

Phase II report (published July 2000)

- surveys wide range of specific technologies
- identifies and describes specific microgravity phenomena important to HEDS technologies
- recommends focused areas of microgravity research
- provides programmatic recommendations

Purpose and Scope

Purpose

To identify opportunities for microgravity research to contribute to the understanding of fundamental scientific questions underlying operation and development of exploration technologies

Scope

- **Considered all HEDS environments (space, lunar, Mars, asteroids)**
- **Does not recommend (to NASA) program balance between HEDS related research and other microgravity research**

Technological Challenges

"If we're going to think of a human Mars mission ... we can't use engineering processes that we have today. The limitations of these systems are the biggest barrier to reducing the costly problem of design uncertainty"

Sam Venneri
NASA Chief Technologist
June 1998
Aerospace America

Hubble Instrument (NICMOS) Faces Shorter Lifespan

"We have no space experience with these things, we're pushing the envelope because we wanted to try to get a four- to five-year lifetime. What we're finding out is that the properties of this stuff are not well understood, not modeled."

Edward Weiler SPACE
NASA AA for Science
Space News 3
March 31 – April 6, 1997

Charge to the Committee on Microgavity Research

- CMGR will undertake an assessment of scientific and related technological issues facing NASA's Human Exploration and Development (HEDS) endeavor.

- The Committee will specifically look at mission enabling technologies which, for development, require an improved understanding of fluid and material behavior in reduced gravity environment.

- The Committee and NASA mutually interpreted the main thrust of the charge to be determination of the gravity-related physicochemical phenomena most relevant to HEDS technology needs and recommendations of fundamental research on those phenomena.

Materials Processing in Microgravity

- Previous CMGR NRC reports
  - "Toward a Microgravity Research Strategy," 1992
  - "Microgravity Research Opportunities for the 1990s," 1995
- For example, solidification of metals is affected by buoyancy forces
  - Microsegragation reduced by microgravity environment
  - Suppression of detrimental convection
  - Growth is diffusion controlled
  - μg eliminates sedimentation

Primary Resources

- Various Workshops
  - Workshop on Research for Space Exploration: Physical Sciences and Process Technologies
  - Sixth International Conference on Engineering Construction and Operations in Space
  - Ninth Annual NASA-JPL Advanced Space Propulsion Research Workshop
- 30 years of reference documents on space technology and fluid/materials behavior
- Detailed technical briefings from NASA, academia and industry

BRIEFINGS - EXAMPLE

Research & Technology Investment Areas for Exploration

Human Support

- Health & Human Performance
- Advanced Life Support
- Advanced Habitation Systems
- EVA & Surface Mobility

Space Transportation

- Affordable Earth-to-Orbit Transportation
- Advanced Interplanetary Propulsion
- Cryogenic Fluid Management
- Aeroassist
- In Situ Resource Utilization

Advanced Space Power

- Advanced Power Generation
- Power Management
- Power Storage

Information & Automation

- Communications & Networks
- Advanced Operations
- Intelligent Systems
- Intelligent Synthesis Environment

Sensors & Instruments

- Science & Engineering Field Labs
- Planetary Prospecting
- Sample Curation
- Environmental & Medical Monitoring

(CONTINUED)

Advanced Space Power

¶ Advanced Power Generation

- Lightweight, high relaibility, high efficiency systems for multi-year missions
  - Megawatt-class systems for efficient spacecraft propulsion
  - 100 KW-class fixed surface power systems
  - 10 KW-class mobile systems
  - 1 KW-class human-portable systems
- *Advanced PV systems for 1-100 KW*
- Solar Dynamic options for 10-1000's KW
- Potential Nuclear options for 100 - Multi-MW

Energy Storage

- High capacity regenerative fuel cell and lightweight battery options for long-term storage and fixed surface operations
- *Compact, mobile systems (batteries, fuelcells or flywheel systems)*

Power Management

- *Very lightweight, high efficiency systems (10-100X better than state-of-the-art)*
- Broad power range: KW to MW
- Reconfigurable, fault tolerant power networks

HEDS Functions

Power Generation and Storage

Space Propulsion

Life Support

Hazard Control

Material Production and Storage

Construction and Maintenance

Approach

Defined broad HEDS functions

Determined capabilities required for each function

Discussed various technologies capable of fulfilling each function

- Current space technologies
- Proposed space technologies
- Current Earth technologies applicable to space

Broke down technologies into subsystems and processes

Identified common subsystems (or processes) affected by gravity levels

Identified phenomena important to operation of subsystem and processes

Approach (Example)

HEDS function

(Space Propulsion)

Capabilities required to fulfill function

(Generation of adequate propulsive force)

System/Technologies that can provide capability

(Solar Electric/Rankine Cycle)

Subsystem/Component

(Two-phase radiator)

Phenomena that affect operation of subsystem in low gravity

(Multiphase flow and heat transfer)

Approach (Example)

HEDS function

(Material Production and Storage)

Capabilities required to fulfill function

(Physical and chemical processing)

System/Technologies that can provide capability

(Sabatier reactor)

Subsystem/Component

(Catalyst bed reactor)

Phenomena that affect operation of subsystem in low gravity

(Flow in porous media)

Capabilities Needed to Carry Out HEDS Functions

Power Generation and Storage
- Generation of adequate energy
- Storage of energy
- Conversion of energy to work

Space Propulsion*
- Generation of adequate propulsive force

Life Support*
- Revitalization of atmosphere
- Reclamation of water
- Management of solid waste
- Control of temperature and humidity
- Production of food

Hazard Control
- Protection of crew and habitat/spaceship from fire
- Protection from radiation
- Protection from chemical and biological contamination

Material Production and Storage*
- Extraction and transport of feedstock
- Concentration and beneficiation of feedstock
- Physical and chemical processing
- Storage of processed materials

Construction and Maintenance
- Site preparation
- Fabrication of components or structural elements from raw or processed materials
- Joining of components or structural elements

Schematic of a generic electric power system.

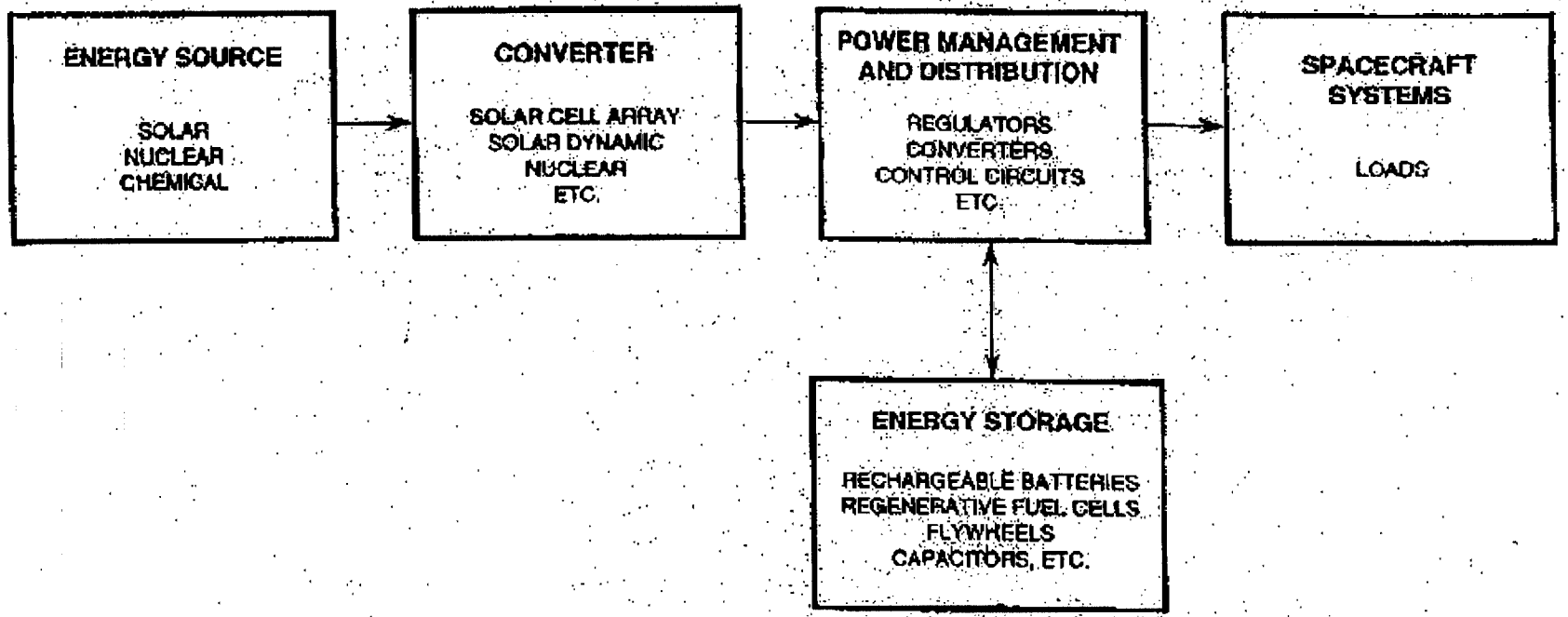

Qualitative diagram illustrating the regimes of applicability of various space power systems.

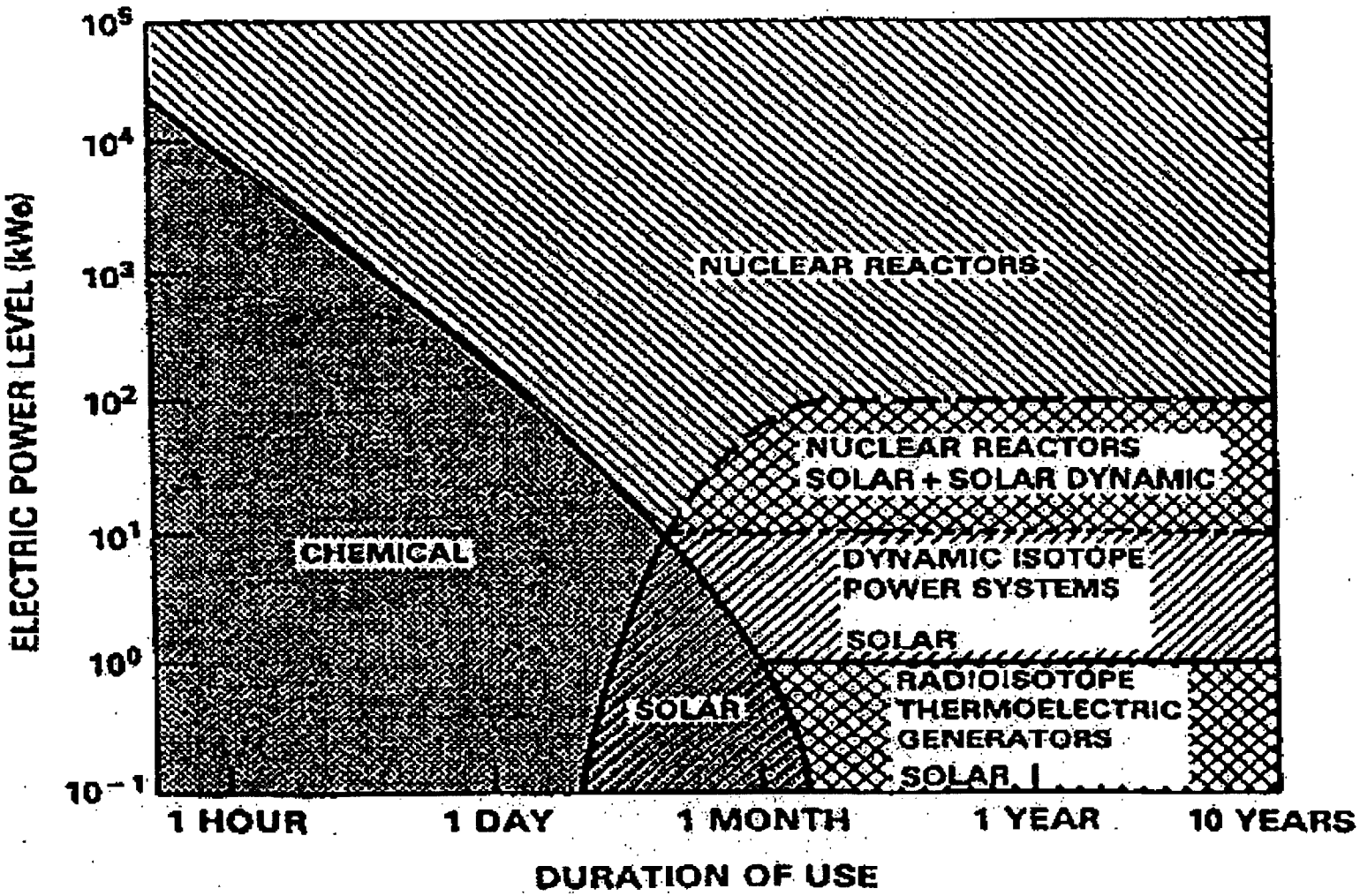

Committee on Microgravity Research

Solar Energy Flux as a Function of Distance From the Sun

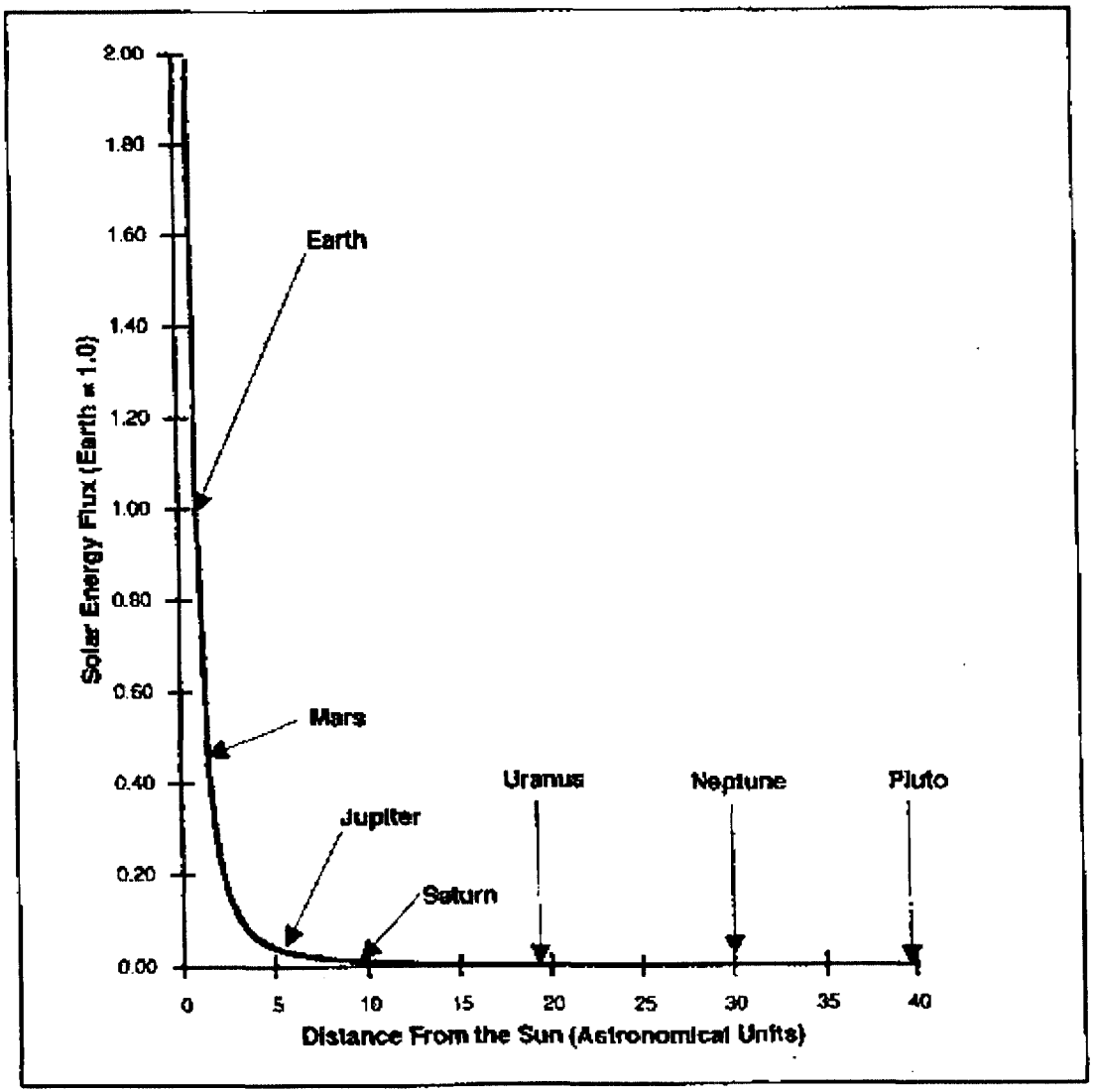

NASA/CP—2000-210470

Schematic diagram of fuel cell-electrolysis cycle.

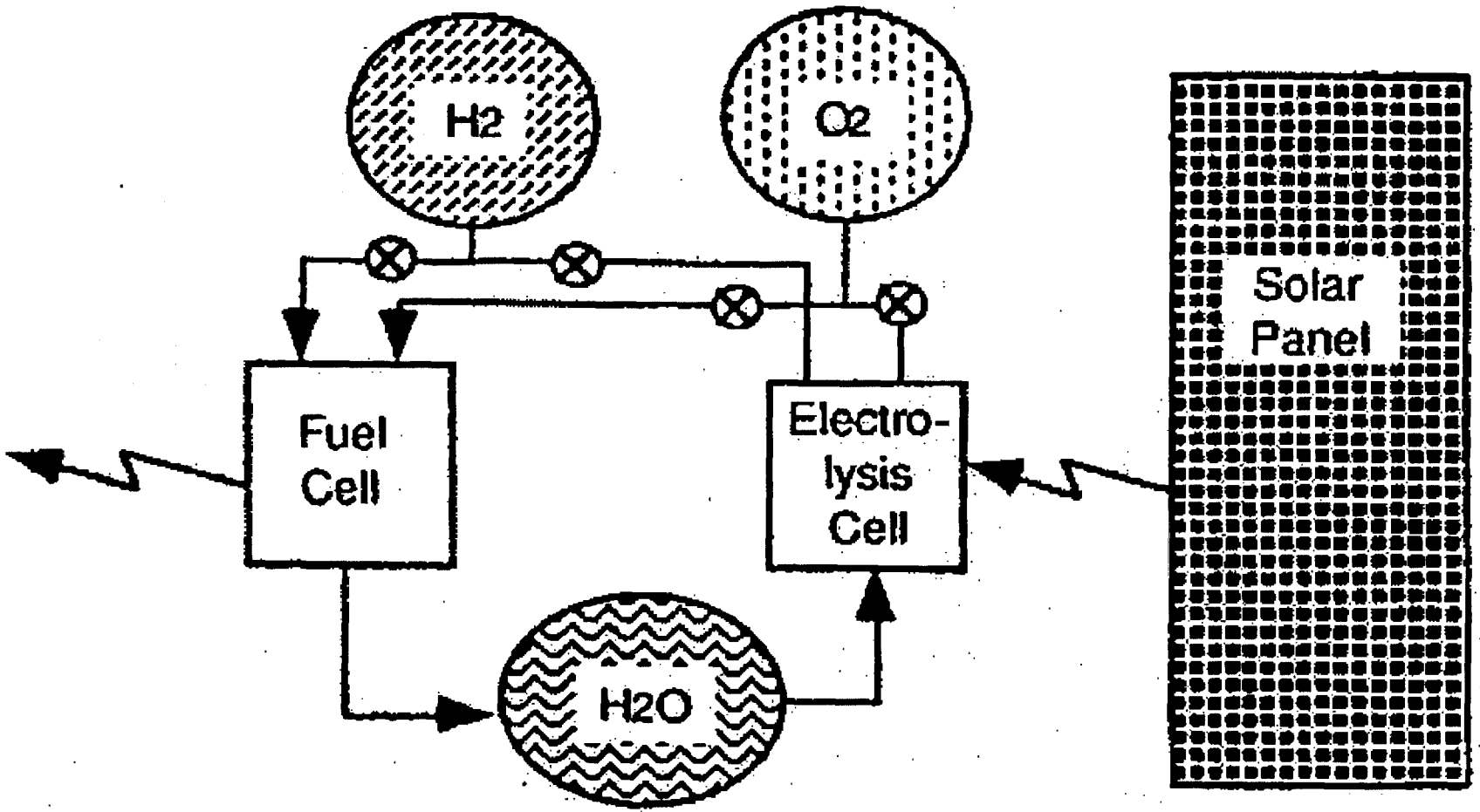

Committee on Microgravity Research

Static feed water electrolysis cell.

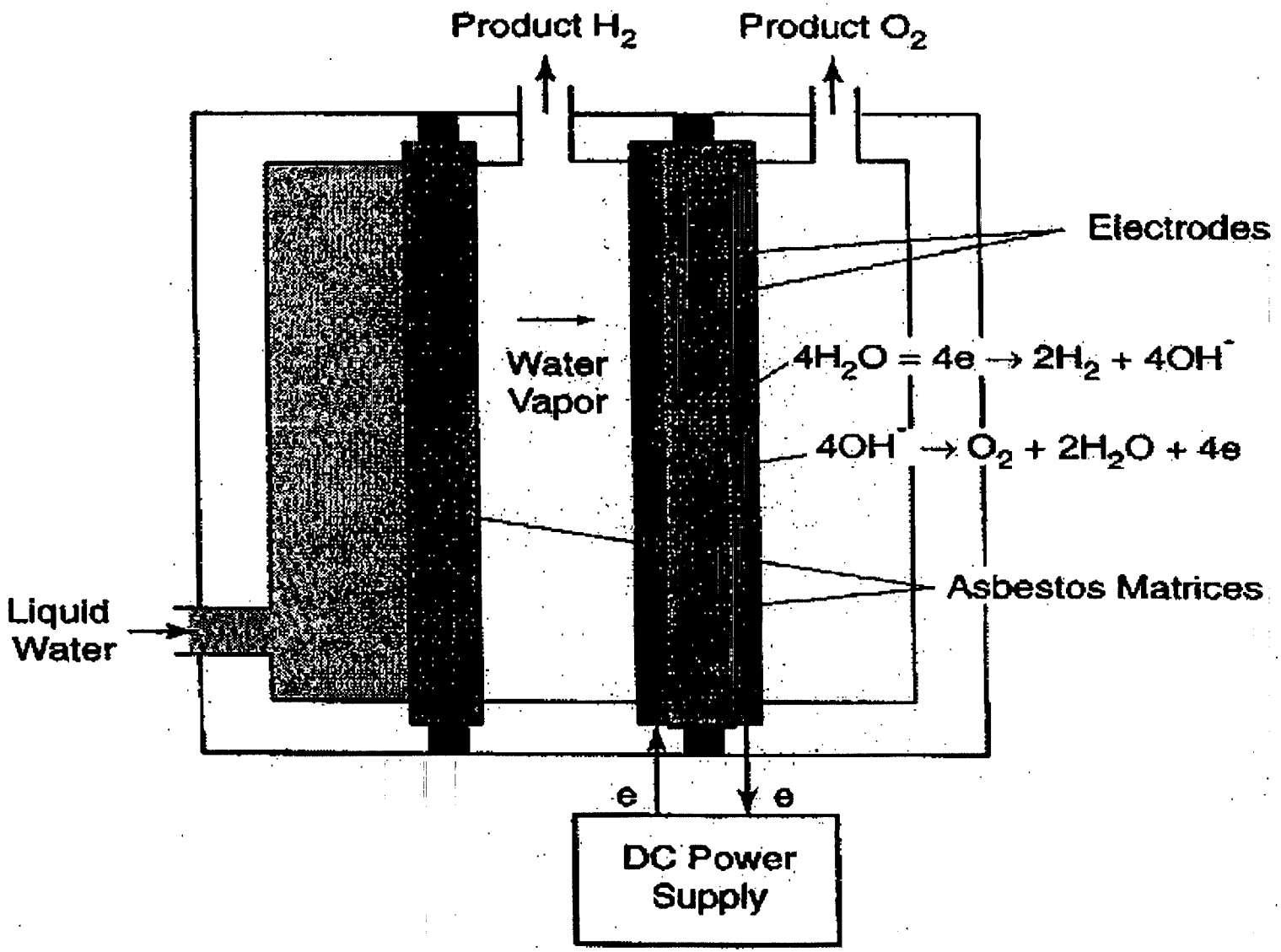

Committee on Microgravity Research

List of Selected Subsystems for Passive and Active Power Generation

Representative Subsystem	Passive				Active			
	PV	TE	TI	TPV	BR	RA	ST	AMTEC
Batteries	L	L	L	L	-	-	-	-
Boiler	-	-	-	-	-	H	-	-
Capillary pumped loop	-	-	-	-	H	H	H	-
Compressor	-	-	-	-	L	-	L	-
Condenser	-	-	-	-	-	H	-	H
Converter	L	L	L	L	-	-	-	-
Controls	L	L	L	L	L	L	L	L
Evaporator	-	-	-	-	-	-	-	H
Heat exchanger	-	-	-	-	M	H	M	M
Heat pipes	-	-	-	-	H	H	H	-
Phase separator	-	-	-	-	-	H	-	-
Pipes	-	-	-	-	L	M	L	-
Pumps	-	-	-	-	-	M	-	-
Radiators	-	-	-	-	M	H	M	-
Regenerative heat exchangers	-	-	-	-	L	H	L	-
Regulators	L	L	L	L	L	L	L	L
Solar array	L	-	-	L	-	-	-	-
Solar collector	-	-	-	-	M	H	M	-
Storage	-	-	-	-	M	M	M	-
Turbine/alternator	-	-	-	-	L	L	L	-
Valves	-	-	-	-	L	M	L	-

NOTE: the abbreviations: **PV**-photovoltaic, **TE**-thermoelectric, **TI**-thermoionic, **TPV**-thermophotovoltaic, **BR**-Brayton, **RA**-Rankine, **ST**-Stirling, and **AMTEC**-alkali metal thermal-to-electric conversion.The letters **L**, **M** and **H** designate low, medium, and high preliminary assessment of the impact of reduced gravity on the phenomena taking place in the subsystem, respectively. Where no letter is given, the subsystem is not applicable to the system listed.

Phenomena Affecting Common Subsystems

Subsystem/ Variant	Phenomenon																		
	Capillarity	Wetting	Marangoni Flows	Two-Phase Flows	Phase Separation/Distrib.	Mixing	Flow in Porous Media	Convection	Boiling Heat Transfer	Condensation Heat	Multiphase Flow and Heat	Evaporation Heat	Phase-Change Heat	Solidification	Multiphase System	Combustion	Pyrolysis	Granular Flow	Structural Dynamics
Storage tanks																			
Gas								•											•
Liquid	•	•	•	•	•	•		•	•			•		•					•
Cryogenic	•	•	•	•	•			•	•	•	•	•			•				•
Pumps																			
Condensate											•								
Liquid line															•				
Microdevices																			
Compressors																			
Rotary											•								
Adsorption											•								
Piping																			
Gas-phase									•	•	•								•
Liquid-phase					•			•	•		•								•
Two-phase	•	•	•		•	•		•	•	•	•				•				•
Radiators																			
Solid-state																			•
Gas-phase								•											•
Two-phase					•	•		•		•	•			•	•				•
Heat pipes																			
Capillary pumped loop	•	•	•		•		•			•	•	•		•	•				
Simple			•		•		•			•	•	•		•	•				
Fans and blowers								•											
Evaporators																			
Boilers			•		•	•			•				•		•				
Vaporizers		•	•		•			•				•	•						
Liquifiers																			
Condensers					•					•					•				
Distillations units								•											
Filters/separators																			
Gas/solid					•						•								
Gas/liquid	•		•		•	•					•								
Liquid/liquid	•				•	•					•								
Liquid/solid	•				•	•					•								
Vortex separators					•						•								
Rotating drum separators					•														
Spargers					•	•					•								
Valves and actuators											•								•
Heaters								•											
Catalyst beds							•												
Seals											•								
Heat exchangers																			
Gas/gas								•											
Gas/liquid								•		•			•						
Gas/solid								•					•						
Fluidized-bed							•												
Fire extinguishers						•		•								•			
Smoke detectors																•			

Phenomena of Importance in Reduced Gravity

Interfacial Phenomena

Capillary Equilibrium and Dynamic Forms
Wetting
Marangoni Effect

Multiphase Flow

Phase Separation and Distribution
Mixing
Multiphase Systems Dynamics
Flow in Porous Media

Heat Transfer

Single-phase Convection
Evaporation Heat Transfer
Boiling Heat Transfer
Condensation Heat Transfer
Two-phase Forced Convection Heat Transfer
Solid/Liquid Phase-change Heat Transfer
Phase Change Heat Transfer in Porous Media

Solidification

Pattern Formation
Casting

Chemical Transformation

Combustion
Pyrolysis
Solution Chemistry

Behavior of Granular Materials

Lunar and Martian Regolith
Kinetics of Granular Flow

Cryogenic Storage

Gravity Issues

Fractional Gravity

- terrestrial storage technologies probably adequate
- other environmental considerations – dust, temperature cycles, etc.

Microgravity

- fluid position
- fluid configuration
- fluid transfer
- heat transfer

Effect of g-Level on Multiphase Flow

Two-phase flow of air and water through a pipe at normal gravity (top), fractional gravity (middle), and very low gravity (bottom). (The gravity vector is directed toward the bottom of the photos.) The flow distribution of gas and liquid in two-phase systems is strongly affected by the gravity level. Currently the impact of that altered distribution on flow dynamics, heat transfer rates, and pressure drop characteristics is poorly understood.

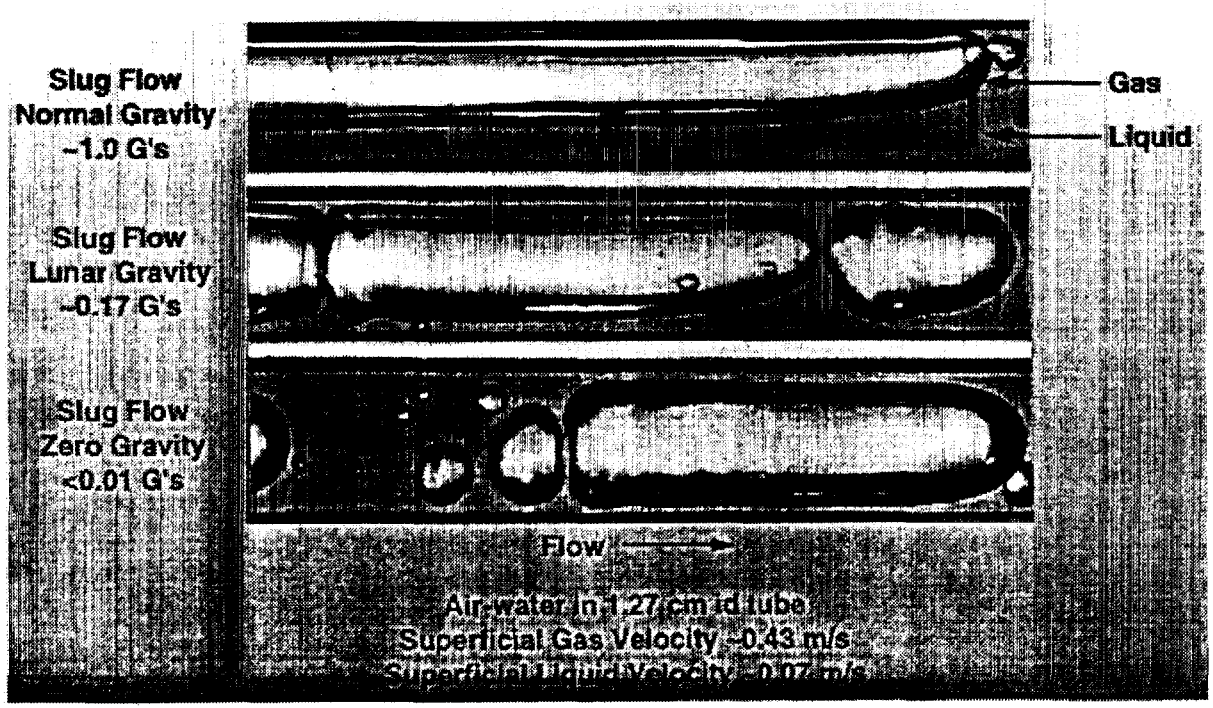

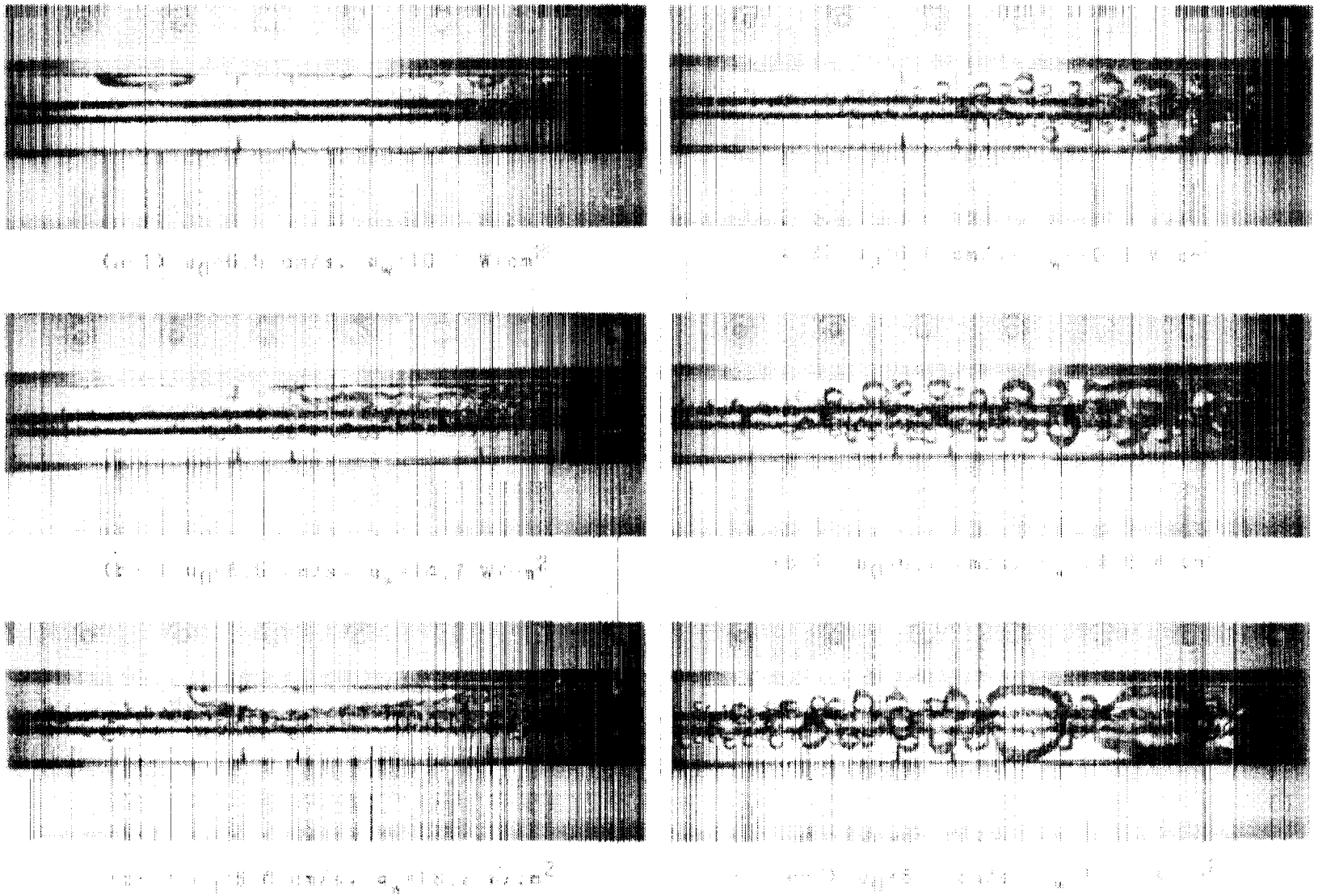

FROM SAITO ET AL., NUCL. ENG. & DESIGN (1994)

Radial void distribution for 1 g_0 and bubbly upflow (Serizawa, 1974) where α is the local void fraction and r/R is the relative radial position.

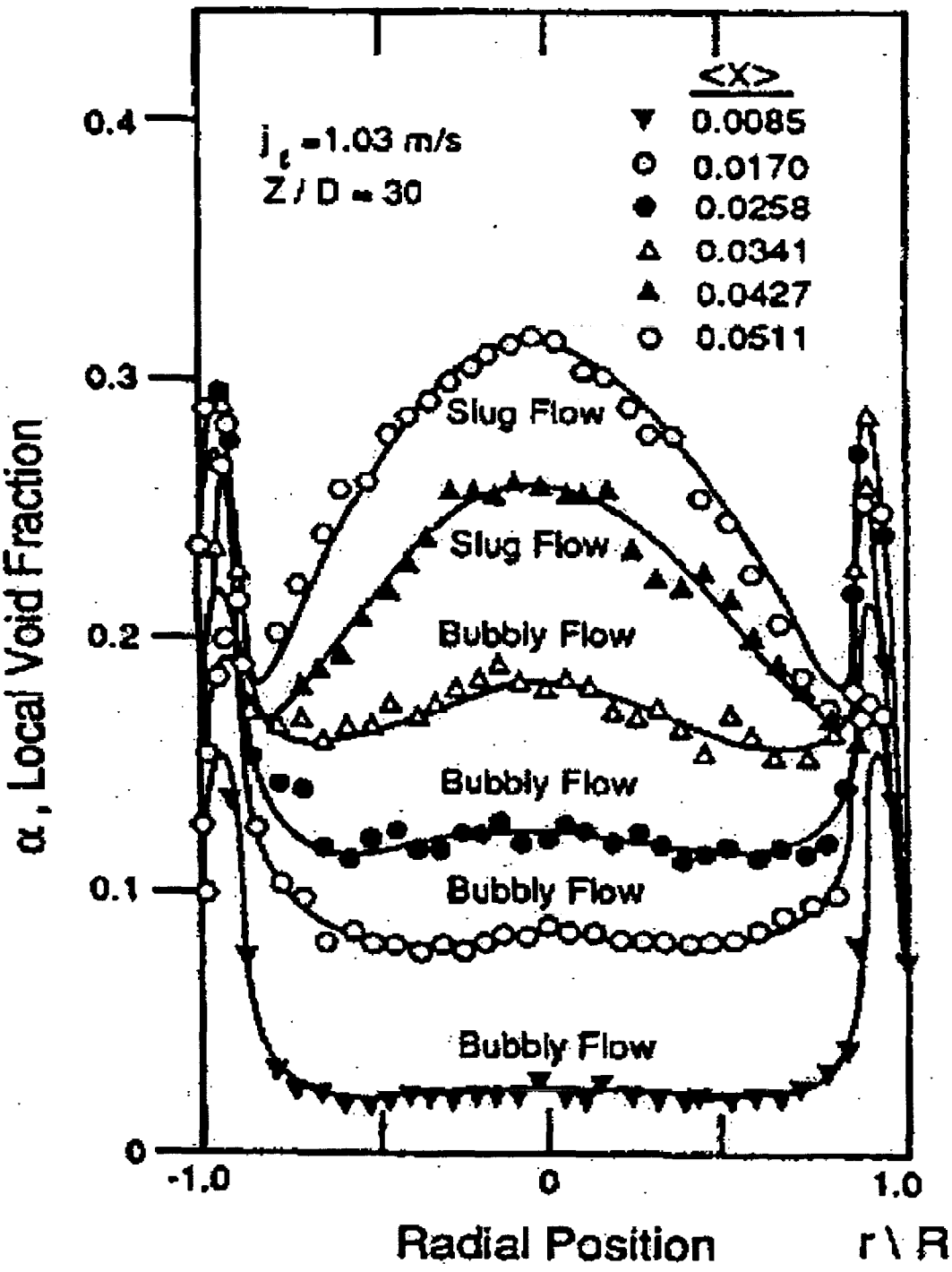

Approximate composite microgravity pool boiling curves for R-113 from steady and quasi-steady measurements made during shuttle flights STS-47, STS-57, and STS-60.

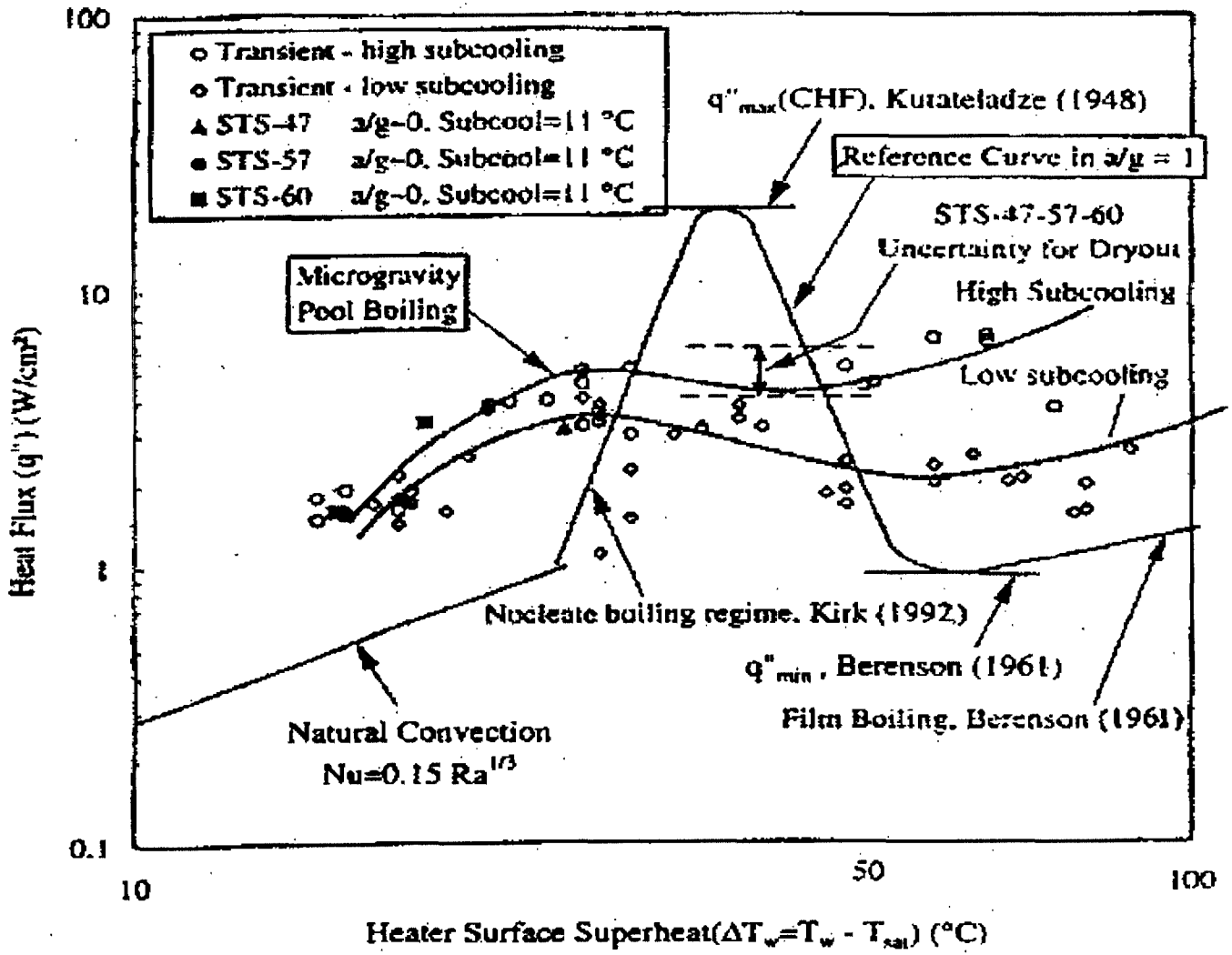

Committee on Microgravity Research

Examples of Phenomena in Heat Pipes in μg Environment – An Example

- Obstruction of liquid transport by incipience of nucleate boiling
- Recession of the evaporating liquid meniscus in a groove can lead to unstable mode of operation in the axially-grooved evaporator
- Formation of vapor zone in a porous structure can increase the overall thermal resistance of evaporator and finally lead to dryout in a heat pipe
- Shear stresses at the liquid-vapor interface combined with the effects of thermocapillarity can lead to flooding of he capillary structure in the condenser of an axially grooved heat pipe
- Existence of thick liquid films attached to the extended evaporating meniscus in a capillary tube can effect performance (dryout) in capillary-driven devices

Schematic of a simple heat pipe.

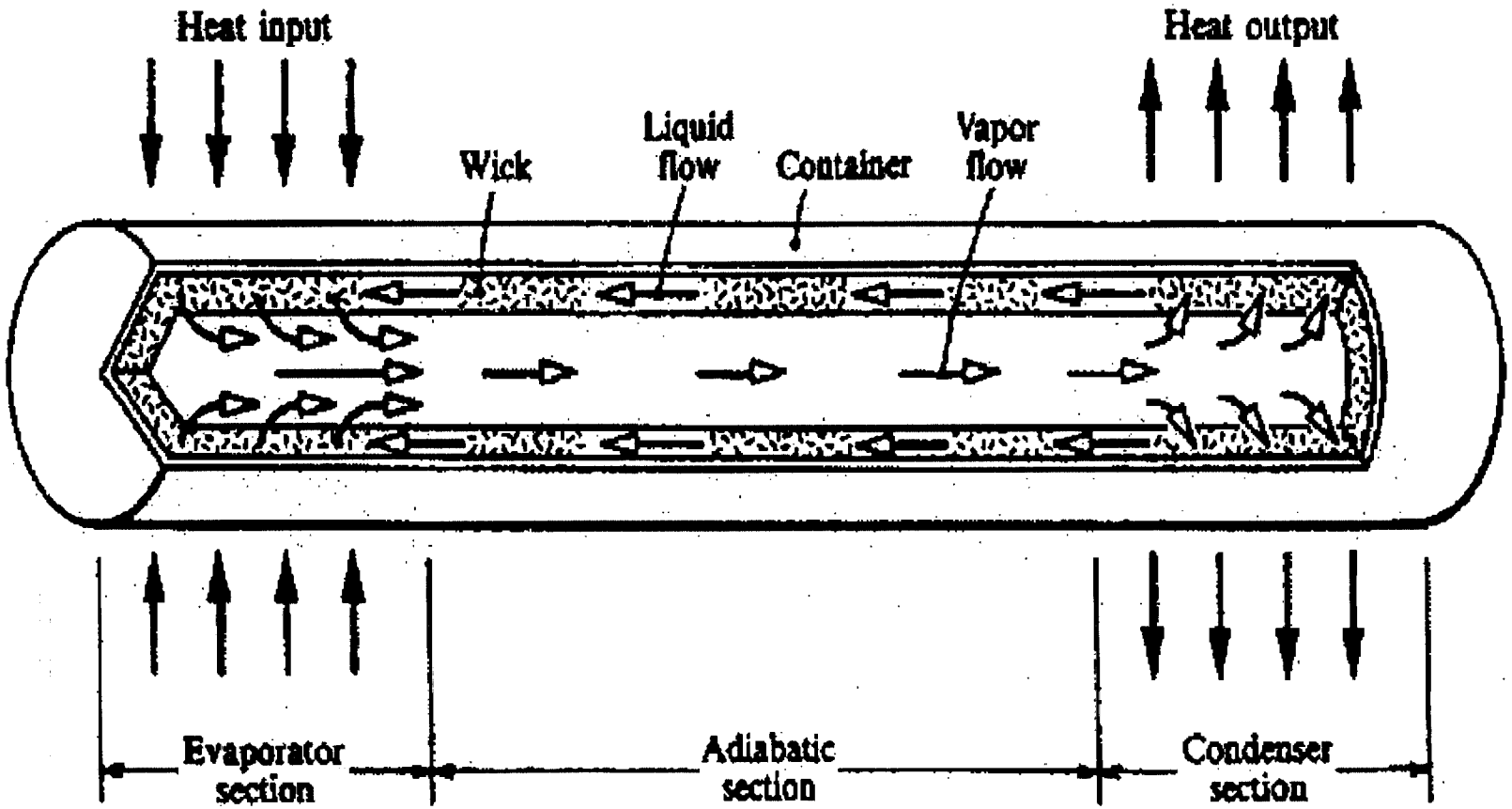

Committee on Microgravity Research

Concrete Production

Cement Production

Quarrying, grinding and blending, clinkering, ball-milling

Concrete Production

Batching of aggregate an cement, mixing, transport, placement, curing

Gravity Issues

Clinkering dependent on rate of fall in kiln

Heat and mass transport in kiln

Sedimentation and buoyancy during/after placement

High Priority Research Areas

- Important ones arising in numerous HEDS technologies where gravity impacts physical phenomena
- Not every phenomena category resulted in high priority research recommendation
- Only those high priority research areas which have a potential of affecting a wide range of HEDS technologies are identified
- Medium priority research aras are listed in the report

Surface or Interfacial Phenomena

High-Priority Research Recommendations:

- Physics of Wetting—hysteresis effect, dynamics of wetting process, wetting below scale of correlation length, empirical and fundamental knowledge of wetting material combinations and conditions

- Capillary Driven Flows—flows and transport regimes during evaporation and heat transfer, scaling of flow regime boundaries, Marangoni convection, effect on dynamics of liquid and bubble oscillation, effect on motion of contained liquid

HEDS Applications

- Welding, liquid phase sintering, the operation of wicks in heat pipes for thermal management, use of capillary vanes in cryogenic storage tanks to control the position and movement of liquids, lubrication, in boiling/condensation heat transfer including the rewetting of hot surfaces

Multiphase Flow and Heat Transfer

High-Priority Research Recommendations:

- Develop physically-based models for predicting flow regimes, flow regime transitions, and multiphase flow and heat transfer in reduced gravity.
- Assess model using reduced-scale and separate-effects experiment in microgravity.
- Assess gravitational effect on forced convective boiling, two-phased forced convective heat transfer and pressure drop.

HEDS Applications

- Power production and utilization systems, life support systems, other phase change systems that require high energy-transport efficiency and high power-to-weight ratios.

Multiphase Flow and Heat Transfer

Other Research Recommendations:

- Assess gravitational effect on convective condensation heat transfer.
- Study methods for enhancing single- and two-phase heat transfer and reducing pressure drop, in order to decrease equipment mass and volume.
- Study effect of gravity on two-phase and boiling flows in porous media.

HEDS Applications

- Power production and utilization systems, life support systems, other systems that require high energy-transport efficiency and high power-to-weight ratios

Multiphase System Dynamics

High-Priority Research Recommendations:

- Collection and analysis of stability data on boiling and condensing systems at reduced gravity for use in testing analytical models of linear stability thresholds and non-linear instability phenomena

HEDS Applications

- Reliable phase change systems. Prevention of operational problems or severe damage due to global system instabilities in multiphase power/propulsion systems.

Fire Phenomena

High-Priority Research Recommendations:

- Experimental, theoretical and computational studies of flame spread over surfaces of solid materials in microgravity and fractional gravity, examining ignition requirements, flame-spread rates, and flame structure.

- Gravity effects in smoldering, including initiation and termination, propagation rates, products of smoldering, and conditions for transition from smoldering to flaming combustion.

HEDS Applications

- Fire detection and suppression aboard spacecraft and in other sealed habitats.

Granular Materials

High-Priority Research Recommendations:

- Development of predictive models of granular deformation and flow under reduced gravity, including the effects of particle size, shape and constitution, particle agitation, and electrostatic charge, expecially at low pressures.

- Predictive models of dust behavior in spacecraft and extraterrestrial environments, including cohesion and adhesion mechanisms.

HEDS Applications

- Site preparation, mining activities, ore processing, structural installations and habitat construction

Programmatic Recommendations

- Integrated multiphase fluid physics research program needed to develop a reliable, computational fluid dynamics model for predicting multiphase flow and heat transfer behavior in reduced gravity systems.
- NASA-wide coordination is needed to ensure continuous exchange of information and ideas, between fundamental research programs and spacecraft designers, on reduced gravity issues.
- A rigorous peer review mechanism has been vital to quality of microgravity research program and should be maintained as HEDS related research is incorporated into the program.
- Research could probably not be accommodated within current μg fluids program
- These recommendations are directed to NASA in general and not just to microgravity program.

Programmatic Recommendations (cont.)

- NASA should utilize ISS and its subsystems for test bed studies of scientific and engineering concepts applicable to HEDS technologies, such as:
  - Multiphase flow and heat transfer experiments to support computational model development
  - Identification of fundamental control loop or system instabilities
  - Instrumentation and control systems for HEDS hardware
  - Development of autonomous operational principles for HEDS systems

August 9, 2000

Session 1A
Multiphase Flow and Phase Change I

PRESSURE-RADIATION FORCES ON VAPOR BUBBLES

A. Prosperetti, Y. Hao, and H.N. Oğuz
Department of Mechanical Engineering, The Johns Hopkins University
Baltimore MD 21218

At normal gravity, the effectiveness of boiling as a heat transfer mechanism relies in no small measure on the rapid removal of vapor bubbles from the heated surface by buoyancy. This process has a two-fold benefit, as it both aids in removing latent heat and in promoting microconvective motion near the surface. At low heat fluxes, in microgravity conditions complex bubble coalescence phenomena help remove bubbles from the heated surface, but the effectiveness of this mechanism is limited and the critical heat flux is reached at much lower wall superheats than on Earth.

In order to increase the critical heat flux at low gravity it is therefore desirable to remove bubbles from the heated surface providing a substitute for buoyancy. The objective of this work is to study the suitability of acoustic pressure forces (also known as Bjerknes forces) as a means to achieve this end. This idea seems promising because small bubbles (smaller than the resonant radius) tend to be attracted by sound pressure antinodes (such as those formed near a solid heating surface), while larger bubbles are repelled by pressure antinodes. One can thus envisage a situation where, as the vapor bubbles grow, they are eventually pushed away from the heated region. Furthermore there would be the additional benefit of the local microconvection induced by the pulsating vapor bubbles.

This argument ignores however the effect of the wall on the pressure field produced by the pulsating bubble itself. This effect can be approximated by replacing the wall by an image bubble, which would be pulsating in phase with the real bubble. It is known that such an image bubble exerts an attractive force on the real bubble whatever its radius, and it is not obvious *a priori* which one of the two effects would prevail.

Our calculations show that, if the wavefronts are parallel to the solid surface, the attractive force of the image bubble prevails and the vapor bubble is attracted by the wall. A typical example is shown in Fig. 1. Obviously, it is impossible to achieve bubble removal with such an arrangement. However, if the wavefronts are perpendicular to the wall, the bubble is pushed along the wall away from the pressure antinode once it grows past its resonant radius and the objective of this investigation can be met (Fig. 2).

This work therefore suggests that acoustic forces can be used to remove bubbles from the heated area provided conditions are such that the force is directed parallel to the rigid wall.

The previous results have been obtained with a pure vapor, spherical bubble model. In the continuation of this work deformation of the spherical shape will be allowed and the simultaneous presence of an incondensable gas in the bubble will be considered.

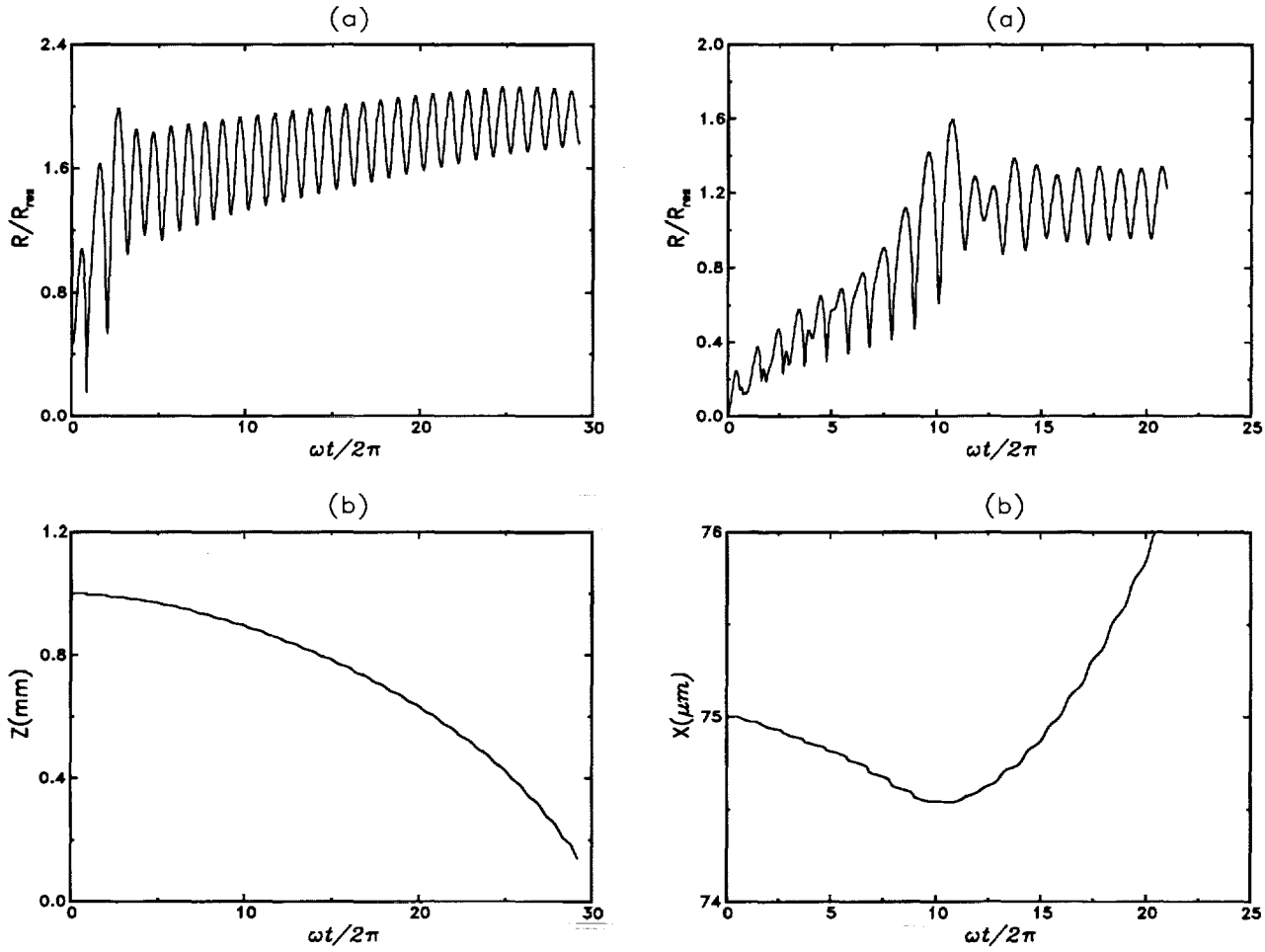

Figure 1: (Left) Bubble radius (a,above) and distance above the wall as a function of time under the action of a 20 kHz sound field with wavefronts oriented parallel to the rigid surface. The pressure amplitude is 0.3 atm, the initial bubble nucleus has a radius of 35 μm, and the resonance radius R_{res} used to normalize the radius in the upper panel is 75 μm. The liquid is water at 100 °C and 1 atm pressure. At time zero the bubble is positioned 1 mm away from the solid wall located at $Z = 0$.

Figure 2: (Right) Bubble radius (a, above) and distance from the pressure antinode located at $X = 0$ (b, below) as a function of time under the action of a 1 kHz sound field with wavefronts oriented perpendicular to a rigid surface. The pressure amplitude is 0.4 atm, the initial bubble nucleus has a radius of 35 μm, and the resonance radius R_{res} used to normalize the radius in the upper panel is 2.71 mm. The liquid is water at 100 °C and 1 atm pressure. At time zero the bubble is positioned 4.4 mm above the solid wall and 75 μm away from the pressure antinode. Note the change of direction of the bubble motion as it grows past the resonant radius.

NASA/CP—2000-210470

PRESSURE-RADIATION (BJERKNES) FORCES ON VAPOR BUBBLES

A. PROSPERETTI, H.N. OĞUZ, and Y. HAO

Department of Mechanical Engineering
The Johns Hopkins University
Baltimore

Supported by NASA

FROM MERTE ETAL.

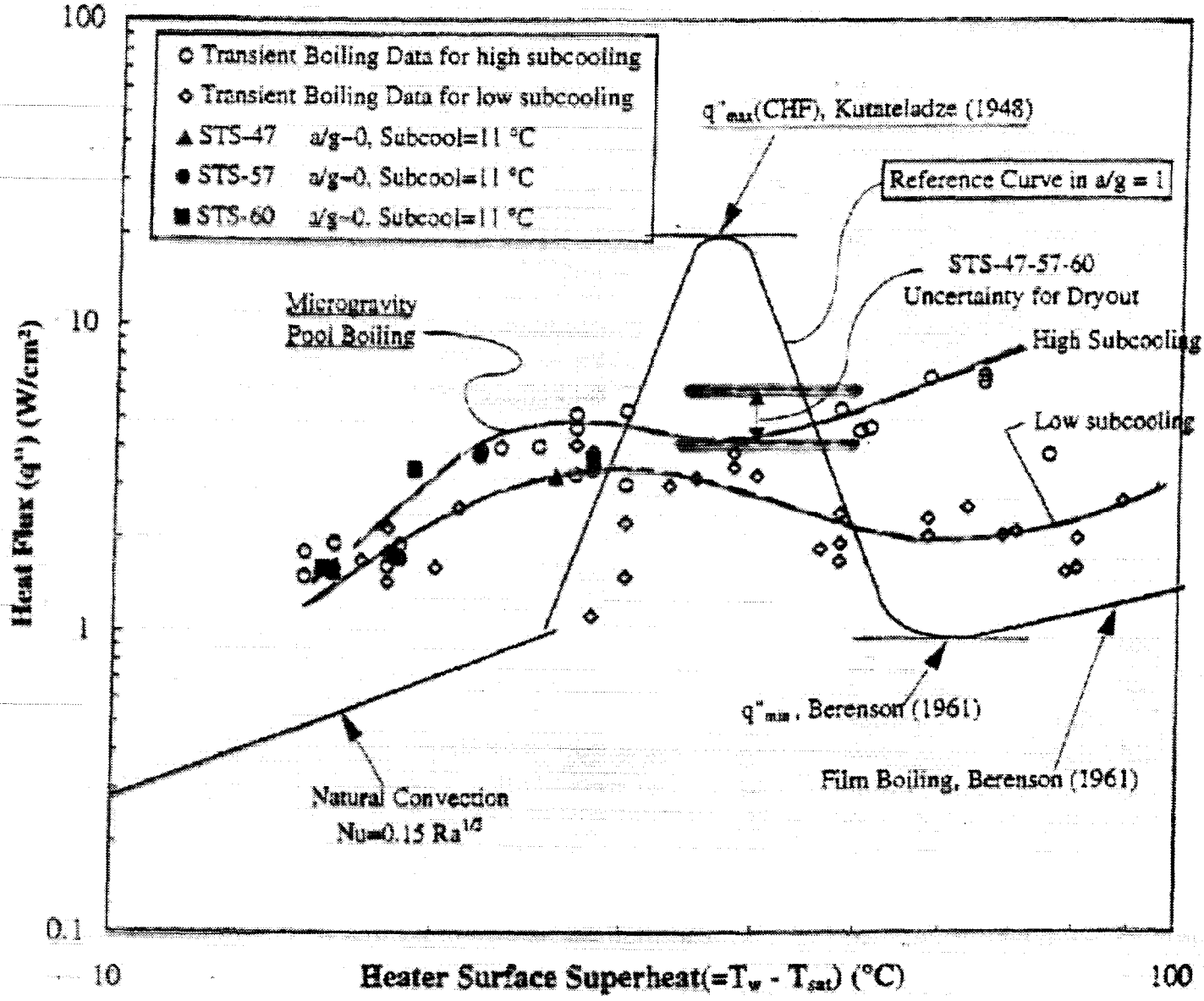

Figure 6.36. Approximate composite microgravity pool boiling curves for R-113 from steady and transient measurements on PBE-IA-IB-IC (STS-47-57-60).

MOTIVATION

- In low gravity bubbles linger near heated surface
  $\Longrightarrow$ Coalescence and dry-out are favored

- Possible means to remove bubbles from the neighborhood of the heater are

  – Electrostatic fields

  – Flow

  $\longrightarrow$ Acoustic pressure radiation forces

- More generally, in microgravity means to "manage" bubbles are necessary

FORCE ON A BUBBLE

Fluid force on bubble

$$\mathbf{F} = \oint_S p(\mathbf{x}, t)\, \mathbf{n}\, dS$$

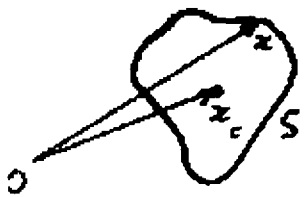

$$p = \begin{cases} p_{acoustic} & \text{sound field} \\ +p_{hydrodin.} & \text{boundaries, other bubbles, flow, etc.} \\ +p_{scattered} & \text{mostly monopole ("self-force")} \\ +\ldots & \end{cases}$$

$$p(\mathbf{x}, t) \simeq p(\mathbf{x}_C, t) + (\mathbf{x} - \mathbf{x}_C) \cdot \nabla p + \ldots$$

$$\Longrightarrow \mathbf{F} \simeq -V \nabla p$$

BUBBLE VOLUME

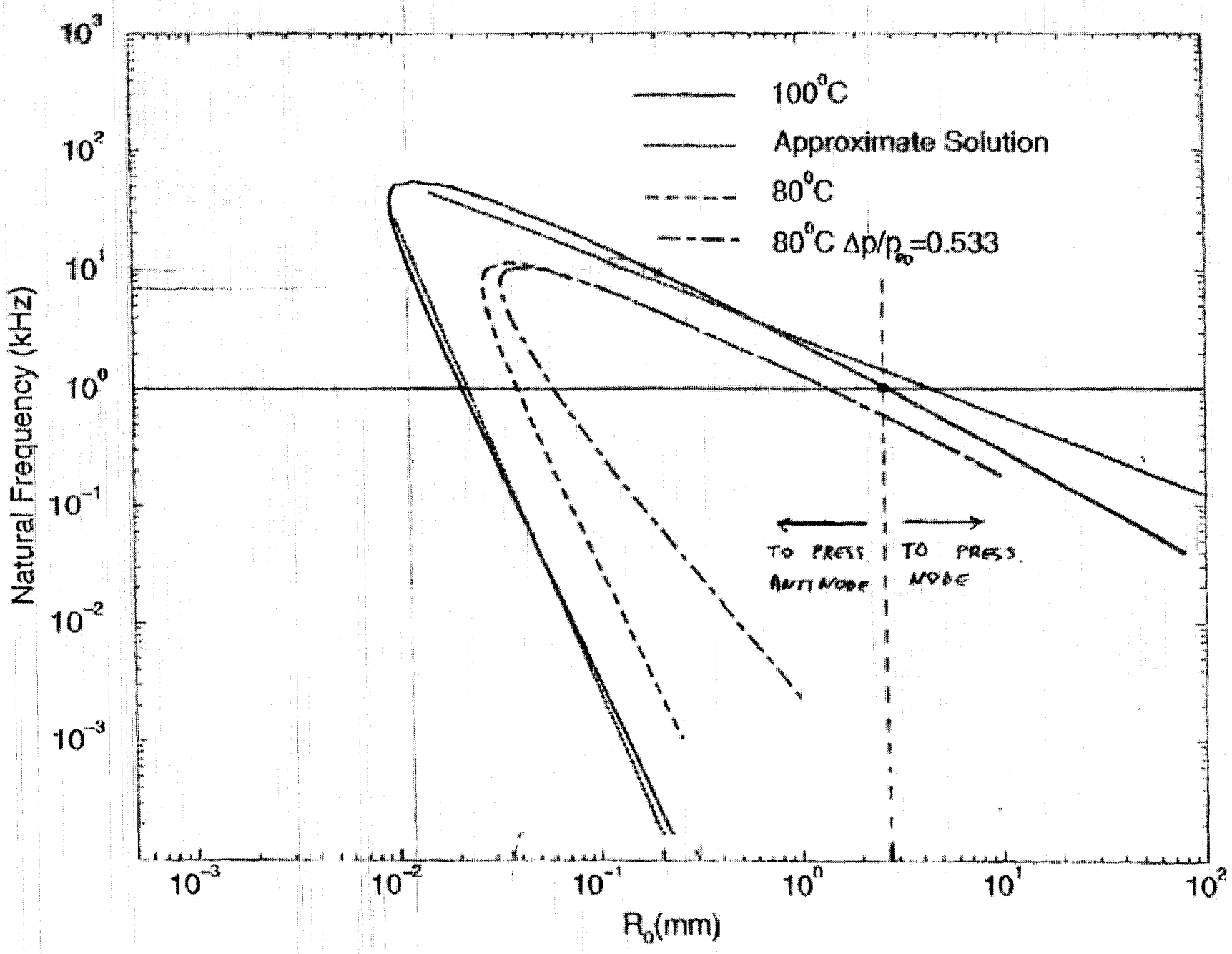
100°C
Approximate Solution
80°C
80°C Δp/p∞=0.533
TO PRESS ANTINODE
TO PRESS NODE
Natural Frequency (kHz)
R0(mm)
10^3
10^2
10^1
10^0
10^-1
10^-2
10^-3
10^-3
10^-2
10^-1
10^0
10^1
10^2

COMPONENTS OF MODEL

- Vapor bubble in oscillating pressure field
- Bubble-liquid relative velocity
- Primary Bjerknes force
- Effect of wall ($\sim$ "image bubble") – Secondary Bjerknes force
- Bubble motion under action of Bjerknes forces
- Bubble deformation (in progress)

BUBBLE-BUBBLE INTERACTION – I

(WALL EFFECTS)

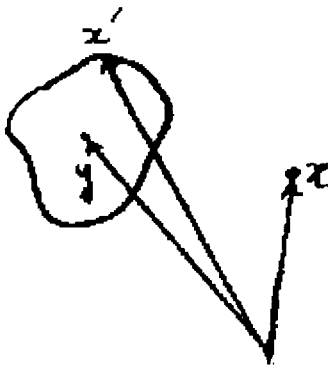

Green's identity for one body

$$\phi(\mathbf{x}) = \int_S \left[G(\mathbf{x} - \mathbf{x}') \frac{\partial \phi}{\partial n'} - \phi(\mathbf{x}') \frac{\partial}{\partial n'} G(\mathbf{x} - \mathbf{x}') \right] dS'$$

$$G(\mathbf{x} - \mathbf{x}') = \frac{1}{4\pi} \frac{1}{|\mathbf{x} - \mathbf{x}'|} \simeq \frac{1}{4\pi} \frac{1}{|\mathbf{x} - \mathbf{y}|} + \frac{(\mathbf{x} - \mathbf{y}) \cdot \mathbf{r}}{|\mathbf{x} - \mathbf{y}|^2} + \ldots$$

Substitute into integral to find

$$\begin{aligned} \phi &= A\, G(\mathbf{x} - \mathbf{y}) + \mathbf{B} \cdot \nabla G(\mathbf{x} - \mathbf{y}) + \ldots \\ &= \sum_{n=0}^{\infty} \mathbf{A}_n (\cdot \nabla)^n G(\mathbf{x} - \mathbf{y}) \end{aligned}$$

For N bubbles centered at $\mathbf{y}^1, \mathbf{y}^2, \ldots \mathbf{y}^N$

$$\phi = \sum_{\alpha=1}^{N} \sum_{n=0}^{\infty} \mathbf{A}_n^{\alpha} (\cdot \nabla)^n G(\mathbf{x} - \mathbf{y}^{\alpha})$$

NASA/CP—2000-210470

BUBBLE-BUBBLE INTERACTION – II

Singularity expansion of the potential

$$\phi = \sum_{\alpha=1}^{N} \sum_{n=0}^{\infty} \mathbf{A}_n^{\alpha} (\cdot\nabla)^n G(\mathbf{x} - \mathbf{y}^{\alpha})$$

Coefficients $\mathbf{A}_n^{\alpha}$ must be determined from boundary conditions

To impose them, use local representation near each bubble

$$\phi = \sum_{\ell=0}^{\infty} \left(C_{\ell m}^{\alpha} r_{\alpha}^{\ell} + D_{\ell m}^{\alpha} r_{\alpha}^{-\ell-1} \right) Y_{\ell}^{m}(\theta_{\alpha}, \phi_{\alpha})$$

Final step: relate $C_{\ell m}^{\alpha}$, $D_{\ell m}^{\alpha}$ to $\mathbf{A}_n^{\alpha}$

TEMPERATURE FIELD

SPHERICAL VAPOR BUBBLE

Energy equation

$$\frac{\partial T_L}{\partial t} + \mathbf{u} \cdot \boldsymbol{\nabla} T_L = D_L \nabla^2 T_L$$

Velocity field near bubble

$$\mathbf{u} = \boldsymbol{\nabla} \left[\sum_{\ell=0}^{\infty} \sum_{m=-\ell}^{\ell} \left(C_\ell^m r^\ell + D_\ell^m r^{-\ell-1} \right) Y_\ell^m(\theta, \phi) \right]$$

Expand T near bubble

$$T_L = T_\infty + \sum_{N=0}^{\infty} \sum_{M=-N}^{M} S_N^M(r,t)\, Y_N^M(\theta, \phi)$$

Substitute into energy equation and separate components to find

$$\frac{\partial S_{NM}}{\partial t} + \sum_{KL} F_{MN}^{KL} \left(C_\ell^m D_\ell^m, S_K^L, \frac{\partial S_K^L}{\partial r} \right)$$

$$= \frac{D_L}{r^2} \left[\frac{\partial}{\partial r} \left(r^2 \frac{\partial S_{NM}}{\partial r} \right) - N(N+1) S_{NM} \right]$$

$$\frac{\partial S_{NM}}{\partial t} + \sum_{KL} F_{MN}^{KL}\left(C_\ell^m D_\ell^m, S_K^L, \frac{\partial S_K^L}{\partial r}\right)$$

$$= \frac{D_L}{r^2}\left[\frac{\partial}{\partial r}\left(r^2\frac{\partial S_{NM}}{\partial r}\right) - N(N+1)S_{NM}\right]$$

Boundary conditions at bubble surface

$$S_{00}(R(t),t) = T_S(t)\,, \qquad S_{NM}(R(t),t) = 0\,, \qquad M,N \neq 0\,.$$

$$4\pi R^2 k_L \left.\frac{\partial S_{00}}{\partial r}\right|_{r=R(t)} = L\frac{d}{dt}\left(\frac{4}{3}\pi R^3 \rho_V\right) + \frac{4}{3}\pi R^3 \rho_V c_s \frac{dT_S}{dt}\,.$$

For $r \to \infty$

$$S_{00} \to T_\infty\,, \qquad S_{NM} \to 0\,, \qquad M,N \neq 0$$

Solution of radial equations effected by mapping

$$x = \left[1 + \frac{r - R(t)}{\ell}\right]^{-1} \qquad \ell \propto \sqrt{\frac{D_L}{\omega}}$$

spectral Chebyshev expansion

$$S_N^M(r,t) = \sum_{k=0}^{\infty} a_{NMk}(t)\, T_{2k}(x)$$

and collocation

SATURATED WATER $P_\infty = 1$ atm $R_{res} = 2.71$ mm $f = 1$ kHz

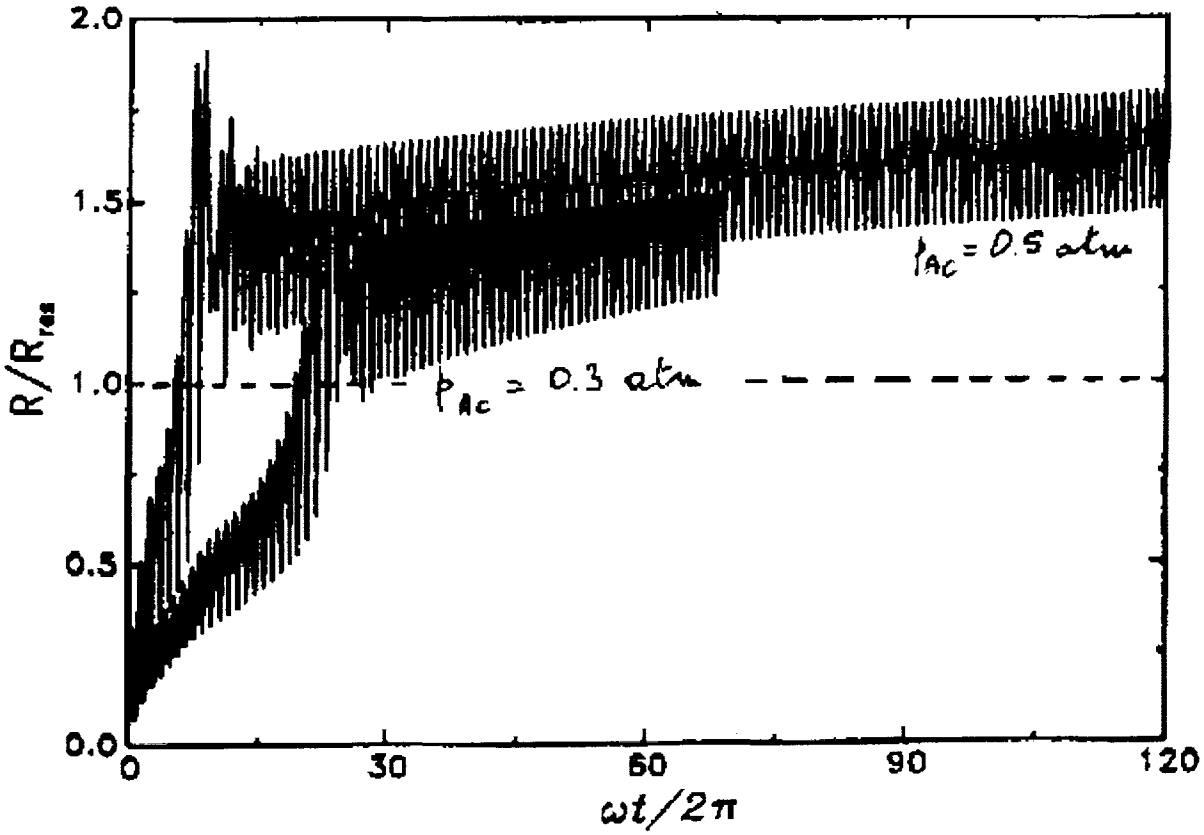

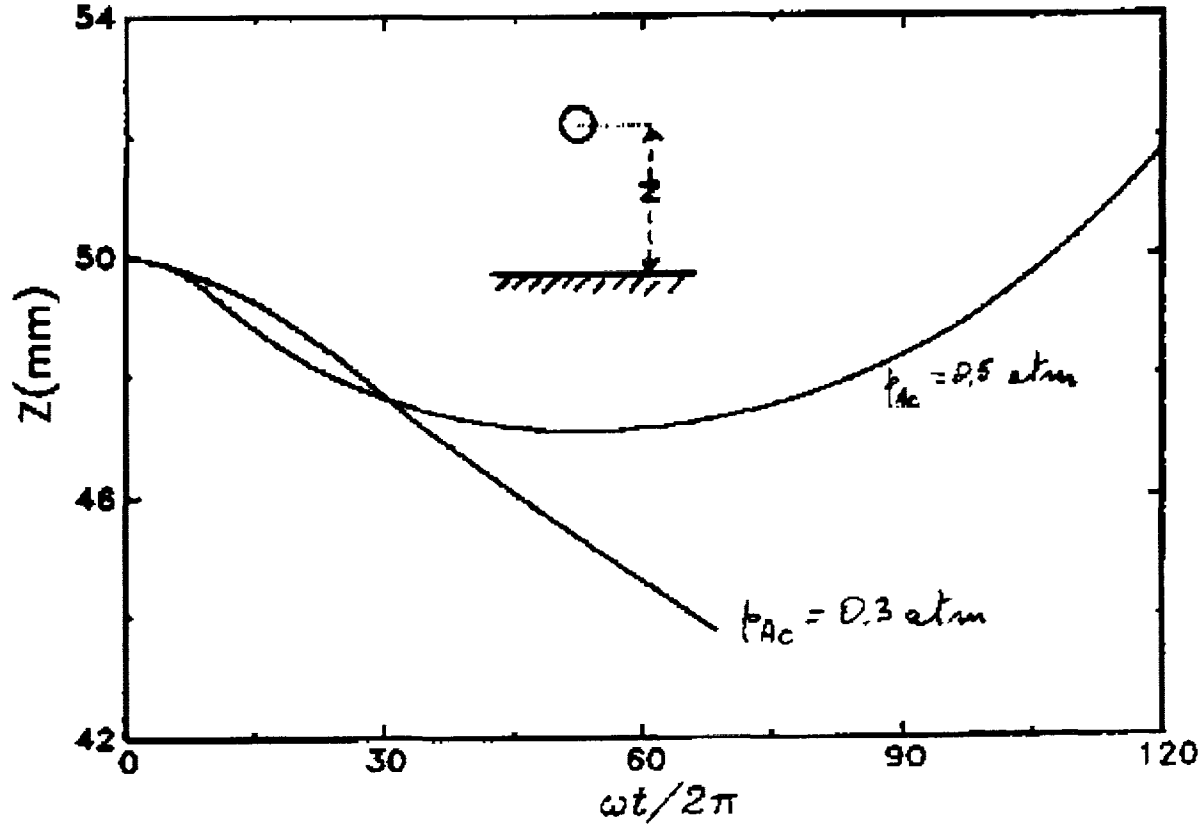

SATURATED WATER $p_\infty = 1$ atm $R_{max} = 2.71$ mm $f = 1$ kHz

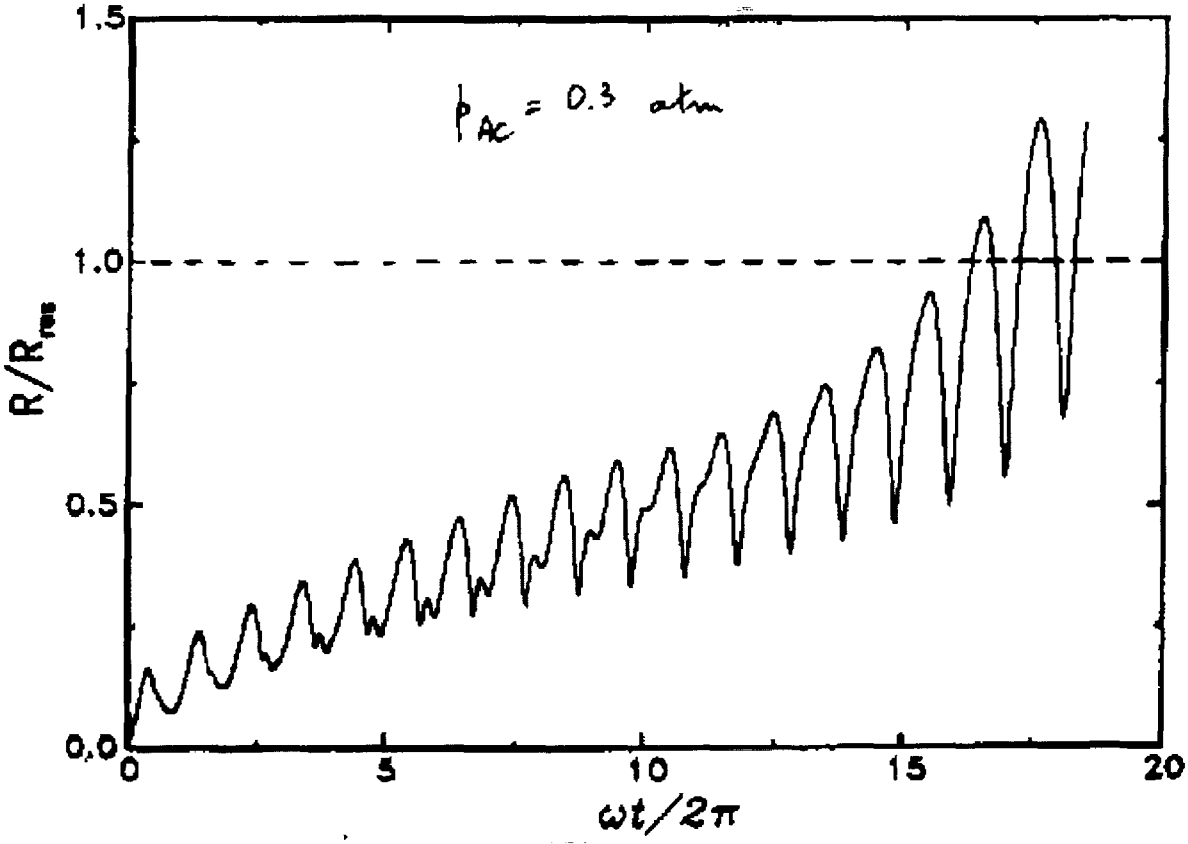

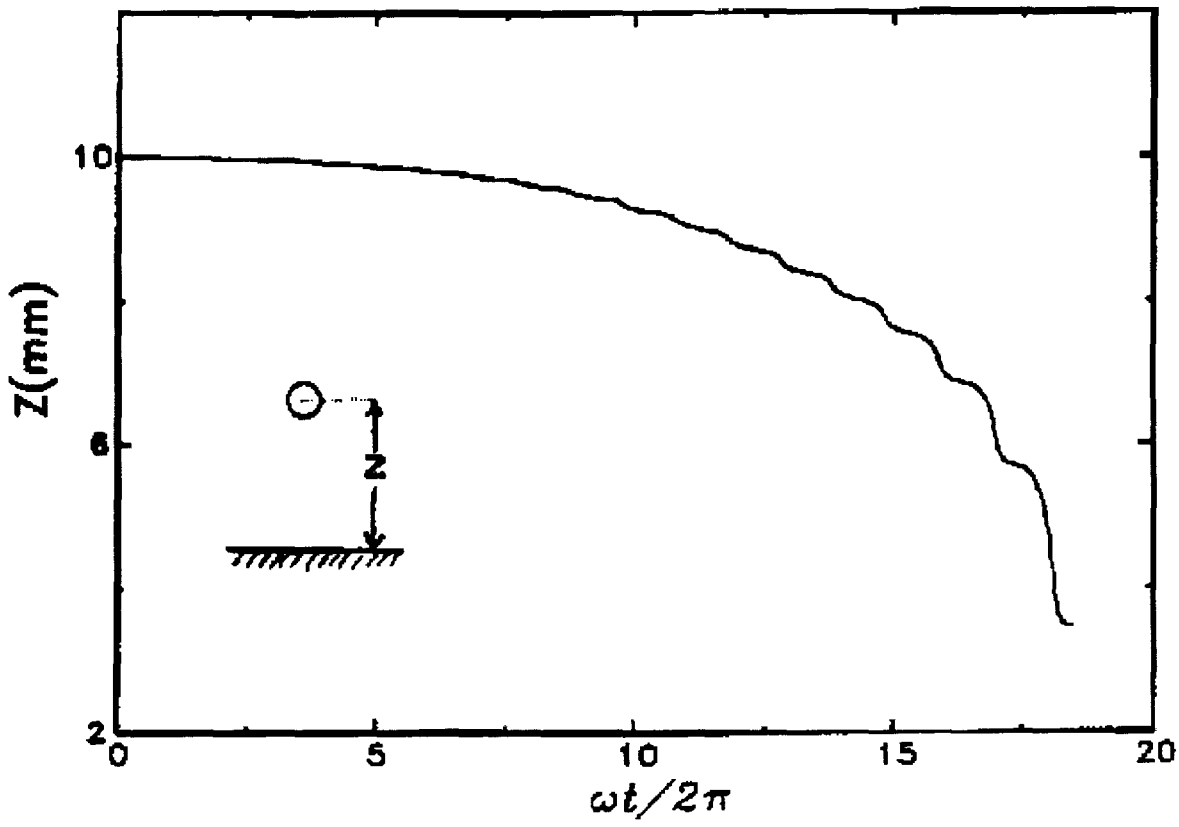

Low Velocity Flow
Vapor Bubble
∇p_{Ac}
∇p_{Ac}
Low Velocity Flow

SATURATED WATER $P_\infty = 1$ atm $R_{eq} = 2.71$ mm $f = 1$ kHz

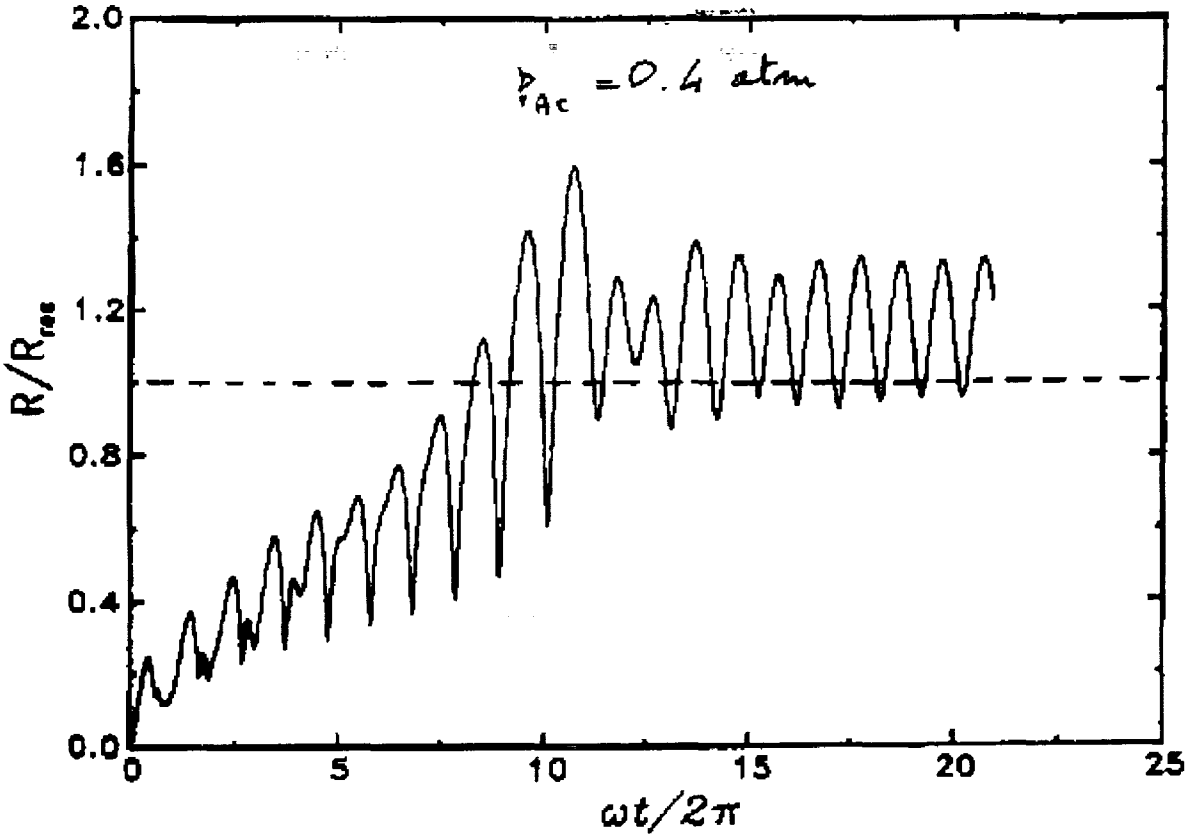

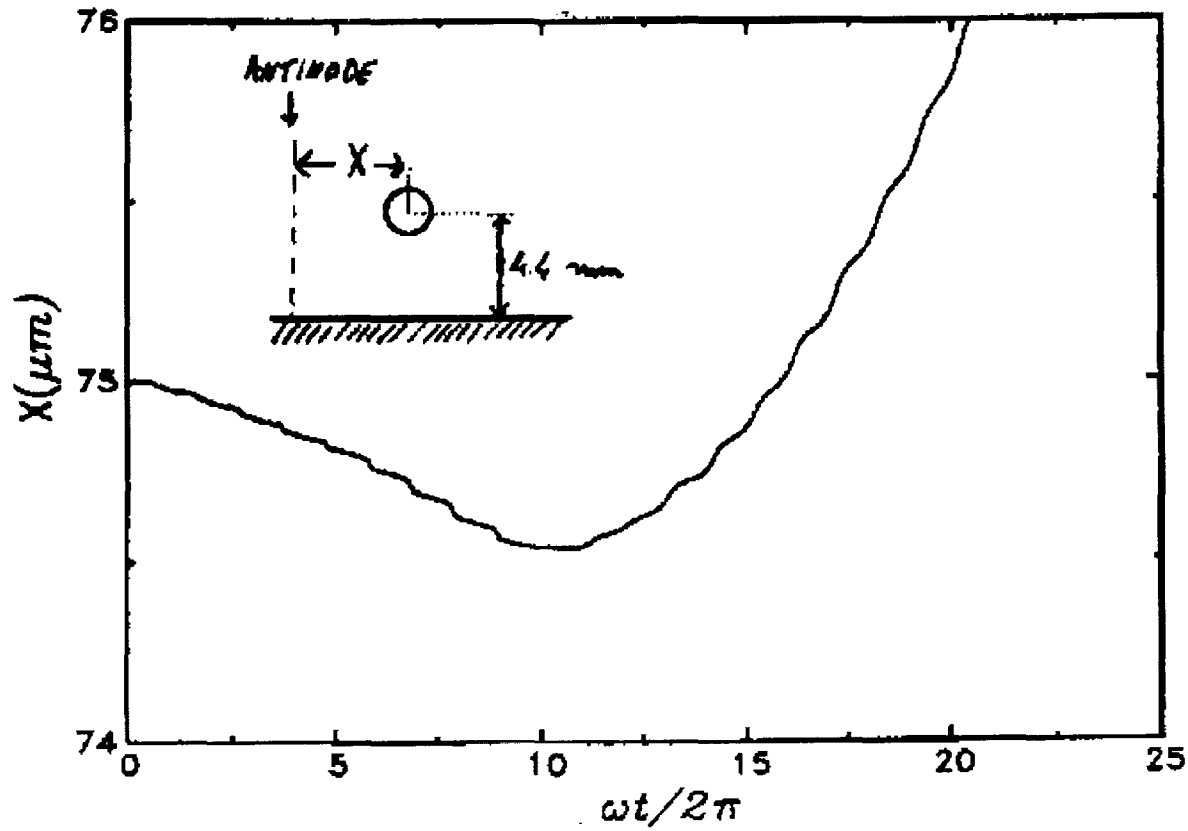

EXPERIMENTAL INVESTIGATION OF POOL BOILING HEAT TRANSFER ENHANCEMENT IN MICROGRAVITY IN THE PRESENCE OF ELECTRIC FIELDS

Cila Herman
Department of Mechanical Engineering
The Johns Hopkins University, Baltimore, MD

Problem statement

The research carried out in the Heat Transfer Laboratory of the Johns Hopkins University was motivated by previous studies indicating that in terrestrial applications nucleate boiling heat transfer can be increased by a factor of 50 when compared to values obtained for the same system without electric fields. Imposing an external electric field holds the promise to improve pool boiling heat transfer in low gravity, since a phase separation force other than gravity is introduced. The influence of electric fields on bubble formation has been investigated both experimentally and theoretically.

Method of study and results

The research carried out within the framework of the NASA project focused on the analysis of bubble formation under the influence of electric fields. In the first phase of the research air was injected into the working fluid PF5052 through an 1.5mm diameter orifice located in the center of the circular ground electrode which is flush with the bottom wall of the test cell. The life cycle of the bubble was captured on videotape with a high-speed camera. Bubble shapes in terrestrial conditions and microgravity (microgravity experiments were carried out in NASA's KC-135 aircraft) with and without electric fields were visualized for a range of operating parameters. In addition to evaluating the effects of ***gravity***, ***the magnitude and polarity of the electric field***, the ***mass flow rate of the air*** injected into the test cell, as well as the ***level of heating*** applied to the bottom electrode were varied during these experiments. Typical bubble sequences for the uniform electric fields (0V and 25kV potential difference between the electrodes) recorded in terrestrial conditions are shown in Figure 1 and in microgravity in Figure 2.

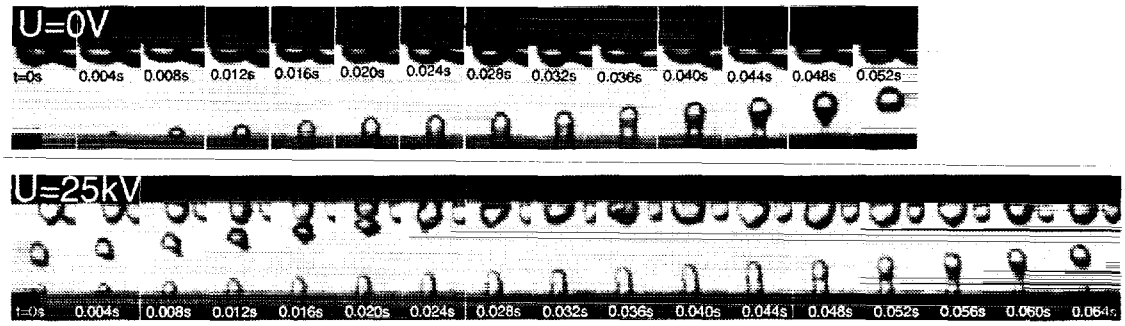

Figure 1. Bubble formation at an orifice without electric field (top) and with 25 kV applied to the electrodes as function time visualized under terrestrial conditions in the Heat Transfer Lab of the Johns Hopkins University.

Experiments were carried out for two ***configurations of the electrodes***. In the first series of experiments the two electrodes were ***parallel***, generating a uniform electric field. In the second series of experiments the shape of the ***high-voltage electrode*** was modified to a ***spherical shape*** (its diamater being one fourth of the diameter of the circular ground electrode) and positioned off-axis with respect to the bottom ground electrode. This electrode configuration yields a nonuniform electric field.

Bubble shapes and sizes were measured using digital image processing. A dedicated digital image processing code was developed for this purpose using the Matlab software. In the analysis, selected image sequences were converted into a digital format using a frame grabber. The images were then enhanced and sequentially read by the image processing code. The size of the bubble during bubble formation, its volume and key dimensions were extracted and stored in a file for further evaluation. Measured bubble shapes are currently being compared with predictions obtained using simplified analytical models.

In addition to the visualization of bubble shapes, **temperature fields** were visualized using **holographic interferometry**. Dedicated image processing codes for the evaluation of interferometric images of bubbles and

tomographic algorithms for the tomographic reconstruction of 3D temperature distributions around the bubble were developed.

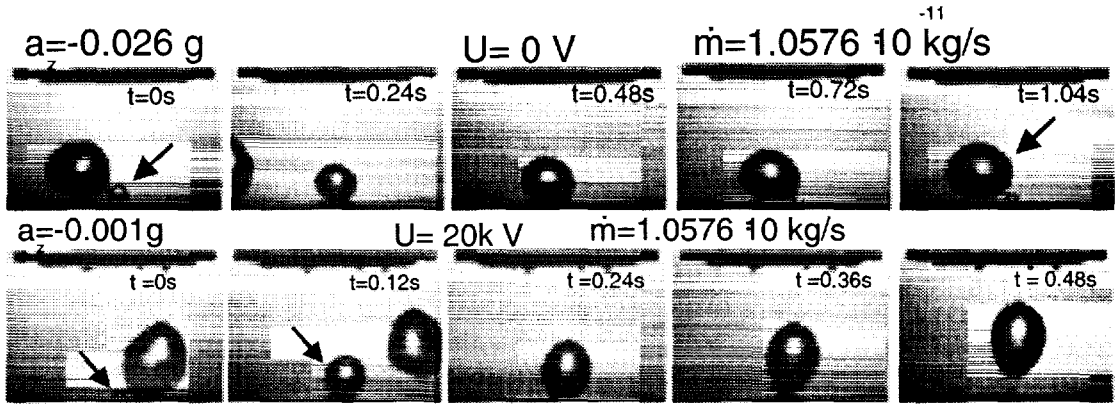

Figure 2. Bubble formation at an orifice without electric field (top) and with 25 kV applied to the electrodes (bottom) as function time visualized in microgravity conditions in NASA's KC-135 aircraft.

The results of visualization experiments clearly indicate that there are significant differences in bubble shape, size and frequency, caused by effects of gravity and electric fields. In terrestrial conditions the bubbles at detachment are much smaller and more elongated in the presence of the electric field than for the reference conditions without the electric field. Microgravity experiments have verified that in the presence of electric fields bubbles do detach from the orifice and move away from the surface as opposed to the situation when large spherical bubbles developing at the orifice remain motionless on the surface in the absence of acceleration. The bubble shape in microgravity is elongated when an electric field is applied between the electrodes, contrasted to the nearly spherical shape in the absence of the electric field. In addition to the change of shape, one key difference in the behavior of the bubbles in the presence of the electric fields is the significantly reduced tendency for coalescence.

Apart from the experimental studies, existing simplified analytical models describing bubble formation at an orifice and during boiling were evaluated and modified to accommodate the physical effects considered in the NASA study. Bubble shapes and sizes at detachment were evaluated for a range of working fluids as function of the magnitude of the electric field and the gravity level.

The influence of gravity level on bubble shapes in the performance fluid PF5052 for two values of the potential difference imposed between the electrodes, U=50kV and U=0V, is illustrated in Figure 3. Results obtained for terrestrial conditions show little difference in bubble shape due to the electric field. Bubble elongation in microgravity is pronounced, as illustrated in Figure 3. The elongation becomes more significant with increasing magnitude of the electric field (50 kV) both in terrestrial conditions and microgravity. The comparison of modeling data with experimental results is currently underway.

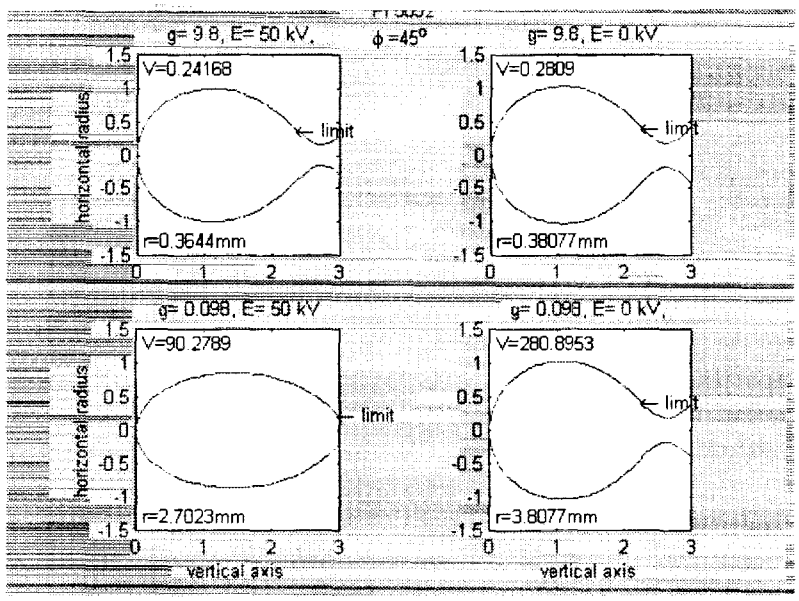

Figure 3. Bubble shapes at detachment for terrestrial conditions and 1/10g for a potential difference between the electrodes of 50 kV (left) and 0 kV (right)

EXPERIMENTAL INVESTIGATION OF POOL BOILING HEAT TRANSFER ENHANCEMENT IN MICROGRAVITY UNDER THE INFLUENCE OF ELECTRIC FIELDS

Cila Herman
Department of Mechanical Engineering
The Johns Hopkins University

Fifth Microgravity Fluid Physics and Transport Phenomena Conference
August 9-11, Cleveland, OH

Laboratory

NASA/CP—2000-210470

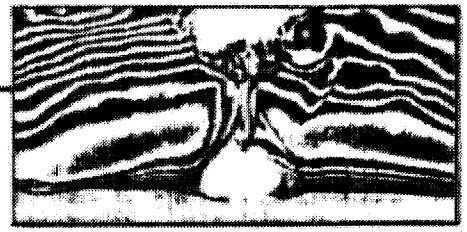

NASA/CP—2000-210470

Acknowledgments

Financial support provided by NASA

Dr. Istvan Foldes
Dr. Ed Scheinerman
Gorkem Suner
Ozan Tutunoglu
Tara Lynn Johnson
Christophe Milburn
Margareta Stefanovic
Curt Ewing
Bill Darling

Support at NASA Glenn Research Center
KC - 135 crew
Ground support team for KC - 135 flights

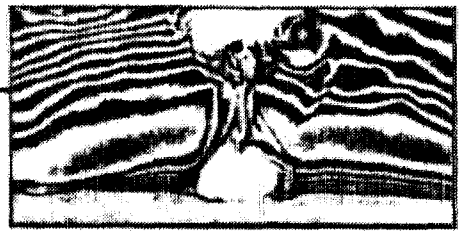

NASA/CP—2000-210470

OUTLINE

1. Introduction and motivation

2. Summary of past research accomplishments

3. Bubble formation at an orifice in microgravity under the influence of electric fields

- Experimental approach
- Experimental setup
- Visualization images and results
- Modeling efforts

4. Outlook and future research

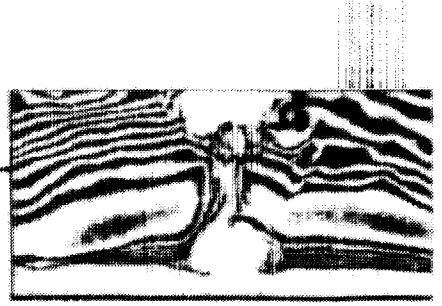

FORCES ACTING ON A BUBBLE DURING DYNAMIC BUBBLE GROWTH

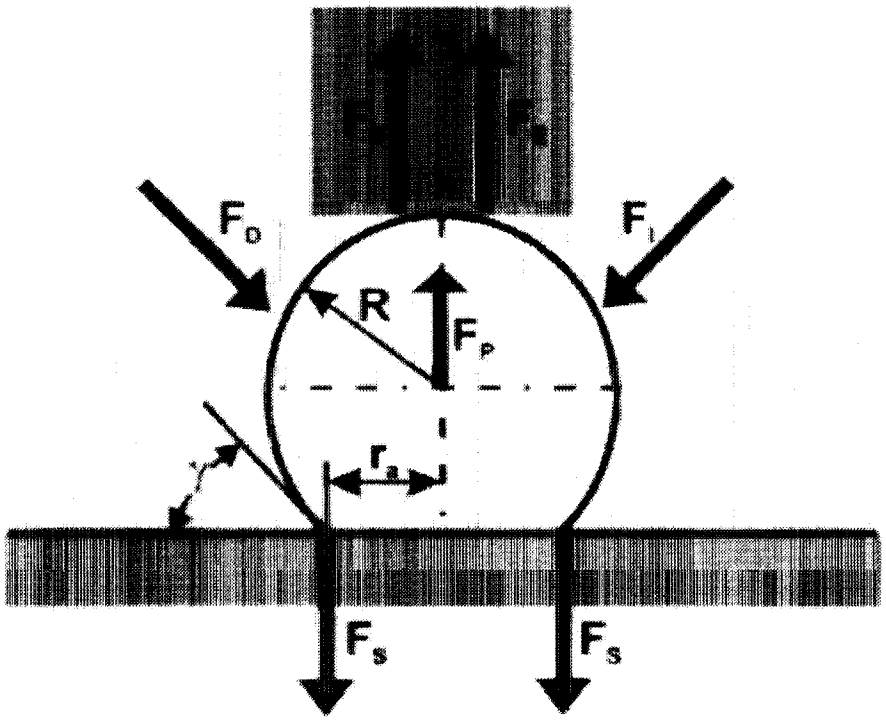

Force balance $F_D + F_S = F_I + F_P + F_B + F_E$

Drag $F_D = C_D \frac{\rho_L}{2} \left(\frac{dR}{dt} \right)^2 \pi r_a^2$

Surface tension $F_S = 2\pi \, r_a \sigma \, \sin\gamma$

Inertia $F_I = \frac{4}{3} \pi R^3 \rho_L \frac{d^2R}{dt^2}$

Pressure $F_P = \left(\frac{2\sigma}{R} + \Delta p_V \right) \pi r_a^2$

Buoyancy

Electric field

NASA/CP—2000-210470

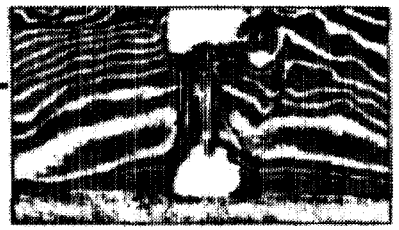

FORCE CAUSED BY THE ELECTRIC FIELD

$$\vec{F}_E = \rho_f \vec{E} - \frac{1}{2} E^2 \nabla \varepsilon - \nabla \left[\frac{1}{2} \rho \, E^2 \left(\frac{\partial \varepsilon}{\partial \rho} \right)_T \right]$$

Coulomb's force (electrophoretic) $\rho_f \vec{E}$

Dielectrophoretic force $\frac{1}{2} E^2 \nabla \varepsilon$

Electrostriction $\nabla \left[\frac{1}{2} \rho \, E^2 \left(\frac{\partial \varepsilon}{\partial \rho} \right)_T \right]$

Gases: $\rho \left(\frac{\partial \varepsilon_G}{\partial \rho} \right)_T = \varepsilon_0 (\varepsilon_G - 1)$ Liquids: $\rho \left(\frac{\partial \varepsilon_L}{\partial \rho} \right)_T = \frac{\varepsilon_0 (\varepsilon_L - 1)(\varepsilon_L - 2)}{3}$

Relaxation time of electrical charges $\tau_\sigma = \frac{\varepsilon}{\sigma}$

Thermophysical and transport properties: $k = k(E)$ and $\mu = \mu(E)$

Electrical properties: $\varepsilon = (\varepsilon)_0 (1 + a \Delta T)$ and $\sigma = (\sigma)_0 (1 - b \Delta T)$

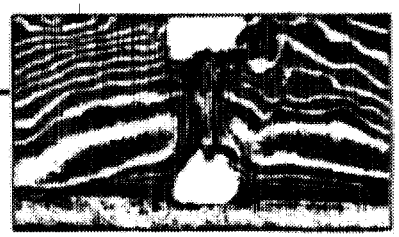

GOVERNING EQUATIONS

Momentum equation

$$\rho\left(\frac{\partial \vec{v}}{\partial t}+\vec{v}\cdot\nabla\vec{v}\right)=-\nabla p+\rho\ \vec{g}+\vec{F}_E+\mu\ \nabla^2\vec{v}$$

Incompressibility condition

$$\nabla\cdot\vec{v}=0$$

Energy equation

$$\frac{\partial T}{\partial t}+\vec{v}\cdot\nabla T=\alpha\nabla^2 T+\sigma\ E^2/\rho c_p$$

Force of electrical origin

$$\vec{F}_E=\rho_f\vec{E}-\frac{1}{2}E^2\nabla\varepsilon-\nabla\left[\frac{1}{2}\rho\ E^2\left(\frac{\partial\varepsilon}{\partial\rho}\right)_T\right]$$

σ electrical conductivity
E electric field strength
ρ_f free charge density
ε dielectric permittivity

NASA/CP—2000-210470

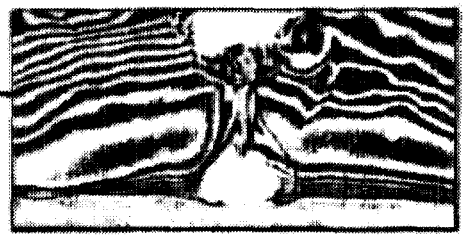

NASA/CP—2000-210470

Past research accomplishments - measurement techniques -

- **Visualization of unsteady temperature distributions around bubbles using real-time holographic interferometry**

- **Accounting for light deflection effects in the reconstruction of temperature distributions from interferometric images**

- **Reconstruction of axially symmetrical temperature distributions from interferometric images**

- **Reconstruction of 3D unsteady temperature distributions from interferometric images using tomographic techniques**

- **Measurement of bubble volume and dimensions using digital image processing**

Pool Boiling in Microgravity

under the Influence of Electric Fields

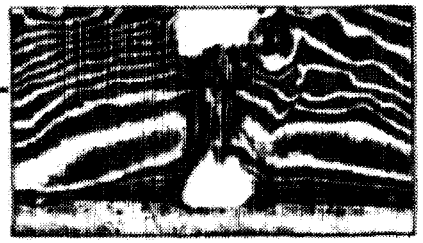

THERMAL PLUME ABOVE THE HEATED DISK VISUALIZED BY HOLOGRAPHIC INTERFEROMETRY

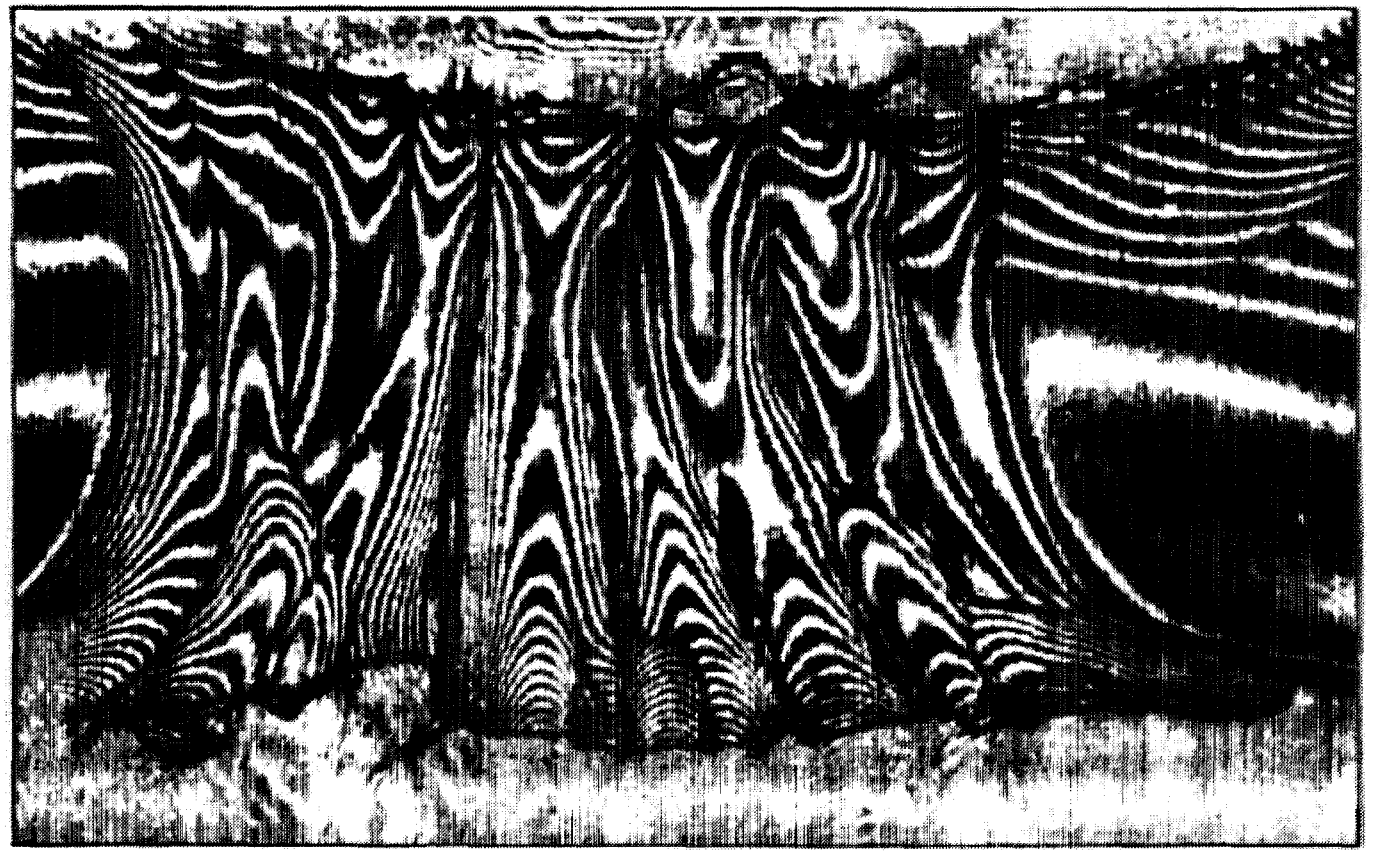

Working fluid: PF-5052
Saturation temperature: T_{sat}=50 °C
Pressure: p= 1 bar

Surface temperature T_s= 29 °C
ΔT/fringe pair=0.05 °C

The Johns Hopkins University
Heat Transfer Laboratory

Cila Herman

Pool Boiling in Microgravity
under the Influence of Electric Fields

AIR BUBBLES INJECTED INTO THE THERMAL BOUNDARY LAYER THROUGH AN ORIFICE

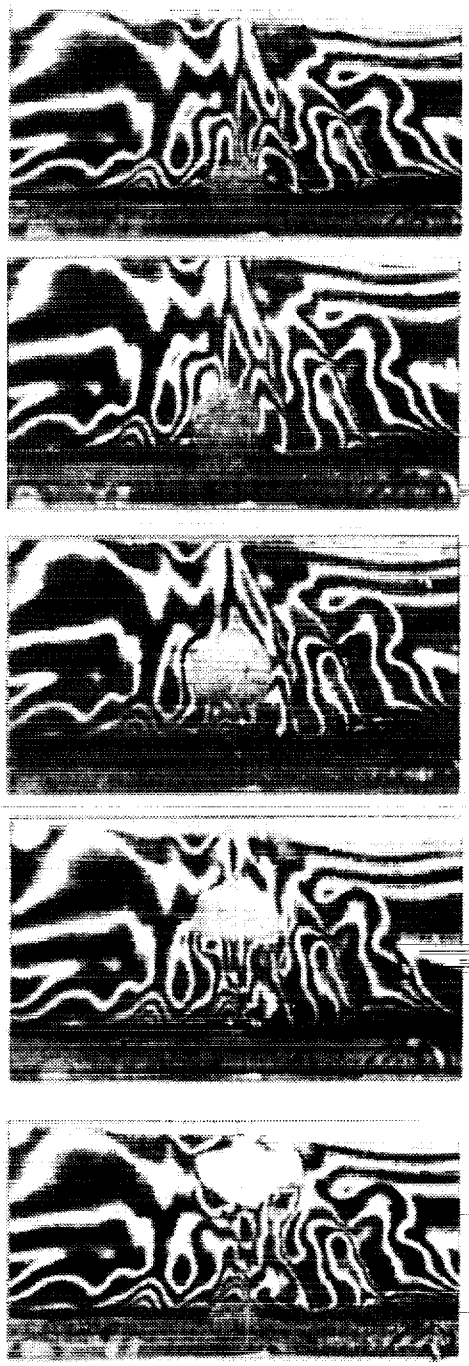

Working fluid: PF-5052
Saturation temperature: T_{sat} = 50 °C
Pressure: p= 1 bar

Surface temperature: T_s = 25 °C
ΔT/fringe pair = 0.05 °C

Time separation between images = 0.01 seconds

The Johns Hopkins University
Heat Transfer Laboratory

Cila Herman

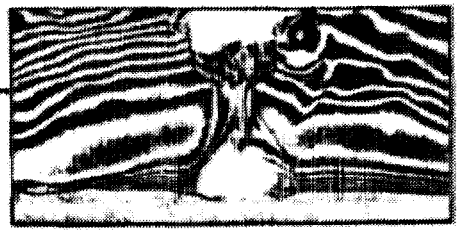

NASA/CP—2000-210470

PHF VAPOR PATTERNS HYDRODYNAMIC THEORY

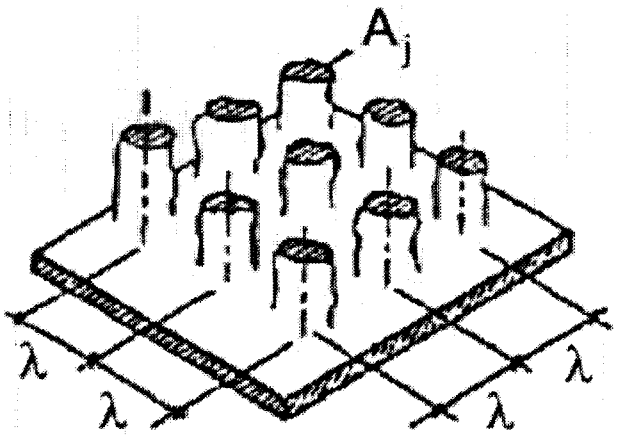

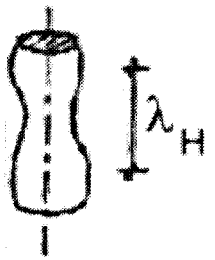

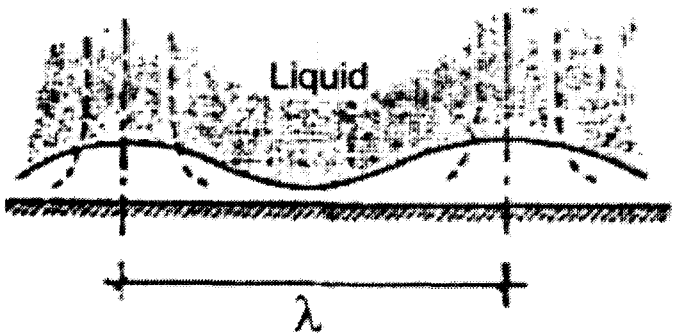

The Johns Hopkins University
Heat Transfer Laboratory

Cila Herman

SCHEMATIC OF THE EXPERIMENTAL SETUP

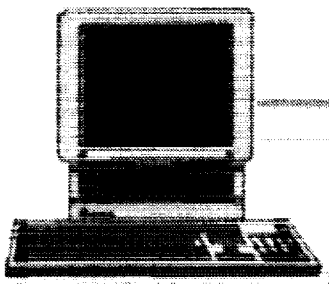

PC for data acquisition & control

Data acquisition & control system

Accele-rometer

30 kV Power supply

PF 5052

Test cell

Electrodes

Injection system

Power supply

Thermocouples

Resistive heater

Grounding

Pool Boiling in Microgravity

under the Influence of Electric Fields

Schematic of the test cell

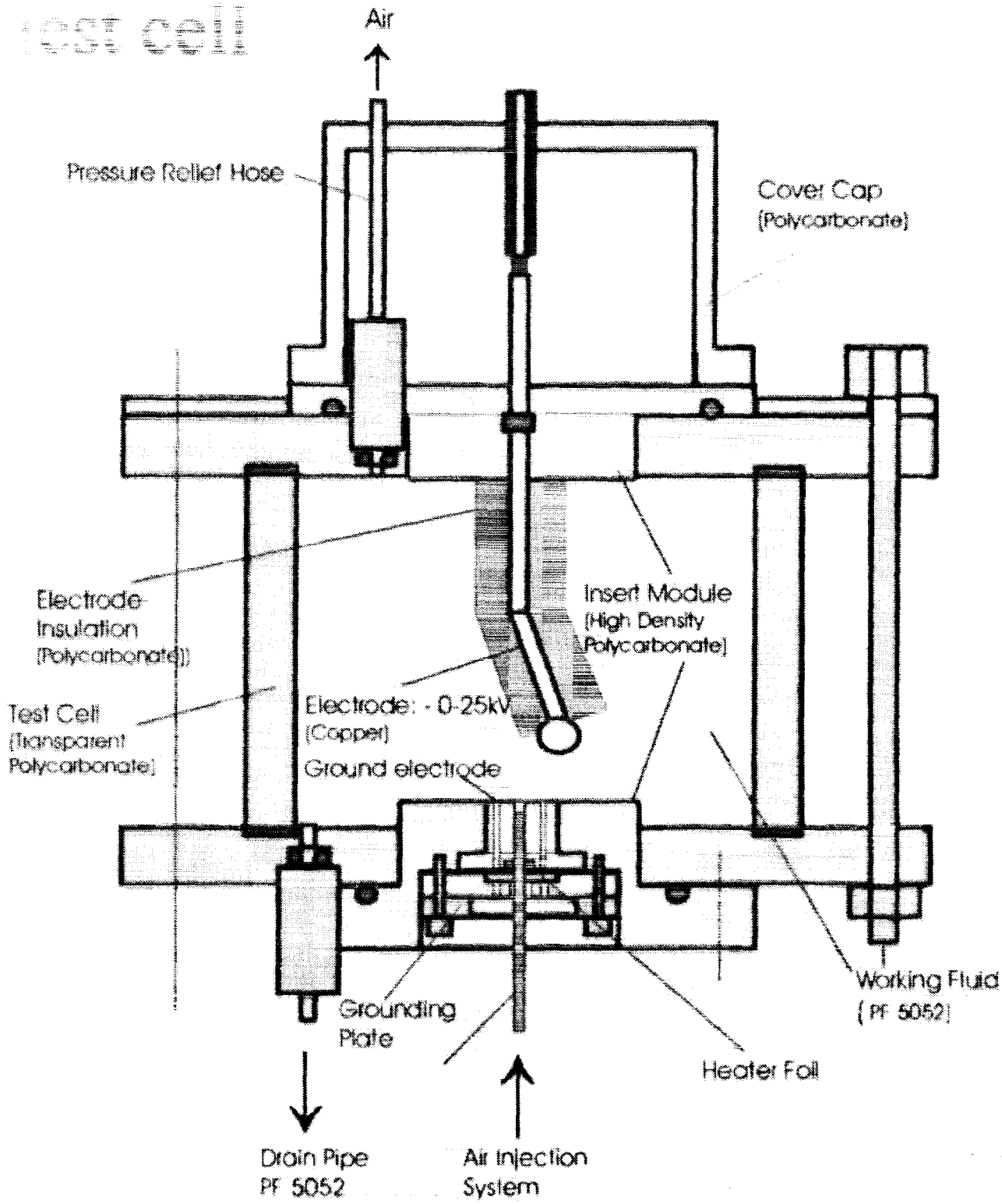

The Johns Hopkins University
Heat Transfer Laboratory

Cila Herman

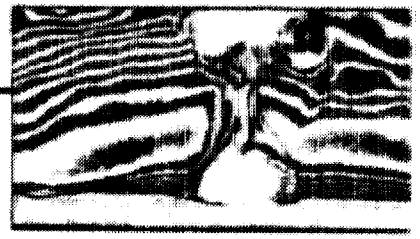

Details of the test cell

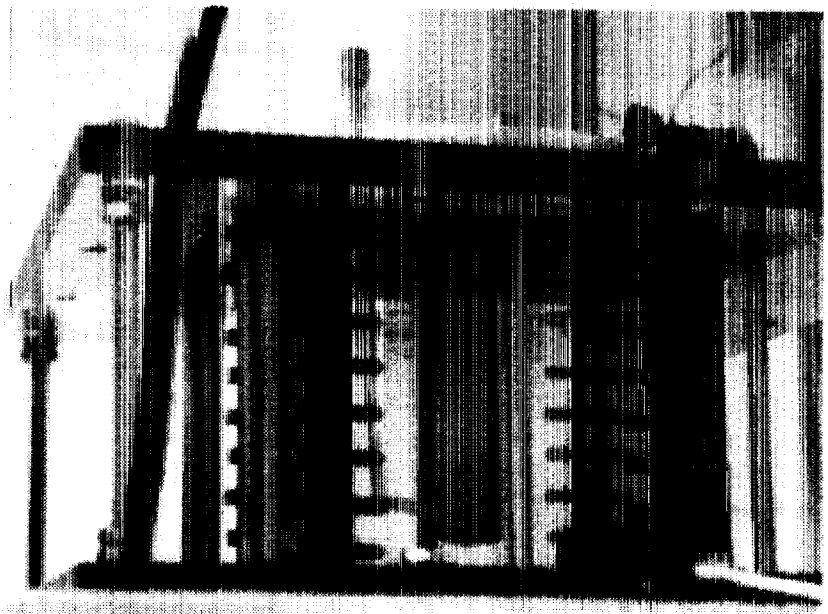

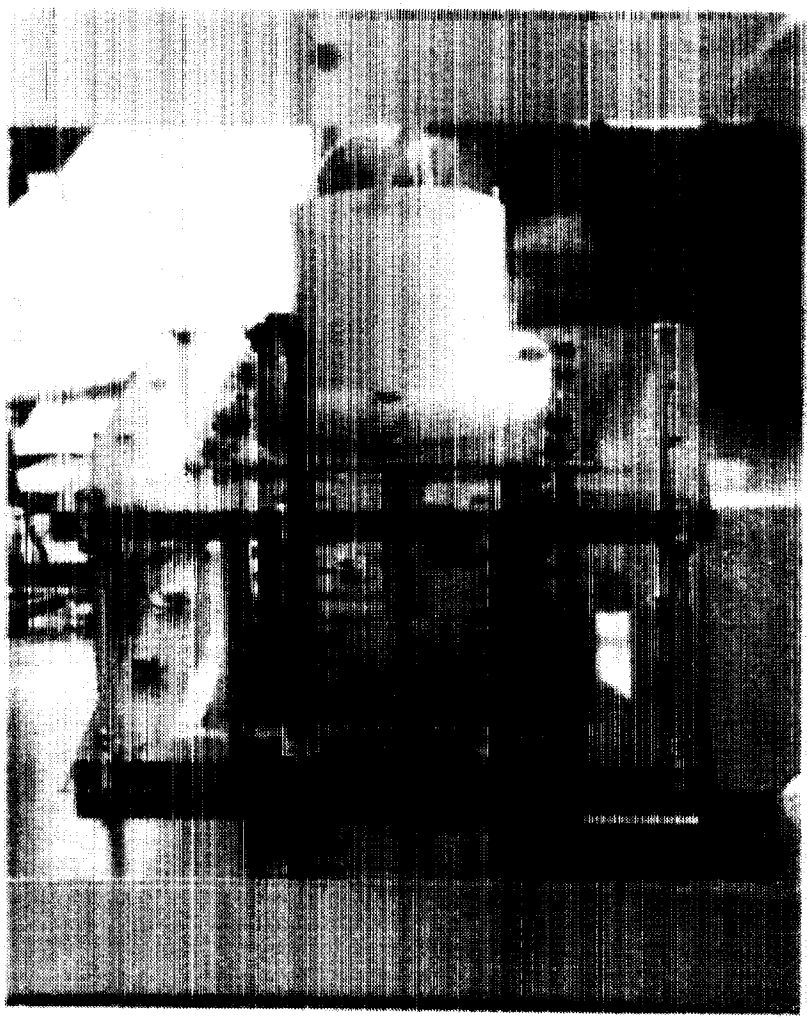

The Johns Hopkins University
Heat Transfer Laboratory

Cila Herman

NASA/CP—2000-210470

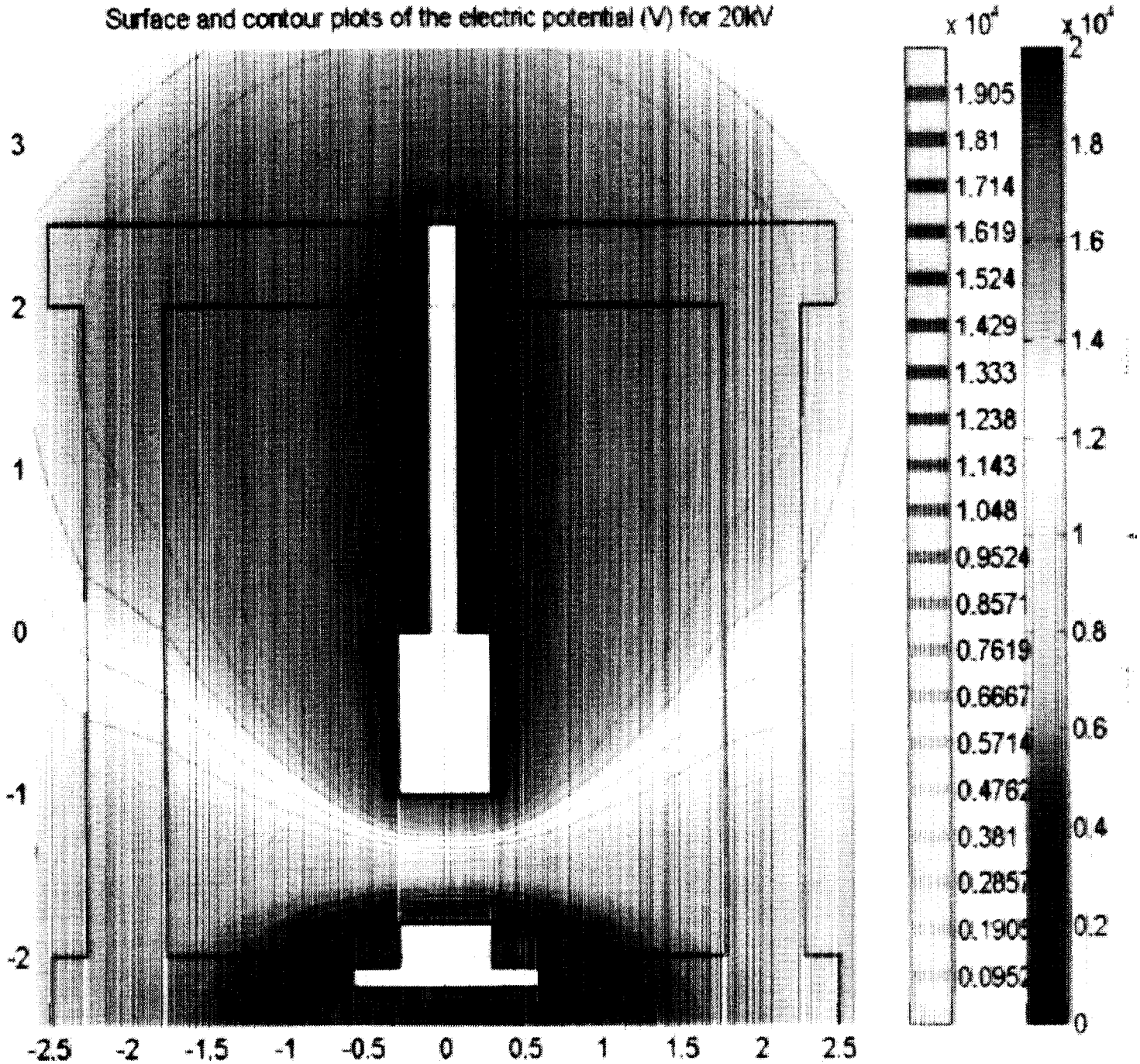
Surface and contour plots of the electric potential (V) for 20kV
x 10^4
1.905
1.81
1.714
1.619
1.524
1.429
1.333
1.238
1.143
1.048
0.9524
0.8571
0.7619
0.6667
0.5714
0.4762
0.381
0.2857
0.1905
0.0952
x 10^4
2
1.8
1.6
1.4
1.2
1
0.8
0.6
0.4
0.2
0
3
2
1
0
-1
-2
-2.5
-2
-1.5
-1
-0.5
0
0.5
1
1.5
2
2.5

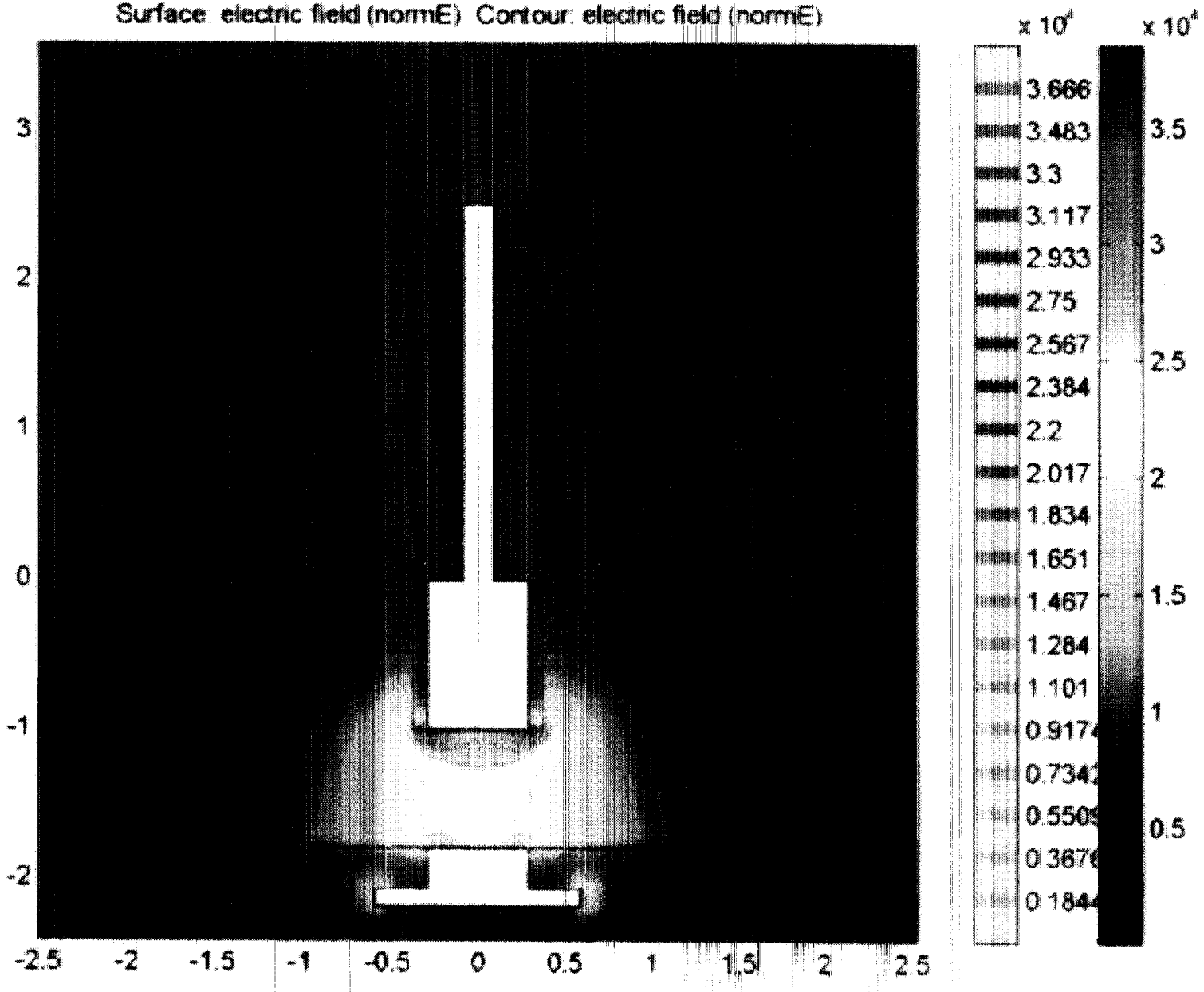
Surface: electric field (normE) Contour: electric field (normE)
x 10^4
3.666
3.483
3.3
3.117
2.933
2.75
2.567
2.384
2.2
2.017
1.834
1.651
1.467
1.284
1.101
0.9174
0.7342
0.5509
0.3676
0.1844
x 10^4
3.5
3
2.5
2
1.5
1
0.5
3
2
1
0
-1
-2
-2.5
-2
-1.5
-1
-0.5
0
0.5
1
1.5
2
2.5

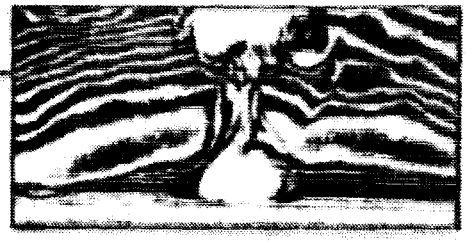

Pressure relief system

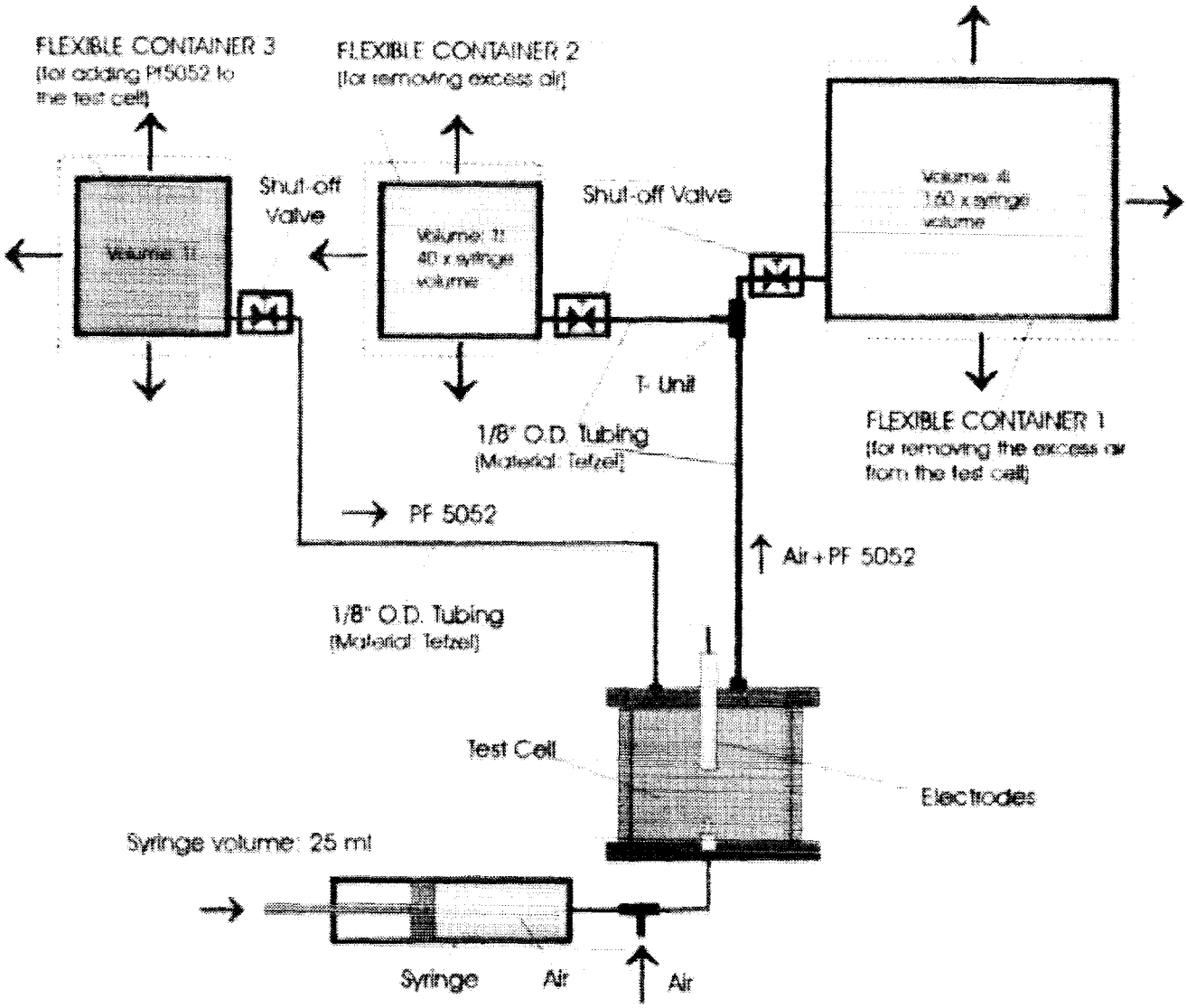

Pool Boiling in Microgravity

under the Influence of Electric Fields

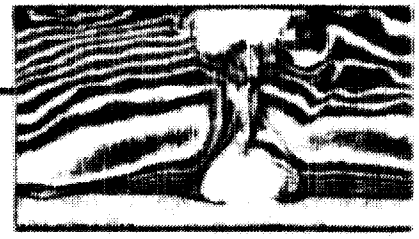

Experimental rack

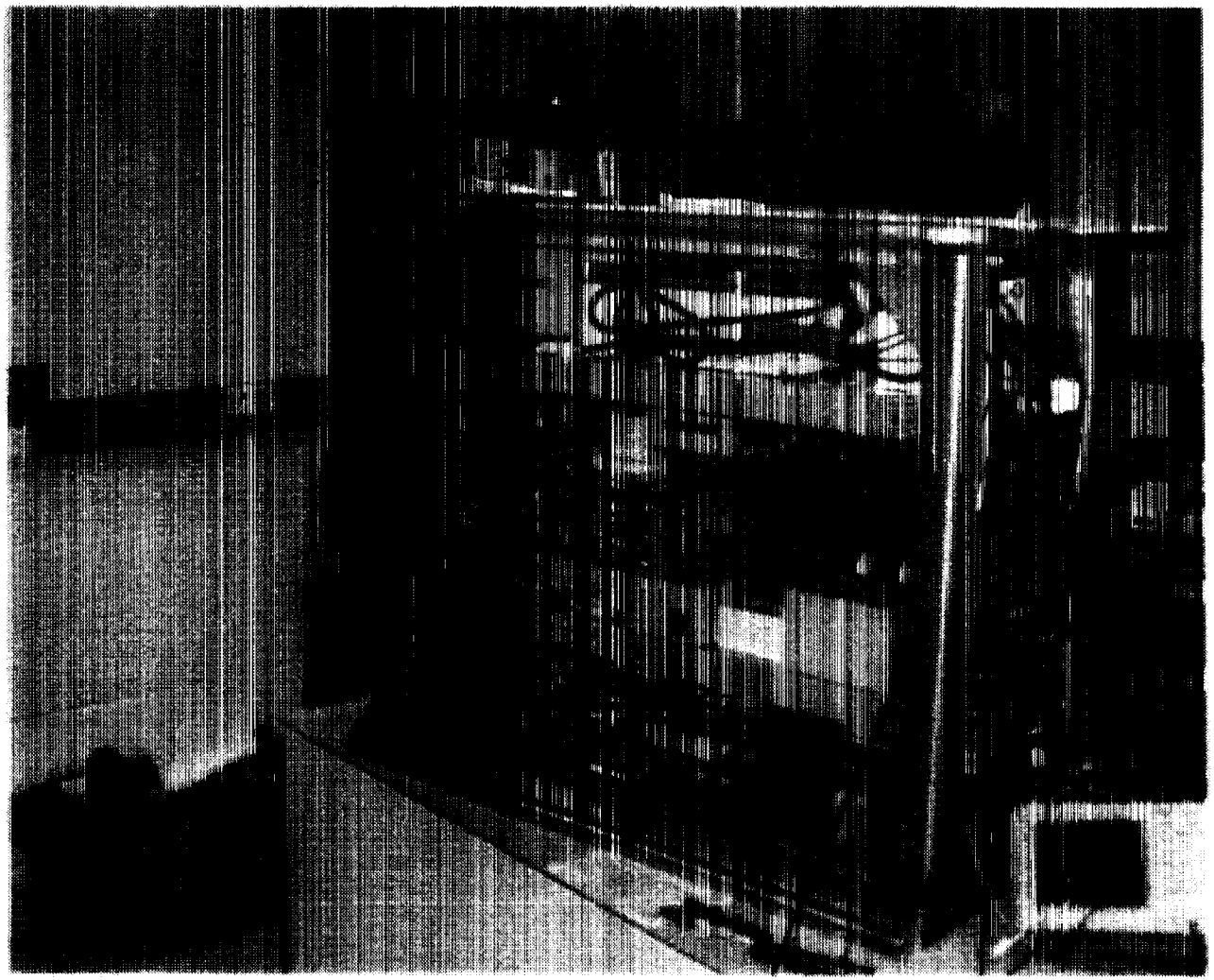

The Johns Hopkins University
Heat Transfer Laboratory

Cila Herman

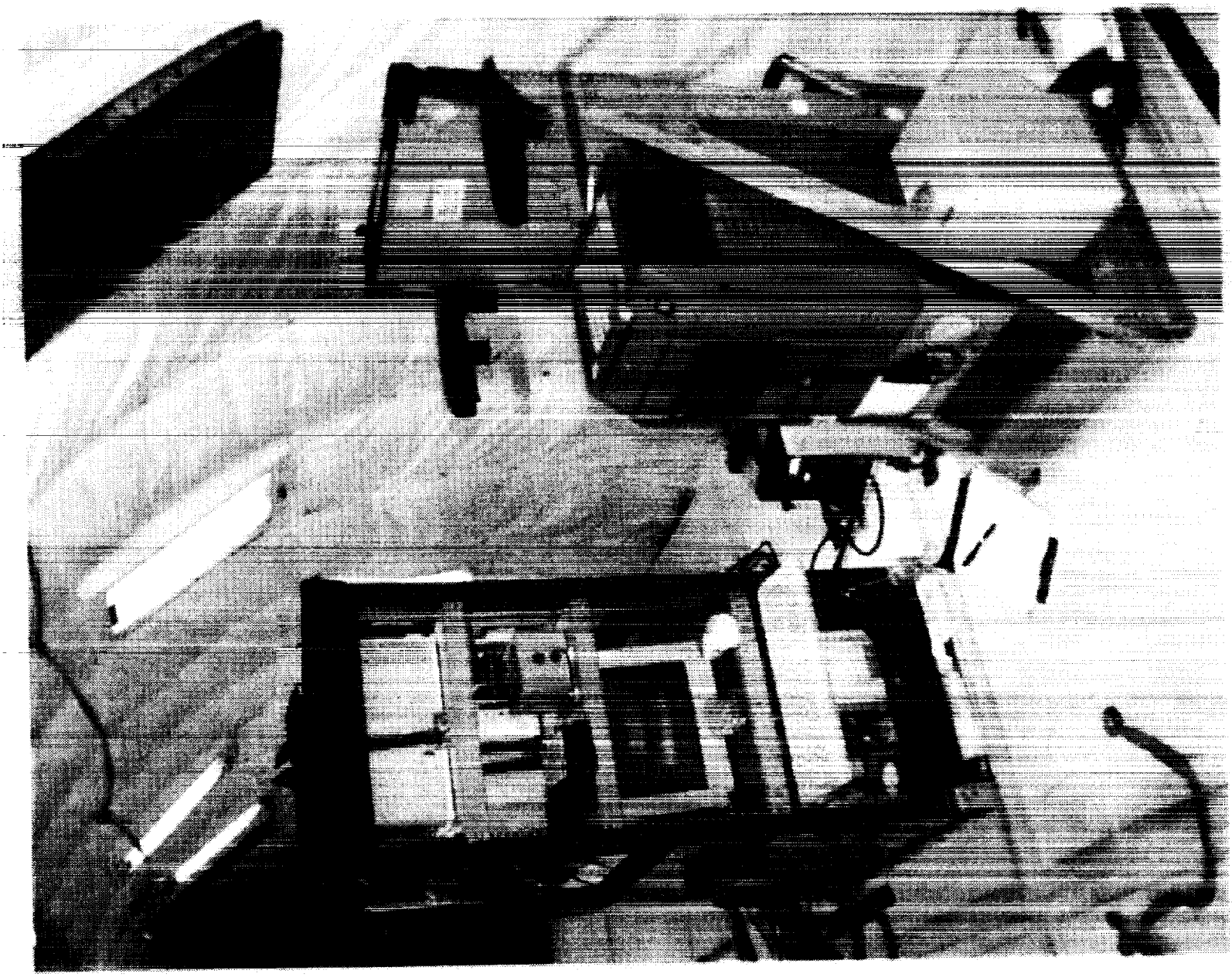

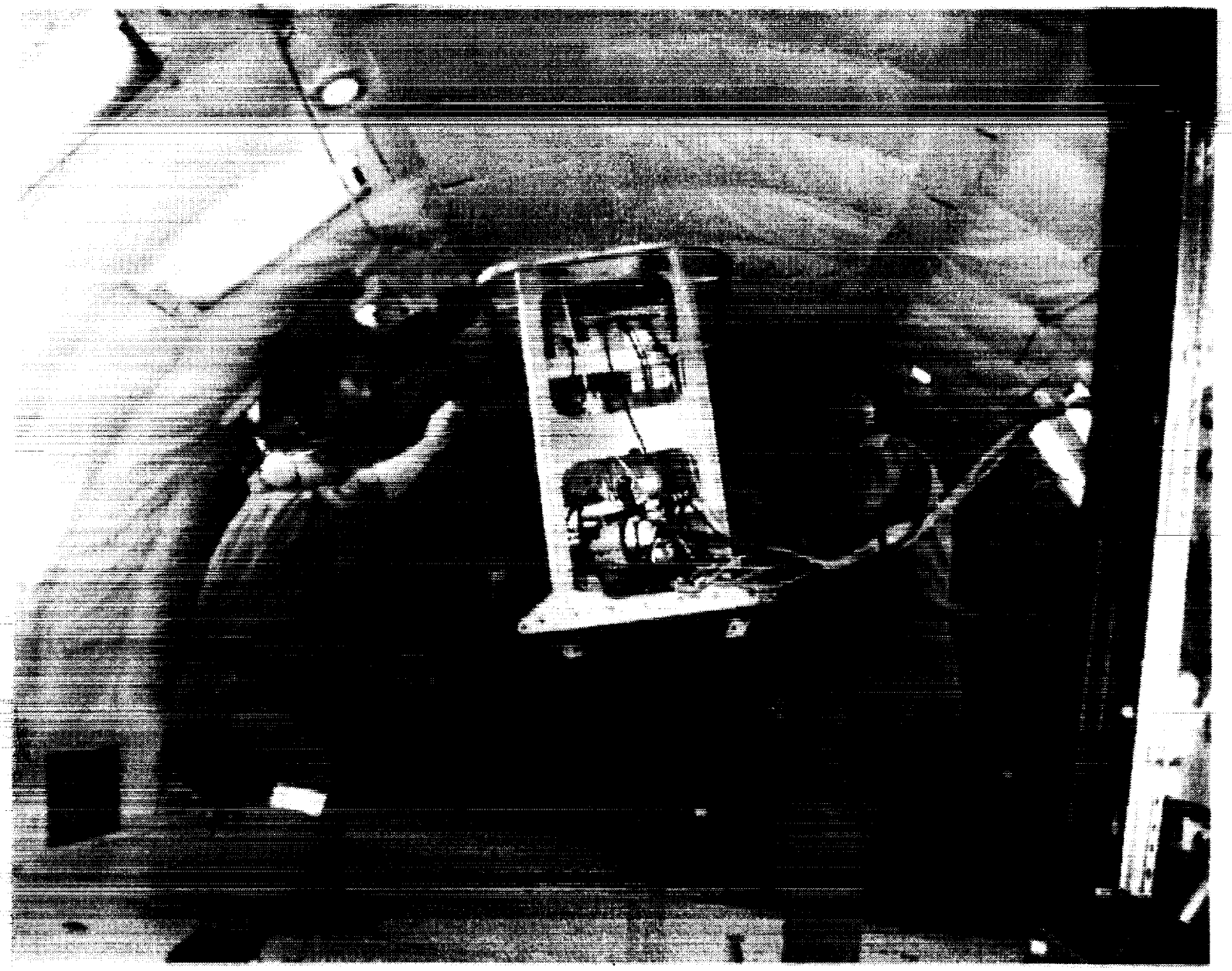

Experimental parameters

- Potential difference between electrodes: 0V, 5kV, 10kV, 15kV, 20kV
- Polarity
- Shape of the high-voltage electrode: cylindrical, spherical
- Heating applied to the ground electrode
- Gravity: 1g, 0g, 0.3g, 0.1g
- Mass flow rate of the injected air

NASA/CP—2000-210470

NASA/CP—2000-210470

PHF VAPOR PATTERNS

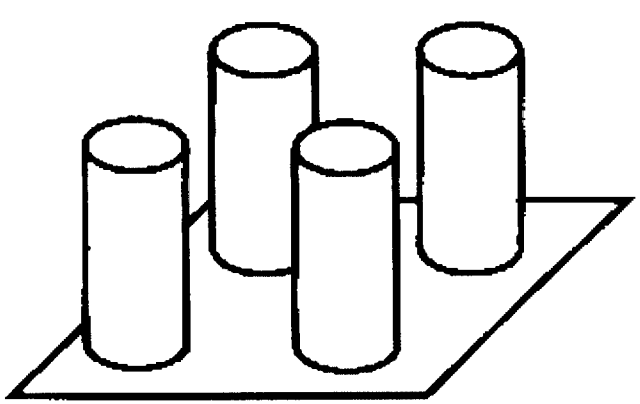

a) without electric field

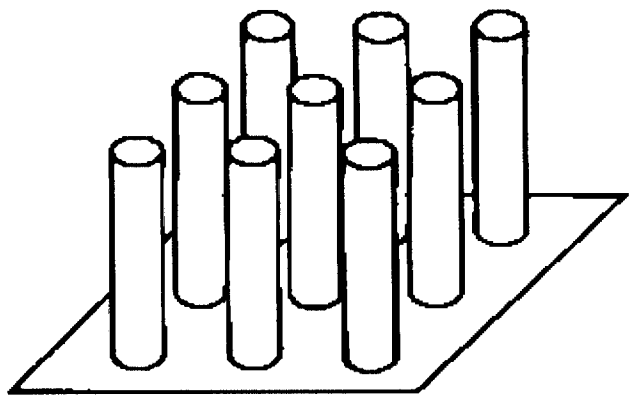

b) with electric field

HYDRODYNAMIC MODEL FOR PEAK HEAT FLUX

$$\frac{(Q/A)_{max}}{h_{fg}\rho_v} = 0.13\left[\frac{\sigma g(\rho_L - \rho_v)}{\rho_v^2}\right]^{\frac{1}{4}}$$

Zuber and Tribus (1958)

based on the Helmholtz - Taylor analysis

ELECTRIC FIELD EFFECT - ELECTROHYDRODYNAMIC APPROACH

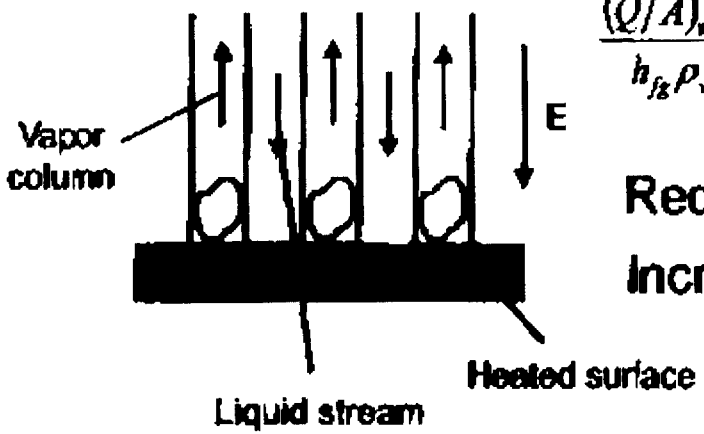

$$\frac{(Q/A)_{max}}{h_{fg}\rho_v} = C_1\left[\frac{(\sigma g(\rho_L - \rho_v))^{\frac{1}{2}}}{\rho_v}\left(\frac{\rho_L}{\rho_L + \rho_v}\right) + \frac{(\varepsilon - \varepsilon_0)^2 E^2}{\rho_v(\varepsilon + \varepsilon_0)}\right]^{\frac{1}{2}}$$

Melcher (1963)

Reduction of bubble departure size $DE = C_2$

Increase of bubble departure frequency $fD^2 = C_3$

Pool Boiling in Microgravity

under the Influence of Electric Fields

Life cycle of an injected bubble in 1g

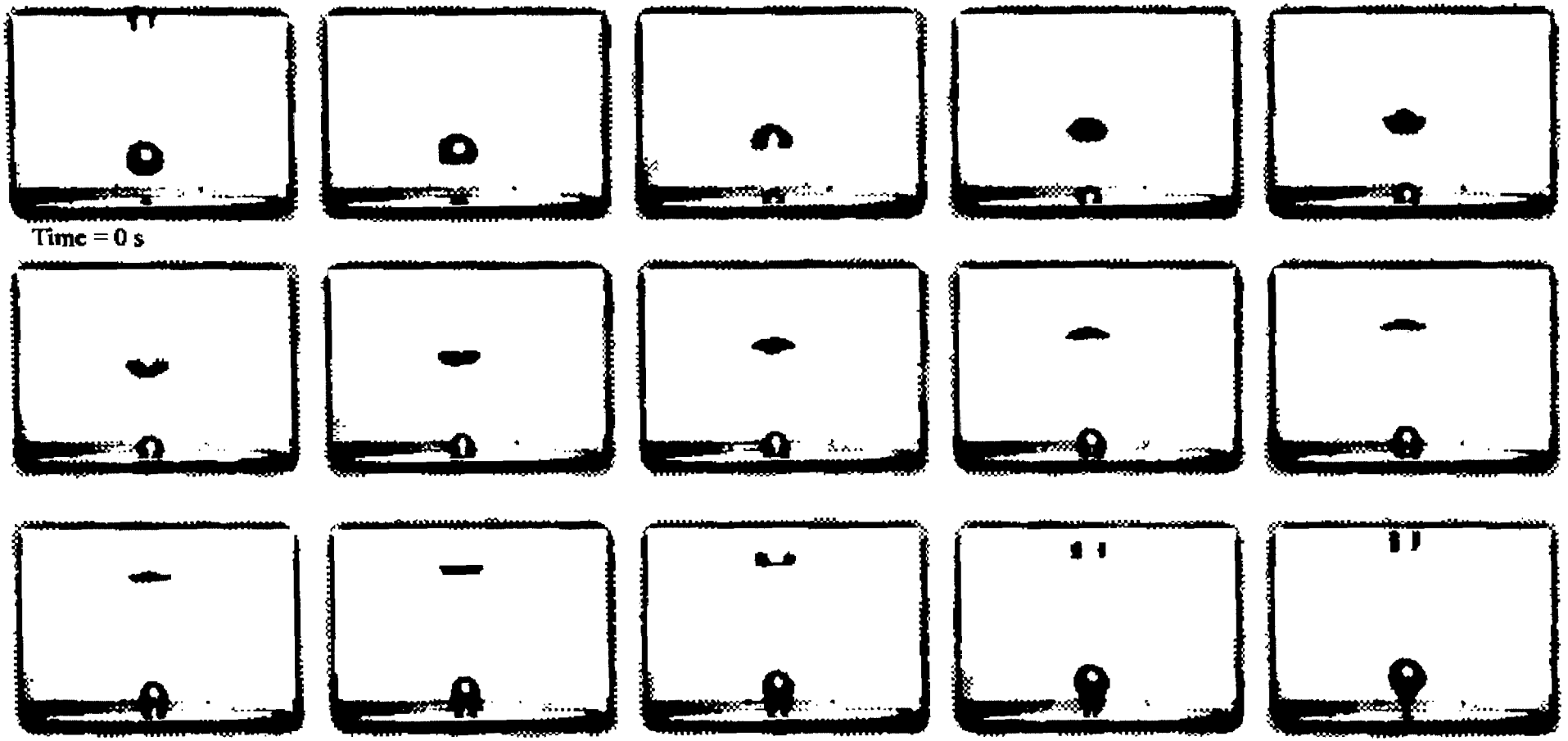

Time = 0 s

Time = 0.056 s
Volume = 4.22×10^{-3} cm^3

Experiment Parameters:

Potential Difference: 0 kV
Mass Flow Rate: 2.58×10^{-7} kg/s
Time Interval: 0.004 s

Average Acceleration:

Acceleration X: 0 g
Acceleration Y: 0 g
Acceleration Z: 1 g

Terrestrial, Cleveland Matrix, Experiment No. 7

The Johns Hopkins University
Heat Transfer Laboratory

Cila Herman

Pool Boiling in Microgravity

under the Influence of Electric Fields

Life cycle of an injected bubble in 1g, 20kV

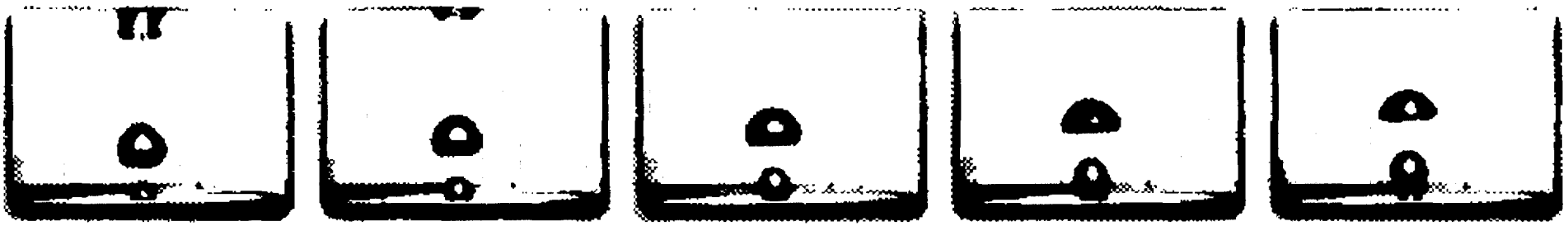

Time = 0 s

Time = 0.024 s
Volume = 8.77×10^{-3} cm^3

Experiment Parameters:

Potential Difference: 20 kV
Mass Flow Rate: 2.58×10^{-7} kg/s
Time Interval: 0.004 s

Average Acceleration:

Acceleration X: 0 g
Acceleration Y: 0 g
Acceleration Z: 1 g

Terrestrial, Cleveland Matrix, Experiment No. 11

The Johns Hopkins University
Heat Transfer Laboratory

Cila Herman

Pool Boiling in Microgravity

under the Influence of Electric Fields

Life cycle of an injected bubble in microgravity, 0V

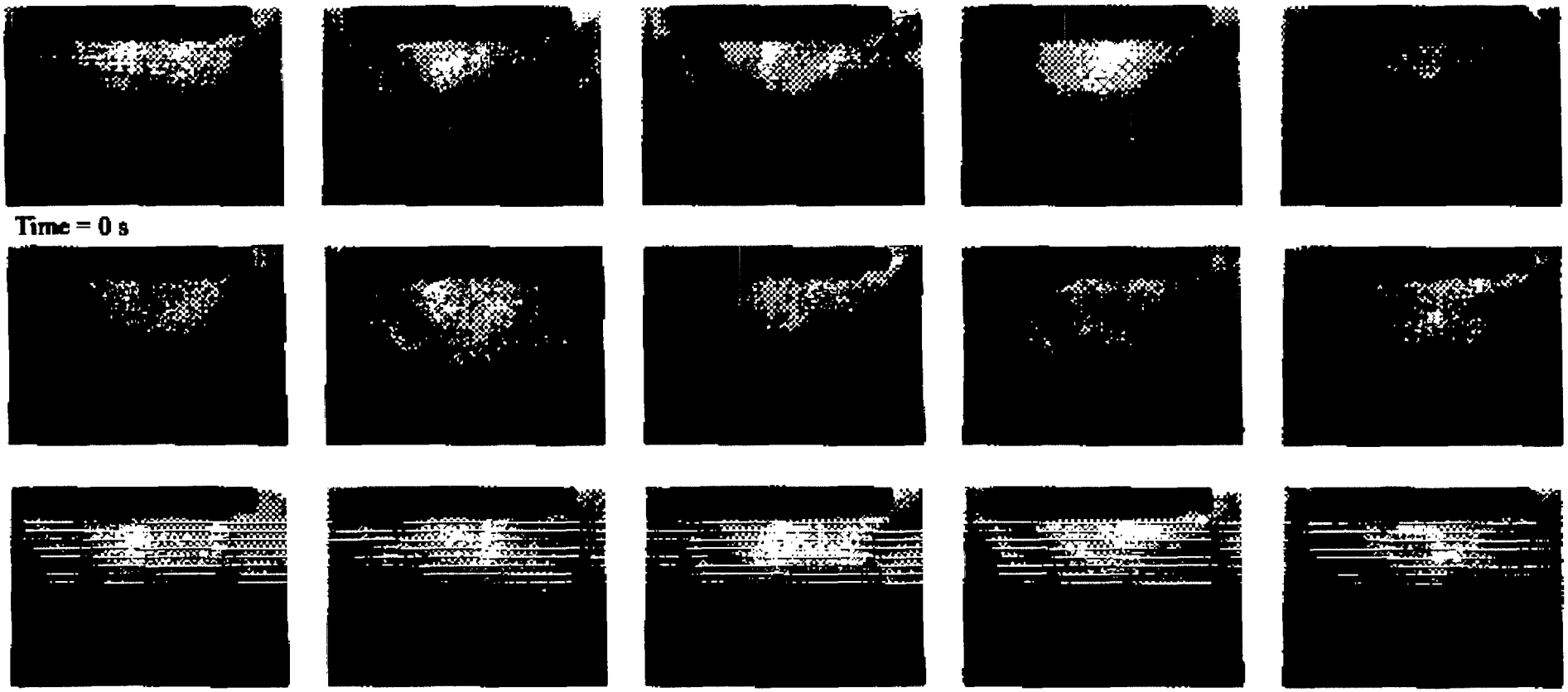

Time = 0 s

Time = 0.72 s
Volume = 0.135 cm^3

Experiment Parameters:

Potential Difference: 0 kV
Mass Flow Rate: 2.58×10^{-7} kg/s
Time Interval: 0.048 s

Cleveland, Day 2: October 20, 1999, Experiment No. 7

Average Acceleration:

Acceleration X: 0.02g
Acceleration Y: 0.04 g
Acceleration Z: 0.02 g

The Johns Hopkins University
Heat Transfer Laboratory

Cila Herman

Typical Acceleration Data: Bolted-Down Configuration

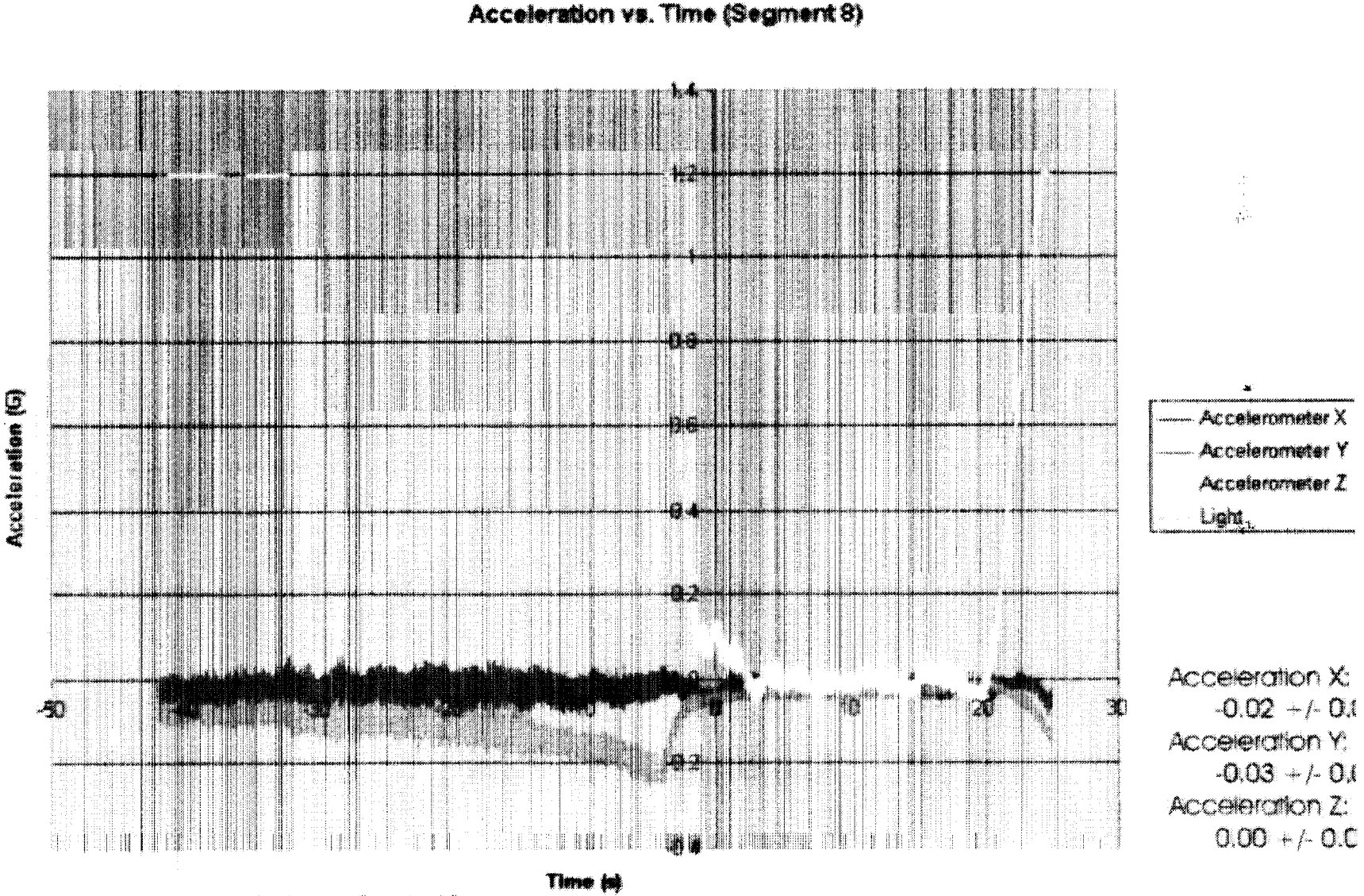

Cleveland Experiment Day 3 October 21, 1999

The Johns Hopkins University
Heat Transfer Laboratory

Cila Herman

Pool Boiling in Microgravity

under the Influence of Electric Fields

Typical Acceleration Data -- 0G Portion

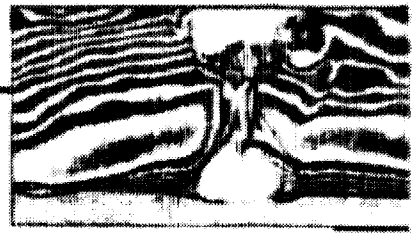

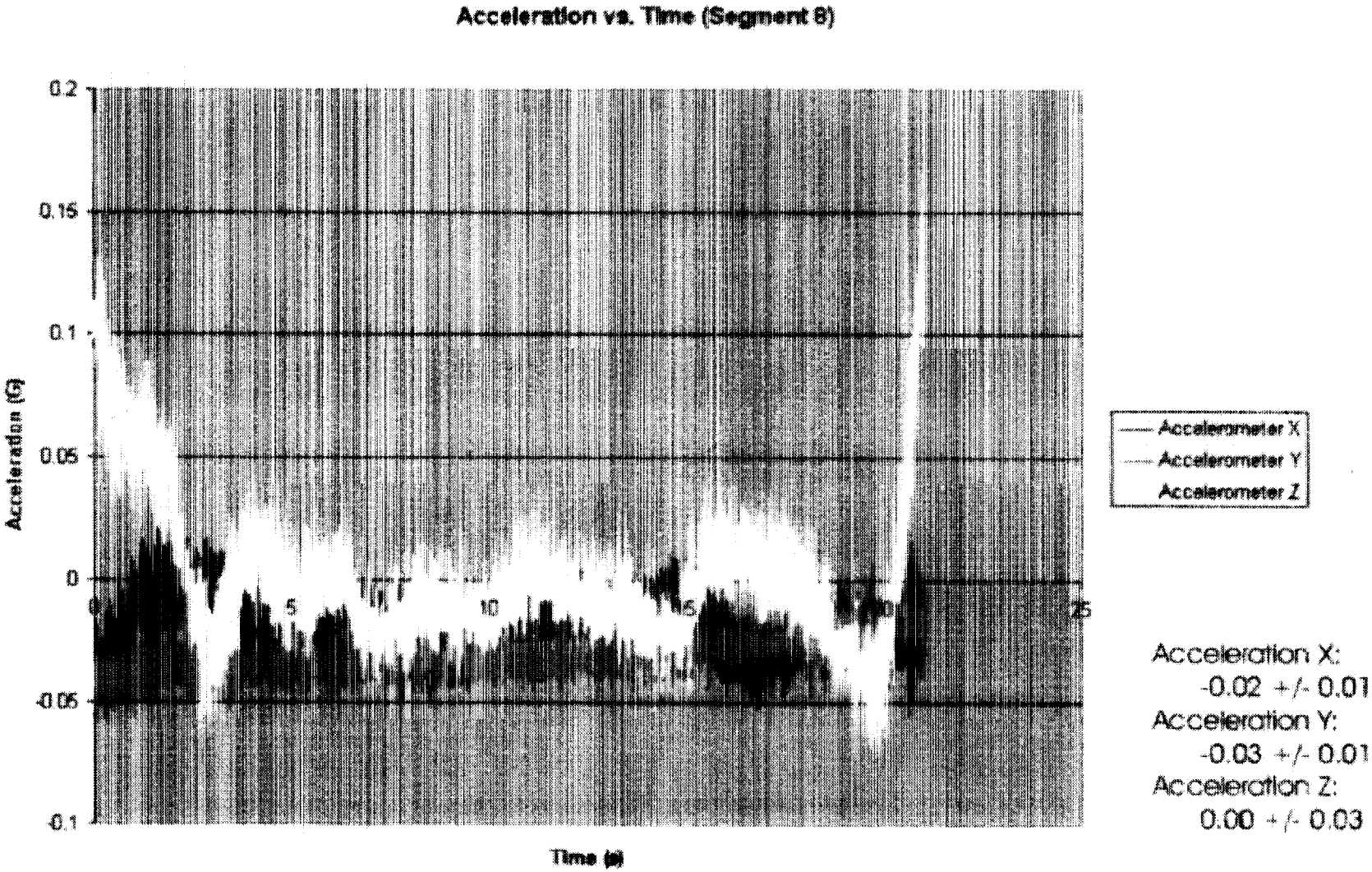

Acceleration X:
-0.02 +/- 0.01
Acceleration Y:
-0.03 +/- 0.01
Acceleration Z:
0.00 +/- 0.03

Cleveland Experiment Day 3 October 21, 1999

The Johns Hopkins University
Heat Transfer Laboratory

Cila Herman

Pool Boiling in Microgravity

under the Influence of Electric Fields

Typical Acceleration Data

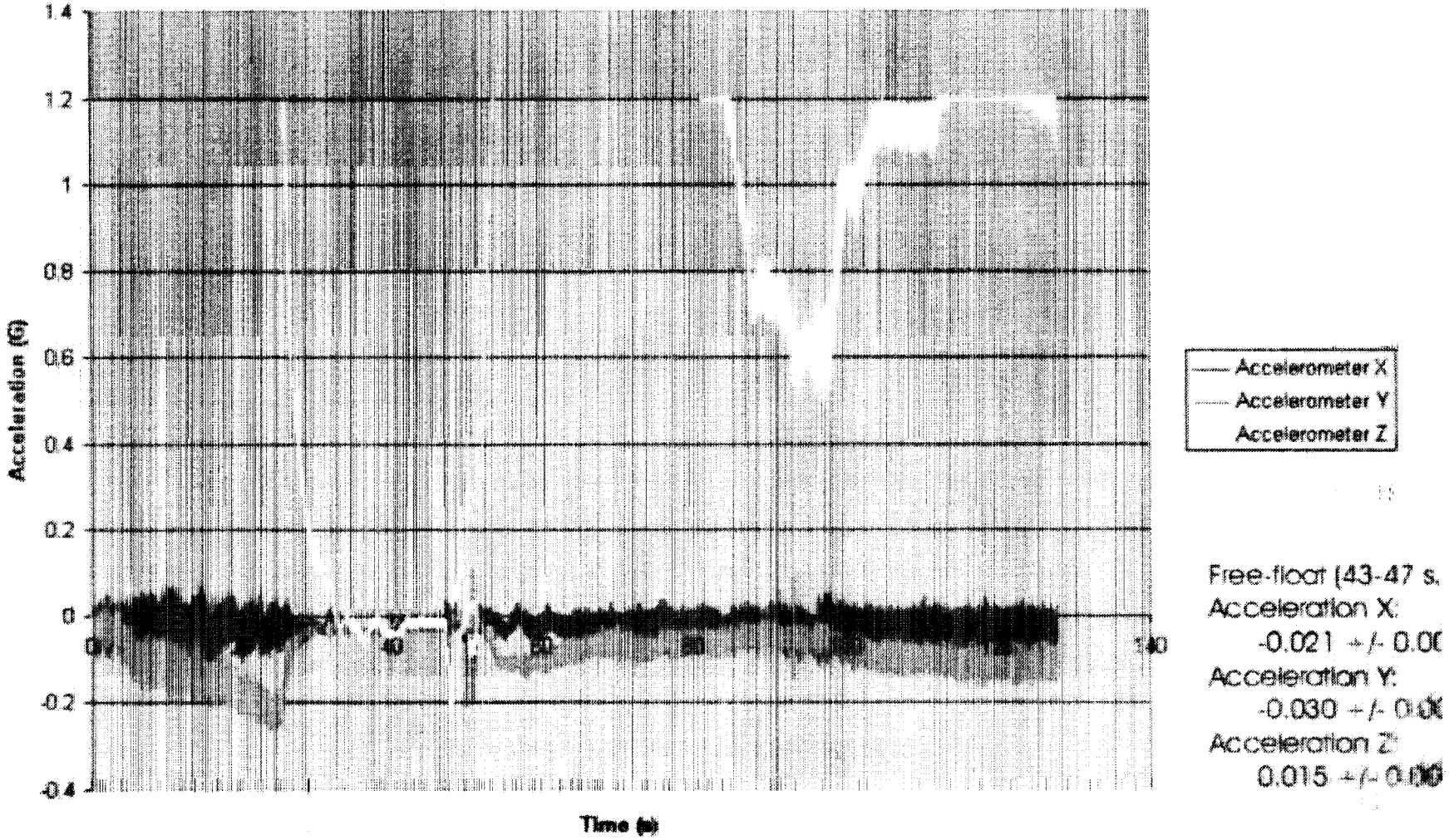

Houston Experiment Day 3 February 3, 2000

The Johns Hopkins University
Heat Transfer Laboratory

Cila Herman

Pool Boiling in Microgravity

under the Influence of Electric Fields

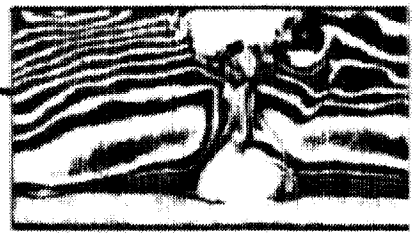

Typical Acceleration Data -- Free-float Portion

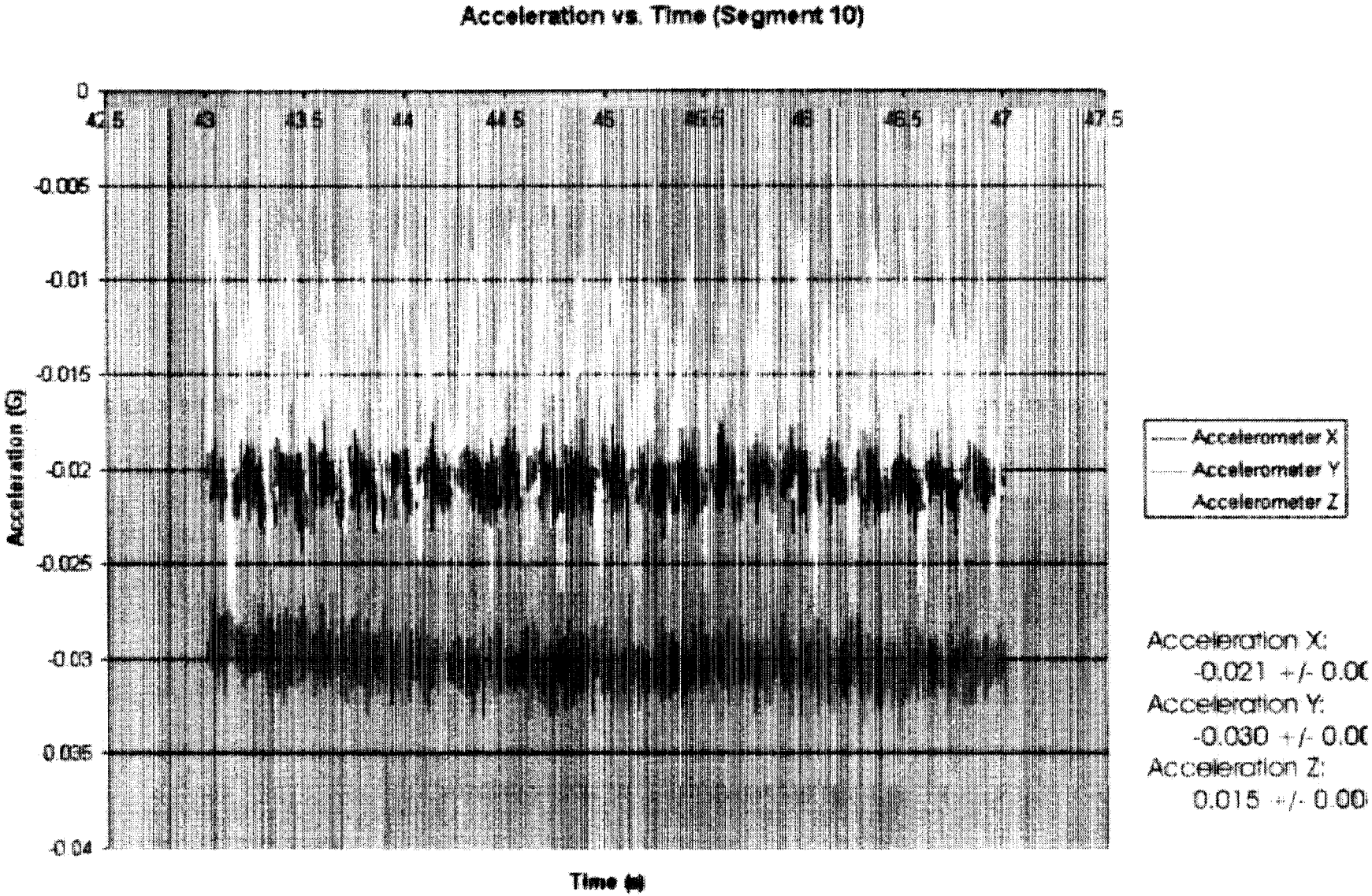

Houston Experiment Day 3 February 3, 2000

The Johns Hopkins University
Heat Transfer Laboratory

Cila Herman

Pool Boiling in Microgravity

under the Influence of Electric Fields

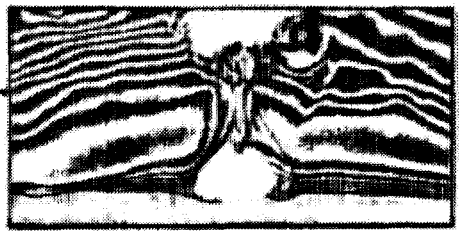

Interfacial instability on bubble surface in microgravity

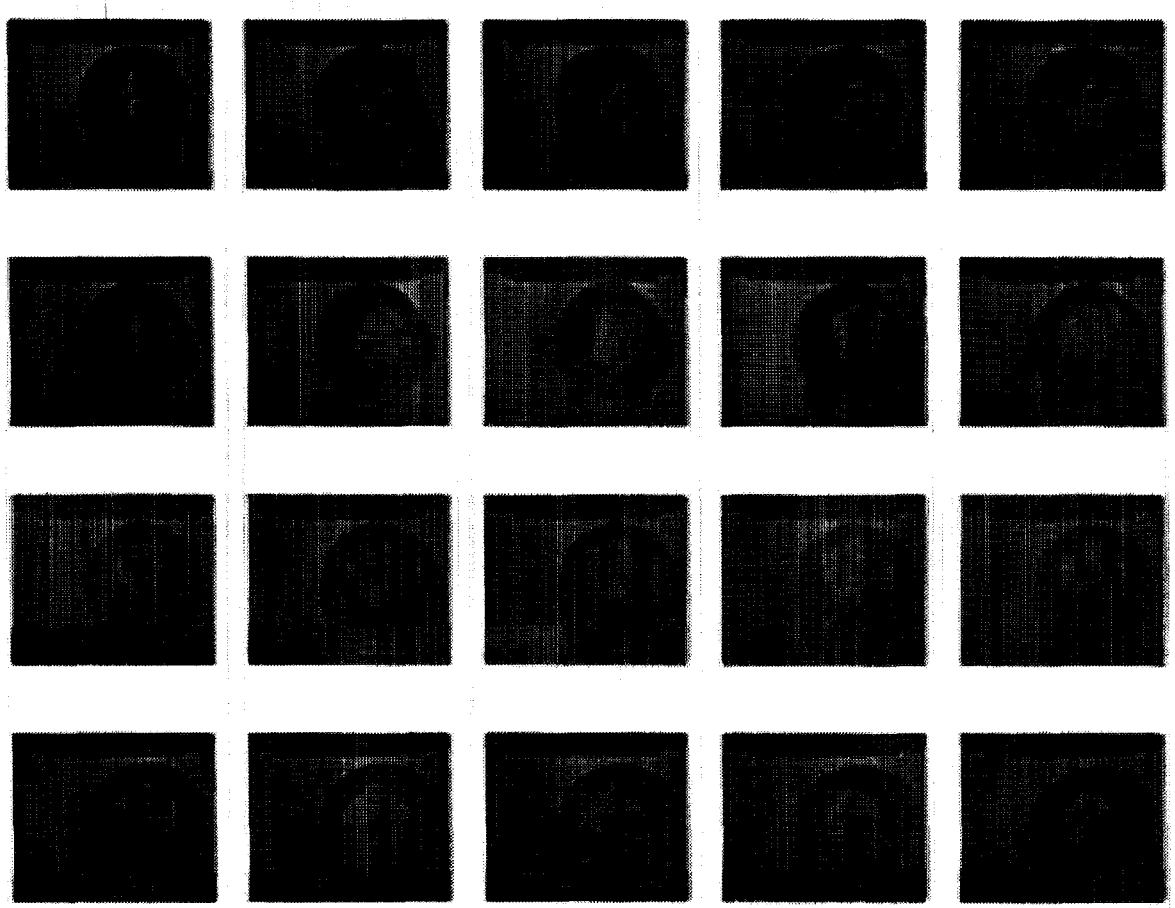

Experimental Parameters:
Potential Difference: 0 kV
Mass Flow Rate: 4.09 x 10 ^ -7 kg/s
Time Interval: 0.004 s

Cleveland Experiment, Day 3, October 21, 1999

The Johns Hopkins University
Heat Transfer Laboratory

Cila Herman

Pool Boiling in Microgravity

under the Influence of Electric Fields

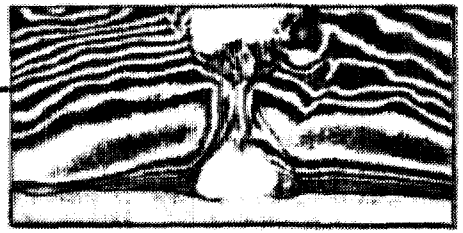

Coalescence of Bubbles in Microgravity

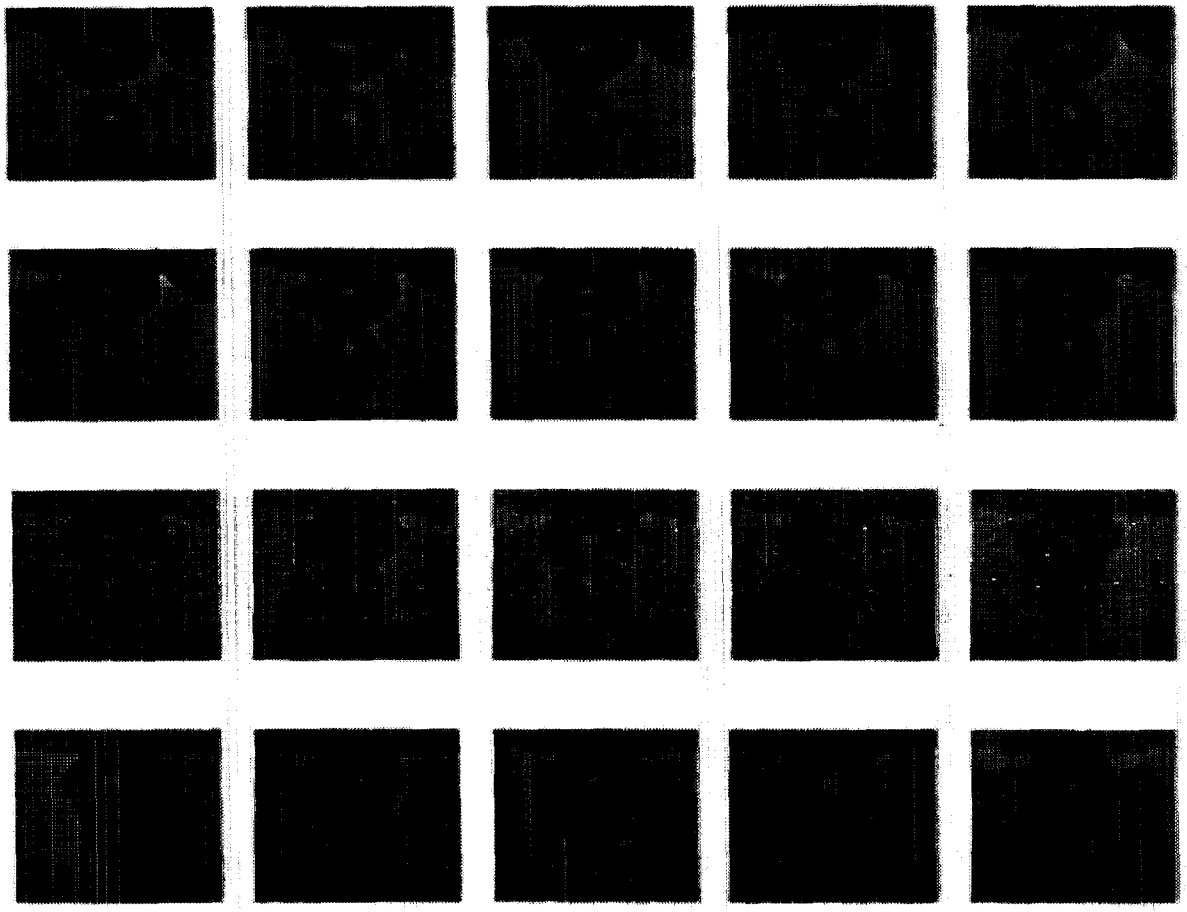

Experiment Parameters:
Potential Difference: 0 kV
Mass Flow Rate: 4.09 x 10 ^ -7 kg/s
Time interval: 0.004 s

Cleveland Experiment, Day 3, October 21, 1999

The Johns Hopkins University
Heat Transfer Laboratory

Cila Herman

Pool Boiling in Microgravity

under the Influence of Electric Fields

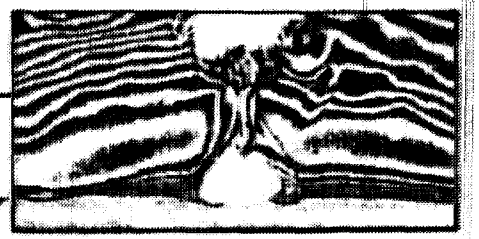

Life cycle of an injected bubble in microgravity, 20kV

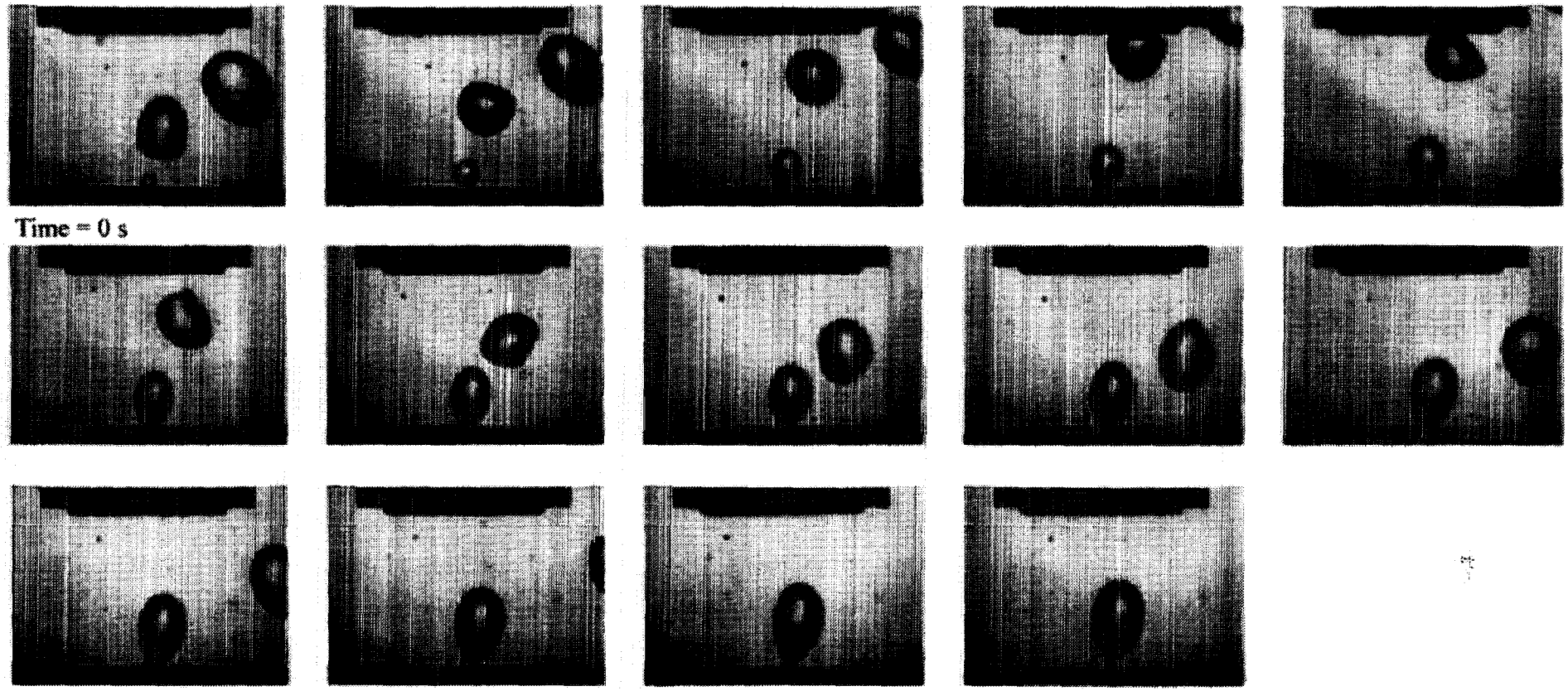

Time = 0 s

Time = 0.52 s
Volume = 9.19×10^{-2} cm^3

Experiment Parameters:

Potential Difference: 20 kV
Mass Flow Rate: 2.58×10^{-7} kg/s
Time Interval: 0.040 s

Average Acceleration:

Acceleration X: 0.03 g
Acceleration Y: 0.02 g
Acceleration Z: 0.02 g

Cleveland, Day 2: October 20, 1999, Experiment No. 11

The Johns Hopkins University
Heat Transfer Laboratory

Cila Herman

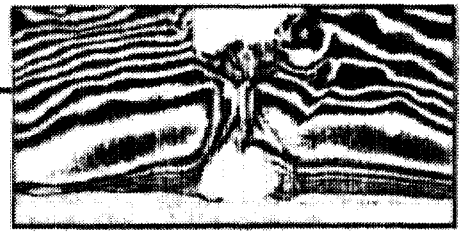

Bubble dimensions: terrestrial, 0V

Experimental Sequence
Terrestrial - Cleveland Matrix
0 kV, 1 g, 0.7 mm

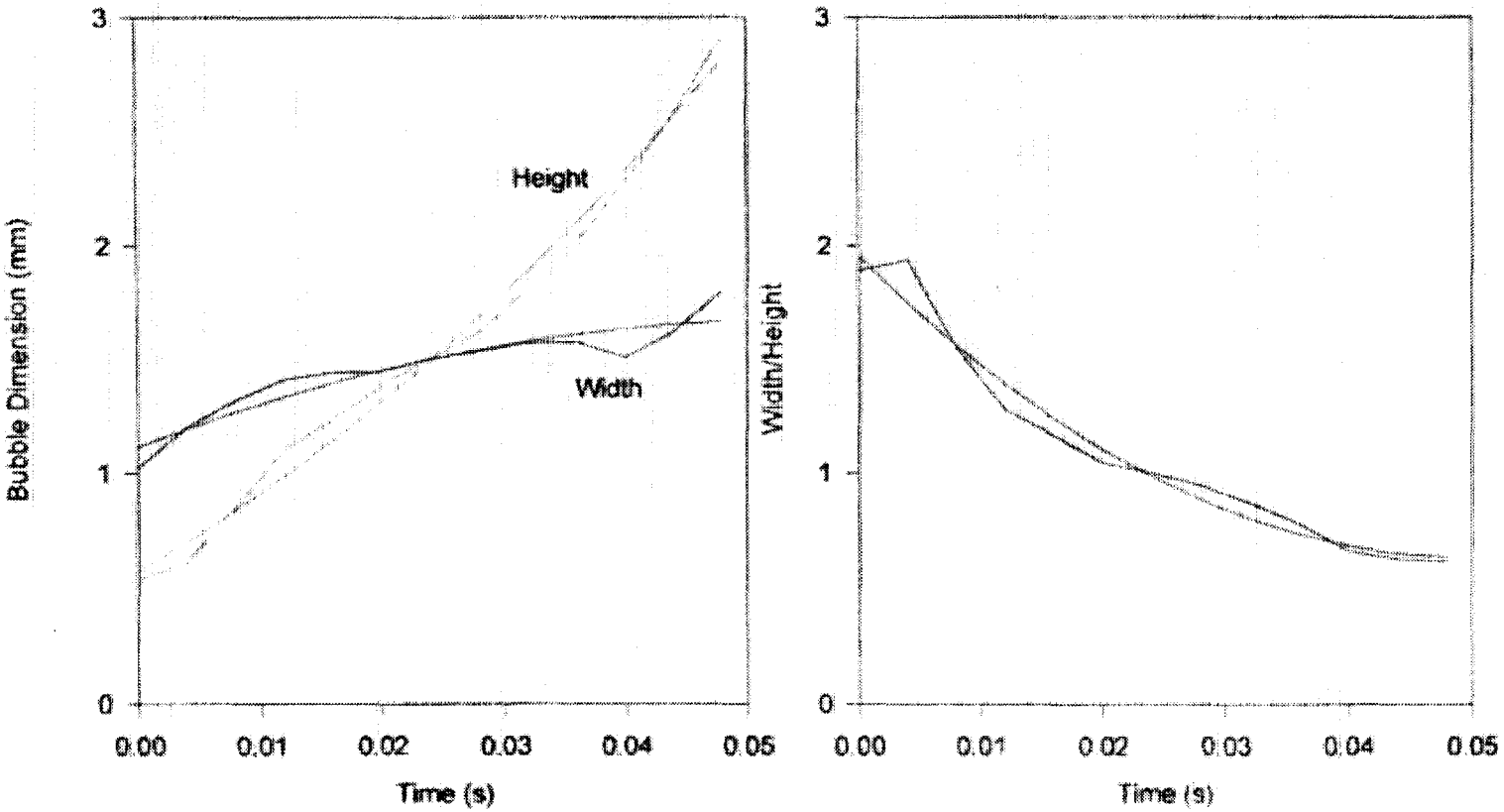

NASA/CP—2000-210470

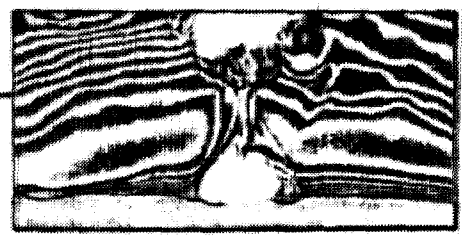

NASA/CP—2000-210470

Bubble dimensions: terrestrial, 20kV

Experimental Sequence
Terrestrial - Cleveland Matrix
20 kV, 1 g, 0.7 mm/s

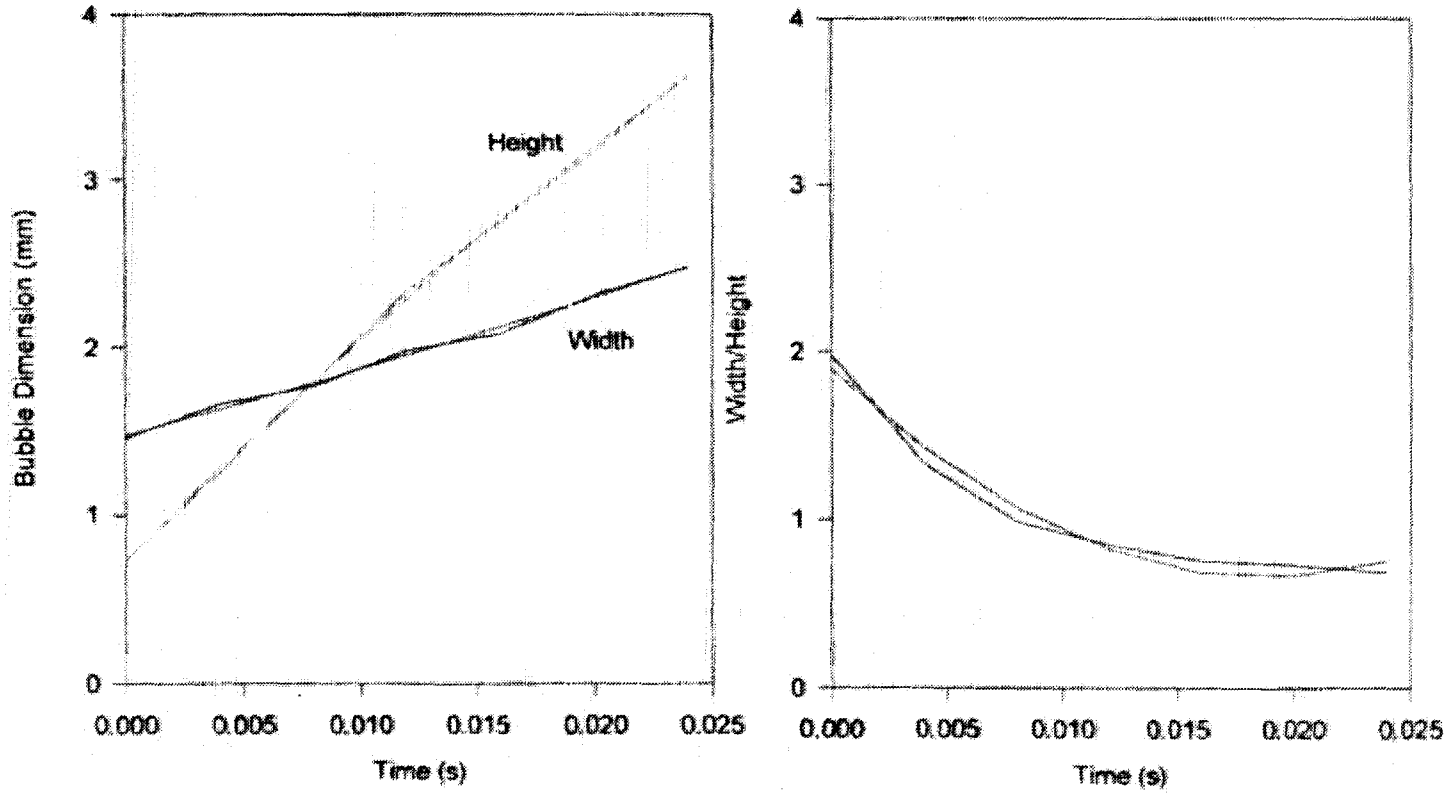

The Johns Hopkins University
Heat Transfer Laboratory
Cila Herman

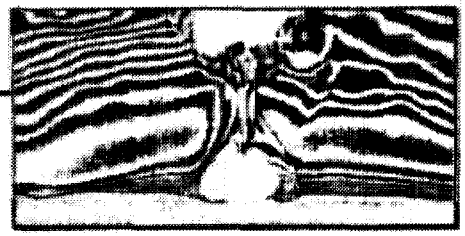

NASA/CP—2000-210470

Bubble dimensions: microgravity, 0V

Experimental Sequence
Cleveland, Day 2 - October 20, 1999
0 kV, 0 g, 0.7 mm/s

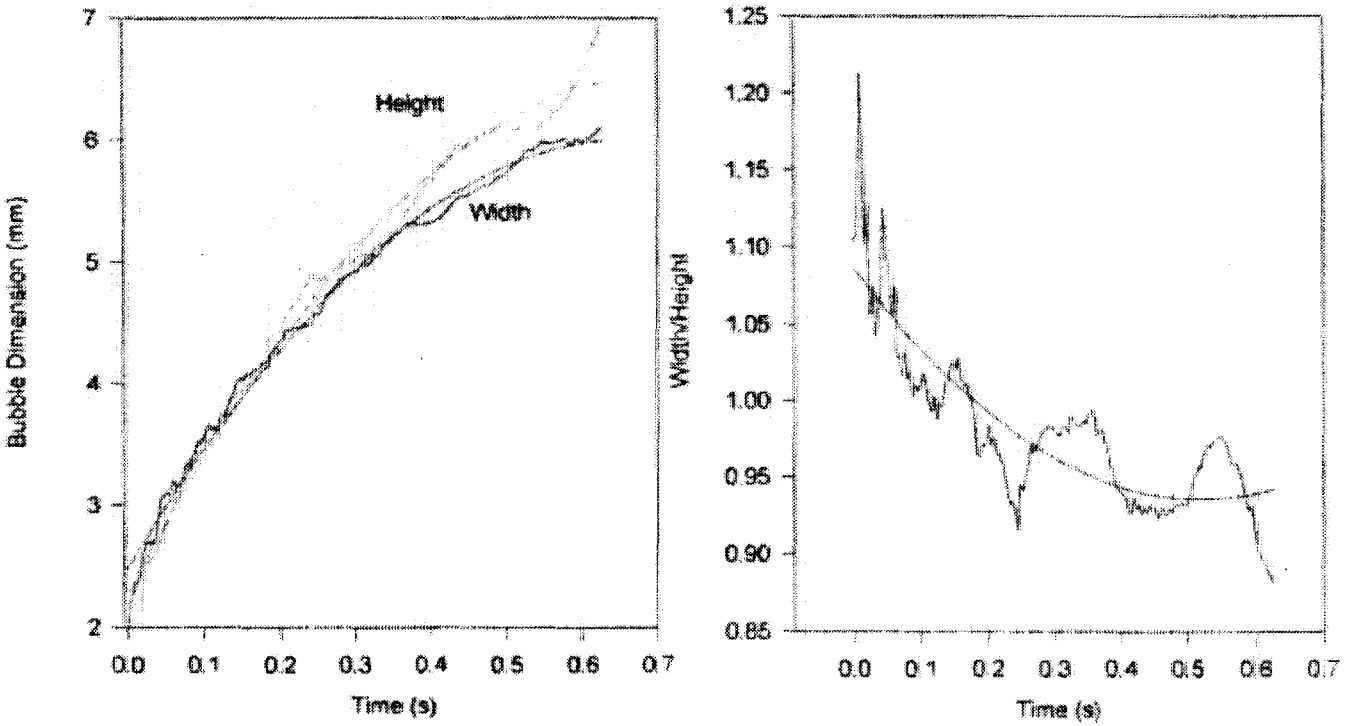

The Johns Hopkins University
Heat Transfer Laboratory
Cila Herman

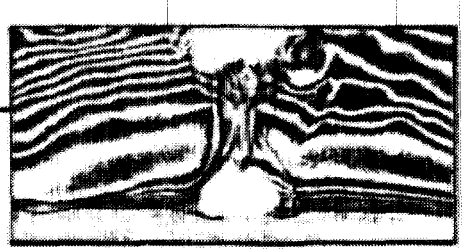

Bubble dimensions: microgravity, 20kV

Experimental Sequence
Cleveland, Day 2 - October 20, 1999
20 kV, 0 g, 0.7 mm/s

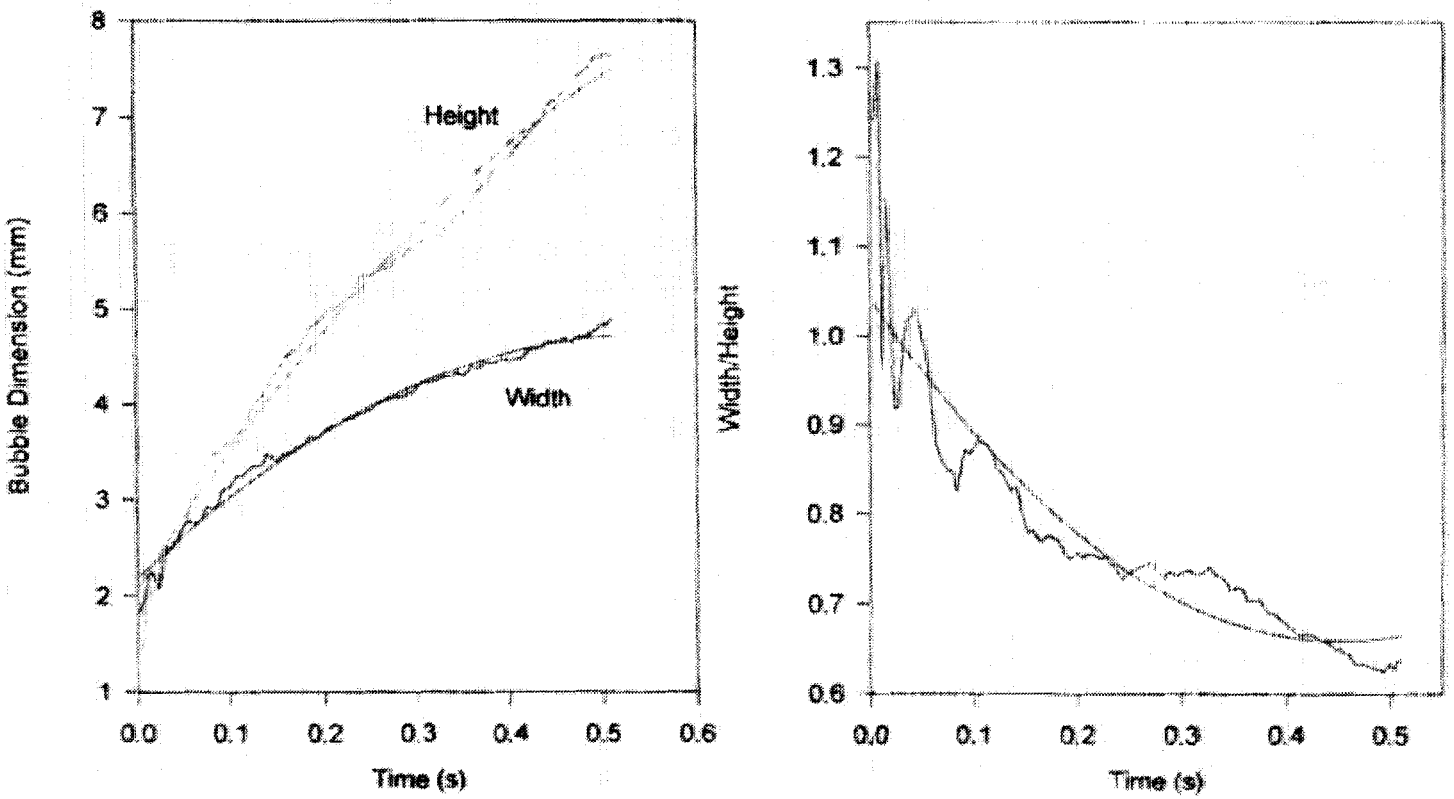

NASA/CP—2000-210470

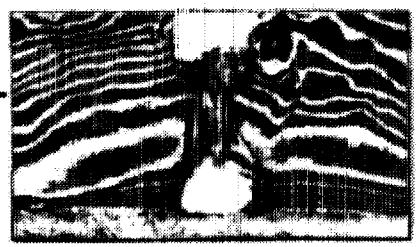

THERMOPHYSICAL PROPERTIES OF PF-5052 AND SELECTED WORKING FLUIDS

Fluid	Chemical Structure	Thermophysical Properties							
		Boiling Point	Critical Point		Density at 25 °C	Thermal Conductivity		Specific Heat Capacity at 25°C	
		T	T_c	p_c	ρ_c	k_{liq}	k_{vap}	$c_{p\,liq}$	$c_{p\,vap}$
		[°C]	[°C]	[bar]	[kg/m³]	[W/mK]	[W/mK]	[J/kgK]	[J/kgK]
PF5052	$C_5F_{11}NO$	50.00	181.00	19.15	1700.0	0.062	0.010	975.2	
R123	$CHCl_2CF_3$	27.78	183.70	3.67	1463.0	0.081	0.011	965.0	721.0
R141b	CCl_2FCH_3	32.15	208.35	4.54	1230.0	0.091		691.4	775.3
Water	H_2O	100.	374.0	219	958.3	0.679	0.025	4220.0	2030.0

NASA/CP—2000-210470

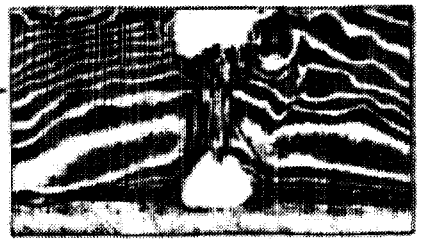

ELECTRICAL AND OPTICAL PROPERTIES OF PF-5052 AND SELECTED WORKING FLUIDS

Fluid	Chemical Structure	Optical Properties	Electrical Properties		
		Index of refraction at 25 °C	Permittivity	Electrical Conductivity	Relaxation Time
		n	ε_{liq}	σ	t
		-	[Farad/m]	[1/Ωm]	[ms]
PF5052	$C_5F_{11}NO$	1.2712	1.541 E-11	1.29E-08	1.20
R123	$CHCl_2CF_3$	1.329	3.984 E-11	4.72E-08	0.84
R141b	CCl_2FCH_3	1.36 (at 10 °C)	7.145 E-11	9.47E-09	7.55
Water	H_2O	100.	7.080 E-10	5.52E-06	0.12

NASA/CP—2000-210470

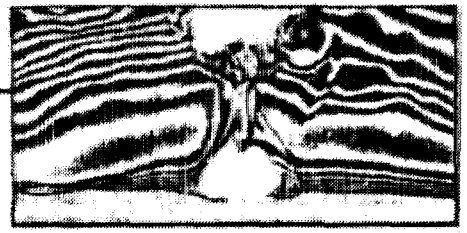

NASA/CP—2000-210470

MAXIMUM BUBBLE SIZE IN THE ABSENCE OF ELECTRIC FIELD (Fritz, 1935)

Basic assumptions:

1. Buoyancy balanced by surface tension forces
2. Orifice diameter much smaller than bubble diameter (?)

Governing differential equation: $$\frac{1}{R}+\frac{\sin\Phi}{x}=\frac{2}{R_{tip}}+\frac{g(\rho_V-\rho_L)}{\sigma}\cdot z$$

Maximum bubble volume: $$V_{\max}^{\frac{1}{3}}\left(\frac{\rho\, g}{\sigma}\right)^{\frac{1}{2}}=0.01667\ \Phi$$

Equivalent departure radius: $$R_d=0.0103\ \Phi\left(\frac{\sigma}{\rho g}\right)^{\frac{1}{2}}$$

Fritz, W., 1935, *Berechnung des Maximalvolumens von Dampfblasen,* Physikalische Zeitschrift, Vol. 36, No.11, pp. 379-384.

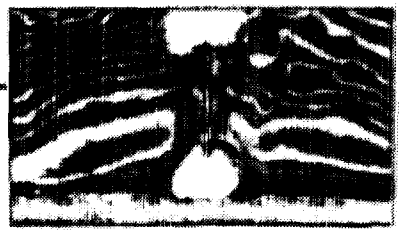

Radius of spherical bubbles as function of contact angle: Fritz model

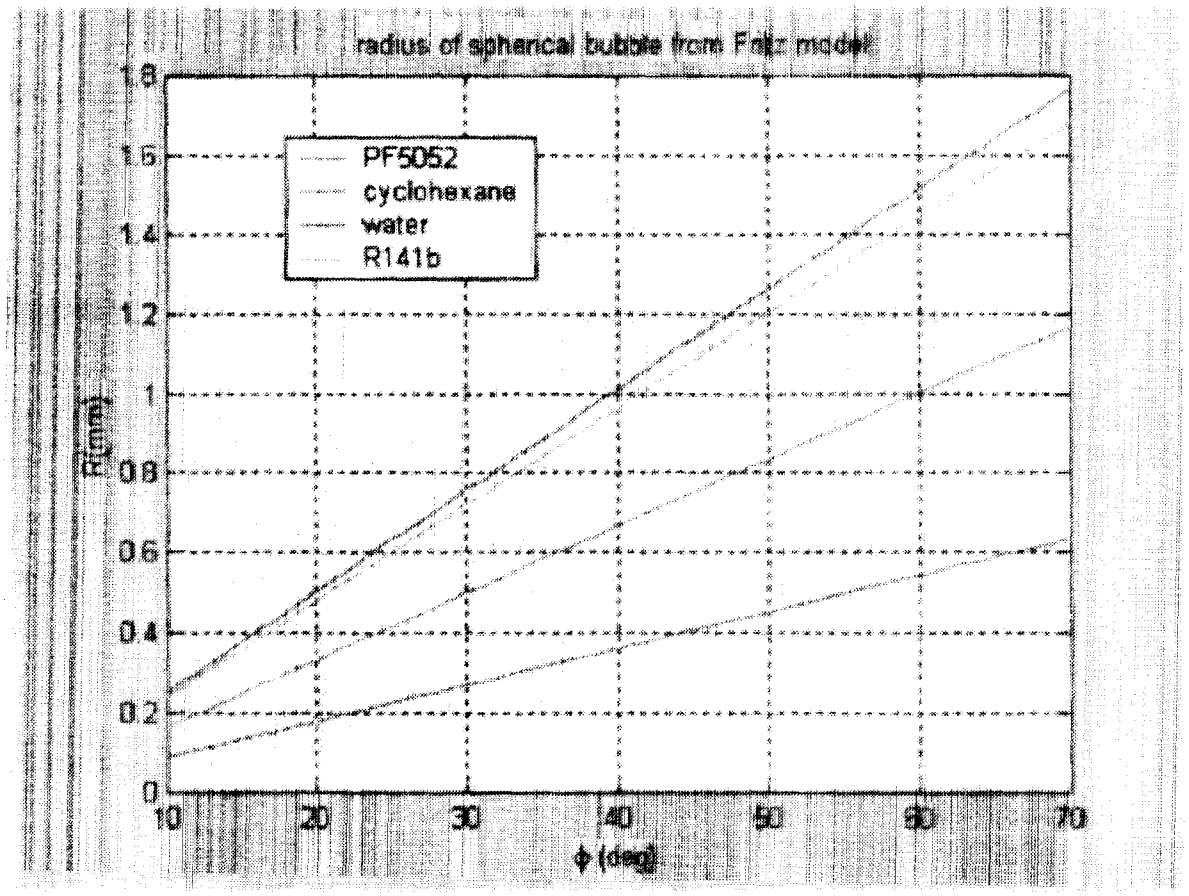

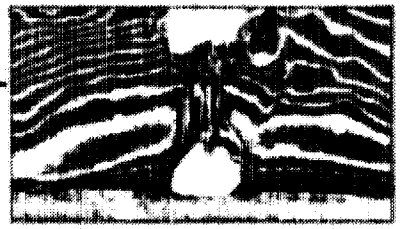

MAXIMUM BUBBLE SIZE IN AN ELECTRIC FIELD

Cheng and Chaddock, 1986

Assumptions:

- Relies on bubble volume and contact angle from Fritz model
- Buoyancy balanced by surface tension and the electric field force
- Orifice diameter much smaller than bubble diameter (?)
- Bubbles with spheroidal profiles

Governing equation:

$$\frac{\partial}{\partial x}\left(\alpha^{-\frac{2}{3}}+\alpha^{\frac{1}{3}}\frac{\sin^{-1}e}{e}\right)-\frac{\varepsilon_0 E^2 r}{3\sigma}\frac{\partial H}{\partial \alpha}=0$$

Parameters:

$e=\left(1-\frac{b^2}{a^2}\right)^{\frac{1}{2}}$ – eccentricity

$H=\frac{(\varepsilon_V-\varepsilon_L)\varepsilon_L}{(1-n)\varepsilon_L+n\varepsilon_V}$,

$\alpha=\frac{\text{major radius}}{\text{minor radius}}$

$n=\frac{1-e^2}{2e^3}\left(\ln\frac{1+e}{1-e}-2e\right)$

Bond number $Bo=\beta\equiv\frac{(\rho_L-\rho_V)R_{tip}^2 g}{\sigma}$

Cheng, K.J., Chaddock, J.B., 1986, *Maximum size of bubbles during nucleate boiling in an electric field.* , Int. J. Heat Fluid Flow, Vol, 7, No. 4, pp.278-282.

NASA/CP—2000-210470

Elongation of the bubble in the electric field

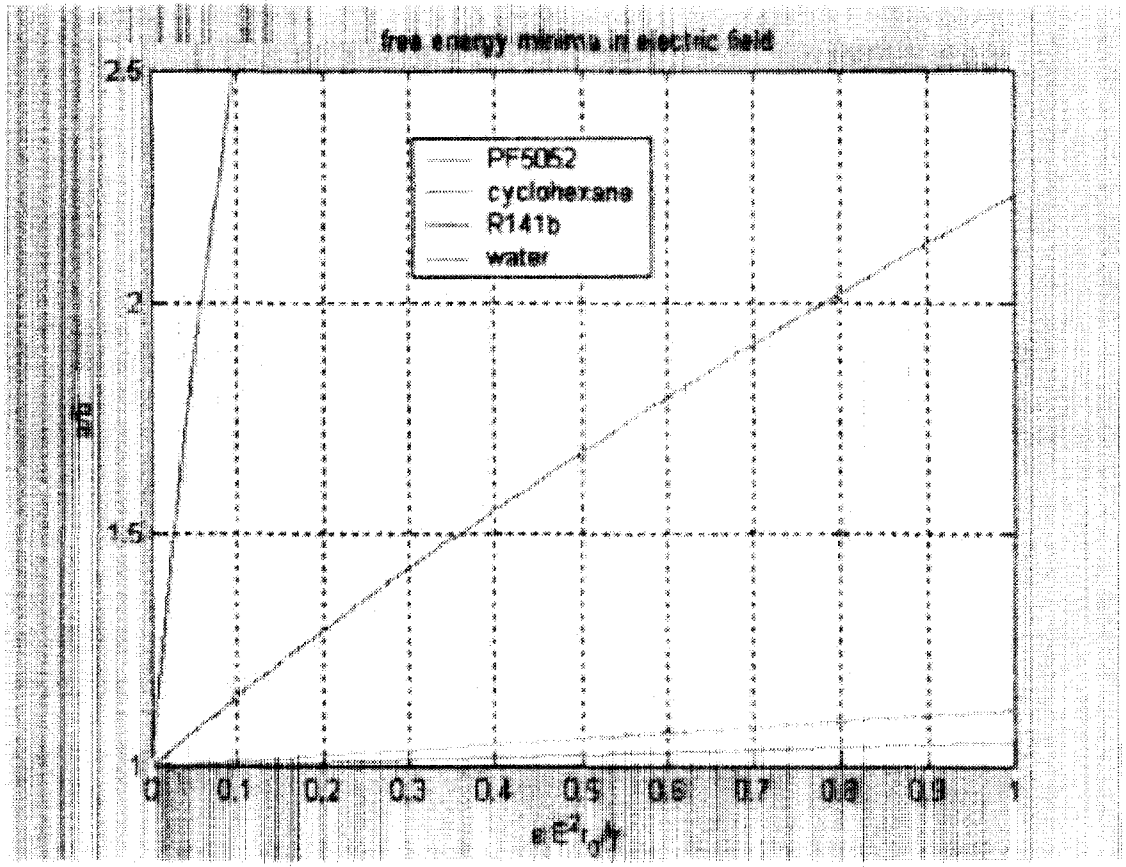

NASA/CP—2000-210470

Elongation of the bubble as function of radius and electric field magnitude

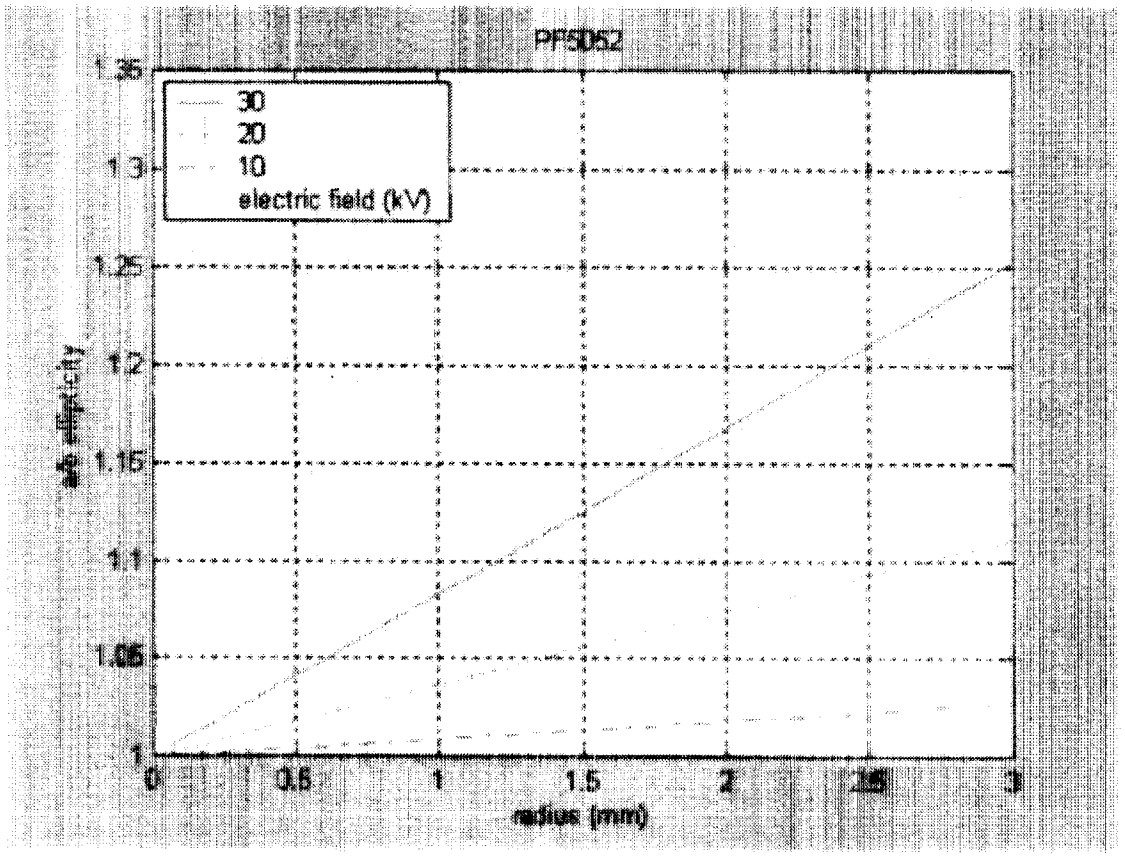

NASA/CP—2000-210470

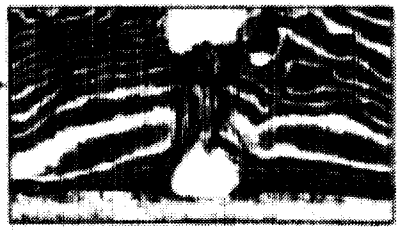

Bubble shapes in PF5052 as function of the parameter β

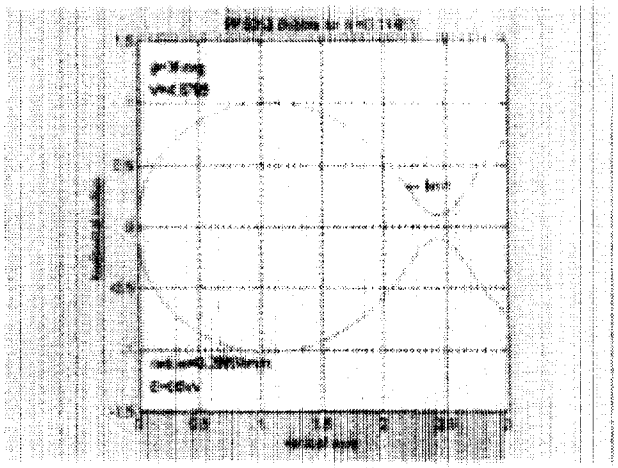

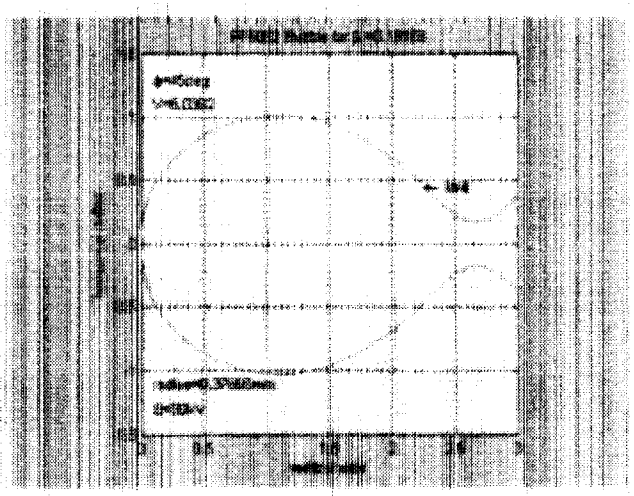

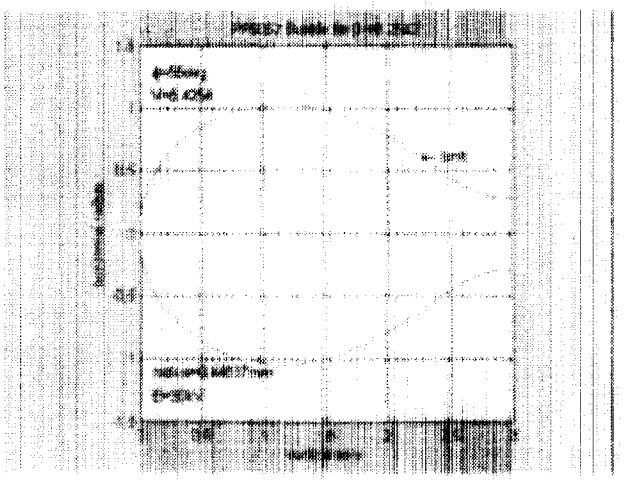

NASA/CP—2000-210470

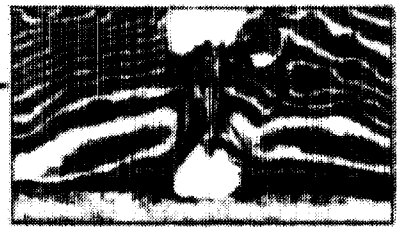

Bubble shapes in PF5052 as function of electric field and gravity

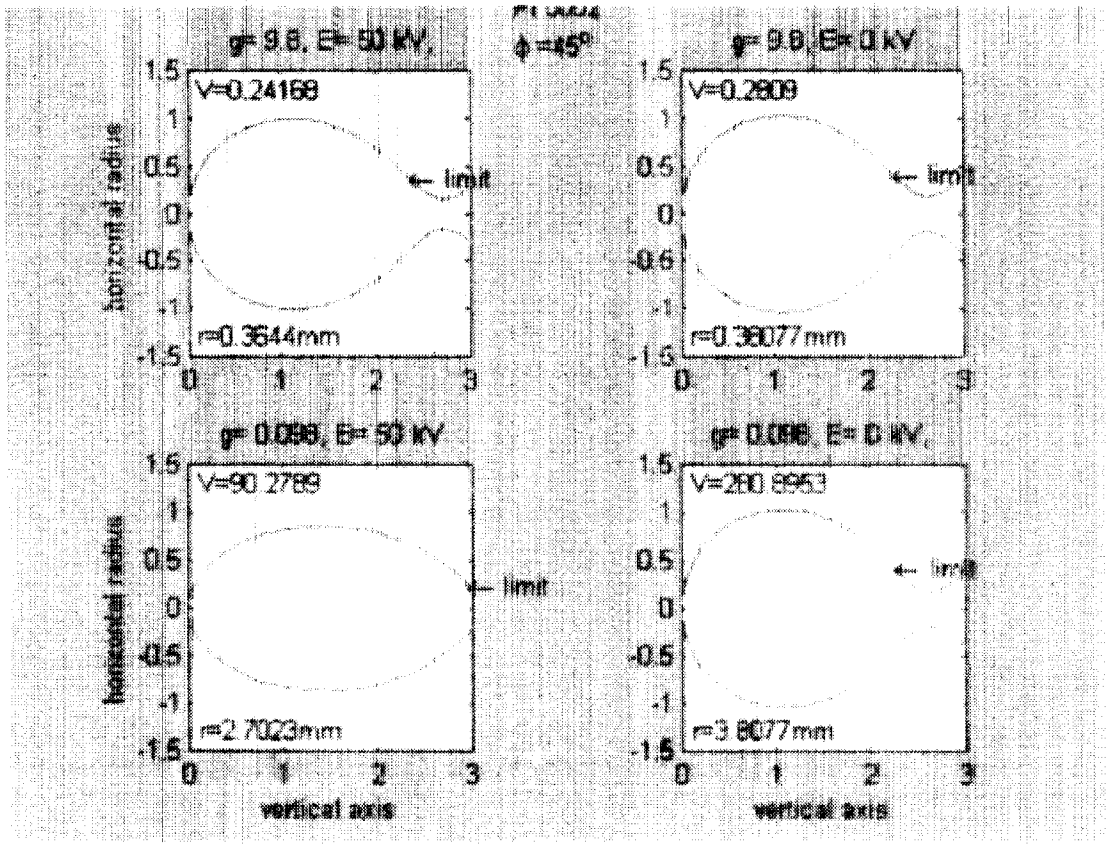

The Johns Hopkins University
Heat Transfer Laboratory

Cila Herman

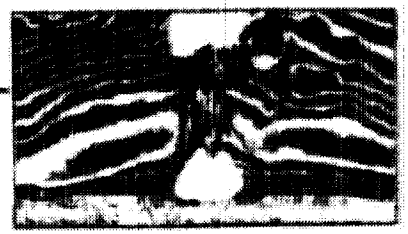

Bubble shapes in R141b as function of contact angle and electric field

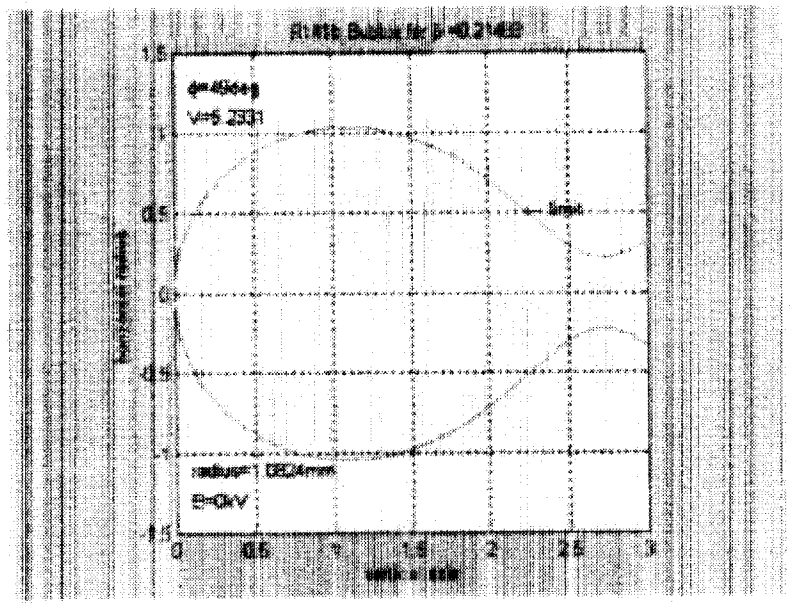

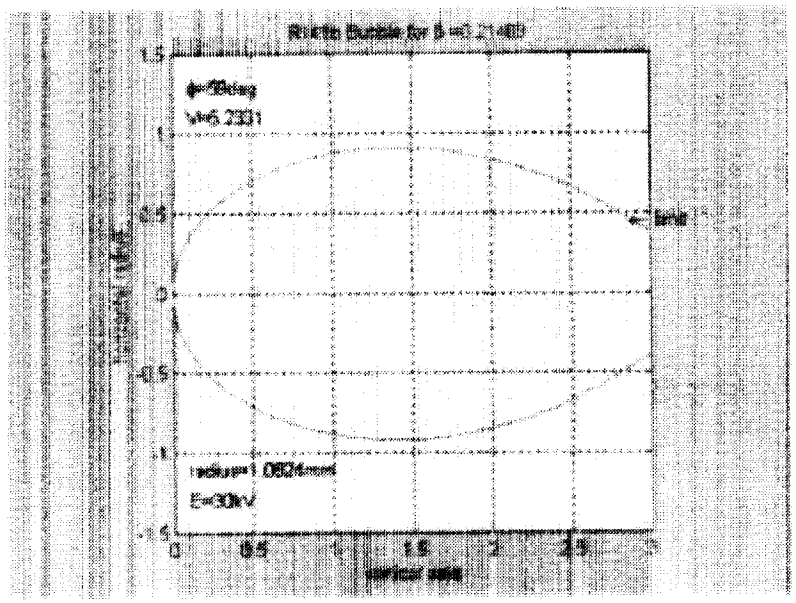

Pool Boiling in Microgravity

Under the Influence of Electric Fields

Bubble shapes in R141b

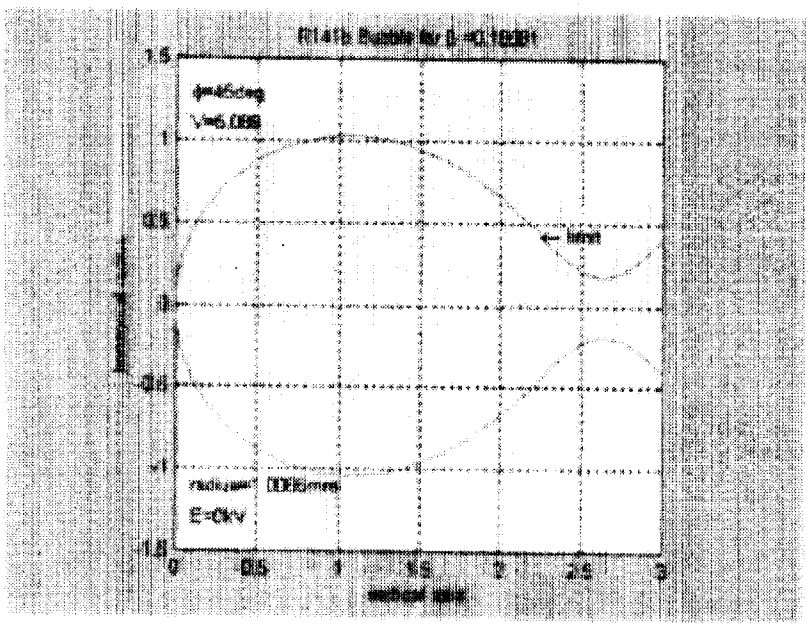

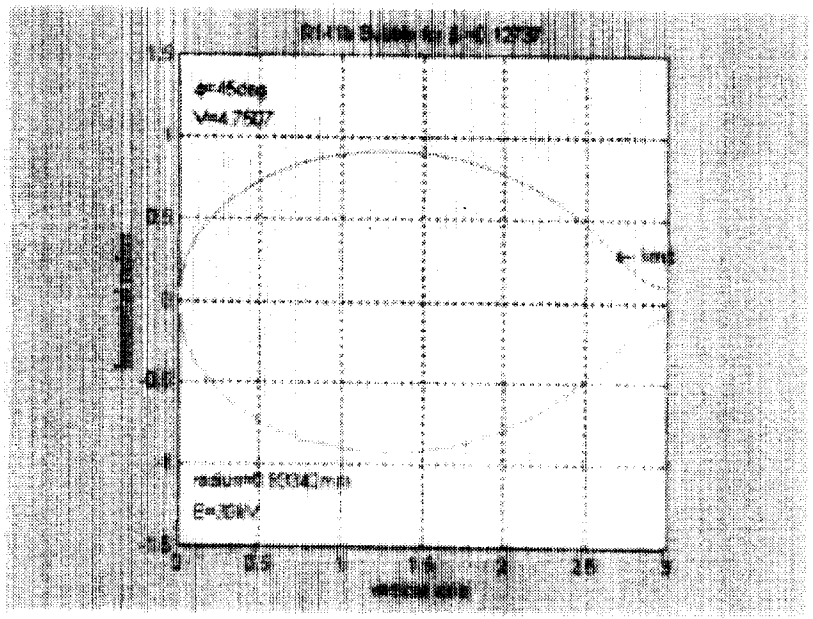

The Johns Hopkins University
Heat Transfer Laboratory

Cila Herman

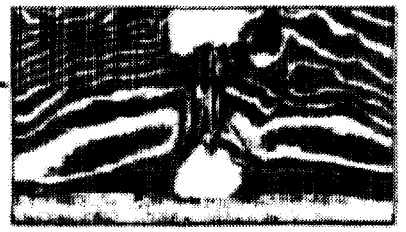

Future work

- Validation of the analytical model *
- Numerical determination of electric field force components for experimental sequences *
- Quantify the impact of electrode shape *
- Establishing the dependence on gravity level *
- Experiments with boiling on a single nucleation site
- Experiments with holographic interferometry

NASA/CP—2000-210470

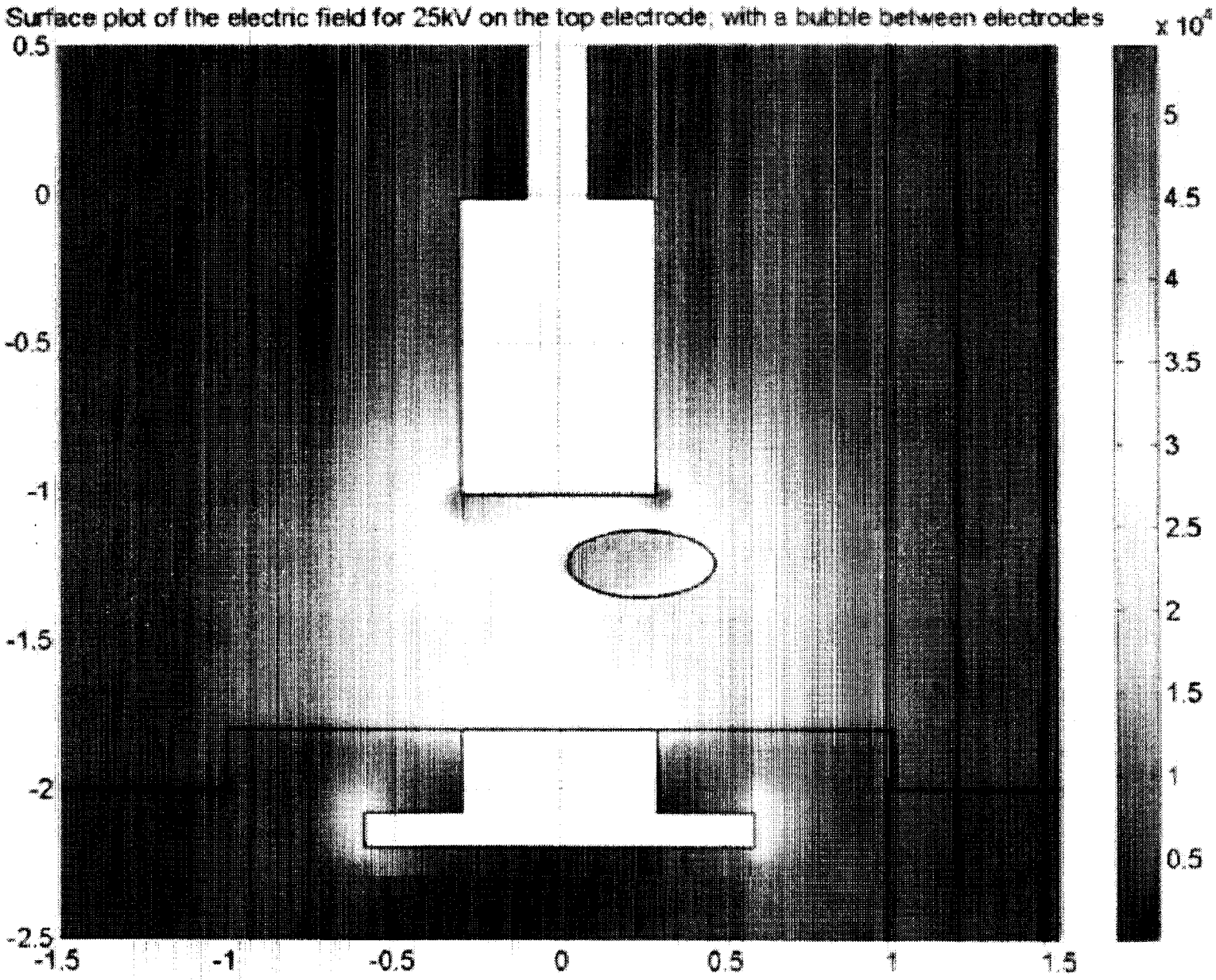
Surface plot of the electric field for 25kV on the top electrode, with a bubble between electrodes
x 10^4
0.5
0
-0.5
-1
-1.5
-2
-2.5
-1.5
-1
-0.5
0
0.5
1
1.5
5
4.5
4
3.5
3
2.5
2
1.5
1
0.5

SATURATED POOL BOILING HEAT TRANSFER MECHANISMS

J. Kim, N. Yaddanapudi
Dept. of Mechanical Engineering
University of Maryland
College Park, MD 20742

ABSTRACT

In the present work, saturated pool boiling was studied in a reduced gravity environment provided by a KC-135 aircraft. The objective of this work was to identify the boiling processes associated with nucleate boiling, critical heat flux (CHF), and transition boiling. Saturated pool boiling of FC-72 at 1 atm on an array of 96 heaters, each 0.27 mm x 0.27 mm in size was studied. Each of the heaters was maintained at a constant temperature by means of electronic feedback circuits, and the time-resolved heat flux from each heater was calculated from the instantaneous voltage across that heater. At each temperature, the voltage across the individual heaters were sampled at a rate of 1250 Hz for 6.4 seconds.

Boiling curves for microgravity and earth gravity are shown in Figure 1. To avoid hysteresis associated with boiling incipience, the measurements were started off at a high wall superheat. The earth gravity data are seen to be very repeatable. The boiling curves for microgravity agreed with each other for superheats up to ~30 K, but differed at higher superheats. The discrepancy between these two boiling curves is probably due to g-jitter, which tends to remove the larger vapor bubbles from the heater surface, allowing liquid to rewet the surface. At lower wall superheats, nucleate boiling was observed wherein multiple bubbles grew, often merged, then departed with relatively small departure diameters. At 35 K and 40 K, a single large bubble was seen to cover the entire heater. In the low heat flux nucleate boiling regime (from 15 K to 25 K on Figure 1), microgravity heat fluxes were slightly larger than the corresponding values in earth gravity due to more nucleation sites and larger bubbles in microgravity. Similar trends were observed by other researchers [1, 2, 3]. A critical heat flux (CHF) of about 7.5 W/cm^2 was observed in microgravity at a wall superheat between 30 K and 35 K. CHF was not reached in earth gravity over the superheats studied. However, a CHF of 22 W/cm^2 was observed in a previous study of saturated pool boiling in earth gravity using a similar heater [4]. The CHF values in microgravity were about 35% of those in earth gravity, similar to that observed by other researchers [2, 3]. The visual observations in microgravity seemed to indicate that bubble coalescence governs CHF.

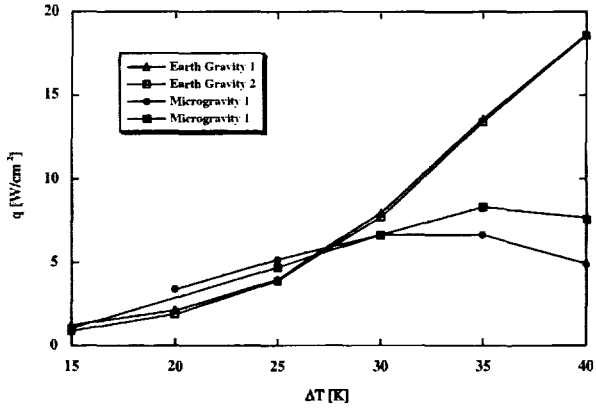

Figure 1: Boiling curves in earth gravity and microgravity.

Images of boiling in microgravity were correlated with time resolved heat flux maps. It was observed that high heat flux was associated with areas covered with small, rapidly

nucleating bubbles, while low heat flux was associated with the large bubbles. The array heat transfer in microgravity is governed by the extent of the surface covered by high heat flux, small bubble boiling.

The time resolved heat flux data were conditionally sampled according to whether or not boiling occurred on the surface, providing an average heat flux during boiling. To do this, a boiling function, B(t), was generated from the time-resolved heat transfer signal whose value is 1 when boiling occurs on the surface and 0 otherwise. The boiling function was used to obtain the boiling heat flux (the heat flux that occurs only when boiling is present on the surface) over the entire heater array. The time and array averaged boiling heat flux is plotted vs. wall superheat in Figure 2 for the earth gravity and microgravity runs. Boiling heat flux for both gravity levels increase monotonically over the range of superheats studied, and collapse onto a single curve. This result is not unexpected since inertia forces dominate bubble growth when the bubbles are small. In microgravity, large heat transfer rates were observed where numerous small bubbles (on the order of the individual heater size) nucleated, with very little heat transfer associated with the large bubble. Since large heat transfer rates are associated with small bubbles, and since small bubbles are not affected significantly by gravity, it is not surprising that the boiling heat flux is relatively insensitive to gravity.

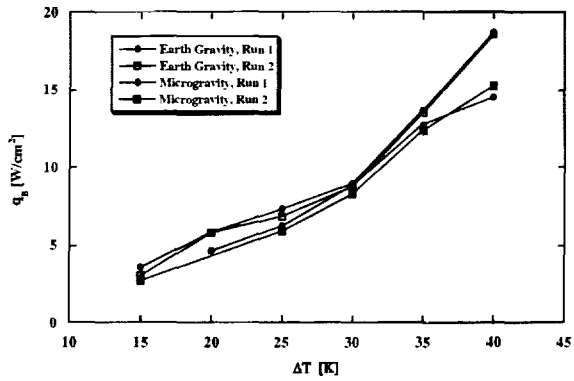

Figure 2: Boiling heat flux in earth and microgravity.

In summary, heat transfer during boiling in microgravity seems to be governed by two parameters: 1). the size of the large primary bubble on the surface, and 2). the heat flux associated with the small scale boiling at a given superheat. The first parameter appears to be governed by bubble coalescence, and determines the extent of the surface covered by small bubble boiling. The second parameter can be obtained from the earth gravity boiling heat transfer data. Future work should concentrate on determining the effect of gravity on coalescence phenomenon.

REFERENCES

1. Straub, J., Zell, M., and Vogel, B., 1992, "Boiling under Microgravity Conditions," Proceedings of the First European Symposium Fluids in Space, Ajaccio, France, ESA SP-353, pp. 269–297.
2. Oka, T., Abe, Y., Mori, Y.H., Nagashima, A., 1995, "Pool Boiling of n-Pentane, CFC-113, and Water under Reduced Gravity: Parabolic Flight Experiments with a Transparent Heater," Journal of Heat Transfer, Vol. 117, pp. 408–417.
3. Merte, H., Lee, H. S., and Ervin, J. S., 1994, "Transient Nucleate Pool Boiling in Microgravity–Some Initial Results," Microgravity Science and Technology VII/2, Hanser Publishers, Munich, pp. 173–194.
4. Rule T.D., and Kim, J., 1999, "Heat Transfer Behavior on Small Horizontal Heaters during Pool Boiling of FC-72," ASME Journal of Heat Transfer, Vol. 121, pp. 386–393.

Pool Boiling Heat Transfer Mechanisms in Microgravity

Jungho Kim, John Benton, Robert Kucner

University of Maryland

Nagaraja Yaddanapuddi

MetaSensors, Rockville, MD

NASA Fluid Physics Conference

August, 2000

Cleveland, OH

JK

Objectives

Determine boiling heat transfer mechanisms in earth, lunar, martian, and microgravity (KC-135, Sounding Rocket)

- **nucleate boiling**
- **critical heat flux**
- **transition boiling behavior**

Measure *Local Heat Flux*

Boiling Heat Transfer Mechanisms

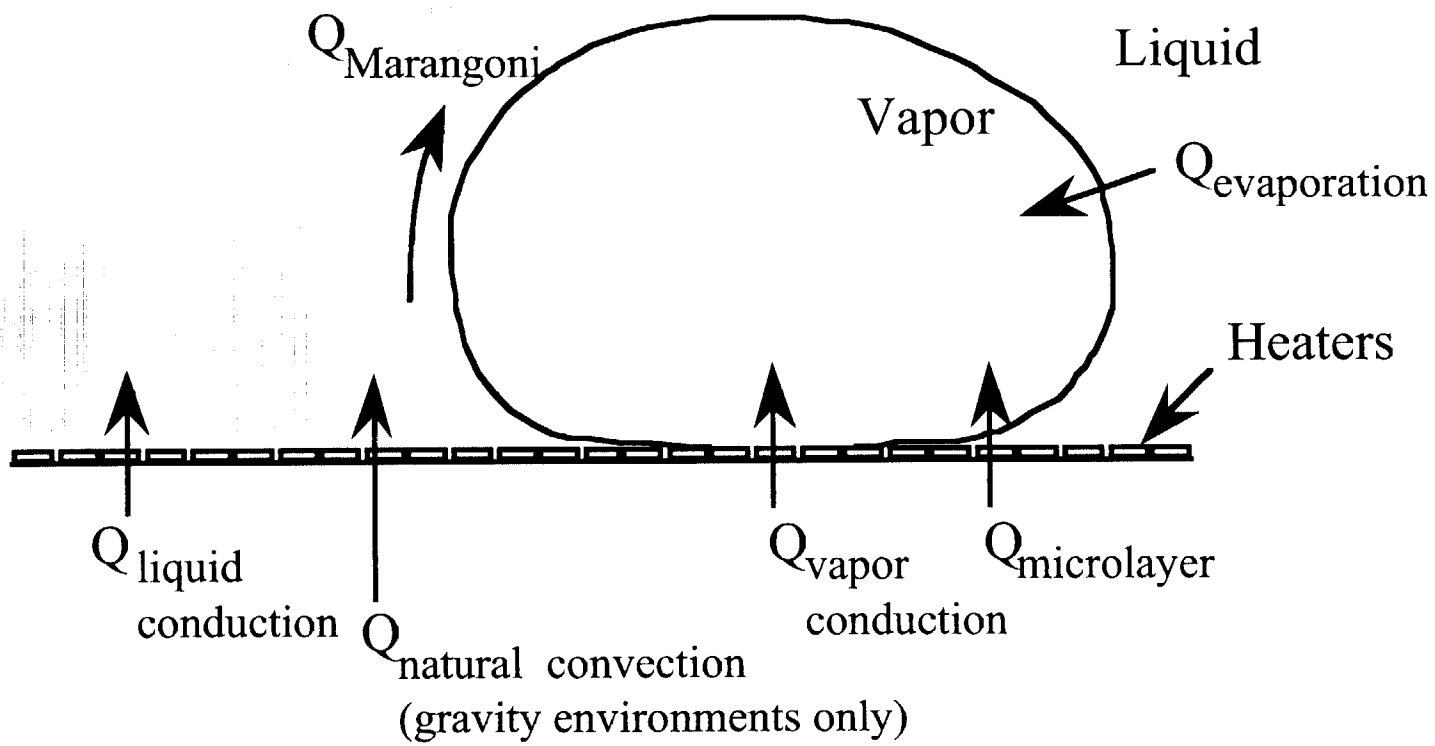

Individual Heaters

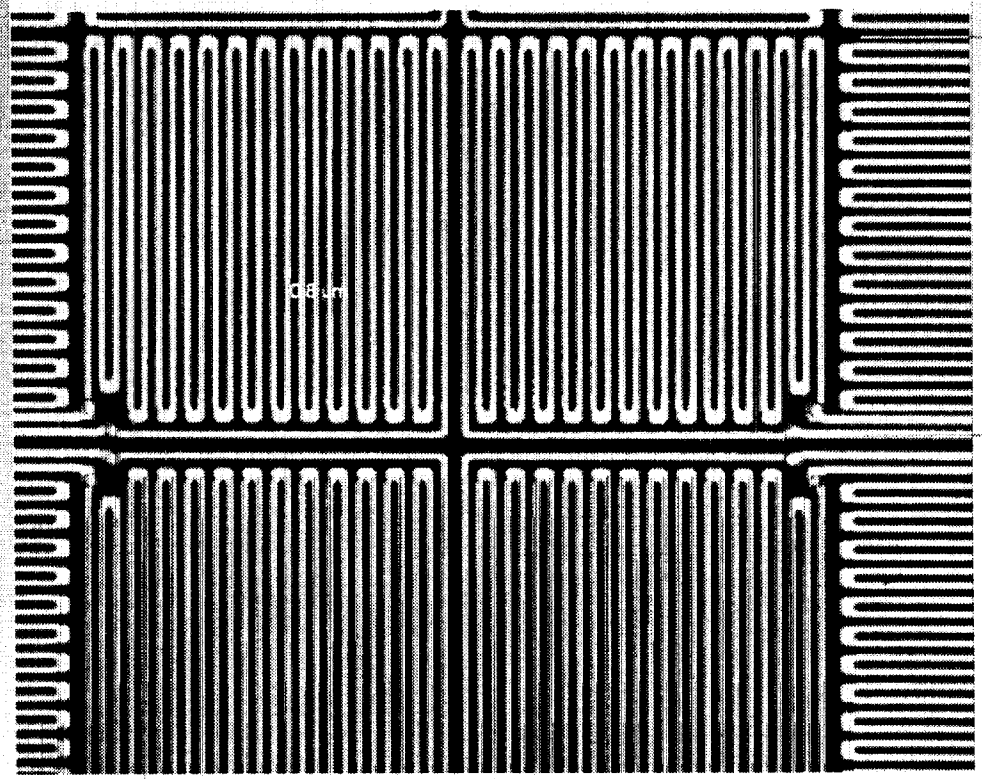

- Pt heaters on quartz substrate
- 5 µm line widths
- Heater size 270 µm
- Heater resistance ~1000 Ω

JK

Boiling on Heater Array

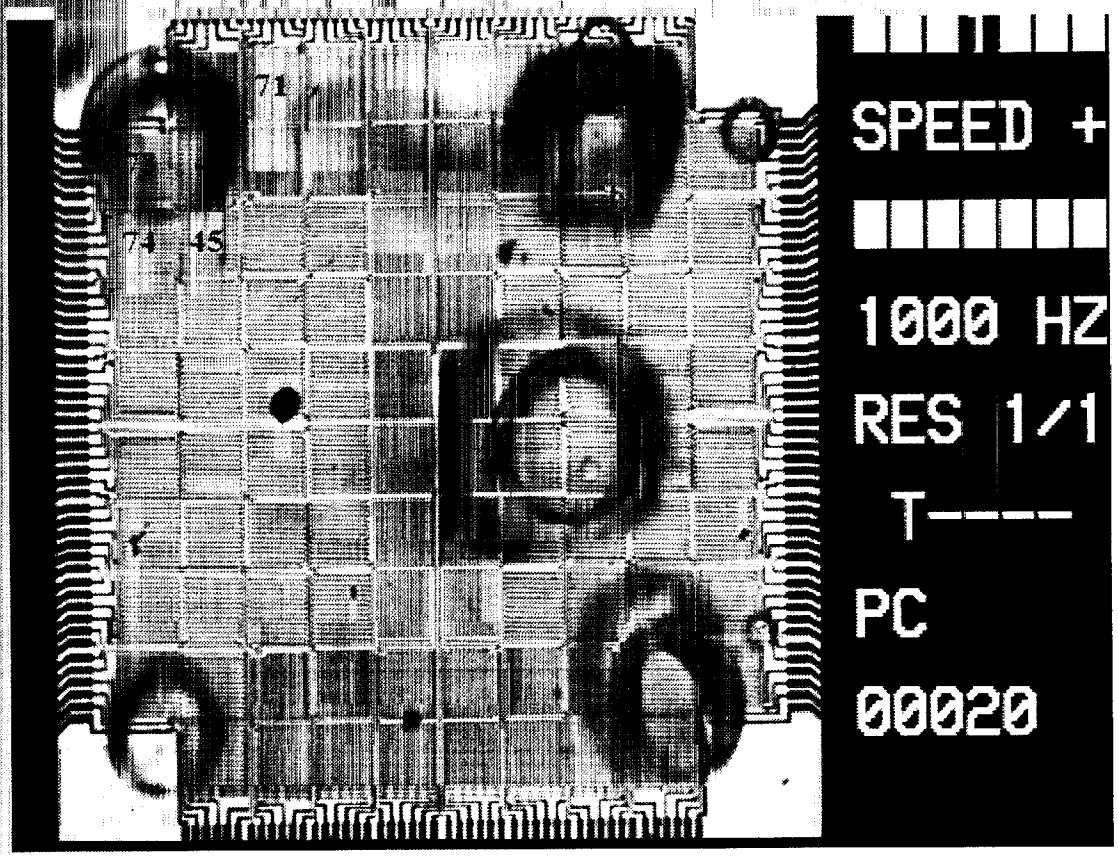

- 96 heaters in array
- 2.7 mm x 2.7 mm array size

JK

Feedback Circuits

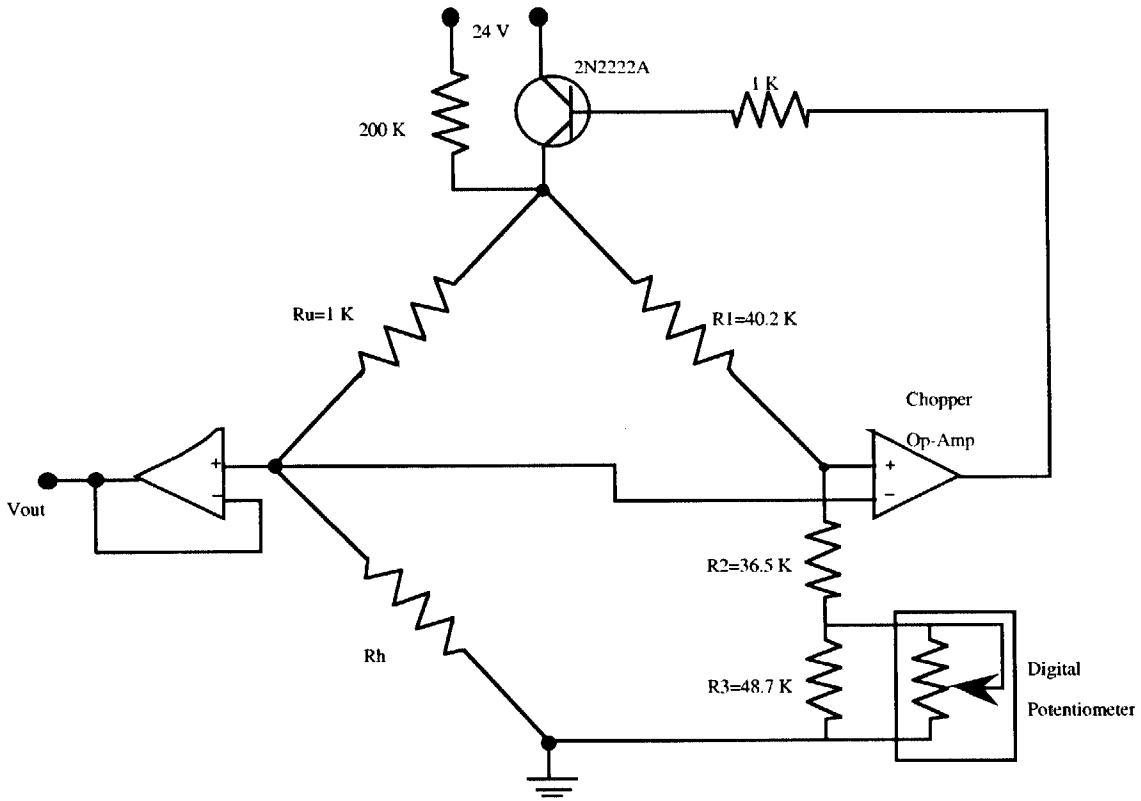

- 96 feedback circuits (one per heater)
- Constant temperature operation
- 15 kHz frequency response

JK

Test Apparatus

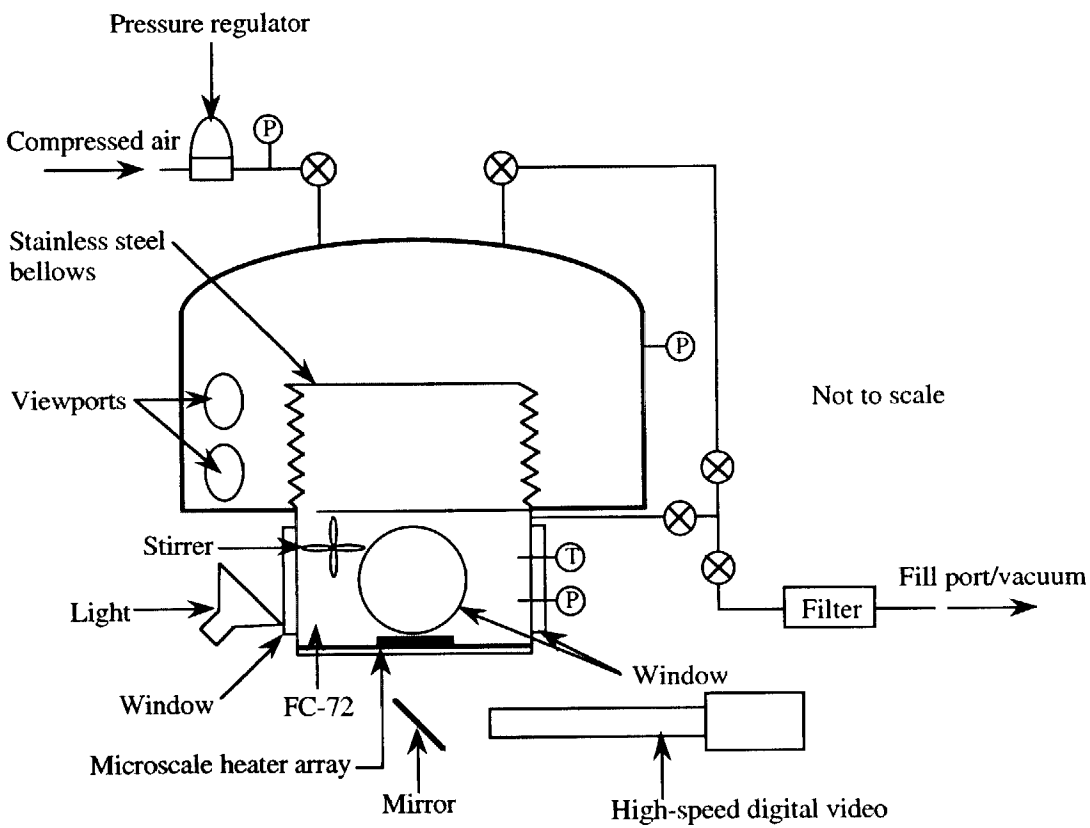

- **Prototype for Dr. H. Merte's shuttle payload**

Test Apparatus, cont'd

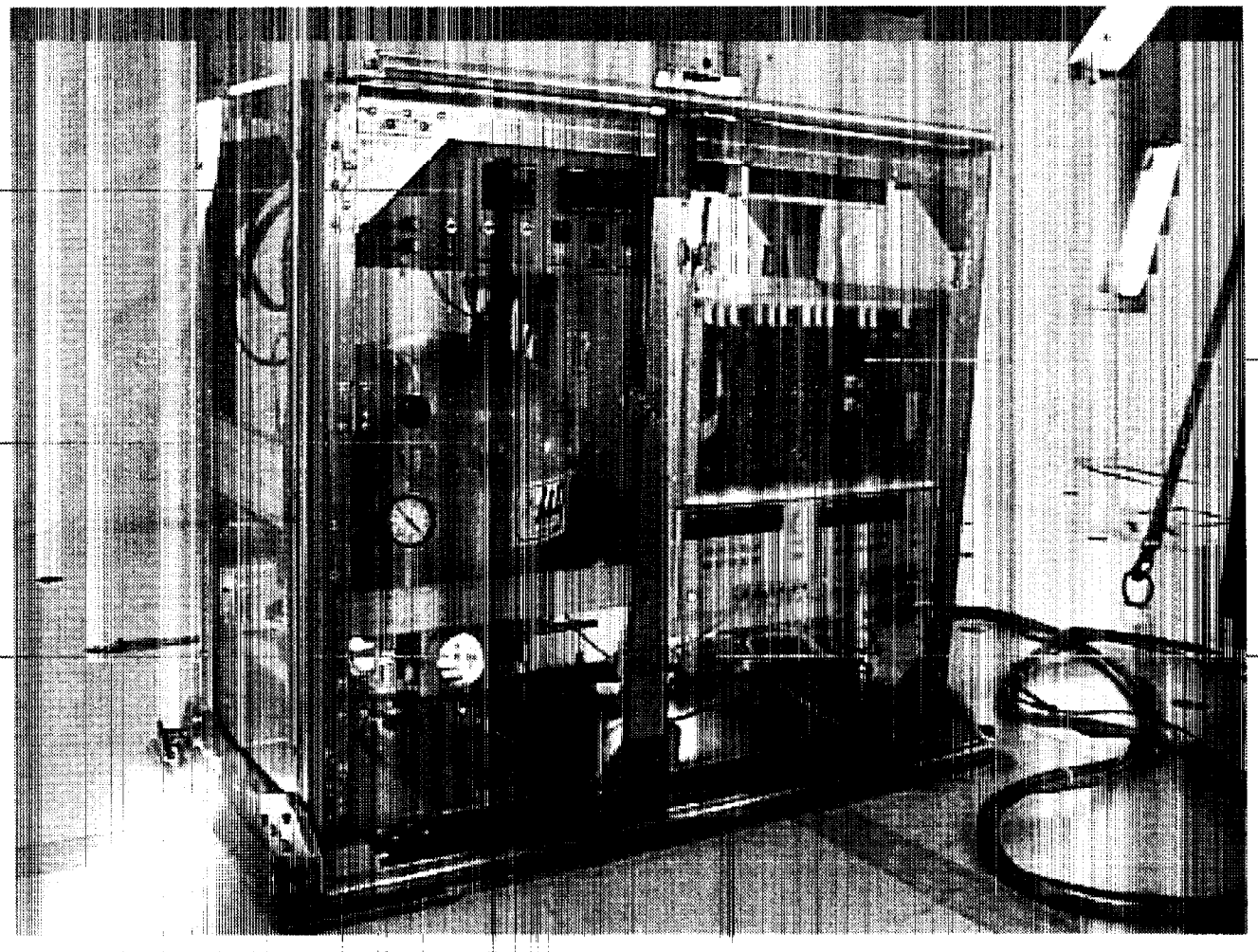

JK

Advantages of Current Approach

- Can obtain data at CHF and in transition boiling without danger of heater burnout
- Can obtain time resolved and local heat flux information
- Semi-transparent substrate allows high-speed images to be obtained simultaneously with heat flux

MICROGRAVITY RESULTS:
KC-135
Saturated Boiling

JK

Microgravity Results: KC-135, August, 1998

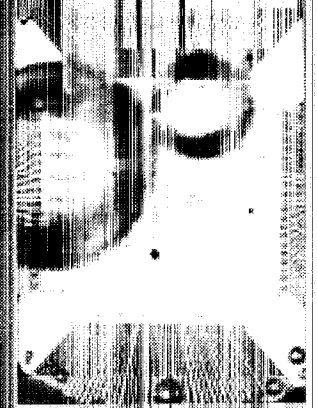

Superheat=15 K

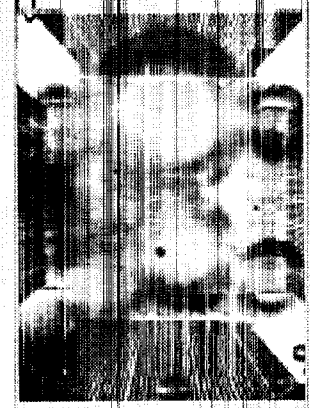

Superheat=20 K

Superheat=25 K

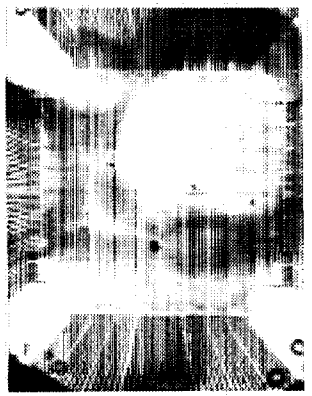

Superheat=30 K

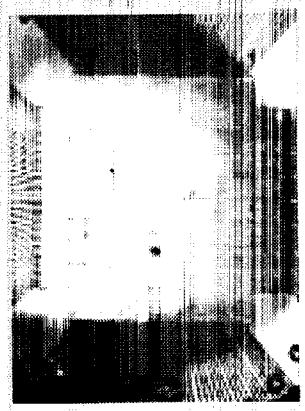

Superheat=35 K

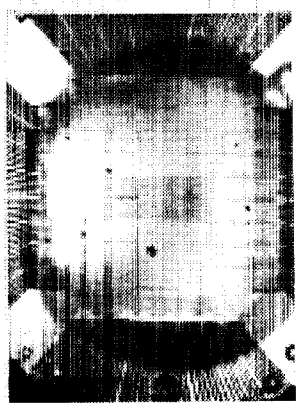

Superheat=40 K

- **Increase in number of bubbles with superheat until 25 K**
- **Coalescence of bubbles above 25 K**
- **Steady state reached?**
- **Effects of g-jitter?**

JK

Boiling Curves

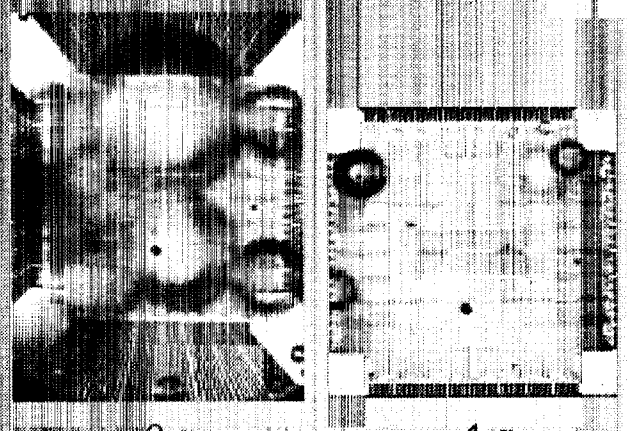

0 g 1 g

Superheat=20 K

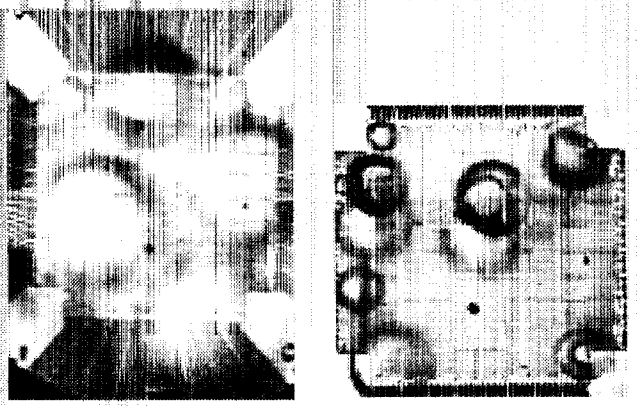

0 g 1 g

Superheat=25 K

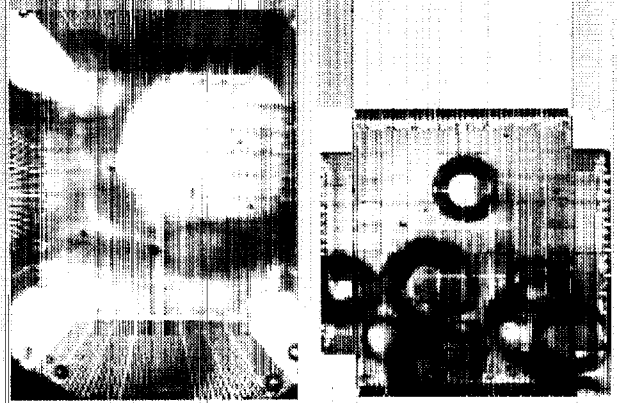

0 g 1 g

Superheat=30 K

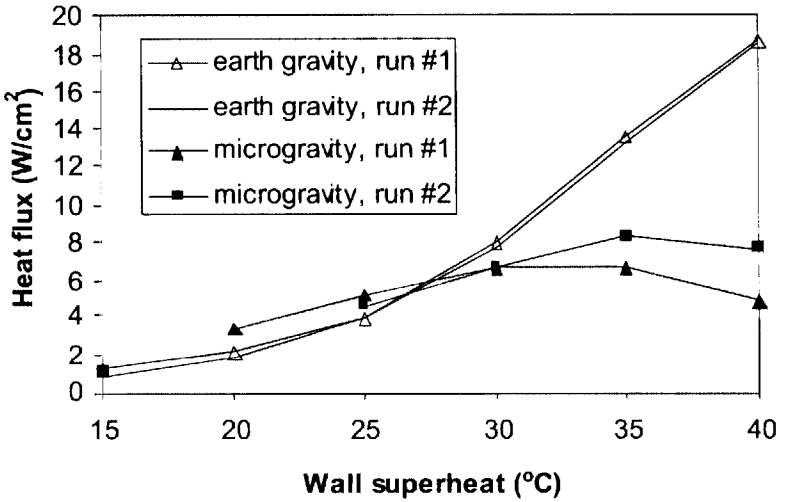

- **Higher heat fluxes in μg at low superheats**
- **Lower CHF in μg**

JK

Comparison Between Images and Heat Flux Map

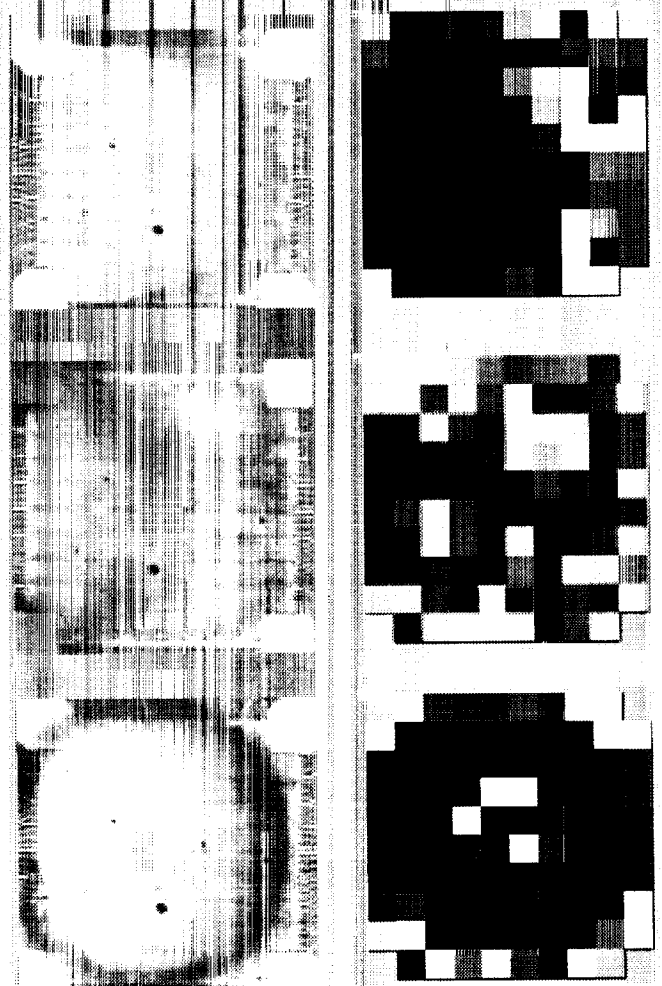

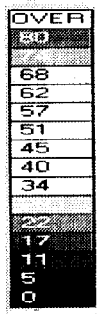

- Wall Superheat= 40 K
- High heat transfer associated with small, rapidly nucleating bubbles
- Low heat transfer associated with large "primary" bubble

JK

Boiling Function Determination

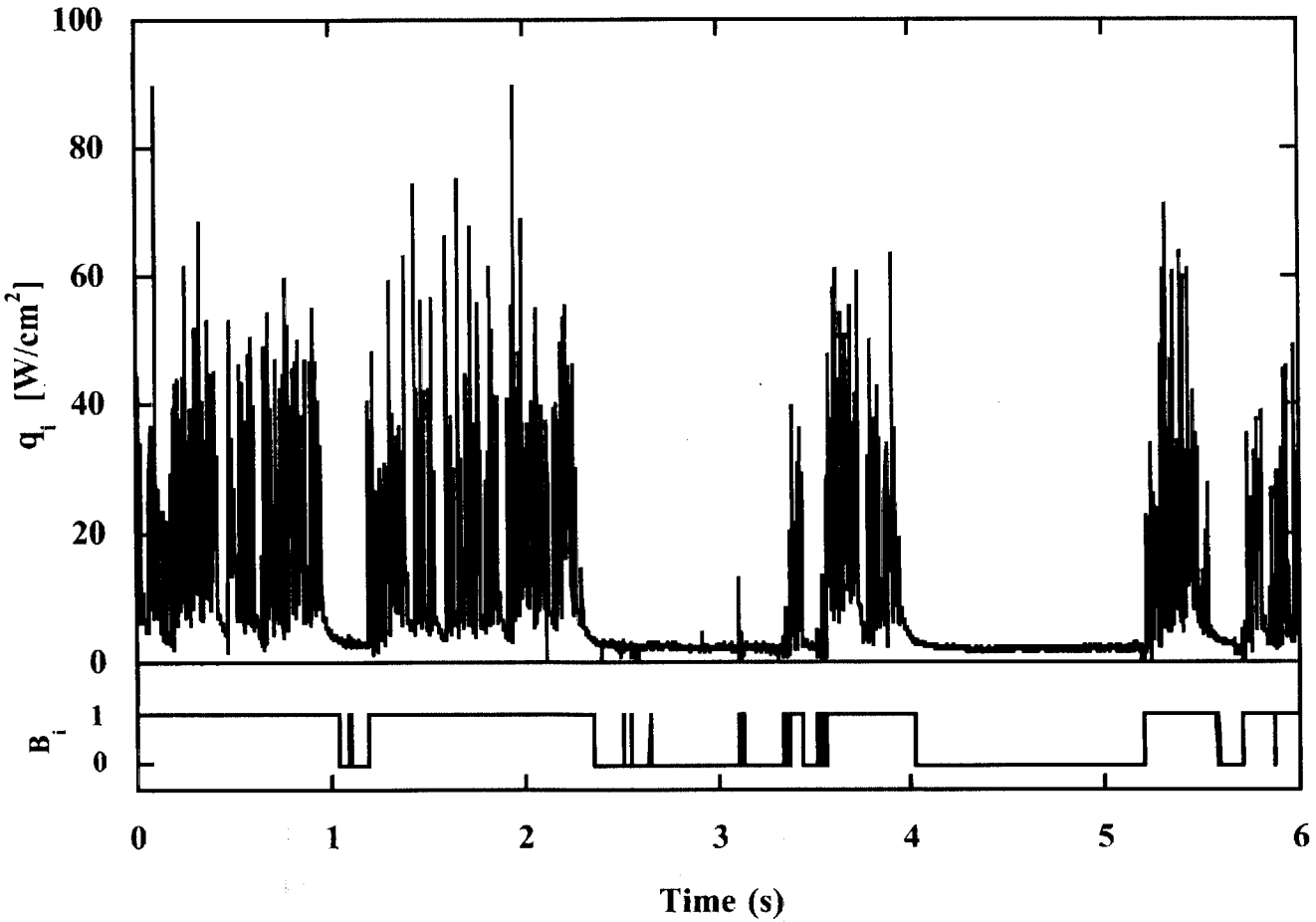

JK

Boiling Heat Flux

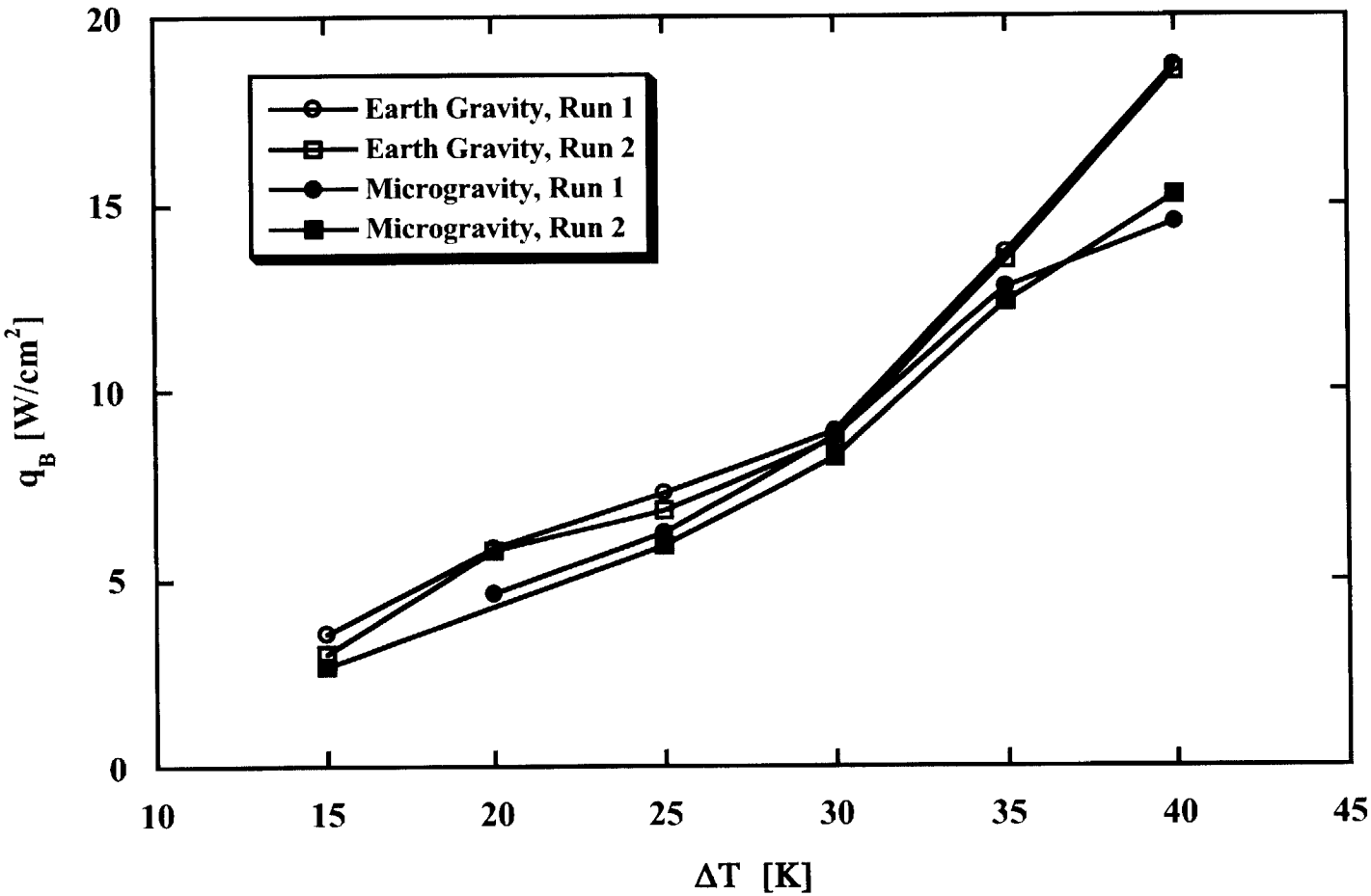

- Boiling heat flux in earth gravity and microgravity are similar
- For small scale bubbles, boiling is not influenced by gravity

JK

Boiling Fraction

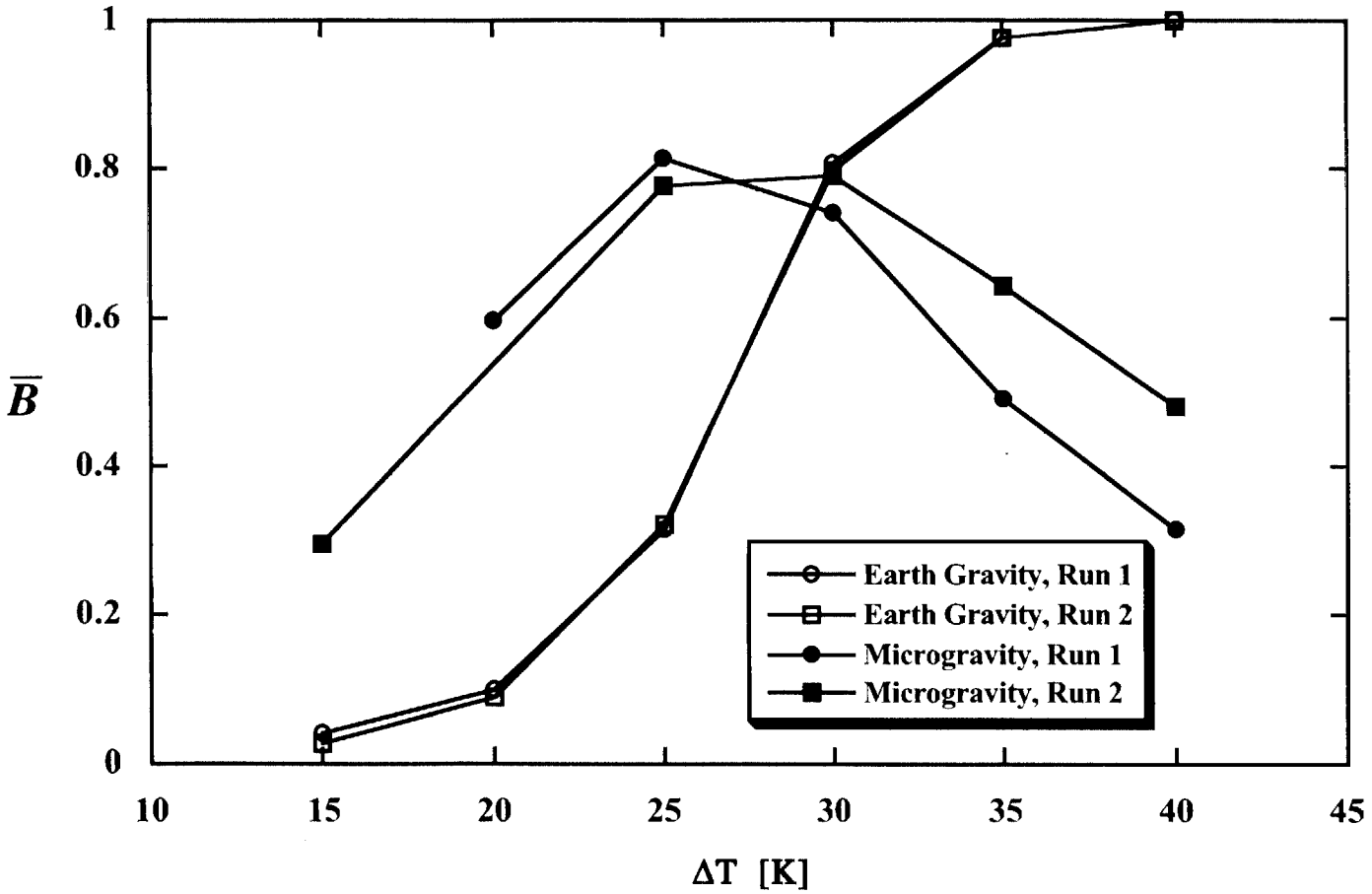

- Increasing amount of vapor on surface above ~30 K in μg

JK

Comparison Between Computed and Measured Heat Flux

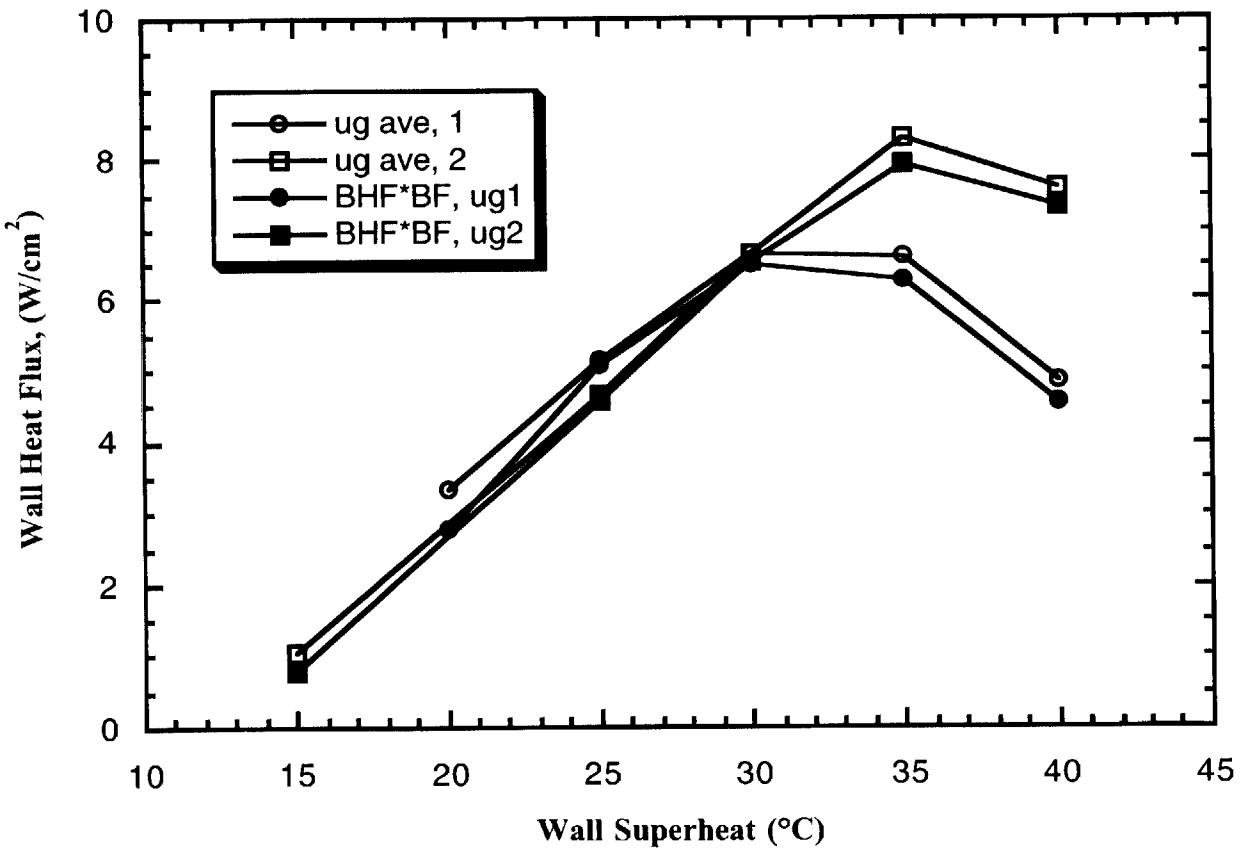

- Can predict boiling curve in microgravity if boiling heat flux in earth gravity and boiling fraction are known.

JK

Conclusions: Saturated Boiling

- CHF values in μg are about 35% of those in earth gravity.
- Heat transfer is associated with small-scale bubbles.
- Heat transfer in microgravity can be predicted from known heat flux in earth gravity along with knowledge of boiling fraction.

JK

MICROGRAVITY RESULTS: SOUNDING ROCKET & KC-135

Subcooling=35 K, 1 atm

JK

Sounding Rocket Payload

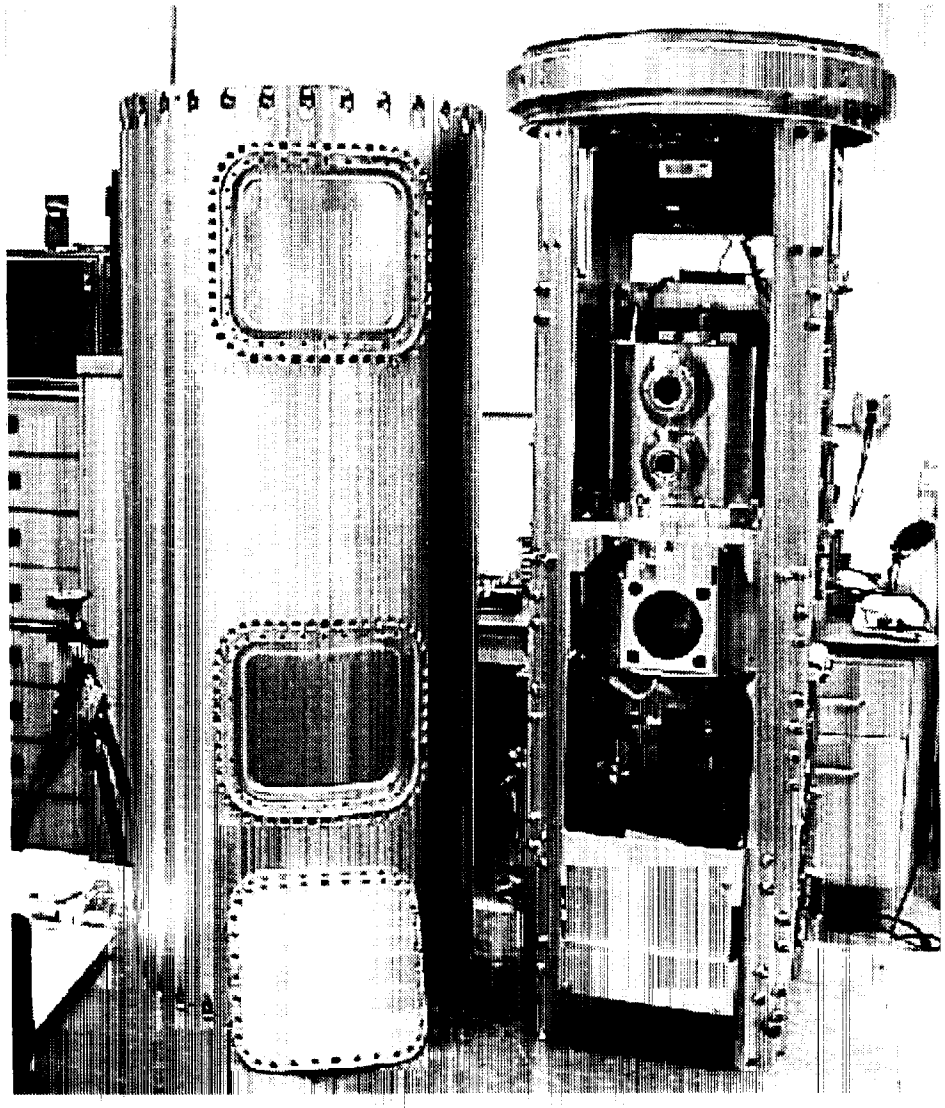

JK

Assembled Payload

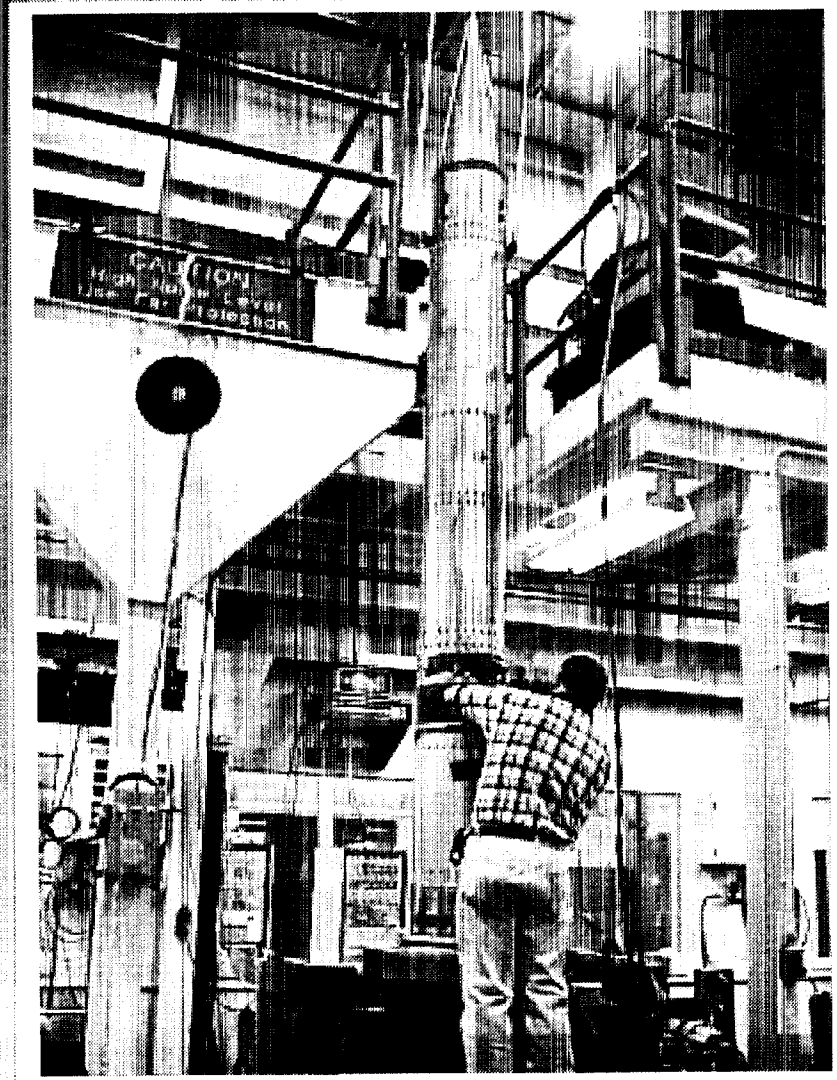

JK

Boosters

JK

Flight Profile, December 1999

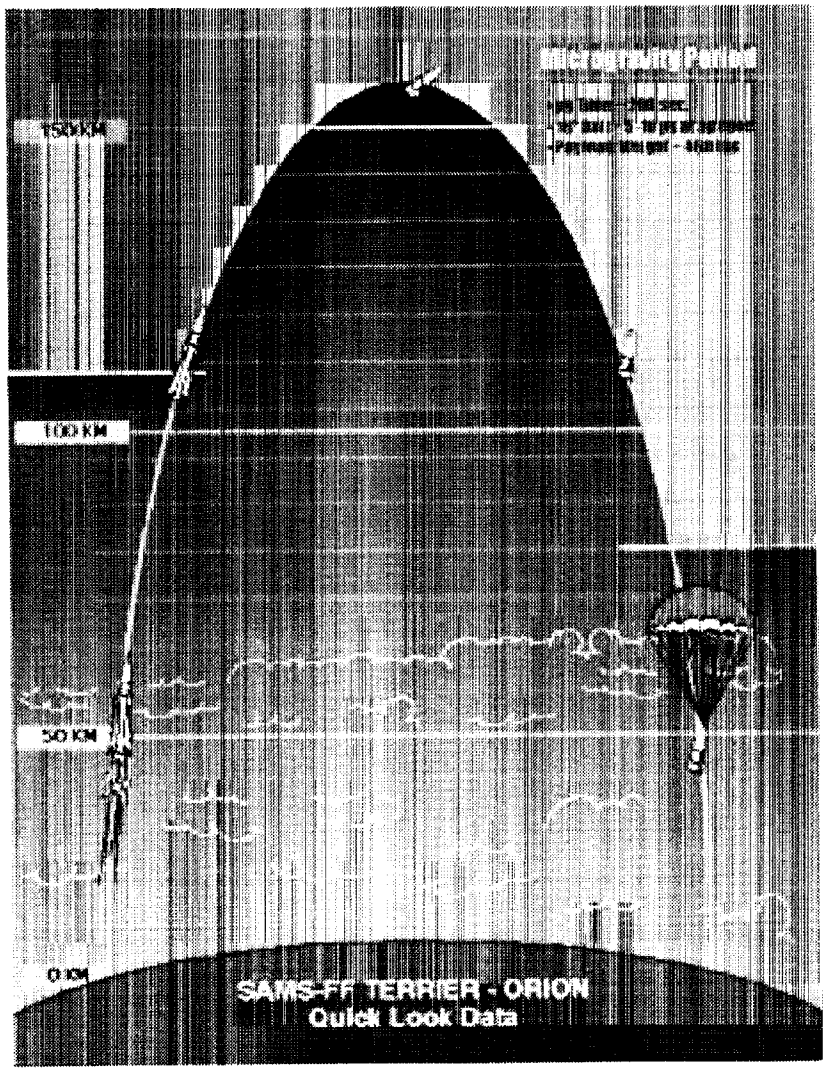

- 200 s of microgravity
- 10^{-6} grms
- Electronics worked well and heat flux data was obtained
- VCR malfunctioned so no video.

JK

Re-Flight on KC-135, April 2000

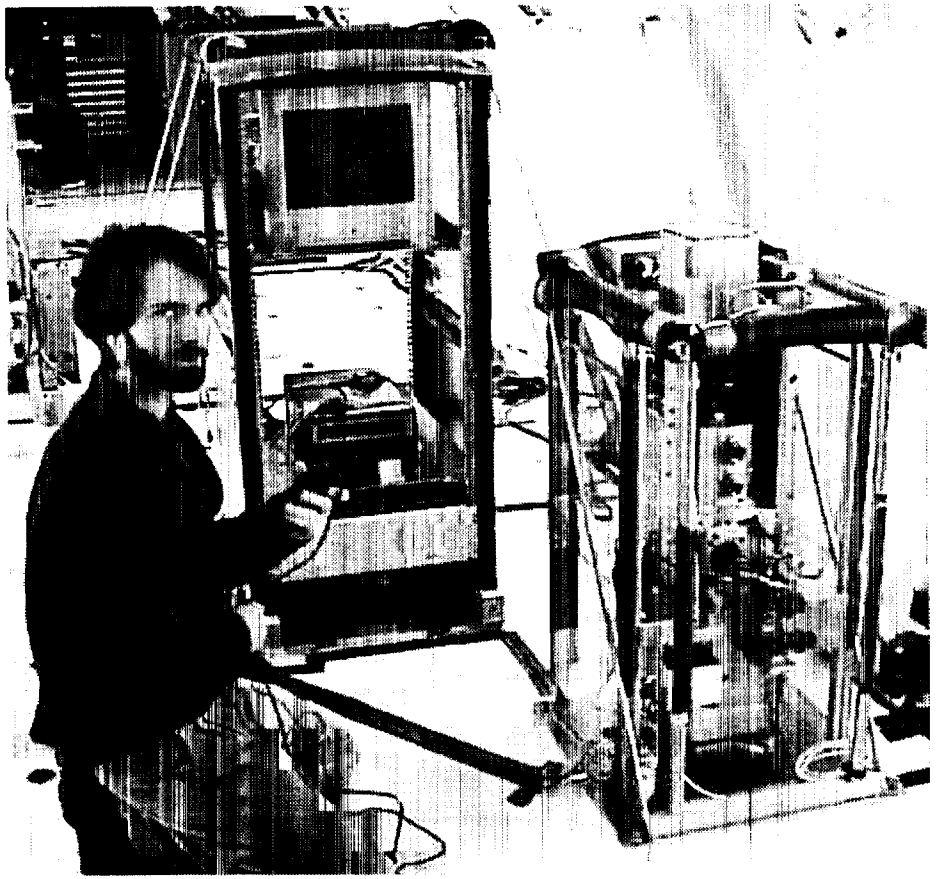

- Heat flux and video obtained using SR payload, same heater array
- Video of bubble motion

JK

Raw Heat Flux Through Parabola

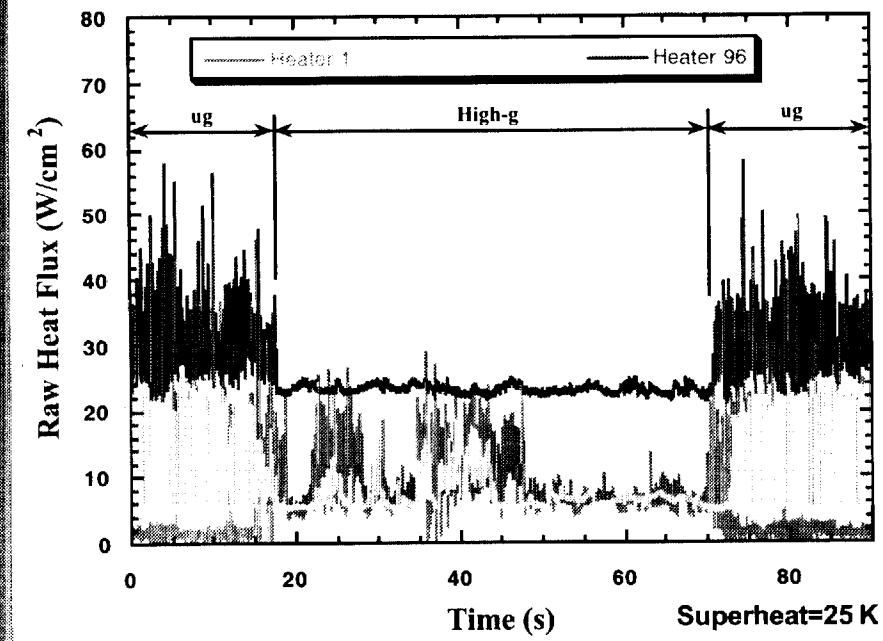

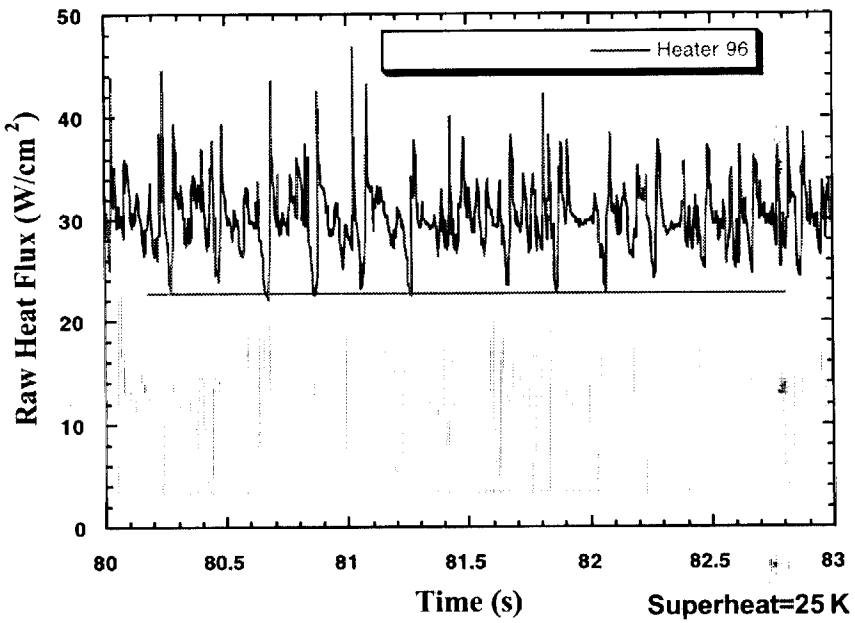

- Raw heat flux calculated from heater voltage, resistance, and area
- Need to correct data for substrate conduction to get heat flux from wall to liquid
- Assume heat flux from wall to fluid is zero when vapor covers heater

JK

Comparison Between KC-135 and SR: Preliminary Results

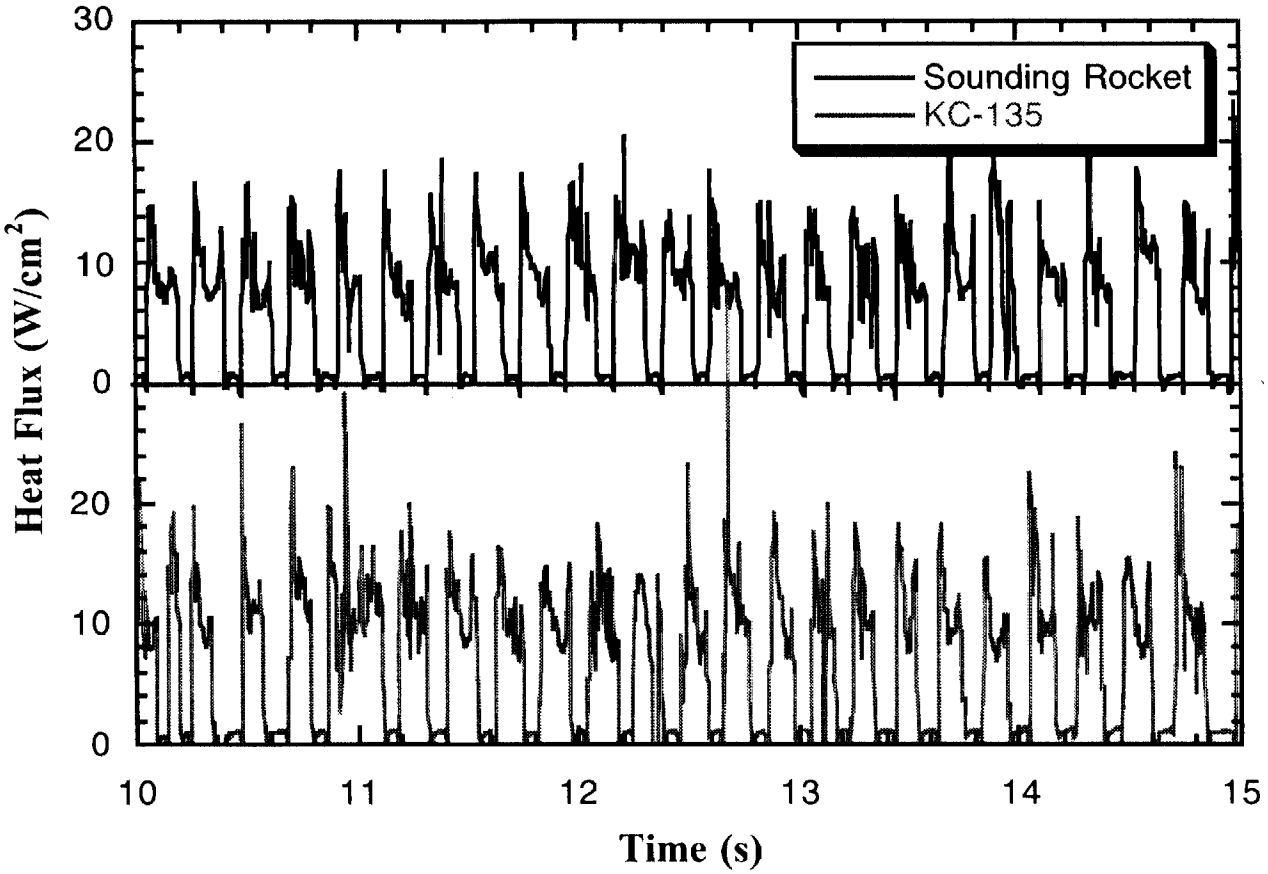

- SR data is more regular, repeatable than KC-135 data
- KC-135 heat fluxes are slightly higher than SR

JK

Comparison Between KC-135 and SR: Preliminary Boiling Curve

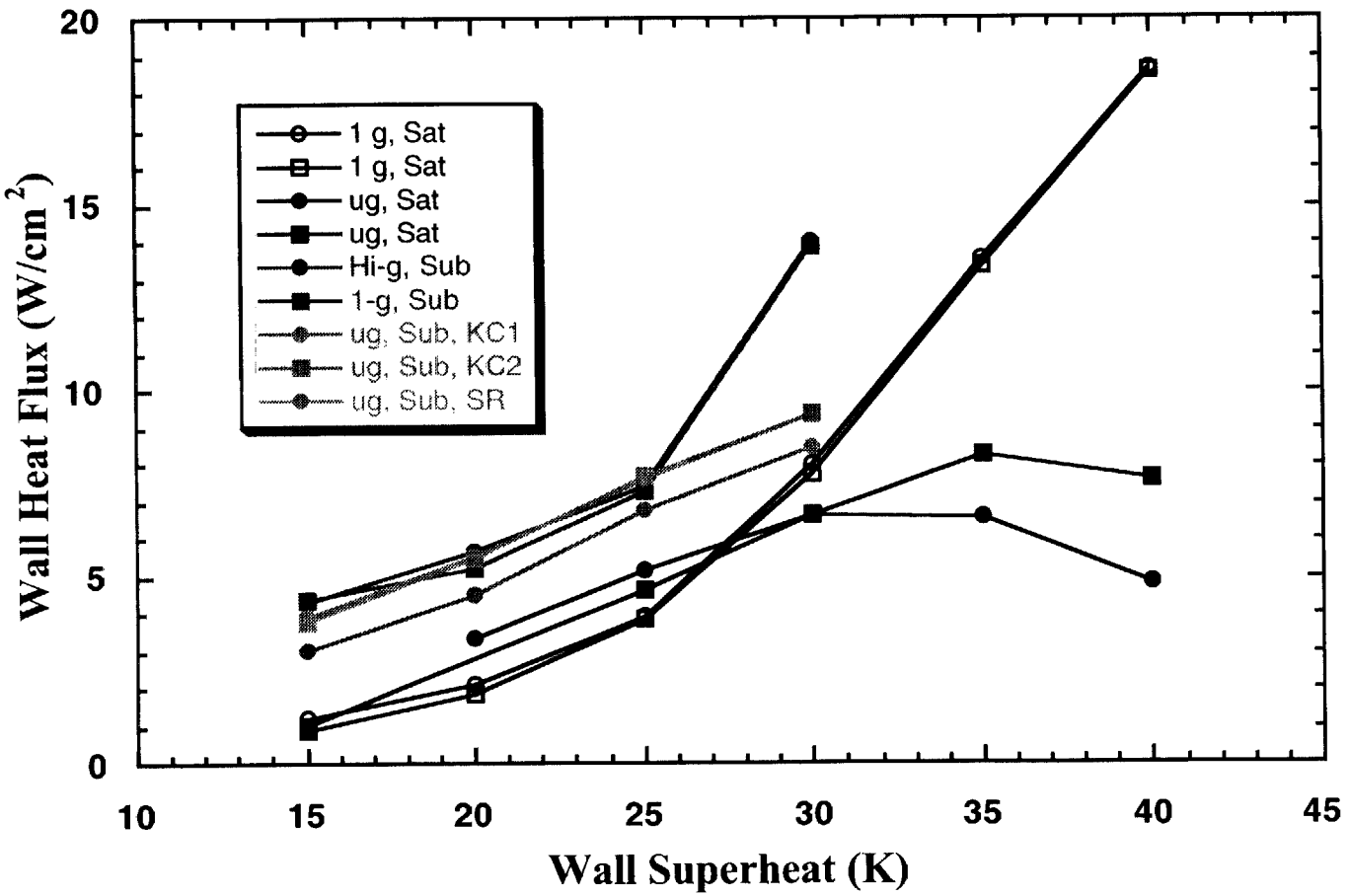

JK

Preliminary Heat Flux Distribution

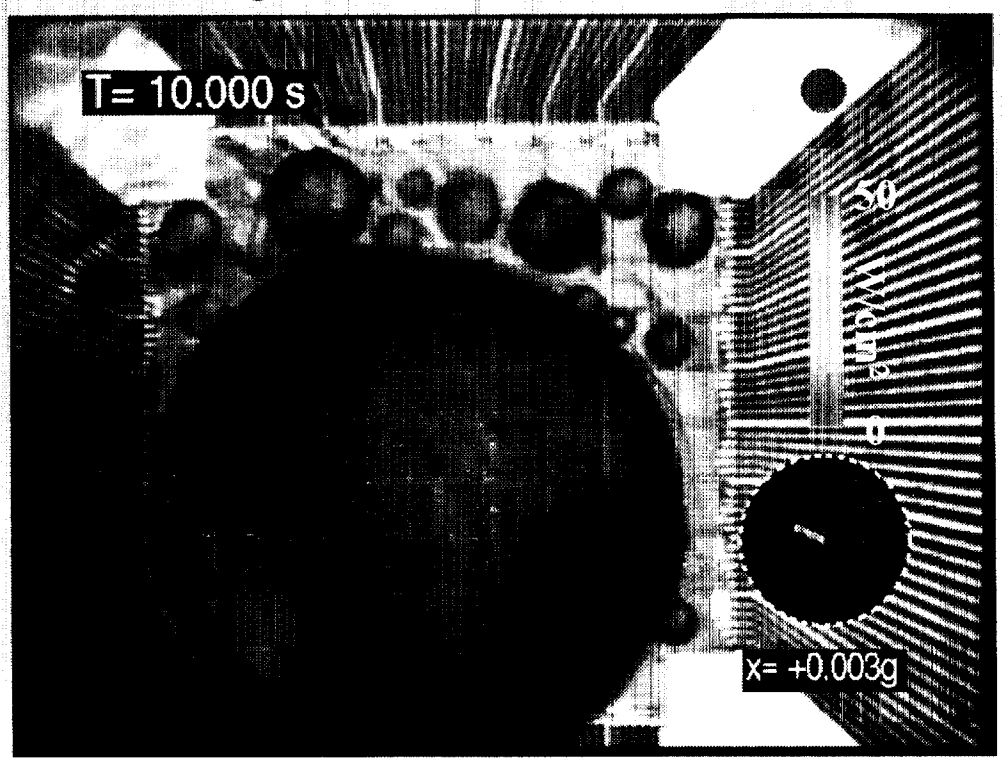

- Images and heat flux data obtained at 60 Hz and 250 Hz
- Large "primary" bubble with smaller satellite bubbles
- Primary bubble moves in circular pattern
- Dry spot underneath bubble
- Higher heat fluxes at contact line

(Colorization of images performed by the NASA GVIS Lab)

JK

Preliminary Heat Flux Distribution, cont'd

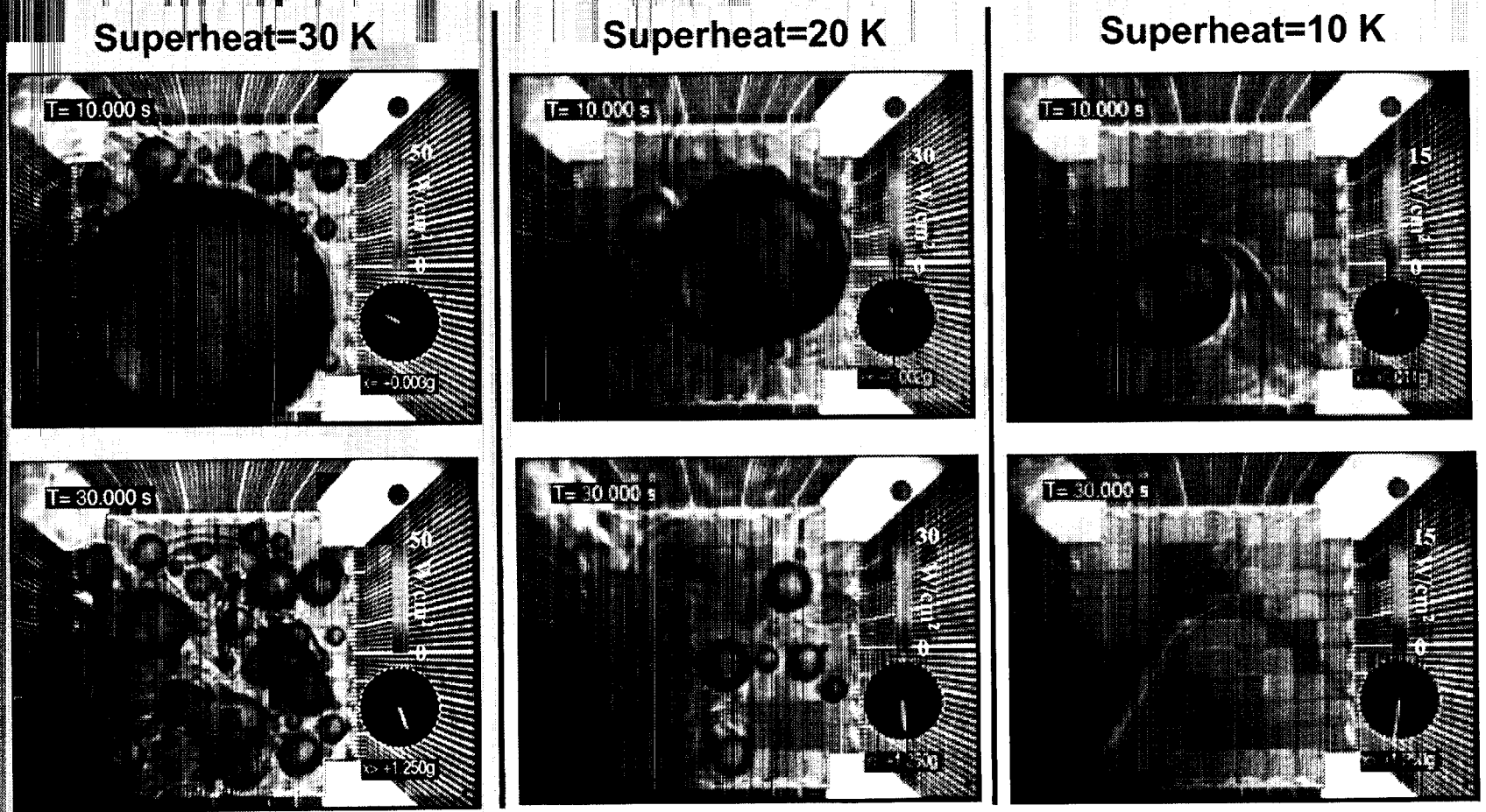

(Colorization of images performed by the NASA GVIS Lab)

JK

Preliminary Conclusions: Subcooled Boiling

- SR environment is quieter that KC-135 environment.
- Not much gravity effect at low superheats (below ~25 K).
- Heat transfer is associated with small-scale bubbles.
- Difference between microgravity and earth gravity heat flux is determined by size of primary bubble.

JK

Acknowledgements

Support for this project was provided by

John McQuillen and Joe Balombin, NASA GRC

Mary Vickerman, GVIS Lab, NASA GRC

Their assistance is gratefully acknowledged.

WETTING AND PARTIALLY WETTING FLUID PROFILES IN A CONSTRAINED VAPOR BUBBLE HEAT EXCHANGER

Y-X Wang, J. Plawsky and P. C. Wayner, Jr.*
The Isermann Department of Chemical Engineering
Rensselaer Polytechnic Institute
Troy, NY 12180-3590
*TEL: (518) 276-6199; FAX: (518)-276-4030; E-mail: wayner@rpi.edu

ABSTRACT

Microgravity experiments using the Constrained Vapor Bubble heat exchanger, CVB, are being developed for the International Space Station. Since the maximum attainable axial heat flux increases with the cell width, systems based on low capillary pressure regions, which require a microgravity environment, are emphasized. Data using a vertical axisymmetric system have been obtained in the earth's environment. The liquid pressure field and resulting fluid flow rates are measured optically through a microscope. Herein, liquid film profiles using a partially wetting system (ethanol/quartz) are compared with those obtained using a completely wetting (pentane/quartz) system.

In particular, we are concerned with the experimental and theoretical study of the Constrained Vapor Bubble, CVB, presented in Fig.1. The liquid-vapor system is formed by evacuating the closed container with sharp internal corners and then underfilling it with a liquid. For an isothermal completely wetting system, the liquid will coat all the walls of the chamber. On the other hand, for a finite contact angle system, some of the walls will have only an extremely small amount of adsorbed vapor which changes the surface properties of the solid-vapor interface. Liquid will fill at least a portion of the corners in both cases. If temperature $T_1 > T_2$ because of an external heat source in the evaporator, Q_{in}, and heat sink in the condenser, Q_{out}, energy flows from End (1) to End (2) by conduction in the walls and by an evaporation, vapor flow and condensation mechanism. The condensate flows from End (2) to End (1) because of the intermolecular force field which is a function of the film profile. The film profile is a function of the thermal conditions on the surface. There is a shape dependent "pressure jump" at the vapor-liquid interface, $P_v - P_l$, due to the anisotropic stress tensor near interfaces. The pressure jump is given by the following extended Young-Laplace equation which includes the effects of both capillarity (σK) and disjoining pressure (Π).

$$P_v - P_l = \sigma K + \Pi \tag{1}$$

For a completely wetting system, $\Pi > 0$. Whereas, for a partially wetting system, $\Pi < 0$. Due to the relatively large cross-sectional area for vapor flow in our system, the vapor space is almost isobaric. The evaporation and condensation regions are connected by an intermediate region which can be approximately isothermal and adiabatic if the system is operated so that Q_{out} (mainly at one end in the condenser) $\cong Q_{in}$ (at the other end in the evaporator). Otherwise, the intermediate region is non-isothermal with an interfacial heat flux and heat losses to the surroundings.

A Constrained Vapor Bubble (CVB) heat exchanger was built to study the evaporation/condensation process in a vertical orientation. Details regarding the experimental setup can be found from Wang et al. [1]. It consists mainly of a quartz cell (square cross section; inside dimensions, 3 mm x 3 mm; outside dimensions, 5.5 mm x 5.5 mm; length, 40 mm), a thermoelectric heater on the top, and coolers on each side of the cell located at 20mm from the top. Naturally occurring interference fringes are viewed and recorded using a microscope. During the presentation, observed liquid film profiles will be discussed. For example, in Fig.2 for the evaporator region of the ethanol/quartz system, bubbles kept generating in the liquid film in the corner. There were no bubbles in pentane for the conditions studied (see Fig.3). In the condenser region, dropwise condensation occurred for the ethanol/quartz (see Fig.4), whereas only film condensation existed for the pentane/quartz system.

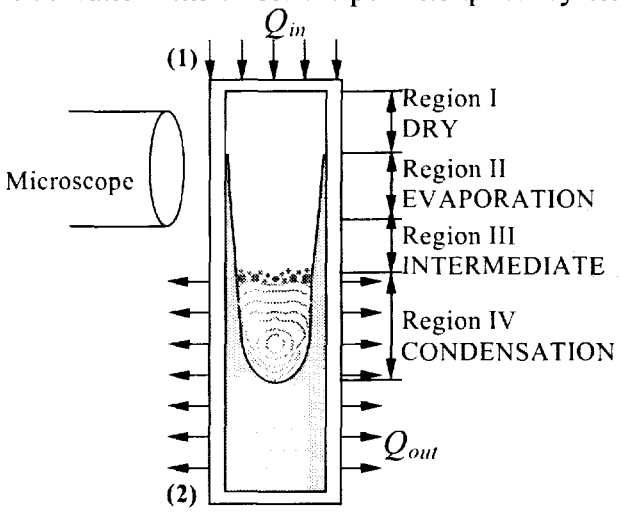

Figure 1. A schematic drawing of the vertical CVB in the earth's gravitational field.

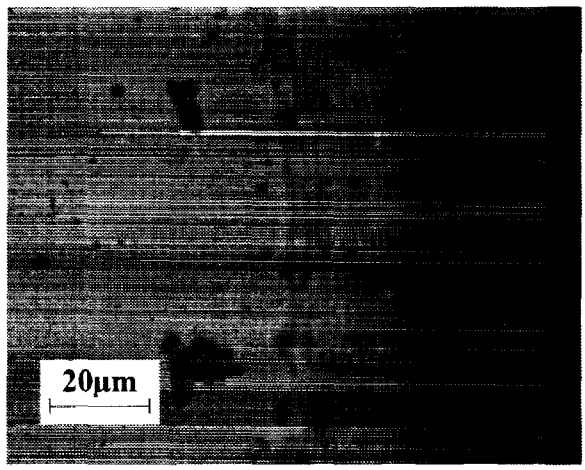

Figure 2. Boiling evaporation of ethanol in Region II

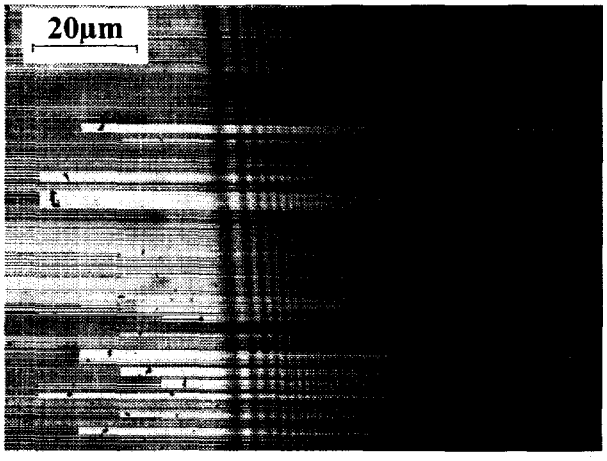

Fig.3. Evaporation of pentane in Region II.

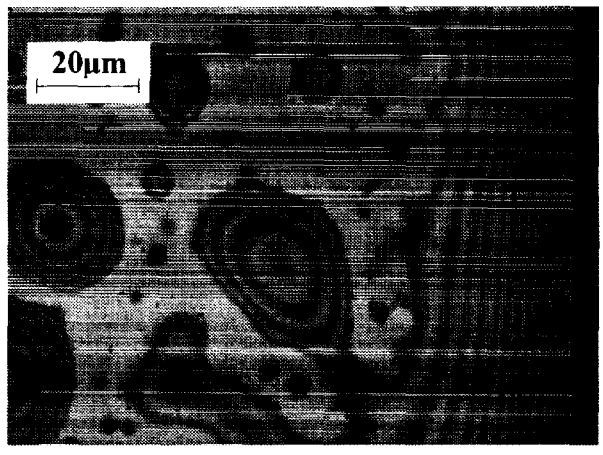

Fig.4. Dropwise condensation of ethanol in Region IV.

[1] Wang, Y-X, Plawsky, J., and Wayner, P. C., Jr., Heat and Mass Transfer in a Vertical Constrained Vapor Bubble Heat Exchanger using Ethanol, *34th National Heat Transfer conference*, Paper number: NHTC2000-12201, Aug. 2000.

WETTING & PARTIALLY WETTING FLUID PROFILES IN A CONSTRAINED VAPOR BUBBLE HEAT EXCHANGER

Y-X Wang, J. Plawsky and P. C. Wayner, Jr.*
Isermann Department of Chemical Engineering
Rensselaer Polytechnic Institute
Troy, NY 12180-3590

5th μg Fluid Physics &
Transport Phenomena Conference

August 9-11, 2000
Cleveland, Ohio

1

OUTLINE

MOTIVATION

JUSTIFICATION FOR μg

GROUND-BASED EXPERIMENTAL STUDIES

- EXPERIMENTAL SET-UP
- PICTURES OF WETTING VERSUS PARTIALLY WETTING FLUIDS
- PICTURE OF DROPWISE CONDENSATION
- SCHEMATIC OF FORCE BALANCE
- DIMENSIONLESS FORCE BALANCE
- AXIAL PRESSURE GRADIANT

CONCLUSIONS

CONSTRAINED VAPOR BUBBLE HEAT EXCHANGER (MICROGRAVITY ENVIRONMENT)

$$P_V = P_\ell + \sigma K + \frac{(-B)}{\delta^n}$$

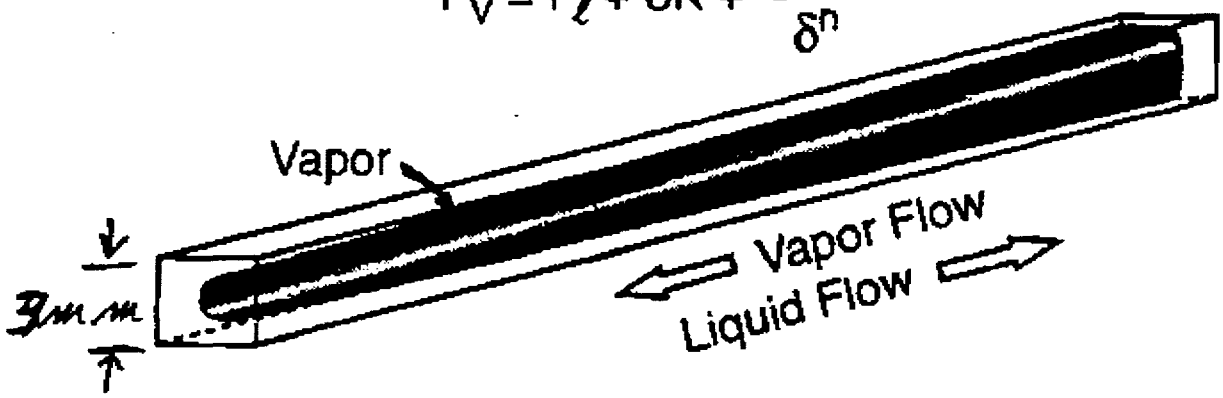

3x3x40mm

$$T_2 > T_1$$

$$P_{v2} > P_{v1} > P_{\ell 1} > P_{\ell 2} < P_{v2}$$

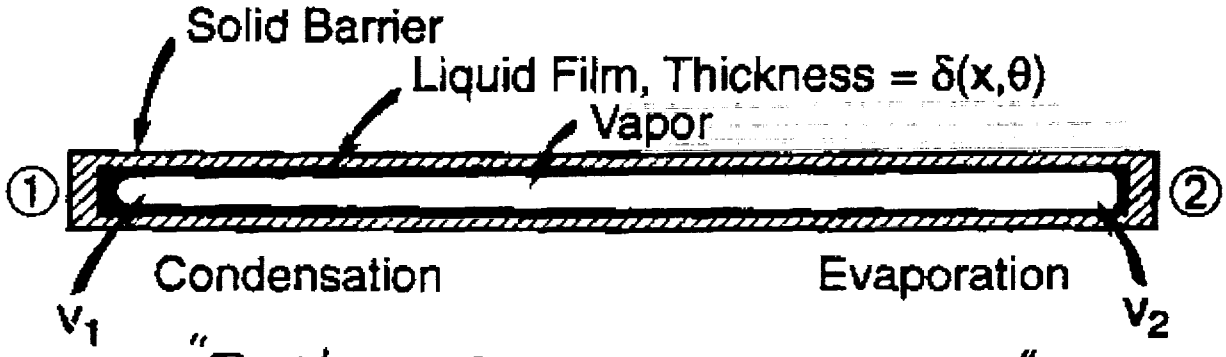

"FIN HEAT EXCHANGER"

CROSS-SECTION OF CVB (g → 0)

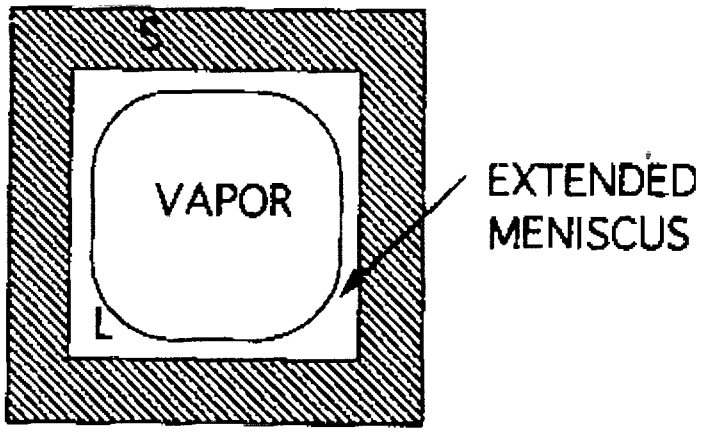

3

A MULTI-FACETED STUDY

1) A BASIC STUDY IN INTERFACIAL PHENOMENA, MICROGRAVITY FLUID PHYSICS, AND THERMODYNAMICS

2) A BASIC STUDY IN THERMAL TRANSPORT AND STABILITY

3) A STUDY OF A HIGH FLUX, PASSIVE HEAT EXCHANGER FOR A MICROGRAVITY ENVIRONMENT

FACETS 1 AND 2 ARE EMPHASIZED

4

JUSTIFICATION FOR μg ENVIRONMENT

A) RELATIVELY LARGE INTERFACIAL SYSTEMS WITH SMALL CAPILLARY PRESSURES IN THE CONDENSER AND INTERMEDIATE SECTIONS GIVE HIGH AXIAL HEAT FLUXES

B) STABILITY AND TRANSPORT PROCESSES WITH SMALL CAPILLARY PRESSURES NEED TO BE STUDIED USING AN AXISYMMETRIC SYSTEM (SMALL BOND NUMBER)

C) TO OBTAIN A SMALL BOND NUMBER WITH SMALL CAPILLARY PRESSURES A MICROGRAVITY ENVIRONMENT IS NEEDED

D) THE UNAVAILABLE DATA ARE MOST JUDICIOUSLY OBTAINED IN A MICROGRAVITY ENVIRONMENT

5

APPROXIMATE EQUATION FOR THE THEORETICAL AXIAL PROFILE OF THE CURVATURE IN THE CORNER: K = 1/r

[BASED ON BALANCE OF VISCOUS SHEAR AND CAPILLARY PRESSURE GRADIENT]

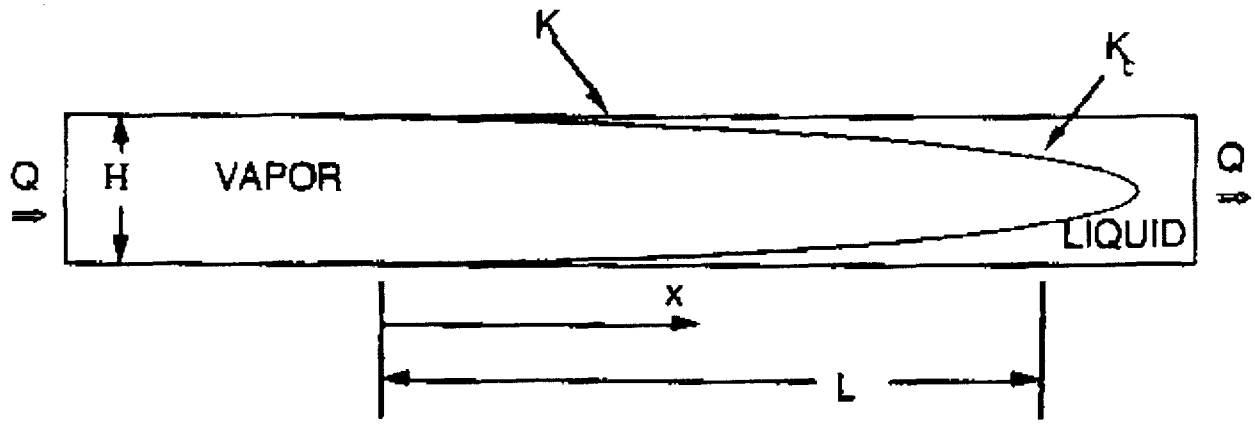

$$\frac{1}{K^3} = \frac{1}{K_c^3} - \frac{3\,\nu\,k_{fl}\,Q\,(L-x)}{C_l^3\,\sigma\,h_{fg}}$$

ν = kinematic viscosity
Q = axial heat flow rate
h_{fg} = heat of vaporization
σ = surface tension
C_L = shape factor = 0.43
k_{fl} = friction coefficient
K_C = curvature in condenser
= $4/(H = 3mm) = 1{,}333\ m^{-1}$)

6

$$\frac{1}{K^3} = \frac{1}{K_c^3} - \frac{3\nu k_{fl} Q (L - x)}{C_l^3 \sigma h_{fg}} \qquad \frac{dK}{dx} = -\frac{\nu k_{fl} Q}{C_l^3 \sigma h_{fg}} K^4$$

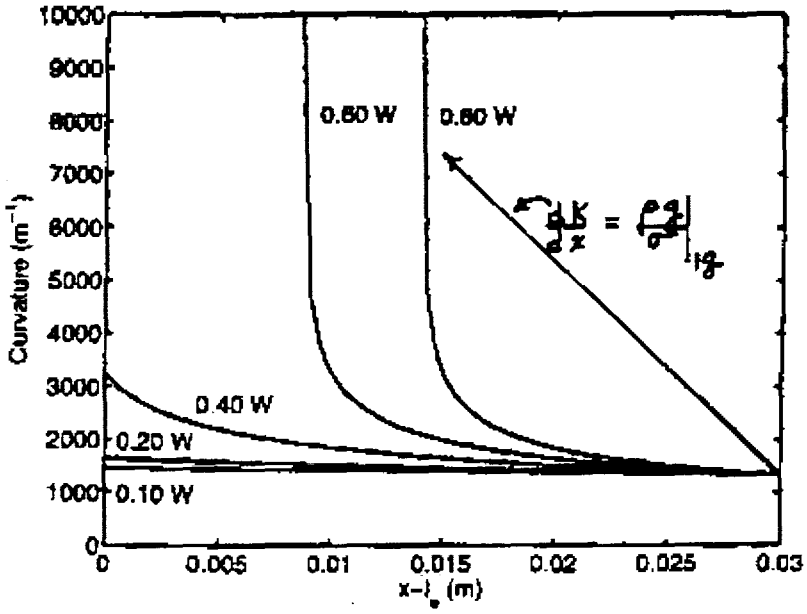

INSIDE DIMENSION, H = 3 mm, K > 1,333 m^{-1}

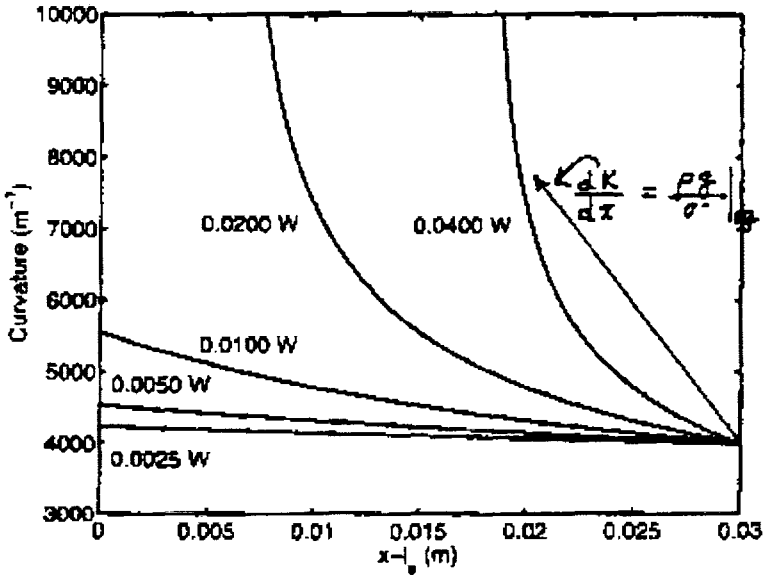

INSIDE DIMENSION, H = 1 mm, K > 4,000 m^{-1},
(K_c' for H = 1mm) = 81 (K_c' for H = 3 mm)'

7

MAXIMUM HEAT FLUX, q_m''

$$q_m'' = \frac{Q_m}{H^2} = \frac{c_l^3 \sigma h_{fg}}{192 \upsilon k_{fl}} \frac{H}{L}$$

"MAXIMUM" HEAT FLUX VERSUS WIDTH OF CELL, H, FOR L = 30 mm,

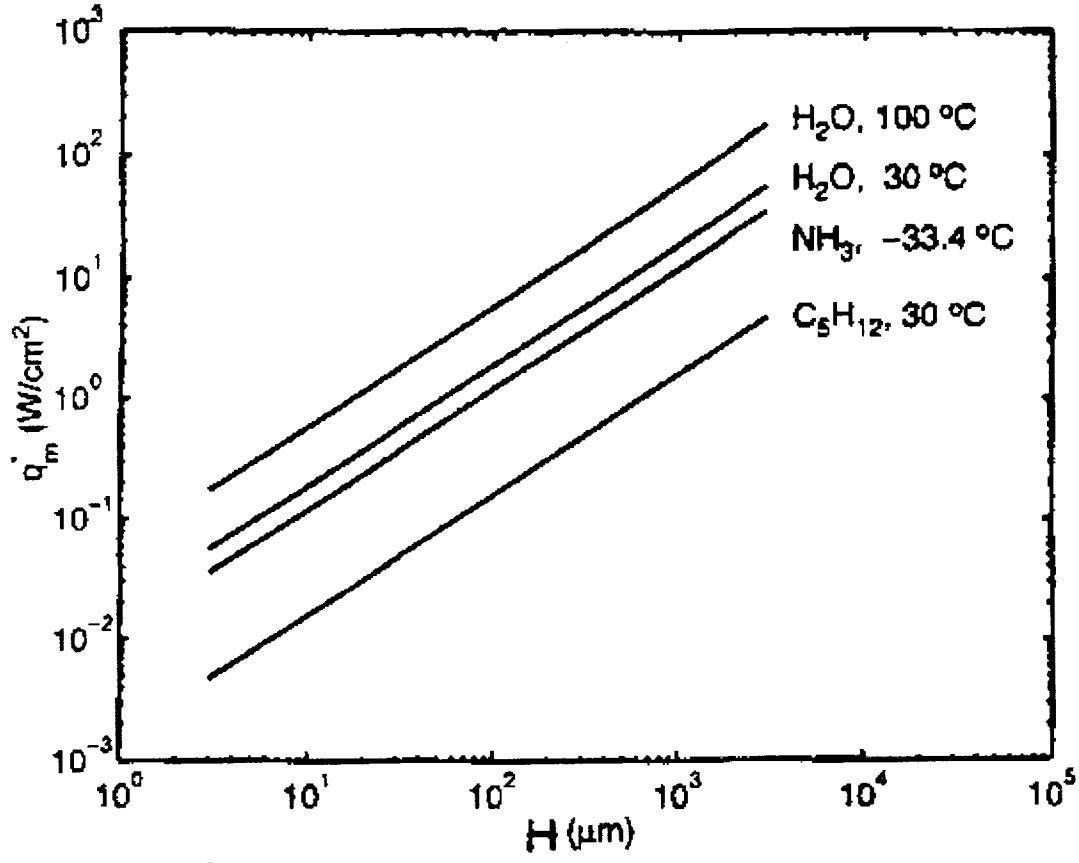

8

OUTLINE

MOTIVATION

JUSTIFICATION FOR μg

* GROUND-BASED EXPERIMENTAL STUDIES

  EXPERIMENTAL SET-UP

  PICTURES OF WETTING VERSUS PARTIALLY WETTING FLUIDS

  PICTURE OF DROPWISE CONDENSATION

  SCHEMATIC OF FORCE BALANCE

  DIMENSIONLESS FORCE BALANCE

  AXIAL PRESSURE GRADIANT

CONCLUSIONS

9

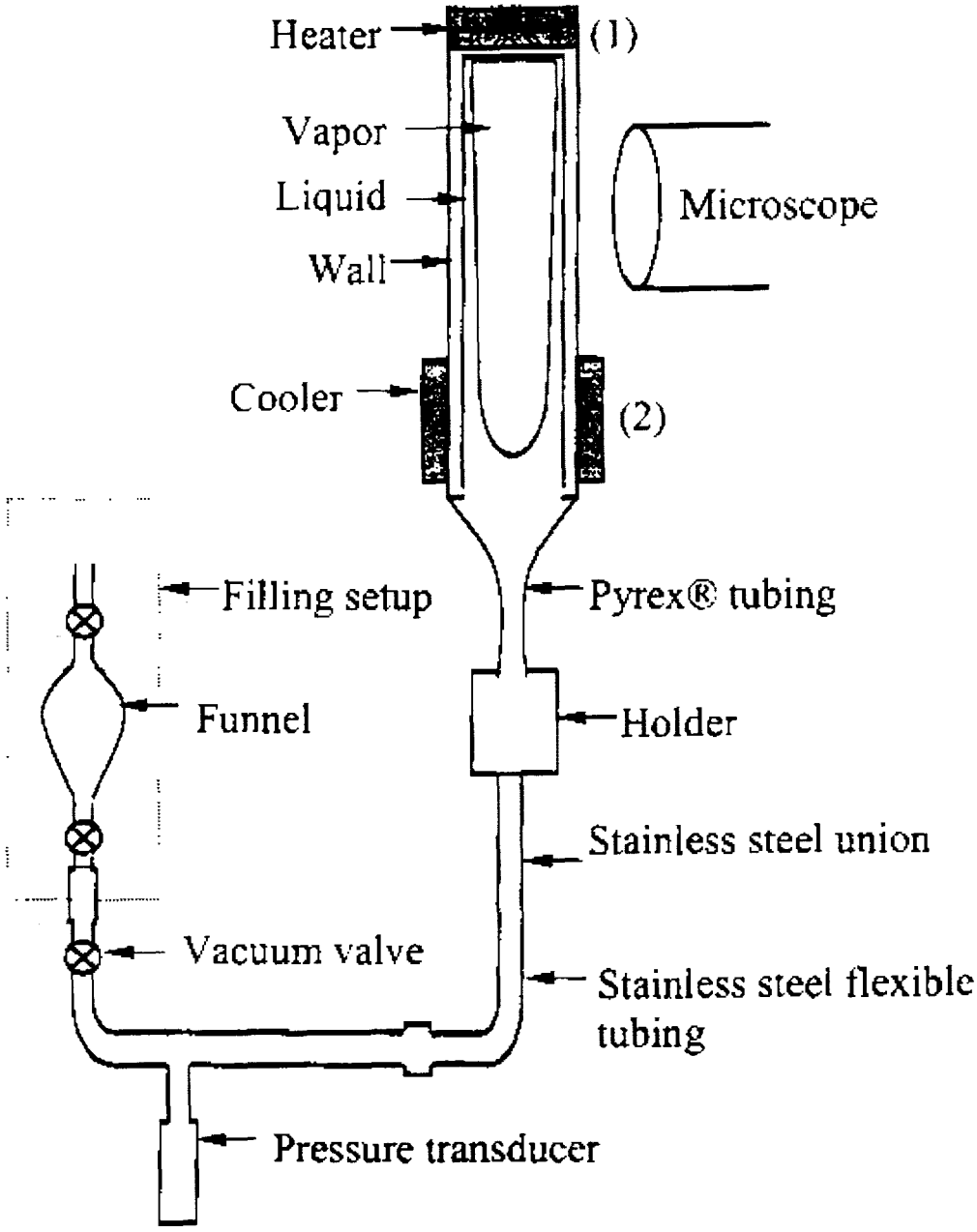

The Vertical Constrained Vapor Bubble System

10

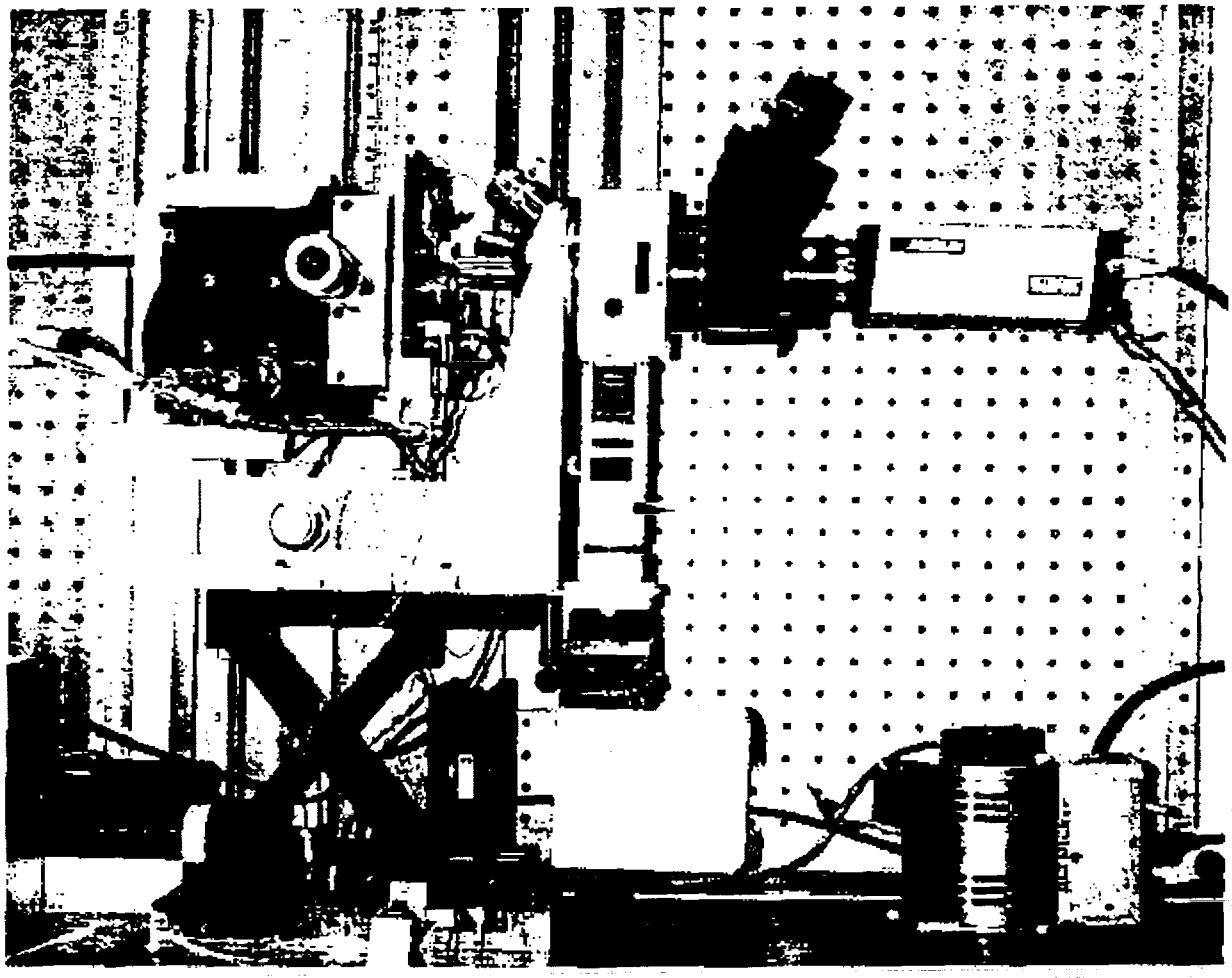

Experimental Setup of the Vertical Constrained Vapor Bubble (CVB)

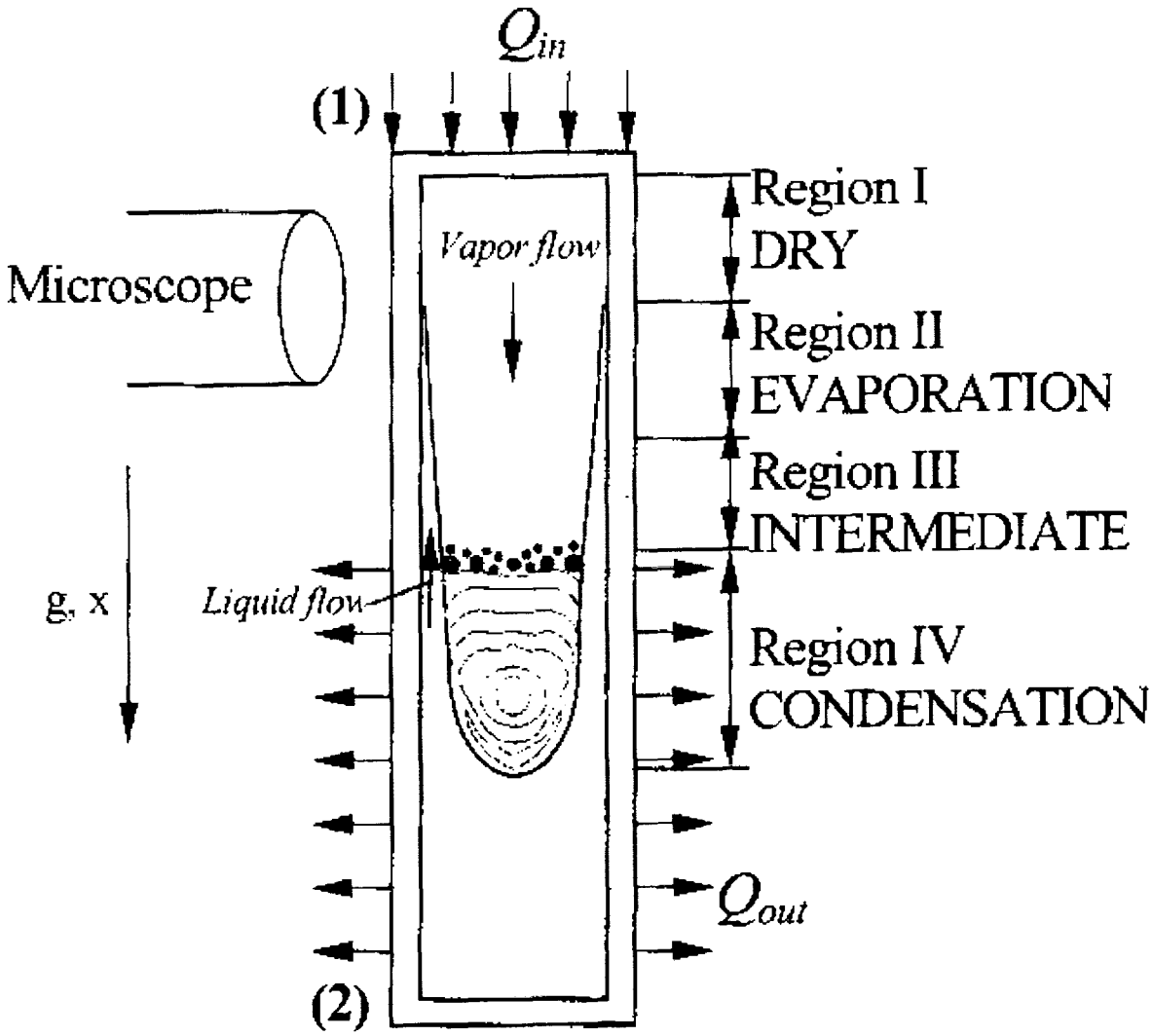

A Schematic Drawing of the Vertical CVB in the Earth's Gravitational Field

12

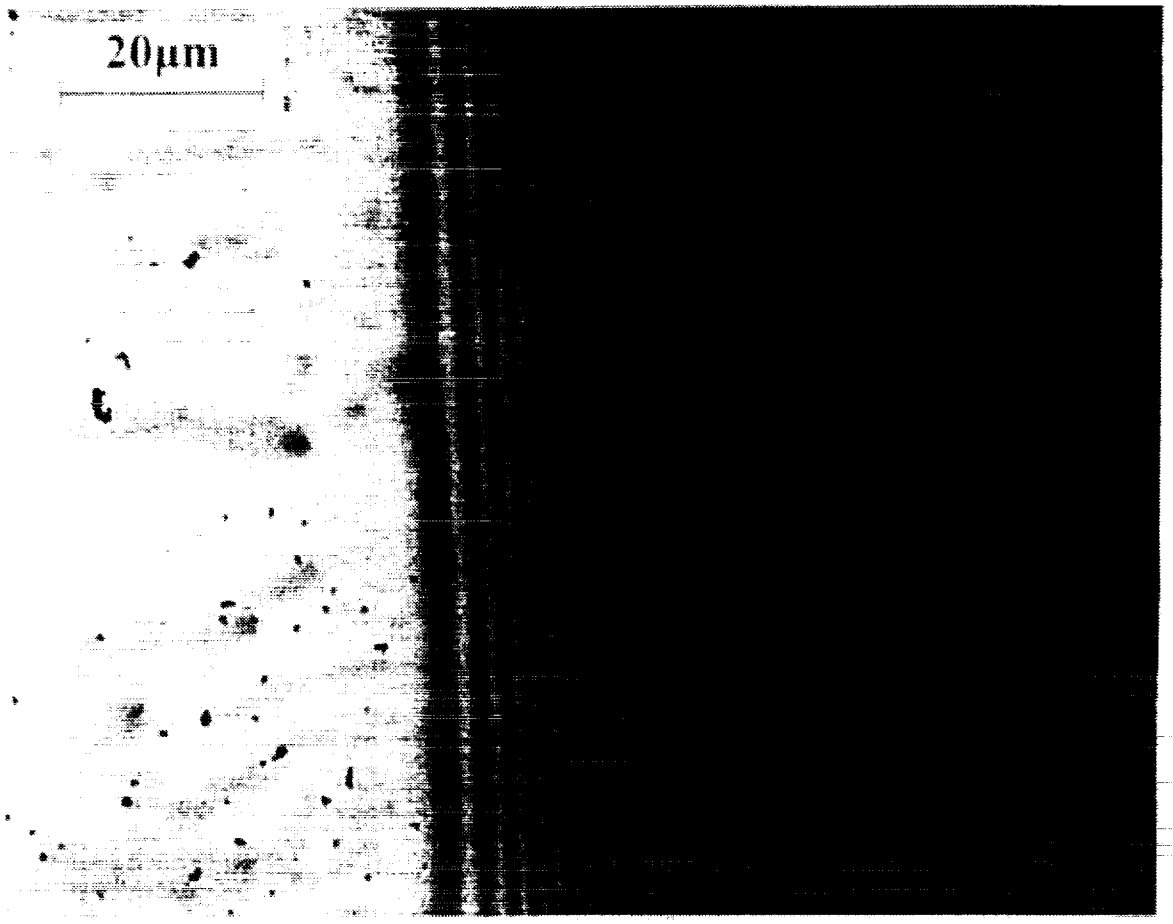

Evaporation of Pentane in Region II

13

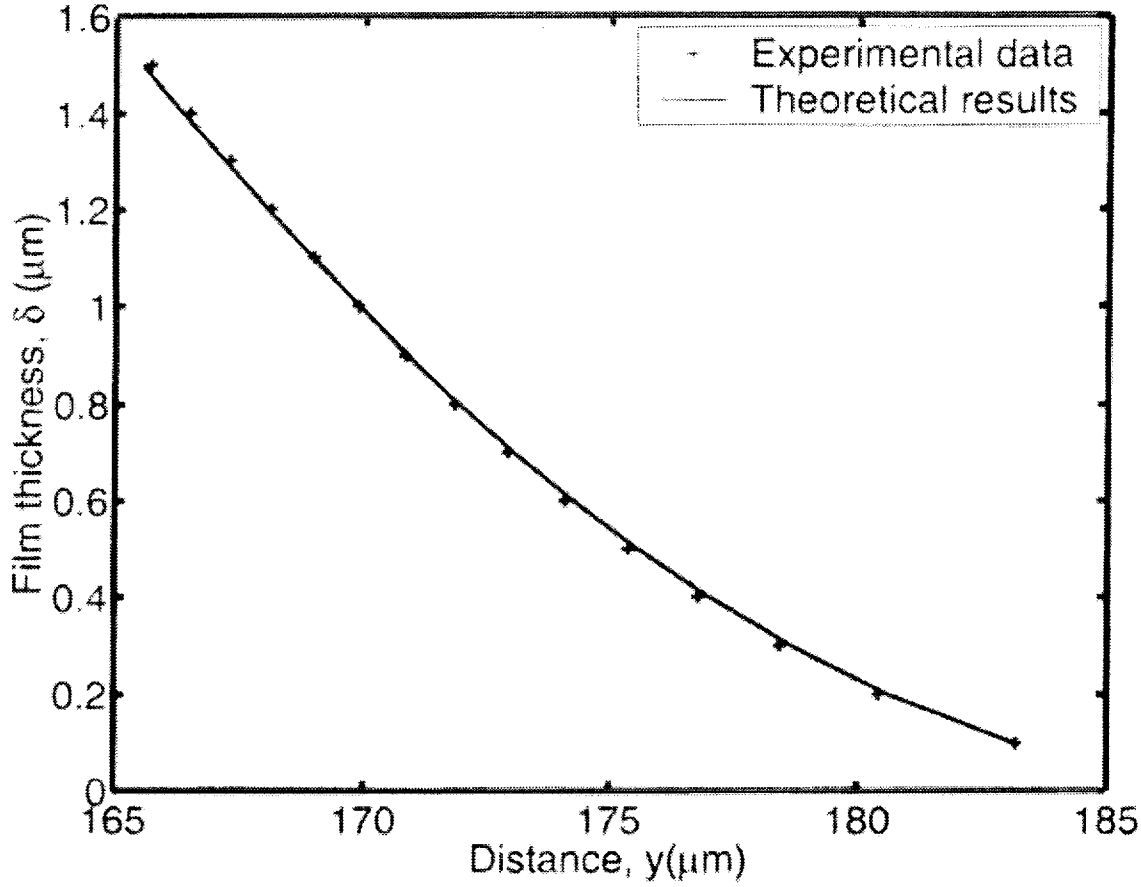

Film Thickness Profiles of Pentane in the Corner of the Cell

Gives: Contact Angle, θ

Curvature, $K = 1/r$

14

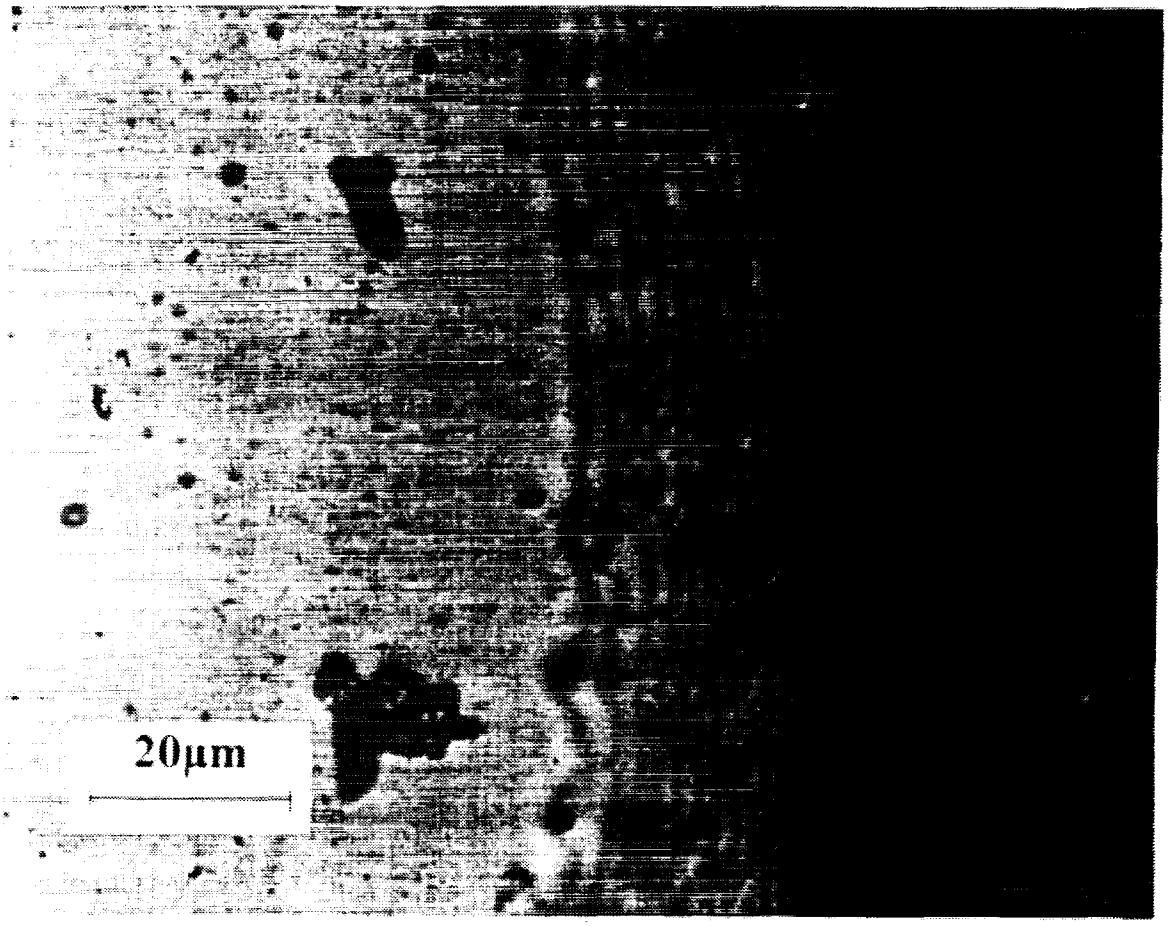

Boiling Evaporation of Ethanol in Region II

$\theta > 0$

15

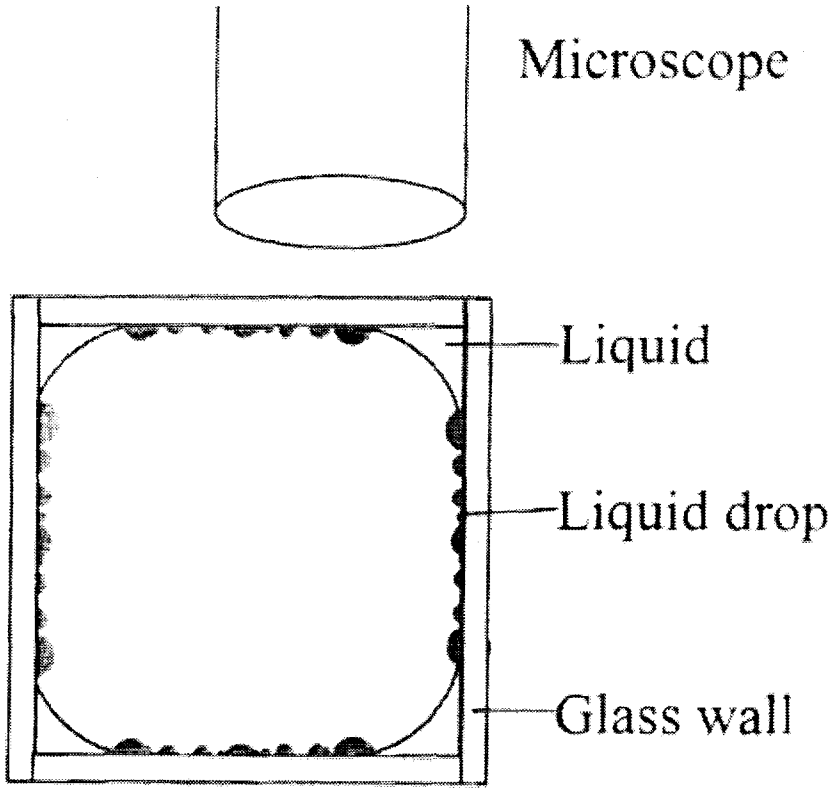

Dropwise Condensation in Region III

Ethanol, $\theta > 0$

16

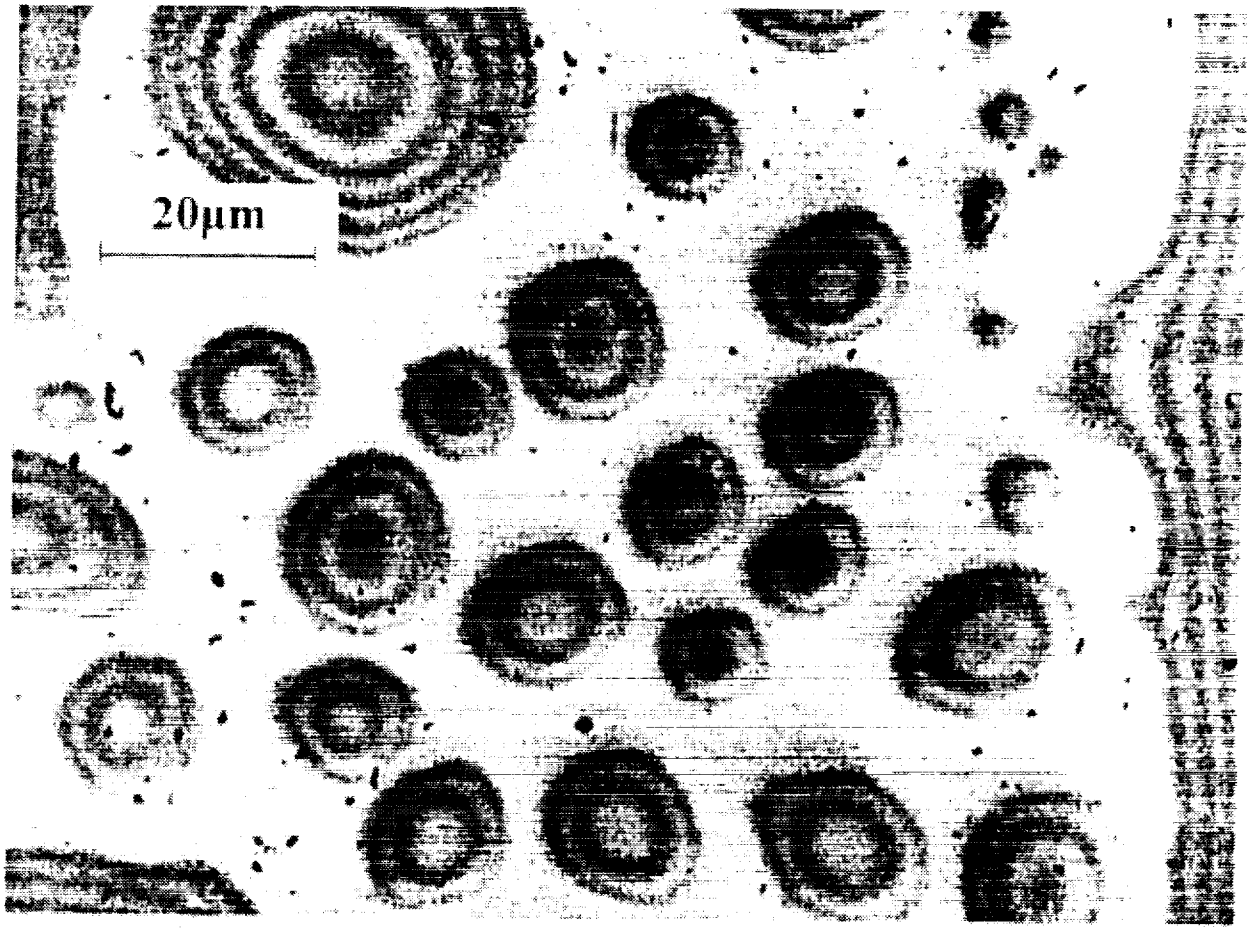

Dropwise Condensation of Ethanol (t = 0 sec)

17

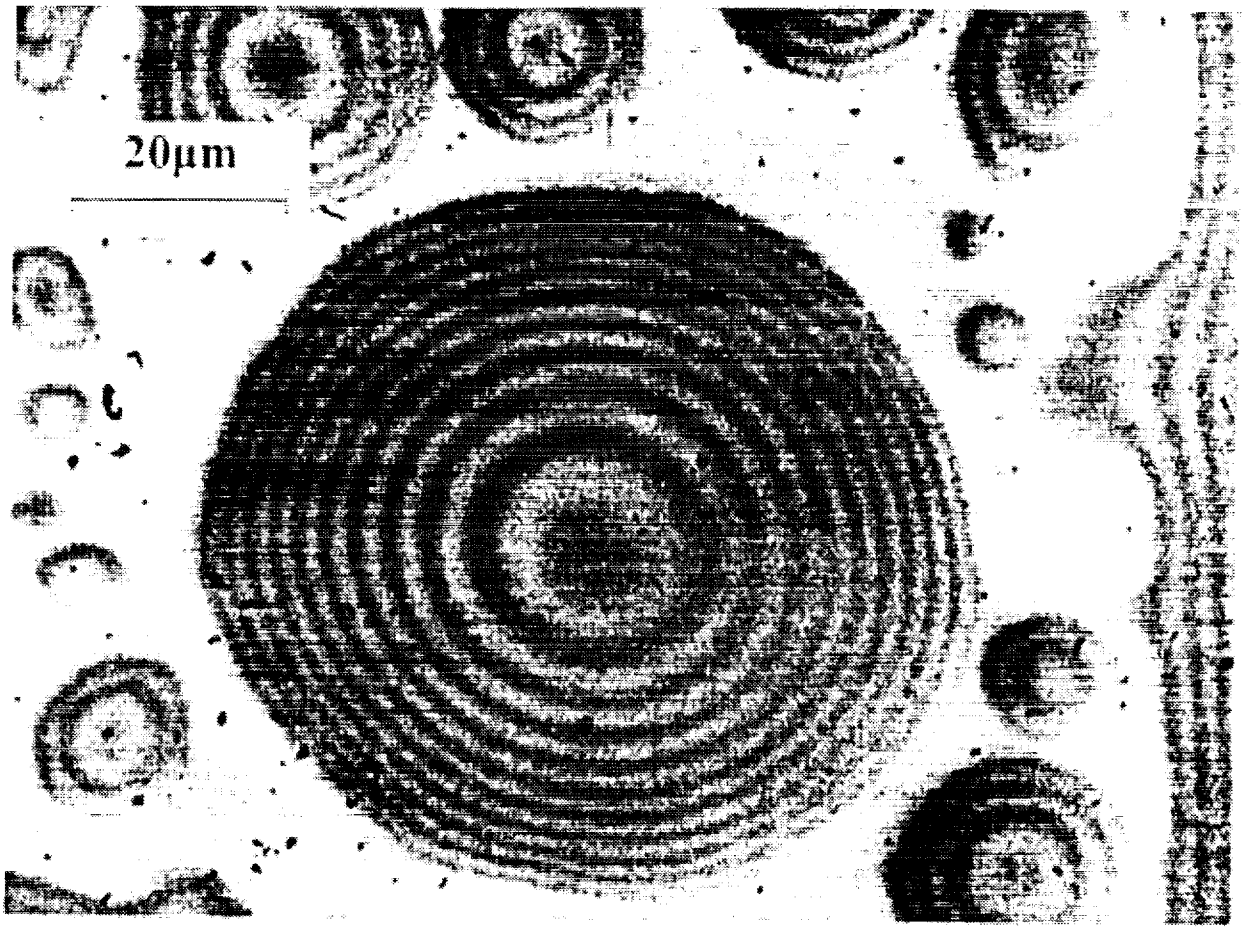

Dropwise Condensation of Ethanol (t = 4 sec)

18

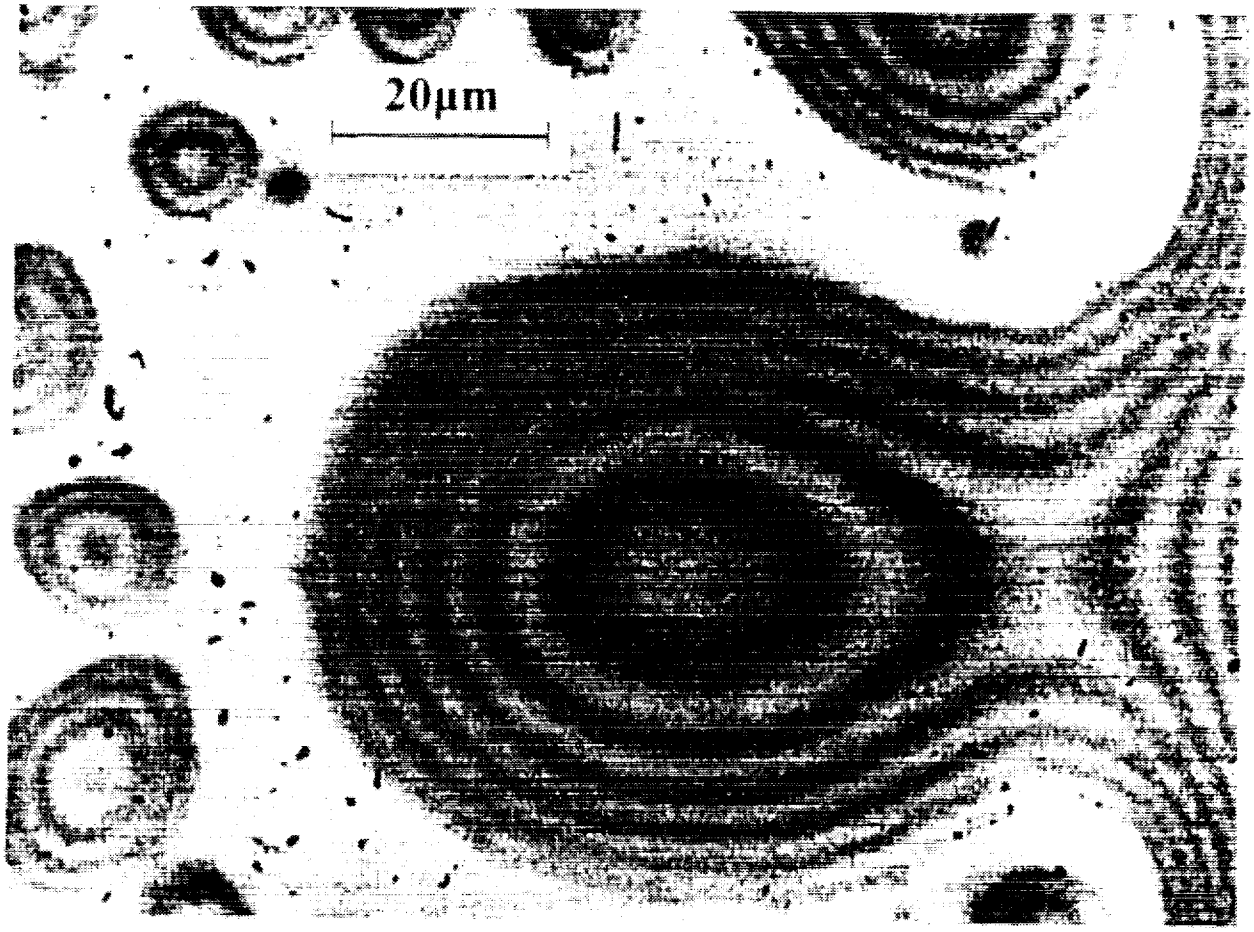

Dropwise Condensation of Ethanol (t = 5 sec)

19

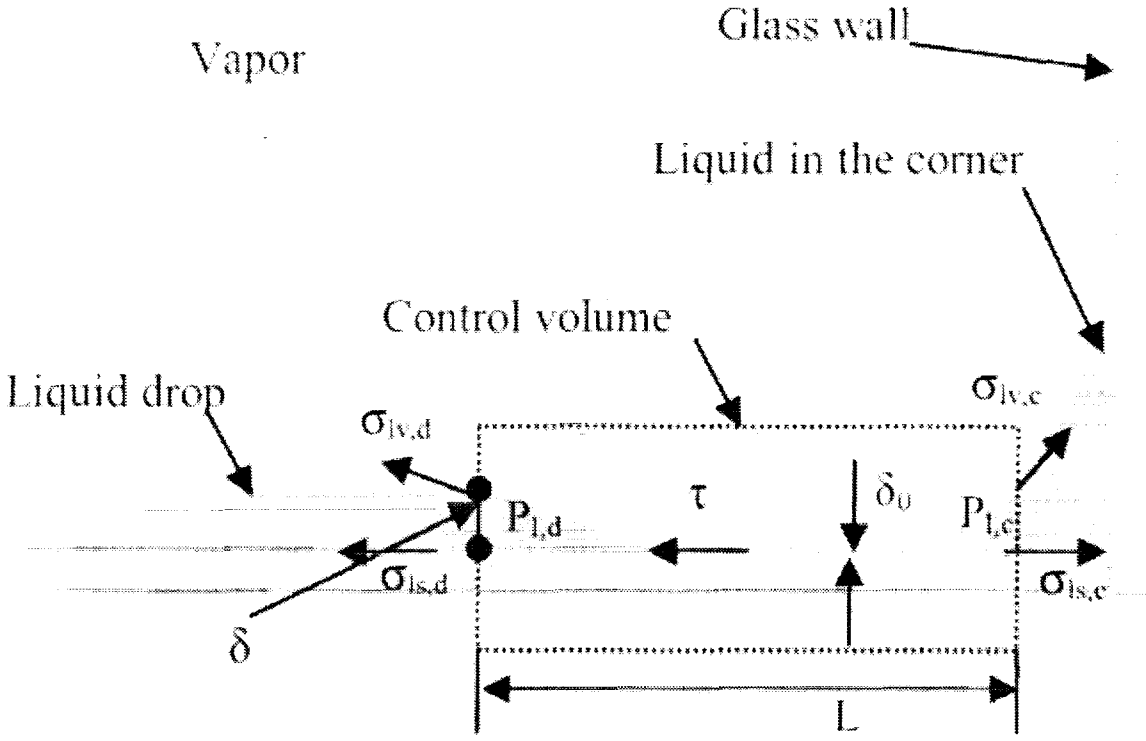

Macroscopic Force Balance

$$\frac{\tau L}{\sigma} = (-\cos\theta_d + \cos\theta_e) + \delta(K_d + K_e)$$

20

Temperature difference, θ, between the outside surface of the CVB cell and the room, vs. the axial distance, x, for the cell operating as a CVB heat exchanger and as a dry evacuated cell.

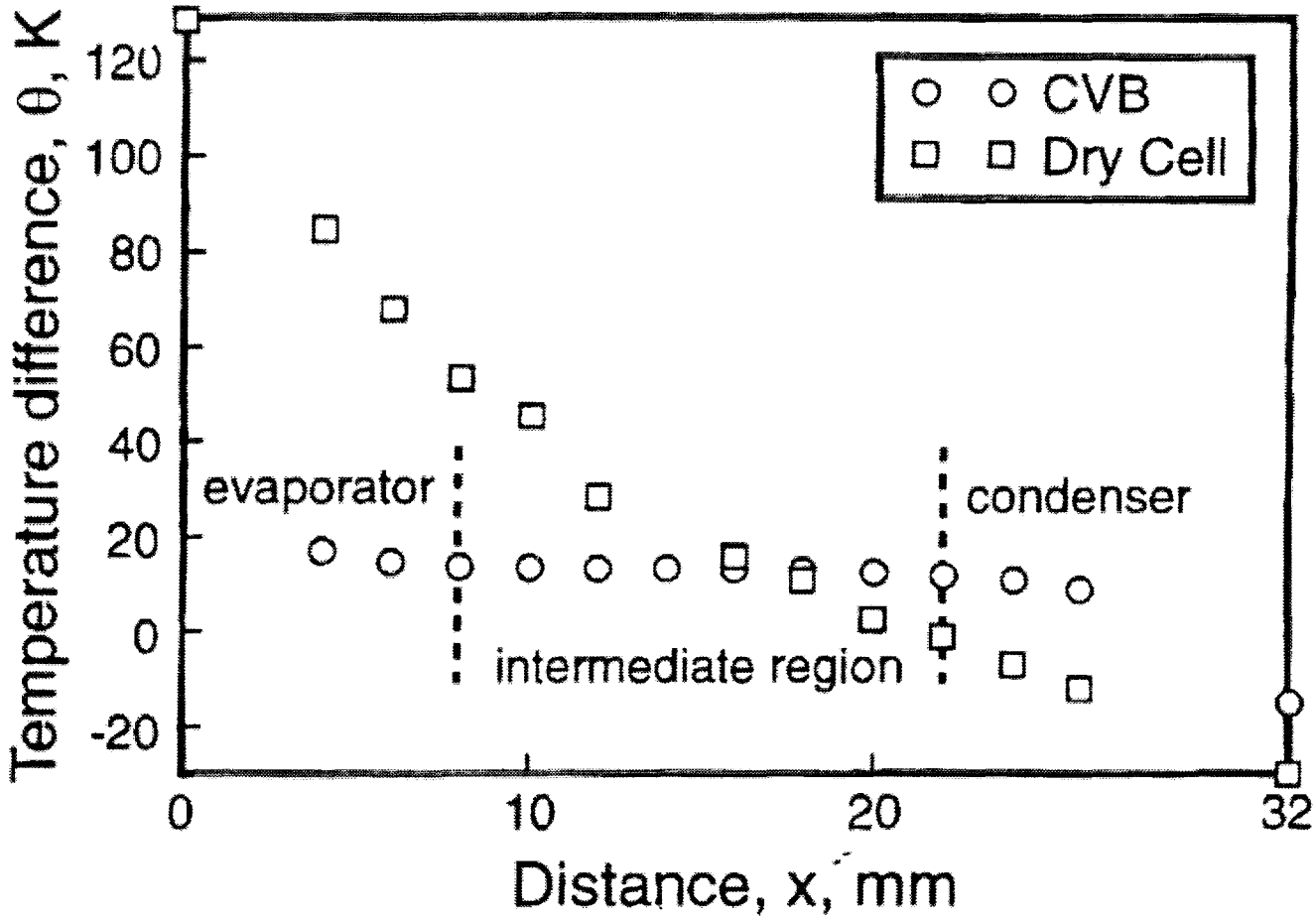

DRY CELL FOLLOWS SIMPLE FIN MODEL

CVB HAS ENHANCED CONDUCTION IN THE INTERMEDIATE REGION

21

Corner radius of curvature profiles obtained using the IAI for both the inclined cell operating as a CVB heat exchanger and at equilibrium.

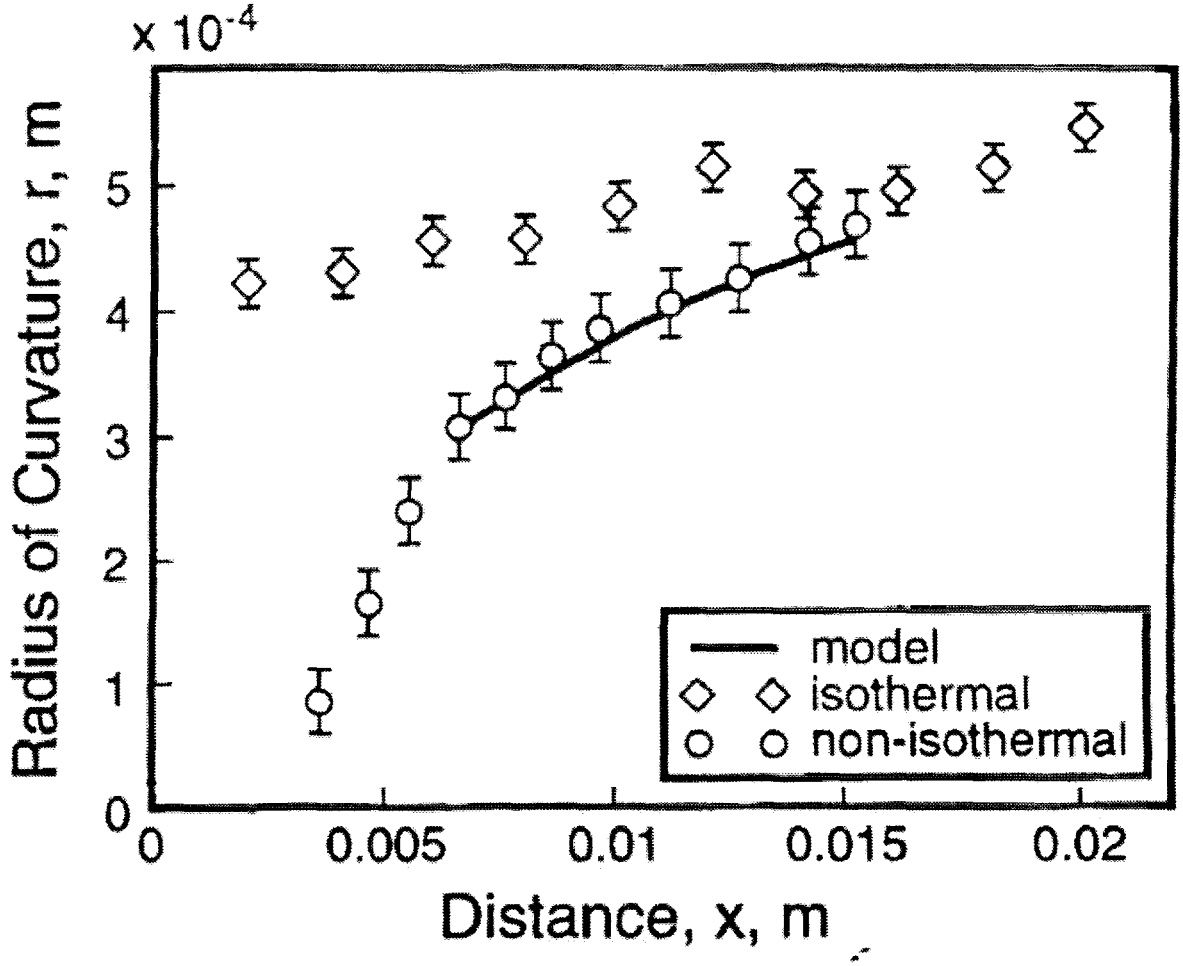

MOMENTUM MODEL CONFIRMS RADIUS OF CURVATURE DATA

22

CONCLUSIONS

GROUND BASED EXPERIMENTS USING AN AXISYMMETRIC VERTICAL CVB HEAT EXCHANGER WITH WETTING AND PARTIALLY WETTING FLUIDS ARE IN PROGRESS.

EFFECTIVE EXPERIMENTAL AND THEORETICAL TECHNIQUES TO DETERMINE THE CHARACTERISTICS OF FLUID FLOW AND HEAT TRANSFER IN A CONSTRAINED VAPOR BUBBLE HEAT EXCHANGER WERE DEVELOPED.

A FLIGHT EXPERIMENT IS PLANNED FOR 2004

23

A MECHANISTIC STUDY OF NUCLEATE BOILING HEAT TRANSFER UNDER MICROGRAVITY CONDITIONS

V.K. Dhir[1] and M.M. Hasan[2]

[1]University of California Los Angeles, Department of Mechanical and Aerospace Engineering, Los Angeles, CA 90095, U.S.A , e-mail: vdhir@seas.ucla.edu

[2]NASA Glenn Research Center, Microgravity Division, Cleveland, OH 44135, USA

ABSTRACT

Experimental studies of growth and detachment processes of a single bubble and multiple bubbles formed on a heated surface have been conducted in the parabola flights of KC-135 aircraft. Distilled water and PF5060 were used as the test liquids. A micro-fabricated test surface was designed and built. Artificial cavities of diameters 10 μm, 7 μm and 4 μm were made on a thin polished Silicon wafer that was electrically heated by a number of small heating elements on the back side in order to control the surface superheat.

Bubble growth period, bubble size and shape from nucleation to departure were measured under subcooled and saturation conditions. Significantly larger bubble departure diameters and bubble growth periods than those at earth normal gravity were observed. Bubble departure diameters as large as 20 mm for water and 6 mm for PF5060 were observed as opposed to about 3 mm for water and less than 1 mm for PF5060 at earth normal gravity respectively. It is found that the bubble departure diameter can be approximately related to the gravity level through the relation $D_d \propto 1/\sqrt{g}$. For water, the effect of wall superheat and liquid subcooling on bubble departure diameter is found to be small. The growth periods are found to be very sensitive to liquid subcooling at a given wall superheat. However, the preliminary results of single bubble dynamics using PF5060 showed that the departure diameter increases when wall superheat is elevated at the

same gravity and subcooling. Growth period of single bubbles in water has been found to vary as $t_g \propto g^{-0.93}$.

For water, when the magnitude of horizontal gravitational components was comparable to that of gravity normal to the surface, single bubbles slid along the heater surface and departed with smaller diameter at the same gravity level in the direction normal to the surface. For PF5060, even a very small horizontal gravitational component caused the sliding of bubble along the surface.

The numerical simulation has been carried out by solving under the condition of axi-symmetry, the mass, momentum, and energy equations for the vapor and the liquid phases. In the model the contribution of micro-layer has been included and instantaneous shape of the evolving vapor-liquid interface is determined from the analysis. Consistent with the experimental results, it is found that effect of reduced gravity is to stretch the growth period and bubble diameter It is found that effect of reduced gravity is to stretch the growth period and bubble diameter at departure. The numerical simulations are in good agreement with the experimental data for both the departure diameters and the growth periods.

In the study on dynamics of multiple bubbles, horizontal merger of 2, 3 4, and 5 bubbles was observed. It is found that after merger of 2 and 3 bubbles the equivalent diameter of the detached bubble is smaller than that of a single bubble departing at the same gravity level. During and after bubble merger, liquid still fills the space between the vapor stems so as to form mushroom type bubbles.

The experimental and numerical studies conducted so far have brought us a step closer to prediction of nucleate boiling heat fluxes under low gravity conditions. Preparations for a space flight are continuing.

NASA/CP—2000-210470

A MECHANICTIC STUDY OF NUCLEATE BOILING HEAT TRANSFER UNDER MICROGRAVITY CONDITIONS

V. K. Dhir

University of California , Los Angeles
Mechanical and Aerospace Engineering Department
Los Angeles , CA 90095

M.M. Hasan

NASA Glenn Research Center, Lewis Field
Cleveland , OH 44135

Presented at the
FIFTH MICROGRAVITY FLUID PHYSICS AND TRANSPORT PHENOMENA CONFERENCE
August 9-11, 2000, Cleveland, Ohio

NASA/CP—2000-210470

OBJECTIVES

- Mechanistic understanding of low gravity nucleate pool boiling process through numerical simulations and experiments.
- Investigation of the scaling of the effect of gravity on the growth and departure of single bubble from a designed nucleation site.
- Effect of liquid subcooling and wall superheat on bubble growth and departure at low gravity.
- Understanding of horizontal merger process of multiple bubbles at low gravity.
- Validation of the predictive model of nucleate boiling under low gravity conditions.

NUMERICAL SIMULATIONS

NUMERICAL SIMULATIONS

Prediction of Nucleate Boiling Heat Transfer

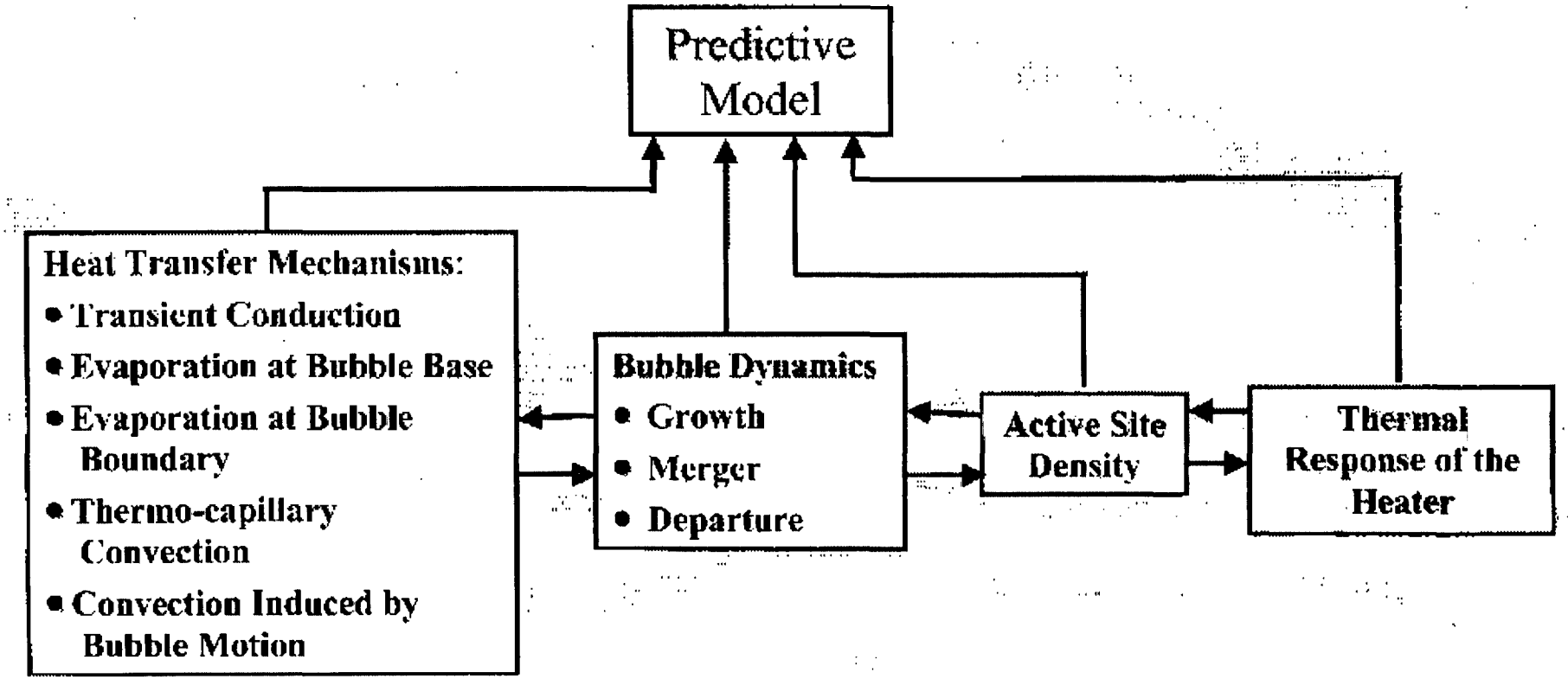

NUMERICAL SIMULATIONS (Cont'd)

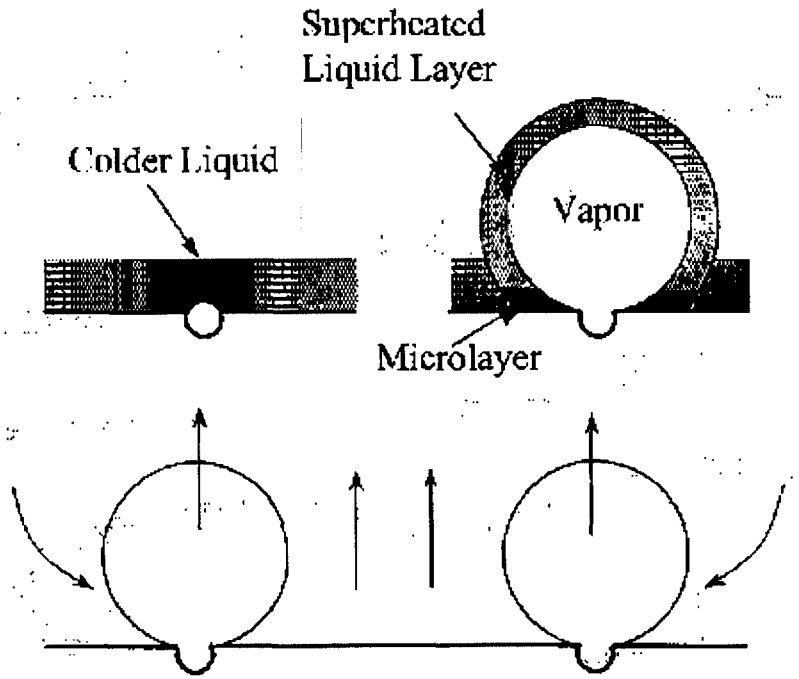

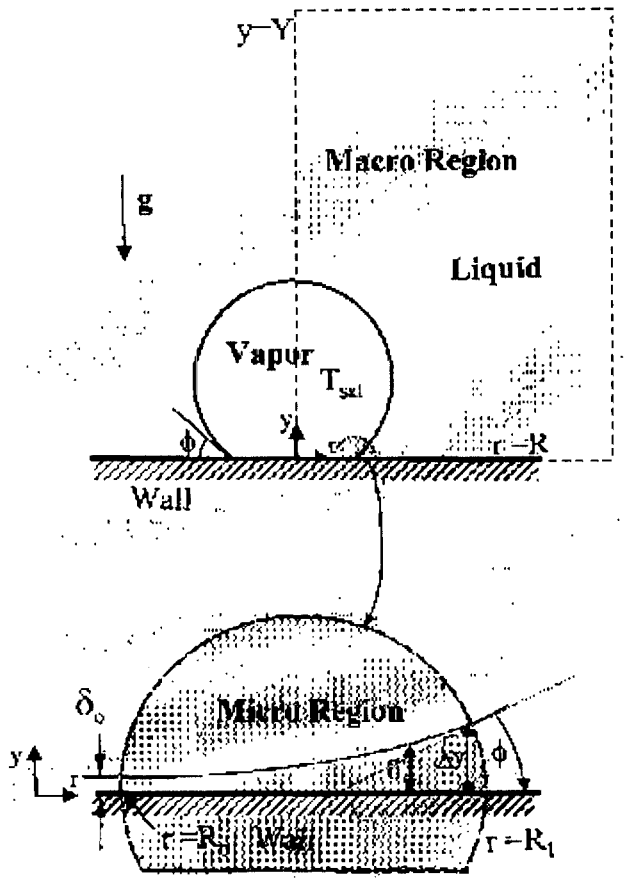

NUMERICAL SIMULATIONS (Cont'd)

Predicted Bubble Growth at Different Gravity Levels

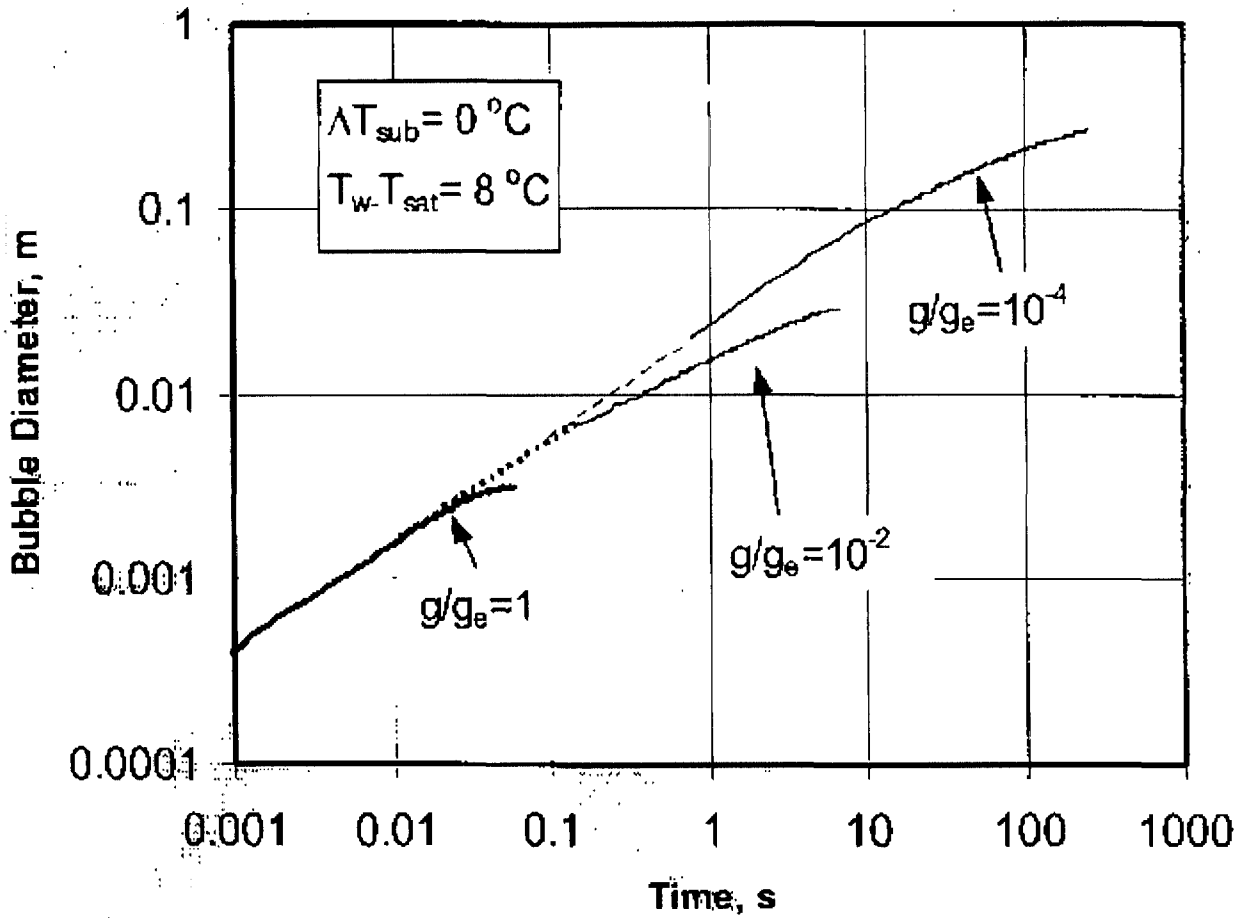

NUMERICAL SIMULATION (Cont'd)

Numerical Simulations - Scaling with Respect to Gravity

Gravity Level	Bubble Departure Diameter (mm)	Bubble Growth Period (sec.)
$1g_e$	2.8	0.056
$10^{-2}g_e$	27	4.5
$10^{-4}g_e$	265	257

Liquid: Saturated Water; System Pressure: 1atm, $\varphi = 50^{\circ}$, $T_w - T_{sat} = 7°C$

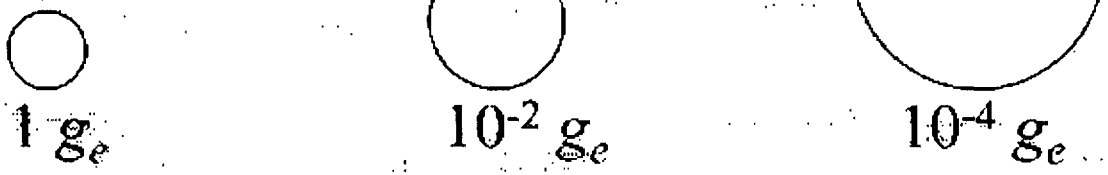

$1\ g_e$ $\quad 10^{-2}\ g_e$ $\quad 10^{-4}\ g_e$

$$D_d \propto g^{-1/2}$$

$$t_g \propto g^{-0.93}$$

EXPERIMENTS

EXPERIMENTS

- **Closed Test Chamber:**
  Feedback control of system pressure, liquid subcooling and superheat of heater surface.

- **Measurements Using Thermocouple Rakes:**
  Liquid temperature near heater surface (thermal boundary layer) and bulk liquid temperature.

- **High Speed Video Cameras:**
  Record the boiling process at large magnification and in two orthogonal directions.

- **Low Gravity Condition during KC-135 Flight:** $g_z \approx \pm 0.04\, g_e$
  in the direction, z, normal to the heater surface with the accidental increase up to 0.065 g_e.

- **Three-Component Accelerometer.**

EXPERIMENTS

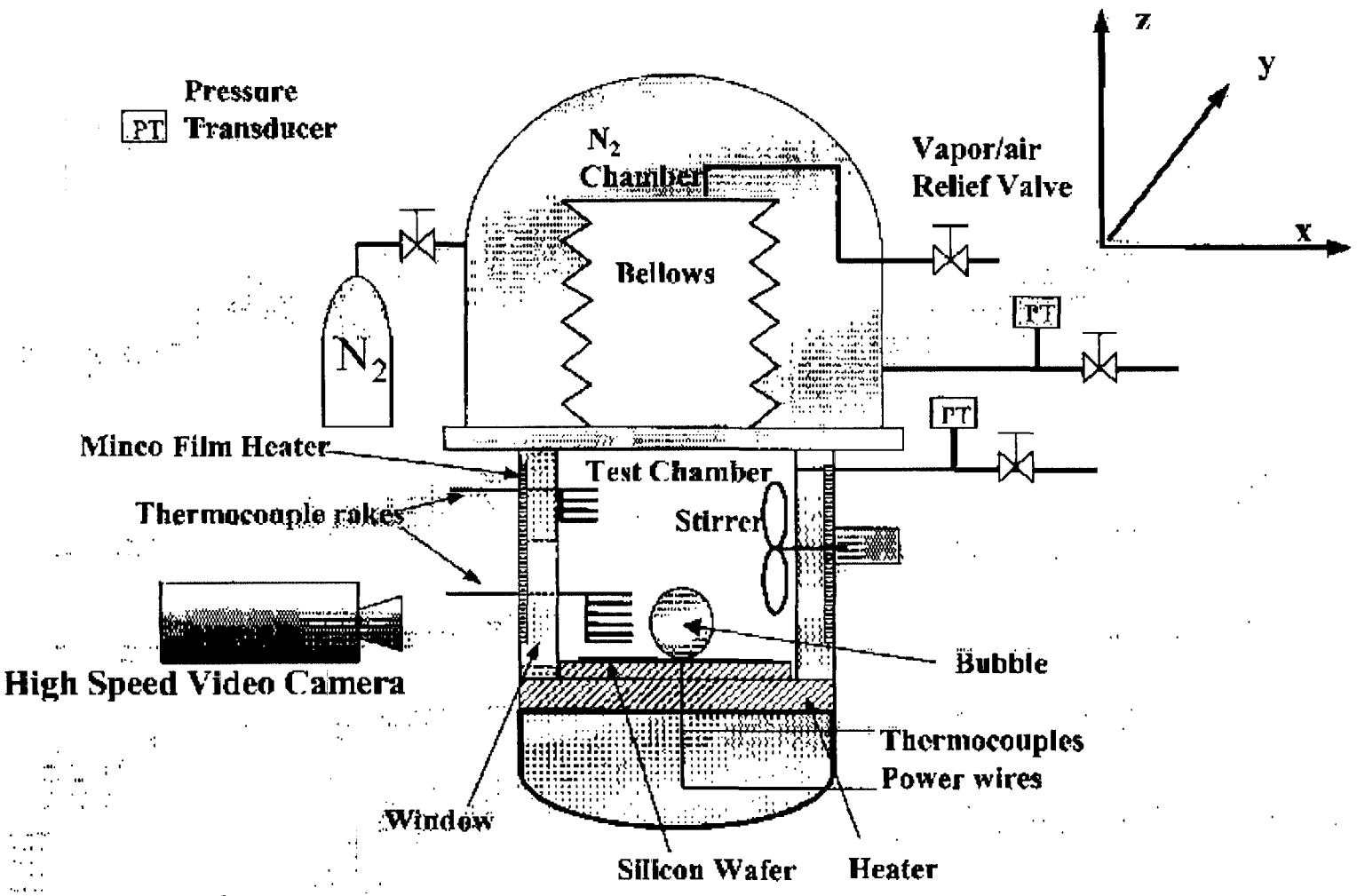

Schematic of Experimental Set-up

EXPERIMENTS (Cont'd)

- **Heater Surface:**
  Polished Silicon wafer (roughness < 5 Å).

- **Nucleation Sites:**
  5 Cavities of 100 μm in depth and 10 μm (one), 7 μm (two), 4 μm (two) in diameter at a spacing of 7 mm made in the wafer center via the Deep Reactive Ion Etching Technique.

- **Heating Elements:**
  Foil-like strain gages bonded at the back of silicon wafer and grouped in different regions for separate control of superheats.

- **Nucleation Activation:**
  Only at the desired cavities before take-off of KC-135.

- **Overall Wall Superheat and Bulk Liquid Subcooling:**
  Set to specified values prior to each parabola (low gravity period).

EXPERIMENTS (Cont'd)

Configuration of Heater with Designed Nucleation Sites

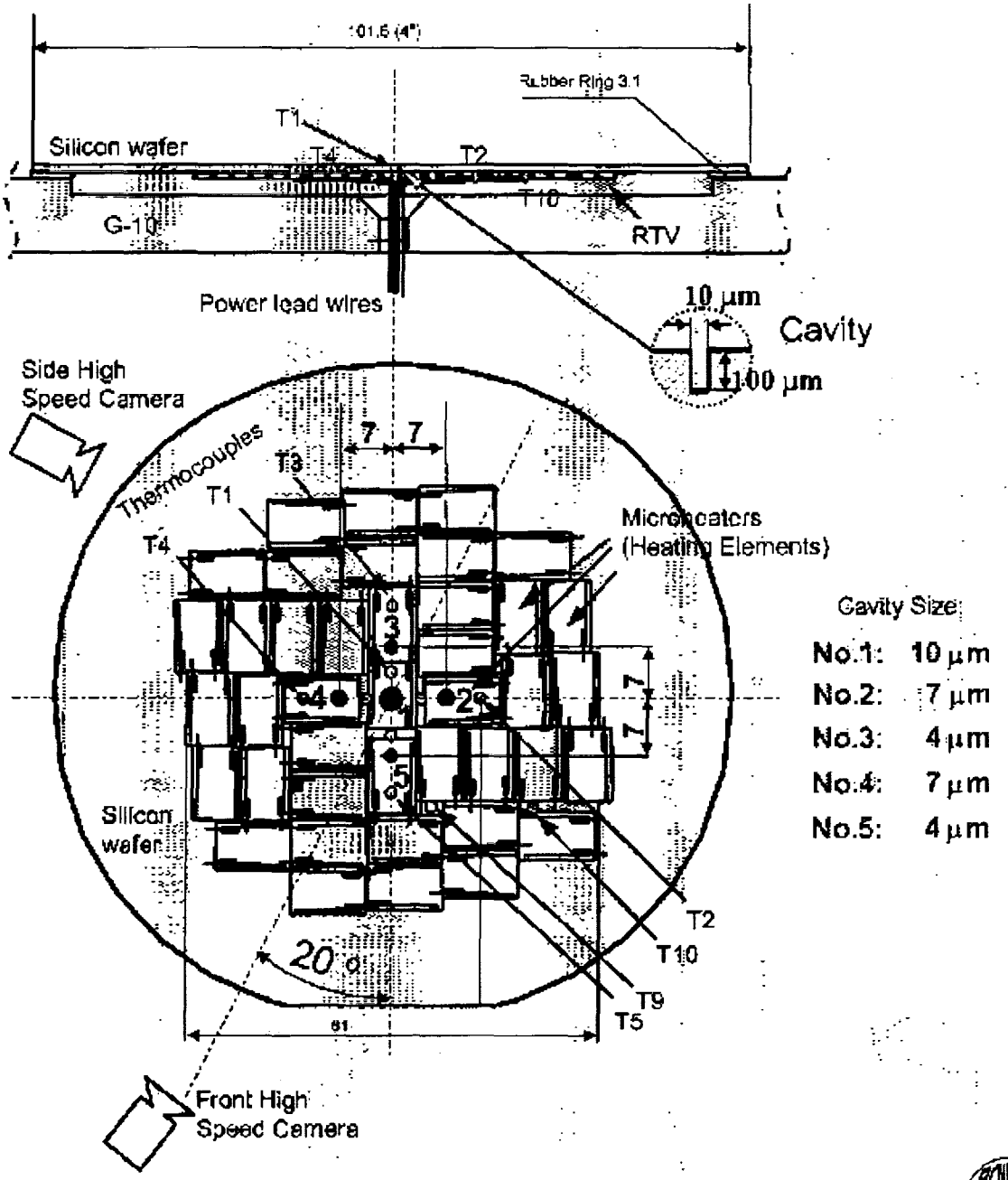

Cavity Size:

No.1: 10 μm
No.2: 7 μm
No.3: 4 μm
No.4: 7 μm
No.5: 4 μm

EXPERIMENTS (Cont'd)

Typical Gravity Level During Parabola Flight

(Run No.389, Oct.6, 1998)

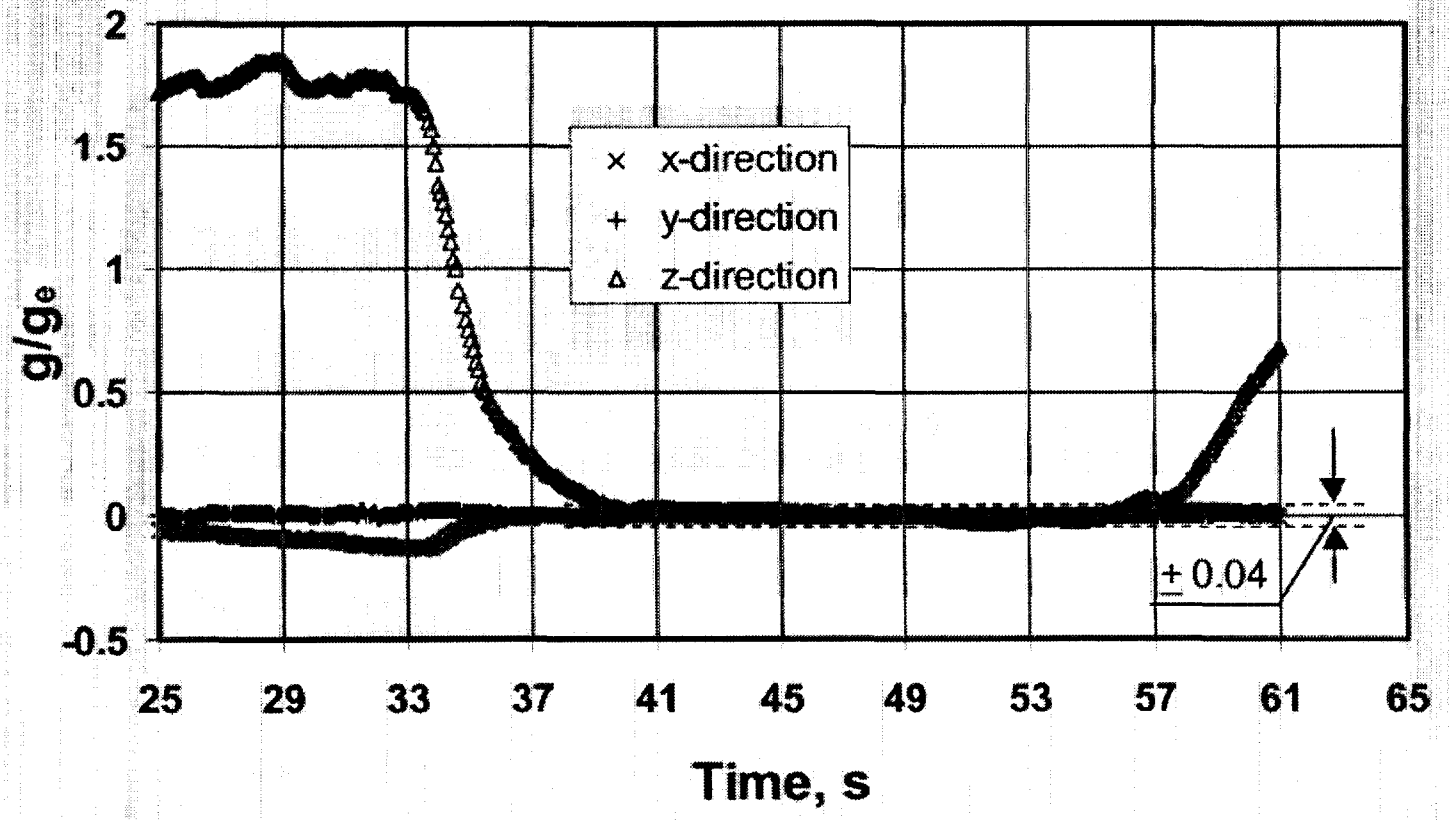

EXPERIMENTAL RESULTS

EXPERIMENTAL RESULTS (Cont'd)

-- Single Bubble at Low Gravity in KC-135

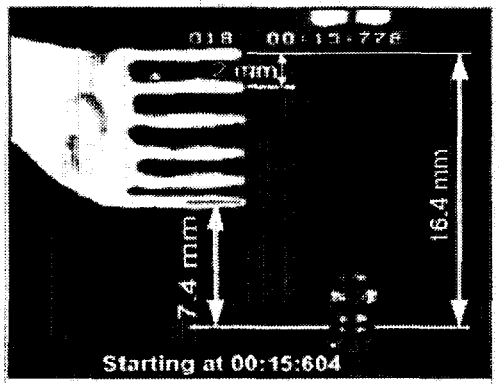

a) t=0.17 s

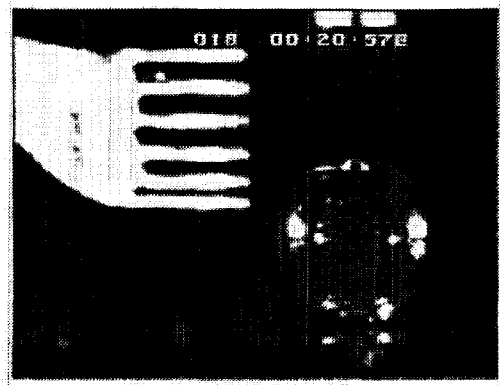

b) t=4.97 s

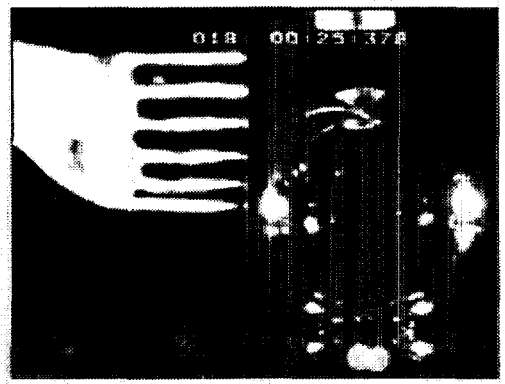

c) t=9.77 s (maximal base)

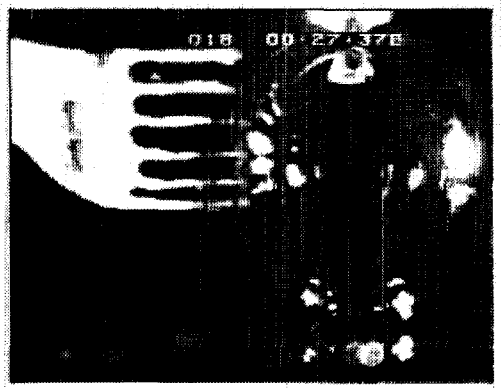

d) t=11.77 s

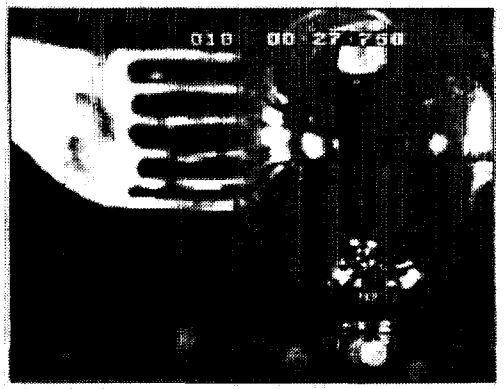

e) t=12.15 (departing)

Pictures of Single Bubble During a Growth-Departure Cycle,
ΔT_{sub}=0.3 °C, T_w-T_{sat}=4.2°C, $g_z \approx 0.02\ g_e$

EXPERIMENTAL RESULTS (Cont'd)

-- Single Bubble at Low Gravity in KC-135

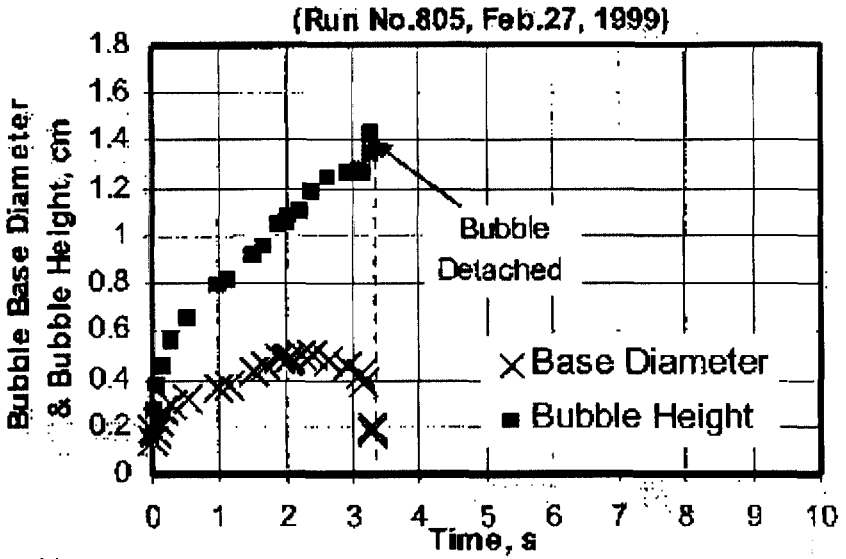

ΔT_{sub}=0.0 °C, T_w-T_{sat}=5.5 °C

$g_z \approx 0.040\ g_e$

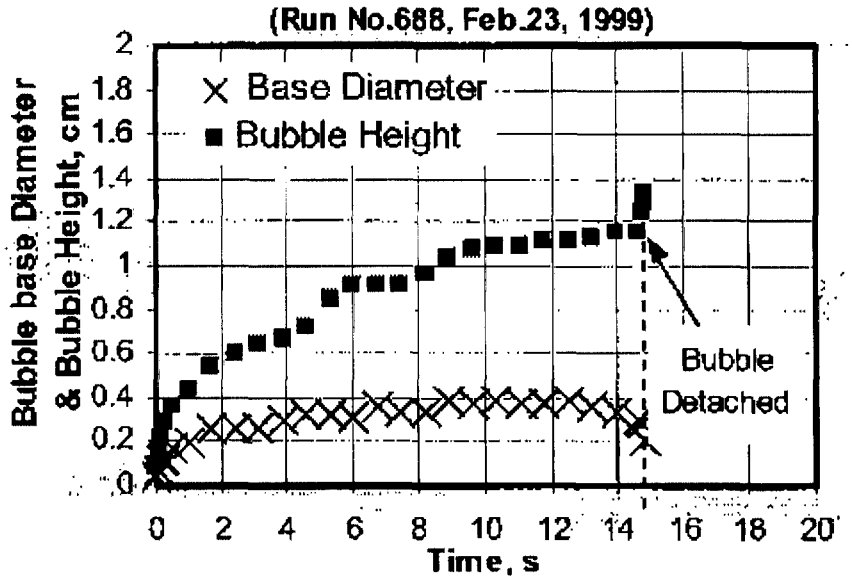

ΔT_{sub}=0.2 °C, T_w-T_{sat}=2.5 °C

$g_z \approx 0.045\ g_e$

Bubble Height and Base Diameter as Function of Time

EXPERIMENTAL RESULTS (Cont'd)

-- Single Bubble at Low Gravity in KC-135

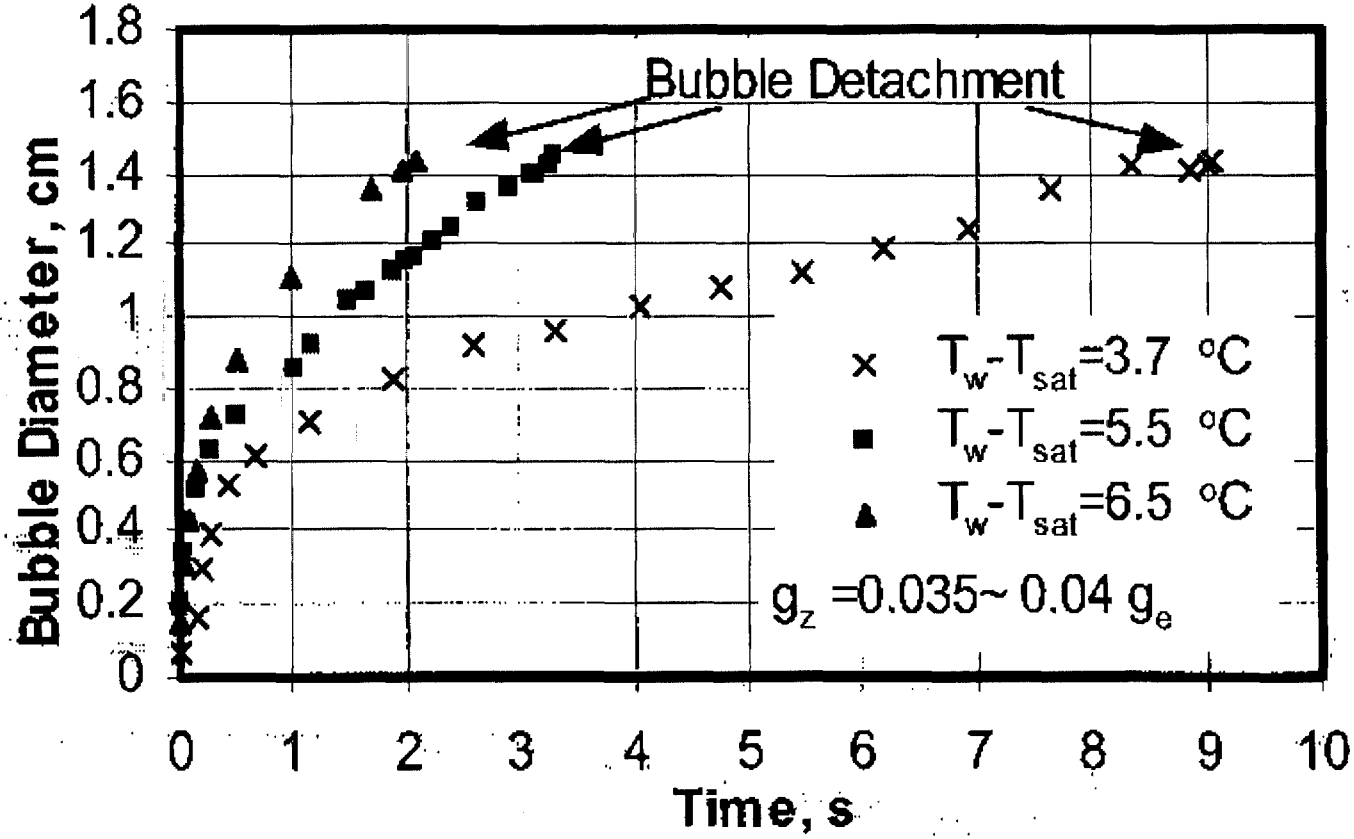

Effect of Wall Superheat on Bubble Growth in Saturated Water

EXPERIMENTAL RESULTS (Cont'd)

-- Single Bubble at Low Gravity in KC-135

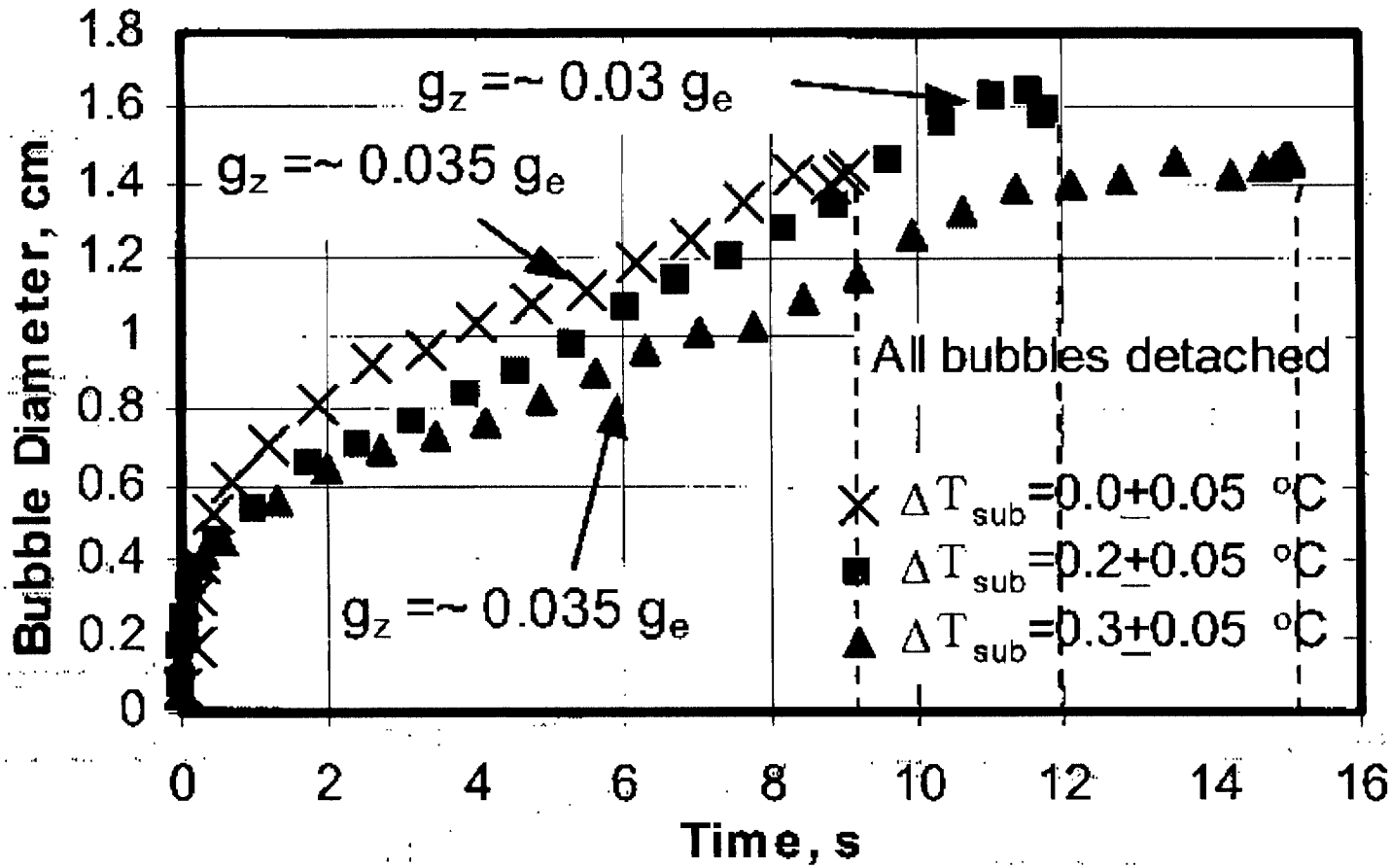

Effect of Liquid Subcooling on Bubble Growth for a Wall Superheat T_w-T_{sat}=3.5 °C

EXPERIMENTAL RESULTS

-- Horizontal Merger of Two Bubbles at Low Gravity

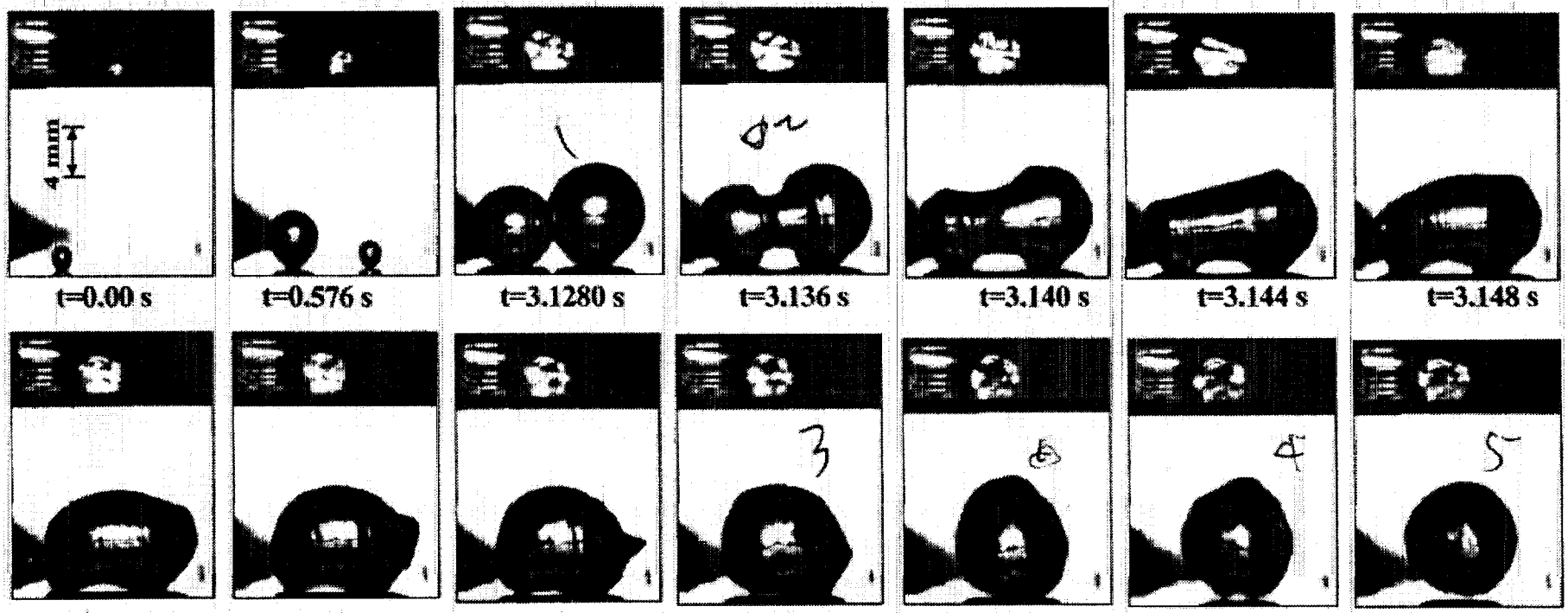

Two Bubble Merger at ΔT_{sub}=3.0 °C, T_w-T_{sat}=5.0°C, g_z=0.0033 g_e, g_x=0.0060 g_e, g_y=-0.0009 g_e

EXPERIMENTAL RESULTS (Cont'd)

-- Horizontal Merger of Three Bubbles at Low Gravity

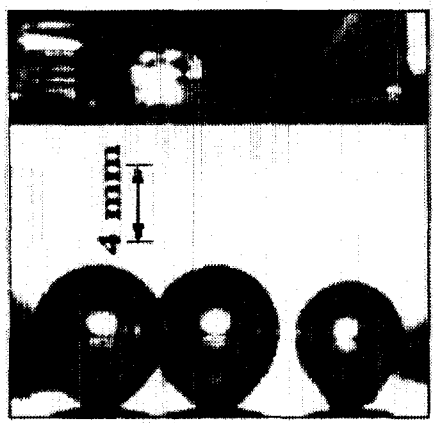

t=0.000 s

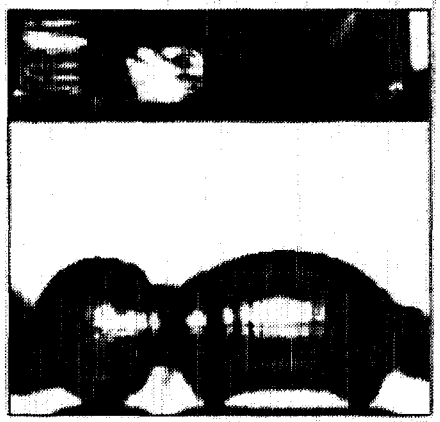

t=0.096 s

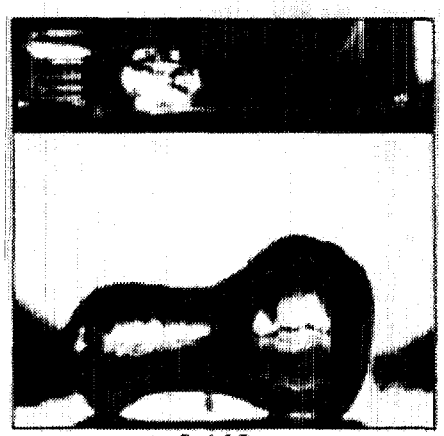

t=0.112 s

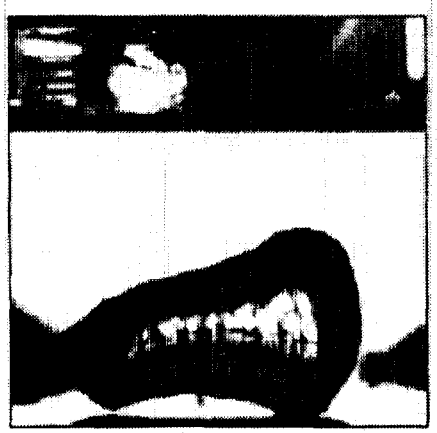

t=0.120 s

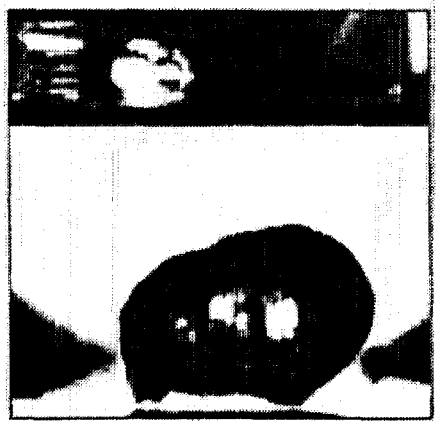

t=0.128 s

Three Bubble Merger at ΔT_{sub}=2.0 °C, T_w-T_{sat}=5.5°C, g_z=0.008 g_e, g_x=0.003 g_e, g_y=~0.000 g_e

EXPERIMENTAL RESULTS (Cont'd)

-- Horizontal Merger of Two Bubbles at Low Gravity

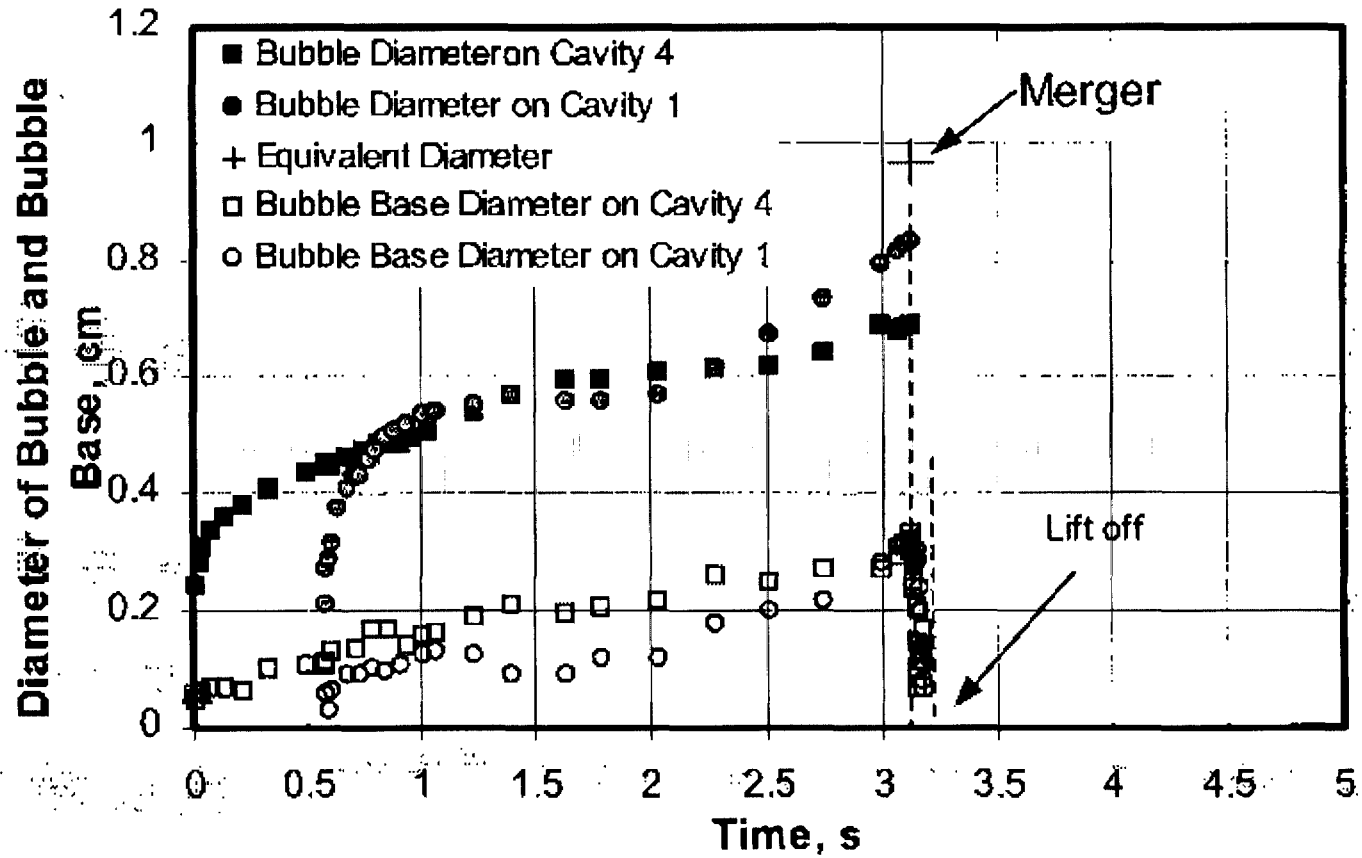

Diameter of Bubbles and Bubble Bases during Two Bubble Merger at ΔT_{sub}=3.0 °C, T_w-T_{sat}=5.0°C, g_z=0.0033 g_e, g_x=0.0060 g_e, g_y=-0.0009 g_e

COMPARISON OF NUMERICAL SIMULATIONS WITH EXPERIMETAL RESULTS

Comparison of Numerical Simulation Results with Data in Subcooled Water
-- at Low Gravity

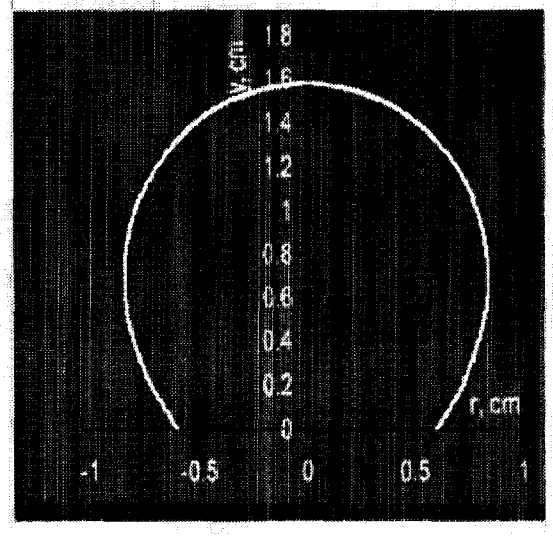

Numerical

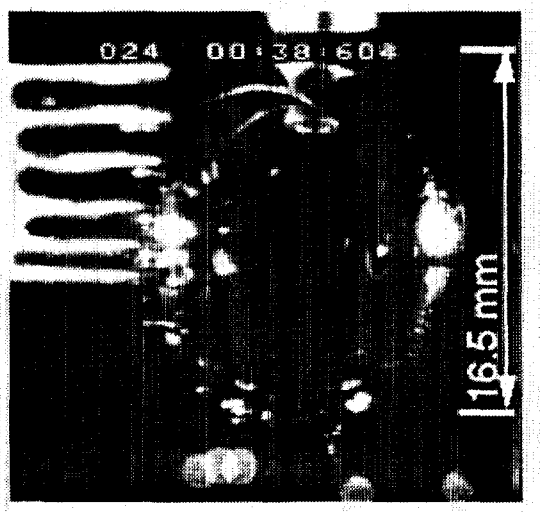

Experimental

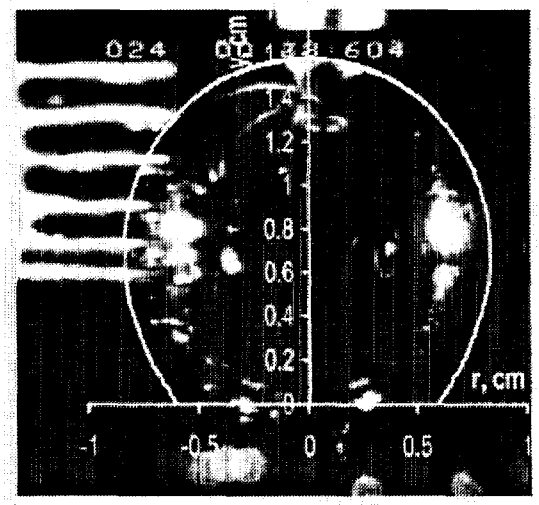

Comparison

$g = 0.02\ g_e$, $T_w - T_s = 3.8\ ^oC$, $\Delta T_{sub} = 0.4\ ^oC$

Comparison of Numerical Simulation Results with Data in Subcooled Water (Cont'd) -- at Low Gravity

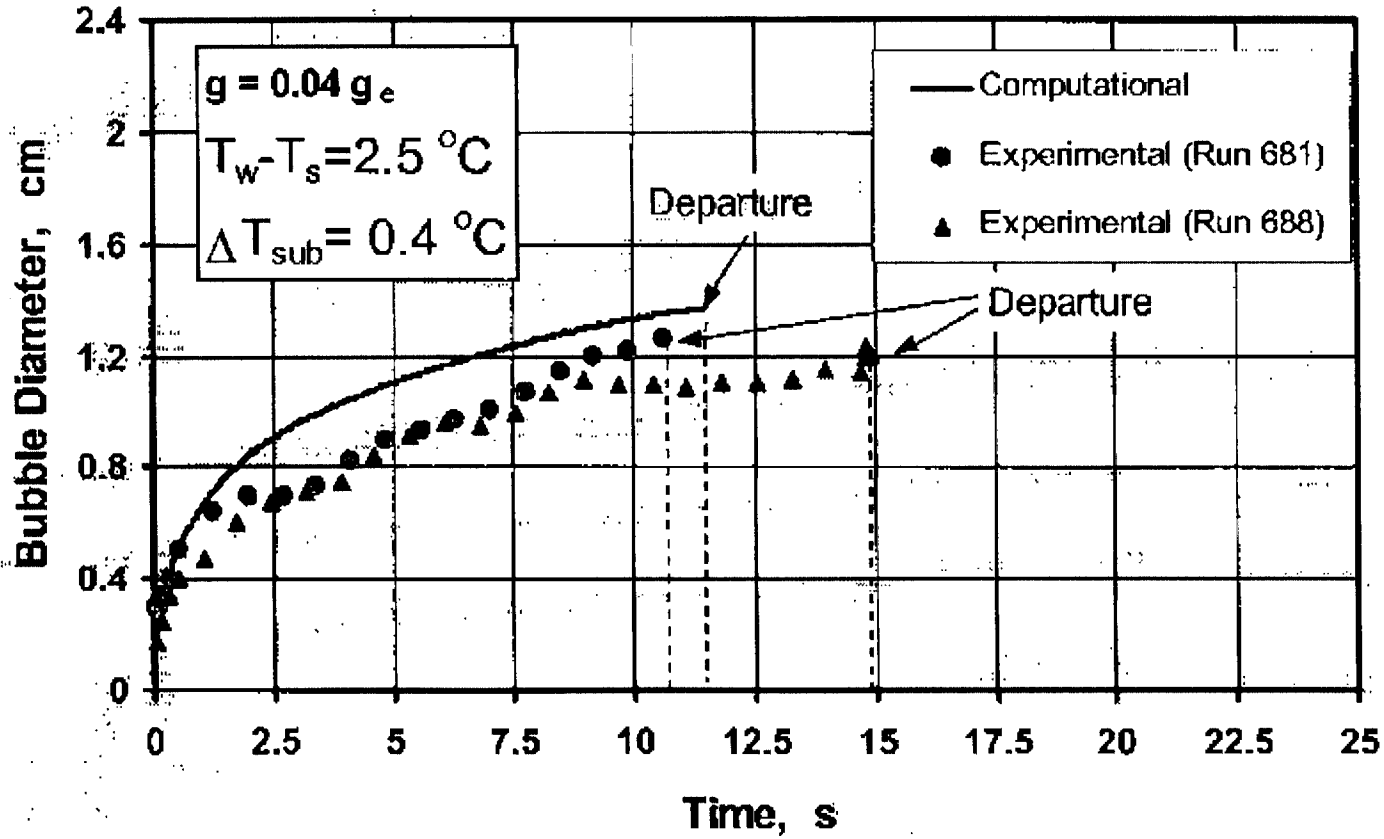

SCALING OF EFFECT OF GRAVITY ON SINGLE BUBBLE DEPARTURE (Cont'd)

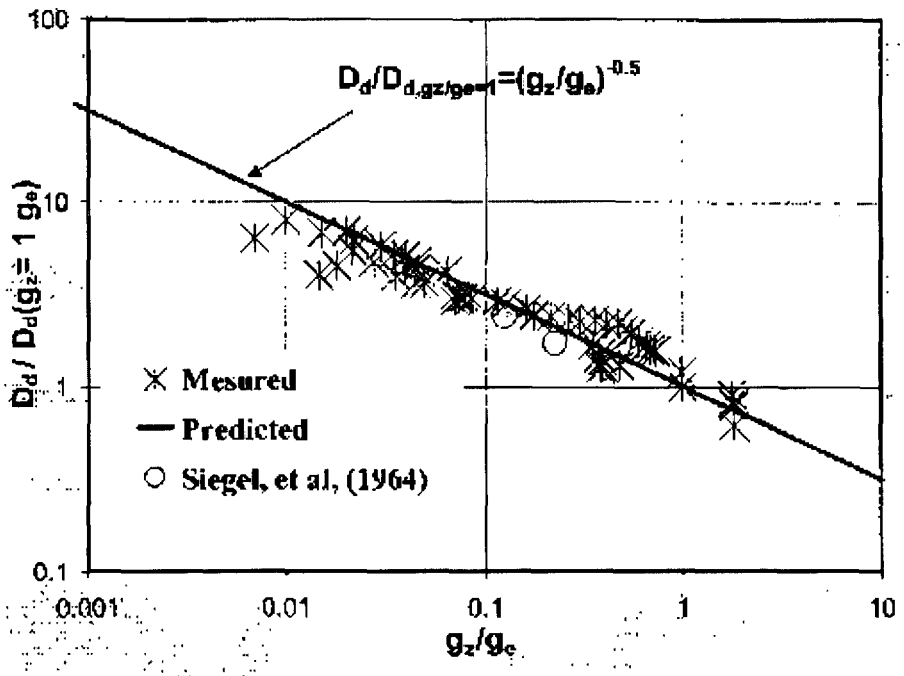

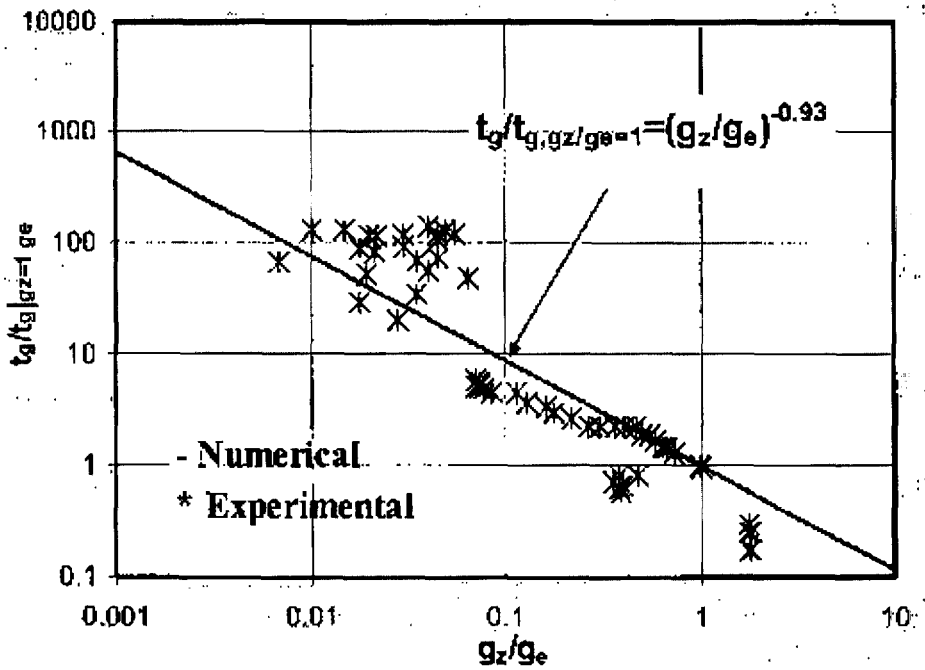

EXPERIMENTAL RESULTS (Cont'd)

-- Horizontal Merger of 2 and 3 Bubbles at Low Gravity

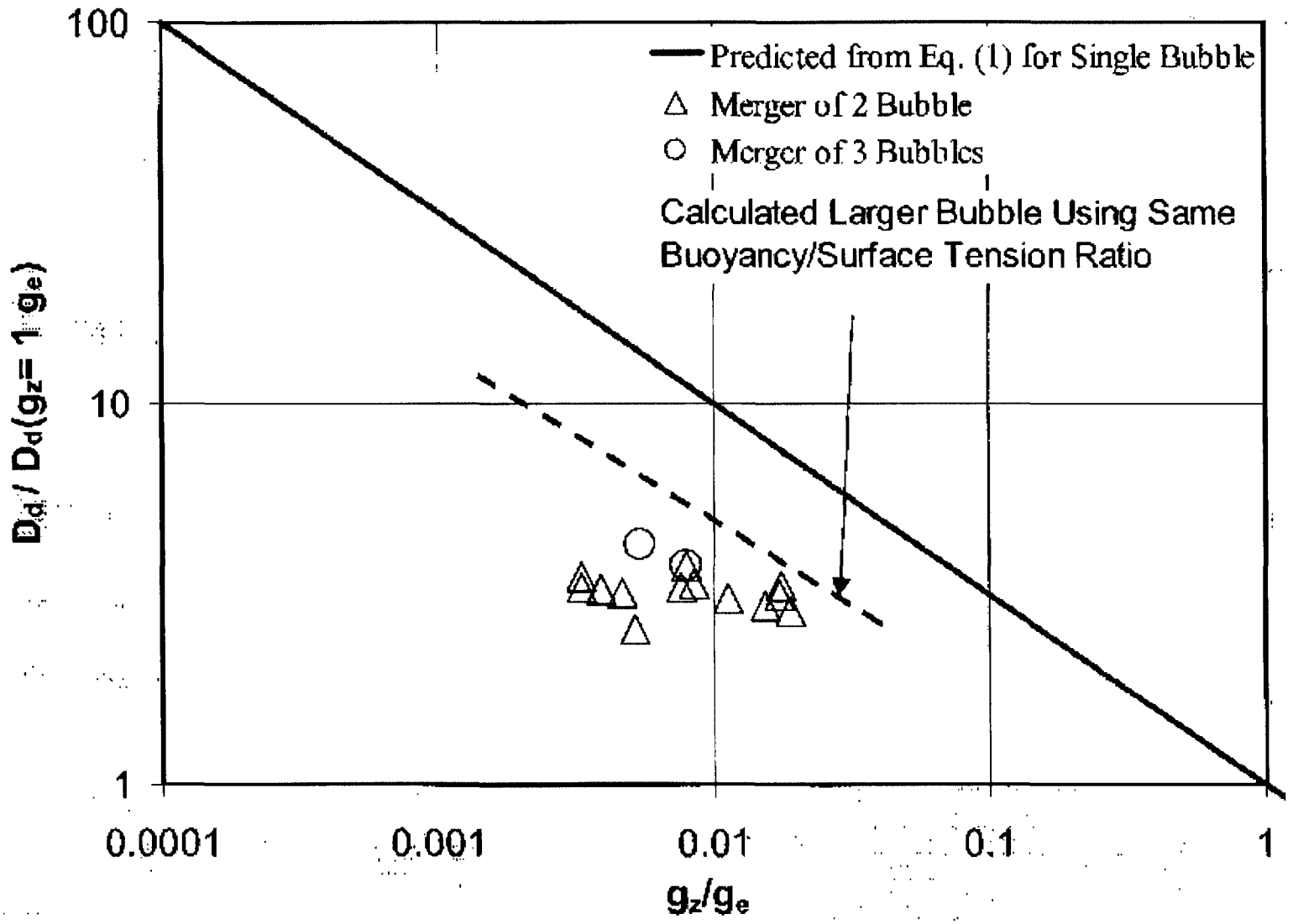

Comparison of Numerical Simulation Results (3-D) with Experimental Data

Experimental

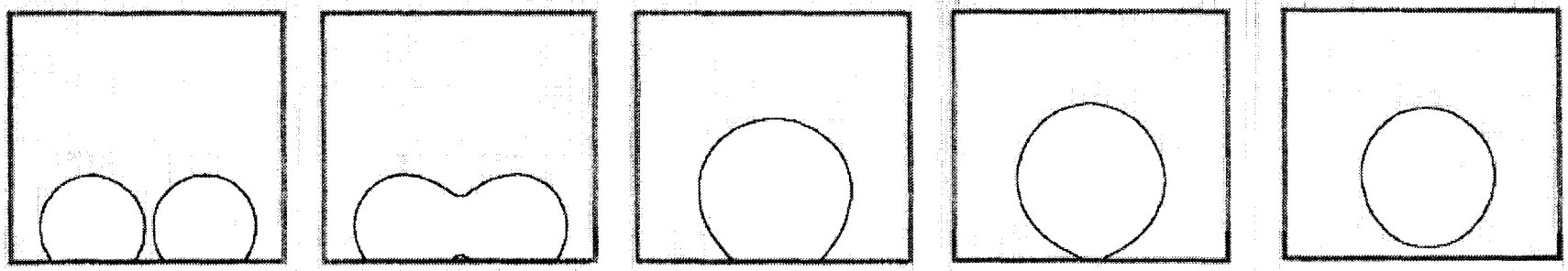

Numerical

NASA/CP—2000-210470

CONCLUDING REMARKS

- Well defined and controllable nucleation sites were obtained by micro-fabricating cavities on the polished Silicon wafer.
- Complete boiling process of single bubble from nucleation inception to departure of bubble was observed on the designed surface at low gravity.
- Larger bubble departure diameters (> ~20 mm) and longer bubble growth periods than those at earth normal gravity were measured.
- The bubble departure diameters and growth periods scale as $D_d \propto g^{-1/2}$ and $t_g \propto g^{-0.93}$ respectively.
- Small subcooling in the liquid can lead to significantly prolonged bubble growth periods and reduced bubble growth rates.
- During bubble merger, mushroom type of bubbles attached to the heater surface via vapor stems were observed to form.
- The merger caused lift-off of the vapor mass from the surface in a smaller equivalent diameter than that of a single bubble at departure at the same gravity level.
- The liquid motion during merger and the resulting lift force probably played a role in early lift-off of the merged bubbles.

August 9, 2000

Session 1B
Complex Fluids I

Physics of Hard Spheres Experiment: Microscopy of Colloidal Particles

Z-D. Cheng, J. C. Ruiz, M. Megens, A. D. Hollingsworth, C. Harrison,
W. B. Russel and P. M. Chaikin
Depts of Physics and Chem. Eng. and Princeton Materials Institute, Princeton University

In preparation for the next phase of the Physics of Hard sphere experiment, an investigation of hard sphere nucleation and growth using a specially designed microscope on the space station, we have developed new colloidal particles, as well as some new techniques. The new colloidal systems are flourescently dyed, index and density matched spheres with screened and unscreened electrostatic interactions, as well as microlithographically prepared disks. Confocal imaging of the nucleation process shows dominant surface nucleation with an amorphous first layer and then well defined crystallite propagation into the bulk.

We have studied the nucleation and growth of colloidal crystals in the confined geometry of a 150 μ thick sample between slide and cover slip in a confocal microscope. The samples were PMMA-PHSA stabilized .956 μ spheres fluorescently labeled with fluorescene using a modification of the techniques developed in ref.1. The initially dyed and washed particles were found to be charged when suspended in the index and density matching solvent decalin-tetralin-cycloheptylbromide . Even in this highly non-polar solvent the coulomb interactions could be effectively screened using the organic salt Tin(II) 2-ethylhexanoate. The confocal images shown in figure 1 correspond to "slices" 1, 4 and 48 μ from the cover slip, for a sample with volume fraction 0.52, 60 minutes after homogenization. What is striking is the low density and amorphous character of the first layer, the crystallinity of the forth layer, and the mixed crystal-liquid character of the 50th layer. The crystallites have clearly nucleated on the surface but the layer closest to the surface is not crystalline. This indicates the two, not necessarily constructive, effects of the surface. One is the wettability, the other is the constraint on particle motion. The excluded volume interaction is repulsive depleting the layer closest to the wall and leaving it below the freezing transition. The next layer has a higher volume fraction but still has restricted motion in the direction perpendicular to the wall. This is where the crystal first nucleates. With confocal microscopy we can scan the volume of the cell with an area of 200x200 μ squared and a depth of 60 μ in a 5 minutes. We can then follow the growth of the crystal liquid front as it propagates into the bulk. The observed front growth goes from 1 μ /10minutes to 1μ /min as the volume fraction changes from .50 to .60.

In the coexistence region the nucleation proceeds incompletely leaving a metastable boundary between the crystal and liquid phases. In the figure we show the three dimensional structure of the crystallites in this situation. The crystal structure of each slice of the sample has been analyzed by an algorithm which locates the particles, finds the local crystal structure and the direction of the crystal axes and assigns the next layer to the same crystal if its orientation is within 5 degrees of the underlying layer. (There is no distinction made here for FCC vs HCP, the structures all conforming to RHCP). The crystals grow epitaxially from the substrate layer with the initial (2^{nd} layer) domain structure unannealed in the growth process. The stalagmite shape of the crystallites indicates the dendritic growth instability.

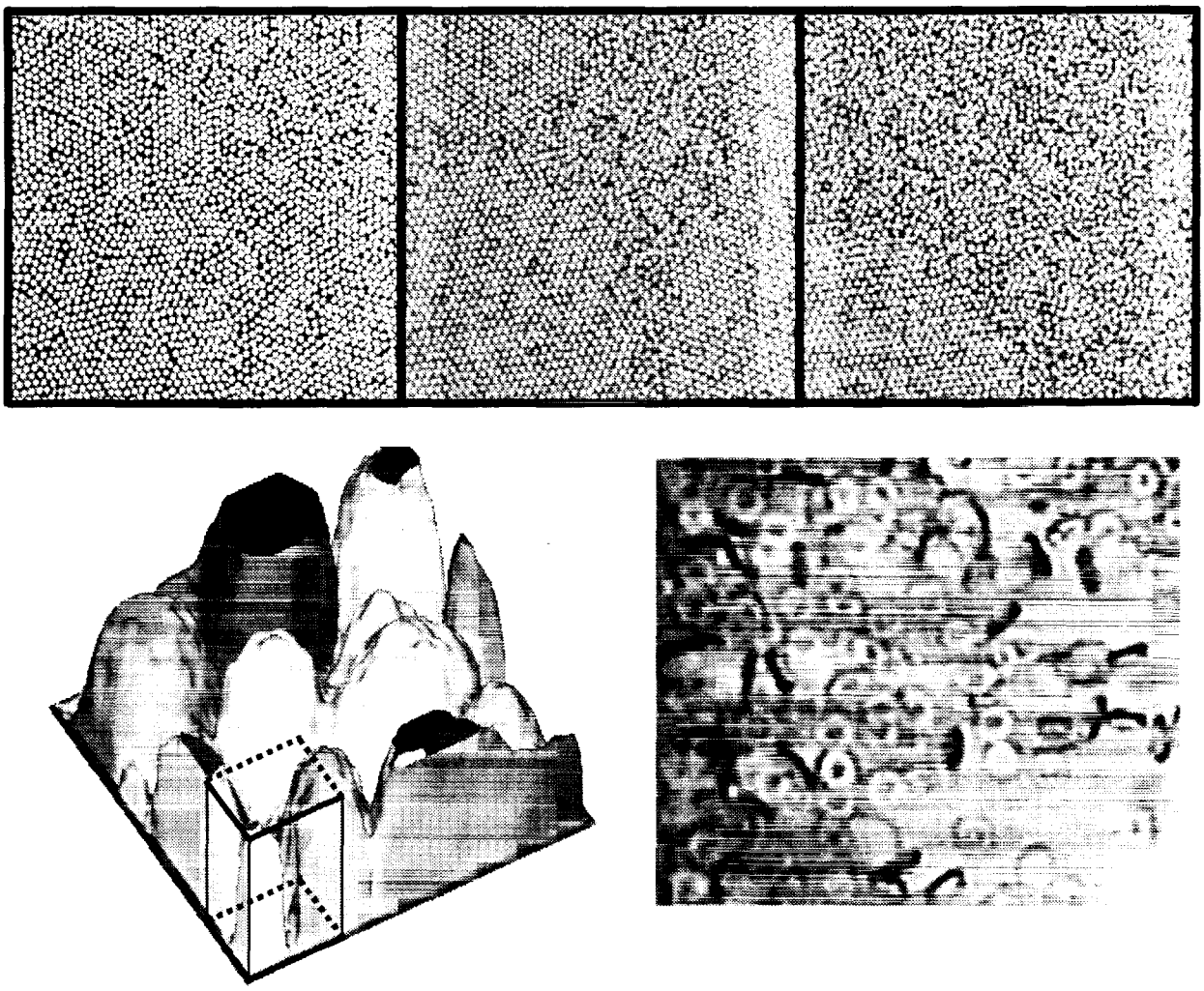

Fig. 1 Top) Confocal images of 1 μ particles at 1, 4 and 48 μ from cover slip. left) 3D crystallites, colors are different orientations. Images from top are in outlined rectangular prism. right) Colloidal PMMA disk/donuts 4μ diameter x 0.4 μ thick produced by photolithography.

Since the design of the flight microscope incorporates sample cells with submicroliter capacity, our initial experiments showed that extensive investigations of colloidal systems could be done with miniscule (by conventional standards) quantities of material. It then became practical to design our own non-spherical, colloidal particles using variations of optical lithography. On a three inch wafer it is possible to make ~ 2 microliters of colloidal particles at volume fraction 0.5. Depending on the size and shape this amounts to ~ 300,000,000 particles, well beyond numerical simulation capabilities. The example presented in the figure is a suspension of 4 x 0.4 μ disk/donuts made of PMMA. Using this technology virtually any two dimensional shape, disk, rod, banana, etc. can be made readily. Three dimensionally shaped colloidal particles can be prepared but with more difficulty.

REFERENCES

1. E.R. Weeks, J.C. Crocker, A.C. Levitt, A. Schofield, and D.A. Weitz, Science 287 627-31 (2000)

Physics of Hard Spheres Experiment: Microscopy of Colloidal Particles

Hard Spheres and μ gravity:
Some previous flights

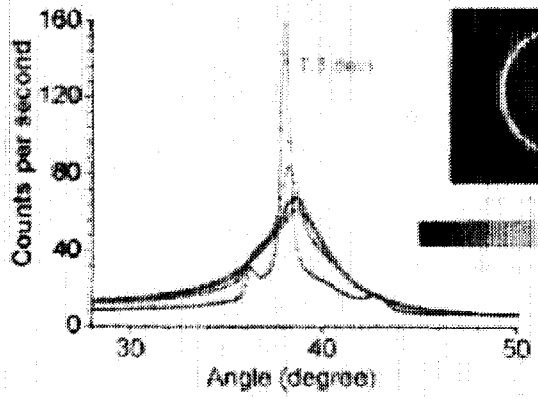

Confocal Microscopy:
Diffusion and 3D Crystal Growth

New Particles:
Designer Colloids from Lithography

PMMA Disks

Who's to Blame

Princeton - Chem Eng.

- **Bill Russel**
- Jesus Carlos Ruiz (also Mexico City)
- Andrew Hollingsworth

Princeton - Physics

- Zhengdong Cheng (XOM)
- Christopher Harrison
- Mischa Megans

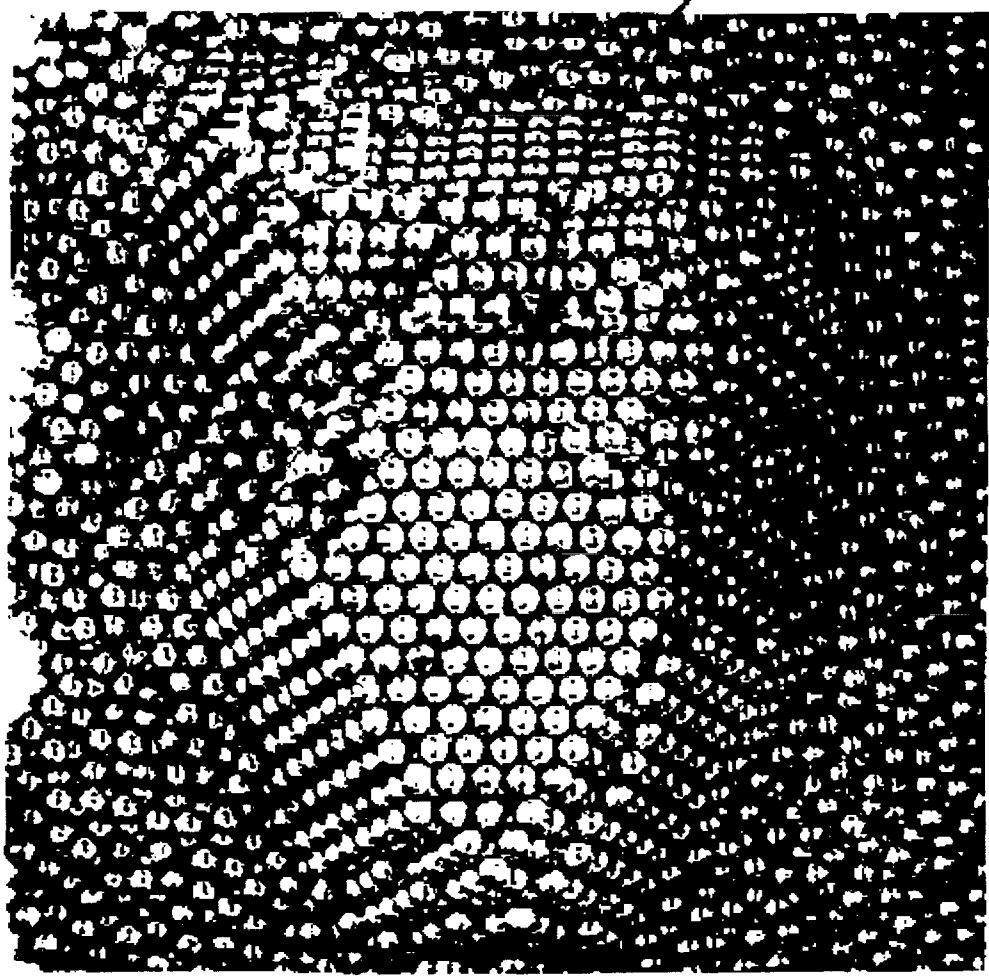

FIGURE 14. Face-centred cubic 'crystal' surrounded by 'liquid' caused by shearing ball-bearing mush. (111 face is shown at the top surface.

Packing Problems are Important
- How much grain in a barrel

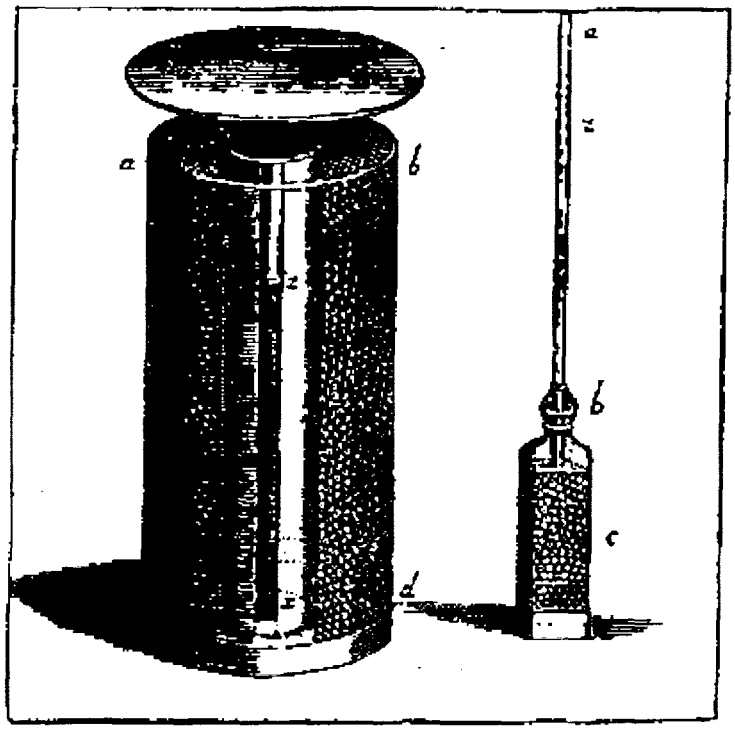

Figure 2.9 Stephen Hales (1727) was a highly gifted biologist whose interests included the uptake of water by plants. The diagram on the left shows the apparatus he used to demonstrate the substantial force exerted by dilating peas. However, when the lid (f) was covered with a weight great enough to prevent its lifting, the dilated peas deformed into the Wigner–Seitz cells of the rep structure. The peas in the bottle at right, used by Hales in a related experiment, would not have served so well to illustrate random close packing because of the presence of the crystallinity-inducing planar walls.

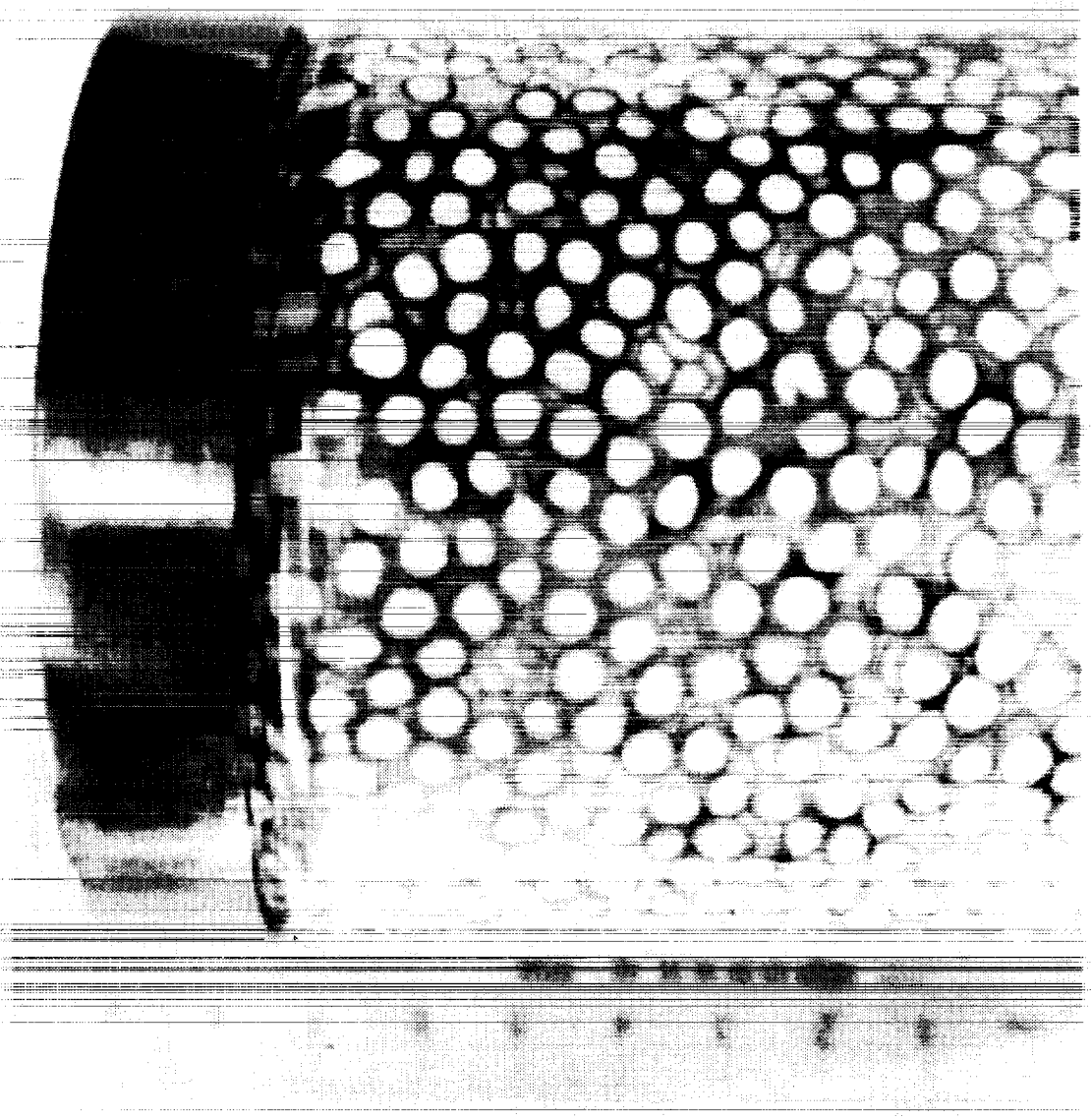

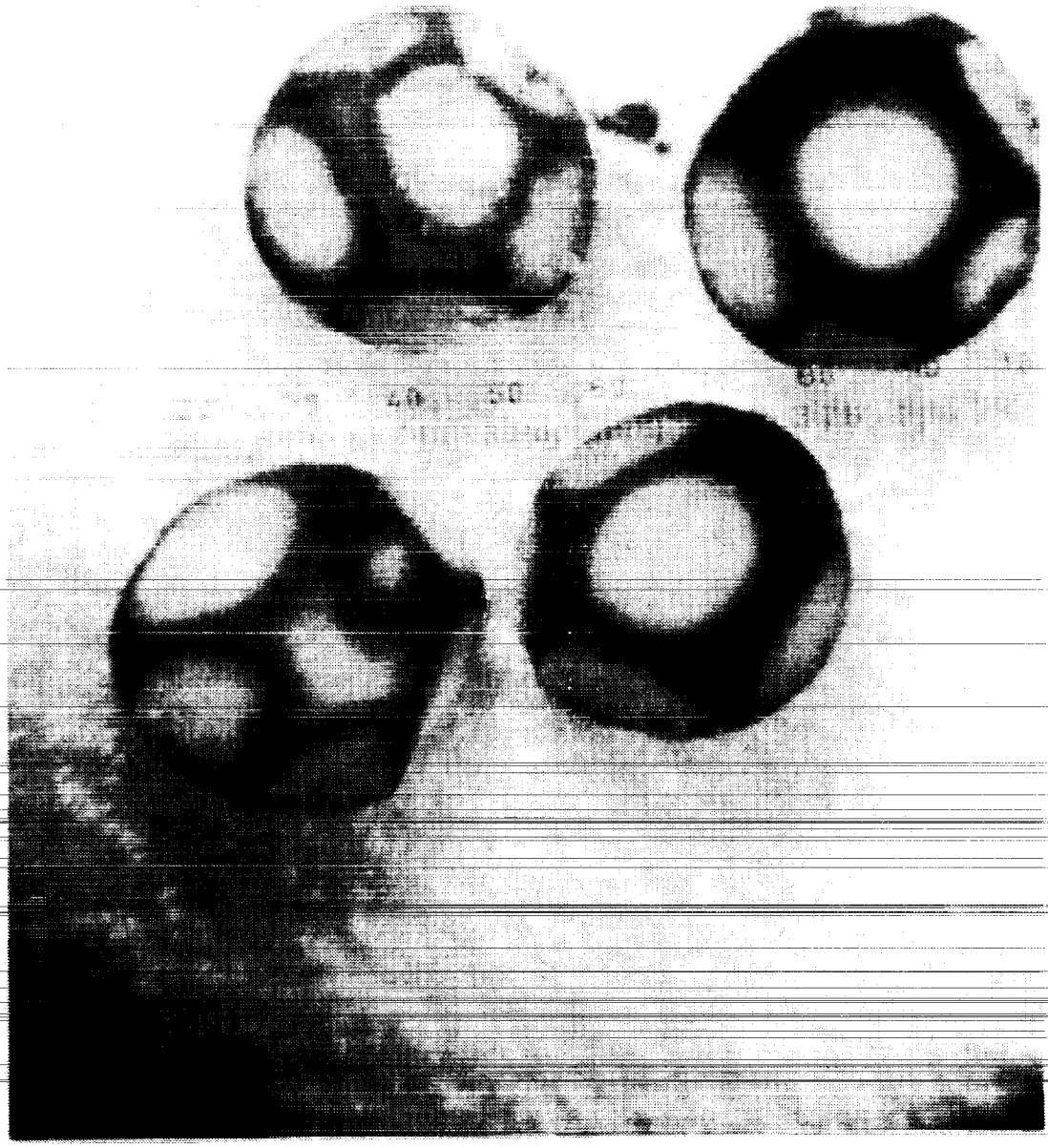

gravitational height

$$mgh = k_B T$$

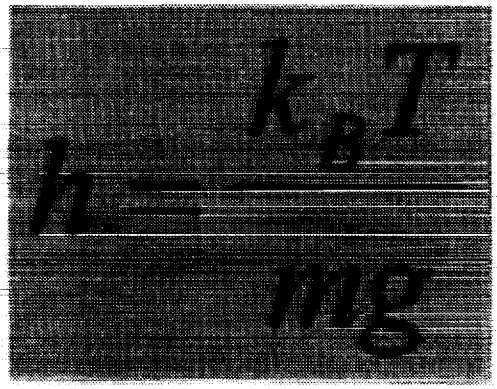

Ball bearings	$h \sim 10^{-18}$ cm
Colloids	$h \sim 1\mu$
N_2 Molecules	h ~ 10 km

h<diameter, gravity dominates

h>container, neglect gravity

Equilibrium Phase Diagram for Hard Spheres

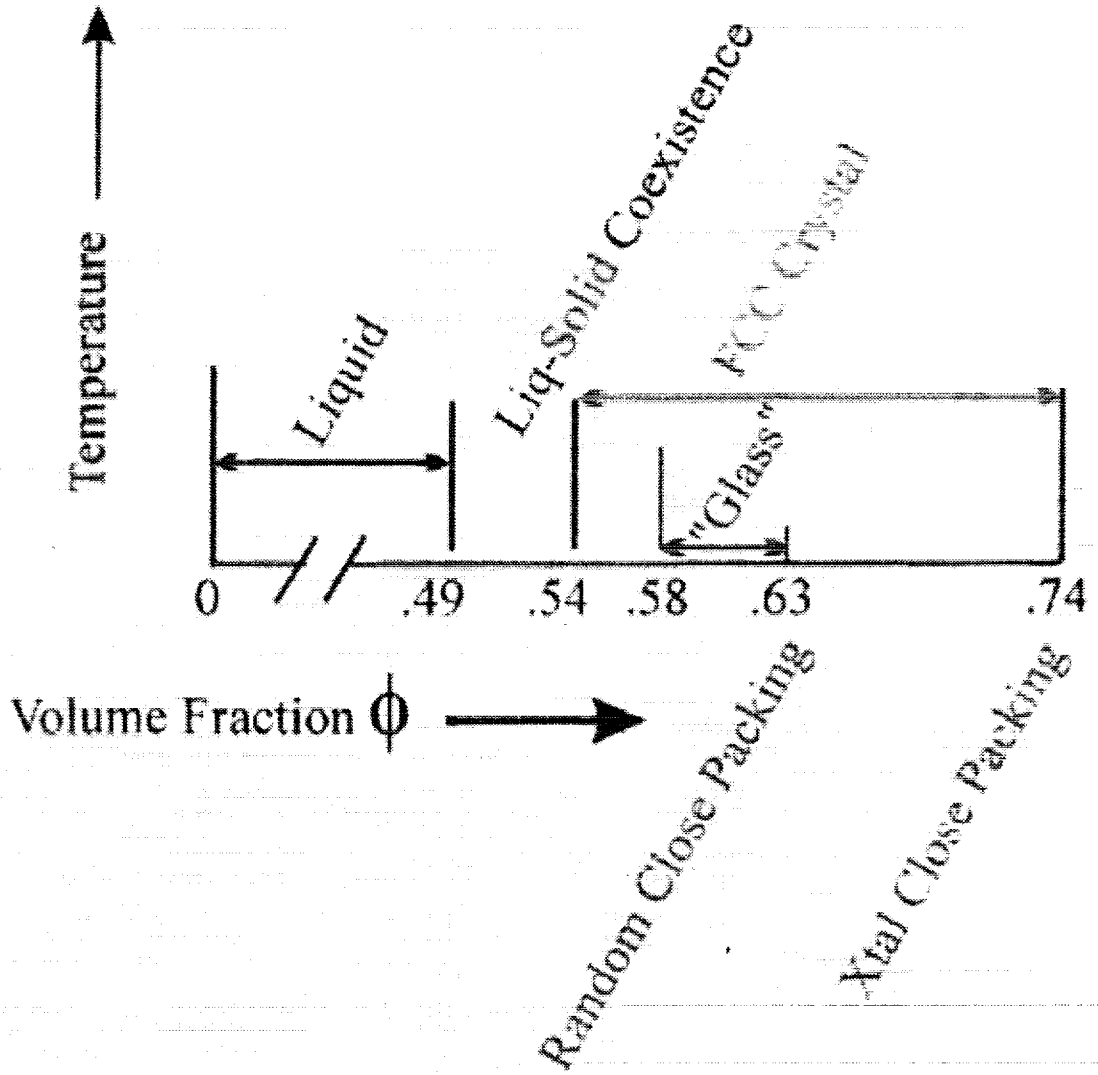

Phase Diagram by 1g Experiment

325 *nm* PMMA/decalin/CS2

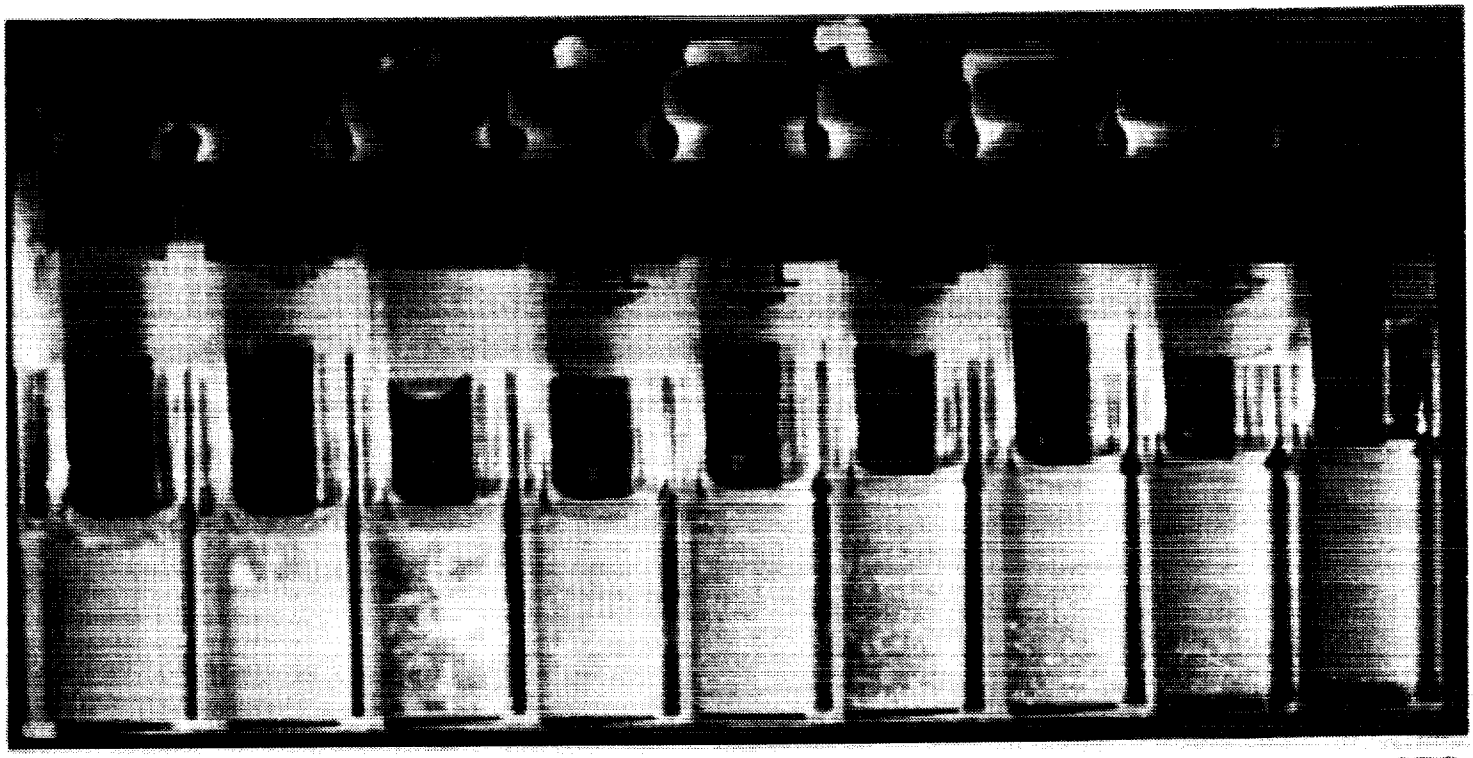

0.637 0.621 0.595 0.578 0.553 0.528 0.512 0.502 0.478

Crystal Coexistence Liquid

Heterogeneous

Pusey & van Megen, *Nature, 320 (1986) 340*

Cheng

CDOT 1998

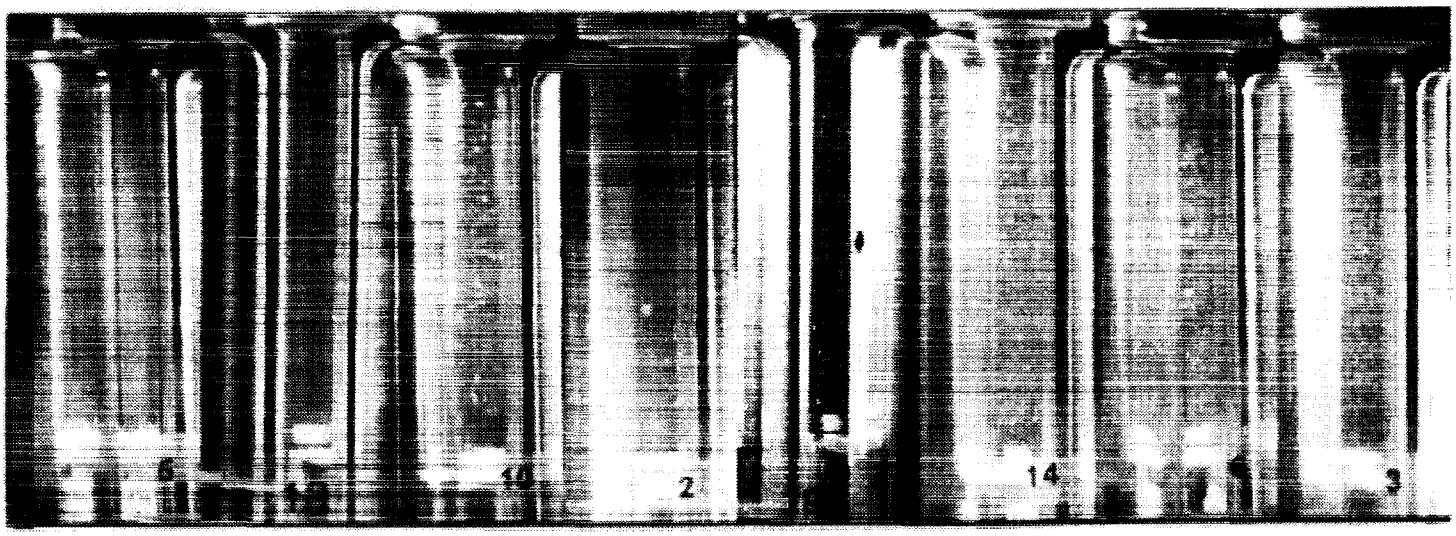

0.50 0.502 0.504 0.512 0.516 0.518 0.524 0.537

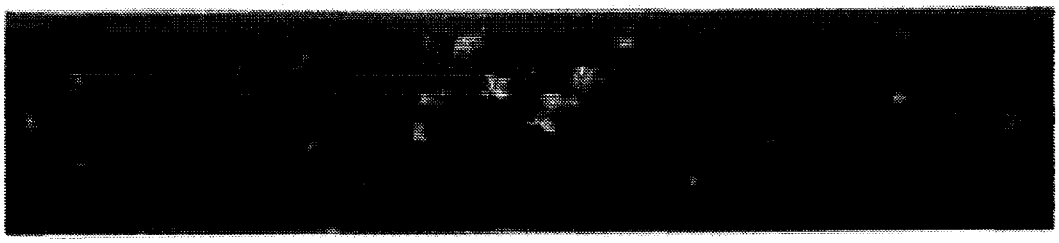

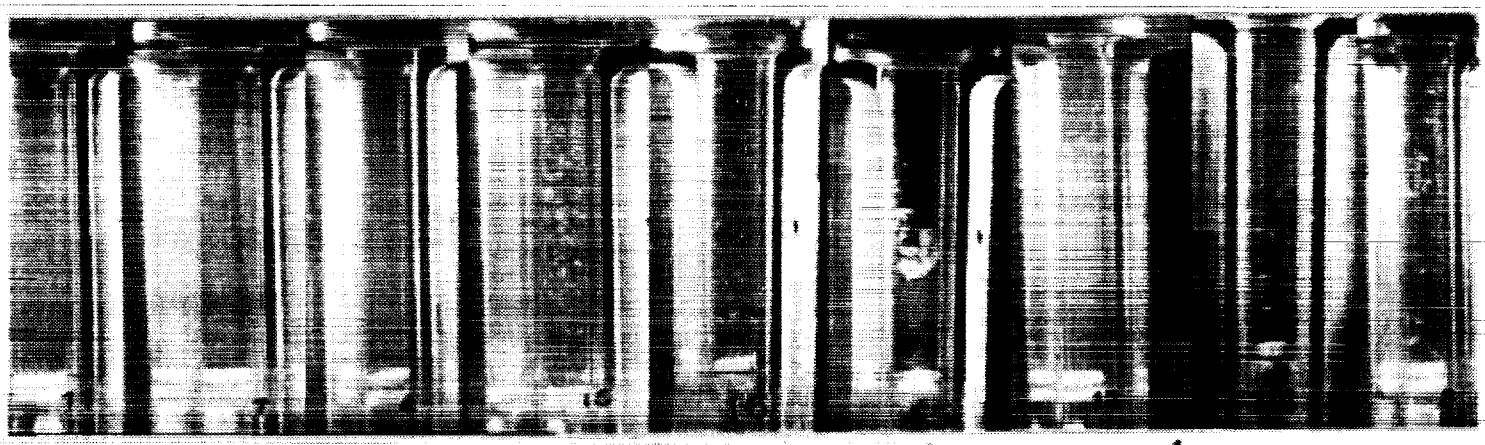

0.5470.549 0.561 0.591 0.605 0.618 0.619 0.633 0.634

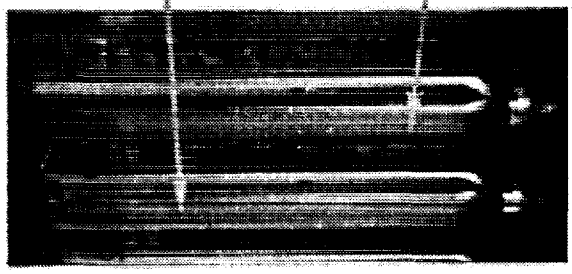

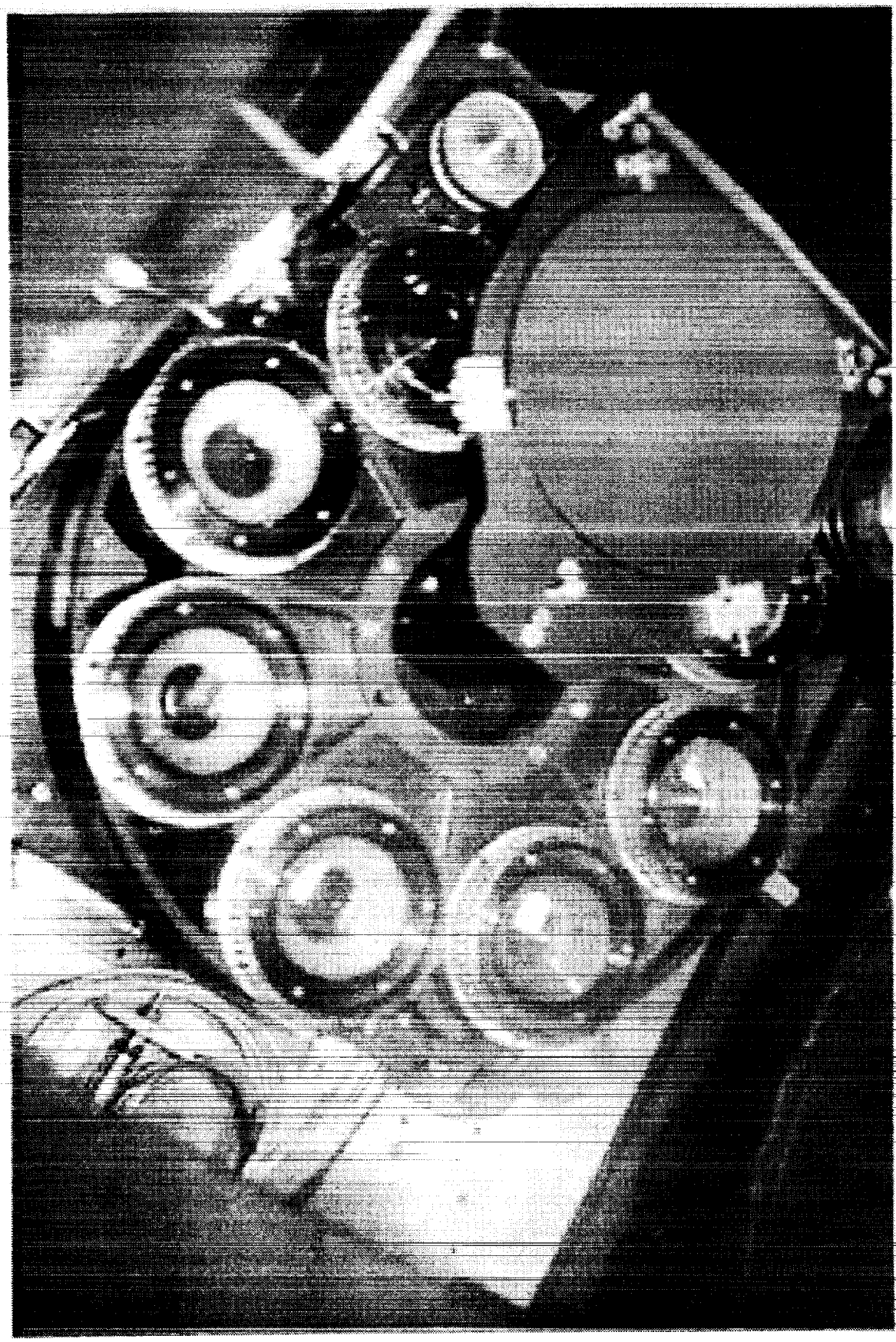

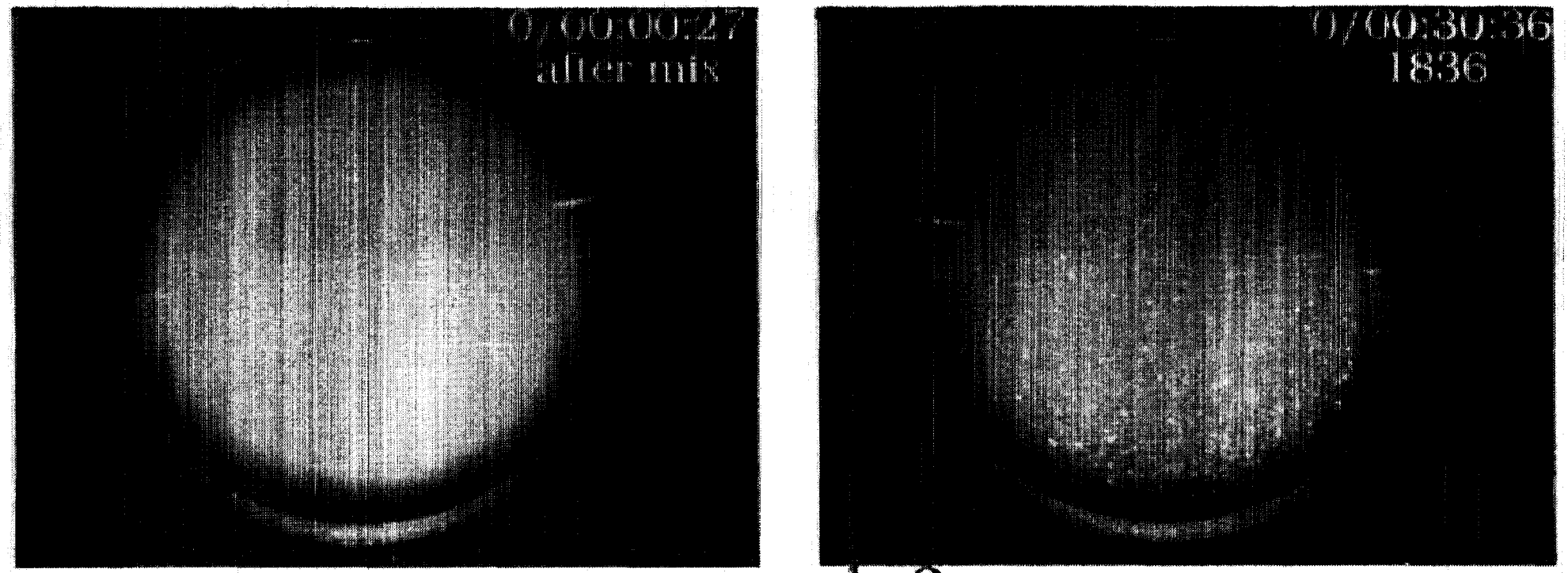

sample 3

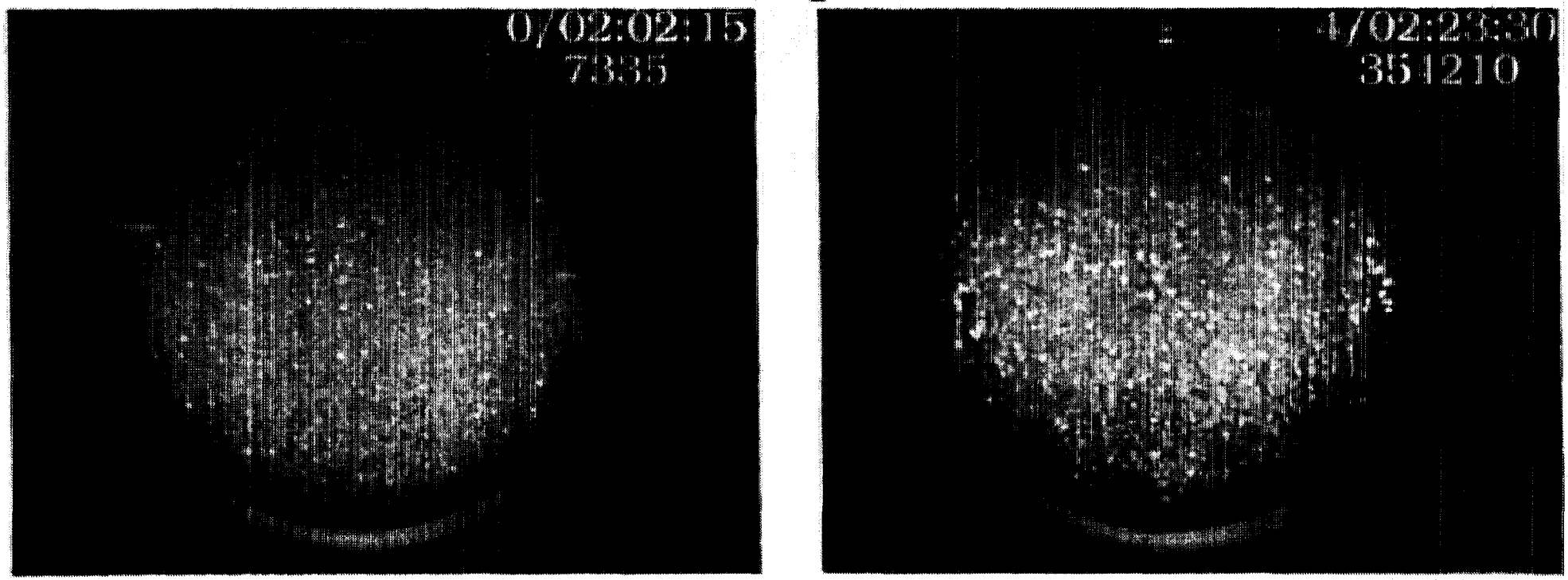

NASA/CP—2000-210470

Cheng

Bragg Scattering

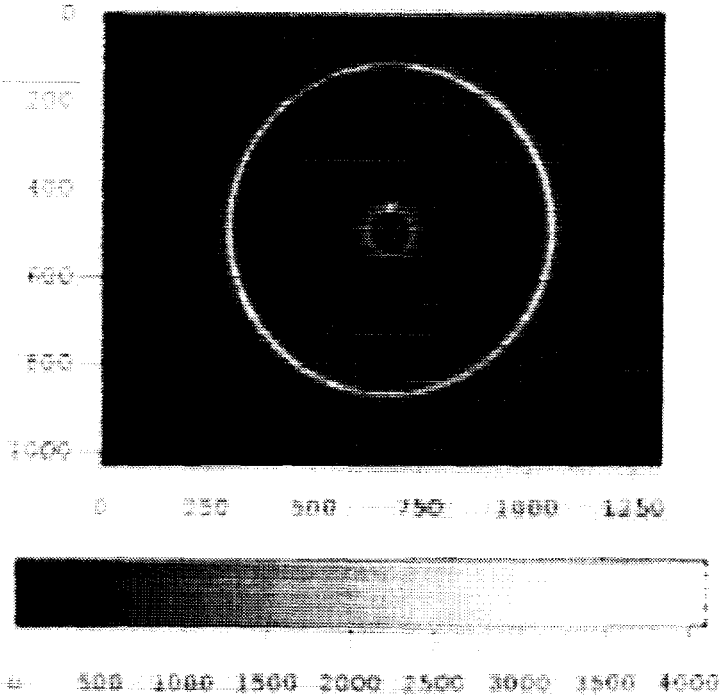

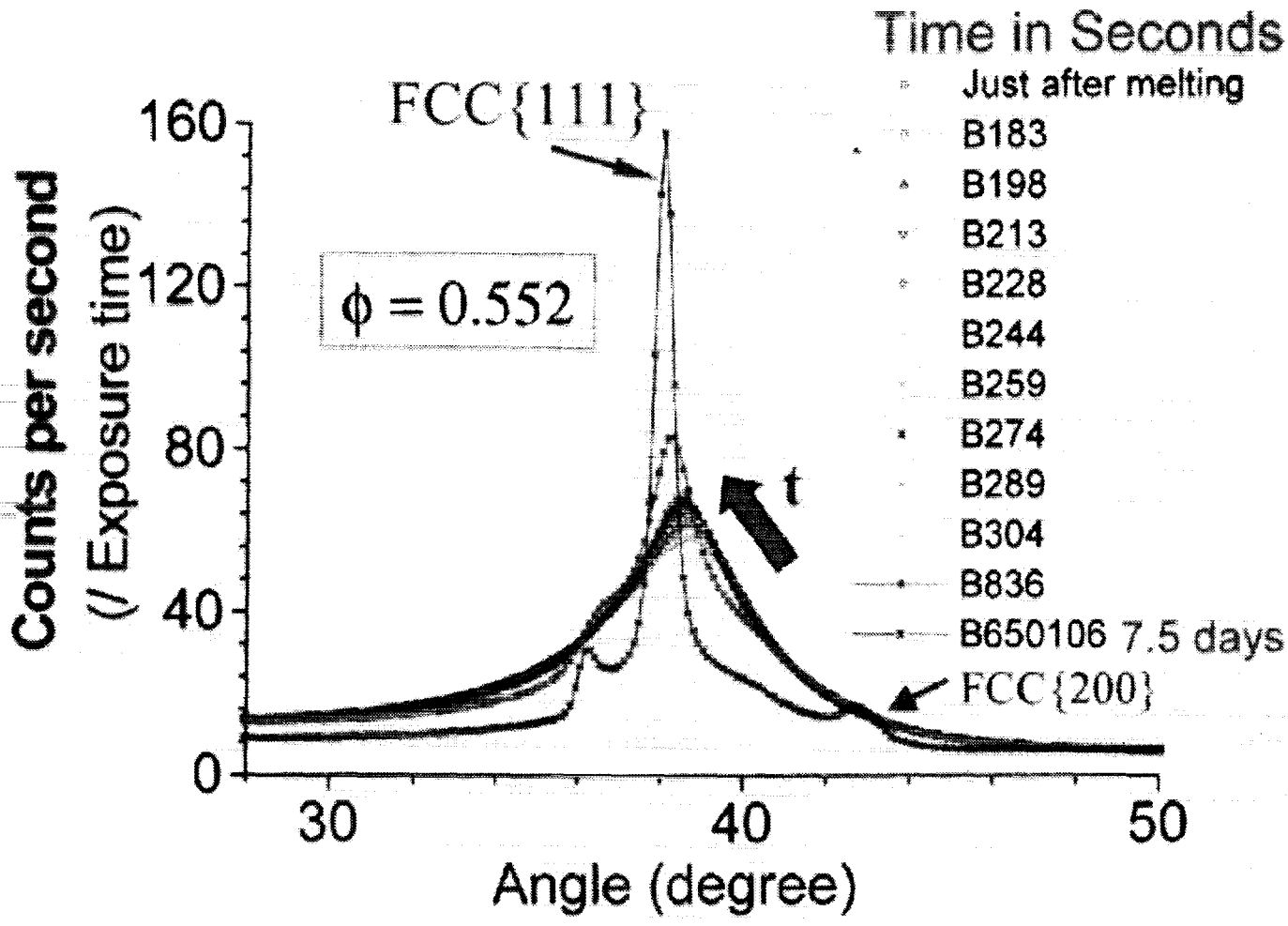

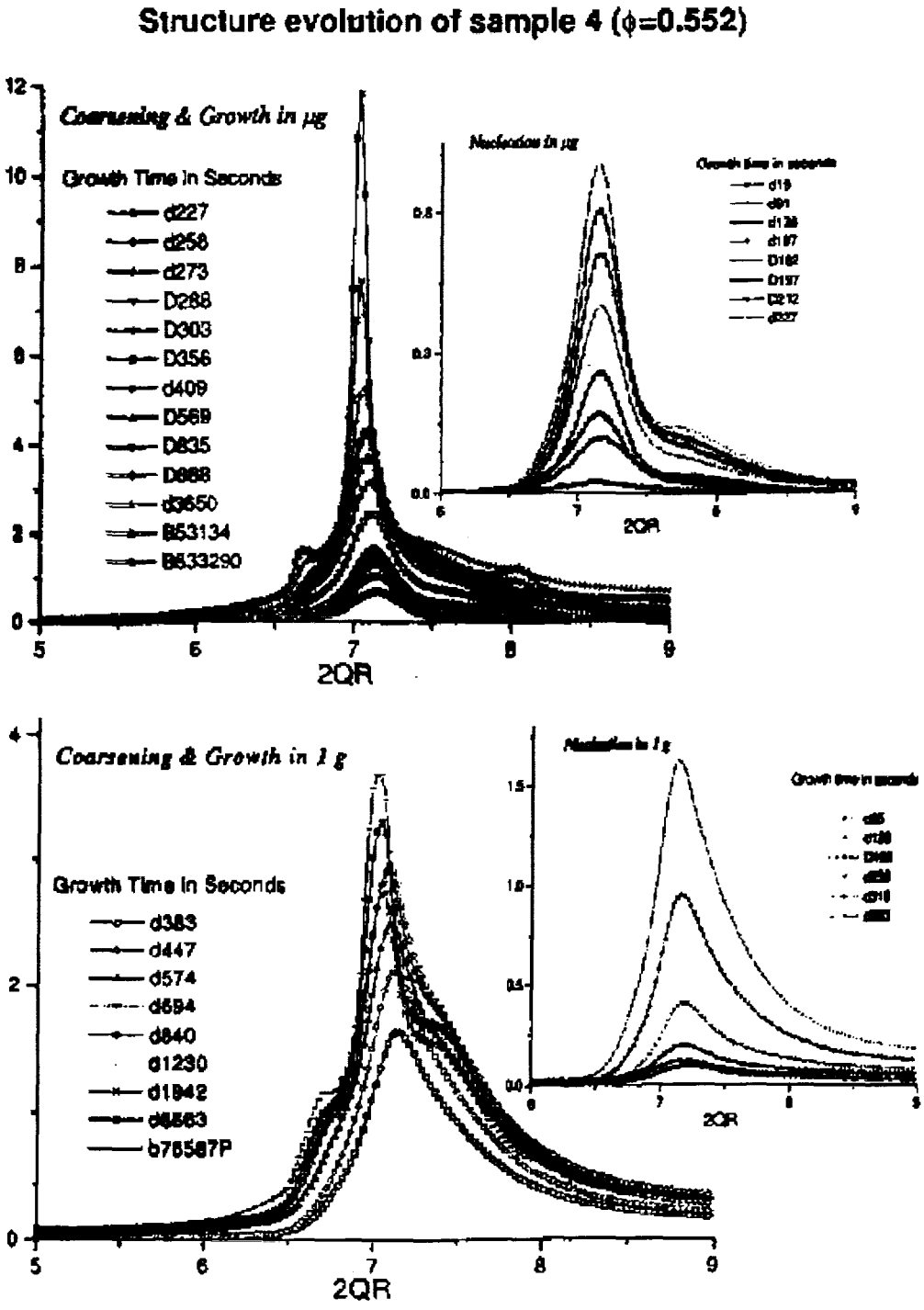

Figure 5.31: The structure evolution of sample 4 in μg and $1g$.

Fully crystallized Sample $\phi = 0.552$

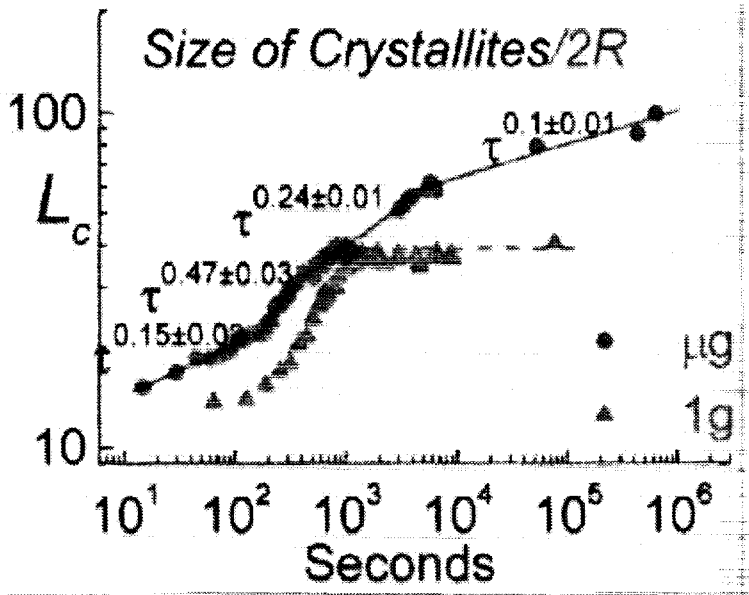

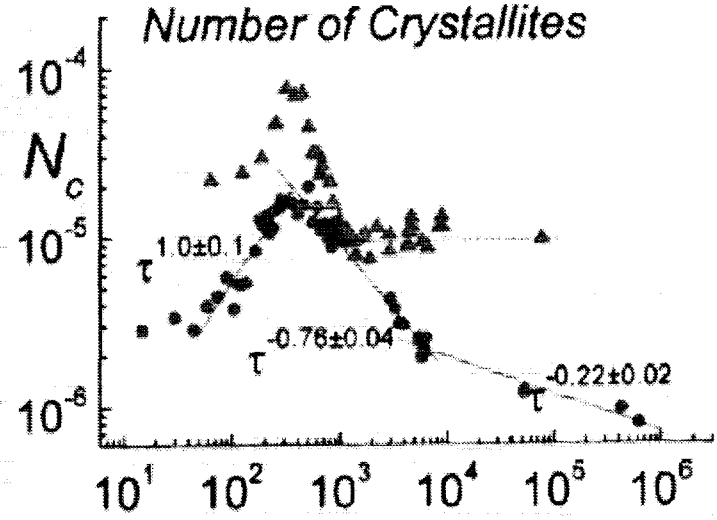

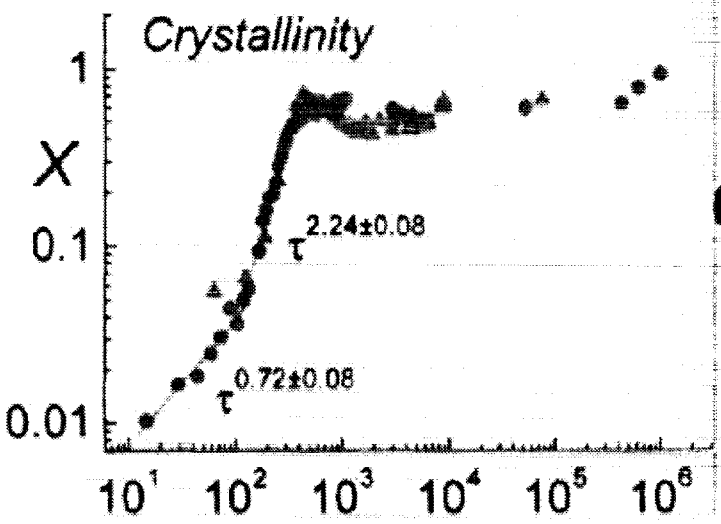

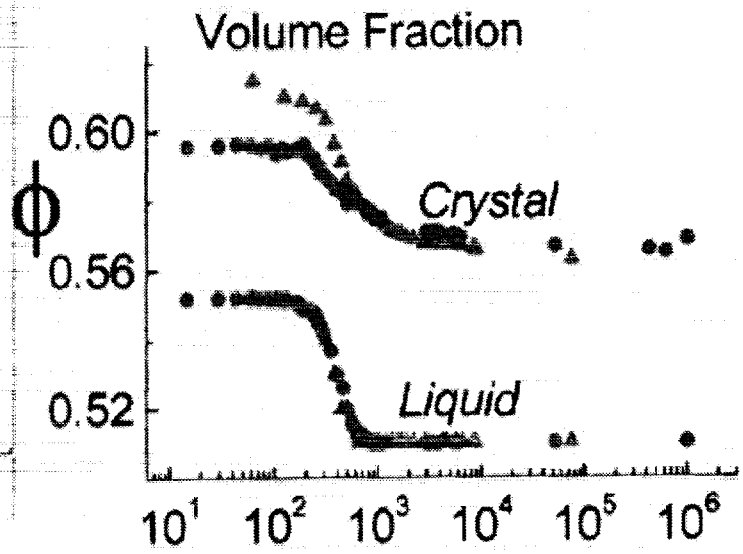

- Compressed and Expanding lattice : Gibbs-Thompson effect
- Nucleation at constant rate
- Growth : (1) diffusion limited < 300s
  (2) intermediate stage
  (3) coarsening non-classically
- Effect of gravity : (1) more small crystal,
  (2) suppress coarsening

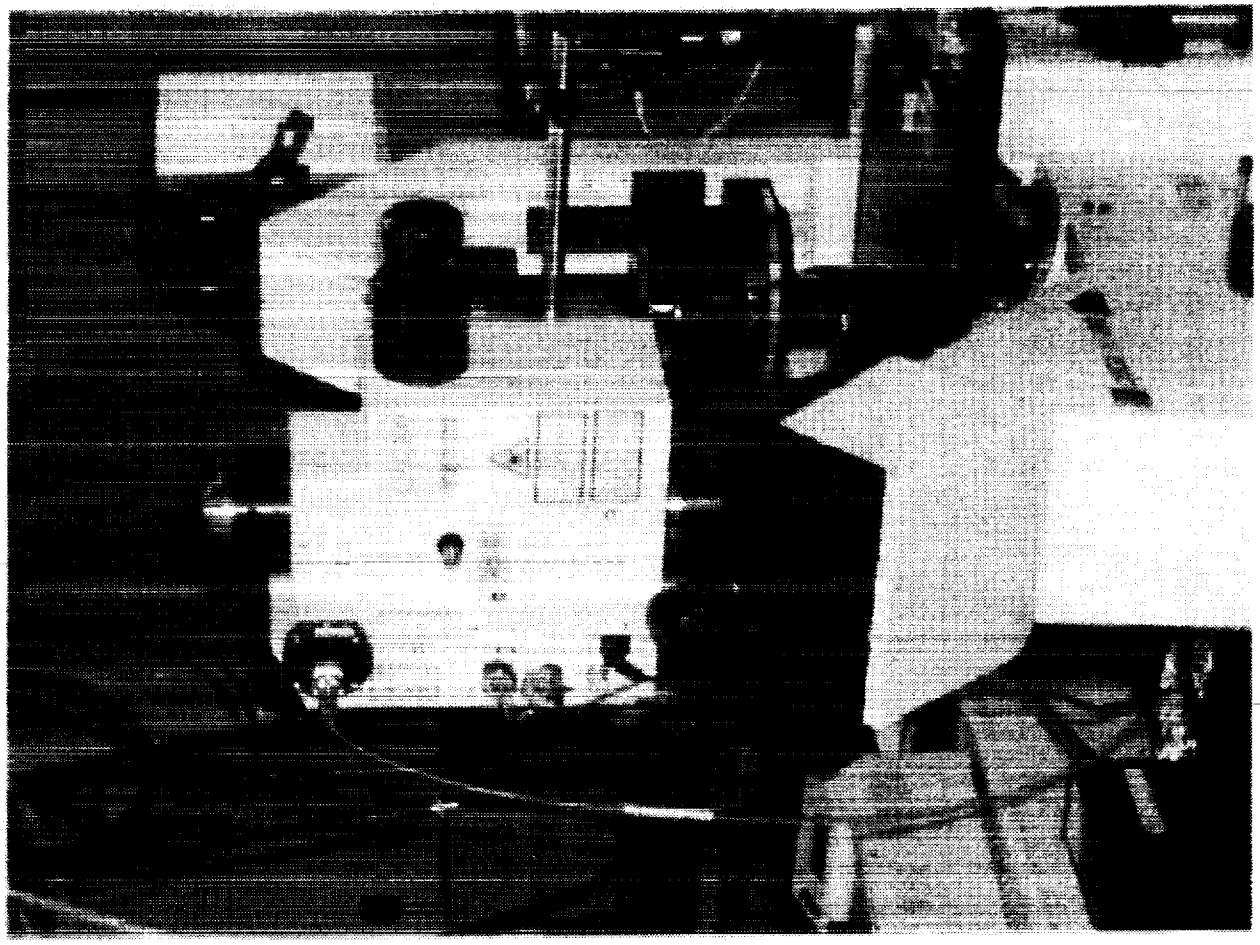

Confocal Setup

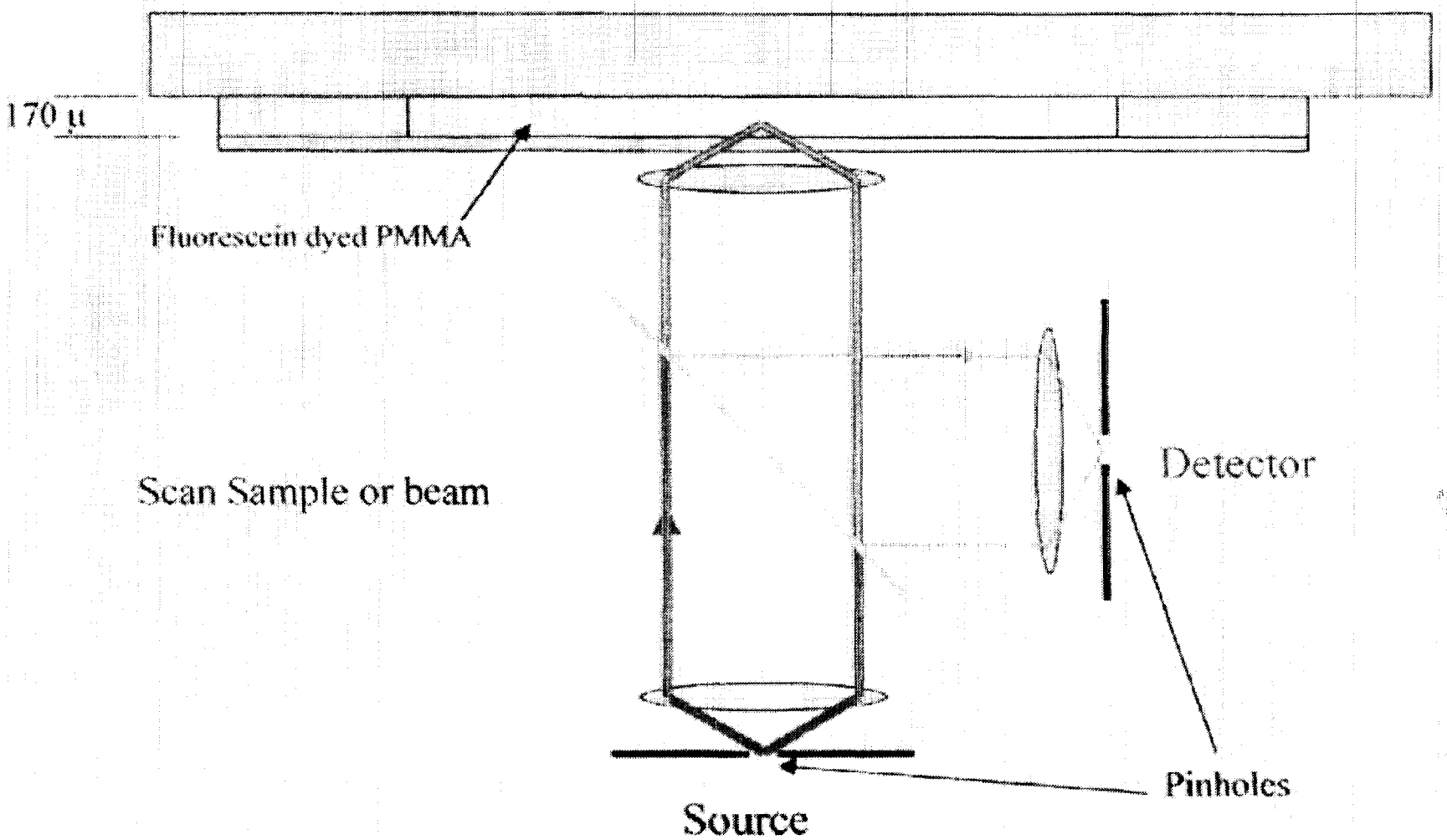

Some Concoctions for PMMA-PHSA Spheres

	Density	Index
PMMA	1.192	1.489
Decane	0.73	1.411
Decalin	0.896	1.475
CHB	1.289	1.508
Tin 2-ethylhexanoate	1.251	1.4930
Tetralin	0.9662	1.5391

For density and index match:
PMMA 0.956μm + PHSA 10nm, Tetralin 4%, Decalin 10%, CHB 87%,
spheres swell ~ 10% in 2 weeks

Charged Spheres:
PMMA 0.956μm + PHSA 10nm, Tetralin 4%, Decane 10%, CHB 87%,
Fluorescein Dye, crystallizes at ~ 10% volume fraction

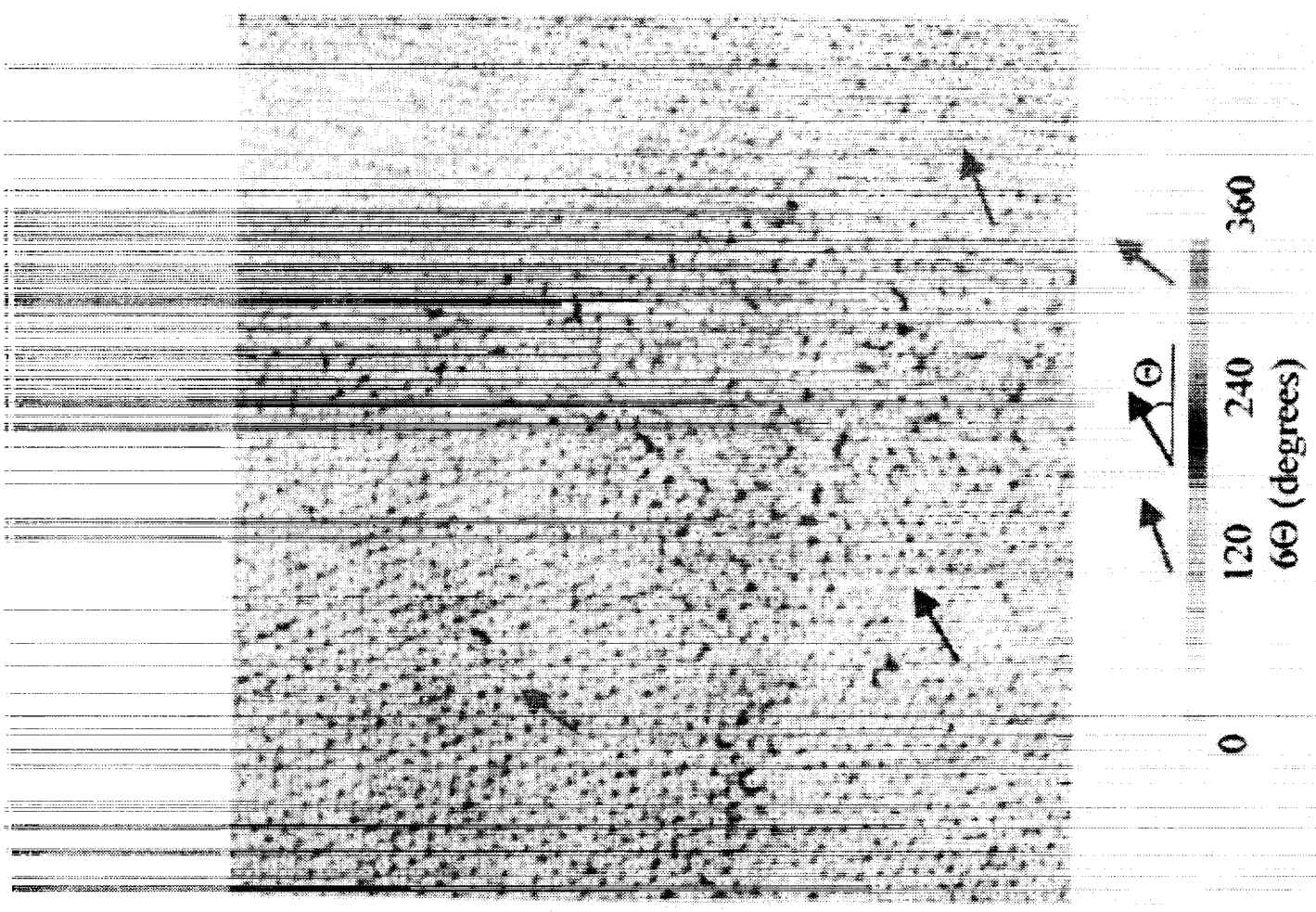
0
120
240
360
6Θ (degrees)
Θ

0 microns

4 microns

48 microns

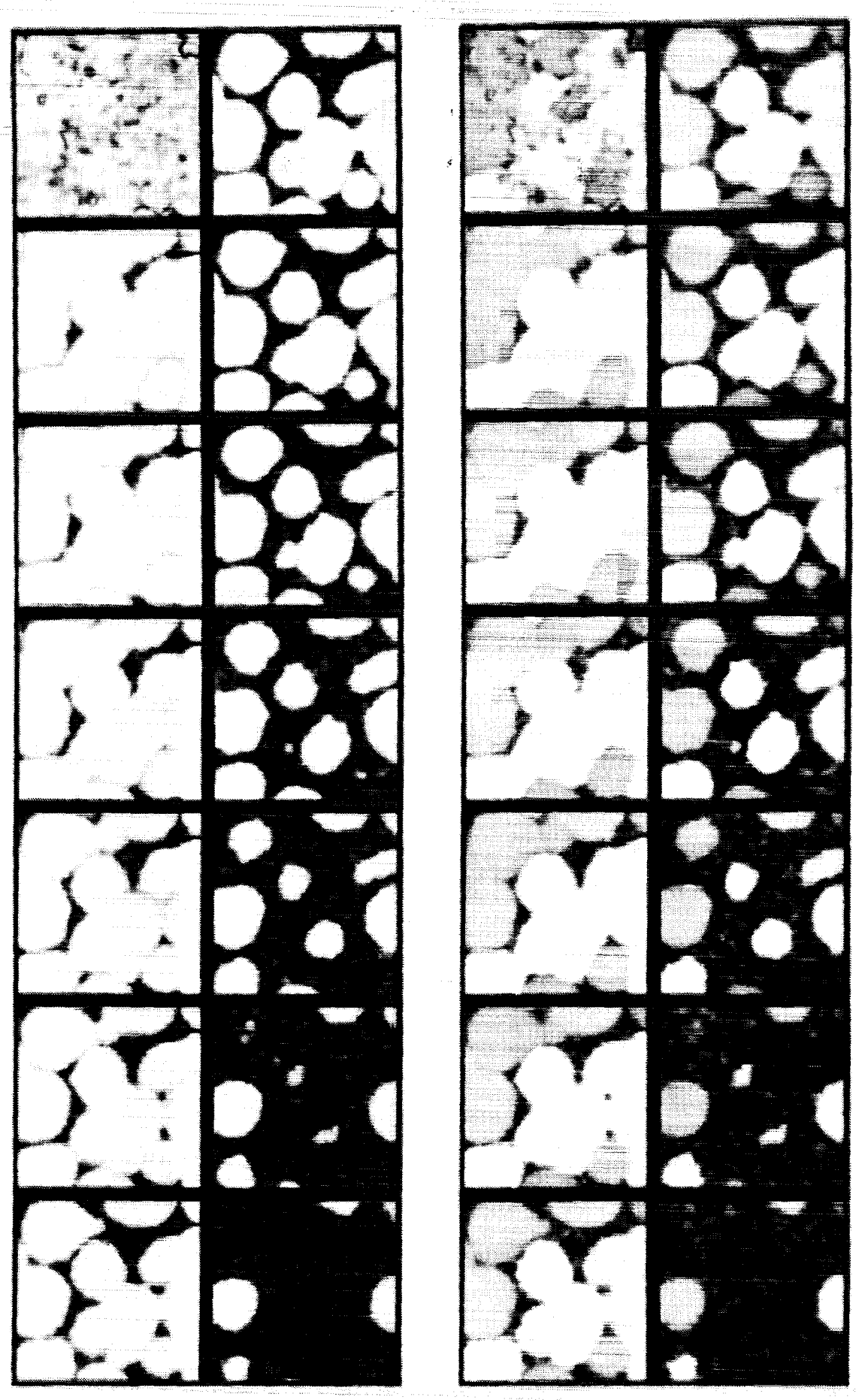

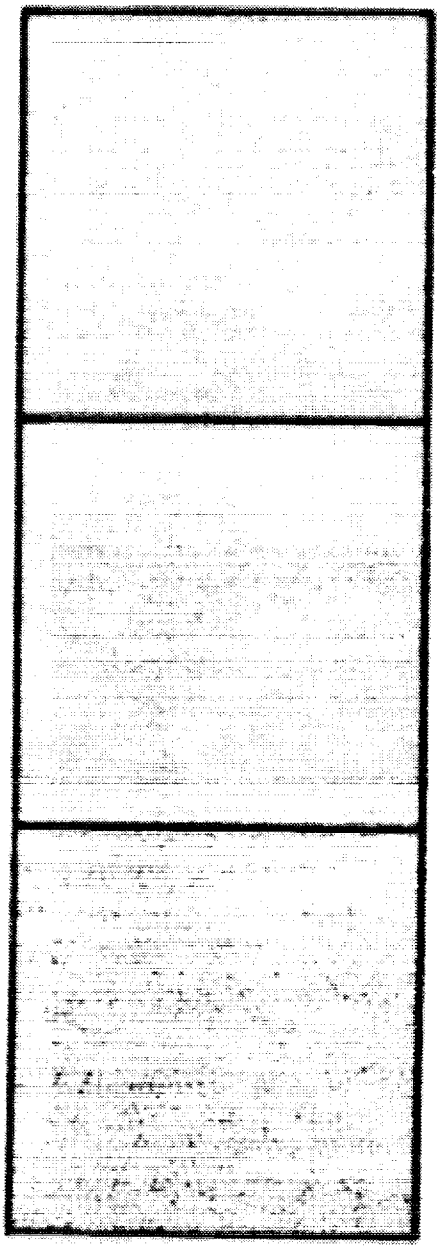

Figure 1

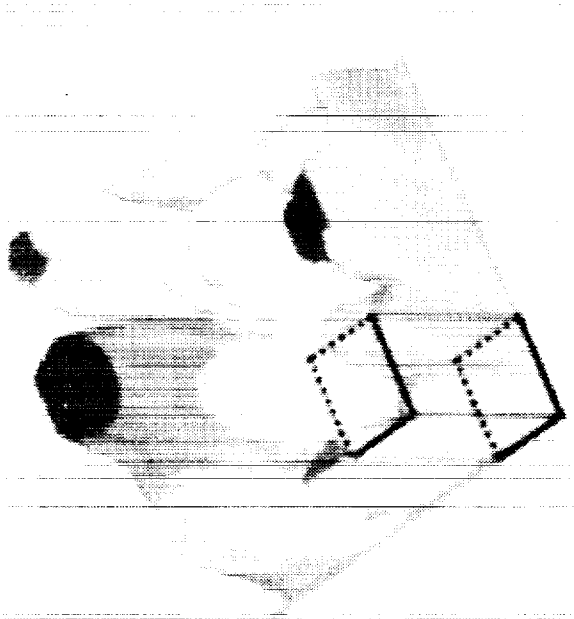

Figure 2

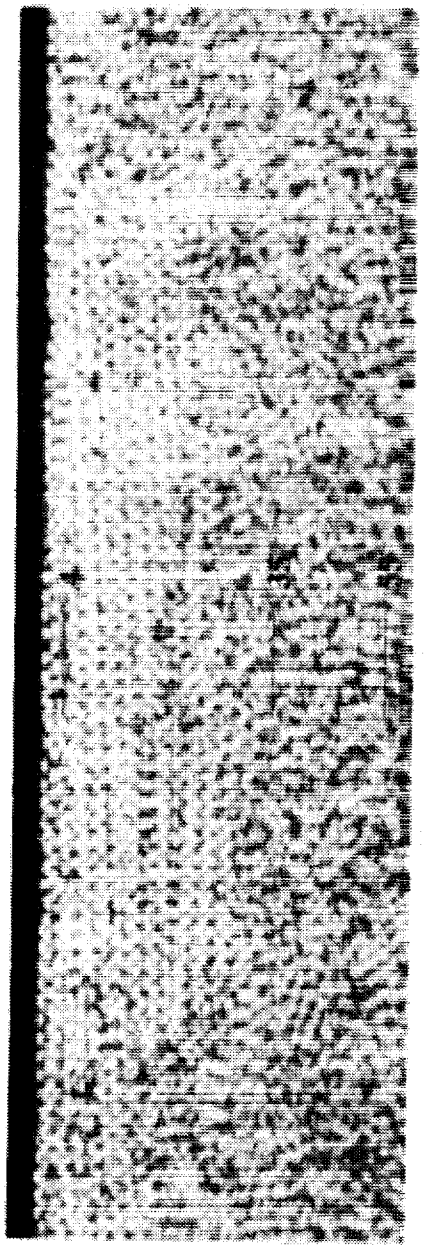

Speed of Growing Fronts

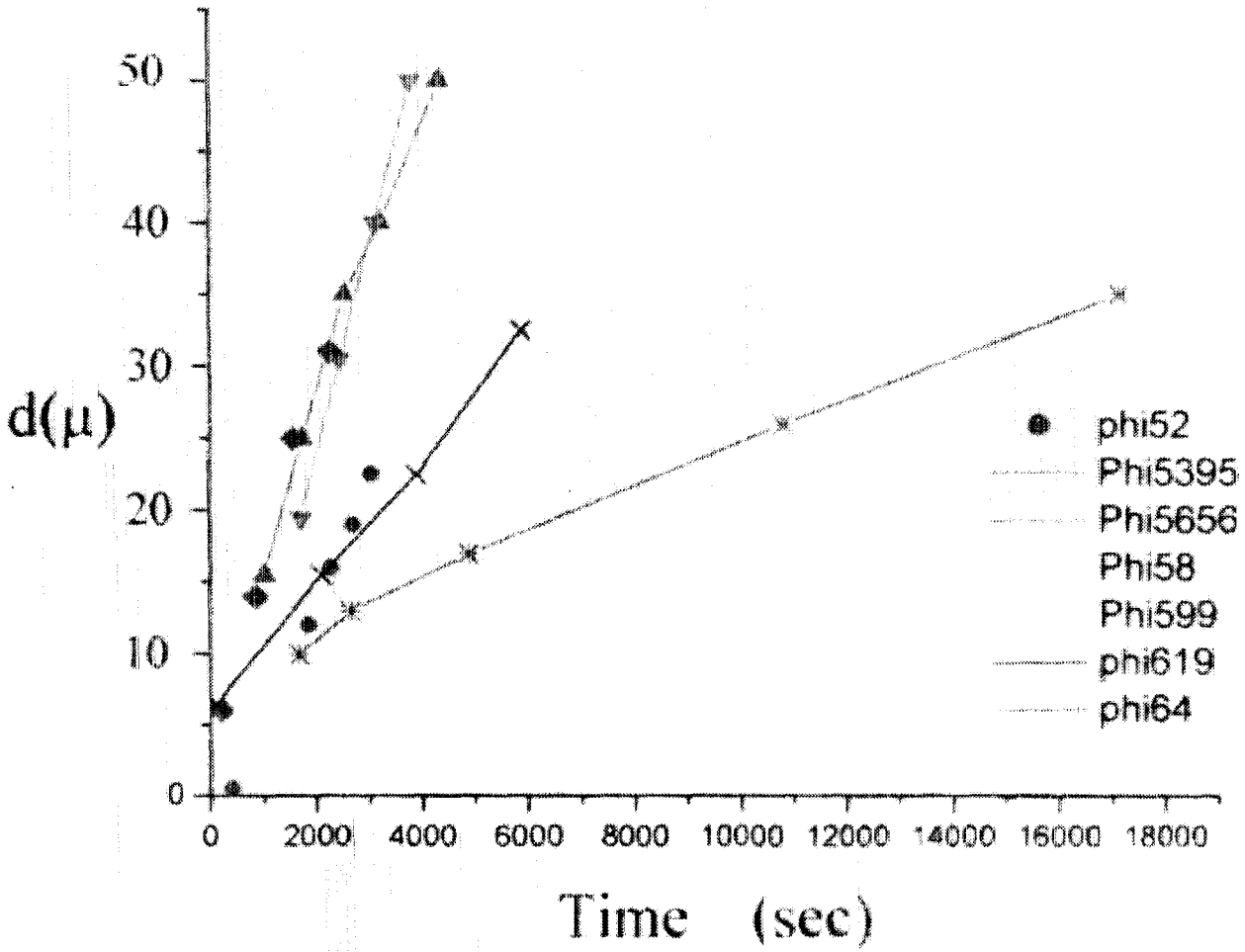

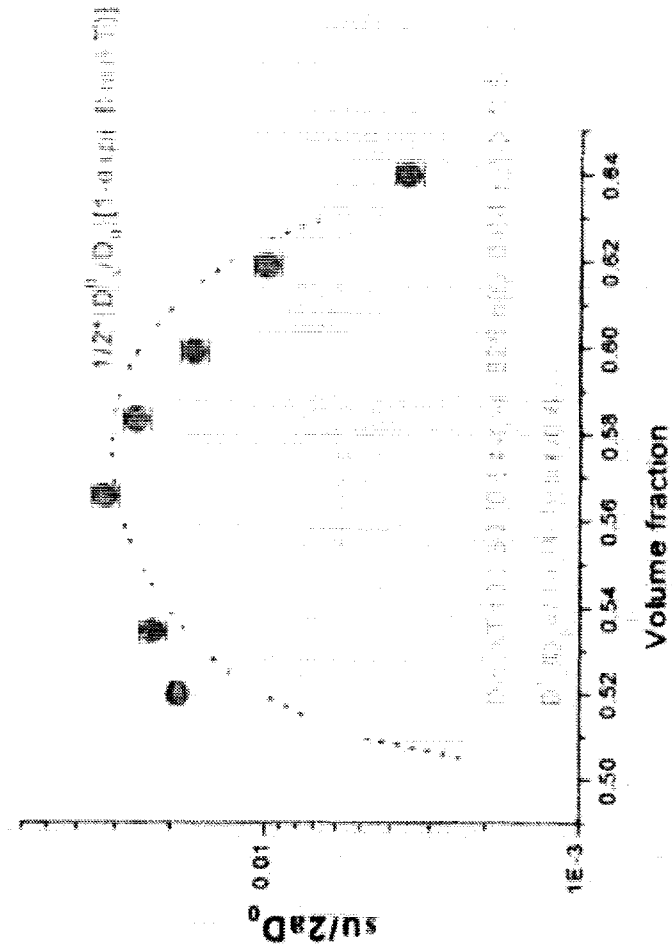
su/2aD0
0.01
1E-3
0.50
0.52
0.54
0.56
0.58
0.60
0.62
0.64
Volume fraction

Figure 4

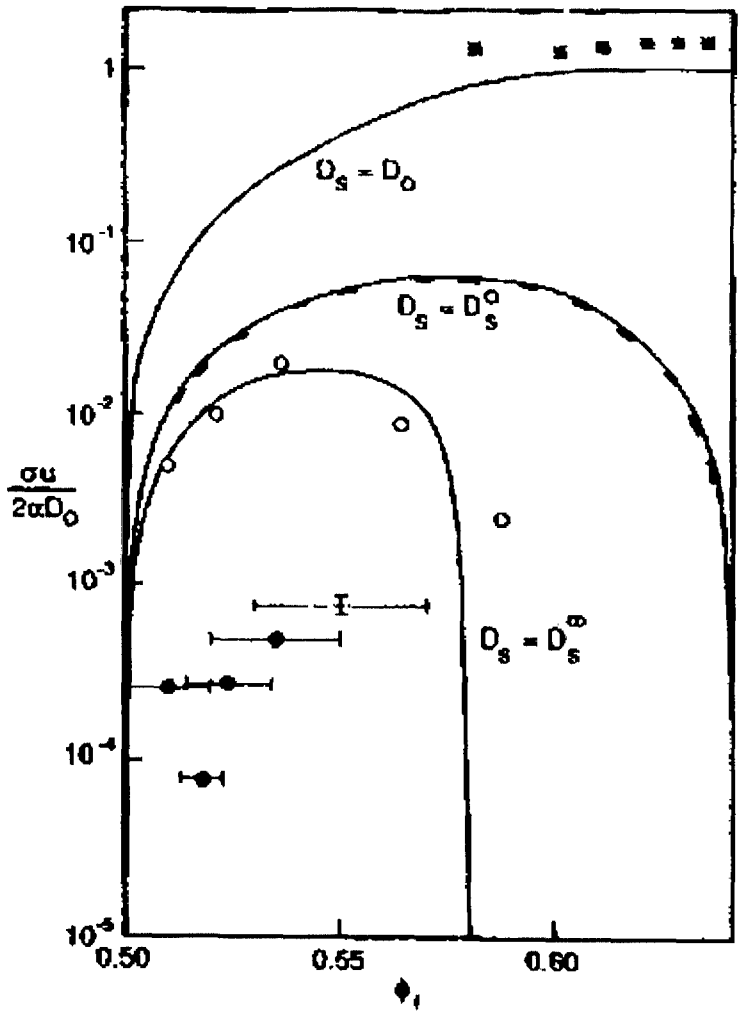

Figure 3 Crystal growth rates $\sigma u/2\alpha D_0$ for hard spheres from (4) and (9) with $D_s = D_s^0$ from (10); for hard spheres from (4) and (9) with $D_s = D_s^\infty$ from (10); for charged spheres from (4) and (11) with $D_s = D_0$. ○ estimates of rates for polymerically stabilized spheres from Pusey and van Megen (1987); * rates for charged spheres from Aastuen, *et al.* (1986) plotted with ϕ_f from (9) and (11); + maximum rate for hard spheres from Davis and Russel (1988). ● rates for hard spheres from x-ray scans of Davis (1989).

Mean Squared Displacement

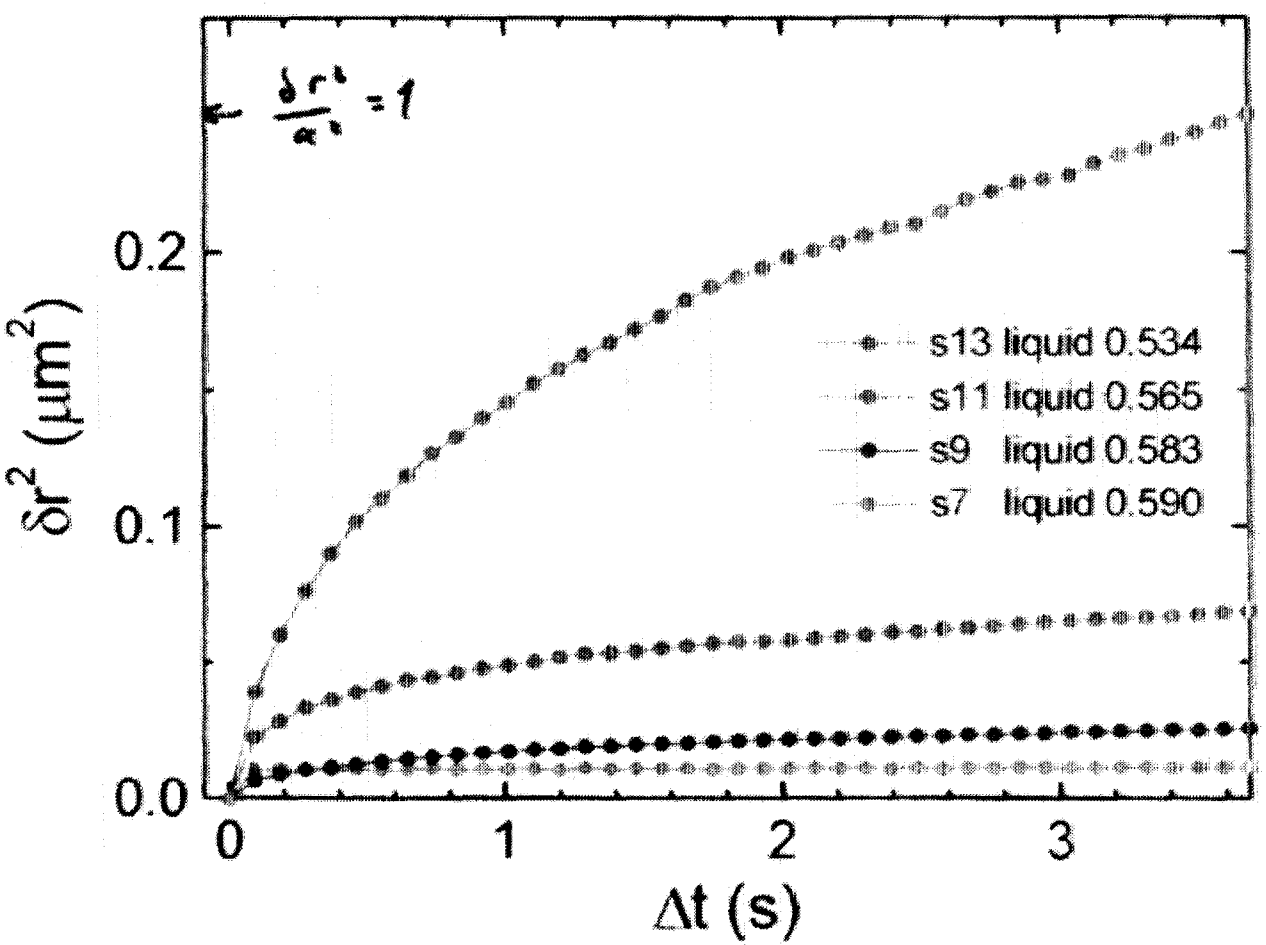

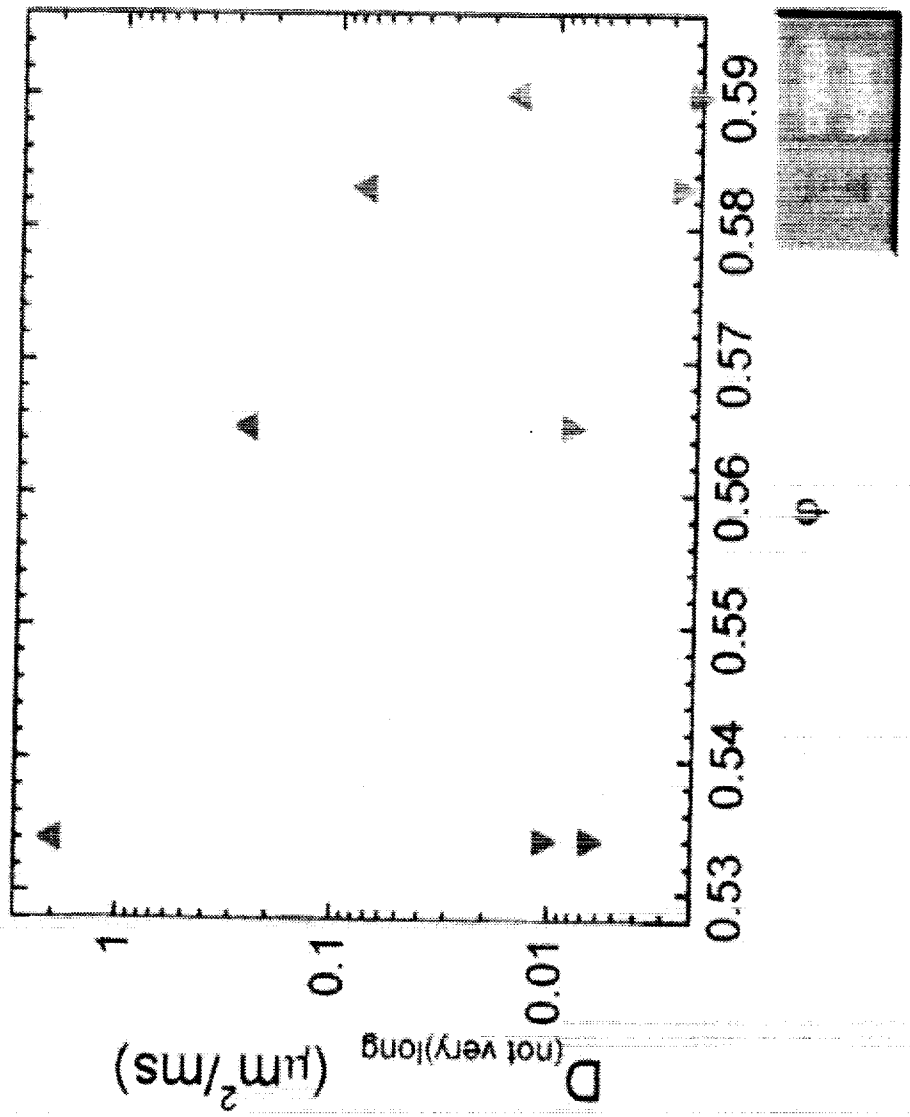
D (not very)long (μm²/ms)
1
0.1
0.01
0.53
0.54
0.55
0.56
0.57
0.58
0.59
φ

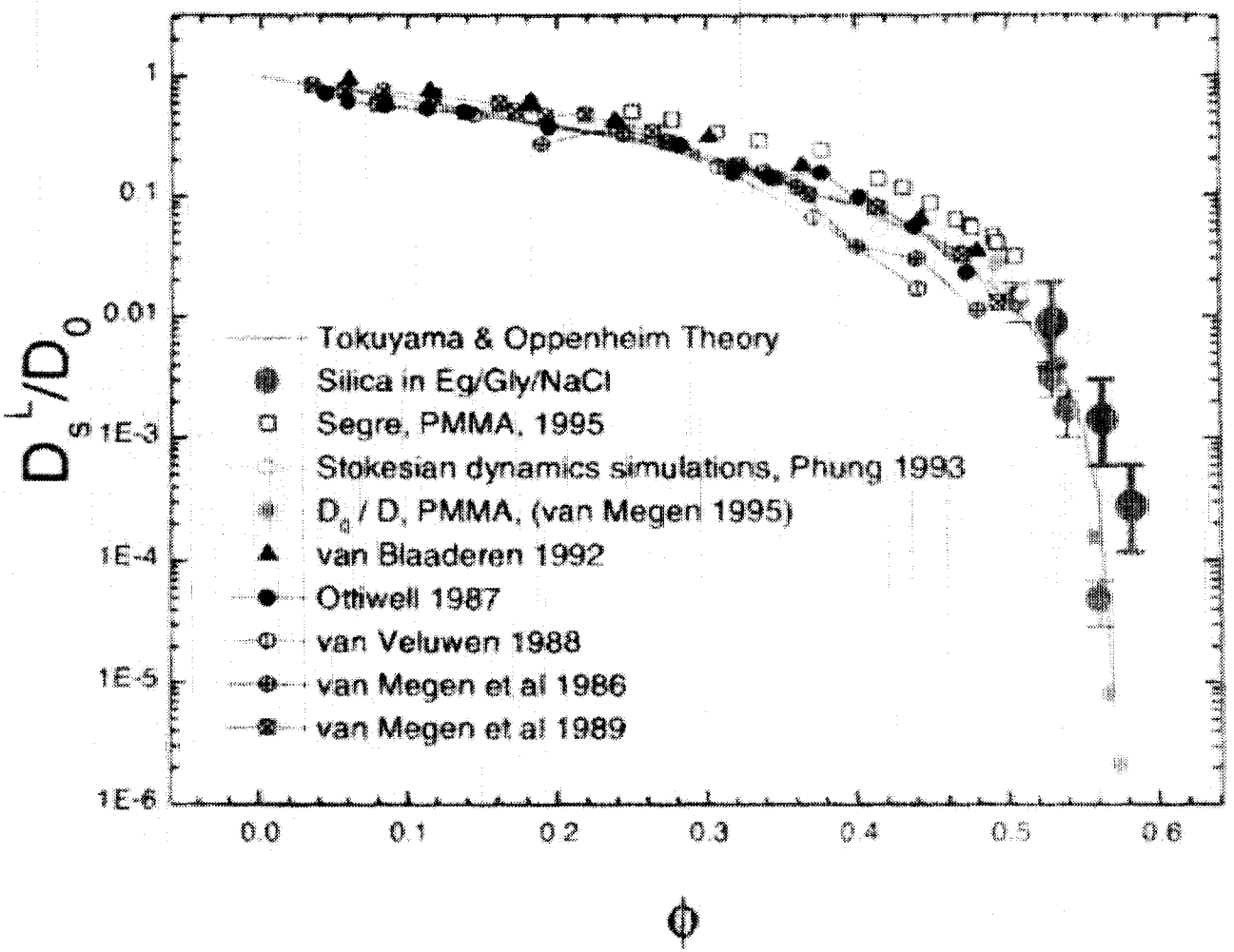

Figure 1.3: Long-time self diffusion. Previous data: Segre et al., 1995 [22]; van Megen & Underwood, 1994 [25]; van Blaaderen, 1992 [26]; van Megen & Underwood, 1989 [27]; van Veluwen & Lekkerkerker, 1988 [28]; Ottewill & Williams, 1987 [29].

Fabrication: Spin Coating

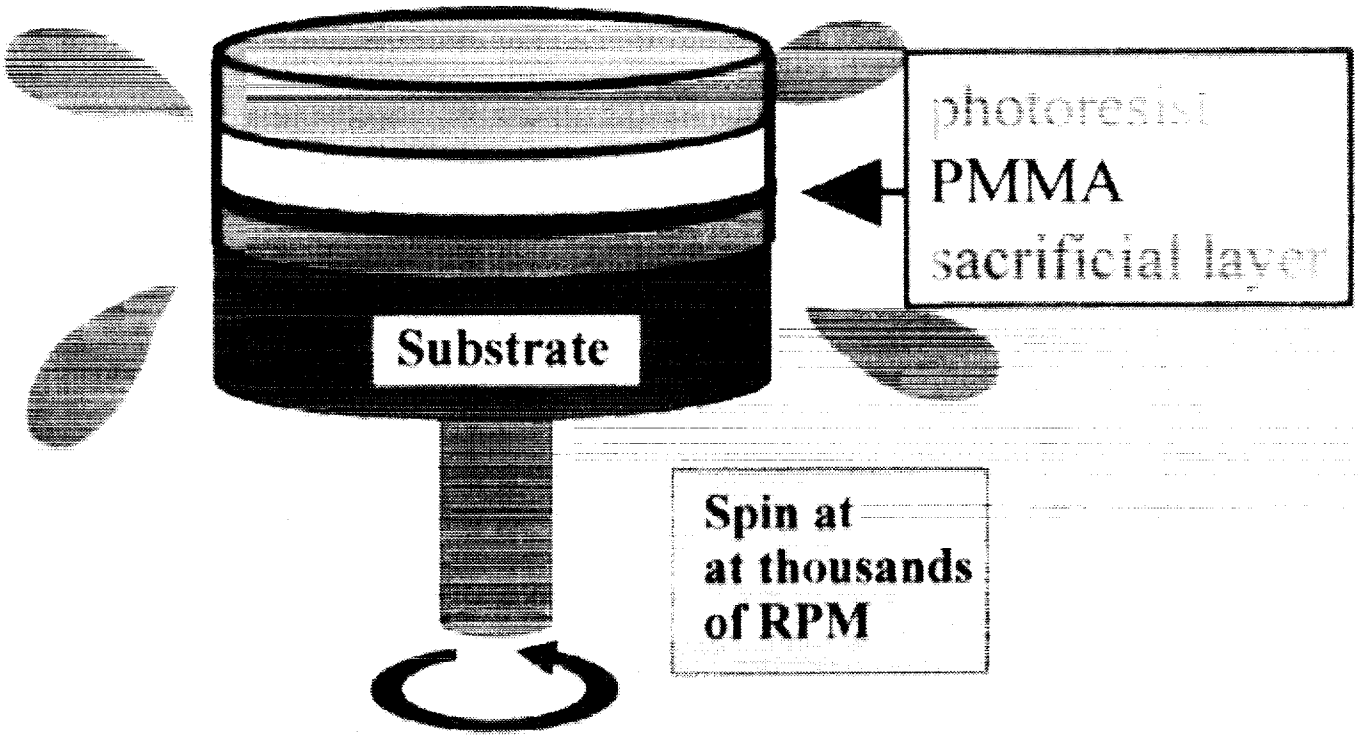

- Polymeric layer spin coated
- Solvents chosen such that each coating does not remove layer underneath

Fabrication: Exposure

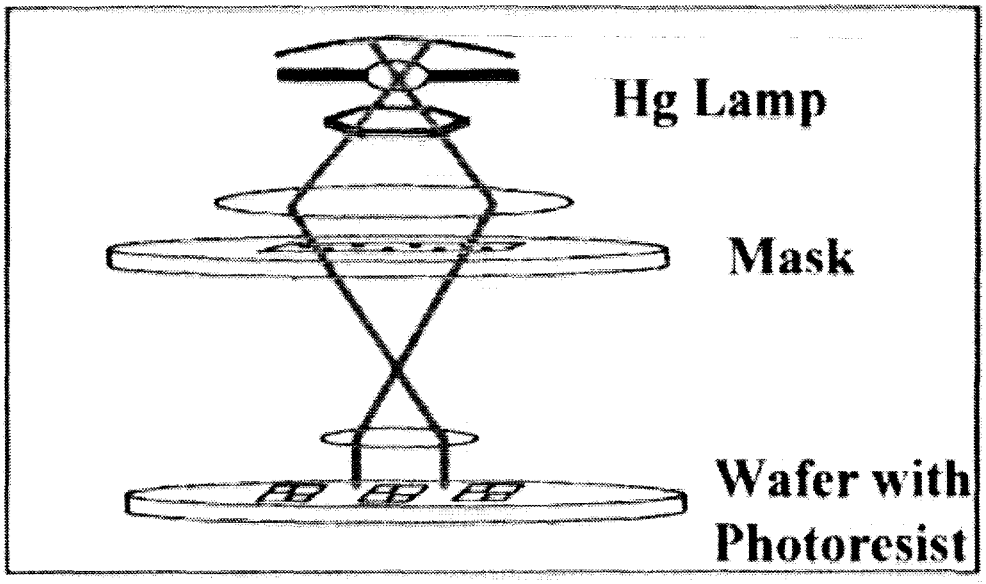

- After exposure and developing, the pattern is "written" into the photoresist.

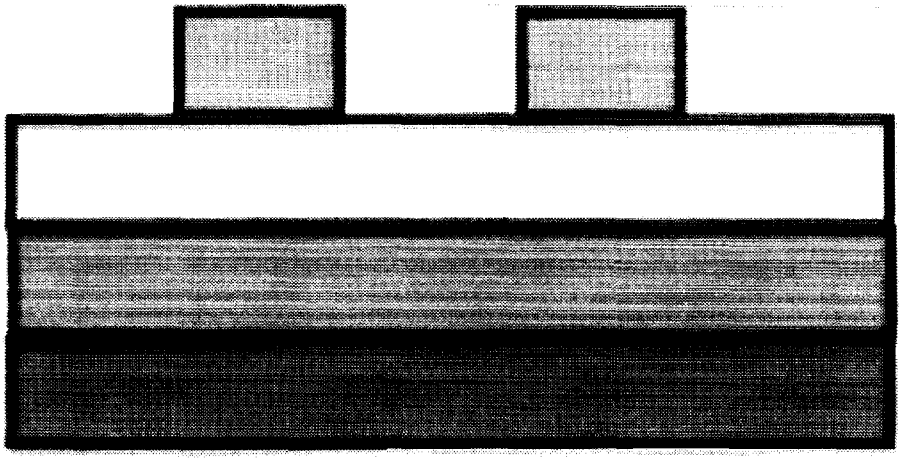

photoresist
PMMA
sacrificial layer
substrate

Fabrication: Pattern Transfer

O_2 Plasma

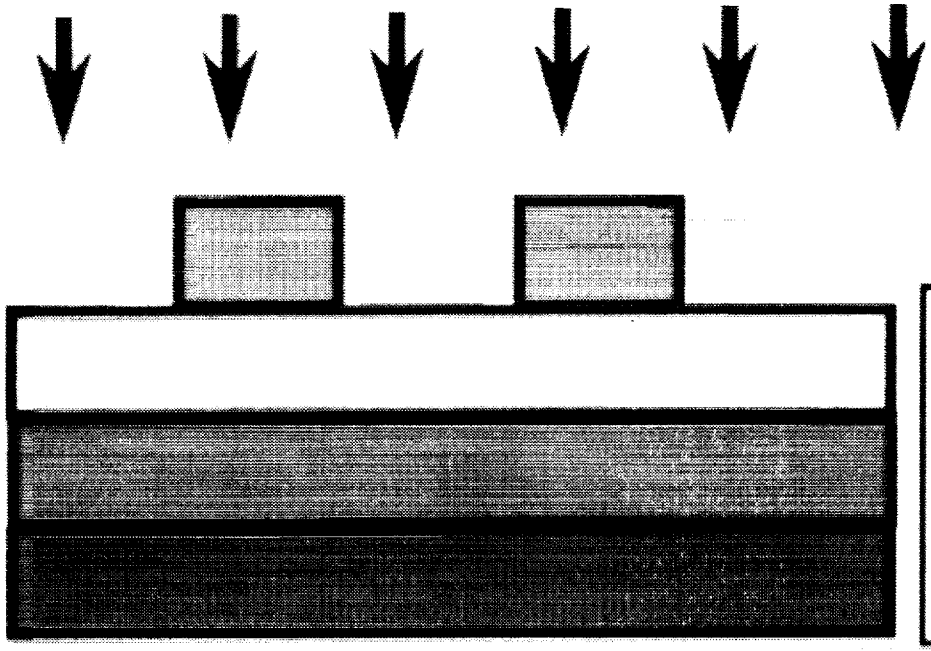

photoresist
PMMA
sacrificial layer
substrate

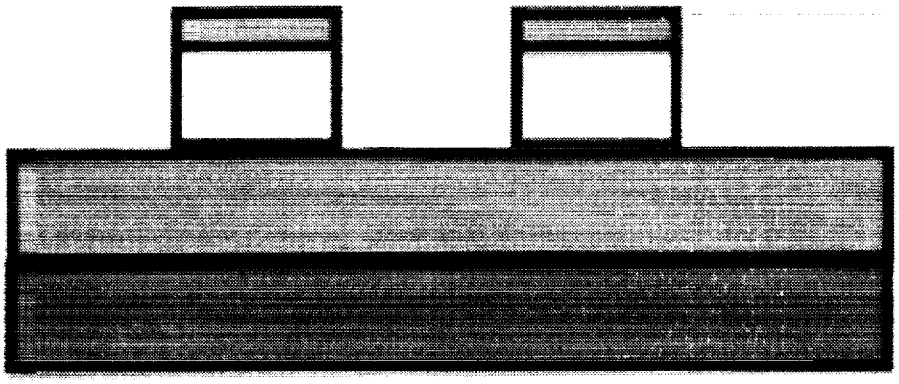

PMMA disks
sacrificial layer
substrate

- Reactive ion etching (RIE) transfers pattern from photoresist to PMMA
- Colloidal particles ready to float off

This talk will present recent results from ground-based research to support the "Physics of Colloids in Space" project which is scheduled to fly in the ISS approximately one year from now. In addition, results supporting future planned flights will be discussed.

PCS
PHYSICS OF COLLOIDS IN SPACE

DAVE WEITZ HARVARD

ERIC WEEKS
URS GASSER
TONY DINSMORE
SULIANA MANLEY

PHIL SEGRE NASA & HUNTSVILLE
LUCA CIPELETTI MONTPELLIER

COLLOIDAL CRYSTALS → BINARY ALLOYS

COLLOIDAL GELS

COLLOID/POLYMER MIXTURES

SCATTERING

MICROSCOPY

PC 5

PAUL CHALKIN SCIENCE

Confocal Microscopy

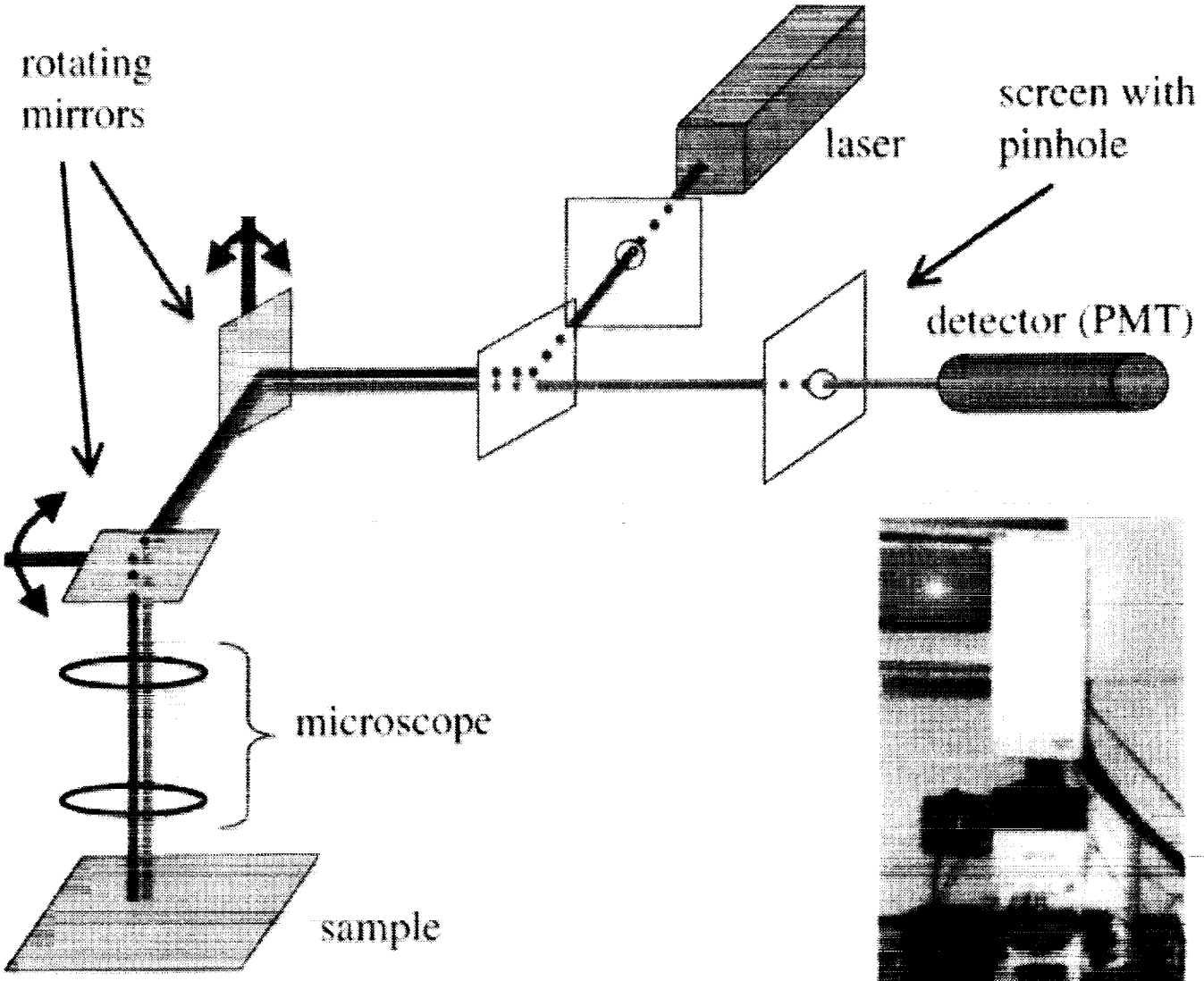

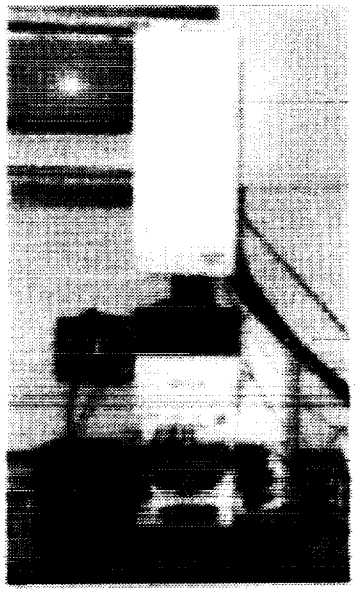

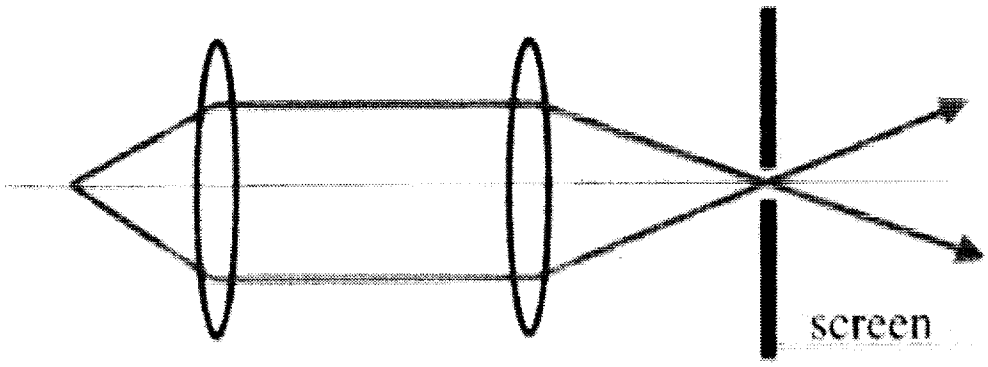

Confocal microscopy for 3D pictures

Scan many slices, reconstruct 3D image

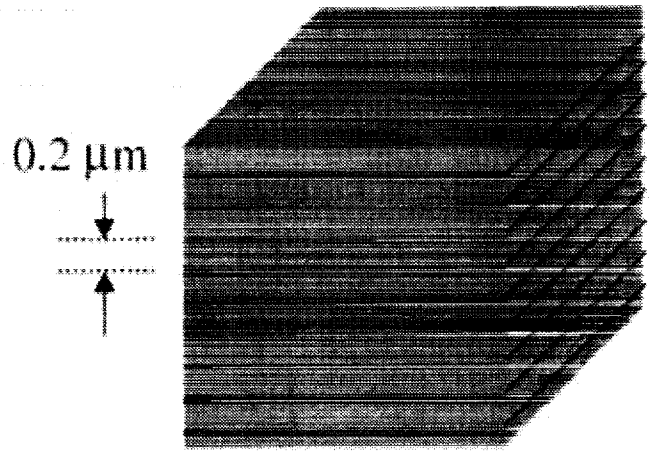

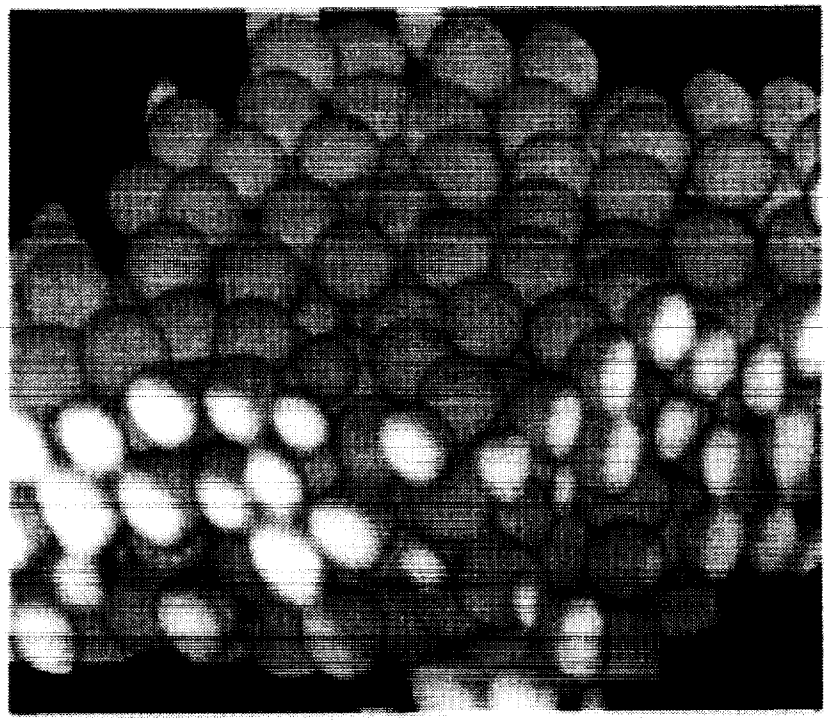

2.3 µm diameter PMMA particles

Microscopy and Tracking

Microscopy:

- 30 images/s (512×480 pixels, 2D)
- one 3D "cube" per 6 s
- $67 \times 63 \times 14\ \mu m^3$
- 100× oil / 1.4 N.A. objective
- Identify particles within 0.03 μm (*xy*)
  0.05 μm (*z*)

Particle tracking:

- Follow 3000-5000 particles, in 3D
- 200-1000 time steps = hours to days
- ≈ 4 GB of images per experiment

PMMA particles:

- made by Andrew Schofield (Edinburgh)
- fluorescent (Andrew Levitt, U. Penn)
- monodisperse, can crystallize
- density matching solvent
- 3D samples: look >30 μm from wall (>10 diameters)

(not to scale)

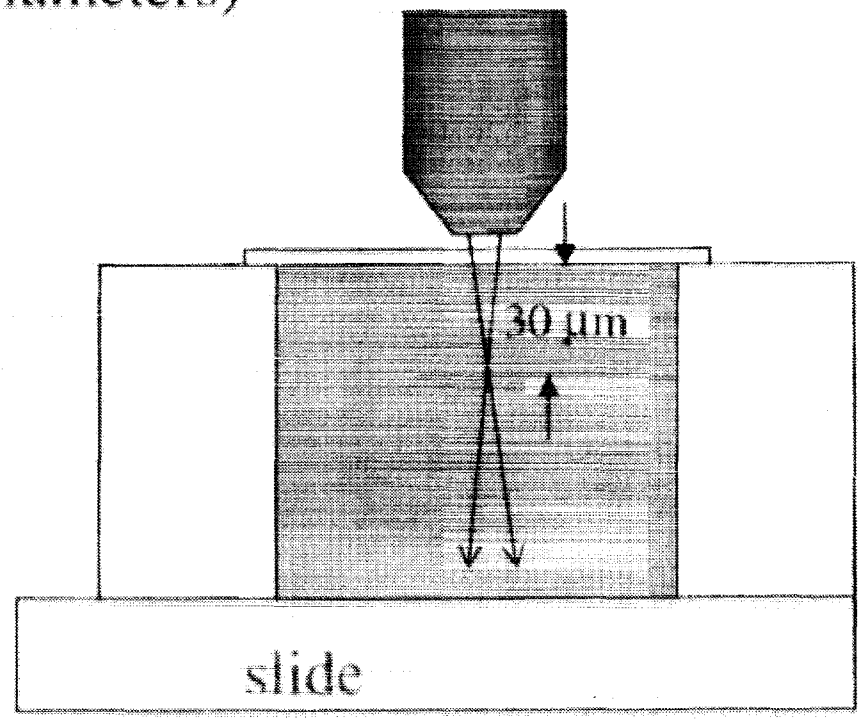

Experimental Details

- 2.3 μm diameter PMMA colloids
- density matched solvent
- act like hard spheres
- equilibrium is random HCP

- confocal microscopy to take 3D pictures
- look 30 μm in from cover slip

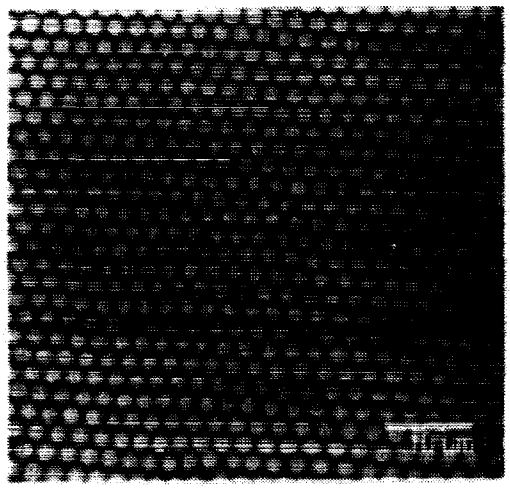

single 2D image

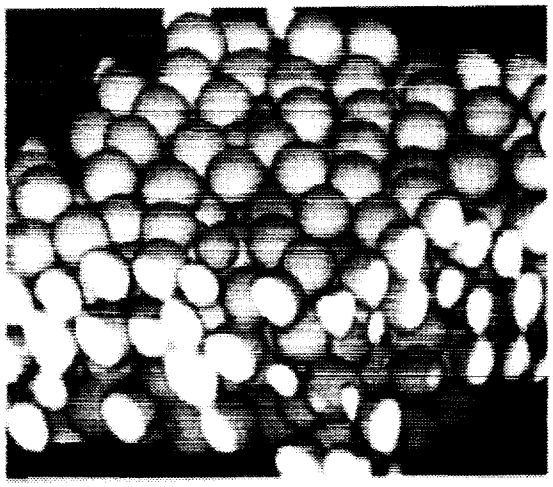

3D reconstruction
from many 2D slices

Brownian Motion

(2 μm particles, **dilute** sample)

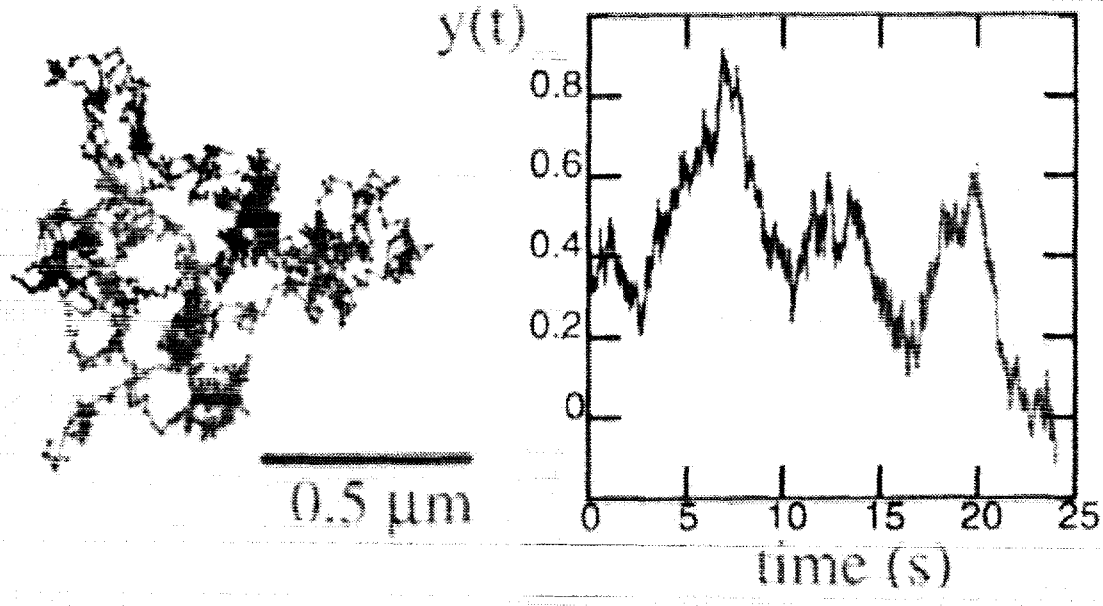

Leads to normal diffusion:

$$\langle \Delta x^2 \rangle = 2Dt$$

$$D = \frac{k_B T}{6\pi\eta a}$$

viscosity η

particle size a

Diffusion: **dilute** samples

Mean square displacement:

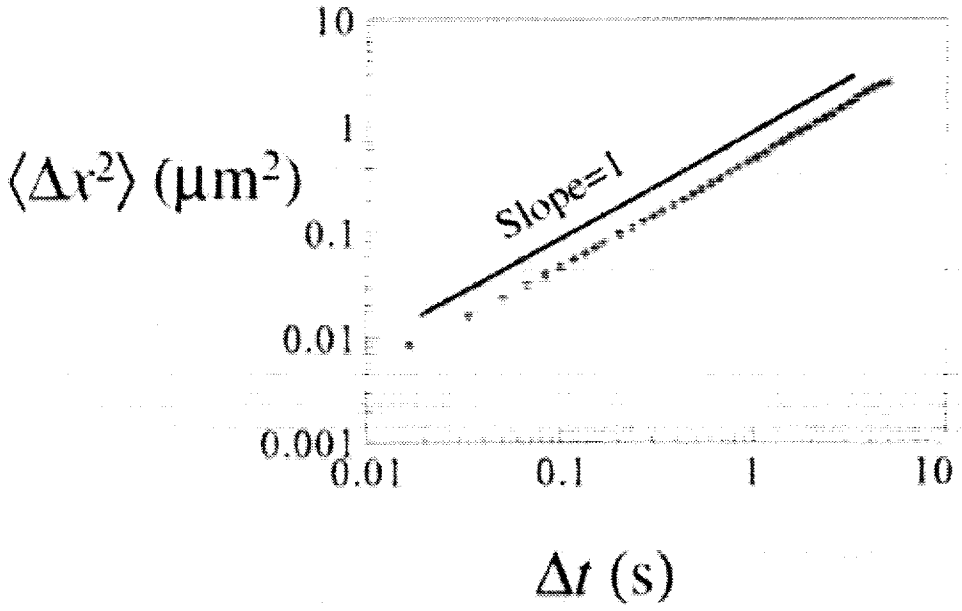

Displacement distribution function:

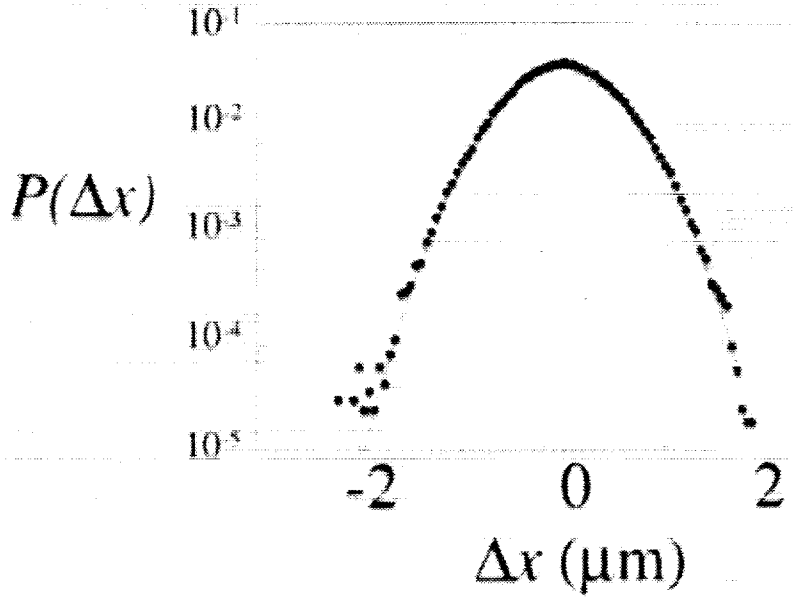

Δt=0.5s

Gaussian

Mean square displacement

Volume fraction ϕ=0.53,
"supercooled fluid"

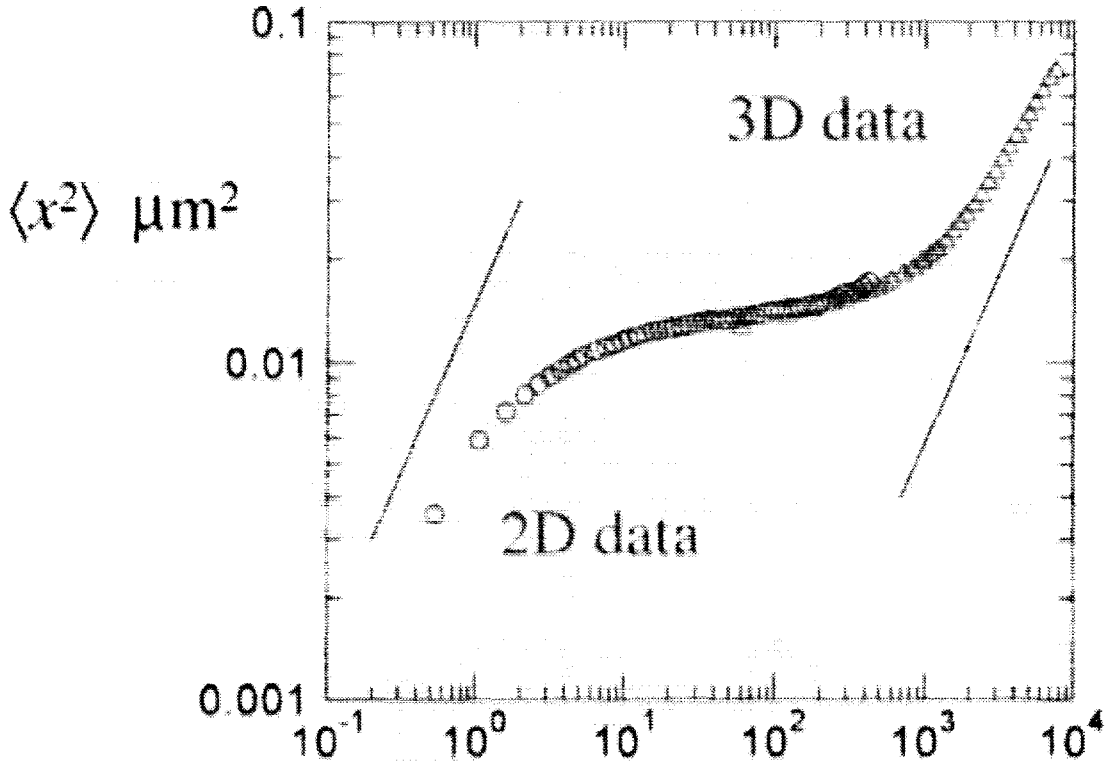

Cage trapping:

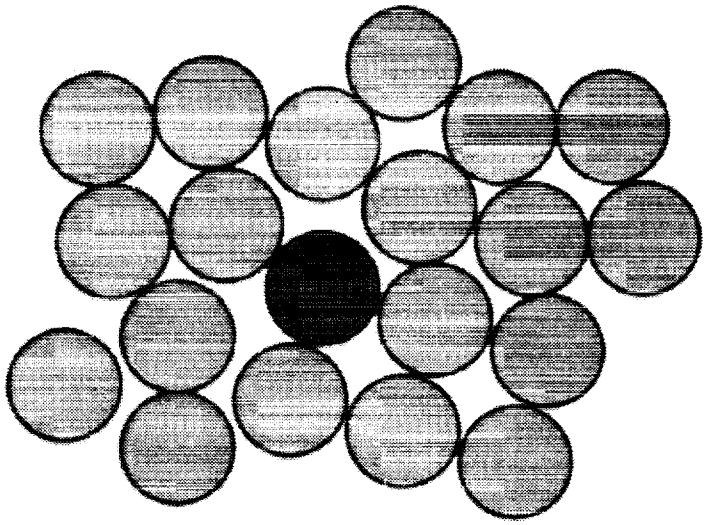

- Short times: particles stuck in "cages"
- Long times: cages rearrange

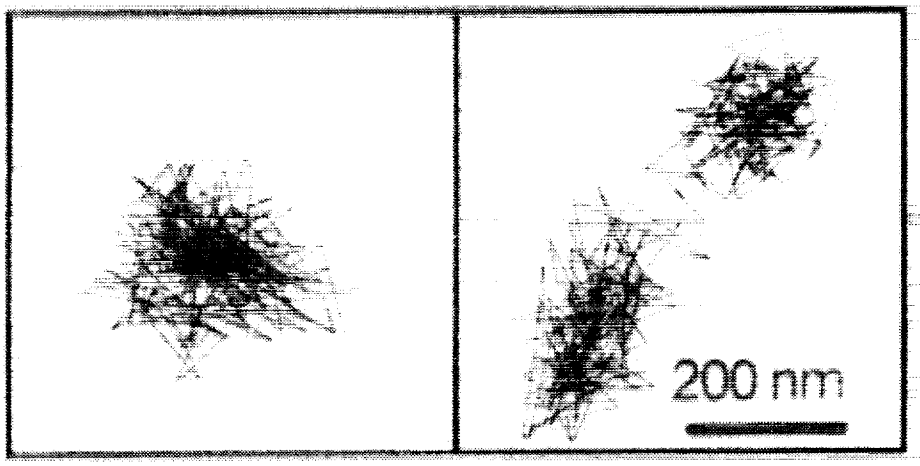

ϕ=0.56, 100 min (supercooled fluid)

Displacement distribution function

Volume fraction ϕ=0.53,
"supercooled fluid"

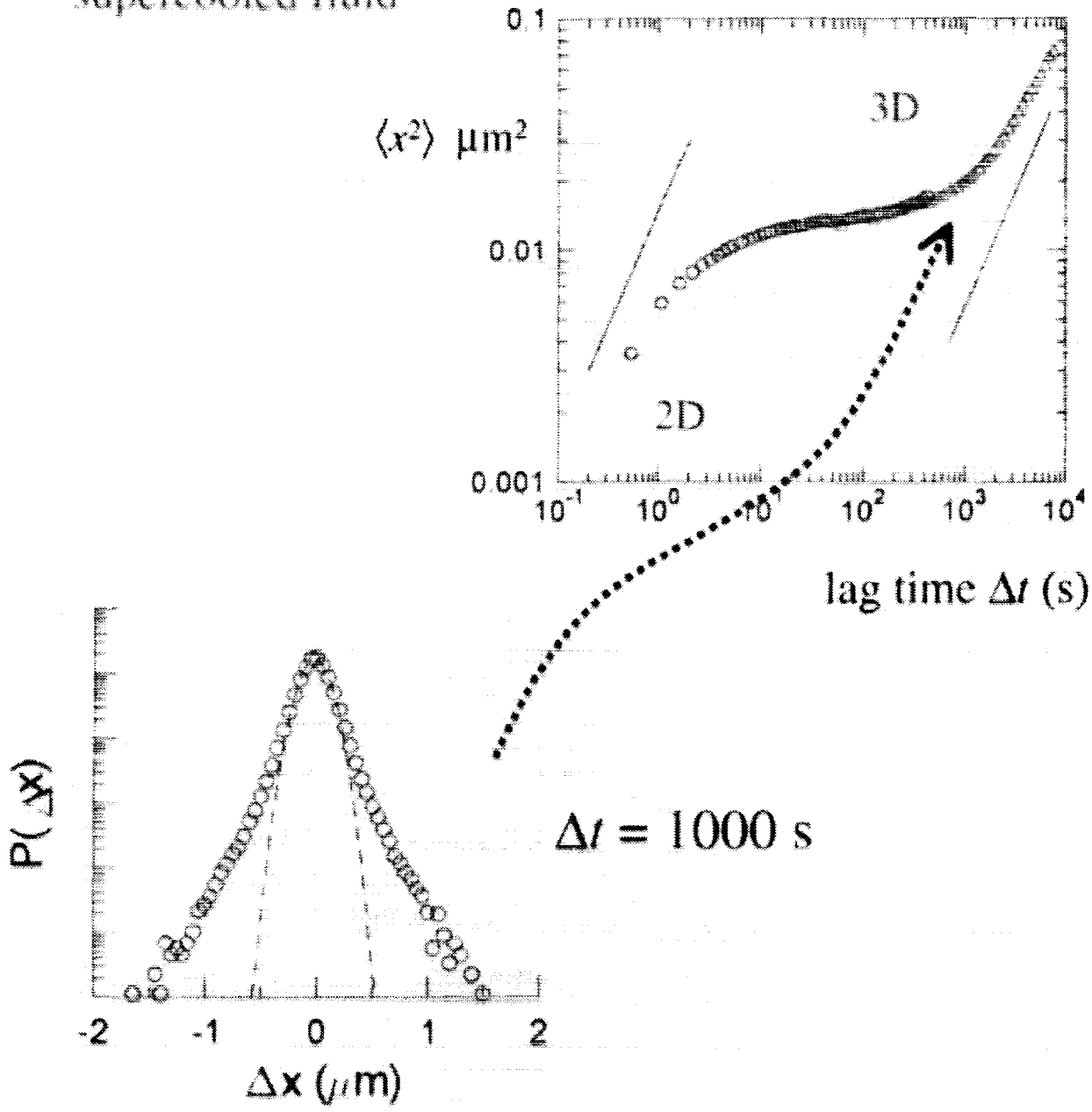

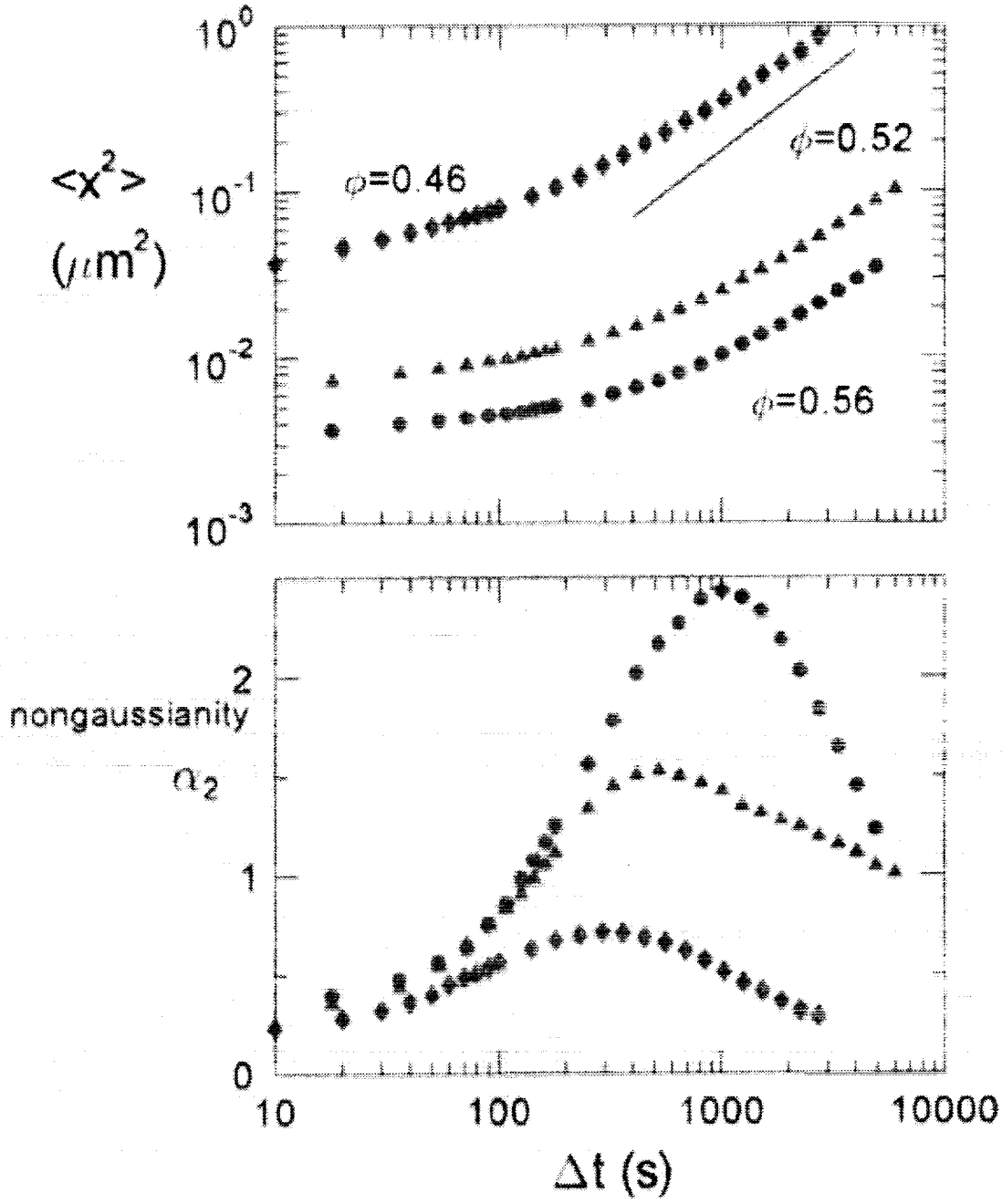
10^0
10^{-1}
10^{-2}
10^{-3}
<x²>
(μm²)
φ=0.46
φ=0.52
φ=0.56
nongaussianity
α_2
2
1
0
10
100
1000
10000
Δt (s)

Time scale:

Δt^* when nongaussian parameter α_2 largest

Length scale:

Δr^* on average, 5% of particles have $\Delta r(\Delta t^*) > \Delta r^*$

≈ cage rearrangements

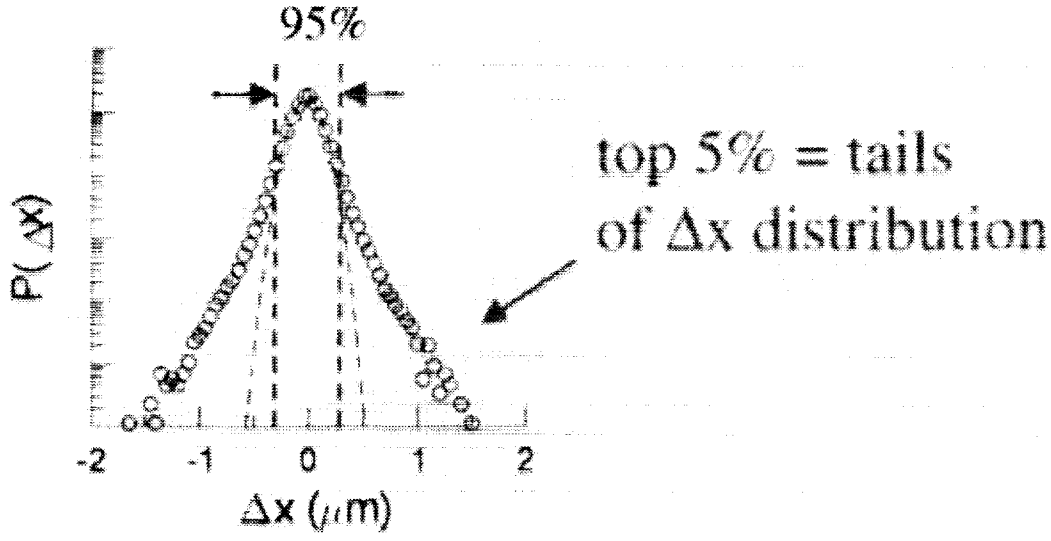

(φ=0.53, supercooled fluid)

Number N_f of fast neighbors to a fast particle:

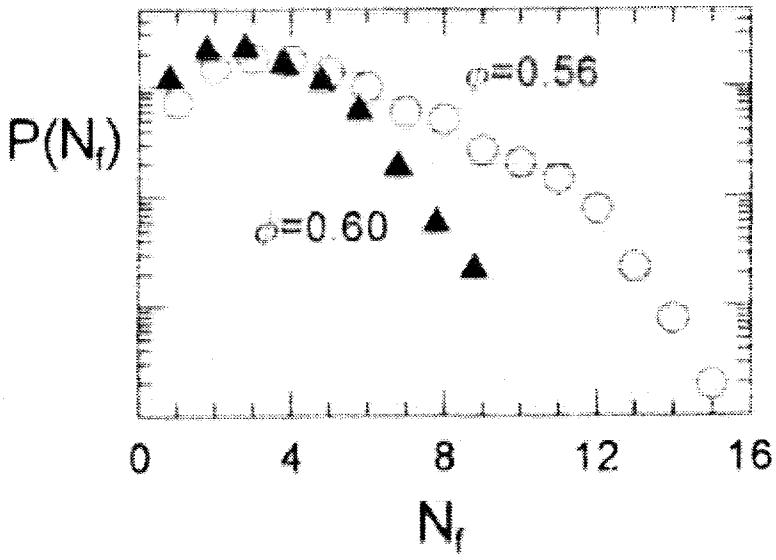

Fractal dimension:

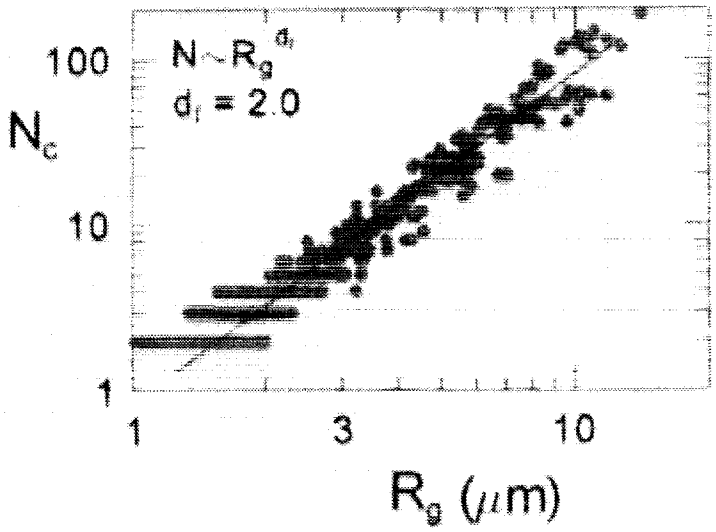

φ=0.56
supercooled fluid

Dynamical Heterogeneity: possible *dynamic* length scale

Adam & Gibbs: "**cooperatively rearranging regions**" (1965)

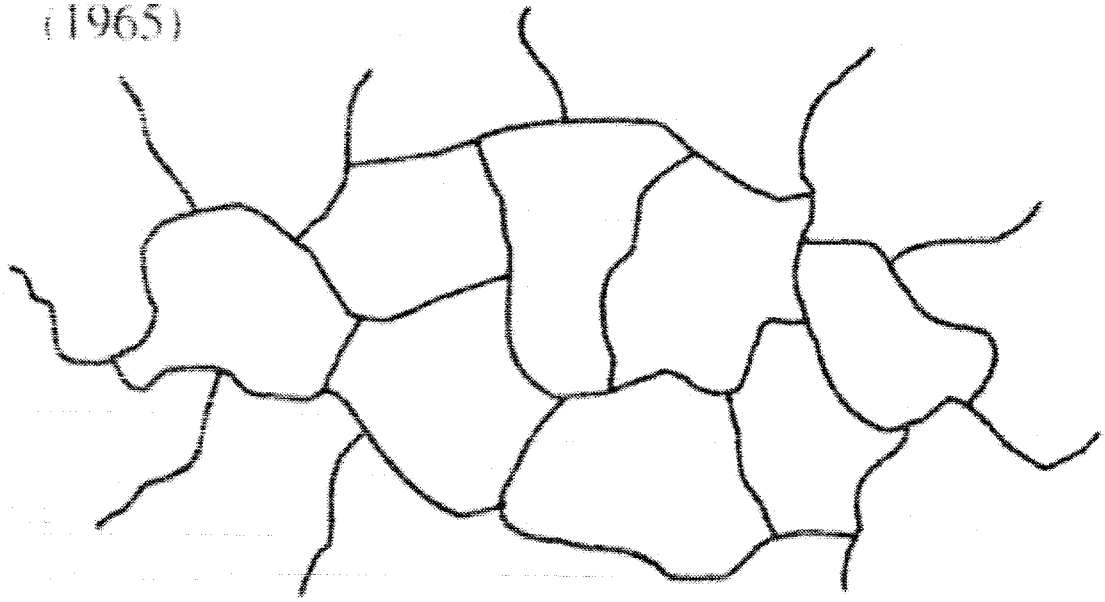

NMR experiments:

- Schmidt-Rohr & Spiess (1991, polymers)
- Tang, Johnson, et al (1998, metallic glasses)
- Silleseu et al (1992, o-terphenyl)

Photobleaching:

- Cicerone & Ediger (1995, o-terphenyl)

Simulations:

- Glotzer, Kob, Donati, et al (1997, Lennard-Jones)

Nucleation and Growth of Colloidal Crystals

by Small Angle Light Scattering

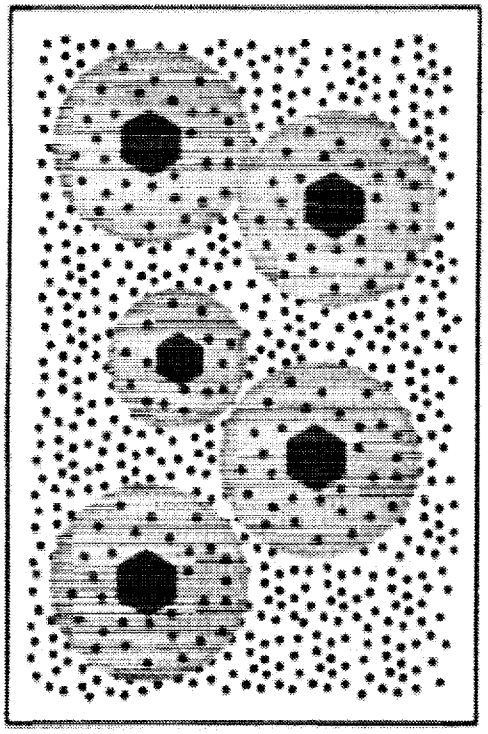

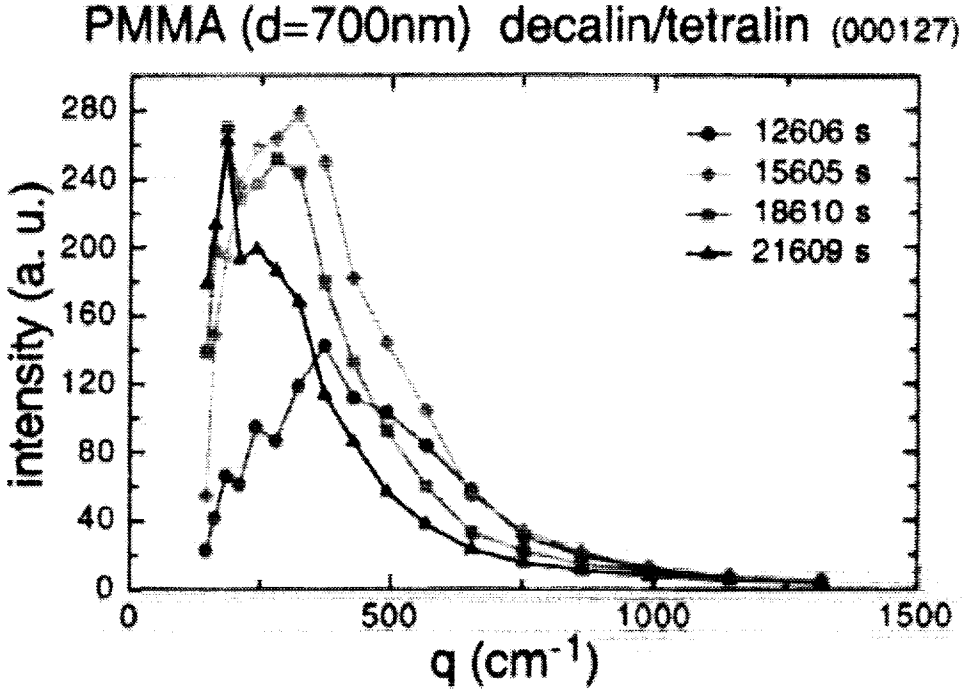

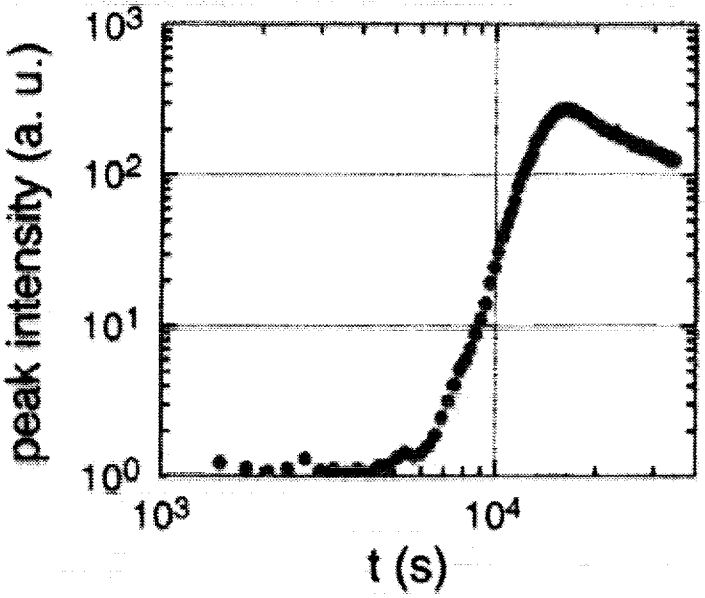

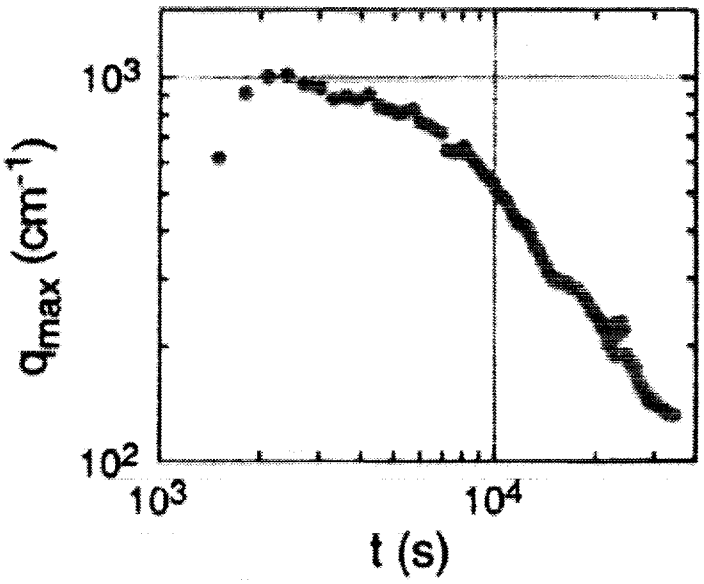

Local crystallization order parameter:

P. R. ten Wolde, M. J. Ruiz-Montero, D. Frenkel: *J. Chem. Phys.* **104**, 9932 (1996)

- Lennard-Jones simulation

- Find nearest neighbor connections r_{ij}

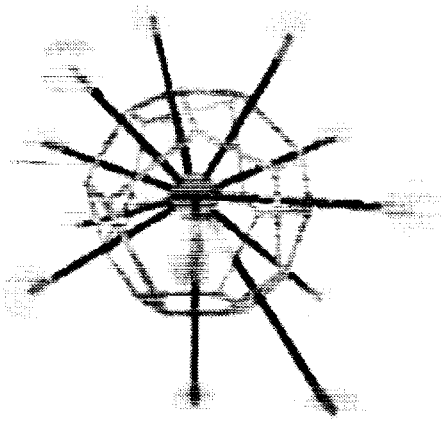

- Resolve connections in spherical harmonics:

$$q_{lm}(i)=\langle Y_{lm}(r_{ij})\rangle_j$$

- Examine $l=6$

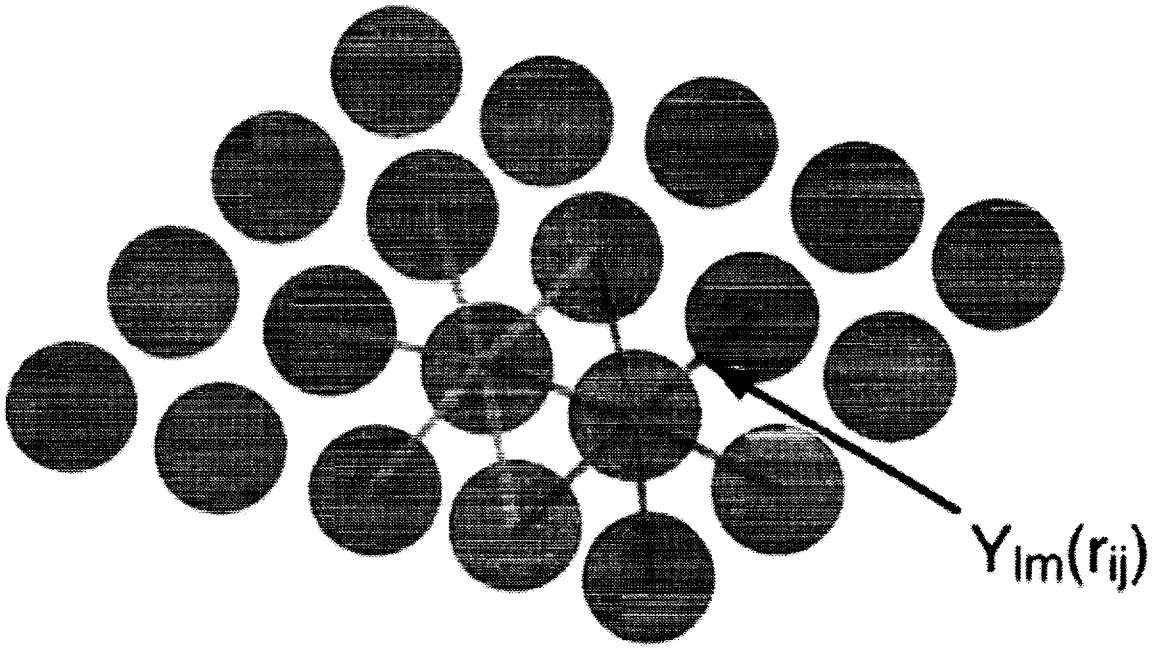

local bond order parameters:

$$q_{lm}(i) = 1/N_i \sum_{j(n.n.)} Y_{lm}(r_{ij})$$

rotationally invariant form:

$$q_l(i) = [\ 4\pi/(2l+1) \sum_m |q_{lm}(i)|^2\ ]^{1/2}$$

crystal-like bonds:

$$\vec{q}_6(i) \cdot \vec{q}_6(j) = \sum_m q_{6m}(i)\ q^*_{6m}(j) > 0.5$$

Gelation:

Non-Equilibrium States

Aggregation in colloid-polymer mixtures

fluid → gel

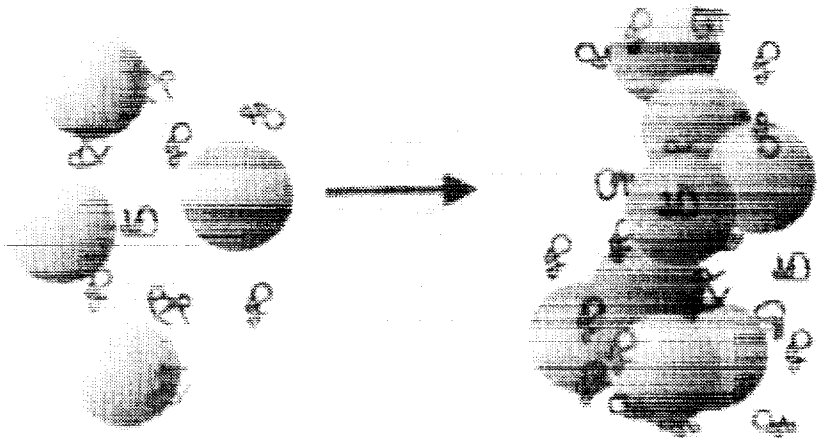

Polystyrene polymer, r_g=37 nm

+

PMMA spheres, r_c=350 nm

↓

Depletion attraction

c_p=5.0

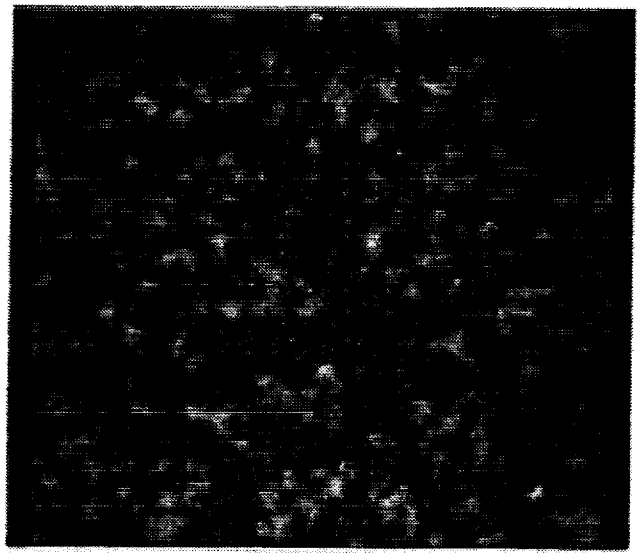

(image is 20 diameters thick)

c_p=8.8 (gel)

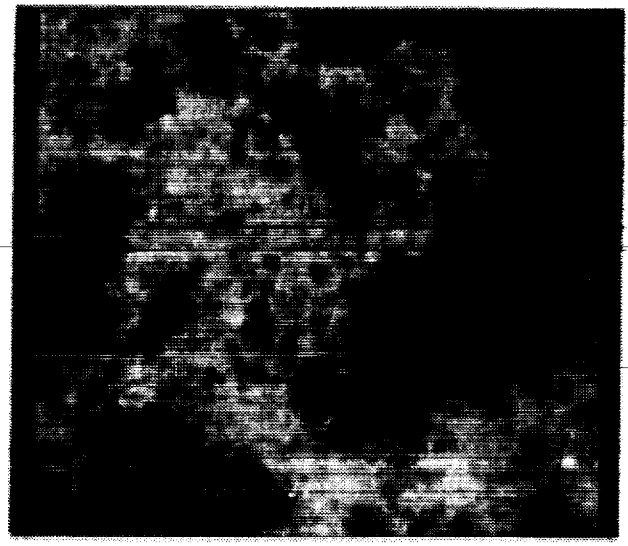

(image is 40 diameters thick)

Reconstructions of 3D images

c_p=5.0
('fluid-
cluster')

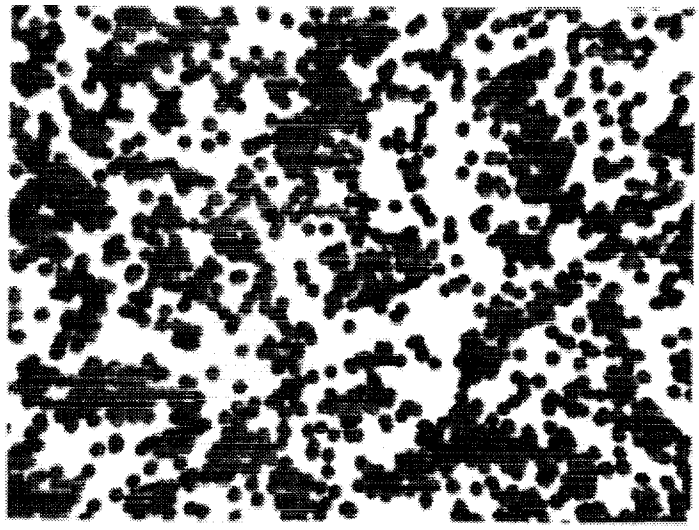

$c_{p=}$11.8
(gel)

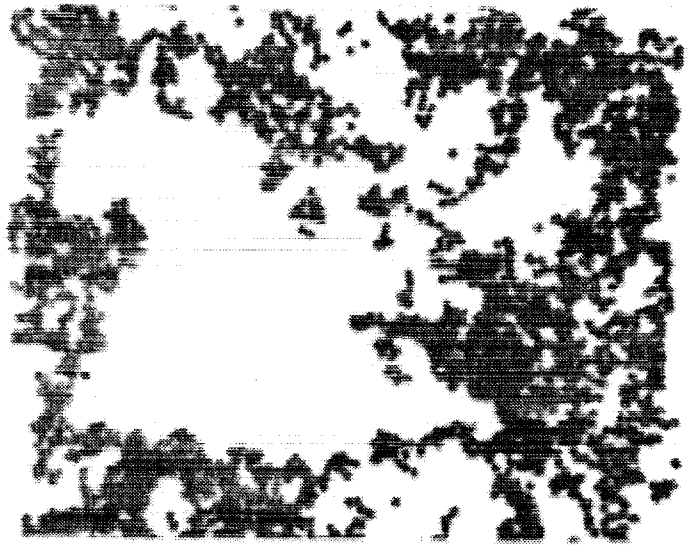

ϕ=0.03

Gel morphology

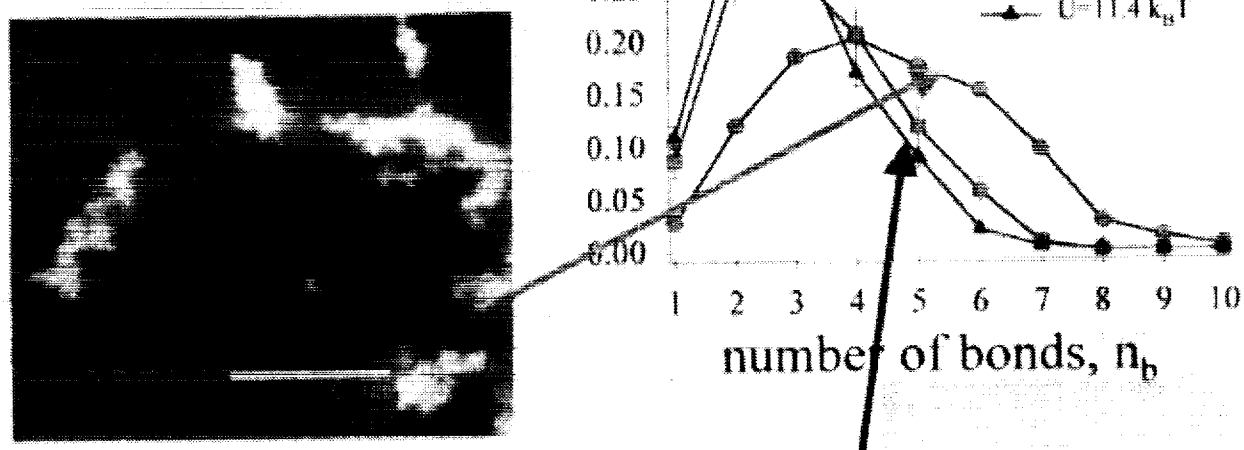

U=5.1 k_BT

U=11.4 k_BT

$\phi = 0.03$
$R_c = 0.35\ \mu m$
images are 2 μm thick

~12 h old

Gel morphology - chains

- Define chain, determine its length
- Find particles in chain (red)

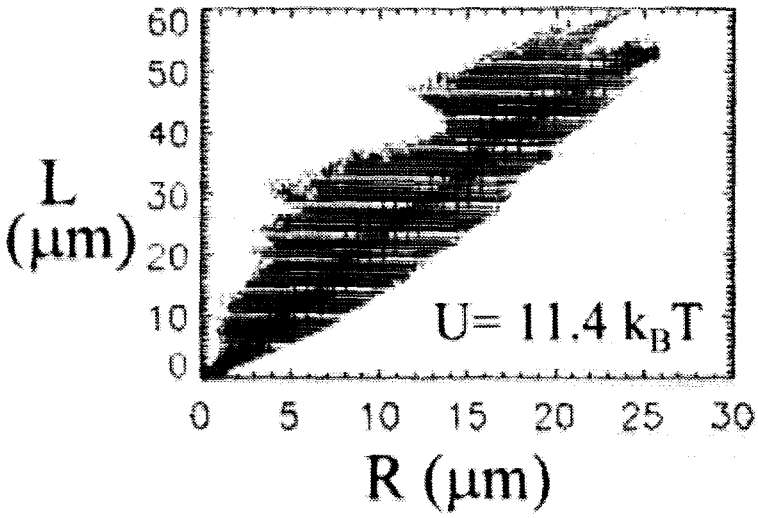

- Shortest-path length, L
  - L=2.3 × R (for all samples, U=5-11 k_BT)

- Chemical dimension, $N_{ch} \propto R^{d_{chem}}$
  - measured $d_{chem} = 1.0 \pm .1$
- Chain cross section = N_{ch}/(L×sphere diameter)
  - 1.5 particles (U= 5.6 k_BT)
  - 1.0 particles (U= 11.4 k_BT)

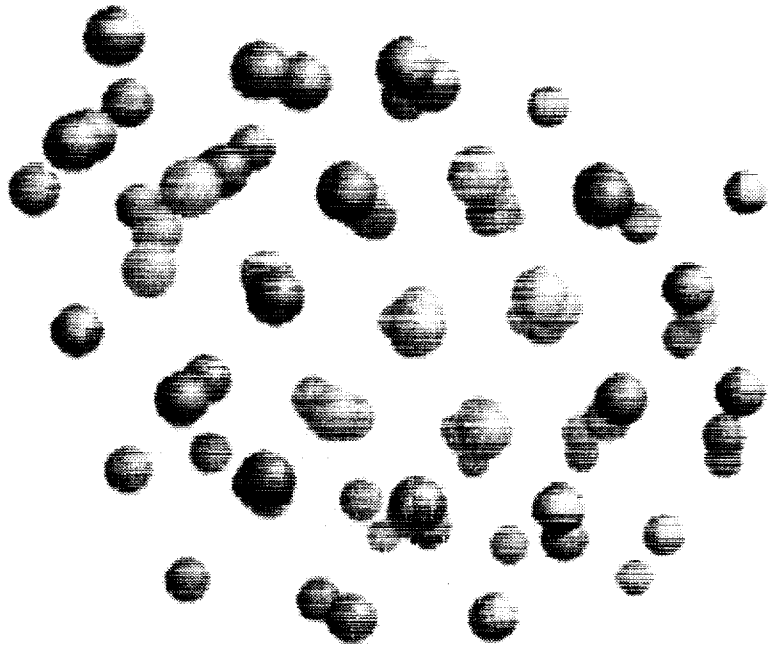

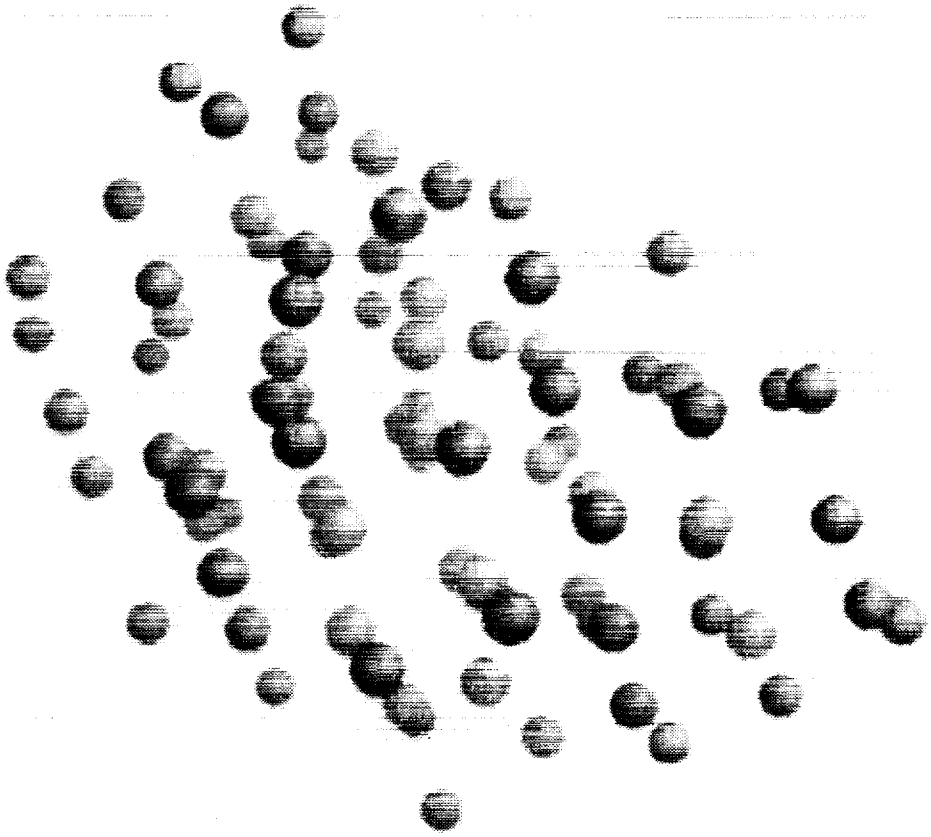

COLLOIDAL ASSEMBLY IN ENTROPICALLY DRIVEN, LOW-VOLUME-FRACTION BINARY PARTICLE SUSPENSIONS

S. Sanyal, J. Zhang, W.J. Work, K-H Lin, and A.G. Yodh, University of Pennsylvania

We describe entropic depletion-induced assembly experiments to synthesize novel colloidal crystals. Our samples are typically a mixture of large and small species suspended in water or in an organic liquid. The larger particles are spherical colloids with diameter ranging from 0.4 to 3 microns, and its type range from polymer-based spheres such as polymethylmethacrylate (PMMA), polystyrene (PS) and silica, to semiconductors such as ZnS, to novel polymer-based spheres that have hollow interiors. The small species can be a polymer (e.g. PS polymer), a micelle (e.g. SDS micelles), a dendrimer, or a very small colloidal particle. Typically an optical grating template is bonded to one wall of our microscope slide cells to select particular colloidal crystal types.

We have investigated the entropic self-assembly of colloidal spheres on periodic patterned templates [1,2]. A variety of two-dimensional structures with quasi-long-range order are observed to form on templates with one- and two-dimensional periodic structure. In particular, on a template commensurate with an FCC (100) plane, entropic forces induced by non-adsorbing polymers form an FCC crystal more than 30 layers thick without random stacking defects [3].

We have also begun particle synthesis experiments to achieve samples of monodisperse colloidal suspensions of the types mentioned above. So far our successes in this endeavor are as follows. (1) We could modify a published technique [4] to synthesize 140 nm and 400 nm ZnS particles with size-dispersity < 5%. In principle this same procedure can be applied to synthesize a range of similar sulfides, e.g. CdS, SnS, PbS, MnS. (2) We have prepared monodisperse particles that have a water-swollen core (precursor to hollow sphere particles) with particle sizes in the 550-650 nm range [5,6]. Initial success of their assembly by depletion techniques has been achieved in our laboratory [7]. (3) We have also succeeded in synthesizing 100 nm, 200 nm, and 600 nm monodisperse (<10%) magnetic particles following a literature technique [8,9].

We will describe experiments to measure the photonic bandstructure of some of these crystals using a spectrophotometer set up in our laboratory, which can perform angle- and wavelength-resolved reflection and transmission experiments on our colloidal crystalline samples.

References

[1] Sanyal, S., Zhang, J., Lin, K-H., Work, W.J., Yodh, A.G., Using Depletion Force to synthesize PBG crystals, Bulletin of the American Physical Society, 45 (1), 768, 2000.

[2] Lin, K-H, Crocker, J.C., Yodh, A.G., Prasad, V., Weitz, D.A., Schofield, A., Entropically Driven Colloidal Crystallization on Patterned Surfaces, Bulletin of the American Physical Society, 45 (1), 698, 2000.

[3] Lin, K-H, Crocker, J.C., Prasad, V., Schofield, A., Weitz, D.A., Yodh, A.G., Entropically Driven Colloidal Crystallization on Patterned Surfaces, Submitted to Physical Review Letters, November 1999.

[4] Sugimoto, T., *et al.*, Journal of Colloid & Interface Science 180, 305-308 (1996).

[5] Kowalski, *et al.*, Sequential heteropolymer dispersion and a particulate material obtainable therefrom, useful in coating compositions as an opacifying agent, US Patent 4,469,825, September 4, 1984, Assigned to Rohm and Hass Company.
[6] Yanase, N., Noguchi, H., Asakura, H., Suzuta, T., Preparation of magnetic latex particles by emulsion polymerization of styrene in the presence of a ferrofluid. Journal of Applied Polymer Science 50, 765-776 (1993).
[7] Zhang, J., Work, W.J., Sanyal, S., Lin, K-H, Yodh, A.G., 3-Dimensional Colloidal Crystals from Hollow Spheres, Bulletin of the American Physical Society, 45 (1), 631, 2000.
[8] Ugelstad, J., Ellingsen, T., Berge, A., Helgee, O.B., Process for preparing magnetic polymer particles, US Patent 4,774,265, September 27, 1988, Assigned to Sintef.
[9] Ugelstad, J., Ellingsen, T., Berge, A., Helgee, O.B., Magnetic polymer particles and process for the preparation thereof, US Patent 4,654,267, March 31, 1987, Assigned to Sintef.

Entropic Effects in Suspension

Anthony Dinsmore, John Crocker, Ritu Verma,
*** Keng Hui-Lin, Eric Weeks, Peter Kaplan Jennifer Rouke, David Thakker, Derek Wong, Joe Mateo**
Jian Zhang, Mohammad Islam, Subrata Sanyal, Ahmed Alsayed, Vikram Prasad, Andy Schofield
Arjun Yodh Dept. of Physics and Astronomy**
University of Pennsylvania

Tom Lubensky, PENN
Randy Kamien, PENN
Phil Nelson, PENN
Dave Weitz Dept. of Physics & Astro., ~~PENN~~ HARVARD
David Pine Dept. of Chemical Eng., UCSB
Wilson Poon
Patrick Warren Dept. Physics, Un. of Edinburgh

For Details See:

Kaplan, Rouke, Yodh, Pine, Phys. Rev. Lett. **72** (1994)
Dinsmore, Yodh, Pine, Phys. Rev. E **52** (1995)
Dinsmore, Yodh, Pine, Nature **383** (1996).
Dinsmore, Warren, Poon, Yodh, Europhy. Lett. **40** (1997).
Dinsmore, Wong, Nelson, Yodh, Phys. Rev. Lett. **80** (1998).
Verma, Crocker, Lubensky, Yodh Phys. Rev. Lett. **81** (1998).
Dinsmore, Yodh Langmuir **15** (1999).
Crocker, Mateo, Dinsmore, Yodh, Phys. Rev. Lett. **82** (1999). 2000
Verma, Crocker, Lubensky, Yodh submitted Macromolecules (~~1999~~).
Lin et. al. PRL (2000) August.

****Acknowledgements: NASA, NSF**

PLAN

1. MOTIVATION

2. DEPLETION Effect

   a. Bulk
   b. Wall
   c. Wall Structures

3. One-, Two-, Three-Dimensional Assembly in Ideal System

4. SUMMARY

General Motivations

• Difficult, but desirable to create patterned nano- and micro-scale materials that are ordered in three-dimensions.

SMART MATERIALS FOR
NEXT GENERATION TECHNOLOGIES.

Lithography
Holography
*Self-Assembly of mesoscopic constituents

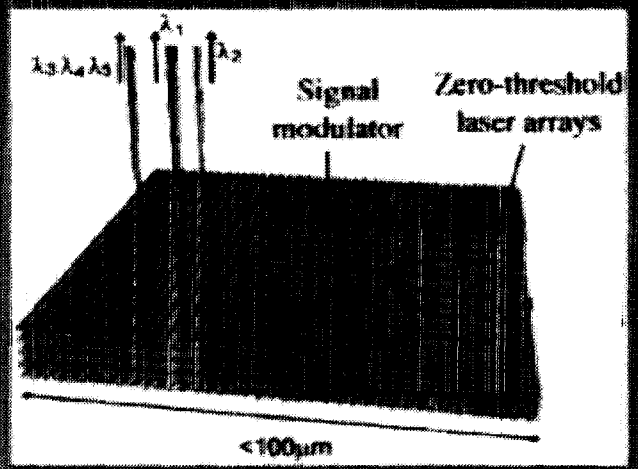

• Colloidal particles ranging in size from ~10 nm to ~3 micron can be assembled into ordered crystalline phases.

*Equilibrium Thermodynamics
Gravitationally-driven
Convectively-driven
Electrohydrodynamically-driven

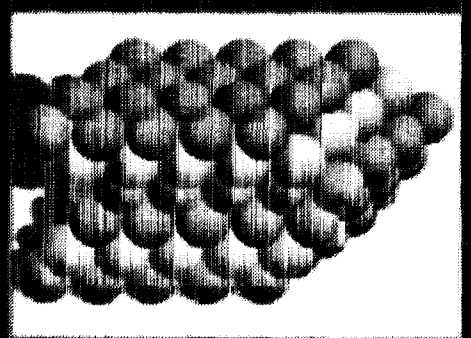

Depletion Force: (HARD SPHERES)

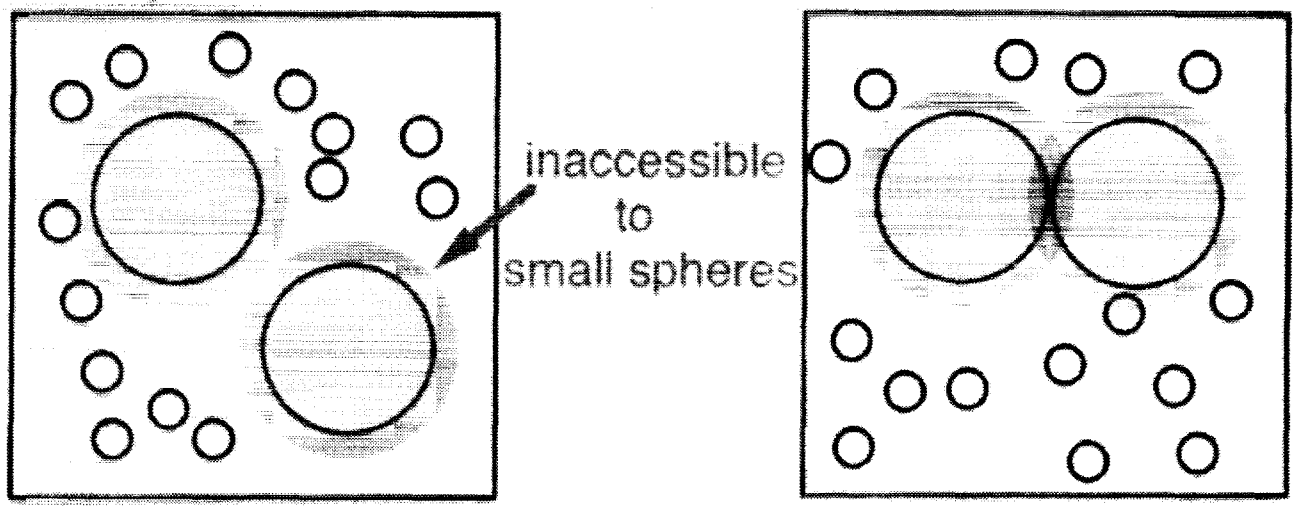

→ Moving 2 large spheres together increases volume accessible to small spheres

↓

increases total entropy

$\Delta F = \Delta U - T\Delta S$

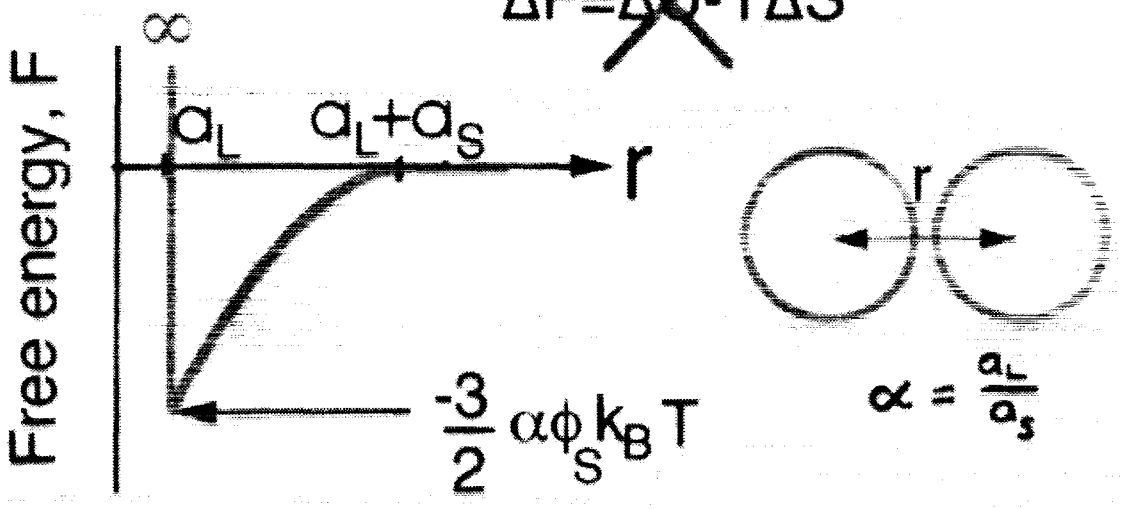

Free-energy gradient ⟷ Force

- S. Asakura and F. Oosawa, J. Chem. Phys. **22**, 1255 (1954).
- A. Vrij, Pure and Applied Chem. **48**, 471 (1976).

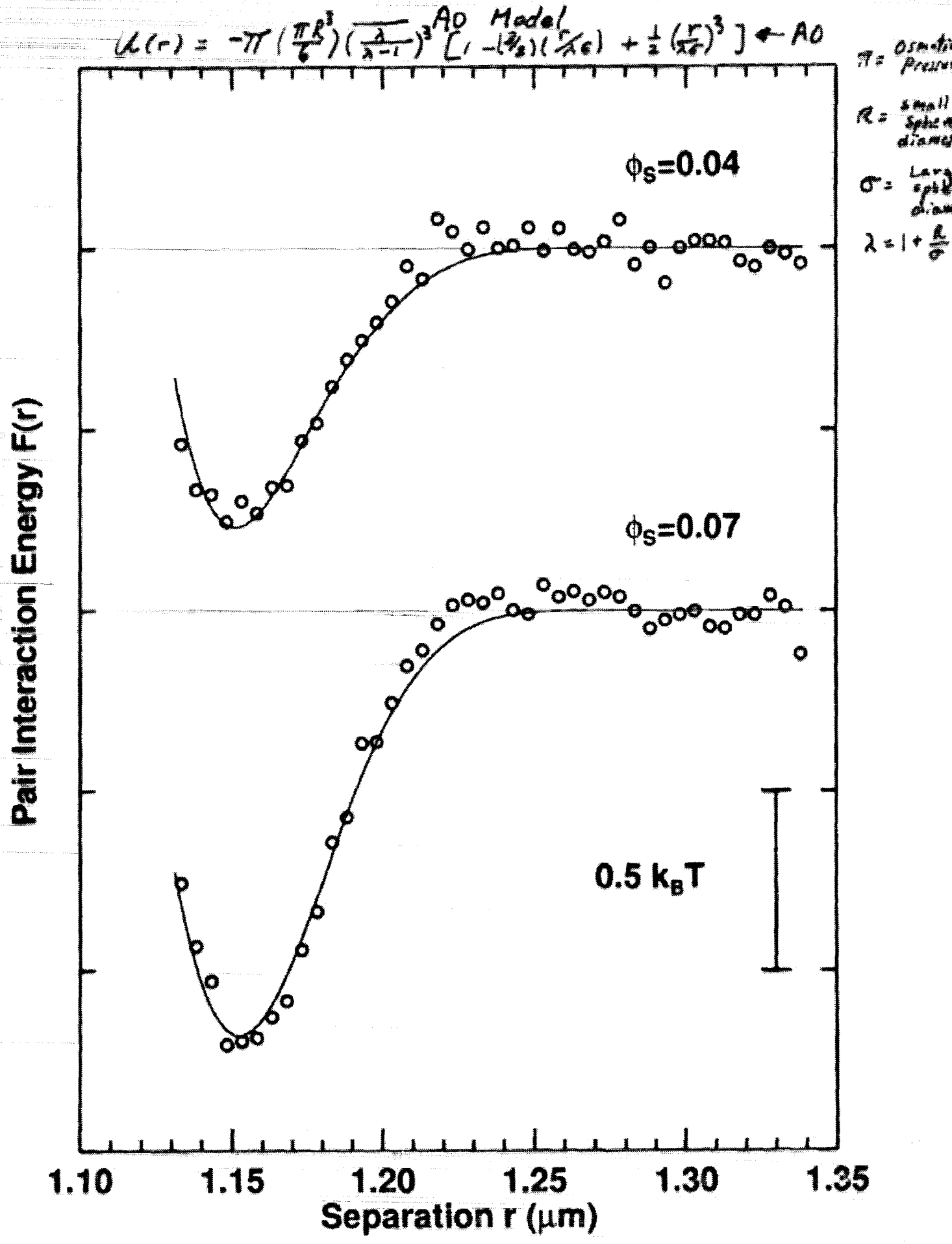

PRL 82 : 4352 (1999)

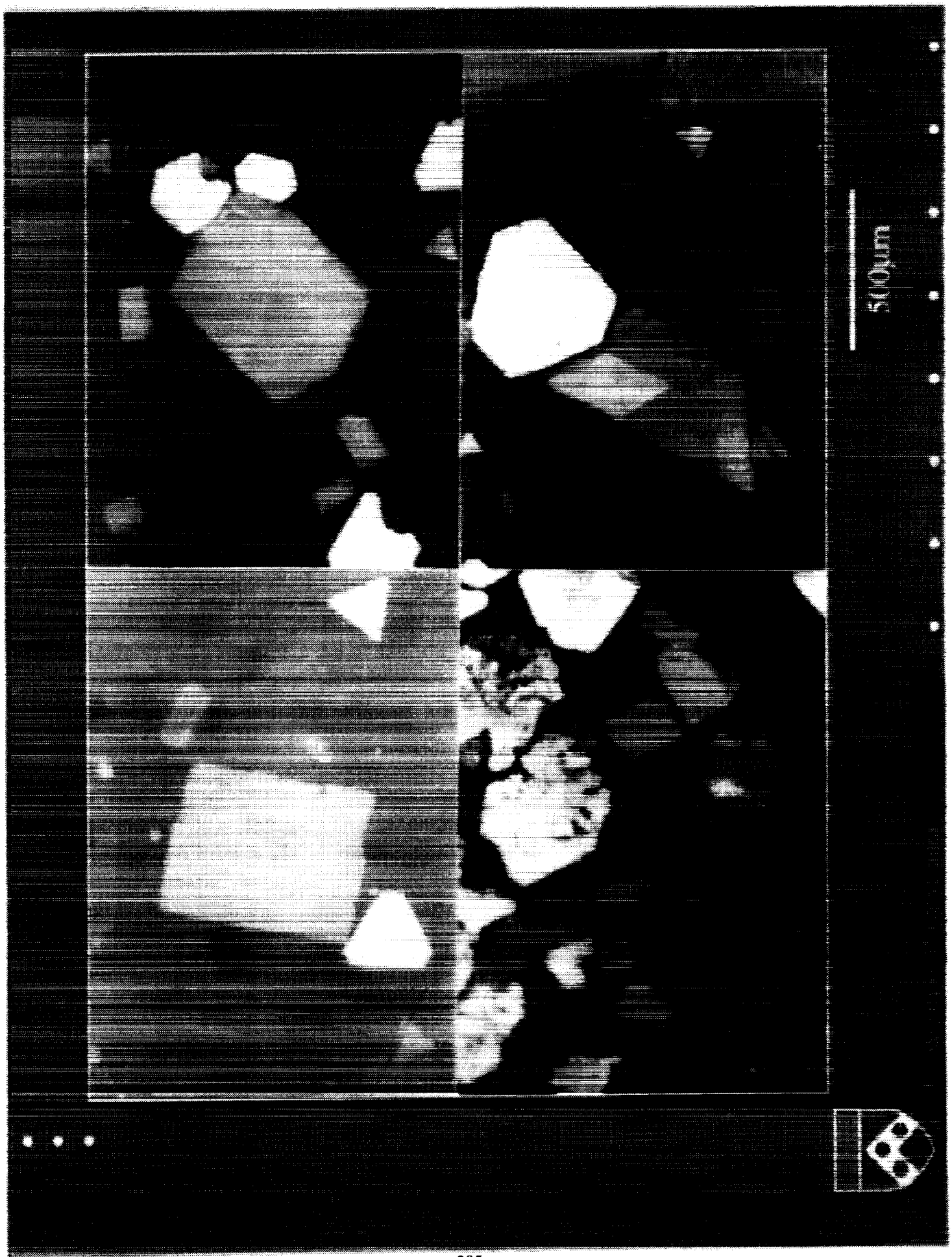
500μm

Phenomenological Approach

Dickman, Yuhl, Tian PRE 52 '95

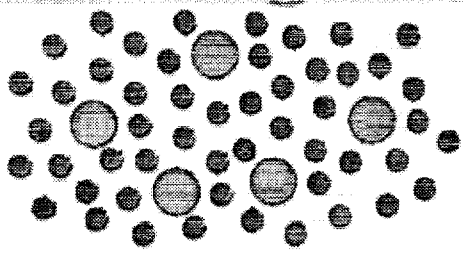

Fluid Phase:

- Gas of Large hard spheres + Gas of Small hard spheres.

Gas Pressures derived from the Carnahan-Starling Equation of State; Volume fractions of the Large (Small) spheres are <u>increased</u> as a result of the volume occupied by the Small (Large) spheres.

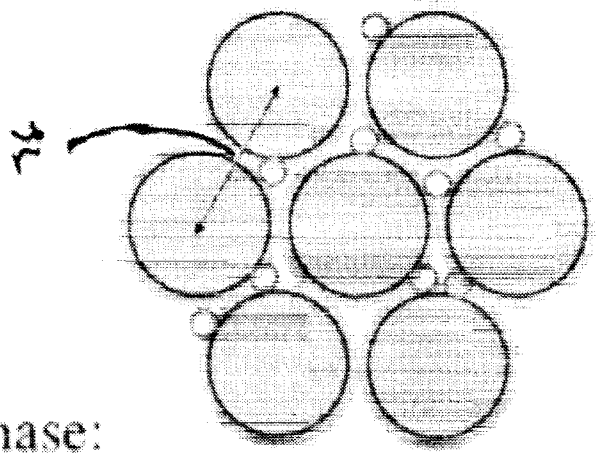

Solid Phase:

- Close-packed lattice of Large Hard-spheres permeated by hard-sphere gas of Small spheres.

<u>Critical Feature Emerging from the Solid Model</u>

Since the Large sphere excluded volumes already overlap in the solid, the entropy of the Small spheres increases as the crystal becomes more tightly packed !

Equate Osmotic pressures of phases, and chemical potentials of large and small spheres within each phase⇒PHASE DIAGRAM

Phase Diagram

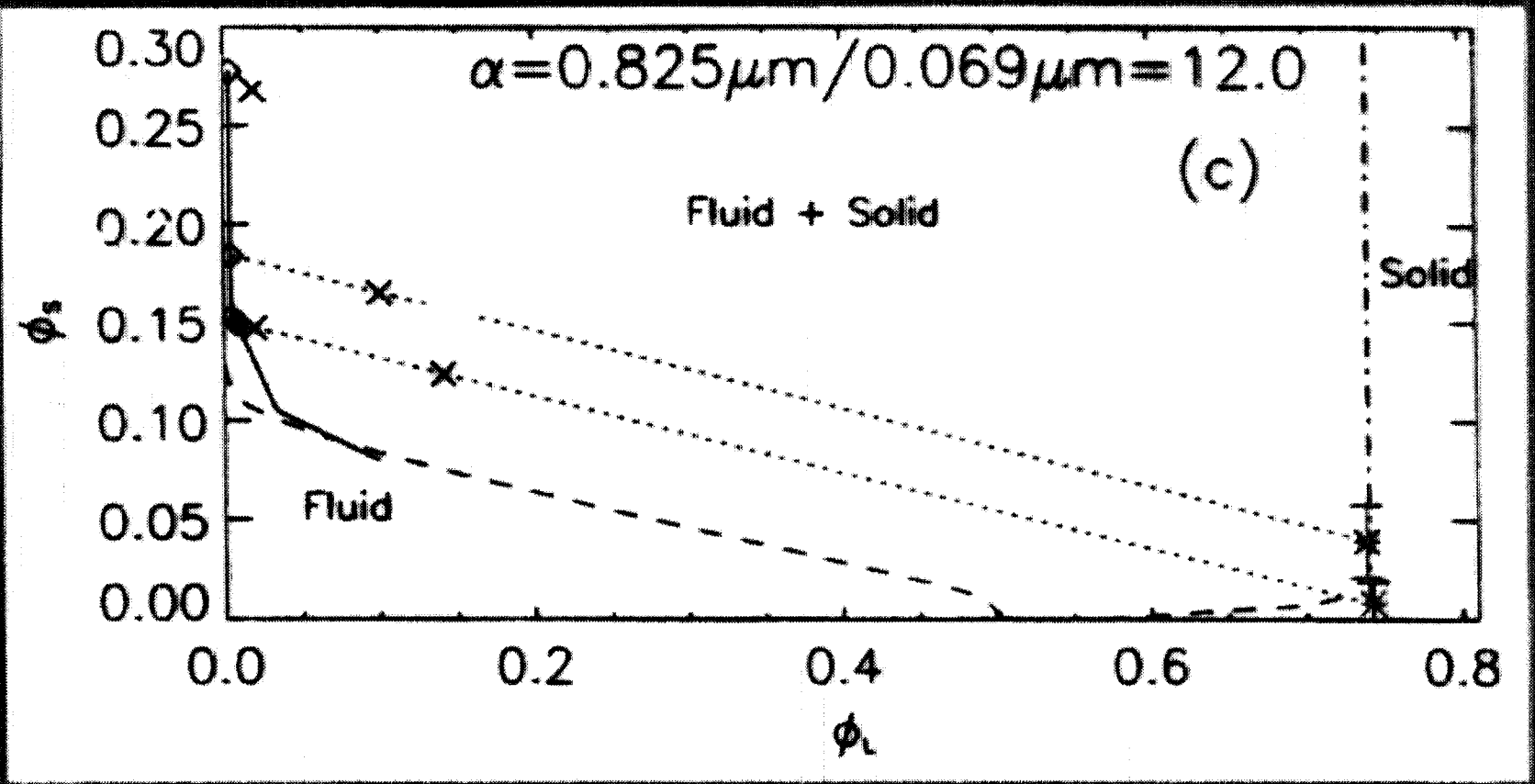

Depletion force at surface: (HARD SPHERES)

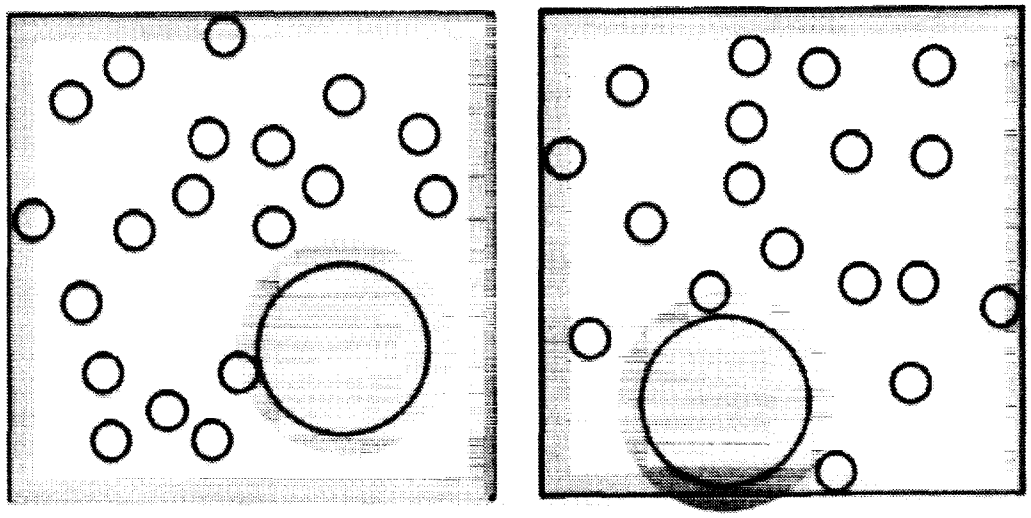

→ Moving large sphere to wall decreases the Free energy even more!

$$\text{Force}_{\substack{\text{sphere}\\\text{-wall}}} \approx 2 \times \text{Force}_{\substack{\text{sphere}\\\text{-sphere}}}$$

$$\approx 3\alpha\phi_S k_B T \qquad \alpha = \frac{a_L}{a_S}$$

ϕ_s = volume fraction small particles

(a few $k_B T$ in strength)

- P. D. Kaplan, J. L. Rouke, A. G. Yodh, and D. J. Pine, Phys. Rev. Lett. **72**, 582 (1994).
- P. D. Kaplan et al, Phys. Rev. Lett. **73**, 2793 (1994).

RANGE OF COMPOSITIONS WHERE "EQUILIBRIUM" COLLOIDAL EPITAXY IS POSSIBLE!

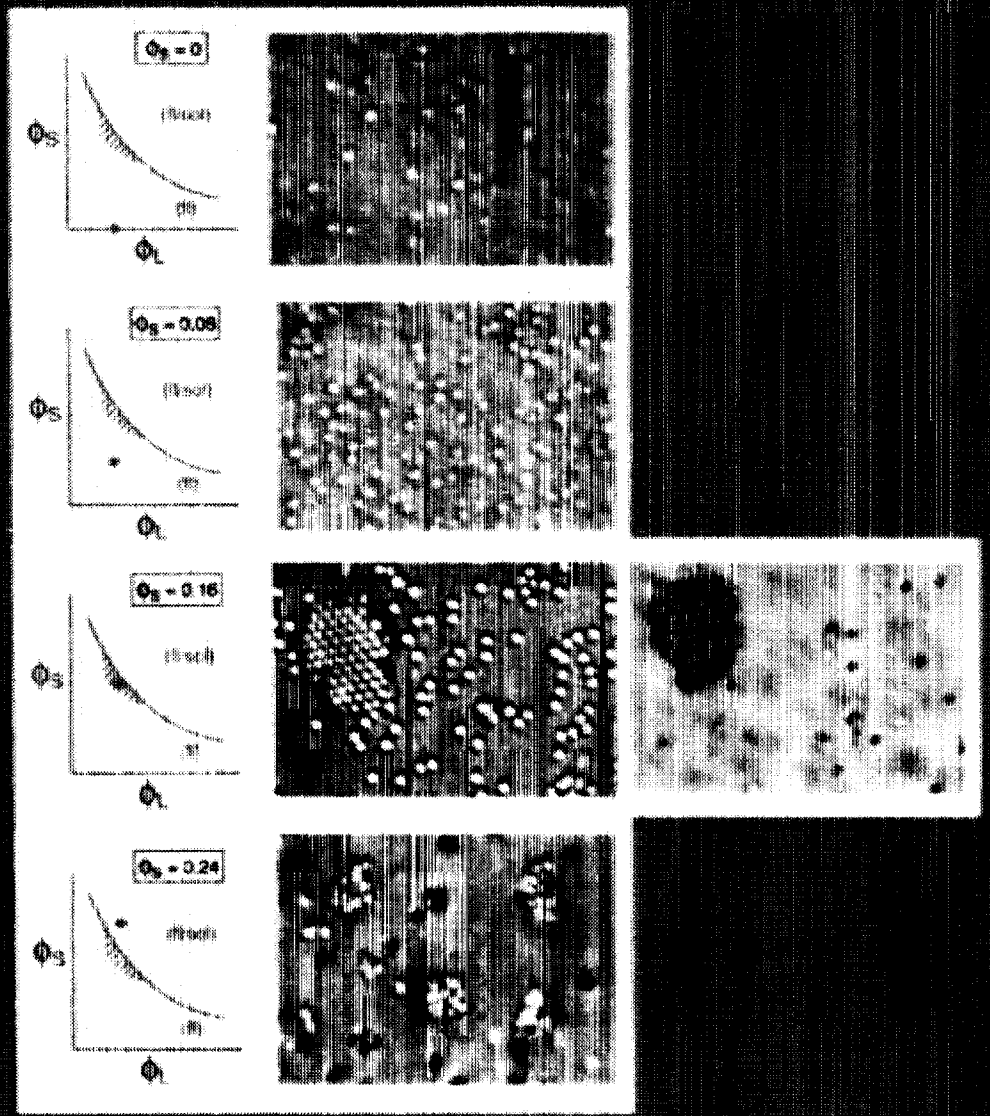

Surface Crystallization

Wall + Attractive Particle Interactions offer:

- Possibility for Surface Nucleation and subsequent Growth without substantial Bulk Nucleation
- Different from more typical "space-filling" crystallization processes that arise in most colloidal systems

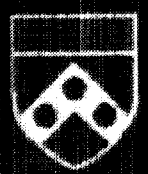

Entropic effects with Structure in the Walls

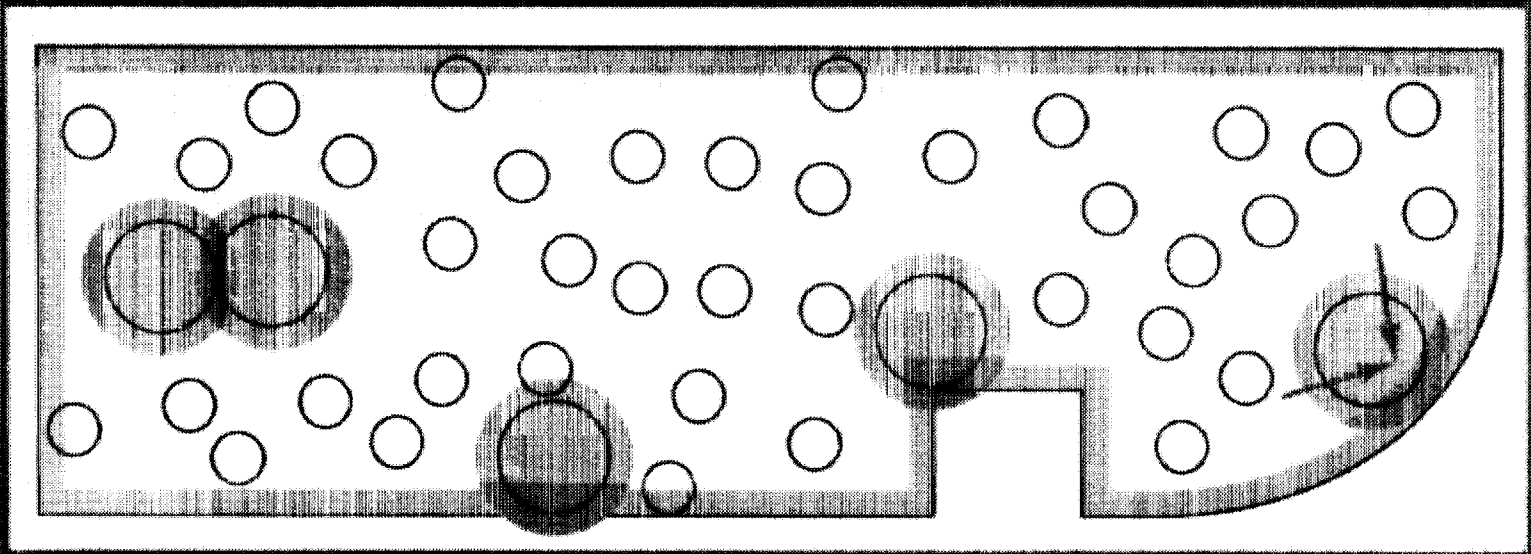

Entropic repulsion from a step edge:

Less excluded-volume overlap here

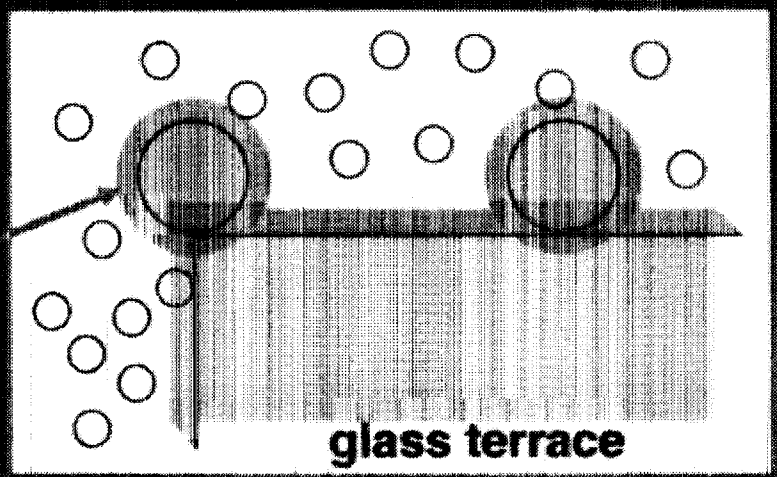

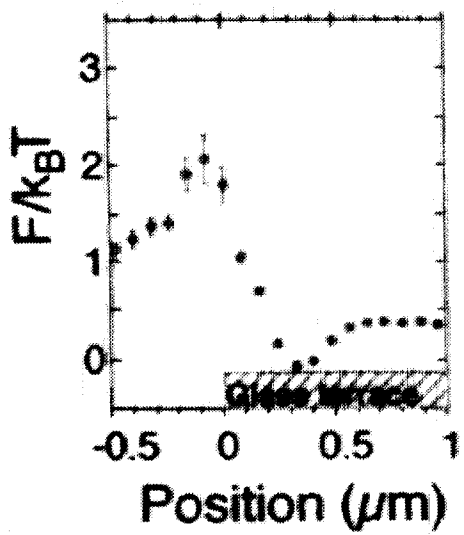

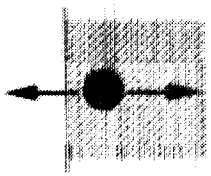

Free-energy barrier $\approx 2k_BT$ at edge of terrace

Maximum force = 0.04 pN

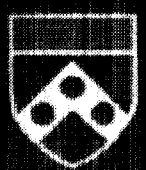

CORNERS

VESICLES

(PARTICLES PUSHED TO WALLS AND REGIONS OF HIGH CURVATURE)

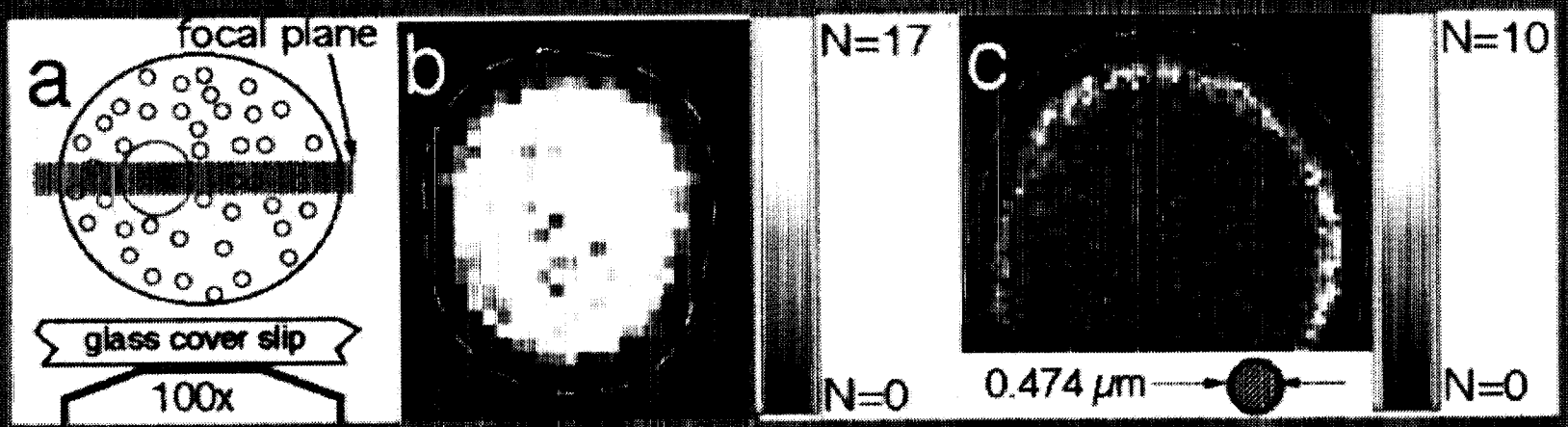

Attractive Depletion Interaction PLUS Topographically Patterned Substrates

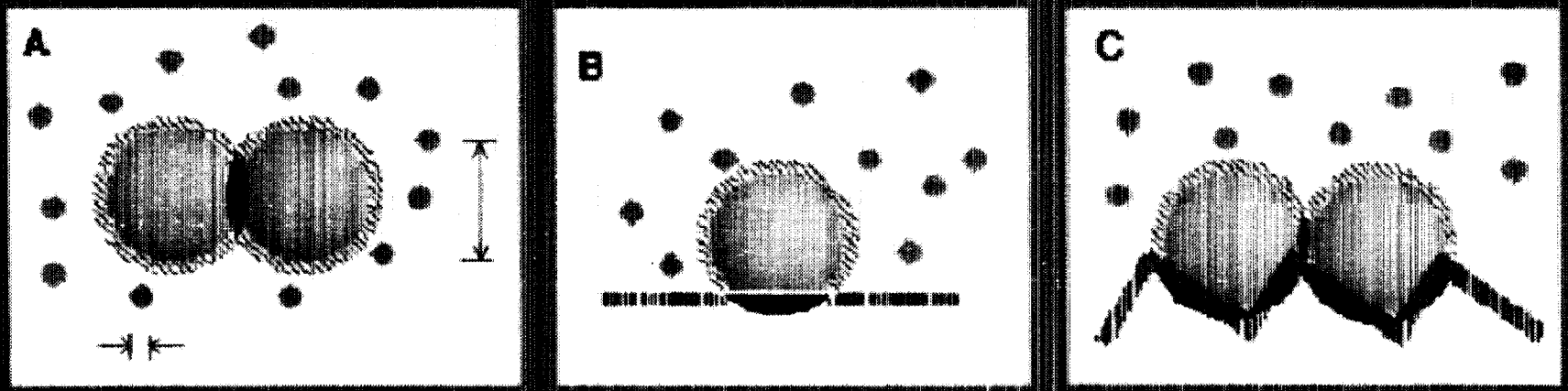

POWERFUL NEW TECHNIQUE FOR COLLOIDAL ASSEMBLY.

Example: How does the template help?

Why do we need a template?

Under certain conditions, colloids self-assemble into random close-packed crystals.

Random stacking

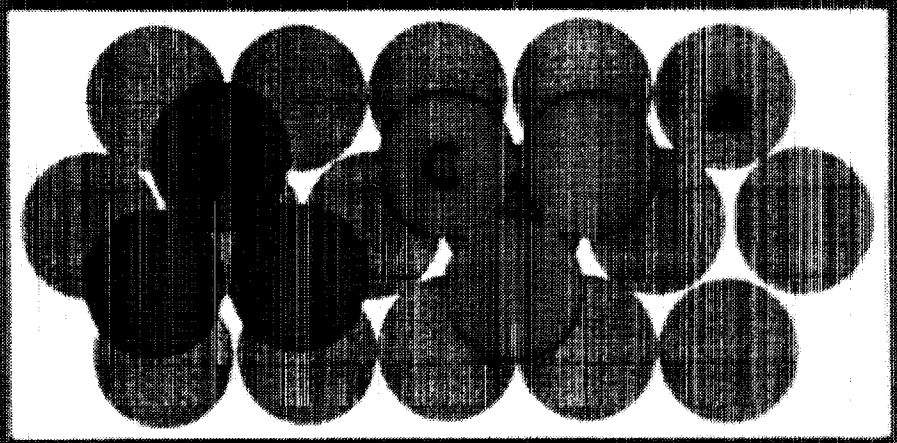

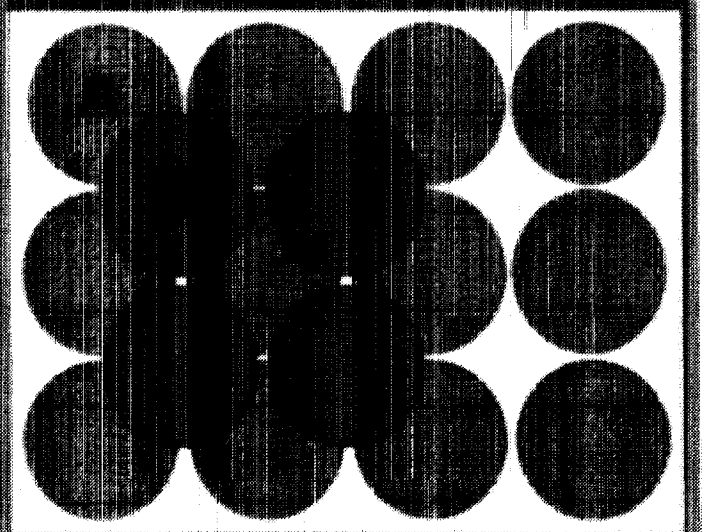

If we have a template such as FCC 100 plane, there is no stacking faults and also we can reduce the grain boundary.

"How to" Manual: PMMA templates

1. Line grating templates:

Press grating on PMMA layer above Tg ~ 120 C

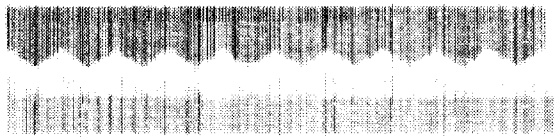

Grating pitch 0.3-10 microns

Remove grating when cool

2. Cross grating templates:

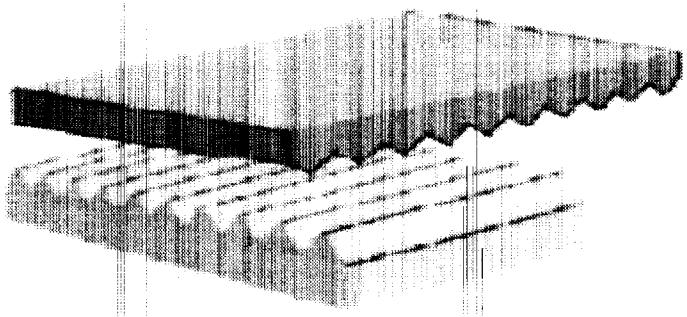

Rotate grating & repeat

Imprint Scheme

a

grating

PMMA layer (thermoplastic)
(>200 nm thick)

glass substrate

Press a grating onto PMMA layer while heating PMMA above its glass temperature.

b

Commercially available grating pitches range from 0.3 micron to 10 micron.

Remove the grating after PMMA is cool.

pitch~0.46 micron

C

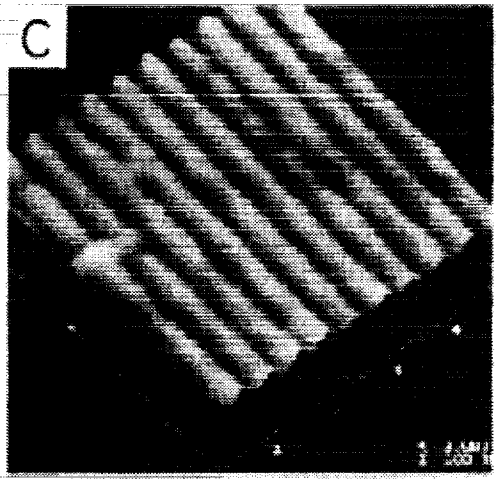

pitch~0.83 micron

D

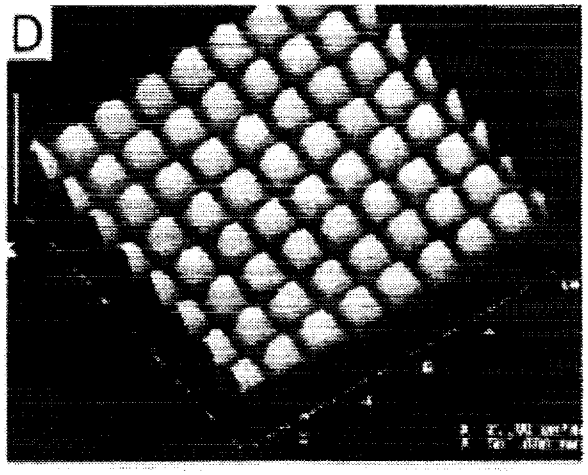

Ref: J Vac. Soc. Tech B 15 2897 (1997)
Steve Chou et al

"How to" Manual: PDMS templates

PMMA cross grating on microscope slide

PDMS pre-polymer + curing agent

Coverslip

Plasma treat to oxidize PDMS after removing PMMA mold

Our System

- PMMA Colloids (0.65~1.1μm) stabalized in organic solvents
- polystyrene polymer to depletion. (Rg~15nm, 2~3% volume fraction)
- solvents: closely index matched with PMMA beads (<0.01 difference in index of refraction) good for 3D microscopy.
- density matched for 2D study (decalin/cycloheyl bromide)
- non-density matched for 3D growth (decalin)

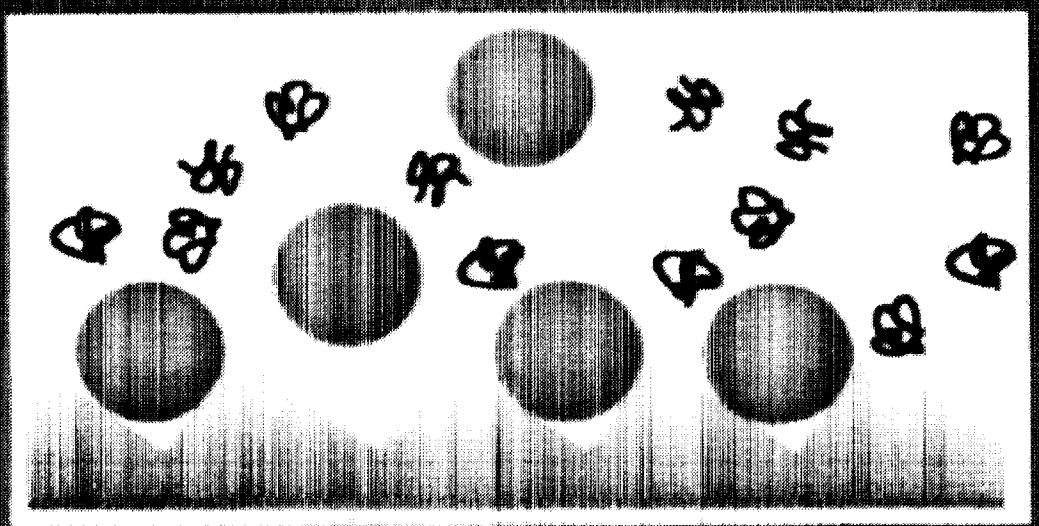

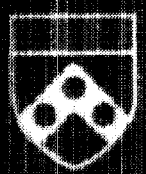

University of Pennsylvania

Line Grating

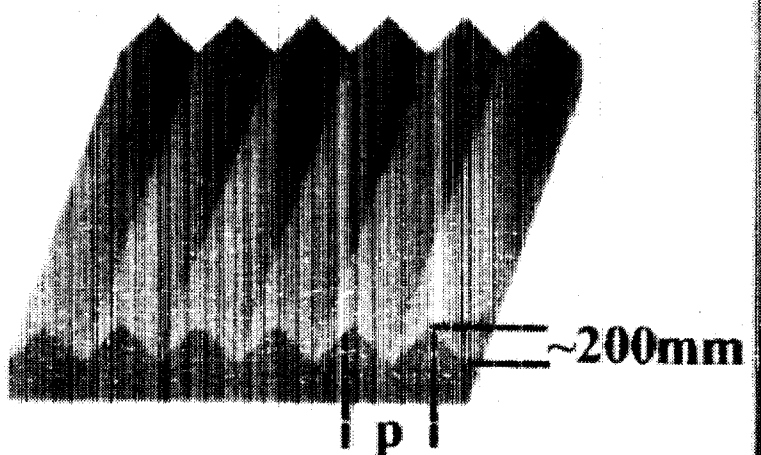

p= 0.833μm, 1.2μm, 1.667μm

Crossed Grating

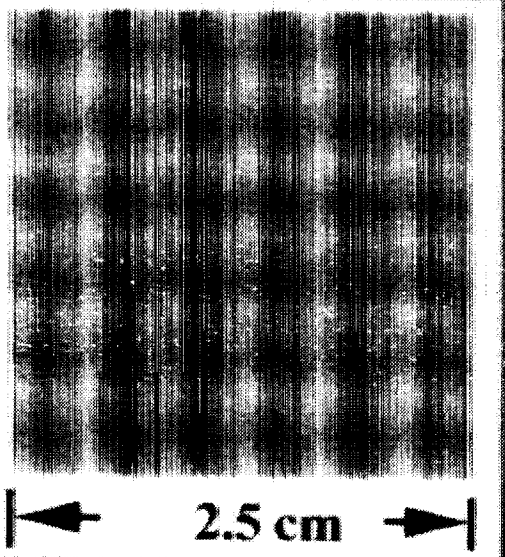

Steven Chou. J. Vac. Sci Tech: B 15 No.6 Nov/Dec '97

On a flat surface

Structure function

On a grating

Structure function

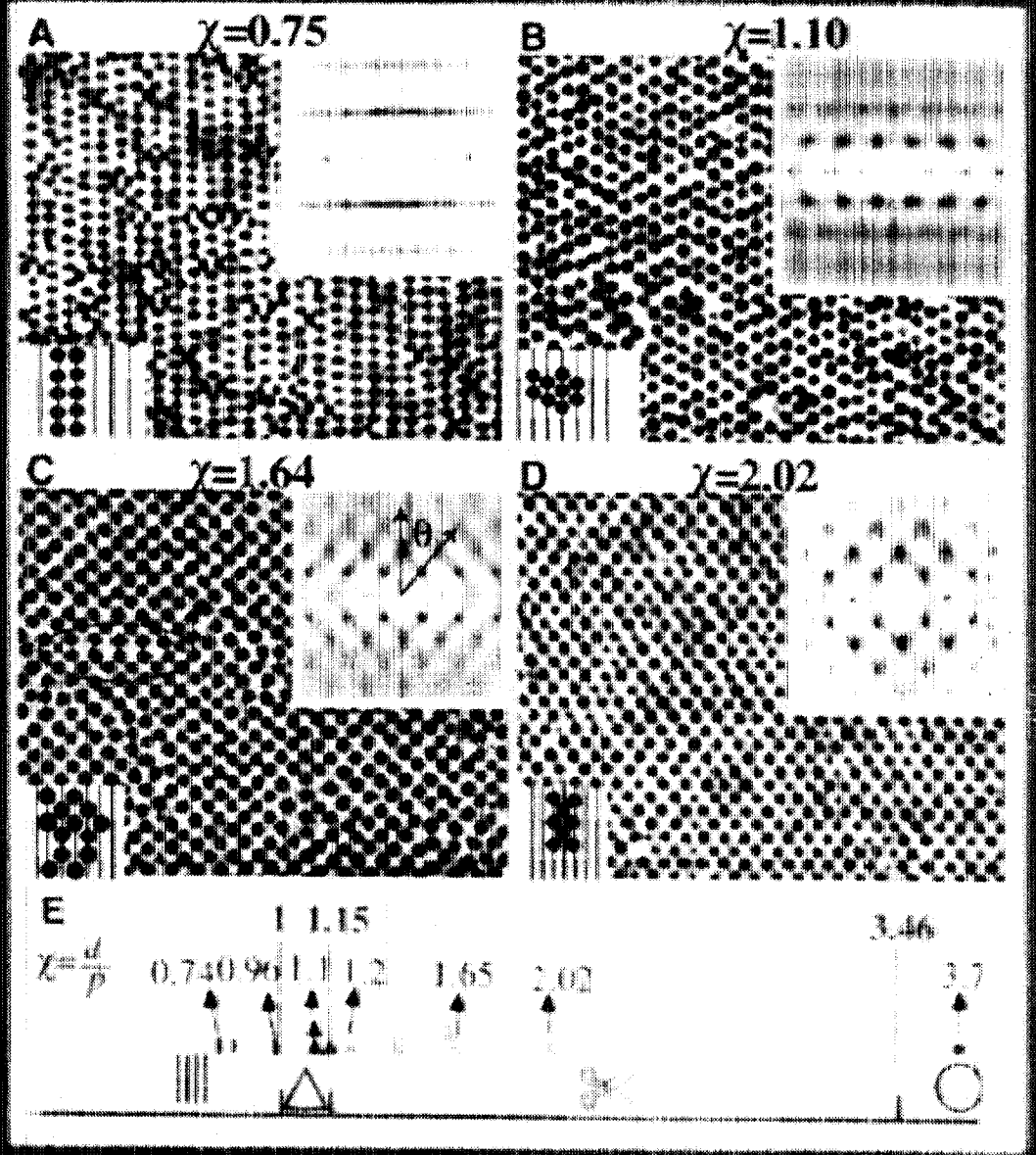

d = mean spacing above groove

scissor angle $\tan\theta = \frac{2p}{d}$

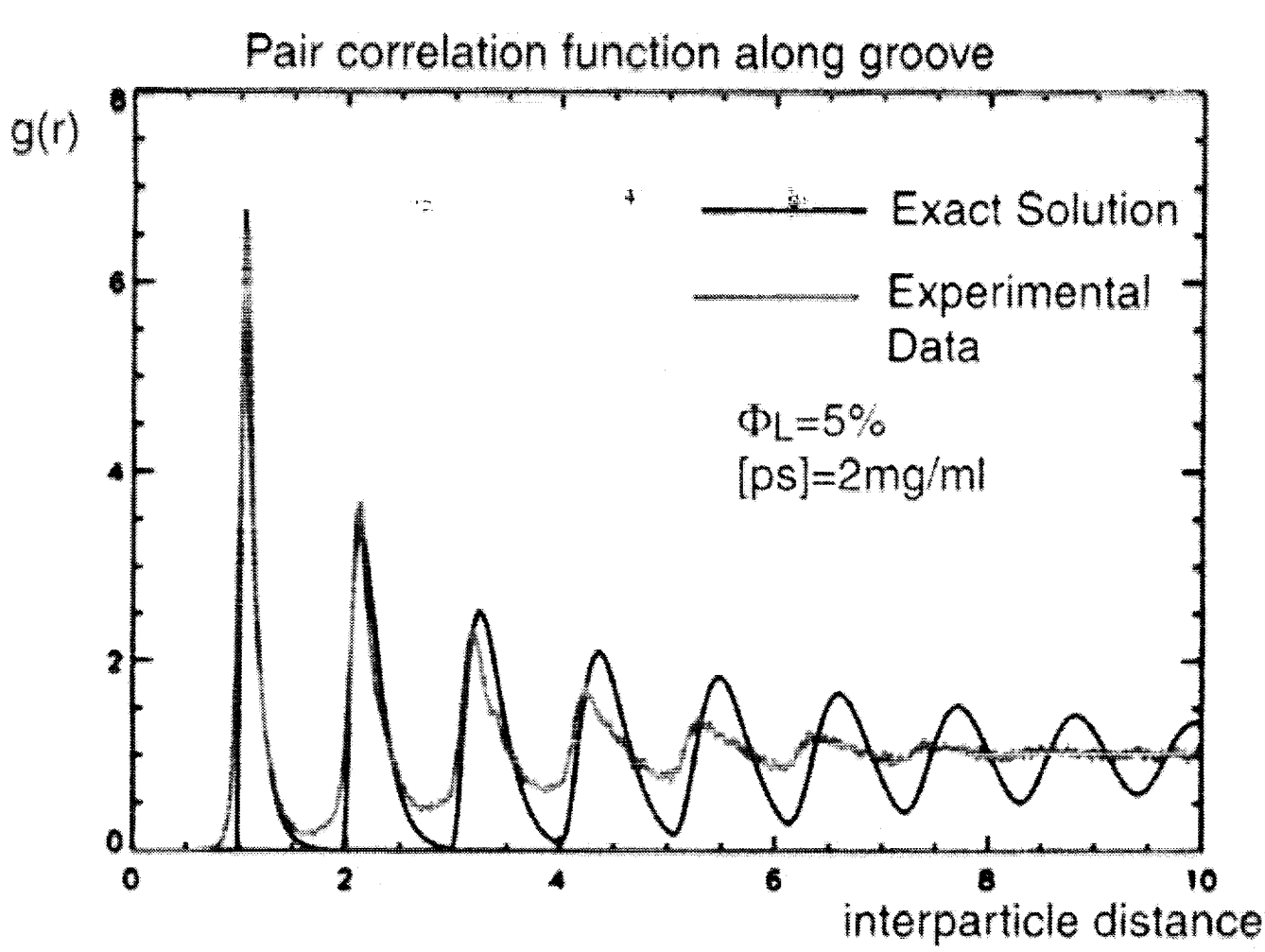

Most likely interparticle distance = 0.93 micron
Hard sphere diameter = 0.86 micron
radius of gyration of polystyrene = 0.015 micron

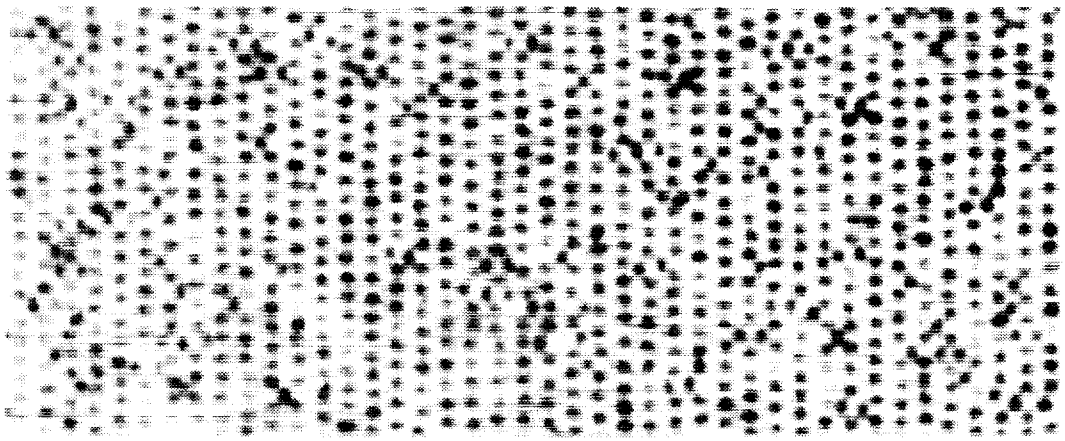

Weakly interacting 1D liquid

$$S_m(k_x) = \frac{A_m e^{-k_x^2 W_m}}{1 + C_m \cos(k_x p)} + B_m$$

$$k_y = m G_y$$

A_m: amplitude

B_m: background

C_m: coupling constant $\quad |C_m| < 1$

W_m: Debye-Waller factor

p: period.

Structure function for Scisoor Phase

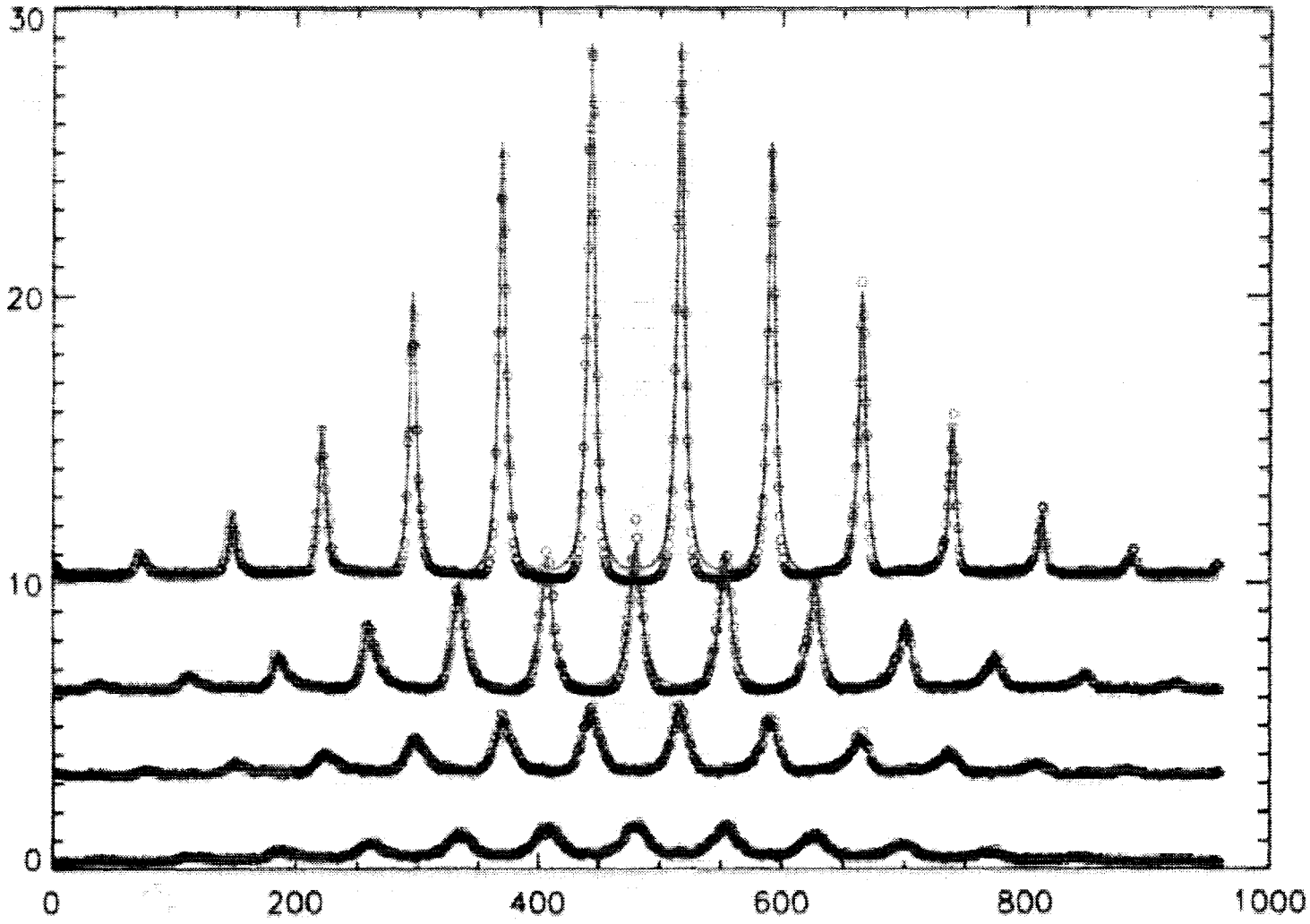

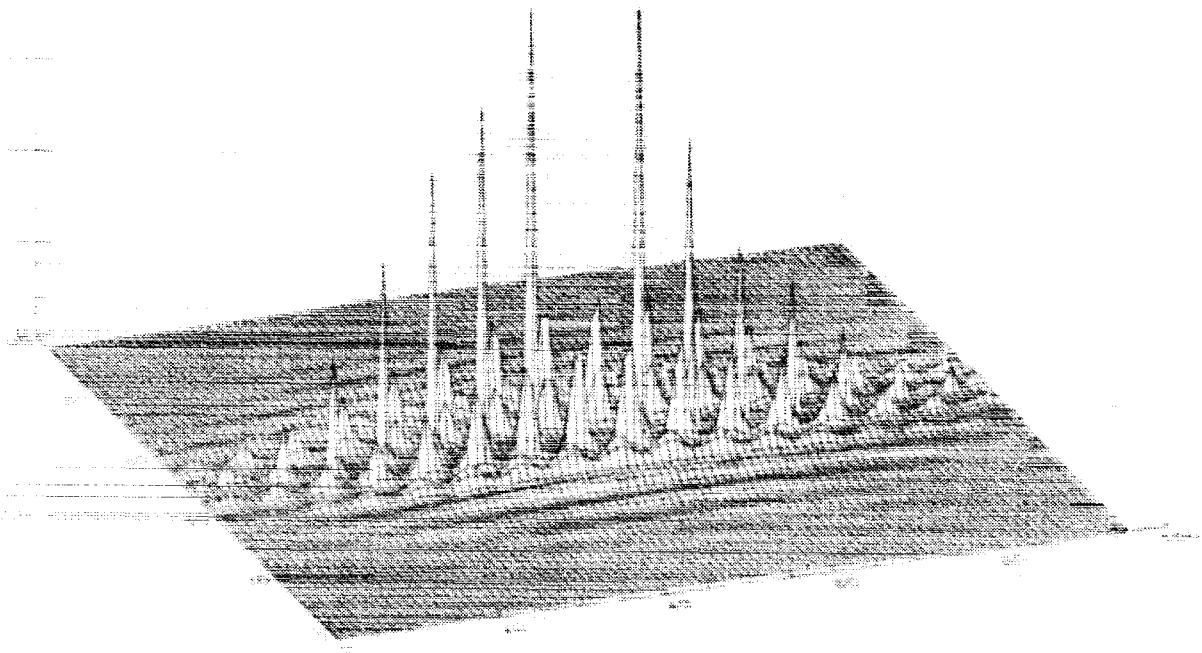

A
B
C
D
= 1
E
$\chi = \frac{d}{p}$
0.707
1
1.414
0.707
0.87
1.05
1.33
1.49

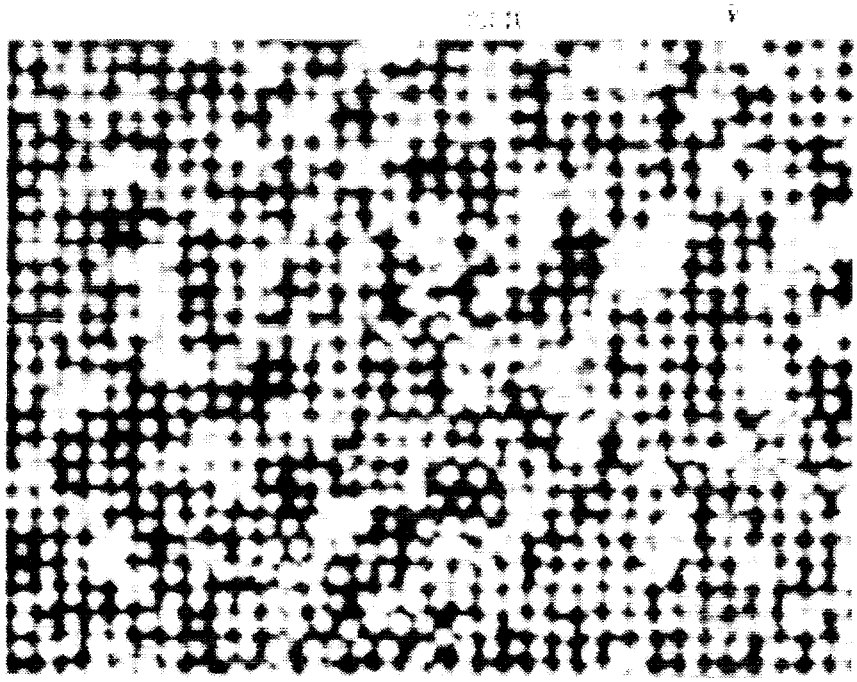

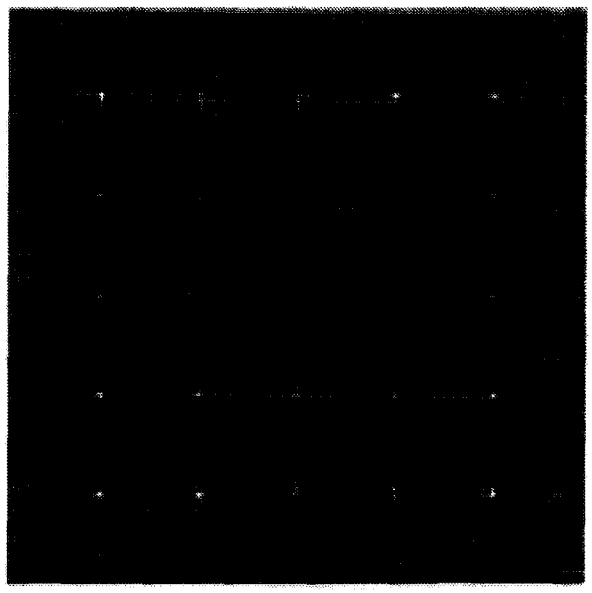

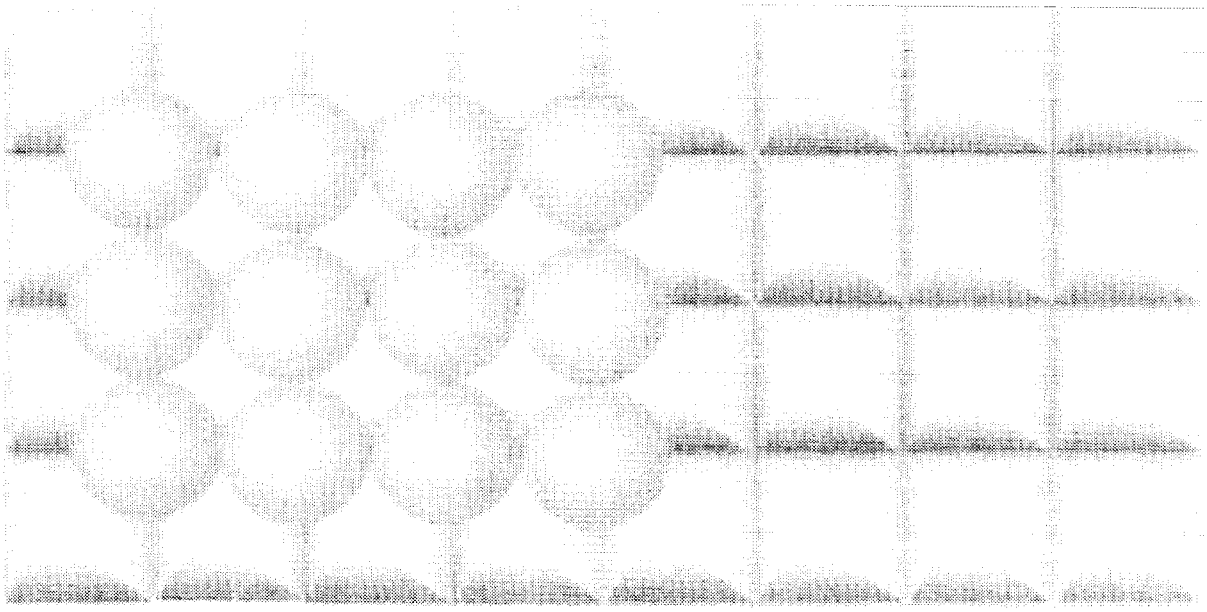

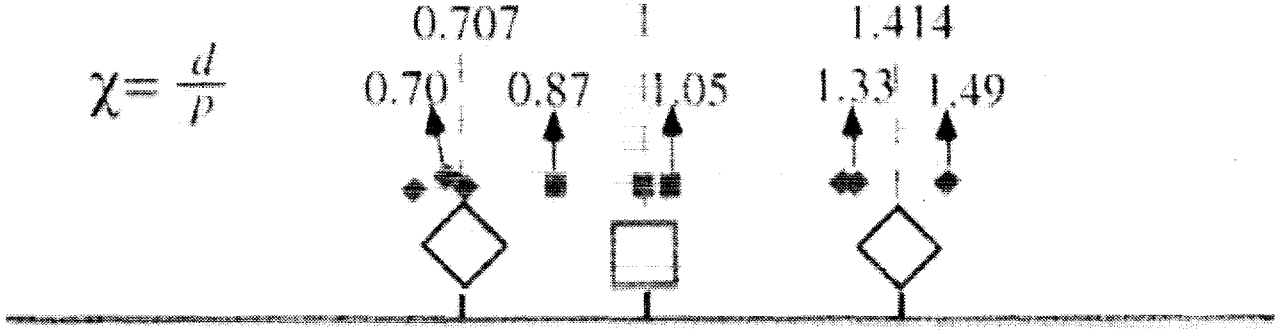
$\chi = \frac{d}{p}$
0.707
1
1.414
0.70
0.87
1.05
1.33
1.49

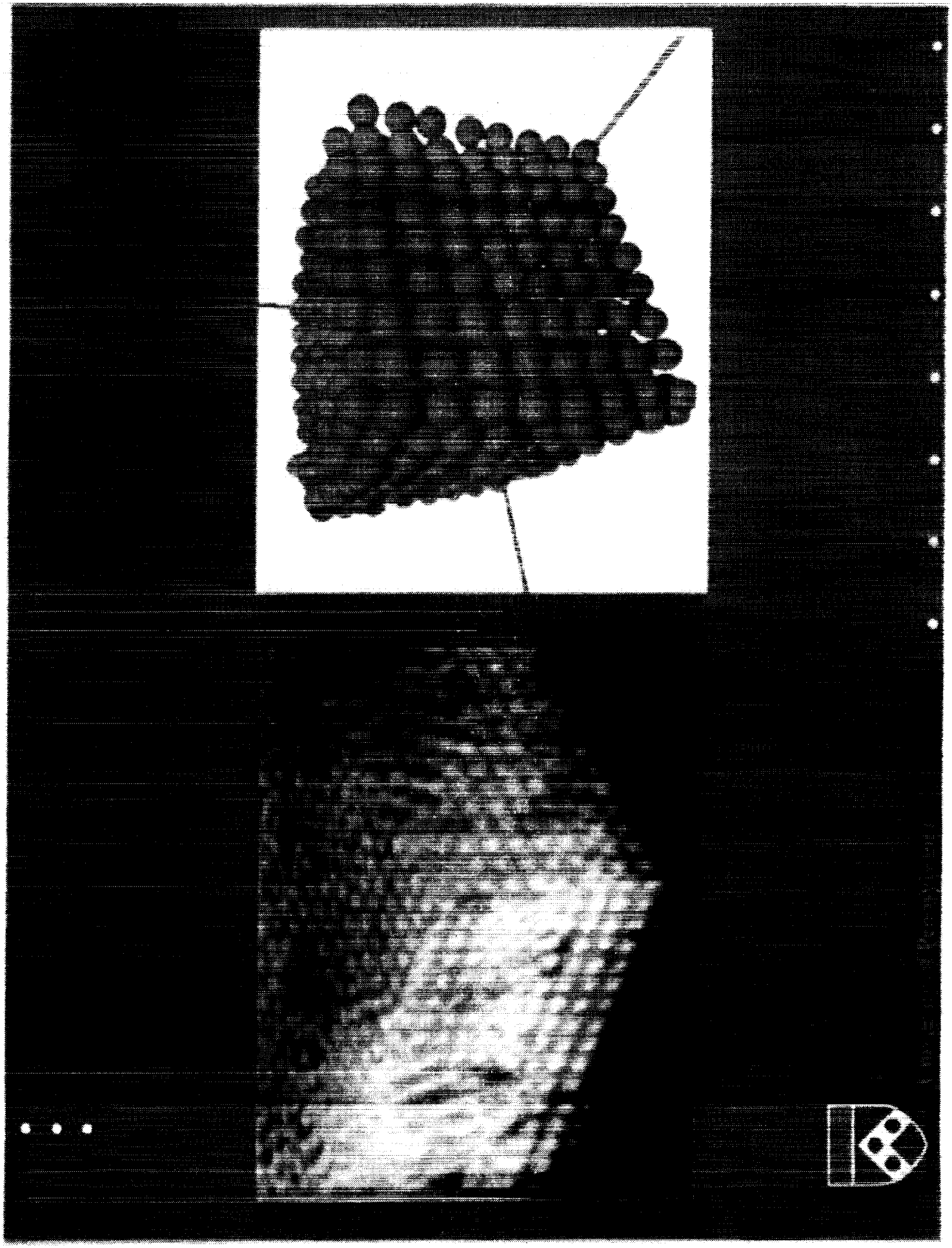

BCC 100 Plane

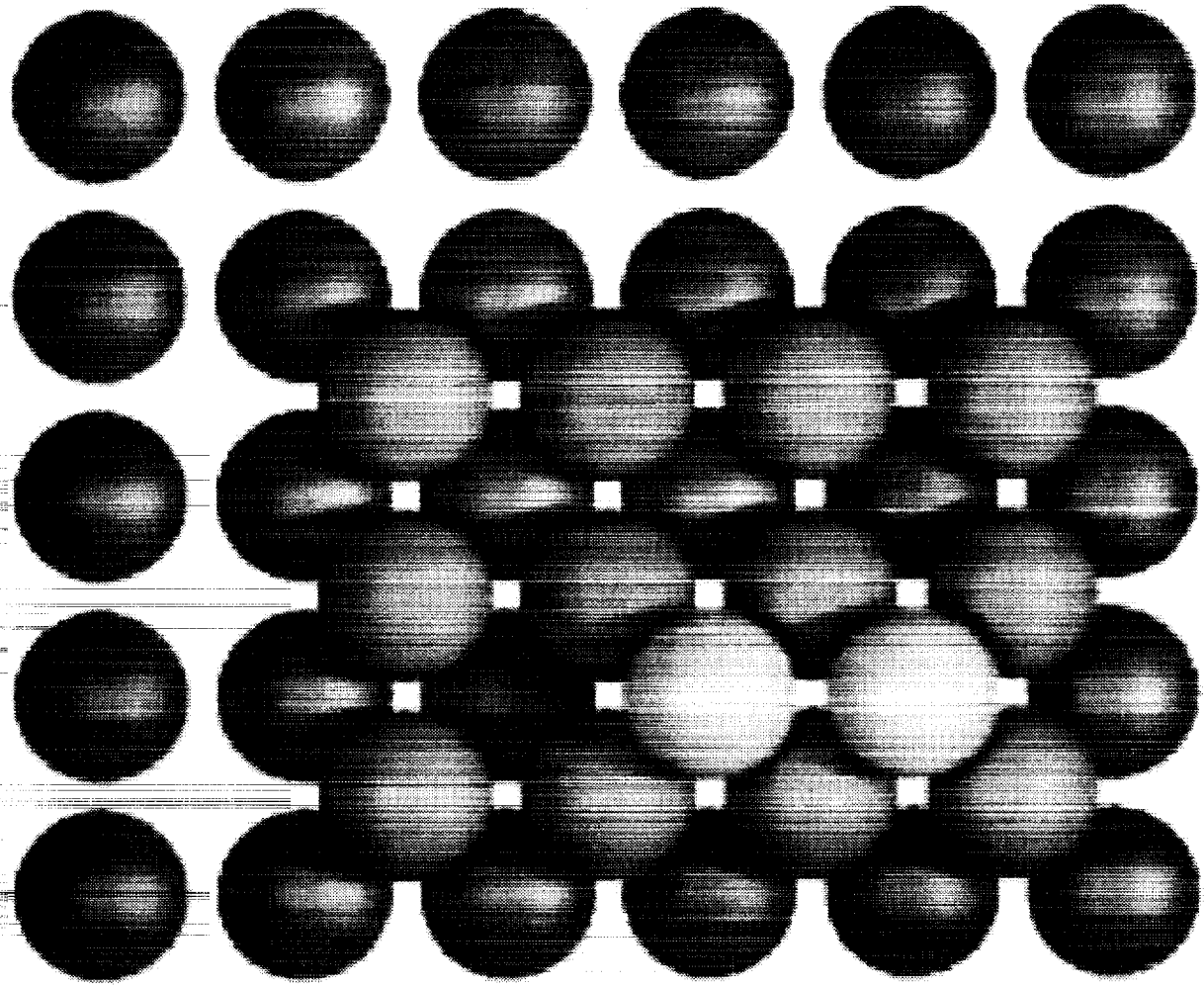

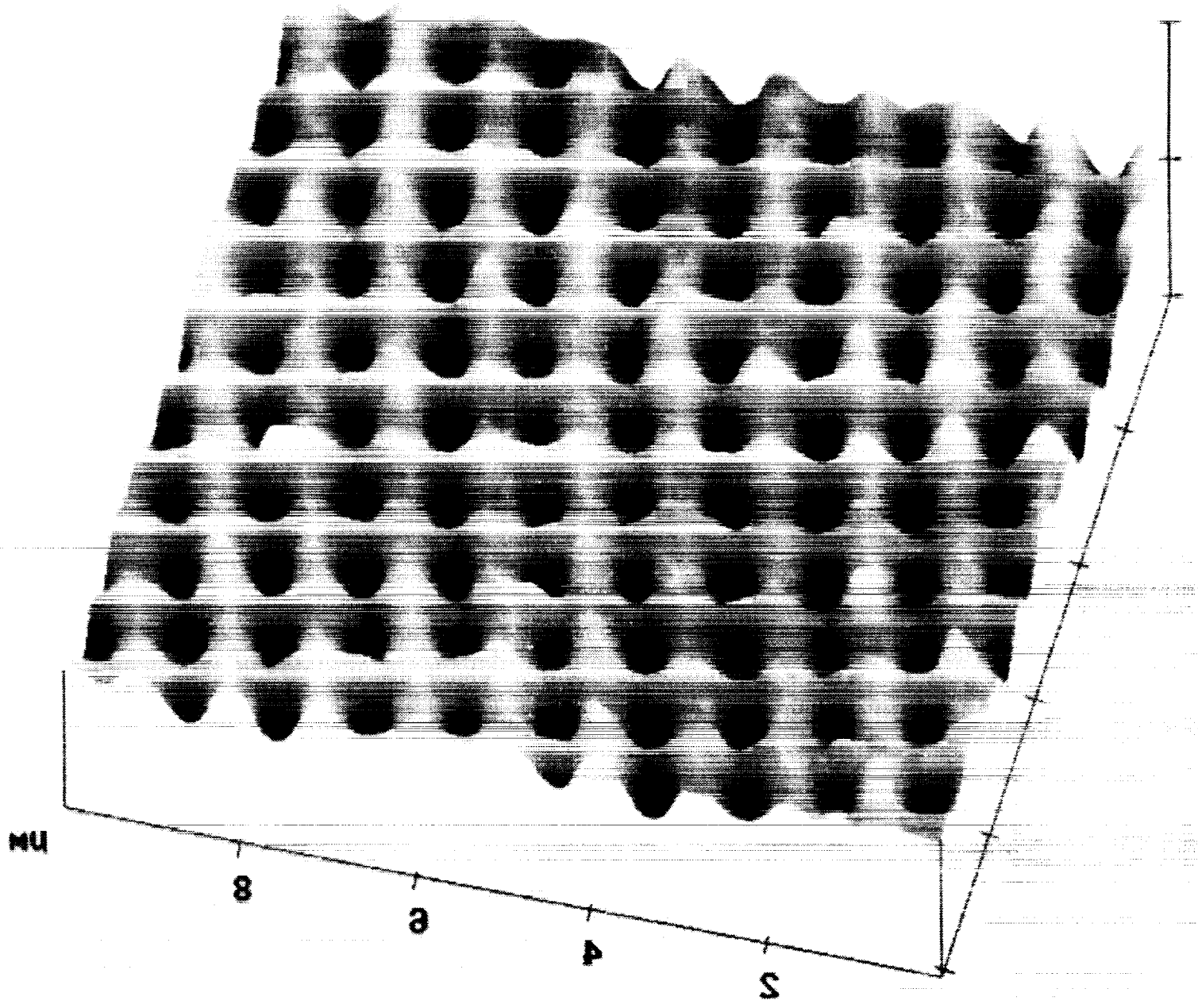
μm
8
6
4
2

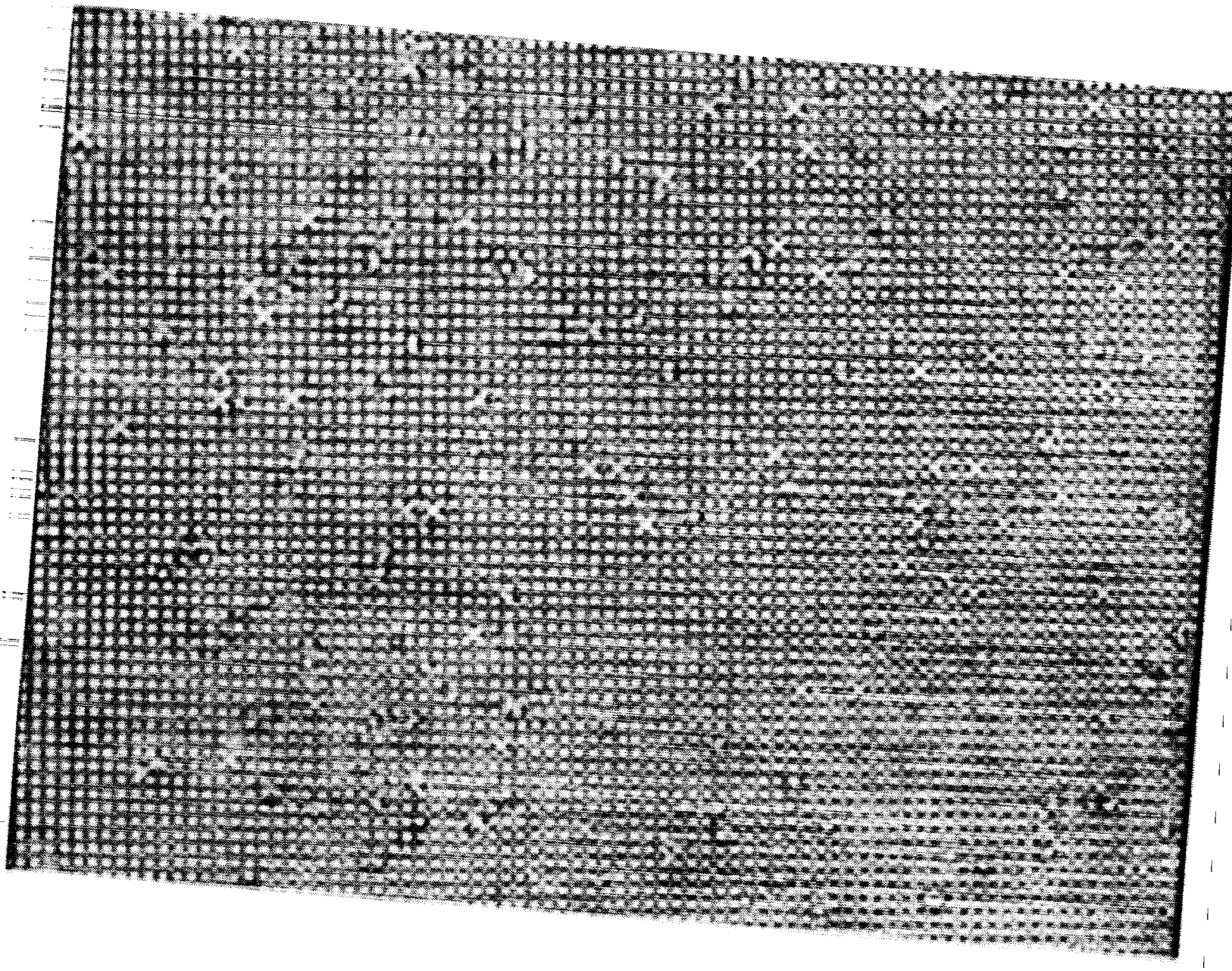

Summary

1. DEPLETION IMPORTANT IN MANY CONTEXTS

2. ENTROPIC ENGINEERING

* Equilibrium approach for Building Novel Colloidal Structures (irrespective of particle density)

Micromechanics and Dynamics in Magnetorheological Suspensions

Alice P. Gast and Eric Furst
Department of Chemical Engineering, Stanford University, Stanford CA 94305-5025, USA

Magnetorheological (MR) suspensions are composed of paramagnetic colloidal particles that acquire dipole moments when subjected to an external magnetic field. At sufficient field strengths and concentrations, the dipolar particles rapidly aggregate to form long chains. Subsequent lateral cross-linking of the dipolar chains is responsible for a rapid liquid-to-solid-like rheological transition. The unique, magnetically-activated rheological properties of MR suspensions make them ideal for electrical-mechanical transducers. Additionally, the ability to experimentally probe colloidal suspensions interacting through tunable anisotropic potentials is of fundamental interest.

In this talk we will describe our work toward a microscopic understanding of magnetorheological behavior. Much of the rheological behavior arises from the cross-linked structure caused by defects and Landau-Peierls thermal fluctuations of dipolar chains. We used the light scattering technique, diffusing-wave spectroscopy, to investigate the fluctuations of dipolar chains. We have prepared monodisperse neutrally buoyant MR suspensions allowing us to probe the dynamics of the dipolar chains using light scattering without complications due to gravitational forces and polydispersity.

Optical gradient force trapping techniques, or laser tweezers, have become increasingly important tools for studying the microscopic structure, mechanics, and interactions in biological, colloidal, and macromolecular materials. We also present our study of the micromechanical properties of dipolar chains and chain aggregates in a magnetorheological suspension. Using dual-trap optical tweezers, we are able to directly measure the deformation of dipolar chains parallel and perpendicular to the applied magnetic field. We observe the field-dependence of chain mechanical properties, such as tensile strain, chain reorganization, defect-annealing and rupture. We discuss the role these forms of energy dissipation take in the yield stress and rheology of MR suspensions.

NASA/CP—2000-210470

Micromechanics and Dynamics in Magnetorheological Suspensions

Alice P. Gast
Department of Chemical Engineering, Stanford University
Eric M. Furst
Laboratoire de Physico-Chimie, Institut Curie

Outline

- MR suspensions

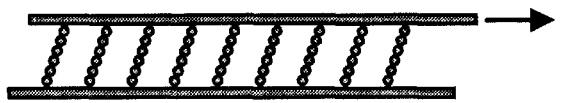

- Optical trapping

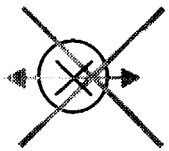

- Bending and stretching dipolar chains

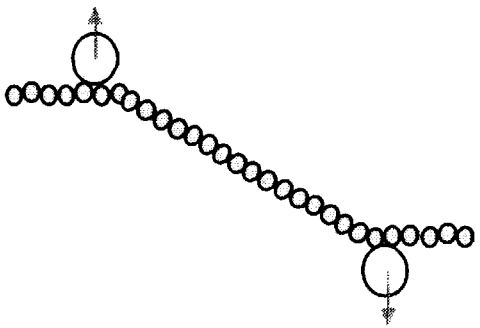

- Chain defects

- Lateral interactions and coarsening

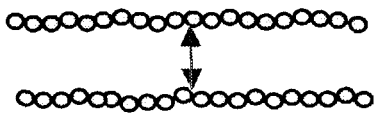

Microstructure and Rheology

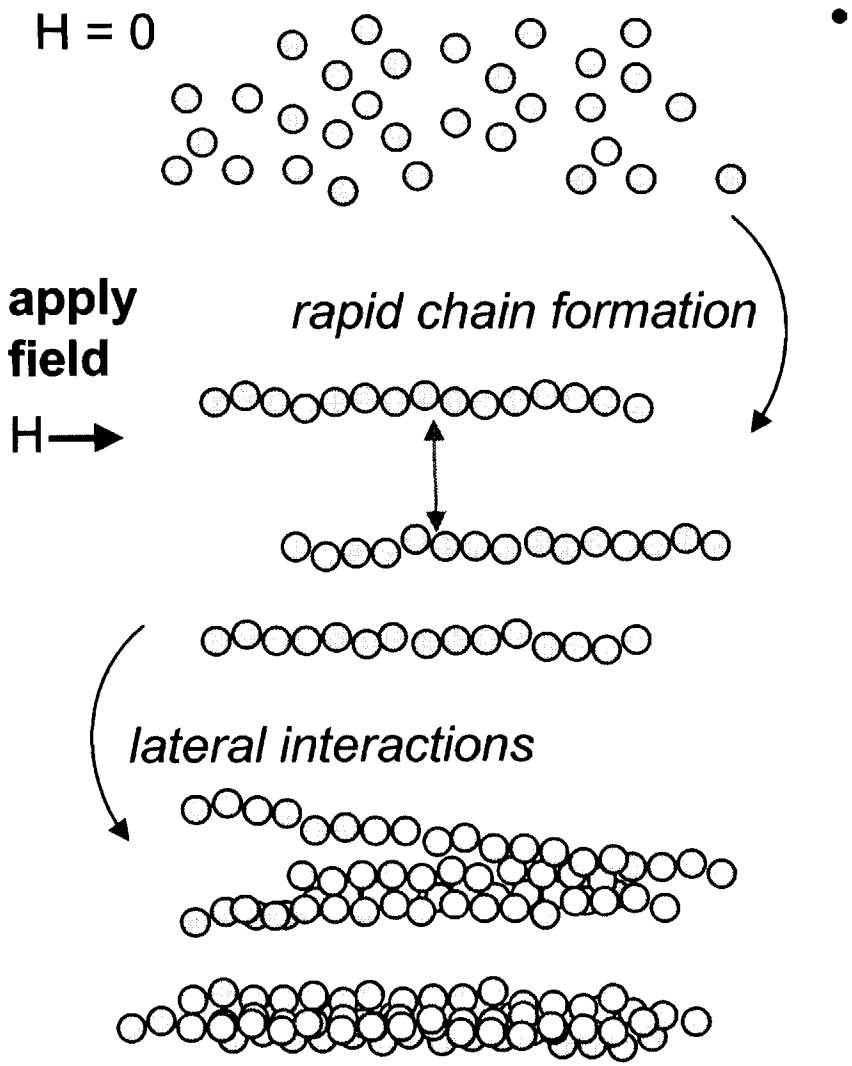

- dipole strength

$$\lambda = \frac{-U_{max}}{kT} = \frac{\pi \mu_0 a^3 \chi^2 H^2}{9kT}$$

- microstructure deformation and rupturing → finite yield stress

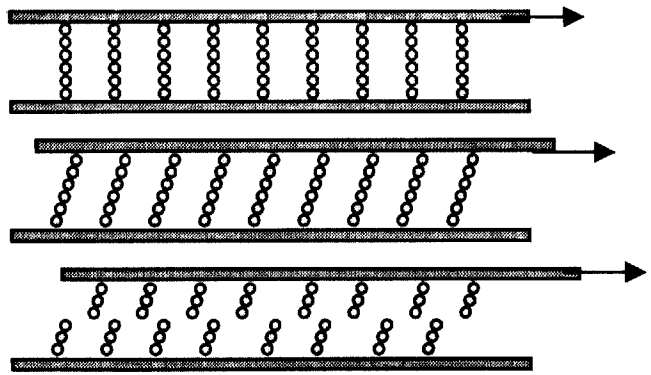

Gast and Zukoski, 1989.
Klingenberg and Zukoski, 1990.
Bonnecaze and Brady, 1992.

Experimental Systems

1. Ferrofluid emulsion

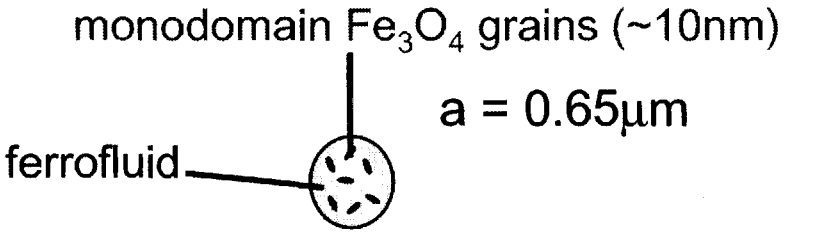

sodium dodecyl sulfate solution

Fractionated - monodisperse

J. Bibette, J. Coll. Int. Sci., 147,474 (1991)

Micrograph of emulsion droplets

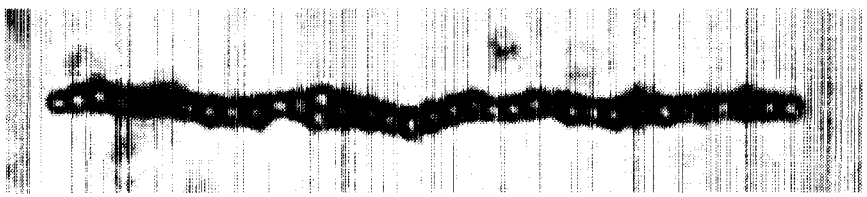

2. Polystyrene (PS) particles - Bangs Lab.

Fe_3O_4 grains embedded in polymer matrix

- polydisperse: a = 0.2-0.43μm
- Magnetic heterogeneity

TEM of PS particles

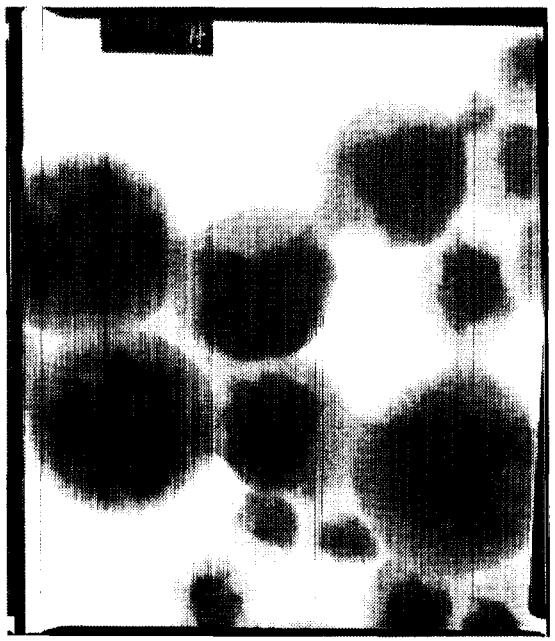

Gradient Optical Trapping

Ray-optic regime:

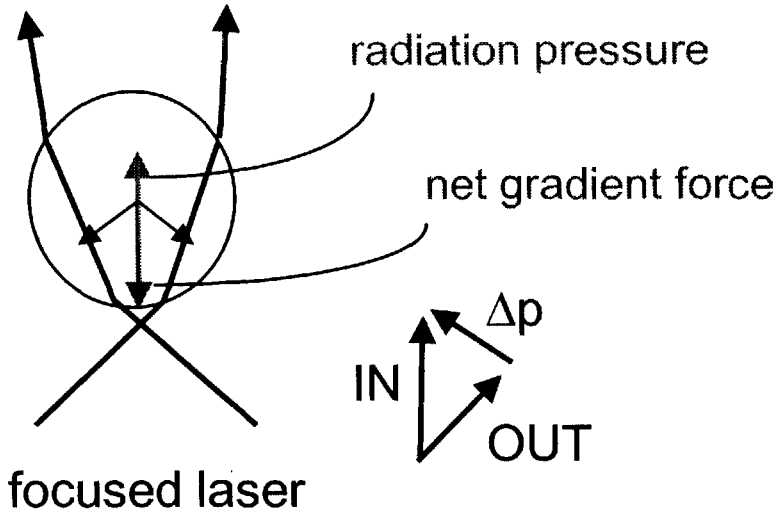

Ashkin,Science, 210, 1081 (1980)
Ashkin, *et al.*, Opt. Lett., 11,288 (1986)

Trapping force calibration:

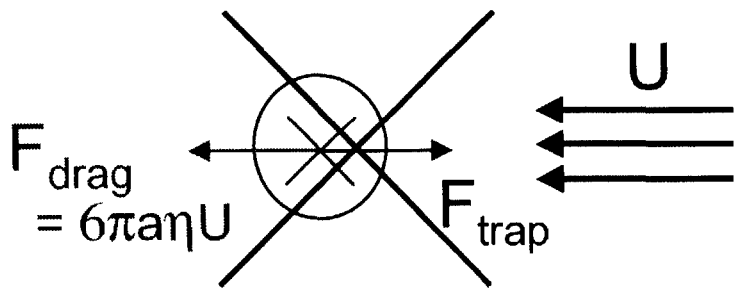

- Micromanipulation and force measurement
- Forces ~ 0.1 - 10 pN

Laser Trapping "Tether-handle" System

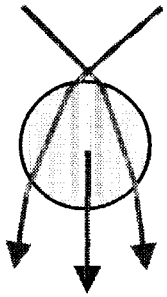

Strong scattering and absorption
pushes MR particles out of laser trap

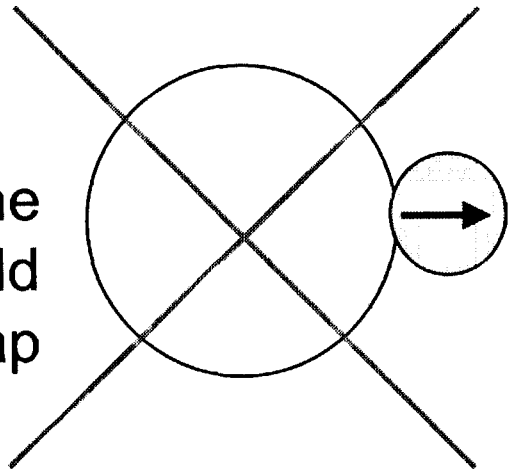

paramagnetic
bead *handle*

3.5 μm polystyrene
bead *tether* held
by trap

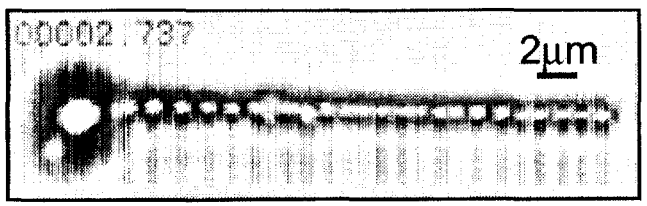

Paramagnetic emulsion droplets
attached to "tether-handle"

Biotin-X-NHS

Streptavidin

$K_a \sim 10^{15}\ M^{-1}$

Dual trap laser tweezers

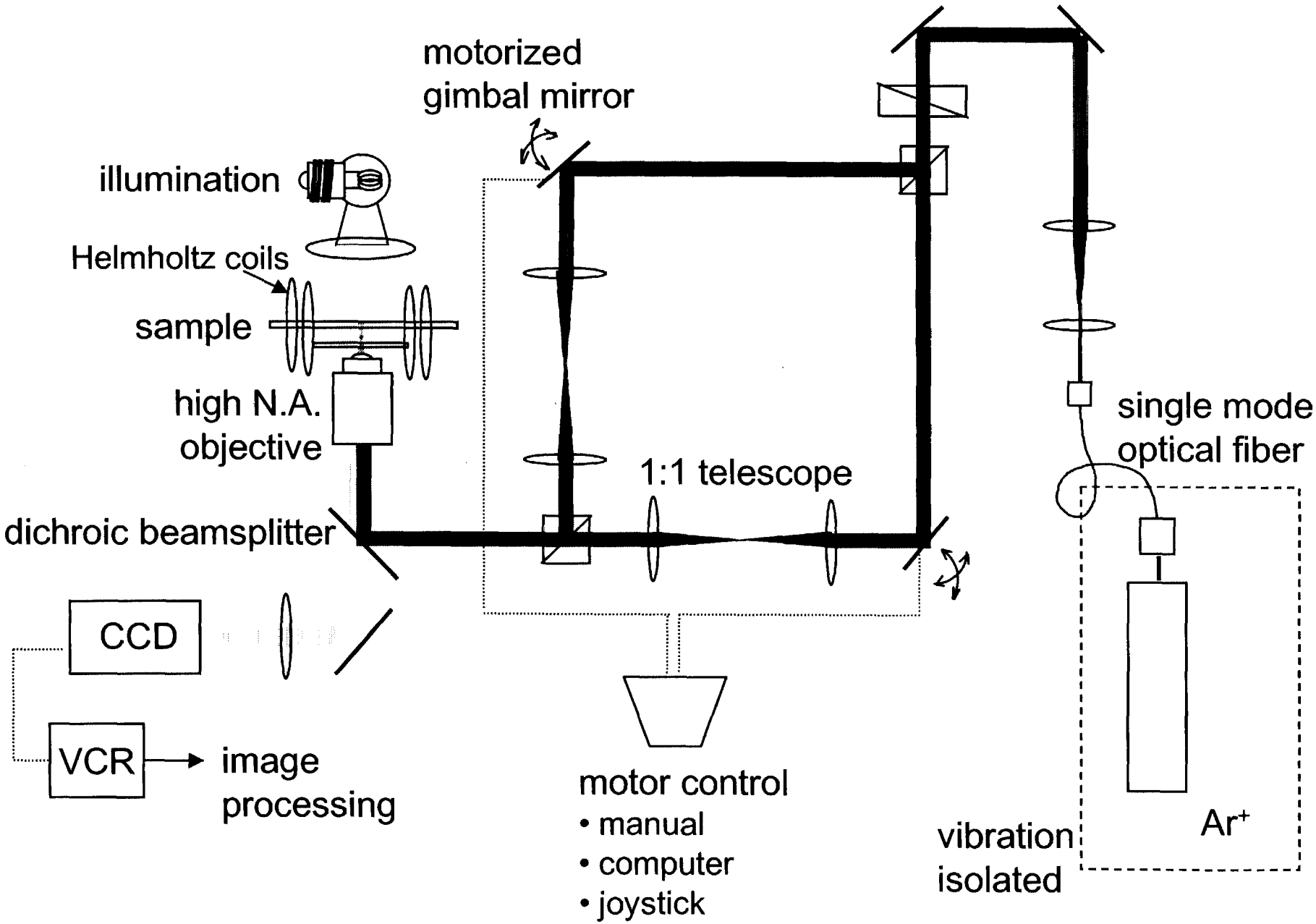

Micromechanics Experiments

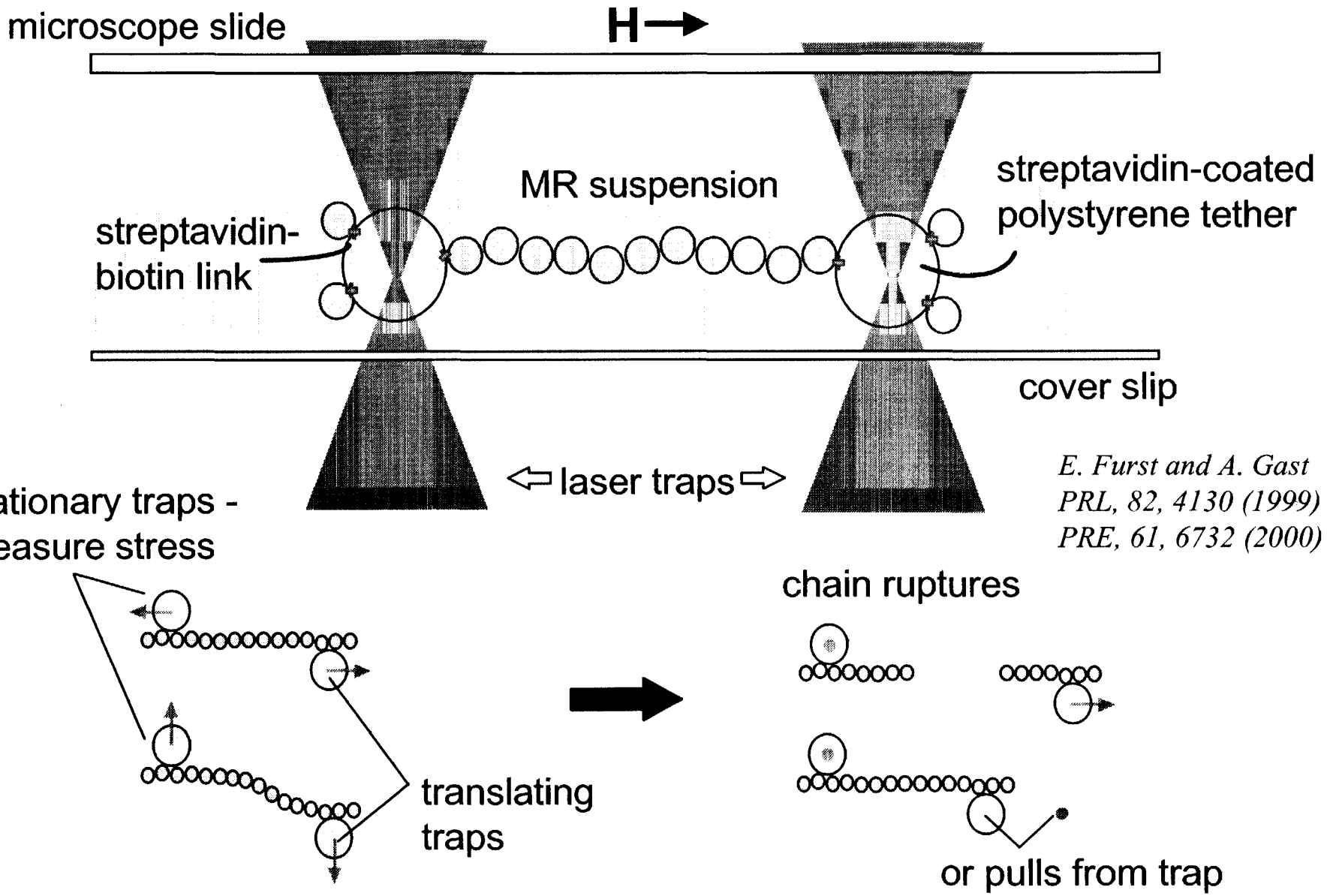

Calculating the Particle Interaction

1. Self-consistent point dipole:

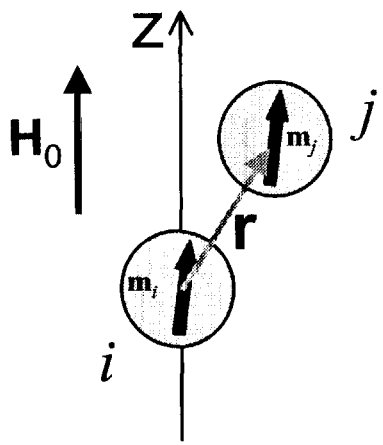

$$\mathbf{m}_i = \frac{4\pi}{3} a^3 \mu_0 \chi \left\{ H_0 \hat{\mathbf{z}} + \sum_{j \neq i} \frac{\left[3\hat{\mathbf{r}}_{ij} \left(\mathbf{m}_j \cdot \hat{\mathbf{r}}_{ij} \right) - \mathbf{m}_j \right]}{4\pi\mu_0 r_{ij}^3} \right\}$$

$$U_{ij} = \frac{1}{4\pi\mu_0} \frac{\mathbf{m}_i \cdot \mathbf{m}_j - 3\left(\hat{\mathbf{r}}_{ij} \cdot \mathbf{m}_i\right)\left(\hat{\mathbf{r}}_{ij} \cdot \mathbf{m}_j\right)}{r_{ij}^3}$$

2. Repulsive double layer:

Derjaguin approximation,
ψ_0 = - 40-45mV, κ = 0.3nm^{-1}

$$U_{el}(r) = 2\pi\varepsilon\varepsilon_0 \psi_0^2 a \ln\left\{1 + \exp\left[-\kappa(r - 2a)\right]\right\}$$

- Mutual induction and chaining effects
- Solve analytically for linear chains
- Numerically for arbitrary particle configurations (defects, etc.)

Emulsion Chain Bending Micromechanics

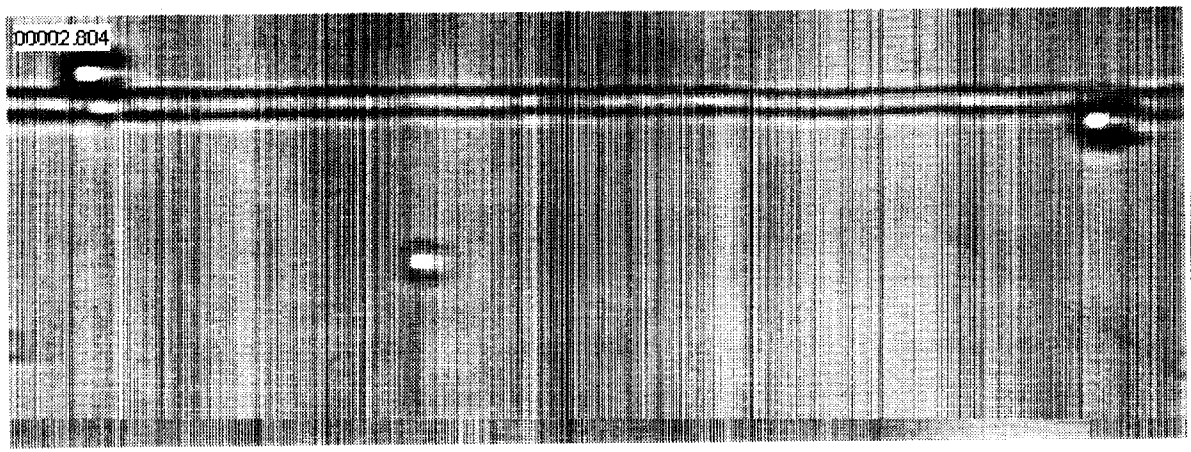

Lateral Deformation of Emulsion Chains

Emulsion chain bending in field

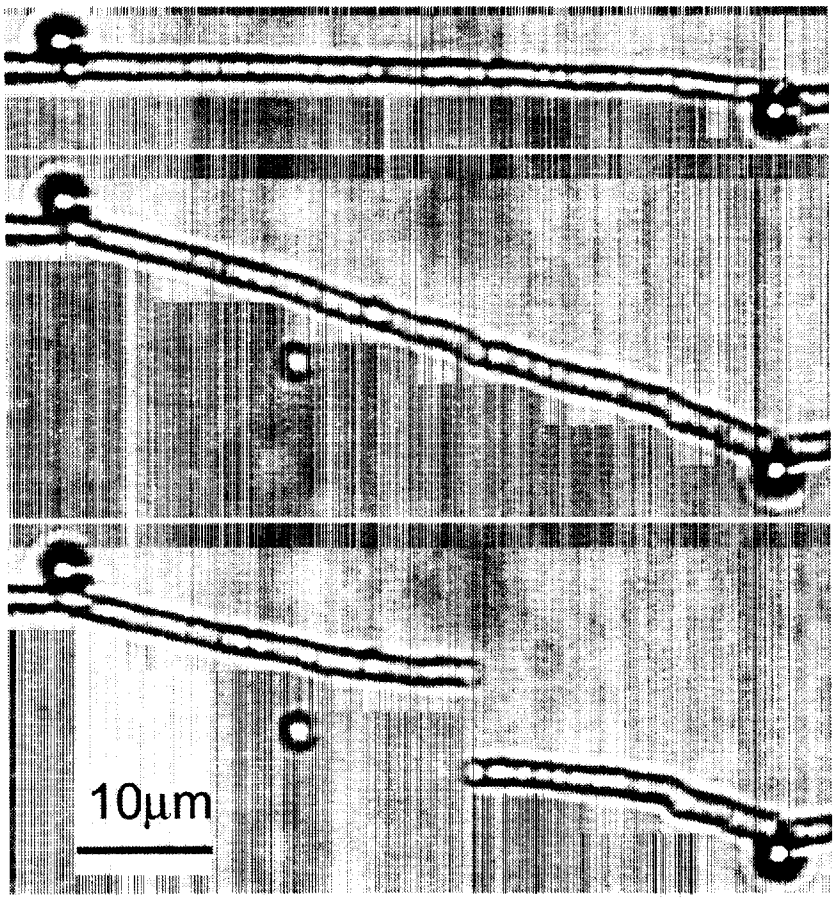

Monodisperse emulsion

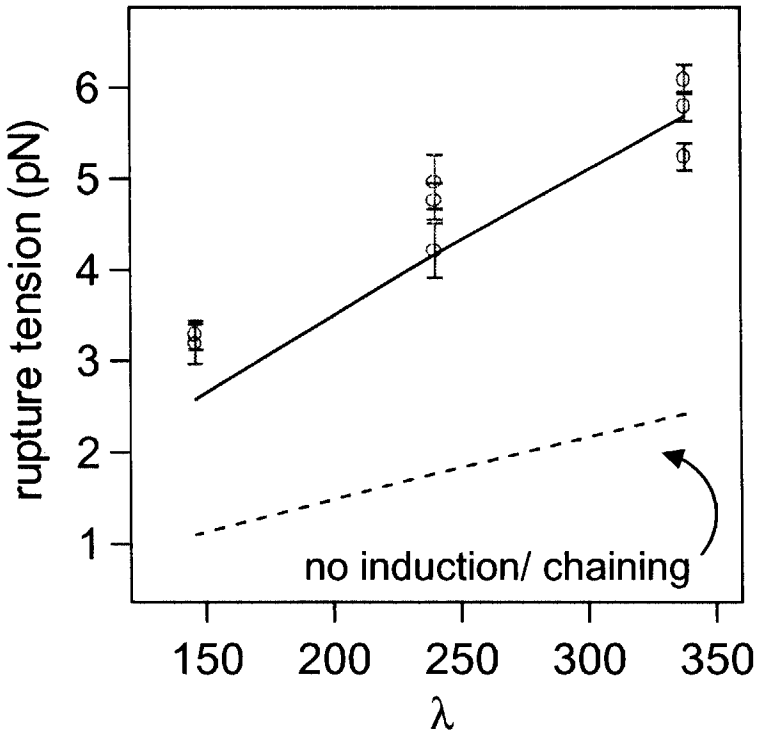

- Agreement with calculated rupture tensions

Bending of defective PS chains

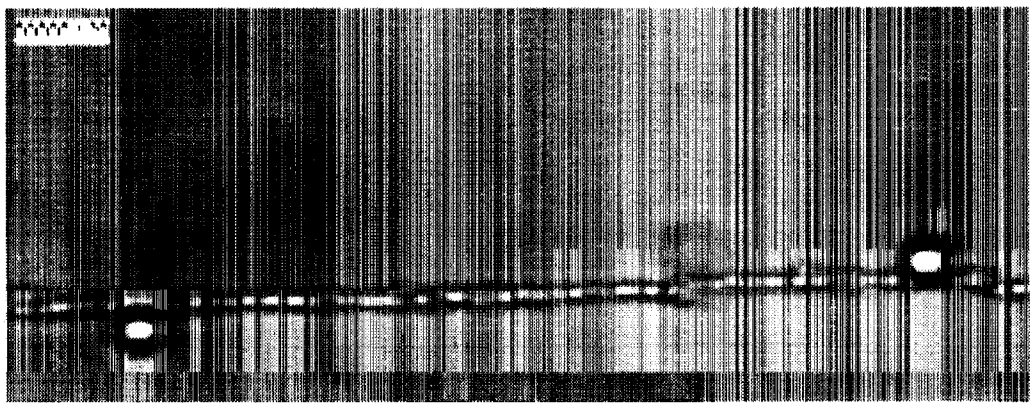

Lateral Deformation of PS Chains

PS chain bending in field - defects

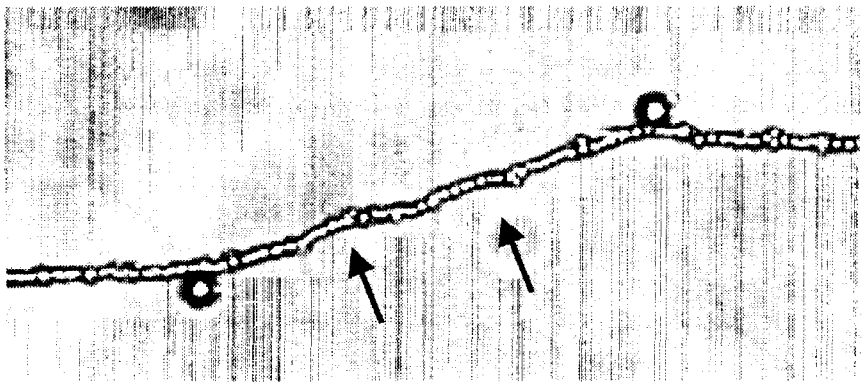

PS chain rupture tensions

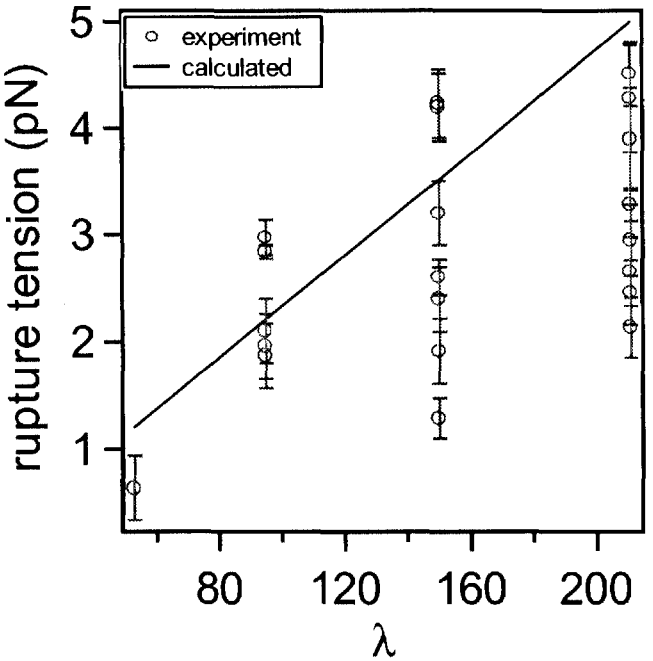

- Greater variability in individual chain behavior.
- Size polydispersity and magnetic heterogeneity
  chains rupture at lower tensions

Emulsion Chain Extension Mechanics

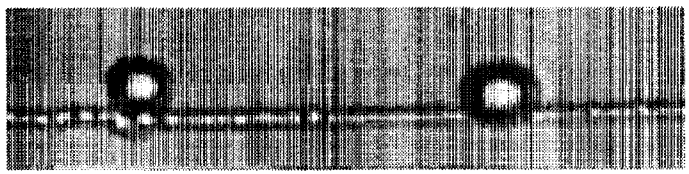

10 μm

Defect Annealing During Extension

Double cruciform

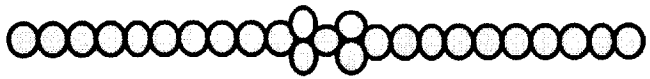

- Strain increase during extension due to defect annealing

Extensional annealing of double cruciform and corresponding tension

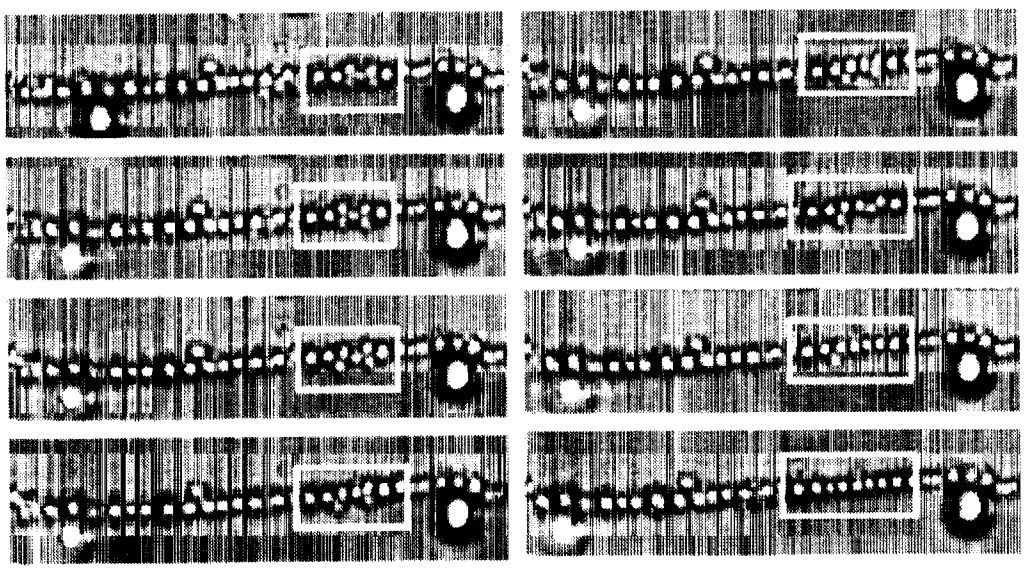

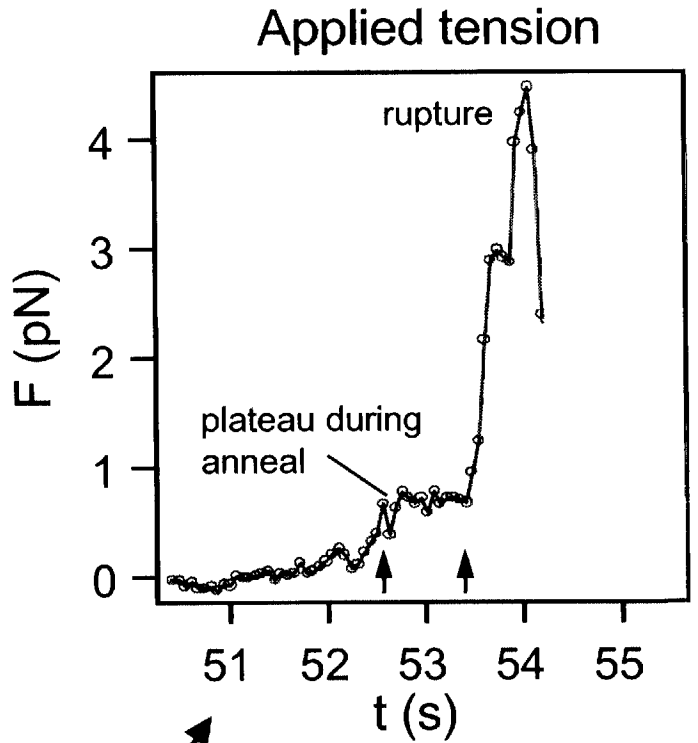

Mechanics of Chain Defects

Characteristic defects

Satellite

Cruciform

Double cruciform

Local rupture tension near defect

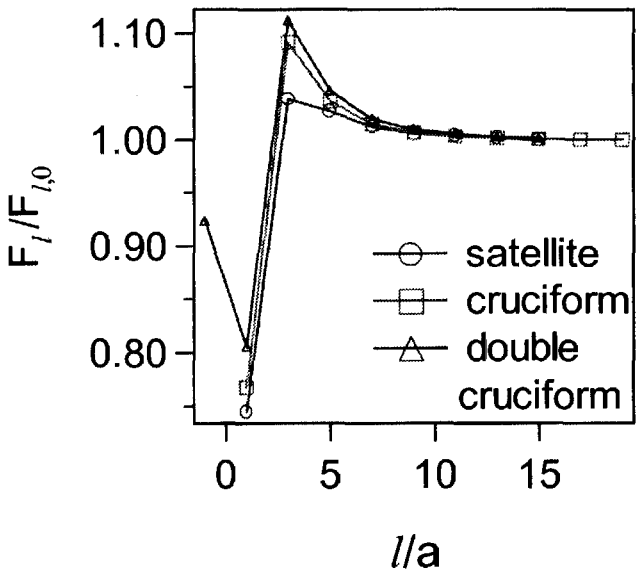

Mason number

$$Mn = \frac{Pe}{\lambda} = \frac{54\eta V_{pull}}{\mu_0 a(\chi H)^2}$$

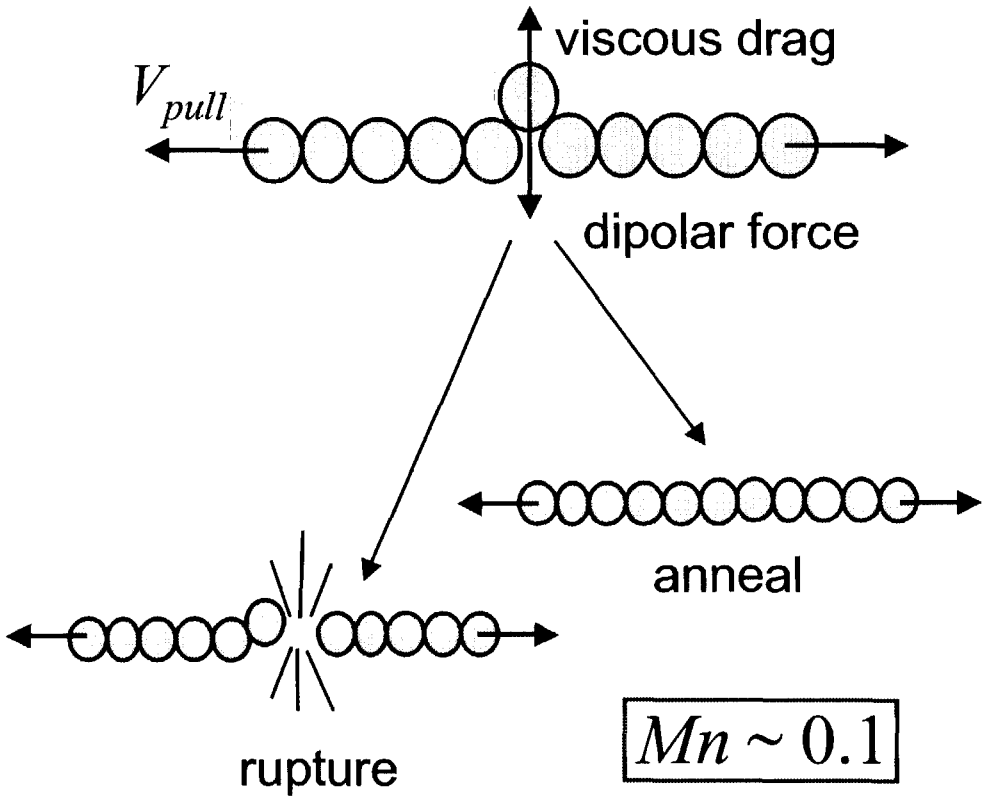

Lateral interactions with optical traps

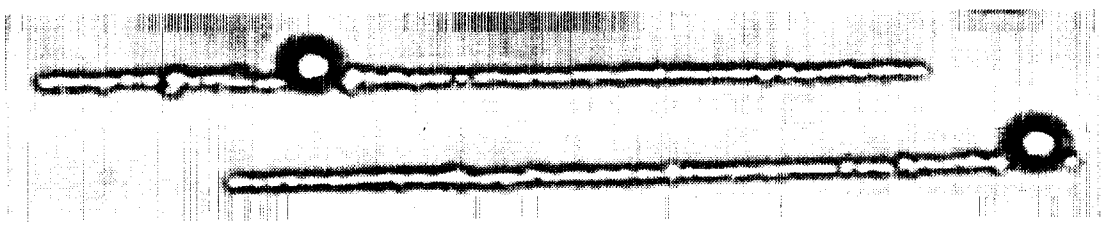

2μm

Regimes of Suspension Coarsening

Fluctuation time
>> coalescence time
(modified Halsey-Toor)

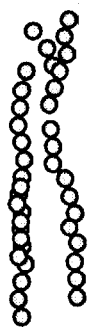

Applies: flexible chains,
close separation
(high concentration)

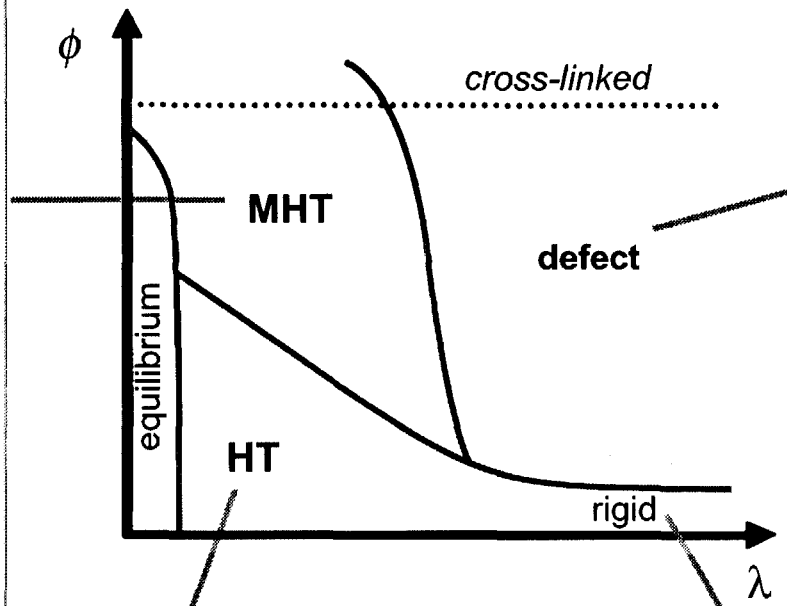

Defective chains,
kinetically pinned

Particle size, shape
and magnetic
inhomogeneity

Inflexible, short chains

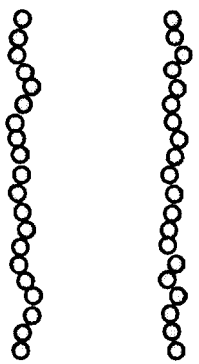

Fluctuation time << coalescence time
(Halsey - Toor)

Applies: flexible chains,
far separation (low concentration)

Halsey and Toor, 1990.
Martin et al., 1992.
Martin et al., 1999.

Rigid Chain Interaction, $\lambda = 610$

Results

- Short, rigid chains
- Ends interact strongly
- Far-field repulsion
  chains repel
- Near-field attraction

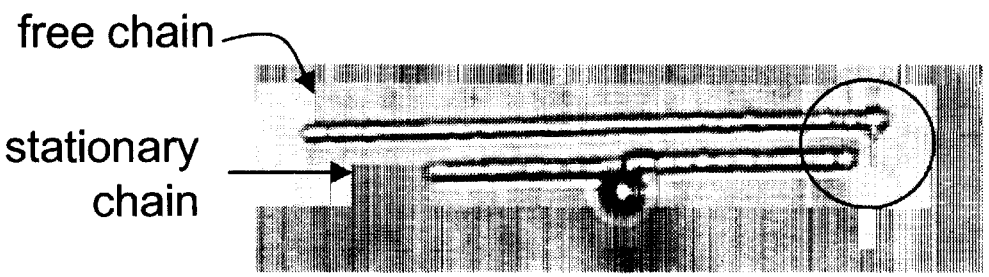

Chain separation

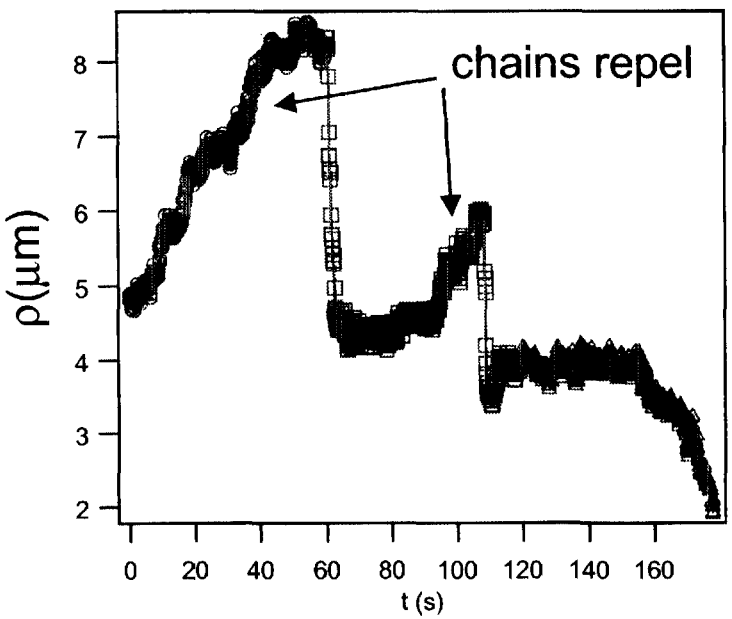

Lateral interaction energy

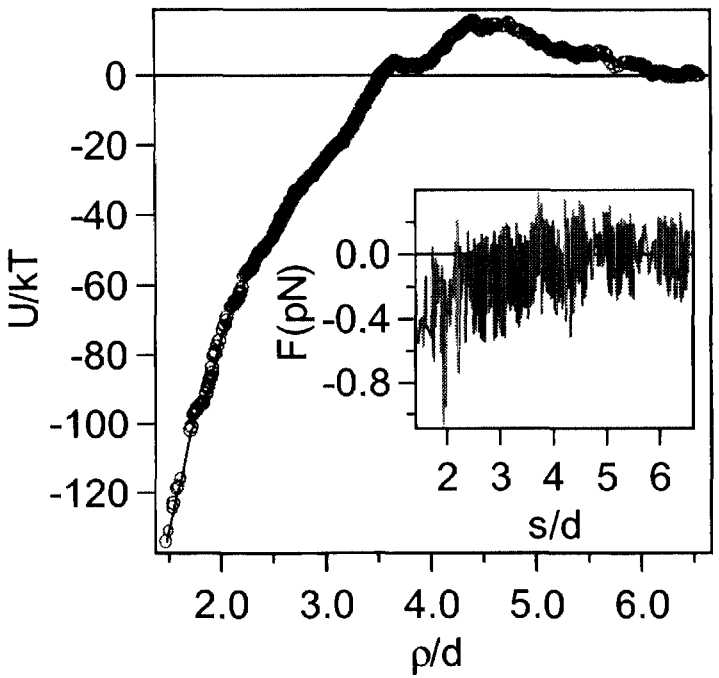

Flexible Chain Interaction, $\lambda = 340$

Results

- Uniform, defect-free chains
- Long-range attraction

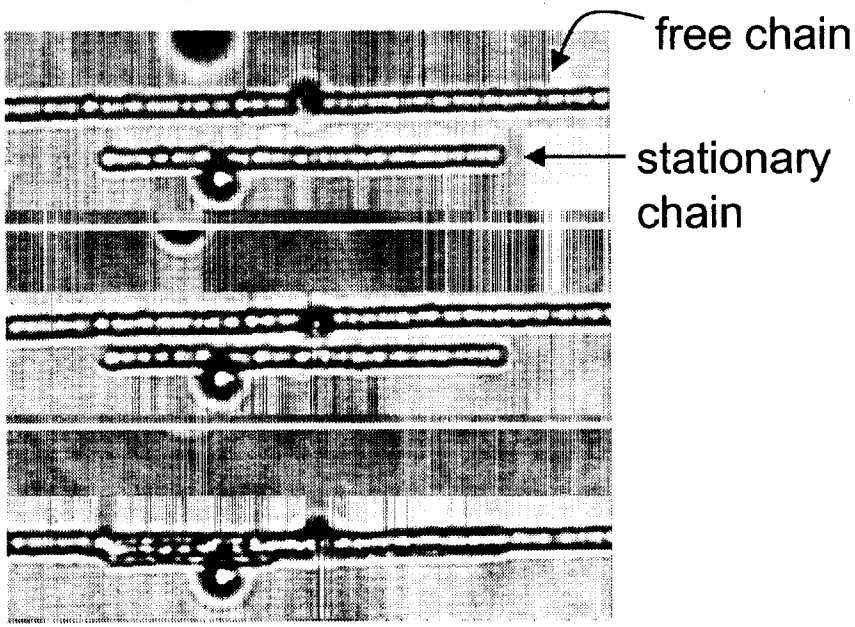

lateral coalescence

Chain separation and lateral force

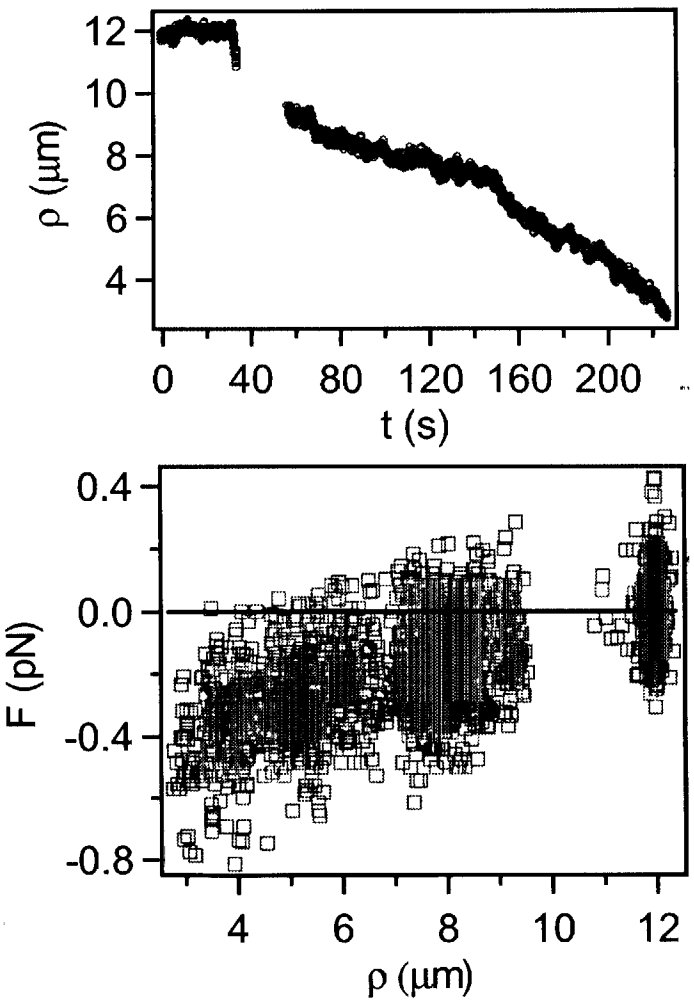

Summary

- Magnetorheological suspension - tunable rheology
  - Unique rheology coupling forces and microstructure
- Optical tweezers - manipulation, dynamics and force measurements
  - Chain rupture and reorganization
  - Chain defects play a key role
  - Coarsening governed by fluctuations and defects

Acknowledgements

- Marc Fermigier - E. S. P. C. I.
- Jim Mikkelsen - Stanford
- Hazen Babcock, Doug Smith, Chu group
- NASA Microgravity Fluid Physics Program

FREELY SUSPENDED SMECTIC FILAMENTS AND THE STRUCTURE OF THE B7 PHASE OF MHOBOW

N.A. Clark, D.R. Link, and J.E. Maclennan
Department of Physics, University of Colorado, Boulder, CO 80309

Abstract

Our recent discovery of the spontaneous formation of chiral domains in fluid smectic phases of achiral bow-shaped molecules [1] opens up a wide variety of possibilities for new liquid crystal phases and phenomena. The basic, spontaneously chiral layer structure of the highest temperature fluid smectic phases, the B2 and B7, are shown in **Figure 1**. One of the most intriguing aspects of this structure is the plethora of possible phases coming from different stacking sequences of the polar ordering and tilt directions. The four possibilities of next-nearest neighbor alternation are shown in **Figure 2**. In the original material studied, NOBOW, the ground states found are antiferroelectric, either the racemic SmC_SP_A or the chiral SmC_AP_A. We are currently studying MHOBOW, synthesized by D. Walba and shown in **Figure 2**, which, by virtue of its methyl hexyloxy tail has a tendency to form anticlinic layer interfaces, in the hope of finding a phase with a ferroelectric ground state, either SmC_AP_S or SmC_SP_A, which can be obtained in NOBOW only by applying a field [2].

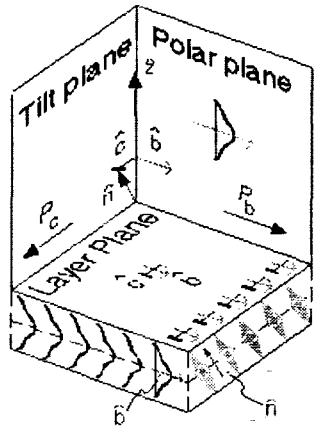

Figure 1: Basic structure of spontaneously chiral layers found in fluid smectic phases of bent-core molecules. Two broken symmetries, polar ordering of the "arrows" and molecular tilt about the arrows, make the layer chiral.

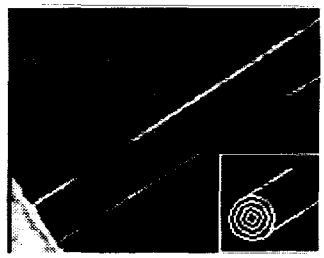

Figure 3: Freely suspended filaments of MHOBOW. These filaments are roughly 20 μm in diameter. X-ray diffraction from the filaments indicates that they have the nested cylinder layer structure shown.

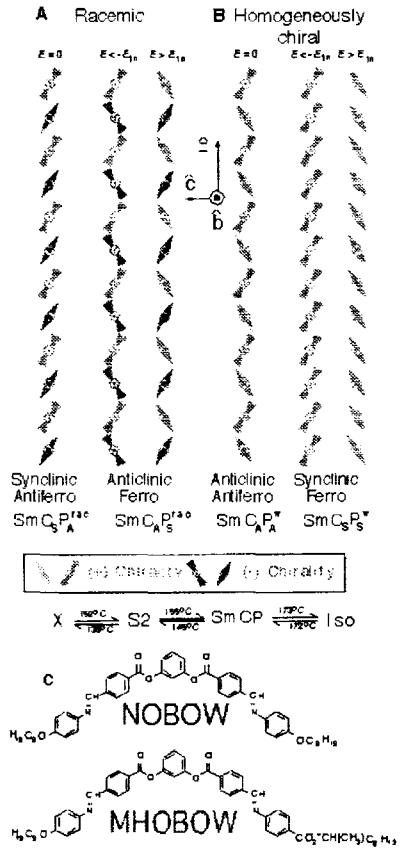

Figure 2: Simplest fluid smectic structures that can be made from the spontaneously chiral layers of **Figure 2**. The B2 phase of NOBOW exhibits both antiferroelectric structures at zero field. MHOBOW has a similar layer structure but a much more complex 3D structure.

Preliminary observations of MHOBOW have made its study, from the point of view of understanding novel LC structures, extremely high priority. The following truly remarkable characteristics have been revealed: (**i**) The smectic phase grows out of the isotropic in the form of helical ribbons. The resulting planar aligned textures of focal conics with layers normal to glass plates exhibit bizarre modulations, including stripes and checkerboards (**Figure 4**). These have also been seen in other materials suggesting that this is a new phase (tentatively called B7), which is a fluid smectic with some kind of in-layer structure. (**ii**) It is virtually impossible to make freely suspended films of MHOBOW. Rather it makes the freely suspended filaments shown in **Figure 3**, which preliminary x-ray scattering experiments reveal to have the nested cylinder layer structure indicated; (**iii**) The powder x-ray diffraction exhibits four resolution-limited smectic layering peaks, very close in layer spacing as indicated in **Figure 5**, which vary continuously with T.. This is further evidence for a more complex three dimensional structure than NOBOW, which as **Figure 5** shows has a typical single layering reflection. (**iv**) The x-ray structure factor of the layering peak of the filaments is extraordinarily complex and rich, as shown in **Figure 6**. Varying in $q_\perp$ (the

scattering vector component along the filament axis) from a double slit-like pattern to modulated layer-like patterns, as q_H (the scattering vector component normal to the filament axis) is varied over the range where the four powder peaks are located. These results suggest some kind of mosaic structure, perhaps with different layer spacings corresponding to the different stacking sequences in **Figure 4**. Recent x-ray diffraction experiments show that the peaks in **Figure 5** are modulated in intensity upon translation along a filament, in domains of several hundred microns dimension.

These preliminary experiments suggest that the B7 is a fluid smectic with extremely unusual and fascinating structures. Of all of the many hundreds of fluid smectic materials we have attempted to study in the freely suspended film geometry over the years, only a few have failed to form films, and none showed any great tendency to form filaments, although this clearly should be a possible freely suspended smectic LC morphology. On several occasions in the past we have intentionally tried to make filaments from a variety of smectics without success. Thus the smectic filament formation property makes the B7 phase unique. It seems quite likely that the stability of filaments is related to the in-plane structure.

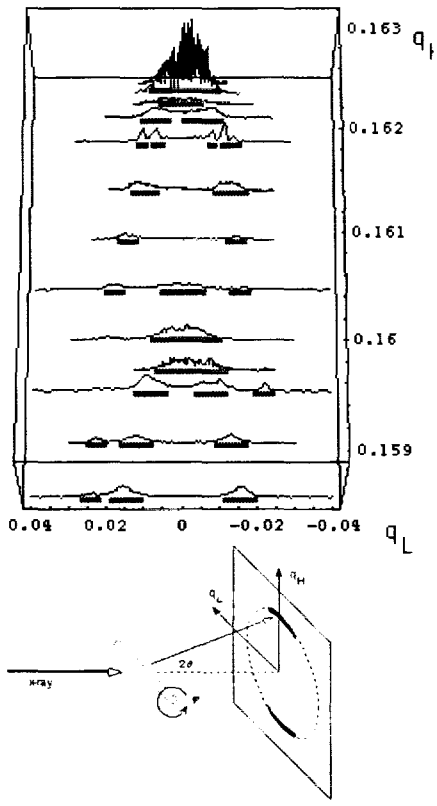

Figure 6: X-ray scattering geometry and intensity from a MHOBOW filament in the B7 phase vs. q_L, the scattering vector component along the filament axis, and q_H, the component normal to the filament axis, both in $Å^{-1}$. The q_H range is roughly that of the multiple peaks in **Figure 5**. This pattern is indicative of a complex, 3D modulated smectic structure that is currently not understood.

The filaments exhibit other interesting structural and optical features. They are birefringent with a local optic axis which is oblique and which can vary continuously along filament and which can be manipulated with an electric field applied normal to the fiber, as if the field were causing a rotation of the optic axis about the fiber axis. Rapid displacement of the ends of the fiber toward one another causes a macroscopic helixing at low T and causes thick regions to transiently appear at high T, a 1D analog of island formation on a rapidly compressed film.

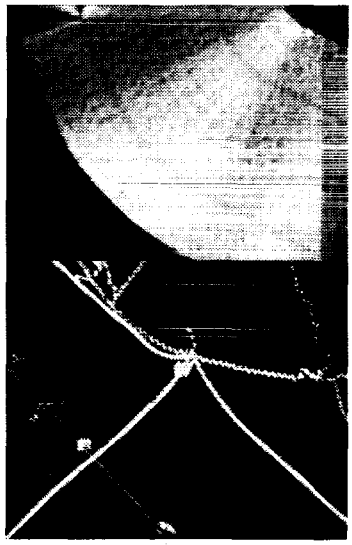

Figure 4: Focal conic texture of r-MHOBOW, showing the complex in-layer modulation of the B7 phase, and helical B7 filmants growing from the isotropic.

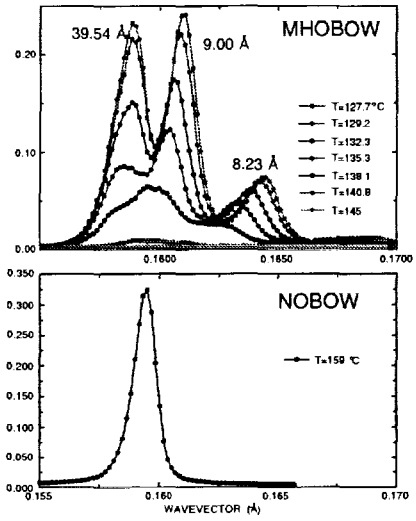

Figure 5: Powder x-ray diffraction peaks showing the unusual multi-peak of MHOBOW and the typical single peak of NOBOW. The NOBOW peak and the individual MHOBOW peaks are resolution limited corresponding to smectic domains > 3000Å in size.

Work supported by NASA Grant NAG3-1846.

References

[1] D.R. Link et al., *Science* **278**, 1924 (1997).
[2] D.M. Walba et al. *Science* **(in press)**

Presentation not available at time of printing.

August 9, 2000

Session 1C
Interfacial Phenomena I

THERMOCAPILLARY-INDUCED PHASE SEPARATION WITH COALESCENCE

R. Davis, M. Rother, and A. Zinchenko
Department of Chemical Engineering, University of Colorado
Boulder, Colorado 80309-0424
robert.davis@colorado.edu, 303-492-7314

ABSTRACT

Understanding the behavior of dispersions of one liquid immersed in a second, immiscible liquid is important in both traditional engineering applications, such as separations and molten materials processing, as well as more fundamental problems in the general sciences. This work examines the interactions of two drops under conditions that viscous forces dominate inertia, focusing on the role of interfacial deformation. The pairwise information may then be used in the study of dilute dispersions, where the probability of three-body interactions is low. Two regimes of deformation are considered: small deformation, where the drops remain spherical except for a small flattening or dimpling between the drops,[1,2] and moderate or large deformation, where the interfaces of both drops distort globally.[3-5] The effects of deformation are significant, because small deformation inhibits drop coalescence, while global deformation promotes alignment of the drops,[6] which may lead to coalescence,[3,4] break-up of the smaller drop,[3,4,7] or even more complicated coalescence-breakup phenomena.[3,4,8]

This paper is focused on the interaction of two drops of different size which experience buoyancy and/or thermocapillary relative motion. Small deformations are considered first, followed by moderate and large deformations. Using methodology from matched asymptotic expansions and a local boundary-integral approach, coupling the lubrication flow in the gap to the internal flow within the drops, the critical horizontal offset demarcating trajectories which lead to coalescence or separation of the drops with small deformations is found. Figure 1 shows the resulting collision efficiencies for slightly deformable (solid curves) and spherical (dashed curves) drops of ethyl salicylate (ES) in diethylene glycol (DEG) in gravitational motion.[1] The collision efficiency of slightly deformable drops is approximately the same for spherical drops until a particular value of the average radius at which the collision efficiencies for spherical and slightly deformed drops rapidly diverge. With a further increase in the average radius, the collision efficiency for slightly deformed drops quickly approaches zero, as the flattening and dimpling in the near-contact region slows the film drainage and reduces the coalescence rate. In Figure 2, population dynamics simulations of droplet growth due to coalescence are shown for the same ES/DEG system, but now in thermocapillary-driven motion,[2] at volume fraction ϕ_0 = 0.05. Although the two distributions for deformable drops in frames a and b begin with different initial conditions, they become nearly indistinguishable later as a result of the retardation of coalescence by small deformations. Coalescence may also be inhibited by appropriated anti-parallel alignment of the gravity vector and temperature gradient.[9]

Turning to larger deformations, computational results[3,4] have been complemented by experiments with glycerol/water drops undergoing gravitational motion in castor oil.[8] A particularly interesting phenomenon observed in the experiments is cyclic capture-breakup, in which the head of a smaller drop does not coalesce with a larger drop after breaking. Instead, the head of the smaller drop passes through the larger drop, moves back around it and is again captured and breaks. Figure 3 shows a typical cyclic process, which we have called 'suckthrough,' for viscosity ratio unity.

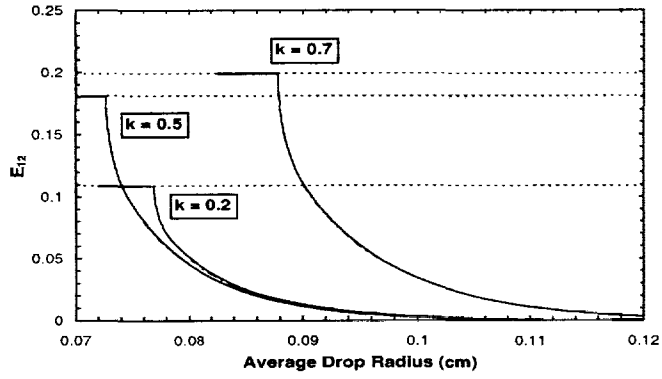

Figure 1: The collision efficiency for sedimentation of drops as a function of the average drop radius for an ES/DEG system for drop size ratios 0.2, 0.5, and 0.7. The dashed lines are for spherical drops, and the solid lines are for slightly deformable drops, both in the presence of van der Waals forces.

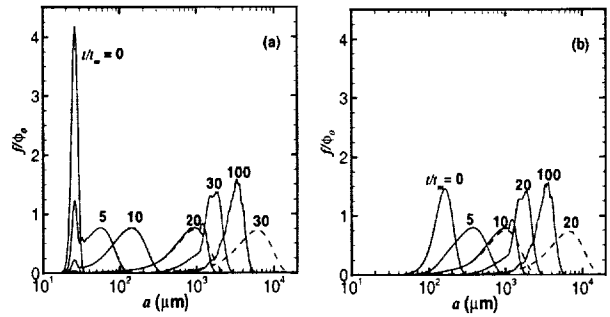

Figure 2: Time evolution of the drop-size distribution for thermocapillary coalescence of an ES/DEG dispersion composed of spherical (dashed lines) and slightly deformable (solid lines) drops with (a) dimensionless standard deviation σ = 0.1 and initial number-averaged radius a_0 = 25 μm and (b) σ = 0.5, a_0 = 100 μm.

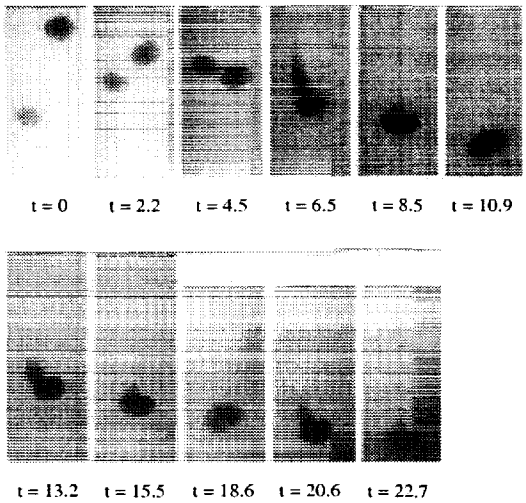

Figure 3: Experimental images of the drop shapes for a trajectory leading to cyclic suckthrough for two glycerol/water drops in castor oil with size ratio 0.87, drop-to-medium viscosity ratio 1.0, and Bond number 7.1. The Reynolds number is 0.16, and the time scale is 1.2 s.

REFERENCES

[1] Rother, M.A., Zinchenko, A.Z. & Davis, R.H. (1997) *J. Fluid Mech.* **346**: 117-148.

[2] Rother, M.A. & Davis, R.H. (1999) *J. Colloid Interf. Sci.* **214**: 297-318.

[3] Zinchenko, A.Z., Rother, M.A. & Davis, R.H. (1999) *J. Fluid Mech.* **391**: 249-292.

[4] Davis, R.H. (1999) *Phys. Fluids* **11**: 1016-1028 (1999).

[5] Zinchenko, A.Z. & Davis, R.H. (2000) *J. Comp. Phys.* **157**: 539-587 (2000).

[6] Manga, M. & Stone, H.A. (1993) *J. Fluid Mech.* **256**: 647-683.

[7] Cristini, V., Blawzdziewicz, J. & Loewenberg, M. (1998) *Phys. Fluids* **10**: 1781-1783.

[8] Kushner, J., Rother, M.A. & and Davis, R.H. *J. Fluid Mech.* (under review).

[9] Zhang, X., Wang, H. & Davis, R.H. (1993) *Phys. Fluids A* **5**, 1602-1613.

Thermocapillary-induced Phase Separation with Coalescence

Robert H. Davis, Michael A. Rother
and Alexander Z. Zinchenko

Department of Chemical Engineering
University of Colorado
Boulder, CO 80309-0424

Outline

1. Spherical drops and bubbles
2. Small deformations
3. Large deformations
4. Concentrated emulsions

Phase Separation

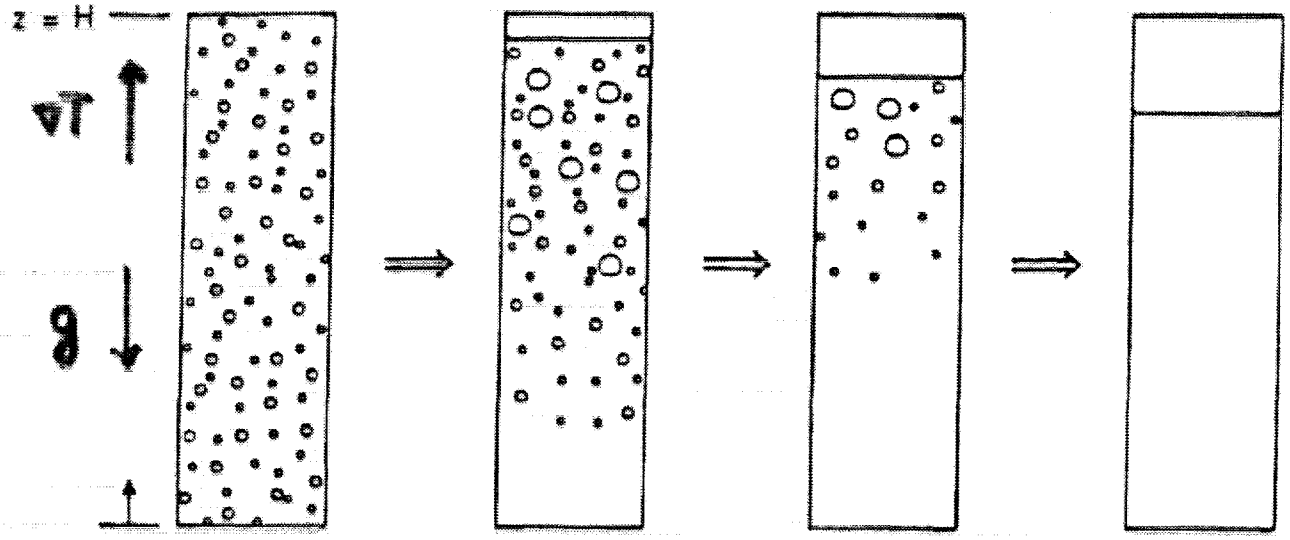

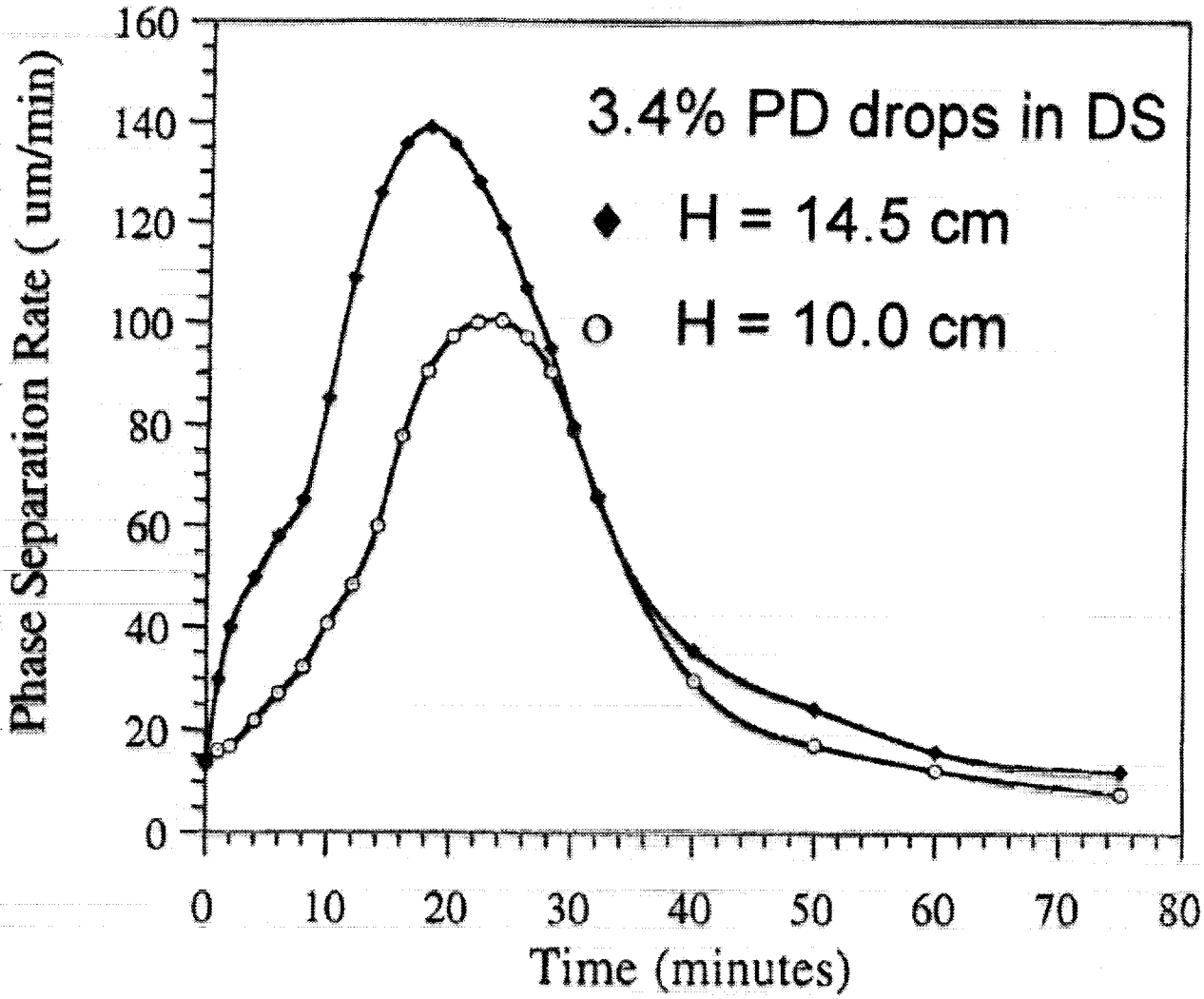

Wang & Davis (1996) *JCIS* **181**: 60

Spherical Drops – Collision Efficiencies

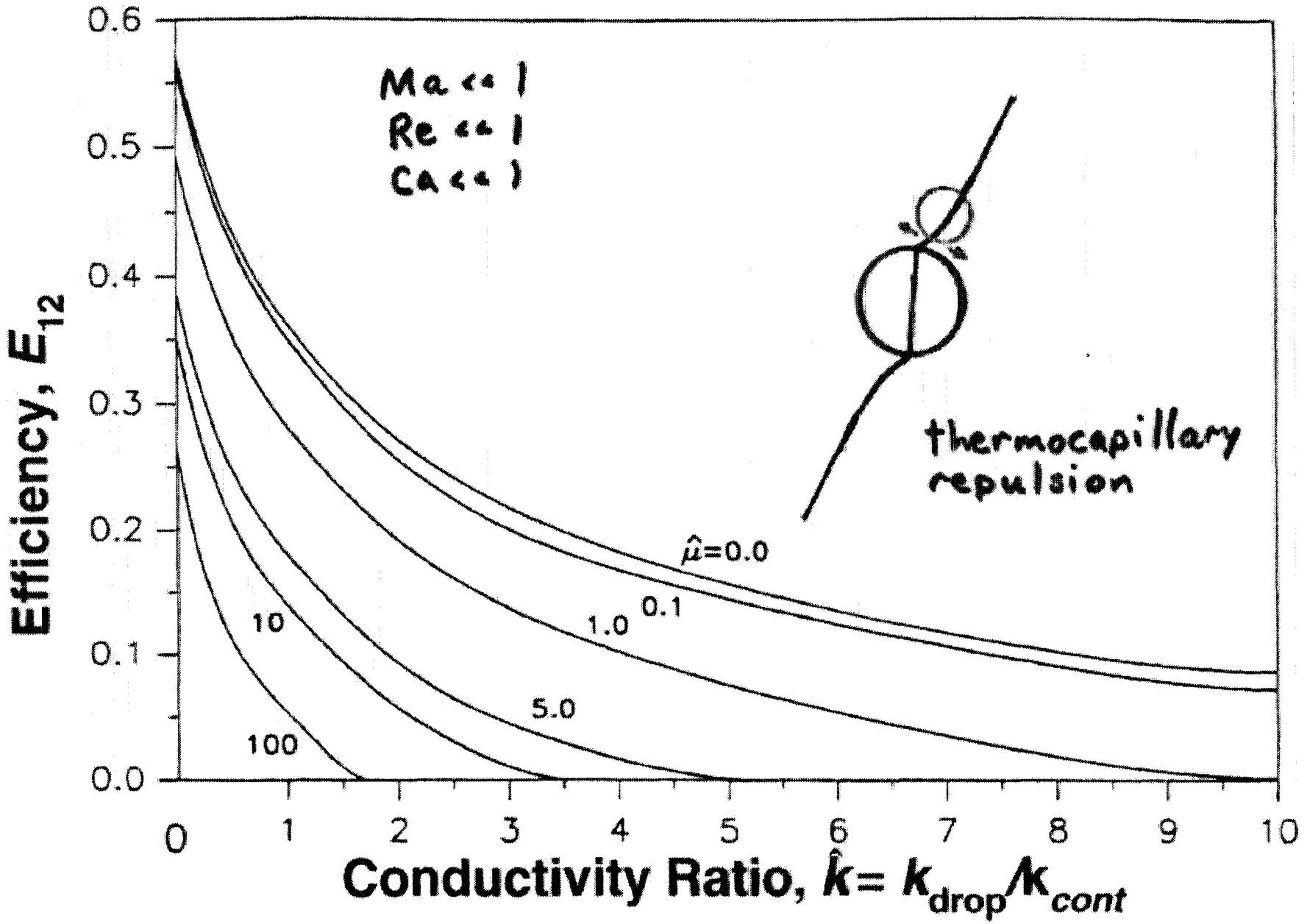

Zhang & Davis (1992) *JCIS* **152**: 548

Small Deformations

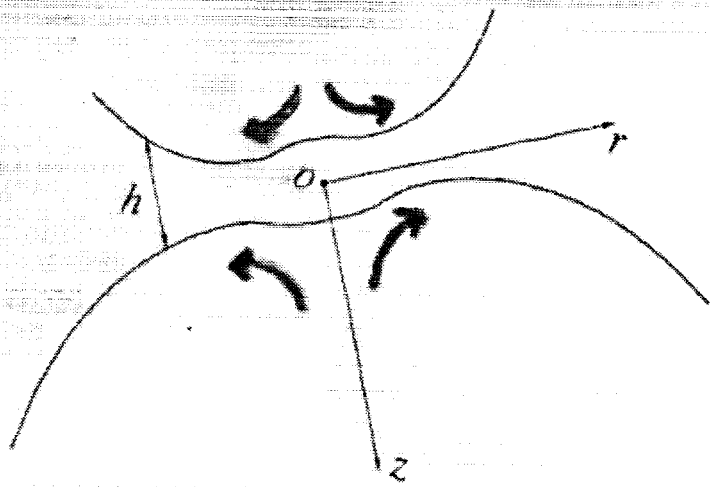

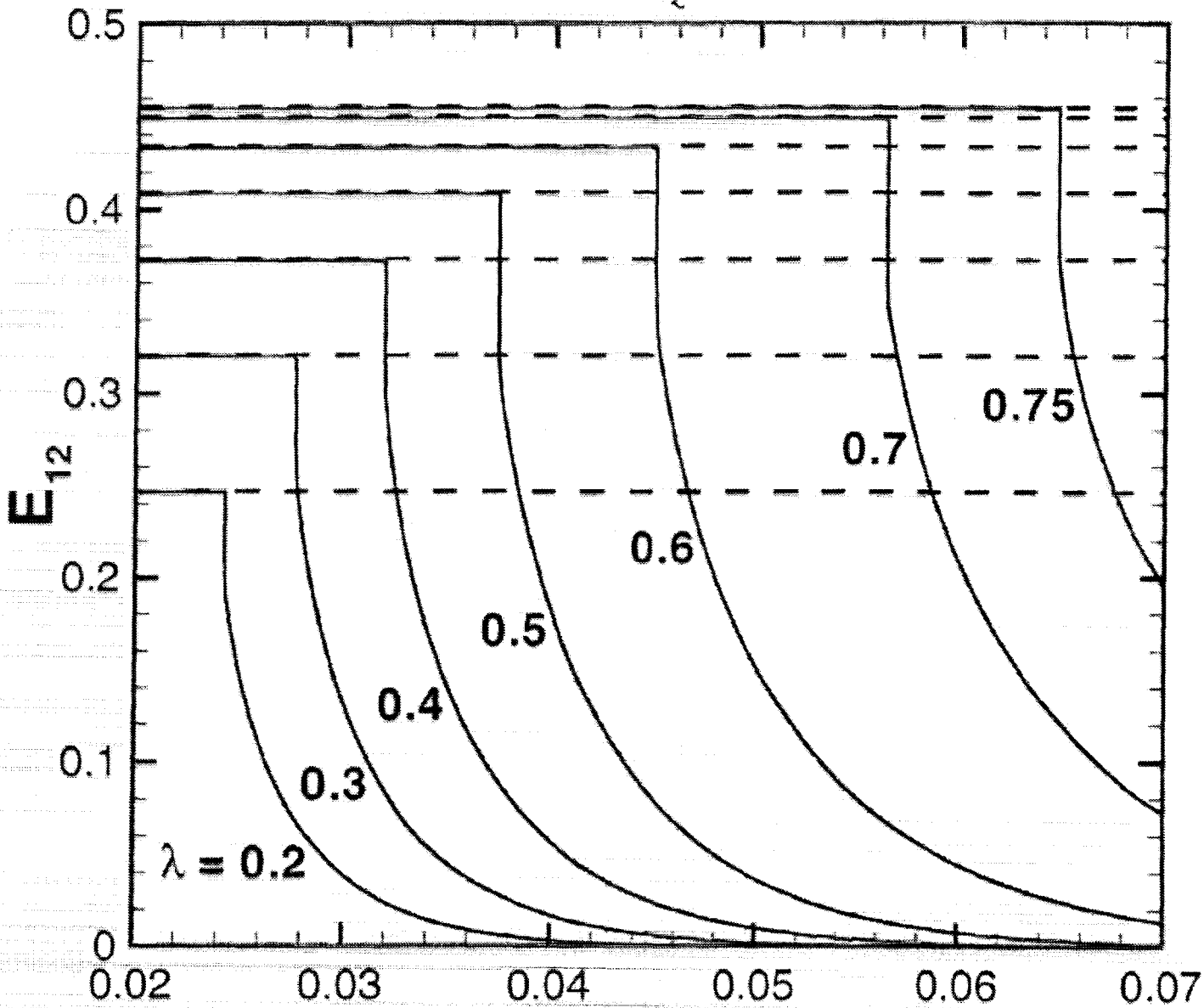

Rother & Davis (1999) *JCIS* **214**: 297

Large Deformations

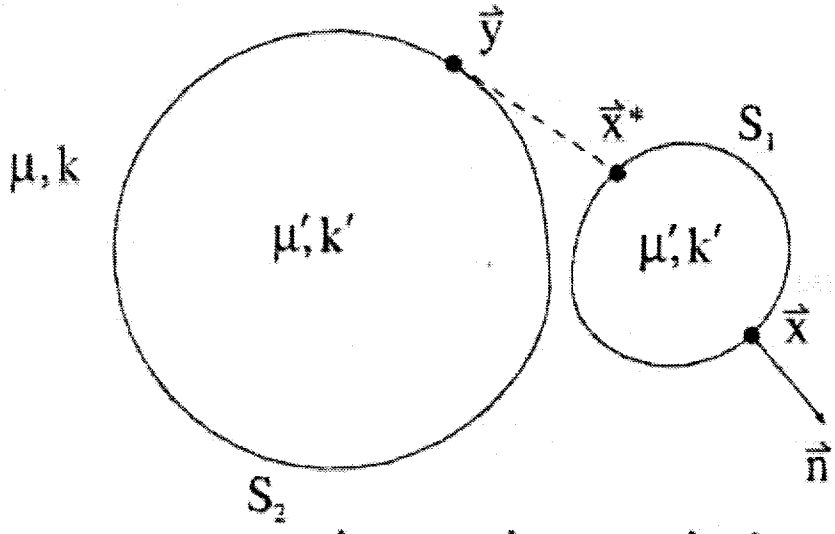

$$\hat{\mu} = \mu' / \mu$$

$$\hat{k} = k' / k$$

boundary-integral method

$$T(\boldsymbol{y}) = \frac{2}{1+\hat{k}}\, T_\infty(\boldsymbol{y}) - \frac{(\hat{k}-1)}{2\pi(\hat{k}+1)} \sum_{\alpha=1}^{2} \int_{S_\alpha} T \nabla(1/r) \cdot \boldsymbol{n} dS$$

$$\boldsymbol{u}(\boldsymbol{y}) = \frac{-1}{4\pi(1+\hat{\mu})} \sum_{\alpha=1}^{2} \left[\frac{1}{\mu} \int_{S_\alpha} \boldsymbol{G} \cdot \Delta \boldsymbol{f} dS - (1-\hat{\mu}) \int_{S_\alpha} \boldsymbol{T} \cdot \boldsymbol{n} \cdot \boldsymbol{u} dS \right]$$

$$\boldsymbol{G} = \frac{\boldsymbol{I}}{r} + \frac{\boldsymbol{rr}}{r^3} \qquad \boldsymbol{T} = \frac{-6\boldsymbol{rrr}}{r^5} \qquad \boldsymbol{r} = \boldsymbol{x} - \boldsymbol{y}$$

$$\Delta \boldsymbol{f} = 2\sigma k_m \boldsymbol{n} - \nabla_s \sigma$$

Singularity Subtraction

$$\int_{S_\alpha} T(\boldsymbol{x}) \nabla(1/r) \cdot \boldsymbol{n} dS = \int_{S_\alpha} [T(\boldsymbol{x}) - T(\boldsymbol{x}^*)] \nabla(1/r) \cdot \boldsymbol{n} dS$$

$$- \begin{cases} 0 & \boldsymbol{y} \text{ outside } S_\alpha \\ 2\pi T(\boldsymbol{x}^*) & \boldsymbol{y} \text{ on } S_\alpha \end{cases}$$

Simulation without Coalescence

$\hat{k} = 1,\ \hat{\mu} = 1,\ k = 0.5,\ x_0/a_2 = 1.0,\ z_0/a_2 = -5.0$

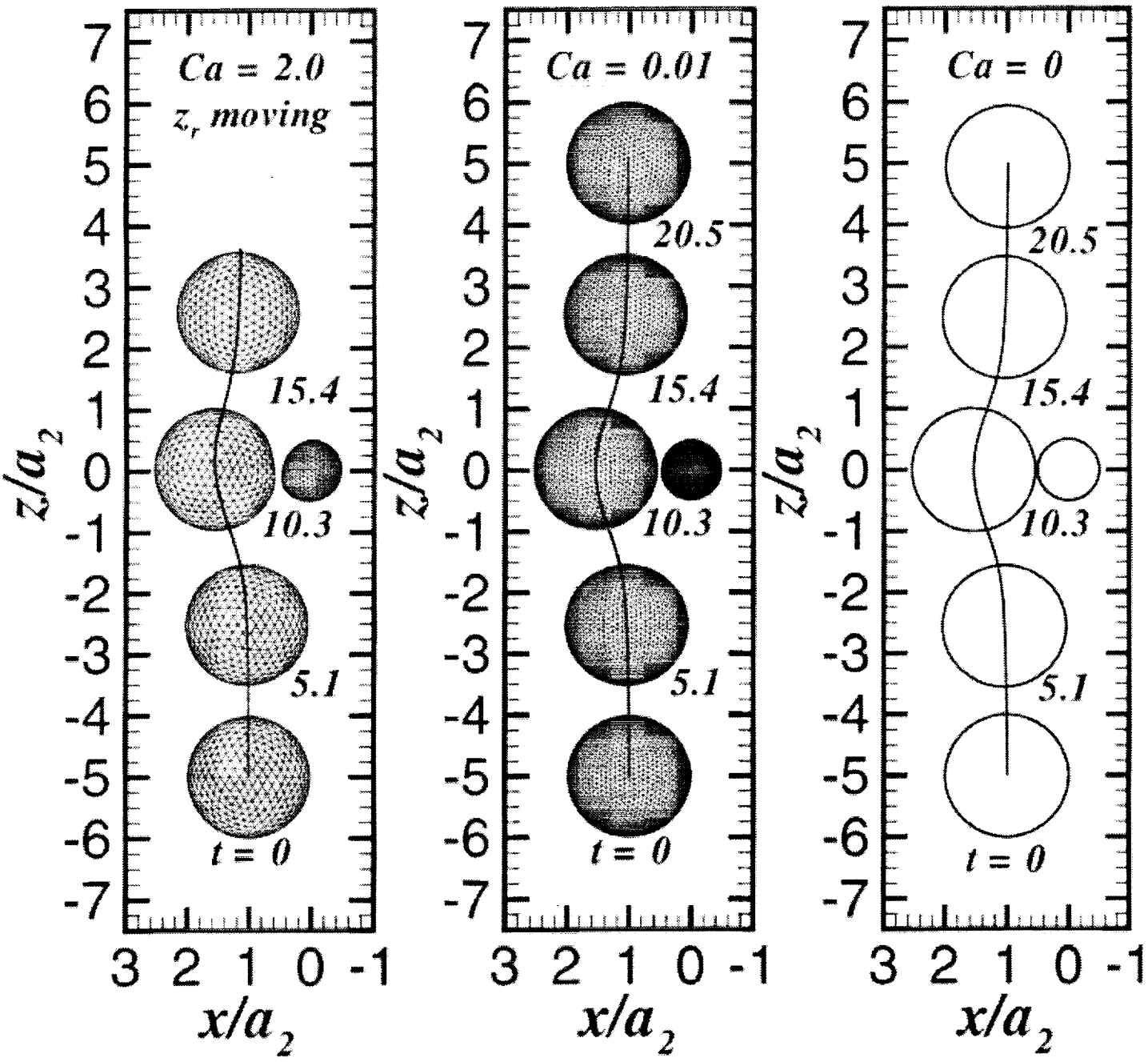

$$Ca \equiv \mu U_2^o / \sigma_o \qquad U_2^o = \frac{a_2\left(-d\sigma/dT\right)\left(dT_\infty/dz\right)}{\mu\left(3\hat{\mu}+2\right)\left(1+\hat{k}/2\right)}$$

$$q \equiv a_2\left(-d\sigma/dT\right)\left(dT_\infty/dz\right)/\sigma_o = \left(3\hat{\mu}+2\right)\left(1+\hat{k}/2\right)Ca$$

Simulation with Coalescence if Spherical

$\hat{k} = 1,\ \hat{\mu} = 1,\ k = 0.7,\ x_0/a_2 = 0.89,\ z_0/a_2 = -2.87$

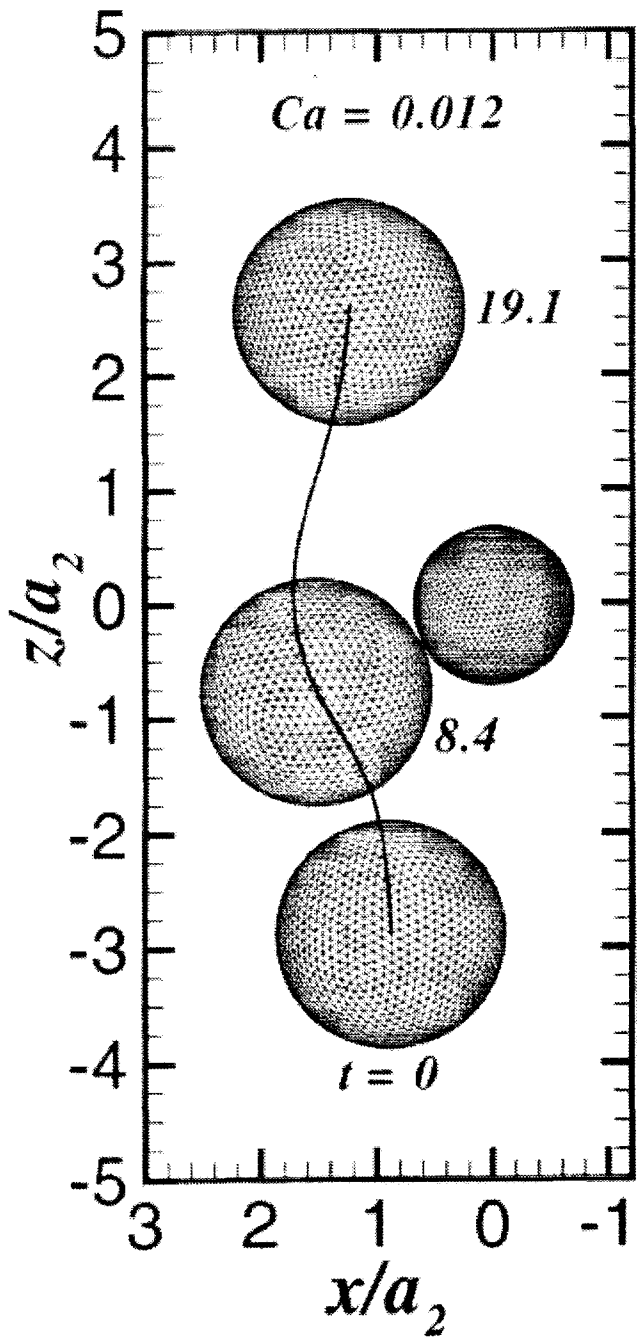

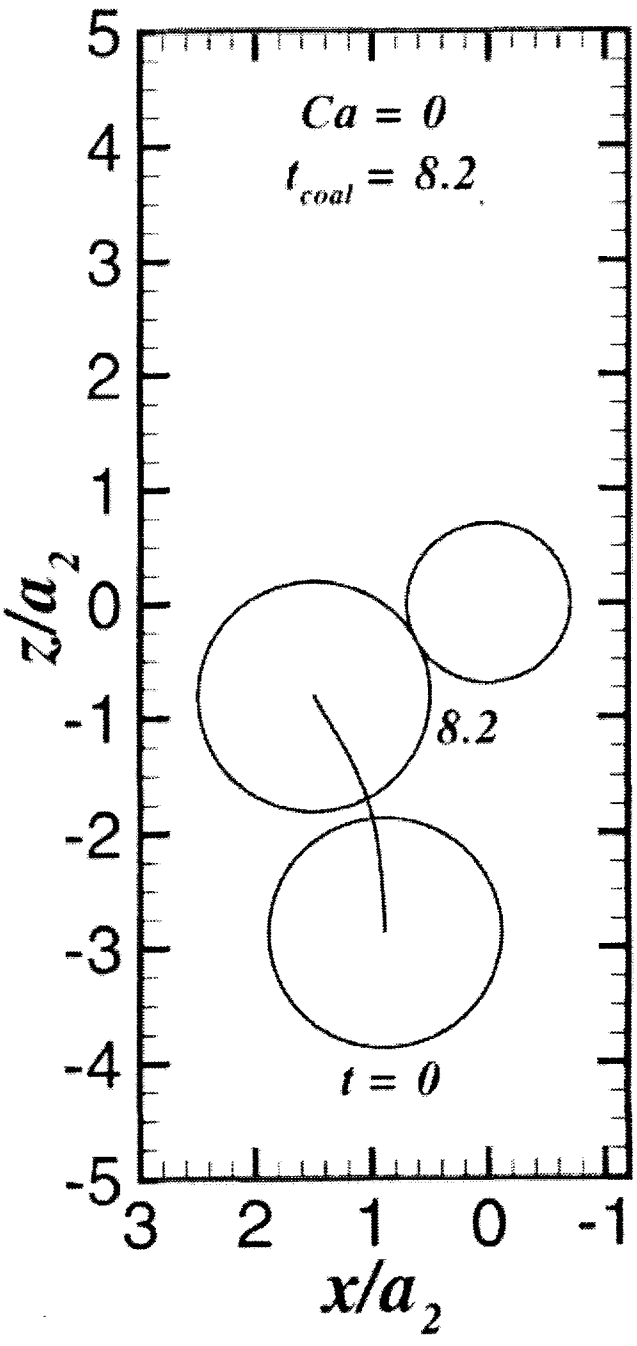

Buoyancy Experiments – Separation

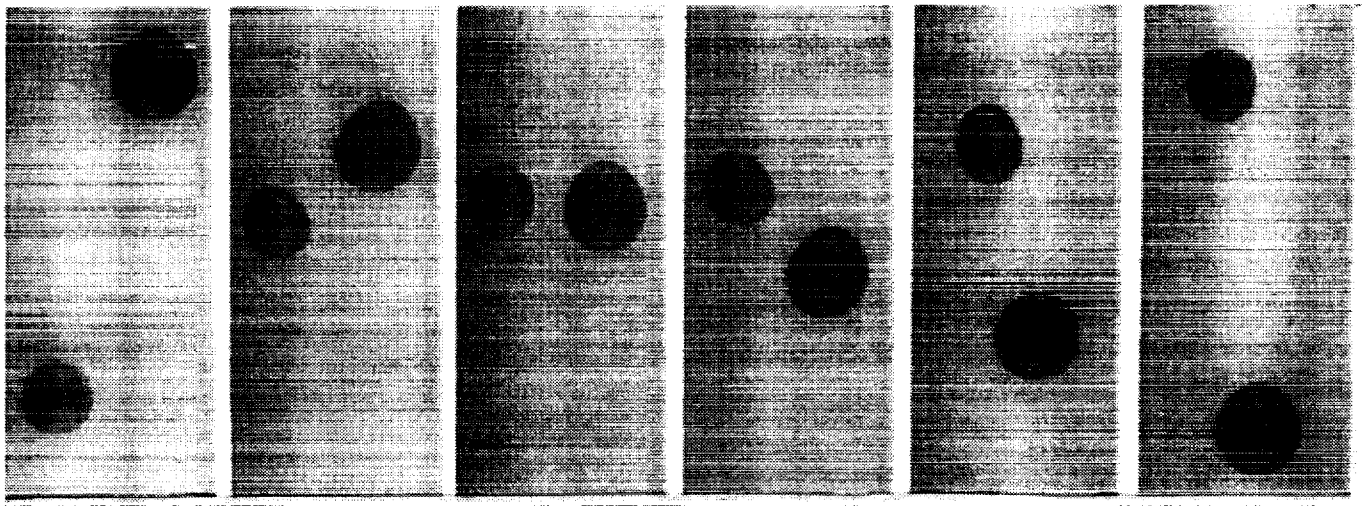

t = 0 s 7.2 s 10.4 s 13.6 s 19.7 s 26.7 s

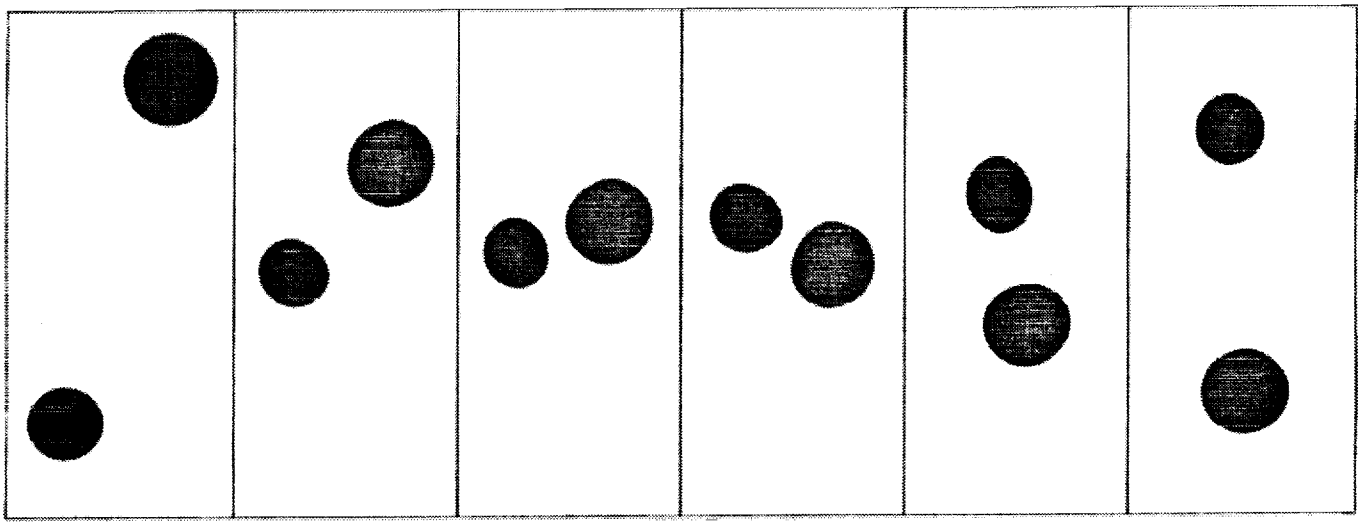

t = 0 s 7.2 s 10.4 s 13.6 s 19.7 s 26.7 s

Glycerol-water drops in castor oil

$a_1/a_2 = 0.8$ $\hat{\mu} = 0.002$ $Bo = 1.8$ $\Delta x_o/a_2 = 2.2$

Kushner, Rother & Davis (2000) *JFM* (submitted).

Buoyancy Experiments – Entrainment

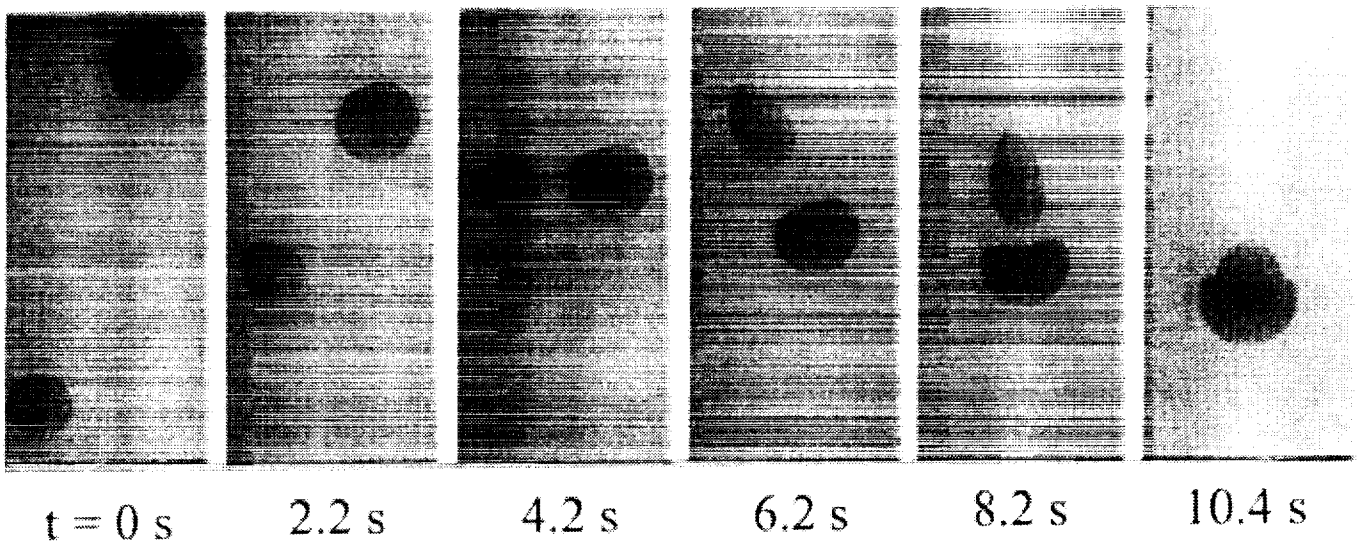

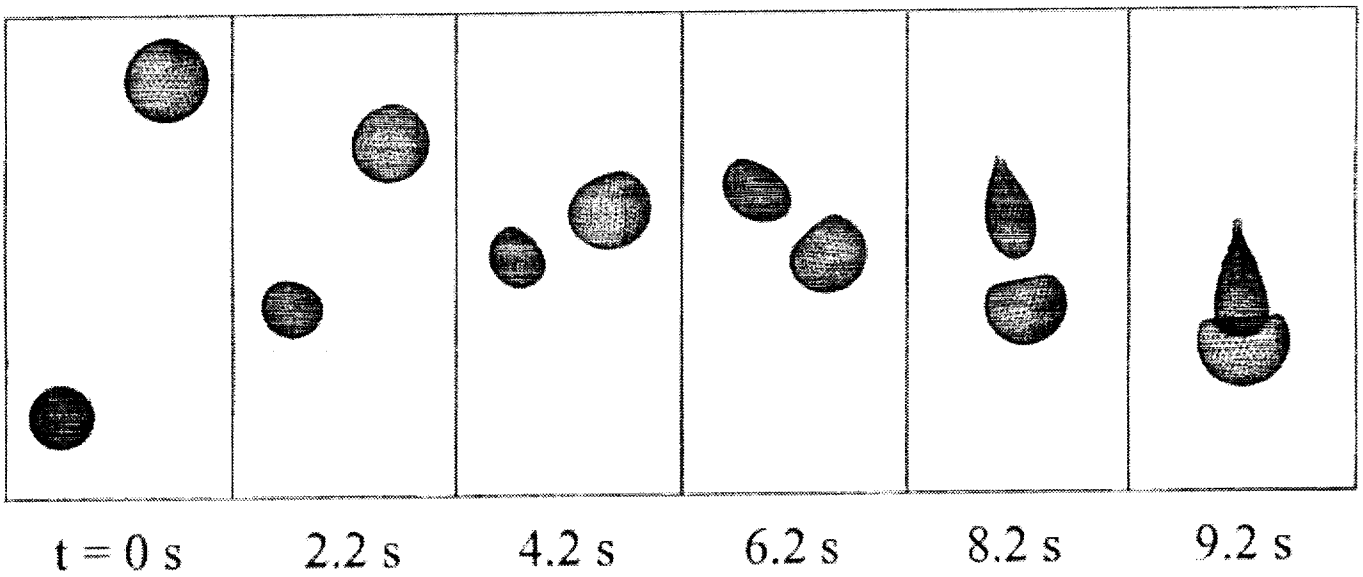

Glycerol-water drops in castor oil

$a_1/a_2 = 0.8$ $\hat{\mu} = 0.1$ **Bo = 5.8** $\Delta x_o/a_2 = 2.5$

Kushner, Rother & Davis (2000) *JFM* (submitted).

Buoyancy Experiments – Coalesence

(1) (2) (3) (4)

$\Delta t \approx 0.5$ s

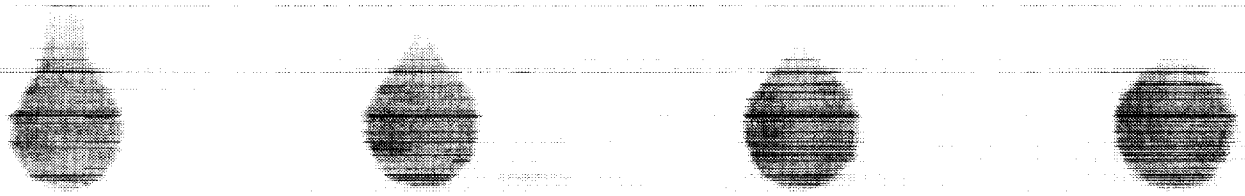

(5) (6) (7) (8)

Glycerol-water drops in castor oil

$a_1/a_2 = 0.8$ $\hat{\mu} = 0.002$ Bo = 0.7 $\Delta x_o/a_2 = 0.2$

Kushner, Rother & Davis (2000) *JFM* (submitted).

Buoyancy Experiments – Breakup

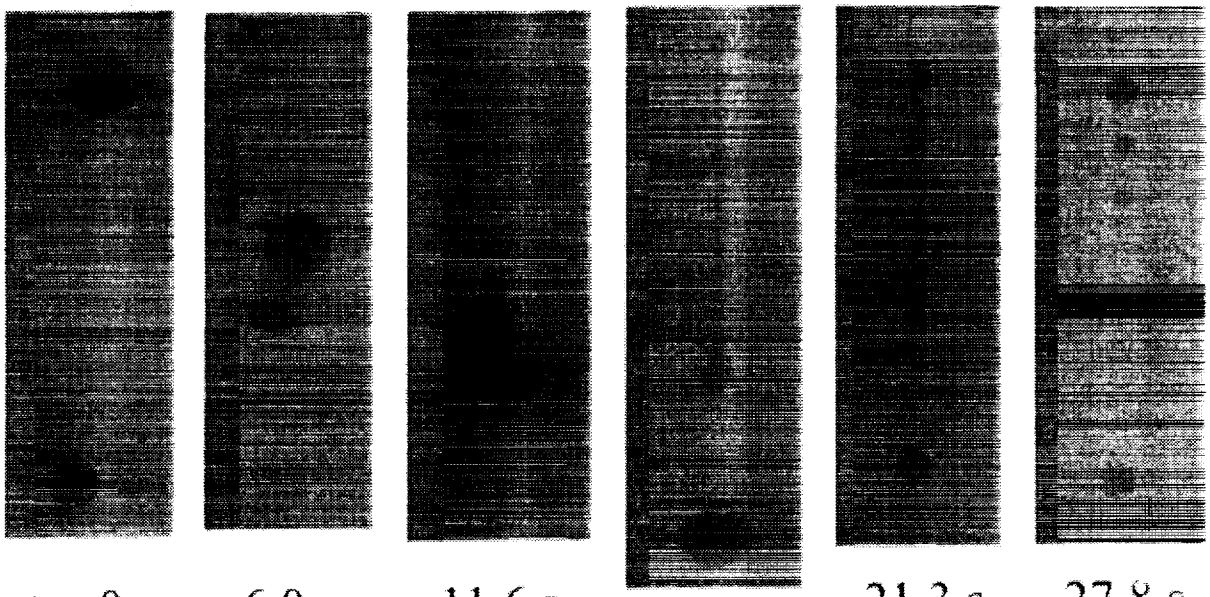

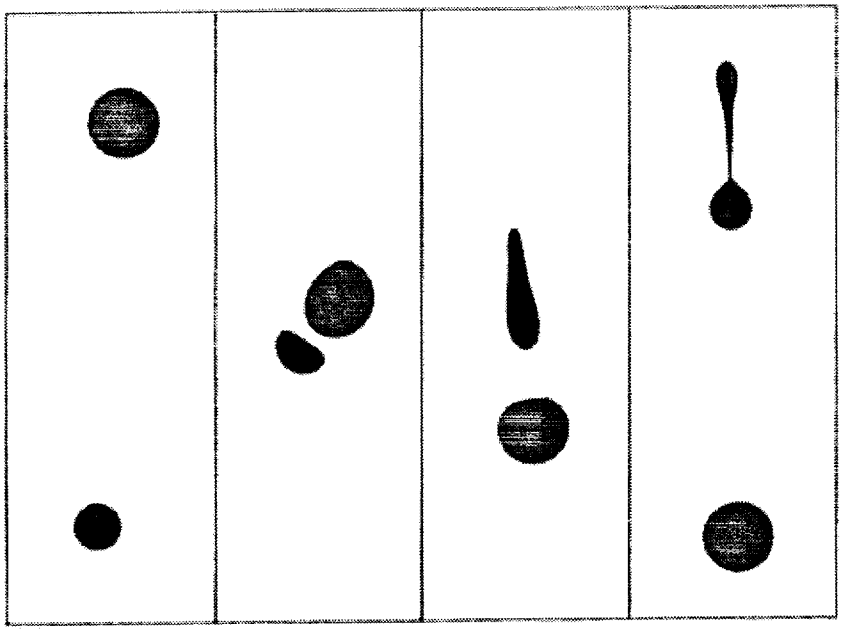

Glycerol-water drops in castor oil

$a_1/a_2 = 0.7$ $\hat{\mu} = 1.0$ **Bo = 5.6** $\Delta x_o/a_2 = 0.8$

Kushner, Rother & Davis (2000) *JFM* (submitted).

Buoyancy Experiments – Suckthrough

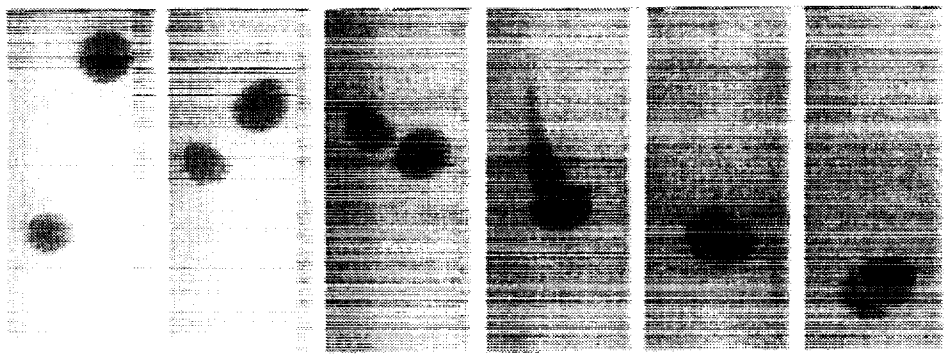

t = 0 s 2.7 s 5.6 s 8.1 s 10.6 s 13.4 s

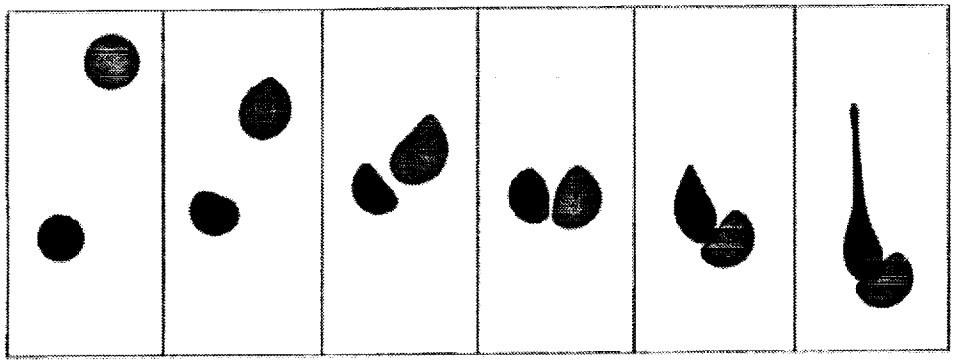

t = 0 s 2.7 s 5.6 s 8.1 s 10.6 s 11.9 s

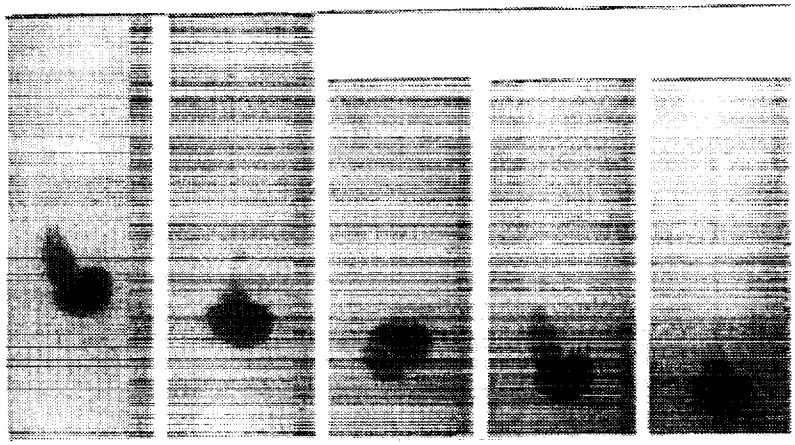

16.3 s 19.2 s 23.0 s 25.4 s 28.0 s

Glycerol-water drops in castor oil

$a_1/a_2 = 0.9$ $\hat{\mu} = 1$ **Bo = 7.1** $\Delta x_c/a_2 = 1.9$

Kushner, Rother & Davis (2000) *JFM* (submitted).

Sedimentation of Concentrated Emulsions

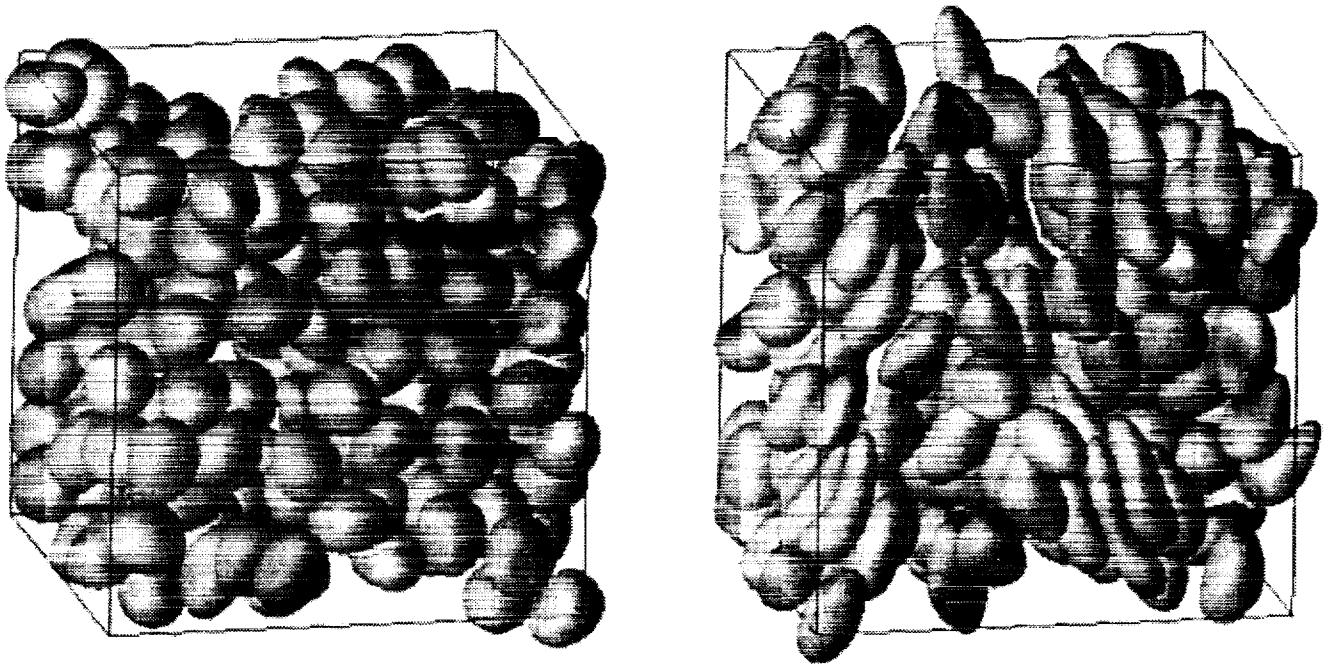

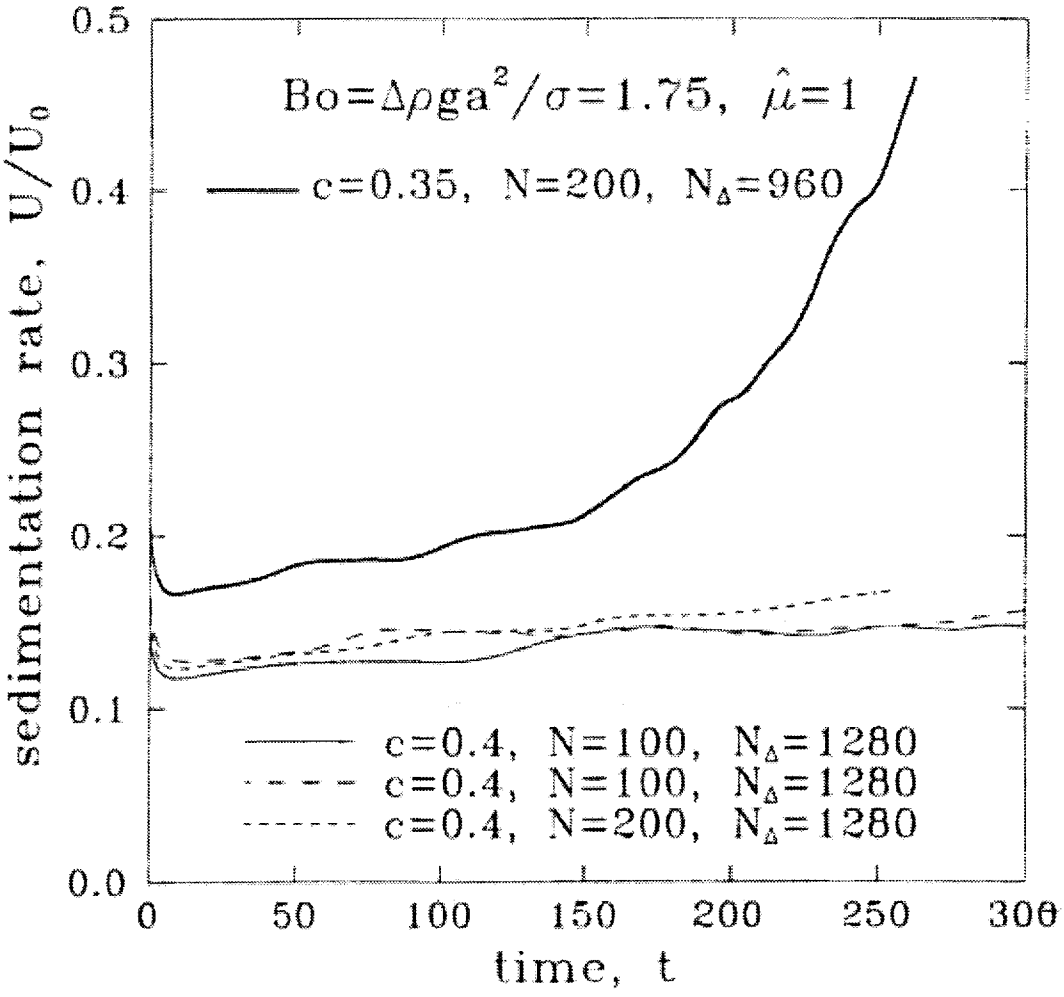

Zinchenko & Davis (2000) *J. Comp. Phys.* **157**: 539.

Simulation of Concentrated Emulsions

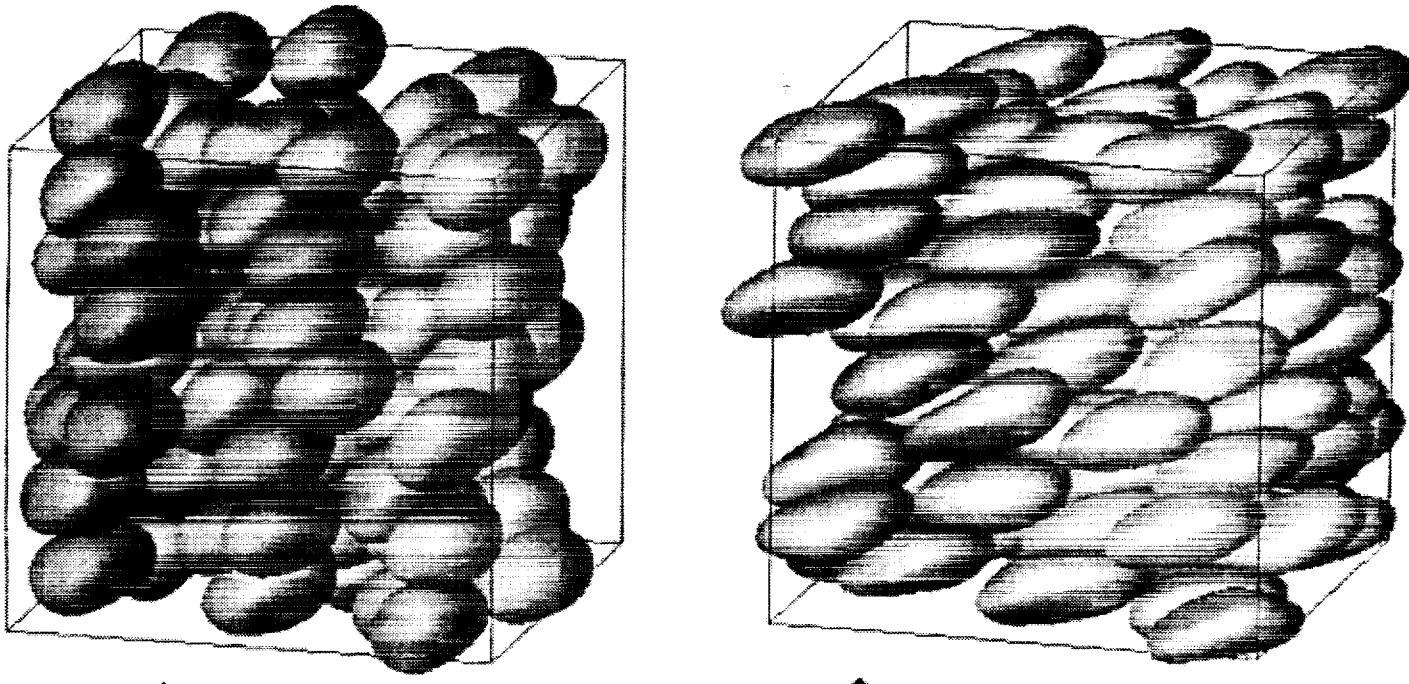

$c = 0.55$, $\hat{\mu} = 3$, $Ca = 0.05$ $c = 0.55$, $\hat{\mu} = 3$, $Ca = 0.2$

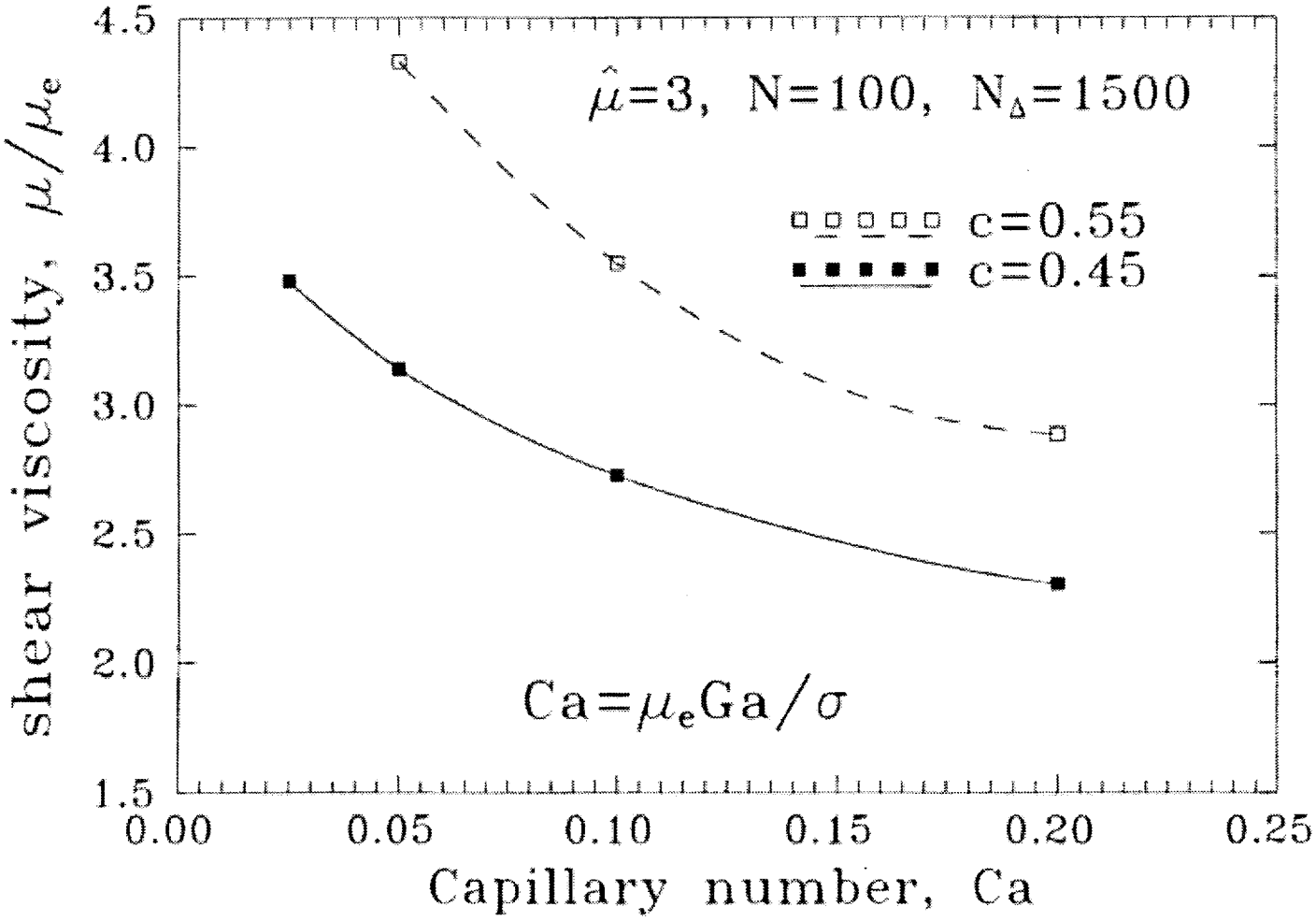

Zinchenko & Davis (2000) *Proc. 13th I. Cong. Rheo.*

Conclusions

- Phase separation enhanced by coalescence
- Nonzero collision rates possible for spherical drops without attractive forces
- Small deformations retard coalescence
- Large deformations unlikely in thermocapillary motion
- Large deformations in buoyancy motion may cause
  - entrainment
  - coalescence
  - breakup
  - suckthrough & cycling

FLUID DYNAMICS AND SOLIDIFICATION OF MOLTEN SOLDER DROPLETS IMPACTING ON A SUBSTRATE IN MICROGRAVITY

C. M. Megaridis[1], D. Poulikakos[2], K. Boomsma[1,2] and V. Nayagam[3]

[1]Department of Mechanical Engineering, University of Illinois at Chicago, cmm@uic.edu
[2]Institute of Energy Technology, Swiss Federal Institute of Technology, Zurich, Switzerland
[3]National Center for Microgravity Research, Cleveland, Ohio

ABSTRACT

This research program investigates the fluid dynamics and simultaneous solidification of molten Sn/Pb solder droplets impacting on flat, smooth, unyielding substrates. The problem of interest combines a fundamental investigation of fluid transport and heat transfer, with the development of the novel technology of on-demand dispension (printing) of microscopic solder deposits for the surface mounting of microelectronic devices. This technology, known as *solder jetting*, features on-demand deposition of miniature solder droplets (30 to 120μm in diameter) in very fine, very accurate patterns using techniques analogous to those developed for the ink-jet printing industry. After ejection, the molten metal droplets collide, spread, recoil and eventually solidify on the substrate. This solder application technology has shown great promise in microelectronic packaging and assembly, therefore, the development of a good understanding of the pertinent fundamental fluid dynamics and solidification phenomena is essential for its successful commercial implementation.

The study consists of a theoretical and an experimental component. The theoretical work uses Navier-Stokes models based on finite element techniques to elucidate the fluid dynamics, heat transfer and solidification phenomena, and in turn, improve fundamental understanding of the miniature solder deposition process. The experimental component of the research tests the numerical predictions and provides necessary input data (contact angles) for the theoretical model. The experiments are performed in microgravity (2.2s drop tower of the NASA GRC) in order to allow for the use of larger solder droplets which make feasible the performance of accurate measurements, while maintaining similitude of the relevant fluid dynamic groups (*Re, Fr, We, Ste*). The work aims to create a science base and identify the influence of the dominant process parameters in solder droplet dispensing. These process parameters are: droplet size and velocity; droplet, substrate and ambient gas temperatures; and contact angle between solder and substrate before and after solidification. The sensitivity of the solidified-droplet (bump) shape and size to variations in the above parameters is critical because solder bump volume, position, and height variation are key metrics for solder jet technology. Through a combination of experiments and numerical modeling, the effect of the dimensionless groups *Re, We, Fr* and the physics these parameters represent are systematically documented [1].

The axisymmetric impingement of solidifying molten solder droplets onto smooth metallic substrates was investigated to provide fundamental information relating to the apparent (macroscopic) contact angle and free surface behavior during fluid spreading, and to determine which parameters govern the process. Molten eutectic 63%Sn–37%Pb solder droplets of approximately 1 mm in diameter were used in simulation of microcasting in normal gravity. In addition, mm-sized droplet impact events in reduced gravity were employed for scale-up

modeling of the impingement of picoliter size droplets used in electronic chip packaging. Experiments were conducted in both normal and reduced gravity with technically relevant impact velocities of ~1m/s and ~0.2m/s, respectively, defining the domain of the dimensionless groups believed to govern the droplet spreading, recoiling and solidification behavior. In normal gravity, the conditions investigated correspond to Re = O(1000), We = O(10), and Fr = O(100). In reduced gravity of 5×10^{-4}g (characteristic of the levels attained at the 2.2s drop tower), the impact conditions correspond to Re = O(100), We = O(1), and Fr = O(10000). In both cases Ca=O(0.001). Figure 1 below displays the experimental apparatus employed in the drop tower experiments. The results, as reported in [2], showed the spreading velocity of the droplets to decrease with time after impact. The apparent contact angle decreased with increasing contact-line speed, contrary to the classic behavior established using creeping flows or rolling droplets. Using previously defined relations for droplet impingement, it was reported in [2] that for the current experimental matrix, viscosity, capillarity, solidification, and surface tension all influence the spreading of the metal droplet and must be simultaneously considered in modeling efforts if accurate results are sought. The results provided a clear demonstration of the effect of the free-surface dynamic motion on the instantaneous value of the contact angle during spreading and recoiling of the bulk fluid. These results do not follow established trends from studies of slow spreading or rolling droplets.

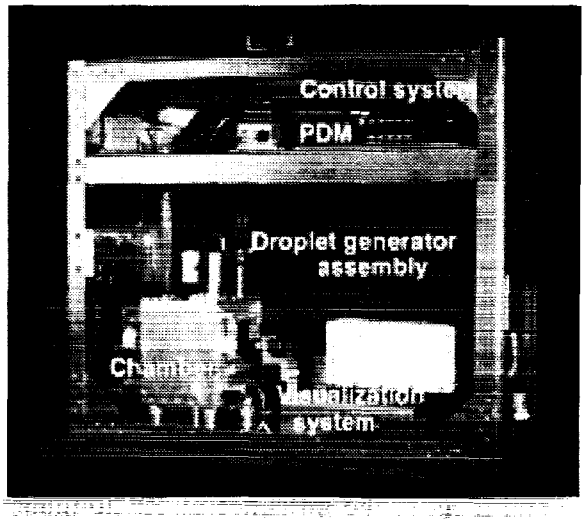

Fig. 1: Photograph of the experimental apparatus designed and constructed for the 2.2s drop tower experiments conducted at the NASA Glenn Research Center. The experiment rig consists of five major components: droplet generator, environmental chamber, visualization system, power distribution module (PDM), and control system. This apparatus was used to perform the experiments reported in [2].

The first phase of the program has investigated the *axisymmetric* impact of liquid-metal droplets on flat stationary substrates. The second phase, which is about to commence, will examine oblique (non-axisymmetric) impact events, which are necessary in high-throughput configurations. The offset impact introduces an array of new scientific challenges and constitutes the main goal of the new generation of this technology.

REFERENCES

1. Xiong, B., Megaridis, C. M., Poulikakos, D. and Hoang, H., 1998, "An Investigation of Key Factors Affecting Solder Microdroplet Deposition," *ASME, J. Heat Transfer*, Vol. 120, pp. 259-270.
2. Boomsma, K., Megaridis, C. M., Poulikakos, D. and Nayagam, V., 2000, "Contact Angle Dynamics of Molten Solder Droplets Impacting onto Flat Metallic Substrates," *Physics of Fluids*, submitted.

Fluid Dynamics and Solidification of Molten Solder Droplets Impacting on a Substrate in Microgravity

C. M. Megaridis, K. Boomsma
Department of Mechanical Engineering
University of Illinois at Chicago

D. Poulikakos
Institute of Energy Technology
Swiss Federal Institute of Technology

V. Nayagam
National Center for Microgravity Research

D. B. Wallace
MicroFab Technologies

Fifth Microgravity Fluid Physics &
Transport Phenomena Conference
August 9-11, 2000
Cleveland OH

• PROBLEM DESCRIPTION

Fluid dynamics and simultaneous solidification of molten solder droplets impacting on a flat substrate

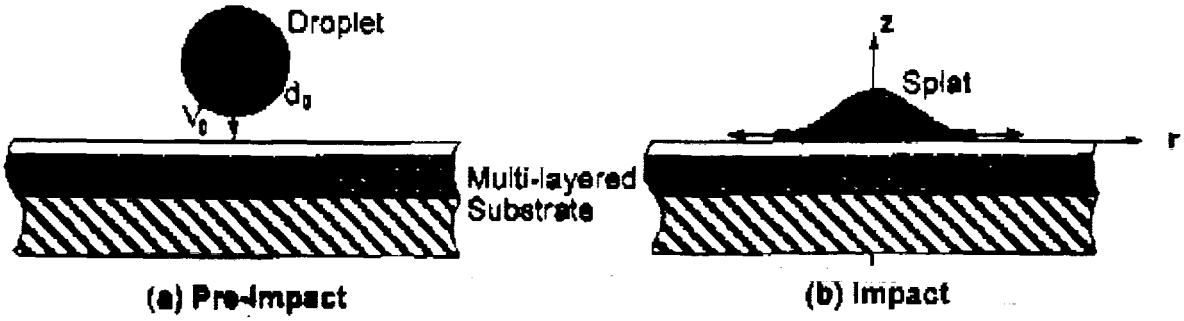

• TYPICAL CONDITIONS STUDIED

63%Sn-37%Pb eutectic solder (T_m=183°C)
Solder injection temperature ~210°C
Droplet diameter 50–100μm
Droplet injection velocity 1–3m/s
Ambient (N_2) temperature 20–150°C
Flight distance 1–5mm
Re **= O(100),** ***We*** **= O(1),** ***Fr*** **= O(1000)**
Multi-layered smooth substrate
Substrate temperature 20–150°C

$Bo = O(10^{-3})$
$Oh = O(10^{-2})$
$Ca = O(10^{-3})$

Demand Mode Solder Jet

1440 pad microprocessor test vehicle, 60μm bumps

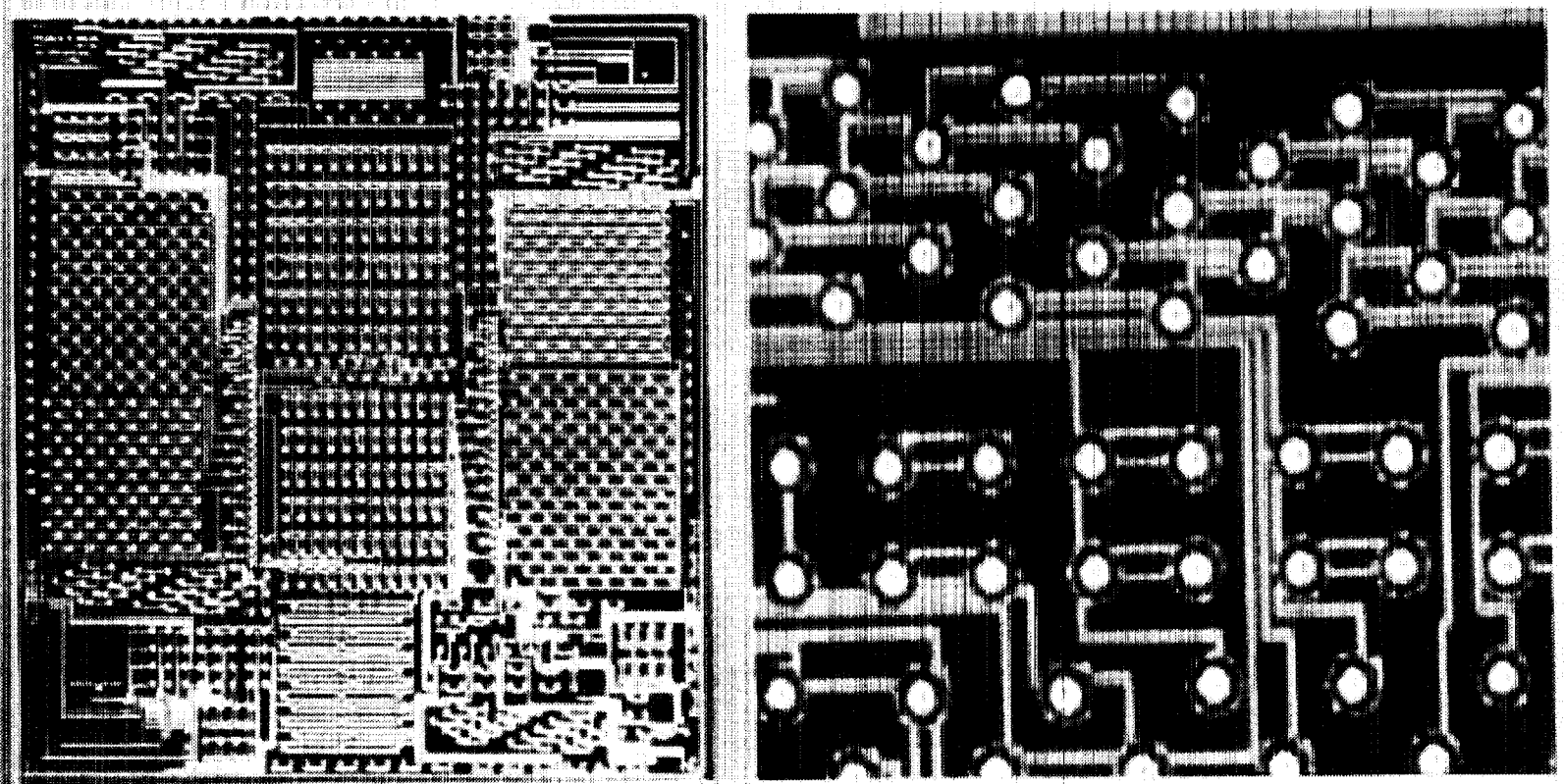

MicroFab
Technologies, Inc.

• OBJECTIVES

1. Investigate fluid dynamics and simultaneous solidification of molten solder droplets impacting on smooth flat substrates.

2. Create science base and identify influence of dominant process parameters in solder microdroplet dispensing. These are: droplet size and velocity; droplet, substrate and ambient gas temperatures; contact angle between solder/substrate before and after solidification.

3. Through a combination of experiments and numerical modeling, document systematically the effect of the relevant dimensionless groups (Re, We, Fr, etc.) and the physics they represent.

- **WHY MICROGRAVITY?**

$$\mathrm{Re} = \frac{V_0 d_0}{\nu}, \quad We = \frac{\rho V_0^2 d_0}{\gamma}, \quad Fr = \frac{V_0^2}{d_0 g}$$

Typical operating conditions in solder micro-droplet dispensing correspond to:

***Re* = O(100), *We* = O(1) and *Fr* = O(1000)**

To achieve similitude (based on Re, We and Fr) with mm-diameter droplet experiments, one should:

- **reduce injection velocity by O(10)**
- **reduce surface tension coefficient of solder by O(10)**
- **reduce gravitational level by O(1000)**

Thus, the microgravity environment is necessary to maintain relevance when performing large solder-droplet impact experiments.

- **METHODOLOGY**

Experimental:

Performed in microgravity (2.2s drop tower of NASA LeRC) to allow for the use of large (mm-diameter) solder droplets, which make feasible the performance of more accurate measurements, while maintaining similitude of the relevant fluid dynamical groups (Re, We, Fr).

Theoretical:

Axisymmetric Navier-Stokes models based on finite element techniques and detailed free-surface tracking. Its goal is to provide fundamental understanding of transport phenomena in miniature solder deposition process.

Experiments test the numerical predictions and provide necessary input data (such as wetting angles) for the numerical model.

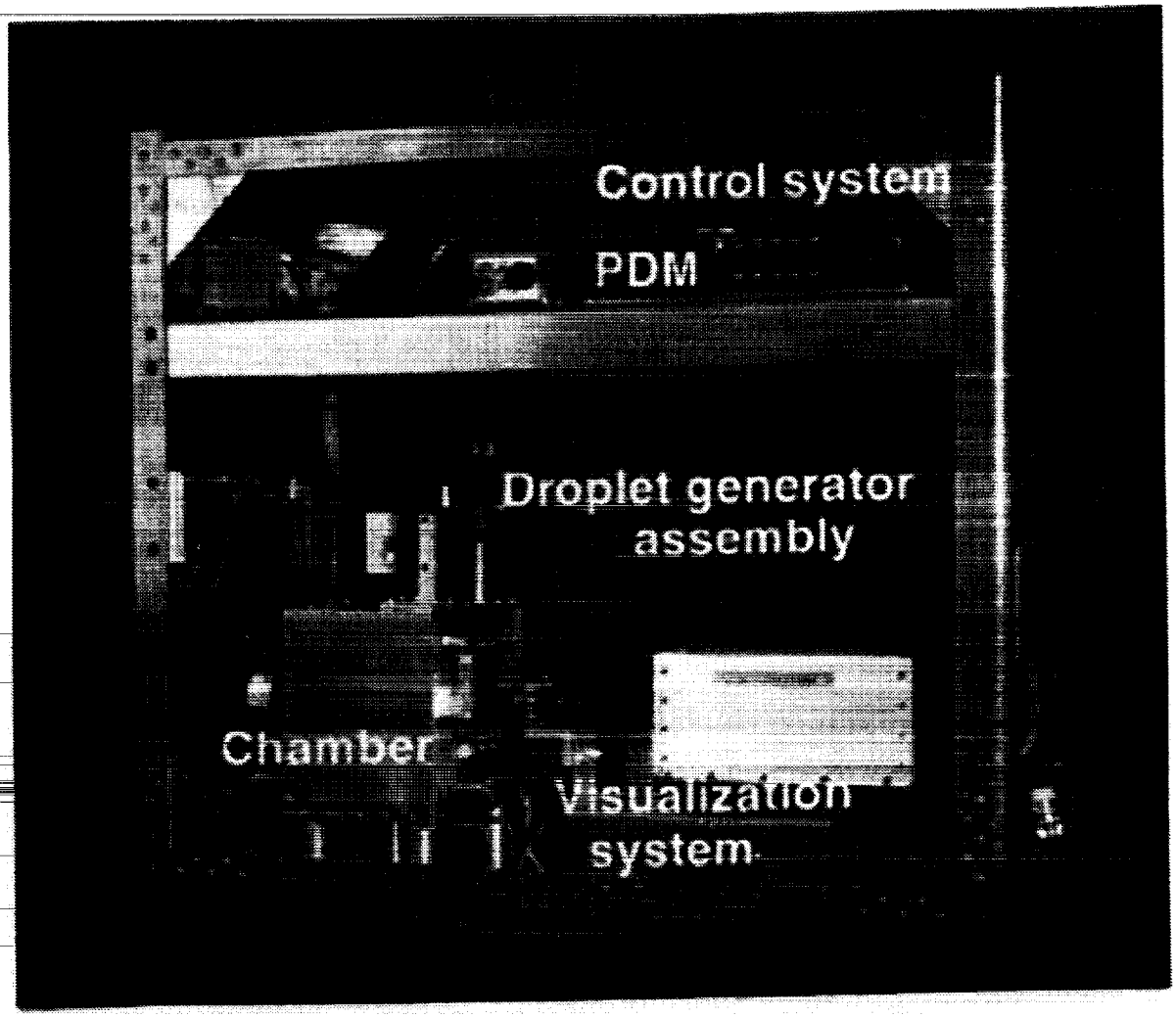
Control system
PDM
Droplet generator assembly
Chamber
Visualization system

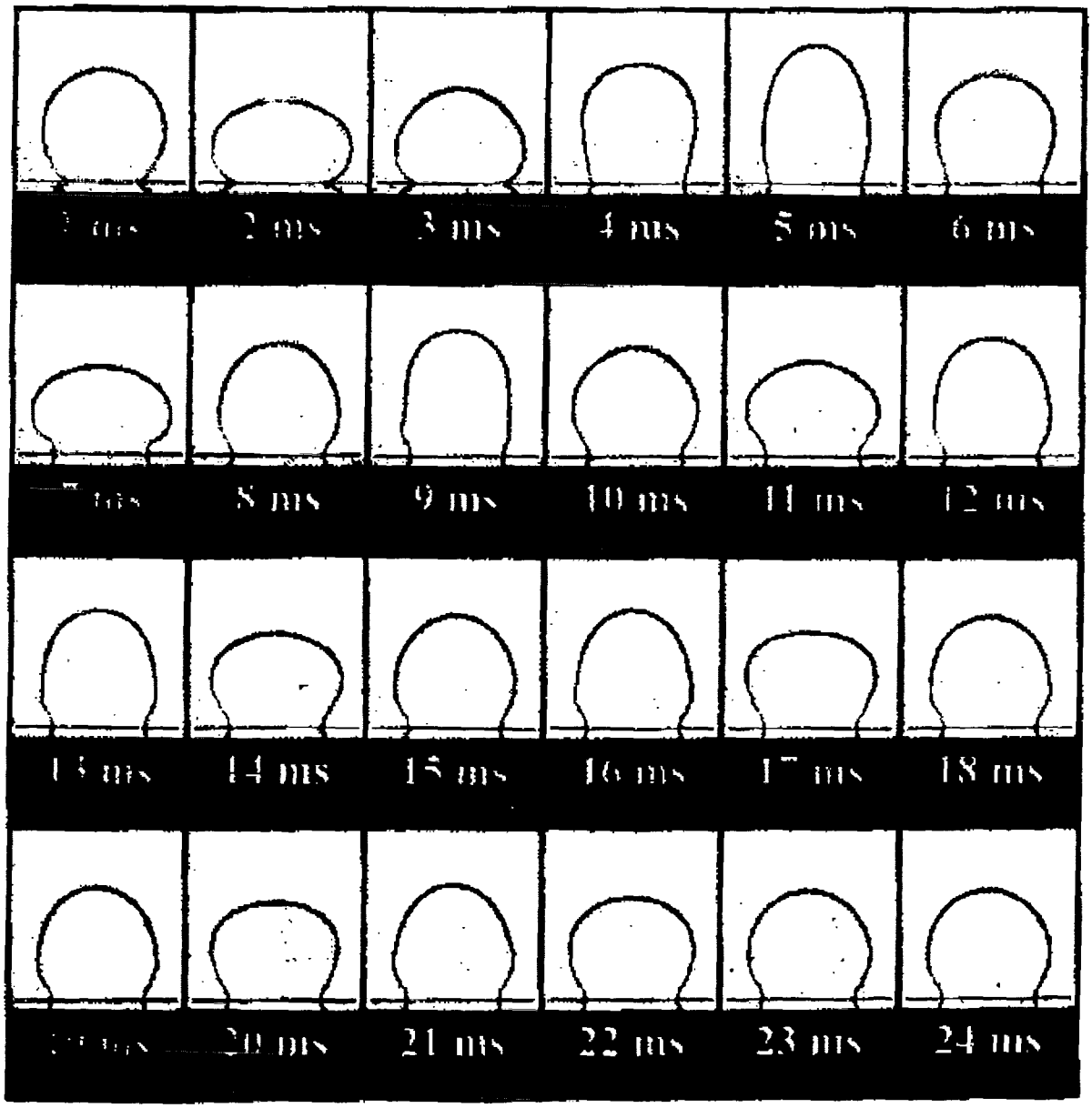
2 ms
3 ms
4 ms
5 ms
6 ms
8 ms
9 ms
10 ms
11 ms
12 ms
14 ms
18 ms
21 ms
22 ms
23 ms
24 ms

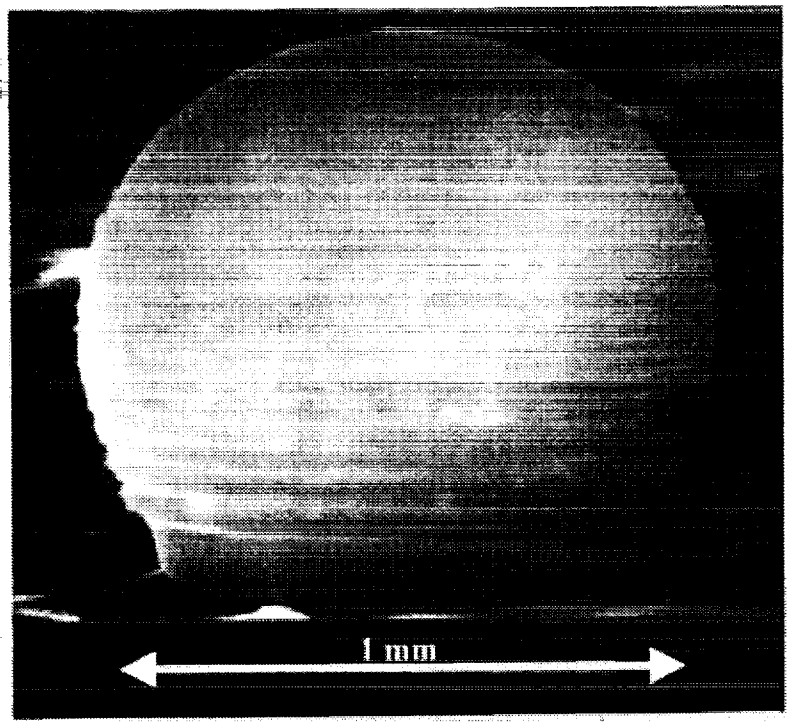

$V_o = 0.23 m/s$, $d_o = 1.1 mm$

$Re = 740$, $We = 1.3$, $Fr = 25000$,

$T_0 = 208\ °C$, $T_{sub} = 25\ °C$ (st. steel)

Effect of thermal contact resistance

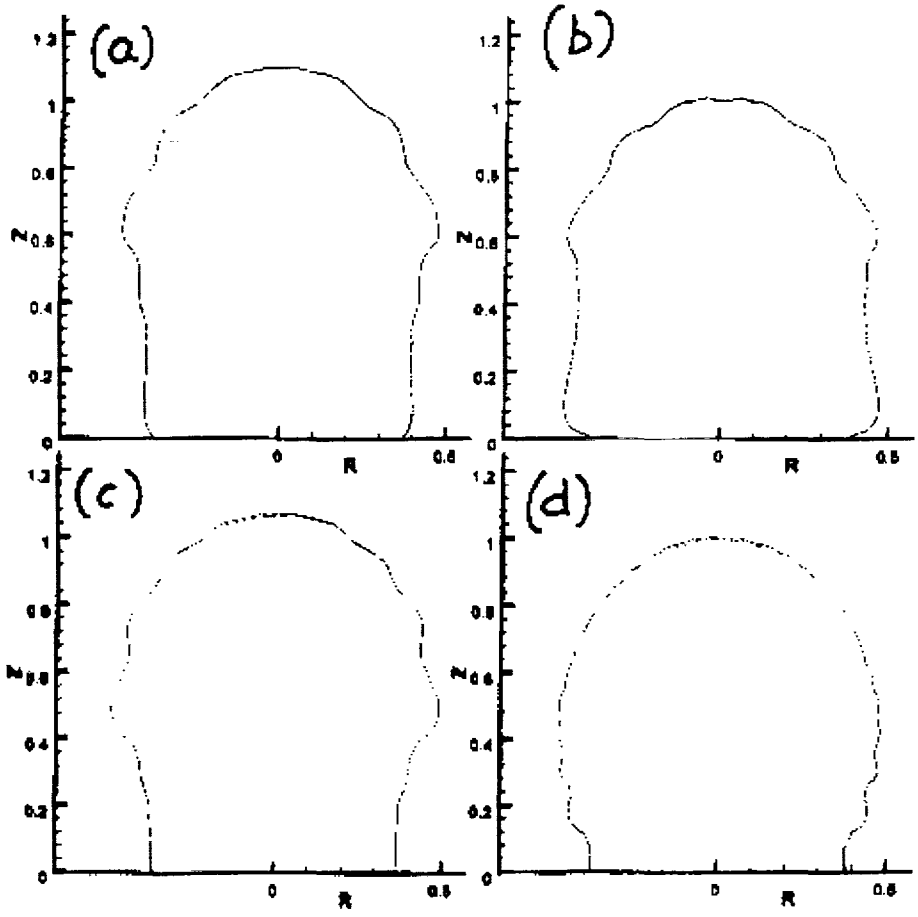

$$Bi = h\, d_o / k$$

(a) $Bi_l = 1.0, Bi_s = 0.5$

(b) $Bi_l = 1.5, Bi_s = 1.0$

(c) $Bi_l = 0.2, Bi_s = 0.2$

(d) $Bi_l = 1.05, Bi_s = 0.07$

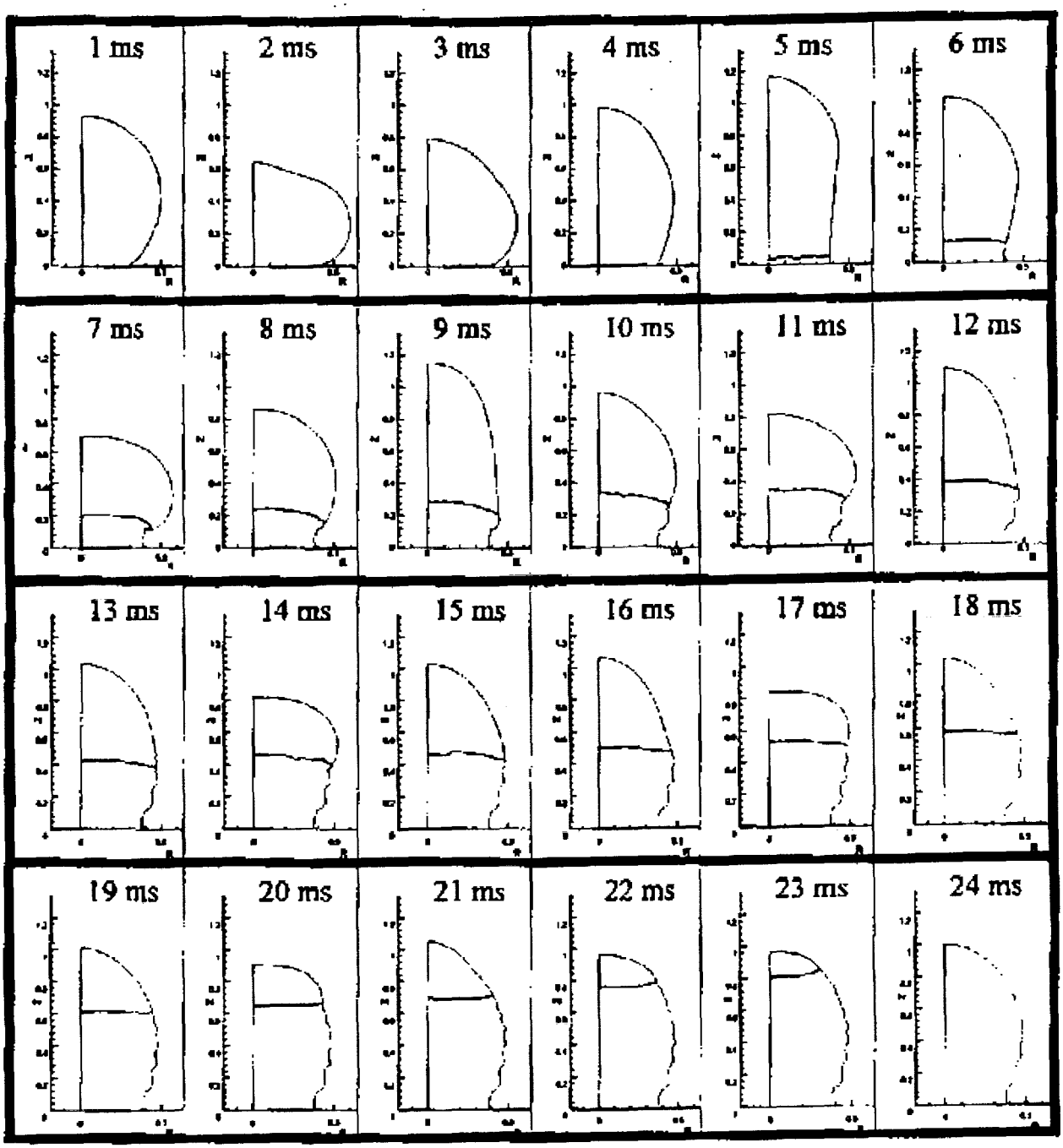
1 ms
2 ms
3 ms
4 ms
5 ms
6 ms
7 ms
8 ms
9 ms
10 ms
11 ms
12 ms
13 ms
14 ms
15 ms
16 ms
17 ms
18 ms
19 ms
20 ms
21 ms
22 ms
23 ms
24 ms

• CONCLUSIONS

Experiments in reduced gravity (2.2s drop tower) have been performed successfully for axisymmetric impact. A numerical model has been developed to investigate the fundamental phenomena.

Conditions investigated:
Re = O(100), We = O(1), Fr = $O(10^4)$,
Ca= $O(10^{-3})$, Bo = $O(10^{-4})$, Oh = $O(10^{-2})$

Large number of frozen ripples formed on droplet surface. Despite complexity of transport and solidification processes, model captures well the main features of the experimental data.

Contact angle vs. contact line speed data showed a clear dependence of contact angle on free-surface deformation dynamics. The measured trend contradicts the classical one established for creeping non-solidifying flows.

FLUID FLOW IN A ROTATING CIRCULAR CYLINDER

Z. Liu[1], W. Schultz[2], and M. Perlin[1]

[1]Naval Architecture and Marine Engineering
[2]Mechanical Engineering and Applied Mechanics
University of Michigan, Ann Arbor, MI 48109

ABSTRACT

We study the motion of a fluid layer confined by a horizontally oriented, axially rotating, circular cylinder. This physical system facilitates a simple framework for investigating the dynamics of a viscous flow with a fluid-fluid interface or that of a free-surface that makes a trijunction with a solid, all in the presence of gravity. The periodicity of the boundary conditions simplifies the analysis. Surface tension is included, and disjoining pressure is applied to avoid a contact line. Two simple limiting cases exist for zero and for infinite rotation speed, and represent that of a fluid pool on the cylinder bottom and that of a uniform film experiencing solid-body rotation, respectively. Two dimensionless quantities are introduced and used in perturbation analyses: δ, the ratio of average film thickness to cylinder radius that represents the fullness of the cylinder; and Γ, the ratio of the Reynolds number to Froude number that therefore represents the ratio of gravitational to viscous forces. Three sets of approximations and their analytic/numeric solutions are presented: steady and unsteady lubrication approximations through three orders in δ; steady high-speed flow approximations through two orders of small Γ; and steady creeping-flow approximations in the limit of large Γ. Also a draining, thin film for zero rotation speed will be presented.

Lubrication theory is used with perturbation expansion of dependent variables in terms of δ to study a thin film for steady and unsteady flow. Γ is assumed order one, and the expansion is conducted and solved through second order (i.e. zeroth, first, and second orders) for the first time. The lowest-order, thin-film thickness profile is evaluated numerically for varying Γ, and the results for the steady solution agree with previously published results. Evaluating the expressions at the next order in δ, some differences are apparent. In figure 1 we present the results for the time invariant case and first order. Although the profile steepens (and exhibits an asymmetric dimple due to surface tension for Γ=0.47) in the vicinity of the maximum thickness with increasing Γ, the position of the maximum remains at θ=90°, in contrast with experiments. At the same order, with the initial condition of a uniform film, we present the temporal evolution; however, as can be seen in figure 2 for Γ=0.47, the unsteady profile exhibiting a dimple evolves until a singularity occurs, and the solution becomes indeterminate—and never achieves a resemblance to the steady solution. Prior to this, the maximum thickness position can be seen to differ significantly from the steady case, and is around 30° gradually shifting in time toward 45°. The last surface is presented for dimensionless time 2.25 (scaled by rotation rate). Solutions for increasing rotation rate (i.e. decreasing Γ) exhibit smaller maximum thicknesses with position shifting from 30° toward 90° (not shown). Results with and without surface tension display interesting differences and will be presented through second order.

We next abandon the thin-film assumption, include inertial effects, and investigate the steady system for $\Gamma \ll 1$, a cylinder rotating at high speed (or equivalently in reduced gravity or with increased viscosity). This case represents the departure from solid-body rotation. We solve through order Γ by the method of Frobenius. Twelve coefficients are determined to complete the series solution, and the results are presented in figure 3. As Γ is increased, initially the position of maximum thickness tends toward the cylinder bottom consistent with physical experiments, goes through a uniform thickness solution, and as Γ is increased further proceeds to a solution with maximum thickness around 270°.

Our final investigation concerns slow rotation speed (equivalently large gravitational to viscous force), or flow where Γ is large. In this case we define a small parameter, $\gamma \equiv \Gamma^{-1}$. Physically, a small pool of fluid is located symmetrically along the bottom of the circular cylinder in the limit of vanishing γ. Solutions are obtained through the first two orders of γ.

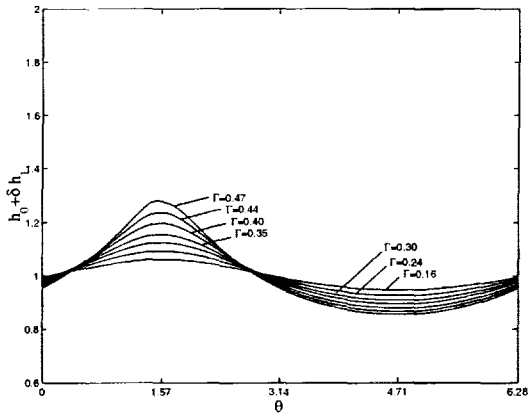

Figure 1. Steady solutions for lubrication theory through first order with δ=0.03 and varying Γ.

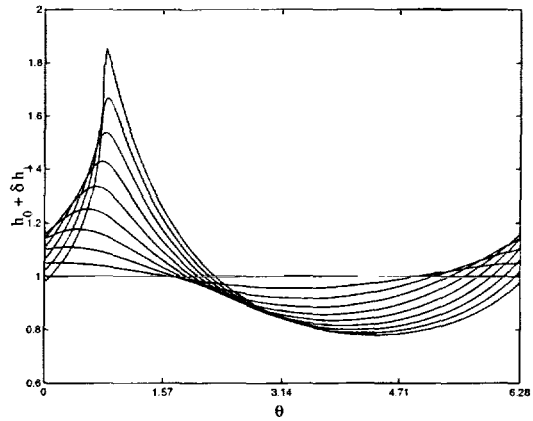

Figure 2. Temporal surface evolution for lubrication theory through first order with δ=0.03 and Γ=0.47.

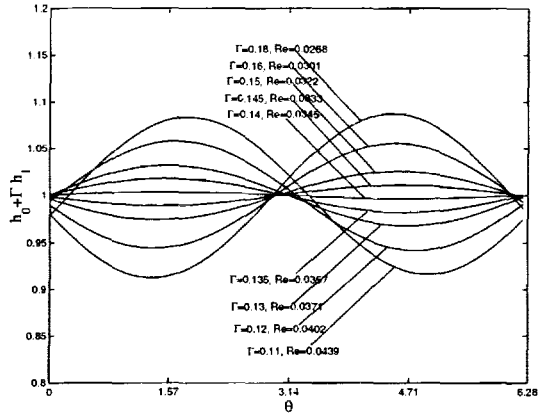

Figure 3. Steady solutions for small Γ.

NASA/CP—2000-210470

Fluid flow in a rotating circular cylinder

Z. Liu, W. W. Schultz & Marc Perlin

The University of Michigan

Motivation

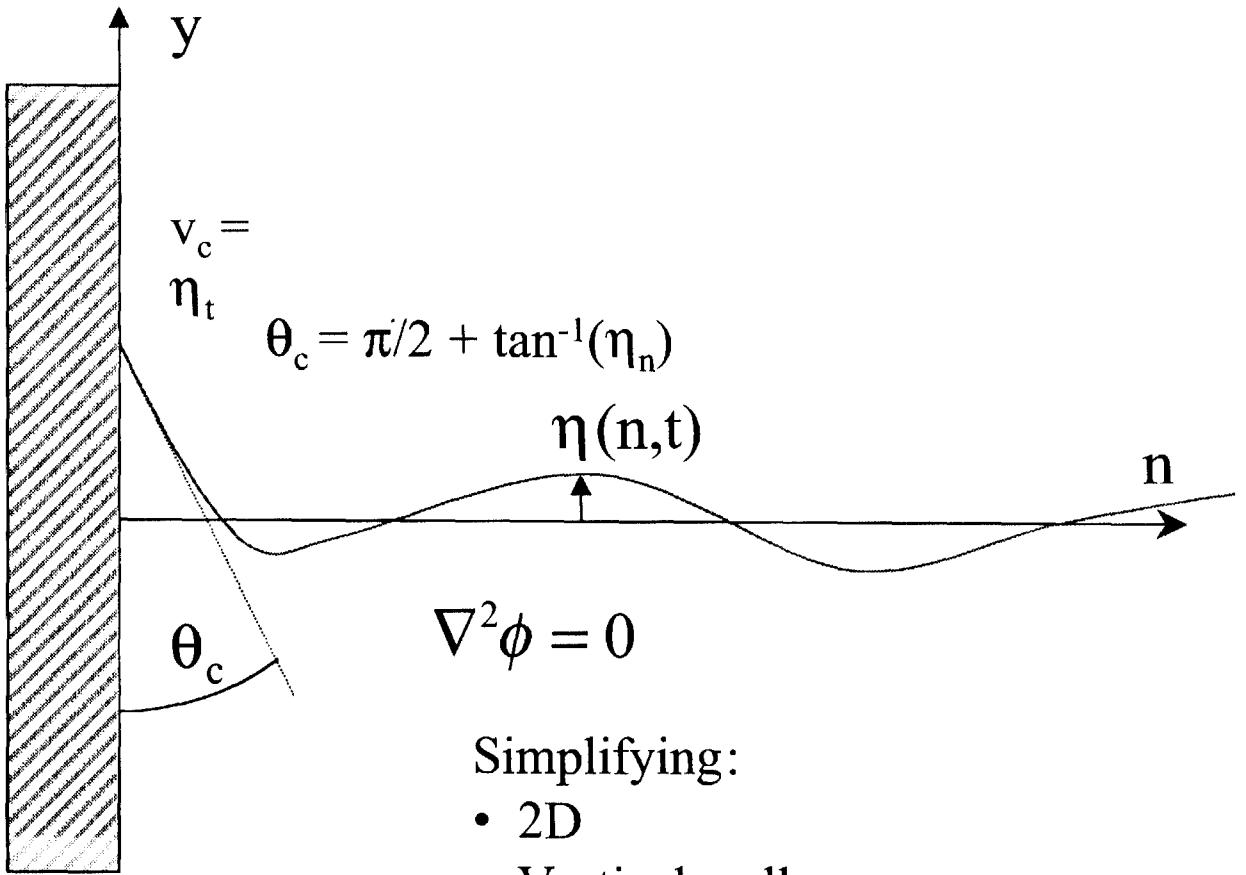

Simplifying:

- 2D
- Vertical wall
- Stainless steel wall not glass

Contact line models

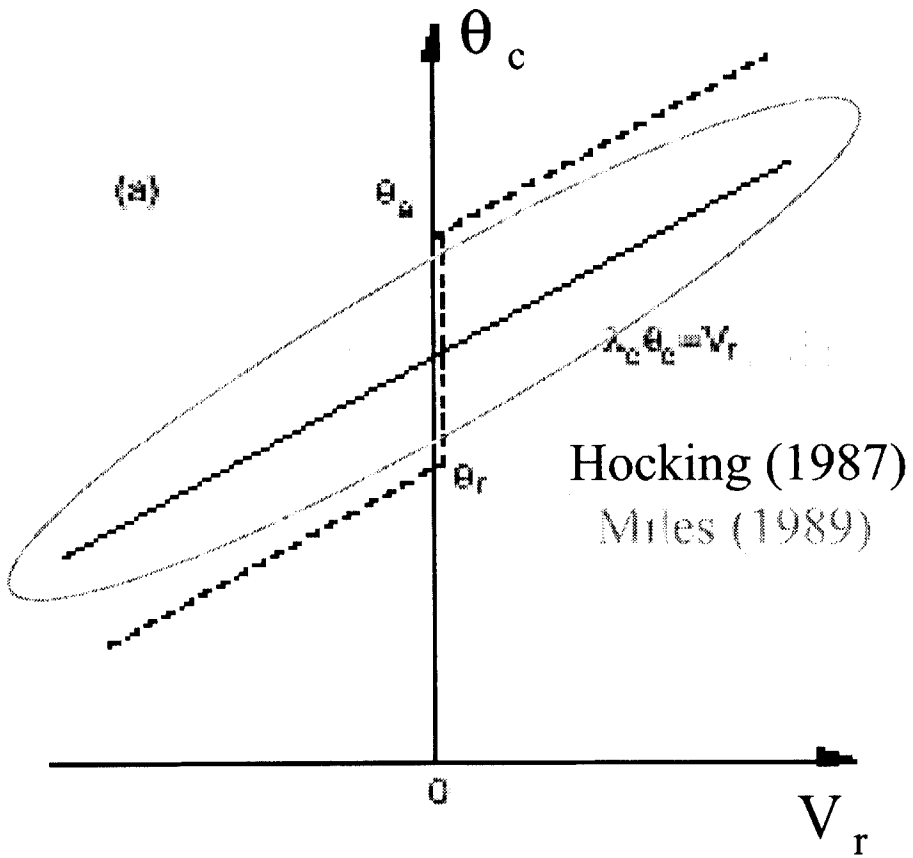

Hocking (1987)
Miles (1989)

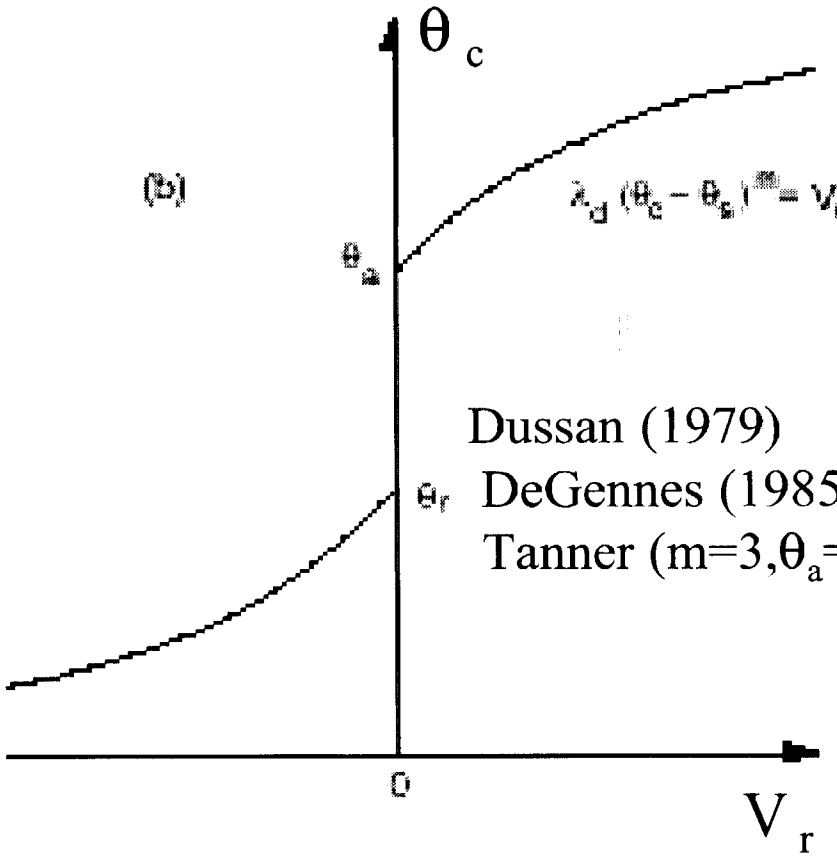

Dussan (1979)
DeGennes (1985)
Tanner ($m=3, \theta_a=\theta_c$)

Experimental Reality

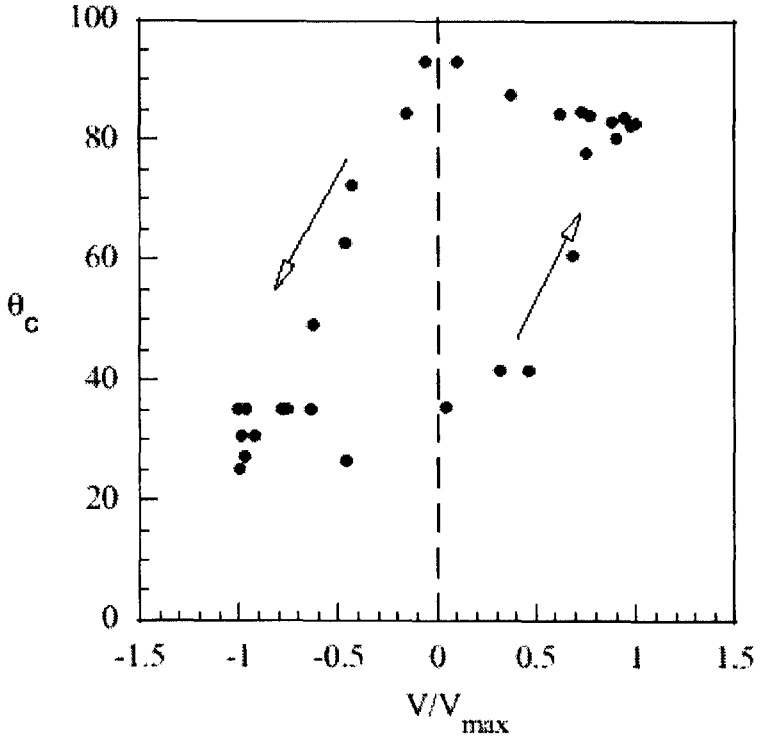

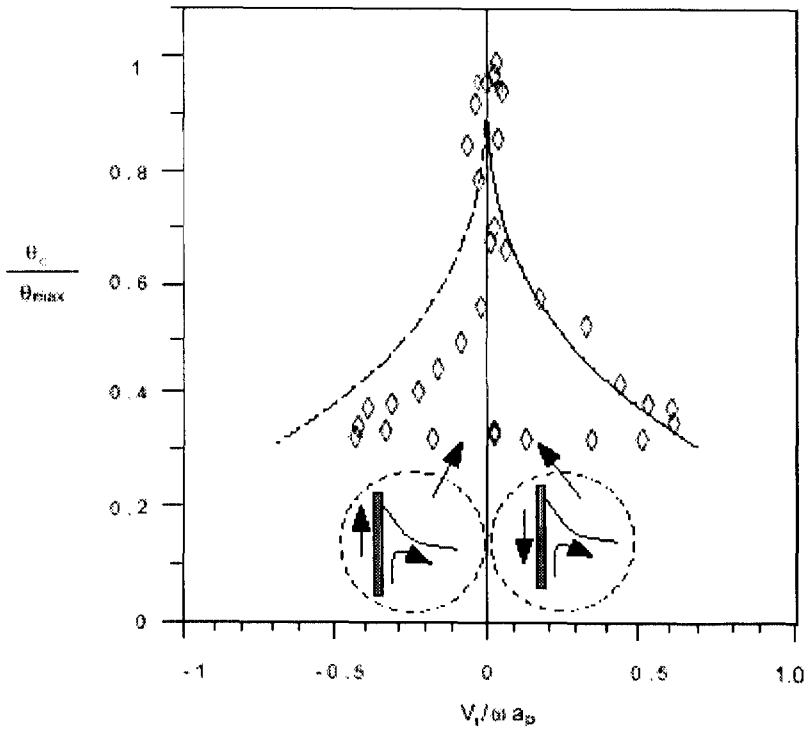

Stick-Slip behavior

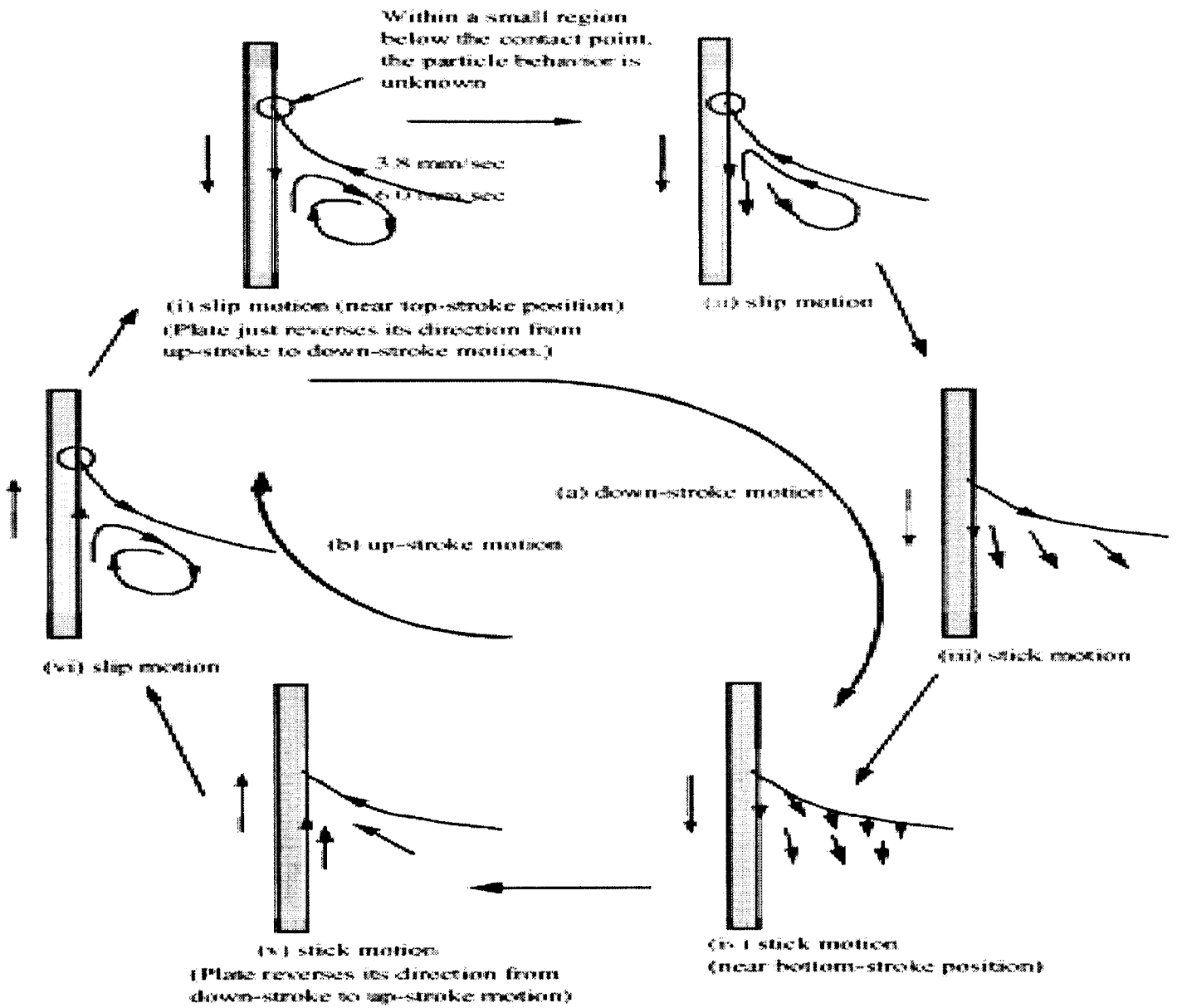

With frequency and amplitude dependence

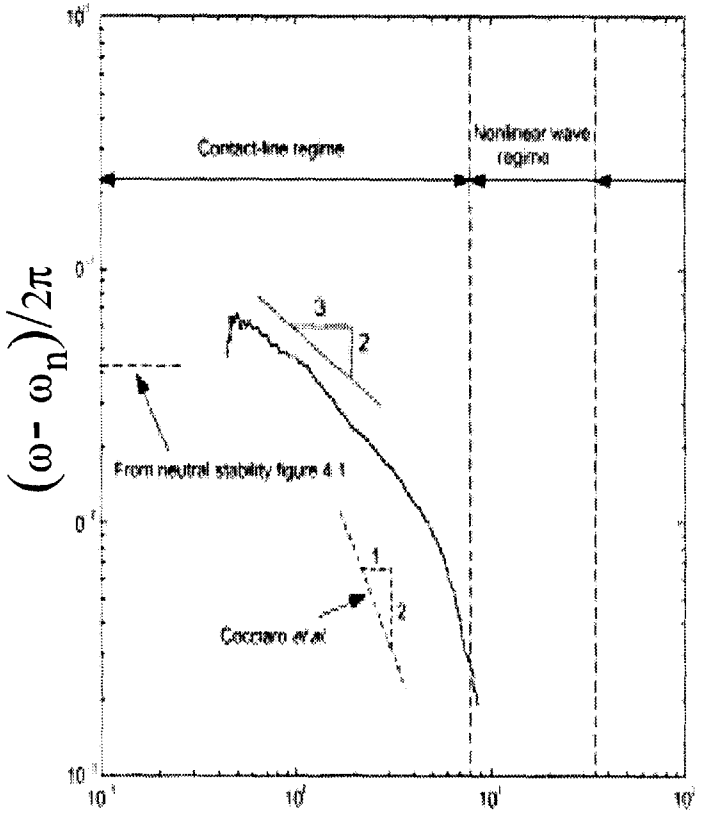

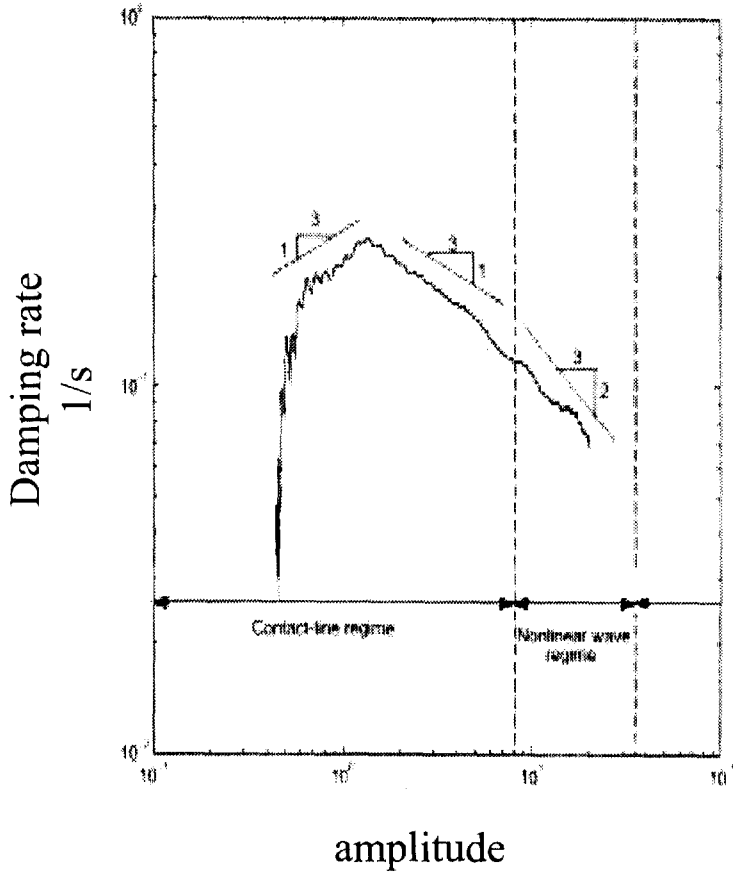

Simplifying further

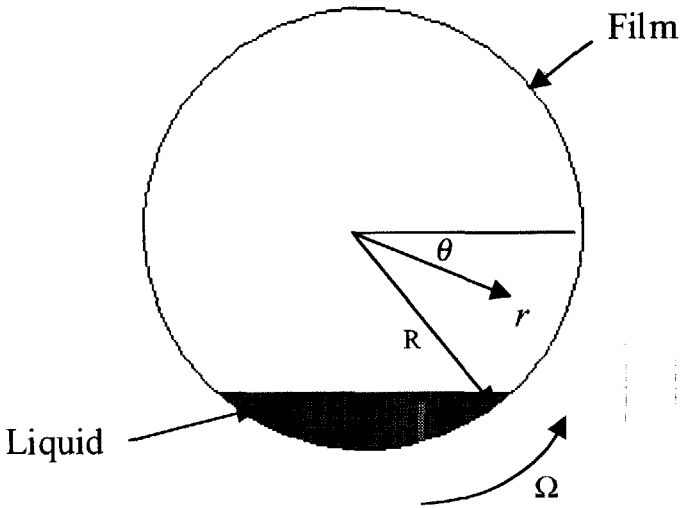

- Spreading behavior of liquid
- Lubrication theory possible

- Relieving thin film assumption;
- Two limiting cases;

$$\Gamma = \frac{R\delta^2 \rho g}{\mu \Omega}$$

$\Gamma << 1$

$\Gamma >> 1$

Experimental Setup

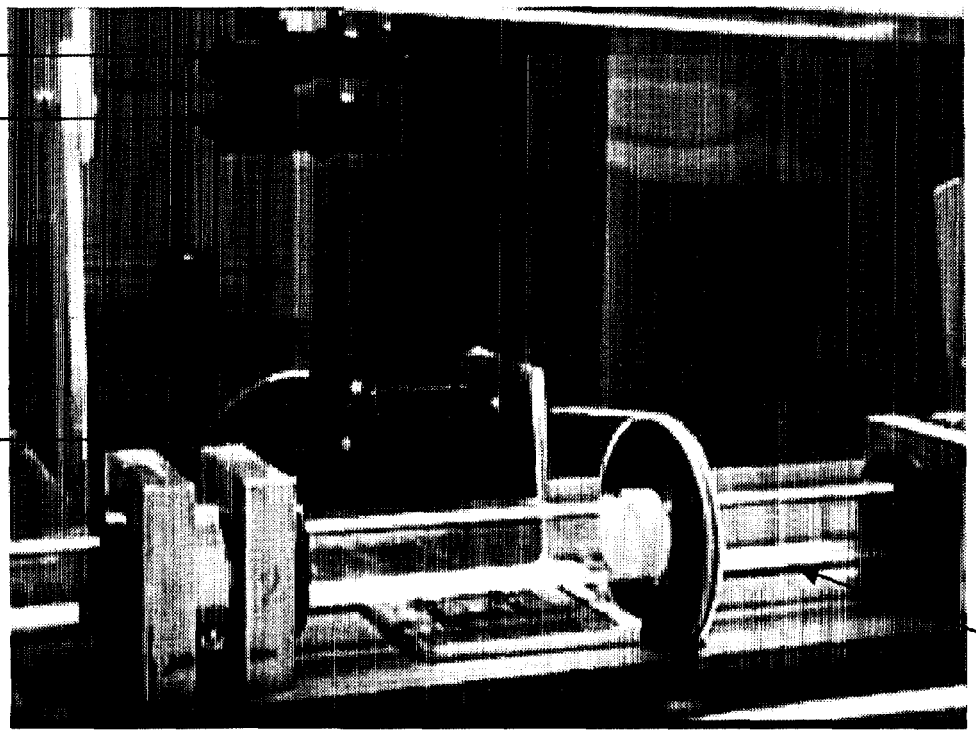

Cylinder size: 660 mm × 33 mm

Resolution: 45 count/deg

Liquid volume: 15cc

Experiments

Γ decreasing

$\rightarrow$

Lubrication assumption

Scaling

$$r = r\hat{}R\ ,\ h = h\hat{}\bar{h},\ u = u\hat{}/\delta R\Omega\ ,\quad v = v\hat{}/R\Omega\ ,\quad p = \hat{p}/(\mu\Omega/\delta),\quad t = \Omega\hat{t},$$

Parameters

$$\delta = \frac{\bar{h}}{R} << 1,\quad \Gamma = \frac{R\delta^2 g}{\upsilon\Omega} \sim O(1),\quad Ca = \frac{\delta\sigma}{\mu\Omega R} \sim O(1)$$

Zero-order film profile equation

$$\frac{\partial h_0}{\partial t} + \boxed{(1 - \Gamma h_0^2 \cos\theta)\frac{\partial h_0}{\partial \theta} = -\frac{\Gamma}{3} h_0^3 \sin\theta}$$

Johnson, 1988

Wilson, 1993

First-order film profile equation

$$\frac{\partial h_1}{\partial t} + \left(1 - \Gamma h_0^2 \cos\theta\right)\frac{\partial h_1}{\partial \theta} + \left(\Gamma h_0^2 \sin\theta - 2\Gamma h_0 \frac{\partial h_0}{\partial \theta}\cos\theta\right) h_1$$

$$= \frac{\Gamma}{6} h_0^4 \sin\theta - \frac{4\Gamma}{3} h_0^3 \frac{\partial h_0}{\partial \theta}\cos\theta - \frac{\Gamma}{3} h_0^3 \frac{\partial^2 h_0}{\partial \theta^2}\sin\theta - 3\Gamma h_0^2 \left(\frac{\partial h_0}{\partial \theta}\right)^2 \sin\theta$$

$$\boxed{-\frac{Ca}{3} h_0^3 \frac{d^2\kappa}{d\theta^2} - Ca h_0^2 \frac{\partial h_0}{\partial \theta}\frac{d\kappa}{d\theta}}$$

where κ is the curvature.

Comparison of different order solutions

$$h = h_0 + \delta h_1 + \delta^2 h_2$$

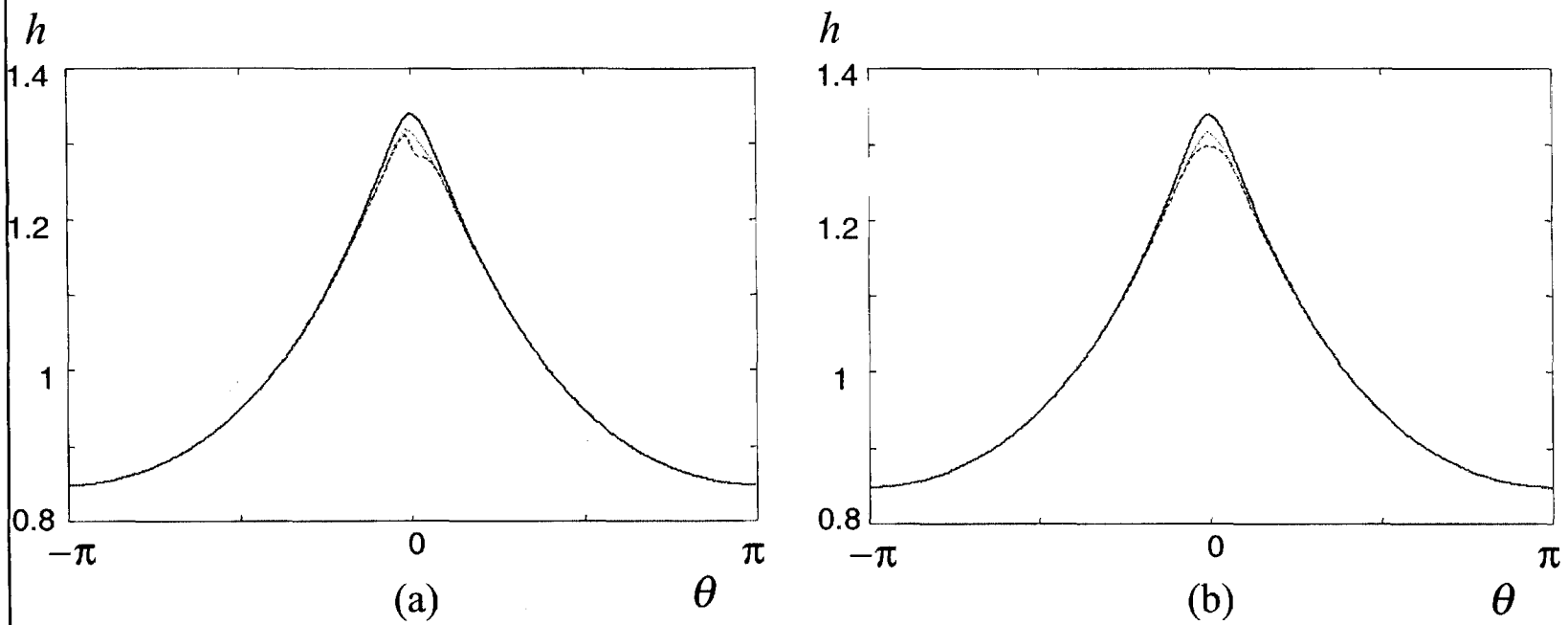

Solid curves: h_0 , dash curves: $h_0 + \delta h_1$, dot curves: $h_0 + \delta h_1 + \delta^2 h_2$

δ=0.014, $\Gamma = 0.486$,(a) $Ca \neq 0$, (b) $Ca = 0$.

Comparison to experimental results

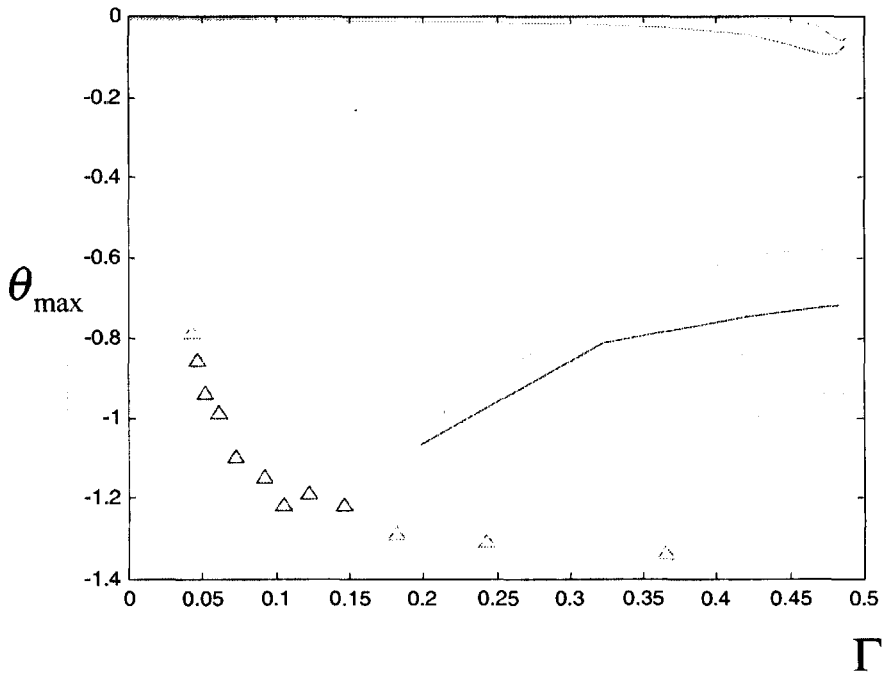

symbols: experimental data;

red-dot curve: lubrication solution;

green curve: including $F_c = \mathrm{Re}$ at order $O(\delta^0)$;

blue curve: including $F_c = \mathrm{Re}\, v_0^2$ at order $O(\delta^0)$;

red-solid curve: including $F_c = \mathrm{Re}\, v_0^2$ at $O(\delta)$.

- Dimple appears in the second order solution.
- Unlike experiment's "maximum" thickness always occurs at $\theta = 0$.
- Including surface tension, symmetry no longer exists at $\theta = 0$.

Numerical solutions for unidirectional rotating cylinder

$\Omega_1 > \Omega_2 > \Omega_3$

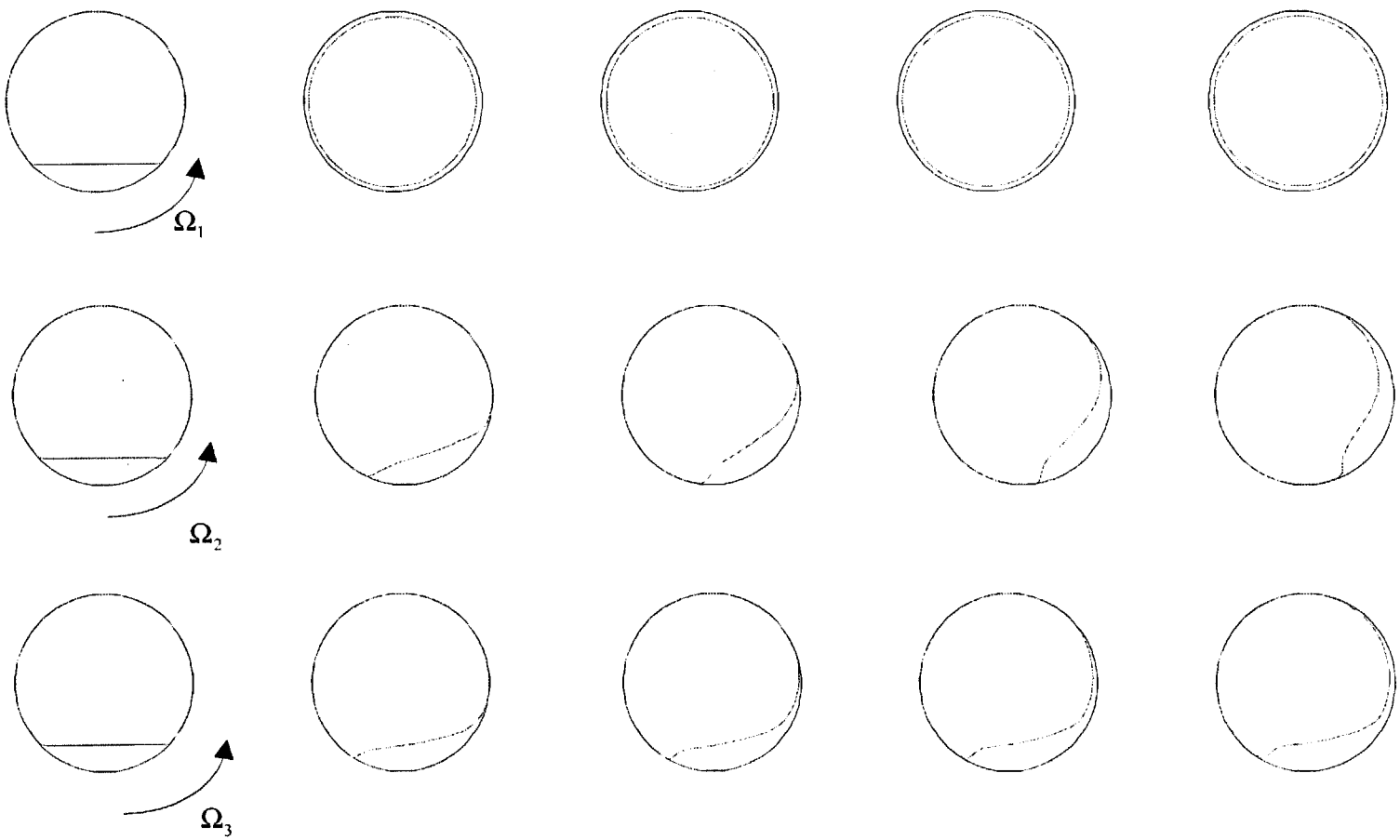

Experiments

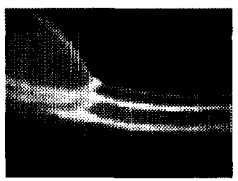

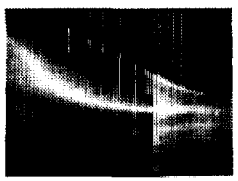

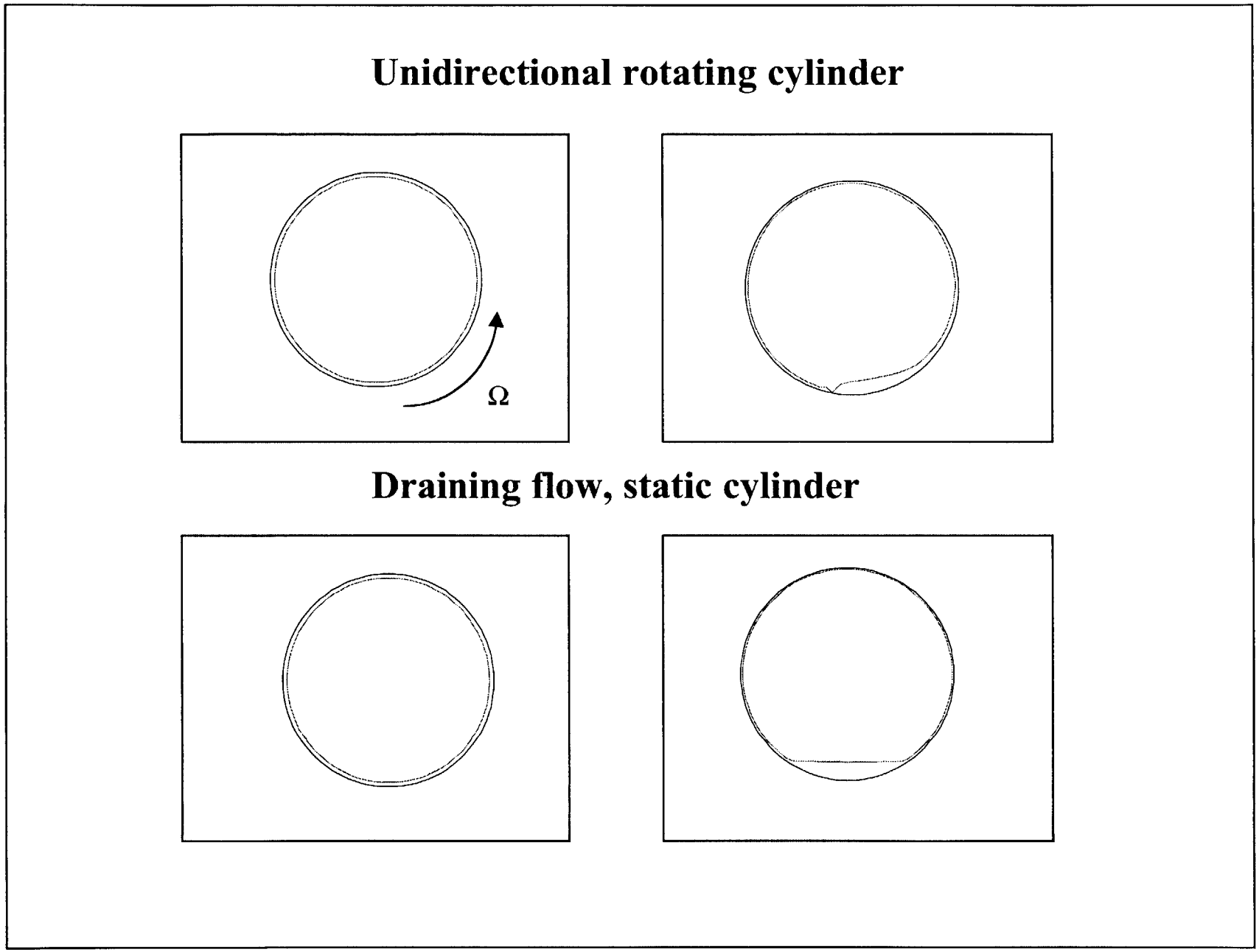
Unidirectional rotating cylinder
Ω
Draining flow, static cylinder

Lubrication approximation correction

Pressure rescaling: $p = \hat{p}/(\rho\delta R\Omega^2)$

Including constant centrifugal force: $F_c = \mathrm{Re}$

$$\frac{\partial h_0}{\partial t} - \frac{h_0^3}{3}\left(\mathrm{Re}\,\delta\frac{\partial^2 h_0}{\partial\theta^2} + \Gamma\cos\theta\right) - h_0^2\frac{\partial h_0}{\partial\theta}\left(\mathrm{Re}\,\delta\frac{\partial h_0}{\partial\theta} + \Gamma\sin\theta\right) + \frac{\partial h_0}{\partial\theta} = 0$$

Including centrifugal force: $F_c = \mathrm{Re}\,v_0^2$

$$\left(1+\delta\,\mathrm{Re}\,h_0^2\frac{\partial h_0}{\partial\theta}\right)^2\frac{\partial h_0}{\partial t} - \frac{\Gamma\cos\theta}{3}h_0^3 - \frac{\delta\,\mathrm{Re}\,\Gamma\cos\theta}{3}h_0^3\frac{\partial h_0}{\partial\theta} - \frac{\delta\,\mathrm{Re}}{3}h_0^3\frac{\partial^2 h_0}{\partial\theta^2}$$
$$- \frac{\delta\,\mathrm{Re}\,\Gamma\sin\theta}{3}h_0^4\left(\frac{\partial h_0}{\partial\theta}\right)^2 + \frac{2\delta^2\,\mathrm{Re}^2}{3}h_0^4\left(\frac{\partial h_0}{\partial\theta}\right)^3 + \frac{\delta\,\mathrm{Re}\,\Gamma\sin\theta}{3}h_0^5\frac{\partial^2 h_0}{\partial\theta^2}$$
$$- \Gamma h_0^2\frac{\partial h_0}{\partial\theta}\sin\theta + \delta\,\mathrm{Re}\,h_0^2\left(\frac{\partial h_0}{\partial\theta}\right)^2 + \frac{\partial h_0}{\partial\theta} = 0$$

Conclusions

- Centrifugal term is important but has not been added formally
- Location of maximum film thickness is highly dependent on expansion technique.
- Expansion and 2D assumption fail for small rotation rate (large Γ)
- We have more work to do …

USING NONLINEARITY AND CONTACT LINES TO CONTROL FLUID FLOW IN MICROGRAVITY

Forced Motion — Slug Moves to Right

Low Speed, Long Duration

High Speed, Short Duration

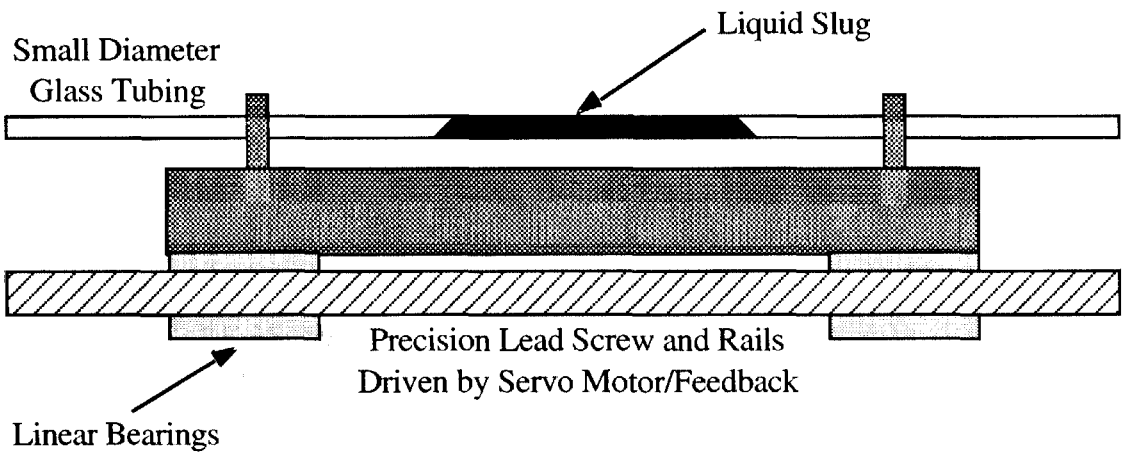

PICTORIAL SKETCH OF EXPERIMENTAL SETUP

AN INTERFEROMETRIC INVESTIGATION OF CONTACT LINE DYNAMICS IN SPREADING POLYMER MELTS AND SOLUTIONS

David G. Fischer[1], Ben Ovryn,[1] Pirouz Kavehpour[2] and Gareth H. Mckinley[2]
[1]National Center for Microgravity Research on Fluids and Combustion,
NASA Glenn Research Center, MS 110-3, 21000 Brookpark Road, Cleveland OH 44135.
[2]Department of Mechanical Engineering, M.I.T., Cambridge, MA 02139.

INTRODUCTION

The objective of this research is to apply interference microscopy to systematically measure the spatial and temporal evolution of surface profiles that develop in the near-contact line region of Newtonian liquids, weakly elastic dilute polymer solutions, inelastic shear thinning fluids and entangled polymer melts. Moving contact-line problems in polymeric materials are encountered in many coating flows, gravity-driven drainage and in spin-coating operations where spreading arises from the combined action of gravitational and/or centrifugal body forces on a deposited droplet. Examples of industrial processes where spreading of a viscous liquid over a flat dry substrate is important include: dip-coating of sheet metal; gravity drainage and drying of colloidal paints; spin-coating of photoresists on silicon substrates and coating of inks on paper. In the latter examples, achieving a spatially uniform coating requires careful control and understanding of the mechanisms that influence the spreading dynamics of a fluid droplet. As the mass fraction of solvent progressively decreases, the viscoelastic properties become increasingly important. The interface profile is therefore governed by a dynamic balance between surface tension and viscous and elastic stresses, and pronounced differences in the shape of the interface between Newtonian and non-Newtonian droplets have been predicted and observed experimentally.

The dynamics of the near contact line region governs the feasibility and stability of future microgravity containerless materials processing operations that might involve spin- or dip-coating of barrier materials or photoresists. In order to investigate such phenomena, it is essential to develop an instrument that can non-invasively and quantitatively image the evolution of the surface topography of fluid layers with high spatial and temporal resolution.

EXPERIMENTAL RESULTS

A phase-modulated laser feedback interferometer has been developed that allows high-resolution measurement of changes in surface height for static and dynamic liquid surfaces [1]. To elucidate the significance of rheological behavior near the contact line, experiments are focusing on a single solid substrate (polished silicon wafers) and four distinct classes of fluids; a simple viscous Newtonian reference standard, a dilute polymer solution, an inelastic shear-thinning fluid and a weakly entangled oligomeric melt. Access to a microgravity environment may ultimately be important since the 'inner scale' region over which elastic, viscous and capillary effects are all important will be physically enlarged as the gravitational driving force is reduced. Present ground-based experiments are proceeding in two parallel efforts:

(i) Analysis of Optical Path Distortions in Transparent Samples

A model has been developed that predicts the effective optical path through a thick refractive specimen on a reflective substrate (e.g. a silicone oil droplet on a silica substrate) as measured by a scanning confocal interference microscope equipped with a high numerical aperture (NA) lens [2]. If the effective pinhole of the confocal microscope is infinitesimally small then only one ray (the 'magic ray') contributes to the measured differential optical path length, OPL. However for a pinhole of finite diameter, rays within a small angular cone contribute to the measured OPL as shown in Figure 1. With an *a priori* estimate of the local surface shape, an iterative algorithm can be used that allows the measured phase to be corrected for refractive effects. In figure 2 we show a scanned image of a static PDMS drop with contact angle 68° and contact radius 18 μm as measured using the laser feedback interferometer.

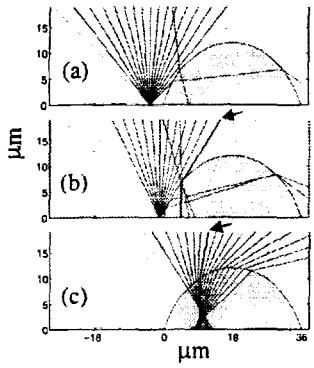

Fig. 1 Ray traces resulting when a high-NA beam is scanned from left to right into a droplet forming a spherical cap. The 2 rays marked by the arrows are the 'magic rays'; see text.

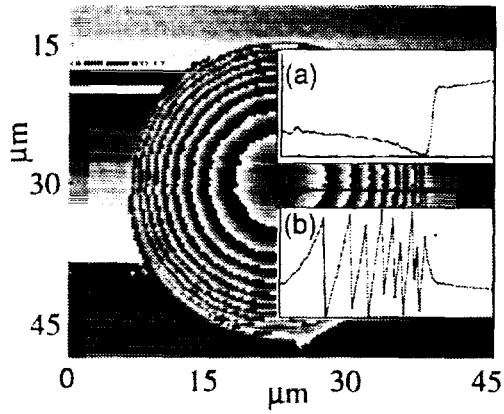

Fig.2 Two-dimensional phase-image of the droplet surface before phase-unwrapping. Insets are (a) the visibility (max. = 0.3) and (b) the phase along the delineated region.

(ii) Development of Instrumentation and Apparatus for Spreading Drops

A temperature-controlled apparatus is being assembled, at MIT, on an x-y scanning stage to permit rasterized imaging of viscous 'gravity currents' flowing down an inclined plane. The resulting profiles will be compared with theoretical predictions for Newtonian and non-Newtonian constitutive models [3,4]. The local shape of the advancing front depends on the boundary condition at the advancing contact line In Figure 3 we show two representative profiles of the local surface profile for a silicone oil ($\mu \approx 10^4$ cPoise) quasi-statically advancing on *(a)* a dry and *(b)* a wet horizontal silicon substrate.

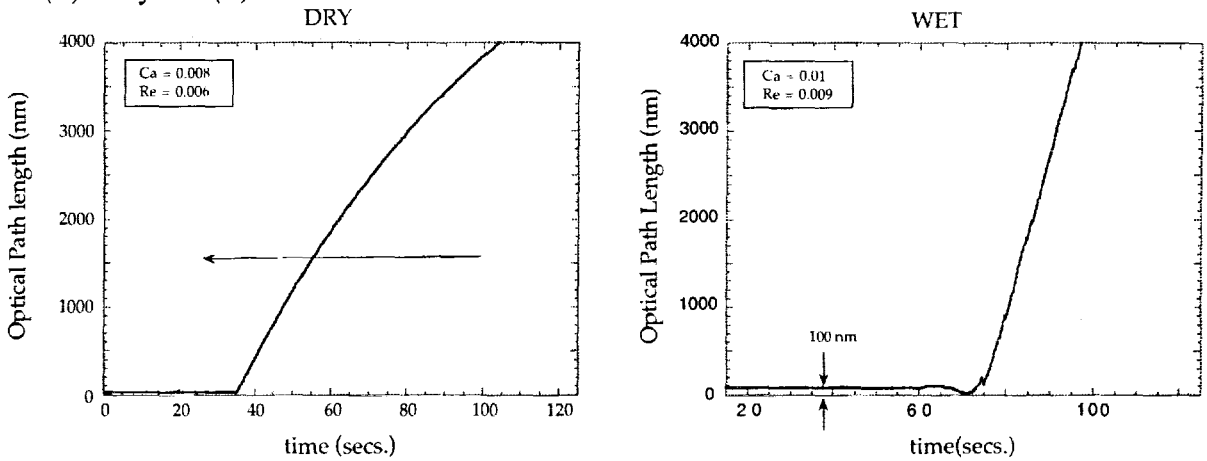

Fig. 3 Evolution in the optical path length (OPL) as a viscous silicone drop slowly spreads under gravity from right to left over (a) a dry silicon wafer and (b) a silicone film that pre-wets the substrate.

In future work, we plan on using this technique to image the spatio-temporal evolution of surface topography in two important commercial processes: (i) the evolution of a solidifying drop [5] and (ii) the drying and cracking of colloidal films coated on glass surfaces.

References:

1. B. Ovryn and J. Andrews, Measurements of changes in optical path length and reflectivity with phase-shifting laser feedback interferometry, *Appl. Opt.*, **38,** 1959-1967 (1999).
2. D. Fischer, B. Ovryn, Interfacial shape and contact angle measurement of transparent samples with confocal interference, *Opt. Lett* **25,** 478-481 (2000).
3. Huppert, H.E., Flow and instability of a viscous current down a slope, *Nature*, **300,** 427-428 (1982)
4. Pascal, H., Gravity flow of a non-Newtonian fluid sheet on an inclined plane, *Int. J. Eng. Sci.*, **29**(10), 1307-1313 (1991).
5. Anderson, D.M., M. Grae Worster, S.H. Davis The case for a dynamic contact angle in containerless solidification, *J. Crystal Growth* **163,** 329-338 (1996).

NASA/CP—2000-210470

AN INTERFEROMETRIC INVESTIGATION OF CONTACT LINE DYNAMICS IN SPREADING POLYMER MELTS AND SOLUTIONS

David G. Fischer, Ben Ovryn, H. P. Kavehpour,
and Gareth H. Mckinley

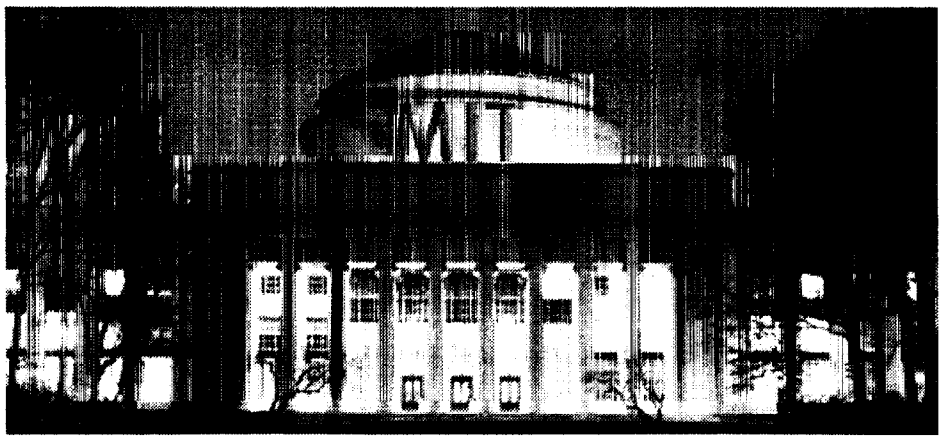

Introduction

- Objective:
  - Apply interference microscopy to systematically measure the spatial and temporal evolution of surface profiles that develop in the near contact line region.
- A phase-modulated laser feedback interferometer has been developed that allows high resolution measurement of changes in surface height for static and dynamic liquid surfaces.
- Applications:
  - Moving contact line in polymeric materials
  - Gravity-driven drainage
  - Spin-coating operation of photoresists on silicon substrate
  - Dip-coating of sheet metal

Interferometer

- Division of amplitude Interferometer (Michelson)

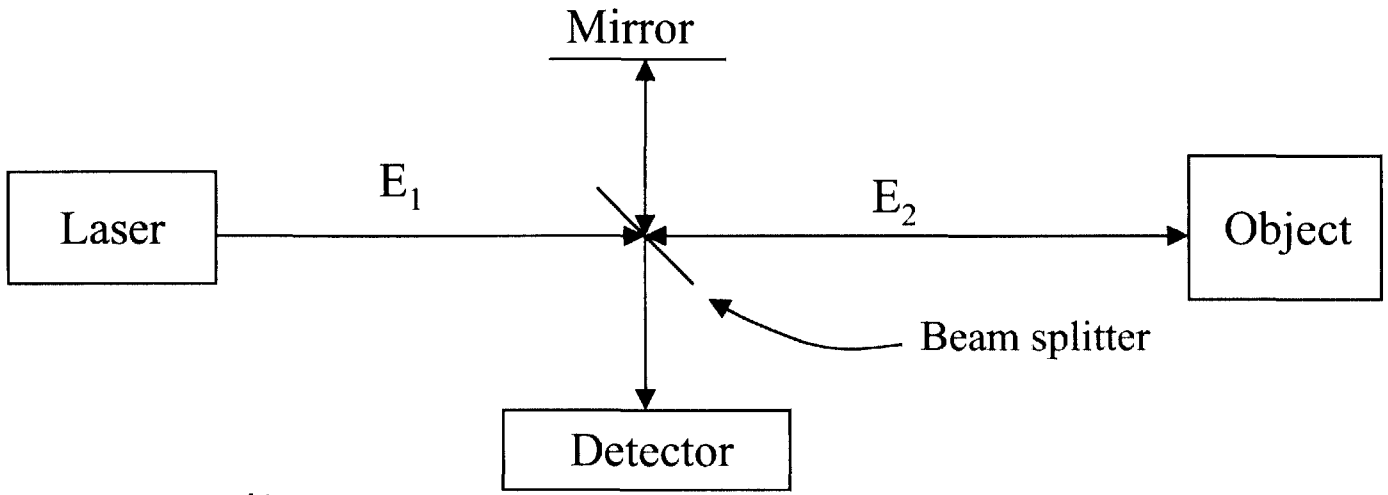

$E_1 = a_1 e^{-i\phi_1}$

$E_2 = a_2 e^{-i\phi_2}$

$I = |E_1 + E_2|^2 = I_0 (1 + m\cos(\phi))$ ⟶ Intensity

$\phi = \phi_2 - \phi_1$ ⟶ Phase

$m = 2(a_1 a_2)/(a_1^2 + a_2^2)$ ⟶ Visibility

Laser Feedback Interferometer (LFI)

- LFI system with multiple reflection:

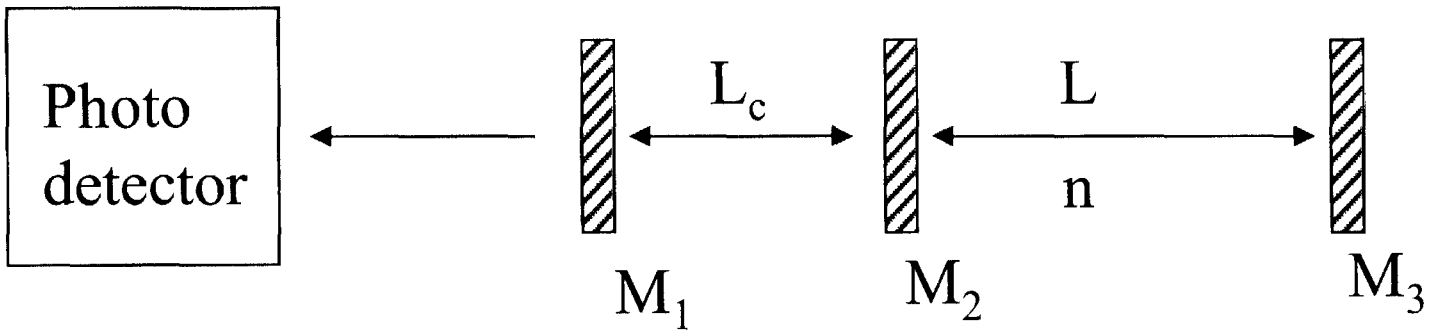

$$I(m,b,\phi) = I_0 \{ 1 + m\cos(\phi)\ \Sigma(-b)^j \cos(j\phi)\}$$

$$\phi = (4\pi/\lambda)\, n\, L,\ \ m = \gamma\, R_3^{1/2}$$

- With only a single reflection (j= 0), behaves like a two beam interferometer:

$$I(m,\phi) = I_0\{1 + m\cos(\phi)\}$$

Phase shifting interferometery applied to LFI

- Measure the change in intensity for a series of experimentally controlled phase changes to electro-optic modulator

$$I_i(m, \phi, \psi) = I_0 \{1 + m \cos(\phi + \psi_i)\}$$

Optical path length: $\delta = \int n \, ds$

Phase: $\phi = (4\pi/\lambda)\,\delta$

- Example: $\psi_i = \{0, \pi/2, \pi, 3\pi/2\}$

$I_1 = I_0 \{1 + m \cos(\phi)\}$ $\quad$ $I_3 = I_0 \{1 - m \cos(\phi)\}$

$I_2 = I_0 \{1 - m \operatorname{cin}(\phi)\}$ $\quad$ $I_4 = I_0 \{1 - m \operatorname{cin}(\phi)\}$

then:

$\tan(\phi) = (I_2 - I_4)/(I_1 + I_3)$ $\quad$ $m = 2((I_1 - I_3)^2 + (I_4 - I_2)^2)^{0.5}/(I_1 + I_2 + I_3 + I_4)$

Determination of the accuracy of LFI

- Cantilever bending of a piezoelectric bimorph

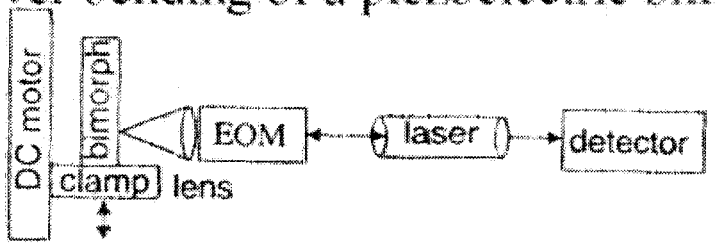

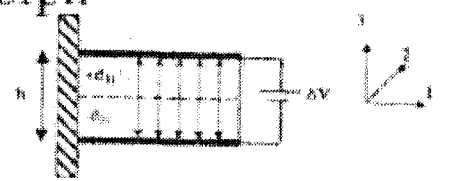

$$u_3 = -\frac{3}{2}\frac{d_{31}\,\Delta V}{h^2}u_1^2$$

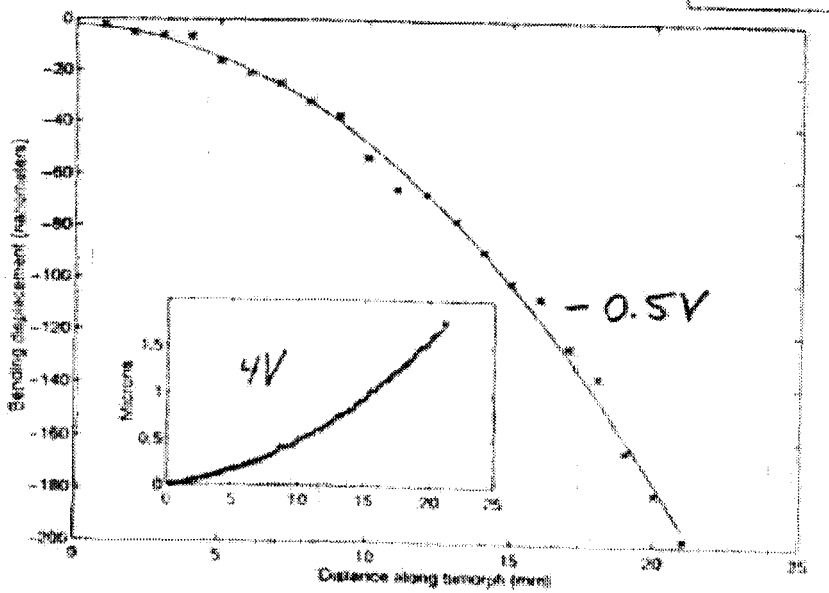

Measurement of static contact angle of drops of PDMS on fluorinated silicon wafer

1) Wipe single crystal silicon wafer with toluene
2) Dip silicon into FC-723 surface modifier and allow to dry
3) Place 60,000 cS PDMS drops using an atomic force microscope cantilever tip

Data Collection

1) Wafer on closed-loop, two dimensional translation stage (100 μm x 100 μm)
2) Image with 50 x 0.8 NA objective
3) Collect two-dimensional image data sample with at least 125 nm/ data point

   Do calculation on-line
   Scanning times are long
   ~50 msec/data point (not yet optimized)

36 μm diameter drop

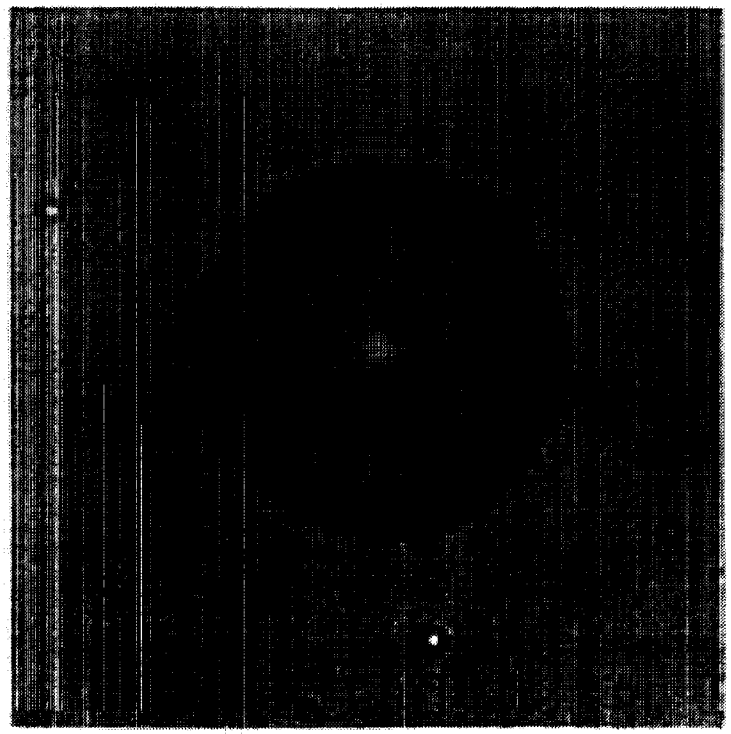

VIDEO IMAGE

Measurements with LFI

- Raw visibility and phase

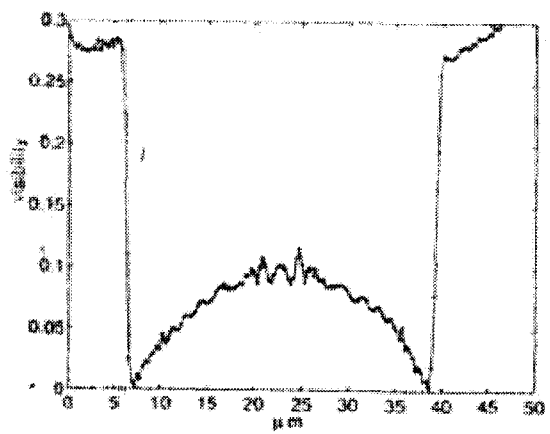

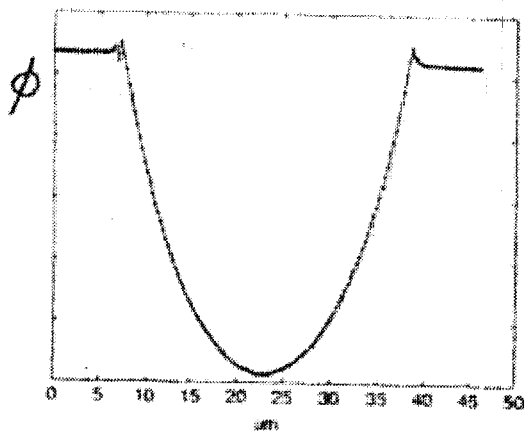

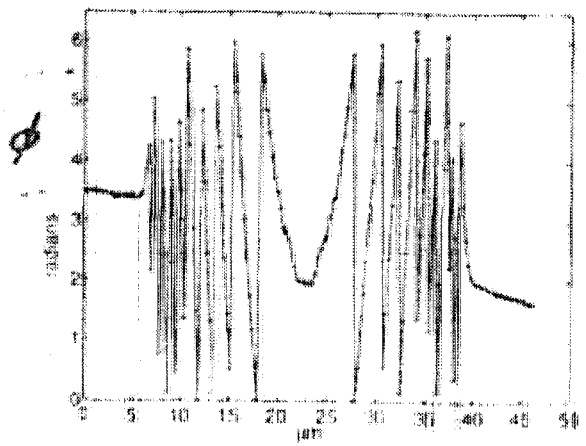

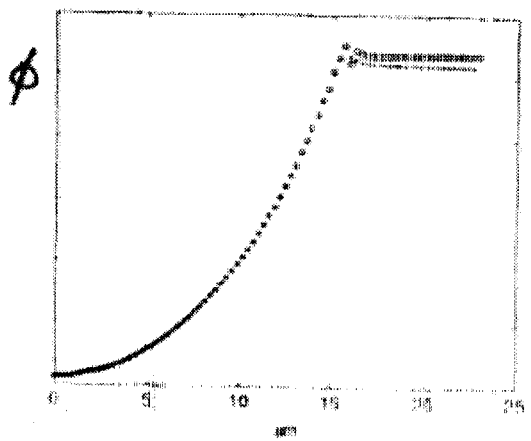

Two dimensional scan of etched silicon wafer

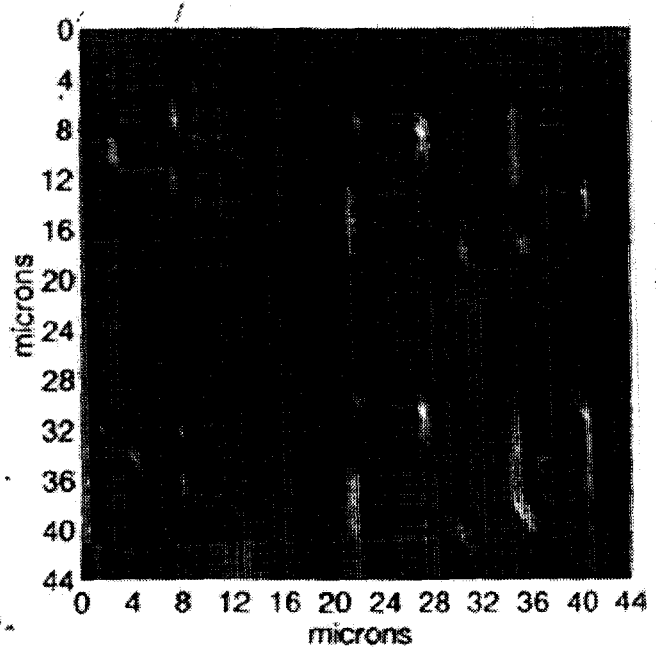

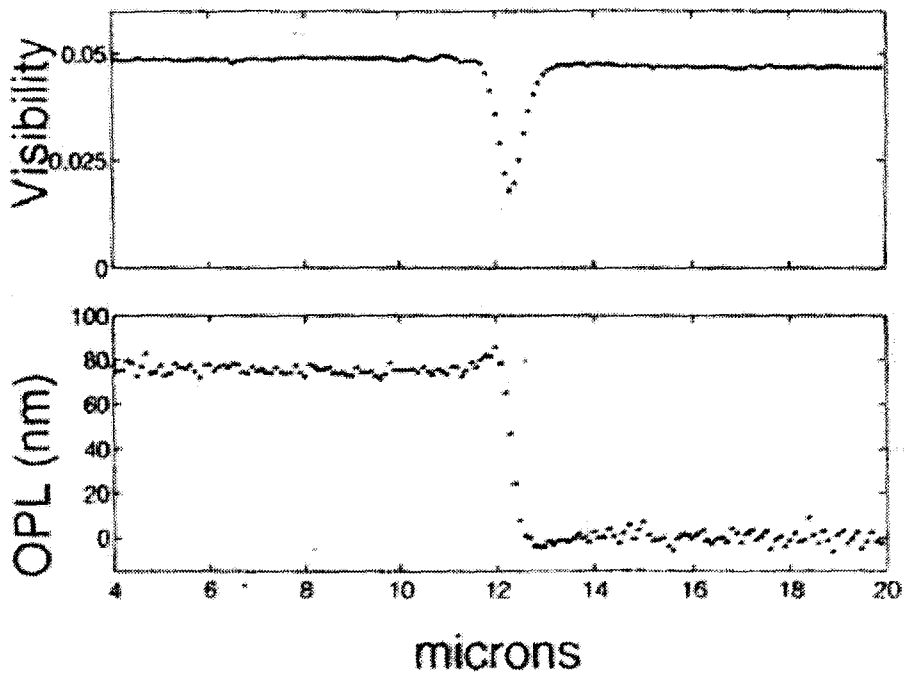

Confocal microscopy results

- Scanning a drop during the wetting process

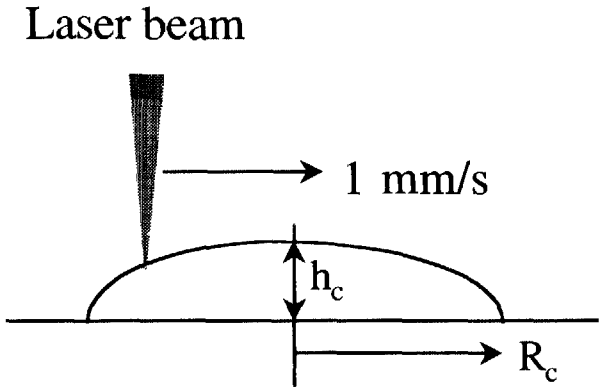

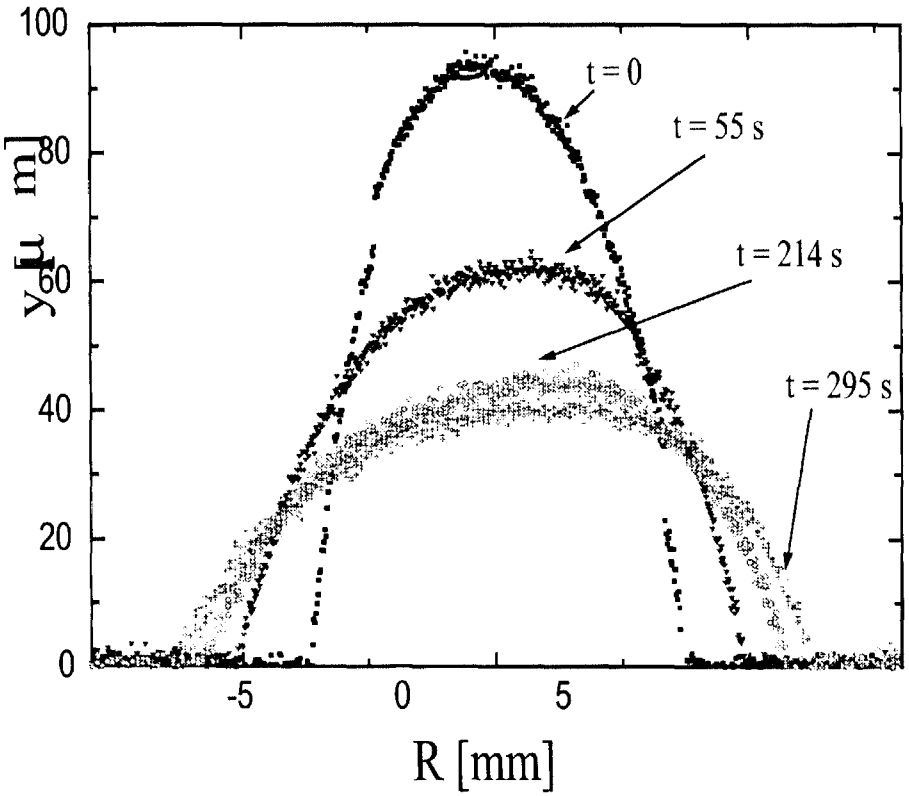

- Spreading of a silicon oil drop (h= 0.1 Pa.s) on a silicon surface.
- Scanning speed is 1 mm/s

Confocal microscopy results (cont.)

- Scaled form of drop spreading

$$\xi = \frac{y(x,t)}{h_c(t)}$$

$$\zeta = \frac{R(x,t)}{R_c(t)}$$

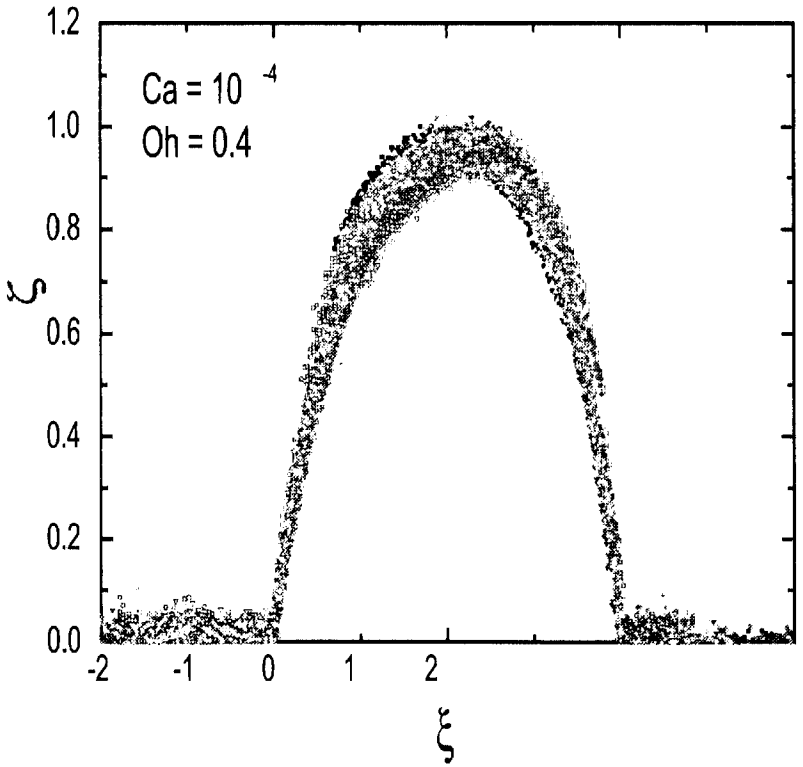

Confocal microscopy results (cont.)

- Comparison of spreading results with theoretical results

- Ohnesroge number , $Oh=\mu/(\rho R\sigma)^{0.5}$
- If $Oh >> 1$, then $\zeta \sim t^{-0.25}$
- If $Oh << 1$, then $\zeta \sim t^{-1.33}$

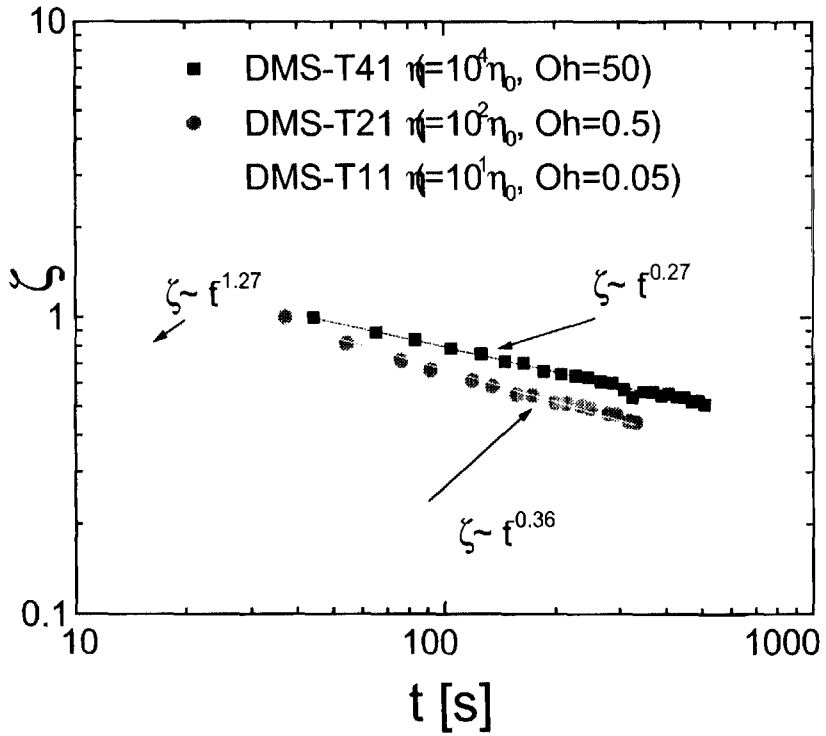

Confocal microscopy results (cont.)

- Comparison of spreading results with theoretical results

- If $Oh >> 1$, then $\xi \sim t^{0.125}$
- If $Oh << 1$, then $\xi \sim t^{0.67}$

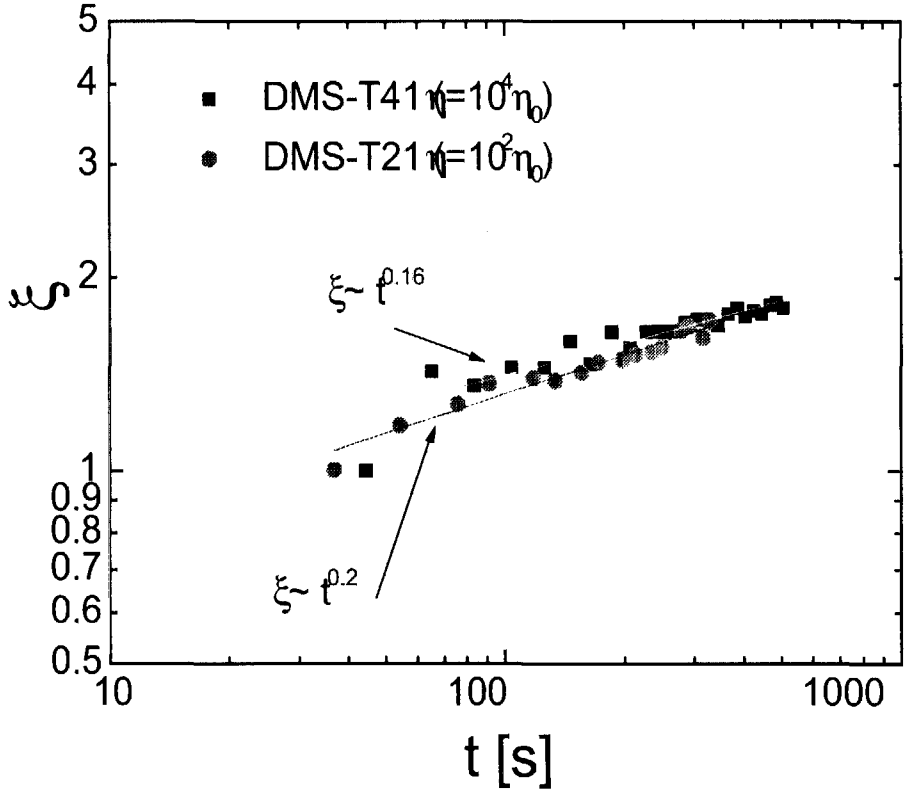

Confocal microscopy results (cont.)

- Evaporation of a coffee drop on a silicon surface (The Coffee Ring problem)

- Ring formation at the contact line

- Scanning speed is 250 μm/s

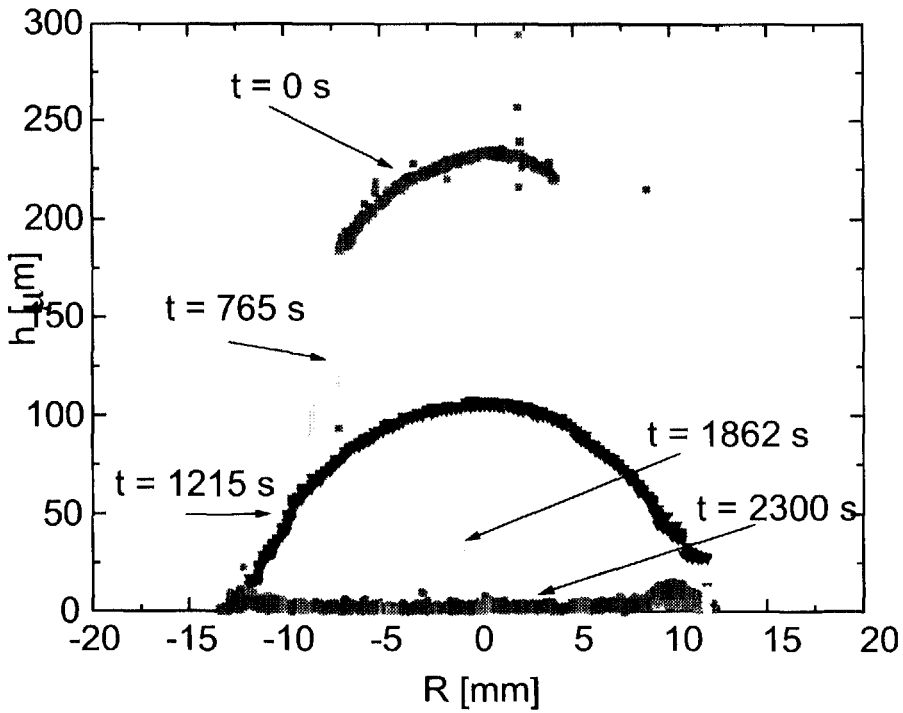

Conclusion

- Laser feedback microscopy has better spatial and vertical resolution as compared to other optical methods (e.g. two order of magnitudes better than confocal microscopy).

- LFI is a non-invasive method therefore it is an excellent tool for measurements close to the contact-line.

- Other applications of LFI are surface profiling of MEMS, measurement of very low amplitude vibrations, and characterization of nano-scale cracks and surface defects.

COALESCENCE AND NON-HYDRODYNAMIC FORCES ACROSS THIN FILMS BETWEEN TWO FLUID INTERFACES

Tonya Kuhl, Charles Park, Hong Yang, Fabio Baldessari, Jacob Israelachvili and L. Gary Leal
Department of Chemical Engineering
University of Calif. at Santa Barbara

This project represents a combined "macroscopic" and "microscopic" investigation of coalescence between droplets in a flow. The **macroscale** studies are being carried out in a very small 4-roll mill that is designed to allow us to work with drops of O(100 microns) or less in diameter. We have obtained comprehensive data on coalescence conditions for two equal size drops in the plane of the various flows that can be produced in the 4-roll mill, both for head-on collisions and for glancing collisions. The data shows quantitative agreement with the expected hydrodynamic scaling behavior for two Newtonian fluids with a contaminant free interface. However, it suggests an unexpected dependence of the critical film "thickness" at coalescence on the drop size, as well as a currently unexplained dependence of the same quantity on the molecular weight when the suspending fluid is a polymeric liquid (though with bulk rheological properties that are still Newtonian under the conditions of the coalescence experiment. We have also recently initiated macroscopic studies of the role of different types of surface forces in setting the conditions for coalescence (e.g. van der Waals forces versus hydrophobic attraction). The **microscale** studies are being done using the surface forces apparatus (SFA). Initially, these studies were focused on the origin of hydrophobic forces across thin films where, for the first time, the full force-law (force versus distance, F vs. D) has been measured from $D > 50$ nm. To $D=0$. More recently, we have begun to investigate the use of the SFA as a means to directly investigate the film thinning and instability problems-under conditions that directly relate to the macroscale coalescence experiments. We have obtained preliminary data that explores the conditions and details of the film collapse process at the moment of coalescence for conditions of very small capillary number (approx. .00001), as well as the separation when the coalesced interface is pulled back apart.

Coalescence and Non-Hydrodynamic Forces across Thin Films between Two Fluid Interfaces

Tonya Kuhl, Charles Park, Hong Yang, Fabio Baldessari, Jacob Israelachvili and L. Gary Leal
Department of Chemical Engineering
University of Calif. at Santa Barbara

Outline:

- **AIM – experimentally based understanding of flow induced coalescence of drops and bubbles**
- **Macroscale vs. Microscale Experiments**
- **Numerical Simulations**
- **OUTCOME – develop realistic models of the interactions between deforming liquid-liquid and vapor-liquid surfaces in coalescence and related processes**

Macroscopic Measurements - 4 Roll Mill

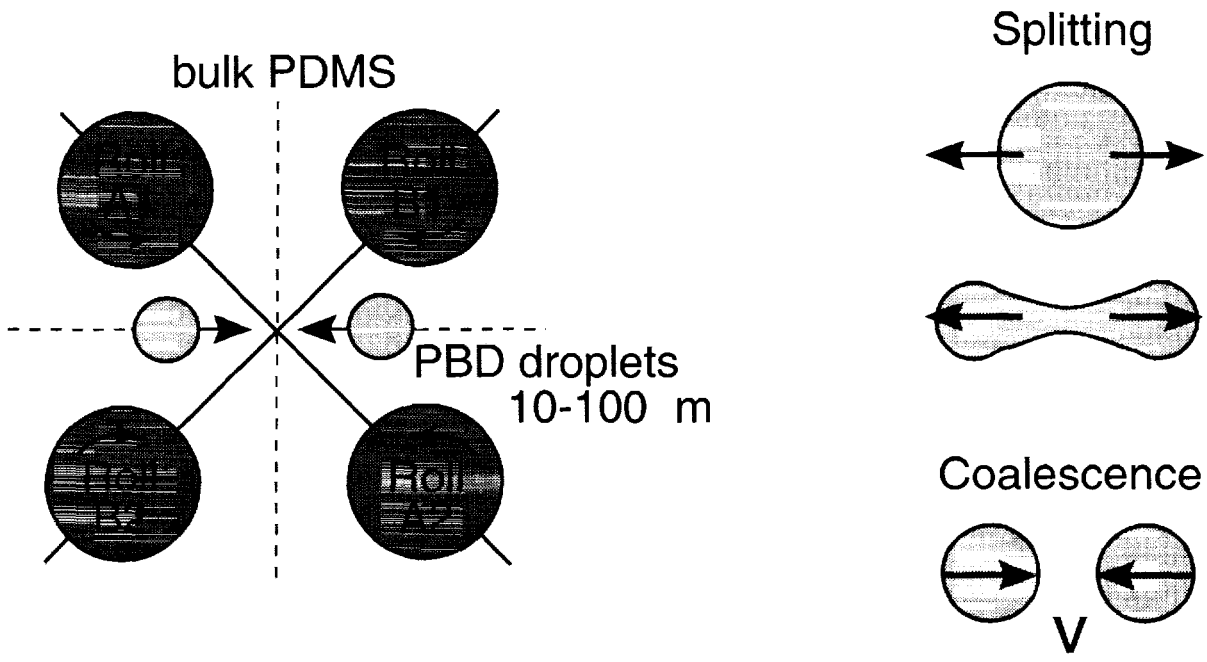

Microscopic Measurements - Surface Force Apparatus

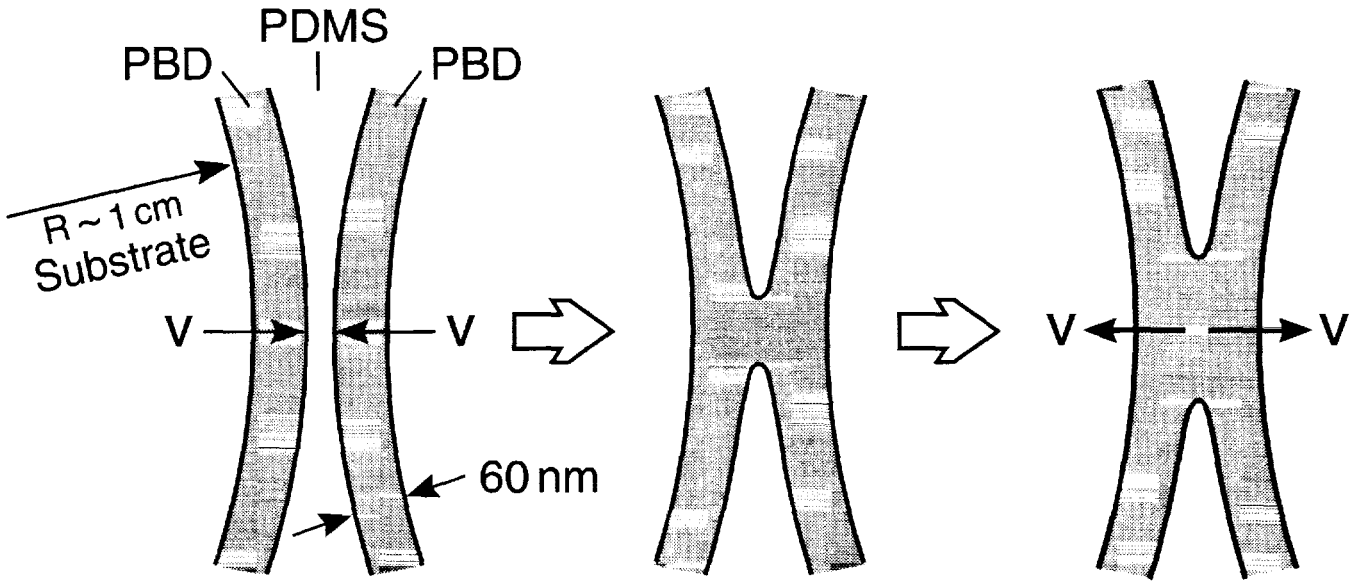

Drop Collision and Separation – $C_a > C_c$

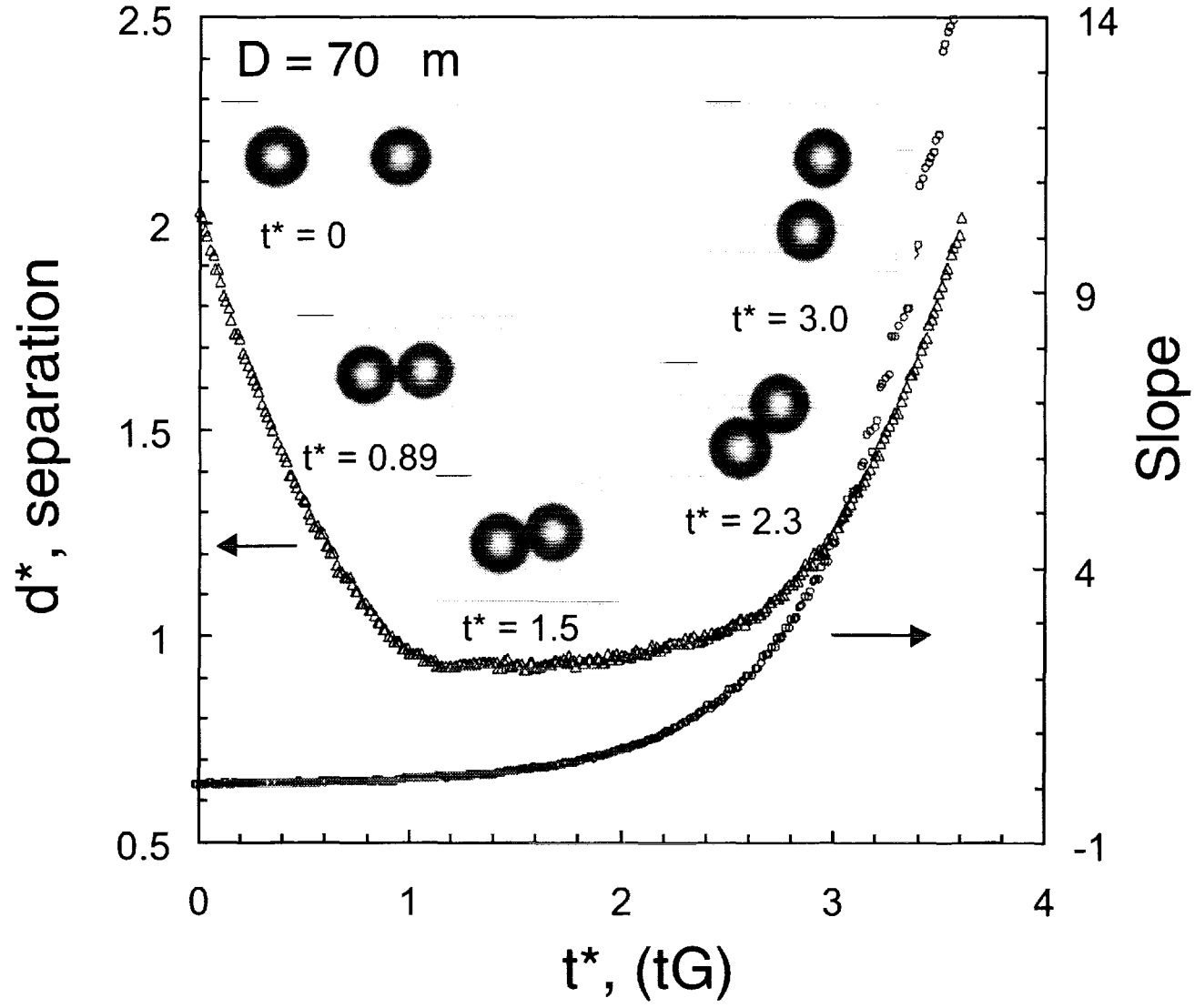

Two Drops - same plane
produced by breakup

$d^*_{initial} = 2$

initial = 0

= 0.9

All controlled by choice of breakup and separation flows

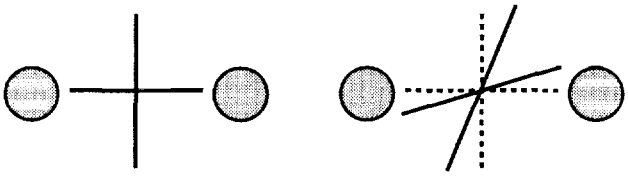

breakup =1 collision =0.9

Drop Collision and Coalescence
$C_a < C_c$

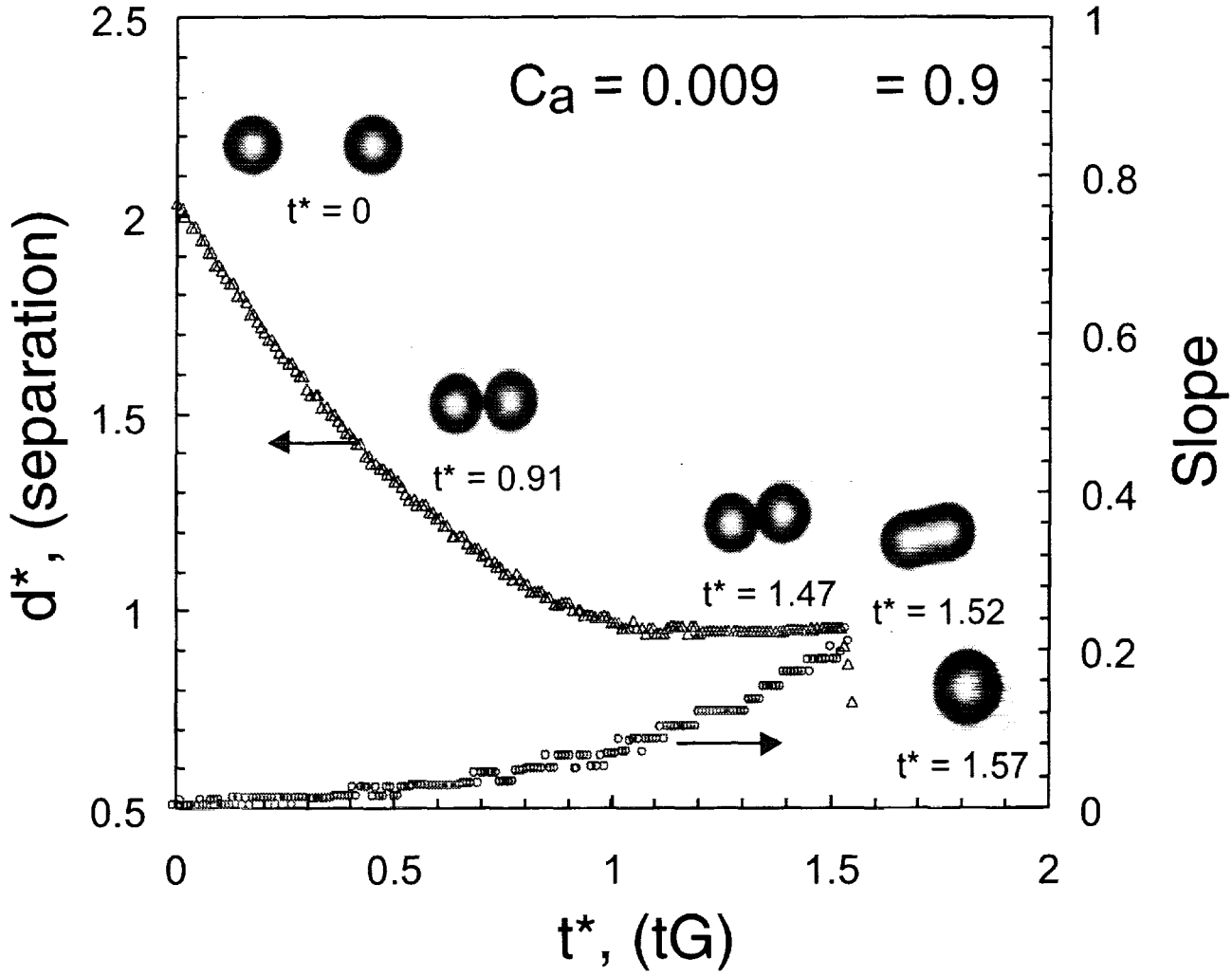

Coalescence $C_a < C_c$ "gentle" collisions

NOTE: $C_{a\ crit}$ << $C_{a\ crit}$
coalescence breakup

Drainage Time
(PB in PDMS, =1.0, offset/2R=0.0)

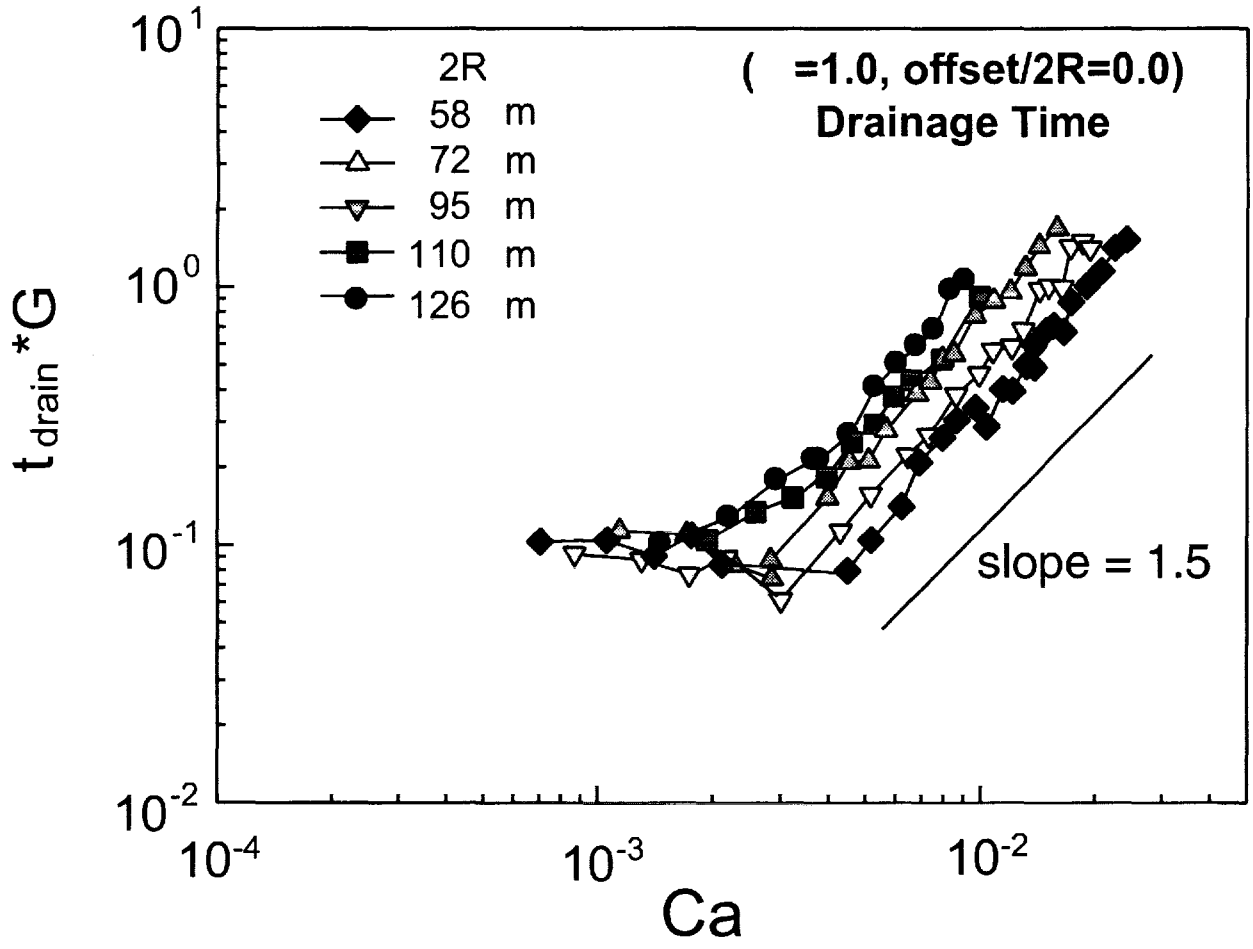

Recall: $(tG)_{drain} \sim \frac{R}{h_c} Ca^{3/2}$ (flat film)

$(tG)_{drain}$ indep of R, Ca (sphere)

Coalescence scaling law

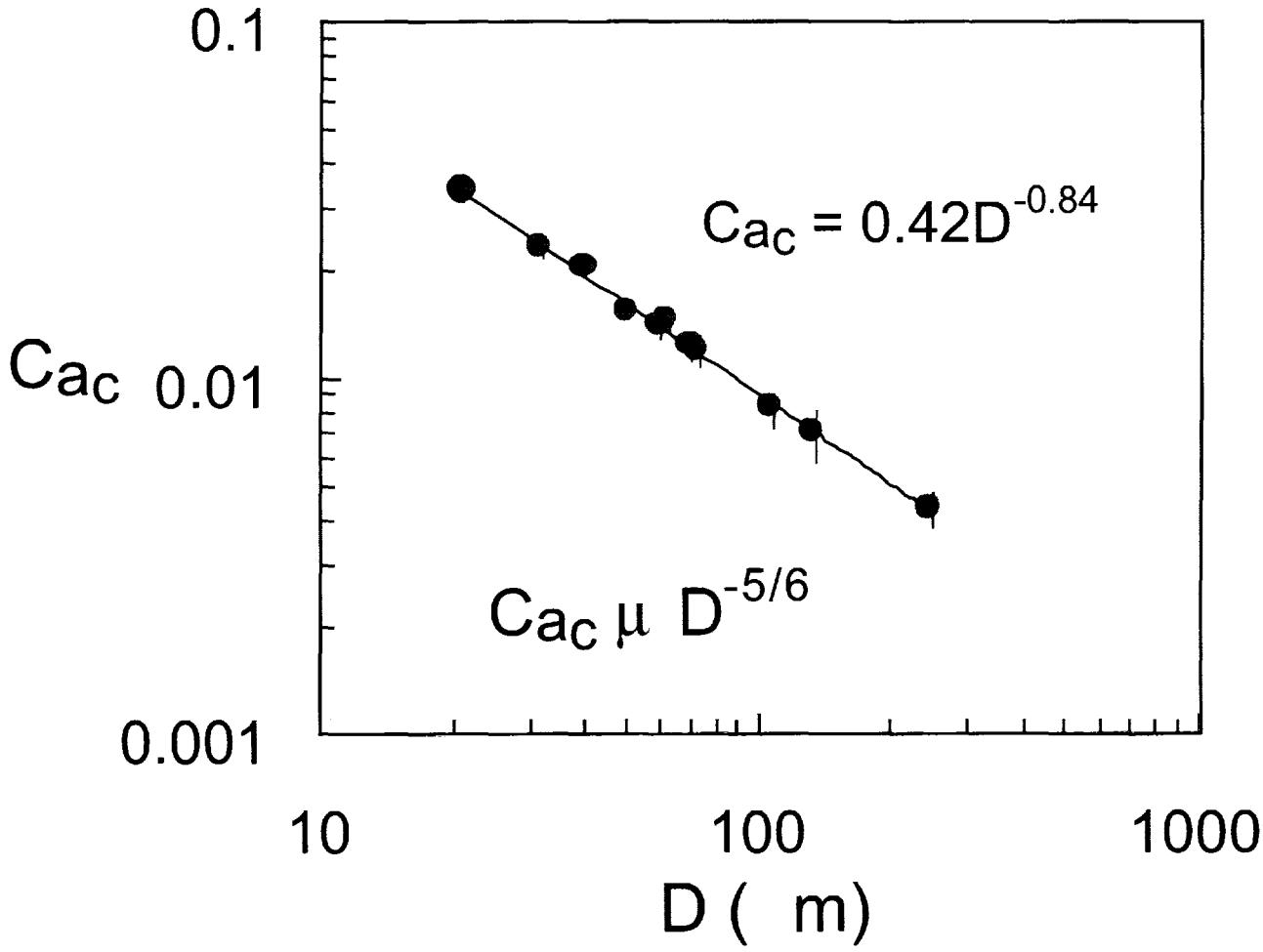

PB5000/PDMS60000, = 0.9

Scaling Law Behavior

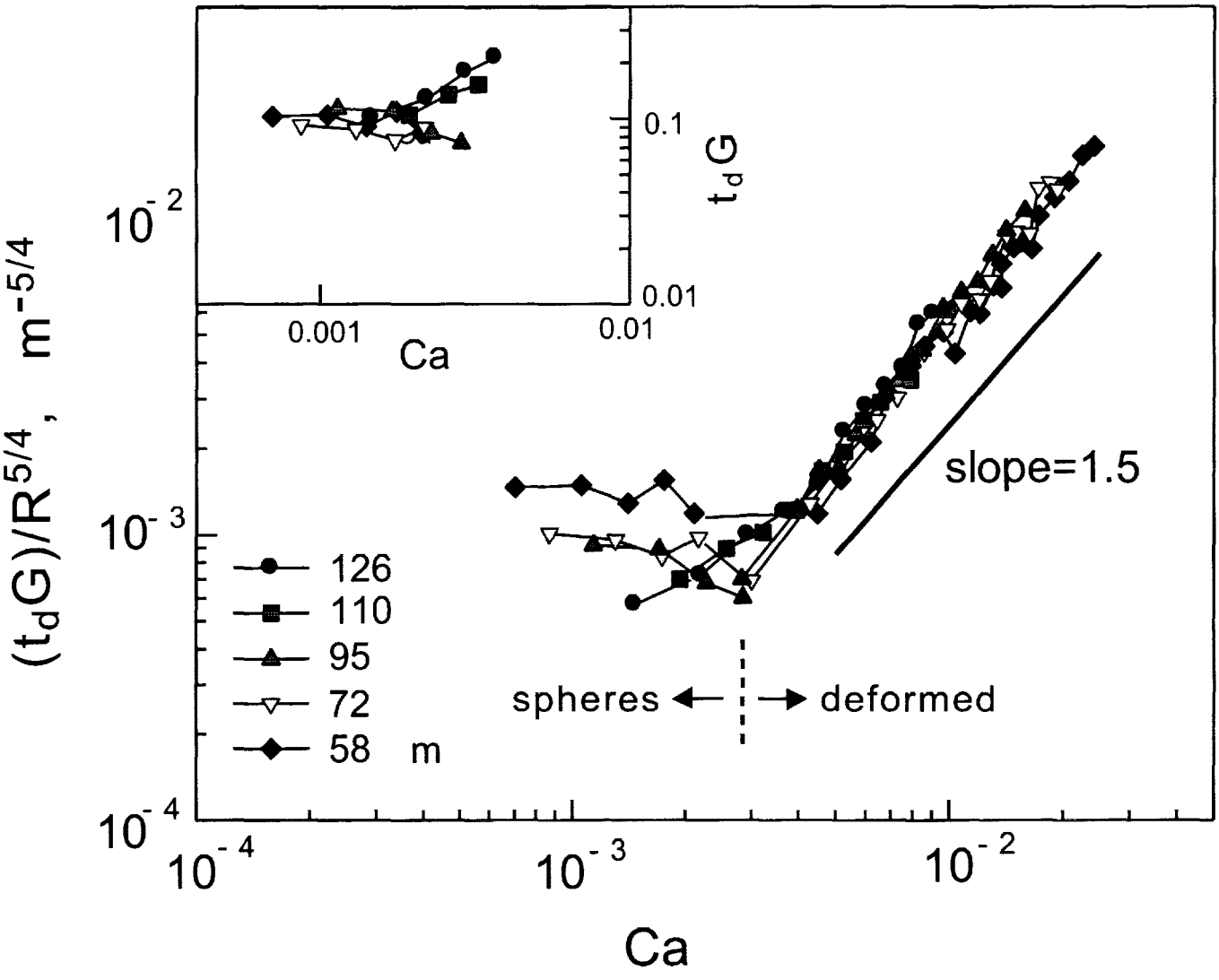

Suggests $h_c \sim R^{-1/4}$

Does not follow Chesters' $h_c \sim R^{+1/3}$

Critical Film Thickness, h_c vs. drop size

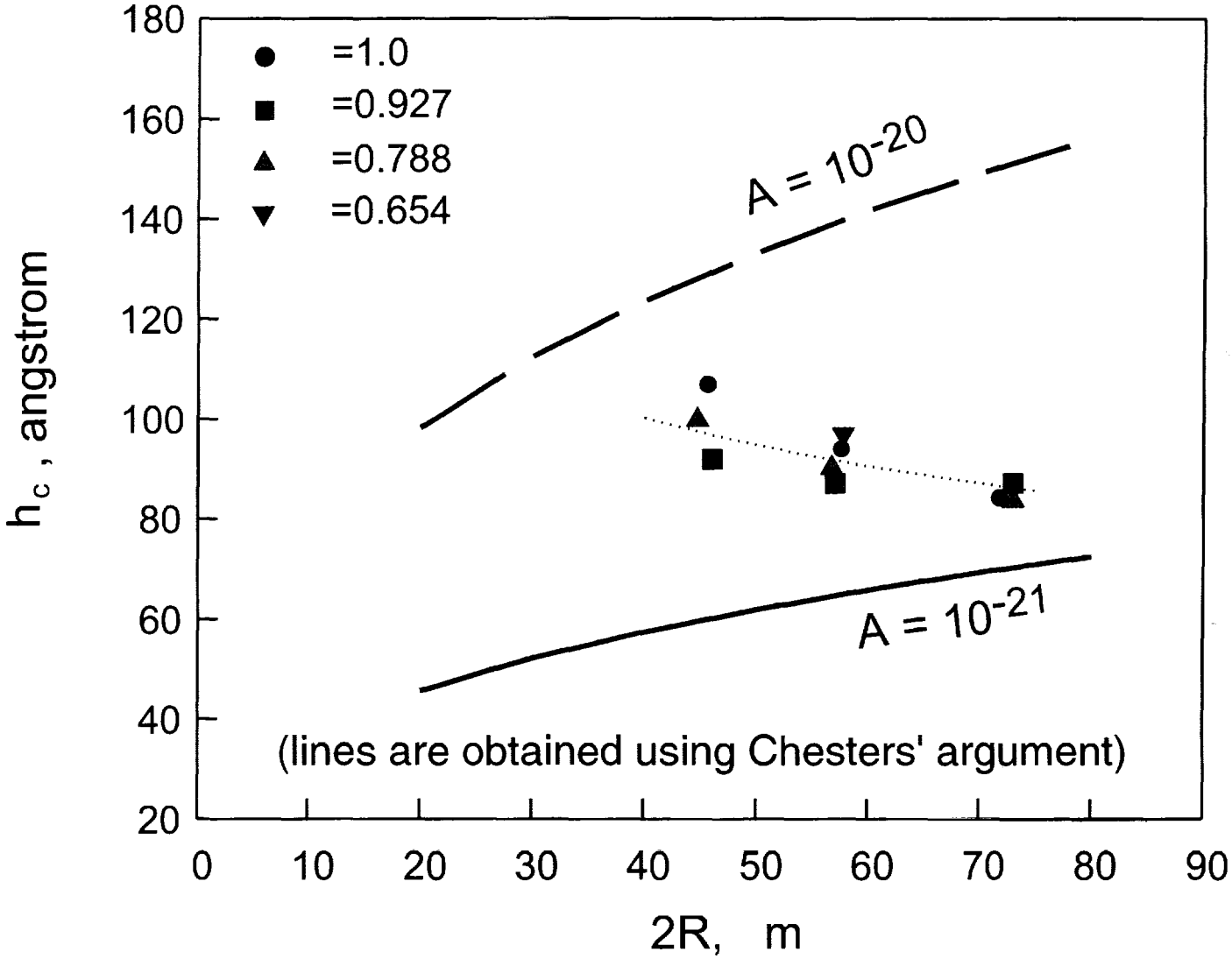

Recall: SFA - $A=6.6\ 10^{-21}J$

$h_c \sim 55Å$

h_c inferred from fit of Ca_c vs. offset to the approx. scaling theory

Ca_c vs. offset
(= 1, R = 29 m)

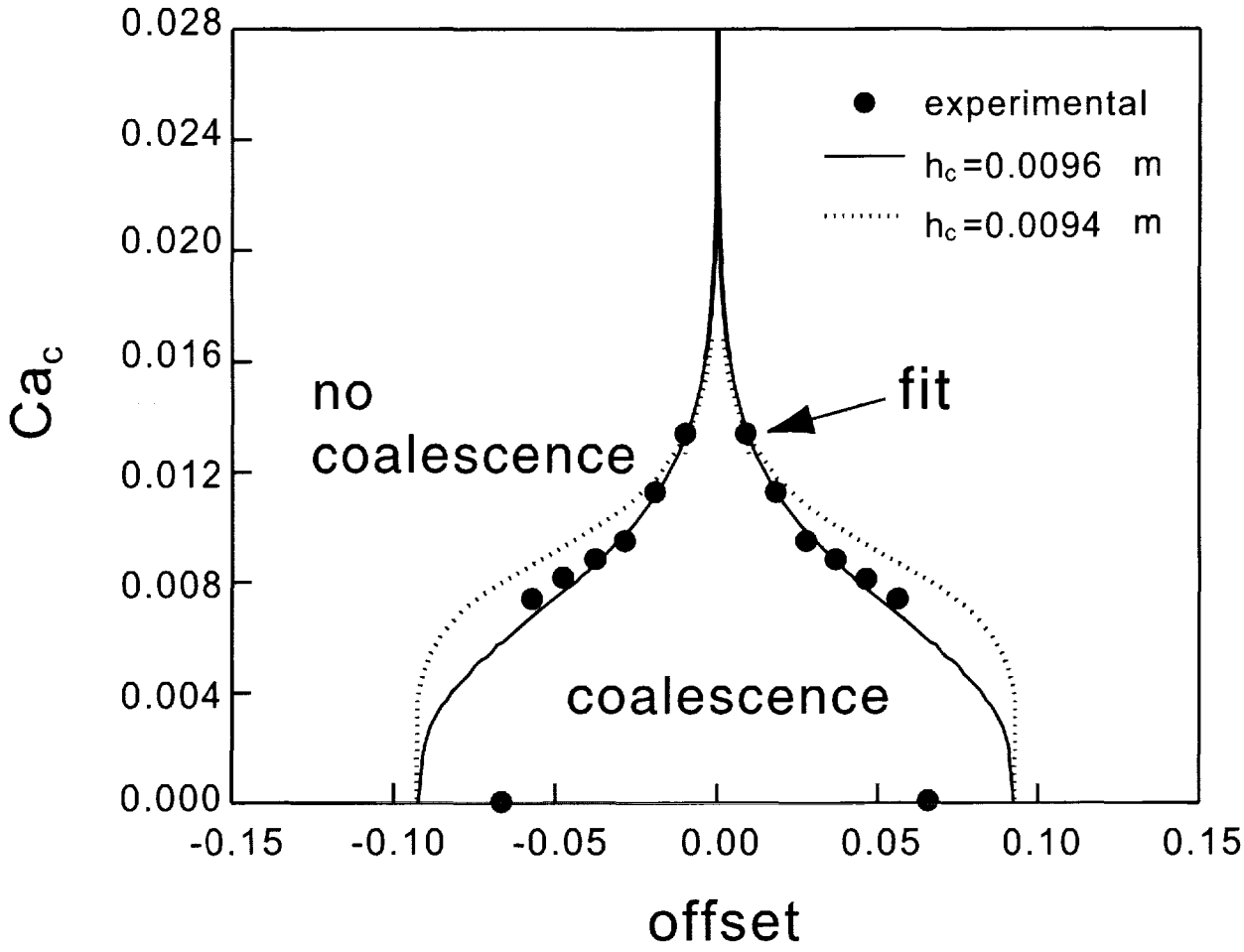

Static Force Measurements – "solid" PBD across liquid PDMS

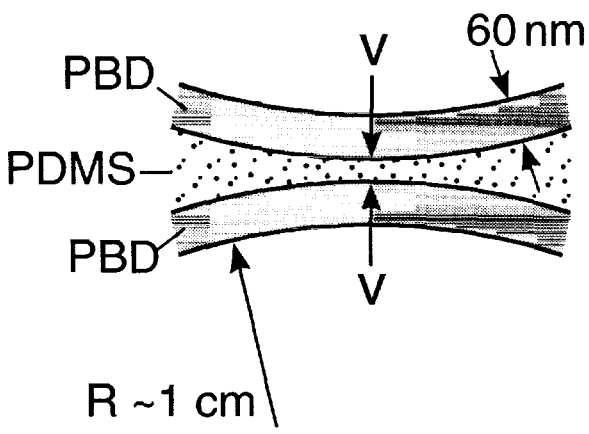

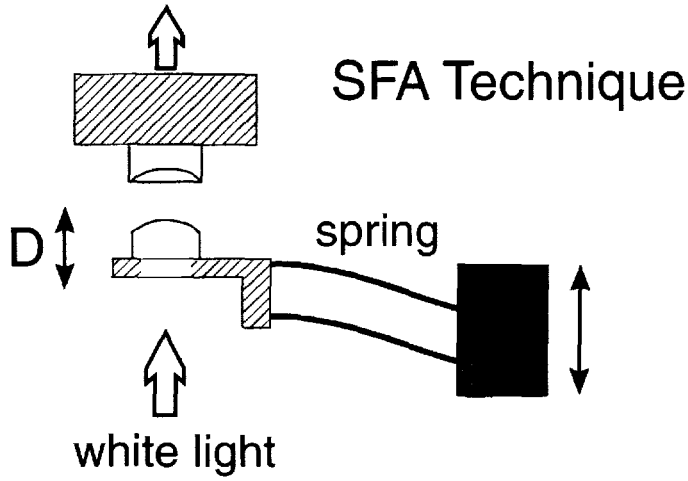

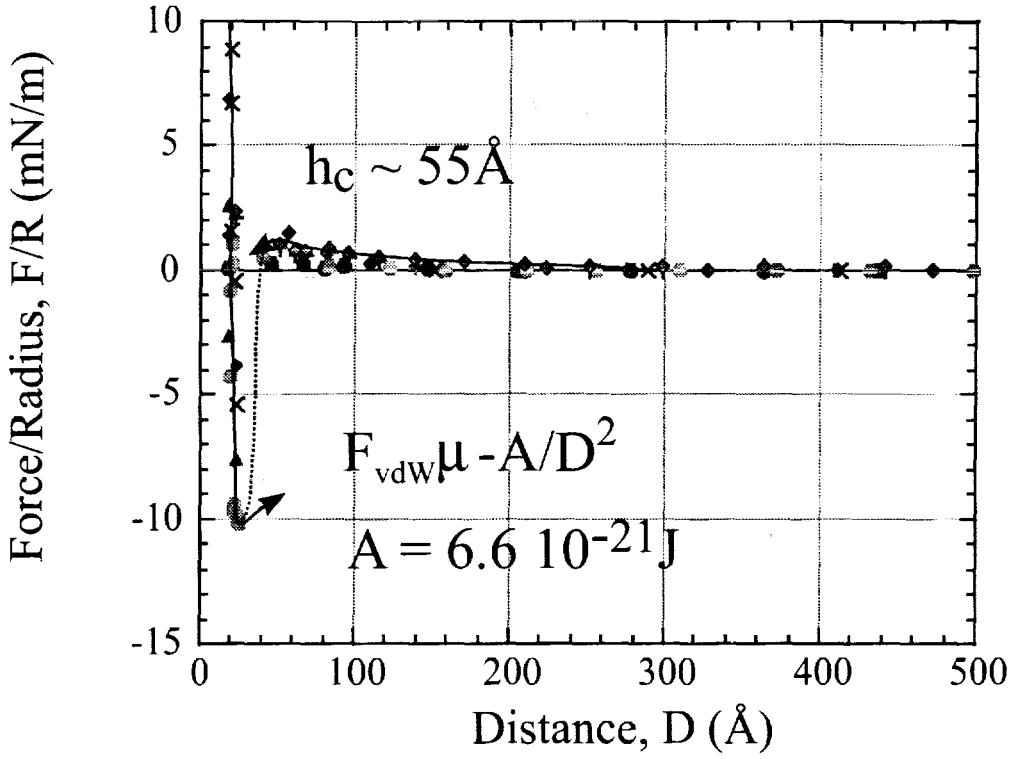

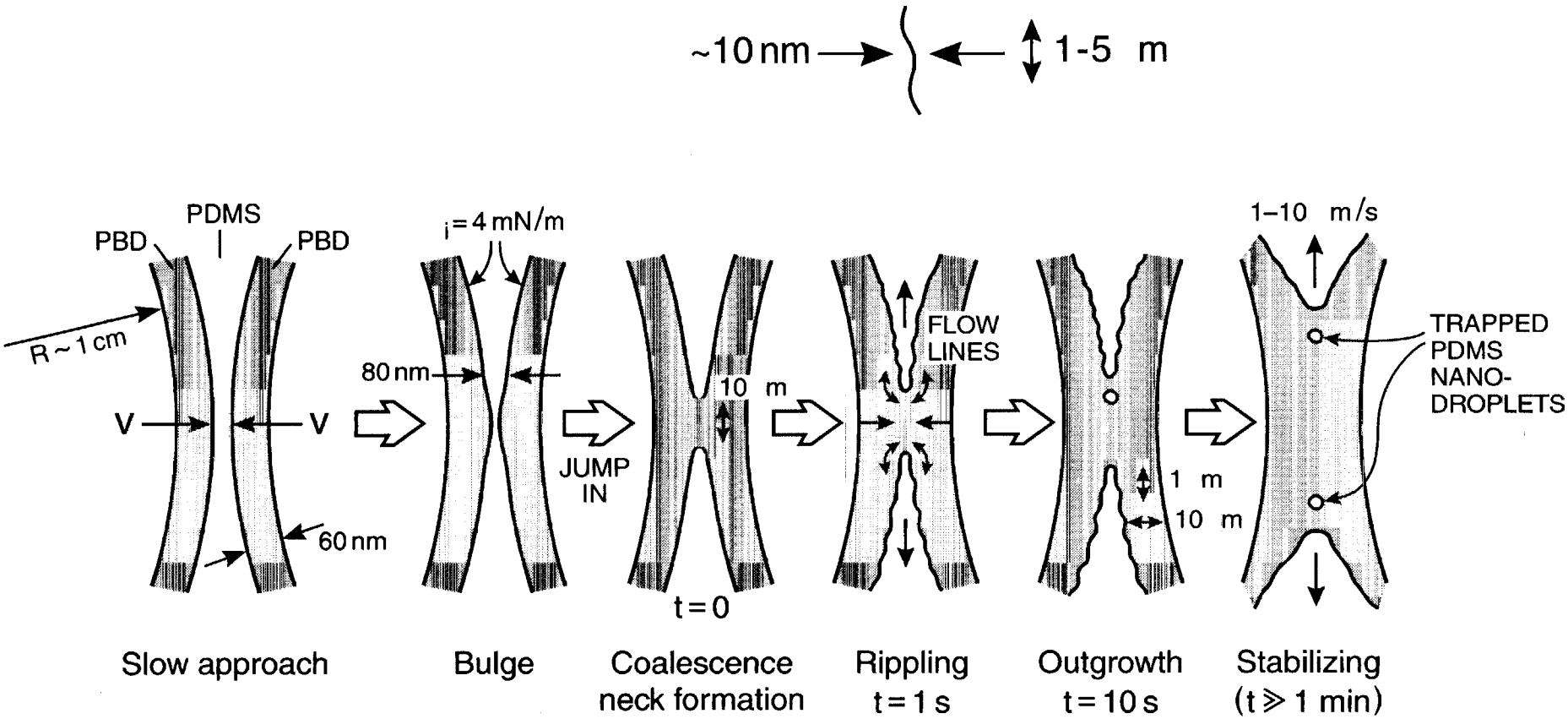
~10 nm
1-5 m
PDMS
PBD
PBD
R ~ 1 cm
V
V
60 nm
Slow approach
80 nm
i = 4 mN/m
Bulge
JUMP IN
10 m
t = 0
Coalescence neck formation
FLOW LINES
Rippling t = 1 s
1 m
10 m
Outgrowth t = 10 s
1–10 m/s
TRAPPED PDMS NANO-DROPLETS
Stabilizing (t ≫ 1 min)

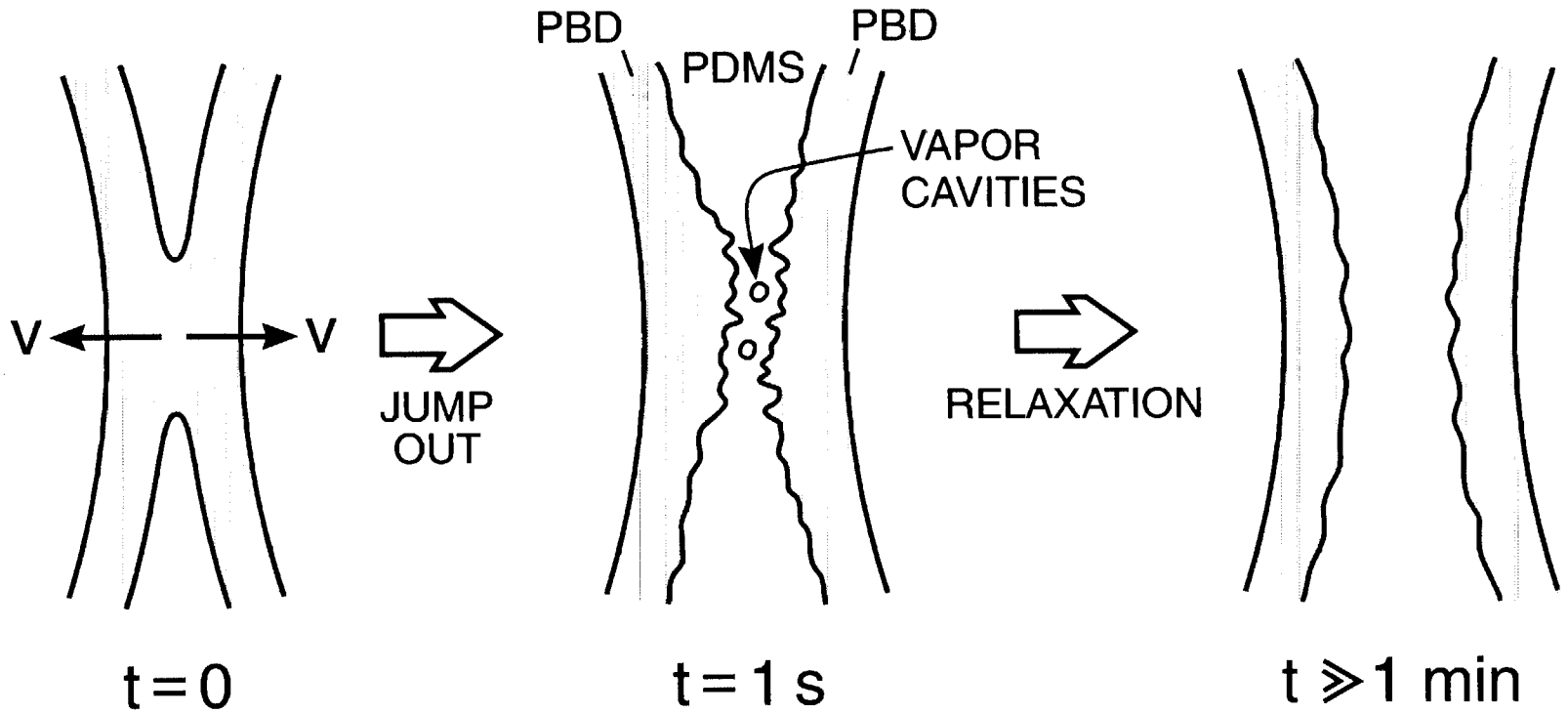
PBD
PDMS
PBD
VAPOR
CAVITIES
V
V
JUMP
OUT
RELAXATION
t = 0
t = 1 s
t ≫ 1 min

Hydrophobic Interactions

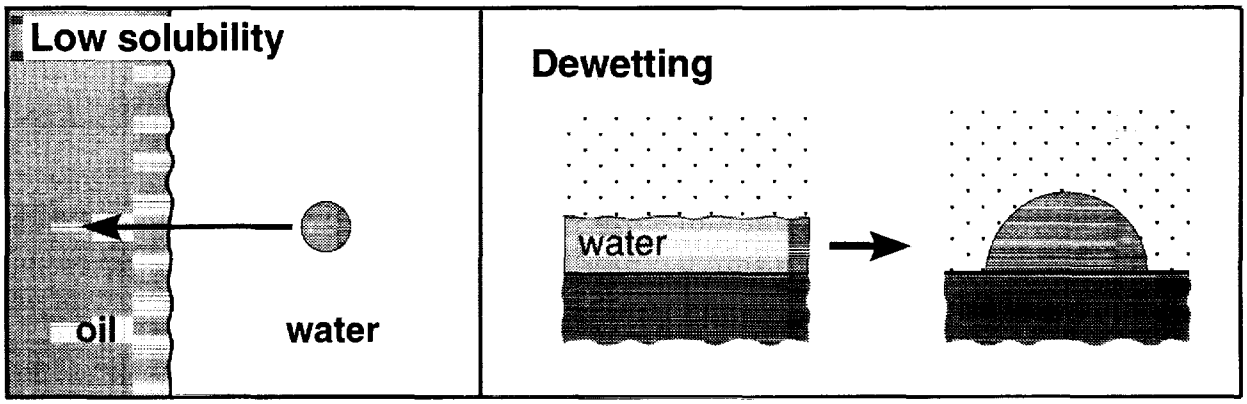

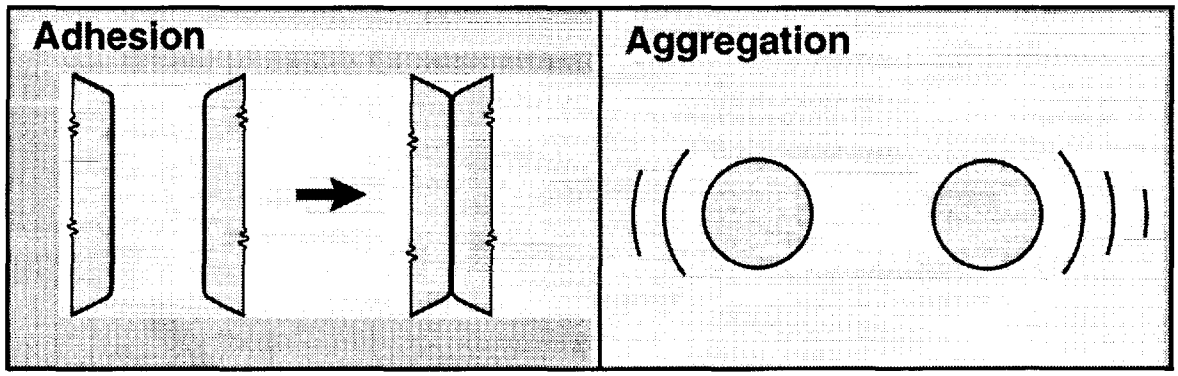

Traditionally,

$$F\mu\ e^{-D/D_0}$$

Hydrophobic Interaction Force Profile

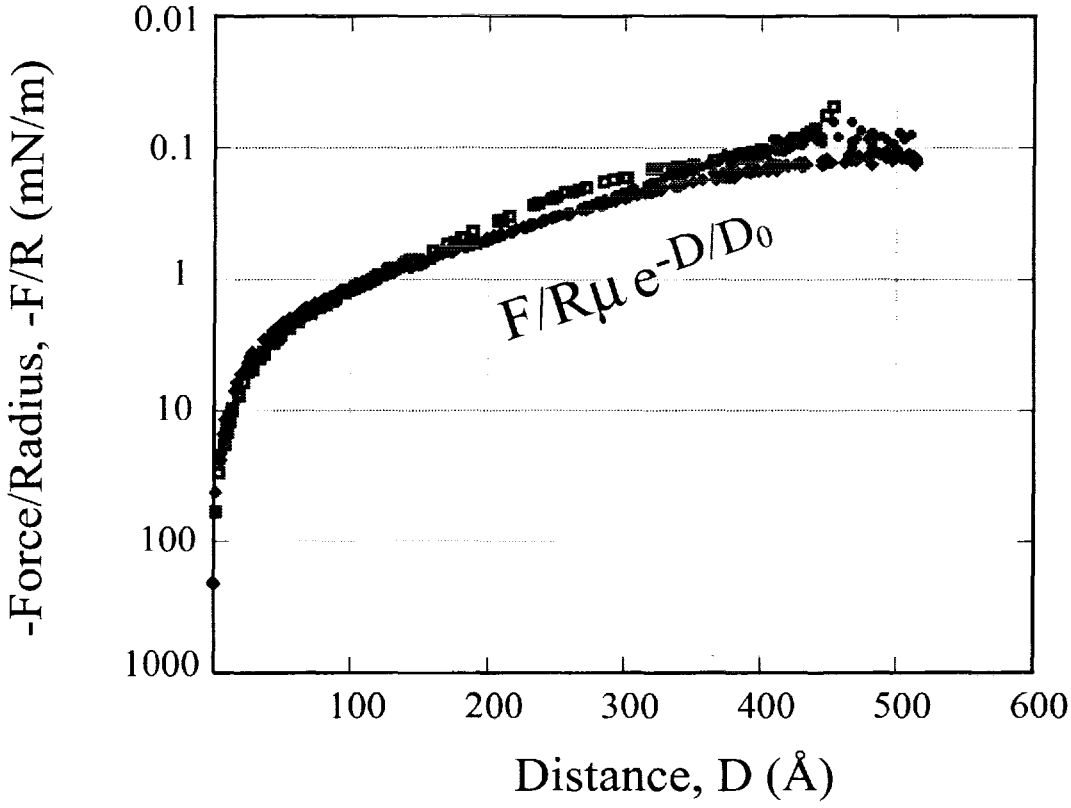

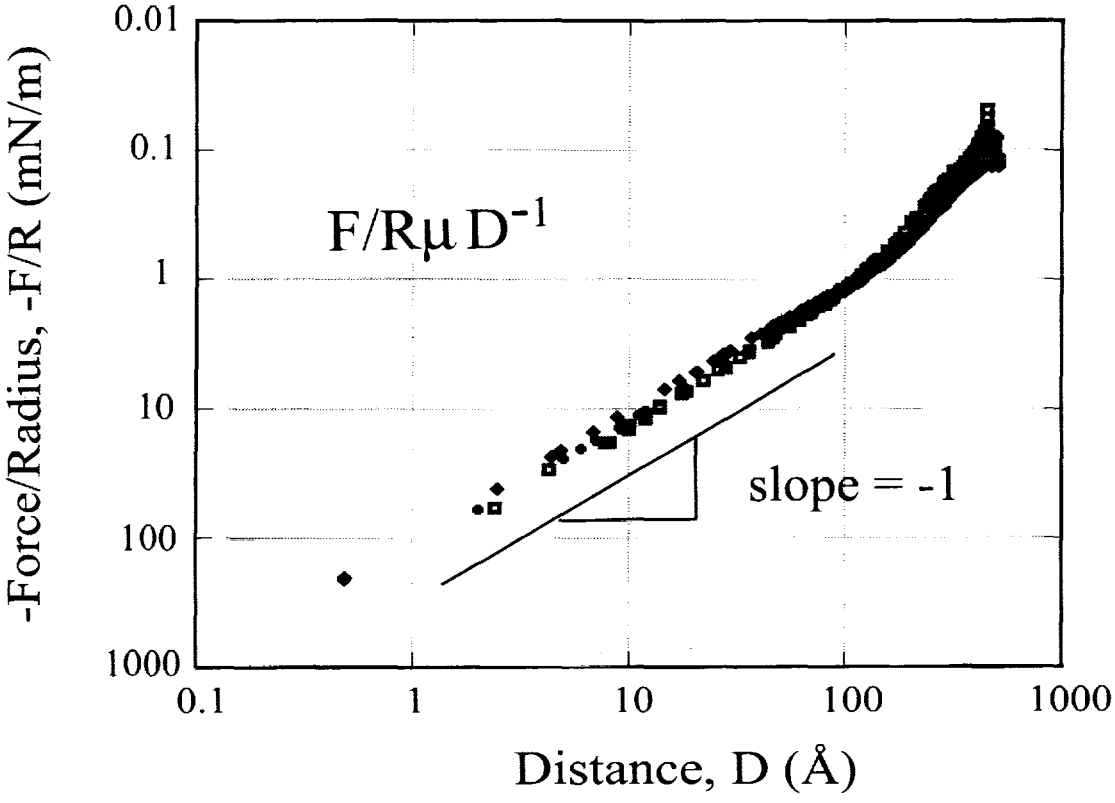

Summary:

- **Experimentally based understanding of flow induced coalescence of drops on the Macro and Microscale**

  $$h_c \sim R^{+1/3}$$

  Intriguing $h_c \sim R^{-1/4}$ **??**

- **Numerical Simulations match well and more improvements in the future**

- **First direct measurement of the hydrophobic interaction as a function of distance to contact**

  $$F \sim \exp(-D/D_0) \quad \text{for } D>150\text{Å}$$

  $$F \sim D^{-1} \quad \text{for } D< 200\text{Å}$$

Macro – **L. Gary Leal, Charles Park, Hong Yang, and Fabio Baldessari**

Micro – **Jacob Israelachvili, Tonya Kuhl**

This work was supported by the Microgravity Science Program of NASA via Grant #NAG 3-2115

August 9, 2000

Session 2A
Multiphase Flow and Phase Change II

Modeling of Transport Processes in a Solid Oxide Electrolyzer Generating Oxygen

G. Tao , K.R. Sridhar , and C.L. Chan
Department of Aerospace and Mechanical Engineering
The University of Arizona, Tucson, AZ 85721

Abstract

Carbon dioxide, the predominant atmospheric constituent on Mars, can be used to produce oxygen using Solid Oxide Electrolyzer Cells(SOEC). The extracted oxygen is of interest for propulsion and life support needs. Several studies have shown that using local resources, ISRU (in-situ resource utilization), can reduce both the launch mass from earth and the landed mass on Mars, thereby providing significant cost savings and reduced risks for future human missions to Mars.

SOEC works on the principle of oxygen ion transport in certain ceramic oxides. The electrochemical cell is made of a solid nonporous oxygen ion conducting electrolyte, such as fully stabilized Zirconia doped with Yttrium(YSZ), that is sandwiched between two porous electrodes. An external DC power supply is applied to the electrodes. The porous electrodes help to form the triple phase boundary (TPB) or electrochemical reaction sites (ERS) that facilitate oxygen transport. TPB or ERS is a location of an interface where an oxygen bearing gas such as carbon dioxide, an electron conductor such as the electrode, and the electrolyte with oxygen ion vacancies intersect. There are several transport processes occurring in a SOEC generating oxygen from carbon dioxide. At cathode side, for example, CO_2 gas impinges on the electrode surface from the bulk flow and then diffuses through the porous electrode. A CO_2 molecule dissociates into oxygen atom and CO. The oxygen atom picks up two electrons from the electrode to become a doubly charged oxygen ion. The oxygen ion, forced by external applied voltage, transports through the vacancies in the crystal lattice of the electrolyte to anode side. The whole process consists of gas diffusion, adsorptive dissociation, electrochemical reaction, and ion migration. Associated with these irreversible processes are three kinds of overpotentials which contribute to the degree of deviation of the cell voltage from its thermodynamic open circuit voltage. The three overpotentials are concentration, activation, and ohmic. Quantification of the different overpotentials is essential to understand the reaction mechanism and to develop efficient SOEC for space applications.

The ohmic overpotential and activation overpotential can be measured by the current interruption method in conjunction with a recording oscilloscope. As the current cut off, the potential differences begin to drop. The voltage drop curve consists of linear and nonlinear parts. The initial linear drop within couple of microseconds corresponds to ohmic losses followed the nonlinear drop which lasts couple seconds account for activation overpotential.

The typical performance characteristics of a SOEC at 800°C is shown in Figure 1. In the beginning, the current density increases with the CO_2 electrode (cathode) potential. Then the current saturates, reaching a plateau for a range of cathode potentials. After the CO_2 electrode voltage exceeds a threshold value, the current density increases sharply. While the CO_2 electrode potential is increased, the anode and cathode activation overpotentials also change as shown in Figure 2. The measured overpotential is the sum of the activation overpotential and ohmic losses. By using the current interruption method at high voltage, we can measure the characteristic

resistance of anode and cathode electrodes and thereby the ohmic overpotetial. From these two measurements, the activation overpotential can be calculated. From the characteristic shapes of the curves shown in Figure 1 and Figure 2, we can classify a cell's typical performance into three regions, namely small current region, constant current region, and high current region.

In region I, the current increases gradually from negative to positive as the CO_2 electrode voltage potential increases in magnitude. The activation overpotential also increases on both sides. The current is caused by the impurity content (O_2, 0.107%) in CO_2 gas source.

In region II, the cell's current stays at a nearly constant level although the CO_2 electrode potential increases in magnitude. The anodic activation overpotential at the oxygen side remains unchanged, while the cathodic overpotential increased sharply. At this point, all O_2 taking part in electrochemical reaction comes from O_2 impurity of CO_2. There is no CO_2 dissociating into CO and O. Because of limited O_2 source, the cell is in a mass limited flow condition. All the increase in applied potential is utilized at the cathode, while the activation overpotential on anode side remains unchanged. The overpotential at the cathode side is still not sufficient to provide the free energy required to crack CO_2.

In region III, the cell's current increases with applied voltage, after the CO_2 electrode voltage reaches a certain threshold value. The activation overpotential at CO_2 side drops sharply, while activation overpotential on the anode side increases. The magnitude of the threshold is a function of temperature. It can be determined by the CO_2 energy of formation and is termed the Nernst potential. In region III the activation overpotentials fit the Tafel plot well. The data on exchange current density and charge transfer coefficients obtained from the Tafel plots can be used to fit the well known Butler Volmer equation.

SOECs have been used in a CO_2 environment to produce O_2. The current-voltage characteristics and overpotentials associated with the process have been measured. Three distinct regions are observed, and been analyzed.

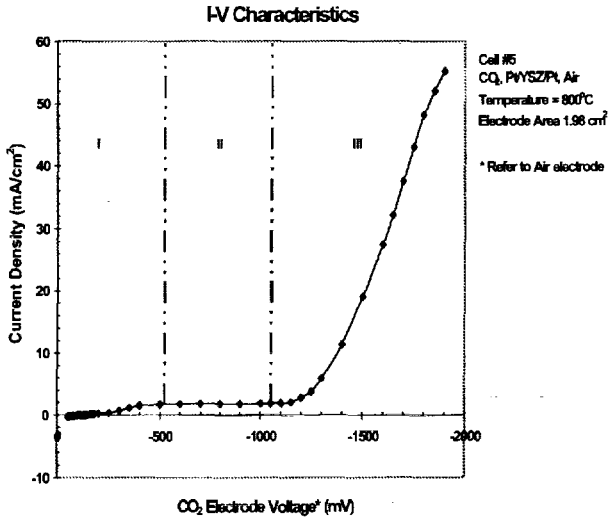

Fig. 1 I-V Characteristic at 800 °C

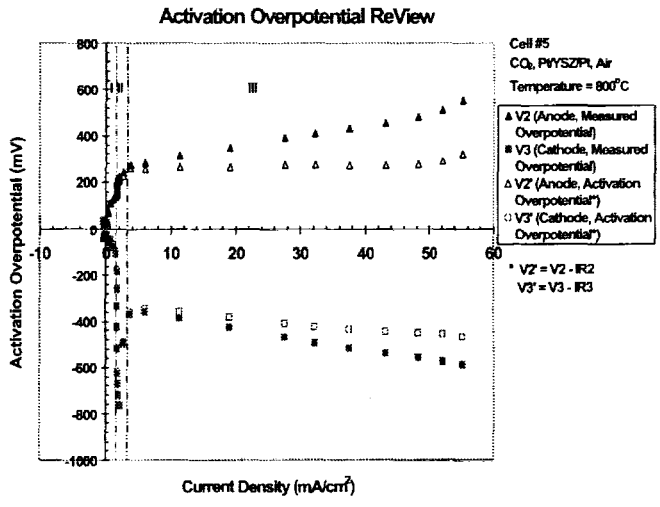

Fig. 2 Activation Overpotential Review

NASA/CP—2000-210470

Modeling of Transport Processes in a Solid Oxide Electrolyzer Generating Oxygen

K. R. Sridhar

C.L. Chan

Gege Tao

NASA/CP—2000-210470

Overview

- **Introduction**
- **Principle of Solid Oxide Electrolysis (SOEC)**
- **Experimental Set-up**
- **Experimental Results and Discussion**
- **Conclusions**
- **Future Work**

- **Certain ceramic oxides conduct oxygen ions at elevated temperatures**

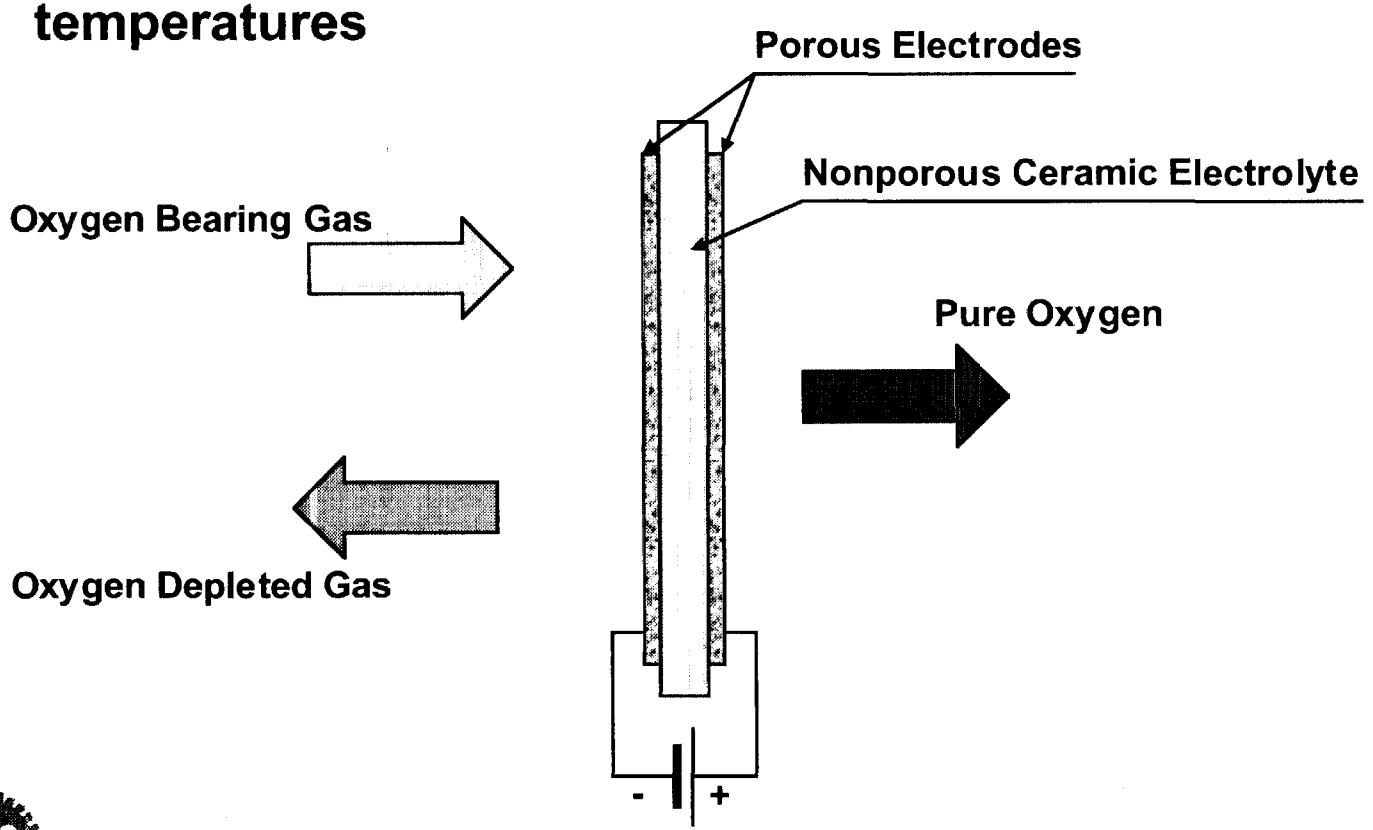

NASA/CP—2000-210470

Crystal Structure of Yttria Stabilized Zirconia (YSZ)

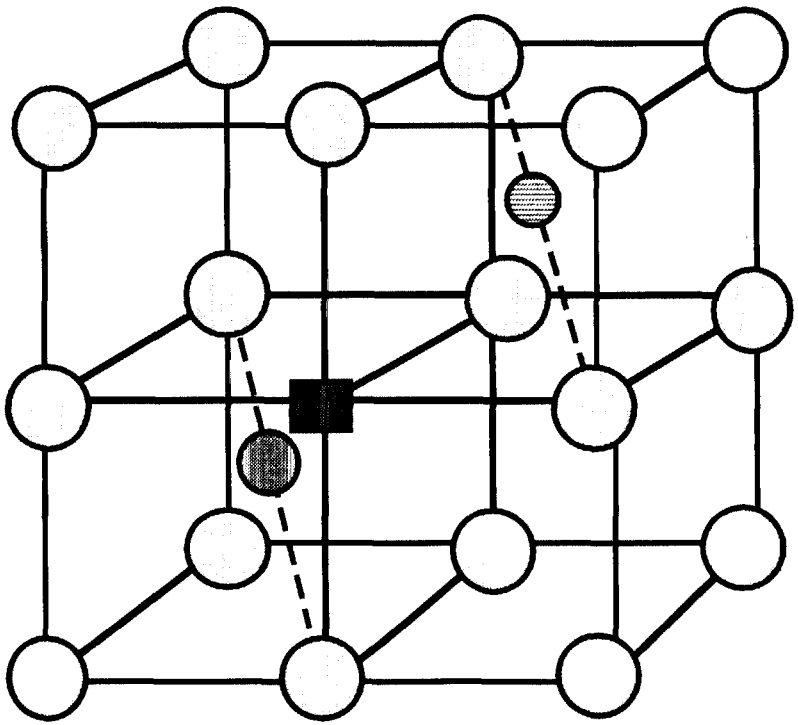

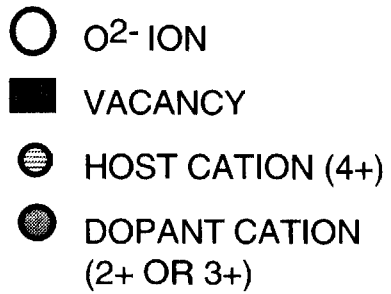

NASA/CP—2000-210470

NASA/CP—2000-210470

Three Phase Boundary (TPB and ERS)

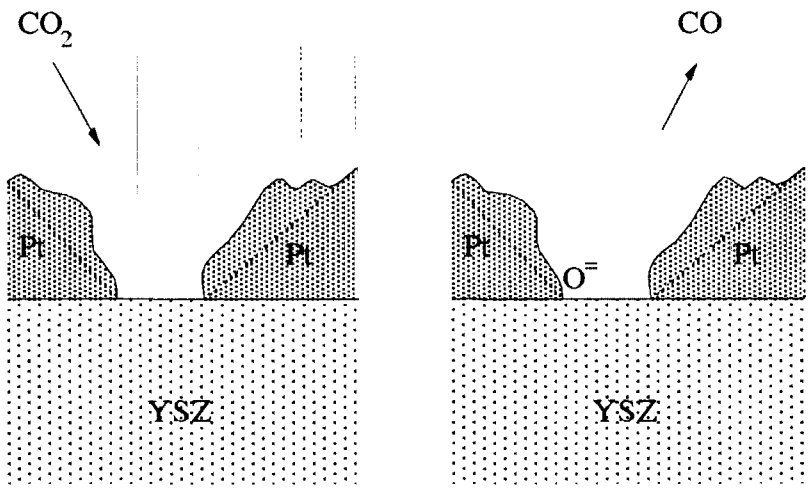

Electrolyzer Stack

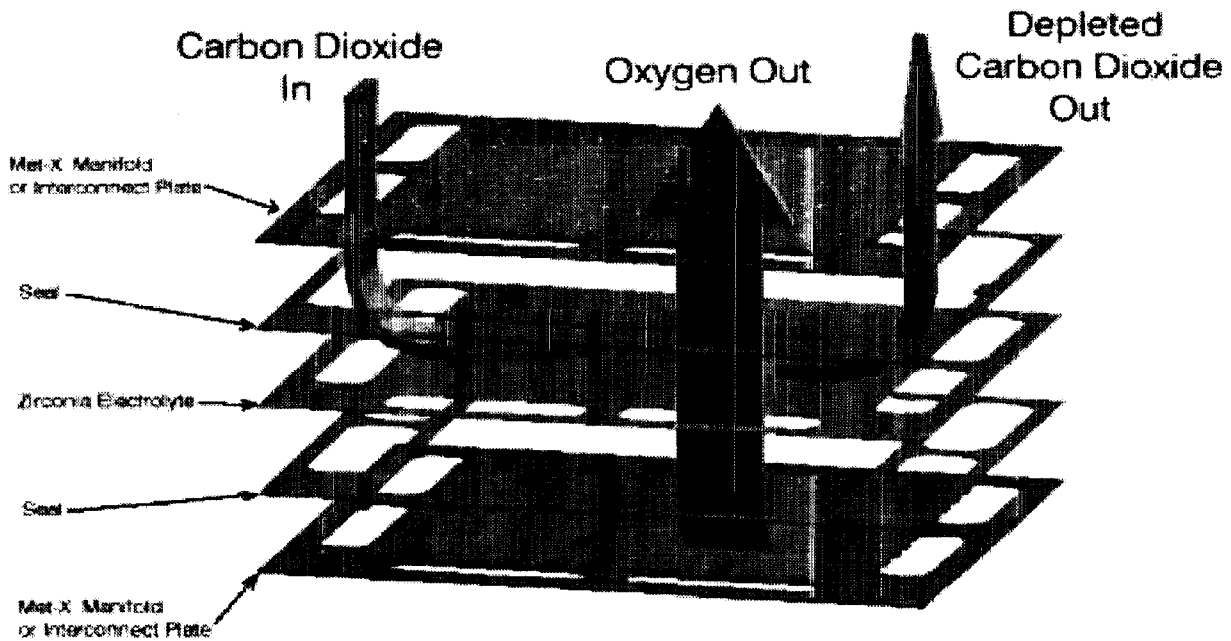

NASA/CP—2000-210470

NASA/CP—2000-210470

Flight Hardware MIP/OGS for Mars Lander

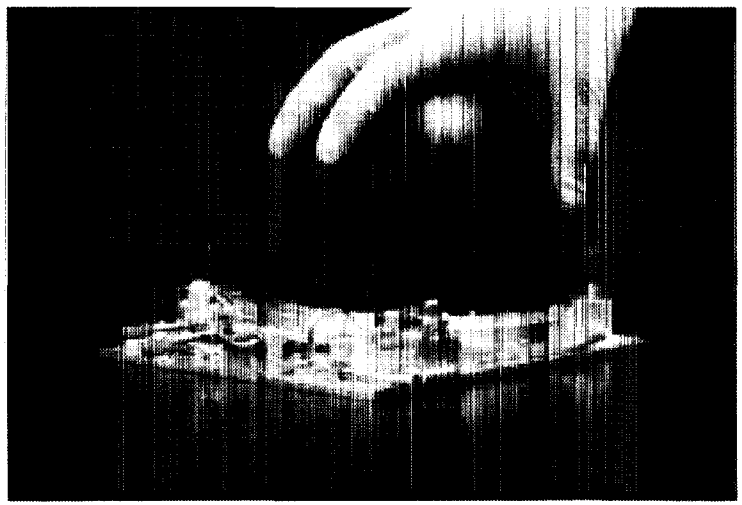

ISRU End-to-End payload for 2005

PROMISE

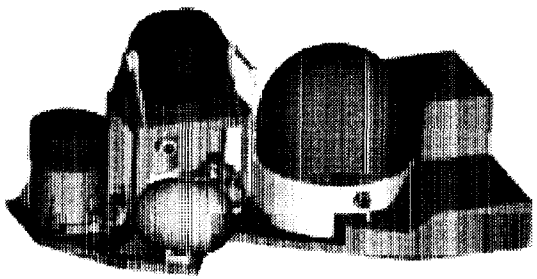

Basic Repeating Element of a SOEC Stack

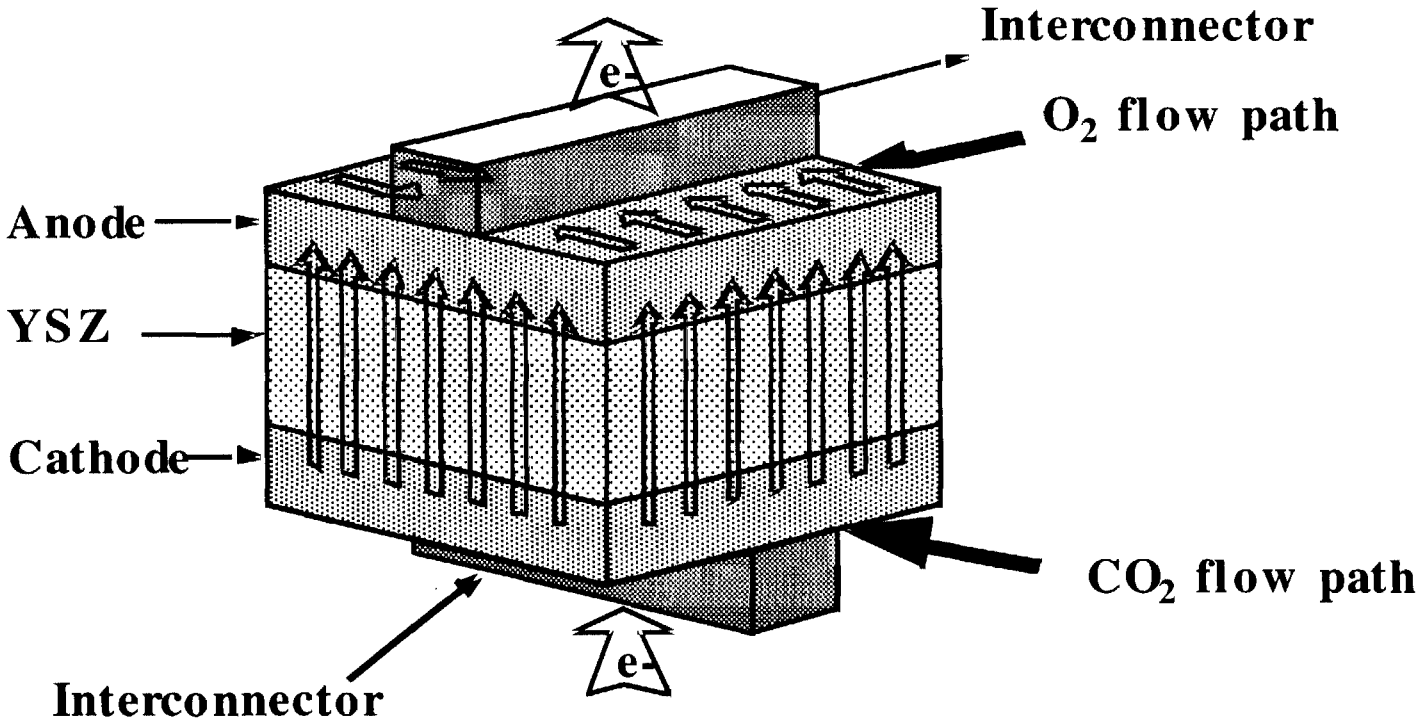

A Plausible Mechanism of Oxygen Transport

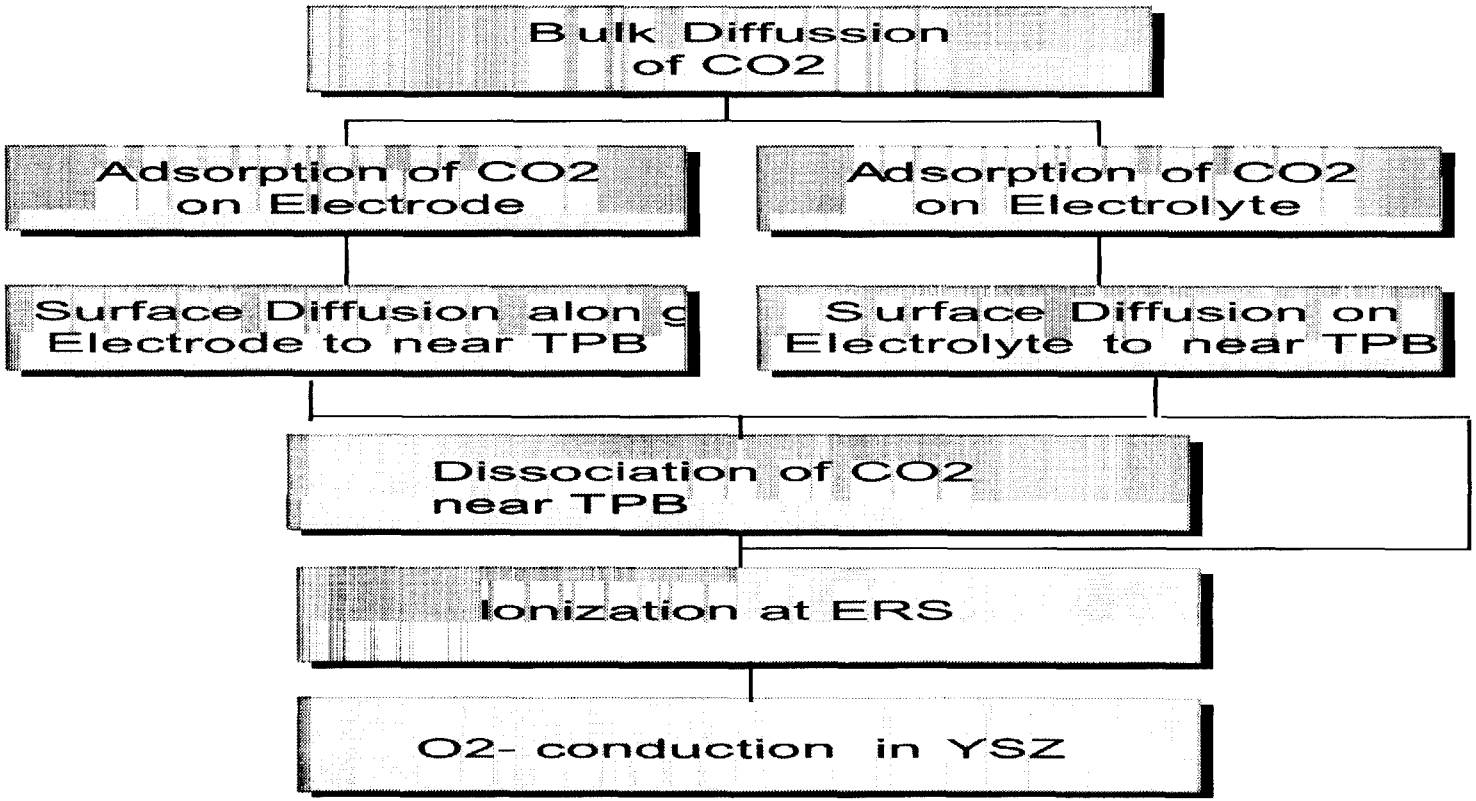

Reactions on the Cathode Side

The Overall reaction on the cathode side

$$CO_{2(g)} + 2e^- \Longrightarrow CO_{(g)} + O^{2-} \quad [1]$$

Plausible Steps:

$CO_{2(g)}$ (bulk gas) $\Rightarrow CO_{2(g)}$ (boundary layer) [2]

$CO_{2(g)}$ (electrode outer surface) $\Rightarrow CO_{2(g)}$ (diffuse into Pt micropore) [3]

$CO_{2(g)}$ (Pt mircropore) $\Rightarrow$ $CO_{2(ads)}$ (adsorbed on Pt particle) [4]

$CO_{2(ads)}$ (on Pt particle surface) $\Rightarrow$ $CO_{2(ads)}$ (transported near TPB) [5]

$CO_{2(ads)}$ (near TPB) $\Rightarrow$ $CO_{(g)}$ + $O_{(ads)}$ (near TPB) [6]

K.R. Sridhar, (520) 621-6111

NASA/CP—2000-210470

$$O_{(ads)}\ (\text{near TPB}) \Rightarrow O_{(ads)}\ (\text{at ERS}) \qquad [7]$$

$$2e^{-}\ (\text{Pt}) \Rightarrow 2e^{-}\ (\text{transport to ERS}) \qquad [8]$$

$$V_O^{\cdot\cdot}\ (ZrO_2) \Rightarrow V_O^{\cdot\cdot}\ (\text{transport to ERS}) \qquad [9]$$

$$O_{(ads)}\ (\text{ERS}) + 2e^{-}\ (\text{ERS}) + V_O^{\cdot\cdot}\ (\text{ERS}) \Rightarrow O_o\ (\text{ERS}) \qquad [10]$$

Where $V_O^{\cdot\cdot}$ is a doubly ionized oxygen vacancy, O_o is an oxygen ion on normal lattice site, and e^- is an excess free electron from electrode.

K.R. Sridhar, (520) 621-6111

NASA/CP—2000-210470

Overpotentials

- Activation overpotential
- Concentration overpotential
- Ohmic losses

$$\eta = \eta_{ohmic} + \eta_{con} + \eta_{act} \qquad [11]$$

Quantification of the different overpotentials is essential to understand the reaction mechanism and to develop efficient SOEC for space applications

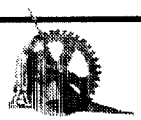

K.R. Sridhar, (520) 621-6111

NASA/CP—2000-210470

Activation Overpotential Measurement

- Current interruption method -- in conjunction with a recording oscilloscope to measure ohmic overpotential and activation overpotential
- The voltage drop curve consists of linear and nonlinear parts
- Linear drop represent ohmic loss, while
- Non-linear drop account for activation overpotential

K.R. Sridhar, (520) 621-6111

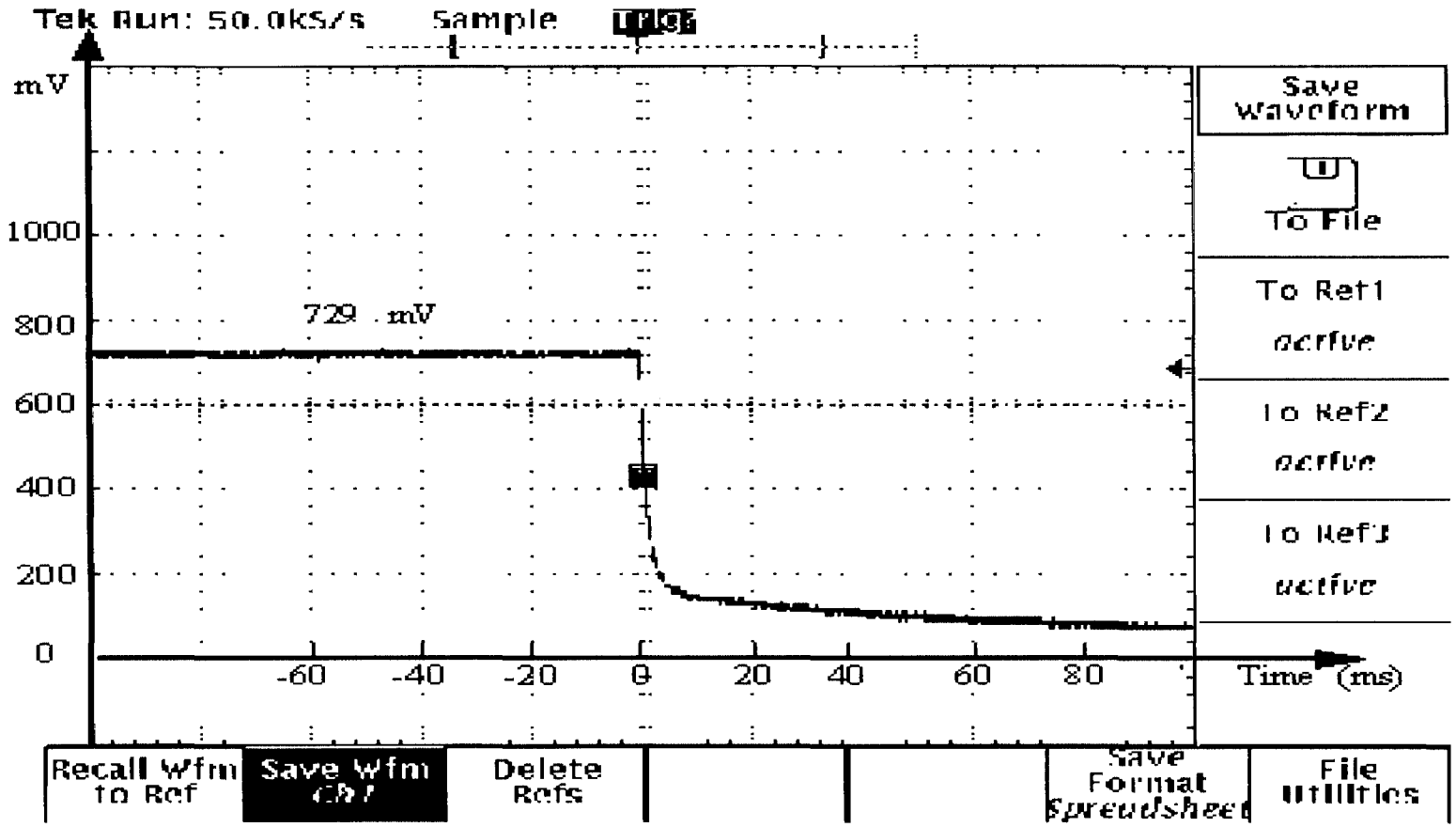

Typical Transient Behavior (trace from current interruption)

K.R. Sridhar, (520) 621-6111

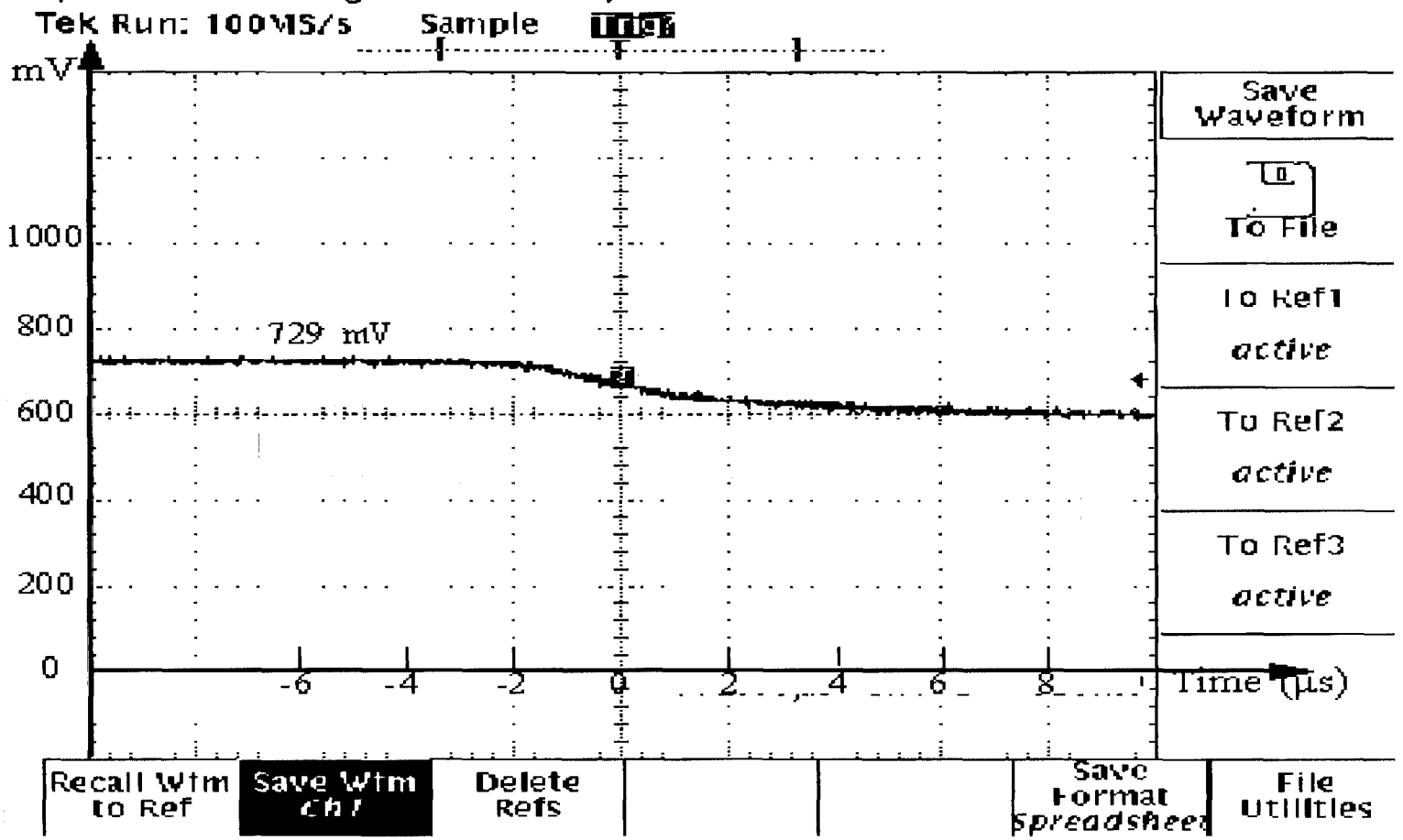

Typical Transient Transient Behavior (small time scale)

K.R. Sridhar, (520) 621-6111

Experimental Setup

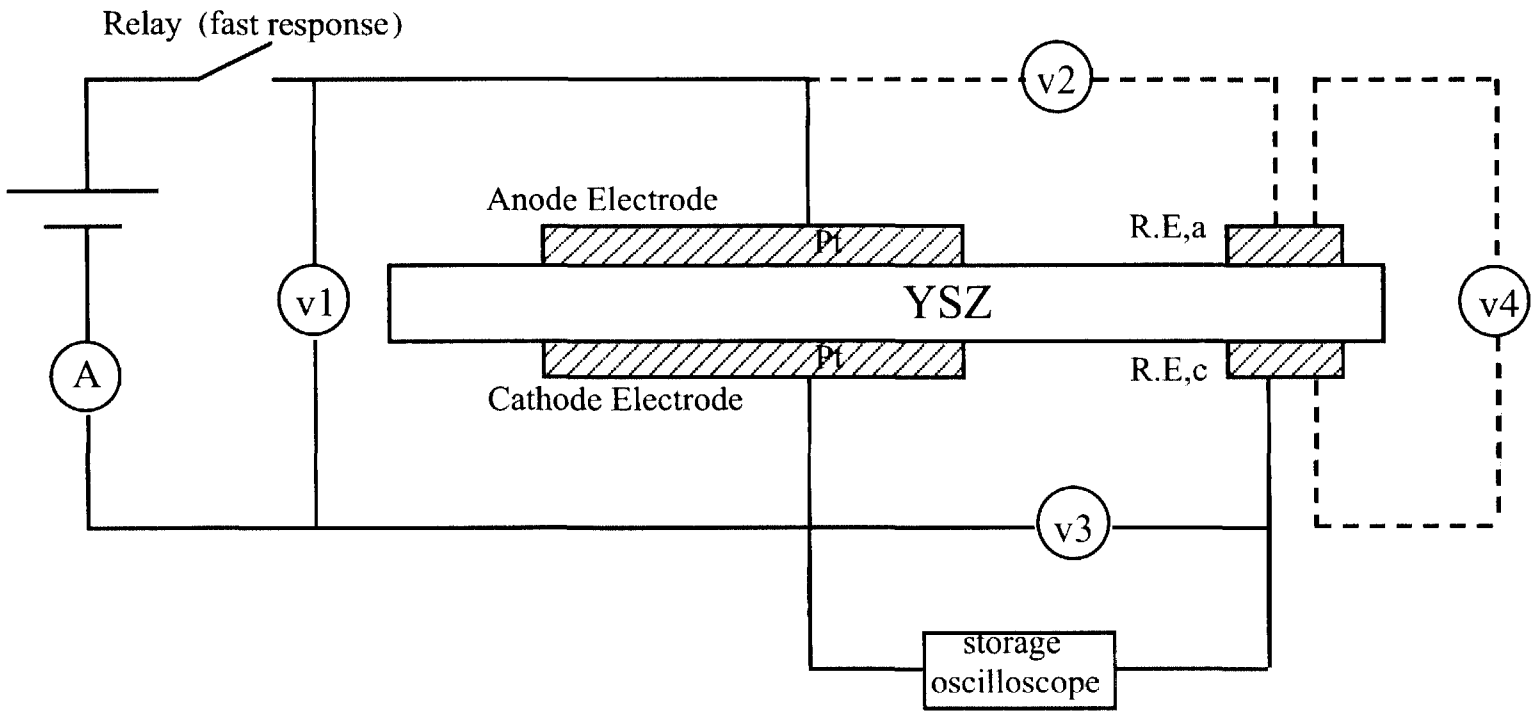

Activation Overpotential Measurement by Current Interruption Method

K.R. Sridhar, (520) 621-6111

Arrangement of Electrodes

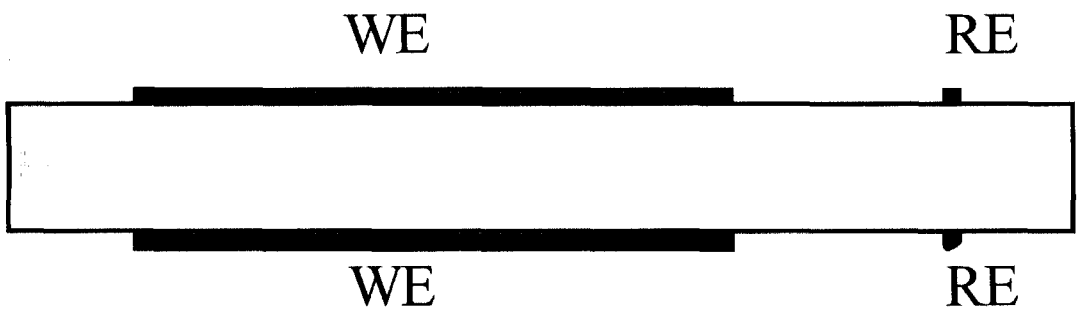

Four - Electrode Arrangement

K.R. Sridhar, (520) 621-6111

NASA/CP—2000-210470

- Electrolyte -- 8% mole YSZ with 300 micrometers thickness
- Electrode -- Pt, ~6 micrometers thickness
- Working Electrode (WE) area -- 1.98 cm^2
- Reference Electrode (RE) area -- 0.02 cm^2
- Distance between WE and RE is ~20 times larger than YSZ thickness

Experimental Equipment

- HP 6641A system DC power supply to provide constant cell voltage
- Tektronix TDS 420 digitizing oscilloscope to record voltage drop signal
- Fluke with high input impedance to monitor steady state potential
- Solid state relay (SSR) for quick response switch
- Tektronix differential preamplifier to eliminate noise
- MTI gas chromatography to measure reaction gas composition

K.R. Sridhar, (520) 621-6111

NASA/CP—2000-210470

Experimental Results and Discussion

Current-Voltage (I - V) Characteristic

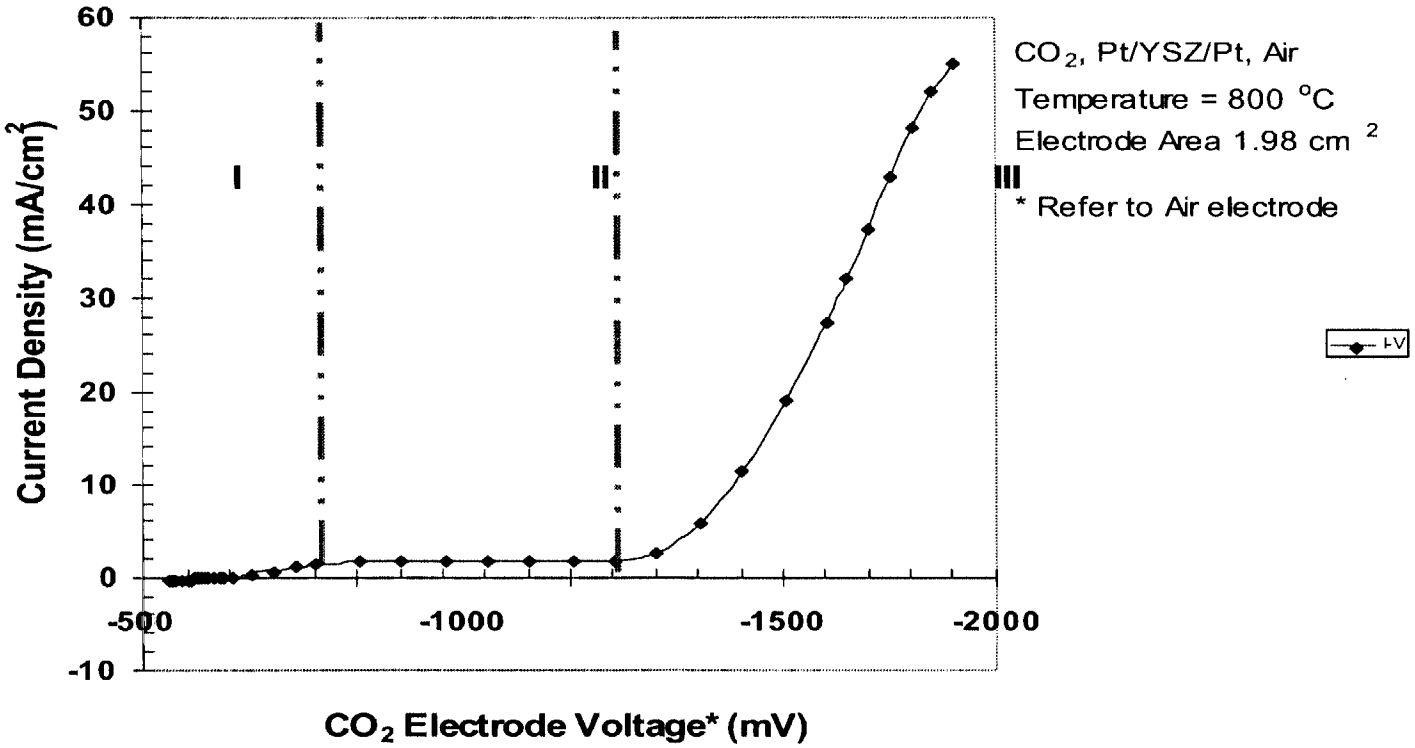

K.R. Sridhar, (520) 621-6111

NASA/CP—2000-210470

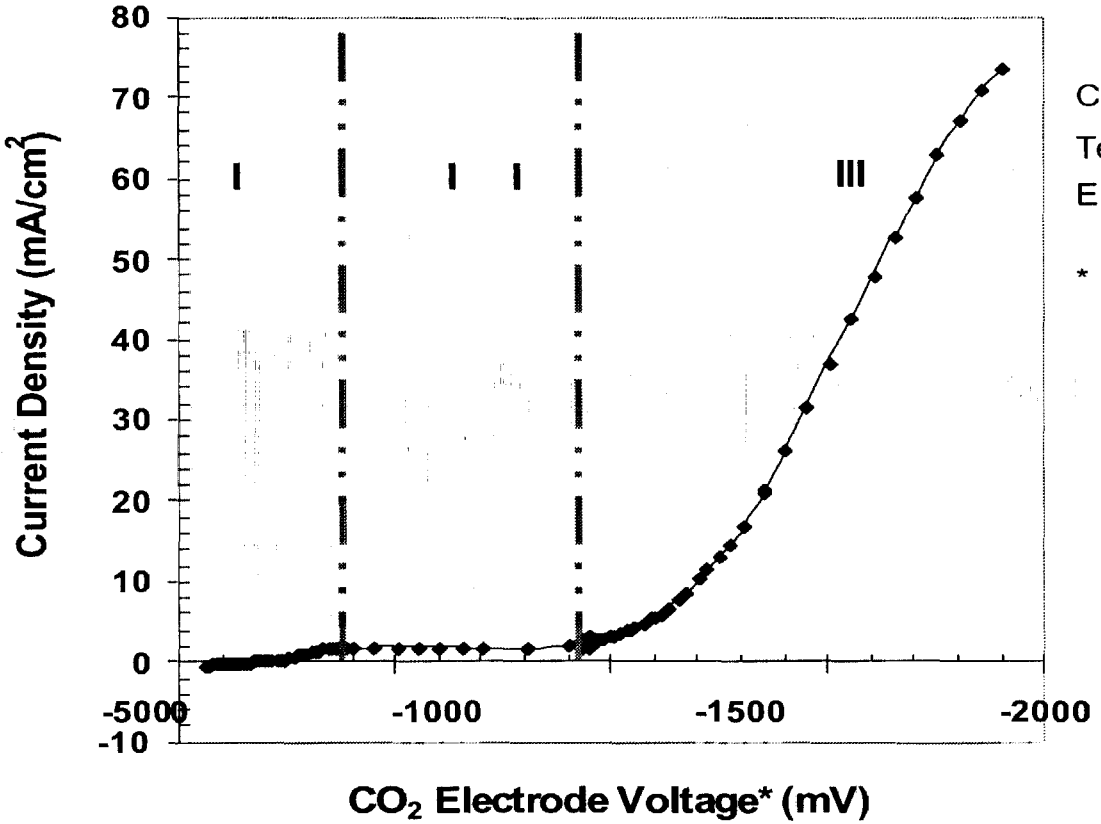

CO_2, Pt/YSZ/Pt, Air

Temperature = 850 °C

Electrode Area 1.98 cm^2

* Refer to Air electrode

Activation Overpotential

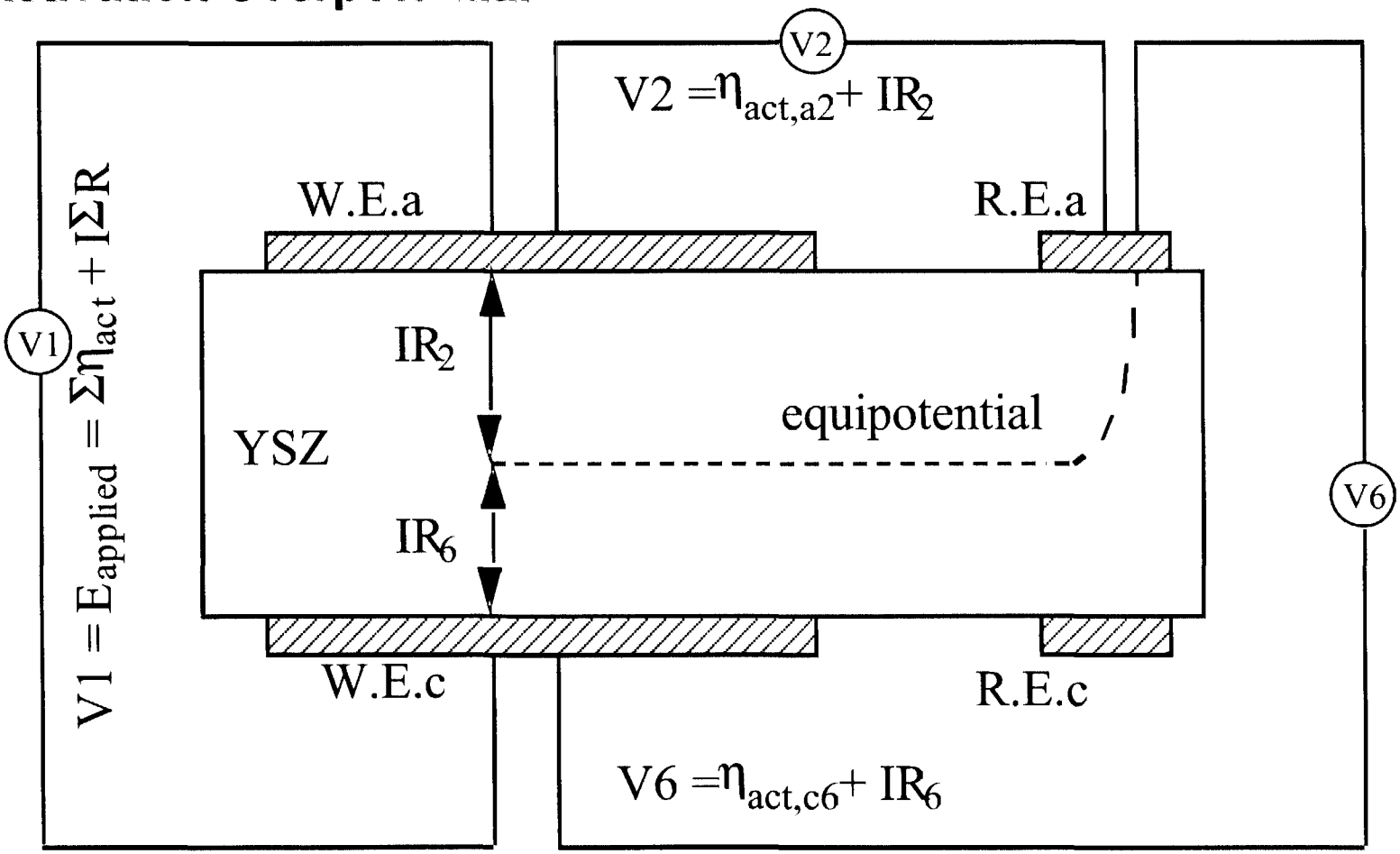

K.R. Sridhar, (520) 621-6111

NASA/CP—2000-210470

$V1 = E_{applied} = \Sigma\eta_{act} + I\Sigma R;$

$V2 = \eta_{act,a2} + IR_2;$ **

$V3 = \eta_{act,c3} + IR_3;$

$V5 = \eta_{act,a5} + IR_5;$

$V6 = \eta_{act,c6} + IR_6;$

V1 is input potential by HP DC power supply (constant voltage control)

V2, V3, V5 and V6 are overpotential directly measured by Fluke, which count ohmic loss and activation overpotential.

R_2 is ohmic loss between W.E.a and the equipotential line of R.E.a.

R_2 is calculated from ** and the current interruption method results.

K.R. Sridhar, (520) 621-6111

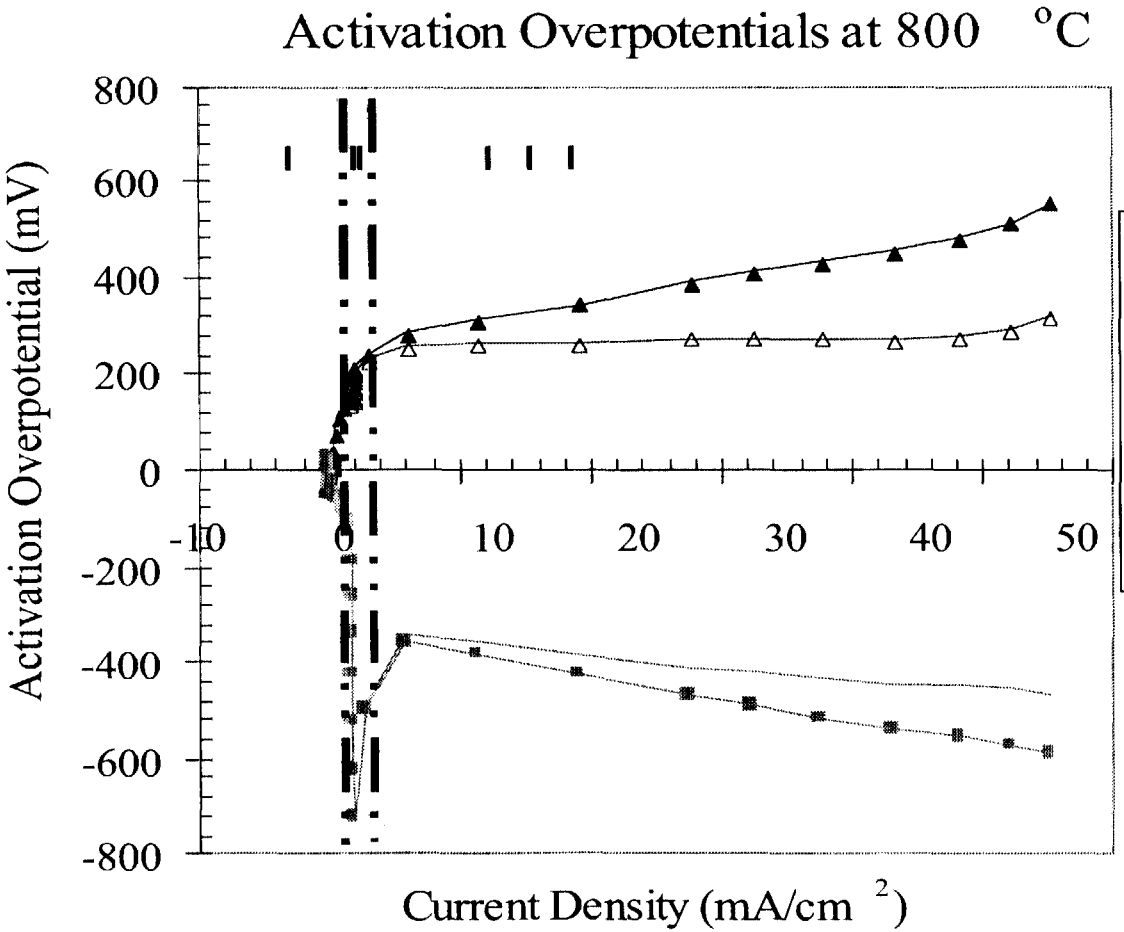

CO_2, Pt/YSZ/Pt, Air

Temperature = 800 °C

- V2 (Anode, Measured Overpotential)
- V2' (Anode, Activation Overpotential*)
- V3 (Cathode, Measured Overpotential)
- V3' (Cathode, Activation Overpotential*)

* $V2' = \eta_2 = V2 - IR_2$

$V3' = \eta_3 = V3 - IR_3$

K.R. Sridhar, (520) 621-6111

NASA/CP—2000-210470

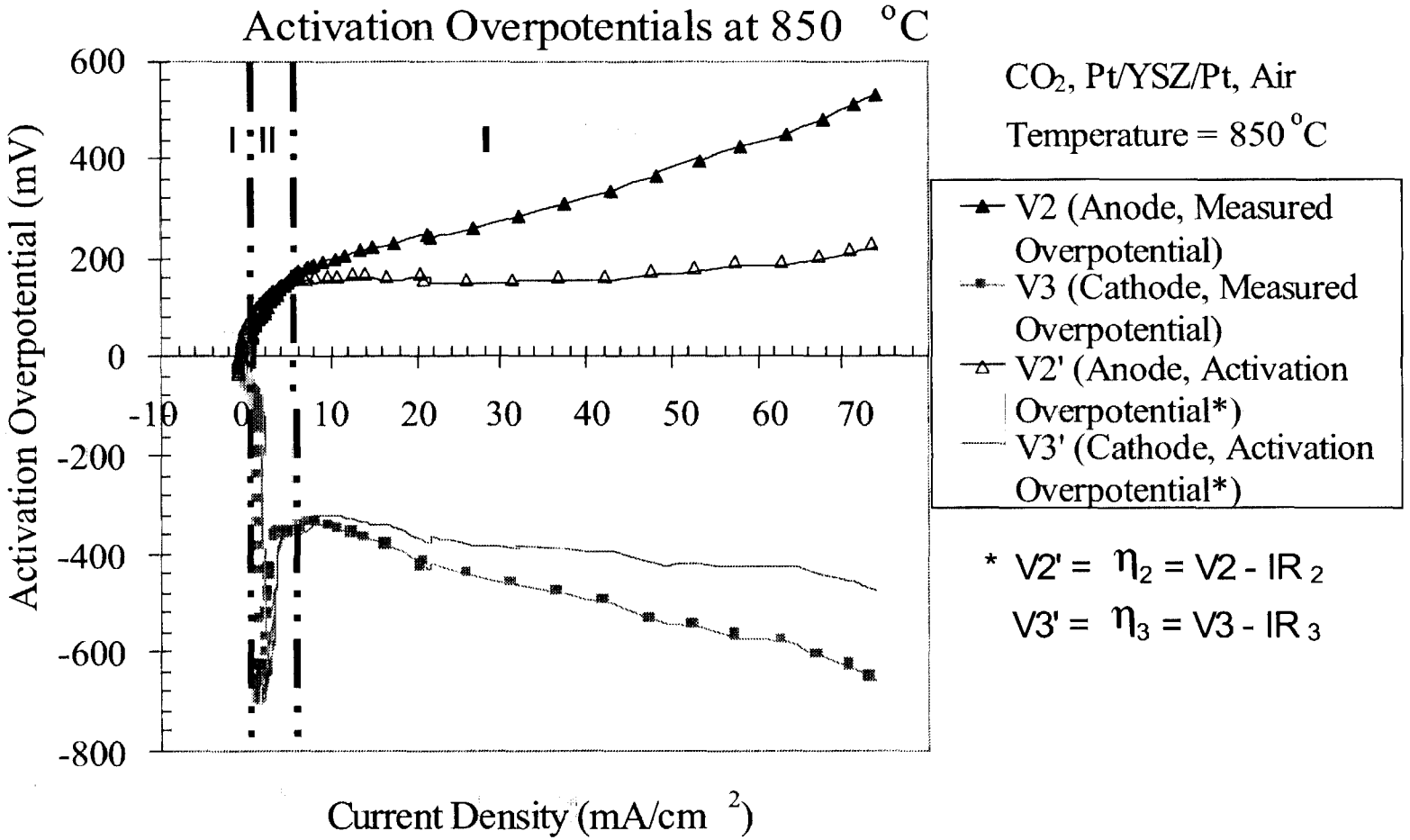

K.R. Sridhar, (520) 621-6111

NASA/CP—2000-210470

Activation Overpotential Results

A: Region I -- Small Current Region

Air, Pt / YSZ / Pt, Air

B: Region II -- Constant Current Region

Current is limited by impurity of O_2 diffusion at cathode side (0.107% of O_2)

C: Region III -- High Current Region

Charge transfer limits reaction rate

K.R. Sridhar, (520) 621-6111

NASA/CP—2000-210470

4.4 Butler Volmer Equation and Data Fitting

$$i = i_{o,a}\left\{\exp\left(\frac{\alpha_{a,a} F \eta_{act,a}}{RT}\right) - \exp\left(\frac{\alpha_{c,a} F \eta_{act,a}}{RT}\right)\right\} \quad [12]$$

For anode side, where $i > 0$, and $\eta_{act,a} > 0$

$$i = i_{o,c}\left\{\exp\left(\frac{\alpha_{a,c} F \eta_{act,c}}{RT}\right) - \exp\left(\frac{\alpha_{c,c} F \eta_{act,c}}{RT}\right)\right\} \quad [13]$$

For cathode side, where $i < 0$, and $\eta_{act,c} < 0$

NASA/CP—2000-210470

Where R is universal gas constant, F is Faraday's constant, T is the cell working temperature.

I is cell's current density, η_{act} is activation overpotential obtained by current interruption method.

$i_{o,a}$, and $i_{o,c}$ are exchange current density.

$\alpha_{a,a}$, $\alpha_{c,a}$, and $\alpha_{a,c}$, $\alpha_{c,c}$ are transfer coefficients of anode and cathode respectively.

Bockris model: $\alpha_{a,a} + \alpha_{c,a} = 2$; $\alpha_{a,c} + \alpha_{c,c} = 2$

K.R. Sridhar, (520) 621-6111

NASA/CP—2000-210470

Two approximations Eq. 12 and Eq. 13:

- Small η:

  linearize Eqs. as

$$\frac{i}{i_o} = \frac{(\alpha + \alpha_c)F}{RT}\eta_{act} \qquad [14]$$

- Large η:

  Tafel plots

$$\eta_{act} = \frac{RT}{\alpha F}\ln\left(\frac{i}{i_o}\right) \qquad [15]$$

K.R. Sridhar, (520) 621-6111

NASA/CP—2000-210470

Butler Volmer Equation Fitting Experimental Data

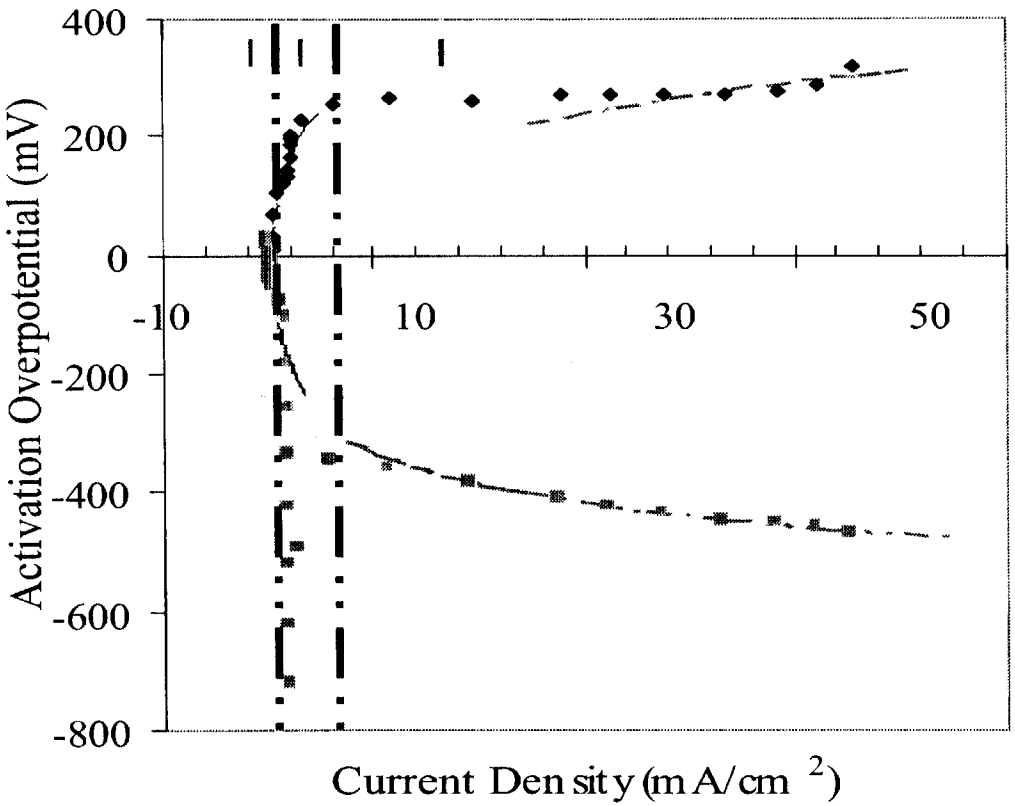

CO_2, Pt / YSZ / Pt, Air

Temperature = 800 °C

- V2' (Anode, Activation Overpotential)
- V2' (Butler Volmer Eq. Fitting Region I)
- V2' (Butler-Volmer Eq. Fitting Region III)
- V3' (Cathode, Activation Overpotential)
- V3' (Butler Volmer Eq. Fitting Region I)
- V3' (Butler Volmer Eq. Fitting Region III)

* $V2' = \eta_2$, $V3' = \eta_3$

Butler Volmer Equation Fitting Experimental Data (800 °C)

K.R. Sridhar, (520) 621-6111

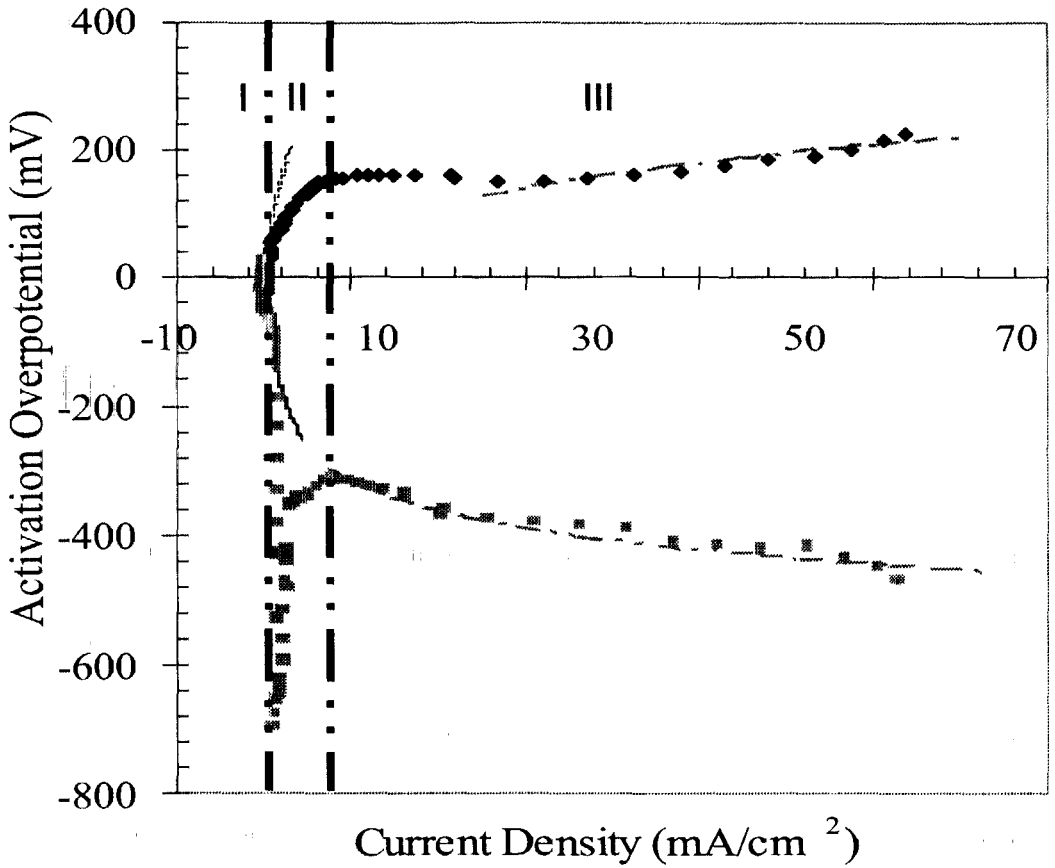

CO_2, Pt/YSZ/Pt, Air

Temperature = 850°C

- V2' (Anode, Activation Overpotential)
- V2' (Butler-Volmer Eq. Fitting Region I)
- V2' (Butler-Volmer Eq. Fitting Region III)
- V3' (Cathode, Activation Overpotential)
- V3' (Butler-Volmer Eq. Fitting Region I)
- V3' (Butler-Volmer Eq. Fitting Region III)

* $V2' = \eta_2$, $V3' = \eta_3$

Butler Volmer Equation Fitting Experimental Data (850 °C)

K.R. Sridhar, (520) 621-6111

NASA/CP—2000-210470

NASA/CP—2000-210470

Region I

	$i_{0,a}$ (mA/cm^2)	$\alpha_{a,a}$	$\alpha_{c,a}$	$i_{0,c}$ (mA/cm^2)	$\alpha_{a,c}$	$\alpha_{c,c}$
800 °C	0.3544 1	1 -0.		2678	1 1	
850 °C	0.363 1	1 -0	319 1	1		

Region III

	$i_{0,a}$ (mA/cm^2)	$\alpha_{a,a}$	$\alpha_{c,a}$	$i_{0,c}$ (mA/cm^2)	$\alpha_{a,c}$	$\alpha_{c,c}$
800 °C	3.031 0.886	1.114	-0.129 0.79	1.21		
850 °C	5.667 1	168 0.832	-0.084	0.532 1.468		

Conclusion

Successful measurement of activation overpotential and ohmic losses.

Three regions of cell's performance:

In region I the charge transfer steps control the reaction rate.

In region II, the gas surface diffusion in the electrode/electrolyte interface is the rate determining step.

In region III, charge transfer steps control the reaction rate.

Butler Volmer Equation can describe the reaction rates and also to predict SOEC performance and O_2 production.

K.R. Sridhar, (520) 621-6111

NASA/CP—2000-210470

Future Work

Analyze electrode structure to model different transport processes in these three regions

Improve electrode and electrolyte to increase ERS, decrease activation overpotential and increase O_2 production rate.

K.R. Sridhar, (520) 621-6111

NASA/CP—2000-210470

PRODUCTION AND REMOVAL OF GAS BUBBLES IN MICROGRAVITY

H.N. Oguz
Johns Hopkins University
Department of Mechanical Engineering
Baltimore, MD 21218

ABSTRACT

This study focuses on two topics relevant in many microgravity applications: formation of gas bubbles from orifices in tubes and removal of individual bubbles from liquids. Bubble injection from an axisymmetric slot is investigated experimentally and numerically. Three dimensional boundary integral simulations of bubble injection from multiple holes along the axial direction of a tube have also been carried out. Several difficulties encountered in the numerical modeling of these flows have been overcome and a stable method has been developed. The main difficulty is the tendency of a growing bubble to touch nearby solid surfaces. An artificial force is introduced to keep bubbles away from the walls and continue the computations without affecting the main characteristics of the problem. It has been observed that downstream bubbles detach earlier when all bubbles start growing at the same time. This is expected because the average flow rate seen by downstream bubbles is higher than the ones seen by upstream bubbles. Bubble shapes obtained from normal gravity experiments are shown in fig. 1. Simulations under similar flow condition (fig. 2) [1] reproduce this flow.

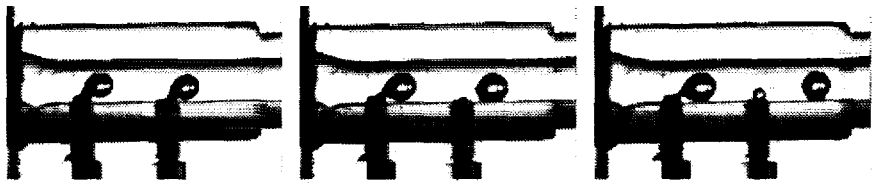

Figure 1. Images of bubble formation from two needles of 0.4-mm radius embedded in a tube of 1.6-mm radius. The average water velocity is 21 cm/s.

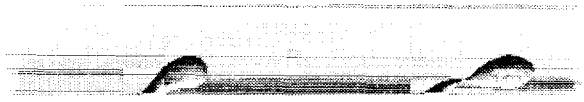

Figure 2. Three-dimensional simulations of multiple bubble formation in a tube. The average velocity is 20 cm/s.

A series of experiments have been carried out to investigate gas injection from an axisymmetric slot in a tube under normal gravity conditions. Three distinct regimes of operation as a function of the gas/liquid flow rate ratios are observed. At high gas flow rates, the injected gas completely fills the tube and blocks the liquid flow. A Taylor bubble is generated in this regime. When the liquid flow rate becomes comparable to the gas injection rate, axial symmetry is broken and a regular single bubble forms. This is

identified as the second regime where the liquid flow is not interrupted by the gas. At even higher liquid flow rates, turbulent conditions and chaotic multi-bubble formations are observed. This is the third regime. Illustrative pictures for these regimes are shown in fig 3.

(a) (b) (c)

Figure 3. Three regimes of bubble injection from a slot: (a) Taylor bubble, (b) single bubble, and (c) chaotic.

An axisymmetric boundary integral code is employed to simulate this flow. Because of the imposed symmetry the range of validity of the simulations were somewhat limited but the results are useful in understanding the basic dynamics of the problem. Simulations suggest the existence of a stable liquid column inside the bubble. Assuming that the bubble front moves with the same velocity as the liquid column, an equilibrium condition that admits one stable solution is derived [2].

Although there have been many investigations of the formation of bubbles from an underwater orifice, the opposite case, i.e. removal of bubbles by an orifice, has received very little attention. The dynamics of a bubble entering a capillary tube is studied. A stream of sparsely spaced bubbles generated from an underwater orifice is positioned just below a capillary tube that is connected to a vacuum reservoir. Sufficiently small bubbles are captured in the capillary. In some cases, a small bubble detaches from the back of the main one as a result of severe surface deformation near the entrance of the capillary. Larger bubbles, on the other hand, break in two while being drawn into the capillary. A boundary integral technique is employed to simulate this process. An artificial repulsive force is introduced to form a thin layer of water around the bubble in the capillary tube. With this scheme, it is possible to simulate bubble motion both outside and inside the capillary. Numerical bubble shapes are found to be in very good agreement with experiment.

REFERENCES

[1] ``Development of a three dimensional boundary integral method and its application to bubble formation from submerged orifices" Jun Zeng Ph.D. Thesis Department of Mechanical Engineering, Johns Hopkins University 1999.

[2] ``Gas bubble injection from an axisymmetric slot in a tube" H.N. Oguz, APS Meeting, New Orleans, LA. November 21-23, 1999.

Presentation not available at time of printing.

Using Surfactants to Control Bubble Coalescence in Nucleate Pool Boiling

Kathleen J. Stebe, Department of Chemical Engineering, Johns Hopkins University, 3400 North Charles Street, Baltimore, MD 21218 kjs@jhu.edu

R. Balasubramaniam, NCMRfc/ NASA Glenn Research Center, 21000 Brookpark Road, Cleveland, Ohio 44135 bala@lerc.nasa.gov

Nucleate boiling is the preferred mode of heat transfer in heat exchangers operating not only on the earth, but also in reduced gravity conditions, where the size of the heat exchanger is constrained. In nucleate boiling, large amounts of heat are transported with small changes in the system temperature as consequence of the latent heat of vaporization. For efficient operation in this regime, the dynamics of the vapor bubbles must be understood and controlled. It has been established experimentally that vapor bubble dynamics are strongly influenced by surfactant additives in that greater heat fluxes are realized at smaller superheat. This effect, however, is non-monotonic in surfactant concentration and depends strongly on the degrees superheat, which determine the rate of bubble growth and detachment.

The aim of this work is to understand the mechanisms behind the non-monotonic heat flux improvement caused by the surfactant additives, and to identify regimes which promote improved heat flux. Surfactants adsorb at fluid interfaces, where they reduce the surface tension and give rise to Marangoni stresses when the rate of surfactant mass transfer is slow compared to the prevailing surface convective flux at the vapor-liquid interface. Surfactant also adsorbs at solid substrates, changing the balance of surface tensions and interfacial energies that determine the wetting conditions on the solid substrate. As bubbles grow, they create liquid-vapor interface. If surfactant transport to these interfaces is far slower than the rate of bubble growth and detachment, surfactant will be ineffective in changing the bubble dynamics. If the mass transfer rates are comparable, reduced surface tensions and Marangoni stresses both favor the formation of smaller bubbles which detach more easily, and hence higher heat flux. If surfactant mass transfer is far faster than the bubble growth rate, the surface tension will be reduced, but no Marangoni stresses will occur. Therefore, it is imperative to understand the surfactant mass transfer kinetics and the hydrodynamic behavior of the growing vapor bubble as a function of surfactant concentration in order to control this process.

We propose to study the dependence on surfactant concentration of the bubble formation, growth and detachment both numerically and experimentally. Ground-based, drop-tower and flight experiments are proposed. In the laboratory, the wetting conditions on the solid surface will be varied independently in a controlled manner using self-assembled monolayers (SAMs). The equilibrium and dynamic surface tension for surfactant systems will be studied for temperatures of interest, where data are extremely scarce. The dynamics of individual vapor bubbles will be studied both in the laboratory and in drop tower experiments. Bubble coalescence will be studied as a function of surfactant properties by creating two neighboring nucleation sites of the substrates. In the numerical modeling of this process, the surfactant effects on the stress conditions at a strongly deforming bubble interface will be studied for a single bubble growing on a heated surface. This is a problem in which the surfactant mass transfer, the temperature field and the momentum equation are coupled. The surfactant data obtained in the laboratory, including the surface equation of state which relates the surface tension to the local surface concentration and the surfactant mass transfer kinetics, will provide the material parameters required in the numerical model.

Using Surfactants to Control Bubble Growth and Coalescence in Nucleate Pool Boiling

Kathleen J. Stebe
The Johns Hopkins University

R. Balasubramaniam
NCMR / NASA Glenn Research Center

Nivedita R. Gupta
The Johns Hopkins University

Surfactants and Heat Transfer

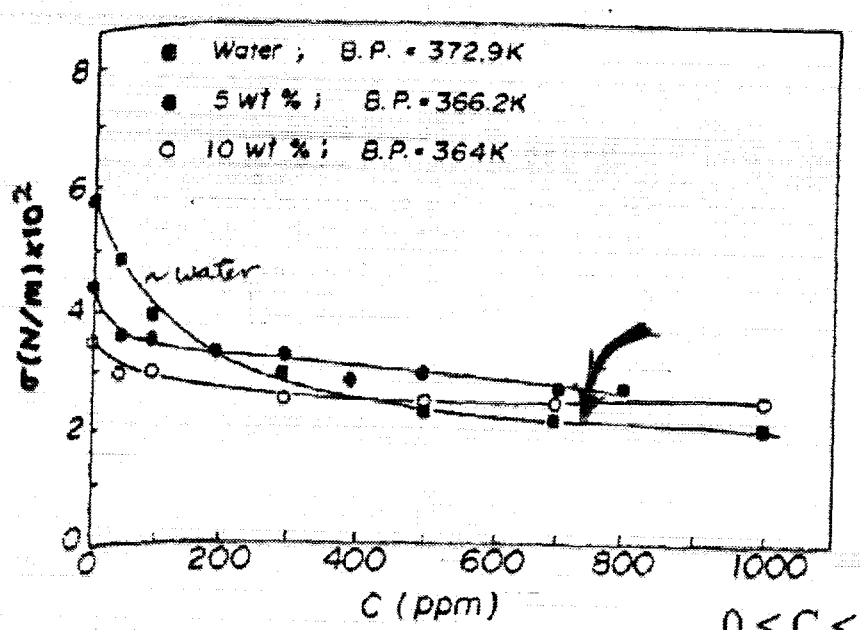

$\int \theta(C)$
$\{$ nucleation (C)

$0 < C < 2000$ ppm
SDS

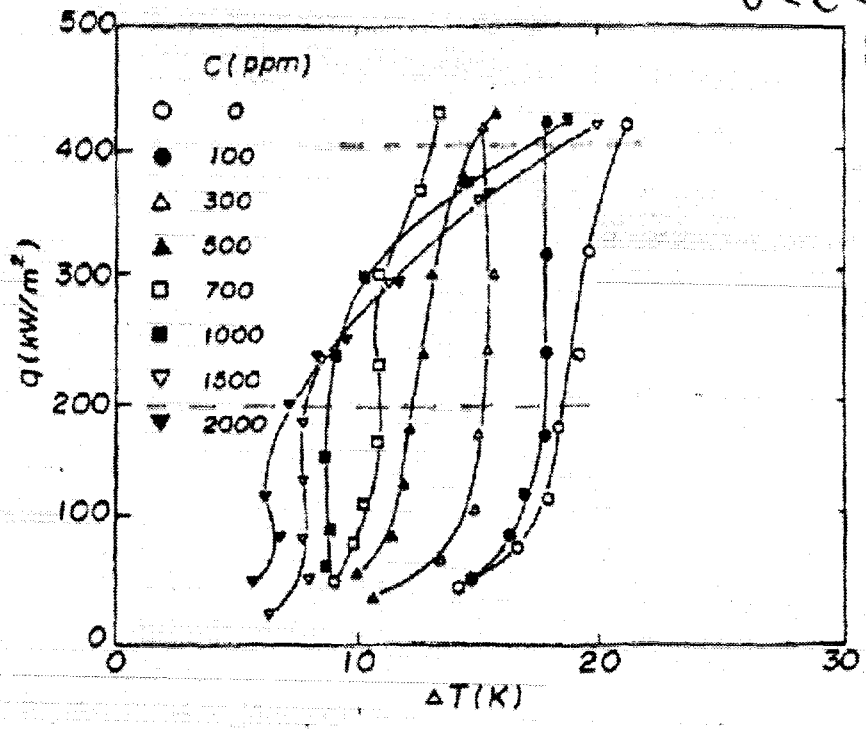

- At low q : ΔT decreases with C — — —
- At high q : ΔT is non-monotonic — — —

Tzan & Yang, 1990

Surfactants : Non-monotonic changes in Heat Transfer

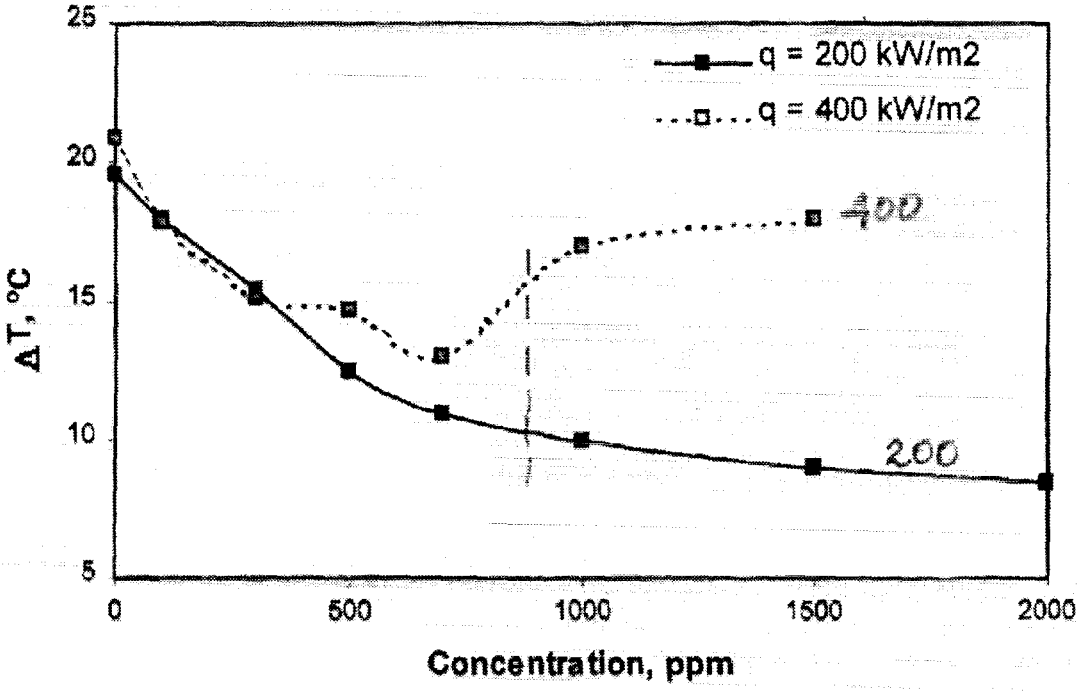

- $< \sigma_{eq} >$ reduces up to C ~ 700 ppm
- Roughly constant for C > 700 ppm

What surfactant-related mechanisms may cause non-monotonic behavior ?

- Surfactants and strong deformations : $\nabla_s \sigma$ & break-up highly dependent on coverage
- Surfactant mass transfer rates / surface dilatation rate
  - Highly dependent on bulk concentration
  - (Remobilizing surfactants)

I. Numerical Study of Rapid Vapor Bubble Growth

- 1st Generation : Growth of an injected bubble at finite Re

  Aim : Surfactant effects on rapidly growing interfaces

- 2nd Generation : Vapor Bubble Growth by Evaporation

  Aim : Incorporate evaporation from microlayer, Coupling of bubble dynamics with heat transfer

II. Experiments

Surfactants May Alter Bubble Detachment

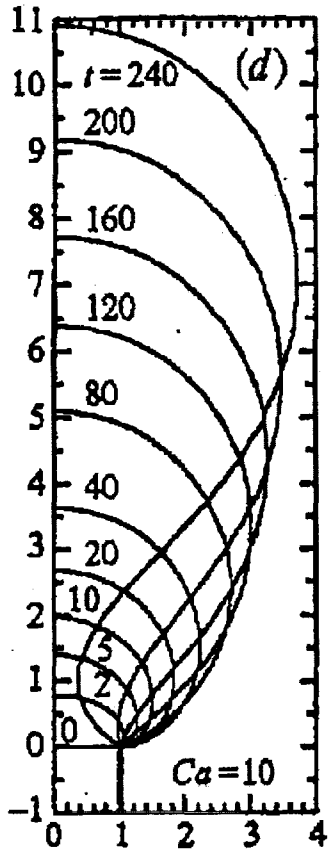

Wong et al., 1998

- Neck Formation : Complex flow, redistribute surfactants
- Surfactants alter neck formation
- A related problem studied by Eggleton, Tsai & Stebe
  - strong dilatation
  - bubble detatchment

Surfactants and the Taylor extensional flow

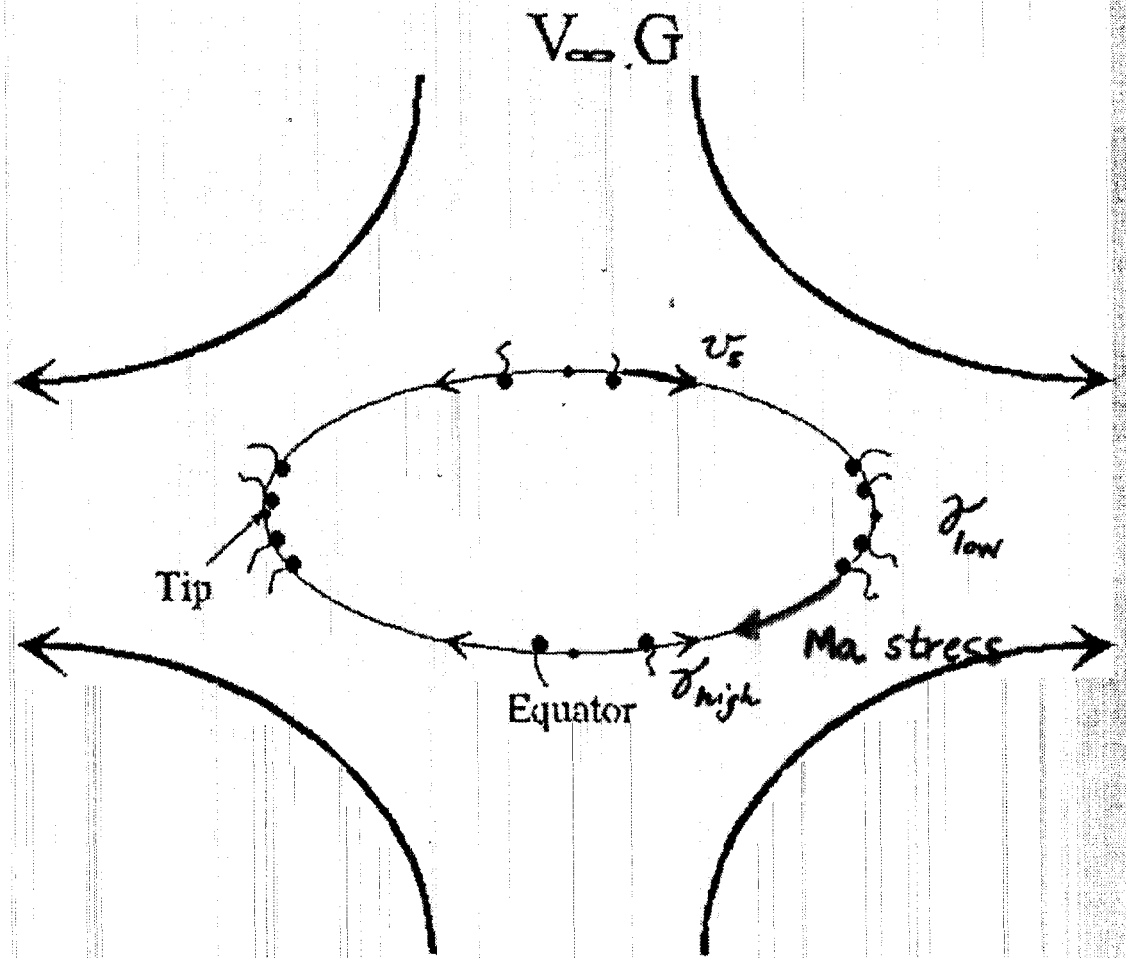

$$(\underline{n}\cdot\underline{\sigma}) = 2H\gamma\underline{n} + \nabla_s\gamma$$

$$Ca = \frac{\mu G a}{\gamma_{eq}}$$

$$\lambda = \frac{\mu_{drop}}{\mu} = 0.05$$

- Linear: Leal & collaborators

Monolayer Saturation

Minimum area/molecule

$A_{min} = 1/\Gamma_\infty$

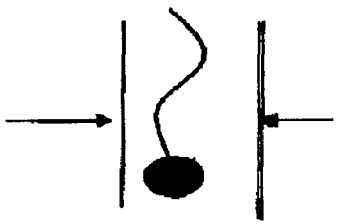

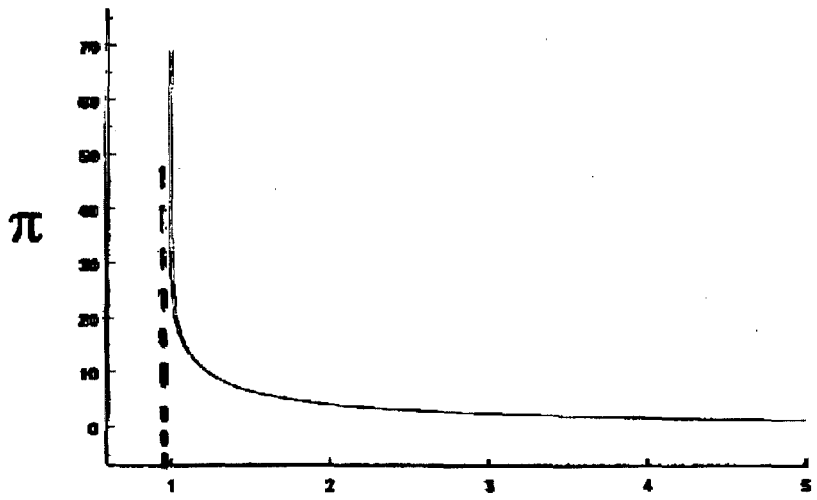

$\Gamma_\infty/\Gamma = A/A_{min} = 1/x$

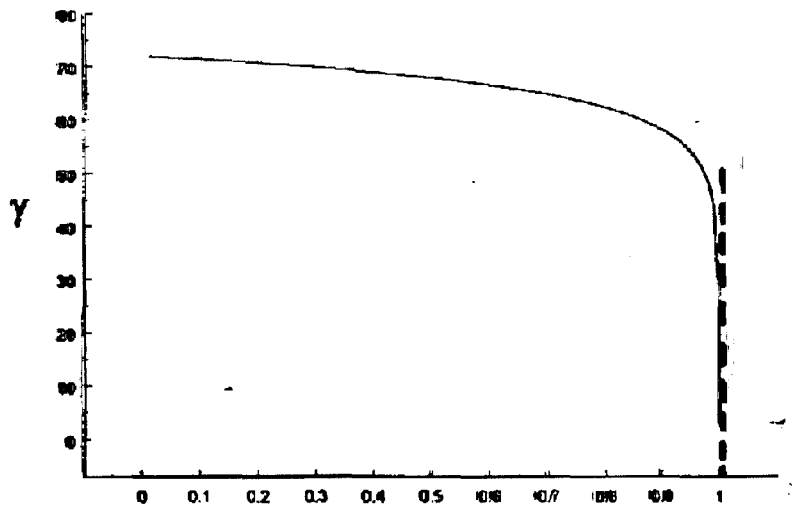

Γ/Γ_∞

$\pi = \gamma_o - \gamma(\Gamma) = -RT\Gamma_\infty \ln(1-\Gamma/\Gamma_\infty)$

2-D ideal gas: $\pi = RT\Gamma$

Surfactants and Deformation Mechanisms

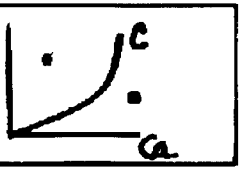

$$\gamma = \frac{\gamma_o}{\gamma_{eq}} + E\ln(1 - x\Gamma)$$

$$E = \frac{RT\Gamma_\infty}{\gamma_{eq}} = 0.2$$

$$-\nabla_s \gamma = \frac{Ex}{(1 - x\Gamma)}\nabla_s \Gamma$$

$$x = \frac{\Gamma_{eq}}{\Gamma_\infty}$$

$x \ll 1$ $\qquad \nabla_s \gamma(t=0) \approx Ex\nabla_s \Gamma$

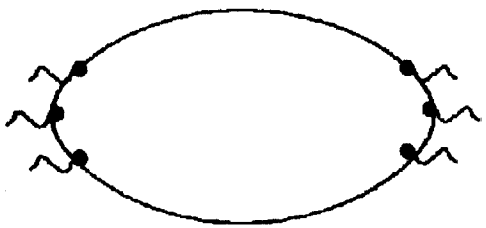

$D_f \uparrow$

$x \to 1$ $\qquad \nabla_s \gamma(t=0) \approx \frac{Ex}{1-x}\nabla_s \Gamma$

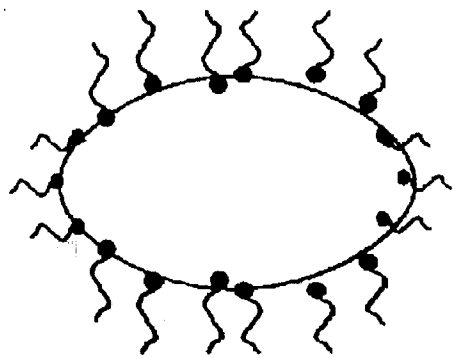

$D_f \downarrow$

Low coverage: large gradients λ=0.05

initially $\frac{\partial \Gamma}{\partial s} \sim Ex \frac{\partial \Gamma}{\partial s}$

Steady state profiles for x=0.1 largest Ca=0.06

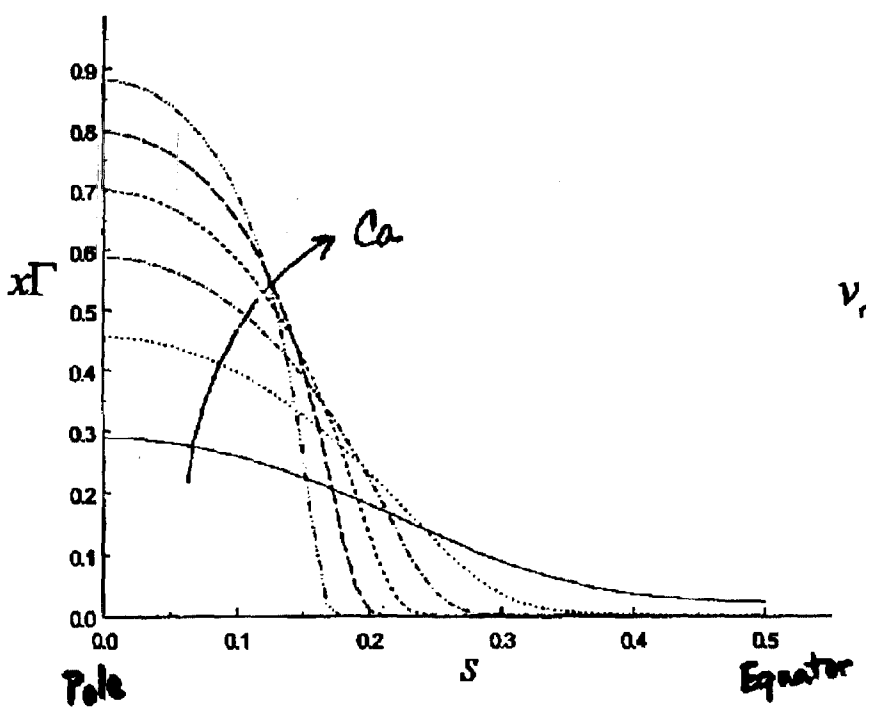

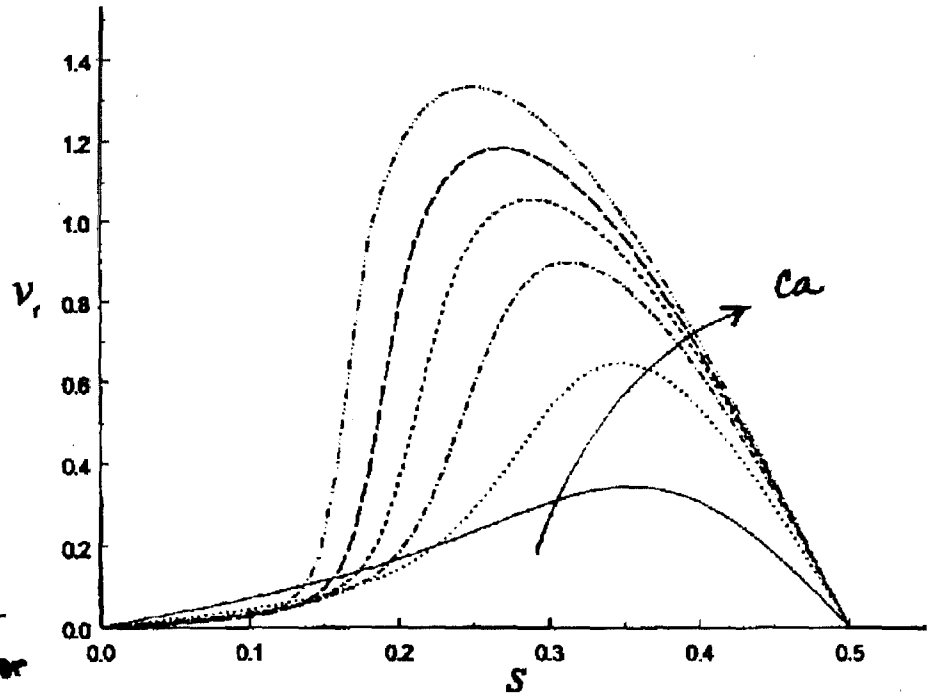

as Ca↑, surfactant swept entirely toward caps at the drop poles

Evolution of the tip curvature x=0.1

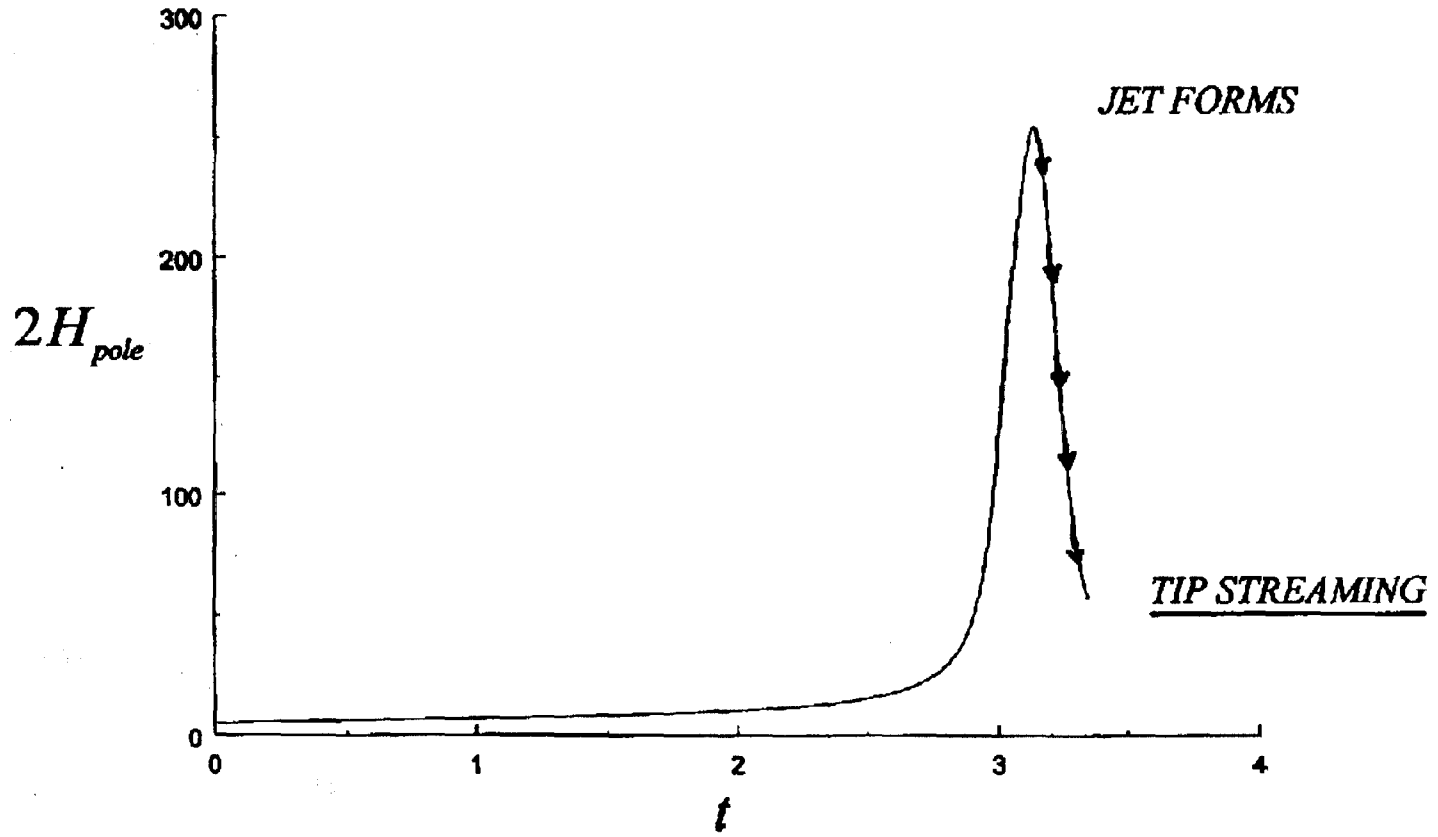

Ca_{cr}=0.065

Evolution of drop shape x=0.1

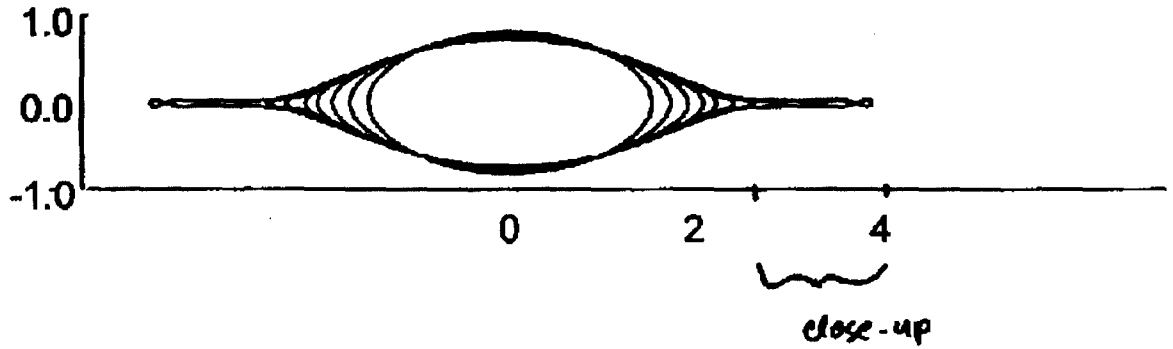

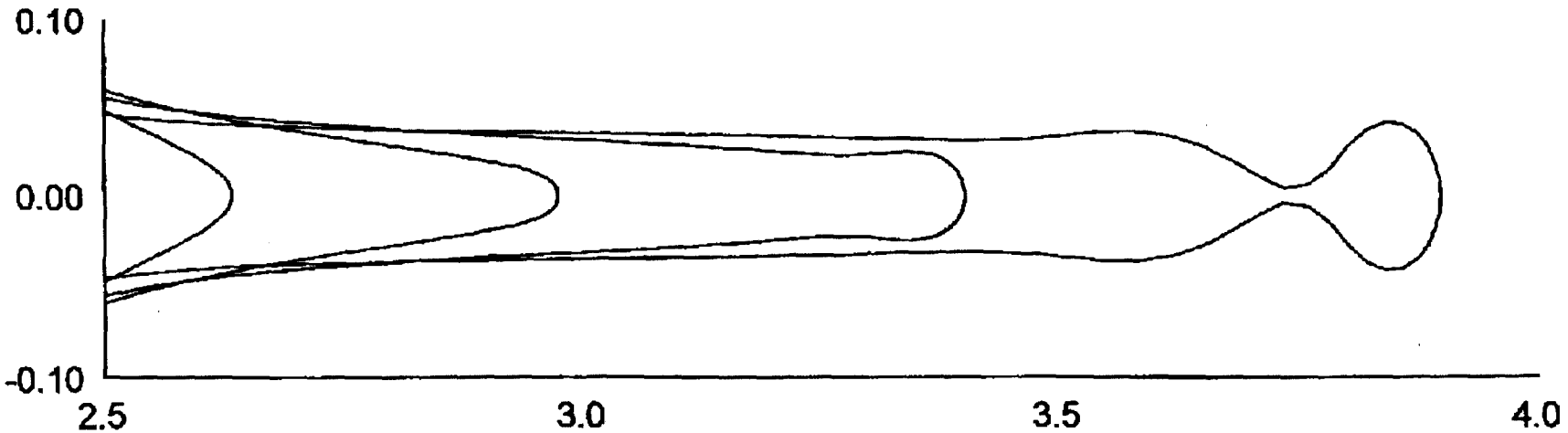

- $Vol_{daughter} \sim 1.3 \times 10^{-4}$ $\gamma_{daughter}$=0.51 Ca_{cr}=0.065

Evolution of $x\Gamma$ x=0.1

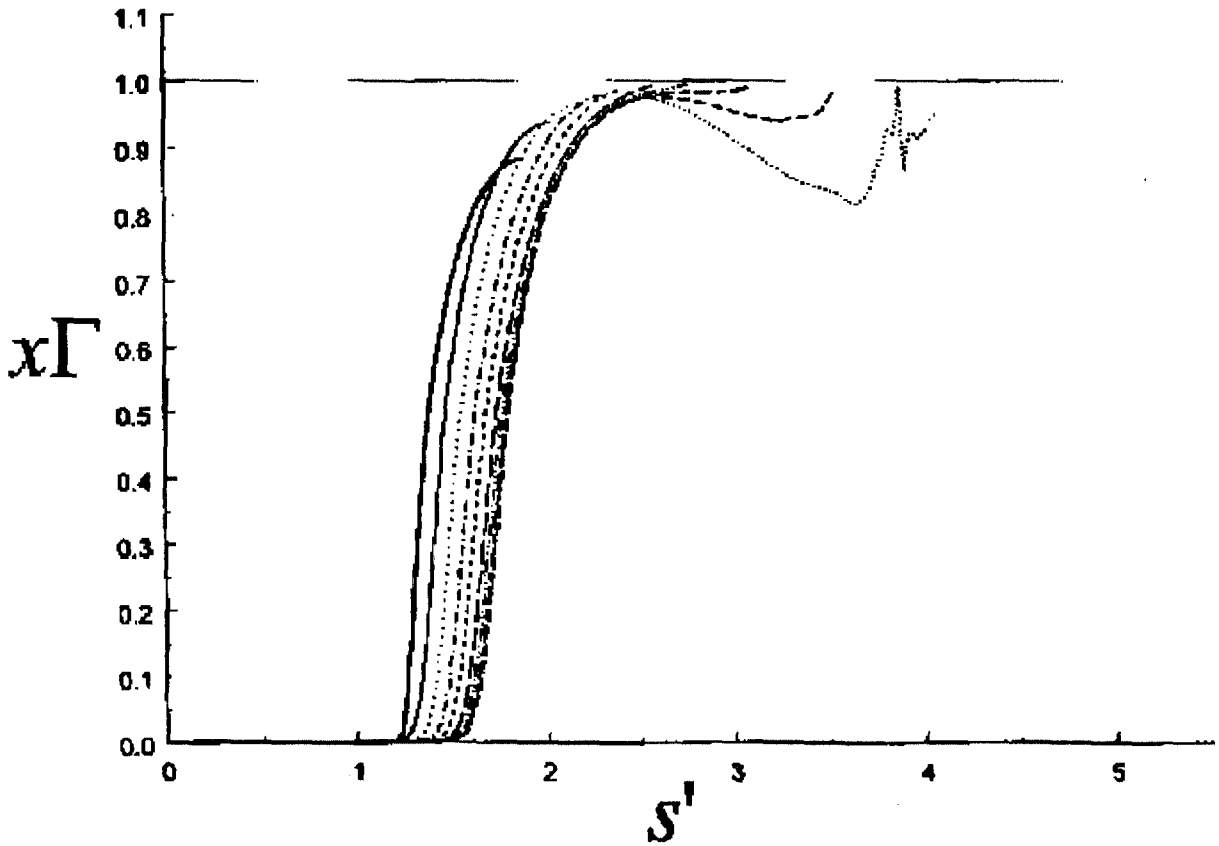

Mass Transfer Rates

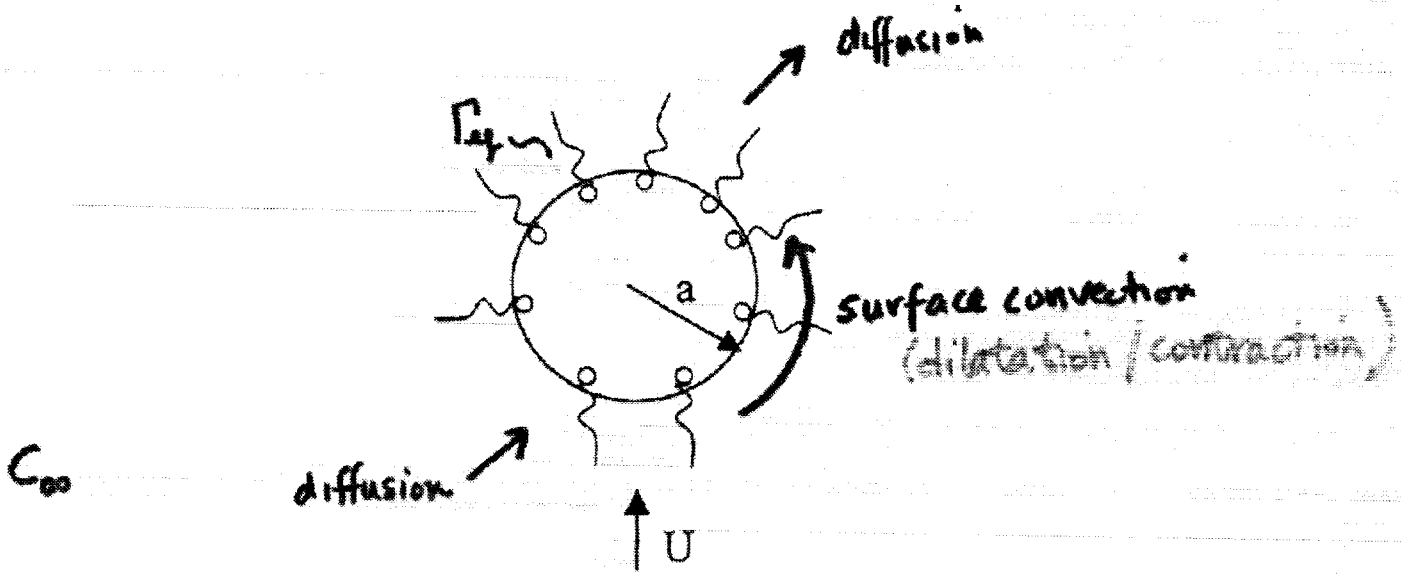

$$\frac{\partial \Gamma}{\partial t} + \nabla_s \cdot \left(\Gamma \vec{V}_t\right) + 2HV_n\Gamma - D_s \nabla_s^2 \Gamma = -\vec{n} \cdot \nabla C|_s D$$

$$length \sim a \qquad \Gamma \sim \Gamma_{eq}$$

$$V \sim U \qquad t \sim \frac{a}{U} \qquad \vec{n} \cdot \nabla C \sim \frac{C_\infty}{a\sqrt{Pe}}$$

In non-dimensional form

$$\frac{\partial \Gamma}{\partial t} + \nabla_s \cdot \left(\Gamma \vec{V}_t\right) + 2HV_n\Gamma - \frac{1}{Pe_s} \nabla_s^2 \Gamma = -\vec{n} \cdot \nabla C|_s \frac{1}{\sqrt{Pe}} \left(\frac{aC_\infty}{\Gamma_{eq}}\right)$$

- $h \sim \dfrac{\Gamma_{eq}}{C_\infty}$: highly dependent on surfactant physical chemistry & concentration

Adsorption Depth

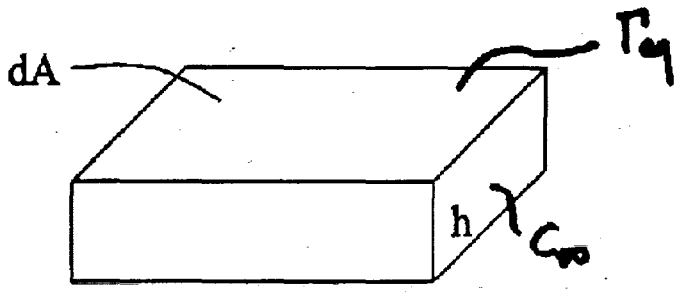

$$\Gamma_{eq}\, dA = C_\infty h dA$$

$$h = \frac{\Gamma_{eq}}{C_\infty}$$

- numerics: mass flux to surface: highly dependent on h
- Can select surfactants with highly differing h values and similar surface tensions

---

- $\tau_D = h^2/D = \left[\frac{\Gamma_{eq}}{C_\infty}\right]^2 \Big/ D$ quiescent system

- Surfynol 104: small h - AOT: large h

II. Experiments

- Lab-based
  - Single bubble growth & detachment
  - Two-bubble studies with coalescence
  - Two surfactants with differing h similar σ_{eq}
  - SAMs : Contact Angle

Pendant Bubble Method

Pendant Bubble Apparatus

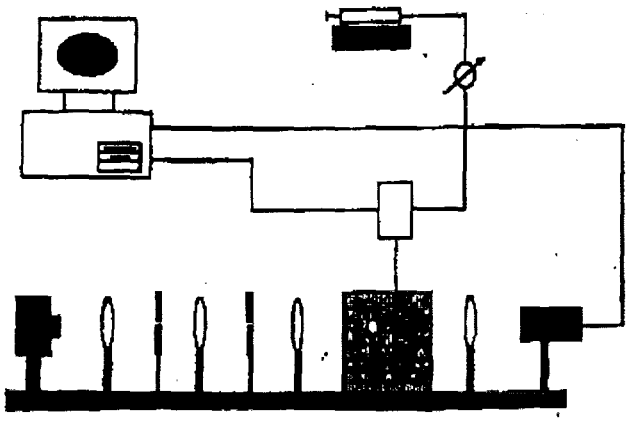

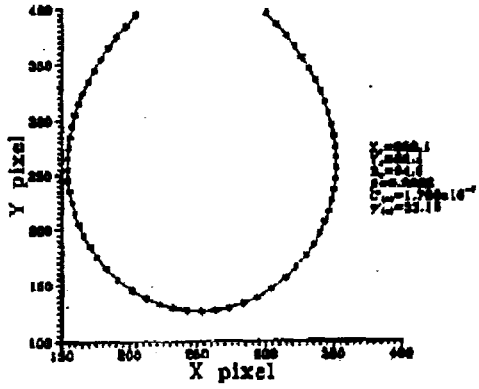

Surfynol 104 Pendant Bubble Data

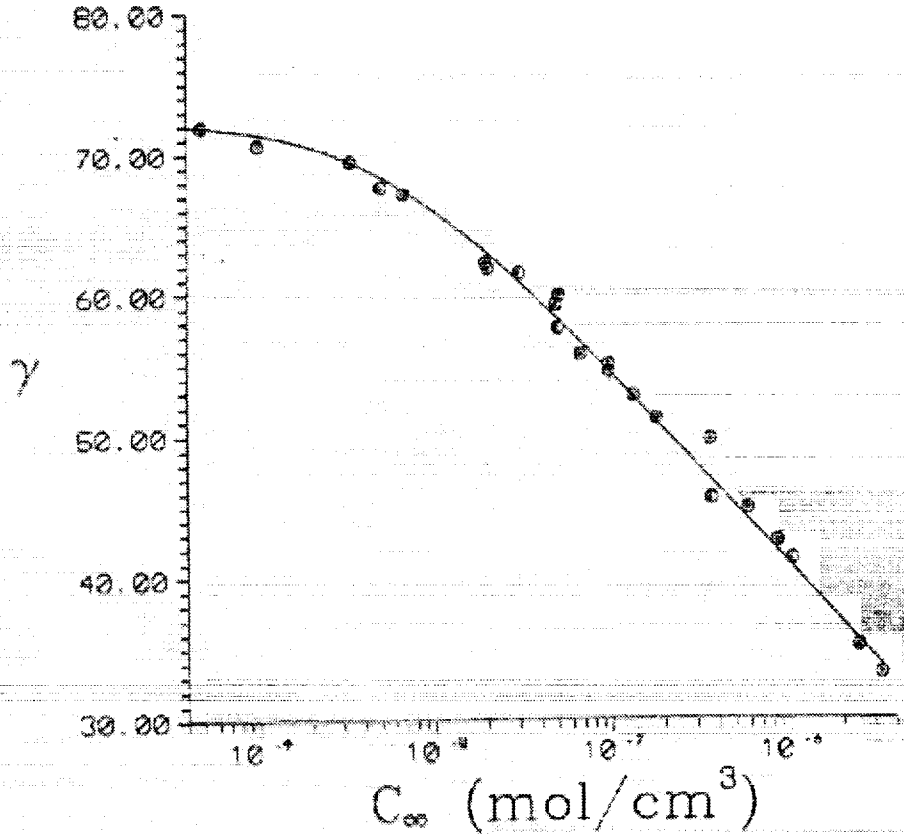

$\Gamma_\infty = 2.42\text{x}10^{-10}$ mol/cm^2

$a = 5.03\text{x}10^{-9}$ mol/cm^3

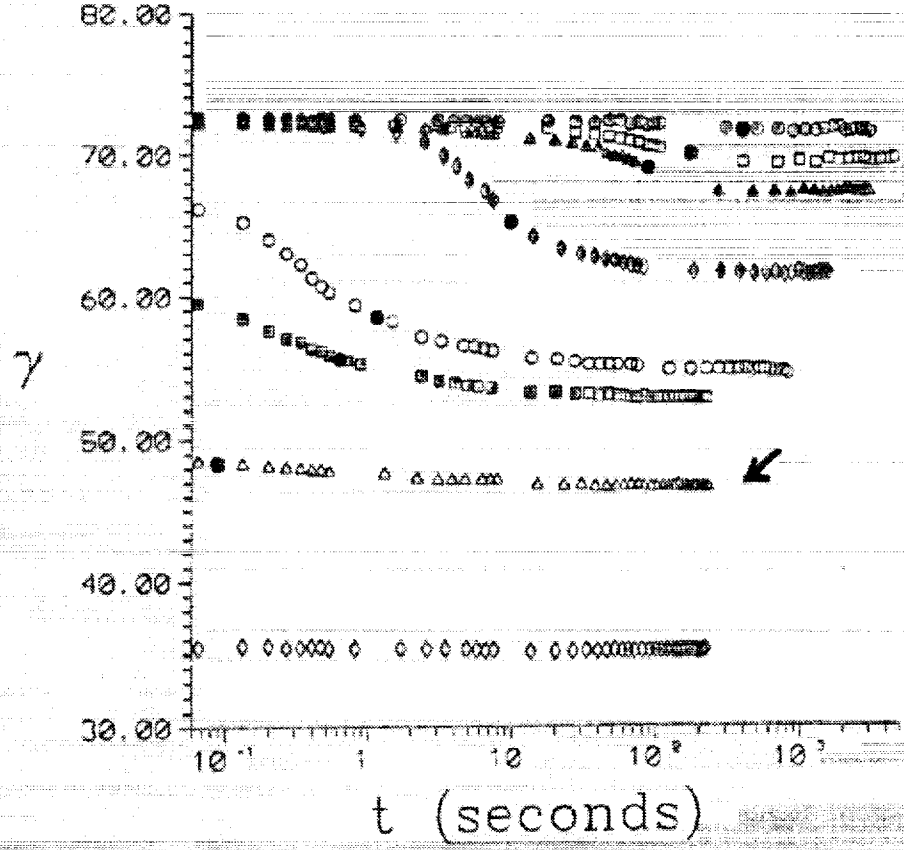

Ferri & Stebe, JHU

Best Fit for Diffusion Controlled Dynamics

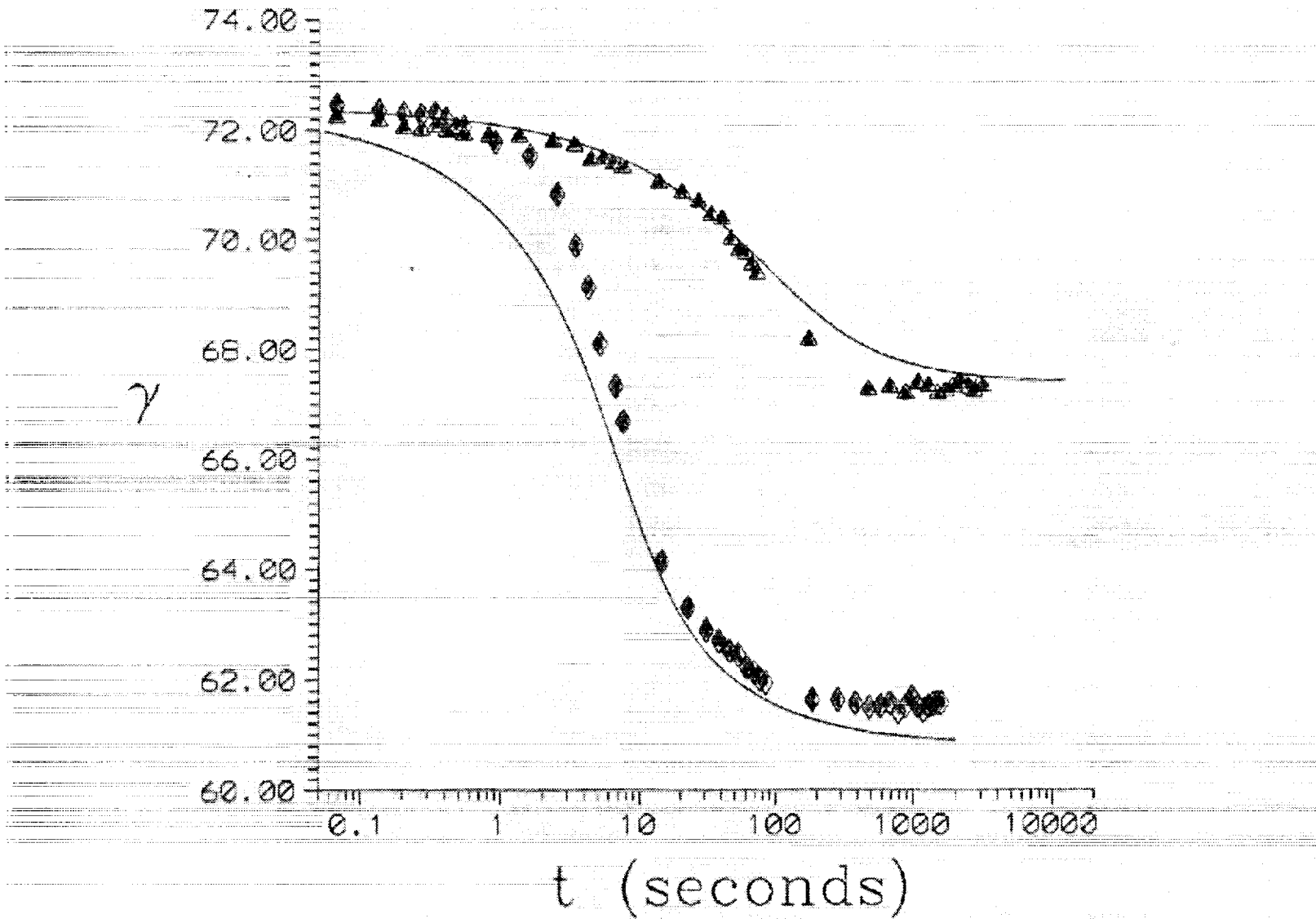

$D_{PFG\text{-}NMR} = 4.8 \times 10^{-6}\ cm^2/s$

$D_{AVG} = 4.4 \times 10^{-6}\ cm^2/s$

Ferri & Stebe, JHU

AOT: Equilibrium and Dynamics by Pendant Bubble

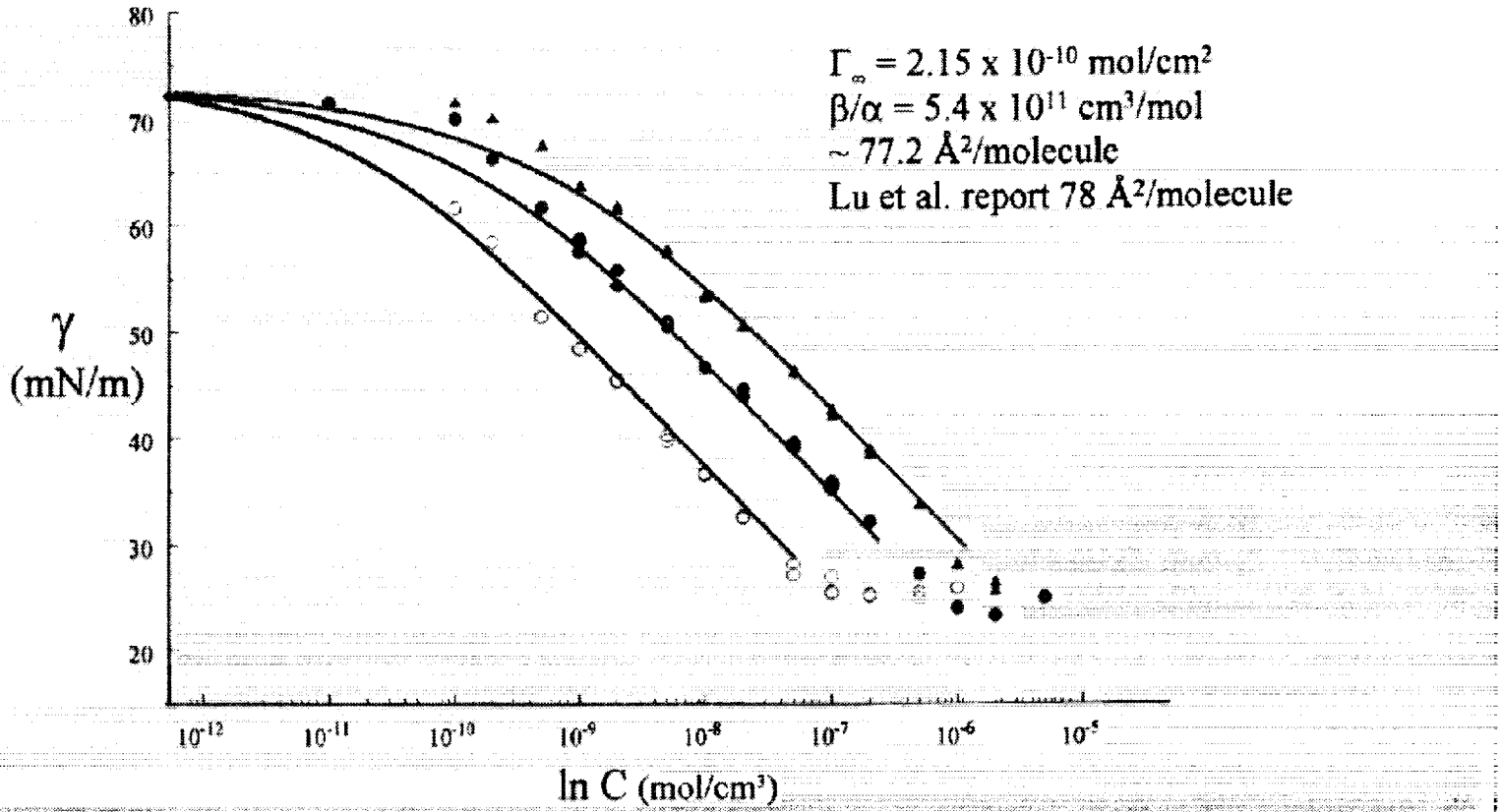

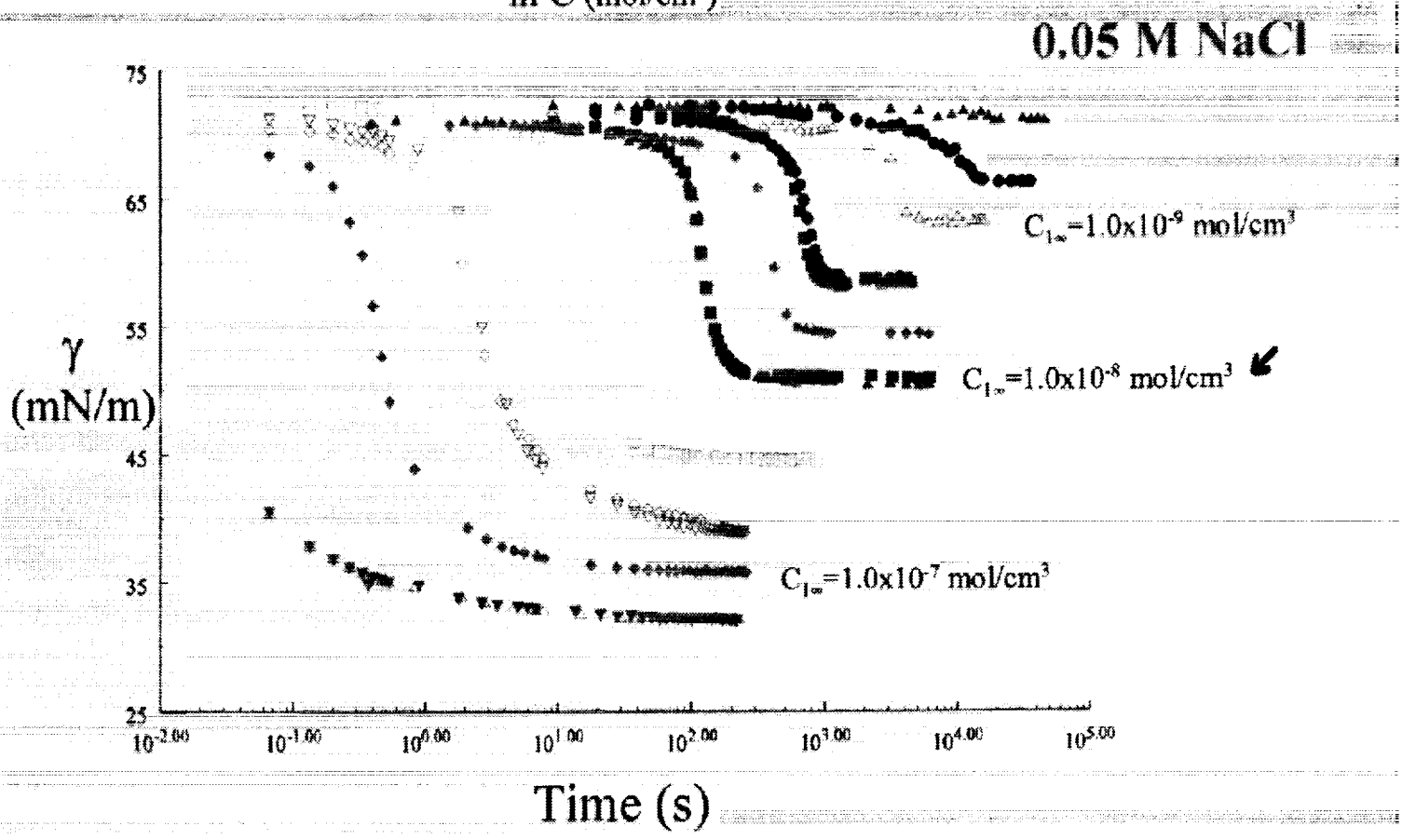

Dynamic Surface Tension:

Diffusion Control Model, $D = 6.5 \times 10^{-6} cm^2/s$

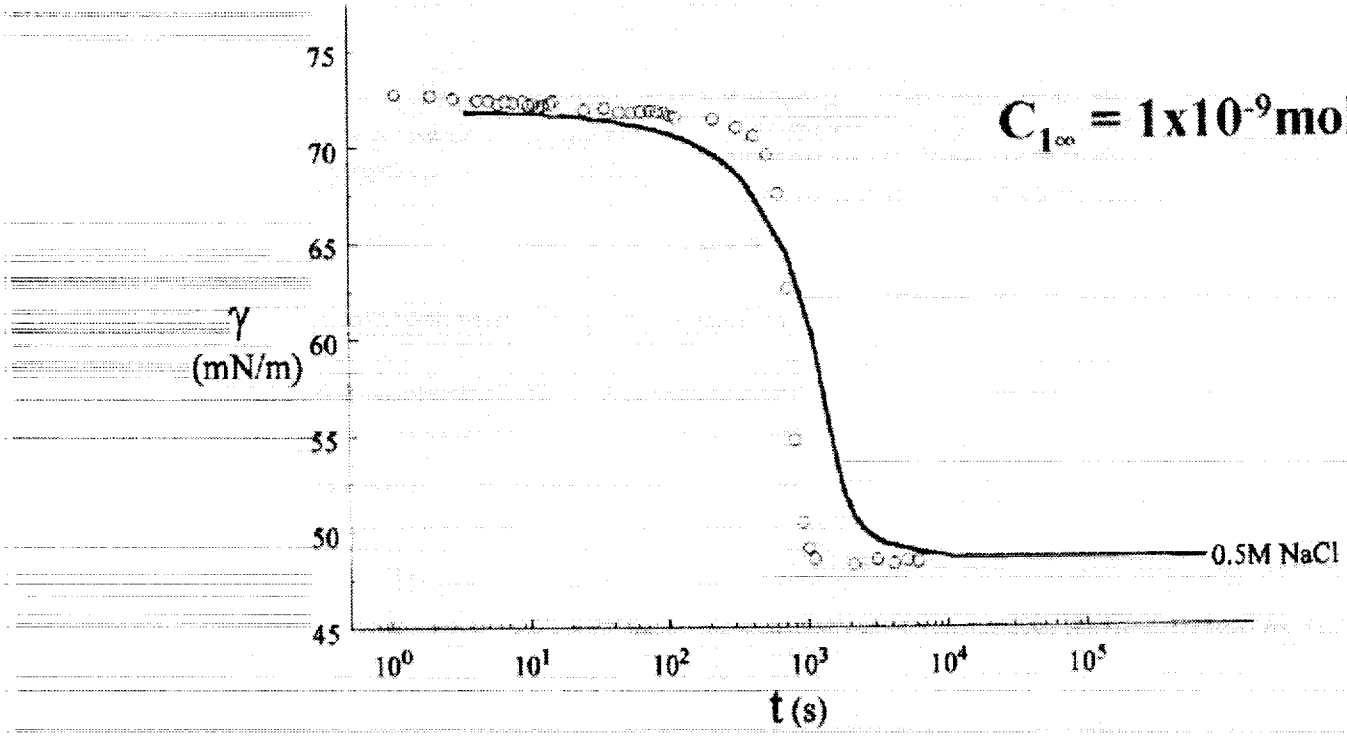

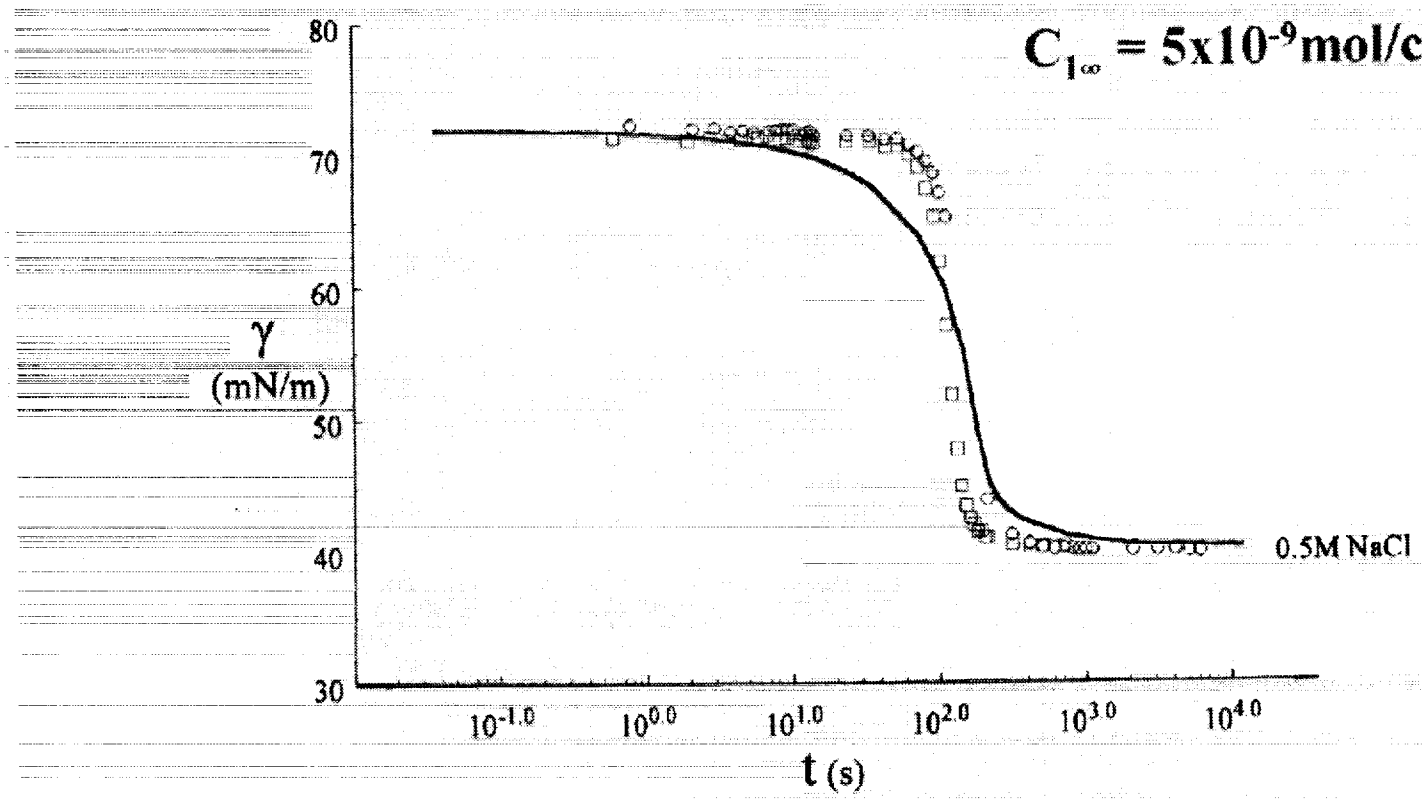

Microgravity Experiments

- Use experimental hardware similar to that used by Prof. Merte in his space shuttle experiments
- Tests will be conducted in drop towers and KC-135 aircraft
- Test liquid is water
- Goal is to obtain the nucleate boiling curve, systematically changing the amount of surfactant added to water
- Dynamics of bubbles will be observed by video or motion picture cameras

THE PHYSICS OF BOILING AT BURNOUT

T.G.Theofanous, J.P. Tu, T.N. Dinh, T.Salmassi, A.T.Dinh, and K.Gasljevic

Center for Risk Studies and Safety
University of California, Santa Barbara, CA 93106, USA

ABSTRACT

The basic elements of a new experimental approach for the investigation of burnout in pool boiling are presented. The approach consists of the combined use of ultrathin (nano-scale) heaters and high speed infrared imaging of the heater temperature pattern as a whole, in conjunction with highly detailed control and characterization of heater morphology at the nano and micron scales. It is shown that the burnout phenomenon can be resolved in both space and time. Ultrathin heaters capable of dissipating power levels, at steady-state, of over 1 MW/m^2 are demonstrated. A separation of scales is identified and it is used to transfer the focus of attention from the complexity of the two-phase mixing layer in the vicinity of the heater to a micron-scaled microlayer and nucleation and associated film-disruption processes within it.

Fifth Microgravity Fluid Physics and Transport Phenomena Conference
August 9-11, 2000, Cleveland, Ohio, U.S.A.

THE PHYSICS OF BOILING AT BURNOUT

Theo G. Theofanous

T.G. Theofanous, J.P. Tu. T.N. Dinh,
T. Salmassi, A.T. Dinh and K. Gasljevic

Center for Risk Studies and Safety
University of California, Santa Barbara

UCSB
Center for Risk Studies & Safety

Outline

- Nucleate Boiling Crisis
- BETA Pool Boiling Experiments
- Infrared Thermometry of Nucleate Boiling Heat Transfer
- Critical Heat Fluxes Quantification
- Visualization and Characterization of Burnout
- Physical Insights and Future Plan

UCSB
Center for Risk Studies & Safety

Nucleate Boiling Crisis

- As the Limit of Coolability in Power and Thermal Management Equipment
- Featuring Complex Two-Phase Flow at High Heat Fluxes
- Involving Interactions of Processes Occurring at Multiple Scales
- Mechanism(s) of CHF were Observed and Investigated Indirectly using
  - ✓ Time- *or* Space-Average Measurement
  - ✓ Integral *or* Local Measurement

UCSB
Center for Risk Studies & Safety

Nucleate Pool Boiling Crisis

- Hydrodynamic Concept

  Kutateladze (1948), Zuber (1959)
  Lienhard & Dhir (1973)

$$q''_{CHF} = C_k \ \rho_V^{1/2} H_{fg} [\sigma g (\rho_L - \rho_V)]^{1/4},$$

$$C_k = 0.15 \ \ (0.131 \ldots 0.168)$$

- Macrolayer Evaporation Model

  Katto (1968, 1983)

- Thermal (Vapor-Stem) Model

  Dhir (1989)

- Controversy due to

  ✓ Remarkable Effect of Heater's Surface on CHF
  ✓ Lack of Direct Observations and Measurements Required to Qualify Theoretical Concepts

NEED FOR NEW FUNDAMENTAL EXPERIMENTS

UCSB
Center for Risk Studies & Safety

BETA Pool Boiling Experiments

Aim: Fundamental, Direct Identification of the Boiling Crisis Phenomenon

Saturated Pool Boiling on Horizontal Upward-Facing Heaters

- Eliminate End Effect with a Heated Area of 20 x 40 mm (Infinite Flat Plate Behavior);
- Minimize Heater Thermal Capacity Effect: 140 nm Titanium Heater Vapor-Deposited on 130 μm Glass
- Cavity-Free Heater Surface: AFM-measured rms roughness ±4nm

KEY OBSERVATION AND MEASUREMENT:

THE HEATER'S THERMAL PATTERN
AND
THE DYNAMIC FINGERPRINT OF BOILING

Using High Speed Infrared Thermometry

UCSB
Center for Risk Studies & Safety

BETA Pool Boiling Experiments

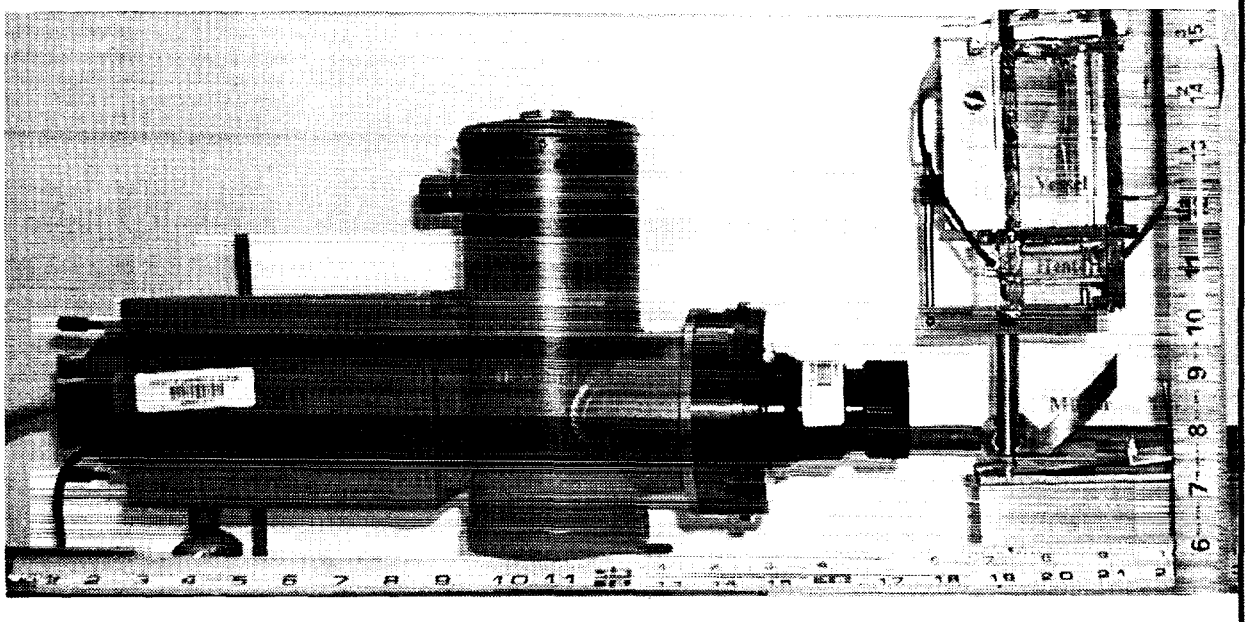

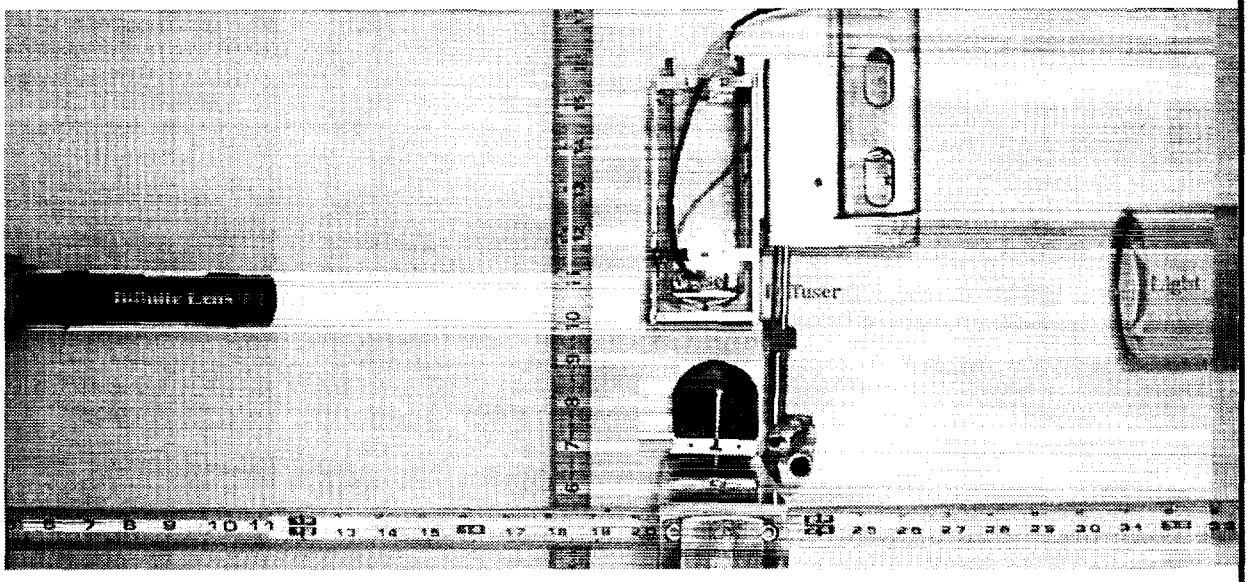

UCSB

Center for Risk Studies & Safety

IR Images of Nucleate Boiling (Fresh Heater A)

29 kW/m^2

56 kW/m^2

259 kW/m^2

303 kW/m^2

557 kW/m^2

635 kW/m^2

UCSB

Center for Risk Studies & Safety

Thermal Footprint of a **Regular Bubble** in Nucleate Pool Boiling

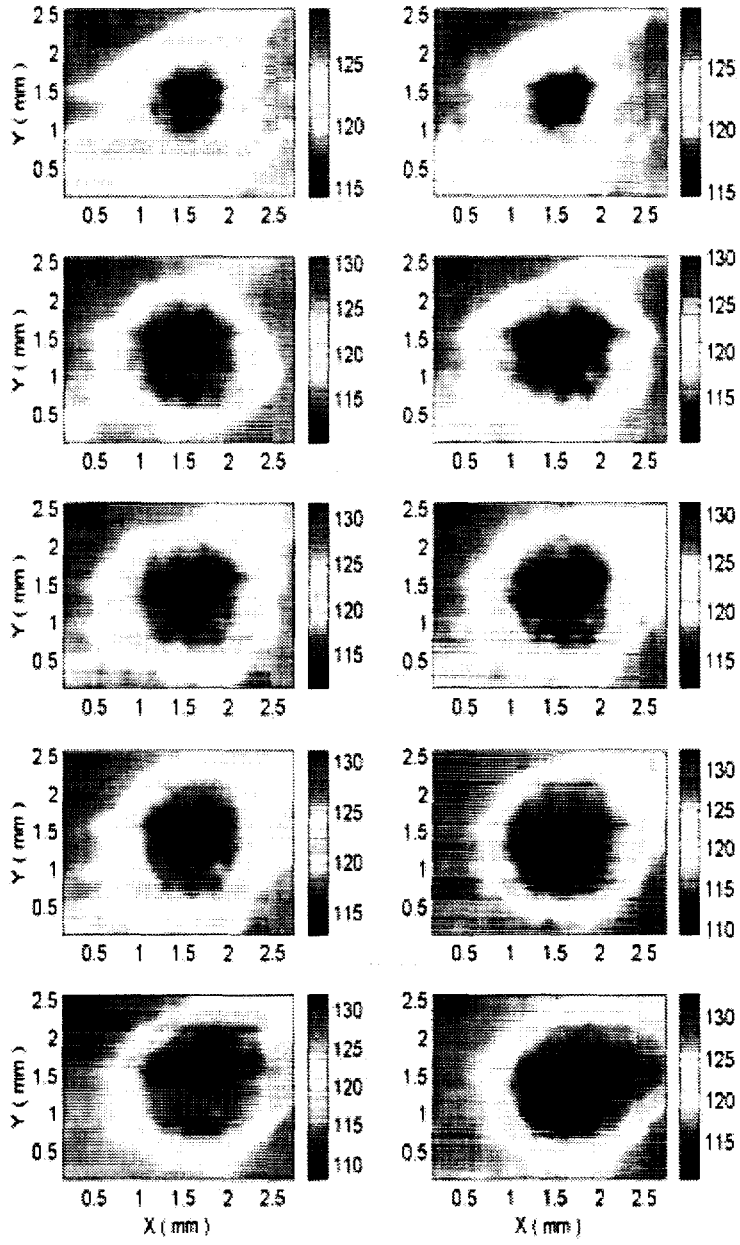

Heat flux q" ≅ 259 kW/m^2. Time interval 30 ms. Heater A.

UCSB

Center for Risk Studies & Safety

Thermal Footprint of a **Regular Bubble**

At 95% of CHF

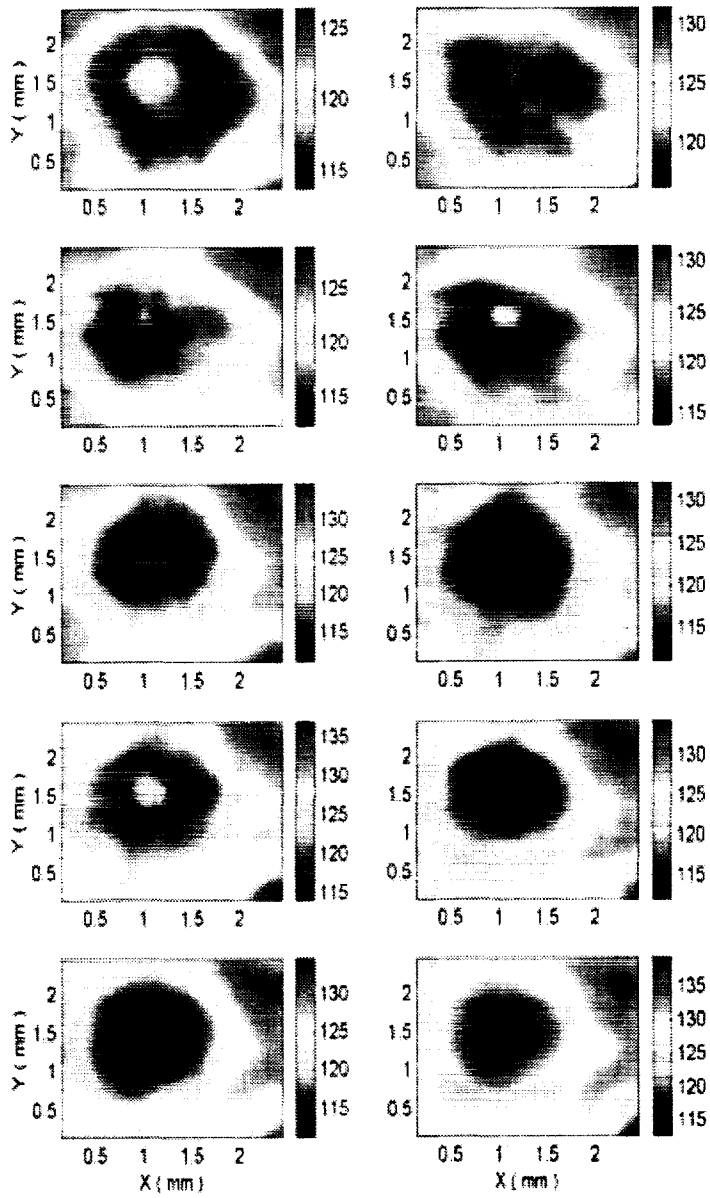

Heat flux q" ≅ 635 kW/m^2. Time interval 30 ms. Heater A.

UCSB

Center for Risk Studies & Safety

Thermal Footprint of an **Irregular Bubble**

At 95% of CHF

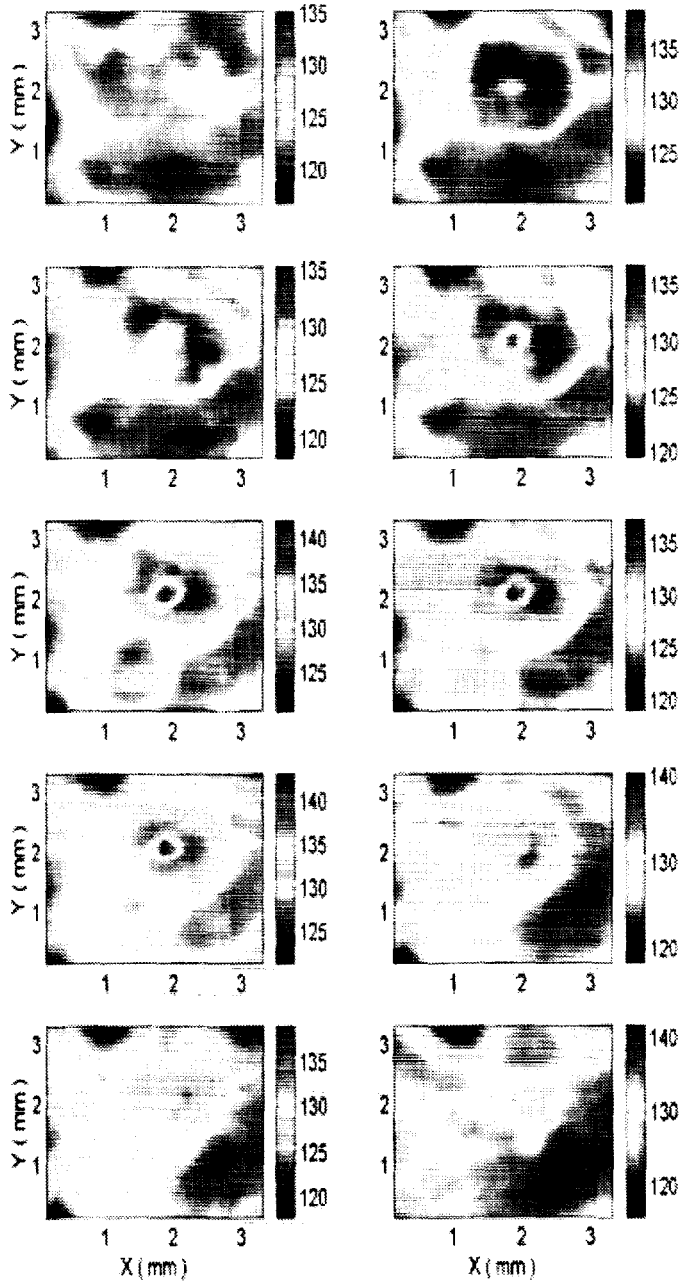

Fig 1. 3. Temperature Distribution (Tidiwa-b17)

Heat flux q" ≅ 625 kW/m^2. Time interval 30 ms. Heater A.

UCSB

Center for Risk Studies & Safety

Thermal Footprint of a Large Bubble with Formation of Hot Spot near Boiling Crisis

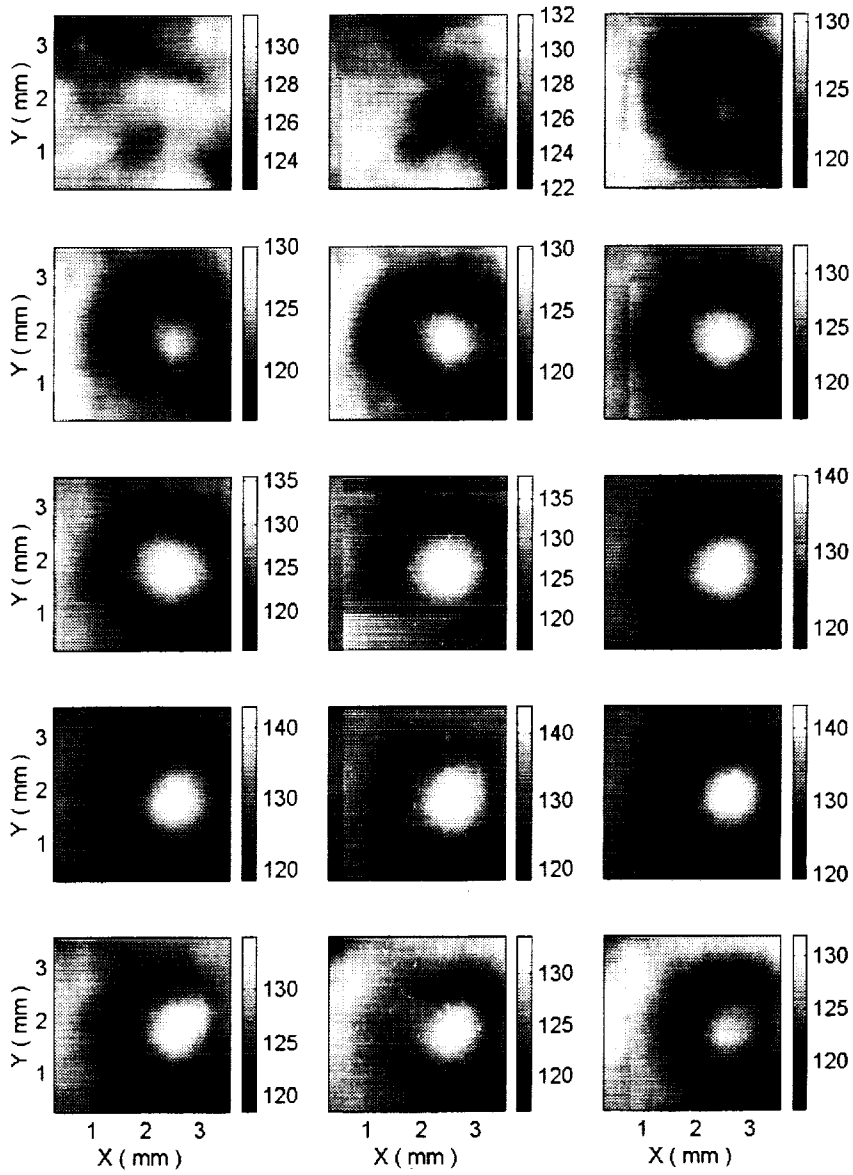

Heat flux q" ≅ 672 kW/m^2. Time interval 1ms. Heater K.

UCSB
Center for Risk Studies & Safety

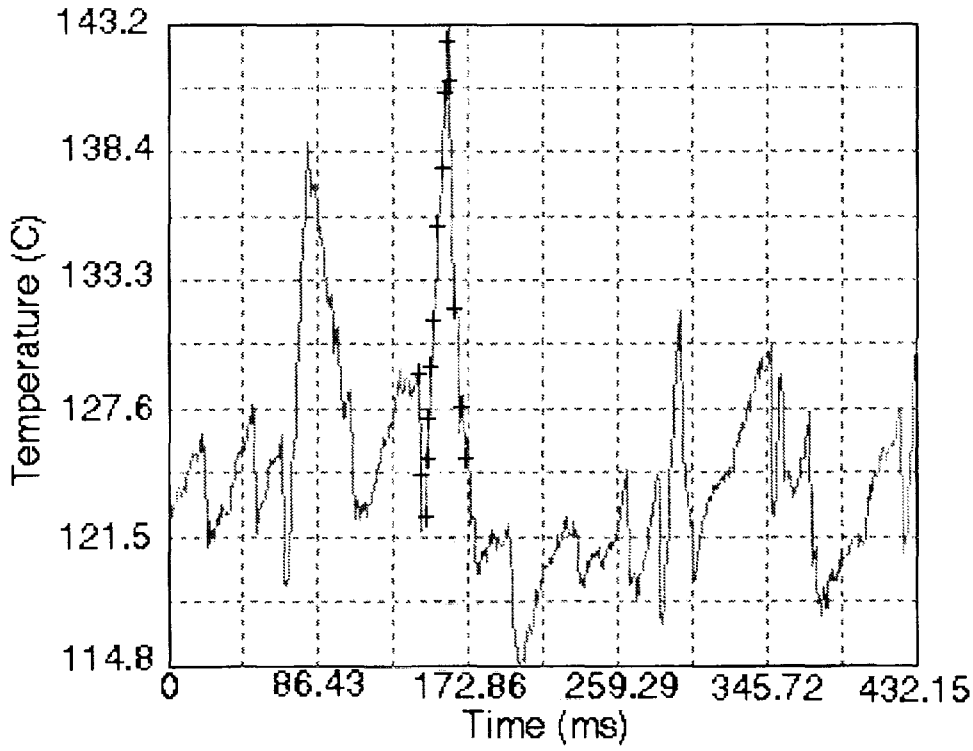

Temperature history at the hot spot location
(crosses correspond to IR images below)

UCSB
Center for Risk Studies & Safety

Thermal Footprint of a Large Bubble with Formation of Hot Spot near Boiling Crisis

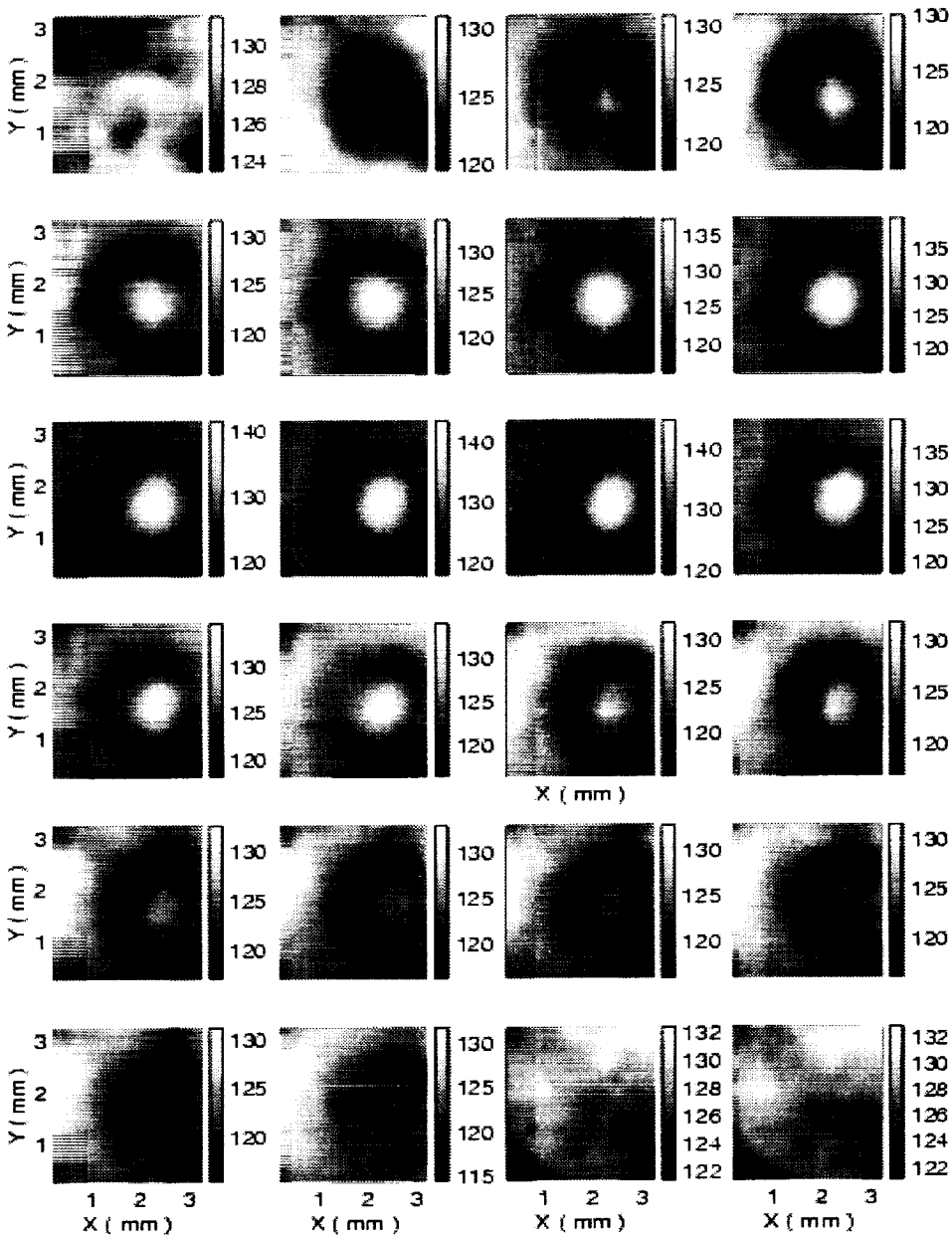

Heat flux q" ≅ 672 kW/m^2. Time interval 2 ms. Heater K.

UCSB

Center for Risk Studies & Safety

Nucleate Boiling Heat Transfer Observations

Pool Boiling Processes were Experimented

- On Ti Heaters with Different Thickness: 140 nm, 270 nm, 500 nm and 1000 nm;
- Using DC and AC (30...1000 Hz, sine and square waves);
- Fresh and Aged Heaters

The Heater's Ageing Degree was Found as the Primary Factor that Affects Boiling Characteristics and CHF

For a Fresh Heater, Nucleation Site Density is Low, and Characteristic Length of Bubble-Induced Cold Spot is Relatively Large.

Regular and Irregular Bubbles were Identified. Formation of Hot Spot in Irregular Bubbles at High Heat Fluxes were Observed.

For an Aged Heater, the Heater's Surface is Cooler and Covered with Numerous Small-Sized Cold Spots (i.e. Significantly Higher Nucleation Site Density).

UCSB

Center for Risk Studies & Safety

FRESH HEATER A

259 kW/m^2

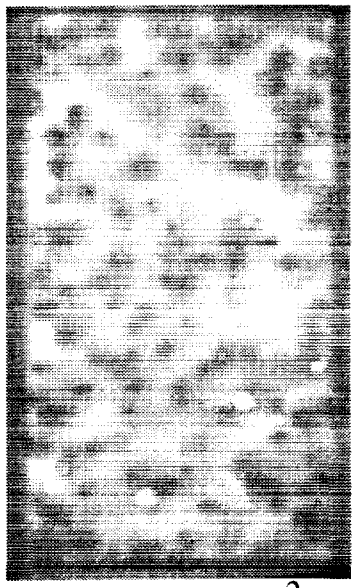

635 kW/m^2

Burned Out

AGED HEATER G

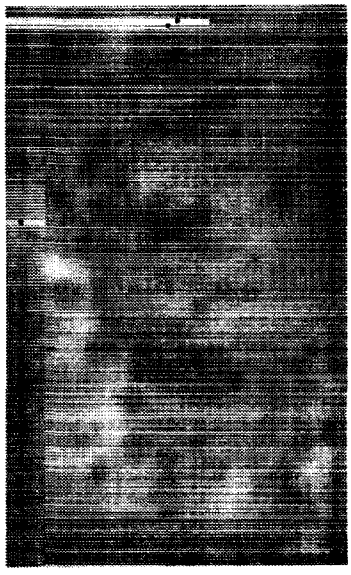

116 kW/m^2

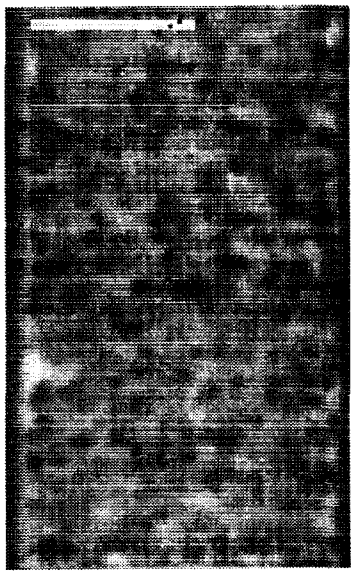

620 kW/m^2

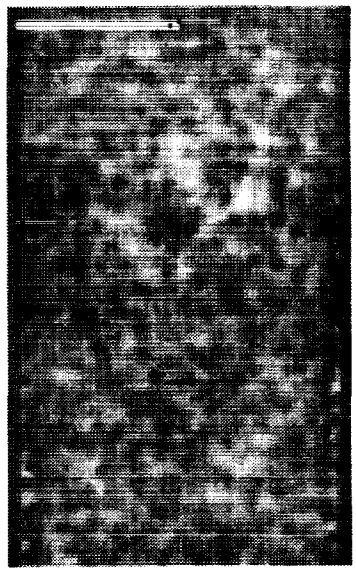

1062 kW/m^2

UCSB

Center for Risk Studies & Safety

AVERAGE SIZE OF COLD SPOTS

FRESH HEATER (Ti10A)

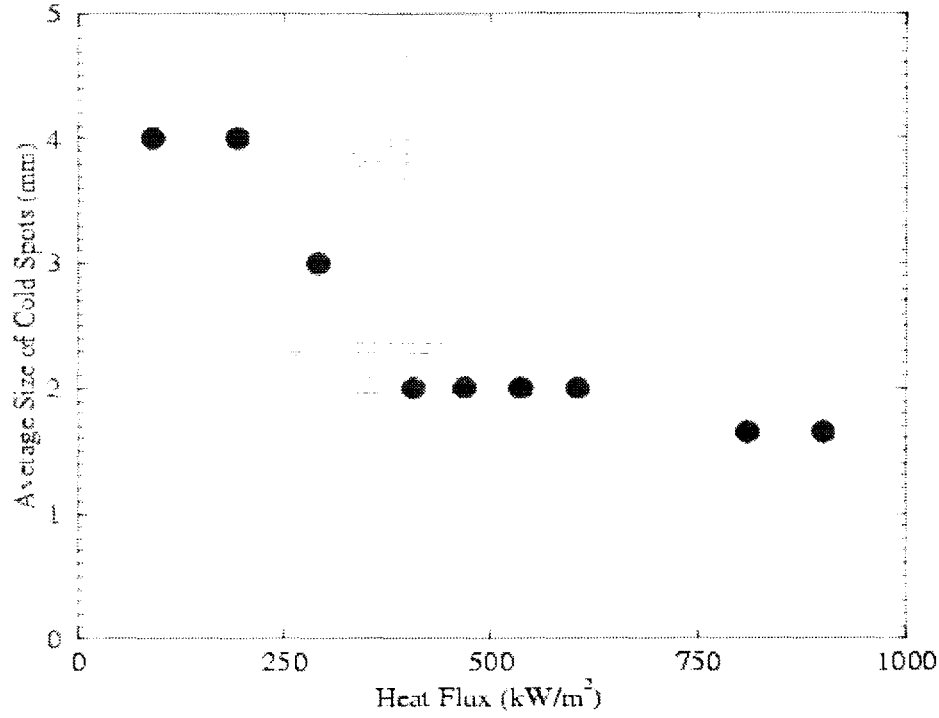

AGED HEATER (2700A01)

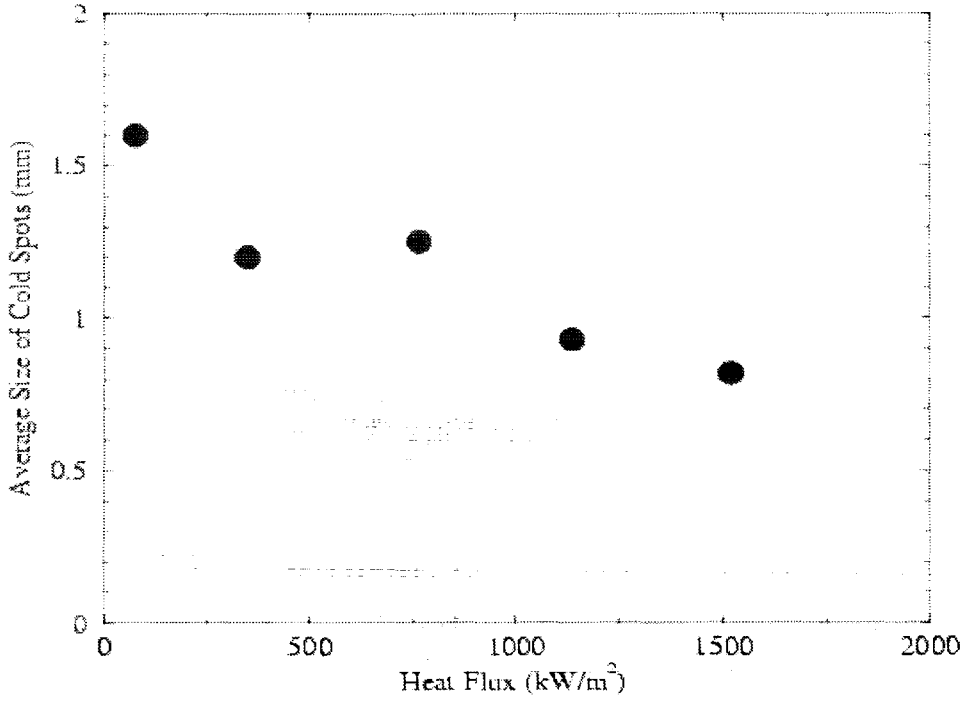

UCSB

Center for Risk Studies & Safety

AVERAGE SUPERHEAT AND NUCLEATION SITE DENSITY

Ideally Fresh and Clean Heater

T10a

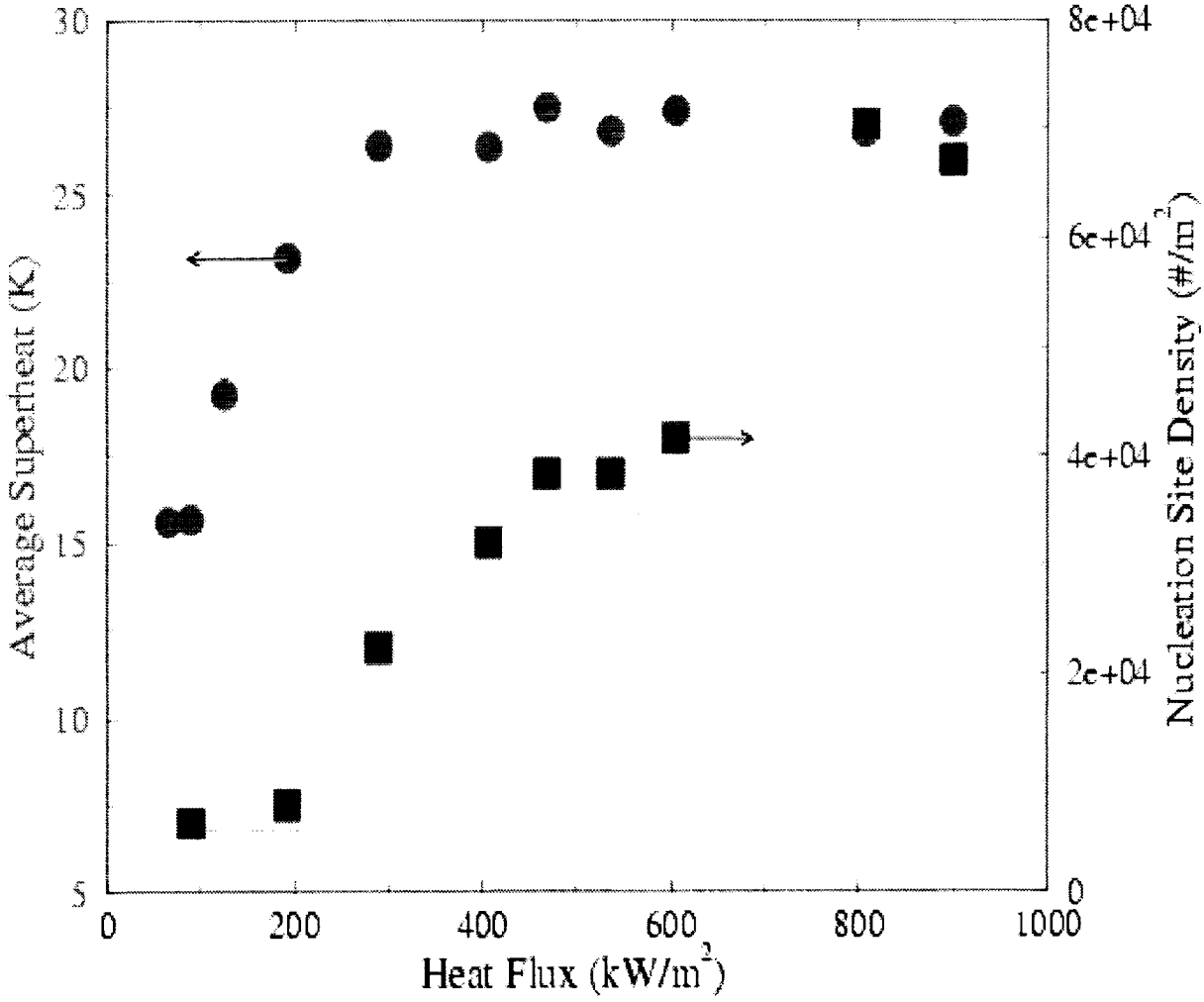

- Superheat Reached Saturation (27 K) at 300 kW/m^2
- Nucleation Site Density Increases Linearly with q"

UCSB

Center for Risk Studies & Safety

AVERAGE SUPERHEAT AND NUCLEATION SITE DENSITY

Aged Heater

2700 A01

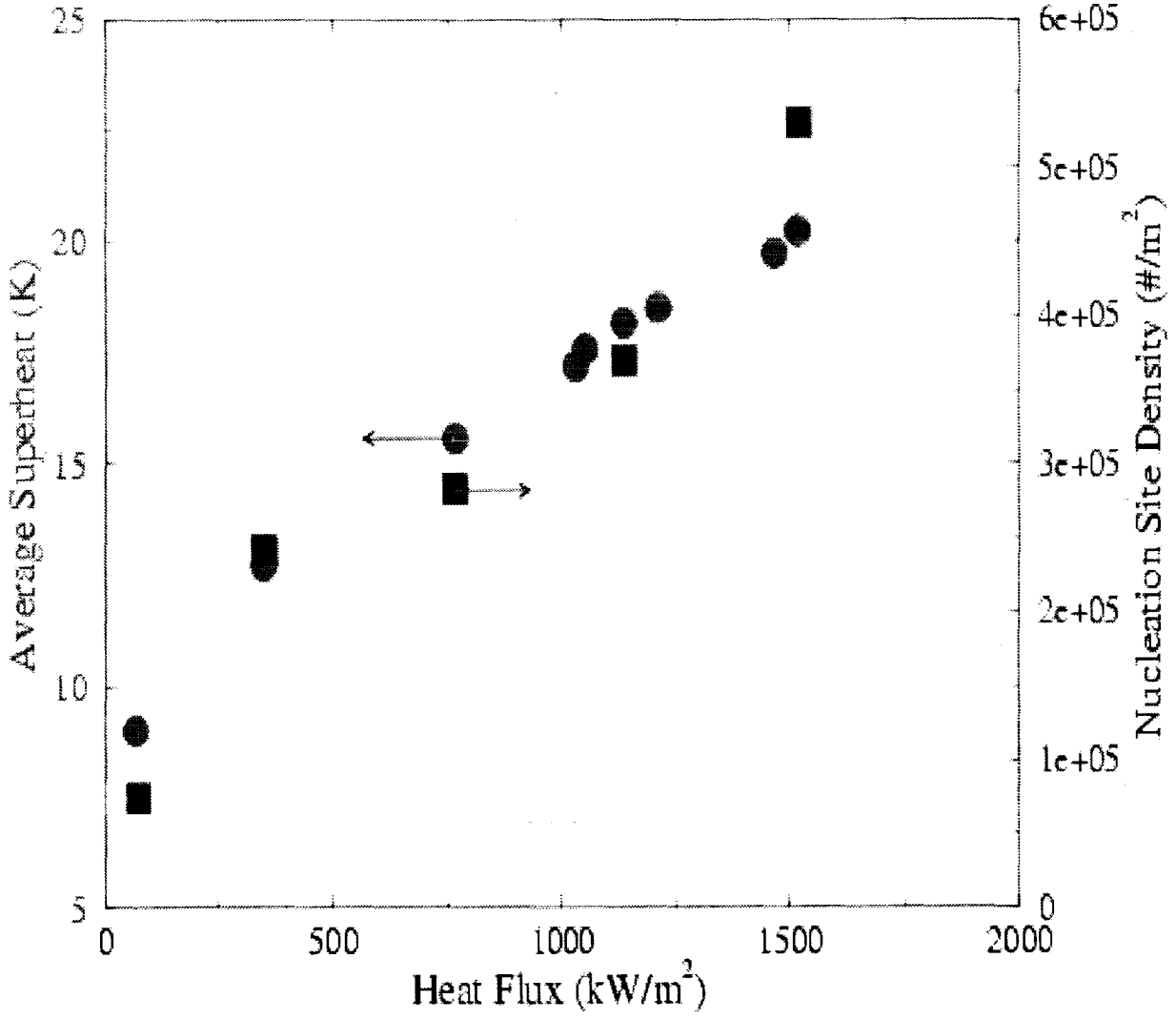

- Nucleation Site Density and Superheat Increase Linearly with Heat Flux q"
- At CHF (1.5 MW/m^2) Superheat is Still Low (20 K)

UCSB

Center for Risk Studies & Safety

NUCLEATION SITE DENSITY

For the First Time, Direct Identification of Active Nucleation Site in a Broad Range of Heat Fluxes up to CHF was Possible

Measured Values are Found Significantly Lower than Values Reported in Literature, Leaving a Significant Fraction of Heater's Surface be Cooled by Liquid (recall the Constant Heat Flux in the Nanoscale Heaters)

A Well-Wet Surface with a Small Contact Angle ($\beta \approx 15^{\circ}$) Features Higher Nucleation Site Density than on a Fresh Heater with a Larger Contact Angle (also in Contrary to the Literature)

The Reason May Be Related to The Vapor-Deposited Nanoscale Heaters, where No Micron-Size Cavities Exist

The Dependence of Nucleation Site Density on Superheat was also Not Confirmed

UCSB
Center for Risk Studies & Safety

NUCLEATION SITE DENSITY

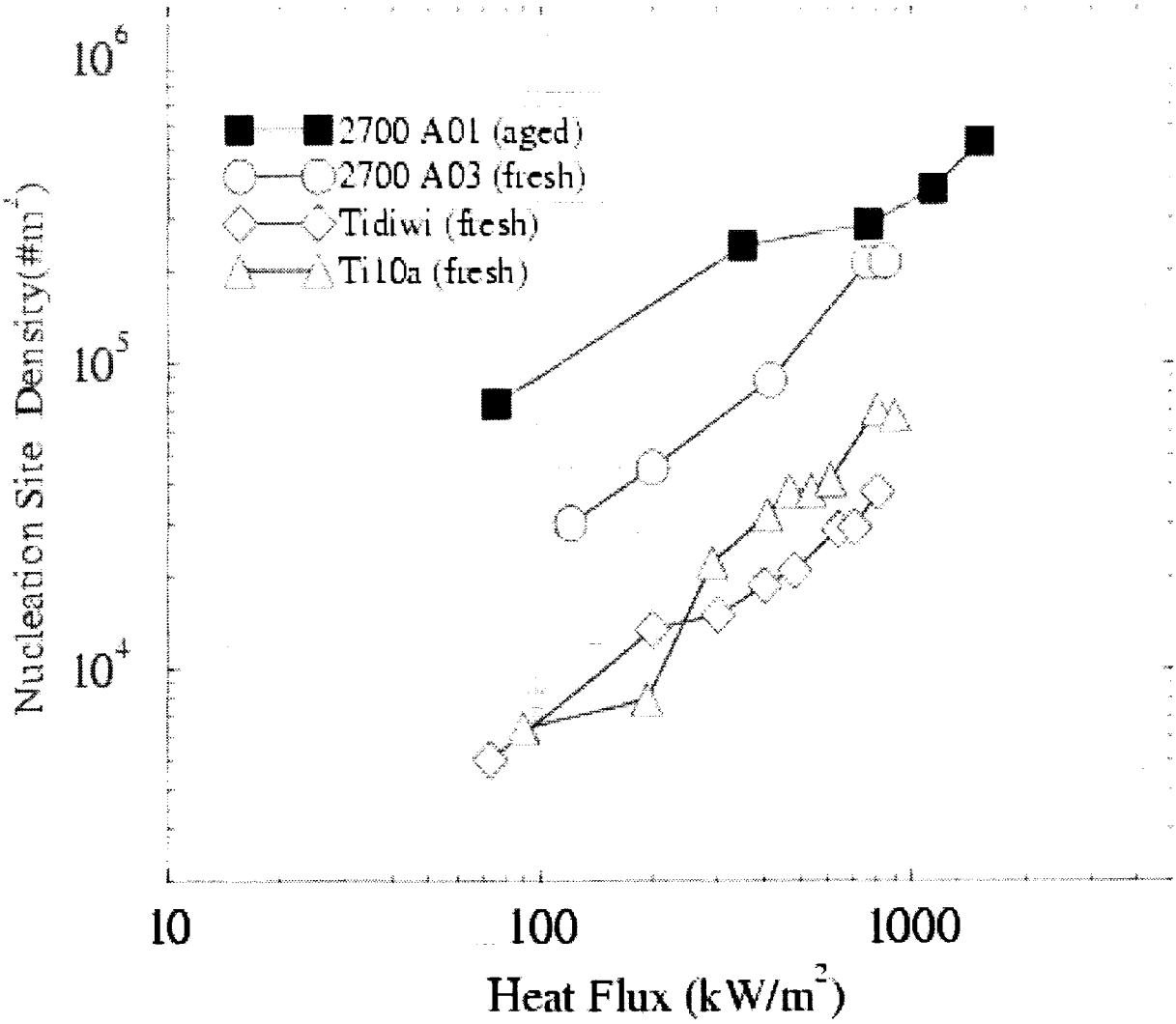

UCSB
Center for Risk Studies & Safety

TRANSIENT TEMPERATURE RESPONSE UNDER BOILING BUBBLE

FRESH HEATER – REGULAR BUBBLE

q" = 90 kW/m^2- Average Bubbling Period ~100 ms

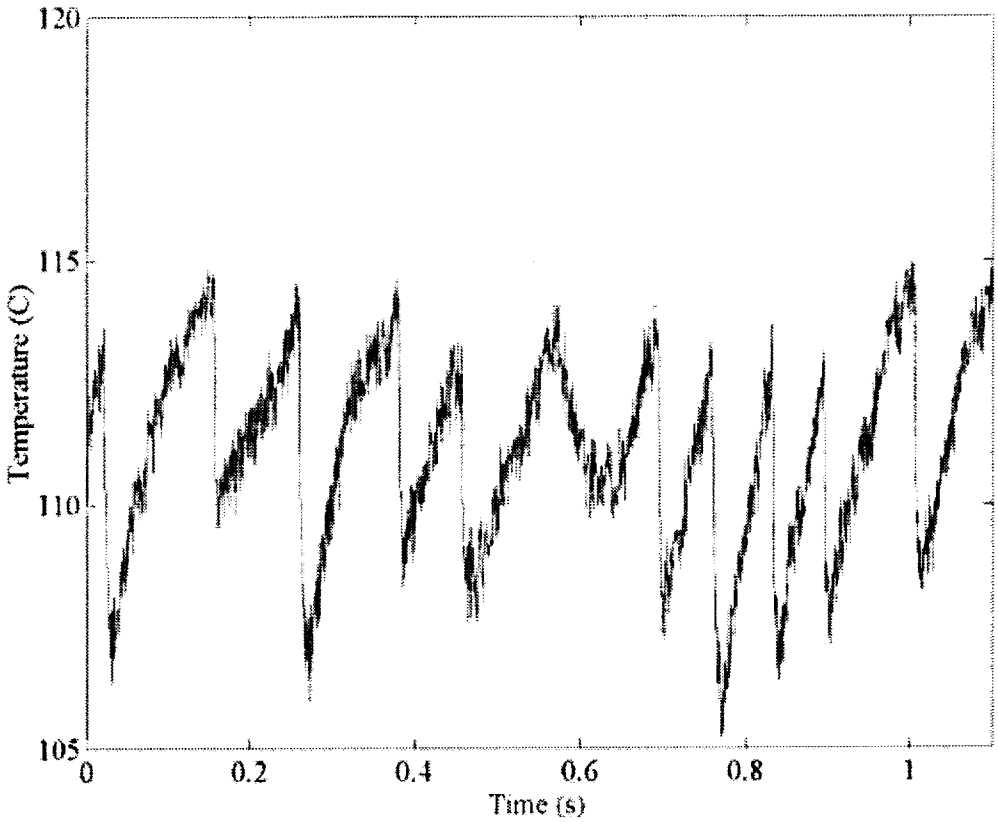

- Bubbles are Identified from the Heater's Cold Spots
- Gradual Heat-up of Liquid up to a Superheat of 15K Followed by Rapid Cooling under a Nucleating Bubble

UCSB
Center for Risk Studies & Safety

q" = 200 kW/m^2- Average Bubbling Period ~ 25 ms

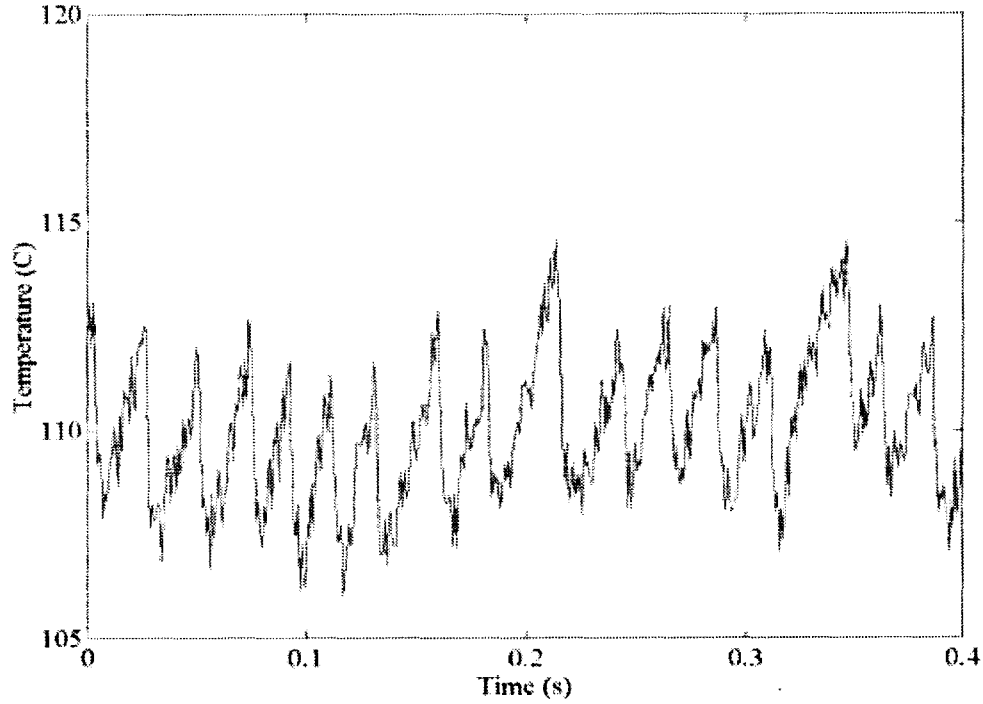

q" = 400 kW/m^2- Average Bubbling Period ~ 15 ms

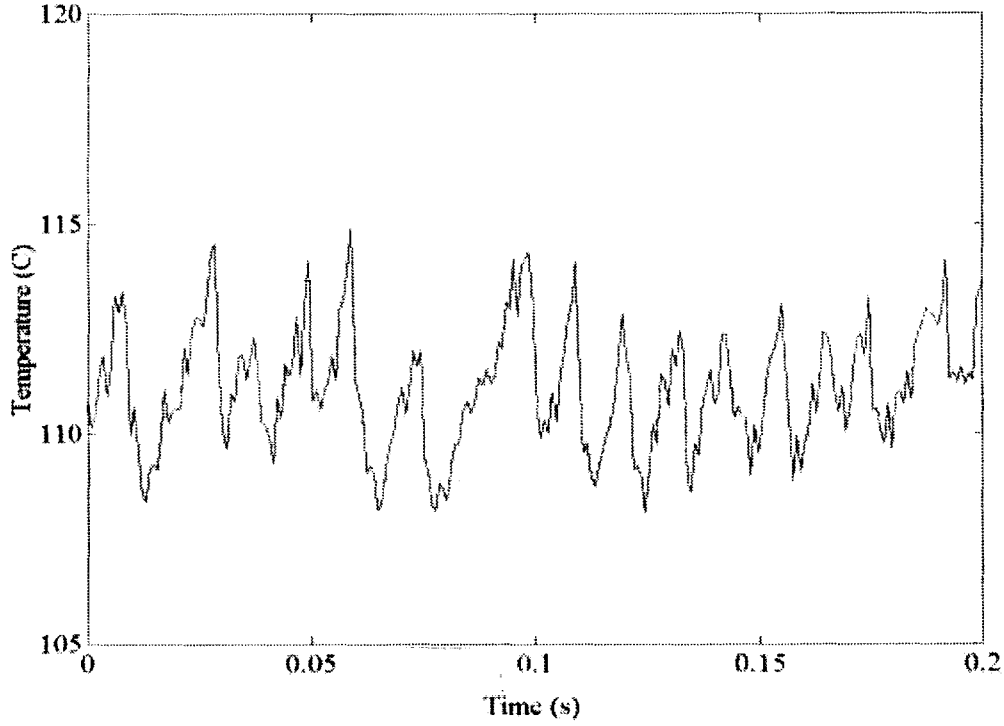

UCSB
Center for Risk Studies & Safety

TEMPERATURE across a COLD SPOT

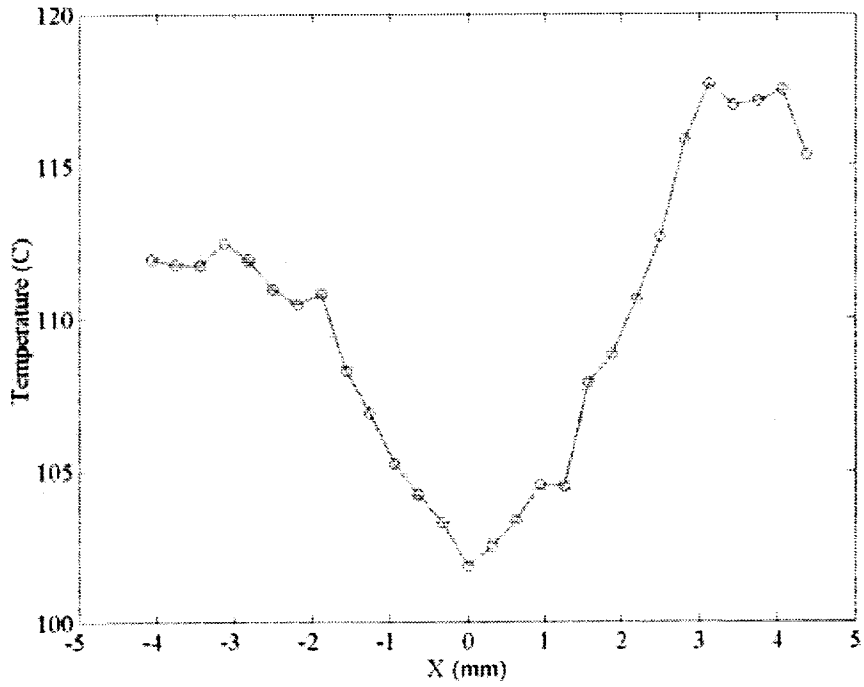

TEMPERATURE across a HOT SPOT

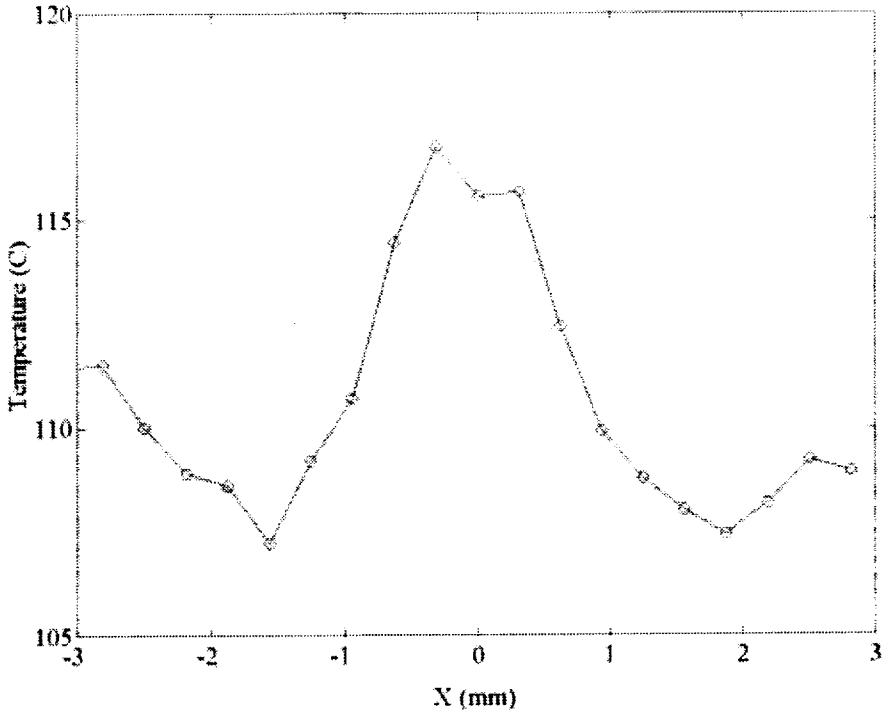

UCSB

Center for Risk Studies & Safety

BOILING BUBBLE with a HOT SPOT

q" = 200 kW/m^2- Average Bubbling Period ~120 ms

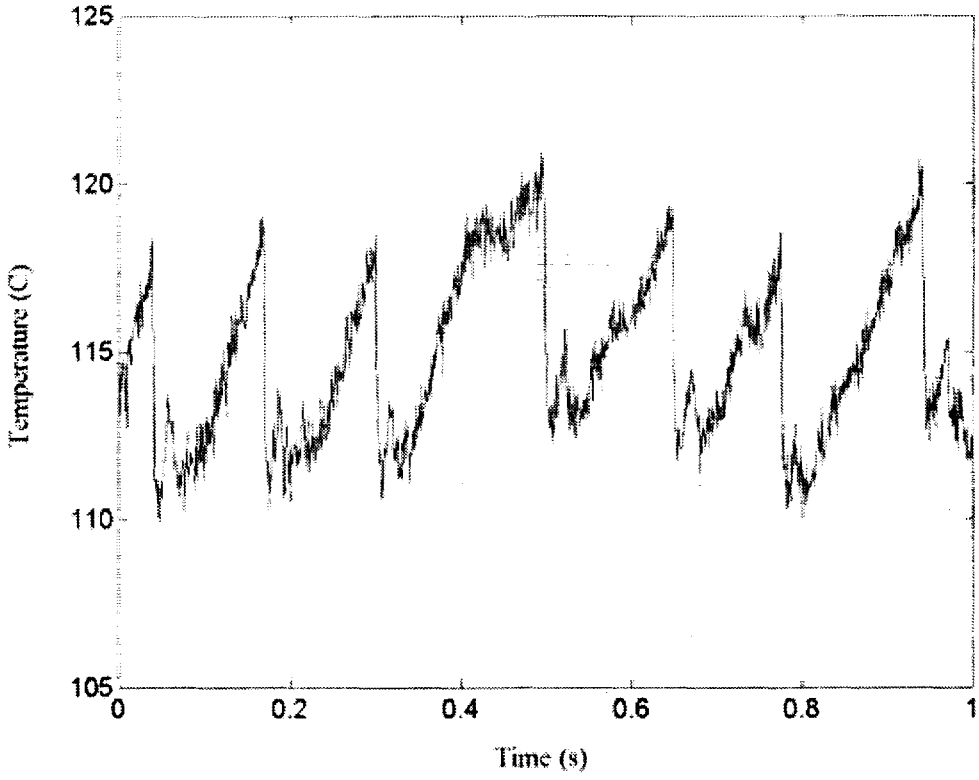

A Hot Spot is Observed to Form within a Cold Spot Induced by the Nucleating Bubble

The Transient Temperature in the Hot Spot is Coupled with the Dynamics of Cold Spot

UCSB
Center for Risk Studies & Safety

CRITICAL HEAT FLUXES

The Limit of Coolability of the Ti Thin-Film Heaters were Achieved at High Fluxes Ranging from:

600 kW/m^2 for Nanoscopically Smooth and Fresh Heaters Surface, and up to

1.5 MW/m^2 for Aged Heaters

For the First Time, High Heat Fluxes (1.2 ...1.5 MW/m^2) were Achieved in Pool Boiling on such Thin Heaters, in Contrary to CHF Data Reported in Literature

For the First Time, Origin of a Boiling Crisis Process was Unambiguously Detected by IR Direct Imaging

The High Speed and High Resolution IR Thermometry Enabled Identification of Nucleate Boiling Heat Transfer Pattern and Flow Behavior under Boiling Crisis

Burnout (Irreversible Dry Spot) was Observed to Form in Areas Not Covered with Cold Spots

Dry Spots are Not Necessarily Associated with Hot Spots

UCSB

Center for Risk Studies & Safety

SURFACE TEMPERATURE RESPONSE

TRADITIONALLY, LOCAL TEMPERATURE MEASUREMENT HAS BEEN USED AS THE BOILING CRISIS DETECTOR

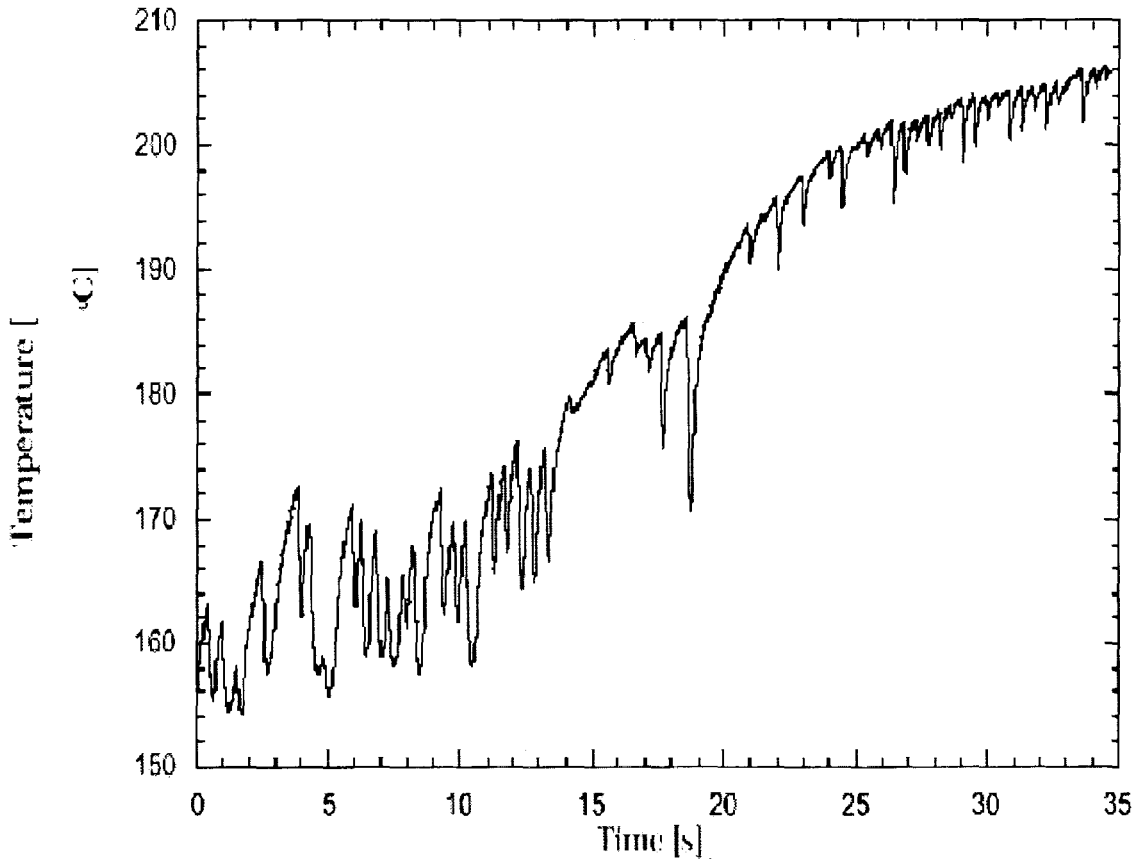

Temperature Measurement on the ULPU Downward Facing Heater during a Burnout Event

UCSB
Center for Risk Studies & Safety

VIDEO VISUALIZATION OF BURNOUT

Time = 0.00 s

Time = 0.05 s

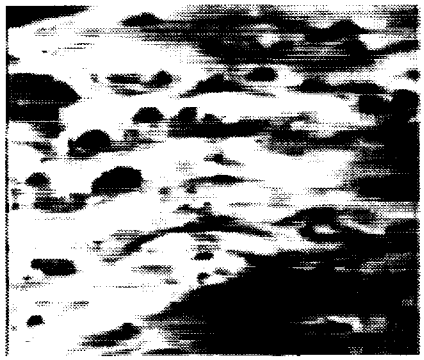

Time = 0.10 s

Time = 0.15 s

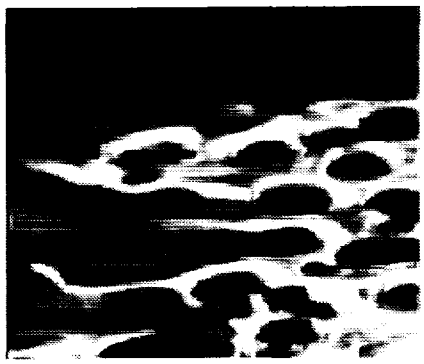

Time = 0.20 s

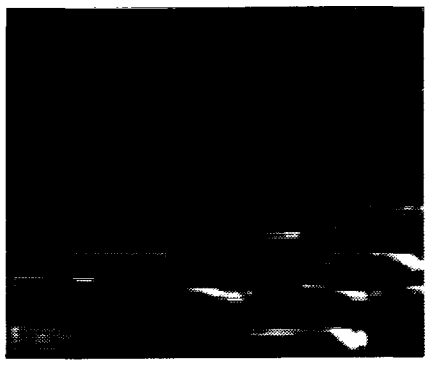

Time = 0.25 s

Dry-out on a Downward Facing Heater
(mini-ULPU Experiment)

UCSB

Center for Risk Studies & Safety

BURNOUT UNDER GAS BUBBLES (200 kW/m^2)

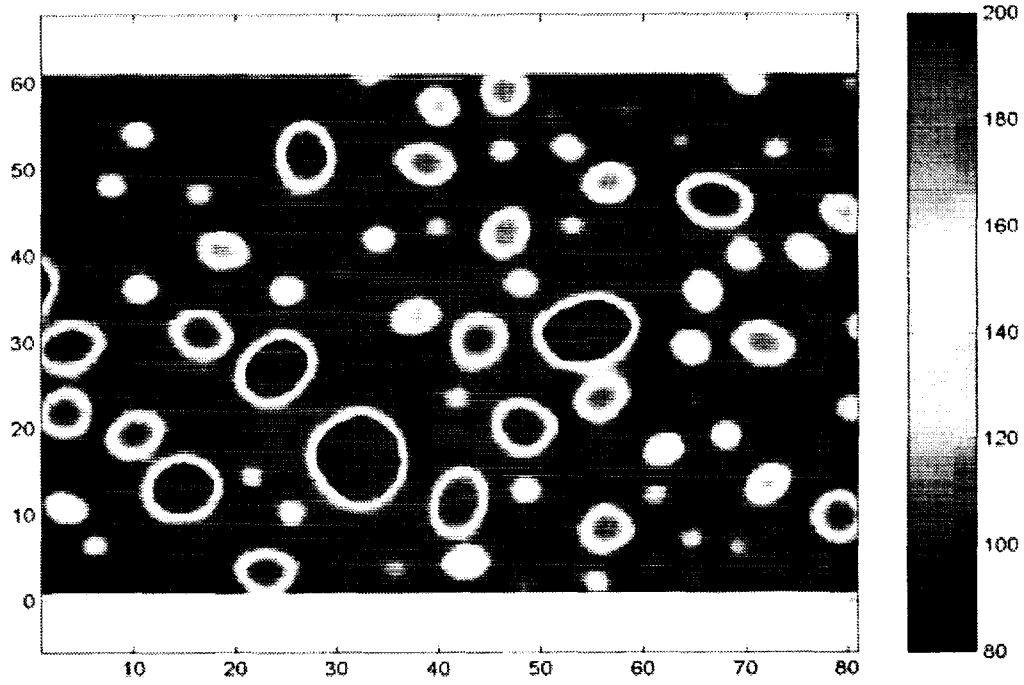

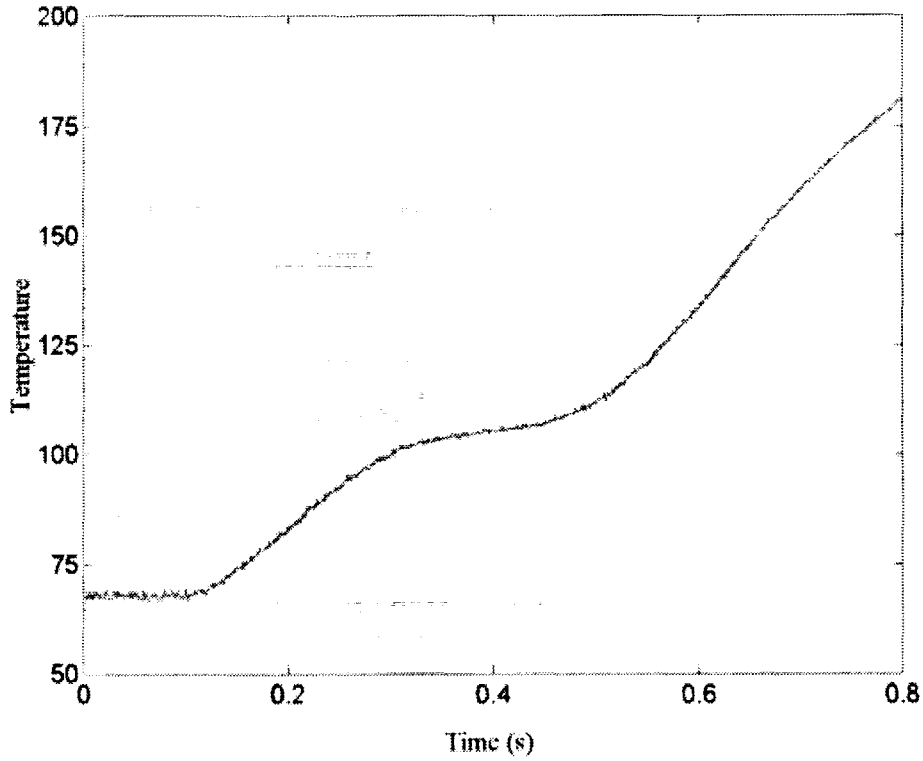

UCSB

Center for Risk Studies & Safety

BURNOUT IN DEGASSED WATER POOL BOILING

Temperature History of at the Center of a Dryspot (Fresh Heater Ti10a)

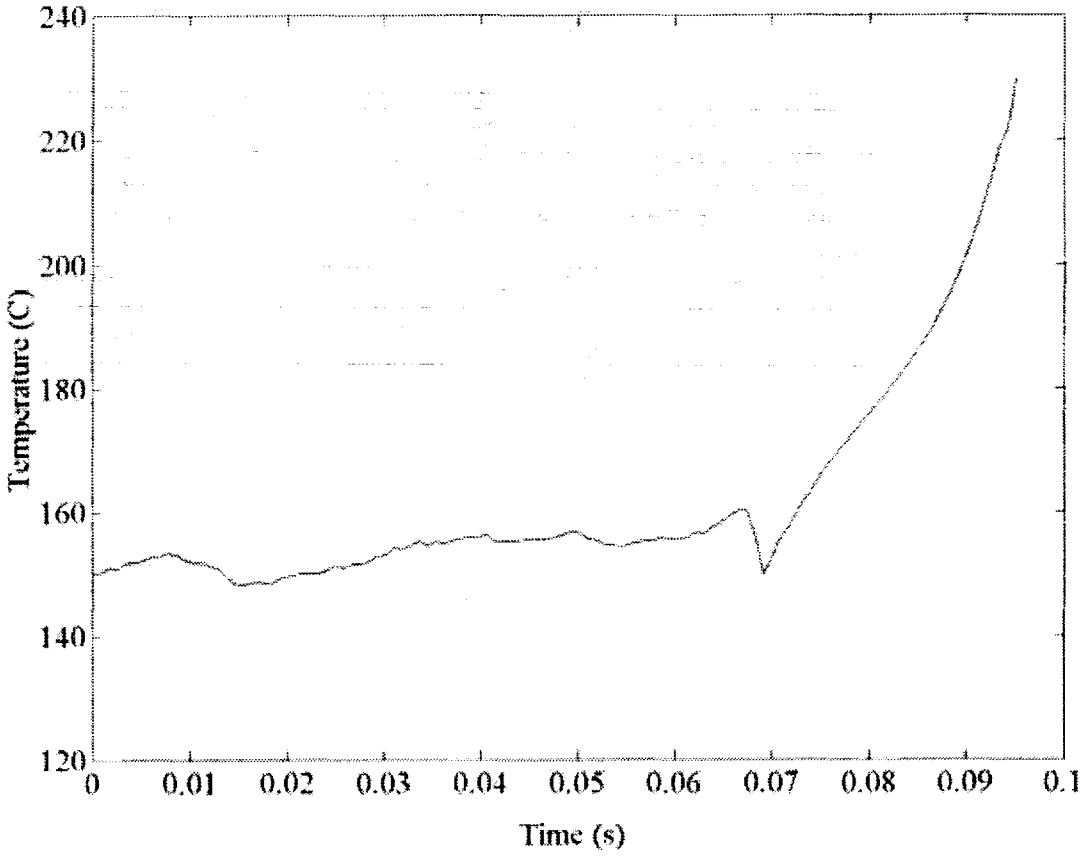

Burnout occurs in areas not covered by regular cooling sites, when heater's superheat typically reaches 50-60 °C

Liquid film evaporation preludes a rapid overheating (3000-4500 K/s at heat flux 1…1.5 MW/m^2)

UCSB
Center for Risk Studies & Safety

BURNOUT HISTORY

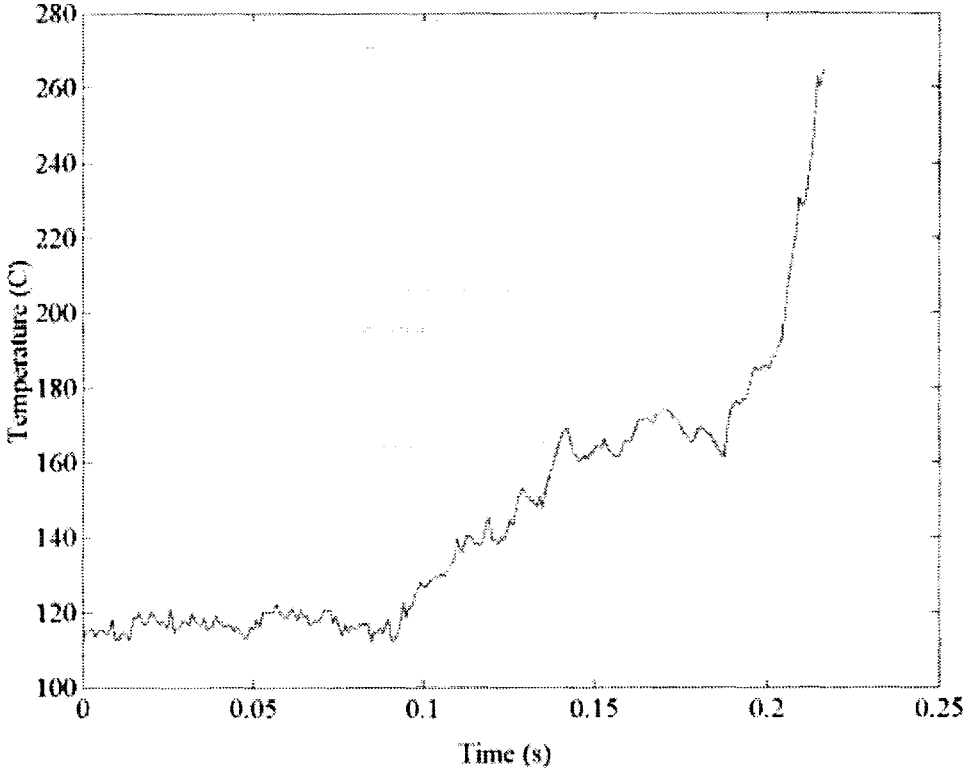

Heater 2700A03

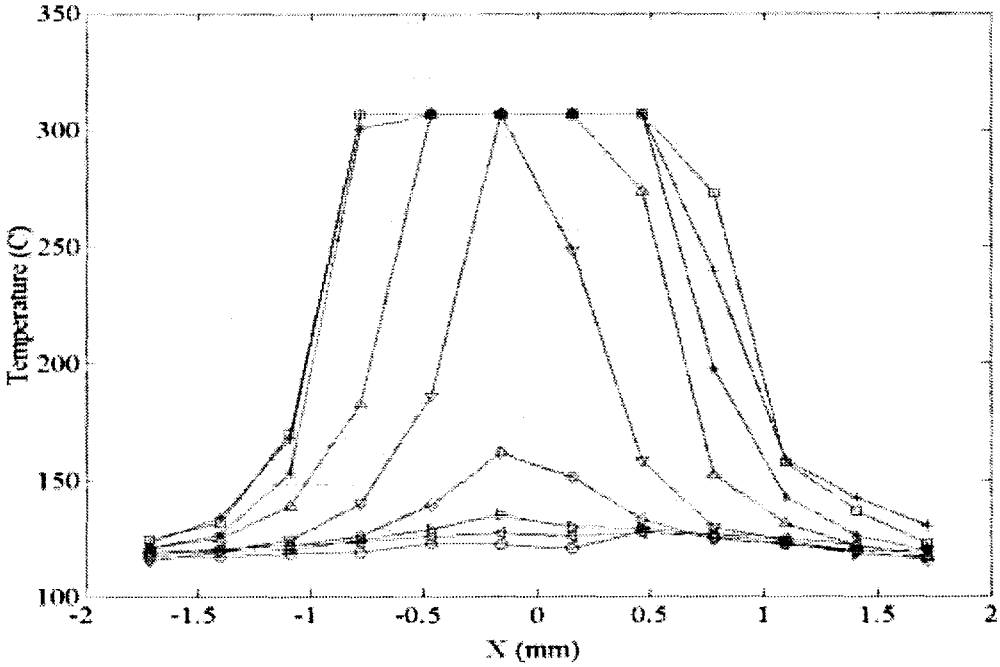

UCSB

Center for Risk Studies & Safety

IR IMAGING OF BURNOUT SEQUENCE

WATER DEPLETION TEST

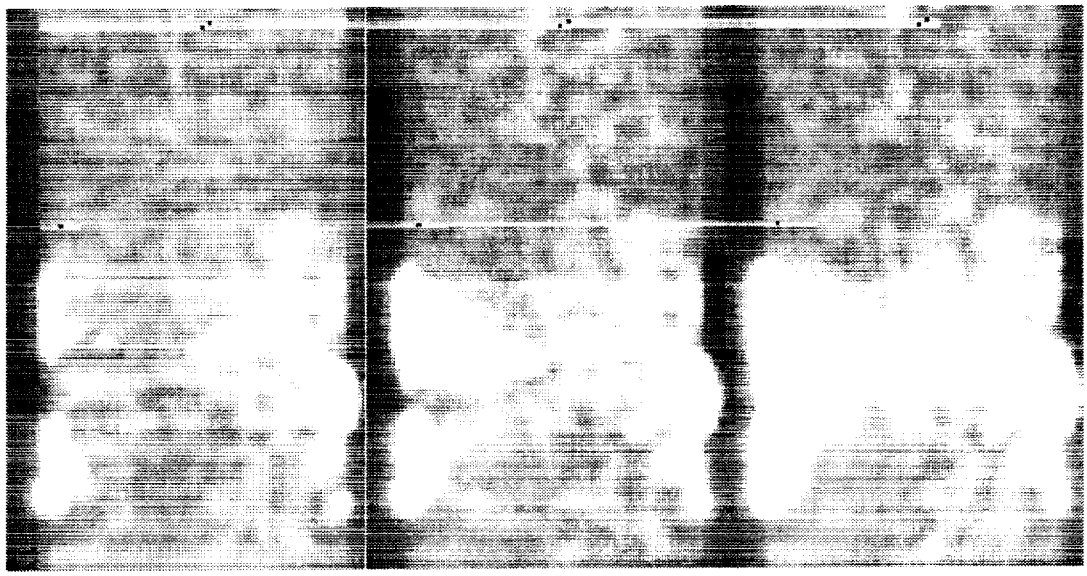

a) b) c)

J heater, run at 730 kW/m^2. Time interval 100 ms

POOL BOILING TEST

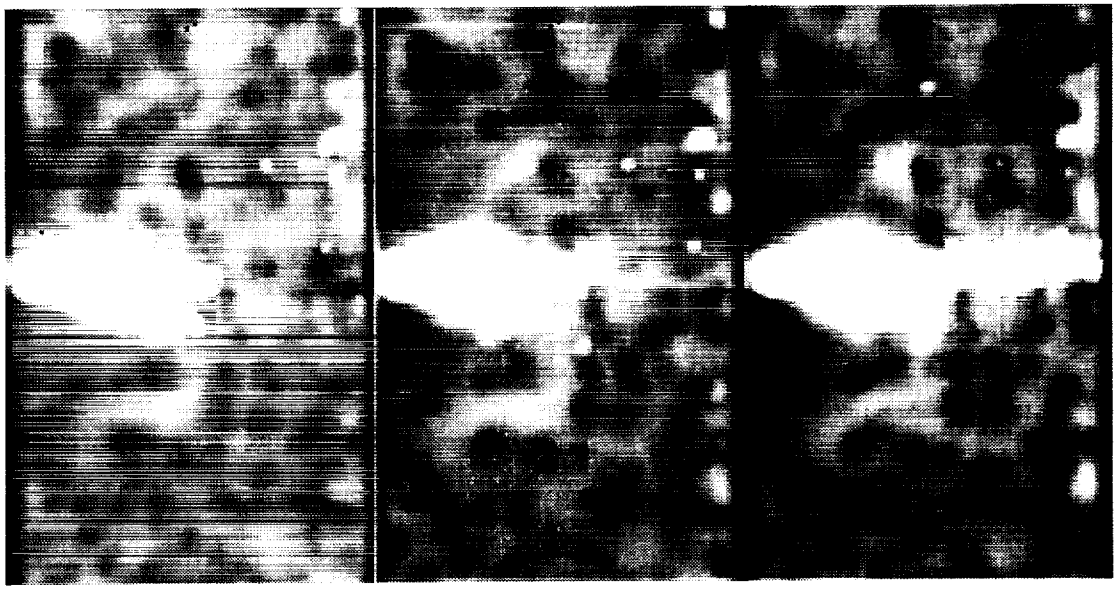

a) b) c)

K heater, run at 756 kW/m^2 . Time interval 30 ms

UCSB

Center for Risk Studies & Safety

ORIGIN OF THE BOILING CRISIS PROCESS

Heater Ti10a – q" = 900 kW/m^2

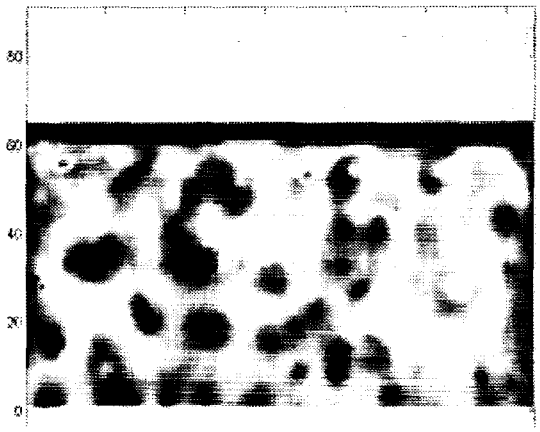

0 ms

500 ms

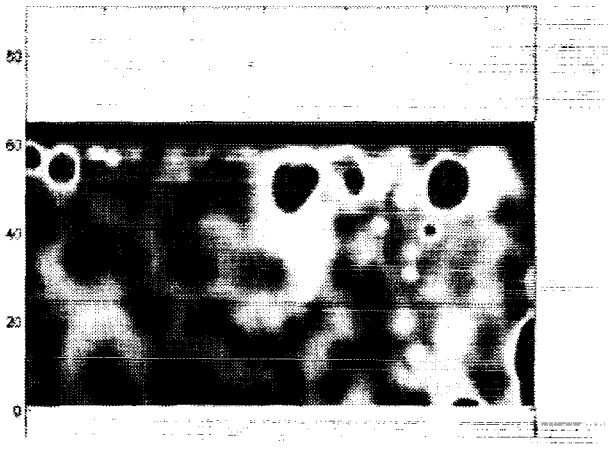

1000 ms

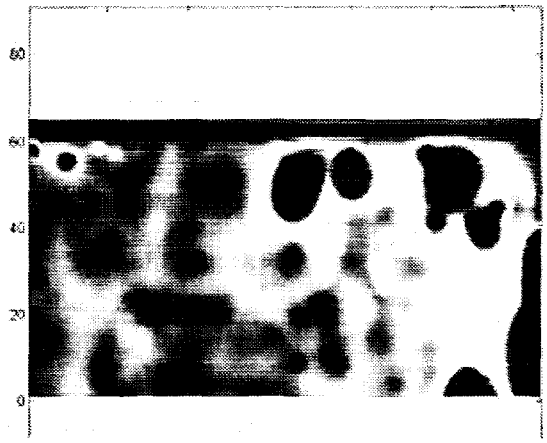

1500 ms

- Formation and Growth of Areas with Rapid Heating
- Thermal Stress Associated with Overheating May Have Caused The Thin Heater and Glass to Break

UCSB

Center for Risk Studies & Safety

CHRACTERIZATION OF HEATER SURFACE

Using

- Optical Microscope (x1000)
- Optical Microscope with a Nomarski Prism
  (small depth of field)
- Scanning Electron Microscope (SEM)
- Atomic Force Microscope (AFM)

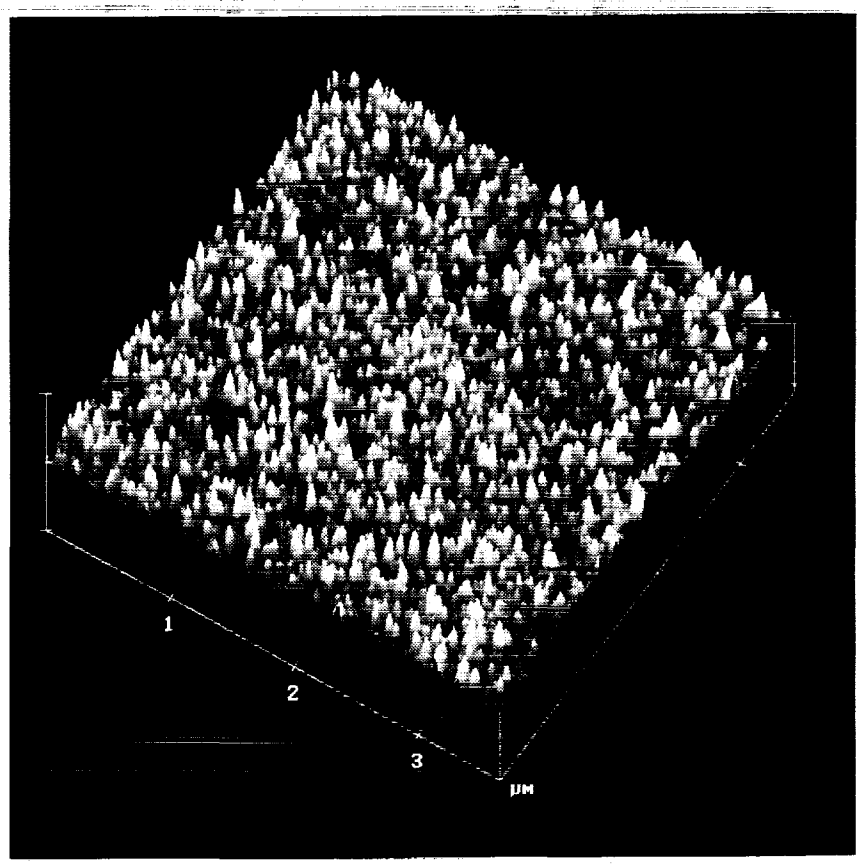

AFM Picture of a Fresh Heater, Before and After Boiling in Chemically Clean and Degassed Water
(scan area 3.5 x 3.5 µm, roughness rms ±4 nm)

UCSB
Center for Risk Studies & Safety

AGED HEATER MORPHOLOGY (CHF 1.5 MW/m^2)

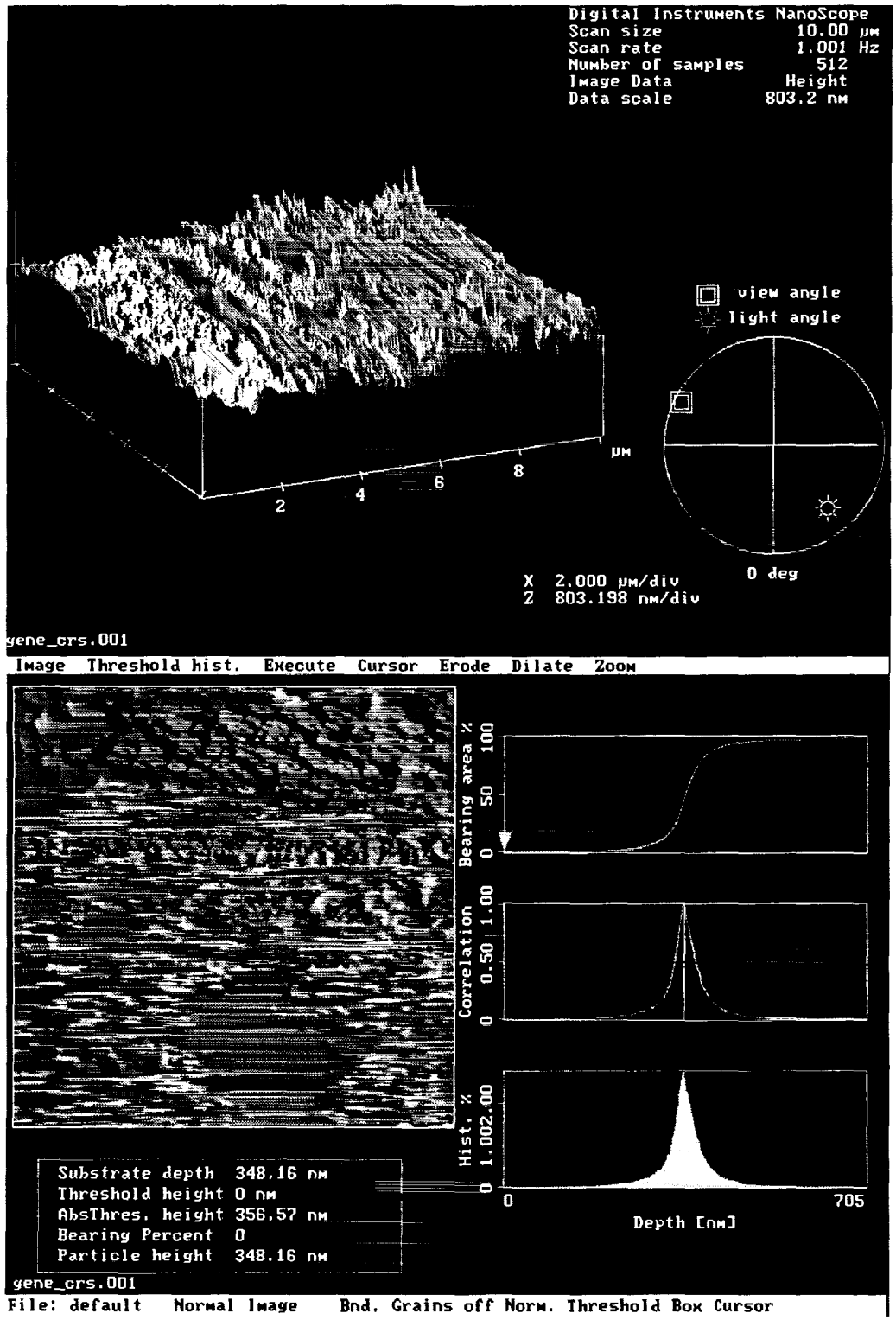

UCSB

Center for Risk Studies & Safety

AGED HEATER (After CHF, 1 MW/m^2)

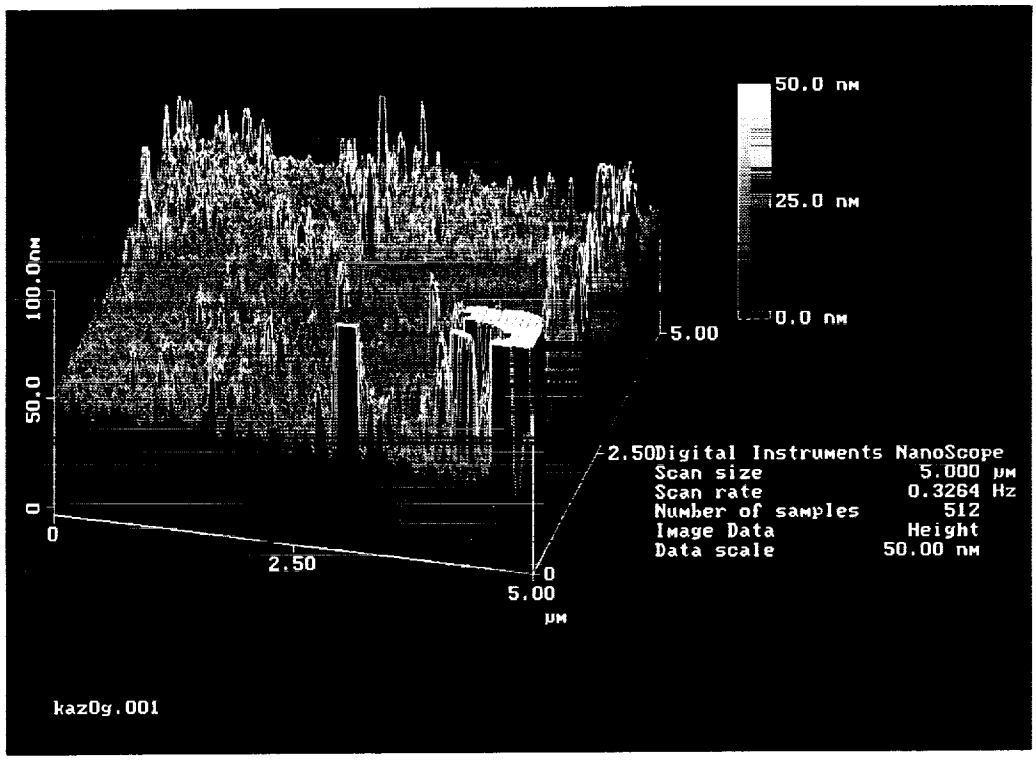

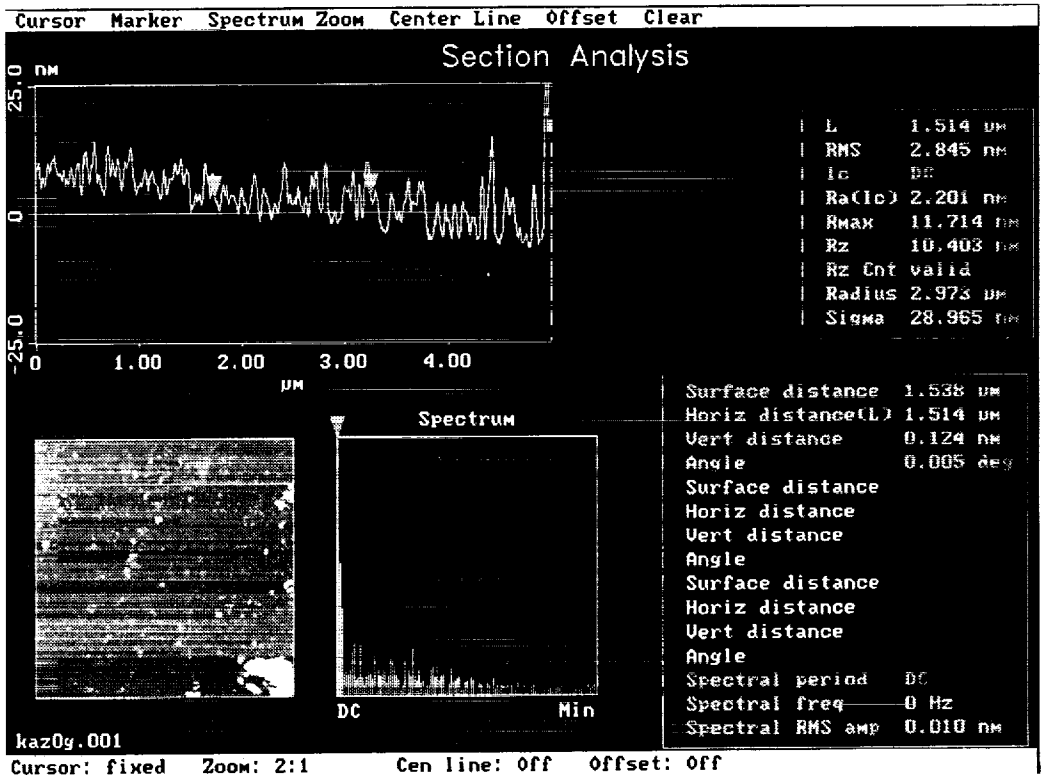

UCSB

Center for Risk Studies & Safety

AGED HEATER SURFACE MORPHOLOGY

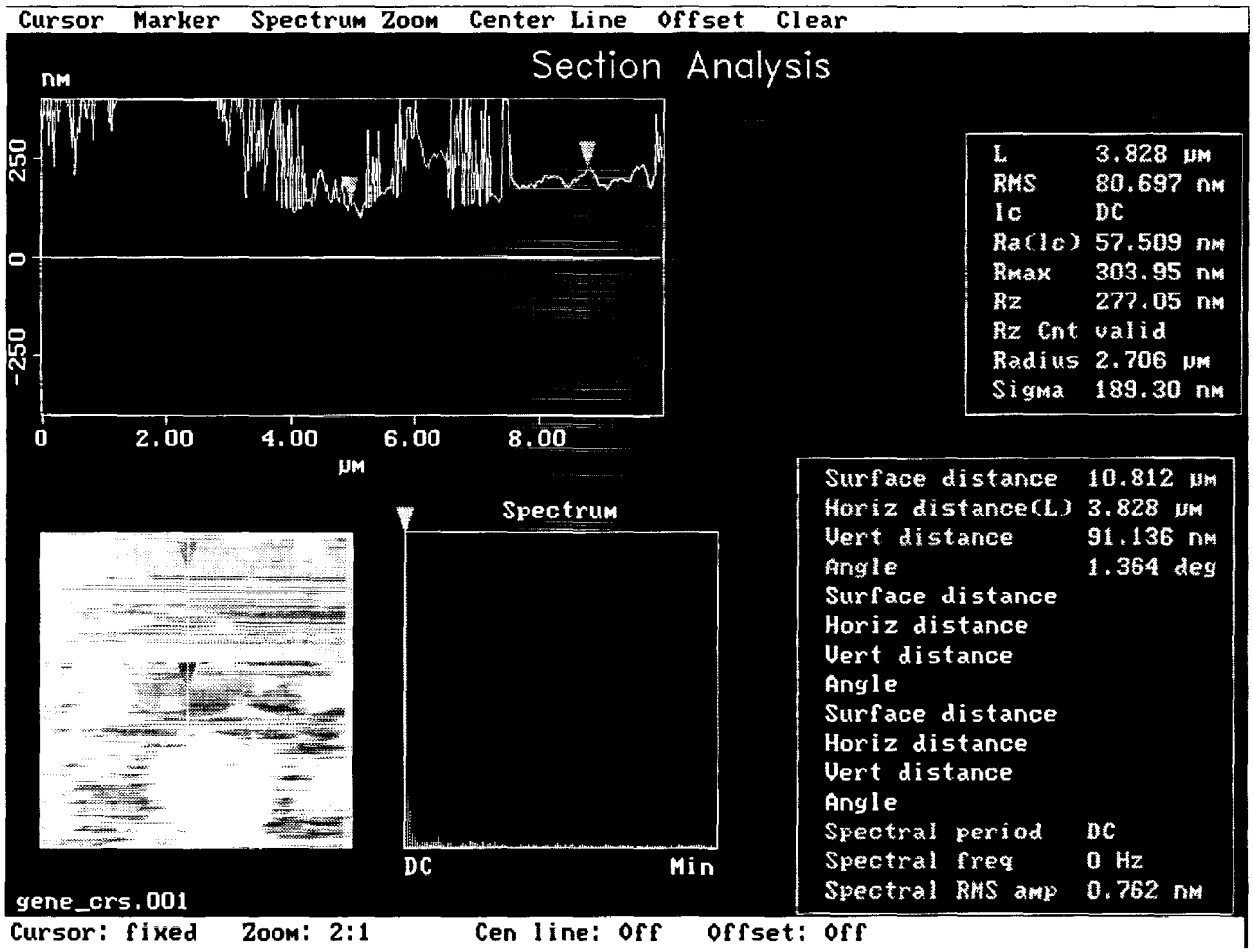

The Aged Heaters have Nanoscopically Rough Surfaces (rms > ±50 nm)

The Heater's Surface Includes Protrusions of 100 nm Scale

The Coverage is Microscopically Non-Uniform.

UCSB

Center for Risk Studies & Safety

CLOSE-UP VIEWS OF THE AGED HEATER

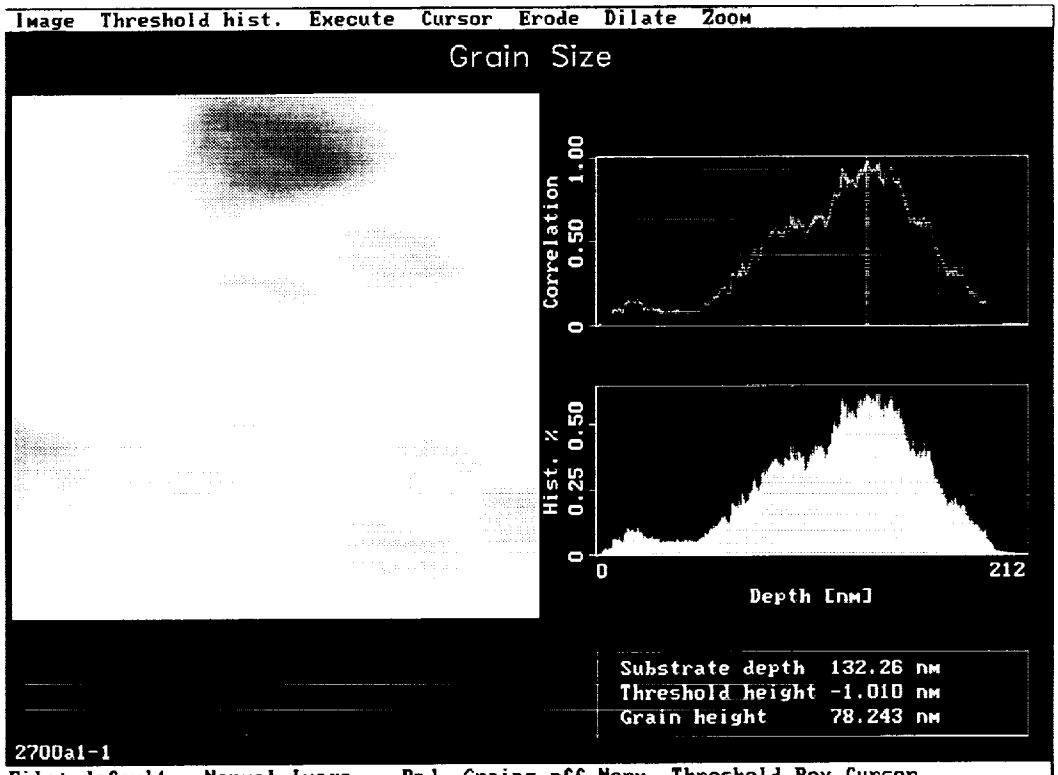

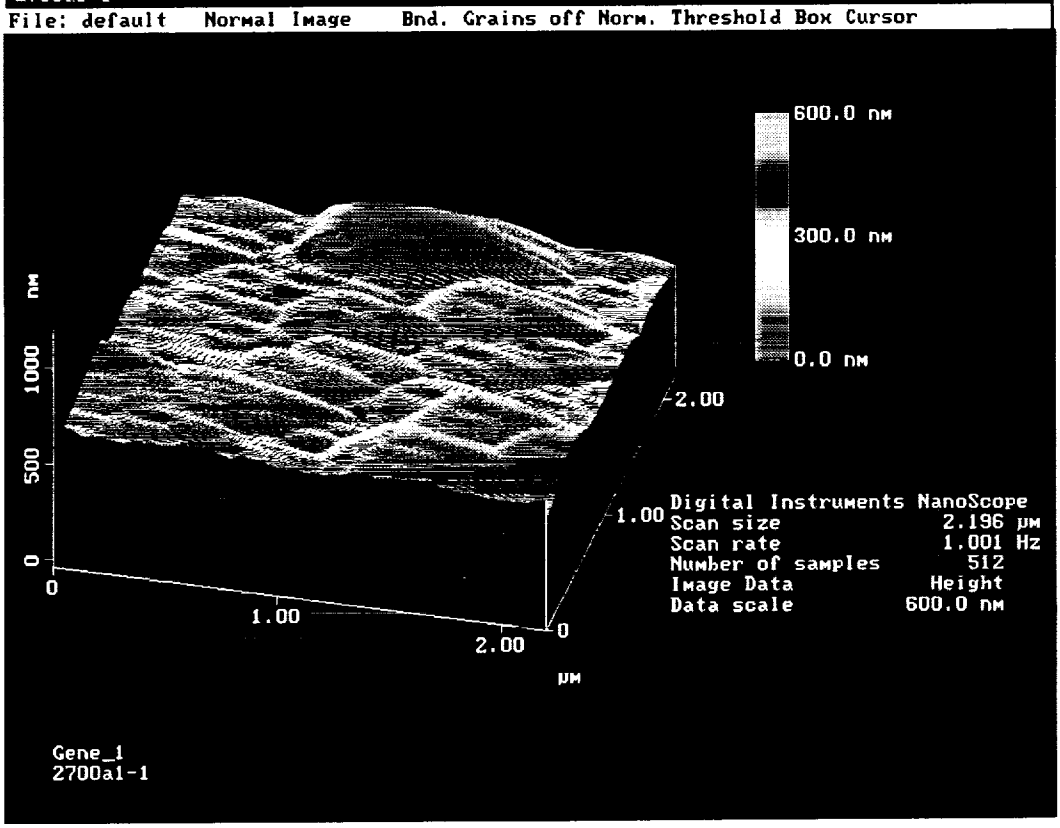

UCSB

Center for Risk Studies & Safety

CHRACTERIZATION OF HEATER SURFACE

The Degree of Heater Ageing Significantly Affects the Wetting Characteristics and Nucleation Behavior

In Addition to Static Contact Angle (β), Advancing (β_{ADV}) and Receding (β_{REC}) Contact Angles were Determined

Heater	β	β_{ADV}	β_{REC}
Fresh			
Before Experiment	60-65°	70-80°	30-40°
After CHF	65-80°	80-100°	25-40°
Aged	90-110°	90-100°	< 10°

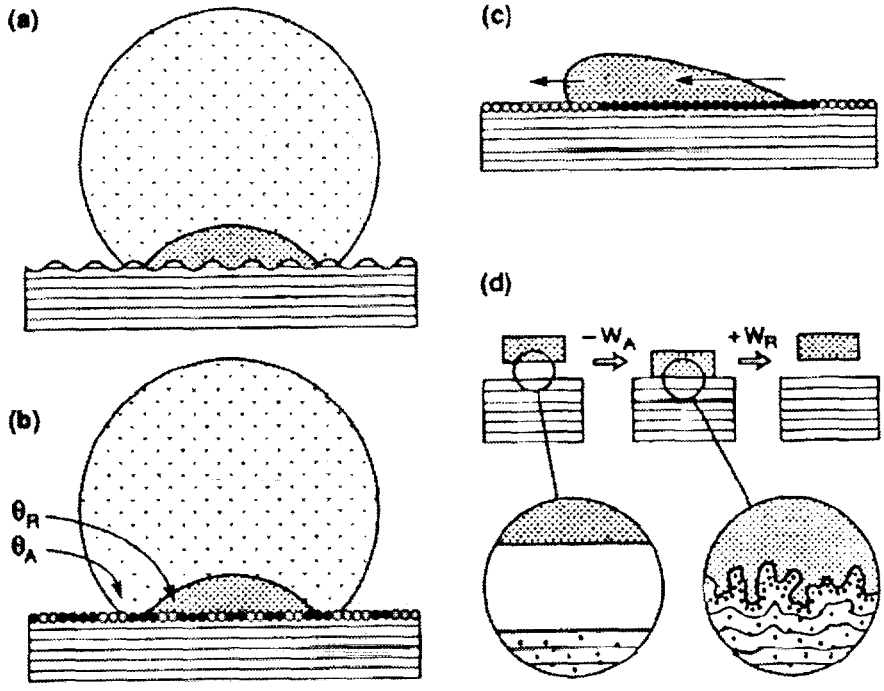

(Israelachvili, 1985)

UCSB
Center for Risk Studies & Safety

CONCLUDINGS REMARKS

- Vapor-Deposited Ultrathin Heaters were Used in Combination with High-Speed IR Thermometry to Study Nucleate Boiling and Boiling Crisis
- The Technique Enables High-Resolution Visualization of Nucleate Boiling Heat Transfer with Incredible Details
- Ultrathin Heaters Feature CHF Similar to Thick Heaters
- High Heat Fluxes (over CHF Values Predicted by the K-Z Correlation) were Achieved on Aged Heaters
- High-Flux Nucleate Boiling and Boiling Crisis were Realized with Significantly Lower Density of Active Nucleation Site on both Fresh and Aged Heaters
- Nucleation Occurs on the Ultra-Smooth Surface for Liquid Superheat As Low as 20-35 °C
- The Nucleation Pattern is Highly Regular at High Heat Fluxes

UCSB

Center for Risk Studies & Safety

CONCLUDINGS REMARKS (contd.)

- Formation and Growth of Hot Spots within Nucleation Sites were Observed, particularly in Fresh Heaters at Relatively High Fluxes
- The Depletion Experiments Show that Bubble Continue to Nucleate in the Thin Microfilm
- Very Thin Liquid Film Persists to Wet the Heater's Surface Until Dry Spots Form Simultaneously in Few Locations and Avalanche
- The Degree of Heaters' Ageing (partly Represented by Receding Contact Angle) was Found to Determine the Nucleation Site Density and Maximum Heat Fluxes
- The Nucleation Site-Related Hot Spots Did Not Serve as the Source for Irreversible Dry Spots (Boiling Crisis)
- Origin of Boiling Crisis was Found to Relate to Areas of Superheated Liquid in Between Nucleation Sites
- The Technique Developed Opens Unique Window to Study the Physics of Boiling and Examine in Details Related Surface Phenomena

UCSB
Center for Risk Studies & Safety

MARANGONI EFFECTS ON NEAR-BUBBLE MICROSCALE TRANSPORT DURING BOILING OF BINARY FLUID MIXTURES

C. Sun, V. P. Carey
Department of Mechanical Engineering, University of California, Berkeley, CA 94704

B. Motil
NASA Glenn Research Center, Cleveland, OH 44315

ABSTRACT

In earlier investigations (see Ahmed, et al. [1]), Marangoni effects were observed to be the dominant mechanism of boiling transport in 2-propanol/water mixtures under reduced gravity conditions. In this investigation we have examined the mechanisms of binary mixture boiling by exploring the transport near a single bubble generated in a binary mixture between a heated surface and cold surface. The temperature field created in the liquid around the bubble produces vaporization over the portion of its interface near the heated surface and condensation over portions of its interface near the cold surface. Experiments were conducted using different mixtures of water and 2-propanol under 1g conditions and under reduced gravity conditions aboard the KC135 aircraft. Since 2-propanol is more volatile than water, there is a lower concentration of 2-propanol near the hot surface and a higher concentration of 2-propanol near the cold plate relative to the bulk quantity. This difference in interface concentration gives rise to strong Marangoni effects that move liquid toward the hot plate in the near bubble region for 2-propanol and water mixtures. In the experiments in this study, the pressure of the test system was maintained at about 5 kPa to achieve the full spectrum of boiling behavior (nucleate boiling, critical heat flux and film boiling) at low temperature and heat flux levels. Heat transfer data and visual documentation of the bubble shape were extracted from the experimental results.

In the 1-g experiments at moderate to high heat flux levels, the bubble was observed to grow into a mushroom shape with a larger top portion near the cold plate due to the buoyancy effect. The shape of the bubble was somewhat affected by the cold plate subcooling and the superheat of the heated surface. At low superheat levels for the heated surface, several active nucleation sites were observed, and the vapor stems from them merged to form a larger bubble. The generation rate of vapor is moderate in this regime and the bubble shape is cylindrical in appearance. In some instances, the bubble interface appeared to oscillate. At higher applied heat flux levels, the top of the bubble became larger, apparently to provide more condensing interface area adjacent to the cold plate. Increasing the applied heat flux ultimately led to dry-out of the heated surface, with conditions just prior to dryout corresponding to the maximum heat flux (CHF). A more stable bubble was observed when the system attained the minimum heat flux (for film boiling). In this regime, most of the surface under the bottom of the bubble was dry with nucleate boiling sometimes occuring around the contact perimeter of the bubble at heated surface. Figure 1 shows a typical bubble in this regime.

Fig. 1. Bubble profile for 2-propanol mole fraction of 0.015, with gap =6.4 mm, pressure = 4.04 kPa, ΔT_c = 2.73°, ΔT_h = 99.79°, T_{bulk} = 27.5° C, q" = 728.7 kW/m^2.

Different variations (e.g. gap between two plates, molar concentration of the liquid mixture) of the experiments were examined to determine parametric effects on the boiling process and to determine the best conditions for the KC135 reduced gravity tests. Variation of the gap was found to have a minor impact on the CHF. However, reducing the gap between the hot and cold surface was observed to significantly reduce the minimum heat flux for fixed molar concentration of 2-propanol.

In the reduced gravity experiments aboard the KC135 aircraft, the bubble formed in the 6.4 mm gap was generally cylindrical or barrel shaped and it increased its extent laterally as the surface superheat increased. In reduced gravity experiments, dryout of the heated surface under the bubble was observed to occur at a lower superheated temperature than for 1g conditions. Observed features of the boiling process and heat transfer data under reduced gravity will be discussed in detail. The results of the reduced gravity experiments will also be compared to those obtained in comparable 1g experiments.

In tandem with the experiments we are also developing a computational model of the transport in the liquid surrounding the bubble during the boiling process. The computational model uses a level set method [2] to model motion of the interface. It will incorporate a macroscale treatment of the transport in the liquid gap between the surfaces and a microscale treatment of transport in the regions between the bubble interface and the solid surfaces. The features of the model will be described in detail. Future research directions suggested by the results to date will also be discussed.

REFERENCES

[1] Ahmed, S. and Carey, V.P., 1998, "Effects of Gravity on Boiling of Binary Fluid Mixtures," *Int. Journal of Heat and Mass Transfer*, Vol. 41, pp. 2469-2483.
[2] Sethian, J. A., 1996, *Level Set Methods*, Cambridge University Press, Cambridge, U.K.

NASA/CP—2000-210470

Marangoni Effects on Near-Bubble Microscale Transport During Boiling of Binary Fluid Mixtures

C. Sun, V.P. Carey
Department of Mechanical Engineering, University of California at Berkeley

B. Motil
NASA Glenn Research Center, Cleveland, OH

Outline

- Background
- Experiments
- Results
- Conclusions and Future Work

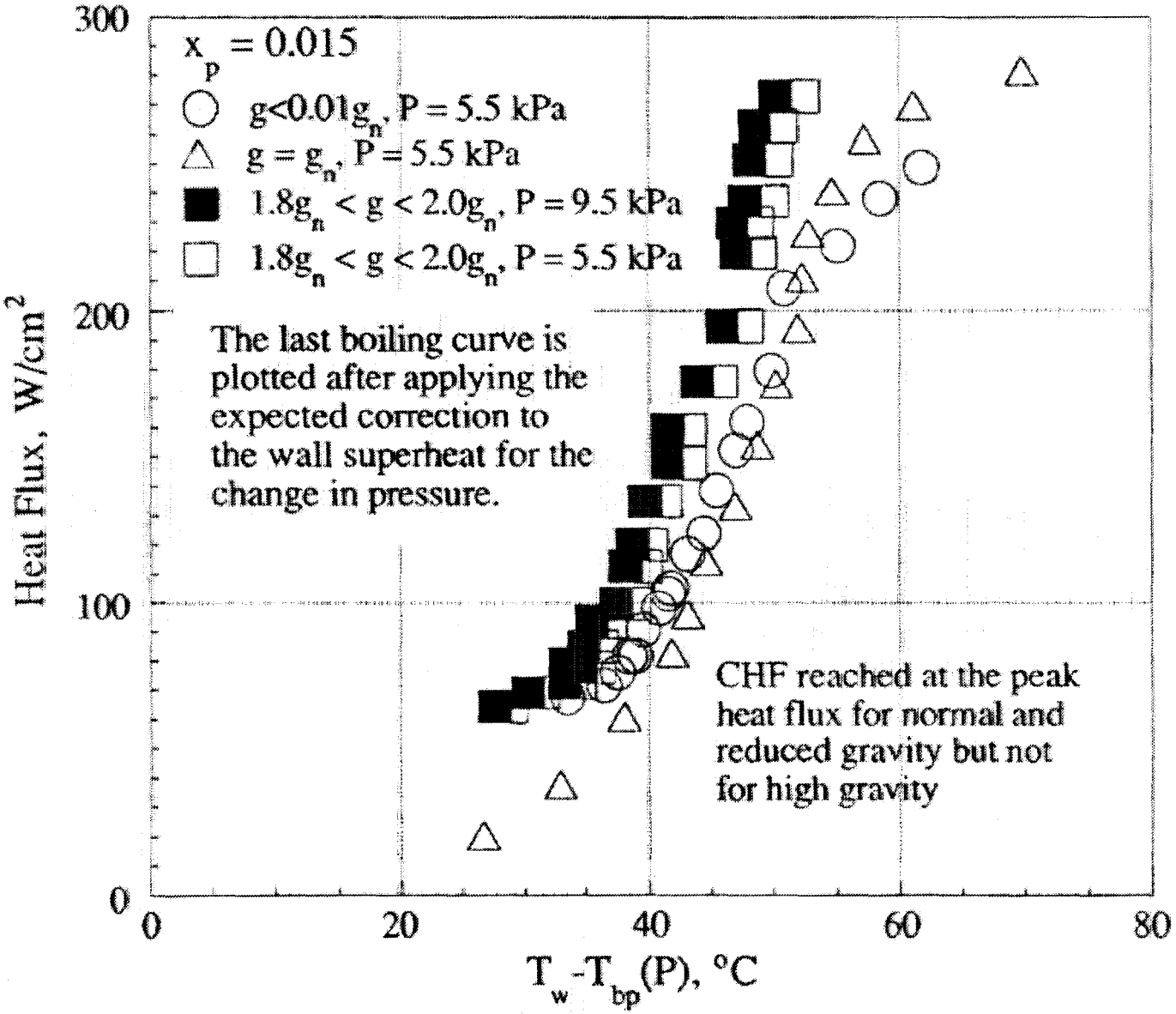

Effect of gravity on the boiling of water/2-propanol mixture for x_p=0.015.

Marangoni Effects on Near Bubble Transport

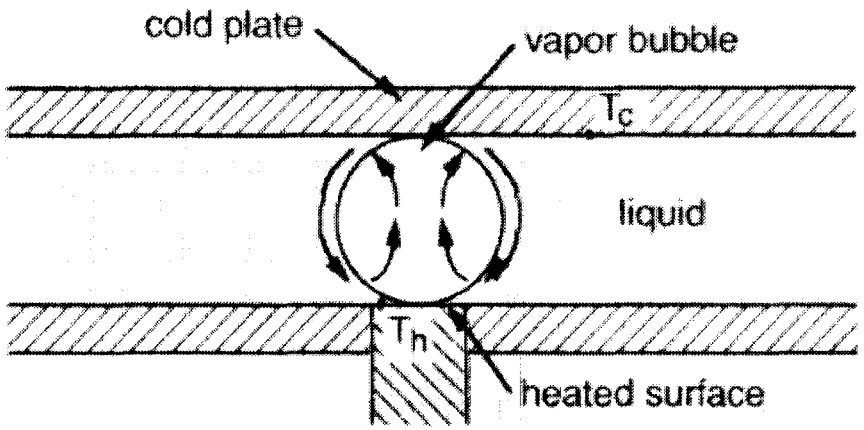

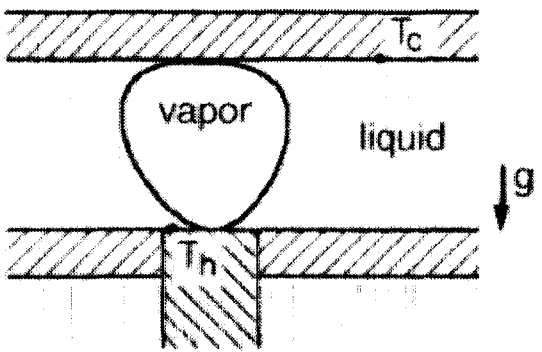

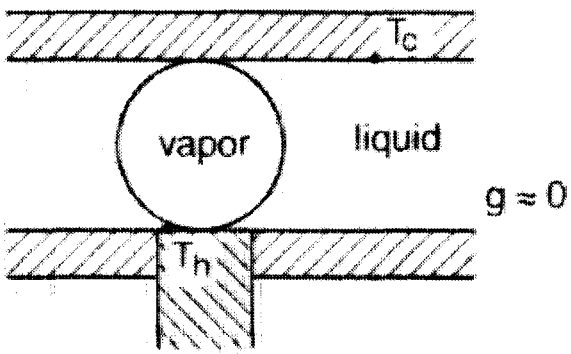

Multiphase Transport Laboratory, August 2000

Marangoni Effects on Near Bubble Transport

- Test section with stationary bubble

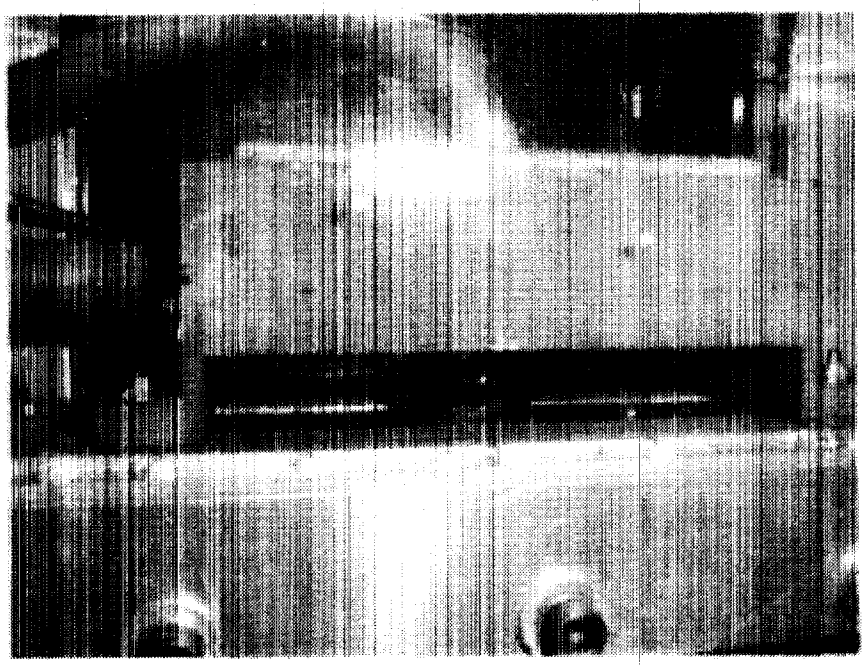

Multiphase Transport Laboratory, August 2000

Marangoni Effects on Near Bubble Transport

- Test system

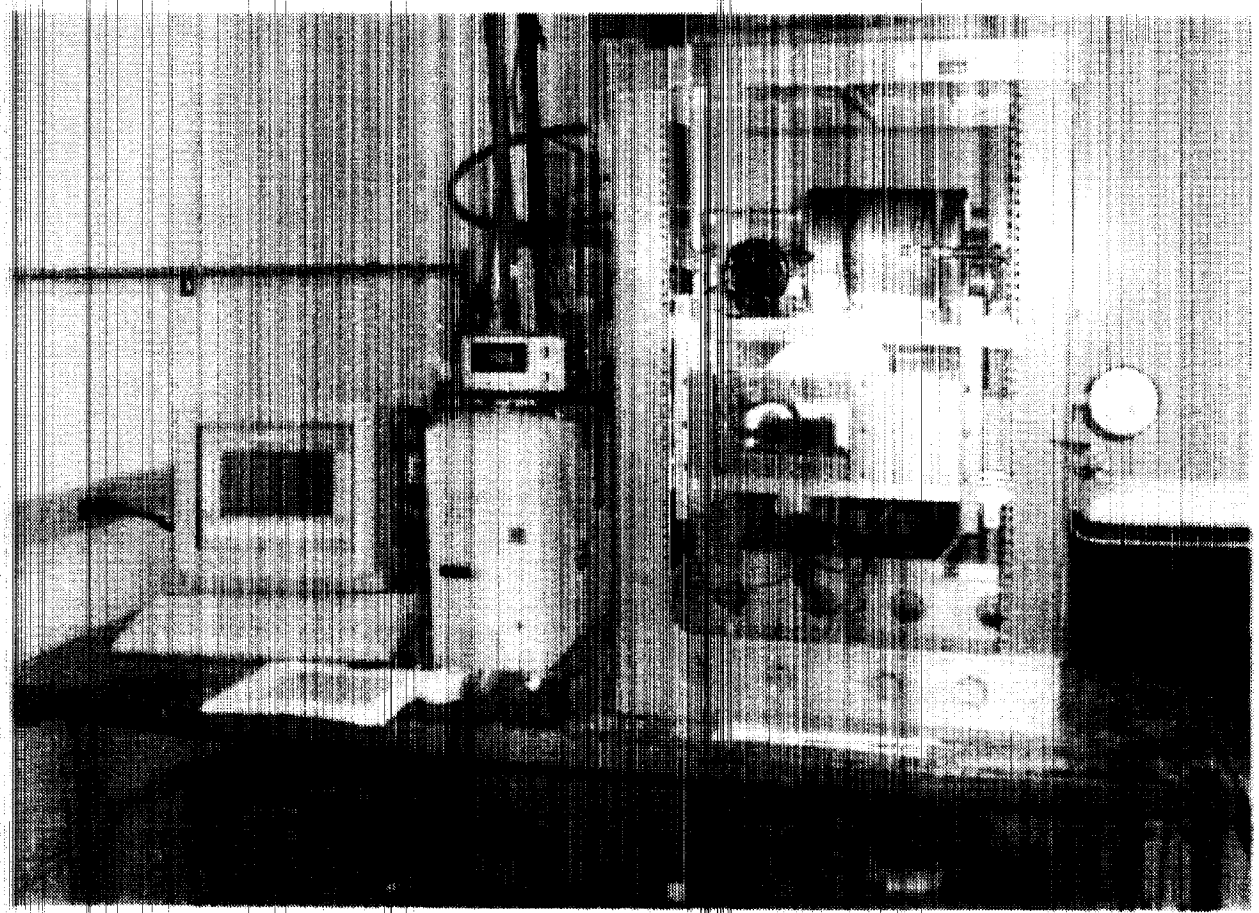

Multiphase Transport Laboratory, August 2000

Marangoni Effects on Near Bubble Transport

- pure water at 4 kPa,
- wall superheat = 34 °C, coldplate subcooling = 15 °C

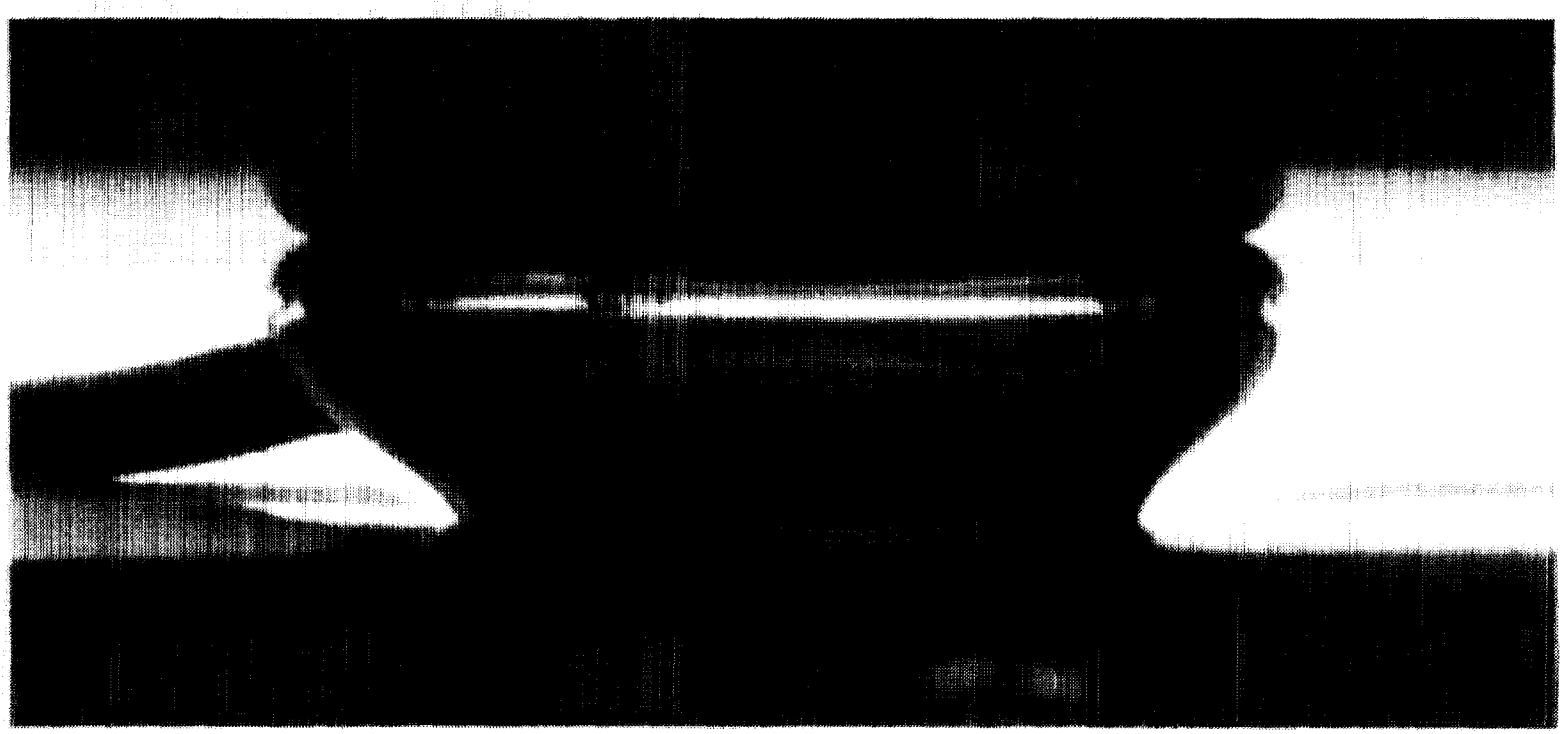

Multiphase Transport Laboratory, August 2000

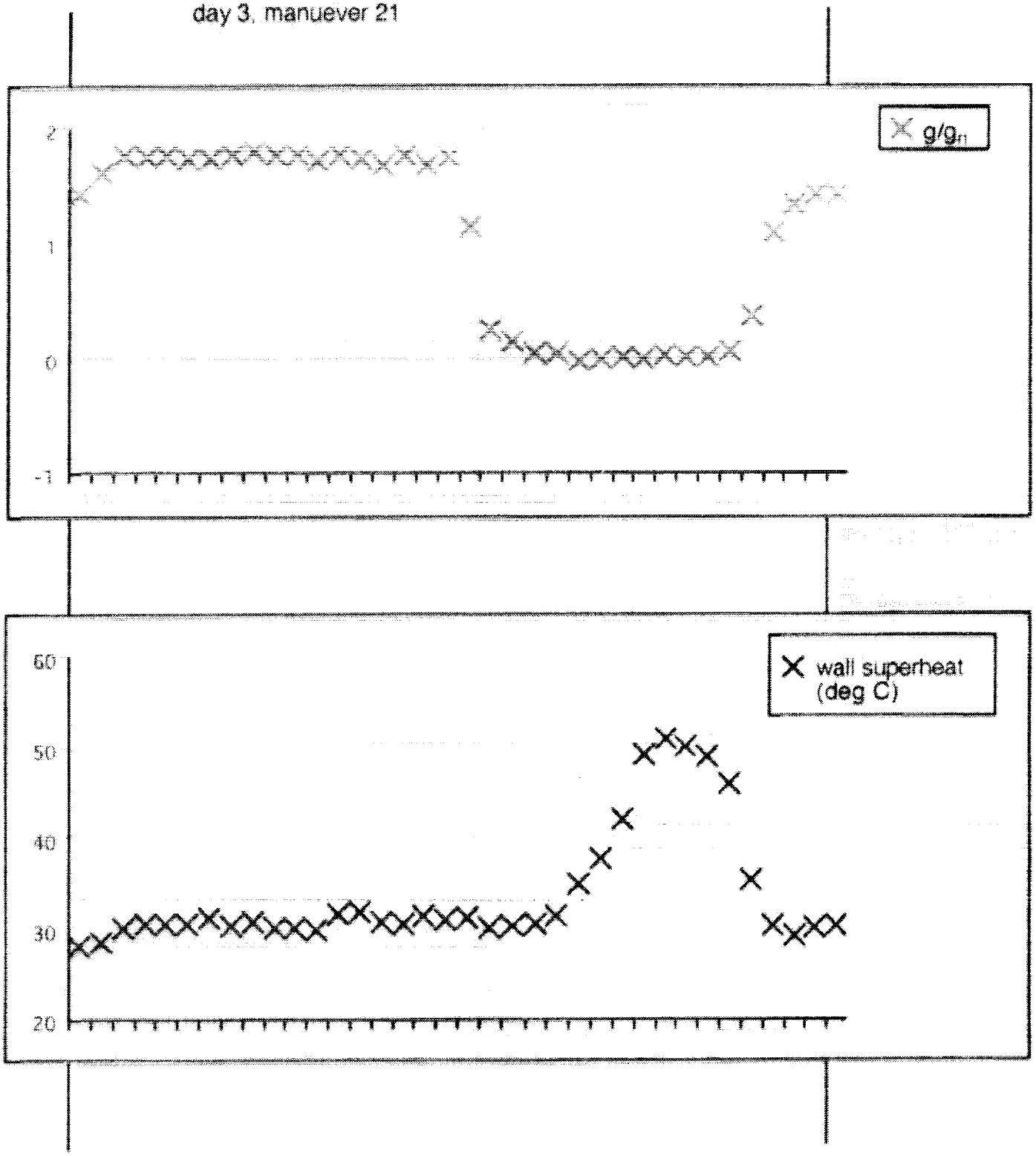
day 3, manuever 21
g/g0
2
1
0
-1
wall superheat (deg C)
60
50
40
30
20

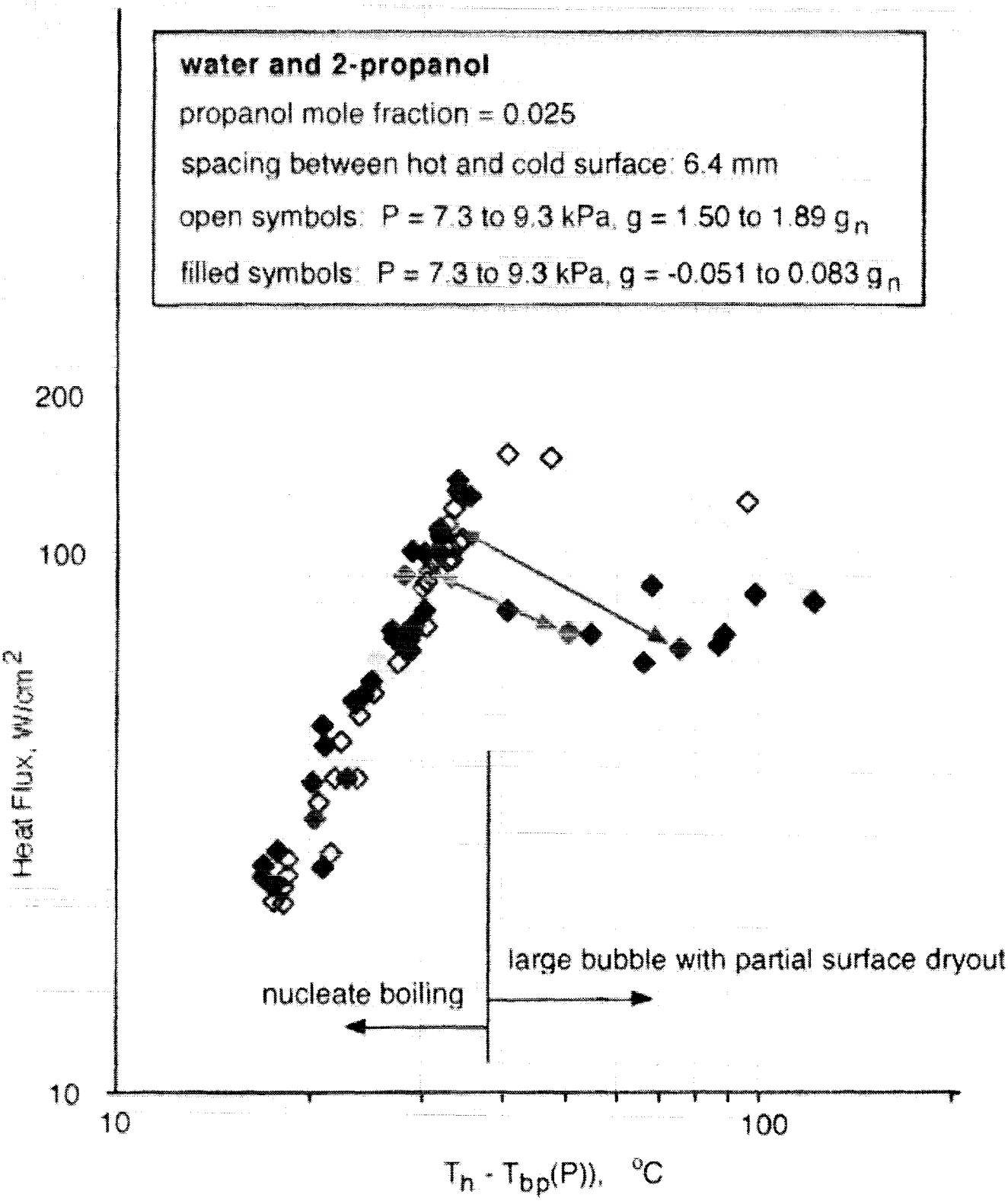
water and 2-propanol
propanol mole fraction = 0.025
spacing between hot and cold surface: 6.4 mm
open symbols: P = 7.3 to 9.3 kPa, g = 1.50 to 1.89 g_n
filled symbols: P = 7.3 to 9.3 kPa, g = -0.051 to 0.083 g_n
200
100
10
10
100
Heat Flux, W/cm^2
$T_h - T_{bp}(P)$, °C
nucleate boiling
large bubble with partial surface dryout

Transition from low g to high g, day 3 maneuver 21

Gap = 6.4 mm, water and 2 propanol at x = 0.025

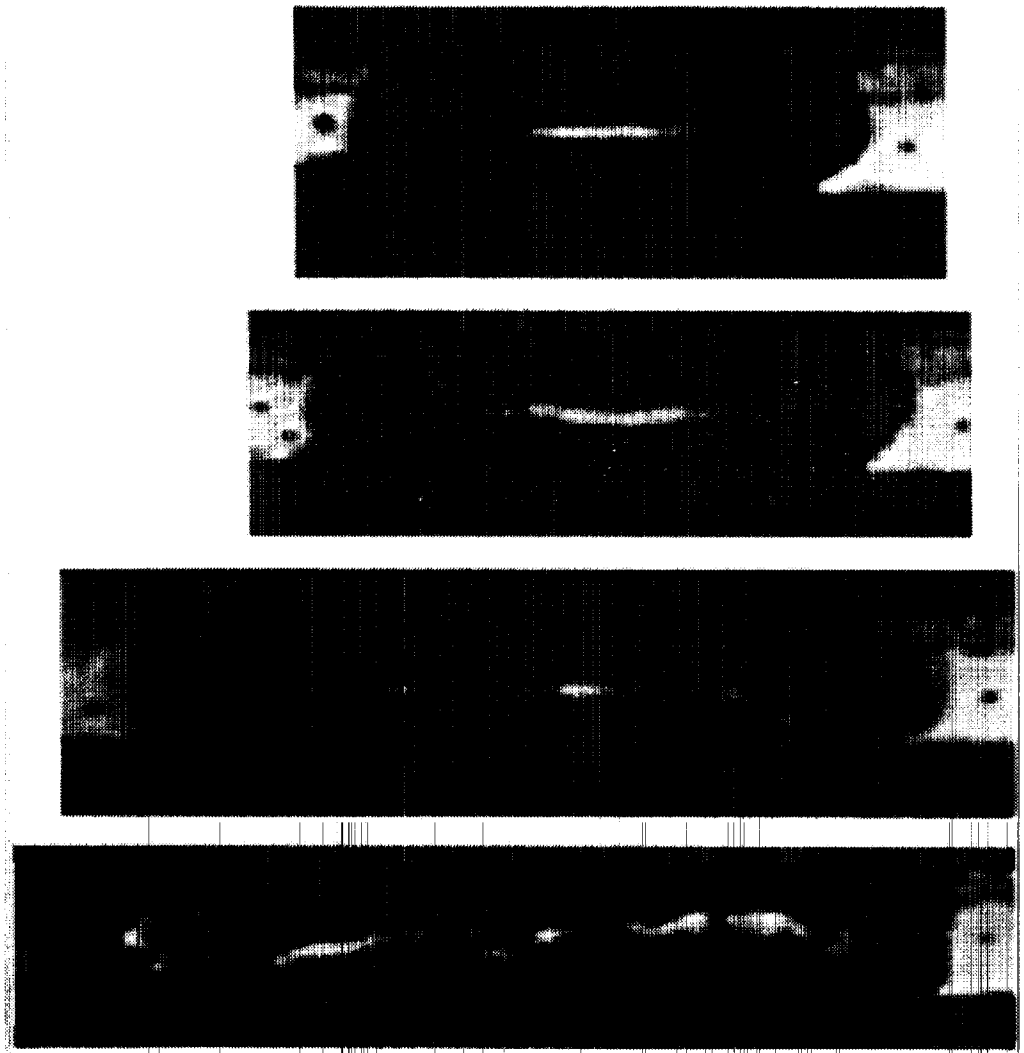

t = 18.485 s

t = 21.018 s

t = 22.026 s

t = 23.414 s

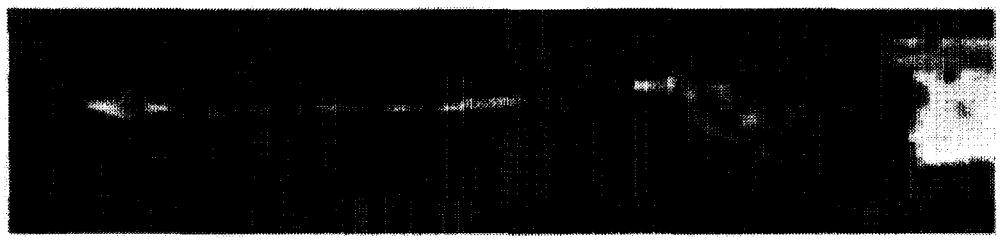

t = 25.974 s

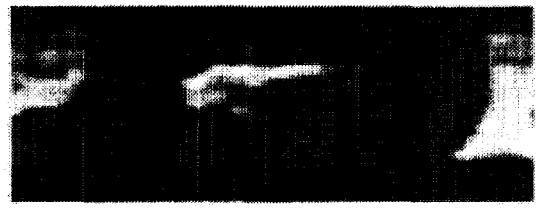

t = 26.690 s

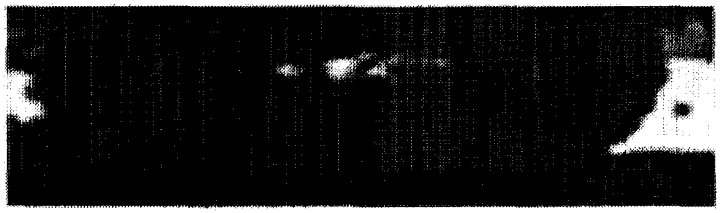

t = 27.158 s

t = 27.848 s

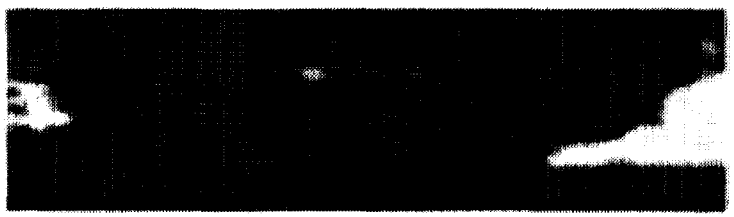

t = 28.078 s

t = 33.598 s
t = 34.508 s
t = 35.508 s
t = 36.510 s
t = 37.508 s
t = 38.506 s
t = 39.494 s

Results of Experiments

- Two boiling modes observed:
  - Nucleate boiling
  - Large stationary bubble with partial surface dryout

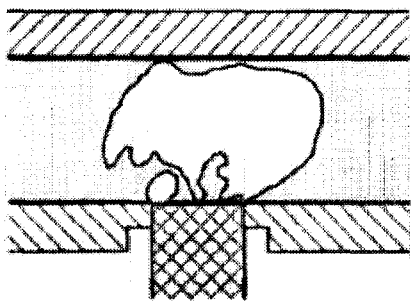

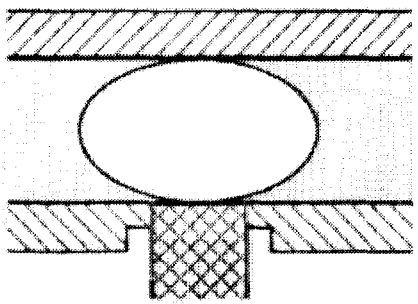

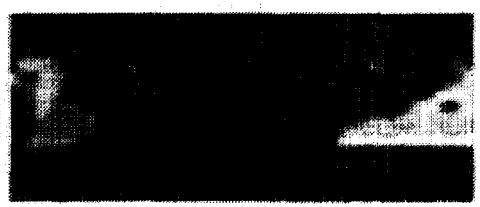

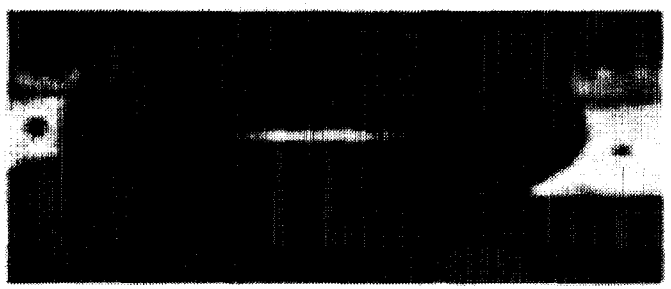

- Phase morphology and heat transfer characteristics determined for each type

Subsequent Work

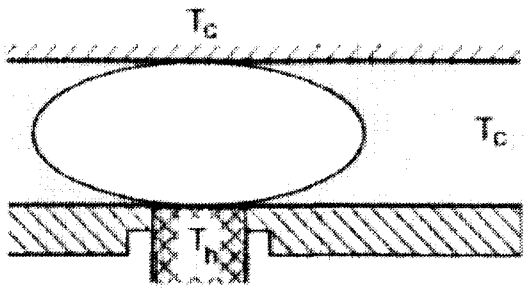

- Development of model of near-bubble transport including
  - Wall conduction
  - Bulk fluid motion
  - Microlayer transport between interface and walls
  - Marangoni effects

- Comparison of experimental data with model predictions for 1g and reduced g results
- Analysis of parametric effects using model

- Experiments with other aqueous mixtures

THERMAL CONTROL AND ENHANCEMENT OF HEAT TRANSPORT CAPACITY OF TWO-PHASE LOOPS WITH ELECTROHYDRODYNAMIC CONDUCTION PUMPING

J. Seyed-Yagoobi[1], J. Didion[2], J.M. Ochterbeck[3], and J. Allen[4]

[1]Department of Mechanical Engineering, Texas A&M University,
College Station, Texas 77843-3123
[2]Thermal Engineering Branch, National Aeronautics and Space Administration
Goddard Space Flight Center, Greenbelt, Maryland 20771
[3]Department of Mechanical Engineering, Clemson University
Clemson, South Carolina 29634-0921
[4]National Center for Microgravity Research, c/o NASA Glenn Research Center
Mail Stop 110-3, 21000 Brookpark Road, Cleveland, Ohio 44135

ABSTRACT

There are three kinds of electrohydrodynamics (EHD) pumping based on Coulomb force: induction pumping, ion-drag pumping, and pure conduction pumping. EHD induction pumping relies on the generation of induced charges. This charge induction in the presence of an electric field takes place due to a non-uniformity in the electrical conductivity of the fluid which can be caused by a non-uniform temperature distribution and/or an inhomogeneity of the fluid (e.g. a two-phase fluid). Therefore, induction pumping cannot be utilized in an isothermal homogeneous liquid. In order to generate Coulomb force, a space charge must be generated. There are two main mechanisms for generating a space charge in an isothermal liquid. The first one is associated with the ion injection at a metal/liquid interface and the related pumping is referred to as ion-drag pumping. Ion-drag pumping is not desirable because it can deteriorate the electrical properties of the working fluid. The second space charge generation mechanism is associated with the heterocharge layers of finite thickness in the vicinity of the electrodes. Heterocharge layers result from dissociation of the neutral electrolytic species and recombination of the generated ions. This type of pumping is referred to as pure conduction pumping.

This project investigates the EHD pumping through pure conduction phenomenon. Very limited work has been conducted in this field and the majority of the published papers in this area have mistakenly assumed that the electrostriction force was responsible for the net flow generated in an isothermal liquid. The main motivation behind this study is to investigate an EHD conduction pump for a two-phase loop to be operated in the microgravity environment. The pump is installed in the liquid return passage (isothermal liquid) from the condenser section to the evaporator section. Unique high voltage and ground electrodes have been designed that generate sufficient pressure heads with very low electric power requirements making the EHD conduction pumping attractive to applications such as two-phase systems (e.g. capillary pumped loops and heat pipes). Currently, the EHD conduction pump performance is being tested on a two-phase loop under various operating conditions in the laboratory environment. The simple non-mechanical and lightweight design of the EHD pump combined with the rapid control of performance by varying the applied electric field, low power consumption, and reliability offer significant advantages over other pumping mechanisms; particularly in reduced gravity applications.

NASA/CP—2000-210470

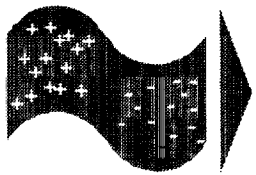

THERMAL CONTROL AND ENHANCEMENT OF HEAT TRANSPORT CAPACITY OF TWO-PHASE LOOPS WITH ELECTROHYDRODYNAMIC CONDUCTION PUMPING

J. Seyed-Yagoobi[1], J. Didion[2], J.M. Ochterbeck[3], and J. Allen[4]

[1]Texas A&M University

[2]NASA-Goddard Flight Center

[3]Clemson University

[4]National Center for Microgravity Research

OBJECTIVES

Electrohydrodynamics Laboratory

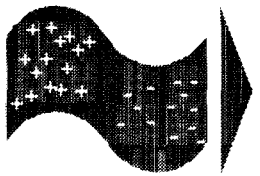

- theoretical and experimental work to understand the EHD driven liquid flow
- EHD pump based on conduction phenomenon
- ground and microgravity environment
- with and without bubbles
- optimum electrode design
- EHD pump performance in single-phase and two-phase systems

BACKGROUND

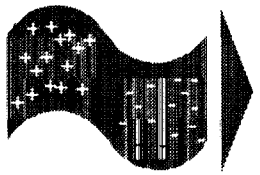

- past microgravity studies with EHD dealt for example with bubble growth
- no work carried out to study an EHD driven flow in microgravity
- fundamental understanding of an EHD pump in microgravity needed
- pave the way for development of EHD technologies for heat transfer and mass transport systems in microgravity

EHD PUMPING

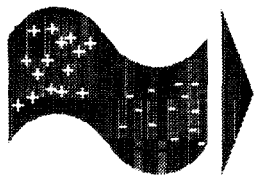

- interaction of electric fields and free charges in a dielectric fluid
- Coulomb force main mechanism of this interaction
- electric field and free charges required

EHD PUMPING ADVANTAGES

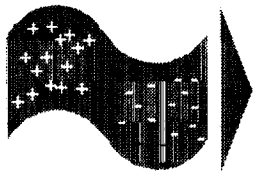

- simple design
- lightweight
- non-mechanical
- rapid control of performance
- low power consumption

ELECTRIC BODY FORCE

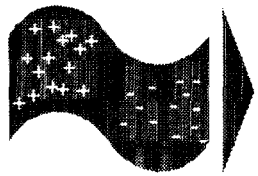

$$\vec{F}_e = \underbrace{q\vec{E}}_{\text{Coulomb Force}} \underbrace{- \frac{1}{2}E^2\nabla\varepsilon + \nabla\left[\rho\frac{E^2}{2}\left(\frac{\partial\varepsilon}{\partial\rho}\right)_T\right]}_{\text{Polarization Force}}$$

Note: In an isothermal liquid, only Coulomb force can sustain a permanent EHD motion.

ELECTRIC CHARGE GENERATION

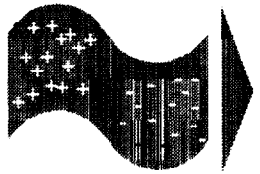

- direct injection, not desirable
- induction, not feasible in isothermal liquid
- conduction

CHARGE GENERATION - CONDUCTION

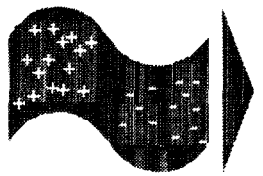

- heterocharge layers of finite thickness in the vicinity of electrodes

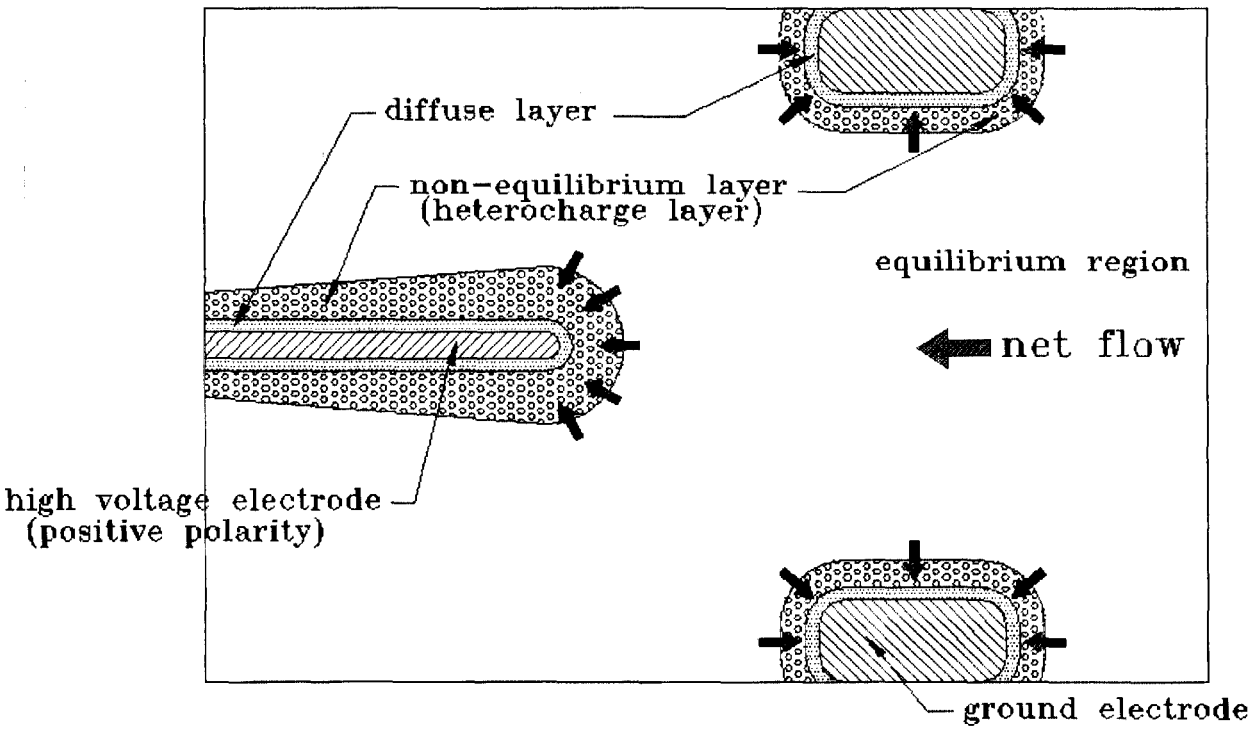

EHD CONDUCTION PUMPING

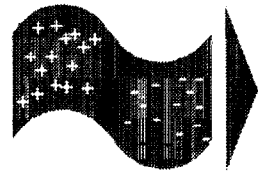

- Atten and Seyed-Yagoobi (1999) presented a theory in point/plane geometry
- Jeong, Seyed-Yagoobi, and Atten (2000) experimentally investigated the phenomenon
- theory indicates $F_e \propto \varepsilon E^2$
- high electric field and permittivity are desirable

STATIC EHD CONDUCTION PUMP APPARATUS

Electrohydrodynamics Laboratory

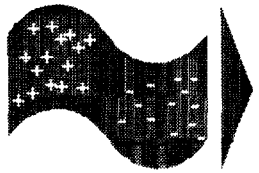

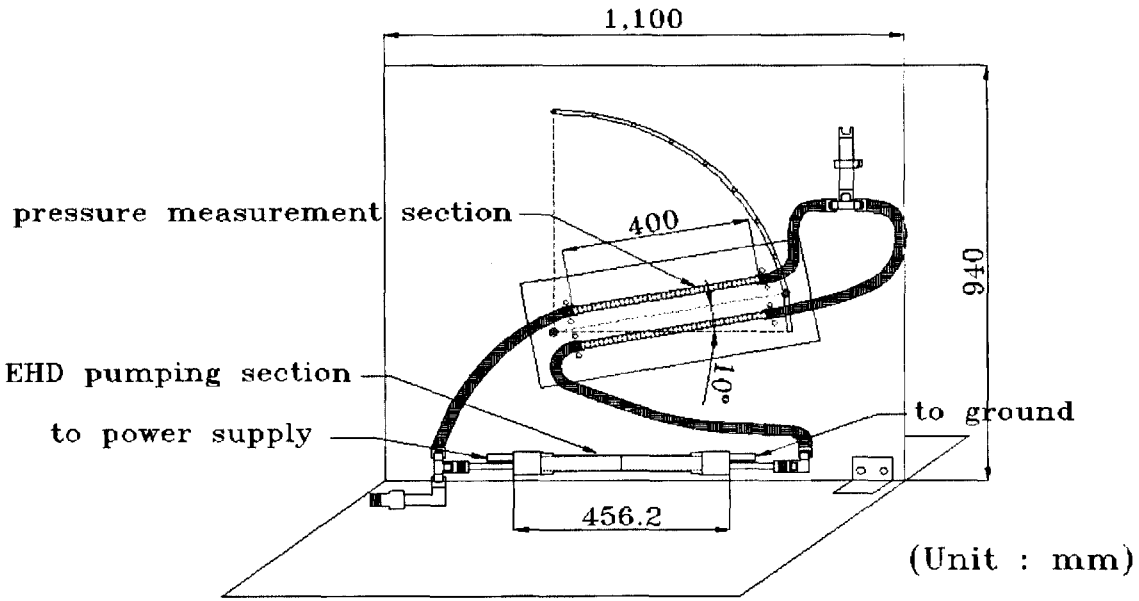

PRELIMINARY ELECTRODE DESIGN

Electrohydrodynamics Laboratory

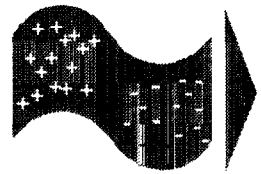

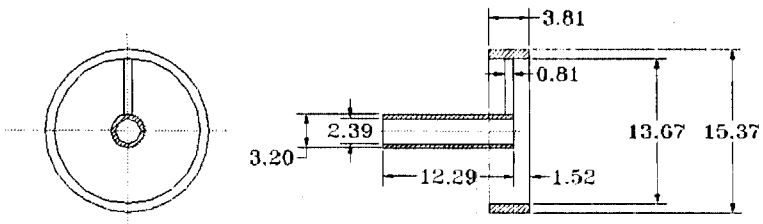

(Unit : mm)

hollow tube (high voltage) electrode

PRELIMINARY ELECTRODE DESIGN (cont.)

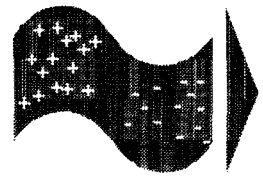

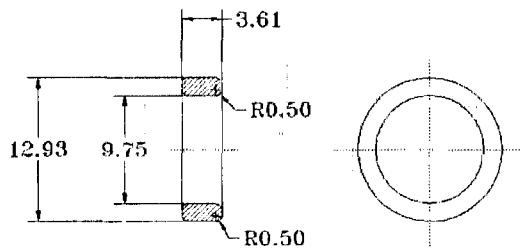

(Unit : mm)

ground electrode

ASSEMBLED HOLLOW-TUBE HIGH VOLTAGE ELECTRODE AND RING GROUND ELECTRODE

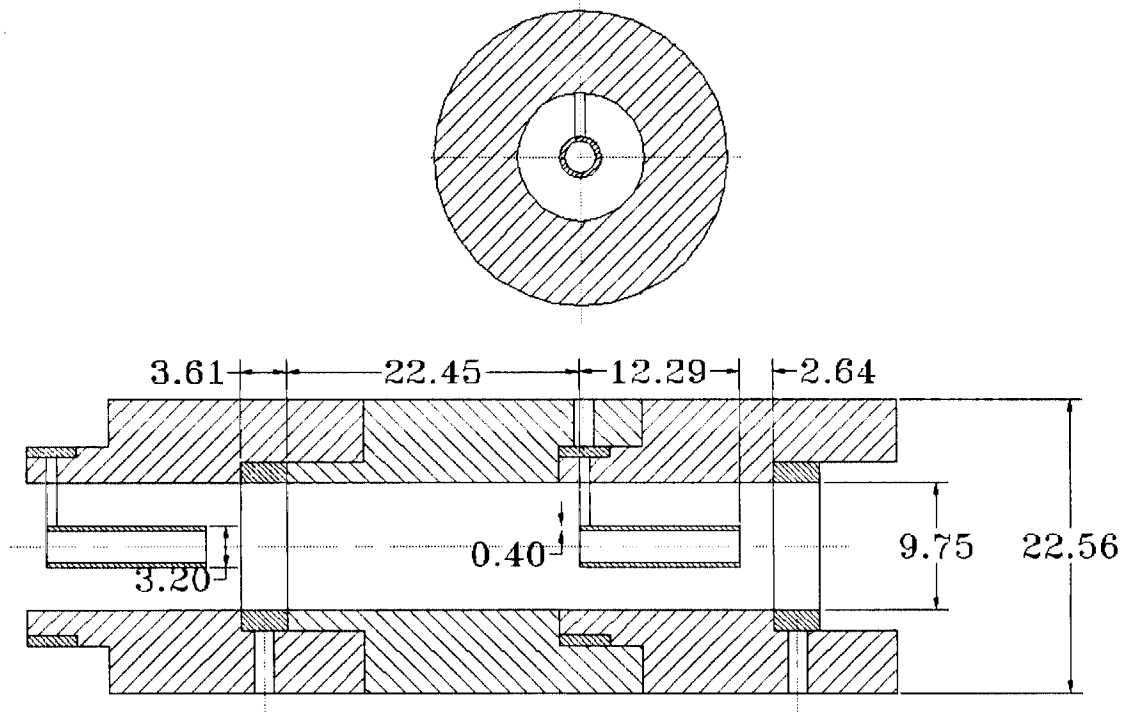

(Unit : mm)

Note: two pairs shown

HOLLOW TUBE - RING ELECTRODE DESIGN

Electrohydrodynamics Laboratory

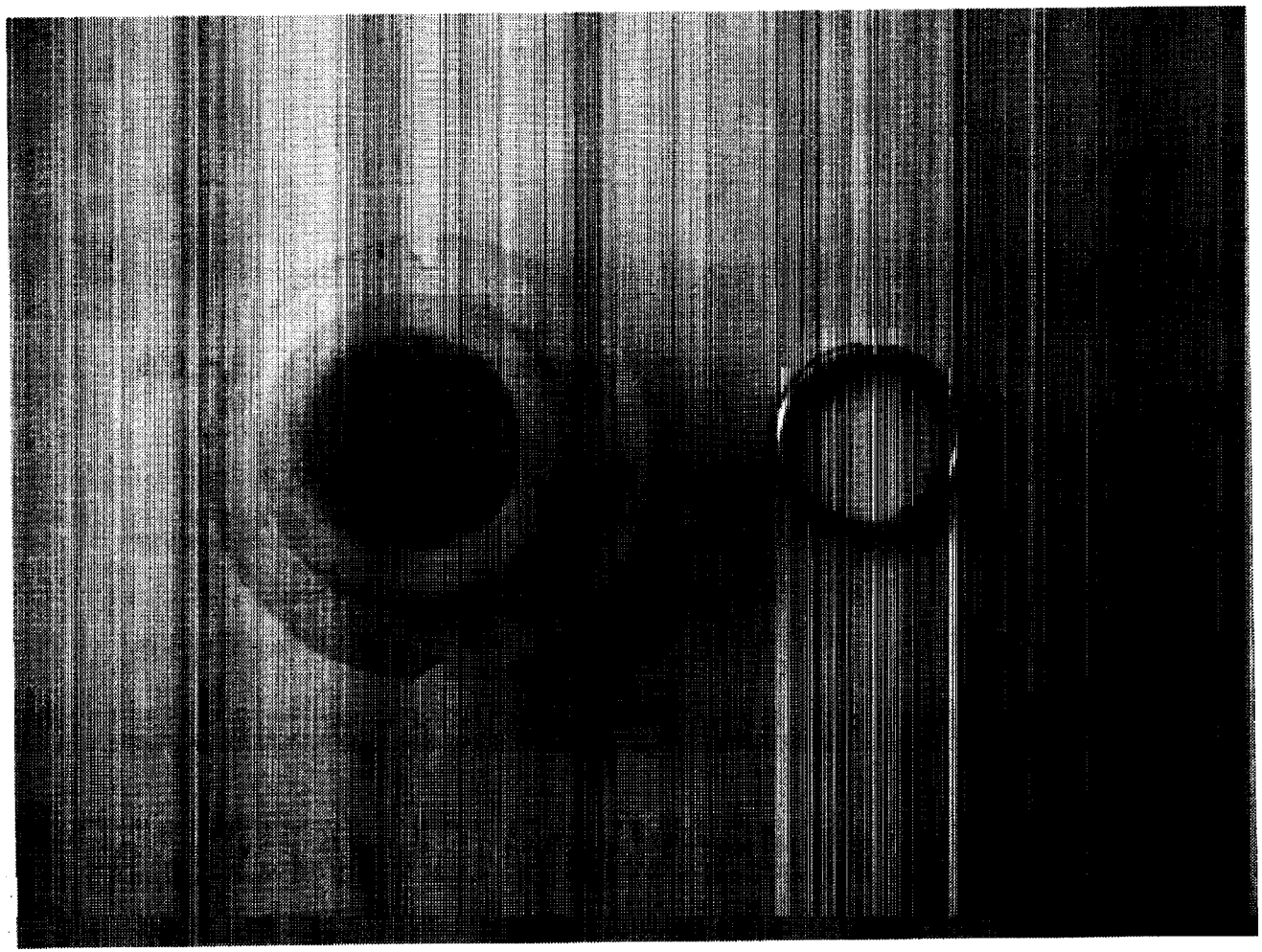

PRESSURE GENERATION

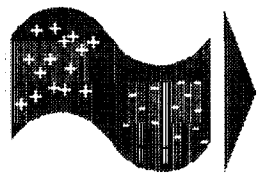

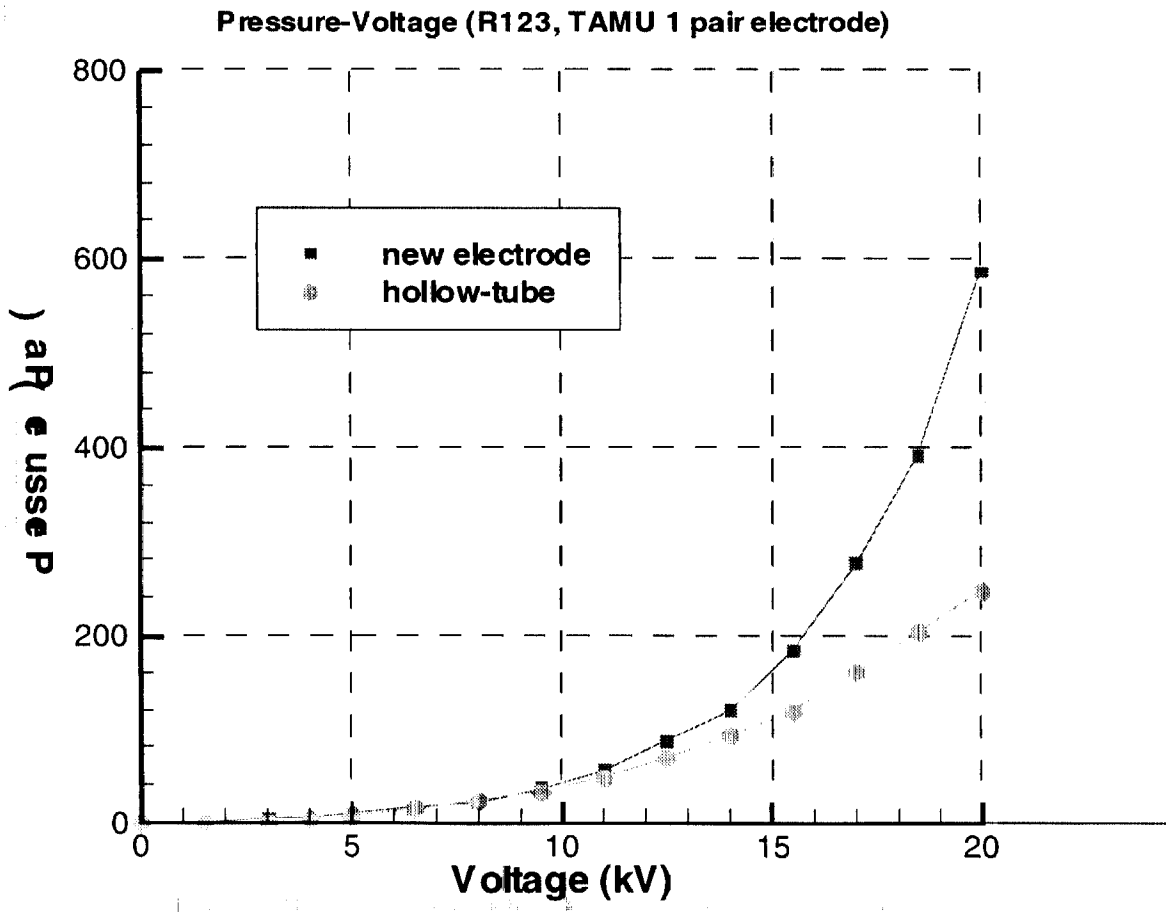

CURRENT CONSUMPTION

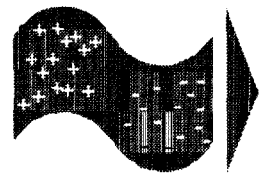

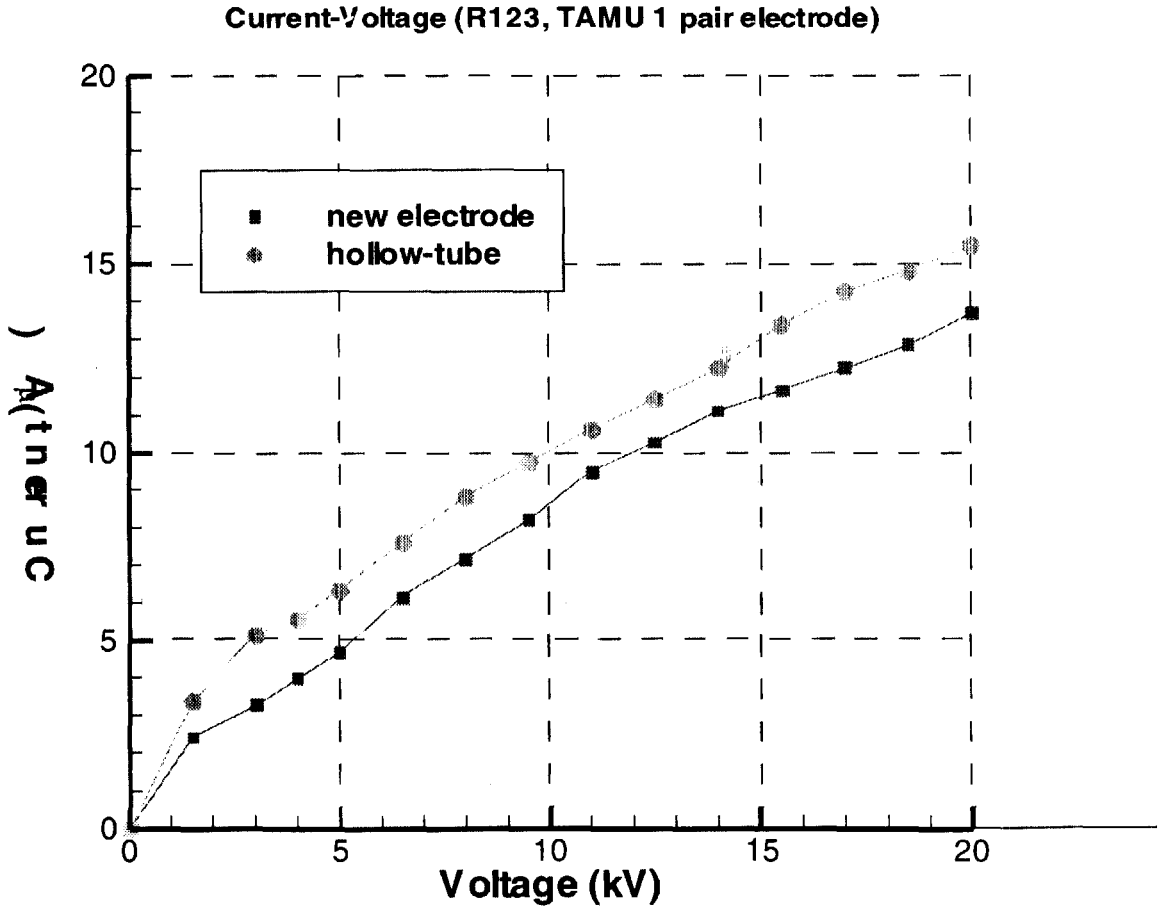

LONG TERM OPERATION

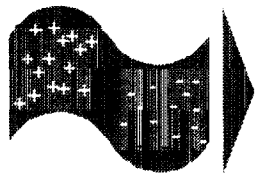

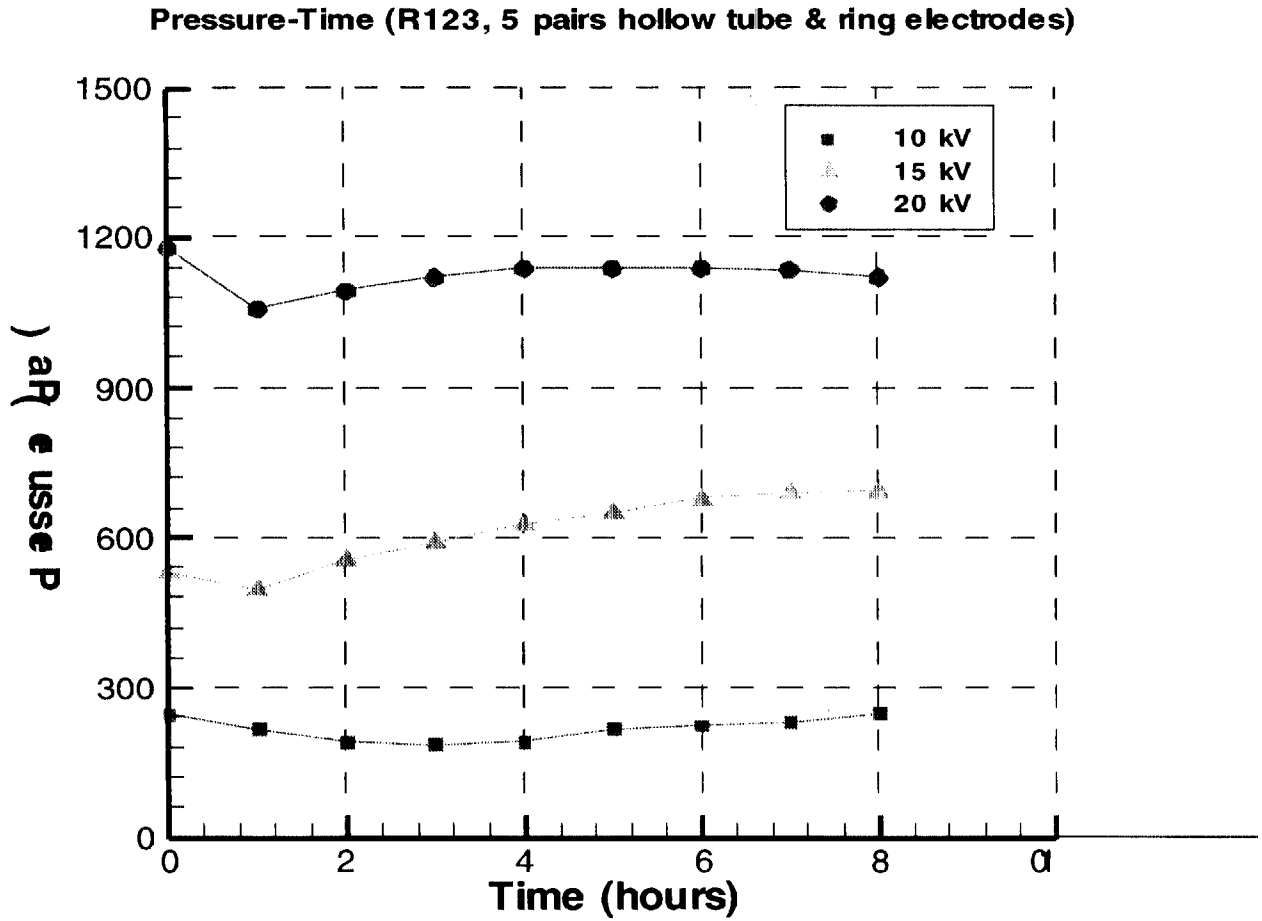

LONG TERM OPERATION (cont.)

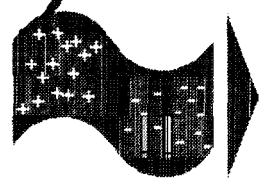

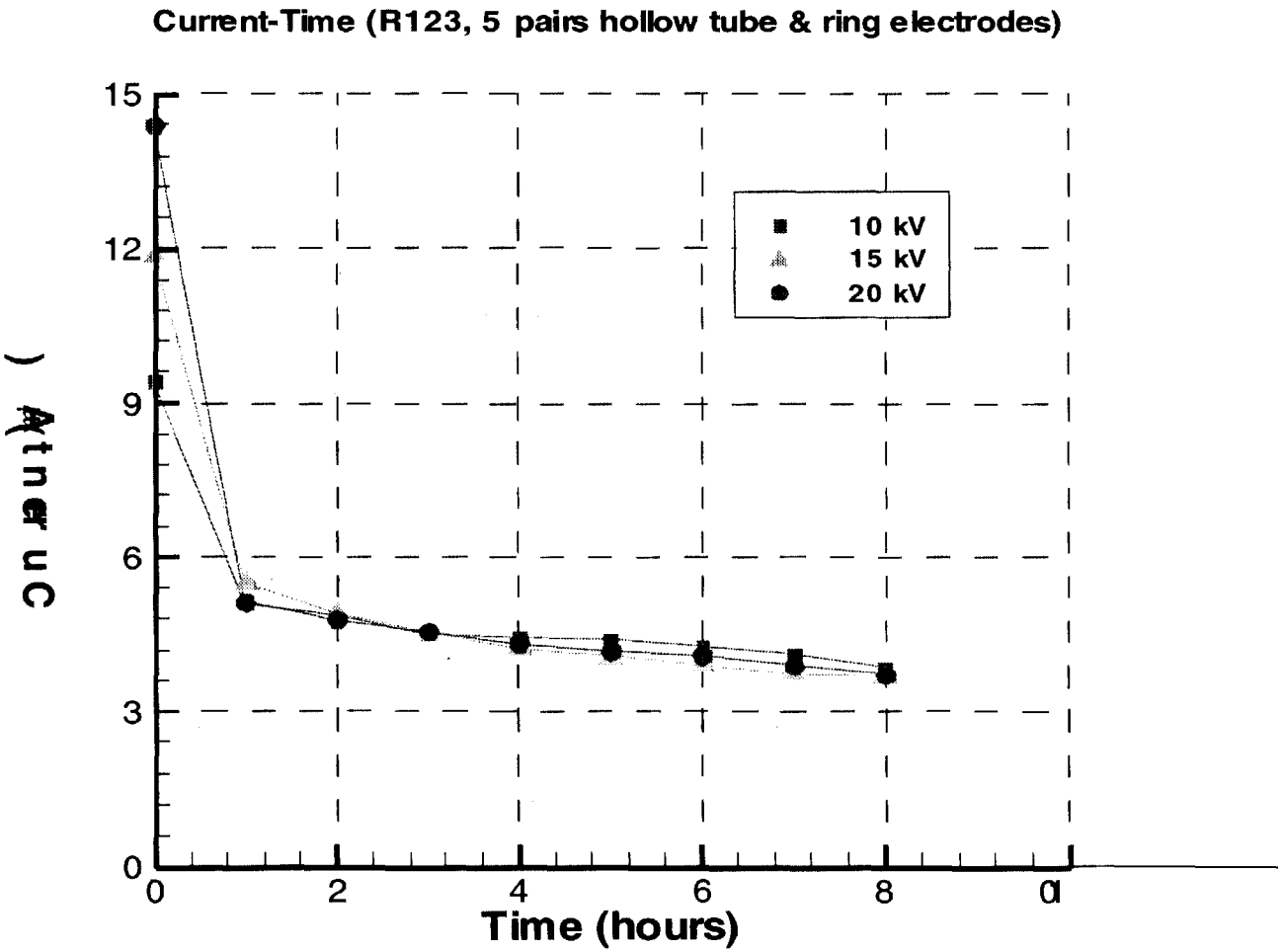

PRESSURE GENERATION - NEW ELECTRODE DESIGN

Electrohydrodynamics Laboratory

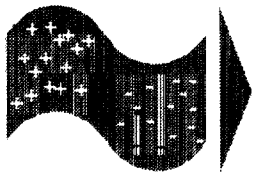

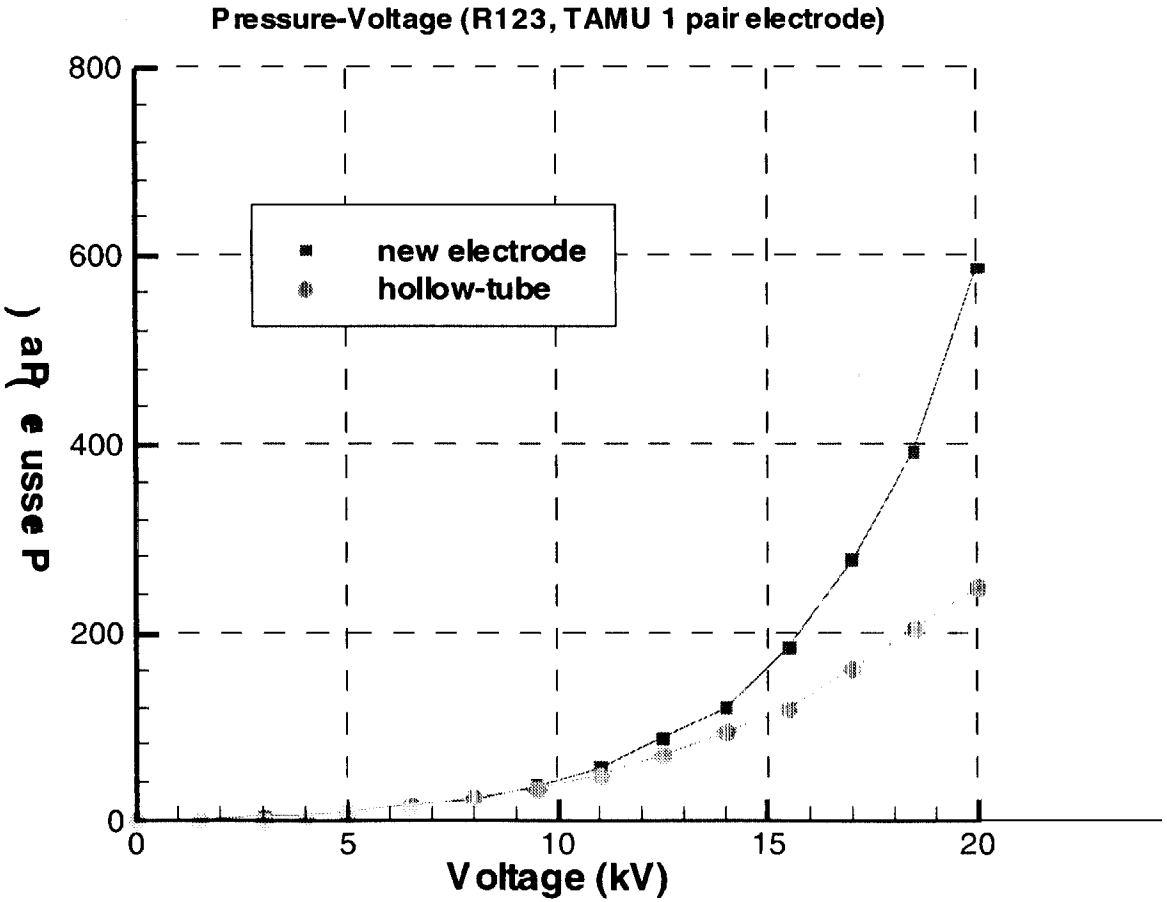

CURRENT CONSUMPTION - NEW ELECTRODE DESIGN

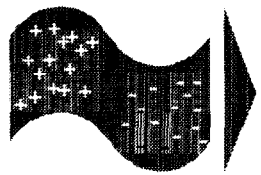

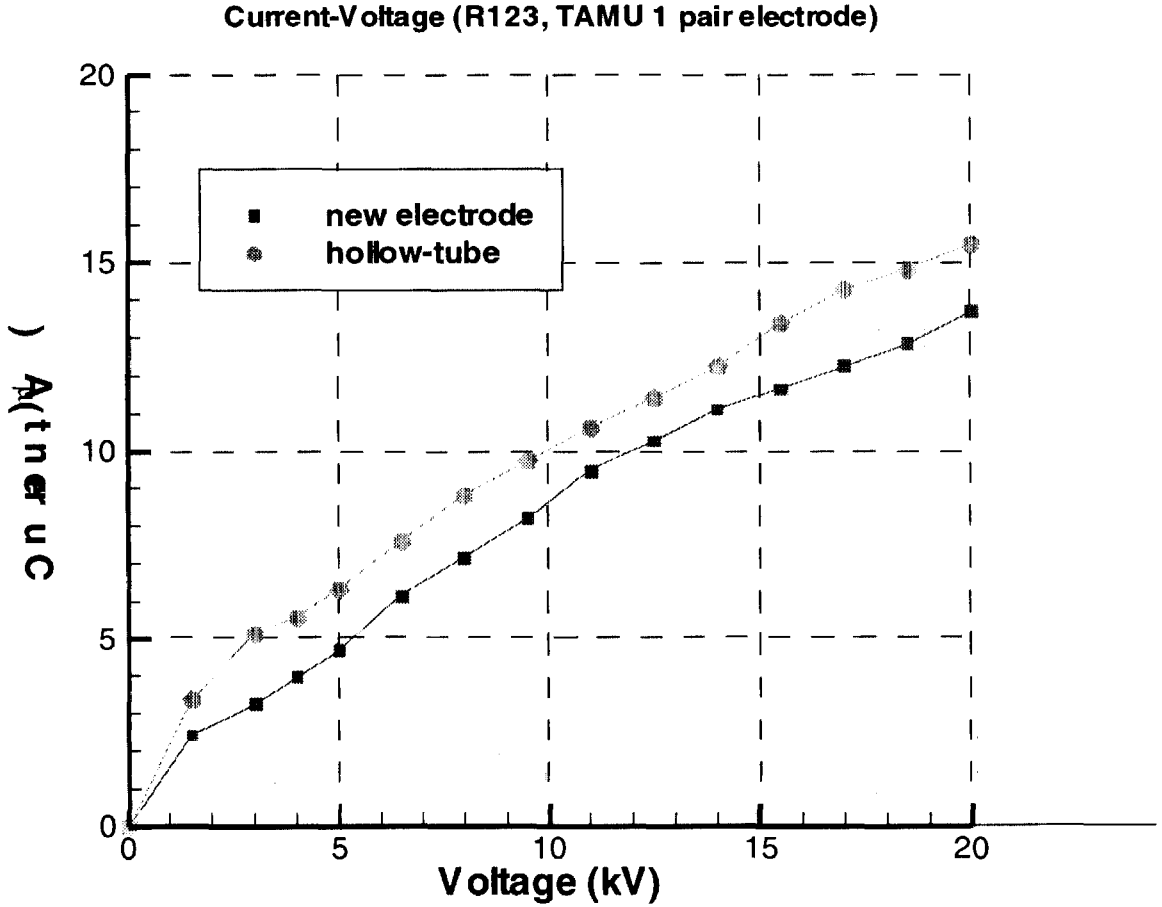

SIMPLIFIED NASA-GODDARD EHD TEST LOOP SCHEMATIC

Electrohydrodynamics Laboratory

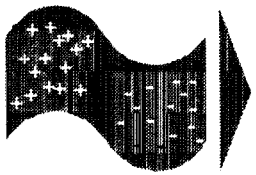

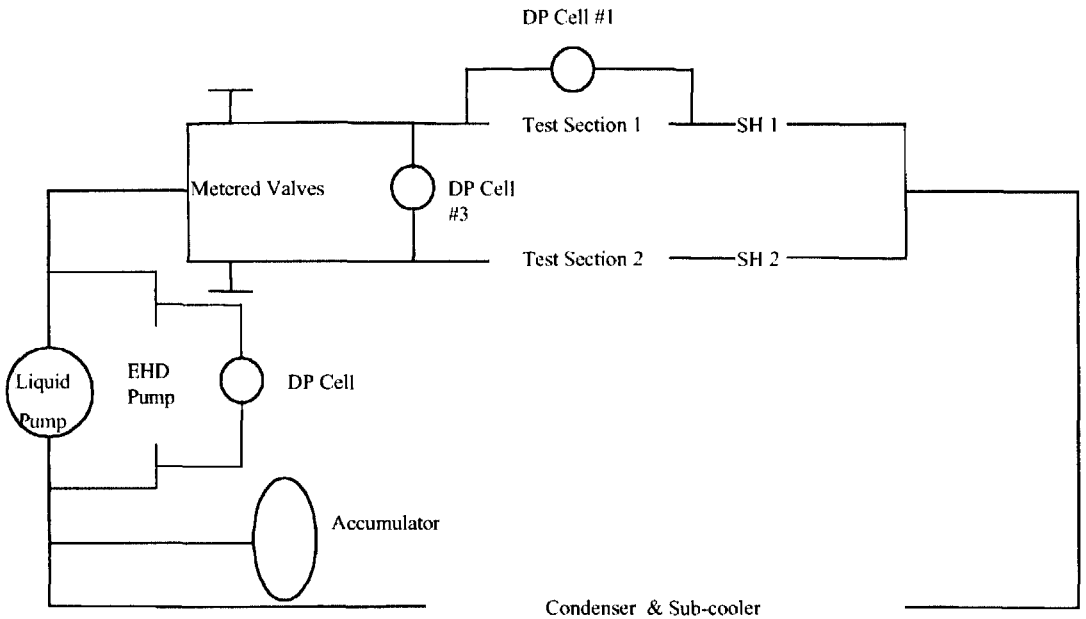

SIMPLIFIED TEST LOOP SCHEMATIC

Electrohydrodynamics Laboratory

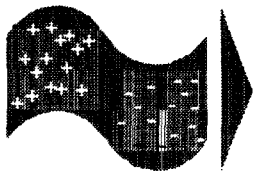

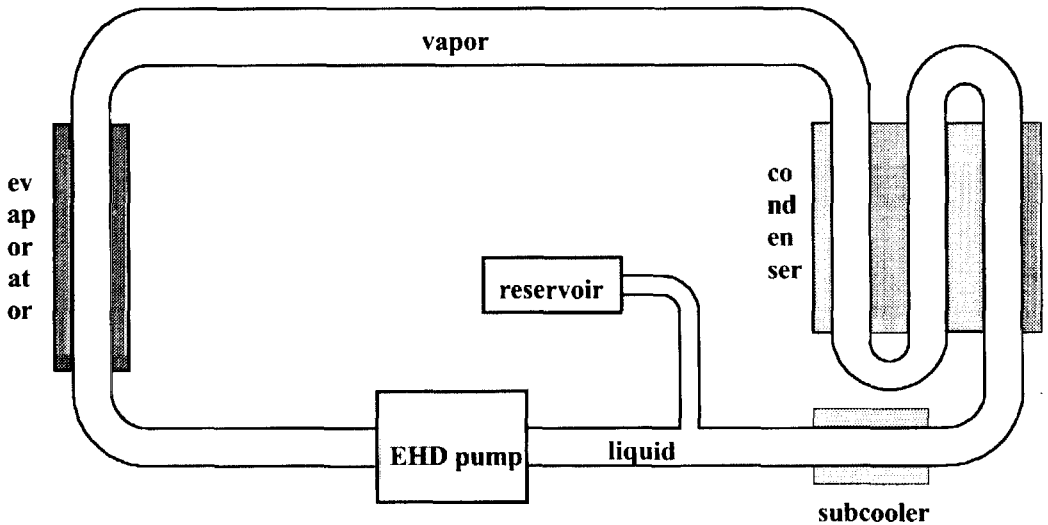

CONCLUSIONS

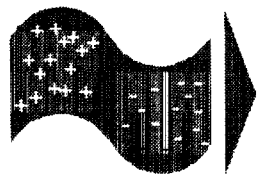

- several electrode designs considered
- EHD conduction pumping confirmed
- significant pressure head generated

August 9, 2000

Session 2B
Flow of Granular Media I

Slide Conveying of Granular Materials - Thinking out of the Glovebox[1]

J. D. Goddard, A. K. Didwania & P.R. Nott[2]
Department of Mechanical and Aerospace Engineering
University of California, San Diego

Abstract

The vibratory conveyor, routinely employed for normal-gravity transport of granular materials, usually consists of a continuous open trough vibrated sinusoidally to induce axial movement of a granular material. Motivated in part by a hypothetical application in zero gravity, we propose a novel modification of the vibratory conveyor based on a closed 2d trough operating in a "slide-conveying" mode, with the granular mass remaining permanently in contact with the trough walls. We present a detailed analysis of the mechanics of transport, based on a rigid-slab model for the granular mass with frictional (Coulomb) slip at the upper and lower walls. The form of the vibration cycle plays a crucial role, and the optimal conveying cycle is not the commonly assumed rectilinear sinusoidal motion. The conveying efficiency for the novel slide conveyor will be presented for several simple vibration cycles, including one believed to represent the theoretical optimum.

Background - Vibratory Conveying

Granular media represent an interesting class of materials that can exhibit a spectrum of complex flow behavior, ranging from solid-like to gas-like. Understanding and describing their mechanical behavior poses a scientific interesting and technologically important challenge, since a many processes involve handling and processing of granular solids. One particular interesting class of mechanical processes are those involving vibratory excitation or "fluidization" of granular masses. Following a long-standing scientific fascination with the wave-like patterns on the surface of vibrated powders and grains, dating back to the celebrated work of Faraday (1831), there has been a resurgence of activity in recent times, accompanying the growth of theoretical interest in pattern formation in non-linear dynamical systems (See, e.g., Bizon *et al.* 1999). There is an almost completely disjoint body of engineering literature on vibratory conveying of granular materials.

Vibratory conveyors, routinely employed in industry for transport of granular materials, generally consist of a continuous trough vibrated sinusoidally in time to induce axial movement of the granular material. Fig.1 presents a schematic cross-sectional view of a vibratory conveyor. Key process variables are inclination α, amplitude A , frequency f and direction β of vibration, along with frictional/mechanical properties of the conveyor surface and the granular material. In recent works, Nedderman & Harding (1990) extend the earlier analysis of Booth and McCallion (1963) and present optimization studies for horizontal and inclined sliding. In most applications, vibratory conveyors work in one of two distinct modes, *slide conveying* or *flight conveying*, accordingly as $N < 1$ or $N > 1$, respectively, where N is the nondimensional *throw number*

$$N = \Gamma \sin\beta / \cos\alpha, \quad \text{with} \quad \Gamma = A\omega^2/g, \tag{1}$$

[1]Partially supported by grants from the National Aeronautics and Space Administration
[2]Permanent address: Indian Institue of Science, Bangalore, India

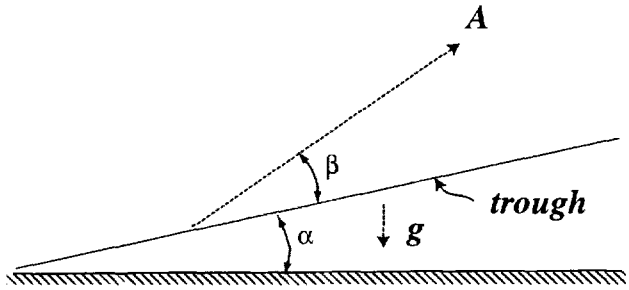

Figure 1: Definition sketch of a vibratory conveyor

in which the various symbols are defined above and g denotes gravity. Assumptions common to most existing models of vibratory transport are: 1.) The granular mass can be treated as a single rigid slab, 2.) side-wall friction and air drag are negligible, 3.) the granular mass interacts with the trough wall as a rigid body with Coulomb friction, and 4.) the trough executes a rectilinear sinusoidal motion (A in Fig. 1), This engineering model corresponds essentially to the lowest Γ states discussed in basic scientific studies (Bizon *et al.* 1999).

Present Work

It is evident that pure slide conveying and/or a closed trough would be required in a zero-g environment, and the intial phase of the current work is concerned with the theoretical analysis of the closed 2d trough with parallel walls, completely filled with a granular mass. As a starting point, we adopt the first three of the assumptions listed immediately above but consider a more general periodic motion than 4.). The basic equations (nonlinear ODEs) are but slight modifications of those given elsewhere (Nedderman and Harding, 1990) and are not repeated here. They lead to an interesting optimal control problem, involving the maximization of axial transport subject to constrained periodic forcings. The present talk will discuss a few preliminary results, including some numerical simulations for simple periodic cycles and a conjectured form of the theoretically optimal cycle.

References

[1] Bizon, C., Shattuck, M.D., & Swift, 1999 *Phys. Rev. E*,**60**,7210.

[2] Booth, J. H. & McCallion, H. 1963 *Proc. Inst. Mech. Eng.*, **178**, 521.

[3] Faraday, M. 1831 *Phil. Tran. Roy. Soc. Lond.* **52**, 299.

[4] Harding, G. H. L. & Nedderman, R. M. 1990 *Chem. Eng. Res. Design*, **68**, 131.

[5] Nedderman, R. M. & Harding, G. H. L. 1990 *Chem. Eng. Res. Design*, **68**, 123.

Slide Conveying of Granular Materials - Thinking out of the Glovebox*

Joe Goddard

Mechanical & Aerospace Engineering

UCSD

NASA 5th Microgravity Fluid Physics and Transport Phenomena Conference

August 9-11, 2000

Cleveland, OH

*Supported in part by a NASA Grant.
Coworkers: A. Didwania, P.R. Nott

Background and Outline of Talk

- Work described is part of a program of research on the mechanics of vibrated granular layers, with objectives:
  1. Development of fluid-mechanical models to explain complex ("Faraday") patterns on vertically-vibrated layers, and
  2. Connection to engineering models of vibratory conveying, with a view to possible variable-g application (e.g. heat transfer)

- Focus of this talk is on results from recent efforts on Item 2, including
  - Review of current modes and models of conveying ("throw" and "slide") and limitations in reduced g
  - Analysis of closed-channel slide conveying, with discussion of optimal vibration cycles and discussion of recently discovered exact solution to the problem
  - Future work

"Throw" Conveying

- (a) Layer in flight - normal gravity g_0
- (b) "Solid-block" model - basic equations:

$$\frac{d\mathbf{v}(t)}{dt} = \mathbf{f}(t) + \mathbf{g}(t), \text{ with } \mathbf{g}(t) = \mathbf{g}_0 - \dot{\mathbf{v}}_c(t)$$

relative to plate, where

  - $\mathbf{g}(t)$ is virtual gravity
  - $\mathbf{f}(t)$ is specific plate-contact force (frictional-elastic, generally impulsive).

- Without a "lid", the plate-displacement amplitude and frequency A, ω give unbounded $\Gamma = A\omega^2/g_0$ in zero-g.

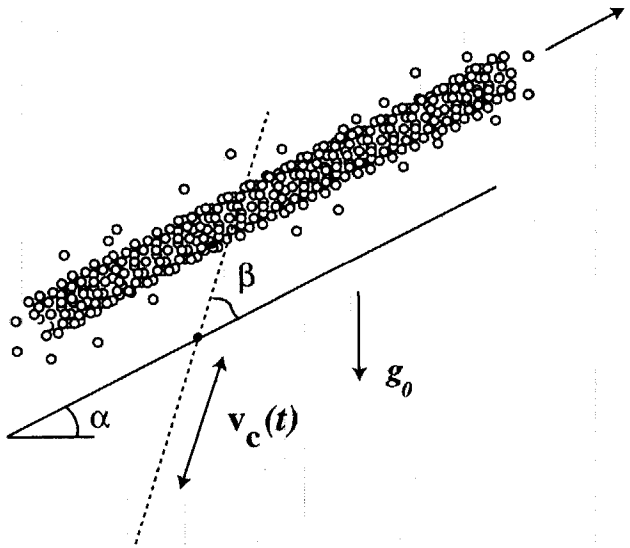

(a)

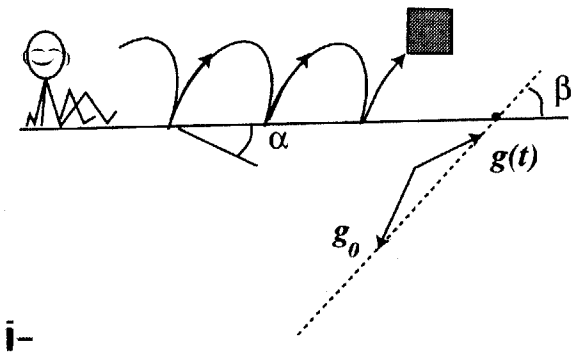

(b)

"Slide" Conveying

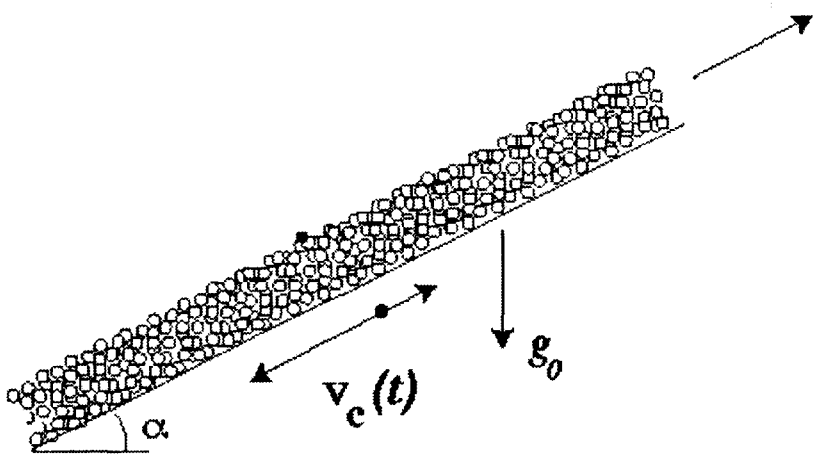

- Employed for fragile materials.
- Layer in permanent contact with surface and active contact force $f(t)$ is purely frictional.
- In-line ($\beta = 0$), unsymmetrical $v_c(t)$ can provide transport:
- Tilt ($\beta > 0$) enhances efficiency but amplitude is limited by magnitude of g_0

Closed-Conduit Slide Conveying

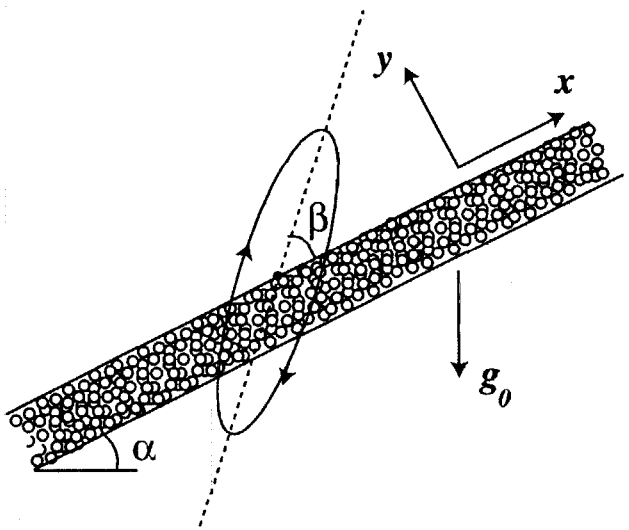

- A, ω not limited by gravity - device can work in zero g.
- "Ideal" cycles with zero frictional dissipation exist.
- A simple theory arises - with constant wall friction μ, length scaled by A and time by ω^{-1}, the x-velocity $u(t)$ satisfies

$$\frac{du}{dt} = T(t) - \mu|N(t)|\mathrm{sgn}(u), \quad \text{for} \quad |T(t)| \geq \mu|N(t)|$$

$$u = 0, \quad \text{otherwise}$$

with 2π-periodic coefficients:

$$T = -(g_0 \sin\alpha + \dot{u}_c)/A\omega^2, \quad N = -(g_0 \cos\alpha + \dot{v}_c)/A\omega^2$$

where pressure "head" should be added to $g_0 \sin\alpha$.

Optimality

- Present effort:
  - establish optimality criteria and ideal cycles
  - investigate optimal real cycles (e.g. elliptical cycle in Fig. above)

  Lack of u-differentiability of ODE for u rules out standard variational methods (mitigated by exact solution below)

- As, e.g., simplest type of optimality, maximize net cyclic displacement:

$$\max_{T,N\in\mathcal{C}} X, \quad \text{where} \quad X = \int_0^{2\pi} u(t)dt$$

  where $\mathcal{C}$ denotes constraint class of $T(t), N(t)$

Solution

With intervals of sliding in $(0, 2\pi)$:

$$F(t) := |T(t)| - \mu|N(t)| \geq 0, \;\; t_i \leq t \leq \tau_i$$

$i = 1, 2 \ldots$,the exact solution is

$$u(t) = \sum_i S_i(t) u_i(t)$$

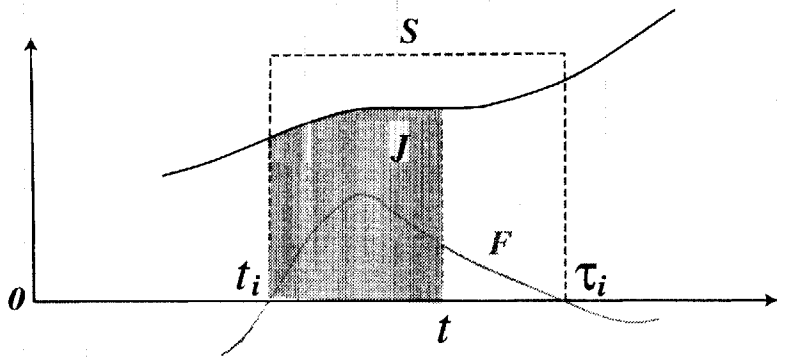

where

$$u_i(t) = R\{J_i^{(+)}(t)\} - R\{-J_i^{(-)}(t)\}$$

$$J_i^{(\pm)}(t) = \int_{t_i}^{t} [T(t') \mp \mu|N(t')|] dt'$$

$$S_i(t) = H(t - t_i) - H(t - \tau_i)$$

$R(u)$, $H(u) \equiv R'(u)$, and S_i denote ramp, Heaviside-step and window functions, and $J^{(\pm)}$ are right- and left-directed "impulses", with $J^{(-)} \geq J^{(+)}$

Ideal and Elliptical Cycles

Exact solution has been employed to:

- establish ideal cycle for bounded forcing,

$$\mu|N(t)|_{\max} \leq |T(t)|_{\max} \leq T_m,$$

found to be square waves, with X=1

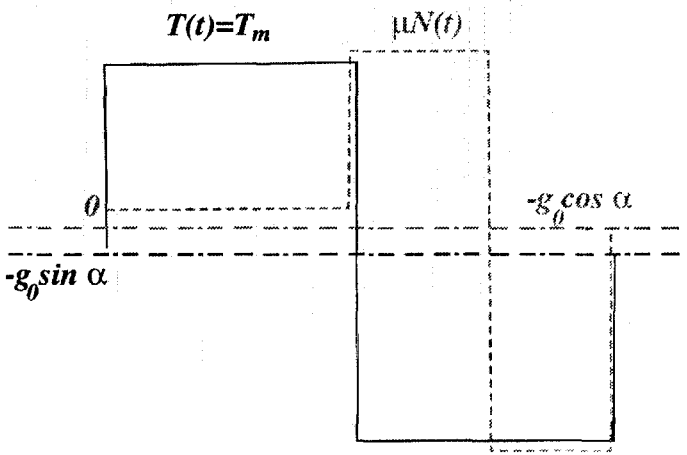

- work out (complicated!) two-parameter algebraic expression for X for the elliptical cycle. The optimal parameter values have as yet not been determined.

Future Work

- Work out details of optimal elliptical cycle for slide conveying with view towards simple experiment
- Consider partially full channel and throw conveying, in conjunction with our other work on stability of vibrated layers

Shaken Granular Systems and the Effects of Gravity

R. Behringer
Department of Physics and Center for Nonlinear and Complex Systems
Duke University
Durham, NC 27708-0305

ABSTRACT

I describe two types of studies that probe the nature of granular systems under the effects of gravity: a) ordinary granular materials such as sand or glass beads contained in a rectangular box and subject to horizontal shaking; and b) spherical particles on a smooth flat substrate. The first type of work involves experimets and MD simulations with collaborators L. Kondic, G. Metcalfe and S. Tennakoon. The second set of studies are in collaboration with M. Dutt L. Kondic, and B. Painter.

Horizontally Shaken Sand This set of studies is intended to probe the transition between granular solid and granular fluid that occurs when the effects of shearing are strong enough to overcomethe effects of a gravitational load. Thus, there are interestingparallels between the present system and avalanches. The basis setup is a box with a rectangular horizontal cross section that is subject to horizontal shaking along the long direction and of the form $x = A\sin(\omega t)$. When the strength of the horizontal shaking, as measured by the dimensionless acceleration, $\Gamma = A\omega^2/g$ exceeds the friction coefficent, μ, Mohr-Coulomb models of granular failure predict that the material will start to deform. In fact, we observe the formation of a fluid layerof material at high enough Γ. However, the Mohr-Coulomb picture does not describe this fluid-like state. To our knowledge, very little is known about the properties of granular systems near this transition, which is the focus of the present studies.

We have carried out a series of experiments[1] and MD simulations to remedy this lack of knowledge. We find that with increasing Γ, the failure of the granular solid occurs at a well defined $\Gamma_{cu} = \mu$, as one might expect from the Mohr-Coulomb picture. At this point, a fluid layerof non-zero thickness H forms. This layeris nucleated locally and then spreads across the top surface of the remaining solid. Unlike what one might expect from the case of frictional failure for solid-on-solid friction, the transition is hysteretic; if Γ is reduced from Γ_{cu}, the fluid layer persists until Γ reaches $\Gamma_{cd} < \Gamma_{cu}$, at which point, H falls discontinuously to 0. This is true for a variety of materials, with the size of the hysteresis loop reflecting the frictional properties of the materials. Within the fluid layer,there is flow both in the direction of shaking and in the horizontal direction transverse to the shaking. For the in-line direction, the flow is generated by the sloshing of the fluid layerand by the opening and refilling of a gap at either end of the container. Flow is induced in the transverse direction by shearing with the walls.

Associated with the transition are divergent time scales for the formation of the fluid layer as Γ increases, and with the disappearance of the layer as Γ decreases. If $\epsilon \equiv |\Gamma - \Gamma_{cu,d}|/\Gamma_{cu,d}$, then a time $\tau_u = A/\epsilon^{-1}$ is required to nucleate the fluid, following a step upward in Γ of size ϵ past Γ_{cu}. An identical power law,$\tau_d = A/\tau^{-1}$ applies following an ϵ step below Γ_{cd} for the time associated with the vanishing of the fluid.

The nature of the transition is substantially affected by a number of changes to the system. If the layer is weakly dilated by a fluidizing air flow, the hysteresis is removed. When we add a thin freely moving strip of plastic that covers the surface of the material and has a mass comparable to half a layer of grains, the hysteresis is also removed. If we add an 'intruder' particle on the top surface of the fluid, it dramatically changes the times for the fluid to vanish when Γ falls below Γ_{cd}.

Thus, the solid-fluid transition under the influence of gravity presents a host of modeling challenges. The symmetry of the divergent relaxation times, τ_u and τ_d suggest an underlying theoretical structure that is identical for both phases.

Spherical Particles of a Flat Substrate Systems of particles on a substrate represent an opportunity to observe particle motion in detail, since 3D systems are by and large not visualizable. Thus, one might hope that systems of spherical particles, rolling with low coefficient of rolling friction, μ_r, might be very valuable for studying 2D granular gases and for testing preditions of clustering due to inelastic effects. We have carried out a series of experiments in this vein, begining with an experiment to observe clustering–i.e. the formation of spatial structure in a granular gas due to inelasticity of the collisions. These experiments show that when spheres collide on a substrate, the collision induces a period of slipping that leads to high energy dissipation. Consequently, the effective restitution coefficent is much higher than it would be in the absence of the substrate.

Indeed, collisions are now moderated through the substrate, and such systems represent a new class of granular materials. We have set out to characterize the properties of this novel fluid state. Necessarily, energy must be continuously supplied if such a system is to be maintained in a dynamic state. We do this by shaking the substrate in the horizontal plane. It is also possible to control gravity, since the relevant component of $\vec{g}$ is set by the tilt from horizontal of the substrate. The dynamics of the system are strongly affected by the relative orientation of the direction of shaking and of $\vec{g}$. If these directions are coincident, a collection of grains undergoes a transition from solid to fluid as the shaking strength Γ increases. Below this transition, the system exhibits subharmonic instabilities to standing waves, such as those seen in thin vertically vibrated 3D layers. The resulting patterns are often chaotic, and this may represent an interesting way to probe spatio-temporal chaos. If the directions of shaking and of $\vec{g}$ are not coincident, large scale convective flow occurs. This flow is reminiscent of granular convection in vertically shaken systems. However, now the relevant control parameter is the velocity of shaking, $A\omega$ rather than Γ, as it is in the 3D vertical shaking case.

This type of system offers an astonishingly rich phenomonology that is accessble to experiment and is a likely candidate for MD simulations. We are pursuing both of these approaches.

[1]S. Tennakoon, L. Kondic and R. Behringer, Europhys. Lett. **45**, 470 (1999).

For images of these and related studies please see: www.phy.duke.edu/ bob, and the links to web pages of other group members.

Shaken Granular Systems
And
The Effect of Gravity

Fifth Microgravity Fluid Physics
And
Transport Phenomena Conference

Cleveland, OH
August 9-11, 2000

Collaborators: Ben Painter, Lou Kondic, Guy Metcalfe

OUTLINE

I. Horizontally Shaken granular materials

- A. Nature of the fluid-solid transition
- B. Divergent time scales
- C. Changing the nature of the transition

II. Systems of particles on a flat substrate

- A. Sliding as a result of collisions
- B. A novel form of convection
- C. Cooling of a granular sample on a substrate
- D. Subharmonic waves

Shaking as a Means to Probing Granular Friction, Failure, and Phase Transitions

Outline

1. **Introduction:** S → F studied F → S ?
   solid-fluid phase transition in granular materials

2. **Horizontal Shaking—fluid-solid transition is**
   - **hysteretic**
   - **sensitive to a small number of surface particles**
   - **hysteresis is eliminated by various simple modifications**
   - **transition shows interesting time-scales**
   - **contrary to naïve friction model**

3. **Vertical and Horizontal Shaking**
   Novel tests of friction laws

4. **Conclusions**

Introduction & Motivation

I. Horizontal shaking of a granular material may look at the:

- change from solid-like to liquid-like motion
- sensitivity to shearing failure under own weight
- role of dilation in failure
- role of bulk surface activity in failure
- onset of avalanches

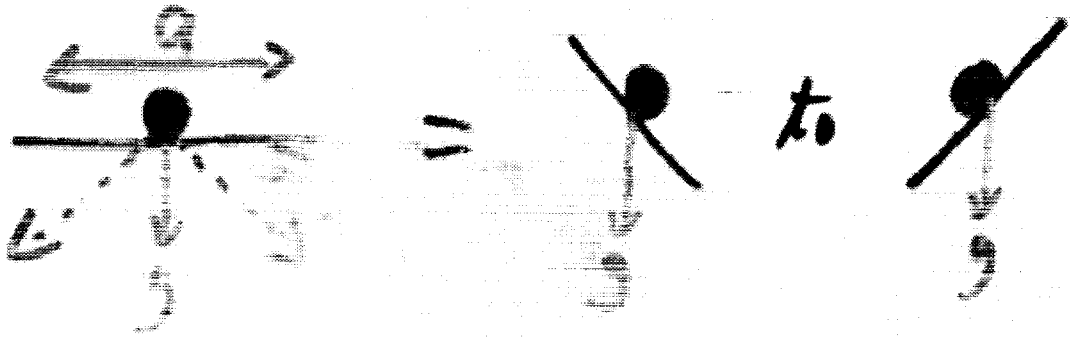

Frictional Failure

For Solid → Fluid

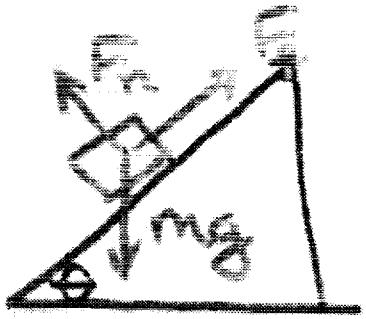

At balance: $F_n = mg\cos\theta$

$F_s = mg\sin\theta$

Largest $F_s = \mu F_n$

Failure: $\tan\theta = \mu$

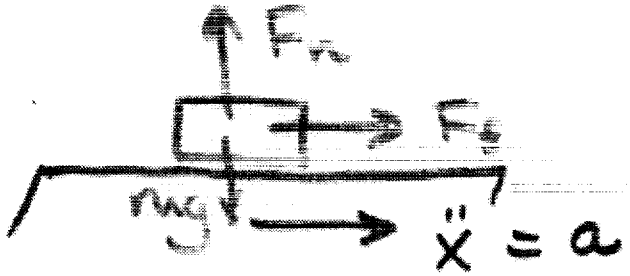

Failure

when $a = \mu g$

Model for Fluid → solid ?

Experiment

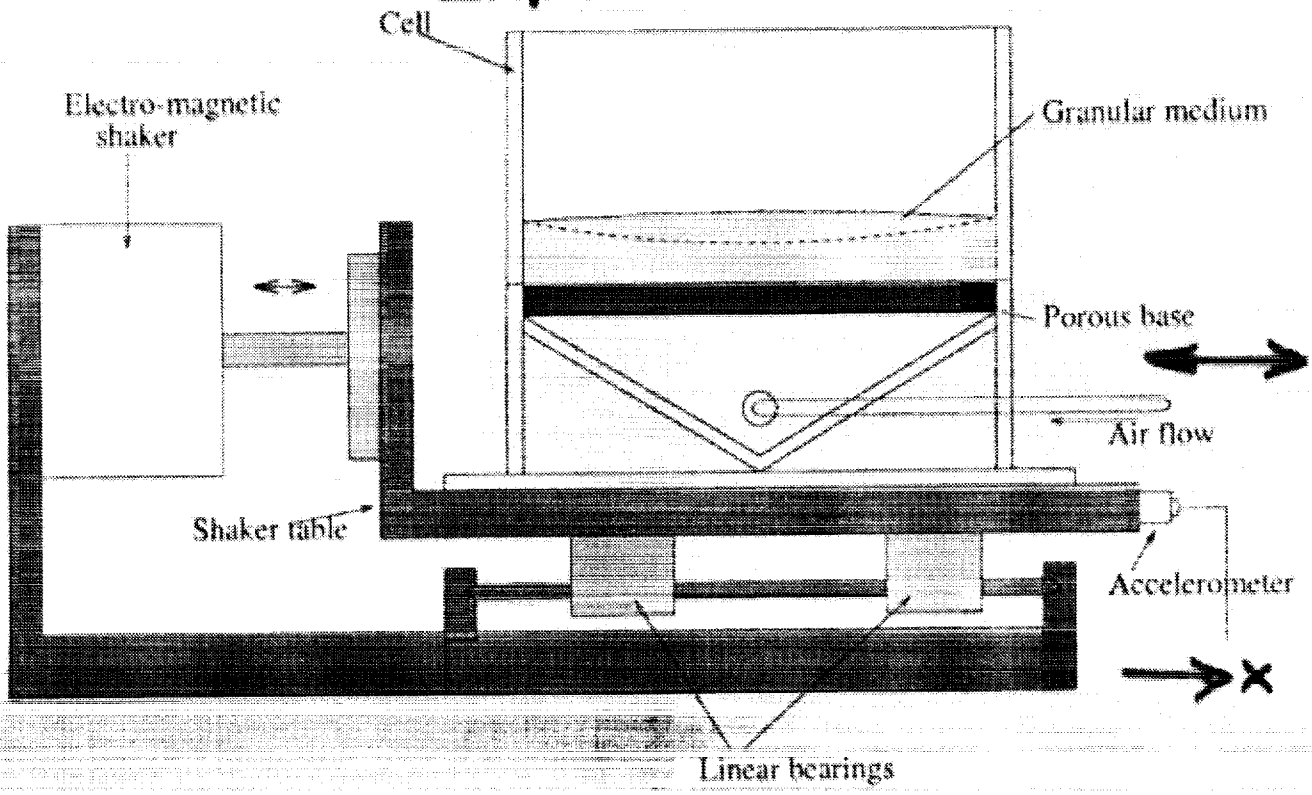

$$x = A\cos\omega t$$

$$\Gamma = \frac{A\omega^2}{g}$$

$$\delta\Gamma/\Gamma = 0.1\%$$

A shaking amplitude
ω shaking frequency
g acceleration of gravity

$\omega = 2\pi(5\text{ Hz})$; A varied; $\Gamma_{max} \simeq 2$

Sand and Cell

Typical material

Ottawa sand: average particle size 0.6 mm
average particle mass 0.5 mg

Cell size: 202×32 grains
121×19 mm
$\frac{3}{4} \times 4\frac{3}{4}$ in

cell depth ≈ 200 grains

+ rough sand,
glass spheres,
:

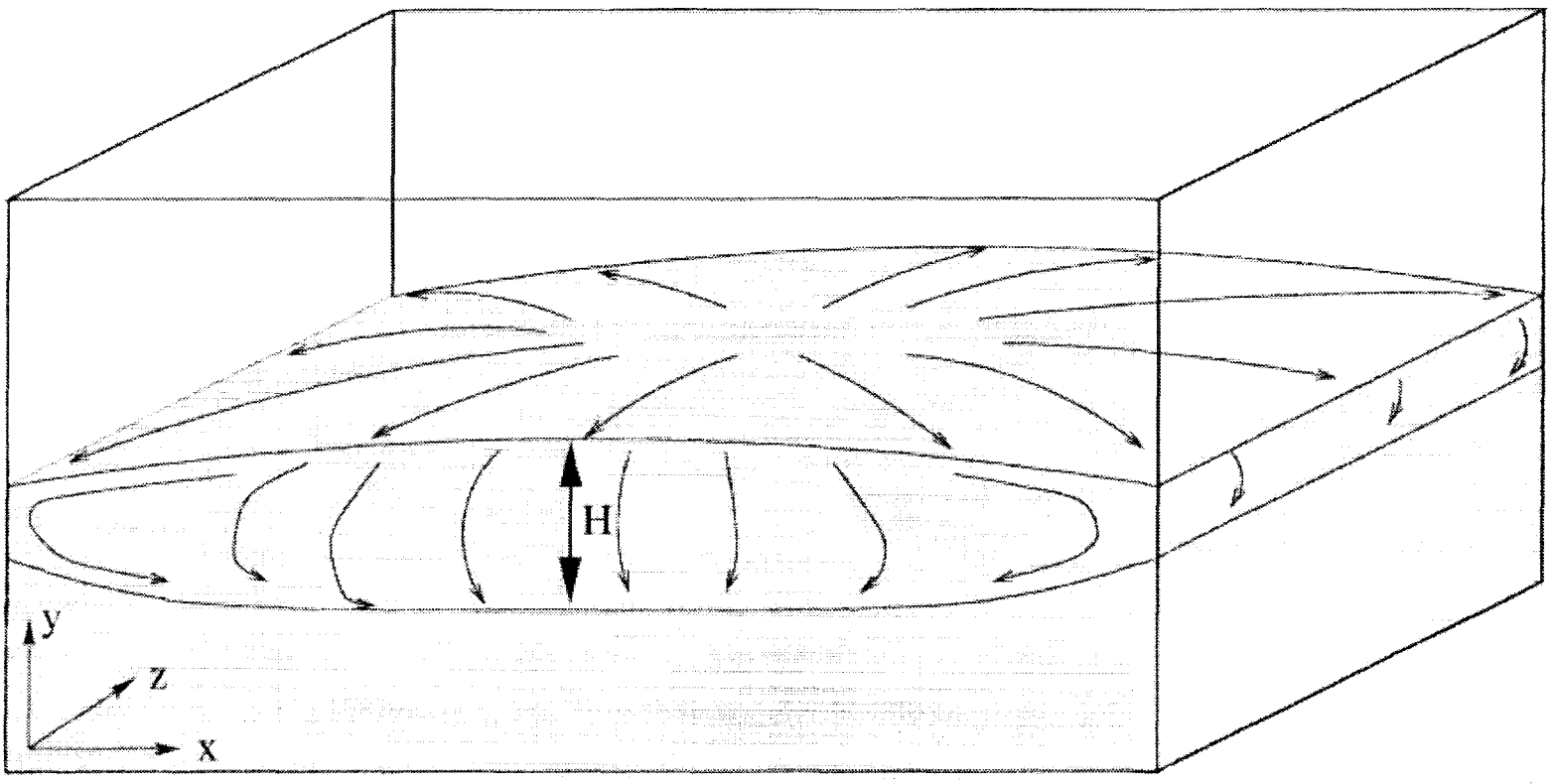
H
y
z
x

Hysteretic transition to 'sloshing' fluid flow

1. $\Gamma_h < \Gamma_{hd}$: solid
2. $\Gamma_{hd} < \Gamma_h < \Gamma_{hu}$ solid or fluid
3. $\Gamma_h > \Gamma_{hu}$ fluid

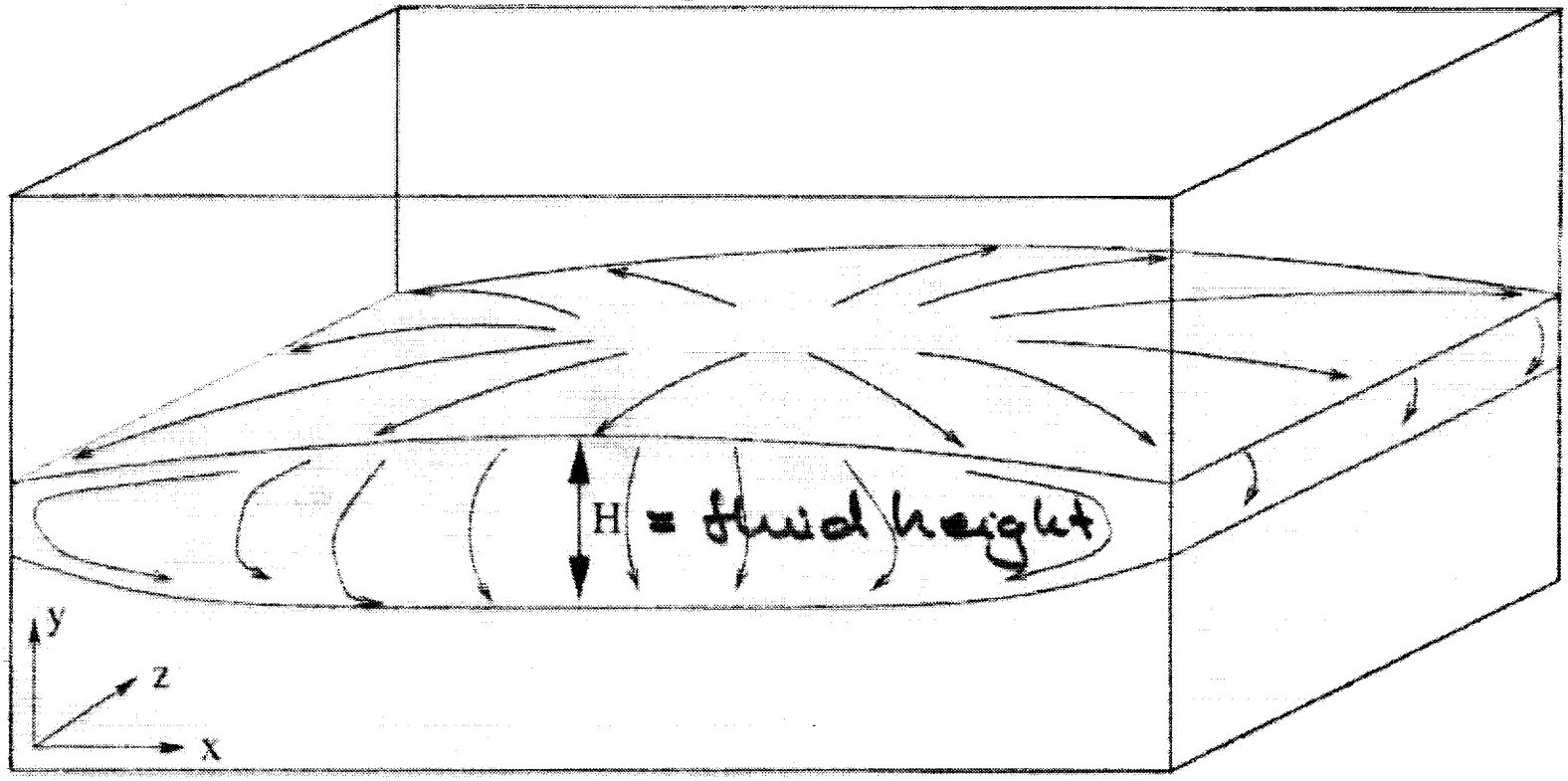

Mean Flows

$\Gamma_h > \Gamma_{hu}$

Backwards Bifurcation/Hysteresis

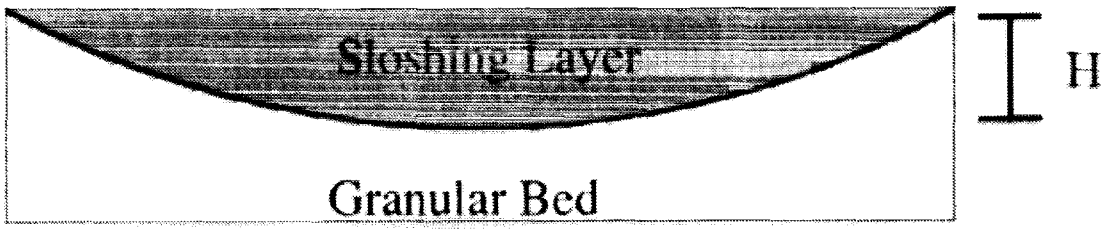

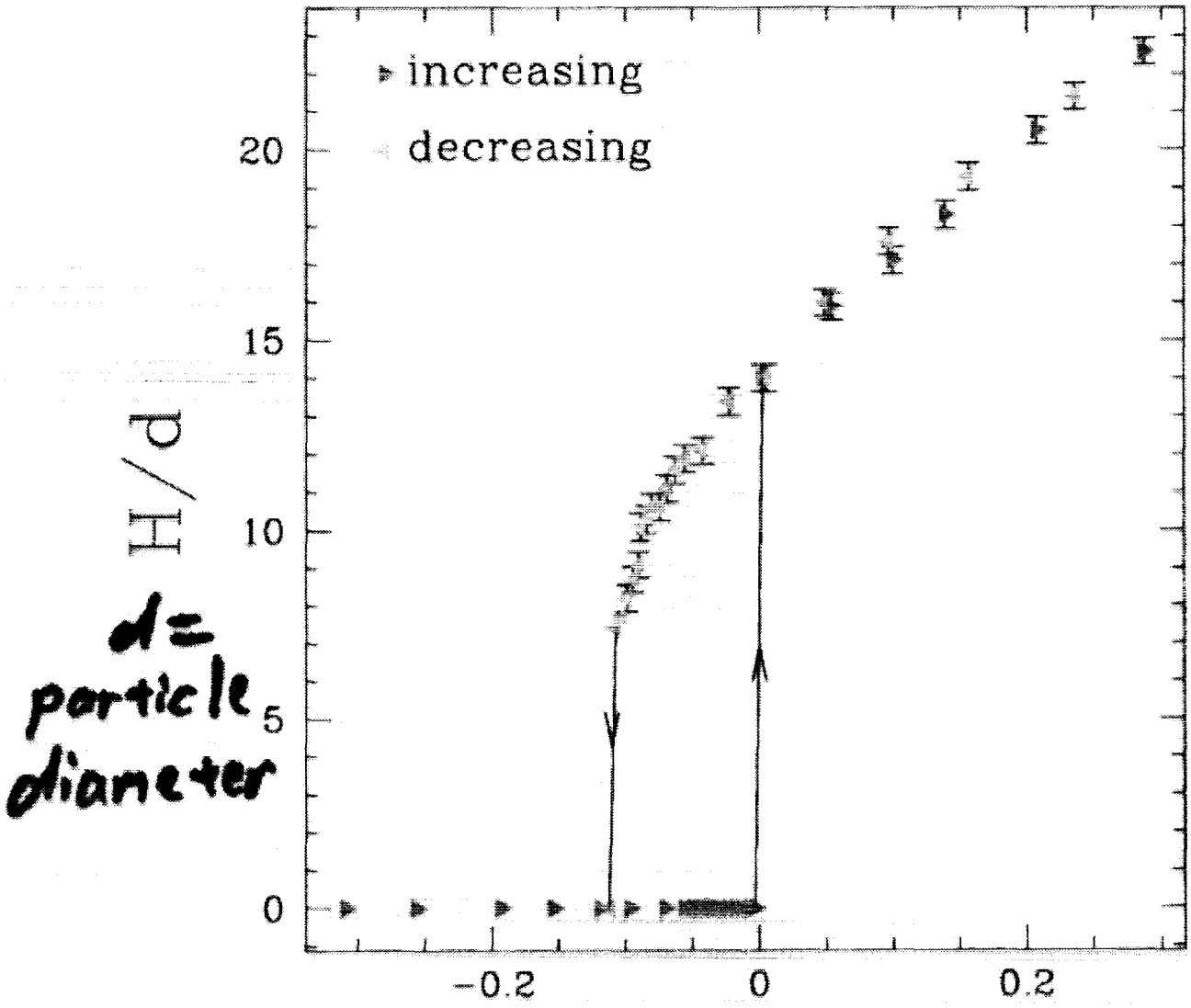

$$\epsilon \equiv \frac{\Gamma - \Gamma_c}{\Gamma_c}$$

Different Material Roughness

rough sand

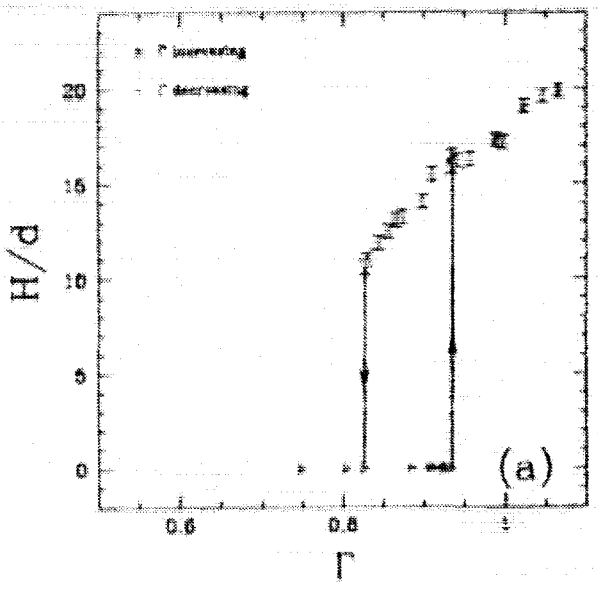

glass beads

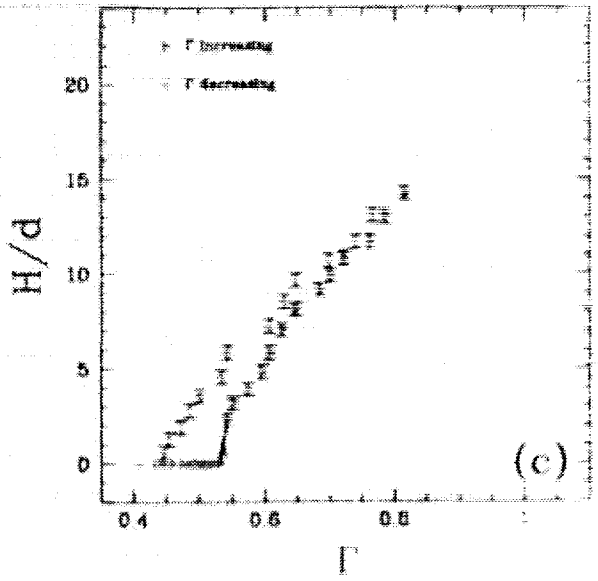

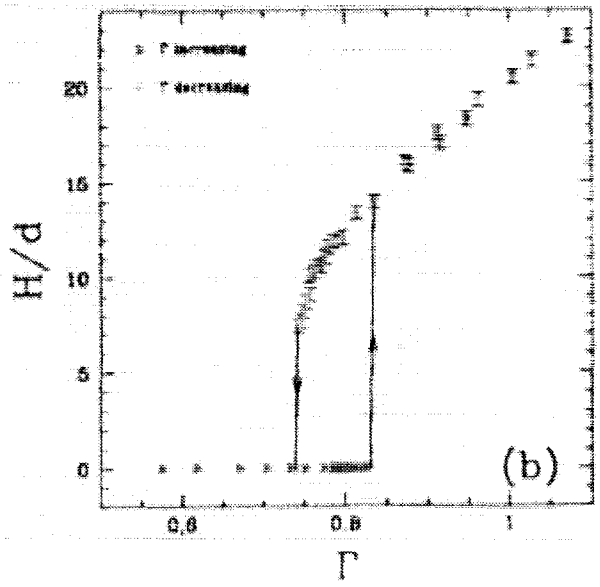

smooth sand

Convection due to sloshing

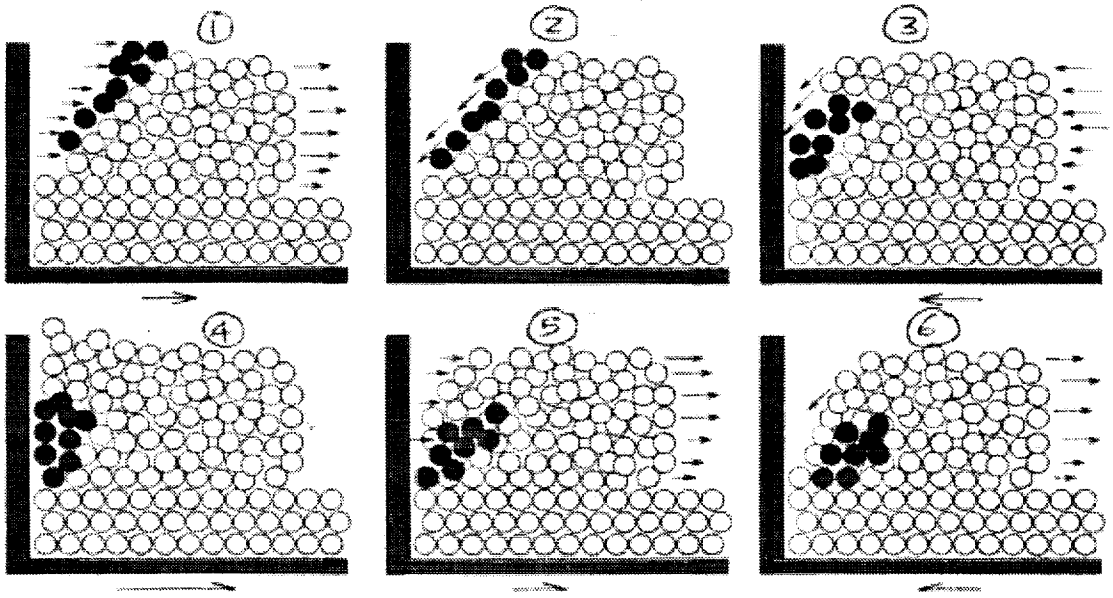

The convective flow parallel to the shaker plane is due to the avalanching of grains at the end walls during the sloshing motion of the liquefied layer.

Convection due to wall shearing

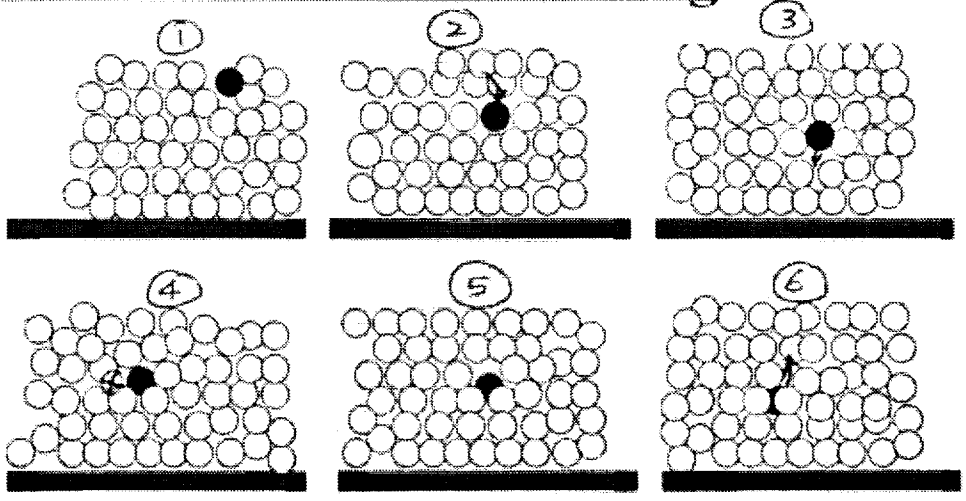

The convective flow transverse to the shaker plane is due to the side wall shearing, which has not, to our knowledge, been previously characterized, but it is likely to occur generally when a 3D material is sheared in the presence of gravitational field.

Convection due to side wall shearing

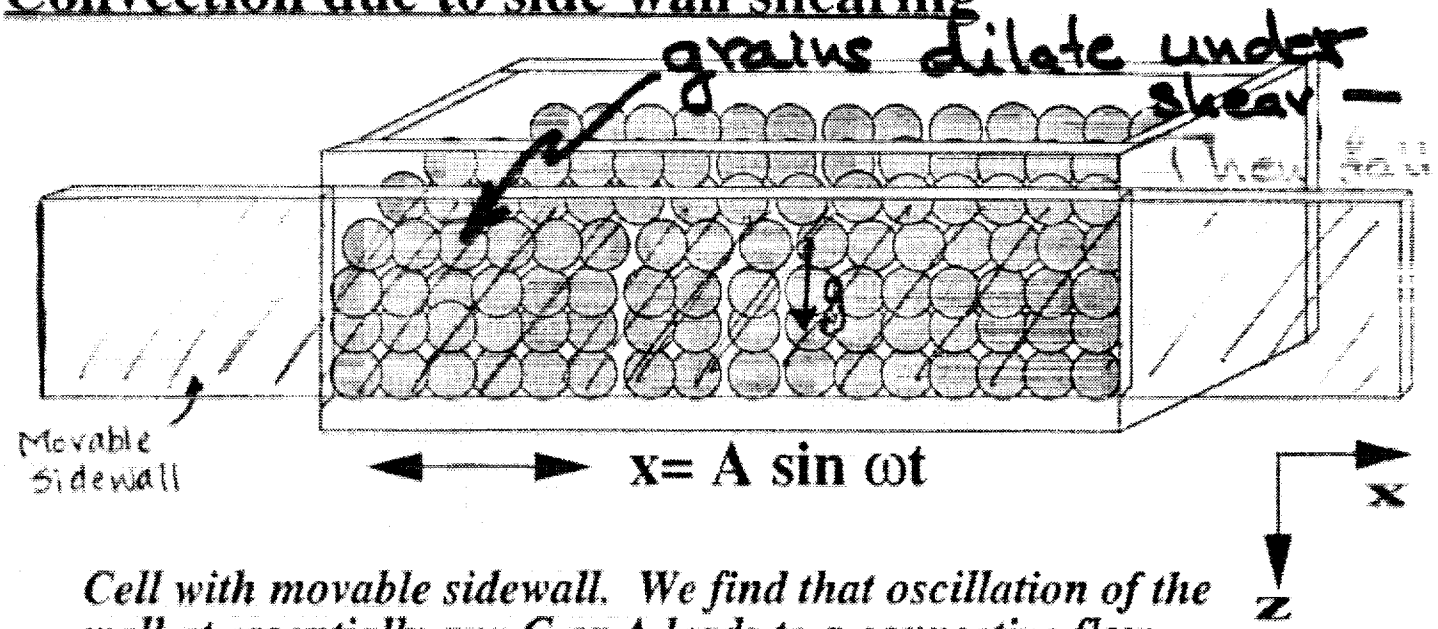

Cell with movable sidewall. We find that oscillation of the wall at essentially any G or A leads to a convective flow where grains fall at the sidewall, and then pushed inward, and upward within a shearing layer of 5–10 grains.

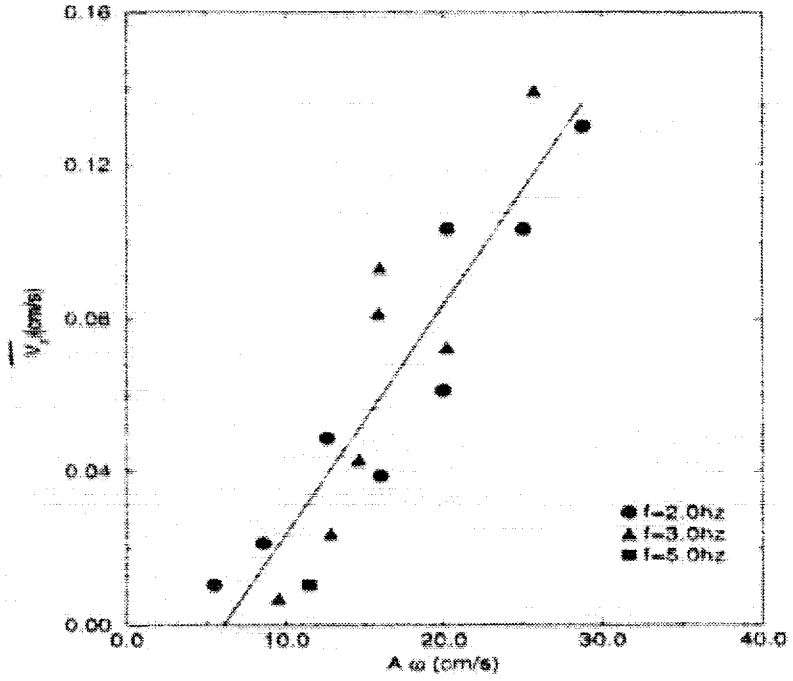

Downward average speed Vz has linear dependency with velocity amplitude Aω .

Sliding Surface Grains

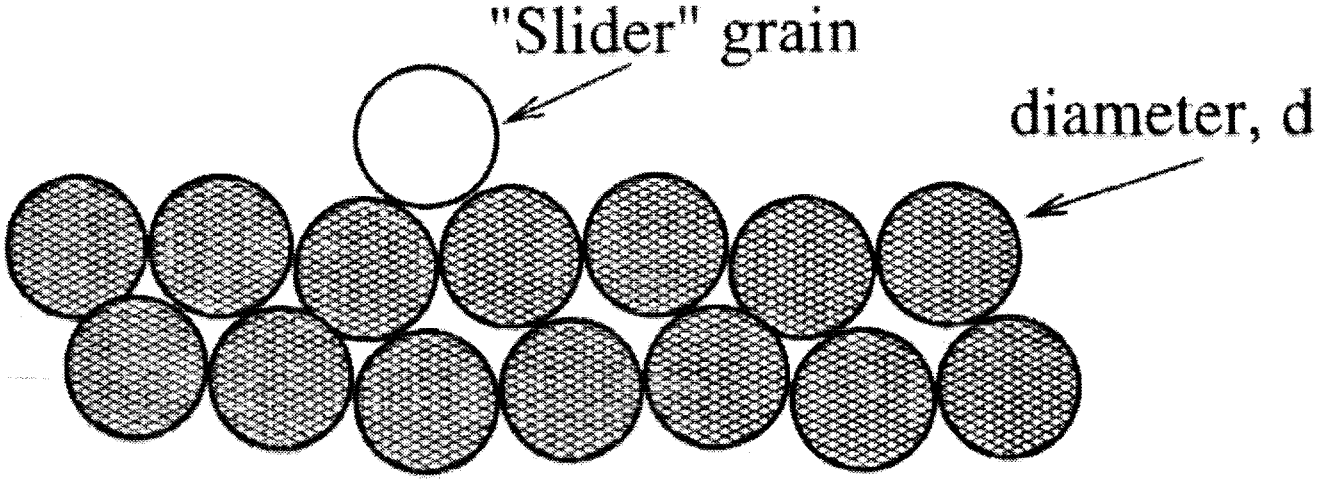

Sliders begin when

$$(A\omega)^2 \sim \alpha g d \qquad \alpha \sim 1$$

(Not frictional)

Timescale

$$\tau \sim \left(\frac{d}{g}\right)^{1/2} \approx 0.01\,s$$

$0.1\,s \leq T$ = shaking period

Further Explorations

- Determine unstable branch of H vs. Γ
- Determine nucleation time scales
- Dilate sample - what is effect on transition
- Increase overload (surprise here!)
- add 'impurities'

Unstable Branch

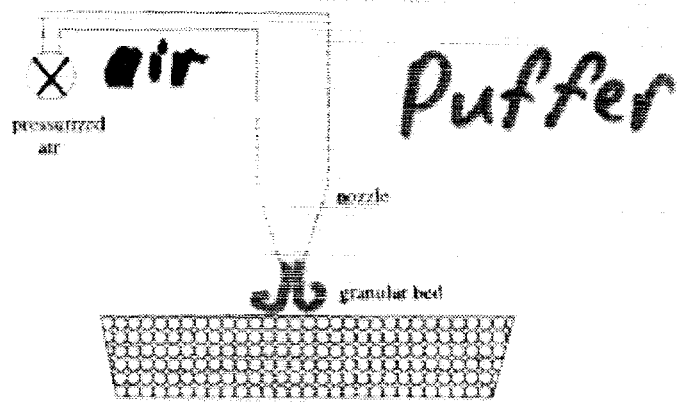

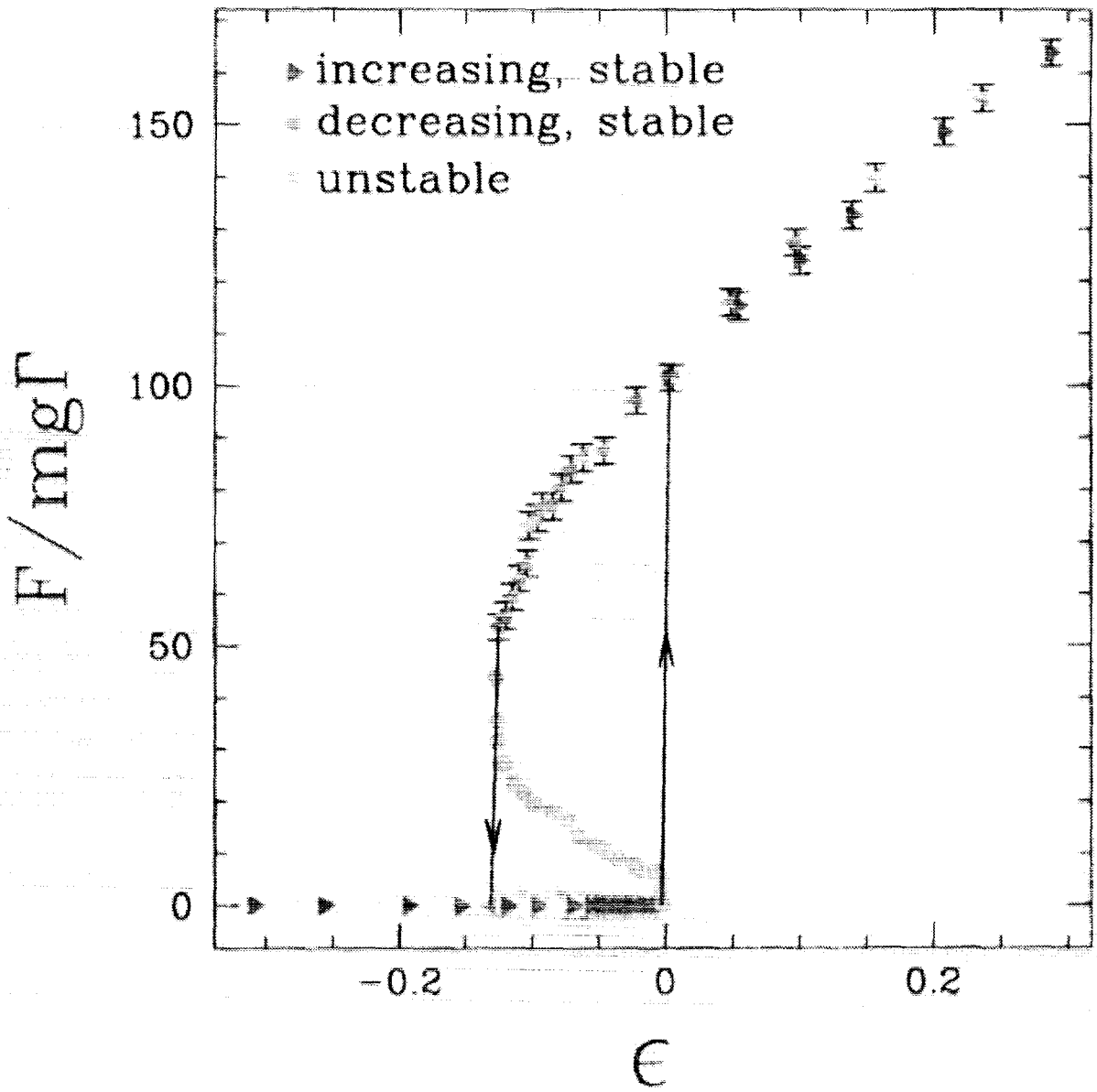

Transistion Timescales

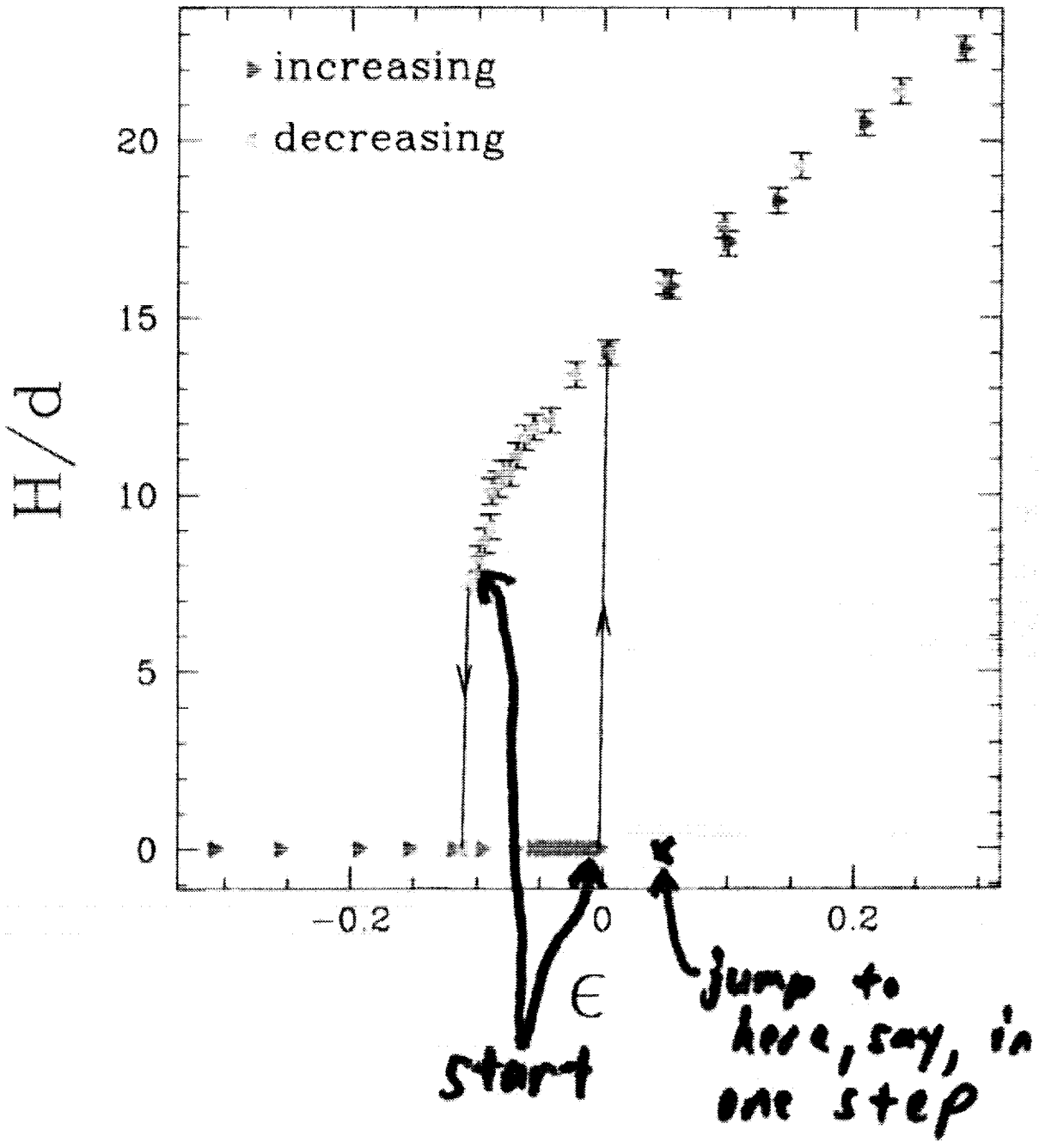

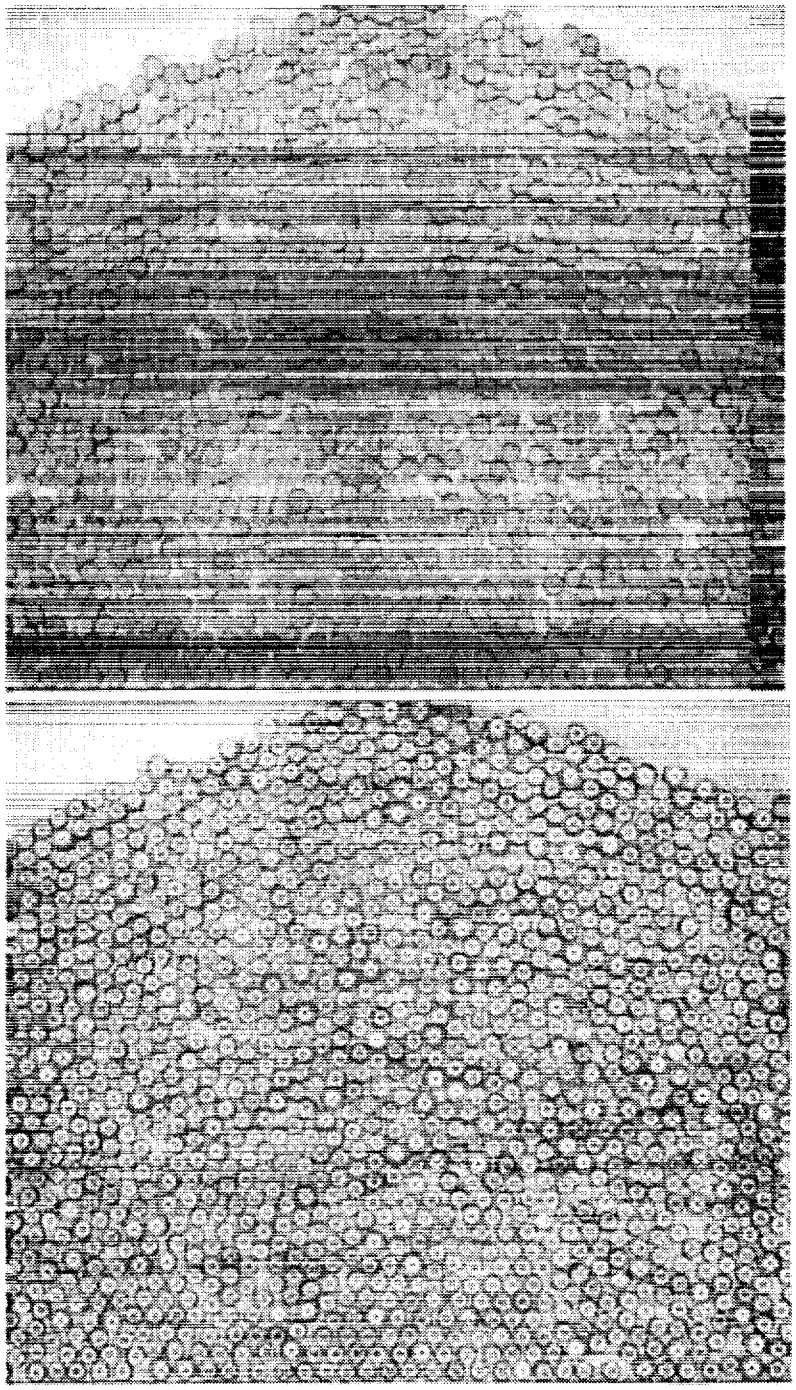

Figure 5.1: Top: Original image of middle section of 2-D pile. Bottom: Same image with center marks found by combination of manual and software methods. Notice that we distinguish large diameter (0.90 cm) and small diameter (0.73 cm) particles.

Timescales are Powerlaws

$$\tau \equiv \tau^* \epsilon^{\beta}$$

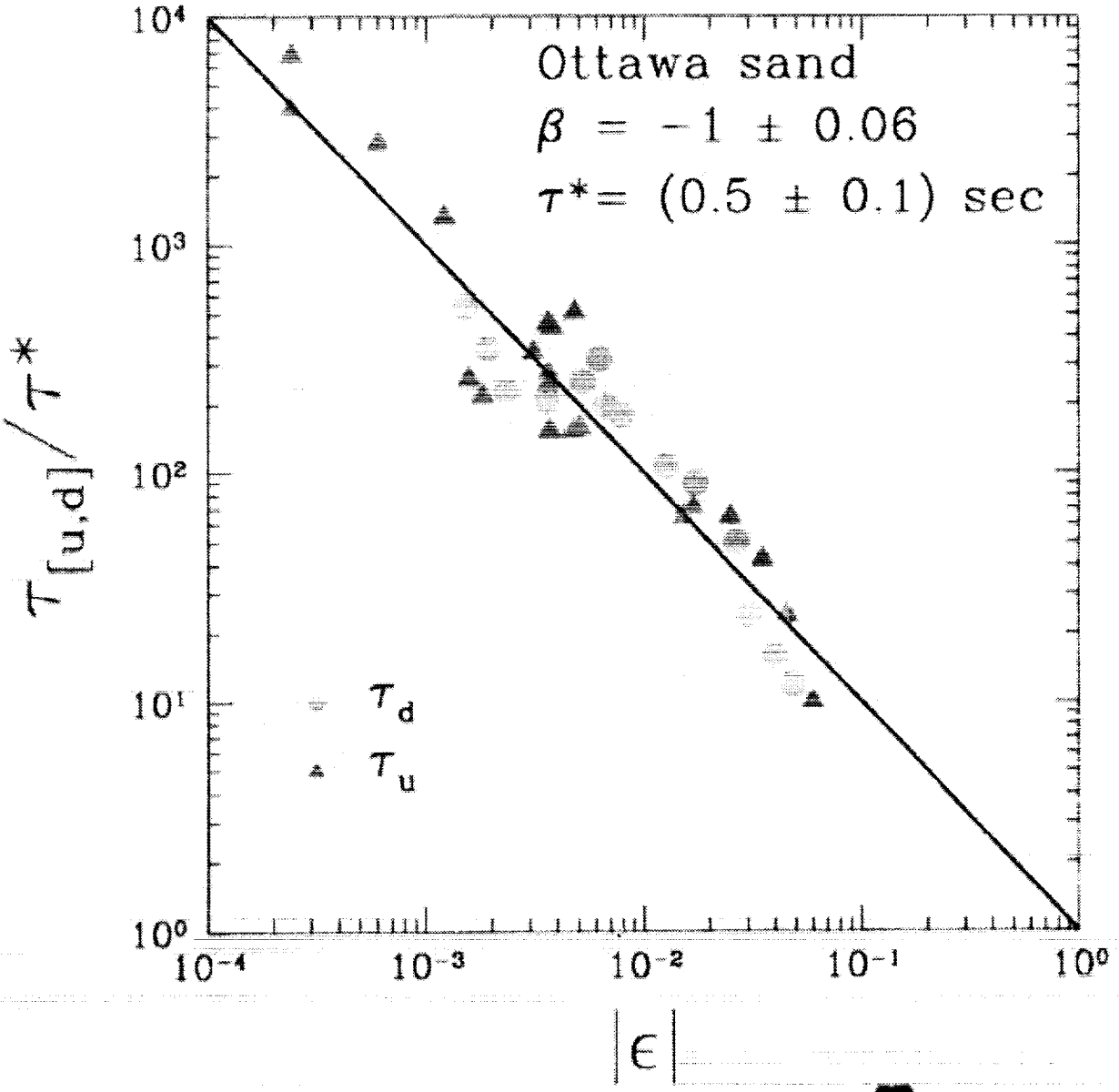

ϵ defined with appropriate Γ_c for up and down transition

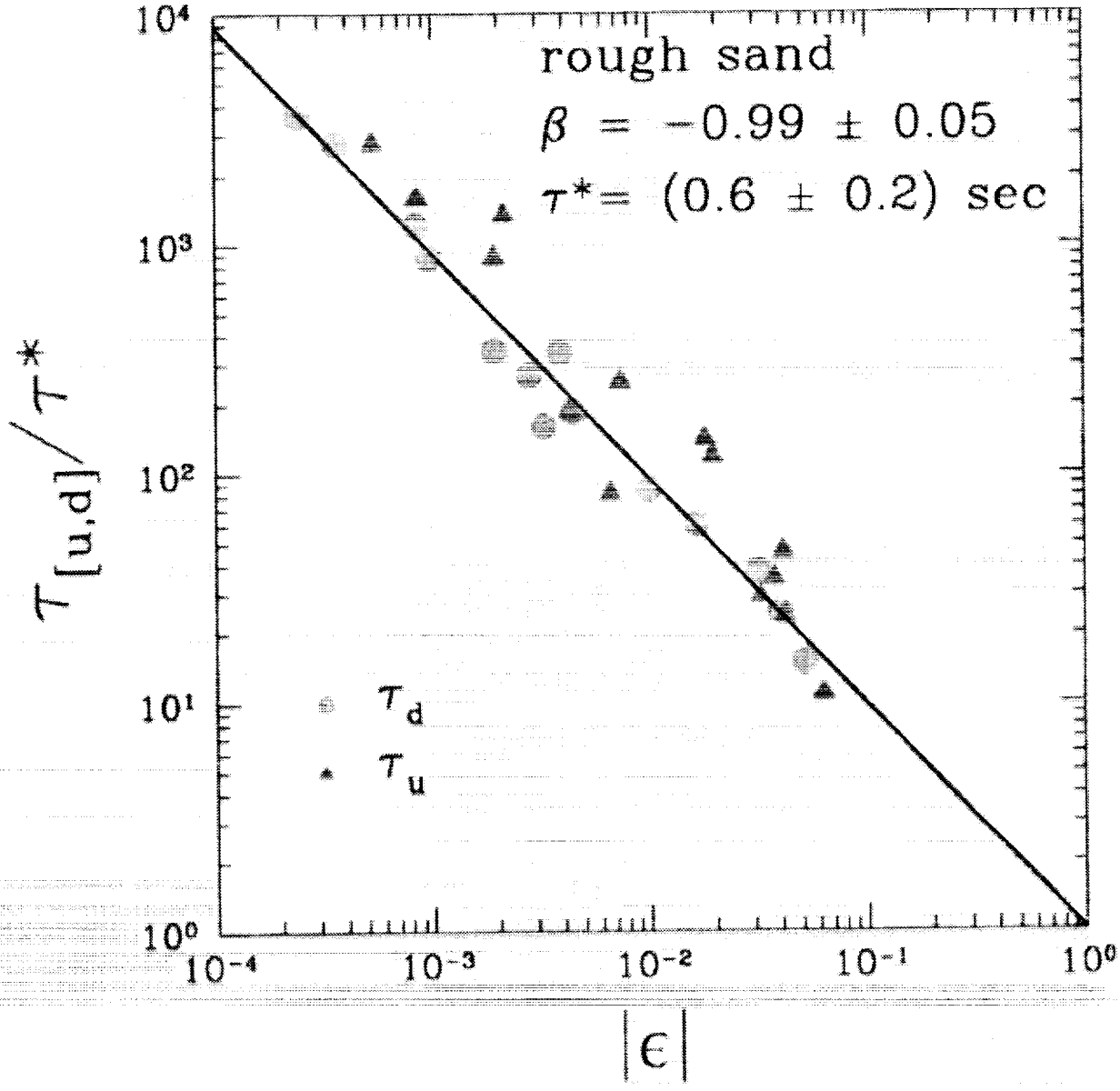

Same result for changing A: All observations well-fit by a powerlaw with $\beta = -1$, $\tau^* \approx 0.5$ sec.

Sloshing Nucleation and Decay

Turn-On

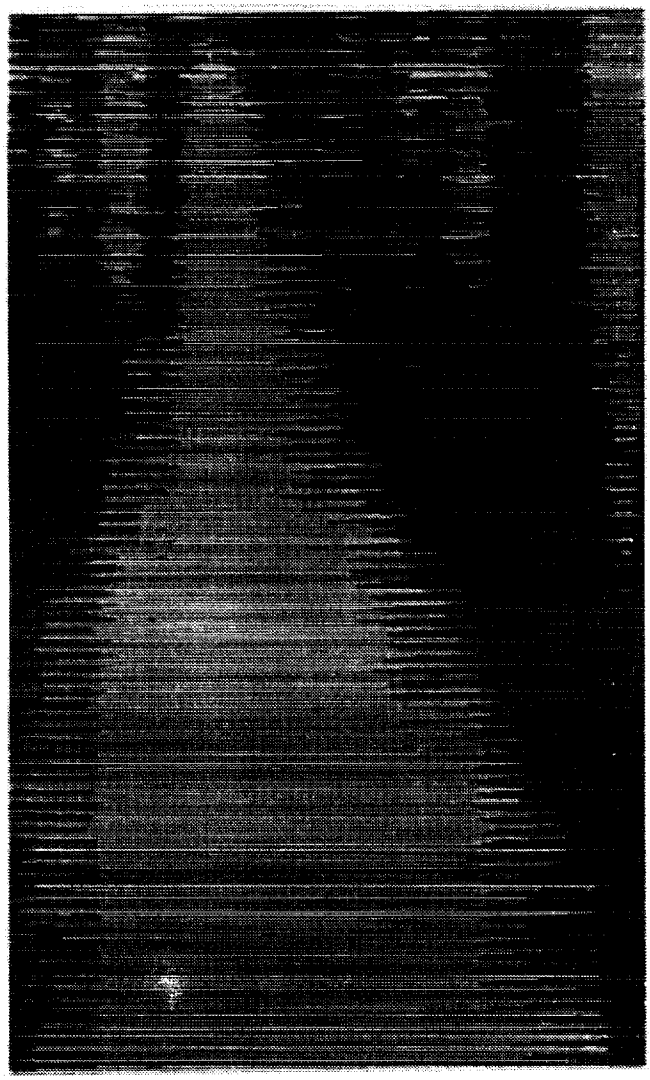

Turn-Off

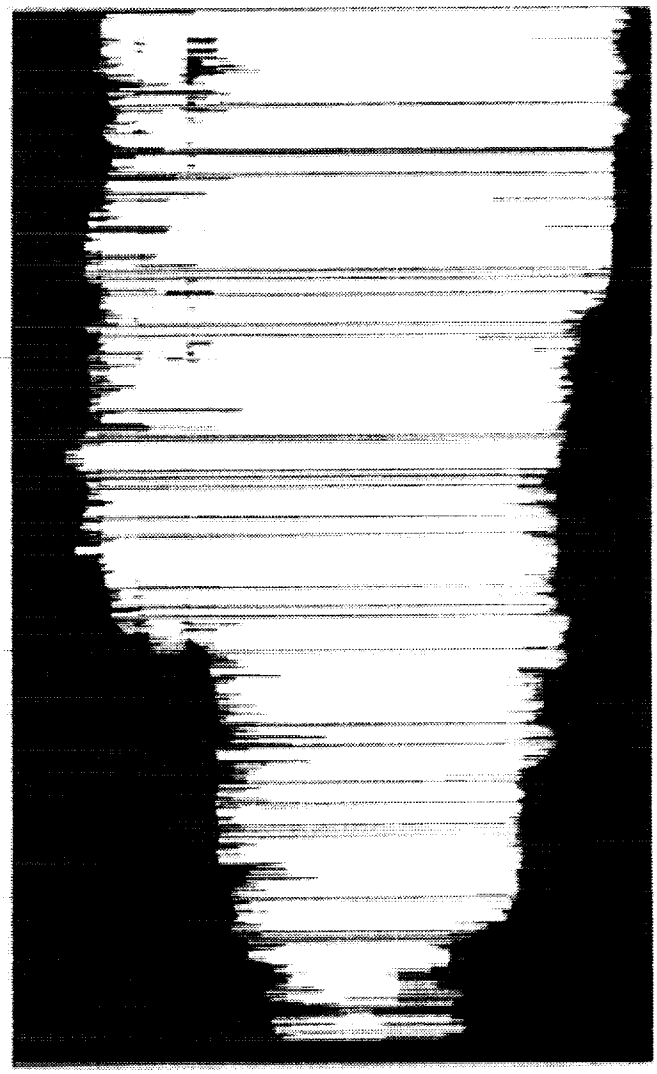

Key Points so far:

Transition to liquefied surface layer

— is hysteretic—exact points may depend on static/kinetic friction

— has same powerlaw timescales for up and down transition—seems robust against changes in material and driving

Modifying the Bifurcation

Fluidize
Suppress Sliders
Add Single Particle Impurities

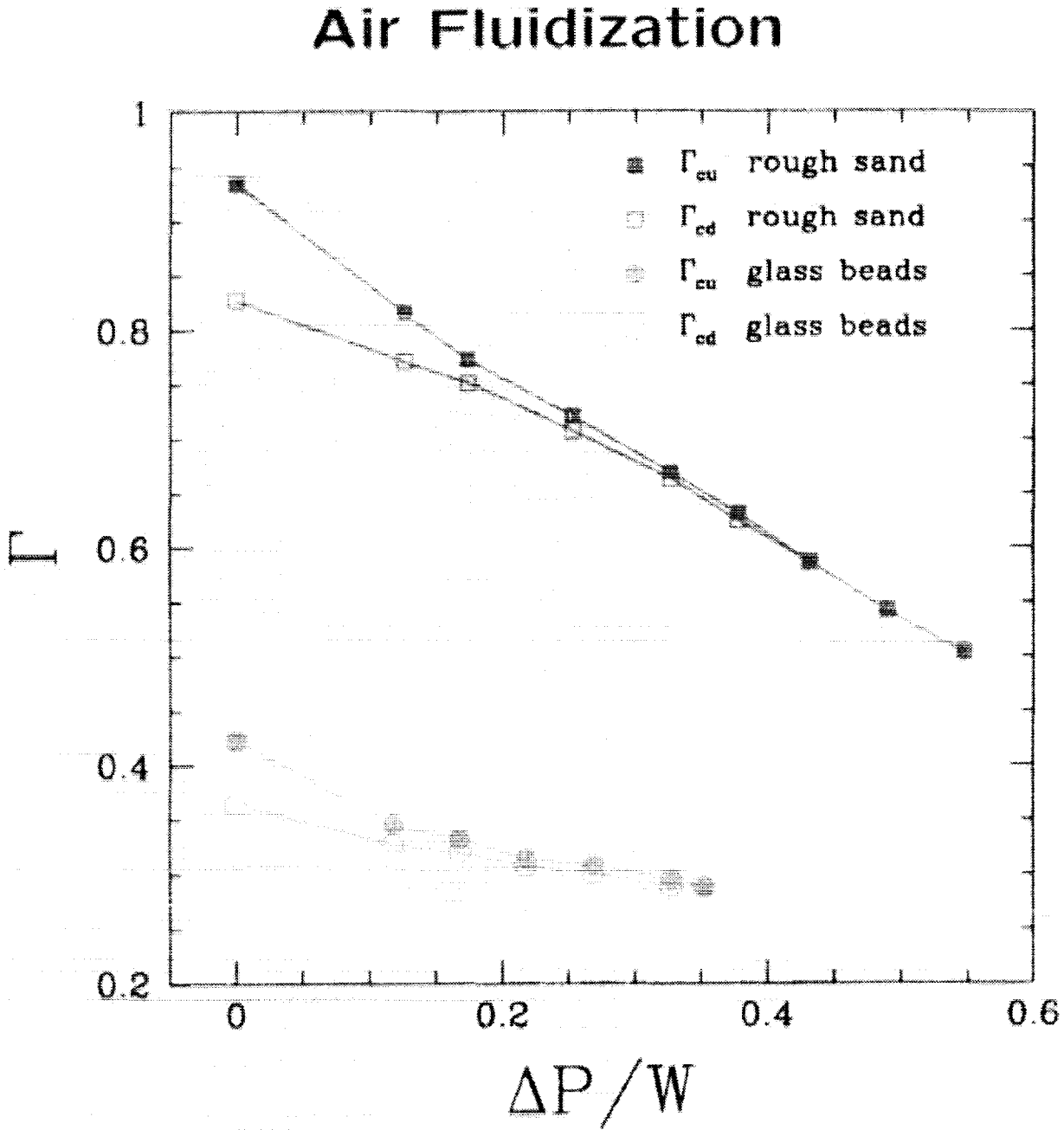
Air Fluidization
1
0.8
0.6
0.4
0.2
Γ
0
0.2
0.4
0.6
ΔP/W
Γcu rough sand
Γcd rough sand
Γcu glass beads
Γcd glass beads

Suppressing Sliders

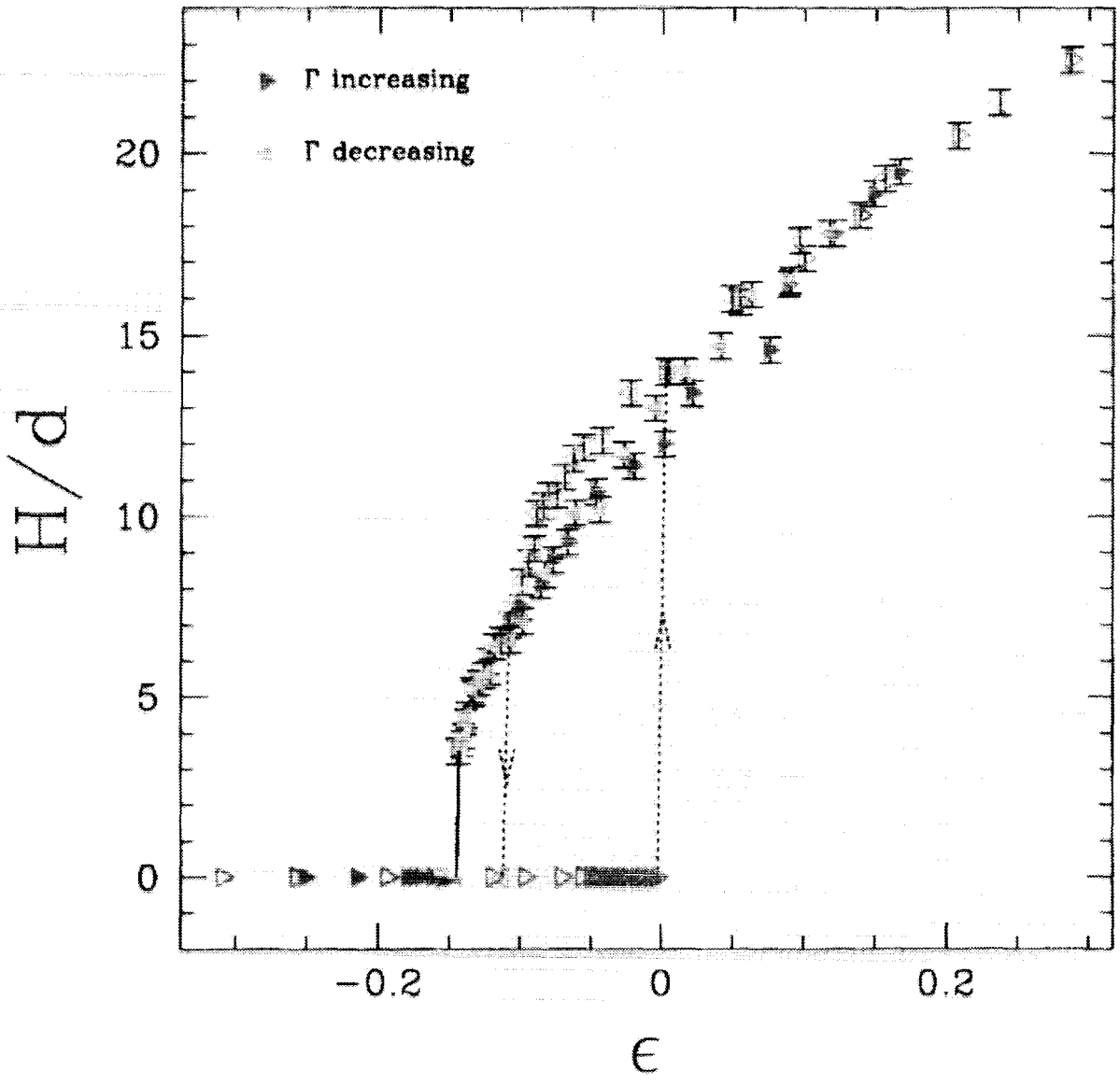

Red + Green: Ordinary

Purple + Blue: add small overload

Impurities Change Exponent

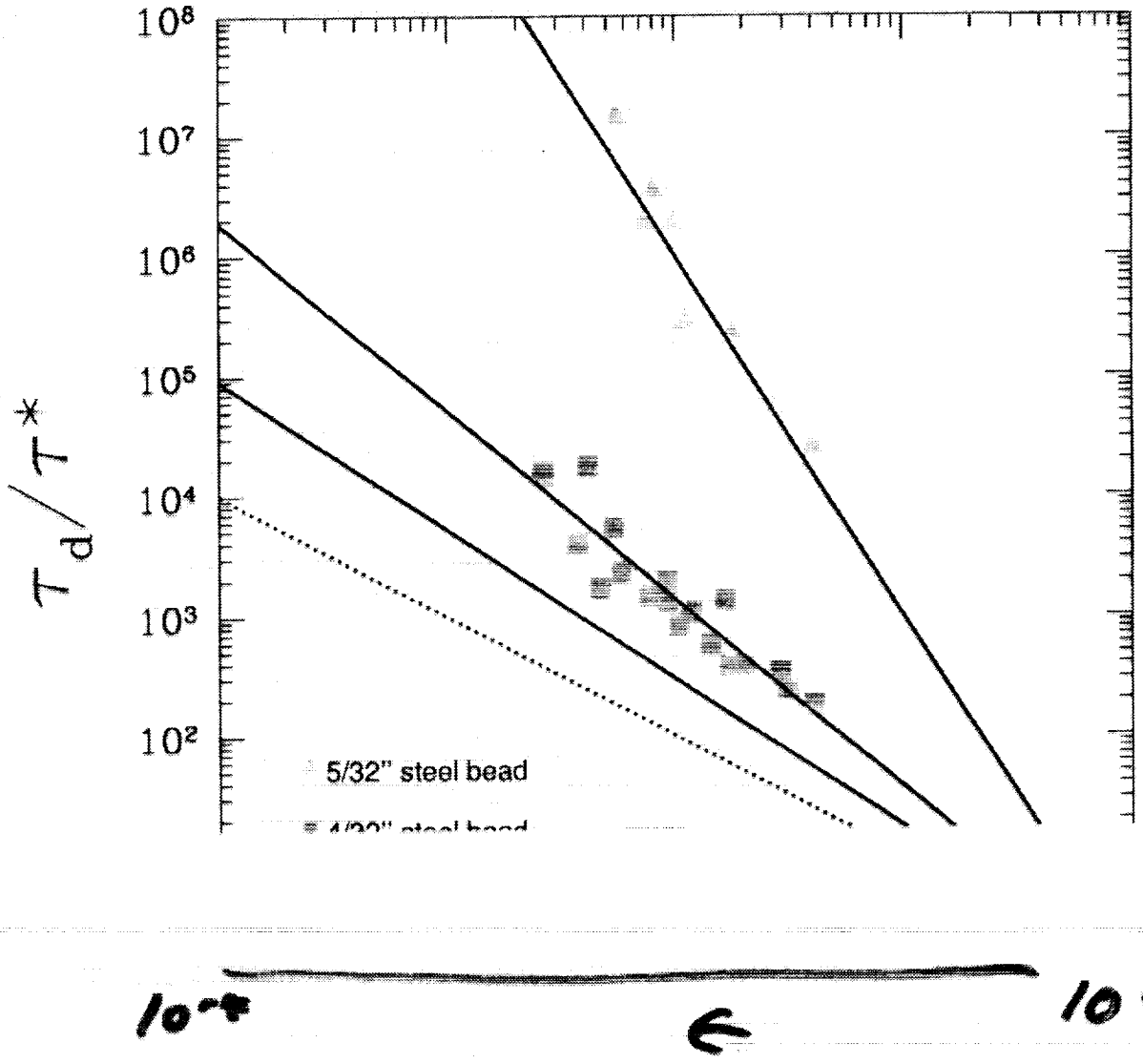

Powerlaw Exponent Correlates to Impurity Mass

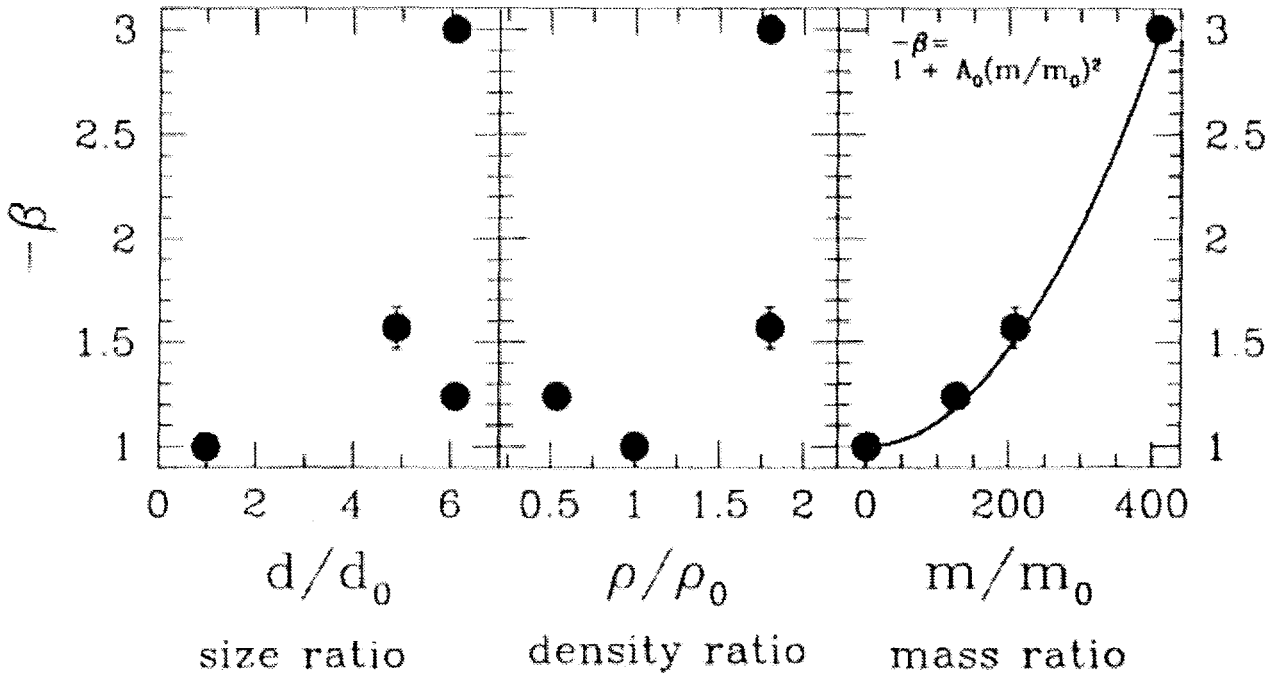

$$-\beta = 1 + A_{\circ}\,(m/m_{\circ})^2$$

$$A_{\circ} = (1.17 \pm 0.02) \times 10^{-5}$$

Block Model

(with D.G. Schaeffer, Duke Math Dept)

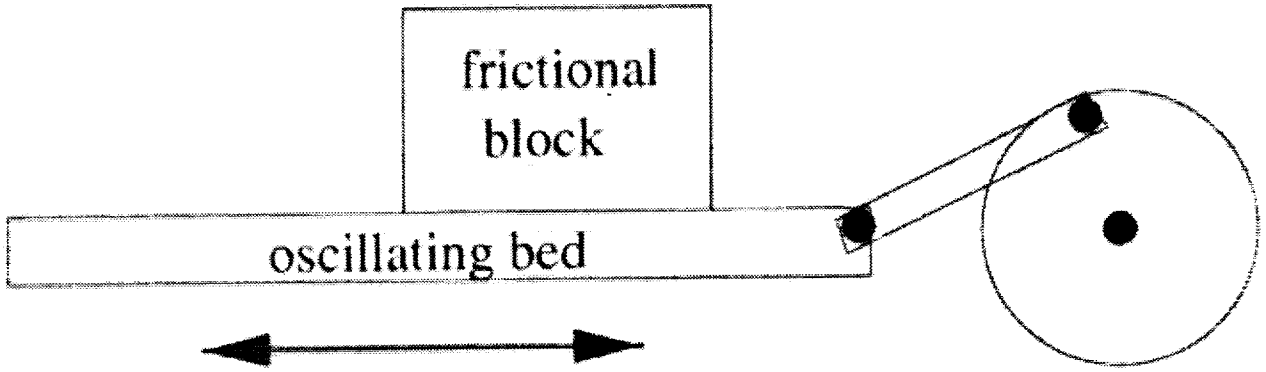

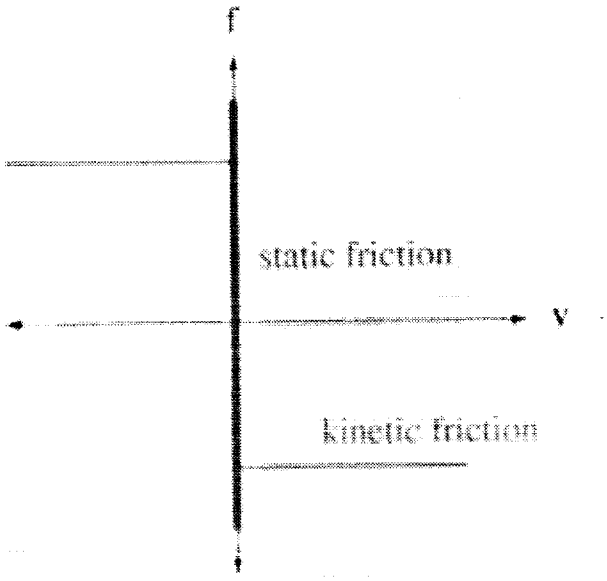

Coulomb friction

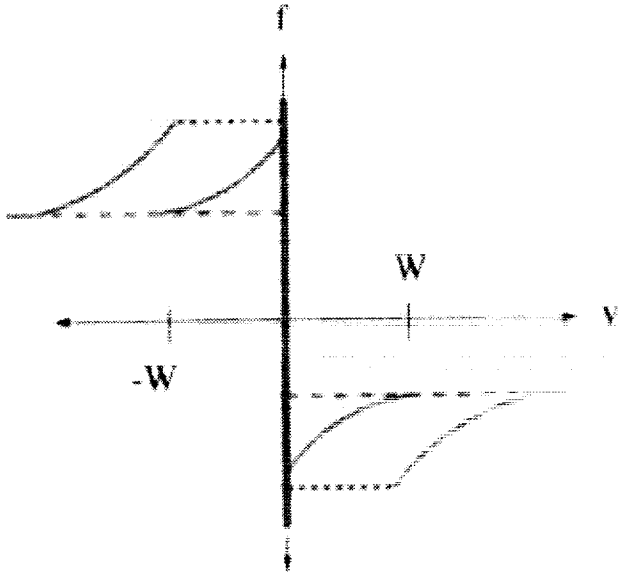

relaxing friction

Introduce timescale σ to relax between static and dynamic friction

Relative velocity y — the usual Coulomb friction

$$\dot{y} = f + A\sin(t)$$

But friction coefficient "relaxes"

$$\sigma\dot{\theta} = 1 - \theta\left(1 + R\frac{|y|}{W + |y|}\right)$$

Frictional force f is

$$y \neq 0 \quad \begin{cases} f = -\text{sign}(y)\theta \end{cases}$$

$$y = 0 \quad \begin{cases} f = -A\sin(t) & \text{if } |A\sin(t)| < \theta \\ f = -\text{sign}(\sin(t))\theta & \text{if } |A\sin(t)| \geq \theta \end{cases}$$

↑ friction coefficient

Model Bifurcations

Coulomb

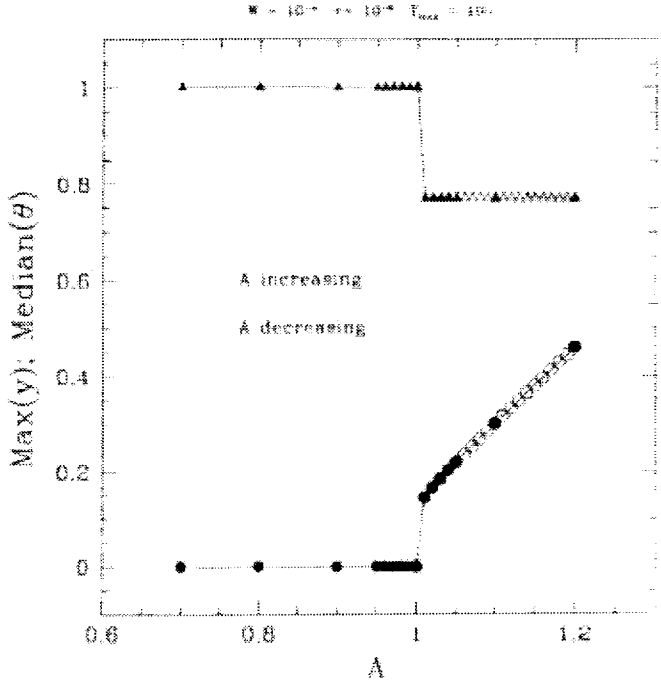

$W = 0 \ \sigma = 10^{-6}$

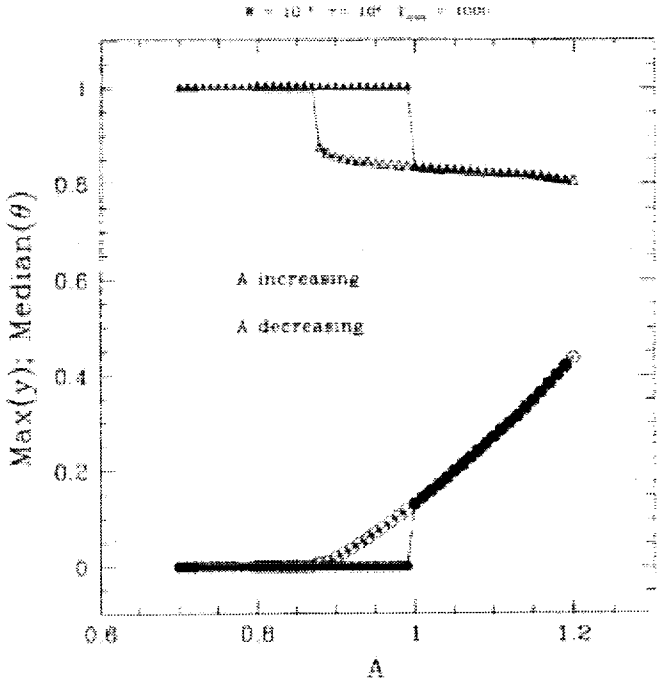

Model Bifurcations

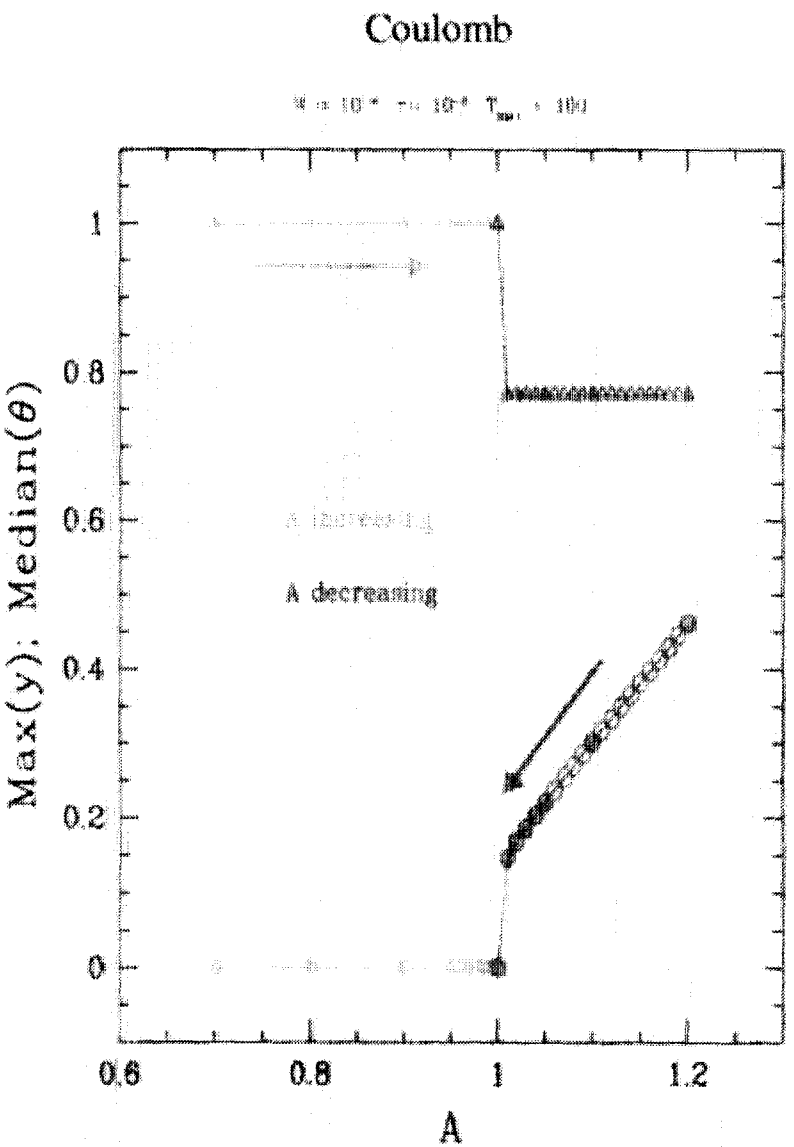

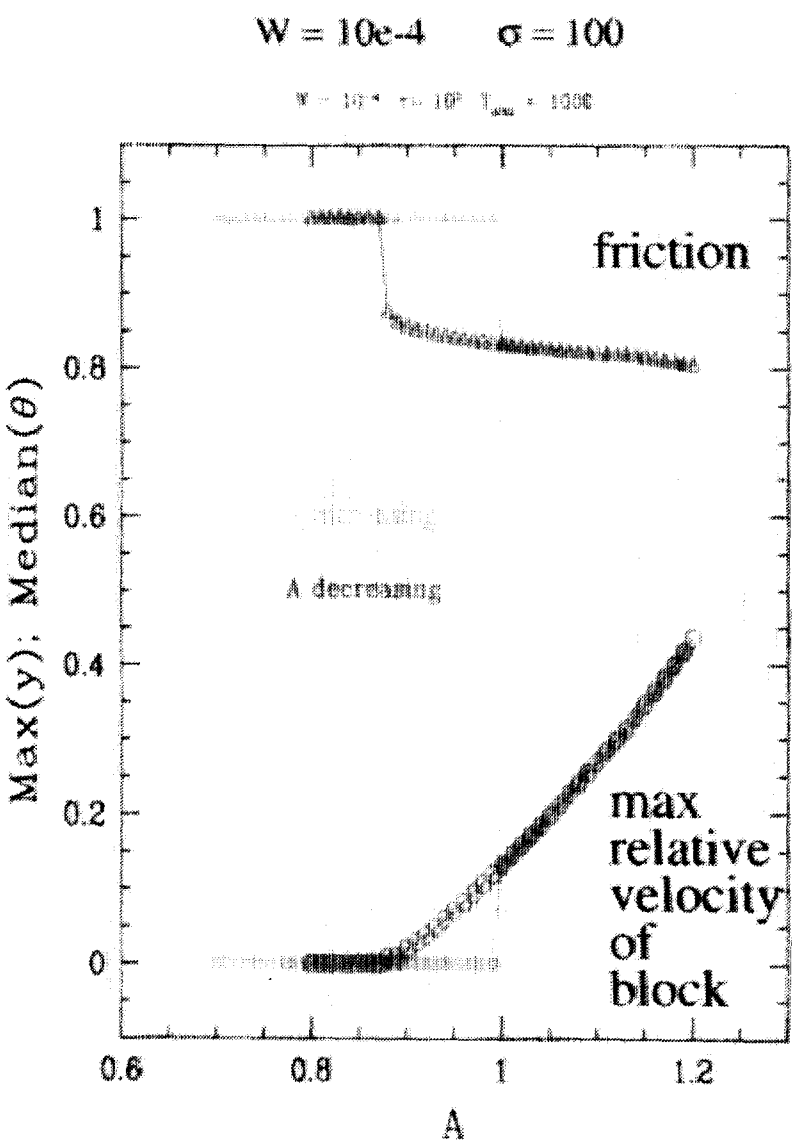

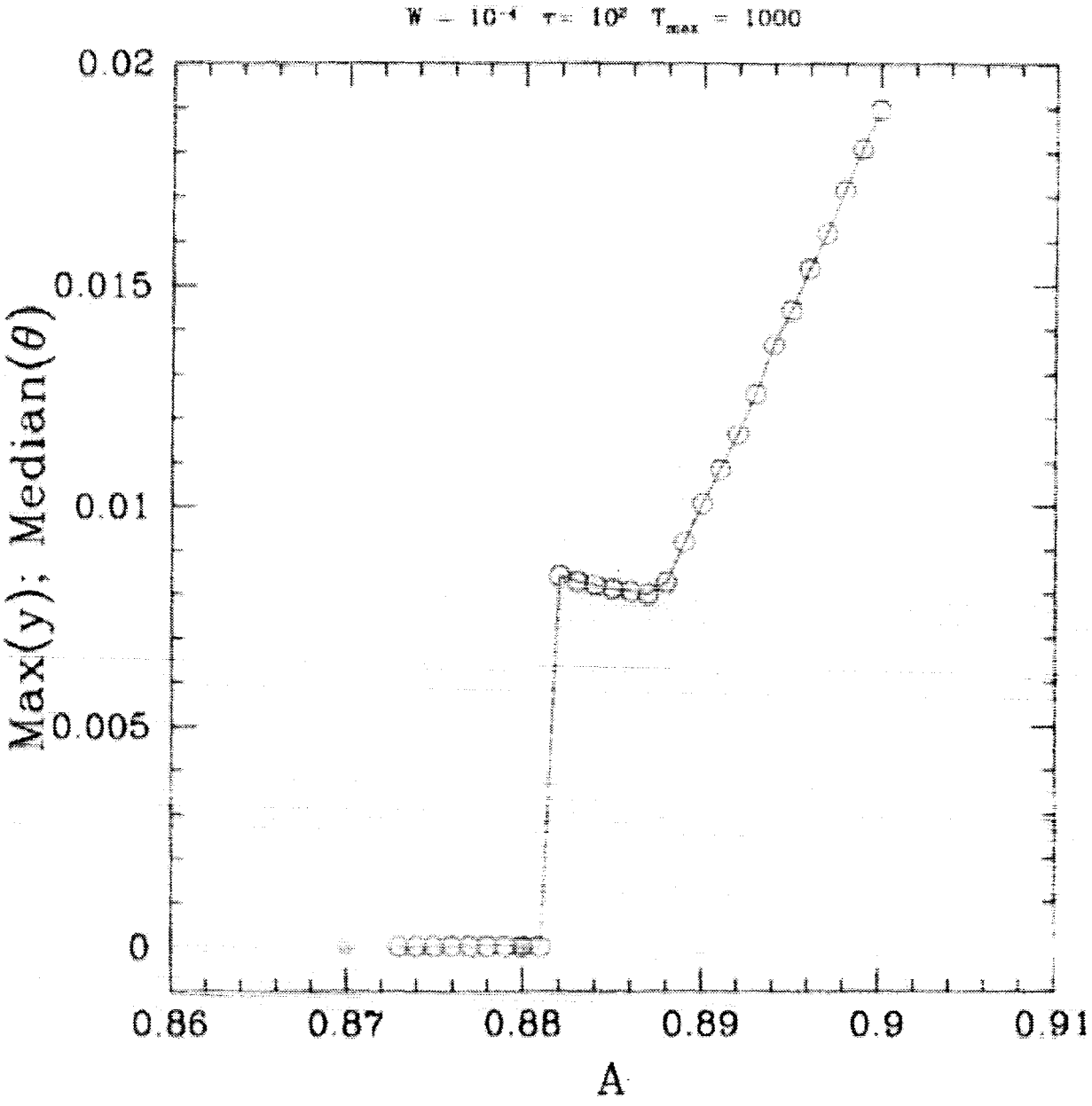

Model with a timescale for changing between static and dynamics friction produces hysteresis but doesn't seem to have powerlaw transitions.

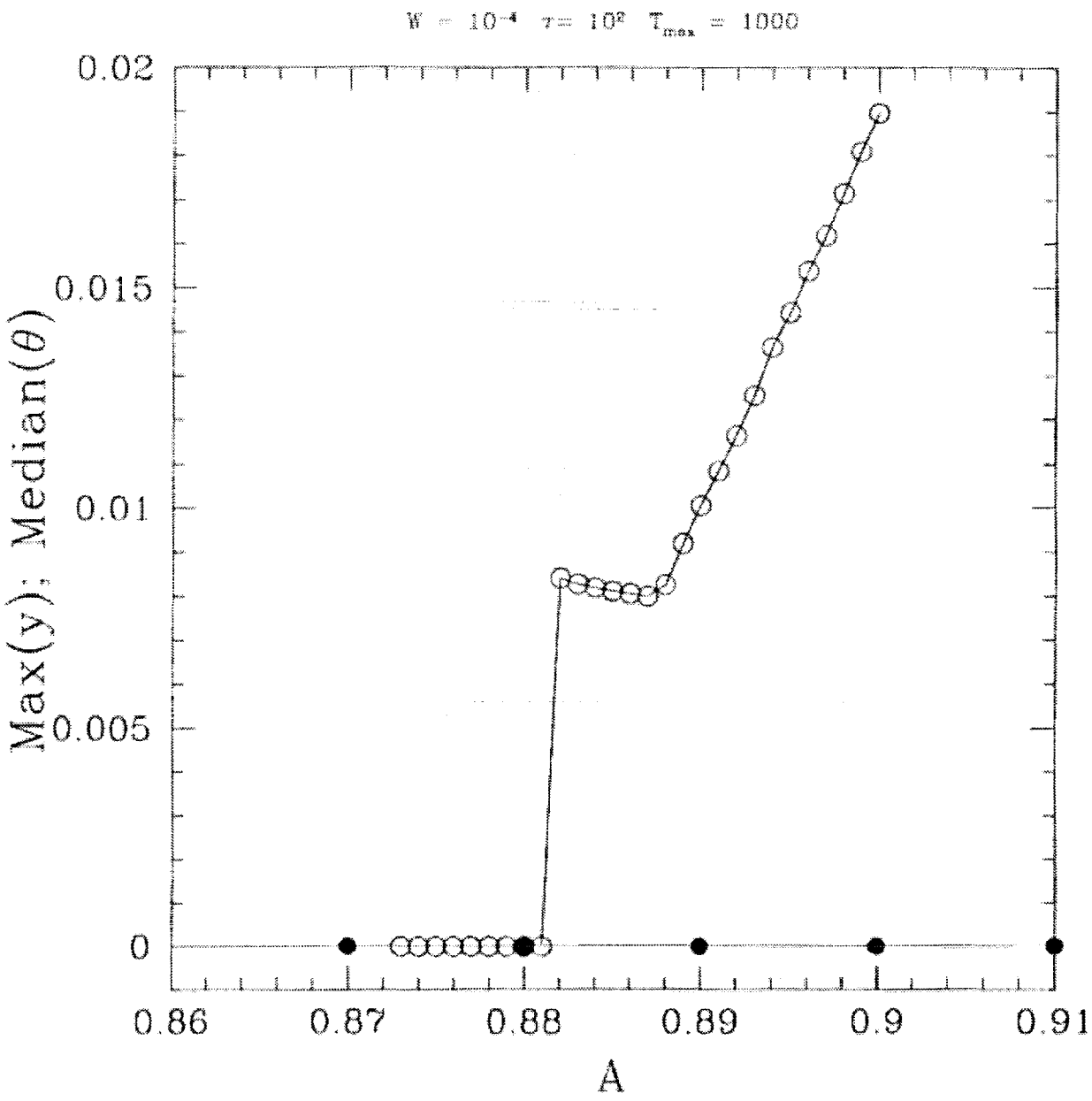

Model produces hysteresis but doesn't seem to have powerlaw transitions.

Conclusions for Initial Transitions of Horizontally Agitated

Dry Granular Materials:

Transition to sloshing is via a backwards bifurcation

Small number of surface particles seem to first stabilize then destabilize the layer

Transition starts locally and spreads

Time scales for the transition follow powerlaws

Powerlaw exponent is strongly affected by single particle impurities

Simple block model with frictional relaxation captures several facets of the experiment

Systems of Rolling Particles

1. Rolling friction (small)
2. Binary collisions → sliding
3. Novel Collective Dynamics
   a) Cluster formation on "cooling"
   b) Convection
   c) Subharmonic Waves

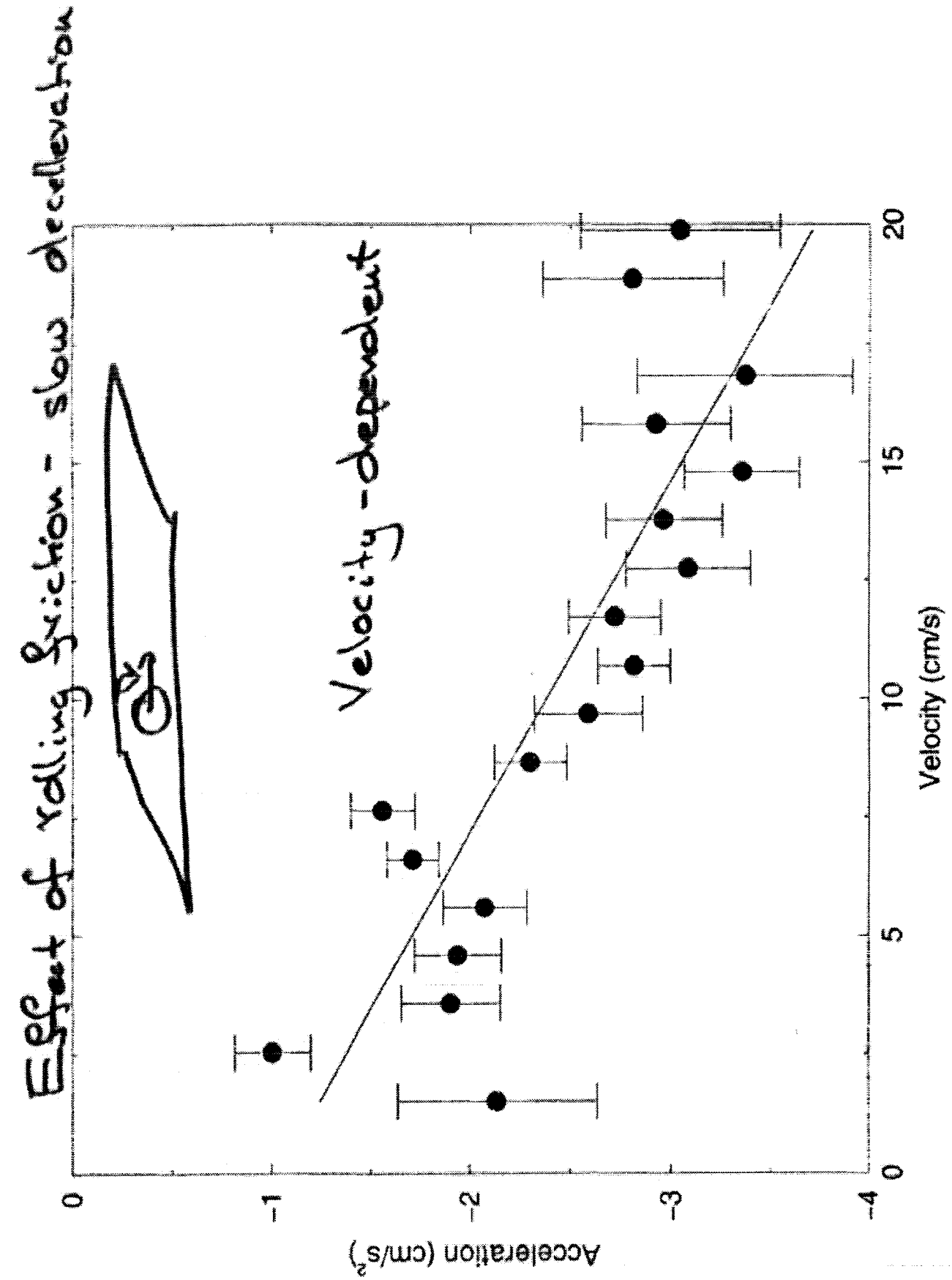
Effect of rolling friction - slow deceleration
Velocity-dependent
Acceleration (cm/s²)
Velocity (cm/s)
0
-1
-2
-3
-4
0
5
10
15
20

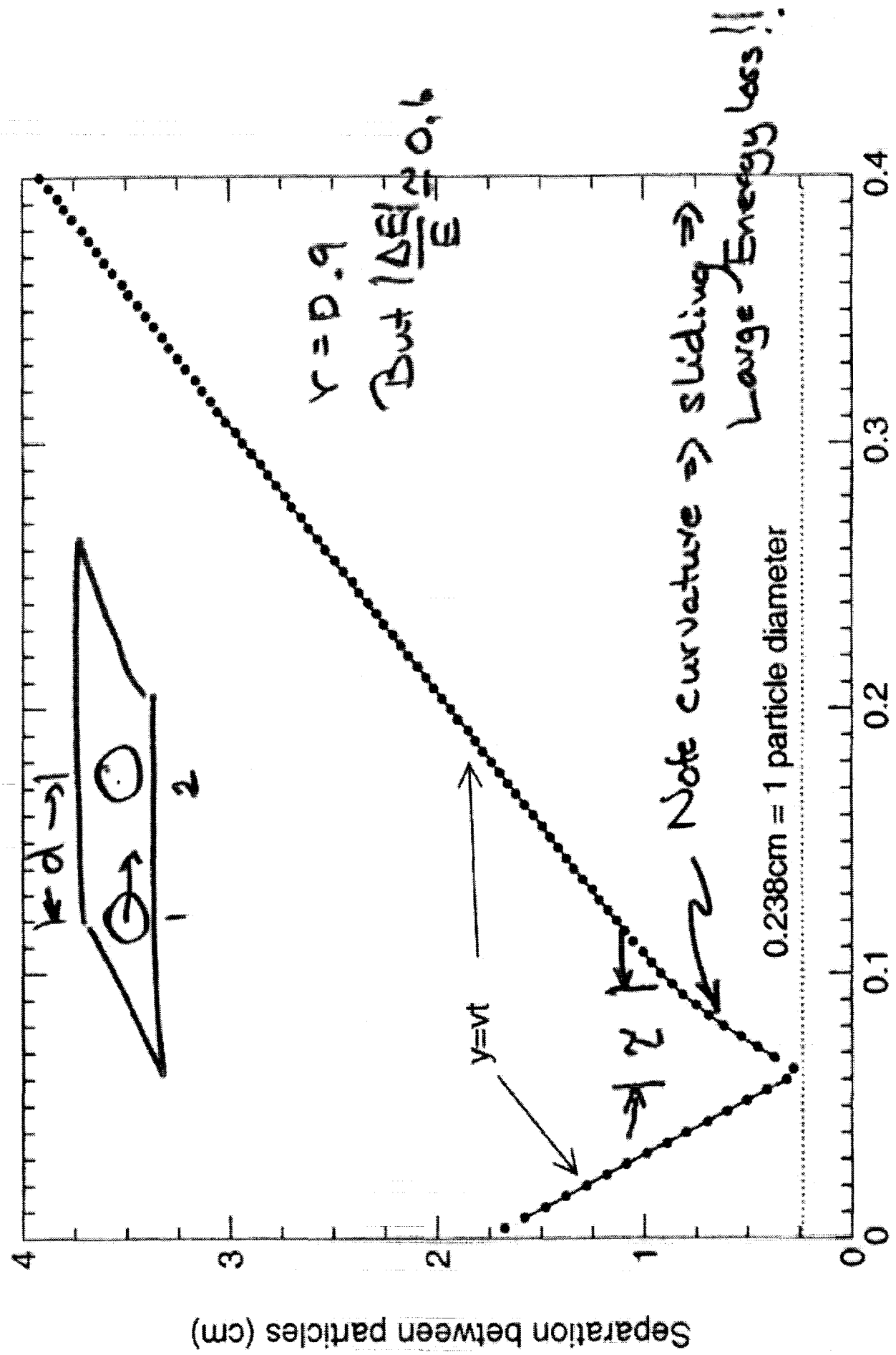
Separation between particles (cm)
Time (sec)
0.238cm = 1 particle diameter
y=Vt
Note curvature => sliding => Large Energy Loss !!!
r = 0.9
(But |Δθ| ≥ 0.6)
1
2

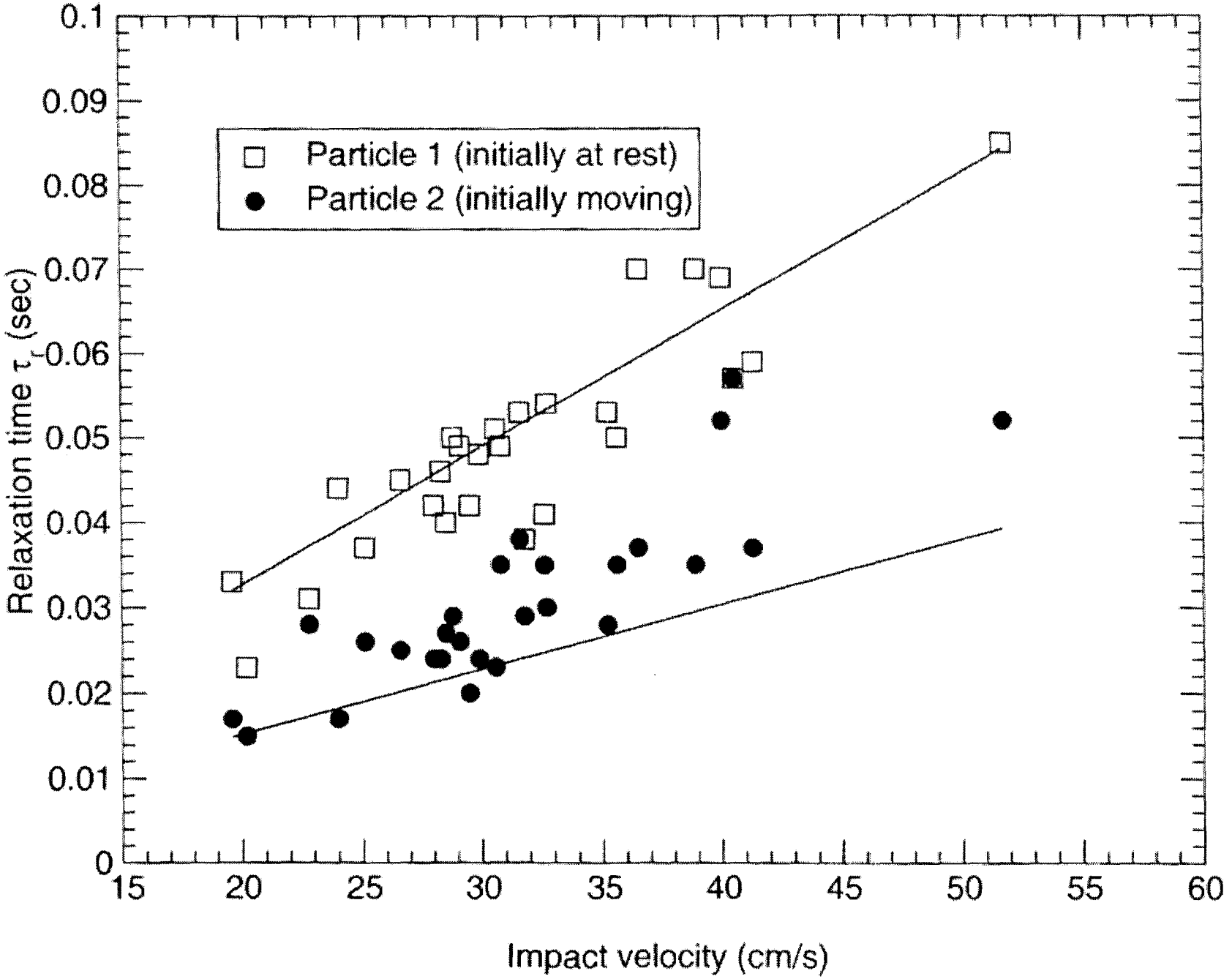
Particle 1 (initially at rest)
Particle 2 (initially moving)
Relaxation time τ_r (sec)
Impact velocity (cm/s)
0
0.01
0.02
0.03
0.04
0.05
0.06
0.07
0.08
0.09
0.1
15
20
25
30
35
40
45
50
55
60

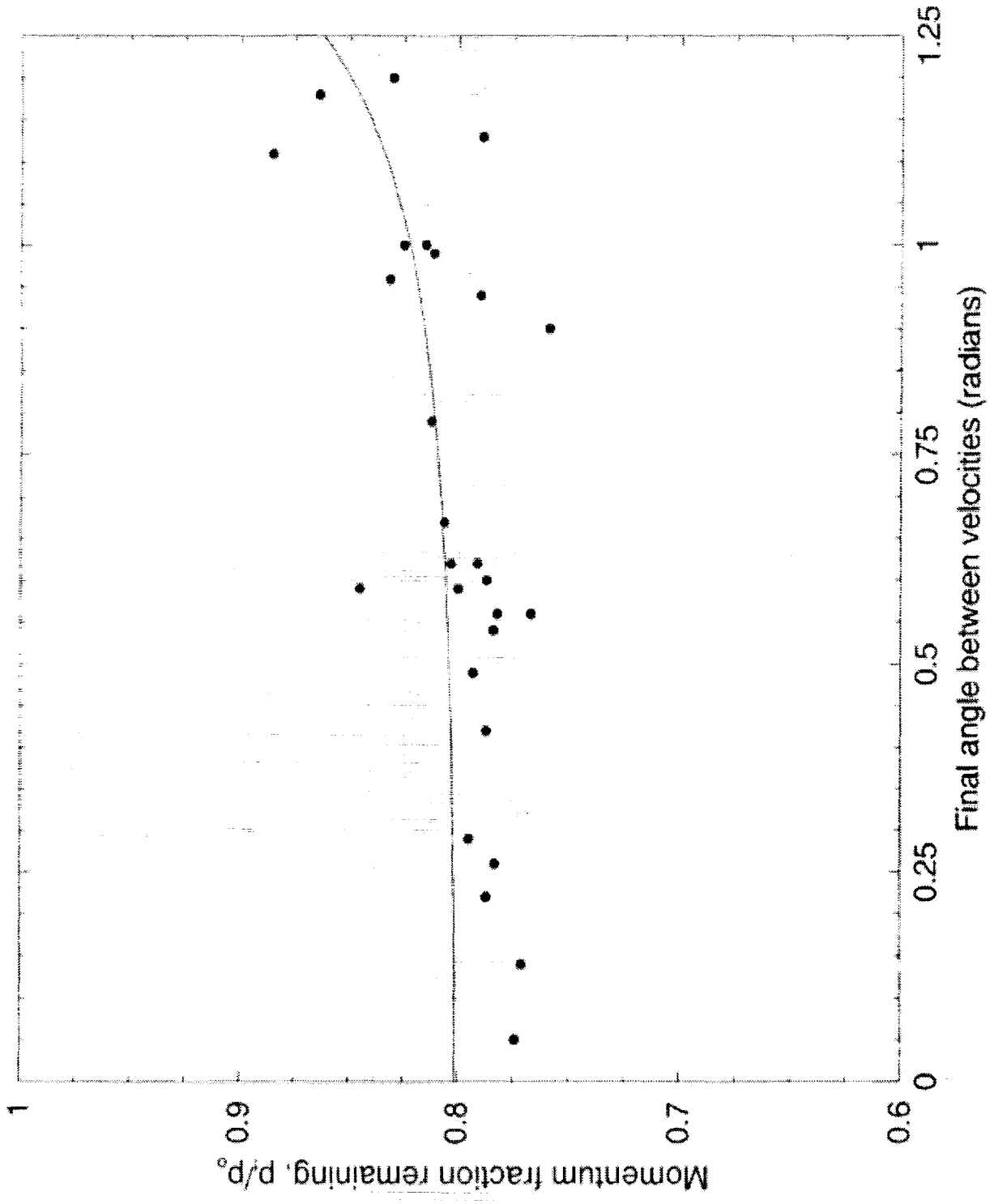
Momentum fraction remaining, p/p$_o$
1
0.9
0.8
0.7
0.6
0
0.25
0.5
0.75
1
1.25
Final angle between velocities (radians)

Shaken Systems -
Variable $\vec{g}$

- Subharmonic waves
- Convection

120

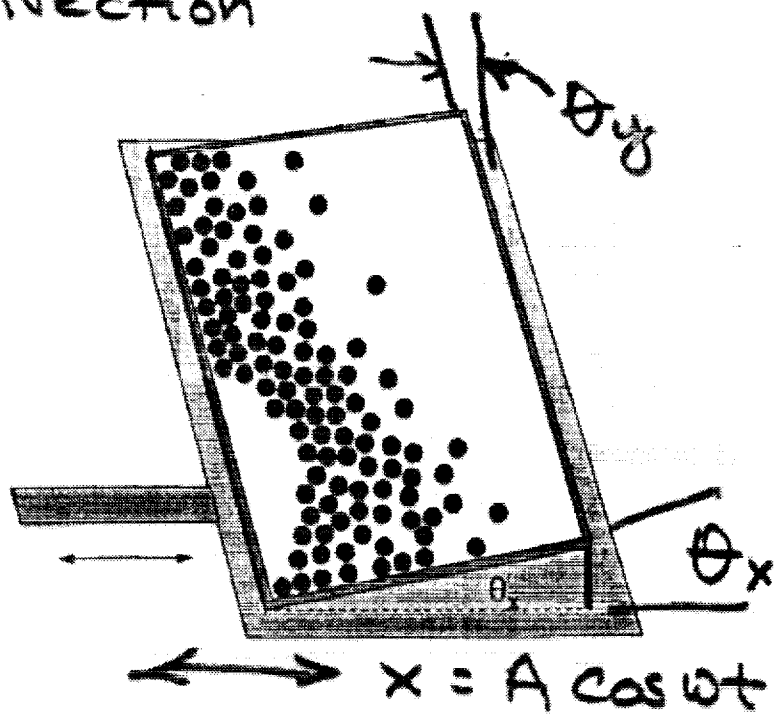

Figure 6.1: Experimental apparatus for wave system.

Subharmonic Waves

$\theta_y = 0$

$\theta_x \sim 1^\circ$ to 5°

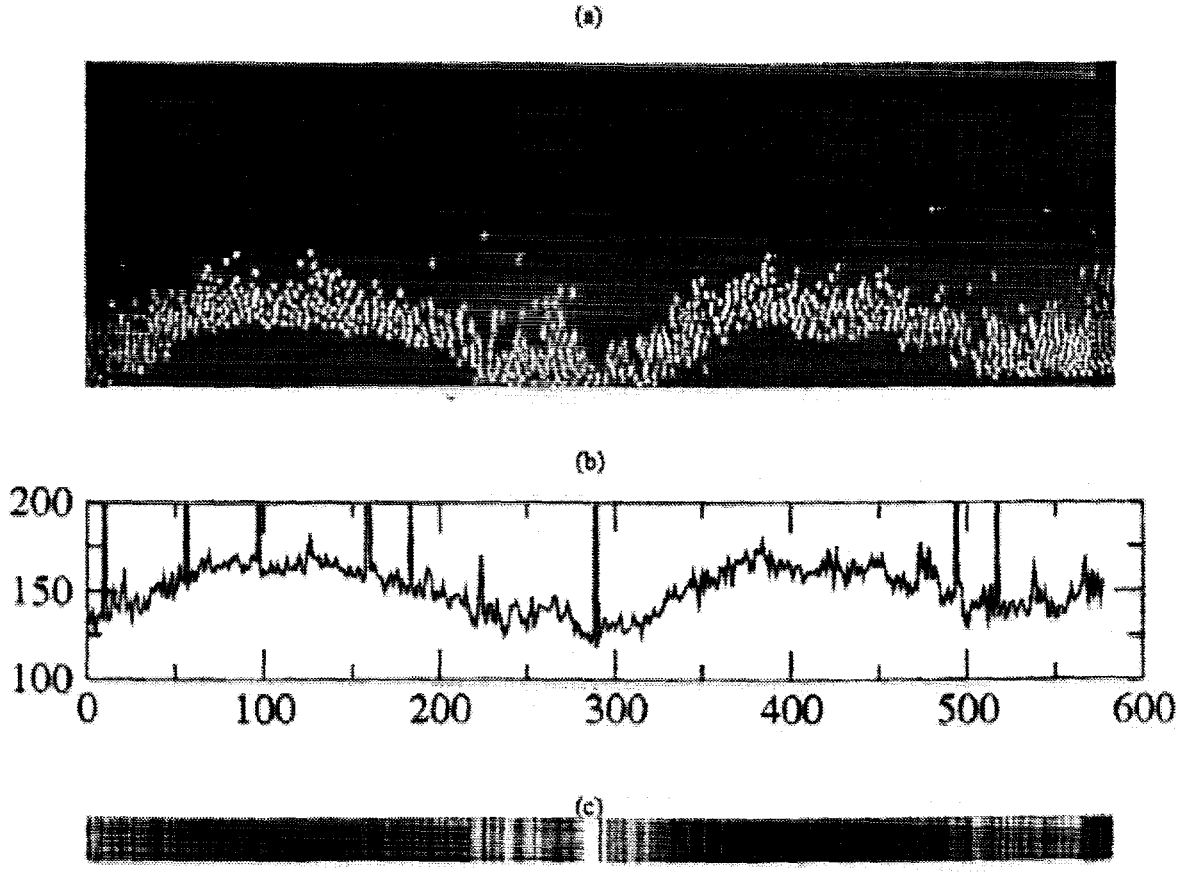

Figure 6.3: The method of creating time series pictures: (a) shows the raw picture, (b) the height profile of the picture, and (c) the corresponding brightness profile, which will become a single row of a time series picture (as, e.g., Fig. 6.4.

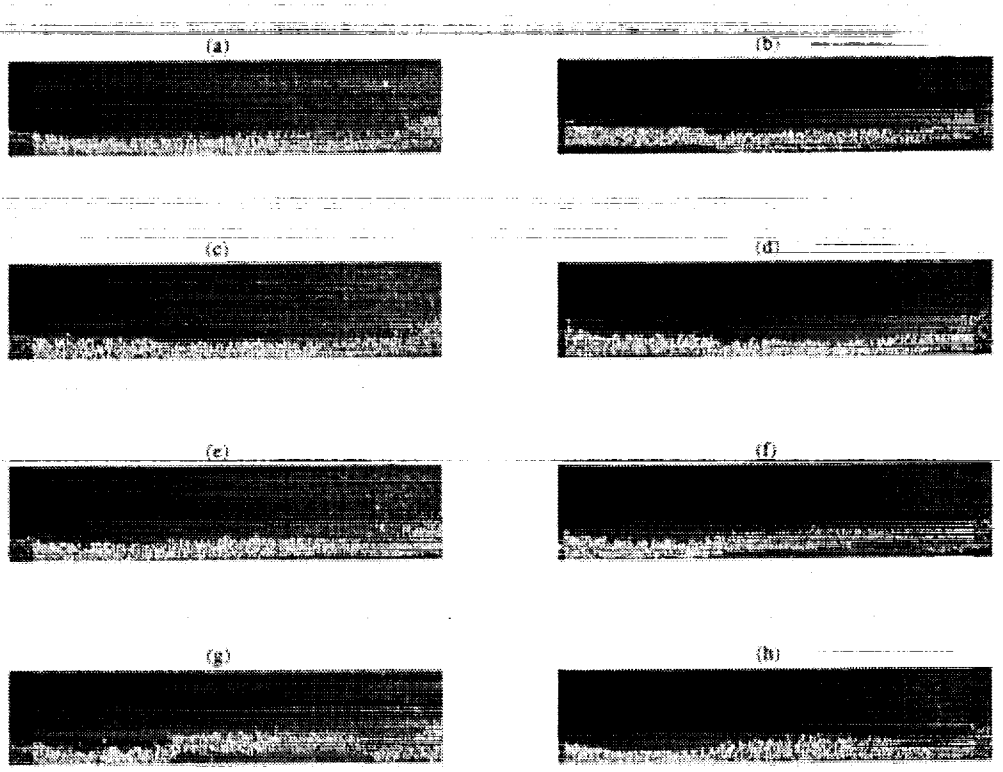

Figure 6.2: Images of the granular system, as viewed from above, through two complete driving cycles. Shown is a stable single wave, located near the center of the system. The frames proceed from (a) to (h), and each is taken 90° out of phase from the previous.

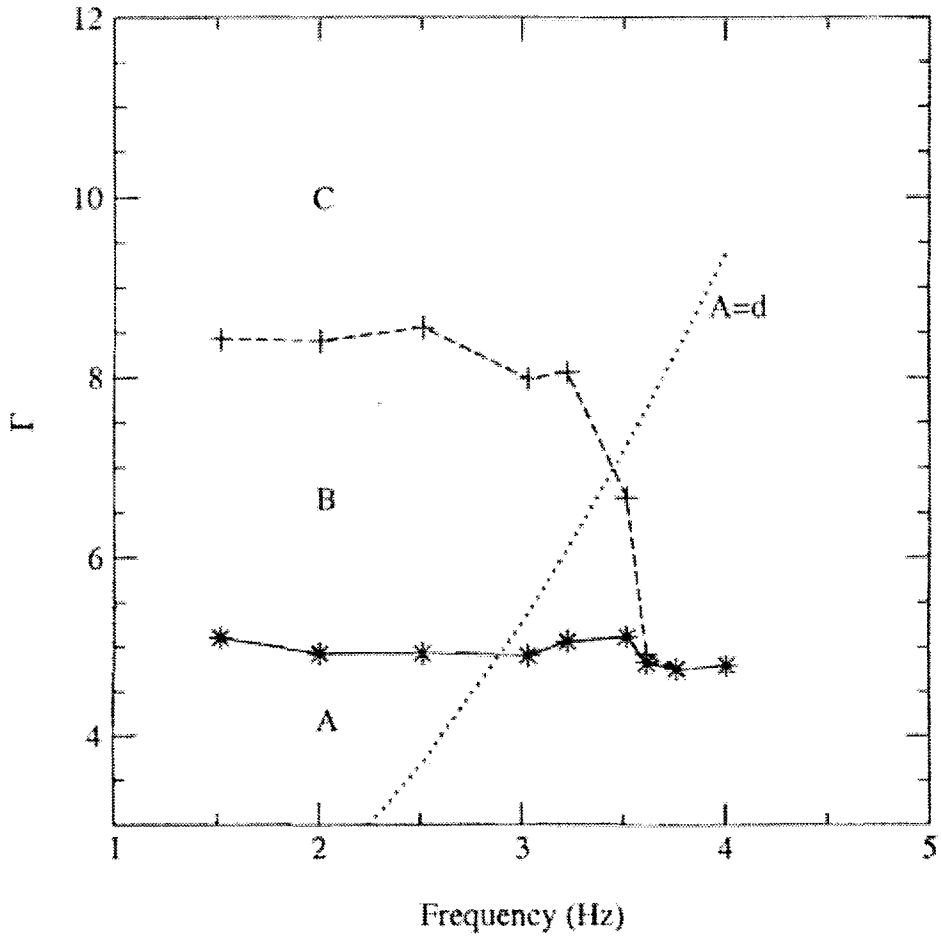

Figure 6.5: Phase space for granular system, showing the regions in parameter space in which (A) no patterns form, (B) induced patterns are stable but do not form spontaneously from the flat state, and (C) the flat state is unstable.

Space - time evolution

$\longrightarrow y$

123

$t \downarrow$

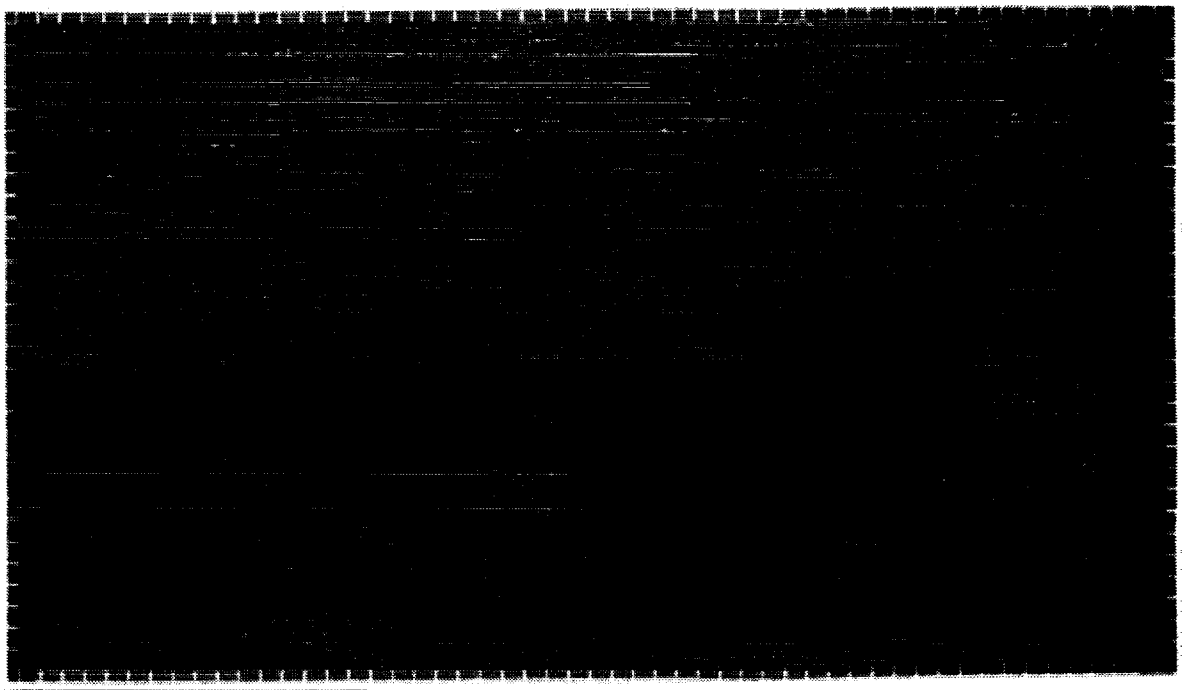

Figure 6.4: Sample time series picture, consisting of the height profile every second driving period for 600 periods (approximately 300 sec.). Shown is a single, unstable wave, which breaks into two waves.

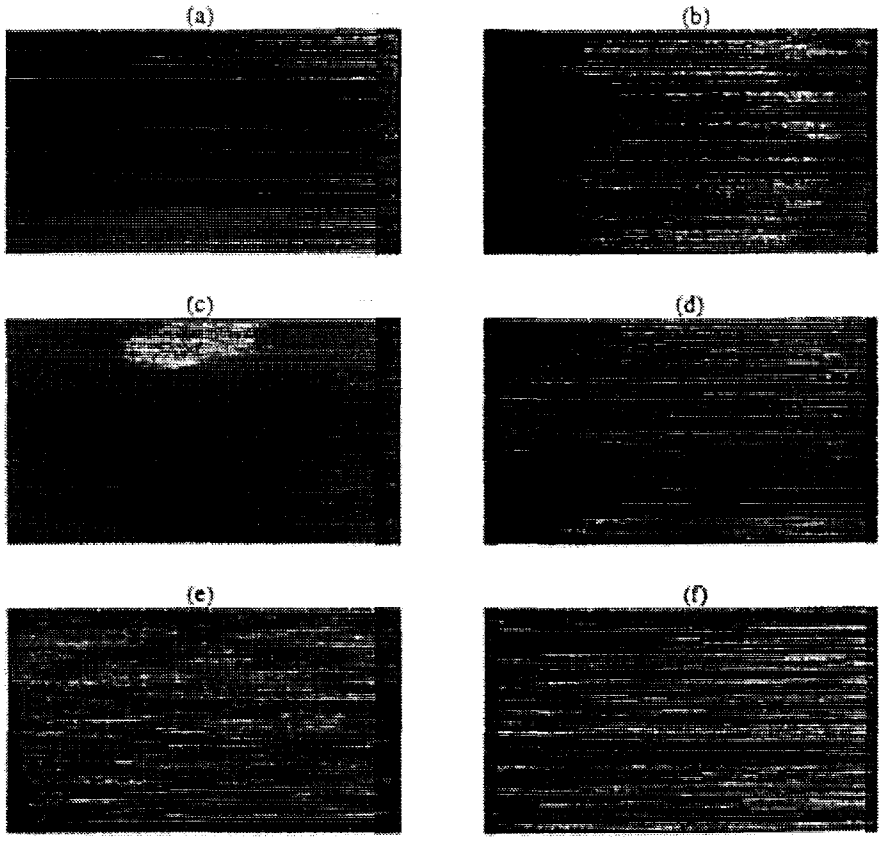

Figure 6.7: Some different states of the system. The states are (a) split, (b) one wave, (c) decaying wave, (d) spontaneously forming two waves, (e) disordered (chaotic) state, (f) disordered state at higher driving. These states are driven at $2.002Hz$, with acceleration $\Gamma =$ (a) 5.42, (b) 5.63, (c) 5.99, (d) 8.49, (e) 10.55, and (f) 13.01.

Surface Convection

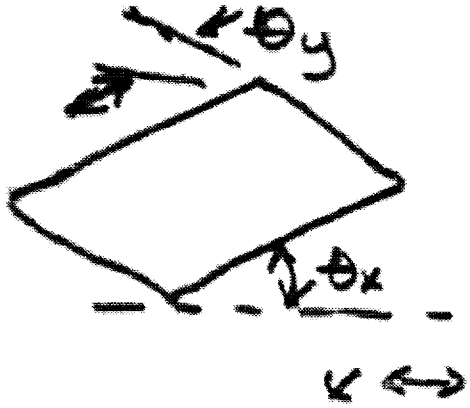

$\theta_x \simeq 1^\circ$ to 5°

$\theta_y \simeq 1^\circ$ to 2°

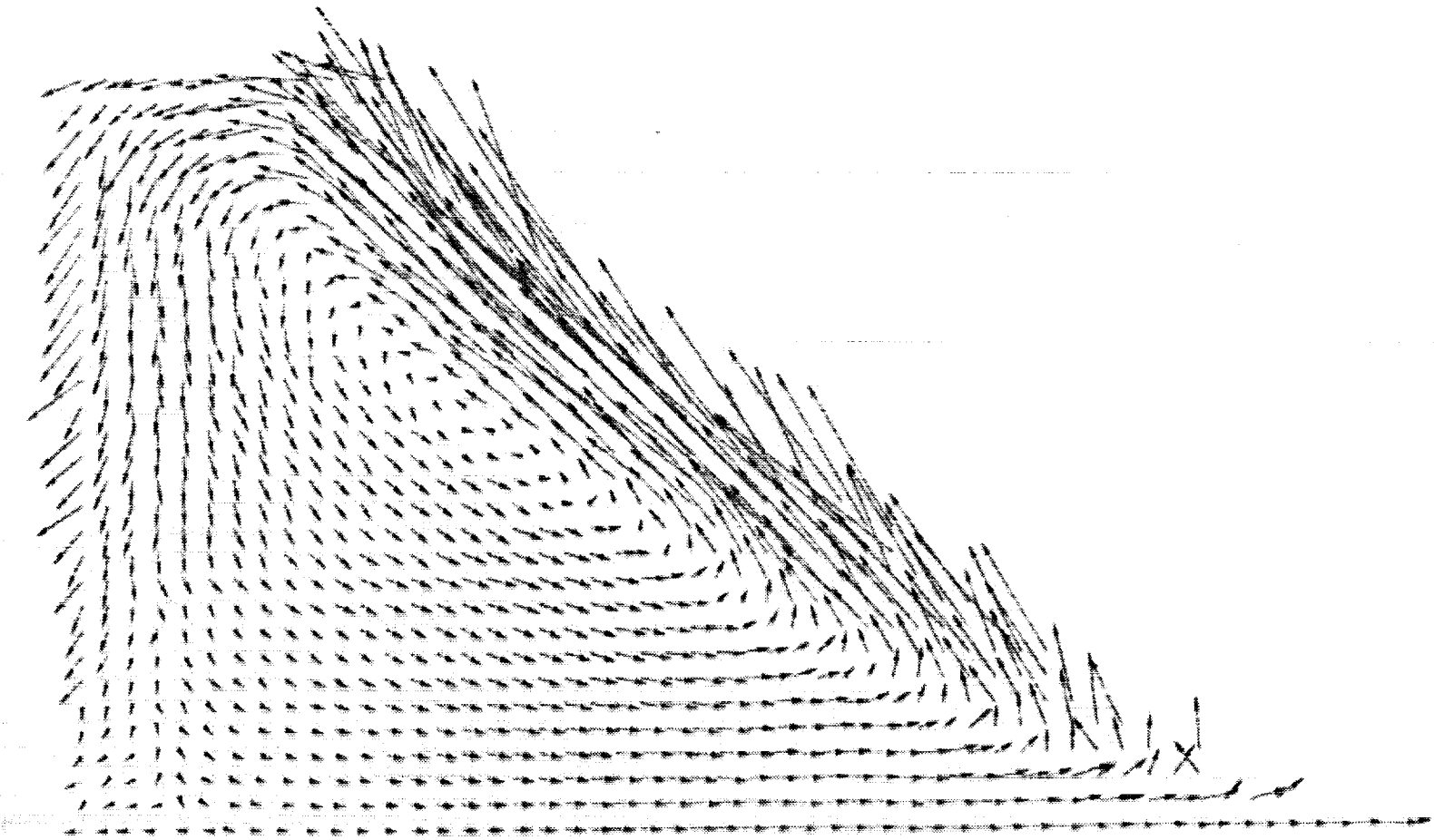

$\Gamma = A\omega$ = key control parameter

As Γ increases:

1. tilt forms
2. convection begins
3. eventually disordered motion

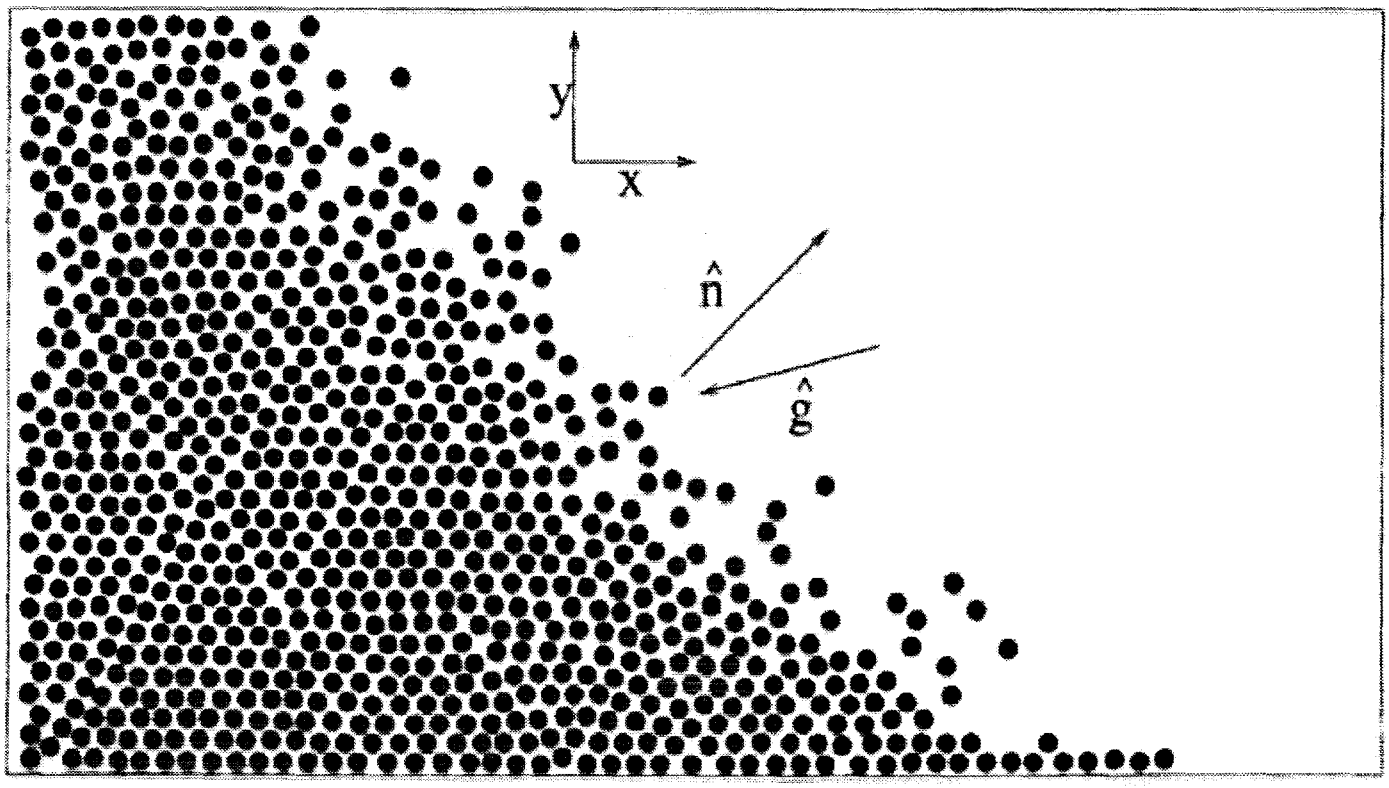

FIGURES

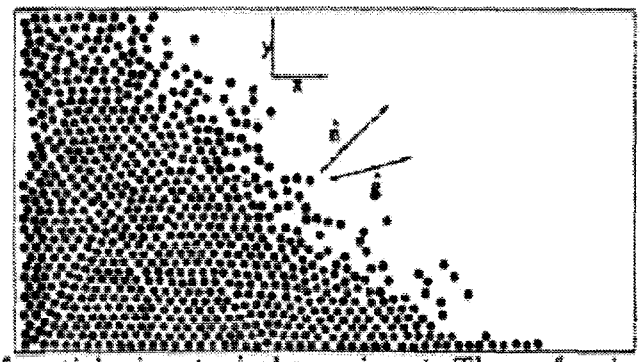

FIG. 1. Positions of particles in a typical experiment. The surface is approximately 35 particle diameters wide, and the system contains 800 particles. Also shown are the $\hat{x}$ (driving) and $\hat{y}$ directions, as well as the approximate directions of the normal to the free surface ($\hat{n}$) and the component of gravity tangent to the substrate ($\hat{g}$).

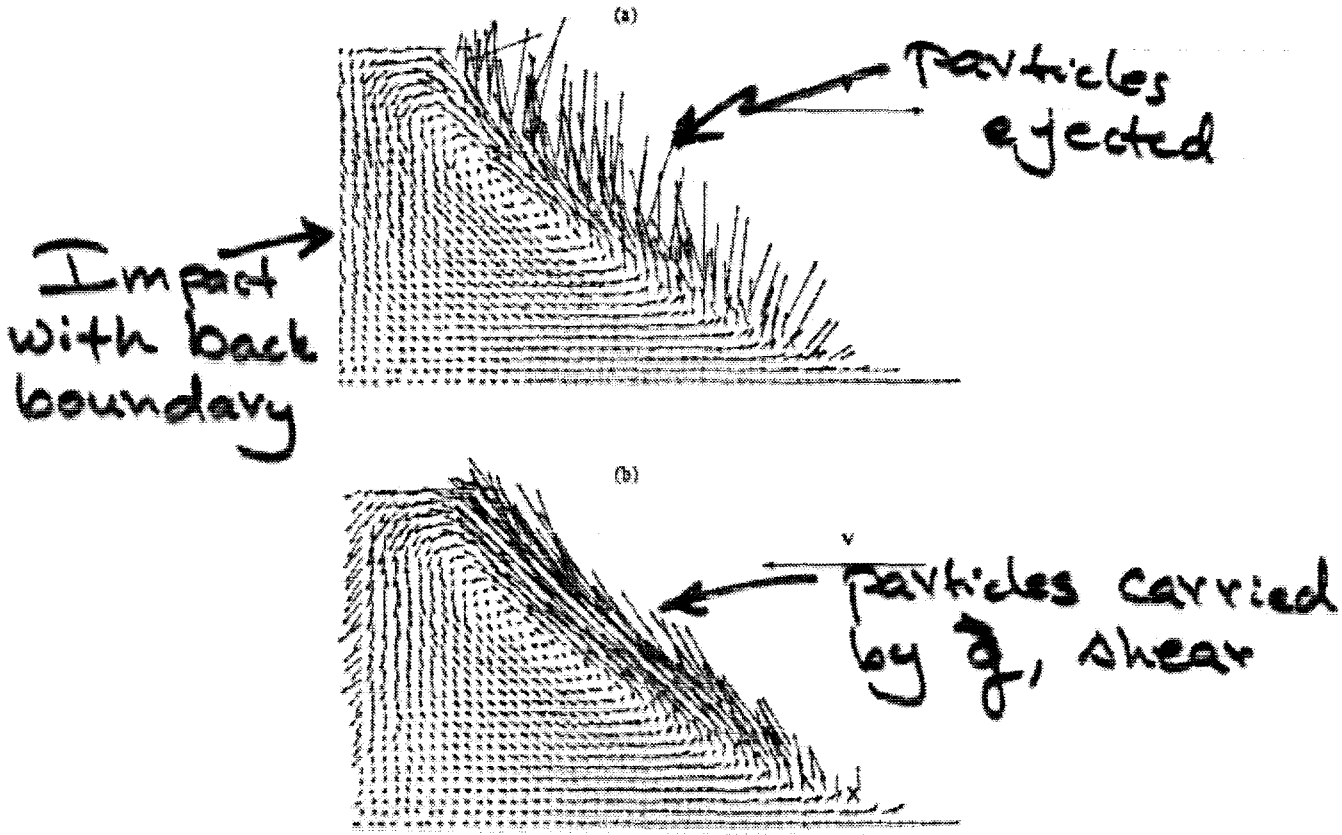

FIG. 2. Velocity field at fixed phases with respect to the driving (at maximum driving velocity to the right (a) and to the left (b)), averaged over 136 driving periods. Here $\omega = 2.0Hz$, $\Gamma = 9.09$ (defined as $\Gamma = A\omega^2/g_{eff}$), and $A\omega = 10.1cm/s$. The direction of motion of the substrate is also indicated.

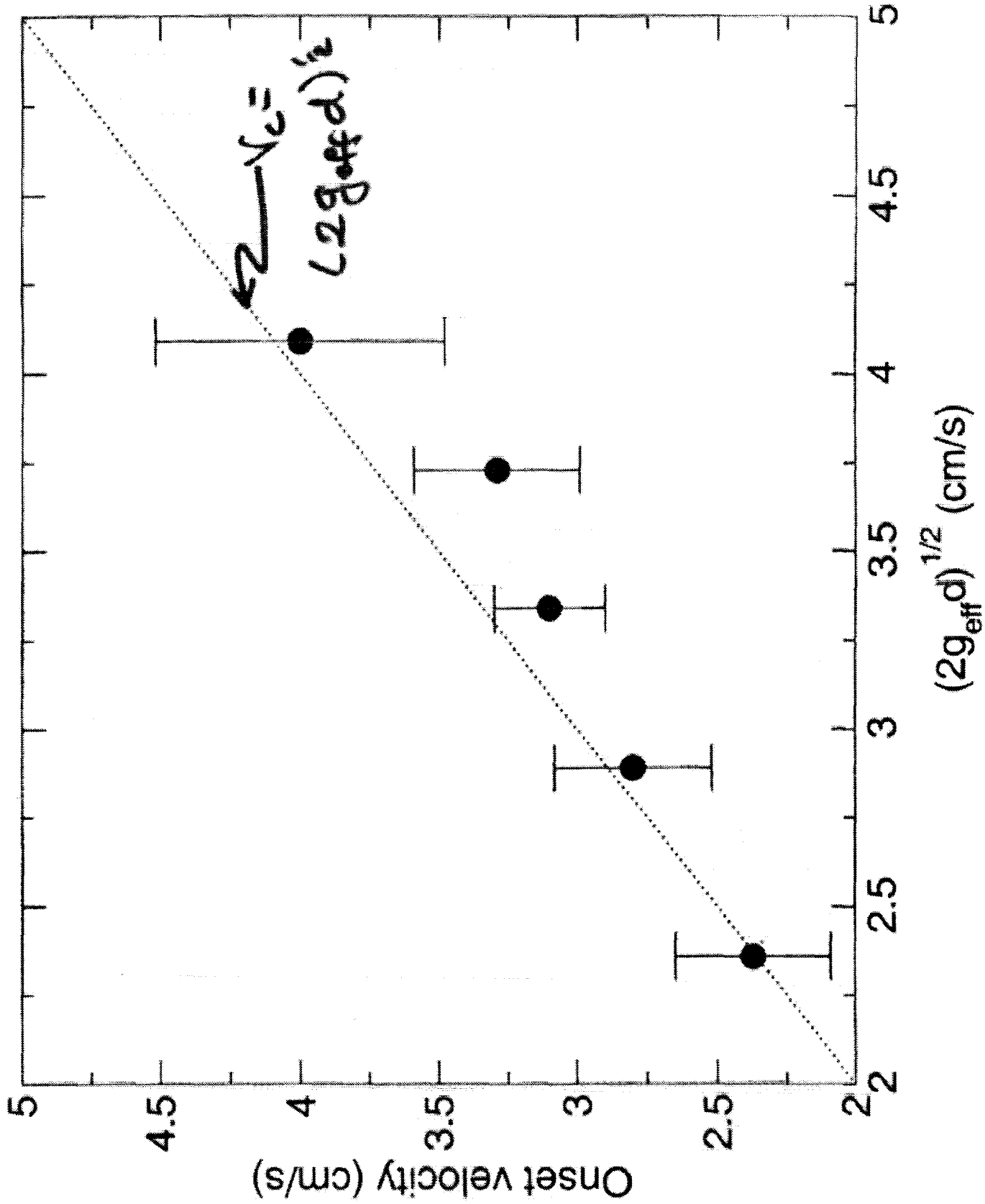
Onset velocity (cm/s)
$(2g_{eff}d)^{1/2}$ (cm/s)
5
4.5
4
3.5
3
2.5
2

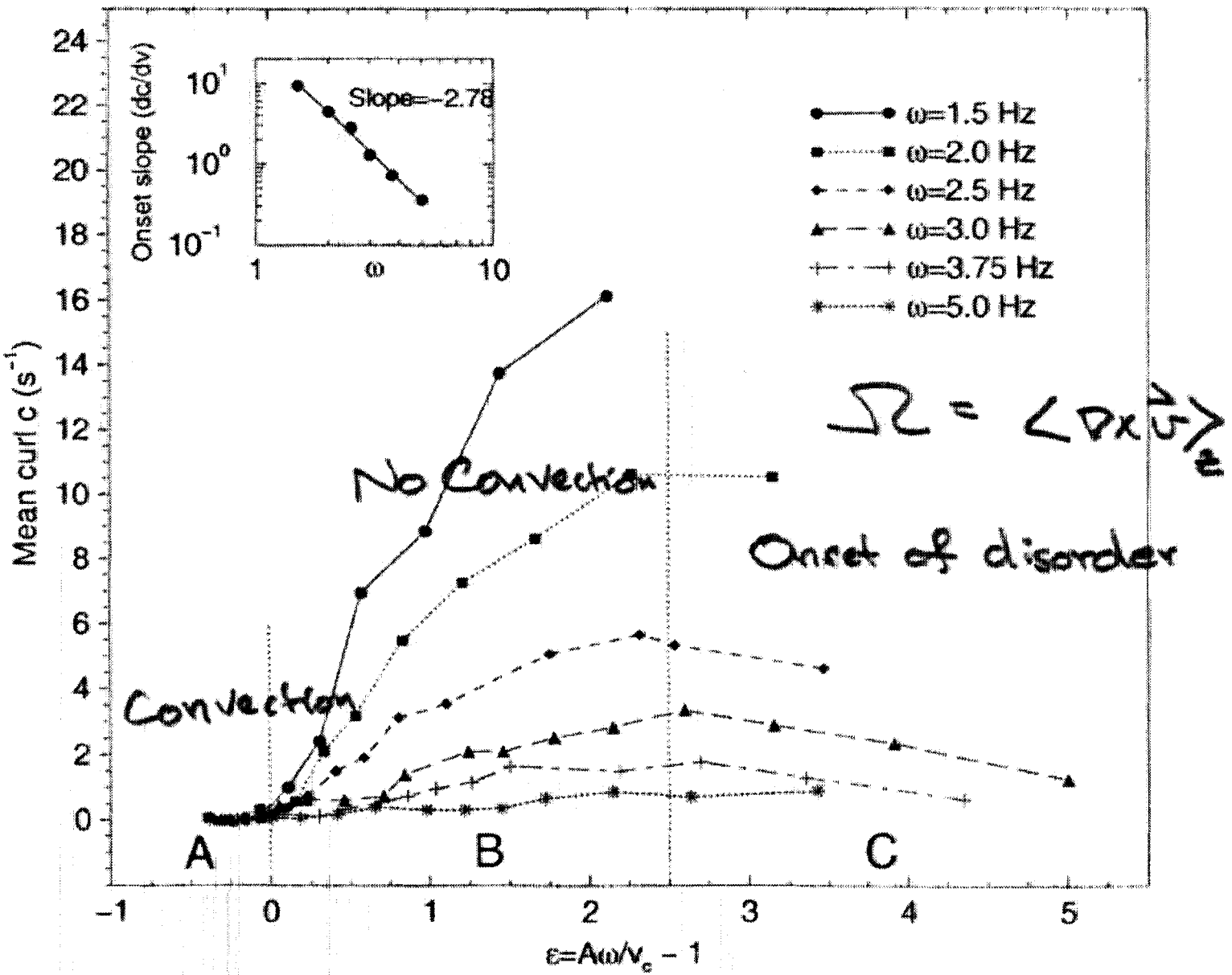
Mean curl c (s^{-1})
ε=Aω/V$_c$ − 1
Onset slope (dc/dv)
Slope=−2.78
ω
ω=1.5 Hz
ω=2.0 Hz
ω=2.5 Hz
ω=3.0 Hz
ω=3.75 Hz
ω=5.0 Hz
No Convection
Convection
Onset of disorder
A
B
C

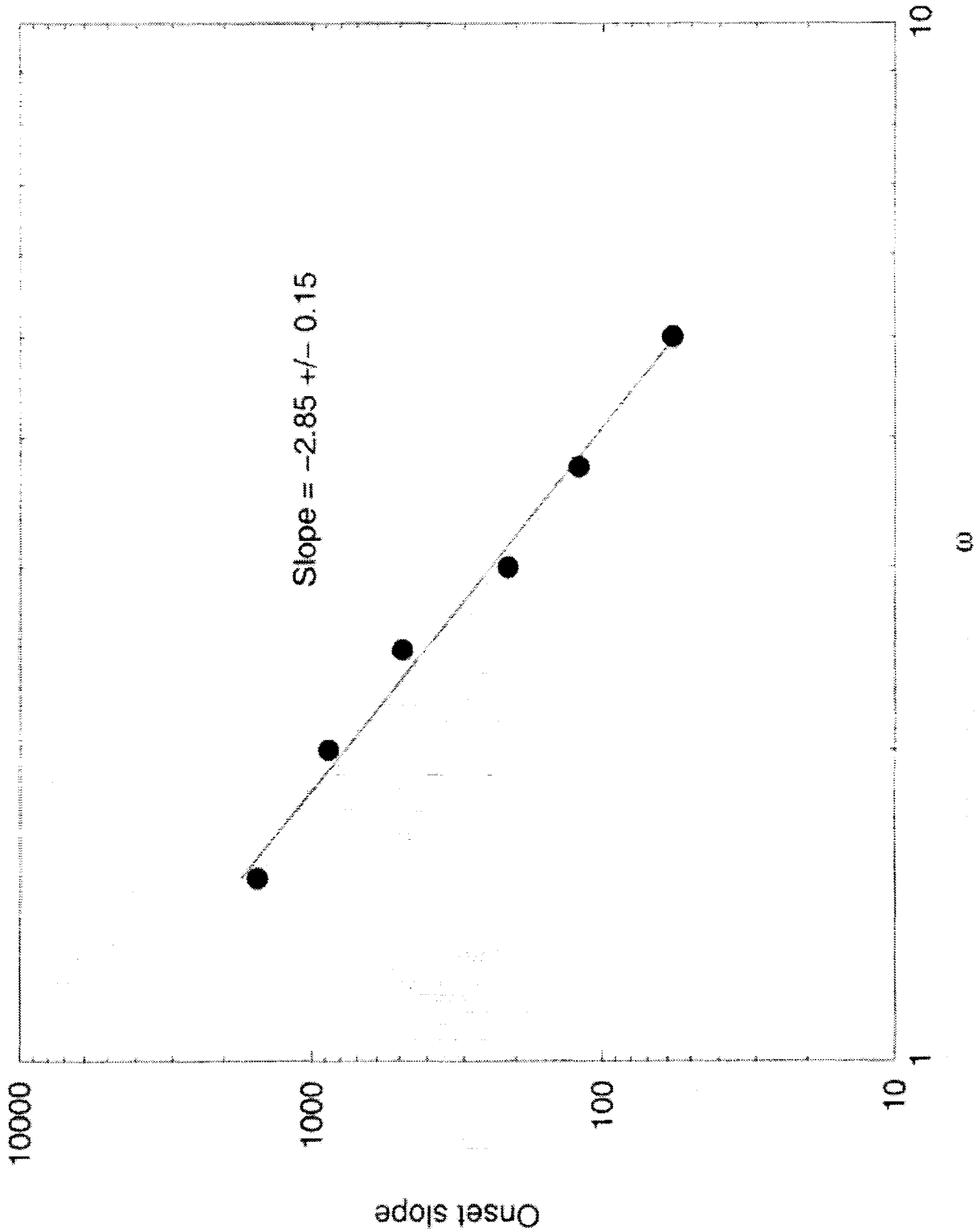
Slope = −2.85 +/− 0.15
Onset slope
ω
10000
1000
100
10
1
10

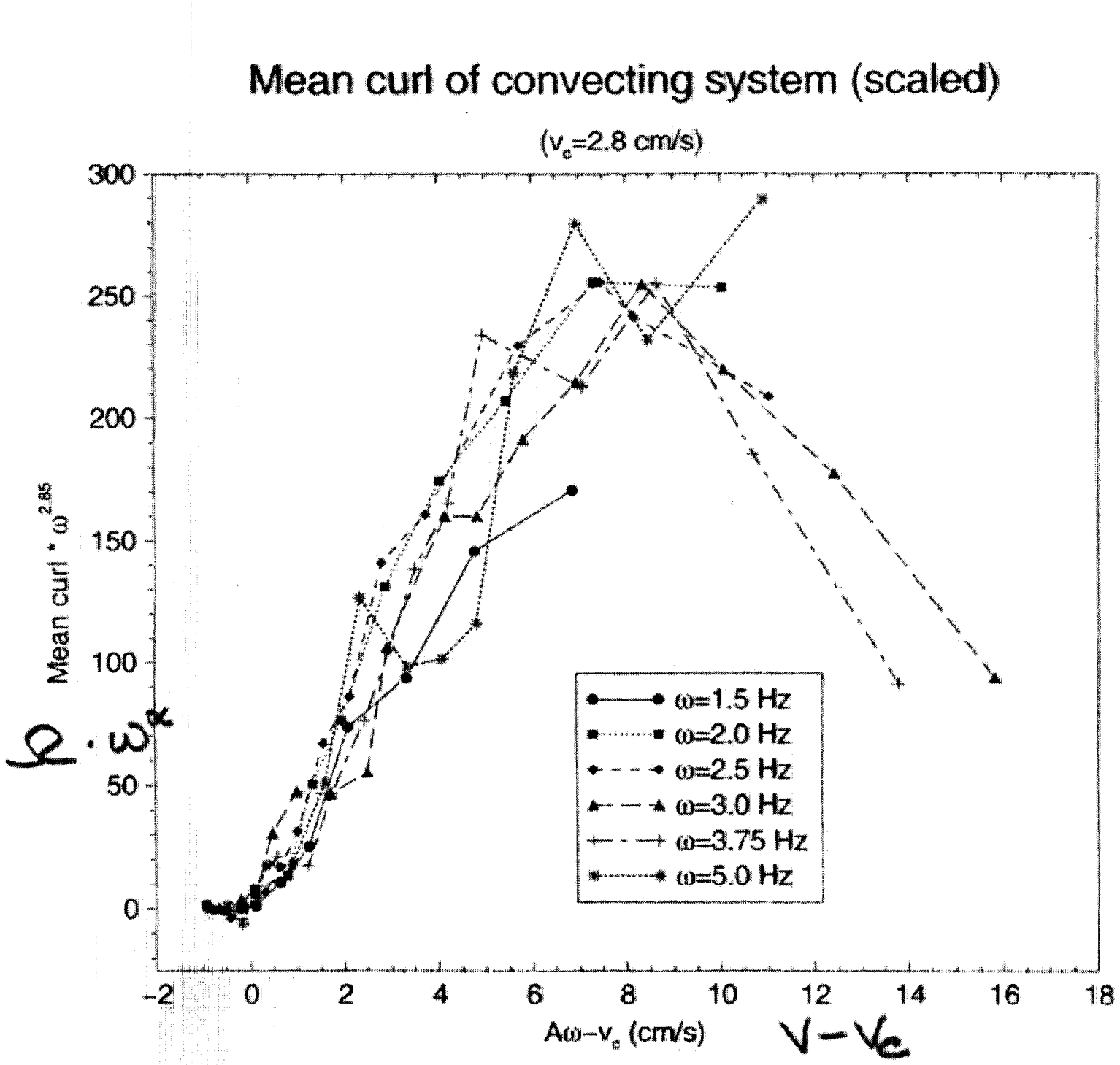
Mean curl of convecting system (scaled)
(v_c=2.8 cm/s)
Mean curl * $\omega^{2.85}$
$A\omega - v_c$ (cm/s)
ω=1.5 Hz
ω=2.0 Hz
ω=2.5 Hz
ω=3.0 Hz
ω=3.75 Hz
ω=5.0 Hz
300
250
200
150
100
50
0
−2
0
2
4
6
8
10
12
14
16
18

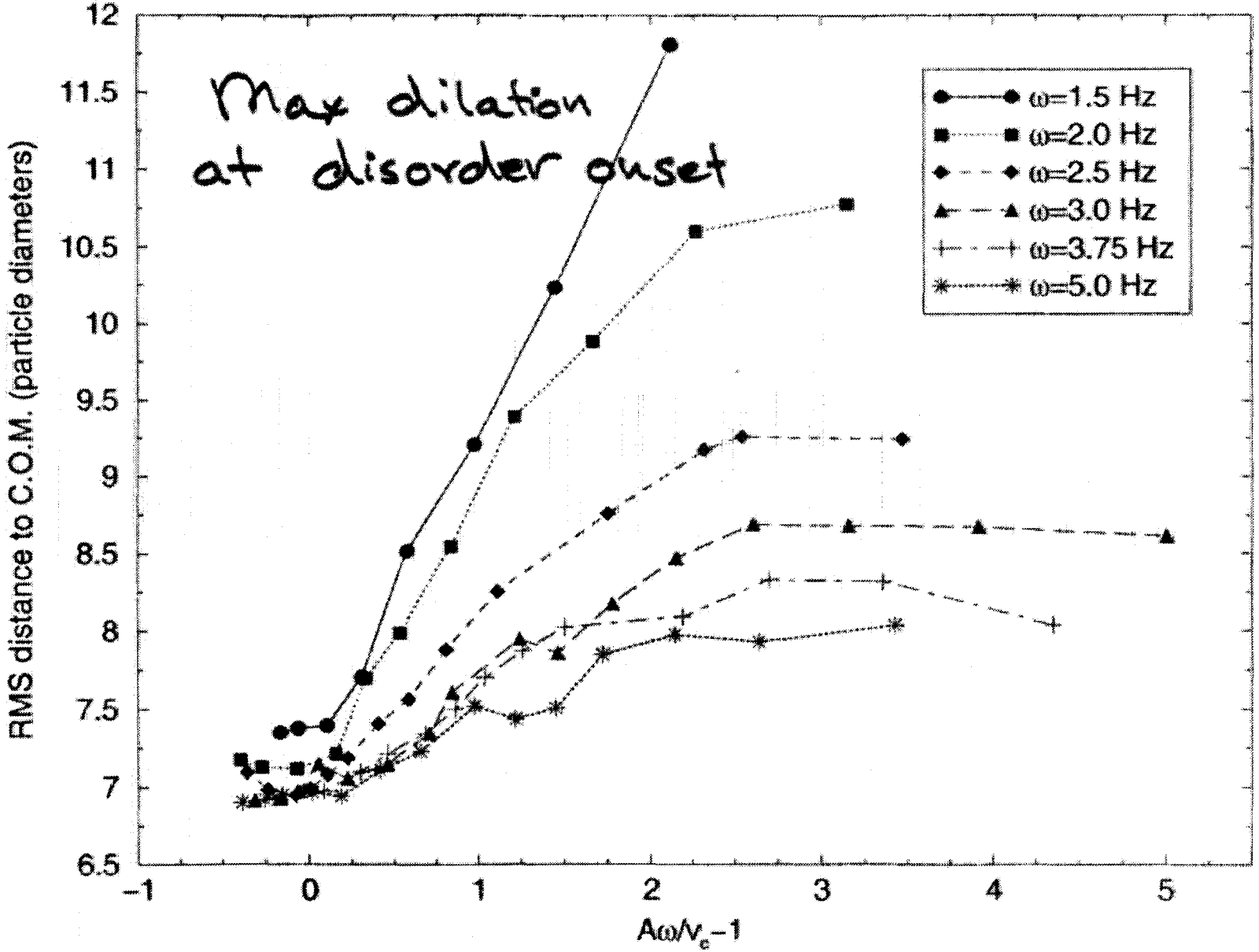
Max dilation
at disorder onset
RMS distance to C.O.M. (particle diameters)
Aω/V_c−1
ω=1.5 Hz
ω=2.0 Hz
ω=2.5 Hz
ω=3.0 Hz
ω=3.75 Hz
ω=5.0 Hz
12
11.5
11
10.5
10
9.5
9
8.5
8
7.5
7
6.5
−1
0
1
2
3
4
5

Cluster Formation in Cooling System

FIGURES

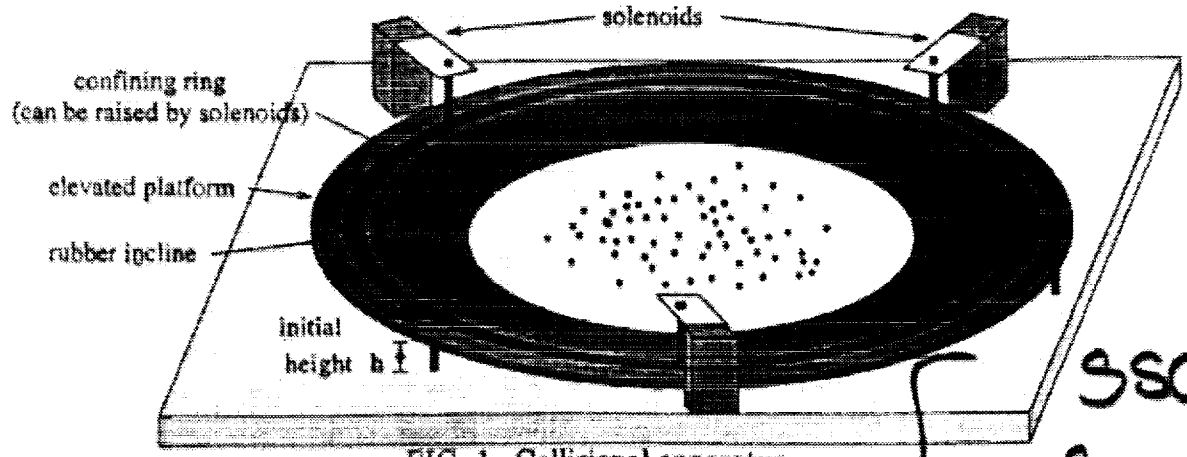

FIG. 1. Collisional apparatus

SSC = surface-sphere collider

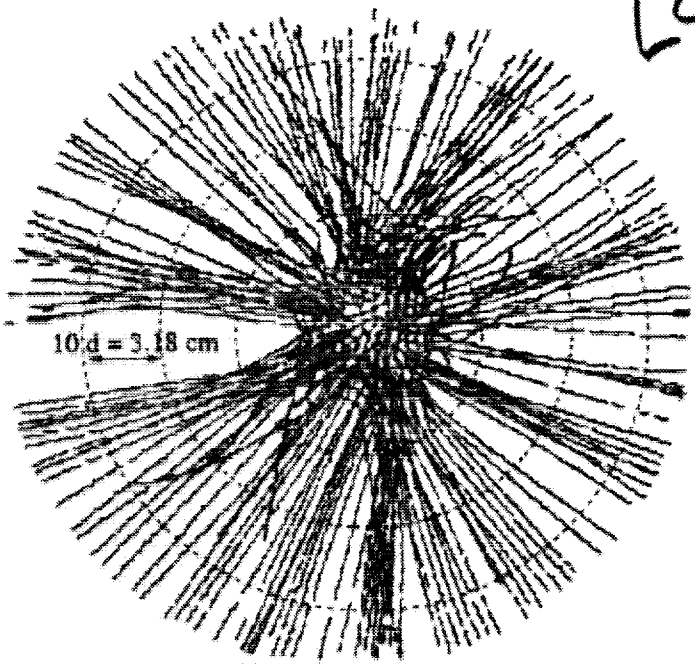

particle tracks

FIG. 2. Sample trajectories over the course of an experiment, with system size $N = 150$ particles. The concentric dotted circles represent the approximate radial positions of the majority of particles at times $t = 0.1, 0.2$, and 0.3 sec. All particles come to rest without escaping the collisional surface.

Final States

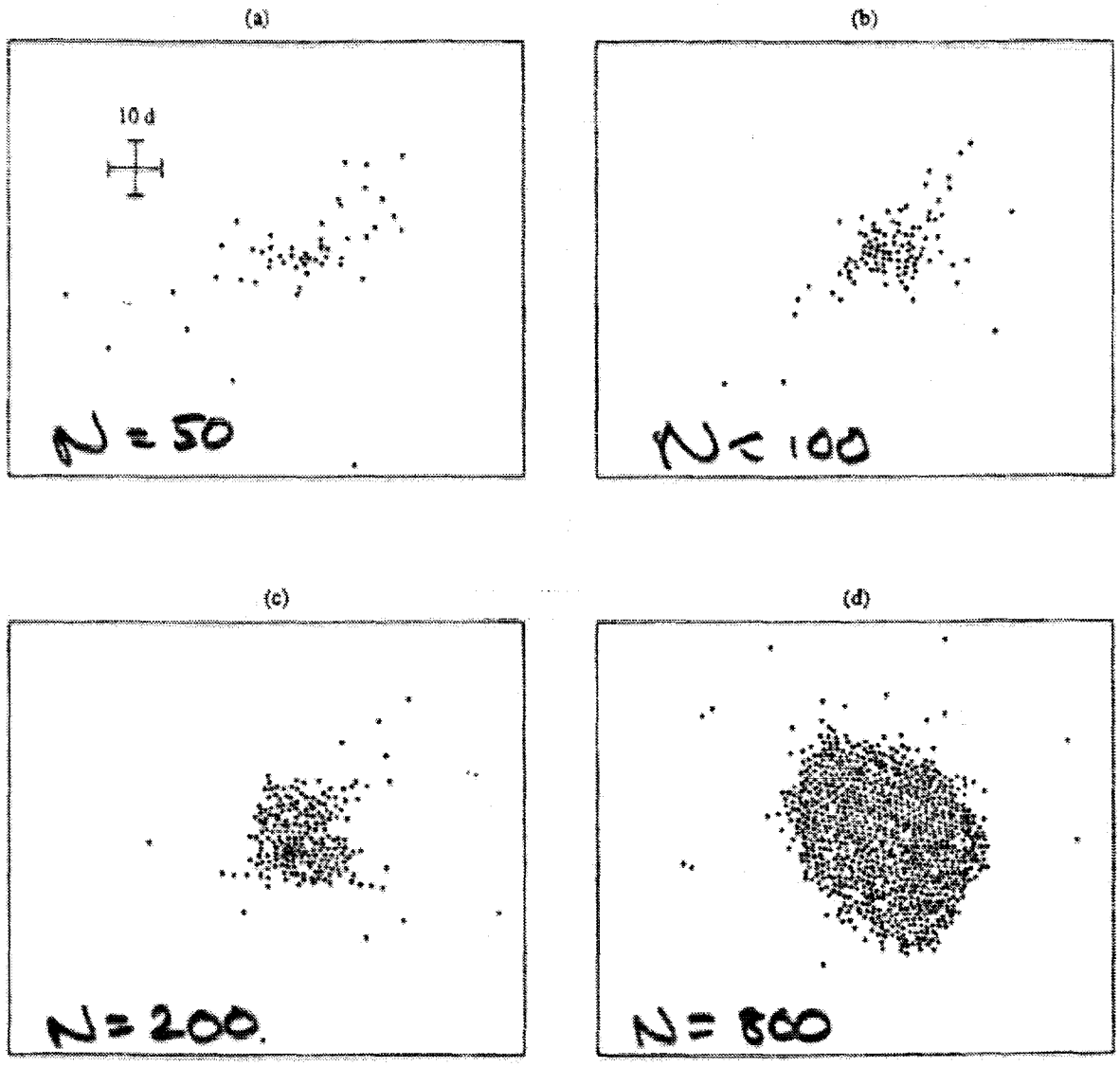

FIG. 3. N = (a) 50, (b) 100, (c) 200, and (d) 800 particles in their final states. In all except the 50-particle case, all particles have come to rest in the field of view. The cross in (a) is provided for scale; each arm is 10 particle diameters long.

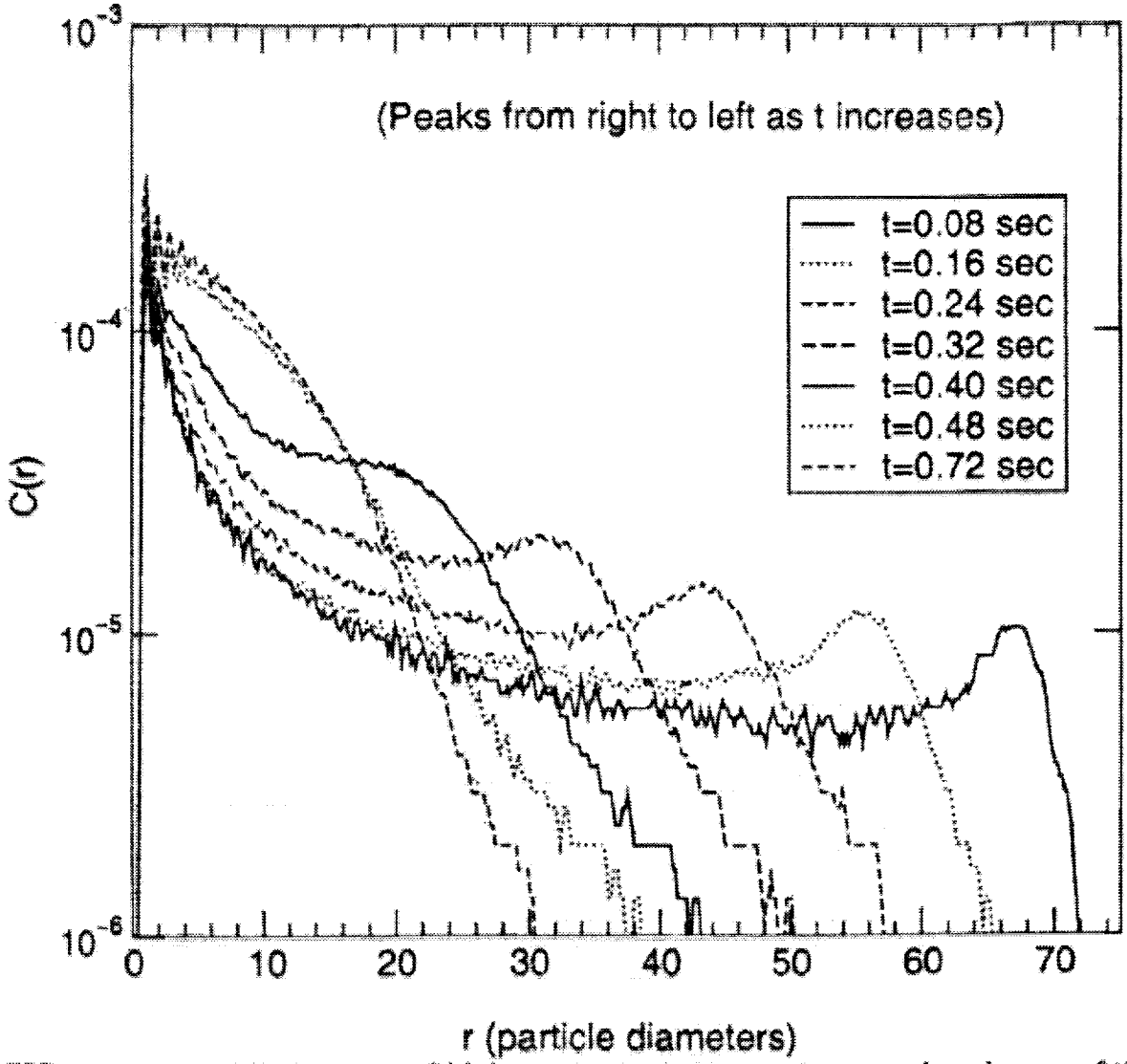

FIG. 4. Autocorrelation function C(r) for a system of 400 particles over a broad range of time containing the collapse. The particles meet in the center at $t \approx 0.44 sec$.

$$C(\vec{r}) = \int \rho(\vec{r}', \vec{r}) \rho(r') \, dr'$$

$$C(r) = \langle C(\vec{r}) \rangle_{angles}$$

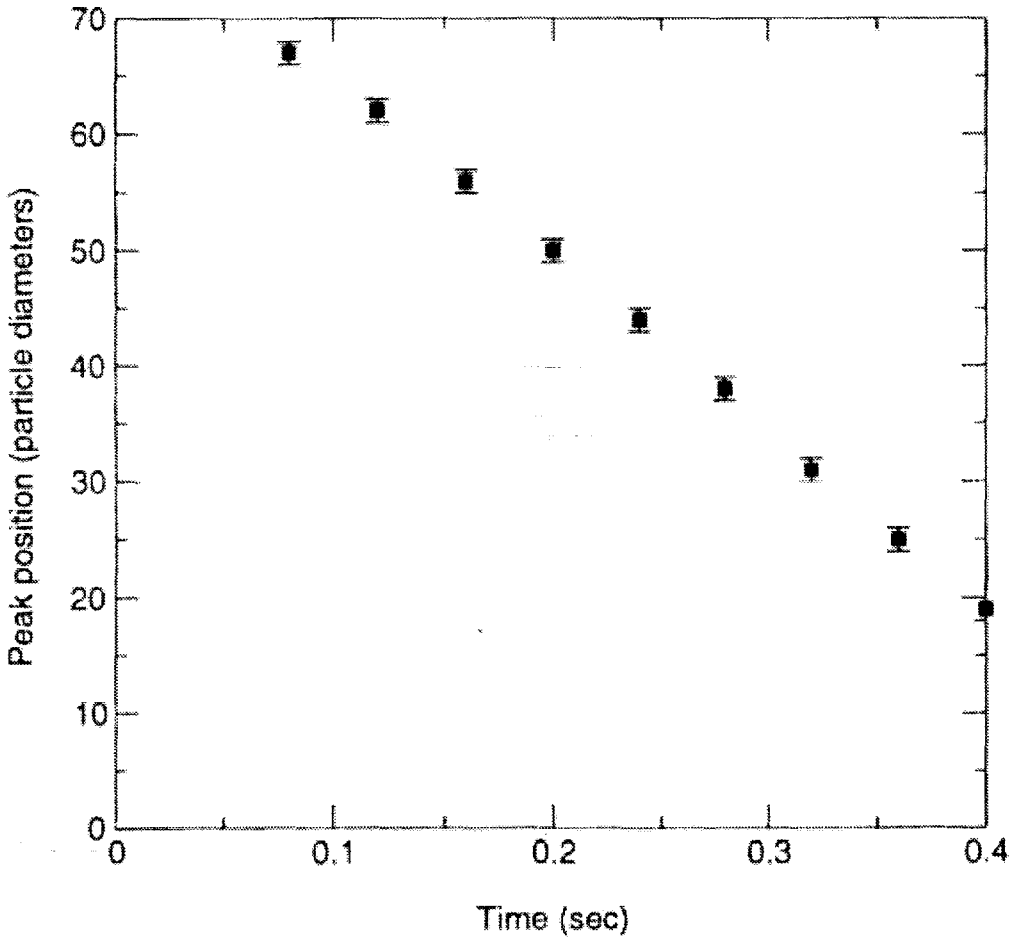

FIG. 6. Position of the peak in the spatial autocorrelation function $C(r)$ in a 400-particle system versus time, for $t < t_c$.

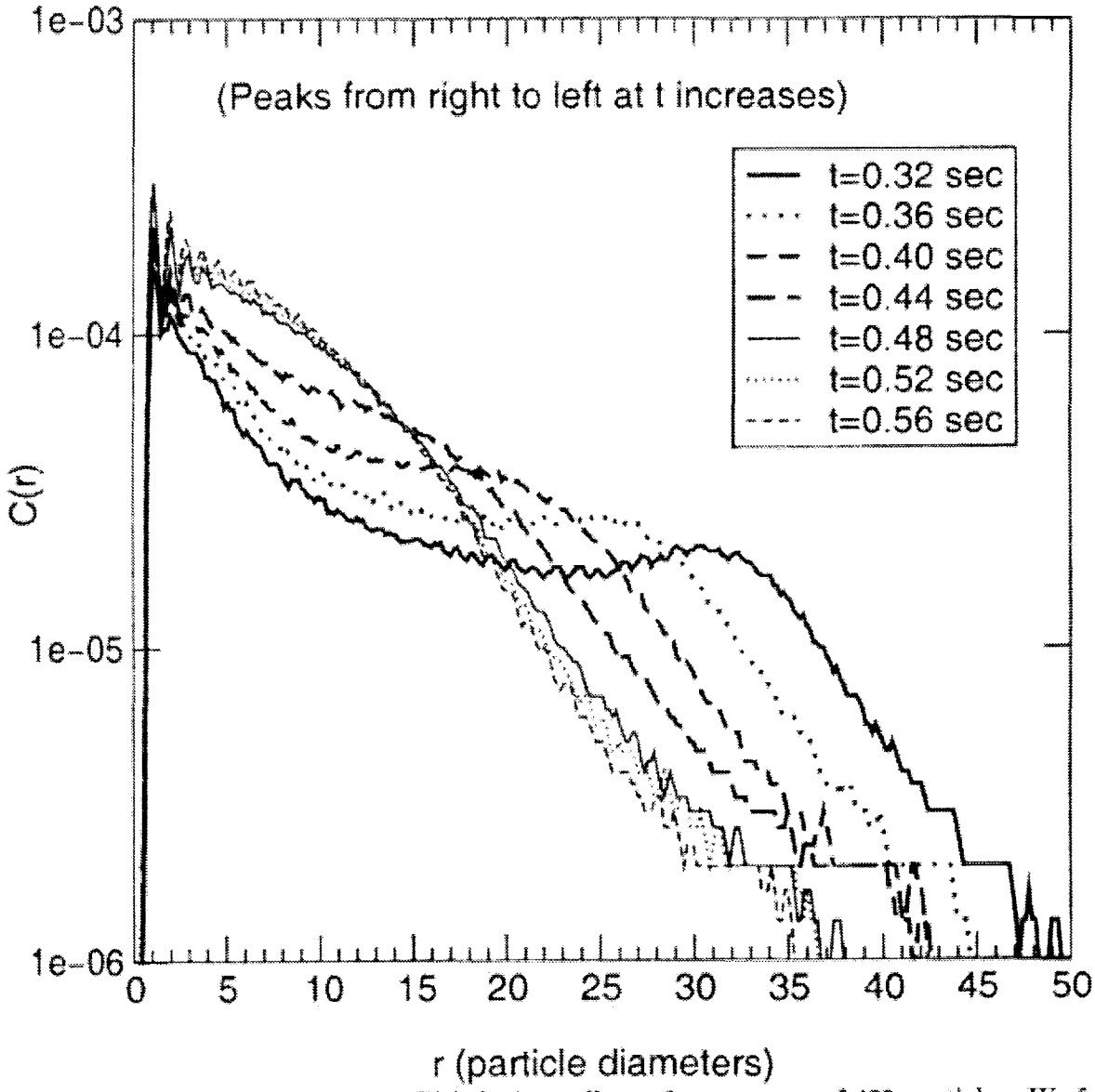

FIG. 5. Autocorrelation function C(r) during collapse for a system of 400 particles. We focus on the time near the collapse.

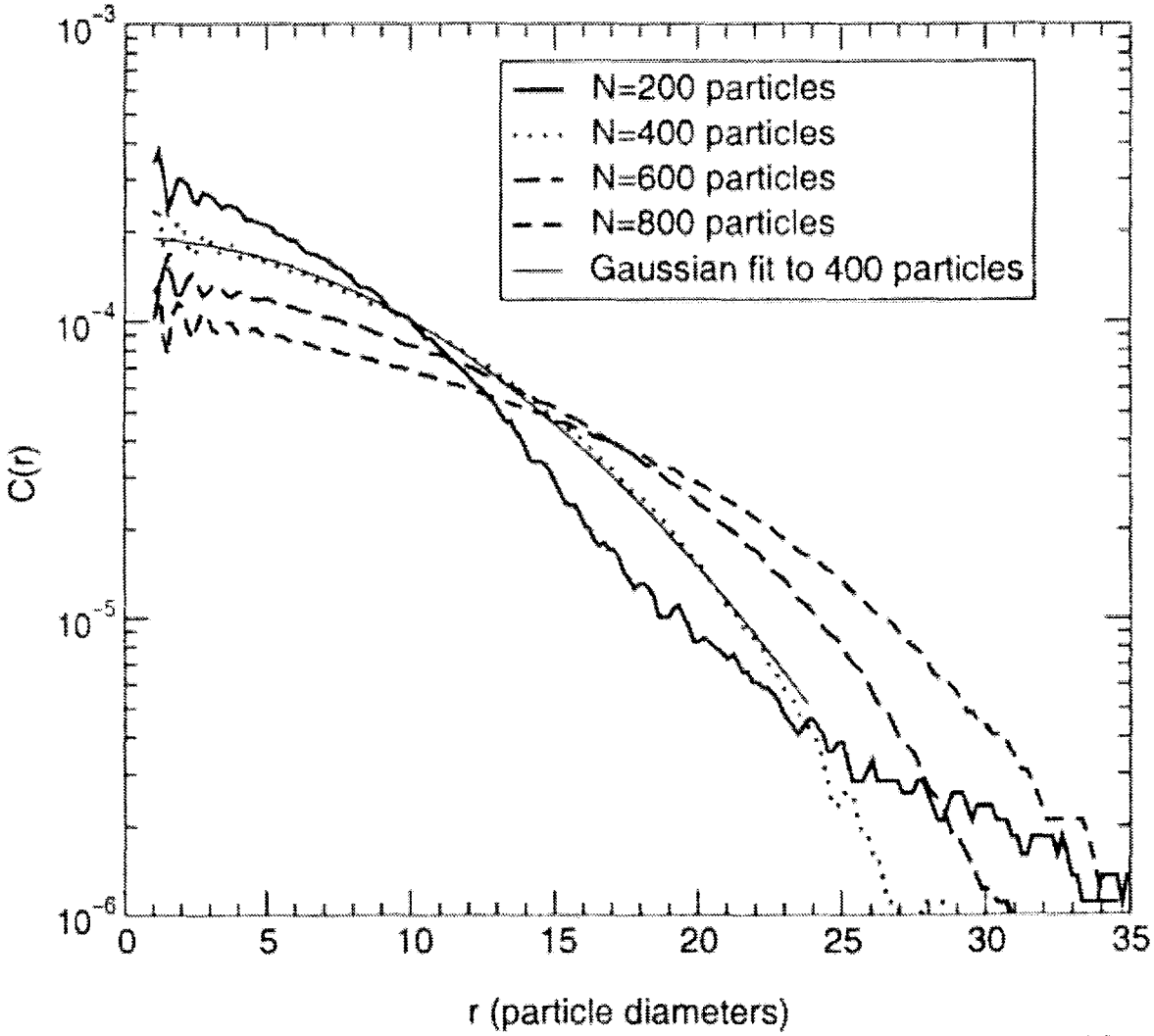

FIG. 7. Autocorrelation function $C(r)$ of final states for different system sizes N. The thin solid line is a least-squares gaussian fit to the $N = 400$ case.

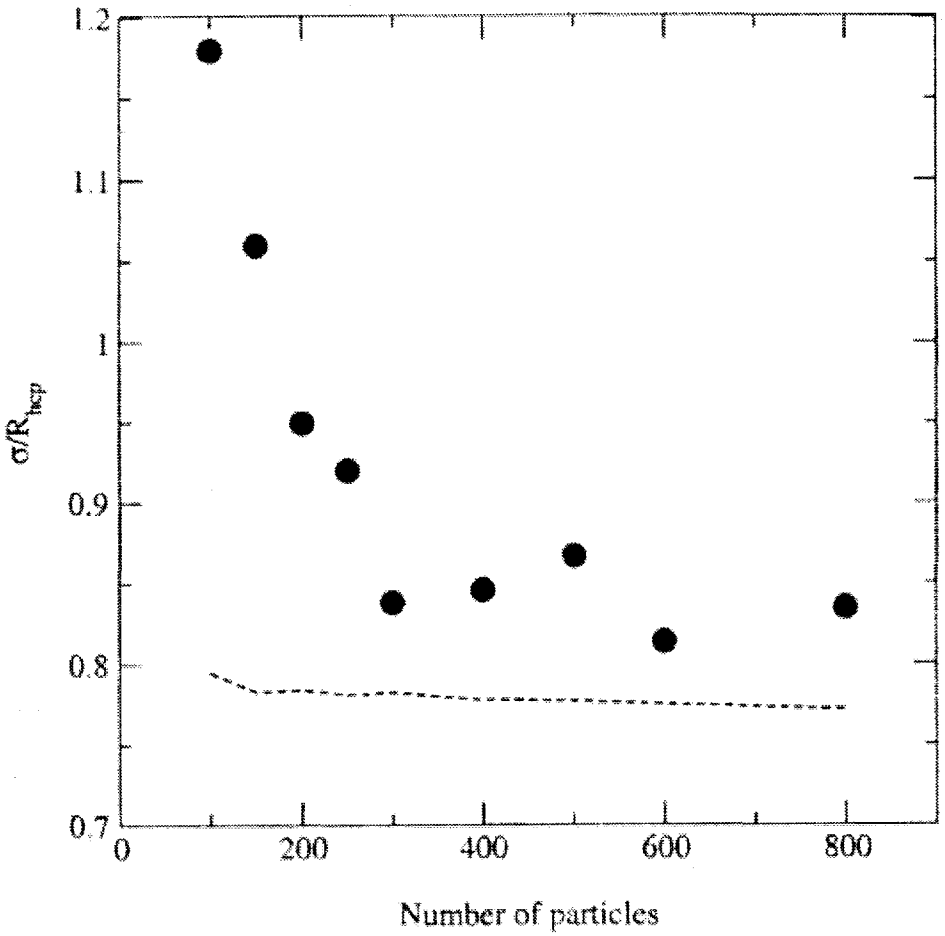

FIG. 9. Gaussian width σ of autocorrelation $c(r)$ normalized by R_{hcp}, the radius of a close-packed system of N particles. The dotted line represents σ for a computer-generated hexagonally close-packed system of N particles.

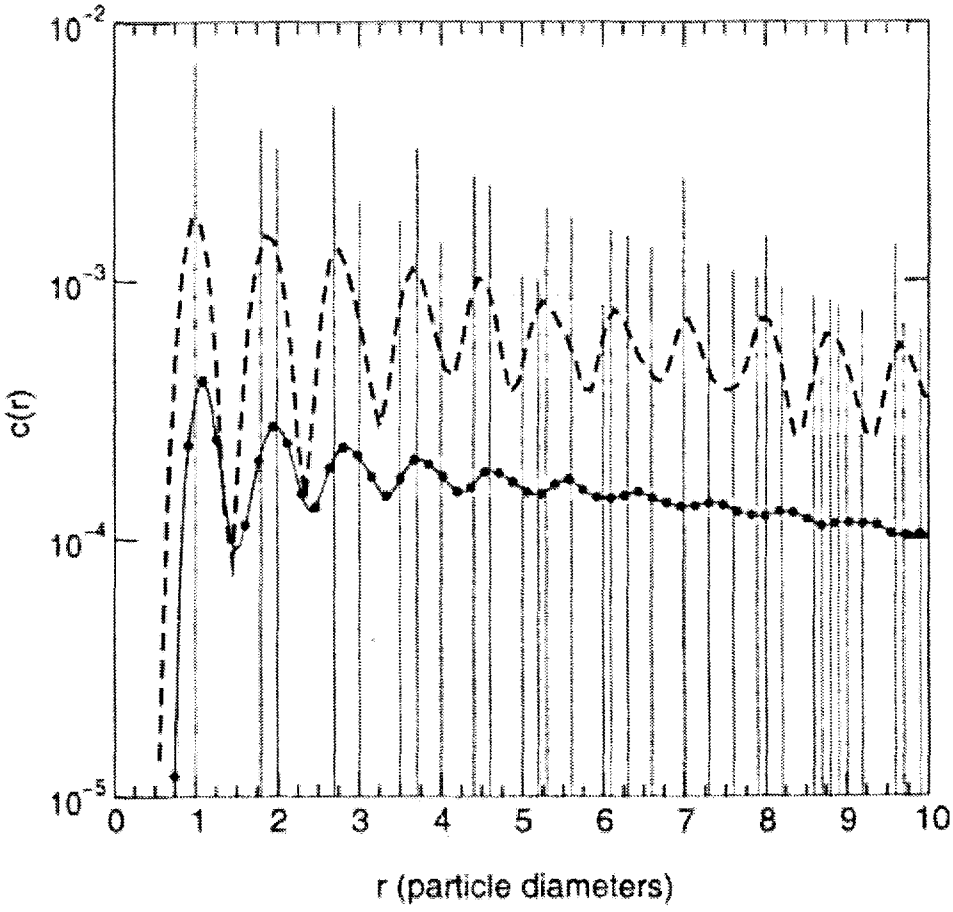

FIG. 10. Autocorrelation function $C(r)$ of a system of $N = 400$ particles at small radius r. The solid curve represents experimental data. Vertical lines are the computed autocorrelation for a set of 397 hexagonally close-packed particles represented by delta functions, and the dashed curve is a smoothed fit to the computed autocorrelation. The distance between the experimentally determined peaks is greater than that of the computed peaks by a factor of approximately 1.04.

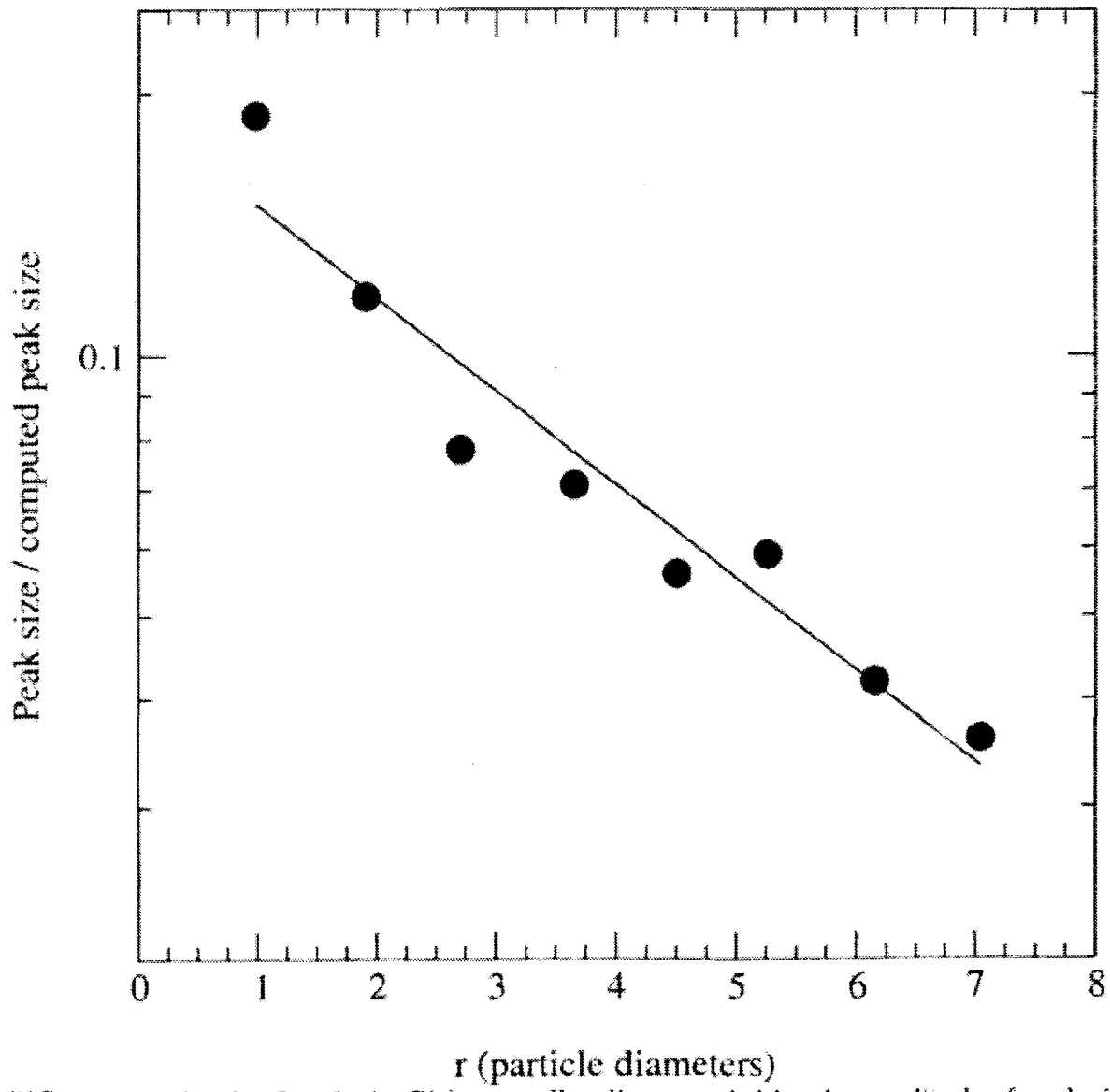

FIG. 11. Amplitude of peaks in $C(r)$ at small radius r, scaled by the amplitude of peaks in a computed hexagonally close-packed system, for $N = 400$ particles.

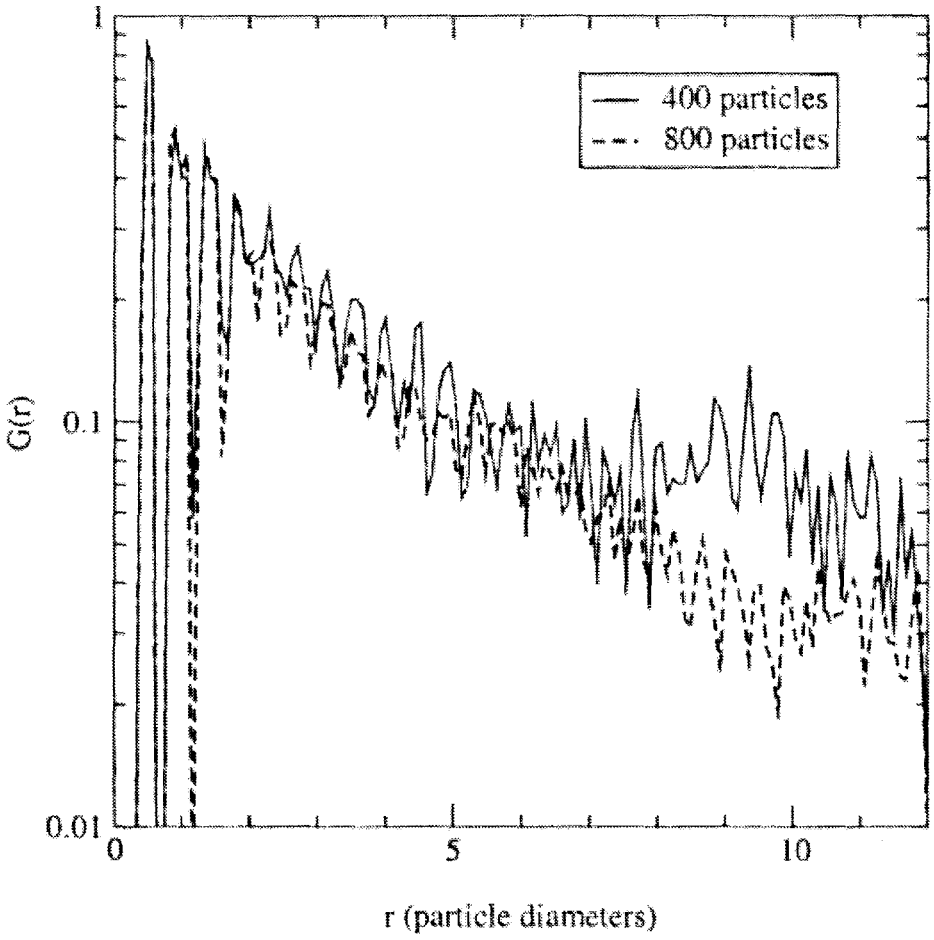

FIG. 12. Orientation autocorrelation length G(r) for 400- and 800-particle systems.

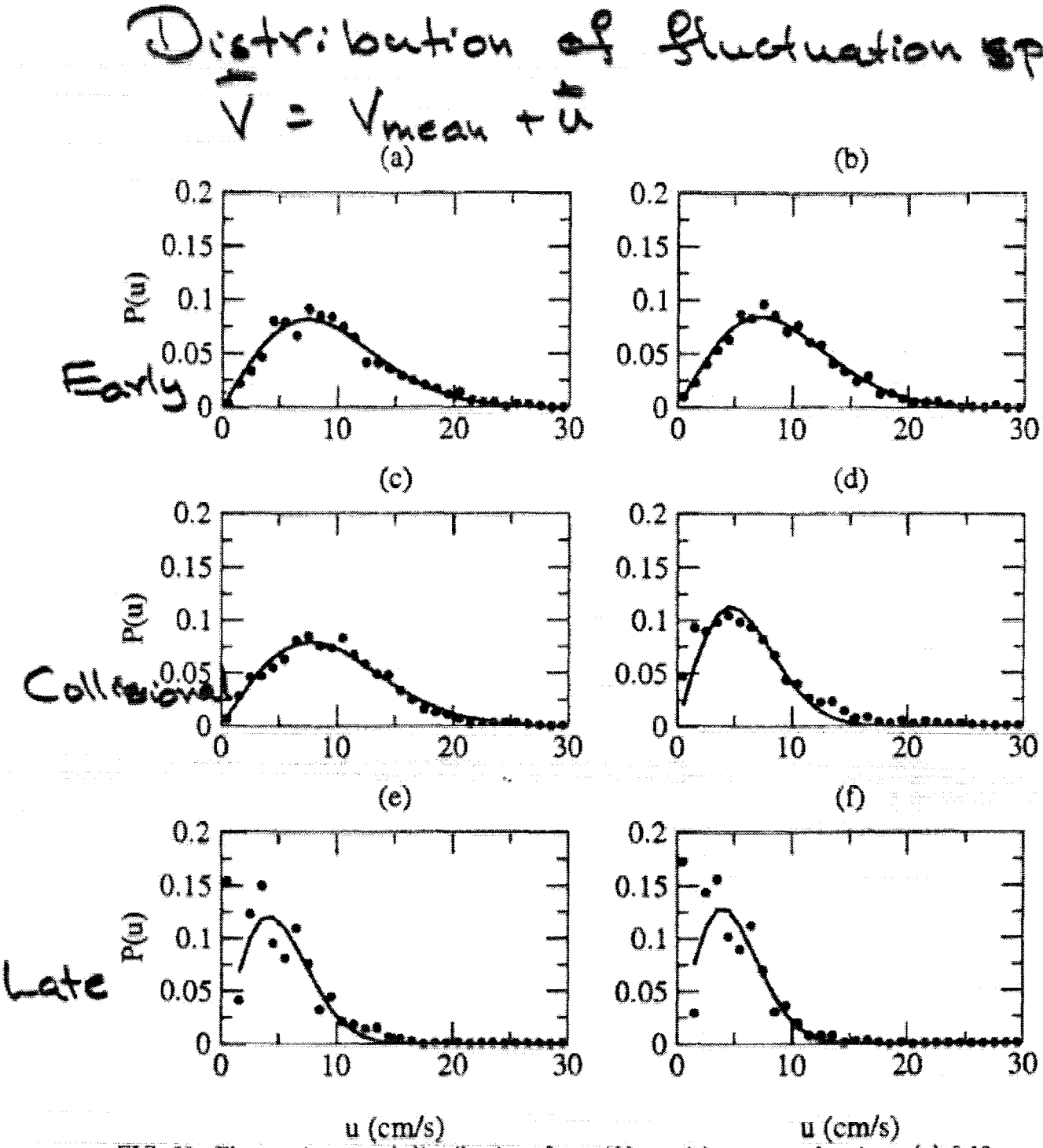

FIG. 23. Fluctuation speed distributions for a 400-particle system, for times (a) 0.12*sec.*, (b) 0.28*sec.*, (c) 0.44*sec*, (d) 0.52*sec*, (e) 0.68*sec*, and (f) 0.88*sec*. The solid lines are least-squares fits of the data to the Maxwell-Boltzmann speed distribution. In each of (e) and (f) the lowest-speed point, representing stationary particles in the condensed state, is disregarded for the fit.

2D Maxwell-Boltzmann:

$P(u) \sim u e^{-(u/\sigma)^2}$

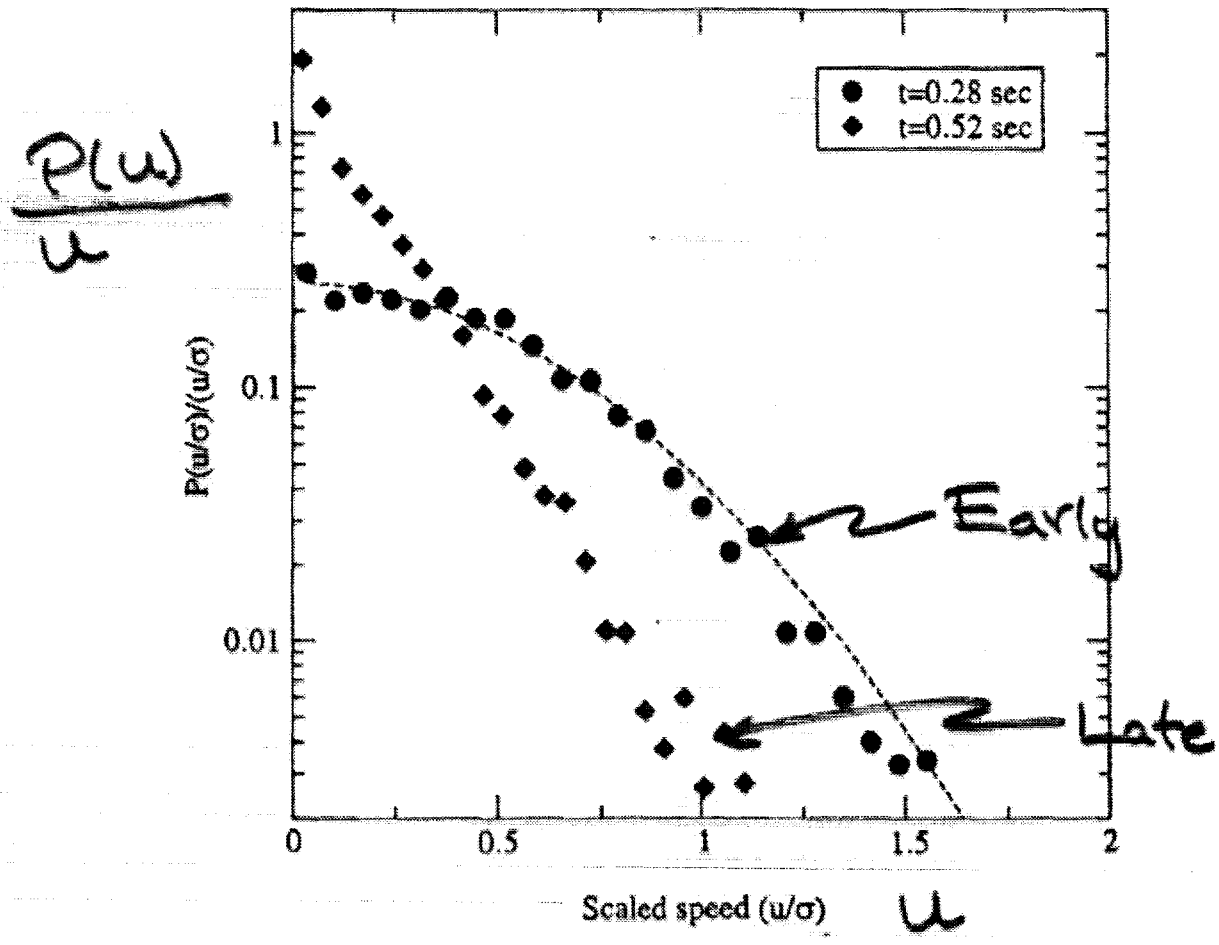

FIG. 24. Fluctuation speed distribution for a 400-particle system, scaled by (u/σ), for times before (0.28*sec.*) and after (0.52*sec.*) the majority of collisions have taken place. Also shown for reference is a least-squares gaussian fit to the data at $t = 0.28sec.$ (dashed line).

Conclusions

Horizontal Shaking - Fluid-Solid

Hysteretic transition

Long time scales

Striking changes from
fluidization
slider suppression
impurities

Coulomb + time delay →
better model

—

Surfaces - Rolling

Novel analogues to
Convection
Subharmonic waves

Strong energy losses from
sliding after collisions

NASA/CP-2000-210470

PARTICLE SEGREGATION IN COLLISIONAL SHEARING FLOWS

J. T. Jenkins and M. Y. Louge
Cornell University, Ithaca, NY 14853

ABSTRACT

During the past four years, we have worked to insure the success of a flight experiment on particle segregation in energetic grain flows. The experiment is meant to test theory and numerical simulations as they apply to shearing flows of colliding grains in micro-gravity. The experiment involves a binary mixture of spheres that differ in diameter and/or mass. A steady, fully-developed flow of the mixture is established between parallel, bumpy boundaries that are in relative motion. Because the energy transferred and dissipated in collisions between the flowing spheres and the boundaries is different from that transferred and dissipated in collisions among the flowing spheres, the energy of the particle velocity fluctuations in the mixture varies across the flow.

The frequency of collisions among and between the two types of spheres depends upon the spatial gradient of this energy and upon the spatial gradients of the concentrations of the two types of spheres. Consequently, the balances of momentum across the flow require that gradients of concentration accompany the gradients of mixture fluctuation energy. In the experiment, we measure how the energy of the velocity fluctuations and the concentrations vary across the flow. The object of the experiment is to determine how well these measured fields compare with those predicted by theory and observed in numerical simulations and to understand why any differences between them occur. The activities of the past four years involved physical experiments, computer simulations, and theory.

We carried out physical experiments on five flights in the KC-135. This involved the design and construction of a prototype shear cell in the shape of a racetrack. We also developed a way to obtain images of flowing spheres made of plastic, ceramic, and metal through the cell side wall and a means for computer interpretation of these images. We then measured profiles of mixture velocity, mixture fluctuation velocity, mixture volume fraction, and species number density in the shear cell during episodes of micro-gravity on the KC-135. The comparison of these profiles with those measured in computer simulations and the predictions of theory led to adjustments in the operating conditions of the shear cell and gave indications of the advantages and disadvantages of each material.

We developed discrete particle dynamics simulations for the full racetrack cell and for a section of fully developed flow that was periodic in the flow direction. The full computer simulation was used to design the racetrack shear cell and to study the properties of the flow in it. We also tested the results of the fully developed simulation against the measurements made in the shear cell during flight and predictions of theory. The latter were obtained in a numerical scheme that we developed to solve the full equations and boundary conditions for the mean mixture velocity, fluctuation velocity, and mixture volume fraction in steady, fully developed shearing flows over the cross section of the shear cell.

Finally, we derived a simplified theory for segregation for mixtures in which the diameters and/or the masses of the two spheres are not too different and a new theory for segregation of disks in planar shearing flows. We extended existing boundary conditions for bumpy frictional boundaries to include terms that are nonlinear in the ratio of the mean slip velocity to the strength

of the velocity fluctuations. We developed simple approximate differential equations with analytical solutions to describe segregation between bumpy boundaries with the influence of the side walls taken into account in an averaged way.

Future research will involve the evaluation of a new cell design. Computer simulations of the full racetrack shear cell indicate that the flow along the straight sections never achieves a fully-developed state. In earlier studies, we were led to believe that a fully-developed flow was attained because, near the ends of the straight sections, the profiles of mixture mean velocity, fluctuation velocity, and volume fraction were all close to their fully-developed values. The flow development seems to be controlled by the end regions in a way that we do not yet understand.

Consequently, we have begun to evaluate an axi-symmetric shear cell configuration in which the flow is fully developed at each section. Such a shear cell involves concentric circular cylinders that are in relative motion. Cylindrical bumps on these are parallel to the axis of the cylinders. When the cylinders rotate in opposite directions, so that there is a streamline of zero circumferential mixture velocity inside the shearing flow, the centripetal accelerations are minimized.

The advantage of such a cell is that the flows will be fully developed at every section. Also, because both boundaries move with respect to the fixed sidewalls, the flows will be more agitated across the gap. A possible disadvantage is that there is always some centripetal accelerations within the gap. However, theory and computer simulations can incorporate at least modest centrifugal forces, so we regard this as an opportunity to test this capability against the physical experiments. Finally, such an axi-symmetric cell is simpler to design and build than the racetrack and its axi-symmetric design seems to offers greater flexibility for a variety of experiments that might involve cylindrical boundaries of different diameters, depths, and bumpiness. Also, the design facilitates studies of time-dependent segregation and segregation in flows that are a single particle in depth.

Because the flow in the axi-symmetric cell is fully developed at every section, it is possible to employ it to carry out unambiguous experiments on time-dependent segregation. In the racetrack design, the time-dependent segregation associated with a change in boundary speed could be confused with that associated with the flow development. The axi-symmetrc geometry makes it possible to carry out measurements of diffusion velocities and time-dependent concentrations across the cell that follow, for example, an abrupt change in boundary speed. The results of such experiments can be tested against computer simulations and simplified versions of existing theories.

The simplicity of the design of the axi-symmetric cell makes it possible to reconfigure it to carry out experiments on segregation in flows that are a single particle in thickness. This provides an opportunity to test theory for the segregation of binary mixtures of disks in planar shearing flows that we have developed during the past four years. Also, this provides an opportunity to complement the work of researchers the University of Rennes who are carrying out physical experiments on the segregation of binary mixtures of circular disks in shearing flows carried out on an air table. We anticipate that because of the simplicity of the two-dimensional experiment, the prototype axi-symmetric shear cell, employed upon the KC-135, could provide sufficient data for meaningful comparison between theory, computer simulations, and the two experiments.

Particle Segregation in Collisional Shearing Flows

Segregation by size and/or mass in a binary mixture of colliding spheres, driven by spatial gradients in the mixture fluctuation energy.

J. Jenkins, M. Louge, A. Reeves
B. Arnarson, H. Xu

T&AM, M&AE, E&CE
Cornell University

Shear Cell Schematic

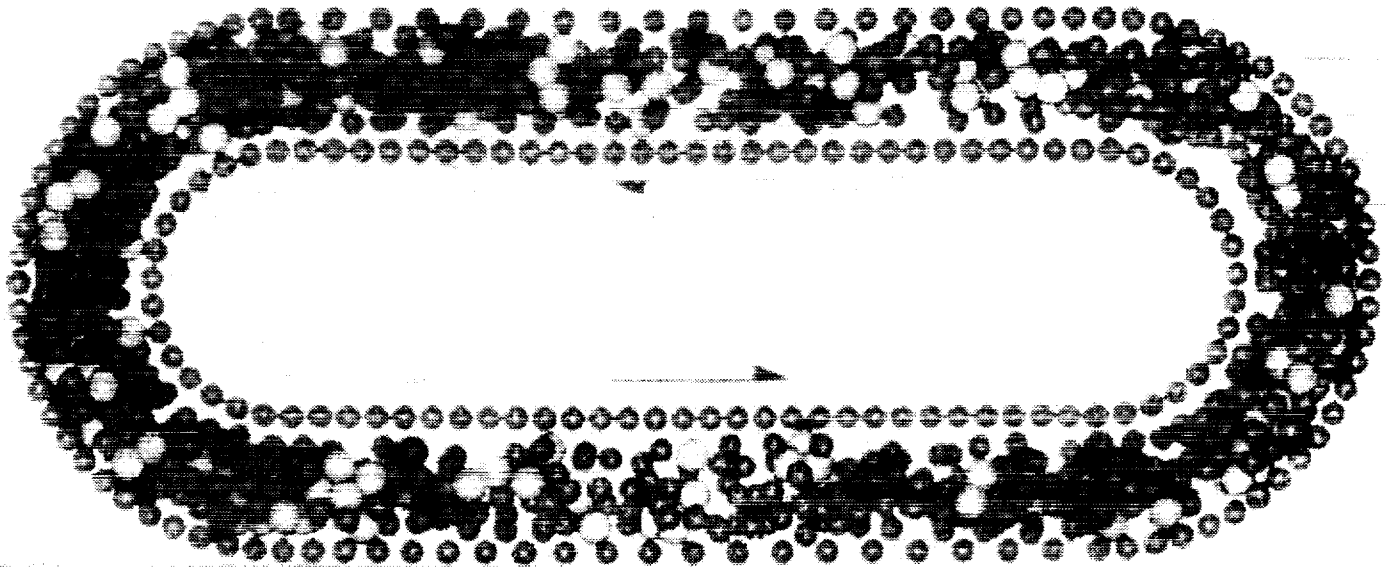

The Region of Fully-Developed Flow

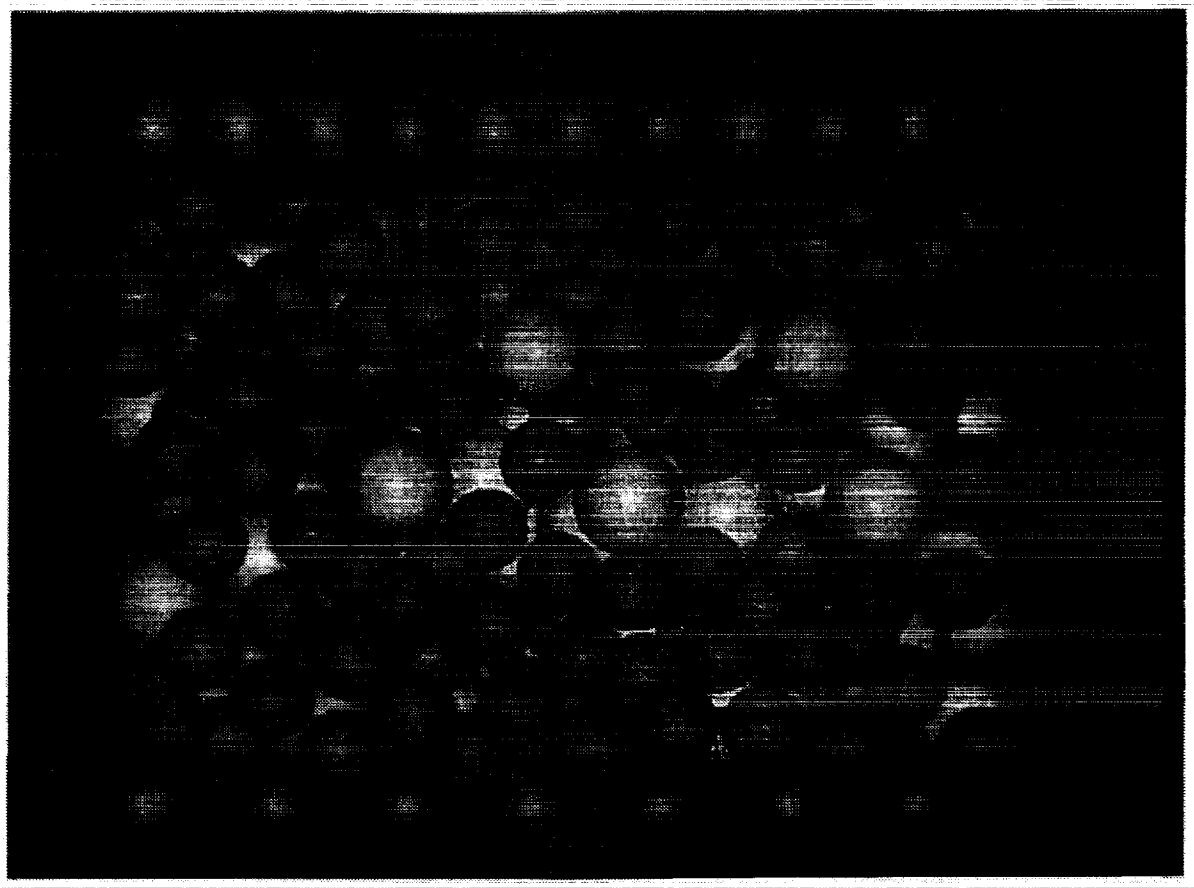

Experiment

Experimental conditions

Test	U m/s	F Hz	Species A	r_A mm	$\bar{\nu}_A$ %	Species B	r_B mm	$\bar{\nu}_B$ %	$t^\dagger$	t_0 s
I	1.4	1000	ceramic	1.59	10	acrylic	1.98	30	300	10
II	0.9	500	acrylic	1.6	28	acrylic	1.98	5	250	10

Impact Properties

sphere 1	r_1 (mm)	ρ_1 (g/cm^3)	sphere 2, bump or wall	r_2 (mm)	ρ_2 (g/cm^3)	e	μ_f	β_0
acrylic	1.6/1.98	1.22	acrylic	1.6/1.98	1.22	0.93	0.12	0.35
ceramic	1.59	3.86	ceramic	1.59	3.86	0.97	0.10	0.24
acrylic	1.6/1.98	1.22	ceramic	1.59	3.86	0.93	0.11	0.10
acrylic	1.6/1.98	1.22	fixed bump	1.59	-	0.97	0.22	0.28
ceramic	1.59	3.86	fixed bump	1.59	-	0.68	0.08	0.29
acrylic	1.6/1.98	1.22	aluminum	∞	-	0.94	0.14	0.51
ceramic	1.59	3.86	aluminum	∞	-	0.61	0.10	0.14
acrylic	1.6/1.98	1.22	glass	∞	-	0.83	0.12	0.34
ceramic	1.59	3.86	glass	∞	-	0.96	0.09	0.00

Experiment

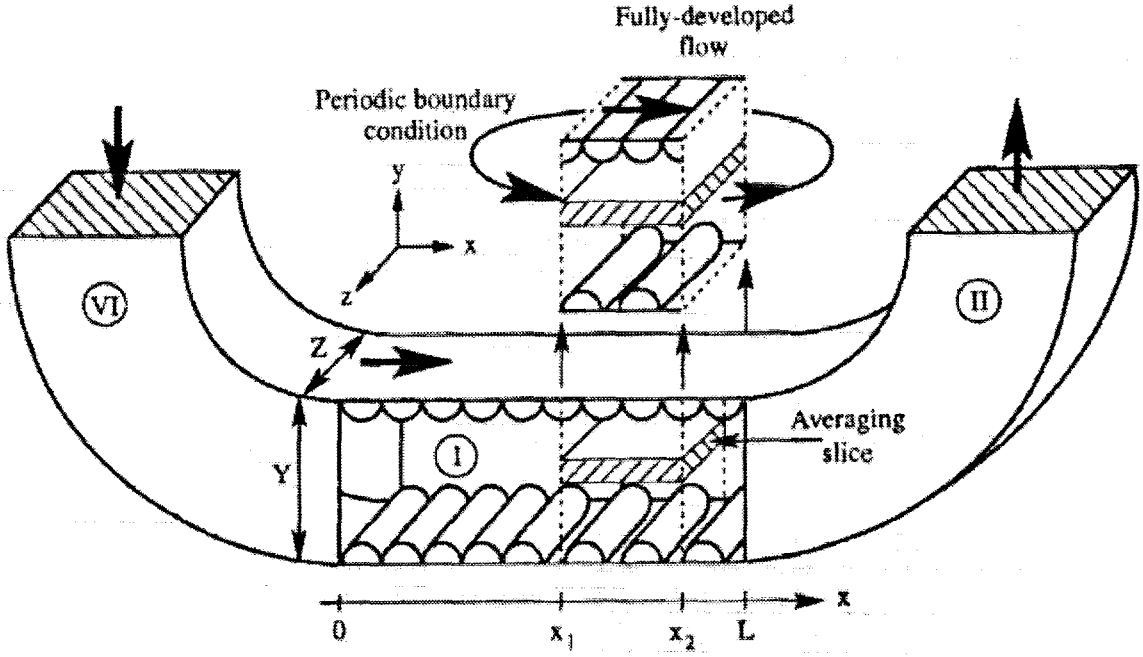
Fully-developed
flow
Periodic boundary
condition
y
x
z
VI
II
Z
Y
I
Averaging
slice
x
0
x_1
x_2
L

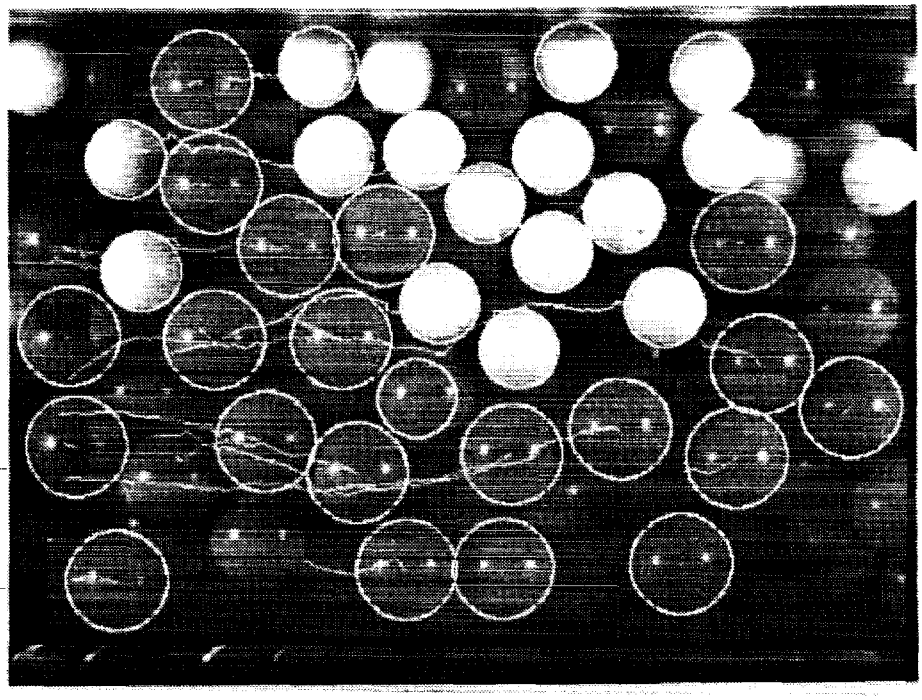

Experiments and Simulation

Test II

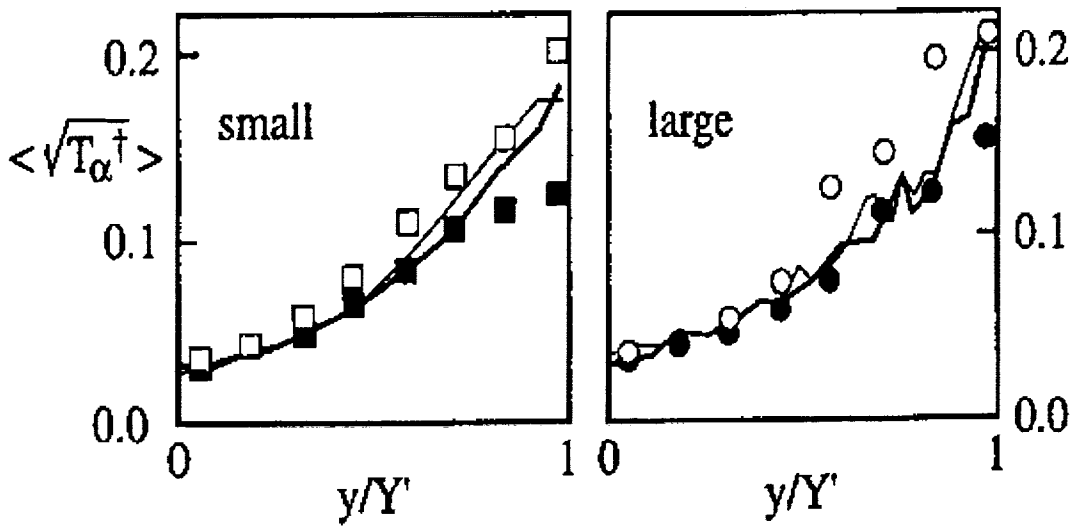

Number fraction: $f_A \equiv \frac{n_A}{n}$, $\phi_A \equiv \frac{f_A}{\bar{f}_A}$

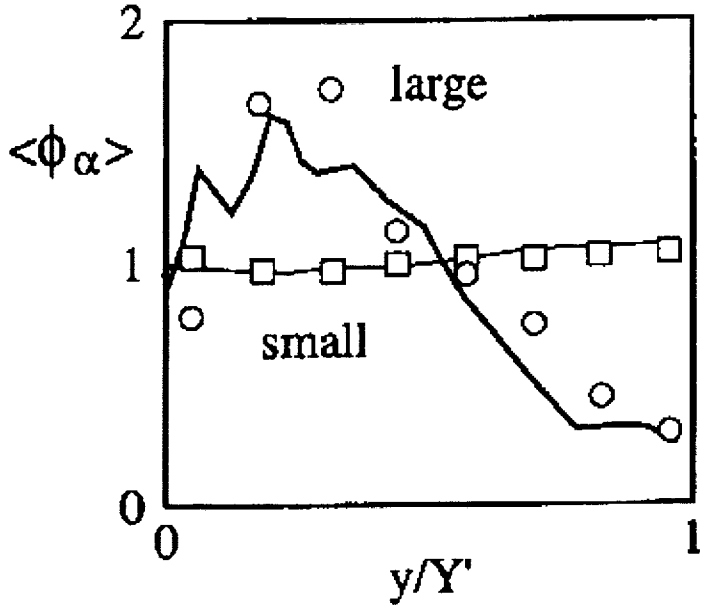

Kinetic Theory

Fluctuation velocity: $w \equiv T^{1/2}$

$$\left(\frac{pM}{F}w'\right)' + \frac{(1-2\bar{x}\delta r)}{r_{AB}^2}\frac{p}{F}\left[\frac{5\pi}{4J}\left(\frac{FS}{p}\right)^2 - 3(1-e_{eff})\right]w = 0$$

where

$$x \equiv \frac{1}{2}\left(\frac{n_A}{n} - \frac{n_B}{n}\right), \quad \delta r \equiv \frac{r_A - r_B}{r_B}, \quad e_{eff} \equiv e - \frac{\pi}{2}\mu$$

Boundary conditions

$$r_{AB}w' = -b_0 w, \text{ at } y = 0, \text{ and } r_{AB}w' = b_1 w, \text{ at } y = Y.$$

Segregation

$$x' = -\left(\frac{1-4x^2}{2}\right)(R\delta r + \Gamma\delta m)\frac{w'}{w}$$

Theory and Simulations

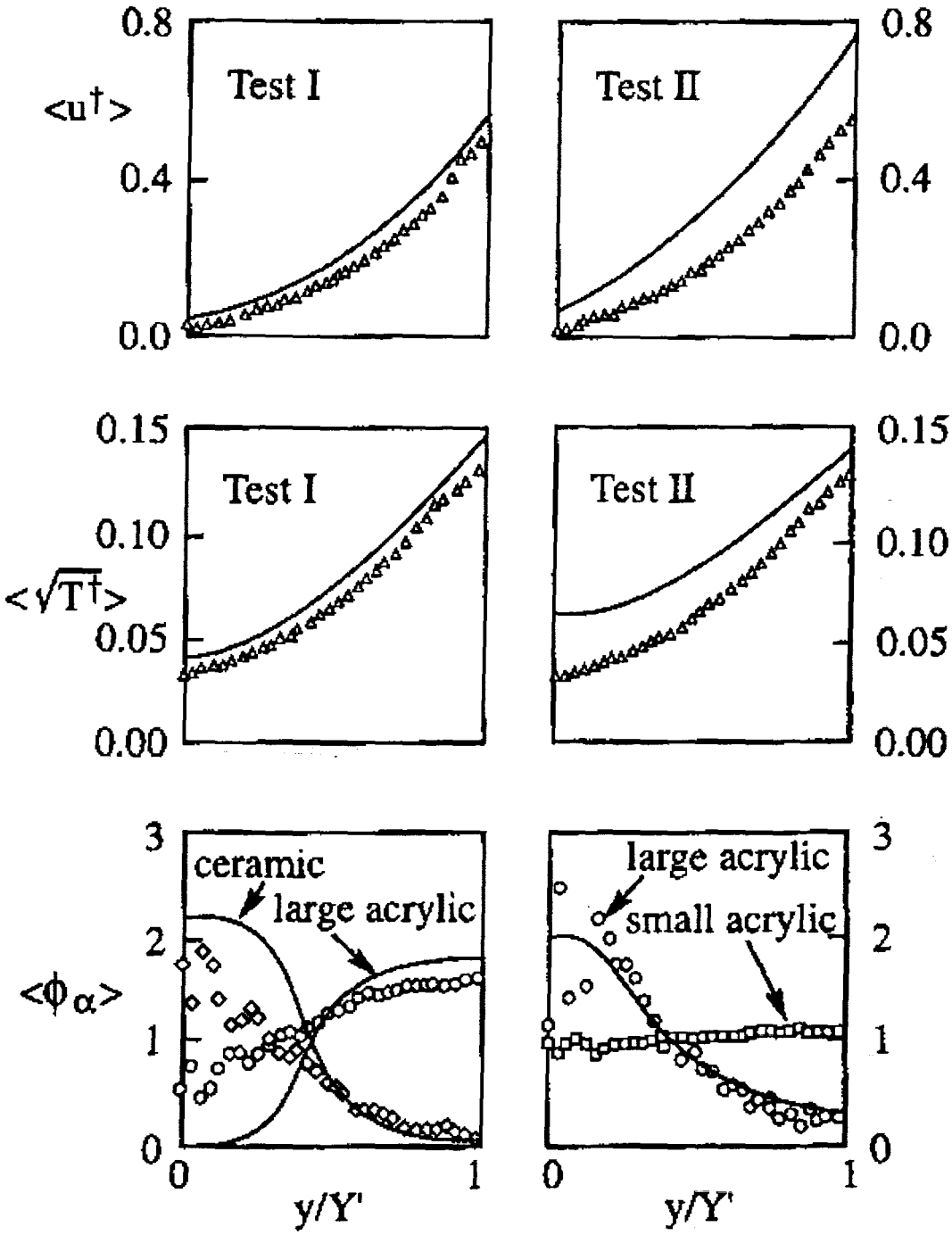

STUDIES OF GAS-PARTICLE INTERACTIONS IN A MICROGRAVITY FLOW CELL

Michel Y. Louge, James T. Jenkins, Haitao Xu and Anthony Reeves
Cornell University
Ithaca, NY 14853

ABSTRACT

The ability to transport particulate materials predictably and efficiently using a flowing gas is likely to play an important role in the development of lunar and martian environments that are hospitable to humans. On earth, the transport and processing of solid materials are also crucial in a number of applications from the chemical, mining, power and oil industries.

For these flows, an appreciation has recently developed for the influence of collisional interactions among particles. Collisions between such particles can transfer a significant amount of momentum within the flow and at the boundaries. A crucial parameter in such suspensions is the fluctuation kinetic energy or agitation of the particles. Its local measure is the granular temperature $T \equiv (1/3)\ \overline{u'_i u'_i}$, where u'_i is the fluctuating velocity of the particles. It is with this parameter that the solid phase can transmit momentum through an effective viscosity.

Sangani, et al. (1996) have determined the contribution of the viscous forces of the gas to the dissipation of particle fluctuation energy in random flights of particles between collisions. They do this over a range of concentrations for simple shearing flows in which the particle Reynolds number is small and the Stokes number is greater than one. We have extended their theory to inhomogeneous, three-dimensional, fully developed, steady shearing flows in practical wall-bounded devices. This involves the introduction of energy transport due to spatial gradients and the extension of boundary conditions for bumpy frictional walls to systems with large slip velocity at the boundaries.

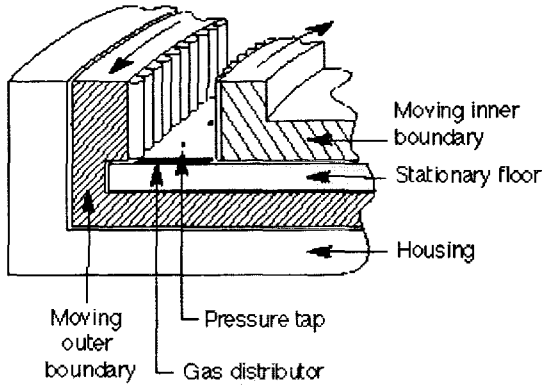

Sketch of the axisymmetric Couette shear cell.

In this context, we are designing an axisymmetric microgravity flow cell in which to study the interaction of a flowing gas with relatively massive particles that collide with each other and with the moving boundaries of the cell (Figure). This cell will permit suspensions to be studied over a range of laminar, steady, fully developed conditions where viscous forces dominate the gas flow and inertial forces proportional to the gas

density are nearly eliminated. Unlike terrestrial flows, where the gas velocity must be set to a value large enough to support the weight of particles, the duration and quality of microgravity on the International Space Station will permit us to achieve suspensions in which the agitation of the particles and the gas flow can be controlled independently by adjusting the pressure gradient along the flow and the relative motion of the boundaries.

In this cell, we will first characterize the viscous dissipation of the energy of the particle fluctuations when there is no relative mean velocity between gas and solids. In the absence of a gas, individual impacts are so fast that the only time scale governing the granular phase is the inverse of γ, the shear rate imposed by the moving boundaries. At small particle Reynolds numbers, the gas introduces an additional viscous relaxation time $\theta_s = \rho_s d^2/18\mu_g$, where ρ_s, d and μ_g are, respectively, the density of the spheres, their diameter and the gas viscosity. In simple shear flows, Sangani et al. (1996) have calculated values of the limiting Stokes number $St = \gamma \theta_s$ at which the particle fluctuation energy is equally dissipated by viscous and collisional interactions. Far above this limit, the shear rate is sufficient to ignore the viscous drag on the spheres.

In contrast, our intention is to reduce the boundary speed in successive tests until the Stokes number becomes small enough for the gas to affect the balance of fluctuation energy of the spheres. We will control the magnitude of the particle Reynolds number by adjusting the absolute pressure in the cell. At sufficiently low Stokes number, Sangani et al. (1996) showed that the granular fluctuation velocity scales as $\sqrt{T}/\gamma d \quad St/R_{diss}$, where R_{diss} is a coefficient characterizing viscous dissipation. In our experiments, we will infer R_{diss} by recording transverse profiles of granular temperature and comparing these with theoretical predictions. The measurements will be accomplished by observing the flow through sidewalls and by using computer vision techniques. In order to evaluate the role of non-continuum lubrication, we will also carry out relatively modest evacuation of the apparatus and measure R_{diss} at increasing values of the molecular mean free path. We will perform experiments at Stokes and Reynolds numbers where the present theory is valid and also, in an effort to inform future theoretical work, at values when it is not.

In another series of experiments, we will impose a gas pressure gradient on the shearing cell sketched above. The gradient will induce a relative velocity between the two phases, while the shearing will independently set the agitation of the solids. These experiments will be unique in exploring a regime where particle velocity fluctuations are determined by a mechanism other than interactions with the gas. In this regime, we will measure the dependence of R_{diss} and the drag coefficient on the solid volume fraction. We will do so by recording transverse profiles of mean gas velocity, mean granular velocity, temperature and volume fraction, and by comparing these with theoretical predictions. By partially evacuating the cell, we will also record the effects of particle Reynolds number on R_{drag}. These tests will require measurements of mean gas velocity. These will be accomplished using a new tracer technique analogous to particle-image-velocimetry.

REFERENCE

Sangani A.S., Mo G., Tsao H.-K., and Koch D.L., "Simple shear flows of dense gas-solid suspensions at finite Stokes number," *J. Fluid Mech.* **313**, 309-341 (1996).

NASA/CP—2000-210470

Studies of Gas-Particle Interactions in a Microgravity Flow Cell

Michel Louge, James Jenkins, Haitao Xu,
Anthony Reeves and Stephen Keast
Cornell University

Microgravity Fluid Physics Conference
Cleveland, OH, August 9, 2000

CORNELL UNIVERSITY

IFPRI
International Fine Particle Research Institute

Background

- Gas-solid suspensions are ubiquitous.
- An appreciation has developed for the importance of particle collisions.
- Theories have recently been proposed for interactions of a viscous gas and agitated solids when the flow is not turbulent.

Fluid-solid suspensions

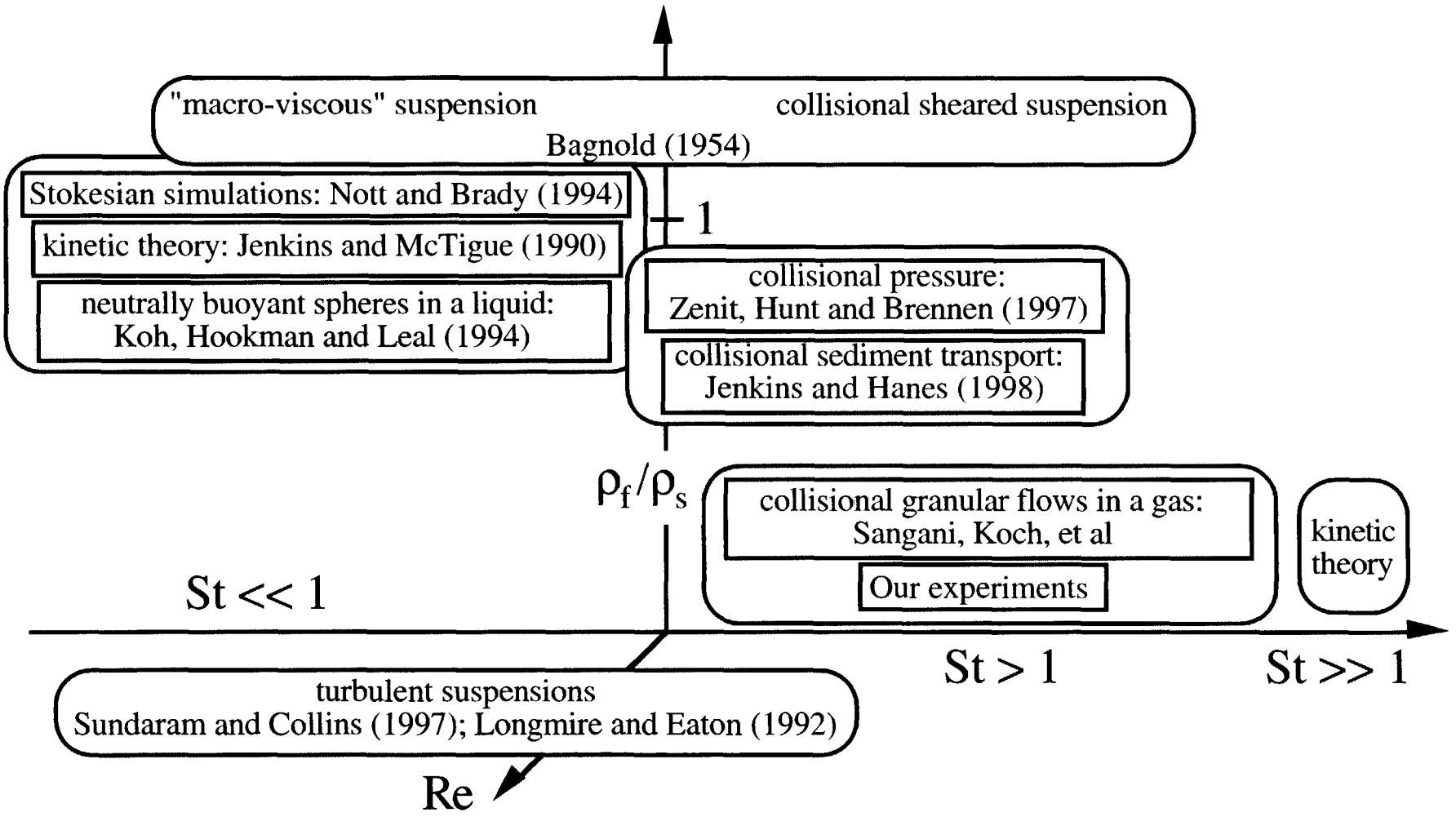

Stokes number $= \theta_s/\theta_{flow}$ with $\theta_s = \rho_s\, d^2/18\mu_g$
particle inertia versus viscous gas resistance

Granular temperature

Solid fluctuation velocity u'_s.

$$T = \frac{1}{3}\overline{u'_{s_i} u'_{s_i}}$$

Fluctuation energy per mass of the grains.

NASA/CP—2000-210470

Objectives

In the context of a viscous gas interacting with an agitated, collisional granular material,

- Measure viscous dissipation of fluctuation energy and viscous drag using a steady, fully-developed, collisional flow of inelastic spheres in a gas.
- Test predictions of existing theories.

Interactions of a viscous gas and agitated solids

solid volume fraction ν , molecular mean free path λ_g, granular temperature T.

(1) Viscous dissipation of T; effects of ν, T, λ_g

(2) Viscous drag; effects of ν, T

Microgravity → Only viscous and collisional interactions.

→ No enduring contacts.

Gas → Minimize forces associated with fluid inertia.

Shear cell → Independent control of fluctuation energy.

(1) Viscous dissipation

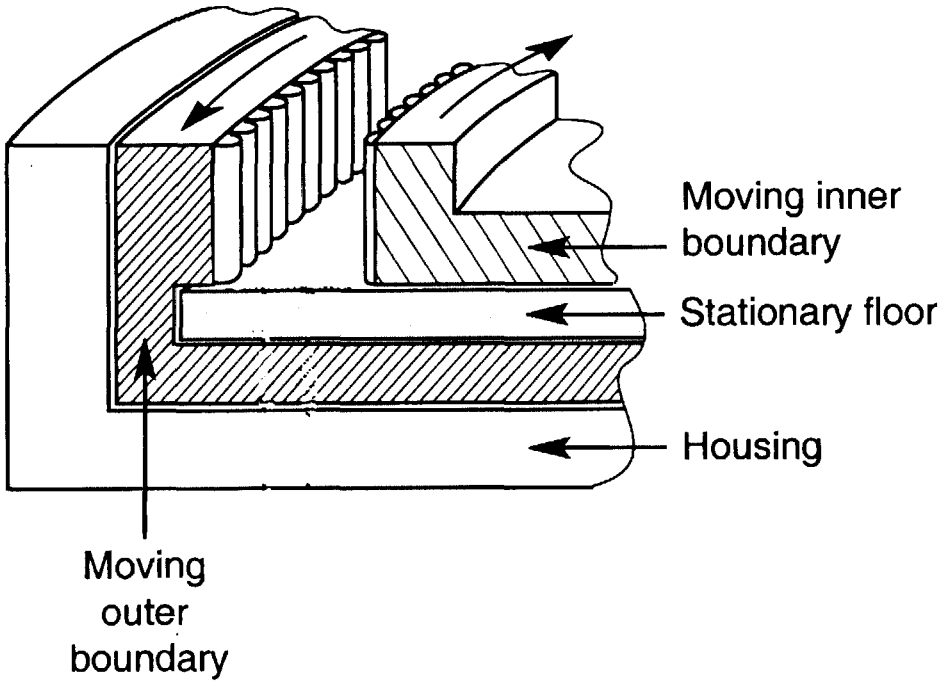

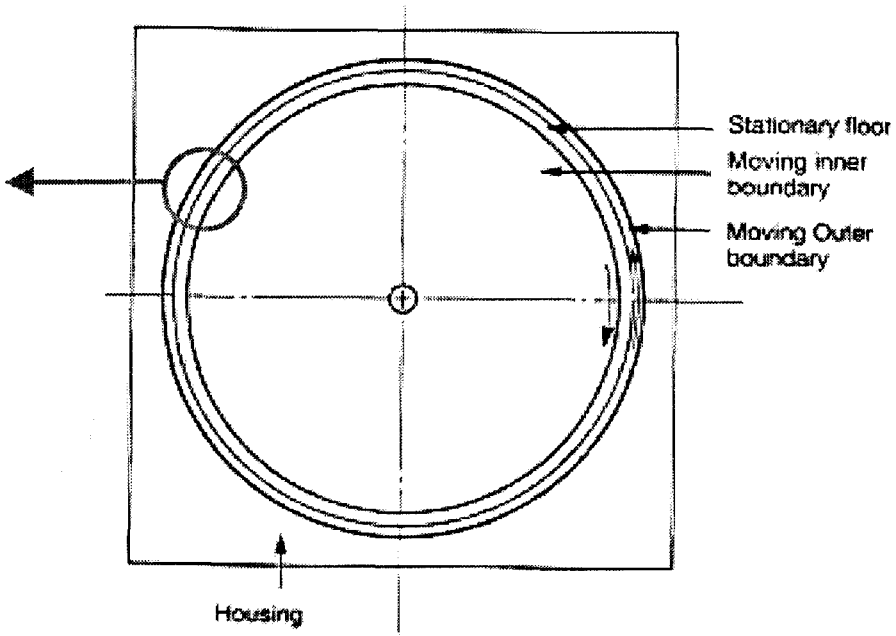

Reduce boundary speed until collisional and viscous dissipation of fluctuation energy are comparable.

Interactions of a gas with colliding spheres in a simple shearing flow

Solid density ρ_s, diameter d, volume fraction ν, pair-distribution function $g_{12}(\nu)$, granular temperature T, normal restitution e, mean shear rate γ, gas viscosity μ_g.

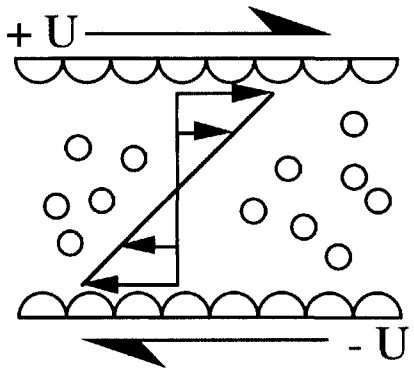

Collisional production ~ $\rho_s\, d\, \sqrt{T}\, f_\eta(\nu)\, \gamma^2$

Collisional dissipation ~ $(1\text{-}e)\, \nu\, \rho_s\, T^{3/2}\, \nu\, g_{12}(\nu)/d$

Viscous dissipation ~ $\mu_g\, \nu\, R_{diss}\, T/d^2$

<u>High U</u>: $\sqrt{T}/\gamma d \sim (1\text{-}e)^{-1/2}$

<u>Low U</u>: $\sqrt{T}/\gamma d \sim (\rho_s\, d^2/\mu_g)\, \gamma\, /R_{diss} \sim \mathrm{St}/R_{diss}$

Method

viscous dissipation

- Reduce boundary speed to achieve low Stokes numbers.
- Fit R_{diss} to the measured granular fluctuation velocity profile.
- Measure granular velocity distribution function.

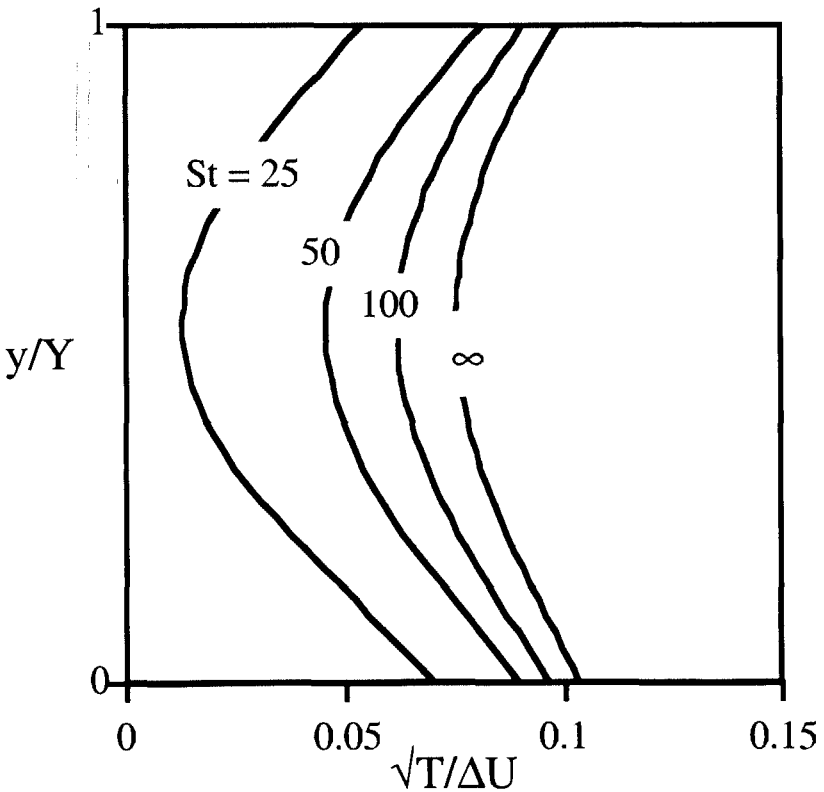

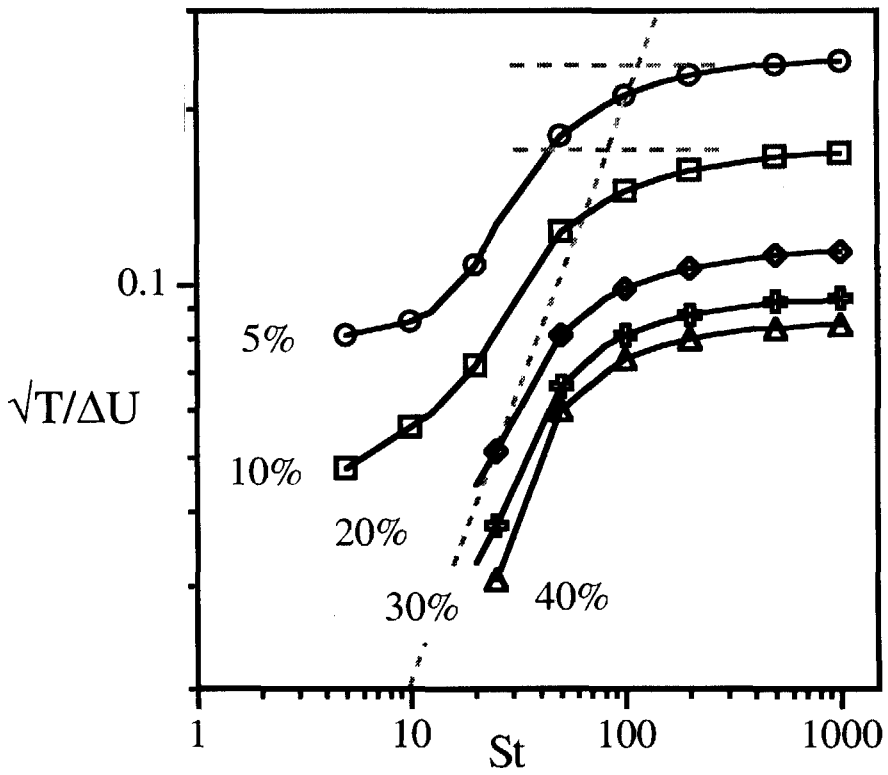

(2) Viscous drag

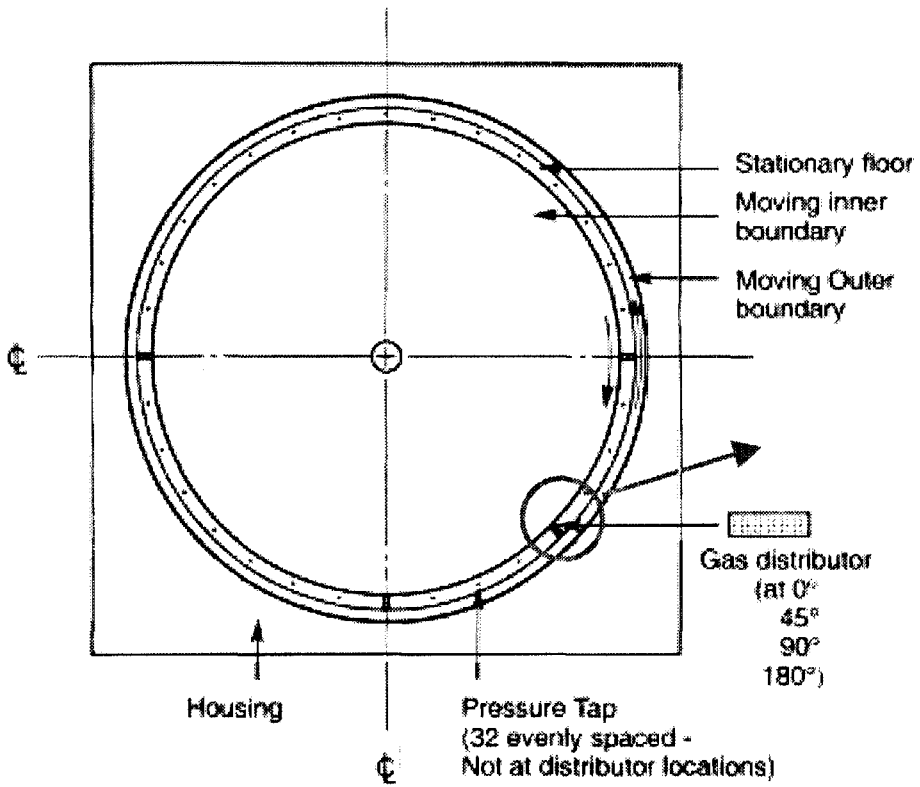

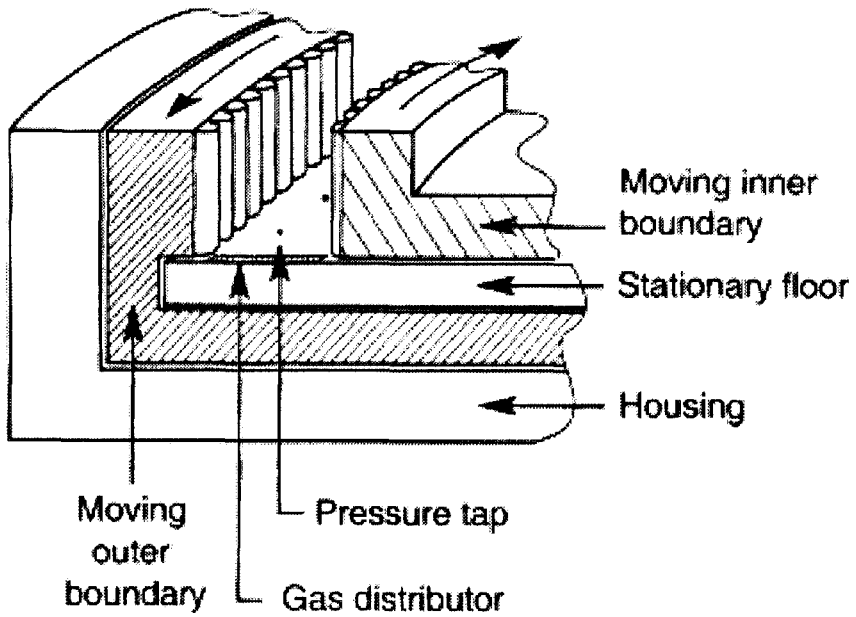

Impose a gas pressure gradient on a sheared granular material

Shearing →control of fluctuation energy
→control of solid mass flux

Uniform, unbounded suspension

Grain diameter d, volume fraction ν, relative velocity u_s-u_g, gas pressure p_g and viscosity μ_g.

Average gas momentum balance:

$$0 = \frac{18\mu_g \nu(1-\nu)^2 R_{drag}}{d^2}\left(u_s - u_g\right) - (1-\nu)\frac{dp_g}{dx}$$

Measure u_s, u_g and dp_g/dx.

Minimize shear stress in the gas phase.

Accomplishments

- Modeled gas-solid flow in wall-bounded cell.
- Prescribed experimental conditions.
- Specified microgravity requirements.
- Designed a new tracer anemometer.
- Carried out preliminary tests on the KC-135.

ELECTROSTATICS OF GRANULAR MATERIAL (EGM): SPACE STATION EXPERIMENT

J. Marshall and T. Sauke, SETI Institute, MS 239-12, NASA Ames, Moffett Field, CA 94035, and W. Farrell, MS 695.0, NASA Goddard, Greenbelt, MD 20771.

ABSTRACT

Aggregates were observed to form very suddenly in a lab-contained dust cloud, transforming (within seconds) an opaque monodispersed cloud into a clear volume containing rapidly-settling, long hair-like aggregates. The implications of such a "phase change" led to a series of experiments progressing from the lab, to KC-135, followed by micro-g flights on USML-1 and USML-2, and now EGM slated for Space Station. We attribute the sudden "collapse" of a cloud to the effect of dipoles. This has significant ramifications for all types of cloud systems, and additionally implicates dipoles in the processes of cohesion and adhesion of granular matter. Notably, there is the inference that like-charged grains need not necessarily repel if they are close enough together: attraction or repulsion depends on intergranular distance (the dipole being more powerful at short range), and the D/M ratio for each grain, where D is the dipole moment and M is the net charge. We discovered that these ideas about dipoles, the likely pervasiveness of them in granular material, the significance of the D/M ratio, and the idea of mixed charges on individual grains resulting from tribological processes --are not universally recognized in electrostatics, granular material studies, and aerosol science, despite some early seminal work in the literature, and despite commercial applications of dipoles in such modern uses as "Krazy Glue", housecleaning dust cloths, and photocopying.

The overarching goal of EGM is to empirically prove that (triboelectrically) charged dielectric grains of material have dipole moments that provide an "always attractive" intergranular force as a result of both positive and negative charges residing on the surfaces of individual grains. Microgravity is required for this experiment because sand grains can be suspended as a cloud for protracted periods, the grains are free to rotate to express their electrostatic character, and Coulombic forces are unmasked. Suspended grains will be "interrogated" by applied electrical fields. In one module, grains will be immersed in an inhomogeneous electric field and allowed to be attracted towards or repelled from the central electrode of the module: part of the grain's speed will be a function of its net charge (monopole), part will be a function of the dipole. Observed grain position vs. time will provide a curve that can be deconvolved into the dipole and monopole forces responsible, since both have distinctive radial dependencies. In a second approach, the inhomogeneous field will be alternated at low frequency (e.g., every 5-10 seconds) so that the grains are alternately attracted and repelled from the center of the field. The resulting "zigzag" grain motion will gradually drift inwards, then suddenly change to a unidirectional inward path when a critical radial distance is encountered (a sort of "Coulombic event horizon") at which the dipole strength supersedes the monopole strength --thus proving the presence of a dipole, while also quantifying the D/M ratio. In a second module, an homogeneous electric field eliminates dipole effects (both Coulombic and induced) to provide calibration of the monopole and to more readily evaluate net charge statistical variance. In both modules, the e-fields will be exponentially step-ramped in voltage during the experiment, so that the field "nominalizes" grain speed while spreading the response time --effectively forcing each grain to "wait its turn" to be measured.

In addition to rigorously quantifying M, D, and the D/M ratio for many hundreds of grains, the experiment will also observe gross electrometric and RF discharge phenomena

associated with grain activity. The parameter space will encompass grain charging levels (via intentional triboelectrification), grain size, cloud density, and material type.

Results will prove or disprove the dipole hypothesis. In either case, light will be shed on the role of electrostatic forces in governing granular systems. Knowledge so gained can be applied to natural clouds such as protostellar and protoplanetary dust and debris systems, planetary rings, planetary dust palls and aerosols created by volcanic, impact, aeolian, firestorm, or nuclear winter processes. The data are also directly applicable to adhesion, cohesion, transport, dispersion, and collection of granular materials in industrial, agricultural, pharmaceutical applications, and in fields as diverse as dust contamination of space suits on Mars and crop spraying on Earth.

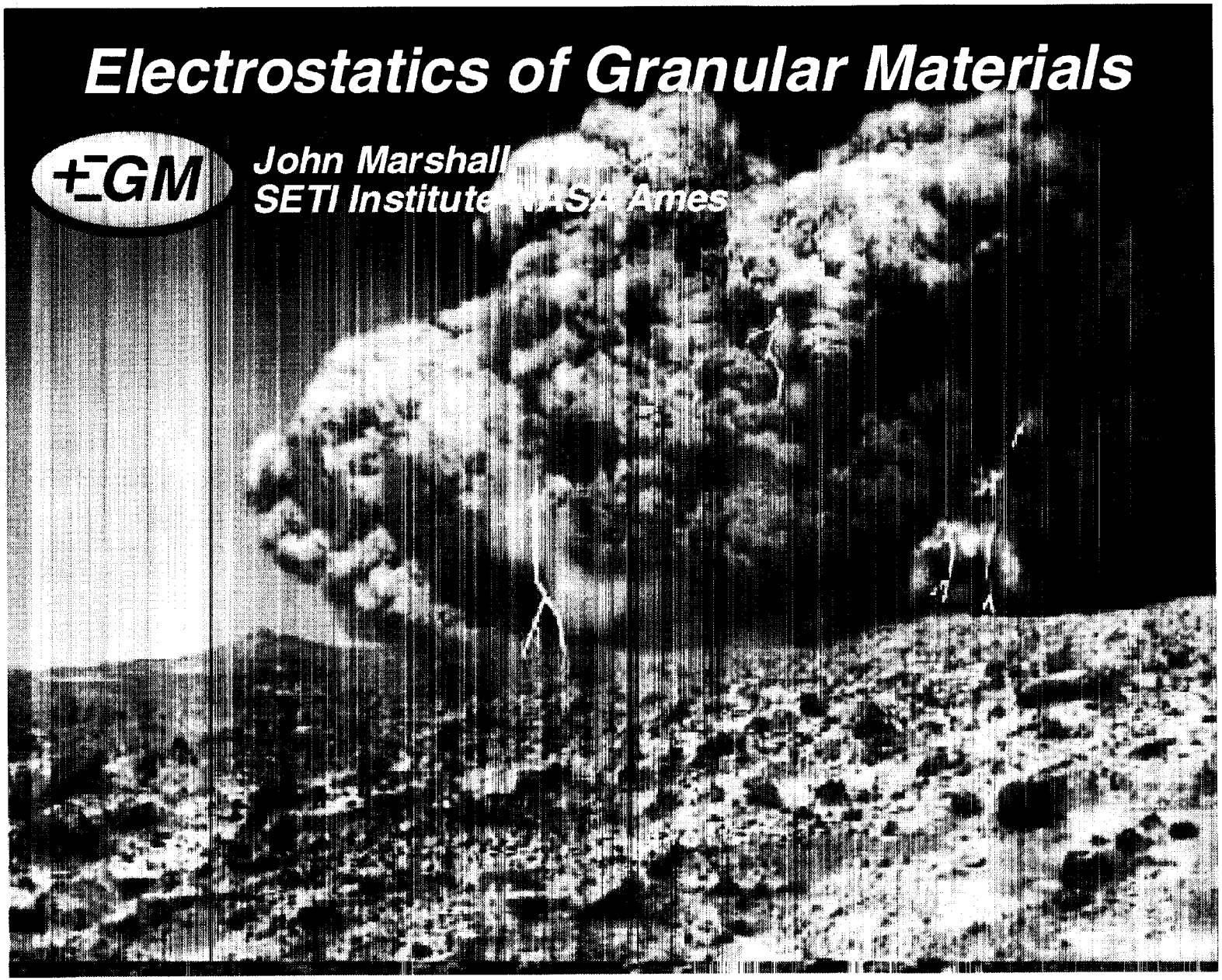
Electrostatics of Granular Materials
±GM
John Marshall
SETI Institute/NASA Ames

Hypotheses Being Tested

Grains of dielectric material must have a dipole moment, D, if they have a non-uniform distribution of positive and negative surface charges (total net charge determines value of monopole moment, M, regardless of the charge distribution)

For certain granular regimes, interaction of grains is strongly a function of D/M ratio and its relationship to intergranular spacing. D/M has not been experimentally determined for triboelectrically interactive grain populations

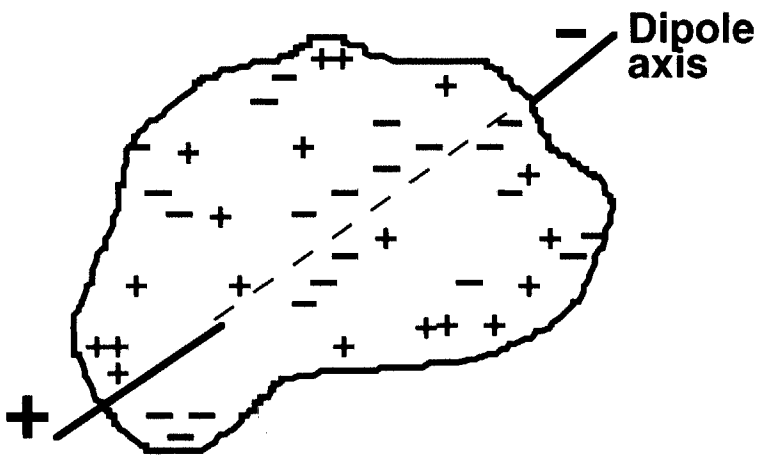

Strength of the dipole is a function of the number of fixed charges, and the distribution of the charges

Current Concepts

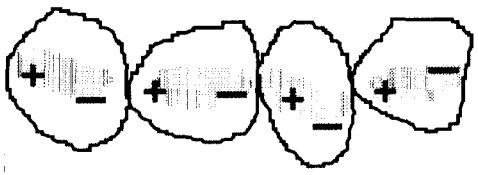

Aggregates formed from
discrete dipoles on each grain

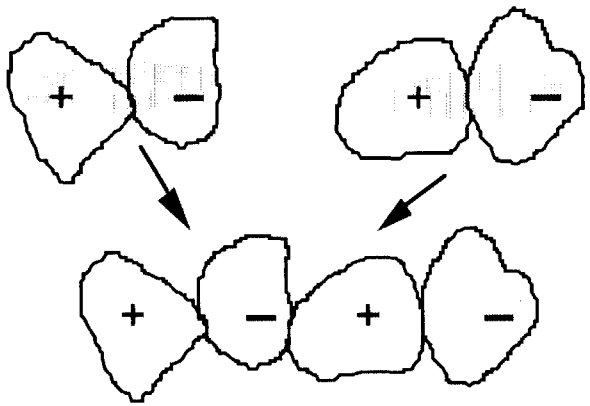

Aggregates formed from
dipole couplets of monopoles

EGM versus conventional aggregation concept

Tribocharging & Dipoles

Grains of like material acquire both + and - charges during grain-grain contact as a result of differential work functions

Causes

- **Microscopic surface configurations causing stress field variation**
- **Structural variation in hardness, surface energy, piezoelectrics, etc**
- **Protruberance dragged across a surface is dramatically heated compared to scratch line on other surface --thermal discrepancy**
- **Surfaces transfer material across tribological boundary. For like materials, it is random which grain acquires or loses material**

Effects

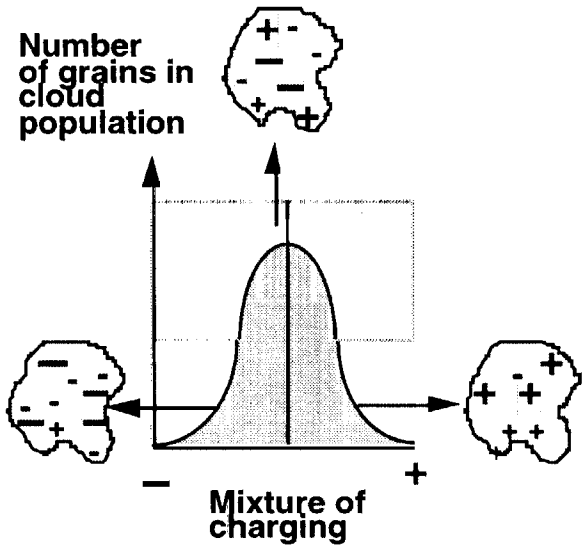

Mixture of monopole and dipole strengths in grain population

Dipoles: Early Clues

t = 0

Dense dust cloud

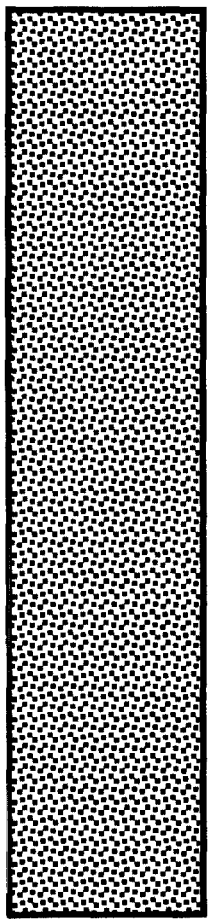

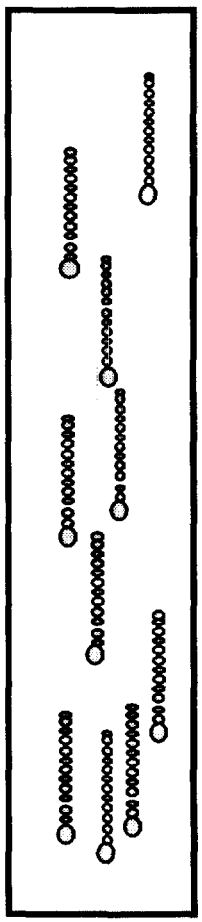

t = 30 seconds

Clear column with 2 cm long settling filament hairs. Catastrophic "phase change"

1 m settling column of dust in 1 g

Undispersable sand mass with filamentary attachments

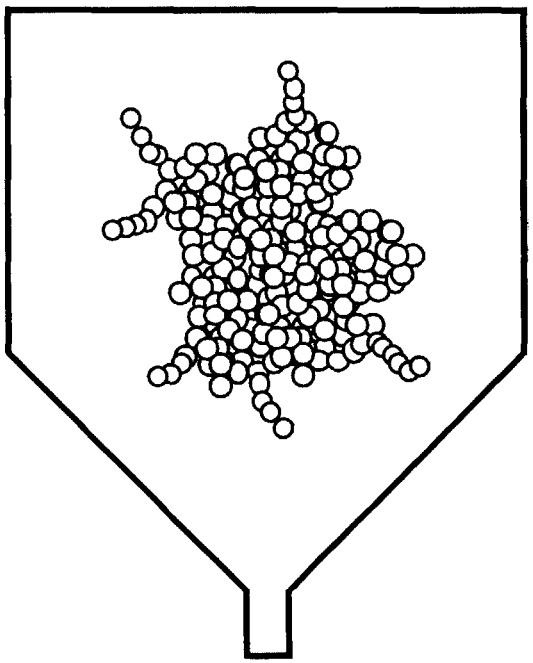

10 liter container in KC-135 zero-g

USML-2 Evidence for Dipoles

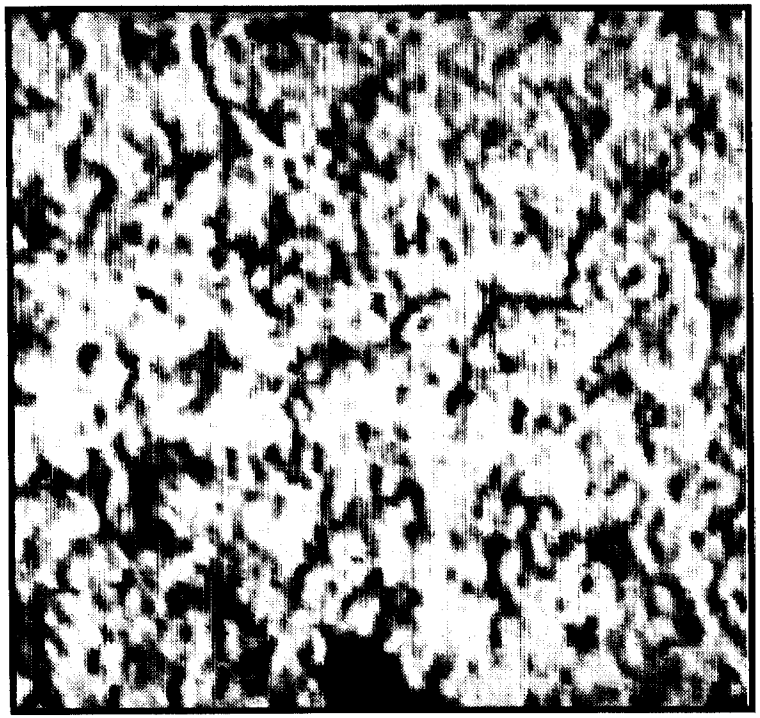

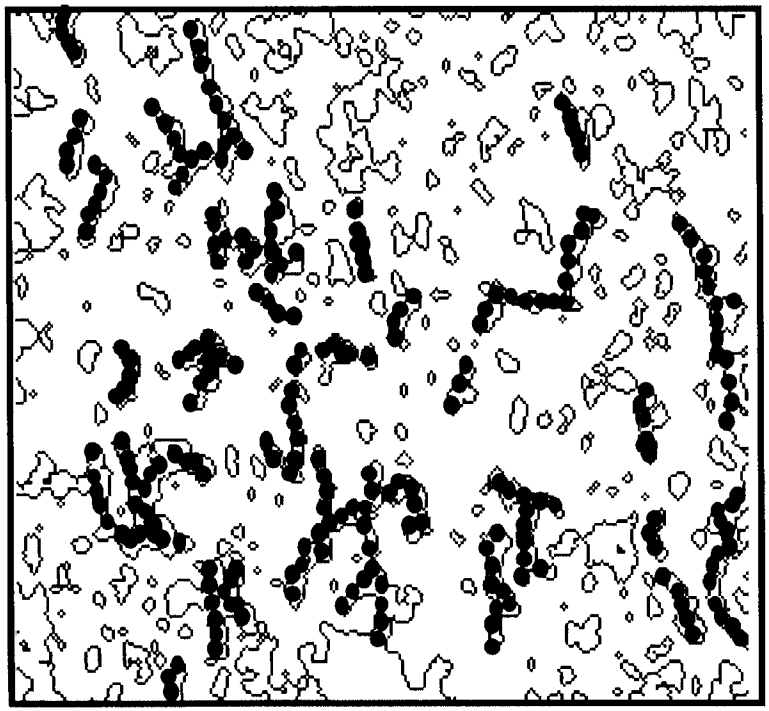

Filamentary aggregates from dense grain cloud in USML-2 Glovebox. Angular grains of 400 micron diameter quartz

Dipoles in Modeling

- 3-D computer modeling produced same results as USML experiments
- Grains "dispersed" with fixed surface charges, randomly distributed. Each charge just a monopole with corresponding Coulombic force
- No dipoles or D/M ratio artifically embedded in the code
- Chain aggregates always produced, implicating dipoles

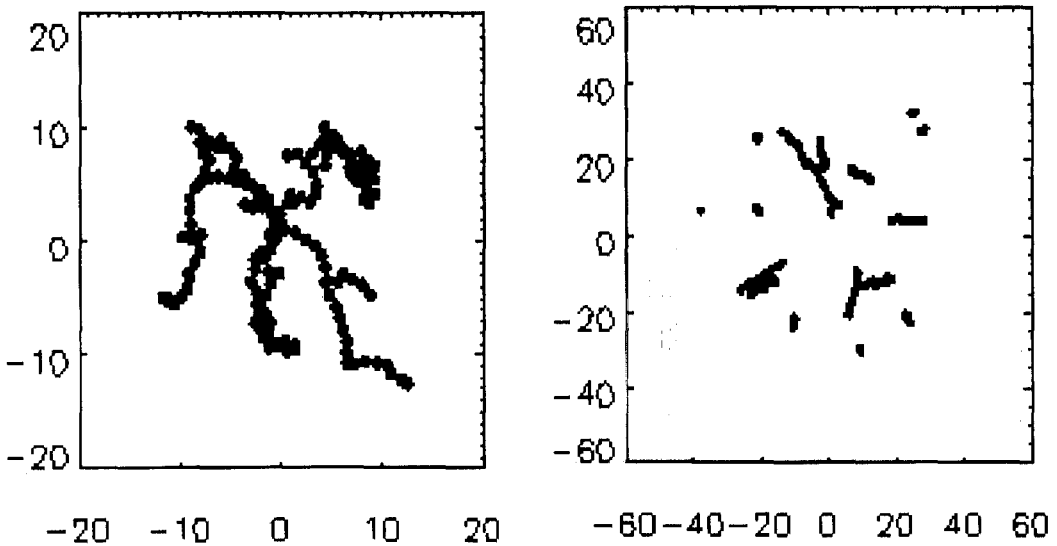

Left: Aggregate from cloud collapse ("neutral" charge-balanced grains with dipoles)

Right: Aggregates (formed by dipole interactions) being dispersed by monopole forces (cloud net charge). Units = grain diam.

Coulombic "Event Horizon"

Interaction of a grain with other grains or with surfaces is function of dipole to monopole (net charge) relationship, and distance between grains and surfaces. Need both D and M

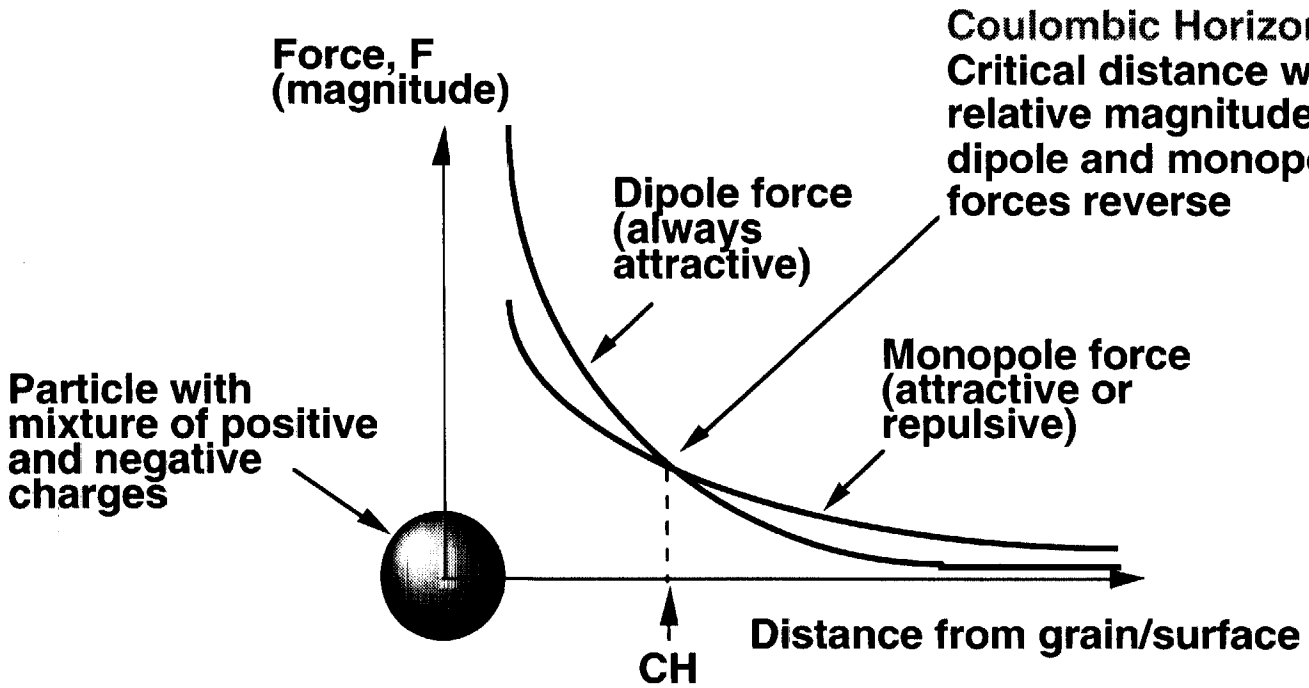

CH can be orders of magnitude larger than grain itself

Experiment Concept

E-Field Manipulation of Suspended Sand Grains

Module Characteristics

IFU

- Inhomogeneous radial (2D) field lines
- Dipoles only move to center. Monopoles can move in or out

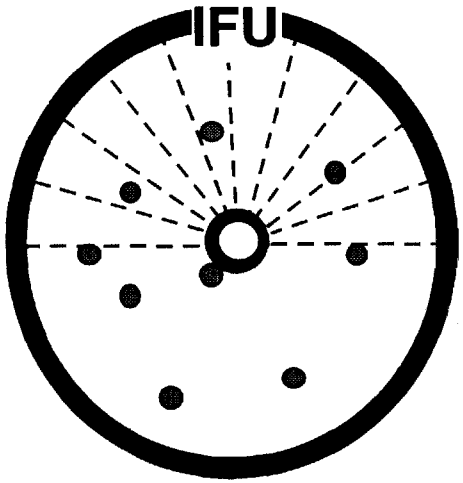

HFU

- Homogeneous parallel field lines
- Both aggregates and single grains studied
- Dipoles cannot move in either direction. Monopoles can move both ways

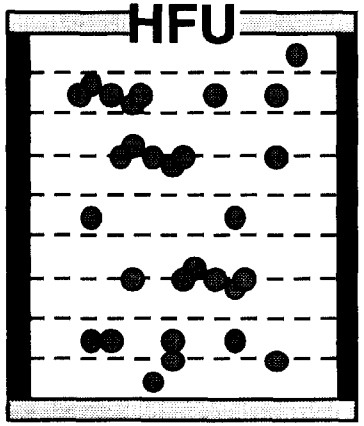

Prime Measurements & Function

- Radial speed indicates D and M
- Event horizon (r) gives D/M ratio
- Forces expressed:
  Dipole
  Monopole
  Induced polarization

- Drift speed of grains & aggregates indicates monopole
- Torque/alignment on aggregates indicates cluster dipole
- Long range forces expressed:
  Monopole

Experiment Description

Preliminary Engineering Concept for the IFU

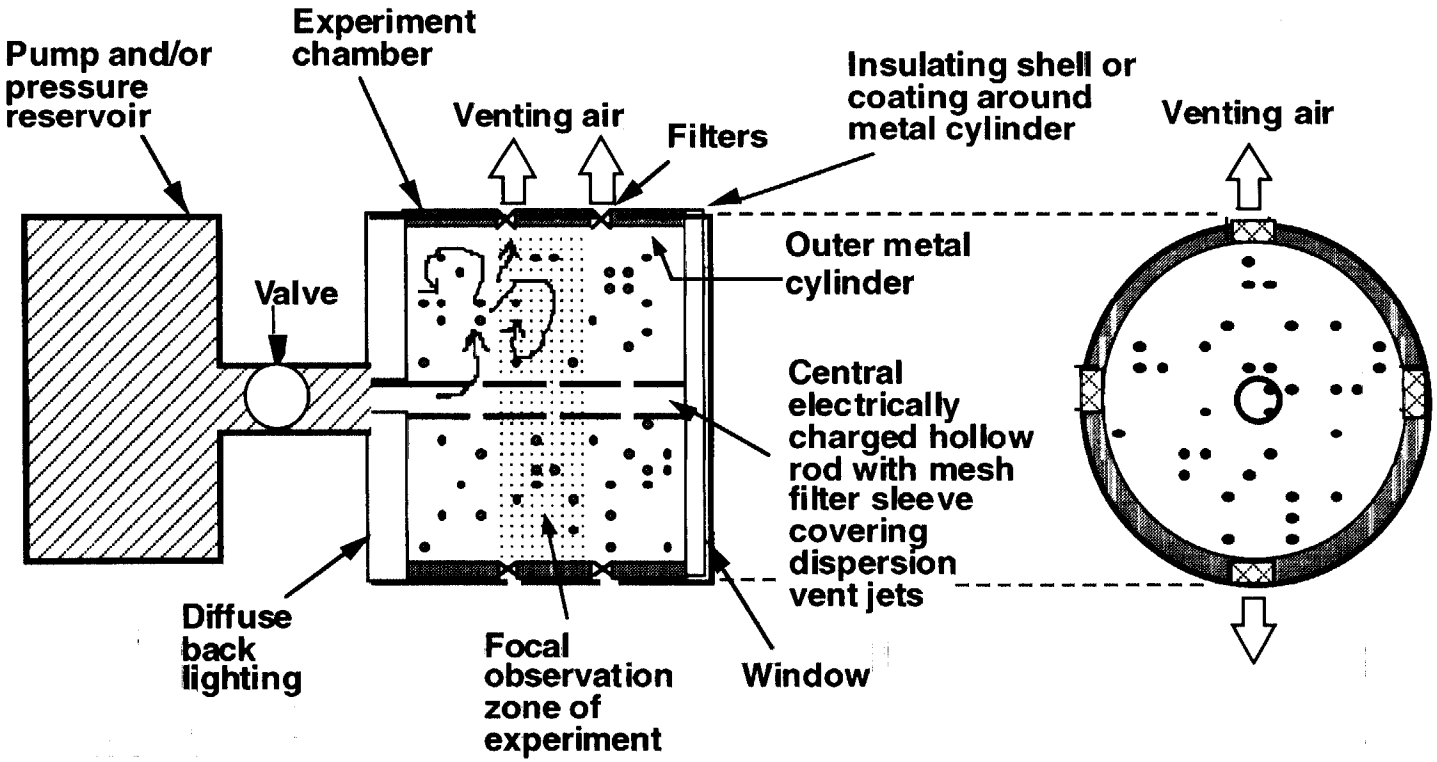

IFU: Grain Interrogation

Method I: Fixed-Polarity Field ---------- Data Acquisition

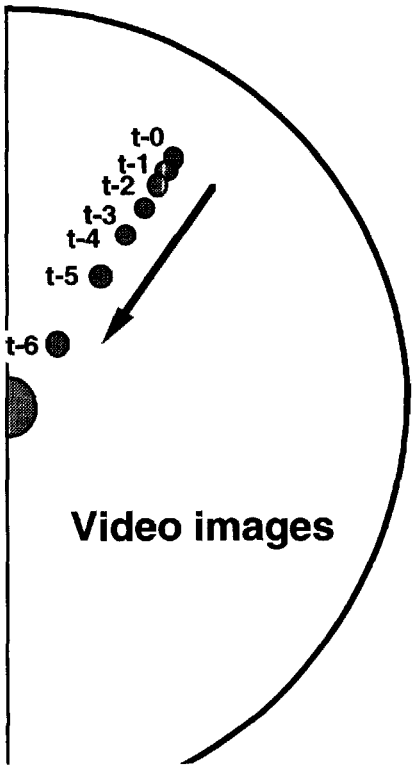

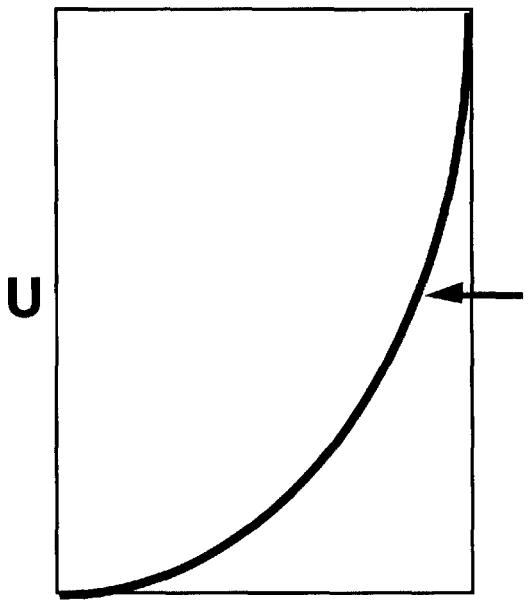

Shape of curve reflects acceleration contributions from: monopole and dipole forces

$1/r$ and $1/r^2$ components

Grain with a dipole rotates dipole axis in alignment with field and is pulled inward. Net charge on grain adds increase or decrease of speed, depending on sign. Depending on distance, net charge can cause drift away from center, but at close range, dipole can override net charge

IFU: Grain Interrogation

Method II: Alternating-Polarity Field --- Data Acquisition For Direct D/M Ratio

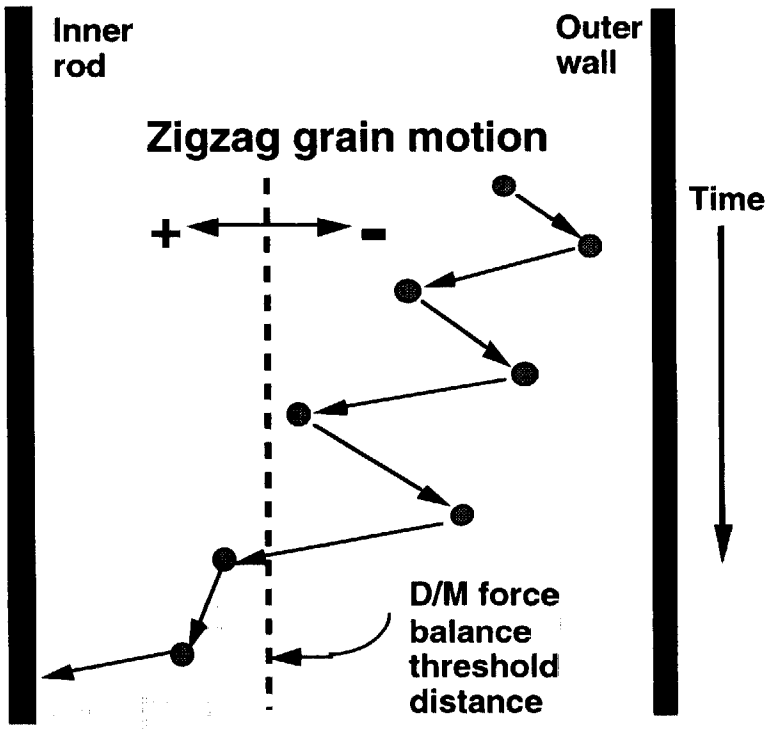

Video images

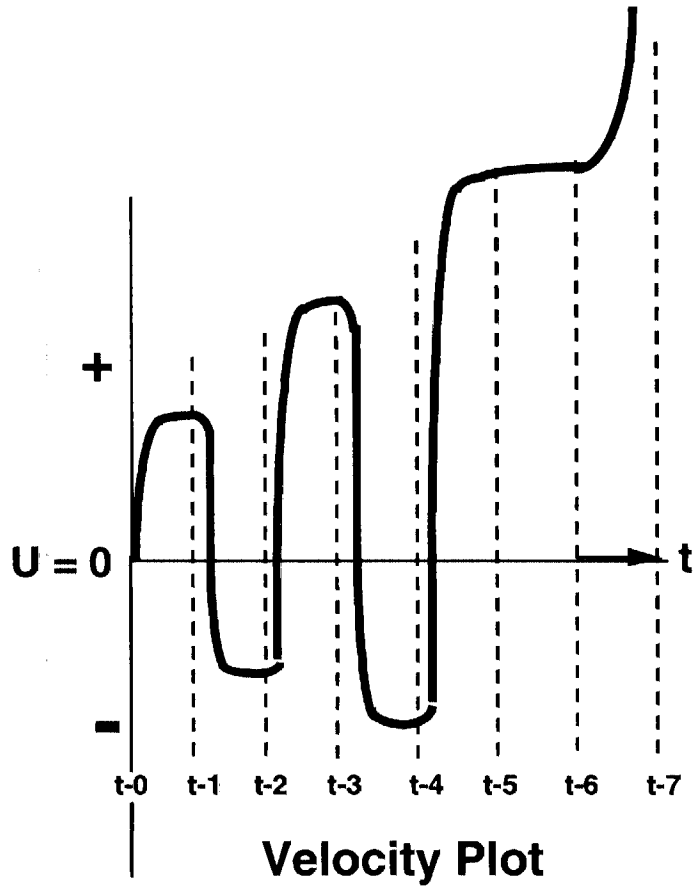

Velocity Plot

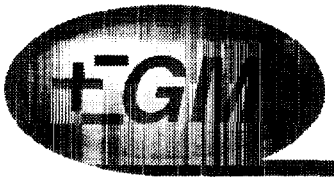

IFU: Grain Interrogation

Definition of the D/M ratio

At the event horizon, where Fd and Fm are equal, and the grain is about to enter the "always attractive" zone, it follows that:

$$-M\ k\ V/r + D\ k\ V/r^2 = 0$$

This solves to: $r = D/M$

Thus, the event horizon for a grain is the grain's D/M ratio, by definition, measured in units of length, r

Example Data Product

Scenarios For IFU Population Statistics

Possible D/M Population Statistics for Methods I & II. (Data Sets Directly Comparable in Units of 'r')

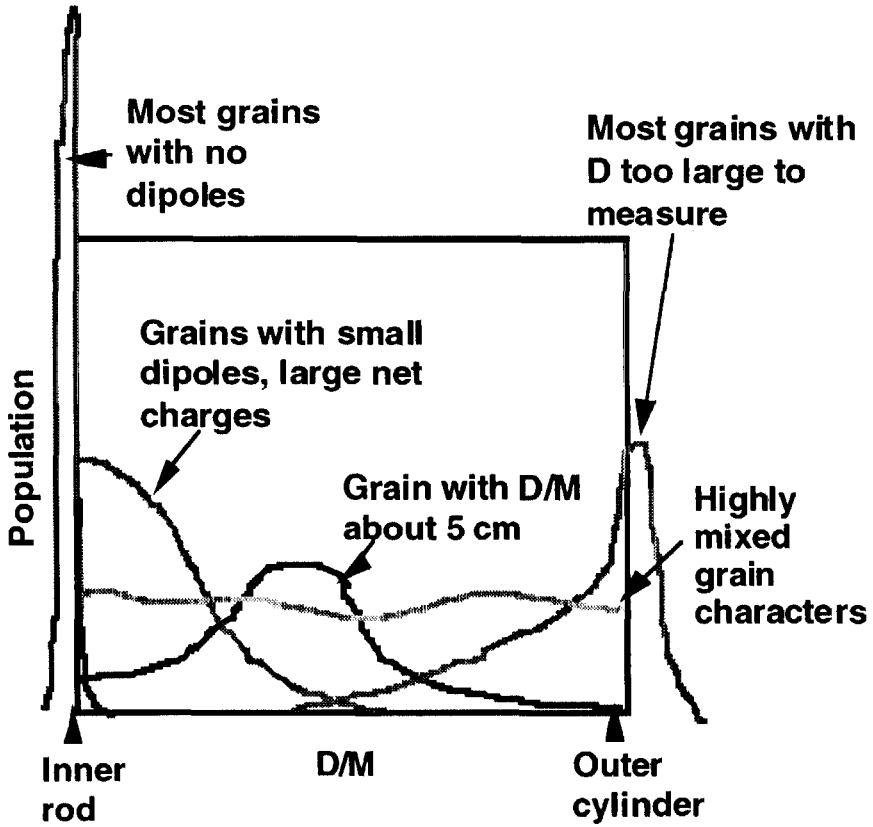

Possible D and M Population Statistics from Method I

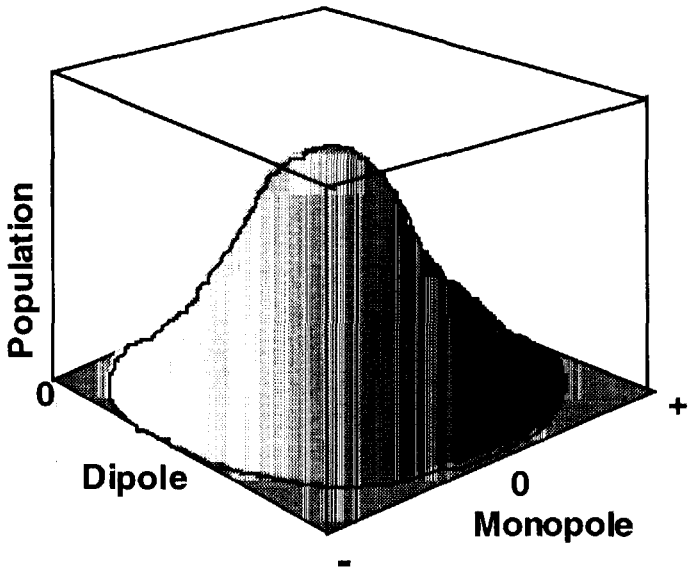

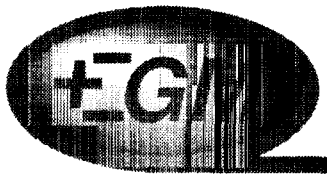

Verification of Hypothesis

- **Measurable values of D in IFU Method I:**
  Proof of dipoles (of magnitude affecting cloud behavior)

- **Measurable D/M ratios in IFU Method II:**
  Proof of dipoles
  Proof of charge mixing on single grains if D/M >grain diameter

- **D/M values too large to measure by IFU Method II:**
  Proves dipoles and that even greater than expected

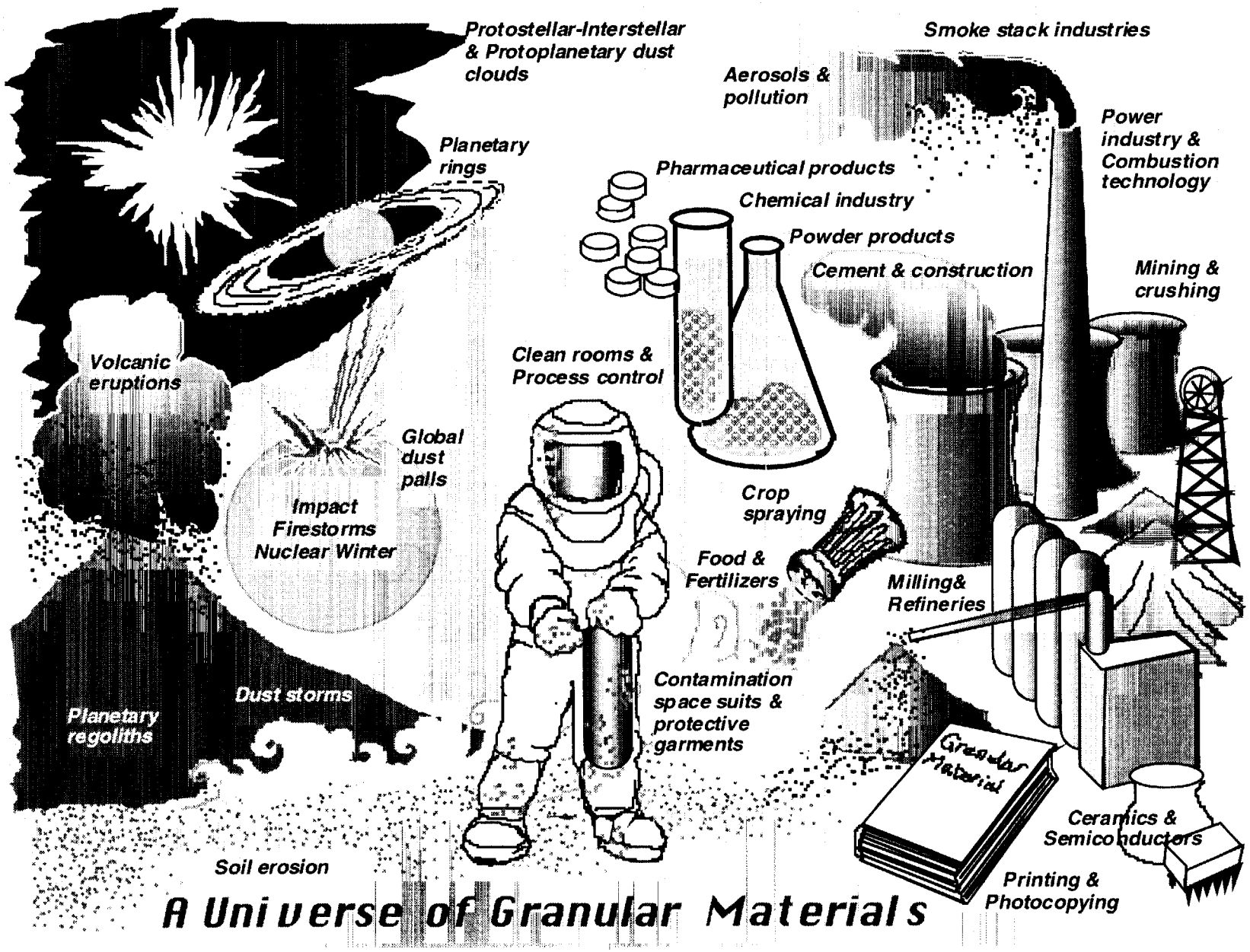
Protostellar-Interstellar & Protoplanetary dust clouds
Smoke stack industries
Aerosols & pollution
Planetary rings
Power industry & Combustion technology
Pharmaceutical products
Chemical industry
Powder products
Cement & construction
Mining & crushing
Volcanic eruptions
Clean rooms & Process control
Global dust palls
Impact Firestorms Nuclear Winter
Crop spraying
Food & Fertilizers
Milling& Refineries
Contamination space suits & protective garments
Dust storms
Planetary regoliths
Granular Material
Ceramics & Semiconductors
Soil erosion
Printing & Photocopying
A Universe of Granular Materials

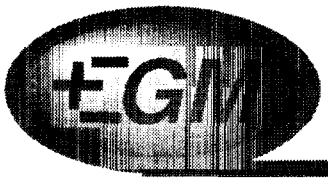

Benefits of Research

- Provides fundamental knowledge for electrostatics, granular materials, surface science. Concept of largely unrecognized adhesive/cohesive force

- Knowledge enables modeling of cloud behavior in protostellar and protoplanetary dust-debris systems, planetary rings, planetary dust palls and aerosols created by volcanic, impact, aeolian, firestorm, nuclear winter processes, and atmospheric pollution

- Data directly applicable to adhesion, cohesion, transport, dispersion, and collection of granular materials in industrial, agricultural, pharmaceutical applications, and in fields as diverse as dust contamination of space suits on Mars and crop spraying on Earth

ASSESSMENT OF CONSTITUTIVE AND STABILITY BEHAVIOR OF SANDS UNDER PLANE STRAIN CONDITION

Khalid A. Alshibli[1] and Stein Sture[2]

[1]*Project Scientist, University of Alabama in Huntsville/ NASA Marshall Space Flight Center, Mail Code SD48, Huntsville, AL 35812, Tel. (256) 544-3051, Fax (256) 544-8029, Email: khalid.alshibli@msfc.nasa.gov.*

[2]*Principal Investigator, Dep. of Civil, Environmental, & Architectural Engineering, Campus Box 428, University of Colorado at Boulder, Boulder, CO 80308-0428, Tel. (303) 492-7651, Email: sture@grieg.colorado.edu.*

ABSTRACT: A series of biaxial (plane strain) experiments were conducted on three sands under low (15 kPa) and high (100 kPa) confining pressure conditions to investigate the effects of specimen density, confining pressure, and sand grains size and shape on the constitutive and stability behavior of granular materials. The three sands used in the experiments were fine, medium, and coarse-grained uniform silica sands with rounded, sub-angular, and angular grains, respectively. Specimen deformation was readily monitored and analyzed with the help of a grid pattern imprinted on the latex membrane. The overall stress-strain behavior is strongly dependent on the specimen density, confining pressure, sand grain texture, and the resulting failure mode(s). That became evident in different degrees of softening responses at various axial strains. The relationship between the constitutive behavior and the specimens' modes of instability is presented. The failure in all specimens was characterized by two distinct and opposite shear bands. It was found that the measured dilatancy angles increase as the sand grains' angularity and size increase. The measured shear band inclination angles are also presented and compared with classical Coulomb and Roscoe solutions.

NASA/CP—2000-210470

Assessment of Constitutive and Stability Behavior of Sands Under Plane Strain Condition

Khalid Alshibli* and Stein Sture†

* Research Assistant Professor and MGM Project Scientist, University of Alabama in Huntsville

† Professor and MGM PI, University of Colorado at Boulder, CO

Presentation Outline

- Introduction
- Plane Strain (PS) experiments:
  - Sand particles properties
  - Specimen density
  - Confining pressure
- Conventional Triaxial Compression (CTC) experiments

Plane Strain versus Conventional Triaxial Compression Experiments

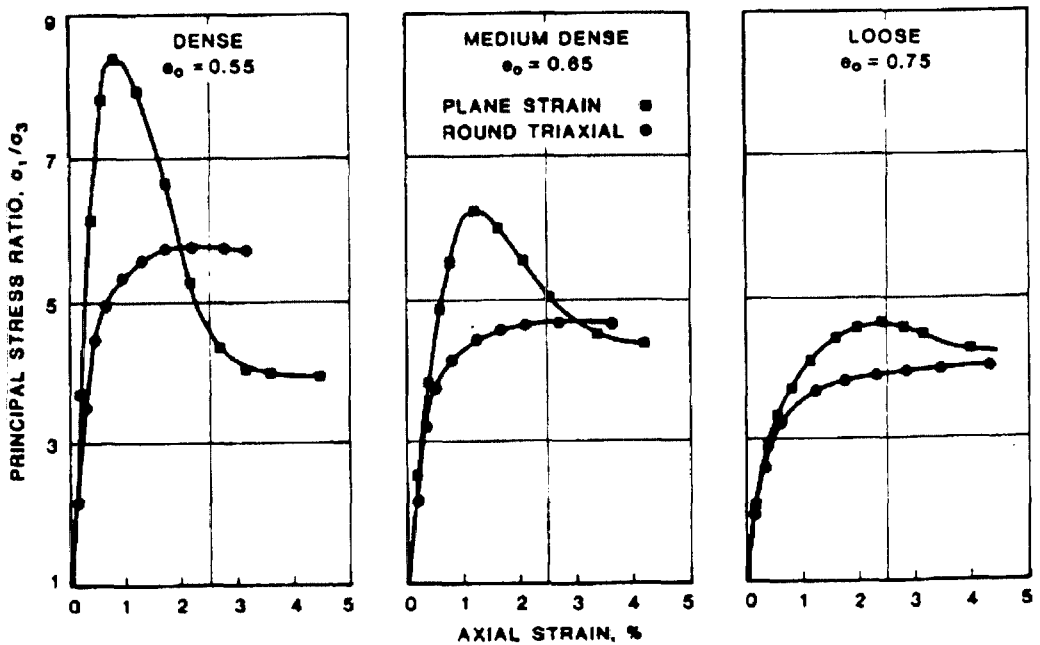

Stress-strain relations for plane strain and triaxial experiments (*After* Marachi *et al. 1988)*

Deformation Modes in Soils

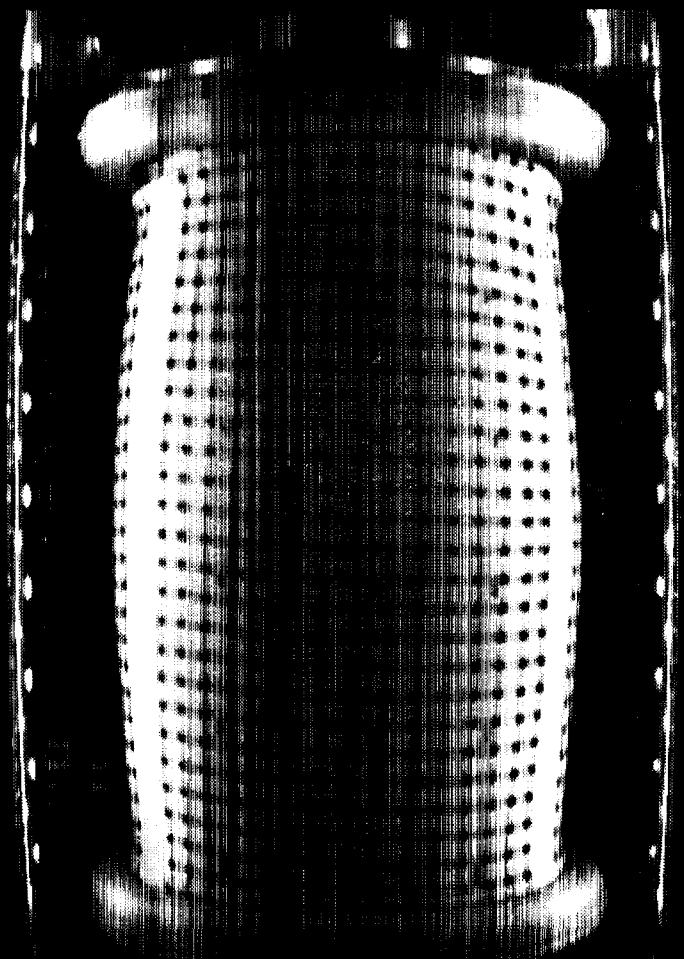

CTC Specimen

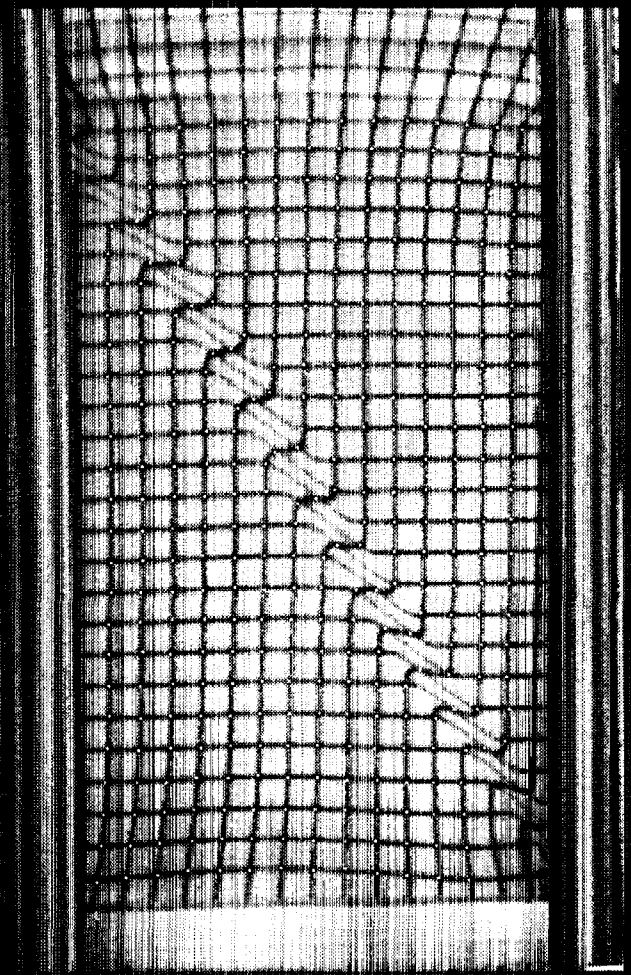

PS Specimen

Specimen Preparation by Air Pluviation

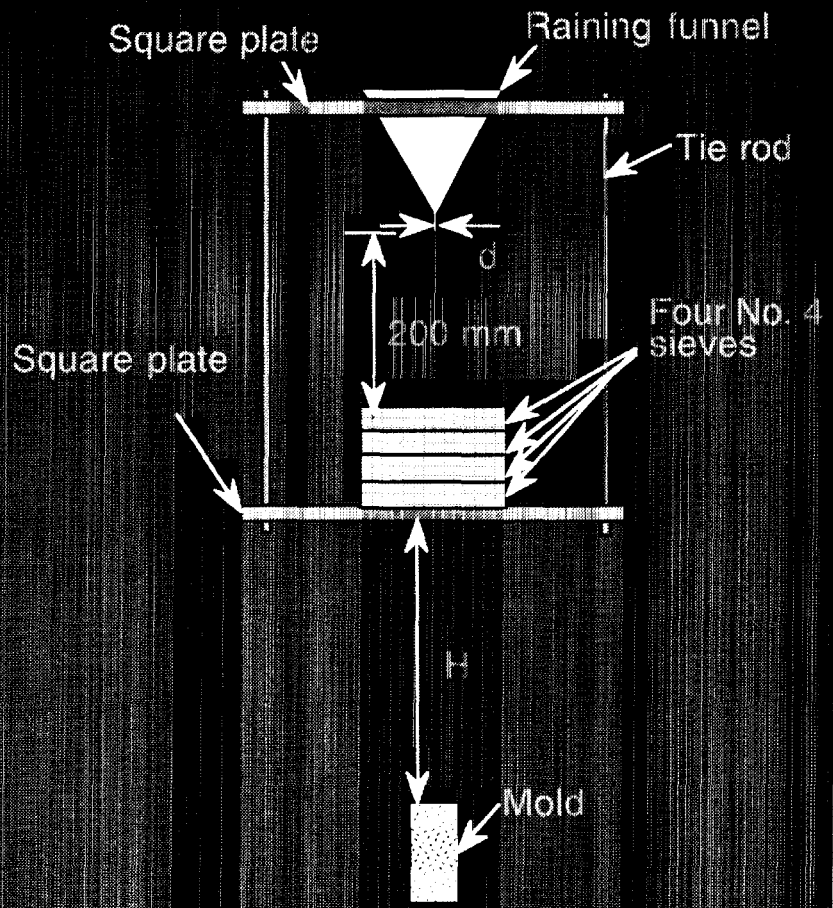

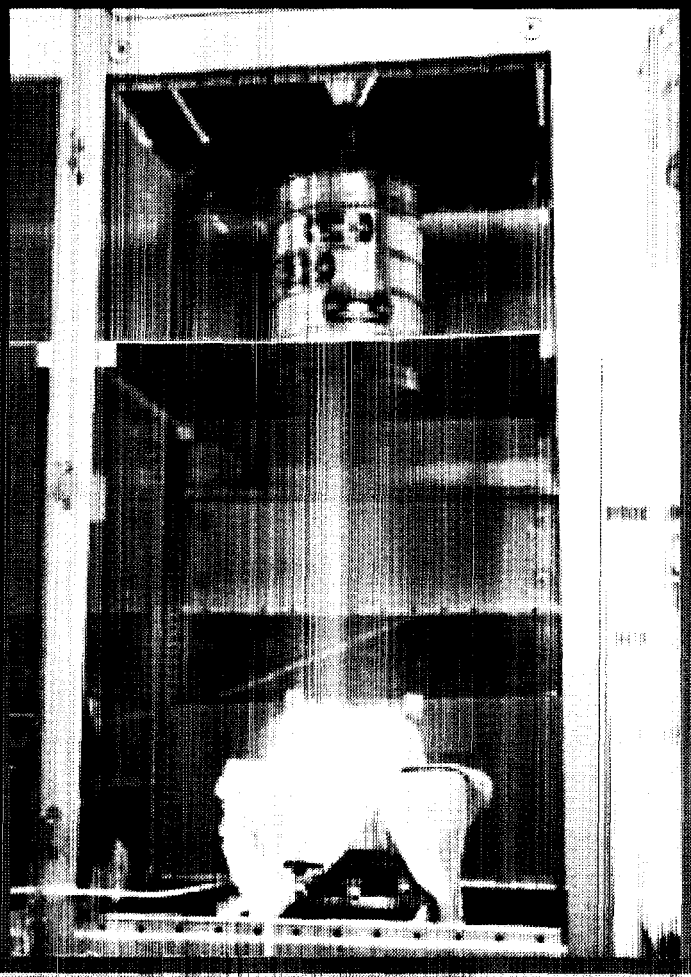

Plane Strain Experiments Investigation Parameters

- Sand Type:
  - Fine-grained (F-sand)
  - Medium-grained (M-sand)
  - Coarse-grained (C-sand)
  - Particles surface texture: rounded, sub-angular, and angular
- Specimen Density:
  - Loose (D_r = 40-50%)
  - Dense (D_r = 88-98%)
- Confining Pressure: Low (15 kPa), High (100 kPa)

Properties of Sands Used in the Plane Strain Experiments

- F-75 Sand (Ottawa sand):
  - d_{50} = 0.22 mm
  - Rounded particles
- M-Sand:
  - d_{50} = 0.55 mm
  - Sub-angular particles
- C-Sand
  - d_{50} = 1.66 mm
  - Angular particles

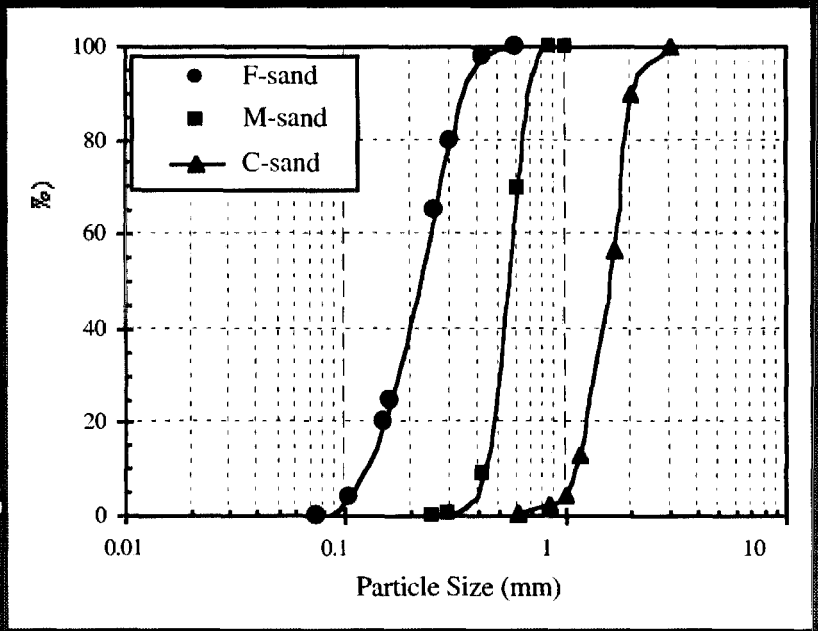

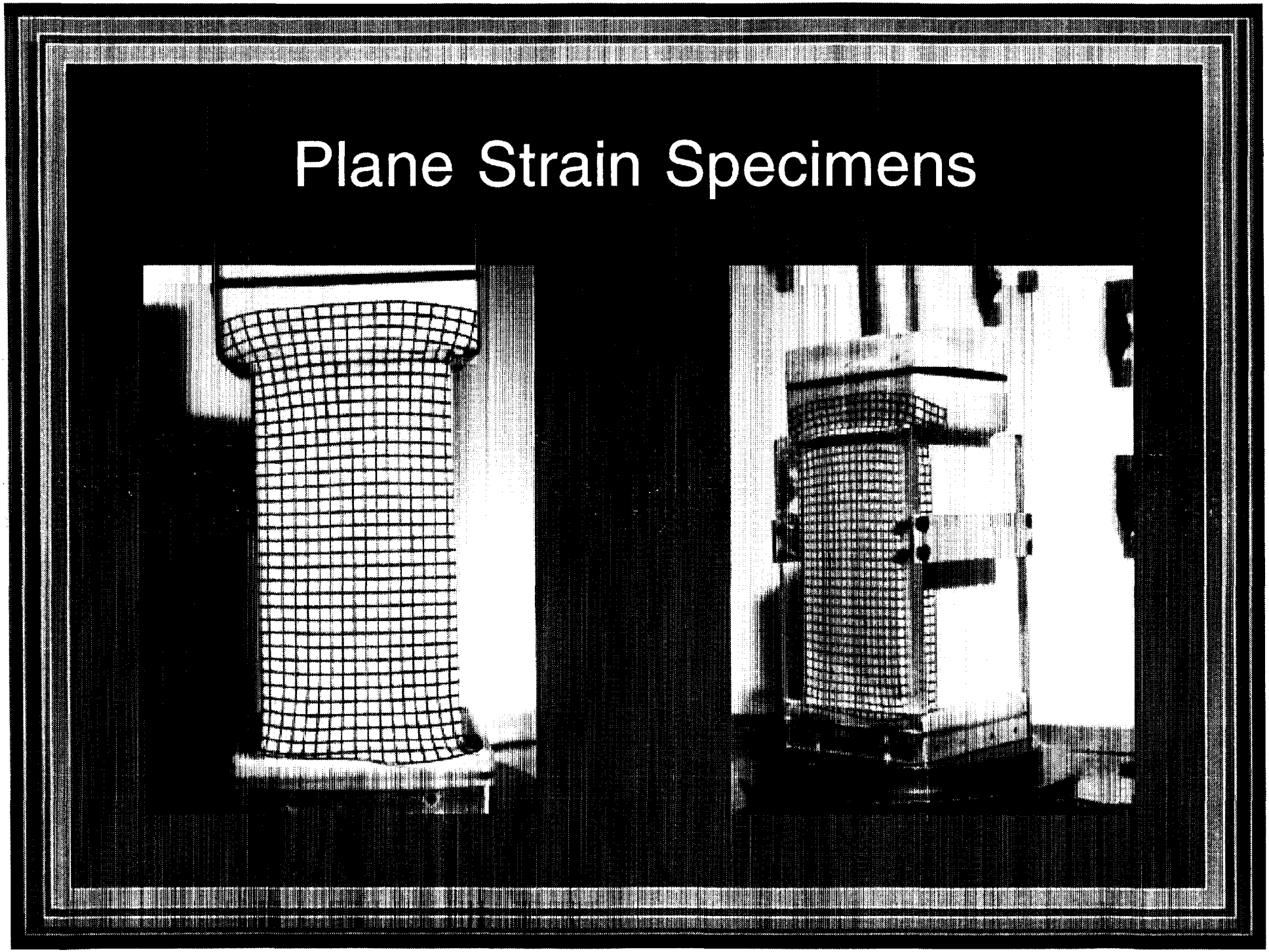
Plane Strain Specimens

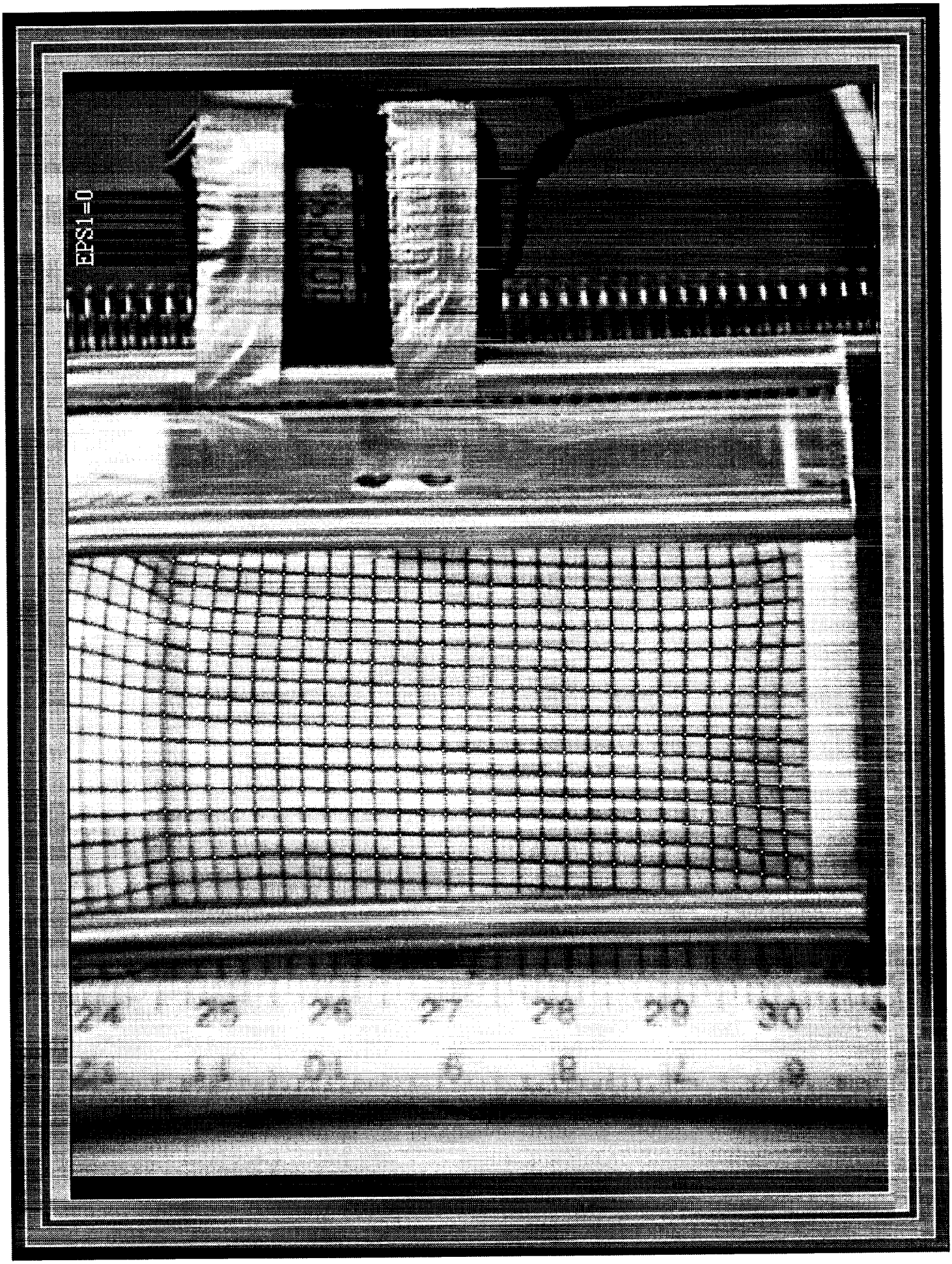
EPSI=0
24
25
26
27
28
29
30

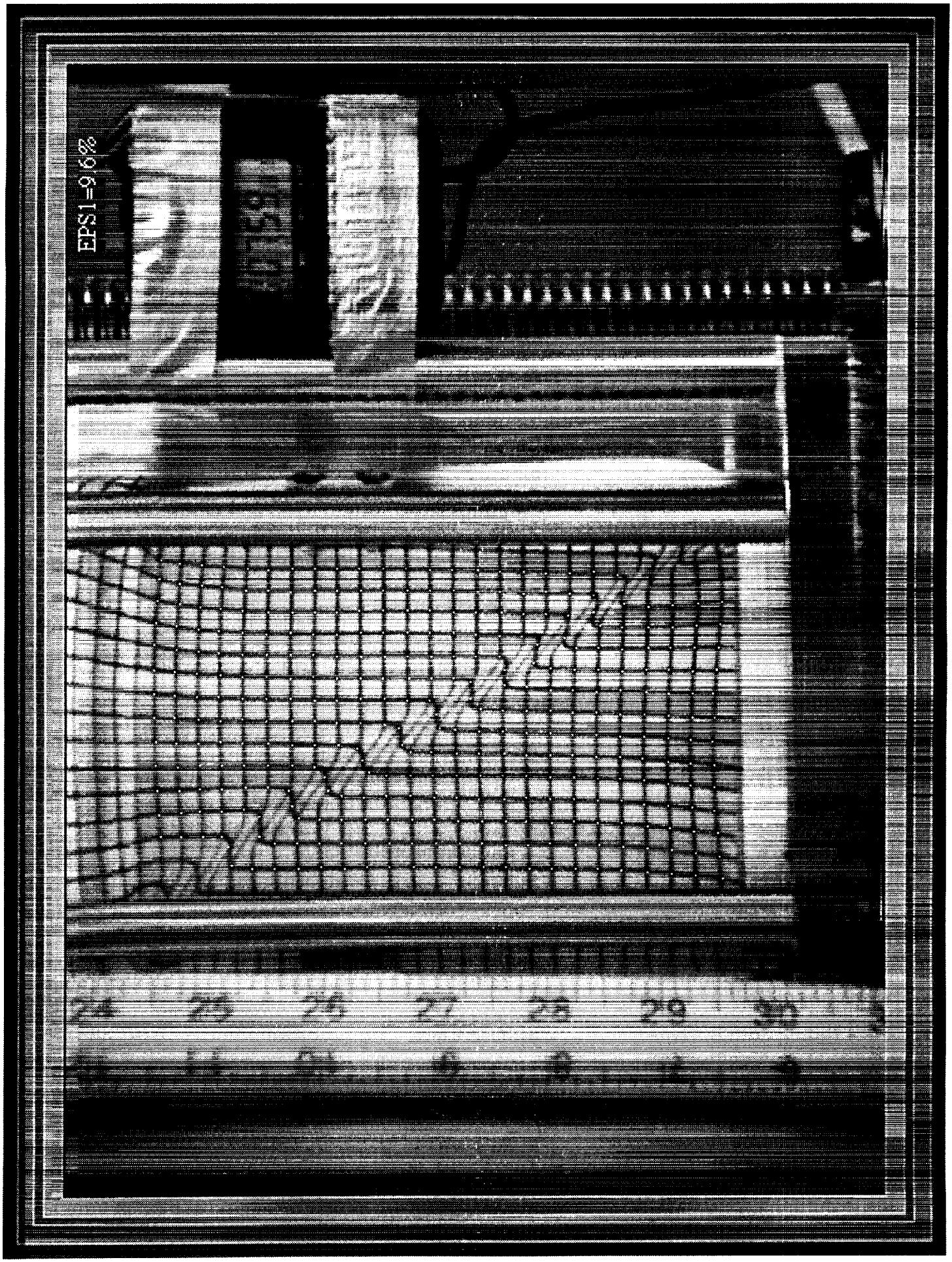
EPS1=9 6%

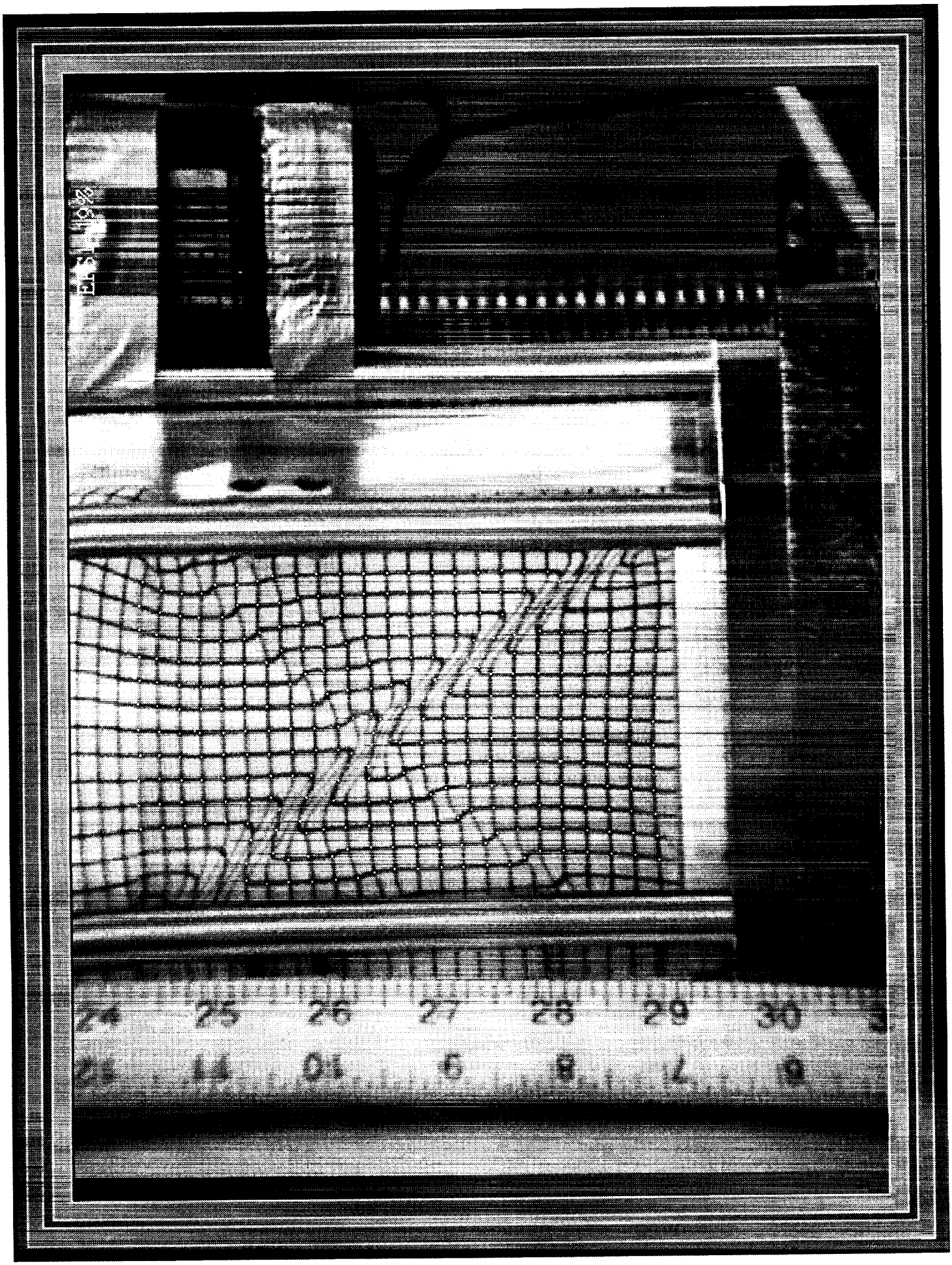

Shear Band Thickness Measurement

Specimens' Stabilization & Thin Sectioning

- A low viscosity epoxy (viscosity = 0.020 poise) was used to stabilize the specimens.
- Specimens were cut into thin sections.
- Back-scatter electron microscope was used to collect images for fabric analysis.

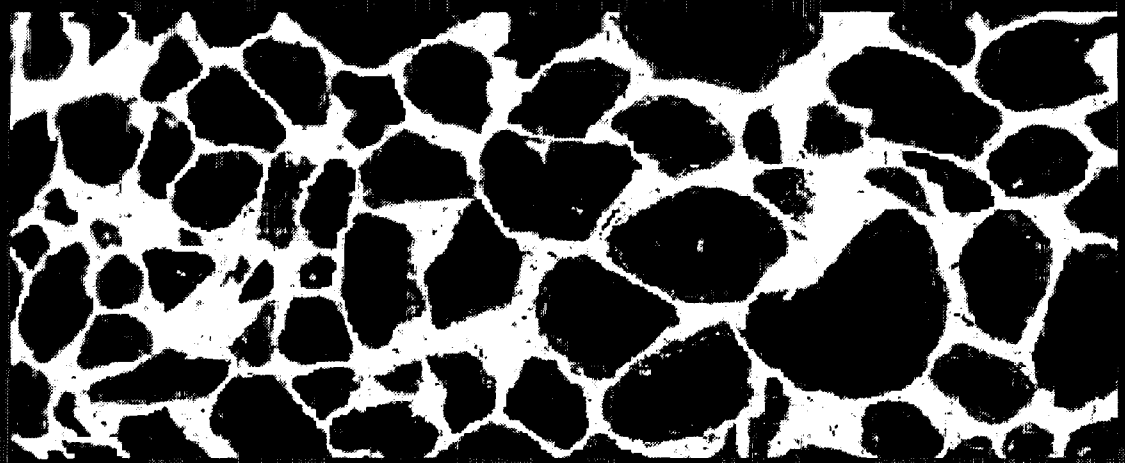

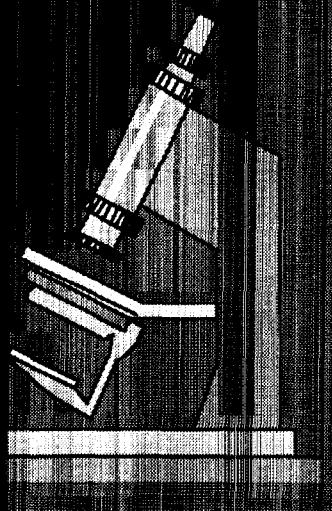

F-75 Sand Specimens (PS Exp.)

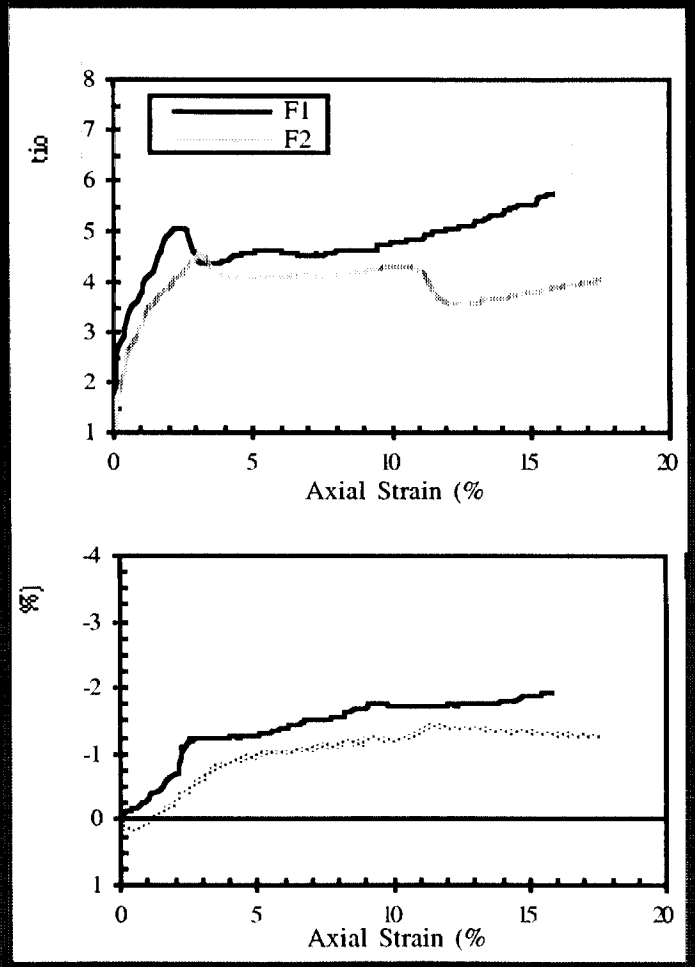

Loose Specimens

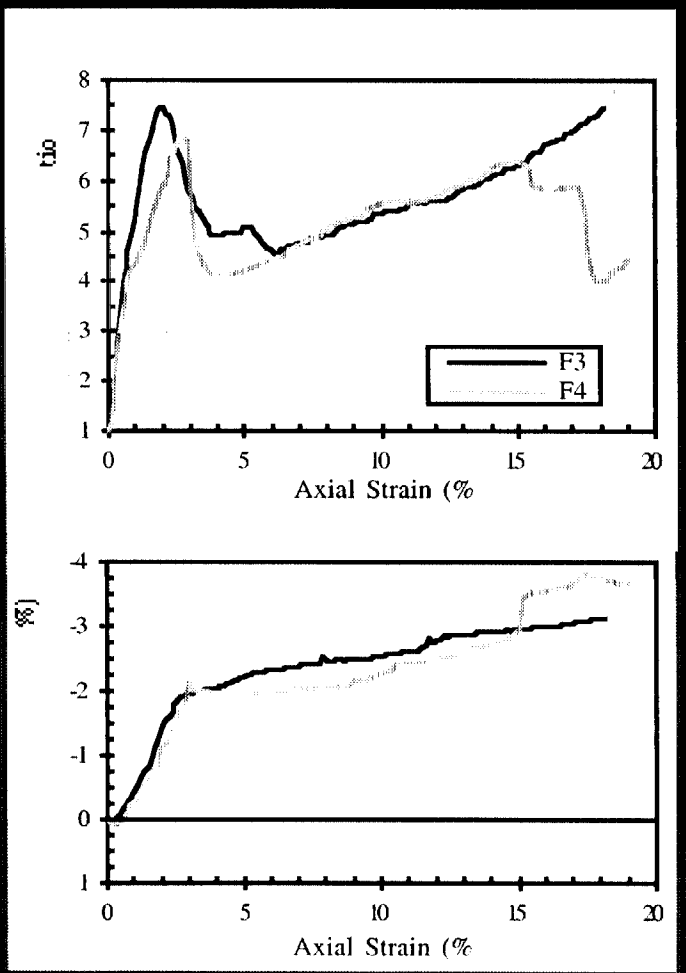

Dense Specimens

M- and C-sand Specimens (PS Exp.)

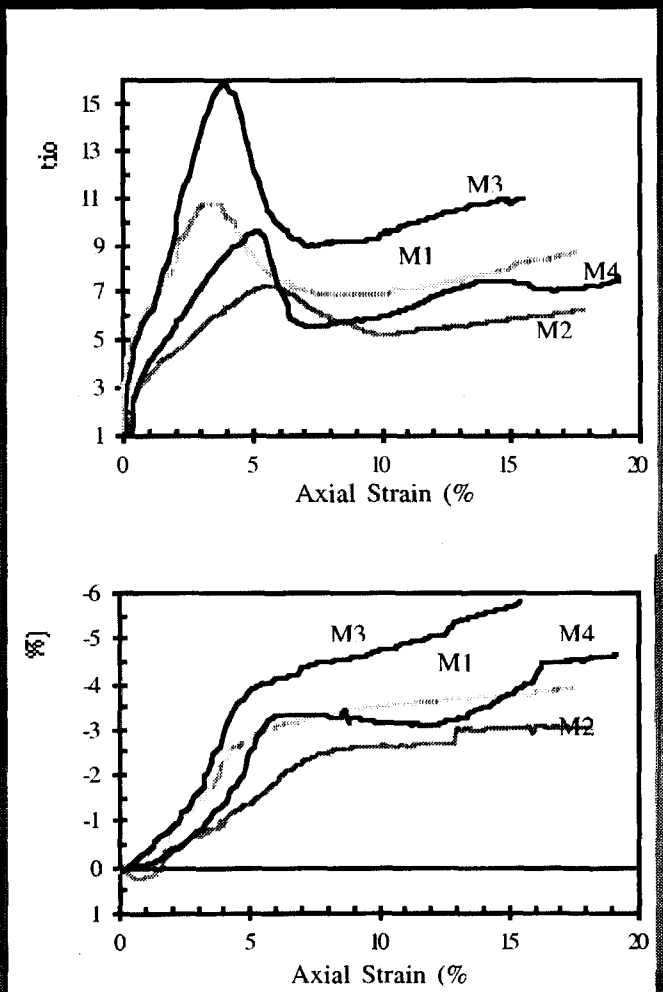

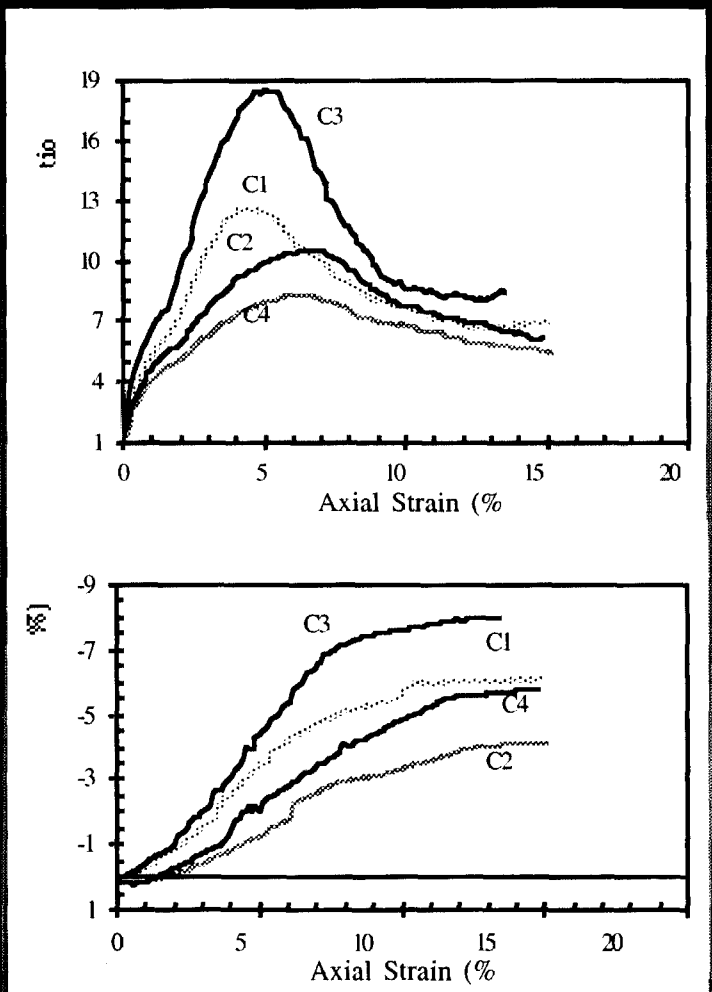

Effects of specimen density and sand type on shear band inclination angle

Confining Pressure = 15 kPa

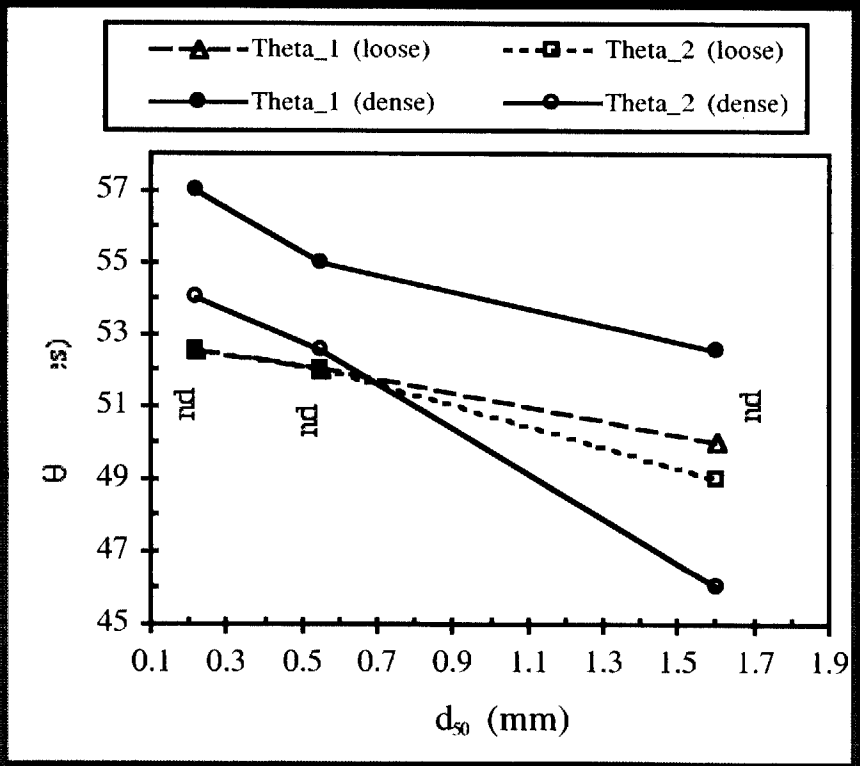

Confining Pressure = 100 kPa

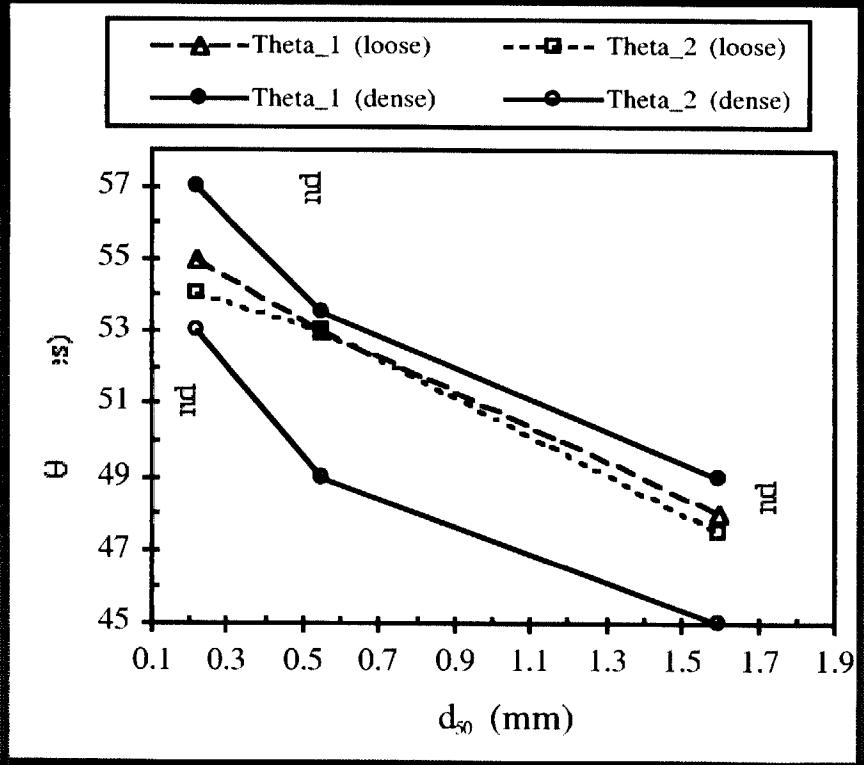

Effects of specimen density and sand type on shear band thickness

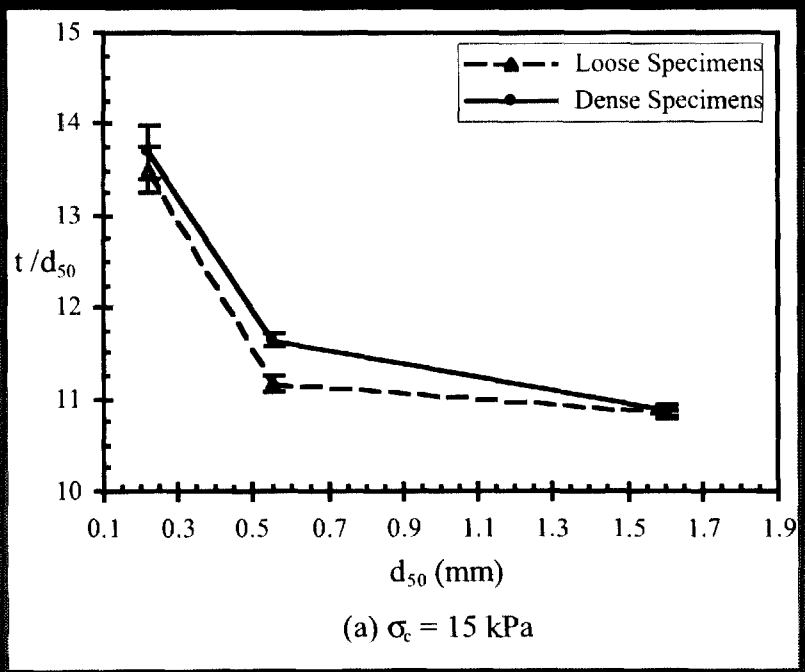

(a) σ_c = 15 kPa

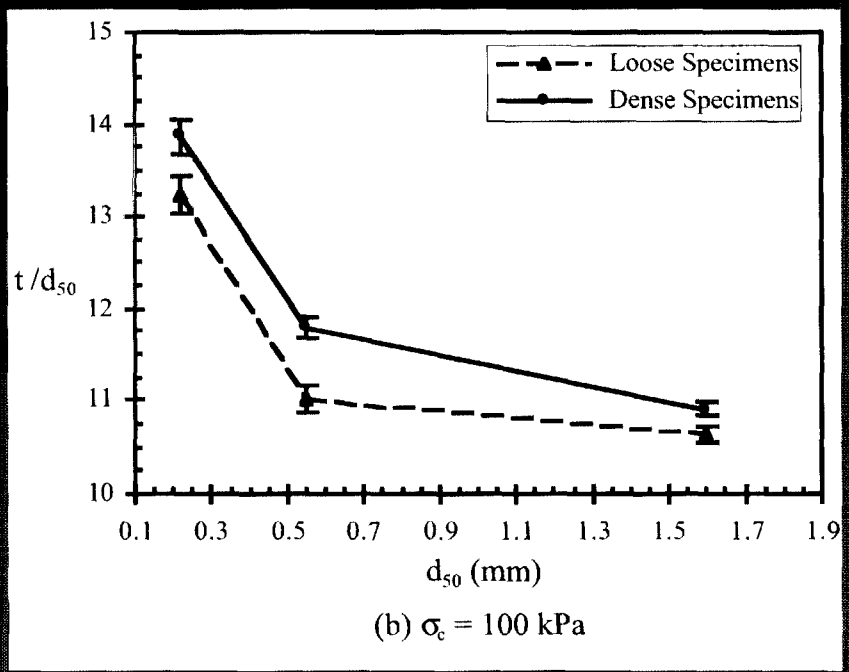

(b) σ_c = 100 kPa

Summary of PS Experiments

- The overall stress-strain response is strongly dependent on specimen density, confining pressure, and sand grain texture.
- For the Fine sand:
  - The confining pressure is the main factor affecting the specimens' stability.
  - The instability was triggered sooner for specimens tested under low confining pressure compared to those tested under high confining pressure, regardless of specimen density.

Summary of PS Experiments

- For the M-sand:
  - The effect of specimen density on the failure pattern is more significant than for the F-sand.
- For the C-sand:
  - There is only one peak in the principal stress ratio regardless of the specimen density and the confining pressure level.
- All specimens show dilative behavior.
- The dilatancy angles were observed to increase as the sand grain angularity increases.

Mechanics of Granular Materials (MGM) Experiments

- A series of Conventional triaxial Compression experiments were performed on Ottawa sand specimens in μg aboard the Space Shuttle during the STS-79 and STS-89 missions.
- Specimens were tested under very low confining pressure conditions (0.007, 0.075, and 0.189 psi).
- Preparation is underway to investigate the behavior of fully-saturated specimens (STS-107).

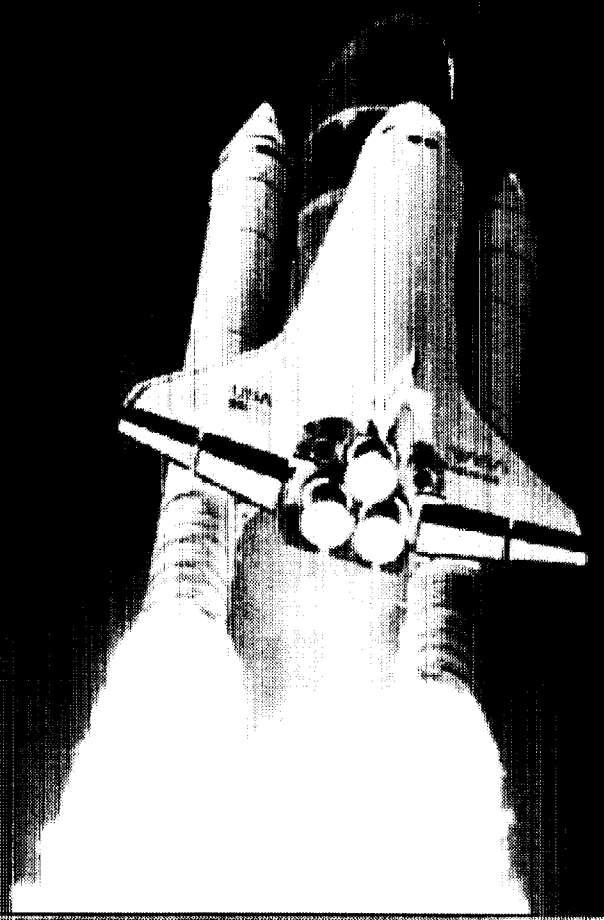

MGM Flight Experiments

Mission	σ_c (kPa)	Density	Loading Mode
F1 (STS-79)	0.05, 0.52, 1.30	Dense (D_r = 85%)	Quasi-static
F2 (STS-89)	0.05, 0.52, 1.30	Loose (D_r = 65%)	Quasi-static
F3 (STS-89)	0.05, 0.52, 1.30	Loose (D_r = 65%)	Cyclic

MGM Twin Double Locker Assembly

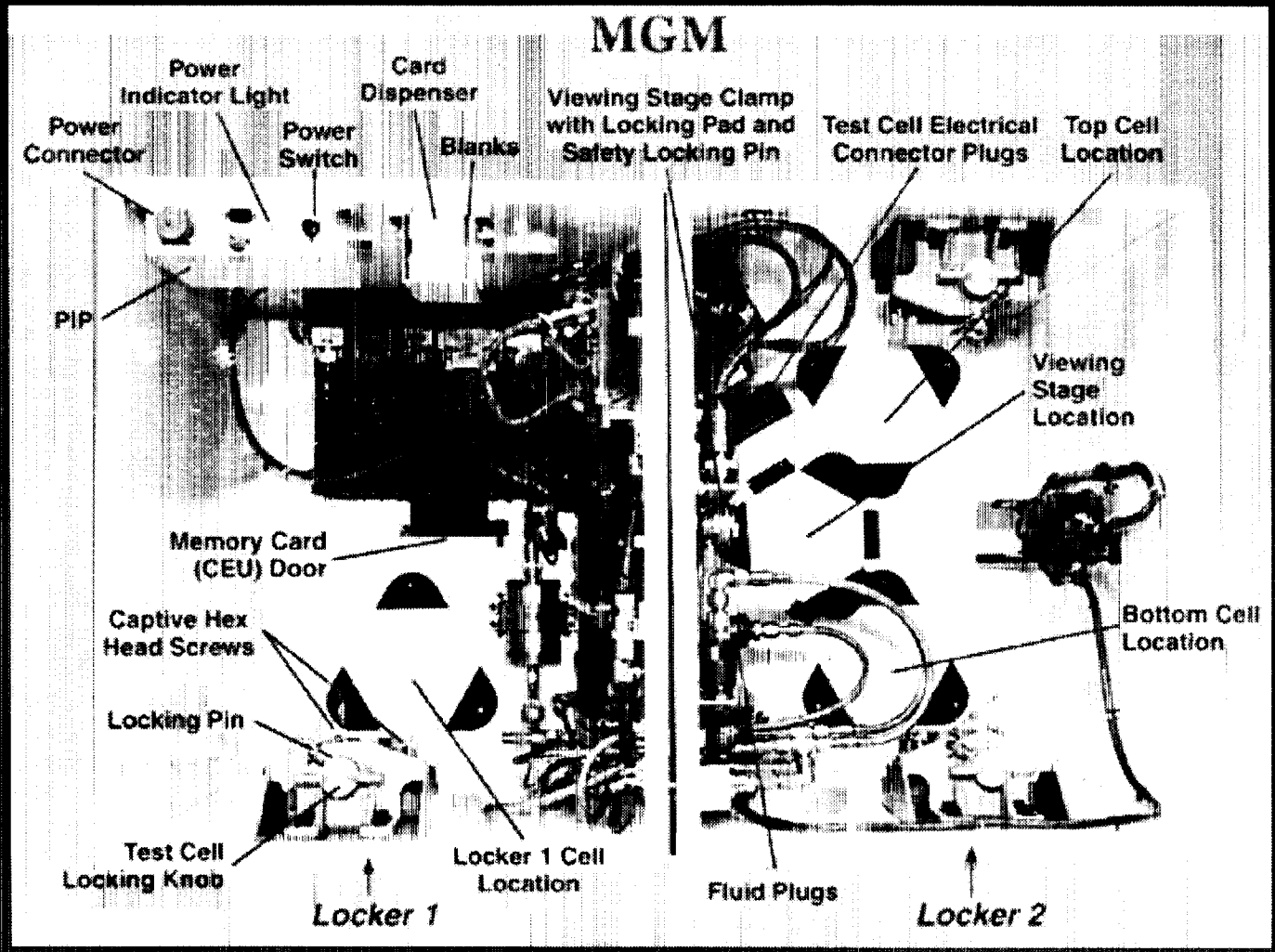

MGM Triaxial Test Cell

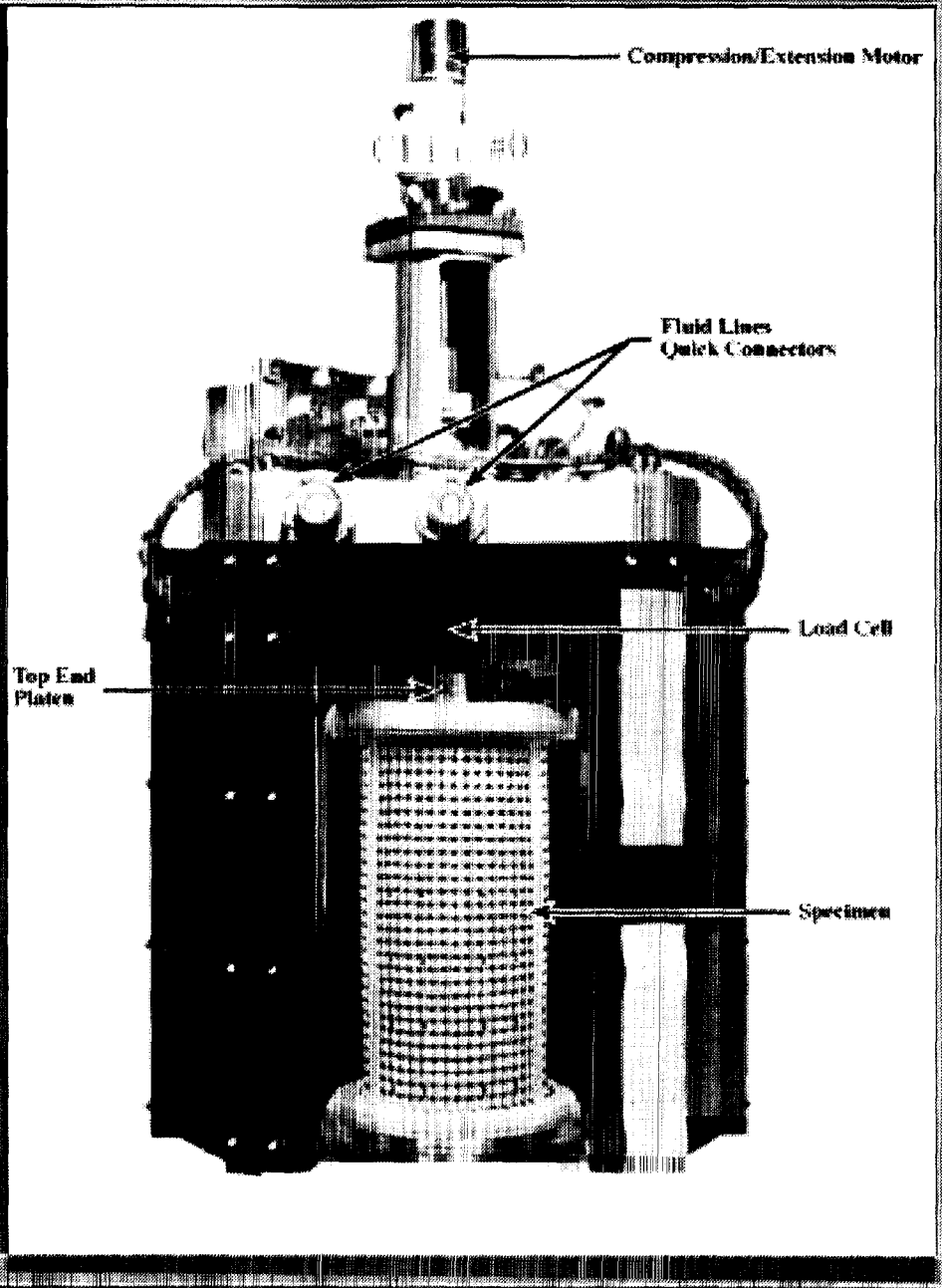

MGM specimen subjected to 25% axial strain

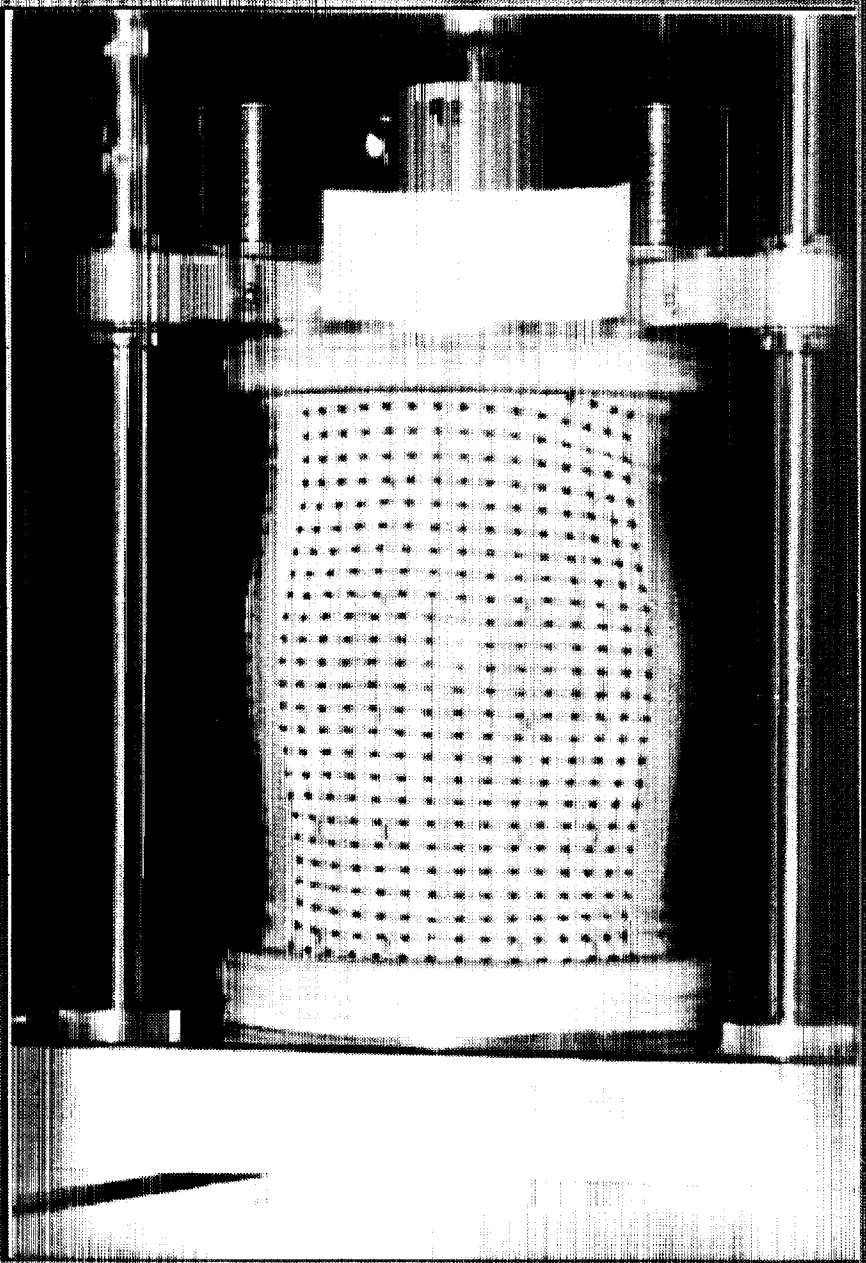

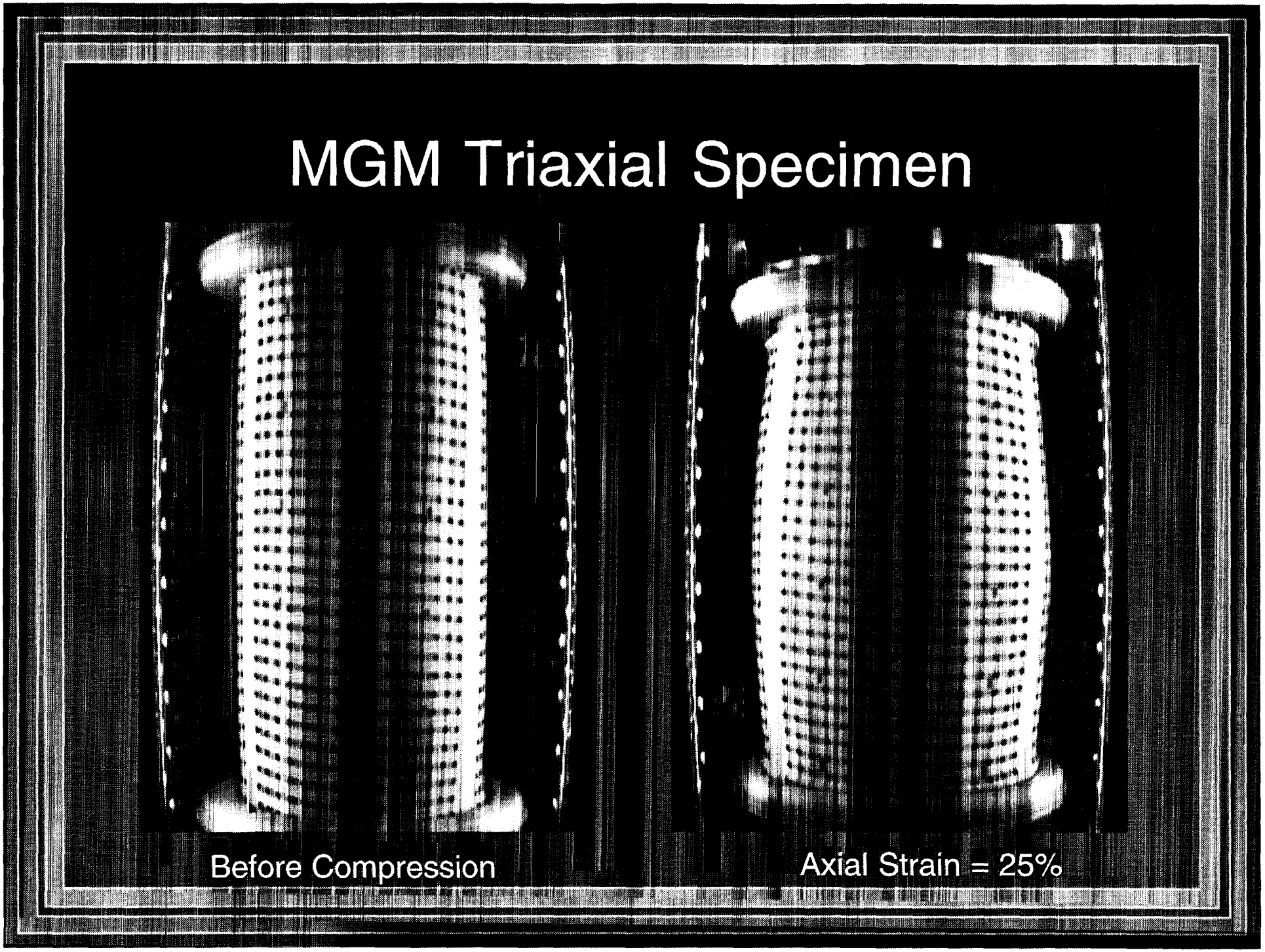
MGM Triaxial Specimen
Before Compression
Axial Strain = 25%

Stress-Strain Relations for Ottawa Sand (μg versus 1-g)

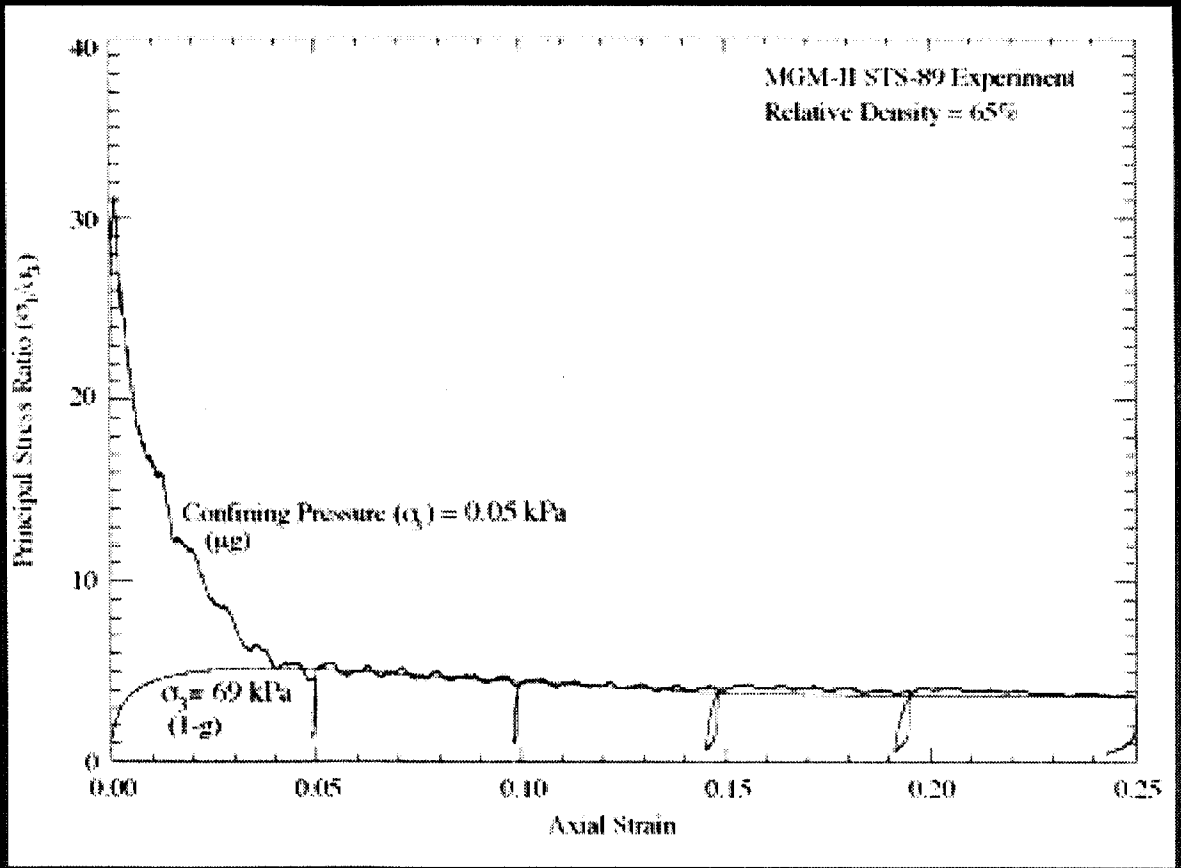

Stress-Strain Relations for Ottawa Sand (μg)

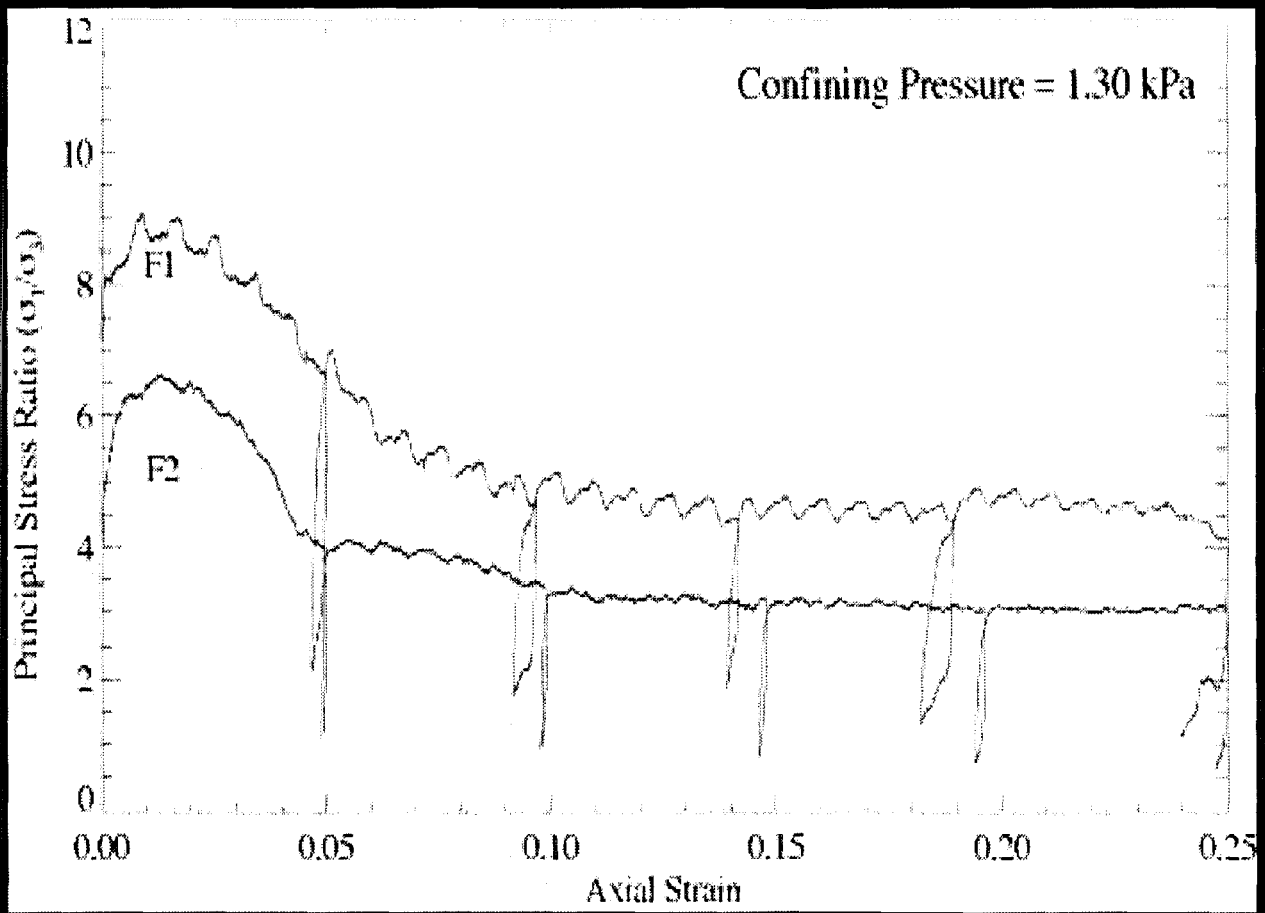

Volumetric Strain-Axial Strain for MGM Specimens (μg)

The specimens show continuous dilation (volume increase). There appears to be a significant departure from the initial and nearly linear volumetric expansion at the 4 to 5% axial strain level, where the rate of expansion seems to be reduced by a factor of almost five.

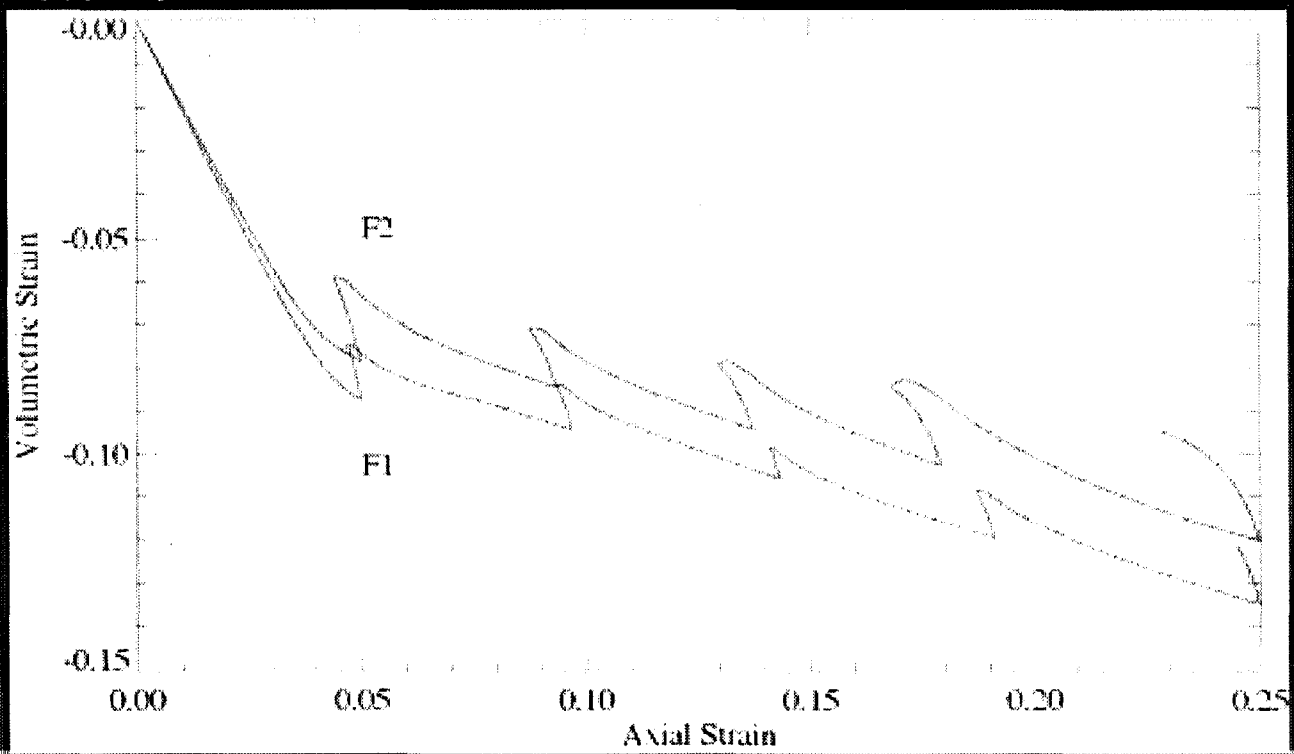

Friction and Dilatancy Angles of Ottawa Sand

- MGM microgravity data yields the first accurate experimental measurements of friction and dilatancy angles at very low effective stresses.
- High peak friction angles (μg: 48°-70° compared to 1-g: 42°-48°).
- Young's Modulus ≈12 - 24 MPa and constant as compression progresses (in 1-g: it decreases)
- Dilatancy angles are nearly twice that seen in 1-g

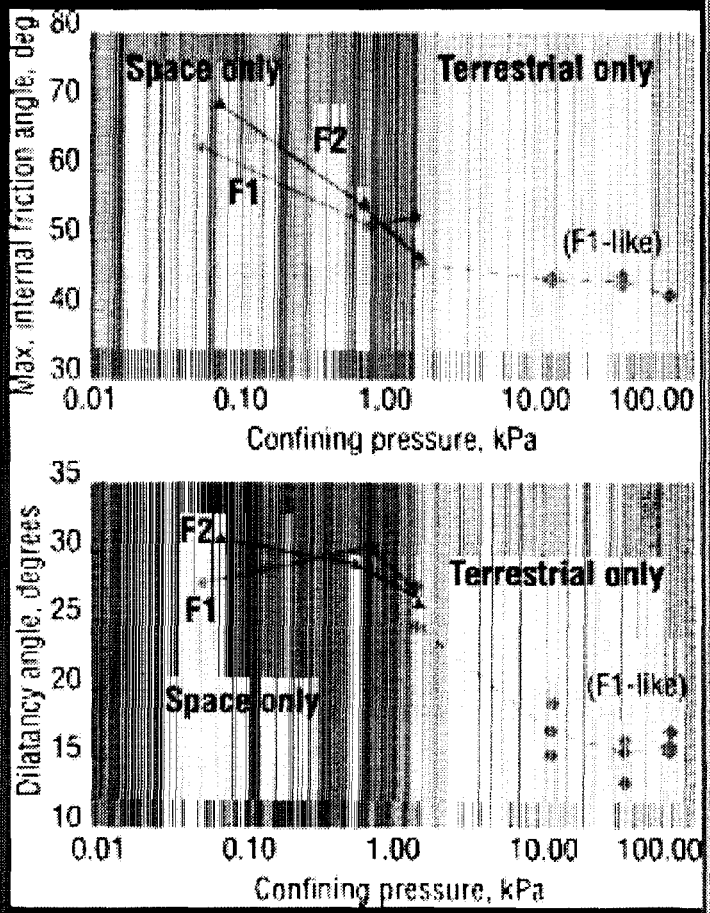

CT Renderings of MGM-F1-130 Specimen

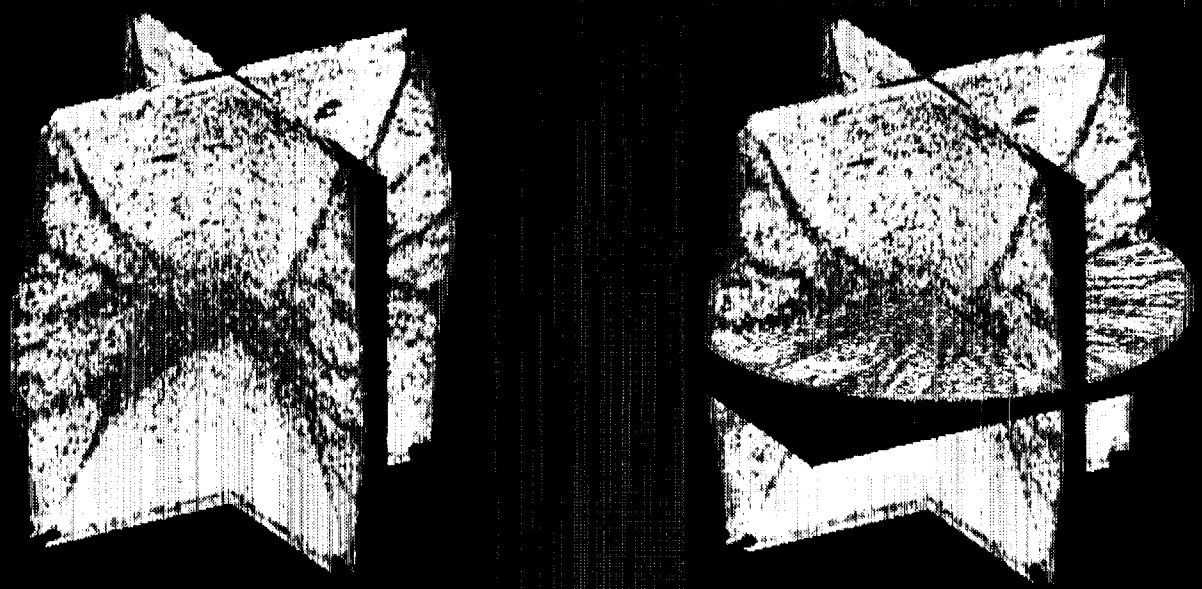

CT Renderings of MGM-F1-130 Specimen

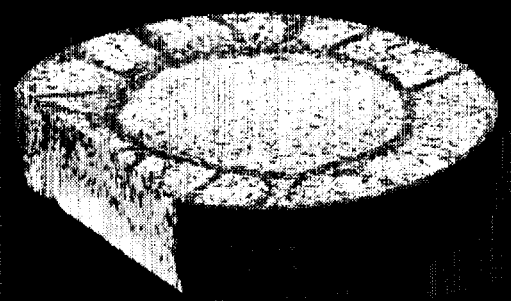

Z = 5-30 mm

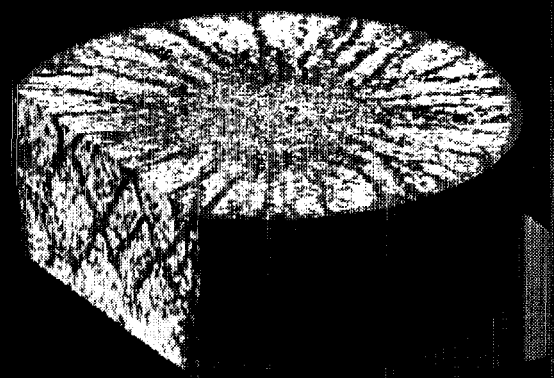

Z = 15-60 mm

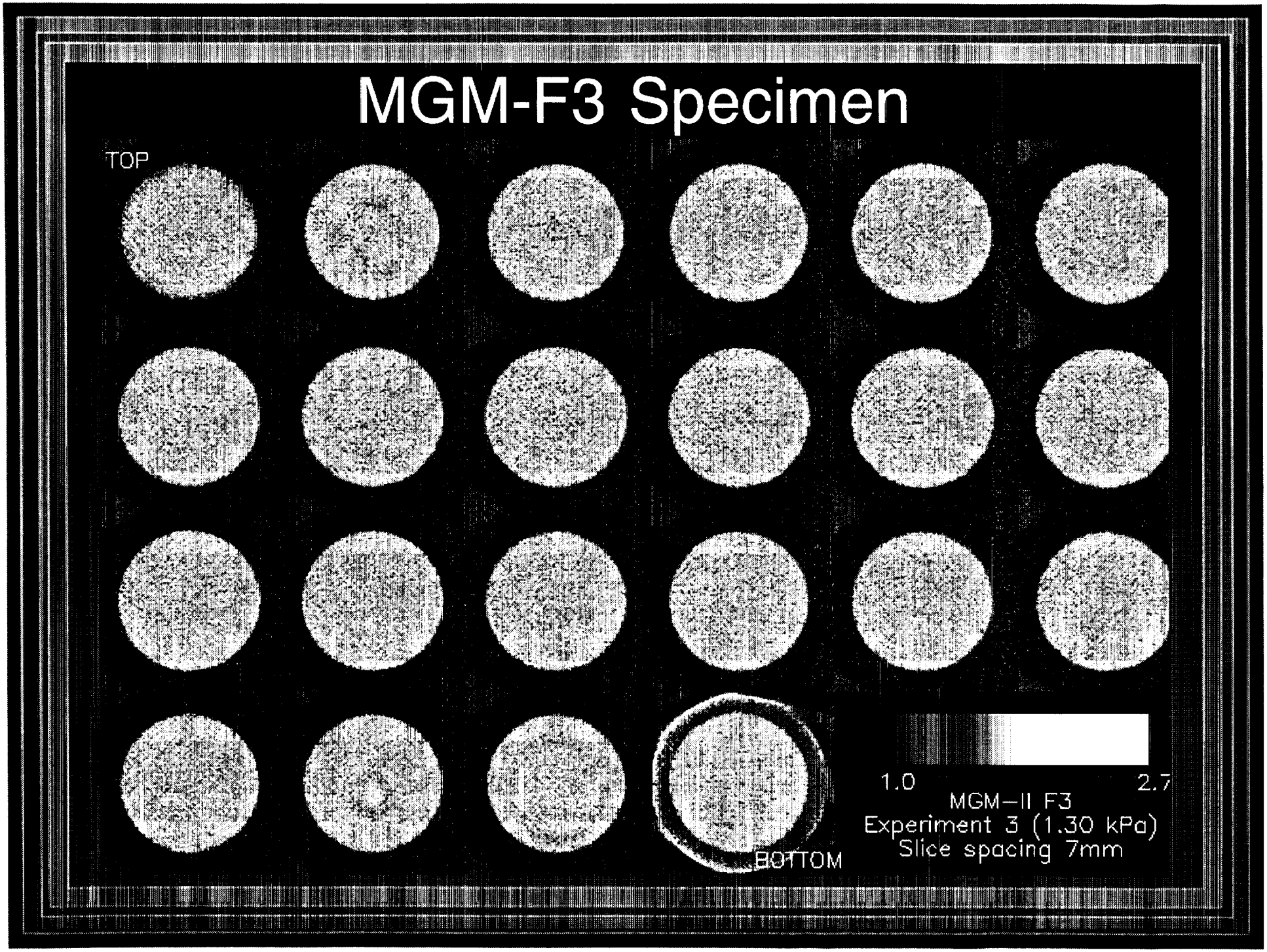
MGM-F3 Specimen
TOP
BOTTOM
1.0
2.7
MGM—II F3
Experiment 3 (1.30 kPa)
Slice spacing 7mm

MGM-F3 Specimen
MGM-II F3 Experiment 3 (1.30 kPa)
Slice spacing 1.5mm
1.0
2.7

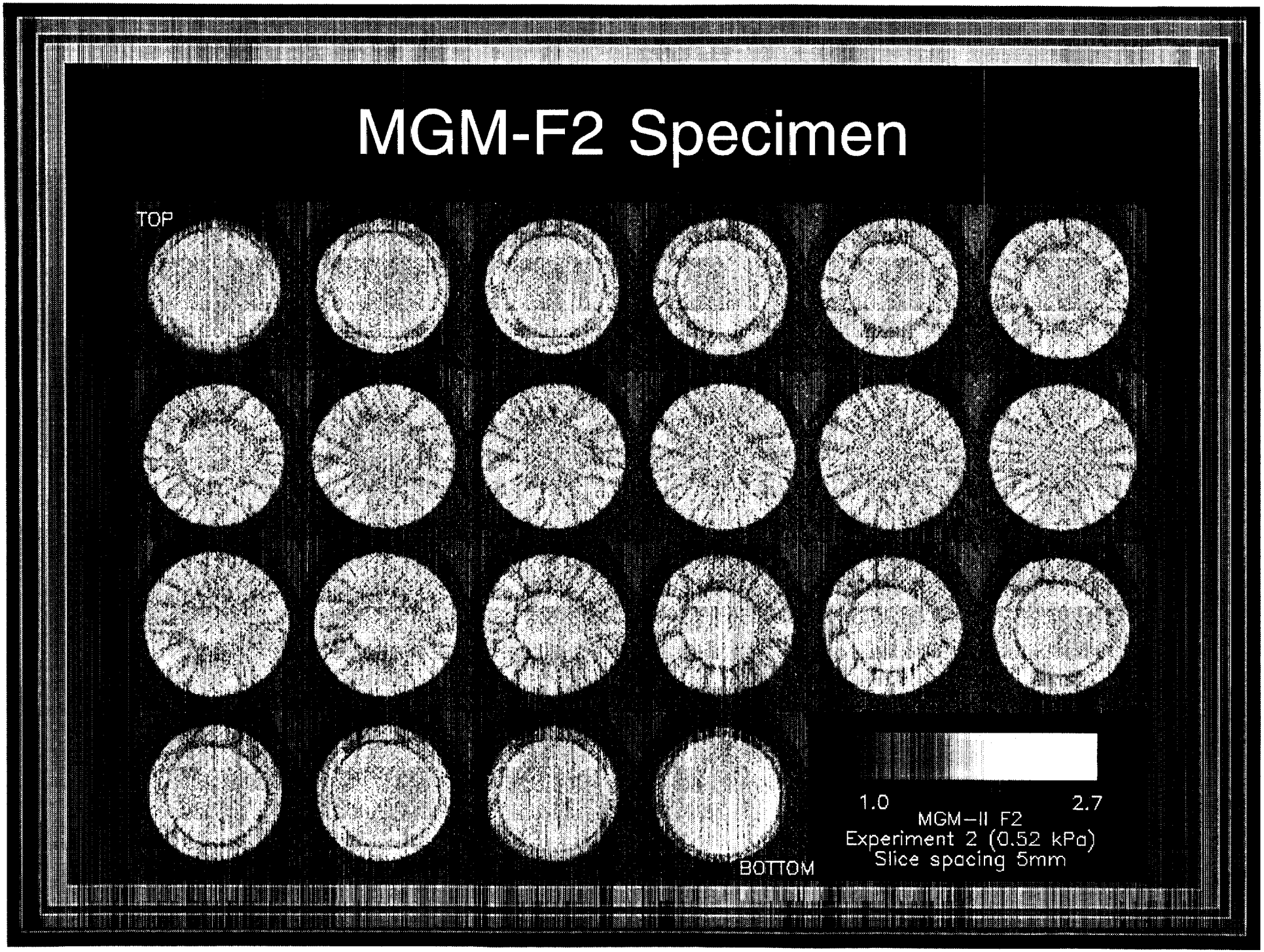
MGM-F2 Specimen
TOP
BOTTOM
1.0
2.7
MGM—II F2
Experiment 2 (0.52 kPa)
Slice spacing 5mm

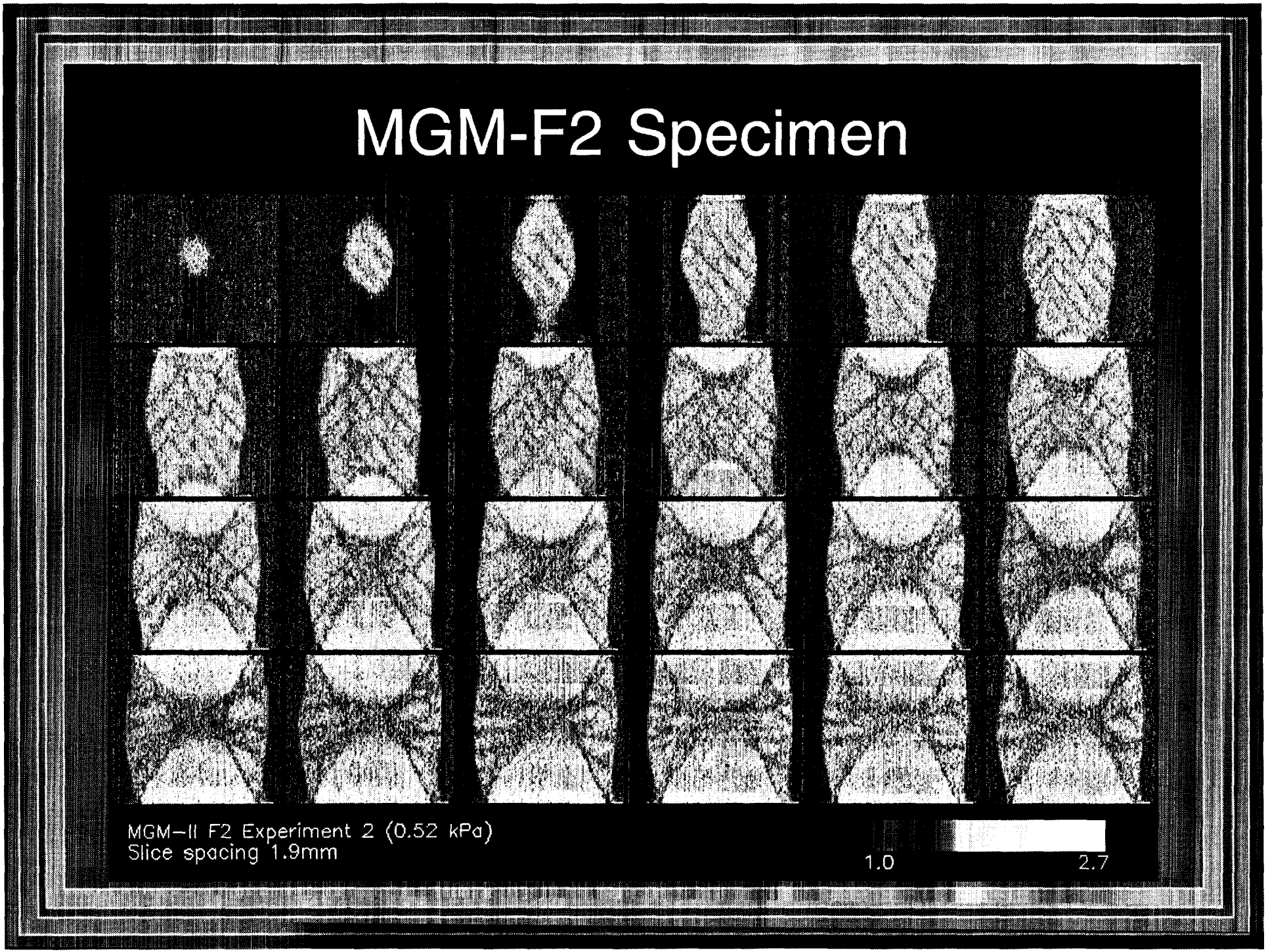
MGM-F2 Specimen
MGM–II F2 Experiment 2 (0.52 kPa)
Slice spacing 1.9mm
1.0
2.7

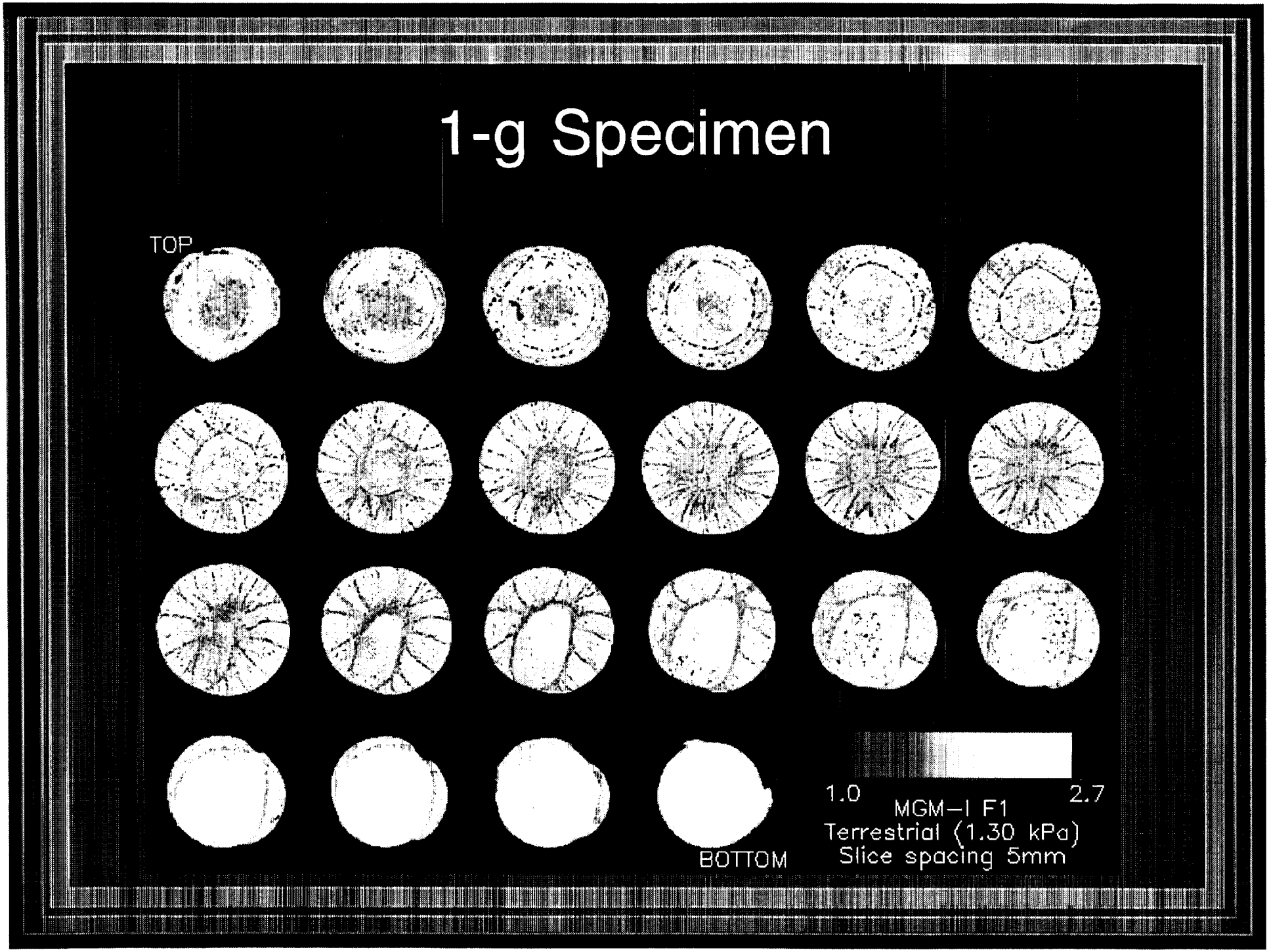
1-g Specimen
TOP
BOTTOM
1.0
2.7
MGM-I F1
Terrestrial (1.30 kPa)
Slice spacing 5mm

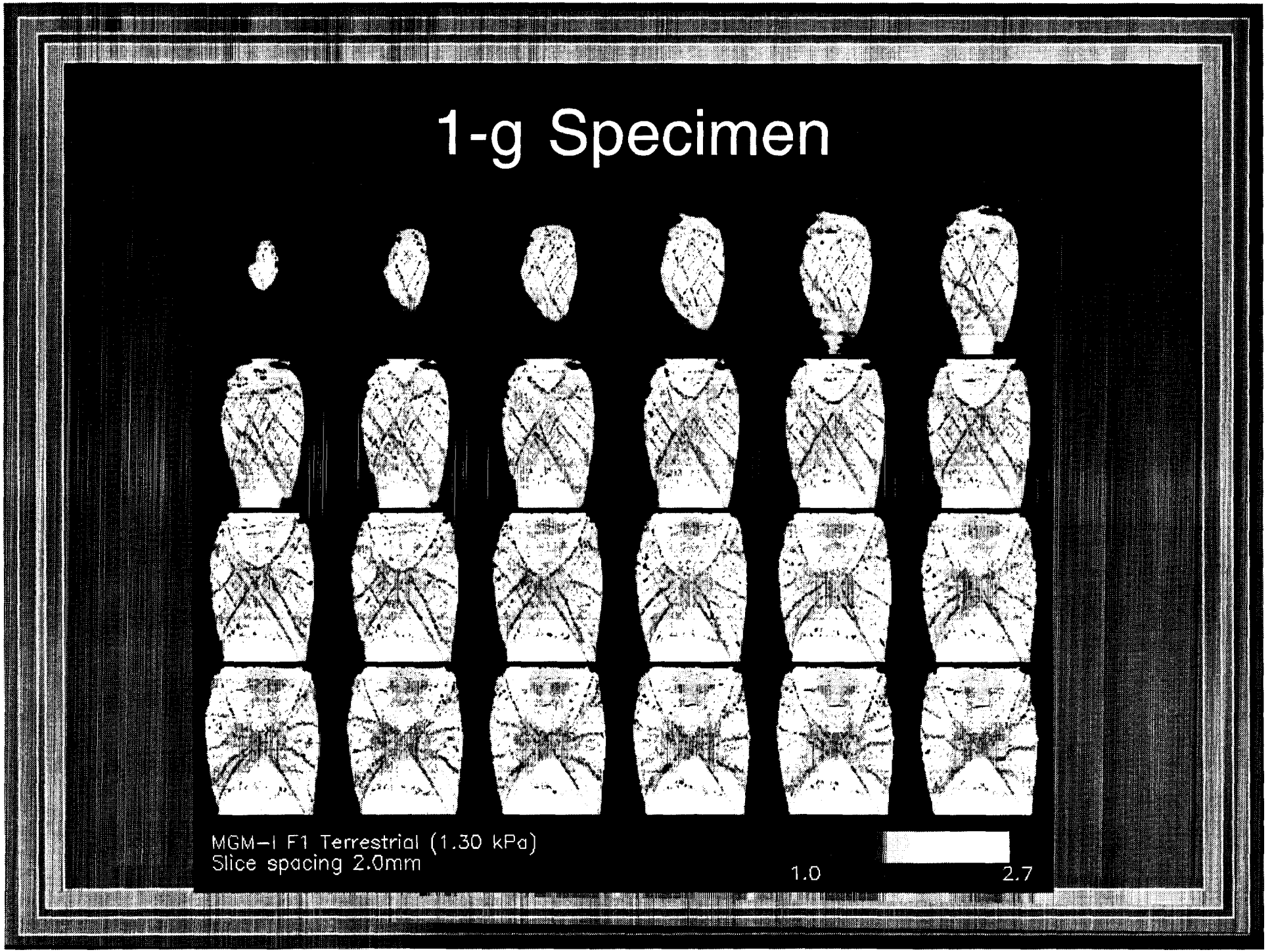
1-g Specimen
MGM–1 F1 Terrestrial (1.30 kPa)
Slice spacing 2.0mm
1.0
2.7

(CT) Analysis of MGM Specimens

- The CT scanning technique demonstrated a good ability to detect specimens' inhomogeneities, localization patterns, and quantify void ratio variation within sand specimens.
- Post-flight CT analysis revealed valuable data about the internal structure of MGM specimens.
- Uniform diffuse bifurcation was observed in flight specimens.
- Non-uniform bifurcation was observed in 1-g specimens.

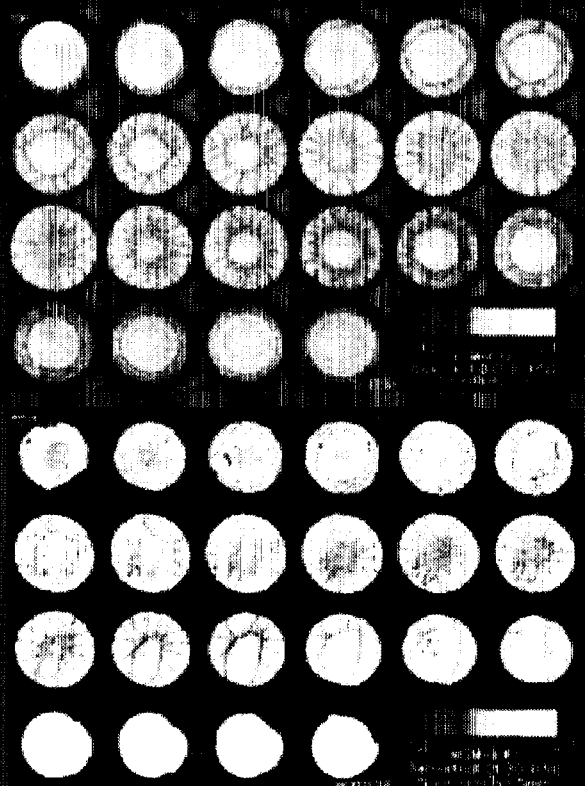

CT Analysis versus Thin-Sectioning and Microscopy

Summary

It is quite clear that the deformation processes and instability phenomena are different for CTC and plane strain conditions. This raises questions about our understanding of soil behavior under these two basic but very different modes of loading.

August 9, 2000

Session 2C
Dynamics and Instabilities I

THERMAL FIELD IMAGING USING ULTRASOUND

D. Andereck[1], S. Rahal and S. Fife
Department of Physics
The Ohio State University
Columbus, Ohio 43210

It is often desirable to be able to determine the temperature field in the interiors of opaque fluids forced into convection by externally imposed temperature gradients. To measure the temperature at a point in an opaque fluid in the usual fashion requires insertion of a probe, and to determine the full field therefore requires either the ability to move this probe or the introduction of multiple probes. Neither of these solutions is particularly satisfactory, although they can lead to quite accurate measurements. As an alternative we have investigated the use of ultrasound as a relatively non-intrusive probe of the temperature field in convecting opaque fluids. The temperature dependence of the sound velocity can be sufficiently great to permit a determination of the temperature from timing the traversal of an ultrasound pulse across a chamber. In this paper we will present our results on convecting flows of transparent and opaque fluids.

Our experimental cells consist of relatively narrow rectangular cavities made of thermally insulating materials on the sides, and metal top and bottom plates. The ultrasound transducer is powered by a pulser/receiver, the signal output of which goes to a very high speed signal averager. The average of several hundred to several thousand signals is then sent to a computer for storage and analysis. The experimental procedure is to establish a convective flow by imposing a vertical temperature gradient on the chamber, and then to measure, at several regularly spaced locations, the transit time for an ultrasound pulse to traverse the chamber horizontally (parallel to the convecting rolls) and return to the transducer. The transit time is related to the temperature of the fluid through which the sound pulse travels. Knowing the relationship between transit time and temperature (determined in a separate experiment), we can extract the average temperature *across* the chamber at that location. By changing the location of the transducer it is then possible to find the average temperature at different locations along the chamber, thereby determining the temperature profile along the system. (In the future we will construct an array of transducers. This will give us the capability to determine the temperature profile much more rapidly than at present, an important consideration if time-dependent phenomena are to be studied.)

To validate our procedure we introduced encapsulated liquid crystal particles into glycerol. The liquid crystal particles' color varies depending on the temperature of the fluid. A photograph of the fluid through transparent sidewalls therefore gives a picture of the temperature field of the convecting fluid, independent of our ultrasound imaging. A representative result is shown in the Figure 1, which reveals a very satisfying correspondence between the two techniques. Therefore we have a great deal of confidence that the ultrasound imaging approach is indeed measuring the actual temperature profile of the fluid. The technique has also been applied to convecting liquid metal flows, and representative data will be presented from those experiments as well.

[1] Supported by NASA NAG3-2138.

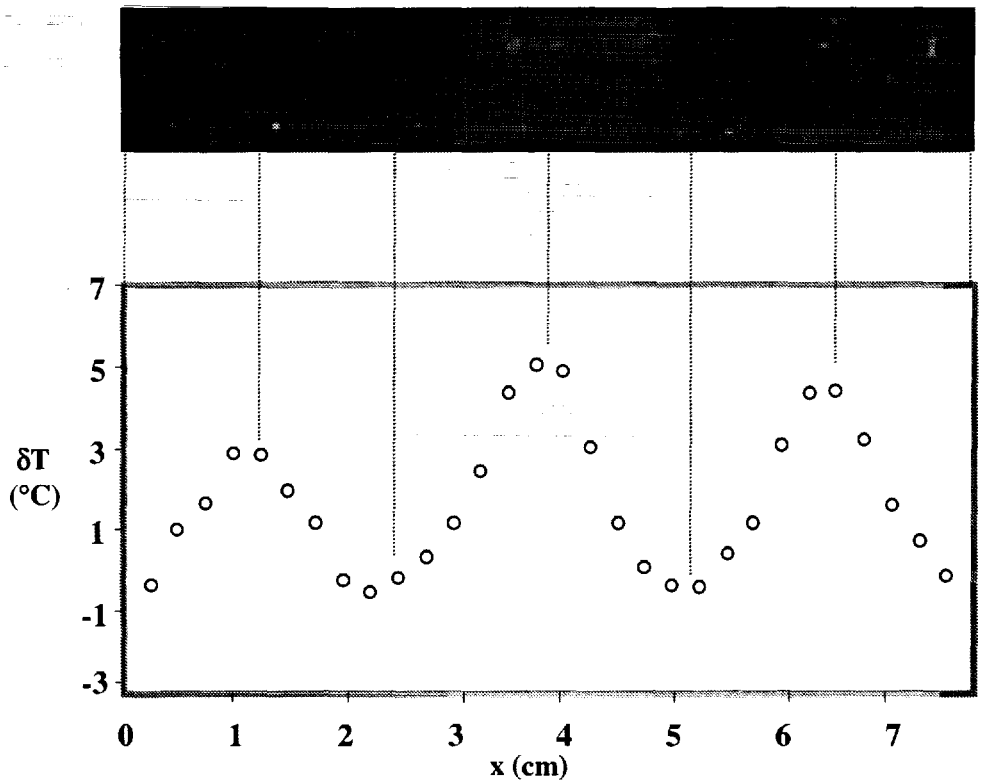

Figure 1: Relation between temperature field in convecting glycerol as revealed by suspended encapsulated liquid crystals, and a temperature profile from ultrasound transit times.

Ultrasound Imaging of Thermal Fields

C. David Andereck, Sean Fife, and Samir Rahal*

Department of Physics
The Ohio State University

*Now at the University of Batna, Algeria

Supported by NASA Grant NAG3-2138

Fifth Microgravity Fluid Physics and Transport Phenomena Conference

August 9, 2000

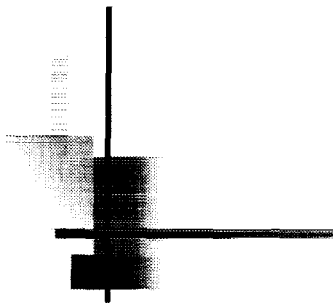

Aim of the work

* Interesting flows of opaque fluids abound: crystal growth, molten metals, polymers

* Current techniques and their limits:

  - Optical techniques (transparent fluids)

  - Thermistors, thermocouples, hot wire probes (invasive and local)

  - Ultrasound velocimetry (requires seeding)

  - X-rays (requires very thin samples)

Therefore, attempt to use
use ***ultrasound*** to map ***thermal fields***

The Concept

Sound velocity is a function of temperature along the path of sound propagation

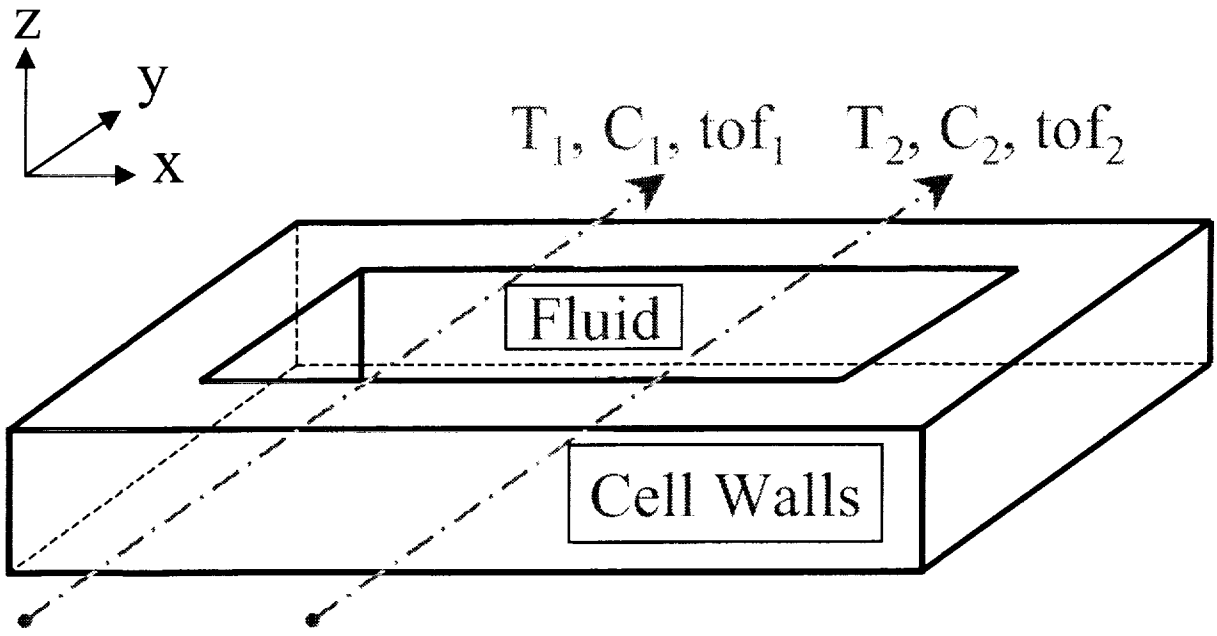

tof (x) → T (x)

Moving transducer

T: temperature

C: sound velocity

tof: time of flight

Experimental Procedure

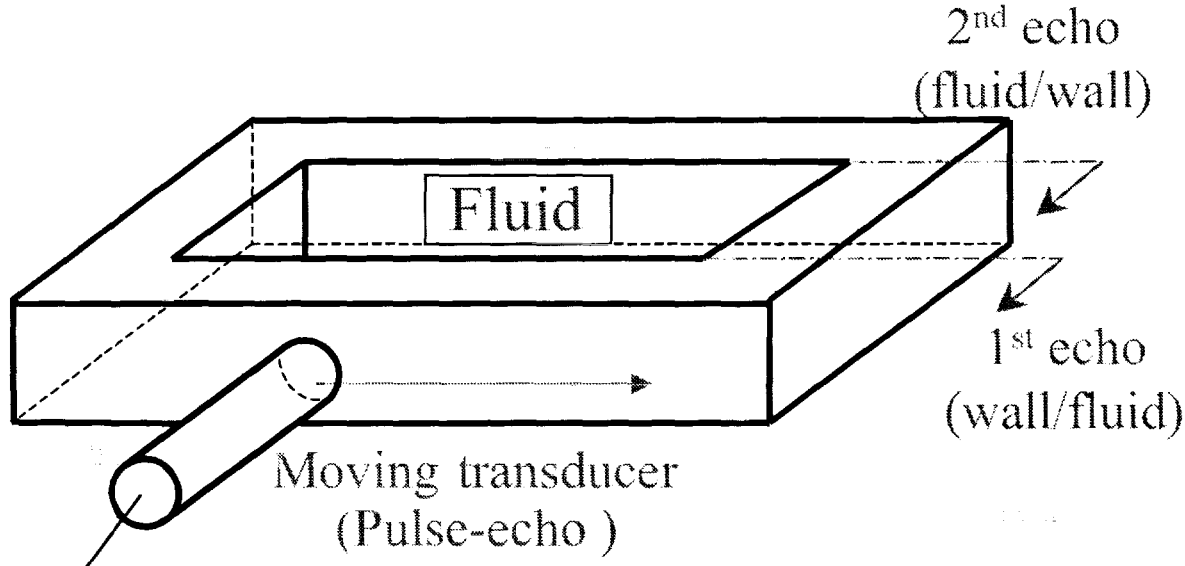

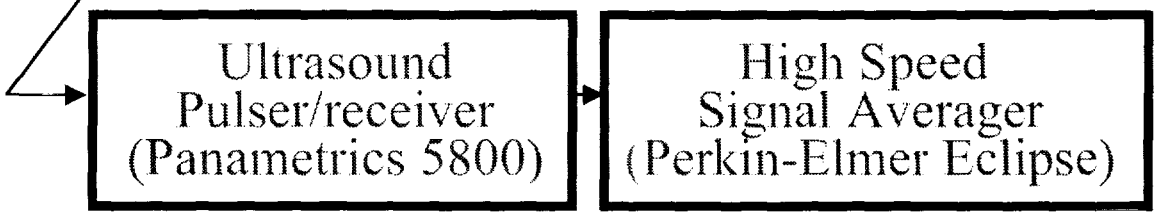

Schematic Ultrasound Signal

(For each location)

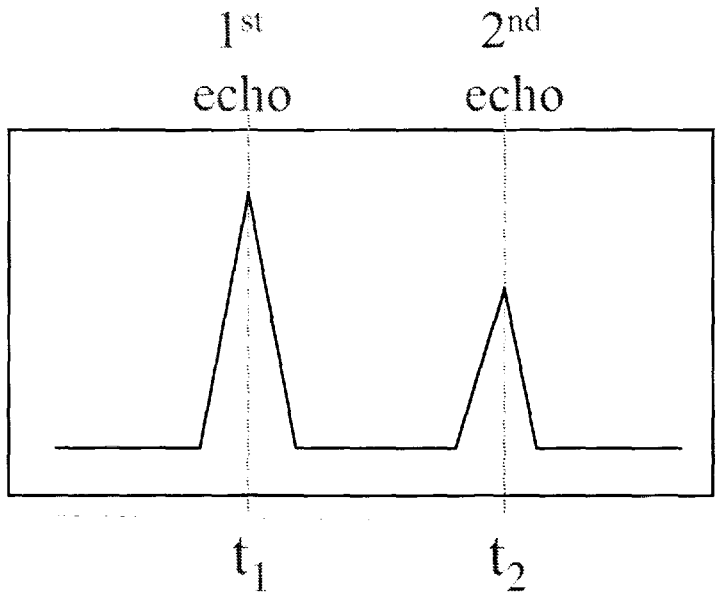

$t_2 - t_1 = 2tof$ (time of flight)

Sample Signal

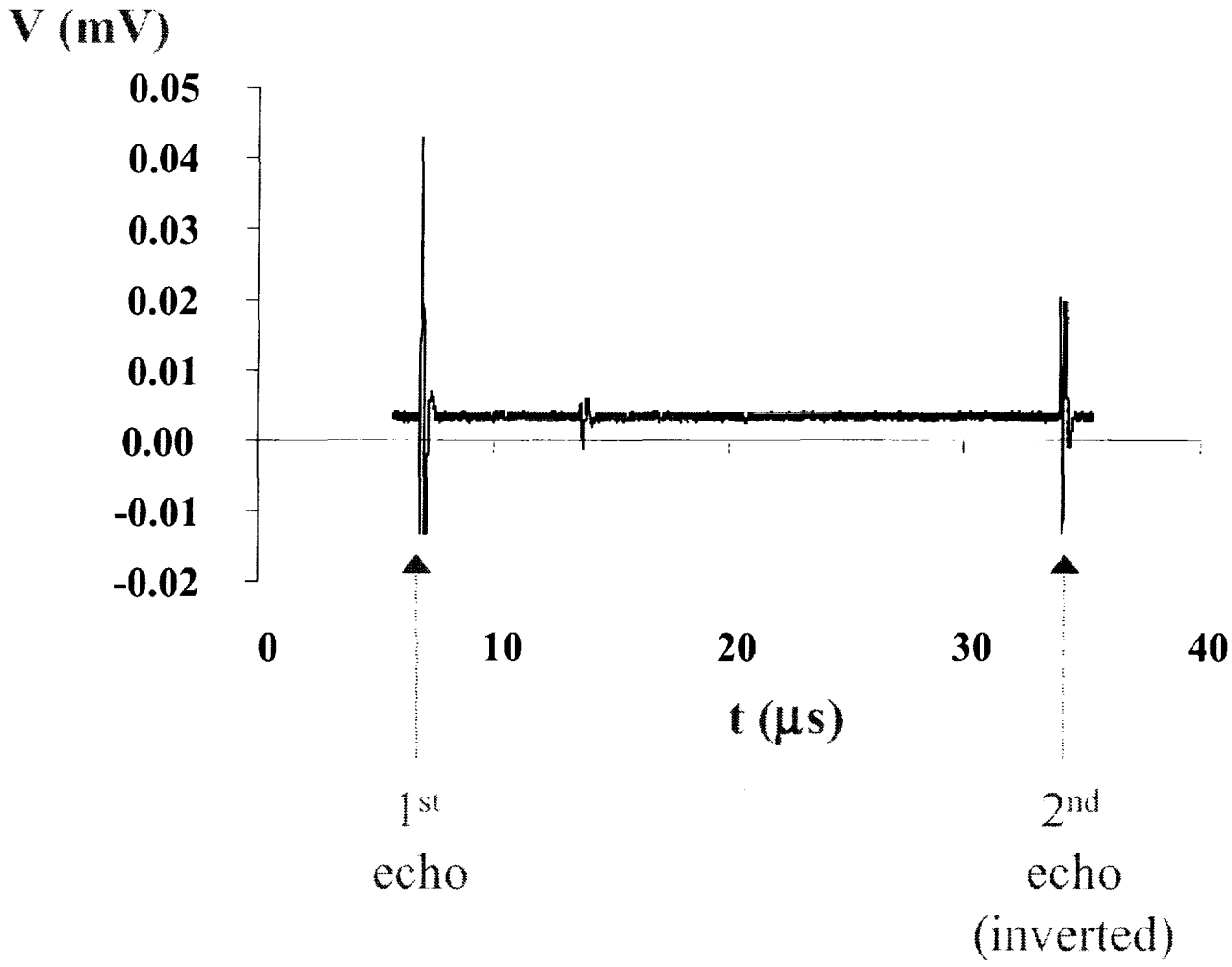

Transducer diameter = 0.35 Inch
Power in pulse = 25 μJ
Resonant frequency = 2.25 MHz
Pulse width = 0.6 μs
Pulse repetition rate = 1 kHz

Calibration for Glycerol

Temperature vs time of flight

Vertical $\Delta T = 0$ °C

➔no convection

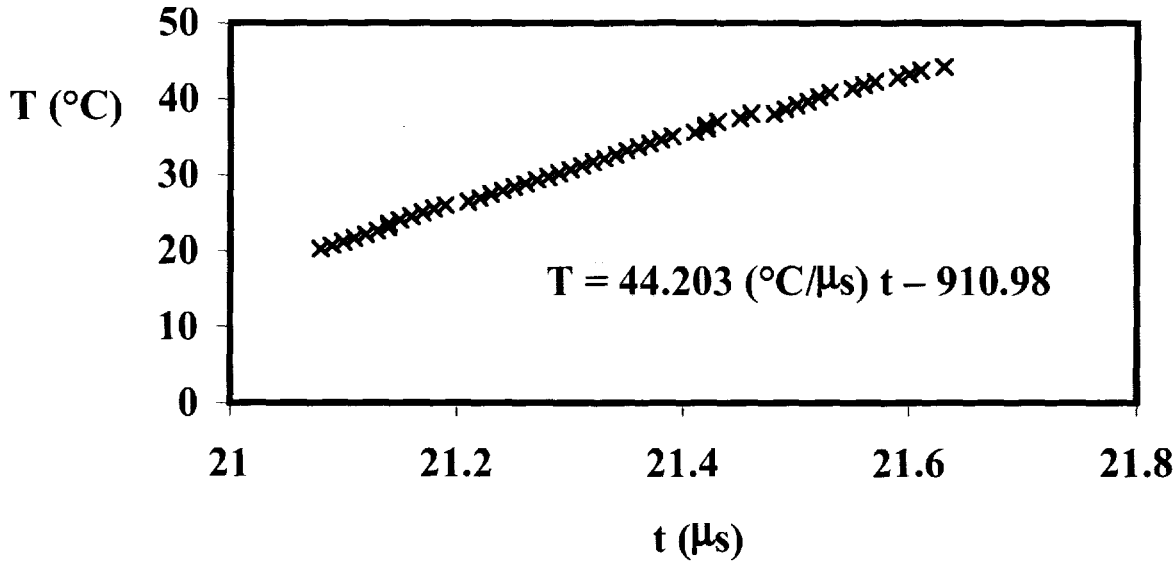

Glycerol : Prandtl Number Pr = 7613

T = temperature

t = 2tof (time of flight)

Rayleigh-Bénard configuration

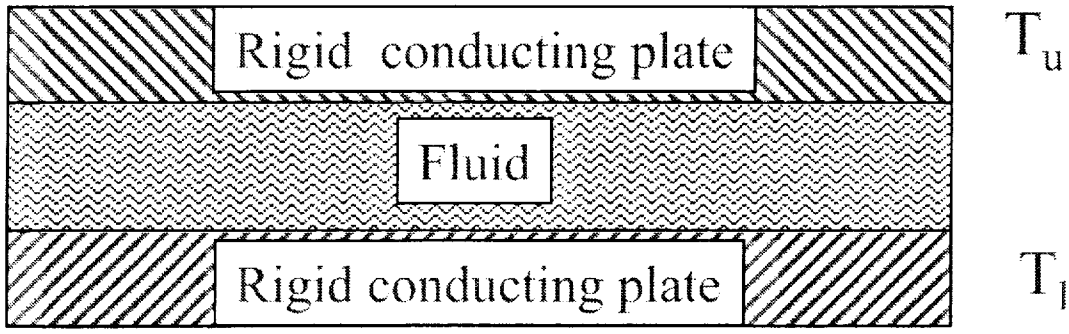

$$\Delta T = T_l - T_u > \Delta T_c$$

(ΔT_c = critical temperature difference for onset of convection)

Convection roll pattern
(schematic)

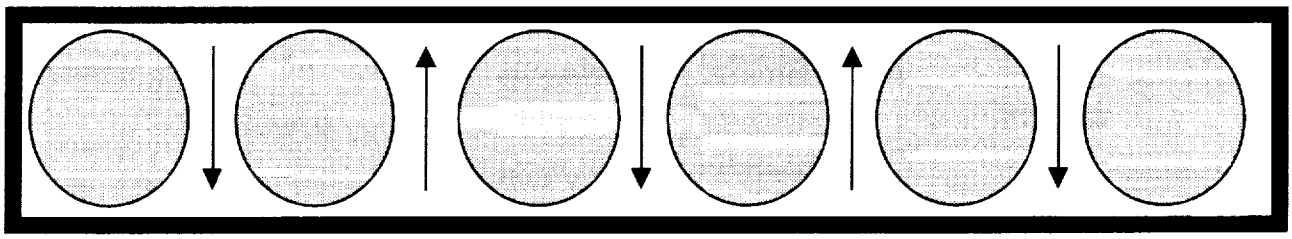

Results with Glycerol

Ultrasound measurements

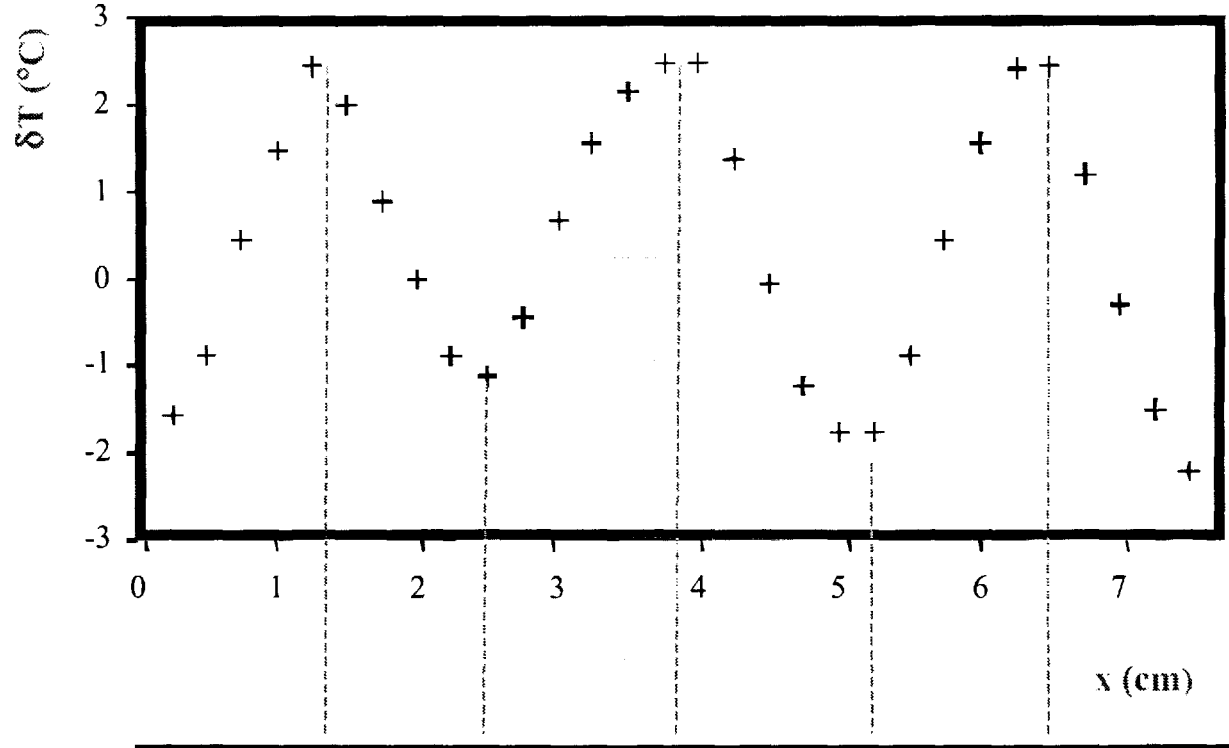

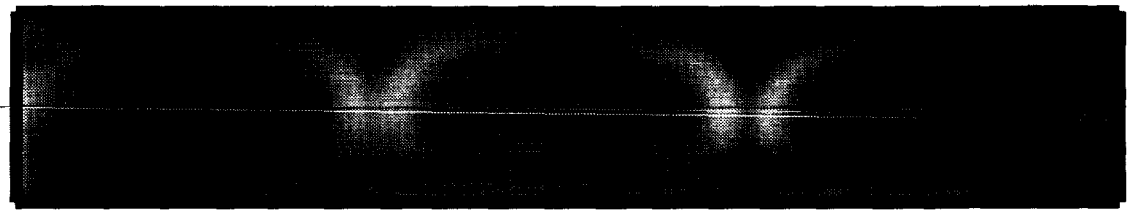

Thermochromic liquid crystals

(T = 29 °C: red start, T = 33 °C: blue start)

δT: deviation from the mean temperature

Cell dimensions: 7.77 cm long, 2.00 cm wide, 1.3 cm high

$\Delta T = 14$ °C ➔ Rayleigh Number $Ra = 1.2\ Ra_c$ (critical value)

Calibration of Mercury

Temperature vs time of flight

Vertical $\Delta T = 0$ °C

➔no convection

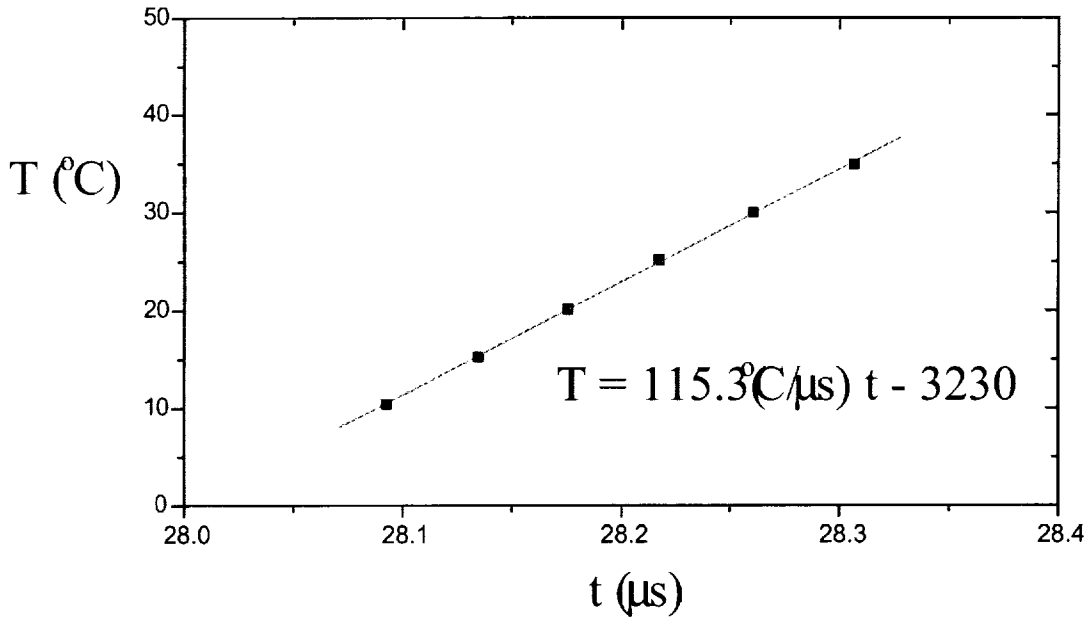

Mercury: Prandtl number Pr = 0.027

T = temperature

t = 2tof (time of flight)

Stainless Cell #1 Background

Cell dimensions: 4.00 cm long,
2.00 cm wide, 5.00 cm tall

T = 20.0 C, DT = 0

→ No convection

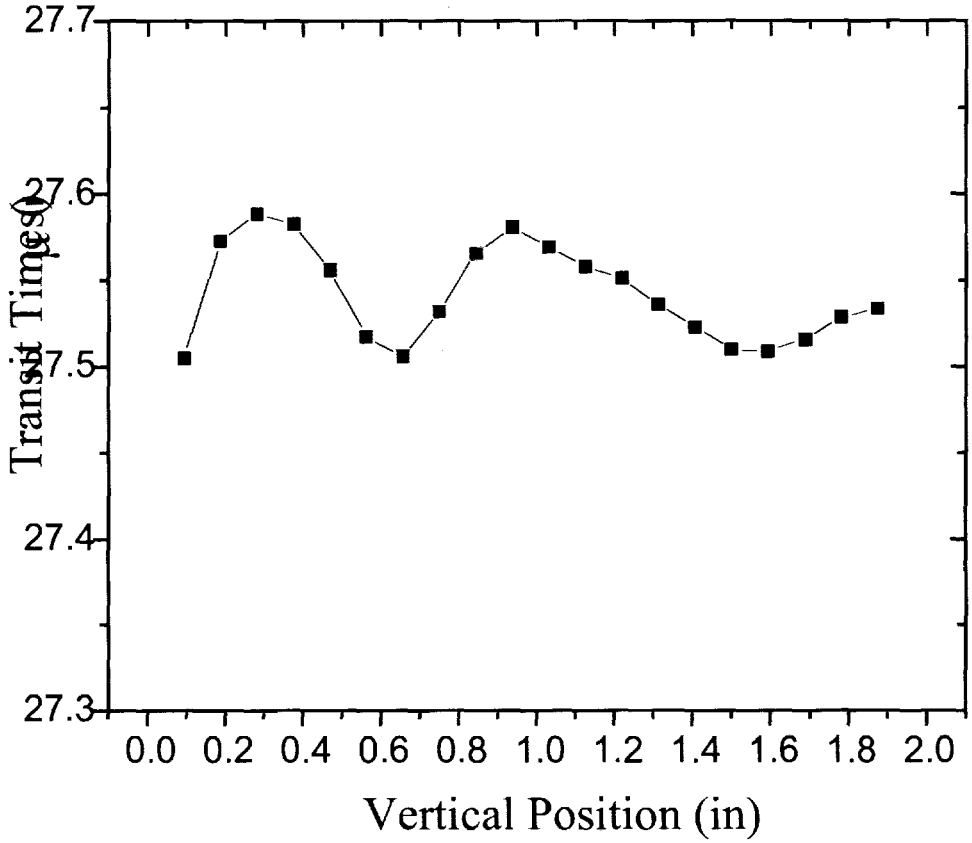

Nonuniform cell width due to
precision of machining

Use these points for background compensation

Tall Cell--Inverted Gradient

Imposed inverted gradient ~15 C

→ No convection

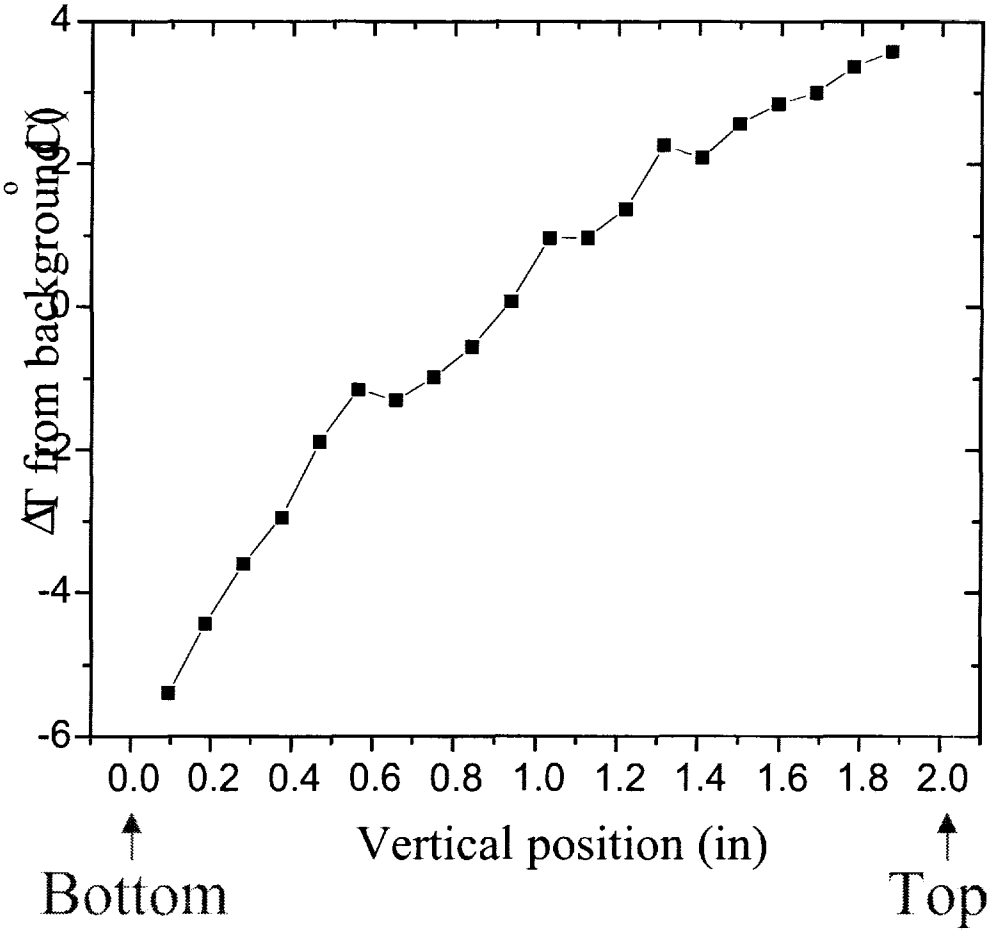

Stainless Cell #2 Background

Cell dimensions same as Plexiglas cell used with Glycerol

T = 20.0 C, DT = 0

=> No convection

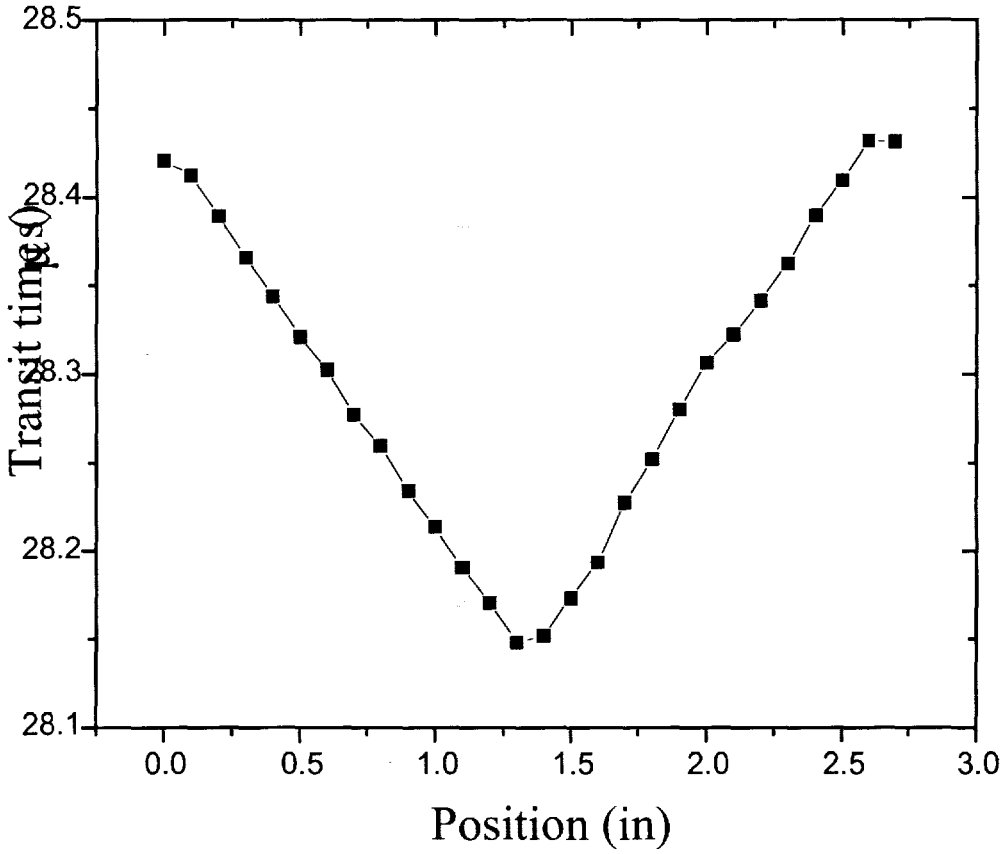

Nonuniform cell width due to precision of machining

Use these points for background compensation

Mercury Convection

$\Delta T = 2.3$ C

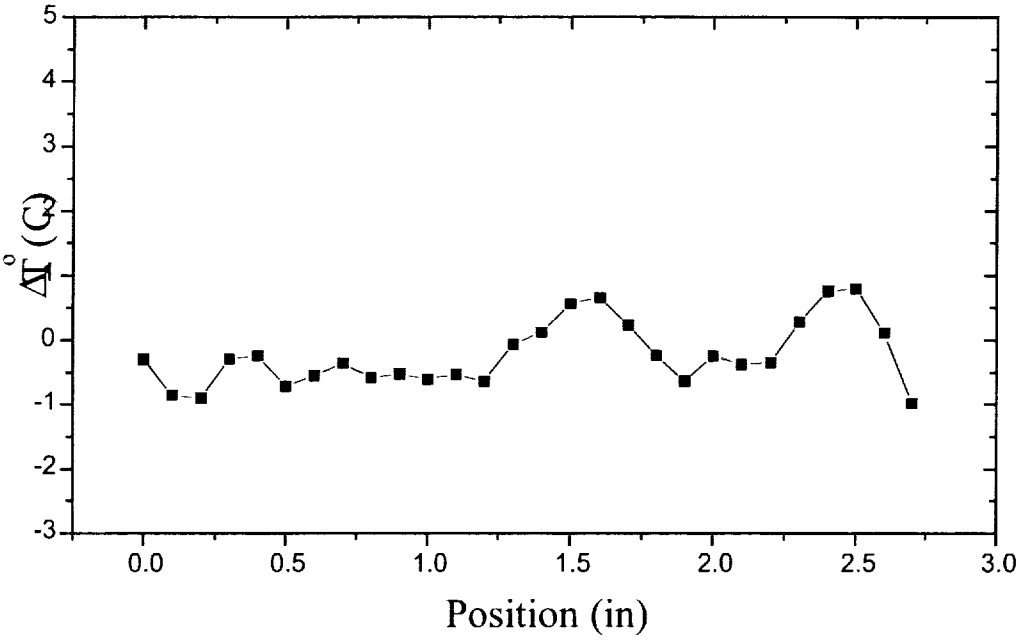

$\Delta T = 5.6$ C

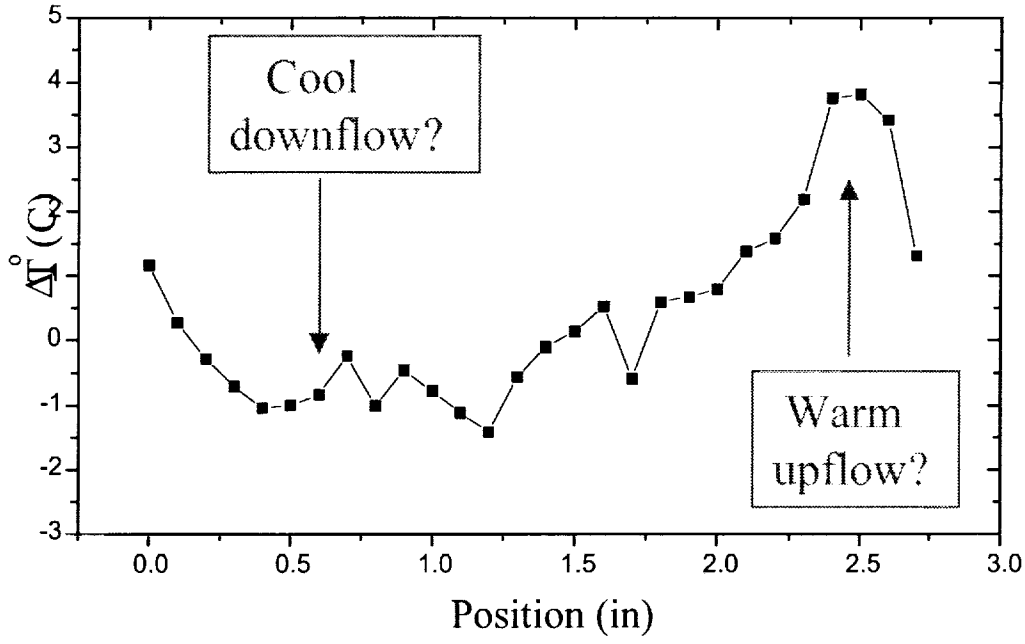

Conclusions

* Development of a new technique: measurement of thermal fields using ultrasound

* Application to a transparent fluid (Glycerol)

--Temperature resolution of ~ 0.1 °C

--Validation: pattern visualization with thermochromic liquid crystals

* Application to an opaque liquid (Mercury)

* Future ➔ Transient states using an array of transducers

STABILITY OF THERMOCAPILLARY RETURN FLOWS UNDER VERTICAL GRAVITY MODULATION

V. A. Suresh, G. M. Homsy, *Department of Chemical Engineering, Stanford University, CA 94305-5025, USA. bud@chemeng.stanford.edu*

INTRODUCTION

G-jitter convection is of general interest to NASA, and the time-dependence of the body force opens the possibility of new physical effects such as resonance [1, 2], streaming [3] and parametric instability [4]. The hydrodynamic stability of fluids in a non-uniform temperature field subject to constant body forces has been extensively studied in the literature, Rayleigh-Bénard convection being the classical example [5]. Later work has shown that time dependent acceleration can significantly affect the stability of such flows [6]. This work considers the effect of the interaction between g-jitter and thermocapillarity in determining the stability characteristics of a model flow.

PROBLEM DEFINITION AND RESULTS

A definition sketch of the system is shown in figure 1. It consists of an infinite horizontal slot of narrow thickness bounded by a rigid boundary at the bottom and a flat free interface at the top. A constant temperature gradient is applied along the length of the slot and a time harmonic gravitational acceleration in the y - direction is used to model the g-jitter. A parallel return flow consisting of a steady thermocapillary component and a time periodic buoyant component is set up in the slot [1]. The relative strength of the two components is characterized by the Rayleigh number, Ra and the Marangoni number, Ma. Our earlier work [1] established that parallel flow solutions exist for all values of the parameters. The presence of vertical jitter leads to the potential for two-dimensional cellular convection due to unstable thermal stratification over a portion of the cycle. The stability limit for no jitter is well known [7].

Linear stability equations were obtained for two dimensional rolls, an equivalent dynamical system was obtained using a truncated Galerkin expansion, and the stability boundaries were determined by Floquet theory. The kinetic energy of the disturbances was calculated and used to study the mechanism of the instabilities.

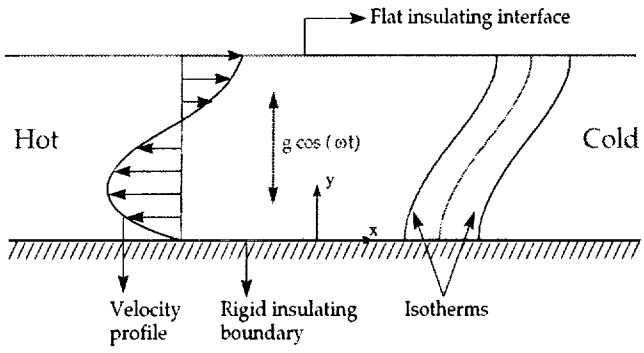

Figure 1

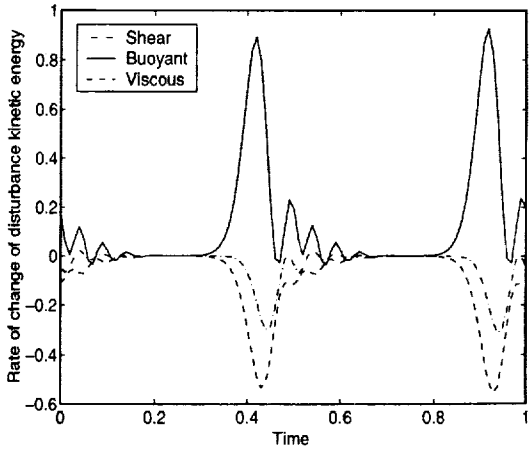

Figure 2

In purely buoyant flows with no thermocapillarity ($Ra > 0, Ma = 0$), buoyant instabilities due to a coupling between the zero mean modulated vertical temperature stratification and the jitter were observed. Figure 2 shows the rate of change of the average disturbance kinetic energy over a time period for an unstable set of parameters for this mechanism, clearly showing its buoyant origins. In the limit of strong thermocapillarity with no body forces ($Ma > 0, Ra = 0$), the results of Smith and Davis [7] were recovered and shear instabilities were observed. The critical Ma was initially found to decrease as Ra was increased from zero, indicating that the two mechanisms reinforce each other in certain parameter ranges. At larger Ra, the opposite trend was observed. A similar behavior was found for critical Ra as Ma was increased from zero. This leads to regions of stability in the $Ra - Ma$ plane: flows in these regions are stable due to the combined effect of buoyancy and thermocapillarity, whereas a purely buoyant or a purely thermocapillary flow at the same Ra or Ma would be unstable. These results are contrasted with those obtained by Nield [8] in the case of steady gravity, for which thermocapillarity and buoyancy reinforce each other.

REFERENCES

[1] P. Grassia and G. M. Homsy, "Thermocapillary and buoyant flows with low-frequency jitter. I. Jitter confined to the plane," *Phys. Fluids.*, **10**, 1273, 1998.

[2] V. A. Suresh, C. I. Christov, and G. M. Homsy, "Resonant thermocapillary and buoyant flows with finite frequency gravity modulation", *Phys. Fluids.*, **11**, 2565, 1999.

[3] A. Farooq and G. M. Homsy, "Streaming flows due to g-jitter-induced natural convection," *J. Fluid. Mech*, **271**, 351, 1994.

[4] A. Farooq and G. M. Homsy, "Linear and nonlinear dynamics of a differentially heated slot under gravity modulation," *J. Fluid. Mech*, **313**, 313, 1996.

[5] S. Chandrasekhar, *Hydrodynamic and Hydromagnetic Stability*, (Dover Publications Inc., New York, 1981).

[6] P. M. Gresho and R. L. Sani, "The effects of gravity modulation on the stability of a heated fluid layer," *J. Fluid Mech.*, **40**, 783, 1970.

[7] M. K. Smith and S. H. Davis, "Instabilities of dynamic thermocapillary liquid layers. Part 1: Convective Instabilities," *J. Fluid Mech.*, **132**, 119, 1983.

[8] D. A. Nield, "Surface tension and buoyancy effects in cellular convection," *J. Fluid Mech.*, **19**, 341, 1964.

NASA/CP—2000-210470

Stability of Thermocapillary Return Flows under Vertical Gravity Modulation

Vinod Suresh and G. M. Homsy
Department of Chemical Engineering,
Stanford University

Grassia & Homsy, *Phys. Fluids* **10**, 1273, 1998

Grassia & Homsy, *Phys. Fluids* **10**, 1291, 1998

Suresh, Christov, & Homsy, *Phys. Fluids* **11**, 2565, 1999

Motivation

- Random, time dependent accelerations ('g-jitter') observed on board spacecraft
- Magnitude of acceleration may be up to 100 times larger than background gravity
- g-jitter can significantly effect fluid mechanics in microgravity through ***Resonances*** and ***Parametric Instabilities***

Flow Geometry: General **g**

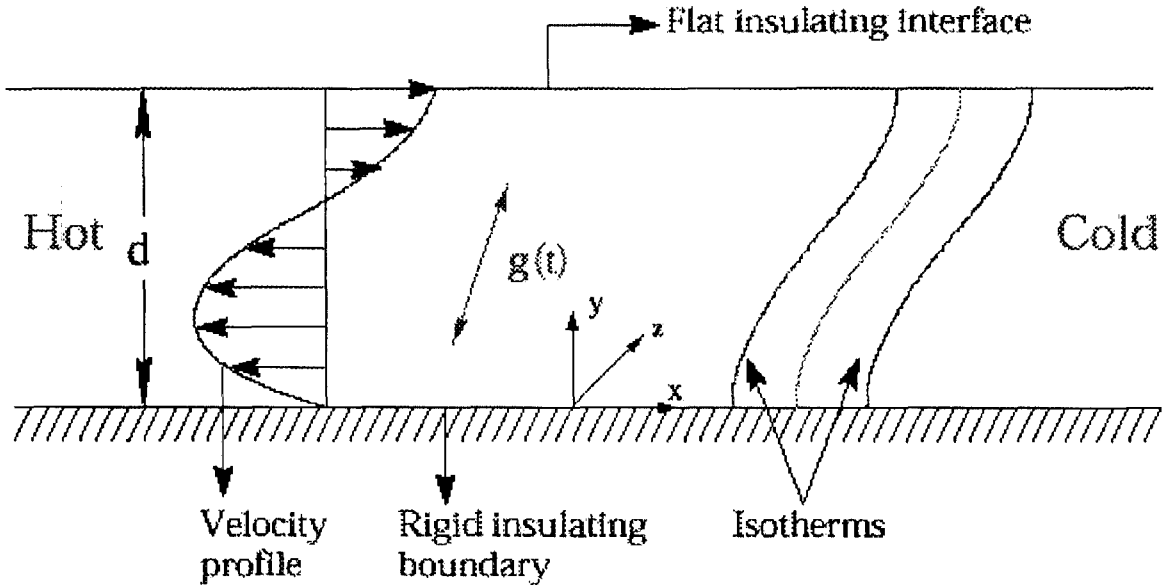

- Base flow driven by complex interaction between thermal gradient, thermocapillarity, convection, and buoyancy
- Dimensionless Parameters

$$\mathrm{Ù} = \frac{\grave{u}d^2}{\hat{e}}\frac{\mathbf{g}}{|\mathbf{g}|} \qquad Pr = \frac{\acute{i}}{\hat{e}}$$

$$Ra = \frac{|\mathbf{g}|d^4\acute{a}_T\hat{a}}{\acute{i}\hat{e}} \qquad Ma = \frac{\tilde{a}_T\hat{a}d^2}{\grave{i}\hat{e}}$$

Flow Geometry: Horizontal Jitter

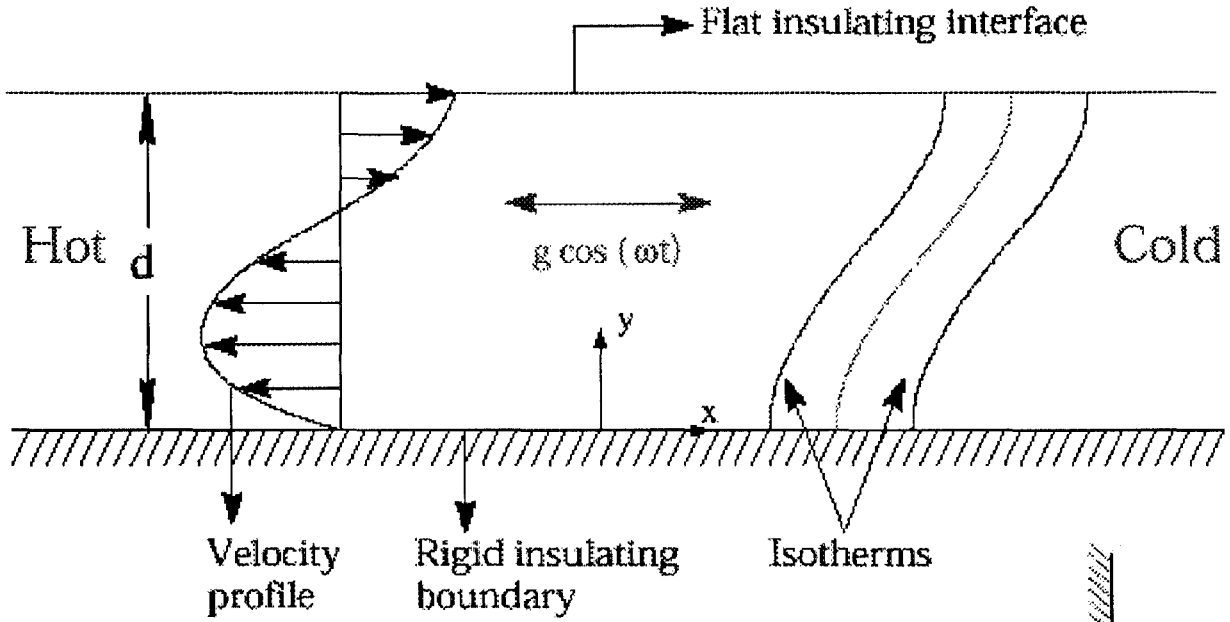

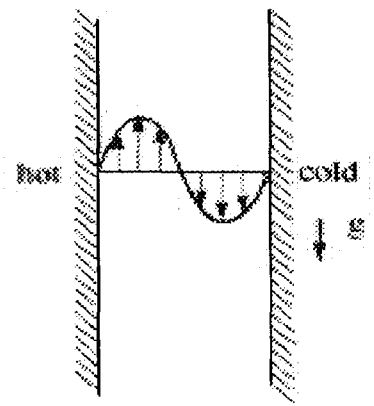

- Quasistatic (low frequency) Case
  - Parallel flow
  - Analogy with stratified slot
  - Buoyancy boundary layers on "stable" part of cycle
  - Run-away to long wave length Rayleigh/Benard modes on "unstable" part of cycle

Flow Geometry: Horizontal Jitter

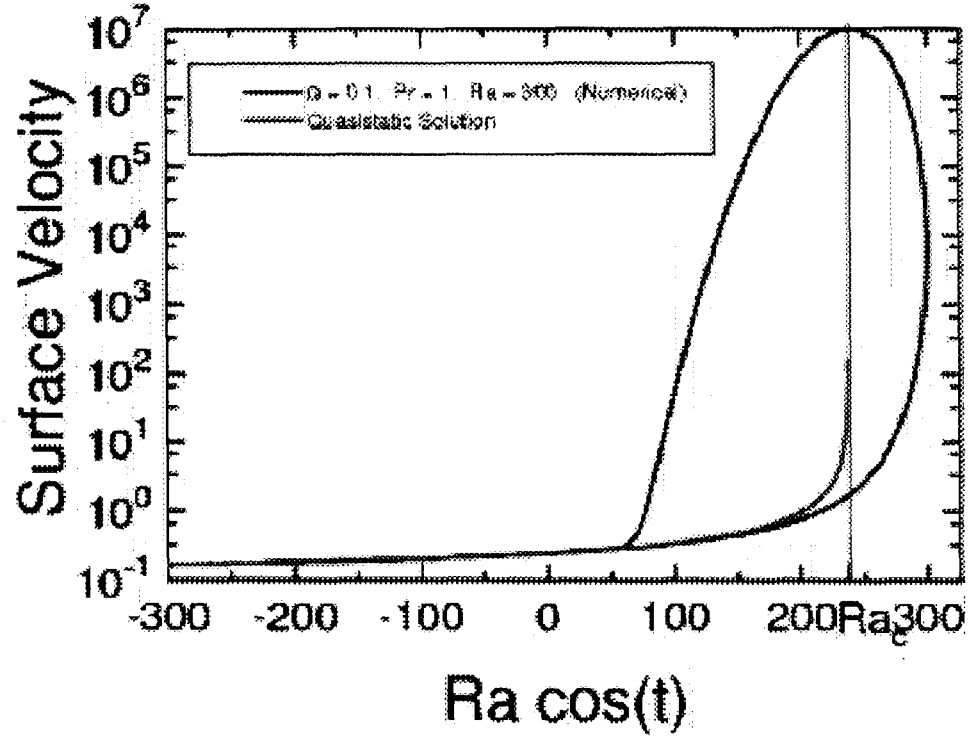

- Finite Frequency Case
  - Parallel flow
  - Finite frequency opens a hysteresis loop
  - Asymptotic scalings determined

Flow Geometry: Vertical Jitter

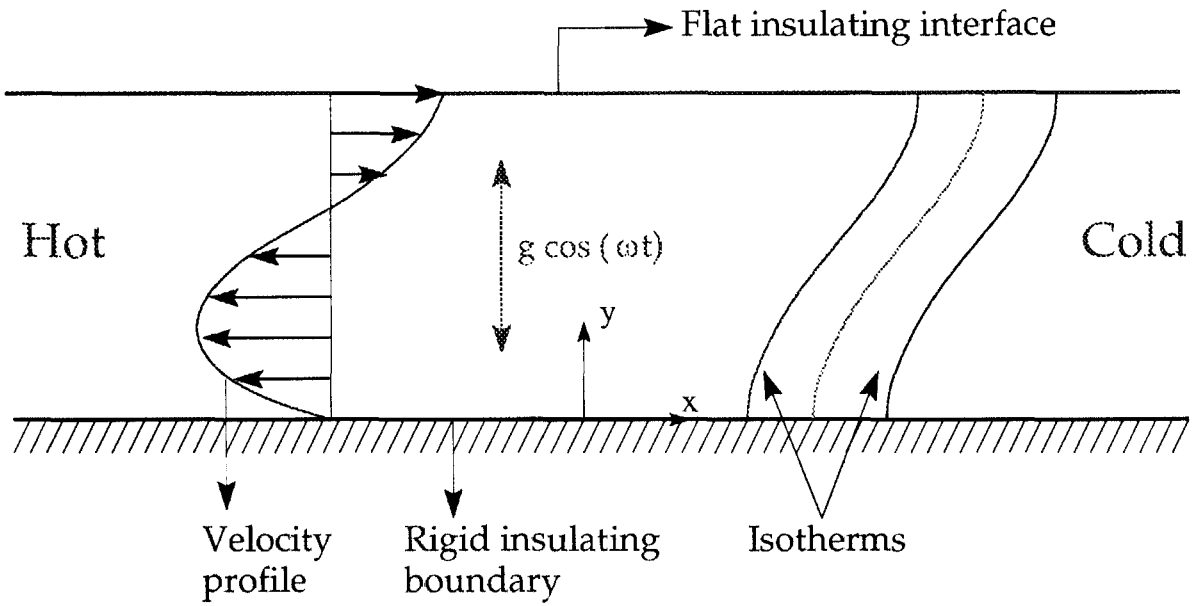

Dimensionless Parameters

$$Ra = \frac{g\beta A \Delta T d^3}{\nu\kappa} \qquad Pr = \frac{\nu}{\kappa}$$

$$Ma = \frac{\sigma_T \Delta T d^2}{\mu\kappa}$$

Flow Geometry: Vertical Jitter

- Base flow consists of gravity driven time-periodic and surface tension driven steady components.

$$\Psi = Ma\,\Psi_0(y) + Ra\,\exp(i\Omega t)\,\Psi_1(y)$$
$$T = -x + Ma\,T_0(y) + Ra\,\exp(i\Omega t)\,T_1(y)$$

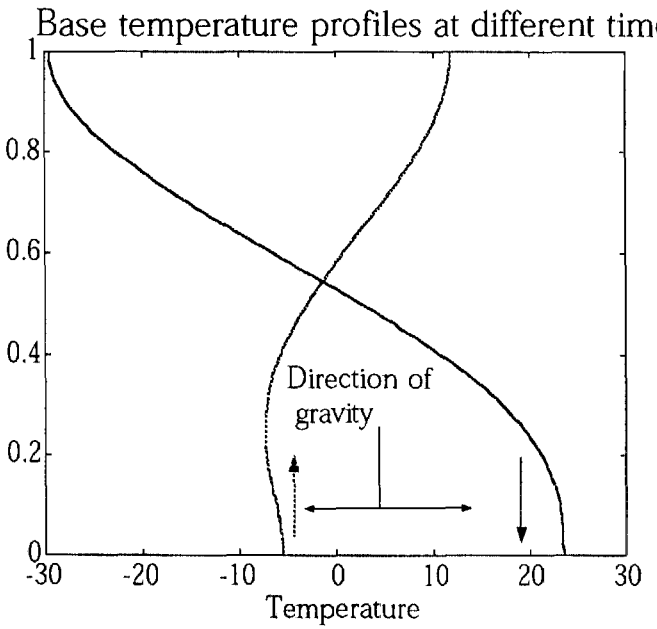

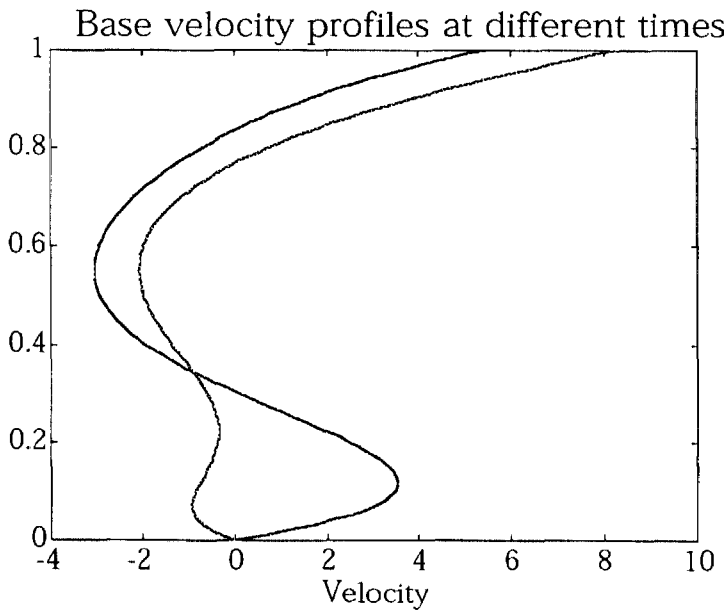

Features of the Base States

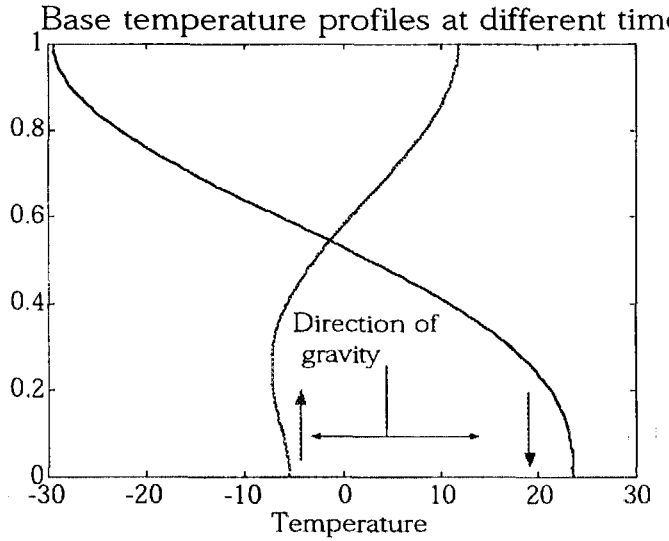

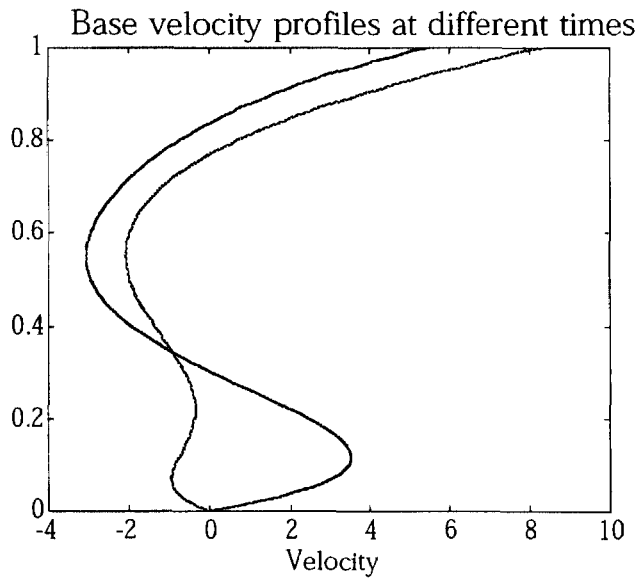

- Potential for buoyant instabilities due to unstable temperature profiles.

- Potential for shear instabilities due to inflectional velocity profiles.

Features of the Base States

Time-periodic base state that has potential for three separate instability mechanisms:

- o Buoyancy instabilities due to unstable stratification
- o Shear instabilities due to inflectional velocity profiles
- o Hydrothermal waves due to coupled T,u,v fields in the presence of thermocapillarity

Linear Stability Analysis

- Introduce a small disturbance into the base flow:

$$\vec{u}(x,y,t)=\vec{U}_B(y,t)+\vec{u}_D(x,y,t)$$
$$T(x,y,t)=T_B(y,t)+T_D(x,y,t)$$

- Linearize the Navier-Stokes equations and integrate equations by Galerkin expansions.
- Follow the evolution of the disturbances in time to determine instability points by Floquet theory.
- Determine mechanisms of instability through interrogation of energy balances.

Results: Stability Map

$Pr = 1, \Omega = 10$

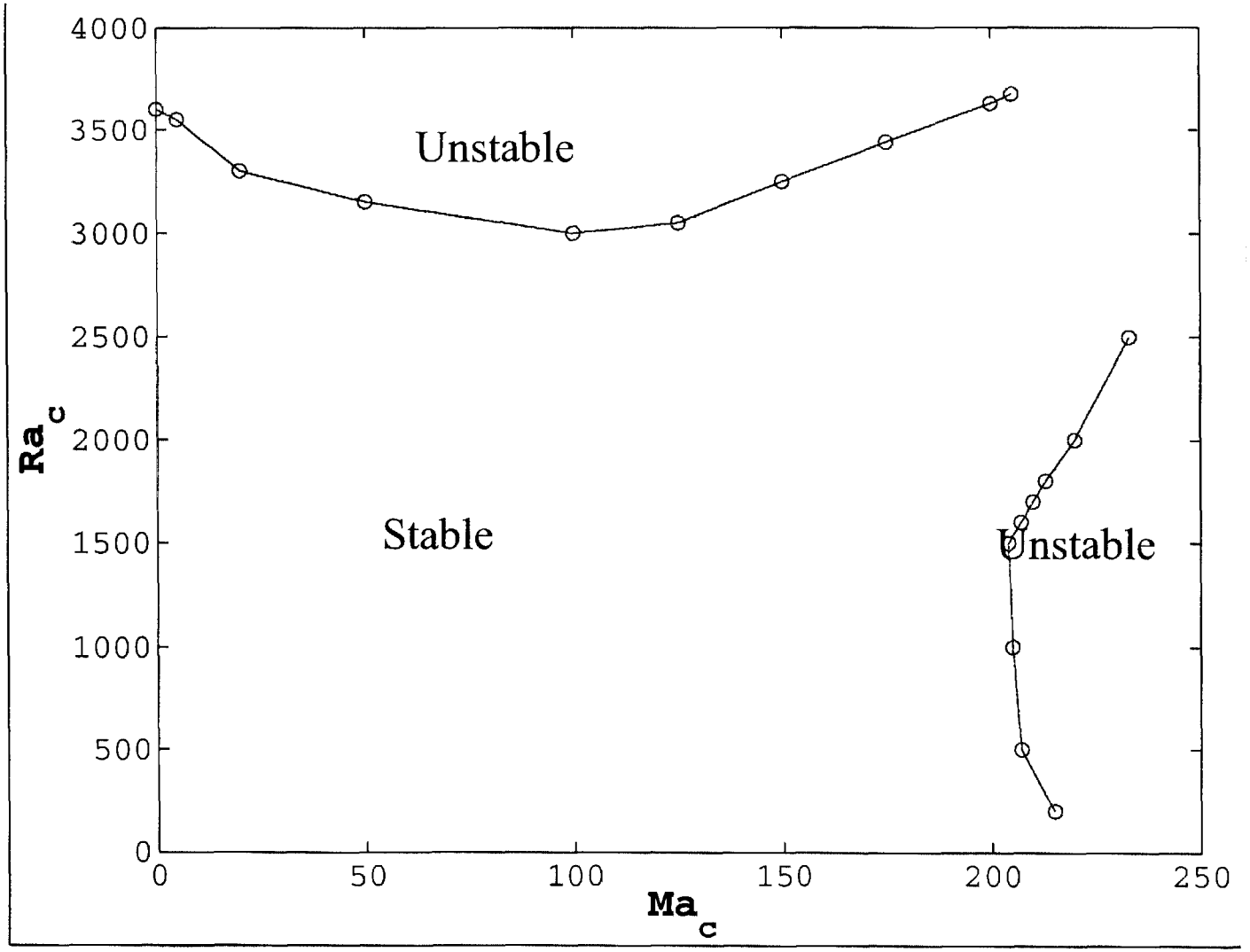

Results: Energy Balances

$$\frac{d\langle E\rangle}{dt} = \underbrace{-\left\langle uv\frac{dU_b}{dy}\right\rangle}_{\text{shear}} \quad \underbrace{-\ Ra\ Pr\ \langle uT\rangle \cos(\Omega t)}_{\text{buoyant}}$$

$$\underbrace{-\ Pr\ \langle \boldsymbol{\nabla u} : \boldsymbol{\nabla u}\rangle}_{\text{viscous}} \quad \underbrace{+\ Pr \int_0^{2\pi k} u\,\frac{\partial u}{\partial y}\bigg|_{y=1} dx}_{\text{surface}}$$

$$\langle\ \ \rangle \equiv \int_0^{2\pi k} dx \int_0^1 dy$$

Results: Energy Balances

$Pr = 1, \Omega = 10$

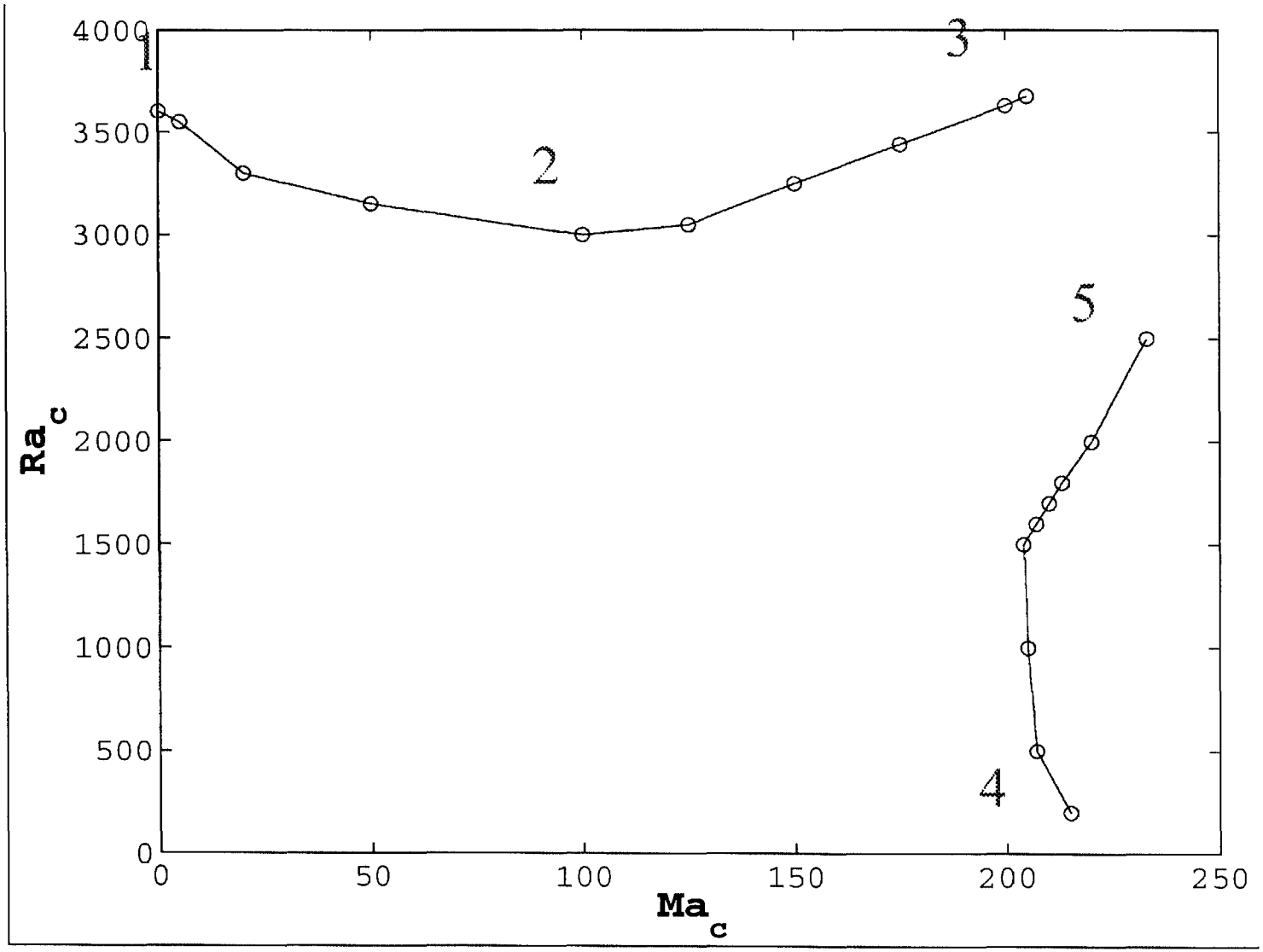

Results: Energy Balances

$Ma = 0, Ra = 3600, Pr = 1, \Omega = 10$

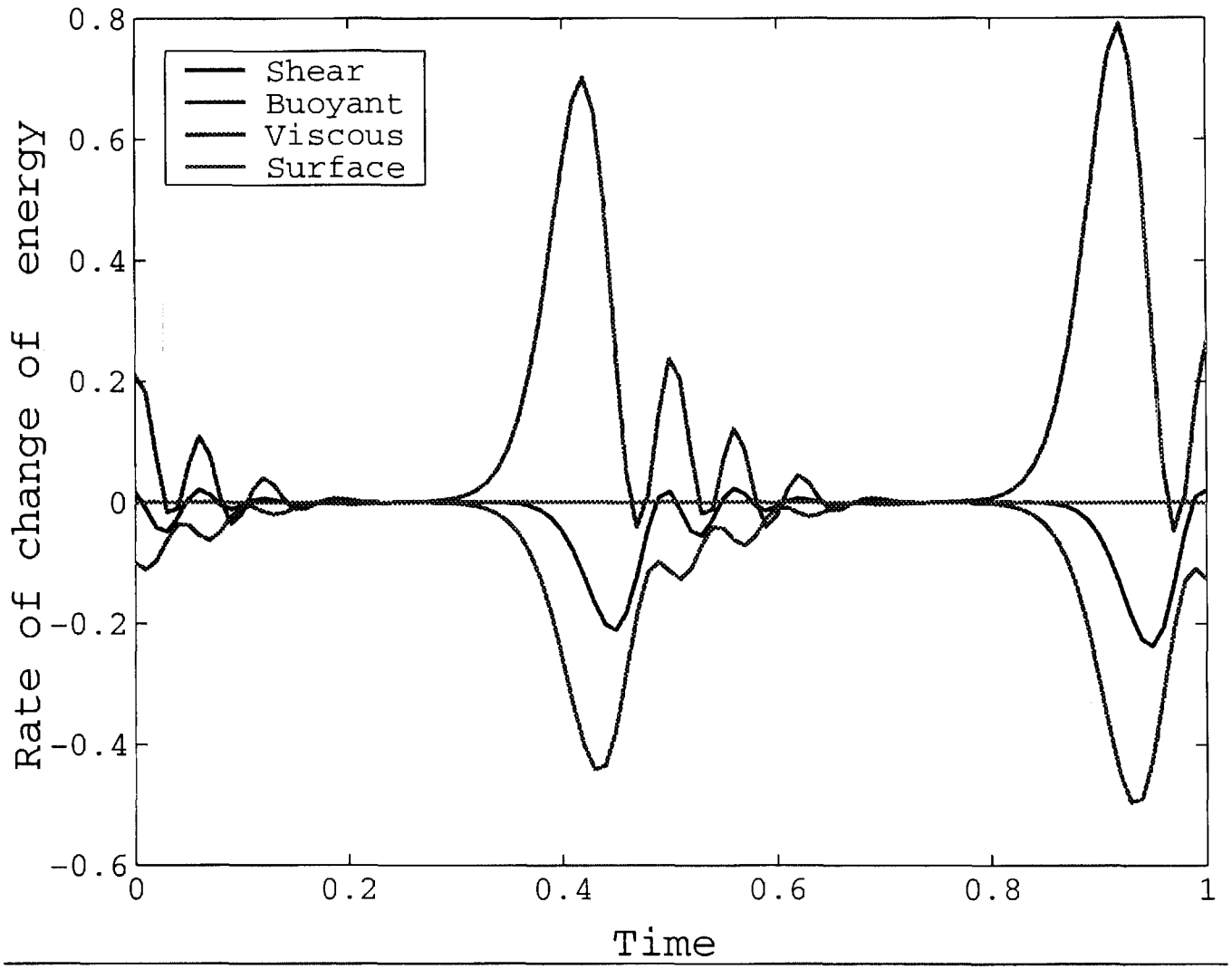

Results: Energy Balances

$Ma = 100, Ra = 3025, Pr = 1, \Omega = 10$

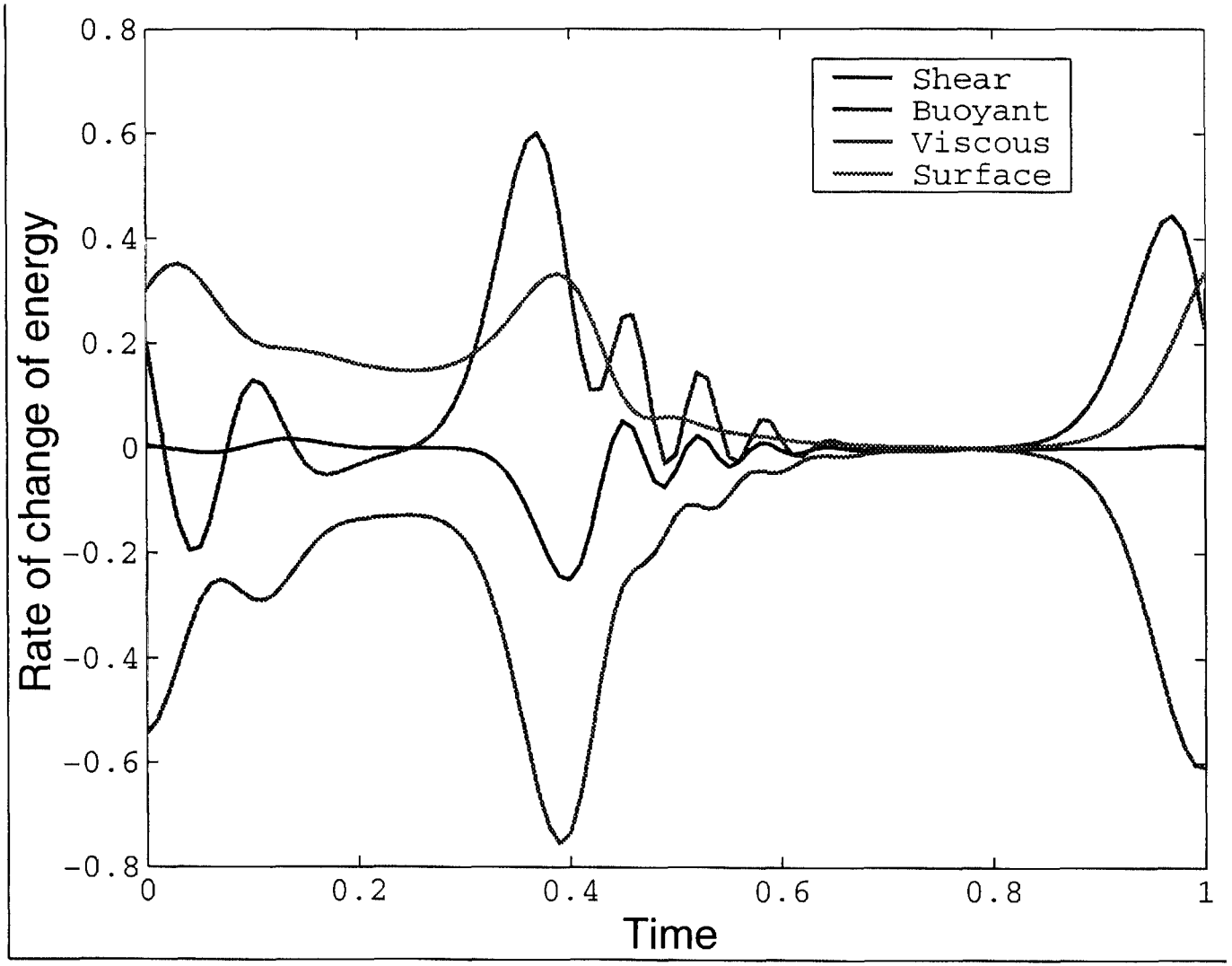

Results: Energy Balances

Ma = 200, Ra = 3630, Pr = 1, Ω = 10

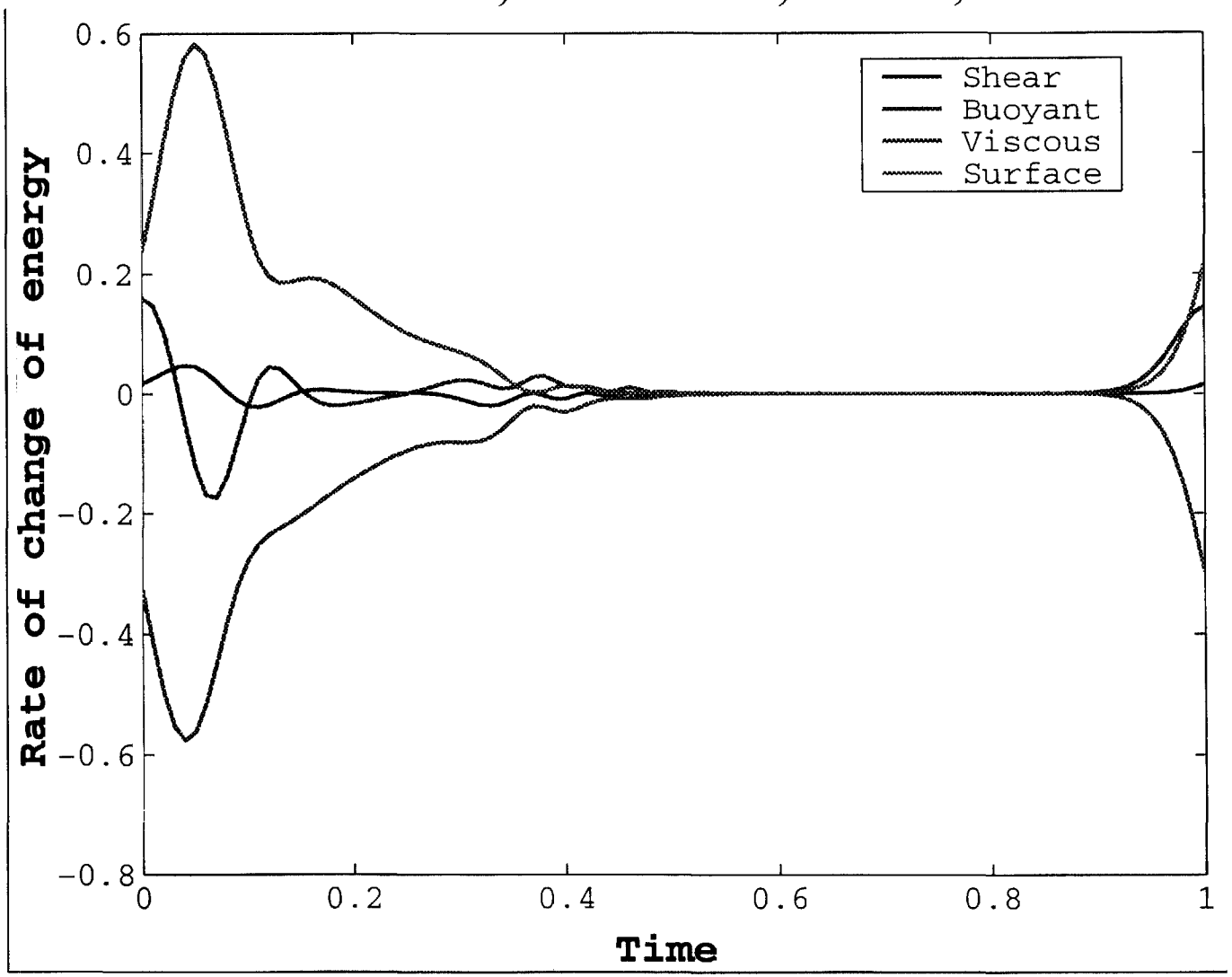

Results: Energy Balances

$Pr = 1, \Omega = 10$

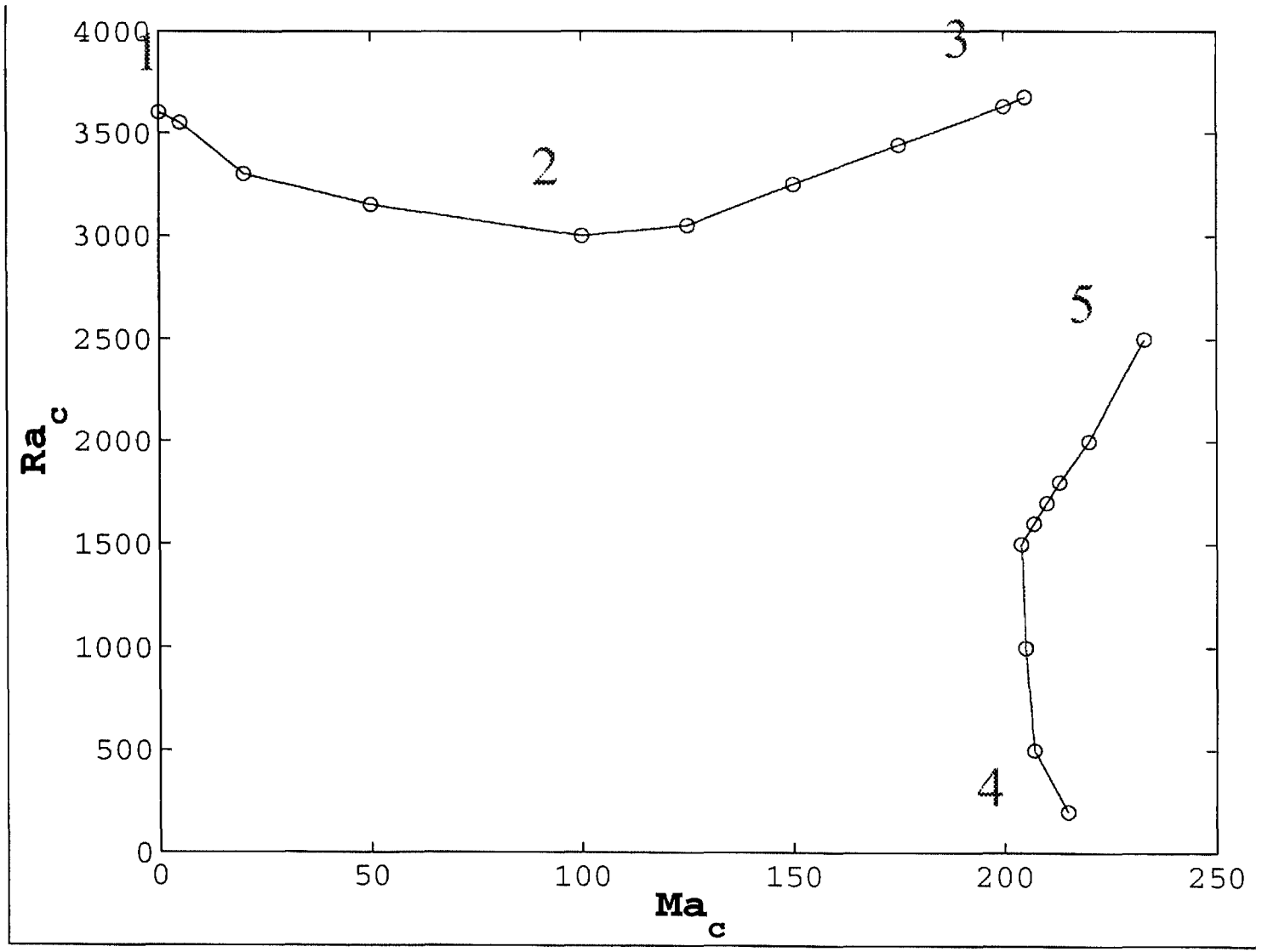

Results: Energy Balances

Ma = 220, Ra = 100, Pr = 1, Ω = 10

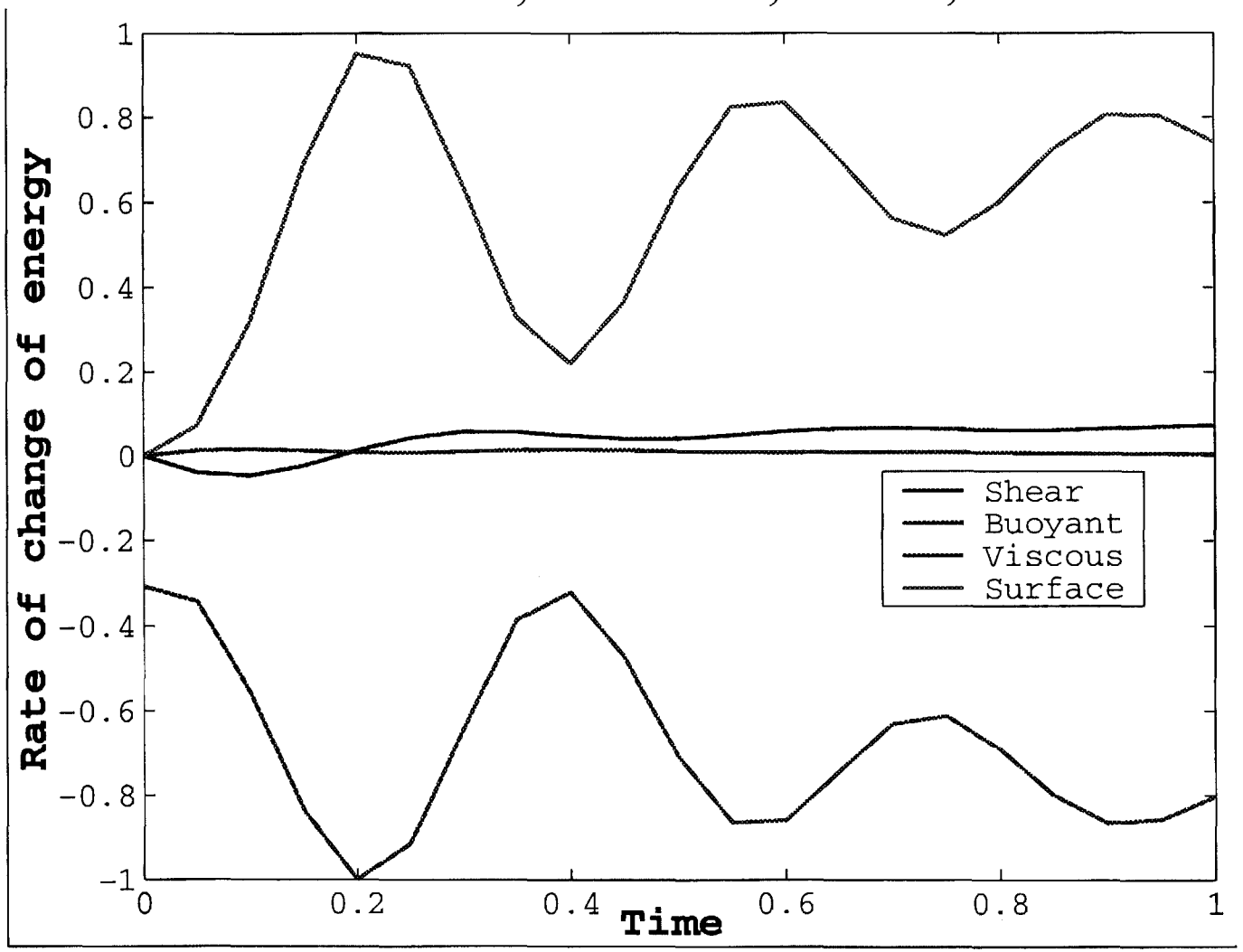

Results: Energy Balances

$Ma = 235, Ra = 2500, Pr = 1, \Omega = 10$

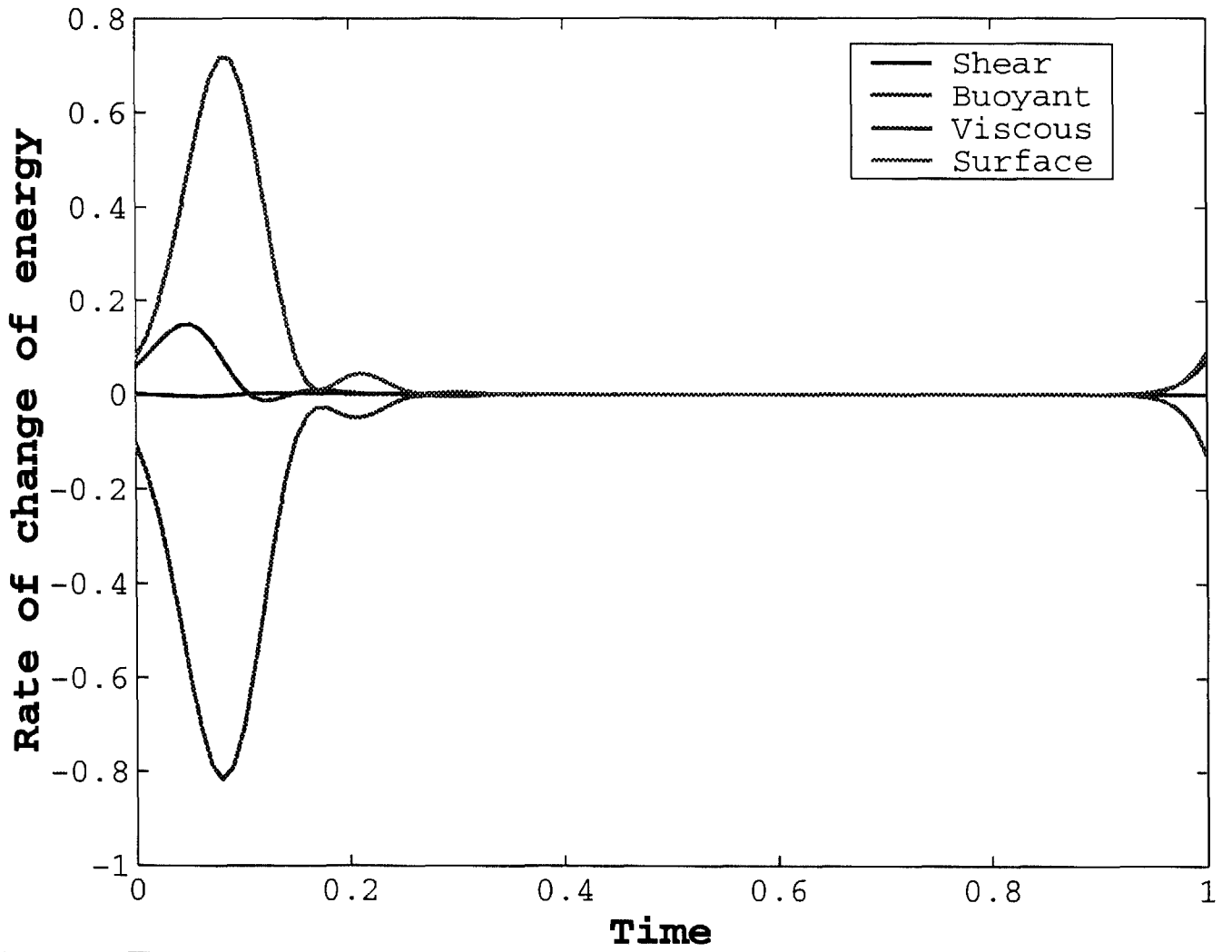

Results: Mechanisms

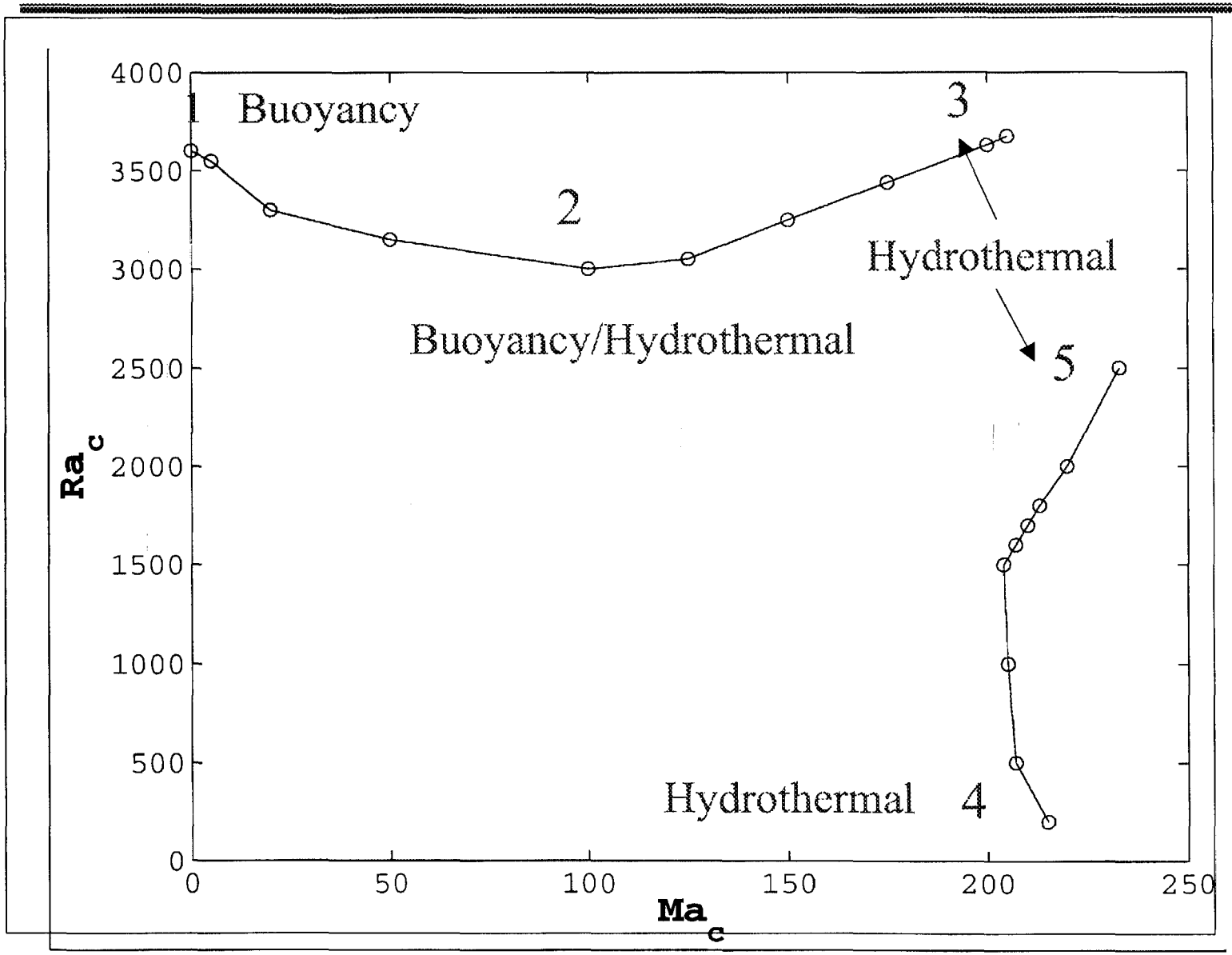

Conclusions

- Time-periodic flows have potential for three basic instability mechanisms
  - Buoyancy (Rayleigh/Benard modes)
  - Shear (finite Reynolds #) instabilities
  - Hydrothermal (Smith/Davis) waves
- Hydrothermal & Rayleigh/Benard modes dominate over the range of parameters studied

Molecular Dynamics of Fluid-Solid Systems

Joel Koplik[1] and Jayanth R. Banavar[2]

[1]Benjamin Levich Institute and Department of Physics,
The City College of the City University of New York; New York, NY 10031
[2]Department of Physics, The Pennsylvania State University; University Park, PA 16802

We will discuss the results of molecular dynamics (MD) simulations [1] of polymer melts. The idea is to specify the interactions between the individual atoms or monomers of a polymer chain in the form of classical two-body potentials, and integrate Newtons equations of motion. These simulations intrinsically study small regions of fluid over microscopic time intervals, usually in the tens of nanometers and nanoseconds, but this often suffices to exhibit continuum behavior. A further limitation here is the restriction to relatively short molecules, lengths up to 100 or so monomers, but fortunately this exceeds the estimated entanglement length. The specific computational polymers studied here are freely jointed FENE [2] chains, whose properties have been determined by previous simulations. The "canonical" rheological properties (shear-thinning etc.) have been measured by Hess, Loose and collaborators [3], while "chemical physics" properties (entanglement, reptation, etc.) have been studied by Binder, Grest, Kremer [4] et al., as well as other groups. The approach taken in this work is the simulation of complete micro-experiments of fluid mechanical phenomena: putting microscopic regions of fluid into motion with appropriate forces, taking full account of bounding surfaces, temperature control and so on.

We employ standard molecular dynamics simulation techniques [1] which have been successfully applied to Newtonian fluid flows for some time [5], and lately polymeric fluid flow as well [6]. In addition to the binding FENE force, any two monomers interact with the familiar cut-off Lennard-Jones 6-12 potential. Bounding surfaces consist of solid atoms attached to lattice sites by a confining potential and interacting with the fluid through a Lennard-Jones potential [7].

A useful generic configuration is that of a liquid drop on a solid substrate, a starting point for several calculations. Since the molecular configurations are crucial, it is important to initialize the system so as to avoid any bias. We begin with FENE chains alone, whose monomers are placed on adjoining regular lattice sites, and randomize them by cooking. The chains are confined to a box with impermeable boundaries (using a simple repulsive force field) at low density and a high temperature. After all spatial distribution functions have become isotropic, the fluid is cooled by kinetic energy rescaling and squeezed by a central force field to produce a constrained spherical drop, and then the force field is gradually removed. The resulting drop is stable if the previous operations are slow enough. The solid is separately equilibrated, and the drop is placed near the solid and allowed to interact with it. If the Lennard-Jones attractive term is 0.8 times the standard value, the liquid is partially wetting, and forms a drop (for chains of lengths 2-100, at least). Higher values, 1.0 or more, will give complete wetting, where the drop will spread until it runs out of molecules.

One easy application of this configuration is to solidify the drop by cooling the substrate. If the temperature of the solid atoms is reduced the liquid above will attempt to come to thermal equilibrium by losing heat to the substrate, and eventually solidifying. The interest

in this process stems from the recent suggestion [8] that if the liquid completely wets its own solid the final state will be a spherical cap (neglecting gravit y), but if instead it partially wets there will be a small dimple on top. In fact, for these in teractions and chains of length 2, 10, 30 and 100, there is no dimple, and as the drop cools it conducts heat sufficiently well as to produce only weak gradients in temperature and mean-square atomic displacements in ternally We are now exploring other choices of interaction.

A more striking simulation which can be readily carried out from the same initial state is coalescence. The drop plus substrate system, i.e., the atomic positions and v elocities, are duplicated and flipped ov er to give two drops opposing each other. In this case the drops are initially separated b y a distance just less than the in teraction range, so that a few nearby monomers in the separate drops are mutually attracted, and pull their respective molecules along with them. These molecules in turn pull their neighbors along, and the two drops smoothly coalesce. The process is qualitatively the same for molecules of any length, even if surrounded b y a second fluid [9].

A third application of this tec hnique concerns liquid bridge dynamics. T ostudy the elongation properties of non-Newtonian fluids in the laboratory, a useful configuration in- v olv esa cylinder of liquid placed between two solid plates [10], which are then stretched at an exponential rate. The quantitative results of these calculations will be presented in detail elsewhere [11], but for example we will exhibit snapshots of the stretched bridges, and such quantities as the minimum radius, normalized force on the plates, and T routonratio as a function of Hencky strain. These results resemble those found in experiment[10] and simulation [12], respectively .

References

1. M. P .Allen and D. J. Tildesley, Computer Simulation of Liquids, Clarendon, Oxford (1987)
2. R. B. Bird, C. F. Curtiss, R. C. Armstrong and O. Hassager, Dynamics of P olymeric Liquids, vol. 2, Wiley, New York (1987).
3. M. Kroger, W. Loose and S. Hess, J. Rheol. 37, 1057 (1993).
4. K. Binder, Monte Carlo and Molecular Dynamics Simulation of Polymer Systems, Oxford, New York (1995).
5. J. Koplik and J. R. Banav ar, Annu. Rev. Fluid Mech. 27, 257 (1995); JSME In t. J. 41, 353 (1998); Computers in Phys. 12, 424 (1998).
6. J. Koplik and J. R. Banav ar,J. Rheol. 41, 787 (1997).
7. P .A. Thompson and M. O. Robbins, Phys. Rev. Lett. 63, 766 (1989)
8. D. M. Anderson, M. Grae Worster and S. H. Davis, J. Crystal Growth 163, 329 (1996).
9. J. Koplik and J. R. Banav ar,Science 257, 1664 (1992).
10. See S.H. Spiegelberg, D.C. Ables and G. H. McKinley, J. Non-Newtonian Fluid Mech. 64, 229 (1996), and earlier references therein.
11. B. Busic, J. Koplik and J. R. Banav ar, in preparation.
12. M. I. Kolte, H. K. Rasmussen and O. Hassager, Rheol. Acta 36, 285 (1997).

Molecular Dynamics Simulations of Non-Newtonian Flows:

Liquid bridge extension
Drop coalescence and solidification

Boris Busic, Jayanth Banavar, JK

General idea:

Simulate 3d microscopic version a of lab experiment

Integrate Newton's equations for monomers with standard FENE and Lennard-Jones interactions

20,000 $\rightarrow$ 120,000 monomers, workstation $\rightarrow$ T3E

Chain lengths 4 to 100; Melts or solutions

Nosé-Hoover or constant-KE thermostats

Newtonian and non-Newtonian drop studies

start: atoms on lattice sites

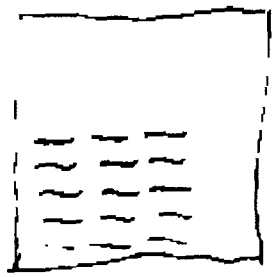

cook: run at high T and low ρ

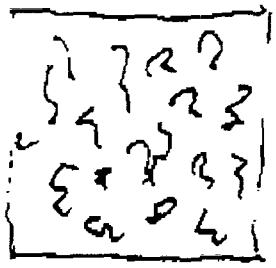

contract: lower T gradually,
apply weak central force

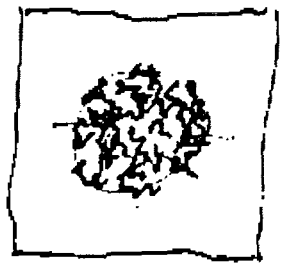

relax: gradually remove central force,
→ equilibrium spherical drop

setup: put half drop on substrate,
re-equlibrate

L=100 chains on a substrate

500 t equilibration

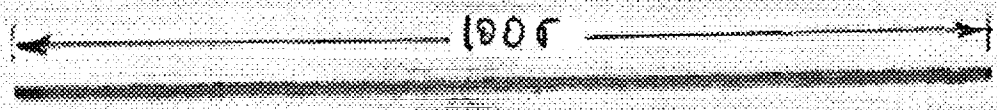

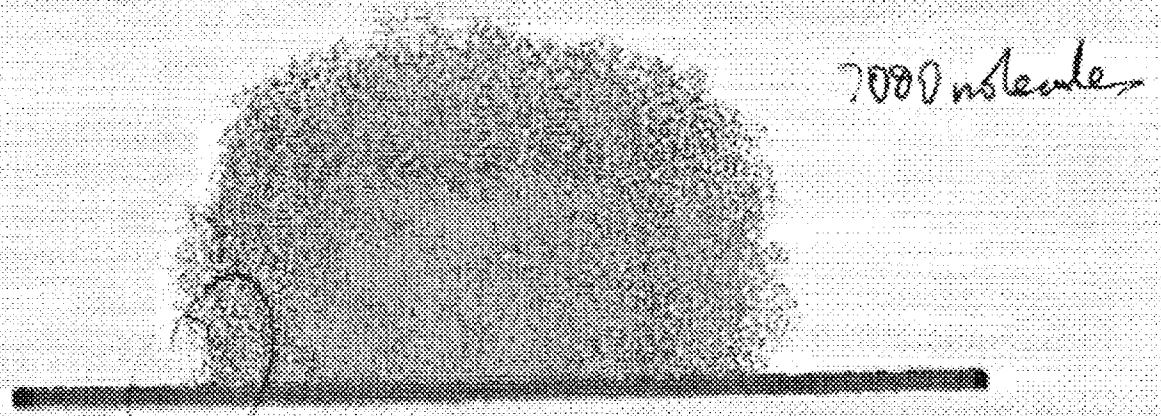

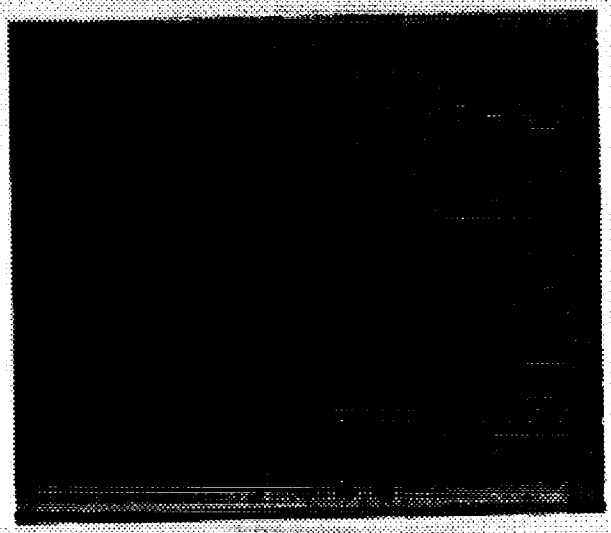

Solidification:

Cooling of a liquid drop on a cold substrate

→ test suggestion (Anderson, Davis & Worster) that a liquid which "does not wet its own solid" forms a dimple when it solidifies:

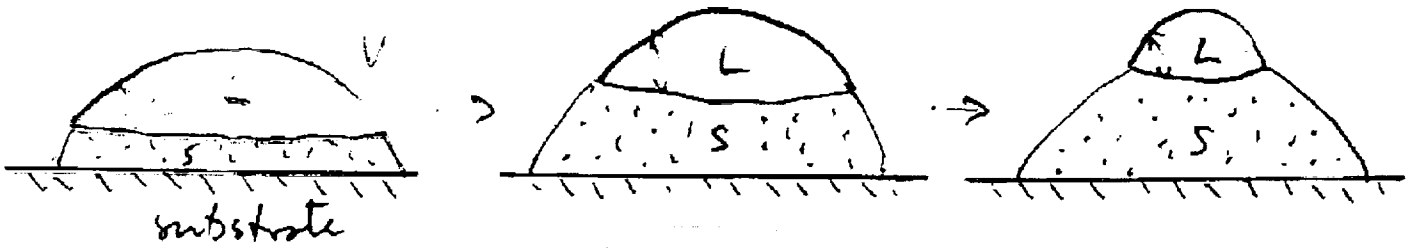

Coalescence:

Place two such drop + substrate systems in proximity
And follow coalescence process:

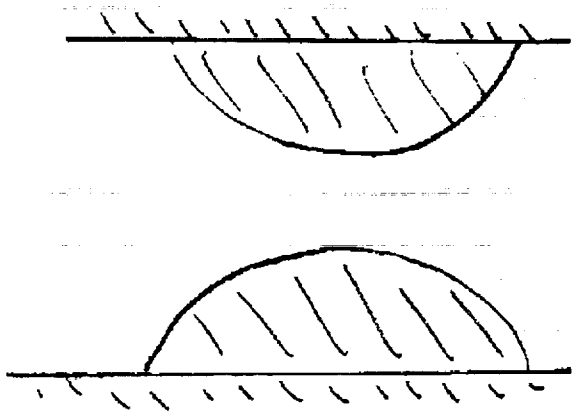

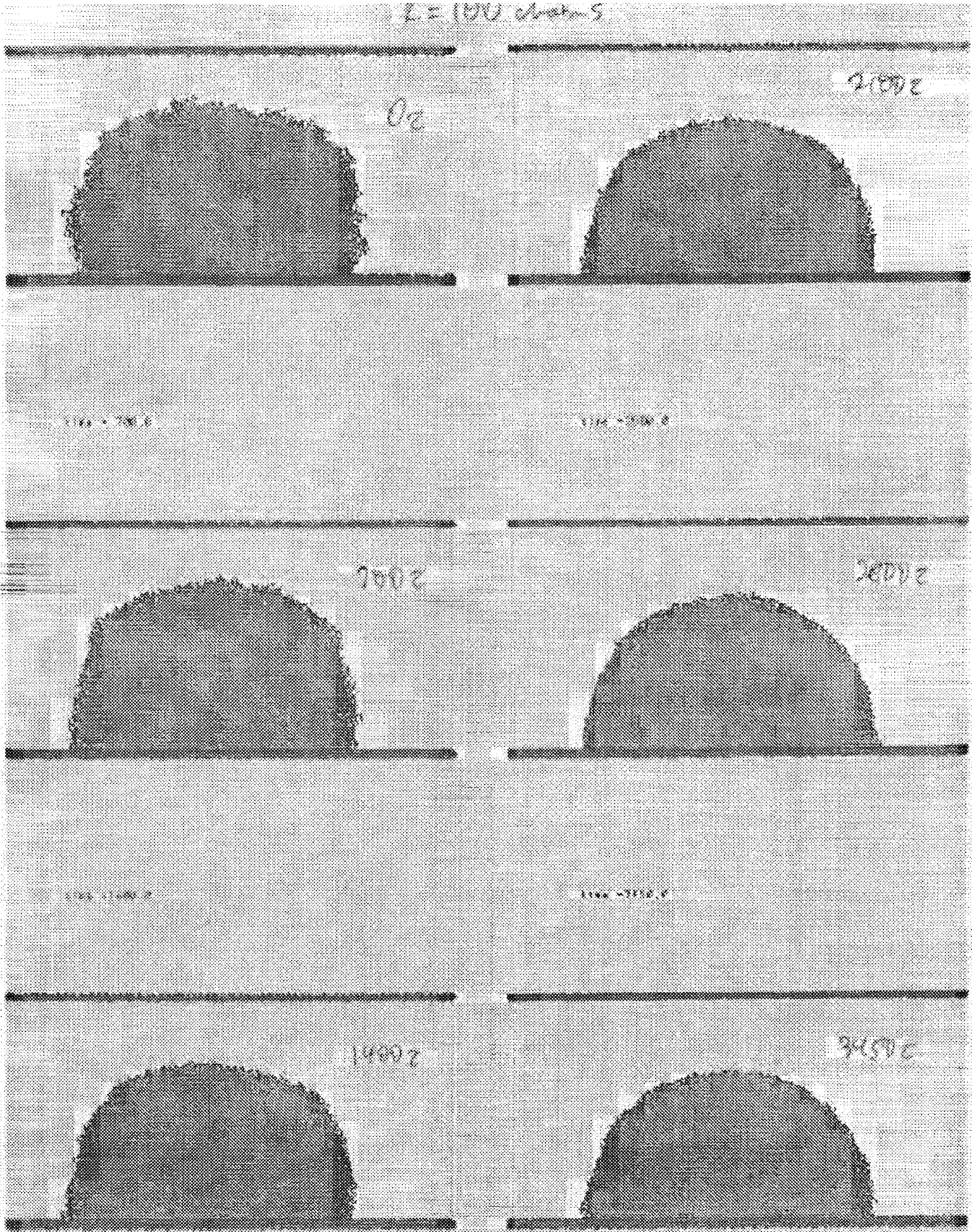
E=100 Volts
0Z
210VE
700E
2800E
1400E
3450E

L = 190 melt

freely-jointed chains

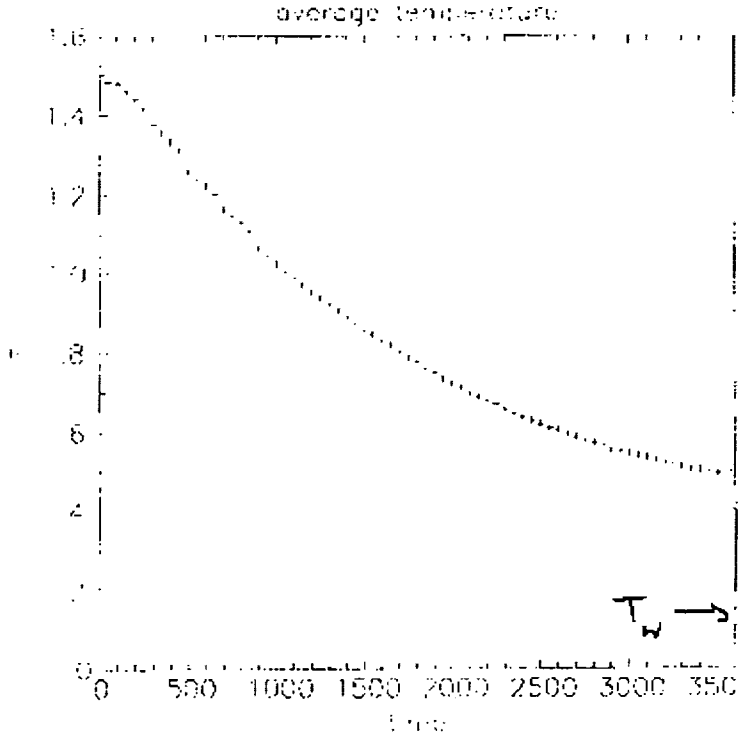

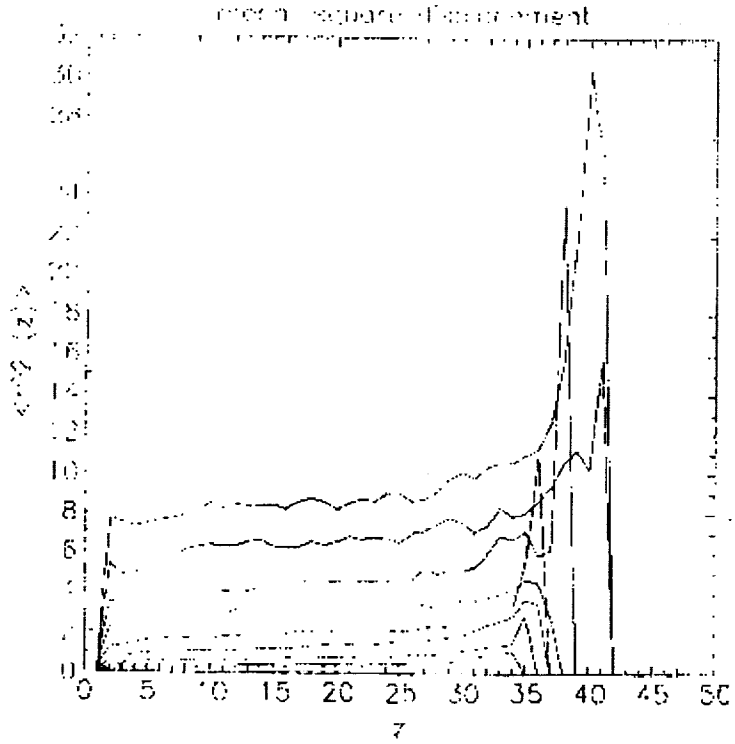

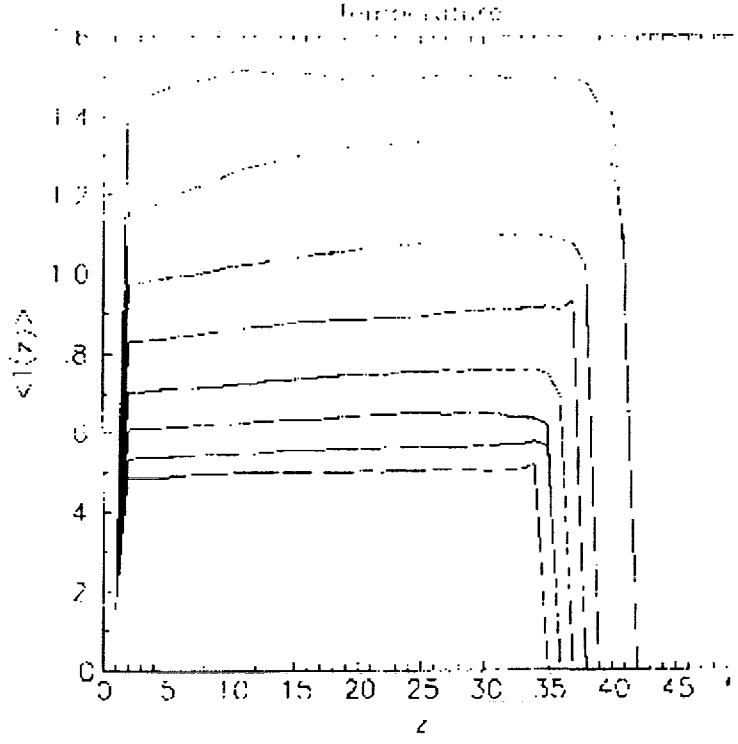

$\ell = 4$ nematic

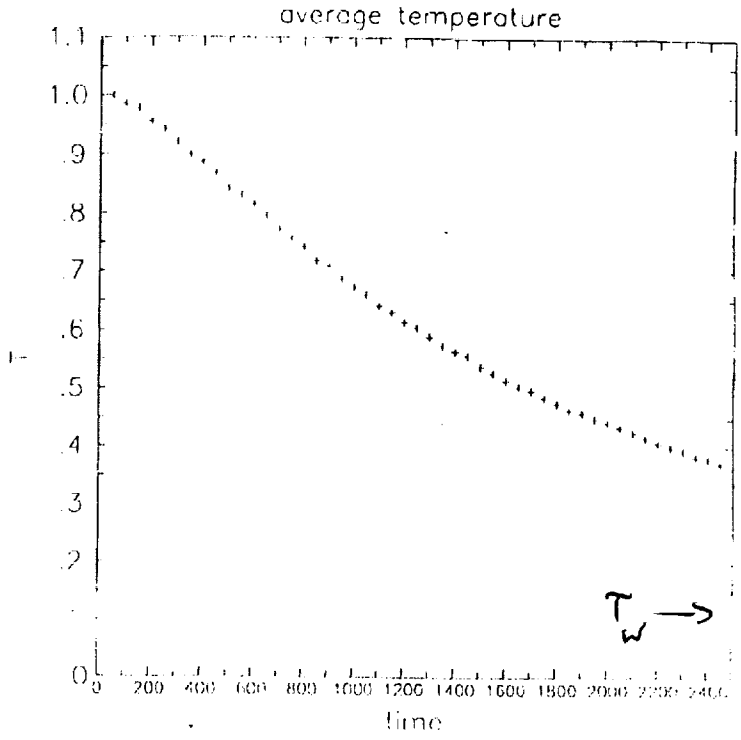

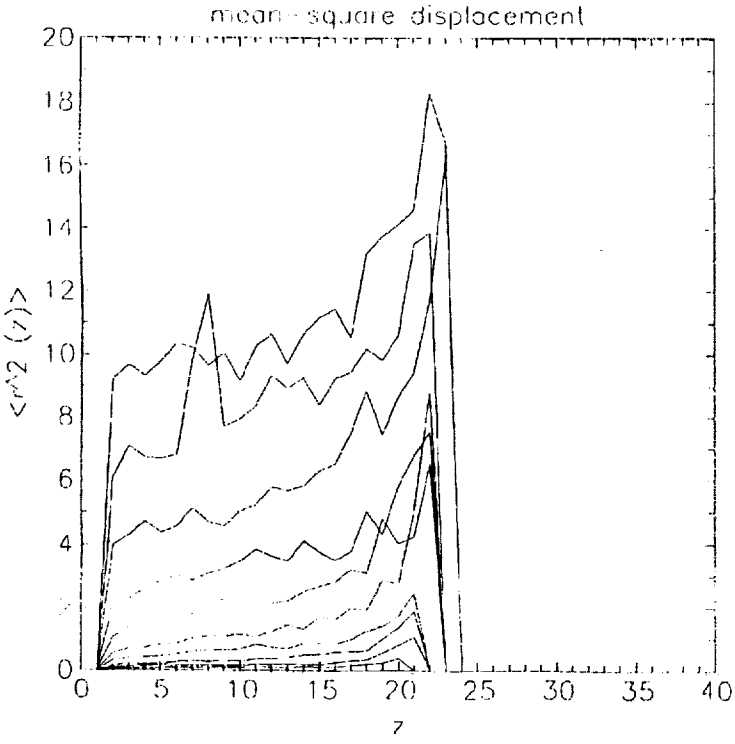

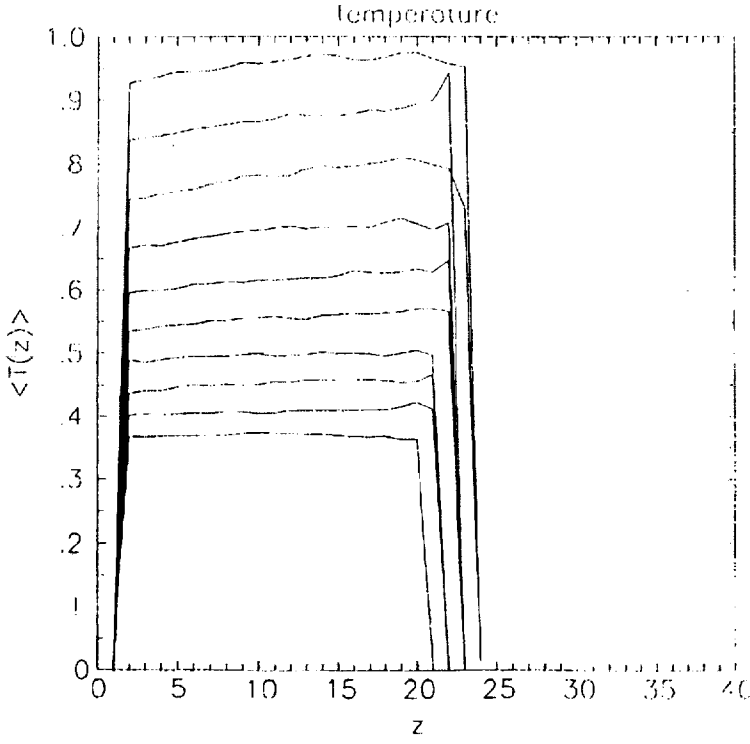

$t = 4$ months

$t = 0$

side

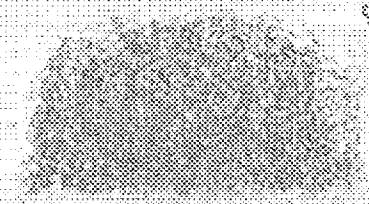

top

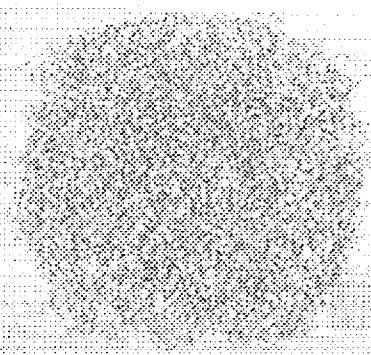

750 C

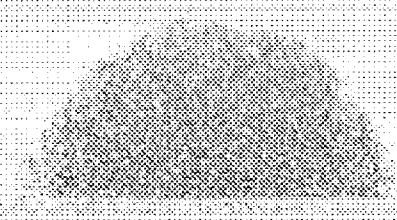

2000 C

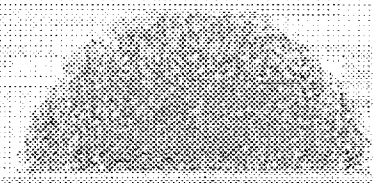

1250 C

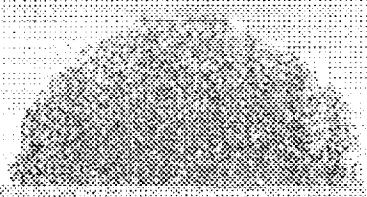

2500 C

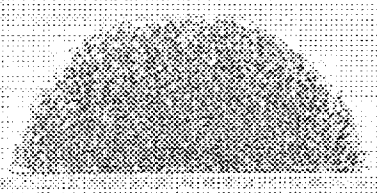

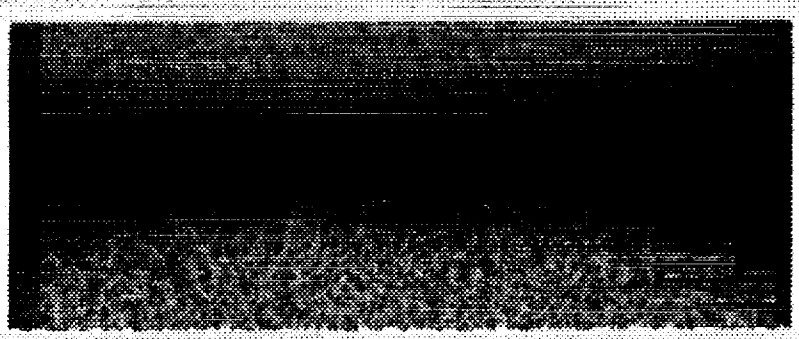

side view

top view of center slab

density profile

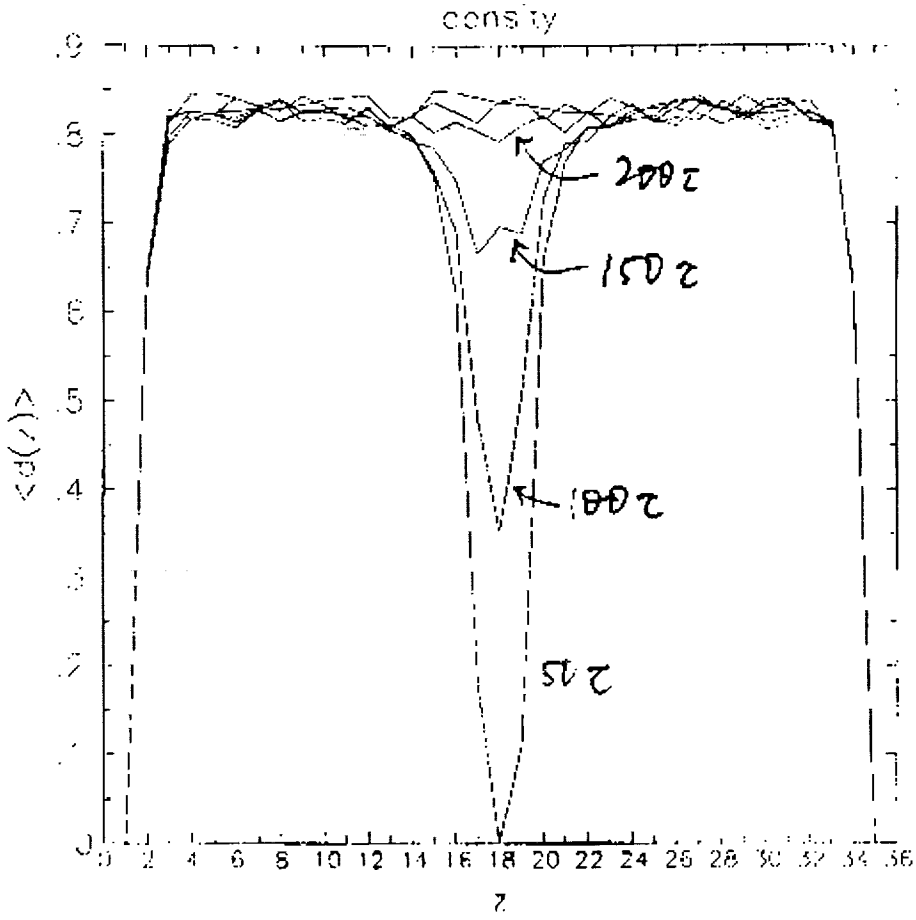

$\langle r^2 \rangle$ profile

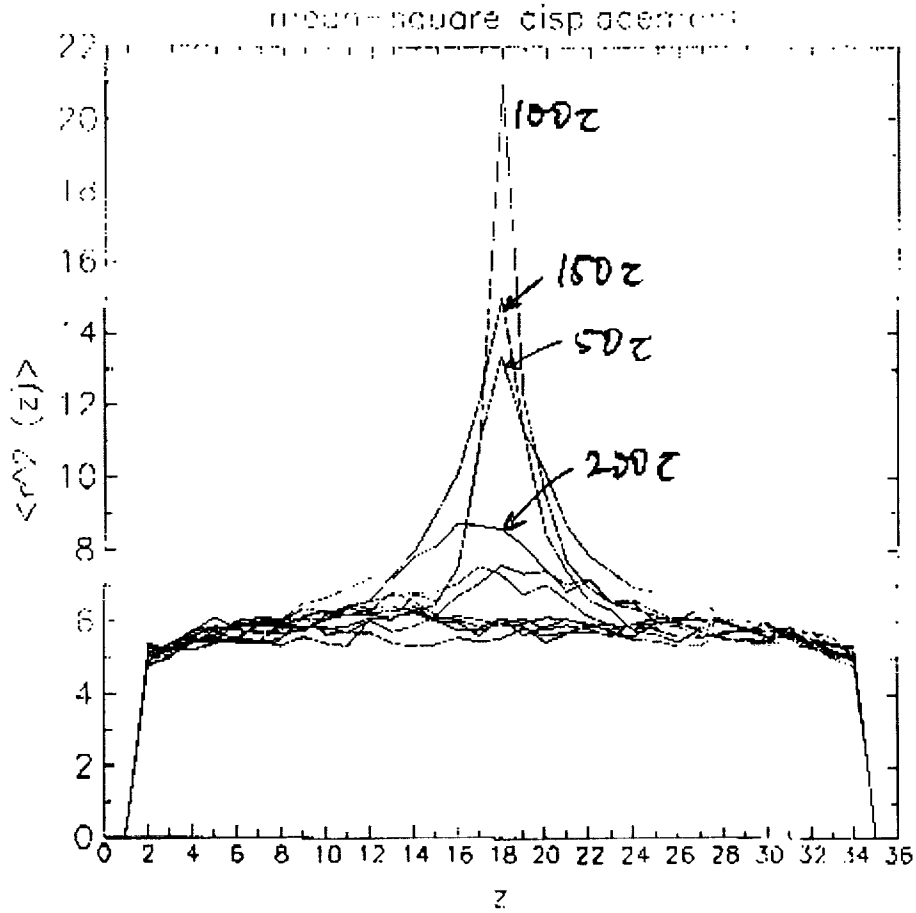

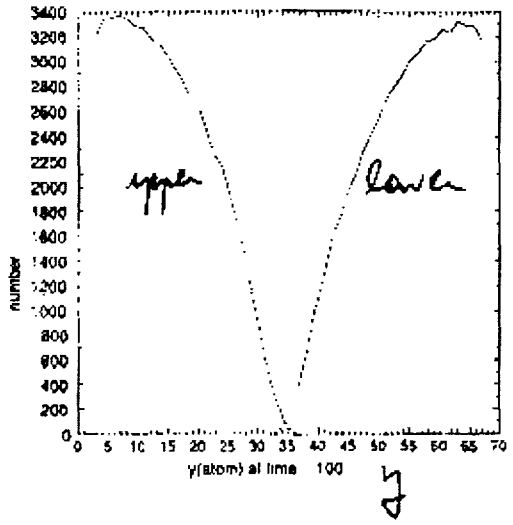
number
y(atom) at time 100

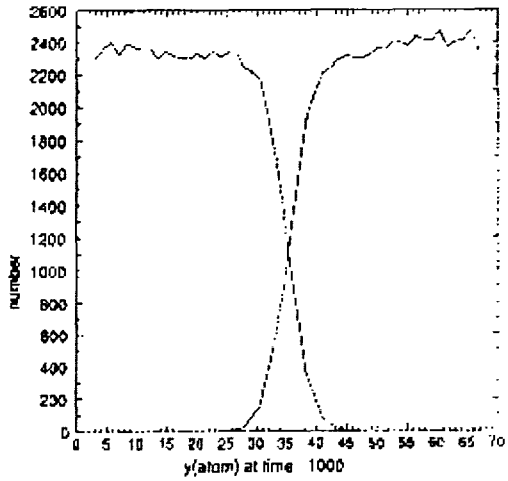
number
y(atom) at time 1000

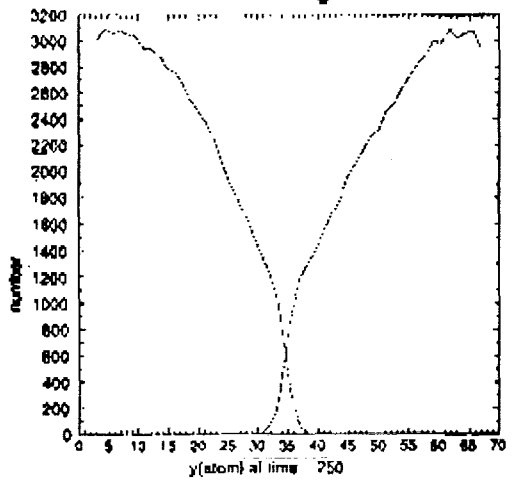
number
y(atom) at time 250

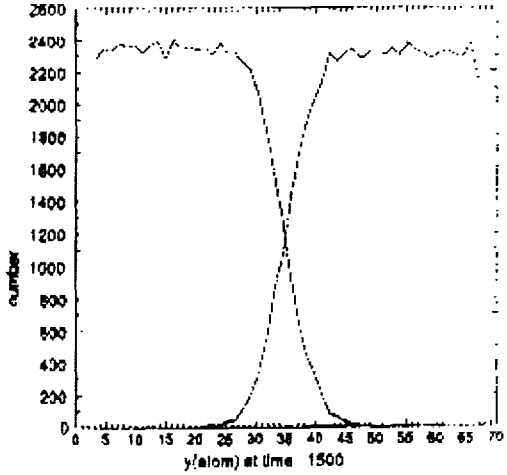
number
y(atom) at time 1500

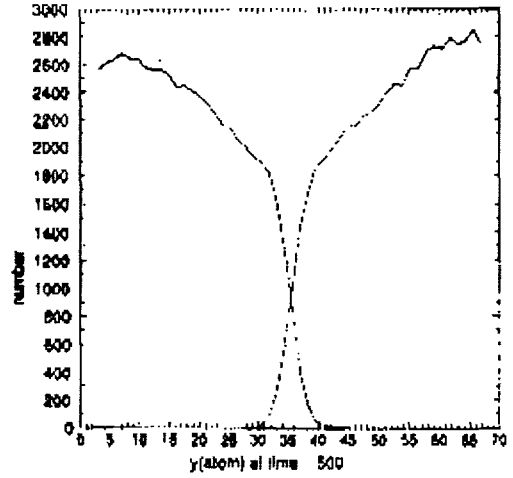
number
y(atom) at time 500

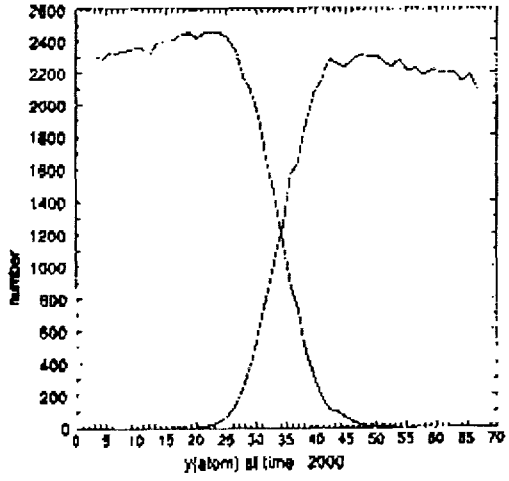
number
y(atom) at time 2000

Coalescence of L=100 chains:

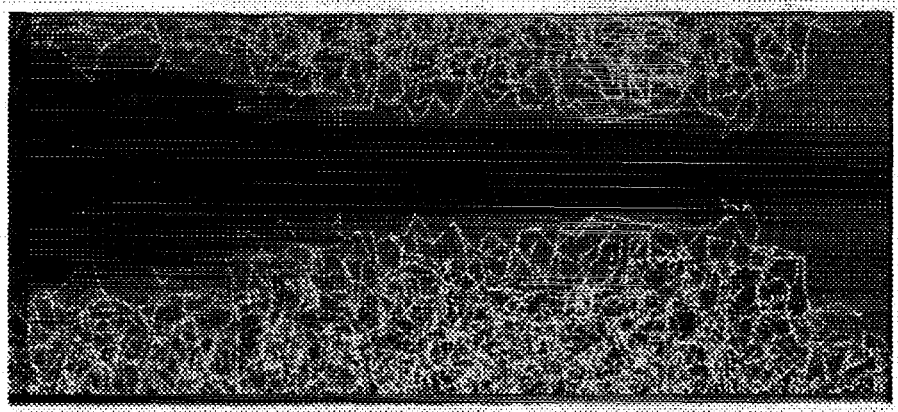

0

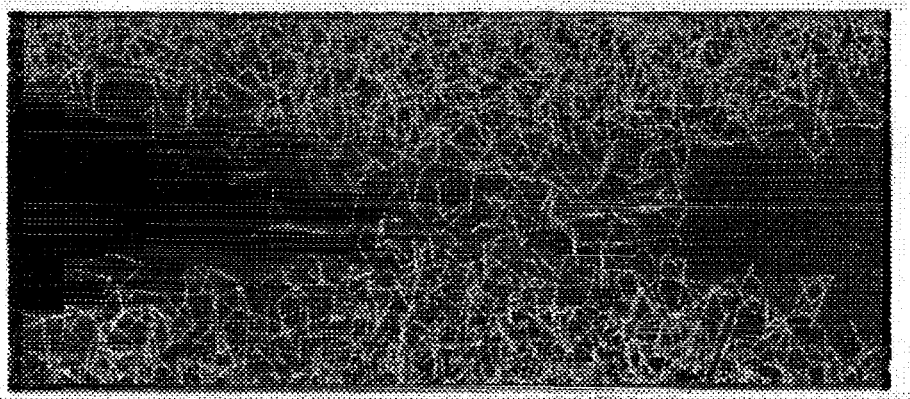

50

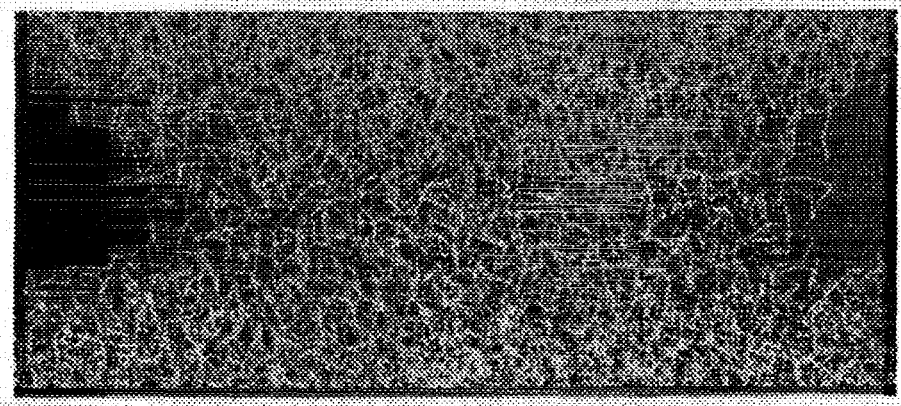

100

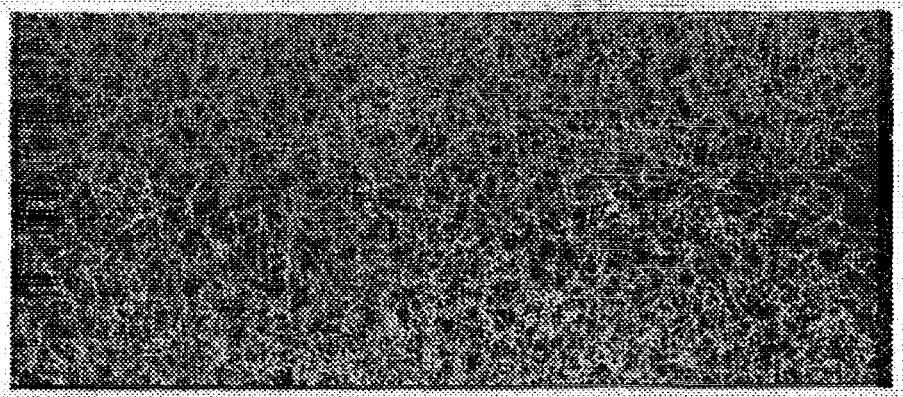

150

Liquid bridge (B. Basaran)

extensional flow of a liquid cylinder

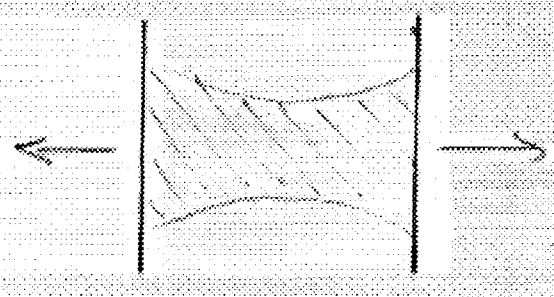

Look at shape evolution

fracture

r_{min}

F on plates

τ_r

$\underline{u}$

shear stress

Fluid properties :

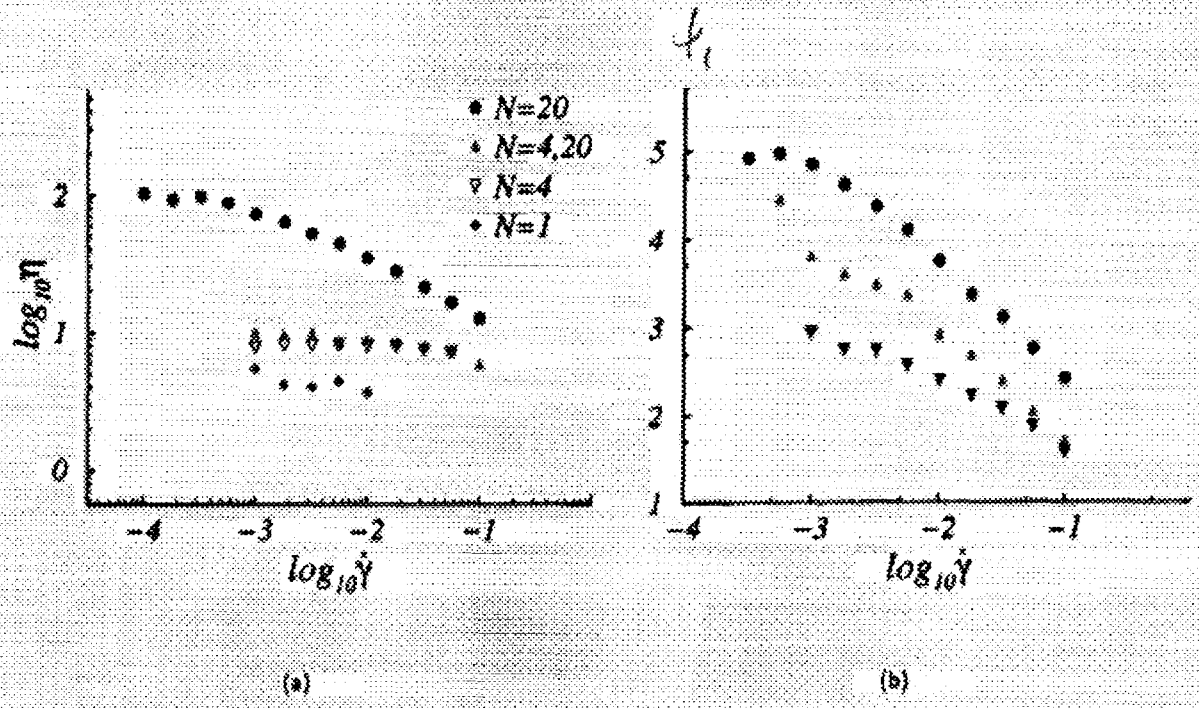

Figure 1: (b) The variation of the normal stress differences with the shear rate as $\log_{10}\Psi$ *vs* $\log_{10}\dot{\gamma}$. The symbols (•) and (▼) represent $\log_{10}\Psi_1$ the melt N=20 and the N=4,20 'solution' respectively.(▲) represents $\log_{10}(-\Psi_2)$

LIQUID	shear viscosity η_0	surface tension α	density ρ
N=20	97.0 ± 2	1.2758 ± 0.0001	1.037 ± 0.005
N=4,20 solution	9.7 ± 0.2	0.6458 ± 0.0006	0.864 ± 0.01
N=4	8.0 ± 0.1	0.6223 ± 0.0005	0.837 ± 0.009
N=1 LJ fluid	4.3 ± 0.7	0.576 ± 0.005	0.786 ± 0.004

Table 1: Physical properties of liquids in MD simulations

$\ell = 20$ melt

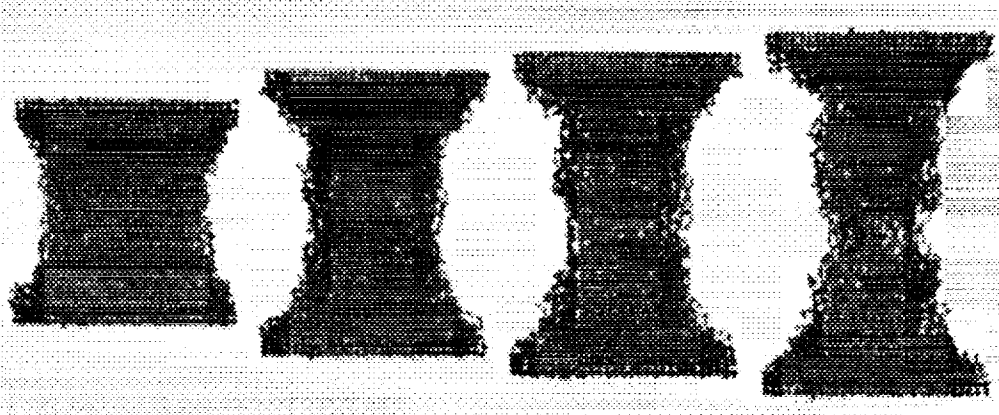

Figure 2: Snapshots of the melt $N = 20$ bridge at Hencky strains $\varepsilon = 0.349, 0.608, 0.749$, and 0.872 respectively.

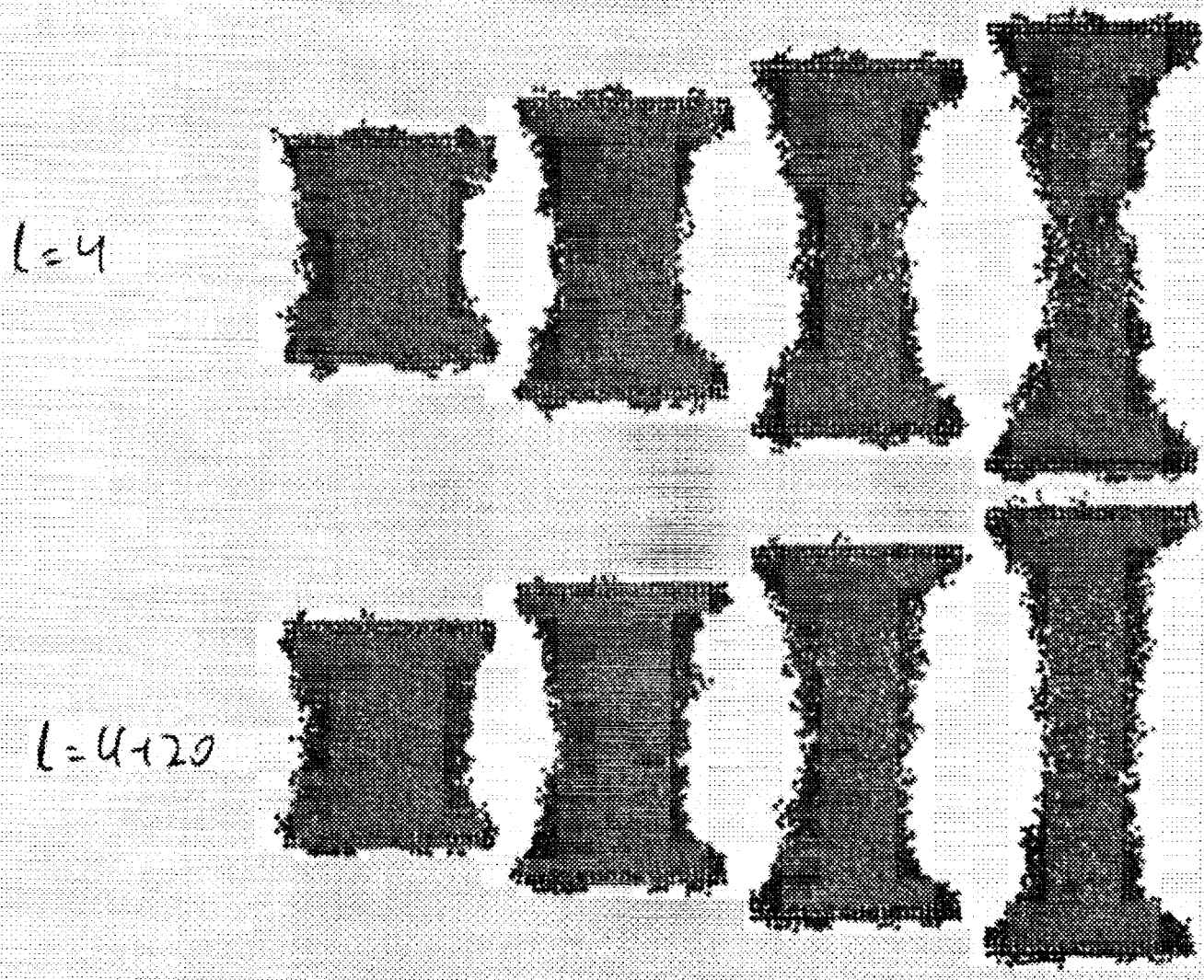

Figure 3: Snapshots of the Newtonian $N = 4$ bridge (top) and the solution bridge with the $N = 4$ fluid as solvent (bottom) at Hencky strains $\varepsilon = 0.443, 0.749, 0.983$ and 1.17 respectively.

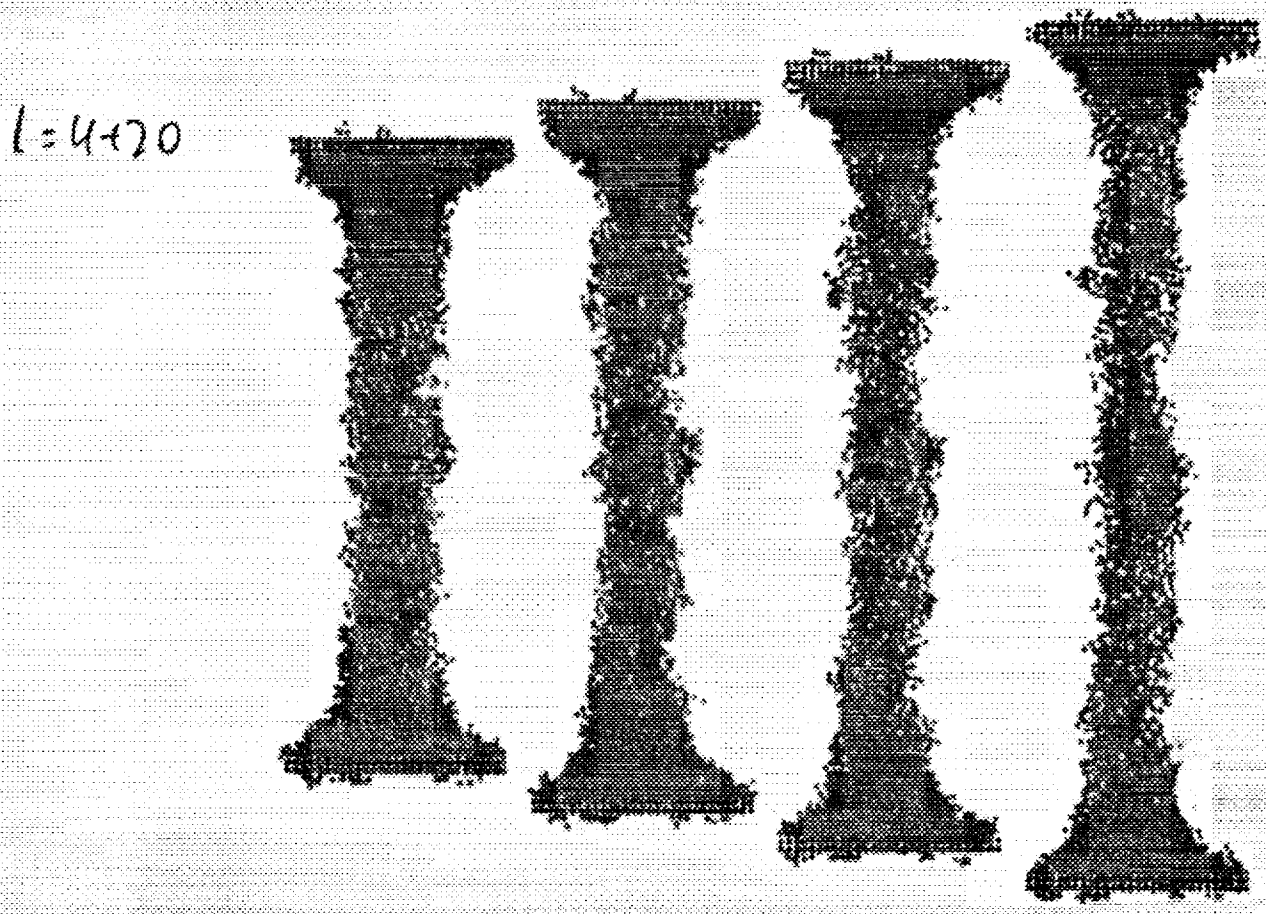

Figure 4: Snapshots of the solution bridge shown in Fig.3 at Hencky strains $\epsilon = 1.47, 1.59, 1.70$ and 1.79 respectively.

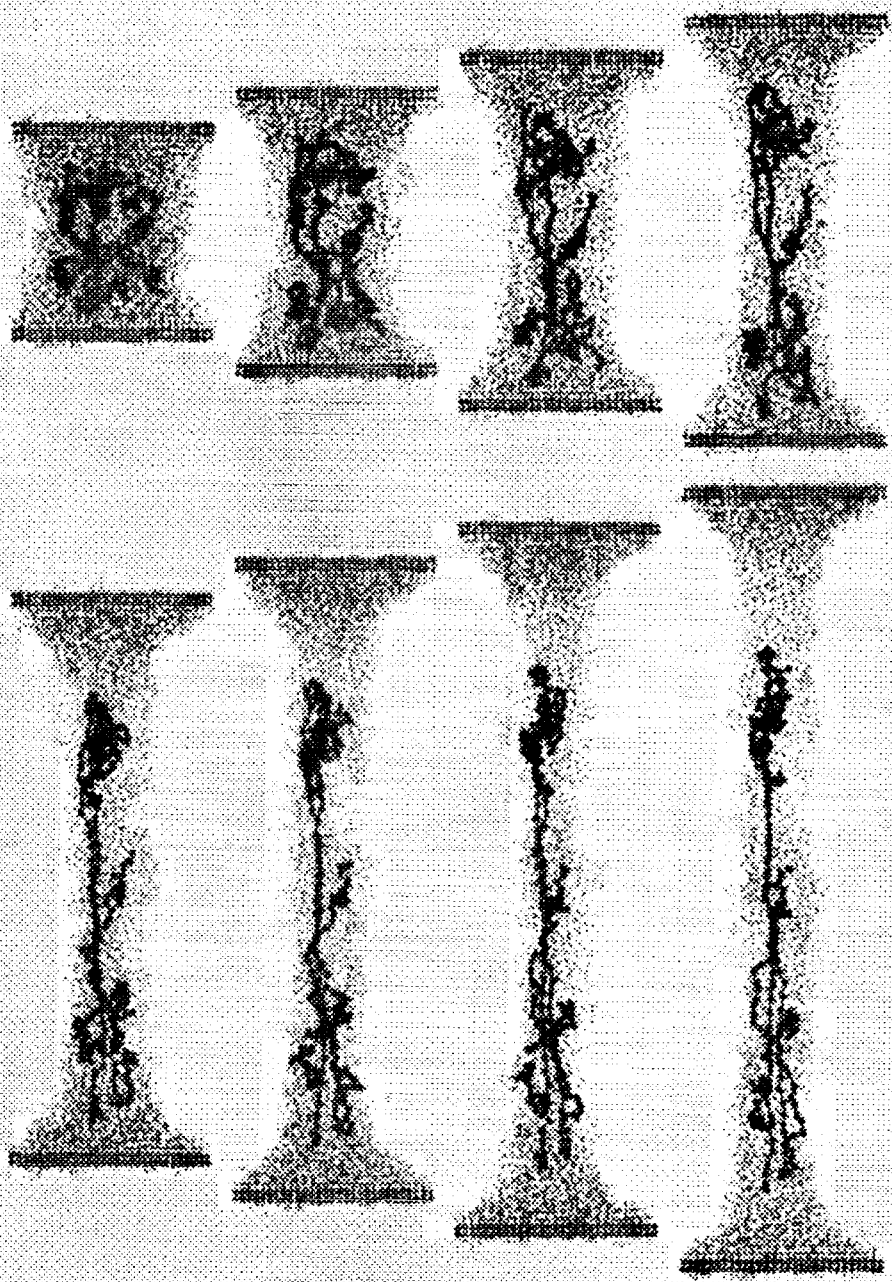

Figure 5: The polymer chain conformations in course of the solution filament elongation

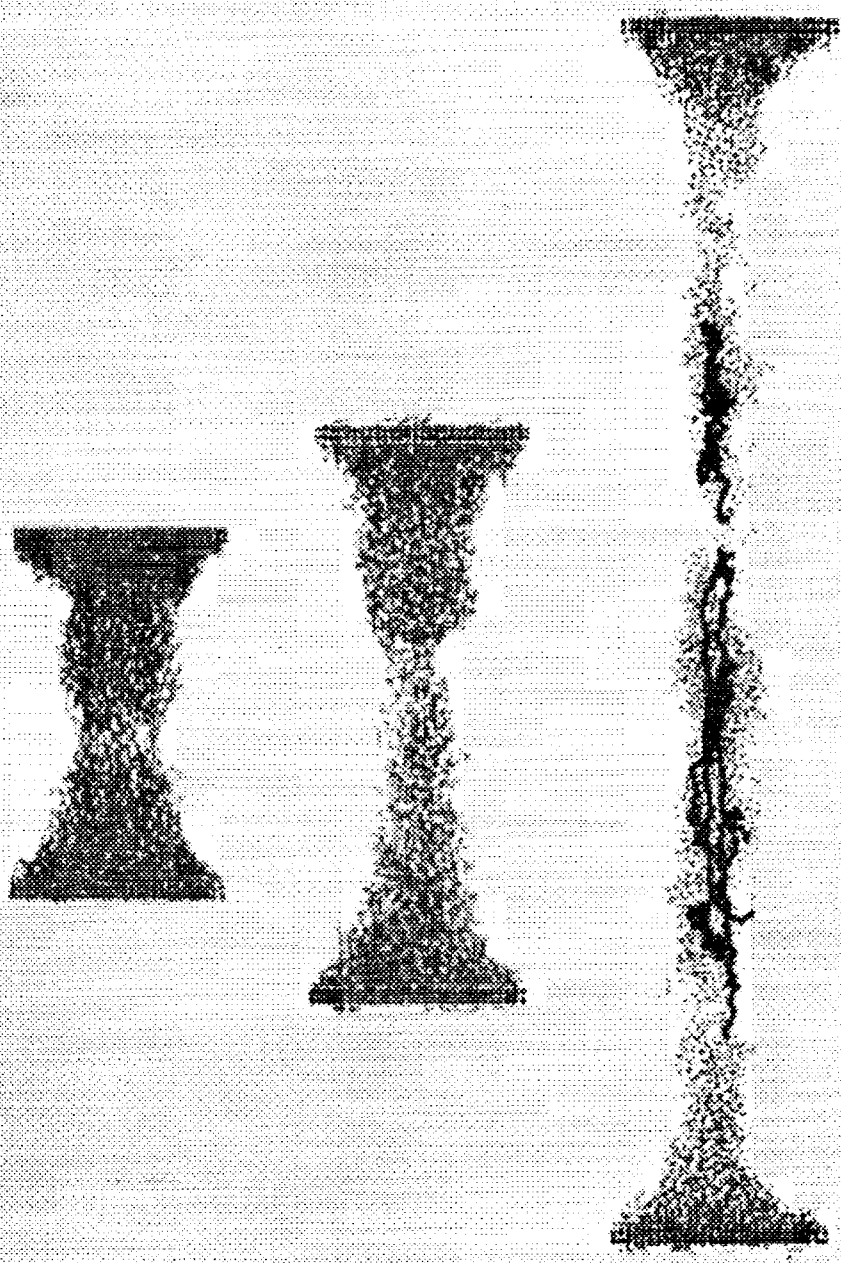

Figure 6: Break-up of the three bridges. The melt bridge is on the left, the $N = 4$ bridge in the middle and the solution bridge on the right.

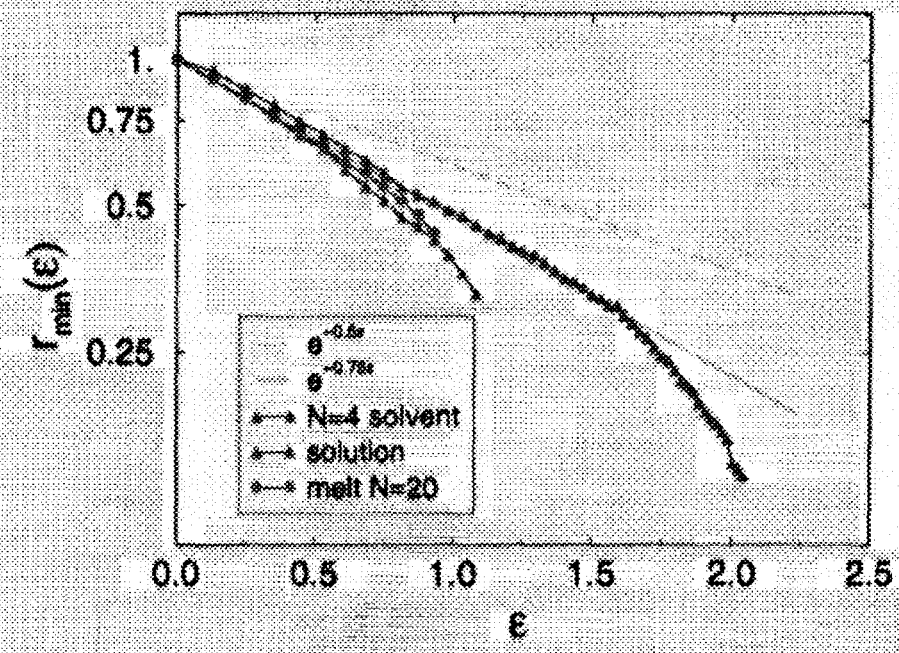

Figure 7: Evolution of the minimum radius of the filaments as a function of Hencky strain for the three bridges discussed in the previous section

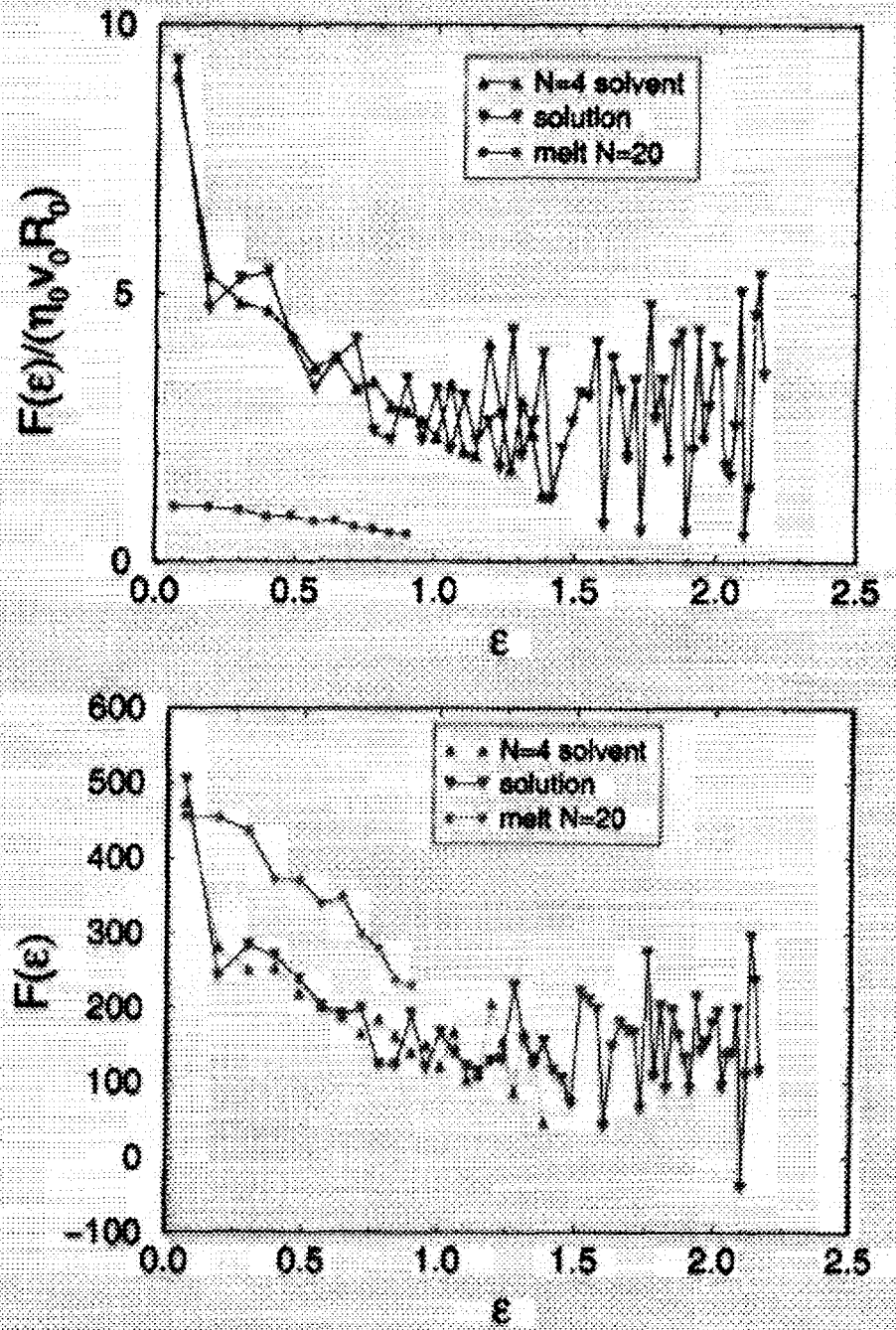

Figure 8: Evolution of the force on the end-plates as a function of Hencky strain for the three bridges discussed in the previous section

$$Tr = \frac{F}{\pi r_{min} \eta_e \dot{\varepsilon}}$$

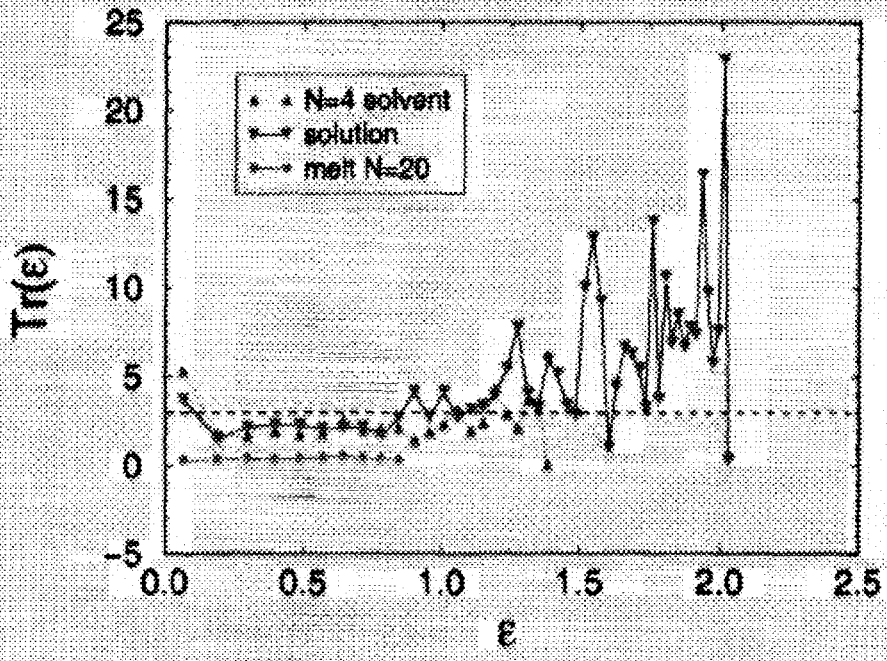

Figure 9: Trouton ratio as a function of Hencky strain for the three bridges discussed in the previous section

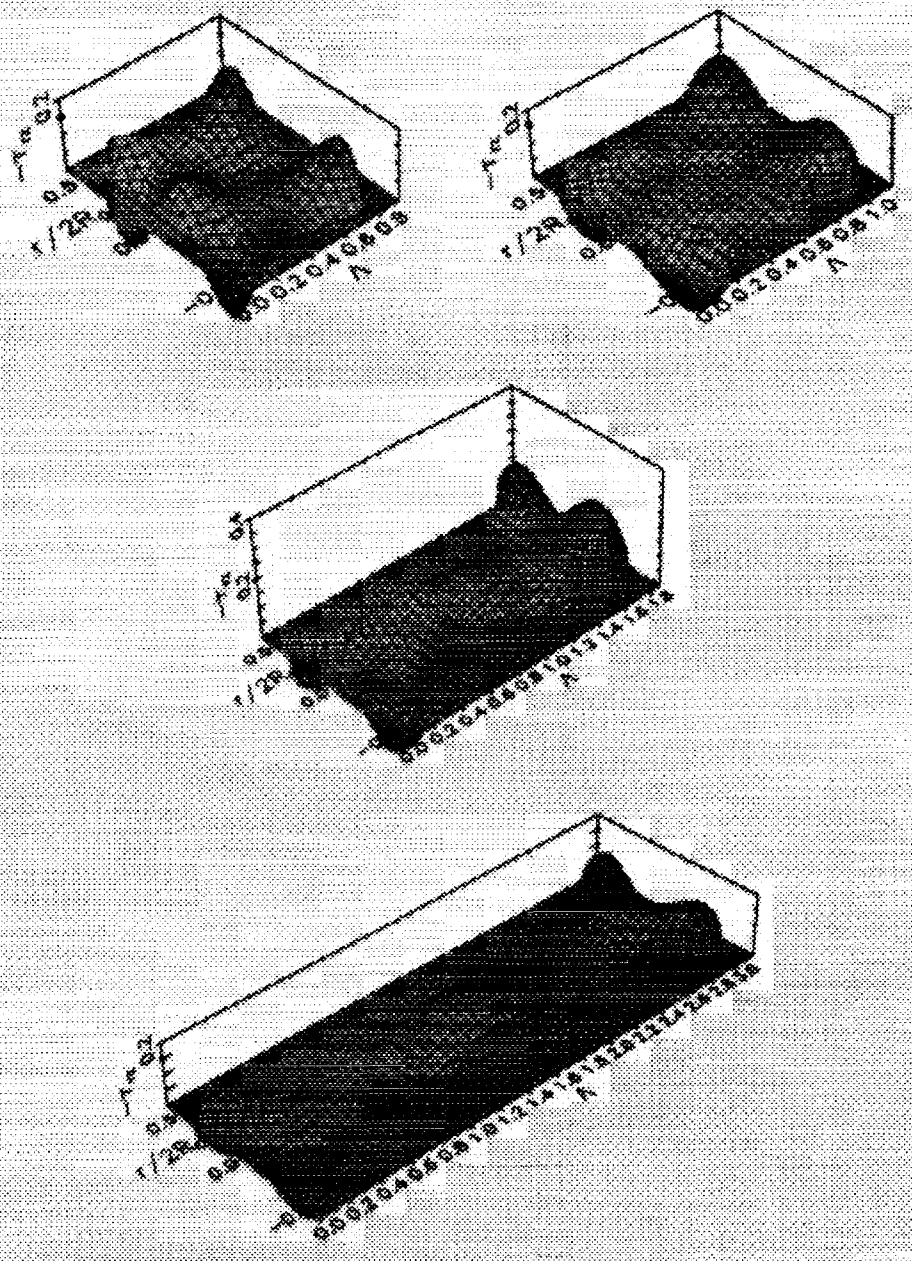

Figure 10: Shear stress for the solution bridge

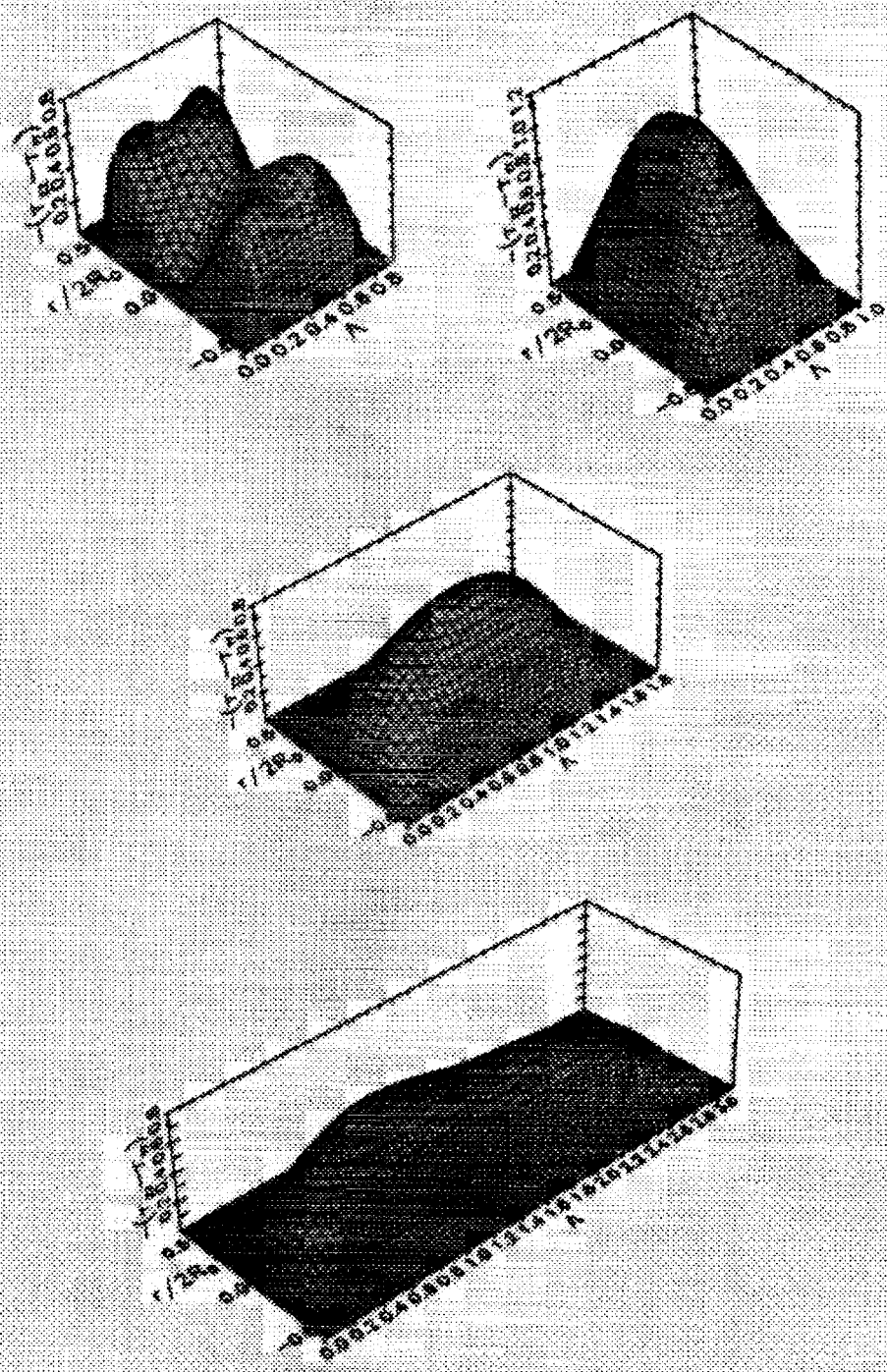

Figure 11: Normal stress difference for the solution bridge

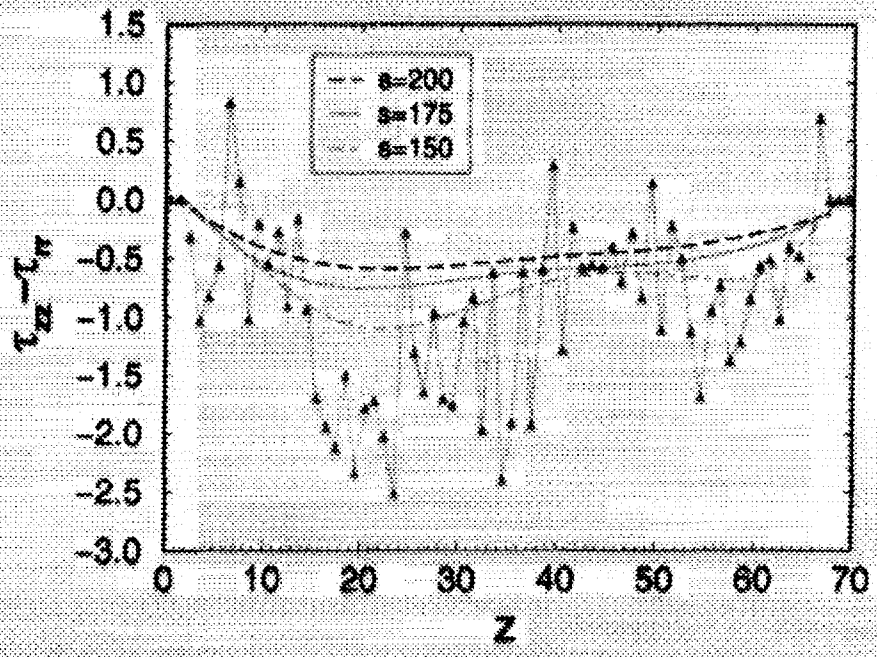

Figure 12: Variation of the normal stress difference, $\tau_{zz} - \tau_{rr}$, along the centerline of the solution liquid bridge at $\Lambda \approx 3$ The least-square polynomial fit is obtained for $s > 230$

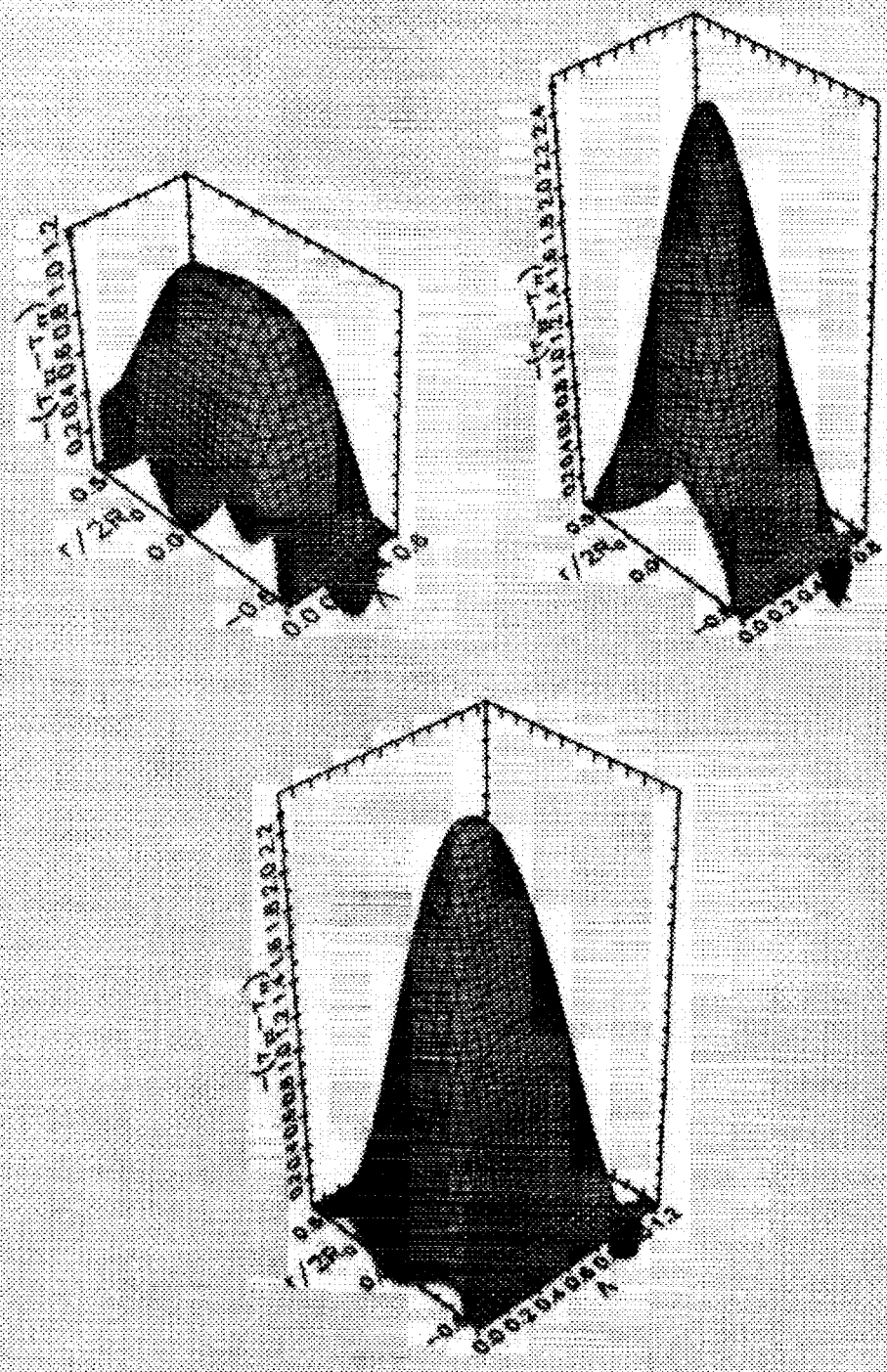

Figure 13: Normal stress difference for the melt bridge

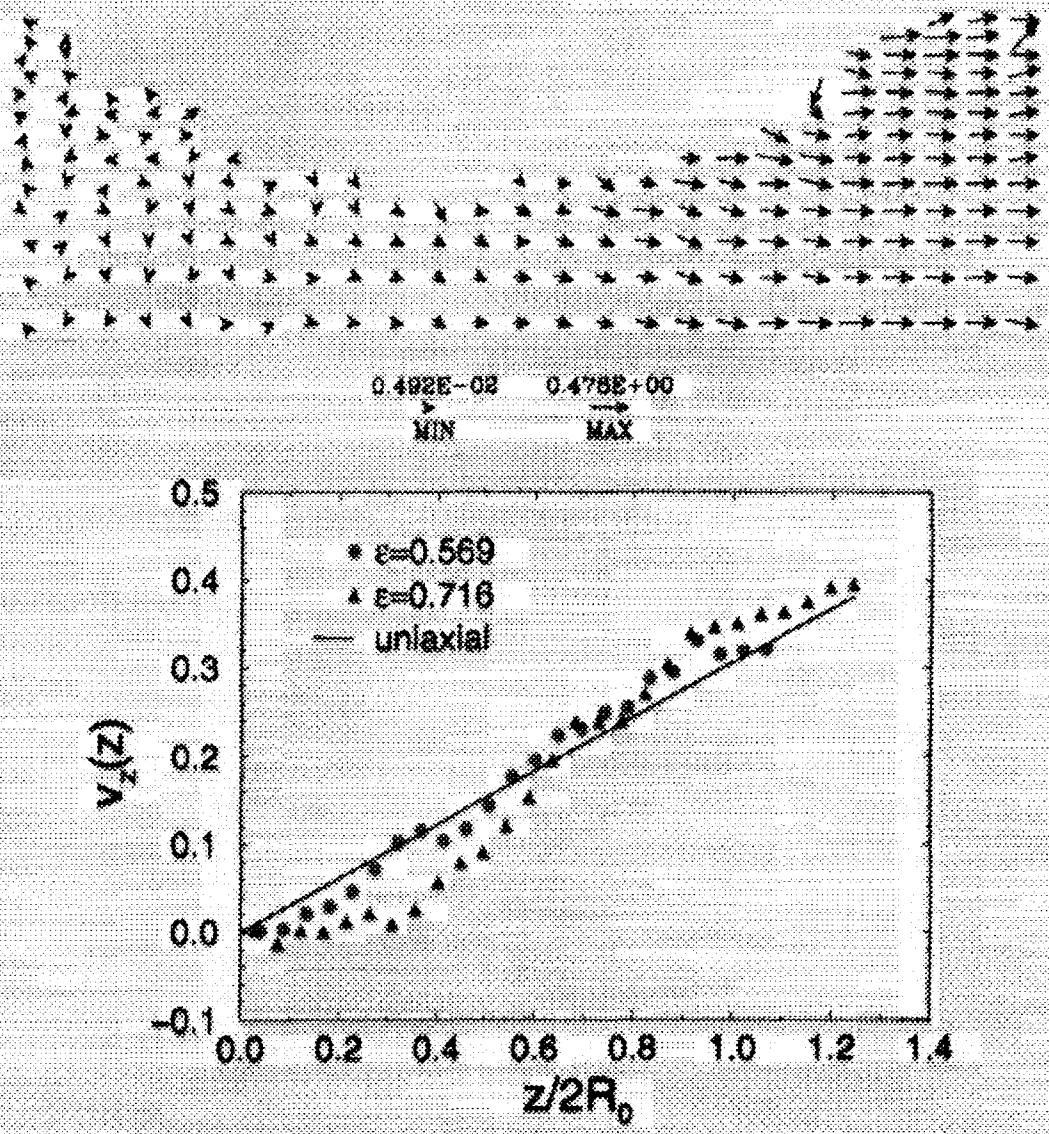

Figure 14: Velocity field of the monatomic liquid bridge at Hencky strain $\varepsilon \approx 0.569$ (top) and the axial velocity profiles along the centerline of the bridge

DIFFUSING LIGHT PHOTOGRAPHY OF CONTAINERLESS RIPPLE TURBULENCE

William Wright and Seth Putterman
Physics Department, University of California, Los Angeles CA 90095

ABSTRACT

The high amplitude motion of the surface of a fluid displays a number of extraordinary phenomena ranging from localized structures to turbulence. Among localized structures there can appear breather [1] and kink [2] solitons [sometimes called darkons] and aspects of turbulence can be studied via the mutual scattering of ripples running along the surface of a fluid[3].

As the height of the surface of a fluid $\zeta(r,t)$ as a function of position and time is the key parameter measurement of the above phenomena requires a technique that can resolve large variations in $\zeta(r,t)$. In our experiments the surface motion is made visible by suspending into the water a .04% solution of polyballs. This concentration is sufficiently dense that light travelling through the water is so strongly scattered that it diffuses. In this way the technique overcomes the problems presented by the appearance of caustics in attempts to apply shadowgraphs to high amplitude fluid motion. The key criterion for the application of diffusing light principles to resolve surface height is that the overall depth of the fluid must be greater than the transport mean free path which in turn must be comparable to the maximum surface heights resolved. The concentration is sufficiently dilute that it does not affect the viscosity. Light is then incident on the fluid from below and a charge coupled device (CCD) records the light to exit the fluid. Typically the image of the surface is broken up into one million pixels [1024x1024] where each pixel is capable of recording a dynamic range of 65,000 gray scales [or 16 bits]. This image is converted into the surface height with the help of a calibration plot.This plot shows the amount of light to exit the surface as a function of fluid depth. The deeper the fluid the smaller is the amount of light to make it to the surface at that location. The dependence on surface slope is weak as demonstrated from photos of jello molds in the shape of sine waves that are formed from these water polyball solutions. The maximum slopes of these molds corresponds to capillary wave mach numbers of about ½, This imaging technique is useful for obtaining an instantaneous realization of the surface height when the illumination is in the form of a short [microsecond] flash of light. The surface height as a function of time at a single point in the fluid can be obtained by reading out the calibrated signal from a single pixel as a function of time.

This technique has been able to resolve, the hyperbolic secant profile of a breather soliton, the hyperbolic tangeant profile of a darkon, the unusal shear thinned states of non-Newtonian fluids, and the Kolmogorov spectrum of ripple turbulence. This last case constitutes the core of a proposed experiment in microgravity and will be described further.

The law for the spectrum in the inertial region can be derived in parallel with Kolmogorov's law of vortex turbulence. If E_k denotes the ripple energy per unit area

between k and 2k then E_k must be sufficiently large that nonlinear reversible processes dominate damping of mechanicalenergy due to viscosity.. Furthermore the density of modes excited must be sufficiently large that their spacing in frequency space is less than their broadening due to nonlinear interactions. In this limit one finds for the power spectrum of surface motion :

$$\zeta^2(\omega) = q^{1/2}\sigma^{1/6} / \rho^{2/3}\omega^{17/6}$$

$$\zeta^2(k) = q^{1/2}\rho^{1/4} / \sigma^{3/4}k^{15/6}$$

where $q, \omega, k, \rho, \sigma$ are energy input [at some low frequency], frequency, wavenumber, fluid density, and surface tension. Measurements reveal reasonable agreement with both of theses formulas. The fact the the temporal spectrum agrees with the spatial spectrum is another test of the imaging technique.

A number of key assumptions underly the 'derivation' of Kolmogorov's law from the theory of interacting propagating waves[4]. They are 1) the random phase approximation and 2) a closure hypothesis. In its simplest form the closure hypothesis says that the average of the product of action of two modes is the product of the averages [this can be called a stosszahl ansatz]. The abiding question of turbulence is the extent to which these assumptions are violated.

These issues will be addressed in a microgravity environment where ripples will be studied on the surface of a positioned fluid sphere that is about 12cm in diameter. The sphere will be held in place and excited by acoustic forces. Light will be brought in with an optical fiber to the center of the sphere. From that point light will diffuse out to the surface where it will be imaged.

On the surface of a sphere the wavenumber k is replaced with l/R where l is an integer and R is the radius of the sphere. For a cascade starting at 1Hz [l about 8], the turbulent regime in k should extend over more than 1.5 decades.

The advantages of microgravity are that the forces of capillarity dominate the motion over a wider ranger of wave numbers than on the ground. This is desirable as the nonlinear properties of capillary waves are much stronger than those of gravity waves. At these longer wavelengths capillary waves also suffer less dissipation and so the effects of turbulent motion are more accessible. In low g it is possible to levitate a large drop of fluid. In this arrangement capillary waves do not scatter off of boundaries but run around the drop and scatter only off other waves which is precisely the effect that we seek. This can be called turbulence without boundaries.

1] J.Wu et al; Phys. Rev. Lett. **52**, 1421 (1984).
2] B. Denardo et al ; Phys. Rev. Lett. **64**,1518 (1990).
3] W. Wright et al;Science, **278**,1609 (1997).
4] S. Putterman, P.H. Roberts; Phys. Rep. **168**,209 (1988).

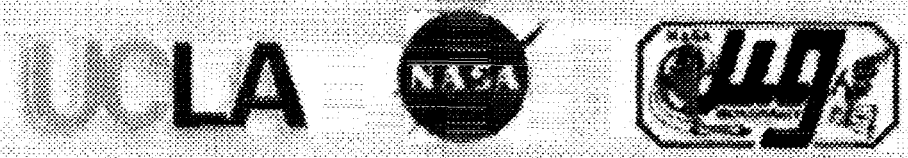

Diffusing Light Photography Of Containerless Ripple Turbulence

Seth J. Putterman & William B. Wright
UCLA — Department of Physics & Astronomy

INTRODUCTION AND BACKGROUND

OVERARCHING PARADIGM

ENERGY FOCUSING IN THE FAR OFF-EQUILIBRIUM MOTION OF FLUIDS

Turbulence: the influence of nonlinear processes on the randomization of energy leads to the appearance of intermittent structures.

Solitons: localized structures that remain stable at high amplitudes.

Sonoluminescence: diffuse sound energy focuses by 12 orders of magnitude to create picosecond flashes of ultraviolet light.

Frictional Electricity: slow relative motion of a conductor on a dielectric accelerates electrons to 1% speed of light.

Stick-slip Friction: uniform macroscopic stresses are focused to 1Mbar by quantum bonding.

Big whorls have little whorls
Which feed on their velocity;
And little whorls have lesser whorls,
And so on to viscosity
(in the molecular sense) ... Richardson 1926

The wind comes in gusts ... attributed to Landau

When I die and go to heaven there are two matters on which I hope for enlightenment. One is quantum electrodynamics and the other is turbulent motion of fluids. And about the former I am really optimistic.

Sir Horace Lamb 1932

Deep Water Traveling Waves
- Dispersion Law -

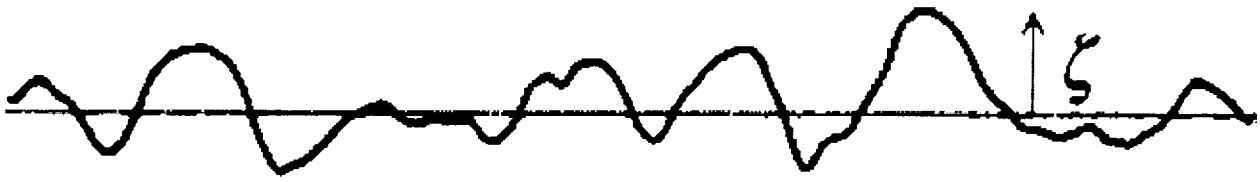

$$\zeta = \zeta_k e^{ikx - i\omega t}$$

$$\omega^2 = gk + \frac{\sigma}{\rho} k^3$$

Capillary length $= 2\pi\sqrt{\frac{\sigma}{\rho g}} \sim 1.7$ cm $= \lambda_c$

$\lambda < \lambda_c \rightarrow \sigma$ waves

f > 14 Hz

[using σ = 70 dynes/cm]

Three Wave Interactions

- Finite Amplitude Ripples –

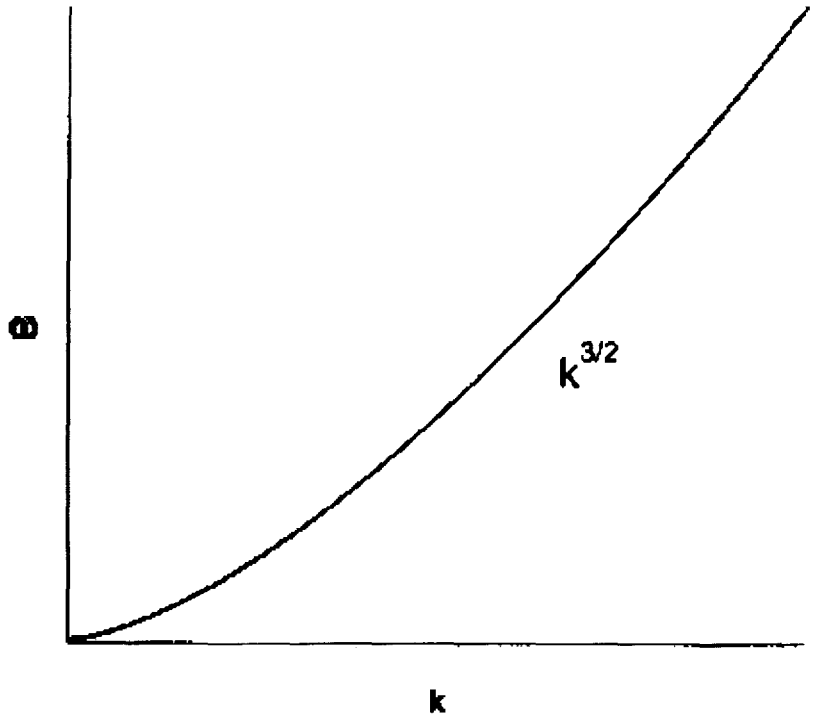

Fundamental Interaction

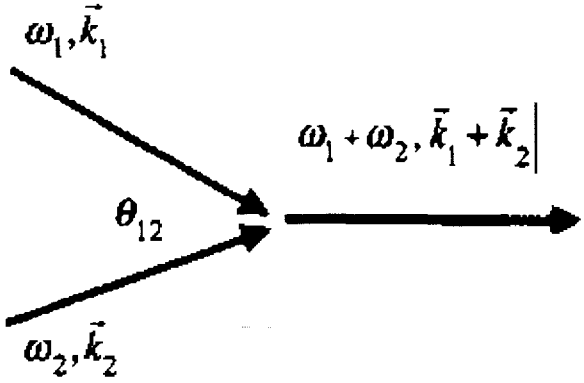

Interaction Condition: $(\omega_1+\omega_2)^2=\frac{\sigma}{\rho}\left|\vec{k}_1+\vec{k}_2\right|^3$

e.g. if $\left|\vec{k}_1\right|=\left|\vec{k}_2\right|$ then $\theta_{12}=74°$

11

OPERATIONAL DEFINITION OF TURBULENCE

$$\left(\frac{\partial E_k}{\partial t}\right)_+ = G^2 \omega_k E_k \frac{E_k}{\sigma} - 4\mu k^2 E_k$$

1) Interaction rate due to nonlinear scattering:

$$\frac{1}{\tau_+} \equiv G^2 \omega_k \frac{E_k}{\sigma} \gg 4\mu k^2$$

$$\text{or } M^2 > 1/G^2 Q,$$

where M is the Mach number and Q is the quality factor.

2) There must be many modes in the bandwidth determined by τ_+:

$$n(\omega)/\tau_+ \gg 1$$

where n is the density of modes

$$n(\omega) = \frac{S\omega^{1/2}}{3\pi(\sigma/\rho)^{2/3}}$$

and S is the surface area.

Turbulence, not Chaos !

POWER SPECTRUM FOR RIPPLE TURBULENCE

$$\omega^2 = (\sigma/\rho)k^3$$

σ = surface tension

cascade from $k \to 2k$ =

$$\left.\frac{\partial E_k}{\partial t}\right]_+ = \omega_k G^2 E_k \frac{E_k}{\sigma} - 4\mu k^2 E_k$$

$E_k = \sigma k^2 \zeta_k^2$ = ripple energy between k and 2k

μ = kinematic viscosity ~ .01 cm^2/s for water,
$G^2 = 8\pi^4/13$ = nonlinear coefficient

$$\left.\frac{\partial E_k}{\partial t}\right]_+ = q = \frac{ergs}{cm^2 s} = \text{energy throughput}$$

in the steady state, $E_k \sim \left[q\sigma/g^2\omega_k\right]^{1/2}$.

therefore spectral density

$$e(\omega) \sim 1/\omega^{3/2}$$

$$\zeta^2(\omega) \propto \frac{\sigma^{1/6} q^{1/2}/\rho^{2/3}}{\omega^{17/6}}; \zeta^2(k) \propto \frac{q^{1/2}\rho^{1/4}/\sigma^{3/4}}{k^{15/4}}$$

$$\langle \zeta^2(r) \rangle = \langle \zeta^2(t) \rangle = \int \zeta^2(k)dk = \int \zeta^2(\omega)d\omega$$

Excitation and Measurement of Ripples [Ground-based]

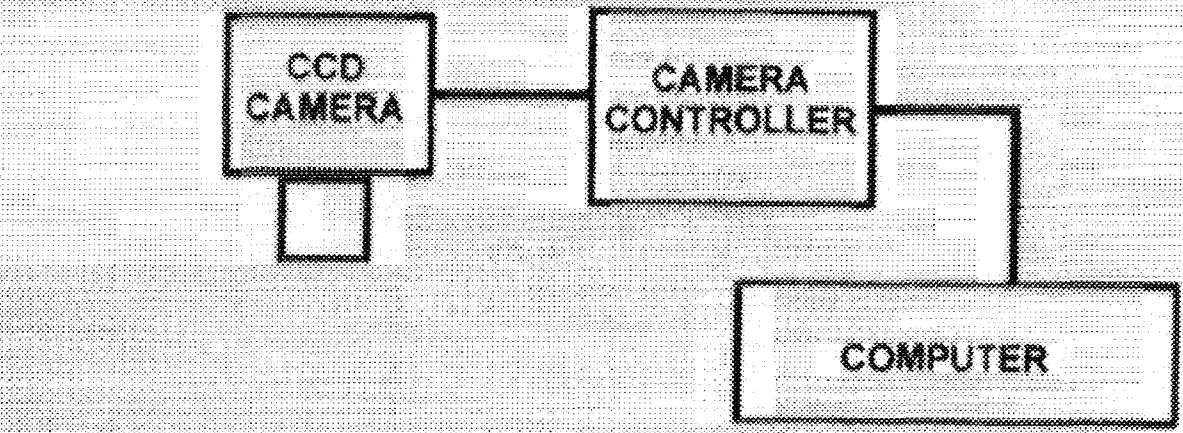

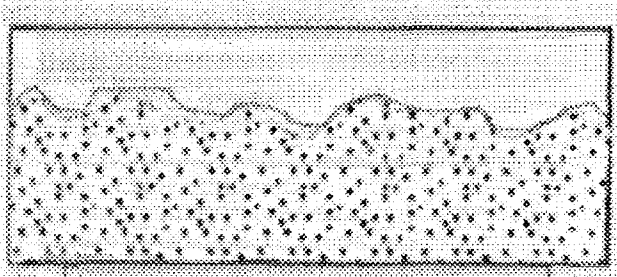

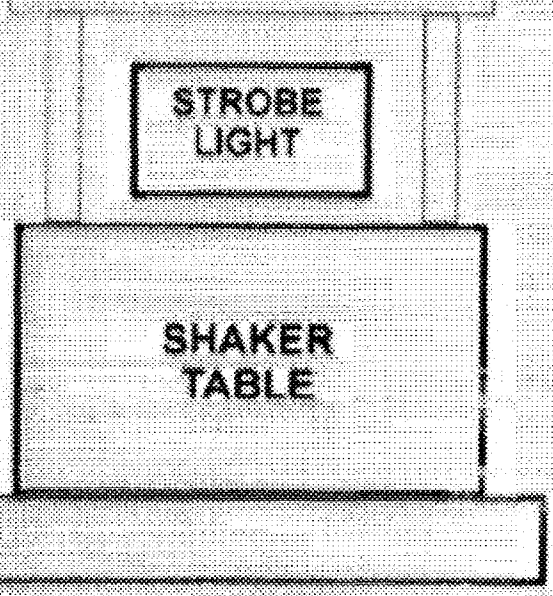

Raw Image

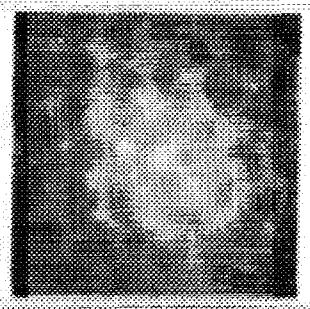

Calibrated Image

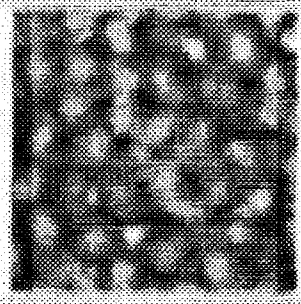

FFT/Power Spectrum

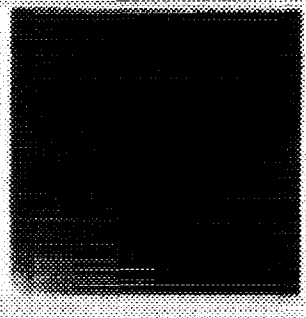

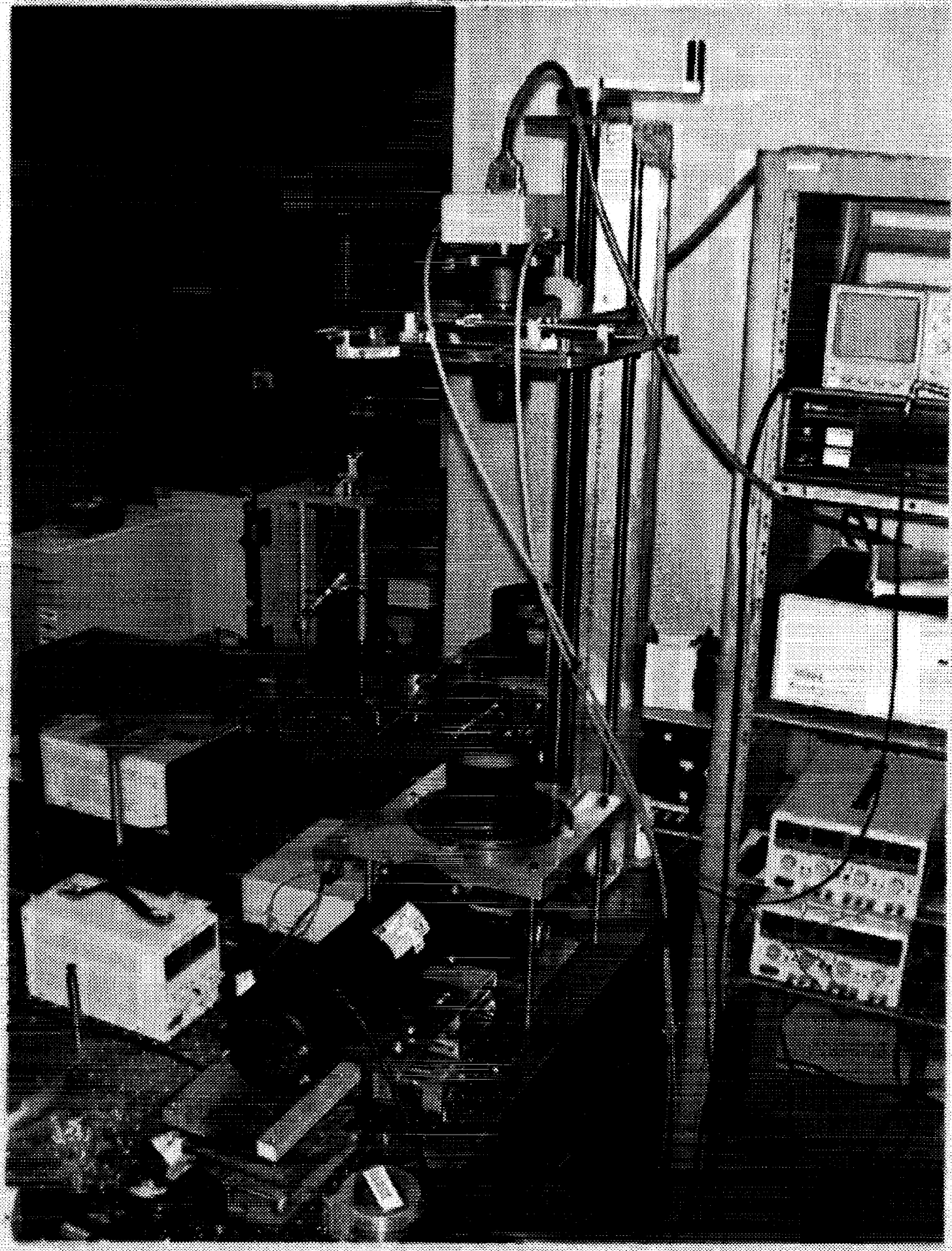

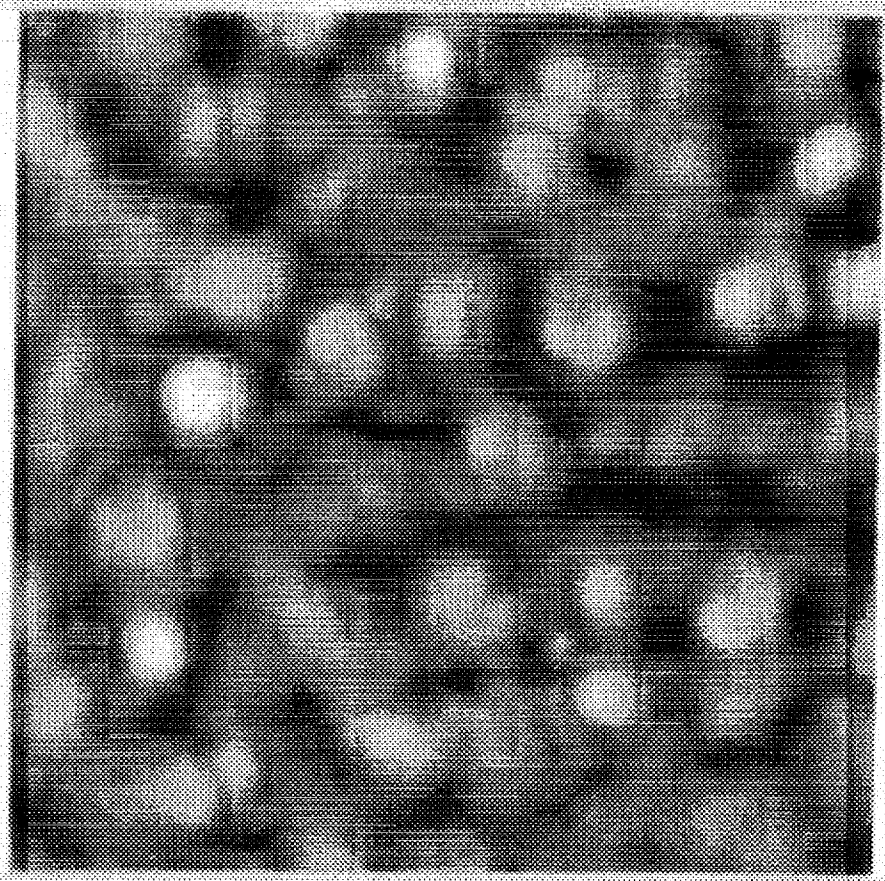

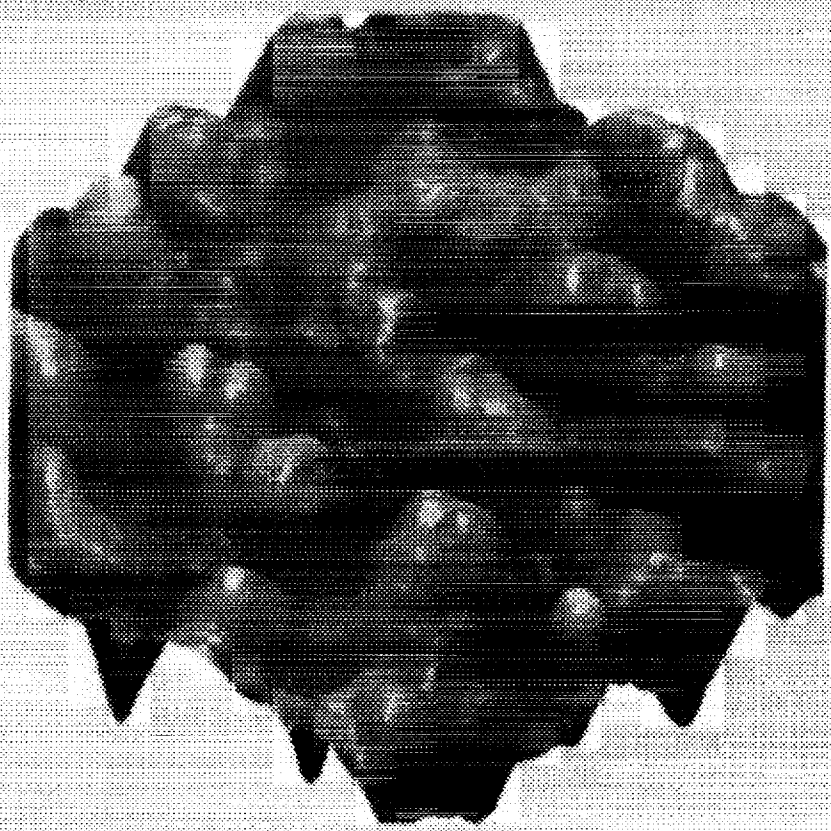

24

Power Spectrum of Ripple Turbulence

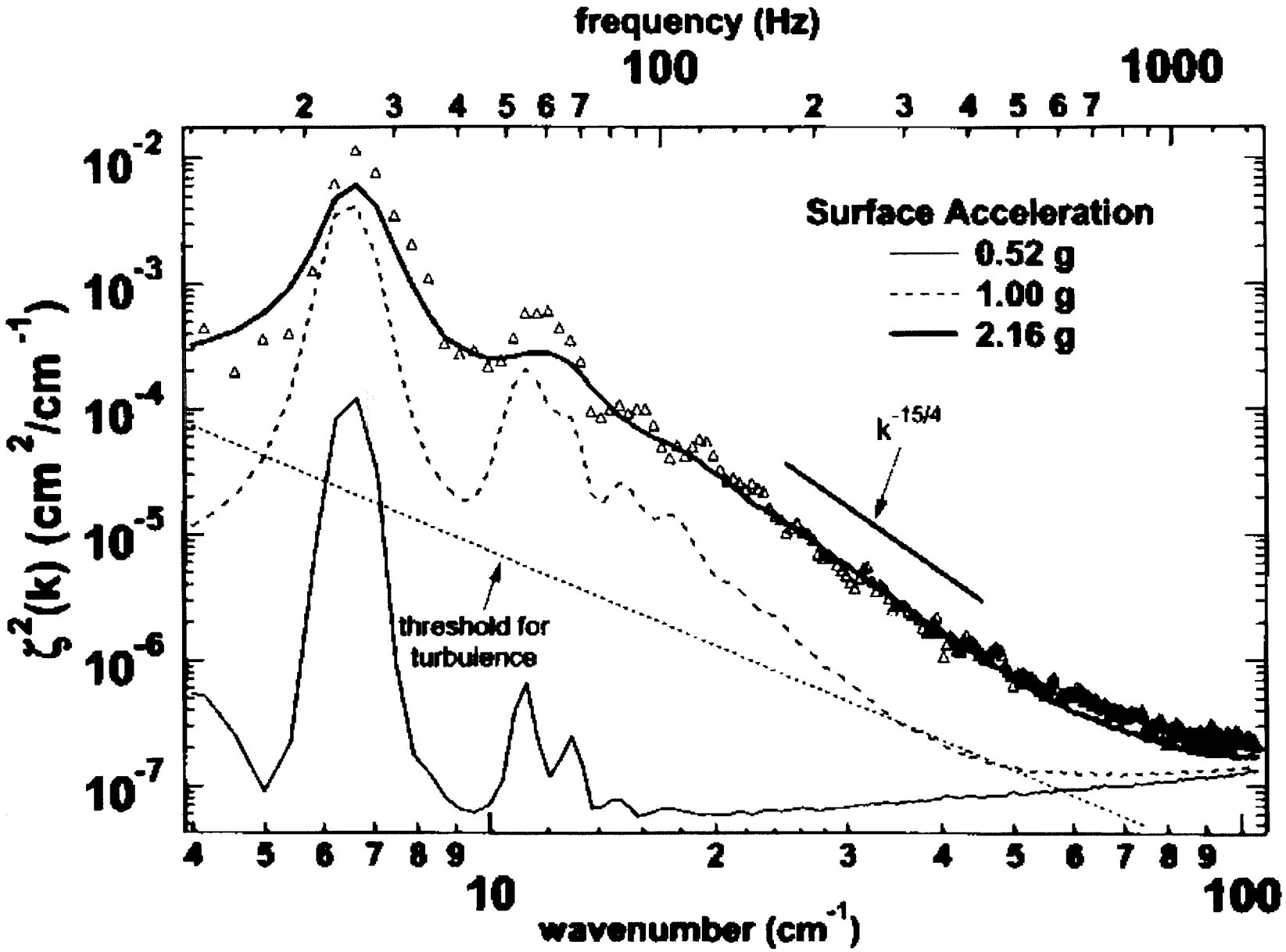

DIAGNOSING INTERMITTENCY

Imaging Technique yields $\zeta(r)$ at some 't'.

The Power Spectrum is proportional to $|\zeta(k)|^2$ which can be compared to Kolmogorov's argument.

Deviations from Gaussian fluctuations around the Kolmogorov Spectrum are diagnosed by calculating the local rate of dissipation of mechanical energy into heat, or:

$$\dot{E}_{mech} \sim \left\{\lambda_0 \nabla^2 \zeta\right\}^2$$

This quantity has been made dimensionless by scaling to the injection wavelength λ_0.

Intermittency is revealed by calculating the contribution to $\dot{E}$ from a finite range of 'k'.

$$\dot{E} \propto \mu k^2 \rho \left(\frac{\partial \zeta}{\partial t}\right)^2 \cdot \frac{1}{k}$$

Intermittency in Turbulence

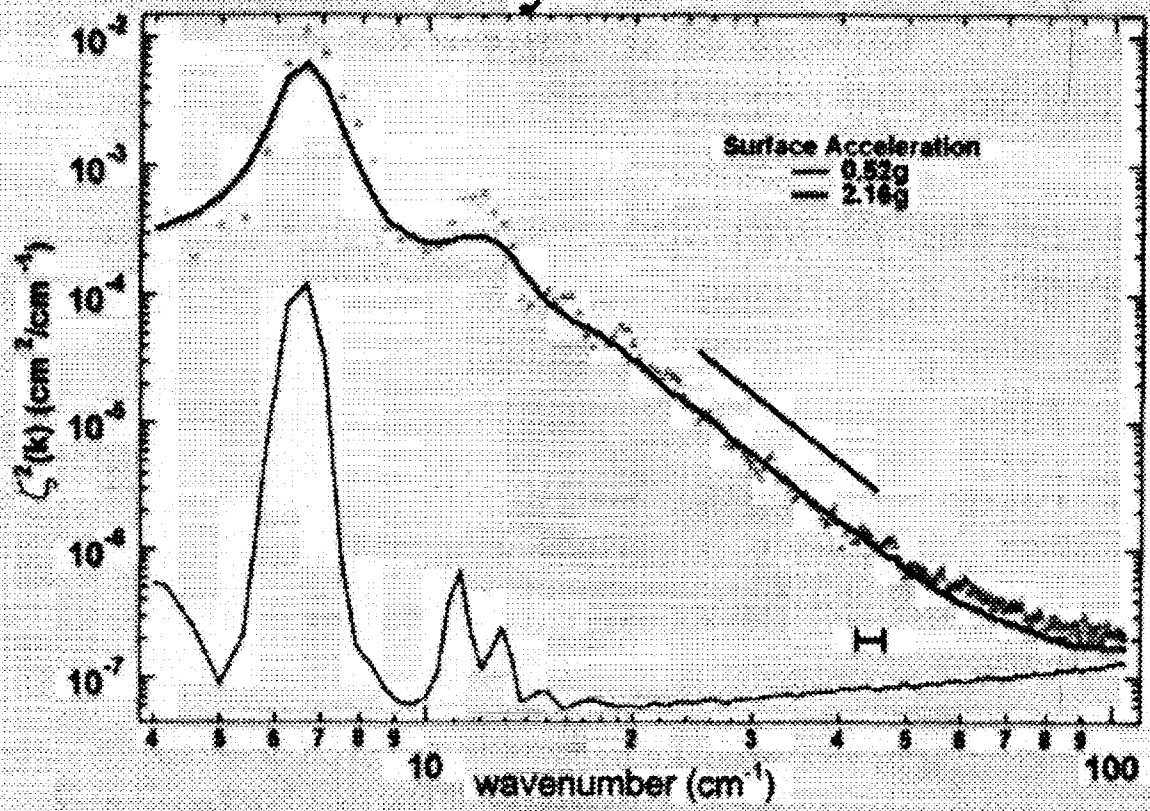

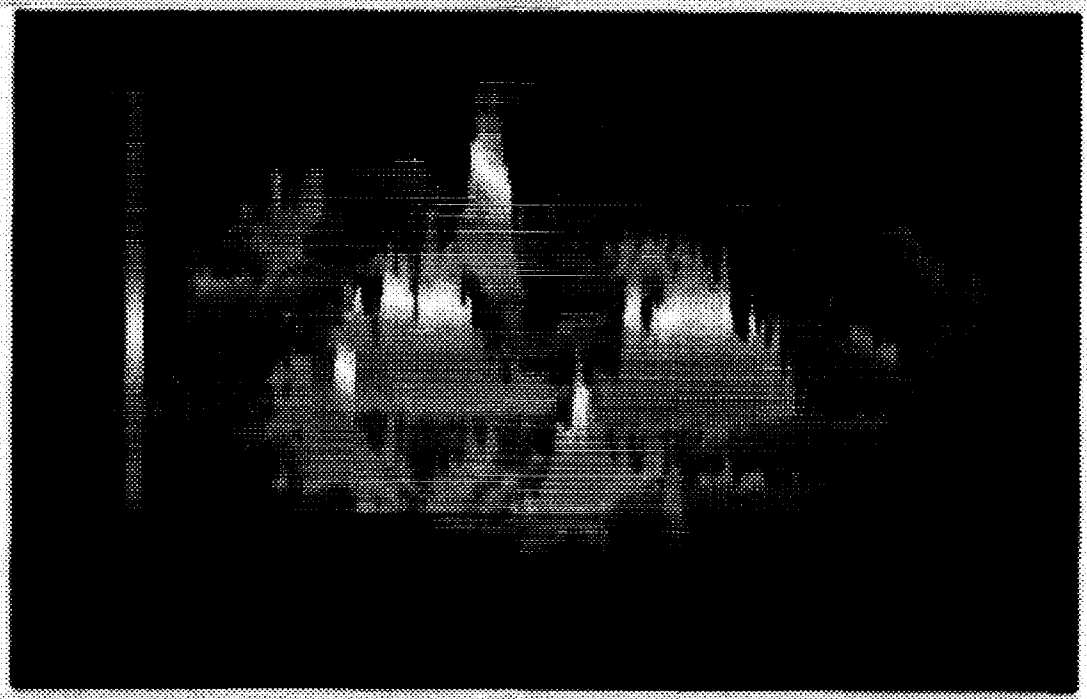

Plot of $\left(\lambda_0 \nabla^2 \zeta\right)^2 \propto$ local dissipation

THEORETICAL OUTLOOK

1) Collective modes of turbulence: Is there turbulent second sound ?

2) Beyond the power spectrum: What are the long term correlations ? Is the Stosszahl Ansatz valid ?

3) Regarding computer simulations, we need a physical system to which all algorithms for turbulence should be compared. (Zakharov)

4) Beyond Fourier analysis: How does one quantify and diagnose structure in turbulence ?

The Kolmogorov spectrum is a balance between competing effects (structure and randomization) that obscures intermittency.

Proposed Space Experiment

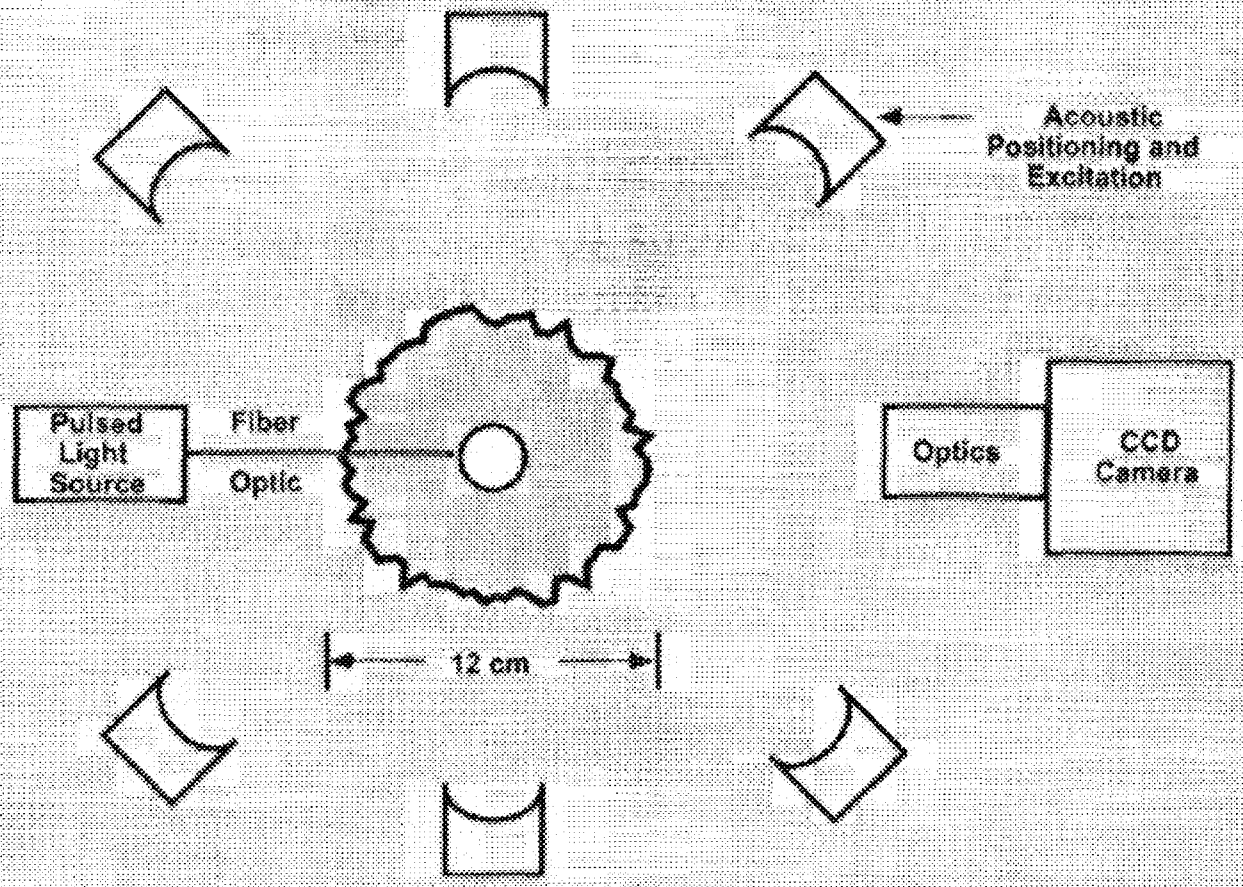

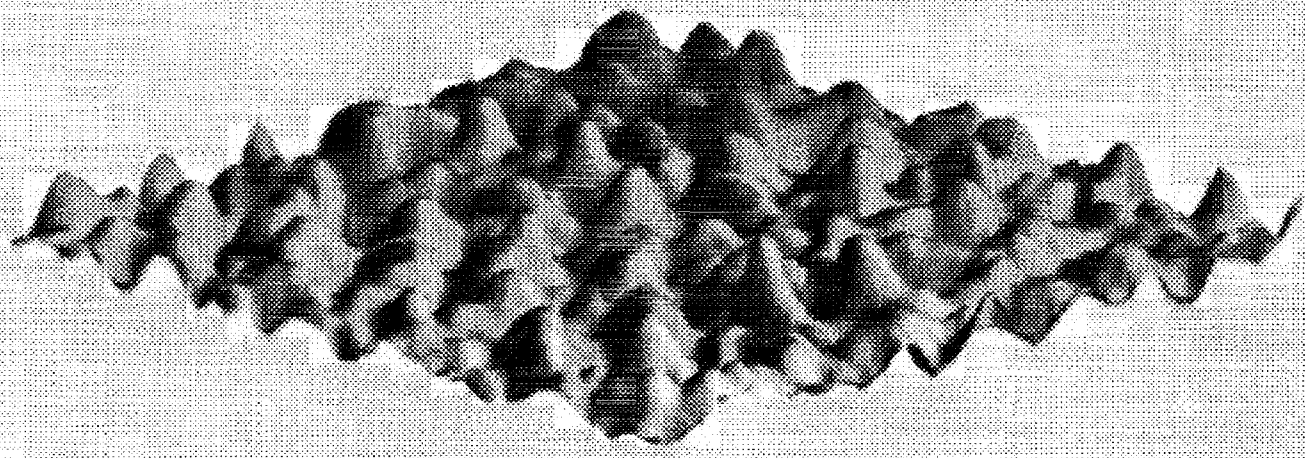

Rendition of ground-based measurement of turbulent motion

BENEFITS

First data on turbulence in a closed system will influence direction of turbulence research.

An understanding of intermittency will lead to new statistical distributions to describe off-equilibrium behavior in many fields of investigation, such as plasma physics.

This experiment represents the largest containerless control of a fluid volume.

STATUS OF THEORETICAL UNDERSTANDING

Good picture of the Kolmogorov cascade, probably because it follows from an energy conservation argument.

Not even the beginnings of a higher-level theory with which to understand intermittency.

STATUS OF EXPERIMENT

Power spectrum spans less than a decade of wave number.

Viscous interaction with the container walls could be affecting data.

Although experiments show evidence of intermittency, this effect cannot be studied as a function of the size of the cascade becuase the ground-based cascade spans less than a decade.

Turbulent Spectrum
$M_f^2 = M_0^2 \sqrt{\frac{f_0}{f}}$
Breaking
μg
g
λ = 0.6mm
Threshold for Turbulence
$M_f^2 = (5)\frac{1}{Q_f G^2} = 4x10^{-4}\left(\frac{f}{Hz}\right)^{1/3}$
M_f^2
0.1
0.01
0.001
1
f_0
10
100
1000
frequency (Hz)

WEAKLY NONLINEAR DESCRIPTION OF PARAMETRIC INSTABILITIES IN VIBRATING FLOWS

Edgar Knobloch[1], José M. Vega[2] and Carlos Martel[2]
[1]Department of Physics, University of California, Berkeley, CA 94720, USA
[2]E.T.S.I. Aeronáuticos, Universidad Politécnica de Madrid, Plaza Cardenal Cisneros 3, 28040 Madrid, SPAIN

June 10, 2000

ABSTRACT

This project [1-7] focuses on the effects of weak dissipation on vibrational flows in microgravity and in particular on (a) the generation of mean flows through viscous effects and their reaction on the flows themselves, and (b) the effects of finite group velocity and dispersion on the resulting dynamics in large domains. The basic mechanism responsible for the generation of such flows is nonlinear and was identified by Schlichting and Longuet-Higgins. However, only recently has it become possible to describe such flows self-consistently in terms of amplitude equations for the parametrically excited waves coupled to a mean flow equation. The derivation of these equations is nontrivial because the limit of zero viscosity is singular. This project focuses on various aspects of this singular problem (i.e., the limit $C_g \equiv \nu/[gh^3 + (Th/\rho)]^{1/2} \ll 1$, where ν is the kinematic viscosity and h the liquid depth) in the weakly nonlinear regime. Several distinct cases are identified depending on the values of the Bond number, the size of the nonlinear terms, distance above threshold and the length scales of interest. The theory provides a *quantitative* explanation of a number of experiments on the vibration modes of liquid bridges and related experiments on parametric excitation of capillary waves in containers of both small and large aspect ratio.

In this presentation we describe our results [6] on nearly inviscid parametrically excited surface gravity-capillary waves in large, finite-depth annular domains. Under explicitly known conditions this system is described by the following coupled equations describing the evolution of the amplitudes of resonant left- and right-traveling waves and their interaction with a mean flow in the bulk:

$$A_t - v_g A_x = \mathrm{i}\alpha A_{xx} - (\delta + \mathrm{i}d)A + \mathrm{i}(\alpha_3|A|^2 - \alpha_4|B|^2)A + \mathrm{i}\alpha_5\mu\bar{B} + \mathrm{i}\alpha_6\int_{-1}^{0} g(y)\langle\psi_y^m\rangle^x\,dy\,A + \mathrm{i}\alpha_7\langle f^m\rangle^x A + HOT,$$

$$B_t + v_g B_x = \mathrm{i}\alpha B_{xx} - (\delta + \mathrm{i}d)B + \mathrm{i}(\alpha_3|B|^2 - \alpha_4|A|^2)B + \mathrm{i}\alpha_5\mu\bar{A} - \mathrm{i}\alpha_6\int_{-1}^{0} g(y)\langle\psi_y^m\rangle^x\,dy\,B + \mathrm{i}\alpha_7\langle f^m\rangle^x B + HOT,$$

$$A(x+L,t) \equiv A(x,t), \quad B(x+L,t) \equiv B(x,t).$$

As part of the derivation explicit expressions for the coefficients are obtained. Here the complex amplitudes A and B are the amplitudes of the two counterpropagating waves driven parametrically by the forcing (with dimensionless amplitude μ), and the notation HOT indicates higher order terms. The first seven terms describe the effects of inertia, propagation at the group velocity v_g, dispersion, damping, detuning, cubic nonlinearity and parametric forcing. The last two terms described the coupling to the mean flow in the bulk (indicated by the superscript m) and are conservative. They are written in terms of (a local average $\langle\cdot\rangle^x$ of) the streamfunction

ψ^m for the mean flow and the associated free surface elevation f^m. These quantities satisfy

$$\psi^m_{xx} + \psi^m_{yy} = \Omega^m, \quad \Omega^m_t - [\psi^m_y + (|A|^2 - |B|^2)g(y)]\Omega^m_x + \psi^m_x \Omega^m_y = C_g(\Omega^m_{xx} + \Omega^m_{yy}) + HOT,$$

$$\psi^m_x - f^m_t = \beta_1(|B|^2 - |A|^2)_x + HOT, \quad \psi^m_{yy} = \beta_2(|A|^2 - |B|^2) + HOT, \quad \text{at } y = 0, \tag{1}$$

$$(1-S)f^m_x - Sf^m_{xxx} - \psi^m_{yt} + C_g(\psi^m_{yyy} + 3\psi^m_{xxy}) = -\beta_3(|A|^2 + |B|^2)_x + HOT, \quad \text{at } y = 0. \tag{2}$$

$$\int_0^L \Omega^m_y \, dx = \psi^m = 0, \quad \psi^m_y = -\beta_4[\mathrm{i}A\bar{B}\mathrm{e}^{2\mathrm{i}kx} + \text{c.c.} + |B|^2 - |A|^2] + HOT, \quad \text{at } y = -1, \tag{3}$$

$$\psi^m(x+L,y,t) \equiv \psi^m(x,y,t), \quad f^m(x+L,t) \equiv f^m(x,t), \quad \int_0^L f^m(x,t)\,dx = 0,$$

valid outside of viscous boundary layers at the free surface ($y = 0$) and the bottom ($y = -1$). Here $S \equiv T/(T+\rho g h^2)$ (T is the surface tension) is the gravity-capillary balance parameter ($S \to 1$ in microgravity). The resulting equations differ from the exact equations forming the starting point for the analysis in the presence of the forcing terms in the boundary conditions and in two essential simplifications: the fast oscillation associated with the surface waves has been filtered out, and the boundary conditions are applied at the unperturbed location of the free surface, $y = 0$. The mean flow itself is forced in two ways. The right sides of the boundary conditions (1a) and (2) provide a *normal forcing mechanism*; this mechanism is the only one present in the strictly inviscid case and does not appear unless the aspect ratio is large. The right sides of the boundary conditions (1b) and (3c) describe two *shear forcing mechanisms*, a tangential stress at the free surface and a tangential velocity at the bottom wall. Neither of these forcing terms vanishes in the limit of small viscosity (i.e., as $C_g \to 0$). Two cases are considered in detail, gravity-capillary waves and capillary waves in a microgravity environment.

Acknowledgement: This work was supported by NASA under grant NAG3-2152.

References

[1] E. Knobloch and J. Moehlis. Bursts in oscillatory systems with broken D_4 symmetry, Physica D 135, 263–304 (2000).

[2] C. Martel, E. Knobloch and J.M. Vega. Dynamics of counterpropagating waves in parametrically forced systems. Physica D 137 (2000) 94–123.

[3] E. Knobloch and J. Moehlis. Burst mechanisms in hydrodynamics. In Nonlinear Instability, Chaos and Turbulence, Vol.2, L. Debnath and D. N. Riahi (eds), WIT Press (2000), pp. 237–287.

[4] J.A. Nicolas and J.M. Vega. Linear oscillations of axisymmetric viscous liquid bridges. Z. angew. Math. Phys. In press.

[5] J.A. Nicolas and J.M. Vega. A note on the effect of surface contamination in water wave damping. J. Fluid Mech. In press.

[6] J.M. Vega, E. Knobloch and C. Martel. Nearly inviscid Faraday waves in annular containers of moderately large aspect ratio. Physica D. Submitted.

[7] M. Higuera, J.A. Nicolas and J.M. Vega. Coupled amplitude-streaming flow equations for the evolution of counter-rotating, nearly-inviscid surface waves in finite axisymmetric geometries. Nonlinearity. Submitted.

Weakly Nonlinear Description of Parametric Instabilities in Vibrating Flows

Edgar Knobloch,
Dept. of Physics, University of California
Berkeley, CA 94720, USA

José Manuel Vega and Carlos Martel (martel@fmetsia.upm.es)
E.T.S.I. Aeronáuticos, Universidad Politécnica de Madrid
28040 Madrid, Spain

- Systems **large** in one spatial direction, x.
- Invariant under **reflections**, $x \to -x$, and **translations**, $x \to x + c$.
- Basic steady solution, u_0, uniform in x.
- Linear stability of u_0,

$$u = u_0 + \varepsilon U e^{ikx+\omega t} + \text{c.c.}, \qquad |\varepsilon| \ll 1.$$

dispersion relation, $\omega(k)$:

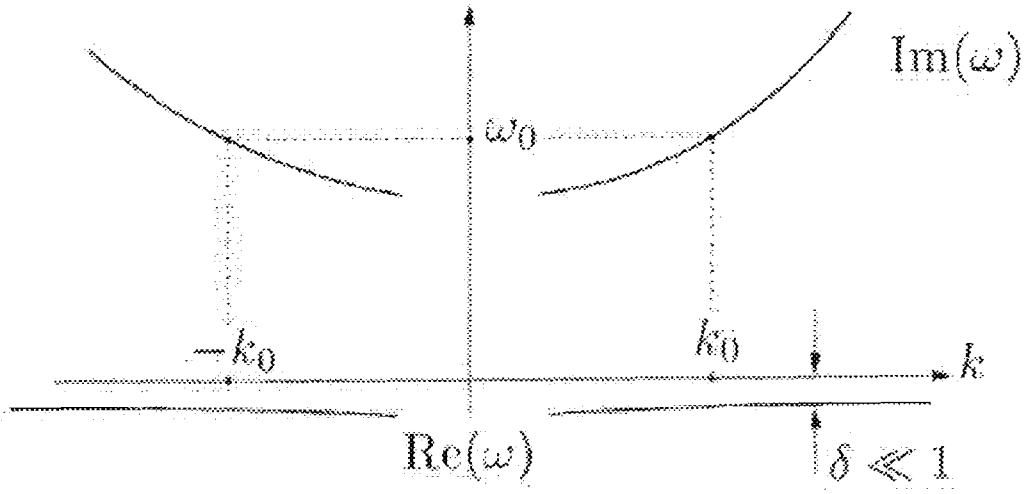

- Small **damping** δ.
- Small **parametric forcing** with frequency $2\omega_0$.

$$(\cdots + \overline{A}e^{-ik_0x-i\omega_0t} + \cdots)(e^{2i\omega_0t} + \cdots) \mapsto (e^{-ik_0x+i\omega_0t}) \text{ eq.}$$

Physical systems

- Faraday problem, nearly inviscid fluid in a large container (surface waves only).

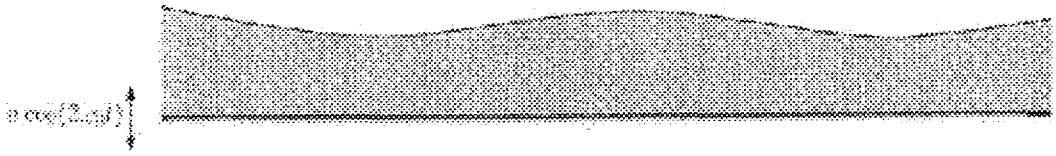

- Light propagation in optical systems.

Weakly nonlinear analisys

Two slowly modulated wavetrains:

$$u = u_0 + A(x,t)Ue^{ik_0x - i\omega_0 t} + B(x,t)Ve^{-ik_0x + i\omega_0 t} + \text{c.c.} + \dots$$

$$|A_t| \ll |A|, \quad |A_{xx}| \ll |A_x| \ll |A| \ll 1,$$
$$|B_t| \ll |B|, \quad |B_{xx}| \ll |B_x| \ll |B| \ll 1,$$

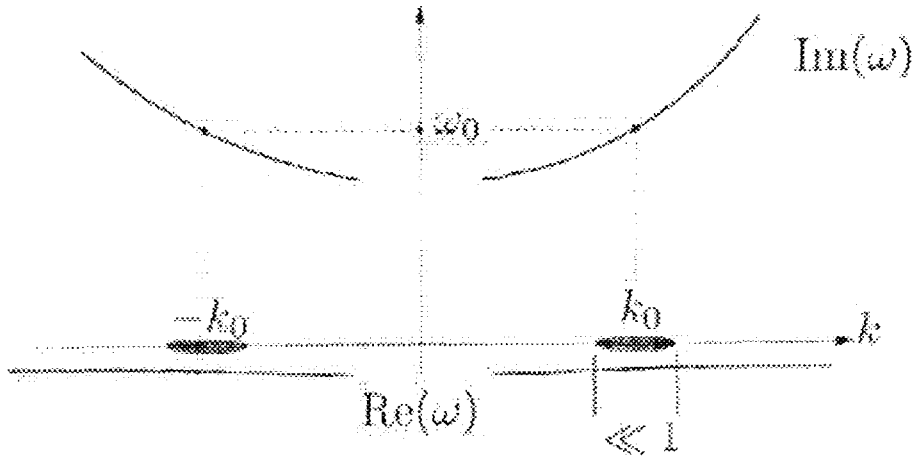

Amplitude equations:

$$A_t = -\delta A + c_g A_x + i\alpha A_{xx} + iA(\beta|A|^2 + \gamma|B|^2) + \mu\overline{B} + \dots$$
$$B_t = -\delta B - c_g B_x + i\alpha B_{xx} + iB(\beta|B|^2 + \gamma|A|^2) + \mu\overline{A} + \dots$$

- δ = damping ($\ll 1$)
- c_g= group velocity
- α = dispersion
- μ = parametric forcing ($\ll 1$)
- β, γ= nonlinear interaction

Amplitude equations

CCCPFDNLS:

$$A_t - A_z = (-\delta + i\nu)A + i\varepsilon A_{zz} + iA(\beta|A|^2 + \gamma|B|^2) + \mu\overline{B}$$
$$B_t + B_z = (-\delta + i\nu)B + i\varepsilon B_{zz} + iB(\beta|B|^2 + \gamma|A|^2) + \mu\overline{A}$$
$$A(x+1,t) = A(x,t) \quad B(x+1,t) = B(x,t)$$

Annular geometry, length $L \gg 1$.

Scalings:

$$(x,t)/L \qquad (A,B)\sqrt{L} \qquad (\beta+\gamma) > 0$$

$$\delta L \to \delta \sim 1,$$
$$\mu L \to \mu \sim 1,$$
$$|\varepsilon| \sim 1/L \ll 1$$

- $\nu \in]-\pi, \pi]$ detuning to the nearest natural mode.
$A(x+L) = e^{i\theta}A(x)$, ..., $\theta \equiv$ spatial mismatch.

- **Fast transport** produced by the group velocity.
- **Small dispersion** (slow modulation).

$$|\varepsilon A_{xx}| \ll |A_x|,$$
$$|\varepsilon B_{xx}| \ll |B_x|,$$

Highest allowed wavenumbers $k \sim 1/\sqrt{|\varepsilon|}$, **intermediate scales**.

Basic steady state

Linear stability of the basic state, $A = B = 0$ (no dispersion):

$$\mu_c = \sqrt{\delta^2 + (\nu + 2k\pi)^2}$$

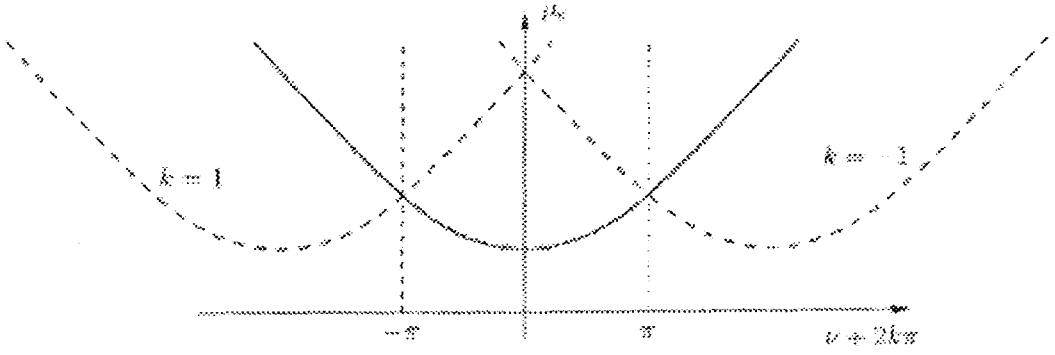

We are near the first resonance tongue.

Uniform Standing Waves

- $A = R_o e^{i\theta + i2m\pi x}$, $B = R_o e^{i\phi - i2m\pi x}$,

$$(R_o^2(\beta + \gamma) + (\nu + 2m\pi))^2 + \delta^2 = \mu^2$$

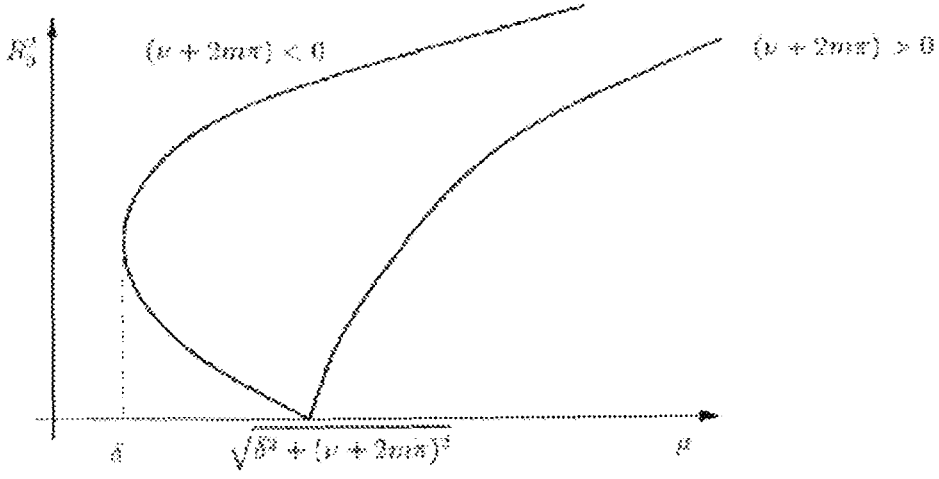

$((\nu + 2m\pi) - R_0^2)$ plane: 1point $\leftrightarrow$ 1 SW

SW linear stability

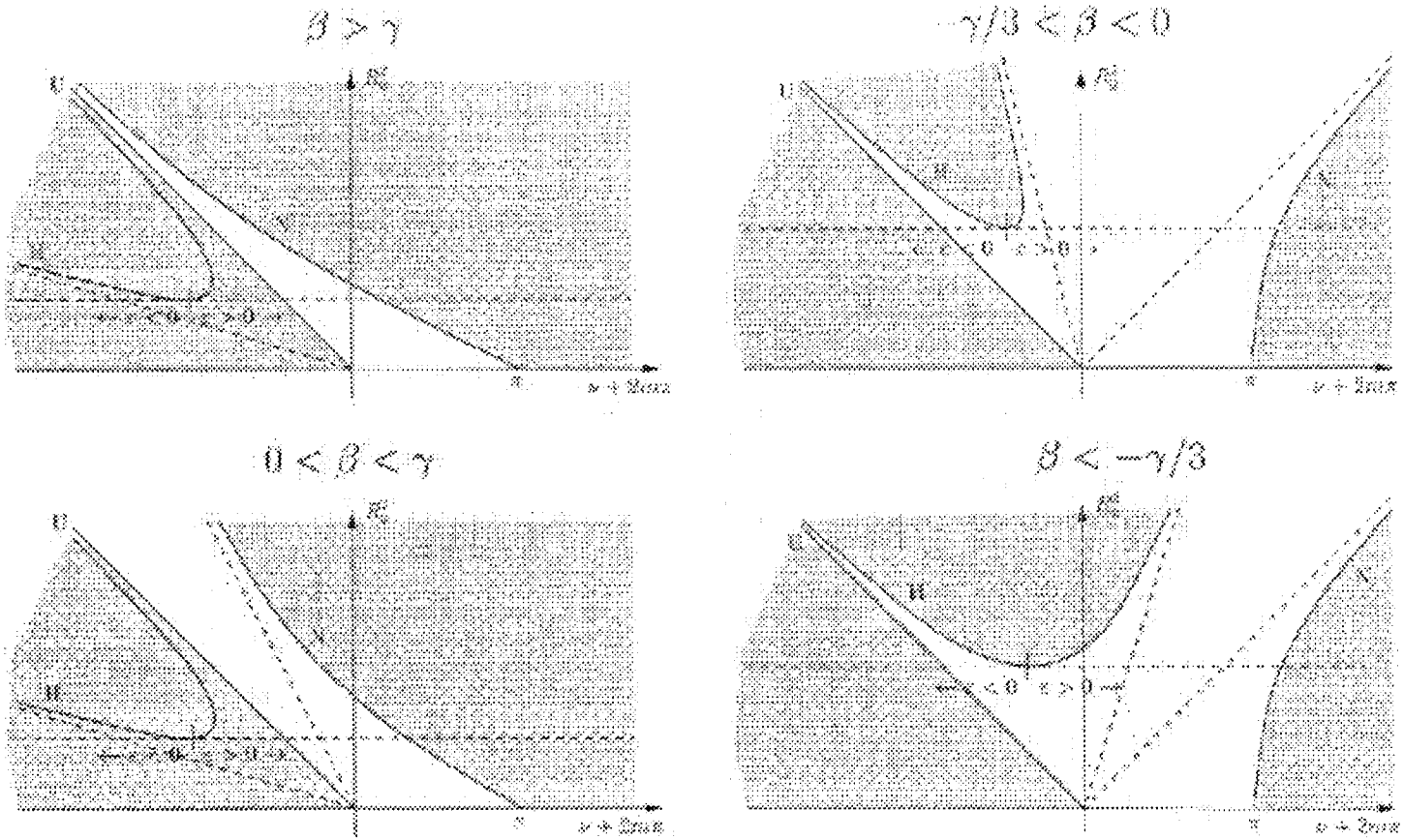

-Dispersion neglected: Uniform pert. (U). Non-uniform pert., $k \sim 1$ (N).

-Pert. with intermediate scales, $k \sim 1/\sqrt{|\varepsilon|} \gg 1$ (H). Shift in the detuning: $\upsilon + 2n\pi \pm \tilde{k}^2$.

More complex solutions for higher forcing

No intermediate scales.

$$\mu = 3.1 \quad \delta = 1 \quad \nu = 0 \quad \beta = 1 \quad \gamma = .5 \quad \varepsilon = -.0001$$

$|A(x,t)|$ $|B(x,t)|$

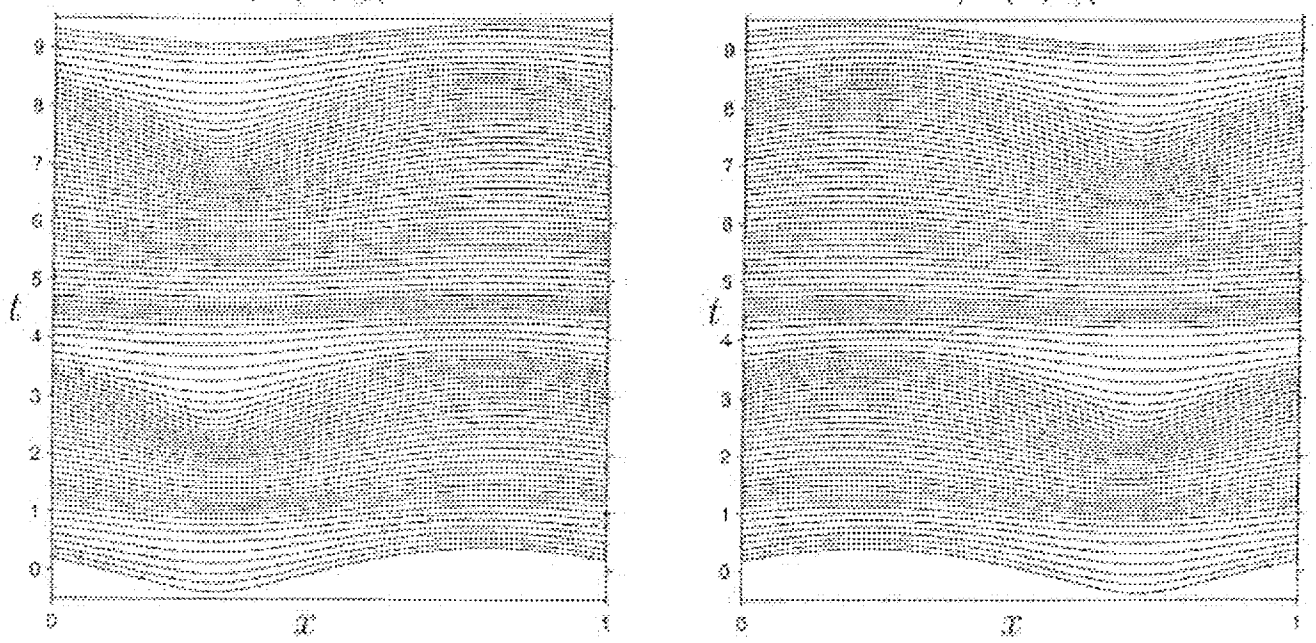

Intermediate scales wavetrain over the SW.

$$\mu = 2.5 \quad \delta = 1 \quad \nu = 0 \quad \beta = 1 \quad \gamma = .5 \quad \varepsilon = .0001$$

$|A(x,t)|$ $|B(x,t)|$

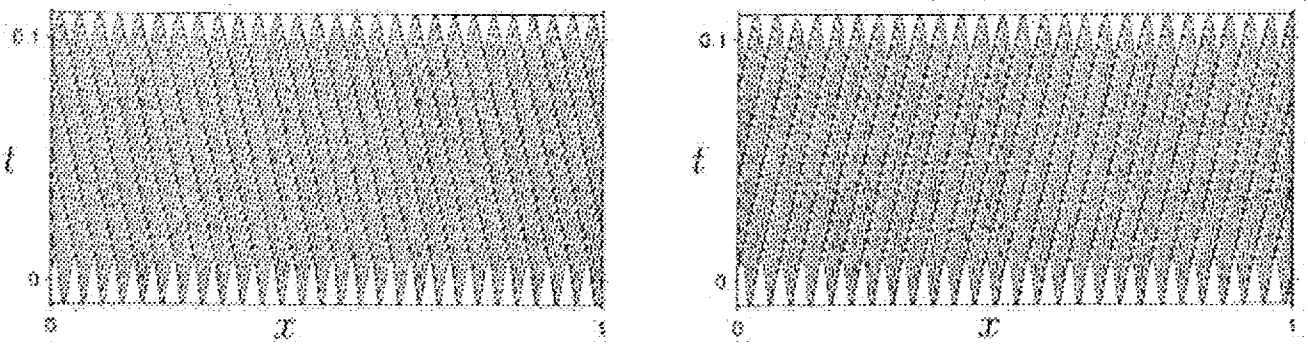

More complex solutions for higher forcing

STC, intermediate scales

$$\mu = 3.5 \quad \delta = 1 \quad \nu = 0 \quad \beta = 1 \quad \gamma = .5 \quad \varepsilon = -.0001$$

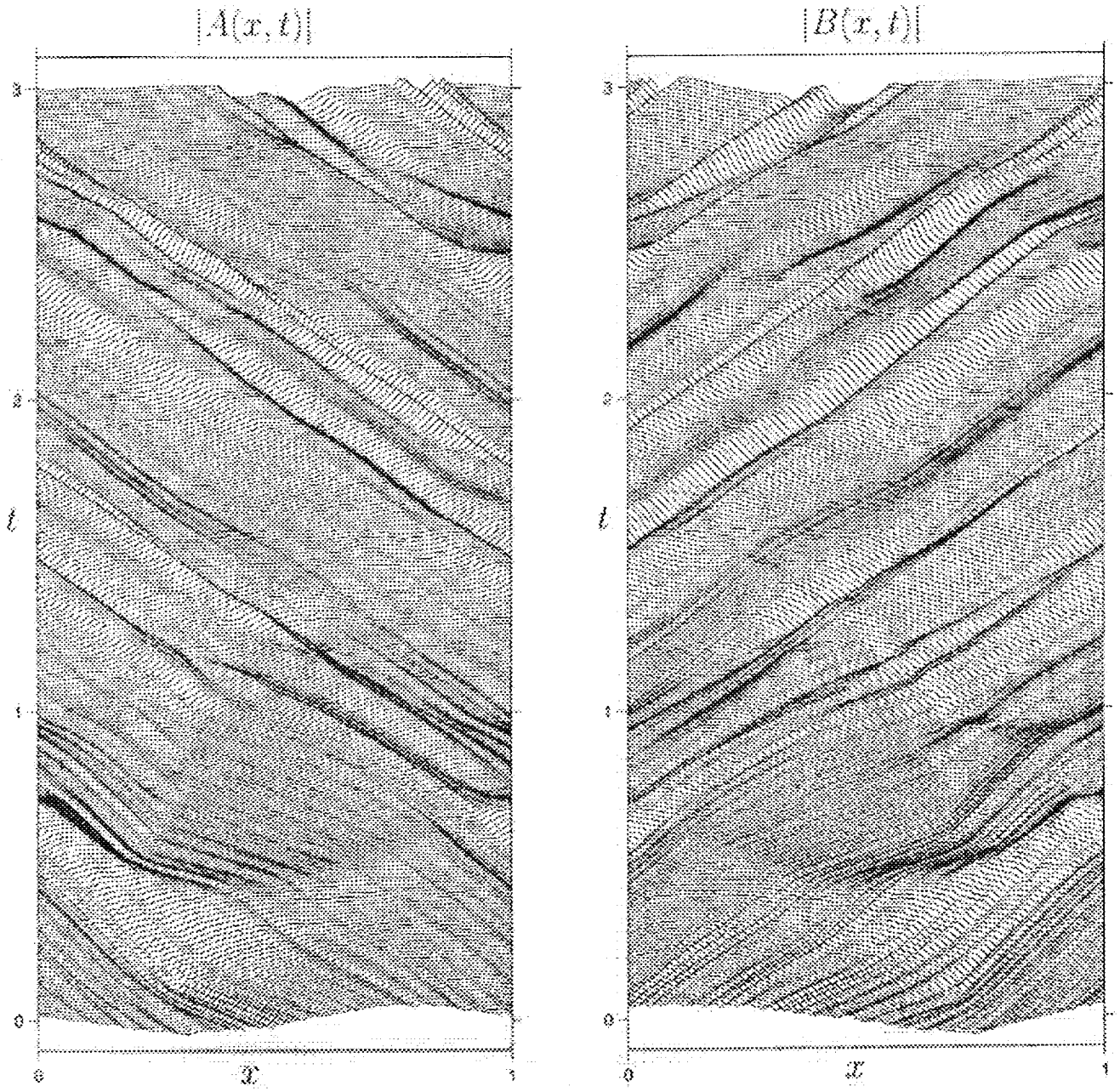

More complex solutions for higher forcing

Shocks.

$$\mu = 2 \quad \delta = 1 \quad \nu = 0 \quad \beta = -1 \quad \gamma = 2 \quad \varepsilon = .0001$$

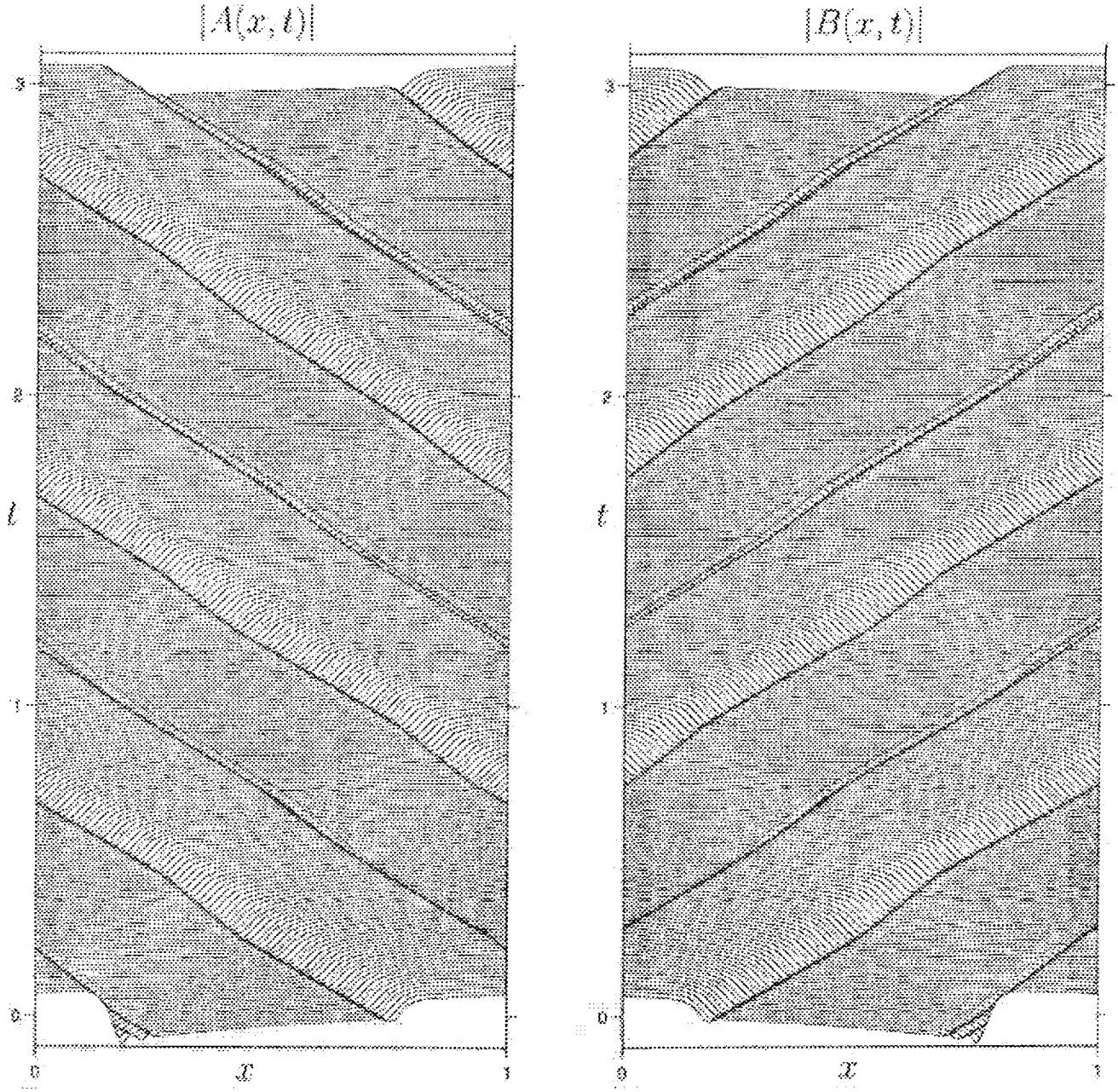

More complex solutions for higher forcing

Solitary waves.

$$\mu = 1.5 \quad \delta = 1 \quad \nu = 0 \quad \beta = -1 \quad \gamma = 2 \quad \varepsilon = -.0001$$

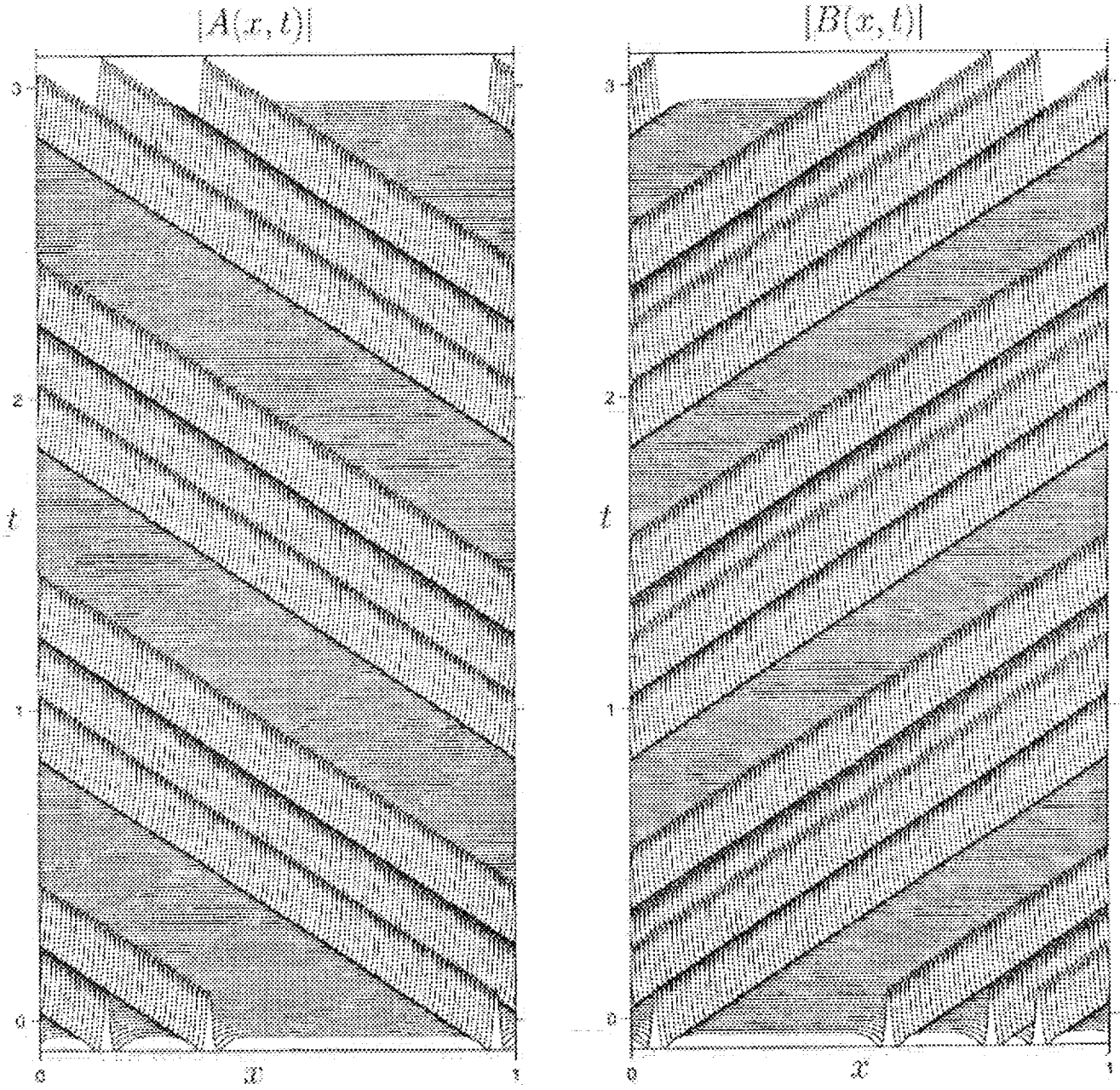

More complex solutions for higher forcing

STC, intermediate scales.

$$\mu = 3 \quad \delta = 1 \quad \nu = 0 \quad \beta = -1 \quad \gamma = 2 \quad \epsilon = .0001$$

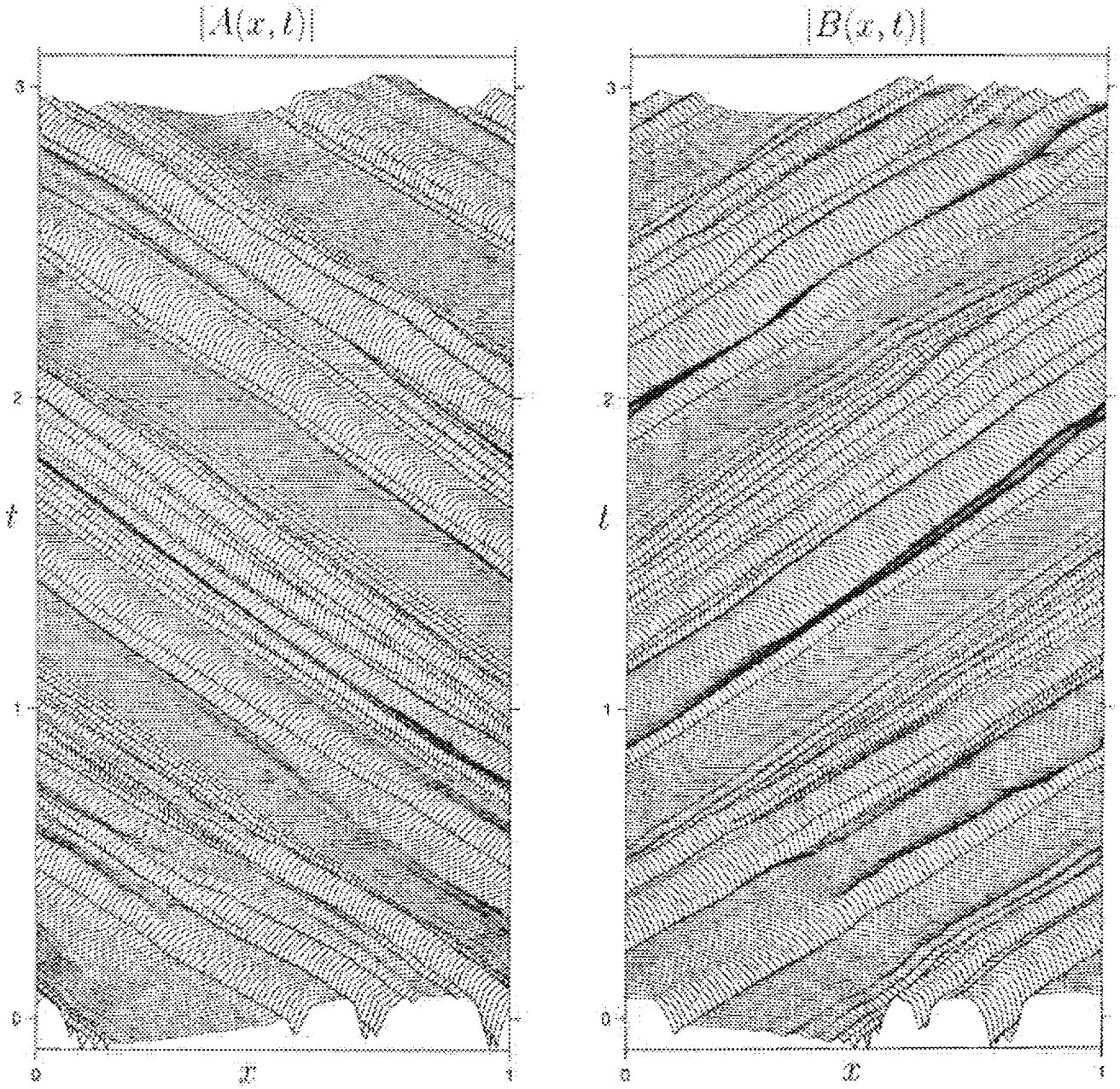

More complex solutions for higher forcing

STC, intermediate scales.

$$\mu = 2.0 \quad \delta = 1 \quad \nu = 0 \quad \beta = -1 \quad \gamma = 2 \quad \varepsilon = -.0001$$

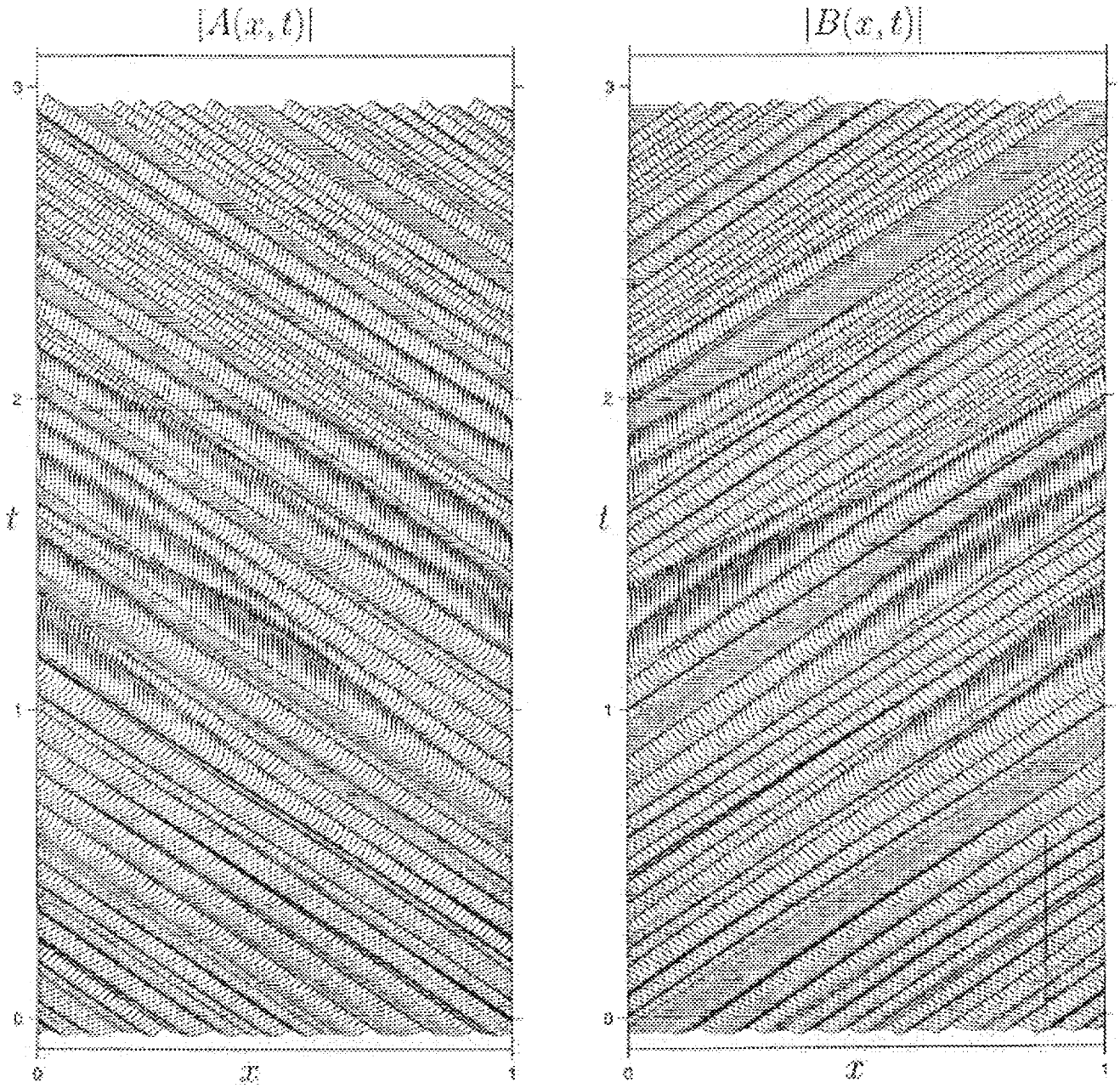

More complex solutions for higher forcing

STC, intermediate scales.

$$\mu = 3.5 \quad \delta = 1 \quad \nu = 0 \quad \beta = -1 \quad \gamma = 4 \quad \varepsilon = .0001$$

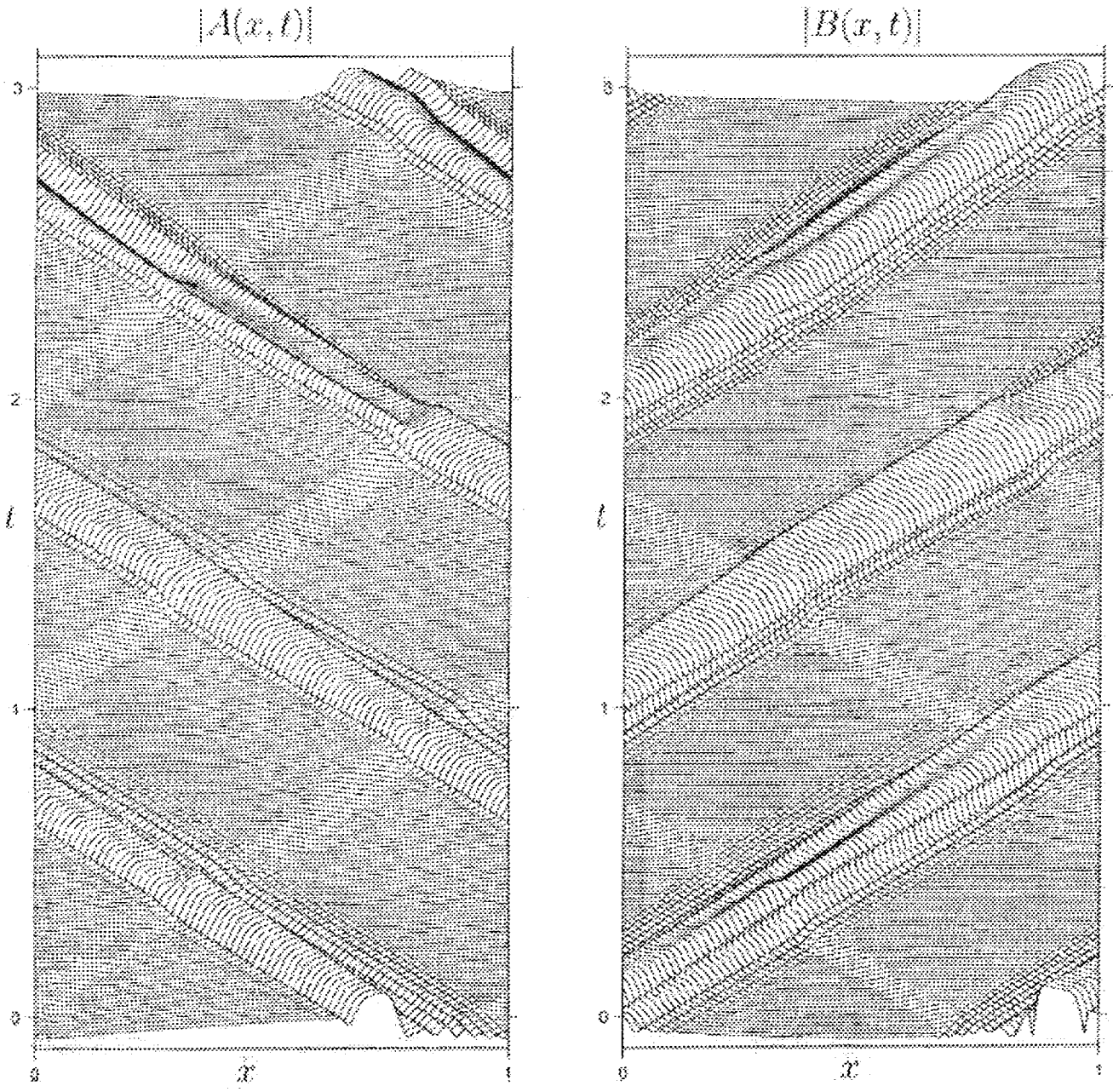

Conclusions

- Dynamics dominated by the group velocity transport.
- No simple condition for the onset of intermediate scales.
- Slow modulation:

$$|k| \ll 1/|\varepsilon|$$

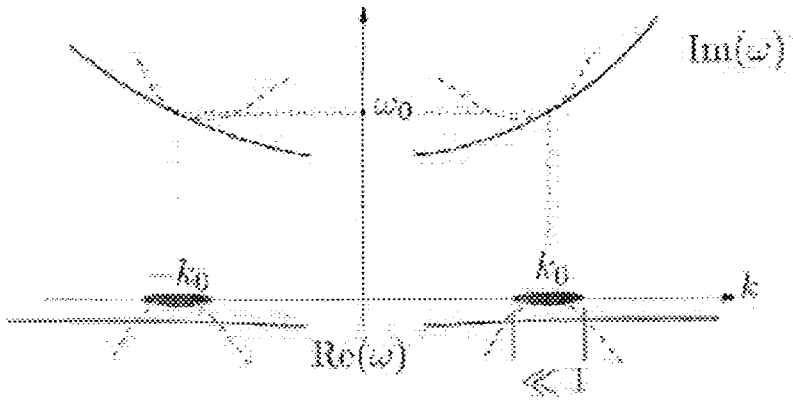

Explicitly imposed.

- Faraday problem. Surface waves, mean flow not included...

Complete description of the Faraday problem

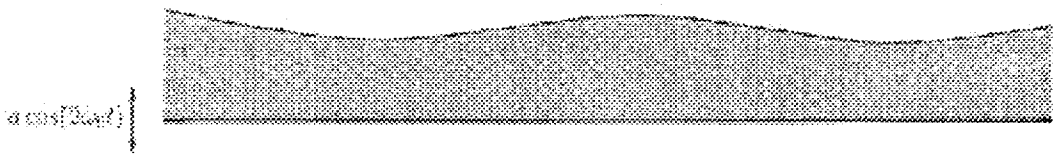

Surface modes (inviscid) + Hydrodynamic modes (viscous)

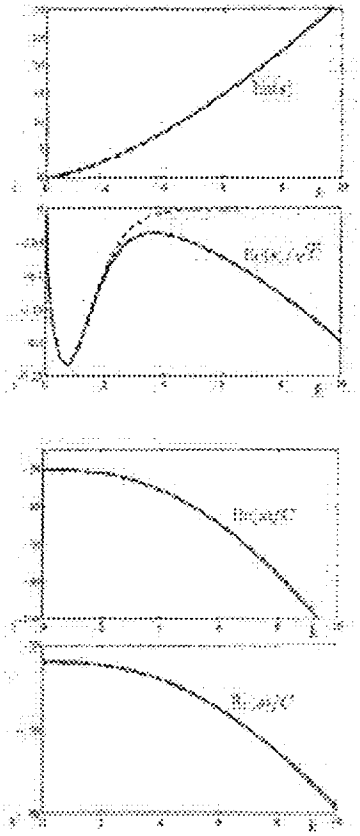

$$\psi^m_{xx} + \psi^m_{yy} = \Omega^m, \quad \Omega^m_t = C_y(\Omega^m_{xx} + \Omega^m_{yy})$$

$$\psi^m_x = 0, \quad \psi^m_{yy} = 0 \quad \text{at } y = 0$$

$$\int_0^L \Omega^m_y dx = \psi^m = 0 \quad \psi^m_y = 0 \quad \text{at } y = -1$$

$$f^m = 0$$

Weakly nonlinear evolution

$$A_t - c_g A_x = i\alpha A_{xx} - (\delta + i\nu)A + iA(\beta|A|^2 + \gamma|B|^2) + \mu\overline{B}$$

$$+i\alpha_1 \int_{-1}^{0} g(y) \left\langle \psi_y^m \right\rangle dy A + i\alpha_2 \left(f^m\right) A$$

$$B_t + c_g B_x = i\alpha B_{xx} - (\delta + i\nu)B + iB(\beta|B|^2 + \gamma|A|^2) + \mu\overline{A}$$

$$-i\alpha_1 \int_{-1}^{0} g(y) \left\langle \psi_y^m \right\rangle dy B + i\alpha_2 \left(f^m\right) B$$

$$\psi_{xx}^m + \psi_{yy}^m = \Omega^m$$

$$\Omega_t^m - \left[\psi_y^m + (|A|^2 - |B|^2)g(y)\right]\Omega_x^m + \psi_x^m \Omega_y^m = C_y(\Omega_{xx}^m + \Omega_{yy}^m)$$

$$\psi_x^m - f_t^m = \beta_1(|B|^2 - |A|^2)_x, \quad \psi_{yy}^m = \beta_2(|B|^2 - |A|^2) \quad \text{at } y = 0$$

$$(1-S)f_x^m - Sf_{xxx}^m - \psi_{yt}^m + C_y(\psi_{yyy}^m + 3\psi_{xxy}^m) = -\beta_3(|B|^2 + |A|^2)_x \quad \text{at } y = 0$$

$$\int_0^L \Omega_y^m dx = \psi^m = 0 \quad \psi_y^m = -\beta_4(iA\overline{B}e^{2ikx} + \text{c.c.} + |B|^2 - |A|^2) \quad \text{at } y = -1$$

$$\int_0^L f^m dx = 0$$

$$S = T/(T + \rho g h^2), \quad C_y = \nu/(gh^3 + (Th/\rho))^{1/2}, \quad (.) = \text{ average in the fast } x.$$

Instabilities and Spatio-Temporal Chaos of Hexagonal Convection Patterns in the Presence of Rotation

H. Riecke, B. Echebarria, F. Sain

Department of Engineering Sciences and Applied Mathematics,

Northwestern University, 2145 Sheridan Rd, Evanston, IL, 60208, USA

A.M. Mancho

Centro de Astrobiología (Associated Member of NASA Astrobiology Institute) INTA,

Ctra. Ajalvir, km. 4, 28850 Torrejón de Ardoz, Madrid, Spain

Under conditions of reduced gravity, surface tension gradients become a dominant force in driving convective flows. In thin layers they lead typically to the classic *hexagonal* convection patterns. Here we are interested in the possible types of spatio-temporal chaos that can arise from instabilities of such patterns.

In buoyancy-driven convection and other pattern-forming systems spatio-temporal chaos has been investigated in great detail. In most of these systems it arises from a stripe-type planform, e.g. convection rolls. As the case of spiral-defect chaos illustrates vividly, the chaotic state can strongly depend on the underlying destabilized pattern. Therefore we expect qualitatively different dynamics if the destabilized convection pattern is hexagonal rather than stripe-like.

To destabilize the hexagonal convection pattern we consider convection in a rotating system. Rotation is known to have a strong impact on convection patterns due to the Coriolis force. A particularly interesting case is rotating buoyancy-driven Boussinesq convection where due to the Küppers-Lortz instability the usually observed steady roll pattern is transformed into a pattern of ever-changing patches of rolls in different orientations.

Within the framework of the full fluid equations for Marangoni convection a detailed stability analysis of hexagonal convection and simulations of the evolution ensuing from the instabilities is a formidable undertaking. We will discuss results for two order-parameter models [1,2] and for coupled Ginzburg-Landau equations [3,4].

As a minimal model for the description of hexagonal patterns in the presence of rotation we discuss an extension of the Swift-Hohenberg equation [1],

$$\partial_t \psi = R\psi - (\nabla^2 + 1)^2 \psi - \psi^3 + \alpha\psi^2 + \gamma\, \hat{e}_z \cdot (\nabla\psi \times \nabla(\nabla^2\psi)). \qquad (1)$$

Here ψ is a typical physical quantity like the temperature of the fluid in the mid-plane and $\hat{e}_z$ is the unit vector perpendicular to the (x, y)-plane. The rotation enters (1) *via* the term proportional to γ, which breaks the chiral symmetry of the system. Linear stability analysis of the weakly nonlinear hexagon patterns described by (1) reveals long- and short-wave instabilities, which can be steady and oscillatory. The oscillatory instabilities can induce a transition to hexagon patterns that are periodically modulated in space and time. Further instabilities can lead to disordered patterns as shown in fig.1a. Strikingly, in this regime the pattern still retains a residual six-fold symmetry reflected in 6 broad peaks in the spatial

Fourier spectrum. Fig.1b shows a space-time plot of the angle dependence of this Fourier spectrum (radially integrated). Most notably, the spectrum exhibits an effective precession in time, which on longer time scales displays intermittent behavior.

For poorly conducting top and bottom boundaries Marangoni convection arises at long wavelengths. For the case of a nondeformable fluid surface we have systematically derived the long-wave equation [2]

$$\psi_t = -b\psi - \lambda\nabla^4\psi - \mu\nabla^2\psi - g_3(\nabla\cdot(\nabla\psi)^3) \quad - \alpha\nabla^2(\nabla\psi)^2 - \beta\nabla\cdot(\nabla^2\psi)(\nabla\psi)$$
$$-\gamma\,\hat{e}_z\cdot(\nabla\psi\times\nabla(\nabla^2\psi)) - g_2\,\hat{e}_z\cdot(\nabla\times(\nabla\psi)^3). \qquad (2)$$

As in (1), the rotation can drastically reduce the stability range of the hexagon patterns. Fig.1c shows a case in which above a certain reduced Marangoni number $\mu_c \approx 0.05$ the steady hexagons become unstable at all wavenumbers. In this regime chaotic dynamics may be expected in analogy to the results found for the Swift-Hohenberg equation (1) [1].

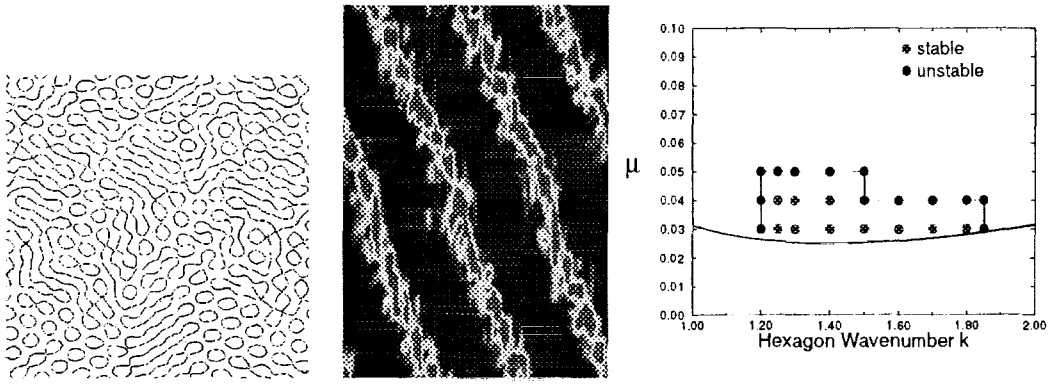

Fig.1 a) Snapshot of hexagon pattern in (1) for $R = 0.036$, $\alpha = 0.1$, $\gamma = 6$. b) Space-time diagram of the angle-dependence of the Fourier spectrum. Parameters as in a). c) Range of stable hexagons in long-wave equation (2) for Marangoni convection for $b = 0.025$ and a rotation rate $\Omega = 3$.

Rotation can induce a Hopf bifurcation to *oscillating* hexagons. Using coupled Ginzburg-Landau equations for the hexagon patterns [3] we have shown that independent of the values of the coefficients in these equations oscillating hexagons with the critical wavenumber are linearly stable. However, larger perturbations induce a transition to persistent defect chaos [4], a state that has been studied in great detail in the single complex Ginzburg-Landau equation but has so far not really been accessible in clean experiments.

[1] F. Sain and H. Riecke. Instabilities and spatio-temporal chaos of hexagonal patterns with broken chiral symmetry. *Physica D*, to appear.

[2] A. Mancho, F. Sain, and H. Riecke. *unpublished.*

[3] B. Echebarria and H. Riecke. Instabilities of hexagonal patterns with broken chiral symmetry. *Physica D*, 139:97–108, 2000.

[4] B. Echebarria and H. Riecke. Defect chaos of oscillating hexagons in rotating convection. *Phys. Rev. Lett.*, 84:4838, 2000.

Instabilities and Spatio-Temporal Chaos of Hexagonal Convection Patterns with Rotation

H. Riecke Northwestern University, USA
B. Echebarria Northwestern University, USA
F. Sain Northwestern University, USA
A.M. Mancho INTA, Madrid, Spain

supported by NASA

Hexagons in Marangoni Convection

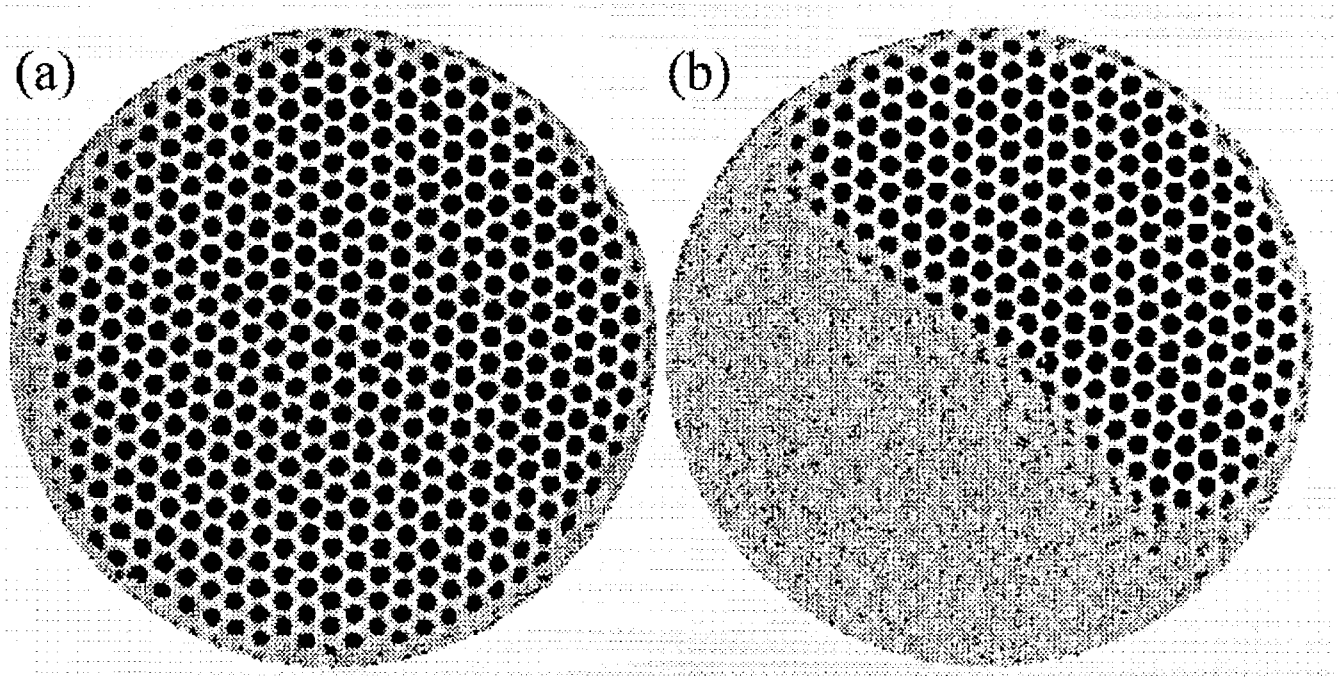

(M.F. Schatz *et al.*, PRL 75 (1995) 1938)

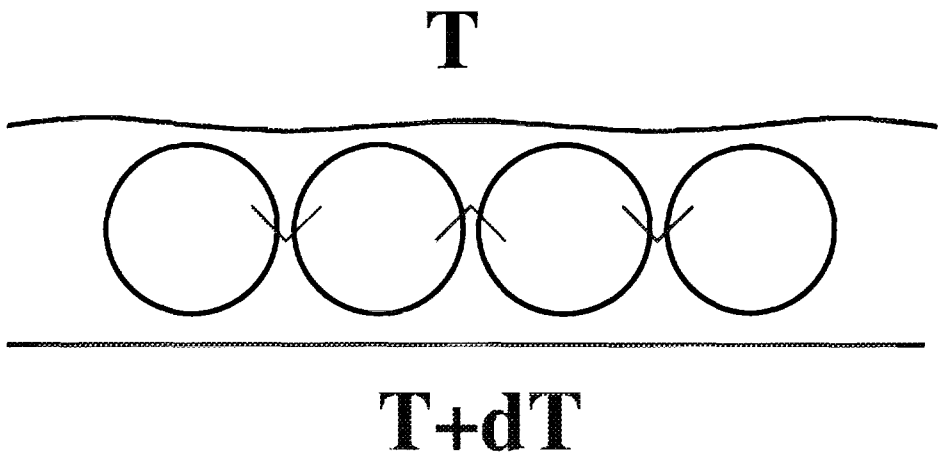

- Hysteresis: transcritical bifurcation

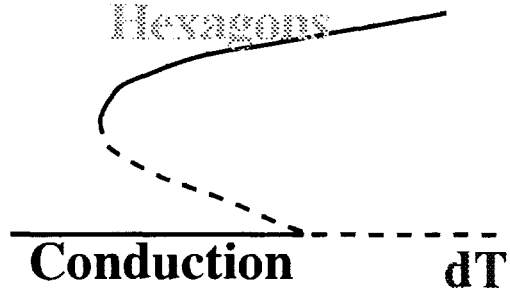

Extended Swift-Hohenberg Equation

- Minimal model equation for order parameter ψ

$$\partial_t \psi = R\psi - (\Delta + 1)^2 \psi - \psi^3 + \alpha\psi^2 + \gamma\, \mathbf{e}_z \cdot (\nabla\psi \times \nabla(\Delta\psi))$$

  - α breaks up-down symmetry: hysteresis
  - γ breaks chiral symmetry: rotation

- Weakly nonlinear analysis:
  - resonances
  - 2 translation modes
  - Hopf mode
  - long- and short-wave instabilities
  - steady and oscillatory instabilities

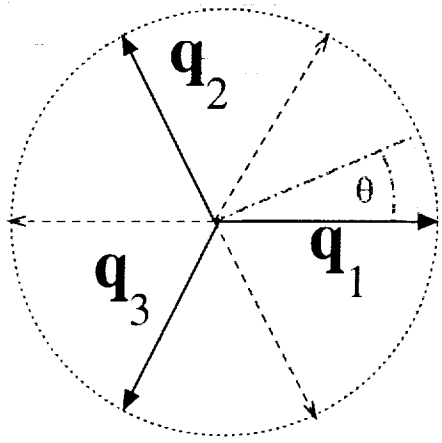

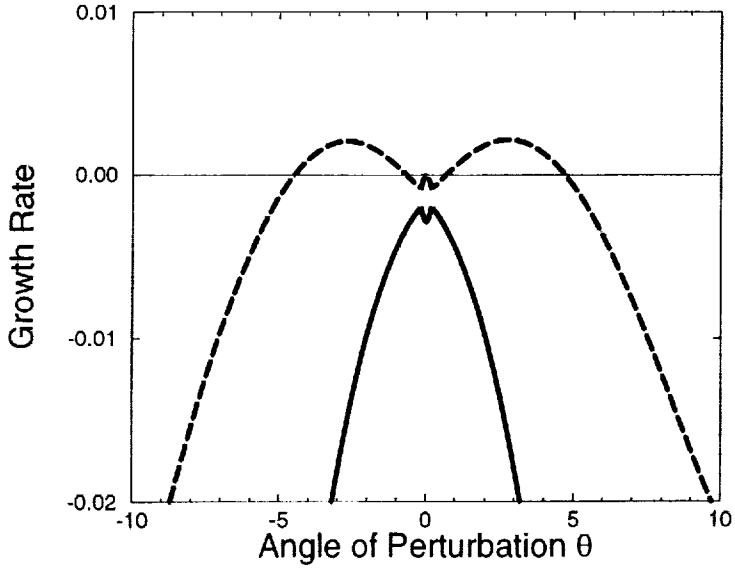

Persistent Disorder

- $\alpha = 0.1\ \gamma = 14$

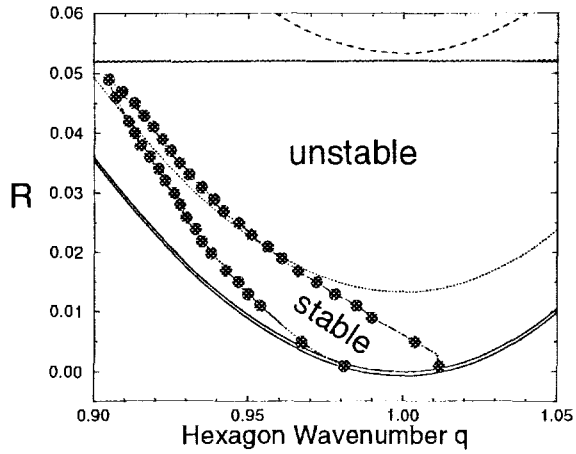

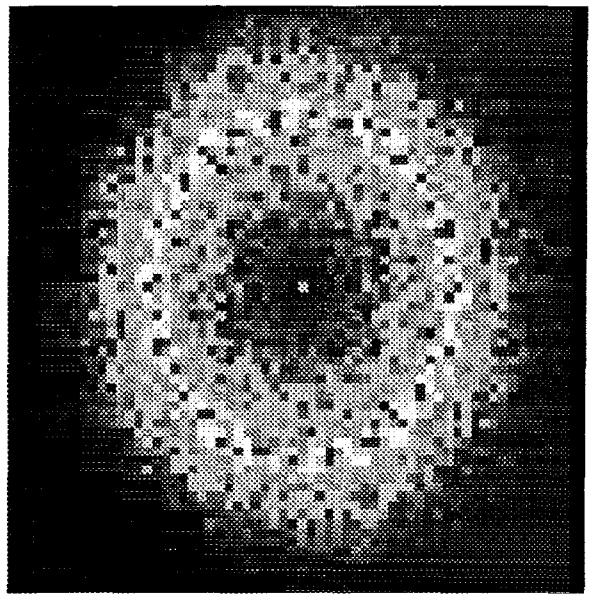

Fourier spectrum isotropic

Real-space snapshot

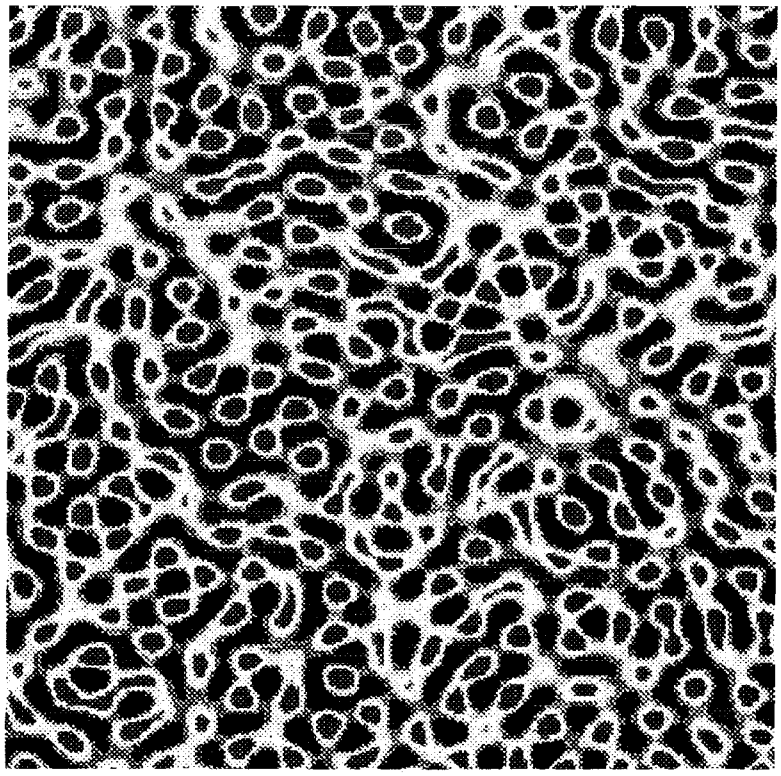

- Stability limits for $\alpha = 0.1$, $\gamma = 6$

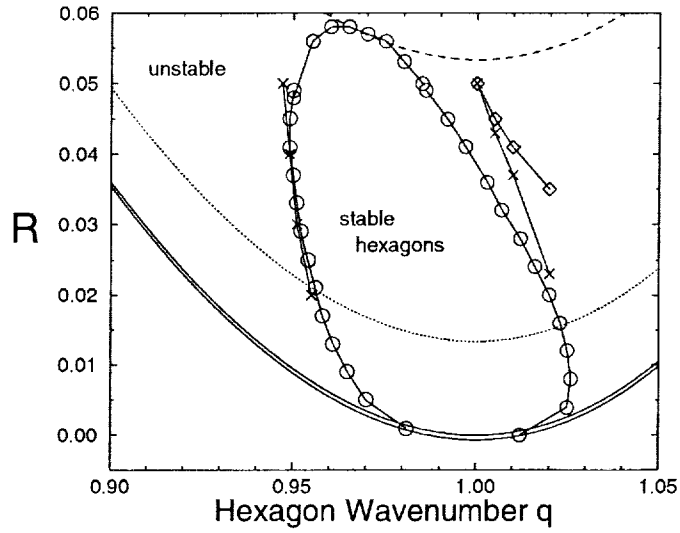

- Real-space zero-level contours of solution ψ.

$t = 0$
$t = 220$

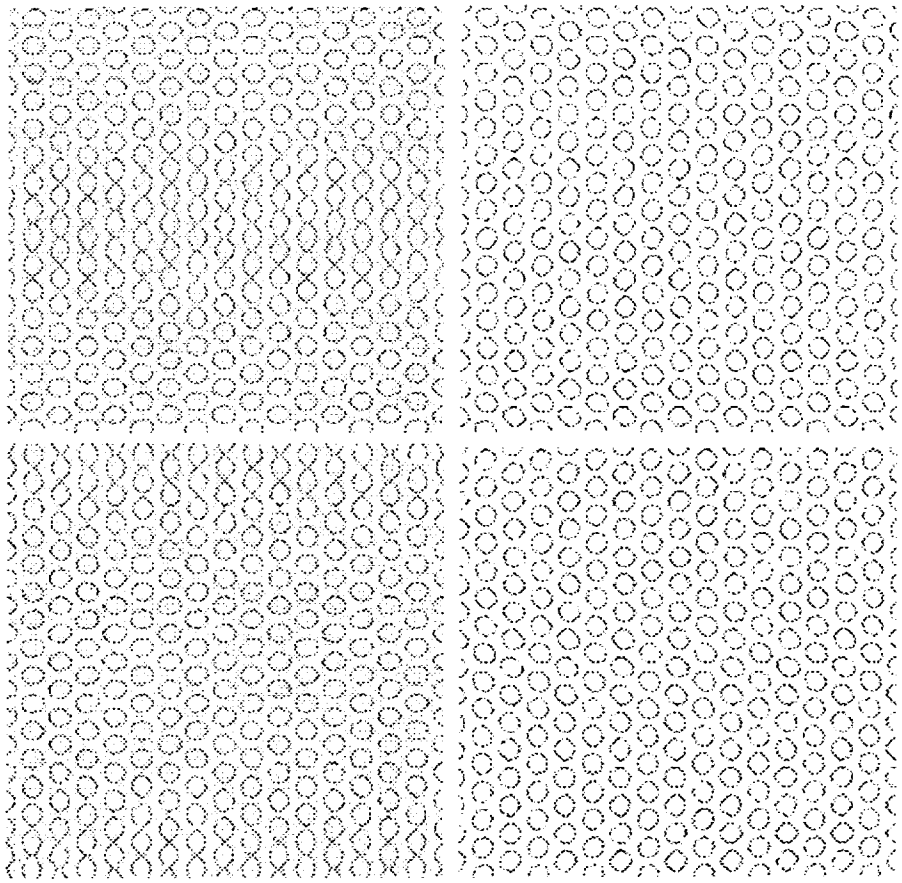

$t = 50$

$t = 110$

$t = 170$

- Standing wave modulation.

Bistability of Disorder and Hexagons

- Real-space zero-level contours

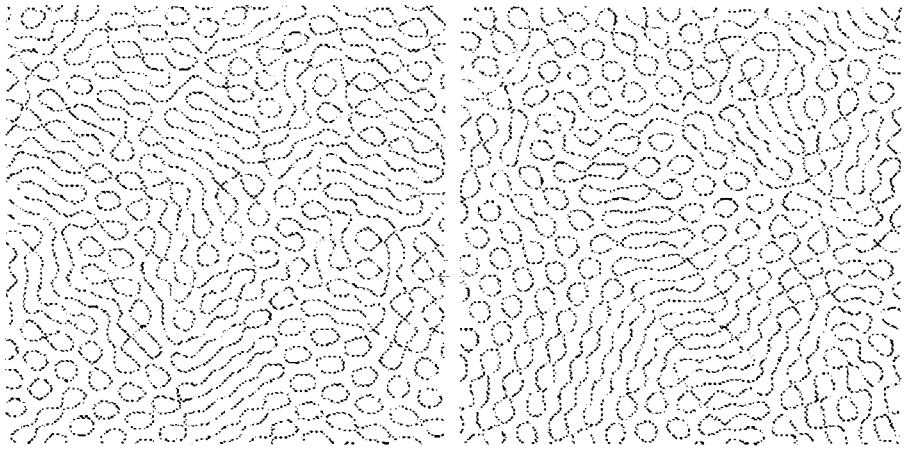

- Sixfold symmetry in Fourier Spectrum

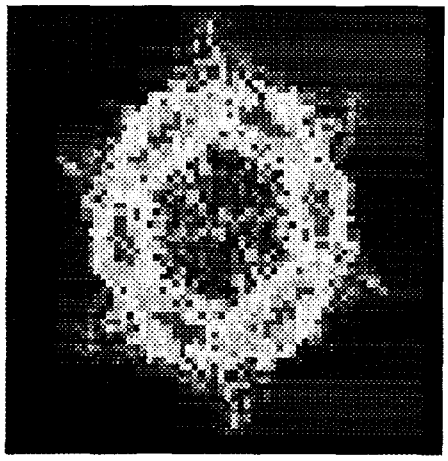

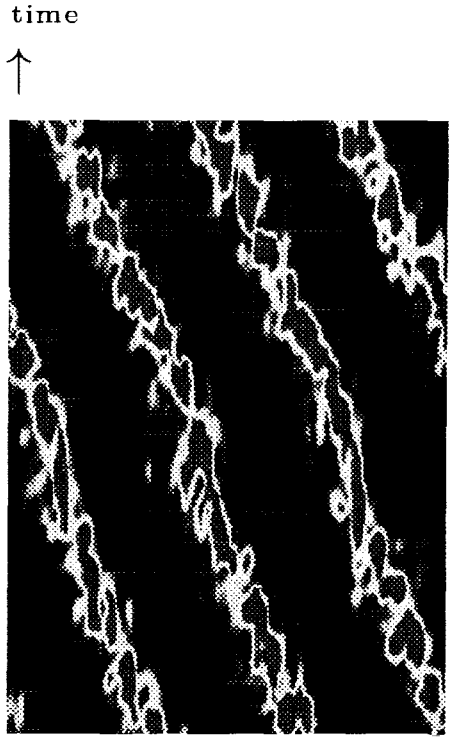

- Temporal evolution of Fourier Spectrum

Longwave Marangoni Convection

Navier-Stokes equations

$$\begin{aligned}
\frac{1}{\mathcal{P}}\left(\partial_t + \mathbf{u}\cdot\nabla\right)\mathbf{u} &= -\nabla p + \mathcal{P}\frac{1}{2}\nabla|\mathbf{\Omega}\times\mathbf{r}|^2 + 2\mathbf{\Omega}\times\mathbf{u} + \\
&\quad +\nabla^2\mathbf{u} \\
\nabla\cdot\mathbf{u} &= 0 \\
\left(\partial_t + \mathbf{u}\cdot\nabla\right)\theta &= \nabla^2\theta
\end{aligned}$$

Boundary conditions:

$$\begin{aligned}
z=1: \quad \partial_z^2 w &= \mathcal{M}\Delta_H\theta \\
z=0: \quad \partial_z\theta &= -\left(1 - Bi_1\theta\right) \\
z=1: \quad \partial_z\theta &= -\left(1 + Bi_2(\theta+1)\right)
\end{aligned}$$

- Rotation rate $\Omega = \omega\frac{d^2}{\kappa}$
- Marangoni number $\mathcal{M} = \gamma d\frac{\Delta T}{\rho\nu\kappa}$
- Prandtl number $\mathcal{P}\to\infty$
- non-deformable interface: large surface tension
- Poor conductors: $Bi_i \equiv h_i\frac{d}{k} \ll 1$

  $\Rightarrow$ critical wavenumber small

- Longwave expansion for poorly conducting boundaries
  $\Rightarrow$ reduction to two dimensions

$$\begin{aligned}\psi_t &= -b\psi - \mu\Delta\psi - \lambda\Delta^2\psi - \alpha\Delta|\nabla\psi|^2 \\ &\quad -\beta\nabla\cdot(\Delta\psi\nabla\psi) - \delta\nabla\cdot\left(|\nabla\psi|^2\nabla\psi\right) \\ &\quad -\mathbf{e}_z\cdot\left(\gamma_1\nabla\psi\times(\nabla\Delta\psi) + \gamma_2\nabla\psi\times\nabla|\nabla\psi|^2\right)\end{aligned}$$

$$\gamma_1 = -\frac{233}{525}\Omega + \ldots \quad \gamma_2 = \frac{8}{35}\Omega + \ldots \quad \lambda = \frac{1}{15} - \frac{7}{1200}\Omega^2 + \ldots$$

- Resonances: weakly nonlinear analysis of limited validity
  $\Rightarrow$ use Galerkin method on hexagonal lattice

- Stability diagram for $\Omega = 3$, $b = 0.025$

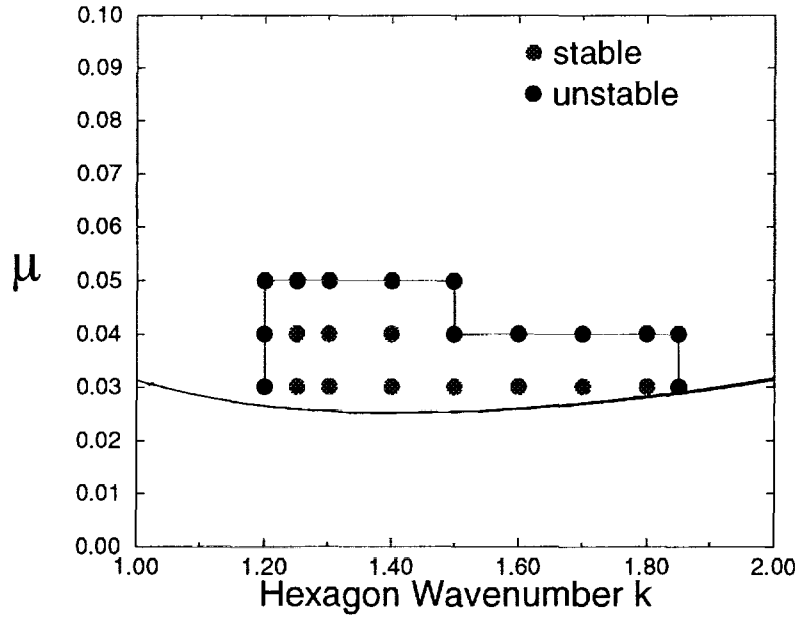

Ginzburg-Landau Equations for Hexagons with Rotation

$$\begin{aligned}\partial_t A_1 &= \mu A_1 + (\mathbf{n}_i \cdot \nabla)^2 A_1 + A_2^* A_3^* - A_1|A_1|^2 \\ &\quad -(\nu+\gamma)A_1|A_2|^2 - (\nu-\gamma)A_1|A_3|^2\end{aligned}$$

- γ breaks chiral symmetry: rotation

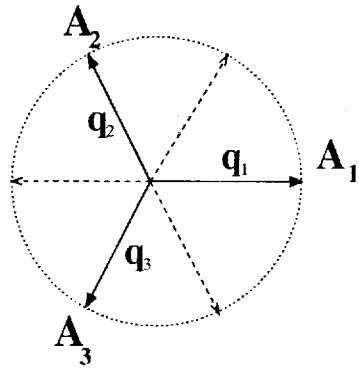

- Bifurcation diagrams

without rotation

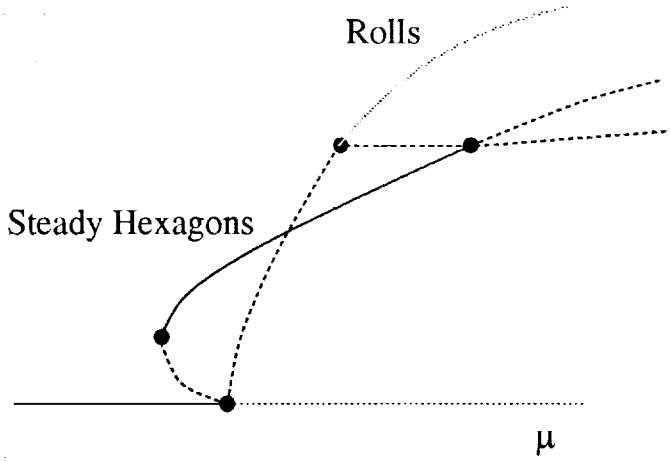

with rotation

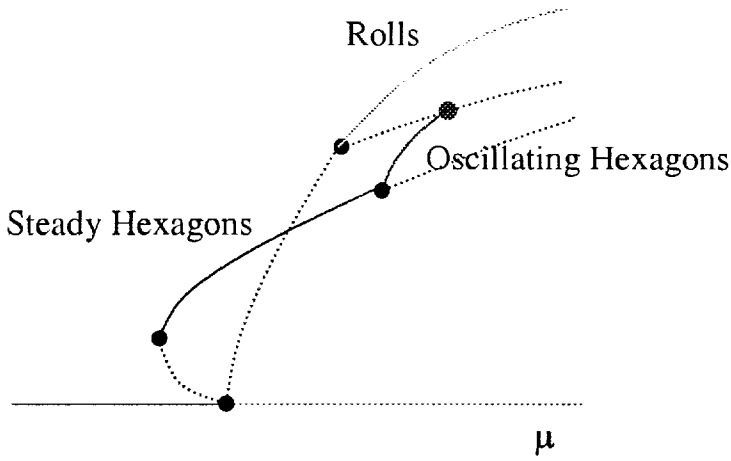

(J.W. Swift (1984), Soward (1985))

- Küppers-Lortz instability: rolls unstable for all μ.
- Oscillating hexagons end in heteroclinic cycle

Oscillating Hexagons

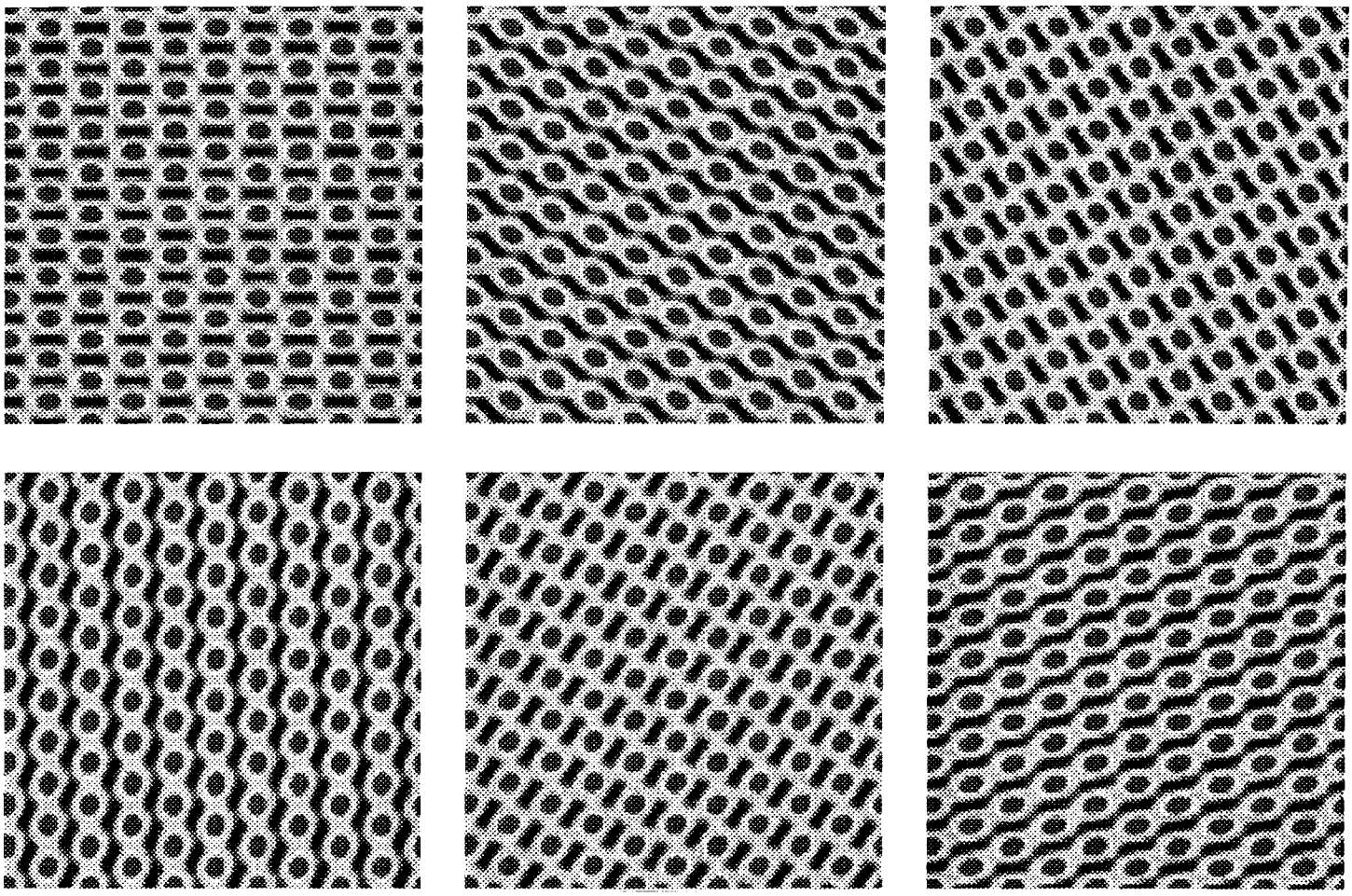

$\gamma < \gamma_{KL}$

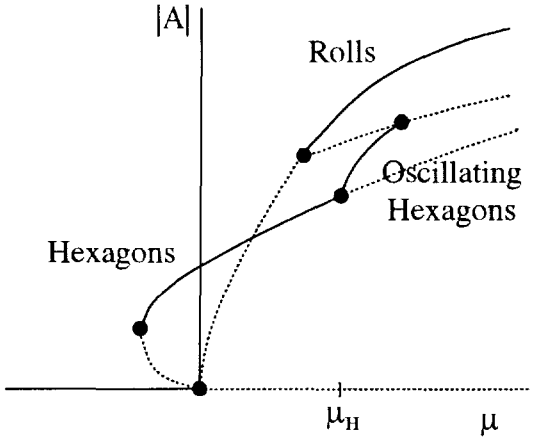

$\gamma > \gamma_{KL}$

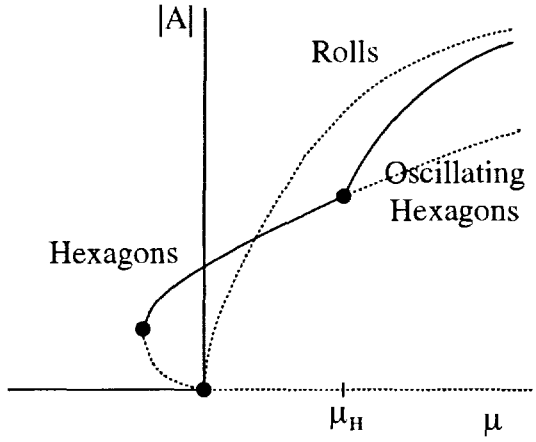

Amplitude-Phase Equations

- Perturbation expansion ($\epsilon \ll 1$):

$$A_n = (R + \epsilon^{1/2}[e^{2\pi n i/3}\mathcal{H}(x,t)e^{i\omega t} + c.c] + \mathcal{O}(\epsilon))e^{i\mathbf{q}_n\cdot\mathbf{x} + i\epsilon^{1/2}\phi_n(x,t)}$$

- CGLE coupled to phase modes:

$$\begin{aligned}
\partial_T \mathcal{H} &= (\mu - \mu_H)\delta\mathcal{H} + \xi\nabla^2\mathcal{H} - q\delta\mathcal{H}\nabla\cdot\vec{\phi} - \rho\mathcal{H}|\mathcal{H}|^2 \\
\partial_T \vec{\phi} &= D_\perp\nabla^2\vec{\phi} + D_{||}\nabla(\nabla\cdot\vec{\phi}) + D_{\times_1}\nabla^2(\hat{e}_z\times\vec{\phi}) \\
&\quad + D_{\times_2}(\hat{\mathbf{e}}_z\times\nabla)(\nabla\cdot\vec{\phi}) - iq\beta(\mathcal{H}\nabla\overline{\mathcal{H}} - \overline{\mathcal{H}}\nabla\mathcal{H}) \\
&\quad + q\alpha\nabla|\mathcal{H}|^2 + iq\eta[\mathcal{H}(\hat{e}_z\times\nabla)\overline{\mathcal{H}} - \overline{\mathcal{H}}(\hat{e}_z\times\nabla)\mathcal{H}] \\
&\quad + q\beta(\hat{e}_z\times\nabla)|\mathcal{H}|^2
\end{aligned}$$

$$\begin{aligned}
\vec{\phi} \equiv (\phi_x, \phi_y) &= (-\phi_2 - \phi_3, (\phi_2 - \phi_3)/\sqrt{3}) \\
\phi_1 + \phi_2 + \phi_3 &= \Phi
\end{aligned}$$

- Form of equations by symmetry: Reflections $\Rightarrow \mathcal{H} \to \mathcal{H}^*$

- Homogeneous oscillations: $\mathcal{H} = \mathcal{H}_0 e^{i\Omega t}$, $\vec{\phi} = 0$

- Amplitude $\mathcal{H}$ and phase $\vec{\phi}$ decoupled at band center $q = 0$
  Stability of oscillations $\mathcal{H}$ + stability of hexagons $\vec{\phi}$

Defect Chaos

- Band center ($q = 0$):
  oscillation amplitude $\mathcal{H}$ and phase $\vec{\phi}$ decouple
- Complex Ginzburg-Landau equation (CGLE)

$$\partial_t \mathcal{H} = \mathcal{H} + (1 + ib_1)\nabla^2 \mathcal{H} - (b_3 - i\,\mathrm{sign}(\omega))\,\mathcal{H}|\mathcal{H}|^2$$

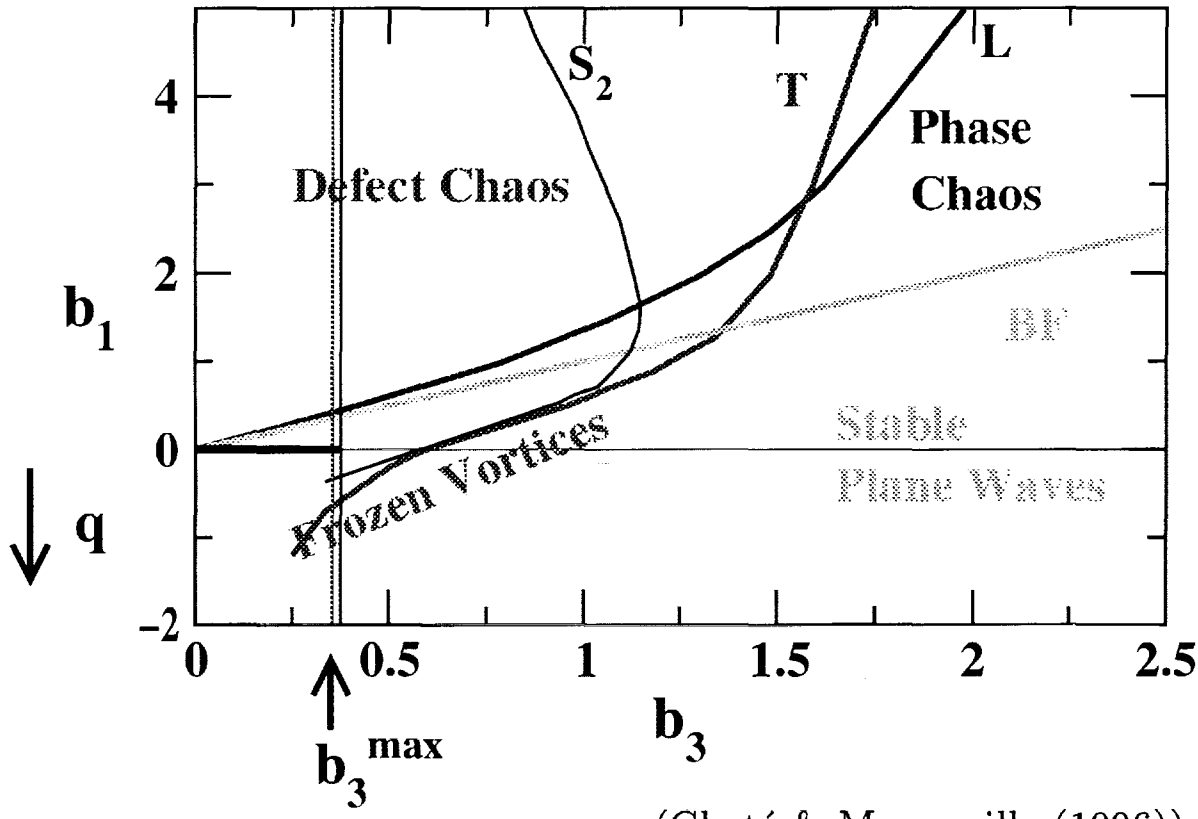

(Chat´e& Manneville (1996))

$$b_1 = \frac{2(9R^2 + 2\omega^2)q^2}{(6q^2R - 9R^2 - \omega^2)\omega}, \qquad b_3 = \frac{2|\omega|R(3R+1)}{\omega^2(1+4R) + 8R^2(1+2R)}$$

- Plane waves bistable with defect chaos

Numerical simulations

- Reconstruction of the hexagonal pattern $\psi = \sum_{i=1}^{3} A_i e^{i\mathbf{k}_i^c \cdot \mathbf{x}}$

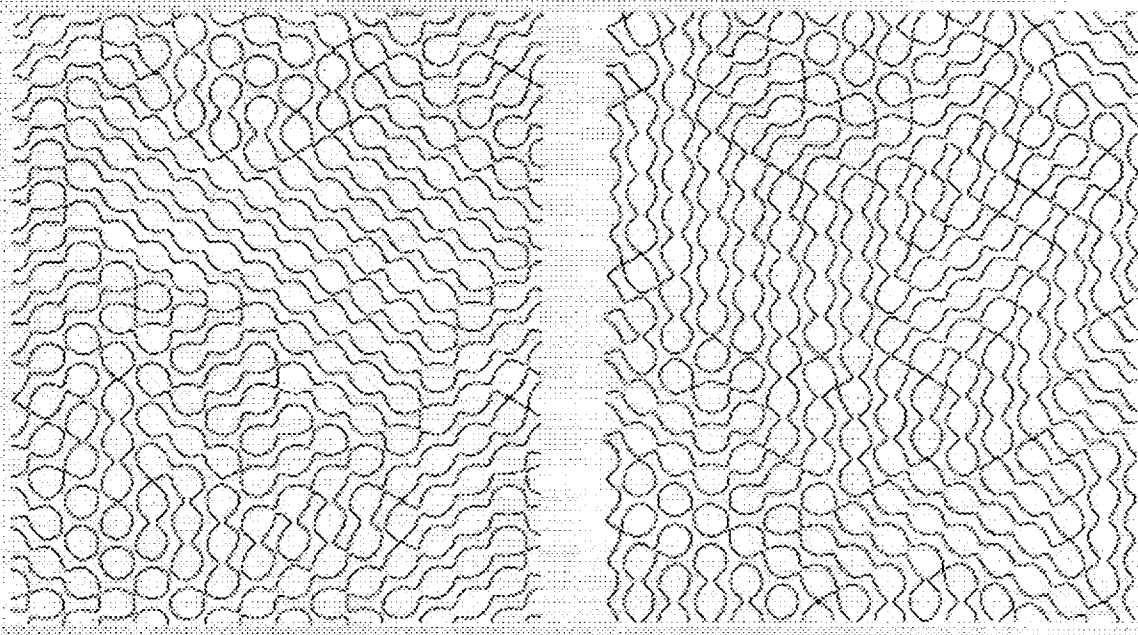

t=0 t=T/2

- Amplitude of oscillation $\mathcal{H} \cong \langle \epsilon^{-i\omega t}(|A_n| - (\sum_{j=1}^{3} |A_j|)/3)\rangle_T$

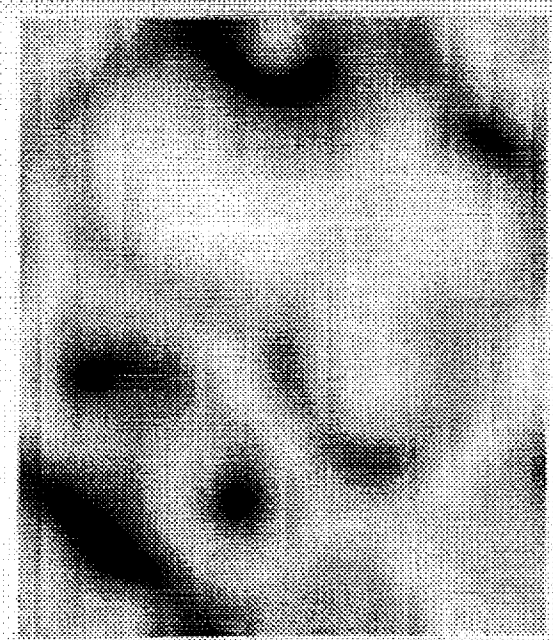

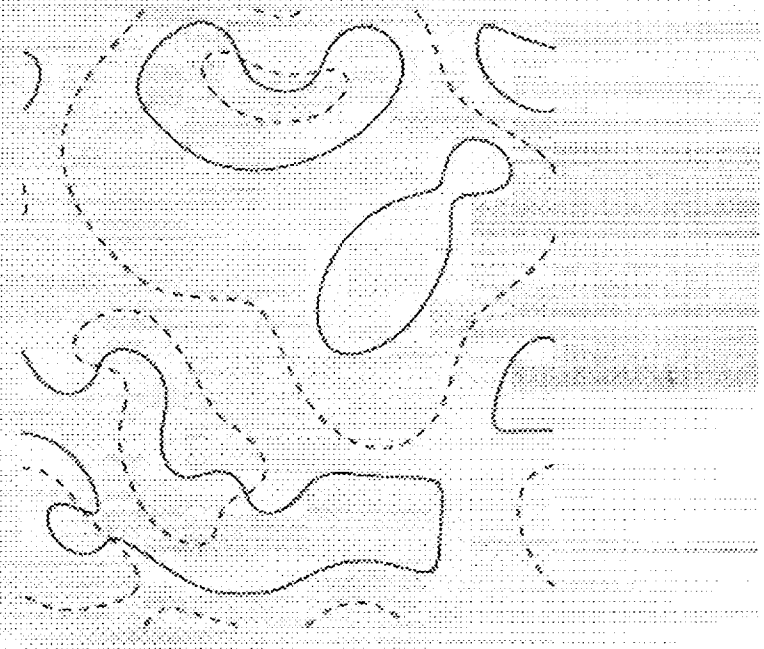

Defect density

- Off-center ($q \neq 0$) $\rightarrow$ coupling to the phase
- Characterization $\rightarrow$ defect density ($n = \langle N \rangle / L^2$)

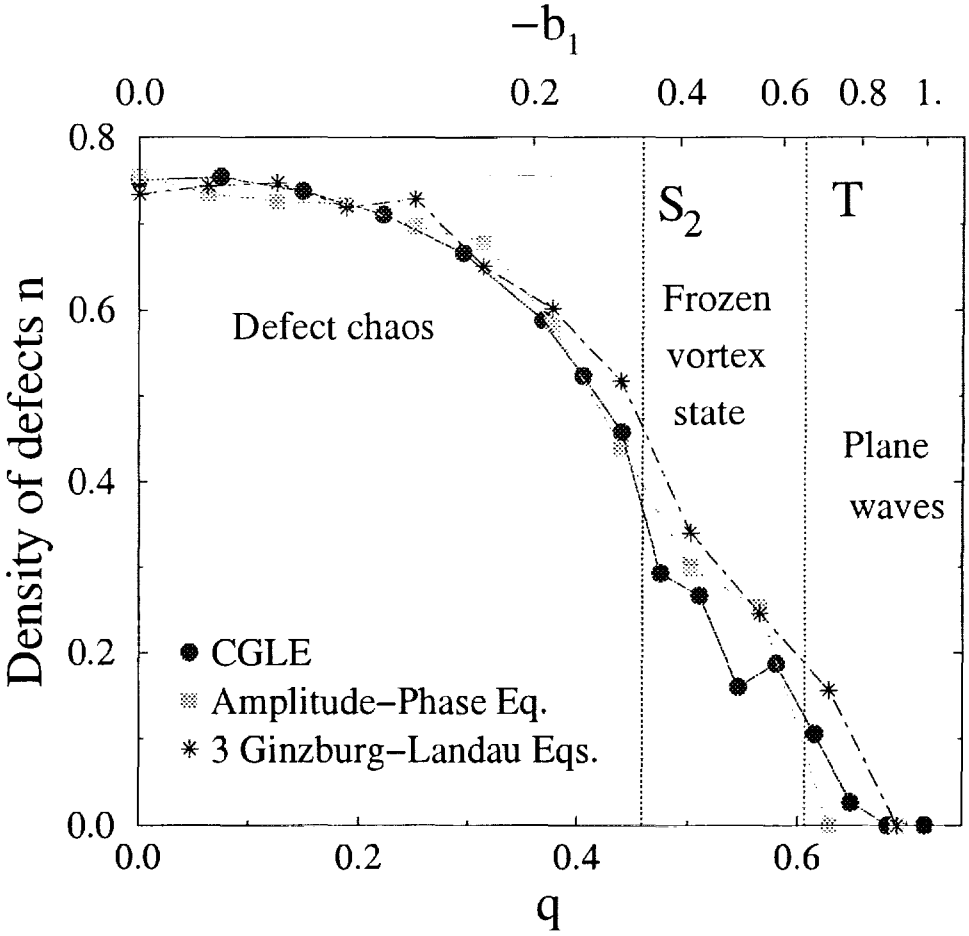

- Coupling with phase seems not important in this regime

Conclusion

Steady Hexagons:

- simple order-parameter model
- long-wave equation for Marangoni convection with poorly conducting boundaries

• steady and oscillatory side-band instabilities

• destabilization of hexagons of all wavenumbers

• spatio-temporal chaos: precessing spectrum

Oscillating Hexagons:

- three coupled Ginzburg-Landau equations
- complex Ginzburg-Landau equation coupled to phase

• CGL-type spatio-temporal defect chaos

Movies at `www.esam.nwu.edu/riecke/research.html`

August 10, 2000
Theme Speaker

An Integrated Exploration Strategy

Mr. Michael Conley
NASA Lyndon B. Johnson Space Center

NASA/CP—2000-210470

An Integrated Exploration Strategy

10 August 2000

Michael Conley

Human Deep Space Exploration

★ ***The Opportunity*** - An explosion of recent discoveries
- Allan Hills Meteorite
- Pathfinder
- Clementine
- Lunar Prospector

★ ***The Challenge*** - Affordable human exploration
- Evolving current systems
- Developing high pay-off technologies
- Leveraging commercial and other agencies technology programs
- Developing core capabilities
- Efficient mission approaches
- Significant reduction in cost

Exploration Strategic Roadmap

Dates dependent on decision to go & available funding

International Space Station

Assembly Complete

Phase 2 | Phase 3 | Operations Transition | Commercial Utilization

Human Support Technology

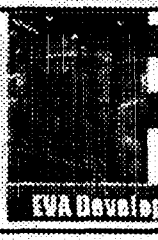

Lunar / Mars Life Support Testbed | BIO-PLEX | Translab | Lunar Lander | Mars Lander

Biomedical | Radiation Data Analysis | Zero-G Data Analysis

EVA Development | Next-Generation EVA System | Mars EVA Systems

Space Operations

Communications Initiatives | Commercial Utilization

Lunar and Mars Missions

Lunar Prospector | Surveyor '98 Orbiter and Lander | System Design Go-Ahead | Mars Sample Return | Operational & Technology Tests @ Moon | Human Mars Missions

Shuttle Upgrades & Shuttle Transition

System Definition | Commercial Utilization

Implementation

Liquid Flyback Boosters | Mars Launcher

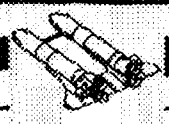

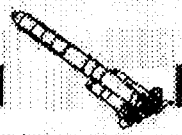

In Situ Resource Utilization

Lunar / Mars Testbed | Mars Flight Demo | Mars Flight Demo | Mars Sample Return | Large Scale Propellant Production

Revolutionary Interplanetary Transportation & Power

High Efficiency Propulsion | In-Space Propulsion Demonstrator | Lunar Propulsion & Power Demo | Full Scale Flight Unit Production

Advanced Space Power

X-38?

High Speed Aerobraking | Human Aerocapture (Earth) | Human Aerocapture (Mars)

Mars Aerocapture Demo | Mars Aerocapture and Precision Landing Demo

Core Capabilities & Technologies

Common Technology Building Blocks (Core Technologies)	Common System Building Blocks (Core Capabilities)	Potential Destinations

Examples

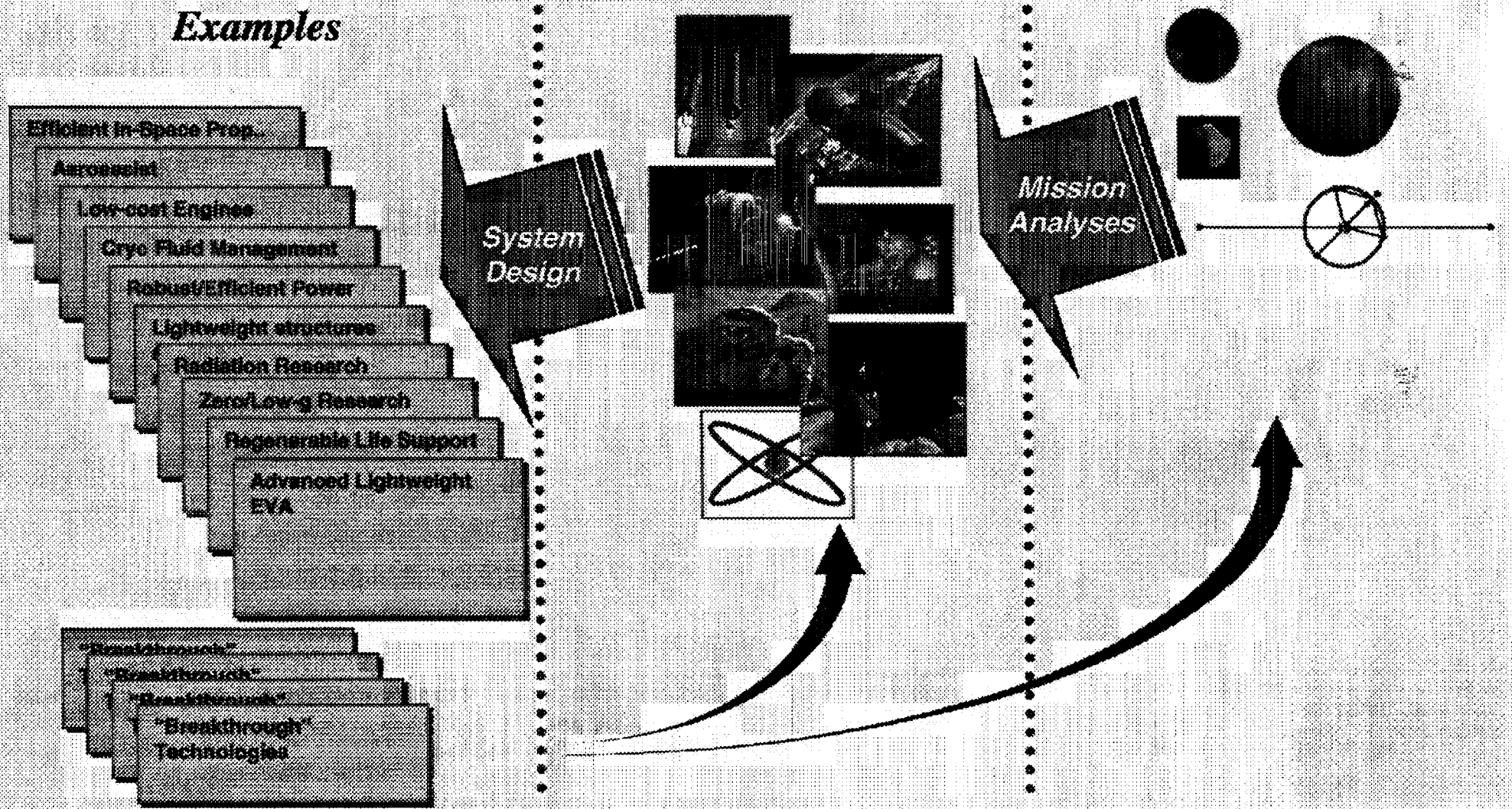

Mission Staging Scenarios

EXPLORATION OFFICE

SEP is assumed based on non-nuclear approach

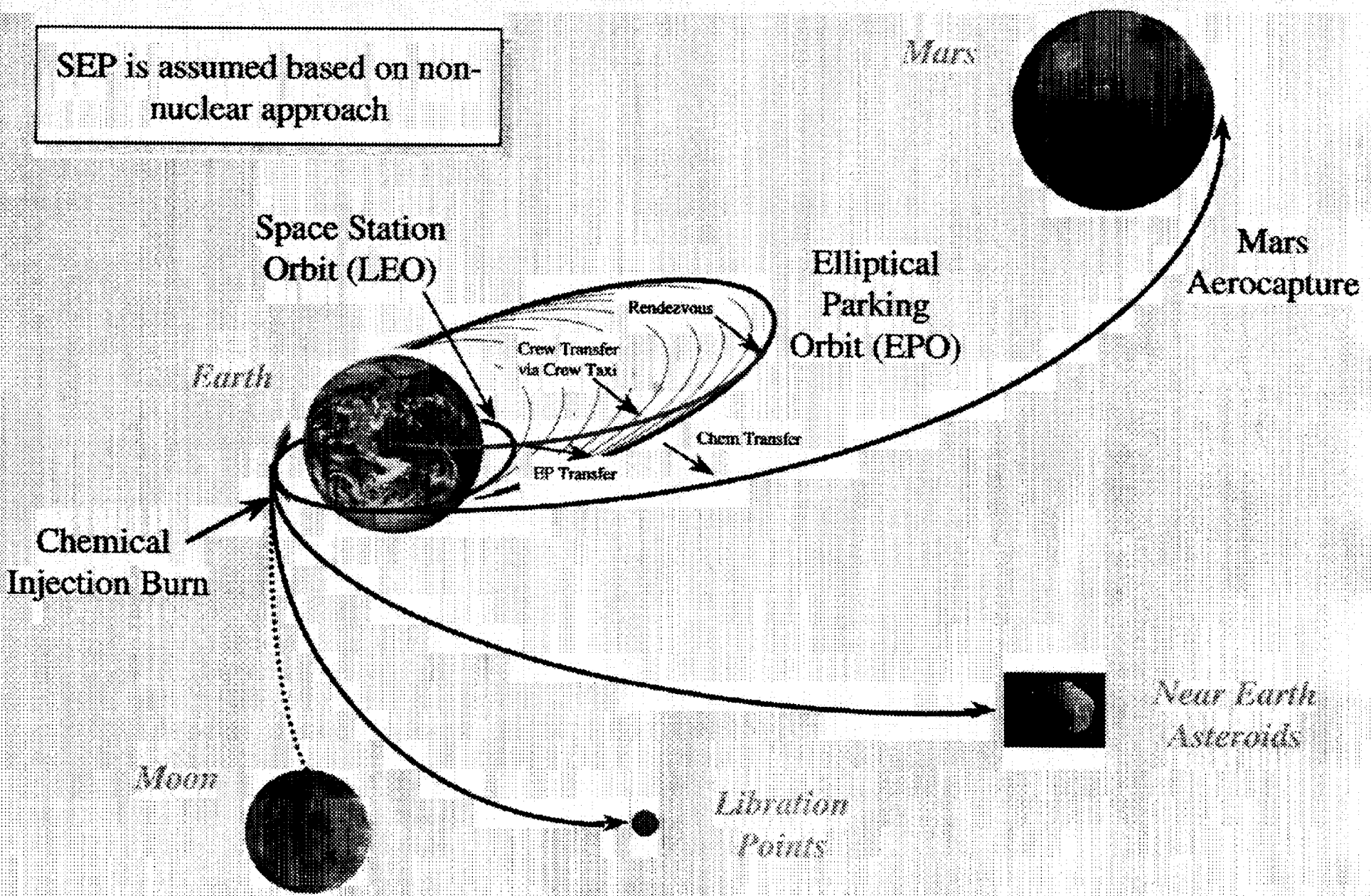

Human Lunar Architecture Concept

EXPLORATION OFFICE

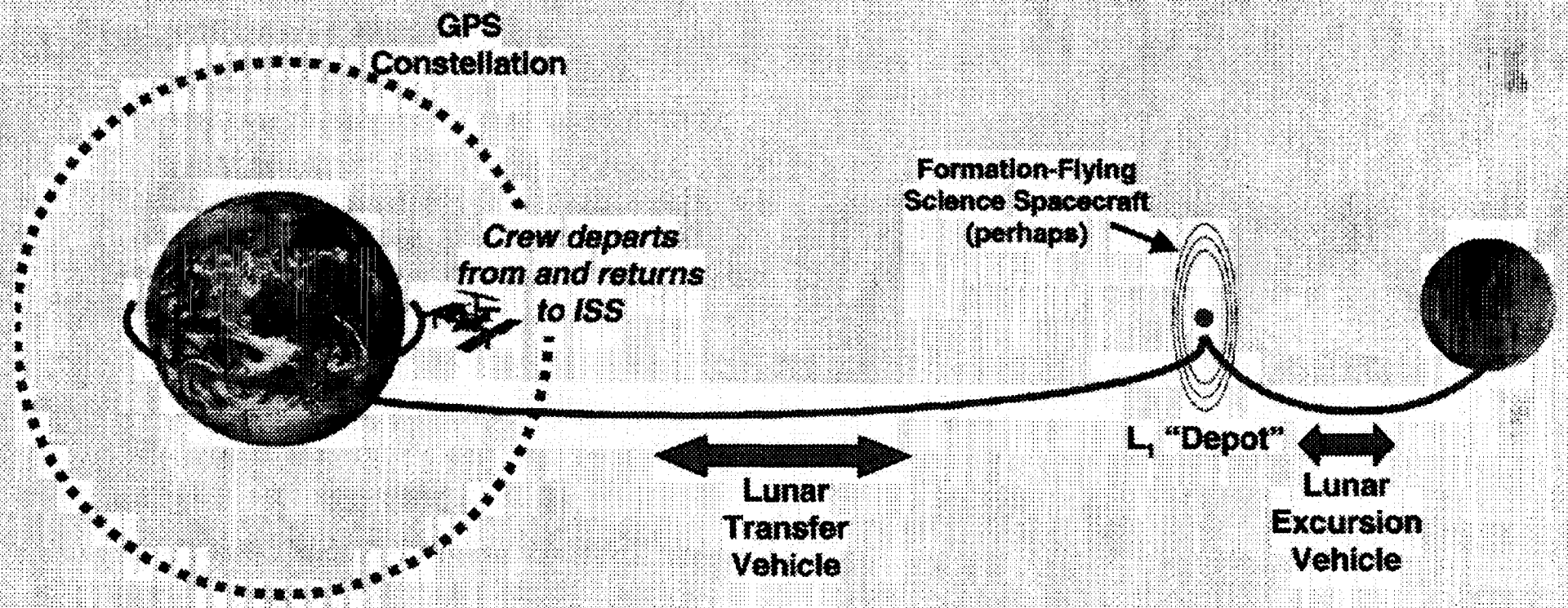

Lunar Transfer Vehicle

EXPLORATION OFFICE

- "Requirements"
  - Based at ISS for timing flexibility
  - Launch and recovery in Space Shuttle
  - Utilizes space storable propellants
  - Crew of 4 with ΔV capability of >1700 m/s
  - Operations in automated mode, or with crew onboard - automated rendezvous and proximity operations
  - Aerocapture manuevers at lunar return speeds to ISS orbit
- Preliminary Concept
  - Lifting body for crew g reduction
  - Integral LOX/CH_4 propulsion system
  - Eighteen day independent mission capability
  - Lightweight docking system

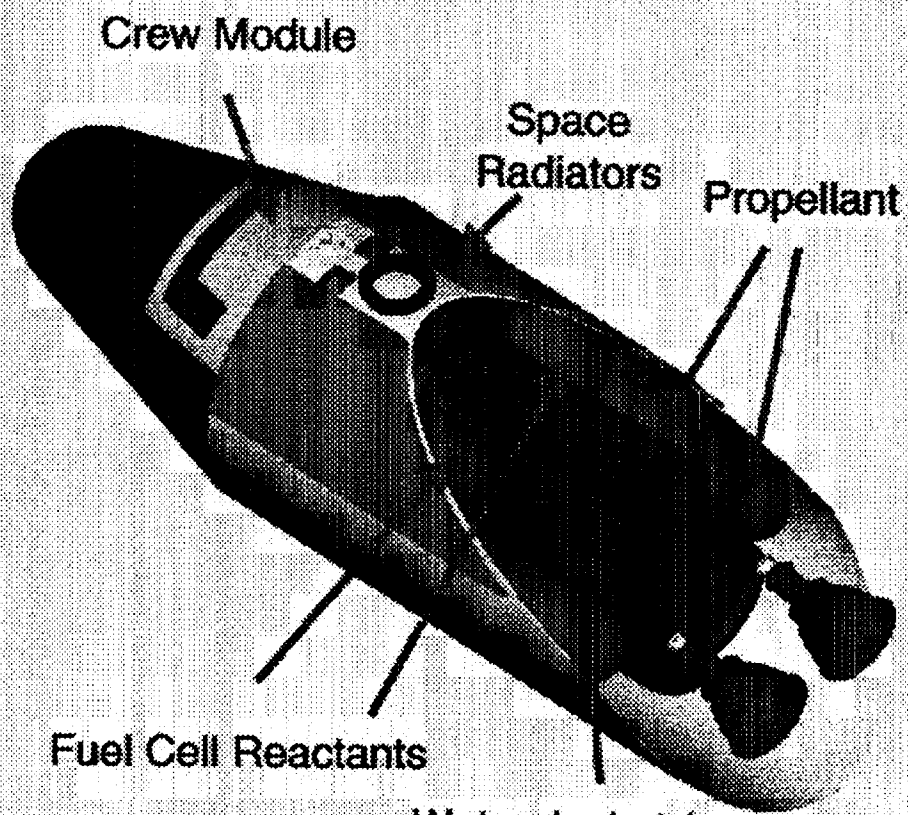

Lunar L_1 "Gateway"

EXPLORATION OFFICE

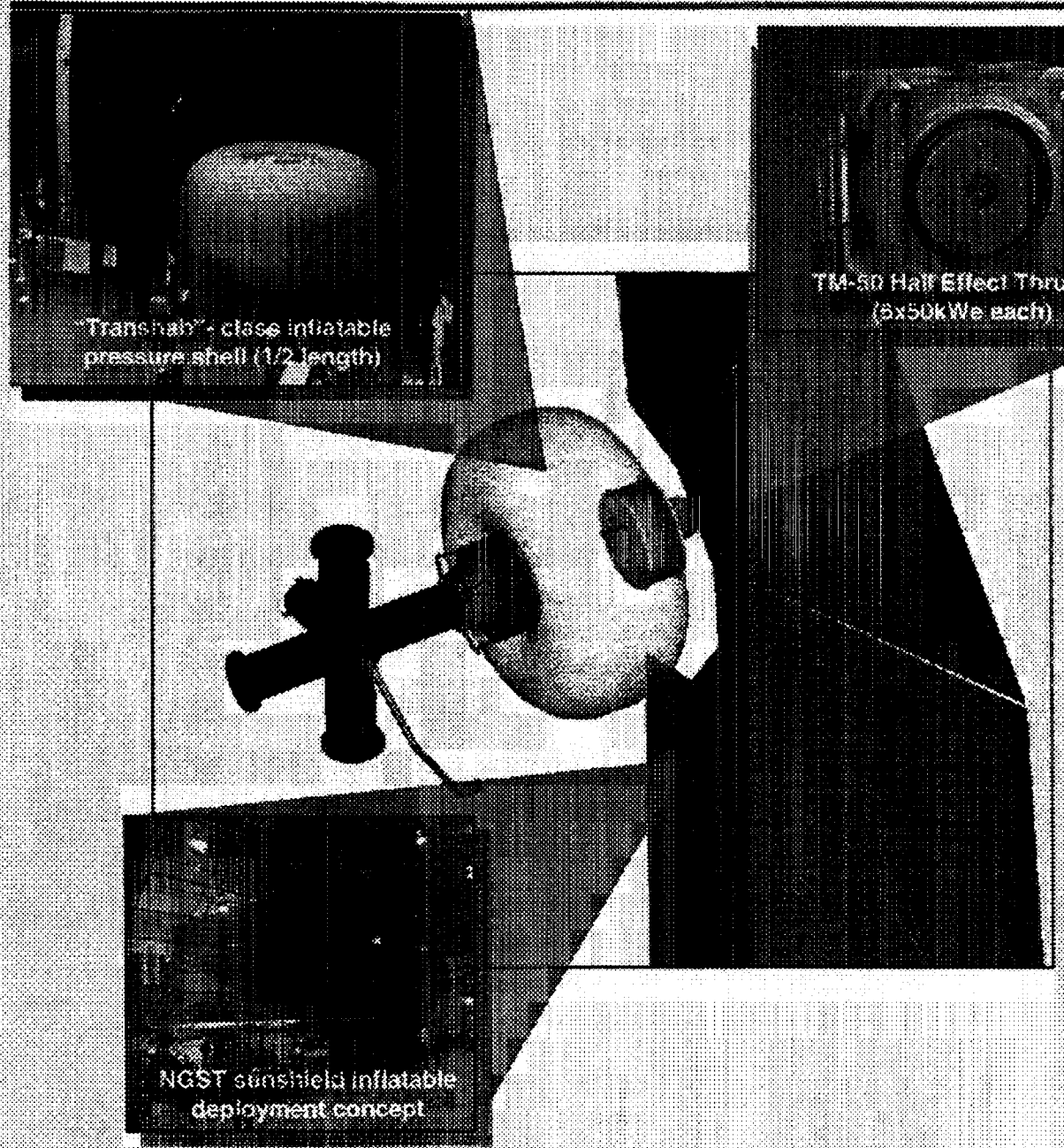

- **"Requirements"**
  - **Docking capability for Lunar Transfer Vehicle and Lander and pressurized crew transfer**
  - **Crew habitation for ≥12 days per lunar mission for return phasing or advanced system testing**
  - **Vehicle support (power, att. control) for Lunar Transfer Vehicle and Lander**
  - **Launch on EELV or Shuttle**
  - **Habitat delivered via solar electric propulsion from LEO to L1**
- **Preliminary Concept**
  - **"Half-length" inflatable habitat**
  - **Delivered to L_1 via Solar Electric Propulsion System**
  - **SEP remains attached to provide power, attitude control**

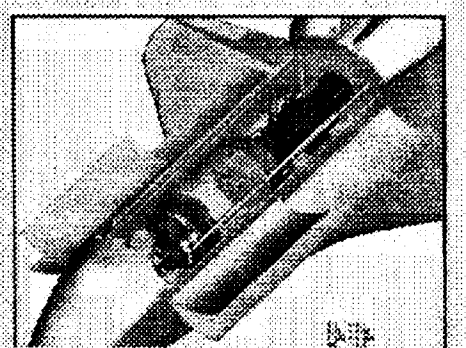

Lunar Excursion Vehicle

EXPLORATION OFFICE

- "Requirements"
  - LEV will be designed for round-trip piloted missions from L_1 to lunar surface and back to L_1
  - LEV will be delivered to L_1 by transfer stage
  - LEV will be able to remain at L_1 for extended period to allow for delay in crew arrival
  - LEV will interface with L_1 Depot
  - LEV will allow easy lunar surface egress/ingress of suited crewmembers
- Preliminary Concept
  - LOX/CH_4 propulsion stages (ascent and descent)
  - Seven day independent mission capability

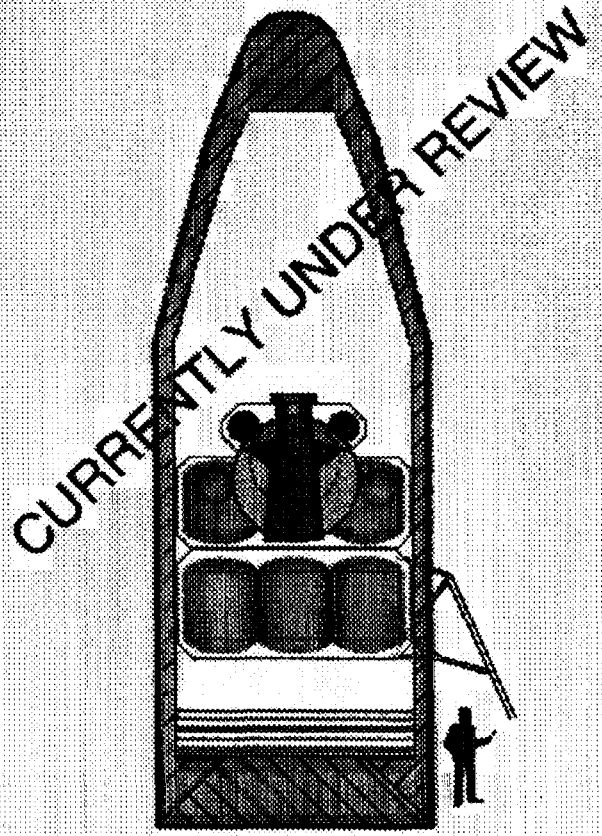

Mission Concept

EXPLORATION OFFICE

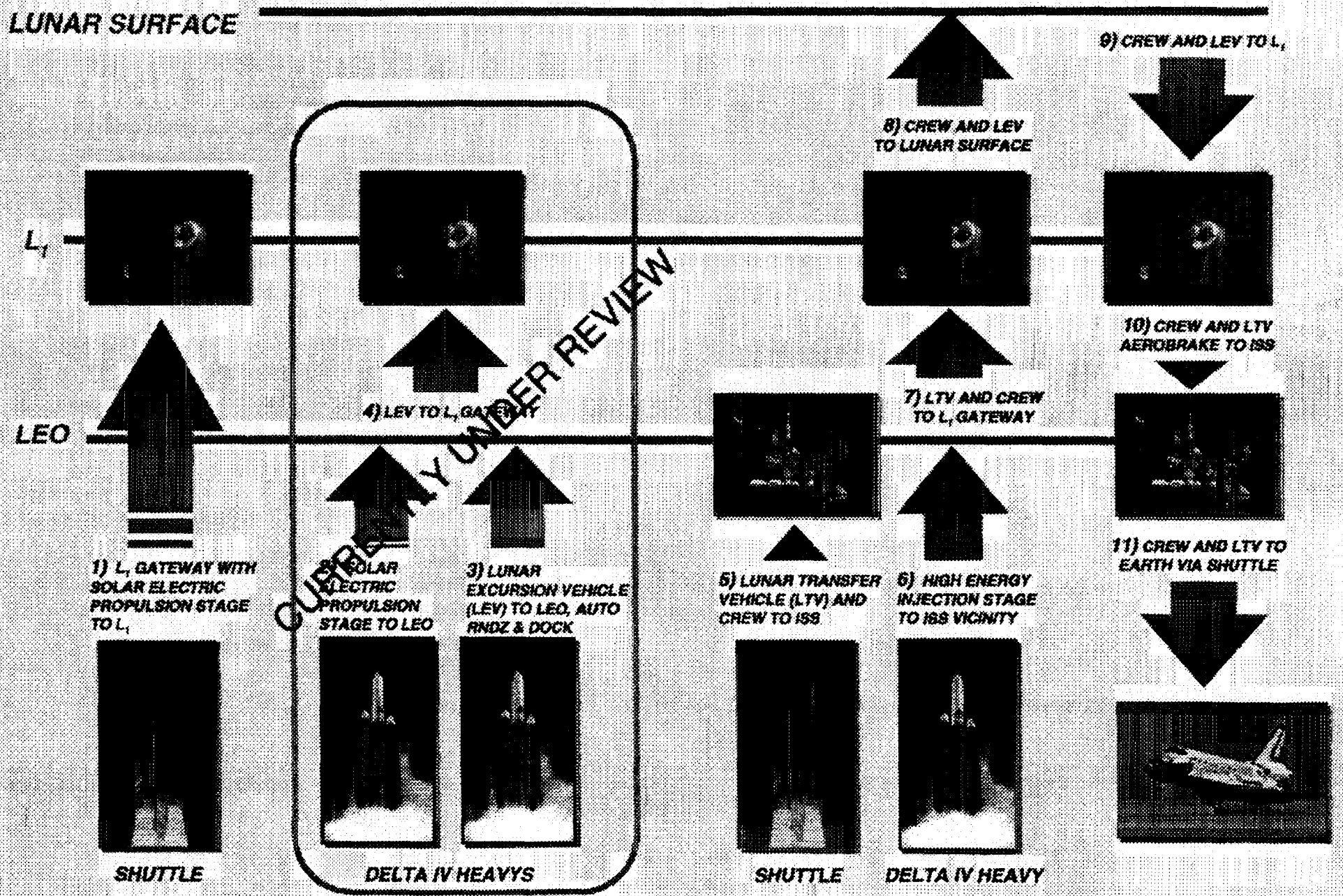

CURRENTLY UNDER REVIEW

Mars Mission Overview (SEP Option)

EXPLORATION OFFICE

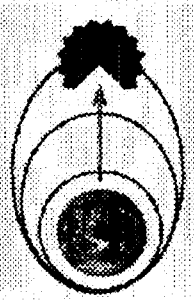

Habitat Lander and Ascent/Descent Vehicles delivered to Low Earth Orbit with "Shuttle Class" launcher. Solar Electric Propulsion stage spirals cargo to High Earth Orbit. Chemical injection used at perigee. SEP spirals back to LEO for reuse.

Surface Habitat and exploration gear aerocaptures into Mars orbit

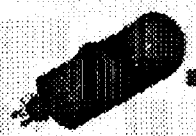

Ascent/Descent Vehicle aerocaptures and remains in Mars orbit for the crew

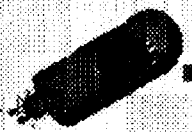

Crew rendezvous with Descent/Ascent Vehicle in Mars Orbit then lands in vicinity of Habitat Lander

Surface Habitat lands and performs initial setup and checkout - Initial outpost established

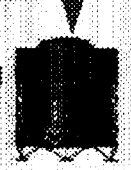

30 days provided to satisfy "long-stay" criteria.

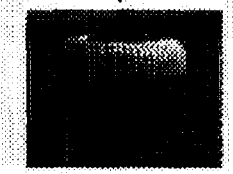

Mars Surface

Crew ascends and rendezvous with waiting Transit Habitat

Habitat remains in Mars orbit

Crew travels to Mars in "fast transit" 180-206 day transfer. Aerobrakes into Mars orbit

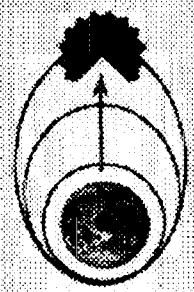

Transit Habitat vehicle delivered to LEO with "Shuttle Class" launcher. SEP spirals Transit Habitat to High Earth Orbit. Crew delivered to vehicle via crew taxi. SEP spirals back to LEO for reuse.

Crew returns to Earth on "fast transit" 180-206 day transfer. Direct entry at Earth

Earth

Mars Mission Vehicles

EXPLORATION OFFICE

Mars Transit Vehicle

- **Supports mission crew of six for up to 200-day transits to and from Mars**
- **Return propulsion stage integrated with transit system**

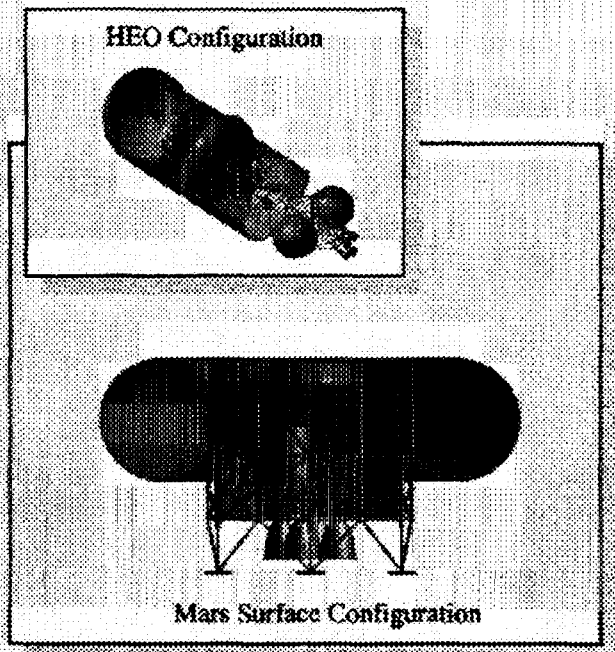

Mars Surface Habitat

- **Vehicle supports mission crew of six for up to 18 months on the surface of Mars**
- **Provides robust exploration and science capabilities**

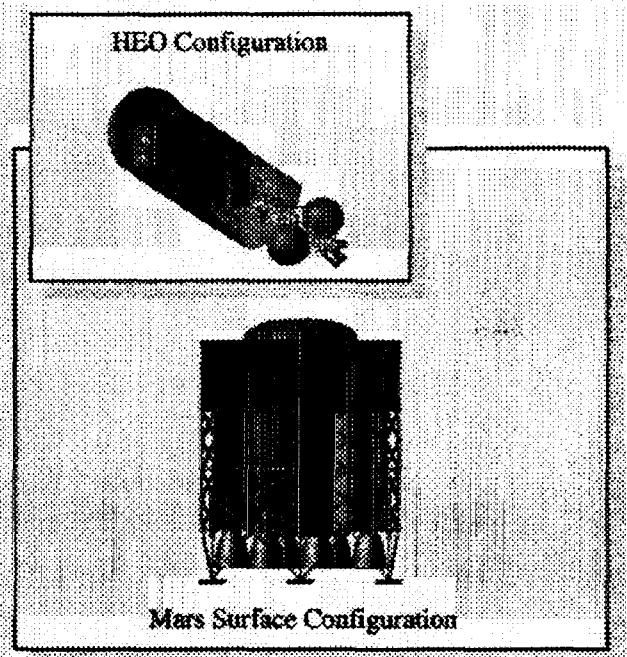

Descent/Ascent Vehicle

- **Transports six crew from Mars orbit to the surface and back to orbit**
- **Provides contingency abort-to-orbit capability**
- **Supports six crew for**

Lunar - Mars Life Support Project

Phase I: 15-day, 1-Person Test
July 1995

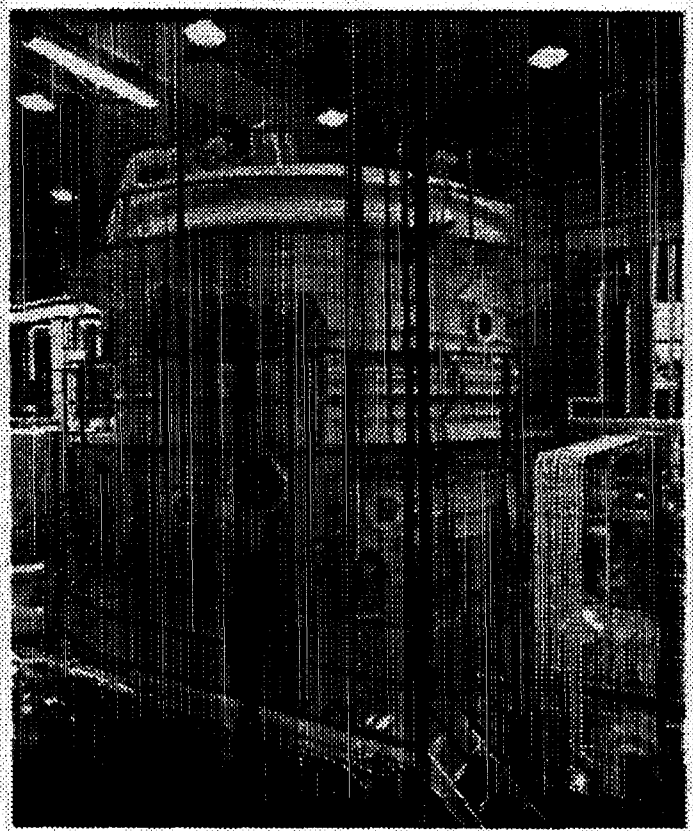

Phase II: 30-day, 4-Person Test - June 1996
Phase IA ISS: 60-day, 4-Person Test - January 1997
Phase III: 90-day, 4-Person Test - September 19, 1997

NASA/CP—2000-210470

TransHab Full Scale Shell Development Unit (SDU-3)

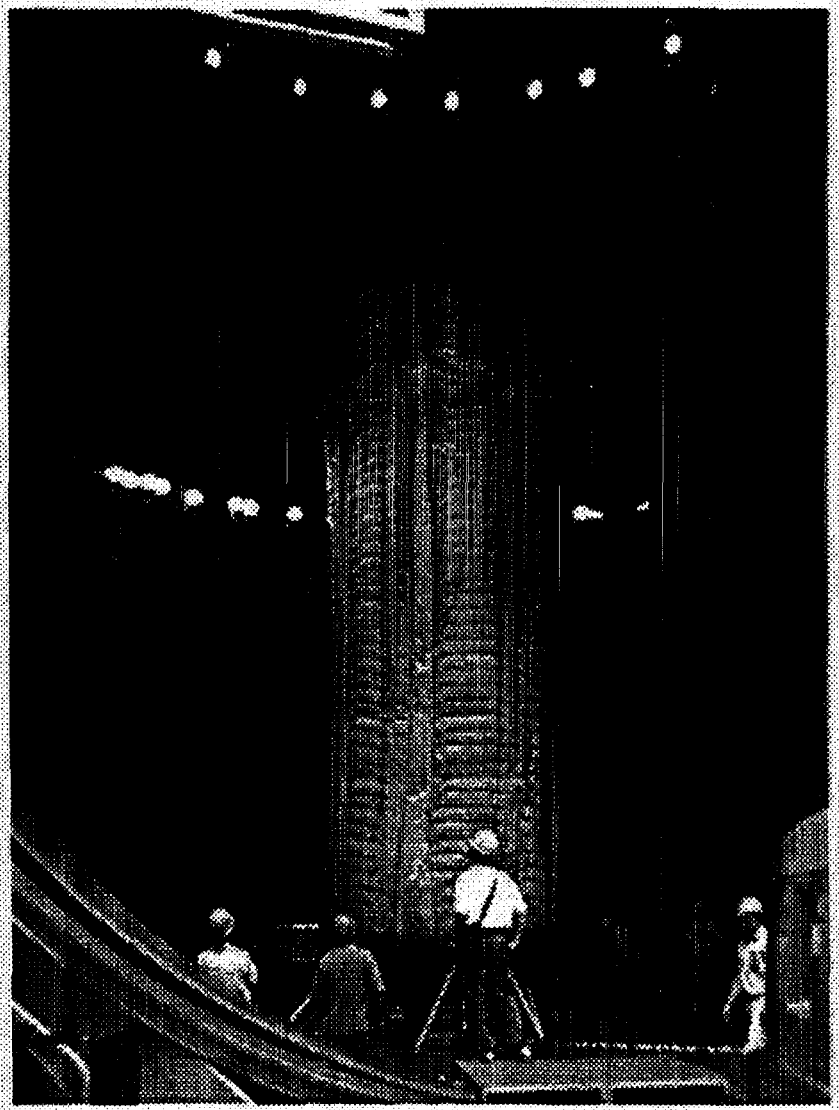

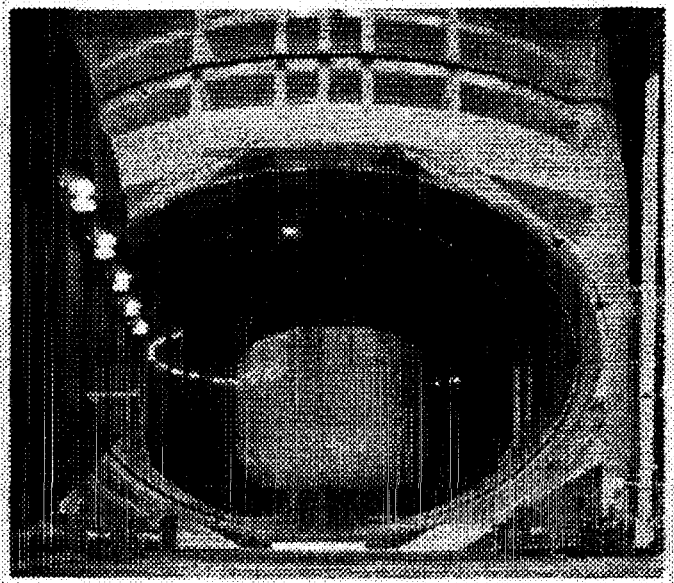

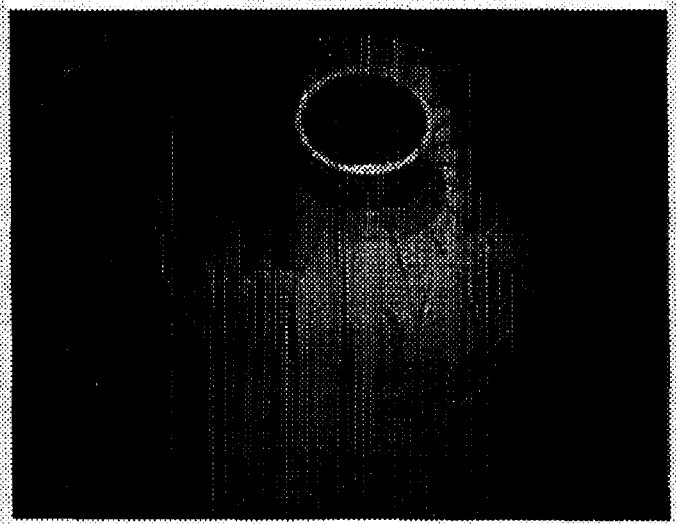

Vacuum Deployment Test 12-21-98

X-38 Technology Testing

Dryden Flight Research Center EC99 45060-25 Photographed 03JUL1999
The X-38 Ship 2, Crew Return Vehicle is released from the B-52 Mothership.
NASA/Dryden Carla Thomas

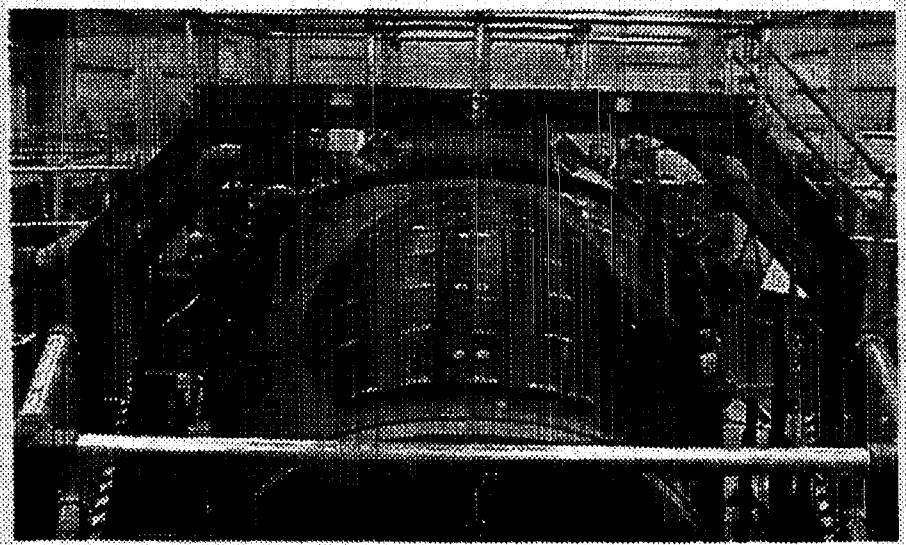

EC99-44923-157 Dryden Flight Research Center 05MAR99
X-38 v132 free flight NASA photo by Bill Ibbell

VASIMIR Laboratory Experiment

Technologies and Designs to Reduce Costs

LOW EARTH ORBIT

Solar Electric Propulsion

TEST AND DEMONSTRATION FLIGHTS

AFFORDABLE HUMAN EXPLORATION

Advanced Life Support

BIO-PLEX

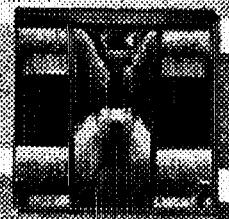

Crew Transfer

MARS

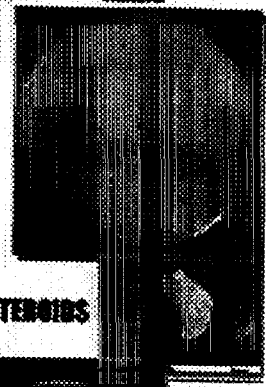

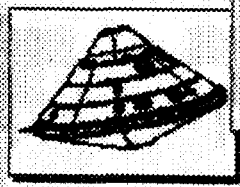

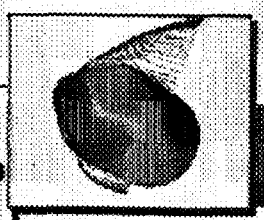

Aerocapture

ASTEROIDS

ROBOTIC MISSION TESTS

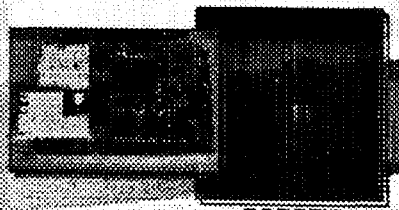

MOON

In Situ Resource Utilization

ROBOTIC MISSION TESTS

LIBRATION POINTS

Lightweight Structures and Systems

INFLATABLES

MINIATURIZED AVIONICS

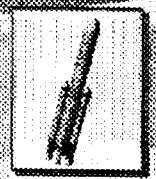

Shuttle - Compatible Heavy Lift

80 METRIC TONS TO LEO

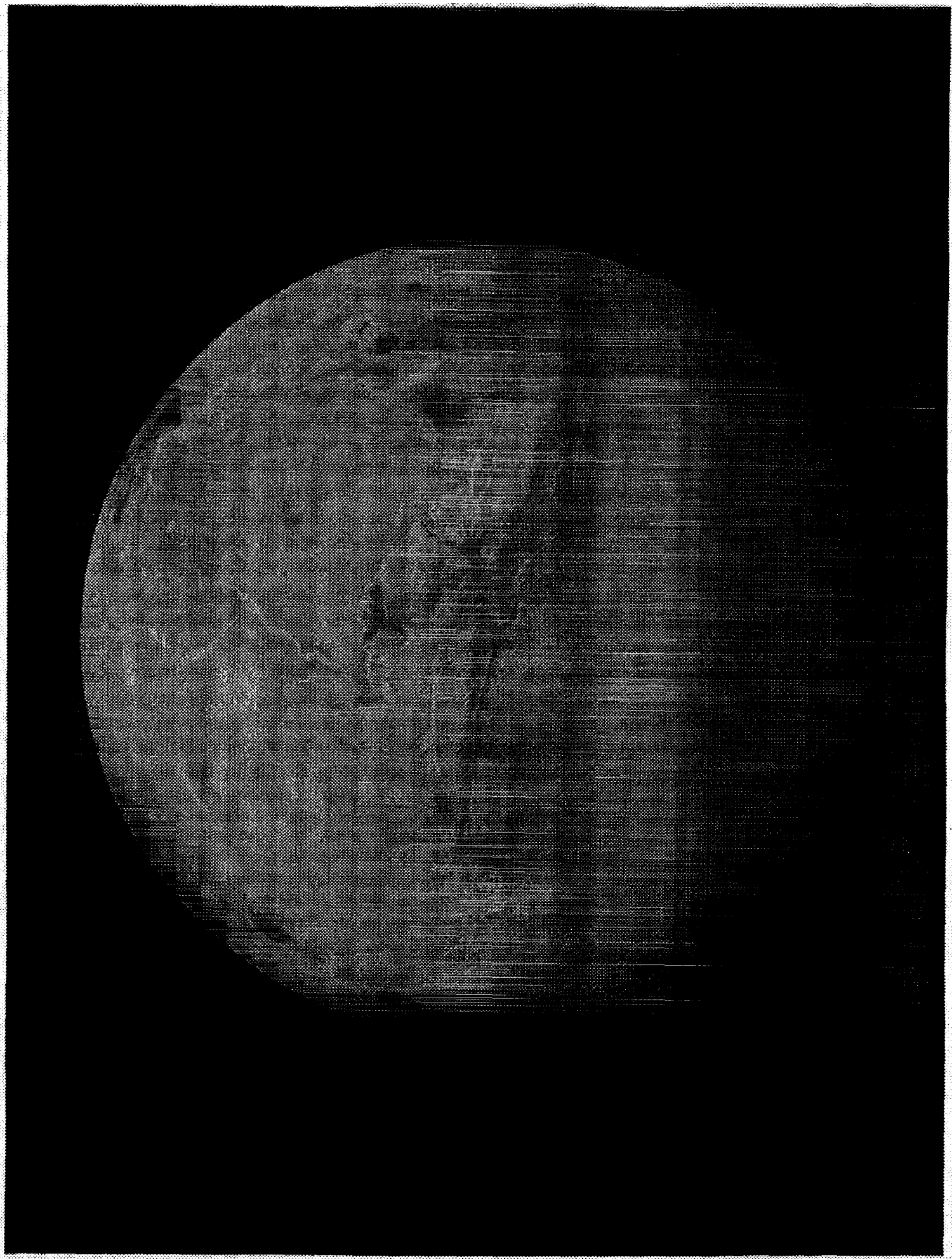

August 10, 2000
Session 3A

Multiphase Flow and Phase Change III

Computations of Boiling in Microgravity

G. Tryggvason
University of Michigan
Ann Arbor, MI 48109

Dave Jacqmin
NASA Glenn Research Center
Cleveland, OH 44135

ABSTRACT

The absence (or reduction) of gravity, can lead to major changes in boiling heat transfer. On Earth, convection has a major effect on the heat distribution ahead of an evaporation front, and buoyancy determines the motion of the growing bubbles. In microgravity, convection and buoyancy are absent or greatly reduced and the dynamics of the growing vapor bubbles can change in a fundamental way. In particular, the lack of redistribution of heat can lead to a large superheat and explosive growth of bubbles once they form. While considerable efforts have been devoted to examining boiling experimentally, including the effect of microgravity, theoretical and computational work have been limited.

Here, the growth of boiling bubbles is studied by direct numerical simulations where the flow field is fully resolved and the effects of inertia, viscosity, surface deformation, heat conduction and convection, as well as the phase change, are fully accounted for. Boiling involves both fluid flow and heat transfer and thus requires the solution of the Navier-Stokes and the energy equations. The numerical method is based on writing one set of governing transport equations which is valid in both the liquid and vapor phases. This local, single-field formulation incorporates the effect of the interface in the governing equations as source terms acting only at the interface. These sources account for surface tension and latent heat in the equations for conservation of momentum and energy as well as mass transfer across the interface due to phase change. The single-field formulation naturally incorporates the correct mass, momentum and energy balances across the interface. Integration of the conservation equations across the interface directly yields the jump conditions derived in the local instant formulation for two-phase systems. In the numerical implementation, the conservation equations for the whole computational domain (both vapor and liquid) are solved using a stationary grid and the phase boundary is followed by a moving unstructured two-dimensional grid. While two-dimensional simulations have been used for preliminary studies and to examine the resolution requirement, the focus is on fully three-dimensional simulations.

The numerical methodology, including the parallelization and grid refinement strategy is discussed, and preliminary results shown. For buoyancy driven flow, the heat transfer is in good agreement with experimental correleations. The changes when gravity is turned off and/or fluid shear is added are discussed, as well as the difference between simulations of a layer freely releasing bubbles versus simulations using only one wavelength initial perturbation. Figure 1 shows the early stages of the formation of a three-dimensional bubble from a thin vapor layer. The boundary conditions are periodic in the x and y direction, the bottom is a hot and the top allows a free outflow. The jagged edge of the surface close to the bottom of the computational domain is due to some of the surface elements being on the other side of the domain and some elements not plotted by our plotting routine. In the second figure, we show the temperature distribution through two perpendicular planes.

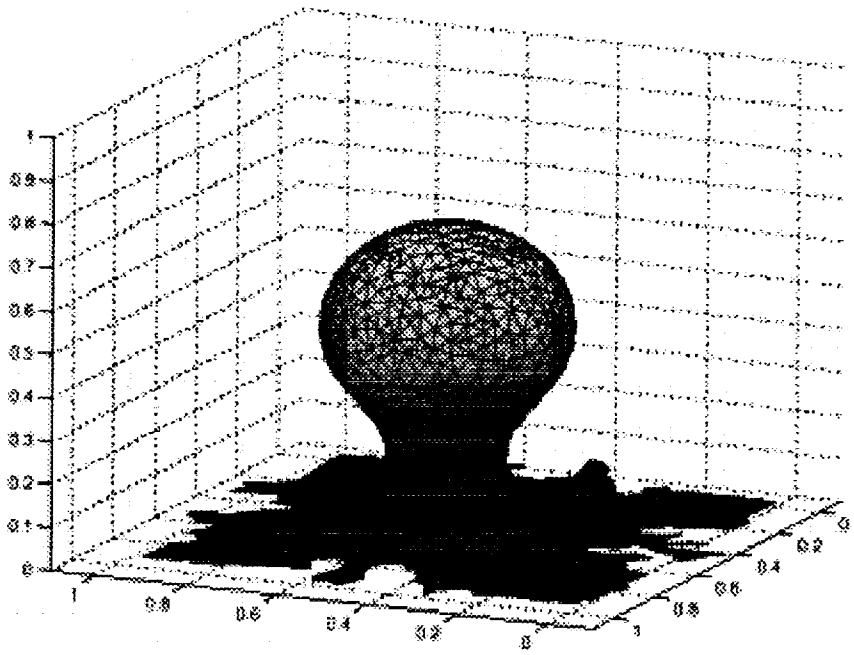

Figure 1. The formation of a bubble from a thin vapor layer. The grid representing the phase boundary is shown after the bubble has formed. The jagged edges of the front are an artifact of plotting of the periodic boundaries.

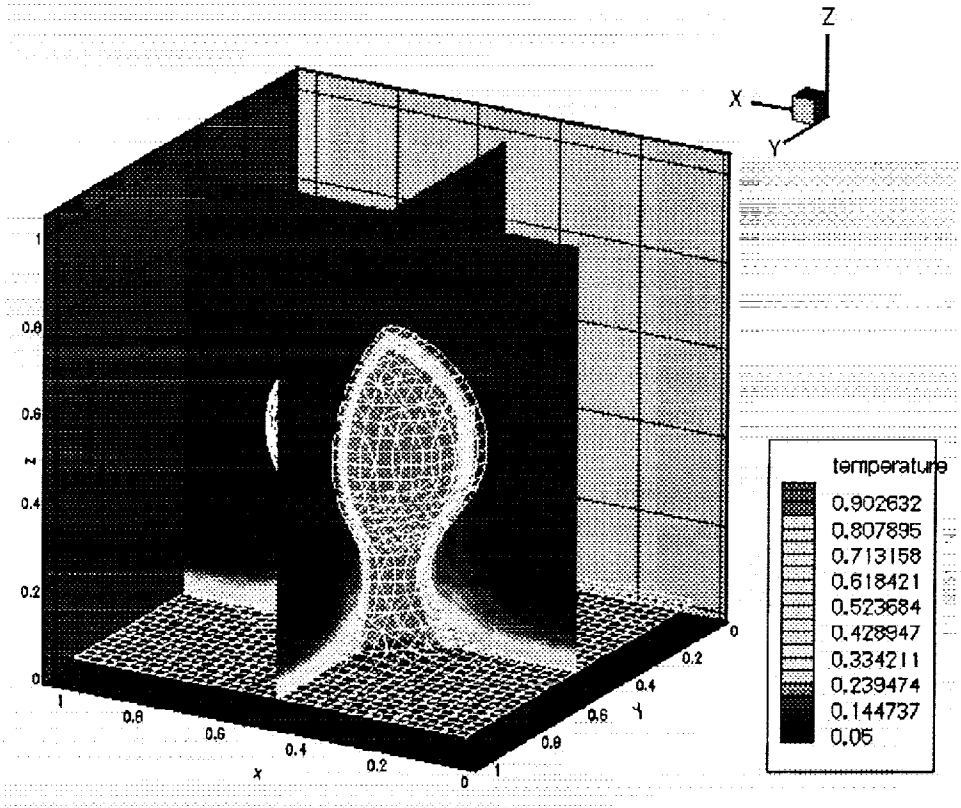

Figure 2. The temperature distribution in a bubble rising from a thin vapor layer. The high temperature in the bubble is represented by a light shades of gray.

NASA/CP—2000-210470

Title

Computations of Boiling Flows

Gretar Tryggvason
Worcester Polytechnic Institute

Dave Jacqmin
NASA Glen Research Center

Asghar Esmaeeli

Ozgur Ince
University of Michigan

Motivation

Phase change is the most efficient way of transporting heat (as in boiling and refrigeration). However, the results of design or operator error can be catastrophic.

Effect of gravity, flow, binary solute, thermocapillary, surfactants, electric fields, acoustic, and so on are important but still poorly understood.

Motivation

Direct numerical simulations of bubbly flows now allow relatively routine predictions of bubbly flows.

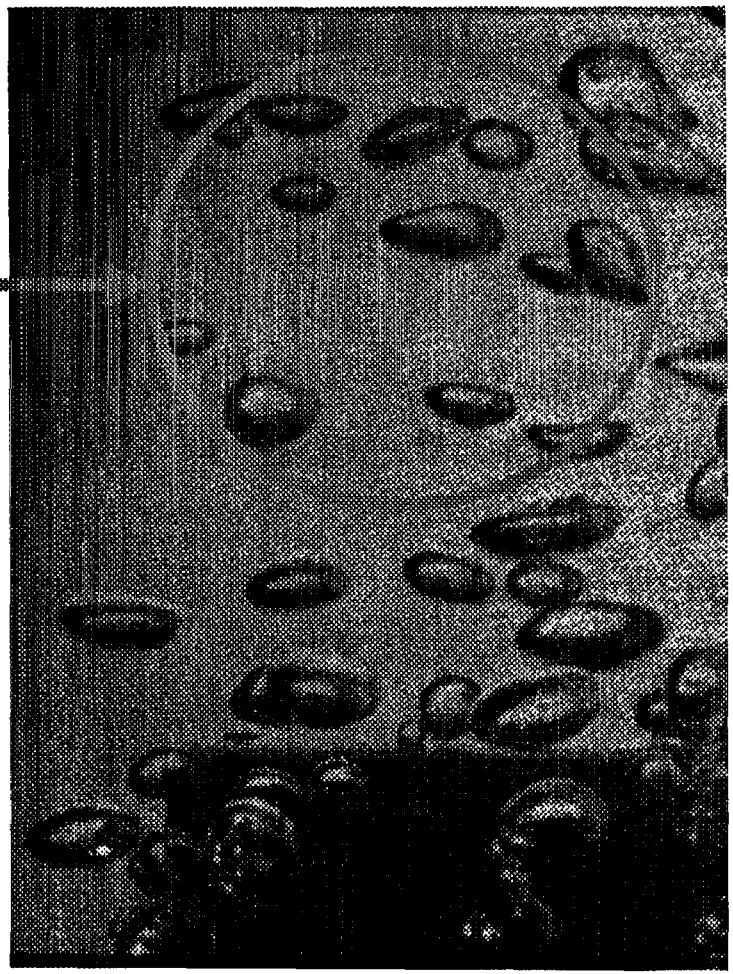

Motivation

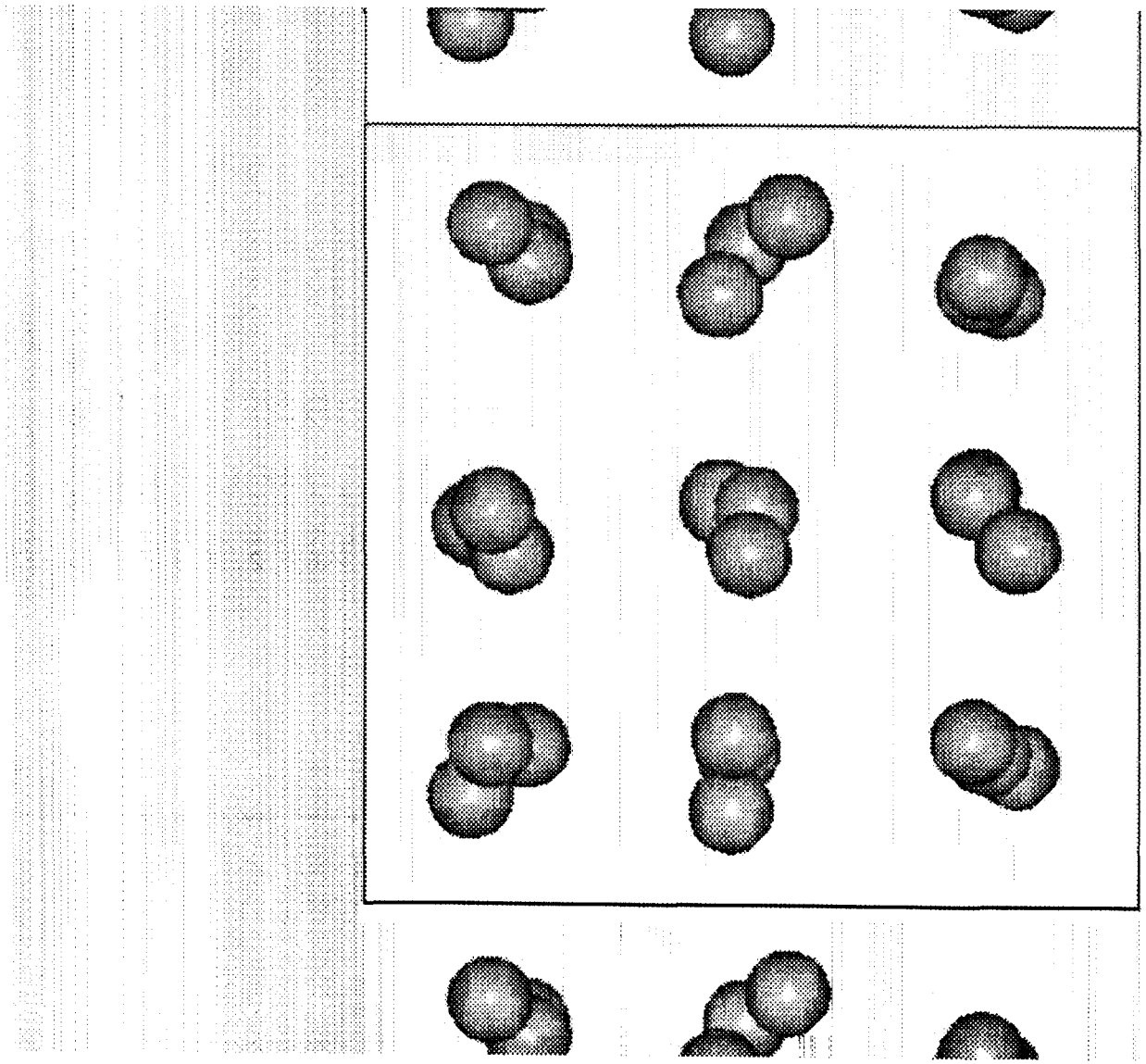

Motivation

The formation of bubbles is the critical part of boiling

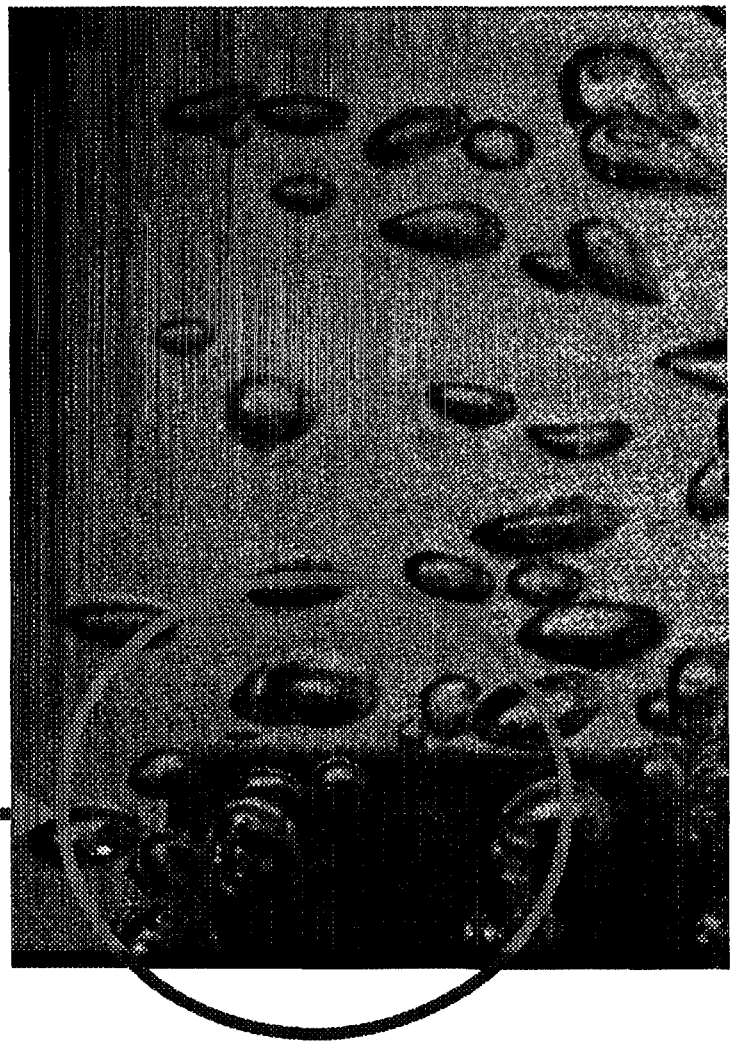

Boiling Flows—Background

2D simulations by:

D. Juric and G. Tryggvason. Computations of Boiling Flows. *Int'l. J. Multiphase Flow*. 24 (1998), 387-410.

G. Son and V.K. Dhir. Numerical simulation of film boiling near critical pressures with a level set method. *J. Heat Trans*. 120 (1998), 183-192.

S.W.J. Welch and J. Wilson. A volume of fluid based method for fluid flows with phase change. *J. Comp. Phys*. 160 (2000), 662-682.

Governing Equations

Momentum (conservative form, variable density and viscosity)

$$\frac{\partial \rho \mathbf{u}}{\partial t} + \nabla \cdot \rho \mathbf{u}\mathbf{u} = -\nabla p + \mathbf{f}$$

$$+ \nabla \cdot \mu\left(\nabla \mathbf{u} + \nabla^T \mathbf{u}\right) + \underbrace{\int_F \sigma \kappa \mathbf{n} \delta\left(\mathbf{x} - \mathbf{x}_f\right) dA}_{\text{Singular Interface Term}}$$

Mass conservation (incompressible flows)

$$\nabla \cdot \mathbf{u} = 0$$

Equations of state (properties of each fluid remain constant)

$$\frac{D\rho}{Dt} = 0; \quad \frac{D\mu}{Dt} = 0$$

Numerical Method

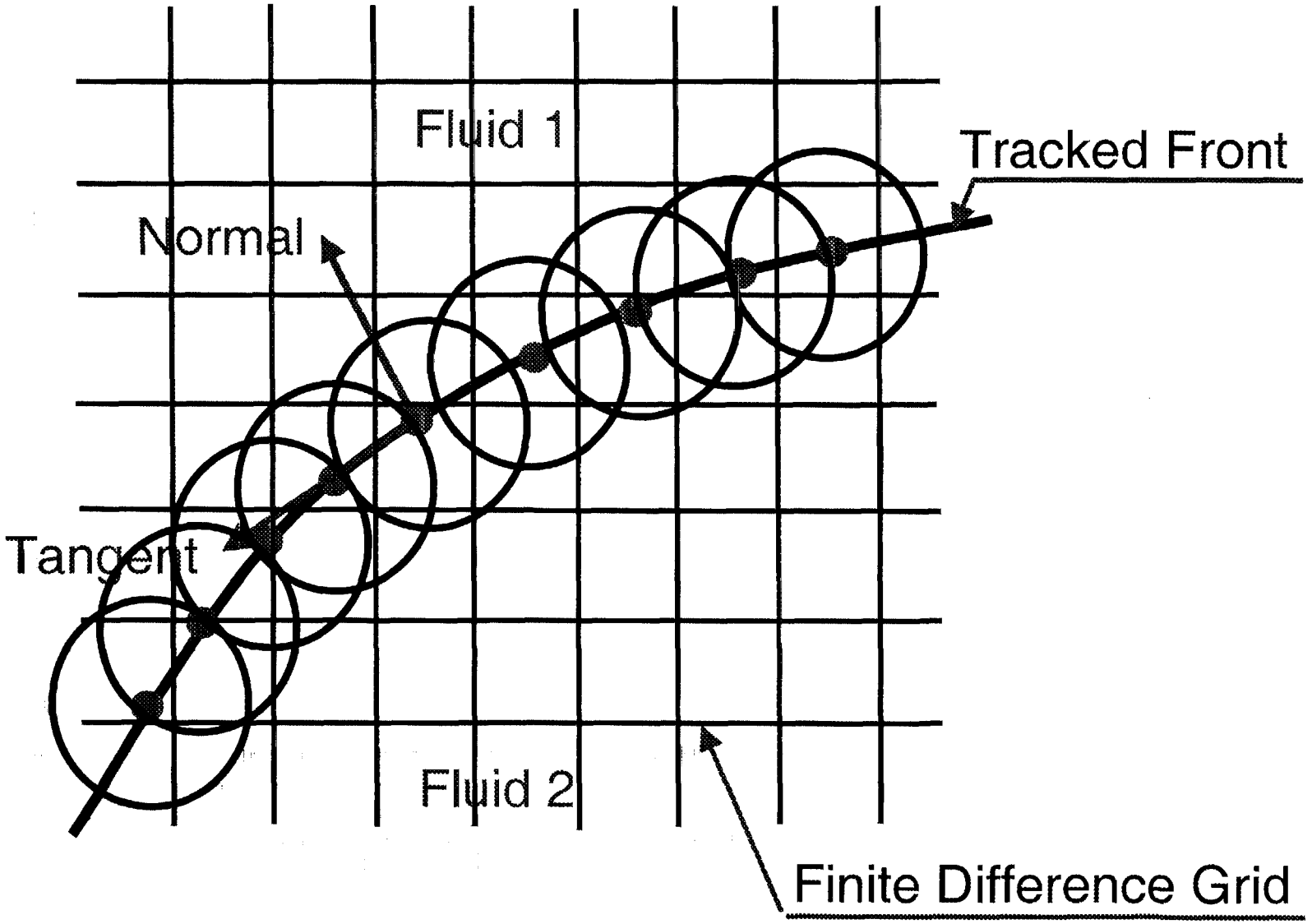

Interpolating from grid

The velocities are interpolated from the grid:

$$\phi_{ijk} = \sum \phi_l w_{ijk}$$

the weights w_{ijk} can be selected in several different ways

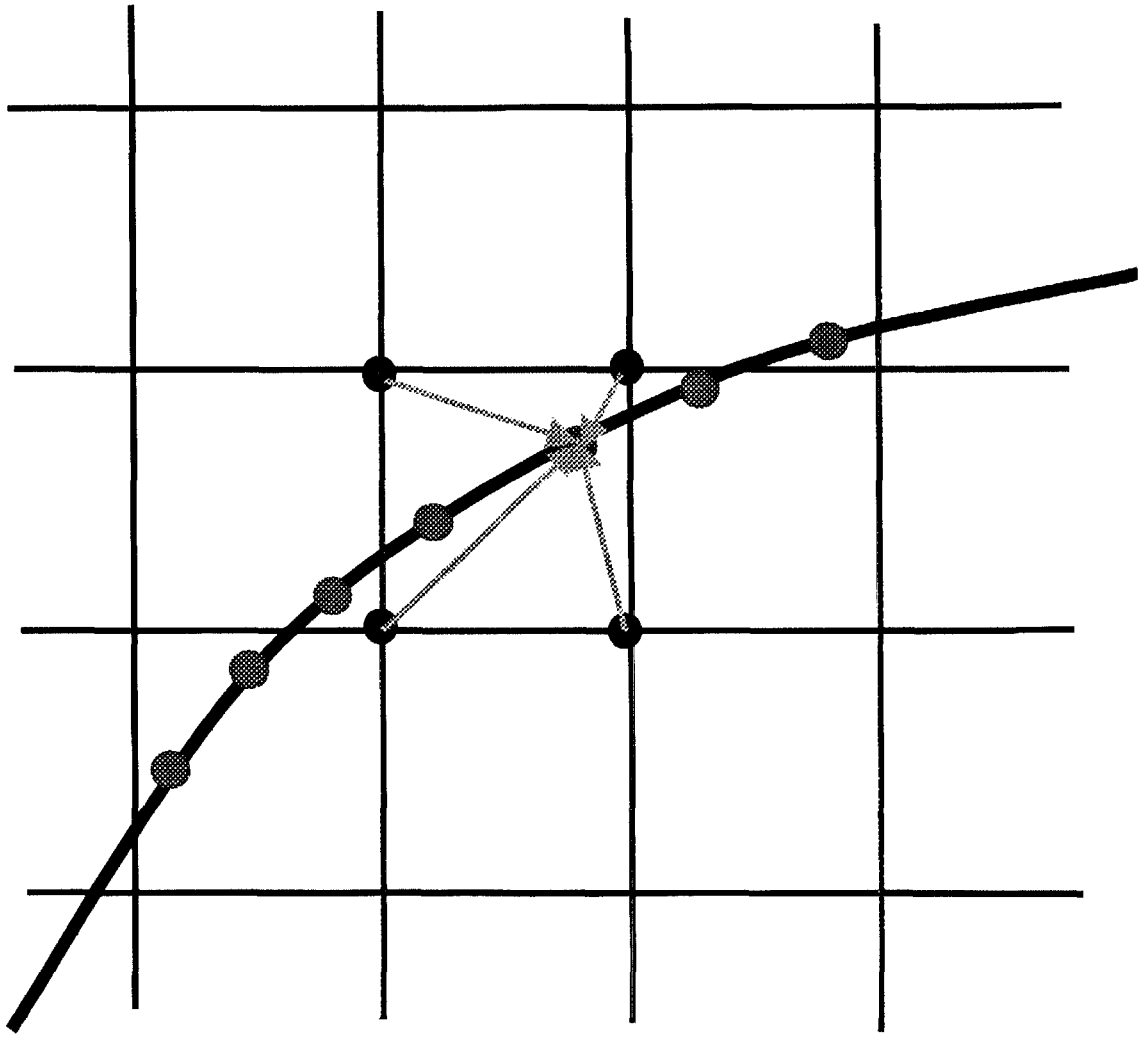

Approximating singular terms

The front values are distributed onto the grid by

On the front: per length
On the grid: per volume

To conserve integrated value

$$\phi_{ijk} = \sum \phi_l w_{ijk} \frac{\Delta s_l}{h^3}$$

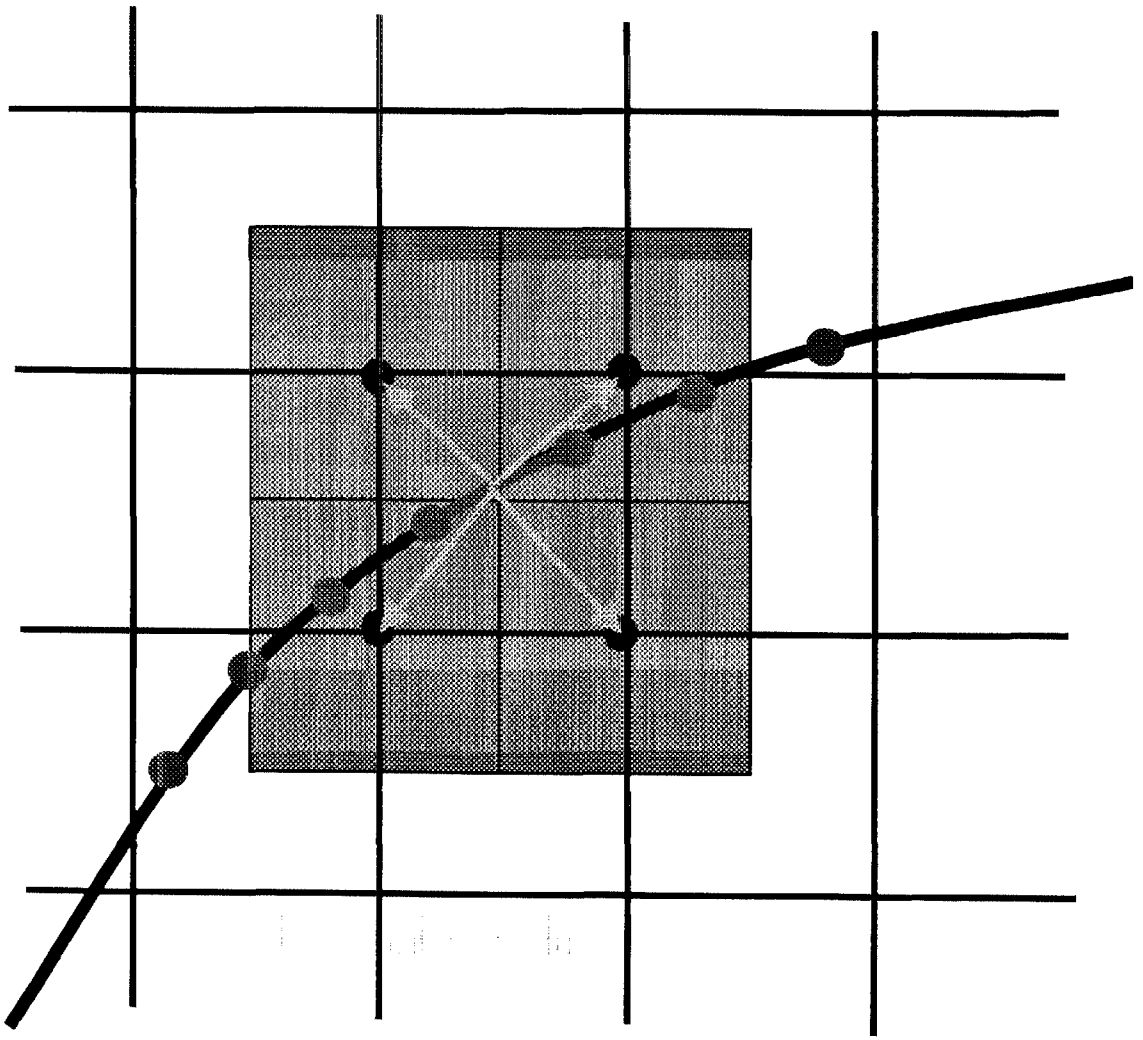

Phase boundary

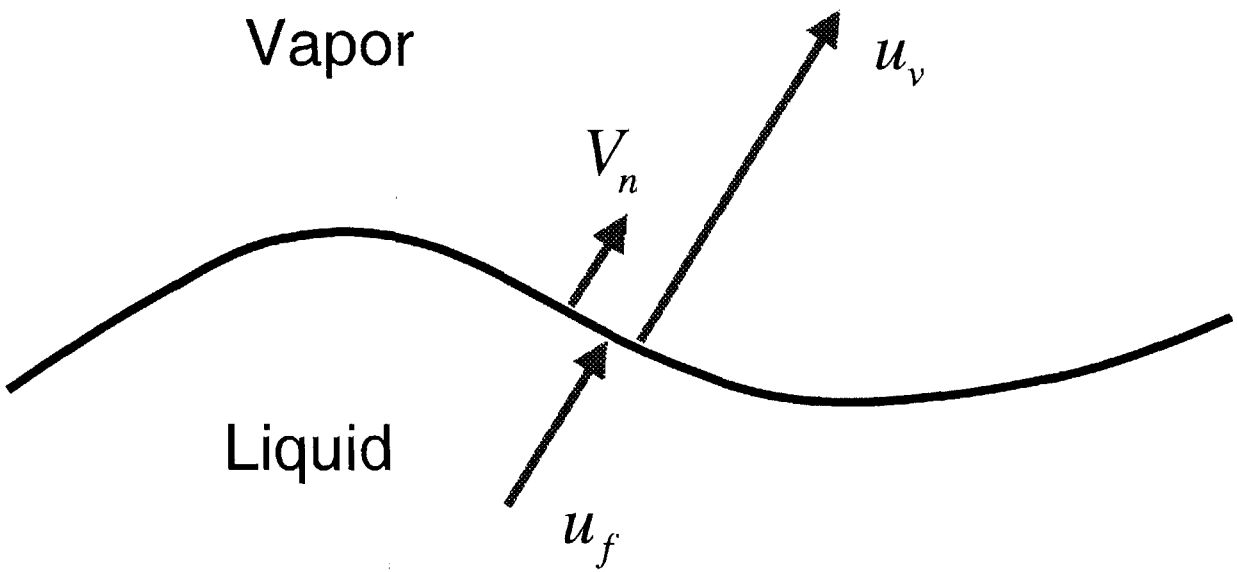

Phase boundary

Mass conservation

$$\frac{\partial \rho}{\partial t} + \nabla \cdot \rho \mathbf{u} = 0$$

The Rankine-Hugoniot conditions give:

$$-V_n\left(\rho_f - \rho_v\right) + \left(u_f \rho_f\right) - \left(u_v \rho_v\right) = 0$$

where

V_n :Velocity of phase boundary

Rewrite:

$$\rho_f\left(u_f - V_n\right) = \rho_v\left(u_v - V_n\right) = \dot{m}$$

Phase boundary

$$\frac{\dot{m}}{\rho_f} = u_f - V_n \quad \text{and} \quad \frac{\dot{m}}{\rho_v} = u_v - V_n$$

Volume Source (subtract)

$$Q = u_f - u_v = \dot{m}\left(\frac{1}{\rho_f} - \frac{1}{\rho_v}\right)$$

Velocity of phase boundary (add)

$$V_n = \frac{1}{2}\left(u_f + u_v\right) - \frac{\dot{m}}{2}\left(\frac{1}{\rho_f} + \frac{1}{\rho_v}\right)$$

Phase boundary

The mass transfer at the phase boundary is proportional to the heat source

$$\dot{m} = \frac{\dot{q}}{L}$$

where

$$\dot{q} = k\frac{\partial T}{\partial n}\bigg|_1 - k\frac{\partial T}{\partial n}\bigg|_2$$

Numerical method

Computing the heat source at the phase boundary

$$\dot{q} = k\frac{\partial T}{\partial n}\bigg|_1 - k\frac{\partial T}{\partial n}\bigg|_2$$

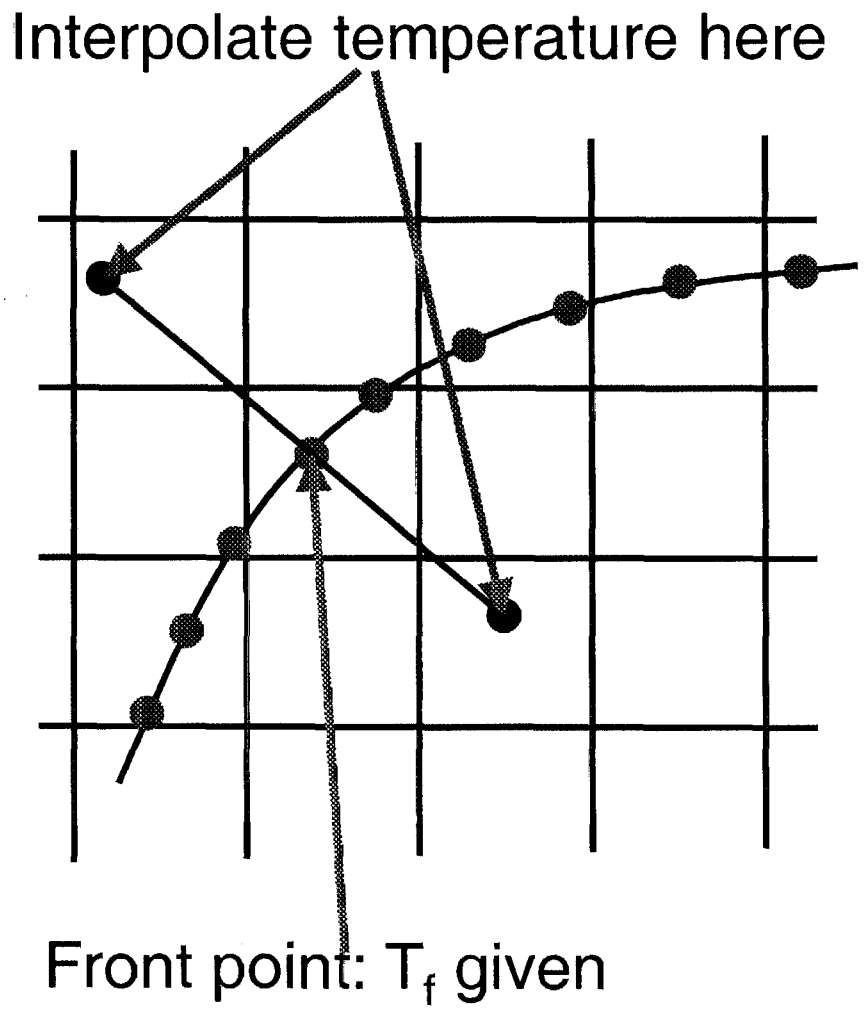

Governing equations

Momentum equation

$$\frac{\partial \rho \mathbf{u}}{\partial t} + \nabla \cdot \rho \mathbf{u}\mathbf{u} = -\nabla p + \mathbf{f}$$

$$+ \nabla \cdot \mu\left(\nabla \mathbf{u} + \nabla^T \mathbf{u}\right) + \int_F \sigma\kappa\, \mathbf{n}\delta\left(\mathbf{x} - \mathbf{x}_f\right) dA$$

Energy equation

$$\frac{\partial c_p \rho T}{\partial t} + \nabla \cdot c_p \rho \mathbf{u} T = \nabla \cdot k \nabla T$$

$$+ \int \dot{q}\delta(\mathbf{x} - \mathbf{x}_f) dA$$

Governing equations

Mass conservation

$$\nabla \cdot \mathbf{u} = \int \dot{m} \left(\frac{1}{\rho_f} - \frac{1}{\rho_v} \right) \delta(\mathbf{x} - \mathbf{x}_f) dA$$

Thermodynamic

$$T_b = T_v(P):$$

Heat source

$$\dot{q} = L\dot{m} \left(\frac{1}{\rho_f} - \frac{1}{\rho_v} \right)$$

Normal velocity of boundary

$$\frac{d\mathbf{x}_b}{dt} = V_n \mathbf{n}$$

Algorithm

- Find heat source at phase boundary
- Interpolate velocity
- Add evaporation to the velocity
- Advance front to new position
- Update material properties
- Smooth heat source onto grid
- Find temperature at next step by solving the energy equation
- Find unprojected velocity
- Smooth volume source onto grid
- Solve for pressure
- Find corrected velocity

Computational Domain

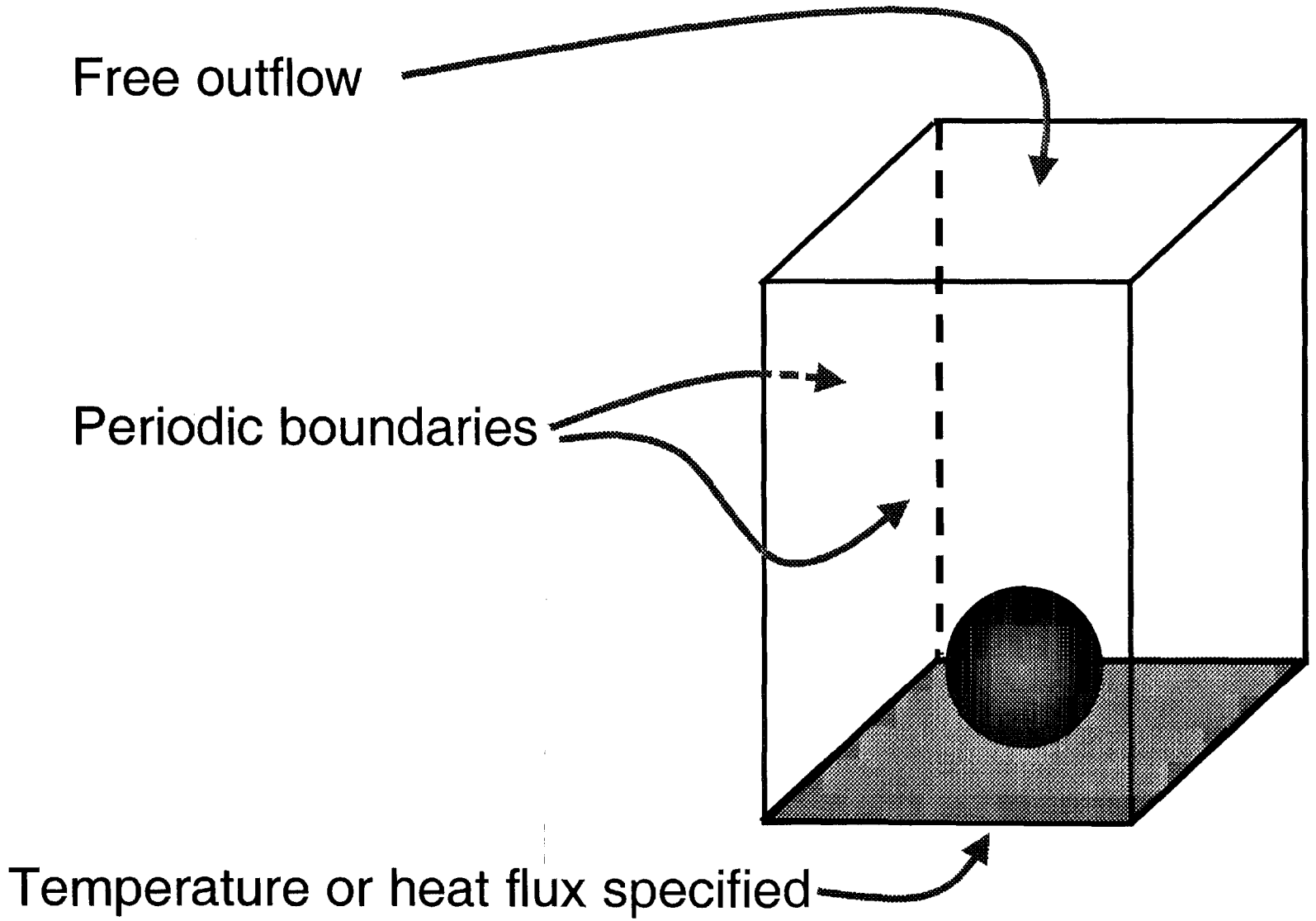

Resolution test

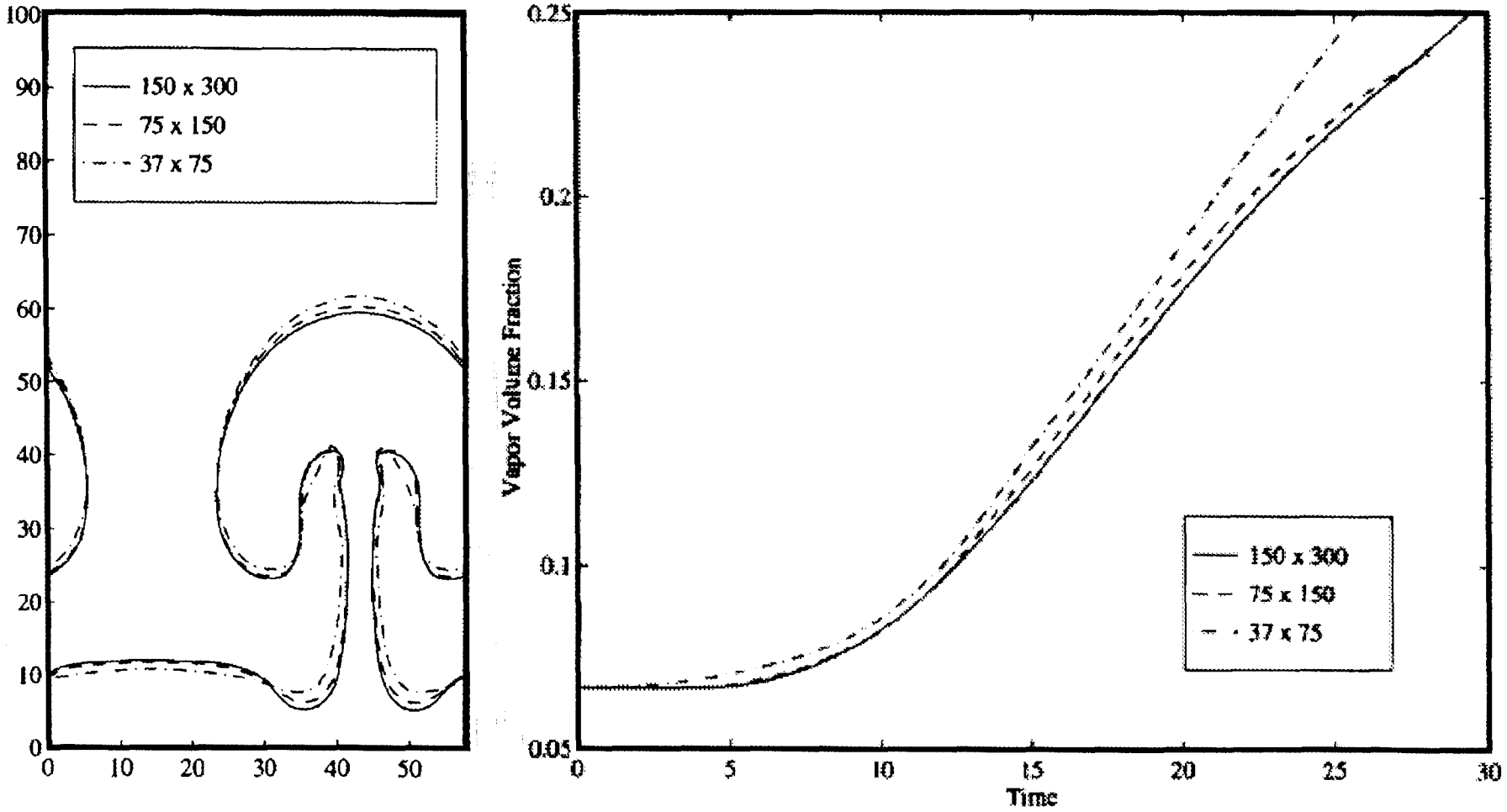

Film Boiling

Four frames from a simulation of the boiling of hydrogen is shown to the right. The color represents temperature, with red hot and blue cold. The bottom wall has a constant heat flux.

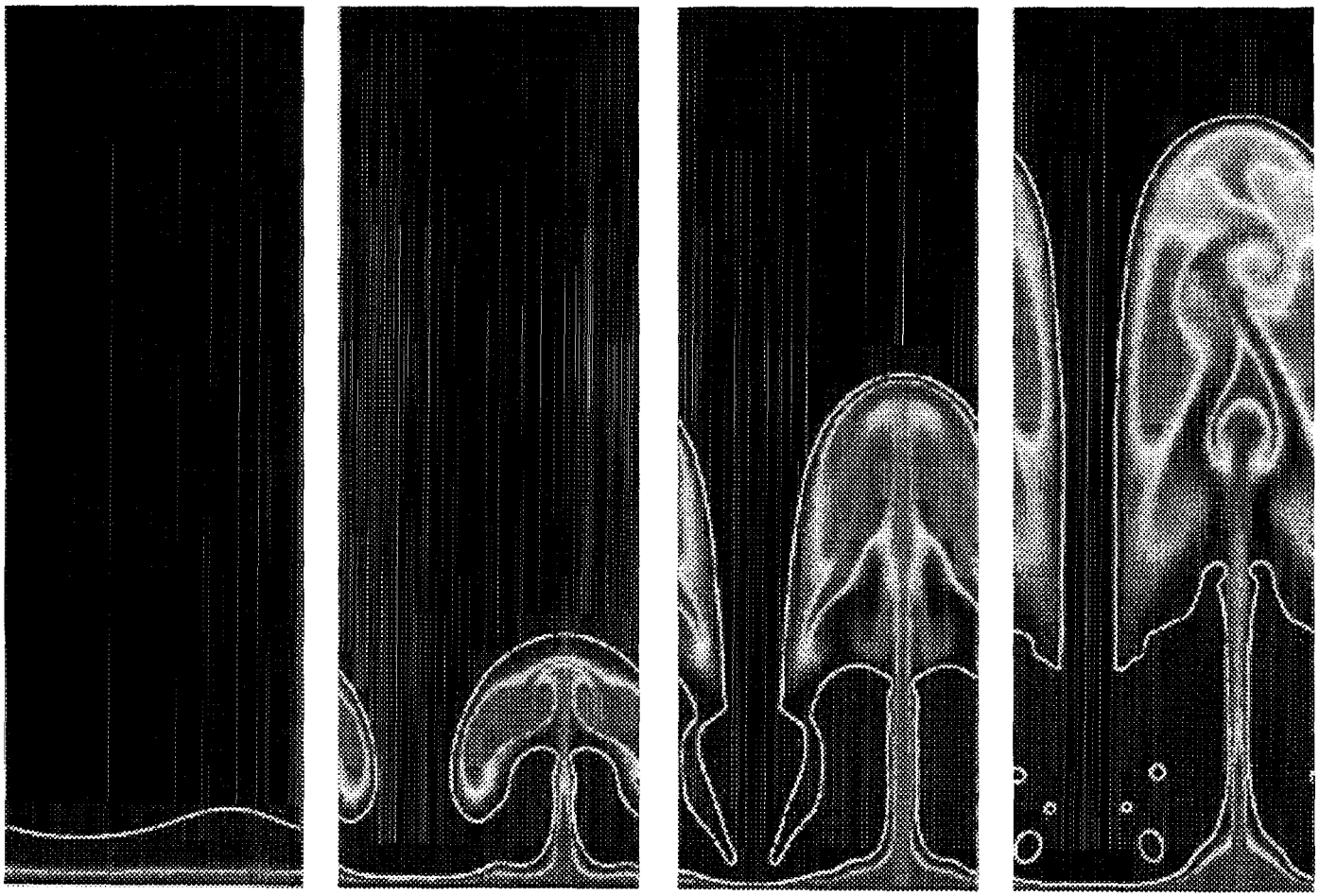

Film Boiling

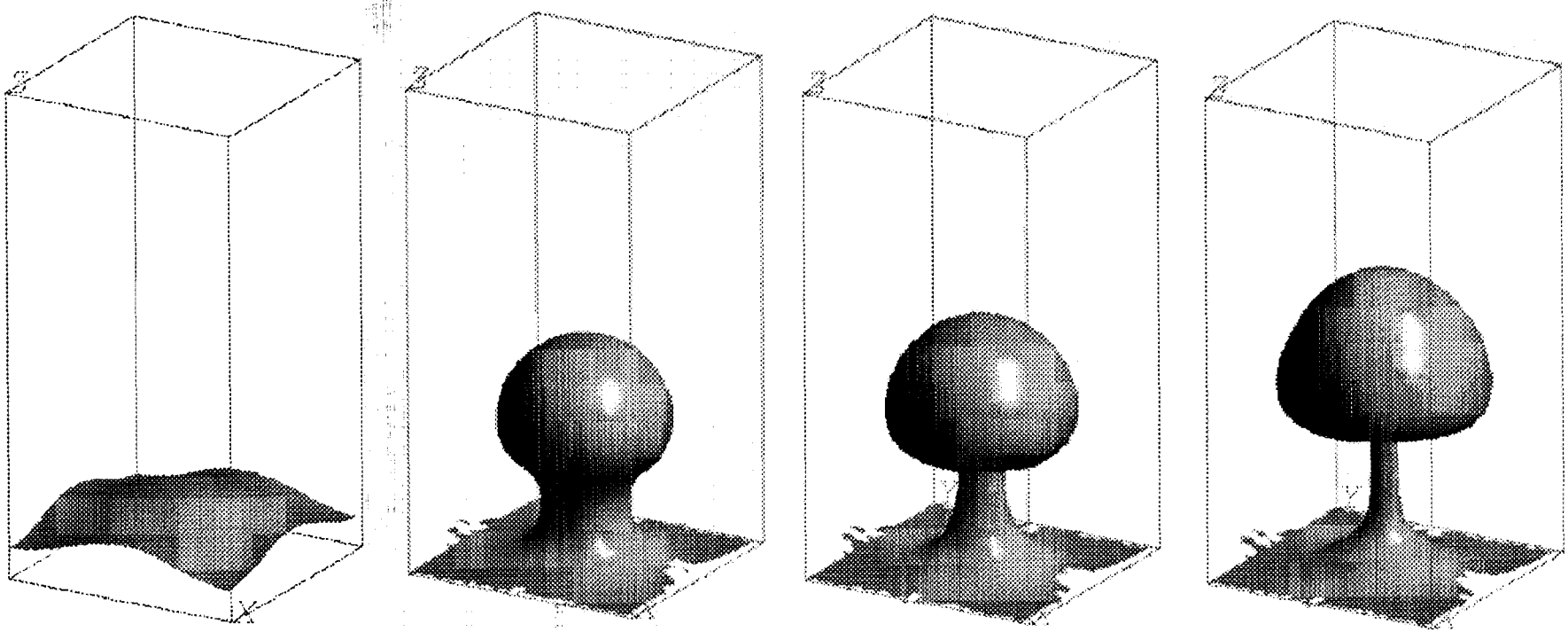

Film Boiling—Velocity

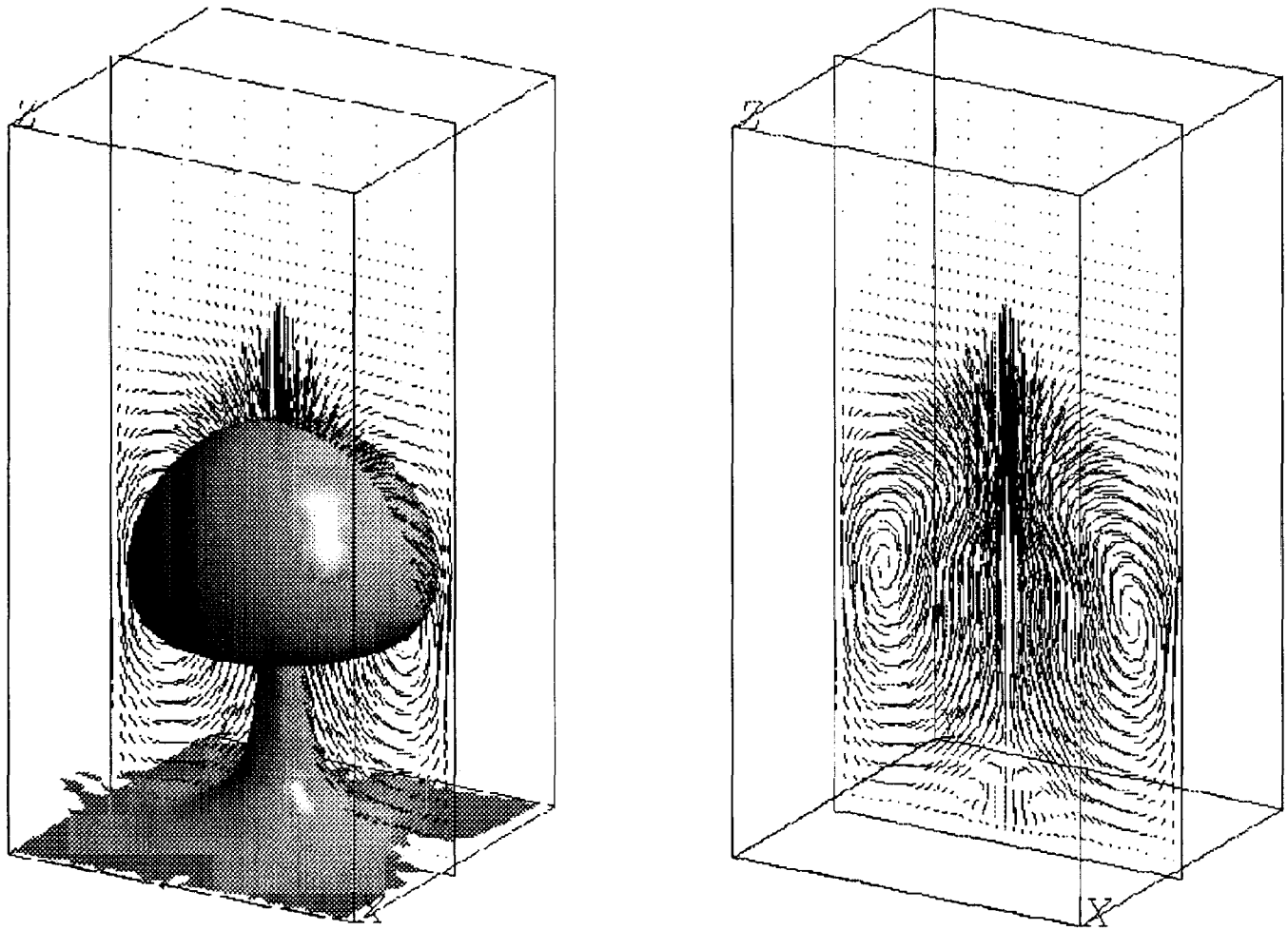

Film Boiling—Temperature

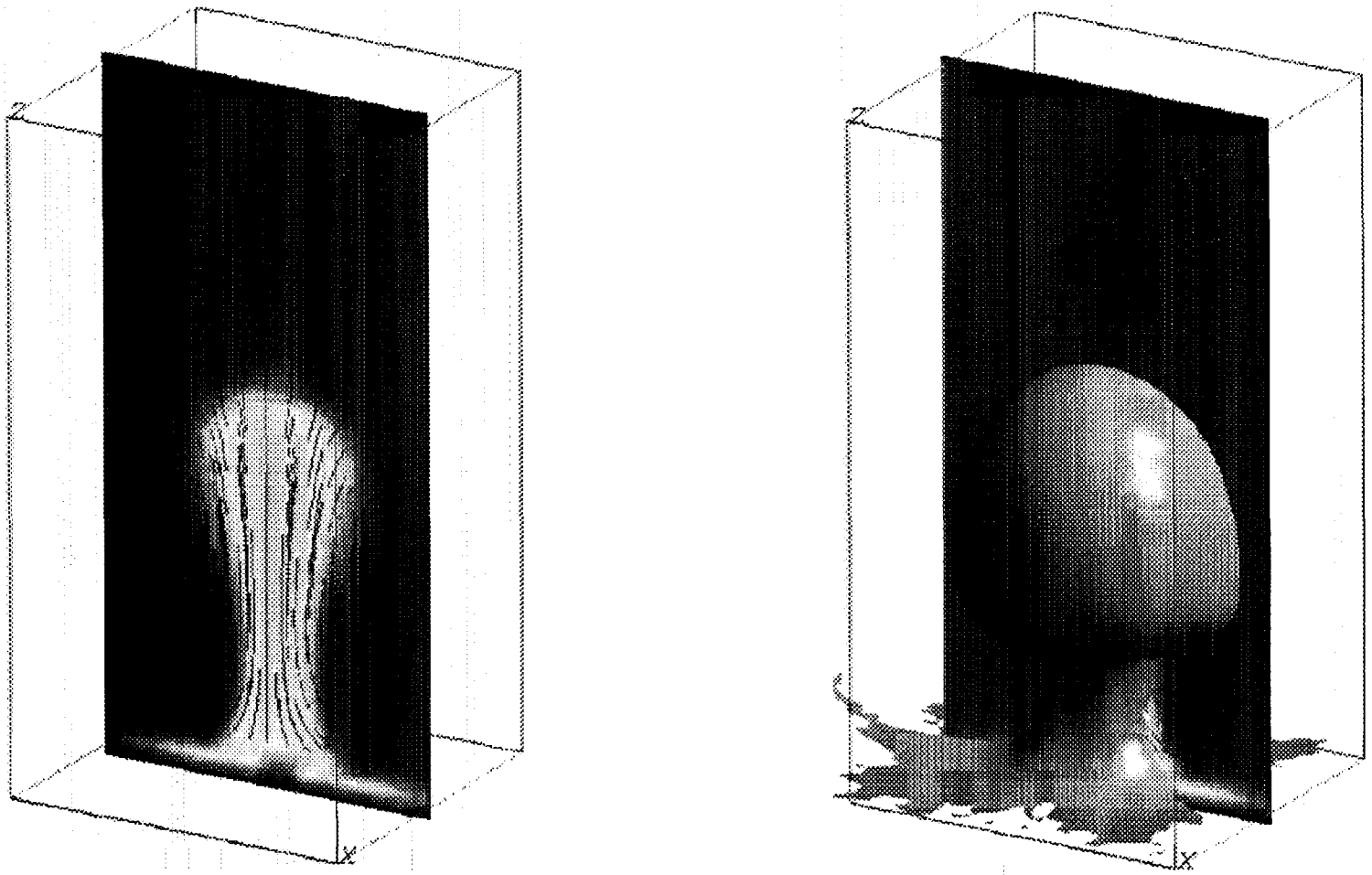

Film Boiling—Temperature

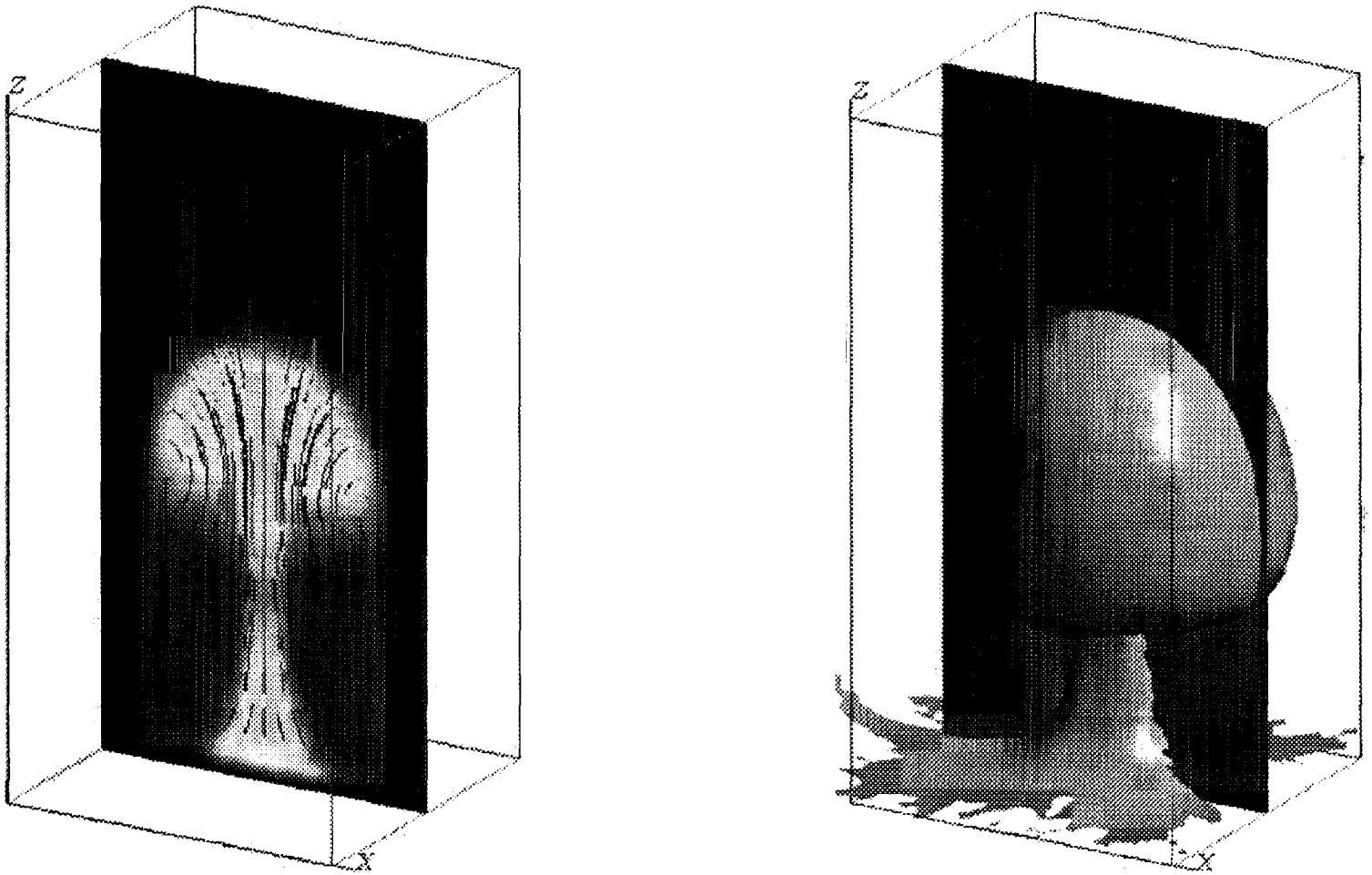

Film Boiling—Heat Flux

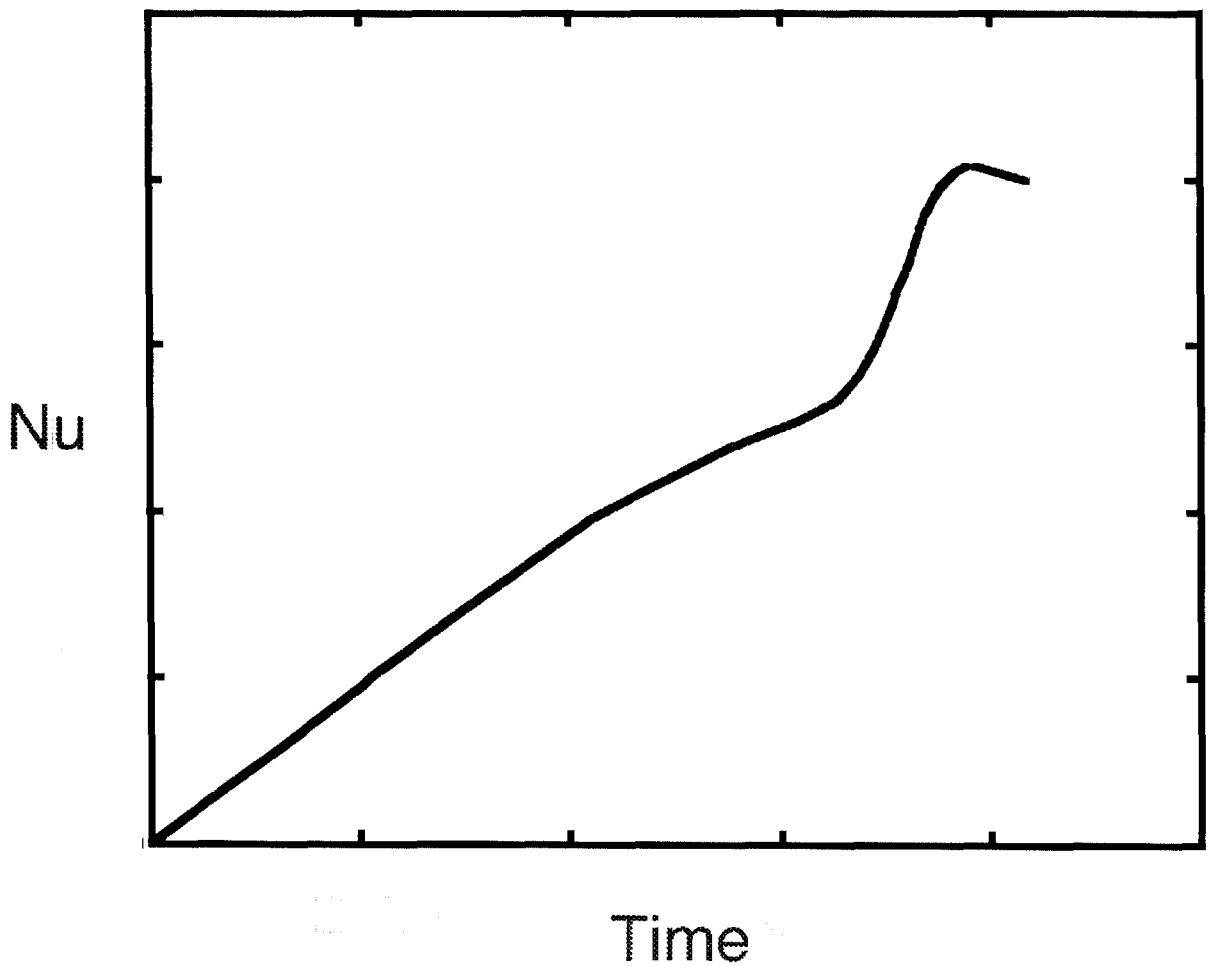

Film Boiling—Resolution

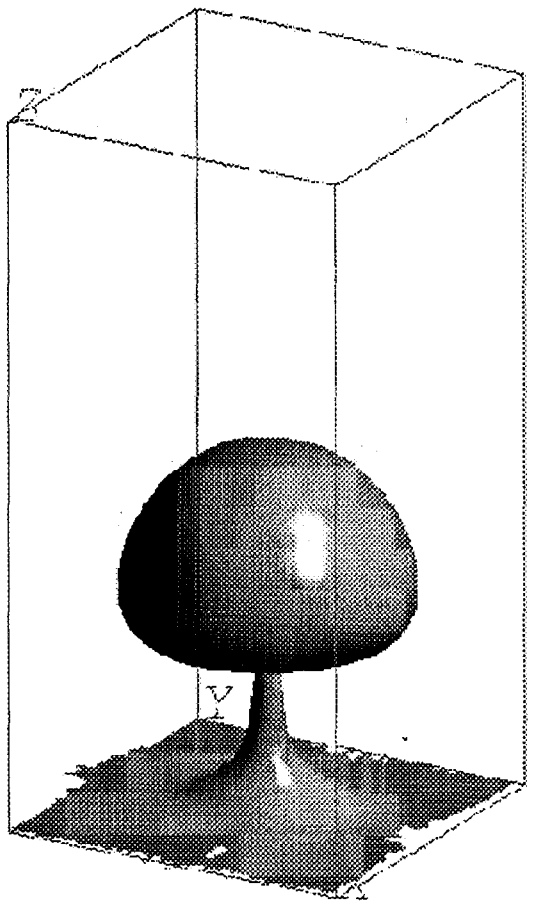

High resolution

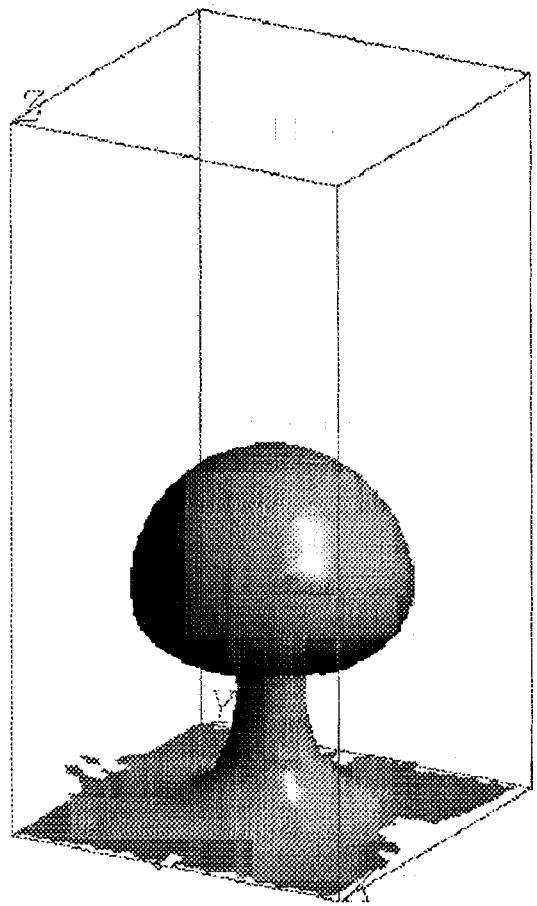

Low resolution

Film Boiling—Heat Flux

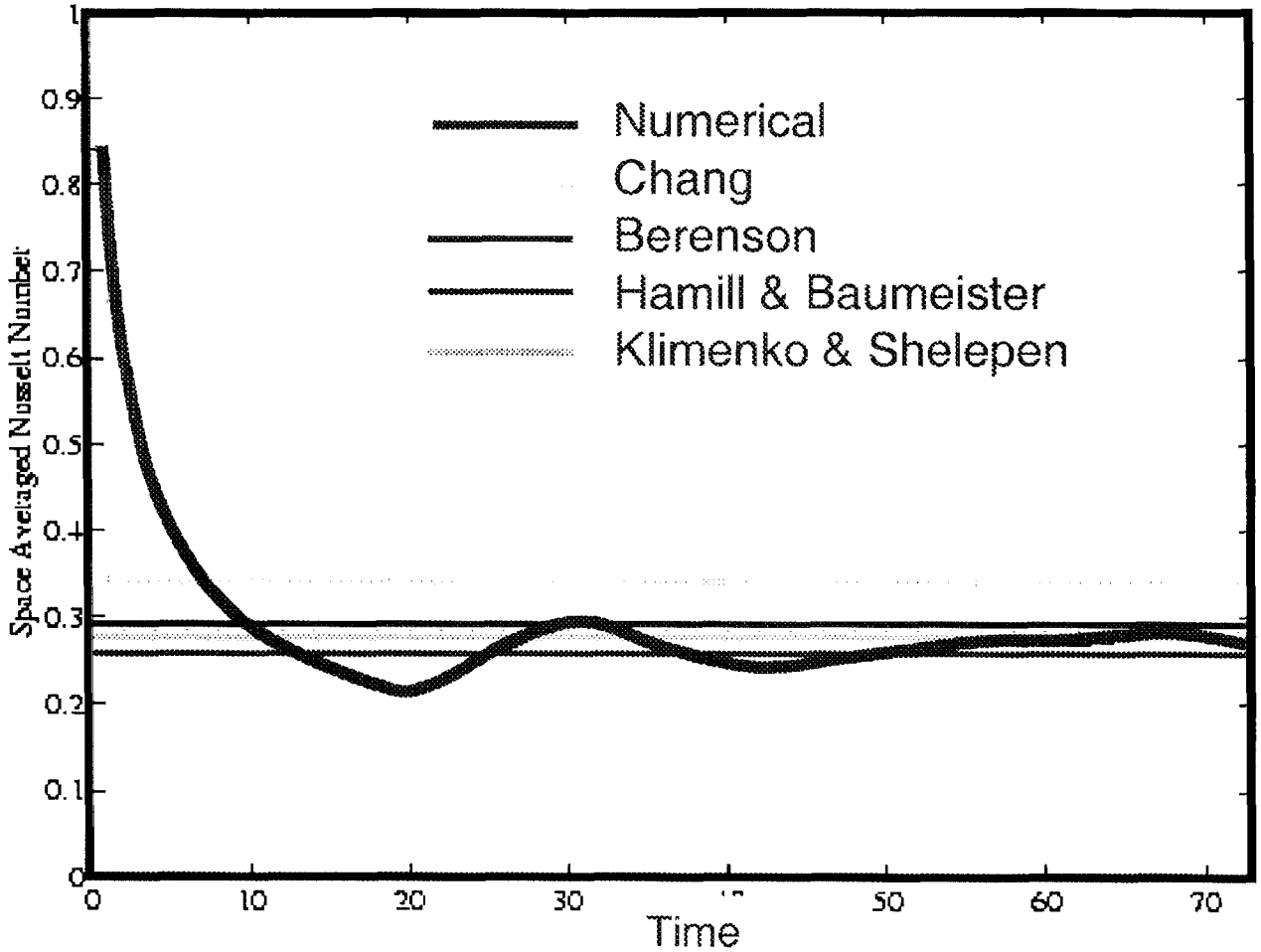

The average heat flux versus time. Predictions by various empirical correlations are shown by horizontal lines.

Nucleate Boiling

In gravity

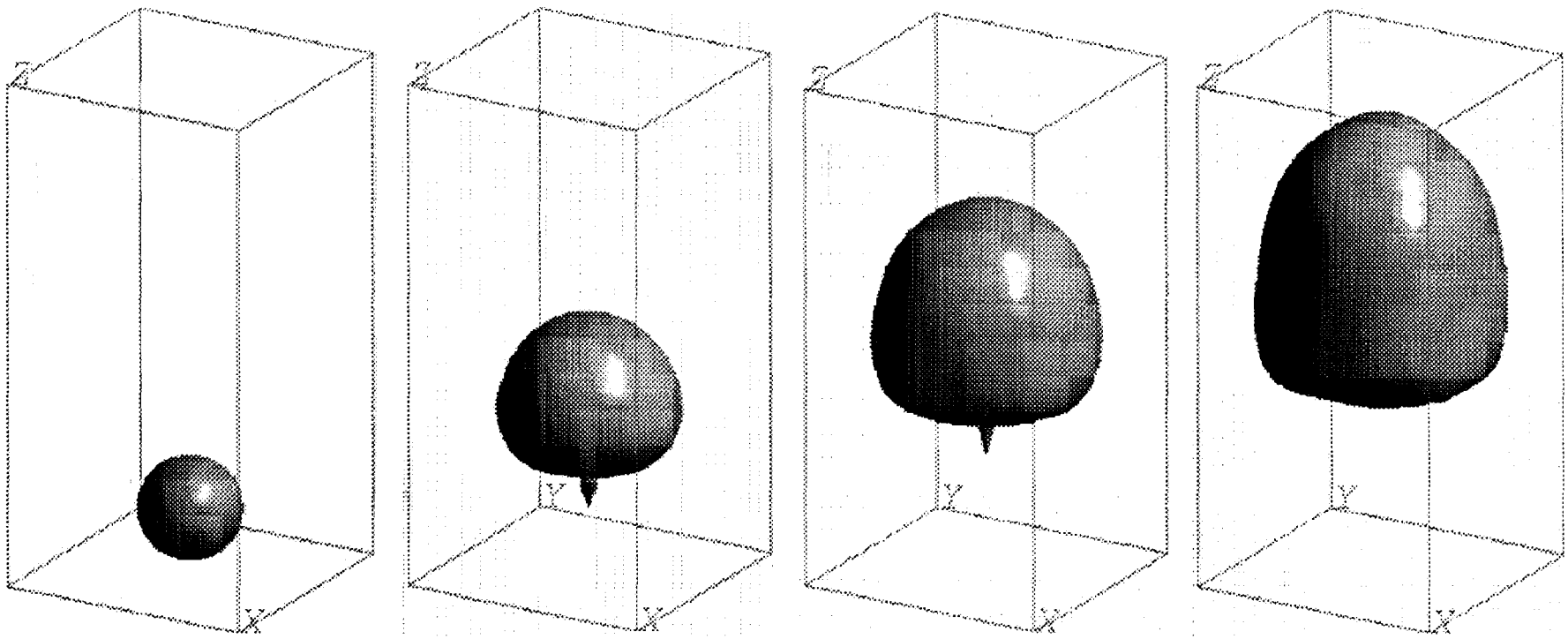

Nucleate Boiling

Zero gravity

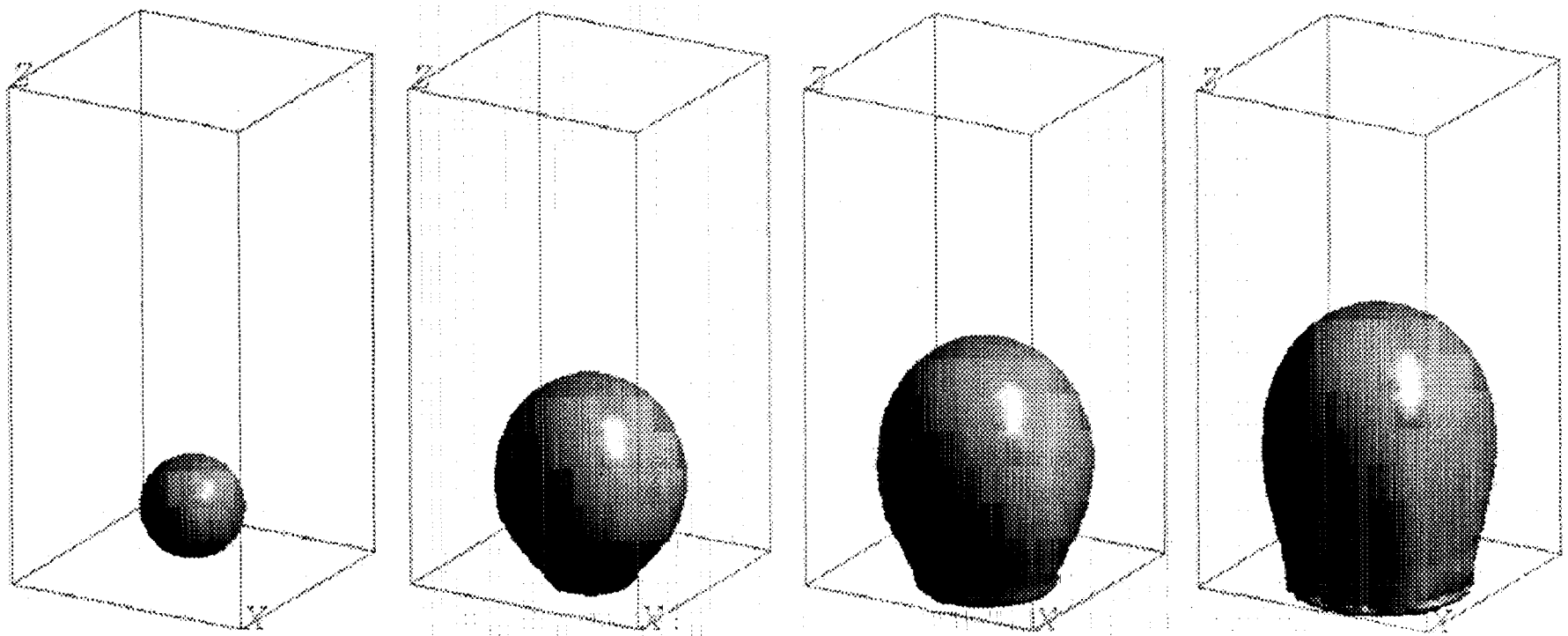

Other Phase Change Problems

Solidification and the effect of flow
on microstructure formation

The effect of flow on solidification

Dendrite growing in a uniform flow

401 by 401grid

Anisotropy=0.4

$$\sigma = \frac{cT_m\gamma}{L^2 Z} =$$

$$\mathrm{St} = \frac{c(T_\infty - T_m)}{L} = -0.3$$

$$\mathrm{Re} = \frac{\rho U Z}{\mu} = 600$$

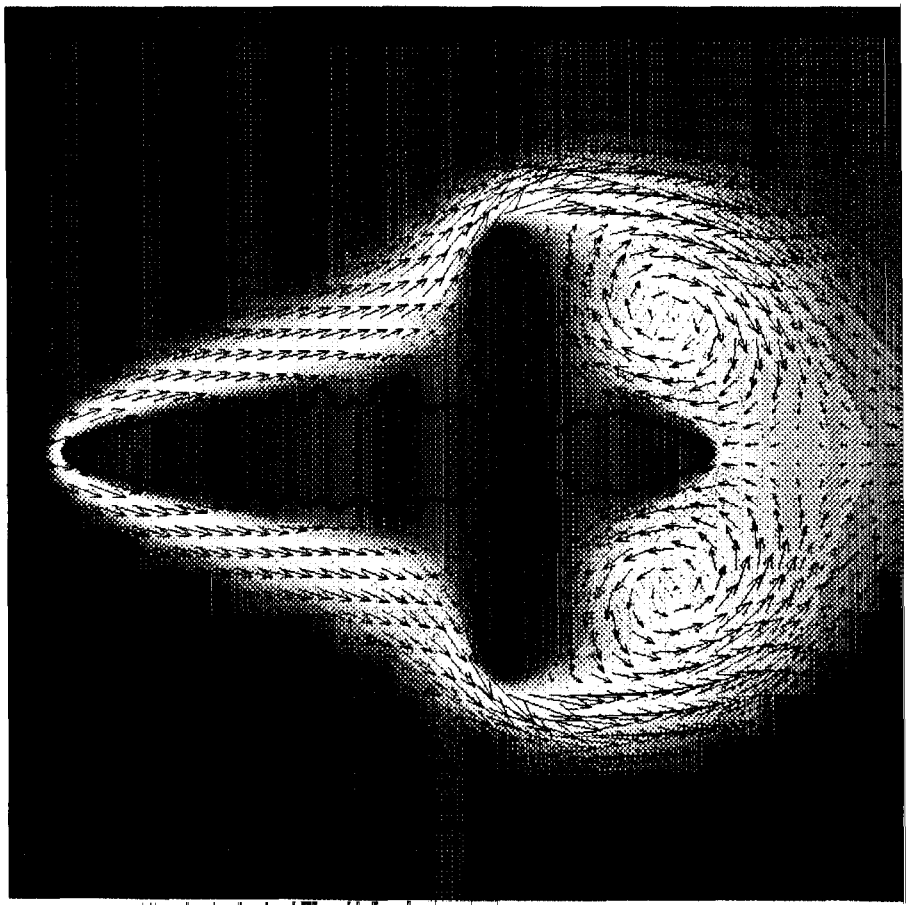

From Nabeel Al-Rawahi

The effect of flow on solidification

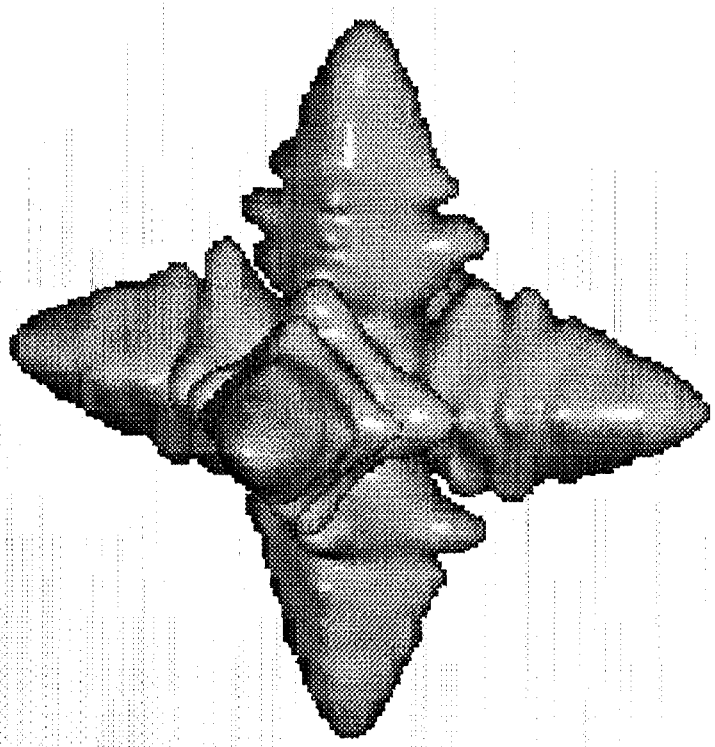

From Nabeel Al-Rawahi

Next Step

- Implementation of the phase change method into our parallel code for fluid flow
- Add adaptive grid refinement capability
- Examination of the effect of gravity and flow on heat transfer
- Adding other effects (electric field, etc)

NUMERICAL SIMULATION OF THREE DIMENSIONAL BUBBLE GROWTH AND DETACHMENT IN A MICROGRAVITY SHEAR FLOW

Vittorio Badalassi
Department of Chemical Engineering
University of California
Santa Barbara, CA 93106, USA
E-mail: badalass@engineering.ucsb.edu

Hiroyuki TAKAHIRA
Department of Energy Systems Engineering
Osaka Prefecture University
1-1 Gakuen-cho, Sakai, Osaka 599-8531, Japan

Sanjoy BANERJEE
Department of Chemical Engineering
University of California
Santa Barbara, CA 93106, USA

ABSTRACT

Bubble growth and detachment in a shear flow are simulated under normal and microgravity conditions, and compared with the experimental results of Misawa et al. (1997). In the experiments, gas was injected through a small hole in one wall and a typical flow configuration is shown in Figure 1. The bubble sizes at detachment depend on shear rate, gravitational conditions and physical properties of the gas and the liquid. To carry out the simulations a transient, 3D code was developed based on Zang et al. (1994) method. The gas- liquid interface was captured implicitly in an Eulerian mesh using the level set technique of Osher and Sethian (1988). The two-phase flow was treated as a single fluid with variable properties, the density and viscosity changing sharply at the gas-liquid interfaces, which are located at the zero level sets. Surface tension was incorporated in the Navier Stokes equation as a delta function force centered about the zero level set.
The results are shown in figure 2, and are in qualitative agreement with the experiments. However, the experiments indicate that the bubbles break off closer to the wall, and the discrepancy with the numerical calculations may arise due to difficulties in founding boundary conditions at the triple interface near the lip of the injection point.

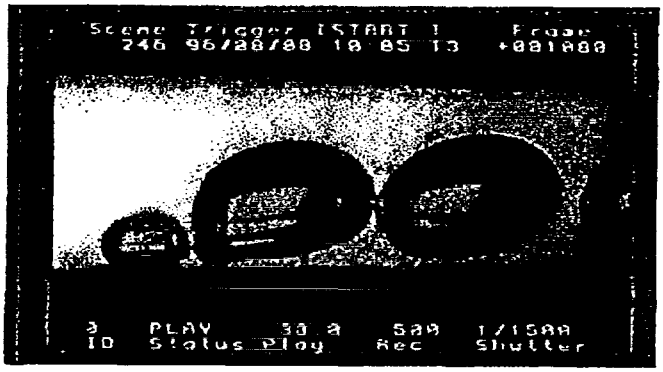

FIG. 1. Bubble Detachment at 0.01 g (Misawa et al., 1996), Velocity of moving belt at the top is 0.114m/s)

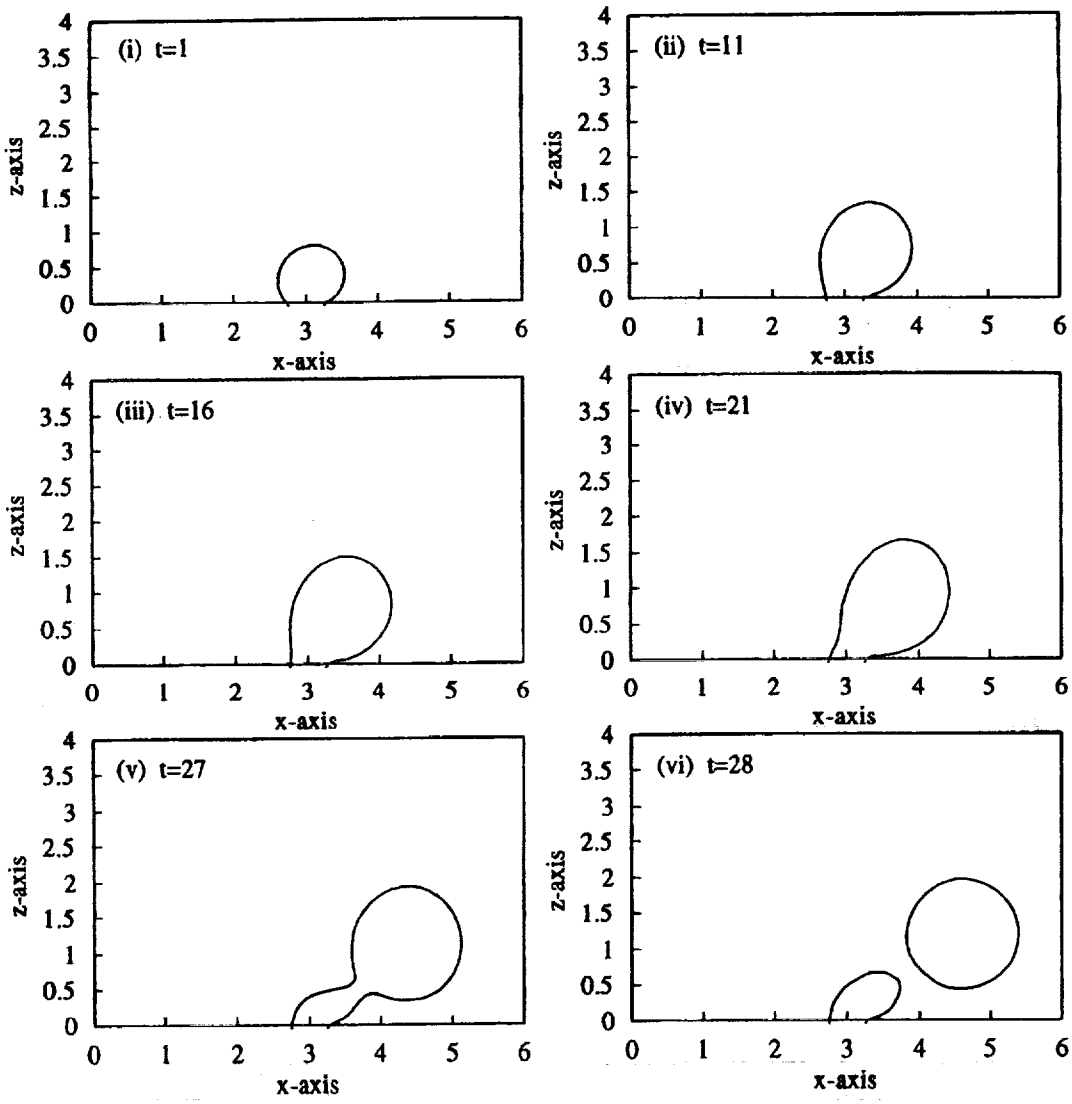

FIG. 2. Evolution of a bubble injected from a wall (without gravity, side view through central plane)

REFERENCES

Misawa, M., et al., 1997, "Bubble Growth and Detach. in Shear Flow under Microgr. Condit.", Exper. Heat Transfer, Fluid Mech. and Thermody. 1997, Ed. Giot M., et al., pp.987-994.

Osher, S., and Sethian, J.,A., 1988, "Fronts Propagating with Curvature-Dependent Speed: Algorithms Based on Hamilton-Jacobi Formulations", J. Comp. Phys., Vol.79, pp.12-49.

Takahira, H. and Banerjee, S. 1999, "Num. Simulation of Three Dimensional Bubble Growth and Detachment in a Microgravity Shear Flow", Microgravity Fluid Physics and Heat Transfer Conference, Oahu, Hawaii

Zang, Y., et al., 1994, "A Non-staggered Grid, Fractional Step Method for Time-Dependent Incompress. Navier-Stokes Eq. in Curvilinear Coordinates", J. Comp. Phys., Vol.114, pp.18-33.

Presentation not available at time of printing.

Three-dimensional oscillations of inviscid drops induced by surface tension

C. P ozrikidis

Department of Mechanical and Aerospace Engineering, University of California, San Diego La Jolla, CA 92093-0411

e-mail: cpozrikidis@ucsd.edu
In ternet URL: http://stokes.ucsd.edu/c_pozrikidis

A n umerical method is developed for simulating three-dimensional oscillations of inviscid liquid drops suspended in a dynamically inert (inviscid and zero density) ambient fluid. The numerical procedure is based on a generalized vortex formulation developed by Baker and cow ork ers that emplos the double-lay er representation for the harmonic potential, and an accompan ying representation in terms of a vortex sheet whose strength derives from the tangential gradient of the density of the double-lay er potential. The density of the double-lay er potential is computed by solving a Fredholm integral equation of the second kind using an isoparametric boundary-element method which in volv esdiscretizing the surface of the drop in to quadratic elements defined by six nodes, and computing the mean curvature by local in terpolation. The gro wthof n umerical instabilities is suppressed by occasional smoothing of the harmonic potential o verthe drop surface, which is done by mapping the deformed shape to the undeformed sphere, expanding the potential o ver the surface of the sphere in a series of spherical harmonics in volving associated Legendre functions, and then reconstructing the potential b y spectrum truncation toeliminate the perturbations. Results of several series of simulations are presented to illustrate the performance of the n umerical method for axisymmetric and non-axisymmetric oscillations. The generalized vortex method is found to be superior to the standard boundary-in tegral method based on Green's third identity, and its performance for moderate-amplitude oscillations is found to range from good to satisfactory depending on the mode of oscillation.

Presentation not available at time of printing.

SCALING OF MULTIPHASE FLOW REGIMES AND INTERFACIAL BEHAVIOR AT MICROGRAVITY

C. J. Crowley
Creare Inc.

ABSTRACT

The purpose of this investigation is to obtain void fraction measurements to support the scaling of microgravity multiphase flow behavior. Void fraction instruments have been built and installed in two existing test loops. Scaling with fluid properties and tube size are being investigated. Preliminary data indicate that interfacial shear and pressure drop in the annular flow regime are less at high gas density (refrigerants) than at low gas density (air/water).

OBJECTIVE AND APPROACH

Our primary objective is to facilitate the confident design of two-phase thermal management systems for spacecraft, by enabling detailed measurement of flow characteristics over a range of pipe sizes and gas densities for scaling of two-phase flow behavior. Our technical approach is to:

1. Obtain design data at several diameters (*e.g.* 12, 19 or 25 mm) with refrigerants.
2. Obtain void fraction data for flow regime transitions (bubbly/slug, or slug/annular), detailed phase distributions (bubble lengths, slug lengths, and film thickness), and interfacial characteristics (wave heights in annular flow), and
3. Develop scaling methods for the key phenomena.

VOID FRACTION INSTRUMENTS

Our void fraction instrument [1] measures capacitance. The instrument enables void fraction measurements with dielectric fluids such as refrigerants, which have high gas density. Previous microgravity void fraction measurements have been made at low gas density (with air and water). Each instrument includes ring sensors (3 mm and 6.5 mm) for measuring film thickness, as well as a helical sensor (135 mm) for average void fraction. We fabricated two void fraction instruments at 12.7 mm ID and installed them in a NASA JSC/Texas A&M flow loop. We refurbished two other instruments at 19 mm ID and installed them in the GRC TEEM flow loop.

We calibrated the instruments with the working fluids in both loops, R-12 and R-134a, respectively. The instruments are first calibrated in a small fluid facility where the output range of the instruments is checked with single-phase vapor and liquid at loop pressures and temperatures. For the 135 mm helical sensors, calibration curves were determined to relate the instrument output to void fraction in a separate flow facility with quick-closing valves and quantitative volume measurements. Calibration curves to relate instrument output to film thickness for the 3 mm and 6.5 mm ring sensors were derived using various calibration plugs made of Macor plastic, each simulating a different film thickness. The film thickness measurements were validated by independent measurements with a falling film of R-134a in a facility at NASA GRC.

RESULTS

Steady-state data have been obtained from one flight test campaign (February, 2000) with the JSC/TAMU facility. Figure 1 is a flow regime map for the data, which were obtained at Mars gravity (0.375g). Most of the data are in the stratified, eccentric annular, and annular flow regimes. Steady-state test data will be obtained with the GRC test loop in future tests.

Figure 2 shows the most interesting result from these tests. Independent measurement of the film thickness (void fraction) allows the interfacial friction factor in the annular flow regime to be evaluated directly from the momentum equation for the gas phase. The interfacial friction factors derived from the data are substantially smaller than expected. Previous microgravity data with air and water [2] showed much higher interfacial shear, consistent with the Wallis correlation [3]. These new data strongly support lower interfacial shear with refrigerant (R-12). The data are in the range of the Chen correlation [4], which was developed without independent void fraction data. These results show that scaling with gas density is important to model interfacial shear in this key (annular) flow regime. Other parameters may also be important. The pressure drop is about a factor of two smaller with the lower interfacial shear. Upcoming tests will focus upon this phenomenon so that we can develop a scaling methodology.

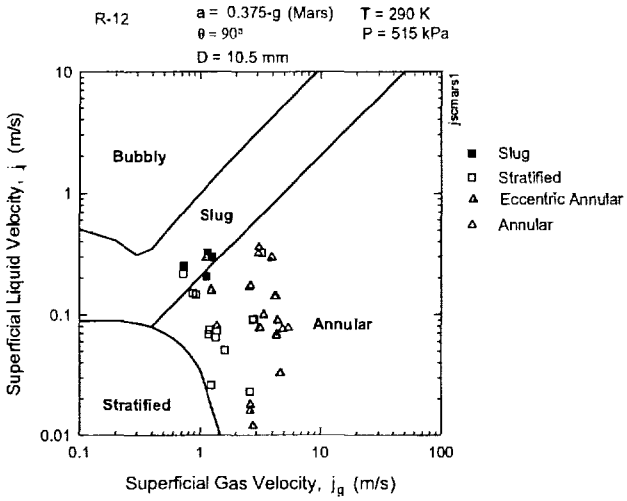

Figure 1. Flow Regime Map for February 2000 Flights of JSC/TAMU Facility

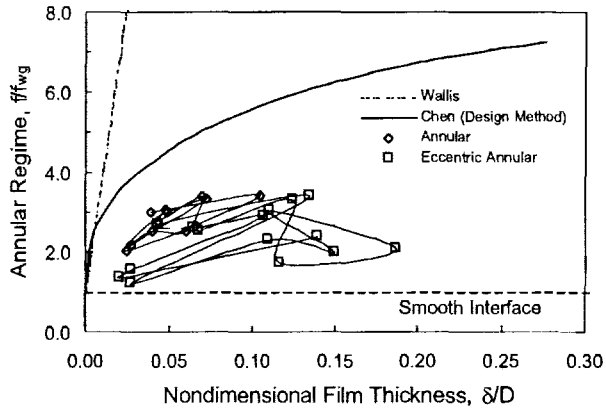

Figure 2. Interfacial Friction Factor for the Annular Flow Regime Derived From Pressure Drop and Void Fraction Data (NASA JSC/TAMU Facility, February 2000)

REFERENCES

[1] Crowley, C.J., Magari, P.J. Martin, C.M. and Hill, M.E.; A Void Fraction Instrument for Two Phase Flow in Dielectric Liquids, AIAA-96-0925, January, 1996.

[2] Bousman, W.S.; Studies of Two-Phase Gas-Liquid Flow in Microgravity; NASA Contractor Report 195434, Prepared for NASA GRC under Grant NA3-510, February, 1995.

[3] Wallis, G. B.; One-Dimensional Two-Phase Flow; McGraw-Hill Book Co., NY, NY, 1969.

[4] Chen, I., Downing, R., Keshock, E. and Al-Sharif, M.; An Experimental Study and Prediction of Two Phase Pressure Drop in Microgravity; AIAA 89-0074, January, 1989.

Scaling of Multiphase Flow Regimes and Interfacial Behavior at Microgravity

Christopher J. Crowley (PI)
Weibo Chen
Graham B. Wallis (Dartmouth College)
Creare Inc.
P.O. Box 71
Hanover, NH 03755

NASA NRA-96 HEDS-01
July 1998 through June 2001

Project/Contract Monitor
NASA Glenn Research Center
Dr. Myron Hill

Creare

Objectives

1. Measure void fraction to supplement flow rate and pressure drop data with refrigerants under microgravity conditions

2. Examine the scaling of interfacial behavior in all flow regimes

3. Develop and improve design models for flow regime transitions and pressure drop in each flow regime

Creare

Approach

- Use void fraction instrument technology developed under the SBIR program
  - -- Based upon capacitance measurement
  - -- Multiple sensors for film thickness and average void fraction
  - -- Proven for KC-135 flight
  - -- Space-qualified design and hardware

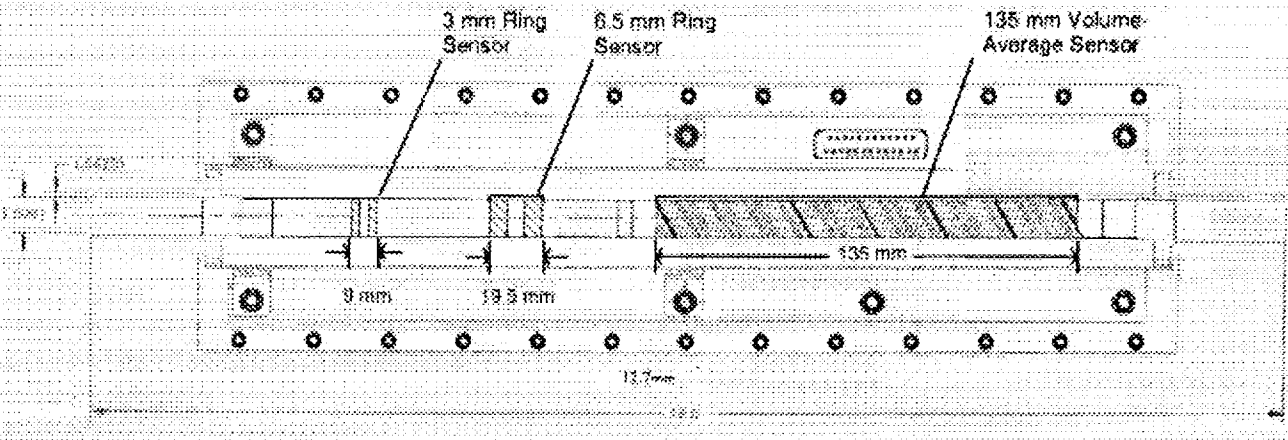

- Use instruments in existing test loops for multiphase flow in microgravity
  - -- Provide void fraction instrument hardware
  - -- Calibrate instruments
  - -- Provide support during microgravity flight tests
  - -- Reduce/analyze void fraction data

Void Fraction Sensors

- Parallel Ring Sensors -- measure local average film thickness in the annular flow regime or liquid height in the stratified flow regime

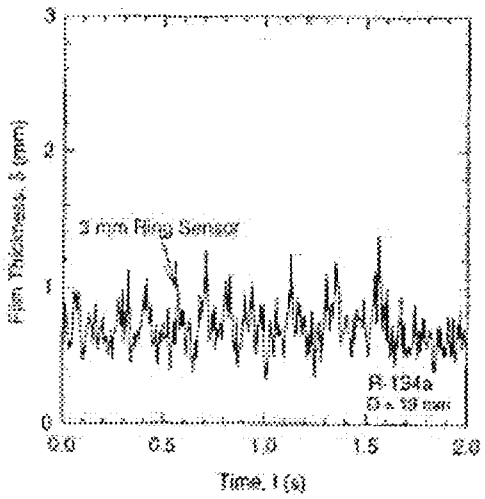

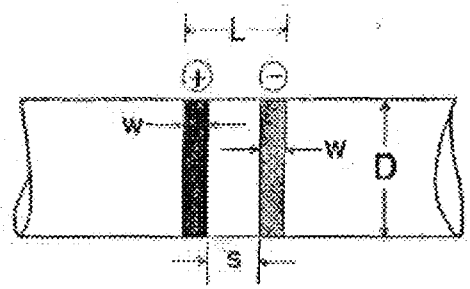

- Helical Sensor – measures average void fraction over a volume about 10 L/D in length

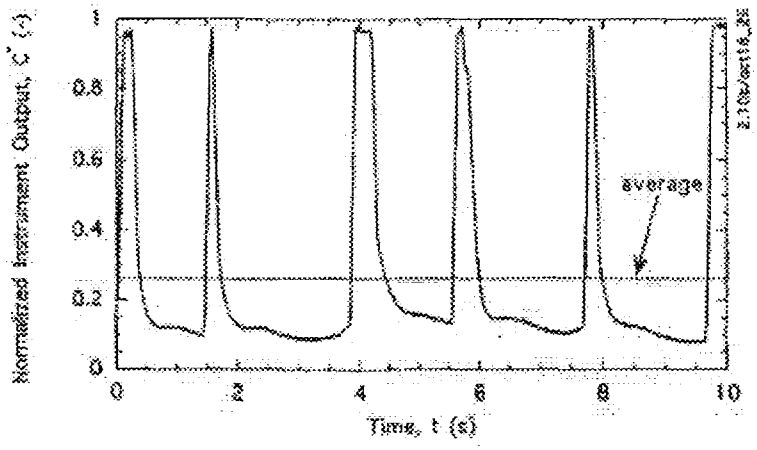

Creare

Flow Loops for Microgravity Tests

Parameter	NASA GRC TEEM Flow Loop	NASA JSC/Texas A&M Flow Loop
Working Fluid	R-134a	R-12
Nominal Pressure	570 kPa @ 293 K	560 kPa @ 293 K
Tube Diameter	19.1 mm	10.9 to 12.7 mm
Test Section Length	2.4 m	1.1 m

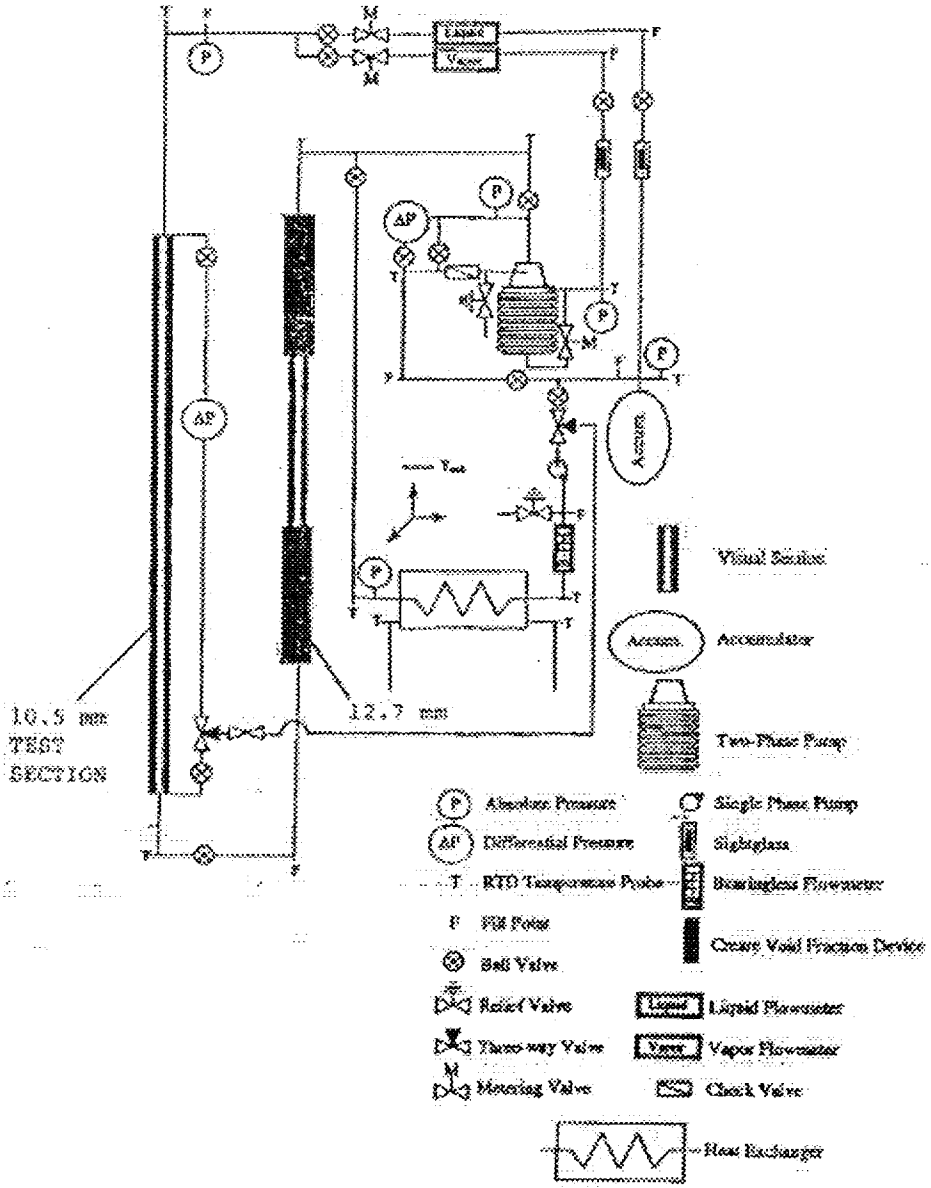

Schematic of NASA JSC/Texas A&M Flow Loop

Creare

Experiments with Refrigerants Vary Scaling Parameters Significantly Compared with Prior Air/Water Experiments

Dimensionless Force Balances		
Parameter	Equation	Force Balance
Froude number	$Fr_v = \frac{\rho_v^{1/2} U_v}{\left[gD(\rho_l - \rho_v)\right]^{1/2}}$	$\frac{inertia}{buoyancy}$
Weber number	$We_v = \frac{\rho_v D U_v^2}{\sigma}$	$\frac{inertia}{surface\ tension}$
Reynolds number	$\mathrm{Re}_v = \frac{\rho_v D U_v}{\mu_v}$	$\frac{inertia}{viscous}$
Bond number	$Bo = \frac{gD^2(\rho_l - \rho_v)}{\sigma}$	$\frac{buoyancy}{surface\ tension}$
Suratman number	$Su = \frac{\sigma D \rho_l}{\mu_l^2}$	$\frac{surface\ tension}{viscous}$
Grashoff number	$Gr = \frac{\rho_v(\rho_l - \rho_v)gD^3}{\mu_v}$	$\frac{buoyancy}{viscous}$

Wider Scaling of Dimensionless Parameters vs. Air/Water (at Given Tube Diameter and Flow Rate)					
Facility	Froude Number	Weber Number	Reynolds or Grashoff No.	Bond Number	Suratman Number
NASA GRC TEEM Flow Loop	L: 1x V: 1.5x	L: 7x V: 200x	L: 4x V: 30x	7x	2x
NASA JSC/Texas A&M Flow Loop	L: 1x V: 2.5x	L: 7x V: 42x	L: 4x V: 7x	6x	2.5x

L = Liquid Phase
V = Vapor Phase

Creare

Status of KC-135 Flight Tests

- NASA JSC/Texas A&M Flow Loop
  - -- About 40 tests at Mars gravity (0.38g) in February 2000
  - -- Corresponding tests at microgravity (0.01g) expected by Fall 2000

- NASA GRC TEEM Flow Loop
  - -- No steady-state data at present
  - -- Microgravity tests anticipated during the upcoming year

Example of Test Data

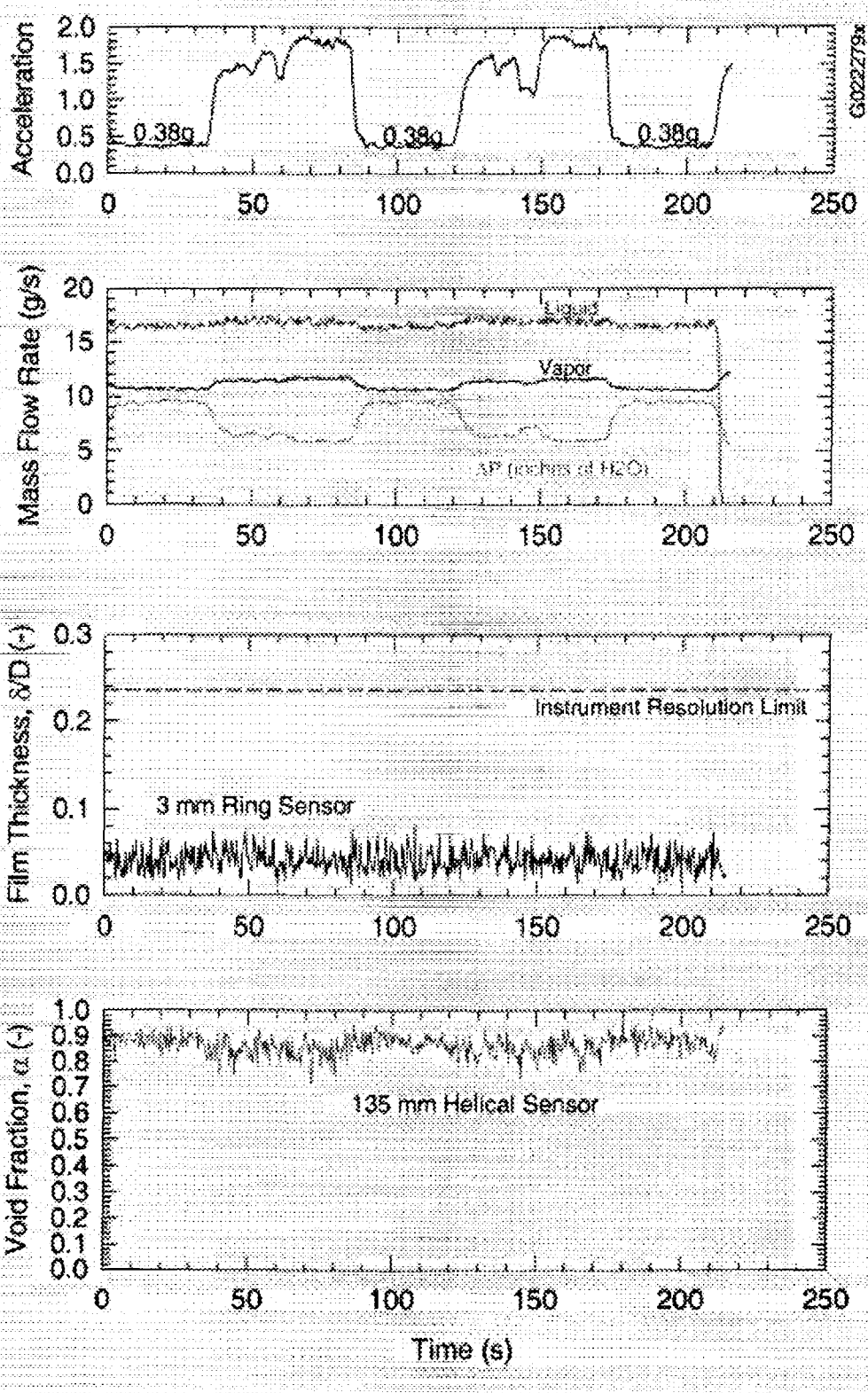

Flow Regime Map for February 2000 Tests

- Most data lie in the annular flow regime
- Stratified flow regime persists to a higher superficial gas velocity than expected
- Eccentric annular flow persists up to a superficial gas velocity of j_g = 4 m/s at 0.38g

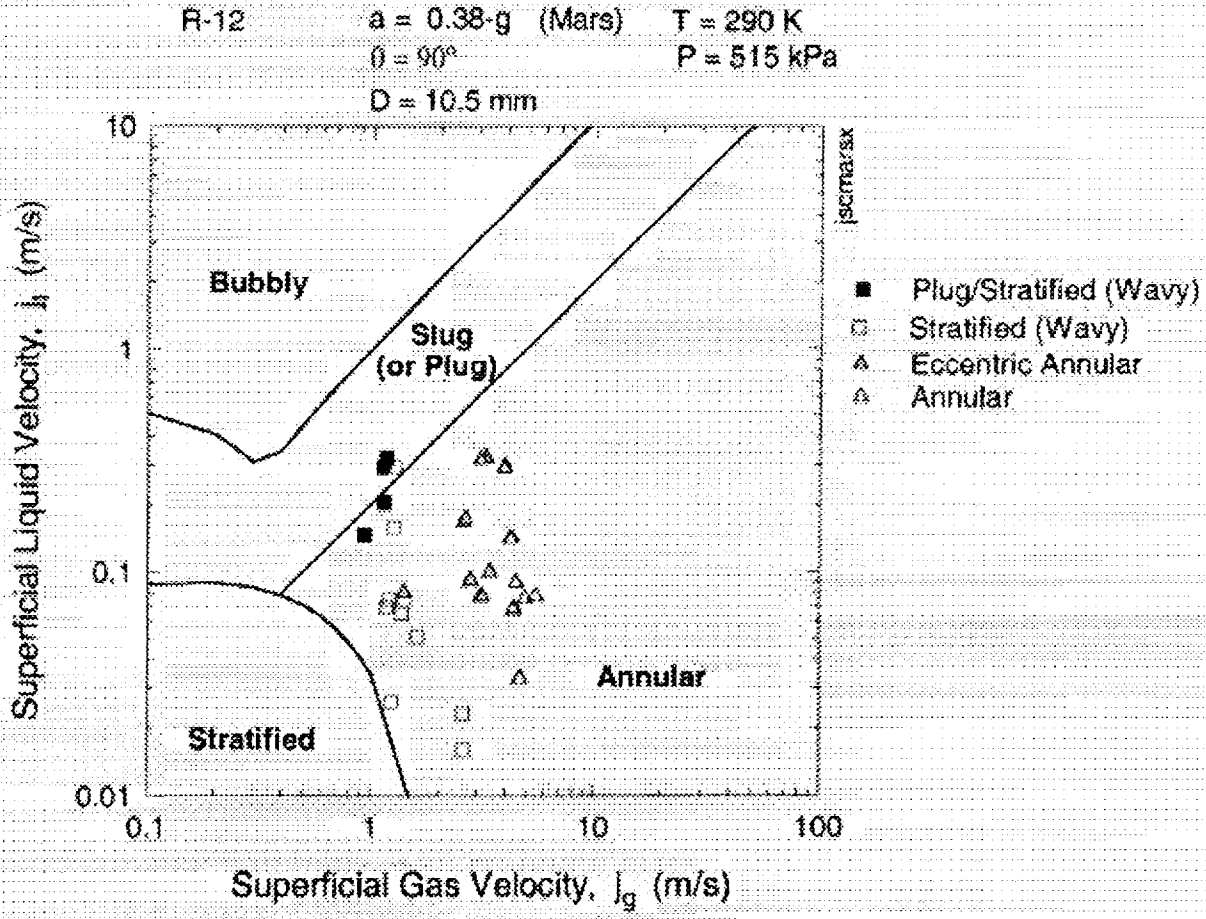

Interfacial Friction Factor for the (Symmetric) Annular Flow Regime

- The interfacial friction factor is smaller than expected with this refrigerant, *i.e.* at gas density 30 times greater than in air/water tests

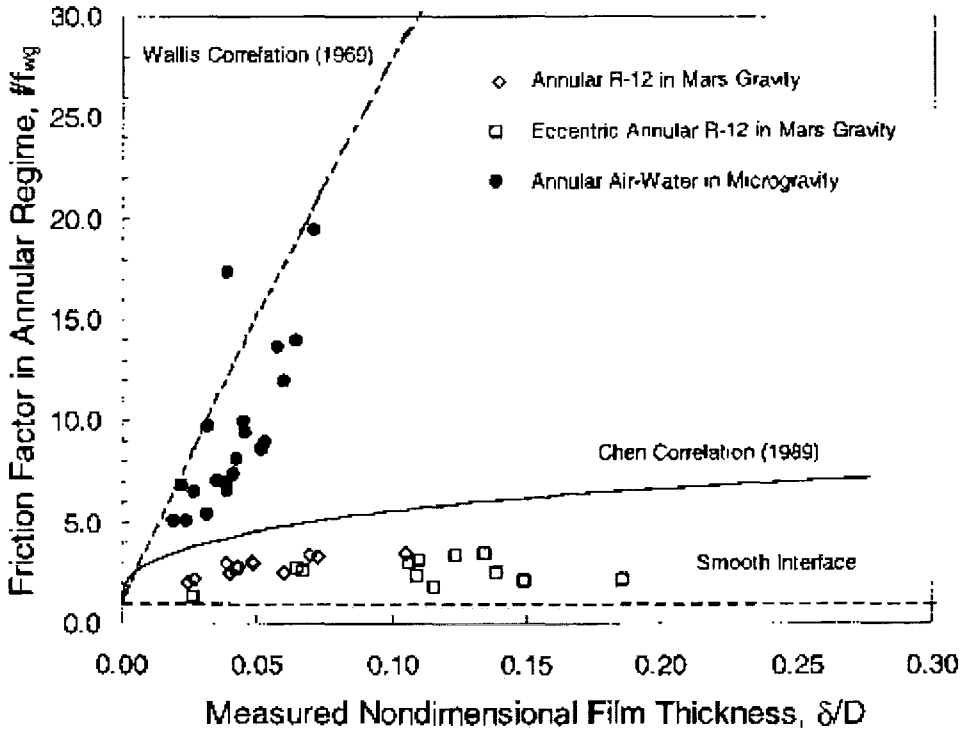

Creare

Conclusions

- The capacitive void fraction instruments enable void fraction and film thickness measurements to be made with refrigerants as the working fluids

- Comparison with prior air/water data indicates that the interfacial shear is smaller for R-12 at a given void fraction or film thickness:

  Therefore gas density may play a role in scaling interfacial shear for the annular flow regime, and this topic is the focus of current investigations.

DEVELOPMENT OF A MAGNETIC RESONANCE IMAGING TECHNIQUE FOR MEASURING EMULSION COALESCENCE

M. d'Avila, N. Shapley, J. Walton*, S. Dungan, R. Phillips and R. Powell
Department of Chemical Engineering and Materials Science,
University of California, Davis
* NMR Facility, University of California, Davis

ABSTRACT

The kinetics of emulsion coalescence determine emulsion stability and also emulsion rheology, which depends on the distribution of droplet sizes in the system. In a concentrated emulsion, which is opaque, conventional optical methods for monitoring the droplet size distribution are often impractical, and cannot distinguish between flocculation and coalescence. Nuclear magnetic resonance (NMR) is uniquely suited to measuring droplet size distributions by observing restricted diffusion, which is unaffected by flocculation. In addition, NMR imaging provides the capability of measuring droplet concentration and velocity profiles in a flowing material.

We wish to quantify the effect of shear flow on coalescence of a concentrated emulsion. We have constructed a combined annular Couette flow cell and magnetic resonance imaging probe. The wide-gap Couette geometry, where the emulsion is sheared between concentric cylinders, produces a planar, axisymmetric shear flow. The imaging probe, consisting of a 300 MHz birdcage coil, is combined with an imaging system utilizing maximum gradients of 95 G/cm. The emulsion is composed of 20-40% volume fraction iso-octane in water, stabilized by Tween 20 surfactant. Blends of the iso-octane with a denser oil can be used to achieve density-matched emulsions, which would simulate systems in microgravity during earth-based experiments.

We have demonstrated the capability of extracting the droplet size distribution in a quiescent emulsion from restricted diffusion data obtained by using a pulsed gradient stimulated echo sequence. Figure 1 shows, for the first time, that this NMR method produces nearly quantitative agreement with light scattering measurements. Also, we have employed NMR imaging to visualize and measure the velocity profile of water in the Couette flow cell, by the time-of-flight method, displayed in figure 2. Data from monitoring the droplet size distribution, droplet concentration and velocity profiles over time in the flowing emulsion system will be presented.

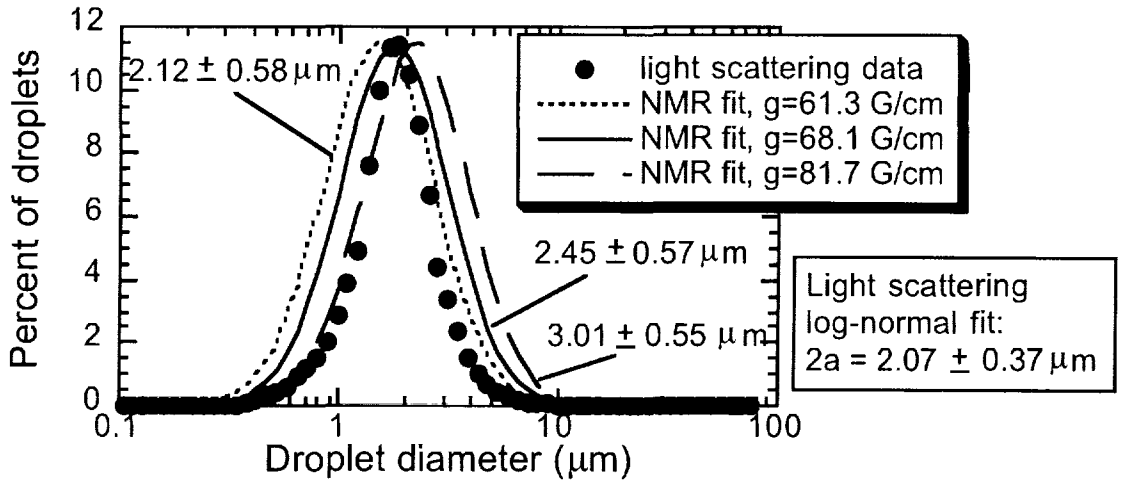

Figure 1. Comparison of droplet size distributions measured in a quiescent emulsion consisting of 15 wt% iso-octane and 0.5 wt% Tween 20 in water. (Droplet volume fraction = 20%). Light scattering data are presented together with distributions fit from several NMR restricted diffusion curves (with varying field gradient values) from the same system.

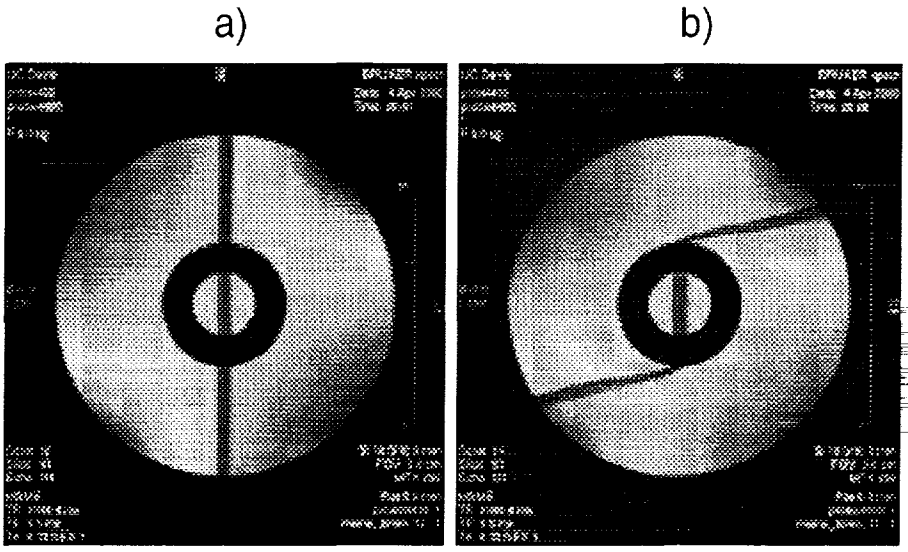

Figure 2. a) Spin-echo cross-sectional image of the stationary flow cell filled with water. The dark vertical line indicates the region tagged by saturation.

b) Identical imaging sequence, run while the outer cylinder rotated at 0.3 rev/s. The delay between tagging and recording the image was 516 ms. The displacement of the tagged plane indicates the motion of the water. From this image, the water velocity profile across the annular gap was quantified.

NASA/CP—2000-210470

Development of a Magnetic Resonance Imaging Technique for Measuring Emulsion Coalescence

N. Shapley, M. d'Avila, J. Walton*,
S. Dungan, R. Phillips and R. Powell

Department of Chemical Engineering and Materials Science
*NMR Facility
University of California, Davis

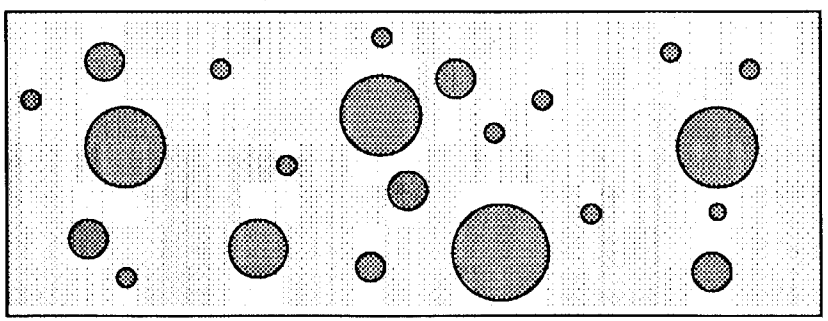

Controlling Emulsion Stability is Critical

- Food storage and processing, pharmaceuticals, separations, multiphase reactions
- Breakdown processes

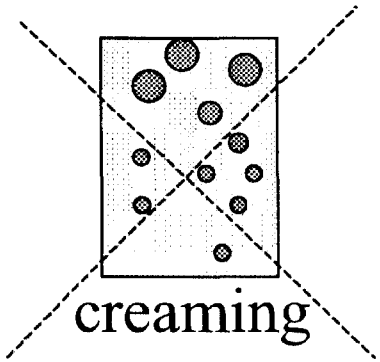

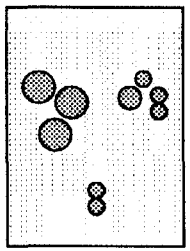

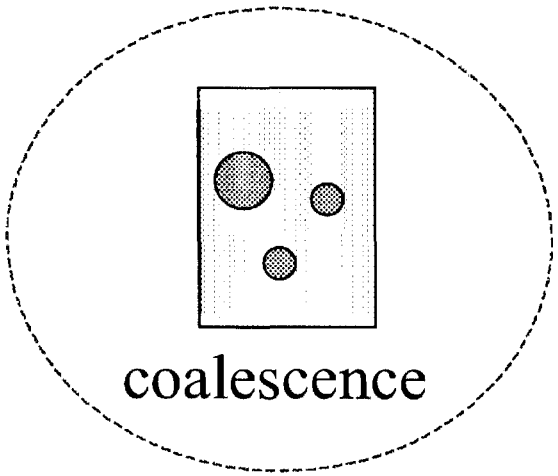

Eliminate creaming in microgravity

- How does flow affect coalescence?

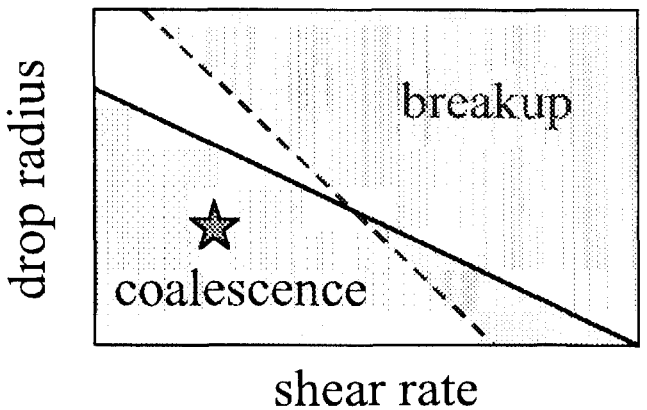

Four Steps in Shear-Induced Coalescence

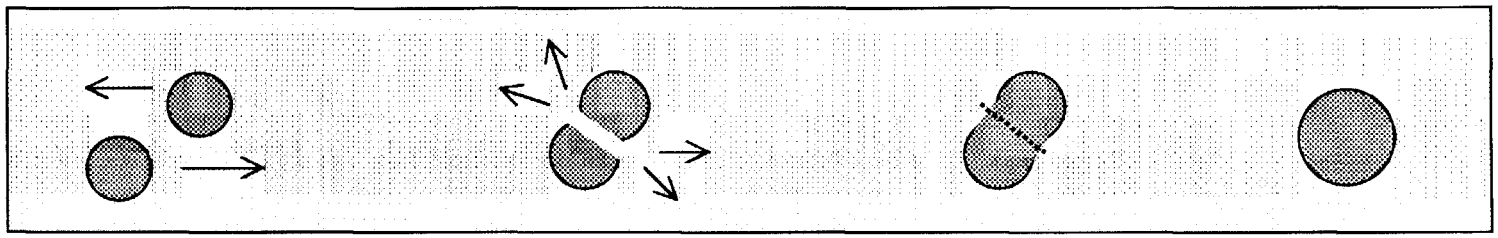

collision (dilute oil/water) | film drainage (polymer blends) | film rupture (foams) | fusion

- Objective: To determine dominant kinetics of coalescence in a concentrated oil/water emulsion during shear flow.

$\longrightarrow$ Scaling with (γ , ϕ , g)

- Approach: Use NMR to measure:
  - Droplet size distribution over time (restricted diffusion)
  - Velocity profile
  - Droplet volume fraction profile

Emulsion Composition and Flow Geometry are Variable

- Emulsion composition:

  ϕ = 20 to 40% iso-octane in water

  Stabilized by 0.5 wt% Tween 20 surfacta

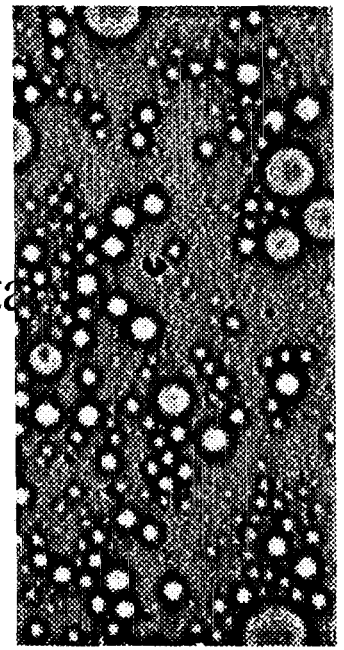

90 μm

- Log-normal initial size distribution

- Oil blends simulate microgravity by density matching

- Flow geometry: combined narrow-gap / wide-gap annular Couette flow

$$\frac{(R_o - R_i)}{R_i} = \begin{cases} 1.75 & \text{wide gap} \\ 0.1 & \text{narrow gap} \end{cases}$$

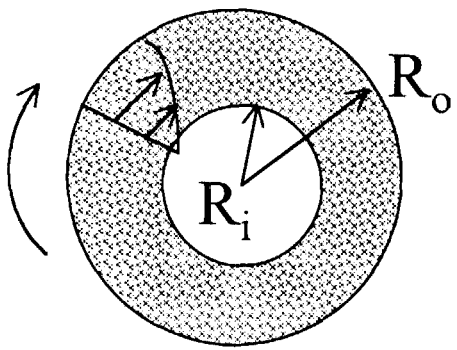

NMR Exceptionally Well-Suited to Measuring Coalescence

•Distinguishes coalescence from flocculation

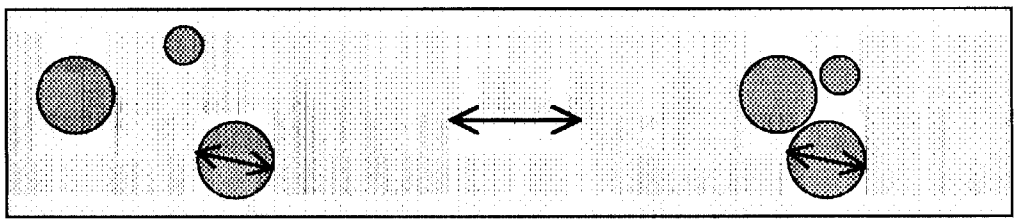

•<u>In situ</u> measurements of emulsions during shearing are difficult
Conventional methods require removing samples
Creaming can bias measurements (Mishra et al., 1998)

•Optical techniques confined to use in dilute systems
(Vinckier et al., 1998; Rusu et al., 1999)
NMR more accurate for concentrated systems

Combined Flow Cell and NMR Probe Displays High Precision Design

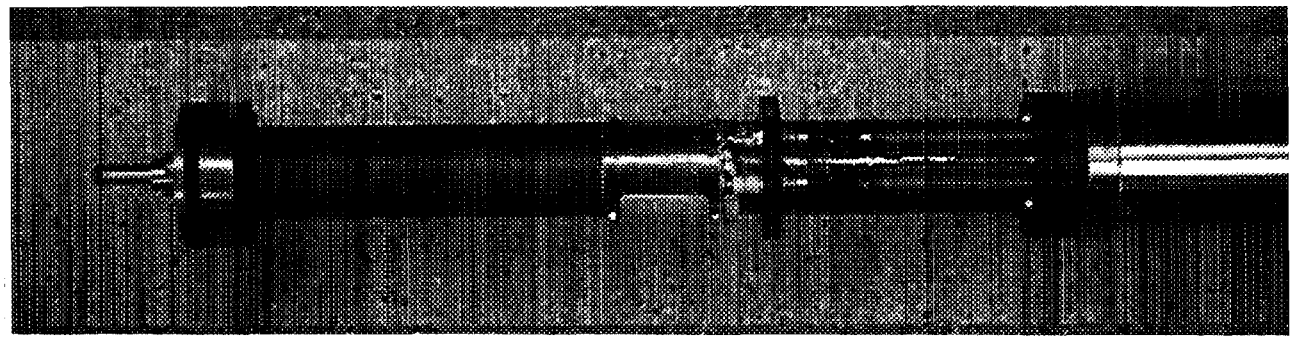

- Outer cylinder rotates to prevent Taylor-Couette instabilities
- $\pm$ 0.25 mm concentricity of cylinders
- $L / (R_o - R_i) = 40 \longrightarrow$ No end effects
- ULTEM housing has high strength, machinability, low dielectric loss
- Custom-built 300 MHz "slotted-tube resonator" RF coil
- Imaging system with maximum gradients of 95 G/cm

Restricted Diffusion Indicates Domain Sizes in Material

Over diffusion time Δ,

bulk restricted

$$\frac{I(G)}{I(G=0)} = F(a, D, \Delta, \delta, G)$$

droplet radius

diffusion coefficient

diffusion time

gradient duration

gradient strength

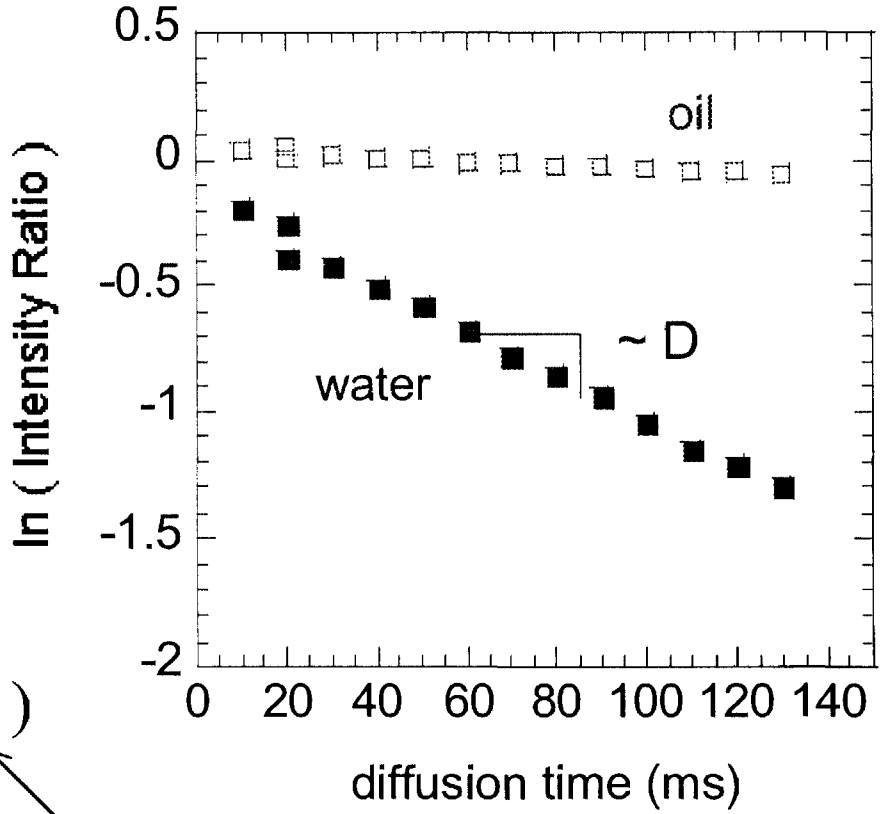

Size Distributions Determined by Observed Restricted Diffusion

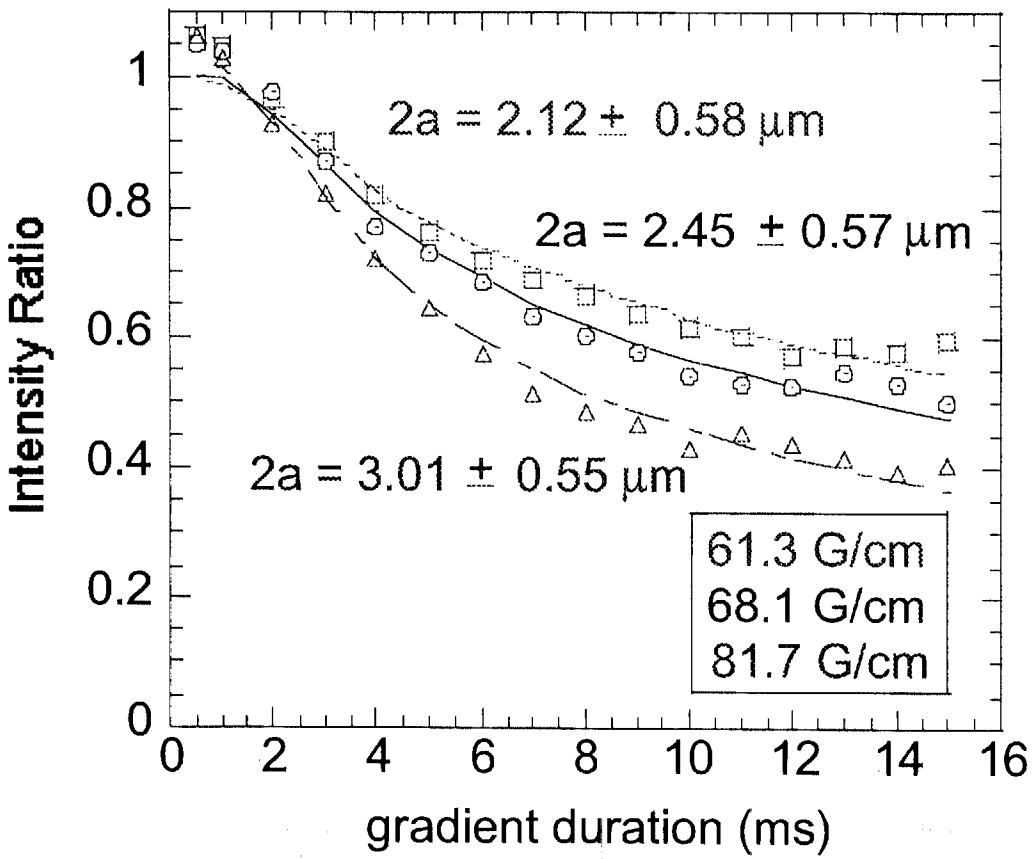

NMR Size Distributions Agree with Light Scattering Data

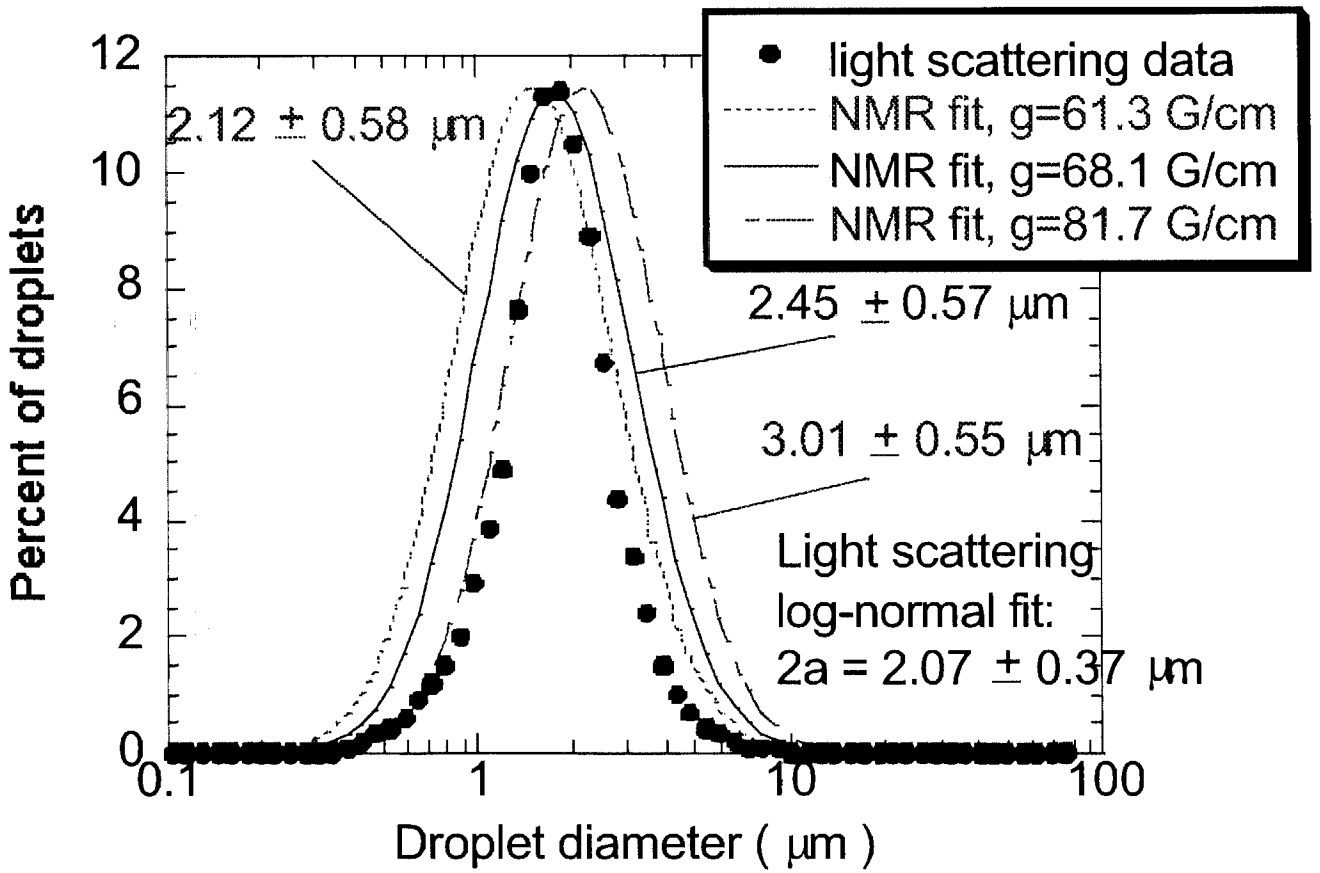

Shear-Induced Coalescence Changes Droplet Size Distribution

Before and after 1.06×10^6 averaged strain units applied

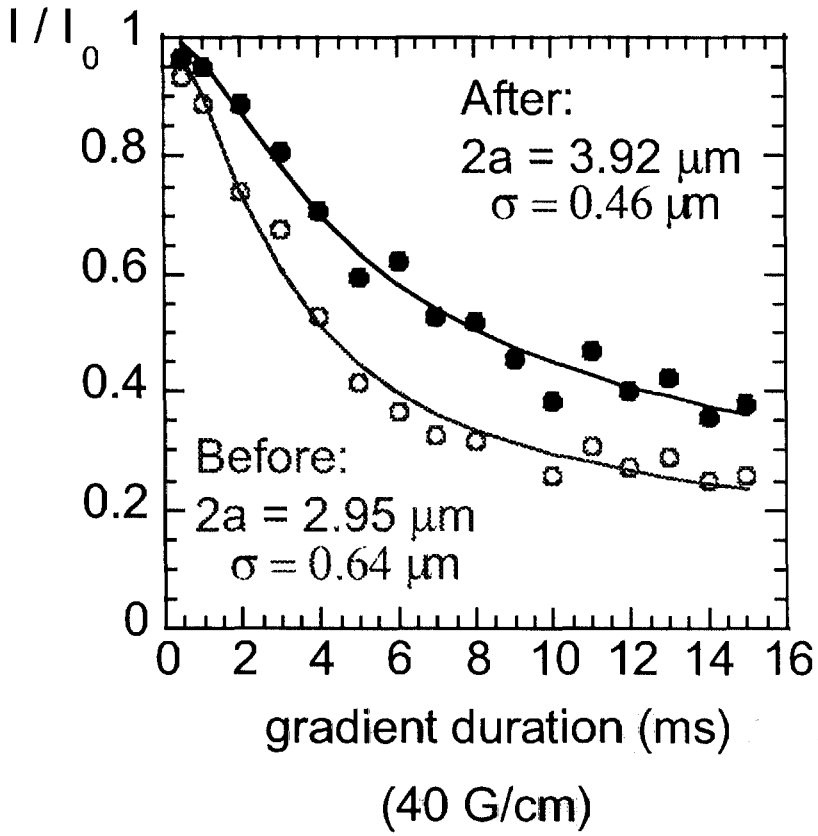

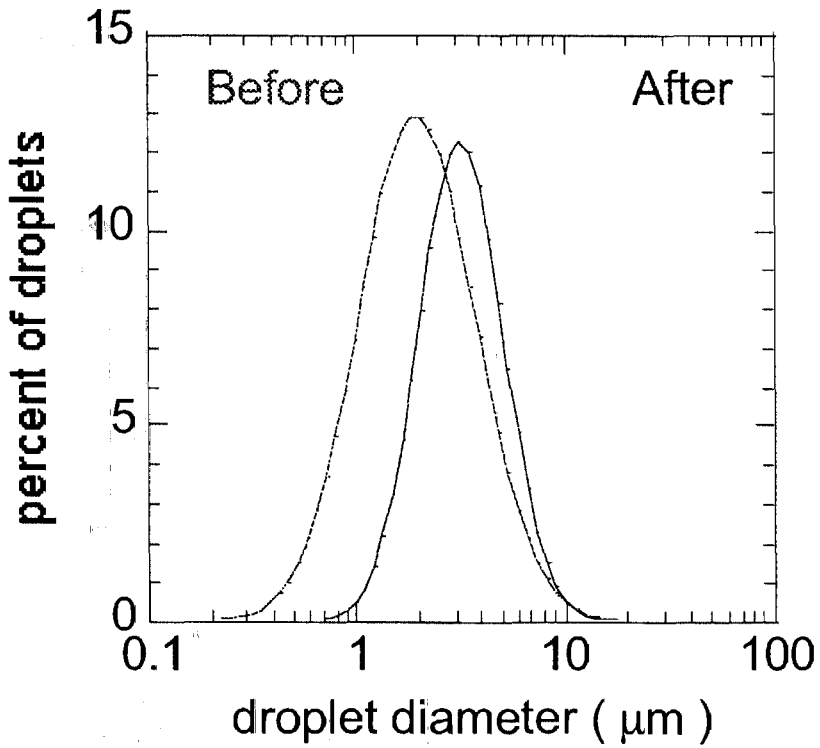

Time of Flight Images Capture Velocity Profile of Water

Displacement of tagged plane indicates motion of water

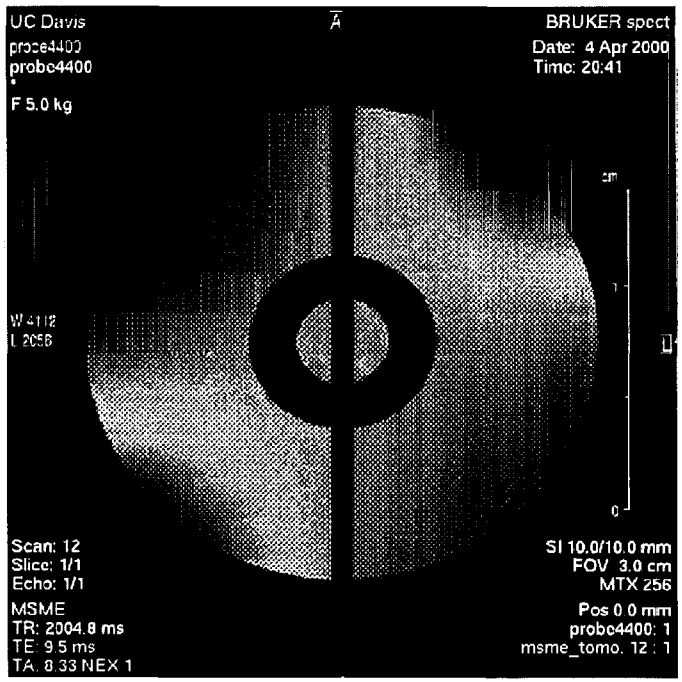

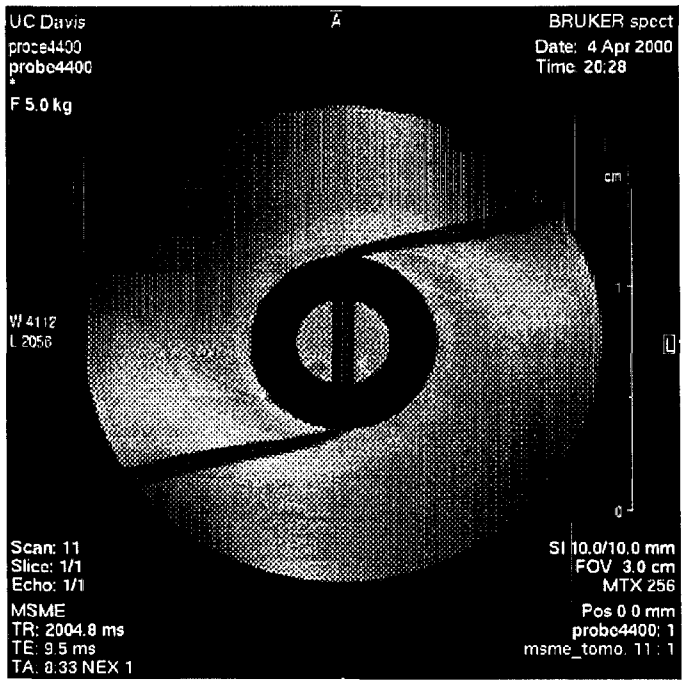

No motion

0.3 rev/s rotation, 516 ms delay

Time of Flight Velocity Profile Matches Newtonian Theory

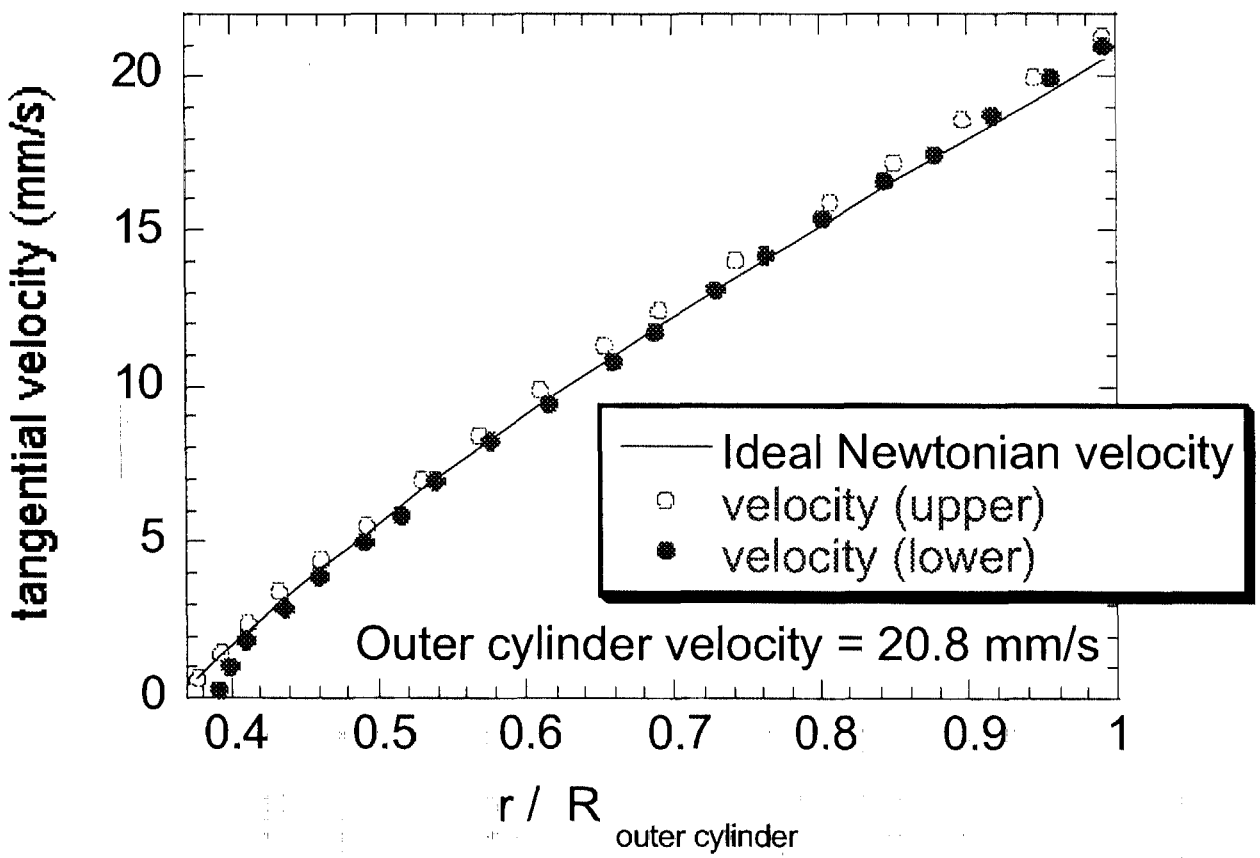

Droplet and Water Concentration Visible Through Chemical Shift Imaging

Emulsion quiescent for 3 hours, before flow

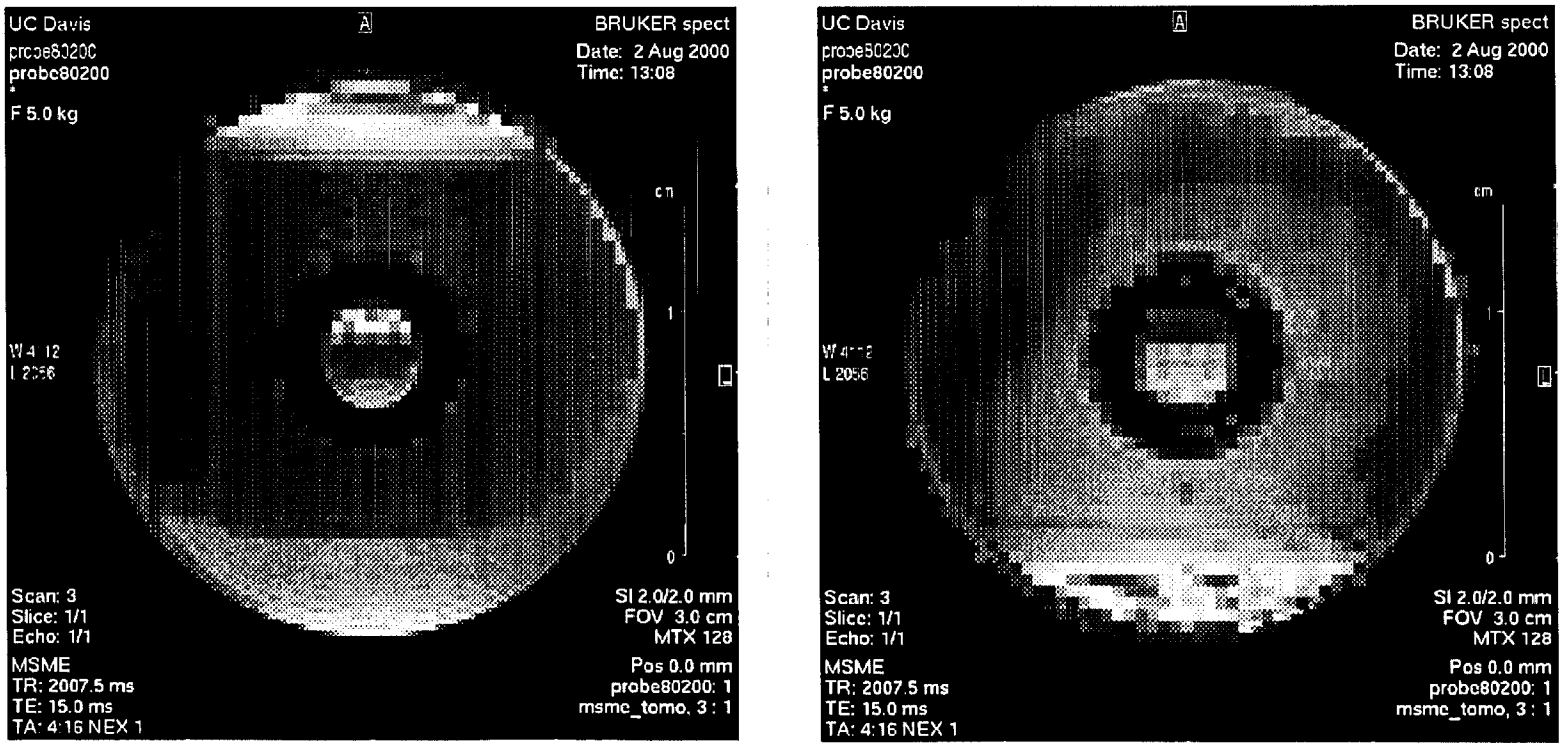

Oil droplets

Scale

0-13% 90-100%

Water

Summary and Future Work

- NMR method can quantify:
  - droplet size distributions
  - velocity profiles
  - droplet volume fraction profiles

- Tune system to move among:

collision, drainage, rupture - dominated regimes

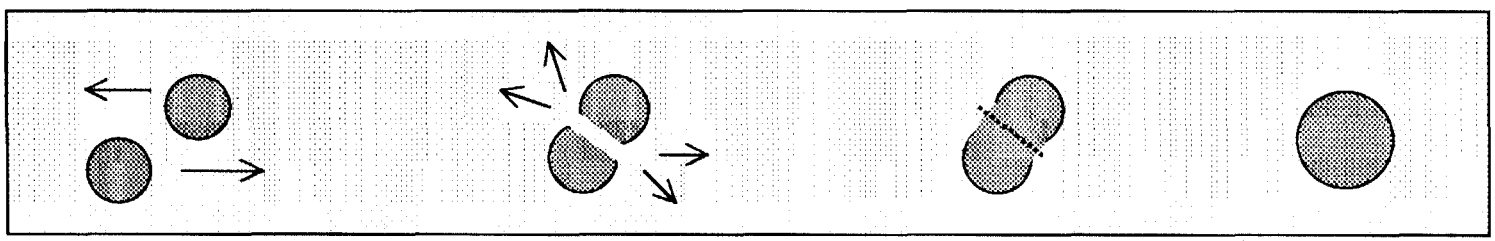

- Quantify influence of gravity through oil density adjustment

August 10, 2000
Session 3B

Complex Fluids II

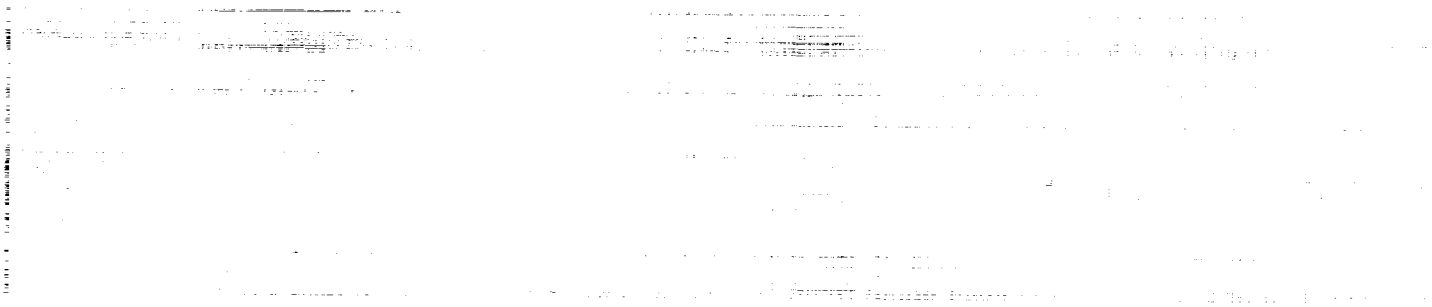

GAS & LIQUID TRANSPORT INSIDE AQUEOUS FOAMS

M.U. Vera and D.J. Durian
UCLA Department of Physics & Astronomy, Los Angeles CA 90095-1547
(12 June 2000)

INTRODUCTION

Foams are nonequilibrium dispersion of gas bubbles packed densely in a relatively small volume of liquid [1]. Surfactants or other surface-active agents must be present in order to prevent rapid collapse through the rupture of the thin liquid films separating adjacent gas bubbles. Even so, foams evolve with time. First, in the presence of earth's gravity, liquid will flow downwards through the random network of Plateau borders at which three films meet. This drainage effect is more pronounced for wetter foams, where the Plateau borders are thicker. It effectively prevents systematic study of the material properties of a sequence of foams as the liquid fraction ε is increased up to the melting transition at ε_c=1-0.634 (where the bubbles become close-packed spheres). For this reason we need prolonged microgravity conditions. But even in microgravity foams will coarsen with time by the diffusion of gas from smaller to larger bubbles. This coarsening effect is driven by surface tension. Whether gravitational drainage or surface tension-driven coarsening, the end results is that the gas and liquid components of a foam tend to separate with time until all that remains is a puddle of liquid and a pocket of gas.

In this talk I will review recent work in our laboratory to understand the physics of drainage and the physics of coarsening, and how the two are coupled. This is interesting for its own right, as well as for applications. It is also important for establishing the extent to which microgravity conditions are truly necessary for our proposed flight experiments on the connection between the microscopic structure and dynamics of foams and their macroscopic rheological properties (FOAM = Foam Optics And Mechanics). After all, a better understanding of drainage could lead to a means by which it may be circumvented.

DRAINAGE & COARSENING

Recent work has been greatly stimulated by the development of a partial-differential "drainage equation" that describes how the local liquid fraction $\varepsilon(z,t)$ in a foam may evolve in response to three basic forces: gravity, capillarity, and viscous drag [2,3]. The basic geometrical assumption is that the film thickness (l) is much smaller than the average Plateau border radius (r), which in turn is much smaller than the average bubble size (R); this implies $\varepsilon \sim (r/R)^2$ and holds for large bubbles and dry foams. One then finds that the flow speed inside the Plateau borders is

$$u_{gravity} = u_o \varepsilon^m \left(1 - \sqrt{\frac{\varepsilon_c}{\varepsilon}}\right) \frac{\xi}{\varepsilon} \frac{\varepsilon}{z} , \qquad (1)$$

where m=1 (1/2) for no-slip (slip) boundary conditions, $u_o \rho gR^2/\eta$, and $\xi \gamma/\rho gR$. The drainage equation is then simply a continuity equation based on Eq.(1). This may be modified to include the variation of container shape with depth [4]; specifically, one can largely eliminate vertical gradients with use of an exponential "Eiffel Tower" sample cell. However, poor agreement with experimental data was observed at long times was attributed to the influence of coarsening [4].

The challenge, then, is to incorporate coarsening effects by allowing the bubble size to vary with depth and time. We believe we have solved with problem. By considering pressure differences between adjacent bubbles in terms of the radii of curvature of the Plateau borders, we have derived the liquid-fraction dependence of the growth law for a uniform polydisperse foam: $RdR/dt=D_o/\varepsilon^{1/2}$. We have also verified this law, and obtained the constant D_o, by fitting bubble-growth data to $R(t)=R_o(1+t/t_o)^{1/2}$ for several liquid fractions. Now consider the effect of spatial variation in bubble size or liquid fraction. The very same coarsening mechanism must drive a net flux of gas in the direction of lower pressures. This gives the full growth law as

$$\frac{R}{t} = D_o \frac{1}{\sqrt{\varepsilon} R} + \frac{R^2}{\alpha} \frac{\partial^2}{\partial z^2} \frac{1}{\sqrt{\varepsilon} R} \quad , \tag{2}$$

where α O(0.02) is the fractional difference between the radii of the average and the crossover bubble (that neither grows nor shrinks). Curvature in the pressure field causes an accumulation or loss of gas and hence contributes to R/ t. Gradients in the pressure field cause a transport of gas, and hence a transport of liquid at speed

$$u_{coarsening} = -\frac{1-\varepsilon}{\varepsilon} u_{gas} = \frac{1-\varepsilon}{\varepsilon} \frac{D_o R}{\alpha} \frac{\partial}{\partial z} \frac{1}{\sqrt{\varepsilon} R} \quad . \tag{3}$$

Note that this increases dramatically for dry foams, where a small gas flow speed requires a correspondingly larger liquid flow speed. The full drainage equation, including effects of both gravitational and coarsening-induced liquid flow is then simply a continuity equation for $\varepsilon(z,t)$ with a liquid speed of $u=u_{gravity}+u_{coarsening}$. Bubble sizes evolve according to Eq.(2) with boundary conditions $u_{coarsening}=0$, such that no gas escapes the sample.

As of this writing, we have collected a complete data set for $\varepsilon(z,t)$ and $R(z,t)$ and are now analyzing it via numerical solution of the above set of coupled PDE's. We are also searching for exact and similarity solutions in the case of coarsening-dominated transport.

REFERENCES

[1] R.K. Prud'homme and S.A. Khan, ed., *Foams: Theory, Measurement, and Application.* Surfactant Science Series **57**, (Marcel Dekker, NY, 1996).

[2] D. Weaire, S. Hutzler, G. Verbist, and E. Peters, Adv. Chem. Phys. **102**, 315 (1997).

[3] S.A. Koehler, S. Hilgenfeldt, and H.A. Stone, Phys. Rev. Lett. **82**, 4232 (1999).

[4] A. Saint-Jalmes, M.U. Vera, and D.J. Durian, Europhys. Lett. **50**, 695 (2000).

FOAM OPTICS AND MECHANICS

UCLA Department of Physics & Astronomy

- Objective
  - elucidate macroscopic properties in terms of microscopic bubble-scale structure and dynamics
    - eg vanishing elasticity vs liquid fraction
    - eg vanishing elasticity vs strain rate
- Approach
  - macroscopics: rheology $G^*(\omega)$, $G(t,\dot{\gamma})$, $\sigma(\dot{\gamma})$
  - microscopics: DWS, DTS, video microscopy
  - vs liquid fraction
  - vs time (and hence vs bubble size)
- Recent studies of *Jamming Phase Diagram*

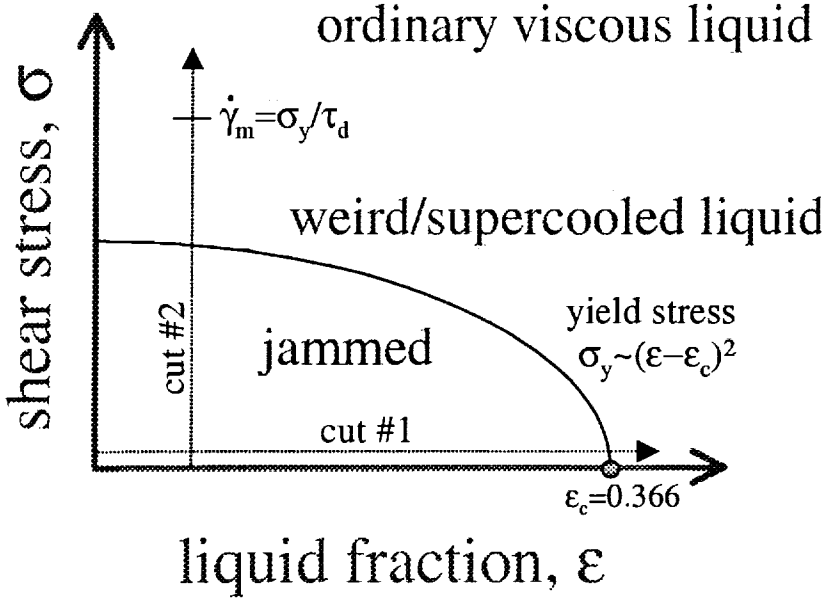

Need for prolonged microgravity

- foams evolve with time
  - **drainage** due to earth's gravity
    - increasingly fast for wetter foams
    - only dry foams can be fully studied on earth
  - **coarsening** due to gas diffusion from smaller to larger bubbles
    - driven by Laplace pressure (cannot be eliminated)
    - slow on scale of bubble dynamics
    - self-similar size distribution
  - **film rupture**
    - negligible for common surfactants

- need microgravity
  - to access wet foams
    - map out full jamming phase diagram
    - behavior near critical point

- need long duration experiments
  - to achieve reproducible size distribution
  - to follow behavior vs bubble size

TODAY: gas and liquid transport

- physics of drainage
  - crucial for many applications
  - not well understood / outstanding puzzles
  - a nuisance for FOAM project
    - extend/delimit range of ground-based studies
- coupling with coarsening
  - drier foams coarsen faster
  - bigger bubbles cause faster drainage
    - eg 30 minutes after shaking SDS solution:

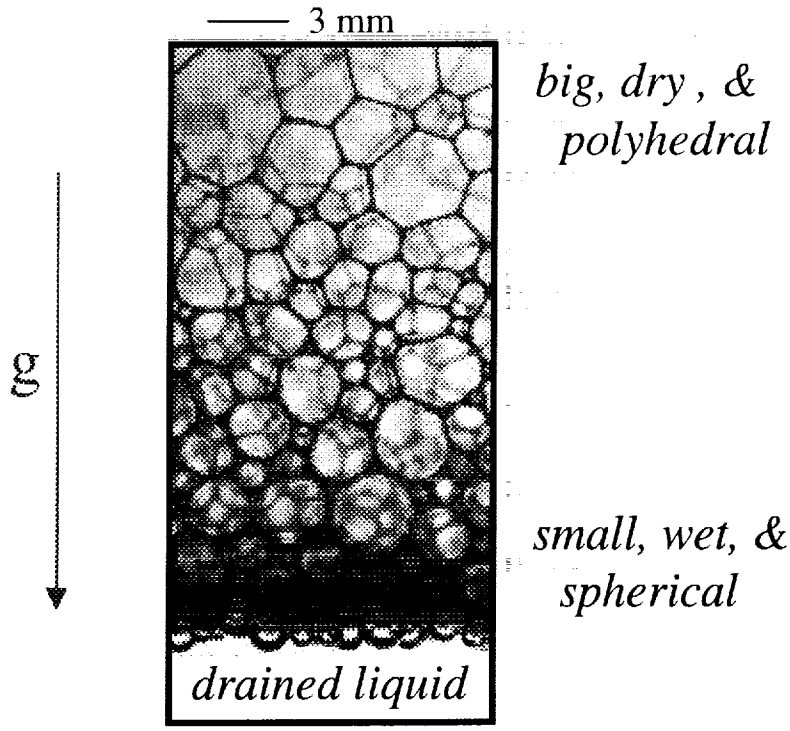

Team FOAM

- UCLA Physics:
  - Anthony Gopal
  - Pierre-Anthony Lemieux
  - Narayanan Menon
  - Rajesh Ojha
  - *Arnaud Saint-Jalmes*
  - Löic Vanel
  - *Moin Vera*

- NASA Glenn:
  - Greg Zimmerli, project scientist
  - Sue Motil, project manager
  - Angela Becker
  - Art Birchenough
  - Ed Hovenac
  - Dan Minjares
  - Robert Skupinski

Bubble-packing geometry

- Foam is dry & bubbles are jammed:
  - static packing of bubbles
  - negligible liquid in films and vertices

3 films per Plateau border

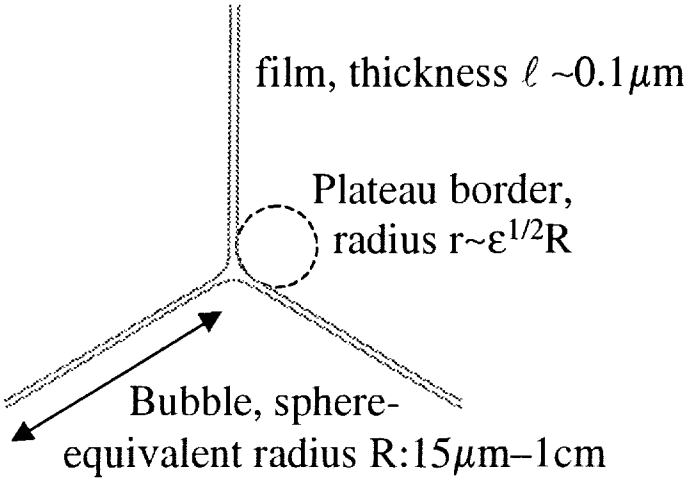

4 Plateau borders per vertex

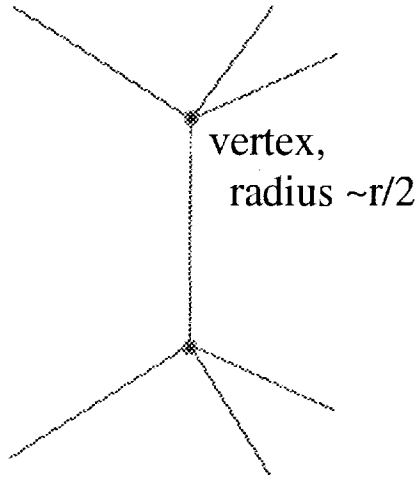

- Liquid fraction (assuming Kelvin cell):

$$\varepsilon \quad 3\frac{\ell}{R} + 0.34\left(\frac{r}{R}\right)^2 + 0.55\left(\frac{r}{R}\right)^3 \quad 0.34\left(\frac{r}{R}\right)^2 \quad \text{since } \ell << r << R$$

most liquid is in the Plateau borders

  - scatter light
  - provide channel for drainage

Foam Optics

- Plateau borders are primary scattering site
  - estimate photon transport mean-free path:

$$l^* = \frac{1}{\rho\sigma^*} \sim \frac{1}{\frac{1}{R^3}(rR)} \sim \frac{R}{\sqrt{\varepsilon}}$$

  - measure diffuse transmission through slab:

$$T_d = \frac{1 + z_e}{(L/l^*) + 2z_e}$$

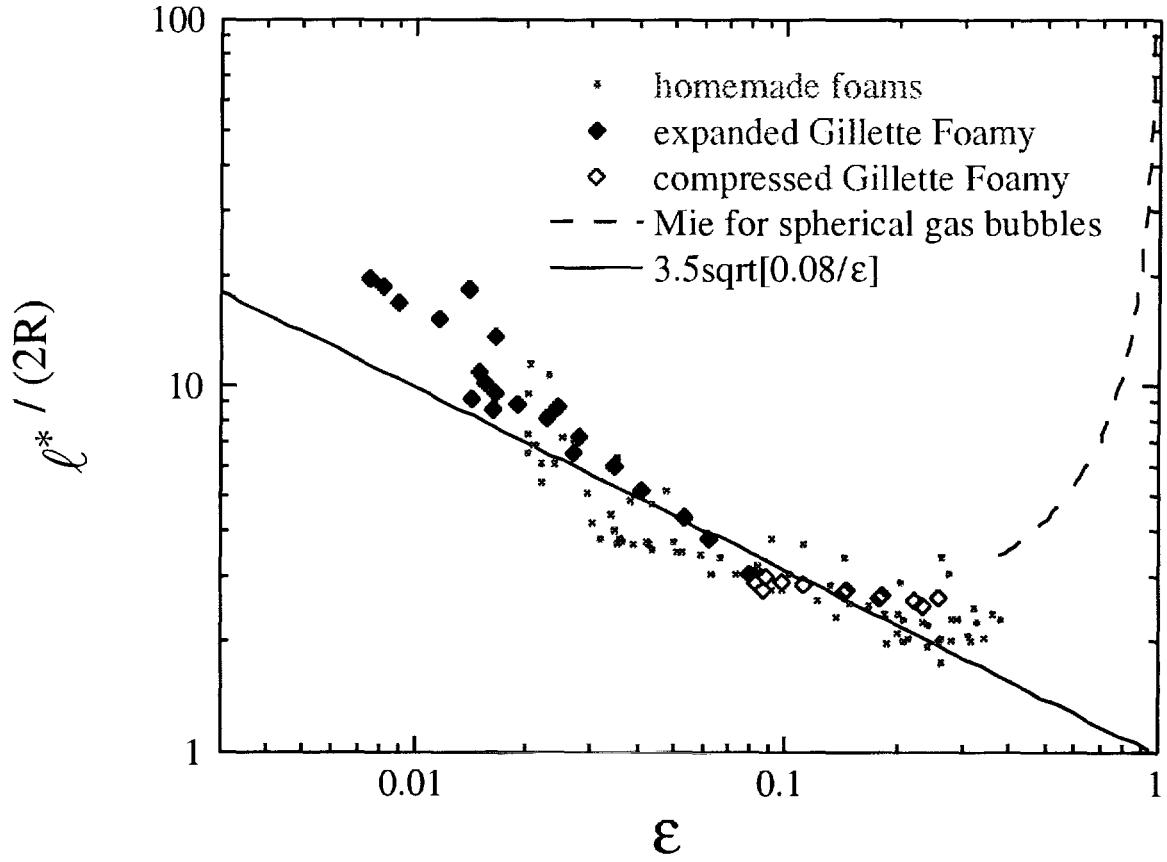

Liquid Flow Speed, u=?

- estimate ΔE/time for the three forces:

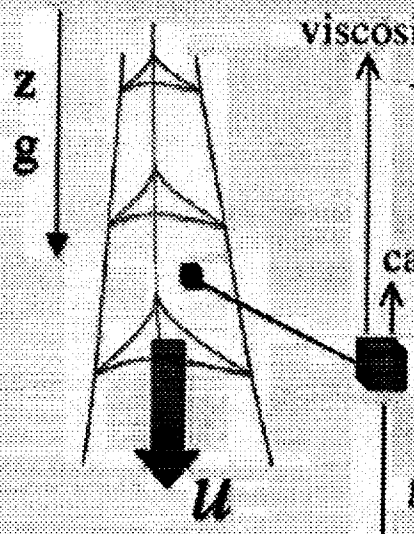

viscosity $-\eta\left(\frac{u}{r}\right)^2 * \begin{cases} r^2 R & \text{rigid films}^* \text{ (shear in PB's)} \\ r^3 & \text{mobile films}^{**} \text{ (shear in vertices)} \end{cases}$

capillarity $-\left(\frac{d}{dz}\left[P_\phi - \frac{\gamma}{r}\right]R\right)r^2 u$

gravity $+\rho(r^2 R)gu$

- use $r \sim \varepsilon^{1/2} R$ and solve $\Sigma(\Delta E/\text{time})=0$ for u :

$$u = K_m \frac{\rho g R^2}{\eta c^3}\left(1 - \frac{\sqrt{\delta_\varepsilon}\,\gamma c}{\rho g R \varepsilon^{3/2}}\frac{\partial \varepsilon}{\partial z}\right) * \begin{cases} \varepsilon & \text{shear in PB's}^* \\ \varepsilon^{1/2} & \text{shear in vertices}^{**} \end{cases}$$

* Goldfarb, Kann, Shreiber, Izv. Akad. Nauk SSR **2**, 103 (1988) & Verbist, Weaire, Kraynik, J. Phys.: Cond. Matt. **8**, 3715 (1996)

** Koehler, Hilgenfeldt, Stone, Phys. Rev. Lett. **82**, 4232 (1999)

The Drainage Equation

- continuity for liquid conservation:

$$0 = \frac{\varepsilon}{t} + \frac{(u\varepsilon)}{z} + \frac{u\varepsilon}{A}\frac{dA}{dz}$$

$\varepsilon(z,t)$ = liquid volume fraction

$u(z,t)$ = liquid flow speed (previous slide)

$A(z)$ = cross-sectional area of container *

- boundary conditions:

$$\varepsilon|_{boundary} = \varepsilon_c \text{ (flow), or } \left.\frac{\varepsilon}{\varepsilon / z}\right|_{boundary} = \xi\sqrt{\frac{\varepsilon_c}{\varepsilon}} \text{ (no flow)}$$

- free drainage starting with $\varepsilon(z,t)=\varepsilon_o$
  - solution for A(z)=constant not known
  - solution for $A(z)=A_o Exp[z/z_o]$ is simple* (ignoring capillarity in boundary conditions)

liquid fraction:

$$\varepsilon(t) = \varepsilon_o / (1 + t/t_o)^{1/m}$$

with $t_o = z_o / (u_o m \varepsilon_o^{\,m})$

vol. of drained liquid:

$$V(t)/V_f = 1 - 1/(1 + t/t_o)^{1/m}$$

* A. Saint-Jalmes, M.U. Vera, D.J. Durian, Europhys. Lett. **50**, 695 (2000).

Eiffel Tower Experiment

- uniform drying (no ε-gradients) as expected

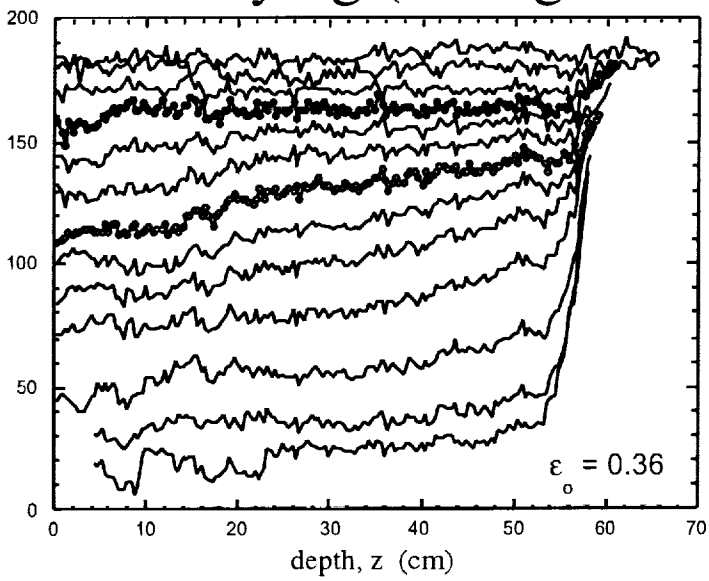

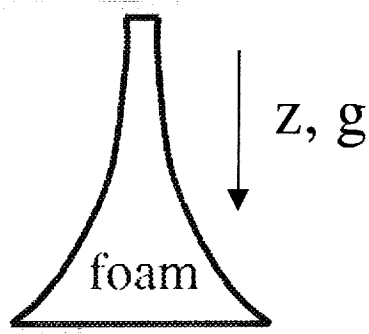

- but much faster than prediction:
  - must include effects of coarsening

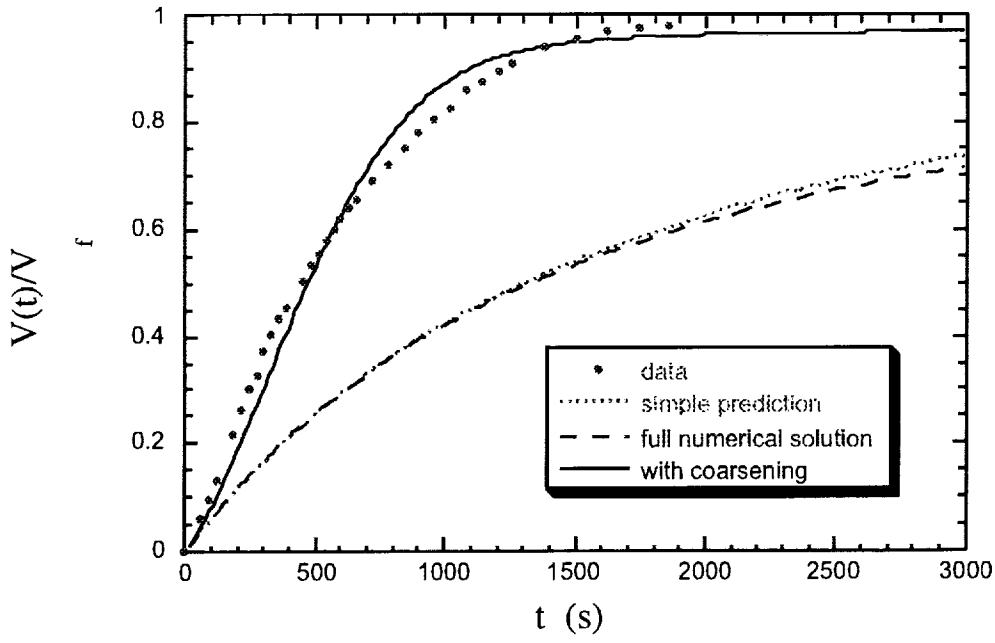

rate of coarsening, R/ t, vs ε

- (volume)/ t = area * flux
- flux to pressure difference between average bubble and one with R_c/ t =0

$$P - P_c = \frac{\gamma}{r} - \frac{\gamma}{r_c} \approx \frac{\gamma}{\sqrt{\varepsilon}} \frac{1}{R} - \frac{1}{R_c}$$

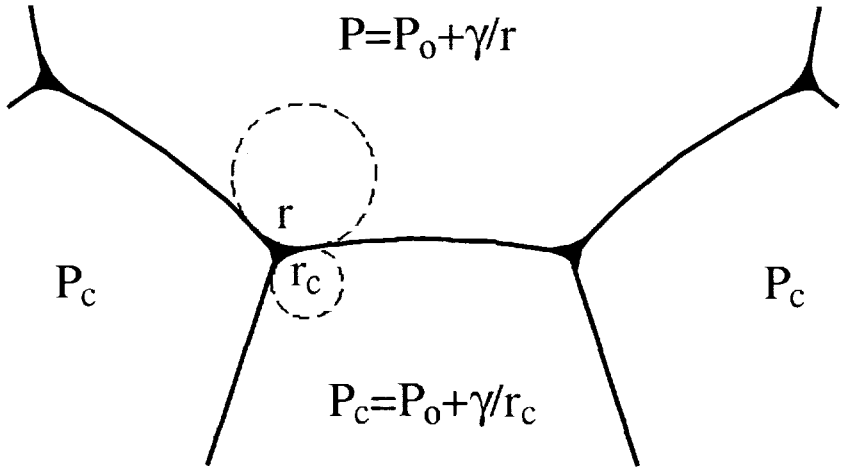

- including vertical pressure variation:

$$\frac{R}{t} = D \frac{1}{\sqrt{\varepsilon} R} + \frac{R^2}{\alpha} \frac{^2}{z^2} \frac{1}{\sqrt{\varepsilon} R}$$

with $[D] = \mathrm{cm}^2/\mathrm{s}$, and

$\alpha \cong R/R_c - 1 \cong 0.01$ (constant)

test R R/ t=D/ε^1/2

- (1) create different foams with uniform ε
  - obtain R(t) from diffuse transmission (green points)
- (2) create one foam with ε_o=0.08, let it drain
  - obtain R(z,t) from video microscopy
  - obtain ε(z,t) from diffuse transmission (red points)
- both results agree with prediction
  - dashed curve shows D(1-sqrt[ε/ε_c])

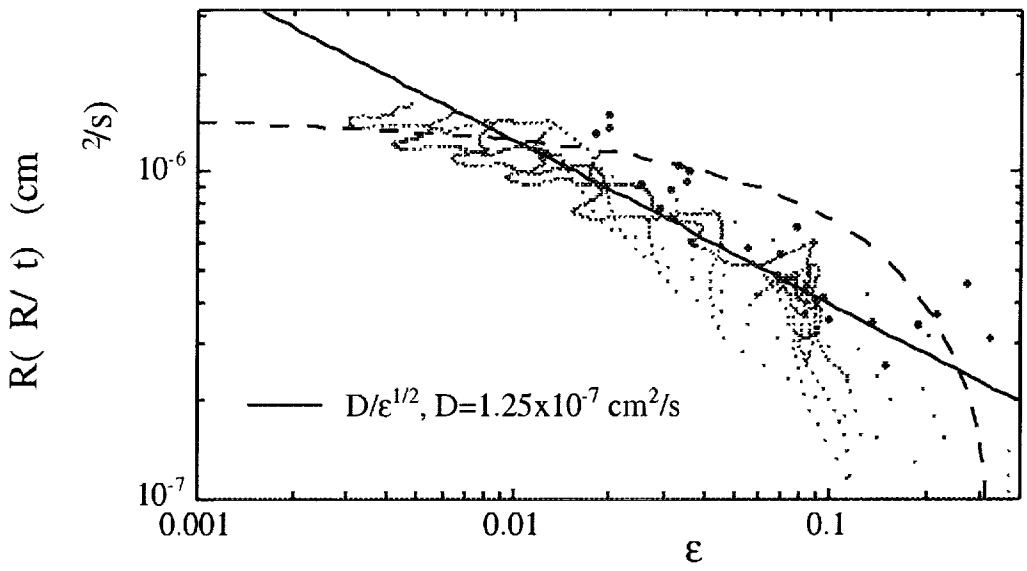

variation in pressure, $P=\gamma/(\varepsilon^{1/2}R)$

- gradient causes gas transport from high to low pressure regions:

$$J = -\frac{DR}{\alpha}\frac{1}{z}\frac{1}{\sqrt{\varepsilon}R}$$

- curvature contributes to growth law:

$$\frac{R}{t} = D\left[\frac{1}{\sqrt{\varepsilon}R} + \frac{R^2}{\alpha}\frac{2}{z^2}\frac{1}{\sqrt{\varepsilon}R}\right]$$

- gas transport means a displacement flow of liquid that must be included in the continuity / drainage equation:

$$u = u_{viscous} + u_{displacement}$$
$$= K_m \frac{\rho g R^2 \varepsilon^m}{\eta c^2}\left[1 + \frac{\sqrt{\delta_e}\gamma c}{\rho g}\frac{1}{z}\frac{1}{\sqrt{\varepsilon}R}\right] + \frac{1-\varepsilon}{\varepsilon}\frac{DR}{\alpha}\frac{1}{z}\frac{1}{\sqrt{\varepsilon}R}$$

free drainage for ε_o=0.08

- volume of drained liquid vs time
  - measure height of liquid under foam (circles)
  - measure $\varepsilon(z,t)$ and integrate (crosses)
  - numerically solve PDE's (solid curves)

    (D=0 case shown as dotted curve)

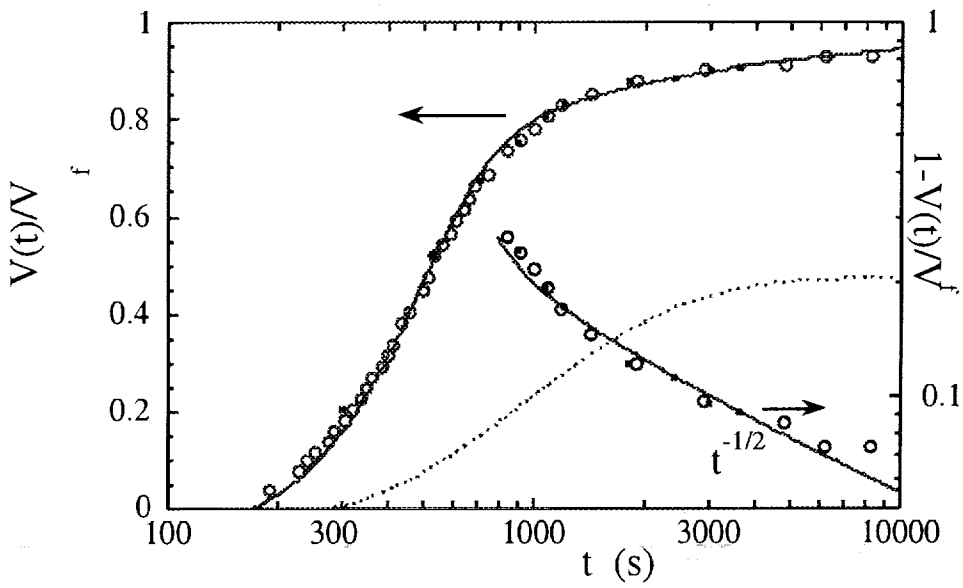

- $t^{-1/2}$ asymptote is easy to understand
  - volume of liquid remaining in sample is of order $\varepsilon_c A\gamma/(\rho g R)$ with $R\sim(Dt)^{1/2}$

    (i.e. liquid is released only as the foam coarsens)

evolution of R(z,t) & ε(z,t) profiles

- video microscopy and DTS (solid)
- numerical solution of PDE's (dashed)

time sequence: red …black corresponds to t = 60, 120, 300, 540, 1080, 2400s

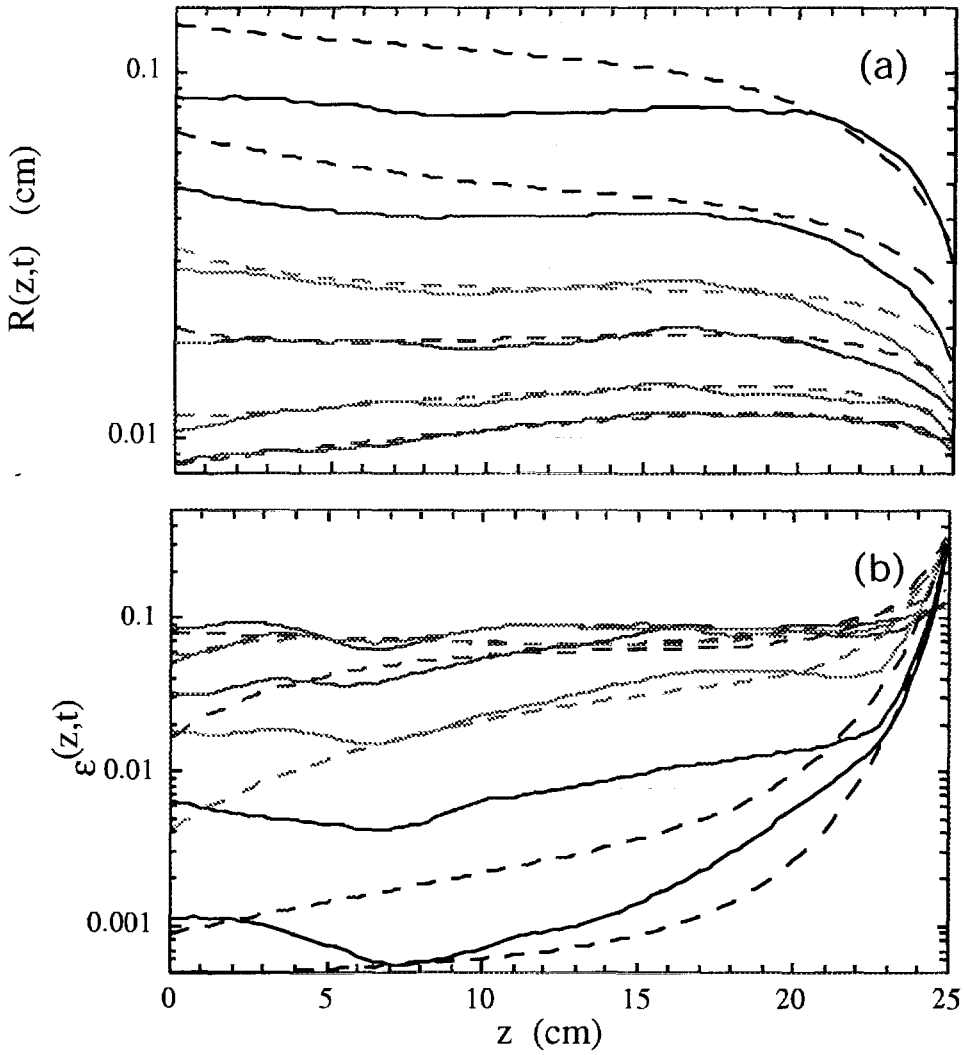

CONCLUSIONS

- bubble-packing geometry of foams
  - Plateau borders
    - contain most of the liquid, $\varepsilon \sim (r/R)^2$
    - scatter light, $l^* \sim R/\varepsilon^{1/2}$
    - provide channel for fluid flow
  - films
    - if mobile (Koehler, Hilgenfeldt, Stone)
      - shear flow inside vertices
    - if rigid (Weaire et al.)
      - shear flow inside Plateau borders
- gravitational drainage of aqueous foams
  - unavoidably coupled to coarsening
  - much faster than otherwise expected
  - growth law: $\frac{R}{t} = D \frac{1}{\sqrt{\varepsilon} R} + \frac{R^2}{\alpha} \frac{2}{z^2} \frac{1}{\sqrt{\varepsilon} R}$
  - displacement flow: $u = \frac{1-\varepsilon}{\varepsilon} \frac{DR}{\alpha} \frac{1}{z} \frac{1}{\sqrt{\varepsilon} R}$

$ the financial support from NASA is gratefully acknowledged

Foam Evolution: Experiments and Simulations

H. Aref, J.M. Sullivan, S.T. Thoroddsen
Theoretical and Applied Mechanics, and Mathematics
University of Illinois, Urbana

We describe several areas of work on the fluid physics of foam evolution and flow, including experimental observations, mathematical models, and numerical simulations. We have made detailed observations of the topological reconnections that occur in an evolving foam, and propose a new model for the flow there. We describe the phase transition which can happen as a foam is expanded until it exerts negative pressure on its container. We are exploring new optical tomography techniques to observe an evolving foam and reconstruct the three-dimensional structure. We compare the evolution of a real foam with simulations in Brakke's Evolver. We can also simulate infinite periodic foams, including new mathematical possibilities for TCP structures.

RECONNECTIONS

The Plateau rules say that in any froth or foam, bubbles meet in threes along the so-called Plateau borders; these curves then meet in fours at the nodes. As a foam evolves (mainly due to diffusion of gas between the bubbles) the nodes will sometimes meet, resulting in a combined node not obeying the Plateau rules, which thus immediately breaks apart into several nodes, connected by a new film or Plateau border which expands very rapidly.

Using high-speed video equipment, we have made accurate observations of these reconnection events, which happen over time scales less than a tenth of a second. We observed reconnections in coarsening foams, but also in a special adjustable triangular-prism wire frame which allows control of a single reconnection. We note that the wetness (or liquid fraction) can have a great effect on the speed and sequence of reconnections, since it changes the size of the Plateau borders and nodes..

We have used our experimental data to construct a simple dynamical model for a reconnection event, incorporating Marangoni effects which are due to the rapid stretching of the surface and the resultant change in surfactant concentration.

In a coarsening forth, the slow diffusion of gas between adjacent bubbles of differing pressure is punctuated by these rapid reconnections. Because each reconnection makes a large local change in geometry, it is likely to lead immediately to further reconnections. Thus reconnections occur in avalanches. We have recorded, with multiple video cameras, the evolution of a coarsening foam over a period of days, and scanned the tapes to collect statistics about these avalanches.

PHASE TRANSITIONS

The structure of a foam results from a balance between pressure in the gas bubbles and surface tension in the liquid films. Under normal conditions, a foam in a box exerts an outward force on the walls of the box, due to the pressure. But when surface tension is much more important (for instance if the foam is greatly expanded from its original volume), the net force on the walls will be inward. This means that the ambient pressure of the foam should be considered negative.

In this regime of negative pressure, an interesting phase transition can happen. The bubbles segragate into two phases, one consisting of a few huge bubbles, and the other consisting of many small bubbles. We have developed a theory to explain this phase transition, which agrees very well with simulations made in the Evolver. We hope to find an appropriate physical system with which we can experiment with this transition.

In many real-world applications of foams, it is very important to control the size of the foam cells: large voids typically make a foamed material much less useful. It seems likely that the undersirable large cells sometimes found in real foams are the result of the phase transition we have described. A better understanding will hopefully lead to processing techniques which can avoid this transition.

TOMOGRAPHY

In collaboration with David Brady of the Beckman Institute's imaging group, We have started an project to use visible-light tomography to capture the three-dimensional structure of a foam. Preliminary results are promising: under appropriate lighting conditions the tomographic Radon transform results in a volumetric density profile from which Plateau border positions can be extracted.

We have already written and tested software which will reconstruct the entire foam structure (suppplying information about the faces and cells) from the Plateau borders (or perhaps just the node positions) alone. This uses the known geometry of foams (with equal angle conditions guaranteed by the Plateau rules) to find successively the edges, faces, and cells, and outputs these in Evolver format.

The tomographic process will allow us to automatically track the coarsening of a foam over a period of many hours, and compare this with a simulation of diffusive coarsening in the Evolver. There are many interesting questions about the statistics of cell growth in three dimensions; we will be able to address these.

SIMULATIONS AND TCP STRUCTURES

We have recently discovered new mathematical constructions for foam structures in the class known as tetrahedrally close-packed (TCP). These are interesting in that the least-energy (ground state) configuration for a foam with equal-volume cells is evidently one of the simplest TCP structures (though this remains unproven mathematically).

Our new structures form an interesting intermediate class, inbetween random foams and completely ordered foams (like Kelvin's foam). We can model them in the Evolver, and use them as interesting starting points for diffusion simulations.

NASA/CP—2000-210470

Foam Evolution:

Experiments and Simulations

H. Aref, J.M. Sullivan, S.T. Thoroddsen
Theoretical and Applied Mechanics, and Mathematics
University of Illinois, Urbana

2000 August 10

Foam Evolution and Flow:

- Topological reconnections
- Phase transitions
- Visual-light tomography
- Numerical simulations
- New TCP structures

NASA/CP—2000-210470

NASA/CP—2000-210470

Reconnections:

- Foams evolve (diffusion, etc) at slow time scales
- When nodes meet, Plateau rules are violated
- New films and borders appear, and expand to equilibrium
- Reconnections happen over time scales less than 100ms

Reconnections

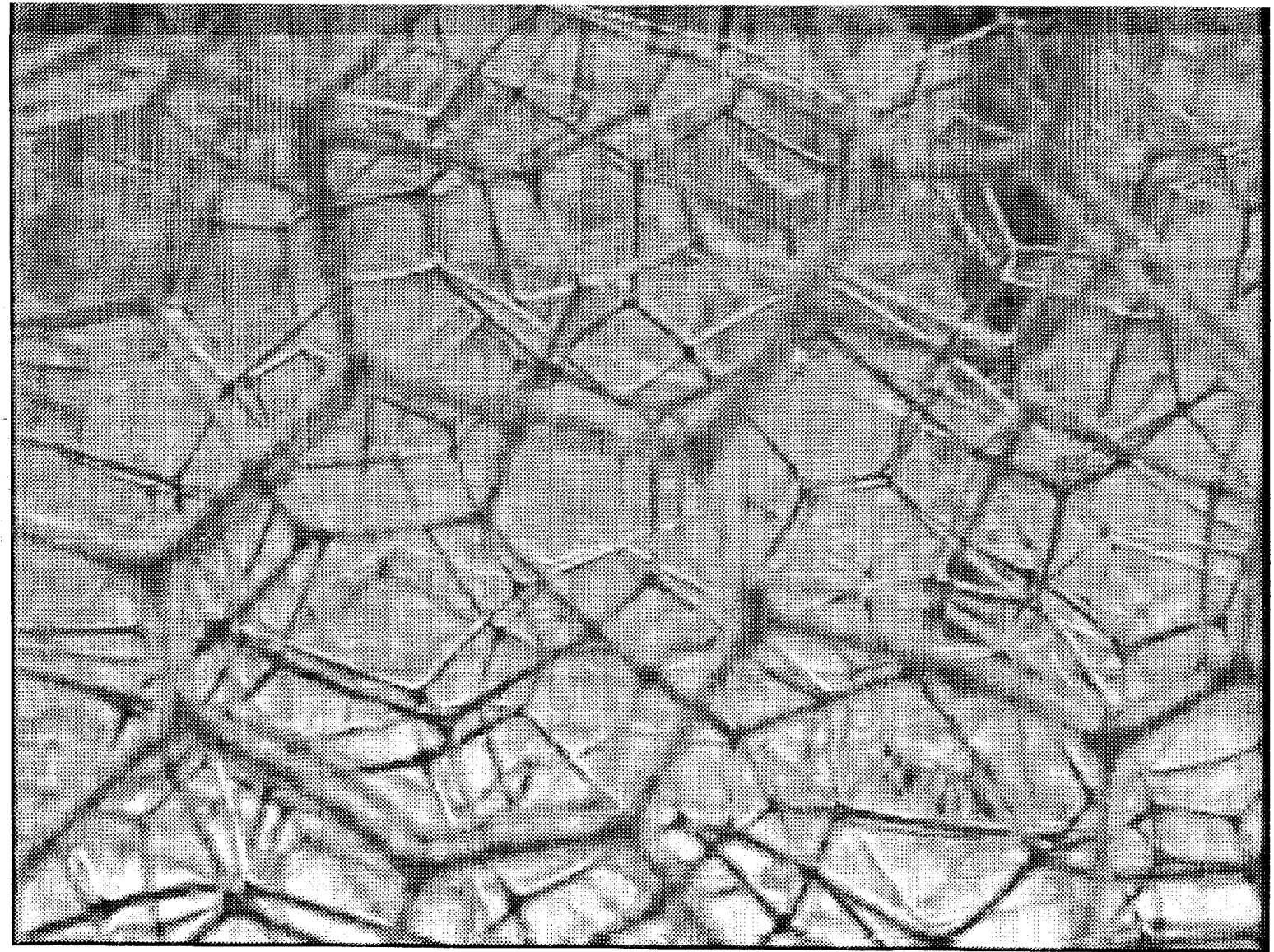

Reconnections

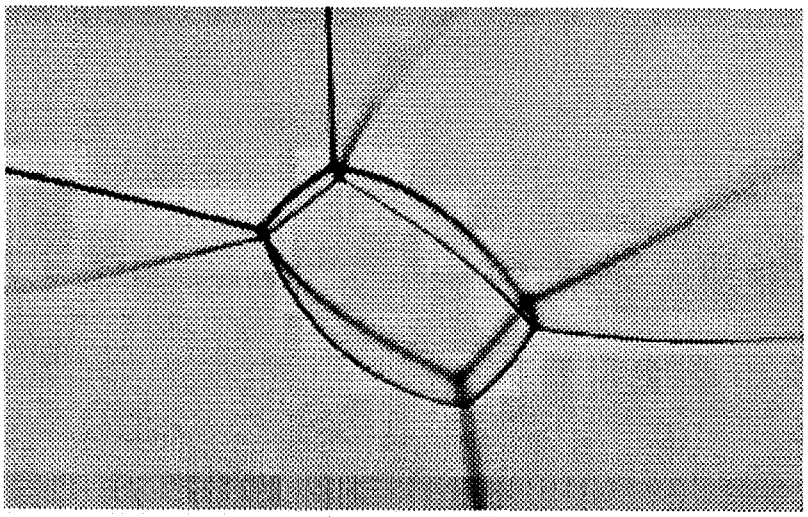

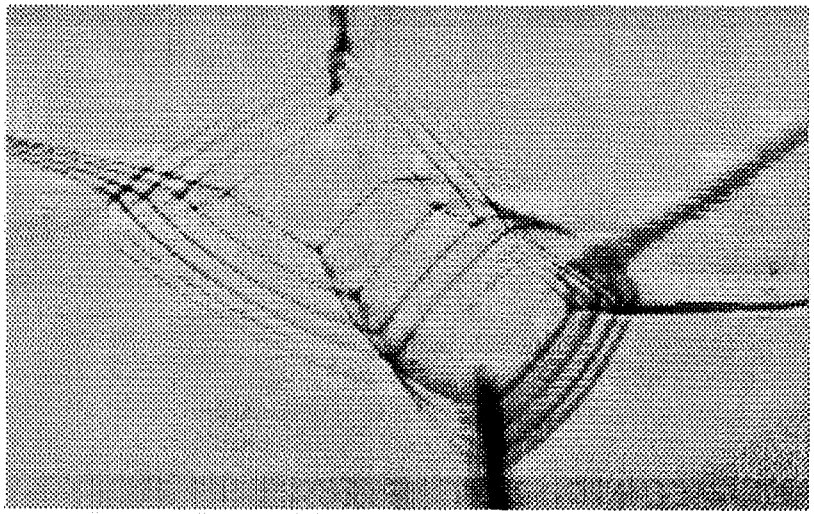

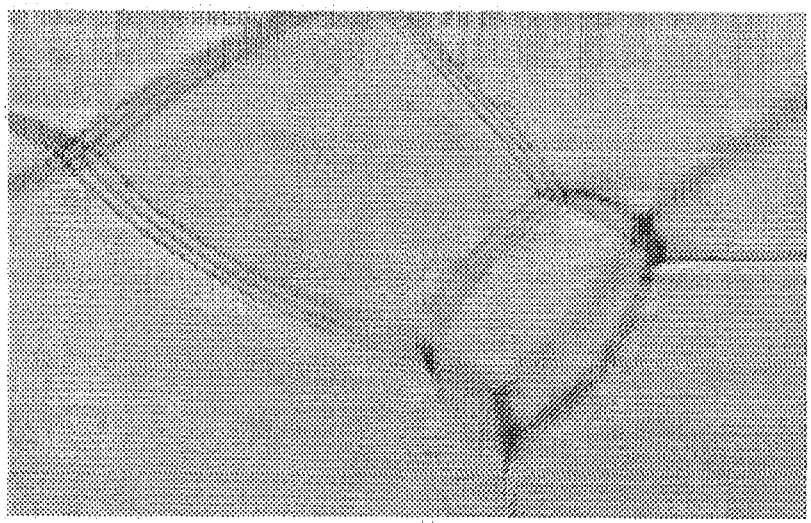

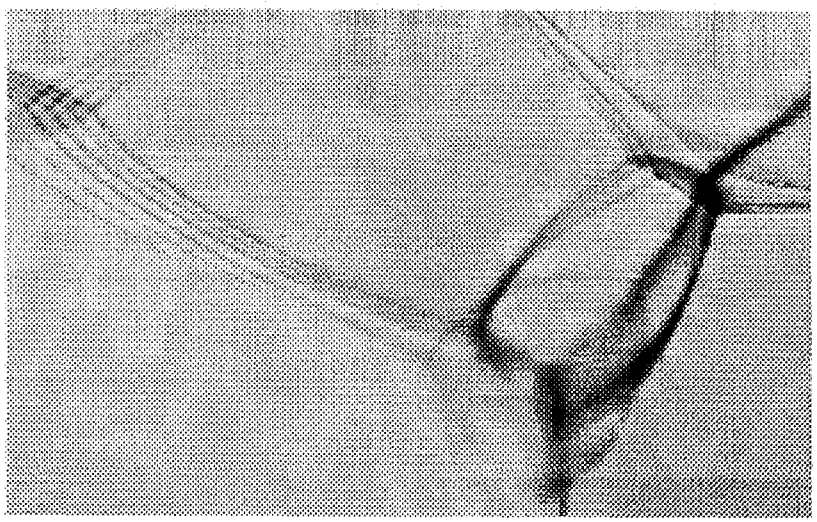

NASA/CP—2000-210470

Experiments:

- High-speed video camera
- Coarsening foams & adjustable wire-frame
- Avalanches of reconnections

Dynamical model:

- Incorporates Marangoni effects
- Adjusted to fit experiments

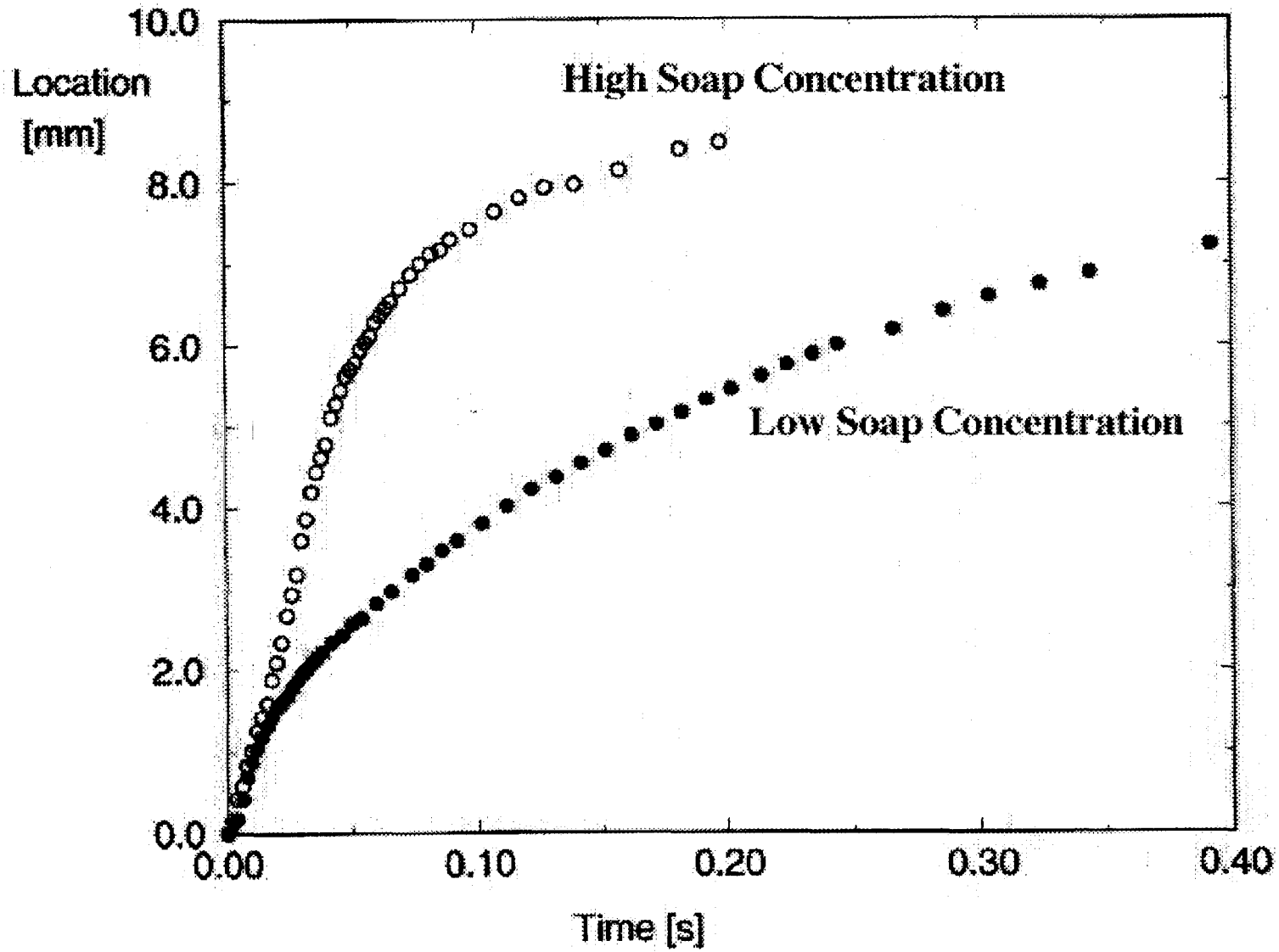
10.0
Location
[mm]
8.0
6.0
4.0
2.0
0.0
High Soap Concentration
Low Soap Concentration
0.00
0.10
0.20
0.30
0.40
Time [s]

Negative Ambient Pressure:

- gas very compressible
- surface tension high
- foam pulls inwards on container

Phase Transition:

- Bubbles separate into two phases
- Few huge bubbles at low pressure
- Many small bubbles at high pressure
- Theory agrees with numerical simulations

NASA/CP—2000-210470

Phase Transitions

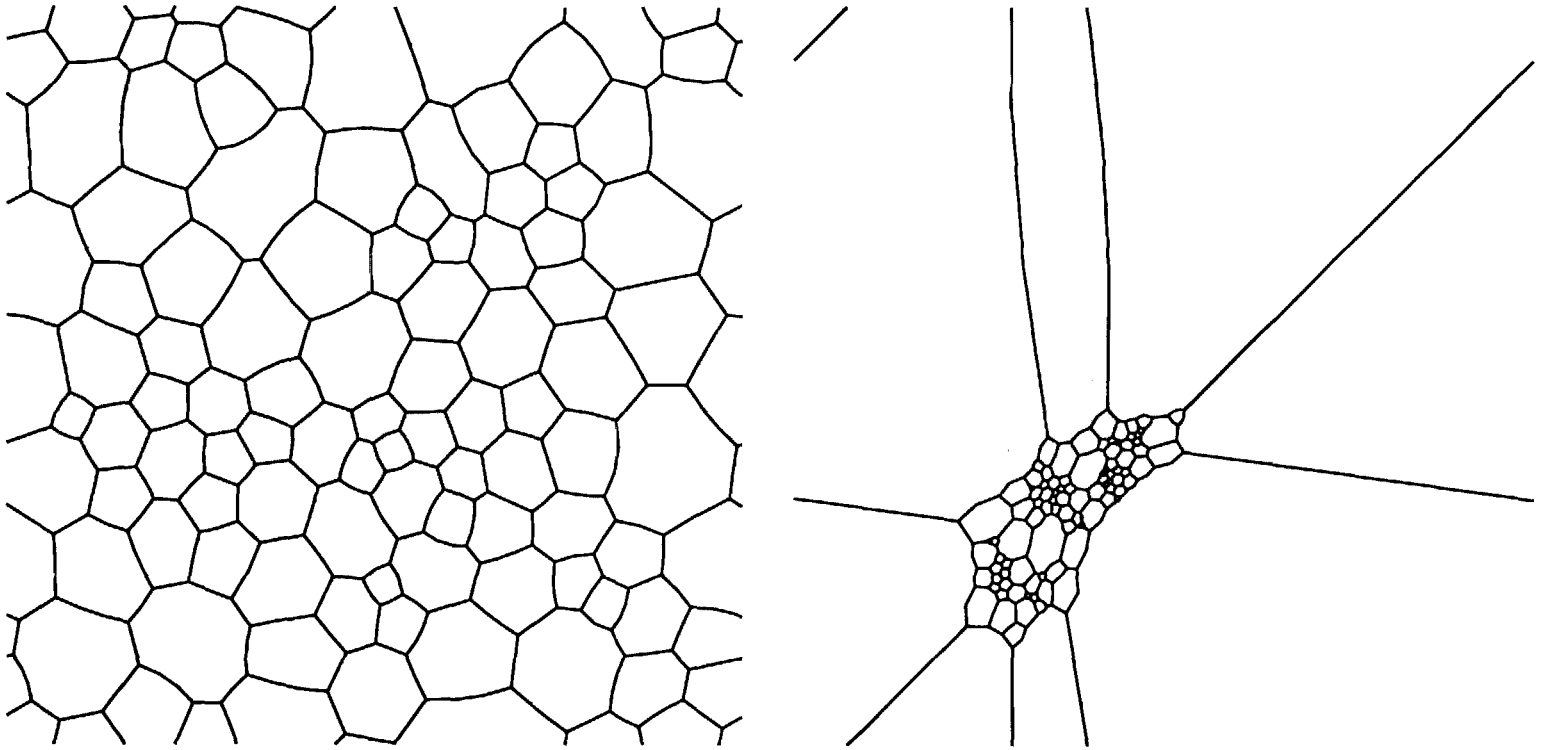

Phase Transitions

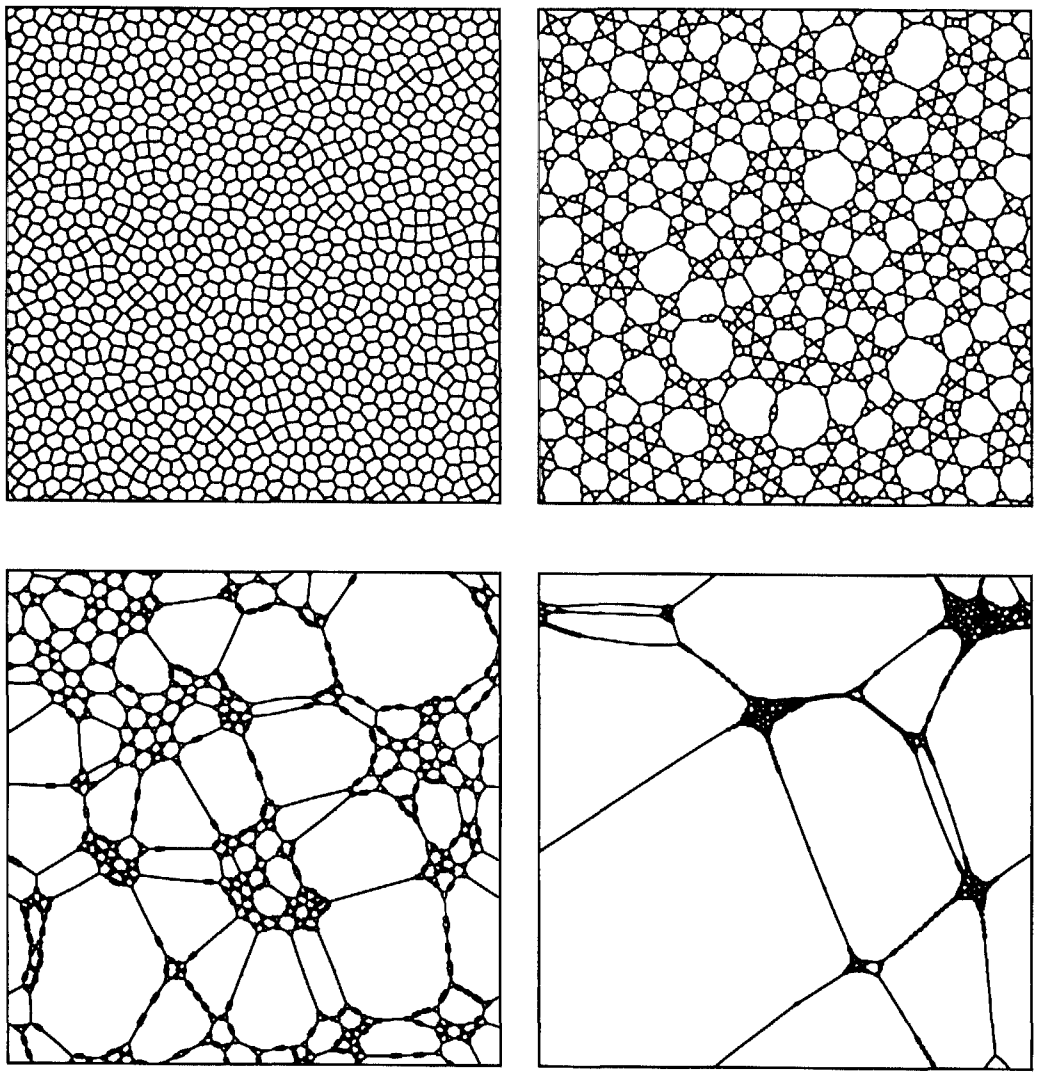

NASA/CP—2000-210470

Experimental setup:

- Cone-beam tomography
- Visible light
- Rotating foam in cylindrical container
- Correction for lensing effect

976

Tomography

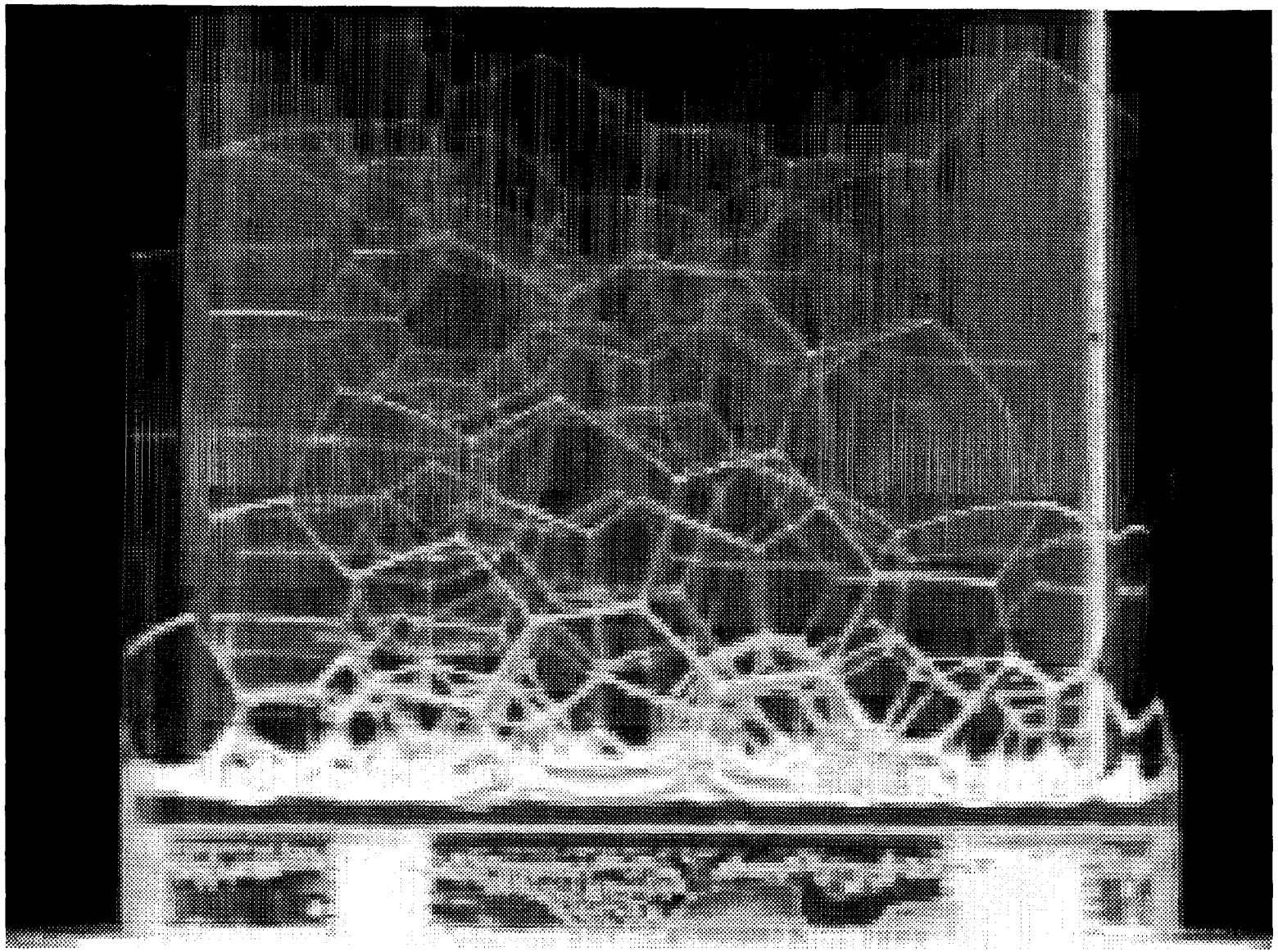

Tomography

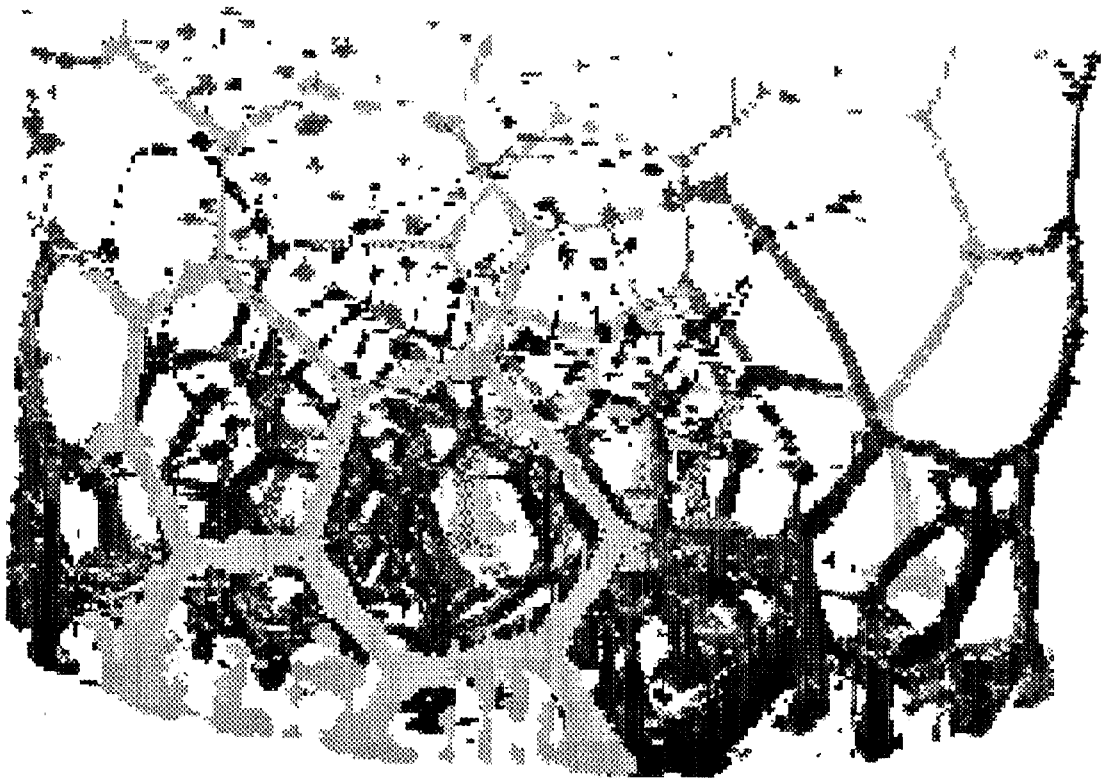

NASA/CP—2000-210470

Surface Evolver:

- Diffusion in 2d
- Varying surface tension in 2d
- Extensions to 3d

979

Simulations

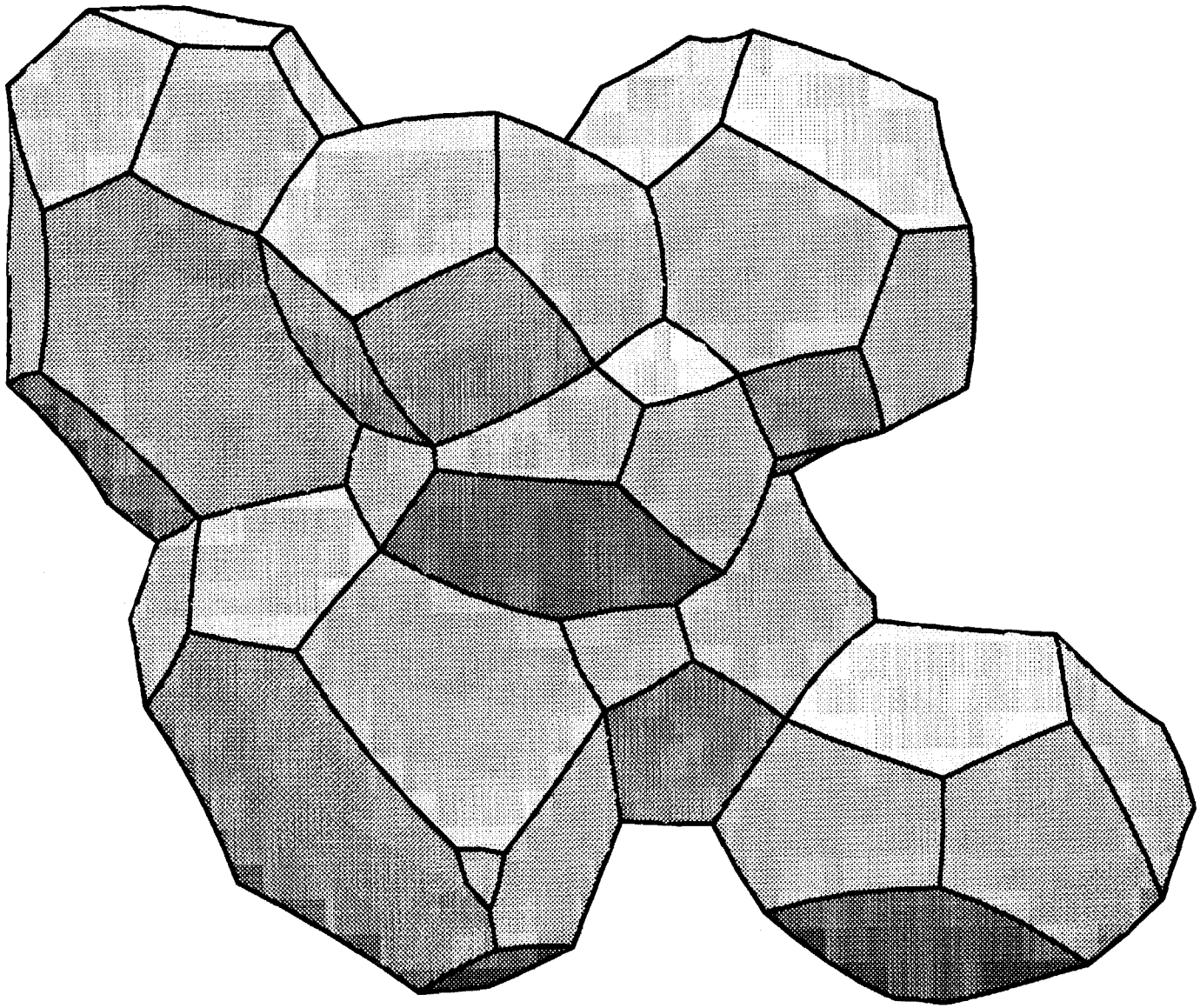

TCP structures:

- Large family of monodisperse foams
- Semi-random structures
- Mathematical interest

NASA/CP—2000-210470

TCP structures

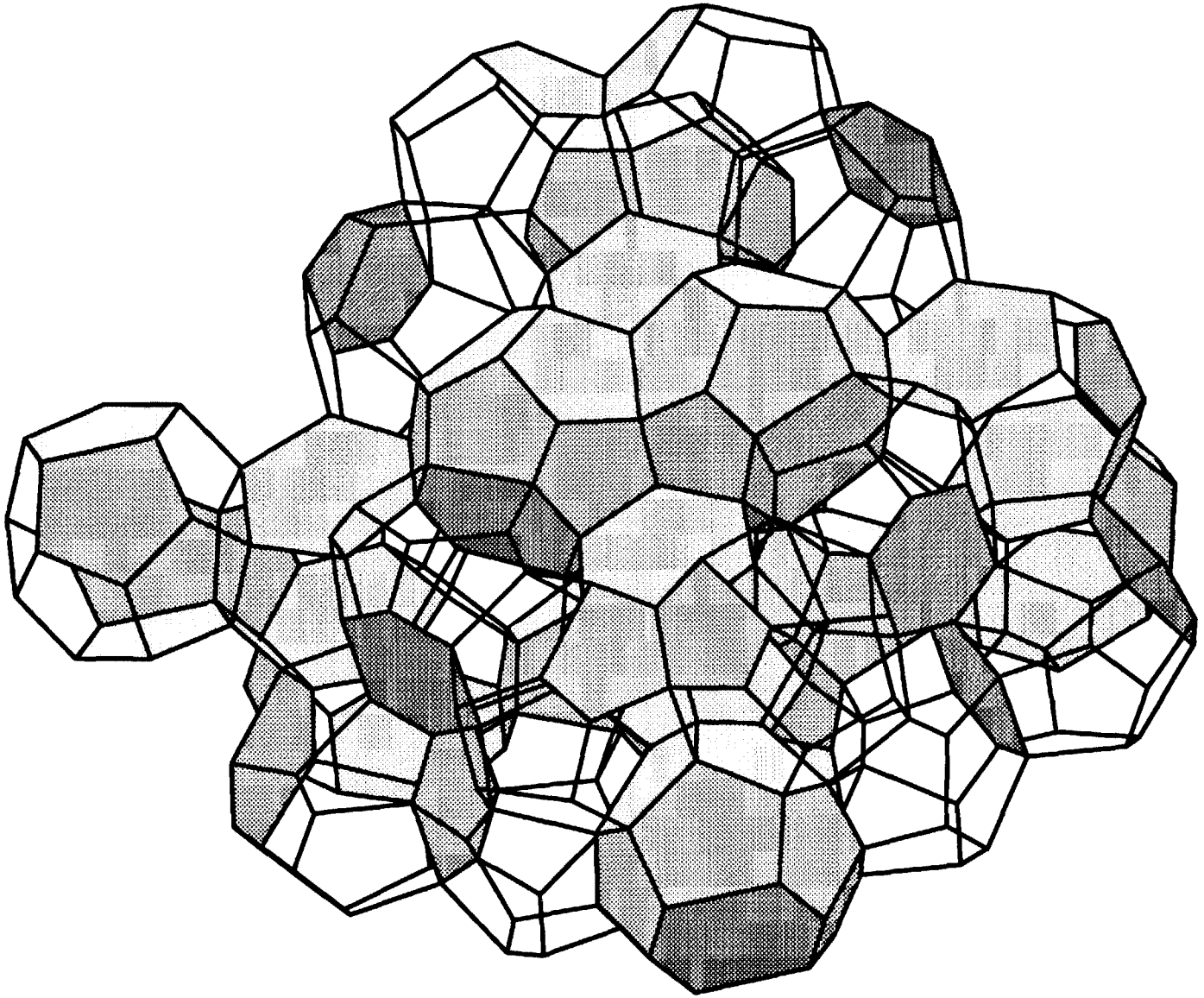

Thoroddsen & Tan, "The speed of topological rearrangements in foam", Bull. Amer. Phys. Soc. **44** (1999), p. 143.

Vainchtein & Aref, "Morphological transition in compressible foam", submitted to Phys. Fluids (July 2000).

Aref & Vainchtein, "The equation of state of a foam", Phys. Fluids **12**:1 (2000), p. 23-28.

Sullivan, "New Tetrahedrally Close-Packed Structures", Proc. Euroconf. on Foams, Delft (June 2000).

Fetterman, Tan, Sullivan, Thoroddsen, *et al*, "Tomographic Imaging of Foam", submitted to Optics Express (July 2000).

NASA/CP—2000-210470

Linear viscoelastic response of a concentrated emulsion

M. Nemer, J. Bławzdziewicand M. Loewen berg

Department of Chemical Engineering, Yale Universit y,New Hav en Connecticut, USA

Abstract

Analytical results for the dynamics of thin inextensible films [1] hav e been incorporated in theoretical models [2] and simulations [3] of the dynamics of two-dimensional systems. In three dimensions the effective-in terparticle-potential model has been supplemented by simple bubble-bubble frictional dissipation [4, 5]. Howev er,these models cannot describe the effect of detailed drop-scale dynamics on the evolution of the system. In general, the development of theories for the rheology of foams and emulsions will require a detailed understanding of the relevant drop-level dynamics. In this presentation, we describe a numerical inv estigation of the role of detailed drop-scale microphysics on the linear viscoelastic behavior of dense two-dimensional emulsions; Stokes equations are assumed and surfactant effects are neglected. We consider an ordered hexagonal lattice of drops for which the linear relation between stress and strain is isotropic [6]. The system is thus characterized by a single frequency-dependent linear viscoelastic modulus. F ordispersed-phase v olume fraction ϕ beyond a critical v alue $\phi_c = \pi/2\sqrt{3}$, the drops are in a state of compression.

F or small-amplitude shape perturbations$\delta\mathbf{x}$, the response of the system of the system is linear

$$\frac{d(\delta\mathbf{x})}{dt} = \mathbf{A}\,\delta\mathbf{x}, \tag{1}$$

where the linearized v elocity operator $\mathbf{A}$ is obtained b y solving the Stokes equations with the boundary-integral method [7]. By projecting the normal modes of $\mathbf{A}$, onto a step strain perturbation, the corresponding contribution to the shear stress is calculated.

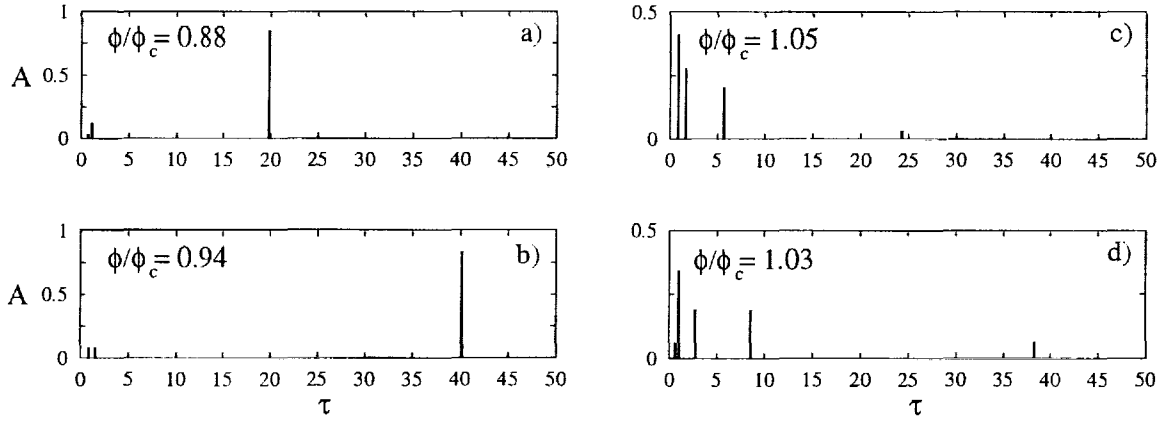

Figure 1: Relaxation spectra: normalized amplitudes A verses relaxation times τ for the indicated volume fractions. Relaxation times are normalized by capillary relaxation time $\mu a/\sigma$, where μ is the contin uous-phase viscosit y,a is the drop radius, and σ is surface tension.

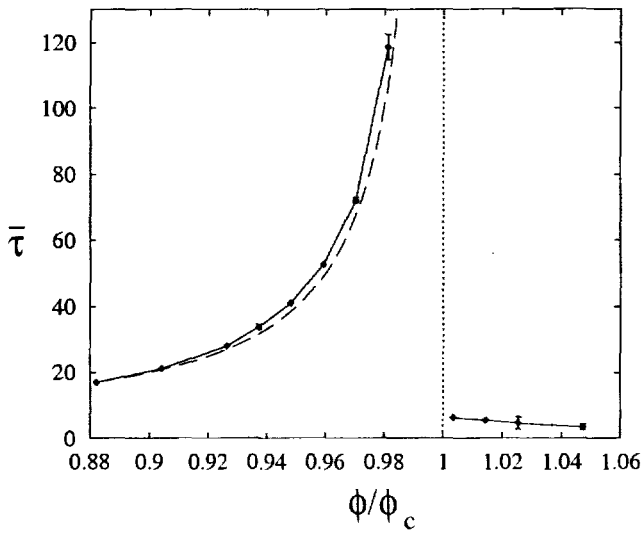

Figure 2: Average relaxation time, $\bar{\tau}$ defined by zeroth moment of relaxation spectrum versus volume fraction (solid line); lubrication theory (dashed line).

The relaxation times and amplitudes corresponding to the normal-mode decomposition are plotted in Figures 1a,b for two subcritical values of ϕ. Only a few modes are significantly excited. The dominant mode corresponds to the largest relaxation time, which is associated with the lubrication resistance between closely spaced drops, and diverges as $\phi/\phi_c \to 1$.

The relaxation times and amplitudes are plotted in Figures 1c,d for two super-critical values of ϕ. In this regime, the response of the system is dominated by decay on capillary relaxation time scale; a long time scale is evident but with small amplitude.

The average relaxation time $\bar{\tau}$ (zeroth moment of relaxation spectrum), shown in Figure 2, indicates that the average relaxation time diverges as $\phi \to \phi_c^-$. This behavior is associated with the lubrication singularity of the zero-frequency viscosity; according to a lubrication analysis, $\bar{\tau}$ diverges as a simple pole at $\phi = \phi_c$. By contrast, $\bar{\tau}$ is nonsingular for $\phi > \phi_c$.

References

[1] K. Shinoda K. J. Mysles and S. Frank el. *So ap Films: A study of Their Thinning and A Bibliography.* P ergamon, 1959.

[2] D. A. Reinelt and A. M. Kraynik. On the shearing flow of foams and concentrated emulsions. *J. Fluid Mech.*, 215:1235–1253, 1990.

[3] T. Okuzono and K. Kaw asaki. Rheology of random foams. *Journal of Rhe olo gy* 37:571–586, 1993.

[4] T. G. Mason, M. D. Lacasse, G. S. Grest, D. Levine, J. Bibette, and D. A. Weitz. Osmotic pressure and viscoelastic shear moduli of concentrated emulsions. *Physical Review E*, 56:3150–3166, 1997.

[5] D. J. Durian. Bubble-scale model of foam mechanics: Melting, nonlinear behavior, and avalanches. *Physical Review E*, 55:1739–1751, 1997.

[6] U. Frisch, B. Hasslacher, and Y. Pomeau. Lattice-gas automata for the navier-stokes equation. *Physical R eview letters*, 56:1505–1508, 1986.

[7] C. P ozrikidis. *Boundary Inte gral and Singularity Methods for Linearize d Visc ous Flow.* Cambridge University Press, 1992.

Presentation not available at time of printing.

DUSTY PLASMA DYNAMICS NEAR SURFACES IN SPACE

S. Robertson, A. Sickafoose, J. Colwell, M. Horányi
(LASP, University of Colorado, Boulder, CO 80309-0392)

ABSTRACT

Illumination of a space-borne object by solar ultraviolet light produces photoelectrons which form a layer, or sheath, near its surface. Typical sheath dimensions are tens of centimeters to one meter at distances of one AU. A vertical electric field, having a sign that returns electrons to the surface, is generated by the emission of photoelectrons into this sheath. Differential charging in a photoelectron layer over small spatial scales, such as along the terminator on a rough surface, leads to horizontal electric fields in addition to the vertical field. Dust grains on a planetary surface can enter the photoelectron layer by levitation or as a result of external disturbances. Levitation can occur when grains in the regolith become electrostatically charged such that the Lorentz force overcomes gravity and adhesive forces. Particles ejected from the surface by external disturbances, such as micrometeorite impacts or human/spacecraft activity, can become charged by photoemission and electron collection when immersed in a plasma. Therefore, particles levitated or ejected from the surface can be trapped in the photoelectron sheath and transported vertically and horizontally above the surface by the electric fields.

Dust grains suspended above the lunar surface have been observed on multiple occasions. A horizon glow tens of centimeters above the surface of the Moon was detected by Surveyors 5, 6, and 7 [1]. At spacecraft sunrise, Apollo astronauts observed high altitude streaks due to light scattered off particles extending from the lunar surface to above the spacecraft [2]. More recently, a horizon glow 10 to 20 km above the lunar surface was detected by the Clementine spacecraft [3]. Furthermore, the Lunar Ejecta and Meteorite Experiment (LEAM) deployed by Apollo 17 detected evidence for horizontal dust transport on the surface of the Moon at terminator crossings [4].

Dust transport is also important in planetary ring systems, as confirmed by Voyager's discovery of spokes in Saturn's B-ring in 1981. These features are most likely clouds of particles electrostatically levitated off the surfaces of larger bodies in the ring and into a plasma cloud created by meteoritic impacts. Many small, airless bodies in the solar system are coated with a dusty regolith; therefore, dust levitation and transport may occur on Mars, Mercury, planetary satellites, asteroids, comets, and even planetesimals [5,6,7,8]. Understanding dust charging and dynamics is thus crucial to interpreting observations of planetary bodies. In addition, surface activity can agitate dust and inject particles into the photoelectron layer, possibly causing contamination of instruments on planetary surfaces. Therefore, the charging and dynamics of dust near planetary surfaces is a necessary component of future manned and unmanned exploration of the solar system.

We have begun the investigation of dust charging and dynamics near surfaces in space by performing experiments in which dust grains are dropped through a beam of UV and dropped past a UV illuminated surface having a photoelectron sheath. The experiments are performed in vacuum, with illumination from a 1 kW Hg-Xe arc lamp having a spectrum extending to ~ 200

nm (~ 6.2 eV). The photoemitter is a 12-cm diameter zirconium plate, which also acts as a Langmuir probe to verify the properties of the photoelectron sheath. We have examined [9] photoelectric charging for particles 90-106 μm in diameter composed of zinc, copper, graphite, glass, SiC, lunar regolith simulant (JSC-1), and martian regolith simulant (JSC Mars-1). We find that the photoelectric charging properties of the metallic materials are consistent with charges calculated from the work function of the materials, the energy of incoming photons or photoelectrons, and the capacitance of the grains. Dust dropped through UV illumination loses electrons due to photoemission, while dust dropped past an illuminated surface gains electrons from the photoelectron sheath. The photoelectric charging properties of the non-conducting materials are difficult to interpret due to large amounts of triboelectric charging. However, the results suggest that the JSC Mars-1 is more susceptible to photoelectric charging than the JSC-1.

In a second experiment, a flat surface is coated in dust (JSC-1 or JSC-Mars-1) and a photoelectron layer is generated above it. Plasma sheath characteristics are determined through Langmuir probe and floating potential probe sweeps. A window in the top of the chamber allows investigation of dust levitation and charging properties as a function of ultraviolet illumination. An agitator under the surface provides external disturbances to eject dust into the photoelectron layer. The charges of individual dust particles in the sheath can be measured by a Faraday cup, and tungsten filaments are used for ambient plasma production. The topography of the surface can be easily altered to simulate a terminator region, in order to create strong horizontal electric fields within the sheath. Dust levitation and transport in the sheath is observed by a CCD camera.

These ground-based studies of dust dynamics near surfaces in space provide information on the transport of micron-sized particles. Particles of this size are in the transitional range between gravitational and electromagnetic control on a planetary surface. A microgravity environment will allow continuation of the experiments to smaller particle sizes. In microgravity, the ratio of electrostatic forces to gravitational forces is high, so the environment will also be more like that of small, dusty planetary bodies. Thus, this research provides a set of experimental techniques upon which subsequent microgravity experiments will be based.

REFERENCES

[1] J.J. Rennilson and D.R. Criswell, The Moon **10**, 121 (1974).
[2] J.E. McCoy, and D.R. Criswell, Proc. 5th Lunar Conf., 2991 (1974).
[3] H.A. Zook, A.E. Potter, and B.L. Cooper, Lunar Planet. Sci. Conf. **26**, 1577 (1995).
[4] O.E. Berg, F.F. Richardson, and H. Burton, NASA Spec. Publ. SP-330, 16 (1973).
[5] R. Grard, Icarus **114**, 130 (1995).
[6] W.H. Ip, Geophys. Res. Lett. **13**, 1133 (1986).
[7] P. Lee, Icarus **124**, 181 (1996).
[8] D.A. Mendis, J.R. Hill, H.L.F. Houpis, and E.C. Whipple, Jr., Astrophys. J. **249**, 787 (1981).
[9] A.A. Sickafoose, J.E. Colwell, M. Horányi, and S. Robertson, Phys. Rev. Lett., in press.

Dusty Plasma Dynamics Near Surfaces in Space

Scott Robertson

Amanda Sickafoose

Joshua Colwell

Mihály Horányi

Laboratory for Atmospheric and Space Physics

University of Colorado

Boulder, CO 80309-0392

The Fifth Microgravity Fluid Physics and Transport Phenomena Conference

Sheraton Cleveland City Centre Hotel

Cleveland, Ohio, USA

August 9-11, 2000

Outline

I. Motivation
   a. Ring dynamics
   b. Lunar exosphere
   c. Surfaces of asteroids, small moons
   d. Operations in a dusty environment

II. Lab experiments
   a. Isolated dust photoemits
   b. Dust above surfaces collects electrons
   c. Shaken dust has triboelectric charge
   d. Levitation

III. Microgravity experiments

Why microgravity?

Forces:

Inertia

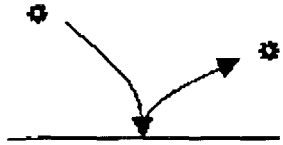

Gravity

Electrostatic

Adhesion

Cohesion

On earth:

Gravity may exceed electrostatic force

$mg > qE$

$m \propto r^3$, $q \propto r$, inequality depends upon size of dust grain

The Moon:

$mg \approx -qE$ at 10 microns, at the surface

at 0.1 microns, at 100 km (E is less)

Asteroids, rings: $mg << qE$,

$qE <$ adhesion, cohesion

What experiments can we do?

In the lab: magnitude of q

magnitude of E above a photoemitter

dust releases when qE exceeds mg

(requires unrealistic E)

In microgravity:

when qE exceeds adhesion, dust levitates or escapes

when qE exceeds cohesion, aggregates disperse

varying illumination releases particles

release of dust by impacts

Surveyor 3

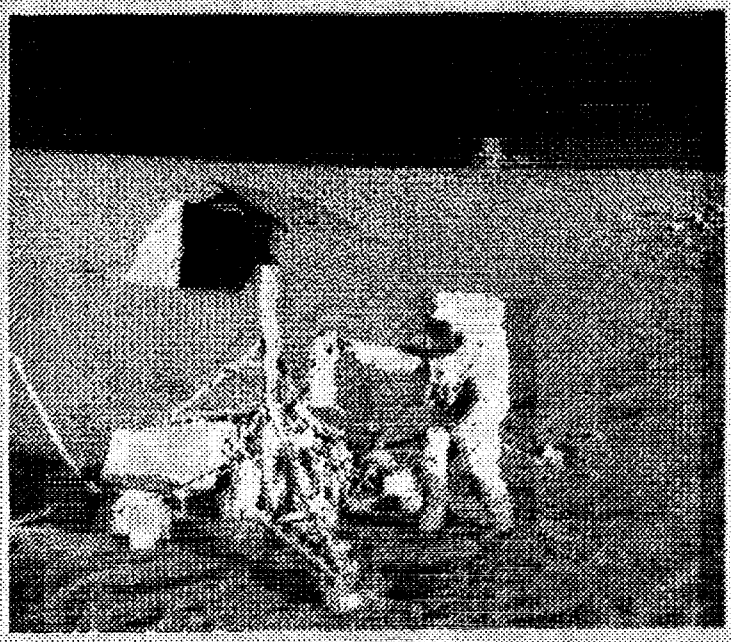

Apollo 12 1969

Instruments photographed horizon glow Horizon glow 10 to 30 cm above the surface

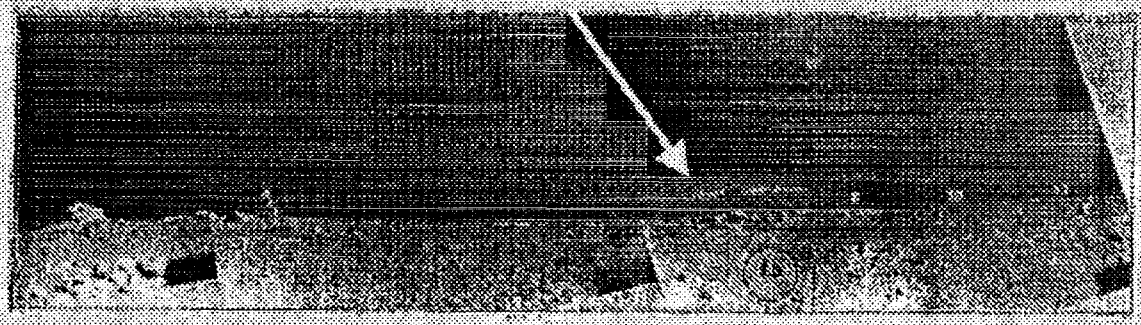

Surveyor 7

Data indicate forward scattering from grains <10 microns

Lunar Horizon Glow

Apollo 17 Astronaut Sketches

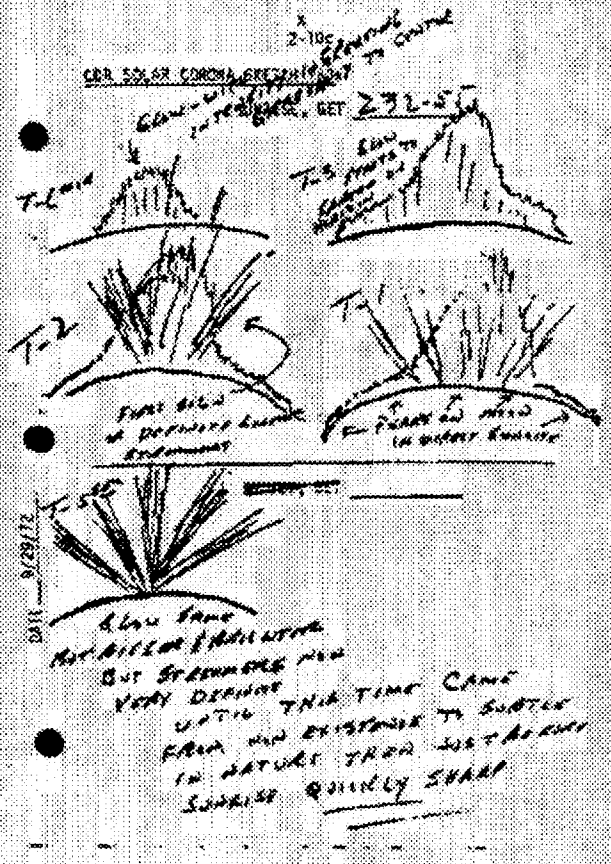

Conclusion: Dusty exosphere,
0.1 micron grain size

Clementine Photo

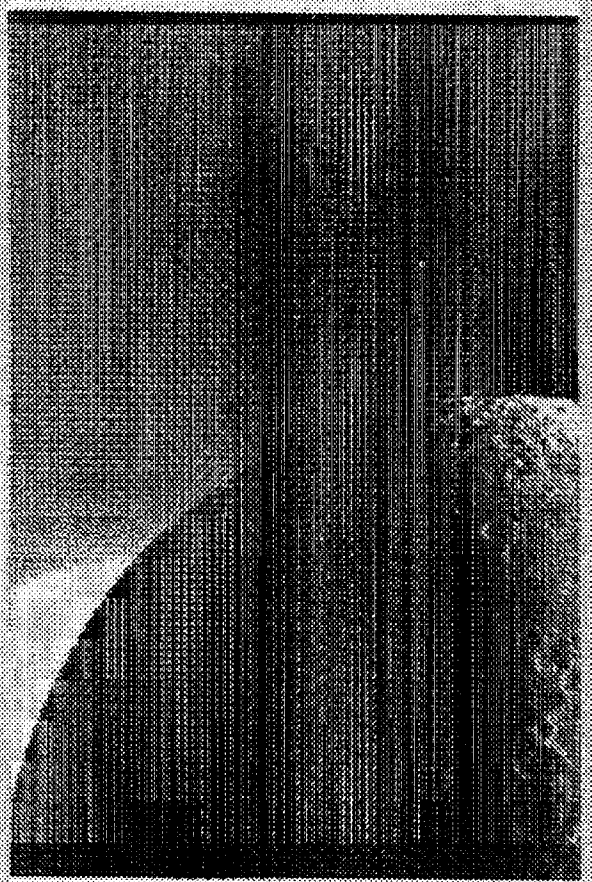

Scale height: 10 km

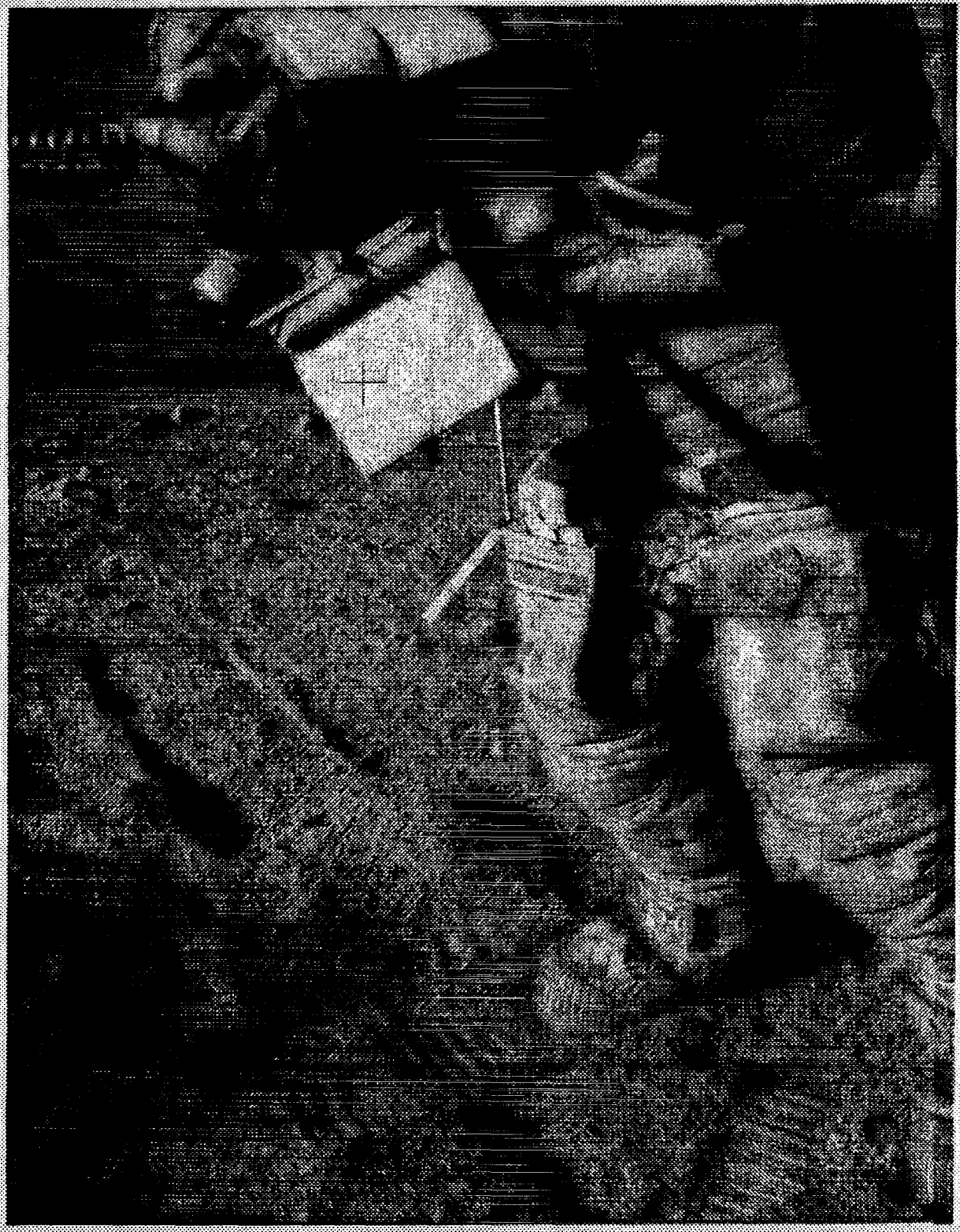

Apollo 15 astronaut suit covered in lunar dust

LEAM instrument detected dust impacts

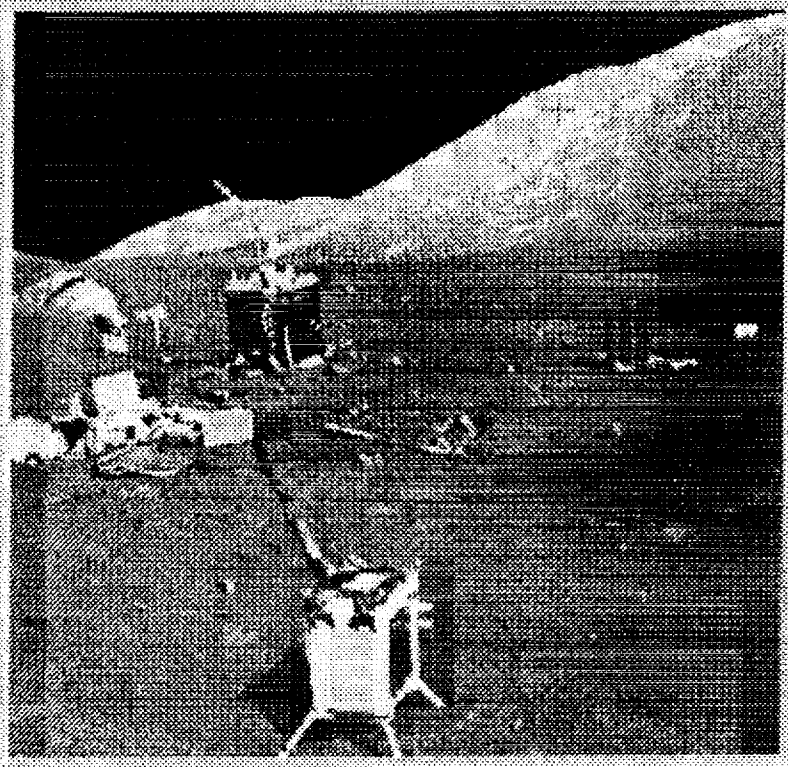

Dust impacts occurred at sunset and sunrise

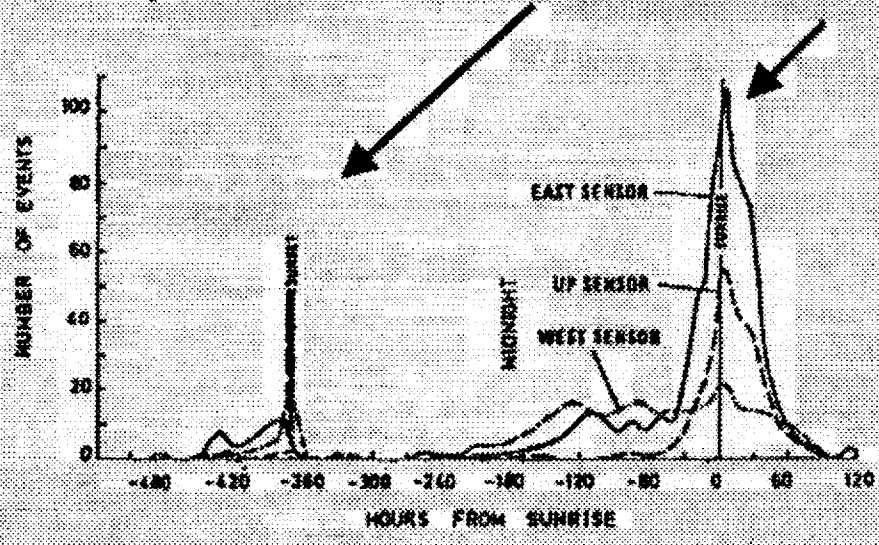

Photoelectric charging caused dust transport.

The dust charging apparatus

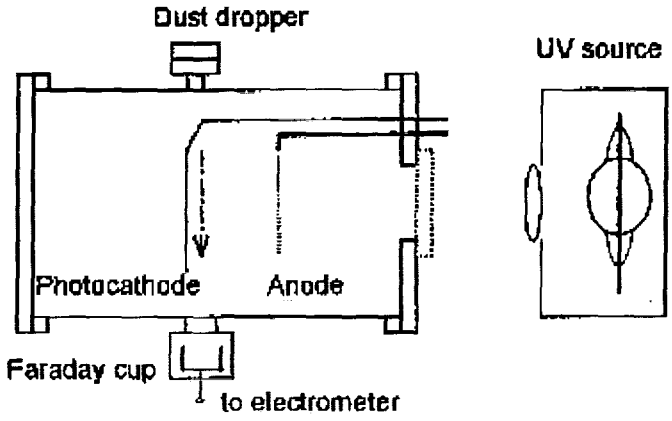

Charge on a dust grain is measured by the Faraday cup

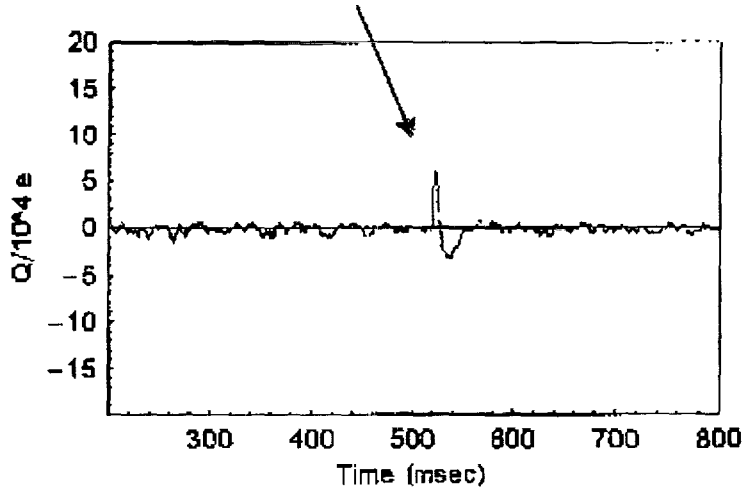

This grain has 50,000 electrons

The dust charging apparatus

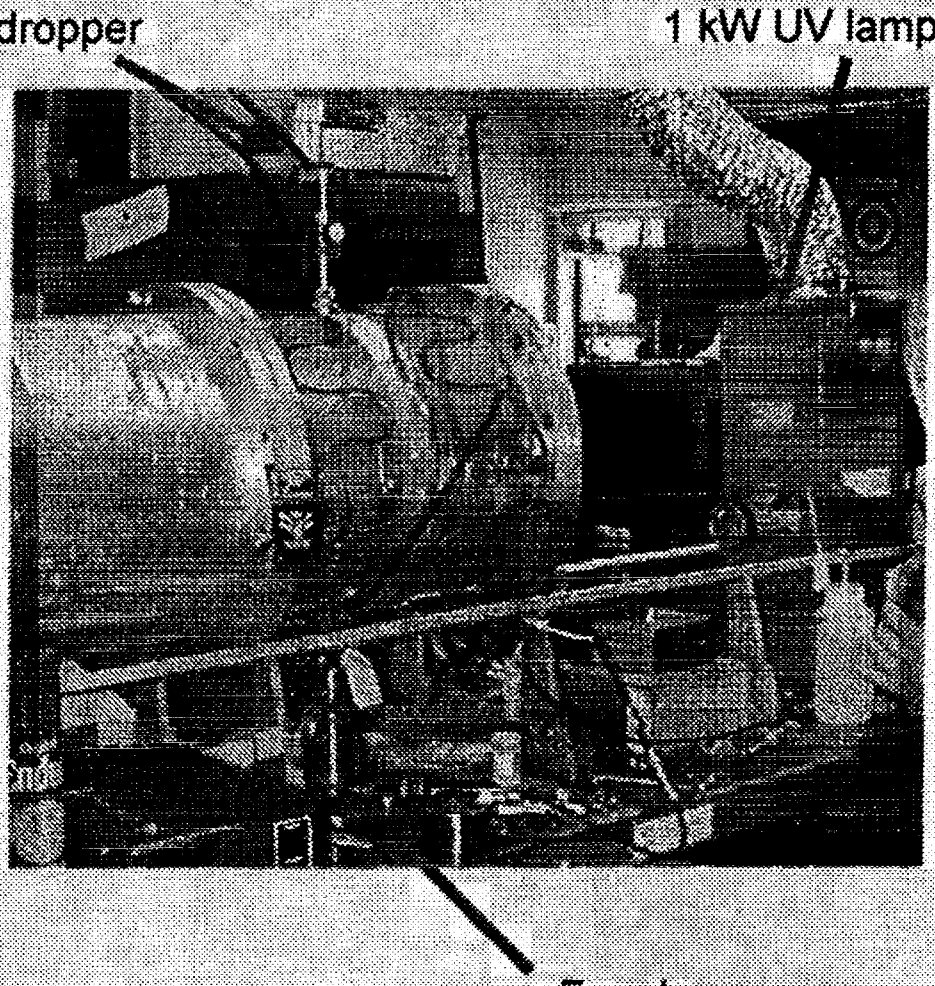

Photomicrographs of dusts

Scale = 100 microns/big division

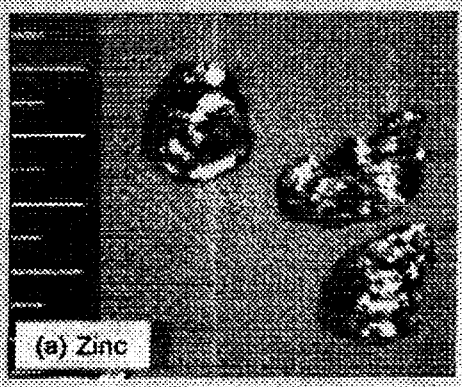

Zinc is selected for high photoelectric yield.

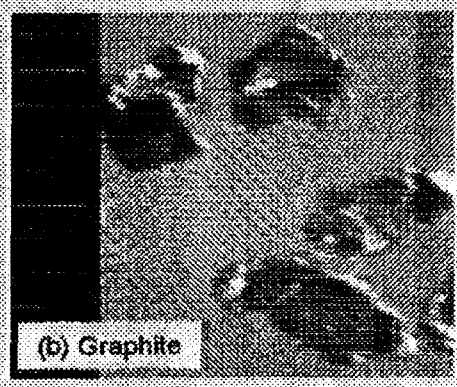

Graphite is selected for low photoelectric yield.

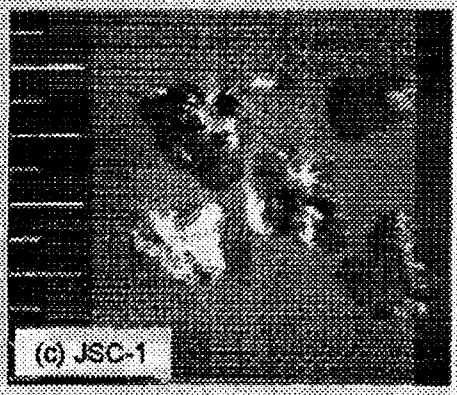

JSC-1 is a lunar regolith simulant

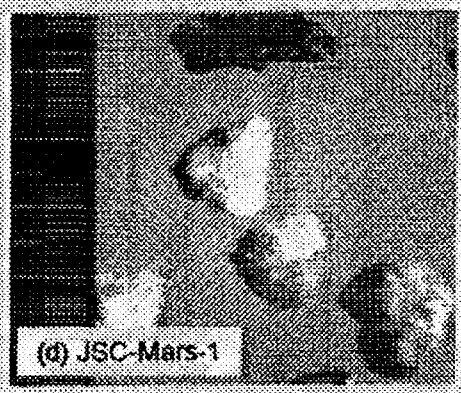

JSC-Mars-1 is a Mars regolith simulant.

Simulation of electron "gas" above the illuminated surface

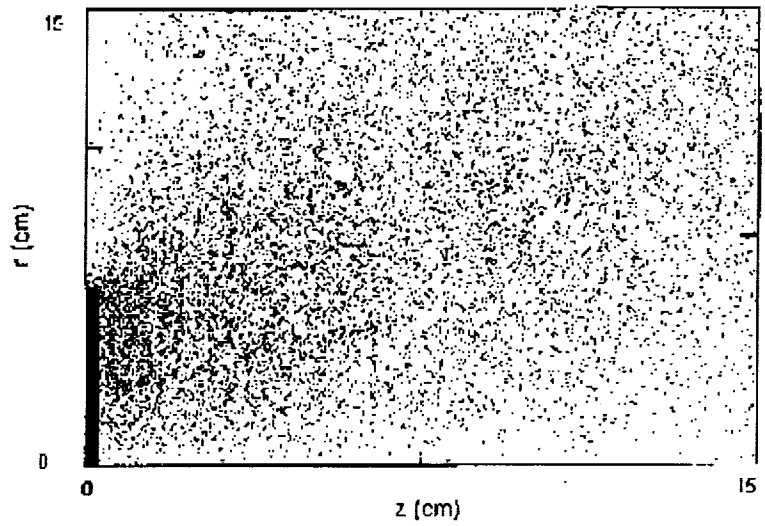

Electron density above the illuminated surface

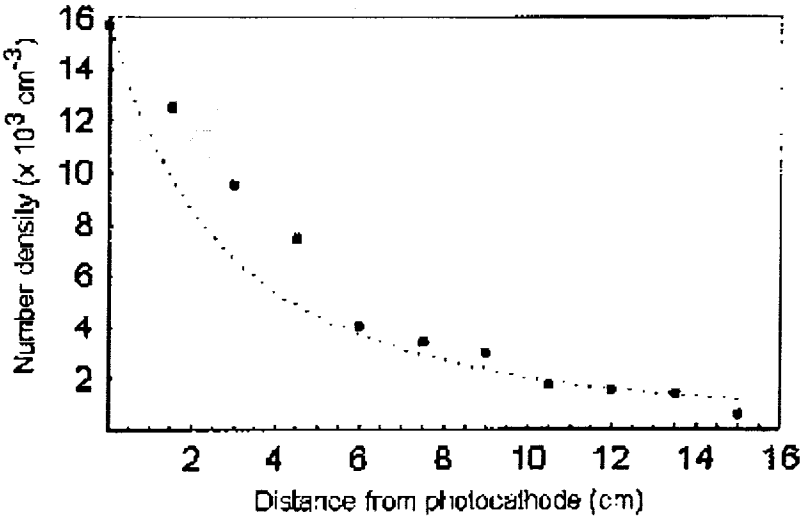

Dotted line is from photoelectron sheath theory.

Grains dropped through UV beam charge positively

(lose electrons by photoemission)

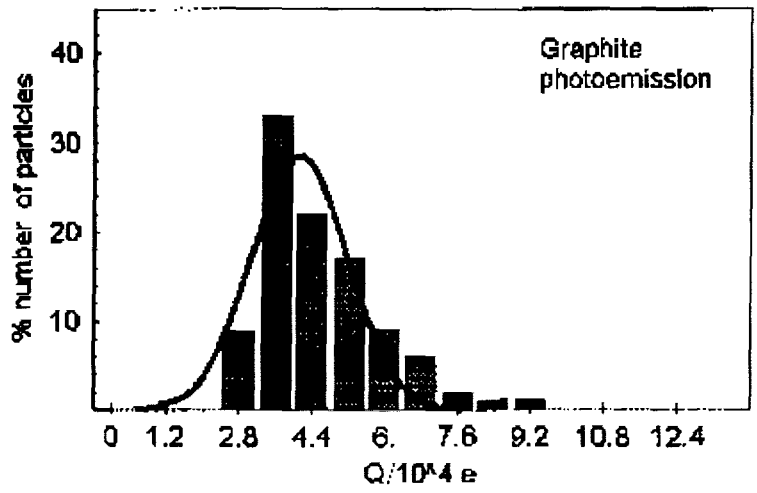

Grains dropped past illuminated surface charge negatively

(Accumulate electrons)

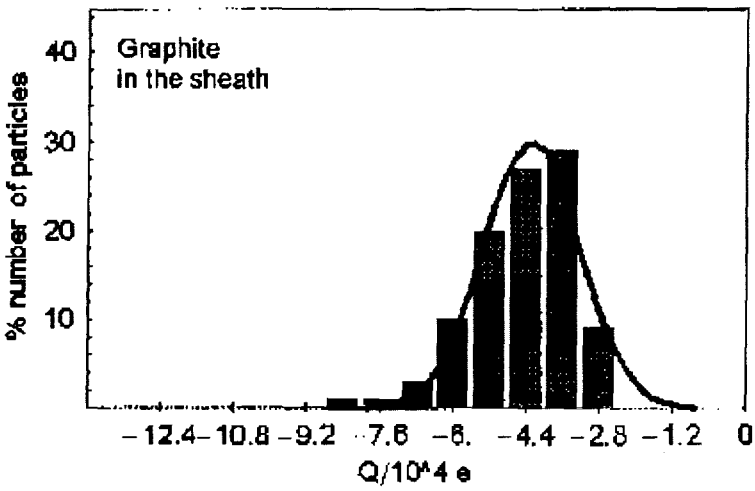

Mars regolith simulant shows triboelectric charge

With *NO* UV

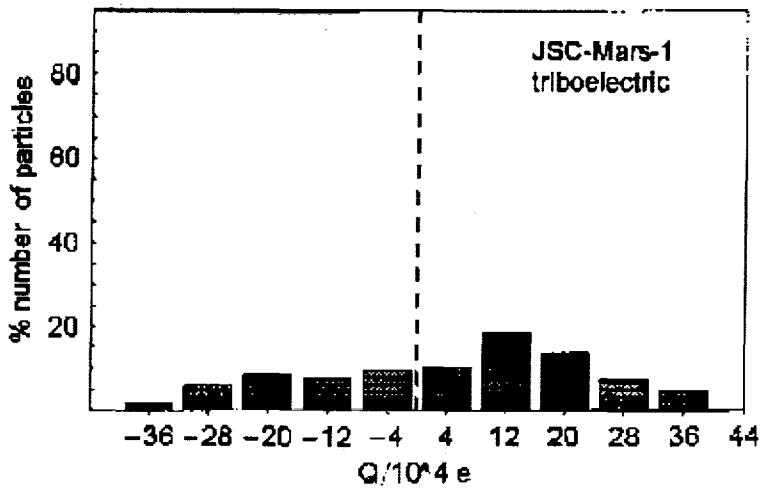

When dropped past a photoemitting surface

JSC-Mars-1 has negative charge (acquires electrons)

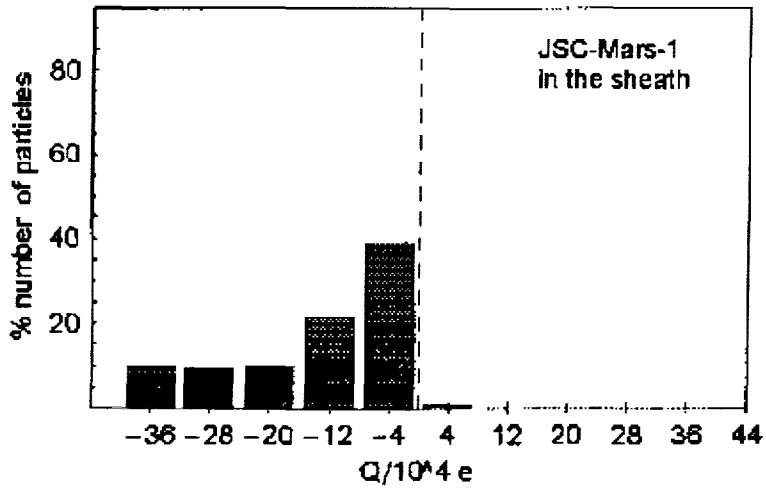

There are no positive grains because these attract electrons which neutralize the charge.

Charge on zinc grains changes sign with distance from an illuminated surface

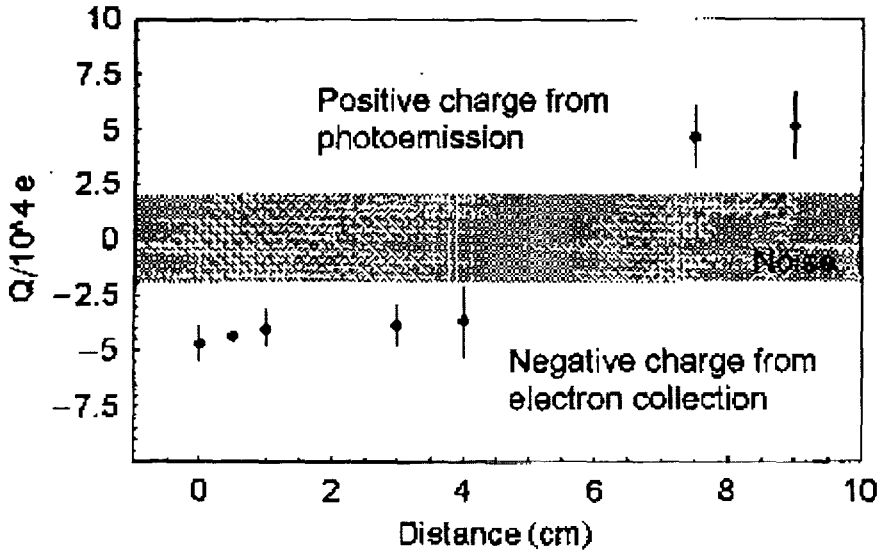

More distant grains have the sign of charge to be levitated. Grains close to the surface do not.

Lunar dust cloud is explained!

Dust levitation experiment (in progress)

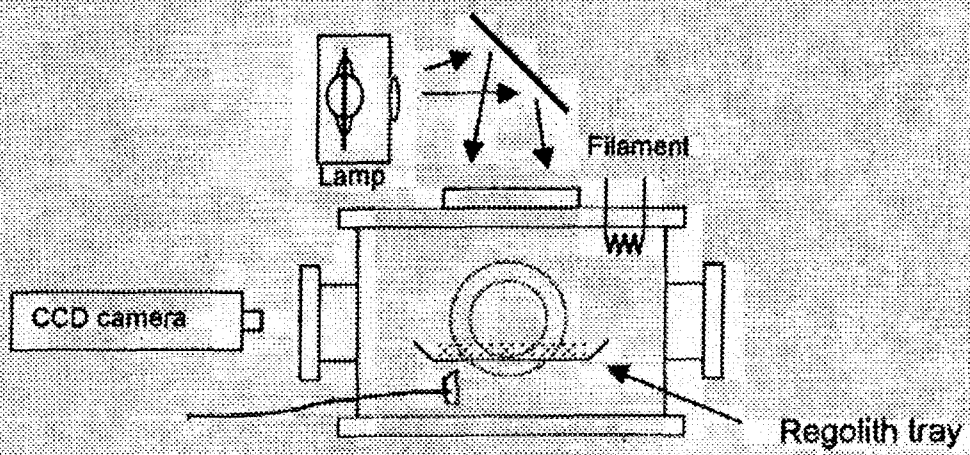

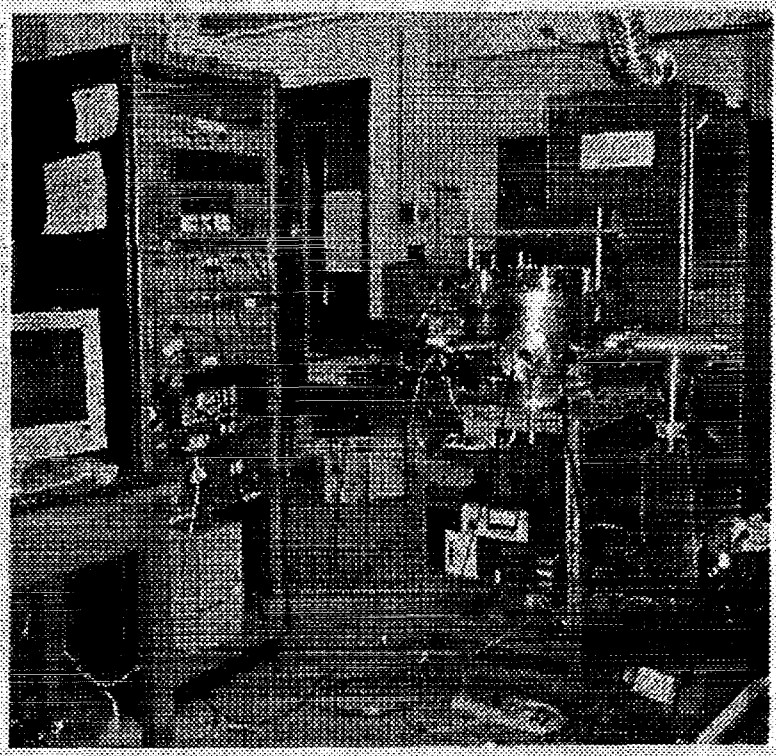

Electrostatic dust transport from sunrise/sunset

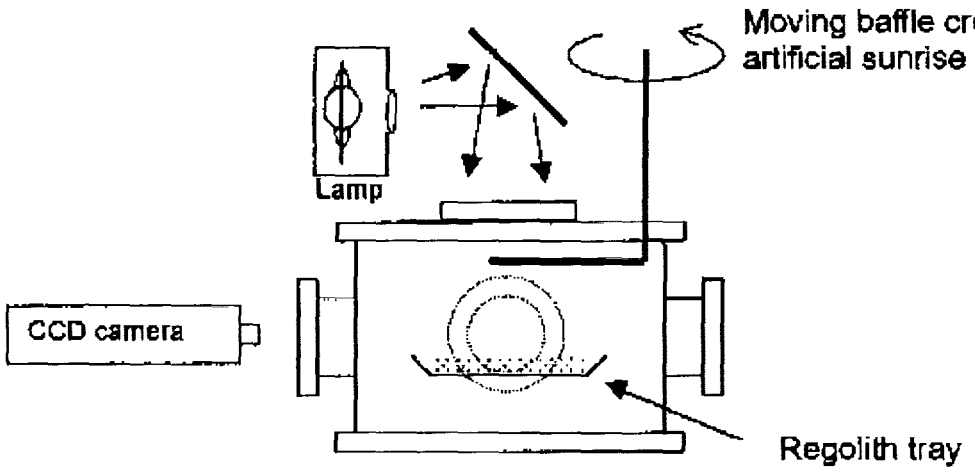

Electrostatic effects in impacts

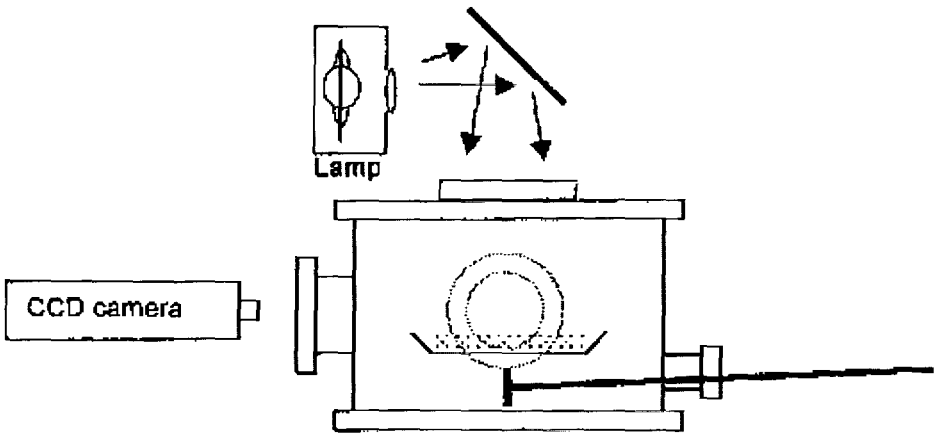

RHEOLOGY OF FOAM NEAR THE ORDER-DISORDER PHASE TRANSITION

R. Glynn Holt (rgholt@bu.edu) and J. Gregory McDaniel (jgm@bu.edu), Boston University, Dept. of Aerospace and Mechanical Engineering, 110 Cummington St, Boston, MA 02215

INTRODUCTION AND MOTIVATION

Foams are extremely important in a variety of industrial applications. They are widely used in firefighting applications, in flow applications such as enhanced oil recovery, and as trapping, transport and separation agents. The most important quality of a foam in many of these industrial processes is its response to imposed strain, or its *rheological* behavior. There exists little experimental data on the rheological properties of real 3D foams, even though such knowledge would likely enhance the efficacy of current applications and suggest other unique applications. The lack of 3D data is due in large part to the earth-based requirements for contact containment, and to the fact that gravity-induced drainage quickly destroys all but the "driest" foams, those with a very high gas volume fraction ϕ. We introduce a unique method to provide non-contact control and manipulation of foam samples. The development of this technique will provide the ability to carry out a set of benchmark experiments in **0g** allowing determination of a foam's yield stress, bulk shear and dilatational moduli and viscosities as a continuous function of gas volume (or 'void') fraction ϕ from the dry limit (ϕ 1) through the order-disorder phase transition to the wet limit ($\phi \ll 1$) of a bubbly liquid.

OBJECTIVES

The goal of the investigation is the determination of the mechanical and rheological properties of foams, utilizing the microgravity environment to explore foam rheology for foams that cannot exist, or only exist for a short time, in **1g**. *The specific objectives of the investigation are:*

1) To refine and utilize a novel, non-contact acoustic technique [1] for experimentally measuring the stress-response of small samples of foam ("foam drops") subjected to both static and time-varying extensional shear and pure dilatational strain. Our efforts will focus on refining a shape-modal oscillation technique, and an ambient (hydrostatic) pressure variation technique to meet our goals, and we will investigate step-function, quasistatic and oscillatory temporal variations in the acoustic and ambient pressures.

2) To experimentally measure the stress-response of small samples of foam ("foam drops") subjected to both static and time-varying extensional shear and pure dilatational strain. Acoustically-imposed strain amplitude, strain rate, and (in the oscillatory case) frequency will be our forcing control parameters. The void fraction, the gas phase density and diffusivity, as well as the multi-component liquid phase shear viscosity, surface tension and surface viscosities, will be our material control parameters.

3) To model the response of foam drops to static and time-varying modulation of the acoustic field to extract rheological properties: the yield stress, the bulk viscoelastic shear and dilatational moduli (complex) and the effective bulk shear and dilatational viscosity numbers. We will use effective elastic [1] and viscoelastic medium theory to explore the small amplitude dry foam limit, bubbly liquid theory to investigate the wet foam limit, and merge the two near the transition region.

4) To define experiments that can be performed in the μg environment, where the effects of drainage and high acoustic fields can be avoided, and ϕ can be varied smoothly through the order-disorder transition.

RESULTS

We can graphically illustrate some of the capabilities of our acoustic method, as well as illustrate our digitized video diagnostic capabilities by considering the following sequence of images. By varying the acoustic levitation pressure amplitude P, we can vary the magnitude of the imposed strain, which is axisymmetric. The amplitude can be varied as a step function, quasi-statically (shown below), or periodically, without affecting stable levitation of the drop. For comparison's sake, in Fig. 1 we present a pure liquid drop as well as a foam sample, both levitated in our 30 kHz levitator. Whereas the liquid drop exhibits more sensitive deformability but can recover its original shape (not shown), the foam sample exhibits a *yield stress*, which is apparently exceeded in the lower sequence, since the final foam sample is no longer the same shape or size, and is levitated at a slightly different location. This clearly demonstrates the capability of exerting a strain in a non-contact manner via acoustics. We should note that we chose a fairly mild deformation to illustrate our point – if necessary, the acoustics can easily flatten and disintegrate the foam sample.

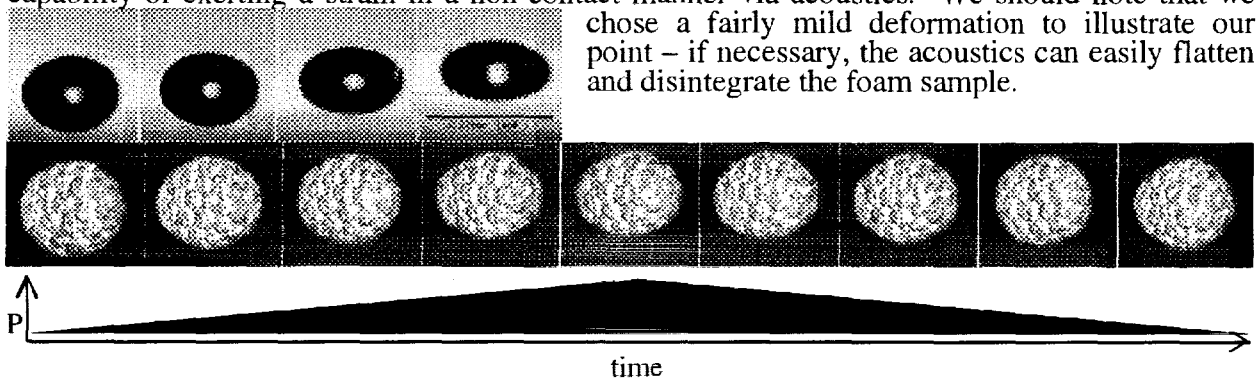

Figure 1. Acoustically levitated sample drops of liquid (top) and foam (bottom) exposed to a slowly increasing and decreasing (left-to-right) acoustic pressure amplitude. The acoustic frequency is 30 kHz.

MICROGRAVITY RELEVANCE AND SIGNIFICANCE

All but the driest foams drain in gravity. The liquid component will flow downward, and the bubbles will rise until a pool of liquid with a dry foam cap will form. Gravity will thus prevent the measurement of foam properties as the gas volume fraction is decreased towards the order-disorder transition, because the foam will be destroyed. There is very little experimental data on the rheological properties of 3D foams, primarily because potential experiments are severely hindered by the requirement for contact containment, and draining and thinning due to gravity. Our experimental technique can provide non-contact control and manipulation of multicomponent and multiphase drops. Coupled with a low-gravity environment, the technique will allow larger scale, near spherical samples to be investigated under nearly ideal conditions for any void fraction.

Understanding the rheological behavior of foams is important as a basic problem in fluid physics, and as a practical problem in many industries. In comparison with existing experimental techniques for rheological measurements, our technique offers at least four advantages. First, it is a non-contact technique that can nevertheless provide stable positioning and straining manipulation of a sample. Second, we can easily levitate and strain samples of arbitrary void fraction continuously from 0 to 1. Third, we can test small samples of foam with variable number and size of bubbles to investigate limiting cases. Finally, we can simultaneously measure shear and compressional parameters, whereas traditional techniques are restricted to either of these.

REFERENCES

[1] McDaniel, JG and Holt, RG, Phys. Rev. E 61, 2204 (2000).

NASA/CP—2000-210470

An Acoustic Levitation Technique to Study Foam Rheology Near the Order-Disorder Transition

Glynn Holt, Greg McDaniel
Dept. of Aerospace and Mechanical Engineering Boston University

Iskander Akhatov*
Ufa Branch of Russian Academy of Sciences
and
Bashkir University

Students at BU:

Cory Clarke, MS candidate
Chris Fox, MS
Xinmai Yang, PhD candidate
Li Liu, PhD candidate

Sponsors: NASA, *NSF via NRC COBASE

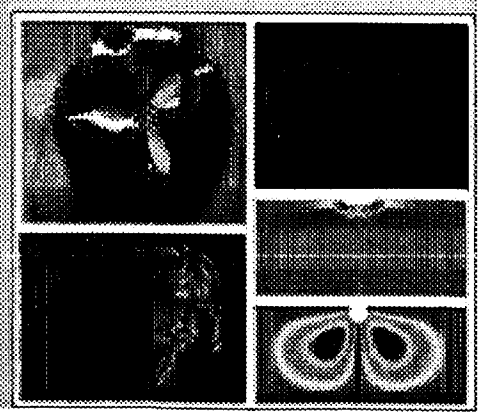

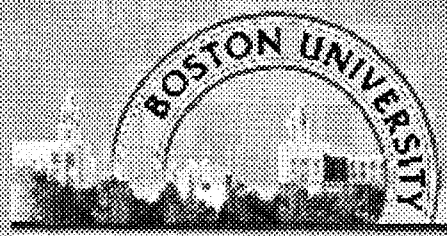

Why Study Foam?

Scientifically interesting:

- » Complex nonlinear material
  - – Sometimes a solid, sometimes a liquid
- » Interesting rheological properties
- » Exhibits a unique order-disorder phase transition *only approachable in 0g*

Lots of industrial applications:

- » Firefighting, oil recovery, separation, transport, trapping, ...

Space applications:

- » Firefighting, transport...

BOSTON UNIVERSITY

What is a Foam?

A distribution of gas bubbles in a liquid host with a gas volume (void) fraction between 0 and 1

- Gas usually air
- Liquid is multicomponent aqueous solution
  - Mostly water
    - One or more surfactants
    - One or more oils (emulsified)

We call a compact foam sample a "Foam Drop"

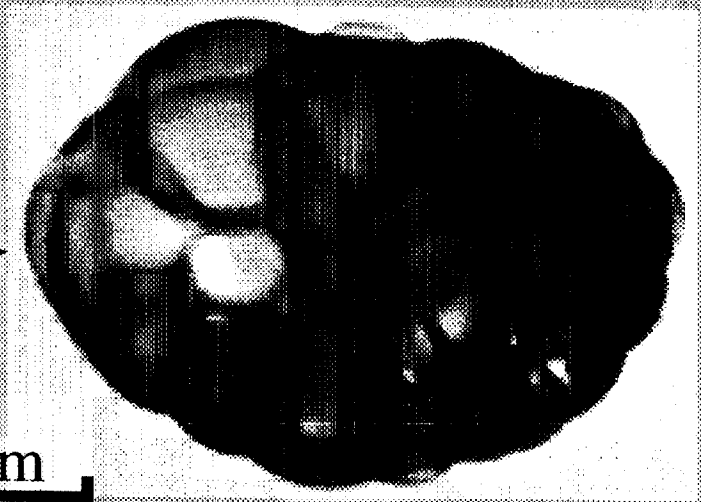

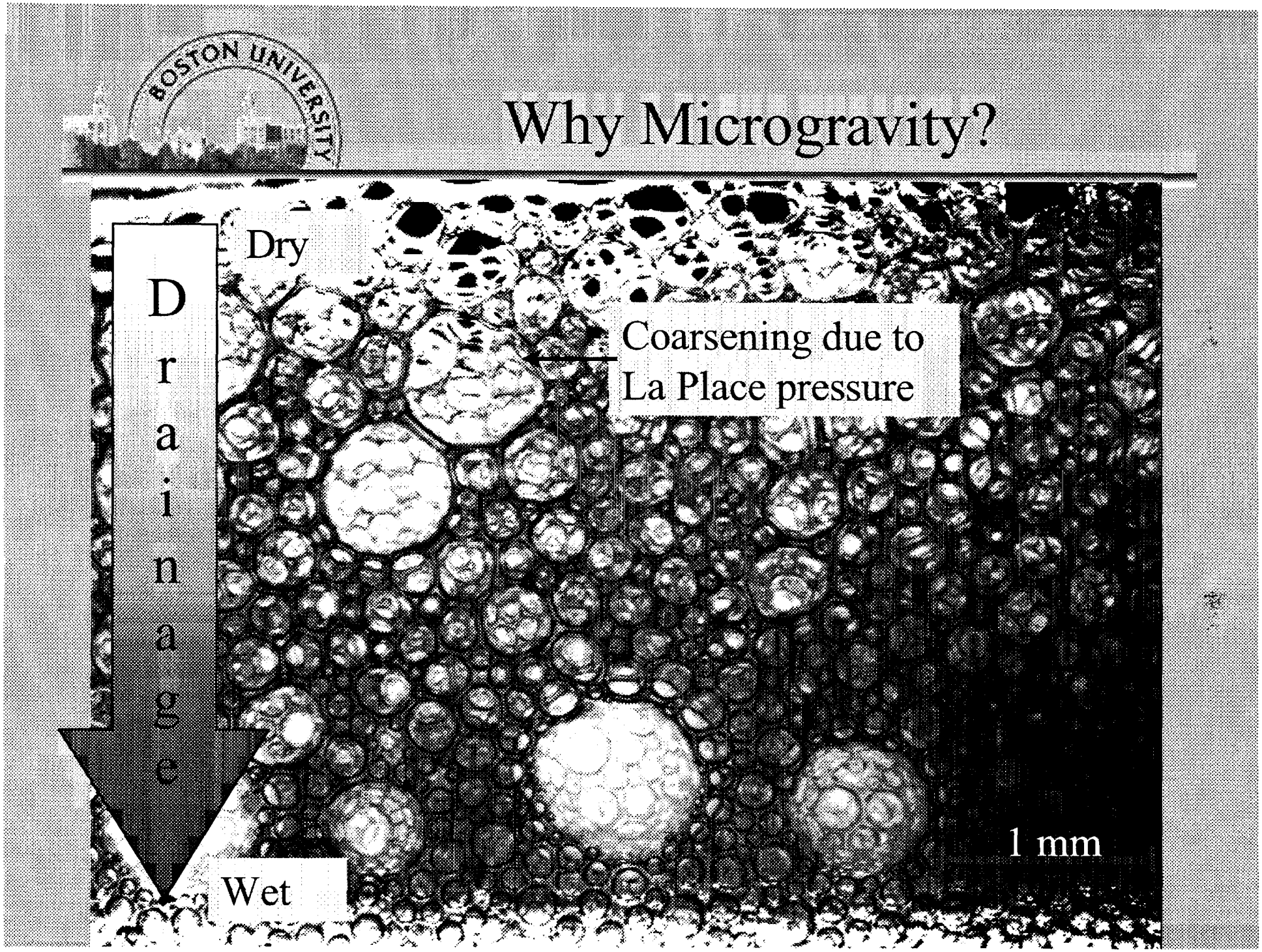
BOSTON UNIVERSITY
Why Microgravity?
Dry
Drainage
Coarsening due to
La Place pressure
1 mm
Wet

BOSTON UNIVERSITY

Why Microgravity?

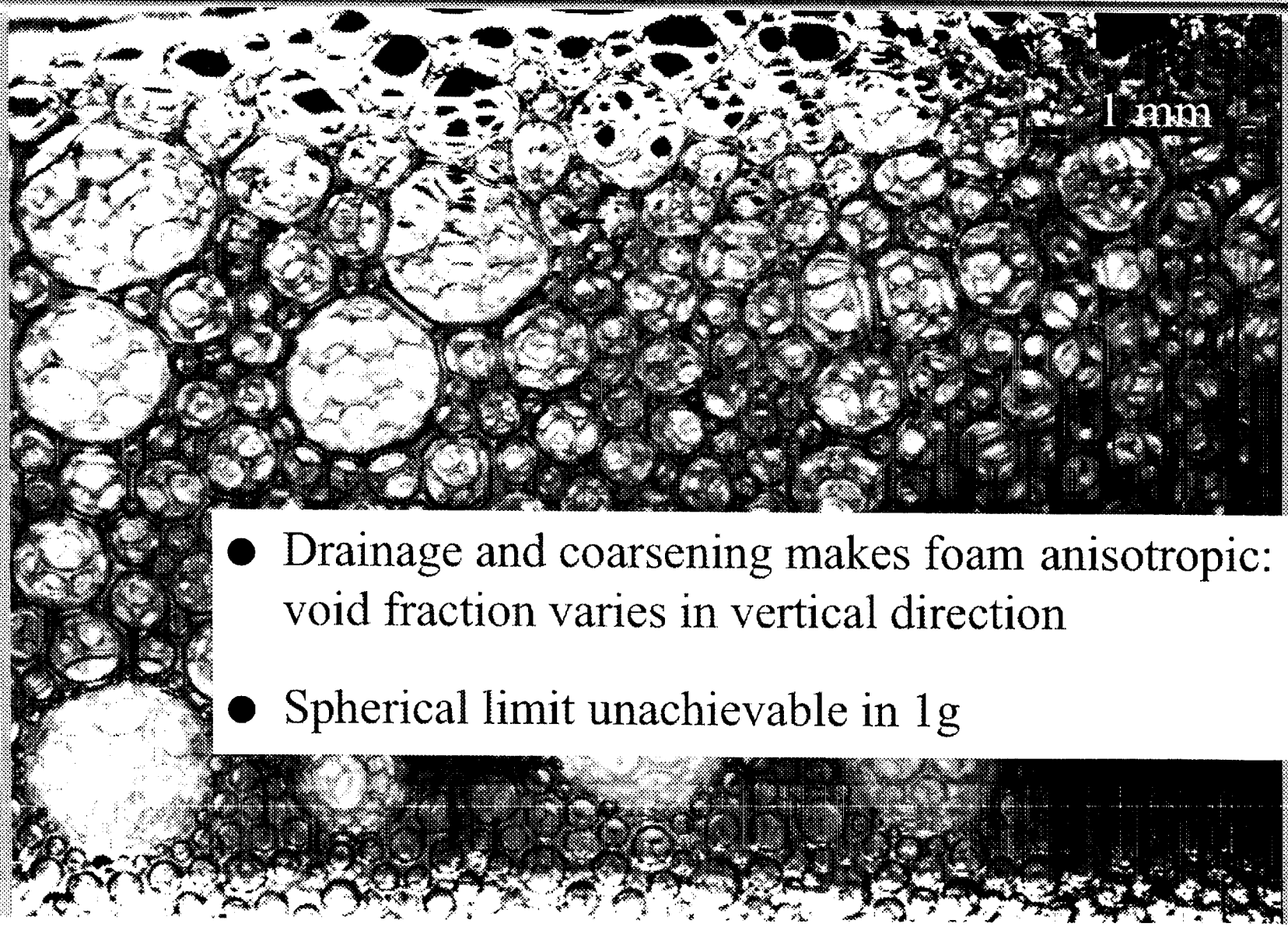

- Drainage and coarsening makes foam anisotropic: void fraction varies in vertical direction
- Spherical limit unachievable in 1g

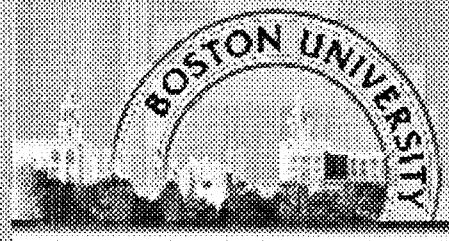

Long-range Goals

- Determination of the mechanical and rheological properties of foams as a function of the gas void fraction.
- Investigate the order-disorder transition as the void fraction increases from a wet to a dry foam.
- Utilize NASA research facilities to defeat drainage to experimentally investigate wet(ter) foams.

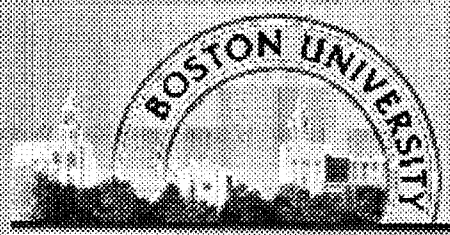

Short-term objectives

Develop novel acoustic levitation technique for foam rheology:

» Non-contact force application yields:

- Stable positioning of sample
- Approximately extensional shear strain (static and oscillatory)
- Dilatational strain (ambient pressure)

» Utilizing the acoustic force we can study either relaxation or oscillatory phenomena

- Oscillatory yields *normal modes*

Short-term objectives (cont.)

To model the response of foam drops to static and time-varying acoustic forces to extract effective rheological properties:

1. Dry limit: treat the foam as an effective continuum, and develop expressions relating experimental measurables to the material properties.

2. Wet limit: model foam as bubbly liquid, include nonlinear bubble dynamics in acoustic environment

Common initial treatment: normal modes analysis

Experimental Technique: Acoustic Levitation

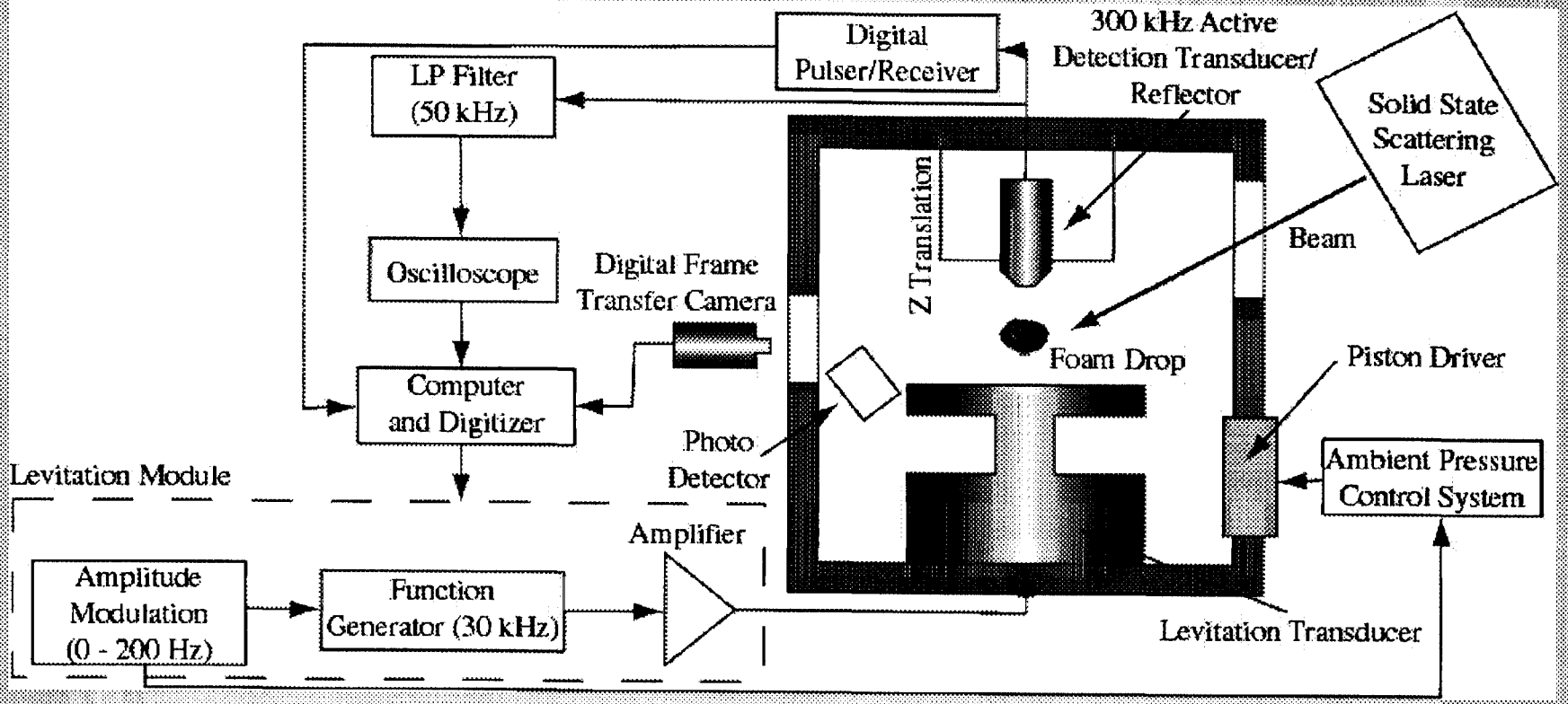

- Non-contact positioning and manipulation
- Acoustic and ambient pressure modulation (excites shear and dilatational motions)
- Imaging, acoustic scattering and optical scattering diagnostics
- Works with wet or dry foams

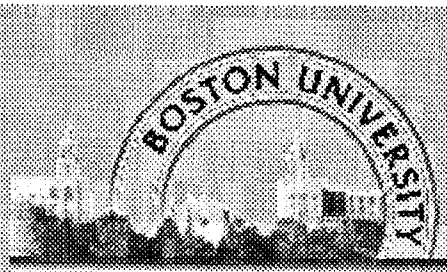

30 kHz, single-axis acoustic levitator movie

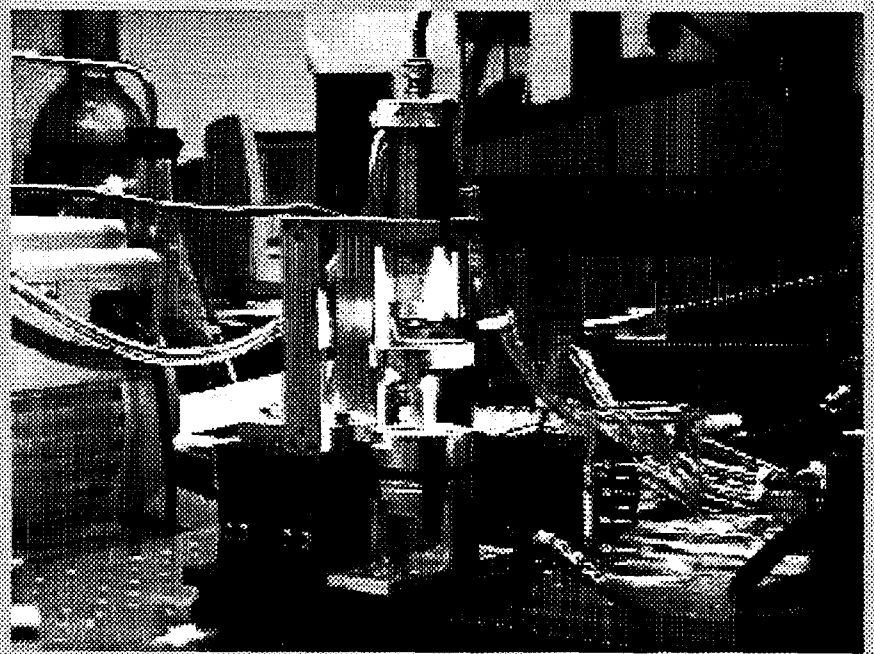

BOSTON UNIVERSITY

Foam Drop Levitation

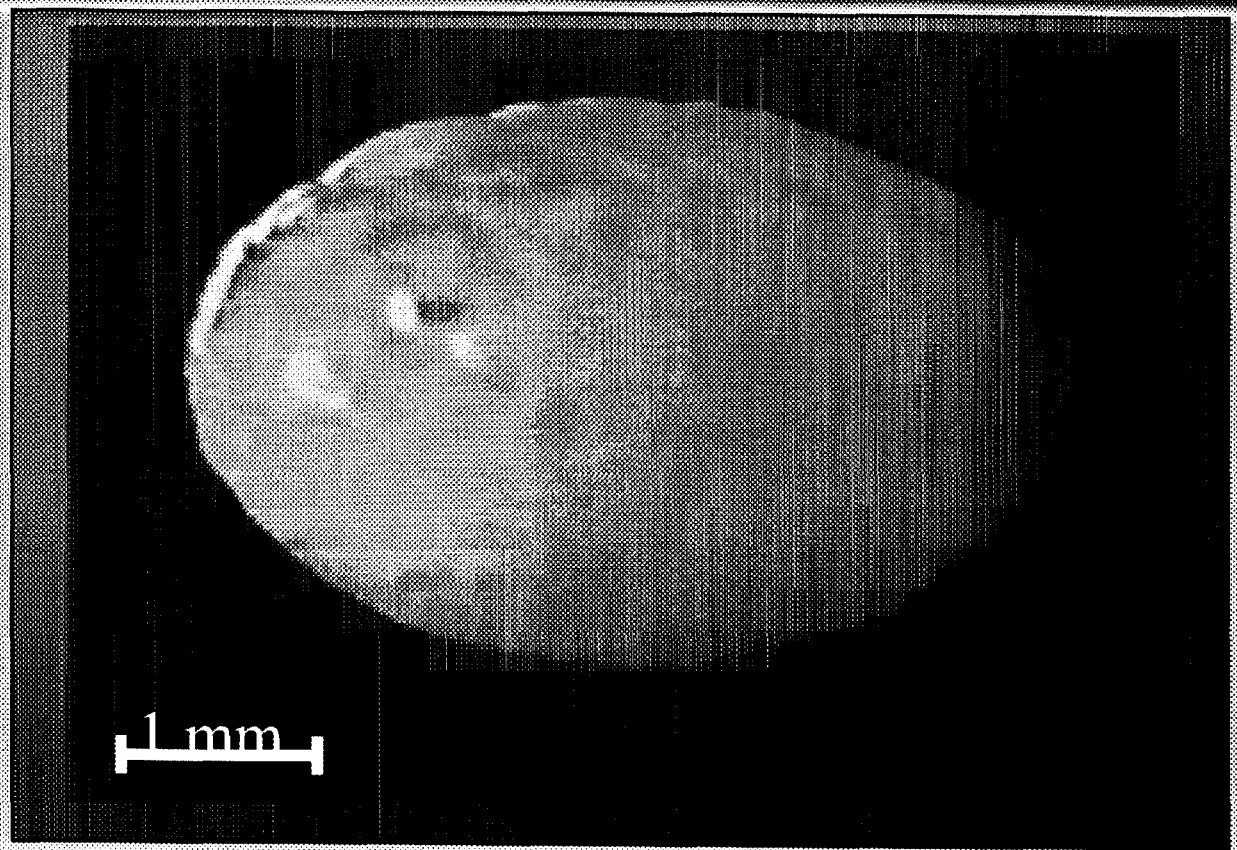

f = 23.0 kHz

P ~ 155 dB re 20 μPa

Shaving cream (Gillette Foamy™)

TX100/glycerol movie

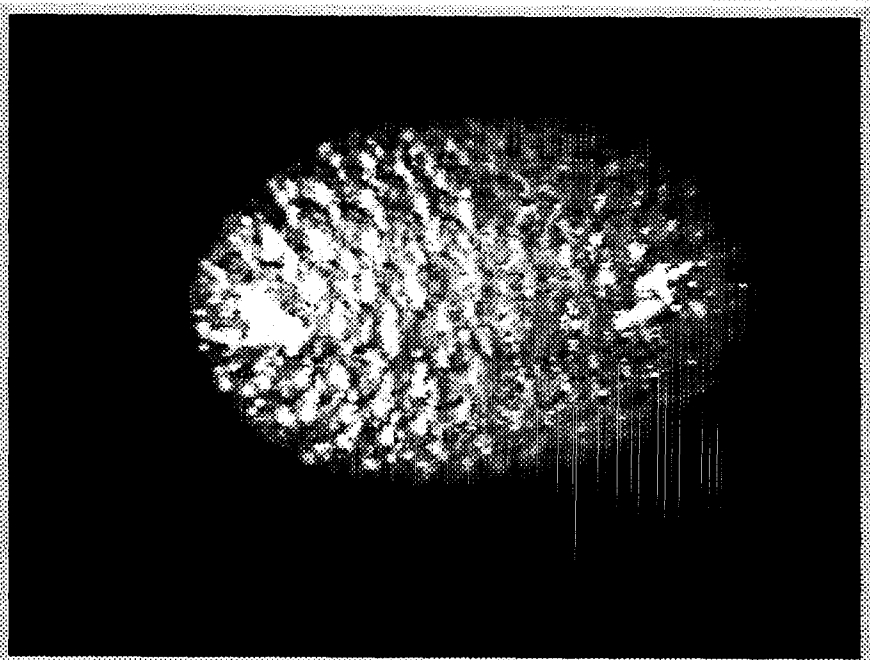

- 30 kHz carrier, no modulation, quasi-static squeeze/release
- 10 CMC Triton-X-100 surfactant, 10% Glycerol/Water, air
- R ~ 2mm, a ~ 200 microns
- Void fraction ~ 0.7

Dry limit

- Void fractions > 0.7
- Low strain rates
- Effective (continuous) elastic medium

Experimental data

Drop parameters from experiment:

Void fraction = 0.77 ($\rho = 231$ kg/m^3)

$R_{eff} = 3.78$ mm, $a_{median} = 0.39$ mm, $f_2 = 63$ Hz (max. response)

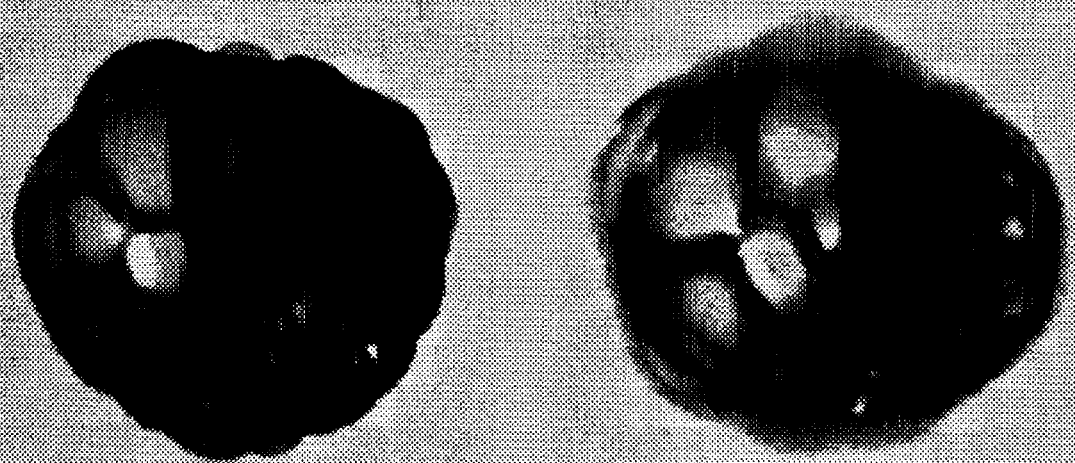

Levitated Levitated & Modulated

Effective Elastic Medium Model for Foam Drop Vibrational Modes

*(McDaniel and Holt, PRE **61**, 2204 (2000)*

- Characteristic equation $C = 0$ yields modal frequencies for the fundamental axisymmetric shape mode ($m = 0$, $n = 2$).

Fundamental mode

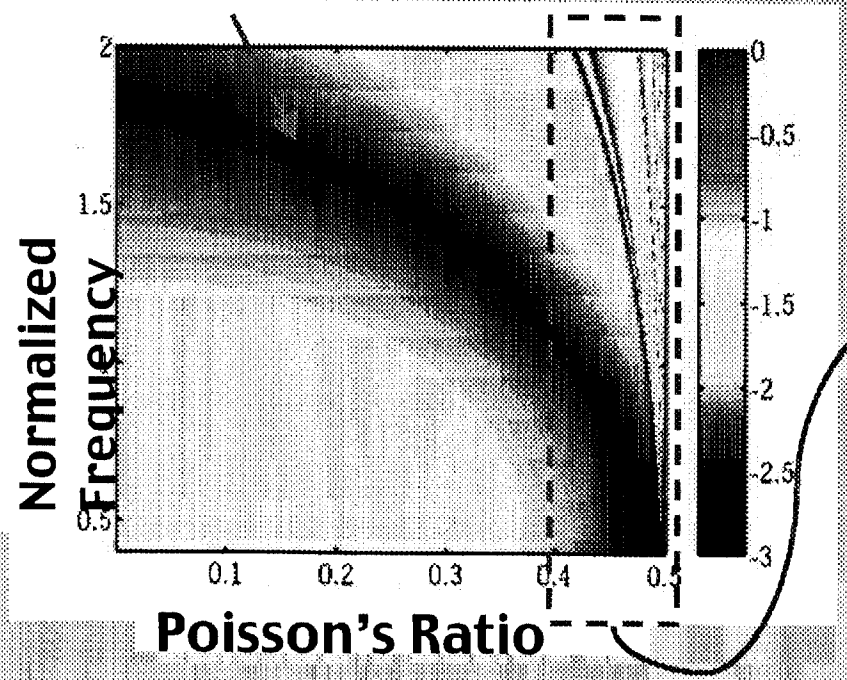

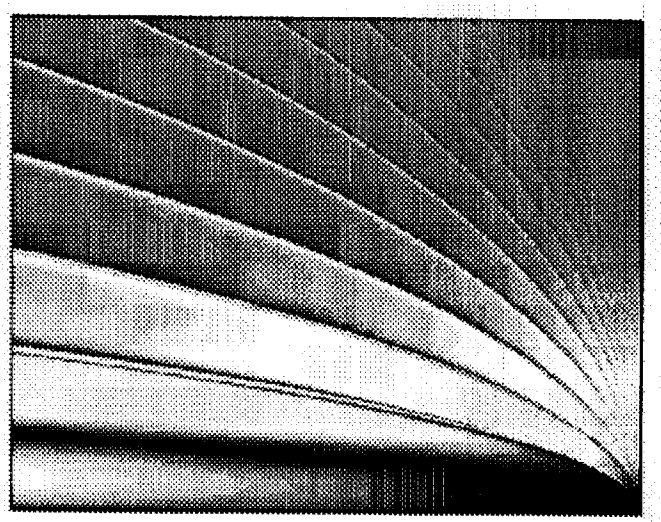

Other modes near the incompressible limit

Effective Elastic Medium Model for Foam Drop Vibrational Modes

- Estimated shear modulus falls in the range of previously measured values

TABLE I. Summary of shear modulus measurements.

Reference	*Void fraction*	*Frequency (Hz)*	*Shear modulus (Pa)*
Cohen-Addad 98	0.926–0.936	0.01–10	100–500
Coughlin 96	0.93–0.941	0	168-251
Princen 86	0.75–0.976	0	61–351
Khan 88	0.92–0.97	0.06–1.6	50–100
Fang 98	Not reported	0.08–16	20–40
Saint-Jalmes 99	0.7–0.94	0–16	10–200
Saint-Jalmes 99	0.5–1	0.16	0–160

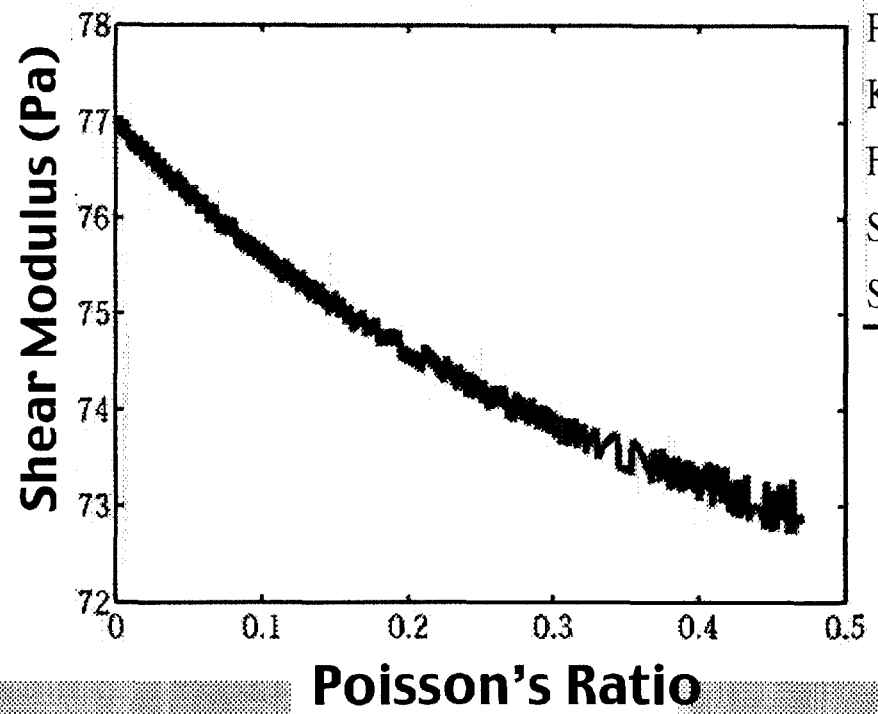

Shear modulus is insensitive to Poisson's ratio.

Wet limit

Bubbly liquid dispersion relation for acoustic waves -- linear acoustics

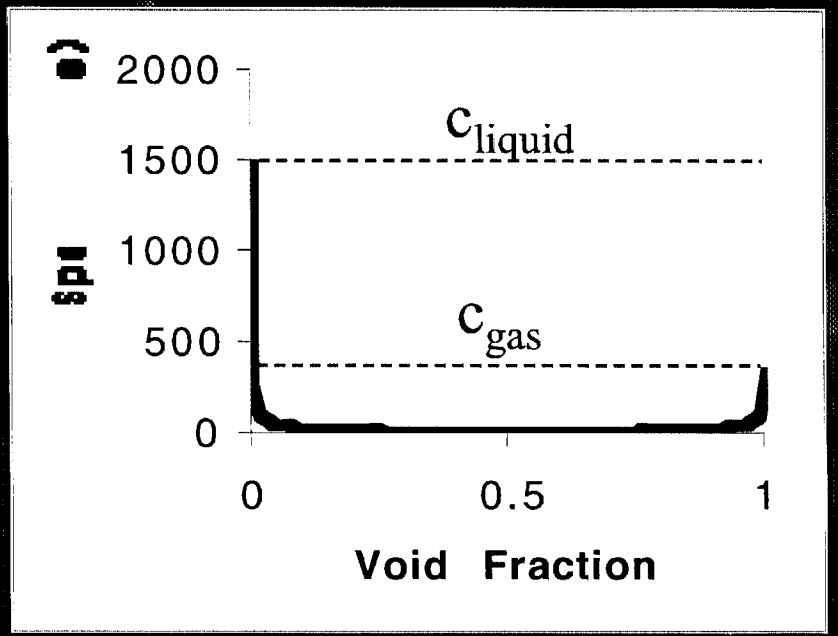

Liquid incompressible

Spatially uniform bubble pressure (bubble Mach # << 1)

Spatially uniform mixture pressure (drop Mach # << 1)

Weak liquid dissipation

Dynamics of wet foam drops in an acoustic field -- modeling results

Incident waves

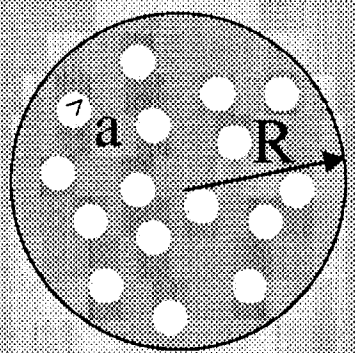

Reflected waves

Main parameters for numerical results:

Liquid –	water
Gas –	air
$f_{acoustic}$ =	30 kHz
R_0 =	3.78 mm
a_0 =	0.39 mm
$f_{sb,\infty}$ =	8.2 kHz

Normal mode frequencies

Shape mode

$$\omega_n^2 \approx \frac{\sigma n(n-1)(n+2)}{\rho_l(1-\phi_0)R_0^3} = \omega_{n,pureliquid}^2 \cdot \frac{1}{(1-\phi_0)}$$

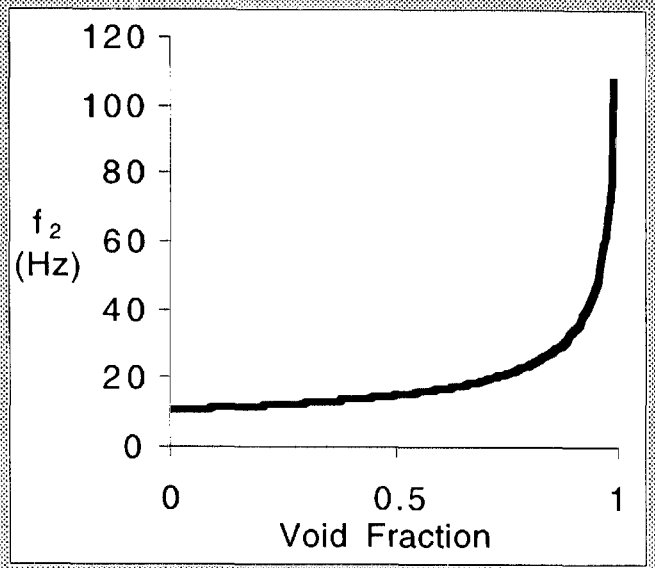

Breathing mode

$$\omega_0^2 \approx \frac{\omega_{SB,\infty}^2}{\frac{3R_0^2}{\pi^2 a_0^2}\phi_0(1-\phi_0)+1-\phi_0^{1/3}}$$

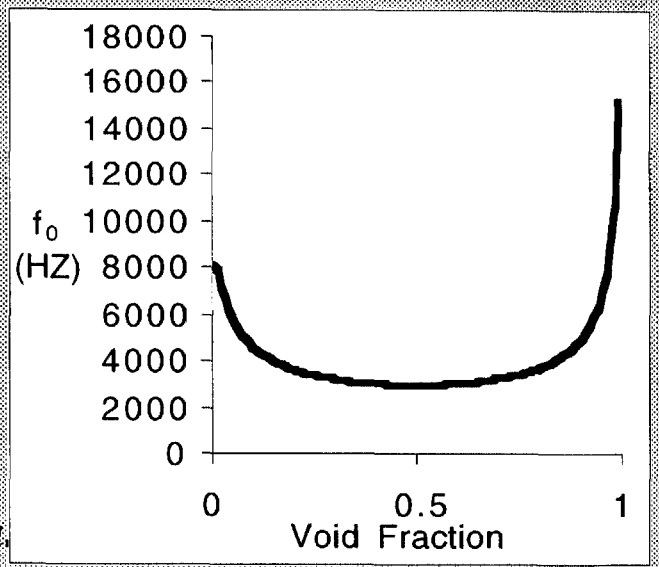

Surface tension σ = 0.031Nt/m (Triton-x-100 sa...

Liquid density ρ_l = 1000 kg/m³ (essentially water)

Foam drop equilibrium radius R_0 = 3.78E-03 m ($\lambda_{air} \sim 10^{-2}$m; $\lambda_{foam} \sim 10^{-4}$ m)

Polytropic exponent κ = 1.33 (ratio of specific heats for air)

P_∞ = 1.00E+05Pa (1 atmosphere)

Bubble equilibrium radius a_0 = 3.9E-04 m (monodisperse)

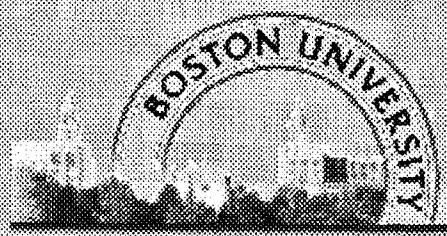

Summary and Future Work

Done:

1. Developed a viable acoustic levitation technique
2. Normal modes analysis for limiting cases
3. Applied analysis to dry elastic case, validated with literature values
4. Fully nonlinear model for wet limit oscillations

To Do:

1. Exploit levitation technique: parameter study, KC experiments for wet and critical v.f.'s
2. Merge analyses to cover transition void fractions:
   - Bjerknes forces
   - dissipation
   - nearest neighbor forces
3. Define microgravity exps.

August 10, 2000
Session 3C

Interfacial Phenomena II

MICRO-FLUID DYNAMICS IN AN EVAPORATING SESSILE DROPLET

Hua Hu and Ronald G. Larson
Department of Chemical Engineering, University of Michigan, Ann Arbor, MI 48109

ABSTRACT

The 3-D time-dependent flow field produced by an evaporating sessile water droplet whose contact line is pinned is studied experimentally and theoretically using the lubrication approximation and finite element analysis.

The experiments are carried out using an optical microscope and small fluorescent tracer particles. Multiple particle tracks are used at each position to average out Brownian motion, which is dominant since flow velocities are small (less than 1 micron/sec). Vertical velocities are obtained using refringence patterns produced by defocused particle images, as shown in f ig.1. When a particle is in focus, the particle image is sharp and small. When a particle is above the focal plane, its images show the ring patterns. However, when a particle is below the focal plane, its images become blurred and the ring patterns disappear. From quantitative measurements of

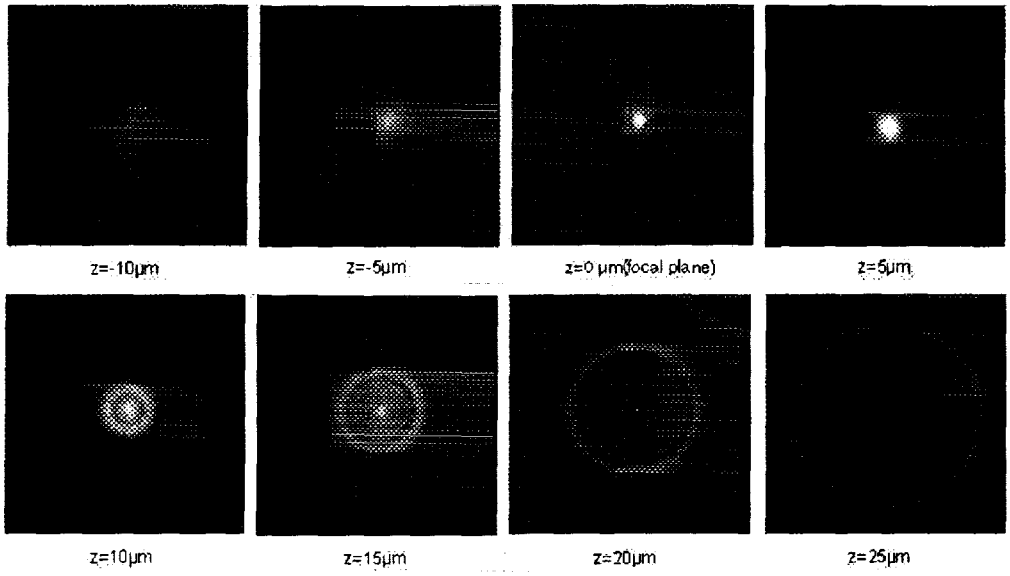

Fig. 2 Refringence of a particle as a function of distance relative to the focal plane

image size to these phenomena, the vertical position and vertical velocity are obtained. The experiments, as illustrated in fig.2, show a hyperbolic flow pattern of fluid moving down and out towards the edge of the droplet, combined with an internal circulation near the surface of the droplet.

In out theoretical analysis of this flow, we divide the problem into three parts: the gas phase, the liquid phase and the air-liquid interface. In the gas phase, the droplet vapor flux can to a good approximation be treated as a quasi-steady-state diffusion problem, where a quasi steady-state solution is obtained at each droplet height, which decreases as the droplet evaporates. This leads to the Laplace equation, which is:

$$^2c = 0 \qquad (1)$$

The boundary conditions for the gas phase are: 1. At r and z , $c = c$; 2. At $r > 1$ and $z = 0$, $q = 0$; 3. At $h = h(t,r)$, $c = c_{sat}$; where r is the radial coordinate, z is the vertical coordinate, c is the water vapor concentration, and h(t, r) is the location of the droplet surface.

In the liquid phase, the flow is very slow (Re < 0.01), and can be regarded as a Stokes flow, which is expressed by the following equation:

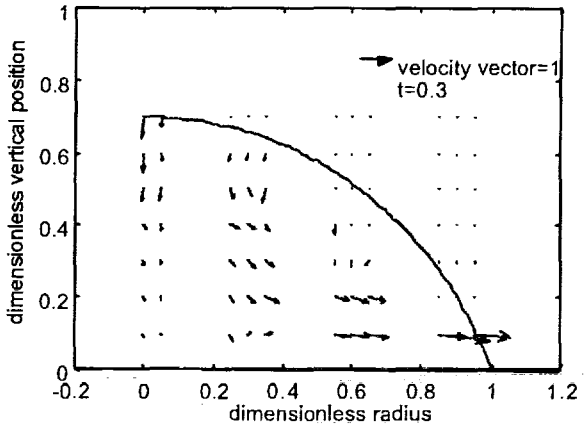

Fig. 2 Velocity field in an evaporating droplet

$$\frac{1}{r}\frac{(rv_r)}{r} + \frac{v_z}{z} = 0 \qquad (2)$$

$$\frac{1}{r}\frac{}{r}(r\tau_{rr}) + \frac{\tau_{rz}}{z} + \frac{\tau_{\theta\theta}}{r} - \frac{p}{r} = 0 \qquad (3)$$

$$\frac{1}{r}\frac{}{r}(r\tau_{zr}) + \frac{\tau_{zz}}{z} - \frac{p}{z} + \rho g = 0 \qquad (4)$$

In addition, the capillary number is high and so the droplet shape at each instant is a spherical cap. Since the contact line is pinned, the contact angle decreases as the droplet evaporates. As the contact angle decreases, the evaporation flux becomes more non-uniform. Because of the heat of vaporization, this leads to a non-uniform distribution of temperature along the air-liquid interface, and hence a non-uniform surface tension, which drives Marangoni flow.

The temperature field in the droplet is solved through the energy equation, again using a quasi-steady approximation, leading to Laplace's equation, since the slow flow produces negligible heat convection. The energy equation is expressed as follow:

$$^2T = 0 \qquad (5)$$

Using a lubrication approximation, an analytic solution to the time-dependent axisymmetric flow field in the evaporating droplet is attained, which accounts for recirculation due to Marangoni flow. We also applied the finite element method obtain a more accurate flow field; however, all qualitative features are captured by the lubrication solution. The theoretical results are then compared to the experimental flow field, and the important role of Marangoni flow is highlighted.

REFERENCES

[1] Jin, Junping, et al., Proc. Natl. Acad. Sci., Vol. 95, pp. 8046-8051, 1998.

[2] Deegan, et al., Nature, vol. 389(6653), pp 827-829, 1997.

[3] Hu, H. and R. G. Larson, Proceedings of '99 international workshop on PIV. Santa Barbara Sep., 1999

Instant DNA Detection

Systems based on electrical signals move from science fiction to reality

Elizabeth K. Wilson
C&EN West Coast News Bureau

In last year's sci-fi movie "Gattaca," the protagonist, attempting to conceal the fact that he's assumed the identity of a genetically "superior" man, scrubs himself daily to rid his body of loose hairs, skin flakes, and anything that might reveal his true identity through his DNA.

His paranoia is understandable. In the "Gattaca" future, vigilant police and employers carry handheld sensors that instantaneously analyze the DNA in snips of hair, drops of blood, or urine in order to expose the genetically "inferior." Parents receive their newborn babies' entire genetic profiles in a few minutes.

Actually, modern-day science is not far behind this technological scenario, though it envisions more humanitarian applications: detecting diseases, monitoring air for biological warfare agents, or checking food-processing plants for bacterial contamination.

Currently, extremely accurate tests for DNA sequences are based on fluorescence signals. The polymerase chain reaction (PCR) multiplies minuscule amounts of DNA into readable quantities. Although these techniques are extremely sensitive and quantitative, they require time, sample preparation, and expensive equipment. And the systems generally aren't portable.

But a number of research groups around the world are now closing in on the technology needed to develop a device that a doctor can use during an office visit or in the field to obtain results within minutes. The key to this technology is electricity.

When a single DNA strand encounters a complementary partner in a sample, it will hybridize. This hybridization can be detected by changes in an electrochemical signal—voltage or current, for example—usually through a redox-active or conducting molecule that behaves differently in the presence of a DNA hybrid than it does in the presence of a single strand.

"If there's a possibility of detecting hybridization in a rapid way using electrical signals instead of fluorescence, that's a tremendous advantage," says David L. Barker, vice president of research and business development at the instrumentation manufacturing company Molecular Dynamics in Sunnyvale, Calif. Electricity can be monitored without regard to the clarity or turbidity of a sample, and it doesn't require excitation lasers or reading by spectroscopic instruments.

"A direct electric reading [to analyze DNA sequences] appears much more elegant and sensitive," notes Francis Garnier, of the molecular materials laboratory at the National Center for Scientific Research (CNRS) in Thiais, France.

If it were small, battery-operated, and cheap, such a device could be a boon for the diagnostics industry and bring a lot of money to its inventors.

"If they can develop a simple test, it's a huge potential market," says Michael J. Powell, new technologies director at Roche Molecular Biochemical in Pleasanton, Calif.

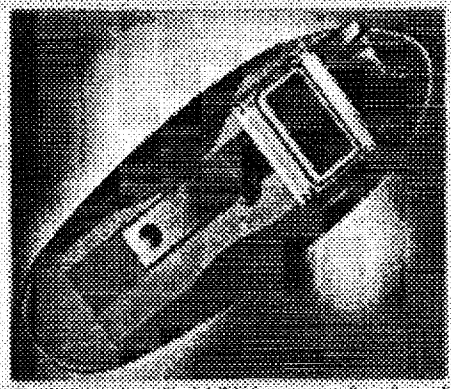

Prototype handheld DNA sensor developed by CMS.

One company hoping to usher in this new wave of technology is Pasadena, Calif.-based Clinical Micro Sensors (CMS), which unveiled a prototype handheld DNA sensor at the Council on Competitiveness' National Innovation Summit, held at Massachusetts Institute of Technology in March.

CMS was founded by Thomas J. Meade, a chemist at California Institute of Technology, and Jon Faiz Kayyem, president of CMS and Meade's former postdoctoral researcher. Meade's lab pioneered research on the fact that double-stranded DNA conducts electricity more efficiently than single-stranded DNA does. CMS is now aggressively pursuing commercialization of the system, tackling the hurdles in this area such as cost, size, and marketing. It is now in pilot production of its handheld DNA sensor.

"Currently, industry can deliver accurate DNA diagnostics, fast DNA diagnostics, convenient DNA diagnostics, and, occasionally, low-cost DNA diagnostics. What it cannot do is combine these attributes into a fast, accurate, convenient, low-cost assay," Kayyem says. "That's where many of us believe biosensors will help."

New Mexico State University chemistry professor Joseph Wang, whose lab specializes in sensor research, has also developed a handheld sensor for detecting lead in blood, which he says can eventually be modified to detect DNA.

Garnier's lab, as well as those of Susan R. Mikkelsen, associate chemistry professor at the University of Waterloo in Ontario; Shigeori Takenaka, head of the molecular systems group at Kyushu University, Fukuoka, Japan; and Peter Bäuerle, chemistry professor at the University of Ulm, Germany, are also publishing ever more ingenious DNA sensor chemistry, filing patents, and working with medical diagnostics companies.

An electrochemical technique is inherently one that involves surfaces. In all the systems, DNA is bound to—"immobilized"—on a solid electrode. For example, Mikkelsen uses carbon-based material as an electrode because it's easy to generate functional groups on its surface. She then covalently binds single strands of DNA, acting as "probes," to the electrode surface. A solution containing DNA strands, known as "targets," is added. If the targets are complementary to the probes, they hybridize to form a double strand.

Meade (left), Kayyem cofounded CMS to develop DNA sensor.

Then she adds a re-

pt. Map. Using A/F Ex. Disk Wi

FIGURE 1

From Schwartz et al.

1272
The gender gap at Harvard and MIT

1279
Dueling geological clocks

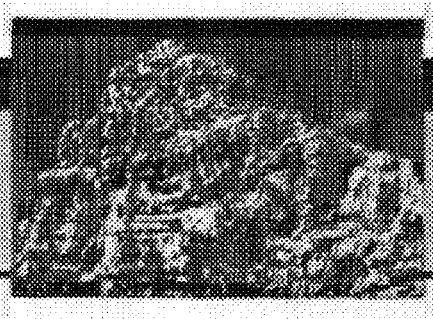

1282
How life got its twist

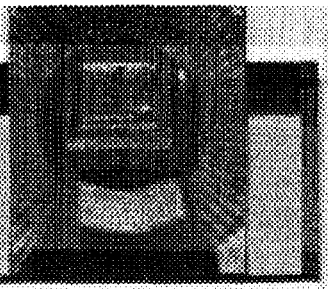

Metspalu recognizes the need to educate Estonians about genetics, but he believes that obtaining informed consent will not be a problem. "In a small pilot study, questioning 111 people resulted in a 90% acceptance rate, and I expect something similar for the general population," he says. –LONE FRANK

Lone Frank is a writer in Copenhagen, Denmark.

INFECTIOUS DISEASES

Malarial Genome Comes Into View

In 1986, Thomas Wellems set out on a seemingly narrow quest. He wanted to find the gene that enabled the malarial parasite *Plasmodium falciparum* to become resistant to chloroquine, the drug that had been a mainstay therapy for decades. But along the way, Wellems, a malaria expert at the National Institute of Allergy and Infectious Diseases (NIAID) in Bethesda, Maryland, accomplished what may be a more far-reaching feat. As reported on page 1351, he and his colleagues from NIAID and from the National Center for Biotechnology Information pinpointed a series of genetic landmarks across the entire 14-chromosome genome of this deadly parasite. It is one of two new maps of the parasite unveiled this

them were inherited along with the drug resistance. The team did this by tracking down microsatellites, short, easily identifiable bits of repetitive DNA that could serve as these landmarks.

For that effort, they also spent more than 5 years developing new resistant and sensitive parasites and then cross-breeding them. Only then could they trace the inheritance of the markers and the drug-resistance trait in the offspring of the hybrids to glean clues to the gene's location.

The map naturally emerged from this effort, as the group determined the patterns of microsatellites in the offspring of the crosses. Markers that are close to one another on a chromosome are more likely to be inherited together than those far apart, and so the team could establish the relative orders of the markers—901 in all—along the chromosomes and the approximate distances between them.

The second map, produced by David Schwartz of the University of Wisconsin, Madison, and his colleagues, pins down the physical locations of its markers. These researchers used a technique called optical

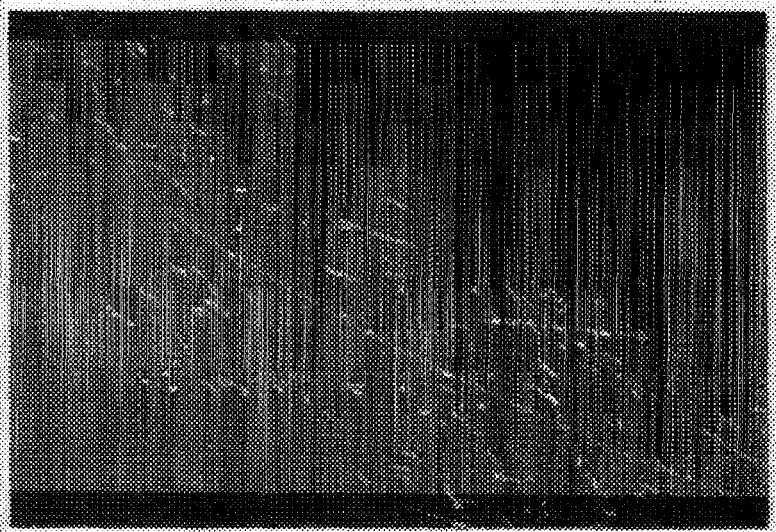

Getting the picture. Computer software merges fluorescence microscopy images to reveal cuts in long stretches of the malarial parasite's DNA.

mapping, which Schwartz devised while at New York University (NYU) in New York City. It uses electrostatic forces to hold pieces of fluorescently labeled *P. falciparum* DNA stretched out on glass. Then, for this

NASA/CP—2000-210470

Prediction and Design of DNA microfluidic devices requires developing experiments and simulations to understand and model:

1) The flow field

2) DNA molecular dynamics in a flow field

3) DNA/surface interactions

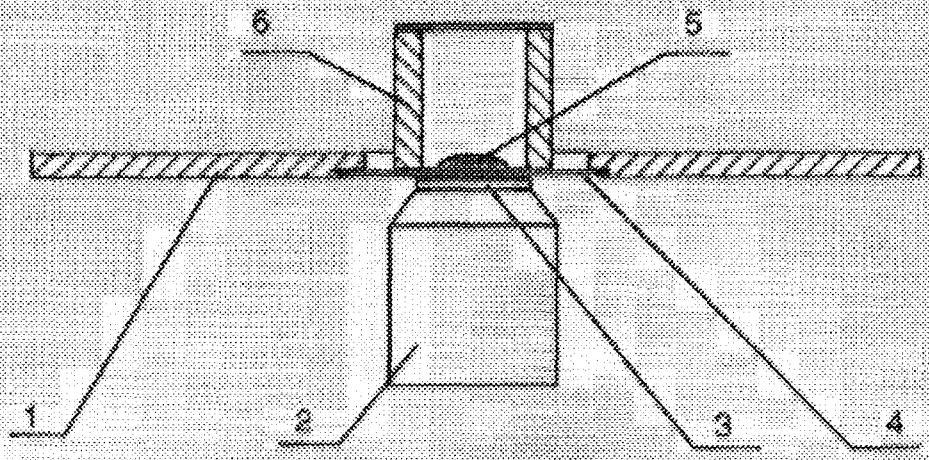

1. Glass cover slip holder 2. Fluorescence objective(40X)
3. Water 4. Glass cover slip 5. Droplet. 6. Sealing cylinder cap

Fig. 1 Sketch of the experimental apparatus

VARIABLES

$v \approx$ flow velocity, ≈ 1 μm/s

$\mu \approx$ viscosity, ≈ 0.01 Poise

$\Gamma \approx$ surface tension, ≈ 70 dyn/cm^2

$R \approx$ droplet radius, $\approx \approx 1$ mm

$h \approx$ droplet height, $\approx \approx 0.3$ mm

$\rho \approx$ liquid density, ≈ 1 gm/cm^3

$g \approx$ gravitational constant, ≈ 980 cm/s^2

DIMENSIONLESS GROUPS

$$\mathrm{Re} \equiv \frac{\rho v R}{\mu} \simeq 10^{-3}$$

$$\mathrm{Ca} \equiv \frac{\mu v}{\Gamma} \simeq 10^{-8}$$

$$\mathrm{Bo} \equiv \frac{\rho g h R}{\Gamma} \approx 0.05$$

=> creeping flow, droplet shape is a spherical cap

contact line is pinned

no slip at substrate, no shear stress at liquid/air surface

imposed evaporation rate + spherical cap => kinematic condition at liquid/air surface

h/R < 0.3: use lubrication approximation

Drying Droplet Model (Deegan, et al.)

- Local Evaporation Rate (Mass Flux)

$$J(\tilde{r},\tilde{t}) = J_0(\tilde{t})\left(1-\tilde{r}^2\right)^{-\lambda}$$

- Depth Averaged Radial Velocity

$$v(\tilde{r},\tilde{t}) = \frac{1}{4}\frac{R}{t_f}\left[\frac{M(\tilde{0})}{M(\tilde{t})}\right]\tilde{r}^{-1}\left(\left(1-\tilde{r}^2\right)^{-\lambda} - \left(1-\tilde{r}^2\right)\right)$$

- Velocity Field

$$v_r = \frac{3}{8}\frac{R}{t_f}\frac{M(\tilde{0})}{M(\tilde{t})}\frac{1}{\tilde{r}}\left[\left(1-\tilde{r}^2\right)^{-\lambda} - \left(1-\tilde{r}^2\right)\right]\left(2\left[\frac{z}{h}\right] - \left[\frac{z}{h}\right]^2\right)$$

$$v_z = -\frac{3}{8}\frac{1}{t_f}\frac{M(\tilde{0})}{M(\tilde{t})}\frac{1}{\tilde{r}}\left[2\lambda\left(1-\tilde{r}^2\right)^{-\lambda-1} + 2\right]\left(\frac{z^2}{h} - \frac{1}{3}\frac{z^3}{h^2}\right)$$

NASA/CP—2000-210470

Fig 12 The velocity field at t=0s according to the theory of Deegan, et al.

NASA/CP—2000-210470

Fig2. Image obtained when there is no water between the lens and the glass cover slip

Fig.3 Image obtained after putting water between the lens and the glass cover slip

NASA/CP—2000-210470

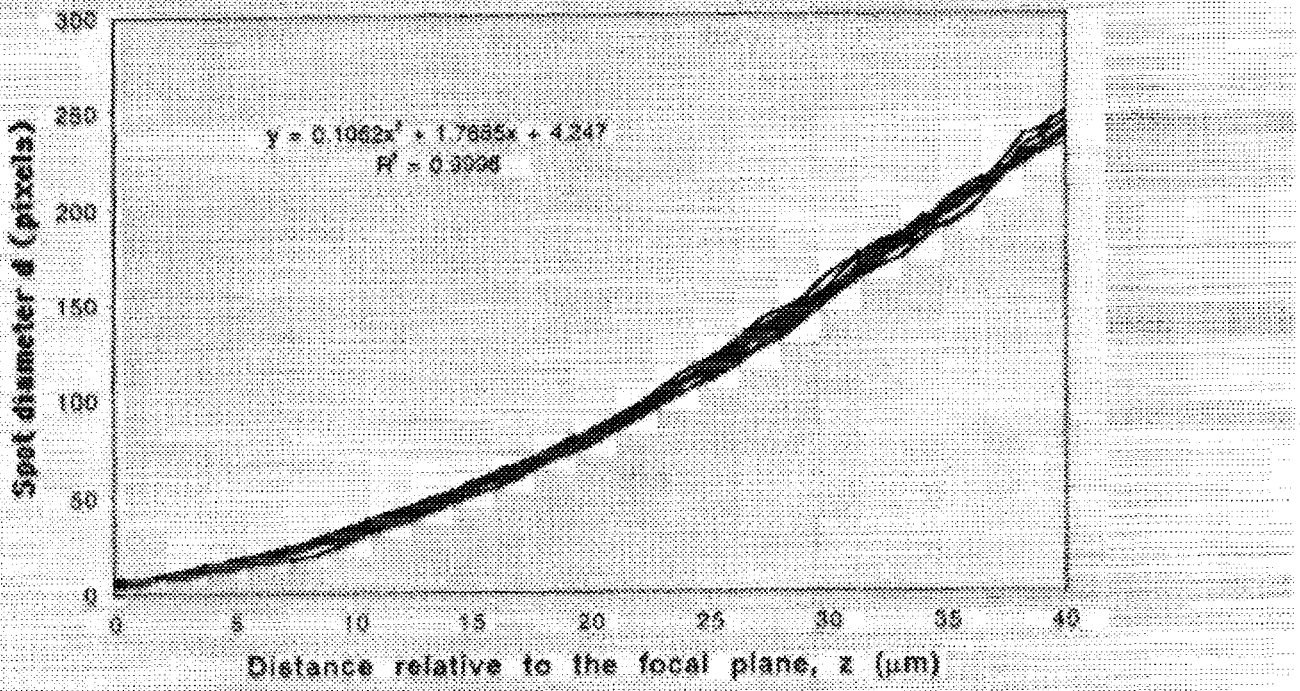

Fig. 6 The standard curve relating the vertical position z of the particle to the diameter d of the particle image

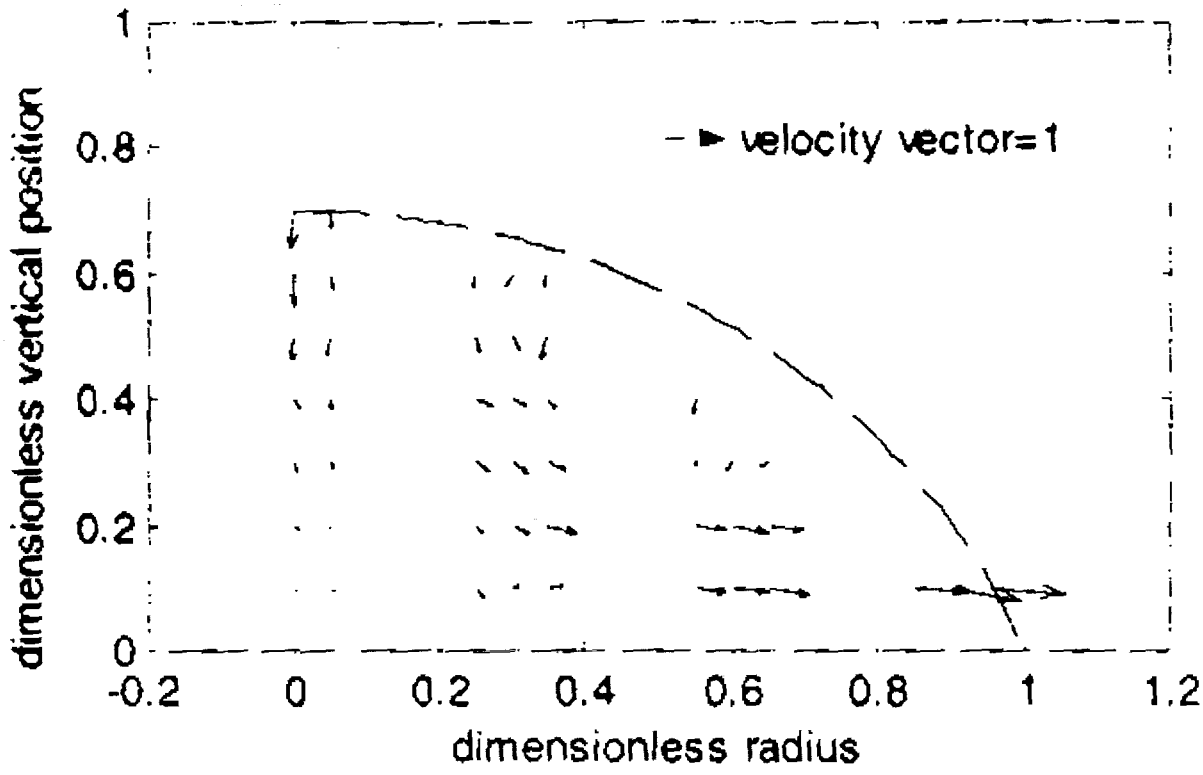

Fig.1 Velocity field at time 0.3

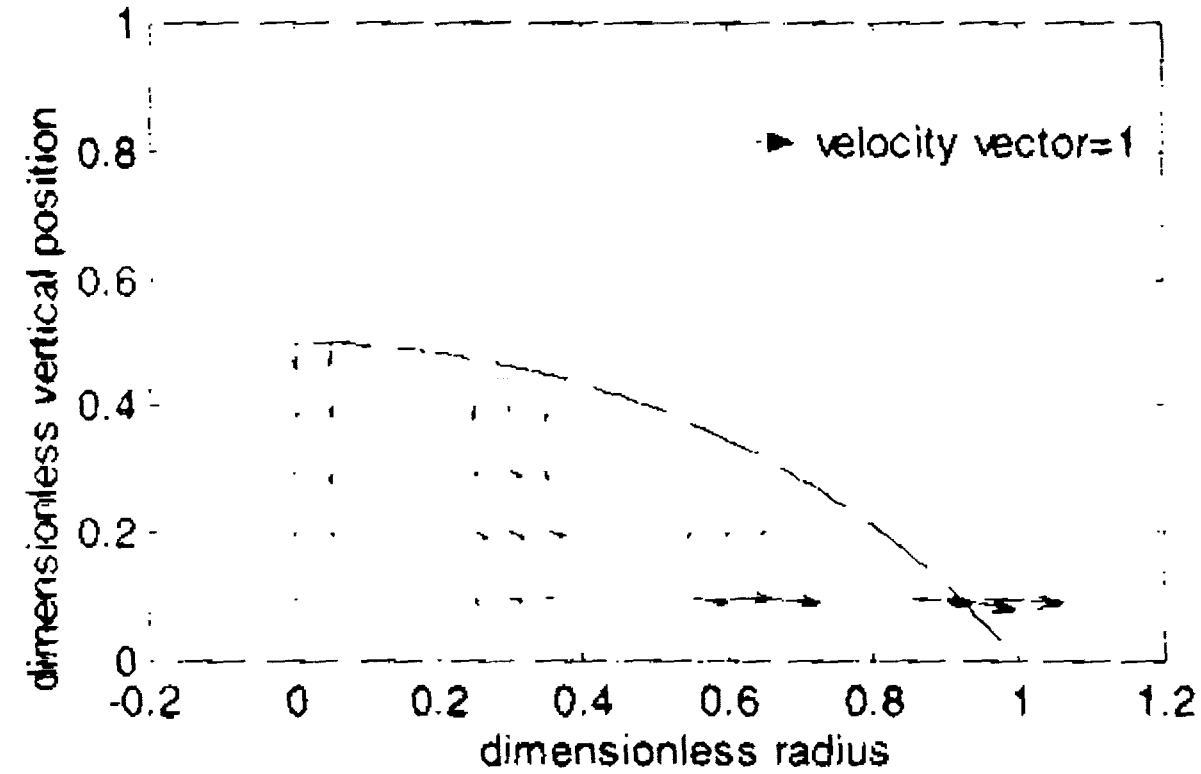

Fig.2 Velocity field at time 0.5

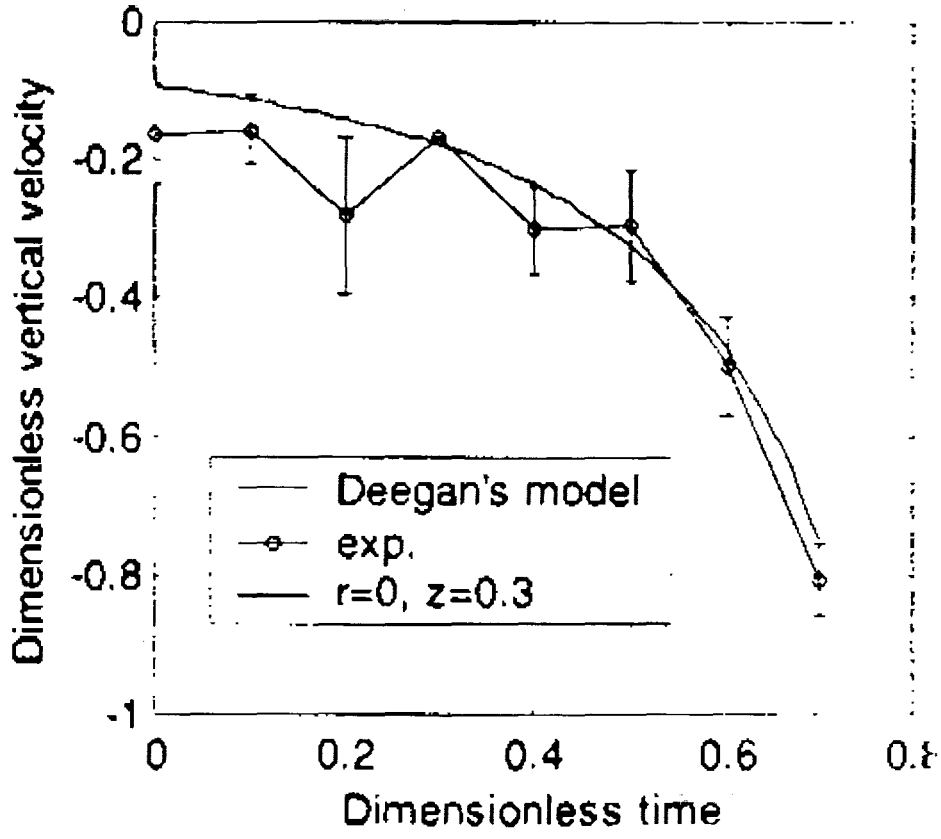
Dimensionless vertical velocity
0
-0.2
-0.4
-0.6
-0.8
-1
0
0.2
0.4
0.6
Dimensionless time
Deegan's model
exp.
r=0, z=0.3

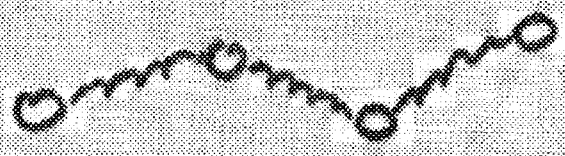

BROWNIAN DYNAMICS METHOD

(Ermak and McCammon 1978; Fixman 1978; Liu et al. 1989; Zylka and Öttinger 1989; Grassia et al. 1995; Grassia and Hinch 1996; Öttinger 1996; Doyle et al. 1997):

$$\underset{\sim}{x}_{m+1} = \underset{\sim}{x}_m + \underset{\sim}{x}_m \cdot \underset{\sim}{\underset{\sim}{\nabla v}}\, dt + (\underset{\sim}{F}^s_m/kT\zeta)\,dt + (6dt/\zeta)^{1/2}\,\underset{\sim}{r}_m$$

$$\frac{F^s(r)\,\lambda_p^{eff}}{kT} = \frac{1}{4}\left(1 - \frac{x}{\ell}\right)^{-2} - \frac{1}{4} + \frac{x}{\ell}$$

$$\underset{\approx}{\sigma}^p = \nu \sum_{i=1}^{N-1} \langle \underset{\sim}{F}^s_i \underset{\sim}{R}_i \rangle$$

L = fully extended length of molecule = 21 μm, 67 μm

ℓ = L/N = fully extended length of spring

λ_p^{eff} = "effective persistence length", = 0.061 μm, 0.096 μm.

(M-1) ζ = kT/D; D = measured translational diffusion coefficient

Each r is randomly distributed on the interval [-1,1]

For N = 40 springs, dt = 10^{-5} sec; = $10^{-5}/\dot{\epsilon}$ sec for large $\dot{\epsilon}$.

ALL PARAMETERS FIXED BY EXP'TL MEASUREMENTS!

11 Bead 10 Chain Simulations on Multiple DNA Molecules

Final Spatial Map for one Quadrant of the Dried Droplet

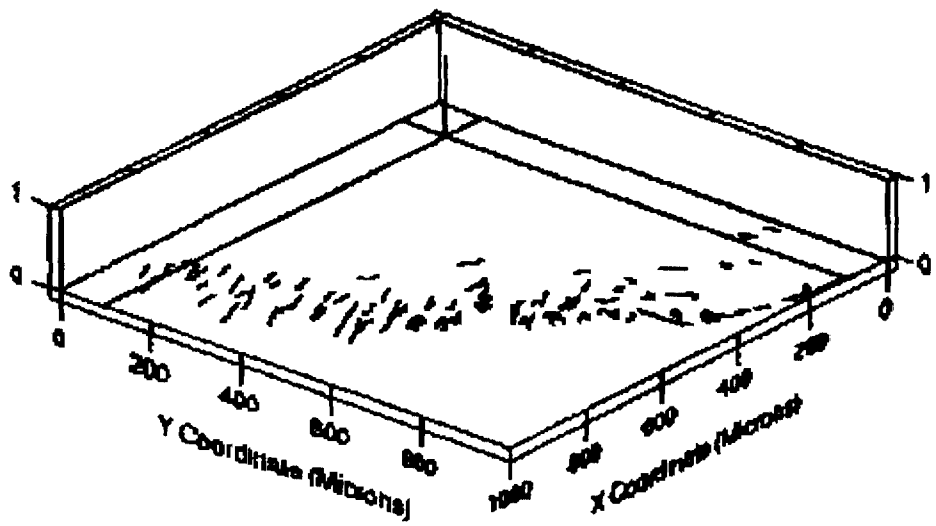

More Molecules

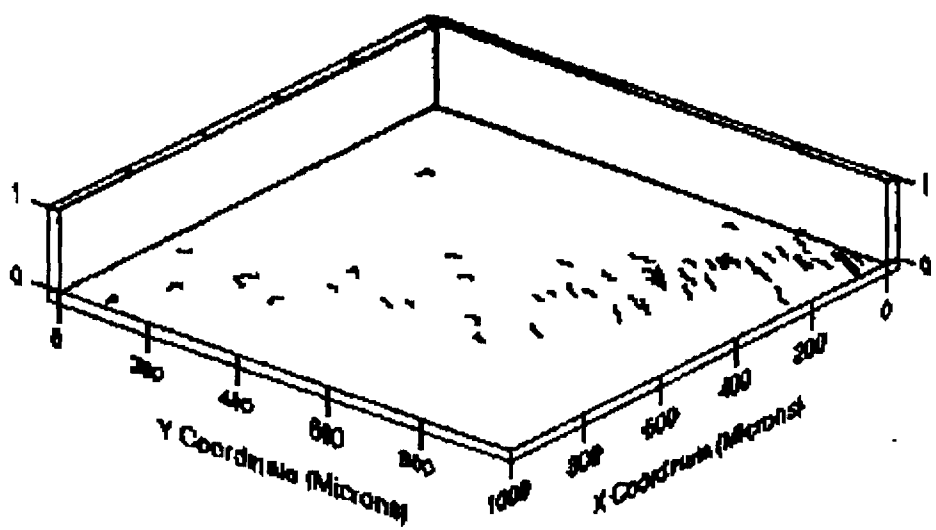

Less Molecules

Final Configurations Essentially Describe the Arc of a Circle

ref. Contact Line Solute Deposits in Drying Droplets

Droplet Dimensions: Radius 1000 micron. Height 300 micron

Various Stretched Final Stuck DNA Configurations

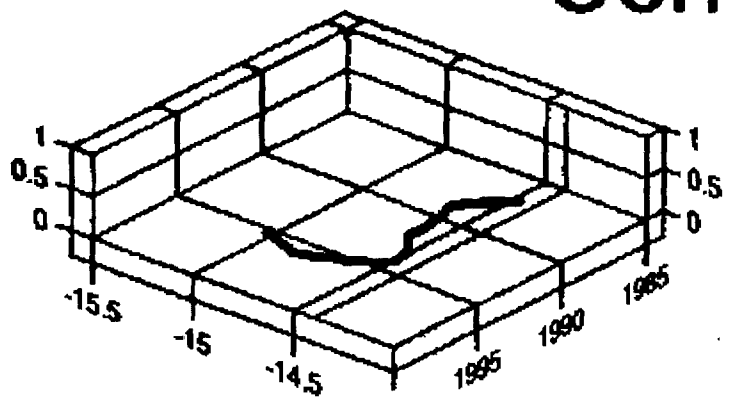

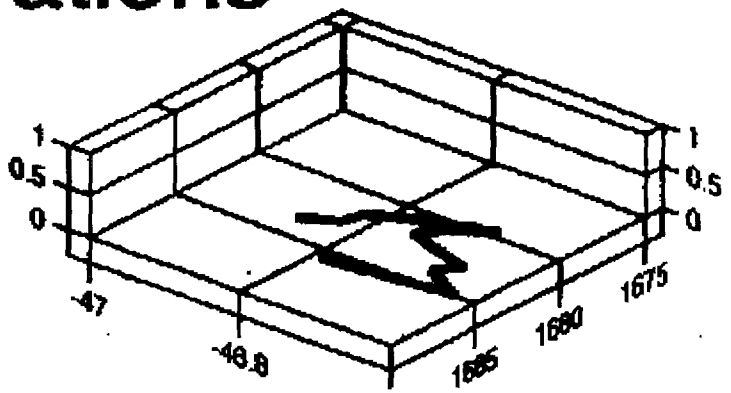

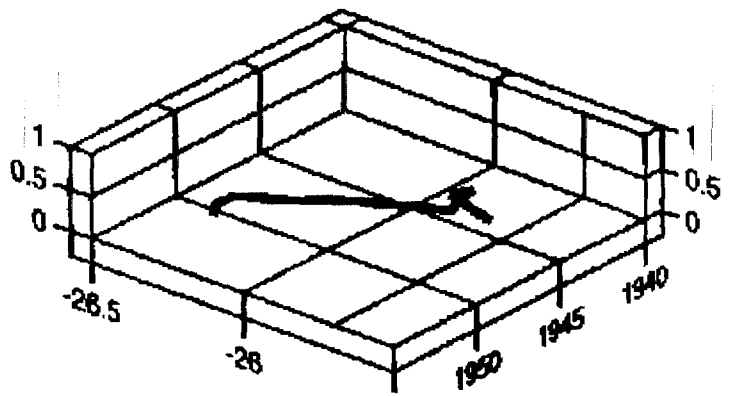

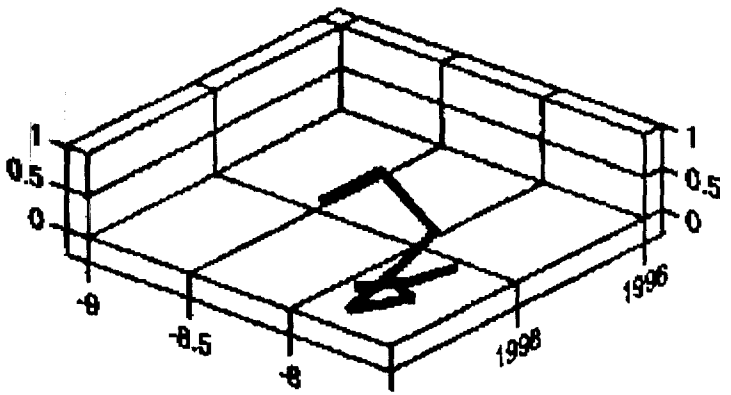

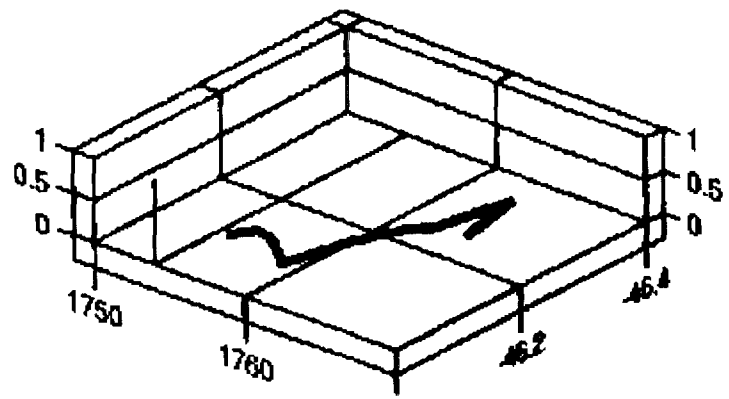

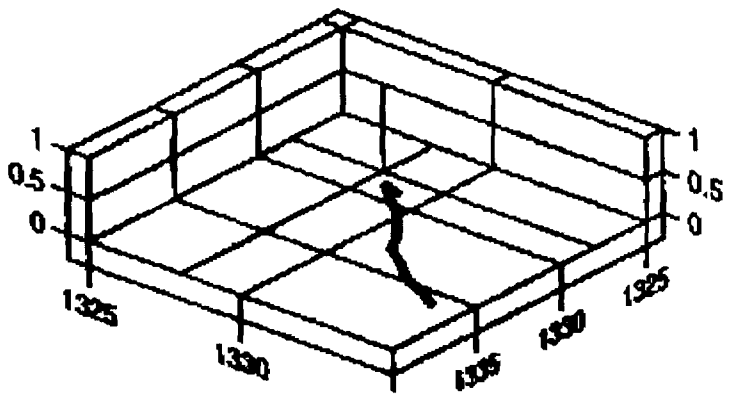

Statistical Analysis : Effect of Model Complexity

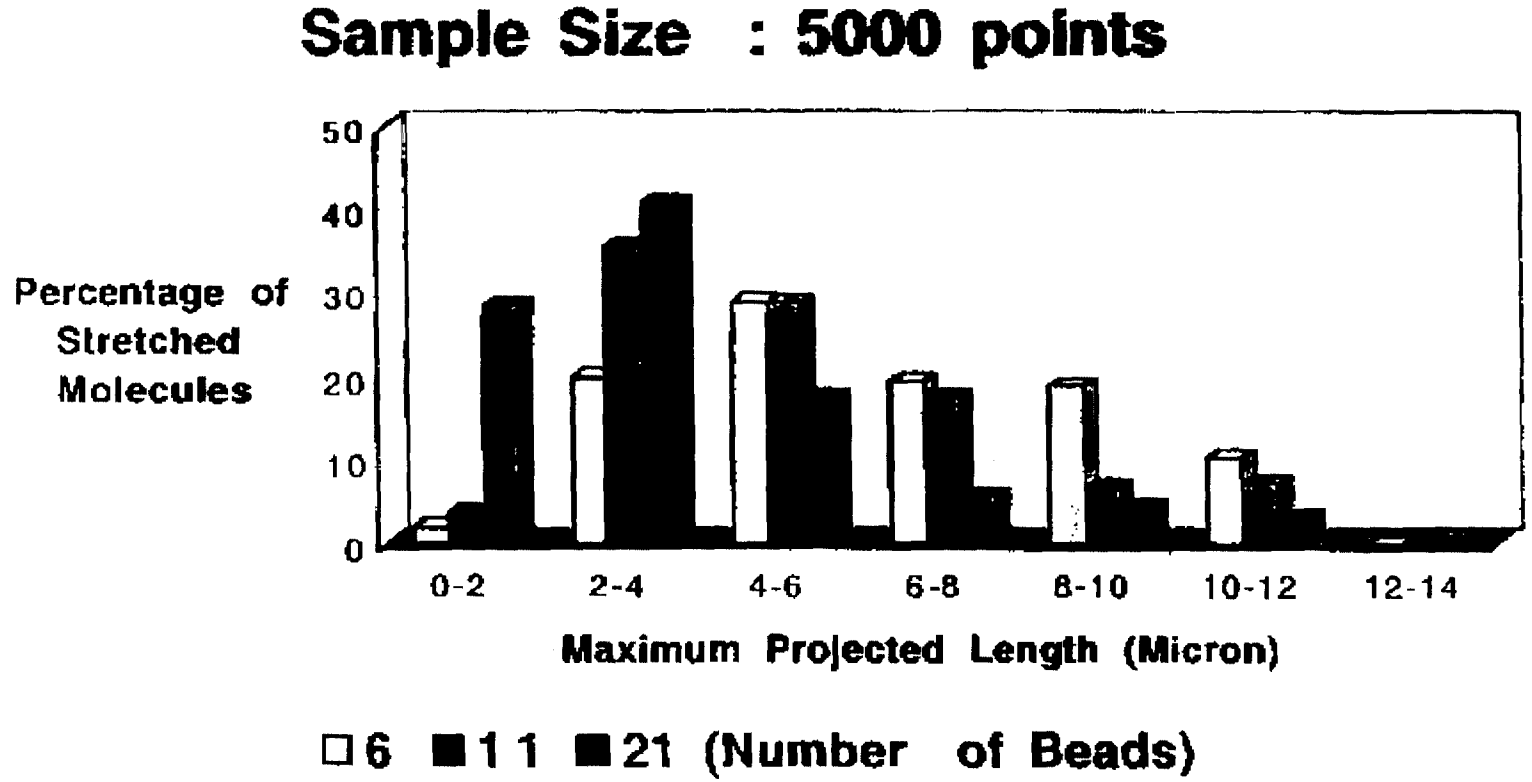

The bias in the Statistical Trends is due to the Infinite Stickiness Criterion used for the Substrate Surface

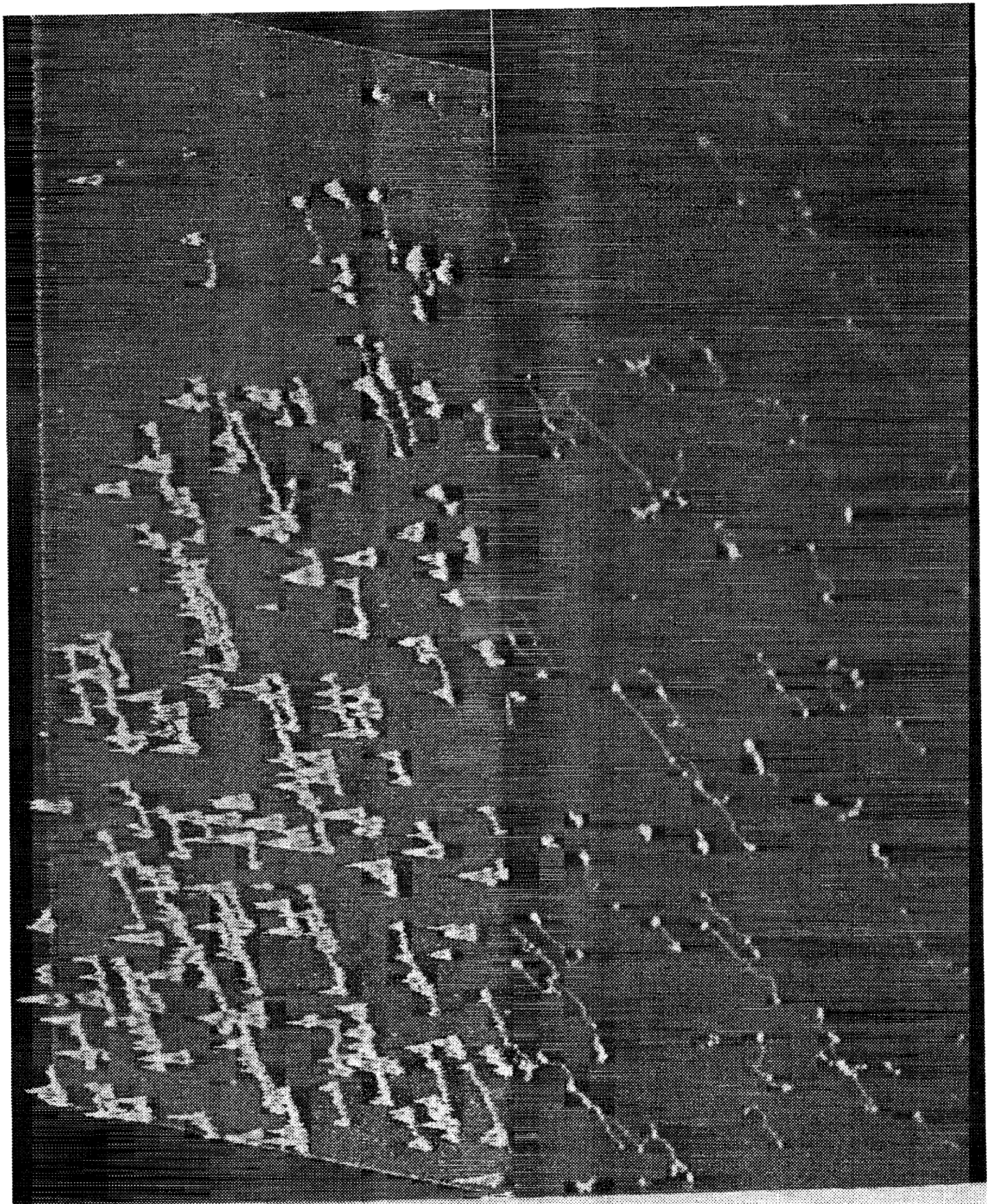

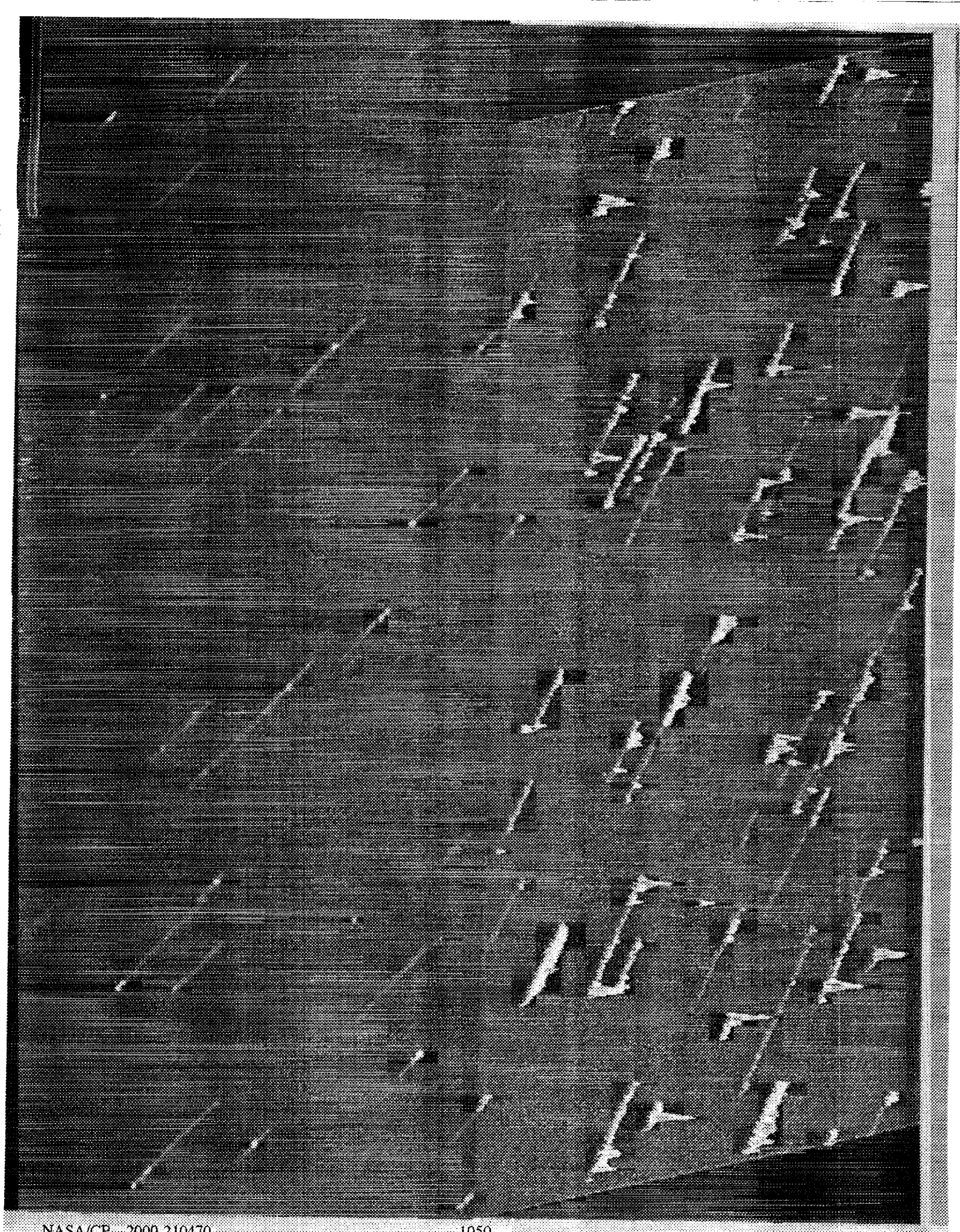

Frequency
Cumulative %
100%
90%
80%
70%
60%
50%
40%
30%
20%
10%
0%
20
18
16
14
12
10
8
6
4
2
0
1
2
3
4
5
6
8
9
10
11
More
Length (µm)

DIMENSIONLESS GROUPS (THERMAL EFFECTS)

$$\mathbf{Ma} \equiv \frac{(\partial\Gamma/\partial T)\Delta T}{\mu v} = \frac{(\partial\Gamma/\partial T)\Delta H_{vap}\rho h}{k\mu} \approx 8 \times 10^4$$

$$\mathbf{Gr} \equiv \frac{\rho^2 \alpha g h^3 \Delta H}{k\mu} \approx 80$$

DIMENSIONLESS GROUPS (THERMAL EFFECTS)

$$St \equiv \frac{k}{C_p \rho h v} \approx \frac{\frac{1}{\Delta T}\frac{dT}{dt}}{\frac{1}{h}\frac{dh}{dt}} \approx 200$$

=> quasi-steady-state temperature field &

convection does not affect temperature distribution

=> temperature distribution satisfies Laplace equation

$$Ma \equiv \frac{(\partial \Gamma/\partial T)\Delta T}{\mu v} = \frac{(\partial \Gamma/\partial T)\Delta H_{vap} \rho h}{k\mu} \approx 8 \times 10^4$$

$$Gr \equiv \frac{\rho^2 \alpha g h^3 \Delta H}{k\mu} \approx 80$$

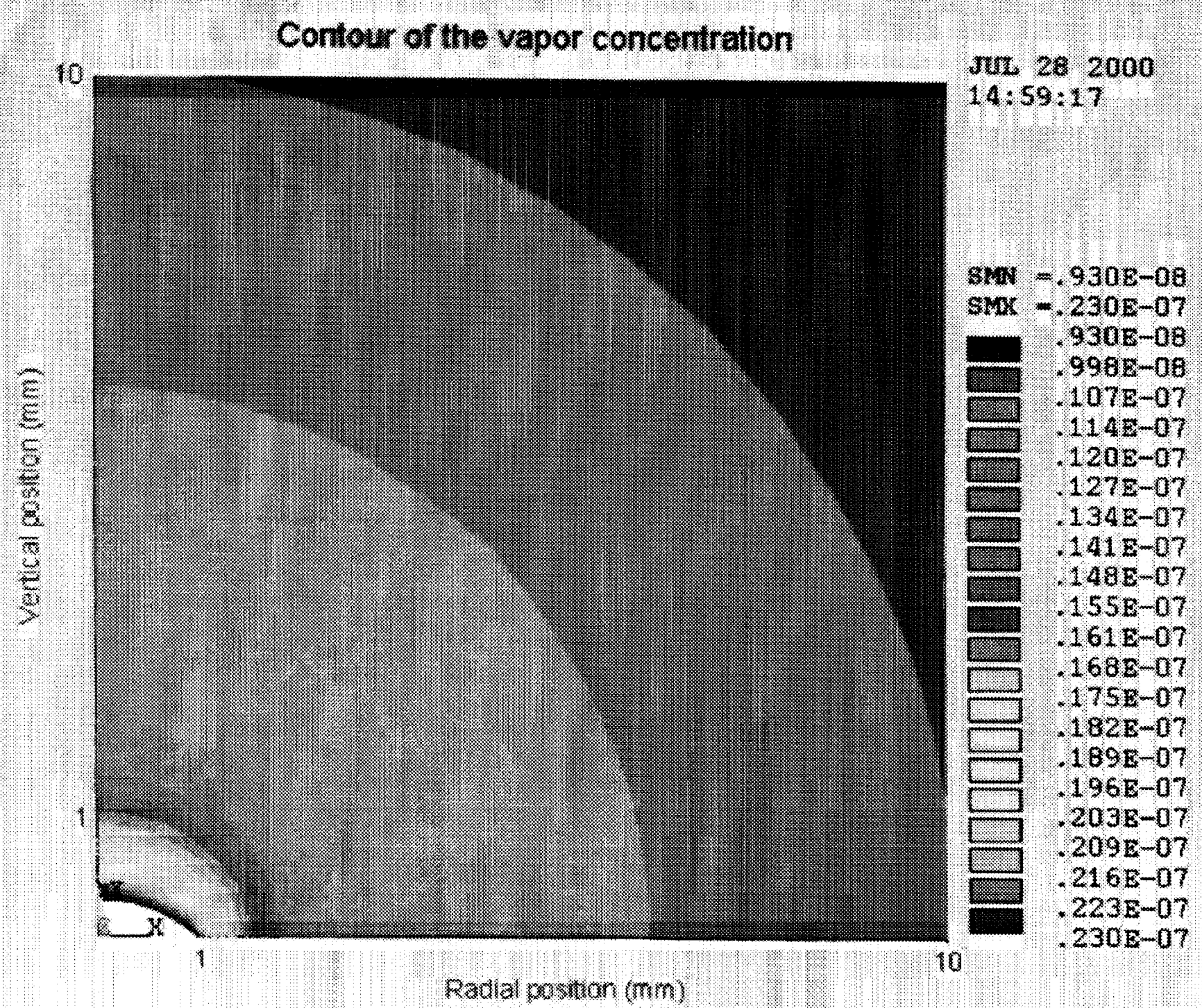
Contour of the vapor concentration
JUL 28 2000
14:59:17
SMN =.930E-08
SMX =.230E-07
.930E-08
.998E-08
.107E-07
.114E-07
.120E-07
.127E-07
.134E-07
.141E-07
.148E-07
.155E-07
.161E-07
.168E-07
.175E-07
.182E-07
.189E-07
.196E-07
.203E-07
.209E-07
.216E-07
.223E-07
.230E-07
10
1
1
10
Vertical position (mm)
Radial position (mm)

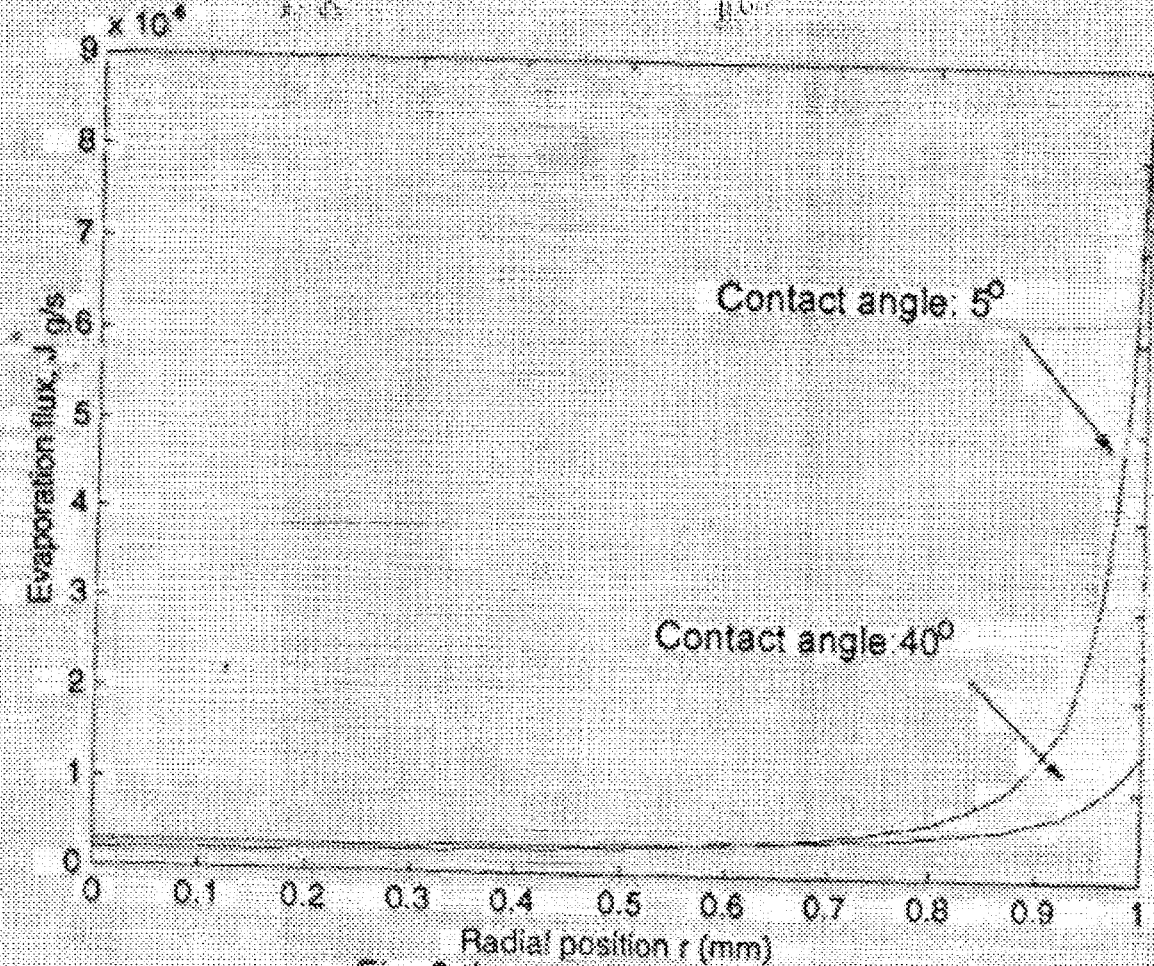

Fig. 2 the evaporation flux vs. r

Contour of the temperature distribution

NASA/CP—2000-210470

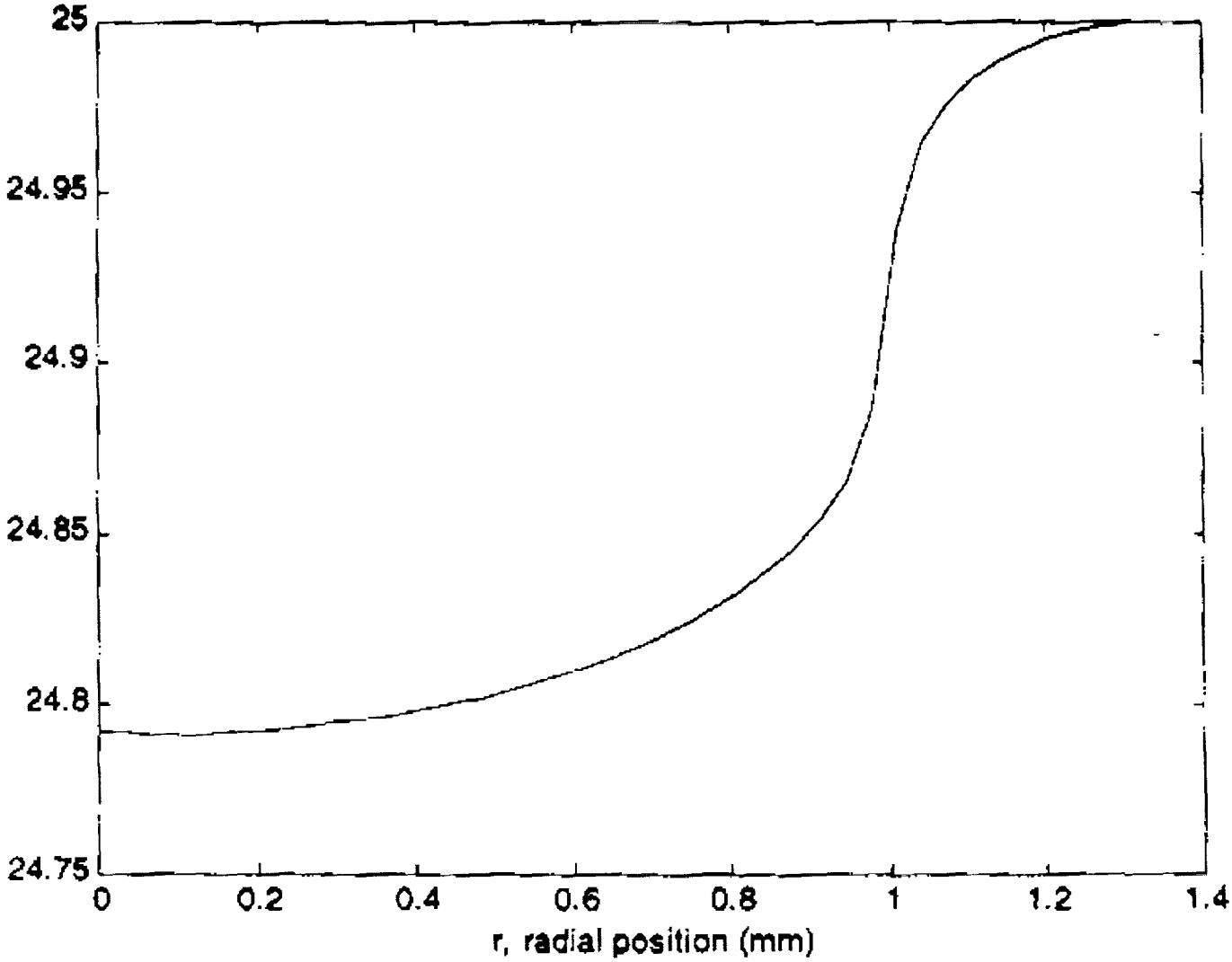

Fig. 5 The suface temperature vs. r

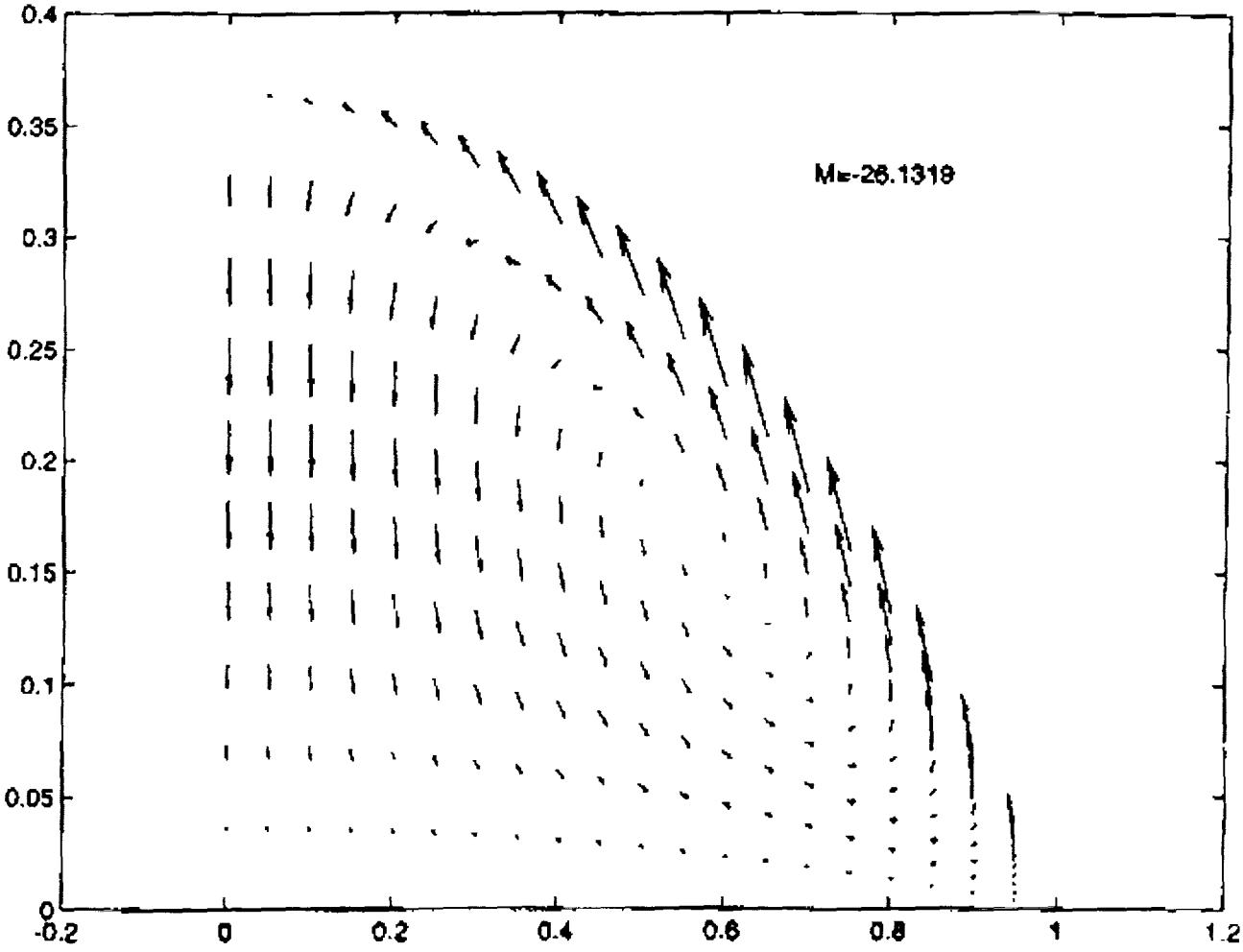
M=-26.1319
0.4
0.35
0.3
0.25
0.2
0.15
0.1
0.05
0
-0.2
0
0.2
0.4
0.6
0.8
1
1.2

SUMMARY

- DNA stretching in an evaporating droplet is sensitive to evaporation rate and surface adhesion.
- Measurement of the flow field in an evaporating droplet is challenging at 1g because of the requirements of small droplets/small tracer particles to avoid sagging/sedimentation.
- Using particle tracking with refringence to determine the z velocity, we find the flow field in an evaporating droplet to be in reasonable agreement with lubrication solution with thermal effects neglected.
- The evaporating droplet problem with thermal effects can be broken into 3 coupled quasi-steady problems: the external vapor field, the droplet thermal field, and the droplet flow field.
- The observed Marangoni flow is much weaker than predicted.
- Accurate prediction of DNA stretching in an evaporating droplet and in microfabricated devices will require combined analyses of the flow field, the DNA molecular dynamics, and the DNA surface adhesion.

INERTIAL EFFECTS ON THE HYDRODYNAMICS OF MOVING CONTACT LINES

S. Garoff[1], Y. Suo[1], K. Stoev[1], E. Ramé[2]
[1]Department of Physics and the Colloids, Polymers and Surfaces Program
Carnegie Mellon University, Pittsburgh, PA
[2]National Center for Microgravity Research, Cleveland, OH

ABSTRACT

The hydrodynamics near steadily moving contact lines have been examined for a variety of material systems for low Capillary number, Ca<<1, and negligible Reynolds number, Re~0. However, in nature and in technological applications, contact lines move under conditions of moderate Re and are often accelerating or decelerating. In both of these cases, the role of inertia in the hydrodynamics controlling spreading must be considered. In this paper, we will discuss these hydrodynamics in both the case of steady state motion of contact lines at moderate Re and the case of unsteady motion as the contact line accelerates or decelerates to a final steady state after a perturbation from another, initial, steady state. In our experiments we test models which incorporate inertia at steady state, and unsteady effects at essentially Re=0.

We first examine the steady state spreading of four ($-CH_3$)-terminated silicone oils on dry pyrex surfaces in the presence of significant inertia. Our measurements of the apparent dynamic contact angle, ω_0, agree qualitatively with Cox's predictions for this macroscopic contact angle and for the interface curvature when inertia is important.[1] However, quantitative comparisons of the hydrodynamics cannot be made because of the lack of a uniformly valid asymptotic solution for the interface shape and the ambiguities arising from the variation in inner physics with contact line speed.

We observe that the presence of inertia reduces the dynamic curvature in the interface shape and thus lowers ω_0. This is consistent with a simple picture of the effects of viscous forces and inertia. When inertia becomes non-negligible with respect to viscous forces, the dynamic pressure gradient near the fluid-vapor interface decreases. This is due to the fact that, when inertia becomes important, and all else being equal, the solid drags less fluid away from the contact line region. By mass conservation, less fluid must be brought into the contact line by flow along the liquid/vapor interface. This, in turn, implies that a smaller pressure gradient would be required along the interface to drive this smaller flow rate into the contact line region. By the dynamic boundary condition, this decreased dynamic pressure leads to a reduced local interface curvature compared to the purely viscous case as found in our experiments. In qualitative agreement with models incorporating inertia, the integrated effect of this reduced curvature at each point along the interface causes the reduction in ω_0 compared to the purely viscous case.

We can contrast the successes and failures in comparing data to theory for the dependence of ω_0 versus Ca, for four methyl-terminated oils. The quantitative success of the purely viscous model in predicting ω_0 versus Ca for the three higher viscosity oils ($3.0\times10^{-2}<\Gamma(\equiv Re/Ca)<2.6\times10^{2}$) is consistent with the success of the model in describing the interface shapes for these cases. We see that the inner scale parameters of these oils are velocity independent within our detectability limit. For our lowest viscosity oil ($\Gamma=3.3\times10^{4}$), no model quantitatively describes the observed dependence of ω_0 versus Ca. Since we do not know if the inner scale physics for this oil has a significant velocity dependence, we cannot draw a firm

conclusion on the moderate Re model. However, we note that the lowest viscosity oil evaporates and this could have an effect on inner scale mechanisms that results in a velocity dependence very different than higher viscosity oils with the same methyl termination.

We have also studied the relaxation of contact line motion and dynamic contact angles after an abrupt change in the relative velocity of the solid surface and the fluid body. In these experiments, Ca remains small and Re~0 throughout the acceleration or deceleration of the contact line. We used a model of the relaxation of the dynamic contact line by assuming that the interface shape is quasi-static, with an apparent contact angle equal to the steady value at the instataneous contact line speed relative to the solid.

Inertial effects are visible in our data for short times after the abrupt change in surface velocity. At these short times, we find that the viscous bending of the interface differs from that of a steadily moving contact line. Thus, we detect a deviation from Stokes flow in the intermediate region near the contact line at early times. At very short times (i.e., less than ~1sec for the lesser viscous fluid, 1000 cPoise) the contact angle relaxation also disagrees with our quasi-static model. Later on after the abrupt change in surface velocity, the interface shape agrees with the predictions of the steady state model, indicating that the flow near the contact line has returned to Stokes flow, and the quasi-static model describes the contact line relaxation well. At long times, near the final steady state, the relaxation becomes exponential as expected near the final point. Our models work equally well for both accelerating and decelerating contact lines. The time scales both for the early time inertial regime and for the later quasi-static regime vary linearly with viscosity. However, these times scales do not differ for -OH and $-CH_3$ terminated oils of the same viscosity even though these oils show very different steady state inner scale physics. Thus, the contact line relaxation we observe is likely due to viscous reorientation of the fluid motion in the intermediate and outer regions and not controlled by relaxation of inner scale hydrodynamic mechanisms.

[1] Cox, R.G., J. Fluid Mech. **357**, pg 249,1998.

EFFECTS OF INERTIA AND UNSTEADY MOTION ON THE HYDRODYNAMICS NEAR MOVING CONTACT LINES

S. Garoff
Y. Suo
K. Stoev
Carnegie Mellon University

E. Ramé
National Center for Microgravity Research

Support: NASA

OUTLINE

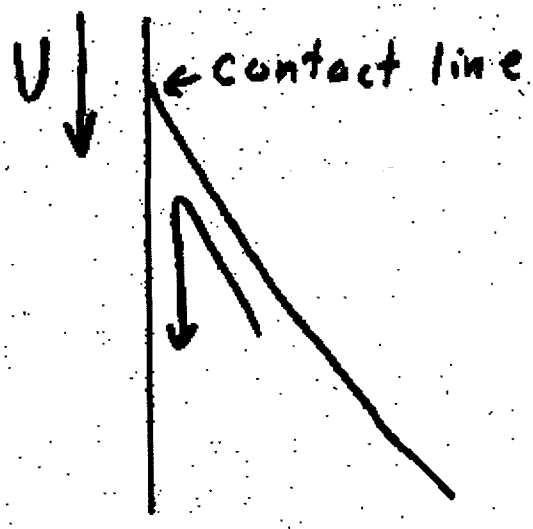

- Effects of dynamics on fluid/vapor interface shape near a moving contact line

- Model and confirming experiments for case of:
  - steady state
  - weak viscous forces (Ca<<1)
  - negligible inertia (Re~0)

- Steady state with "moderate" inertial effects (Ca<<1, Re~1)

- Unsteady motion

OUTLINE

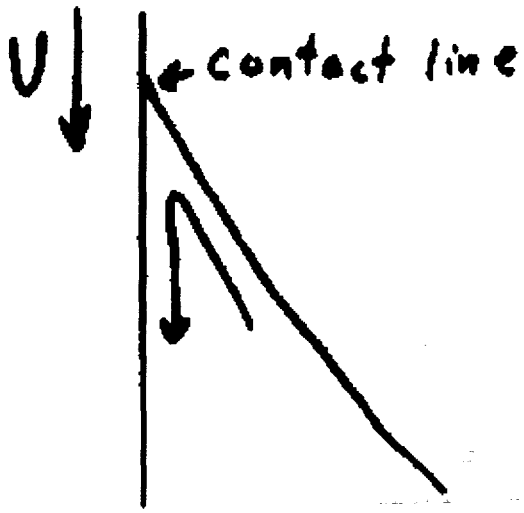

- Effects of dynamics on fluid/vapor interface shape near a moving contact line

- Model and confirming experiments for case of:
  - steady state
  - weak viscous forces (Ca<<1)
  - negligible inertia (Re~0)

- Steady state with "moderate" inertial effects (Ca<<1, Re~1)

- Unsteady motion

EXPERIMENTAL GEOMETRY FOR STUDYING MOVING CONTACT LINES: CYLINER FORCED INTO LIQUID BATH

- Steady State:

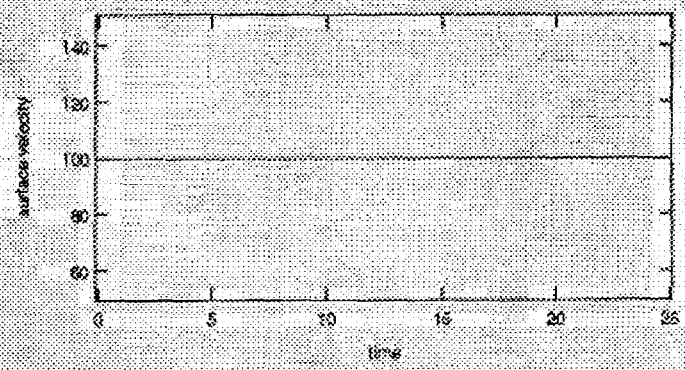

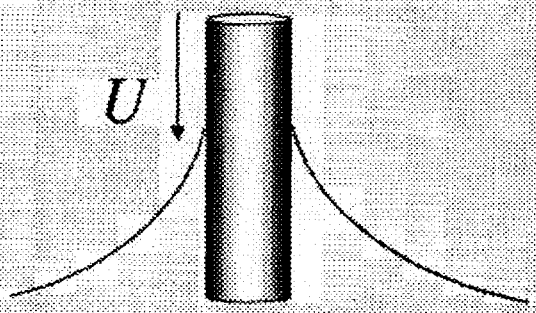

- Unsteady State:

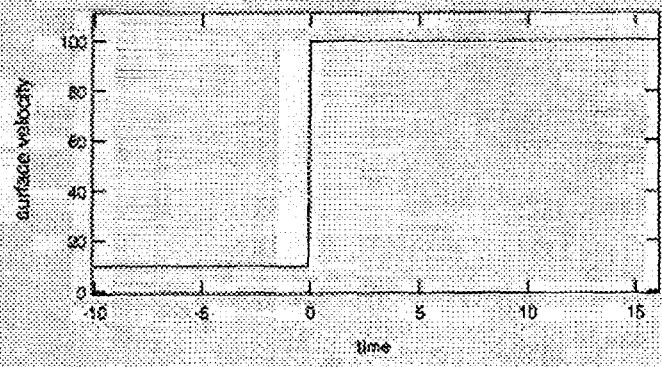

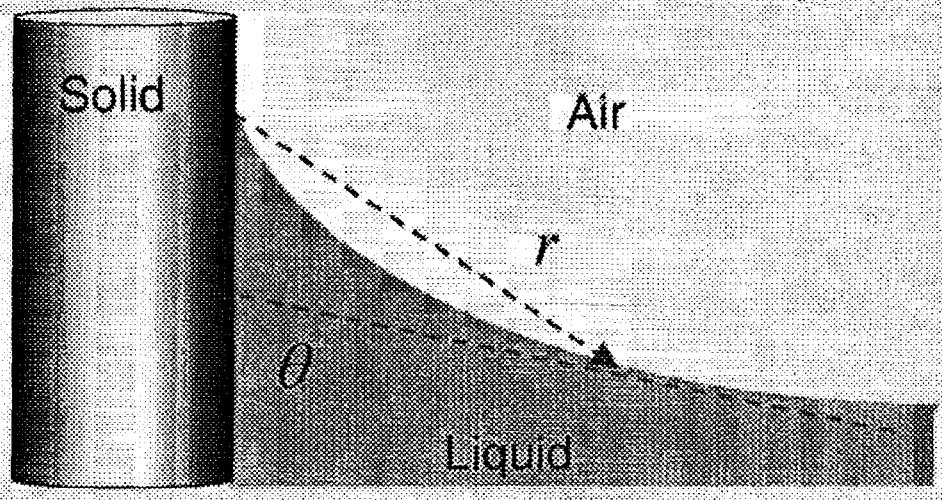

Statics ≠ Dynamics

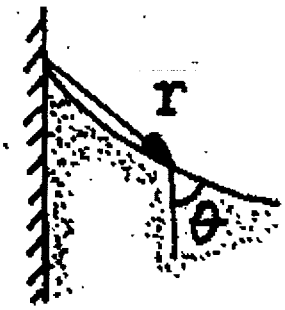

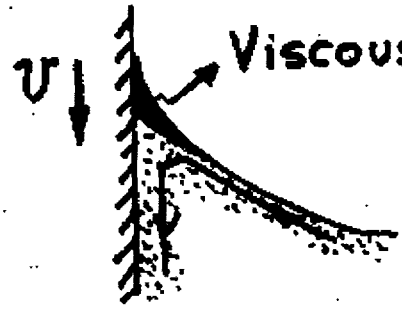

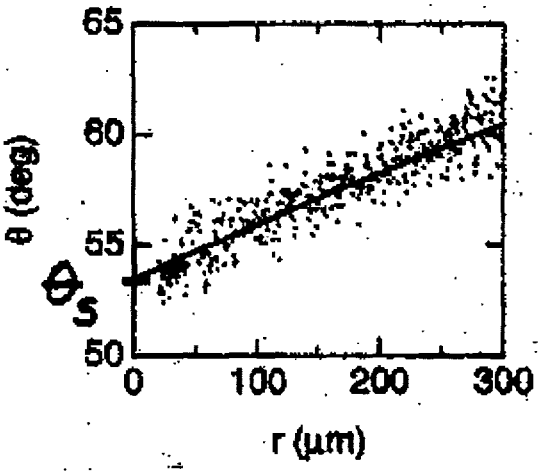

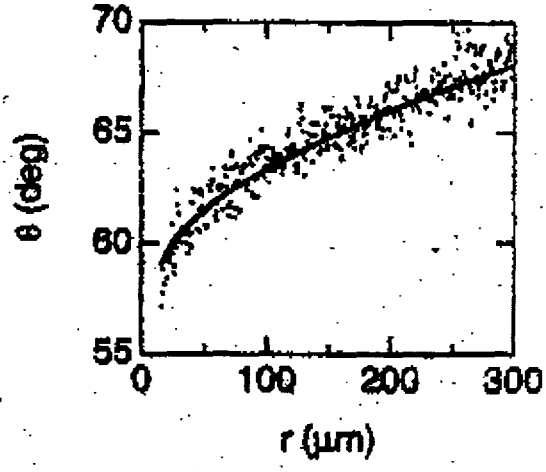

Statics **Dynamics**

FLUID MOTION NEAR CONTACT LINE CAUSES "EXTRA" BENDING OF INTERFACE

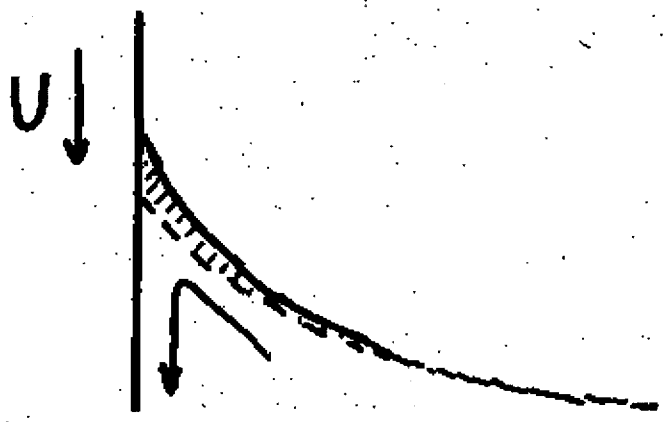

- Stress jump across the fluid/vapor interface balanced by interfacial curvature

$$\Delta\left[P_{dyn} + P_{static} + Ca\ \hat{n} \bullet \left\{\nabla\vec{u} + \nabla\vec{u}^{T}\right\} \bullet \hat{n}\right] = \kappa$$

Ca = capillary number = $\mu U/\gamma$

U = contact line speed — μ = viscosity

γ = surface tension — u = scaled fluid velocity

P = scaled pressure — κ = scaled interface curvature

- Viscous forces bend interface

- Focusing of flow near contact line causes increased bending as contact line approached
(- curvature actually diverging)

Experimental

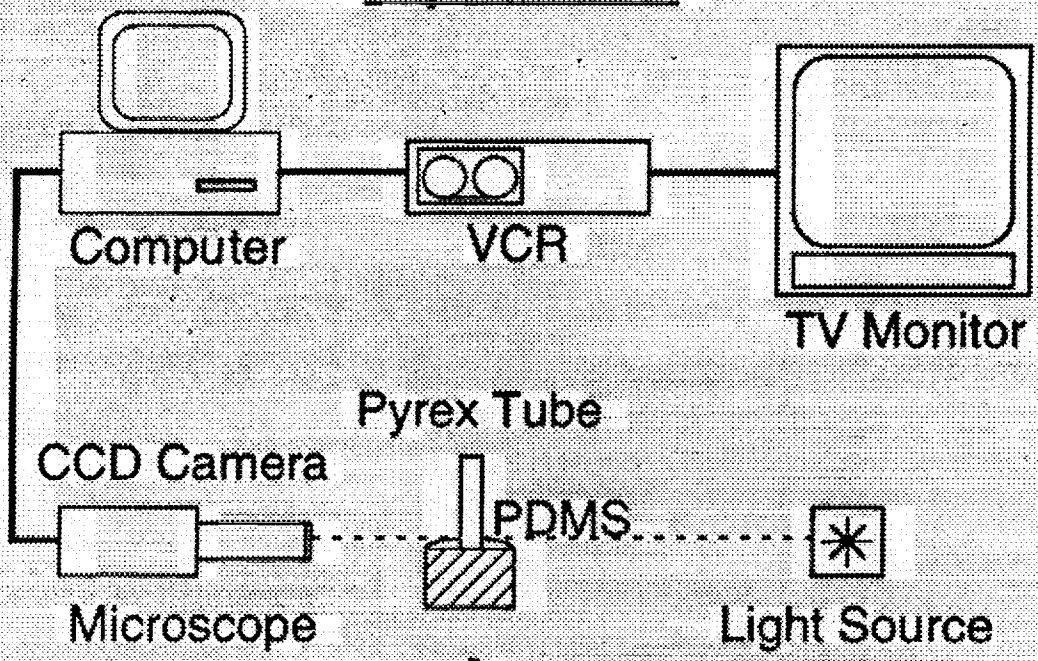

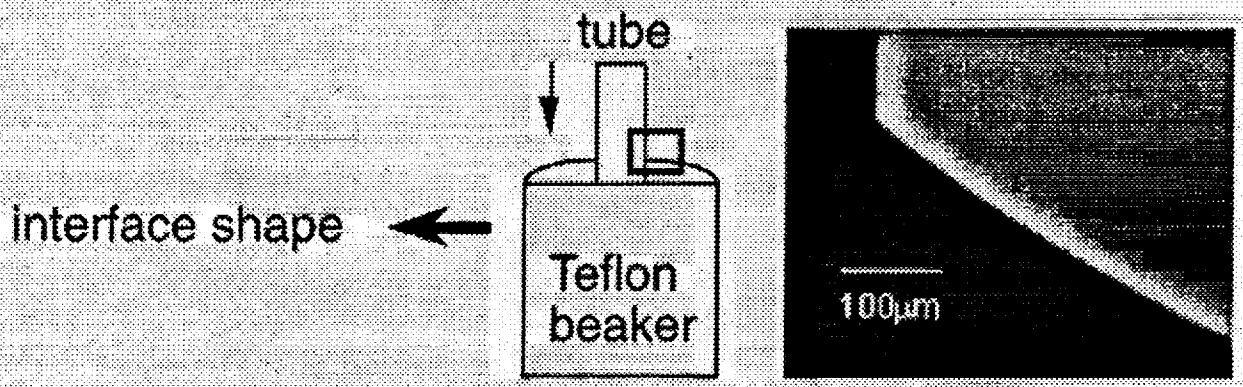

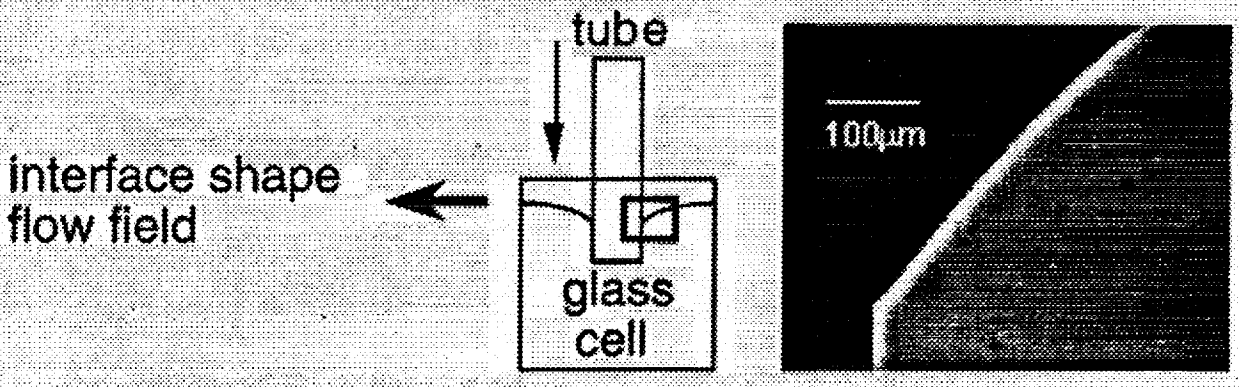

Statics ≠ Dynamics

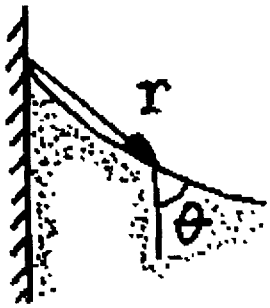

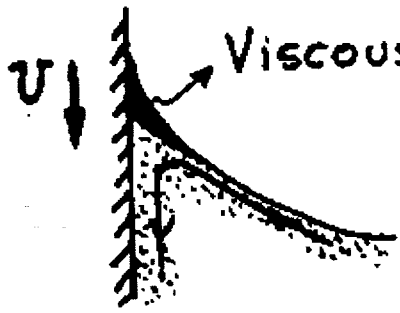

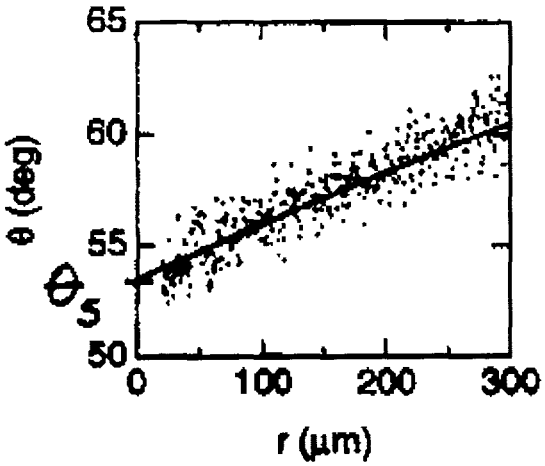

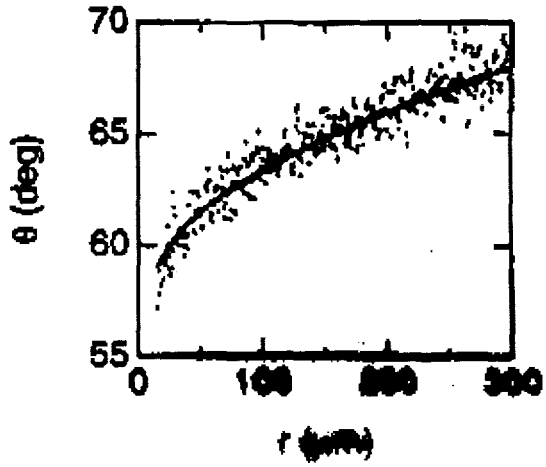

Statics **Dynamics**

INERTIA EFFECTS STEADY STATE INTERFACE SHAPE AND APPARENT DYNAMIC CONTACT ANGLE

- $\cancel{\mathrm{Re}\frac{\partial u}{\partial t}} + \mathrm{Re}\,Ca\left(u\cdot\tilde{\nabla}u\right) = -\tilde{\nabla}\tilde{P} + Ca\tilde{\nabla}^2 u$
- Moderate Re, asymptotic model (for Re~0) fails
- Examine local dynamic curvature = $\gamma\kappa_{measured} - \rho g y$
- At moderate Reynolds number, interface curved less than predicted from pure viscous bending

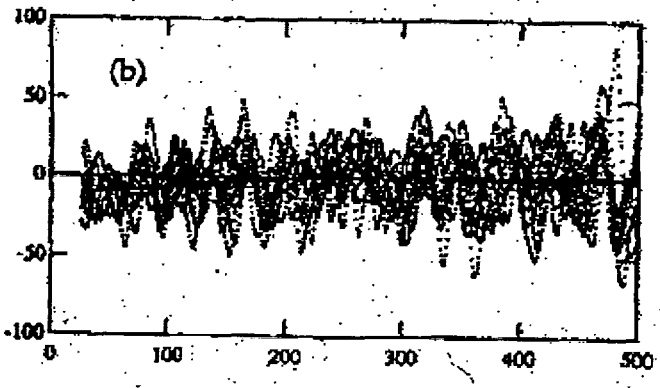

$Re = 1.6$

$Ca = 5 \times 10^{-5}$

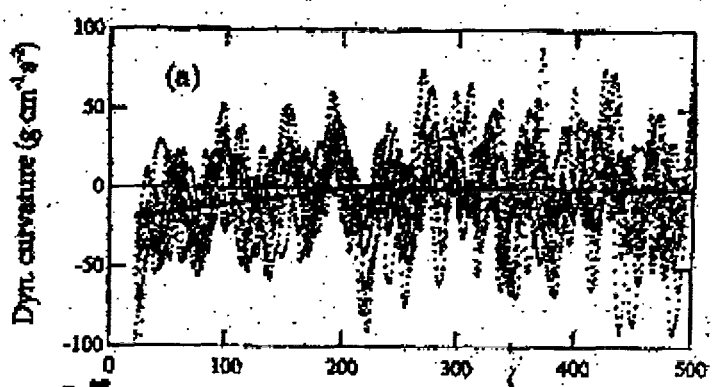

$Re = 10^{-4}$

- Apparent contact angle decreased by inertia (Cox)

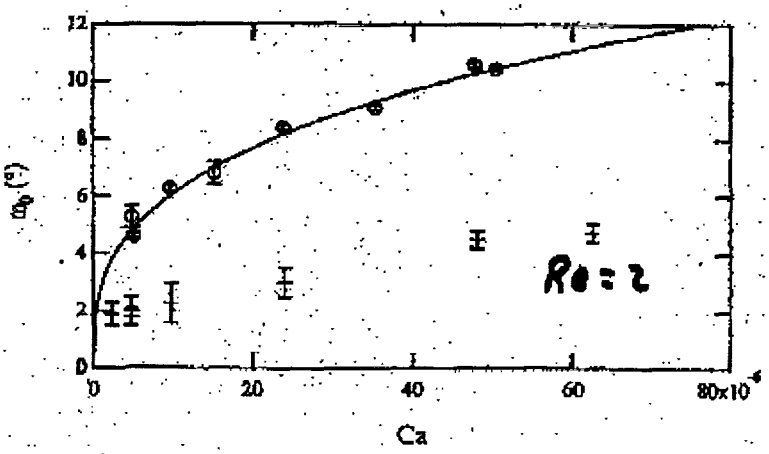

$$\frac{Re_{bottom}}{Re_{top}} \doteq 10^4$$

FLUID MOTION NEAR CONTACT LINE CAUSES "EXTRA" BENDING OF INTERFACE

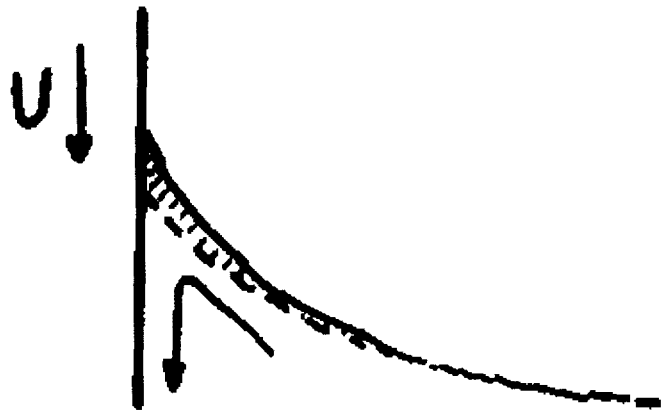

- **Stress** jump across the fluid/vapor interface balanced by interfacial curvature

$$\Delta\left[P_{dyn} + P_{static} + Ca\ \hat{n} \bullet \left\{\nabla\bar{u} + \nabla\bar{u}^{T}\right\} \bullet \hat{n}\right] = \kappa$$

Ca = capillary number = $\mu U/\gamma$

U = contact line speed — μ = viscosity

γ = surface tension — u= scaled fluid velocity

P = scaled pressure — κ = scaled interface curvature

- Viscous forces bend interface

- Focusing of flow near contact line causes increased bending as contact line approached
(- curvature actually diverging)

ASYMPTOTICALLY MATCHED SOLUTION PREDICTS STEADY STATE INTERFACE SHAPE WHEN Ca<<1 and Re~0

- Solve Stokes Equation:

$$\cancel{\mathrm{Re}\frac{\partial u}{\partial t} + \mathrm{Re}\,Ca\left(u\cdot\tilde{\nabla}u\right)} = -\tilde{\nabla}\tilde{P} + Ca\tilde{\nabla}^2 u$$

- Solution:

$$\theta(r) = g^{-1}\left(g(\omega_0) + Ca\ln(\frac{r}{a}) \right) + f(\frac{r}{a}) - \omega_0$$

$$g(x) = \int_0^x \frac{y - \cos y \sin y}{2\sin y} dy$$

a : capillary length

f : interface shape far from contact line

- ω_0 : "apparent contact angle"
  - single fitting parameter
  - connected to shape far from contact line

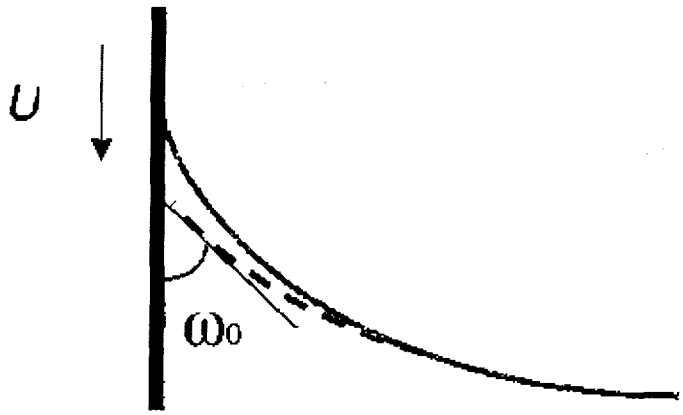

MODEL ACCURATELY DESCRIBES INTERFACE SHAPE AND FLOW FIELD FOR Ca<0.1

(PDMS on Pyrex)

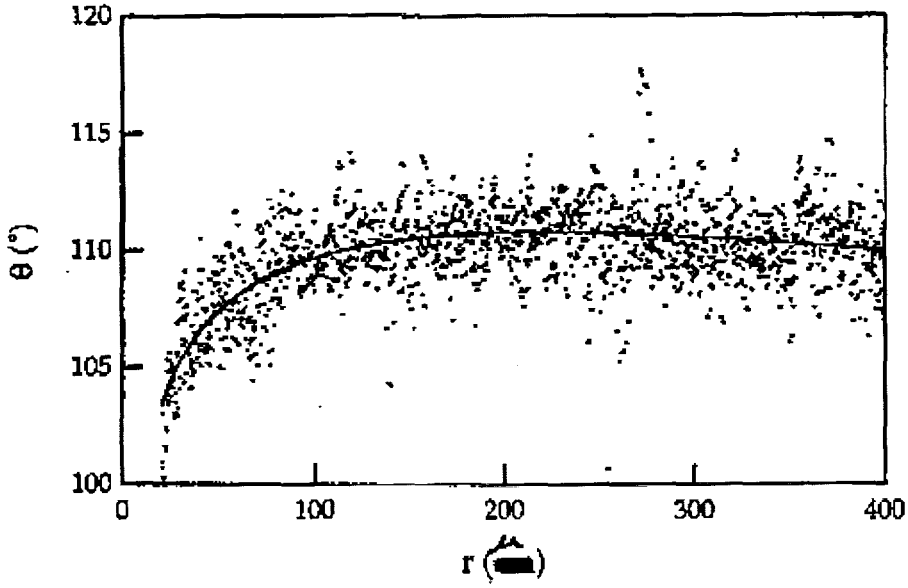

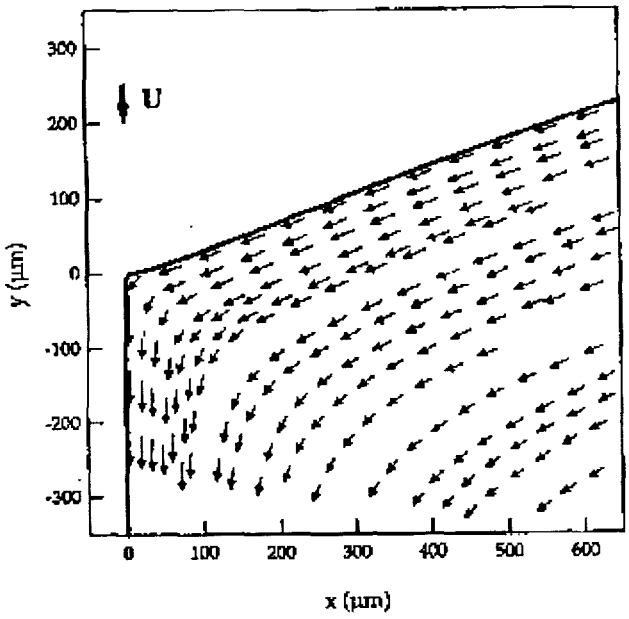

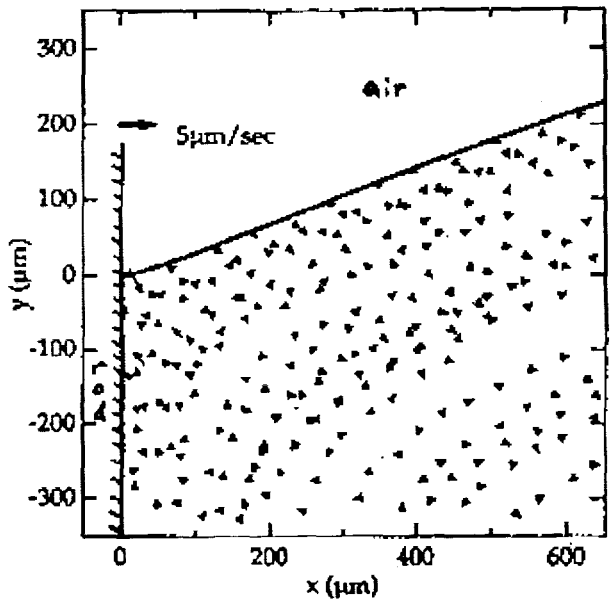

Ca = 0.1
u = 33 μm/s

- Asymptotic model describes flow field and resulting viscous bending
  - Ca measured independently; experiment strong test of model of bending
  - places restrictions on asymptotic behavior of inner physics

INERTIA EFFECTS STEADY STATE INTERFACE SHAPE AND APPARENT DYNAMIC CONTACT ANGLE

- $\cancel{Re\frac{\partial u}{\partial t}} + Re\,Ca\,(u\cdot\tilde{\nabla}u) = -\tilde{\nabla}\tilde{P} + Ca\tilde{\nabla}^2 u$
- Moderate Re, asymptotic model (for Re~0) fails
- Examine local dynamic curvature = $\gamma\kappa_{measured} - \rho g y$
- At moderate Reynolds number, interface curved less than predicted from pure viscous bending

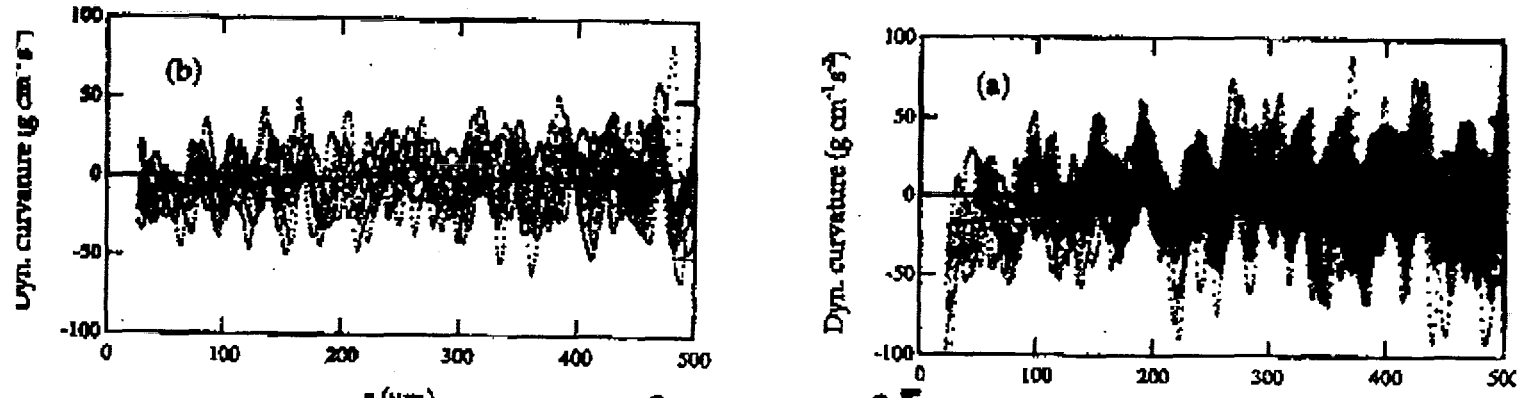

- Apparent contact angle decreased by inertia (Cox)

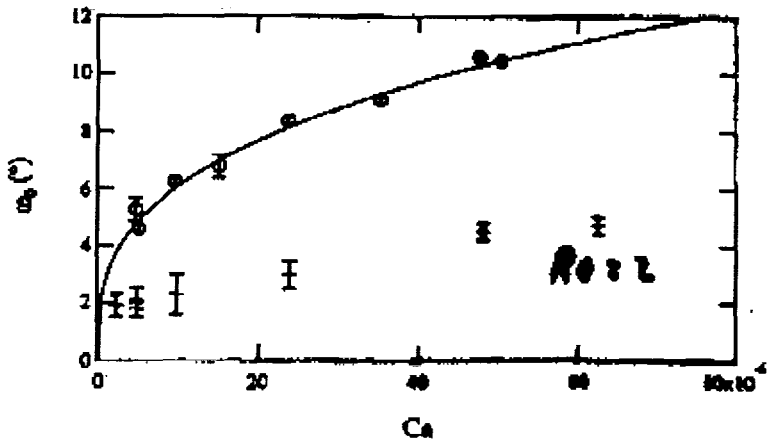

$$\frac{Re_{bottom}}{Re_{top}} = 10^4$$

PROBE UNSTEADY EFFECTS USING STEP CHANGE IN SURFACE VELOCITY

- Probe interface as it relaxes to new steady state
  - measure $\omega_0(t)$

- Experiments run with Re~0

- N-S without convective term

$$\mathrm{Re}\frac{\partial u}{\partial t} + \mathrm{Re}\,Ca\,u\cdot\tilde{\nabla}u = -\tilde{\nabla}\tilde{P} + Ca\tilde{\nabla}^2 u$$

- Compare data to quasi-steady model for temporal relaxation of $\omega_0(t)$
  - only holds when Stokes flow describes hydrodynamics near contact line

- Disagreement with asymptotic model and/or quasi-steady model $\Rightarrow$ unsteady flow effects detectable

Model Using Asymptotic Match Describes Quasi-Steady Relaxation

- Acceleration ($U_i < U_f$)

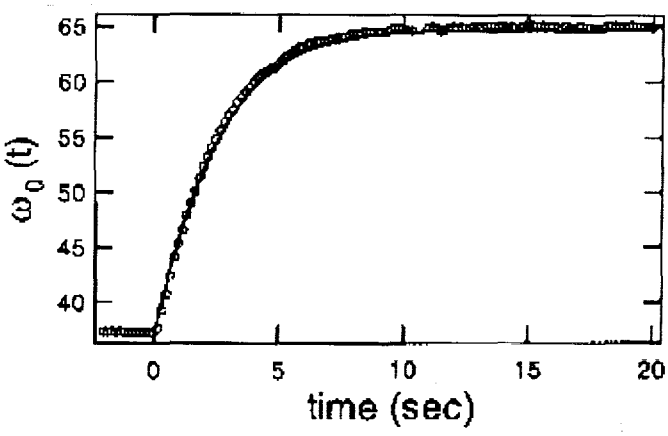

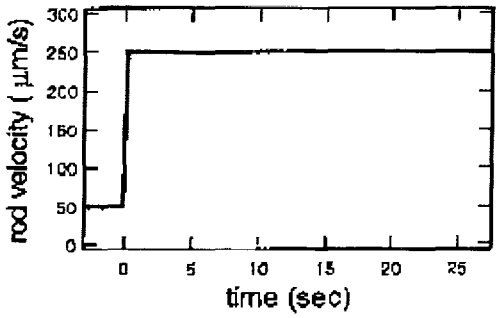

- Deceleration ($U_i > U_f$)

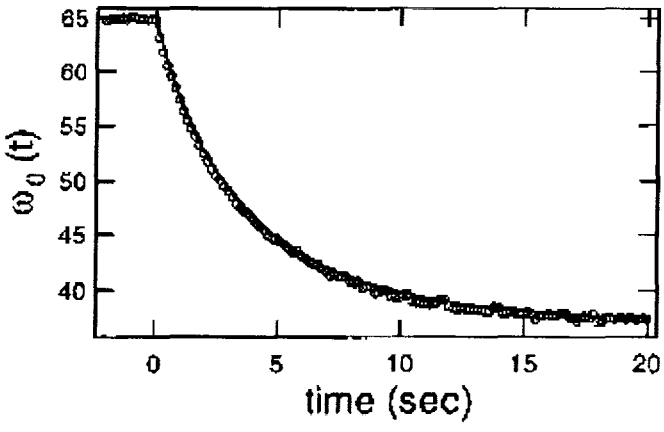

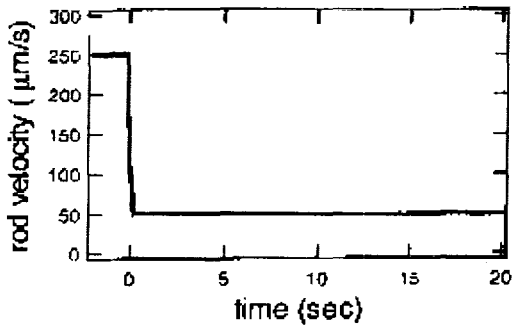

suo@andrew.cmu.edu

Early time: deviations from Stokes flow

- Stokes flow model (asymptotic matched solution) fails

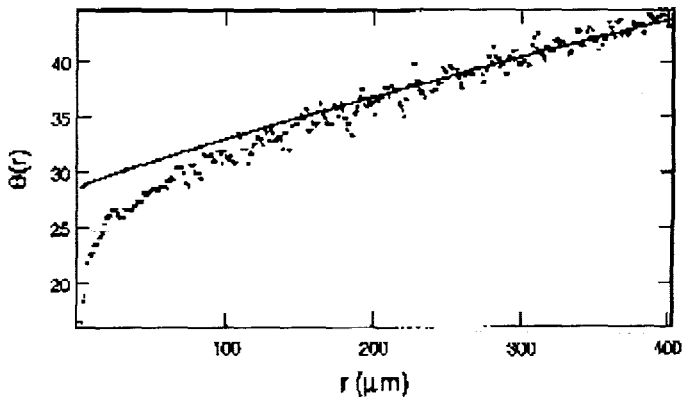

- Deviations from quasi-steady model

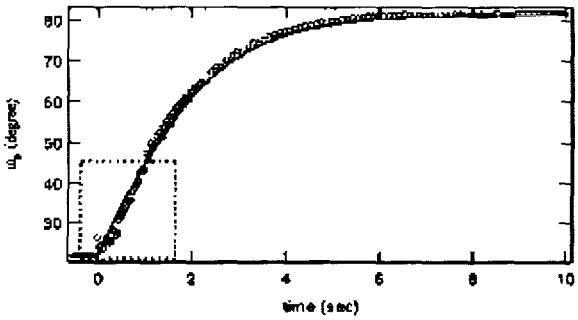

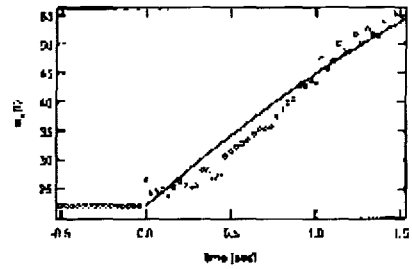

- Deviation is larger when rod velocity change is larger

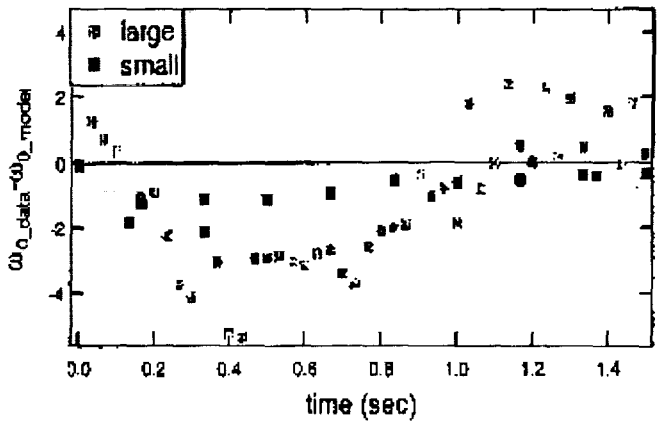

suo@andrew.cmu.edu

EFFECTS OF INERTIA AND UNSTEADY MOTION ON HYDRODYNAMICS NEAR MOVING CONTACT LINES

- Fluid flow near contact line causes bending of the interface and raising of apparent contact angle

- Model for bending quantitatively successful for steady state with $Ca<0.1$ and $\tilde{R}e \sim 0$
  - surface appears "less wettable" than static case

- Effects of steady state inertia:
  - decrease of curvature near contact line
  - increase in apparent contact angle
    - surface appears more wettable than purely viscous case

- Effects of step change in velocity of surface
  - contact line relaxes toward new steady state (mainly governed by viscous forces in our case)
  - unsteady motion does affect interface curvature and contact line relaxation at early times
    - a sign of inertial effects
  - clear implications for motion of contact lines and contact line dissipation on oscillating surfaces

LIQUID BRIDGE STABILIZATION WITH ACOUSTIC RADIATION AND MAXWELL STRESS

D. B. Thiessen, M. J. Marr-Lyon, and P. L. Marston, Department of Physics, Washington State University, Pullman, WA 99164-2814; marston@wsu.edu

ABSTRACT

The stability of a liquid cylinder which bridges two solid cylinders has implications for the management of fluids in low-gravity. It is well known that a cylindrical liquid bridge in zero gravity becomes unstable and breaks when the length of the cylinder exceeds its circumference. The ratio of length to diameter of a cylindrical liquid bridge is defined as the slenderness, $S = L/2R$, and the stability limit $S = \pi$ is known as the Rayleigh-Plateau limit. A stable cylindrical liquid bridge has many modes of oscillation corresponding to different volume-conserving surface deformations. The lowest-frequency mode, known as the (2,0) mode, is the first to become unstable when the slenderness exceeds π. The (2,0) mode is an axisymmetric surface deformation in which one end of the bridge becomes fat and the other end thin. At the point of instability, the deformation grows until the thin end of the bridge breaks. The stabilization schemes explored in this work are based on counteracting the growth of this surface deformation by applying a surface stress distribution which either preferentially pushes radially inward on the fat part of the bridge or pulls radially outward on the thin part. We used active control of acoustic radiation stress [1] and Maxwell electrostatic stress [2] to stabilize liquid bridges in a Plateau tank. Passive acoustic stabilization as well as the active electrostatic method were demonstrated in air in the simulated low gravity of NASA's KC-135 aircraft.

Considering only the (2,0) mode, the dynamics of the bridge is similar to the dynamics of a damped harmonic oscillator in which the mode amplitude corresponds to the oscillator's displacement. The (2,0) mode surface deformation has an associated change in surface area which provides a restoring force proportional to the (2,0) mode amplitude. The effective spring constant for this restoring force is proportional to $\left[(\pi/S)^2 - 1\right]$. Thus the natural spring constant becomes negative when $S > \pi$ which results in instability. An applied stress distribution which couples into the (2,0) mode can act as an additional generalized force on the oscillator's mass. If this applied force is proportional to the amplitude of the (2,0) mode deformation, with the appropriate feedback gain the effective spring constant can be made positive for $S > \pi$, thus allowing for longer stable bridges. Active feedback stabilization involves optically sensing the (2,0) mode amplitude and altering the stress distribution on the bridge [1,2]. For the case of passive acoustic stabilization, an additional restoring force from acoustic radiation stress naturally arises from the interaction between the bridge shape and the sound field. The acoustic wavelength is chosen such that the radiation pressure due to the sound field is a function of the local bridge radius, such that fat regions are squeezed and thin regions are expanded.

Laboratory experiments: We currently stabilize liquid bridges in a Plateau tank by actively controlling Maxwell electrostatic stresses [2]. The aqueous bridge is made slightly electrically conducting by adding a small amount of NaCl. Two ring electrodes concentric with the bridge are positioned near the ends of the bridge in an insulating liquid. The diameter and spacing of the electrodes are chosen in such a way that the stress distribution couples strongly into the (2,0) bridge mode when a voltage is applied to either electrode. When one end of the bridge begins to thin, the electrode voltages are adjusted to expand that end of the bridge counteracting the tendency to break. Stabilization has been accomplished with $S = 4.49$ by this method. Beyond this S, the (3,0) mode becomes unstable, though in principle the (3,0) mode may be stabilized by adding a third electrode. New algorithms for selecting the electrode potentials improved the preliminary results noted in [3].

KC-135 based experiments: Significant advances on the stabilization of liquid bridges in air were facilitated by freely floating the experimental package and by improving the control algorithm and the bridge deployment. Long bridges broke immediately when stabilization was turned off. Liquid bridges (a water, glycerol, NaCl solution) were stabilized to $S = 3.8$ using active control of Maxwell stresses. Figure 1 shows a bridge stabilized for over 2 seconds with $S = 3.8$ prior to breaking in response to an increased g-level. Passive acoustic stabilization (obtained by improving the method in [3]) made it possible to hold bridges with $S = 4.0$ and longer for intervals exceeding 5 seconds. Figure 2 is an example with $S = 4.0$ where the bridge breaks in response to g-jitter. Bridges stabilized in this way have an elliptical profile in response to the radiation pressure of the ultrasonic standing wave. It is anticipated that stabilization in air by either method may be significantly improved on a space-based platform and that the response to g-jitter may be suppressed.

This research was supported by NASA grants NAG3-1918 and NAG3-2378.

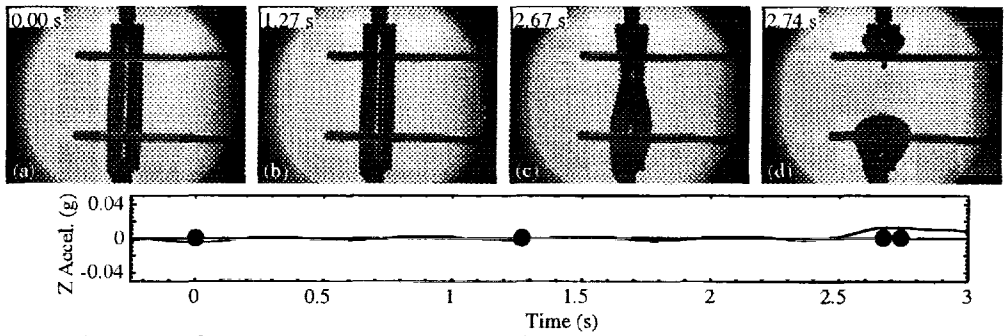

Figure 1: A capillary bridge stabilized to S=3.8 with active control of Maxwell stresses on the KC-135.

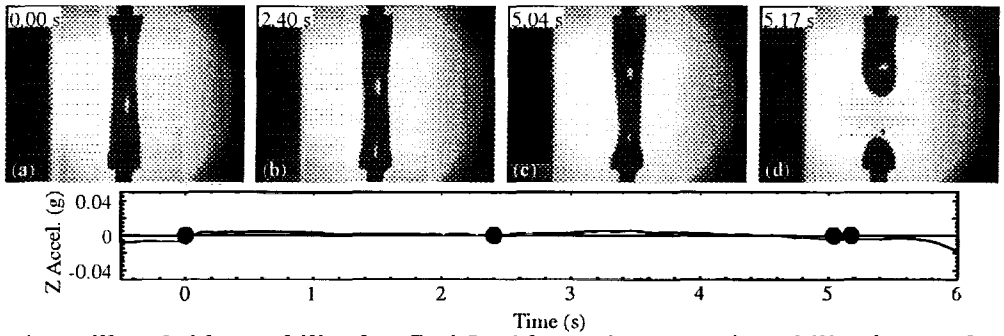

Figure 2: A capillary bridge stabilized to S=4.0 with passive acoustic stabilization on the KC-135.

REFERENCES

[1] M. J. Marr-Lyon, D. B. Thiessen, and P. L. Marston, "Stabilization of a cylindrical capillary bridge far beyond the Rayleigh-Plateau limit using acoustic radiation pressure and active feedback," J. Fluid Mech. **351**, 345-357 (1997).

[2] M. J. Marr-Lyon, D. B. Thiessen, F. J. Blonigen and P. L. Marston, "Stabilization of electrically conducting capillary bridges using feedback control of radial electrostatic stresses and the shapes of extended bridges," Phys. Fluids **12**, 986-995 (2000).

[3] M. J. Marr-Lyon, D. B. Thiessen, F. J. Blonigen, and P. L. Marston, "Radiation and Maxwell stress stabilization of liquid bridges," in Proceedings of the 4th Microgravity Fluid Physics Conference (1998) pp. 570-574.

Passive and Active Stabilization of Liquid Bridges in Low Gravity

Philip L. Marston
→ Mark J. Marr-Lyon
→ David B. Thiessen

Department of Physics
Washington State University
Pullman, WA 99164-2814

marston@wsu.edu

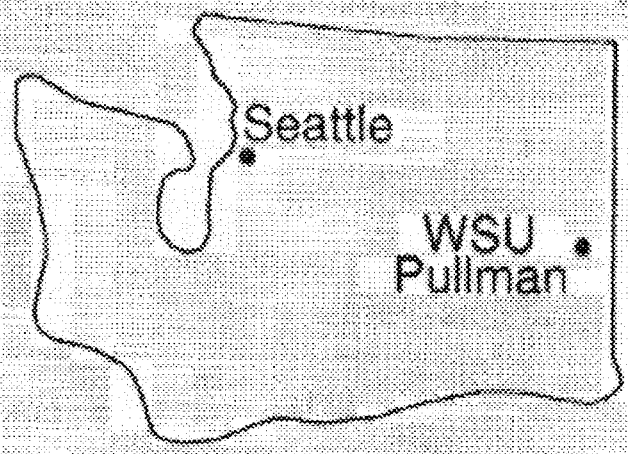

Work supported by NASA Grant NAG3-2378.

1. Review of Plateau-tank experiments:
   "Stabilization of electrically conducting capillary bridges using feedback control of radial electrostatic stresses and the shapes of extended bridges," Phys. Fluids **12**, 986-995 (2000).
2. Stabilization of bridges in air on the KC-135:
   (a) Active control of electrostatic stresses (AES),
   (b) Passive acoustic stabilization (PAS) with radiation pressure.

Introduction

Long bridges naturally become unstable to an axisymmetric mode in which one half bulges while the other thins — the (2,0) mode.

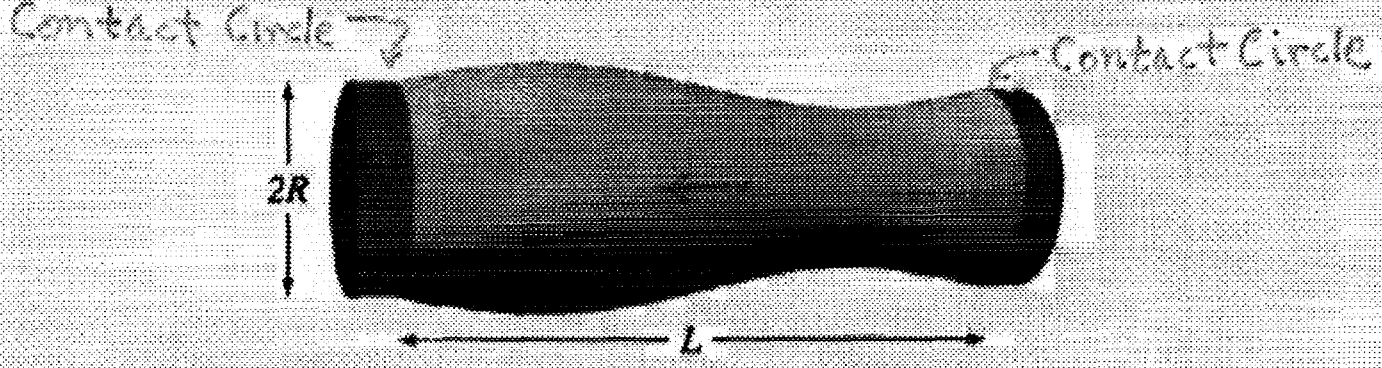

For a cylindrical bridge ($V = \pi R^2 L$) in low gravity of radius R and length L, the slenderness $S = L/2R$ has a natural limit of π, beyond which the bridge breaks (Rayleigh–Plateau instability).

Slenderness $S = L/2R$

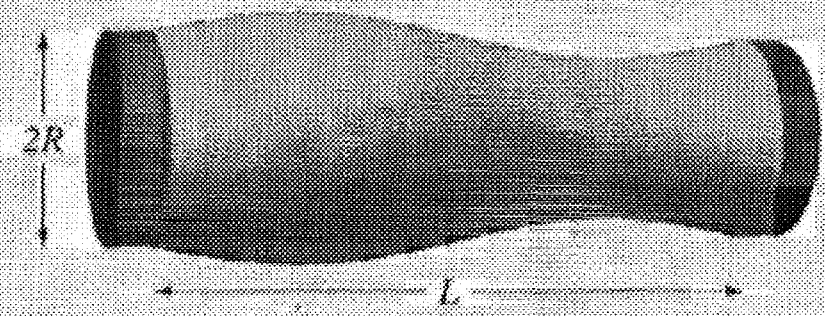

(2,0) mode

Rayleigh–Plateau limit $S_2 = \pi$ for $V = V_{cyl}$.

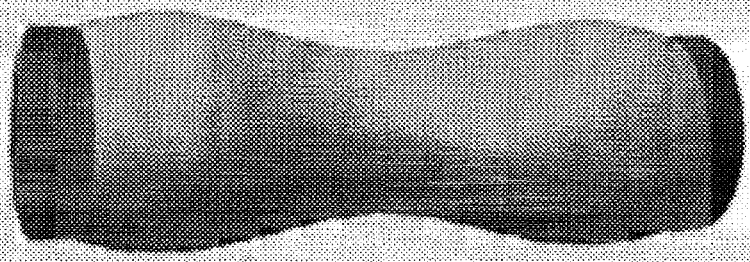

(3,0) mode

Stability limit $S_3 \approx 4.4934$ for $V = V_{cyl}$, the lowest nonzero solution of $\tan S = S$.

Bauer, JFM (1985).

Lowry & Steen, Proc. Roy. Soc. (1995).

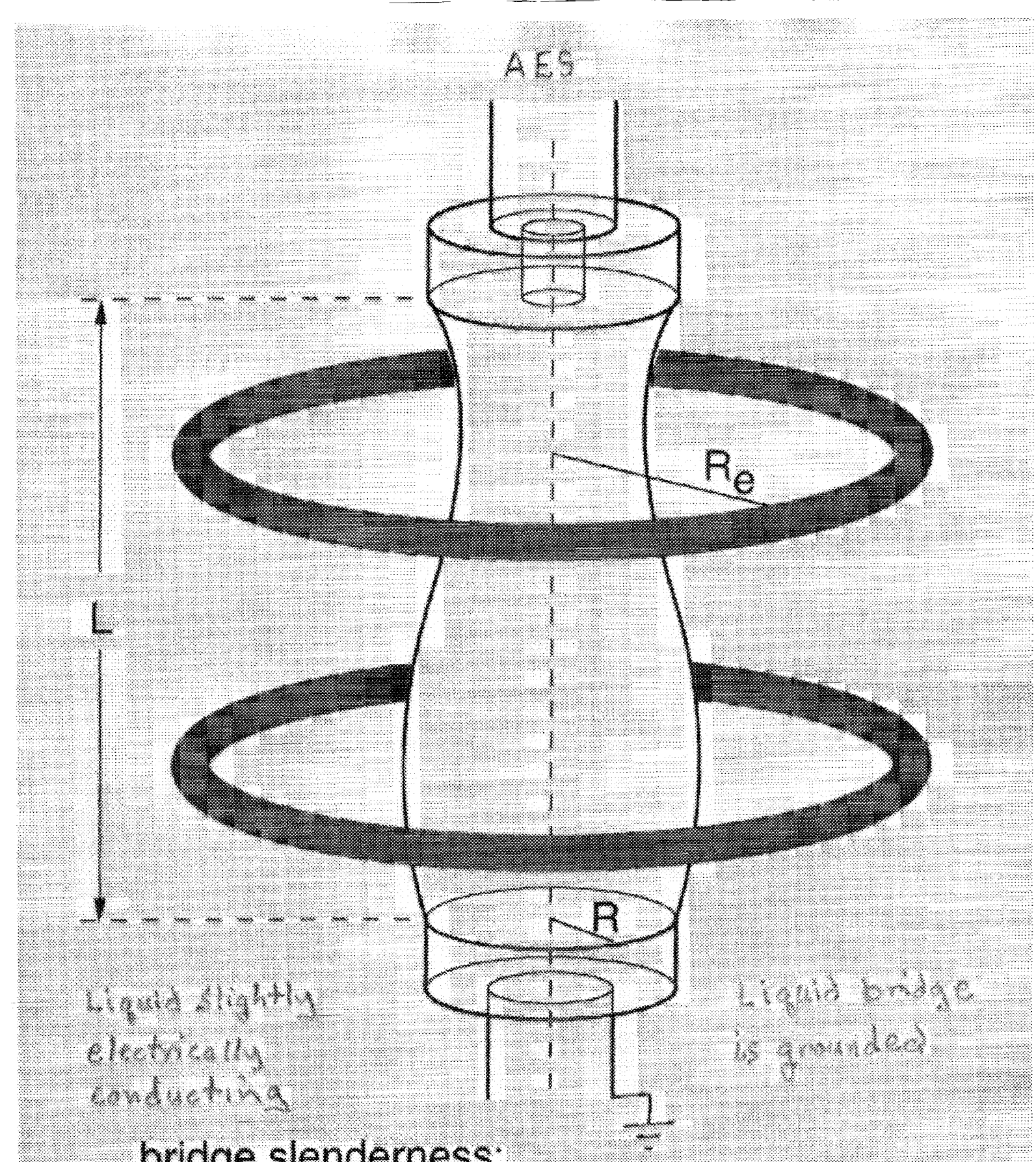

bridge slenderness:

$S = L/2R$

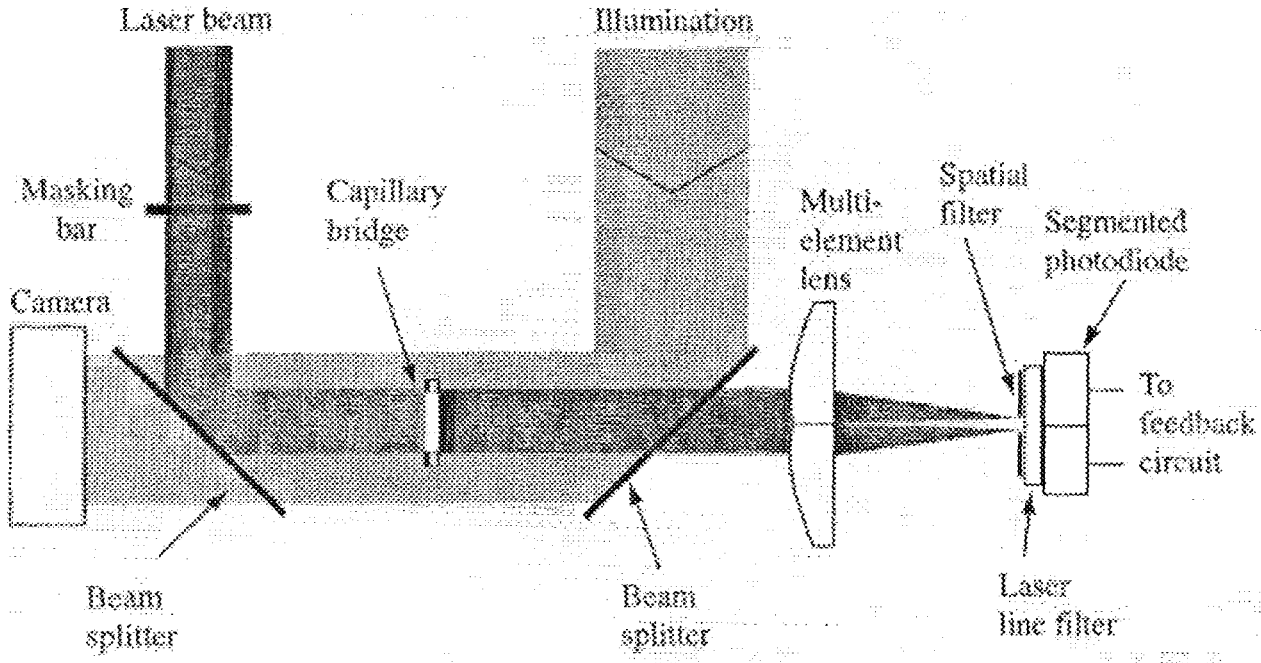

Optics diagram

Modal Feedback Force $\propto V_L^2 - V_R^2$

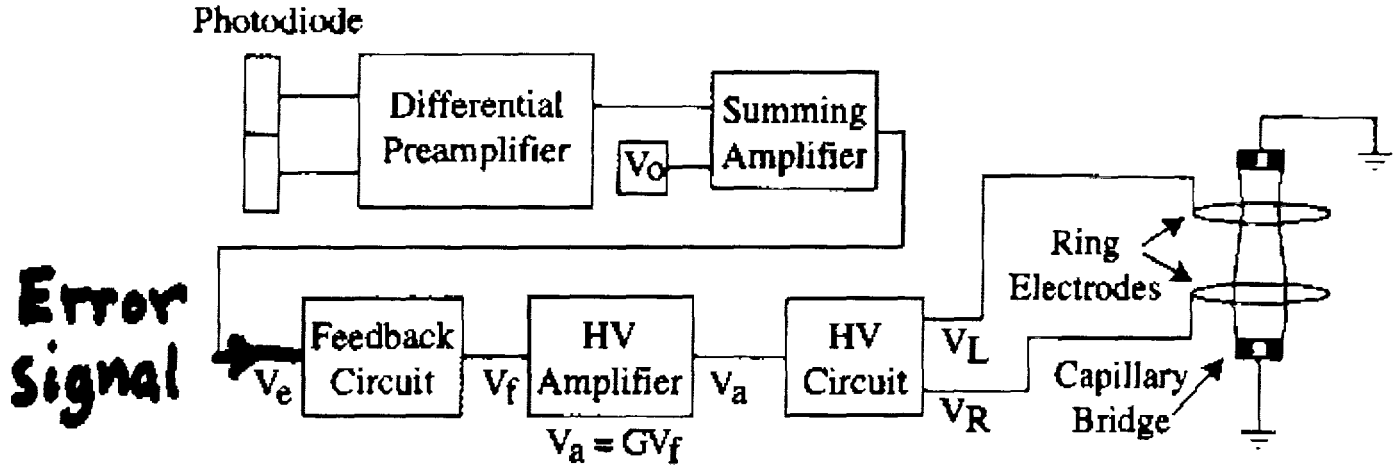

Feedback Circuits

(A) $V_f = KV_e$ (B) $V_f = K\frac{V_e}{\sqrt{|V_e|}} = \pm K\sqrt{|V_e|}$

HV Circuits

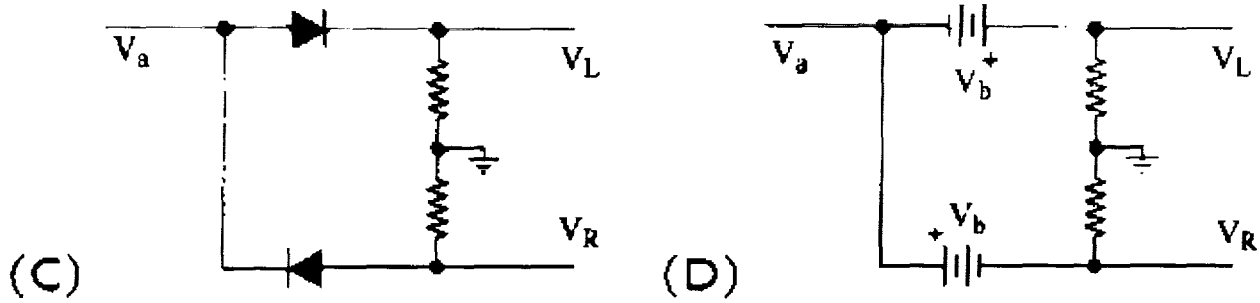

Feedback Method	Feedback Circuit	HV Circuit	$V_L^2 - V_R^2$ $\propto$
Simple	A	C	$\pm V_e^2$
→ Square-root	B	C	V_e
Bias potential	A	D	$V_b V_e$

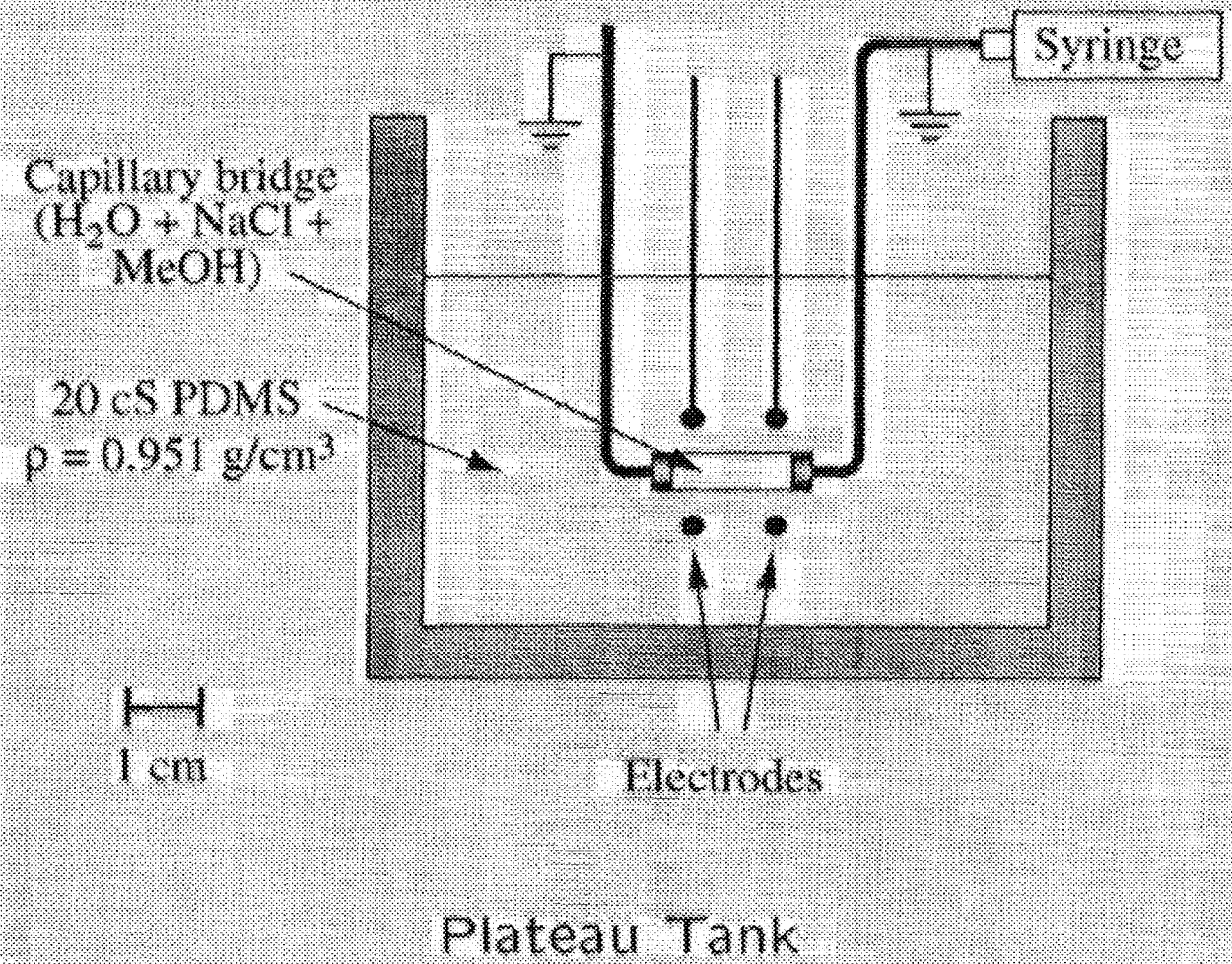

Plateau Tank

Square-root feedback method

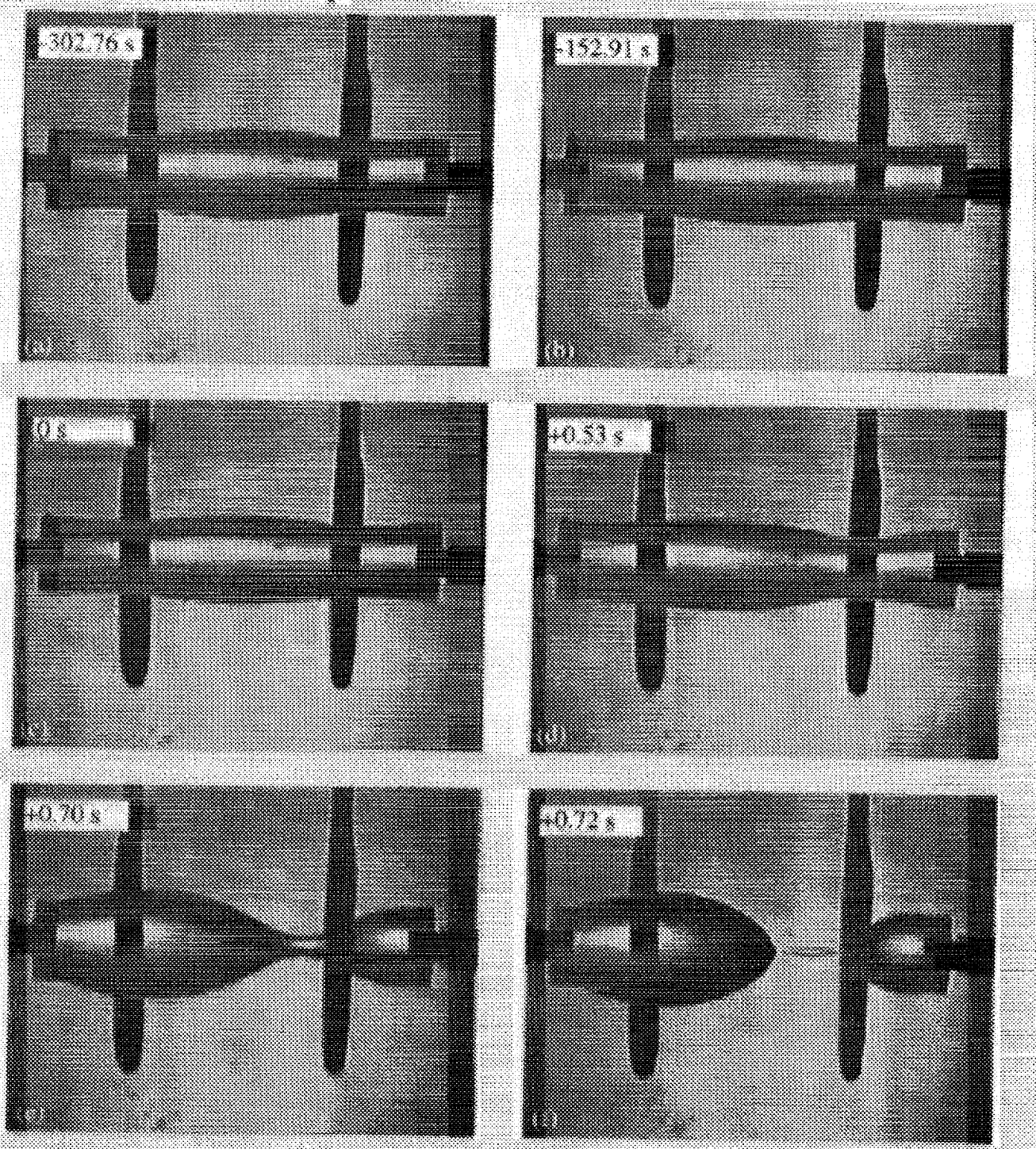

$S = 4.48$, $V = 1.029 V_{cyl}$

The control is turned off at $t = 0$ s.

Electrical conductivity σ_e of the liquid must be sufficiently large for the electrical time constant:

$\tau_{electrical} < \tau_{feedback}$

$\tau_{feedback} \approx 0.1$ ms (limiting feedback delay time)

$\tau_{electrical} \approx R_e C_e$

$C_e \approx 200$ pF electrical capacitance

$R_e \approx L/(\sigma_e 4\pi R^2)$ bridge electrical resistance

Yields: $\sigma_e \gtrsim 10$ μS/cm

Our salt solution: $\sigma_e > 20$ mS/cm

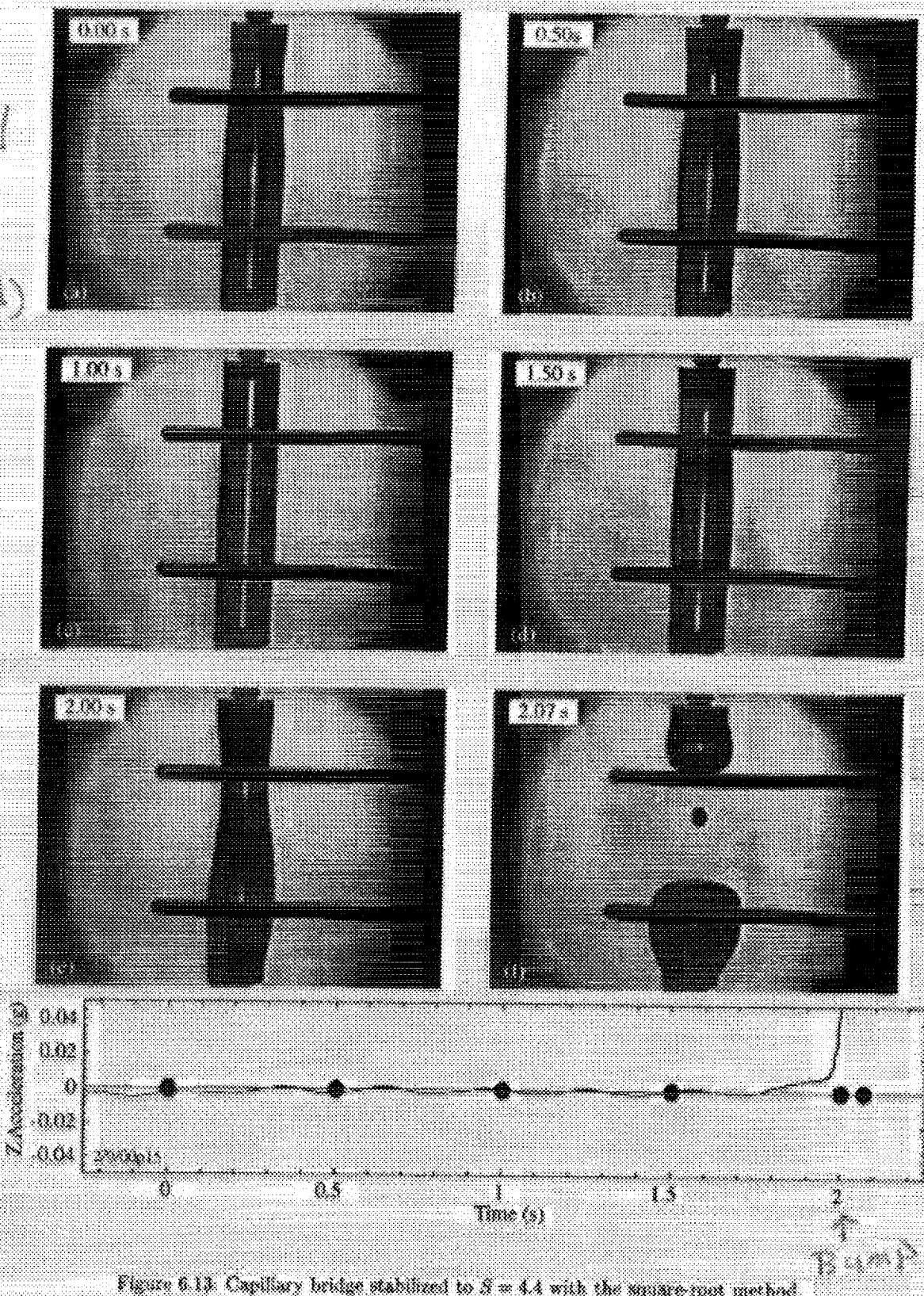

Figure 6.13: Capillary bridge stabilized to $S = 4.4$ with the square-root method.

Approximate Equation of Motion for Modal Amplitude

Feedback gain

$$m_b \frac{d^2x}{dt^2} + \gamma \frac{dx}{dt} + kx(t) + Gx(t-\tau) + \alpha\sqrt{\frac{2}{\pi}} \int_{-\infty}^{t} \frac{1}{(t-t')^{1/2}} \frac{d^2x}{dt'^2} dt' = 0$$

delay time τ

where the spring constant varies with slenderness as

$$k \propto \left[\left(\frac{\pi}{S}\right)^2 - 1\right]$$

solutions are of the type

$$x = x_0 e^{i\Omega t}$$

$x = (2,0)$ mode amplitude

so that

$$F_{\text{feedback}} = -Gx_0 e^{-i\Omega\tau} e^{i\Omega t}$$

(Marston, 1980; Asaki & Marston, JFM 1995)

$$\omega_n^2 - \Omega^2 + \alpha_n i(1+i)\Omega^{3/2} + i\gamma_n\Omega = 0$$

where

ω_n = shifted natural frequency (with feedback)

$$\omega_n^2 = \frac{\omega_b^2 + G_e}{1 + \frac{1}{2}G_e\tau^2}$$

$$\alpha_n = \frac{\alpha / m_b}{1 + \frac{1}{2}G_e\tau^2}$$ ← Boundary layer damping and inertia

$$\gamma_n = \frac{\gamma_e - G_e\tau}{1 + \frac{1}{2}G_e\tau^2}$$ ← Simple damping

Natural frequency of "bare" invscid bridge = ω_b

$$\omega_b^2 = k / m_b$$

$\omega_b^2 < 0$ if $S > \pi$

$$G_e = G / m_b$$

$$\gamma_e = \gamma / m_b$$

Stability Window and Active Damping

- With feedback based on only displacement information, the stability window is

$$-k < G < \gamma_e m_b / \tau$$

so long bridges may be stabilized only if $-k < \gamma_e m_b / \tau$.

- The instability at $G = \gamma_e m_b / \tau$ may be shifted to larger G by incorporating velocity data.

- Amplitude and/or velocity feedback may be used to increase the effective damping giving reduced sensitivity to g-jitter.

Acoustic

Passive stabilization

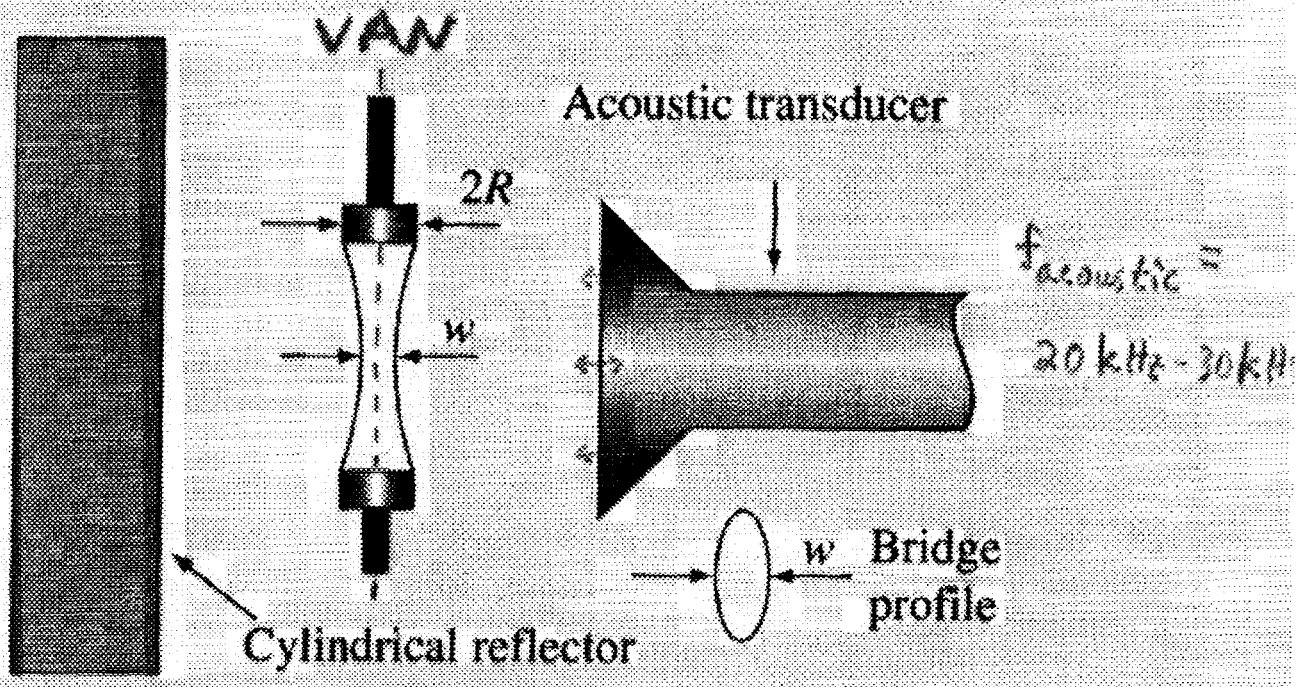

A bridge placed at a velocity antinode of an acoustic standing wave can be stabilized against breakup.

In the frequency range of interest, the bridge will be deformed into an approximately elliptical cross section.

Solving the acoustic problem of an infinite circular cylinder in a planar standing wave yields a partial wave series solution for the time and angle averaged acoustic radiation pressure.

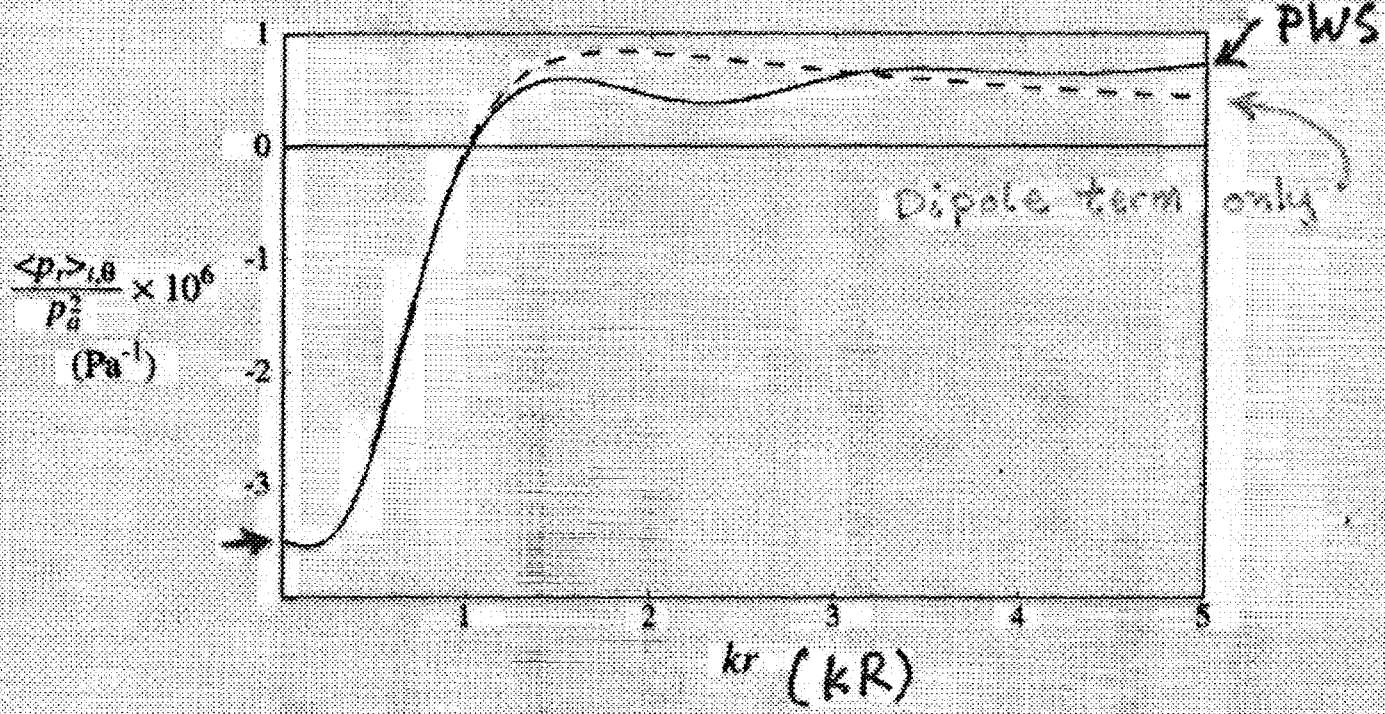

When the slope is positive, areas of larger radius are squeezed more than areas of smaller radius.

In this region, the sound field will passively stabilize the bridge against breakup.

Acoustic Radiation Pressure on High Impedance Objects in Air

Strong form of Bernoulli equation:

$$-\frac{\partial \phi}{\partial t} + \frac{1}{2}v^2 + h = \text{constant}, \quad h = \text{enthalpy}$$

For adiabatic sound with:

1st-order pressure p_1 and velocity $v_1 = -\nabla\phi_1$,

the 2nd-order mean Eulerian excess pressure:

$$\langle p_2 \rangle = \langle V \rangle - \langle K \rangle + \text{Constant}$$

$$\langle K \rangle = \frac{1}{2}\rho \langle v_1^2 \rangle = \text{time-averaged kinetic energy density}$$

$$\langle V \rangle = \langle p_1^2 \rangle / 2\rho c^2 = \text{time-averaged potential energy density}$$

c = speed of sound

(Wang and Lee, 1998)

NASA/CP—2000-210470

ODIS

From a one-dimensional inviscid-slice model of a capillary bridge including a radially varying pressure field, an acoustic parameter q may be defined as

$$q = \frac{R^2}{\sigma} \frac{d\langle P_r \rangle_{t,\theta}}{dR}$$

where the maximum bridge length is a function of q.

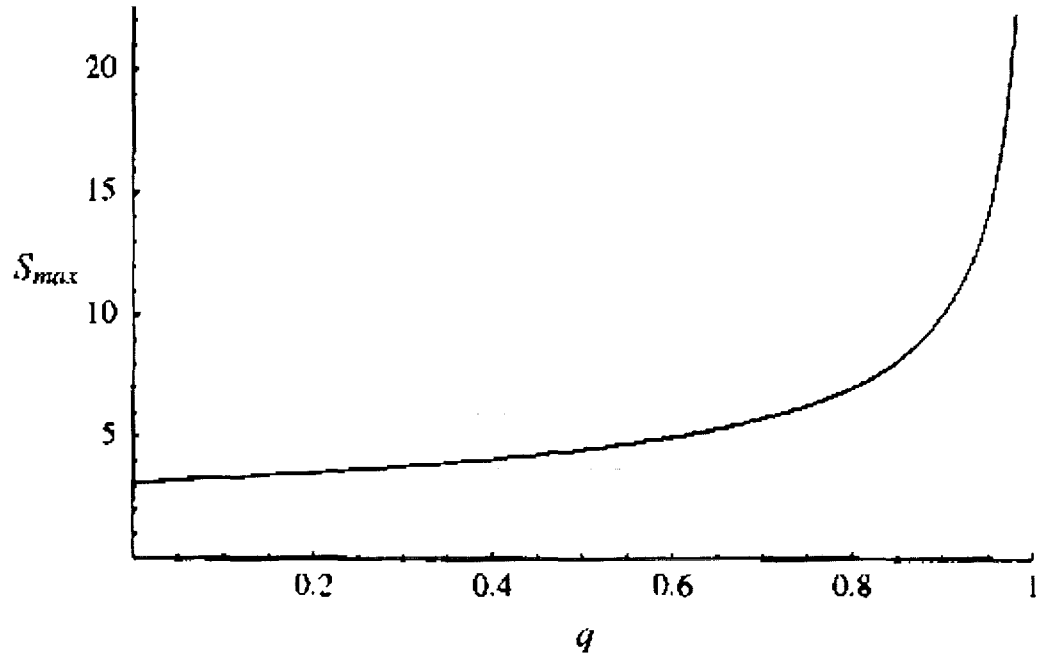

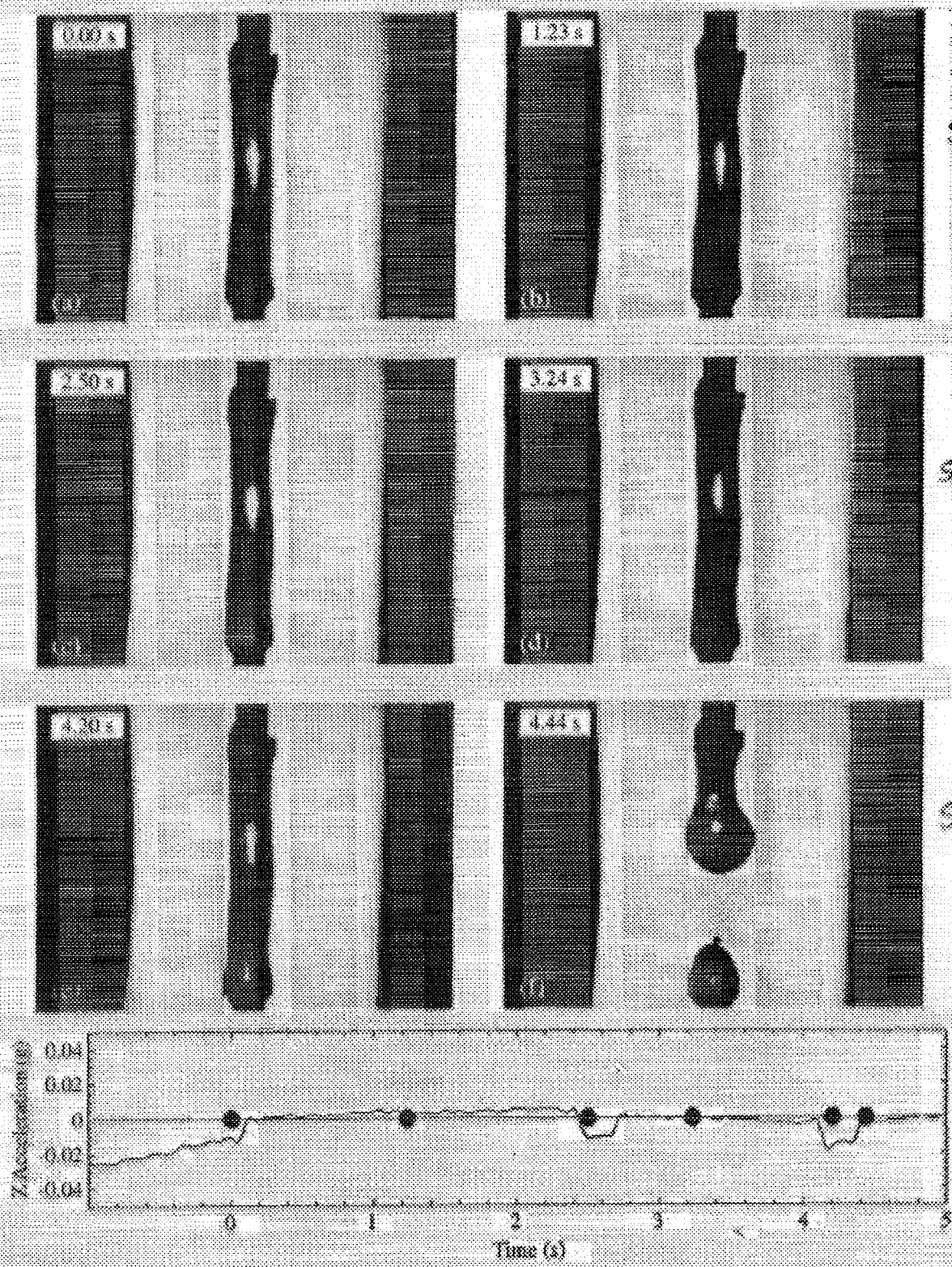

Figure 5.11: A bridge stabilized to $S = 4.5$ using the resonant-plate style transducer.

Summary

- Plateau Tank Experiments:
  Stabilization with Active Control of radial Electrostatic Stress (AES)

- KC-135 based experiments on bridges in air:
  1. AES
  2. Passive Acoustic Stabilization (PAS)

- Requirement that the feedback delay time is short for AES

- Exploration of the limitations of PAS and AES methods for the stabilization of liquid bridges in air may require a space-based platform

Current and Future Research (Near Term)

- AES stability window:
  (1) modeling and verification
  (2) extend by including velocity data
- PAS: Effect of changing kR away from optimum value ≈ 0.8 (KC-135 based tests)

THE EFFECT OF CONVECTION ON MORPHOLOGICAL INSTABILITY

S. H. Davis
Northwestern University

ABSTRACT

The interaction of convection and a solidifying front is known to give microstructures quite different than the case when the melt is quiescent. However, until now little quantitative, or even qualitative information has been available for the diagnosis of anomalous patterns that are seen. The lecture will discuss the response of a front in the directional solidification of a dilute, binary alloy to cellular, convective fields. When the convection is of transverse scale much larger than the morphological scale (absent the flow), it is found that the response is localized spatially with morphological cells confined to localized envelops. In a 2D case like solidification in a Hele-Shaw geometry the localization is due to the tangential component of the flow and appears midway between stagnation points of the frontal flow. In a 3D case the localization is due to the component of flow normal to the front and appears at inward stagnation points on the front independent of the pattern of forcing. The results can be used to "design" microstructural patterns by the imposition of the appropriate convection or they can be used to discover what flow was present in a processing cycle. The analyses find the responses to imposed flows, and thus are mass-transfer calculations. What remains to be done is the full coupled system in which the flow is altered by the morphology. This would involve a 3D, time-dependent calculation of the full free-boundary problem – a daunting task. However, the cases discussed would guide the computationalist in this effort.

REFERENCES

1) Chen, Y.-J. and Davis, S. H. 1999 "Directional solidification of a binary allow into a cellular convective flow: localized morphologies" *J. Fluid Mech.* **395**, 253-270.
2) Chen, Y.-J. and Davis, S. H. 2000 "Flow-induced patterns in directional solidification: localized morphologies in three-dimensional flows" *J.Fluid Mech.* (in press).

Presentation not available at time of printing.

THE DYNAMICS OF MISCIBLE INTERFACES: A SPACE FLIGHT EXPERIMENT

T. Maxworthy
University of Southern California

E. Meiburg
University of California at Santa Barbara

ABSTRACT

Experiments as well as accompanying simulations are described that serve in preparation of a space flight experiment to study the dynamics of miscible interfaces. The investigation specifically addresses the importance of both nonsolenoidal effects as well as nonconventional Korteweg stresses in flows that give rise to steep but finite concentration gradients.

The investigation focuses on the flow in which a less viscous fluid displaces one of higher viscosity and different density within a narrow capillary tube. The fluids are miscible in all proportions. An intruding finger forms that occupies a fraction of the total tube diameter. Depending on the flow conditions, as expressed by the Peclet number, a dimensionless viscosity ratio, and a gravity parameter, this fraction can vary between approximately 0.9 and 0.2. For large Pe values, a quasi-steady finger forms, which persists for a time of O(Pe) before it starts to decay, and Poiseuille flow and Taylor dispersion are approached asymptotically. Depending on the specific flow conditions, we observe a variety of topologically different streamline patterns, among them some that leak fluid from the finger tip. For small Pe values, the flow decays from the start and asymptotically reaches Taylor dispersion after a time of O(Pe).

Comparisons between experiments and numerical simulations based on the 'conventional' assumption of solenoidal velocity fields and without Korteweg stresses yield poor agreement as far as the Pe value is concerned that distinguishes these two regimes. As one possibility, we attribute this lack of agreement to the disregard of these terms. An attempt is made to use scaling arguments in order to evaluate the importance of the Korteweg stresses and of the assumption of solenoidality. While these effects should be strongest in absolute terms when steep concentration fronts exist, i.e. at large Pe, they may be relatively most important at lower values of Pe. We subsequently compare these conventional simulations to more complete simulations that account for nonvanishing divergence as well as Korteweg stresses. While the exact value of the relevant stress coefficients are not known, ballpark numbers do exist, and their use in the simulations indicates that these stresses may indeed be important. We plan to evaluate these issues in detail by means of comparing a space experiment with corresponding simulations, in order to extract more accurate Korteweg stress coefficients, and to confirm or deny the importance of such stresses.

Dynamics of Miscible Interfaces

Eckart Meiburg

Department of Mechanical and Environmental Eng.
University of California at Santa Barbara
Santa Barbara, CA 93106, USA

Tony Maxworthy

Department of Aerospace and Mechanical Eng.
University of Southern California
Los Angeles, CA 90089, USA

- **Introduction and background**
  - **effects of non-vanishing divergence**
  - **non-conventional stresses**
- **Principle experiment: Miscible flow in a capillary tube**
- **Simulations**
- **Preliminary conclusions**

Supported by NASA Microgravity Fluids Program

Introduction and background

- **Many applications give rise to steep concentration gradients in the 'miscible interface' region that separates miscible liquids:**
  - **mixing devices**
  - **chemical reactors**
  - **materials processing applications**
  - **biology and biomedical applications**
  - **enhanced oil recovery**
  - **....**
- **Conventional analysis of such flows is based on**
  - **divergence free velocity field**
  - **Stokes or Navier-Stokes equations with standard stress tensor**
- **How accurate is this approach?**

a) Divergence effects:

* **continuity equation** $$\frac{\partial \rho}{\partial t} + \nabla \cdot (\rho \vec{u}) = 0$$

→ $$\frac{D\rho}{Dt} + \rho \nabla \cdot \vec{u} = 0$$

* **conventional assumption**

$$\frac{D\rho}{Dt} = 0 \rightarrow \nabla \cdot \vec{u} = 0$$

but: when the density of a fluid particle can change as a result of diffusion

$$\frac{D\rho}{Dt} \neq 0 \rightarrow \nabla \cdot \vec{u} \neq 0$$

this also leads to modifications in the conventional Stokes or Navier Stokes equations

→ How important are these divergence effects in real world applications?

b) Non-conventional stresses:

- **Korteweg (1901): additional stresses could potentially be important in regions of large concentration gradients ('Korteweg stresses')**

- **Mathematical form of these stress terms?**

- **Suggestions by Davis (1988), Joseph et al. (1996)**
  - **how can the mathematical form be validated?**
  - **what are the signs and numerical values of the stress coefficients?**
  - **estimates by Smith et al. (1981), Davis (1988), Petitjeans and Maxworthy(1996):**

    ~1 dyn/cm, but time-dependent

Indications that these stresses may be important in many applications, e.g.:

- **Joseph and Renardy (1993): drop of glycerin in water (miscible), drop shape is similar to that of immiscible drops**
- **Hu and Joseph (1992): miscible displacement in a Hele-Shaw cell, evidence of an effective surface tension?**
- **Petitjeans and Maxworthy (1996), Chen and Meiburg (1996): displacement of glycerin by glycerin/water mixture in a capillary tube: discrepancy between flow visualization and simulations based on Stokes equation and non-divergent velocity field**
- **additional attempts to extract 'effective surface tension': Kurowski and Misbah (1994), Petitjeans (1996), Petitjeans and Kurowski (1997)**

Principle experiment: Miscible flow in a capillary tube

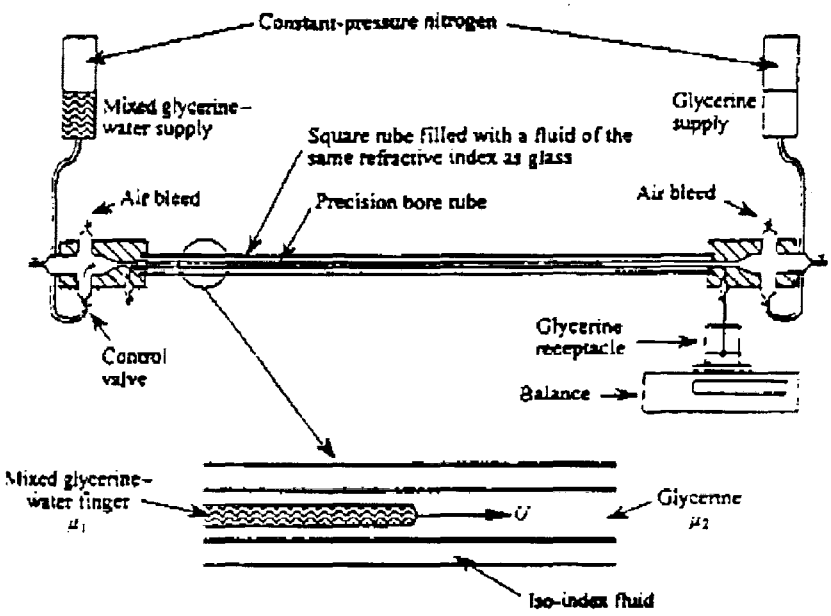

Experiments: Petitjeans & Maxworthy (1996)

'Conventional' simulations: Chen & Meiburg (1996)

Main feature:

A finger of the injected, less viscous fluid propagates along the centerline of the tube, leaving behind a film of the resident fluid on the wall.

Experimental and numerical observations:

- **Miscible displacements: no truly steady state, eventually Taylor dispersion is approached**

- **Large Pe: a quasisteady state evolves for the finger. Tip velocity and fraction of more viscous fluid left on the wall can be measured. They depend on**

  * **Peclet number** $$Pe = \frac{Ud}{D}$$

  * **viscosity ratio** $$At = \frac{\mu_2 - \mu_1}{\mu_2 + \mu_1}$$

  * **density ratio** $$F = g \frac{\Delta\rho}{\rho} \frac{d^2}{\nu U}$$

- **Small Pe: no quasisteady finger forms. Finger quickly decays.**

Preliminary simulations

from Chen and Meiburg (1996), non-divergent,

conventional Stokes eqns. (Pe=1,600, At~100, F=0)

'standard' case:

concentration

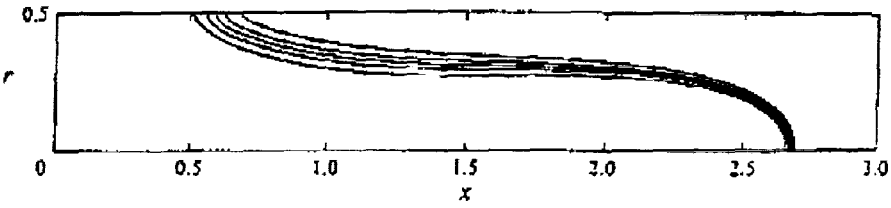

streamlines

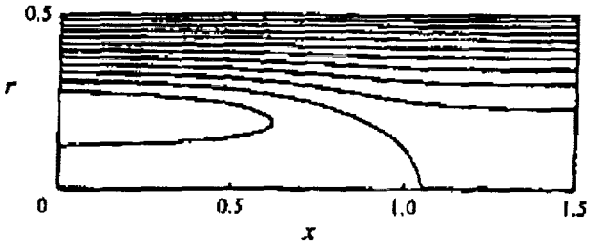

thickness of fluid film left on the wall:

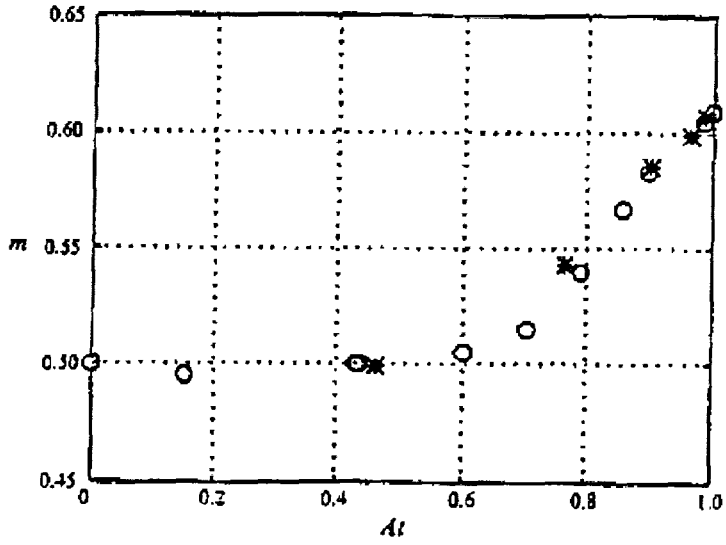

o exp.

* sim.

good agreement experiments/simulations

Experiment (Petitjeans and Maxworthy 1996):

measure fraction of more viscous fluid left behind on the wall as function of Pe

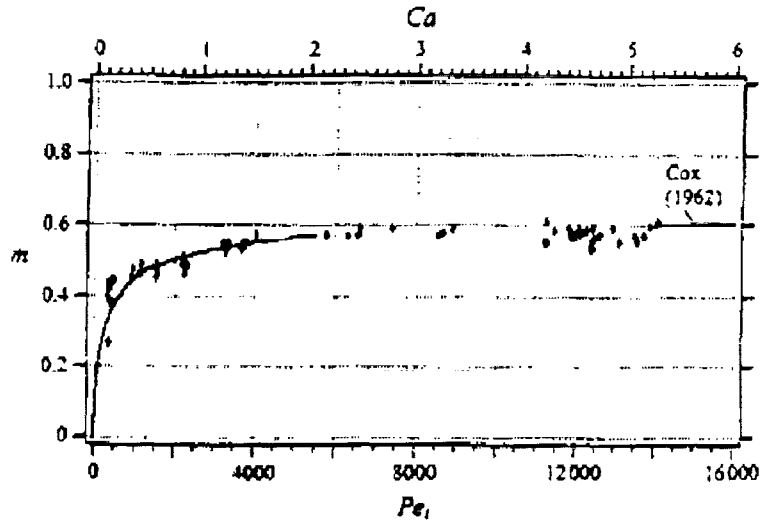

Comparison with immiscible data of Taylor (1961) and Cox (1962) suggests value for an effective surface tension coefficient

formation of spike:

concentration field

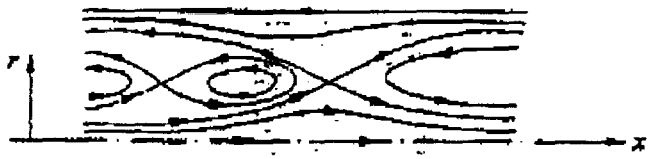

FIGURE 16. (*a*) Unsteady evolution of the concentration field for $R = 3$, $F = -49.78$, and $Pe = 1600$. Times are $t = 4$, 12, and 18. Also shown is the streamline pattern in the reference frame moving with the $c = 0.5$ contour at $t = 18$, as well as a sketch of its topology (*b*). A closed, toroidal recirculation region forms that leads to a 'pinch-off'-like phenomenon near the finger tip.

streamline topology

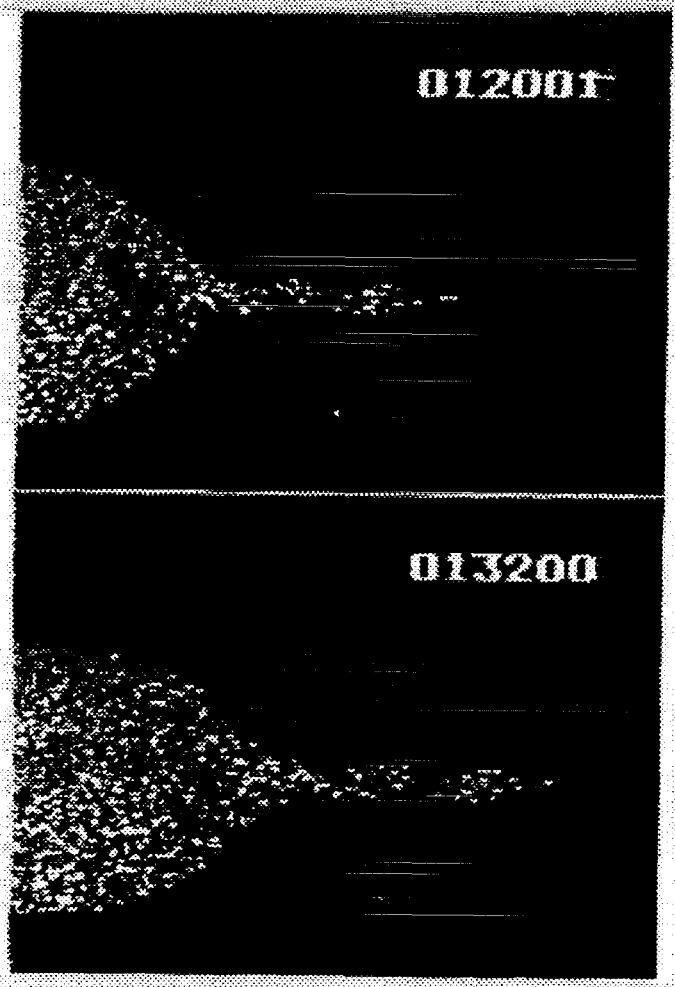
012001
013200

- **Low Pe: discrepancy between experiments and numerical simulations: Experiments show quasisteady finger at substantially lower values of Pe than the numerical simulations**

Indication of nonconventional stresses?

Note: these stresses should be largest when concentration gradients are steep (large Pe), but they could be *relatively* more important at lower values of Pe.

preliminary simulations to evaluate the influence of divergence and Korteweg stresses:

*** perform simulations based on Joseph's suggestions for the form of the governing equations:**

- split velocity field into solenoidal part and divergent part

- postulate Korteweg stress terms with coefficients of unknown size

$$
\begin{aligned}
\frac{\partial \phi}{\partial t} + W_x \frac{\partial \phi}{\partial x} + W_r \frac{\partial \phi}{\partial r} &= D \nabla^2 \phi \\
\nabla \left(p + Q(\phi) \right) &= \nabla \cdot \left(2 \mu D \left[\vec{u} \right] + \delta \left(\nabla \phi \otimes \nabla \phi \right) \right) + \rho g \\
Q(\phi) &= \frac{1}{3} \delta \left| \nabla \phi \right|^2 + \frac{2}{3} \xi \mu D \nabla^2 \phi - \frac{2}{3} \gamma \nabla^2 \phi \\
\frac{\mu}{\mu_1} &= e^{R \phi} \\
\vec{u} &= \vec{W} + \vec{u}_e \\
\nabla \cdot \vec{W} &= 0 \\
\vec{u}_e &= \xi D \nabla \phi \\
\rho &= \frac{\rho_1}{\rho_1 - \rho_2} - \phi \\
\xi &= \frac{\rho_1 - \rho_2}{\rho_1}
\end{aligned}
$$

empirical parameter variations:

* influence of Korteweg stresses:

- no such stresses

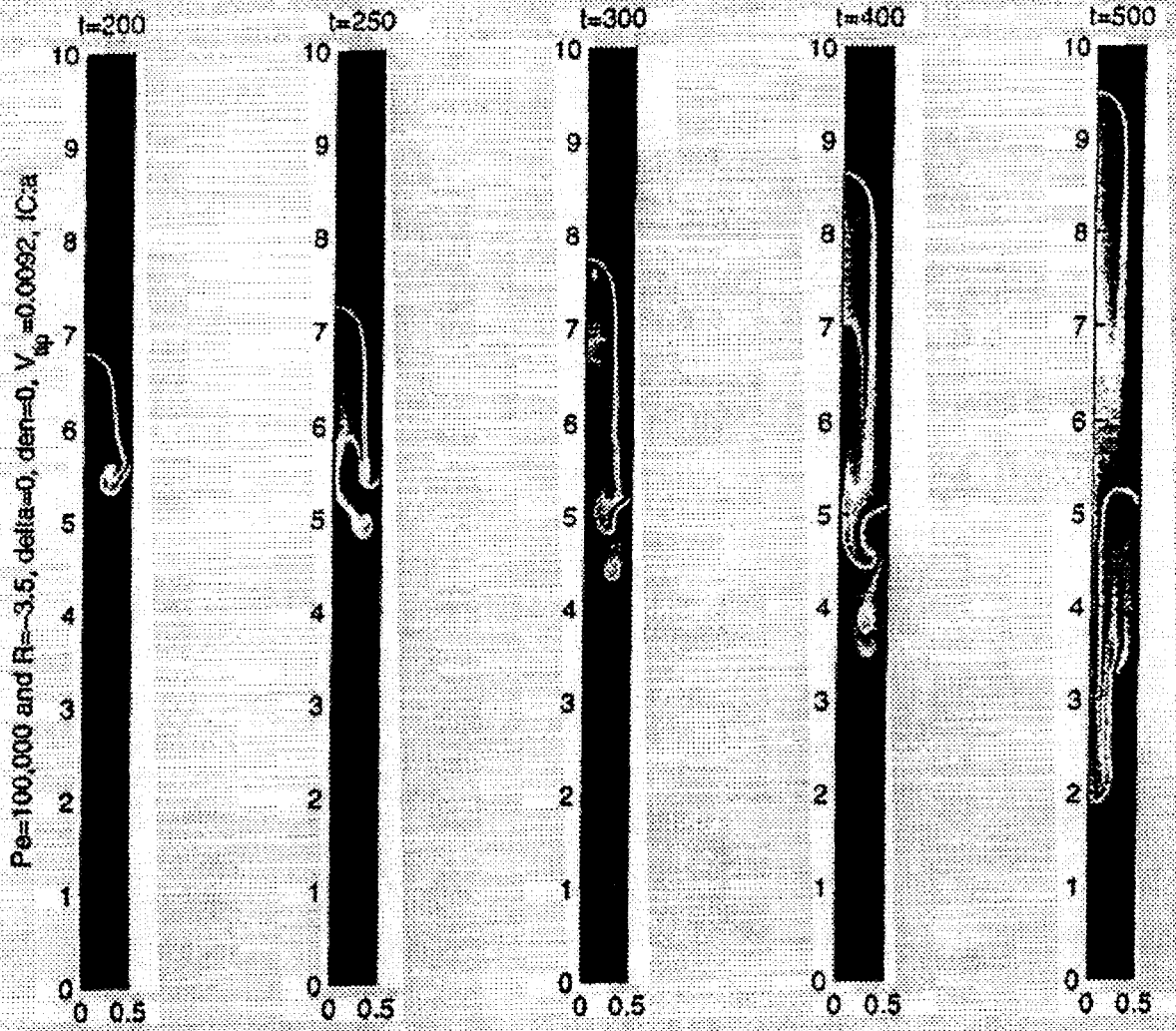

- small positive Korteweg stress coefficient 0.0001

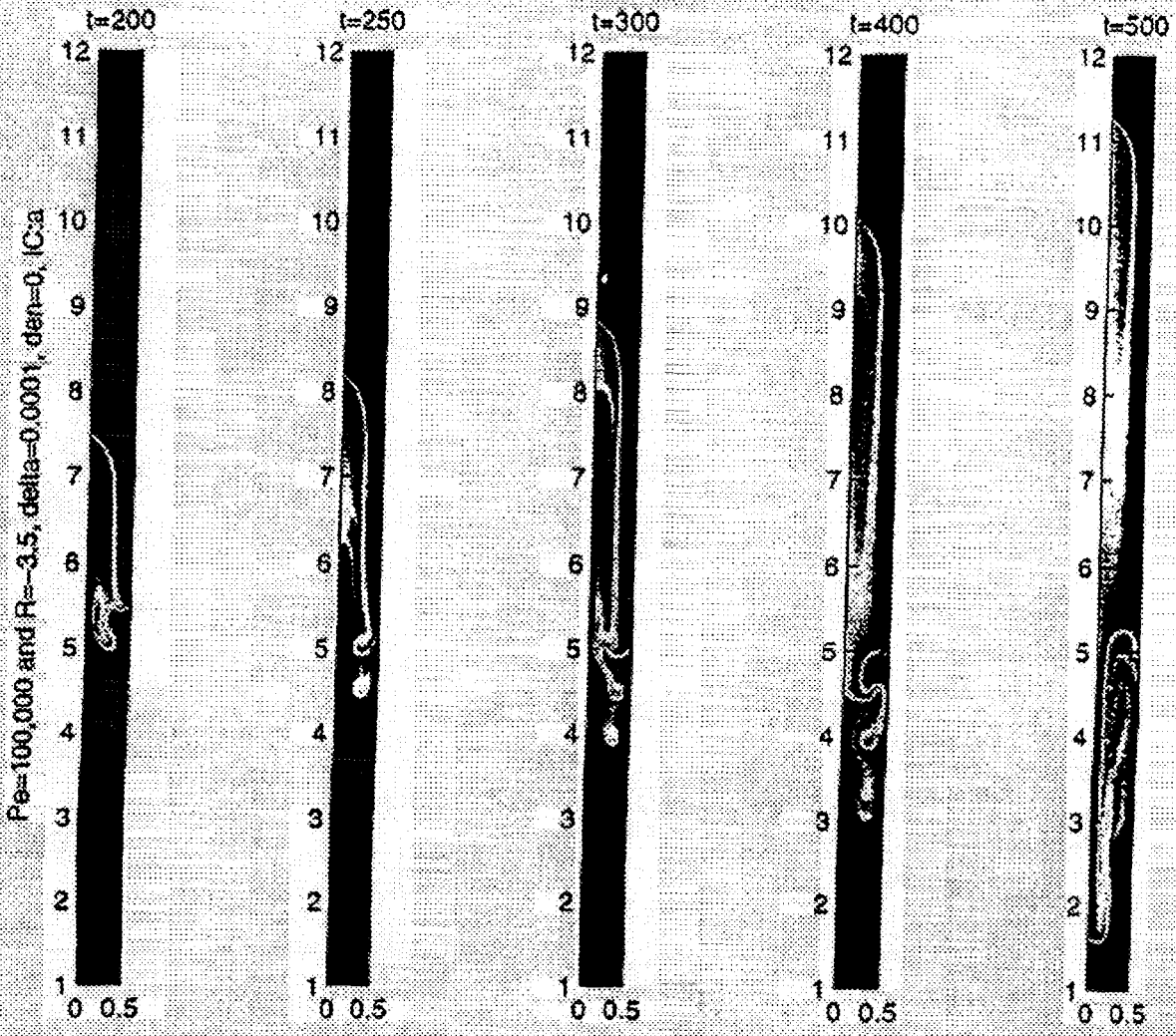

- small negative Korteweg stress coefficient -0.0001

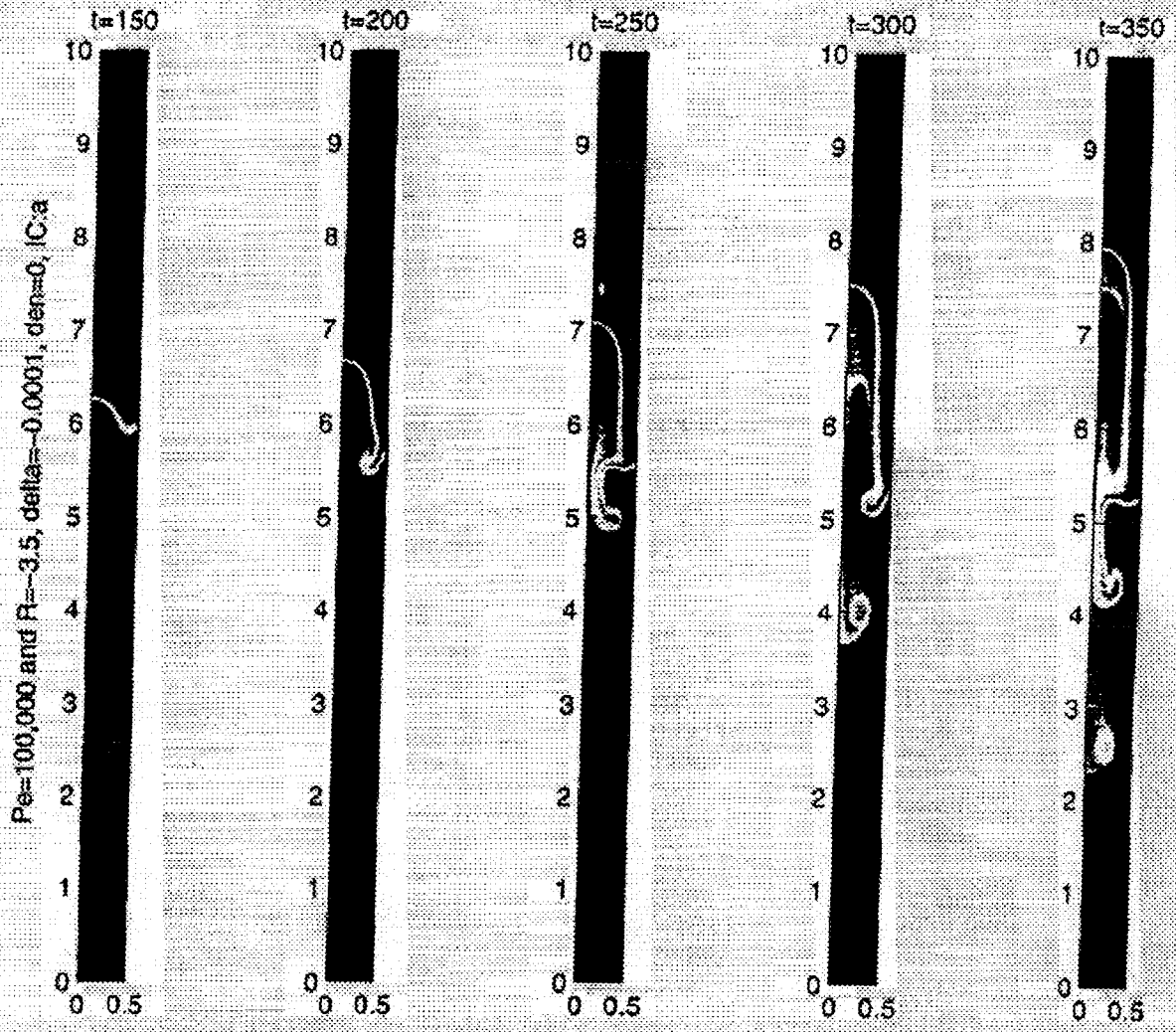

* influence of divergence:

- no divergence

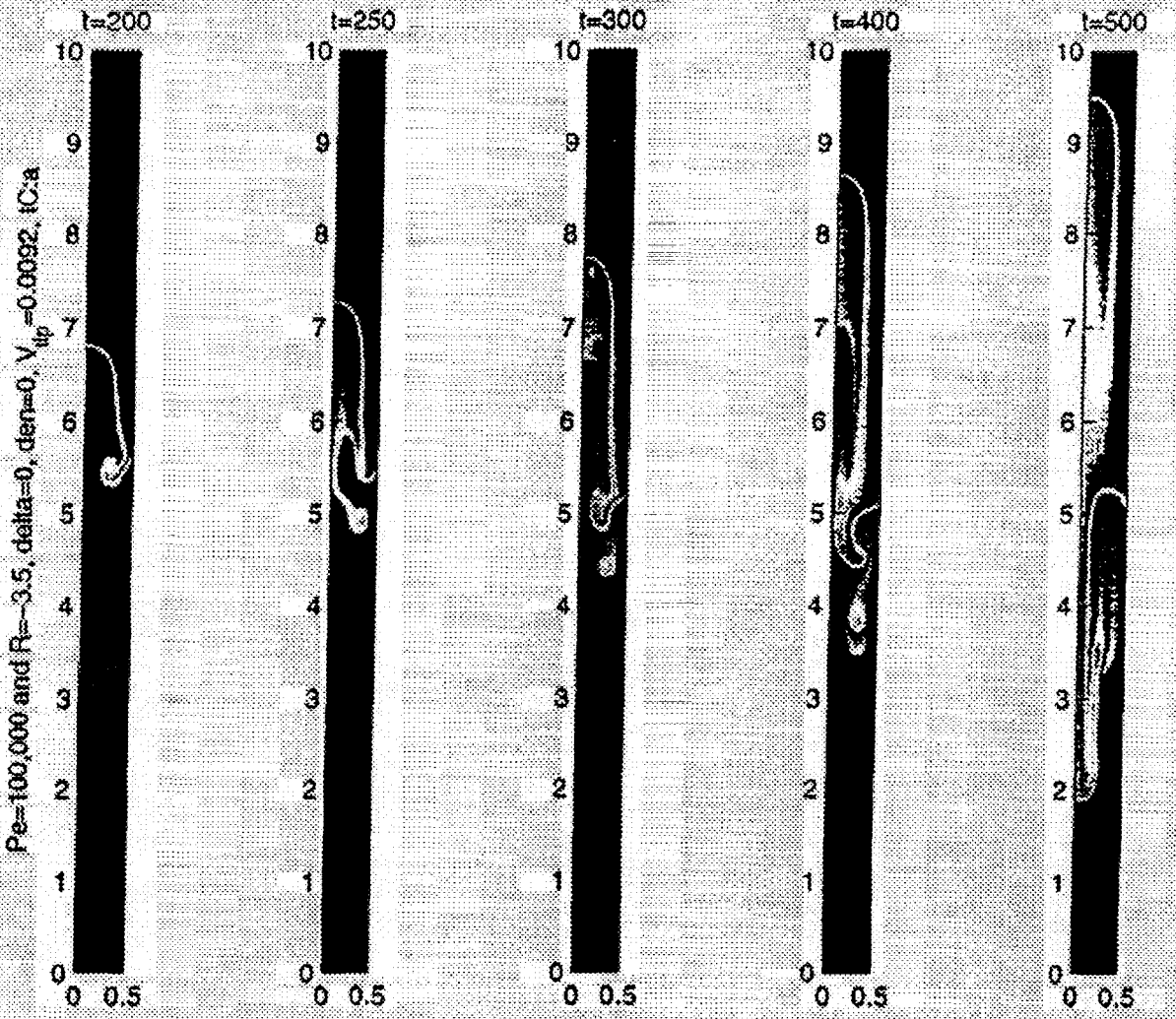

- density parameter 0.25

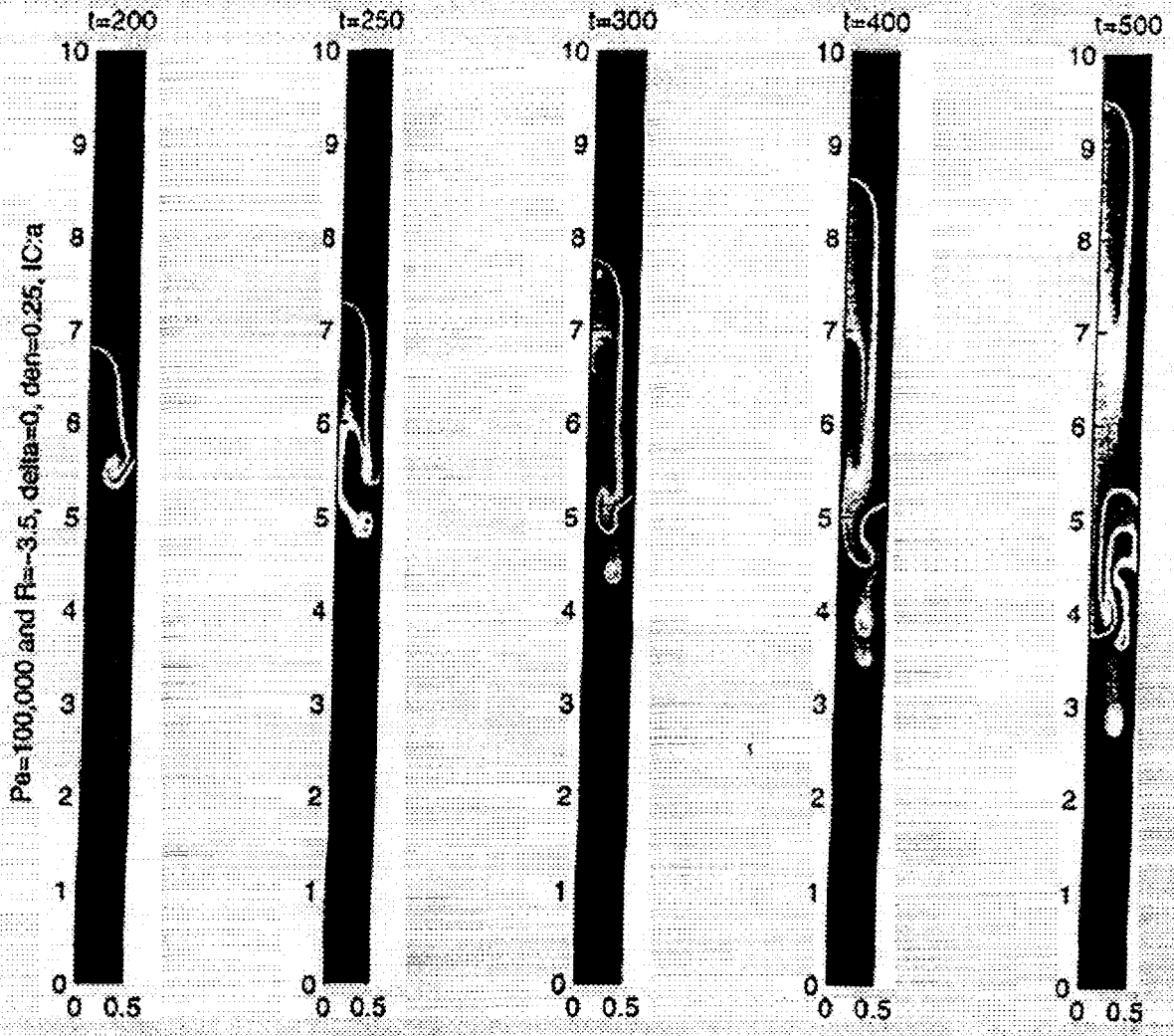

Possible space experiment

Need *detailed* comparison between experiments and numerical simulations at *low* Pe

- **can't use horizontal tube on the ground, because experimental flow is 3-d**
- **can't use vertical tube on the ground, because the experimental flow develops a 3-d instability at low flow rates (low Pe)**
- **have to go to microgravity environment in order to obtain an axisymmetric flow in the experiment**

Peliminary conclusions

- **Fundamental questions regarding the validity of the 'conventional' continuity and Stokes/Navier Stokes equations in regions of steep concentration gradients**
- **mathematical formulation and magnitude of Korteweg stress coefficients are unknown, although there are suggestions**
- **there are indications from experiments and simulations that these stresses can be important**
- **plan to perform detailed comparison between microgravity experiment and numerical simulations in order to obtain more accurate information**

August 10, 2000
Exposition Session

LONGITUDINAL AND TRAVERSE WAVES IN COULOMB CRYSTALS FORMED IN A DUSTY PLASMA

A. Bhattacharjee, X. Wang, S. Hu
The University of Iowa

ABSTRACT

A unified theoretical treatment of longitudinal (or compressional) and transverse modes in Coulomb crystals formed in a dusty plasma is given. Dispersion relations are obtained for two-dimensional and three-dimensional triangular lattices with hexagonal symmetry. Although the acoustic limit is isotropic in all cases, the functional dependence of the dispersion relations on the screening parameter κ is shown to depend sensitively on the dimensionality of the crystal. Dispersion relations are obtained for compressional and transverse lattice waves dominated by near-neighbor interactions. Theoretical predictions are compared quantitatively with two recent experiments, and new dispersion relations that can be tested by future experiments are identified.

Presentation not available at time of printing.

DIFFUSIVE COARSENING OF LIQUID FOAMS IN MICROGRAVITY

I. Veretennikov and J. A. Glazier,
Department of Physics, University of Notre Dame, Notre Dame, IN 46556

INTRODUCTION

Foams could be used very extensively in space (liquid foams in everything from shaving cream, to fire extinguishers, and solid foams in thermal insulation, anti-explosion fuel tanks and structural support elements). One interesting question is whether liquid foams under gravity differ in their fundamental physics from foams in microgravity conditions.

Foam experiments during parabolic flights have shown new phenomena [1]. An initially dry foam sucks liquid from a reservoir located below the foam and an upwards moving wetting front develops. The liquid now redistributes inside the foam, while preserving the total wetness. As a result, the membrane thickness distribution will differ from that on Earth, which will change the stability and viscosity of the foam. A new scenario for foam aging could develop in microgravity. Possibly, foam could reach a new metastable configuration, containing several large bubbles with thick membranes. For the foam to reach the global, no bubble, equilibrium (which is the only final state for foam evolution on the Earth) will require almost infinite time, suggesting that defoaming could be a real problem in microgravity. Once created, foam could persist almost forever.

GOALS

On Earth separating the influence of diffusion-driven coarsening on foam structure and stability from gravity-driven decrease of wetness is difficult. Our main goal is to simulate, to some extent, microgravity conditions in the presence of gravity, by reducing or precisely controlling gravitational drainage, to check some stages of the proposed scenario for the aging of "space" foams. We would like to study the coarsening of foams of different wetnesses stabilized by continuous liquid supply from the top, and to determine the relations between foam structure, wetness and rheological properties.

Another goal is to investigate how the fluid redistributes through foams. Our earlier experiments on flow of two-dimensional foam through a constriction suggest the significance of the fluid redistribution between membranes in determining foam's effective viscosity. In the presence of gravity, however, the total flow through membranes is less than 5% of the total flow through the Plateau borders [2,3]. We hope that using a slowly increasing liquid supply, we will be able to estimate membrane thickness changes during the froth to wet foam transition.

We also would like to develop and test different techniques for foam analysis, which may be suitable for microgravity experiments on the ISS in the future.

PROPOSED STUDIES

We will study both wet and dry foams, continuing our Magnetic Resonance Imaging (MRI) experiments on foam structure to correlate foam's structure and rheological properties. Since our MRI sample is aligned vertically, the only way to stabilize the foam is to supply additional fluid from the top. Varying the flow rate could change the foam wetness.

First, we will examine the coarsening of such "frozen" foams. We can obtain images of the complete three-dimensional structure of foams of different wetnesses. These images will allow us to obtain bubble size and topology distributions directly. For stabilized foams with controlled wetness we will obtain the effective diffusion constants and hence the estimate for the average membrane thickness and its possible variation during coarsening. This technique will allow us to study the dry-wet foam transition, and possibly observe the transition from the von Neumann/Glazier growth law $r=t^{1/2}$ to the Lifschitz-Slyozov $r=t^{1/3}$ behavior, which corresponds

to the growth of non-interacting bubbles. Another proposed set of MRI experiments will relate foam structure and rheology. We would like to measure effective foam viscosity by means of a modified method, used by Callaghan [4] to study the rheological properties of non-Newtonian fluids. Foam will be pumped with different speeds into the RF section of the MRI. Measuring the radial velocity distribution and the pressure drop across the RF section, we can obtain an effective foam viscosity [4]. We hope that these MRI experiments will allow us to correlate effective foam viscosity with basic fluid viscosity, foam wetness and structure. While MRI seems to be the only non-invasive technique available, it is relatively slow, with limited sample size. Hence, we would like to test two alternative techniques to compare their data to those obtained using MRI.

For wet foams, we propose to use a foam analyzer [5] to measure bubble size distribution as a function of time. This technique is faster than MRI and permits a much larger sample. In this device, a thin glass fiber is inserted repeatedly at different locations vertically through foam at known speed. A test light is sent into the fiber. The amount of reflected light depends on the refractive index of the medium surrounding the tip. Thus, more light is reflected when the tip is in gas, than when the tip is in liquid. The reflected light goes back to the sensor, where the light intensity is converted into an electronic signal by a photo-diode. This signal is digitized at a high frequency compared to the probe velocity and recorded on a computer for later analysis. A method to calculate the three-dimensional size distribution from the one-dimensional chord length distribution has been proposed by Weibel [6]. One disadvantage of this technique is that the deconvolution requires statistics on thousands of chord lengths to give a reasonable estimate of the bubble volume distribution.

For dry foam, we would like to try an optical tomographic technique. Scanning a laser beam through the foam, we will be able to reconstruct the full foam structure including the bubble topologies. In the foam, where laser light crosses a lamella, a very bright point appears. Making three simultaneous video images, from the top and sides, allow us to determine the position of the lamella and to determine the bubble diameter. The accuracy will be mostly determined by the rate of scanning and will be limited by the number of bubbles scanned. New software should be developed to get structural and topological information from such images.

We hope the proposed experiments will provide valuable information on structure and coarsening of foams with finite controlled wetness, which could predict foam behavior both in space and on Earth. The techniques developed for this proposal could also be adapted for use on the ISS in the future.

REFERENCES

1. D. Noever and R. Cronise, "Weightless Bubble Lattices: a Case of Froth Wicking," *Phys. Fluids* **6**, 1993, p. 2493.
2. D. Weaire, S. Hutzler, G. Verbist and E. Peters, ''A Review of Foam Drainage," *in Advances in Chemical Physics* **102**, edited by I. Prigogine & S. Rice, John Wilky & Sons, 1997.
3. A. Bhakta and E. Ruckenstein, ''Decay of Standing Foams: Drainage, Coalescence and Collapse," *Advances in Colloid & Interface Science* **70**, 1997, p. 1.
4. P.T. Callaghan, M.E. Gates, C.J. Rofe and J.B.A.F. Smeulders, " A Study of the "Spurt Effect" in Wormlike Micelles Using Nuclear Magnetic Resonance Microscopy," *Journal de Physique II* **6**, 1996, p. 375.
5. C.G.J. Bispernik, A.D. Roneltap and A. Prins, ''Bubble Size in Foams," *Advances in Colloid & Interface Science* **38**, 1992, p. 13.
6. E.R. Weibel, ''*Stereological Methods*," vol. 2, Academic Press, N.Y. London, 1980.

Foams on Earth (Gravity Presents)

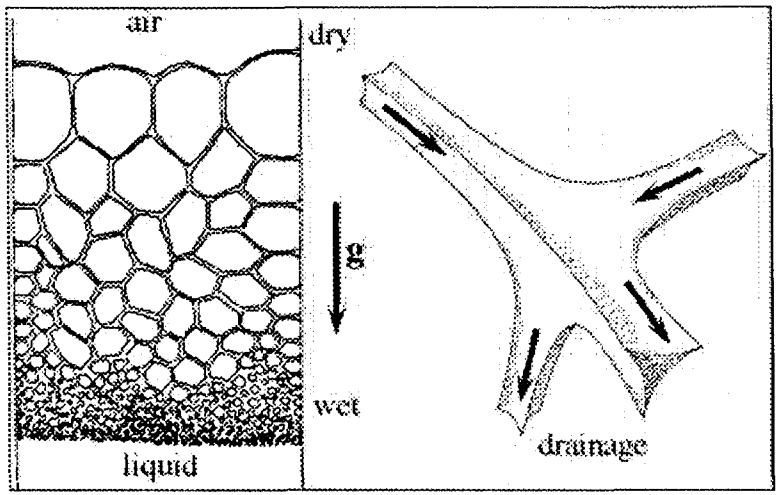

- Fluid drains out of membranes and leaves the foam through the network of Plateau borders.
- Draining liquid flushes surfactants from the soap films.
- Buoyancy pushes bubbles upward:
  1. Bubble packing $\Phi \ll \Phi_{max} \approx 36\ \%$
  2. promotes membrane breakage at the top
- Vertical wetness gradient $\Rightarrow$ faster aging at the top $\Rightarrow$ foam destabilization
- Coarsening and drainage CANNOT be separated.

Foams in Microgravity Conditions

Parabolic flight experiments show (D. Noever & R. Cronise, NASA, Huntsville, 1993):

- Initially dry foam sucks liquid from reservoir.
- Wetting front moves upward.

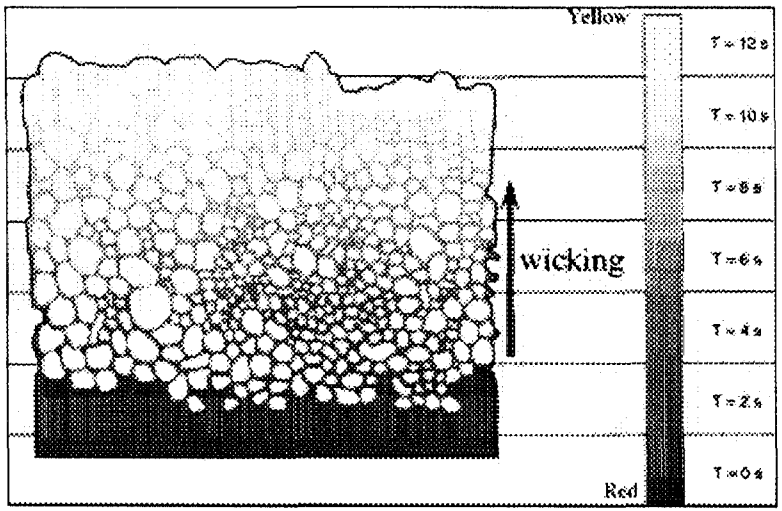

The color spectrum from red to yellow corresponds to the forward time progression in low gravity (each color shade corresponds to 2 s). The solid red area at the bottom is the soap solution reservoir.

Foam Evolution under Steady Microgravity Conditions

- All fluid available is sucked into the foam (fast). The overall wetness is strictly preserved during further evolution, liquid can only redistribute inside the foam.
- Gas diffuses from the smaller bubbles to the larger ones regardless of gravity conditions (slow).
- Decay or growth of bubbles reduces or enhances gas diffusion until the additional fluid from shrinking membranes redistributes inside the foam.
- Diffusion cause the smallest bubbles to disappear. $\Rightarrow$ Total boundary area in the foam decreases. $\Rightarrow$ Average membrane thickness increases. $\Rightarrow$ Rate of gas diffusion can drop dramatically.
- Foam may reach a metastable configuration, containing several large bubbles with thick membranes.
- The global, no bubble equilibrium (which is the only final state of foam evolution on Earth) may require almost infinite time.

$\Downarrow$	$\Downarrow$	$\Downarrow$
Dry/wet foam stability to soap film rupture/ structural changes increases.	Defoaming could be difficult.	One can separate effects of drainage and gas diffusion on foam structure and stability.

Is $\Phi > \Phi_{max}$ possible?

Goals

- Simulation, to some extent, of microgravity conditions on Earth — foam is stabilized by continuous liquid supply to the top of the column.

  ⇓

  * Precise control of foam wetness.
  * Effects of gas diffusion and gravity on foam aging are partially separated.

- Experiments on diffusive coarsening of such "frozen" foams of various wetnesses.

  ⇓

  * Full structural information about foams.
  * Growth law.

- Relation of foam rheology to foam structure.

  ⇓

  * Prediction of flow properties for "space" foams.

- Development and testing of different techniques for foam analysis which may be suitable for microgravity experiments on the ISS in the future.

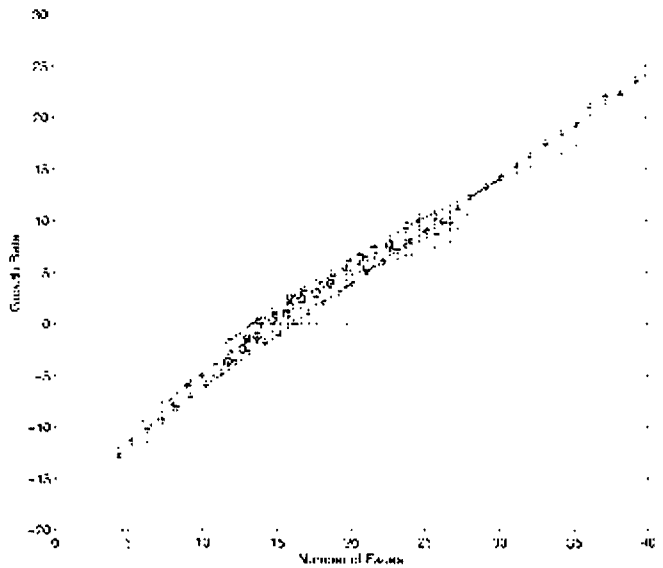

Earlier analytical and numerical predictions of diffusion-driven growth for the ideal dry ($\Phi \to 0$) foam.

Stabilized Aqueous Foam

(Low Viscosity)

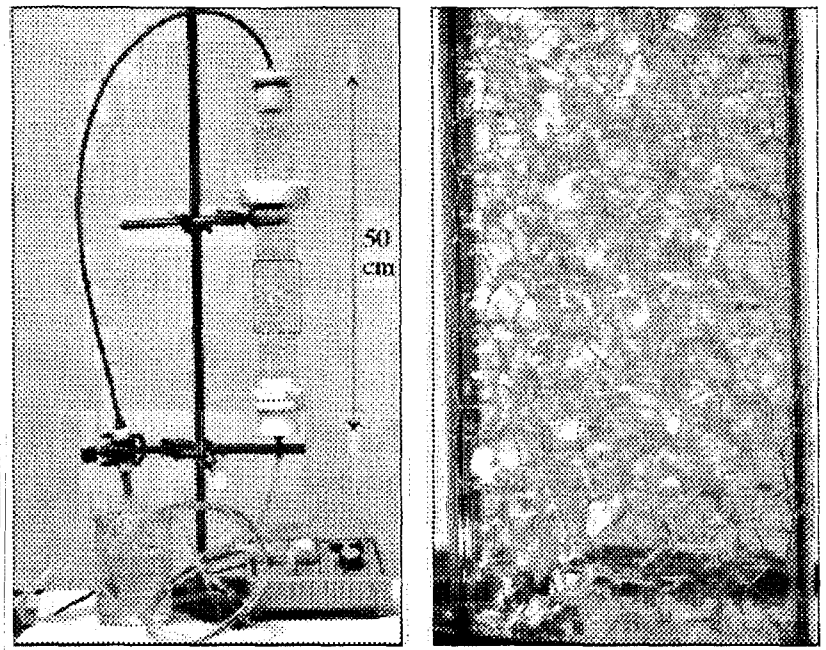

Draining Gelatine-Based Foam

(High Viscosity)

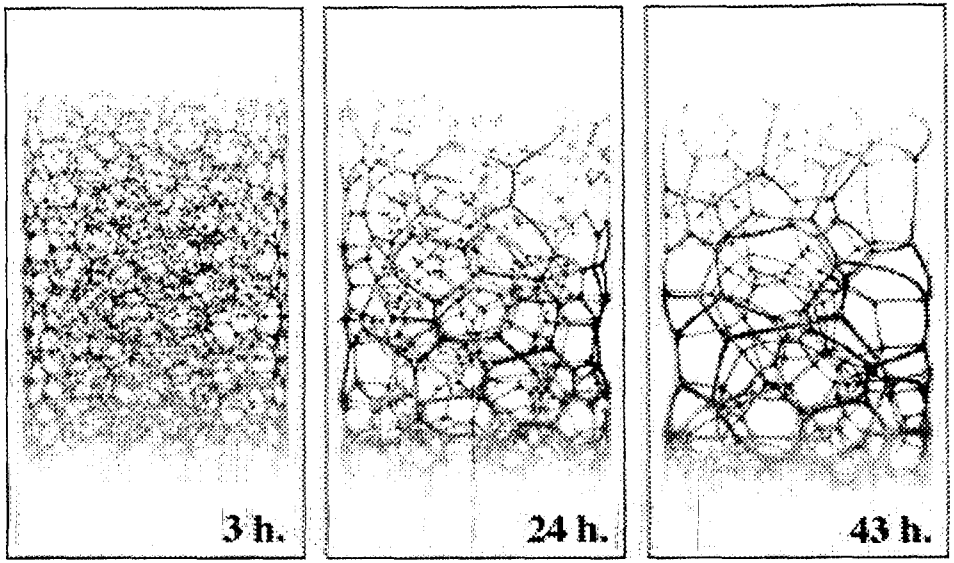

Foam remains stable even after 2 weeks of coarsening, while without liquid supply to top of the foam head, the foam will collapse after 1 hour. No significant wetness gradient, even for relatively tall foam head ($\approx$ 50 cm). Larger membrane thickness provides better signal to noise ratio for MRI. The slowness of MRI is less critical for stabilized foam.

Vertical wetness gradient evident at almost all stages of foam evolution even for 4 cm tall foam head. The above images are the maximum intensity projections of full 3D MRI images of liquid foams. One $256 \times 128 \times 128$ image with spatial resolution approximately 100 μm requires between 30 minutes and 1 hour acquisition, depending on number of averages.

MRI of Liquid Foams

- MRI images of liquid foams contain all necessary information to reconstruct individual bubbles and extract structural and topological information.
- To eliminate strong magnetic inhomogeneities at the gas/liquid interfaces the diamagnetic fluid is doped with paramagnetic $DyCl_3$ and $CuSO_4$ to reduce imaging artifacts and to enhance spin-lattice relaxation (to reduce the longitudinal relaxation time T_1).
- Liquid foams are difficult to image due to their very low signal level caused by their low liquid content. For early times we run 2 to 4 averages, yielding integration times of about 1 hour. For very dry foams we acquire up to 16 averages should.
- Only Plateau borders are visible.
- Modified PGSE method (used by Callaghan for measurements of the rheological properties of Non-Newtonian fluids) can be adapted to study the rheological properties of liquid foams.

University of Notre Dame MRI facility: The 300 MHz (7 Tesla) Bruker SWB Imager.

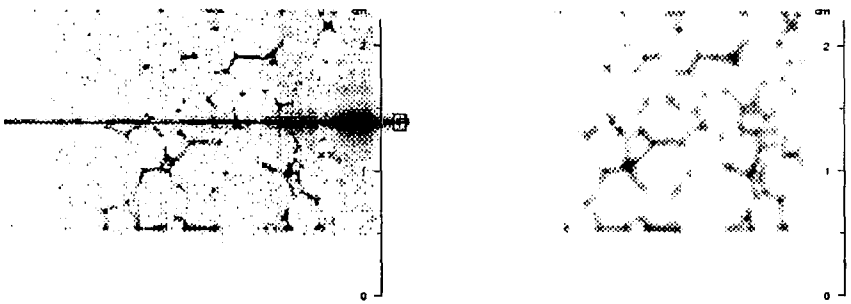

(a) Original central slice of a 3D image of a foam showing noise and artifacts. *(b)* The same slice after filtering.

Prior Results: Coarsening of Non-Stabilized Gelatine-Based Foams.

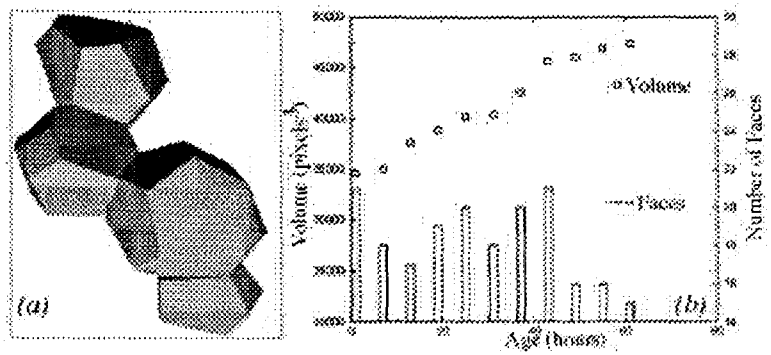

From 3D MRI images we can reconstruct individual bubbles *(a)* and determine the bubble volumes, number of faces, *etc.* Tracking individual bubbles over time *(b)* provides data about the dependence of bubble growth rate on topology. The accuracy and statistics of this data are mostly limited by the semi-automatic reconstruction algorithm.

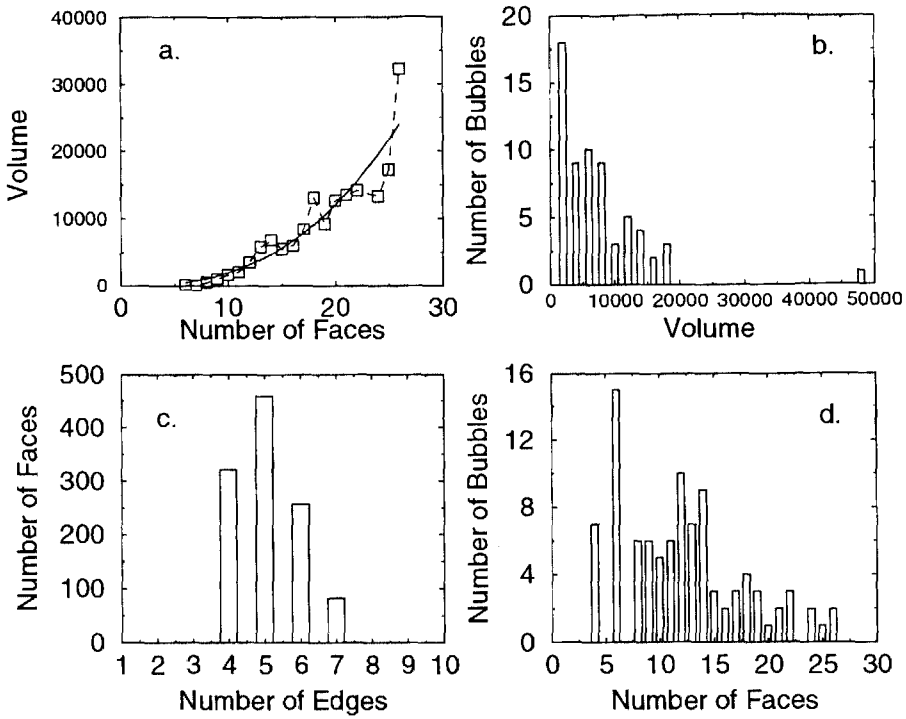

Sample of data for a foam: *(a)* Average bubble volume vs. number of faces. Distributions of volumes *(b)*, edges *(c)* and faces *(d)*.

Wet Foams: Foam Analyzer

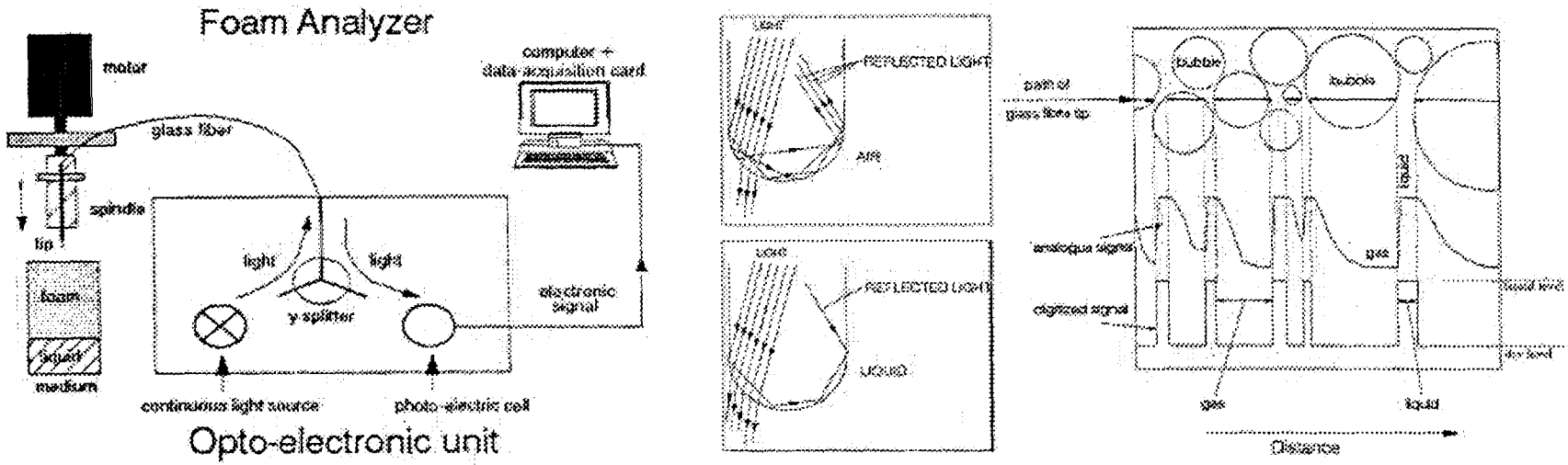

(C. G. J. Bispernik, A. D. Ronteltap and A. Prins, *Advances in Colloid & Interface Science*, **38**, 1992, 13).

- With proper surface treatment, the thin probe will not destroy foam lamellae.
- The measured chord length distributions will allow us to reconstruct the bubble size distribution of the foam and to estimate the membrane thickness distribution. (E. R. Weibel, *"Stereological methods"*, vol.2, Academic Press, London, 1980).
- To reduce the amount of data needed for accurate reconstruction we will try to use parametrized distributions, obtained from MRI experiments, and obtain these parameters by fitting measured chord distributions.

Non-Stabilized Very Dry Foams: Laser Scanner

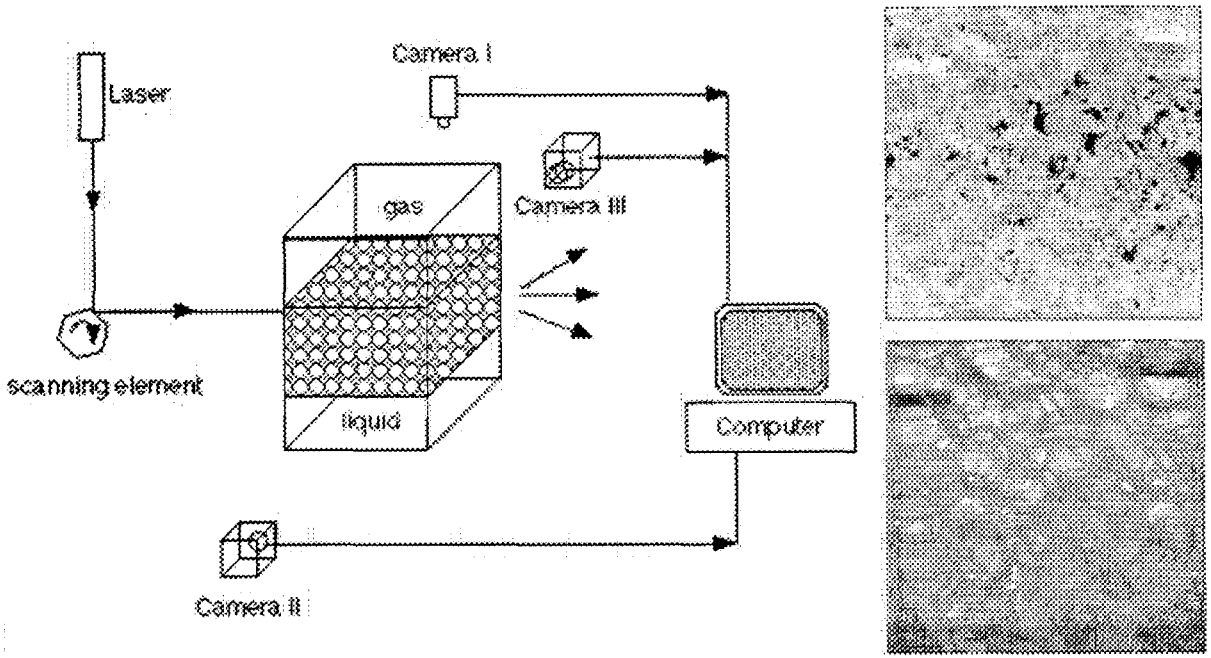

- In the beam, where laser light crosses a lamella, a very bright point appears.
- Making simultaneous images, from the top and sides, allows us to determine the membrane position. Three images may be needed to eliminate spurious points from multiple reflections.
- Scanning the laser beam through the foam, we will be able to reconstruct the full structure of very dry foam. Such foams cannot be analyzed by MRI because of their extremely low liquid content.
- The accuracy will be mostly determined by the rate of scanning and will be limited by the number of bubbles scanned.

◇ Relatively small sample ◇ Fast measurements

Current Status

- Designed and built cell for MRI imaging of stabilized aqueous foams.
- Conducted preliminary experiments on foam wetness/liquid flow rate/foam life-time calibration.
- Designing and acquiring parts to build foam analyzer.
- Developing code for fast (up to 30 fps) image acquisition with Dalsa high resolution (1024×1024) digital video camera. This code will be used for optical tomography.

PHASE-SHIFTING LIQUID CRYSTAL POINT-DIFFRACTION INTERFEROMETRY

DeVon W. Griffin[1], Kenneth L. Marshall[2] and Carolyn R. Mercer[3]

[1] M/S 110-3, NASA Glenn Research Center, 21000 Brookpark Road, Cleveland, OH 44135
[2] Laboratory for Laser Energetics, University of Rochester, 250 East River Road, Rochester, NY 14623
[3] M/S 77-1, NASA Glenn Research Center, 21000 Brookpark Road, Cleveland, OH 44135

Microgravity fluid physics experiments frequently measure concentration and temperature. Interferometers such as the Twyman Green illustrated in Figure 1 have performed full-field measurement of these quantities. As with most such devices, this interferometer uses a reference path that is not common with the path through the test section. Recombination of the test and reference wavefronts produces interference fringes. Unfortunately, in order to obtain stable fringes, the alignment of both the test and reference paths must be maintained to within a fraction of the wavelength of the light being used for the measurement. Otherwise, the fringes will shift and may disappear. Because these interferometers are extremely sensitive to bumping, jarring and transmitted vibration, they are typically mounted on optical isolation tables.

Schlieren deflectometers or the more recent Shack-Hartmann wavefront sensors also measure concentration and temperature in laboratory fluid flows. Ray optics describe the operation of both devices. In a schlieren system, an expanded, collimated beam passes through a test section where refractive index gradients deflect rays. A lens focuses the beam to a filter placed in the rear focal plane of the decollimating lens. In a quantitative color schlieren system, gradients in the index of refraction appear as colors in the field of view due to the action of the color filter. Since sensitivity is a function of the focal length of the decollimating lens, these systems are rather long and filter fabrication and calibration is rather difficult.

A Shack-Hartmann wavefront sensor is an array of small lenslets. Typical diameters are on the order of a few hundred microns. Since these lenslets divide the test section into resolution elements, the spatial resolution can be no smaller than an individual lenslet. Such a device was recently used to perform high-speed tomography of heated air exiting a 1.27 cm diameter nozzle.[1] While these wavefront sensors are very compact, the limited spatial resolution and the methods required for data reduction suggest that a more useful instrument needs to be developed.

The category of interferometers known as common path interferometers can eliminate much of the vibration sensitivity associated with traditional interferometry as described above. In these devices, division of the amplitude of the wavefront following the test section produces the reference beam. Examples of these instruments include shearing and point diffraction interferometers. In the latter case, shown schematically in Figure 2, a lens focuses light passing through the test section onto a small diffracting object. Such objects are typically either a circle of material on a high quality glass plate or a small sphere in a glass cell. The size of the focused spot is several times larger than the object so that the light not intercepted by the diffracting object forms the test beam while the diffracted light generates a spherical reference beam. While this configuration is mechanically stable, phase shifting one beam with respect to the other is difficult due to the common path. Phase shifting enables extremely accurate measurements of the phase of the interferogram using only gray scale intensity measurements and is the *de facto* standard of industry. Mercer and Creath[2] demonstrated phase shifting in a point diffraction interferometer using a spherical spacer in a liquid crystal cell as the diffracting object. By changing the voltage across the cell, they were able to shift the phase of the undiffracted beam relative to the reference beam generated by diffraction from the sphere. While they applied this technology to fluid measurements, the device shifted phase so slowly that it was not useful for studying transient phenomena. We have identified several technical problems that precluded operation of the device at video frame rates and intend to solve them to produce a phase-shifting liquid crystal point-diffraction interferometer operating at video frame rates.

The first task is to produce high contrast fringes. Since the diffracted beam is much weaker than the transmitted beam, interferograms have poor contrast unless a dye is added to the liquid crystal to reduce the intensity of the undiffracted light. Dyes previously used were not rigorously characterized and suffered from hysteresis in both the initial alignment state of the device and the electro-optic switching characteristics. Hence, our initial effort will identify and characterize dyes that do not suffer from these difficulties and are readily soluble in the liquid crystal host.

Since the ultimate goal of this research is to produce interferometers capable of phase shifting at video frame rates, we will quantify the difference in switching times between ferroelectric and nematic liquid crystals. While we have more experience with nematic crystals, they typically switch more slowly than ferroelectric cells. As part of that effort, we will investigate the difference in the modulation of the interferograms as a function of the type of liquid crystal in the cell.

Because the temporal switching response of a liquid crystal cell is directly related its thickness, we intend to explore techniques required to produce cells that are as thin as possible. However, the cells must still produce a total phase shift of two pi radians.

References:

1. McMackin, L., Hugo, R.J., Pierson, R.E. and Truman, C.R., "High Speed Optical Tomography System for Imaging Dynamic Transparent Media," Optics Express, **1**, 302-311 (1977).
2. Mercer, C.R. and Creath, K., "Liquid-Crystal Point-Diffraction Interferometer for Wave-Front Measurements, Applied Optics, **35**, 1633-1642 (1996).

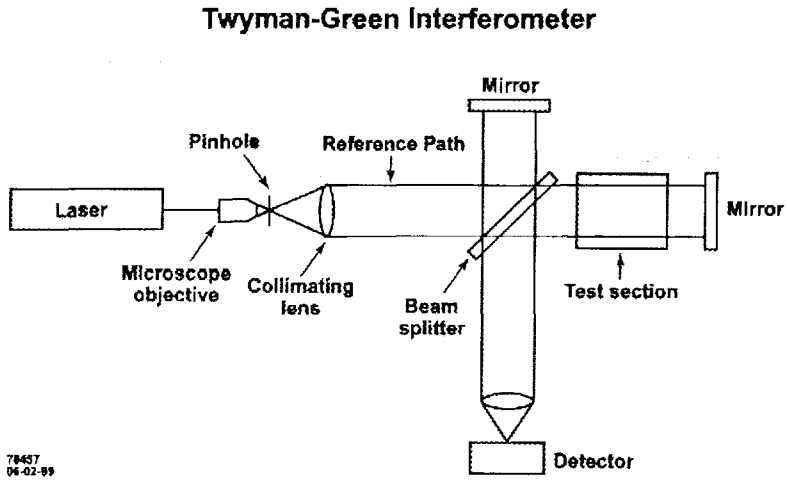

Figure 1

Figure 2

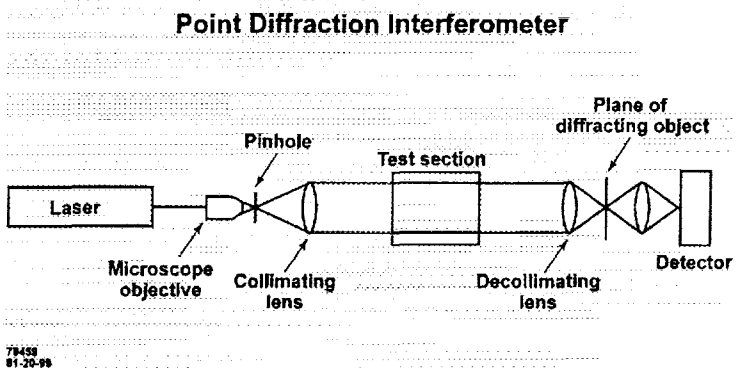

Presentation not available at time of printing.

DSD - A PARTICLE SIMULATION CODE FOR MODELING DUSTY PLASMAS

G. Joyce, M. Lampe, and G. Ganguli

Plasma Physics Division
Washington, DC 20375

ABSTRACT

The NRL Dynamically Shielded Dust code (DSD) is a particle simulation code developed to study the behavior of strongly coupled, dusty plasmas. The model includes the electrostatic wake effects of plasma ions flowing through plasma electrons, collisions of dust and plasma particles with each other and with neutrals. The simulation model contains the short-range strong forces of a shielded Coulomb system, and the long-range forces that are caused by the wake. It also includes other effects of a flowing plasma such as drag forces. Magnetic fields may also be included in the formalism.

In order to model strongly coupled dust in plasmas, we make use of the techniques of molecular dynamics simulation, PIC simulation, and the "particle-particle/particle-mesh" (P3M) technique of Hockney and Eastwood. We also make use of the dressed test particle representation of Rostoker and Rosenbluth. Many of the techniques we use in the model are common to all PIC plasma simulation codes. The unique properties of the code follow from the accurate representation of both the short-range aspects of the interaction between dust grains, and long-range forces mediated by the complete plasma dielectric response. If the streaming velocity is zero, the potential used in the model reduces to the Debye-Huckel potential, and the simulation is identical to molecular dynamics models of the Yukawa potential. The model basically represents the dust as simulation particles interacting via the dressed potential. The plasma appears only implicitly through the plasma dispersion function, so it is not necessary in the code to resolve the fast plasma time scales.

The following studies will be investigated using the DSD particle simulation code:

CRYSTAL STRUCTURES

We will determine the crystal structures which occur under both gravity and microgravity conditions, as a function of system parameters such as plasma density, neutral gas pressure, T_e, T_i, dust grain size, ion flow velocity, location in the discharge. In full gravity, structures will occur in the sheath edge region where the ion flow velocity is on the order of the Bohm velocity. In microgravity, the structures will be formed in the presheath where the flow velocity is less than Bohm. In many cases, more than one crystal structure is possible and the free energy difference between structures is very small. Thus we will determine any metastable crystal states as well, by starting from very low dust temperature. We will determine the free energy differences between states. We will attempt to categorize and explain the different crystal structures seen in various regions of the discharges, and in particular to explain the differences between the typically 2-D structures seen in terrestrial experiments and the 3-D structures which occur in some regions of microgravity experiments.

LATTICE EXCITATIONS AND MELTING TRANSITION

We will determine the lattice vibration spectra of the various configurations and compare this to experimental measurements by Goree et al in terrestrial experiments, and by Morfill et al in microgravity experiments. As the dust temperature, T_d, is increased, we will also look at the percentage of condensed defects and isolated dislocations in the lattice, and these results will be compared directly to the experimental results of Goree based on Delaunay triangulation. We can reproduce the diagnostics used by the experimenters, and in addition we can increase understanding by using techniques that are not available in experiments, e.g. we can deliberately introduce lattice defects of various types, and study their stability, how they spread and merge, and how they affect lattice vibrations. We will study in detail the microscopic processes that occur as T_d increases further and the lattice melts. We will focus on the role played by defects and by vibrational modes, and by break-up into domains separated by flowing regions. We will determine whether the melting transition is a first- or second-order phase transition, and in the former case will determine directly the specific heat of melting. We will compare results with the KTHNY melting theories, and later theories (Glaser (1993)), to determine quantitatively which if any of the existing theories are adequate to describe dusty plasma crystal melting in 2-D and 3-D situations.

LIQUID STATE

We will study the structure factors governing short-range order in the dust liquid state, such as the pair correlation function and orientational correlation functions, and compare the results to measurements by the Goree group, and by the Morfill group in microgravity. We will determine the excitation spectrum in the liquid state. We will study the liquid-solid phase transition from the liquid side, to develop understanding of the basic dynamics of crystal formation. Because plasma streaming leads to a partially attractive force between dust grains, it is possible that there is a first-order liquid-gas phase transition in the dust plasma. (In an ordinary electron-ion plasma, there is no such phase transition, but only a gradual and smooth transition from liquid to gas.) We will determine whether there is such a phase transition in any of the parameter regimes accessible to terrestrial or microgravity experiments.

REFERENCES

Glaser, M. A. and N. A. Clark *Adv. Chem. Phys.* **83** 543 (1993)

Hockney, R. W., and J. W. Eastwood Computer Simulation Using Particles, Chs. 8 & 12 Adam Hilger Bristol 1988

Morfill, G. E., H. M. Thomas, U. Konopka, H. Rothermel, and M. Zuzic "Plasma Crystals and Liquid Plasmas", Physics of Dusty Plasmas p. 184 AIP Conference Proceedings 446 Woodbury, New York (1998)

Morfill, G. E., H. M. Thomas, U. Konopka, H. Rothermel, and M. Zuzic "Plasma Condensation under Microgravity", preprint Max-Planck-Insuitut fuer extraterrestriche Physik. (1998a)

Pieper, J. B., J. Goree, and R. A. Quinn *J. Vac. Sci Technol. A* **14(2)** 519 (1996)

Rostoker, N. and M. Rosenbluth *Phys. Fluids.* **3** 1 (1960)

Thomas, H., G. Morfill, V. Demmel, J. Goree, B. Feuerbacher, and D. Moehlmann, "Plasma Chrystal: Coulomb Crystallization in a Dusty Plasma, *Phys. Rev. Lett.* **72** 652, (1994)

Presentation not available at time of printing.

AGGREGATION AND GELATION OF ANISOMETRIC COLLOIDAL PARTICLES: PRELIMINARY RESULTS AND RESEARCH PLAN

Michael J. Solomon and Priya Varadan, Department of Chemical Engineering, University of Michigan, Ann Arbor, MI 48109-2136. (mjsolo@umich.edu)

ABSTRACT

A research plan for the study of the structure and dynamics of aggregates and gels of colloidal rods and platelets by means of static and dynamic light scattering is presented. Studies under both quiescent and flow conditions are envisaged. For purposes of comparison, preliminary results of the structure and dynamics of spherical colloidal gels are reported. The materials studied, sterically stabilized spherical colloidal silica suspended in hexadecane, form stable, reversible gels that can be studied by light scattering in the volume fraction range 0.01 - 0.10. The gels allow divergences of characteristic times at the gel point to be sensitively probed by manipulating temperature.

INTRODUCTION AND RESEARCH PLAN

The structure and dynamics of colloidal aggregates and gels have been long investigated by the fluid physics community; however, most research has focused on suspensions of spherical particles. Yet, aggregates and gels of anisometric particles - colloidal rods and platelets - may exhibit structure and dynamics that are quite different from spherical colloids. For example, suspensions of colloidal rods gel at extremely low volume fractions and form birefringent sediments and the rheology of solutions and gels of colloidal rods and platelets differs dramatically from that of colloidal spheres.[1] Scientifically, studies with anisometric particles offer the opportunity to assess the role of anisotropic excluded volume and particle orientation in aggregates and gels. Technologically, anisometric colloids find use in a wide range of materials such as ceramics, polymer nanocomposites, well-bore drilling fluids and magnetic storage media.

The specific aim of this research is to use small and wide-angle light scattering, flow light scattering, dynamic light scattering and rheology to study the structure and dynamics of aggregates and gels of anisometric particles. Quiescent aggregates and gels will be studied, as well as gels subjected to shear deformation. The anisometric particles will be prepared by two methods. The first, after Ho et al., will allow the production of anisometric polymer colloids that can be density matched in mixtures of H_2O and D_2O.[2] Because of the elimination of sedimentation effects, these materials can be used for ground-based studies at low volume fraction. The aqueous solutions of anisometric polymer colloids are not suited for high volume fraction studies because the large refractive index contrast between particle and solvent causes multiple scattering. At high volume fraction, studies will be performed with inorganic rods (boehmite) and platelets (gibbsite) that are coated with silica and grafted with octadecyl chains.[1] These now organophilic colloids can be dispersed in non-polar solvents (such as hexadecane) in which spherical colloids of similar surface chemistry are known to gel. Advantages of such thermoreversible gels are that the interparticle potential is believed to be well characterized and their approximate refractive index matching allows single scattering studies up to $\phi = 0.12$.[3] However, because inorganic colloids are prone to sedimentation since

they cannot be density matched on the ground, the microgravity environment presents opportunities for studies that probe a more extensive range of volume fraction, size and shape. Specific studies that are planned: (1) Effect of aspect ratio on the fractal dimension and cluster radius of quiescently formed anisometric particle aggregates and gels. (2) Effect of shear deformation on the structure of anisometric particle gels. (3) The effect of particle shape on the dynamic structure factor. (4) Comparison of scattering and rheological studies.

PRELIMINARY RESULTS

For purpose of future comparison, the static and dynamic structure factor of high volume fraction gels of spherical colloids have been characterized by means of small and wide-angle static light scattering and dynamic light scattering, respectively (Figures 1 and 2). The effect of shear deformation on spherical colloidal gels has also been quantified (Figure 3). Interestingly, Figure 3 demonstrates that anisotropic scattering is observed even for gels of spherical particles. The materials studied are silica colloids (a = 40 nm) with surface grafted octadecyl chains dispersed in the solvent hexadecane. The materials gel below a critical temperature. The results illustrate that ground-based experiments with inorganic colloidal gels are possible, provided that the deleterious effects of sedimentation can be ameliorated by means of studies at sufficiently high volume fraction. Note that the ability to sensitively probe the divergences of characteristic times associated with the gelation transition (Figure 2) by precise control of temperature provides a means to study the relationship between colloidal gelation and the glass transition.

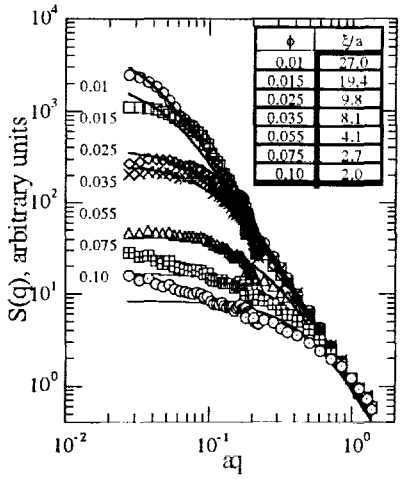

Figure 1. Static structure of a silica sphere/ hexadecane gel. ξ is the cluster radius. Fits are for the model of Sinha et al., 1984. [4]

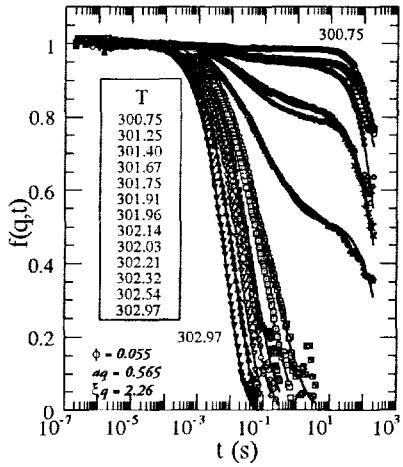

Figure 2. Gel dynamic structure (T_{gel} = 301.94). Fits are for the model of Krall and Weitz modified to account for the additional aging decay. [5]

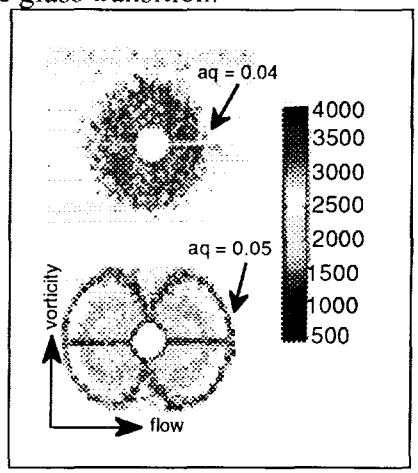

Figure 3. Scattering anisotropy of a quiescent (t) and sheared (b) silica/ hexadecane gel (ϕ = 0.10) in the flow - vorticity plane. The shear rate is 120 s^{-1}.

REFERENCES

[1] A.P. Philipse, A.-M. Nechifor and C. Pathmamanoharan, Langmuir **10**, 4451 (1994). M.J. Solomon and D.V. Boger, J. Rheology **42**, 929 (1998).

[2] C.C. Ho, A. Keller, J.A. Odell and R.H. Ottewill. Colloid Polym. Sci **271**, 469 (1993). M. Carpineti and M. Giglio, Phys. Rev. Lett. **68**, 3327 (1992).

[3] M.C. Grant and W.B. Russel, Phys. Rev. E **47**, 2606 (1993).

[4] S.K. Sinha, T. Freloft and J. Kjems, in *Kinetics of Aggregation and Gelation*, 87 (1984).

[5] A.H. Krall and D.A. Weitz, Phys. Rev. Lett. **80**, 778 (1998).

Presentation not available at time of printing.

Gelation Kinetics in Aerosols

C. Sorensen, A. Chakrabarti, W. Hagemann, D. Fischbach, D. Shi, and D. Fry

Department of Physics, Kansas State University, Manhattan, KS 66506-2601

Abstract

Our recent work has demonstrated that an aerogelation process occurs in acetylene diffusion flames and is responsible for the formation of millimeter sized soot [1]. This work is the first demonstration of gelation in the aerosol phase. Furthermore, our measurements indicate that the aggregates grow too quickly (by a factor of 400) to be described by the Smoluchowski Equation (SE). Based on our previous measurements of the rate constant in dilute aerosol systems which were in agreement with kinetic theory [2], we concluded that this too fast kinetics was a result of a breakdown of the SE as the system became concentrated, i.e., as the gel point was approached.

The goal of our present work is to understand aggregation kinetics when a particulate system becomes concentrated. Aerosols are the idea system for such a study because, unlike colloids, there are no solvent mediate effects influencing the particles. Moreover, this allows us to make direct comparison between experiment and simulation. We are currently advancing our work on three fronts: 1) further studies of acetylene soot formation, 2) aggregation in dense Ti02 aerosols and 3) large-scale simulation of diffusion-limited cluster aggregation in both two and three dimensional systems. Our preliminary simulations suggest that a fast aggregation kinetics takes place for concentrated systems, while for dilute system the aggregation kinetics is consistent with a mean-field kinetic theory. Understanding this fast kinetics in dense systems and the corresponding breakdown of the mean-field theory is the main motivation for the theoretical research.

References:

[1] C. M. Sorensen, W. B. Hagemann, T. J. Rush, H. Huang, and C. Oh. Phys. Rev. Lett. **80**, 1782 (1998).

[2] C. Oh and C. M. Sorensen, J. Aerosol Sci. **28**, 973 (1997).

Presentation not available at time of printing.

NOVEL OPTICAL DIAGNOSTIC TECHNIQUES FOR STUDYING PARTICLE DEPOSITION UPON LARGE CYLINDERS IN A SHEARED SUSPENSION

M. Yoda and B. C. Bailey
School of Mechanical Engineering, Georgia Institute of Technology

ABSTRACT

On a twelve-month voyage to Mars, one astronaut will require at least two tons of potable water and two tons of pure oxygen. Efficient, reliable fluid reclamation is therefore necessary for manned space exploration. Space habitats require a compact, flexible and robust apparatus capable of solid-fluid mechanical separation over a wide range of fluid and particle densities and particle sizes. In space, centrifugal filtration, where particles suspended in fluid are captured by rotating fixed-fiber mat filters, is a logical candidate for mechanical separation. Non-colloidal particles are deposited on the fibers due to inertial impaction or direct interception. Since rotation rates are easily adjustable, inertial effects are the most practical way to control separation rates for a wide variety of multiphase mixtures in variable gravity environments. Understanding how fluid inertia and differential fluid-particle inertia, characterized by the Reynolds and Stokes numbers, respectively, affect deposition is critical in optimizing filtration in a microgravity environment.

This work will develop non-intrusive optical diagnostic techniques for directly visualizing where and when non-colloidal particles deposit upon, or contact, solid surfaces: "particle proximity sensors." To model particle deposition upon a single filter fiber, these sensors will be used in ground-based experiments to study particle dynamics as in the vicinity of a large (compared with the particles) cylinder in a simply sheared (*i.e.*, linearly-varying, zero-mean velocity profile) neutrally-buoyant, refractive-index matched solid-liquid suspension.

The objectives of this new research project are:

1. To develop new optical diagnostic techniques for directly visualizing where and when particles deposit on a solid surface using fluorescent activation or quenching of an indicator species bound to the particle when it approaches (comes within O(100 nm) of) the ligand-bound surface;
2. To design and test a compact, self-contained experimental apparatus to study sheared refractive index-matched suspensions; and
3. To use this apparatus in ground-based experiments to study particle deposition on one large cylinder immersed in simple shear flow of a neutrally buoyant suspension.

Particle proximity sensors are based upon the ligand-specific nature of many common fluorescent species. Fluorescent emission from these so-called "fluorescent indicators" will

either be quenched or activated in the presence of some minimum concentration of a specific ion. For example, the fluorescent intensity of disodium fluorescein decreases by nearly an order of magnitude as pH decreases from 7 to 5. We have already identified several candidate fluorescent indicators that are quenched by pH and calcium ion concentration gradients.

Given that most of these indicators are used in biochemical applications, these fluorescent indicators have been mainly characterized for aqueous chemistries. The suspension liquids currently used by most investigators are, however, organic solvents. We are therefore developing new alternative suspension systems based upon aqueous salt solutions that will match both the refractive index and density of commercially available polymethylmethacrylate (PMMA) particles. An aqueous neutrally-buoyant, refractive index-matched suspension system will allow us to use pH- and Ca^{++}-specific fluorescent indicators with their well-characterized behavior, and take advantage of standard techniques for binding these indicators to the surface of and/or incorporating these indicators within the bulk of PMMA particles. Using these fluorescent indicators would also greatly simplify preparation of the solid surface; binding H^{+}, OH^{-} or Ca^{++} ions to solid glass surfaces using silanes is standard chemical procedure. Development of a novel water-based suspension system would also greatly simplify suspension mechanics experiments in terms of cost and chemical hazards.

We plan to use particle proximity sensors to study particle dynamics near a large cylinder immersed in a simply sheared suspension. As the dyed particles approach the cylinder, whose surface is bound with the appropriate ion, the fluorescent indicator bound to the particle surface will be quenched when the particle is within $O(100$ nm) of the cylinder. The kinetics of this quenching should be virtually instantaneous, occurring within $O(10$ nsec). If the flow is illuminated by light at the appropriate exciting wavelength, the quenched particles can be imaged at the illumination wavelength to determine particle deposition upon the cylinder, while the unquenched particle dynamics away from the cylinder can be imaged at the fluorescence wavelength. The effects of fluid inertia, flow confinement (due to finite test section width), and ratio of particle to cylinder diameter will be explored. The results will be compared with our previous studies of a cylinder immersed in a simply sheared Newtonian liquid.

This ground-based project is the first step towards "heavy" and "light" suspension flow experiments in microgravity. Considering the current limitations of computational techniques in many-particle suspension simulations and the impossibility of decoupling inertial and buoyancy effects upon Earth, microgravity environments are ideal for studying the effects of differential particle-fluid inertia. In addition, particle proximity sensors could be a valuable diagnostic techinque in studying several multiphase flow problems of importance in manned space exploration, such as dust deposition on solar arrays and seal degradation in dusty environments.

NASA/CP—2000-210470

Novel Optical Diagnostic Techniques for Studying Particle Deposition

M. Yoda and B. C. Bailey
Mechanical Engineering

Georgia Institute of Technology

NASA Microgravity 8/00

Motivation

- Study interaction of noncolloidal particles with solid surfaces in sheared particle-liquid suspensions
- Fluid and particle inertia (*Re* and *St*) effects on
  - Particle contact and deposition upon solid surfaces
- Nonintrusive "particle proximity sensor"
  - Indicator on particle reversibly and rapidly triggered when particle within small distance (< 1 μm) of surface
  - Optical changes (*e.g.* color, intensity) easily detectable without disturbing flow
- Reduced-gravity application: centrifugal filtration
  - Separate particles from fluid to reclaim water and air

Objectives

- Develop "particle proximity sensors": techniques for visualizing noncolloidal particle contact with (deposition on) solid surfaces
  - Fluorescent particles "turn off" as they approach solid surface due to ligand concentration gradient
  - Reversible, nonintrusive technique
- Use technique to study particle deposition upon cylinders in simple shear flow of neutrally buoyant suspension
  - Model filter fiber in centrifugal filtration
  - Basic bluff body flow

Model Suspension Systems

- Optical techniques used in suspension systems with refractive index- and density-matched phases
- Current suspension systems use organic liquids
  - Three liquids to match n, ρ of PMMA or PS particles
  - Viscosity of liquid phase $O(100$ cP)
- New aqueous suspension system
  - Two liquids (water, glycerin) + one salt (ammonium thiocyanate) to match n, ρ of PMMA particles
  - Fluorescent indicators require aqueous chemistry:
  - Lower viscosity liquid phase
  - Less chemical hazard

Suspension Characteristics

- 59.8% (w/w) water and 11.2% (w/w) glycerin solutions of NH_4SCN match n of 100–200 μm dia. PMMA particles (n = 1.487)
- Mix in different proportions to vary liquid density
  - At 1g, match PMMA density (ρ = 1.19 g/cm^3) with 54.0% (w/w) aqueous solution
  - At low g, heavy and light index-matched suspensions
- Transmission for 1 cm thick suspension >95% at 5% particle volume fraction, 23°C, 514.5 nm
- Viscosity of liquid phase O(10 cP)

NASA/CP—2000-210470

1155

Particle Proximity Sensor

- Use one of the common fluorescent Ca^{++} indicators
  - Can be irreversibly bound to PMMA surfaces
  - Add Ca^{++} in low (ppm) concentrations to suspension
  - Coat solid surface with porous polymer layer that binds $Ca^{++} \Rightarrow Ca^{++}$ concentration gradient next to surface
- Ca^{++} indicator on particle quenches within $O(100$ nm) of Ca^{++}-depleted solid surface
  - Reversible: particle leaving surface fluoresces again
  - Instantaneous: indicator responds within $O(10$ ns)
- Use as tracer particles in new aqueous suspension to study suspension mechanics and particle contact

Cylinder in Simple Shear

- Centrifugal filtration
  - Particles deposited upon rotating filter basket
  - Cylinder in simply sheared suspension models particle deposition upon single filter fiber in body-fixed frame

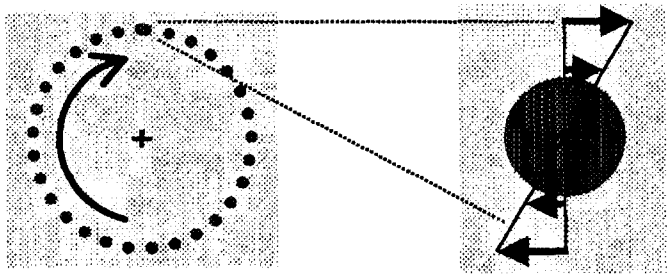

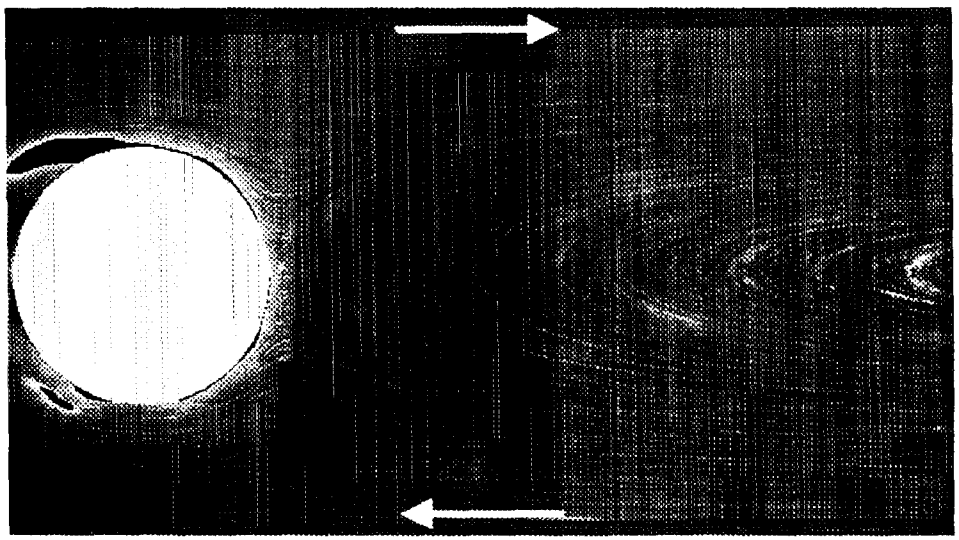

Streamlines for torque-free circular cylinder in single-phase simple shear at $Re_G = 8$

(Zettner and Yoda 2000)

NASA/CP—2000-210470

1157

Experimental Setup

Cylinder in simply sheared suspension

- Two cameras imaging different wavelengths
  - Illuminating $\lambda \Rightarrow$ Particle trajectories
  - Fluorescent $\lambda \Rightarrow$ Particle contact, deposition

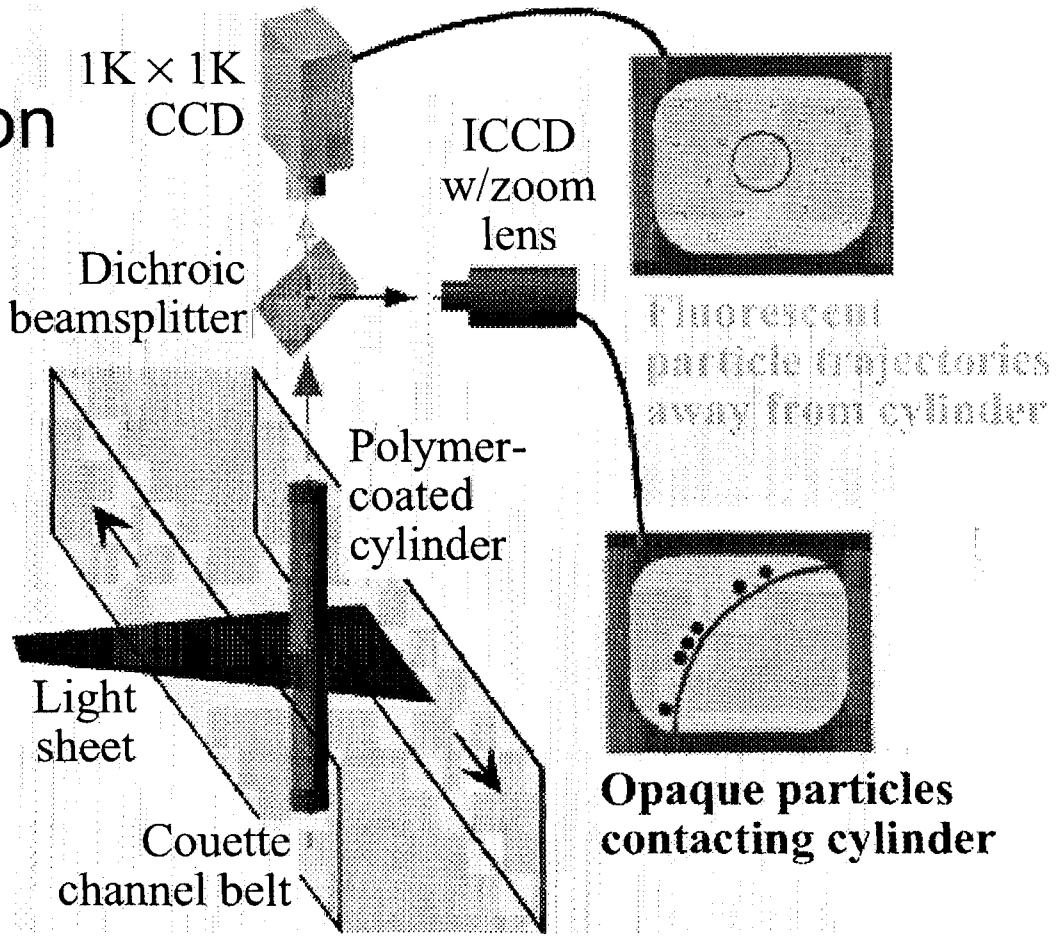

Future Work

- Year 1: Technique Development
  - Test various Ca^{++} indicators for PMMA particles; develop porous polymer layer for glass surfaces
- Year 2: Technique Calibration
  - Calibrate particle contact sensor in basic sedimentation flow (heavy particles)
- Years 3 and 4: Cylinders in Simply Sheared Inertial Suspension
  - Fixed and torque-free circular and elliptical cylinders: cylinder diameter $\gg$ particle diameter
  - Suspension mechanics and particle deposition

Effect of Pressure on Microstructure of $C_{12}E_5$/n-Octane-in-D_2O Microemulsions

S. Ferdinand, D. Bossev, and M. E. Paulaitis

Department of Chemical Engineering
The Johns Hopkins University
Baltimore, Maryland 21218

Forced Rayleigh scattering was used to measure the self-diffusion coefficients of oil droplets dispersed in a water-continuous phase of the $C_{12}E_5$/n-octane-in-D_2O microemulsion at atmospheric pressure as a function of temperature from 17.34 to 24.55°C, and at 26.2°C as a function of pressure up to 534 bar. Droplet self-diffusion coefficients were found to decrease by a factor of two with increasing temperature from the emulsification failure boundary to the phase boundary for this phase and the lamellar phase. This decrease is attributed to a reduction in the spontaneous curvature of the oil/water interface, leading to a transition from spherical to larger non-spherical oil droplets in water with increasing temperature. The effect of increasing pressure, like decreasing temperature, leads to a comparable increase the oil droplet self-diffusion coefficients, which is attributed to an increase in the spontaneous curvature of the oil/water interface, and a transition from non-spherical to smaller spherical oil droplets in water. We conclude from these results that the spontaneous curvature of the oil/water interface is sensitive to pressure, with increasing curvature corresponding to increasing pressure. This conclusion is consistent with the observed pressure-induced sequence of phase transitions observed for mixtures of C_iE_j surfactants, liquid alkanes, and water. These results motivate further studies to determine the extent to which pressure will stabilize certain morphologies that can be used as organic templates for inorganic polymerizations in the aqueous phase. The use of oil-in-water microemulsions takes advantage of the fact that the oil phase is compressible, and as such, pressure can control microstructure during the synthesis reaction. By uncoupling self-assembly from the inorganic synthesis using pressure as an additional process variable, existing synthesis strategies may benefit from enhanced control of the reaction process, and entirely new strategies may be contemplated.

Abstract

- Forced Rayleigh scattering was used to measure the self-diffusion coefficients of oil droplets dispersed in a water-continuous phase of the $C_{12}E_5$/n-octane-in-D_2O microemulsion at atmospheric pressure as a function of temperature from 17.34 to 24.55°C, and at 26.2°C as a function of pressure up to 534 bar. Droplet self-diffusion coefficients were found to decrease by a factor of two with increasing temperature from the emulsification failure boundary to the phase boundary for this phase and the lamellar phase. This decrease is attributed to a reduction in the spontaneous curvature of the oil/water interface, leading to a transition from spherical to larger non-spherical oil droplets in water with increasing temperature. The effect of increasing pressure, like decreasing temperature, leads to a comparable increase the oil droplet self-diffusion coefficients, which is attributed to an increase in the spontaneous curvature of the oil/water interface, and a transition from non-spherical to smaller spherical oil droplets in water.

Specific Aims

- The specific scientific objective of our research is to characterize experimentally and theoretically both the kinetics of phase separation and the metastable structures produced during phase separation in a microgravity environment. The particular systems we are examining contain surfactants. The larger length scales and slower times of phase separation in surfactant-containing systems make observations of critical fluctuations and metastable structures convenient. A key feature of our approach is to use ground-based measurements of critical phenomena in which density differences are minimized or eliminated by control of phase densities using compressible fluids. These experiments will define the key measurements and systems for study in shuttle experiments in which density differences are irrelevant. As part of this work we will also investigate the size and shape of surfactant aggregates and the interparticle interactions between them.

$C_{12}E_5$-Water-Octane Phase Diagram

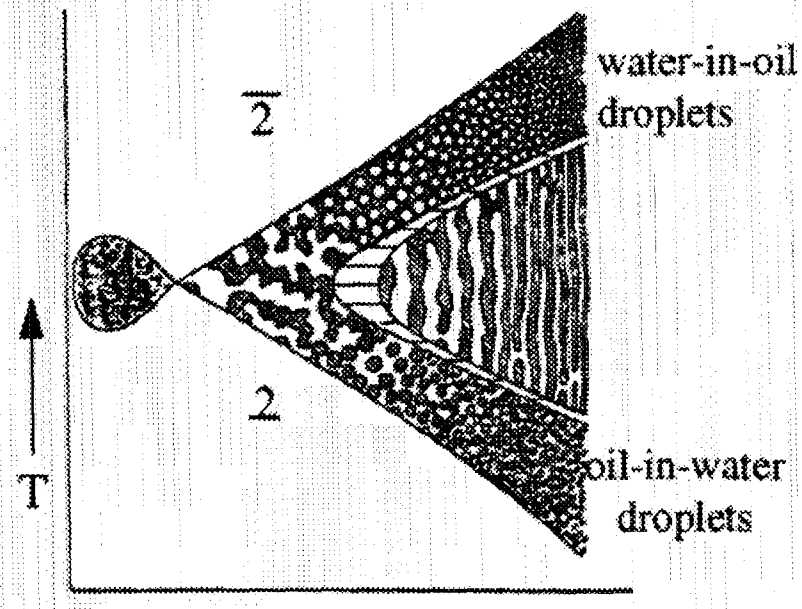

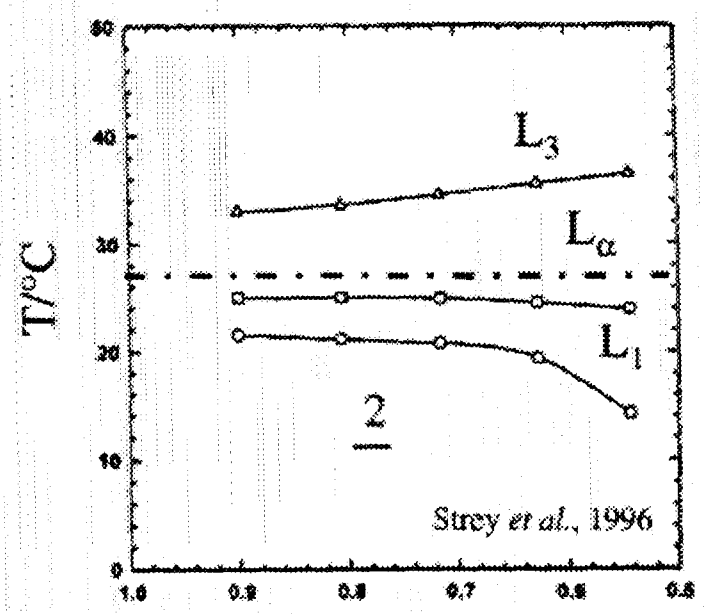

In this study, we determined the effect of pressure on a nonionic surfactant/oil-in-water microemulsion consisting of 3.7 wt% pentaethylene glycol monododecyl ether ($C_{12}E_5$), 4.3 wt% n-octane, and 92.0 wt% D_2O at 26.2°C and pressures up to ~500 bar. For this system, we expect pressure to stabilize single-phase dispersions of oil droplets in water over the formation of a lamellar phase

High-Pressure Forced Rayleigh Scattering

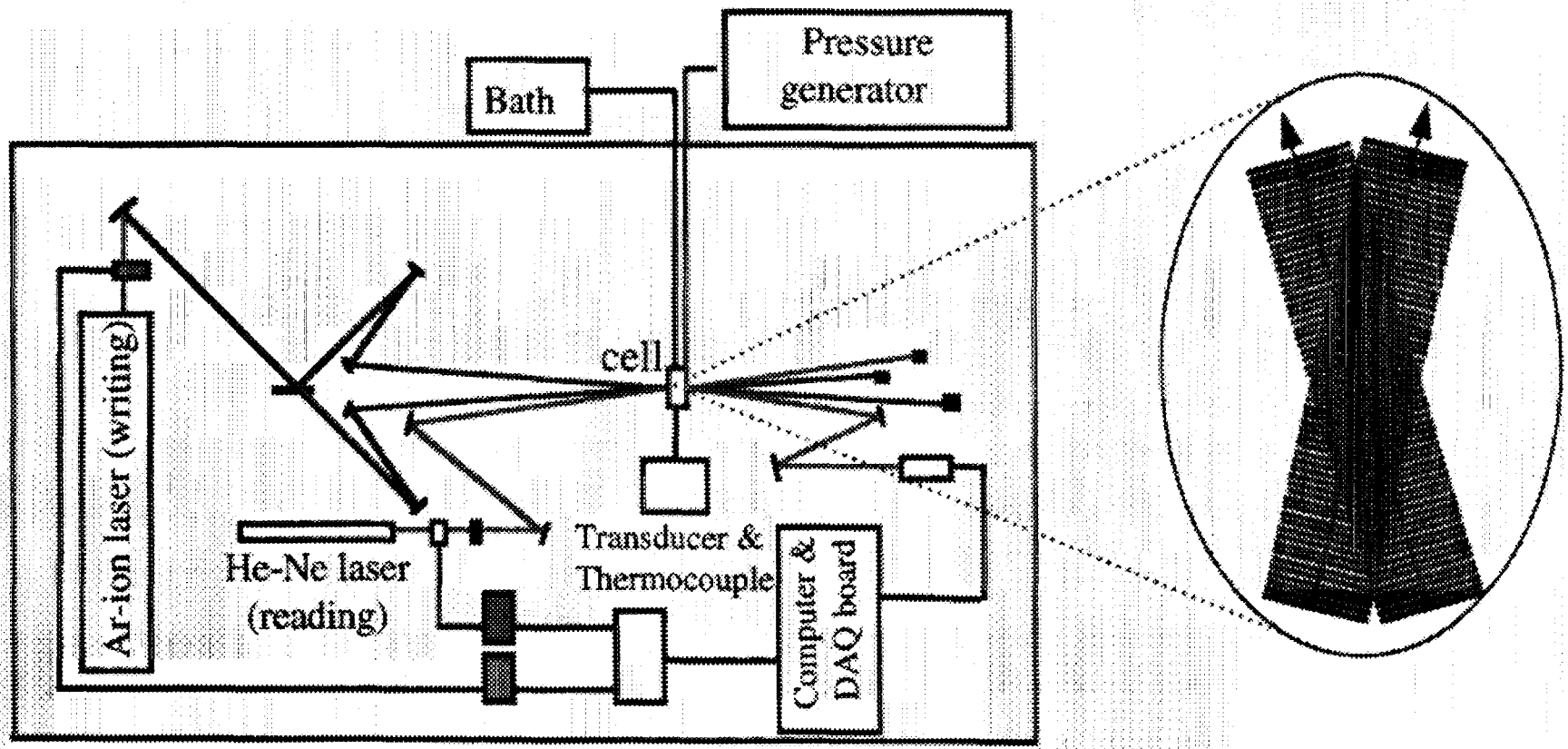

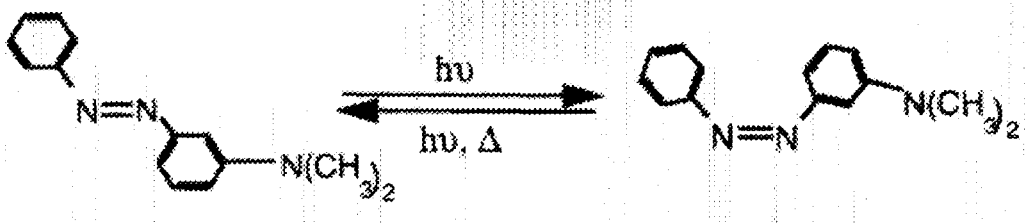

Diffusion Coefficients of Oil Droplets in $C_{12}E_5$-Oil-in-Water Microemulsions

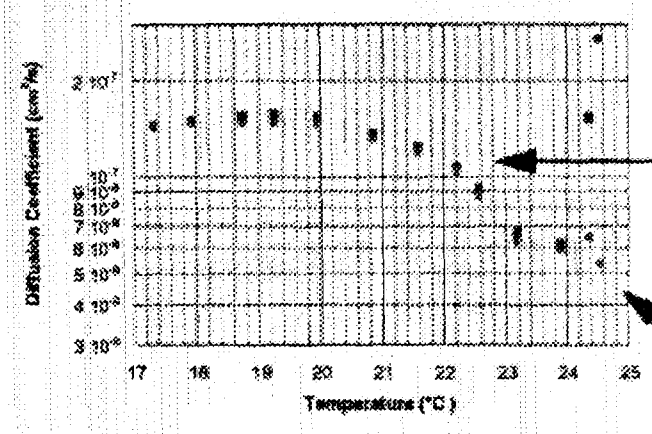

TEMPERATURE CONTROLS MICROSTRUCTURE THROUGH SURFACTANT HEADGROUP-WATER INTERACTIONS

- **droplet diffusion coefficients decrease with increasing temperature due to spherical-to-nonspherical shape change**

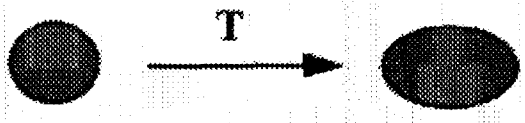

- **phase boundaries between single-phase oil-in-water dispersion and lamellar phase**

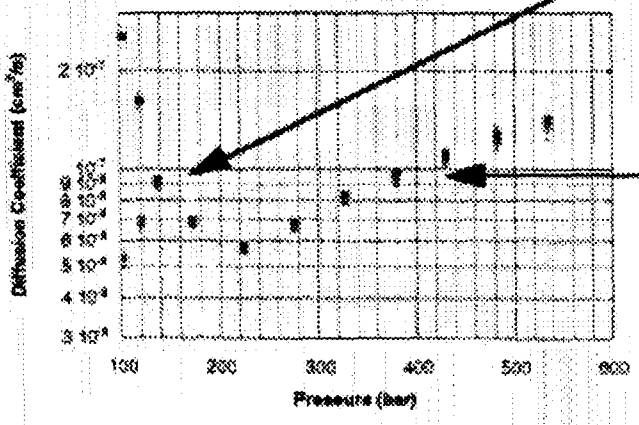

PRESSURE CONTROLS MICROSTRUCTURE THROUGH SURFACTANT TAILGROUP-OIL INTERACTIONS

- **droplet diffusion coefficients increase with increasing pressure due to nonspherical-to-spherical shape change**

Conclusions

- We conclude from these results that the spontaneous curvature of the oil/water interface is sensitive to pressure, with increasing curvature corresponding to increasing pressure. This conclusion is consistent with the observed pressure-induced sequence of phase transitions observed for mixtures of C_iE_j surfactants, liquid alkanes, and water. These results motivate further studies to determine the extent to which pressure will stabilize certain morphologies that can be used as organic templates for inorganic polymerizations in the aqueous phase. The use of oil-in-water microemulsions takes advantage of the fact that the oil phase is compressible, and as such, pressure can control microstructure during the synthesis reaction. By uncoupling self-assembly from the inorganic synthesis using pressure as an additional process variable, existing synthesis strategies may benefit from enhanced control of the reaction process, and entirely new strategies may be contemplated.

Work In Progress

- Preliminary high-pressure SANS measurements on $C_{12}E_5$/n-octane/D_2O microemulsions show a pressure-induced shape change from cylindrical to spherical oil-in-water droplets at 26.2°C.
- The pair distance distribution function, p(r), gives a spherical droplet radius of 89 Å, while a Guinier analysis gives a cylinder radius of 76 ± 5Å and a sphere radius of 102 ± 9Å.

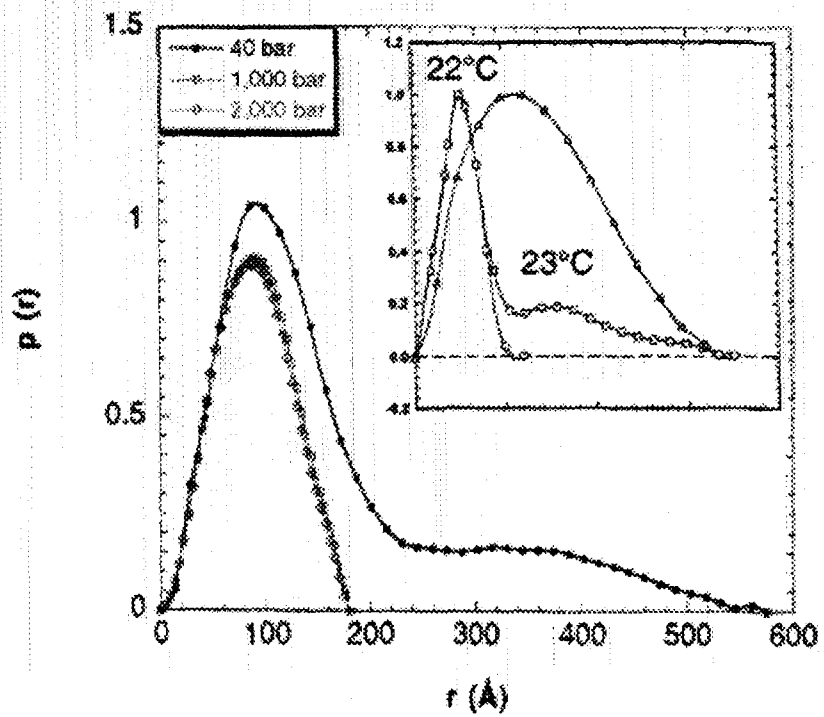

Work In Progress

- We are measuring the kinetics of phase separation for the $C_{12}E_5$/n-octane/D_2O system at isopycnic conditions using low angle light scattering. Isothermal pressure quenches from the one-phase region into the two-phase, liquid-liquid equilibrium region are used to initiate phase separation.
- Our preliminary results indicate that, under isopycnic conditions, droplet size can be controlled by pressure during phase separation for droplets on the order of a micron in diameter. We plan to probe the phase separation kinetics on submicron length scales using small angle neutron and forced Rayleigh scattering.

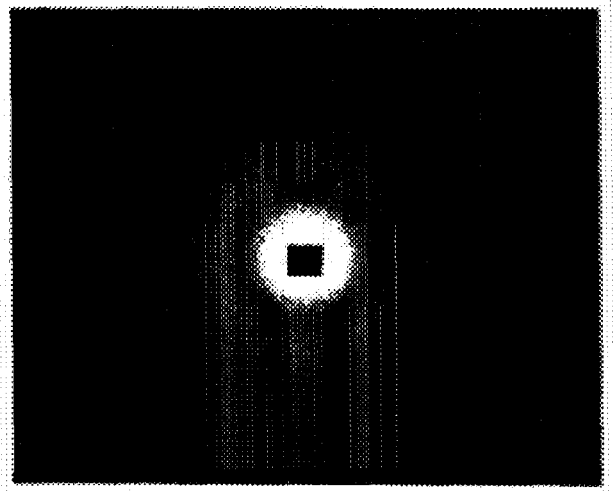

NON-EQUILIBRIUM PARTICLE CONFIGURATION IN SEDIMENTATION

X.-Y. Lei, B. J. Ackerson and P. Tong

Department of Physics, Oklahoma State University, Stillwater, OK 74078

ABSTRACT

In the study of the settling of large non-Brownian particles, one is interested in understanding the effect of the long-range hydrodynamic interactions on the microstructures formed in the settling suspension and finding the direct link between the microscopic particle configuration and the macroscopic properties of the suspension, such as the mean sedimentation velocity and the velocity fluctuations (the rms velocity) as a function of the particle concentration. We have recently proposed [1] that statistical or spontaneous number fluctuations of the particles can produce regions having more (or less) particles than the average. These heavier (or lighter) regions are convectively unstable, when the size becomes larger than the diffusive dissipation length δ_d. Using the Rayleigh criterion, the value of δ_d is calculated and the result agrees with experiment. Above the length δ_d, a set of coarse-grained equations of motion is used to describe the concentration and velocity fluctuations in sedimentation. The model provides a physical interpretation for the emergence of a velocity cut-off length, which prevents hydrodynamic dispersion coefficients from being divergent.

To test these theoretical ideas, we conduct measurements of the particle configuration in a settling suspension of large non-Brownian particles. The particles used in the experiment are 40 μm diameter polymer latex spheres suspended in polyalkylene glycol at the volume fraction 0.4%. A sheet of laser light is used to illuminate a vertical section of the settling suspension and images of the particles are obtained using a CCD camera situated normal to the illuminating light sheet. Figure 1 shows a typical particle configuration in sedimentation. Superimposing a series of such pictures taken at 15-second intervals shows a turbulent looking velocity field with rather large velocity fluctuations. The particle configurations in sedimentation look random but the number fluctuations of the particles are found to be suppressed when compared with Poisson statistics for pure random configurations. Figure 2 compares typical number fluctuations (number of particles in a circle of fixed area) measured in sedimentation (upper curve) with those in pure random configurations (lower curve). Systematic statistical analysis shows that the number fluctuations of the settling particles become more and more suppressed with time. At the later stage of the settling process, the suppression is most striking at large length scales. These findings are consistent with the notion that the convective response of the suspension to ordinary number fluctuations reduces and eliminates them, bringing the suspension to a marginally stable state, in which the statistics are such that unstable convection is minimized.

[1] "A two-fluid description of particle sedimentation," P. Tong and B. J. Ackerson, submitted to Phys. Fluids.

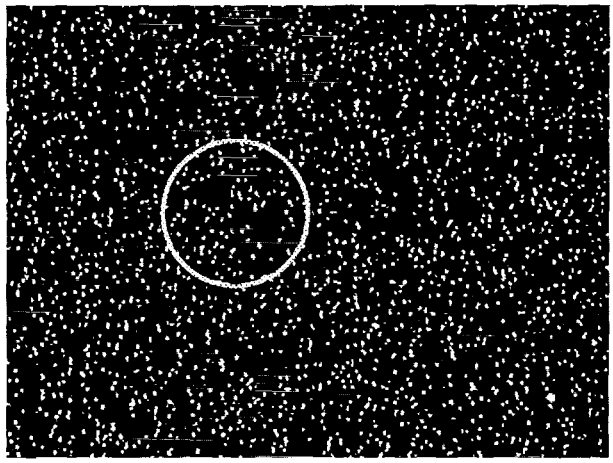

Fig. 1 A typical configuration of non-Brownian particles in sedimentation.

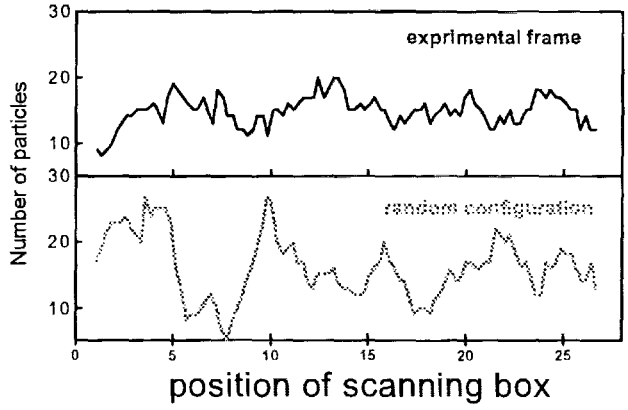

Fig. 2 Typical number fluctuations (number of particles in a circle of fixed area) measured in sedimentation (upper curve) and those with Poisson statistics in pure random configurations (lower curve).

Presentation not available at time of printing.

DYNAMICS OF GRAIN BOUNDARIES IN 2D COLLOIDS

Q. -H. Wei and X. -L. Wu
Department of Physics and Astronomy, University of Pittsburgh, Pittsburgh, PA 15260

Abstract

Grain boundaries are the longest known crystal defects and the development of grain structures plays a critical role in the properties of many kinds of materials such as ceramics, metals, and semiconductors [1]. While the equilibrium structures of grain boundaries have been known very well to atomic resolution through electron microscopy [2] and soap bubble model studies [3], the dynamics process of grain boundary migration driven by external forces or thermal fluctuation is not well established.

In this presentation, we report the non-equilibrium behavior of grain boundaries in a model system, consisting of a monolayer of colloidal particles confined in a soap film. A great advantage of this model system is that structure and dynamics of grain boundaries can be studied instantaneously. The 2D film is formed by drawing a thin plastic frame with a hole in the center from a bulk monodispersed colloidal suspension. Due to the gravity and water evaporation, the thickness of the soap film becomes comparable to the particle diameter, leading to the curving of the water-air interface. This curved meniscus between particles poses an attractive interaction between colloidal particles, which are otherwise hard-sphere like. This attractive capillary force causes the colloidal particles to self-assemble forming crystals which are usually polycrystalline with an average grain size up to hundreds of lattice constants, as shown in Fig. 1a. Using a larger magnification, one can easily distinguish large- and small-angle grain boundaries, which, as indicated respectively by L and S in Fig. 1b, are different from those commonly seen in textbooks [4].

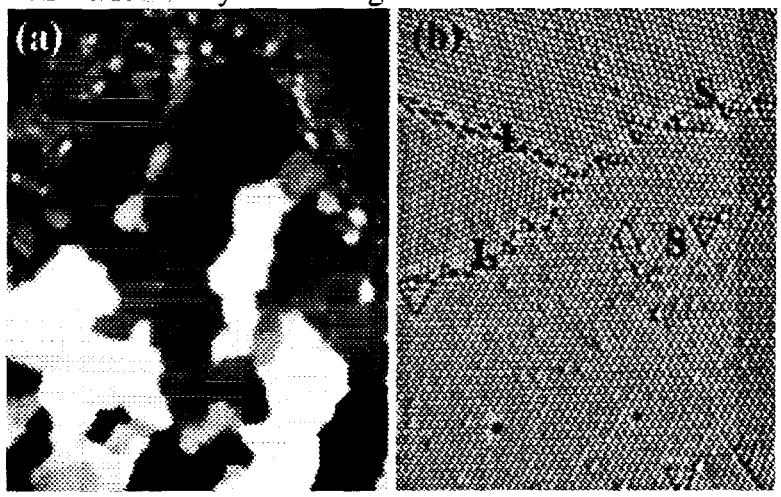

An interesting observation is that when an external periodic vertical vibration is applied to the particle suspension, the grain boundaries are observed to move if the vibration amplitude is large enough. Here, the lower boundary of the film is in contact with the bulk suspension, and the mechanical vibration is coupled to the film through capillary waves excited on the bulk surface due to the Faraday instability. A series of pictures in Fig. 2 show how typically grain boundaries evolve under vibration with a frequency of ~100 Hz. The total length of the grain boundaries decreases, usually in a monotonic fashion, and finally disappears. The detail process of grain boundary migration is in general rather complex, because the mobility of a grain boundary depends not only on the relative orientation of the two grains, but also on the direction of the

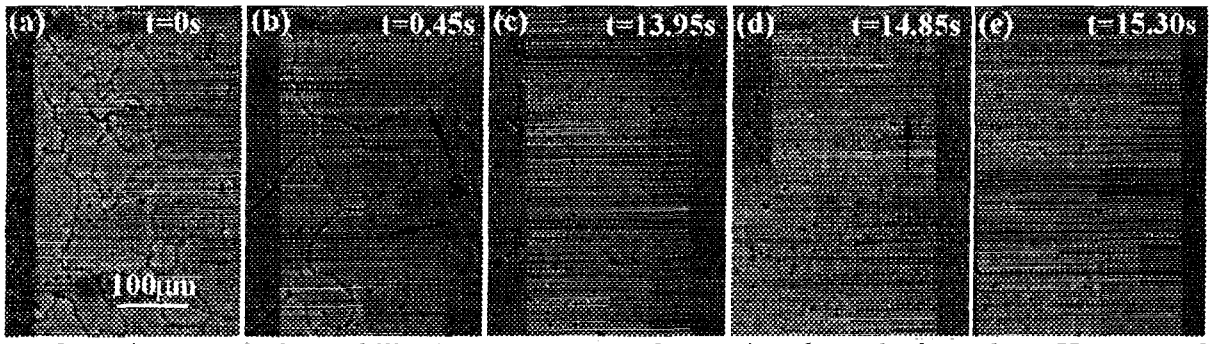

boundary. As a result the mobility is not a constant but varies along the boundary. However, the evolution of grain boundaries under external forcing does show certain simple features: (1) Small loops of defect lines are eliminated first, as seen in Fig. 2a-b, and the effect is somewhat similarly to domain coarsening seen in phase-separating fluids. (2) Before the merging of two domains, the boundary between them becomes fuzzy and discontinuous (Fig. 2b and 2c). Observations under the high power magnification show a rather continuous transition from the large- to the small-angle grain boundaries. In the process, domains are seen to rotate coherently. (3) The elimination of small-angle grain boundaries is much more rapid than the large-angle ones (Fig. 2c-d).

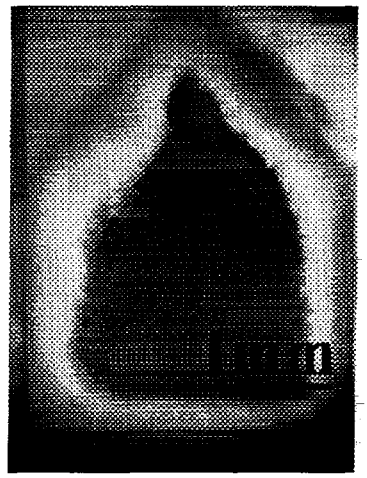

The application of the external vibration not only offers a mean of studying defect dynamics but also provides a robust way to grow high-quality 2D single colloidal crystals of size never achieved before (Fig.3) [5]. Because the assembly process relies on the capillary force, particles of different materials and with various surface properties can be crystallized in this way. Since the freely suspended film provides an environment similar to biological membranes, the technique may be potentially useful for growing 2D crystals of membrane proteins, of which only a handful have been successfully crystallized.

Reference

[1] G. Gottstein, and L. S. Shvindlerman, *Grain Boundary Migration in Metals: Thermodynamics, Kinetics, Applications* (CRC Press, 1999)

[2] See *Grain Boundary Structure and Related Phenomena*, (Minakami, Gunma Prefecture, Japan, 1985).

[3] W. L. Bragg, and J. F. Nye, Proc. Roy. Soc., **A19**, 474(1947).

[4] P. M. Chaikin, and T. C. Lubensky, *Principles of Condensed Matter Physics*, (Cambridge University Press 1995).

[5] Q. –H. Wei, D. Cupid, X. –L. Wu, (submitted).

NASA/CP—2000-210470

Dynamics of Grain Boundaries in 2D Colloids

Q. -H. Wei, X. –L. Wu

Department of Physics and Astronomy
University of Pittsburgh, Pittsburgh, PA 15260

NASA/CP—2000-210470

Abstract

A unique model system for 2D grain boundaries is presented, which consists of monolayer of monodispersed colloidal beads embedded in a soap film. External mechanical vibrations of sufficient strength are observed to initiate grain boundary migration and annihilation, and grain rotation. The total length of grain boundaries are found to decay with time logarithmically. This phenomenon, called "mechanical annealing", also provides a robust way to grow large 2D single colloidal crystals.

System

Bulk suspension: 35% 1μm PS particle+0.03%IGEPAL+water

Polycrystalline

L large-angle grain boundary
S small-angle grain boundary

Mechanical Annealing

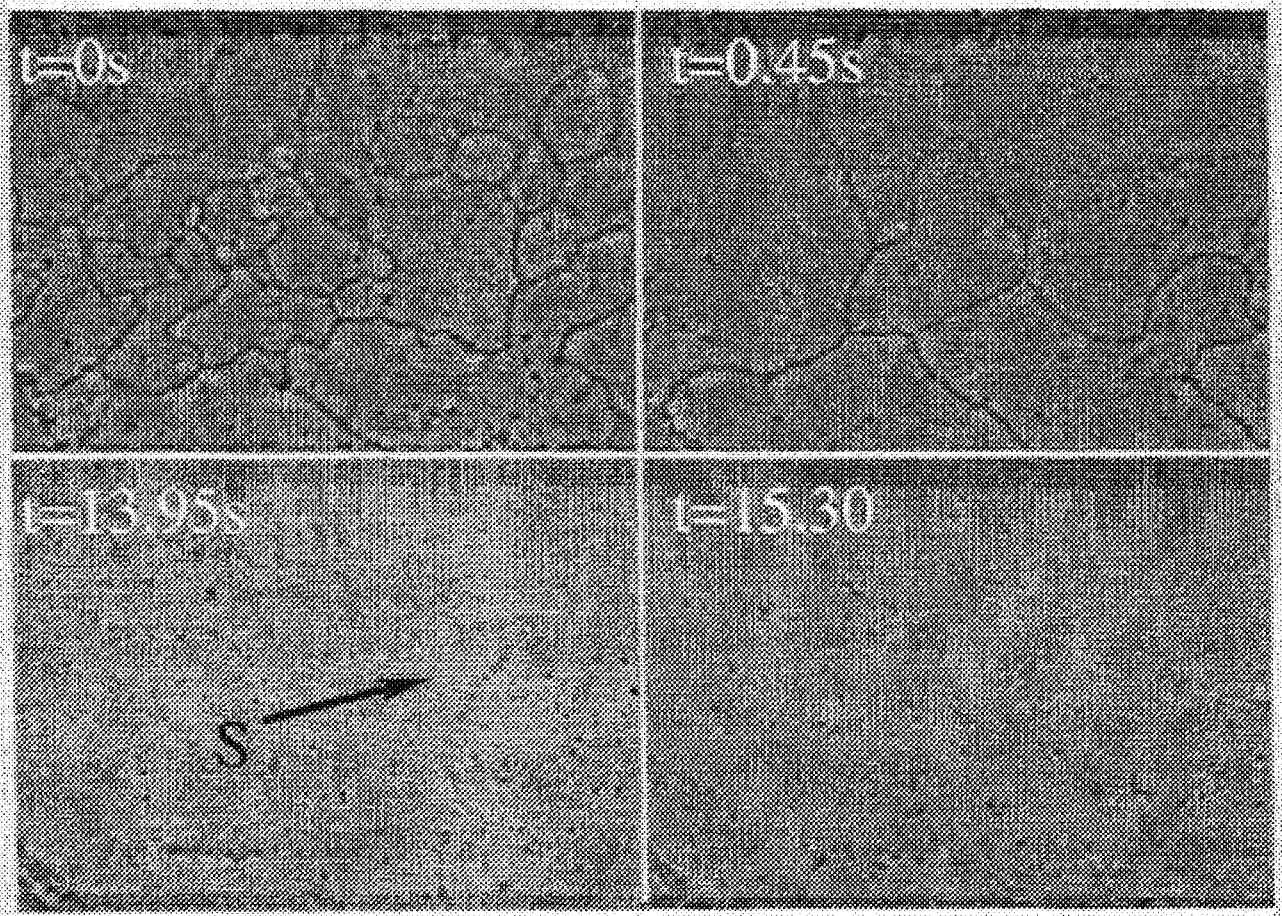

By vertically shaking the bulk suspension, mechanical energy is coupled to the polycrystalline film, and initiates the grain boundary migration and grain coarsening.

Grain rotation

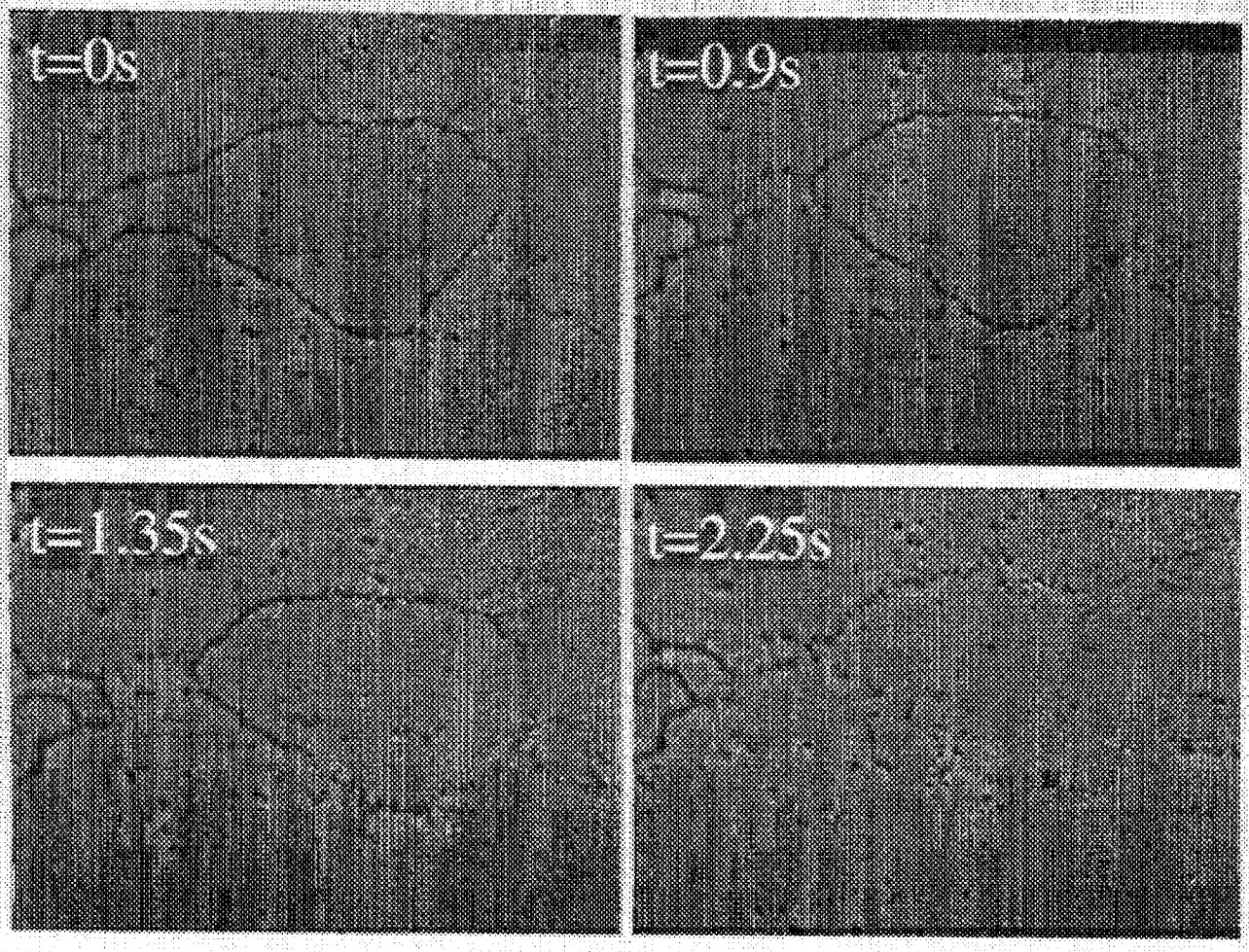

The grain rotation induces transformation of a large-angle grain boundary to a low-angle one which diminishes immediately through dislocation motions.

Grain boundary length vs time

Controlled assembly of 2D single crystals

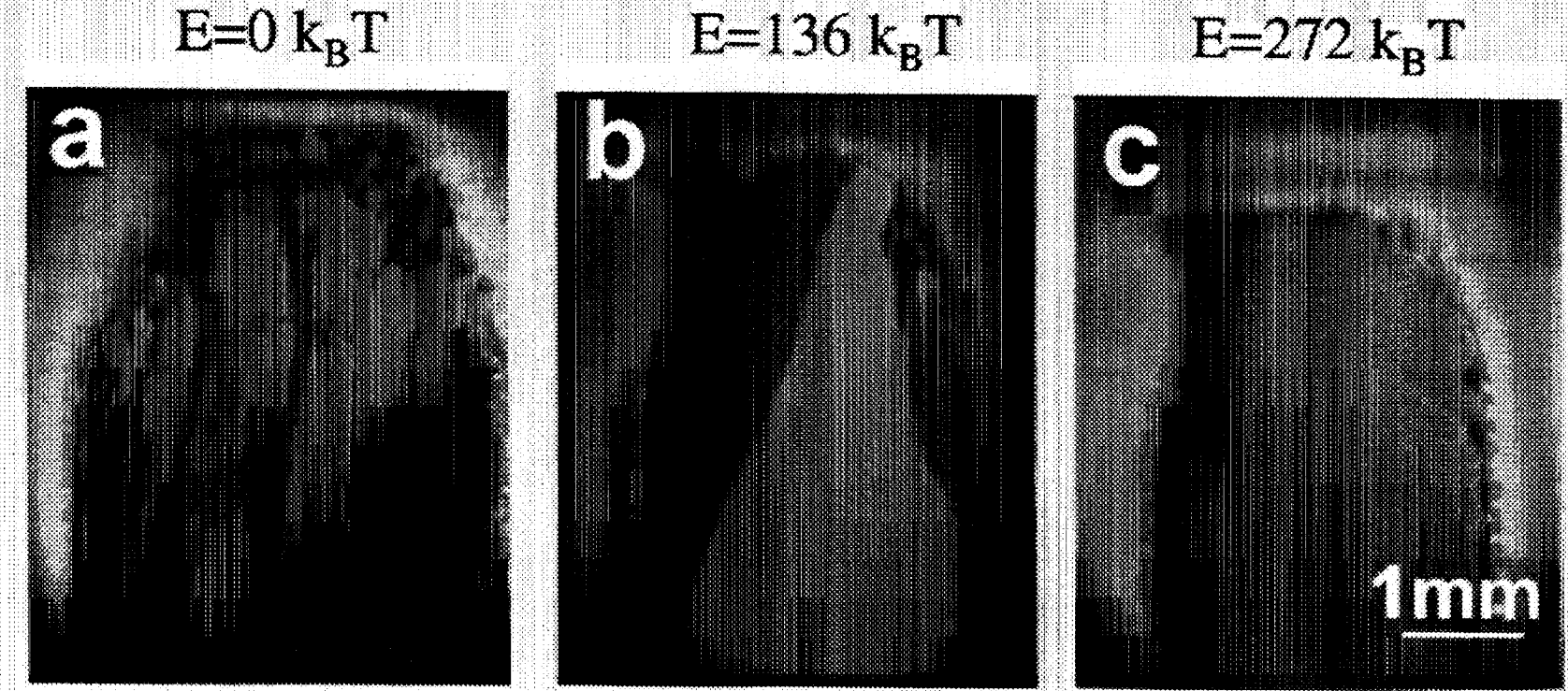

Vibration Energy $E=4\pi^2mf^2A^2$ with f=106Hz

Single crystal

Reference

1. W.T. Read, & W. Shockley, *Phys. Rev. 78*, 275(1950).
2. P.M. Chaikin, &T.C. Lubensky, *Principles of condensed matter physics* (Cambridge, 1995)
3. G. Gottstein, and L.S. Shvindlerman, *Grain boundary migration in metals (CRC press, 1999).*
4. Q. –H. Wei, D.M. Cupid & X.-L. Wu, Appl. Phys. Lett. (accepted).
5. Financial support from NASA is acknowledged.

Photonic Crystals Based on Self-Assembly of Colloidal Particles

D. Weitz
Harvard University

Photonic crystals are systems in which the refractive index periodically changes in space. These structures show interesting optical properties which may lead to the suppression of propagation of light within a certain frequency range. During the last years there have been strong efforts to fabricate such materials with spatial periodicities lying in range of the wavelength of visible light.

One possible approach to fabricate these materials is the use of colloidal particles. We use self-organization of colloidal particles to produce these periodic structures. By using organic and inorganic materials we control both the elastic and scattering properties of the particles and the lattice. We determine the structures and optical properties of the colloidal crystal by optical microscopy and light scattering experiments. By performing light scattering measurements in the optical microscope simultaneously with imaging, we study the scattering from a region with known defect structure. These new materials have great potential for a variety of optical communication devices. Possible technical applications are discussed.

Literature

Photonic Crystals:

Joannopulos, J. D., P. R. Villeneuve, et al. (1997). "Photonic Crystals: putting a new twist on light." *Nature***386**: 143-149.

Yablonovitch. E. (1993). "Photonic Bandgap Structures." *J. Opt. Soc. Am. B* **10**(2): 283-295.

A. D. Dinsmore, M. L. Breen, S. B. Qadri, B. R. Ratna, "Photonic Crystals from Core-Shell Colloidal Spheres" (to be submitted).

M. L. Breen, R. H. Pink, S. B. Qadri, A. D. Dinsmore, B. R. Ratna (to be submittted).

Monodisperse Emulsions:

Bibette, J. (1991). "Depletion interactions and Fractionated Crystallization for Polydisperse Emulsion Purification." *J. Colloid Interf. Sci.* **147**: 474-478.

Umbanhowar, P. B., V. Prasad, et al. (2000). "Monodisperse Emulsion Generation Via Drop Break Off in a Coflowing Stream." *Langmuir* **16**: 347-351.

Encapsulation:

Brown, R. W. and R. P. Bowman (1985). Capsule Manufacture. USA, Appleton Papers Inc., US patent 4552811

Donath, E., G. B. Sukhorukov, et al. (1998). "Novel hollow polymer shellsby colloid-templated assembly of polyelectrolytes." *Angew. Cem. Int. Ed.* **37**(16): 2201-2205.

Foris, P. L., R. W. Brown, et al. (1977). Capsule manufacture. USA, NCR Corporation, Dayton, Ohio, US patent 4001104.

Monodisperse Emulsions

Method 1:

Single Droplet Break-Off

P. B. Umbanhowar et al., Langmuir **16**, 347 (2000)

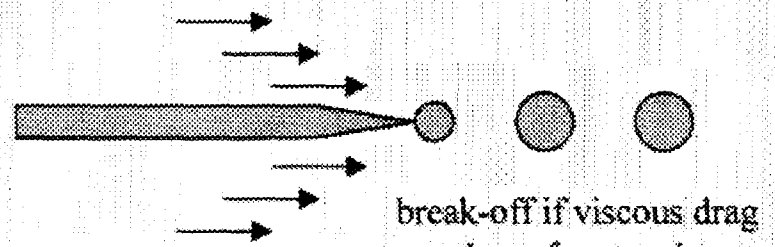

Method 2:

Fractionated Crystallization (Depletion Forces)

J. Bibette, J. Colloid Interf. Sci. **147**, 474 (1991)

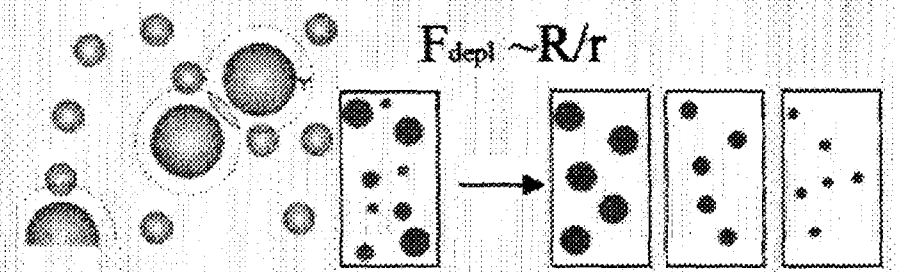

Examples (oil-in-water emulsions):

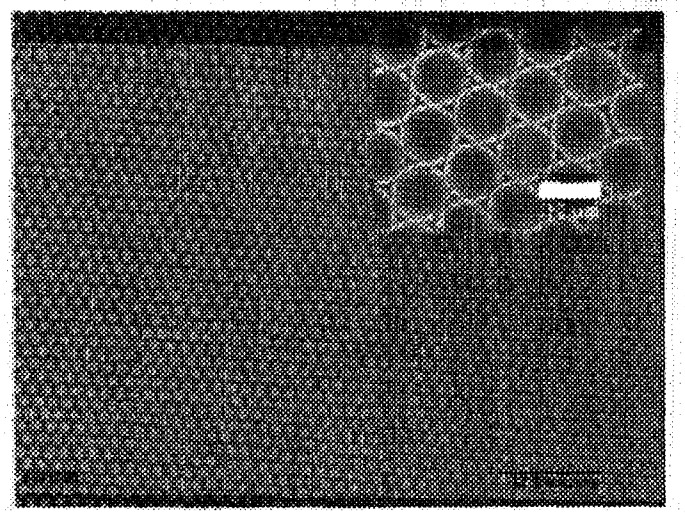

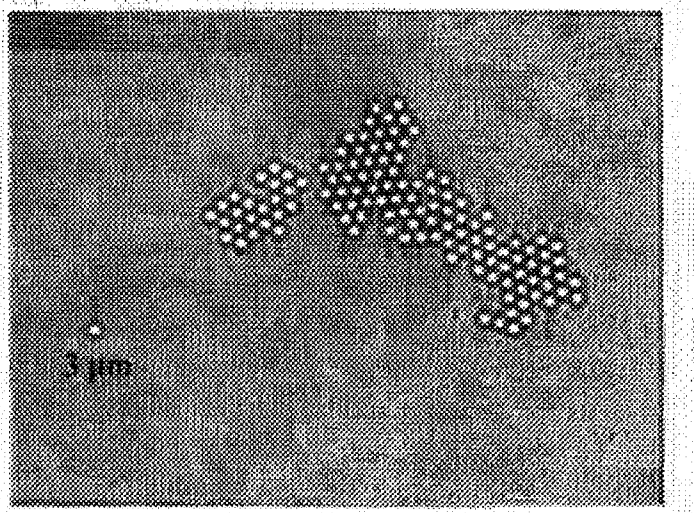

Liquid Crystal Droplets as Bragg-Switch

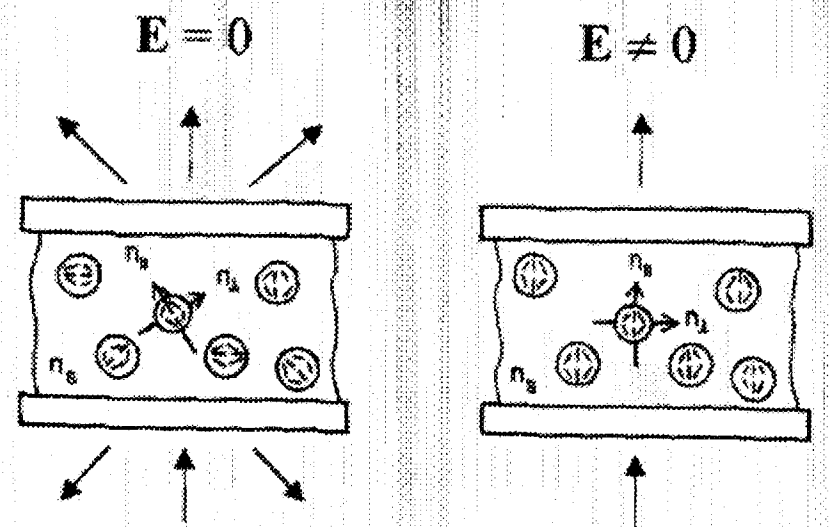

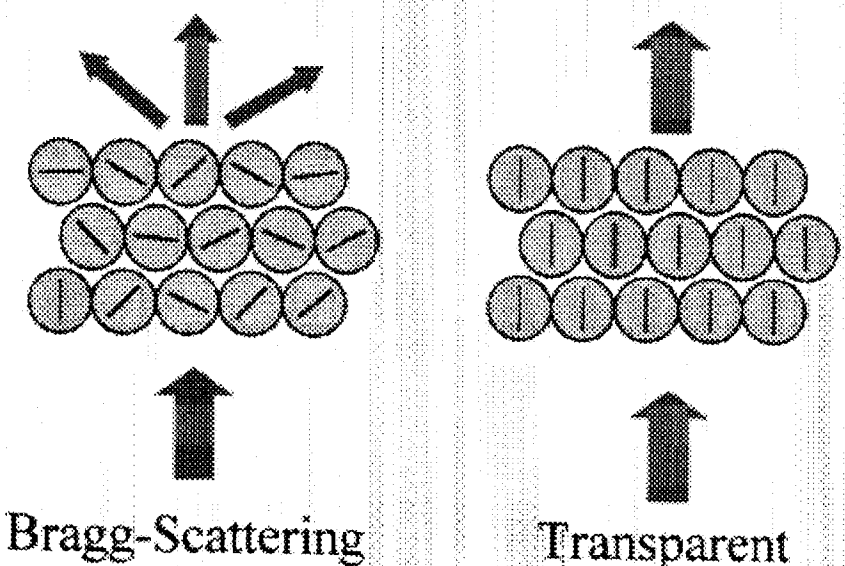

With monodisperse droplets formation of crystals is possible

⇨ Bragg-Switch

Photonic Crystals

- Periodic variation of refractive index (Δn sufficiently high)
- lattice constant comparable to wavelength of light

→ Depending on the crystal structure the formation of a complete photonic bandgap may occur

→ New class of optical materials, many application in optoelectronics

Examples:

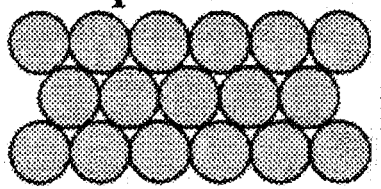

colloidal crystal

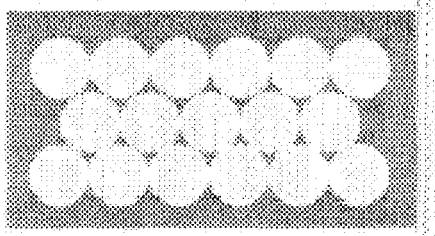

inverse structure

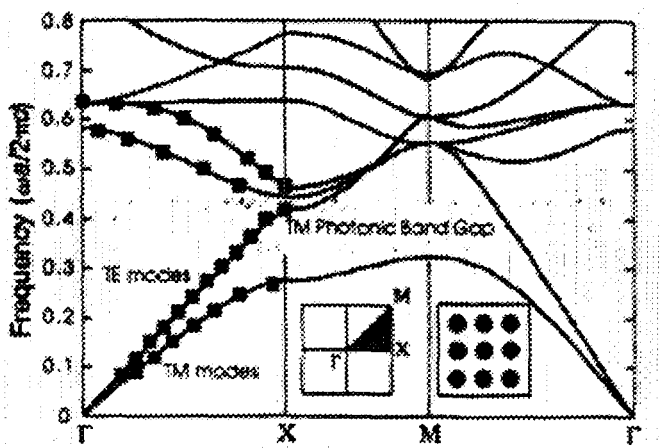

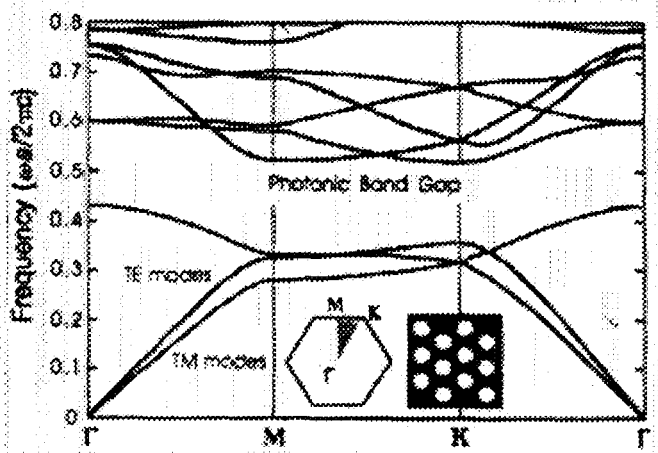

J.D. Joannopoulos et al., Nature **386**, 143 (1997)

Metal-Coated Particles (Optical Hollow Spheres)

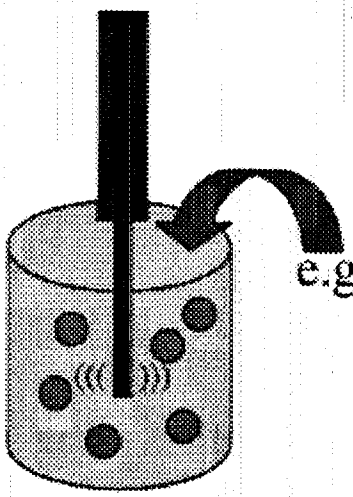

e.g. : Zinc acetate, thioacetamide (also Au, Pd, Mg…)

Strong ultrasonic fields (cavitation)

(N.A. Dhas et al.)

ZnS coated spheres

(TEM picture)

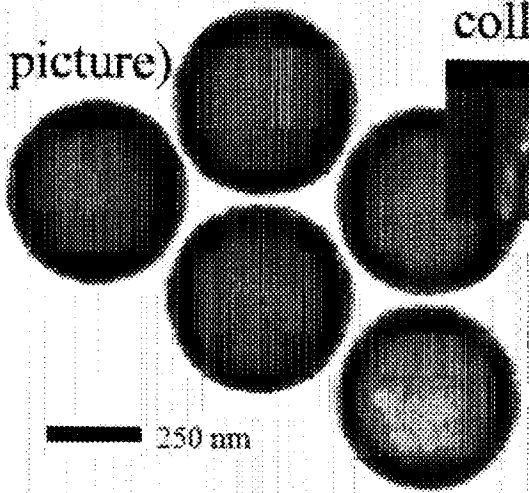

Bragg-scattering of the colloidal crystal

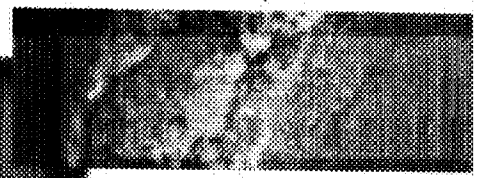

A. D. Dinsmore, M. L. Breen, S. B. Qadri, B. R. Ratna, Naval Research Lab.

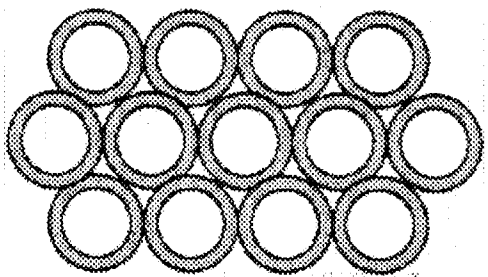

Advantages of photonic crystal structures made of optical hollow spheres:

- wider band gap
- no sintering (which may destroy long-range order)

Encapsulation (mechanical stabilization)

Encapsulation of droplets allows stable crystals even when the solvent is evaporated (e.g. higher contrast of index of refraction).

Adsorption of polyelectrolytes on charged surfaces

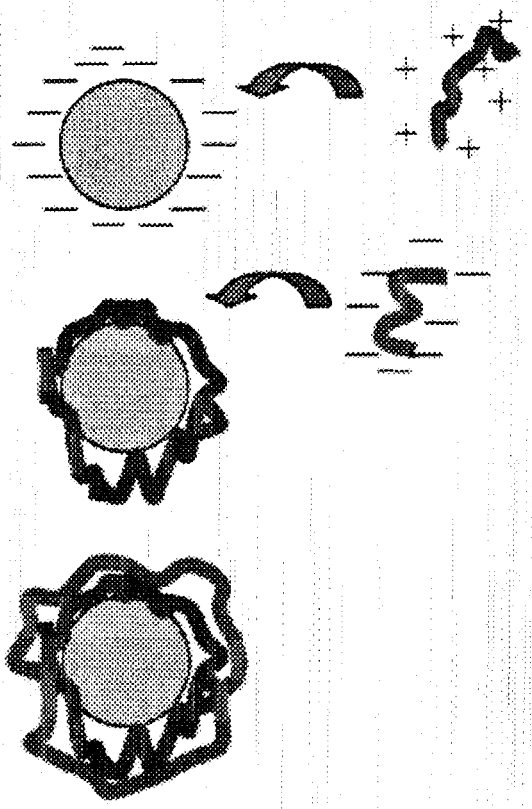

(F. Caruso et al.)

In situ polymerization reaction

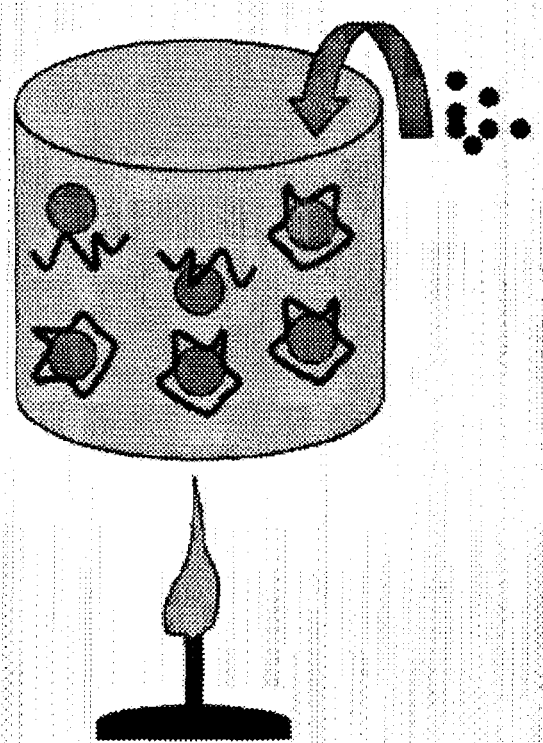

Foris et al., US patent 4001140 (1977)

GRAVITATIONAL EFFECTS ON FLOW INSTABILITY AND TRANSITION IN LOW DENSITY JETS

A.K. Agrawal[1], K. Parthasarathy[1], K. Pasumarthi[1], and D.W. Griffin[2]
[1]School of Aerospace and Mechanical Eng., University of Oklahoma, Norman, OK 73019
[2]NASA Glenn Research Center, 21000 Brookpark Road, Cleveland, OH 44135

ABSTRACT

Recent experiments (e.g., Monkewitz et al, 1990; Subbarao and Cantwell, 1992; Kyle and Sreenivasan, 1993) have shown that low-density gas jets injected into a high-density ambient gas undergo an instability mode, leading to highly-periodic oscillations in the flow-field for certain conditions. The transition from laminar to turbulent flow in these jets is abrupt, without the gradual change in scales. Even the fine scale turbulent structure repeats itself with extreme regularity from cycle to cycle. Similar observations were obtained in buoyancy-dominated and momentum-dominated jets characterized by the Richardson numbers, $Ri = [gD(\rho_a-\rho_j)/\rho_j U_j^2]$ where g is the gravitational acceleration, D is the jet diameter, ρ_a and ρ_j are, respectively, the free-stream and jet densities, and U_j is the mean jet exit velocity. At high Richardson numbers, the instability is presumably caused by buoyancy since the flow-oscillation frequency (f) or the Strouhal number, $St = [fD/U_j]$ scales with Ri. In momentum-dominated jets, however, the Strouhal number of the oscillating flow is relatively independent of the Ri. In this case, a local absolute instability is predicted (e.g., by Monkewitz and Sohn, 1988) in the potential core of low-density jets with $S [= \rho_j/\rho_a] < 0.7$, which agrees qualitatively with experiments.

Although the instability in gas jets of high Richardson numbers is attributed to buoyancy, direct physical evidence has not been acquired in experiments. If the instability is indeed caused by buoyancy, the near-field flow structure of the jet will change significantly when the buoyancy is removed, for example, in the microgravity environment. Thus, quantitative data on the spatial and temporal evolutions of the instability, length and time scale of the oscillating mode and its effects on the mean flow and breakdown of the potential core are needed in normal and microgravity to delineate gravitational effects in buoyant jets.

In momentum dominated low-density jets, the instability is speculated to originate in the potential core. However, experiments have not succeeded in identifying the direct physical cause of the instability. For example, the theory (Monkewitz and Sohn, 1988) predicts an oscillating mode for $S<0.62$ in the limit of zero momentum thickness, which contradicts with the experimental findings of Kyle and Sreenivasan (1993). The analyses of momentum-dominated jets neglect buoyancy effects because of the small Richardson number. Although this assumption is appropriate in the potential core, the gravitational effects are important in the annular region surrounding the jet, where the density and velocity gradients are large. This reasoning provides basis for the hypothesis that the instability in low Richardosn number jets studied by Kyle and Sreenivasan (1993) and Monkewitz et al. (1990) is caused by buoyancy. The striking similarity in characteristics of the instability and virtually the identical conclusions reached by Subbarao and Cantwell (1992) in buoyant ($Ri>0.5$) helium jets on one hand and by Kyle and Sreenivasan (1993) in momentum-dominated ($Ri<1x10^{-3}$) helium jets on the other support this hypothesis. However, quantitative experiments in normal and microgravity are necessary to obtain direct physical evidence of buoyancy effects on the flow instability and structure of momentum-dominated low-density jets.

The primary objective of this new research project is to quantify how buoyancy affects the flow instability and structure in the near field of low-density jets. The flow will be described by

the spatial and temporal evolutions of the instability, length and time scales of the oscillating mode, and the mean and fluctuating concentration fields. To meet this objective, concentration measurements will be obtained across the whole field using quantitative Rainbow Schlieren Deflectometry (Al-Ammar et al. 1998), providing spatial resolution of 0.1mm and temporal resolution of 0.017s to 1ms. The experimental effort will be supplemented with linear stability analysis of low-density jets by considering buoyancy.

- The first objective of this research is to investigate the effects of gravity on the flow instability and structure of low-density jets. The flow instability in these jets has been attributed to buoyancy. By removing buoyancy in our experiments, we seek to obtain the direct physical evidence of the instability mechanism. In the absence of the instability, the flow structure will undergo a significant change. We seek to quantify these changes by mapping the flow field (in terms of the concentration profiles) of these jets at non-buoyant conditions. Such information is presently lacking in the existing literature.

- The second objective of this research is to determine if the instability in momentum-driven, low-density jets is caused by buoyancy. At these conditions, the buoyancy effects are commonly ignored because of the small Richardson based on global parameters. By eliminating buoyancy in our experiments, globally as well as locally, we seek to examine the possibility that the instability mechanism in self-excited, buoyant or momentum-driven jets is the same. To meet this objective, we would quantify the jet flow in normal and microgravity, while systematically decreasing the Richardson number from buoyancy-driven to momentum driven flow regime.

- The third objective of this research is to perform a linear stability analysis of low-density gas jets by including the gravitational effects. The flow oscillations in these jets are attributed to an absolute instability, whereby the disturbance grows exponentially at the site to ultimately contaminate the entire flow field. We seek to study the characteristics of both convective and absolute instabilities and demarcate the boundary between them.

REFERENCES

Al-Ammar, K., Agrawal, A.K., Gollahalli, S.R., and Griffin, D., 1998, "Application of Rainbow Schlieren Deflectometry for Concentration Measurements in an Axisymmetric Helium Jet," *Experiments in Fluids*., vol. 25, pp. 89-95.

Kyle, D.M., and Sreenivasan, K.R., 1993, "The Instability and Breakdown of a Round Variable-Density Jet," *Journal of Fluid Mechanics*, vol. 249, pp. 619-664.

Monkewitz, P.A., Bechert, D.W., Barsikow, B., and Lehmann, B., 1990, "Self-Excited Oscillations and Mixing in a Heated Round Jet," *Journal of Fluid Mechanics*, vol. 213, pp. 611-639.

Monkewitz, P.A., and Sohn, K.D., 1988, "Absolute Instability in Hot Jets," *AIAA Journal*, vol. 26, pp. 911-916.

Subbarao, E.R., and Cantwell, B.J., 1992, "Investigation of a Co-flowing Buoyant Jet: Experiments on the Effect of Reynolds Number and Richardson Number," *Journal of Fluid Mechanics*, vol. 245, pp. 69-90.

Presentation not available at time of printing.

LATTICE-BOLTZMANN METHODS FOR MULTIPHASE FLOWS IN MICROGRAVITY ENVIRONMENTS

R. Chella
Florida State University
Tallahassee, Fl 32310

ABSTRACT

This is a newly funded project to use lattice-Boltzmann techniques to provide a computationally efficient and robust approach to study multiphase flow and transport in microgravit y en vironments. The project objectives and approach are summarized, and some preliminary results provided.

Objectives

- **Phase Separation Under Externally Applied Flows** — Study of the influence of externally applied flows in retarding phase separation and stabilizing non-equilibrium morphologies in binary fluids undergoing spinodal decomposition and n ucleation and growth of droplets. Analysis of time-dependent shear and normal stresses developed in these complex fluids.

- **Phase Separation In Confined Geometries** — Study of the role of short-range and long-range interactions at solid surfaces on phase separation of binary fluids in confined geometries. Quantitatively , to study the range of parameters where the transition from one morphology to the other occurs, and the scaling behavior of the structure factor and the growth law of the characteristic length scale of the growing domains.

- **Contact Line Dynamics** — Study of droplet spreading, in particular the ev olution of the contact angle in droplet spreading, influence of the short-range and long-range solid-fluid in teractions on the equilibrium droplet shape and scaling relations for the slip v elocity in terms of the surface tension, viscosity of the advancing fluid, and the deviation of the contact angle from its equilibrium value. Dynamics of the contact line at a moving solid surface, in particular, the ev olution of the advancing and receding contact angles, and their dependence on the in terfacial tension, fluid viscosities, and v elocity of the moving solid surface.

Approach

A mesoscopic approach, with the system characterized by a coarse-grained free-energy functional of a conserved order parameter. The evolution of the order parameter field is described b y a Cahn-Hilliard type equation. The velocity field satisfies a modified Navier-Stokes equation that includes an explicit coupling term to the order parameter field, arising from the non-ideal particle in teractions. The differential in teractions of binary fluids with solid surfaces are taken in to account b y appropriate modification of the free-energy functional. This approach allo ws for the inclusion, in a consistent manner, of in teraction with solid walls that that cannot be easily included in a classical contin uum formulation. Numerical solution is carried out using a lattice-Boltzmann tec hnique. The computational advantages of this tec hnique include ease of handling boundary conditions at solid boundaries and free surfaces, and amenability to parallelization due to the local nature of the formulation. This makes the study of multiphase flows in irregular geometries and three-dimensions feasible.

Preliminary Results

Phase Separation Under Externally Applied Flows

The structure factor for spinodal decomposition under shear flow is shown in Fig. 1. In accordance with published small-angle light scattering studies, an ellipse quickly develops which elongates and rotates at early times, and the relative intensity in the direction of the major axes decreases with time and finally disappears.

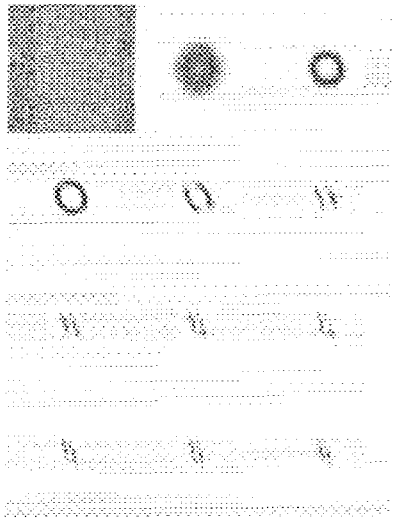

Phase Separation In Confined Geometries

In confined geometries, both the morphology and kinetics of phase separation can be affected by varying the ratio of interfacial tension to wetting forces. In Fig. 2, bicontin uous, capsule, or plug configurations are observed with increase in wetting forces.

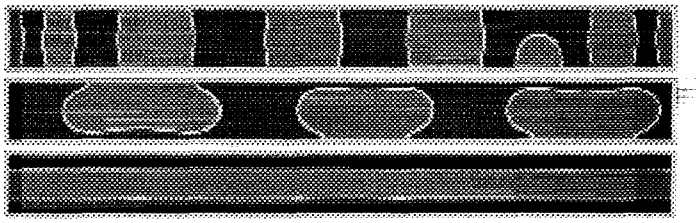

Contact Line Dynamics

Shown in the figure below, is a comparison of the ev olution of droplet shape under the influence only of short-range forces (upper figure), and of both short-range and long-range forces (lo wer figure).

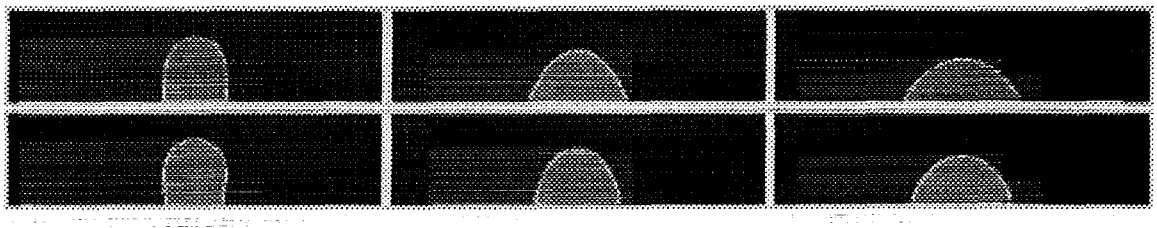

Presentation not available at time of printing.

RESONANCE EFFECTS IN A HORIZONTAL DOUBLE-DIFFUSIVE LAYER UNDER GRAVITY MODULATION

C. F. Chen and Cho Lik Chan
Department of Aerospace and Mechanical Engineering
The University of Arizona, Tucson, AZ 85721-0119 USA

ABSTRACT

A ground-based research effort is planned to investigate the effect of gravity modulation on single- and double-diffusive convection systems, particularly the resonance effect. Two convection systems are selected for the proposed study. One is a horizontal double-diffusive fluid layer stably stratified by a solute gradient being heated from below. The other is a differentially heated layer of fluid. These two systems share a common characteristic: Under steady gravity, the first bifurcation is in the oscillatory mode, hereafter referred to as the internal mode. Our linear stability theory results show that, under gravity modulation, the first bifurcation onsets in a quasi-periodic mode in which the instability oscillates at two incommensurate frequencies whose sum is the forcing frequency. When the forcing or modulation frequency is increased to approximately twice the frequency of the internal mode, resonance occurs and manifests in two aspects: the instability oscillates in the subharmonic mode, exactly half of the forcing frequency, and the critical Rayleigh number is lowered, quite dramatically in some instances for a double-diffusive layer of low Prandtl number fluid under reduced gravity.

We plan to conduct experimental investigations and numerical simulations concurrently for both systems. An oscillating platform will be designed and constructed at a constant amplitude but with variable frequency. The test tanks will be designed with transparent walls for flow visualization and for flow field measurement by PIV. Flow oscillations will also be measured by differential thermocouples fixed in fluid layers. For the vertical layer experiment, a 39% ethanol-water solution with Pr = 26 will be used in a tank 0.4 cm in width. Based on linear stability theory, resonance will occur at the oscillation frequency of 1.5 Hz. For the horizontal double-diffusive layer, we plan to use a salt-water solution to examine the more subtle aspects of the effect of resonance, such as the switchover of the instabilities in the non-resonant modulation regime from a quasi-periodic oscillation mode to the subharmonic oscillation mode in the resonant case.

For the numerical simulations, we plan to modify an existing code capable of solving two-dimensional, time-dependent, double-diffusive convection driven by surface-tension gradients and buoyancy. This code has been validated and yielded good results when compared with experiments. A three-dimensional code will be developed to capture the full complexity of the problem.

Both modes of investigation will be used to ascertain (i) the evolution of the quasi-periodic and subharmonic instabilities into fully nonlinear flow fields, (ii) the effect of gravity modulation on the heat transfer and mixing of solutes in the supercritical states, and (iii) the boundary effects due to finite geometry on the critical condition, as well as the nonlinear state. Comparisons of results between experiments and simulations will validate the code. Once the code has been validated, it will be used to investigate the effect of gravity modulation on convection systems in reduced gravity and microgravity applications. The code will also be used to carry out parameter studies to optimize the design of space experiments.

RESONANCE EFFECTS IN SINGLE- AND DOUBLE-DIFFUSIVE SYSTEMS UNDER GRAVITY MODULATION

C. F. Chen and Cho Lik Chan
Department of Aerospace and Mechanical Engineering
The University of Arizona
Tucson, AZ 85721-0119 USA

- Ground-based research is planned to investigate the effect of gravity modulation on single- and double-diffusive convection systems, particularly the resonance effect.

- Two convection systems are selected for study: a differentially heated vertical fluid layer with Pr > 12.5 and a horizontal stably stratified fluid layer being heated from below. Under steady gravity, both systems bifurcate into an oscillatory mode, hereafter referred to as the internal mode.

- Linear stability theory shows that, under gravity modulation, the first bifurcation onsets in a quasi-periodic mode in which the instability oscillates at two incommensurate frequencies whose sum is the forcing frequency.

- When the modulation frequency is approximately twice the frequency of the internal mode, resonance occurs; the instability oscillates in the subharmonic mode; and the critical Rayleigh number is lowered, quite dramatically in some instances for a double-diffusive layer of low Pr.

- Experimental investigations and numerical simulations will be carried out concurrently for both systems.

LINEAR STABILITY RESULTS FOR A HORIZONTAL DOUBLE-DIFFUSIVE LAYER

A horizontal fluid layer stably stratified by solute is heated from below under gravity modulation. Using the formulation by Terrones and Chen (*JFM*, **255**, 301-321, 1993), we obtained the following resonance results for Pr = 0.01, $R_s = 3200$, and Le $= 3.33 \times 10^3$ at three different amplitude ratios, $h = g_1 / g_0$.

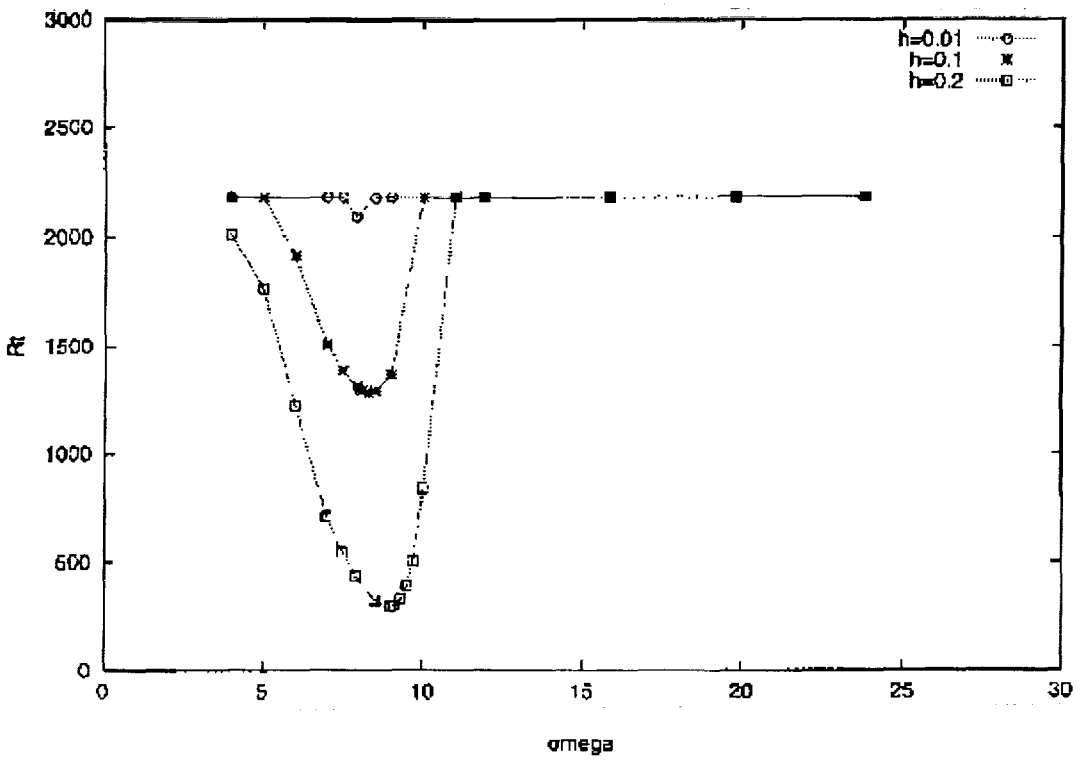

In the figure, $R_t = g\alpha\Delta T D^3 / \nu\kappa$; $\omega = \Omega D^2 / k$; ····· is the subharmonic mode; and ——— is the quasi-periodic mode.

RESULTS OF LINEAR STABILITY ANALYSIS FOR THE VERTICAL LAYER

(Chen & Chen, *JFM*, **395**, 327-344, 1999)

A vertical fluid layer of thickness D is heated differentially with temperature difference ΔT. The oscillatory gravity is $g = g_0 + g_1 \cos \Omega t$. Linear stability analysis by Floquet theory was carried out. Results of the critical Grashof members G_{0c} are shown for constant $g_1/g_0 = 0.5$, with increasing frequency, for a fluid with Pr = 25. Resonant interaction is clearly exhibited for $45 < \omega < 60$.

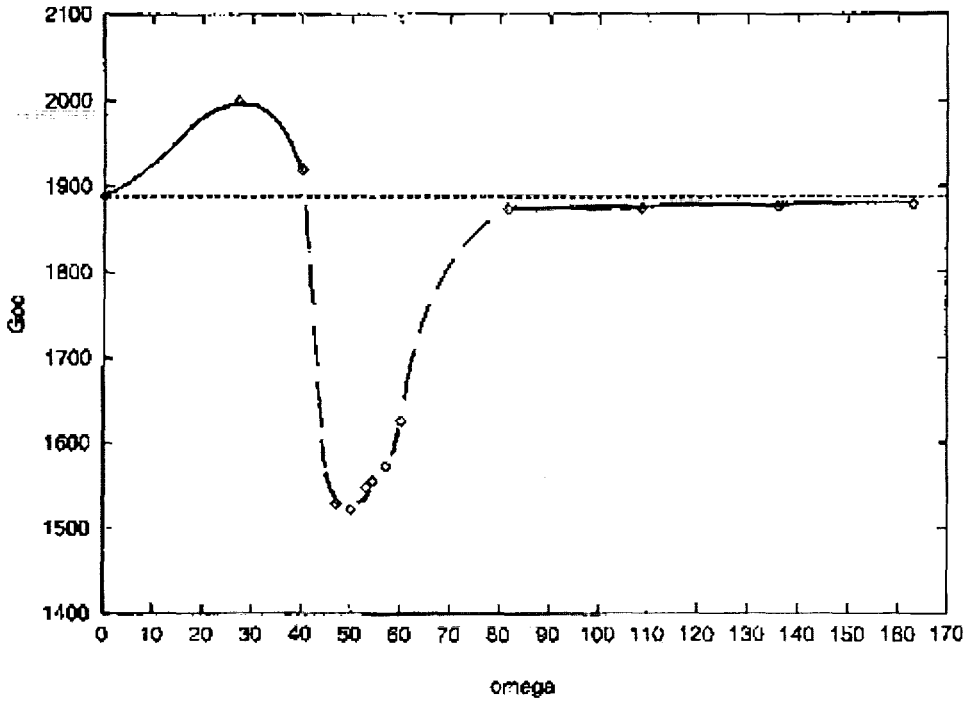

In the figure, $G_{0c} = g_0 \alpha \Delta T D^3/\nu^2$, $\omega = \Omega D^2/\nu$, – – – is the subharmonic mode, ——— is the quasi-periodic mode.

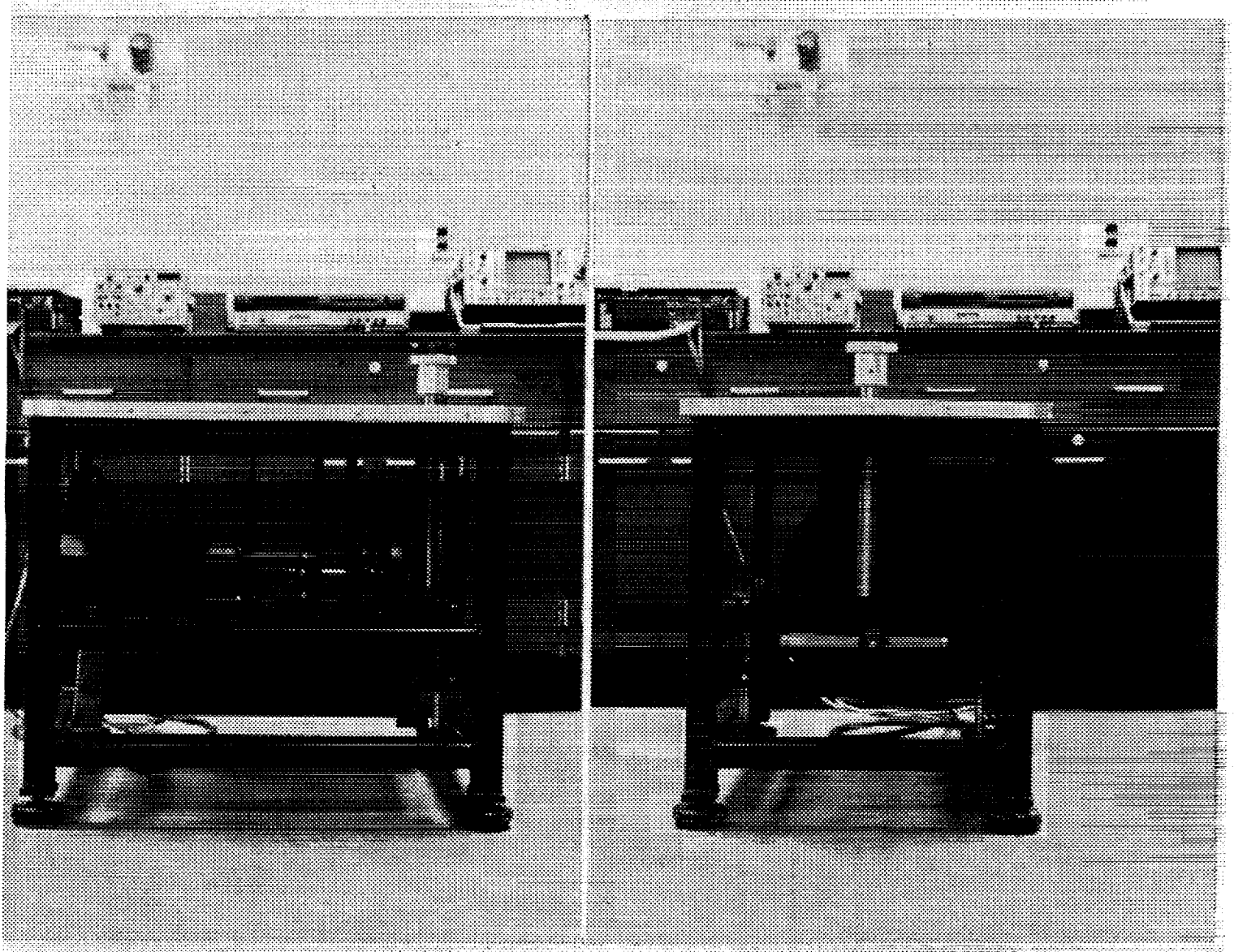

Two views of the oscillating platform showing the variable speed motor, speed reduction gear, bearings, flywheel, and Scotch yoke mechanism.

OSCILLATING PLATFORM

Frequency: Up to 1.6 Hz

Amplitude: 10 cm

Amplitude Ratio g_1/g_0: Up to 1.0

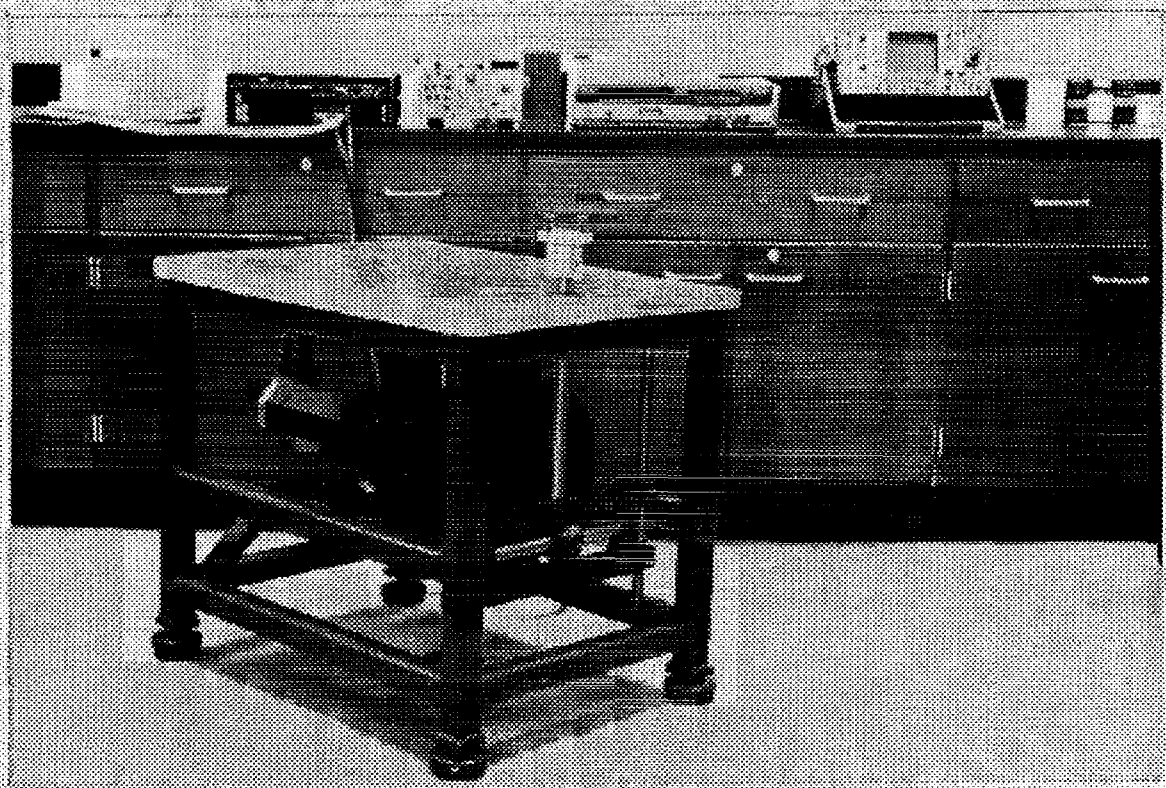

NUMERICAL SIMULATIONS

- **Two-Dimensional Transient Simulation**

  The two-dimensional fluid flow equations are cast in vorticity and stream function form. The dimensionless equations are

$$\frac{\partial \omega}{\partial t}+\frac{\partial}{\partial x}(u\omega)+\frac{\partial}{\partial y}(v\omega)=\mathrm{Pr}(\nabla^2\omega)+\mathrm{Pr}\left(\mathrm{R}_T\frac{\partial T}{\partial x}-\mathrm{R}_S\frac{\partial S}{\partial x}\right)$$

$$\nabla^2\psi=-\omega$$

$$\frac{\partial T}{\partial t}+\frac{\partial}{\partial x}(uT)+\frac{\partial}{\partial y}(vT)=\nabla^2 T$$

$$\frac{\partial S}{\partial t}+\frac{\partial}{\partial x}(uS)+\frac{\partial}{\partial y}(vS)=\mathrm{Le}\nabla^2 S$$

with the dimensionless parameters

$$\mathrm{Pr}=\frac{\nu}{\kappa},\quad \mathrm{Lc}=\frac{\kappa}{D},\quad \mathrm{R}_T=\frac{g\beta_T H^3\Delta T}{\nu\kappa},\quad \mathrm{R}_S=\frac{g\beta_S H^3\Delta S}{\nu\kappa}$$

To render the equations nondimensional, we used the following characteristic quantities: the height H for length, H^2/κ for time, κ/H for velocity, ΔT for temperature, and ΔS for solute (water). The domain is rectangular. The algorithm is capable of handling specified temperature, heat flux, or mixed boundary conditions for the energy equation. Similarly, it can handle specified concentration, mass flux, or mixed boundary conditions for the mass transport equation. As for the fluid flow equation, velocity can be specified on all surfaces. Furthermore, surface tension gradient-driven flow conditions can also be simulated on the top surface.

The finite difference method (FDM) is used to solve these equations. The Laplacian operator is discretized using a central difference, the convection term is approximated by an upwind difference, and the time marching is modeled by the Crank-Nicholson method. The discretized equations are solved by successive over-relaxation (SOR), which is parallelized using a domain decomposition method. The algorithm is validated using previous results for the square cavity problem. The vorticity predictions along the moving boundary are within 0.1%.

This program has been used to simulate the transient two-dimensional thermal and solutal capillary motion in a stratified fluid (Chan & Chen, *Int. J. Heat Mass Transf.*, **42**, 2143-2159, 1999). The program has been modified to include the effect of gravity modulation. We will be using this program to simulate some experiments, especially those dominated by 2-D effects.

- **Three-Dimensional Transient Simulations**

  We plan to develop a full three-dimensional transient algorithm for double-diffusive convection with gravity modulation in a rectangular domain. We plan to use the primitive variables algorithm with a Poisson equation for pressure. Central difference will be used for the diffusion terms, and upwind difference will be employed for the convection terms. A Crank-Nicholson method will be used for marching in time. These discretized equations are solved by SOR, which will be vectorized and parallelized using a domain decomposition method. We will perform simulations to investigate the onset of convection under gravity modulation and nonlinear effects. Simulations of experimental configurations will also be done.

SEPARATION OF CARBON MONOXIDE AND CARBON DIOXIDE FOR MARS ISRU – CONCEPTS

M. Douglas LeVan
Department of Chemical Engineering, Vanderbilt University
Box 1604, Station B, Nashville, TN 37235
John E. Finn
Astrobiology Technology Branch, M/S 239-15
NASA Ames Research Center, Moffett Field, CA 94035-1000
K. R. Sridhar
Department of Aerospace and Mechanical Engineering
The University of Arizona, P.O. Box 210016, Tucson, AZ 85721

ABSTRACT

Solid oxide electrolyzers, such as electrolysis cells utilizing yttria-stabilized zirconia, can produce oxygen from Mars atmospheric carbon dioxide and reject carbon monoxide and unreacted carbon dioxide in a separate stream. The oxygen-production process has been shown to be far more efficient if the high-pressure, unreacted carbon dioxide can be separated and recycled back into the feed stream. Additionally, the mass of the adsorption compressor can be reduced. Also, the carbon monoxide by-product is a valuable fuel for space exploration and habitation, with applications from fuel cells to production of hydrocarbons and plastics.

In our research, we will design, construct, and test an innovative, robust, low mass, low power separation device that can recover carbon dioxide and carbon monoxide for Mars ISRU. Such fundamental process technology, involving gas-solid phase separation in a reduced gravitational environment, will help to enable Human Exploration and Development of Space.

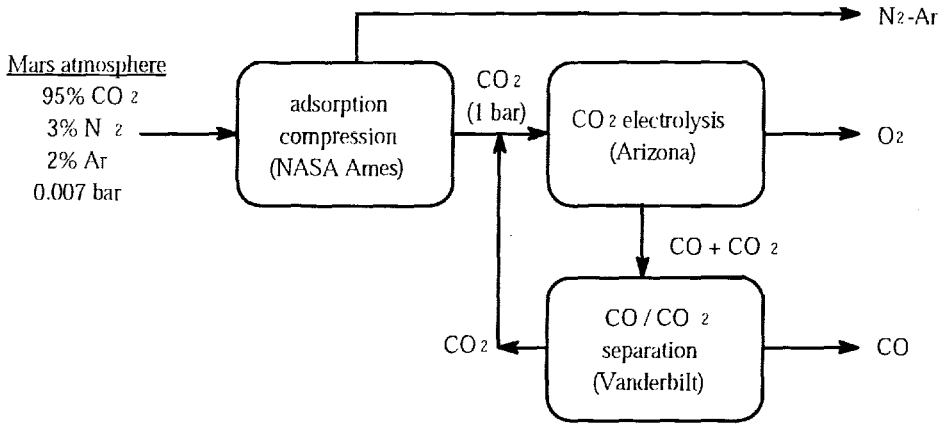

Figure 1. Diagram of system for conversion of the Mars atmosphere to a N_2-Ar mixture, high-pressure CO_2, O_2, and CO.

The separation device will be scaled to operate with a CO_2 sorption compressor and a zirconia electrolysis device built at the NASA Ames Research Center and the University of Arizona,

respectively. Figure 1 is a diagram of the overall system, incorporating the three critical elements of compression, electrolysis, and separation.

For the CO/CO_2 separator, we envision a thermally-driven adsorption-based separation system that combines elements of TSA, PSA, and adsorption compression. One such possible system is shown in Figure 2.

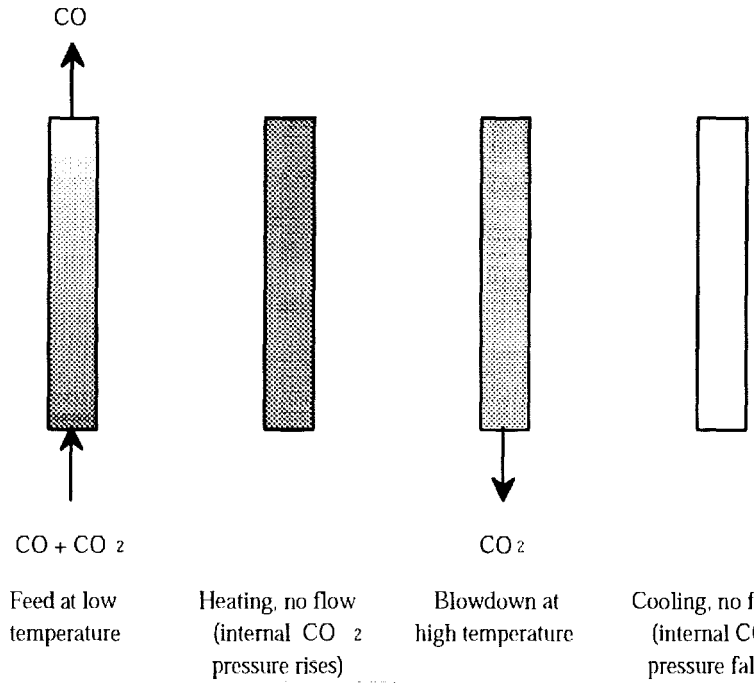

Figure 2. Four-step adsorption cycle for separation of CO and CO_2. CO is produced at the feed pressure (e.g., 1 bar); CO_2 product is expanded to a pressure determined by the requirements of the zirconia cell. Two beds are needed. The steps are as follows: (1) Feed step: the bed is fed with the CO/CO_2 mixture. The bed contains a CO_2 selective adsorbent, and CO is produced as product. Little CO is adsorbed. (2) Heating step: as the bed is heated, the pressure increases. (3) Blowdown step: CO_2 at high pressure is allowed to pass into a storage tank at a pressure sufficient to feed the zirconia cell. (4) Cooling step: the bed is cooled prior to returning it to the feed step.

Research needs for the design shown in Figure 2 are as follows:

- The best adsorbent for the process must be determined.
- Adsorption isotherms must be measured, both for pure components and mixtures.
- Mathematical modeling must be performed to provide a solid framework for design.
- The separation system must be constructed and tested.
- System integration must be studied.

NASA/CP—2000-210470

1206

Separation of Carbon Monoxide and Carbon Dioxide for Mars ISRU – Concepts

M. Douglas LeVan, Vanderbilt University,
Nashville, TN 37235

John E. Finn, NASA Ames Research Center,
Moffett Field, CA 94035

K. R. Sridhar, The University of Arizona,
Tucson, AZ 85721

Introduction

Solid oxide electrolyzers, such as electrolysis cells utilizing yttria-stabilized zirconia, can produce oxygen from Mars atmospheric carbon dioxide and reject carbon monoxide and unreacted carbon dioxide in a separate stream. The oxygen-production process has been shown to be far more efficient if the high-pressure, unreacted carbon dioxide can be separated and recycled back into the feed stream. Additionally, the mass of the adsorption compressor can be reduced. Also, the carbon monoxide by-product is a valuable fuel for space exploration and habitation, with applications from fuel cells to production of hydrocarbons and plastics.

In our research, we will design, construct, and test an innovative, robust, low mass, low power separation device that can recover carbon dioxide and carbon monoxide for Mars ISRU. Such fundamental process technology, involving gas-solid phase separation in a reduced gravitational environment, will help to enable Human Exploration and Development of Space.

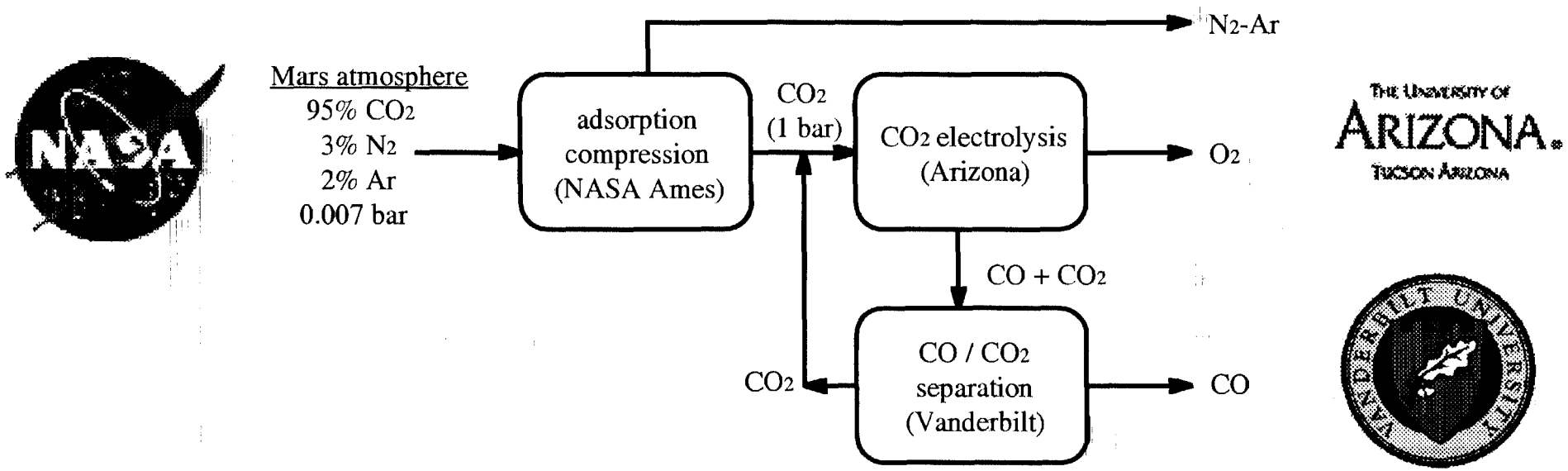
Mars atmosphere
95% CO2
3% N2
2% Ar
0.007 bar
adsorption
compression
(NASA Ames)
CO2
(1 bar)
CO2 electrolysis
(Arizona)
N2-Ar
O2
CO + CO2
CO / CO2
separation
(Vanderbilt)
CO2
CO

Adsorption Compressors

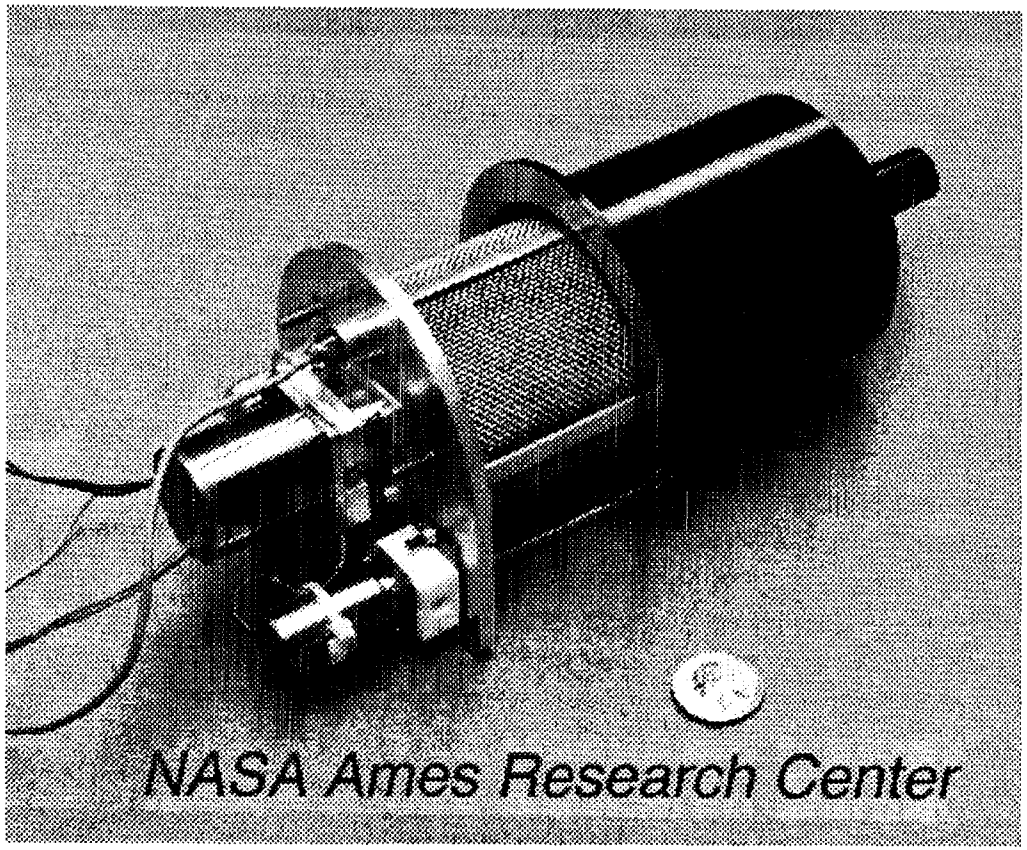

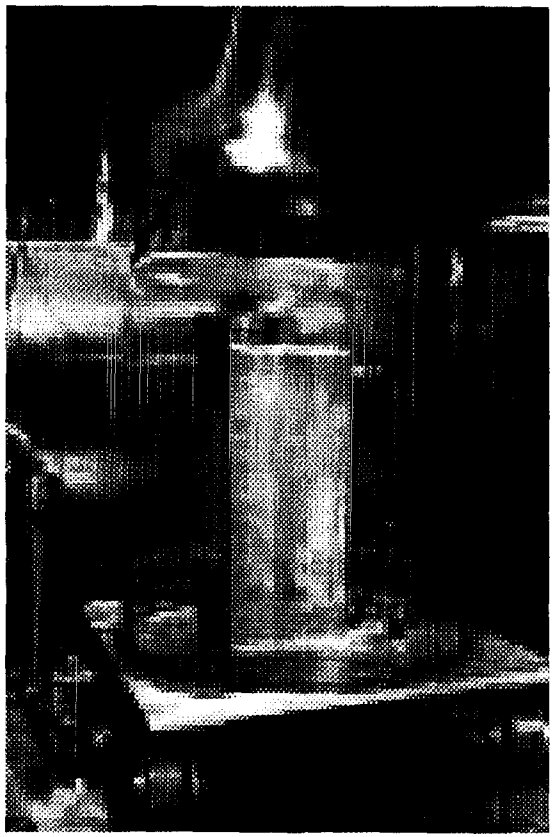

Solid Oxide Electrolysis Cell: Yttria-Stabilized Zirconia (YSZ)

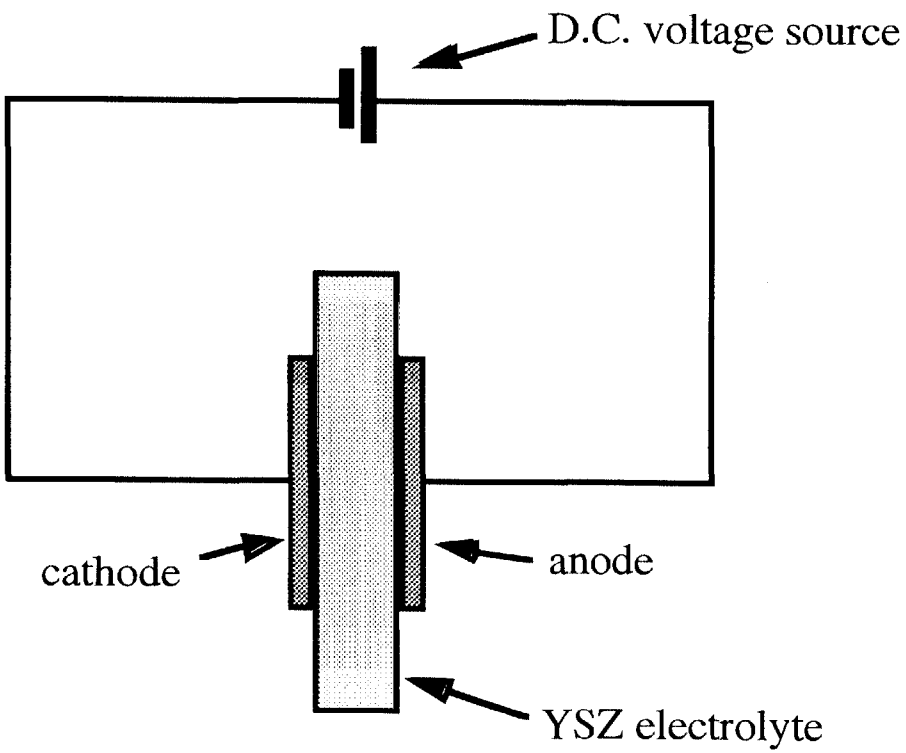

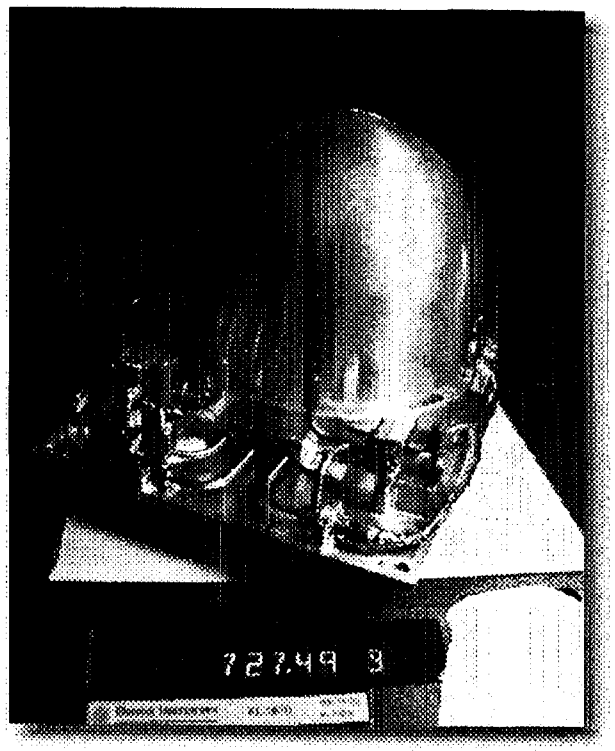

Possible Separation Device

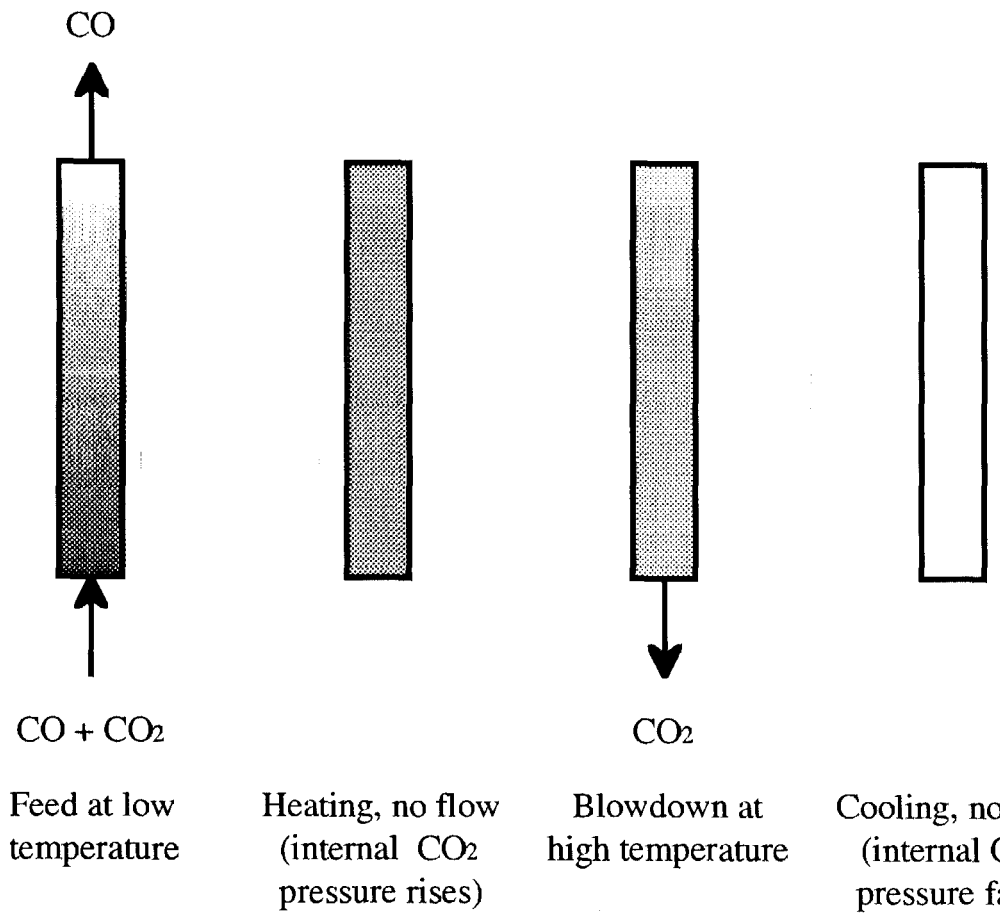

We envision a thermally-driven adsorption-based separation system that combines elements of TSA, PSA, and adsorption compression. A four step cycle is shown. CO is produced at the feed pressure (e.g., 1 bar); CO_2 product is expanded to a pressure determined by the requirements of the zirconia cell. Two beds are needed.

Cycle Steps & Path

(1) Feed: bed is fed with CO/CO_2 mixture. It contains an adsorbent selective to CO_2. CO is produced as product. Little CO is adsorbed.

(2) Heating: as the bed is heated, the pressure increases.

(3) Blowdown: CO_2 at high pressure is allowed to pass into a storage tank at a pressure sufficient to feed the zirconia cell.

(4) Cooling: the bed is cooled prior to returning it to the feed step.

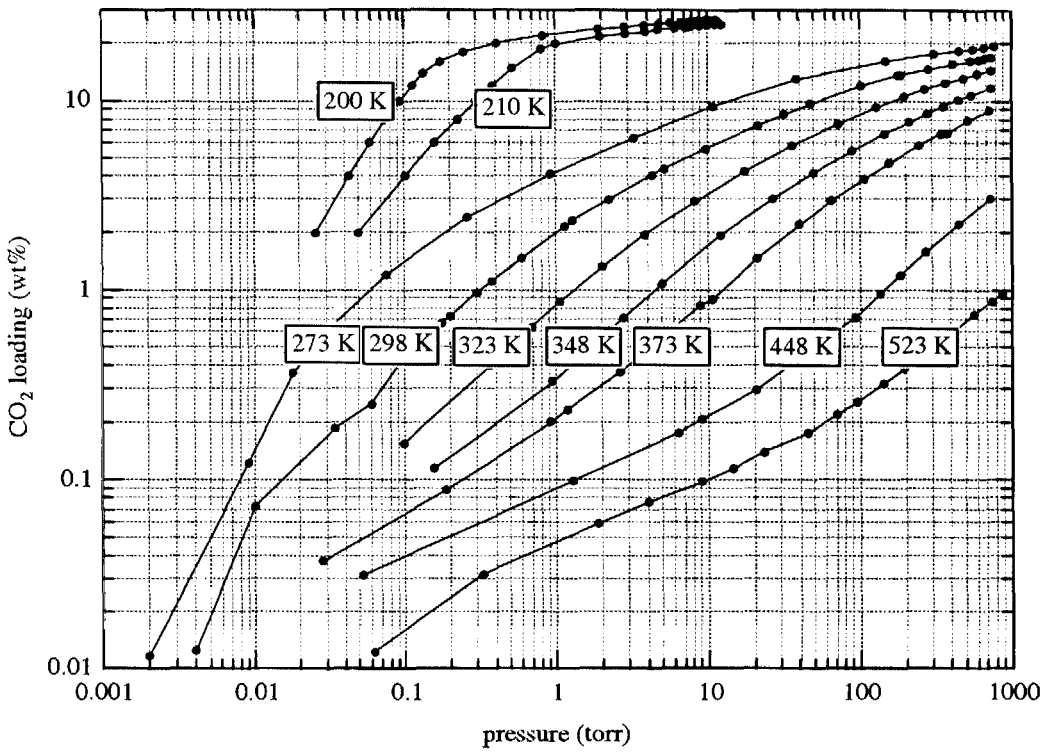

CO_2 isotherms on NaX zeolite (Finn).
Path is for cycle between 273 K and 373 K.

Sample Calculations

Basis: 1 kg/day O_2; 50% conversion/pass in YSZ cell; NaX adsorbent; adsorption at 273 K and heating at 373 K (integrated with Martian day and zirconia cell thermal envelope).

From material balance, 2.75 kg/day of CO_2 must be compressed.

Path points (equilibrium loadings and pressures):

- End of feed: loading of CO_2 (at 273 K, 0.5 bar) will be 18 wt %.
- End of blowdown: loading of CO_2 (at 373 K, 1 bar) will be 9 wt %.
- End of cooling: pressure of CO_2 (at 9 wt %, 273 K) will be 10 torr. (The product of the feed step will be more than 98% CO.)

Desorbing at higher temperatures will increase the CO product purity. For example, if desorption were at 448 K, the residual loading would be only 3 wt %, giving a residual partial pressure of CO_2 in the feed product stream of only 0.4 torr, corresponding to 99.95% CO in the product.

Calculations show the following:

- Losses of CO_2 will be small. With the 373 K desorption temperature, the CO_2 partial pressure in the CO stream is only 10 torr.

- With 50% conversion in zirconia cell, only about half the CO_2 needs to be compressed by the compressor, compared to a process without the separator. The adsorption compressor and zirconia cell can be smaller.

- The purity of the CO stream can be adjusted by changing the desorption temperature (or the adsorption temperature).

- Although residual CO_2 pressures are small after regeneration, the CO_2 loading is not small, e.g., 9 wt %. (A vacuum step would waste CO_2).

- Beds of NaX for a process to make 1 kg O_2 and 1.75 kg CO over a 6 hr period would contain 3.8 kg NaX or over a 25 hr period would contain 0.92 kg NaX. Basis: a bed on stream for CO_2 recovery for 30 minutes; 6 wt % CO_2 loading swing on adsorbent (e.g., 9 wt % to 15 wt %).

Design Goals

Design goals for the separator are as follows:

- to permit essentially complete conversion of CO_2 to products O_2 and CO
- to permit essentially complete recovery of CO
- to separate unreacted CO_2 such that it can be recycled back to the zirconia cell
  - this requires a CO_2 product pressure of 1 bar
  - high purity CO_2 in the recycle is not required since the reaction continues to produce CO
- to be able to generate CO product at various purities

Research Needs

Research needs for the design shown are as follows:

- The best adsorbent for the process must be determined.
- Adsorption isotherms must be measured, both for pure components and mixtures.
- Mathematical modeling must be performed to provide a solid framework for design.
- The separation system must be constructed and tested.
- System integration must be studied.

RIVULET DYNAMICS WITH VARIABLE GRAVITY AND WIND SHEAR

J.S. Marshall and R. Ettema
Iowa Institute of Hydraulic Research
University of Iowa
Iowa City, Iowa

ABSTRACT

This study investigates rivulet dynamics under conditions of variable gravity and wind shear. Particular attention is focused on the dynamics of systems comprising a large number of interacting rivulets, which typically form following breakup of a liquid sheet. Rivulets form when the upper free surface of a liquid sheet flowing over a rigid plate deflects downward and connects to the plate. The flow within the liquid layer may be driven by forces such as wind shear or gravity. The onset of rivulet formation may be triggered by a variety of effects, such as surface roughness of the solid plate, turbulence in the air stream, or thermocapillary instability of the liquid-gas interface. At the head of the rivulet, the liquid-gas-solid contact line forms a U-shaped pattern on the plate. Downstream of the formation point, rivulets exhibit a variety of instabilities, including lateral meandering and vertical instabilities that lead to beading and drop fall-off from the rivulet tip.

Rivulets play an important role in a wide variety of applications in the energy, chemical and aerospace industries. Rivulet formation on the wings of an airplane flying in rain decrease the aerodynamic efficiency and (under freezing conditions) control the pattern of ice formation on the wings. Rivulet formation enhances heat transfer rate to the liquid stream due to the large ratio of liquid surface area to cross-sectional area. This fact has been used in a variety of cooling systems, including cooling streams of solar panels, tubes of mist-cooled heat condensers, and liquid-metal blanket cooling of fusion reactors. Mass transfer rates to rivulets is important for applications such as trickle-phase chemical reactors, flow over a catalytic pellet bed, and flow within columns with structured packing. Rivulet formation in two-phase liquid-gas flow in a tube controls the transition between annular flow to droplet flow. Rivulet formation is an undesirable feature in several coating processes that limits the minimum thickness of the coating sheet and results in inefficient and non-uniform coating of the substrate.

The project will utilize microgravity conditions to investigate rivulet dynamics with variable gravity and wind shear. The planned experiments will be conducted using a centrifugal "Couette flume", consisting of inner and outer cylinders and a liquid water layer of a prescribed thickness coating the inner surface of the outer cylinder. Rotation of the outer cylinder produces different effective gravitational conditions due to the radial centrifugal force. Differential rotation of the inner cylinder is used to generate a prescribed wind shear. Data on rivulet formation and geometry will be obtained using two different laser-induced fluorescent imaging methods. The experiments will be

conducted through the NASA Parabolic Flight Program. A computational study of the rivulet field will simultaneously be performed and used to aid in interpretation of the experimental results. Particular focus is placed on the effect on the rivulet system dynamics of different models for the moving contact line at the liquid-gas-solid interface. Comparison of the experimental data with computational predictions will be used to develop a capability to accurately model liquid sheet breakup and its later evolution as a field of interacting rivulets.

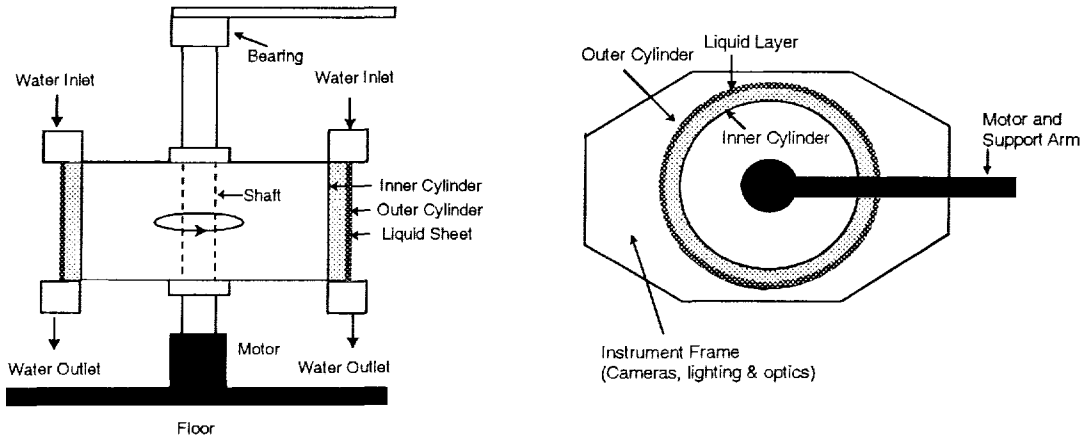

(a) (b)

Fig. 1. Schematic diagram showing the Couette flume device in (a) planform (left) and (b) cross-sectional (right) views. Shaded (gray) regions indicate the annular test section between the two rotating cylinders.

RIVULET DYNAMICS WITH VARIABLE GRAVITY AND WIND SHEAR

J.S. Marshall and R. Ettema
Iowa Institute of Hydraulic Research
University of Iowa
Iowa City, Iowa

Student Participant: Jeff McAllister

Objective

To examine the effect of gravitational acceleration on the following three stages of liquid sheet development in the presence of wind shear:

1. sheet breakup into rivulets

2. system of interacting rivulets

3. rivulet breakdown into droplet flow

The research will examine both the transition between these stages and the dynamics of interacting rivulet systems.

Applications of Rivulet Systems

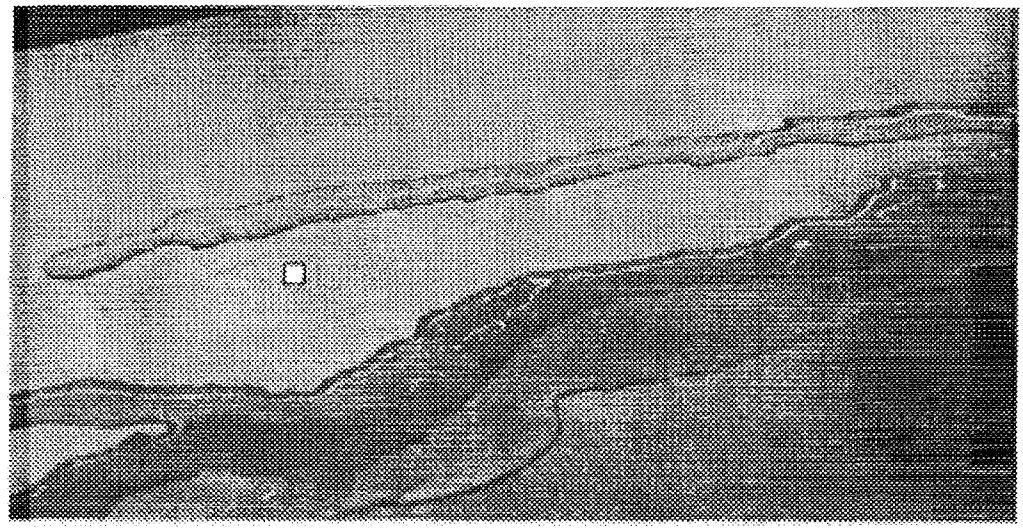

Water-rivulet flow at frigid temperature over an inclined smooth aluminum surface

- "Ribbing" instabilities during material coating processes
- De-icing of aircraft wings
- Heat-transfer enhancement (condensers, solar collectors)
- Mass-transfer enhancement (flow in porous bed)
- Cleaning processes (e.g., in circuit board manufacturing)
- Aerodynamic drag (via surface roughness changes)

Computational Methodology

Flow Field

- Two immiscible fluid layers in a Couette channel with vertical gravity and temperature gradient
- Includes wall roughness and themocapillary advection
- Models to be introduced for contact line formation, motion and healing

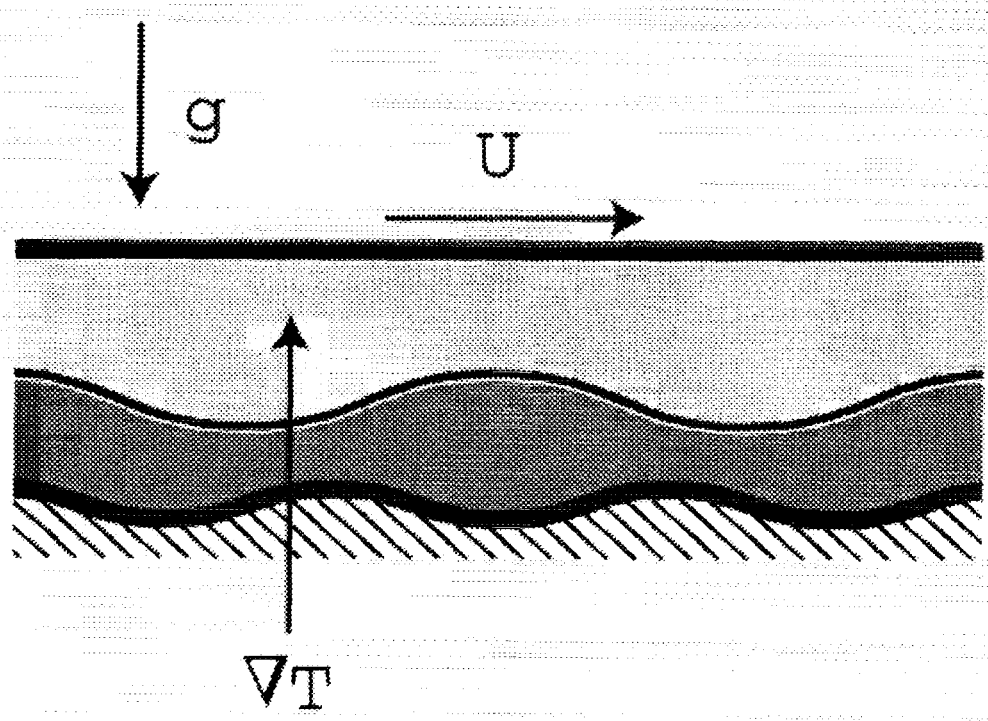

"Page missing from available version"

Numerical Method

- Vertical: Galerkin method with polynomial test functions
- Horizontal: Finite-difference method with periodic boundary conditions

Experimental Methodology

- Apparatus: rotating Couette flume
- LIF to quantify variations in liquid sheet thickness
- PIV to measure flow velocities

Experimental Apparatus

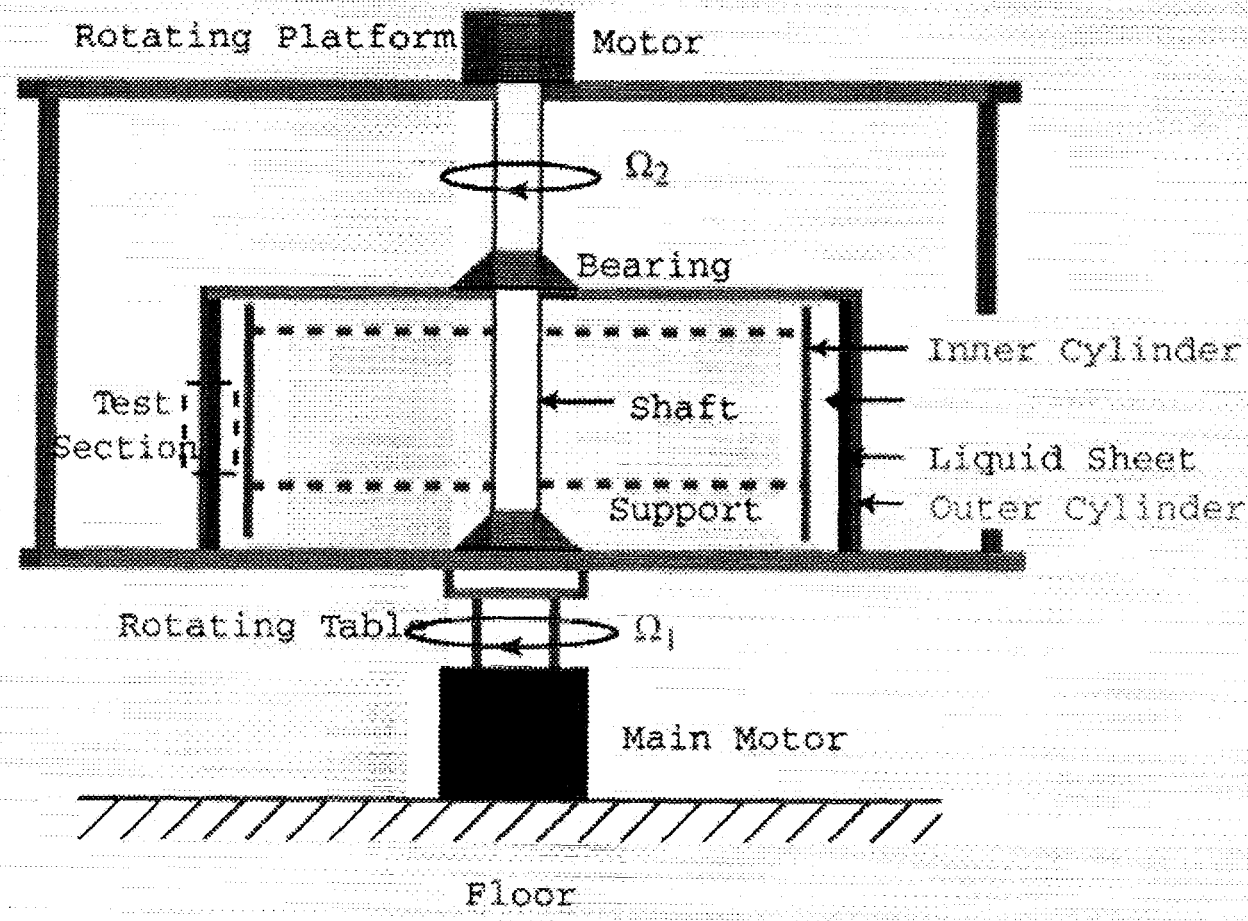

Optical Transmission System

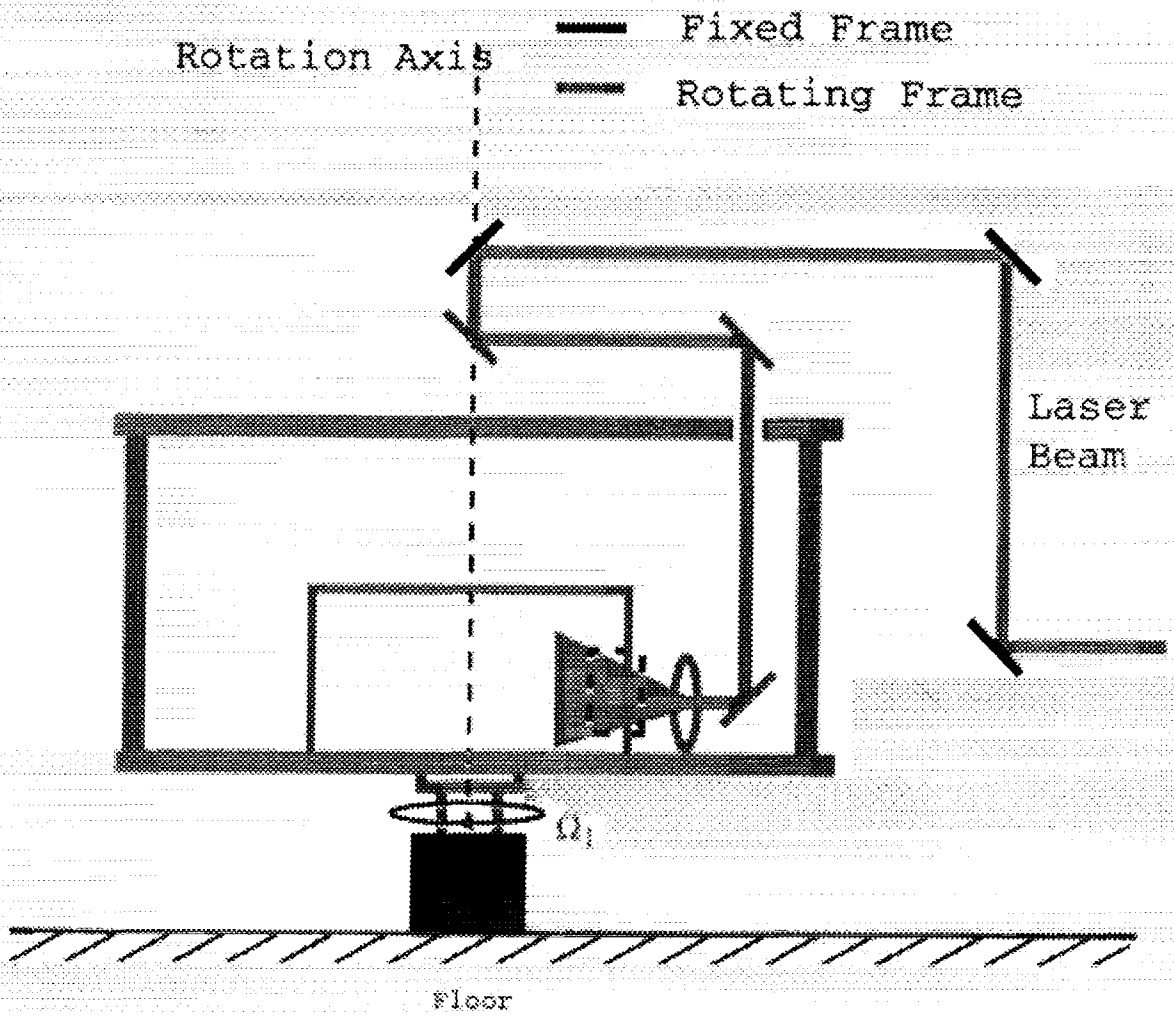

Image Acquisition System

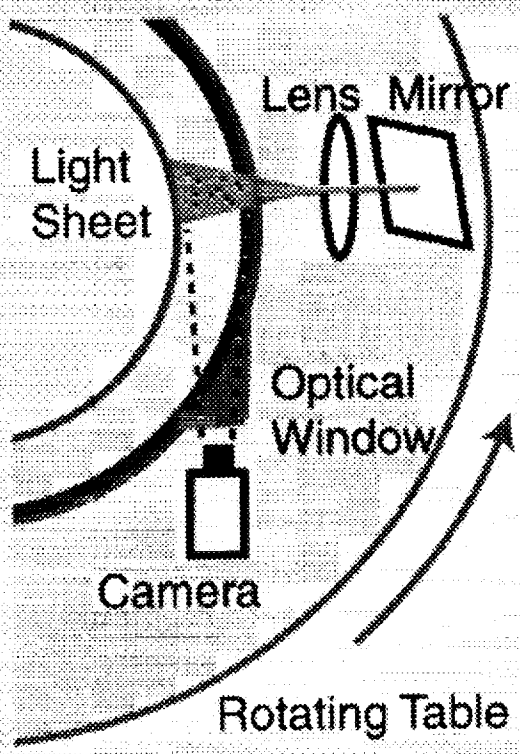

Time Table

Year 1: May, 2000 - November 2000

- Design and perform preliminary testing of experimental apparatus
- Develop computational method without contact lines

Year 2: December, 2000 - November, 2001

- Construction and laboratory testing of experimental apparatus
- Computational study of rivulet formation mechanisms
- Develop computational model with moving contact lines

Year 3: December, 2001 - November, 2002

- Parabolic flight test experiments for isothermal flow
- Compute systems of interacting rivulets
- Compare experimental and computational results

Year 4: December, 2002 - November, 2003

- Parabolic flight test experiments with heat transfer
- Compute rivulet breakup
- Compare experimental and computational results

PERIODIC FLOW AND ITS EFFECT ON THE MASS TRANSFER OF A SPECIES

A. Thomas and R. Narayanan
Department of Chemical Engineering
University of Florida
Gainesville, FL 32611

ABSTRACT

Separating species from air is of great importance to many industries, and of special interest to the space program as one seeks novel ways to revitalize the air environment. Periodic flow can be used to aid in the separation of dilute species in a diluant known as a carrier. Calculations show that the mass transfer in the presence of periodic flow gives a great enhancement of the total mass transfer of a dilute species over that of pure molecular diffusion. If two dilute species are introduced in a mixture such that one has a higher diffusion coefficient making it the faster diffuser, the total mass transfer of the faster diffuser may either be higher or lower than the total mass transfer of the slower diffusing species. As the periodicity of the flow changes, so does the ratio of the mass transfer of the faster diffuser to the slower diffuser, the slower diffuser having the higher mass transfer for a region of frequencies. The qualitative nature of the results depend upon the diffusion coefficients, the frequency of oscillations and the geometry. Consequently a CO_2-He system in a nitrogen carrier will yield qualitatively different results than a CO_2-CH_4 system, and these will both differ from an Ethanol-Glucose system in water. These findings will be presented with an explanation of the physics of mass transfer and its relationship to the diffusivities of each species, the periodicity of the system, and the kinematic viscosity of the carrier fluid. Details of an existing experimental set-up, built to verify these findings, will be given in the poster presentation.

NASA/CP—2000-210470

Periodic Flow and Its Effects on Mass Transfer of Species

Aaron M Thomas

Ranga Narayanan

University of Florida

Department of Chemical Engineering

Outline

- Motivation
- General Theory
- Objective
- Periodic Flow Setup
- Results
- Parameters Effects on the Velocity Profile and Overall Mass Transfer
- Conclusions and Further Work

Motivation

- Periodic flow greatly enhances the total mass transfer over pure molecular diffusion
- Can be used for separations which are important in the chemical industry
- Is of interest to the space program in removing CO2 from the air and returning revitalized air to human environments

General Theory
Carrier
Species

Explanation of General Theory

Imagine a tube connecting two reservoirs. The reservoir on the right has a pure carrier gas while the one on the left has a dilute amount of another species. As shown in the top left figure, if left undisturbed, the dilute species will diffuse from left to right due to pure molecular diffusion. If the fluid exhibits pulsatile flow, the nearly parabolic flow profile will initially cause the species to axially diffuse down the tube and radially diffuse to the boundary (top right). When the flow reverses itself, the species at the boundary now diffuses to the core of the tube (bottom left). On the next cycle, the species is now convected down the tube and again radially diffuses (bottom right) thus transporting the species down the tube in a zig-zag fashion. If two dilute species were present, each would transport at different rates because of differing diffusion coefficients.

General Objective

- It has been observed that periodic flow significantly enhances the total mass transfer of a dilute species. It is our goal to understand how the important operating and thermophysical parameters affect the mass transfer and separation that can be achieved.

Pressure Driven System Between Two Flat Plates

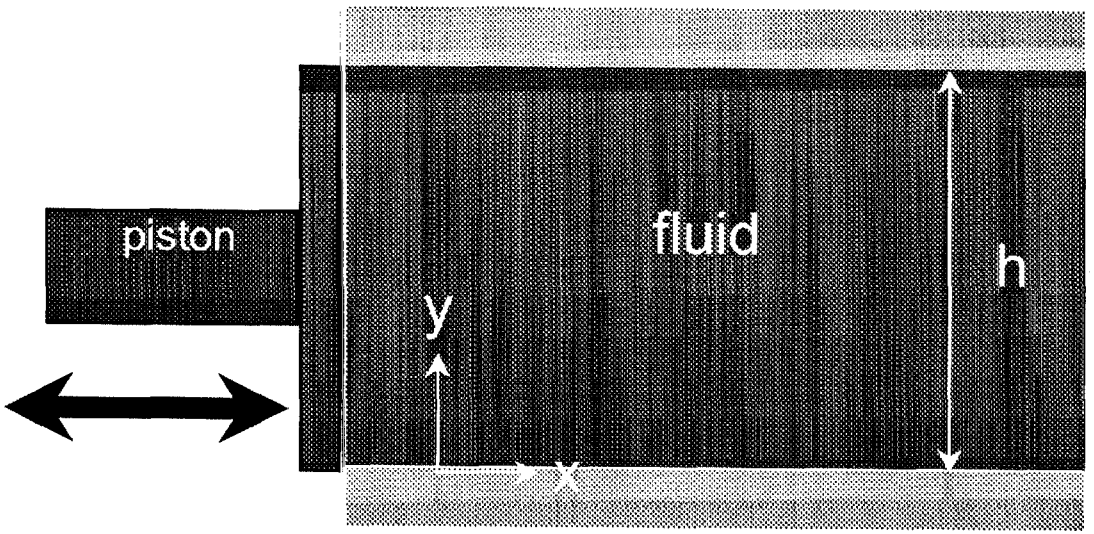

Piston Movement

$$x = A\sin(\omega t)$$

Flow Rate $= h\frac{dx}{dt}$

$$= A\omega h\left(e^{i\omega t} + e^{-i\omega t}\right)$$

Velocity Boundary Conditions

$V_x = 0$ at $y = 0$ and $y = h$

Concentration Boundary Conditions

$$\frac{\partial c}{\partial y} = 0 \text{ at } y = 0 \text{ and } y = h$$

Equations Used

Velocity

$$\rho \frac{\partial V_x}{\partial t} = -\frac{\partial P}{\partial x} + \mu \frac{\partial^2 V_x}{\partial y^2}$$

$$V_x = \hat{V}_x e^{i\omega t} + \tilde{V}_x e^{-i\omega t}$$

Concentration

$$\frac{\partial c}{\partial t} + V_x \frac{\partial c}{\partial x} = D \frac{\partial^2 c}{\partial x^2} + D \frac{\partial^2 c}{\partial y^2}$$

Time Averaged Axial Flux

$$\bar{J} = -D \frac{\partial \bar{c}}{\partial x} + \overline{V_X C}$$

$$= -D \frac{\partial \bar{c}}{\partial x} + \frac{\omega}{2\pi} \int_0^{\frac{2\pi}{\omega}} V_X C dt$$

$$= -\frac{D(c_2 - c_1)}{L} + 2\Re\left(\tilde{V}_X \hat{C}\right)$$

Total Mass Transfer

$$\bar{Q}_{tot} = \frac{1}{h} \int_0^h \bar{J} dy$$

$$= \frac{-D(c_2 - c_1)}{L} + \frac{2}{h} \Re \int_0^h \tilde{V}_X \hat{C} dy$$

Mass Transfer vs Frequency for a He–CO_2 Binary System

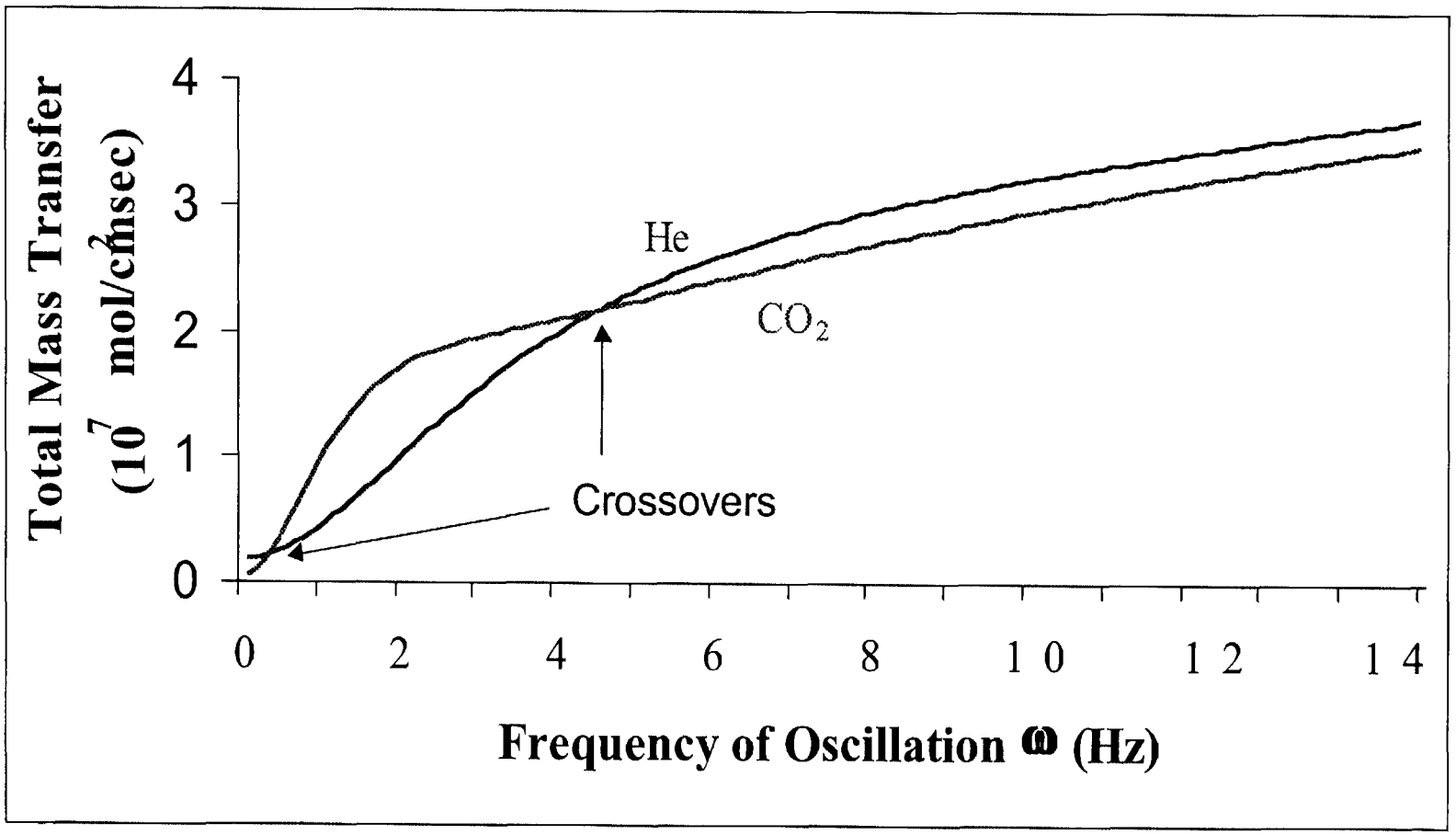

Crossovers

Up to three crossover frequencies where the mass transfer is the same can occur. The first crossover occurs because faster diffusing helium reaches the slow moving boundary more than the slower diffusing carbon dioxide. This retards the mass transfer of helium more than the carbon dioxide. This is similar to Taylor diffusion. The second crossover, if it occurs, is when neither species has enough time to reach the slow moving boundary before the next cycle begins. Because helium initially has the advantage, it will overtake the carbon dioxide to produce a second crossover. As the frequency increases, "wiggles" in the flow profile become more apparent where areas of reverse flow can hinder the mass transfer of a species that diffuses into these areas. The faster moving species has more of a chance to reach these areas thus it could produce a third crossover where the slower diffusing species again will have the higher mass transfer.

Ratio of the Total Mass Transfers for 3 Binary Systems

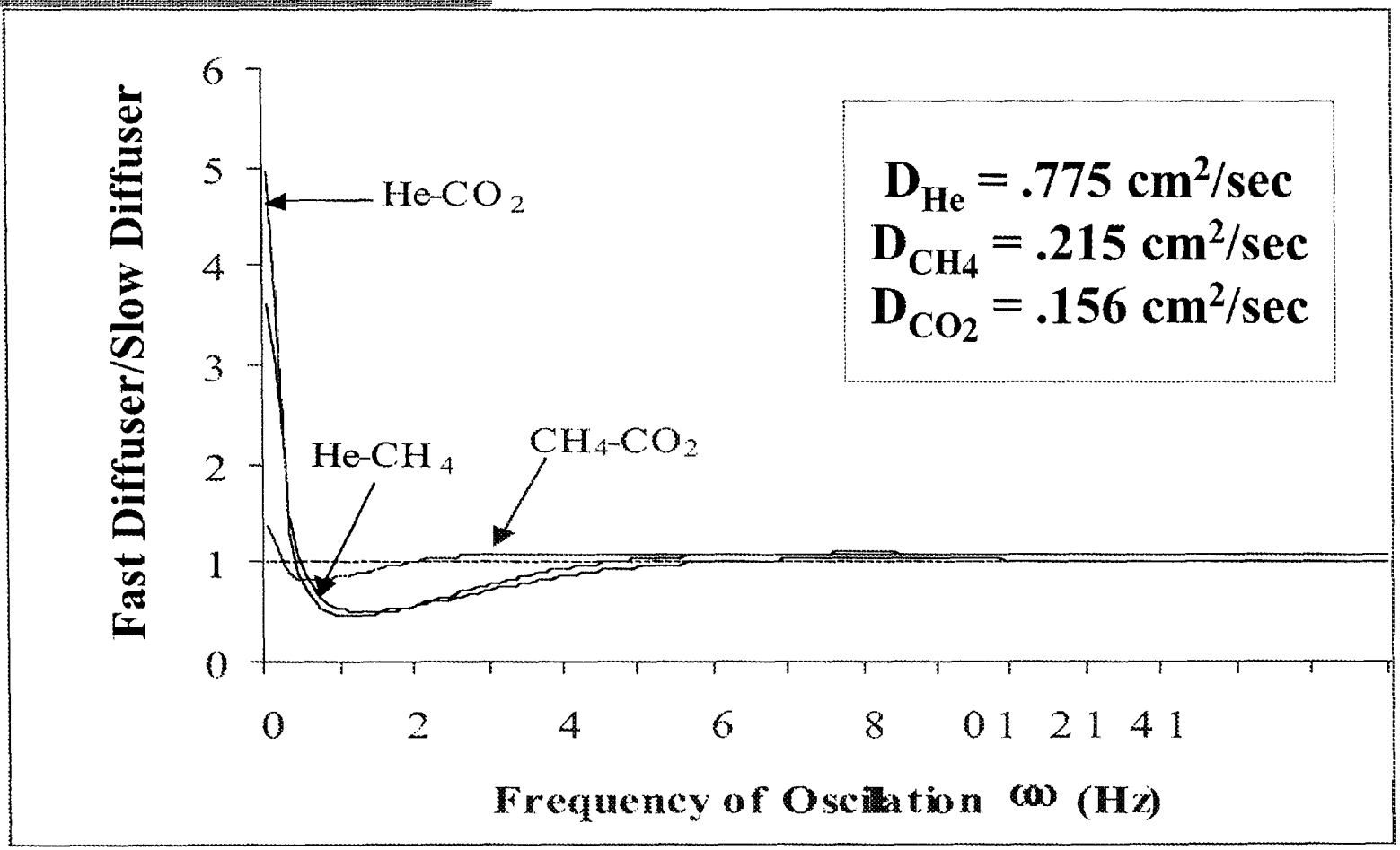

Three Binary System

These three binary systems exhibit the crossovers that can occur in pulsatile flow. The He-CO_2 and CH_4 - CO_2 system exhibit two crossovers while the He- CH_4 system shows three crossovers.

The ratio of the mass transfer also shows the separation that can be achieved and which species will separate out more. If the ratio is greater than unity, the faster diffusion species will separate out more. Less than unity will have the slower diffusing species separate out more, and unity indicates no separation.

Three Major Parameters

- Diffusion Coefficient (D) – indication of the response of the mass transfer of a specie in the presence of a concentration gradient
- Kinematic Viscosity (ν) – indication of the response of the fluid to mechanical perturbations
- Periodicity (ω) – the amount of time it takes to complete one cycle

Velocity Profiles

The following slides depict the velocity profiles at different frequencies in between the flat plates. These profiles, along with the diffusion coefficients and frequency of oscillation previously discussed, are a major factor in the shape of the mass transfer curves. The three slides show the the velocity profile that produces each crossover that may occur. Keep in mind that the kinematic viscosity will alter the shape of the curves as a higher kinematic viscosity will keep the velocity profiles more parabolic for higher frequencies.

Initial Decrease in Total Mass Transfer Ratio

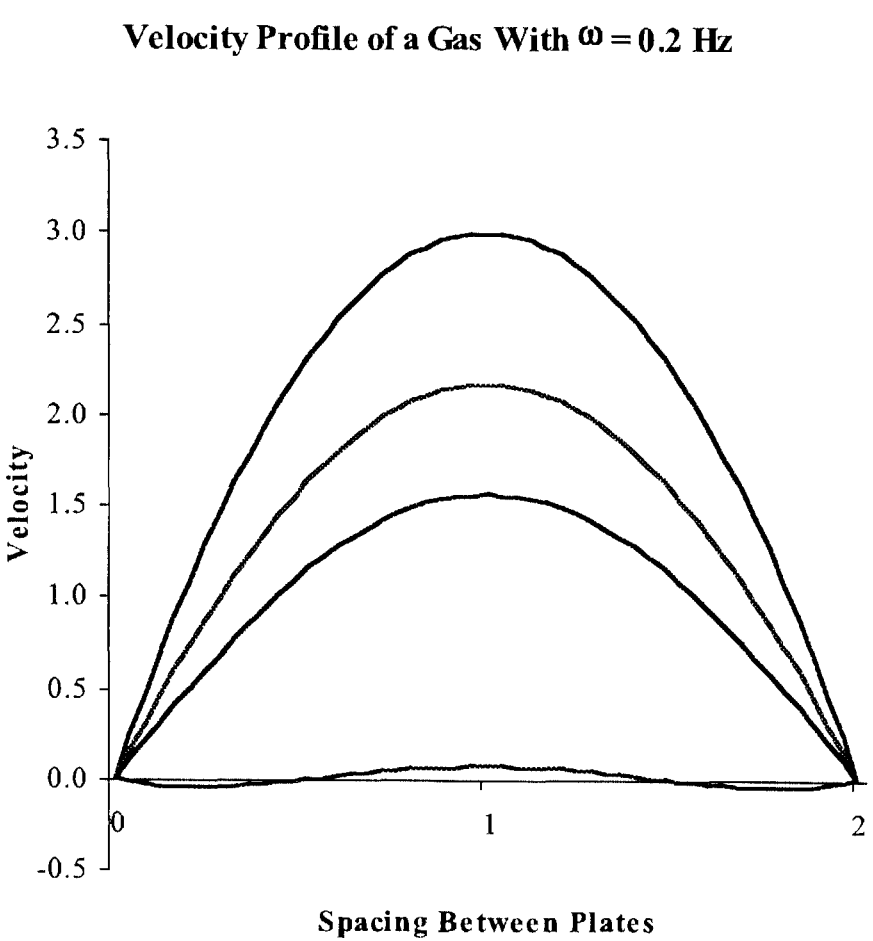

1. Nearly Parabolic Flow Profile
2. Slow Moving Fluid (Low Frequency)
3. Slower Moving Species Has the Advantage

Middle Increase in the Ratio of Total Mass Transfer

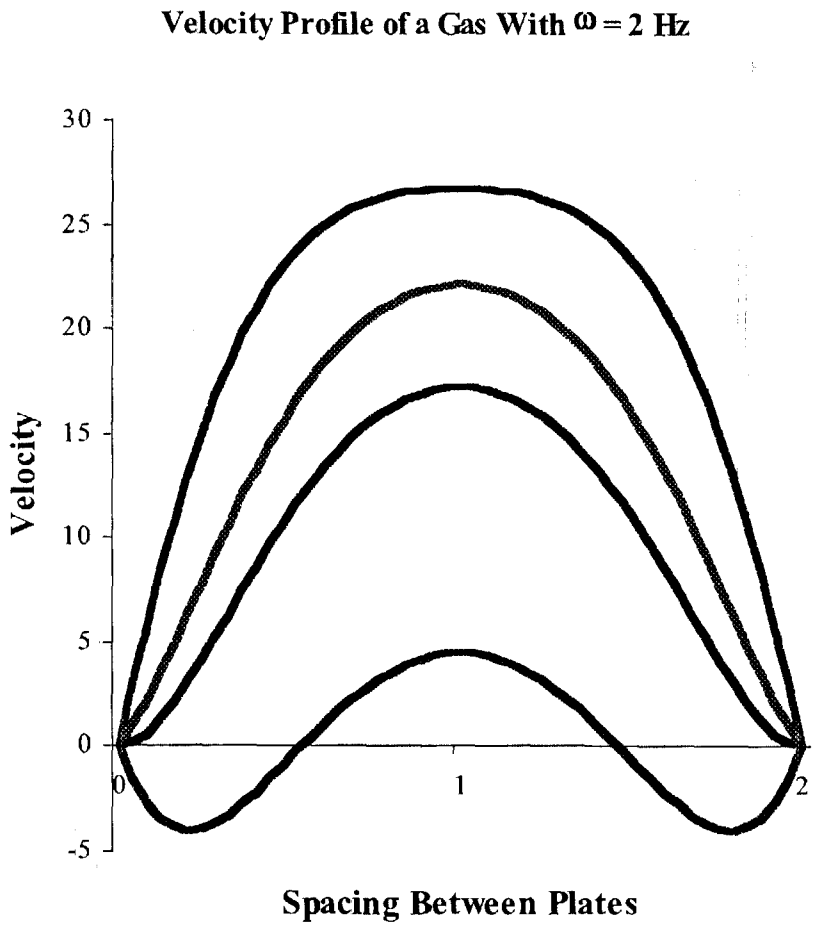

1. Smaller Periodicity (Larger Frequency)
2. Small Regions of Reverse Flow Appear
3. Faster Diffusing Species Has the Advantage

Final Decrease in the Ratio of Total Mass Transfer

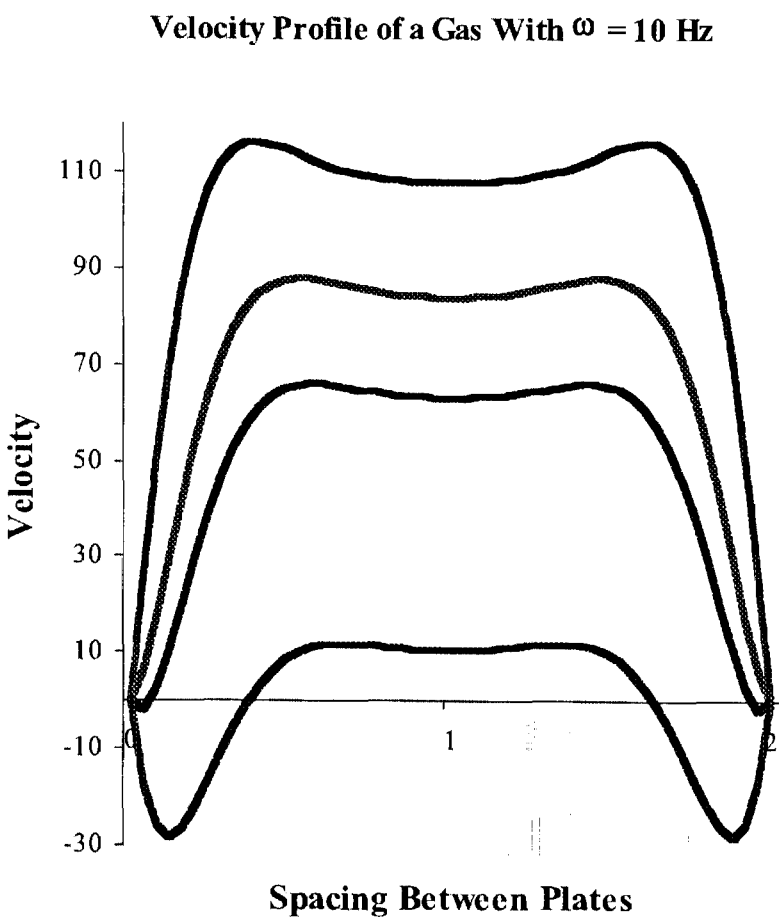

1. Large Frequency. Very Short Cycle Time

2. Reverse Flow Becomes a Factor

3. Slower Diffusing Species Regains the Advantage

Experimental Apparatus

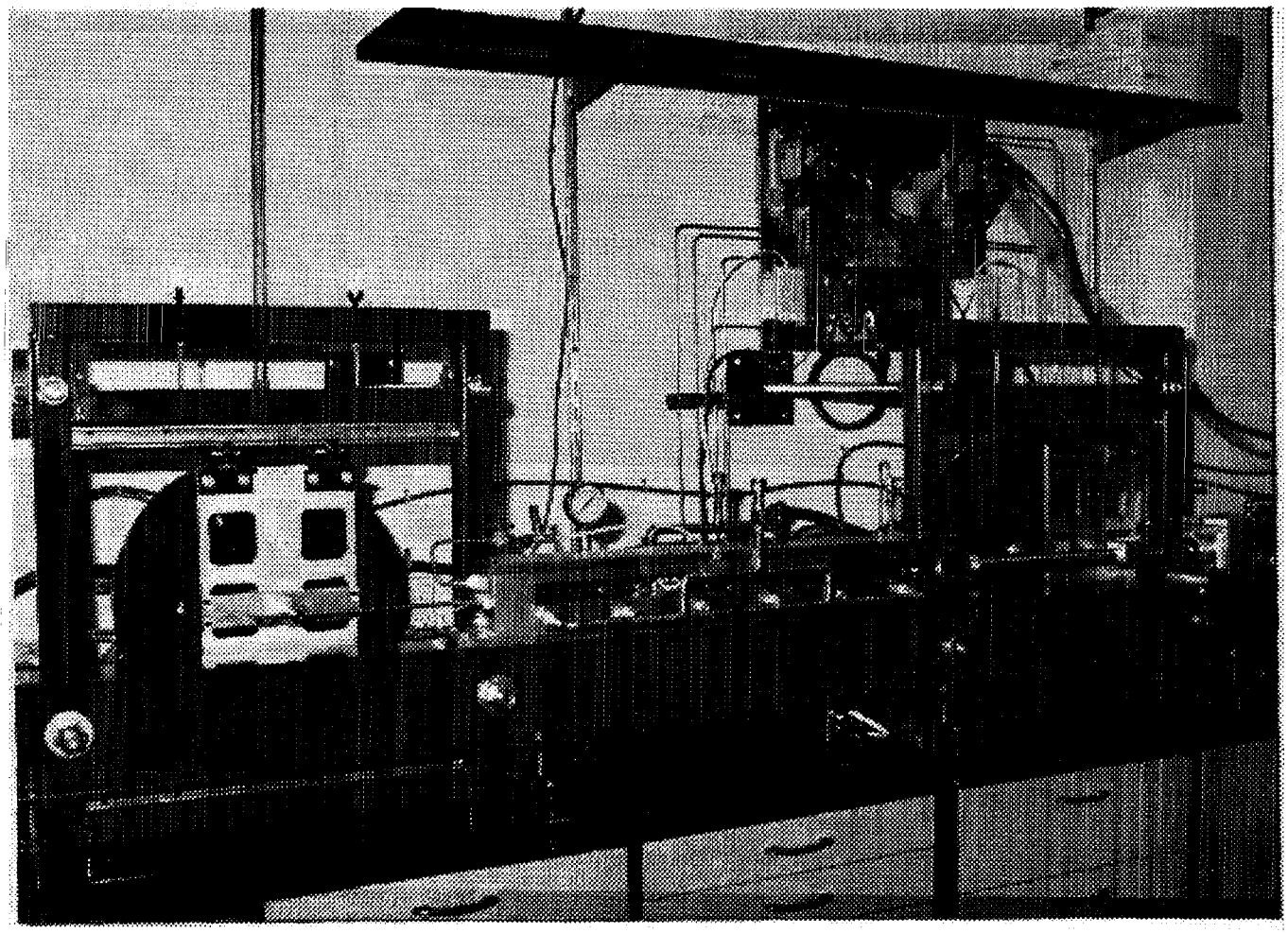

Experimental Setup

Pulsatile flow is produced by oscillating two concentric tubes connected to two reservoirs. It does not make a difference in the physics whether the tubes are oscillated or an oscillating pressure drop produces the flow. Flywheels are used to convert circular motion into oscillatory linear motion. Experiments can be done with two tubes oscillating in phase, out of phase, or only one tube oscillating to produce flow in an annular region. One of the tubes can be removed to produce flow in an open tube. Concentration samples are taken from the flow that enters and leaves both reservoirs in order to determine the mass transfer.

Further Research and Experiments

- Under what conditions does the flow become non-laminar?
- Experiments needed to verify the phenomena observed theoretically
- Effect of geometry on the mass transfer and separation
- Enhance separation due to the Soret effect?

INSTABILITY AND BREAKUP OF GAS JETS INJECTED IN COFLOWING LIQUIDS

R. N. Parthasarathy and S. R. Gollahalli
School of Aerospace and Mechanical Engineering
The University of Oklahoma
Norman, OK 73019

ABSTRACT

A number of practical applications, such as gas dissolution in liquids in gas-liquid reactors and blood oxygenators, coal and mineral purification by flotation, and large-scale mixing in liquids, involve the bubble formation from the breakup of gas jets injected into liquids. Inherent instabilities in the gas flow get amplified and result in the breakup of the jet into bubbles. Thus, important properties, such as the breakup distance, and the size distribution of the bubbles formed as a result of breakup, are determined by the nature of instabilities that lead to the breakup.

Recent theoretical analyses [1-3] indicate that the nature of instabilities that develop in a gas jet injected into a liquid are markedly different from those found in liquid jets injected into gaseous media. The growth rates are smaller and the maximum growth rates occur at longer wavelengths for comparable conditions. Also, the phase velocity of the instabilities is controlled by the liquid coflow. Validation of these theoretical results in ground-based experiments is precluded because of the dominance of buoyancy effects.

The breakup of gas jets injected into liquids is considerably different in the absence of buoyancy. This implies that in order to utilize the breakup phenomena of gas jets injected into liquids for space-processing applications, effects of buoyancy must be isolated. The present investigation aims at delineating the various regimes of instabilities found in gas jets injected into liquid media and isolating and quantifying the effects of buoyancy on the instabilities leading to breakup. To this end, a combination of ground-based and microgravity experiments will be used.

The experimental configuration consists of a round plexiglass test section in which a liquid is pumped vertically upward with a uniform velocity profile at the inlet. The pumped liquid is collected from the top of the test section and recirculated. The liquid coflow velocity is varied with suitable valves. A small round tube (of nominal diameter 1 mm) is used to inject the gas (nitrogen or helium) at the center of the liquid inlet. Compressed gas is supplied at known flow rates using pressure regulators and rotameters. Provision is also made to vibrate the gas inlet tube with known frequency and amplitude. A fluorescent dye (such as Rhodamine) is added to the liquid to help visualize the gas-liquid interface. Flow visualization and image analysis will be used to document the growth of instabilities, and the resulting bubble properties over a wide range of governing parameters: the gas Weber number, Ohnsorge number, liquid-to-gas density ratio, and liquid-to-gas velocity ratio.

The microgravity experiments will be conducted in the 2.2-second drop tower at NASA Glen

Research Center. Analysis indicates that 2.2 seconds is sufficient to observe the characteristics of the instability. The rig that will be constructed is envisioned to be roughly 0.9 m long, 0.4 m wide, and 0.8 m high, to fit in the frame used in the drop-tower experiments. The rig will house the experimental set up and the data-acquisition and photography systems. The experimental set up will be identical to that used in the ground-based experiments. The gas and liquid coflow will be injected vertically upward; the injected gas will collect at the top and will be vented out. Photographs of the gas jet will be obtained using a high-speed motion picture camera. The images will be analyzed to measure the disturbance growth rates and velocities. The electrical system will be designed to enable remote operation of the experiment.

Theoretical work to be undertaken includes analysis to demarcate the mode of instability: absolute or convective for general three-dimensional disturbances over the range of operating parameters. Also, a non-linear stability analysis will be used to study the growth of large-amplitude disturbances, with and without buoyancy effects.

REFERENCES

[1] Parthasarathy, R. N. and Chiang, Kai-Ming (1998) "Temporal Instability of Gas Jets Injected in Viscous Liquids to Three-Dimensional Disturbances," *Physics of Fluids*, Vol. 10, pp. 2105-2107.
[2] Subramaniam, K., Parthasarathy, R. N. and Chiang, Kai-Ming (1999) "Three-Dimensional Temporal Instability of Compressible Gas Jets Injected in Liquids," *AIAA Journal*, Vol. 37, pp. 202-207.
[3] Subramaniam, K. and Parthasarathy, R. N. (2000) "Effects of Confinement on the Temporal Instability of Gas Jets Injected in Viscous Liquids," *Physics of Fluids*, Vol. 12, pp. 89-91.

APPLICATIONS

- Gas dissolution systems in chemical and pharmaceutical industries, oxygenators
- Hybrid Fuel Combustion (propane + LNG)
- Coal and mineral purification by flotation

AIR JET SURROUNDED BY WATER JET
(Lee and Chen, 1991)

Air jet (10 mm ID tube) surrounded by water jet (77 mm ID tube)

Water velocity = 0.5 m/s, Air velocity = 7.7 – 28 m/s

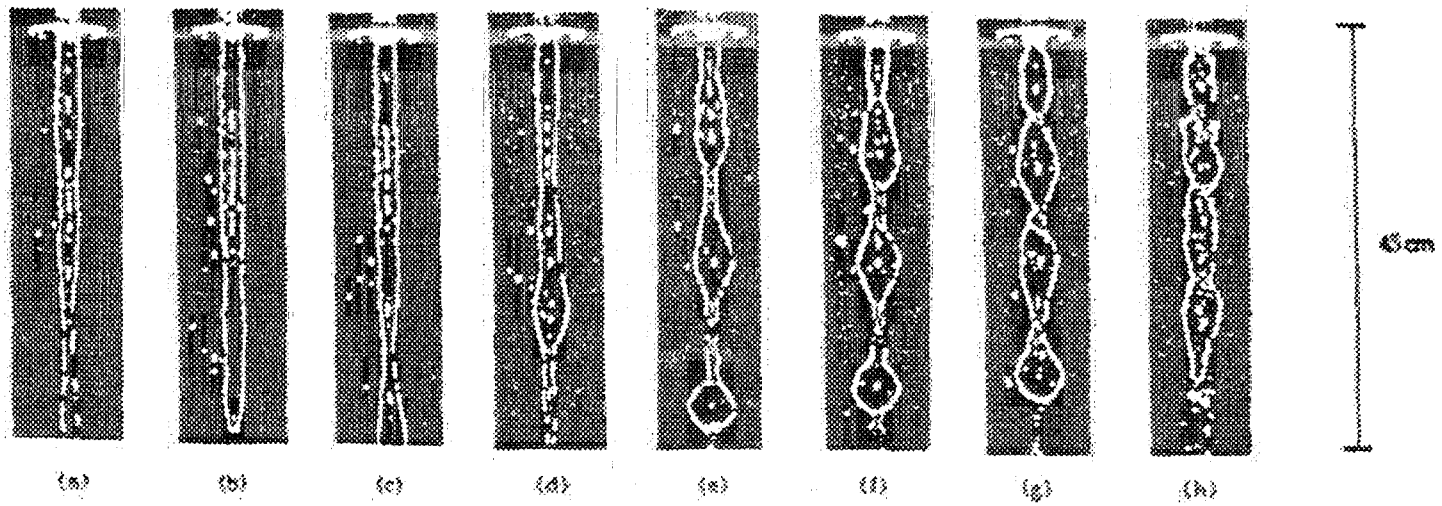

LINEAR STABILITY ANALYSIS

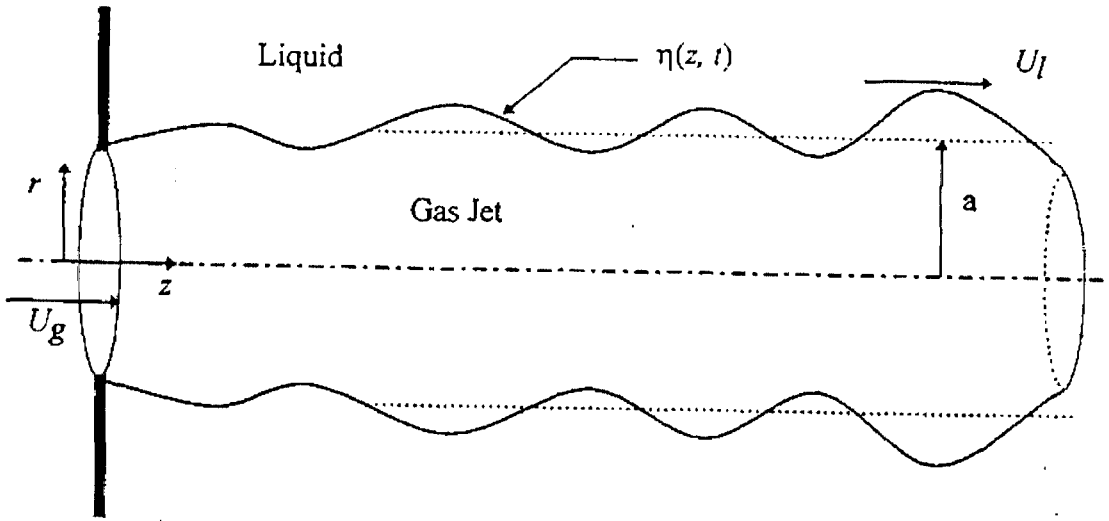

Growth rate of small disturbances is a function of wavenumber ($2\pi/\lambda$) and azimuthal mode

Flow parameters:

Gas Weber number [$\rho_g U_g^2 a/\sigma$],

Ohnsorge number [$\mu_l/(\rho_l a\sigma)^{0.5}$],

Density ratio (ρ_l/ρ_g) and Velocity ratio (U_l/U_g)

Weber number = 40, Density ratio = 1000, Velocity ratio = 0

n = 0, 1

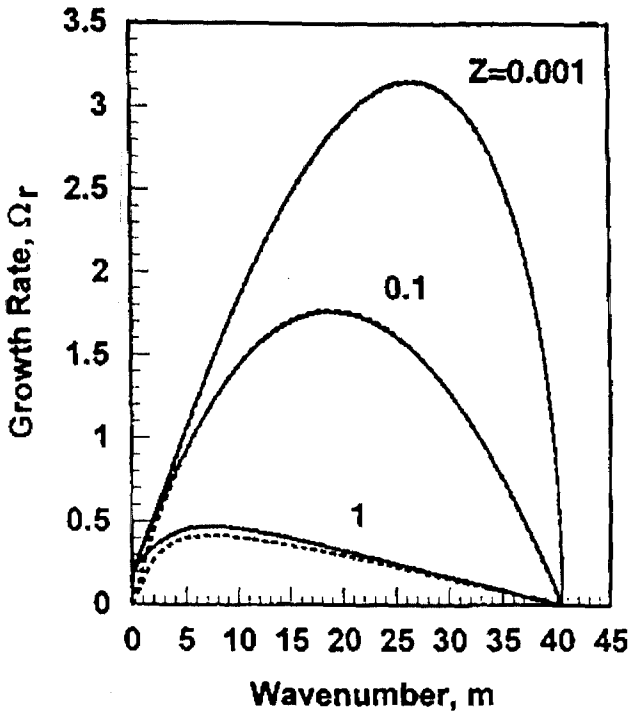

n = 2, 3

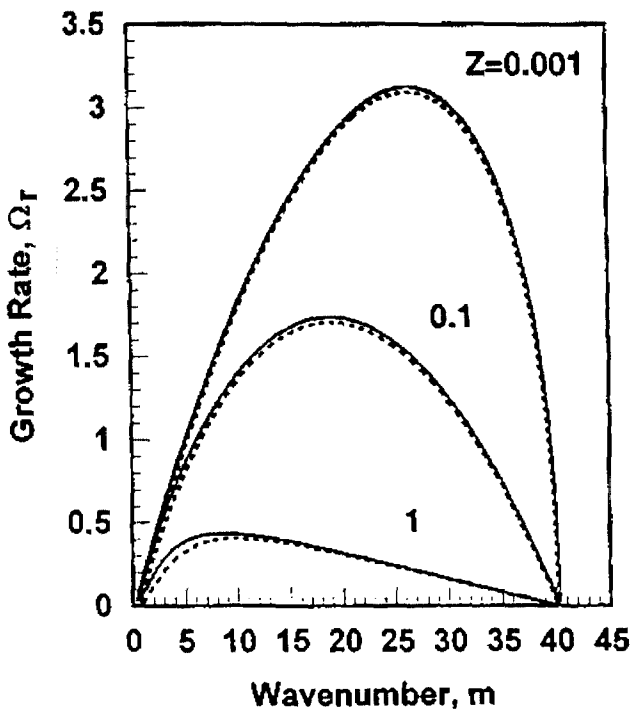

Ohnsorge number = 0.001, Density ratio = 1000, Velocity ratio = 0.2

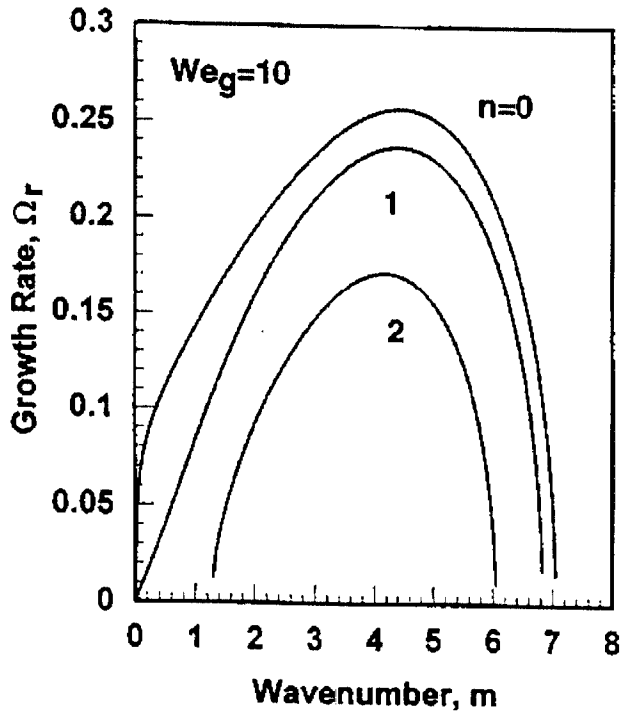

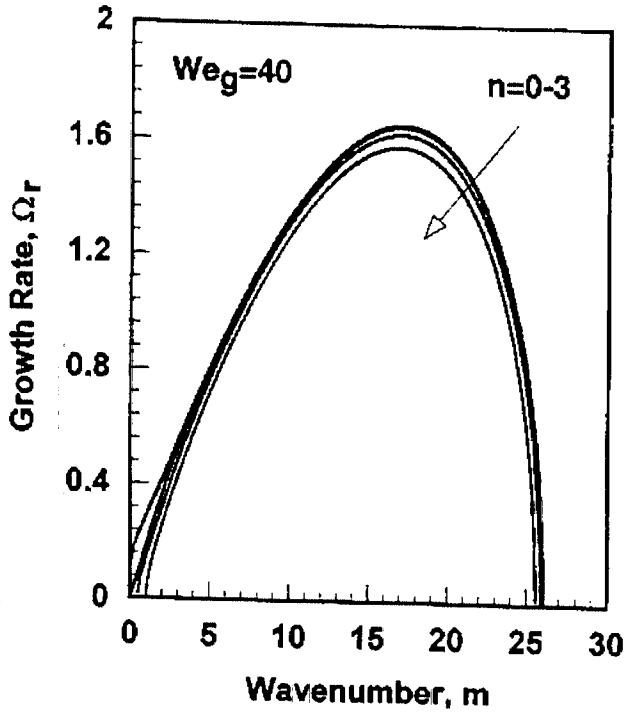

Need for microgravity

- Significant buoyancy effect on ground

- Air jet injected into water through 2 mm tube

  Velocity = 1 m/s $We_g = 0.017$ Fr = 0.12 (on ground)

  Velocity = 10 m/s $We_g = 1.7$ Fr = 12 (on ground)

  Low We and high Fr achieved in microgravity,

  NASA 2.2 second drop tower

- Problems with liquid hydrostatic pressure eliminated

Experimental Set-up

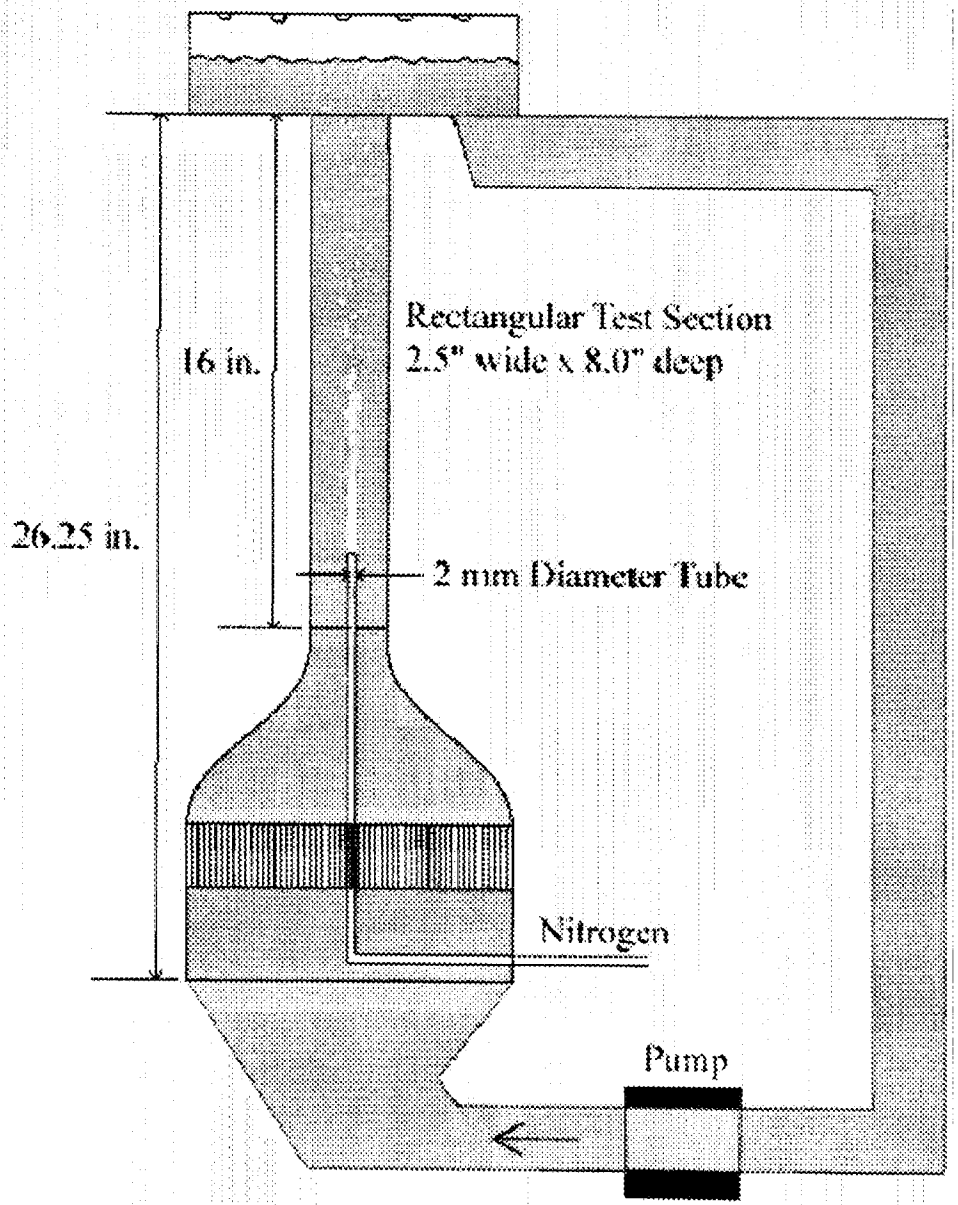

NASA MICROGRAVITY FLUID PHYSICS
UNIVERSITY OF OKLAHOMA

NASA/CP—2000-210470

PLAN

Experiments

- Ground-based and drop tower
- Image gas-liquid interface
- Document instability characteristics for various flow parameters

Theory

- Absolute vs Convective instability
- Non-linear stability analysis

FLUID PHYSICS AND MACROMOLECULAR CRYSTAL GROWTH IN MICROGRAVITY

M. Pusey, E. Snell, R. Judge,
NASA Laboratory for Structural Biology, Code SD48, MSFC, Huntsville, AL 35812, USA.

N. Chayen,
Division of Biomedical Sciences, Imperial College of Science Technology and Medicine, London, SW7 2AZ, UK.

T. Boggon, & J. Helliwell,
Chemistry Department, University of Manchester, Oxford Road, Manchester, M13 9PL, UK.

ABSTRACT

The molecular structure of biological macromolecules is important in understanding how these molecules work and has direct application to rational drug design for new medicines and for the improvement and development of industrial enzymes. In order to obtain the molecular structure, large, well formed, single macromolecule crystals are required. The growth of macromolecule crystals is a difficult task and is often hampered on the ground by fluid flows that result from the interaction of gravity with the crystal growth process.

One such effect is the bulk movement of the crystal through the fluid due to sedimentation. A second is buoyancy driven convection close to the crystal surface. On the ground the crystallization process itself induces both of these flows. Buoyancy driven convection results from density differences between the bulk solution and fluid close to the crystal surface which has been depleted of macromolecules due to crystal growth. Figure 1 is a Schlieren photograph of a growing lysozyme crystal illustrating a 'growth plume' resulting from buoyancy driven convection. Both sedimentation and buoyancy driven convection have a negative effect on crystal growth and microgravity is seen as a way to both greatly reduce sedimentation and provide greater stability for 'depletion zones' around growing crystals. Some current crystal growth hardware however such as those based on a vapor diffusion techniques, may also be introducing unwanted Marangoni convection which becomes more pronounced in microgravity (Chayen et al.1997). Negative effects of g-jitter on crystal growth have also been observed (Snell et al. 1997).

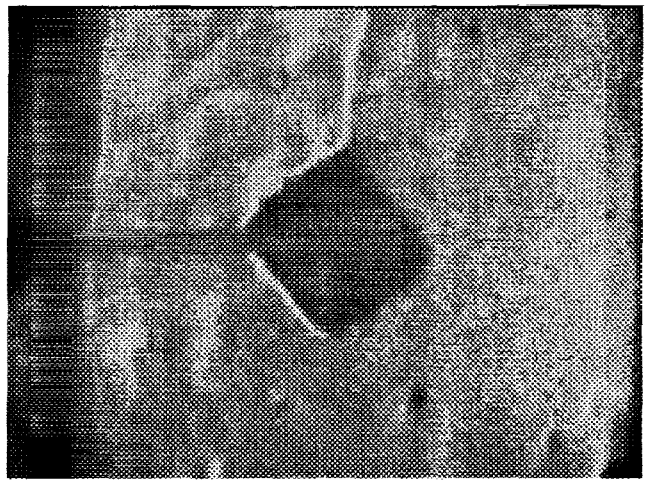

Figure 1. Buoyancy driven convection observed during lysozyme crystal growth.

To study the magnitude of fluid flows around growing crystals we have attached a number of different fluorescent probes to lysozyme molecules. At low concentrations, <40% of the total protein, the probes do not appear to effect the crystal growth process (Figure 2). By using these probes we expect to determine not only the effect of induced flows due to crystal growth hardware design but also hope to optimize crystallization hardware so that destructive flows are minimized both on the ground and in microgravity.

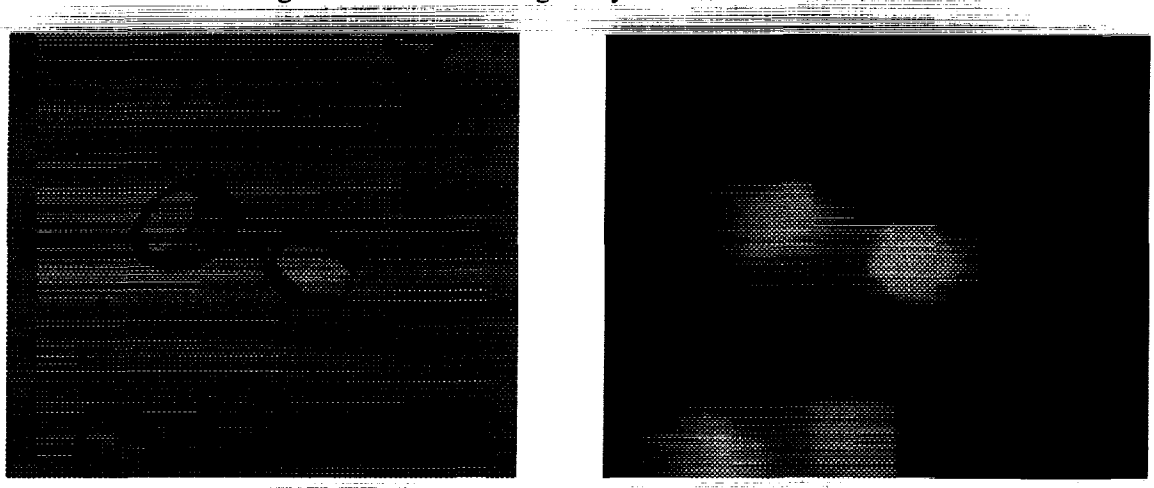

Figure 2. Two photographs showing fluorescently tagged lysozyme (an enzyme that prevents bacterial infection) crystals under white light (left) and UV light (right). These are identical in morphology to untagged samples.

REFERENCES

Chayen, N.E., Snell, E.H., Helliwell, J.R. & Zagalsky, P.F. CCD video observation of microgravity crystallization of apocrustacyanin C1. J. Cryst. Growth 171 (1997) 219-225.

Snell, E.H., Boggon, T.J., Helliwell, J.R., Moskowitz, M.E. & Nadarajah, A. CCD video observation of microgravity crystallization of lysozyme and correlation with accelerometer data. Acta Cryst. D53 (1997), 747-755.

Presentation not available at time of printing.

ELECTROHYDRODYNAMIC FLOWS IN ELECTROCHEMICAL SYSYTEMS

D. A. Saville
Department of Chemical Engineering
Princeton University, Princeton NJ

ABSTRACT

Recent studies disclose that electrohydrodynamic flow is often present in electrochemical systems. Nevertheless, our understanding of electrohydrodynamics (EHD) is largely confined to situations involving fluid interfaces with apolar liquids or electrokinetics in aqueous systems. Neither addresses events involving electrodes. This work centers on this new class of flows – electrohydrodynamic motion in systems with electrochemical reactions

Experiments on well-characterized systems are proposed along with theoretical work on the relevant model equations. In addition to their scientific value, the results will have technological applications since they provide insight into ways of controlling small-scale fluid motion* – EHD pumping or patterning, for example.

A two-part program is envisioned. In the experimental part, flows in the region between two electrodes will be studied with homogeneous and patterned electrodes. With homogeneous electrodes, motions arising from electrohydrodynamic instabilities will be investigated. With patterned electrodes, flow is engendered by lateral current inhomogenities on an electrode. Because currents are low and the cells thin, buoyancy driven convection is weak and the experimental set-up is relatively simple. Flow visualization techniques will be used to image the flows. Preliminary experiments to establish the feasibility of the approach have been completed.

A parallel component of the program involves solving the relevant equations to describe: (i) the hydrodynamic stability of the homogeneous electrode configuration and (ii) the flow structure in a patterned electrode set-up. Because the model equations are "stiff" a new methodology is proposed to handle matters in the thin layers near the electrodes. The technique is based on well-tested ideas used effectively in electrokinetics. It promises to simplify the numerical work considerably.

Results from the two parts complement one another and provide a definitive test of electrohydrodynamic models, especially the roles of current and charge induced near electrodes. Since the experimental set-up is simple, flow visualization will provide qualitative and quantitative tests of the theory.

*See "Downsizing Chemistry" by M. Freemantle in *Chemical & Engineering News,* February 22, 1999 **77** pp. 27-36 or "Microfluidics – a review" by P. Gravesen, J.

Branebjerg, & O.S. Jensen *J. Micromech.Microeng.* **3** 168-82 (1993) for a discussion of applications to miniaturizing chemical processes with microfluidic systems.

Electrohydrodynamics offers exciting possibilities for applications. For example, electroconvection can be used in deposition-patterning processes. Since ITO is a semi-conductor photochemical/photo electric effects enhance some electrochemical processes. Accordingly, electrohydrodynamic flows present in colloidal deposition can be modulated by UV light. The figure shows a recent example [Hayward, Saville & Aksay "Electrophoretic assembly of colloidal crystals with optically tunable micropatterns" *Nature* **405** 56-59, 2000].

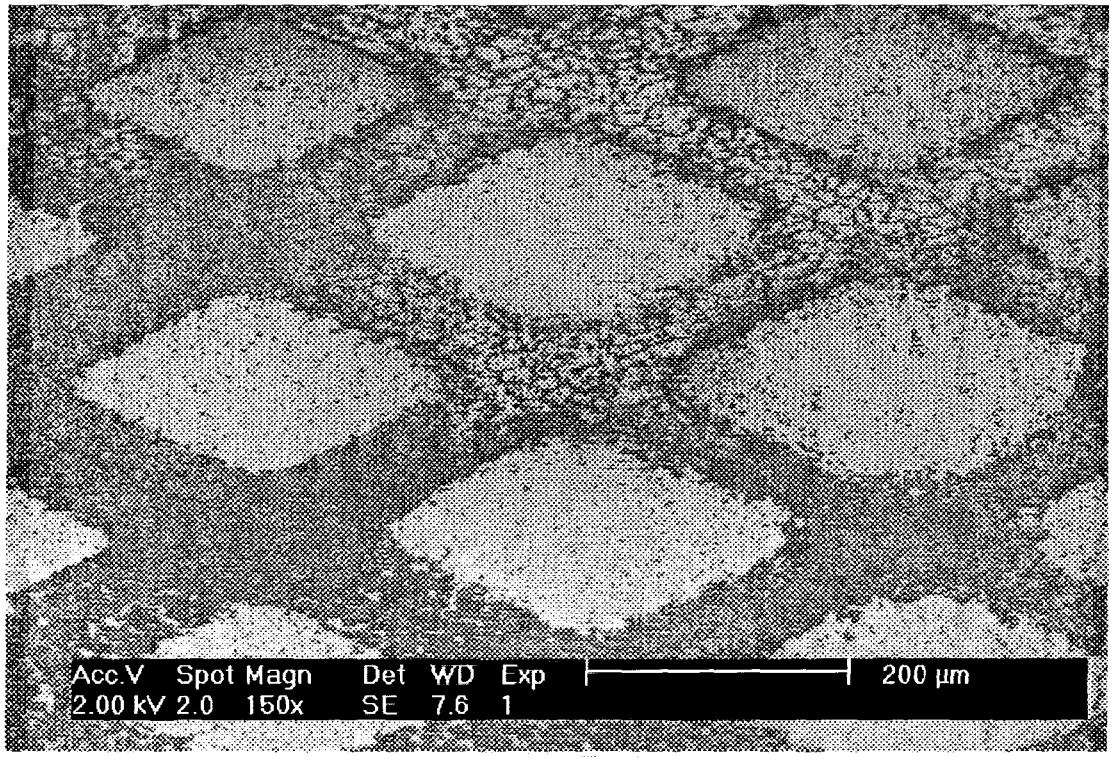

An SEM image of an ITO electrode with a pattern of colloidal crystals (intersecting stripes) induced by the interaction of UV light with the semi-conductor surface during electrodeposition. A mask was used to filter UV light from the diamond-shaped regions to alter the deposition and assembly processes. These regions are almost entirely free of colloidal particles having been swept clear by an electrohydrodynamic flow. The intersecting stripes are polycrystalline. The density of the crystal images varies from point to point due to the density of particles and SEM imaging processes.

NASA/CP—2000-210470

Department of Chemical Engineering
Princeton Center for Complex Materials - Princeton University

Electrohydrodynamic Flows In Electrochemical Systems

D. A. Saville

NAG3-2380

March 2000 - November 2003

NASA/CP—2000-210470

Department of Chemical Engineering
Princeton Center for Complex Materials - Princeton University

BACKGROUND

Our current understanding of electrohydrodynamics centers on motions in apolar liquids - usually involving sharp interfaces - or electrokinetic effects such as electro-osmosis in aqueous systems. For example, electro-osmotic pumping in small capillaries relies on the equilibrium charge derived from the chemistry of the solid-liquid interface. A new class of electrically driven flows has recently come to the fore – some associated with current flow across membranes, others associated with electrodeposition or electrolysis. These differ from the familiar examples in that the electrical body force is associated with current from an electrode. In "electro-chemical pumping" one might provide much more flexibility by modulating the charge in the solution with current crossing the electrode-solution interface. A coordinated program of experiments and modeling in well-defined geometries is proposed .

Background:

Downsizing Chemistry by M. Freemantle
Chemical & Engineering News, February 22, 1999 77 pp. 27-36.

Microfluidics by P. Gravesen, J. Branebjerg, & O.S. Jensen
J. Micromech.Microeng. 3 168-82 (1993).

NASA/CP—2000-210470

Objective:

To provide a broad picture of electrohydrodynamics in thin cells.

By examining processes near a uniform electrode, we will establish the conditions for the appearance of motion due to electrohydrodynamic instabilities. Studies with patterned electrodes will elucidate the structure of steady flows. Experiments with thin cells will provide a test of the theoretical model and insight into how "stirring" influences electrochemical processes. Studying patterned or segmented electrodes will provide another test, along with information on the design of electrodes for manipulating fluids in specified ways. Both aqueous and non-aqueous systems will be investigated. Our work is motivated in part by the results reported in a recent paper in *Nature.*

Department of Chemical Engineering
Princeton Center for Complex Materials - Princeton University

Electrophoretic assembly of colloidal crystals with optically tunable micropatterns

R. C. Hayward, D. A. Saville & I. A. Aksay
Nature 405 56-59 (2000).

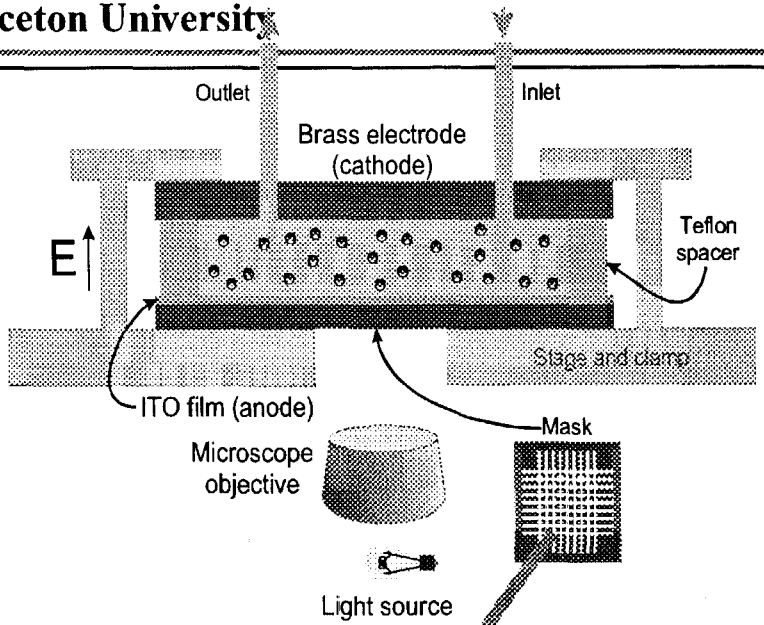

Patterned electrode flow pattern (postulated)

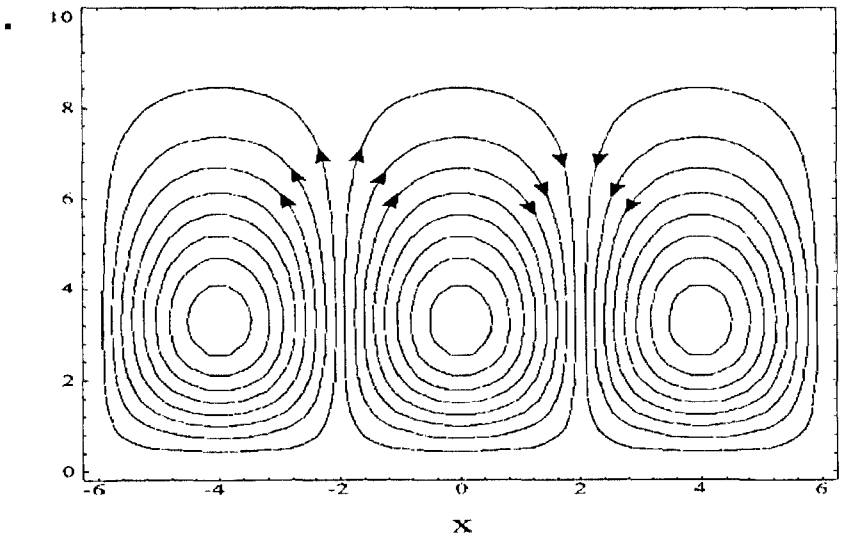

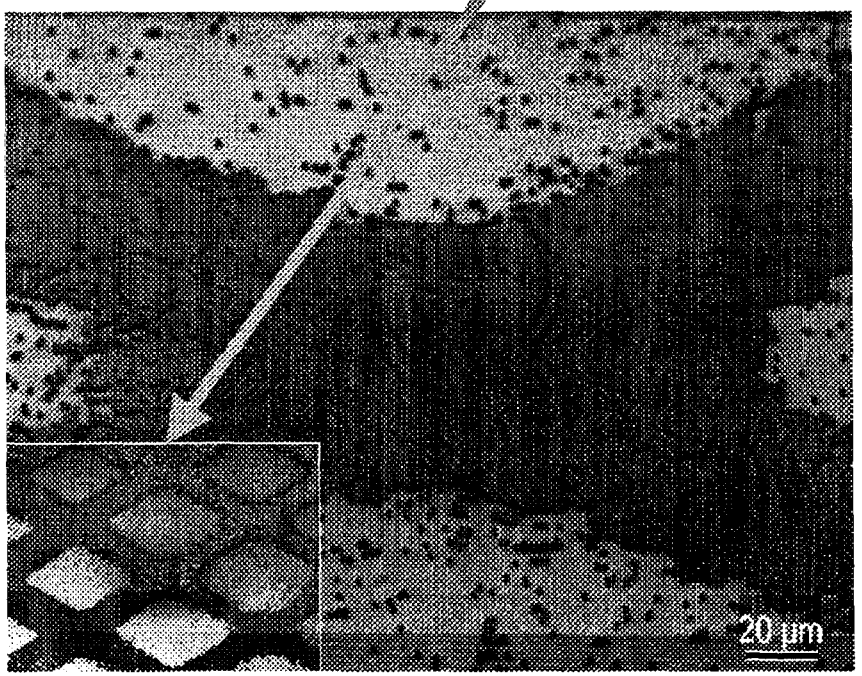

Current Problems Under Study -

- Electrophoretic Deposition of Colloidal Particles
  Provides insight into flow processes in an 'interesting' system.
- Electrohydrodynamic Stability of a Thin Layer
  Provides a tractable system to study the coupling between electrochemistry and fluid mechanics.
- Flow Near a 'Patterned' Electrode
  Provides insight into the coupling between electrode current patterns and flow.

Department of Chemical Engineering
Princeton Center for Complex Materials - Princeton University

Recent Work - Electrohydrodynamic Stability of a Thin Layer

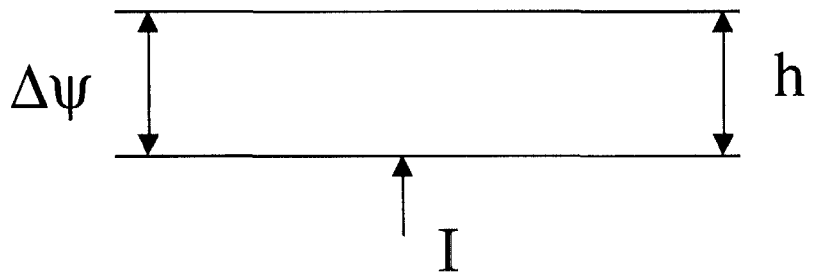

Parameters:

Dimensionless current, $I\ (\Delta\psi)$; Wavenumber, $2\pi h/\lambda$

$$\kappa h = \sqrt{\frac{e^2 \sum n_i^{\infty} z_i^2}{\varepsilon \varepsilon_o k_B T}}\, h \qquad Pe = \frac{\varepsilon \varepsilon_o}{\mu D}\left(\frac{k_B T}{e}\right)^2 \approx 0.5$$

M. E. Buchanan

NASA/CP—2000-210470

Results:

1. Electroneutral models (no diffuse layers) are always stable. This is contrary to extensive calculations by:

   I.Rubinstein, T. Zaltzman, & B. Zaltzman, *Phys. of Fluids* 7 11467-82 (1995).

   B. Zaltzman, B. *Phys. of Fluids* 8 936-43 (1996).

2. Instability occurs at currents well below the limiting value (I= 2) with diffuse layers. Previous (incorrect) studies indicated instability only at or near the limiting current.

3. The presence or absence of an instability is (not surprisingly) very sensitive to the electrochemical boundary conditions.

Department of Chemical Engineering
Princeton Center for Complex Materials - Princeton University

Stability diagram with vanishing ion concentration gradients at the boundaries.

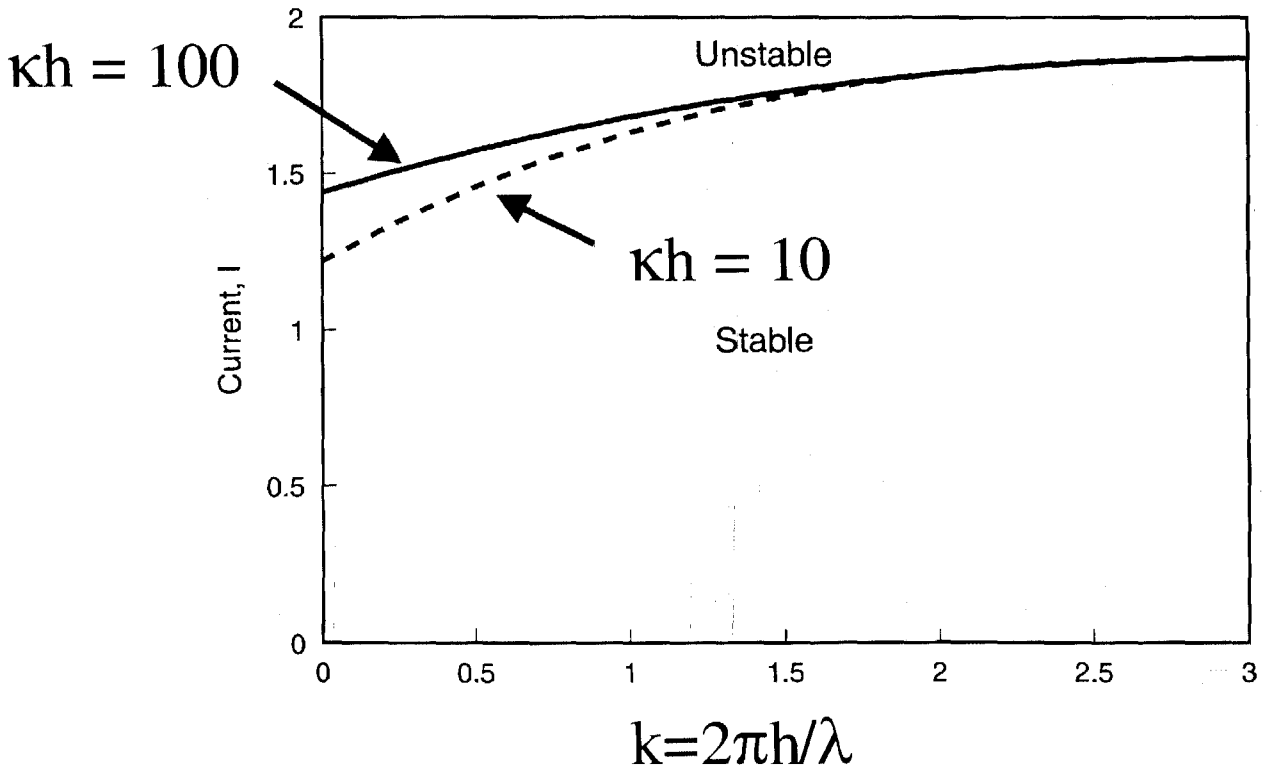

Department of Chemical Engineering
Princeton Center for Complex Materials - Princeton University

Stability diagram with vanishing ion fluxes due to electrical forces at the boundaries

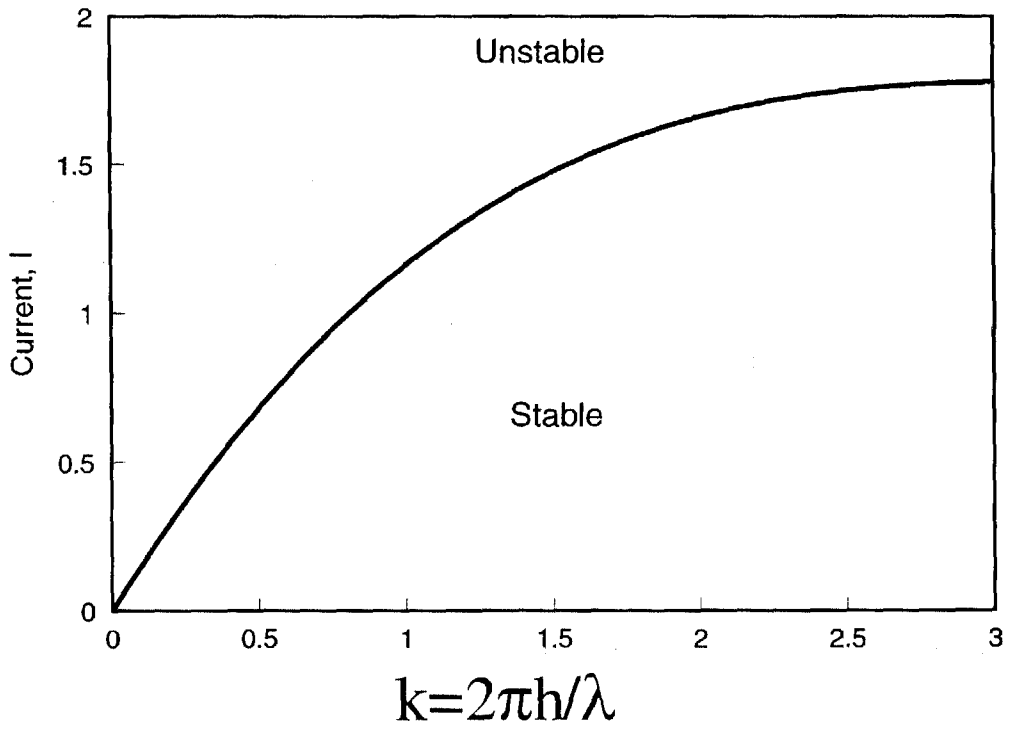

$$k=2\pi h/\lambda$$

A summary of progress to date:

- The theory of hydrodynamic stability for a thin electrolyte layer supporting a current has been completed. Current efforts focus on extending the theory to predict the structure of steady flows near patterned electrodes.

- Experimental studies of the flow near electrodes, including effects of mechanical and optical patterning have been initiated.

COMPETING HARMONIC AND SUBHARMONIC INSTABILITIES AND PARAMETRICALLY EXCITED SURFACE WAVE PATTERNS

M. Silber and C.M. Topaz, Northwestern University

Standing wave patterns may be parametrically excited on the free surface of a fluid layer when the gravitational acceleration is periodically modulated. In the classic Faraday wave experiment sinusoidal forcing is employed, leading to excitation of subharmonic standing waves. However, over the last decade, it has been demonstrated that harmonic response is also possible; for example, when two-frequency periodic forcing is used [1], or when the fluid layer is sufficiently thin [2], or for certain viscoelastic fluids [3]. For each of these systems it is possible to tune the periodic forcing function in order to access a transition between harmonic and subharmonic response. At the bicritical point, both instabilities set in simultaneously but with different spatial wavenumbers. Near this codimension-two point, a variety of unusual patterns have been observed, including quasipatterns [1] and superlattice patterns [4, 5]. Superlattice patterns have also been observed recently in Rayleigh Bénard convection subjected to vibration, near the harmonic/subharmonic transition point [6].

Much of the theoretical work on the Faraday wave pattern formation problem has focused on the role that resonant triads play in the pattern selection process (see for example [7]). Resonant triads are comprised of three critical wave vectors $\mathbf{k}_1$, $\mathbf{k}_2$, and $\mathbf{k}_3 = \mathbf{k}_1 \pm \mathbf{k}_2$, where $|\mathbf{k}_1| = |\mathbf{k}_2|$ is the wavenumber of one critical mode and $|\mathbf{k}_3|$ is the wavenumber of the other critical mode. Associated with each resonant triad is an angle θ_r which separates the two wave vectors of equal magnitude; two examples are given in Figure 1.

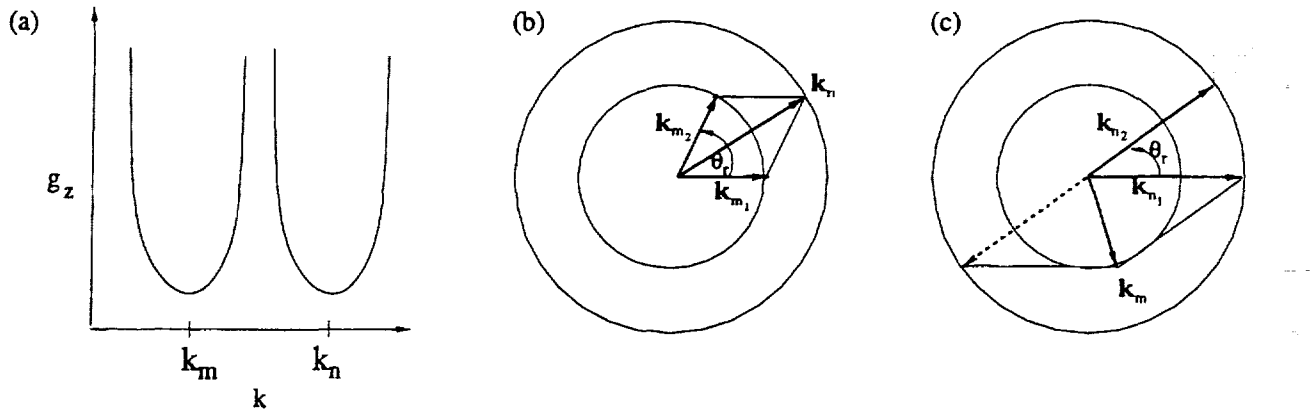

Figure 1: (a) A schematic neutral stability curve $g_z(k)$ showing the forcing amplitude g_z at which the flat fluid surface first becomes unstable to perturbations of wavenumber k. The curve represents a bicritical situation. (b) An associated spatially resonant triad $\mathbf{k}_{m_1}$, $\mathbf{k}_{m_2}$ and $\mathbf{k}_n = \mathbf{k}_{m_1} + \mathbf{k}_{m_2}$ with resonant angle θ_r indicated. (c) Another example of a spatially resonant triad $\mathbf{k}_{n_1}$, $\mathbf{k}_{n_2}$ and $\mathbf{k}_m = \mathbf{k}_{n_1} - \mathbf{k}_{n_2}$.

Our bifurcation analysis of the two-frequency Faraday wave problem shows that weakly damped *harmonic* modes strongly influence the pattern selection process near onset, whereas near critical *subharmonic* modes do not [8, 9]. This work reveals a surprising mechanism responsible for stabilizing the superlattice patterns observed in laboratory experiments of

Kudrolli, Pier and Gollub [4]. Specifically, our study indicates that modes associated with a harmonic resonance tongue at *small* wavenumber k_s are critical to stabilizing the observed wave patterns with onset critical wavenumber k_c, where $k_c = \sqrt{7}k_s$. The experimentally observed superlattice pattern exhibits structure on both these lengthscales. These results are based on a weakly nonlinear analysis of equations derived by Zhang and Viñals [10], which describe small amplitude surface waves on a semi-infinite weakly inviscid fluid layer. We have recently extended parts of our analysis to the full hydrodynamic equations, which apply to a layer of viscous fluid of finite thickness, and will present these results.

We are currently extending our analysis to the vibrational Rayleigh-Bénard convection problem, with the immediate goal of determining the role of Boussinesq symmetry in the pattern formation problem. We are also extending our linear analysis to Faraday waves on the interface between two immiscible fluids, and to the case of waves that are parametrically excited by a piecewise constant, periodic acceleration. Preliminary results will be presented.

References

[1] W.S. Edwards and S. Fauve. Patterns and quasi-patterns in the Faraday experiment. *J. Fluid Mech.* **278** 123–148 (1994).

[2] H.W. Müller, H. Wittmer, C. Wagner, J. Albers and K. Knorr. Analytic stability theory for Faraday waves and the observation of the harmonic surface response. *Phys. Rev. Lett.* **78** 2357–2360 (1997).

[3] C. Wagner, H.W. Müller and K. Knorr. Faraday waves on a viscoelastic liquid. *Phys. Rev. Lett.* **83** 308–311 (1999).

[4] A. Kudrolli, B. Pier and J.P. Gollub. Superlattice patterns in surface waves. *Physica D* **123** 99–111 (1998).

[5] H. Arbell and J. Fineberg. Spatial and temporal dynamics of two interacting modes in parametrically driven surface waves. *Phys. Rev. Lett.* **81** 4384–4387 (1998).

[6] J.L. Rogers, M.F. Schatz, J.L. Bougie and J.B. Swift. Rayleigh-Bénard convection in a vertically oscillated fluid layer. *Phys. Rev. Lett.* **84** 87–90 (2000).

[7] W. Zhang and J. Viñals. Pattern formation in weakly damped parametric surface waves driven by two frequency components. *J. Fluid Mech.* **341** 225–244 (1997).

[8] M. Silber and A.C. Skeldon. Parametrically excited surface waves: two-frequency forcing, normal form symmetries, and pattern selection. *Phys. Rev. E* **59** 5446–5456 (1999).

[9] M. Silber, C.M. Topaz and A.C. Skeldon. Two–frequency forced Faraday waves: weakly damped modes and pattern selection. *Physica D* in press (2000).

[10] W. Zhang and J. Viñals. Pattern formation in weakly damped parametric surface waves. *J. Fluid Mech.* **336** 301 (1997).

Presentation not available at time of printing.

Dynamics and Stability of Liquid Bridges

J. Iwan D. Alexander, Lev A Slobozhanin*, Andrew H. Resnick†
Department of Mechanical and Aerospace Engineering and National Center for Microgravity Research on Fluids and Combustion,
*Center for Microgravity and Materials Research, University of Alabama in Huntsville,
Federal Data Corporation, Brook Park, Ohio

Abstract

Liquid bridges are liquid volumes that are held, by surface tension, between two or more rigid supports. They occur in a variety of natural and technological processes ranging from the float-zone crystal growth technique to porous media flow and are important in situations as diverse as low-gravity fluids management and fluid behavior in microairways during respiration. In this work we have examined the dynamical behavior and stability of a variety of liquid bridge configurations with emphasis on bridges that are held between coaxial circular supports, although liquid configurations in partially filled containers are also considered. The poster presentation will summarize our experimental, theoretical and numerical work on the stability and dynamics of liquid bridges, with particular emphasis on nonaxisymmetric bridges and axisymmetric bridge configurations that lose stability to nonaxisymmetric perturbations.

Presentation not available at time of printing.

DROPLET FORMATION BY VORTEX RINGS

Choongil Kim & Luis P. Bernal
Department of Aerospace Engineering
University of Michigan
Ann Arbor, MI 48109-2140

ABSTRACT

An experimental investigation of droplet formation by vortex rings impinging normal to a liquid/air or a liquid/liquid interface has been conducted.[1-4] Experiments included microgravity drop tower tests and 1-G tests to determine the effect of Weber number, Reynolds number, as well as density ratio, and viscosity ratio on the interaction. Microgravity is an ideal environment to experimentally study the dynamics of fluid interfaces. Of particular interest is the dynamics of droplet formation by vortical flows under surface tension controlled dynamics. These flow phenomena arise in a wide variety of engineering problems both in space systems and on Earth. For example, liquid atomization is an important component of many systems including: aerosol generators for drug delivery, fuel injectors, paint sprays, and inkjet printers. In these applications surface tension is the dominant stabilizing force of the liquid interface because the drop size is very small. In microgravity, these flow processes can be studied at much larger scale which facilitates experimental observation. The interaction of a vortex ring with the interface between immiscible fluids is a relatively simple flow configuration where the phenomena of liquid breakup and droplet formation can be studied in controlled experiments.

The microgravity experiments were conducted in the 2.2 *s* drop tower at NASA Glenn Research Center. The drop tower rig was equipped with a fluid test cell (15 *cm* × 15 *cm* × 300 *cm*) and a piston-type vortex ring generator attached to the bottom of the test cell. The piston diameter is 1.9 *cm*. The fluid interface was stabilized with a knife-edge. The flow was visualized using flat panel light source and a standard format video camera. For the drop tower experiments a control box detects the release of the drop tower rig and initiates the vortex ring motion and timing lights shown in all the video recordings. The 1-G experiments were conducted in the same rig.

One of the main focus of the research is to determine the effects of density and viscosity ratio.[4] The tests results show two very distinct behaviors. At very small density and viscosity ratio, for a gas/liquid interface ratio, the interaction results in a long liquid column that breaks into one or more small droplets at both ends of the column as illustrated in Figure 1. The diameter of the droplets is significantly less than the initial vortex ring diameter. In this case change of the liquid viscosity does not change the flow evolution significantly. In contrast, for a density ratio of order one, i.e. liquids of matched density, the vortex ring propagates through the interface and forms a droplet and smaller secondary droplets as illustrated in Figure 2. The droplet shape is approximately spherical and, the dye patterns inside the droplet indicate that the fluid inside the droplet carries some vorticity from the initial vortex ring. For density ratio of order one, the effect of viscosity ratio is to change the size and structure of the liquid column during droplet formation and the number and size of satellite droplets formed. These effects are characterized in terms of the Ohnesorge number defined as $Oh = \mu_l/(\rho_l \sigma D)^{0.5}$. As the Ohnesorge number is increased, the liquid column thickness becomes thinner and the duration of lower fluid column within the upper layer fluid is shorter as shown in Figures 3 and 4. These results suggest that density and viscosity ratio effects are more important than previously recognized in computational and experimental studies of multiphase flows.

REFERENCES

[1] L.P. Bernal, P. Maksimovic, F. Tounsi & G. Tryggvason. "An experimental and numerical investigation of drop formation by vortical flows in microgravity." AIAA paper 94-0244, AIAA 32nd Aerospace Sciences Meeting & Exhibit. Reno, NV. January 10-13, 1994.

[2] L.P. Bernal & P. Maksimovic. "The propagation of a vortex ring through multiple liquid interfaces in microgravity." AIAA paper 96-0593, AIAA 34th Aerospace Sciences Meeting & Exhibit. Reno, NV. January 15-18, 1996.

[3] L.P. Bernal & P. Maksimovic. "Velocity field measurements during drop formation by vortical flows in microgravity." AIAA paper 98-0734, AIAA 36th Aerospace Sciences Meeting & Exhibit. Reno, NV. January 12-15, 1996.

[4] C. Kim & Luis P. Bernal. "Density and Viscosity Ratio Effects in Droplet Formation." AIAA paper 00-0855, AIAA 38th Aerospace Sciences Meeting & Exhibit. Reno, NV. January 10-13, 2000.

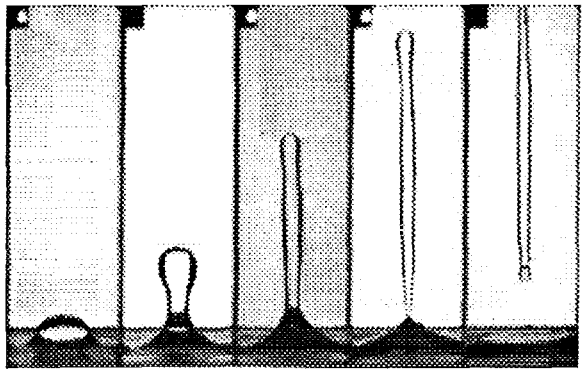

Figure 1. Top layer: Air – Bottom layer: Silicon Oil (2 *cS*) at μ-G conditions, ρ_2/ρ_1 = 0.00143, μ_2/μ_1 = 0.01, Re 4720, We 220, Oh 0.003, Δt 0.17 *sec.*

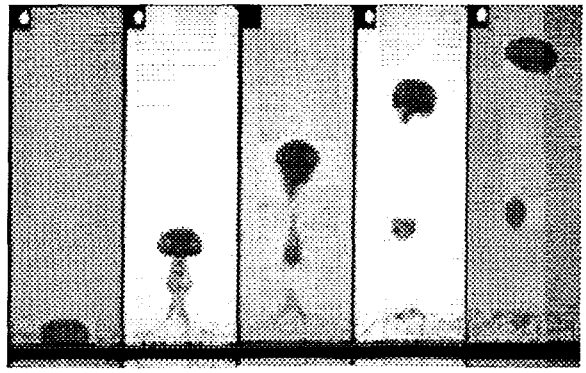

Figure 2. Top layer: Silicon Oil (2 *cS*) – Bottom layer: Glycerol/Water solution at μ-G conditions, ρ_2/ρ_1 = 0.785, μ_2/μ_1 = 0.39, Re 4800, Δt 0.17 *sec.*

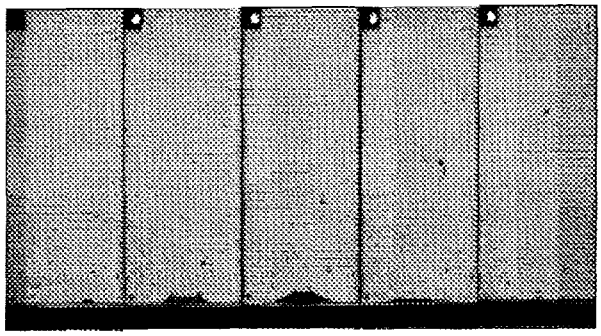

Figure 3. Top layer: Methanol/Water solution, Bottom layer: Silicon Oil (10 *cS*). ρ_2/ρ_1 = 0.973, μ_2/μ_1 = 0.186, Re 616, We 210, Oh 0.0232, Bo 9.66, Fr 21, Δt 0.22 *sec.* 1-G Experiment.

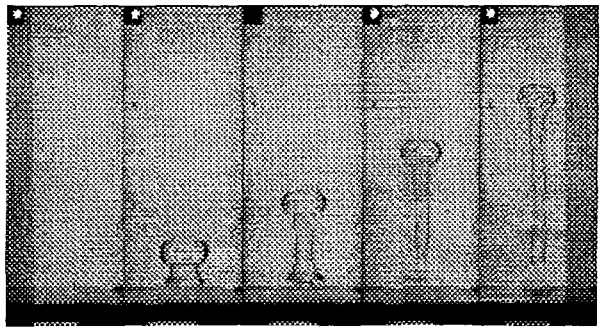

Figure 4. Top layer: Silicon Oil (10 *cS*), Bottom layer: Water, ρ_2/ρ_1 = 0.94, μ_2/μ_1 = 7.19, Re 7300, We 190, Oh 0.00172, Bo 7.09, Fr 23, Δt 0.22 *sec.* 1-G Experiment.

Presentation not available at time of printing.

THERMOPHORETIC FORCE MEASUREMENTS ON SINGLE SPHERICAL AND NONSPHERICAL PARTICLES

E. James Davis, Feng Zheng
University of Washington, Department of Chemical Engineering

ABSTRACT

Thermophoretic forces (TF) play important roles in many areas including microparticle transport phenomena under microgravity conditions. However, to our knowledge no experimental study has been done on the dependence of thermophoretic force on particle shape. We have measured the thermophoretic force on two- and three-sphere aggregates, as well as single spheres of polystyrene latex (PSL) particles in nitrogen gas in the transition regime (Knudsen number 0.1 to 10). Our data indicate that particle aggregation may be accelerated by thermophoresis.

Wang and Davis [1][2] have successfully used an electrodynamic balance (EDB) to measure the thermophoretic force on single microsphere particles. In an EDB a vertical dc field cancels the gravitational force on a particle and the thermophoretic force is measured in terms of this dc voltage. Another superimposed ac field keeps the levitated particle stable. However, there are two challenges in using an EDB to measure thermophoretic forces. One is to keep trapped particles stable at the very low ac voltage that is necessary to avoid gas glow discharge at reduced pressure. The other is to determine the size and mass of the single particles, especially non-spherical ones, accurately in order to interpret the data.

Particle stability was improved by adding two independent dc fields in the radial direction with a new octuple double-ring design for the EDB electrodes, as shown in Fig. 1. A conventional double-ring EDB was modified by splitting each ring into four equal electrically independent sections. Three dc sources were combined such that eight potentials were applied to the eight sections of the electrodes. An additional ac voltage was superimposed on each ring section as in the conventional double-ring EDB. The resulting electric field has dc components in the x, y and z-directions, which can be controlled independently by the three dc supplies. The z component is equivalent to the dc field in the conventional EDB and can be used to balance and measure any vertical force such as gravity. The x and y fields can be used to suppress radial oscillations of the trapped particles that arise due to gas convection or distortion of the electric field by the view ports in the chamber walls.

The aerodynamic size of the trapped particles can be determined by a stable oscillation technique that we have developed previously [3]. This technique involves partially balancing the particle against gravity and allowing the particle to oscillate in the ac field. The oscillation trajectories are recorded with a fast linescan camera and are fit to the solutions of the particle equation of motion. With the aid of a video microscopy system the shape and orientation of the particle with respect to the electric field is determined. The geometric dimensions and mass of the particles can be calculated from the aerodynamic size, the shape and the orientation with the knowledge of particle density. Using this method we were able to determine the size and mass of PSL particles of two- and three-sphere aggregates.

We have measured the thermophoretic force on these PSL aggregates in nitrogen gas in the Knudsen regime. The thermophoretic force data, as well as particle shapes and equivalent volume diameters, are shown in Fig. 2. At a Knudsen number of one, the normalized thermophoretic force on the two- and three-sphere aggregate is, respectively, 23% and 10% greater than that on a single sphere. This implies that two- and three-sphere aggregates drift faster due to thermophoresis than single spheres. Once aggregate particles form there may be a positive feedback mechanism for more aggregation due to the higher mobility of the aggregate spheres.

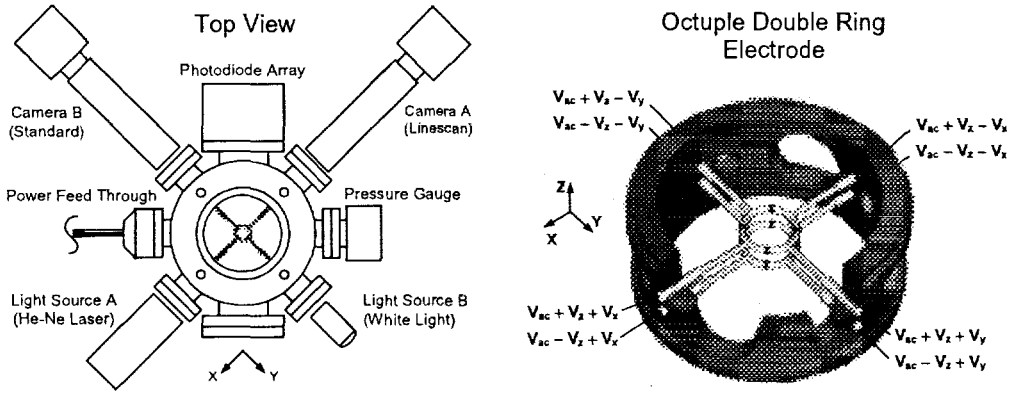

Fig. 1 Thermophoresis electrodynamic balance

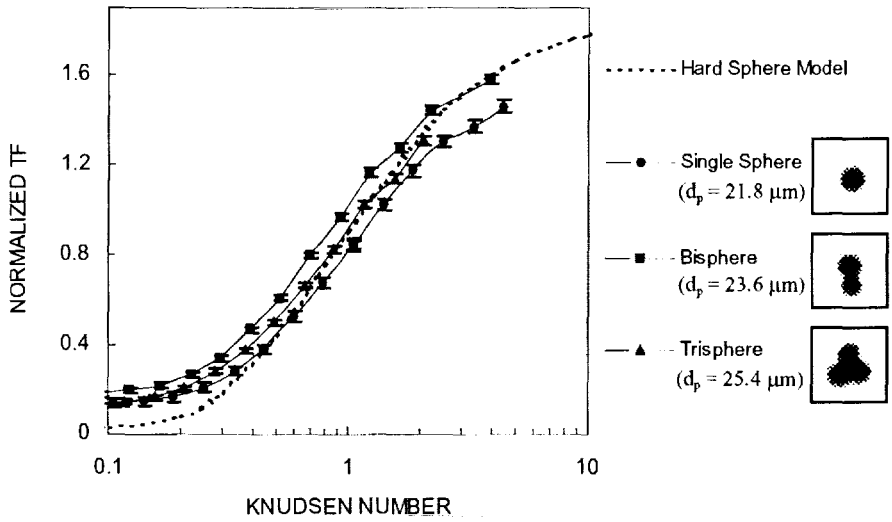

Fig. 2 Thermophoretic force on PSL sphere aggregates in nitrogen gas

REFERENCES

[1] Li, W. and Davis, E. J. (1995a) *J. Aerosol Sci.* **26**, 1063-1083.
[2] Li, W. and Davis, E. J. (1995b) *J. Aerosol Sci.* **26**, 1085-1099.
[3] Zheng, F., Laucks, M. L., and Davis, E. J. (2000) *J. Aerosol Sci.* in press.

Presentation not available at time of printing.

CAPILLARY INSTABILITES IN THE MICROGRAVITY ENVIRONMENT

James B. Grotberg and Steven W. Benintendi
Biomedical Engineering Department
University of Michigan
Ann Arbor, MI 48109

David Halpern
Department of Mathematics
University of Alabama
Tuscaloosa AL 35487

ABSTRACT

The lung is comprised of a network of bifurcating airway tubes which are coated with a thin viscous film. Often times, especially in the case of disease, the liquid film can form a meniscus which fills the whole tube, thus obstructing airflow. The formation of the liquid meniscus is due to capillary driven instabilities which can arise in the lining, causing the lining to close up. In addition, airflow can also be obstructed if the airway tube collapses in on itself. This occurs when the elastic forces of the tube are not large enough to sustain the negative fluid pressures inside the tube caused by surface-tension, and the tube collapses. In both cases, the instability is dependent on the surface tension of the liquid lining. In normal gravity, airway closure occurs at the end of a forced expiration as a normal event even in health lungs. The amount of air remaining in the lungs when this happens is called the closing volume. Fortunately, because of gravity the closure process tends to occur in the lower regions of the lung, due to the weight of the tissue above. In microgravity, it is likely that closure occurs more homogeneously and thus exposes the lung to potential risks. Once the airway is closed, it then must be reopened, usually this is done by taking a deep breath which forces the liquid plug to move and deposit its volume onto a trailing film.

There are other important issues regarding airway closure which relate to pulmonary disease. For example, premature babies, whose lungs have not developed sufficient surfactant to maintain the surface tension of the lung at a sufficiently low level for healthy functioning, are especially predisposed to problems caused by airway closure. In such cases, the patients are sometimes put on high frequency ventilation machines to improve oxygenation. The frequency of the breathing cycle, as well as the tidal volume, are two control parameters at the disposal of the clinician. Little is known, however, of the effect that these two parameters can have on the occurrence of airway closure. Indeed, if airways can be kept open by using some given imposed frequency, then this would important in the treatment of such patients. In addition to medical applications, the general topic of multiphase flows over flexible boundaries is important for a number of technical fields including flows in poroelastic media.

We have investigated the closure phenomenon in flexible tubes in the past. Recently, we developed a theoretical model of perturbed airway closure to study the effects of forced oscillatory air flow on the closure phenomenon. It consists of a single rigid tube coated with a thin viscous

layer. To examine the stability of the layer, we derived an evolution equation for the position of the interface. An oscillatory shear stress was imposed at the interface to simulate the effect of the core airflow. This was derived from an uncoupled problem since the core airflow perceives the film as a rigid boundary. Results from numerical solutions of the evolution equation show the shear stress from the core-flow can saturate the capillary instability and that there is a critical film thickness, dependent on the amplitude and frequency of the airflow, below which closure does not occur. This thickness is larger than the unperturbed critical film thickness. An example of the results is in Figure 1.

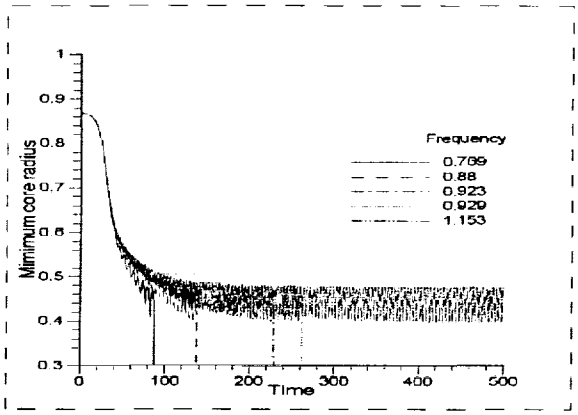

Figure 1. Minimum core radius vs time, for various values of frequency, α. For α = 1.153 closure is prevented.

With regard to airway reopening, we have studied the propagation of a liquid plug in a tube in previous work to examine the relationship of the trailing film thickness to the driving pressure and fluid-interfacial properties. One of the interesting features of the lung airways is the sequence of bifurcations that a liquid plug encounters during inspiration. At the bifurcation is a sharp edge which may act to create an entrance effect. We have modeled the motion of a semi-infinite finger of air through a liquid filled rigid channel subject to a constant pressure gradient. The air-liquid interface is initially semi-circular, making contact with the channel walls. Using the boundary element method, we follow the evolution of the interface. After a certain period of time, dependent on the applied pressure drop, the interface tip reaches a steady state velocity, and a uniform film is deposited behind the advancing interface. In some instances, the distance traveled by the tip to reach steady state can be on the order of the length of an airway Both the tip velocity and thickness of the film increase with increasing pressure drop. Figure 2 shows an example calculation.

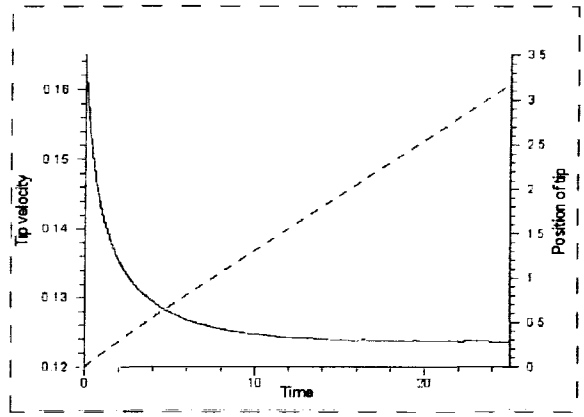

Figure 2. Tip velocity and position vs time for capillary number of 0.1, showing that it takes approximately 3.0 channel half-widths for steady state to be reached.

The delivery of a liquid bolus into the airways is also used in some medical therapies, such as surfactant replacement therapy and liquid ventilation for drug delivery.

Presentation not available at time of printing.

EXPERIMENTS ON THE RICHTMYER-MESHKOV INSTABILITY OF INCOMPRESSIBLE FLUIDS

J. Jacobs
University of Arizona

C. Niederhaus
NASA Glenn Research Center

ABSTRACT

Richtmyer-Meshkov (R-M) instability occurs when two different density fluids are impulsively accelerated in the direction normal to their nearly planar interface. The instability causes small perturbations on the interface to grow and possibly become turbulent given the proper initial conditions. R-M instability is similar to the Rayleigh-Taylor (R-T) instability, which is generated when the two fluids undergo a constant acceleration. R-M instability is a fundamental fluid instability that is important to fields ranging from astrophysics to high-speed combustion. For example, R-M instability is currently the limiting factor in achieving a net positive yield with inertial confinement fusion. The experiments described here utilize a novel technique that circumvents many of the experimental difficulties previously limiting the study of the R-M instability. A Plexiglas tank contains two unequal density liquids and is gently oscillated horizontally to produce a controlled initial fluid interface shape. The tank is mounted to a sled on a high speed, low friction linear rail system, constraining the main motion to the vertical direction. The sled is released from an initial height and falls vertically until it bounces off of a movable spring, imparting an impulsive acceleration in the upward direction. As the sled travels up and down the rails, the spring retracts out of the way, allowing the instability to evolve in freefall until impacting a shock absorber at the end of the rails. The impulsive acceleration provided to the system is measured by a piezoelectric accelerometer mounted on the tank, and a capacitive accelerometer measures the low-level drag of the bearings. Planar Laser-Induced Fluorescence is used for flow visualization, which uses an Argon ion laser to illuminate the flow and a CCD camera, mounted to the sled, to capture images of the interface.

This experimental study investigates the instability of an interface between incompressible, miscible liquids with an initial sinusoidal perturbation. The amplitude of the disturbance during the experiment is measured and compared to theory. The results show good agreement (within 10%) with linear stability theory up to nondimensional amplitude ka = 0.7 (wavenumber × amplitude). These results hold true for an initial ka (before acceleration) of $-0.7 < ka < -0.06$, while the linear theory was developed for $|ka| << 1$. In addition, a third order weakly nonlinear perturbation theory is shown to be accurate for amplitudes as large as ka = 1.3, even though the interface becomes double-valued at ka = 1.1. As time progresses, the vorticity on the interface concentrates, and the interface spirals around the alternating sign vortex centers to form a mushroom pattern (see Figure 1). At higher Reynolds Number (based on circulation), an instability of the vortex cores has been observed. While time limitations of the apparatus prevent determination of a critical Reynolds Number, the lowest Reynolds Number this vortex instability has been observed at is 5000.

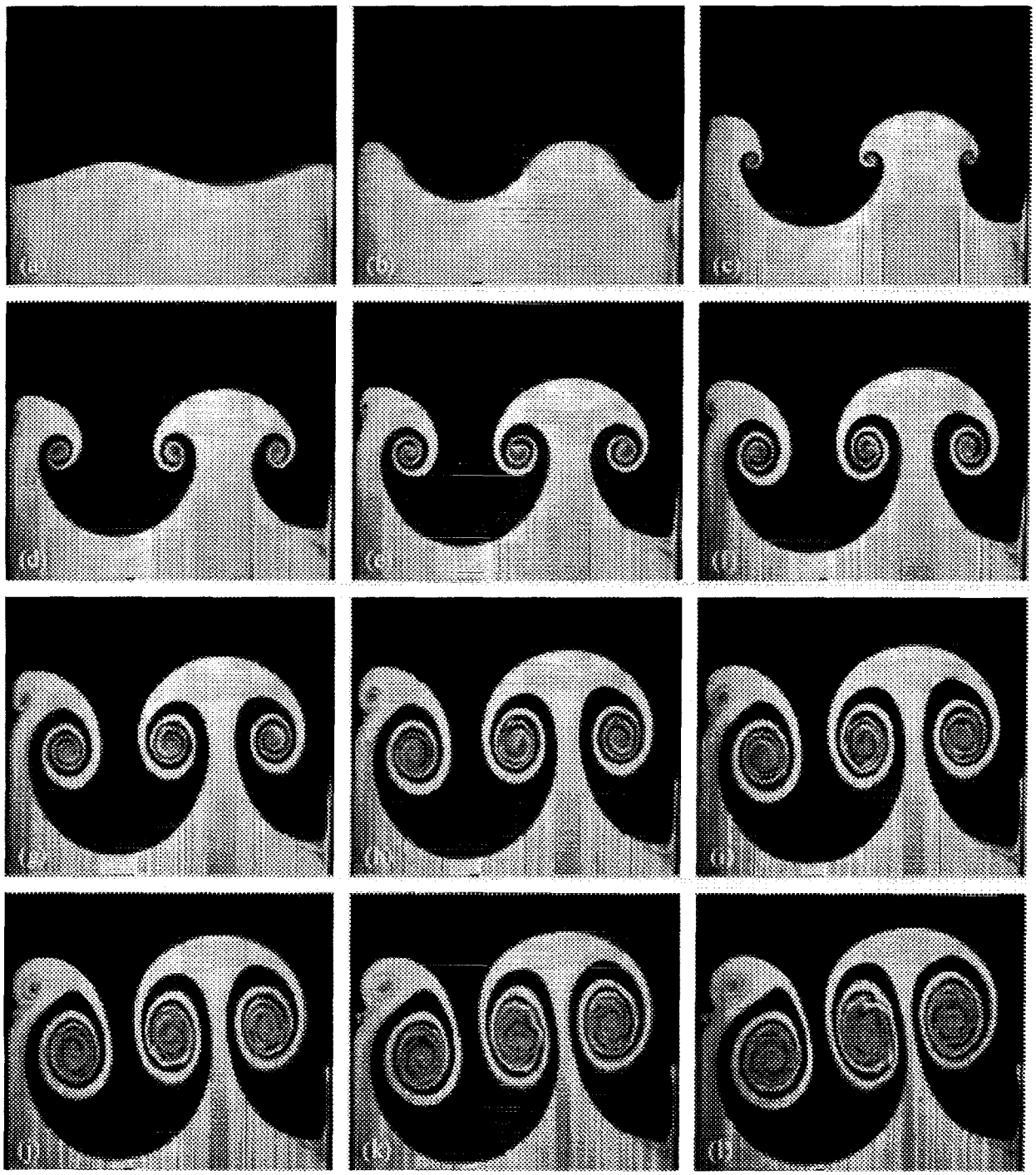

Figure 1. A sequence of images from an experiment with a Reynolds Number of 28700.

Presentation not available at time of printing.

ABSOLUTE AND CONVECTIVE INSTABILITY AND SPLITTING OF A LIQUID JET AT MICROGRAVITY

S.P. Lin, Clarkson University, Potsdam, NY 13699

ABSTRACT

Neglecting gravity and the ambient gas, Leib and Goldstein [1,2] showed theoretically that the formation of drops from a circular cylindrical liquid jet issued from a nozzle is caused by convective instability which forces the growing disturbance to propagate in the downstream direction. However, when the Weber number defined as $We \equiv \rho U^2 a/S$ (ρ, U, a and S being respectively the density, the jet velocity, the jet radius, and the surface tension) is reduced to below a critical value the convectively unstable jet becomes absolutely unstable at a given Reynolds number. The Reynolds number is defined by $Re \equiv a U\rho/\mu$, where μ is the liquid viscosity. They also obtained the critical transition Weber number as a function of Re. As $Re \rightarrow \infty$, the critical Weber number approaches the inviscid limit $We = \pi/2$. Lin and Lian [3] showed that the absolute instability still exists in the presence of ambient gas. As the density of gas is increased the transition Weber number is increased as shown in Fig. 1. The invisid limit indicated by the dashed line and the curve indicated with Q = 0 were obtained by Leib and Goldstein. Q is the ratio of the gas to the liquid density ratio. As the viscosity of the gas is increased, the transition Weber number is reduced slightly [4]. The transition from convective to absolute instability has been observed for the first time in the 2.2-sec drop tower at the NASA Glenn Research Center. Figure 2 is a photograph of a convectively unstable jet in air at We = 17.6, Re = 5.4. Figures 3(a) and 3(b) are photographs of an absolutely unstable jet. They are taken at 0.2 sec and 0.4 sec after the test rig was dropped in the tower. The upstream propagating disturbance suddenly rushed toward the nozzle tip to form a pendant while the downstream propagating disturbance grows along the thin thread of liquid downstream of the forming pendant. The transitions from convective to absolute instability at different Reynolds numbers have been observed by Vihnen, Honohan, and Lin [5]. They are shown in Fig. 4. The range of Reynolds number in this figure is quite small limited by the dimension of the drop rig and the small duration available in the tower. Experiments covering a wider range of Re will have to be carried out in other facilities. As one moves away from the transition curve toward a higher Weber number region at a given Re, the amplification rate of the disturbances become larger and the wavelength above which the disturbances can be amplified becomes shorter. When $We >> \rho_g/\rho$ a spray with droplet diameter of $O(S/\rho g U^2 a)$ is formed, where ρ_g is the gas density. It is shown theoretically that a spray cannot be formed without ρ_g. By use of the energy equation Lin and Chen [6] showed that mechanism of the drop formation is mainly due to capillary pinching but that of atomization (spray formation) is mainly due to the interfacial shear and pressure fluctuation. The disturbance which causes the drop or spray formation can be amplified at a rate k_i only in a range of frequency depending on the flow parameters. An example is shown in Fig. 5. When an external forcing of a given frequency within the range of amplification frequency is imparted on a jet, a particular Fourier mode can be selectively amplified, and the motion of the drop can be frozen in space by use of a Strobe. When the amplitude of external forcing exceeds a limit, however a jet will fork. A forking jet can be observed if twice of the forcing frequency is smaller than the cut off frequency. An example is given in Figs. 5 and 6 (Web and Lin [7]). A theoretical explanation is not yet available and the observation in μ-g is yet to be made.

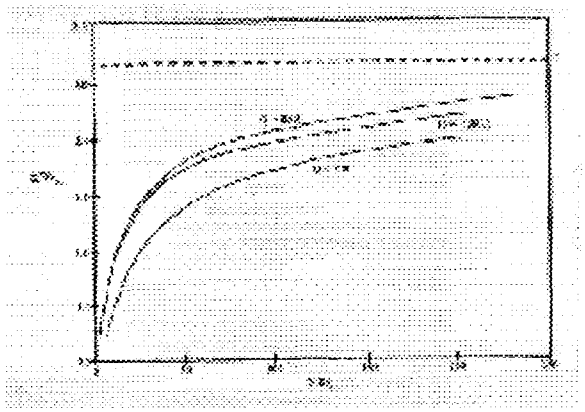

Figure 1

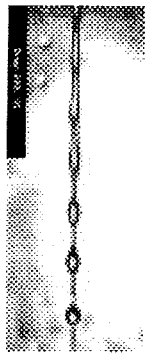

Figure 2

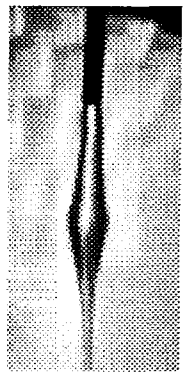

Figure 3(a)

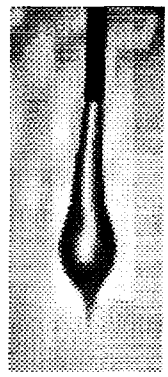

Figure 3(b)

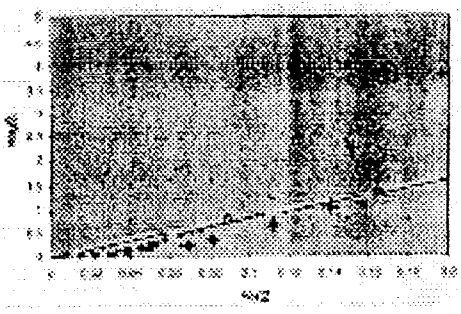

Figure 4

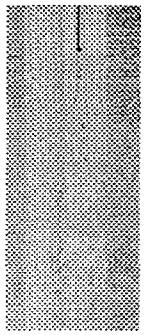

Figure 5

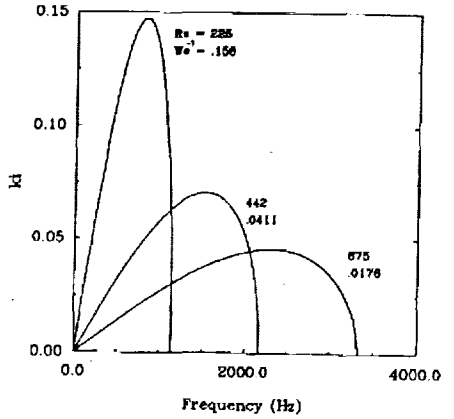

Figure 6

REFERENCES

[1] Leib, S.J. and Goldstein, M.E. 1986a, Phys. Fluids **29**, 952.
[2] Leib, S.J. and Goldstein, M.E. 1986b, J. Fluid Mech. **168**, 479.
[3] Lin, S.P. and Lian, Z.W. 1990, AIAA J. **28**, 120.
[4] Lin, S.P. and Lian, Z.W. 1993, Phys. Fluids A, **5**, 771.
[5] Vinihen, I. Honohan, A. And Lin, S.P. 1997, Phys. Fluids **9**, 3117.
[6] Lin, S.P. and Chen, J.N. 1998, J. Fluid Mech. **376**, 37.
[7] Lin, S.P. and Webb, R.D. 1994, Phys. Fluids **6**, 2545.
[8] Lin, S.P. and Reifz, R.D. 1998, Ann. Rev. Fluid Mech. **30**, 85.

Presentation not available at time of printing.

A COMPACT LASER VELOCITY STRAIN AND VORTICITY PROBE FOR MICROGRAVITY RESEARCH

M. Volkan Otugen, Wei-Jen Su and George Papadopoulos

Mechanical, Aerospace and Manufacturing Engineering
Polytechnic University
Six Metrotech Center
Brooklyn, NY 11201 / U.S.A.

ABSTRACT

A compact laser-based probe for the direct, non-intrusive measurement of temporally- and spatially-resolved velocity gradient and vorticity is presented. The probe's principle and design makes it suitable for microgravity fluid mechanics and combustion research. The measurement technique is based on the collection and direct heterodyning of coherent light scattered from particles in two adjacent locations allowing the determination of a velocity gradient. The beat frequency of the heterodyned light gives the difference in the Doppler shift and is proportional to the velocity difference of two points. This frequency is analyzed using a conventional laser Doppler velocimetry (LDV) signal processor. The angle between the laser beam and the direction of the scattered light determines the measured component of velocity. Therefore, a component of the vorticity vector is measured by using two sets of transmitting and collecting optics, focused at a single location, along with two LDV processors. The technique is non-intrusive, straightforward and inexpensive since it uses standard, off-the-shelf optical and electronic components. It also allows the development of a compact probe with integrated instrumentation using diode lasers and optical fibers. The technique affords, for the first time, non-intrusive, high-accuracy dynamic measurement of velocity gradient and vorticity. The direct, non-contact measurement of the velocity gradients and vorticity will lead to analysis of turbulent flow physics and combustion phenomena.

Measurement Principle:

The technique is based on the direct measurement of velocity difference of particles at two locations by coherent heterodyning of the scattered laser light form the particles at a detector. This is accomplished by collecting the coherent Mie scattered light from two individual particles using a single set of collecting lenses and coupling them into a single mode optical fiber. The fiber is split into two at the receiving end and allows for the easy combination of the scattered light from two locations colinearly. When the output of the fiber is shone on a photodetector, the beat frequency is easily observed. This frequency carries velocity difference information and is analyzed by an LDA processor. Since the distance between the two laser beams is known, $\Delta U_j/\Delta x_j$ is easily calculated. In order to overcome the ambiguity in the sign of the derivative, one of the beams is frequency shifted by using a Bragg cell. Laser light scattered from

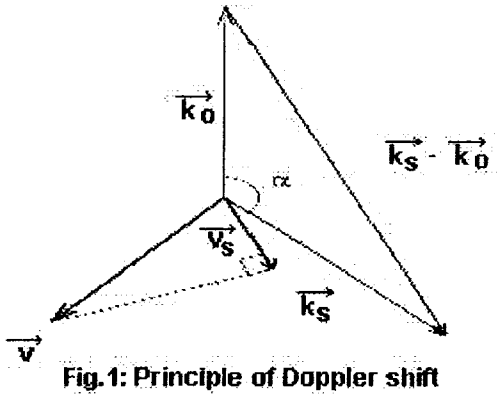

Fig. 1: Principle of Doppler shift

a moving particle will exhibit a Doppler shift that is dependent on the angle between the incident laser beam and the scattering direction as well as the magnitude of the particle velocity. This principle of light scattering is illustrated in Fig. 1, where $\mathbf{k_0}$ and $\mathbf{k_S}$ are the wave vectors for the incident laser light and the scattered light, respectively. The scattered light from a particle with a velocity of **V** will be Doppler shifted by an amount $\Delta f=(1/2\pi)(\mathbf{k_S}-\mathbf{k_0})\,\mathbf{V}$. With the assumption that the magnitude of the wave vectors is $2\pi/\lambda$, this shift is expressed by $\Delta f=(2V_X/\lambda)\sin(\alpha/2)$ where, λ is the incident laser wavelength and V_X is the component of velocity along the direction $(\mathbf{k_S}-\mathbf{k_0})$. Therefore, by judicially placing the laser beam and the collecting optics, one can select a component of velocity to measure.

Optical Setup:

As an example, a wall-mounted compact (2 cm in diameter) velocity gradient probe is shown in Fig. 2. The probe measures the gradients of the wall-normal velocity. It is to be embedded in the wall inside a jacket that is movable in the direction normal to the surface. This allows for measurements in a large physical range in flow including very near the wall at any desired y^+ location. Further, it also would rotate about its axis. This way, both the spanwise and the streamwise gradient measurements can be made by rotating the probe head in the appropriate direction. In the current design, the probe is "mezzo-scale" with about 2 cm diameter and 3 cm length. However in the future, it can be built progressively smaller with smaller optical and mechanical components. The probe head has both transmitting and collecting optics and is connect to the laser and the detector via single mode, polarization preserving fibers. The transmitting side components include fiber couplers F1 and F2, beam transmitting lens, L1, and beam steering wedge, W1. The collecting side include signal collecting lens, L1, steering wedge, W2, refocusing lens, L3, and the fiber couplers F3 and F4.

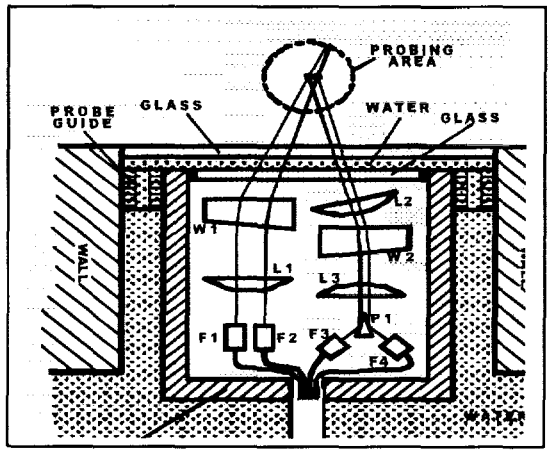

Figure 2: Wall-Mounted velocity gradient probe

The overall size of the probe volume can be changed by adjusting the optics inside the probe head. The measurement concept and the current design allows for a small, light weight, compact and rugged probe. Therefore it is suitable for both drop tower and in-flight experiments.

Some preliminary experiments have been carried out to test viablity of the measurement concept (Otugen et. al., 1998). In these experiments, the velocity difference at two radial locations in a laminar flow between two concentric cylinders was measured and compared to the exact solution to this flow problem. Very good agreement between the experiments and the exact solution has been obtained which validates the method (Otugen et. al., 1998).

REFERENCE

M.V. Otugen, W.J. Su and G Papadopoulos, "A New Laser-Based Method for Strain Rate and Vorticity Measurements", *Measurement Science & Tech*, Feb. 1998, Vol.9, pp. 267-274

Presentation not available at time of printing.

DECOUPLING THE ROLES OF INERTIA AND GRAVITY ON PARTICLE DISPERSION

D. Groszmann and C. Rogers
Tufts University, Department of Mechanical Engineering, Medford, MA 02155

ABSTRACT

The motion of solid particles in a turbulent flow field is dictated by their response to inertial and gravitational forces. Gravity plays the dominant role in this motion by pulling the particles through adjacent regions of fluid turbulence, masking the inertial effects. By examining the dispersion of solid particles in a turbulent flow in the absence of gravity, we can improve our understanding of the mechanisms responsible for particle motion and develop new models for these effects. In this paper we present the particle dispersion experiments conducted on NASA's KC-135 Reduced-Gravity Aircraft, which generates microgravity conditions for 20 seconds.

The turbulent flow field was generated in a closed Lexan box measuring 30.5 cm x 30.5 cm x 30.5 cm by 8 small fans mounted in the corners. Laser Doppler velocimetry measurements inside the box were used to characterize the flow parameters before conducting the microgravity experiments. The measurements show the turbulence to be nearly isotropic, having an isotropy ratio of 0.97, with up to two orders of magnitude in turbulent scales and with a near-zero mean flow in the center region. To cover a broad range of flow regimes of interest, particles with Stokes numbers of about 0.1, 1, and 10 were released in the turbulence box and the particle motion in two and three dimensions were measured.

The two-dimensional measurements were made by recording and measuring particle concentrations in a 4 cm thick light sheet that highlighted a plane in the flow. Results show preferential concentration of particles with a Stokes number of about unity in microgravity conditions but with no preferential concentration in Earth's gravity, suggesting that particle dispersion has a strong dependence on gravitational forces (Fallon, 1999). Figure 1a shows a sample video image highlighting the preferential concentration of 300-350 micron glass particles. Figure 1b compares the average minimum distance between particles (D_P) with DNS results (Coppen et al., 2000).

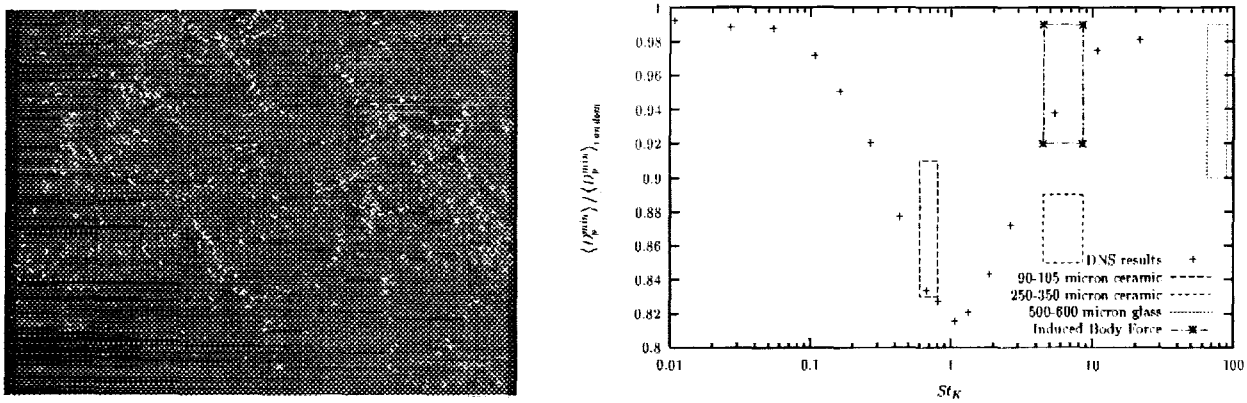

Figure 1. (a) Preferential concentration of 300-350 micron glass particles; (b) Comparison with DNS of average minimum distance.

Three-dimensional measurements of particle motion were made using a three-camera (monochrome 60 Hz) stereo imaging system with a particle-tracking algorithm. Standard photogrammetric techniques were used to determine the particle location in three-dimensional space from the calibrated camera images (Maas et al., 1993). To simplify the camera recording process, the monochrome images from each of the three cameras were encoded in red, green, and blue, combined into one color image, and recorded digitally on a DV recorder. Figure 2a shows a portion of a sample image with all three-camera views of 600-700 micron glass particles superimposed. A single particle is highlighted in each of the three camera views (or color planes). The epipolar geometry constraint was used to identify matching particles from the three different views and these are shown for one particle in the image. Once a particle's position is determined in each of the three camera views, its coordinates in three-dimensional space are determined from the camera calibration parameters. Using velocity and acceleration constraints, particles in a sequence of frames can be matched resulting in particle tracks. A sample track in three-dimensional space for a 600-700 micron glass particle is shown in Figure 2b.

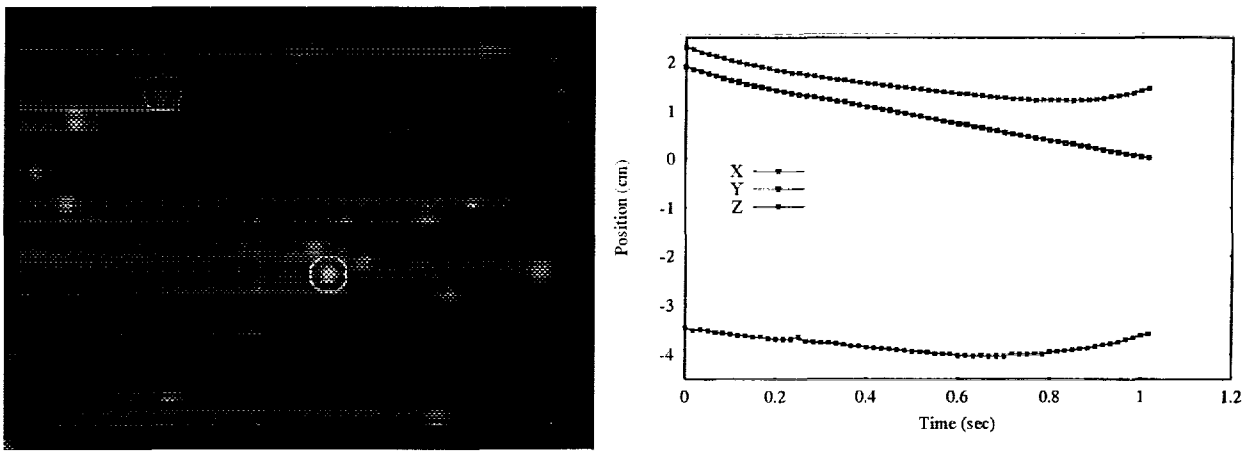

Figure 2. (a) Superimposed images of particles from three-camera system; (b) is resulting particle track in three dimensional space.

Quantitative three-dimensional particle dispersion results together with our previous work in preferential concentration will provide additional insight into the mechanisms of particle-laden turbulent flows. We can compare the dispersion rates of different Stokes number particles in zero g. In addition, we are continuing work with the turbulence box, using a microcontroller to adjust the speeds of individual fans in an attempt to improve the isotropy of the turbulence.

REFERENCES

Coppen, S.W., V. Manno, C.B. Rogers, 2000. "Turbulence characteristics along the path of a heavy particle," J. of Computers and Fluids, in press.

Fallon, T., 1999. "Particle concentration fields in microgravity," Masters Thesis, Tufts University.

Maas H.G., A. Gruen and D. Papantoniou, 1993. "Particle tracking velocimetry in three-dimensional flows: Part 1. Photogrammetric determination of particle coordinates," Exp Fluids, Vol. 15, pp. 133-146.

NASA/CP—2000-210470

ABSTRACT

The motion of solid particles in a turbulent flow field is dictated by their response to inertial and gravitational forces. Gravity plays the dominant role in this motion by pulling the particles through adjacent regions of fluid turbulence, masking the inertial effects. By examining the dispersion of solid particles in a turbulent flow in the absence of gravity, we can improve our understanding of the mechanisms responsible for particle motion and develop new models for these effects. In this poster we present the particle dispersion experiments conducted on NASA's KC-135 Reduced-Gravity Aircraft, which generates microgravity conditions for 20 seconds.

The turbulent flow field was generated in a closed Lexan box measuring 30.5 cm x 30.5 cm x 30.5 cm by 8 small fans mounted in the corners. Laser Doppler velocimetry measurements inside the box were used to characterize the flow parameters before conducting the microgravity experiments. The measurements show the turbulence to be nearly isotropic, having an isotropy ratio of 0.97, with up to two orders of magnitude in turbulent scales and with a near-zero mean flow in the center region. To cover a broad range of flow regimes of interest, particles with Stokes numbers of about 0.1, 1, and 10 were released in the turbulence box and the particle motion in two and three dimensions were measured.

The two-dimensional measurements were made by recording and measuring particle concentrations in a 4 cm thick light sheet that highlighted a plane in the flow. Results show preferential concentration of particles with a Stokes number of about unity in microgravity conditions but with no preferential concentration in Earth's gravity, suggesting that particle dispersion has a strong dependence on gravitational forces.

Three-dimensional measurements of particle motion were made using a three-camera (monochrome 60 Hz) stereo imaging system with a particle-tracking algorithm. Standard photogrammetric techniques were used to determine the particle location in three-dimensional space from the calibrated camera images. To simplify the camera recording process, the monochrome images from each of the three cameras were encoded in red, green, and blue, combined into one color image, and recorded digitally on a DV recorder. Once a particle's position is determined in each of the three camera views, its coordinates in three-dimensional space are determined from the camera calibration parameters. Using velocity and acceleration constraints, particles in a sequence of frames can be matched resulting in particle tracks.

Effects of Inertia: Preferential Concentration

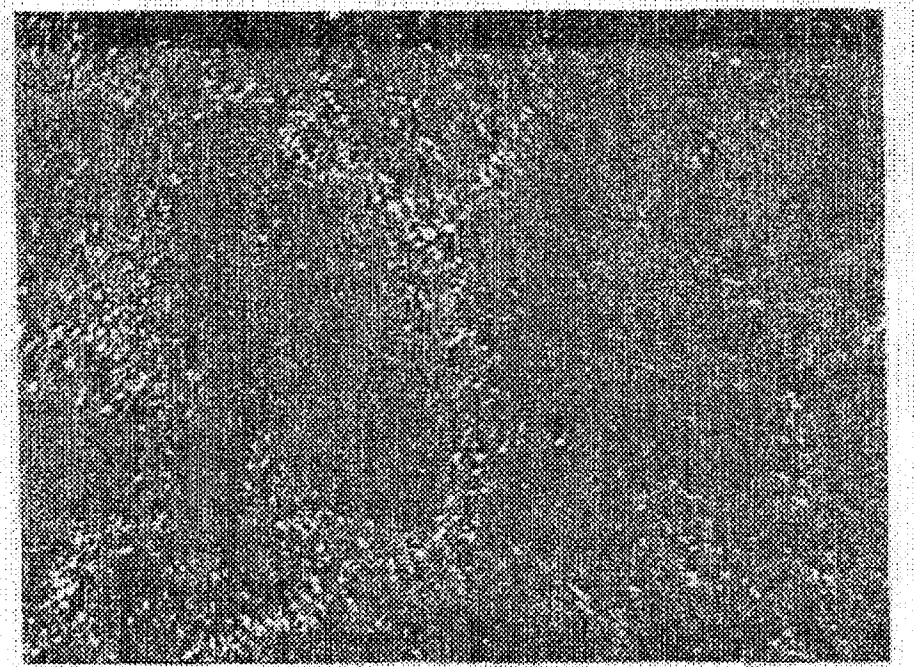

250-350 μm ceramic

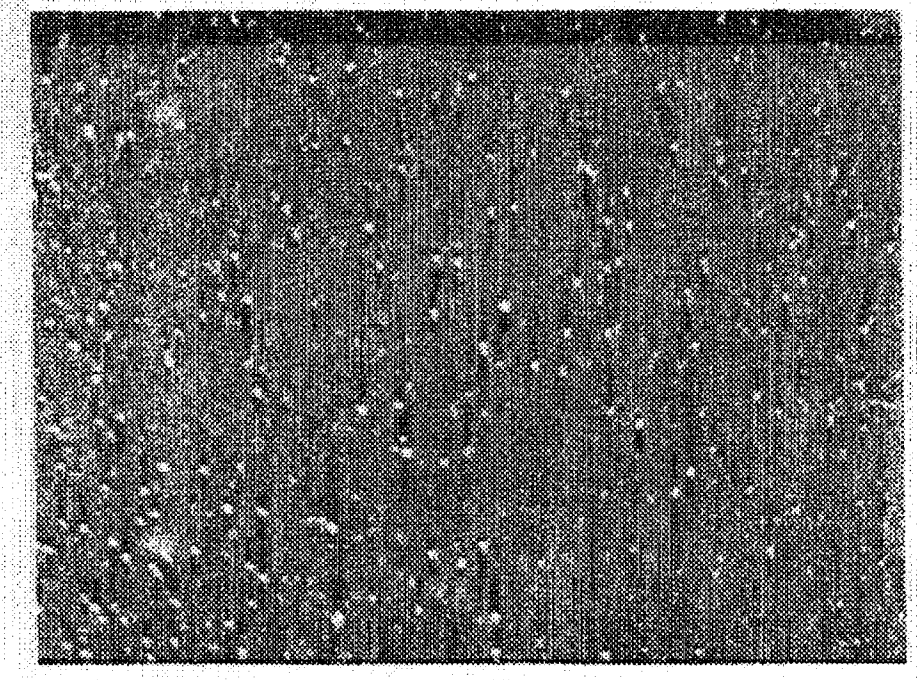

500-600 μm glass

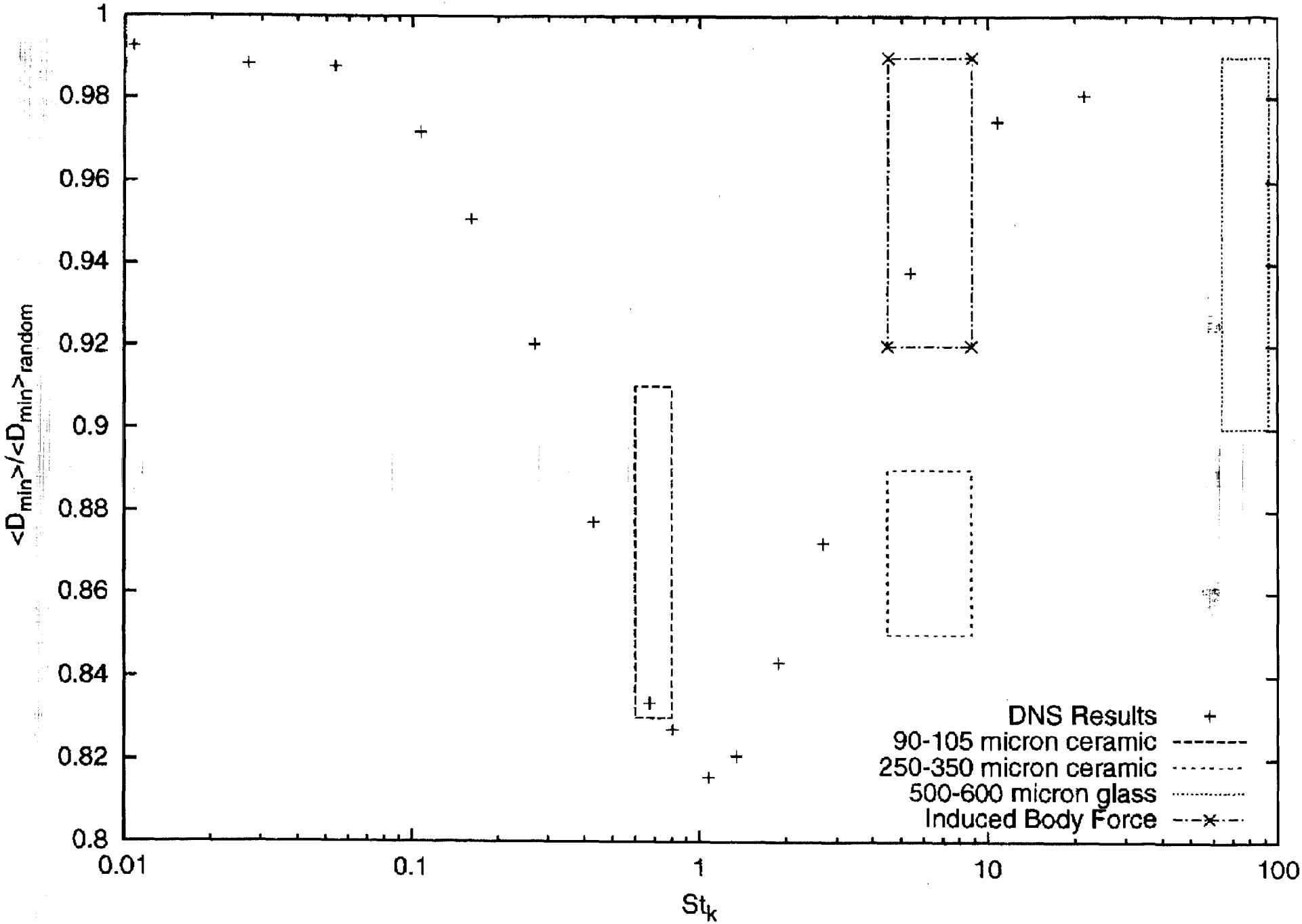
1
0.98
0.96
0.94
0.92
0.9
0.88
0.86
0.84
0.82
0.8
0.01
0.1
1
10
100
St_k
$<D_{min}>/<D_{min}>_{random}$
DNS Results
90-105 micron ceramic
250-350 micron ceramic
500-600 micron glass
Induced Body Force

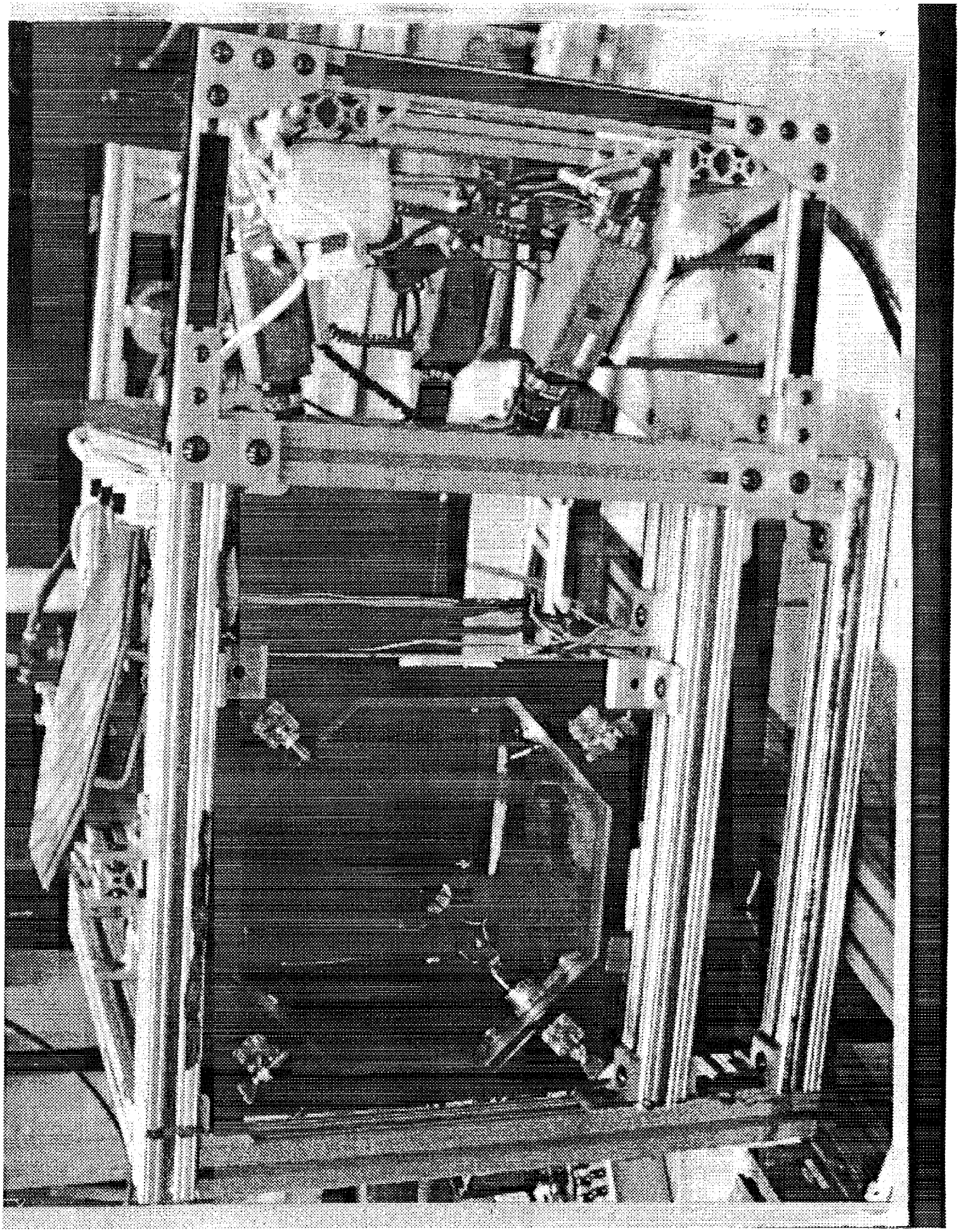

LIGHT SHEET GENERATOR
CAMERA
Air flow out
Air flow in
Slits along walls

(a) (b)

Particle Position vs Time
Position (cm)
Time (sec)
4
2
0
-2
-4
-6
-8
2.4
2.6
2.8
3
3.2
3.4
3.6
3.8
4
X - 650 micron
Y - 650 micron
Z - 650 micron
X - 100 micron
Y - 100 micron
Z - 100 micron

Particle Velocity vs Time
X - 650 micron
Y - 650 micron
Z - 650 micron
X - 100 micron
Y - 100 micron
Z - 100 micron
Velocity (cm/s)
20
15
10
5
0
-5
-10
-15
2.4
2.6
2.8
3
3.2
3.4
3.6
3.8
4
Time (sec)

GROUND BASED STUDIES OF THERMOCAPILLARY FLOWS IN LEVITATED LASER-HEATED DROPS

S.S. Sadhal, A. Rednikov and K. Ohsaka
Department of Aerospace & Mechanical Engineering
University of Southern California
Los Angeles, CA 90089-1453
email: sadhal@usc.edu

ABSTRACT

Glovebox Studies

The IFFD (Internal Flows in Free Drops) investigation were carried out on STS-95 produced good video images with optimal resolution of the internal tracer particles will allow the accurate measurement of the internal motion of the liquid. The first demonstration of non-contact fissioning of a single drop into two parts was obtained with a static sound field. In addition, the new technique for the accurate, acoustically-assisted drop deployment in microgravity has also been verified together with the feasibility of quiescently positioning a partially wetted drop at the end a sting. Thermocapillary flows were observed with a free drop in microgravity, and clear evidence of an increase in the internal circulation in the drop was detected as the sting heater was activated in the vicinity of the drop. Both contacting and non-contacting heater configurations were studied. A much higher rate of successful drop deployment has been obtained in STS-95 when compared to STS-94. This has been attributed to the elimination of the protective cover around the ultrasonic levitator.

Ground-Based Experiments

We have continued ground-based measurement of the thermocapillary flows in electrostatically levitated and laser-heated drops. Convincing evidence is being gathered that these thermocapillary-driven flows quickly couple to a drop rotational motion. This results in a very complicated motion and in the termination of the experiment because of the inability to control the spot heating location. In order to circumvent this drawback, we have investigated mostly two-dimensional flows in drastically flattened ultrasonically levitated drop and spot heated at one end. Flattened drops can be created and held in a stable horizontal position for high-viscosity liquids ($\mu > 10$ poise). By using suspended tracer particles and laser illumination, we have been able to resolve the three-dimensional flows within the disk-shaped drop. The flattening of the drop in a plane perpendicular to gravity minimizes the influence of natural buoyancy, and reveals the essential features of thermocapillary flows in the major plane of the drop.

By suppressing in-plane rotational motion with a glass fiber, we have been able to observe the effects of heating raising the local surface temperature in a range between 10 and 100 °C. We have been able to record steady thermocapillary motion in the plane of the flattened drop. Close examination revealed a double set of dipole-like circulation pattern. A higher velocity (1 to 5

cm/s) small vortex is located near the heated spot region, while a larger counter-rotating vortex extends over the majority of the drop cross-section. These measurements were carried out for fairly low values of the Marangoni between 100 and 250.

Analytical Results

The effects of air compressibility have been accounted for in a greater detail than in the previous analyses. These include possible influence of the thermal boundary layer and, if the surrounding gas is a multi-component mixture, of the diffusional boundary layer. Acoustic streaming around a drop in a liquid, with comparable viscosities inside and outside, has been considered.

It is well known that acoustic streaming originates in the viscous boundary layer at the surface of a particle, where flow is genuinely rotational and thus, a steady flow component is generated as soon as nonlinearities take effect. While this crucial role of the viscous boundary layer has been widely recognized, little attention has been paid to the role the thermal boundary layer. The special case of a solid sphere acoustically levitated in a gas medium has been studied. As solids are generally much more thermally-conductive than gases, the temperature is practically constant within the solid body while oscillating in a sound wave (consisting of velocity, pressure and density oscillations). Therefore, a thermal boundary layer is formed at the surface, in addition to the viscous one. Since density is a function of temperature, a sharp temperature variation in the boundary layer gives rise to the corresponding density variation. The latter in turn influences the flow field (continuity equation). In the final analysis, the acoustic streaming intensity proves to be globally affected.

Furthermore, if we deal with a multicomponent gas, the effect of thermodiffusion emerges as another factor that may also affect the streaming. The temperature gradient brings about a concentration gradient, and therefore, as density depends on composition, there appears an additional contribution to density, and consequently, to the acoustic streaming.

A remarkable new result is that acoustic streaming proves to be much more intense for the drop-in-liquid system, than for a solid sphere in a liquid. This flow originates in the external and internal boundary layers at the drop surface. Now that there is the velocity continuity condition to be satisfied, the acoustic streaming becomes more pronounced with a mobile interface.

The streaming around a rigid sphere has been studied in the long wavelength approximation for a general acoustic field of a given frequency. In particular, the acoustic torque on the sphere has been calculated. Generalizing Riley's (1966) work, we studied the steady streaming around a motionless sphere with the fluid oscillating with a complex velocity amplitude. The result for the steady streaming velocity at the outer edge of the boundary layer is found in a very general form in terms of the velocity amplitude and the oscillation frequency. Since the oscillation velocity has a general form admitting phase differences with respect to the vector components, there is, in general, a net torque with an expression given in terms of the velocity amplitude, the frequency, and the kinematic viscosity.

Ground-Based Experimental Studies

Measurement of Thermocapillary Flows

- Thermocapillary-induced flows in levitated drops quickly couple to a drop rotational motion. This results in a very complicated motion and in the termination of the experiment because of the inability to control the spot heating location.
- In order to circumvent this drawback, we have devised two approaches:
  - The first one consists in heating a rotating drop with its rotation axis perpendicular to the laser incident beam. This provides a belt-shaped heated region on the drop surface.
  - The second approach is to investigate mostly two-dimensional flows in drastically flattened ultrasonically levitated drop and spot heated at one end (Figure 1).

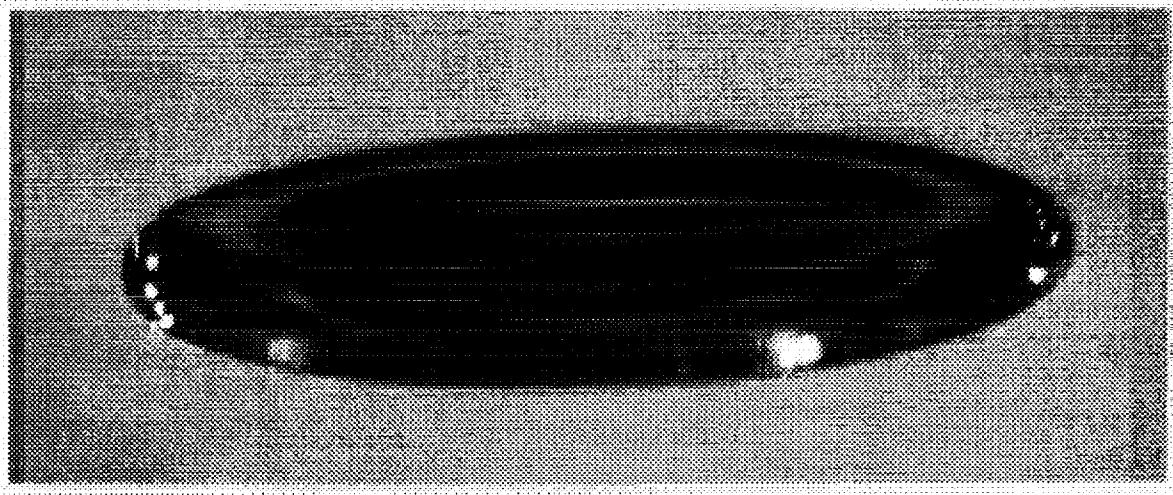

Figure 1: A disk-shaped ultrasonically levitated drop of glycerol. The aspect ratio can be continuously varied by adjusting the acoustic pressure level. The drop side dimension is 4.5 mm.

Flattened Drops

- By using suspended tracer particles and laser illumination, we have been able to resolve the three-dimensional flows within the disk-shaped drop.

- Using a high-viscosity liquid ($\mu > 10$ poise) and an ultrasonic levitator, a drop can be held in a very thin disk-like shape for a substantial time without the onset of shape instability, i.e., the shape remains stationary for a long time.
- Drops of 200 cSt silicone oil (Polydimethylsiloxanes) were ultrasonically levitated in ambient air and under atmospheric pressure.
- The acoustic pressures were adjusted in order to induce a drastic flattening of the drop (see Figure 1) in order to achieve very high aspect ratio (up to 20).
- Shape aspect ratios between 1.5 to 50 can easily be achieved using silicone oil at 1-G. A focused CO_2 laser is aligned to heat a small area (on the order of 200 microns diameter) at one side of the drop.
- Diametrically opposed is a very thin glass fiber contacting the drop surface used to arrest the drop rotation. Flow visualization is carried out with 10 to 50-micron suspanded polymeric tracer particles along with a He-Ne laser sheet illumination.
- Under careful examination, a circulatory motion directed normal to the drop main cross section can be seen at the edge of the drop. This circulatory motion increases in extent towards the drop center for lower viscosity liquids.
- With 200 cSt silicone oil, this outer circulatory motion is restricted to a region within the first 5% of the drop diameter. It appears that this steady circulation is induced by the acoustic streaming flow induced by the levitation field.
- With laser heating raising the local surface temperature in a range between 10 and 100°C, we have been able to record steady thermocapillary-induced motion in the plane of the flattened drop. Figure 2 shows the general flow pattern for a laser spot heated impacting the drop surface at the left edge.
- Close examination reveals a double set of dipole-like circulation pattern. A higher velocity (1 to 5 cm/s) small vortex is located near the

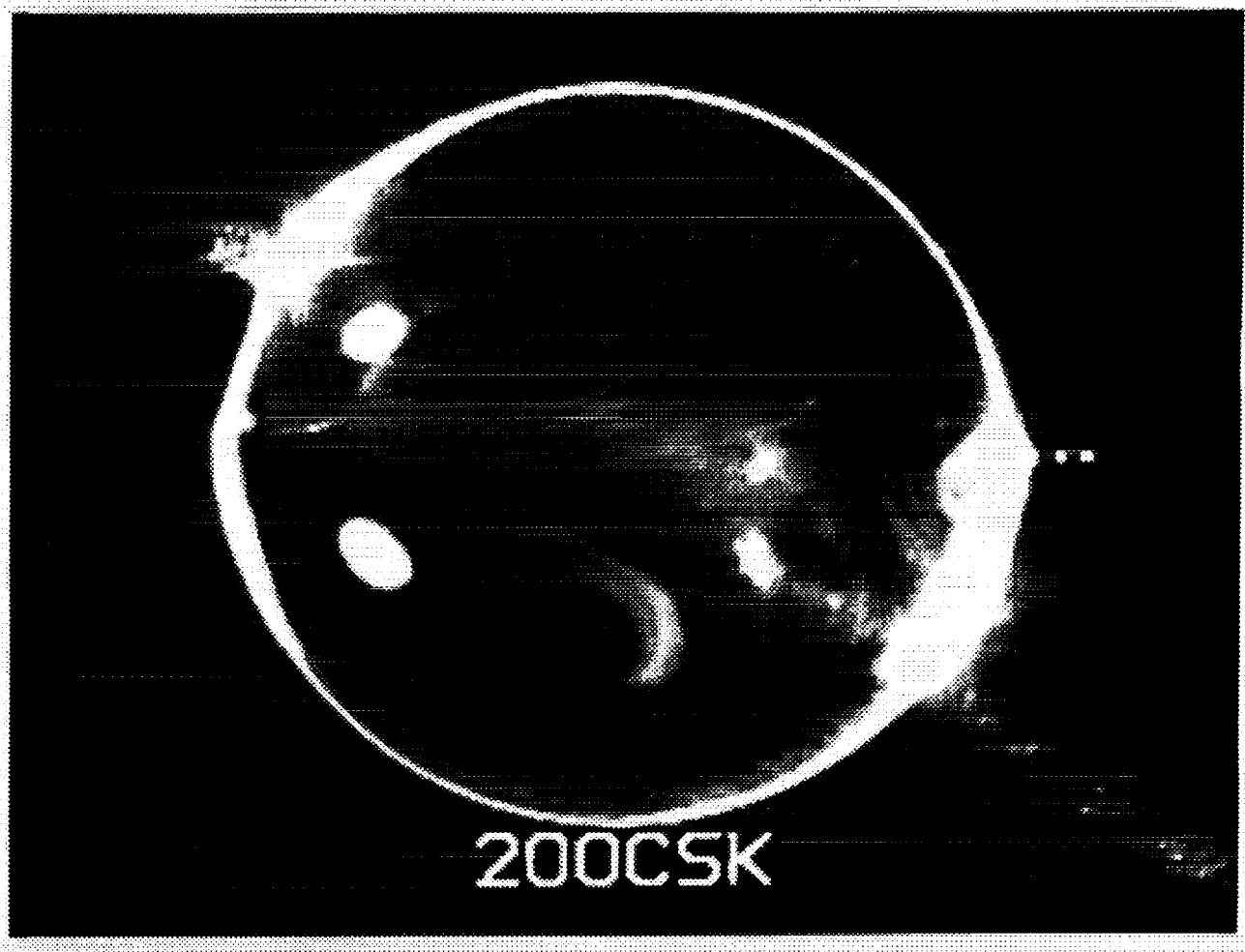

Figure 2: Time-lapse video image of circulatory flow induced in a flattened levitated drop heated with a focused laser on the left side. The 200 cSt silicone oil drop is ultrasonically levitated at 1-G in air at STP, and the flow pattern is made visible by suspended tracer particles illuminated with a laser sheet.

heated spot region, while a larger counter-rotating vortex extends over the majority of the drop cross-section. ($100 < Ma < 250$).

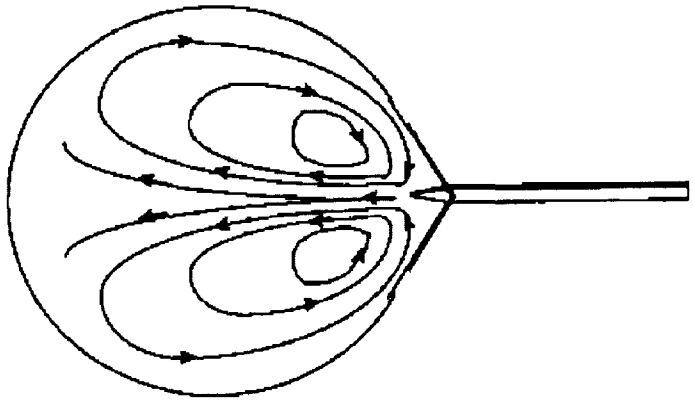

Thermocapillary motion inside a flat drop generated by a hot sting

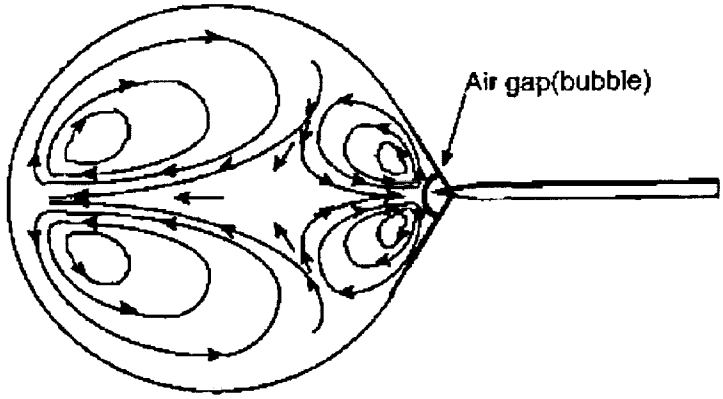

Thermocapillary motion inside a divided flat drop with a hot sting inside the smaller region

Analytical Results

Compressibility and Related Thermal and Diffusional Effects in Levitation Acoustics

- While the crucial role of the viscous boundary layer in generating vorticity has been widely recognized, little attention has been paid to the role of the thermal boundary layer.
- Not only is the latter one essential when studying purely thermoacoustic phenomena, but it may also affect the streaming itself – a phenomenon that has not been studied so far.
- A solid sphere acoustically levitated in a gas medium is considered. With thermal conductivity $k_s \gg k_g$, a thermal boundary layer is formed at the surface, in addition to the viscous one.
- Since density is a function of temperature, a sharp temperature variation in the boundary layer gives rise to the corresponding density variation. The latter in turn influences the flow field (continuity equation).
- In the final analysis, the acoustic streaming intensity proves to be globally affected. The following dimensionless parameter determines the extent of this effect:

$$N_T = \frac{\beta^2 T_0 c^2}{c_p} = \gamma - 1.$$

$\gamma = c_p/c_v$, T_0 = mean (background) temperature,
c = sound speed, β = thermal expansion coefficient.

- The effect is most pronounced for monoatomic ideal gases ($\gamma = \frac{5}{3}$), and negligible for $\gamma \simeq 1$.
- *Viscosity* is also a function of temperature. For gases, it is usually has a power-law dependence. As the acoustic streaming is a second order effect, the variation of viscosity may also contribute to the same order.

- *Multicomponent gas.* Indeed, owing to the effect of thermodiffusion, the temperature gradient brings about the concentration gradient. Therefore, as density depends on composition, there appears an additional contribution to density, and consequently, to the acoustic streaming.

- *Two-component gas.* The steady tangential velocity component persisting beyond the viscous boundary layer (the limiting velocity) is known to be

$$\begin{aligned}\bar{u}_\theta = -\epsilon U_\infty \Big[&\tfrac{15}{16}\sin^2 kz_0 \sin\theta\cos\theta \\ &+\tfrac{5}{8}(ka)\sin kz_0\cos kz_0\sin\theta(13\cos^2\theta - 3) \\ &+\tfrac{25}{36}(ka)^2\cos^2 kz_0\sin\theta\cos\theta(8\cos^2\theta - 3)\Big]\end{aligned} \tag{1}$$

for a standing sound wave of the form $u_z = U_\infty \sin kz e^{i\omega t}$.
$\epsilon = U_\infty/(\omega a) \ll 1; \quad ka \ll 1;$
z_0 = position of the center of the sphere.

- When the thermal and concentrational effects are both taken into account, the following additional contribution to the limiting velocity results

$$\begin{aligned}v_\theta = \epsilon U_\infty A \Big[&\tfrac{3}{4}(ka)\sin kz_0\cos kz_0\sin\theta \\ &+\tfrac{5}{6}(ka)^2\cos^2 kz_0\sin\theta\cos\theta\Big]\end{aligned} \tag{2}$$

where

$$A = [(N_T + Q_T)(Sc+1) + N_C + Q_C] \times \frac{b_1^{1/2}b_2^{1/2}(b_1^{1/2} + b_2^{1/2})}{(1+b_1)(1+b_2)(Sc + b_1^{1/2}b_2^{1/2})},$$

with $2b_{1,2} = Pr + Sc + GPr \pm \left[(Pr+Sc+GPr)^2 - 4PrSc\right]^{1/2}$

$$N_C = \left(\frac{\partial\rho}{\partial C}\right)_{T,p}\frac{K_T\beta c^2}{\rho_0 c_p}, \quad Q_T = -\left(\frac{\partial\mu}{\partial T}\right)_{C,p}\frac{T_0\beta c^2}{\mu_0 c_p},$$

$$Q_C = -\left(\frac{\partial\mu}{\partial C}\right)_{T,p}\frac{K_T\beta c^2}{\mu_0 c_p}, \quad G = \frac{K_T^2}{c_p T_0}\left(\frac{\partial\tilde{\mu}}{\partial C}\right)_{T,p}$$

Here

D = diffusion coefficient
α = thermal diffusivity
K_T = thermodiffusion ratio
$\tilde{\mu}$ = chemical potential
C = concentration

- In the limit of a single-component gas, we have $K_T \to 0$, and the expression for A simplifies to

$$A = (N_T + Q_T)\frac{Pr^{1/2}}{Pr + 1}$$

corresponding to purely thermal contribution to the steady acoustic streaming.

- The result (2), unlike (1), does not contain terms of order $O((ka)^0)$. This is due to the fact that, in the leading order of the long wavelength approximation $ka \ll 1$, the flow is incompressible, while the contribution (2) is associated with compressibility. The further the sphere is located from the velocity antinode, the stronger is the effect (2), being the most pronounced when at the node, as (1) and (2) become of the same order.

- The effect of thermal and diffusional boundary layers has been illustrated for a sphere. However, it may take place in any geometrical configuration. For example, for the classical (Schlichting) problem of the the acoustic streaming near a plane due to a parallel standing wave $u_z = v_0 \cos kz e^{i\omega t}$, we find the following velocity:

$$\bar{u} = \frac{u_0^2}{c}\left(\tfrac{3}{8} + \tfrac{1}{4}A\right)\sin 2kz. \qquad (3)$$

where the term A corresponds to the additional contribution under consideration here.

Liquid-Liquid Systems

- Similar properties in both phases.
In the limit of small streaming Reynolds numbers, the acoustic streaming is determined by

$$\psi_s = B\ (1/r^2 - 1)\bar{\mu}\ (1 - \mu^2), \qquad \hat{\psi}_s = B\ (r^3 - r^5)\bar{\mu}\ (1 - \bar{\mu}^2)$$

in terms of the stream function outside and inside the drop, respectively, and

$$B = \epsilon|M|\frac{9}{80\sqrt{2}}\frac{\kappa^{-1}\phi_\nu^{1/2}}{(1+\kappa^{-1})\phi_\nu^{1/2})(1+\kappa^{-1})}$$

r = radial coordinate, $\kappa = \mu/\hat{\mu}$,
a = drop radius $|M| = (\omega a^2/\nu)^{1/2} \gg 1$,
$\bar{\mu} = \cos\theta$, $\epsilon = U/(\omega a) \ll 1$,
$\phi_\nu = \nu/\hat{\nu}$, U = medium-particle relative velocity.

- A remarkable result is that B is not simply $B \sim \epsilon$, but $B \sim \epsilon|M|$ here. Thus, the acoustic streaming proves to be much more intense ($|M|$ times for $|M| \gg 1$) for the drop-in-liquid system, than for a solid sphere in a liquid.

- This flow originates in the external and internal boundary layers at the drop surface. Now that there is the no-slip condition to be satisfied, the acoustic streaming becomes more pronounced.

- The limit of a highly viscous drop ($\kappa \to 0$), that may, for example, correspond to a drop in a gas, or to a solid sphere, yields

$$B = \epsilon|M|\frac{9}{80\sqrt{2}}\kappa$$

that tends to zero as $\kappa \to 0$.

- Thus, we arrive to an apparent contradiction, since it is well-known that the acoustic streaming does not vanish for a solid sphere. This demonstrates a singular nature of the limit $\kappa \to 0$.

- Therefore, a separate treatment is needed for the case $\kappa \to 0$, and this has been already done in. Herewith, the most interesting asymptotic case corresponds to $\kappa|M| \sim 1$.

Generalization of the Acoustic Field Interacting with a Particle

- Generalizing Riley's (1966) work, we studied the steady streaming around a motionless sphere with the fluid oscillating as $\boldsymbol{U}_\infty \exp(i\omega t)$ far away from the sphere, where $\boldsymbol{U}_\infty$ is generally a complex vector, so that there may be a phase shift between its components.

- This problem is clearly of interest from the acoustic point of view, since the velocity field $\boldsymbol{U}_\infty \exp(i\omega t)$ may often serve as the leading order approximation to a general acoustic field of the frequency ω in the vicinity of a particle, whose size is much smaller than the wavelength.
- This is also a generalization of Lee & Wang (1989), who studied the streaming due to two orthogonal standing waves, that is, in our terms, the case when the vector $\mathrm{Re}\boldsymbol{U}_\infty \exp(i\omega t)$ always remains coplanar.
- The result for the steady streaming velocity at the outer edge of the boundary layer is

$$\boldsymbol{u}_r = \frac{45}{16\omega a}\left(\boldsymbol{A}\cdot\boldsymbol{n} - \boldsymbol{n}\cdot\boldsymbol{A}\cdot\boldsymbol{n}\boldsymbol{n}\right) + \frac{27}{8\omega a}\mathbf{B}\cdot\boldsymbol{n} \qquad (4)$$

  with the tensors $\mathbf{A}$ and $\mathbf{B}$ defined as

$$\mathbf{A} = \mathrm{Re}\ \boldsymbol{U}_\infty \mathrm{Re}\ \boldsymbol{U}_\infty + \mathrm{Im}\ \boldsymbol{U}_\infty \mathrm{Im}\ \boldsymbol{U}_\infty,$$
$$\mathbf{B} = \mathrm{Re}\ \boldsymbol{U}_\infty \mathrm{Im}\ \boldsymbol{U}_\infty - \mathrm{Im}\ \boldsymbol{U}_\infty \mathrm{Re}\ \boldsymbol{U}_\infty$$

  and $\boldsymbol{n}$ being the unit vector in the radial direction.
- While the first term in equation (4) is a trivial generalization of the corresponding axisymmetric result, the second term, with the anti-symmetric tensor $\mathbf{B}$, yields a rotational contribution to the velocity field.
- As expected, the necessary condition for the rotation to exist is a phase shift between the components of $\boldsymbol{U}_\infty$. Otherwise, we have $\mathbf{B} = 0$.
- Note that

$$\mathbf{B}\cdot\boldsymbol{n} = \left[Re\ \boldsymbol{U}_\infty \times Im\ \boldsymbol{U}_\infty\right]\times\boldsymbol{n}.$$

  The rotational motion gives rise to the torque acting on the sphere

$$\boldsymbol{\Gamma} = 3\pi\rho_0 a^2 \left(\frac{2\nu}{\omega}\right)^{1/2} Re\ \boldsymbol{U}_\infty \times Im\ \boldsymbol{U}_\infty.$$

Particle Rotation by Orthogonal Acoustic Fields

- We have examined the response of either solid or liquid particles, when placed in an acoustic field which consists of two orthogonal waves. These have the same amplitude and wave number, but differ in phase by $\frac{1}{2}\pi$.
- One wave is a vertical levitation field and the other is horizontal
- The effect of the second wave, superimposed upon the levitation field, is to create a time-averaged torque on the particle causing it to rotate with a uniform angular velocity.
- The analysis has been carried out in the limit of large Strouhal number. At the leading order, it is shown that solid and liquid cylinders behave in a similar manner, in the sense that the liquid is in solid-body rotation.
- The dominant time-averaged motion of a liquid droplet is also solid-body type; however, superimposed on this is a time-averaged recirculatory flow within the drop in the form of a pair of toroidal vortices.
- For a solid cylinder of radius a, the dimensionless rotational velocity may be expressed as a perturbation expansion,

$$\Omega = \Omega_0 + \varepsilon\Omega_1 + O(\varepsilon^2), \tag{5}$$

where $\varepsilon = U_0/\omega a \ll 1$ with U_0 being the velocity amplitude of the waves, and ω, the frequency.

- Detailed calculations show that

$$\Omega_0 = -\left(\frac{R_s}{2}\right)^{\frac{1}{2}}, \tag{6}$$

where $R_s = U_0^2/(\omega\nu)$. In the limit of $R_s \gg 1$, however, the angular velocity is expressed as

$$\Omega \sim \varepsilon^{-1}\overline{\Omega}_0, \tag{7}$$

where $\overline{\Omega}_0$ is given by the roots of

$$-\overline{\Omega}_0(1+\overline{\Omega}_0)^{\frac{1}{2}} = \left(\frac{\alpha_s}{2}\right)^{\frac{1}{2}}, \tag{8}$$

with $\alpha_s = R_s\varepsilon^2$. Considering that $\overline{\Omega}_0 < 0$, we see that the left-hand side of (8) has a maximum at $\overline{\Omega}_0 = \overline{\Omega}_{0m} = -2/3$ which corresponds to $\alpha_s = \alpha_{sm} = 8/27$.

- For the case of a solid sphere, the expansion

$$\Omega = \varepsilon^{\frac{1}{2}}\Omega_1 + \varepsilon\Omega_2 + O(\varepsilon^{\frac{3}{2}}) \tag{9}$$

is used, resulting in $\Omega \sim \varepsilon^{\frac{1}{2}}\Omega_1 = -\frac{3}{8}(2R_s)^{\frac{1}{2}}$.

Drop Levitated Between Nodes

- The general case of a liquid drop positioned arbitrarily between the velocity node and the antinode has been examined.
- While the leading-order solution is a linear combination of the two groups of solutions when the sphere is placed at the node and antinode of a standing wave, the first-order solutions show that the steady streaming inside and outside the sphere also includes nonlinear terms.
- The flow pattern in the boundary layer is found to have a complex structure with some cases having saddle points.
- For a solid sphere, the flow pattern does not depend much on the frequency parameter $|M|$, while the liquid sphere case depends significantly on $|M|$.
  In fact, the pattern is very sensitive to surface mobility even when the liquid viscosity is high.
- The flow characterization goes through various transitions that depend on several sets of relationships between $|M|$ and $\kappa = \mu/\hat{\mu}$.
- An interesting case is

$$|M| < \frac{15(\kappa+7)(\kappa+3)}{\sqrt{2}\kappa\,(23+5\kappa)},$$

  which has large recirculatory region on the 'front side' of the drop with respect to the outer streaming which is downward (Figures 4 and 6).
- An experimental result is shown in Figure 5 which is qualitatively consistent with the theoretical prediction.

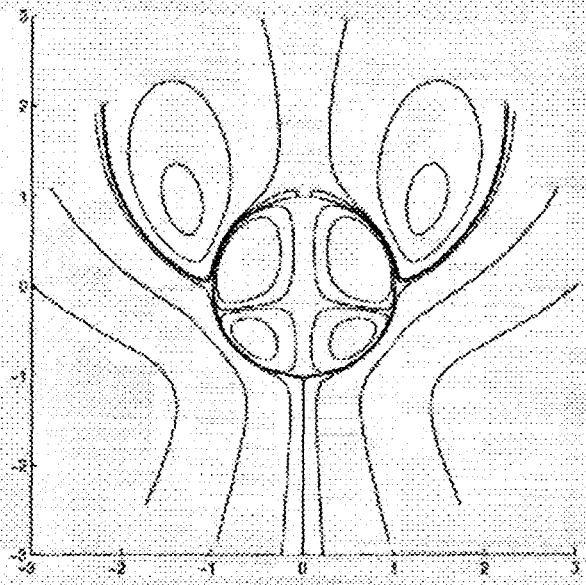

Figure 4: Streaming about a drop displaced between velocity node and antinode for $kZ_0 = \pi/4$, $ka = 0.3$, $\kappa = 0.0156$, and $|M| = 600$.

Figure 5: An experimental result. The tested particle is a drop of water with diameter 1.8 – 1.85mm. The acoustic frequency is 37kHz, corresponding to $|M| = 113$.

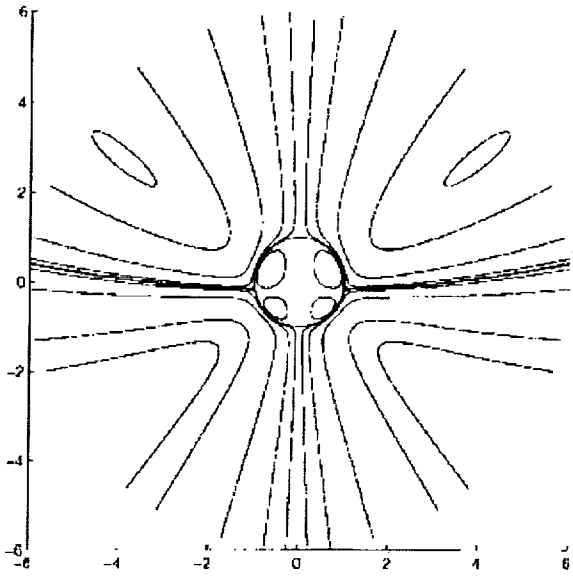

Figure 6: Streaming about a drop displaced between velocity node and antinode for $kZ_0 = \pi/4$, $ka = 0.3$, $\kappa = 0.0156$, and $|M| = 200$.

Journal Publications – 1999-2000

- Zhao, H., Sadhal, S.S. & Trinh, E.H., "Singular Perturbation Analysis of an Acoustically Levitated Sphere: Flow About the Velocity Node," *J. Acoust. Soc. Am.* **106:** 589-595 (1999).
- Zhao, H., Sadhal, S.S. & Trinh, E.H., "Internal Circulation in a Drop in an Acoustic Field," *J. Acoust. Soc. Am.* **106:** 3289-3295 (1999).
- Zhao, H., Sadhal, S.S., Rednikov, A. & Trinh, E.H., "Perturbation Analysis of a Spherical Drop Positioned Between Nodes in an Acoustic Levitation Field," submitted, *J. Fluid Mechanics* (2000).
- Rednikov, A., Riley, N. & Sadhal, S.S., "The Behaviour of a Levitated Particle in Orthogonal Acoustic Fields," submitted, *J. Fluid Mechanics* (2000).

STABILITY OF SHAPES HELD BY SURFACE TENSION AND SUBJECTED TO FLOW

P.H. Steen
Cornell University

ABSTRACT

Capillarity dominates the shape of a liquid/gas or liquid/liquid interface when surface area is large relative to volume (short physical length) or when gravity is small relative to surface tension (long capillary length). Stability of such interfaces is important to applications on earth such as micro-fluidics and in orbit such as the management of liquids in a space station.

REAL-TIME FLOW CONTROL OF UNSTABLE CAPILLARY SHAPES

Three-dimensional capillary interfaces can be destabilized by long wave disturbances since pressure distributions associated with the two principal curvatures can compete, as illustrated by the cylindrical interface: waves longer than the circumference are destabilized by the 'axial curvature pressure'. A time-dependent lubrication pressure is set up using a flow external to such an interface. Real-time feedback control using this pressure, based on video images of the interface shape, suppresses the first mode of instability. In this way, the subdominant mode is revealed for wavelengths between instability of the dominant (first) and subdominant (second) modes. A quantitative comparison to weakly nonlinear stability predictions is favorable [1].

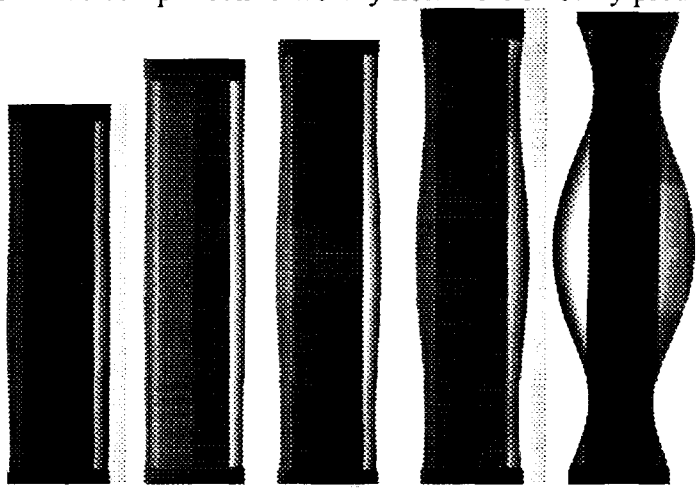

Photos of stabilized liquid bridges, except right which is "collapsed". Lengths (l to r) are 6.76, 7.57, 8.07, and 8.25 where the first mode is unstable at 6.28 (scaled). The center rod amplifies the pressure of the external flow.

BUBBLE DISCONNECTION: SELF-SIMILARITY AND CASCADING PHYSICS

Surface tension disconnects a bubble from a capillary bridge while driving a surrounding inviscid flow. Spatial and temporal behavior is studied just prior to and just after disconnection, via computation and experiment. They are in agreement both before and after the event but anticipated self-similarity is observed only beforehand. Computation coincides with observation due to modeling that identifies the cascade of physics probed over decades of length scales [2].

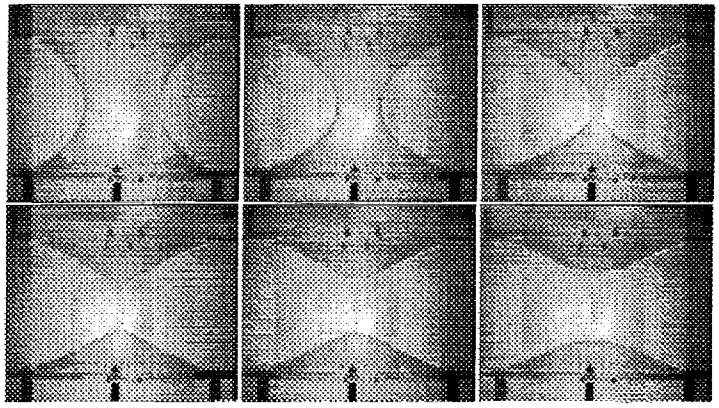

Video images of the collapsing soap film and bubble disconnection at times (l to r): 0 ms, 349 ms, 449 ms, 462 ms, 466 ms and 479 ms). Solid white line is computation.

SINGULAR AXISYMMETRIC SURFACES

To the extent that unconstrained disconnection or pinchoff of any surface will tend to be axisymmetric, at least locally near the pinchoff location, constraints on curvature signatures for axisymmetric surfaces frame the development of singularities in general surfaces. We show, based on differential geometry alone, that is, regardless of the underlying fluid flow, be it viscous or inviscid, how the spatial distribution of curvatures are constrained as singularities in principal curvatures develop. This framework is illustrated by a pinchoff via inviscid dynamics [3].

A NOVEL APPROACH TO COMPUTING BIFURCATION DIAGRAMS

A new approach to the computation of bifurcation diagrams is illustrated on axisymmetric equilibria of liquid droplets and bridges. The new technique has an architecture that solves boundary-value problems in parallel and delivers a global bifurcation diagram, capturing isolated branches. In contrast, conventional techniques deliver solutions in sequence using local path-continuation. A suitable mathematical formulation for the classical problem of predicting shapes of droplet and bridge equilibria is introduced and it is shown how the new technique yields global diagrams. Properties of these diagrams allow families of equilibria to be organized in a way that reveals common structures [4].

REFERENCES

[1] Robinson ND, Steen PH. 2000. *Stabilization of a liquid bridge using time-dependent external flow*. In preparation.

[2] Boratav ON, Chen Y-J, Steen PH. 2000. *Bubble disconnection: self-similarity and cascading physics*. To appear in Lecture Notes in Physics: "Fluid mechanics and the environment: Dynamical approaches", Springer-Verlag.

[3] Boratav ON, Steen PH. 2000. *Singular axisymmetric surfaces and pinchoff via inviscid dynamics*. In preparation.

[4] Domokos G, Szeberenyi I, Steen PH. 2000. *Simultaneously resolved bifurcation diagrams: A novel global approach applied to liquid figures of equilibrium*. J. Comp. Phys. 159, 38-57.

Presentation not available at time of printing.

INSTABILITY OF MISCIBLE INTERFACES

R. Balasubramaniam, N. Rashidnia, R.G. Wilson, J.I.D. Alexander
National Center for Microgravity Research on Fluids and Combustion,
NASA Glenn Research Center, Cleveland, Ohio
and
T. Maxworthy
University of Southern California, Los Angeles

ABSTRACT

The dynamics of miscible displacements in a cylindrical tube will be studied experimentally and numerically, specifically when a more viscous fluid displaces a less viscous fluid. In the converse situation where a less viscous fluid displaces a more viscous fluid, a fingering instability is known to occur (Petitjeans and Maxworthy, 1996), and a flight experiment proposed by Maxworthy and Meiburg (2000) to investigate the interface dynamics in this case is currently being developed by NASA.

From the current theory of miscible displacements, developed for a porous medium satisfying Darcy's law (see review by Homsy, 1987), it can be shown that in the absence of gravity the interface between the fluids is destabilized and thus susceptible to fingering only when a more viscous fluid is displaced by a less viscous one. Therefore, the initial flat interface in the displacement of a less viscous fluid by a more viscous one ought to be stable. However, numerical simulations by Chen and Meiburg (1996) for such displacement in a cylindrical tube show that for a viscosity ratio equal to e, a finger of the more viscous fluid is indeed formed. These calculations were restricted to axisymmetric solutions of the Stokes equations that are valid for negligible values of the Reynolds number.

Preliminary experiments that we have performed show that not only can fingering occur when the more viscous fluid displaces a less viscous one in a cylindrical tube, but also that under certain conditions the advancing finger achieves a sinuous or snake-like spatial pattern. These experiments were performed using silicone oils in a vertical pipette of small diameter. In the initial configuration, the more viscous fluid rested on top of the less viscous one, and the interface was nominally flat. The top fluid also had a slightly larger density than the lower fluid. A dye was added to the upper liquid for ease of observation of the interface between the fluids. The tube diameter and the density and viscosity of the fluids were such that buoyancy induced flow was not observed. The flow was initiated by draining the lower fluid from the bottom of the pipette. The draining velocity was in the range 10 to 50 microns per second. When the viscosity ratio between the fluids is two, an axisymmetric finger of the more viscous fluid was observed to form. When the viscosity ratio is ten, the steady state shape attained by the interface is not axisymmetric. Rather, the upper liquid has a sinuous shape as it flows down the pipette. The density difference for this liquid pair is 0.01 g/cc. Since the upper fluid is heavier, this raises a question whether the instability is due to buoyancy. To explore this, a small amount of carbon tetrachloride was added to the lower fluid

such that the lower fluid is slightly heavier than the upper fluid. The sinuous shape of the interface persists in this case as well, suggesting that the instability might not be due to buoyancy, but is a shear instability. However, carbon tetrachloride diffuses across the interface, and the results must be interpreted with caution.

We plan to modify our apparatus so that the more viscous fluid can be injected from either end of the tube. This will not only enable better control of the displacement compared to the draining technique we have used, but also ascertain the role played by buoyancy forces in the experiments. Thus we will perform experiments where the more viscous, heavier fluid, is pumped from below, where buoyancy has a stabilizing influence. The goal is to obtain the stability map of the system for transition to sinuous interface shapes. We will vary the viscosity ratio, the volumetric flow rate in the tube and the Peclet number for mass transfer. The fluids used will be silicone oils of various viscosities. We will simulate reduced gravity conditions by matching the density of the fluids in some cases by the addition of solvents such as carbon tetrachloride or decane to one of the fluids.

We will also perform numerical simulations of the miscible displacement process, starting from an initially flat interface, to identify the conditions when the interface achieves a sinuous shape. When such a shape is computed, we will obtain the post onset wavelength and compare it to experimental results. The computations will involve time accurate three dimensional simulations of the momentum and mass transport equations. Joseph and Renardy (1993) show that, in general, one must consider the following effects in the mixing region (i) a non-vanishing of the divergence of the velocity field caused by density changes of a fluid element due to diffusion (ii) Korteweg stresses, which accounts for forces in the fluids caused by concentration gradients. We will perform computations without and with these effects, for various values of the system parameters, chiefly the viscosity ratio, density ratio, Peclet number for mass transport and non-dimensional parameters associated with the Korteweg stresses. The Reynolds number will be small compared to one; however, we will retain the non-linear inertial terms in the momentum equations recognizing that they might be important in predicting the complex interface shapes.

References

Chen, C.H. and Meiburg, E. 1996. Miscible displacements in capillary tubes. Part 2. Numerical simulations. *J. Fluid Mech.*, **326**, 57-90.

Homsy, G.M. 1987 Viscous fingering in porous media. *Ann. Rev. Fluid Mech.*, **19**, 271.

Joseph, D.D. and Renardy, Y. 1993. Fundamentals of Two-Fluid Dynamics. Springer-Verlag.

Maxworthy, T, Meiburg E. and Balasubramaniam, R. 2000. The Dynamics of Miscible Interfaces: A Space Flight Experiment. Science Requirements Document, NASA Glenn Research Center, March 2000.

Petitjeans, P. and Maxworthy, T. 1996. Miscible displacements in capillary tubes. Part 1. Experiments. *J. Fluid Mech.*, **326**, 37-56.

NASA/CP—2000-210470

INSTABILITY OF MISCIBLE INTERFACES

R. Balasubramaniam, N. Rashidnia
R.G. Wilson, J.I.D. Alexander

National Center for Microgravity Research on Fluids and Combustion,
NASA Glenn Research Center, Cleveland, Ohio

and

T. Maxworthy

University of Southern California, Los Angeles

Fifth Microgravity Fluid Physics and Transport Phenomena Conference, Cleveland, Ohio, August, 2000.

Objectives

Study the dynamics of miscible displacements experimentally and numerically

- in a cylindrical tube
- more viscous fluid displaces a less viscous fluid
- evaluate effects of (i) non-vanishing velocity divergence in the mixing region (ii) fluid stresses due to concentration gradients (Korteweg stresses)

NASA/CP—2000-210470

Motivation

- Current theory (see Homsy, 1987) developed for a porous medium satisfying Darcy's law shows that the interface is destabilized only when a less viscous fluid displaces a more viscous fluid.

- Numerical simulations (axisymmetric) by Chen and Meiburg (1996) shows that for such displacement a finger of the more viscous fluid is indeed formed.

- Our preliminary experiments show that not only can fingering occur when a more viscous fluid displaces a less viscous one in a cylindrical tube, but also that under certain conditions the advancing finger achieves a sinuous spatial pattern.

Preliminary Experiments

- Silicone oils of various viscosites used in a vertical pipette of diameter 3 mm. Dye added to the upper fluid for observing the interface.
- Flow initiated by draining the pipette (velocity $\sim$ 10 to 50 $micron/s$)
- Axisymmetric finger observed when the viscosity ratio is 2
- Interface has a sinuous shape when the viscosity ratio is 10, both for
  - A heavier upper fluid ($\frac{\Delta\rho}{\rho} \approx 0.01$) (pure silicone oils)
  - A heavier lower fluid ($\frac{\Delta\rho}{\rho} \approx -0.01$), (carbon tetrachloride added to the lower fluid)

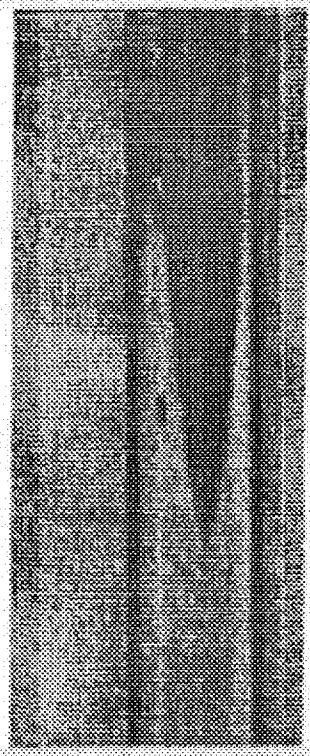

Figure 1a: Axisymmetric finger of a more viscous silicone oil that displaces a less viscous silicone oil. Viscosity ratio = 2.

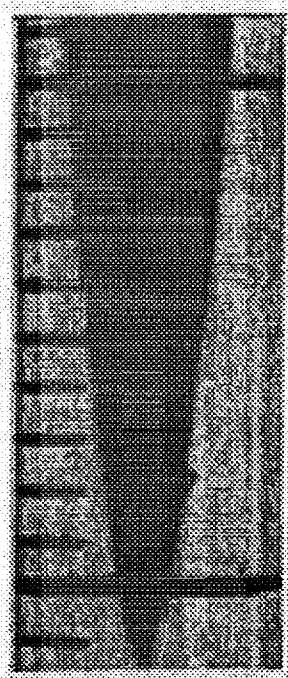

Figure 1b: Axisymmetric finger of a less viscous silicone oil that displaces a more viscous silicone oil. Viscosity ratio = 0.5.

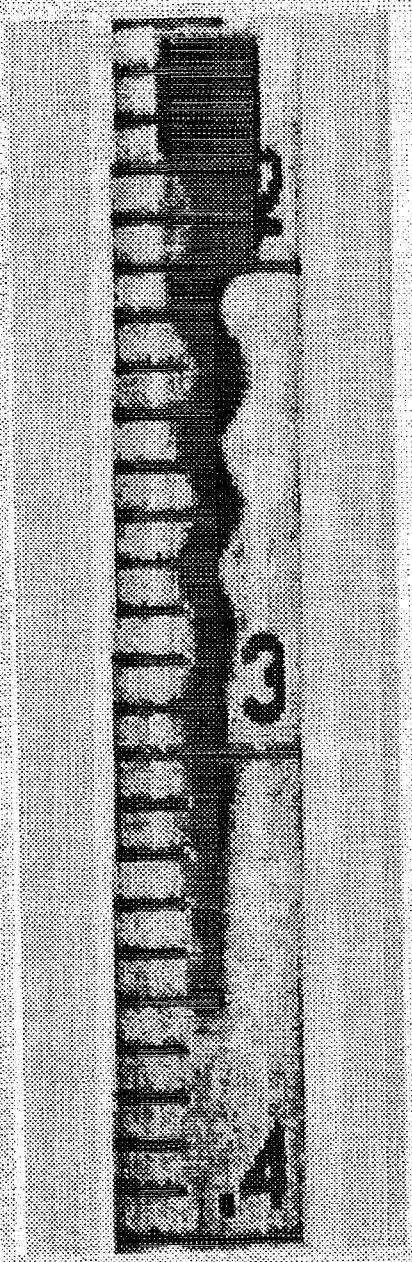

Figure 2: Sinuous shape of the interface between the silicone oils. Viscosity ratio = 10.

Proposed experiments

- Modify experimental apparatus and inject more viscous fluid from either end of the tube.

- Vary the viscosity ratio, density ratio, volumetric flow rate and Peclet number for mass transfer and obtain stability map of the system for transition to sinuous interface shapes.

- Explore density matching of the fluids further using solvents such as carbon tetrachloride, decane.

Proposed numerical simulations

- Time accurate three dimensional calculations of the governing equations will be performed starting from a quiescent, flat interface.

- Identify the conditions when the interface achieves a sinuous shape

- Following Joseph and Renardy (1993), we will consider the following effects in the mixing region, and evaluate their effect on the interface shape

  - Non-vanishing divergence of the velocity field caused by density changes of a fluid element due to diffusion

  - Korteweg stresses, which account for fluid forces due to concentration gradients.

LOW VELOCITY IMPACT EXPERIMENTS IN MICROGRAVITY

J. E. Colwell, Laboratory for Atmospheric and Space Physics, Univ. of Colorado, Boulder, and S. Sture, Dept. of Civil, Env., and Arch. Engineering, Univ. of Colorado, Boulder.

BACKGROUND

Protoplanetary disks, planetary rings, the Kuiper belt, and the asteroid belt are collisionally evolved systems. Although objects in each system may be bombarded by impactors at high interplanetary velocities, they are also subject to repeated collisions at low velocities ($v<10$ m/s). In some regions of Saturn's rings, for eample, the typical collision velocity inferred from observations by the Voyager spacecraft and dynamical modeling is a fraction of a centimeter per second [1]. These interparticle collisions control the rate of energy dissipation in planetary rings and the rate of accretion in the early stages of planetesimal formation. In the asteroid belt collisions typically occur at several km/s (e.g. [2]); however secondary craters are formed at much lower impact speeds. In the Kuiper belt, where orbital speeds and eccentricities are much lower, collisions between Kuiper belt objects (KBOs) can occur at speeds below 100 m/s. In the early solar system, KBOs accreted in the same way planetesimals accreted in the inner solar system, however some regions of the Kuiper belt may now undergo erosional collisions [3,4].

Dust may be present on the surface of all of these objects in the form of a fine regolith created from micrometeoroid bombardment (rings, asteroids, KBOs), high speed interparticle collisions (asteroids, KBOs) or as a product of accretion from protoplanetary dust. Dust released in these collisions is often the only observable trace of the source objects and may be used to infer the physical properties of those larger bodies (e.g. [5,6]).

EXPERIMENTAL PROGRAM

We are conducting a broad program of microgravity impact experiments into dust to study the dissipation of energy in low energy collisions and the production of dust ejecta in these impacts. The Collisions Into Dust Experiment (COLLIDE) flew on STS-90 in April 1998 [7]. The principal results of that experiment were measurements of the coefficient of restitution for impacts into powders at impact speeds below 1 m/s. Almost no ejecta was produced in impacts at 15 cm/s into JSC-1 powder, and the coefficient of restitution was ~ 0.03. COLLIDE-2 is undergoing final preparations for a flight in 2001. The experiment will conduct six impact experiments at impact speeds between 1 and 100 cm/s. The target material will have a low relative density to mimic the regolith on low surface gravity objects in space, such as planetesimals, planetary ring particles, and asteroids.

A new experimental program, the Physics of Regolith Impacts in Microgravity Experiment (PRIME) will use NASA's KC-135 aircraft to explore a much broader range of parameter space than is possible with COLLIDE, at slightly higher impact velocities. PRIME will be capable of conducting up to 16 impact experiments each flight day on the KC-135. Impact velocities between 50 cm/s and 5 m/s will be studied into a variety of target materials and size distributions. The experiment will consist of an evacuated canister with 6 to 8 impact chambers on each of two rotating turntables. Each impact chamber will include a target sample and a launcher with a unique set of parameters. Two viewports will allow high speed video photography of impacts from two orthogonal views with the use of a mirror mounted inside the canister.

Data from COLLIDE and ground-based experimental studies suggest that particle size distribution is an important parameter in controlling the response of granular media to low velocity impacts. Individual grain shapes may also play an important role in the conversion of impactor kinetic energy to target grain kinetic energy. We will also make use of numerical simulations of the impact process to understand the relevant parameters for experimental study.

High speed video of the impact and ejecta patterns will be analyzed to determine the ejecta mass and velocity distributions. This in turn will have direct application for understanding the behavior of dust on the surfaces of planetary objects including asteroids and small moons when disturbed by low velocity impacts and perturbations. These include naturally occurring impacts as well as disturbances to the surface from human and spacecraft activity. The velocity distribution of the ejecta determines the amount of material launched to various altitudes above the surface and escaping the parent body. This information is important for spacecraft instruments landing on airless bodies with low surface gravity and powdery regoliths.

REFERENCES

[1] Esposito, L. W., Understanding Planetary Rings, *Annu. Rev. Earth Planet. Sci., 21*, 487-523, 1993

[2] Bottke, W. F. Jr., M. C. Nolan, R. Greenberg, and R. A. Kolvoord, Velocity Distributions among Colliding Asteroids, *Icarus, 107*, 255-268, 1994.

[3] Stern, S. A., and J. E. Colwell, Accretion in the Edgeworth-Kuiper Belt: Forming 100-1000 km Radius Bodies at 30 AU and Beyond, *Astron. J., 114*, 841-849, 1997a.

[4] Stern, S. A., and J. E. Colwell, Collisional erosion in the primordial Edgeworth-Kuiper Belt and the generation of the 30-50 AU Kuiper Gap, *Astrophys. J. 490*, 879-882, 1997b

[5] Colwell, J. E., and L. W. Esposito, A numerical model of the Uranian dust rings, *Icarus, 86*, 530-560, 1990a.

[6] Colwell, J. E. and L. W. Esposito, A model of dust production in the Neptune ring system, *Geophys. Res. Lett., 17*, 1741-1744, 1990b.

[7] Colwell, J. E., and M. Taylor, Low Velocity Microgravity Impact Experiments into Simulated Regolith, *Icarus 138*, 241-248, 1999.

NASA/CP—2000-210470

1337

Low Velocity Impact Experiments in Microgravity

Joshua E. Colwell

Laboratory for Atmospheric and Space Physics

Stein Sture

Dept. of Civil, Eng., and Arch. Engineering

University of Colorado, Boulder

NASA/CP—2000-210470

1338

Introduction

Collisions play an important role in the evolution of the solar system. High velocity impacts produce craters and fragment asteroids and small moons. Low velocity impacts (V<100 m/s), however, occur much more frequently in some systems, such as planetary rings. Such low speed collisions also dominated the early stages of planet formation, occur in the production of secondary craters in the asteroid belt, and control the collisional evolution in the Kuiper Belt of comets.

The amount of energy dissipated and the amount of dust ejected from the surface in the impact determines whether the collisions are accretional or erosional for planetesimal formation. Such collisions also release dust into planetary dust rings at each of the giant planets.

NASA/CP—2000-210470

1339

Description of Experiments

The Collisions Into Dust Experiment (COLLIDE) is a space shuttle experiment which performs 6 impact experiments into simulated planetary regolith at speeds between 1 and 100 cm/s (Fig. 1). COLLIDE flew on STS-90 in April 1998 and has completed modifications and improvements for a flight in 2001 as COLLIDE-2. Results from STS-90 showed low coefficients of restitution and no ejecta produced (Fig. 2). Ground-based experiments indicate that launch vibrations resulted in a hardening of the target surface inhibiting dust ejecta. COLLIDE-2 will use a different target sample (rounded quartz sand) which does not significantly harden after vibration.

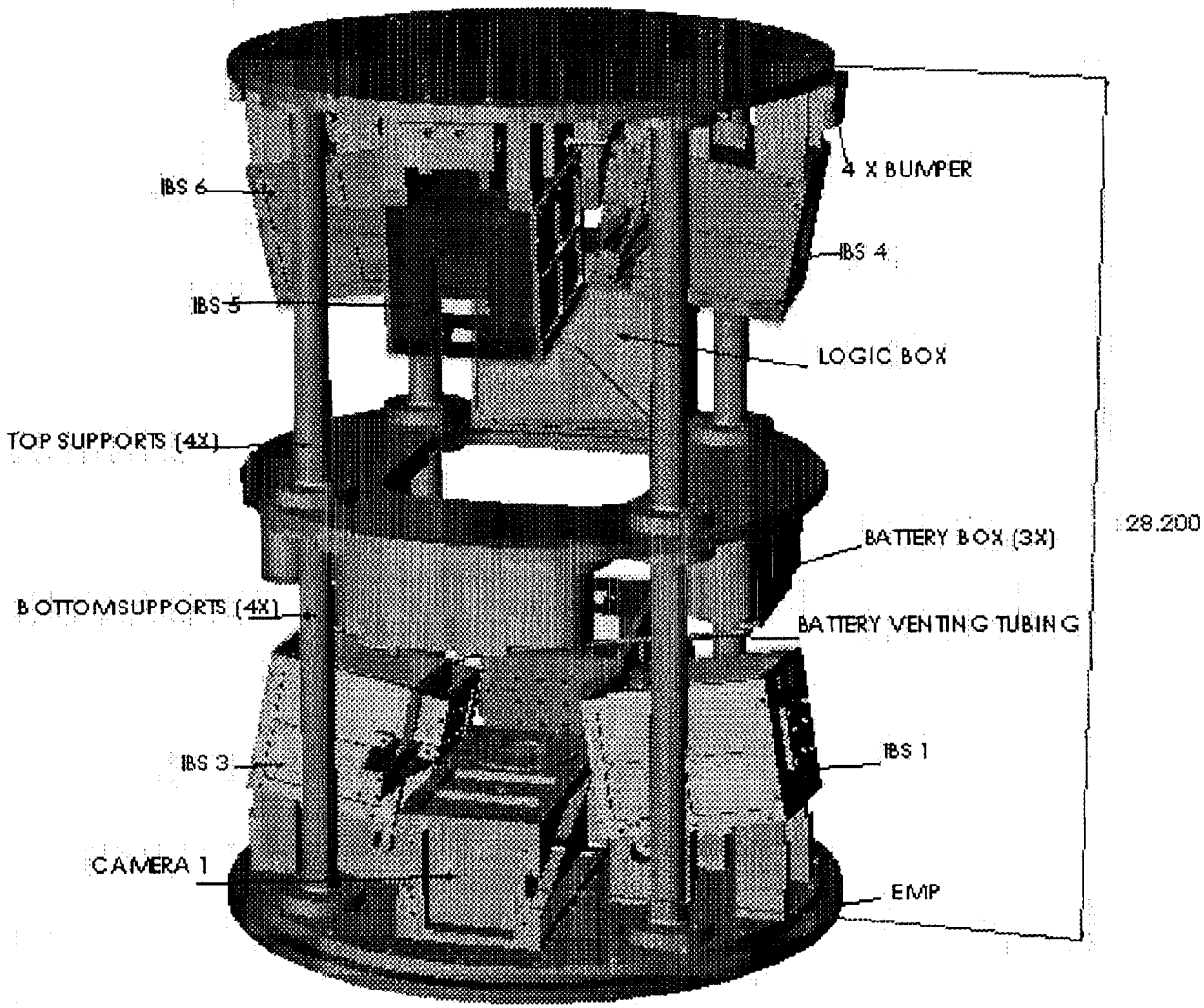

Fig. 1: Space Shuttle payload COLLIDE-2. IBS's are 6 independent impact experiments.

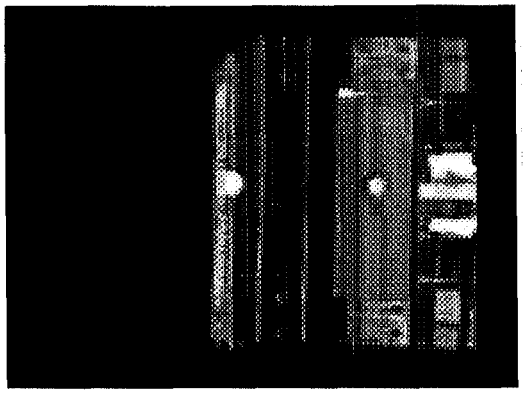

One frame from the COLLIDE-1 experiment on STS-90. The projectile is in contact with the target surface at left and an orthogonal view is visible in the mirror. White grid lines are 2 cm apart.

COLLIDE-1 Coefficients of Restitution

IBS	Projectile Speed (cm/s)	Normal Rebound Velocity (cm/s)	Coefficient of Restitution (ε_n)
1	14.80±0.09	0.41±0.02	0.028±0.002
2	12.18±0.14	6.86±0.12	0.56±0.01*
	6.6±0.2	2.7±0.2	0.41±0.04*
3	28±2.8	13±1.3	0.46±0.1*
4	17.10±0.21	0.37±0.02	0.022±0.002
5	0	N/A	N/A
6	90±15	2.8±0.5	0.03±0.01

Notes: *: rebound off painted aluminum door instead of JSC-1 powder. The projectile in IBS 2 bounced off the door a second time, allowing measurement of ε_n for two impact velocities. Uncertainties are standard deviations from linear regression fits to displacement measurements, except for IBS 3 and IBS 6 which are higher due to the poor image quality and are based on estimates of error in measuring position. ε_n is the ratio of the normal component of the rebound velocity to the impact velocity.

Fig. 2: Results from COLLIDE-1 low velocity impacts into JSC-1 powder at v=15-90 cm/s.

PRIME

The Physics of Regolith Impacts in Microgravity Experiment (PRIME) will expand on COLLIDE and will generate a much larger data set of low velocity impacts into granular media. PRIME will study the impact velocity regime from v=0.1 to 10 m/s. PRIME is designed to operate in the NASA KC-135 and will perform 12-16 low velocity impact experiments per flight day. The larger data set (compared to 6 experiments per shuttle flight for COLLIDE) will enable us to explore a much broader parameter space. PRIME hardware is based on COLLIDE but takes full advantage of the additional space and human operators on the KC-135 (Fig. 3).

NASA/CP—2000-210470

1343

Experimental Plan

Various target powders will be used to study the effects of material strength (or cohesion), friction angle, particle shape, and particle size, and we will vary target depth. Ground-based experiments performed at LASP have shown that more ejecta is produced in materials with low relative density. Significant dust ejecta has been produced at impact speeds of 1.5 to 2.0 m/s in the lab at 1 g. Microgravity is needed to accurately simulate the regolith properties, to reach impact speeds of less than 1 m/s, and to measure the mass and velocity distributions of all ejecta produced in the impacts. We will supplement our experiments with granular media simulations (Fig. 4).

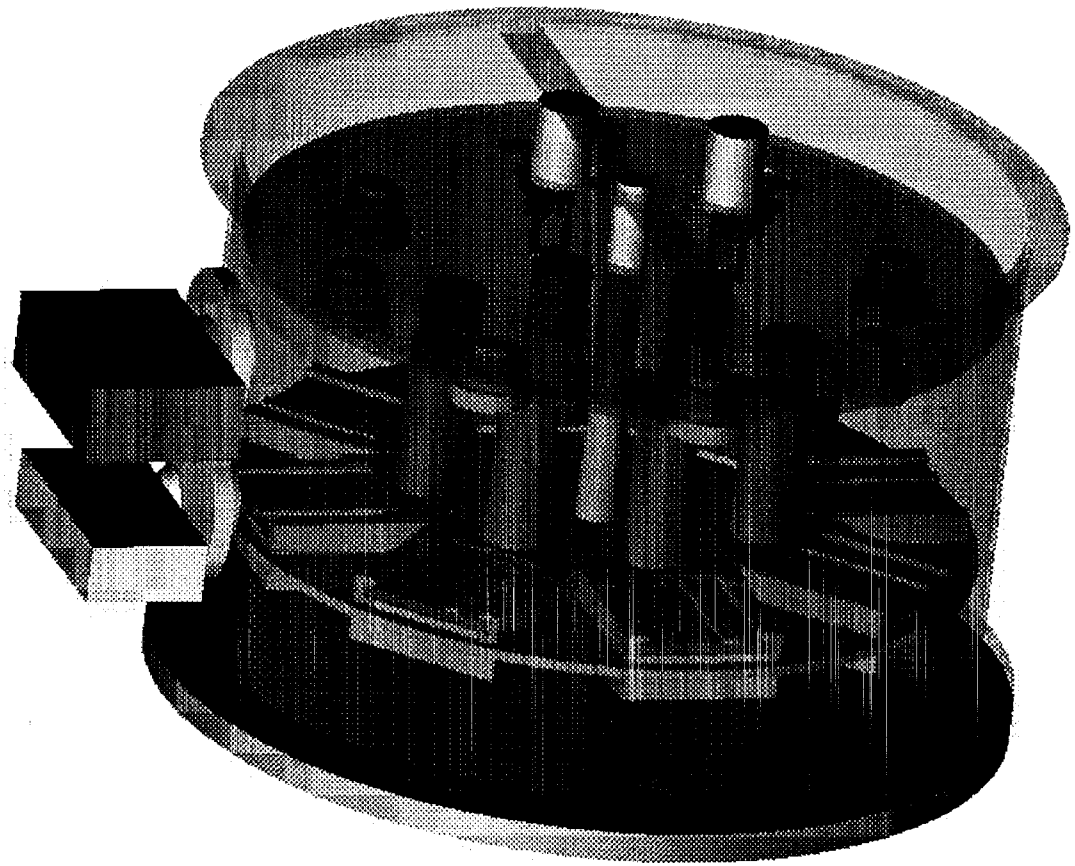

Fig. 3: Conceptual view of PRIME showing two external high speed cameras and 8 impact experiments inside the vacuum chamber. External cameras, power supply, and control electronics free up space inside the container for additional impact experiments. 48-64 impact experiments will be performed per flight campaign on the KC-135.

Numerical Simulations

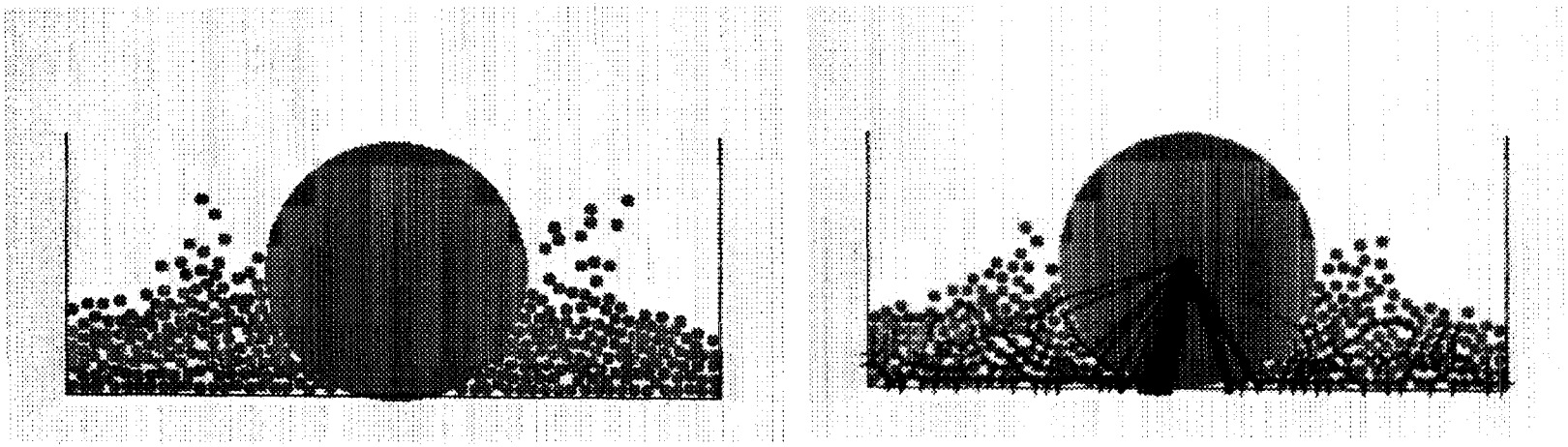

Fig. 4: Example of 2-D simulation of a 2 cm impactor hitting a bed of smaller particles at 2 m/s. Interparticle contact forces are indicated by lines in the figure on the right. (Simulations performed by M. Nakagawa, Colorado School of Mines.) We will carry out 2-D and 3-D simulations of low velocity impacts to compare with our experimental results and to explore regions of parameter space (e.g. large scale; v<10 cm/s; v>10 m/s; etc.) which cannot be achieved with PRIME.

NASA/CP—2000-210470

1346

Summary

PRIME and COLLIDE-2 will allow us to identify the transition in multi-dimensional parameter space between several important regimes in low-velocity impacts: (1) ejecta production with rebound of the impactor; (2) rebound with no ejecta; (3) sticking of the impactor with no ejecta; and (4) sticking of the impactor with ejecta. Our exploration of parameter space will show the importance of the following parameters: (1) impact velocity; (2) impact energy; (3) target size distribution; (4) target relative density; (5) target mechanical properties; and (6) gravitational acceleration.

These data will have direct application to several problems in planetary science and exploration of the solar system.

SURFACE COLLISIONS INVOLVING PARTICLES AND MOISTURE (SCIP'M)

R. Davis, H. Wilson, D. Rager, and Y. Zhao
Department of Chemical Engineering
University of Colorado
Boulder, Colorado 80309-0424
303-492-7314; robert.davis@colorado.edu

ABSTRACT

Collisions of particles with wet surfaces are important in many industrial and natural applications, including filtration, agglomeration, wet granular flow, and pollen capture. A fundamental study of such collisions is underway in our laboratory. Current experimental work involves dropping small plastic and metal balls onto a surface which is overlaid with a thin layer of a viscous fluid and tilted at an angle to the gravity vector. Critical conditions at which the spheres bounce instead of sticking to the surface are determined with the aid of high-frequency strobotic photography. When bouncing does occur, the rebound velocity, angle, and rotation are determined from image analysis of the photographs. Preliminary results show that bouncing increases with increasing ball size and impact speed, and with decreasing viscosity and thickness of the fluid layer. The results are interpreted using elastohydrodynamic theory, accounting for lubrication pressure in the thin viscous layer and Hertzian deformation of the solid ball and opposing surface.

The laboratory experiments are restrict to high impact velocities (~ 1 m/s, or higher), as otherwise gravitational acceleration obscures the rebound. As a result, relatively thick and viscous fluids layers on the surface are required to observe the transition between bouncing and sticking. Future experiments with lower impact speeds (~ 0.1 m/s, or lower) and surfaces wetted with water are planned for a low-gravity environment.

Presentation not available at time of printing.

STEREO IMAGING VELOCIMETRY OF MIXING DRIVEN BY BUOYANCY INDUCED FLOW FIELDS

W.M.B. Duval, D. Jacqmin, B.M. Bomani, I.J. Alexander, M. Kassemi, C.Batur, B.V. Tryggvason, D.V. Lyubimov, T.P. Lyubimova

Microgavity Fluid Physics Branch
NASA Glenn Research Center
Cleveland, Ohio 44135

ABSTRACT

Mixing of two fluids generated by steady and particularly g-jitter acceleration is fundamental towards the understanding of transport phenomena in a microgravity environment. We propose to carry out flight and ground-based experiments to quantify flow fields due to g-jitter type of accelerations using Stereo Imaging Velocimetry (SIV), and measure the concentration field using laser fluorescence. The understanding of the effects of g-jitter on transport phenomena is of great practical interest to the microgravity community and impacts the design of experiments for the Space Shuttle as well as the International Space Station. The aim of our proposed research is to provide quantitative data to the community on the effects of g-jitter on flow fields due to mixing induced by buoyancy forces. The fundamental phenomenon of mixing occurs in a broad range of materials processing encompassing the growth of opto-electronic materials and semiconductors, (by directional freezing and physical vapor transport), to solution and protein crystal growth. In materials processing of these systems, crystal homogeneity, which is affected by the solutal field distribution, is one of the major issues. The understanding of fluid mixing driven by buoyancy forces, besides its importance as a topic in fundamental science, can contribute towards the understanding of how solutal fields behave under various body forces. The body forces of interest are steady acceleration and g-jitter acceleration as in a Space Shuttle environment or the International Space Station. Since control of the body force is important, the flight experiment will be carried out on a tunable microgravity vibration isolation mount, which will permit us to precisely input the desired forcing function to simulate a range of body forces. To that end, we propose to design a flight experiment that can only be carried out under microgravity conditions to fully exploit the effects of various body forces on fluid mixing.

Recent flight experiments, by the P.I. through collaboration with the Canadian Space Agency (STS-85, August 1997), aimed at determining the stability of the interface between two miscible liquids inside an enclosure show that a long liquid column (5 cm) under microgravity isolation conditions can be stable, .ie. the interface remains sharp and vertical over a short time scale; thus transport occurs by molecular mass diffusion. On the other hand, when the two liquids were excited from a controlled vibration source (Microgravity Vibration Isolation Mount) two to four mode large amplitude quasi-stationary waves were observed. The data was limited to CCD recording of the dynamics of the interface between the two fluids. We propose to carry out flight experiments to quantify the dynamics of the flow field using Stereo Imaging Velocimetry and measure the concentration field using laser fluorescence. The results will serve as a basis to understand effects of g-jitter on transport phenomena, in this case mass diffusion. As the

quasi-sationary waves for such a long liquid column can only occur in microgravity conditions, measurement of the kinematics of the flow field will shed light on the instability mechanism.

The research will allow measurement of the flow field in microgravity environment to prove two hypotheses:
(1) Maxwell's hypothesis: finite convection always exists in diffusing systems, and
(2) Quasi-stationary waves inside a bounded enclosure in a micogravity environment is generated by Kelvin-Helmholtz instability; resonance of the interface which produces incipient mixing is due to Rayleigh-Taylor instability.

The first hypothesis can be used as a benchmark experiment to illustrate diffusive mixing. The second hypothesis will lead to the understanding of g-jitter effects on buoyancy driven flow fields which occur in many situations involving materials processing, and other basic fluid physics phenomena. In addition, the second hypothesis will also provide insight in how Rayleigh-Taylor and Kelvin-Helmholtz instabilities propagate concentration fronts during mixing. Measurement of the flow field using SIV is important because it is the flow field which causes instability at the interface between the two fluids.

Mixing driven by buoyancy induced flow fields will be addressed both experimentally and computationally. The experimental effort will address the kinematics of mixing: stretching, transport and chaos. Quantification of the mechanisms of mixing will consists of measuring the flow field using the SIV system at Glenn and capturing the dynamics of the interface, to measure mass transport, using a CCD camera. These experiments will be carried out within the framework of Earth's gravity and g-jitter microgravity acceleration as in a Space Shuttle environment or the International Space Station. The g-jitter will be induced and controlled using a tunable vibration isolation platform to isolate against vibration as well as input periodic and random vibration to the system. The parametric range of the microgravity experiment will be extended from the experiments on STS-85 to investigate higher mode quasi-stationary waves (8 to 12), as well as resonance regions which leads to chaos and turbulence. Ground-based experiments will focus on effects of vibration on stably stratified fluid layers in order to scale for possible scenarios in a microgravity environment. These vibrations will be subjected perpendicular to the concentration field on the ground since the parallel case can only be carried out in a microgravity environment.

The concept of dynamical similarity will be applied to tune the experiments as closely as possible to a Space Shuttle environment or the International Space Station. The computational effort will take advantage of the Computational Laboratory at Glenn to corroborate the experimental findings with predictions of the dynamics of the flow field using the codes FLUENT (finite difference based) and FIDAP (finite element based). We will investigate two important cases, single-fluid model to address dilute systems with negligible jump in viscosity and the more general two-fluid model which accounts for finite jump in viscosity. Apart from its microgravity relevance, this experiment is well suited to study dynamics in nonlinear systems.

Presentation not available at time of printing.

GRANULAR MATERIAL FLOWS WITH INTERSTITIAL FLUID EFFECTS

M. L. Hunt, C. S. Campbell and C. E. Brennen
California Institute of Technology
Pasadena, CA 91125

ABSTRACT

Modern granular flow theory began with the work of Bagnold in 1954 [1]. In his seminal experiments, 1-mm wax spheres suspended in a glycerin-water-alcohol mixture were sheared in a coaxial cylinder rheometer. The rheometer was cleverly designed to measure both the shear and normal forces applied to the walls. From the experiments, Bagnold identified two distinct flow regimes: the macroviscous and the grain inertia. These regimes can be distinguished using a quantity that is now referred to as the Bagnold number, $Ba = \rho d^2 \lambda^{1/2} \dot{\gamma}^2 / \mu$, where ρ is the density (generally taken as the value for the particle phase), d is the particle diameter, λ is a function defined by Bagnold that depends on the solid fraction, $\dot{\gamma}$ is the imposed shear rate, and μ is the dynamic viscosity. In the macroviscous regime, the normal and the tangential stresses were linearly proportional to the liquid's viscosity and the shear rate. In the grain-inertia regime, the stresses were independent of the fluid viscosity, and instead depended on the density, the square of the shear rate and the square of the particle diameter. The dependence on the function λ also differed in the two regimes.

Despite its importance and the almost universal acceptance of these results, there are still questions regarding the analyses and the conclusions. For example, the stress behaviors predicted by Bagnold's analyses also result from simple dimensional analysis, if the assumption is made that in one regime the stresses are independent of the particle (diameter dependence) and in the other regime the stresses are independent of the fluid viscosity. More importantly, the interpretation of the experiments is problematic because the experiments involved a suspension and only a single particle size was studied. In a density-matched suspension, the inertia of the particle and that of the fluid are indistinguishable; hence, the results for the scaling of the stresses may not be applicable to situations in which the densities differ. Additional questions surround the normal stress, which was measured by using a flexible membrane for the inner stationary cylinder that would deflect in response to the applied pressure. The system was insensitive to small pressure changes, and the membrane deflection may have altered the gap size and the mean solid concentration.

The current work at Caltech focuses on experiments and simulations for conditions similar to those originally examined by Bagnold. The low-gravity environment offers the opportunity to reexamine Bagnold's experiments for particles of varying densities. These experiments should provide an opportunity to separate the effects of the inertia of both the fluid and solid phases on the shear and normal stresses. We plan to conduct experiments using different particle sizes and density, varying particle concentrations and shear rates that would extend the Bagnold number well into the grain inertia regime. In addition, the work involves a computational component that

uses a combination of smooth-particle hydrodynamics and the discrete element method to compute liquid-solid flows.

The experimental apparatus will consist of a coaxial shear cell with a rotating outer cylinder. The inner cylinder will be mounted on a friction-free air bearing and constrained from rotation by a load cell to measure the shear force. For the flight instrument, pressure sensors will be inserted in the wall of the inner cylinder to simultaneously measure the normal force [2,3]. The granular material and the fluid will be contained in the annular region of the experiment. We have a prototype shear cell already constructed that we are using as a basis for the design of the flight instrument.

In addition to the experimental measurements, the project also involves a computational phase that uses a combination of the smoothed particle hydrodynamics technique (SPH) and the discrete element method (DEM) to model flows containing a viscous fluid and solid macroscopic particles. The two-dimensional numerical simulations are validated by comparing with experimental measurements for wake size, drag coefficient and heat transfer for flow past a circular cylinder at Reynolds numbers up to approximately 100. The comparisons demonstrate that the technique can be successfully used for incompressible flows at Reynolds numbers up to approximately 100.

The central focus of the work, however, is in computing flows of liquid-solid mixtures. Hence, the simulations were run for neutrally buoyant particles contained between two shearing plates for different solid fractions, fluid viscosities and shear rates. The simulations involved up to 18 solid particles sheared between two plates separated by a distance of approximately 8 particle diameters. The no-slip boundary condition was satisfied on the surface of the particles and the bounding walls. The tangential force resulting from the presence of particles shows an increasing dependence on the shear rate, from a linear regime for macro-viscous flows to a square dependence for grain inertia flows. The normal force showed considerable variation with time, which is not fully understood and is part ongoing numerical simulations. In addition, the simulations indicated stability problems at higher shear rates; the instability has also been observed in other SPH simulations. Hence, the focus of the current work involves the effect of the smoothing function and other features of the simulation technique on the flow parameters.

REFERENCES

[1] R.A. Bagnold, Experiments on a Gravity-Free Dispersion of Large Solid Spheres in a Newtonian fluid under Shear, ***Proc. R. Soc. London* 225**, 49-63 (1954).

[2] C.S. Campbell & K. Rahman, An Improved Particle Pressure Transducer, ***Meas. Sci. Techn.* 3,** 709-712 (1992).

[3] R. Zenit, M.L. Hunt & C.E. Brennen, Collisional Particle Pressure Measurements in Solid-Liquid Flows, ***J. Fluid Mech.* 353**, 261-283 (1997).

[4] A.V. Potapov, M.L. Hunt & C.S. Campbell, Liquid-Solid Flows using Smoothed Particle Hydrodynamics and the Discrete Element Method, submitted to ***Powder Technology*** (2000).

Presentation not available at time of printing.

SHEET FLOWS, AVALANCHES, AND DUNE MIGRATION ON EARTH AND MARS

D. Bideau, Université de Rennes I, 35042 Rennes Cedex, France
D. Hanes, University of Florida, Gainesville, FL 32611 USA
J. Jenkins, Cornell University, Ithaca, NY 14853 USA

ABSTRACT

We have begun a study of sheet flows and avalanches of granular materials in terrestrial and Martian environments. Sheet flows are relatively thin, highly concentrated regions of grains flowing near the ground under the influence of a strong turbulent wind. In them, grains are suspended by inter-particle friction, inter-particle collisions, and/or the velocity fluctuations of the turbulent gas. Avalanches are flows of dry, cohesionless granular materials that are driven by gravity down inclines against the frictional and collisional resistance of the grains.

The study will employ and extend existing theories involving particle-particle and gas-particle interactions to apply to the evolution of a typical terrestrial sand dune during a sandstorm. Experiments will explore the generation of airborne particles in collisions, the flow of air and particles over particle beds, and the dependence of the angle of repose on particle packing and friction. We will also investigate the influence of particle size, reduced gravity, gas density, and gas viscosity in order to extend our results to the Martian environment.

The focus will be on modeling mechanisms for the transport of granular materials by the wind and gravity. The anticipated result of this activity will be continuum equations for the balance of mass, momentum, and energy for both the particle phase and the gas phase that may be employed in numerical codes to study unsteady, inhomogeneous flows.

In the study of suspension and transport by the wind, an effort will be made to understand the transition between successive regimes of flow that are observed as the strength of the wind increases. In particular, the means by which momentum and energy are exchanged between particles and between particles and the gas will be described and quantified. Also, the interface between the bed and the flow will be studied in experiments and computer simulations in order to understand better the balance of momentum and energy there. This will lead to improved boundary conditions for the continuum equations.

In the study of gravitational avalanches, an effort will be made to distinguish between frictional and collisional regimes and to introduce or improve upon models appropriate to each. Computer simulations and existing experimental data will form the basis of the study of flow. Slope failure and flow initiation will also be studied using computer simulations and physical experiments.

The continuum equations and boundary conditions will be employed to describe the flow of sand and air over a dune with its long axis transverse to a steady wind. The idea is that the dune fed with a given volume flux of sand that flows as sheets up its front face and avalanches down its back face. The goal is to predict the evolution of the shape of the dune and its motion for winds and feeds of various strengths. The predicted air and sand flow will be compared with that seen in field studies.

Finally, the continuum equations will be applied to the reduced gravity and thinner atmosphere of Mars. Here, images indicate that sand motion and dune formation and motion are possible; the reduction of the gas viscosity associated with the lower density and temperature of

the Martian atmosphere is compensated for by very high winds. The expertise developed in this part of the research is also expected to apply to problems in materials handling associated with both pneumatic transport and gravitational flows in reduced gravity.

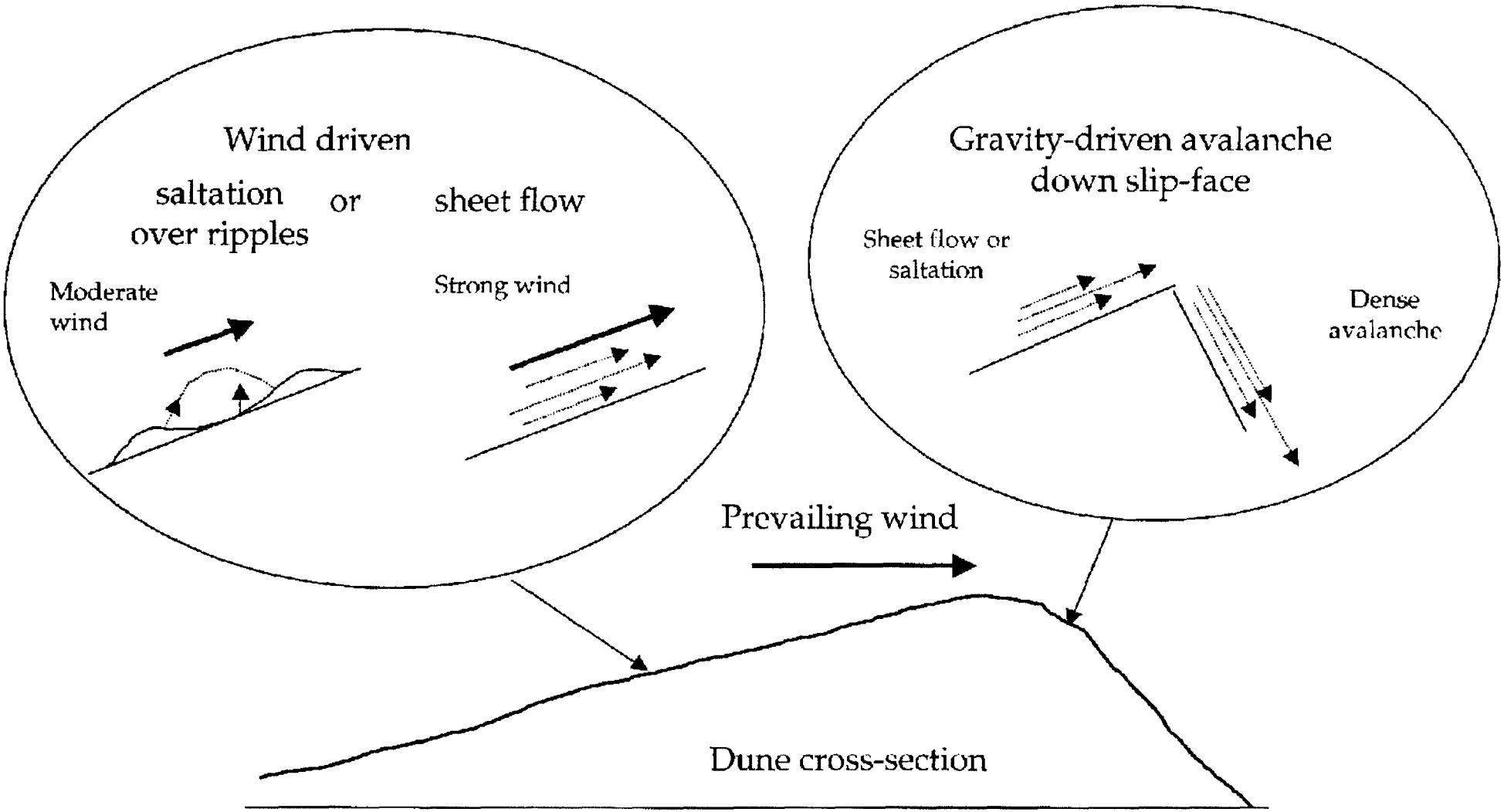

Mechanisms of Dune Formation and Migration

DENSE, FRICTIONAL AVALANCHES

Frictional RUB/Gravitational BUMP

$$S = \mu N + u'\mu\Im$$

Steady:

$$\tan\theta - \mu = \left(\frac{D}{g\cos\theta}\right)^{1/2}\left(1 - \beta\mu\frac{H-z}{2D}\right)^{1/2}\beta u'$$

Dimensionless:

$$u' = \frac{\tan\theta - \mu}{\mu}\frac{1}{\beta}\left(1 - \beta\mu\frac{H-z}{2}\right)^{-1/2}$$

RUB, FALL & BUMP

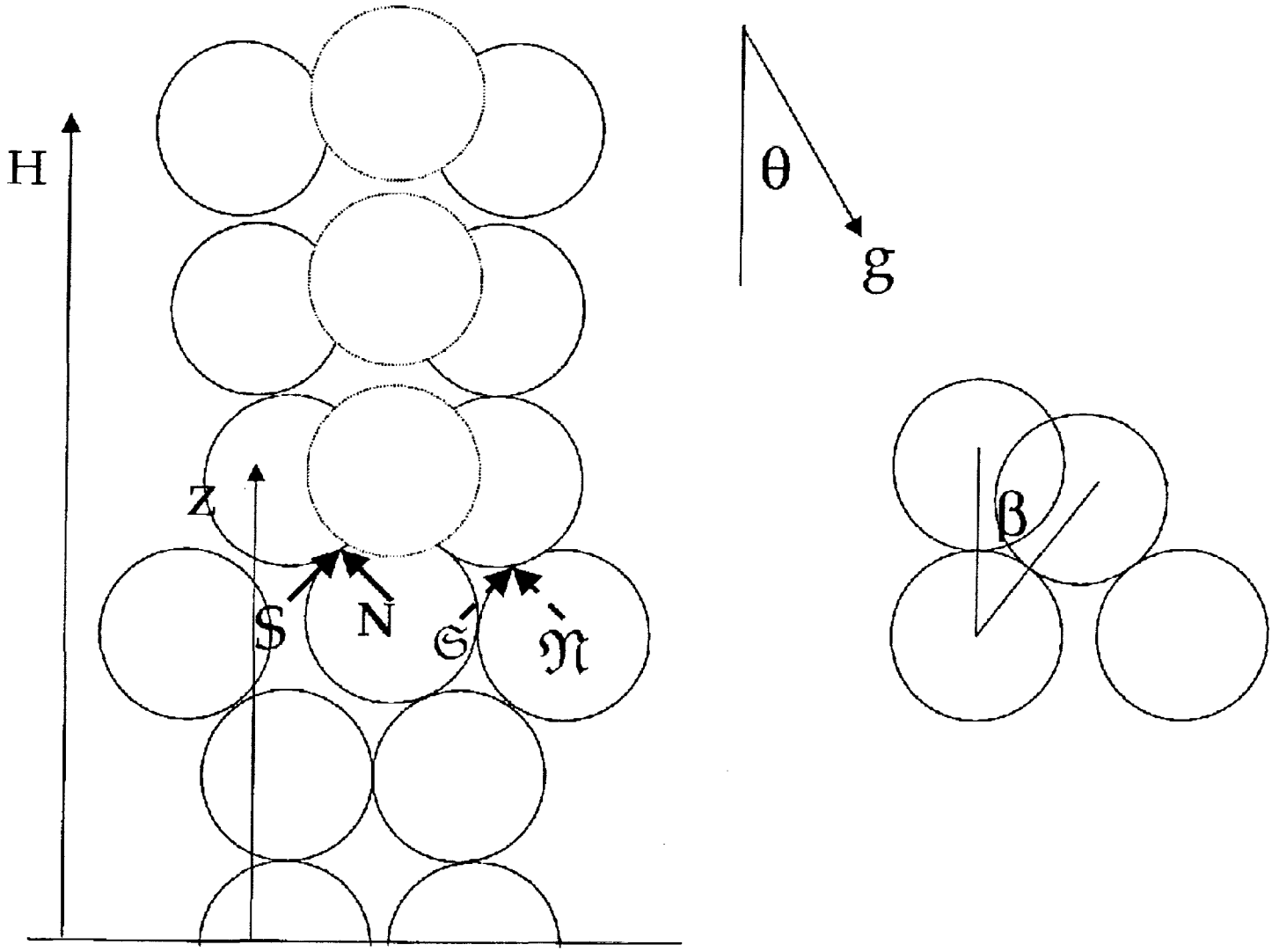

Frictional Rubbing:

$$S = \mu N = \mu mng\cos\theta \doteq \mu m\frac{H-z}{D}g\cos\theta$$

Frictional Fall:

$$v^2 = g\cos\theta\left(1-\beta\mu\frac{H-z}{2D}\right)D\beta^2$$

Frictional Bump:

$$\mathfrak{S} = \mu\mathfrak{N} = \mu mv$$

MECHANISMS OF SAND TRANSPORT

1. SALTATION

Jumping and splashing of individual grains driven by a turbulent wind.

2. SHEET FLOWS

Dense flows of sand near the bed in the presence of strong winds.

Dispersion due to collisions between grains and suspension by the turbulent velocity fluctuations of the wind.

2. DENSE, FRICTIONAL AVALACHES

Gravitational flows of sand down the back of a dune.

Grains rub, fall, and bump rather than colliding.

SALTATION

Turbulent boundary layer:

$$u(z) = u_* \ln\left(\frac{z}{k}\right)$$

$u_* \equiv (S_T / \rho_f)^{1/2}$ Shear velocity

S_T Turbulent shear stress

ρ_f Air density

k Bed roughness

Splash

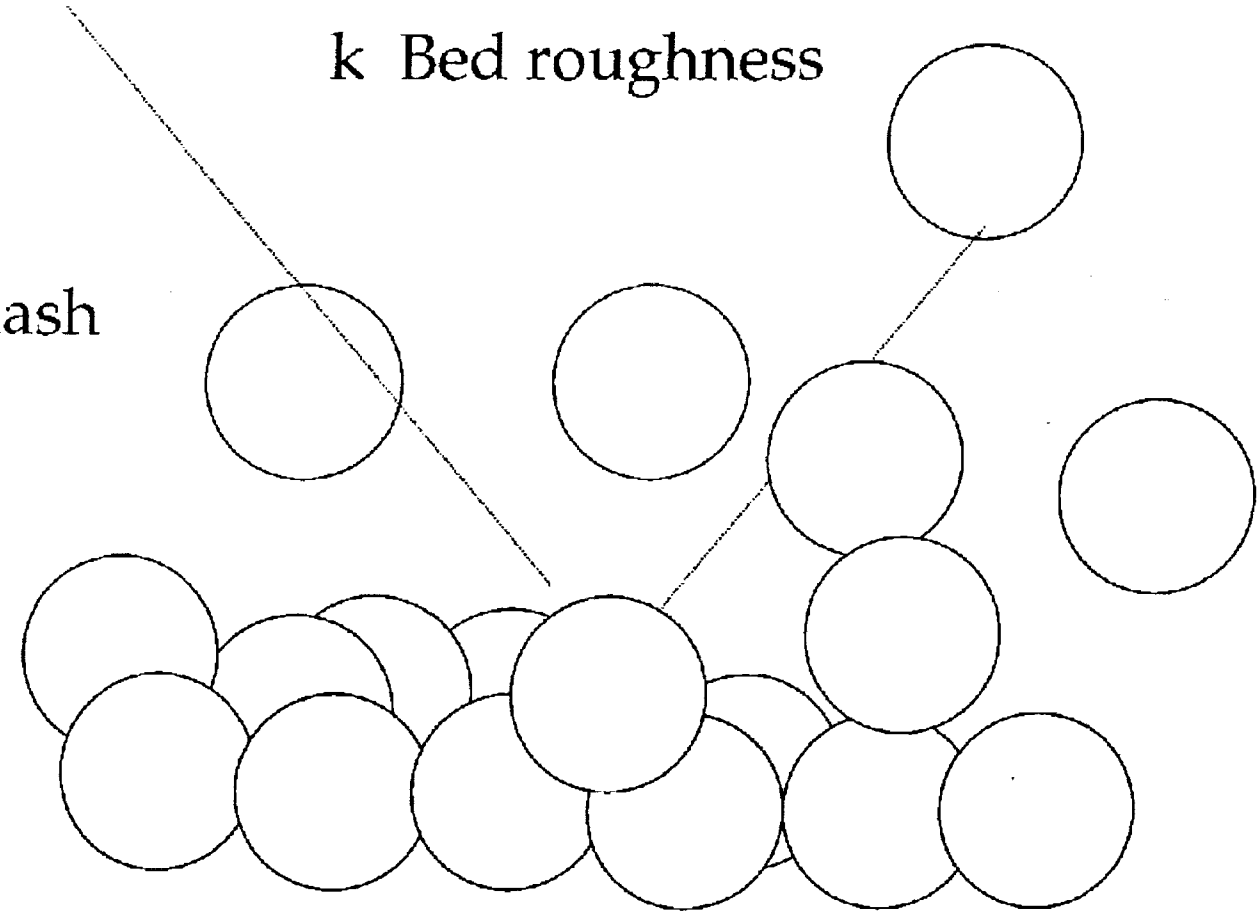

SHEET FLOWS

Concentrated flows in a region near the bed driven by a strong turbulent wind.

COLLISIONAL DISPERSION

Particle pressure: $p = \rho_s \phi [1 + 4G(\phi)]T$

Particle velocity fluctuations **C**: $T \equiv \frac{1}{3}\langle C^2 \rangle$

TURBULENT SUSPENSION

Vertical force: $\langle \phi' w' \rangle = -\nu_t \frac{\partial \langle \phi \rangle}{\partial z}$

VERTICAL BALANCE:

$$-\frac{\partial p}{\partial z} - C_D \nu_t \frac{\partial \phi}{\partial z} = -\rho_s \phi g$$

Collisions dominate when the terminal velocity of the grains is greater than the shear velocity of the turbulence.

Terminal Velocity: v_F

$$\left(\frac{3}{10}\frac{\rho_f}{D}|v_F|+18.3\frac{\mu_f}{D}\right)v_F=\rho_s g$$

D Grain diameter

μ_f Air viscosity

ρ_s Quartz density

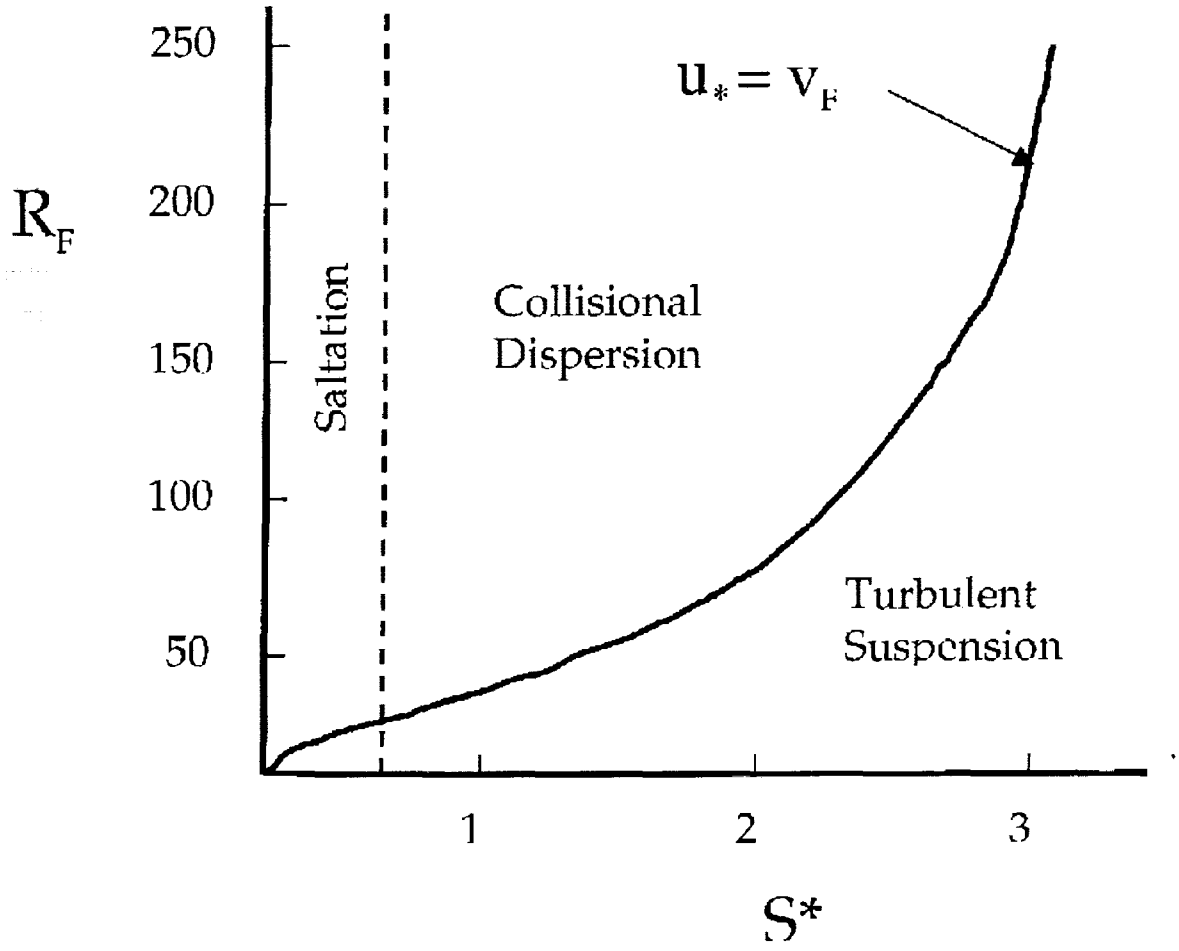

$$\text{Shields number: } S^* \equiv \frac{S_T}{\rho_s g D} = \frac{\rho_f}{\rho_s}\frac{u_*^2}{gD}$$

$$\text{Fall parameter: } R_F \equiv \left(\frac{\rho_s}{\rho_f}\right)^{1/2} \frac{D(gD)^{1/2}}{\mu_f}$$

TURBULENT COAGULATION OF AEROSOL PARTICLES

D. L. Koch and C. Cohen
School of Chemical Engineering, Cornell University
Ithaca, NY 14853

ABSTRACT

Coagulation affects the size distribution of particles produced in aerosol reactors. It influences the production of particulate pollutants in flames and their elimination by electrostatic precipitators, fibrous filters, cyclones, etc. Coagulation of raindrops plays an important role in cloud dynamics, precipitation, and the scavenging of pollutants by precipitation. Turbulent coagulation is particularly important for particles with diameters of one to several microns and pollutants of this size pose the greatest risk to human health.

Coagulation occurs when Brownian motion, differential sedimentation, or turbulent flows force two particles or drops into contact and the particles stick to form an aggregate or larger drop. The rate of coagulation depends on both the forces driving the relative motion of the particles and the hydrodynamic, van der Waals and electrostatic interparticle interactions. A good fundamental understanding of the mechanisms of coagulation leading to quantitative predictions of coagulation rates has been achieved for colloidal particles suspended in liquids. This achievement is largely attributable to the ability of researchers to isolate each of the various driving forces (Brownian motion, laminar shear, turbulent shear and sedimentation) in turn by judicious use of density-matching of the fluid and particles and adjustment of the fluid viscosity.

In contrast, the current understanding of aerosol aggregation processes is rudimentary. Two important features that distinguish the coagulation of aerosols and hydrosols are: (a) the importance of particle inertia in aerosols; and (b) the non-continuum gas flow between colliding aerosol particles. These features present interesting challenges for the theoretical prediction of aerosol flocculation. In experimental measurements on Earth, it is difficult to obtain the ideal situation in which aerosols coagulate solely due to turbulent flows. Instead, one is likely to observe mixed effects of Brownian motion, sedimentation and turbulence, making a critical test of the theory difficult.

We are planning an initial ground-based program of theoretical analysis and experimental measurements of aerosol coagulation due to isotropic turbulence. These studies will provide the necessary background to plan and propose a microgravity experiment on aerosol coagulation four years from now.

For the experiments, we will produce an aerosol of nearly monodisperse aerosol particles with a mean diameter of 1-5 •m using a Condensation Monodisperse Aerosol Generator (TSI 3475). This aerosol will flow slowly through a turbulence chamber stirred by an oscillating grid. The pressure in the chamber will be varied to change the mean-free path of the gas. The turbulent flow will be characterized using laser Doppler anemometry and known scaling relationships for oscillating grid turbulence. In this way, we will obtain an accurate assessment of the flow field to which the aerosol is subjected. The particle concentration and size distribution will be measured *in situ* at various points in the chamber using Dantec's Particle Dynamics Analyzer (PDA). The PDA is based on the latest

fiber optic technology and obtains the local particle concentration, velocity, and size distribution from the light scattered by the particles. Efforts will be made to extract data representative of singlet-singlet coagulation events by limiting the residence time of the aerosol in the turbulent reactor. By using monodisperse drops with a mean diameter of 1-3 •m, we can maximize the importance of turbulence relative to Brownian motion (which dominates for smaller particles) and sedimentation (important for larger particles). However, the extent to which we can isolate turbulence from these other mechanisms will be limited and this forms the motivation for our future microgravity experiment.

To predict coagulation rates, we must first determine the resistivity tensor describing the viscous resistance to the various modes of relative motion of a pair of aerosol particles. The particles of interest have diameters comparable with or slightly larger than the mean-free path of the gas and the interparticle separation becomes smaller than the mean-free path during the interparticle collision. Thus, we must solve a rarefied gas flow problem to determine this resistance. We will adapt the direct-simulation Monte Carlo method for calculations at low Mach numbers in order to obtain a solution of the Boltzmann equation for the non-continuum gas flow between the colliding drops.

The viscous resistivity tensor can be used together with a description of the van der Waals attractions between the particles to specify the interparticle forces. We must then solve Newton's laws of motion for the dynamic encounter of pairs of coagulating drops. The fine particles under consideration have radii much smaller than the Kolmogorov length scale. Exploiting this fact, we will conduct numerical simulations in which pairs of particles are subjected to a temporally fluctuating linear flow field, whose statistics are chosen to reproduce results from previous direct numerical simulations for the Lagrangian correlation functions of the strain and rotation rates in isotropic turbulence. Ensemble and time averages of these stochastic flow simulations will provide the rate constant for turbulent coagulation. In addition to simulations corresponding to the ideal case of turbulent coagulation of non-Brownian particles in microgravity, we will also consider mixed turbulent/sedimentation and turbulent/Brownian simulations.

Presentation not available at time of printing.

Microscopic Flow Visualization in Demixing Fluids during Polymeric Membrane Formation in Low-G

W.B. Krantz[†], A.R. Greenberg[‡], P. Todd[*]

[†]University of Cincinnati, Cincinnati, OH 45221-0171
[‡]University of Colorado, Boulder, CO 80309-0427
[*]Space Hardware Optimization Technology, Inc., Greenville, IN 47124

Macrovoids (MVs) are large (10–50 μm) pores often found in polymeric membranes prepared via phase-inversion techniques. They are generally considered undesirable since they can adversely affect the performance of polymeric membranes. However, MVs can be useful in certain thin-film applications in which vapor transmission is necessary or for use as reservoirs for enzymes or liquid membrane material. The goal of this research is to determine the mechanism of formation for MVs in order to control their formation. The hypothesis to be tested in this research is that MV growth is determined by an interplay of solutocapillary convection, viscous drag, and buoyancy forces. The results of preliminary ground-based experiments employing flow-visualization videomicroscopy to study polymeric membrane formation via dry-casting (evaporative casting) are presented. These experiments establish the viability of this real-time noninvasive technique for studying the MV formation process. Moreover, they indicate that surface-active agents can significantly influence MV formation during the dry-casting process. This flow-visualization videomicroscopy technique will be adapted to studying polymeric membrane formation via the wet-cast (precipitation bath) process in both ground-based as well as KC-135 flight experiments in order to assess the role of both buoyancy as well as surface-tension forces on MV formation.

NASA/CP—2000-210470

Microscopic Flow Visualization in Demixing Fluids During Polymeric Membrane Formation in Low-G

W.B. Krantz[1], A.R. Greenberg[2], and P. Todd[3]

[1]University of Cincinnati, Cincinnati, OH
[2]University of Colorado, Boulder, CO
[3]Space Hardware Optimization Technology, Inc., Greenville, IN

NASA Project Number NAG3-2451
Performance Period: 5/9/00 –1 1/30/03

Fifth Microgravity Fluid Physics and Transport Phenomena Conference
August 9-11, 2000

Macrovoids (MVs)

- "Oversized pores" in polymeric membranes.
- Compromise mechanical integrity of porous sublayer.
- MV-containing membranes unusable in high-pressure separations applications (RO).
- MVs useful in specialized applications:
  - **Breathable fabrics**
  - **Screen printing**
  - **Transdermal drug delivery**
  - **Bioreactors**

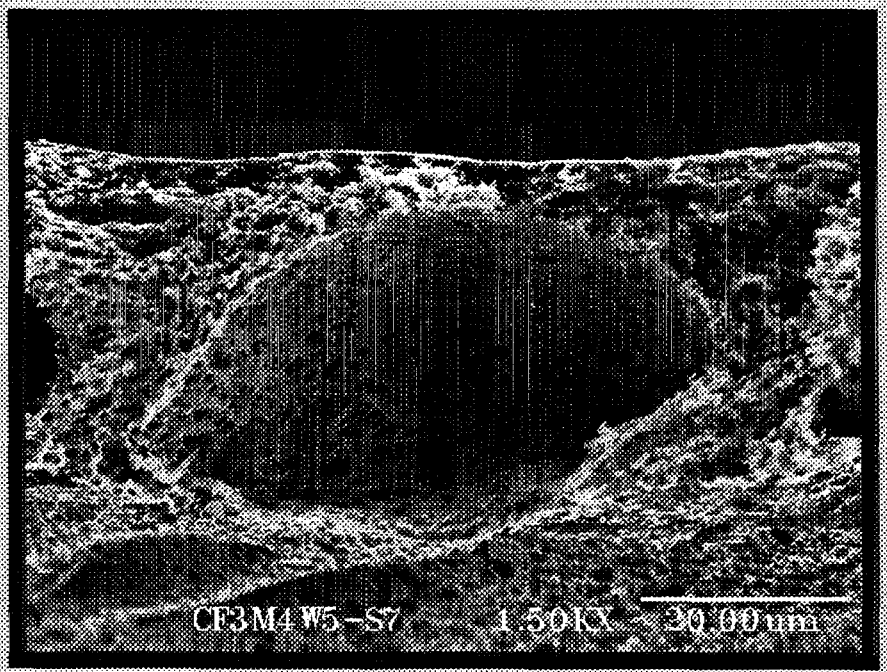

20 μm

Growth Hypotheses
Diffusion versus Solutocapillary Convection

- **Diffusion** (Reuvers, *et al.*)
  - Not influenced by surface tension or buoyancy.
  - Cannot explain MVs that form in < 5 sec.
- **Solutocapillary Convection** (Shojaie, Krantz, Greenberg)
  - Fast solvent loss creates steep nonsolvent (water) concentration gradient.
  - Concentration gradient creates a steep surface tension gradient at MV/bulk interface.
  - Surface tension gradient drives MV growth by solutocapillary convection.
  - $\rho_{MV} < \rho_{soln}$. Buoyancy and viscous drag resist growth into casting solution.

MV Growth via Solutocapillary Convection

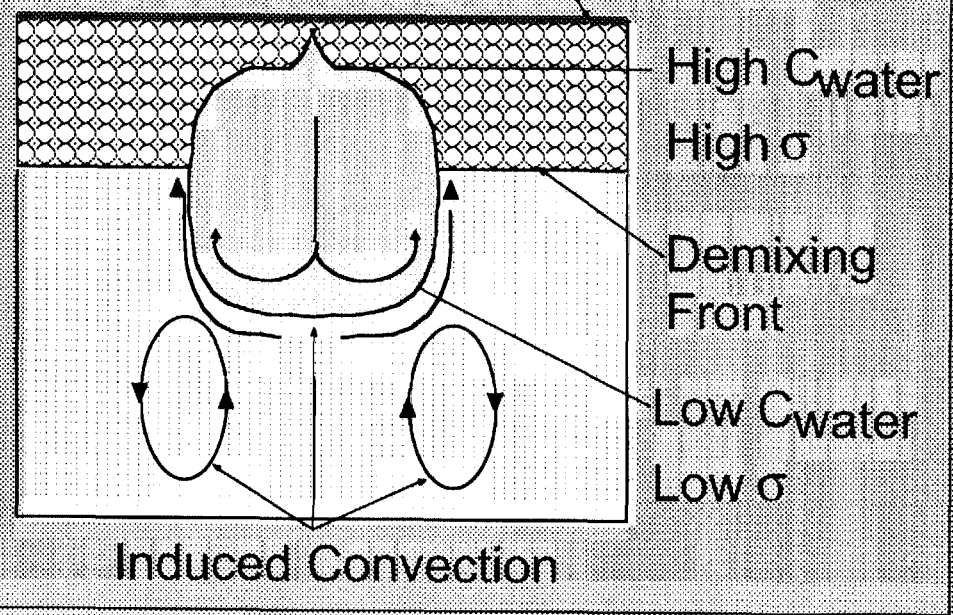

Low - Gravity Experiments

Performed October 1998 on a NASA KC-135A

- ***Diffusive Hypothesis:***
  Eliminating gravity should have no effect on MV growth.
- ***Solutocapillary Hypothesis:***
  A force that restricts MV growth has been removed. More extensive MV growth should be observed.

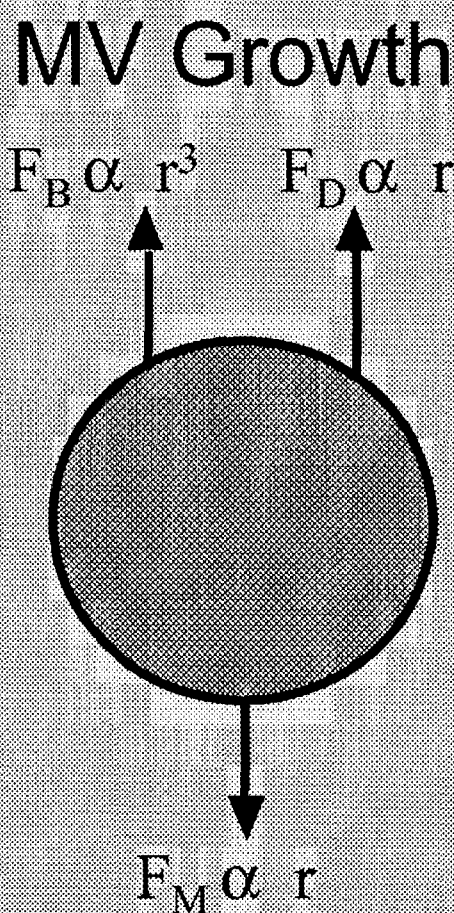

Buoyancy force increasingly important as MV grows

Effects of Low-Gravity on MV Growth

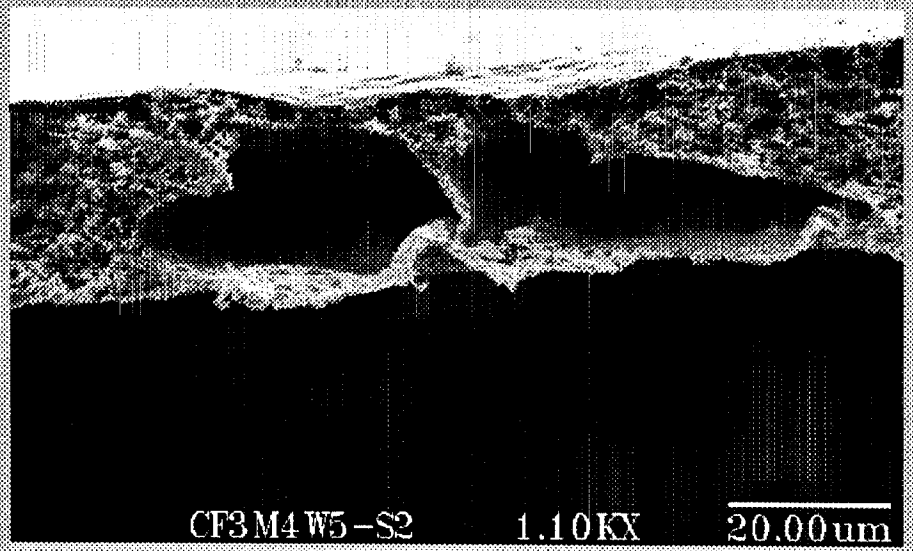

Ground-cast (1-g)

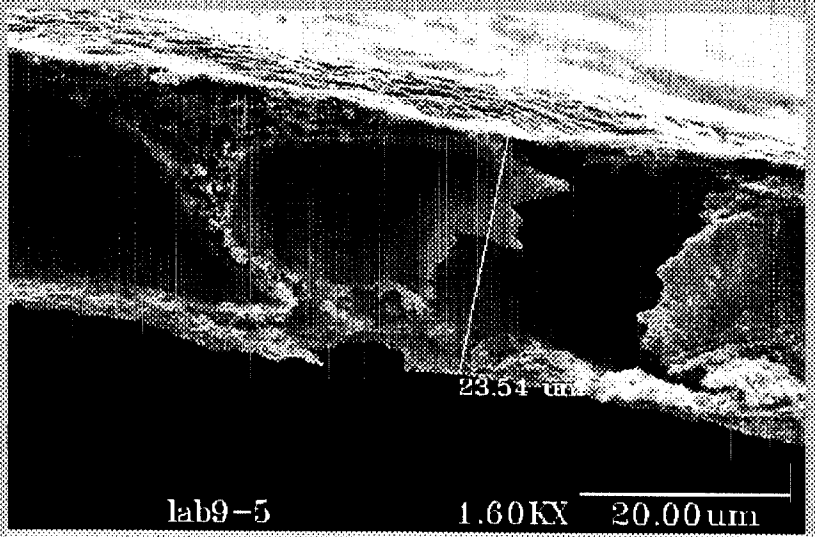

Cast on KC-135 (low-g)

Membranes cast from 10% CA / 30% Water / 60% Acetone solution.
Initial Thickness = 150 microns. No surfactant added.

- The number and size of MVs cast in low-gravity are significantly greater than equivalent membranes cast in 1-g.
- However, this finding does not apply to all casting solution compositions.

MV Growth via VMFV: Three Phases

- **Phase I: Infancy**
  - –Growth is rapid due to large concentration gradient
  - –Begins shortly after demixing

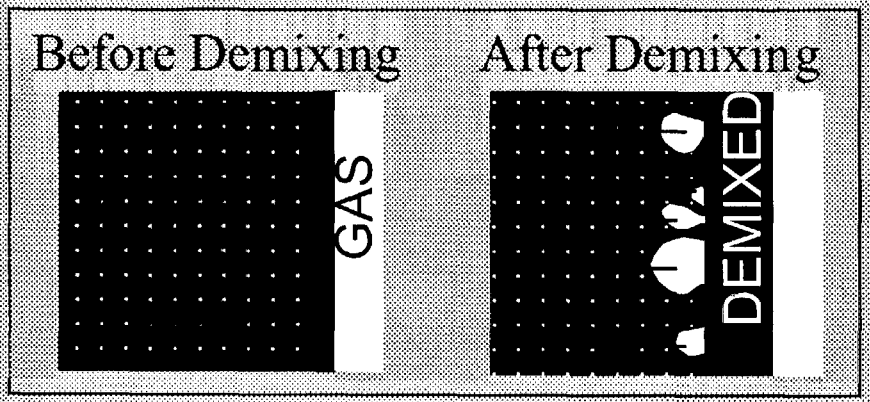

- **Phase II: Adolescence**
  - –Growth is much slower
  - –Convective flow patterns visible.

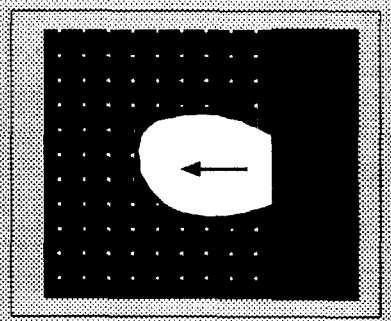

- **Phase III: Death**

Two mechanisms of MV collapse

  - –Diffusive Collapse
  - –Skinning

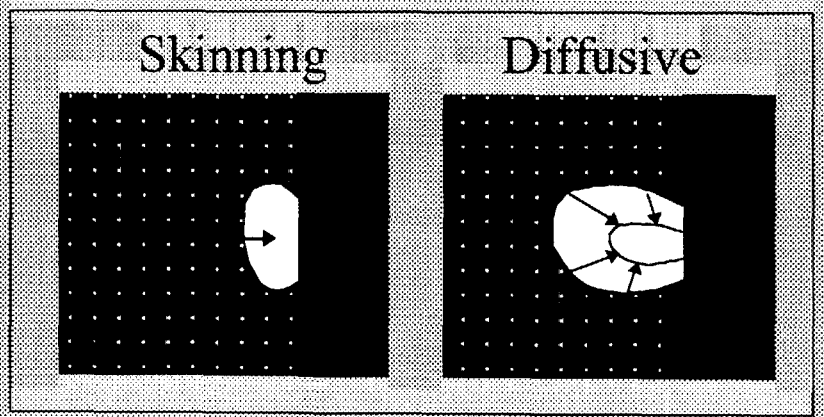

Modified Solutocapillary Convection Hypothesis

- Material enters MV from layer of supersaturated fluid at MV tail.
- Growth occurs when transport in > transport out.
- Collapse occurs when transport out > transport in.

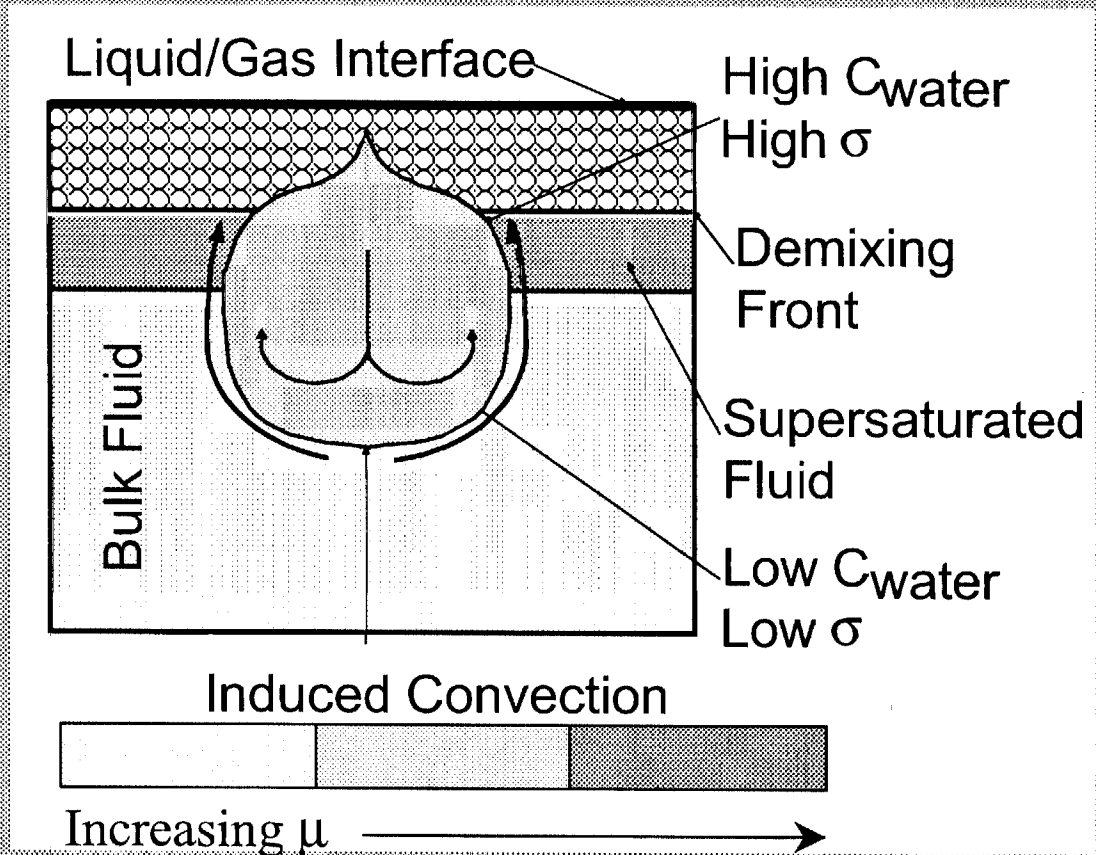

σ-driven convection supplies material to supersaturated layer

Summary

- Low-g, surfactant and VMFV studies support the contention that solutocapillary convection can occur at the MV/bulk interface in membrane dry-casting.
- Results suggest that solutocapillary convection augments the growth of MVs during membrane dry-casting from CA/acetone/water solutions.
- VMFV particle measurements indicate that MV growth is a complex process with three well-defined stages.
- A modified solutocapillary convection hypothesis better explains the phenomena observed during MV growth.

Future Work –
Tasks for NAG3-2451

- Construct apparatus for studying MV growth during wet-casting of polymeric membranes in low-g
- Study MV growth in KC-135 experiments using real-time light-reflection, video-microscopy, and flow visualization
- Develop a model for MV growth caused by solutocapillary convection

MICROGRAVITY DRIVEN INSTABILITIES IN GAS-FLUIDIZED BEDS

Anthony J.C. Ladd
Chemical Engineering Department, University of Florida

David A. Weitz
Department of Physics, University of Pennsylvania

ABSTRACT

A dense pack of solid particles can be fluidized by an upward flow of liquid, which counterbalances the gravitational force on the particles. The resulting suspension is stable for sufficiently small fluid velocities, although the particle dynamics are complex and still not fully understood. A packed particle bed can also be fluidized by a gas flow, but in this case a stable suspension of moving particles cannot be produced in earth's gravitational field. As the gas flow is increased, a stable "expanded" bed can be produced that has a lower solids concentration than the packed bed, but recent Diffusing Wave Spectroscopy (DWS) experiments have shown that the particles are stationary. At slightly higher gas flows, necessary to set the particles in motion, the bed is immediately unstable, with bubbles (large regions essentially void of particles) transporting a significant fraction of the gas through the solid phase. A kinetic theory of gas-fluidized beds predicts that the bed is always unstable to particle inertia, which is several orders of magnitude larger than fluid inertia in this case. In order to study the onset of this particle-induced instability, the minimum fluidization velocity must be reduced by several orders of magnitude; we believe that this can be most successfully accomplished in a reduced gravity environment. These microgravity experiments will offer the first opportunity to experimentally study the effects of low-Reynolds number hydrodynamic interactions in a suspension where there is no liquid, and the particle motion is predominantly ballistic. We expect that in a microgravity environment we can explore the transition between stable and unstable flow regimes in gas-fluidized beds, and contrast the behavior of particle inertia (gas-fluidized) and fluid inertia (liquid fluidized) driven instabilities.

In this work we plan to investigate the effects of small amounts of inertia on the stability of fluidized beds. We will compare and contrast the stability conditions and flow patterns arising from increasing fluid inertia ($Re > 1$, $St \sim Re$) and increasing particle-inertia ($Re < 1$, $St > 1$). In particular we will discover if the progression of instabilities in gas-fluidized beds is similar to that in liquid-fluidized beds, or whether the effects of inter-particle collisions make a fundamental change to the observed flow patterns. However, the inherent mismatch between the index of refraction of a gas and that of a solid particle makes detailed visualization of the particle motion in a gas-fluidized bed difficult, if not impossible. Therefore, an important feature of this proposal is the use of computer simulations to provide insight into the particle dynamics in gas-fluidized beds. The code will first be validated, by comparing simulations of particle motion in liquid-fluidized beds with ground-based experiments using Particle Image Velocimetry. Numerical simulations can then be used to gain insight into the behavior of gas-fluidized systems under microgravity conditions, and guide a suitable set of experiments for a Future Flight Opportunity. Experimental measurements aboard the Mir space station demonstrate that there is a residual gravitational field of about 1 μg, which is fairly steady on a time scale of at least

several hours. A gravitational field of this magnitude should enable gas fluidization under conditions where a stable flow would be expected; by increasing the particle size the onset of a particle-inertia driven instability can be studied.

The results of this research will augment and extend recent developments in our understanding of liquid-fluidized beds at very low Reynolds numbers. New and interesting scientific questions will be addressed, including the role of inertia, the limits of stability in fluidized beds, and the onset of unstable flow patterns. In addition to their intrinsic scientific interest, gas-fluidized beds are widely used in industrial processes; an improved understanding of the hydrodynamic interactions and particle dynamics in gas-fluidized beds may therefore be helpful in the design and scale up of commercial fluidized beds. The proposed research will address flow regimes that are important in industrial applications of fluidized beds, which typically are gas fluidized and operated at moderate to high particle Reynolds number. Future microgravity experiments could address fundamental questions about the behavior of gas-fluidized beds, which are masked by the strength of the earth's gravitational field. In addition, the computational demands of this program will lead to a significant enhancement of our simulation capabilities in the area of particle-fluid systems.

The proposed research will support the goals of the Microgravity Research Division in several ways. First, it aims to uncover fundamental new physics that cannot be observed in earth's gravitational field, namely the onset of instabilities in gas-fluidized beds, which are driven by particle inertia, rather than fluid inertia. This will be accomplished in the present proposal through the use of computer simulations, but we expect that these simulations will form the basis for a Future Flight Opportunity. In addition, flow visualization of gas-fluidized beds will require a new set of experimental diagnostics that may well be applicable to other microgravity experiments. The development of sophisticated computer simulations of gas-particles systems will enable us to better focus future experimental work on the critical physics issues and help ensure that any flight experiments are effectively utilized. Moreover, these computer codes could eventually be used to address issues related to the settling of dust in reduced gravity environments.

Presentation not available at time of printing.

THE DYNAMICS OF PARTICULATE DEPOSITION AND RESUSPENSION PROCESSES AT MODERATE TO HIGH REYNOLDS NUMBERS

E. Meiburg
University of California at Santa Barbara

T. Maxworthy
University of Southern California

ABSTRACT

This very recent project concerns an integrated computational-experimental investigation into the mechanisms that govern the deposition and resuspension dynamics of heavy particles in turbulent boundary layer flows over a sediment bed. The goal is to check if resuspension can be predicted to occur when an effective fluidization velocity in the sediment bed is exceeded. To this end, we will pay special attention to the coupling between the effective Darcy flow inside the sediment bed and the coherent, longitudinal, counterrotating vortical structures that dominate the turbulent boundary layer in the Navier Stokes flow above the bed. The goal is to identify the dimensionless parameters that govern the resuspension processes, and to obtain quantitative information about their threshold values that need to be exceeded for resuspension to occur.

As a first step, we have focussed on identifying efficient ways to implement the computational coupling of the Darcy flow inside the sediment bed to the Navier Stokes flow above. This is being done for the vorticity streamfunction formulation of the governing equations, based on the Beavers-Joseph relationship between the shear stress and the velocity jump at the boundary. On the experimental side, the apparatus is currently assembled that will be able to generate in a controlled fashion the well known longitudinal hairpin vortices that are typically formed by the self induction of disturbed boundary layer vorticity. This is accomplished by blowing through a slot in the wall. It is expected that the detailed understanding to be obtained by comparing the experimental and numerical results will lead to the formulation of accurate boundary conditions that can be employed for simulating deposition and resuspension phenomena in flows over complex topographies.

Dynamics of Particulate Deposition and Resuspension Processes at Moderate to High Reynolds Numbers

Eckart Meiburg

Department of Mechanical and Environmental Eng.
University of California at Santa Barbara
Santa Barbara, CA 93106, USA

Tony Maxworthy

Department of Aerospace and Mechanical Eng.
University of Southern California
Los Angeles, CA 90089, USA

- **Motivation**
- **Investigative approach**
  - **Experiment**
  - **Simulation**
- **Preliminary results**

Supported by NASA Microgravity Fluids Program

Motivation

- **deposition and resuspension important in many natural and technological processes, e.g.**

  - **sediment transport in rivers**
  - **turbidity currents in oceans**
  - **formation and propagation of sediment ripples, sand dunes, avalanches**
  - **mining and operation of machinery in dusty and windy environments (e.g., Mars)**

  .
  .
  .

Investigative approach

- **consider coupled dynamics of fluid motion in sediment bed (Darcy region) and suspension above sediment bed (Navier-Stokes region)**

- **focus on effect of dominant flow structures in typical turbulent boundary layer, i.e., counter-rotating streamwise vortex pair**

- **perform joint computational/experimental investigation in order to access largest possible parameter range, and to extract maximum information**

Experiment

- **free surface water channel**

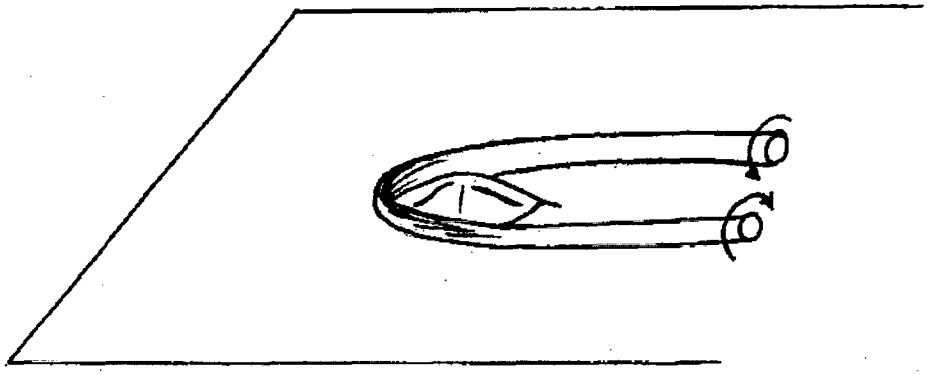

- **generate counterrotating streamwise vortex pair by means of smooth bump on a flat plate, so that no separation results. Implemented by means of flexible rubber diaphragm**

- **qualitative information by means of dye injection**

- **quantitative information by means of DPIV**

Simulation

- **cut through streamwise vortex pair**

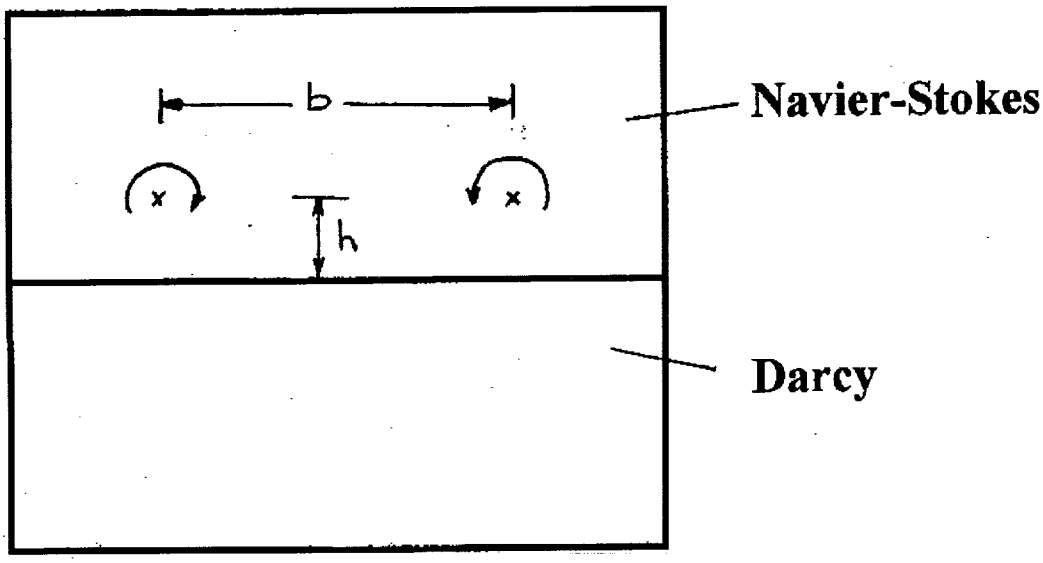

Navier-Stokes region:

$$\begin{aligned} \nabla \cdot \vec{u} &= 0 \\ u_t + (\vec{u} \cdot \nabla)u &= -p_x + Re^{-1}\nabla^2 u \\ v_t + (\vec{u} \cdot \nabla)v &= -p_y + Re^{-1}\nabla^2 v - nG \\ n_t + un_x + (v - V)n_y &= Pe^{-1}\nabla^2 n \end{aligned}$$

Darcy region:

$$\begin{aligned} \nabla \cdot \vec{u}_D &= 0 \\ \vec{u}_D &= -T \cdot Re \cdot \nabla p_D \end{aligned}$$

Dimensionless Parameters

With: Γ **vortex strength**

U_s **settling velocity**

Reynolds number $Re = \frac{\Gamma}{\nu}$

Peclet number $Pe = \frac{\Gamma}{D}$

dimensionless permeability $T = \frac{k}{h^2}$

gravity parameter $G = \frac{3\pi n_0 d_p \nu U_s h^3}{\Gamma^2}$

dimensionless settling velocity $V = \frac{U_s h}{\Gamma}$

aspect ratio $A = \frac{h}{b}$

Boundary conditions at sediment bed surface

- **continuous normal velocity** $v = v_D$
- **normal stress balance** $-p + \frac{2}{Re} v_y = -p_D$
- **empirical shear stress balance (Beavers and Joseph 1967)**

$$u_y = \frac{\alpha}{\sqrt{T}}(u - u_D)$$

Numerical implementation

- **spectral method in spanwise direction**
- **compact finite differences in normal direction**

Preliminary computational results

- **test flow: model of bioreactor**

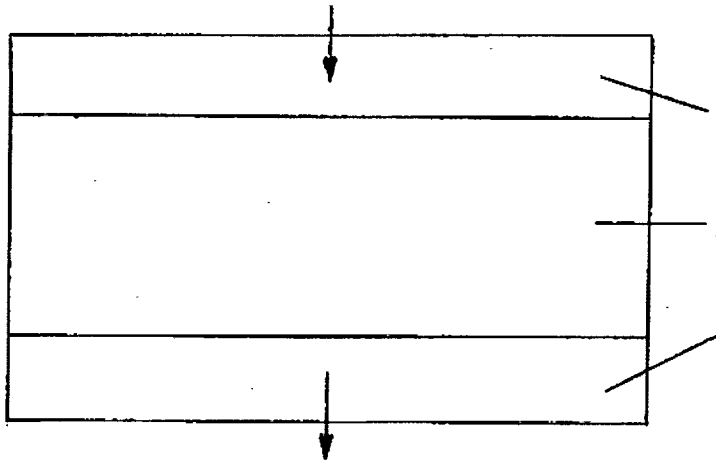

- **small permeability**

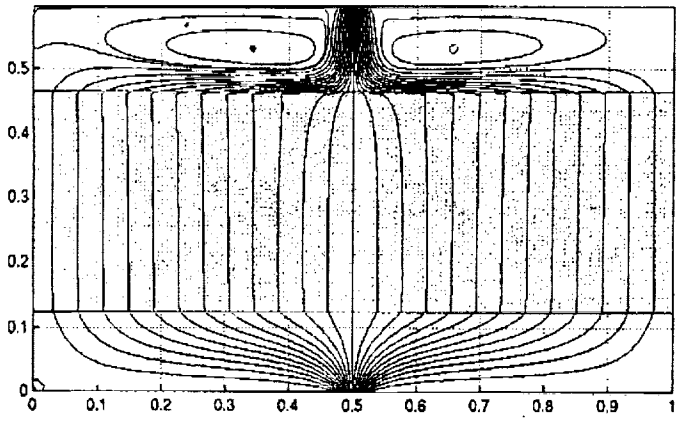

flow is nearly uniform inside porous medium

- **larger permeability**

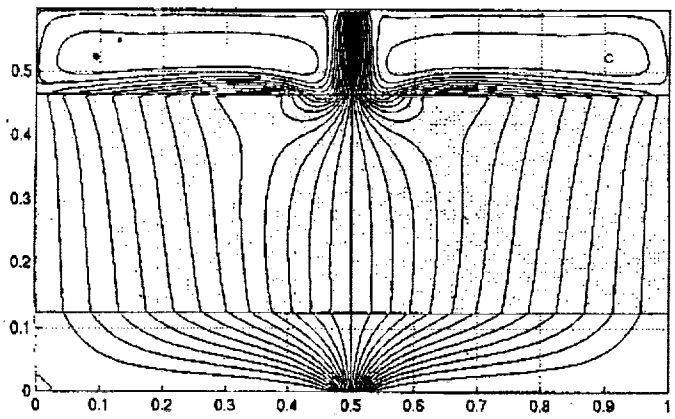

nonuniform flow

STUDIES OF WET GRANULAR MEDIA

P. Schiffer, A.-L. Barabási, P. Tegzes, R. Albert, I. Albert
Physics Dept., 225 Nieuwland Science Hall, University of Notre Dame, Notre Dame, IN 46556

ABSTRACT

Granular materials have long been the subject of scientific studies due to their fascinating physical properties which differ significantly from materials in bulk liquid or solid form. These studies have focused primarily on *dry* granular materials in which the intergrain forces are purely repulsive, but the addition of a wetting fluid to the material adds an attractive force to the system and therefore a new dimension to the underlying physics. Indeed the physics of such a wet granular system is relatively unexplored, and there is no basic understanding of how exactly the addition of a small quantity of wetting fluid affects physical properties of granular media. This problem is of great scientific interest, but it is also of practical importance since granular materials relevant to many industrial and commercial applications often contain significant liquid between the grains. Recent work by our group has demonstrated that large changes in the physical properties of granular materials can be induced by even a nanometer-scale layer of liquid on the grains, offering a glimpse of the complex physical behavior which wetting can induce (see references below). For example, in glass beads coated with oil, we find three different regimes of correlated behavior among the grains with different dynamics and stability (see figure 1 below).

A study of the effects of liquid on the properties of granular materials is of particular interest in the context of microgravity. A reduction in the gravitational force would change not only the distribution and strength of contact forces between the grains in a granular sample, but also the capillary forces due to the liquid bridges between the grains and the dynamics of the liquid draining from the grains. Furthermore, in the microgravity environment where grains will not come to rest at the bottom of a container, liquid-induced adhesive forces would lead to the agglomeration of grains which would otherwise move independently. Wetting will thus significantly affect all physical properties of granular media in microgravity, and there is a significant potential to observe new physical phenomena in wet granular materials in reduced gravity which are otherwise hidden by the presence of gravity.

Since there is currently only a very limited fundamental understanding of the effects of interstitial liquid on granular materials, we are conducting a ground-based research program to establish a basic understanding of the phenomena on Earth. This program combines the efforts of two principal investigators in order to simultaneously investigate both the experimental and theoretical aspects of wet granular media. The goal of the research program is to understand how the addition of liquid changes both the static and dynamic macroscopic physical properties of granular materials, and in particular to understand how the liquid-induced cohesion leads to the development of correlations between the grains. We are probing the liquid-induced phenomena systematically by experimental investigations of various granular properties as a function of liquid content using a variety of liquids and grains. We plan three research thrusts: **a)** Investigations of surface phenomena and the development of correlations through clumps on the surface of a rotating granular sample. **b)** Studies of the impact of interstitial liquid on flow properties through measurements of the drag force in a granular material. **c)** Examination of liquid-induced effects on granular segregation dynamics through magnetic resonance imaging of

vibrated granular materials and studies of segregation during flow. The experimental results will guide the theoretical efforts, while at the same time theoretical research will both provide the basis for interpretation of the experimental data and suggest new experiments to be performed.

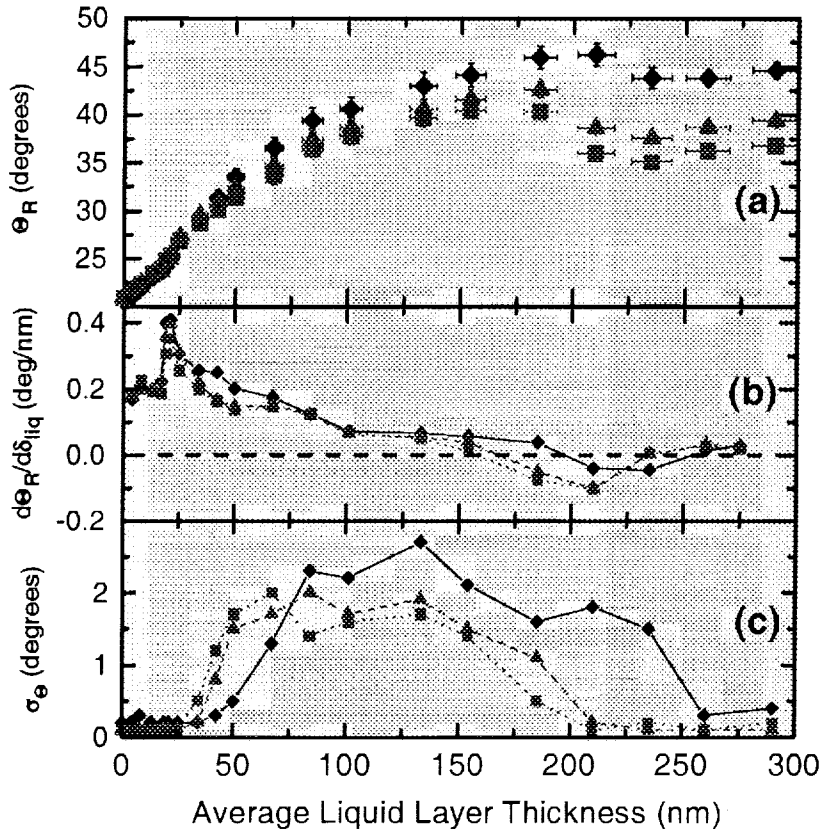

Figure 1. Summary of the results of recent experiments at Notre Dame on wet granular materials. **(a).** The angle of repose as a function of liquid content. The three different symbols in the plot are for measurements conducted on samples with different sample sizes (horizontal diameters of the samples are ◆, d_c = 10.3 cm; ▲, d_c = 15.6 cm; and ■, d_c = 20.4 cm) Note the three distinct regimes of behavior with increasing liquid content, marked by the background color. Note also that the angle of repose depends on the size of the sample for larger liquid contents, but not for the regime of smallest wetting. **(b).** The derivative of the data in figure 1a, showing the sharpness of the transitions between the regimes of wetting. **(c).** The roughness of the surface as quantified through the variation in measured values of the angle of repose (the standard deviation σ_Θ). The much larger roughness in the intermediate wetting regime is indicative of the development of correlated clumps breaking off the surface during flow. At the largest liquid contents studied, the medium again flows smoothly and coherently so that σ_Θ again becomes small.

References: D. J. Hornbaker et al., Nature **387**, 765 (1997); R. Albert et al., Physical Review E **56**, R6271 (1997); R. Albert et al., Physical Review Letters **82**, 205 (1999); A.-L. Barabási et al., Physica A **266**, 366 (1999); P. Tegzes et al., Physical Review E **60**, 5823 (1999); I. Albert et al., Physical Review Letters **84** 5122 (2000).

Presentation not available at time of printing.

Superfluid Contact Line Dynamics

P. Taborek, P. Presser, and J.E. Rutledge
University of California, Irvine

Liquid ^{4}He wets all conventional solid materials. Below 2K, the viscosity drops dramatically as the superfluid fraction increases. These two properties imply that thin films of helium immediately and seamlessly coat all the solid surfaces of a conventional apparatus. A familiar example of this phenomenon is film flow that will empty a suspended beaker of superfluid by crawling up and over the walls of the beaker. Because helium strongly wets most solids, fluid mechanical investigations of contact line phenomena such as spreading and contact angle hysteresis have not been possible with superfluids, and contact line dynamics has not been addressed in the classical superfluid literature.

This situation has changed with the recent development of methods of forming alkali metal substrates, particularly cesium, which are not wet by superfluid helium. We have thermodynamically characterized the Cs/^{4}He system, which displays wetting and prewetting transitions[1], as well as non universal superfluid onset[2]. Below the wetting transition, it is possible to form drops[3] of superfluid on a cesium substrate with contact angles in the vicinity of 40°. We have begun to investigate the dynamics of the superfluid contact line by making videos of superfluid drop flows. Some of the surprising findings of these studies are that superfluid droplets are "sticky" in the sense that they exhibit an anomalously large contact angle hysteresis, and that superfluid drops require a substantial force to initiate flow. Despite the very low viscosity, the drops have a mechanical Q factor similar to water.

We are in the process of developing a next generation ^{3}He based optical cryostat that will allow us to extent our studies to lower temperatures. We plan to study superfluid spreading on a dry wettable surface, which requires a cesium dam to form a dry spot. Temperatures below 0.3K are required to eliminate vapor phase mass transport. We will also study the mechanical Q of drops in the limit of zero vapor pressure and unity superfluid fraction. The dynamics of dewetting and film rupture can be studied by forming metastable films of superfluid on a substrate whose thermodynamically stable state is dry.

1. J.E. Rutledge and P. Taborek, Phys. Rev. Lett 69, 937 (1992)
2. J.A. Phillips, P. Taborek, and J.E. Rutledge, J. Low Temp Phys. 113, 829 (1998)
3. D. Ross, J.E. Rutledge, and P. Taborek, Science 278, 664 (1997)

Presentation not available at time of printing.

SPLASHING DROPLETS

Dr. R. L. Vander Wal
The National Center for Microgravity Research c/o NASA-Glenn
Prof. Gretar Tryggvason
The University of Michigan
Dr. John P. Kizito
The National Center for Microgravity Research c/o NASA-Glenn
Prof. Iwan Alexander
Case Western Reserve University

ABSTRACT

In practical applications involving sprays for cooling, atomization, coating and fuel injection, the small spatial scales and short temporal scales prohibit detailed study of the internal fluid dynamics and surface and internal temperature profile during the droplet-surface interaction. Such information is critical to defining ranges of behavior, testing existing models of droplet-wall interactions and providing benchmark data for development of theoretical models. In a low-gravity environment, enhanced spatial and temporal scales may be achieved while maintaining comparable ranges of surface tension, viscous and inertial effects, typical of practical applications with well-defined initial conditions uninfluenced by gravity.

The relative magnitude of surface tension and viscosity effects will depend upon the kinematics of the impaction process, liquid properties and ambient conditions. Experiments in both the film evaporation and film boiling regimes will be conducted to illuminate surface tension gradient and viscosity effects upon droplet breakup. Parameters that will be varied include the initial bulk liquid surface tension, viscosity, degree of liquid subcooling, impact Weber number, ambient pressure and impact angle. Comparison between results will be used to delineate the role and quantify the relative magnitude of surface tension effects compared with inertial, viscous and wetting contributions to droplet breakup or "splashing".

A second thrust of the work proposed here will be to test equivalent dimensionless groups: for example, for droplets of different size, adjustment of velocity, surface tension and viscosity will be used to equalize Weber and Reynolds numbers to test for hidden property dependencies. These tests will be used to evaluate the applicability of droplet breakup studies using widely different conditions. Experiments in the film evaporation region will provide tests of theory apart from phase change while including wetting behavior and contact angle effects. Experiments in the film boiling regime will include phase change effects while eliminating surface wetting and contact angle effects. Experiments in the nucleate and transition boiling regimes will determine whether splashing can occur prior to droplet disruption by boiling and serve to identify alternative droplet breakup behavior. The experimental data is expected to serve as input to practical spray models while detailed numerical modelling will be developed by comparison to experimental results.

The experimental studies will be complemented by detailed simulation of the drop collision with the walls. A so-called on-fluid formulation will be used where a single set of equations is

written for all the phases involved. In this approach the phase boundary is treated as an imbedded interface by adding the appropriate source terms to the conservation laws. These source terms are in the form of delta functions localized at the interface and are selected in such a way to satisfy the correct matching conditions at the phase boundary.

More specifically, the head-on impact of a drop on a hot surface will be simulated using an axisymmetric numerical model. The model will include local grid refinement to capture the draining of the film between the drop and the surface, the energy equation to compute the temperature distribution, temperature dependent surface tension, and mass transfer from the surface due to evaporation. For the case of drops colliding with solid walls where no slip boundary conditions must be enforced, quantitative predictions will require very fine resolution.

The simulations will be set up to mimic the experimental setup as closely as possible and detailed comparisons will be made. By turning various physical properties on and off and examining the sensitivity of the results to changes in the modeling of the relation between the surface tension and the temperature, for example, it will be possible to determine exactly what forces are important during the collision of drop with a hot surface and the evolution of splashed products.

Presentation not available at time of printing.

CAPILLARY FLOW IN INTERIOR CORNERS

Mark M. Weislogel, TDA Research Inc., 12345 W 52 Ave., Wheat Ridge, CO 80033
Ph; 303-940-2320, Fax; 303-422-7763, mmw@tda.com

Capillary flows in interior corners have an established place in fluids-handling operations in reduced gravity environments. A quantitative understanding of corner flows is essential for the myriad fluid management tasks in space including flows in liquid-fuel tanks, heat pipes, energy systems, condensers, and life-support systems.

Though low-g fluid system designs are largely successful, current techniques for predicting system performance are primarily limited to order of magnitude estimates, delicately guided by the experience of the designer, or direct numerical simulation which can be prohibitively time consuming. A reliable and quantitative design tool serving between these extremes would be a welcome contribution to the low-g fluids management community.

Recently, closed form solutions for a variety of corner flows in simple geometries were derived, (see [1], and references contained therein); these results compare favorably with an extensive set of low-g experiments, [1-2]. These results are limited to flows of perfectly wetting fluids (zero contact angle) along a single straight corner for reasonably long times. An example of sudden capillary rise (imbibition) in a partially filled container of equilateral triangular section is shown in Figure 1. An example of a spreading drop in an interior corner is shown in Figure 2. In applications however, the fluids may be partially wetting (aqueous systems) and the non-ideal corners may be rounded, irregular, bent, and may bifurcate or join other corners. Furthermore, one is often interested in "startup" transients. While these inertia-dominated flows are mostly insignificant in 1-g due to the small size of earth-bound capillary flows, inertia often dominates for long periods in the large-scale capillary flows attainable in low-g.

We propose to carry out an applications-oriented experimental and theoretical study to understand inertia-dominated capillary flows in interior corners as well as flows in complex corner networks. For the experimental investigation, inertia-dominated flows in simple geometries will be studied. This work will complement previous research on flows which occur *after* the inertial phase is complete. For the complex corner network experiments, flows in planar and subsequently three-dimensional geometries of increasing complexity will be quantified in terms of corner geometry, size, fluid volume, and fluid properties.

An important aspect of this work is the integration of experiment with theory. In particular, we hope to provide not only the theoretical foundations, but to use comparison with comprehensive experiments utilizing NASA's drop tower(s) and aircraft to provide a practical guide to the utility, error, and limitations of theory. This is expected to be most valuable for the case of partial wetting, in which hysteresis and other non-ideal effects can be large. For flows through the complex networks to be studied, numerical solutions would be prohibitively expensive. We will investigate techniques that combine asymptotics along straight corners with numerical results at joints between corners.

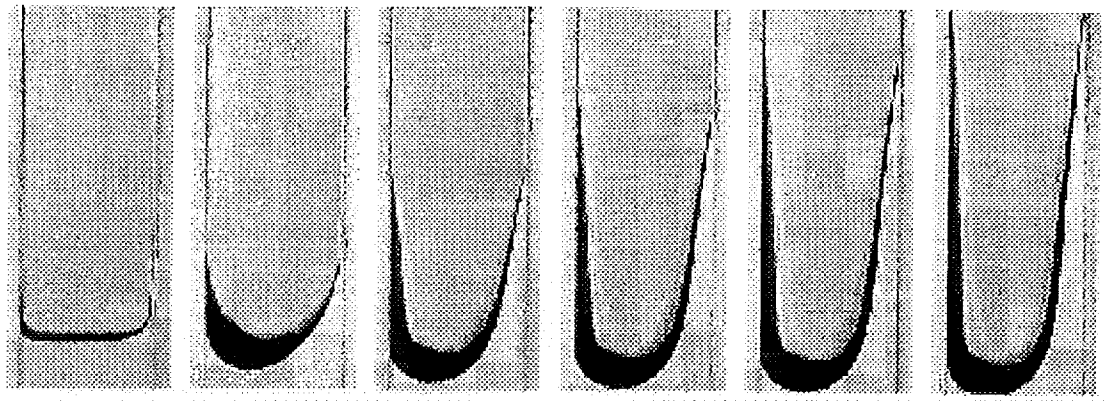

Figure 1. Capillary rise after step reduction in gravity in 2.2s drop-tower test (NASA GRC). A perfectly wetting liquid partially fills the equilateral triangular section container. Time interval between figures is 0.2s.

The overall goal of the proposed research is to provide a firm experimental and theoretical footing for the design of corner-flow devices so that transient flow rate, interfacial configuration and stability can be reliably predicted.

References:

[1] Weislogel, M.M., Lichter, S., Capillary Flow in Interior Corners, *J. Fluid Mech.*, **373**:349-378, November 1998.

[2] Weislogel, M.M., Lichter, S., A Spreading Drop in an Interior Corner: Theory and Experiment, *Microgravity Sci. Technol.* **IX**/3, 1996, pp. 175-184.

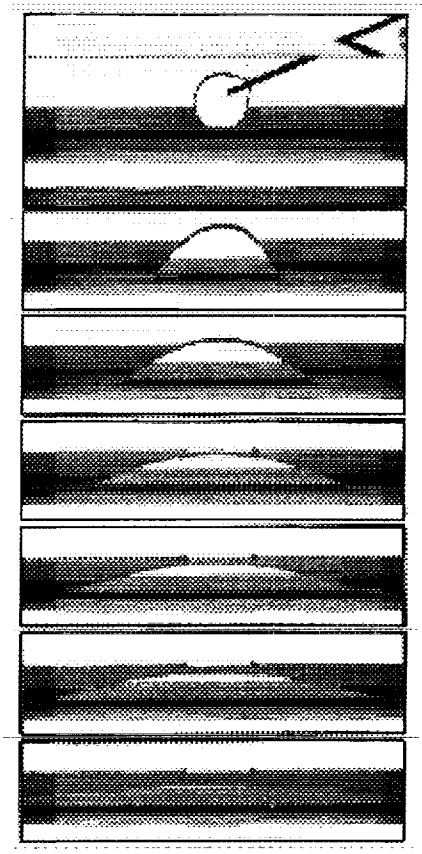

Figure 2. 7s low-g spreading of 20ml drop in 50° interior corner (NASA GRC DC-9 aircraft).

Presentation not available at time of printing.

DRIVEN TWO-DIMENSIONAL TURBULENCE

M. Rivera and X. Wu
University of Pittsburgh

ABSTRACT

Two-dimensional (2D) driven turbulence has been studied in experimental systems in which the length scale at which energy is injected, l_{inj}, and the largest length scale which contains significant energy, l_{out}, are separated by less than a decade [1]-[3]. One such system is an electromagnetically forced soap film [1], called an e-m cell, in which the length scale limitation is imposed by the systems size, l_{sys}. Experiments done in an e-m cell are presented and the effects of l_{sys} on the turbulence are explored. One important result demonstrates that 2D driven turbulence possesses little inertial range if l_{out} is less than a decade removed from l_{inj}. Another result demonstrates that statistical homogeneity is lost if l_{out} approaches l_{sys}. Thus, for the e-m cell to have a significant amount of inertial range as well as maintain homogeneity (two requirements which must be satisfied if results are to be compared with theory) l_{sys} must be at least two decades removed from l_{inj}. Unfortunately in the current manifestation of the e-m cell , l_{sys} is constrained to be little more than a decade removed from l_{inj}. This constraint, however, is imposed by the earth's gravitational field and could be alleviated in a microgravity environment, an experiment for which these earlier results are preliminary explorations.

REFERENCES

[1] M. Rivera and X.L. Wu (submitted to PRL)
[2] M. Rutgers (submitted to PRL)
[3] J. Paret and P. Tabeling, Phys. Fluids **10,** 3126 (1998).

Presentation not available at time of printing.

TAYLOR CONES ON THIN FLOWING FILMS

S. G. Bankoff, Northwestern University

ABSTRACT

An Electrostatic Liquid Film Radiator (ELFR) has been proposed as an option for heat rejection in space. The coolant in this radiator flows along the outer wall in a thin film. In lieu of thick walls to protect the radiator from micrometeorites, an electrostatic field is used to prevent leaks when the wall is damaged. The field exerts a pressure on the coolant interface. If the field pressure is greater than the electrostatic head at a possible leak hole, leakage can be prevented. A possible point of failure is due to an instability of the coolant surface, which is analogous to that seen by Taylor and McEwan [5]. The field is accentuated at the surface of a short wave. A cone forms locally, and a jet of fluid is emitted from the cone towards the electrode, shorting it. This instability sets an upper limit on the field which can be used, thereby limiting the design possibilities.

Earth-based experiments with Hg show that the critical field, F_c, for this instability is much greater than that required to stop leaks in radiator designs [1]. This favorable result was observed over a wide range of the Reynolds number (Re), angle of inclination (β), and height (H), length (L), and position (D) of the electrode along the plate in the direction of flow. The critical field was quite insensitive to the above parameters, as well. For $100 < Re < 600$,$20 < \beta < 90$, and $3 < L < 15cm$, F_c changed by only 30%. The main difference between our experiments and radiator operating conditions is the fluid depth. We have to extrapolate from an experimental depth of $0.1mm$ to a design depth of $2mm$. The depth is likely to be important, because the growth rate of the linear disturbance varies with the square root of the depth at these parameter ranges.

Taylor's experiments showed that critical voltages could be predicted by linear stability theory for a horizontal fluid of infinite depth. He varied electrode height and fluid, and showed agreement to within $10-20\%$, depending on the height of the electrode. The error was speculated to be due to variations in surface tension produced by oxides on the fluid interface. The theory provides the following result for neutral stability,

$$\frac{\varepsilon V_0^2}{4\pi h^2} = tanh(kH)[Tk + g(\rho_1 - \rho_2)/k].$$

This equation assumes that a second fluid (with density ρ_2) exists above the first, and that the electrode is immersed in the second fluid. The parameters $\varepsilon, V_0, h, k, T$, and g are the dielectric constant of fluid 2, the potential of the electrode, the height of the electrode above the fluid interface, the wavenumber of the disturbance, the surface tension, and the accelleration due to gravity. The surface tension term stabilizes short wavelengths and the gravity term stabilizes long wavelengths.

In contrast, the critical voltages can not be so conveniently calculated for a falling film. The linear stability was first done by Kim, Bankoff and Miksis [4]. They showed that in the long wave limit, the critical Reynolds number is given as,

$$Re < \frac{5}{6}cot(\beta) - \frac{10K}{9}\frac{H^2(1-1/e_f)^2}{(\frac{1}{e_f}-1+H)^3} + \frac{5}{9}\frac{\xi^2}{Ca}k^2.$$

Here, K is a dimensionless electric field number, Ca is the capillary numberand ξ is a perturbation parameter for small slope. For flow down a vertical plate, the long waves are unstable for any value of Re without the field. For a mercury film on a vertical plate, waves are visible to the eye within a few centimeters from the inlet. However, these waves do not lead to Taylor cones below fields of $60\ kv/cm$.

A non-linear theory is required on a falling film to determine critical voltages for the onset of Taylor cones. Gonzalez and Castellanos [2] [3] show that for subcritical and supercritical Re, weakly nonlinear theory predicts stable finite amplitude waves. Our experiments show these waves to be unstable to high fields. Figure 1 shows plots of F_c as a function of Re for various values of the plate angle, electrode position and length. Plot (a) shows F_c increases with Re, at a distance of 1.6 cm downstream, decreases with Re 9 cm downstream, and remains nearly constant 15 cm downstream. The trend for 1.6 cm downstream may be caused by the entrance flow region. Dimensional analysis shows this to be 3 cm for $Re = 100$ and 20 cm for $Re = 600$. In this region, the film is thinner than the Nusselt depth, and is travelling at a higher velocity. The trend at a downstream distance of 9 cm may be caused by a plug in the plate which was used for leak stopping experiments. Plot (b) shows that a cylindrical electrode, which produces a pulse field spatially, allows for a higher peak field than a flat plate electrode. For plates longer than 3 cm, however, the length of

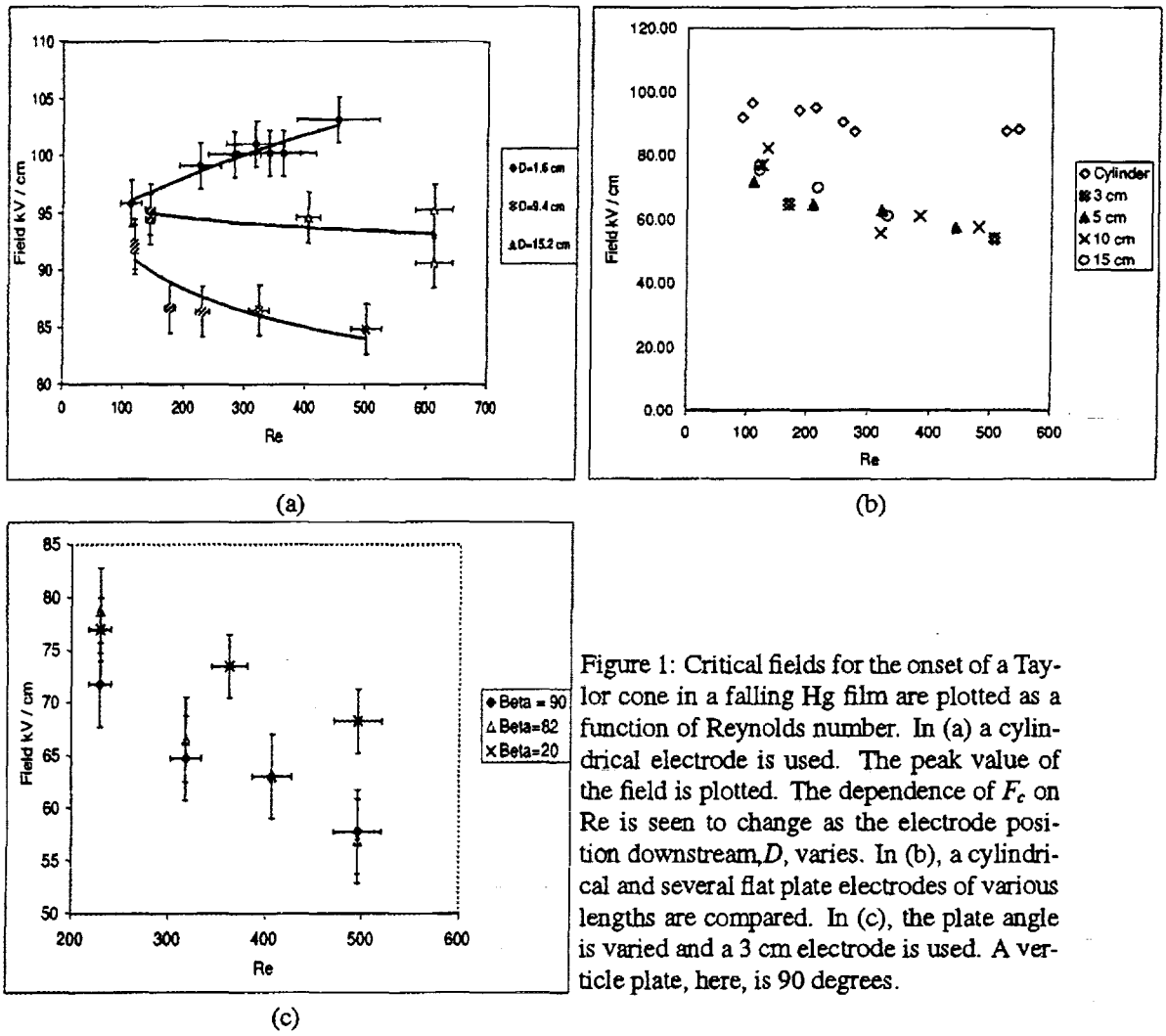

Figure 1: Critical fields for the onset of a Taylor cone in a falling Hg film are plotted as a function of Reynolds number. In (a) a cylindrical electrode is used. The peak value of the field is plotted. The dependence of F_c on Re is seen to change as the electrode position downstream, D, varies. In (b), a cylindrical and several flat plate electrodes of various lengths are compared. In (c), the plate angle is varied and a 3 cm electrode is used. A verticle plate, here, is 90 degrees.

the plate has no effect on F_c. Plot (c) shows an increase in F_c of 15% as the plate angle is decreased and the normal gravitational component is increased.

References

[1] S.G. Bankoff, M.J. Miksis, H. Kim, and R. Gwinner. Design considerations for the rotating electrostatic liquid-film radiator. *Nuclear Engineering and Design*, 149, 1994.

[2] A. Gonzalez and A. Castellanos. Nonlinear electrohydrodynamic waves on films falling down an inclined plane. *Physical Review E*, 53(4), 1996.

[3] A. Gonzalez and A. Castellanos. Nonlinear electrohydrodynamics of free surfaces. *IEEE Transactions on Dielectrics and Electrical Insulation*, 5(3), 1998.

[4] H. Kim, S.G. Bankoff, and M.J Miksis. The effect of an electrostatic field on film flow down an inclined plane. *Phys. Fluids*, 4(10), 1991.

[5] G.I. Taylor and A.D. McEwan. The stability of a horizontal fluid interface in a vertical electric field. *J. Fluid Mech.*, 22(1), 1965.

NASA/CP—2000-210470

Electrohydrodynamic Liquid Film Radiator (ELFR): Leak Stoppage and Stability Results

S. G. Bankoff, E.M. Griffing, R.A. Schluter

- Concept: Lightweight pumped loop membrane radiator
- Leakage of coolant from a puncture prevented by surface tension and electric field
- Early design calculations[1] give 0.074 kg / kW for lithium coolant in a rotating conical radiator with inlet Reynolds number 400, T_{in} = 800K, T_{out} = 700 K
- More conservative T_{in} = 700 K to minimize gas breakdown possibility —> 0.126 kg / kW thermal.
- Both rotating (conical) and non−rotating (cylindrical) designs possible
- Long−wave thin film analysis[2,3] shows surface waves induced by local switching on of electric field harmlessly wash out downstream
- Electrode shorting due to gas breakdown or Taylor cone formation[4] at very high electric fields have been studied experimentally

1 Bankoff, Miksis, Kim, and Gwinner, Nuclear Eng. And Design, 149 441 (1994)
2 Kim, Bankoff, and Miksis, Phys. Fluids A 4 (10), 2117 (1992)
3 Kim, Bankoff, and Miksis, J. Porpul. Power, 9, 245 (1993)
4 Taylor and McEwan, J. Fluid Mech., 22 (1965)

High Electric Field, Vacuum, Falling Film Experiments

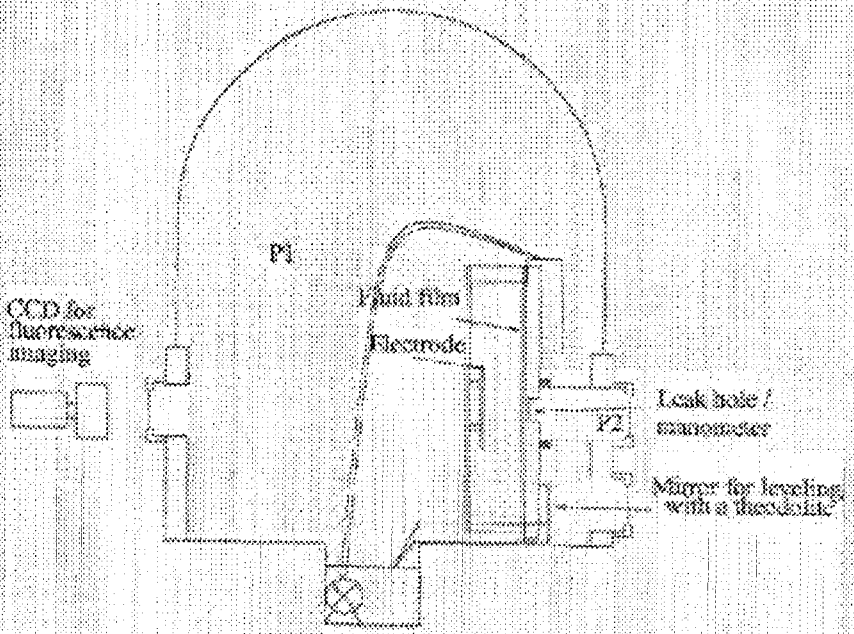

- Electric fields up to 100 kV / cm
- Liquids: Ethanol, diffusion pump oil, Hg
- Film depth measurements: Fluorescent imaging
- Pressure measured at bottom of fluid by calibrated manometer
- Threshold voltages measured for Taylor cone instabilities and / or gas phase breakdown

- The bottom images show the oil and mercury films The flow is top to bottom.
- The oil film had a Reynolds number of ~0.25. No waves were detected by the fluorescence imaging system with or without the field, which had an accuracy of ~ 2 %.
- The mercury film showed waves developing at various positions downstream depending on the Reynolds number. This is a typical image. The top is 8 cm and the bottom is 14 cm from the inlet. The electrohydrodynamic instability was insensitive to these fluid disturbances.

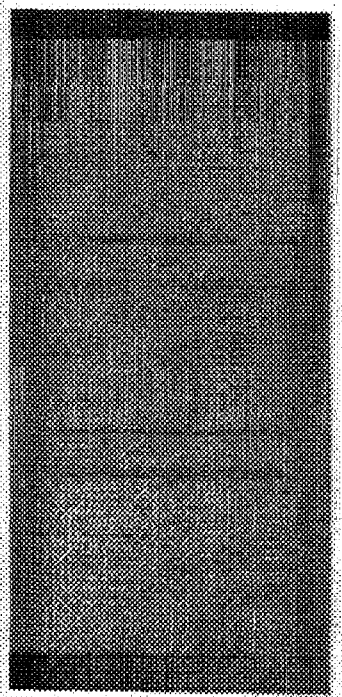

Oil Re ~ 0.25

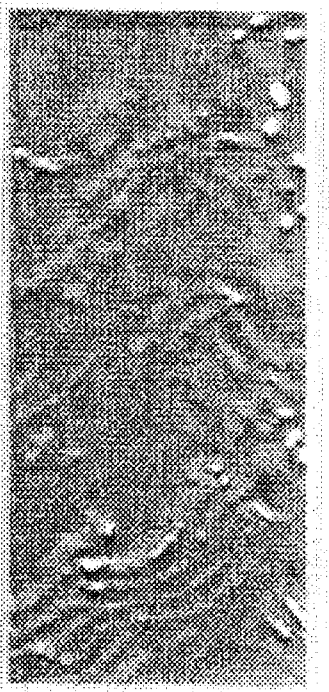

Hg Re ~ 500

Taylor Cone Instability with Mercury

- Electrohydrodynamic instability is a potential problem. However, high surface tension of liquid metals suppresses instability.
- If electric field (E) is above some critical value, a cone forms in the fluid. Jet of fluid bridges the electrode gap producing electric breakdown.
- With Hg, high electric fields (*E~70 kV/cm*) can be used without instability. This gives a large margin for leak stoppage (8–10 kV/cm).

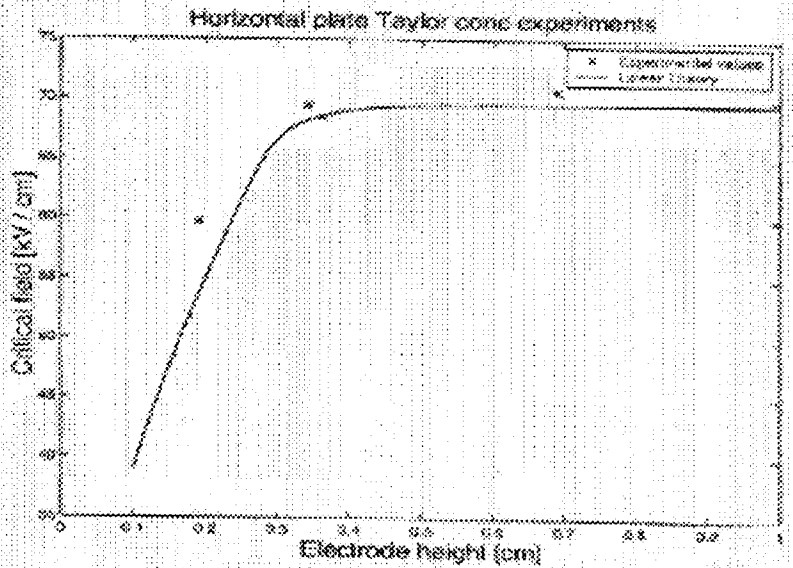

Taylor cone threshold measurements made with Hg on a horizontal plate matched the results of Taylor and McEwan[6] to within experimental error and can be predicted with linear stability.

Threshold electric field for Taylor cone formation (Hg falling film)

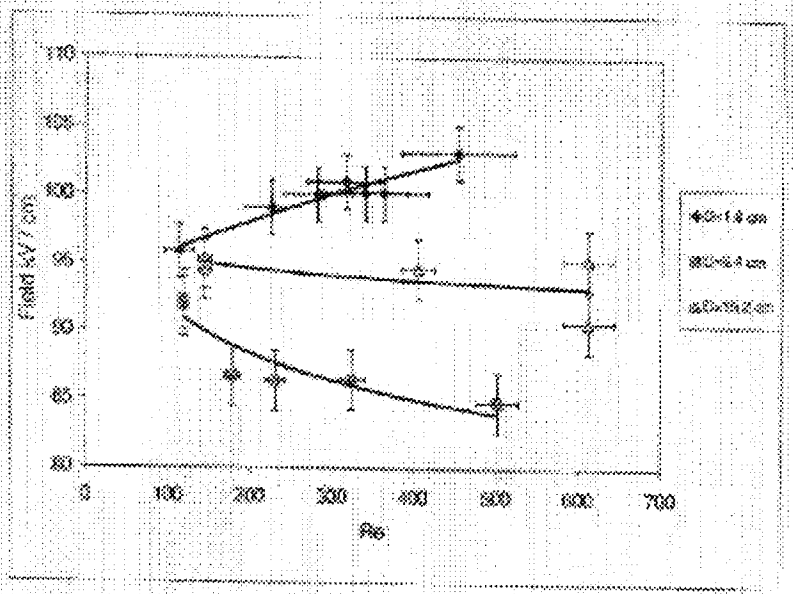

A cylindrical electrode was oriented with the axis transverse to fluid flow . Electric field profile in direction of flow was similar to Gaussian. The electrode position was moved to various distances (D) from the inlet to determine the effect of surface waves.

- For a falling film, the Taylor cone threshold is insensitive to angle of inclination, electrode length, position downstream and Reynolds number. High values of the field *~70 kV / cm* were reached for conditions similar to high temperature radiator design.

Taylor Cone Instability with Mercury

➢ The normal component of gravity produces a minor increase in stability, which means that rotation of the radiator may not be necessary.

➢ In the linear theory, it stabilizes the fluid. For the horizontal case this results in an increase in threshold that is matched by experiment.

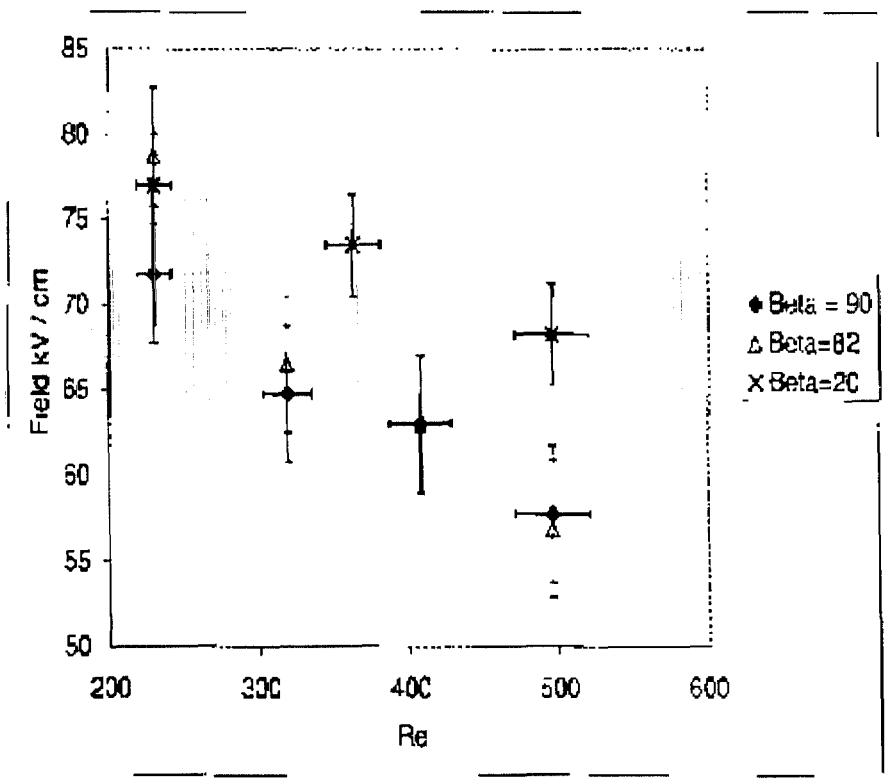

A 5 cm long electrode was held *0.11 cm* above the mercury film, and the angle of inclination of the plate with the horizontal, beta (deg) was varied.

➢ Electrode length has an insignificant effect on fluid stability. The plot below shows no difference in critical field as the electrode length is varied from *3 to 15 cm*.

➢ It is possible that a single electrode could cover the length of the radiator, and be electrified at all times.

➢ For a cylindrical electrode, which corresponds to a quasi-gaussian field, an increase in peak field of *~50%* can be realized.

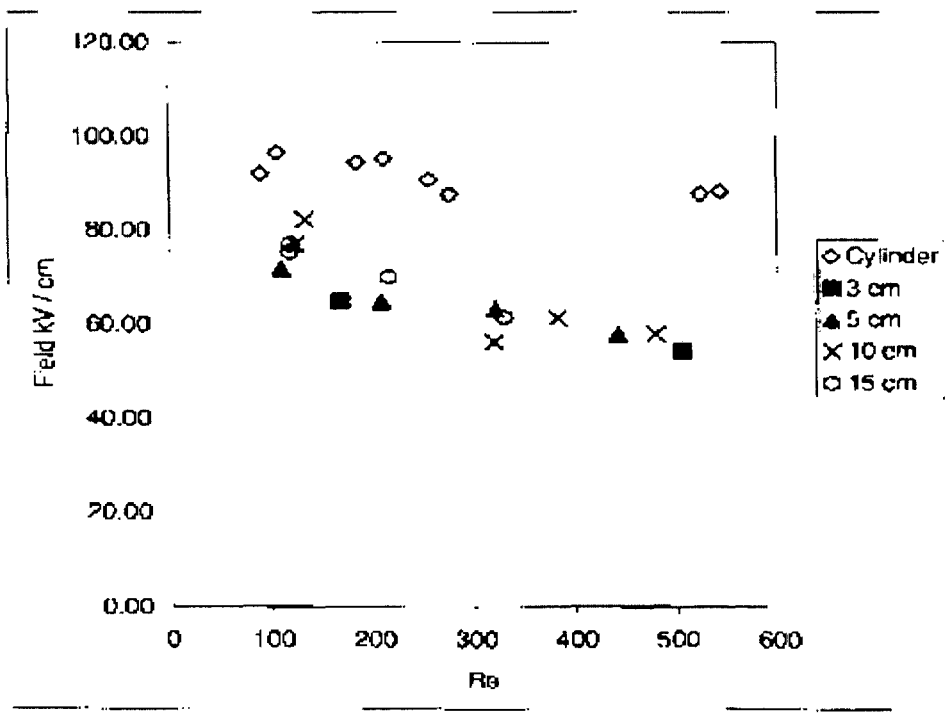

Electrodes of various lengths were held *0.11 cm* above the mercury film and centered *7.5 cm* from the inlet.

Pressure Profile

- The pressure under flowing ethanol and oil films was measured with a U–tube manometer as shown on the right. The manometer was calibrated with a known pressure drop. By moving the electrode, the pressure was then measured as a function of position in the direction of flow.
- For ethanol, the measured pressure matches the calculated pressure jump at the interface.
- For uncontaminated diffusion pump oil, though, the peak negative pressure matches calculations for a conducting fluid. This is nearly twice the expected result for the oil (dielectric constant ~2.3).
- This effect may be due to the field within the dielectric in the vicinity of the leak hole. The diagram in the bottom right shows what the field lines, which exert a body force on the oil, might look like.

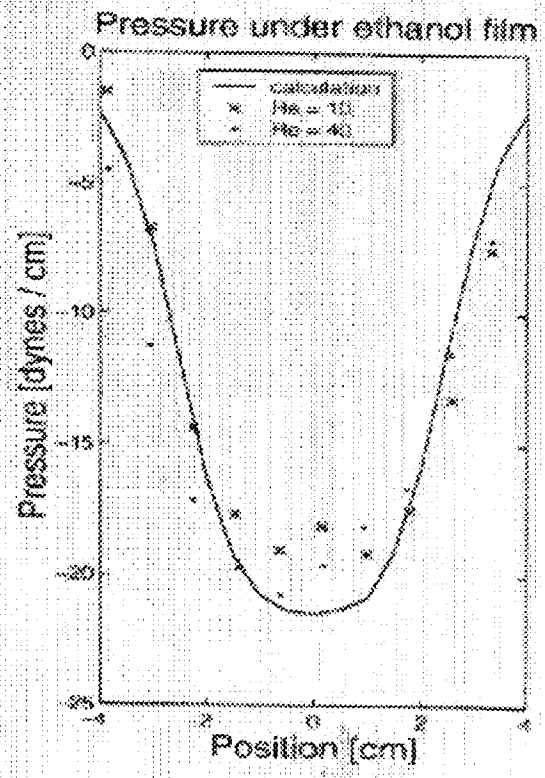

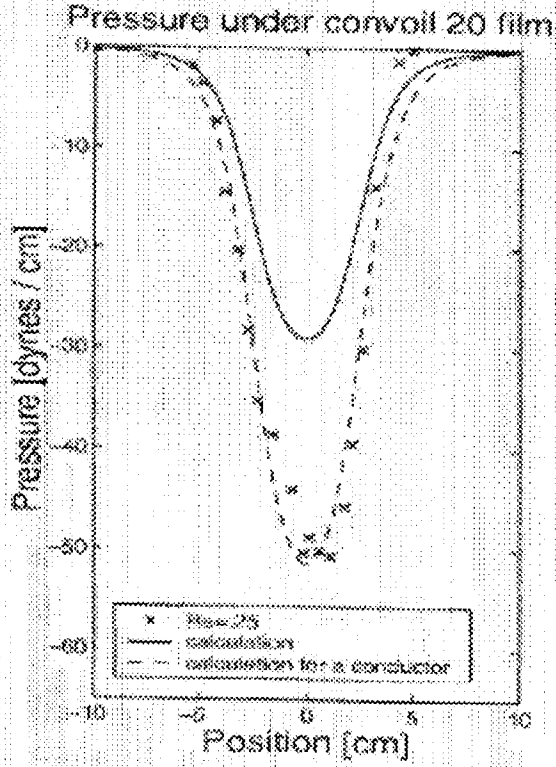

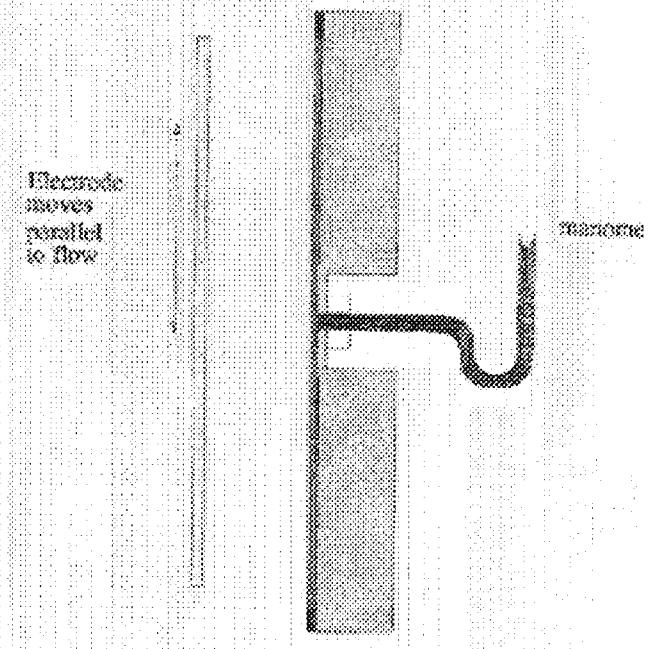

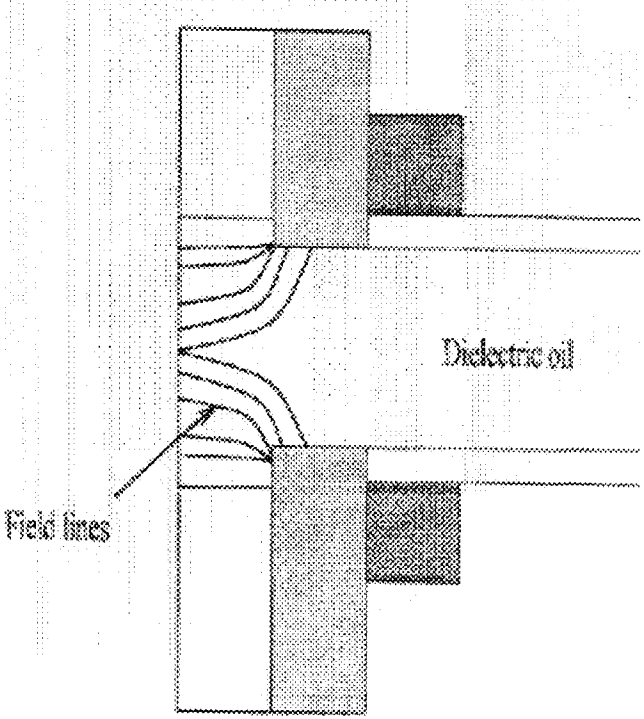

NASA/CP—2000-210470

Leak Stoppage

➢ Non–wetting fluids in zero g are likely to leak when the pressure at the leak hole is greater than the capillary pressure, which prevents leaking. This is confirmed by experiment with falling Hg film. Earth gravity complicates the problem for wetting fluids. We show here that leaks can be stopped in these conditions with fairly low electric fields.

➢ A leak through a 1 mm hole was started with a pressure pulse, and stopped with an electric field. The working fluid was ethanol. The back of the brass plate was coated with an enamel paint. Upon leaking, a rivulet of ethanol flowed down the back of the plate.

➢ Fluorescence imaging was used to measure the depth profile of the rivulet, from which the flow rate was calculated. When the field is raised above a critical value, the leak abruptly stops.

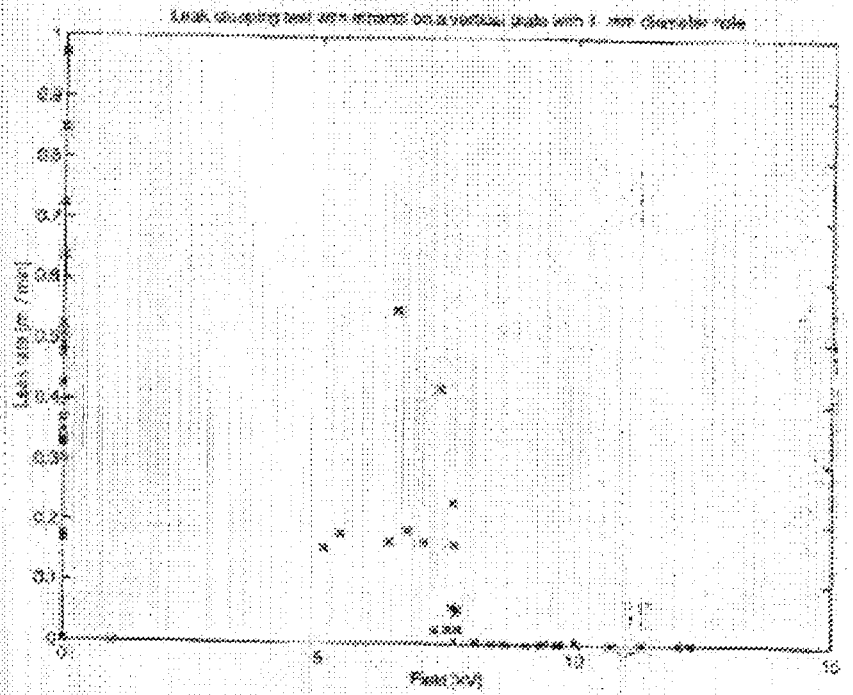

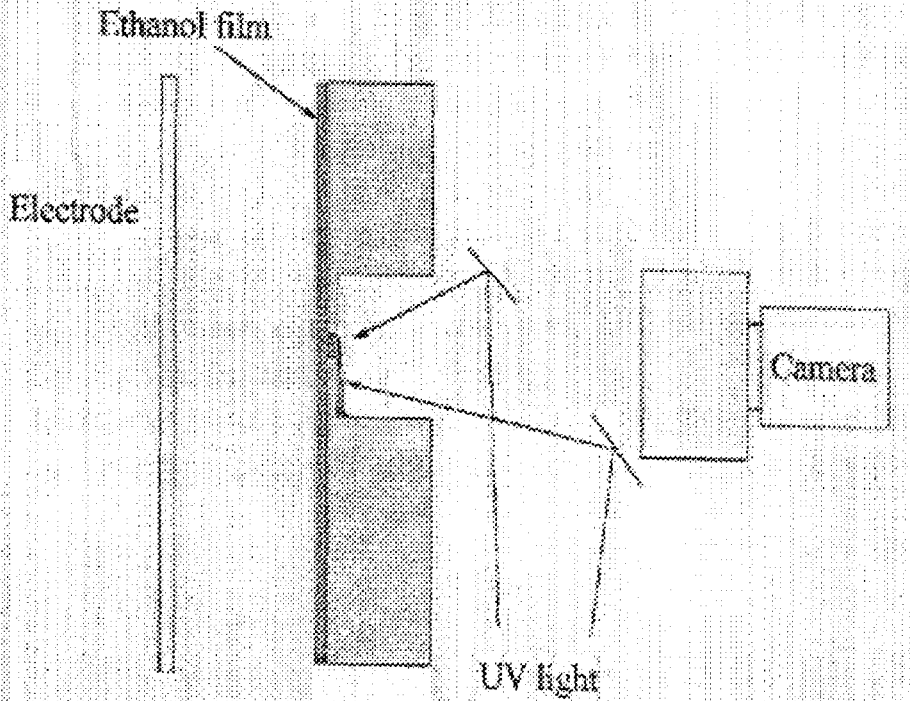

➢ Ethanol filled the hole, producing a hydrostatic head of ~ *90 dynes/cm²* at the bottom of the hole ($P2=P1+\rho g d_h$).

➢ The field required to stop the leak was *8 kV/cm*, which corresponds to *30 dynes/cm²*.

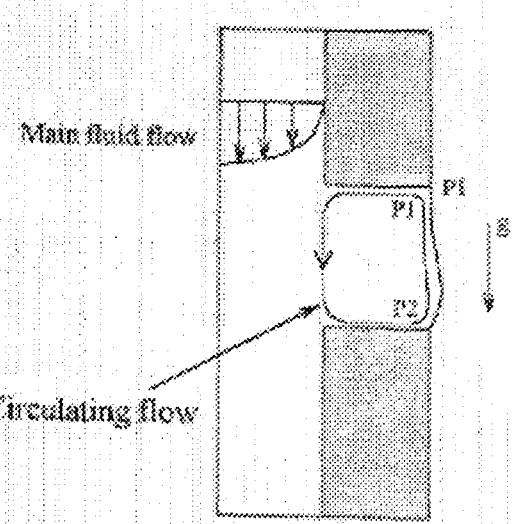

Gas Phase Electrical Breakdown

- Electrical breakdown in the vapor phase will effectively set the maximum operating temperature of a Li radiator. The radiator power per unit weight varies roughly as 1^{st}.
- An estimate of the pressure where vacuum breakdown begins to dominate, can be made from experiments by Hackam and Altcheh[5]. The transition occurs at $P \sim 10^{-3} - 10^{-2}$ Torr, for air depending on the electrode material. Our observations with various geometries and Hg vapor with brass and stainless steel electrodes show $P \sim 3x10^{-3}$ Torr. Alkali metal electrodes are not reported by Hackam, but the effect is to lower the breakdown voltage and shift the Paschen minimum to a lower pressure[6]. This effect is more pronounced when the negative electrode is the alkali metal. One could lessen the effect by making the fluid film positive. Little work has been done to determine the effect of various electrode geometries on breakdown[7].
- As the chart on the right shows, the maximum temperature of a Lithium radiator is $730 - 800$ K. The maximum temperature of a NaK radiator is $430 - 500$ K.

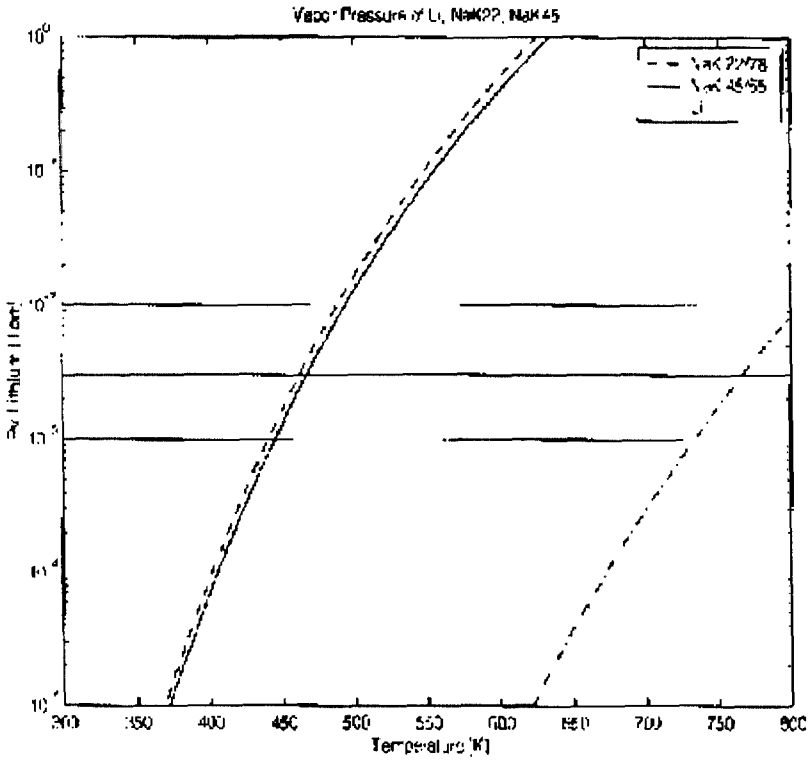

5. Hackam, R. and Altcheh, L, J. App. Phys., **46**, 2, (1975).
6. Penning, F.M., London, 1957.
7. Parker, A.B, Johnson, P.C., Proc. R. Soc. Lond. A., **325**, (1991).

NASA/CP—2000-210470

Design Calculations

1. Several designs have been proposed
   a. spinning (adds flow stability) —> may not be needed
   b. non spinning (reliability)
   c. cone, cylinder – weight is insensitive to geometry. depends on the size of the plenum and distribution and pumping systems

2. Considerations involved
   a. fluid heights between 0.1 and 1mm
   b. flow stability
      long wave calculations —> positive
      experimental observations —> positive
   c. gas breakdown stability —> limits temp. range
   d. leak stopping —> well–wetted materials are acceptable / non–wetted materials are more robust
   e. materials of construction / safety —> needs corrosion and erosion data / directly affects cost
   f. view factor calculations —> a good view factor is obtained over a variety of geometries. Not a critical design issue

Estimated weight breakdown for radiator components

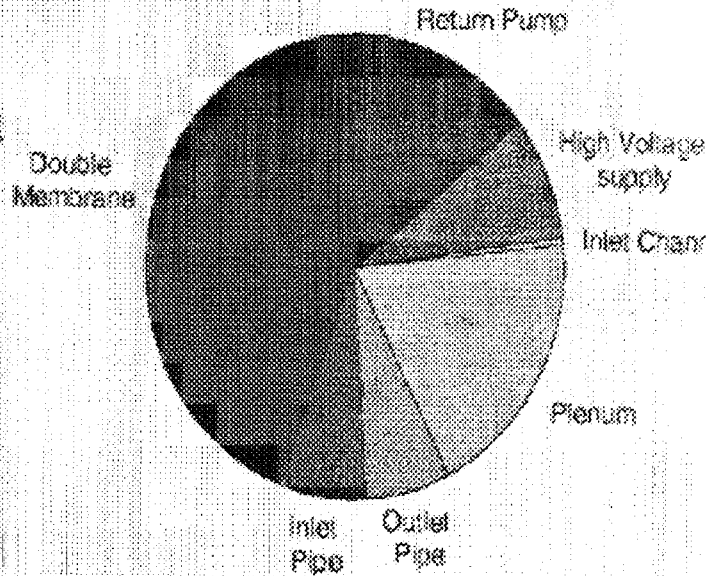

Cross–section of double membrane radiator (% by weight)

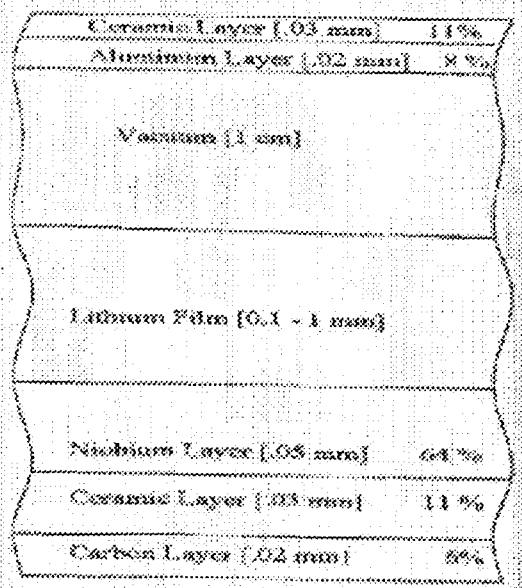

Thicknesses are estimates which need further study.
Ceramic —> rigidity
Niobium —> barrier to Li
Carbon —> leak detection
The Nb needs to be thick enough to protect against lon term erosion.
The solubility of Nb in Li and Na is low, 1 ppm and .03 ppm at 1073 K and 873K respectively.

Conclusions / Recommendations

- Weight savings over heat pipe radiator designs are large.
- Taylor cone and gas breakdown instabilities invcstigated with favorable results. Further work with real materials and realistic geometry is needed.
- Litcrature is favorable about wetting, corrosion, and erosion. Further work on these issues and safe handling are needed.
- Fluid collcction and pumping details need to be tested.

DYNAMICS AND ARREST BY FREEZING OF A MOLTEN CONTACT LINE ADVANCING OVER A COLD SUBSTRATE

A. A. Sonin, G. M. Duthaler, M. Liu, T. Qiu, M. A. Quintella

Massachusetts Institute of Technology
Cambridge, MA 02139, USA

The motion of a molten contact line as it advances over a cold solid and eventually arrests by freezing is a central problem in many materials processing applications, but has received virtually no attention in the literature until only a few years ago. This talk gives an overview of our efforts during the past four years to arrive at a fundamental understanding of the molten contact line problem, based on experimentation and theory. Most of our work deals with what we consider to be the most interesting case: the one where the melt and solid are of the same material.

Our early experimental work addressed the conditions for contact line arrest and was done with molten waxes spreading on solid waxes of the same kind. Using a novel method of producing a molten front with controlled contact line speed[1,2], and interpreting the data with dimensional analysis, we showed[2] that a molten contact line advancing quasi-steadily over a subcooled solid is arrested when the apparent liquid contact angle is reduced to a critical value that depends on the Stefan number based on the solid's subcooling. Subsequent observations of water drops deposited on ice and liquid mercury drops deposited on frozen mercury, both at low a Weber number, yielded similar results[3].

The theory of the moving molten contact line is a challenge because it involves scales from the molecular to the macroscopic. The problem is to find a relationship between the contact line speed and the liquid's apparent contact angle, and to deduce the conditions for arrest. A conventional continuum formulation of the problem contains two singularities at the contact line, the familiar shear stress singularity (which is weak) and also a singularity in heat flux[4]. As a result of the heat flux singularity, the continuum formulation yields no meaningful solution for the apparent liquid slope at the contact line. However, by comparing a continuum finite element simulation with experiments, Schiaffino and Sonin[4] estimated that the physical mechanism that limits the heat flux singularity occurs within 0.1-1 μm of the contact line for wax.

Duthaler and Sonin[5] have recently formulated a theoretical model for the velocity –angle relationship at the contact line of a molten material spreading over a cold solid of its own kind, using as input a simple parametric model for the near-contact-line fusion fron shape, and assuming contact line motion is capillary driven and retarded by viscous forces. The main unknown input parameter in this model is the length scale associated with the wedge-like part of the fusion front at the contact line, which is unknown except for Schiaffino and Sonin's estimate for wax[4], and the wedge angle, which, being the same as the arrest angle in controlled circumstances, can in principle be obtained empirically as a function of the Stefan number, and is available for our wax[2]. In a separate paper Duthaler and Sonin show[6] that their theory agrees well with data taken during wax drop deposition, using Schiaffino and Sonin's estimate for wedge length and limiting the data to conditions where inertial effects are indeed small.

The most important unknown in the molten contact line problem is the physical mechanism that actually limits the heat flux at the contact. On this mechanism rests the success of any theory for molten contact line motion and freezing.

An important part of our experimental program was to be the development and fabrication of micron-scale temperature sensors for measuring the temperature distribution near a moving molten contact line. Our hope was that this would yield some important clues about the physics of the near-contact-line processes, and help discover the heat flux mechanism. This work is described by Liu[7]. Arrays of thin film thermistors, either 1.5μm square or 2.5 μm square on both silicon and silicon dioxide substrates were designed, and fabricated with standard silicon-based integrated-circuit techniques. Tests showed (Liu[7]) that the sensors had more than adequate time response. However, several unavoidable factors rendered these arrays problematic for our purpose. The substrates had much higher thermal diffusivity than our melts, which affected the temperature in the whole system, and the slightly protruding (c:a 0.5 μm) sensors and their leads interfered with the contact line's natural motion via. Perhaps most importantly, the 1.5 μm square sensors were still not small enough for our purpose.

Quintella[8] has performed a computational exploration of how the nature of heat flux distribution near the contact line is affected when the conventional boundary condition of constant temperature at the fusion interface is replaced with some relatively simple alternative models (e.g. a "resistive layer") near the contact line. He shows that, while it is mathematically possible to in essence eliminate the singularity with some of such models, or at least push it to molecular scales, the model inputs require values that are not easy to justify on physical grounds. It would appear that the solution is to be sought in the physics rather than the mathematics.

[1] F. Gao, "Molten microdrop deposition and solidification processes," Ph. D. Thesis, Department of Mechanical Engineering, MIT, May 1994

[2] S. Schiaffino and A. A. Sonin, "Motion and arrest of a molten contact line on a cold surface: an experimental study," *Phys. Fluids* **9** (1997) 2217-2226

[3] S. Schiaffino and A. A. Sonin, "Molten droplet deposition and solidification at low Weber numbers", *Phys. Fluids,* **9** (1997) 3172-3187

[4] S. Schiaffino and A. A. Sonin, "On the theory for the arrest of an advancing molten contact line on a cold solid of the same material," *Phys. Fluids* **9** (1997) 2227-2233

[5] G. M. Duthaler and A. A. Sonin, "A theoretical model for the velocity-angle relationship at the contact line of a molten material spreading over a cold solid of its own kind," submitted to *Phys. Fluids* (2000)

[6] G. M. Duthaler and A. A. Sonin, "Experiments on the velocity-angle relationship at the contact line during molten drop deposition on a cold solid of its own kind," submitted to *Phys. Fluids* (2000)

[7] M. Liu, "Micron-scale thermistors for rapid transients in interfacial temperature," M. S. Thesis, Department of Mechanical Engineering, MIT, September 1998

[8] M. A. Quintella, "Numerical investigation of the heat flux singularity at an advancing molten contact line," M. S. Thesis, Department of Mechanical Engineering, MIT, February 1999

Fuquan Gao and Ain A. Sonin, "Precise deposition of molten microdrops: the physics of digital microfabrication," *Proc. R. Soc. Lond. A* **444** (1994) 533-554

Gregg M. Duthaler, "Design of a drop-on-demand delivery system for molten solder microdrops," M. S. Thesis, Department of Mechanical Engineering, MIT, January 1995

Stefano Schiaffino, "The fundamentals of molten microdrop deposition and solidification", Ph. D. Thesis, Department of Mechanical Engineering, MIT, August 1996

Stefano Schiaffino and Ain A. Sonin, "Formation and stability of liquid and molten beads on a solid surface", *J. Fluid Mech.* **343** (1997) 95-110

Stefano Schiaffino and Ain A. Sonin, "Motion and arrest of a molten contact line on a cold surface: an experimental study," *Phys. Fluids* **9** (1997) 2217-2226

Stefano Schiaffino and Ain A. Sonin, "On the theory for the arrest of an advancing molten contact line on a cold solid of the same material," *Phys. Fluids* **9** (1997) 2227-2233

Stefano Schiaffino and Ain A. Sonin, "Molten droplet deposition and solidification at low Weber numbers", *Phys. Fluids,* **9** (1997) 3172-3187

Javier Torresola, "Solidification properties of certain waxes and paraffins," M. S. Thesis, Department of Mechanical Engineering, MIT, February 1998

Michael Liu, "Micron-scale thermistors for rapid transients in interfacial temperature," M. S. Thesis, Department of Mechanical Engineering, MIT, September 1998

Gregg M. Duthaler, "Molten drop deposition and the dynamics of the molten contact line," Ph. D. Thesis, Department of Mechanical Engineering, MIT, February 1999

Marcelo A. Quintella, "Numerical investigation of the heat flux singularity at an advancing molten contact line," M. S. Thesis, Department of Mechanical Engineering, MIT, February 1999

Presentation not available at time of printing.

STABILITY AND HEAT TRANSFER CHARACTERISITCS OF CONDENSATE FLUID LAYERS IN REDUCED GRAVITY

James C. Hermanson, Andreas N. Alexandrou and William W. Durgin
Mechanical Engineering Department
Worcester Polytechnic Institute, Worcester, MA

Peder C. Pedersen
Electrical and Computer Engineering Department
Worcester Polytechnic Institute, Worcester, MA

Jeffrey S. Allen
National Center for Microgravity Research
Cleveland, OH

ABSTRACT

The focus of this ground-based program is the study of film condensation phenomena under variable, reduced-gravity conditions. Experimental tests, combined with numerical modeling, are employed to gain an improved understanding of the fundamental fluid physics responsible for condensate film growth, film instability and the resulting interfacial motion under variable gravity, and the corresponding implications for heat transfer. There has been relatively little research on the mechanisms operative at the film interface between condensed liquid and its vapor under reduced gravity conditions. Of particular interest are the stability characteristics of the condensate layer, and how they differ from those of films of comparable scale in the absence of condensation.

A schematic diagram of the principal fluid phenomena expected to be operative during a typical condensation experiment when the acceleration (at a normal or reduced gravity level) is directed away from the condensing surface is shown in the figure below.

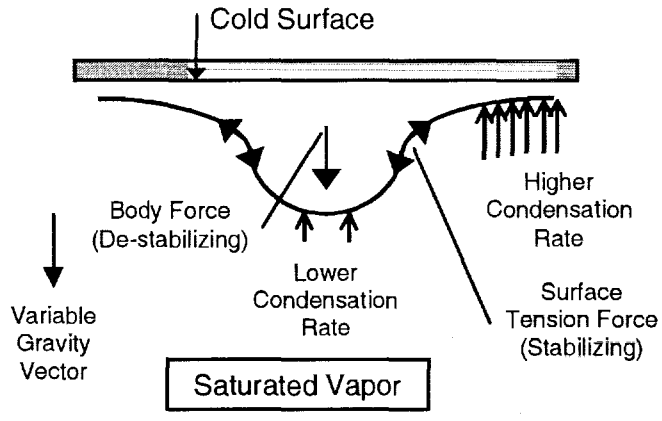

In the presence of a body force directed away from the plate, the condensate fluid layer will be unstable. This density-driven motion will be opposed by the surface tension, which will attempt to stabilize the fluid interface. In addition, the relatively higher thermal resistance associated with the thick fluid film at the crest will lead to a locally retarded condensation rate compared with that in the thin film regions in the fluid troughs.

The opposite sign of the temperature gradient across a condensing film versus that in the more commonly studied heated fluid layer will likely have significant implications for thermocapillary effects. In the case of a condensing layer, thermocapillary forces are expected to have a stabilizing influence on the film surface. Consideration of the combined effects of body

force and thermocapillary forces also suggests that unique convective patterns may arise in the presence of condensation under low-gravity conditions.

The experimental effort will involve three distinct experimental arrangements using identical test cells. First, laboratory tests will be conducted with a steady, stable condensing film on an upwards-facing, cooled surface to validate the experimental hardware and diagnostics. In the second series of experiments, the test cell will be inverted, using the resulting body force to generate fluid instabilities in the presence of condensation. Finally, in a third series of tests, the test cell will be mounted on a rotating platform to be flown on board a parabolic-trajectory aircraft to yield levels of de-stabilizing artificial gravity ranging from residual levels to approximately 0.1 g. This will allow the study of fluid phenomena in film condensation, such as thermocapillary effects, that are not detectable under normal gravity conditions. The dynamic response of the film layer a mechanical perturbation will also be examined.

For these experiments, three distinct fluid environments will be created to reveal particular features of the fluid physics associated with condensation in reduced gravity conditions. The first fluid condition is a condensing film in the presence of saturated vapor. Second, a non-condensing, cooled film surrounded by a non-condensing gas will be studied. In this case, thermocapillary effects will potentially be present owing to the cooling of the film, but there will be no effects of mass addition and film growth. Third, an isothermal, non-condensing film with mass addition will allow the study of the effects of film growth on layer stability in the absence of thermocapillary effects.

The thermal instrumentation will consist of standard thermocouples and heat transfer gauges. Direct photography and shadowgraph imaging will be employed to determine the features of the resulting instabilities, such as the wavelengths, surface deformation, and droplet formation and departure rates. Laser particle tracking will be employed to reveal the convective motion of the liquid film. Finally, the film thickness and growth rate (hence the condensation rate) will be determined using ultrasound gauging. The applicability of this technique has been recently demonstrated at WPI [1]. The technique can measure fluid film thicknesses as small as 50 μm, using a single transducer at a frequency of 10 MHz, with a lateral resolution of as little as 1 mm. Through multiplexing, multiple sites will be monitored sequentially to provide information on the spatial uniformity of the condensate film and the wavelength and amplitude of surface disturbances.

Detailed numerical calculations will be performed for each configuration to model the film layer growth due to condensation, the development of interfacial disturbances, and to predict the heat transfer rate. The numerical modeling will be an extension of previous work at WPI on solidification and droplet dynamics [2]. The liquid-vapor interface will be followed exactly using the Inverse Finite Element Method, which has been shown to have the advantages and accuracy in both two-dimensional and three dimensional problems [2]. According to this approach, the discretization is based on an inverse approach where the isotherms are a priori fixed and the non-linear problem is solved for the location of the discrete nodes. This method allows a "complete" solution to this free-and-moving type of problem.

[1] Pedersen, P.C., Cakareski, Z., and Hermanson, J.C., "Ultrasonic Monitoring of Film Condensation," *Ultrasonics* Vol. 38, 486-490, 2000.

[2] Alexandrou, A., "An Inverse Finite Element Method for Directly Formulated Free and Moving Boundary Problems", *International Journal of Numerical Methods in Engineering* Vol 28, 2383-2855, 1989.

NASA/CP—2000-210470

STABILITY AND HEAT TRANSFER CHARACTERISTICS OF CONDENSATE FLUID LAYERS IN REDUCED GRAVITY

J.C. Hermanson*
P.C. Pedersen†
A.N. Alexandrou*
W.W. Durgin*

*Mechanical Engineering Department
†Electrical and Computer
Engineering Department
Worcester Polytechnic Institute
Worcester, MA

Jeffrey S. Allen

National Center for Microgravity Research
Cleveland, OH

PROBLEM STATEMENT

The focus of this ground-based program is the study of film condensation phenomena under reduced-gravity conditions. Experimental tests, combined with numerical modeling, are employed to gain an improved understanding of the fundamental fluid physics responsible for condensate film growth, film instability and the resulting interfacial motion under variable levels of gravity, and the corresponding implications for heat transfer.

There has been relatively little research on the mechanisms operative at the film interface between condensed liquid and its vapor under reduced gravity conditions. Of particular interest are the stability characteristics of the condensate layer, and how they differ from those of films of comparable scale in the absence of condensation.

PROGRAM PLAN

- 1-g Laboratory Experiments (WPI)
  - Condensing films
  - Non-condensing films with fluid addition
  - Non-condensing, cooled films
- Reduced gravity experiments (NASA/NCMR)
  - Parabolic trajectory aircraft
  - Slowly Rotating Breadboard to get gravity levels from residual to approximately 0.1 g
- Numerical modeling (WPI)
  - Inverse Finite Element Method
  - Isotherms fixed; location of corresponding nodes calculated
- Define follow-on flight experiment (All)

RESEARCH QUESTIONS

- What is the effect of gravity level on the condensation rate and heat transfer of films on downwards-facing surfaces?
- What are the relative roles of mass addition and thermocapillary forces on the stability of condensate film layers subject to a body force?
- How do condensing films respond to perturbations under normal and reduced gravity conditions?
- What unique structures will be revealed in condensing films under reduced gravity conditions?
- What does the competition between increasing film thickness due to condensation and convection due to body force imply for the overall heat transfer?

EXPERIMENTAL APPROACH

- Closed condensation test cell
- Quasi-steady and perturbed films
- Mounting configurations
  - Cooled surface upwards (+1g, stable interface)
  - Cooled surface downwards (-1g, unstable interface)
  - Slowly rotating breadboard (-0.01 to –0.1 g, unstable interface)
- Diagnostics
  - Surface/fluid thermocouple temperature measurements
  - Direct photography and shadowgraph visualization
  - Particle tracing imaging
  - Ultrasound gauging of dynamic film thickness

STABILIZING/DE-STABILIZING MECHANISMS IN CONDENSATION EXPERIMENTS

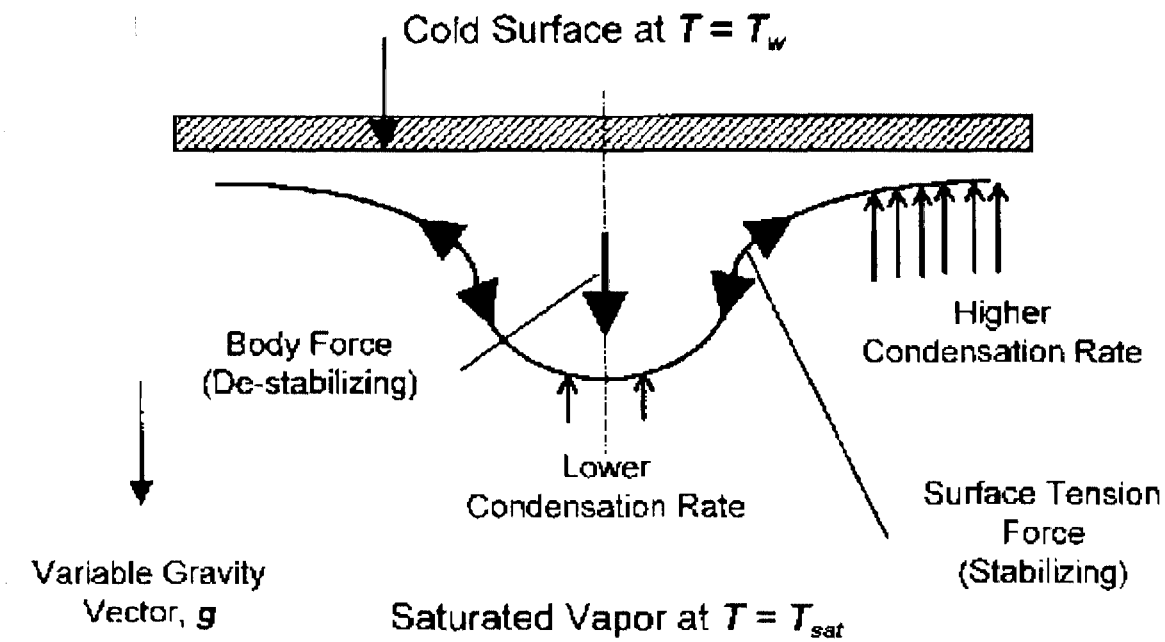

This sketch shows the principal phenomena operative during a typical film condensation experiment when the body force is directed away from the cooled surface. The body force (at normal or reduced gravity) is de-stabilizing to the fluid film, while surface tension has a stabilizing influence. The higher condensation rate in the "troughs" owing to the decreased thermal resistance also plays a stabilizing role.

ROLE OF THERMOCAPILLARY FORCES IN CONDENSING (COOLED) VS. HEATED FILMS

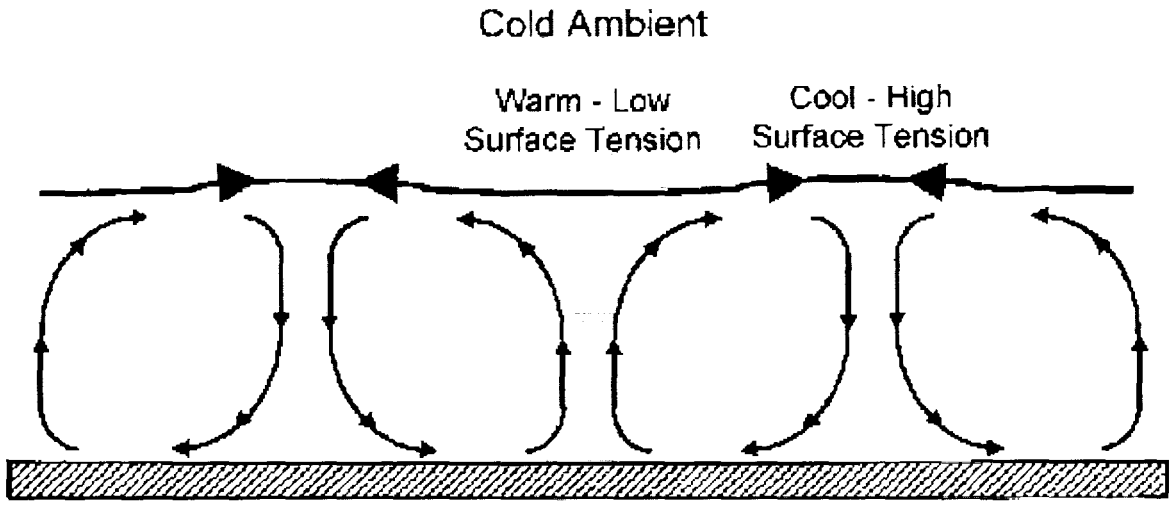

HEATED SURFACE

Thermocapillary forces for the (commonly studied) fluid layer heated from below can serve to drive convective motion.

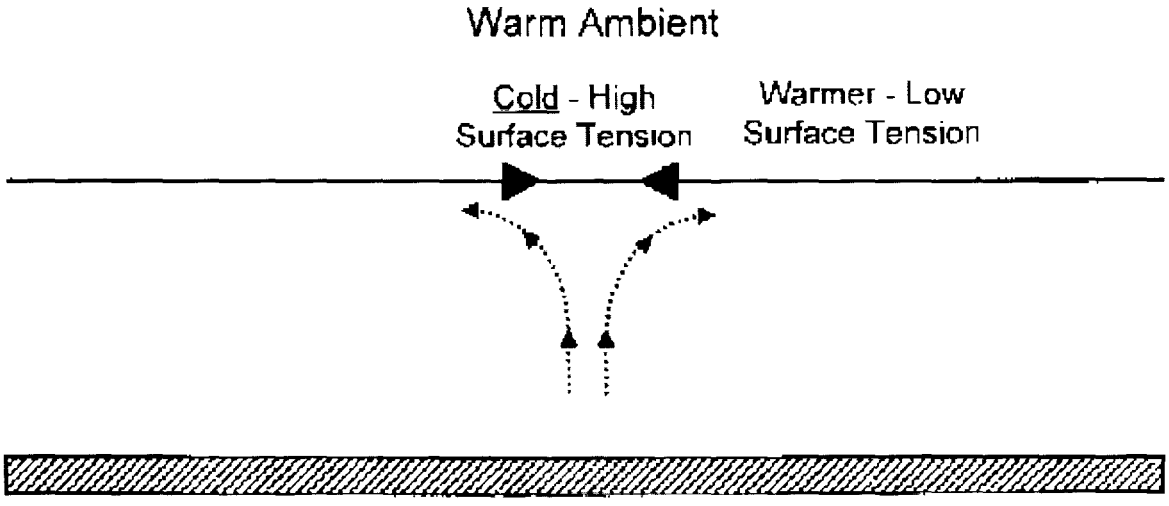

COOLED SURFACE

Thermocapillary forces for a fluid layer cooled from below (current investigation) oppose fluid motion and are a stabilizing influence on the film.

SCHEMATIC SIDE VIEW OF CONDENSATION TEST CELL

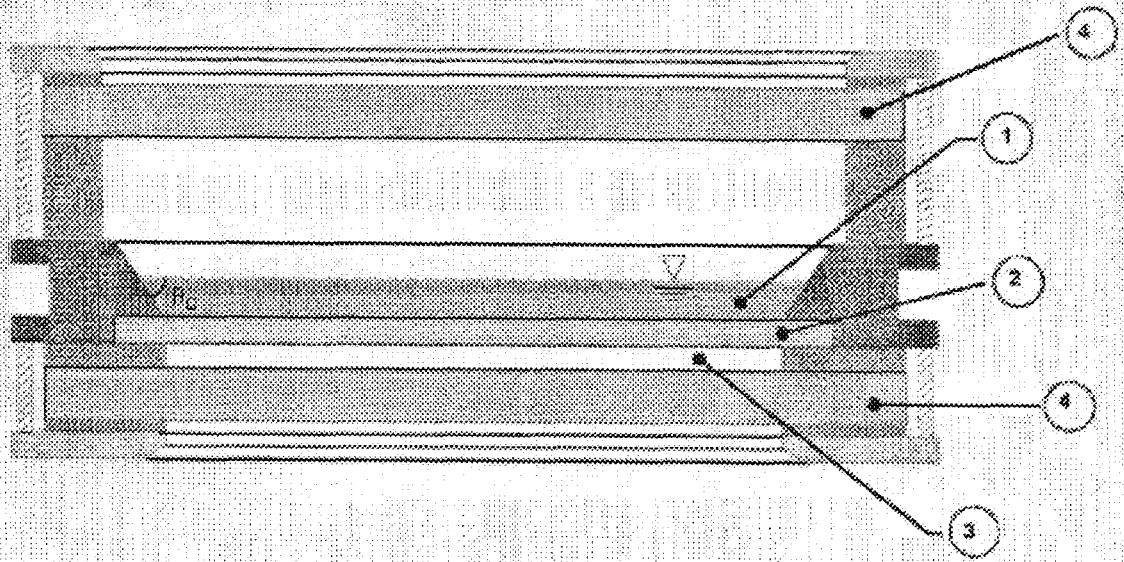

Schematic side view of condensation test cell. 1. Condensate film layer; 2. thin optical window (condensing surface); 3. cooling fluid passage; 4. outer optical windows.

SIMPLIFIED PHYSICAL MODEL OF ACOUSTIC REFLECTIVITY FROM FILM LAYER

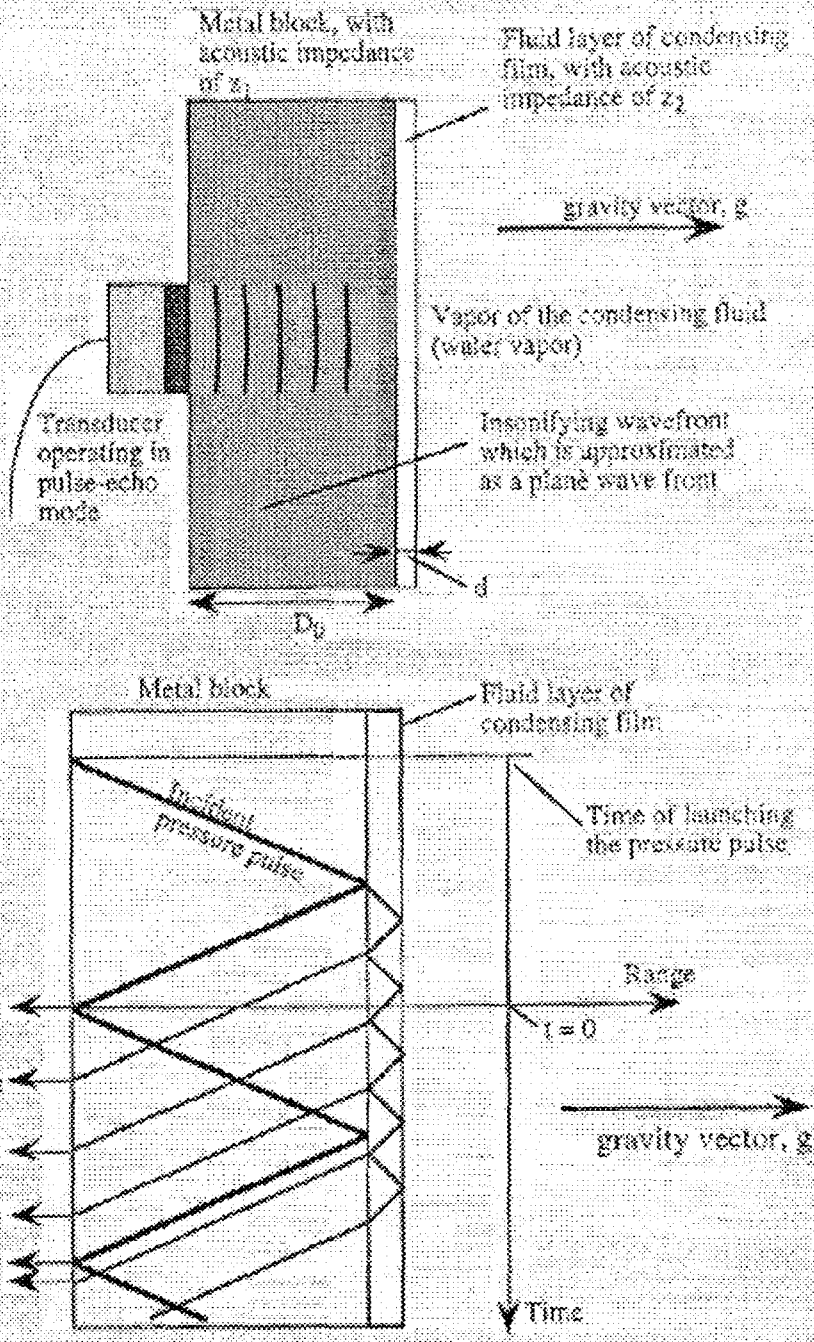

A series of reflections arise due to reflections inside the metal block and multiple reflections inside the condensing film.

MEASURED THICKNESS OF CONDENSING FLUID FILMS

Downward facing surface (-1 g)

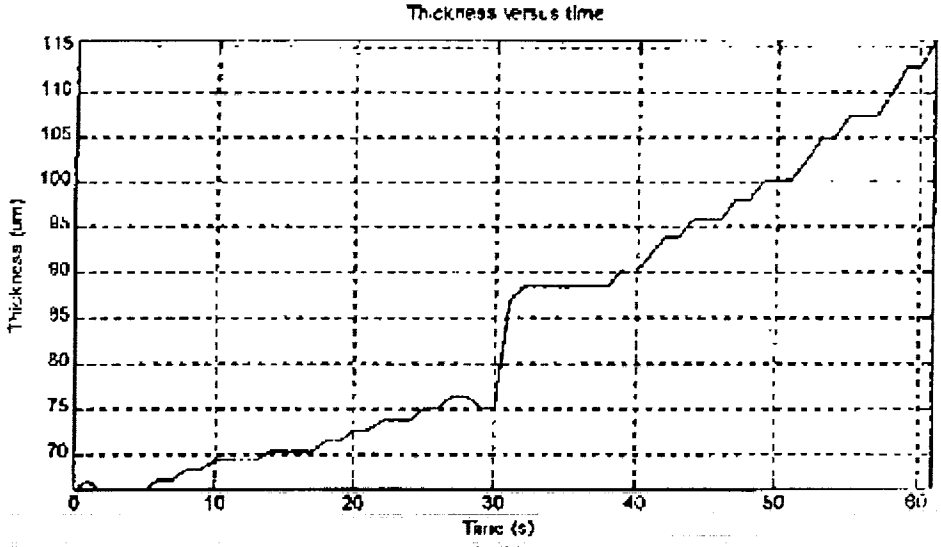

Film thickness growth water vapor in air. Water bath temperature 75 C; cooled surface temperature 25 C.

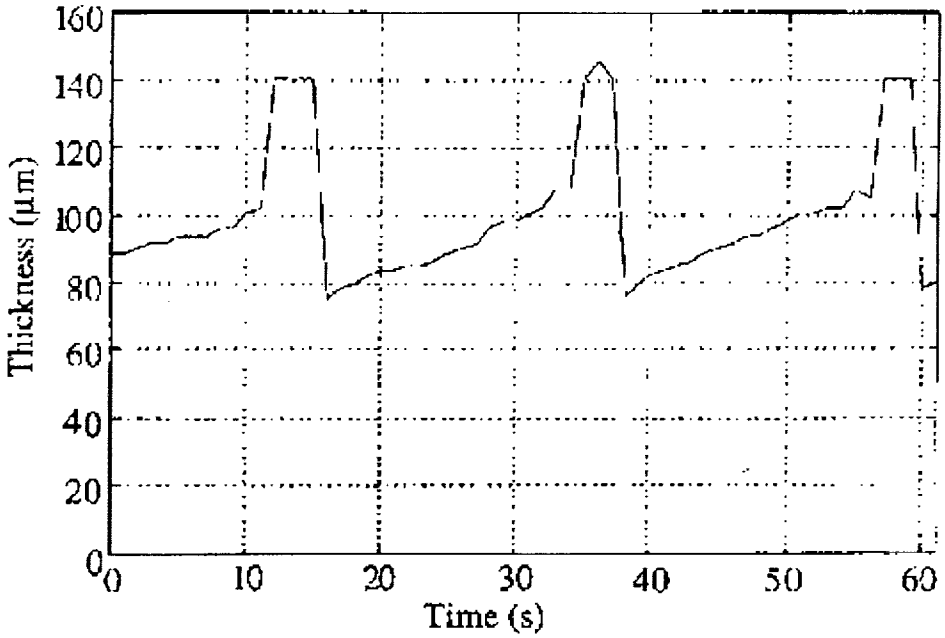

Changes in film thickness for water vapor in air. Water bath temperature 85 C; cooled surface temperature 20 C. The periodic peaks were due to a fluid instability, such as droplet release or droplet motion across the measurement location.

SUMMARY OF RESULTS TO DATE

- Preliminary laboratory experiments of film condensation on the downward-facing surface of a cooled plate have been conducted.

- Condensation experiments were performed using water and methanol. For a given film thickness, the Bond number of the water was less than that of the methanol film by a factor of 2.5, simulating a modest change in gravity level.

- The lower Bond number of the water film appeared to result in longer disturbance wavelengths and a more stable layer than for the methanol film.

- Single-point ultrasound measurements of layer thickness for both static films and condensing films have been performed. The acquired ultrasound signals and spectra agreed well with those predicted by both theoretical principles and a finite-difference model.

TWO PHASE FLOW IN MULTI-CHANNELS – LIQUID HOLDUP AND CAPILLARY FLOW

Farrokh Issacci,[1] Jeff Allen[2]
[1]Honeywell Aerospace, Torrance, CA
[2]National Center for Microgravity Research on Fluids and Combustion, Cleveland, OH

ABSTRACT

This combined experimental and theoretical study will investigate the fundamental aspects of two-phase flow, at low to moderate flow rates, in a multi-channel flow manifold. Some aspects of this investigation are the liquid holdup phenomena in the stagnation points, as well as the capillary force effects on the flow characteristics, and the liquid motion due to the surface-tension effects in such geometries. The results of this study will be basic information required in applications in space environment control and life support systems (ECLSS) such as fuel cells, biroreactors, thermal management systems, phase separators, etc. The advancement of fundamental knowledge of microgravity fluid flow is critical to the successful development of advanced ECLSS equipment used for space utilization and exploration.

This study will use the low gravity environment to single out inertia and capillary forces in a two-phase flow in rectangular channels with different cross-sectional dimensions, from sub-millimeter to centimeters. These configurations are common in many flow systems of space and terrestrial applications. The low gravity environment will allow for investigation of these effects in larger channels, which provide larger liquid drops and liquid films, and better measurement and understanding of these phenomena. The laboratory experimentation of small channels (normal-gravity conditions) will provide database for comparison and verification of low-gravity findings, as well as the theoretical modeling.

This effort will combine theoretical studies with experimentation. Our technical approach will include: identification of the needs for modeling development (based on applications and design issues), development of a test plan for normal and low gravity experimentation, conduct the experiments, compare theoretical results with the experimental data, modification/enhancement of the models based on the experimental data, and develop a plan for more low-gravity testing. This integrated experimental and theoretical approach is believed to result in a successful effort that with a minimum number of experiments will enhance our knowledge of two-phase flow in a rather complicated system of multi channels.

The benefit of this program to NASA and its mission is development of modeling tools critical to development of space systems. Also, a plan will be developed for more flight experimentation with longer reduced-gravity time. The results of this program will be building blocks for development of experimental data and analysis to help expedite the development of critical technology for the space power and life support systems, as well as terrestrial applications, and reduce the technology risks in these developments.

Presentation not available at time of printing.

Buoyancy-Driven Instabilities in Single-Bubble Sonoluminescence

T. Matula
University of Washington

Single-bubble sonoluminescence (SBSL) refers to the emission of light from an acoustically trapped bubble undergoing large-amplitude, nonlinear, predominantly radial oscillations. A sinusoidal acoustic standing wave causes the bubble to grow ten-fold during the tensile portion of the sound wave. Soon after the start of the acoustic compression phase, the bubble is free to collapse, driven by both the acoustic pressure and (more importantly) the inertia of the in-rushing fluid. Very near to the minimum of the collapsed state, the bubble emits broadband electromagnetic radiation. In addition to forcing the bubble into highly nonlinear radial oscillations, the standing wave also produces an acoustic radiation force that opposes the buoyancy force, and thus levitates the bubble.

Currently, the most accepted model for sonoluminescence is based on a variation of the "hot-spot" model, in which the interior gases heat up as the bubble collapses, resulting in an incandescence of a cool dense plasma generated near the final stages of bubble collapse [Moss, 1997]. However, the aggregate experimental evidence is relatively sparse, and precludes the complete dismissal of some competing theories. For instance, the "cool dense plasma" model assumes spherical symmetry throughout the bubble's oscillatory cycle. It is well known that with larger bubbles, observations clearly show that during the bubble's collapse, spherical asymmetries and instabilities (such as liquid jetting, capillary waves, and shape oscillations) develop. The question is not *if* sonoluminescence bubbles develop asymmetries, but rather, are the time scales over which asymmetries develop great enough to become a factor that can influence the light emission mechanism for the bubble?

This work addresses the particular question of whether or not buoyancy-driven instabilities result in a degradation of light emission from single-bubble sonoluminescence, and whether or not the bubble extinction at high forcing amplitudes is due to buoyancy-driven instabilities.

Preliminary observations of sonoluminescence in microgravity show that the light emission intensity does in fact increase during the microgravity phase, by as much as 40%. Laboratory-based experiments have shown that at least some of the increase in intensity is due to the loss of hydrostatic pressure (approximately 5%). This result is exciting, as it may demonstrate that buoyancy instabilities are present in sonoluminescence experiments. Future experiments are planned, including determining whether or not the extinction threshold can be increased in microgravity.

Presentation not available at time of printing.

A Study of Bubble and Slug Gas-Liquid Flow in a Microgravity Environment

J. McQuillen
NASA Glenn Research Center

The influence of gravity on the two-phase flow dynamics is obvious. As the gravity level is reduced, there is a new balance between inertial and interfacial forces, altering the behavior of the flow. In bubbly flow, the absence of drift velocity leads to spherical-shaped bubbles with a rectilinear trajectory. Slug flow is a succession of long bubbles and liquid slug carrying a few bubbles. There is no flow reversal in the thin liquid film as the long bubble and liquid slug pass over the film. Although the flow structure seems to be simpler than in normal gravity conditions, the models developed for the prediction of flow behavior in normal gravity and extended to reduced gravity flow are unable to predict the flow behavior correctly. An additional benefit of conducting studies in microgravity flows is that these studies aide the development of understanding for normal gravity flow behavior by removing the effects of buoyancy on the shape of the interface and density driven shear flows between the gas and the liquid phases.

The proposal calls to study specifically the following:

1) The dynamics of isolated bubbles in microgravity liquid flows will be analyzed: Both the dynamics of spherical isolated bubbles and their dispersion by turbulence, their interaction with the pipe wall, the behavior of the bubbles in accelerated or decelerated flows, and the dynamics of isolated cylindrical bubbles, their deformation in accelerated/decelerated flows (in converging or diverging channels), and bubble/bubble interaction. Experiments will consist of the use of PIV and LDV to study single spherical bubble and single and two cylindrical bubble behavior with respect to their influence on the turbulence of the surrounding liquid and on the wall

2) The dynamics of bubbly and slug flow in microgravity will be analyzed especially for the role of the coalescence in the transition from bubbly to slug flow (effect of fluid properties and surfactant), to identify clusters that promote coalescence and transition the void fraction distribution in bubbly and slug flow, to measure the wall friction in bubbly flow.

   These experiments will consist of multiple bubbles type flows and will utilize hot wire and film anemometers to measure liquid velocity and wall shear stress respectively and double fiber optic probes to measure bubble size and velocity as a function of tube radius and axial location.

OBJECTIVES:

1) Analysis of the dynamics of ***isolated*** bubbles in microgravity liquid flows including the dynamics of spherical isolated bubbles in order to study their dispersion by turbulence, the interaction with the pipe wall, the behavior of the bubbles in positive or negative pressure gradient (bubbles in accelerated or decelerated flows), the dynamics of cylindrical isolated bubbles in order to analyze their velocity with respect to liquid flow regime, their deformation in accelerated/ decelerated flows (in converging or diverging channels), and bubble/bubble interaction.

2) the dynamics of bubbly and slug flow in microgravity and especially the analysis of the role of the coalescence in the transition from bubbly to slug flow (effect of fluid properties and surfactant), the void fraction distribution in bubbly and slug flow with an identification of clusters that can promote coalescence and transition, the wall friction in bubbly flow

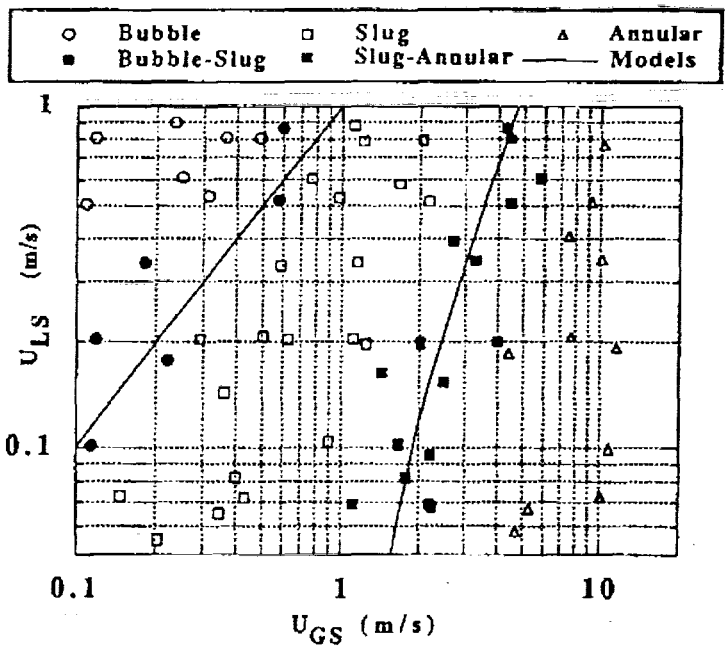

FIGURE 4
MICROGRAVITY FLOW PATTERN MAP FOR 1.27 CM ID TUBE, AIR-WATER

NASA
Lewis Research Center

SPACE EXPERIMENTS DIVISION
MICROGRAVITY SCIENCE AND TECHNOLOGY BRANCH

SFSD
Space Flight Systems Directorate

EFFECT OF G-LEVEL ON MULTIPHASE FLOW

SLUG FLOW
NORMAL GRAVITY
~1.0 G'S

SLUG FLOW
LUNAR GRAVITY
~0.17 G'S

SLUG FLOW
ZERO GRAVITY
<0.01 G'S

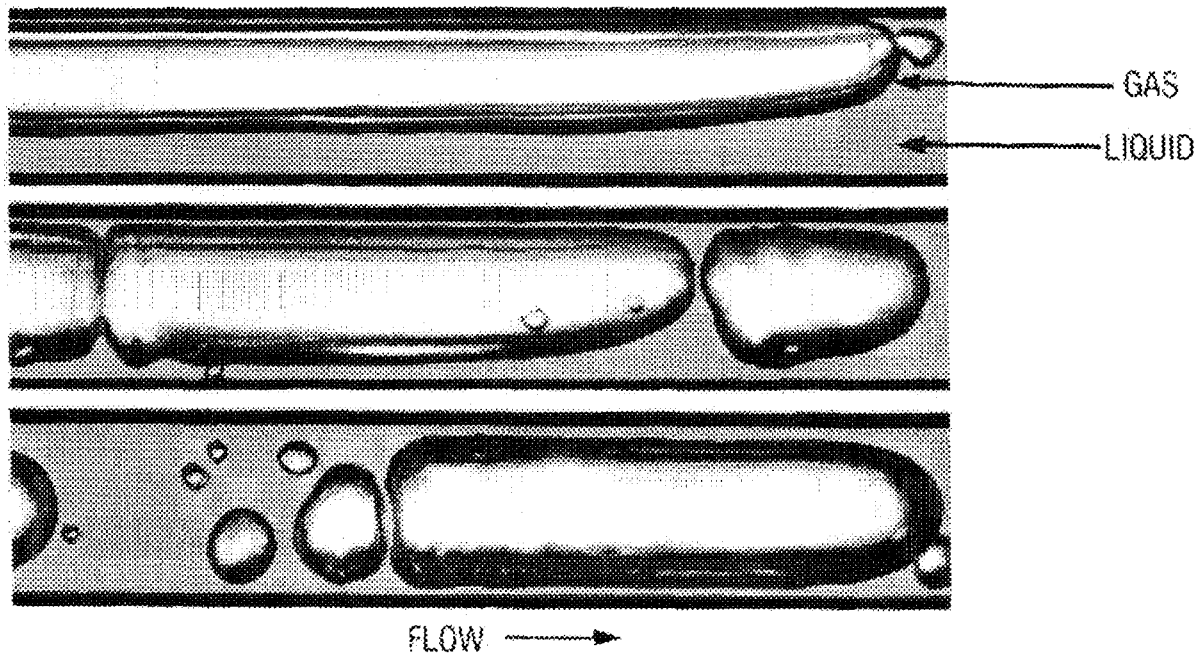

AIR-WATER IN 1.27 CM ID TUBE
SUPERFICIAL GAS VELOCITY ~ 0.43 M/S
SUPERFICIAL LIQUID VELOCITY ~ 0.07 M/S

NASA Lewis Research Center | SPACE EXPERIMENTS DIVISION | SFSD Space Flight Systems Directorate

TWO PHASE FLOW

NORMAL GRAVITY
ANNULAR FLOW

REDUCED GRAVITY
ANNULAR FLOW

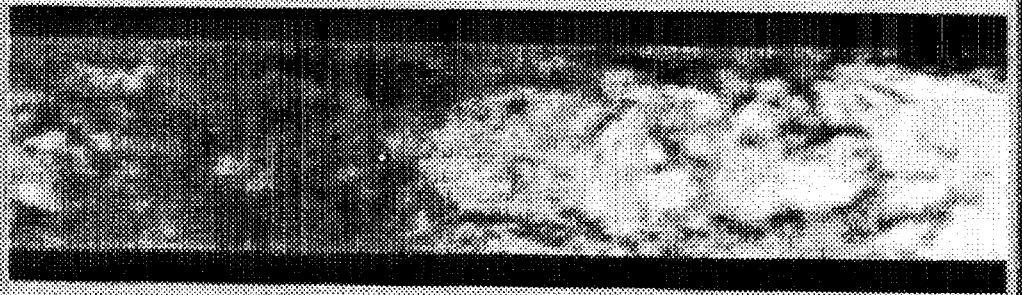

FLUIDS: AIR AND WATER
TUBE DIAMETER: 1.27 cm
SUPERFICIAL GAS VELOCITY: 11.0 m/s
SUPERFICIAL LIQUID VELOCITY: 0.5 m/s

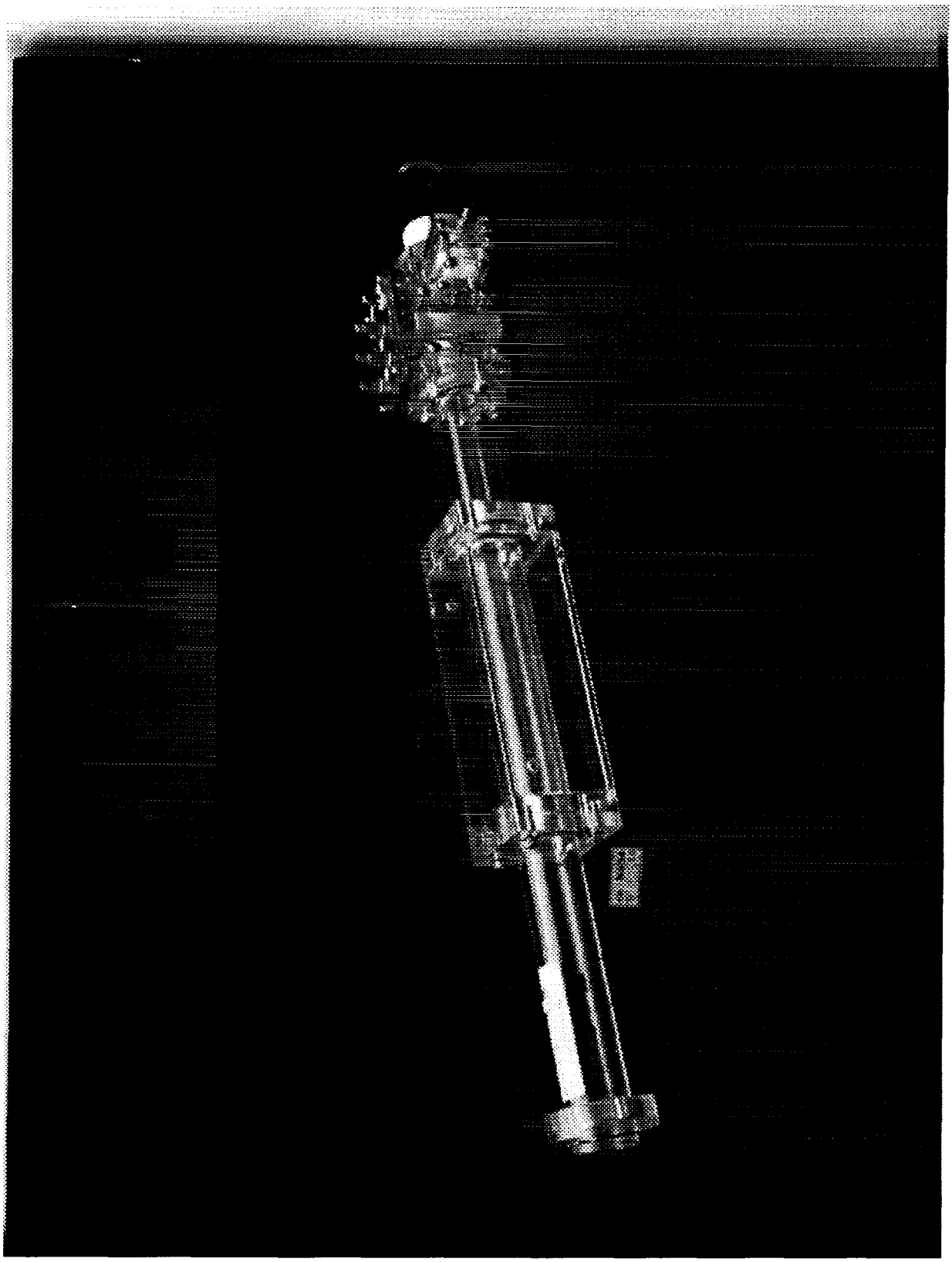

NASA
Lewis Research Center

SPACE EXPERIMENTS DIVISION
MICROGRAVITY SCIENCE AND TECHNOLOGY BRANCH

SFSD
Space Flight Systems Directorate

EFFECT OF G-LEVEL ON MULTIPHASE FLOW

STRATIFIED FLOW
NORMAL GRAVITY
~1.0 G'S

SLUG FLOW
LUNAR GRAVITY
~0.17 G'S

SLUG FLOW
ZERO GRAVITY
<0.01 G'S

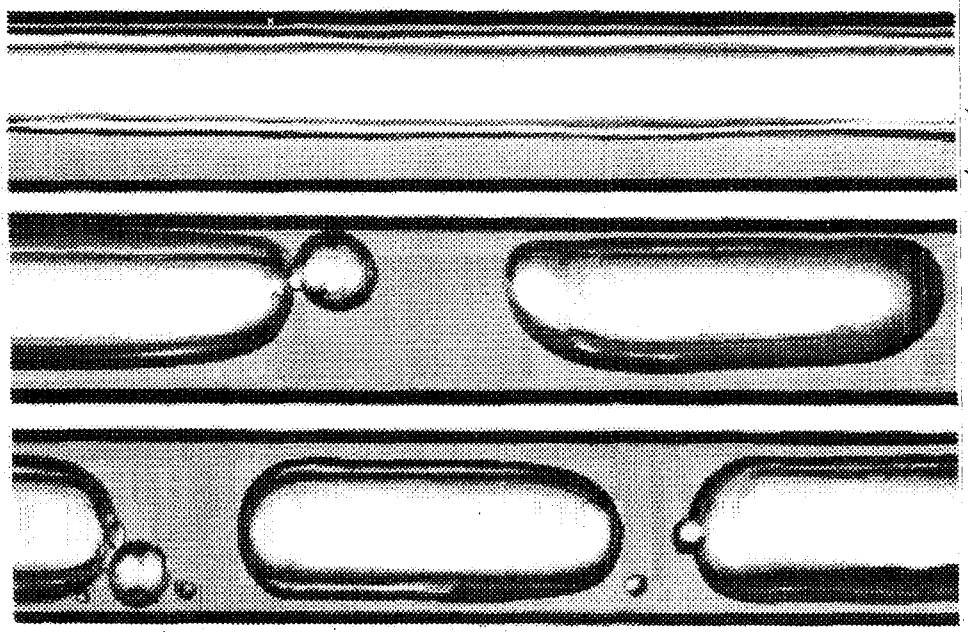

AIR-WATER IN 1.27 CM ID TUBE
SUPERFICIAL GAS VELOCITY ~ 0.14 M/S
SUPERFICIAL LIQUID VELOCITY ~ 0.07 M/S

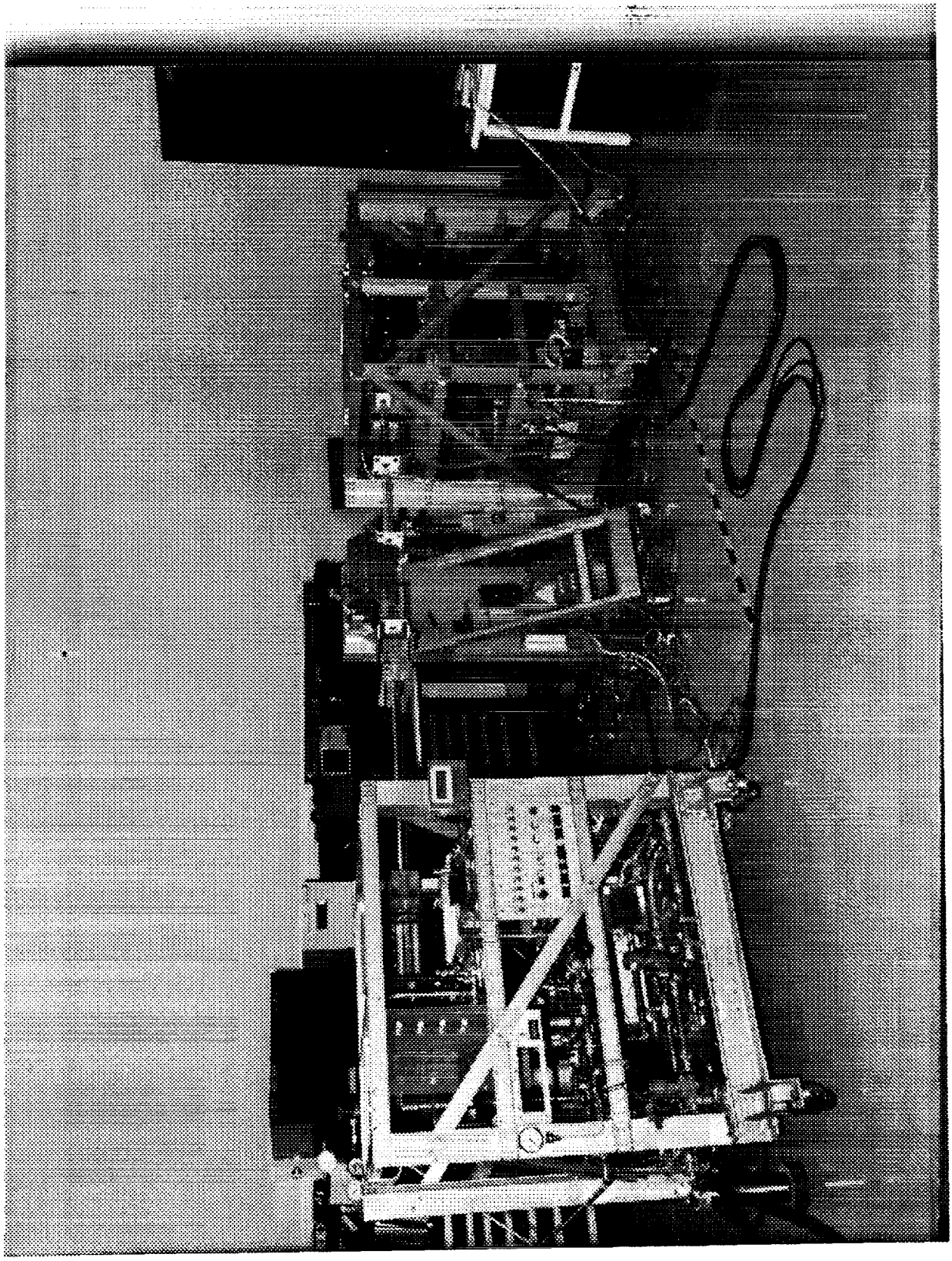

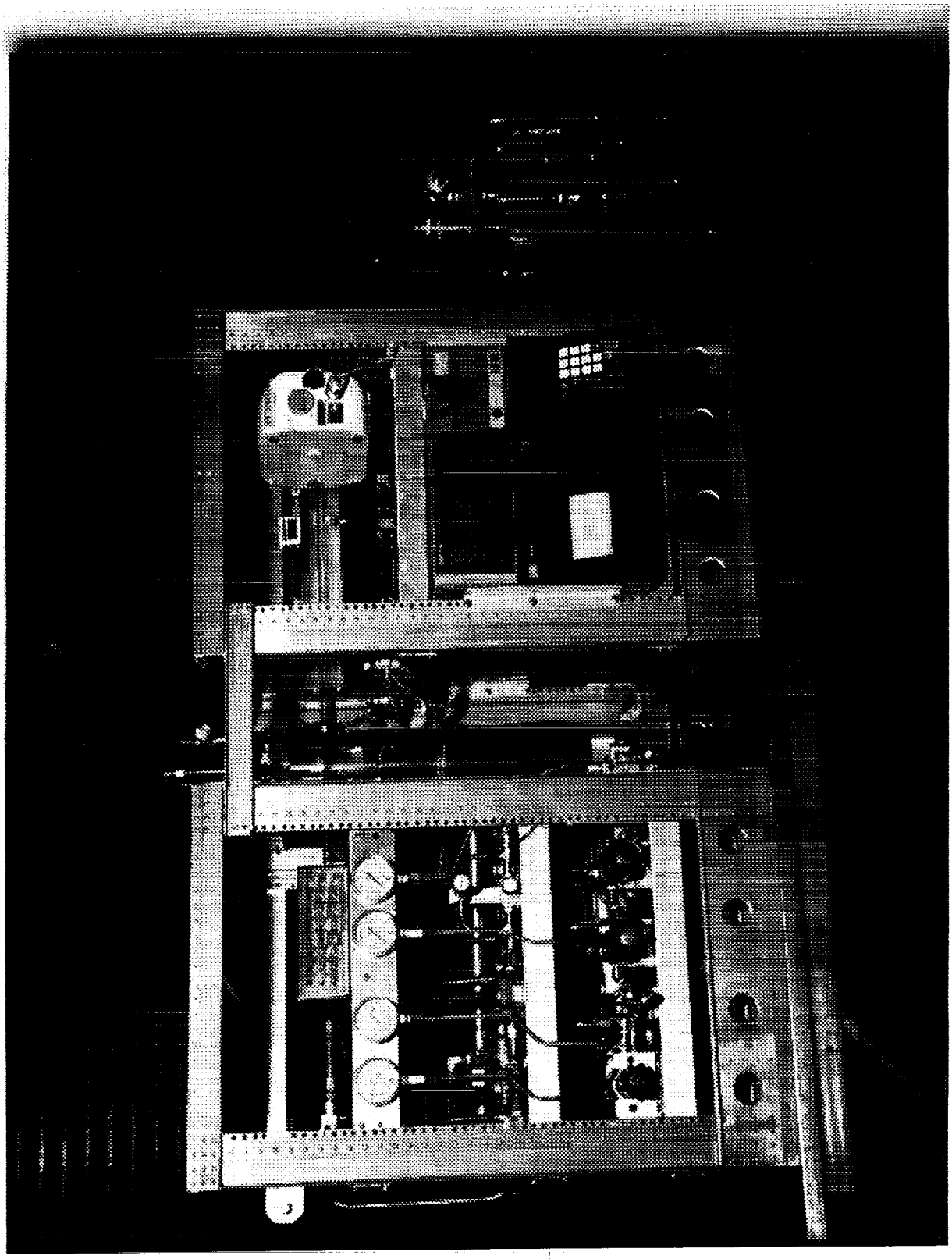

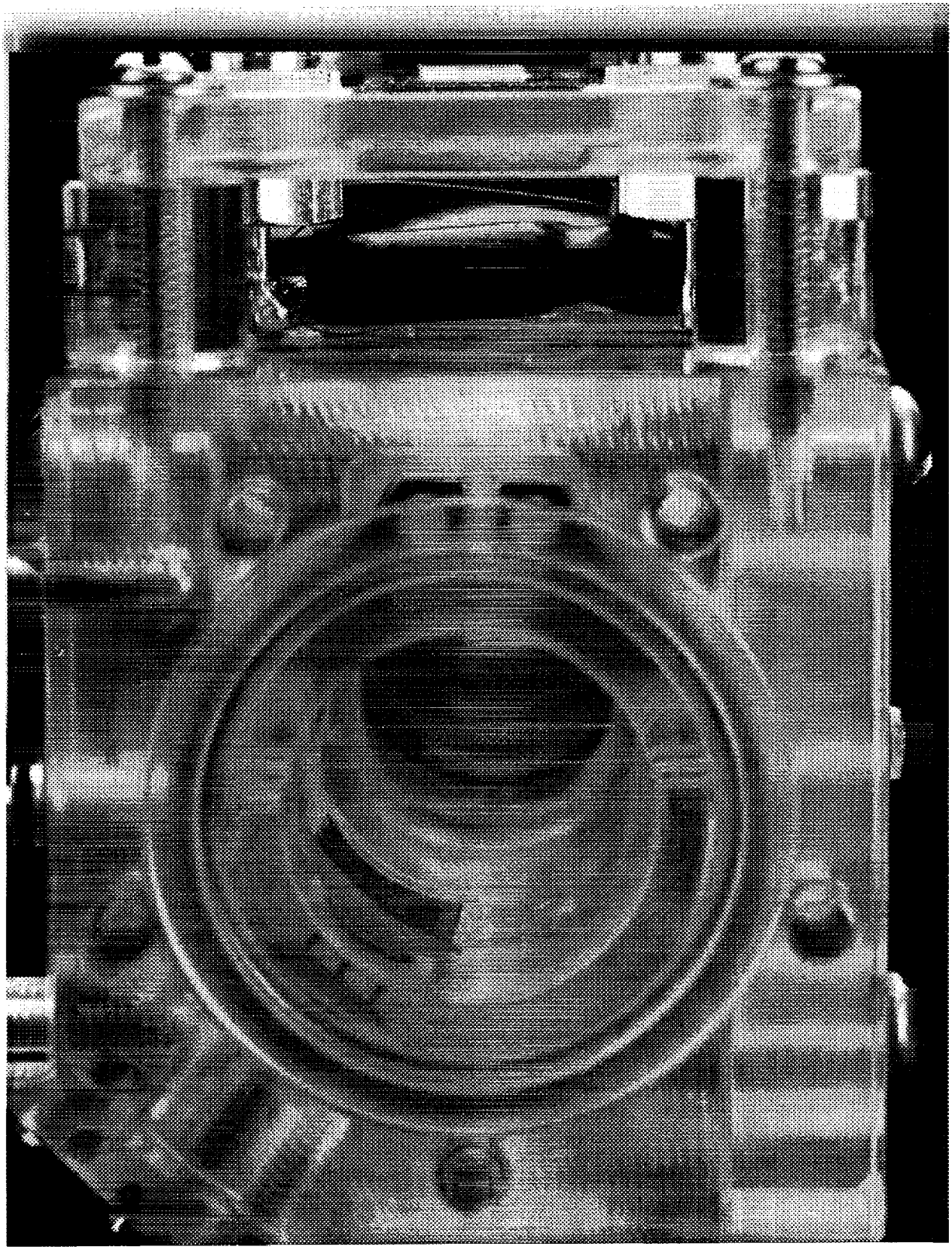

INVESTIGATION OF CRITICAL HEAT FLUX IN REDUCED GRAVITY USING PHOTOMICROGRAPHIC TECHNIQUES

I. Mudawar and H. Zhang
Boiling and Two-Phase Flow Laboratory
School of Mechanical Engineering
Purdue University
West Lafayette, IN 47907

ABSTRACT

This study concerns the theoretical modeling of critical heat flux (CHF) in reduced gravity flow boiling. Throughout the study, the near-wall conditions at heat fluxes approaching and exceeding CHF will be examined with the aid of photomicrography. The proposed work will aim for (a) developing a test apparatus for exploring flow boiling and CHF in reduced gravity, (b) developing photographic methods for investigating vapor layer interfacial instabilities, (c) constructing a phenomenological model for flow boiling CHF in reduced gravity, and (d) providing detailed plans for testing of the same hardware in a future Space Shuttle follow-up study.

During the initial stages of the study, experiments will be performed with vertical upflow at 1*g* to insure proper operation of the flow module, test heater, instrumentation, and flow loop, and to validate previous observations of CHF for vertical upflow. Experiments will then be repeated for different flow orientations to explore any differences in the CHF trigger mechanism in the presence of a smaller body force perpendicular to the heated wall. Finally, the test apparatus will be prepared for future microgravity experiments onboard the Space Shuttle during a follow-up study.

Much of the rationale for the CHF modeling is based upon recent work at Purdue University which has successfully yielded a theoretically-based model for flow boiling CHF, albeit for vertical upflow at 1*g*. High-speed motion analysis revealed bubbles coalesce into a wavy vapor layer at fluxes well below CHF. Hydrodynamic instability of the vapor layer interface facilitates bulk liquid contact with the wall, painting a thin liquid sub-film upon the wall. The sub-film is consumed by a combination of vigorous boiling and interfacial evaporation. CHF commences when the momentum of the vapor issued from the sub-film exceeds the pressure force exerted upon the perturbed interface in the regions of interfacial contact with the wall. This causes the wavy interface to lift away from the wall, precluding any sustained wetting and resulting in wall dryout.

The role of interfacial instability is paramount to establishing the necessary conditions for the dryout. Since interfacial wavelength is sensitive to surface tension forces, inertia, and body force, the proposed experiments will help isolate the individual effects of these forces by measuring the instability features (mainly wavelength and amplitude) at different flow velocities and different orientations. At high g's, interfacial instability is dominated by a balance between surface tension and body forces (Taylor instability). On the other hand, instabilities below 1g are far more complex, exhibiting sensitivity even to minute body forces for small flow velocities, but becoming completely dominated by a balance between surface tension forces and inertia (Helmholtz instability) for high velocities.

Particular attention will be given in this study to (a) the sensitivity of interfacial instabilities at low flow velocities to small body forces, and (b) the nonlinear attributes of interfacial instability such as vapor wave stream-wise stretching and merging of adjacent waves. This information will be used to construct a phenomenological CHF model applicable to reduced gravity conditions which can be used as a design tool to guard against burnout of electronic and power devices in space thermal management systems.

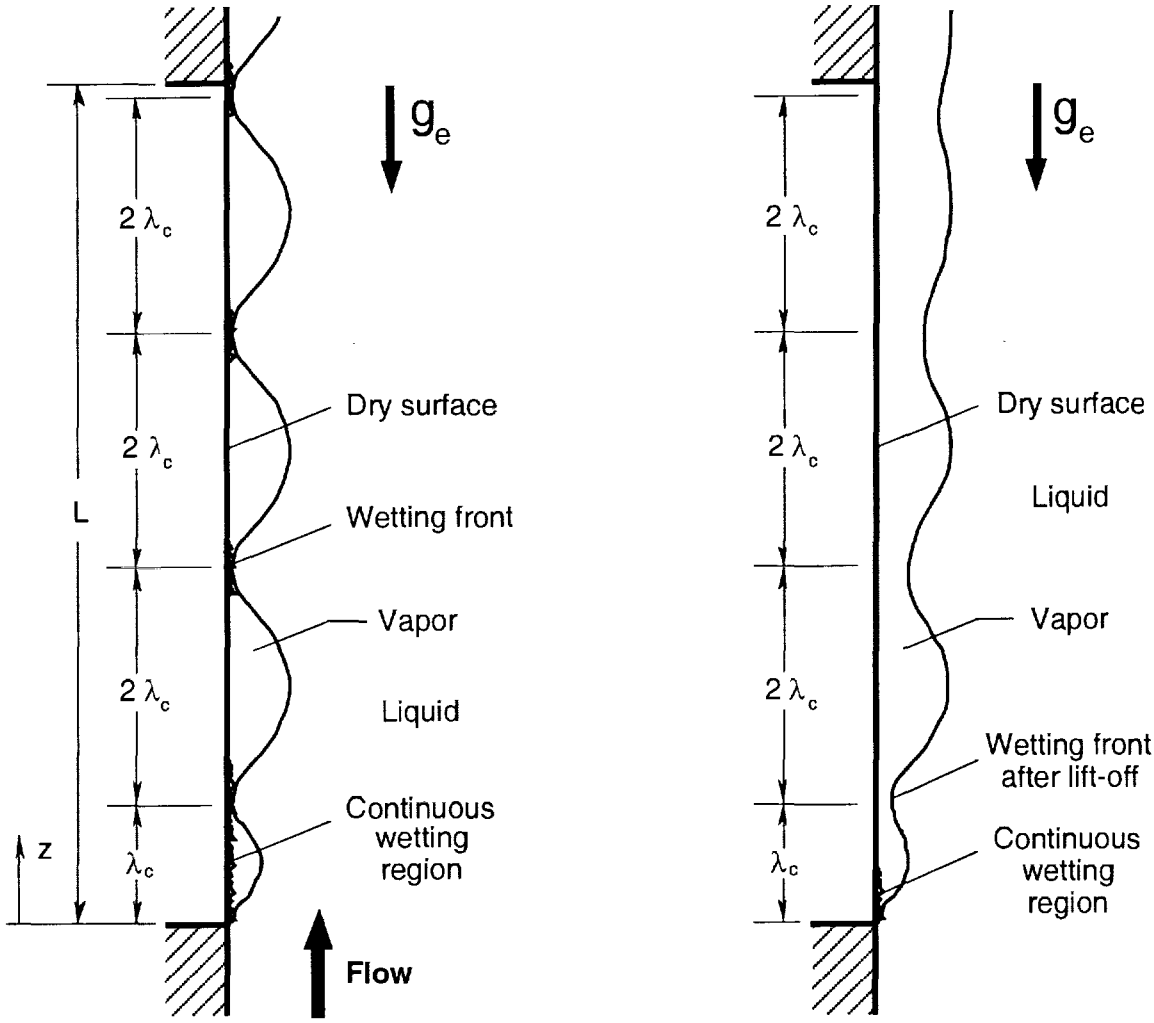

Fig. 1 Vertical upflow at (a) CHF- and (b) CHF+.

Presentation not available at time of printing.

COMPUTATIONAL MODELING OF THE EFFECT OF SECONDARY FORCES ON THE PHASE DISTRIBUTION IN DISPERSED MULTIPHASE CHANNEL FLOWS

G. Tryggvason and S.L. Ceccio
Department of Mechanical Engineering
University of Michigan
Ann Arbor, MI 48109

ABSTRACT

In microgravity, several secondary effects that are usually masked by gravity under terrestrial condition can become important. This is particularly true in multiphase flows, when buoyancy effects are eliminated. A detail understanding of such phenomena is of both scientific and practical interest. Recent progress in numerical simulations of multiphase flow has now made it possible to simulate the full unsteady motion of several bubbles and drops.

It is proposed to examine how two secondary effects will affect dispersed multiphase flow in channels and pipes. Thermocapillary migration generally moves bubbles and drops in the direction of the temperature gradient and would, for example, push bubbles toward the centerline of a pipe if hot fluid entered a cold pipe. The phase distribution in the cross section of a channel has a very strong impact on the pressure drop due to the flow and variations in wall temperature could therefore lead to large changes in the pressure required to pump the fluid. The second effect that will be investigated is electric fields. An electric field can induce both normal and tangential forces on a fluid interface and it is well known that depending on the ratio of the conductivities and the dielectric properties of the continuous and dispersed phase, drops will deform into a prolate or oblate shape. While the interaction of two drops has been examined for two drops in zero Reynolds number flow, nothing has been done to examine how many drops in electric fields interact with each other or the flow. It is likely that the deformation of the drops will affect the pressure drop in major ways. Although two different physical effects will be examined, the key physical questions are similar and much of the numerical technology is essentially identical. Considering these effects together should therefore be both efficient as well as allowing insight for one phenomenon be used to explore the other. Combined effects, where both a variable temperature as well as an electric field is present may also lead to unexpected new phenomena.

Both of those investigations will build on numerical methodology developed already, in part with NASA support. The addition of thermocapillary and electrical forces to the numerical methodology has already been demonstrated, but new numerical development will be required to allow efficient simulations of channel flow with a large number of bubbles and drops.
In addition to uncovering and explaining phenomena of scientific interest that can not be addressed on the earth, the understanding sought here has considerable practical applications. Those include both the prevention of unforeseen design difficulties as well as the possibility of using temperature changes and electrostatic fields for the control of multiphase flow.

Preliminary results are shown in Figure 1 and 2.

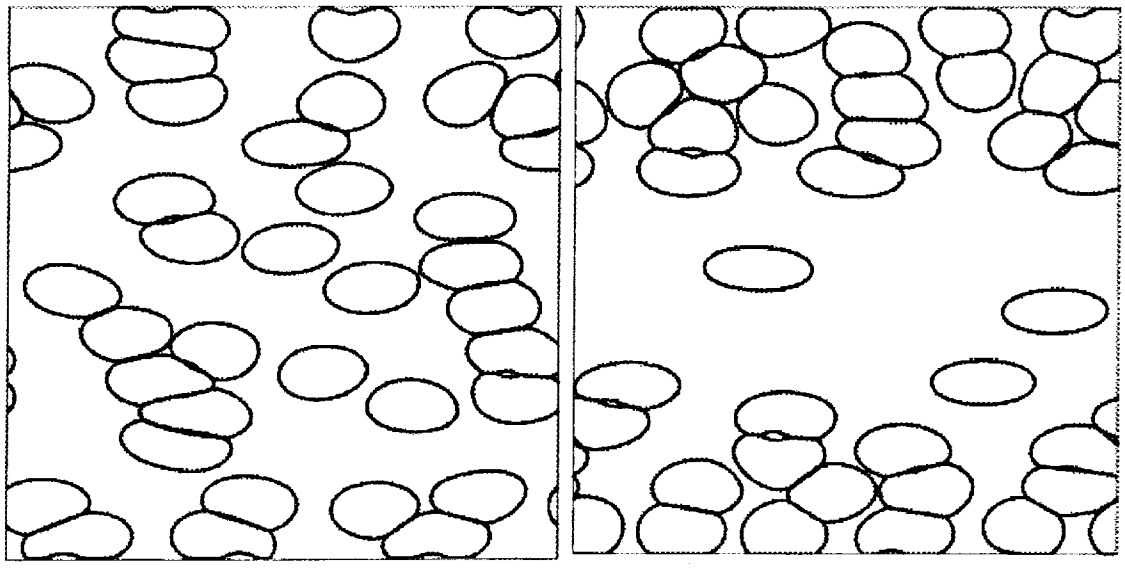

Figure 1. Preliminary two-dimensional simulations of the effect of an electric field on the phase distribution in a pressure driven channel flow. The drops are initially uniformly distributed. In the first frame (left), the drops have become prolate and started to form clusters consisting of two or more drops. In the second frame, most of the drops have moved toward the channel walls.

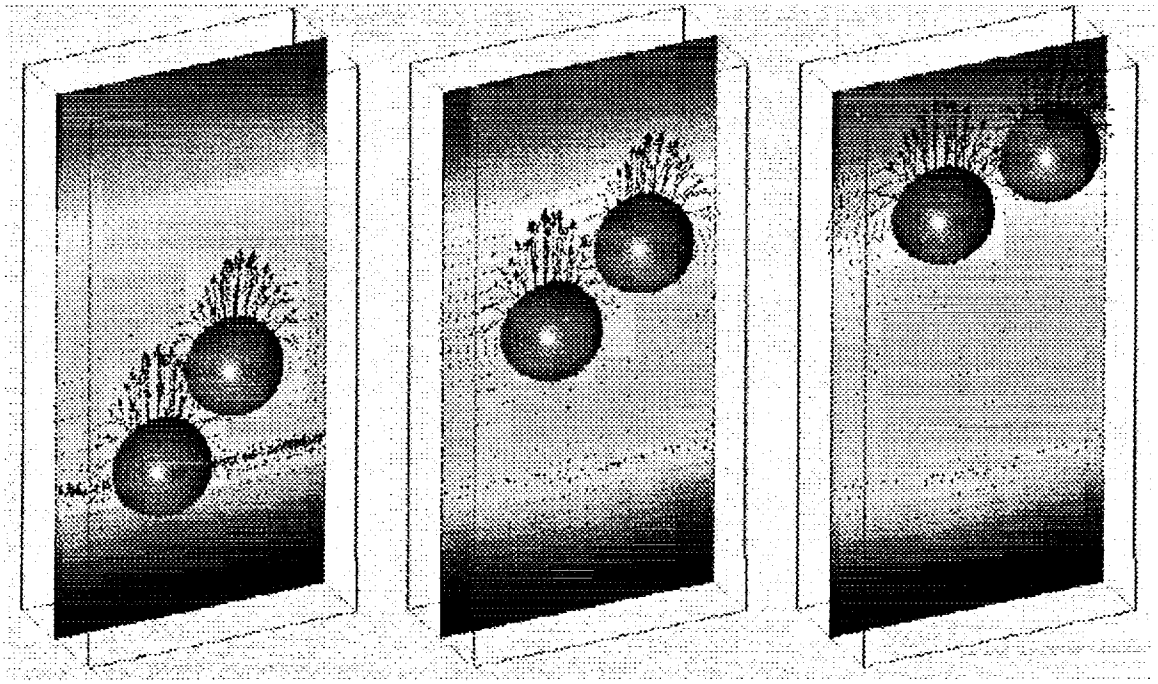

Figure 2. A computation of the thermocapillary migration of two drops in an initially quiescent fluid. The figure shows the bubble shape and the temperature field for two light drops at finite Reynolds and Marangoni numbers. Although each drop starts at a different distance from the hot wall, they move toward a side-by-side configuration as they rise. Simulations of two-dimensional systems, where the interaction is stronger, show this evolution even better and for a large range of parameters we find that two or more drops line up perpendicular to the temperature gradient and space themselves evenly across the channel.

NASA/CP—2000-210470

Computational Modeling of the Effect of Secondary Forces on the Phase Distribution in Dispersed Multiphase Channel Flows

Gretar Tryggvason
Mechanical Engineering
Worcester Polytechnic Institute
Worcester, MA 01609

Steven.L. Ceccio
Mechanical Engineering
University of Michigan
Ann Arbor, MI 48109

Proposed Research

The effect of two secondary effects on on the phase distribution of dispersed multiphase flow in channels and pipes will be studied by direct numerical simulations.

Radial temperature gradient can lead to thermocapillary migration of bubbles and drops in the direction of the temperature gradient.

Electric field can deform drops into prolate or oblate shapes, depending on the ratios of the conductivities and the dielectric properties of the continuous and dispersed phase. Electrically induces motion can also lead to migration and coalescence.

Numerical Approach

A finite volume/front tracking technique

$$\frac{\partial \rho \bar{u}}{\partial t} + \nabla \cdot \rho \bar{u}\bar{u} = -\nabla p + \bar{f} + \nabla \cdot \mu\left(\nabla \bar{u} + \nabla^T \bar{u}\right) + \int_F \sigma \kappa \bar{n} \delta\left(\bar{x} - \bar{x}_f\right) da$$

$$\nabla \cdot \bar{u} = 0$$

$$\frac{D\rho}{Dt} = 0$$

$$\frac{D\mu}{Dt} = 0$$

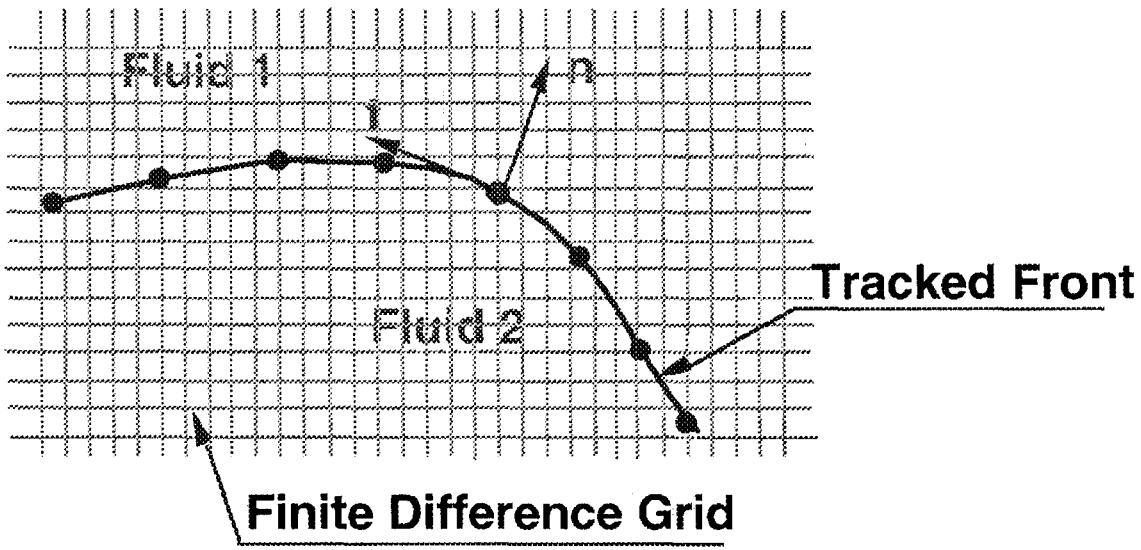

Second order time and space discretization on a staggered grid

Reference

Unverdi and Tryggvason: J. Comput. Phys 100 (1992), 25-37
Unverdi and Tryggvason: Physica D 60 (1992), 70-83

Thermocapillary migration-I

The temperature is found by solving the energy equation

$$\frac{\partial \rho c_p T}{\partial t} + \nabla \cdot (\rho c_p T \overline{u}) = \nabla \cdot k \nabla T$$

where we have assumed that the fluid is incompressible and that viscous heating can be neglected. This equation is solved on a fixed grid by an explicit second order method in the same way as the momentum equation. The temperature on the surface of the bubble or drop is found by interpolating it from the grid and surface tension is found by

$$\sigma = \sigma_o - \beta(T - T_o)$$

Here, $\beta > 0$, since surface tension generally is reduced with increasing temperature.

Thermocapillary migration-II

The collective interactions of many fluid particles can lead to "structure" formation at finite Re and Ma.

Here, the drop initially behind, catches up with the one in front

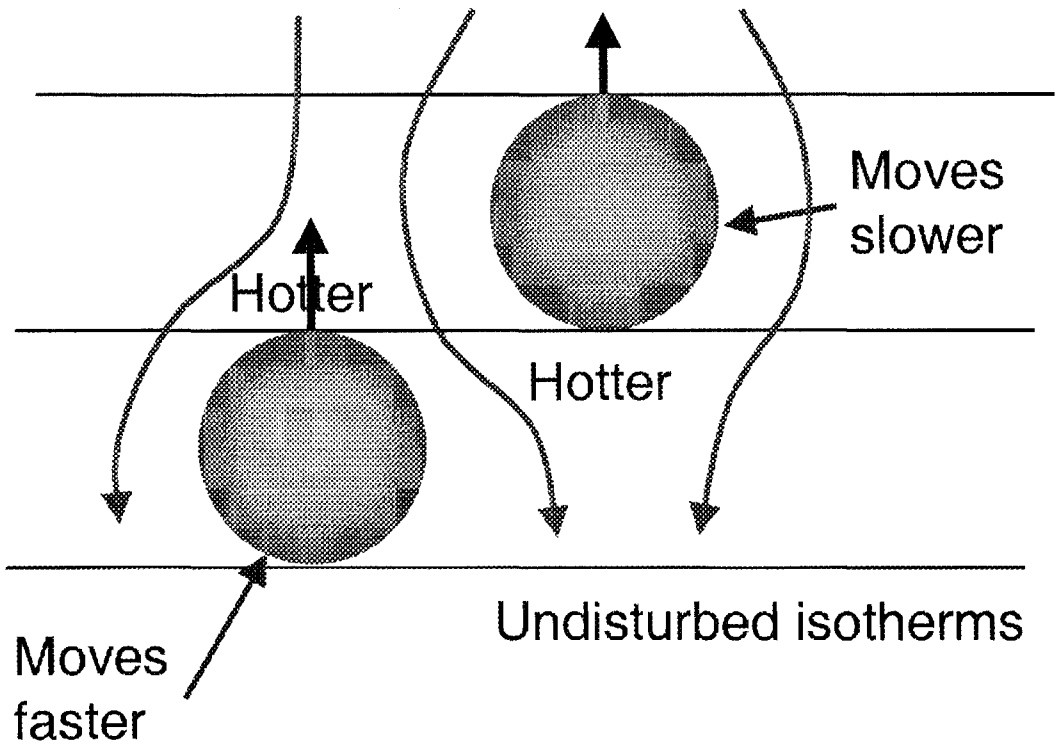

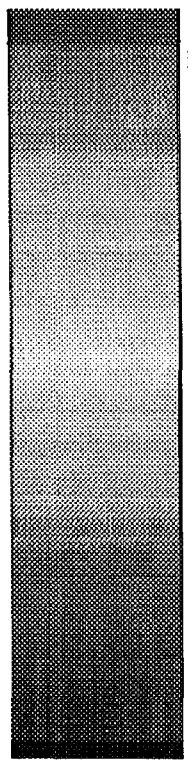

Thermocapillary migration-III

Thermocapillary motion of two three-dimensional drops. The top wall is hot and the bottom wall is cold. Initially the drops are placed near the cold wall. As they rise, the drops line up perpendicular to the temperature gradient. Here, Re=60, Ma=20, Ca=0.0166. Drop density is half of the fluid density.

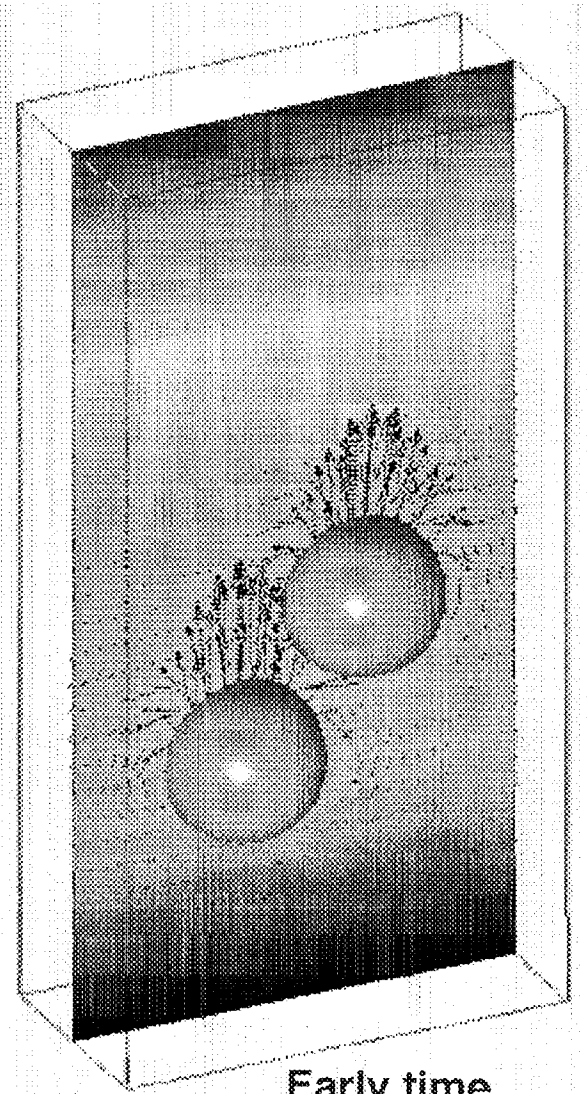

Early time

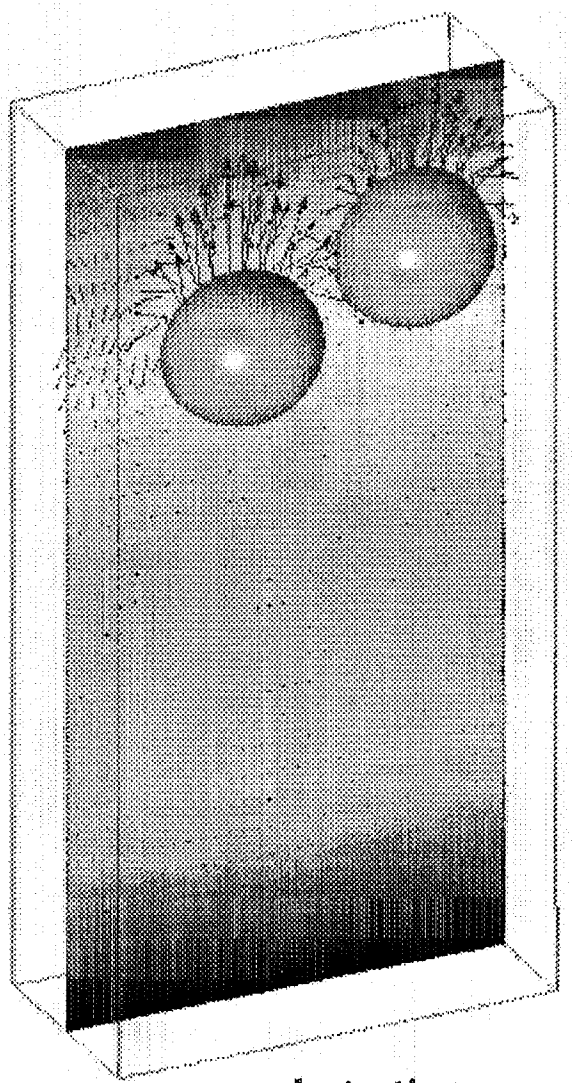

Late time

Electrostatic motion—I

For fluids with small but finite conductivity, Taylor and Melcher (1969) proposed the "leaky dielectric" model. This model allows both normal and tangential electrostatic forces on a two fluid interface.

The electric field is obtained from the electric potential by

$$\nabla \cdot \sigma \nabla \phi = 0$$

where

$$\mathbf{E} = \nabla \phi$$

The force on the fluid is then found by:

$$\mathbf{f} = q\mathbf{E} - \tfrac{1}{2}(\mathbf{E} \cdot \mathbf{E})\nabla \varepsilon$$

where the charge accumulation is

$$q = \nabla \cdot \varepsilon \mathbf{E}$$

Electrostatic motion—II

Electrostatic deformation of axisymmetric drops. The steady state obtained after following the transient motion of an initially spherical drop. For the oblate drop in (a) the ratio of the dielectric constant of the drop to the dielectric constant of the suspending fluid is much larger than the conductivity ratio, but for the prolate drop in (b) both ratios are comparable

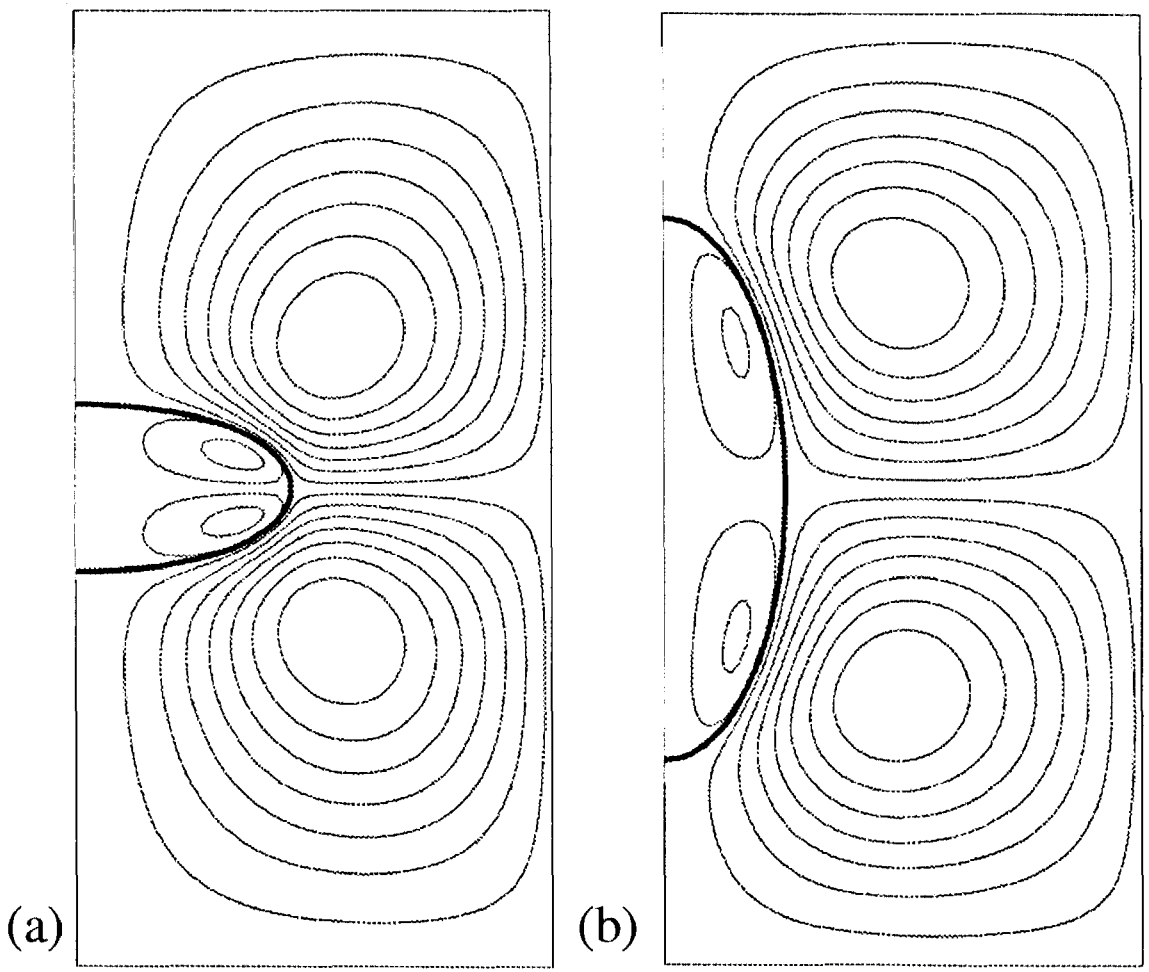

Electrostatic motion—III

Two-dimensional simulations of oblate drops in a channel flow. The volume fraction is 0.44 and E=0.2; We_d=0.125; Re_p=0.078; Re_H=20.0

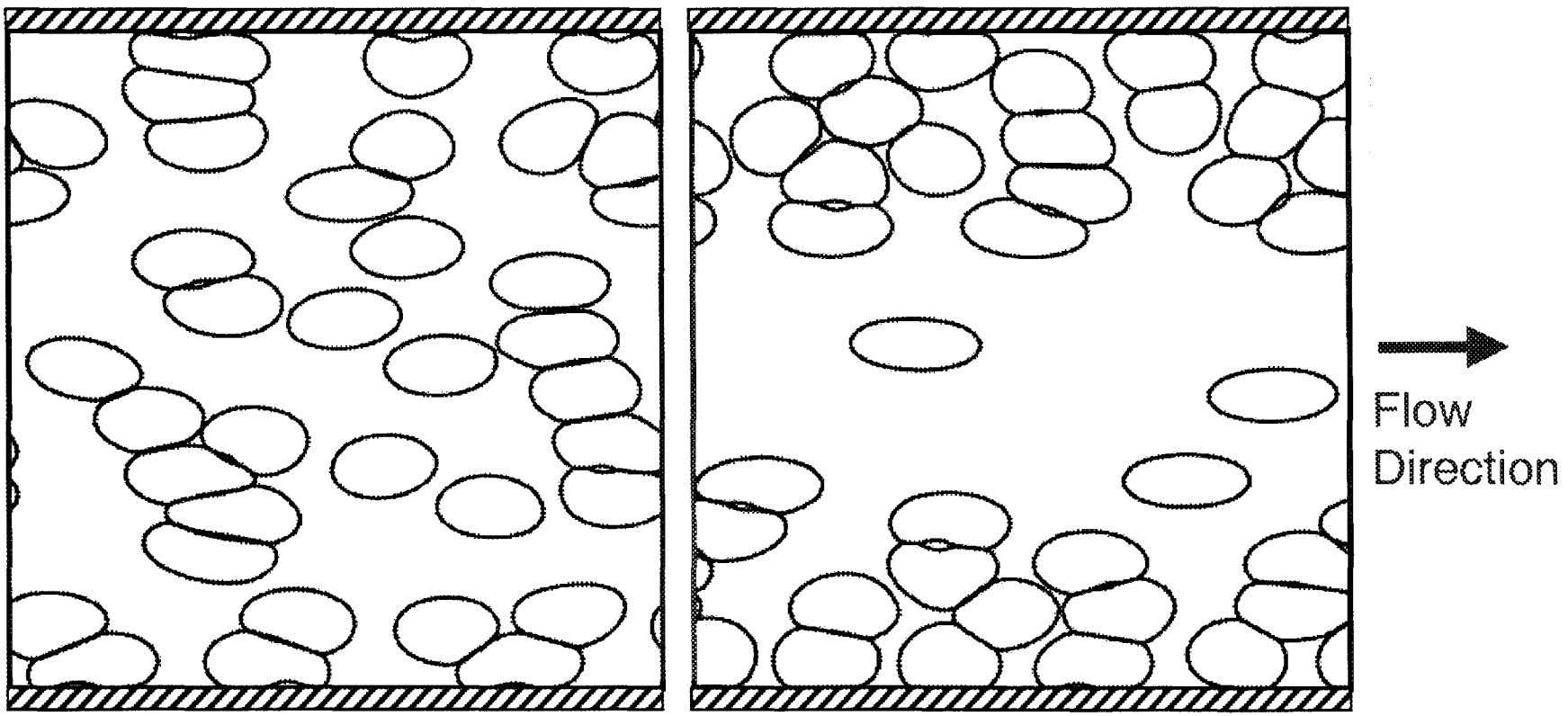

HEAT TRANSFER PERFORMANCES OF POOL BOILING ON METAL-GRAPHITE COMPOSITE SURFACES

Nengli Zhang
Ohio Aerospace Institute/NASA Glenn Research Center
Cleveland, Ohio 44135

David F. Chao
NASA Glenn Research Center
Cleveland, OH 44135

Wen-Jei Yang
Department of Mechanical Engineering and Applied Mechanics, University of Michigan
Ann Arbor, Michigan 48109-2125

ABSTRACT

Nucleate boiling, especially near the critical heat flux (CHF), can provide excellent economy along with high efficiency of heat transfer. However, the performance of nucleate boiling may deteriorate in a reduced gravity environment and the nucleate boiling usually has a potentially dangerous characteristic in CHF regime. That is, any slight overload can result in burnout of the boiling surface because the heat transfer will suddenly move into the film-boiling regime. Therefore, enhancement of nucleate boiling heat transfer becomes more important in reduced gravity environments. Enhancing nucleate boiling and critical heat flux can be reached using micro-configured metal-graphite composites as the boiling surface. Thermocapillary force induced by temperature difference between the graphite-fiber tips and the metal matrix, which is independent of gravity, will play an important role in bubble detachment. Thus boiling heat transfer performance does not deteriorate in a reduced-gravity environment.

Based on the existing experimental data, and a two-tier theoretical model, correlation formulas are derived for nucleate boiling on the copper-graphite and aluminum-graphite composite surfaces, in both the isolated and coalesced bubble regimes. Experimental studies were performed on nucleate pool boiling of pentane on cooper-graphite (Cu-Gr) and aluminum-graphite (Al-Gr) composite surfaces with various fiber volume concentrations for heat fluxes up to 35 W/cm^2. It is revealed that a significant enhancement in boiling heat transfer performance on the composite surfaces is achieved, due to the presence of micro-graphite fibers embedded in the matrix. The onset of nucleate boiling (the isolated bubble regime) occurs at wall superheat of about 10 °C for the Cu-Gr surface and 15 °C for the Al-Gr surface, much lower than their respective pure metal surfaces. Transition from an isolated bubble regime to a coalesced bubble regime in boiling occurs at a superheat of about 14 °C on Cu-Gr surface and 19 °C on Al-Gr surface.

According to a two-tier configuration and its mathematical model [1], and based on the existing experimental data, correlations for the boiling heat transfer performance in the isolated bubble regime and in the coalesced bubble regime are obtained as follows: The boiling heat flux in the low heat flux boiling region (isolated bubble regime) is mainly contributed by micro bubbles, with negligible heat conduction across the microlayer, and can be expressed as

$$q_l = \frac{\pi D_m^{\ 3}}{6} \rho_v h_{fg} C_s (\Delta T_{sat})^m \tag{1}$$

where C_s and m are constants determined by the experimental data, ρ_v is the vapor density, h_{fg} is the latent heat of the working fluid, ΔT_{sat} is the superheat. For the composite surfaces, the maximum diameter of bubbles, D_m, is related to the fiber diameter, d, and the area fraction of the fibers in the base material, α, by

$$D_m = \frac{d}{2}\sqrt{\frac{\pi}{\alpha}} \tag{2}$$

In the case of $\alpha = 0.5$ and $d = 8$ μm, the value of D_m is calculated at 10.03 μm.

In the high heat flux boiling region (coalesced bubble regime), the boiling heat flux consists of two parts: latent heat transport by micro bubbles under the vapor stems and by evaporation on the interface along the macrolayer, which equals heat conduction across the macrolayer. The total heat flux is

$$q_h = \frac{\pi D_m^3}{6} \rho_v h_{fg} C_s (\Delta T_t)^m + k_l C_l (\Delta T_{sat} - \Delta T_t) \tag{3}$$

where, k_l is the thermal conductivity of working fluid, C_l is the constant, ΔT_t is the superheat at transition from isolated to coalesced bubble regime. The first term of Eq. (3) is the maximum value of the heat flux in the isolated bubble regime.

It is obvious that both q_l and q_h are independent from gravity, and therefore, the boiling performance on the metal-graphite composite surfaces would not deteriorate with reduced gravity.

A new model to predict the critical heat flux (CHF) on the composites is proposed to explain the fundamental aspects of the boiling phenomena. The CHF for the metal-graphite composite surface is given by

$$q_C = q_{C,Zuber}\left(1 + \frac{4}{3\pi^2\sigma}\zeta\frac{\partial\sigma}{\partial T}\Delta T_{wb} - \frac{\eta\cos\theta}{12\pi^2}\right)^{1/4} \tag{4}$$

where $q_{C,Zuber} = \frac{\pi}{24}\rho_v h_{fg}\left(\frac{32\sigma\Delta\psi_g}{\pi\lambda_d^4\rho_v^2}\right)^{1/4}$, ζ is a correction factor, σ is the surface tension, ΔT_{wb} is the temperature difference between the heating surface and the bulk liquid, η is a correction factor, θ is the contact angle, $\Delta\psi_g$ is the available gravitational energy that equals $\pi(\rho_l-\rho_v)\lambda_d^4 g/32$, and ρ_l is the fluid density.

It can be seen that the CHF is enhanced through the third term in Eq. (4) for the composite surfaces. Undoubtedly, this kind of materials is suitable to space applications.

We also suggest that using liquid with positive surface tension gradient with temperature, such as dilute aqueous solution of long-chain alcohols, as the working fluid. Then, the role of the second term in Eq. (4) will change from keeping the vapor volumes pressed to the heating surface to driving vapor volume detachment from heat surfaces, and therefore will enhance the CHF.

References

1. N. Zhang, W. J. Yang, and G. W. Yang, Two-tier Model for Nucleate Pool Boiling Heat Transfer on Microconfigured Surfaces, *International Communication Journal of Heat and Mass Transfer,* **19,** 767-779 (1992).

Presentation not available at time of printing.

Thermocapillary Migration of Bubbles

Asghar Esmaeeli and Vedat Arpacı

Department of Mechanical Engineering and Applied Mechanics
The University of Michigan, Ann Arbor, MI 48109

Abstract

We use direct numerical simulation to investigate motion of a few two- and three-dimensional bubbles at $O(1)$ Reynolds and Marangoni numbers due to thermocapillarity. The full Navier-Stokes and energy equations for the flows inside and outside the bubbles are solved using a front tracking/finite difference technique which accounts for the bubble deformation.[1-4] The nondimensional parameters that govern the problem are Marangoni number; Ma, Reynolds number; Re, Capillary number; Ca, volume fraction; α, and the ratios of the material properties of the fluid inside the bubbles and the ambient fluid.

Our goal is to investigate the collective behavior of large systems of bubbles. We are primarily concerned with the effect of the microstructural mechanics on the macroscopic properties of the flow. However, the computations are limited by the high expenses of the three-dimensional simulations as the grid resolution increases. As a compromise between our goal and the expenses, we have chosen to reduce one of the dimensions of the system in most of our computations, therefore, to study large two-dimensional systems (up to 120 bubbles). Although this reduction in dimensions seems to raise some questions on relevance of the results, comparison of motion of solitary bubbles in two and three dimensions at the same volume fractions (keeping all the other nondimensional numbers the same) reveals that the migration velocities have small differences during the relaxation period and are very close at steady state.

As the bubbles migrate, they interact with each other and the flow. Interesting phenomena such as pairing and tripling of the bubbles and formation of horizontal layers of bubbles are observed. These changes in the spatial arrangement of the bubbles have implications in the evolution of the macroscopic properties. To understand that, we compute the pair density function; $G(r,\theta)$, average cluster size; $\langle s \rangle$, and the velocity variances; $\langle \mathbf{V}_b' \mathbf{V}_b' \rangle$.

Figure 1 shows streamlines and the bubbles from one of our simulations of motion of eight bubbles at volume fraction 0.0194. The domain is periodic in the horizontal directions and wall-bounded in the vertical direction. However, the computations are done in a frame moving with the centroid of the bubbles so that we can investigate the long term evolution of the flow. The domain size is $6d_e$ in

each direction where d_e is the initial diameter of the bubbles. The grid resolution is 146^3 and initially about 21000 triangular elements are used to discretize the front. The flow is uniform away from the bubbles and has a vortical structure near the bubbles. Initially, the bubbles migrate impulsively but after a relatively short relaxation time reach to an essentially steady state.

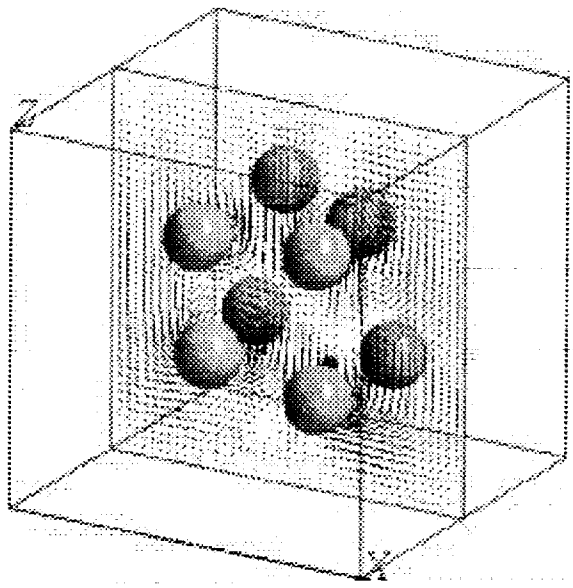

Figure 1: Streamlines and the bubbles at $\alpha = 0.0194$.

References

[1] Unverdi, S. O. and Tryggvason, G., 1992, "A front-tracking method for viscous, incompressible, multi-fluid flows," J. Comp. Physics, Vol. 100, pp. 25-37.

[2] Nas, S. 1995, "Computational investigation of thermocapillary migration of bubbles and drops in zero gravity," Ph.D. Thesis. The University of Michigan.

[3] Esmaeeli, A., Tryggvason, G., and Arpacı, V., 1996, "Thermal Migration of Bubbles in Zero Gravity" Heat Transfer in Microgravity Systems, Editors: A. Gopinath & S. S. Sadhal, HTD-Vol. 332 (ASME, Atlanta, Georgia), pp. 55-63.

[4] Esmaeeli, A. and Arpacı, V., 1999, "Thermocapillary-Driven Migration of Bubbles in Shear Flows" Paper Number FEDSM99-7376. Proceedings of 1999 ASME-FED Summer Meeting. July 18-23, San Francisco, CA.

Research Objective

Motion of bubbles and drops as a result of variations of surface tension with temperature is called thermocapillary migration and can be of importance in the situations where the usually dominant force of buoyancy is negligible. The research in this area is mostly motivated by its potential applications in space operations. For example, it has been suggested (Uhlmann, 1982) that certain high quality metals can be produced in space where due to the absence of gravity the disturbing effect of buoyant convection vanishes. Thermocapillary is a possible mechanism for removal of gas bubbles generated during such processes. Other examples of possible use of thermocapillary include vapor bubble management in liquid rockets used to power space vehicles in orbit (Ostratch, 1982), and containerless glass processing in reduced-gravity (Weinberg, 1978). In fact, even on earth, thermocapillary can be used to control motions of droplets of very small size or of nearly equal density with ambient fluid.

This study aims to investigate the collective behavior of large systems of bubbles moving due to thermocapillarity. We are primarily interested in the effect of the microstructural mechanics on the macroscopic properties of the flow. Dynamics of freely evolving arrays of bubbles is compared to that of solitary bubbles at the same parameters. Effect of inertia is investigated by comparing the evolution bubbly flows at $O(1)$ Reynolds and Marangoni with the flows at zero Reynolds and (or) Marangoni numbers. Other effects such as shear velocity, buoyancy, and coalescence on the average migration velocity of bubbles is also studied.

Governing Equations

$$\frac{\partial \rho \overline{u}}{\partial t} + \nabla \cdot \rho \overline{u}\,\overline{u} = -\nabla p + \nabla \cdot \mu(\nabla \overline{u} + \nabla \overline{u}^T)$$

$$+ \int (\sigma \kappa \overline{n} + \nabla_s \sigma)\delta(\overline{x} - \overline{x}^f) ds.$$

$$\frac{\partial \rho c T}{\partial t} + \nabla \cdot \overline{u} \rho c T = \nabla \cdot k \nabla T$$

$$\nabla \cdot \overline{u} = 0$$

$$\frac{D\rho}{Dt} = 0; \quad \frac{D\mu}{Dt} = 0; \quad \frac{Dk}{Dt} = 0; \quad \frac{Dc}{Dt} = 0.$$

$$\sigma = \sigma_0 + \sigma_T (T - T_0)$$

Numerical Technique

- Front Tracking/Finite Difference
- Full Resolution of Flow Inside and Outside the Bubble
- Inclusion of Bubble Deformability
- Second Order Space and Time Discretization
- Unverdi & Tryggvason (1992), Nas & Tryggvason (1993), Esmaeeli, Tryggvason, and Arpacı (1996a, 1996b, 1997)

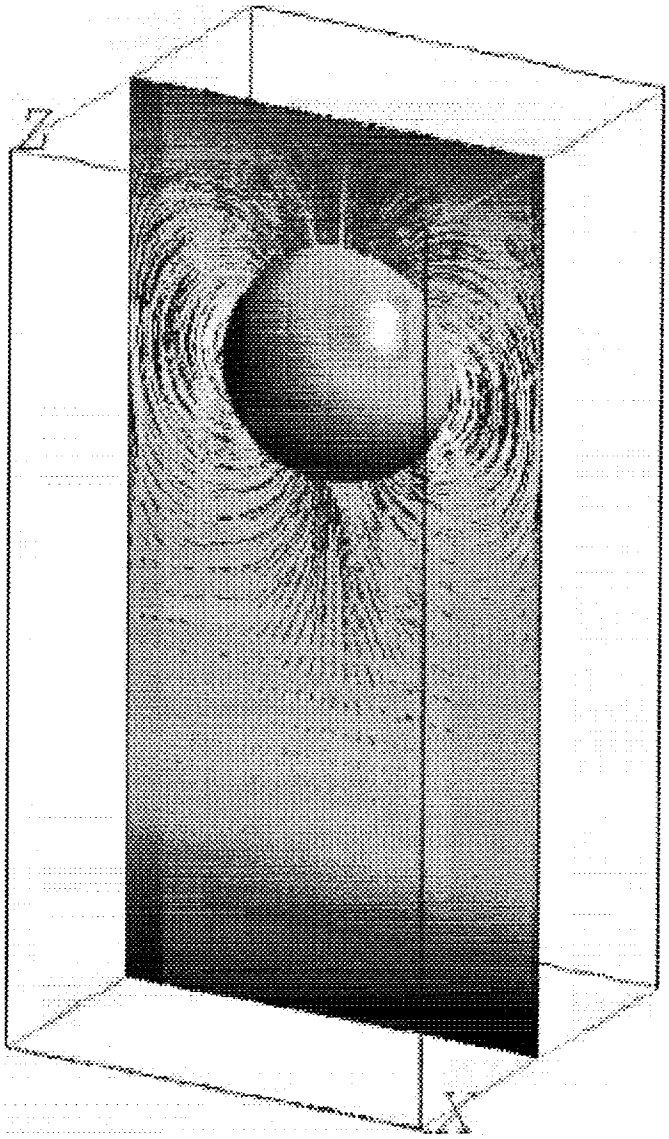

A midplane cross section of streamlines and isotherms of a single bubble rising due to thermocapillarity in zero gravity. Here, the nondimensional numbers are $Re = 10$, $Ma = 1$, and $Ca = 0.06$. The flow is resolved on a $32 \times 32 \times 64$ staggered grid in a $1 \times 1 \times 2$ box.

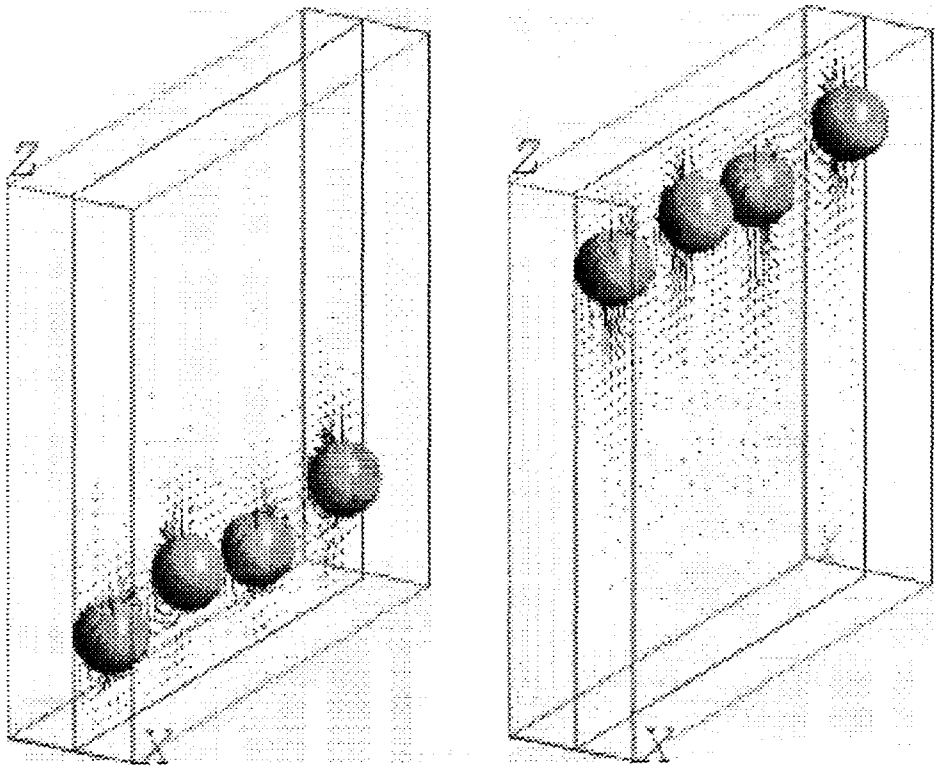

A midplane cross section of streamlines of four bubbles rising in a channel at early time (left frame) and the end of the run. Here, an initially perturbed array of four bubbles evolves to a horizontal chain. The nondimensional numbers are $Re = 30$, $Ma = 30$, and $Ca = 0.05$. The flow is resolved on a $32 \times 128 \times 128$ grid in a $1 \times 4 \times 4$ box.

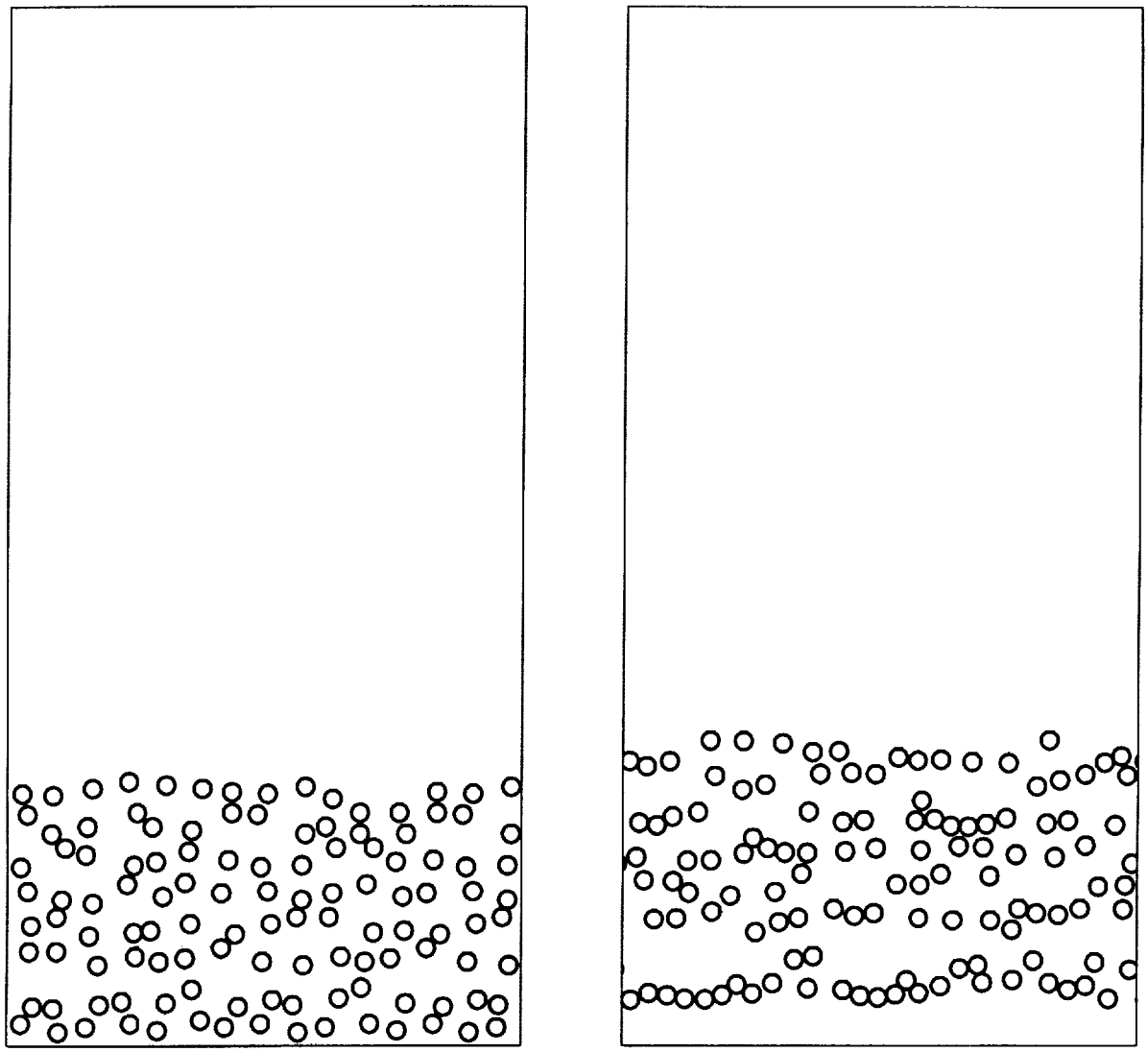

Interactions of 120 two-dimensional bubbles rising in a channel. The left frame shows the initial positions of the bubbles and the right frame shows the positions of the bubbles after a relatively long time. The microstructure evolves from a random configuration to a structured one where bubbles try to form local horizontal chains. Here, $Re = 40$, $Ma = 40$, and $Ca = 0.05$. The flow is resolved on a 962×1923 grid in a 15×30 box.

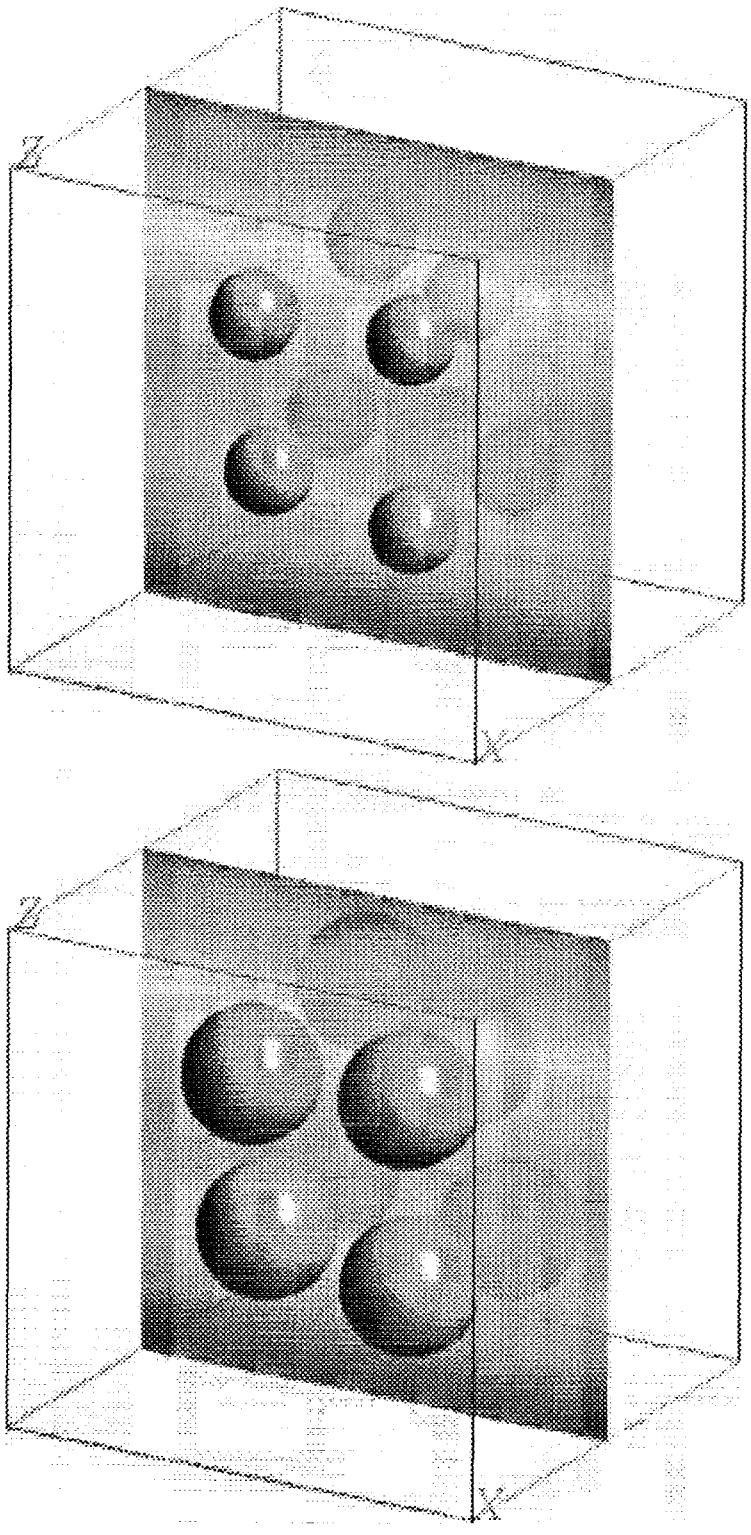

Volume fraction is one of the key parameters that affects the macroscopic properties of bubbly flows. Here, we show isotherms and eight bubbles at volume fractions of 0.019 (top frame) and 0.079 (bottom frame). The computations are done using a moving frame and the nondimensional numbers are $Re = 1$, $Ma = 1$, and $Ca = 0.01$. The flow is resolved on a $146 \times 146 \times 146$ gird in a $3 \times 3 \times 3$ box.

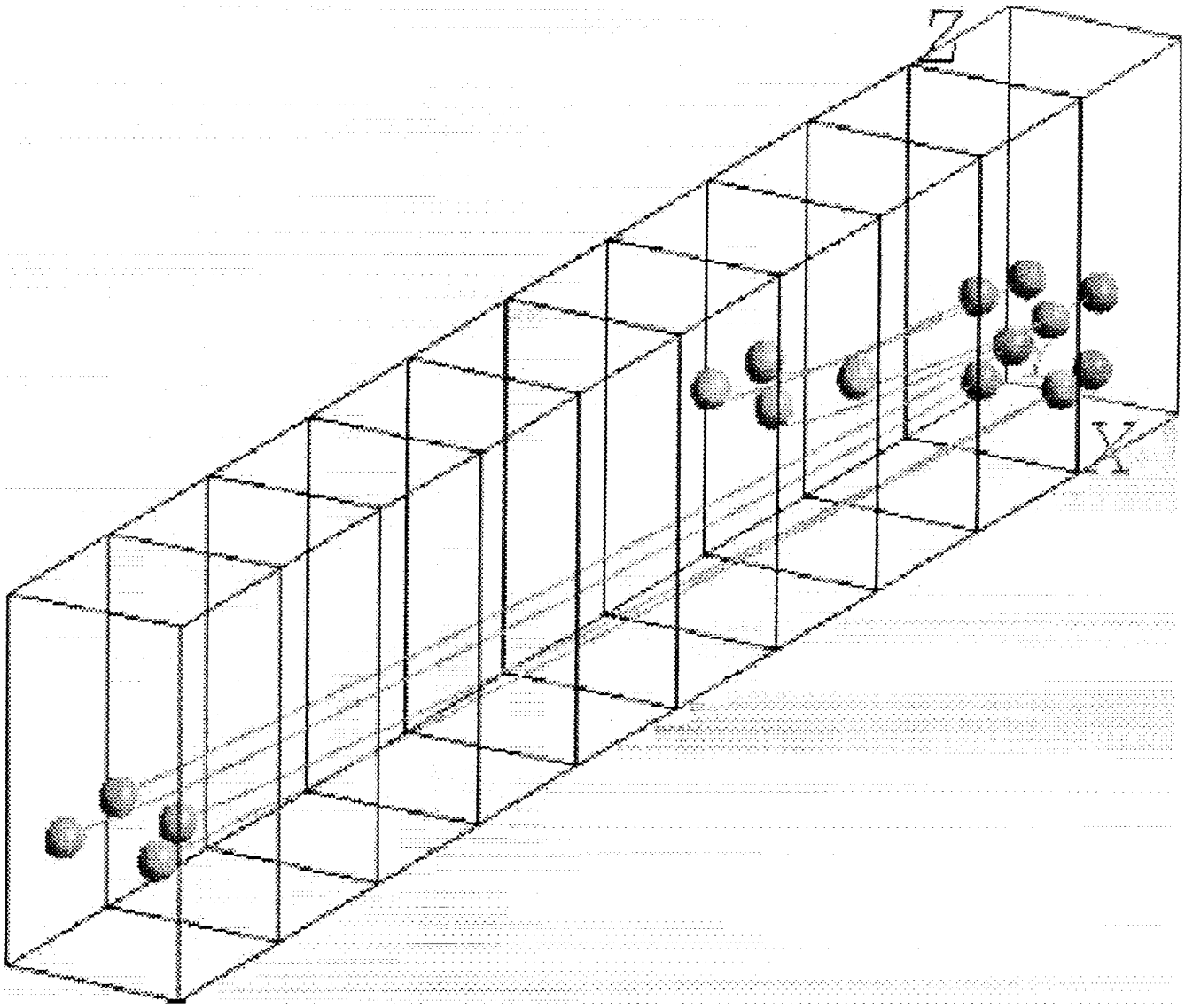

Shear velocity may decrease or increase migration velocity of the bubbles depending on the governing parameters. Here, we show evolution of eight bubbles in a shear flow. The top wall moves in the positive Y direction and the bottom wall moves in the negative Y direction. The first box at the right shows the initial positions of the bubbles. The bubbles are scattered over seven boxes at the end of simulation as a result of shear. The solid lines connecting the bubbles show the trajectories. The nondimensional parameters are $Re = 10$, $Ma = 1$, $Ca = 0.06$, and $Re_g = 32$ and the flow is resolved on a $64 \times 64 \times 128$ in a $2 \times 2 \times 4$ box. For the current simulation, the average migration velocity of the bubbles is about 13 % higher than that of a flow with zero shear.

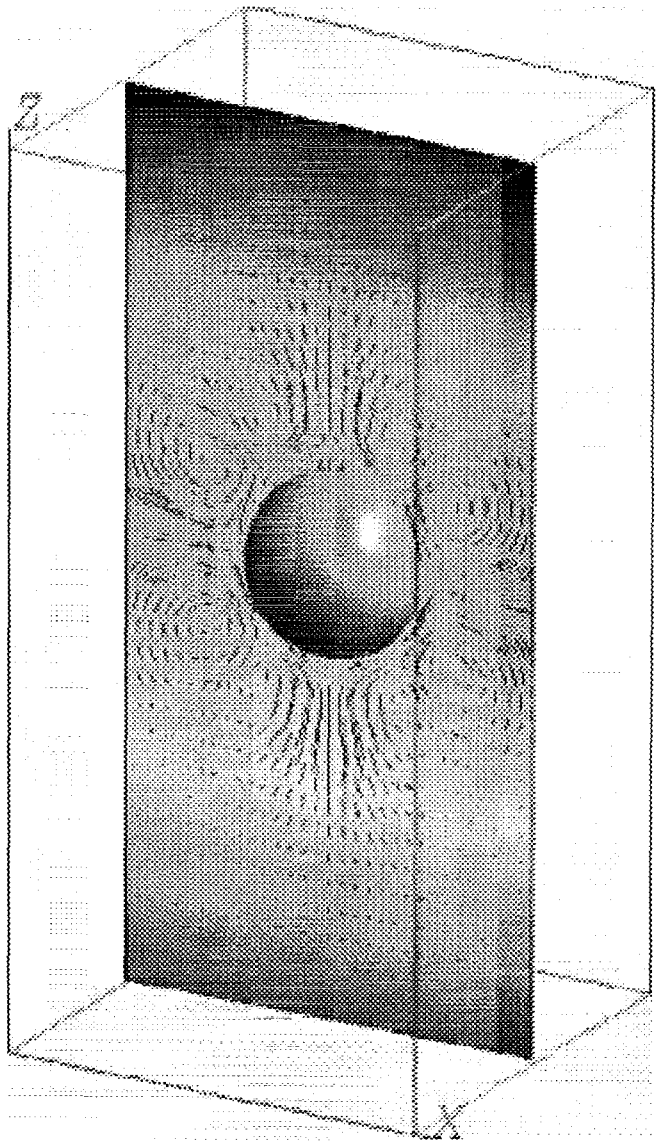

A midplane cross section of streamlines and isotherms of a single bubble in microgravity. Here, the buoyancy and thermocapillary act in opposite directions. The far field is influenced by buoyancy and the near field by thermocapillary. The nondimensional numbers are $Re = 10^{-4}$, $Ma = 10^{-4}$, and $Ca = 10^{-3}$. The flow is resolved on a $32 \times 32 \times 64$ in a $1 \times 1 \times 2$ box.

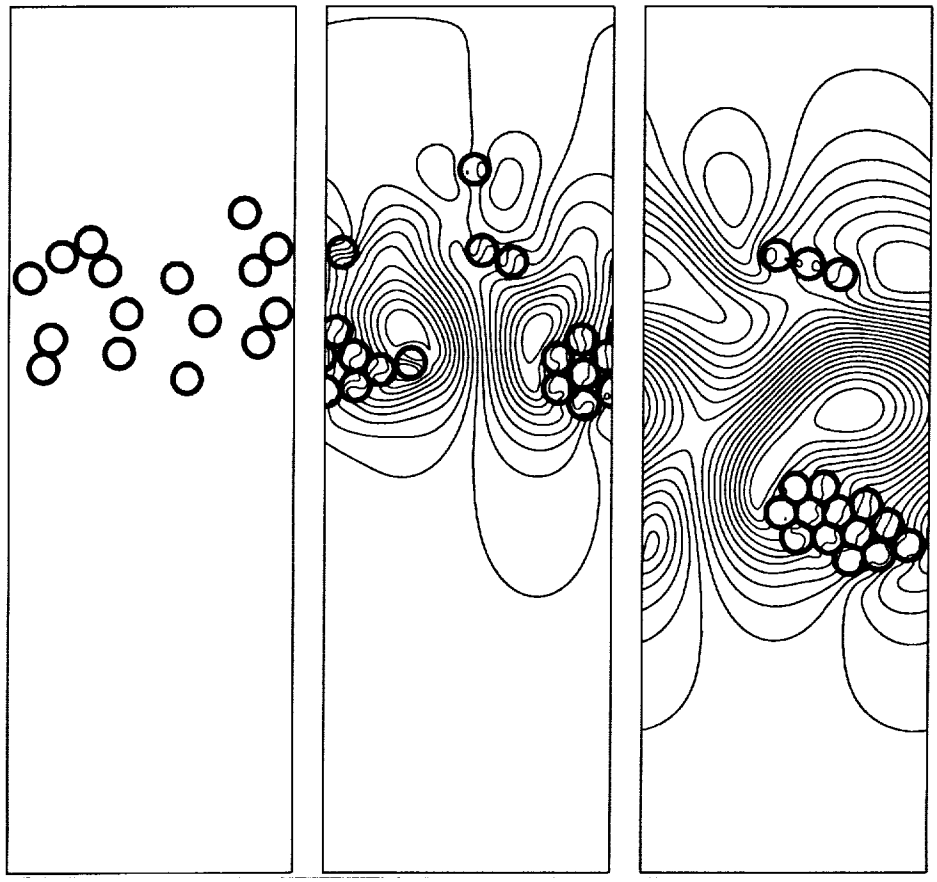

Evolution of sixteen two-dimensional bubbles in microgravity. The first frame shows the initial positions of the bubbles. Here, the thermocapillary forces try to move the bubbles upward while the buoyancy is trying to move the bubbles downward. The outcome is formation of a large cluster of bubbles which moves downward. The nondimensional numbers are $Re = 40$, $Ma = 40$, $Ca = 0.03$, and $\Pi = 4.16$. Π is a nondimensional parameter that characterizes the importance of thermocapillary compared to buoyancy. The flow is resolved on a 130×387 grid in a 4×12 box. grid.

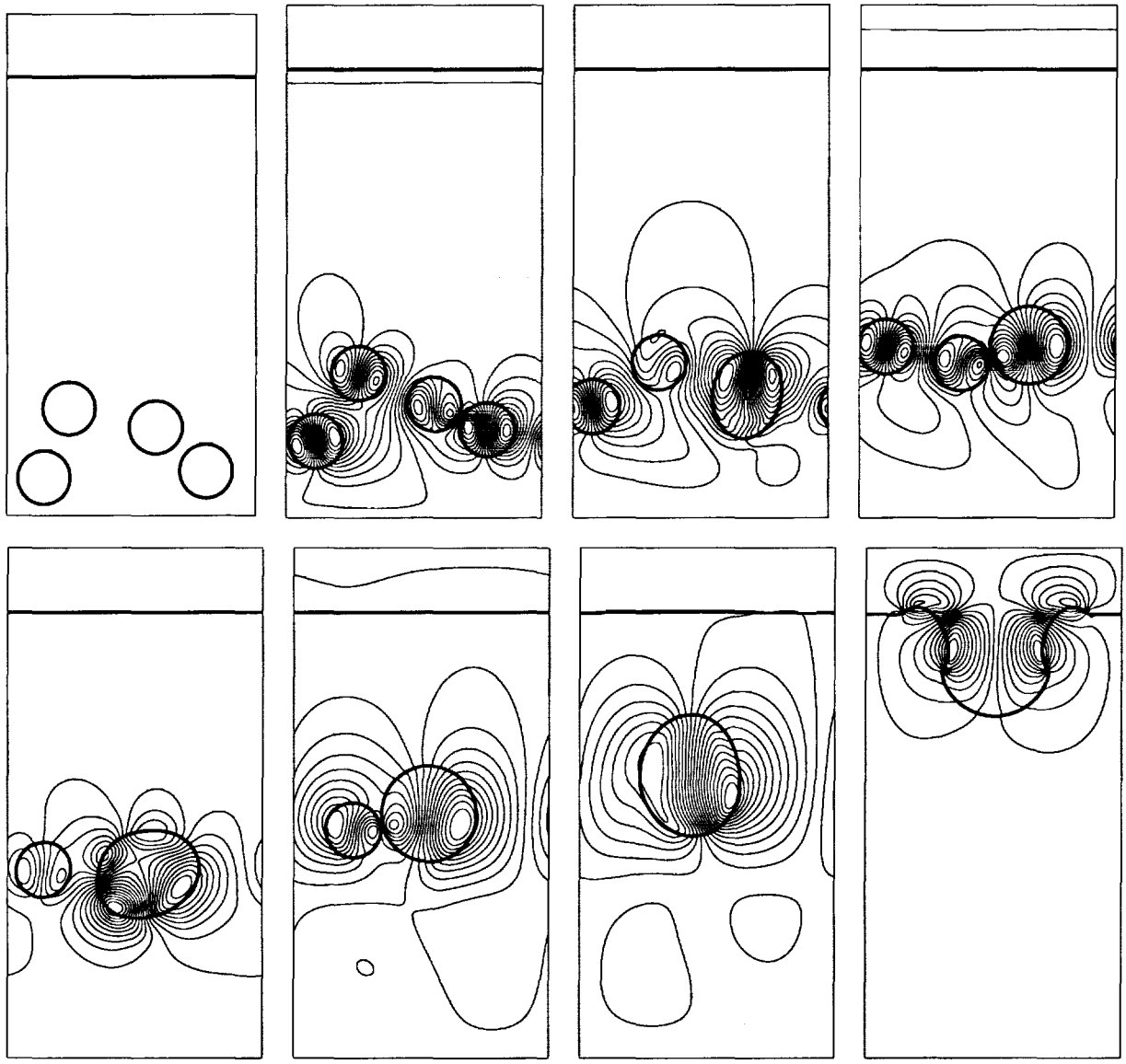

Coalescence of bubbles affects the microstructure and may increase the average migration velocity. The figure shows interaction of four bubbles rising toward an initially flat interface. Time increases from the left to the right and the top to the bottom. Here, $Re = 10$, $Ma = 1$, and $Ca = 0.01$ and the flow is resolved on a 128×256 grid in a 2×4 box.

Determination of the Accommodation Coefficient Using Vapor-Gas Bubble Dynamics in an Acoustic Field

N. Gumerov, C.-T. Hsiao, A. Goumilevski
DYNAFLOW, INC.

ABSTRACT

Nonequilibrium liquid/vapor phase transformations can occur in superheated or subcooled liquids in fast processes such as in evaporation in a vacuum, in processing of molten metals, and in vapor explosions. The rate ξ at which such a phase transformation occurs can be described by the Hertz-Knudsen-Langmuir formula [1]

$$\xi = \frac{\beta(T_a)}{\sqrt{2\pi R_v T_a}}[p_s(T_a) - p_v],$$

where p_s is the saturation pressure, p_v the pressure in the vapor, T_a the temperature of the interface, R_v the gas constant of the vapor, and β the "condensation" or "accommodation" coefficient which is a property of the interface.

Existing measurement techniques for the accommodation coefficient are complex and expensive. Moreover, this coefficient depends on the temperature and is sensitive to the conditions at the interface. Thus development of a relatively inexpensive and reliable technique for measurement of the accommodation coefficient for a wide range of substances and temperatures is of great practical importance.

Our preliminary study showed that in certain range of parameters *the dynamics of the bubble in an acoustic field strongly depends on the value of the accommodation coefficient.* It is known that at temperatures close to the saturation temperature small vapor bubbles grow in a liquid under the action of an acoustic field due to nonlinear effects called "rectified heat transfer", e.g., see [2]. This is particularly true of the bubble average radius in isotropic acoustic fields and of the bubble motion in standing waves. This finding can be used as the basis for an effective measurement technique of this coefficient.

During the current effort the model and theory were substantially extended [3-5]. We developed a theory of vapor bubble behavior in an isotropic acoustic wave and in a plane standing acoustic wave including physical effects such as liquid inertia, heat transfer inside and outside the bubble, surface tension, diffusion of the inert gas inside and outside the bubble, the Soret and Dufour effects in the gas phase, liquid viscosity and compressibility, and nonequilibrium phase transitions in two-component systems. A numerical code was developed which enables simulation of a variety of experimental situations and accurately takes into account slowly evolving temperature.

Using the theory and computational tools developed we performed a parametric study, which showed that the measurement of β can be made over a much broader range of frequencies and bubble sizes than it is commonly thought. We found several interesting regimes and conditions that can be efficiently used for measurements of β, including steady fast oscillations of the bubble radius, low frequency oscillations of the mean bubble size/position and bubble growth/shrinkage near threshold and resonance values. Our results show that measurements of β can be performed both in a reduced gravity environment and in a normal gravity environment.

The reduced gravity conditions provide less masking effects, specific regimes beneficial for measurements, and better temperature control. Some results are shown in Fig. 1-3.

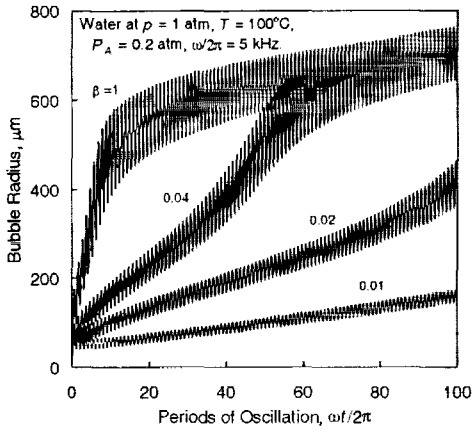

Fig. 1. The dynamics of a vapor bubble in an isotropic acoustic field of amplitude P_A = 0.2 atm at different accommodation coefficients shown near the curves.

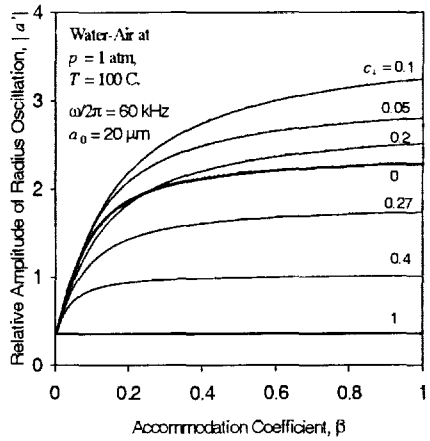

Fig. 2 The relative amplitude of a vapor-gas bubble radius oscillation, $|a'| = \max|a-a_0|p/P_A$ vs the vapor accommodation coefficient at different mass concentrations of air inside the bubble shown near the curve.

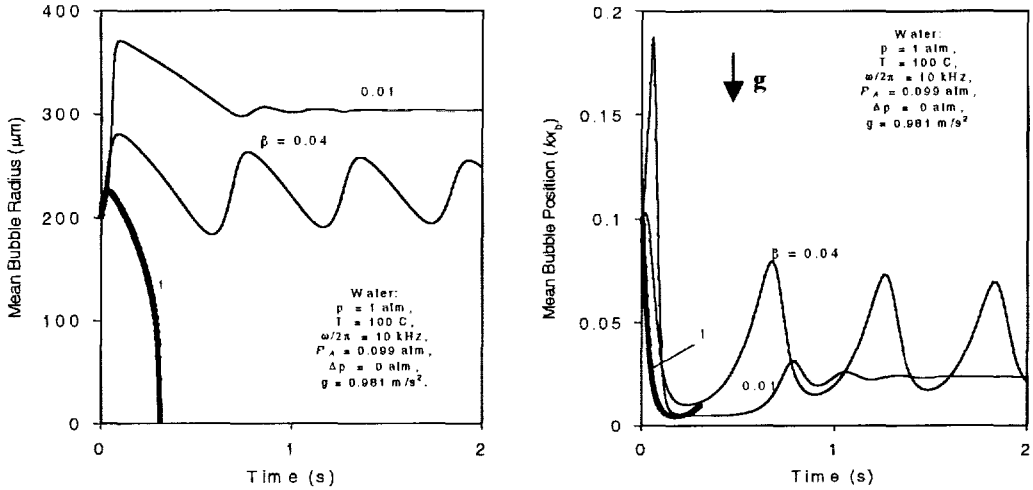

Fig. 3. The dynamics of the mean bubble radius and the mean vapor bubble position in a standing acoustic wave at 0.1 g and different values of the accommodation coefficient shown near the curves. Coordinate of the bubble center $x_b = 0$ corresponds to the pressure node and $x_b = 1/(4k)$ corresponds to the pressure antinode. k is the wavenumber.

REFERENCES

[1] M. Volmer, Kinetik der Phasebildung, Dresden-Leipzig: Steinkopff, 1939.

[2] V.A. Akulichev, Acoustic cavitation in cryogenic and boiling liquids. In: L. van Wijngaarden (ed.) Mechanics and Physics of Bubbles in Liquids, Martinus Nijhoff, the Netherlands, 1982.

[3] N.A. Gumerov, Dynamics of vapor bubbles with nonequilibrium phase transitions in isotropic acoustic fields, Physics of Fluids, **12**(1), 71-88, 2000.

[4] N.A. Gumerov, Rectified heat transfer to vapor bubbles in standing acoustic waves, UEF Conference "Microgravity Fluid Physics and Heat Transfer", HI, 1999.

[5] N.A. Gumerov, C.-T. Hsiao & A.G. Goumilevski, Determination of the accommodation coefficient using vapor/gas bubble dynamics in an acoustic field. DYNAFLOW, INC., Rep. 98001, 2000.

Presentation not available at time of printing.

GAS-EVOLVING EFFECT ON MASS TRANSFER IN ROTATING ELECTROCHEMICAL CELLS UNDER MICROGRAVITY

Y. Kamotani
Department of Mechanical and Aerospace Engineering
Case Western Reserve University
Cleveland, Ohio 44106

ABSTRACT

On earth, gas evolution in electrochemical reactors occurs widely in the electrochemical industry. In water electrolysis and electrochemical machining and electrosynthesis, the gas bubbles agitate the electrolytic cells and enhance the mass transfer, thereby improving the yield of the electrochemical cells. In fact, there are relatively few major electrochemical processes in which evolved gases do not appear. Therefore, the design of life support systems in space requires sufficient electrochemical information related to the behavior of bubbles generated on an electrode. For example, the processes of carbon dioxide removal, oxygen generation, water reclamation and human waste treatment in spaceflight involve gas generation in the systems. Although much research work has been done on electrolytic gas evolution in the presence of gravity or forced flow, much less work is available on electrolytic gas evolution in microgravity. In the absence of gravity the conventional electrochemical cells would be inefficient as the generated bubbles tend to stay near the electrodes.

In the present work we propose rotating electrochemical cells as a means of enhancing the mass transfer significantly and removing the generated gas bubbles effectively in microgravity. Moreover, the design of electrochemical cells becomes relatively compact because it does not require additional pumps and separators to process the bubble-electrolyte flow. The subject of gas evolution in rotating electrochemical cells has never been investigated. Most studies of gas bubbles in electrolytic cells were performed in the presence of natural convection or forced convection. Forced convection can be used to remove gas bubbles from the electrodes of an electrochemical system in microgravity but the bubbles still need to be removed from the electrolyte somehow. By rotating the cells one can remove the bubbles from the electrodes and the electrolyte.

The main objective of the proposed work is to gain basic knowledge of bubble behavior and its effect on mass transfer in rotating electrochemical cells under microgravity as well as normal gravity conditions. The mass transfer rates and various bubble layer characteristics will be measured and analyzed under various conditions in rotating electrochemical cells in normal gravity as well as during parabolic flights. Based on the results, a theoretical model will be constructed to predict the bubble-induced convection in rotating electrochemical cells.

The test section, shown in Fig. 1, consists of two horizontal electrode disks, which serve as cathode (top) and anode (bottom), and a vertical annular Lexan side wall. The anode is made of copper. The cathode is divided into eight ring-shaped sections. The reason for the sectioned cathode is to measure local mass transfer rate. With this arrangement only hydrogen bubbles are generated from the top cathode. The generated bubbles move toward the center along the top wall. A tube is attached to the top plate at the center to remove the bubbles. The gap between the electrodes is variable. A cupric sulfate-sulfuric acid solution ($CuSO_4$ - H_2SO_4 - H_2O) is used as the test fluid. The test section is placed in a rotating system.

The bubble layer along the cathode surface is illuminated by a laser light sheet and a video camera records the bubbles. The bubbles move in the radially inward direction as well as in the azimuthal direction due to Coriolis force. The camera and laser light source are placed on the rotating frame. To minimize the impact of high-g on the equipment, they are placed near the center of the rotating frame. Mirrors and a fiber optic cable are used to illuminate and take pictures of the inner test section. From this measurement we will determine the bubble layer thickness distribution and the bubble velocities (radial components) and sizes at various locations. The mass transfer rate will be determined from the amount of electrodeposited copper on each sectioned platinum cathode using the anode dissolution method. Applied current density in the present experiment is a combination of the partial current density consumed by hydrogen gas generation and that for copper electrodeposition on each sectioned cathode. In the anode dissolution method the electrolytic cell is charged, with the polarity reversed, at a constant current density to dissolve the electrodeposited copper on the platinum anode. The passivation of the cell occurs when the deposited copper is completely depleted on the anode. The amount of electrodeposited copper on each sectioned platinum can then be calculated from the current density and the time to passivate. The local mass transfer rate and partial current density for copper deposition is determined from the amount of deposition.

After the data analysis, we will construct a theoretical model to predict the average mass transfer coefficient, or the average Sherwood number, as a function of the important dimensionless parameters. It is known that generally there are three different mass transfer mechanisms acting at gas evolving electrodes with an intensity depending on the operating conditions: (i) bubble-induced microconvection owing to periodic microflows in the vicinity of gas bubbles adhering to and detaching from the electrode surface, (ii) bubble-induced macroconvection owing to buoyancy flow of a gas-liquid dispersion along the electrode, the flow is caused by the density difference between the dispersion and that of the (nearly) bubble-free liquid, and (iii) single-phase free convection owing to density gradients in the liquid phase near the electrode surface. We will take basically the same approach in constructing our model. In the present work, since the solutal boundary layer is relatively thin, we have basically the microconvection and the bubble-induced macrconvection.

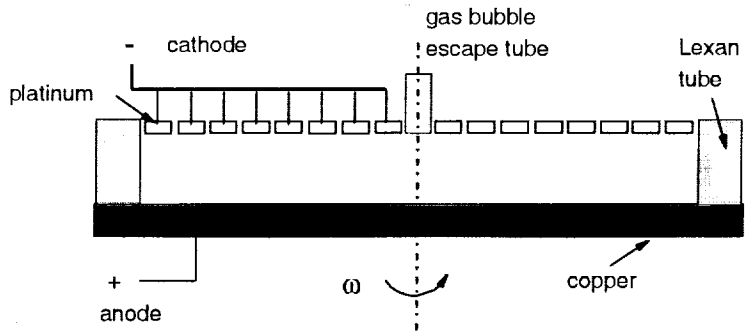

Figure 1 Cross- section of rotating electrochemical cell

NASA/CP—2000-210470

GAS-EVOLVING EFFECT ON MASS TRANSFER IN ROTATING ELECTROCHEMICAL CELLS UNDER MICROGRAVITY

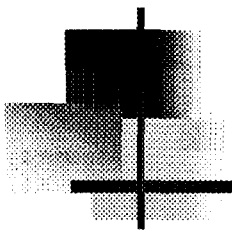

Principal Investigator

Prof. Yasuhiro Kamotani

Department of Mechanical & Aerospace Engineering

Case Western Reserve University

Cleveland, OH 44106

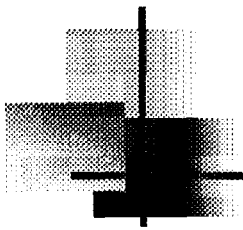

Introduction

To support human exploration and development of space, high performance, efficient electrochemical systems need to be developed. Electrochemical process can reclaim air and water and treat human wastes effectively, precisely and safely. Electrolytically generated gases can affect the performance of electrochemical cells. Very little information is available on the subject of gas evolution in electrochemical cells and its effect on their performance in microgravity. We propose a rotating electrochemical cell to enhance performance and to remove bubbles from the electrodes and electrolyte in a compact design.

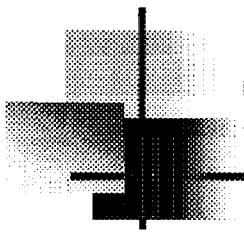

Objectives

- To gain basic knowledge of bubble behavior in rotating electrochemical cells in normal- and micro-gravity
- To study generation, detachment, and motion of gas bubbles in a rotating liquid system
- To analyze mass transfer in the presence of bubble flow in microgravity

Analysis

Complex mass transfer problem due to following factors:

existence of three boundary layers

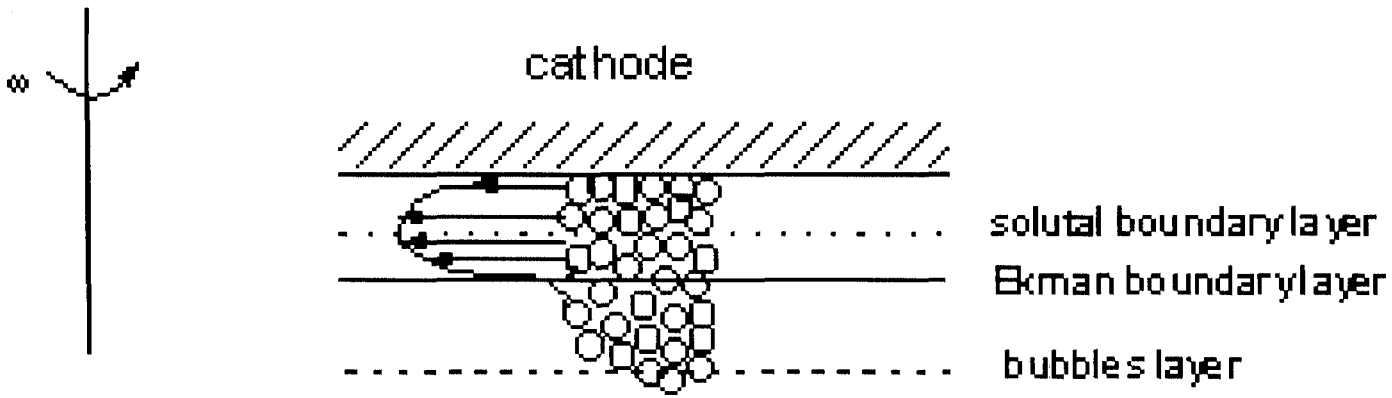

existence of bubble buoyancy and solutal buoyancy

existence of micromixing and macromixing

Experimental Approach

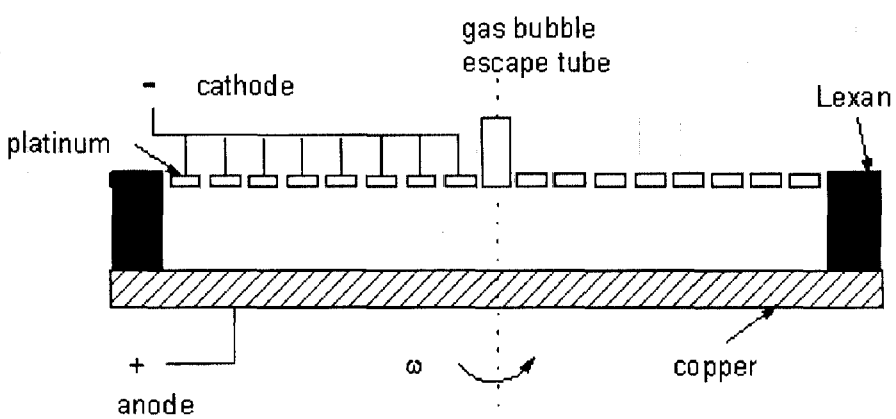

Cross- section of rotating electrochemical cell

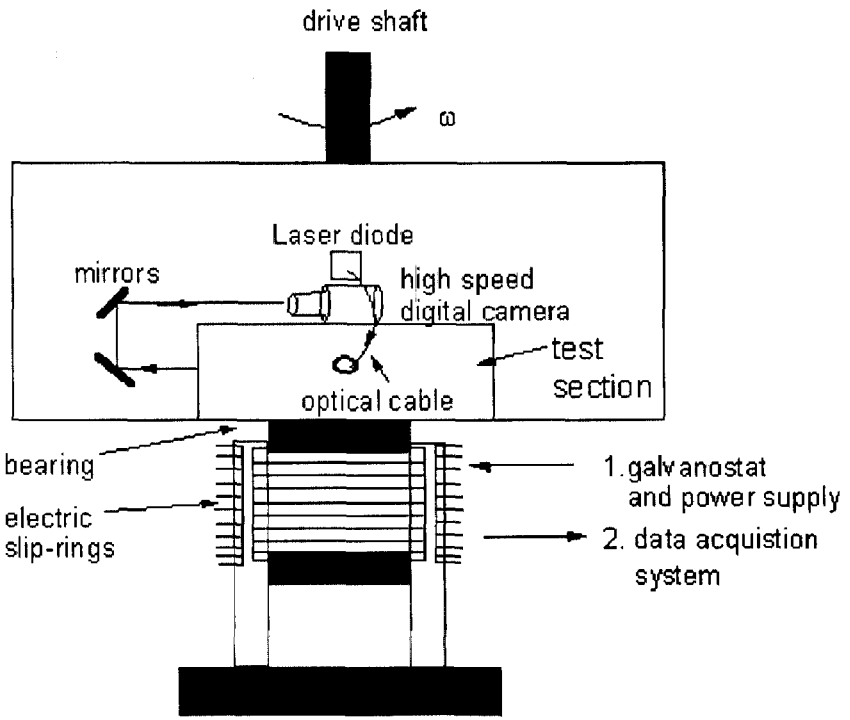

Rotating facility and measurement systems

Experimental Approach

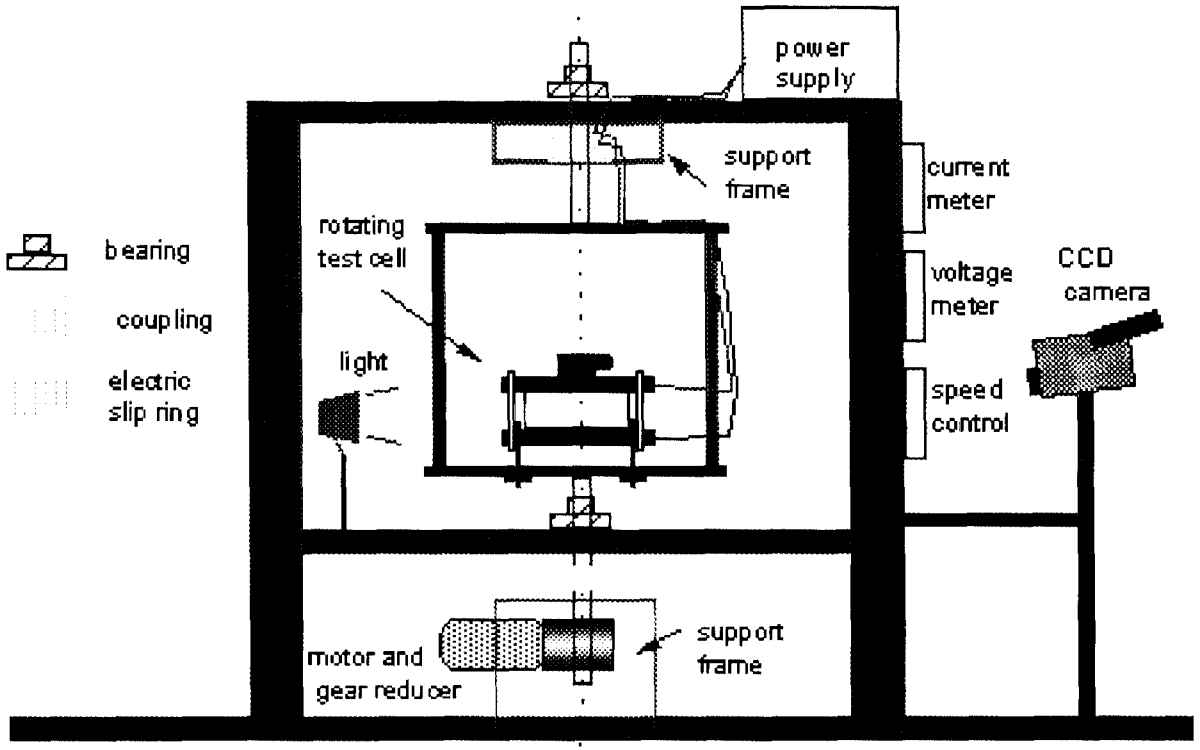

Apparatus for Parabolic Flight Tests

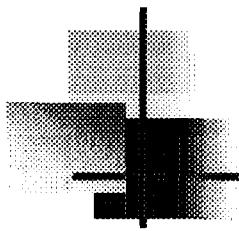

Important Parameters

Ekman number, $Ek = \nu/\omega H^2$

Rossby number, $Ro_s = \beta\Delta C$

Schmidt number, $Sc = \nu/D$

Cylinder aspect ratio, $Ar = H/R$

Centrifugal acceleration level, $Ac = R\omega^2/g$

Centrifugal Rayleigh number, $Ra_{SR} = \omega^2 R\, \beta\Delta C R^3/\nu D$

Rayleigh number for mass transfer, $Ra_{bR} = \Omega^2 R^4/\nu D(\varepsilon/(1-\varepsilon)$

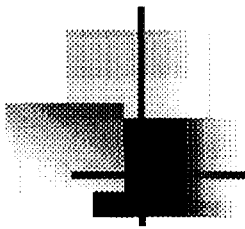

Data to be taken

- **Flow visualization**

  bubble velocity, bubble size, bubble layer thickness

- **Mass transfer measurement**

  copper deposition rate (anode dissolution method), void fraction

INDUSTRIAL PROCESSES INFLUENCED BY GRAVITY

Y. Kamotani, S. Ostrach, F.B. Weng, and J.P. Kizito
Department of Mechanical and Aerospace Engineering
Case Western Reserve University
Cleveland, Ohio 44016

ABSTRACT

We have been investigating gravity-dependent transport phenomena in various industrial processes. The purpose of the study is to address a broader range of microgravity phenomena and to develop new applications of microgravity and normal gravity. Recently we have been investigating the following two subjects: rotating electrochemical systems and coating flow.

We have investigated, experimentally and theoretically, laminar mass transfer in rotating electrochemical cells [1]. As the rotating systems scale up for large battery applications, the mass transfer could become transient and turbulent. The Coriolis and gravity-gradient effects of rotating cells become increasingly important. For that reason, turbulent mass transfer in a rotating shallow electrochemical cell is investigated experimentally with a larger test section than in our previous work. The detail of the test section is shown in Fig. 1. Six local miniprobes embedded in the cathode are used to measure the local mass transfer rate and to detect unsteady turbulent convection. The limiting current method with a cupric sulfate -sulfuric acid system is employed. It is found in most of the present tests that the current is not exactly steady near the limiting current, unlike in our earlier tests with smaller test sections. One typical case of local limiting current as a function of time is presented in Fig. 2. The fact that the limiting current density changes from steady to unsteady in a large diameter cell implies that there is a critical parameter that marks the onset of instability or turbulence in the rotating electrochemical cell. In the present electrochemical system, the $ScRo_S$ number (Schmidt number times solutal Rossby number) is larger than unity, so that the total mass transfer is dominated by centrifugal convection. In that situation, the ratio of convection to diffusion is represented by the centrifugal Rayleigh number, Ra_R. The present data shows that a laminar-to-turbulent transition takes place when Ra_R is between $5x10^{11}$ and 10^{12}. Some results from this work have been published in [2].

The work on coating flow is a combined experimental and numerical study of dip coating flow in a broad parametric range. Emphasis is placed on the stability of a coating flow and identification of the critical parameters, which might lead to the onset of instability. The effect of capillary number and Reynolds number on coating flow is studied. A linear stability analysis of the basic rising film configuration is carried out. The character of waviness is recorded with the aid of digital photography and non-invasive capacitance probes.

The results show that the final non-dimensional thickness in dip coating flow is a function of both capillary number and Reynolds number. At a high parametric range the coating thickness reaches an asymptotic limit and then there is a drop in thickness above a certain parametric value. This drop in thickness is attributed to the appearance of non-sinusoidal waves on the film surface.

Linear stability analysis is performed on a basic rising film configuration. Figure 3 shows the neutral stability curve and the effect of the surface tension parameter on instability. It shows that there is no critical Reynolds number to characterize the onset of instability in a rising film: it is unstable to infinitesimal disturbances for any finite Reynolds number. The main cause of

instability of a dip coating flow is a surface mode of instability having long wavelengths. Surface mode is attributed to the presence of a deformable free surface. A laser reflection method is used to detect instability at small Reynolds numbers. Figure 4 shows a comparison of a numerically computed wavelength having the maximum growth rate and the experimentally observed wavelength, which are in close qualitative agreement. It is suggested that the angled dip coating configuration, where the motion of substrate is at an angle with the horizontal, is hydrodynamically more stable than vertical dip coating.

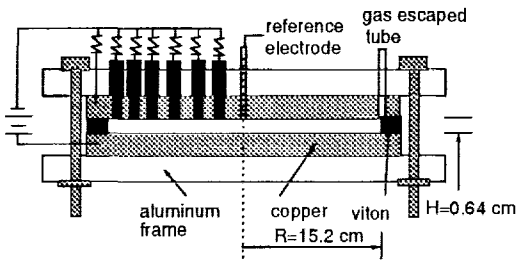

Figure 1. Test cell

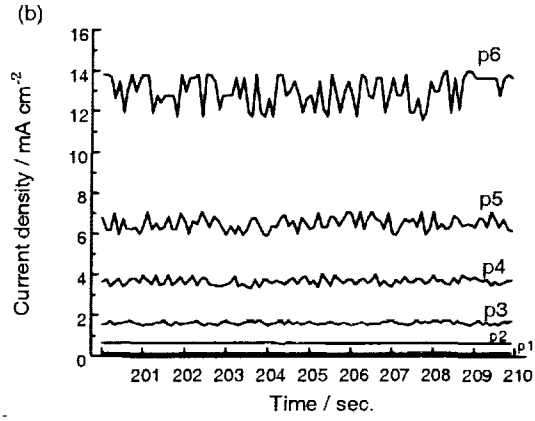

Figure 2. Local limiting current against time

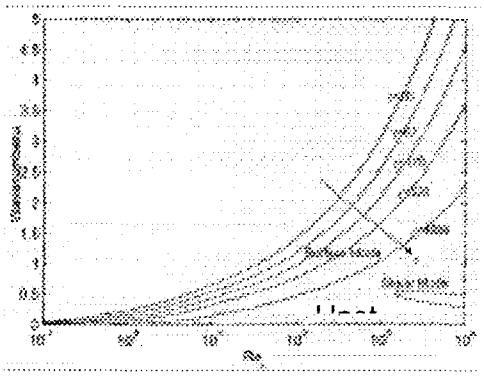

Figure 3. Neutral stability curve for vertical dip coating (γ is surface tension parameter)

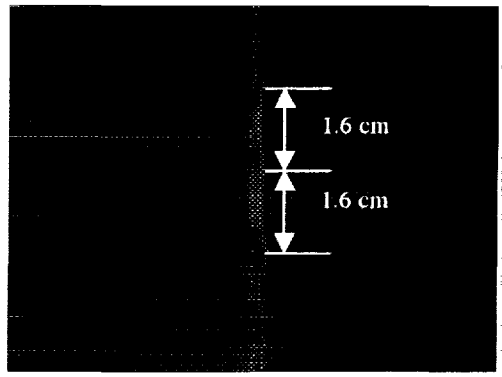

Figure 4. Photograph of wavy film (computed wavelength=1.66 cm)

REFERENCES

1. F. -B. Weng, Y. Kamotani and S. Ostrach, Int. J. Heat & Mass Trans. 41, 1998, 2725-2733.
2. F. -B. Weng, Z. Cheng, Y. Kamotani and S. Ostrach, J. Appl. Electrochem. 29, 1999, 1291-1296.

NASA/CP—2000-210470

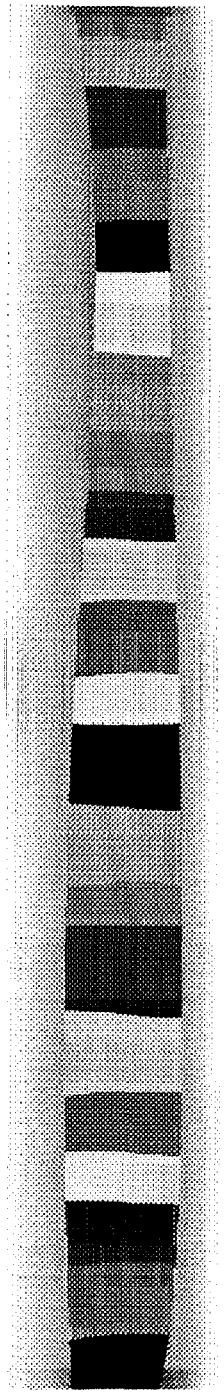

1490

INDUSTRIAL PROCESSES INFLUENCED BY GRAVITY

Y. Kamotani, S. Ostrach, F.B. Weng, and J.P. Kizito

Principal Investigator
Prof. Yasuhiro Kamotani
Department of Mechanical & Aerospace Engineering
Case Western Reserve University
Cleveland, OH 44106

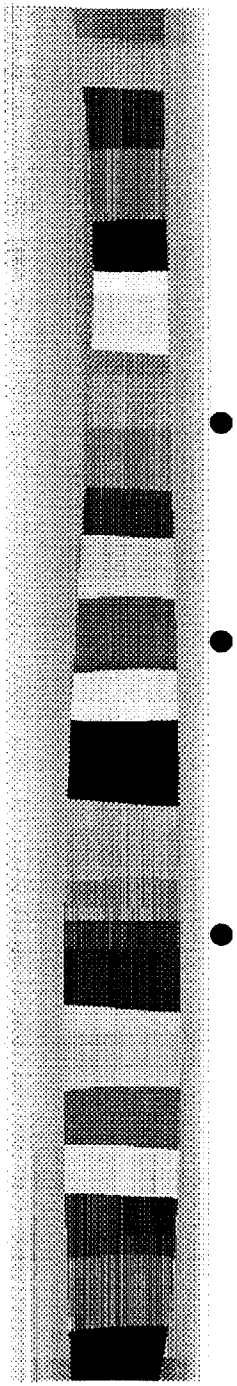

Introduction

- Investigation of gravity-dependent transport phenomena in various industrial processes
- To address a broader range of microgravity phenomena and to develop new applications of microgravity and normal gravity
- Current subjects:
  - Mass transfer in rotating electrochemical cells
  - Coating flow instability

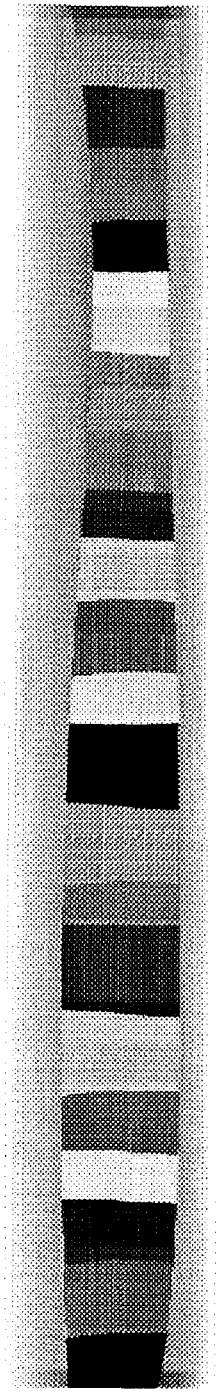

Experimental Setup

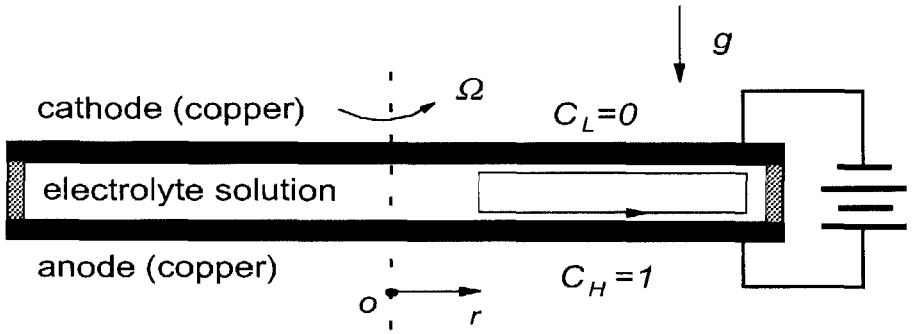

reaction at electrodes:

cathode: $Cu^{++} + 2e^{-} \rightarrow Cu$

anode : $Cu \rightarrow Cu^{++} + 2e^{-}$

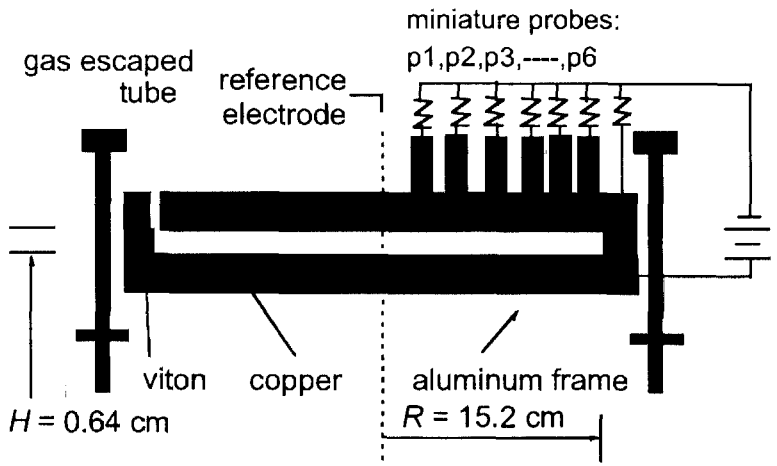

Mass transfer rate fluctuations

(a)

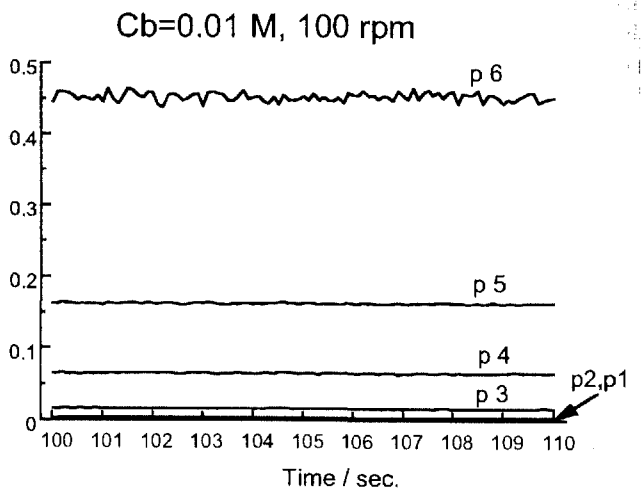

(b)

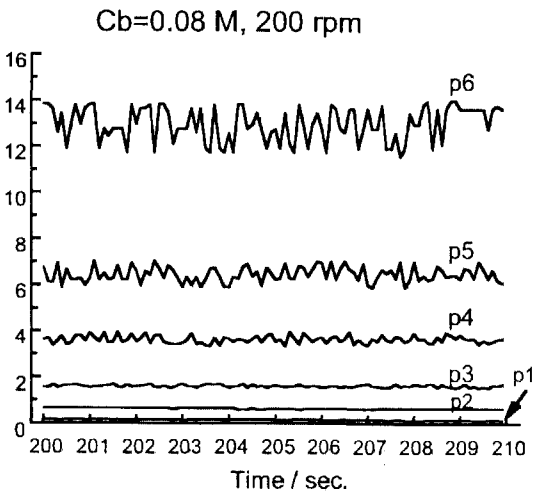

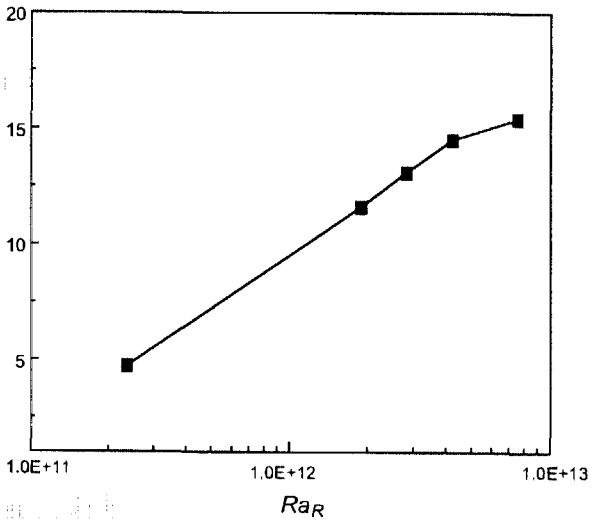

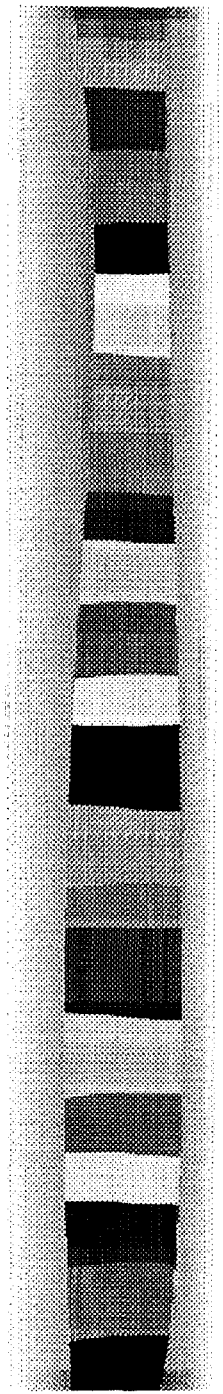

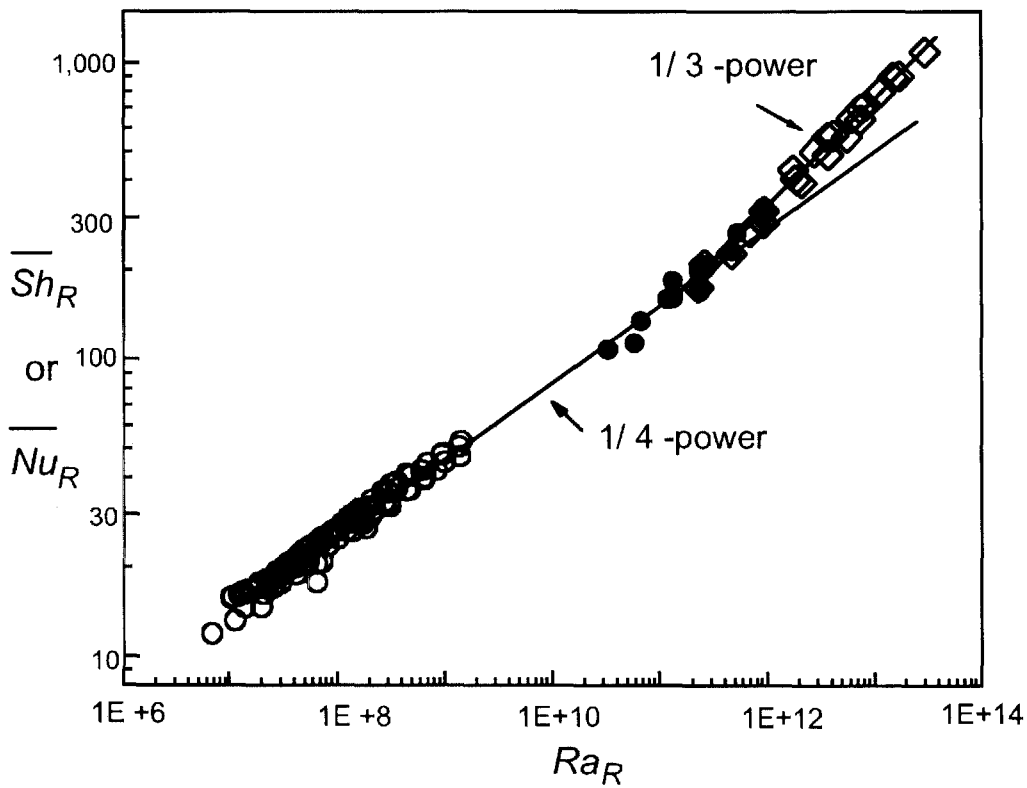

Total Sherwood (or Nusselt) number vs. centrifugal Rayleigh number

Experimental Setup for Coating Flow

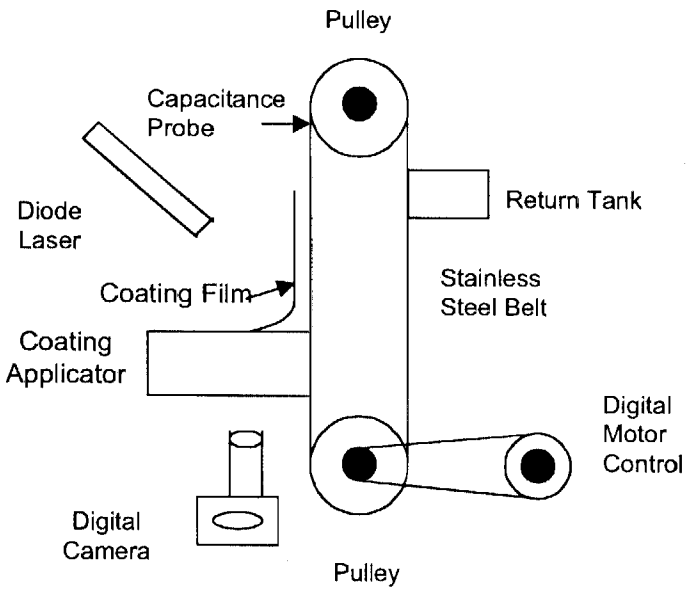

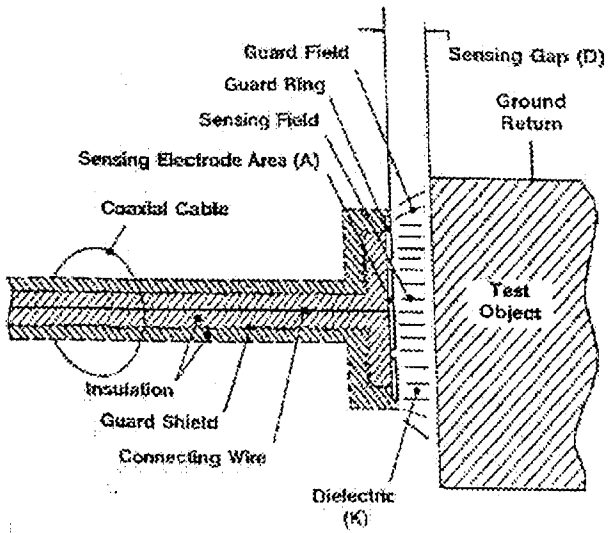

Capacitance probe

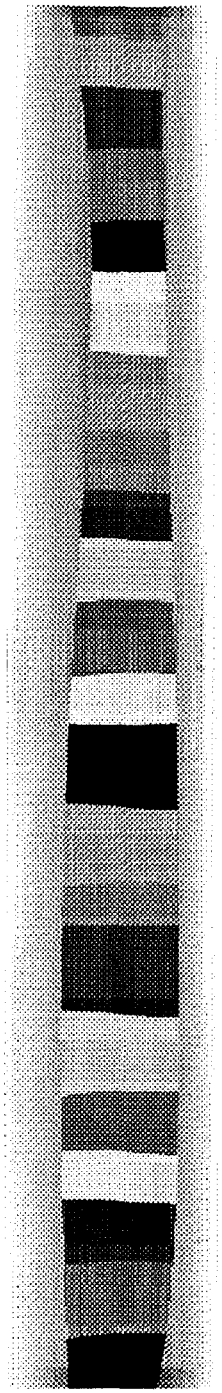

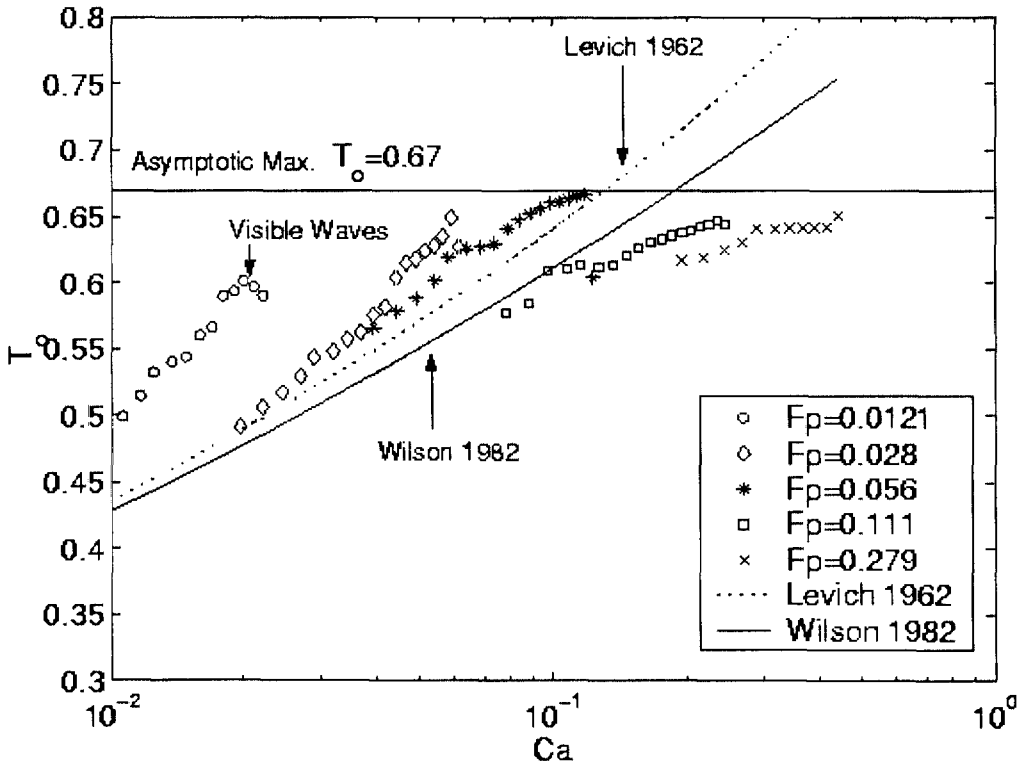

Non-dimensional final thickness as a function of Ca

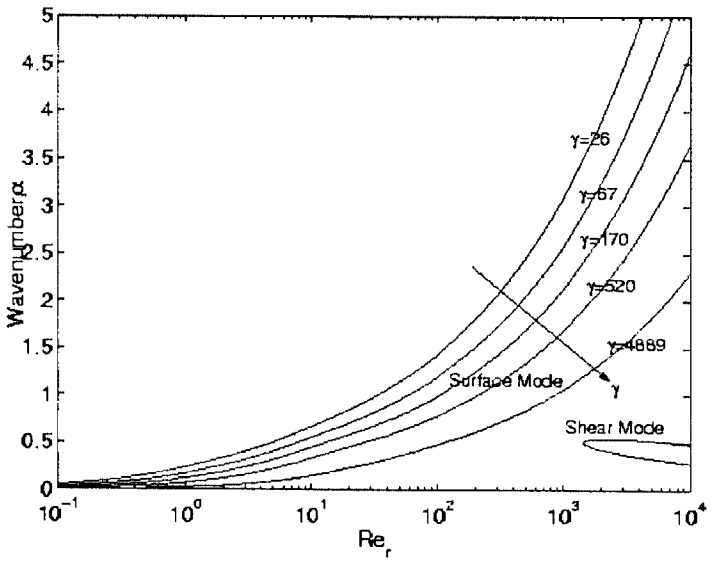

Neutral Stability Curve for a Rising Film

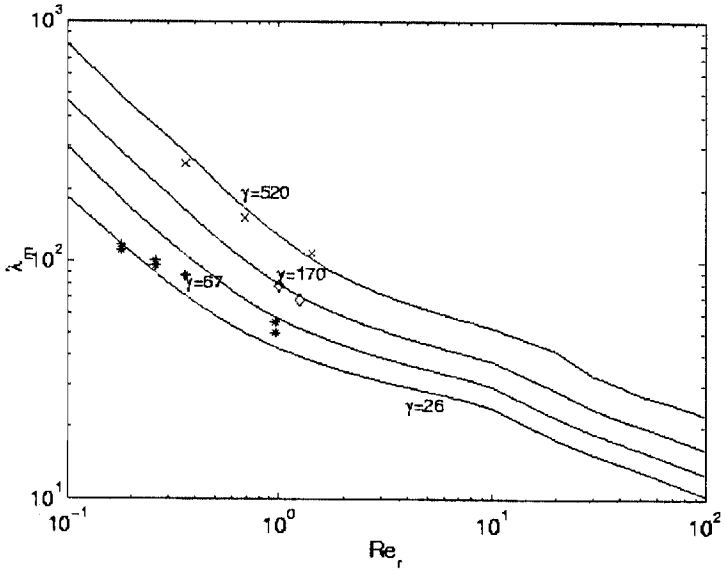

Effect of surface tension on wavelength having maximum growth rate

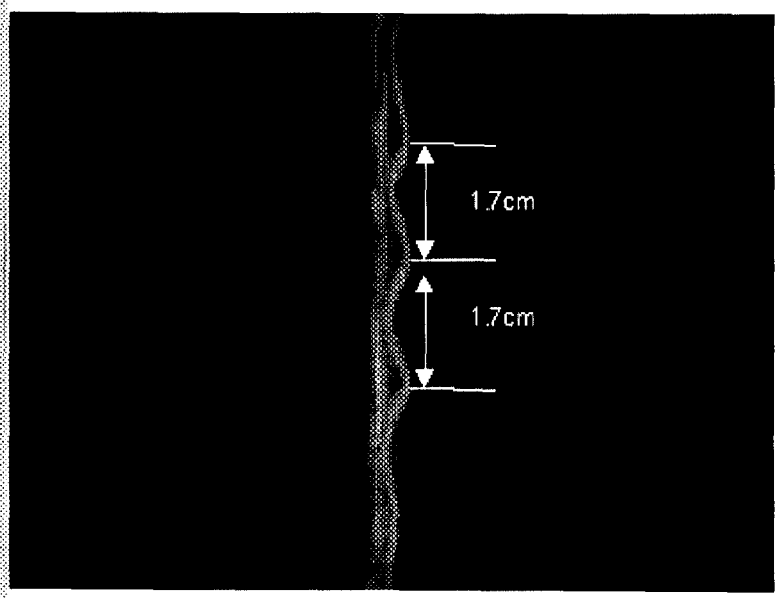

Observed Wavelength at Re_r=1.0,Fp=0.028

Computed wavelength :λ_m=1.72 cm

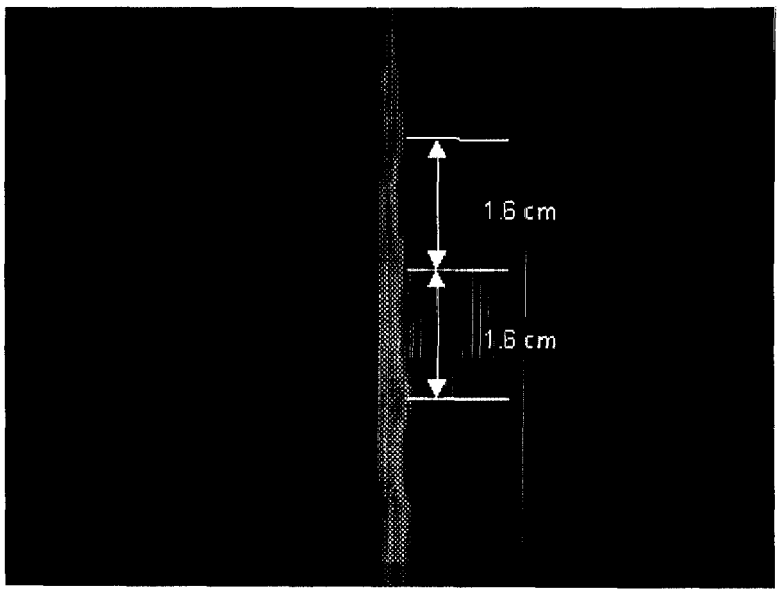

Observed Wavelength at Re_r=1.25,Fp=0.028

Computed wavelength :λ_m=1.66

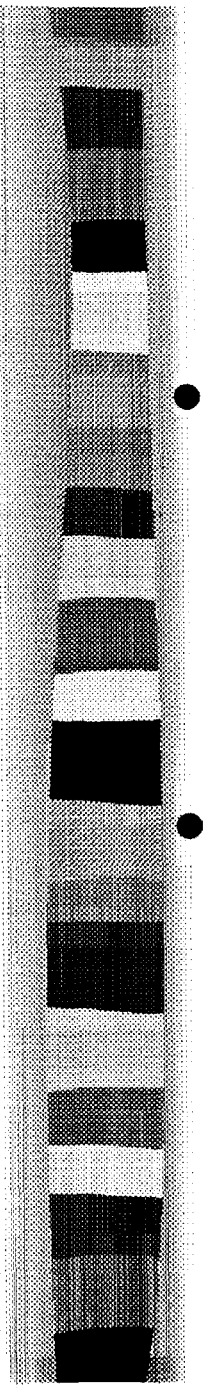

Conclusions

- Mass transfer in rotating shallow electrochemical cells is investigated experimentally. It is found that a laminar-to-turbulent transition takes place when Ra_R is between $5x10^{11}$ and 10^{12}.

- Stability of a dip coating flow is investigated theoretically and experimentally. The film flow is always unstable. The main cause of wavy film is a surface mode of instability having long wavelengths.

BUBBLE FORMATION ON A WALL IN CROSS-FLOWING LIQUID AND SURROUNDING FLUID MOTION, WITH AND WITHOUT HEATING

Avijit Bhunia[1], Yasuhiro Kamotani[2] and Henry K. Nahra[3]
[1,2] Department of Mechanical & Aerospace Engineering, Case Western Reserve University, Cleveland, OH 44106, [2] Corresponding Author, e-mail: yxk@po.cwru.edu
[3] NASA-GRC Lewis Field, MS 500-102, Cleveland, OH 44135

ABSTRACT

Application of gas-liquid two-phase flow systems for space-based thermal management and for the HEDS program demands a precise control of bubble size distribution in liquid. The necessity of bulk liquid motion for controlling bubble size and frequency in the space environment has been suggested by recent studies on pool [1], forced convection boiling [2] and bubble formation in flowing liquid [3, 4]. The present work, consisting of two parts, explores bubble generation at wall in a cross-flowing liquid, i.e., in a forced convection boiling configuration. A schematic is shown in figure 1. The first part looks into the bubble formation process under isothermal conditions in a reduced gravity environment, by injecting gas through a hole in the wall of a flowing liquid channel. In the latter part with channel wall heating, flow and temperature fields near a single bubble are studied under normal (1-g) and micro-gravity (μ-g) conditions.

The objective of the isothermal experiments is to experimentally investigate the effects of liquid cross-flow velocity, gas flow rate, and orifice diameter on bubble formation. Data were taken mainly under reduced gravity conditions but some data were taken in normal gravity for comparison. The reduced gravity experiment was conducted aboard the NASA DC-9 Reduced Gravity Aircraft. The results show that the process of bubble formation and detachment depends on gravity, the orifice diameter (D_N), the gas flow rate (Q_g), and the liquid cross-flow velocity (U_L). The reduced gravity data are shown in figure 2. The data are analyzed based on a force balance, and two different detachment mechanisms are identified. When the gas momentum is large, the bubble detaches from the injection orifice as the gas momentum overcomes the attaching effects of liquid drag and inertia. The surface tension force is much reduced because a large part of the bubble pinning edge at the orifice is lost as the bubble axis is tilted by the liquid flow. When the gas momentum is small, the force balance in the liquid flow direction is important, and the bubble detaches when the bubble axis inclination exceeds a certain angle.

With wall heating, liquid motion around an air bubble in cross-flowing 2cs silicone oil is experimentally investigated in 1-g. A spectral element based steady 2D numerical model is also developed. The traces of particles from experimental flow visualization and the corresponding computed streamlines are shown in figure 3. At the upstream side of the bubble facing the cross-flow, thermocapillary and forced convection create liquid motion away from the wall, up along the surface. At the downstream side, a competing interaction between the two creates a recirculation cell, causing the bulk liquid to stagnate on the surface and separate thereafter. The important dimensionless parameters are - Surface tension and local cross-flow Reynolds numbers $R_\sigma(U_{ref}a/\nu)$ and $Re_{loc}(U_L a/\nu)$, respectively based on reference thermocapillary $U_{ref}(\sigma_T \Delta T/\mu$, $\Delta T=T_{wall}-T_{liquid})$ and local cross-flow velocity U_L, Prandtl number Pr and Grashoff number $Gr(\rho g\beta\Delta T a^3/\mu\nu)$. Variation of the stagnation point with R_σ and Re_{loc} is shown in figure 4. Figures 3 and 4 show good agreement between experimental and numerical results in 1-g. The

computational model is extended to μ-g condition to investigate temperature and velocity on the bubble surface, stagnation and reattachment points of the recirculation cell and wall heat transfer. It is observed that wall heating significantly alters the flow field around the bubble and thus the forces acting on the bubble, which control its detachment. Thus a combination of heating and liquid cross-flow can be utilized to precisely control bubble formation in a μ-g environment.

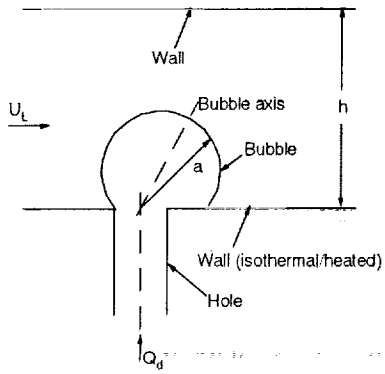

Figure 1: Schematic of bubble generation in Cross-flowing liquid.

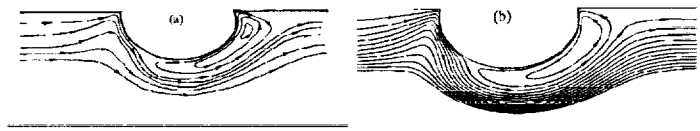

Figure 3: Streamlines for Re_{loc}=3.6, R_σ=194 (a) Experimental and (b) Computational.

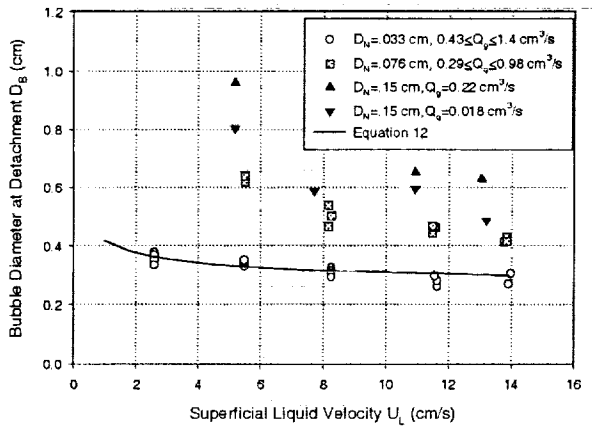

Figure 2: Schematic of bubble generation in Cross-flowing liquid.

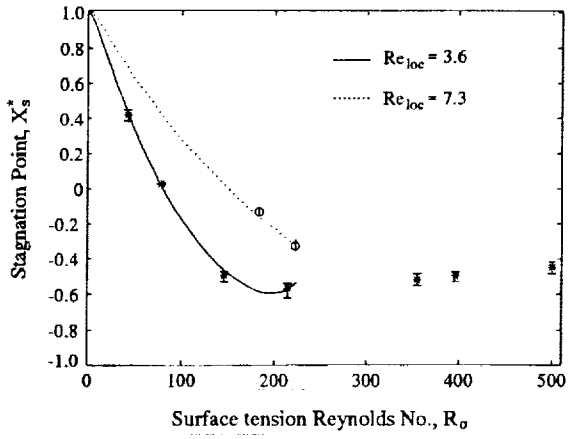

Figure 4: Dimensionless stagnation point in 1-g. Lines - computational. Symbols - exp.

REFERENCES

1. H. S. Lee and H. Merte, Int. J. Heat & Mass Trans., 39 (12), 1996, 2449-2461.
2. Y. Ma and J. N. Chung, Int. J. Heat & Mass Trans., 41 (15), 1998, 2371-2382.
3. I. Kim, Y. Kamotani and S. Ostrach, AIChE J., 40 (1), 1994, 19-28.
4. A. Bhunia, S. C. Pais, Y. Kamotani and I. Kim, AIChE J., 44(7), 1998, 1499-1509.

NASA/CP—2000-210470

BUBBLE FORMATION ON A WALL IN CROSS-FLOWING LIQUID AND SURROUNDING FLUID MOTION, WITH AND WITHOUT HEATING

Avijit Bhunia, Yasuhiro Kamotani and Henry K. Nahra

Principal Investigator
Prof. Yasuhiro Kamotani
Department of Mechanical & Aerospace Engineering
Case Western Reserve University
Cleveland, OH 44106

- **Two-phase flow applications**
  - HEDS program
  - Cryogenic storage
  - Thermal management
  - Propulsion system
- **Bubble detachment in stagnant liquid**

  Uncontrolled bubble size and frequency
- **Need for an additional control mechanism**
  - Flowing liquid
    - Co-flow and cross-flow
    - Wall injection in cross-flow
  - Combination of cross-flow and wall heating

Bubble generation from wall injection in a cross-flowing liquid

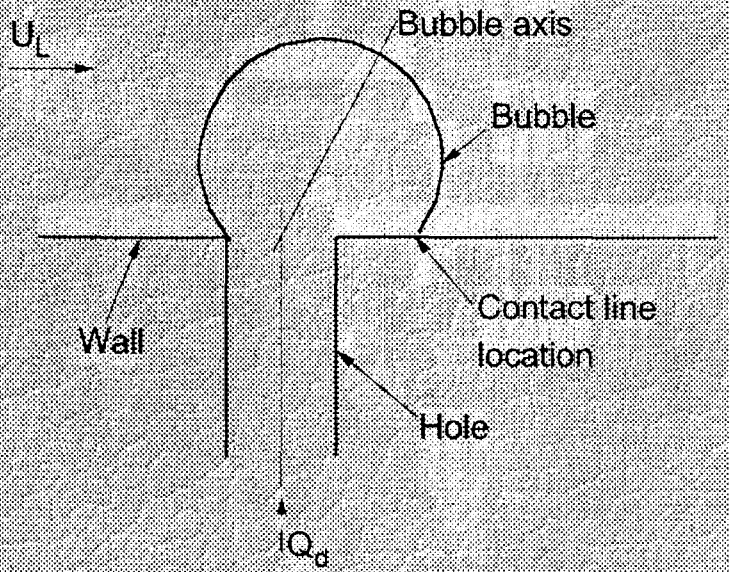

- Parabolic flight experiment
- Analytical modeling based on

$$\mathbf{F_B} + \mathbf{F_D} + \mathbf{F_I} + \mathbf{F_M} + \mathbf{F_\sigma} = 0$$

- F_B - Buoyancy
- F_D - Liquid drag
- F_I - Liquid inertia
- F_M - Gas momentum
- F_σ - Surface tension at bubble base

Sequence of Bubble formation process

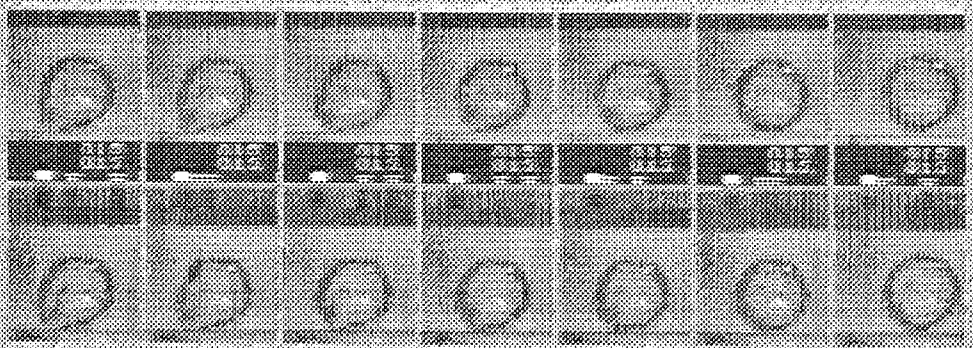

Reduced gravity

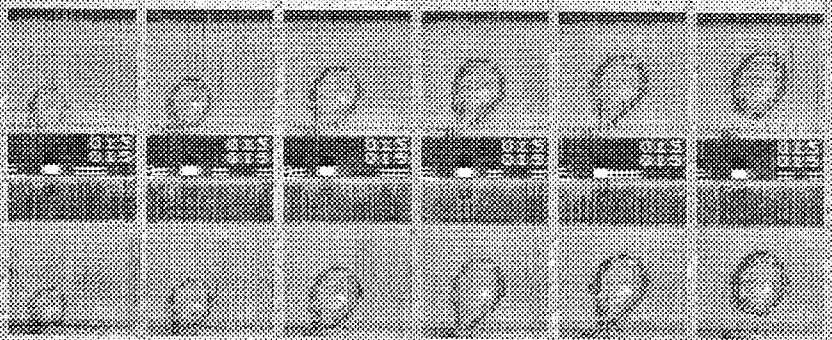

2-g period

$D_N = 0.15$ cm, $Q_g = 0.2$ cc/s, $U_L = 7.7$ cm/s

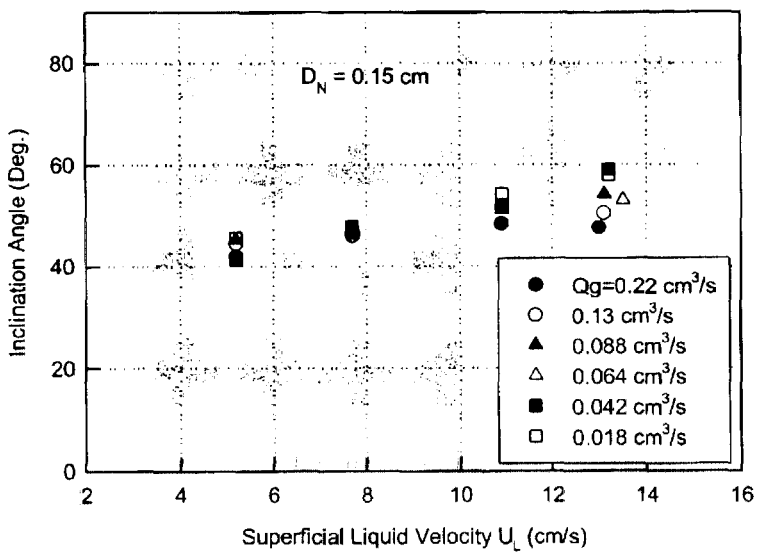

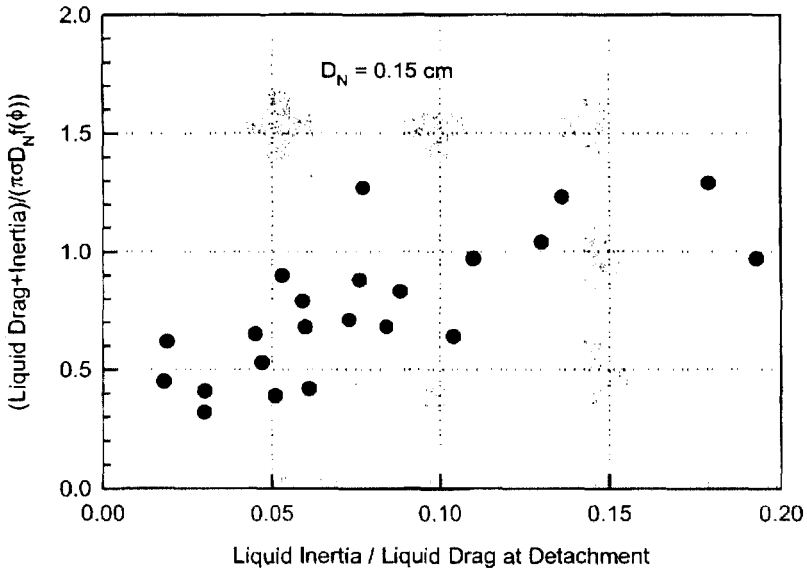

Bubble axis inclination angle vs. U_L

$(F_D + F_I)/F_\sigma$ vs. F_I/F_D

Bubble generation on heated wall of a flowing liquid channel

Focus

Flow and temperature fields around the bubble, 1-g & μ-g.

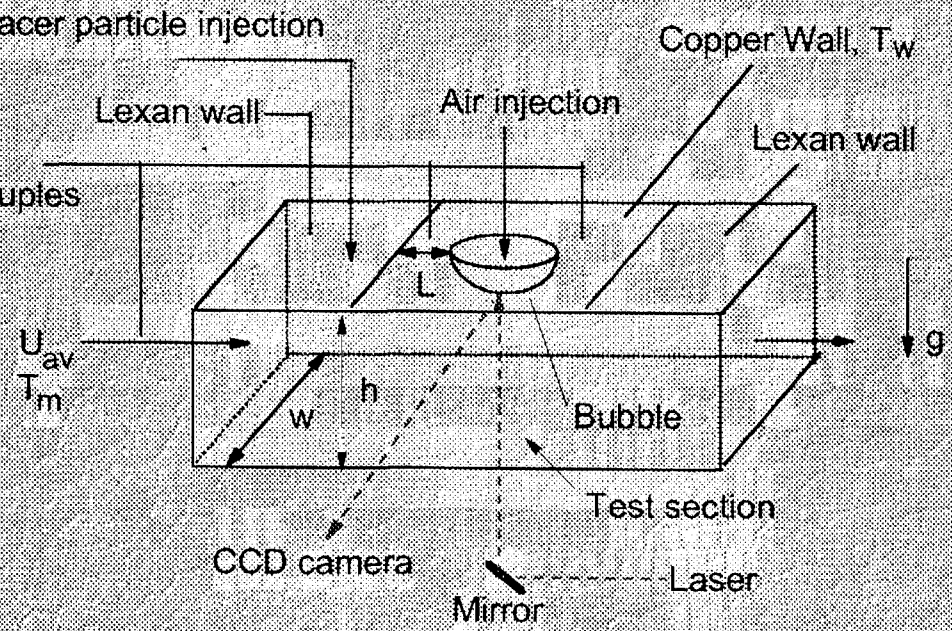

2 cs silicone oil

U_{av} = 1 - 2 cm/s

T_m ~ 23°C

ΔT = 0 - 12°C

Bubble radius a ~ 2 mm

Objectives

Understand the role of convection mechanisms -

- Thermocapillary
- Forced
- Natural

Importance

Flow field governs forces on the bubble $\Longrightarrow$

bubble size & frequency $\Longrightarrow$ Two-phase flow and heat transfer.

Approach

- 1-g experimental work
- 2-D numerical model - Spectral element method - 1-g & μ-g

Flow & Temperature fields $\sim f(R_\sigma, Re_{loc}, \delta_T/a, B_d, Pr)$

$\sim f(V, Re_{loc}, \delta_T/a, B_d, Pr)$

$R_\sigma = U_{ref} a/\nu_l = \sigma_T \Delta T a/\mu_l \nu_l$ $\quad Re_{loc} = U_{loc} a/\nu_l$ $\quad \overline{V} = \dfrac{U_{ref}}{U_{loc}} = \dfrac{\sigma_T \Delta T}{\mu_l U_{loc}}$

$B_d = \rho g \beta \Delta T a^2/\mu_l U_{ref}$ $\quad \delta_T(L)/a = 5L/(aRe_{loc}^{0.5} Pr^{0.33})$

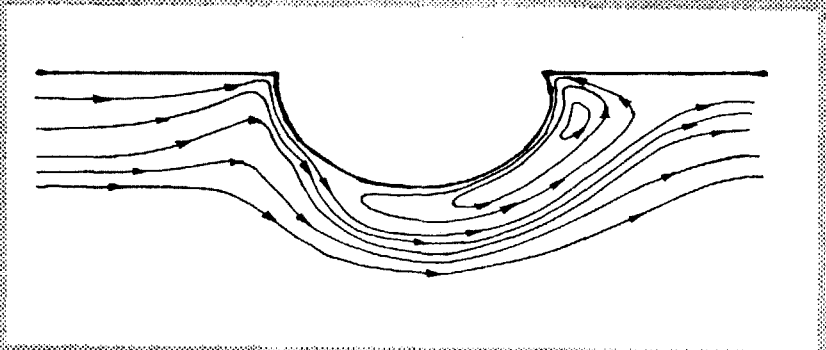

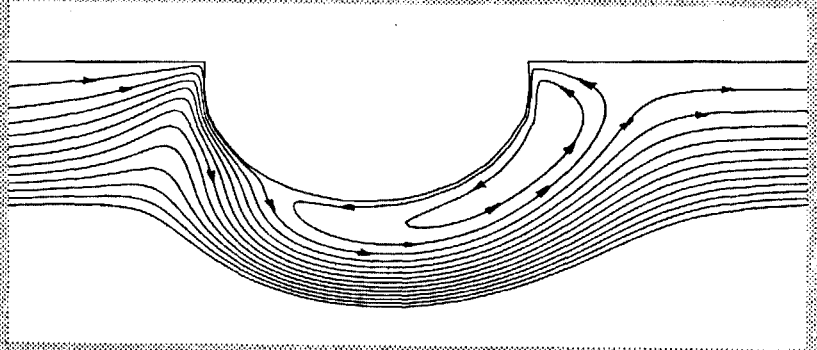

Experimental Numerical

Pr = 27, V = 43.9 (R_σ = 155), Re_{loc} = 3.6, δ_t/a = 3.0, B_d = 0.6

Favoring and opposing effects: Forced & Thermocap. convection

- Stagnation point on bubble surface
- Re-circulation cell at the downstream side

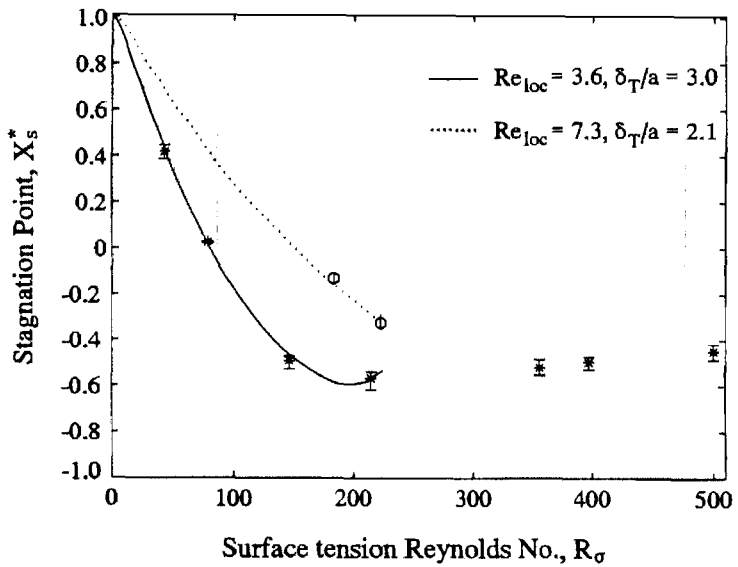

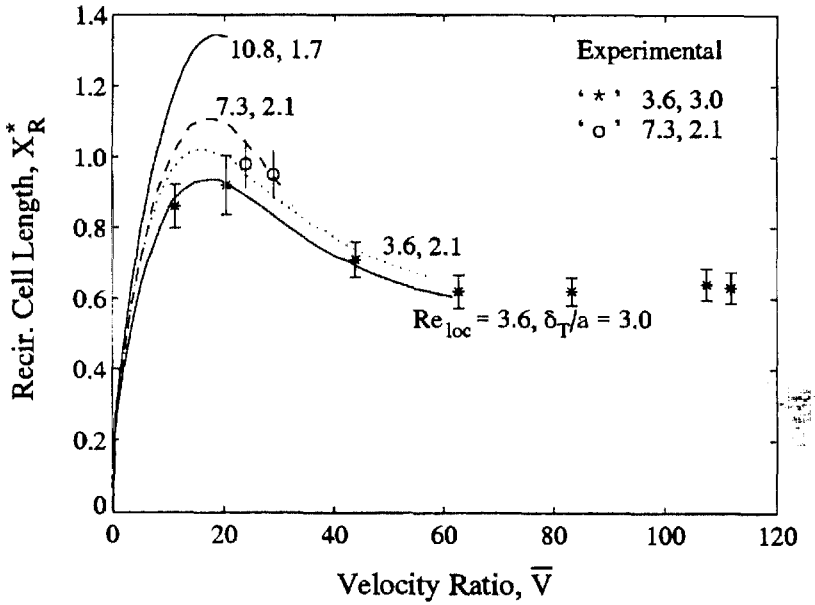

Stagnation point

Length of recirculation cell

Conclusions

- Flowing liquid promotes bubble detachment
  - Various forces interact in complex manner during detachment
  - Wall plays an important role (Loss of pinning edge)
- Effects of wall heating -
  - 3 convection modes govern Flow & Thermal fields -
    - ° Thermocapillary ° Forced ° Natural
    - –Favoring interaction at front & Competing interaction at downstream end - Recirculation
    - –Significant change in flow field → Forces on bubble → Bubble size and frequency can be controlled better

BUBBLE DYNAMICS ON A HEATED SURFACE

M. Kassemi(1), N. Rashidnia(2), (1),(2) NCMR, NASA GRC,
Cleveland OH 44135, Mohammad.Kassemi@grc.nasa.gov,
Nasser.Rashidnia@grc.nasa.gov

ABSTRACT

In this work, we study the time evolution of the thermocapillary flow and temperature fields generated by a bubble on a heated surface below and above the critical Marangoni number for oscillatory convection. A combined numerical-experimental approach is adopted whereupon direct numerical simulations of the temperature and flow fields were used in conjunction with Wollaston Prism Interferometric measurements to capture the dynamic characteristics of the time-dependent convection. Index of refraction fringe distribution fields are constructed from the computed temperature fields using an inverse Abel transform. The numerically predicted fringe patterns are directly compared to Wollaston Prism interferograms for both steady state and oscillatory convection and the agreement is excellent in all cases. It is shown that below a critical Marangoni number, steady state conditions are attainable. However, with increasing Ma number, there is a complete transition from steady state up to a final non-periodic fluctuating flow regime through several complicated symmetric and asymmetric oscillatory modes.

The most prevalent oscillatory mode corresponds to a symmetric up and down fluctuation of the temperature and flow fields associated with an axially travelling wave. This oscillatory mode is captured experimentally through a sequence of WP interferograms. Careful examination of the numerically generated temperature and flow fields, and the associated fringe patterns and comparison to experimental results, reveals that the origin of this class of convective instability is closely related to an intricate temporal coupling between large scale thermal structures within the flow field (in the form of cold fingers) and the temperature sensitive free surface of the bubble.

The temperature and velocity data from supercritical simulations were used to determine the critical Marangoni number for transition to the axially oscillatory thermocapillary convection. In the oscillatory regime, time-dependent thermocapillary flow is characterized by temperature fluctuations on the surface of the bubble. For supercritical bifurcation, as is the case here, when the critical Ma number, is approached at a fixed bubble aspect ratio, Ar, from within the unsteady regime, the temperature fluctuation amplitude decreases becoming zero at the critical point. Thus a scheme to predict the critical Marangoni number is constructed by quadratic extrapolation of (Ma, amplitude) to zero amplitude for fixed Ar. The critical Marangoni number for onset of the axially oscillatory thermocapillary convection is numerically determined using this extrapolation procedure to be around 8500 for a bubble aspect ratio of one. The accuracy of the extrapolated critical Ma number is validated by numerical simulations through spot checking (Ar, Ma) combinations near the estimated critical value. The numerically

predicted critical Ma number is in good agreement with our experimental measurements and with other published experimental results which report a value between 8000 and 9000.

Buoyancy force and natural convection play important roles in the development of the thermal structures in the flow and the initiation of oscillatory convection. Consequently, at low-g, not only the shape of the bubble, but also the time evolution of the temperature and flow fields generated by the bubble are very different from those observed on earth.

Finally, the physical evolution of the azimuthally-driven transverse oscillatory modes observed experimentally could not be captured by the present 2-D analysis. Detailed 3-D simulations are required to investigate the origin and physical characteristics of the transverse oscillations more closely.

NASA/CP—2000-210470

National Center for Microgravity Research on Fluids and Combustion

5th Microgravity Fluid Physics and Transport Phenomena Conference

1514

Bubble Dynamics on a Heated Surface

M. Kassemi and N. Rashidnia

National Center for Microgravity Research (NCMR)
NASA Glenn Research Center
Cleveland, OH

August 2000

Interaction Between Voids/Bubbles With The Surrounding Fluid Environment

- Important in Many Industrial Applications Involving Liquid-Gas Free Surfaces:
  - Storage And Management Of Fluids
  - Manufacturing and Materials Processing (E.g. Crystal Growth)
  - Boiling
- Fluid Motion Usually Driven By Two Cooperating Or Competing Mechanisms:
  - **Thermocapillary Convection** ====>> Surface Force ====>> Temp-Dependent Surface Tension
  - **Natural Convection** ====>> Volumetric Force ====>> Temp-Dependent Density Gradients

Experimental Setup

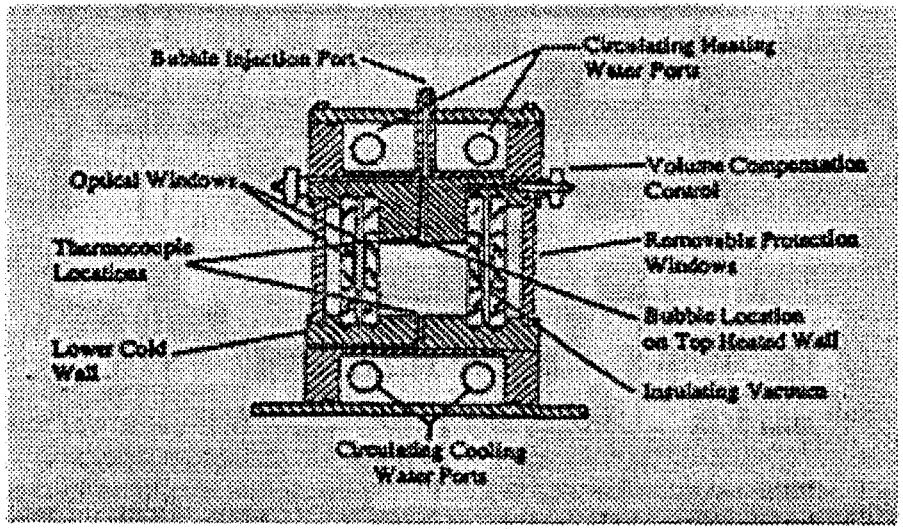

- Test Cell
  - Bubble Injector
  - Silicon Oil
  - Water Cooled/heated Top/bottom Plates
- Laser Sheet Flow Visualization
- WP Interferometry == >> Index Of Refraction Fringes ===>> Temperature Distribution

CASE 1: STEADY STATE 1-G RESULTS

$$\mathrm{Ma} = 2440,\ \mathrm{Ra} = 500,\ \mathrm{Pr} = 122$$

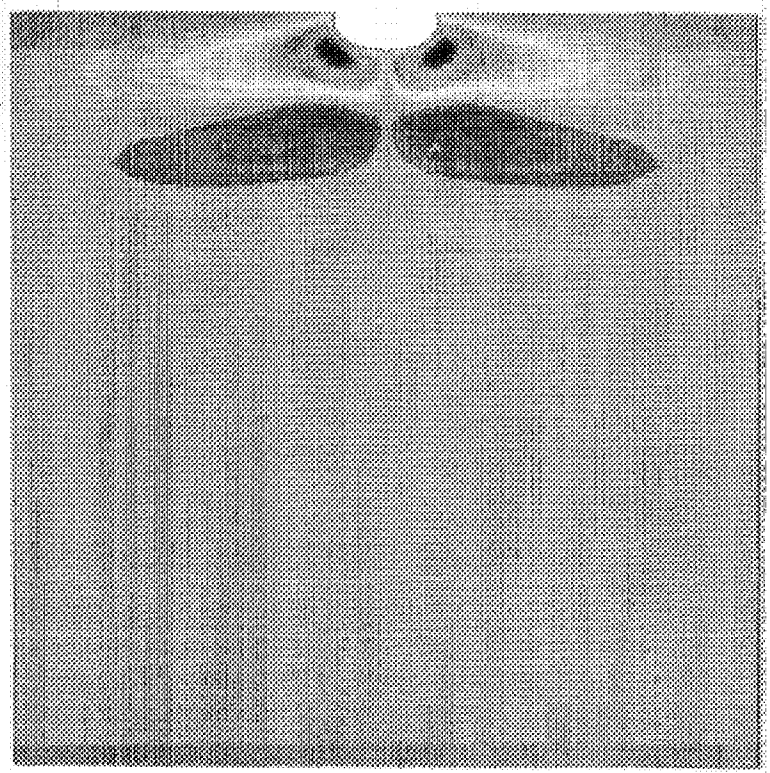

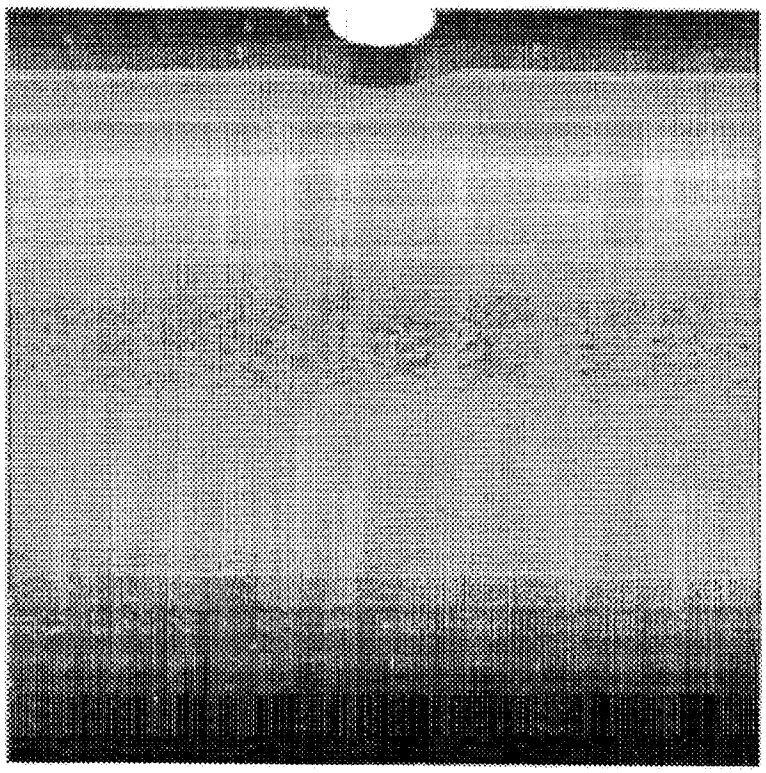

CASE 2: STEADY STATE LOW-G RESULTS

$G_o = 10^{-4}$

$Ma = 1830$

$Ra = 0.244$

$Pr = 122$

1-G CASE: INTERFACIAL TEMPERATURE & SPEED HISTORIES: Ma = 170,000, Ra = 70,000, Pr = 7.3

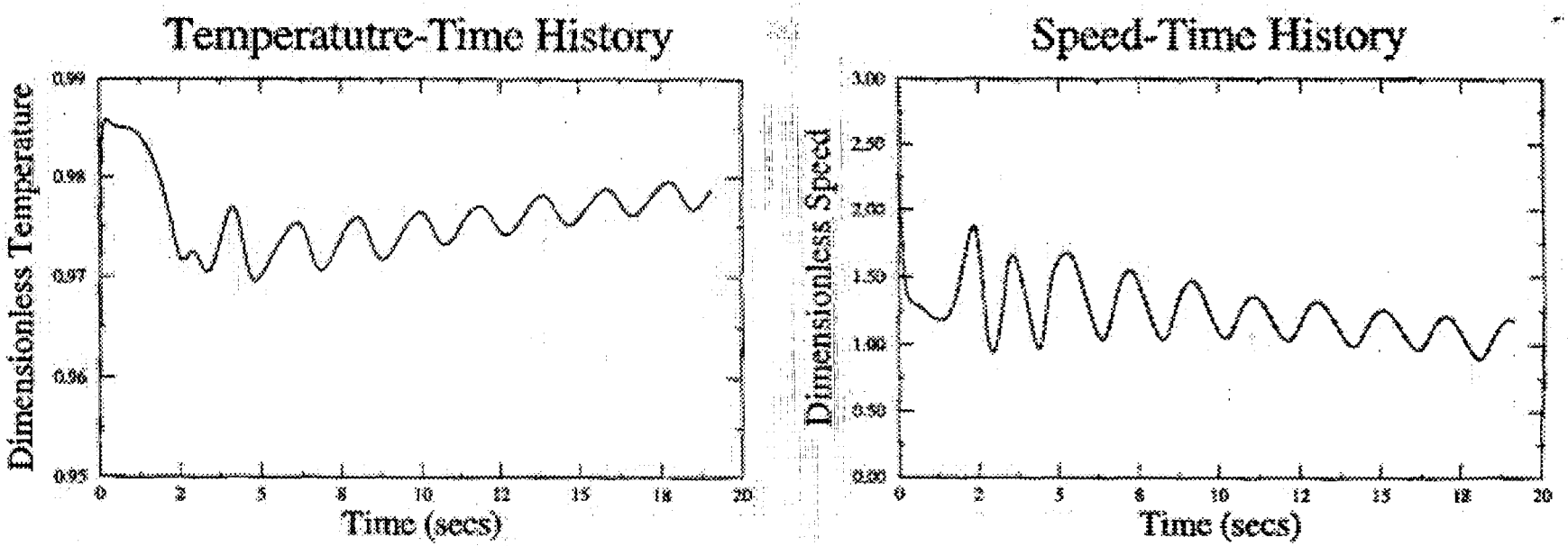

WP INTERFROGRAMS SHOWING ONE SEQUENCE OF THERMAL OSCILLATIONS

Ma = 170,000, Ra = 70,000, Pr = 7.3

0

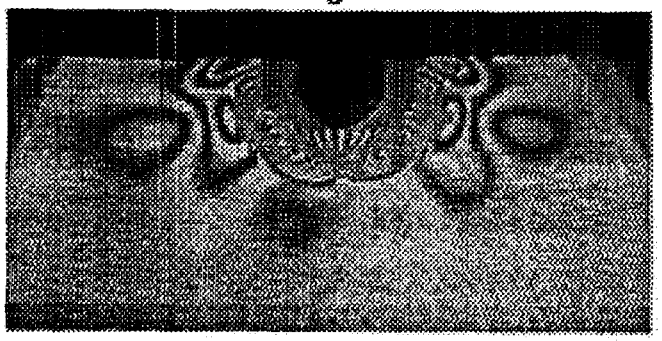

6π/5

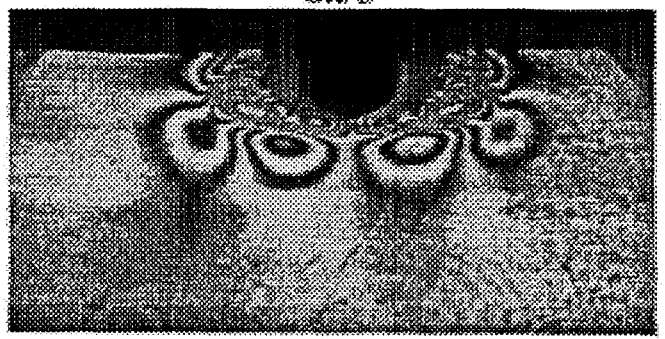

2π/5

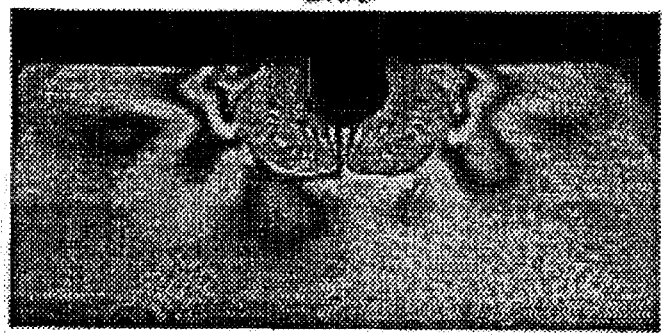

8π/5

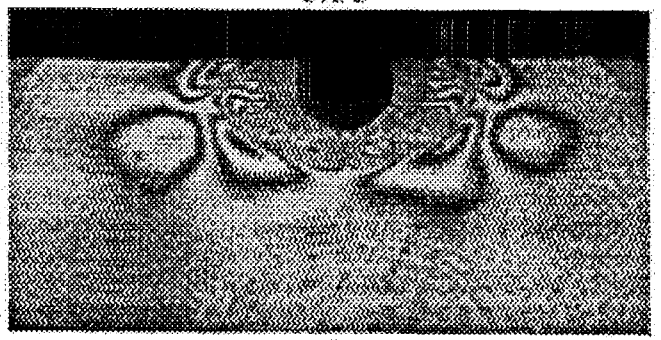

4π/5

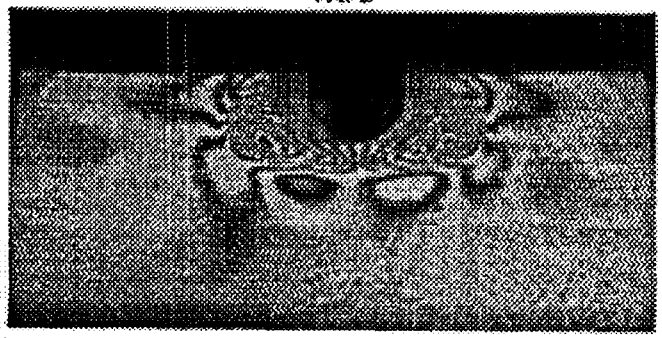

2π

COMPARISON BETWEEN *EXPERIMENTAL* AND *NUMERICAL* WP INTERFEROGRAMS

Experiment: WPI | **Numerical Simulation**

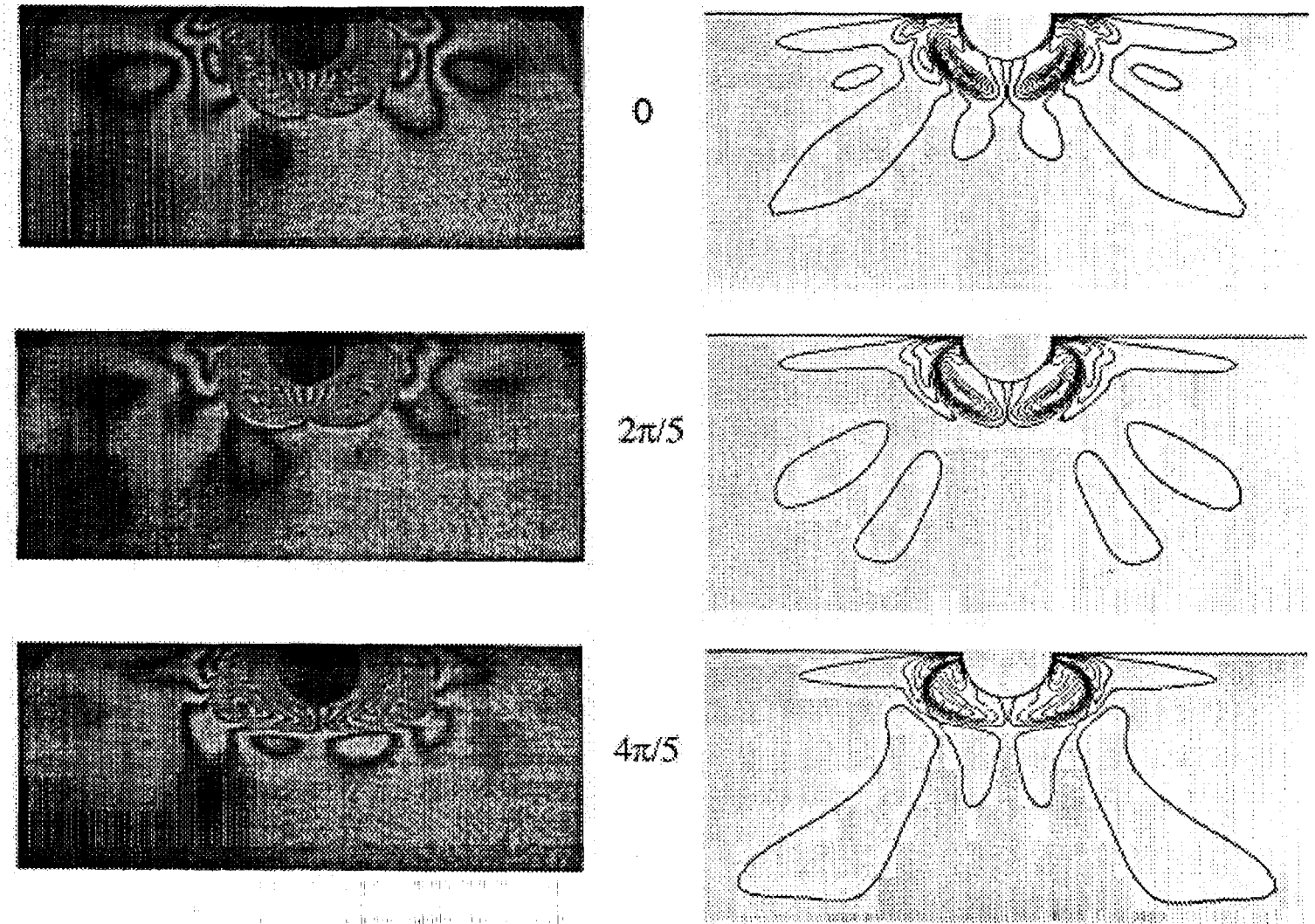

COMPARISON BETWEEN *EXPERIMENTAL* AND *NUMERICAL* WP INTERFEROGRAMS

Experiment: WPI

Numerical Simulation

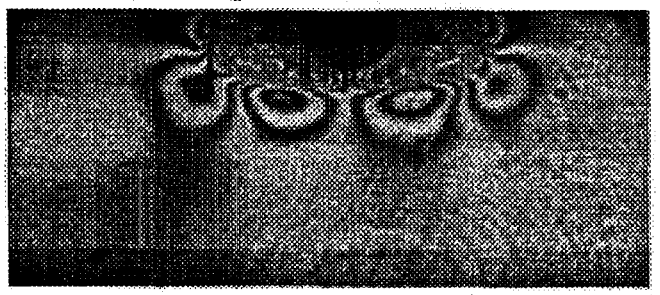

$6\pi/5$

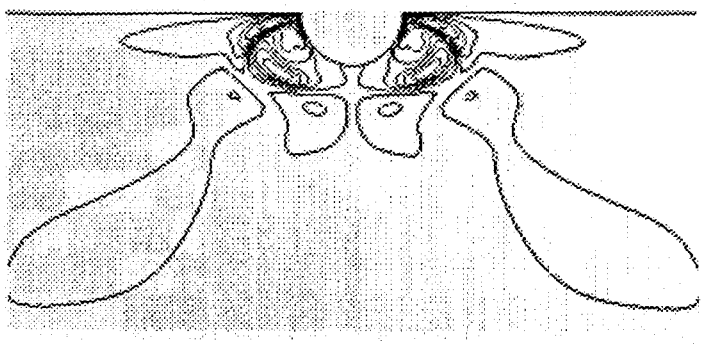

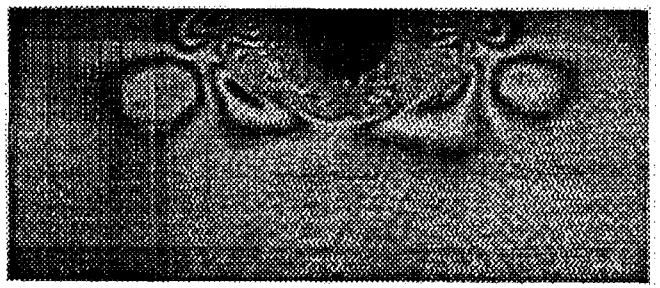

$8\pi/5$

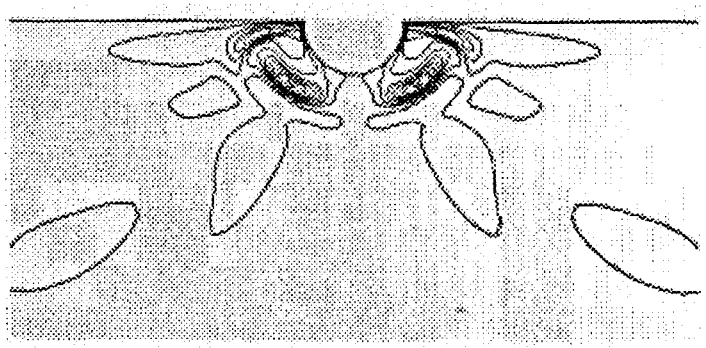

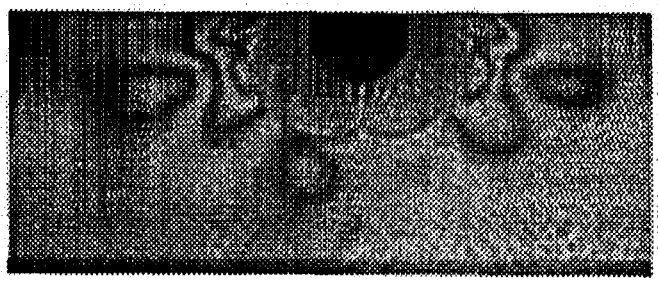

2π

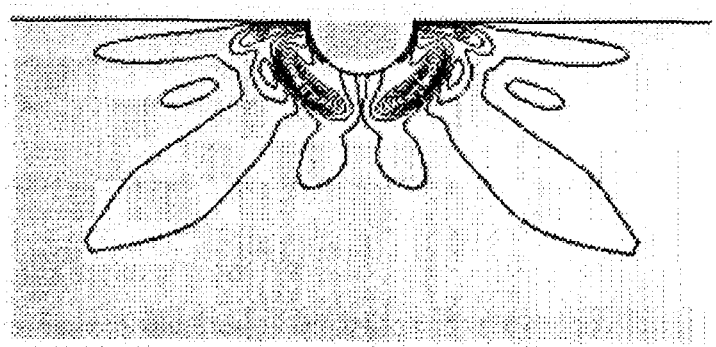

0
2π/5
4π/5

COMPUTATIONAL MATERIALS LABORATORY

NASA

1-G CASE: INTERFACIAL TEMPERATURE & SPEED:
Ma = 170,000, Ra = 70,000, Pr = 7.3

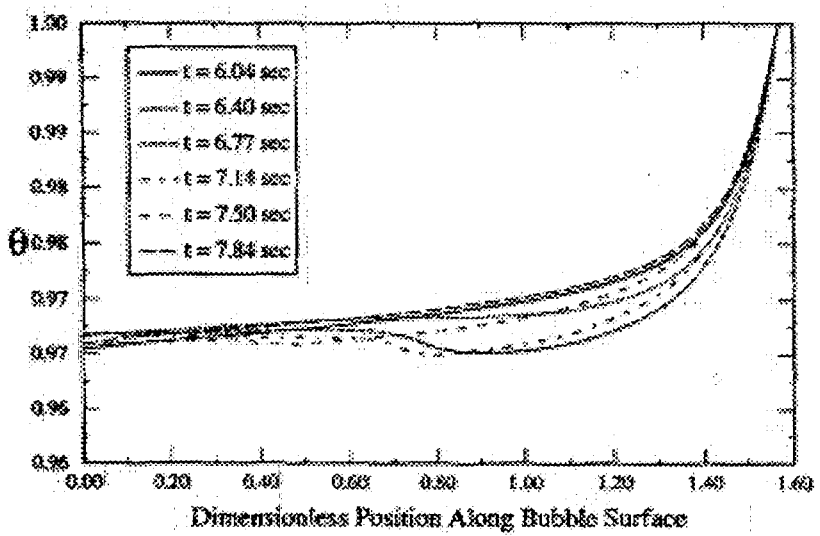

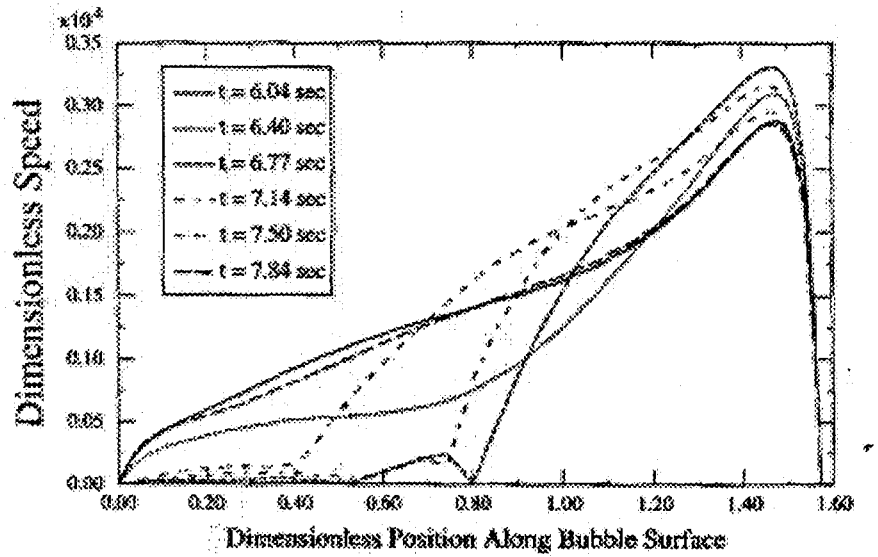

COMPUTATIONAL MATERIALS LABORATORY

NASA

LOW-G CASE TIME-DEPENDENT INTERFACIAL TEMPERATURE:

Ma = 90,000, Ra = 0.50, Pr = 8.4

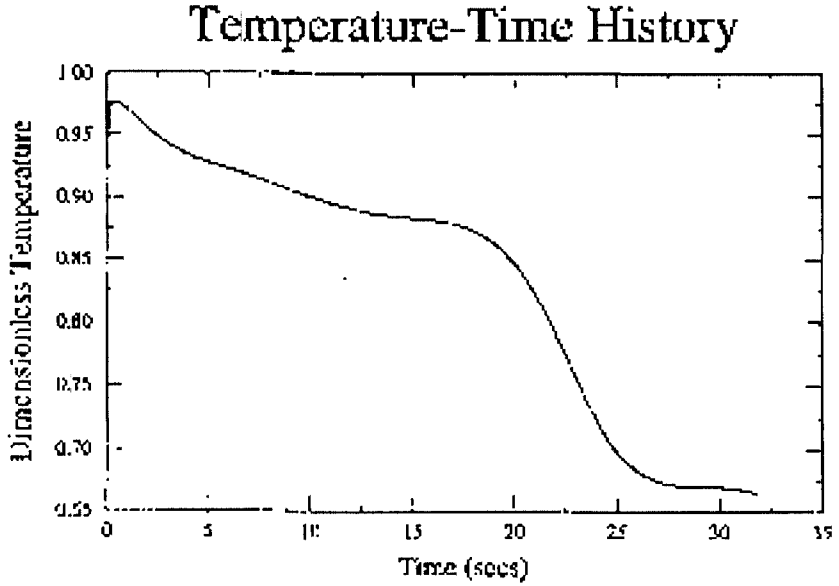

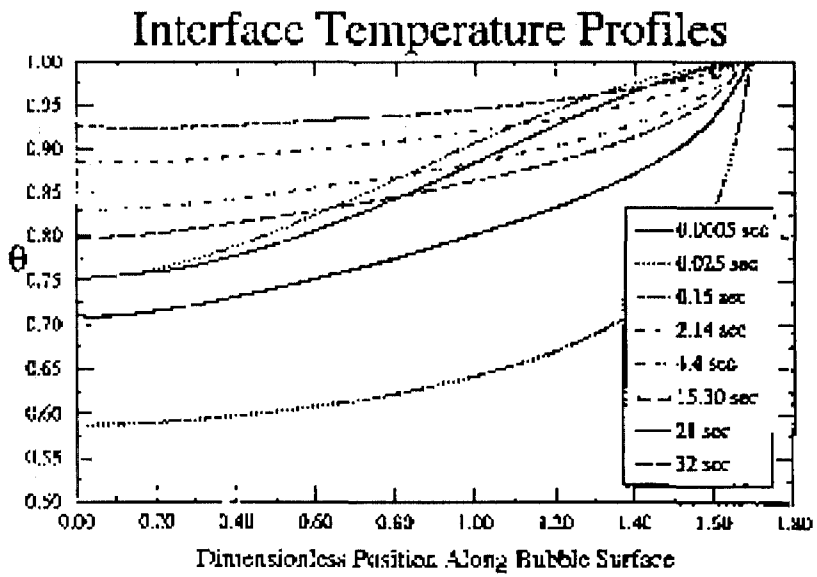

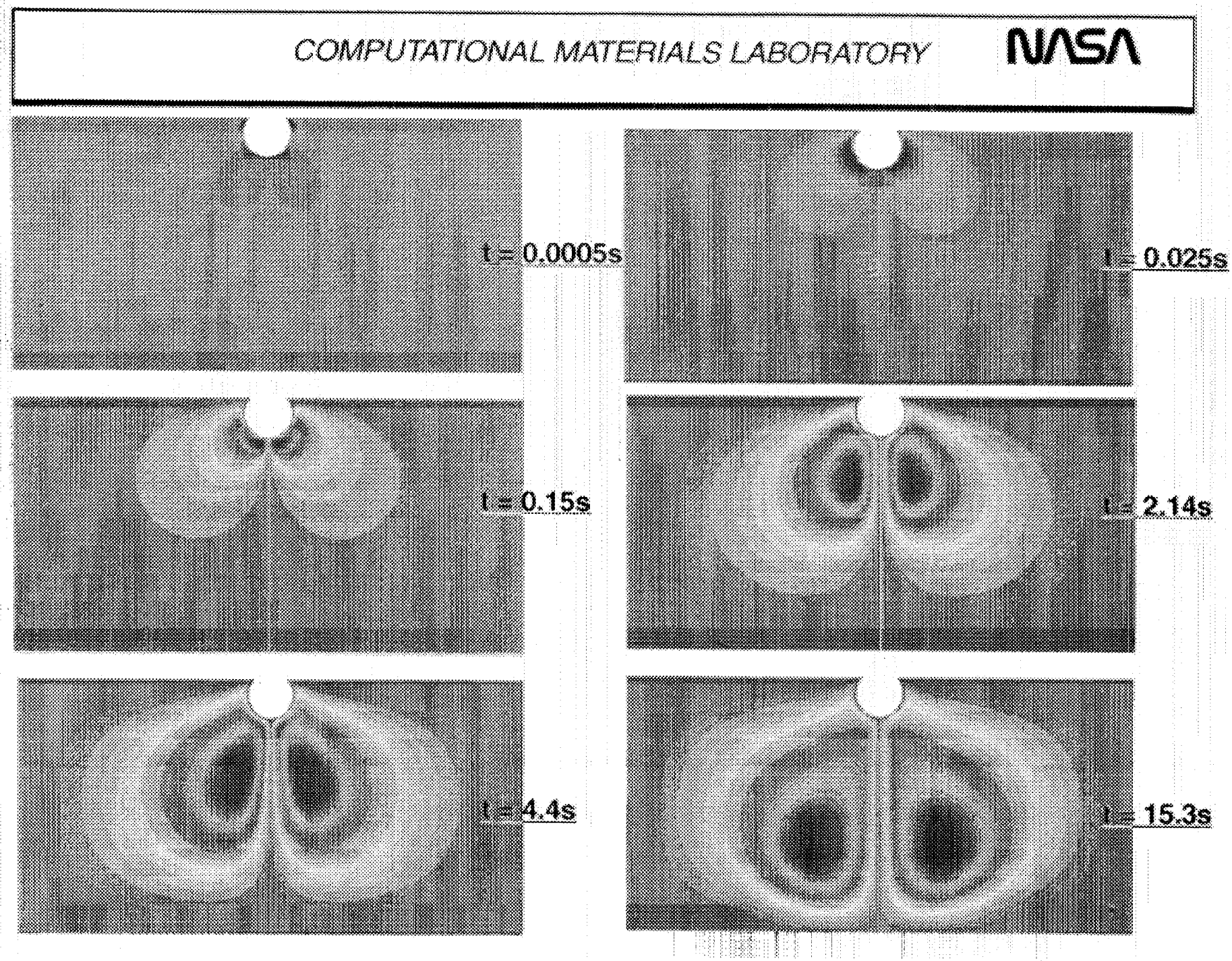
COMPUTATIONAL MATERIALS LABORATORY
NASA
t = 0.0005s
t = 0.025s
t = 0.15s
t = 2.14s
t = 4.4s
t = 15.3s

COMPUTATIONAL MATERIALS LABORATORY
NASA
= 21s
= 32s

THE INVESTIGATION OF THE EFFECTS OF GRAVITY ON SINGLE BUBBLE SONOLUMINESCENCE

Ben Dzikowicz, David B. Thiessen, Philip L. Marston,
Washington State University, Department of Physics, Pullman, WA, 99163

Abstract

In single bubble sonoluminescence (SBSL), a bubble in water emits a flash of light following it's rapid collapse each cycle of oscillation of an ultrasonic field. Since widely varying length and time scales affect the bubble dynamics and optical emission processes, it is difficult to anticipate the importance of the effects of gravity present for observations on earth.

Our bubble is driven in an acoustically resonating cavity at it's first harmonic mode. The acoustical radiation pressure (Bjerknes force) will then keep it suspended in the center near the pressure antinode. When driven in a region where the diffusive processes balance the bubble it acts in a nonlinear but regular way [1], emitting a short (approx. 150ns) each acoustic cycle.

Balancing the Bjerknes force with buoyancy, as in [2], we can see that the bubble should be displaced from the velocity node approximately 20μm at normal gravity. Therefore, water flows past the bubble at the time of collapse. Gravitation also changes the ambient pressure at the bubble's location, as $\Delta P = \rho dg$ this gives a change of approximately –0.5% in our experiment when going from 1.8g to 0g. Studies of ambient pressure changes were also done in order to assess these effects.

Inside a pressure sealed chamber a spherical glass cell is filled with distilled water which has been degassed to 120mmHg. A bubble is then trapped in the center and driven by a piezoelectric transducer at 32.2kHz attached to the side of the cell. An optical system is then set up to take strobbed video images along and light emission data simultaneously. Temperature, pressure, drive voltage, and listener voltage are also monitored.

Figure 1. shows the change in light output with the change in acceleration on the KC-135 aircraft. Figure 2. shows the bubble radii for the same set of data. Note that each 'spike' in the radius plot represents the growth and collapse of many cycles over a one second period. From these graphs we can see that the light output and the maximum bubble radius both increase as the gravity decreases.

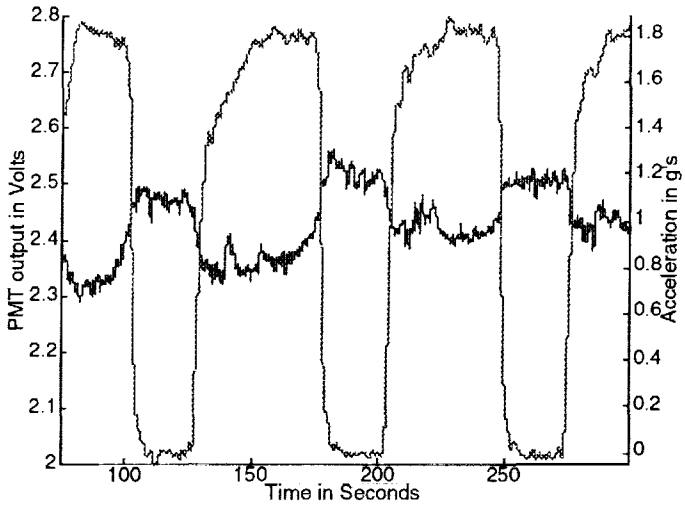

Figure 1.

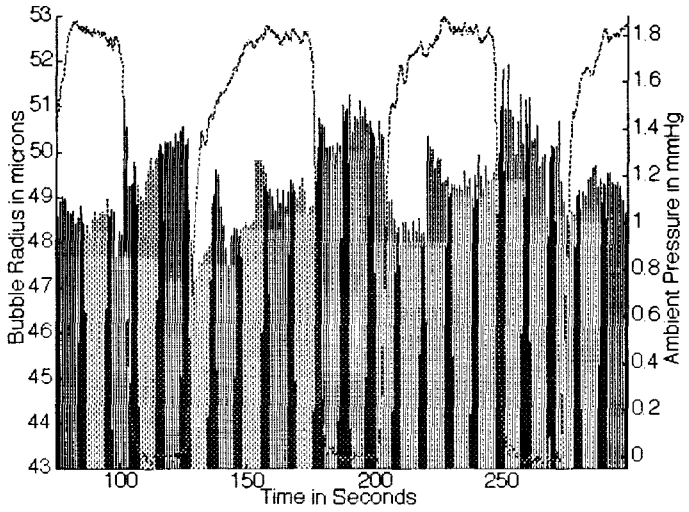

Figure 2

The radii of the bubbles for both experiment s are fit using the Rayleigh-Plesset equation and the acoustic drive amplitude and the ambient bubble radius are found. There is little change in the acoustic drive amplitude as we expect, since we are not varying the drive voltage. However. the ambient bubble radius goes up considerably. These changes (increased light output, increased maximum bubble radius, and increased ambient bubble radius) are also observed when the ambient pressure is varied in the laboratory by an amount similar to that due to gravitation. The changes in the ambient bubble radius and light output with a change in ambient pressure are predicted by the "dissociation hypothesis"[3] and have been observed by other groups in the laboratory[4]. It seems clear that buoyancy's effect on light output and bubble radius, are at best on the same order as the effects of ambient pressure.

[1]Holt, R.G., Gaitan, D.F., Observation of Stability Boundaries in the Parameter Space of Single Bubble Sonoluminescence, Phys. Rev. Lett., vol 77, 3791-3794, 1996

[2]Matula, T.J., Cordry, S.M., Roy, R.A., Crum, L.A., Bjerknes force and Bubble Levitation Under Single-Bubble Sonoluminescence Conditions, J. Acoust. Soc. Am., vol 102, 1522-1525, 1997

[3]Kondic, L., Yuan, C., Chan, C.K., Ambient Pressure and Single-Bubble Sonoluminescence, Phys. Rev. E, vol 57, R32-R35, 1998

[4]Dan, M., Cheeke, J. D. N., Kondic, L., Ambient Pressure Effect on Single Bubble Sonoluminescence, Phys. Rev. Lett., vol 83, 1870-1873, 1999

The Investigation of the Effects of Gravity on Single Bubble Sonoluminescence

Ben Dzikowicz, David B. Thiessen, Philip Marston, Washington State University, Department of Physics, Pullman, WA, 99164

Abstract

In single bubble sonoluminescence (SBSL), a bubble in water emits a flash of light following its rapid collapse each cycle of oscillation of an ultrasonic field. Since widely varying length and time scales affect the bubble dynamics and optical emission processes, it is difficult to anticipate the importance of the effects of gravity present for observations on earth.

Our bubble is driven in a spherical cavity at its fundamental mode. The acoustical radiation pressure (Bjerknes force) will then keep it suspended close to the center near the pressure antinode. When driven in a region where the diffusive processes balance the bubble it acts in a nonlinear but regular way [1], emitting a short (approx. 200ps) burst of light each acoustic cycle.

Balancing the Bjerknes force with buoyancy, as in [2], we can see that the bubble should be displaced from the velocity node approximately 20μm at normal gravity. Therefore, water flows past the bubble at the time of collapse. Changes in gravity also change the ambient pressure at the bubble's location, as $\Delta P = \rho g h$, where h is the depth of the bubble. This gives a change of approximately –0.5% in our experiment when going from 1.8g to 0g. Studies of ambient pressure changes were also done in order to assess these effects.

Inside a pressure sealed chamber a spherical glass cell is filled with distilled water that has been degassed to 120mmHg. A bubble is then trapped in the center and driven by a piezoelectric transducer at 32.2kHz attached to the side of the cell. An optical system is then set up to take strobed video images and light emission data simultaneously. Temperature, pressure, drive voltage, and listener voltage are also monitored.

Figure 2 (two rows down on the left) shows the change in light output with the change in acceleration on the KC-135 aircraft. Figure 3 (below Fig 2) shows the bubble radii for the same set of data. Note that each 'spike' in the radius plot represents the growth and collapse of many cycles over a one-second period. From these graphs we can see that the light output and the maximum bubble radius both increase as the gravity decreases.

The radii of the bubbles for both experiments are fit using the Rayleigh-Plesset equation and the acoustic drive amplitude and the ambient bubble radius are found. There is little change in the acoustic drive amplitude as we expect, since we are not varying the drive voltage. However, the ambient bubble radius goes up considerably. These changes (increased light output, increased maximum bubble radius, and increased ambient bubble radius) are also observed when the ambient pressure is varied in the laboratory by an amount similar to that due to effective changes in the acceleration. The changes in the ambient bubble radius and light output with a change in ambient pressure are predicted by the "dissociation hypothesis"[3] and have been observed by other groups in the laboratory [4]. It seems clear that buoyancy's effect on light output and bubble radius are at best on the same order as the effects of ambient pressure.

Work funded by NASA NAG3-2114

[1]Holt, R.G., Gaitan, D.F., Observation of Stability Boundaries in the Parameter Space of Single Bubble Sonoluminescence, Phys. Rev. Lett., vol 77, 3791-3794, 1996

[2]Matula, T.J., Cordry, S.M., Roy, R.A., Crum, L.A., Bjerknes force and Bubble Levitation Under Single-Bubble Sonoluminescence Conditions, J. Acoust. Soc. Am., vol 102, 1522-1525, 1997

[3]Kondic, L., Yuan, C., Chan, C.K., Ambient Pressure and Single-Bubble Sonoluminescence, Phys. Rev. E, vol 57, R32-R35, 1998

[4]Dan, M., Cheeke, J. D. N., Kondic, L., Ambient Pressure Effect on Single Bubble Sonoluminescence, Phys. Rev. Lett., vol 83, 1870-1873, 1999

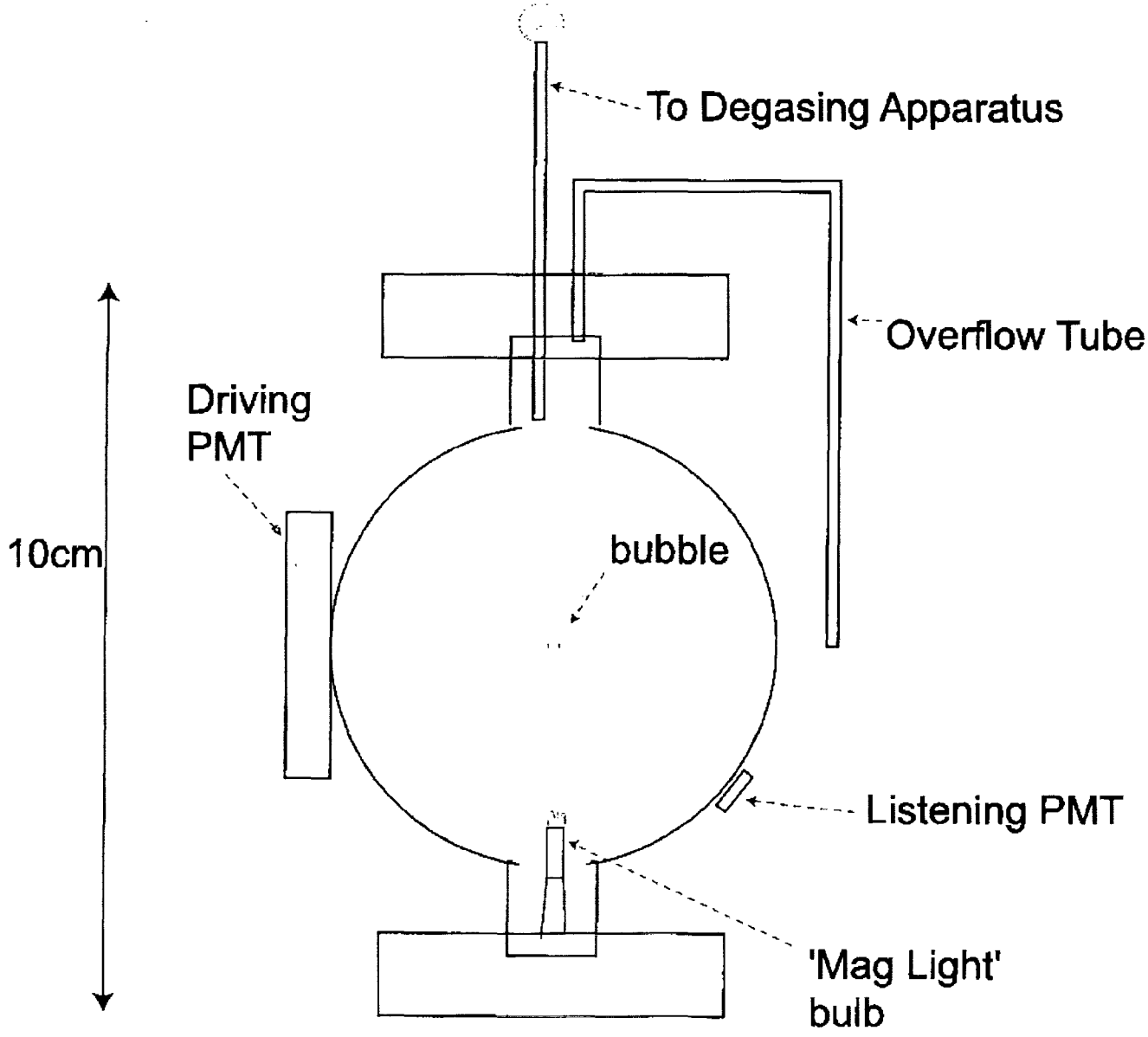

- Driving Frequency ~ 32.4kHz
- Water is degased to ~ 120mmHg
- Maximum bubble size for this frequency ~50 microns.
- Driven at first radial mode.
- Velocity Node and Pressure Anti-Node at Center.
- Light flash occurs at collapse, each acoustic cycle primarily UV and visible light.

Top View of Microgravity Sonoluminescence Experiment
Showing PMT/Laser Diode Switcher and Piezoelectric Devices

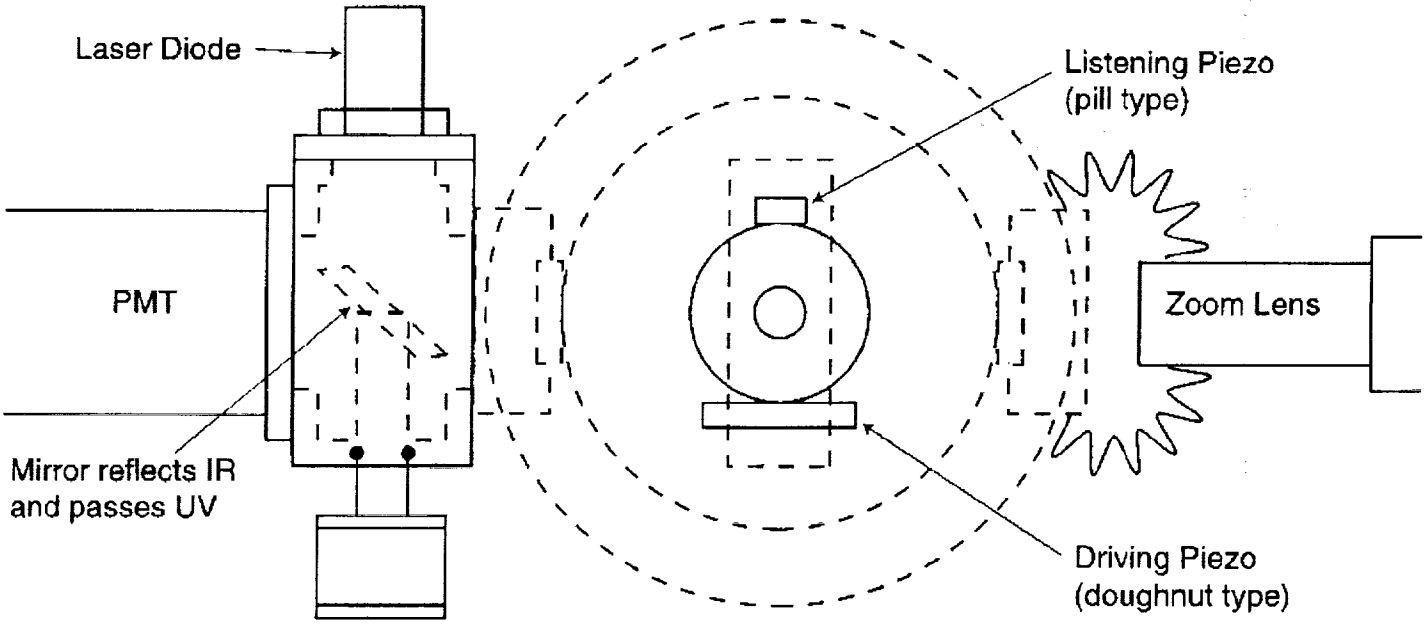

Figure 1

Video Investigation of the Effects of Gravity on Single-Bubble Sonoluminescence

Ben Dzikowicz, David B. Thiessen, Philip L. Marston
Washington State University
Physics Department
Pullman, WA 99164
dzikowic@wsunix.wsu.edu

In single bubble sonoluminescence (SBSL), a bubble in water emits a flash of light following its rapid collapse each cycle of oscillation of an ultrasonic field. Since widely varying length and time scales affect the bubble dynamics and optical emission processes, it is difficult to anticipate the importance of the effects of gravity present for observations on earth. In normal gravity, buoyancy displaces the bubble from the velocity node of the sound field so that water is flowing past the bubble at the time of collapse. Other gravitational effects include the variation in ambient pressure. Our measurements of SBSL light emission for a spherical resonator in NASA's KC-135 aircraft confirm that emission is not automatically quenched in the reduced and enhanced effective gravity conditions created during parabolic flight trajectories. We also measured the bubble radius as a function of time in the reduced gravity environment using strobed video. These measurements were fit to the Rayleigh-Plesset equation to infer the size and pressure conditions of spherical bubble oscillations. These were found to be similar to those reported by other groups for measurements in normal gravity. There are also indications that changes in the effective gravity are accompanied by small changes in the maximum bubble radius as well as by more easily observed changes in the light emission. Work supported by NASA.

Introduction

An air bubble in water will naturally rise due to the effects of buoyancy. We can prevent this from happening by placing the bubble in an acoustically resonating cavity driven at its first harmonic mode. The Bjerknes force will then keep it suspended in the center near the pressure antinode. The sinusoidally changing pressure will then drive the bubble to react as described by the Rayleigh-Plesset equation[1]:

$$R\ddot{R}+\frac{3}{2}\dot{R}^2=\frac{1}{\rho}(P_g(R)-P_0-P_a(0,t))-\frac{4\eta\dot{R}}{\rho R}-\frac{2\sigma}{\rho R}+\frac{R}{\rho c}\frac{d}{dt}(P_g-P_a)$$

Where P_a is the acoustical pressure, P_g is the pressure of the gas in the liquid and P_0 is the ambient pressure. At low pressure amplitudes the bubble simply reacts sinusoidally. At higher amplitudes the concentration of the gas in the water becomes important (related to P_g). When P_g is too small the bubble will eventually dissolve in the water, when P_g is too big then the bubble will grow too large and the buoyancy will take over[2]. However, there is a large region where the neither of these two things occurs and the bubble acts in a nonlinear but regular way.

In this region the bubble will slowly grow to a large size (50 to 200μm) and then collapse violently, only to rebound a few times and then repeat the process. In a resonant cell of about 4cm radius this occurs at a rate of about 34kHz. This is much slower than the monopole resonance of the bubble itself. At the collapse a short burst of broad spectrum, UV and visible light appears. This burst lasts a very short time, around 150ps[3]. Light output due to cavitation is only beginning to be understood.

Gravitational Issues

For some time the symmetry of the collapse and its contribution to the light output has been debated. The bubble is not exactly at the velocity node[4], as the buoyant force is acting on the bubble as well as the Bjerknes force to push the bubble away from the node. Therefore there is fluid motion around the bubble which may cause it to react to the pressure change in a non-symmetrical way. It is difficult to directly observe the collapse of a bubble since it happens so fast and is so small at its final collapse (~1μm). We cannot then tell if the bubble is still spherical

when it emits light. We can, however, remove gravity and observe changes in the bubble's light output, maximum bubble size, and bubble position to try and understand the effects of buoyancy.

There is a problem however, removing gravity does not only change the buoyancy of the bubble, but it also changes the hydrostatic pressure around the bubble. This pressure change appears as a change in ambient pressure, P_o, in the Rayleigh-Plesset equation. There is a pressure drop of about 4mmHg for a change of 1.8g to 0g (a typical transition on NASA's KC-135 aircraft). Other ground based work indicates that with constant driving pressure a decrease in ambient pressure should be accompanied by an increase in light output and maximum bubble radius[5]. Increased maximum bubble radius typically accompanies increased light output when various parameters are altered, and is therefore a good indication that nothing unexpected is going on. With larger size comes more violent collapse and hence brighter light, but without larger size brighter light would indicate another mechanism is affecting the light output.

Not only is the ambient pressure at the bubble's location affected, but when gravity is present, there is a pressure gradient from the top of the cavity to the bottom. At reduced gravity this gradient is gone and the whole cavity is at atmospheric pressure. This may alter the acoustic field in a manner that would affect light output.

Experimental Set Up

We use a 4cm radius spherical glass cell with necks at the top and bottom. Then distilled water, which has been degassed to a pressure of about 120mmHg, is drawn into the top neck of the flask. The entire water system is continuous and sealed so the gas concentration remains constant during filling. Epoxied to one side of the flask is a doughnut shaped piezoelectric transducer to drive the cell, and on the other is a smaller transducer that we monitor in order to tune the system. The system is driven using a function generator into an audio amplifier then into a step-up matching transformer. This allows us to get the 100 to 300V signal we use to drive the cell. The frequency of our system is about 34.2kHz, this varies day to day with temperature and other environmental factors. Once the cell is in the correct mode a 'MagLite' flashlight bulb, which extends through the bottom neck of the flask, is used to create a bubble. By sending a short burst of current through the filament the water is quickly boiled and a bubble rises quickly to the center of the cell. We can then adjust the drive amplitude to give us good light output.

The entire cell is enclosed in a pressure tight chamber in order to block cabin pressure changes that occur on the KC-135 due to dramatic altitude changes. There are quartz windows on each side of the chamber. Into one goes a CCD camera to take strobed video of the bubble, and into the other goes a Photomultiplier Tube (PMT) for the measurement of the bubble's light output. Since the camera needs be strongly backlit to get good images and the PMT must measure the very small light output of the bubble simultaneously, a system was developed to keep these separate using separate wavelengths for each measurement. A mirror which passes UV and visible but reflects IR is placed at a 45° angle and the PMT is placed behind it. In addition a colored glass filter is placed on the PMT to keep stray IR light out. An IR laser diode pointing into the mirror is then able to provide the backlighting necessary for the CCD. This diode is then set to deliver a 100ns pulse, 1Hz slower than the drive frequency. Then we are able to observe 30μs bubble collapses over a period of one second. This setup is unique and allows us to obtain both light output and bubble simultaneously [Figure 1.].

This whole apparatus is then strapped to the floor of NASA's low-gravity KC-135 aircraft which flies in a parabolic trajectory giving cycles consisting of about 20 seconds of 0g and 45s of 1.8g. During the flight we monitor many parameters, besides the light output and the video data, we also record pressure and temperature within the chamber, drive transducer voltage, listener transducer voltage and acceleration. These are recorded at a rate of 20Hz using LabView software.

In order to simulate a change in pressure due to the varying gravity lab experiments were also done. The sealed chamber was attached to a small volume of low pressure, this was then used

to draw the ambient pressure around the bubble down 5mmHg from atmospheric. Then the pressure was released simulating the change in pressure due to gravity. This data was analyzed in the same manner as the flight data.

Data Analysis

The 20Hz parameter data is averaged using a sliding average over 0.5 seconds. The video data is less straightforward, since the optical system used limits the contrast of the images. First the frames are deinterlaced, and then background subtraction is done. After that a FFT filter is applied to reduce high frequency noise. An edge finding program is used to extract the radius and location of the bubble. Events such as turning on and off the PMT and the backlighting simultaneously are then used to line up the two data sets.

Results and Conclusions

Note: Accompanying graphs of radii show peaks not smooth lines. This is due to time scale differences, each peak is actually an acoustic cycle showing the growth and collapse of the sonoluminescing bubble. At this scale these appear as spikes.

Preliminary analysis shows, as confirmed elsewhere[6], that the light output increases as the gravity is reduced [Figure 2.]. We have also shown that the maximum bubble radius increases along with the light output [Figure 3.]. The bubble also moves, but not in a vertical direction as we would expect by just removing the buoyancy. It moves instead in a diagonal direction. For further insight into these results we can look to the ambient pressure tests done in the laboratory.

The tests done in the lab to mimic the pressure changes due to gravity show very similar results. Light output increases and maximum bubble radius increases [Figures 4 and 5.]. This suggests that the increase in light output is due, at least in part, by the change in hydrostatic pressure. As for the bubble's location, it also moves in a similar diagonal way as the bubble in the flight. This is more difficult to interpret, but it suggests that the sound field in the cell is changing in manner not anticipated as the pressure changes. In attempting to predict results the assumption is made that the geometry of the acoustic field is symmetrical and static. This may not be the case, as the changes in pressure and gravity may be altering the field near the center of the flask.

In conclusion, any changes in the light output due to buoyancy will not be easy to detect. Changes in the ambient pressure and the acoustic field make buoyant effects and the symmetry of the collapse difficult to measure. Running the experiment at a lower frequency (i.e. a larger cell) would produce bubbles with higher volume and hence greater buoyancy. This upscaling may allow the observation of buoyant effects. However, the bubble's response to ambient pressure may prove at least as interesting as the changes in buoyancy.

Figures

Figure 1. Top View of Microgravity Sonoluminescence Experiment Showing PMT, Laser Diode, and Piezoelectric Devices.

Figure 2. Gravity and Light Output

Figure 3. Gravity and Bubble Radius

Figure 4. Pressure and Light Output

Figure 5. Pressure and Bubble Radius

References

[1]Barber, B. P., Hiller, R.A., Lofstedt, R., Putterman, S.J., Weninger, K. R., Defining the Unknowns of Sonoluminescence, Physical Reports, vol 281, 65-143, 1996

[2]Holt, R.G., Gaitan, D.F., Observation of Stability Boundaries in the Parameter Space of Single Bubble Sonoluminescence, Phys. Rev. Lett., vol 77, 3791-3794, 1996

[3]Gompf, B., Gunther, G.N., Nick, G., Pecha, R., Eisenmenger, W., Resolving Sonoluminescence Pulse Width with Time Correlated Single Photon Scattering, Phys. Rev, Lett., vol 79, 1405-1408, 1997

[4]Matula, T.J., Cordry, S.M., Roy, R.A., Crum, L.A., Bjerknes Force and Bubble Levitation under Single-Bubble Sonoluminescence Condtions, J. Acoust. Soc. Am, vol 102, 1522-1525

[5]Dan, M., Cheeke, J. D. N., Kondic, L., Ambient Pressure Effect on Single Bubble Sonoluminescence, Phys. Rev. Lett., vol 83, 1870-1873, 1999

[6]Matula, T. J., private communication

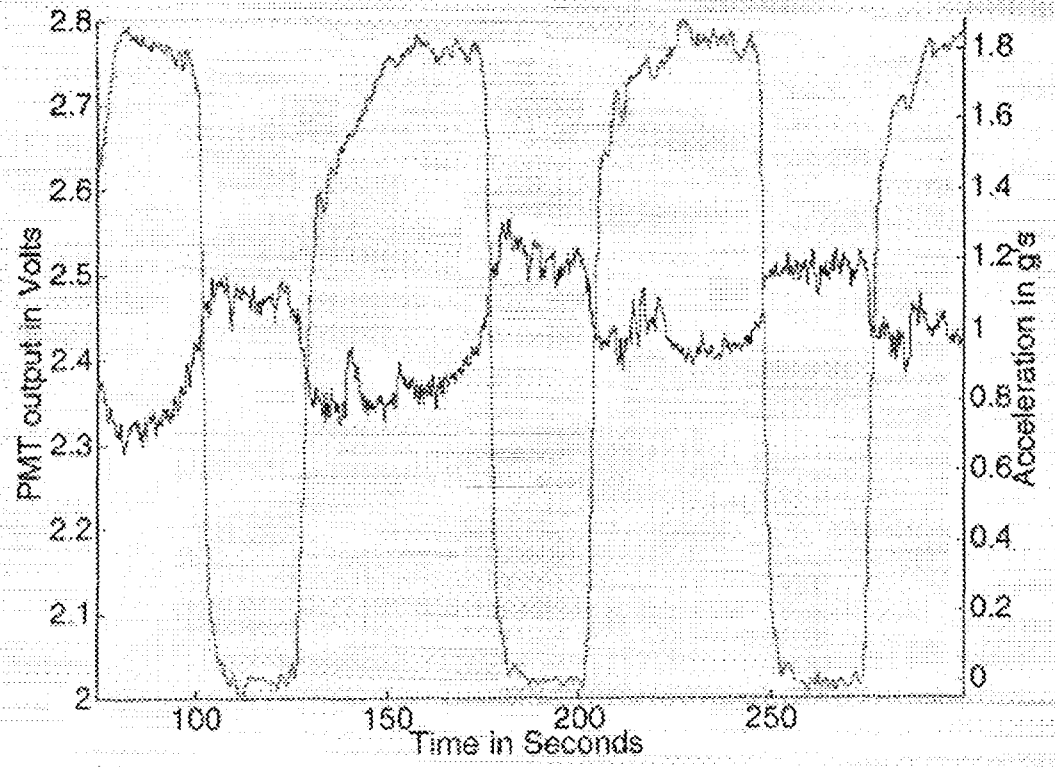

Figure 2 – Acceleration in red

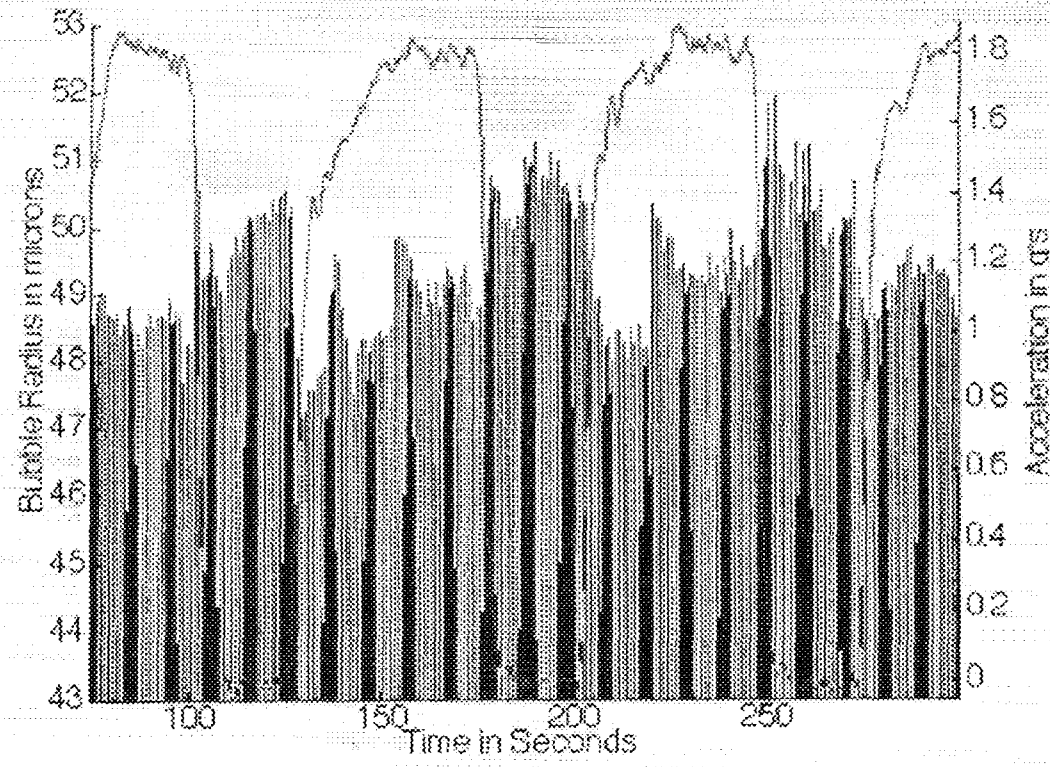

Figure 3 – Acceleration in red

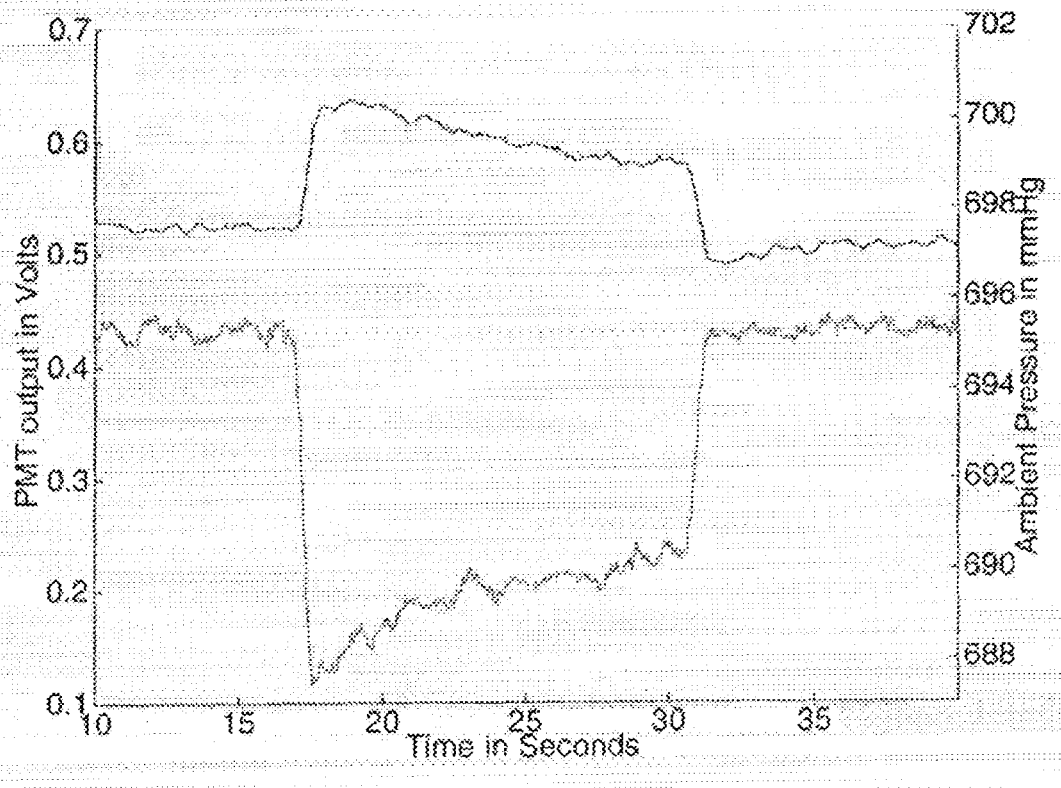

Figure 4 – Ambient Pressure in red

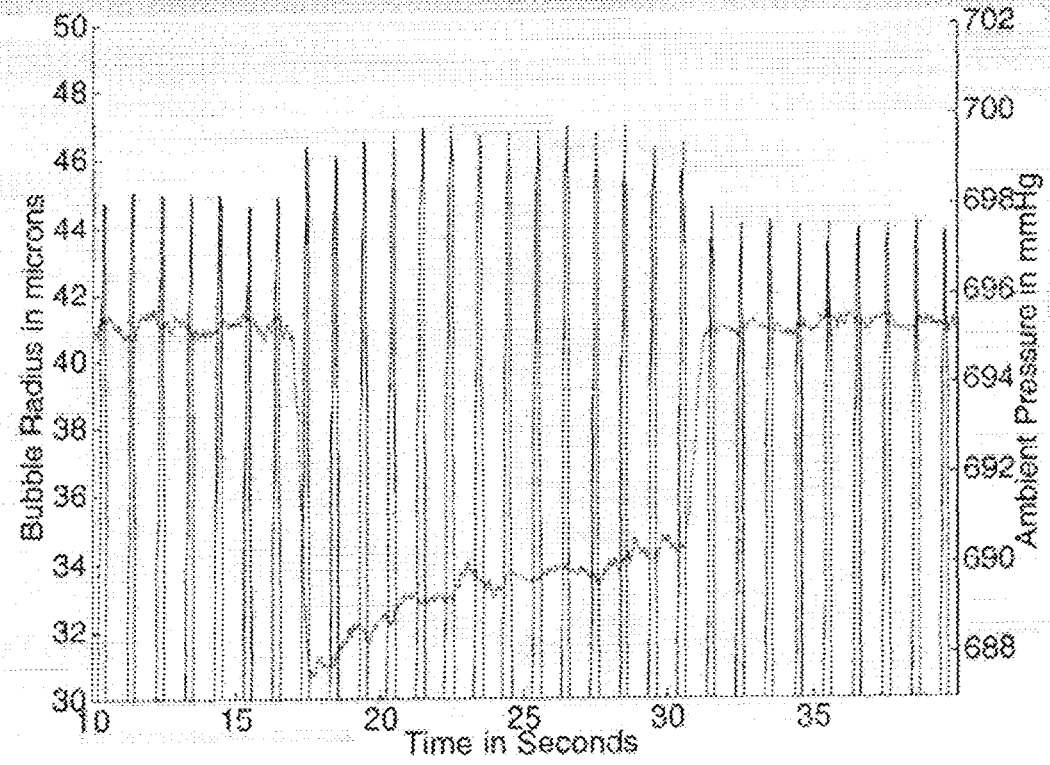

Figure 5 – Ambient pressure in red

Rayleigh – Plesset equation fit to radius data at high g, showing reduced R0

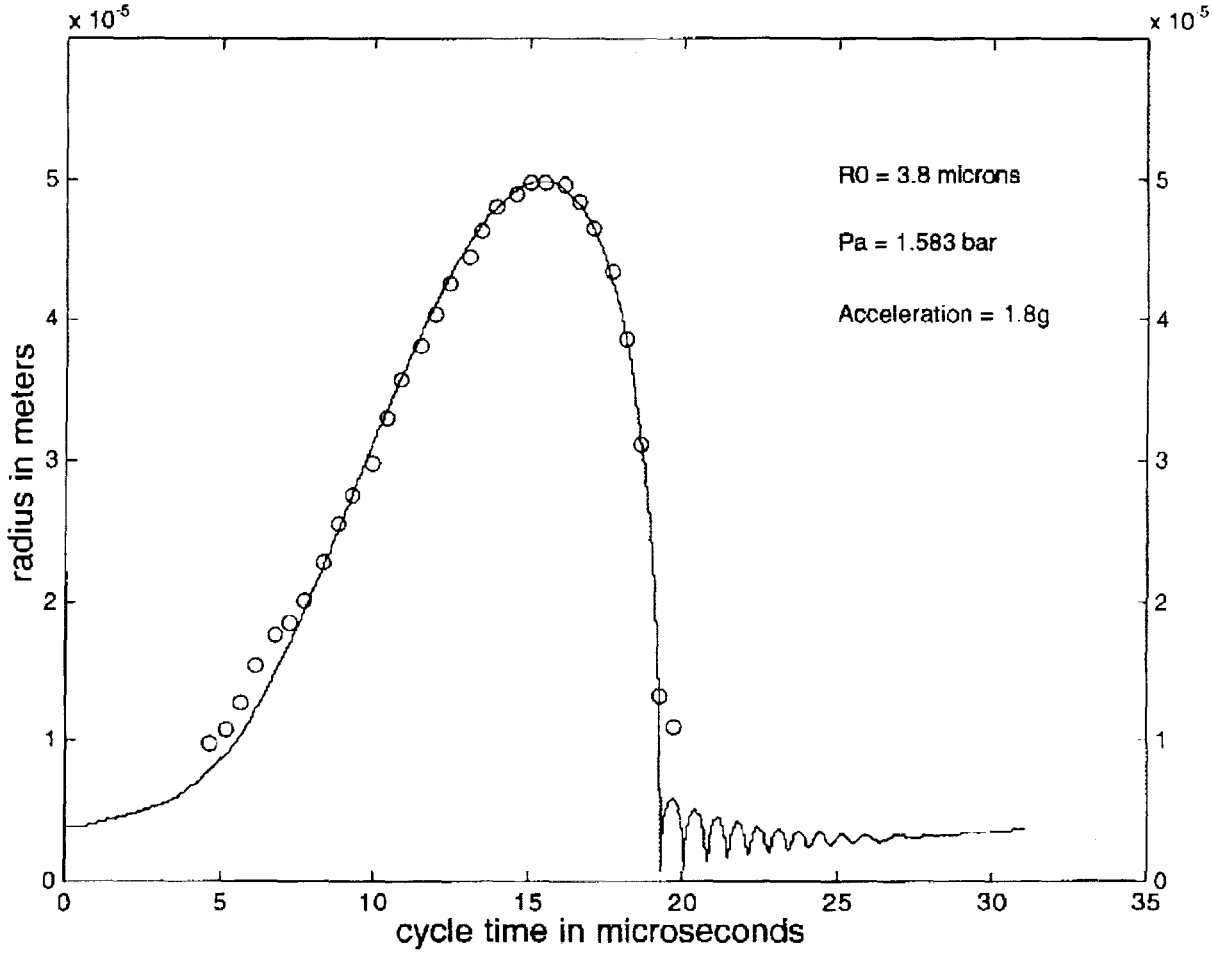

Rayleigh – Plesset equation fit to radius data at low g, showing increased R0

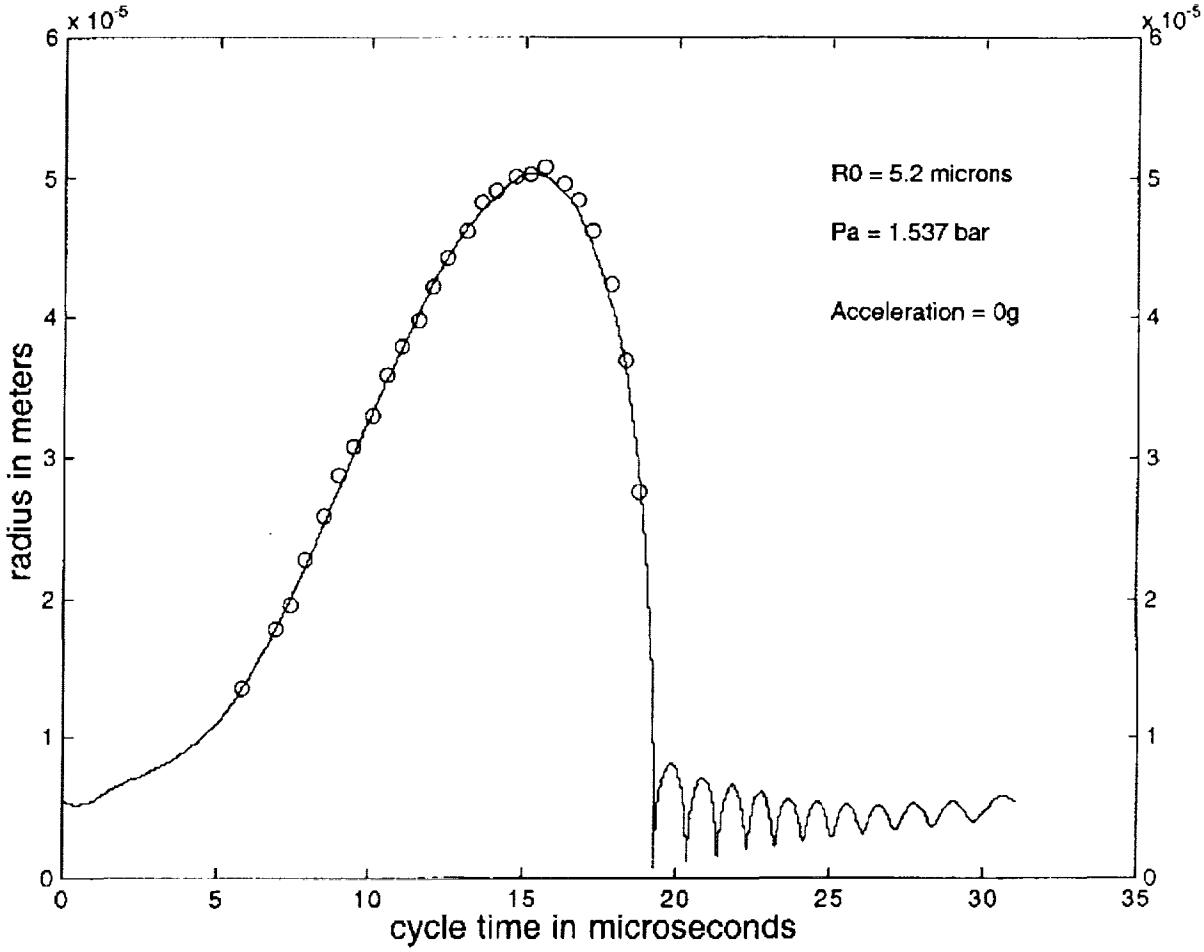

This series of images is taken from the video data at reduced gravity. Each frame represents about 2 microseconds of time. It is actually strobed data taken with a standard video camera; therefore each image is actually thousands of images averaged together.

The frames are deinterlaced and a blank frame is chosen as a background image and subtracted from the remainder of the frames.

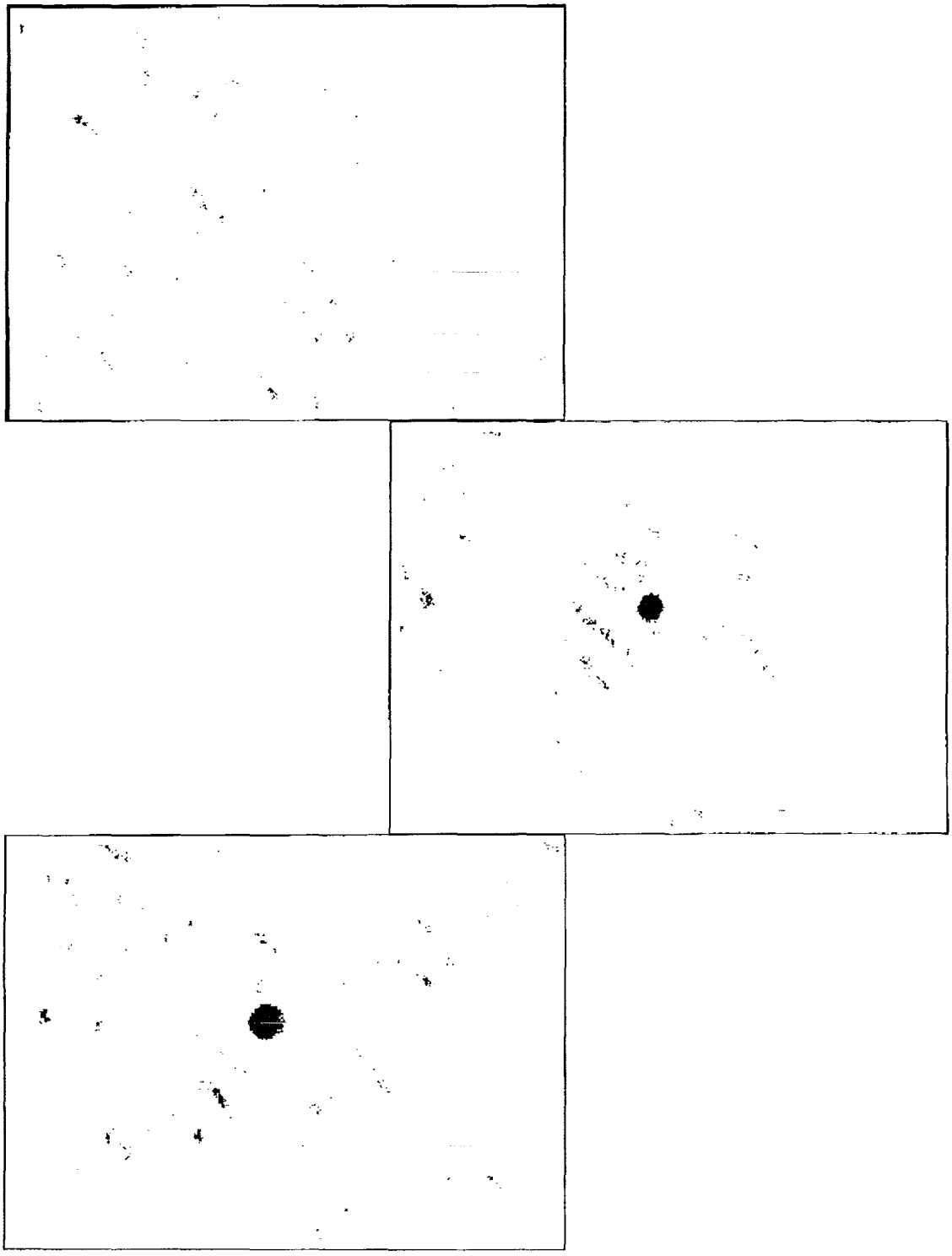

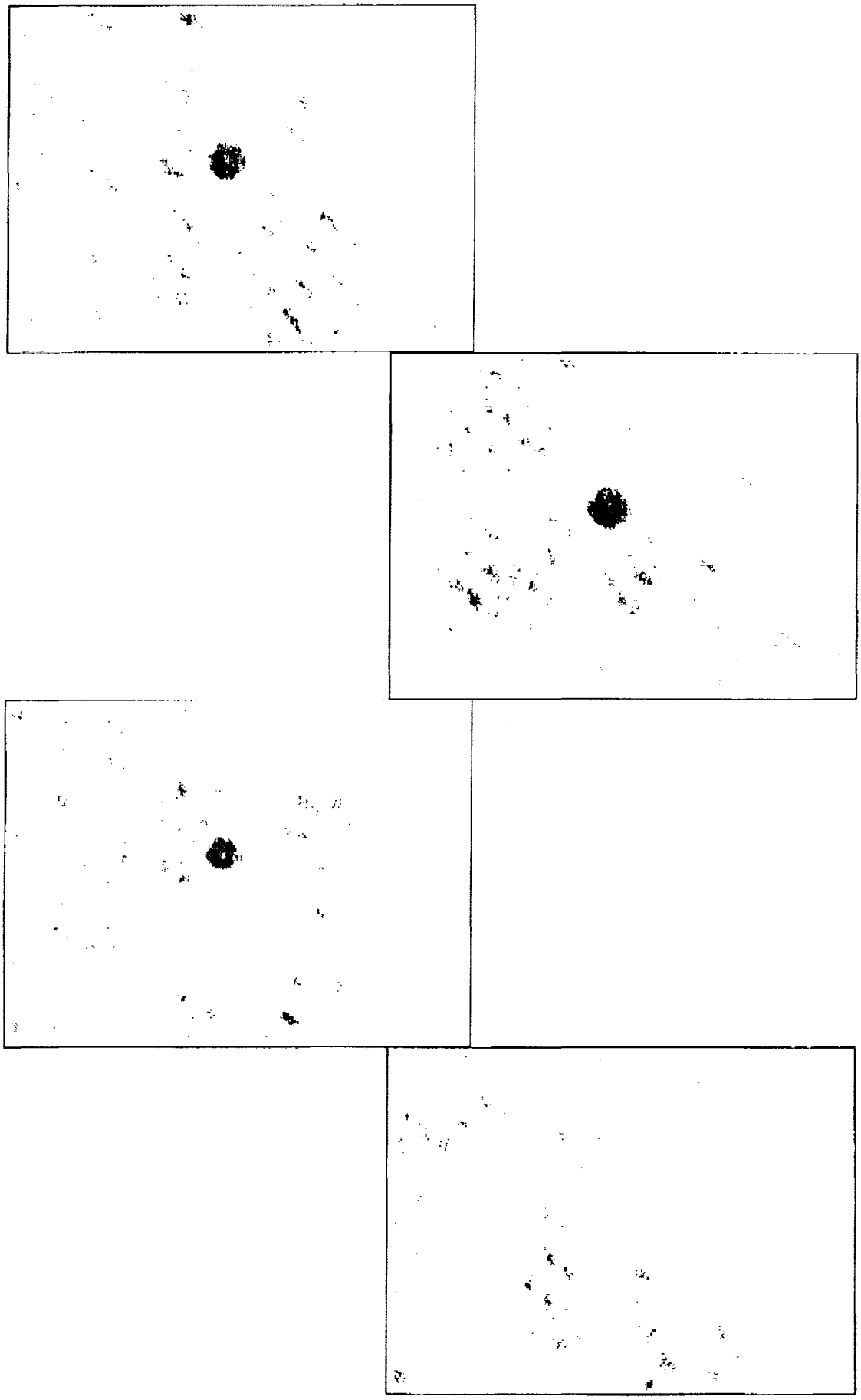

Approximate changes

		flight data	lab data
Ambient Pressure	$\Delta P_0/P_0$	-0.45%	-0.70%
Light Output	$\Delta I/I$	5%	15%
Maximum Bubble Radius	$\Delta R_{max}/R_{max}$	5%	5%
Ambient Bubble Radius	$\Delta R_0/R_0$	25%	27%

flight data -

Data taken on the KC-135 from two cycles 20s apart the first at 1.8g and the second at 0g.

lab data-

Data taken in the lab from two cycles 10s apart, the first at atmospheric pressure and the second .007 bar below that.

Conclusions

- Light output is not quenched with reduced gravity.

- Light output increases with reduced gravity.

- Maximum bubble radius increases with reduced gravity.

- R_0 increases with reduced gravity

- Diffusion models and lab experiments suggest that much of the light and radius increases may be due in part to hydrostatic changes.

- Asymmetries in the acoustic field make buoyant effects difficult to detect.

Optical manipulation of bubbles in water using solid-state laser technology

P. S. Jian
W. E. Torruellas*
D. B. Thiessen
Philip L. Marston

Department of Physics
Washington State University
Pullman, WA 99164-2814

marston@wsu.edu

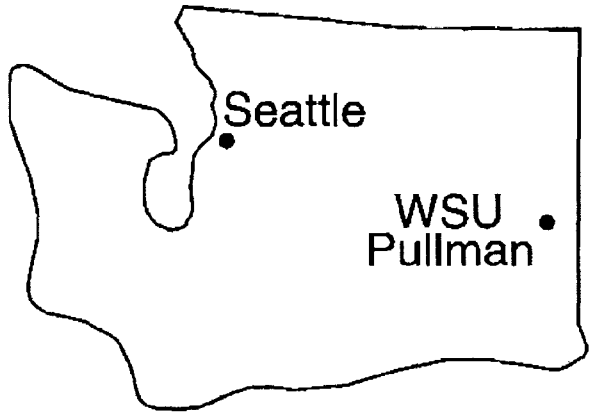

*Present address: Corvis Corp., Columbia, MD.

Research supported by NASA NAG3-2114

1. Unger and Marston, "Optical levitation of bubbles in water by the radiation pressure of a laser beam: An acoustically quiet levitator," J. Acoust. Soc. Am. **83**, 970-975 (1988).

2. P. S. Jian, "Spatio-Temporal Control in Intracavity Nonlinear Optics," PhD. Thesis, WSU (2000).

3. R. Iliew et al, "Generation of donut-like patterns in intracavity-second-harmonic-generation," submitted to JOSA B.

Optical Trapping of a Bubble in a Focused Beam

Bubbles are trapped near the high intensity focal region of a beam with a minimum intensity at the center as a result a donut-like laser beam is required.

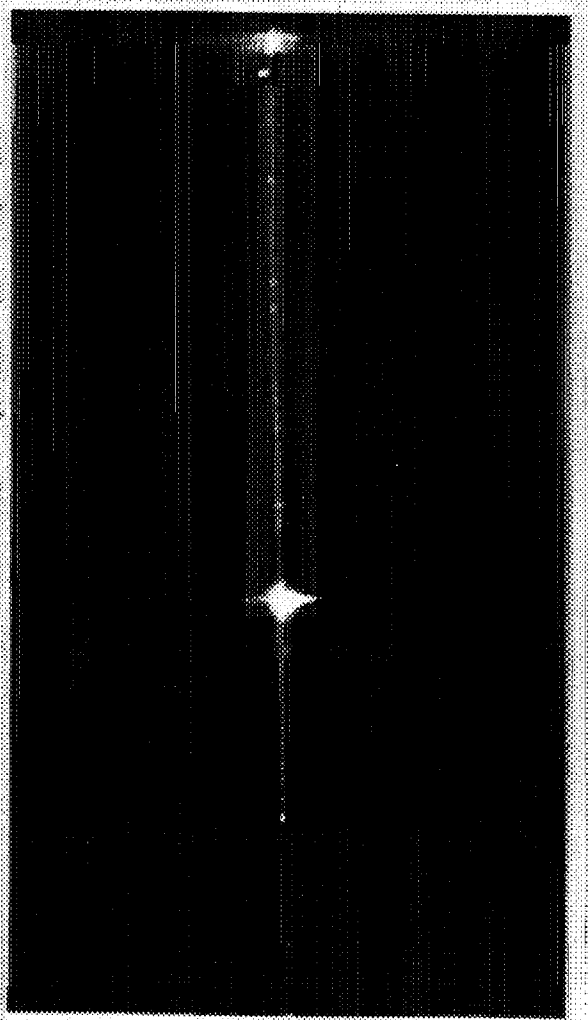

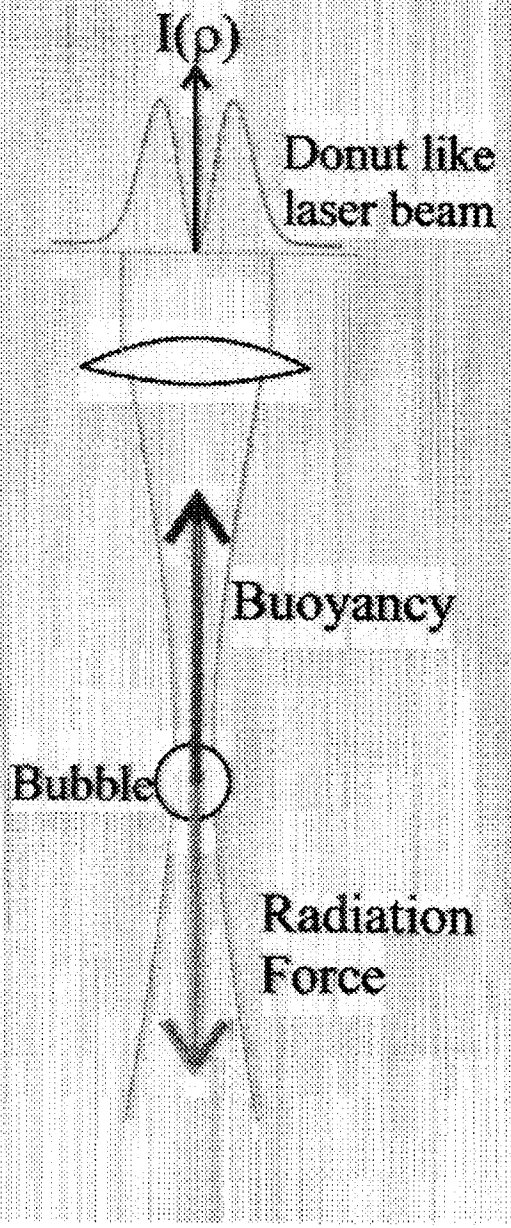

Experimental Setup and the Beam Profile used to Trap the Bubbles in the Water

Schematic of Frequency Doubling Laser Setup

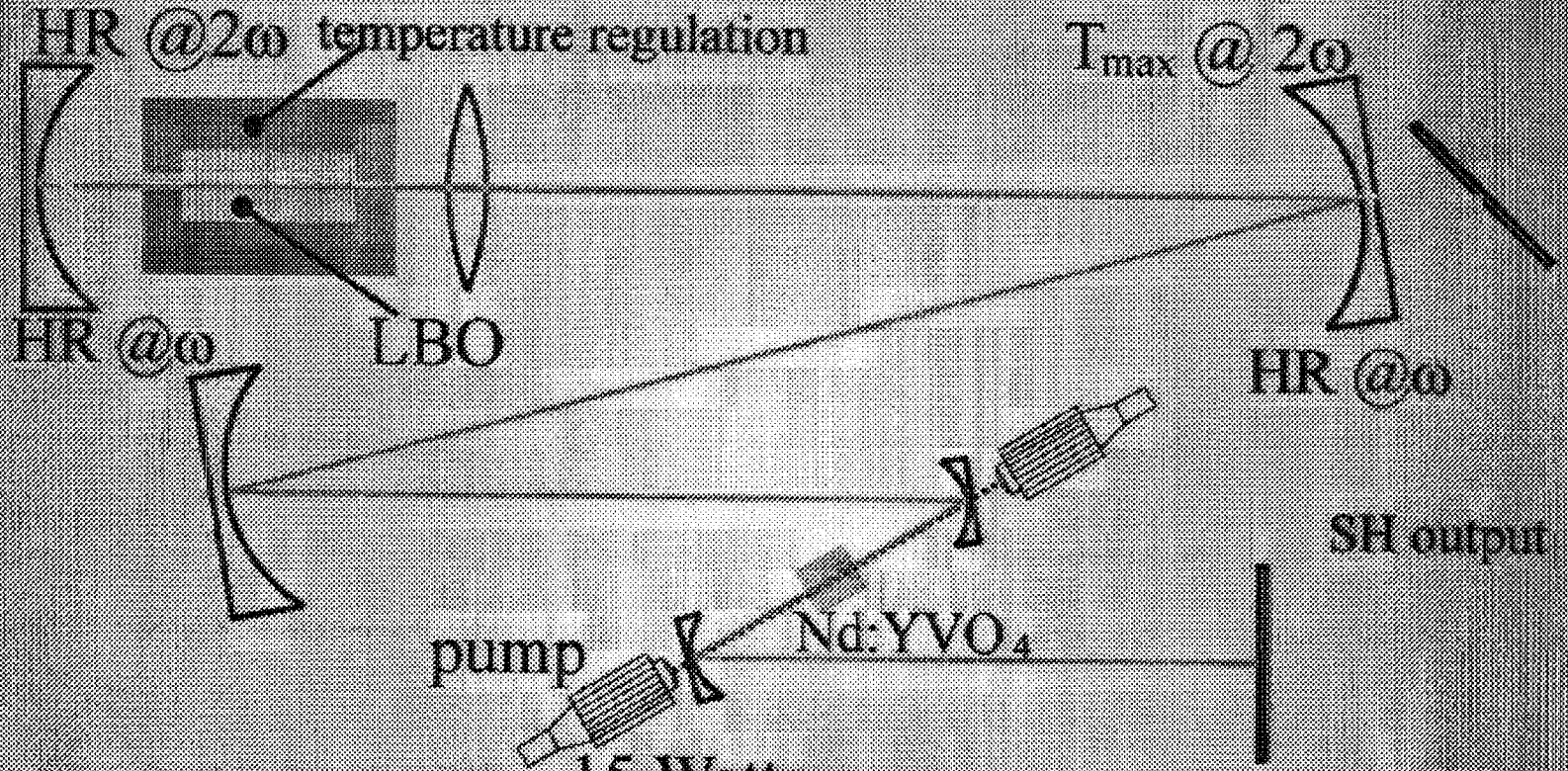

ω: frequency at λ=1064nm, 2ω: frequency at λ=532nm
LBO: second order nonlinear crystal, Nd:YVO_4: the laser rod

Laser Crystal:

Neodymium doped Yttrium-Vanadate (Nd:YVO_4)

Wavelength = 1064 nm

Pumped with water cooled CW diode lasers

Second Harmonic Crystal:

Lithium-TriBorate (LBO)

Second Harmonic Wavelength = 532 nm

CW Power Output: 5.5 W

Laser and second-harmonic generation model in:

"Generation of doughnut-like patterns in intracavity-second-harmonic-generation" submitted to JOSA B.

R. Iliew, P. Jian, Y. Frignac, W. Torruellas, F. Lederer

Support for laser development: NSF, WSU, NASA

ATOMIZATION PROCESSES IN FLUID-FLUID FLOWS: PREDICTION OF THE FREQUENCY OF THE PRECURSOR SOLITARY WAVES

M. J. McCready, B. D. Woods, D. T. Leighton
Department of Chemical Engineering, University of Notre Dame, Notre Dame, IN, 46556,USA,
mccready.1@nd.edu

ABSTRACT

Atomization is an important issue for both process scale fluid-fluid flows on earth and possible energy exchange devices in microgravity. Currently the fraction of entrained liquid in process flows (e.g., annular gas-liquid flow) is predicted with correlations [1] based on dimensional analysis and tuned with data over limited ranges of parameters. These correlations, while the best available, are generally inaccurate and unreliable as they are not based on the fundamental mechanisms. Improvements will require better understanding of atomization, that occurs from the crests of the largest waves and deposition which depends on the turbulent structure and the droplet concentration of the dispersed flow within the center of the pipe. A further crucial issue is prediction of the frequency of solitary waves, that strongly affects the atomization rate and for which there are no current theories.

Our work on this topic is intended to examine all aspects of the atomization process. Linear and nonlinear theory is applied to the two-layer base film with the intention of predicting wave formation. Evolution equations are applied to the finite amplitude waves to determine if they will grow to large amplitude. Experiments are used to verify the wave formation mechanism and to verify the scaling with system parameters. The mechanism of atomization is directly examined experimentally in our matched-density, two-fluid rotating Couette experiment.

This poster will report on our theoretical and experimental efforts characterize the frequency of the waves from which atomization occurs. The first issue in any wave formation problem is prediction of the linear stability of the gas-liquid basestate. We have used a separated flow model, that uses measurements of turbulent flow over wavy surfaces to predict the pressure and shear stress boundary conditions. The liquid phase is computed from the Orr-Sommerfeld equation. We have also used a k-ε turbulence model and solved the Orr-Sommerfeld equations for both phases. For both cases we present general scaling relations for the growth rates and fastest growing wavelengths. This information is used with measurements of solitary wave frequency to develop a predictive procedure for the frequency of solitary waves as a function of shear and fluid properties. It is found that the turbulence stability models give growth rates much higher (e.g., factors of 5 or more) than would be predicted by any laminar theory at similar interfacial shear. Wavelengths of the fastest growing waves also differ from laminar predictions. A correlation for solitary wave frequency that relies on the liquid substrate thickness and the balance between dispersion and nonlinear sharpening of a solitary wave is compared to a method that uses only linear stability predictions.

REFERENCES

[1] Schadel, S. A., G. W. Leman, J. L. Binder and T. J. Hanratty, "Rates of atomization and deposition in vertical annular", *Int. J. Mult. Flow* , **16** , 363-374 (1990).

NASA/CP—2000-210470

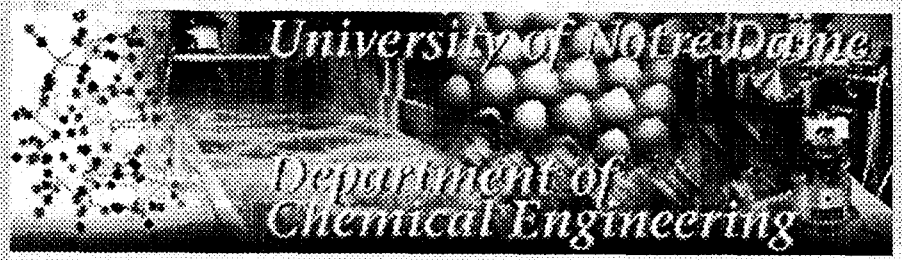

Atomization Processes in Fluid-Fluid Flows: Prediction of the Frequency of the Precursor Solitary Waves

Mark J. McCready, Bennett D. Woods
Department of Chemical Engineering
University of Notre Dame

http://www.nd.edu/~mjm mjm@nd.edu

The big issue in two-phase flows

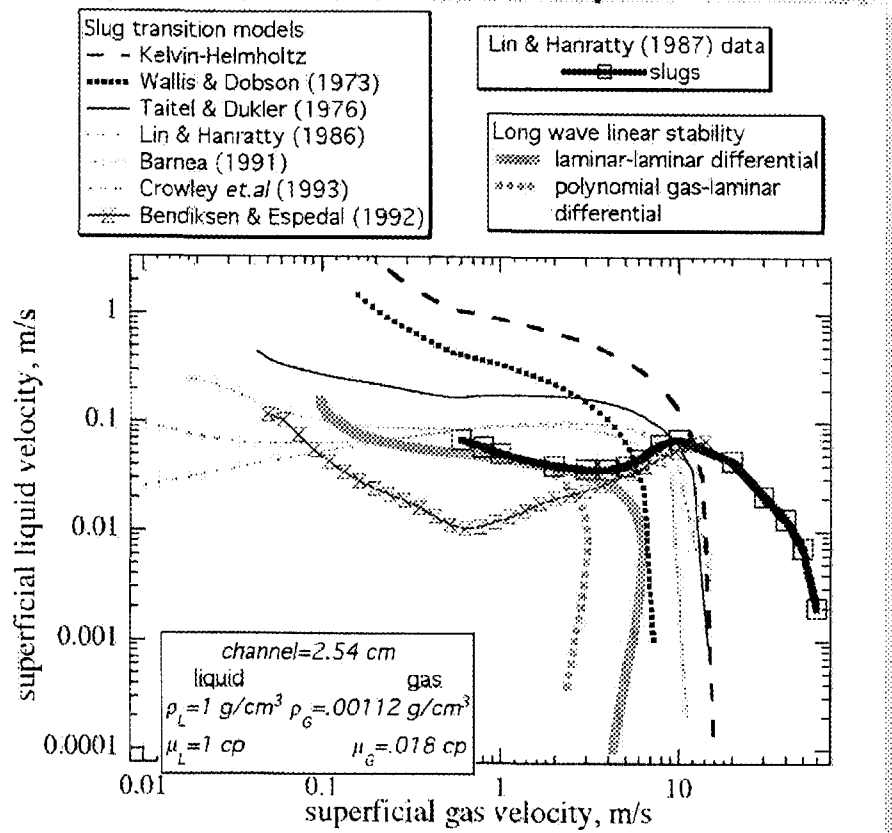

http://www.nd.edu/~mjm mjm@nd.edu

Importance of atomization

- Phase change process affected by liquid on the wall
- Pressure drop, transport rates in annular flow
- Applications
  - Power bus for long duration space flight
  - "Optimal" gas-liquid mass transfer process will involve some atomization,and some special overall fluid geometry

http://www.nd.edu/~mjm mjm@nd.edu

Starting geometry of interest

Two-fluid stratified flow

http://www.nd.edu/~mjm mjm@nd.edu

Classic result: Atomization Mechanism (Woodmansee, Hanratty, 1969)

Questions remaining:
Is this a generic result?
What parameters are involved?

http://www.nd.edu/~n

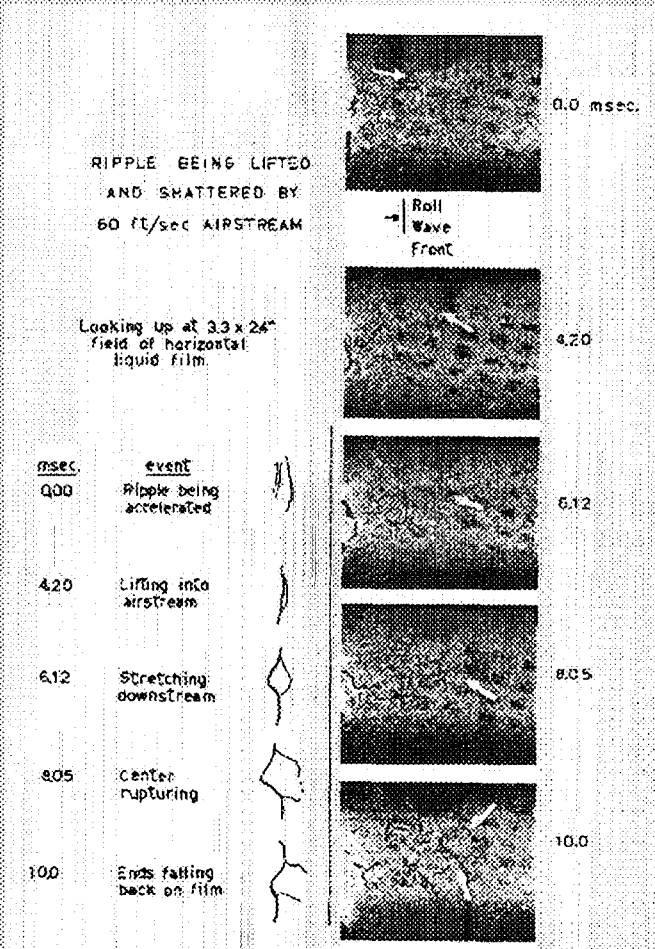

Fig. 5. Ripples being lifted and shattered by 60 ft/sec airstream.

Two-(matched density) liquid, rotating
Couette device
Steady and Oscillatory Flows were studied

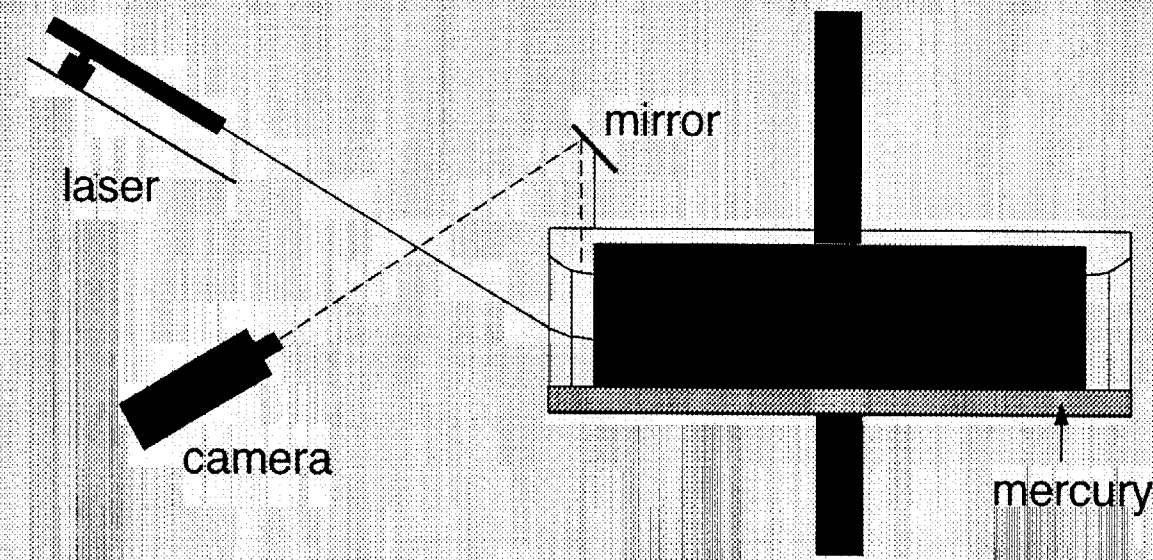

http://www.nd.edu/~mjm
mjm@nd.edu

Rotating Couette experiment

http://www.nd.edu/~mjm mjm@nd.edu

Wave map for rotating Couette flow experiment

Gallagher, Leighton and McCready, *Phys. Fluids*,1997

Left of the line, only short waves are unstable

Regions of "no waves" exist where long waves are unstable

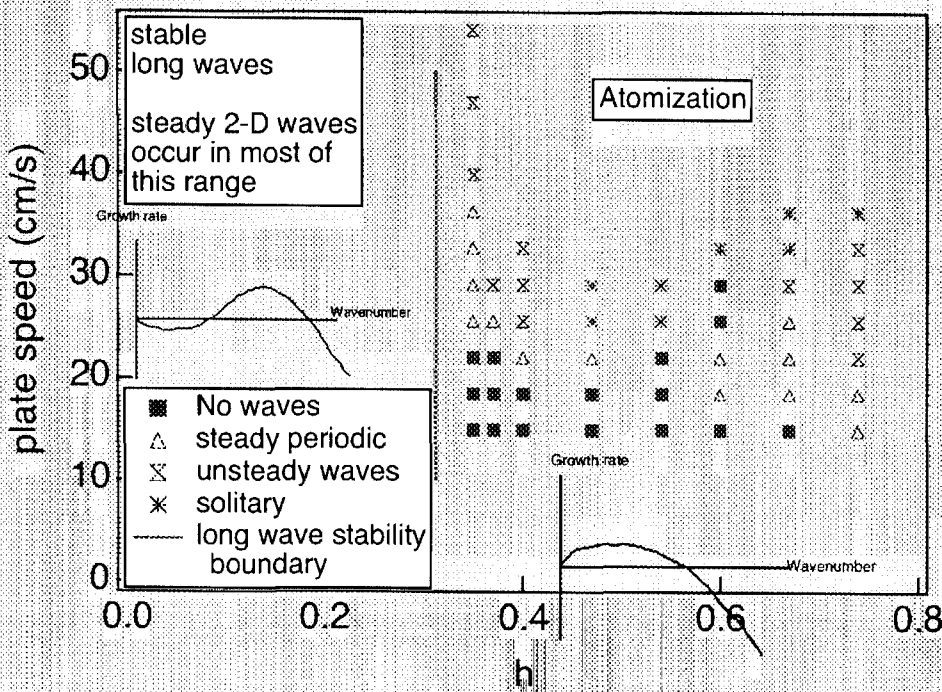

http://www.nd.edu/~mjm mjm@nd.edu

Figure 3: A roll wave for m=0.0159, σ = 0.01 N/m, I = 0.66, and U_p = 84 cm/s. ("Dark" phase is more viscous and it is being atomized)

vRe_{light} = 560 Re_{dark} = 9.5

http://www.nd.edu/~mjm mjm@nd.edu

Figure 4: A sheet-like structure for m=0.0159, σ = 0.01 N/m, I = 0.66, and U_p = 84 cm/s. ("Dark" phase is more viscous and it is being atomized)

http://www.nd.edu/~mjm mjm@nd.edu

Figure 5: A sheet-like structure just prior to break off for m=0.0159, σ = 0.01 N/m, I = 0.66, and U_p = 84 cm/s. ("Dark" phase is more viscous and it is being atomized)

http://www.nd.edu/~mjm mjm@nd.edu

A series of frames 2 milliseconds apart showing the breakup.

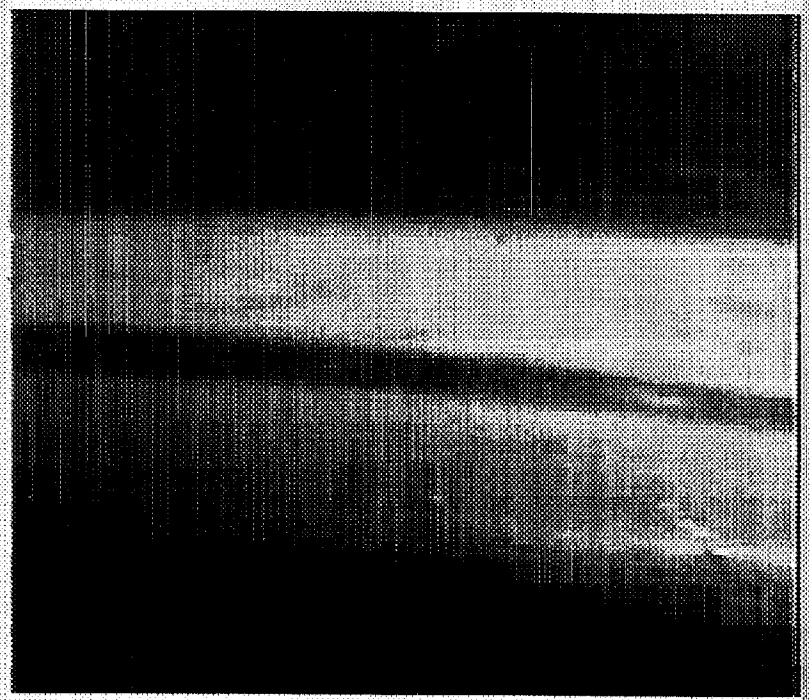

http://www.nd.edu/~mjm mjm@nd.edu

A series of frames 2 milliseconds apart showing the breakup.

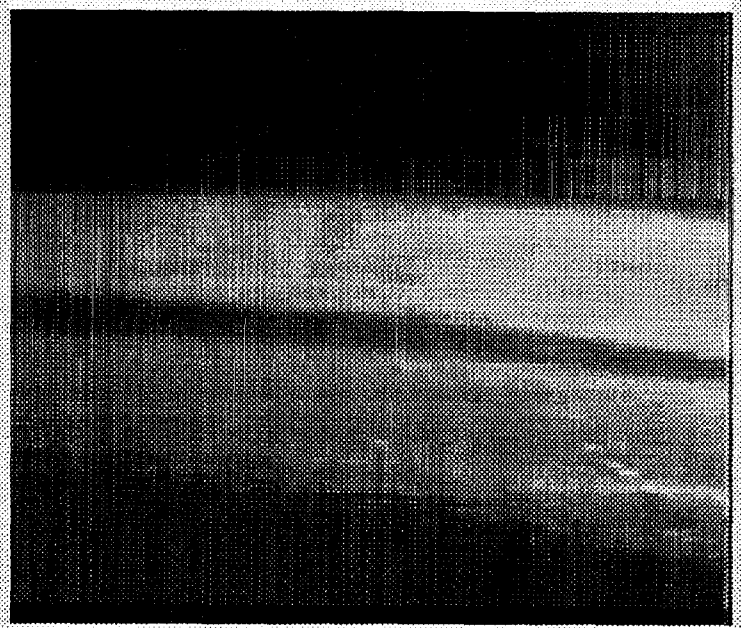

http://www.nd.edu/~mjm mjm@nd.edu

A series of frames 2 milliseconds apart showing the breakup.

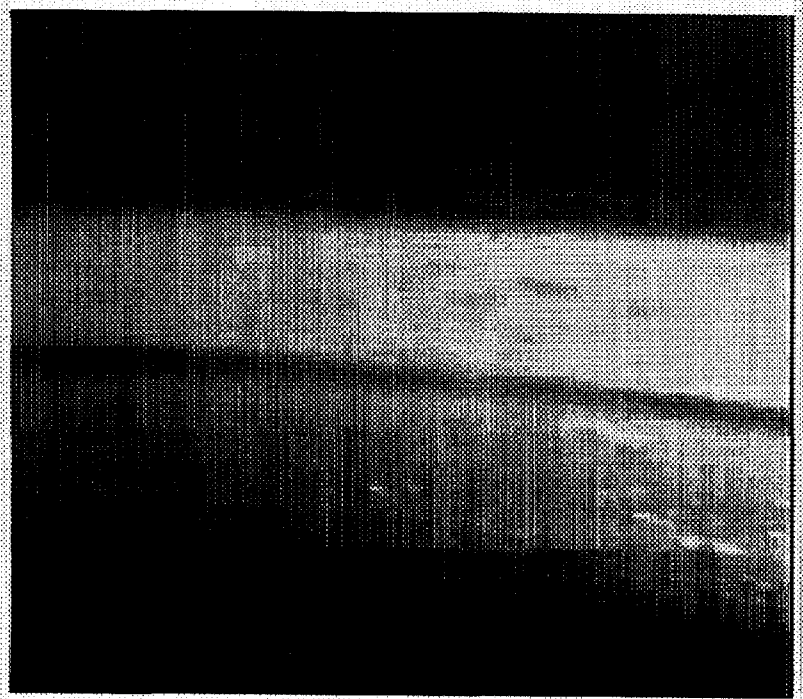

http://www.nd.edu/~mjm mjm@nd.edu

Breakup Occurs

http://www.nd.edu/~mjm mjm@nd.edu

Oscillatory results

- Interfacial wave formation by a unique mechanism that involves generation of an internal mode in the less viscous phase
  - Caused by inflection of the velocity profile similar to Fjortoft's mechanism
- Atomization is not observed in oscillatory flows

http://www.nd.edu/~mjm mjm@nd.edu

Oscillating Couette experiment

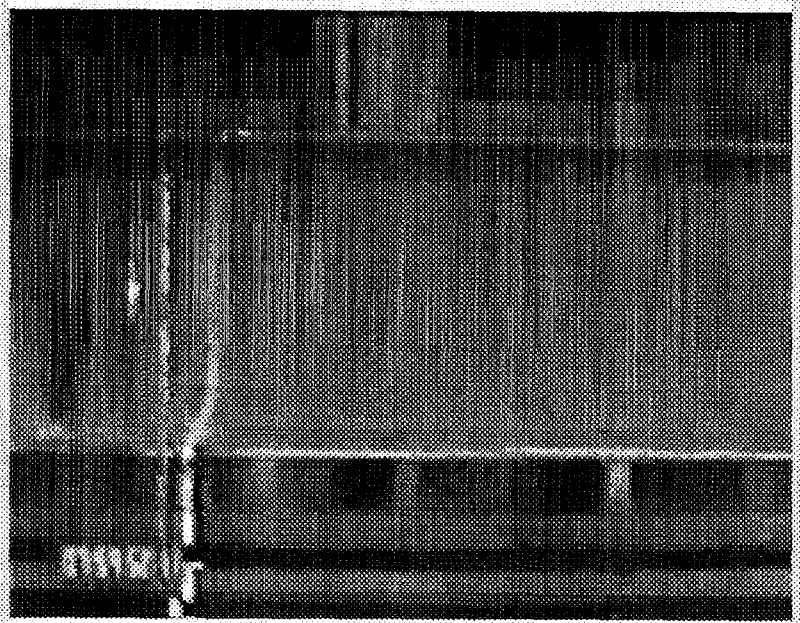

http://www.nd.edu/~mjm mjm@nd.edu

Measured and predicted growth rates

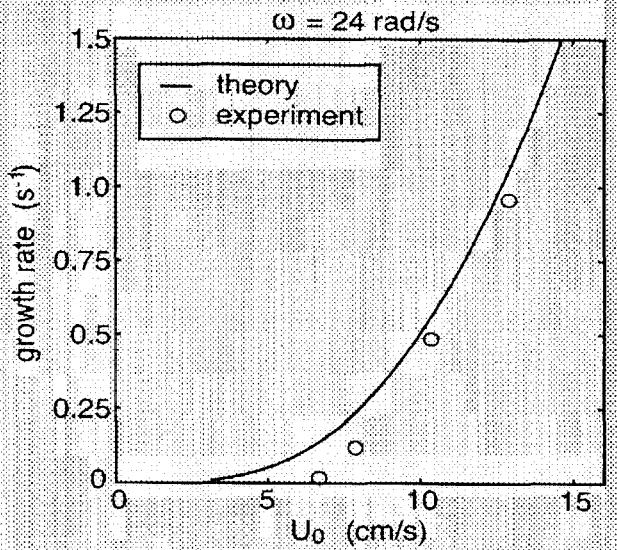

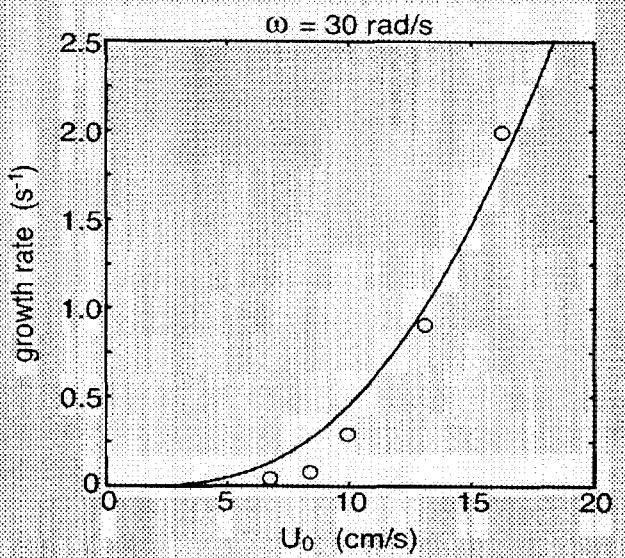

http://www.nd.edu/~mjm

mjm@nd.edu

Mechanism of Instability

- Internal mode in less viscous phase is excited during certain parts of the cycle.

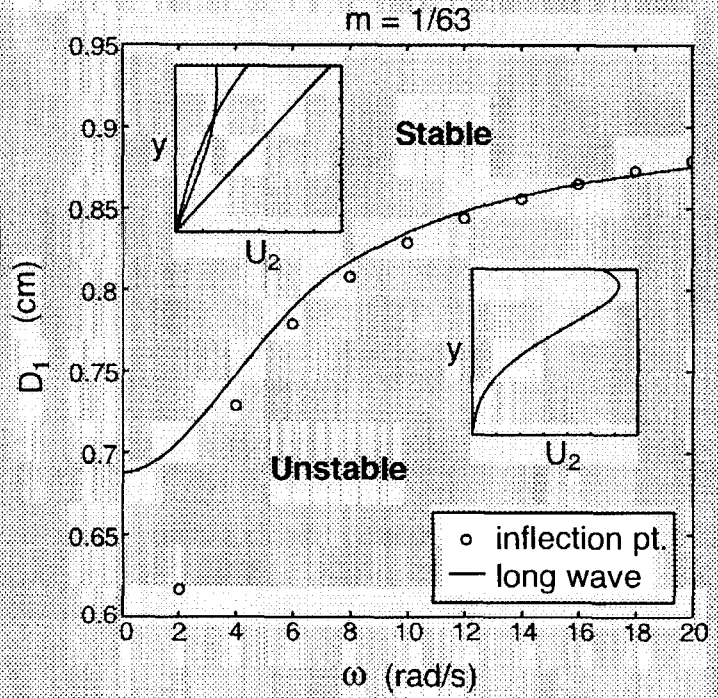

http://www.nd.edu/~mjm mjm@nd.edu

Snapshots of disturbance

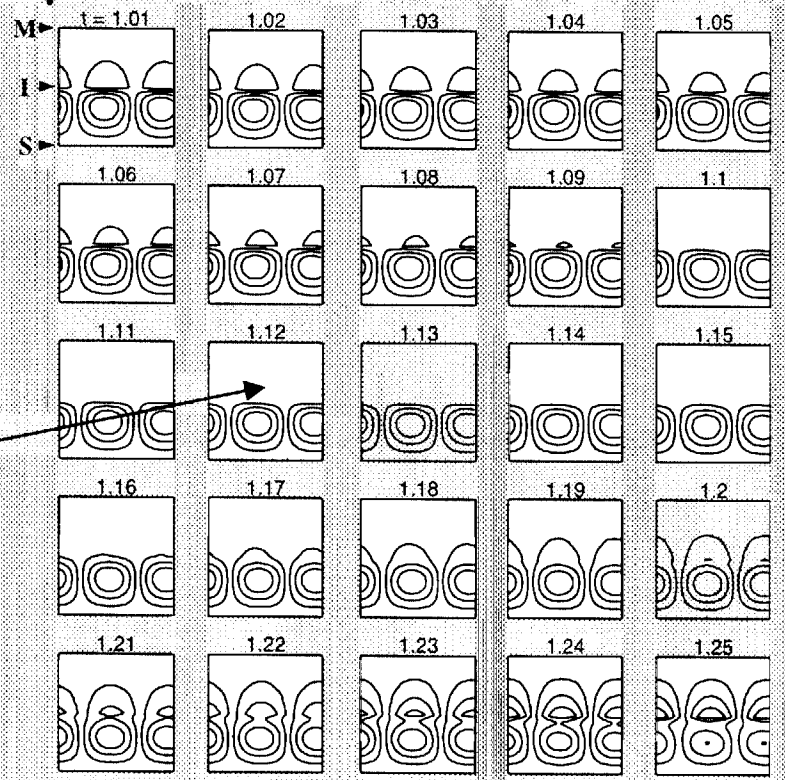

Internal Mode dominates, strongest growth

http://www.nd.edu/~mjm

mjm@nd.edu

Diagram of mechanism
t = 0.89 (1.39)
a)
t = 1.05
b)
t = 1.11
c)
http://www.nd.edu/~mjm
mjm@nd.edu

Spectra as a function of distance

nonlinear effect important in low peak

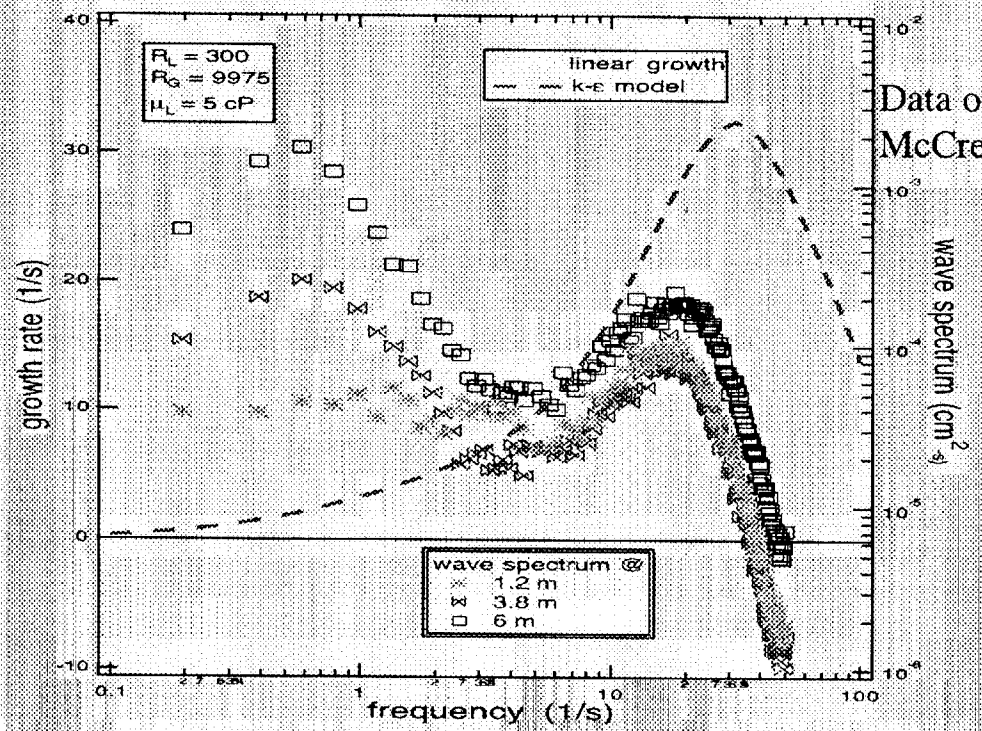

Data of Bruno and McCready, 1988

http://www.nd.edu/~mjm mjm@nd.edu

Slug formation from waves

At least three period doublings occur

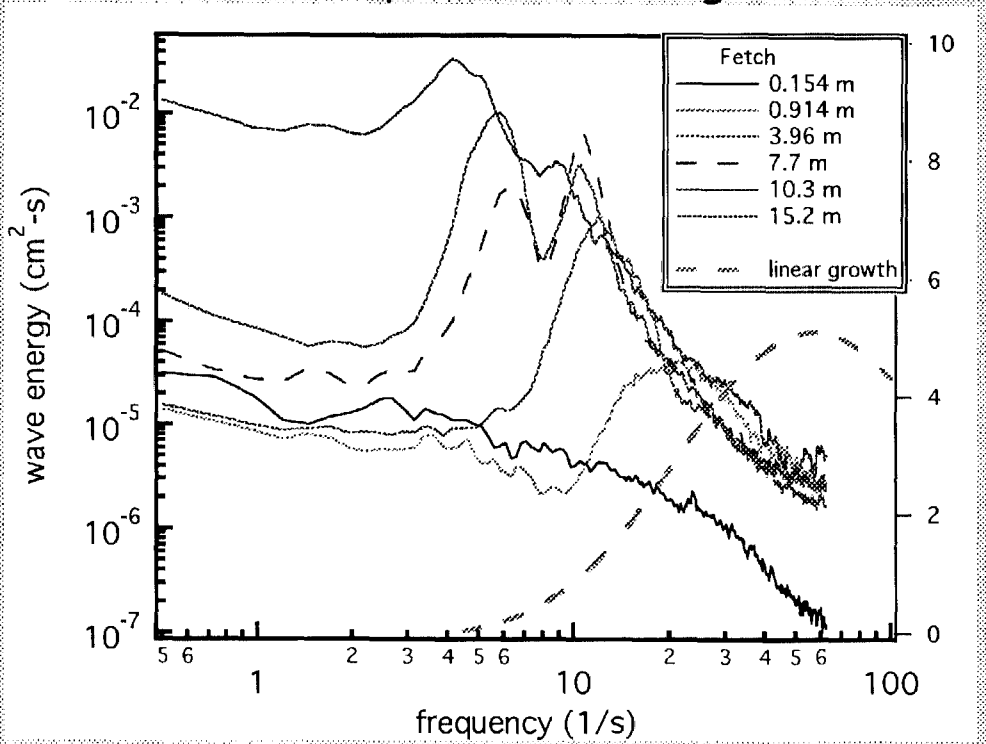

$U_{SG} = 1.8$ m/s
$U_{SL} = 0.18$ m/s
$h/d = .6$

Data of Woods, Hanratty 1998

http://www.nd.edu/~mjm mjm@nd.edu

Formation of a slug from waves

<---------- Flow direction

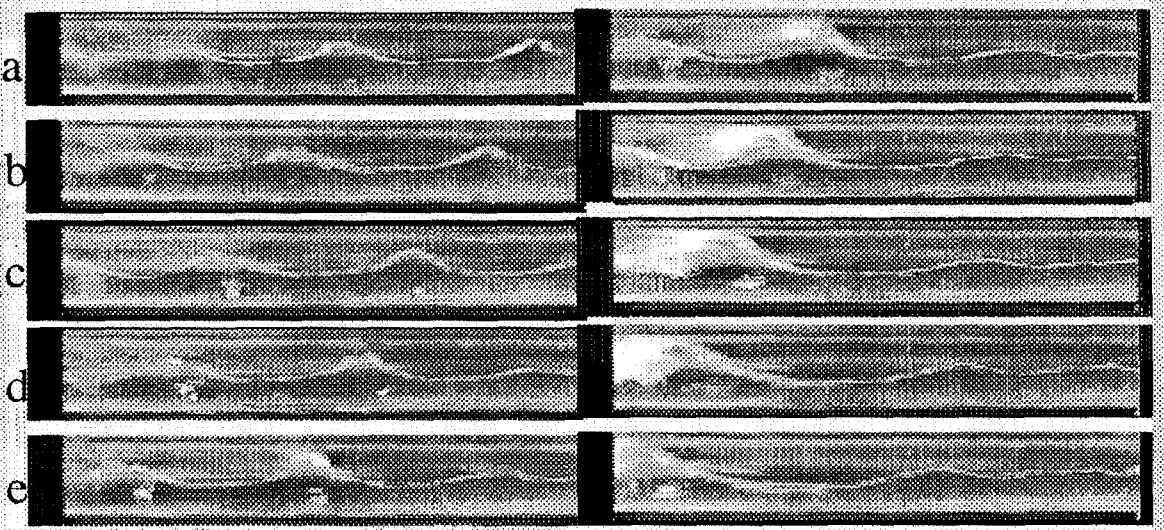

Data of Woods, 1998 U_{SG} = 1.8 m/s, U_{SL} = 0.12 m/s

Photos are 1/30 second apart for air-water in a 7.63 cm pipe.)

http://www.nd.edu/~mjm mjm@nd.edu

Wave spectra across the transition

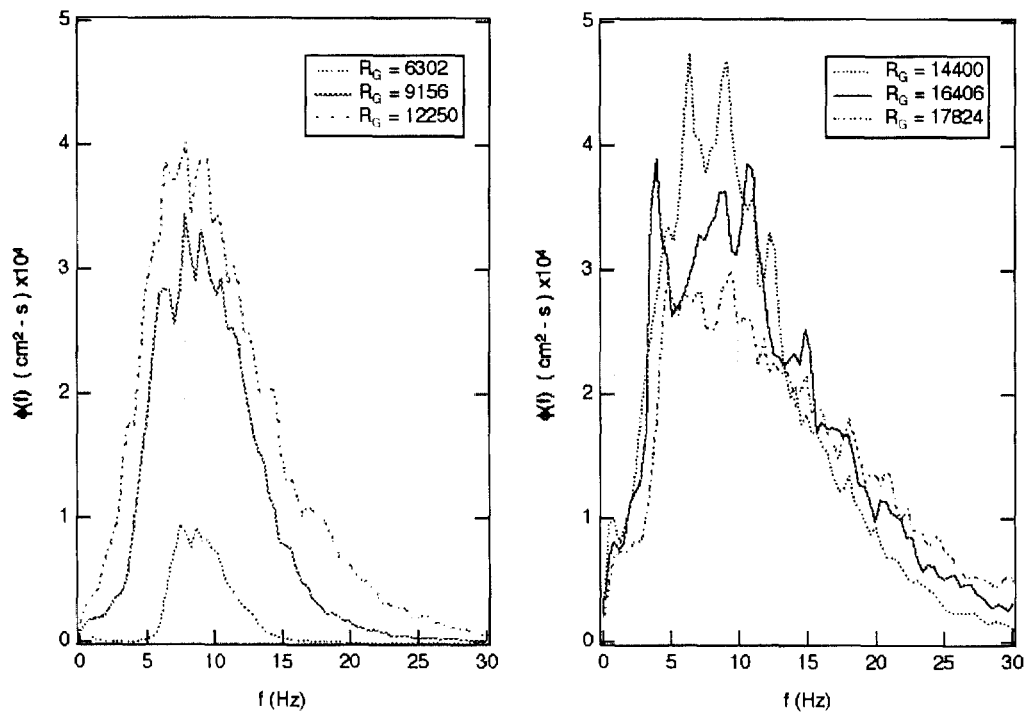

Figure 3. Interfacial wave spectra, R_L = 10, μ = 15 cP

http://www.nd.edu/~mjm mjm@nd.edu

Wave tracings across the transition

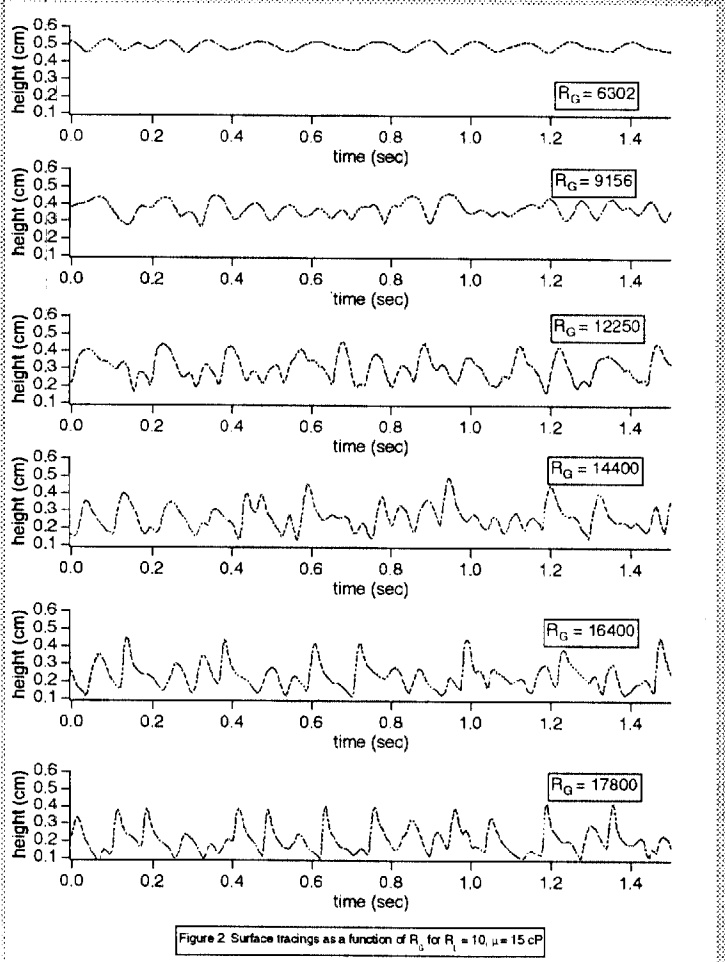

Figure 2. Surface tracings as a function of R_G for R_1 = 10, μ = 15 cP

http://www.nd.edu/~mjm mjm@nd.edu

Gas-liquid flow interfacial stability problem

turbulence model: k-ε

Solve the base state with either a smooth or rough interface (try to match data).

then

Solve the differential stability problem the best we can

Liquid-phase: $0 \le y^* \le d_1$

$$\rho_1\left[\frac{\partial u_i^*}{\partial t^*}+u_j^*\frac{\partial u_i^*}{\partial x_j^*}\right]=\pm\frac{\partial p^*}{\partial x_i^*}+\rho_1 g^*\sin(\theta)+\frac{\partial}{\partial x_j^*}\left[(\mu_1+\mu_t^*)(2s_{ij}^*)\right]$$

$$\rho_1\left[\frac{\partial k^*}{\partial t^*}+u_i^*\frac{\partial k^*}{\partial x_i^*}\right]=\frac{\partial}{\partial x_i^*}\left[\left(\mu_1+\frac{\mu_t^*}{\sigma_{k^*}}\right)\left(\frac{\partial k^*}{\partial x_i^*}\right)\right]+\mu_t^*(2s_{ij}^*)\frac{\partial u_i^*}{\partial x_j^*}\pm\rho_1\varepsilon^*\pm 2\mu_1\left(\frac{\partial\sqrt{k^*}}{\partial x_i^*}\right)^2$$

$$\rho_1\left[\frac{\partial \varepsilon^*}{\partial t^*}+u_i^*\frac{\partial \varepsilon^*}{\partial x_i^*}\right]=\frac{\partial}{\partial x_i^*}\left[\left(\mu_1+\frac{\mu_t^*}{\sigma_\varepsilon}\right)\left(\frac{\partial \varepsilon^*}{\partial x_i^*}\right)\right]+c_1 f_1\mu_t^*\frac{\varepsilon^*}{k^*}(2s_{ij}^*)\frac{\partial u_i^*}{\partial x_j^*}\quad+2\mu_1\mu_t^*\left(\frac{\partial^2 u_i^*}{\partial x_j^*\partial x_i^*}\right)^2\pm\rho_1 c_1 f_1\frac{\varepsilon^{*2}}{k^*}$$

http://www.nd.edu/~mjm mjm@nd.edu

Stability equations continued

Gas-phase: $d_1 \le y^* \le d_1 + d_2$

$$\rho_2\left[\frac{\partial u_i^*}{\partial t^*} + u_j^*\frac{\partial u_i^*}{\partial x_j^*}\right] = \pm\frac{\partial p^*}{\partial x_i^*} + \rho_{2g}^* \sin(\theta) + \frac{\partial}{\partial x_j^*}\left[\left(\mu_2 + \mu_t^*\right)\left(2s_{ij}^*\right)\right]$$

$$\rho_2\left[\frac{\partial k^*}{\partial t^*} + u_i^*\frac{\partial k^*}{\partial x_i^*}\right] = \frac{\partial}{\partial x_i^*}\left[\left(\mu_2 + \frac{\mu_t^*}{\sigma_{k\omega}}\right)\left(\frac{\partial k^*}{\partial x_i^*}\right)\right] + \mu_t^*\left(2s_{ij}^*\right)\frac{\partial u_i^*}{\partial x_j^*} \pm \rho_2\varepsilon^* \pm 2\mu_2\left(\frac{\partial\sqrt{k^*}}{\partial x_i^*}\right)^2$$

$$\rho_2\left[\frac{\partial \varepsilon^*}{\partial t^*} + u_i^*\frac{\partial \varepsilon^*}{\partial x_i^*}\right] = \frac{\partial}{\partial x_i^*}\left[\left(\mu_2 + \frac{\mu_t^*}{\sigma_\varepsilon}\right)\left(\frac{\partial \varepsilon^*}{\partial x_i^*}\right)\right] + c_1 f_1 \mu_t^*\frac{\varepsilon^*}{k^*}\left(2s_{ij}^*\right)\frac{\partial u_i^*}{\partial x_j^*} \qquad + 2\mu_2\mu_t^*\left(\frac{\partial^2 u_i^*}{\partial x_j^*\partial x_i^*}\right)^2 \pm \rho_2 c_1 f_1\frac{\varepsilon^{*2}}{k^*}$$

http://www.nd.edu/~mjm mjm@nd.edu

Stability equations continued

k=1 (liquid-phase) $0 \le y \le 1$

k=2 (gas-phase) $1 \le y \le n_2 + 1$

$$\frac{\left(\mu_k \hat{u}'_{b,k}\right)''}{m_k} + \left(\Gamma_{b,k}\hat{\phi}''_k\right)'' \pm 2\alpha^2\left(\Gamma_{b,k}\hat{\phi}'_k\right)' + \alpha^4\Gamma_{b,k}\phi_k = i\alpha R\frac{r_k}{m_k}\left\{\left(u_{b,k} \pm c\right)\left(\hat{\phi}''_k \pm \alpha^2\hat{\phi}_k\right) \pm u\right.$$

$$\frac{\left(\mu_k \hat{k}'_{b,k}\right)' + \mu_k \hat{u}''_{b,k}}{m_k} + \Gamma_{b,k}\left(\hat{k}''_k \pm \alpha^2\hat{k}_k\right) + \Gamma'_{b,k}\hat{k}_k + 2\frac{\mu_{b,k}\hat{u}'_{b,k}}{m_k}\left(\hat{\phi}''_k + \alpha^2\hat{\phi}_k\right) + \frac{k'_{b,k}}{k_{b,k}}\left(\frac{k'_{b,k}}{2k_{b,k}}\hat{k}_k \pm\right.$$

$$= i\alpha R\frac{r_k}{m_k}\left\{\left(u_{b,k} \pm c\right)\hat{k}_k \pm k'_{b,k}\hat{\phi}_k\right\}$$

$$\frac{\left(\mu_k \hat{\varepsilon}'_{b,k}\right)'}{m_k} + \Gamma_{b,k}\Gamma_{b,k}\left(\hat{\varepsilon}''_k \pm \alpha^2\hat{\varepsilon}_k\right) + \Gamma'_{b,k}\hat{\varepsilon}_k + 2c_1 f_1\frac{\mu_{b,k}\hat{u}'_{b,k}}{m_k}\left(\hat{\phi}''_k + \alpha^2\hat{\phi}_k\right) + r_k R c_2 f_2\frac{\varepsilon_{b,k}}{k_{b,k}}\left(\frac{\varepsilon_{b,k}}{k_{b,k}}\right.$$

$$+ \frac{\left(\hat{u}''_{b,k}\right)^2}{m_k}\left[c_1 f_1\frac{\varepsilon_{b,k}}{k_{b,k}}\left(\mu_k + \varepsilon_k \pm \frac{m_k\mu_{b,k}}{k_{b,k}}\hat{k}_k\right) + \frac{2m_k}{r_k R}\left(\mu_k + 2\mu_{b,k}\hat{\phi}''_k\right)\right]$$

$$= i\alpha R\frac{r_k}{m_k}\left\{\left(u_{b,k} \pm c\right)\varepsilon_k \pm \varepsilon'_{b,k}\hat{\phi}_k\right\}$$

$$\mu_k = c_\mu f_\mu r_k R\frac{k_{b,k}}{\varepsilon_{b,k}}\left(2\hat{k}_k \pm \frac{k_{b,k}}{\varepsilon_{b,k}}\varepsilon_k\right)$$

http://www.nd.edu/~mjm mjm@nd.edu

Stability Equations cont.

Boundary conditions

$$\hat{\phi}_1 = \hat{\phi}_2 \tag{3-18c}$$

$$\hat{\phi}_1 + u_{b,1}\hat{h} = c\hat{h} \tag{3-18d}$$

$$\hat{\phi}_1' \pm \hat{\phi}_2' = \hat{h}\left(u_{b,1}' \pm u_{b,2}'\right) \tag{3-18e}$$

$$\hat{\phi}_1'' + \alpha^2\hat{\phi}_1 + \hat{h}u_{b,1}'' = m_2\left(\hat{\phi}_2'' + \alpha^2\hat{\phi}_2 + \hat{h}u_{b,2}''\right) \tag{3-18f}$$

$$\left(\hat{\phi}_1''' + \Gamma_{b,1}'\hat{\phi}_1'' + u_{b,1}'\Gamma_1' \pm 3\alpha^2\hat{\phi}_1'\right) + i\alpha R\left(u_{b,1}'\hat{\phi}_1 \pm u_{b,1}\hat{\phi}_1'\right) \pm m_2\left(\hat{\phi}_2''' + \Gamma_{b,2}'\hat{\phi}_2'' + u_{b,2}'\Gamma_2' \pm 3\alpha^2\hat{\phi}_2'\right)$$
$$\pm i\alpha\sigma_2 R\left(u_{b,2}'\phi_2 \pm u_{b,2}\phi_2'\right) \pm i\alpha R\left[\left(1 \pm r_2\right)F + \alpha^2 S\right]\hat{h} = i\alpha R c\left(r_2\hat{\phi}_2' \pm \hat{\phi}_1'\right) \tag{3-18g}$$

$$\hat{k}_1 = \hat{\varepsilon}_1 = \hat{\mu}_1 = \hat{k}_2 = \hat{\varepsilon}_2 = \hat{\mu}_2 = 0 \tag{3-18h}$$

http://www.nd.edu/~mjm mjm@nd.edu

How close is the base state?

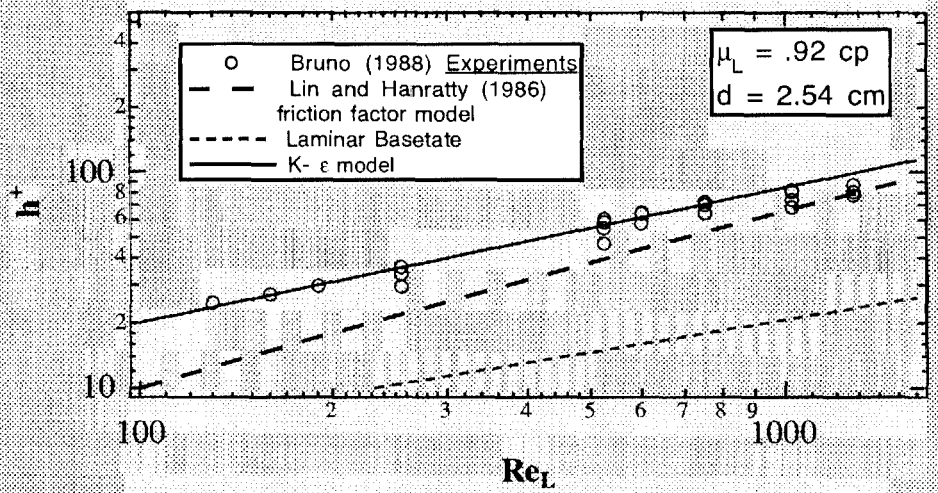

Figure 4.7 h^+ - Re_L correlation for horizontal gas-liquid channel flow. Re_G = 4,000 - 15,000

http://www.nd.edu/~mjm mjm@nd.edu

Friction velocity -- Re

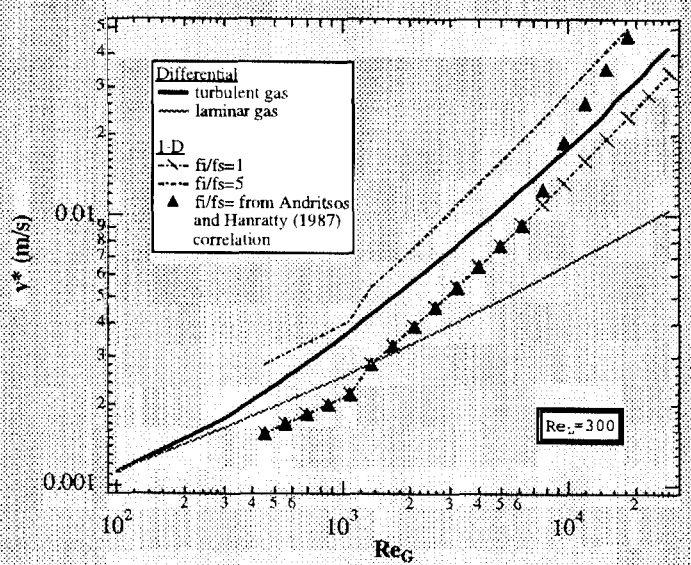

Figure 4.5 Friction velocity versus Re_G at constant Re_L. d = 2.54 cm, μ_L = 1 cp, P=14.7 psia, T=298 K

http://www.nd.edu/~mjm mjm@nd.edu

Laminar growth rate scaling

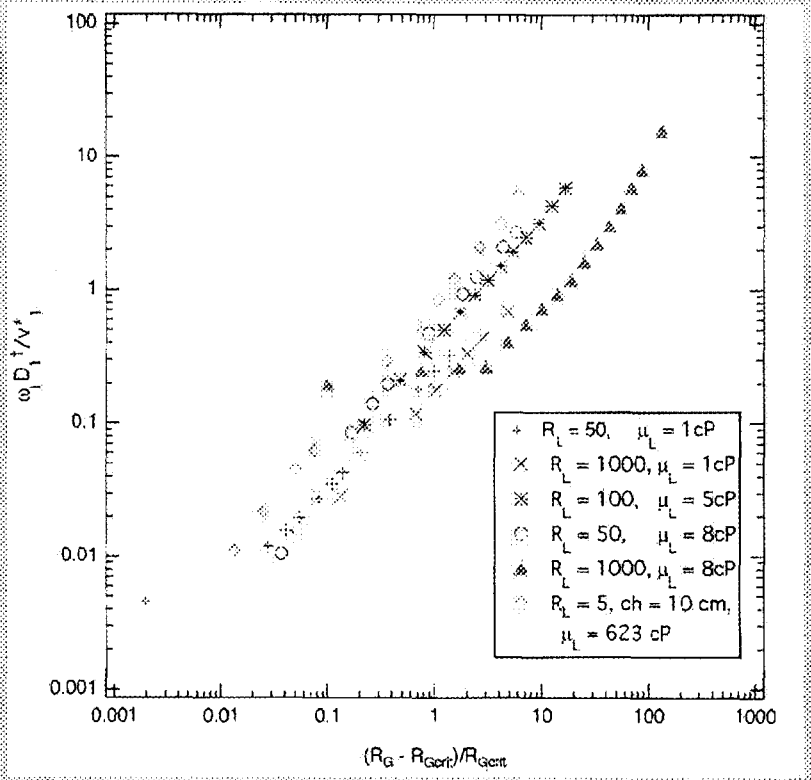

http://www.nd.edu/~mjm mjm@nd.edu

Wave growth in turbulent flow

some similarity to laminar flow?

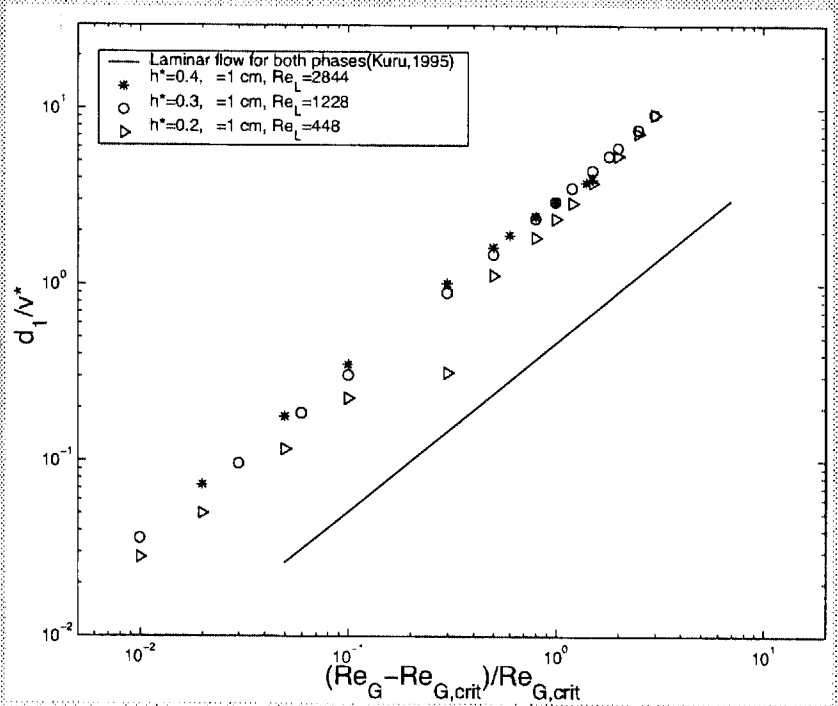

http://www.nd.edu/~mjm

mjm@nd.edu

Weakly- nonlinear theory

$$\frac{D\mathbf{u}}{Dt} = -\nabla p + \frac{1}{R}\nabla^2\mathbf{u}$$

Spectral reduction of Navier-Stokes equations and boundary conditions.

The interface is represented by, $\psi \equiv (\mathbf{u}, p, h)$

We make the assumption that the waves can be represented by a series of modes which have a complex amplitude, A, multiplying a linear eigenfunction, ζ,

$$\psi = \Sigma A_i \zeta_i$$

A series of amplitude coupled amplitude equations is integrated.

$$\frac{\partial A_i}{\partial t} = L(k_i) + \alpha_{ji} A_j A_j^* + \beta_{ji} A_i A_j + \gamma_{kji} A_i A_j A_k$$

Both the dynamic and steady state behavior are watched.

http://www.nd.edu/~mjm mjm@nd.edu

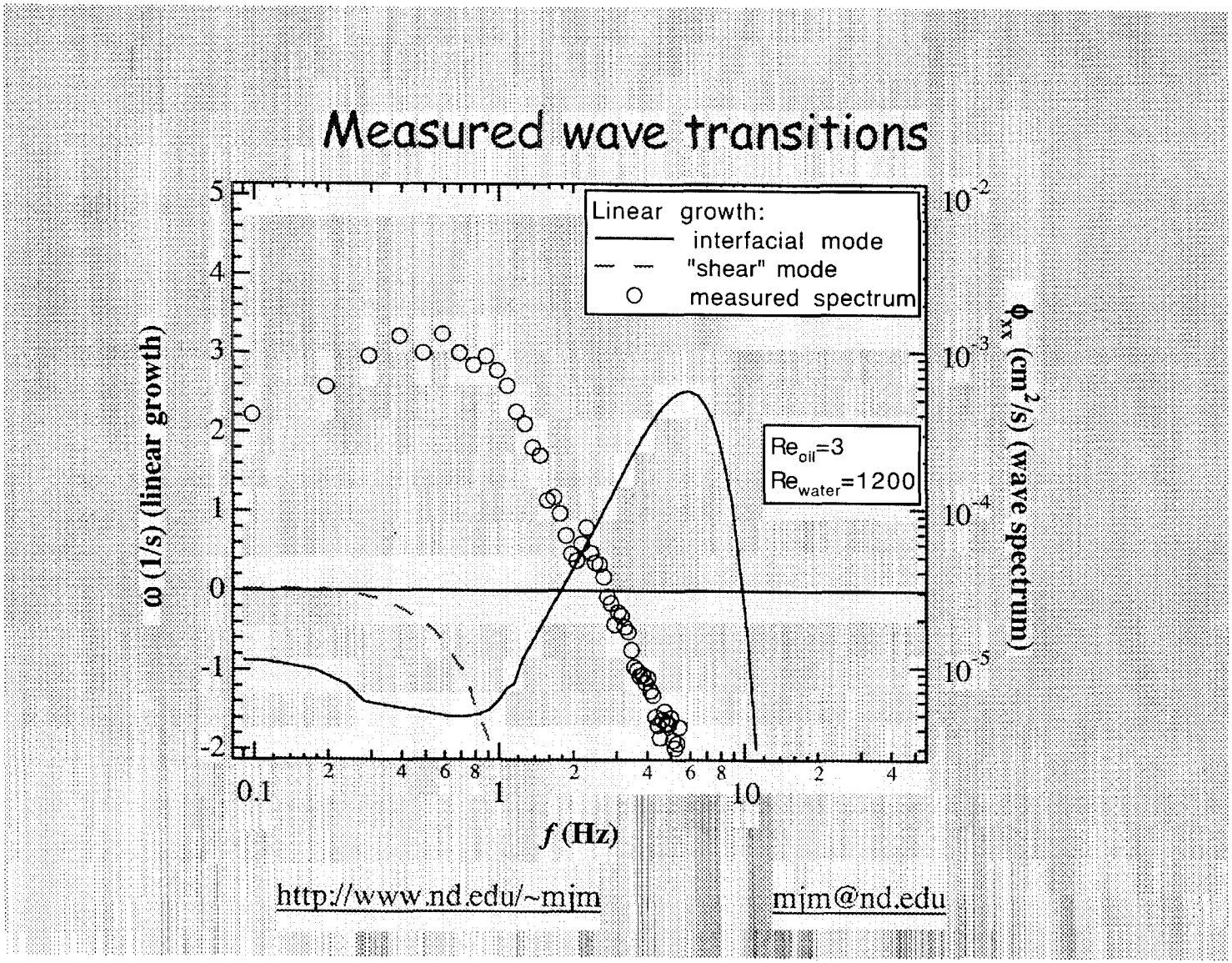
Measured wave transitions
Linear growth:
interfacial mode
"shear" mode
measured spectrum
Re_oil=3
Re_water=1200
ω (1/s) (linear growth)
φ_xx (cm²/s) (wave spectrum)
f (Hz)
http://www.nd.edu/~mjm
mjm@nd.edu

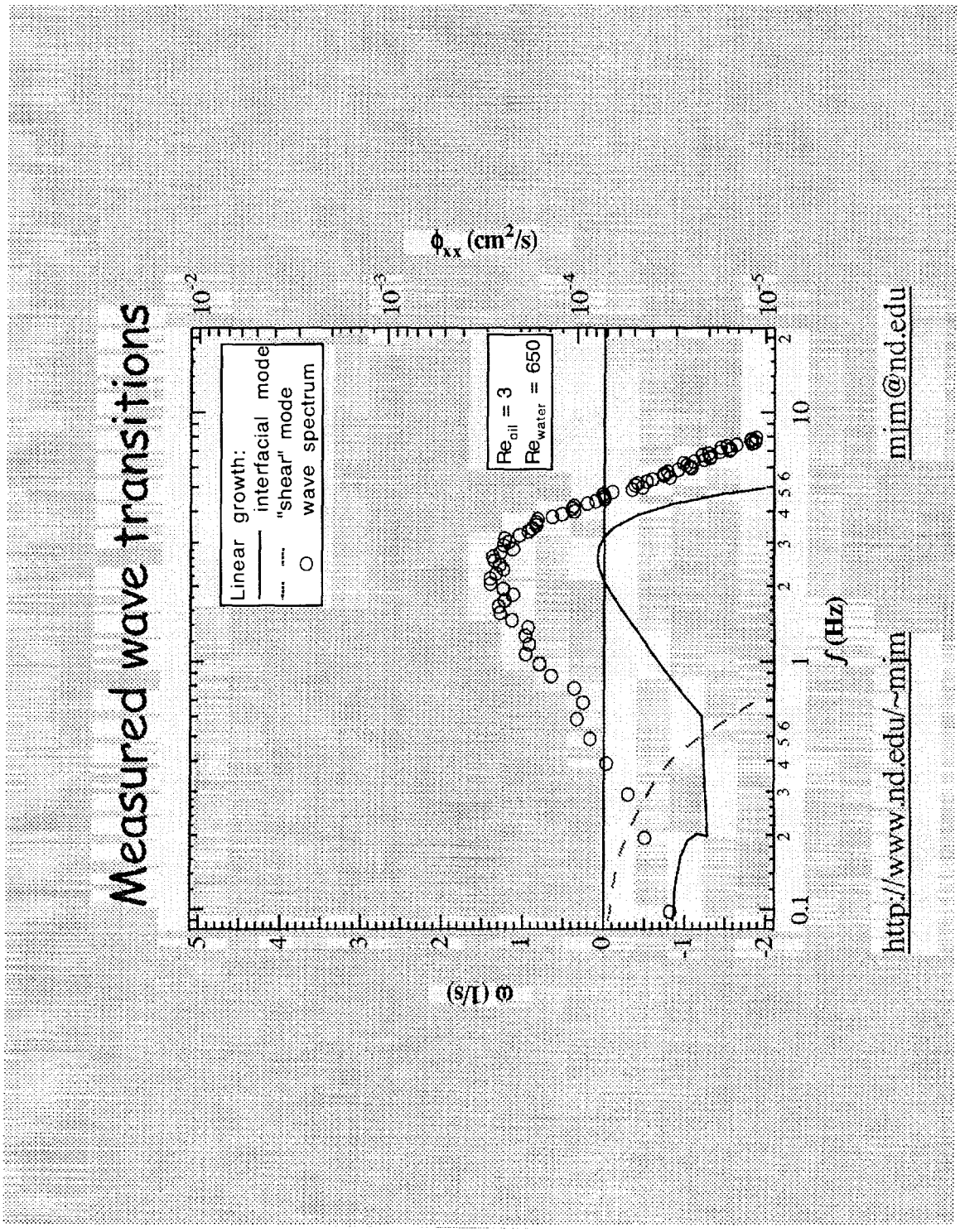
Measured wave transitions
ϕ_{xx} (cm^2/s)
10^{-2}
10^{-3}
10^{-4}
10^{-5}
Linear growth:
interfacial mode
"shear" mode
wave spectrum
Re_{oil} = 3
Re_{water} = 650
ω (1/s)
5
4
3
2
1
0
-1
-2
0.1
1
10
f (Hz)
http://www.nd.edu/~mjm
mjm@nd.edu

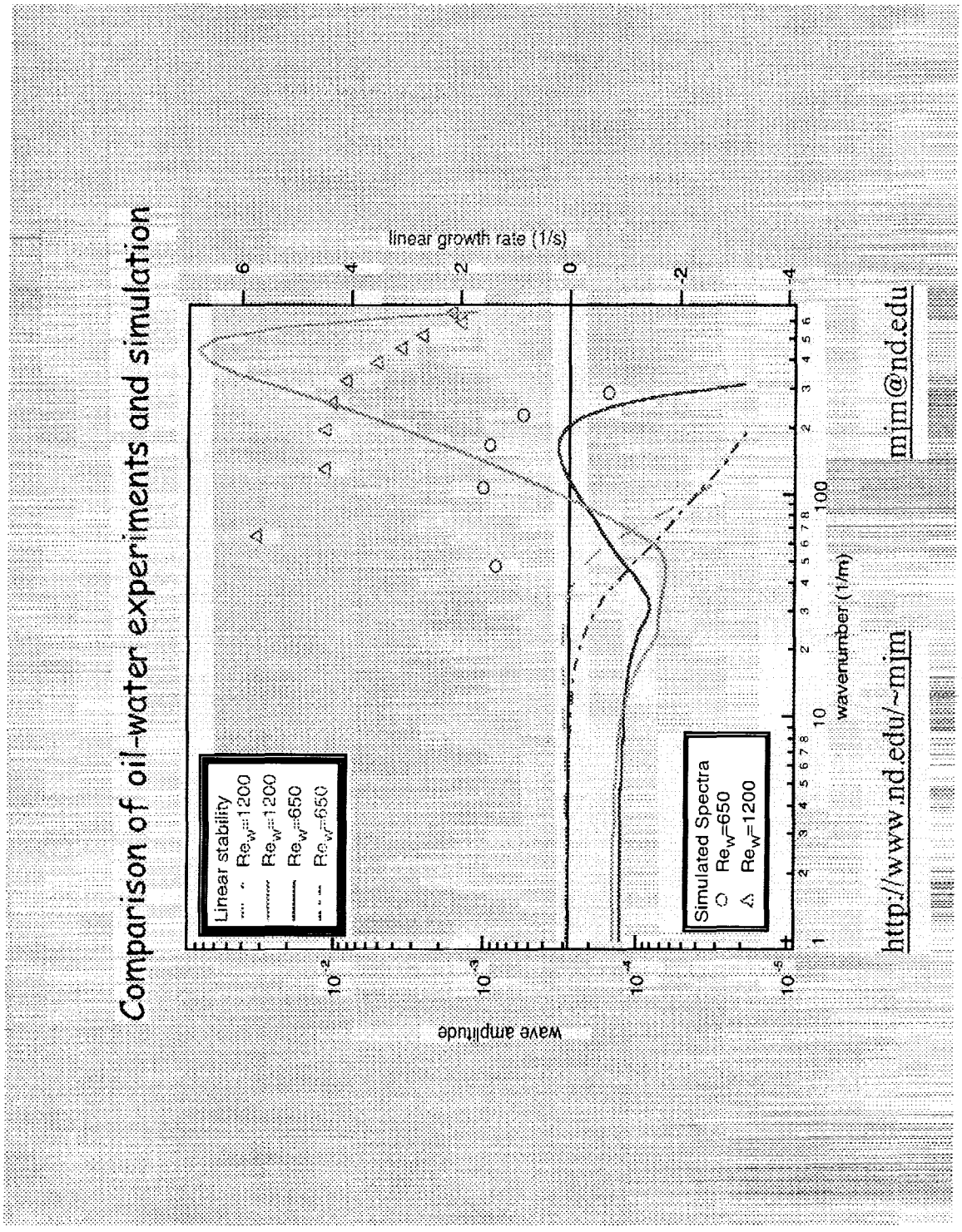
Comparison of oil-water experiments and simulation
linear growth rate (1/s)
wave amplitude
wavenumber (1/m)
Linear stability
Re_w=1200
Re_w=1200
Re_w=650
Re_w=650
Simulated Spectra
Re_w=650
Re_w=1200
http://www.nd.edu/~mjm
mjm@nd.edu

Nonlinear effect on long wave formation

Re_w=650, cubic nonlinear coefficients are more balanced

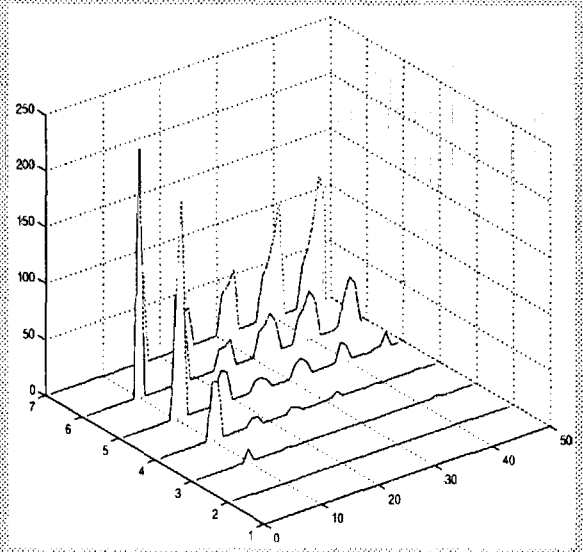

Re_w=1200, large cubic nonlinear coefficients between large and small wavenumbers

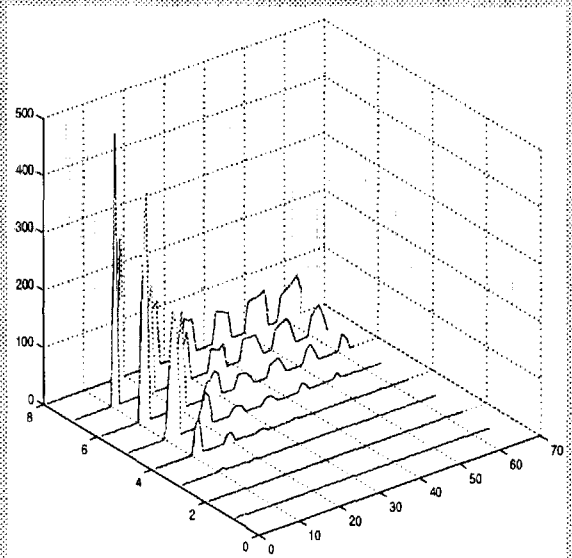

http://www.nd.edu/~mjm

mjm@nd.edu

Conclusions

- 1. Atomization is a generically important process that is not understood very well.
  - Making quantitative predictions is very difficult
- 2. Atomization in parallel two-layer flows will be associated with the waves that are already present.
  - Quantitative prediction of these waves is not possible at present
- 3. In the general case it is the more viscous fluid that is atomizing from crests of large waves
  - Lift and shatter
  - Stretch and break

http://www.nd.edu/~mjm mjm@nd.edu

Conclusions

- 4. Prediction of the precursor waves from linear theory is not possible but some progress is possible using weakly nonlinear theory
  - Turbulent base state/ stability problem is not solved
  - Nonlinear simulation is computationally intensive
    - » Still needs direct experimental verification
    - » Some insight is gained from the coefficient spectrum

http://www.nd.edu/~mjm mjm@nd.edu

Acknowledgements

- NASA, Microgravity Program
- CoWorkers
  - Chia Chang, David Leighton
  - Ben Woods, Mike King, Massimo Sangalli
  - Bill Kuru, Xiaohong Wang, Don Uphold

http://www.nd.edu/~mjm mjm@nd.edu

RECENT DEVELOPMENT IN THE STUDIES OF ANNULAR TWO-PHASE FLOW AT MICROGRAVITY

Kamiel S. Rezkallah and Pieter deJong, Microgravity Research Group, University of Saskatchewan, Saskatoon, S7N-5A9 CANADA

ABSTRACT

Two-phase flows regularly occur in heat transfer systems operating in both terrestrial and space environments. Of particular interest is the annular flow regime which commonly occurs in power plants, heat transfer equipment and chemical processes. In such a flow, the heat transfer rates and the pressure drop are strongly influenced by the film structure. The film structure itself is very much dependent on the gravitational acceleration and the liquid and gas/vapor properties and mass fluxes.

An experimental study of the film structure in annular two-phase flow was carried out at reduced gravity conditions made available onboard NASA's zero gravity aircraft. Film thickness and pressure drop measurements were taken under conditions of minimum gravitational pull on the film, and over a wide range of liquid and gas mass flow rates.

DATA SOURCE

Data was collected in a 9.525 mm inside diameter test section. Gauge and absolute pressure measurements were taken 18.8 cm (~20D) downstream of the mixer. This was followed by a pair of viewing sections and a capacitance type void fraction sensor. The film thickness sensor has dual probes 30 mm (~3D) apart, located 1.05 m (~110D) downstream of the mixer. The two-phase flow temperature and gauge pressure at the outlet of the test section are taken 1.24 m (~130D) downstream the mixer, which extends the differential pressure measurement over 1.052 m (~110D).

Data was collected at liquid mass fluxes ranging from 55 to 318 kg/m^2s, and gas mass fluxes ranging from 2.3 to 25 kg/m^2s. The original data included only the film thickness time traces. Further analysis of the film thickness time traces show variations in terms of the average wave height, the substrate thickness, the average film thickness, the wave frequency, and the wave velocity.

SAMPLE RESULTS

A sample of the film thickness time trace collected in microgravity is given in Figure 1a. A corresponding earth gravity in vertical upwards flow sequence is shown in figure 2a. Video images of the flow pattern associated with the film thickness traces are shown in Figures 1c and 2c, respectively. The probability distribution functions of the film thickness traces at μ-g and 1-g are shown in figure 1b & 2b, respectively.

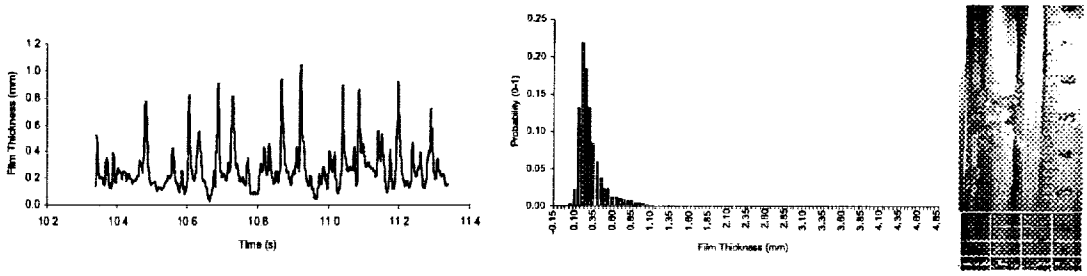

(a) (b) (c)

Figure 1: Sample results at microgravity: (a) Film thickness time trace; (b) Probability Density Function; and (c) sample image.

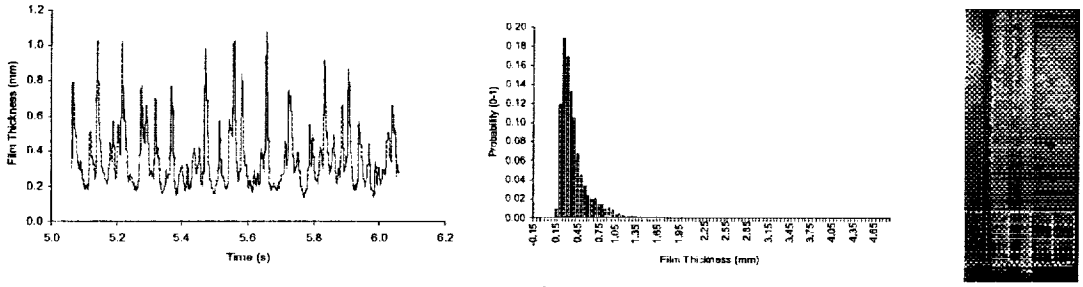

(a) (b) (c)

Figure 2: Sample results at earth gravity: (a) Film thickness time trace; (b) Probability Density Function; and (c) sample image.

The average film thickness is a time average value that is calculated over the length of the measurement window (0.2 to 0.7 mm seems typical).

REFERENCES

1. Azzopardi, B. J. (1986). Disturbance Wave Frequencies, Velocities and Spacing in Vertical Annular Two-Phase Flow. Nuclear Engineering and Design, Vol. 92, pp. 121-133.
2. Bousman, W.S. (1995). Studies of Two-Phase Gas-Liquid Flow in Microgravity. NASA Contractor Report 195434.
3. De Jong, Pieter (1999). An Investigation of Film Structure and Pressure Drop in Microgravity Annular Flow. M.Sc. Thesis, University of Saskatchewan, Canada
4. Lowe, Devin C. (1997) A Study on Flow Regime Identification in Microgravity Gas-Liquid Flows Using a Capacitance Sensor. M.Sc. Thesis, University of Saskatchewan, Canada.
5. Willetts, I.P (1987). Non-Aqueous Annular Two-Phase Flow. Ph.D. Thesis, University of Oxford, UK.

FLUID/SOLID *BOUNDARY CONDITIONS* IN NON-ISOTHERMAL SYSTEMS

PI: Daniel E. *Rosner*, Prof. ChE/ME Yale University, ChE Dept.
Collaborators: A. V. Filippov, M. Zurita-Gotor

The 'thermal creep' boundary condition relates the fluid 'slip' velocity to the tangential fluid temperature gradient one mfp from a solid wall. 'Creep-driven' flows are responsible for particle 'phoresis', as well as circulatory flows in crystal growth ampoules, even in zero-g!

If one *defines*: $C_{tc} \equiv V_{x,fluid} / \{ \nu [(1/T)(dT/dx)] \}$ **and** $Kn_\sigma \equiv l/\sigma$
then we can state our *GOALS*:

- **How does C_{tc} depend on α_{mom}, kT/ε, $l \cdot |grad(\ln T)|$, Kn_σ?**
- **Implications of *dense-vapor kinetic theory* for ordinary particles, nano-particles, and 'heavy' molecular 'solutes'?(Enskog-Boltzmann for hard spheres (HS))**
- **Dependence of suspended particle phoresis on morphology, orientation and thermal conductivity?**
- **Combined effects of thermophoresis and Marangoni convection for small liquid drops; *eg*, in 'spray' flames,...**
- **Implications for future microgravity experiments (inferences of C_{tc} *via* photophoretic 'space-race'), and for ground-based nano-materials processing (ThFFF,...)?**

Presentation not available at time of printing.

FLUID/SOLID *BOUNDARY CONDITIONS* IN NON-ISOTHERMAL SYSTEMS (cont.)

Computational Techniques:

- **Quasi-MC* *free-molecule* simulations**
- **Direct-Simulation Monte-Carlo (DSMC)**
- **Truncated multi-pole expansion method* (aggregates) in near-continuum limit**
- **Higher-order Enskog dense hard sphere vapor kinetic theory**

Recent results collected below for:

- ***fractal aggregates* in gases at both Kn extremes; effects of D_f, pre-factor and thermal conductivity ratio**
- ***straight chains* of spherules in the fm limit; orientation effects (drag, thermophoresis)**
- ***dense vapor kinetic theory* for and isolated *nano-sphere* or 'heavy' molecule (PAH?)**

*see: Filippov, A.V., Zurita M., and Rosner, D.E.(2000), "Fractal-like Aggregates: Relation Between Geometry and Physical Properties", (*J. Colloid Interface Sci.*; in press 2000)

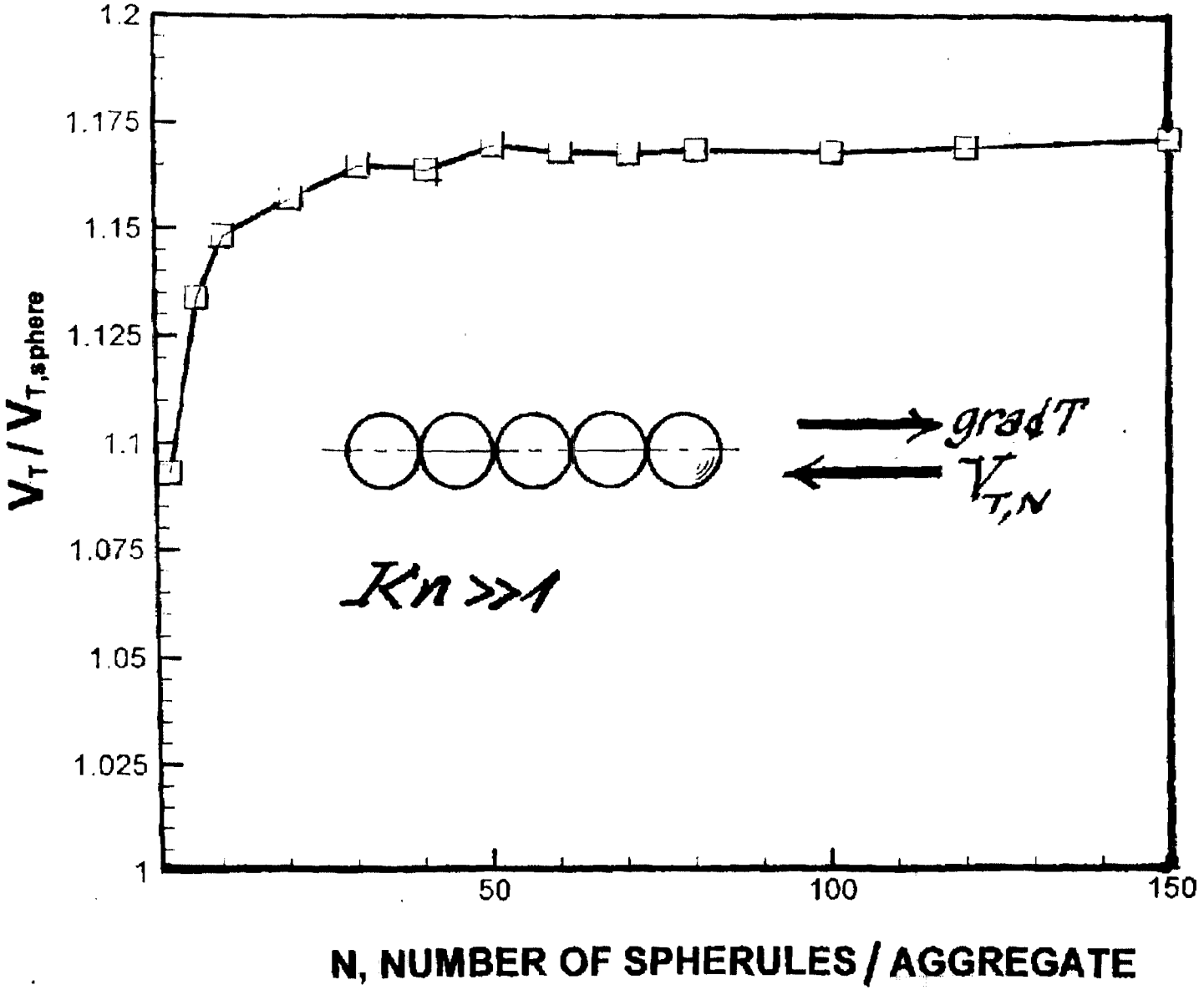
1.2
1.175
1.15
1.125
1.1
1.075
1.05
1.025
1
$V_T / V_{T,sphere}$
50
100
150
N, NUMBER OF SPHERULES / AGGREGATE
gradT
$V_{T,N}$
Kn >>1

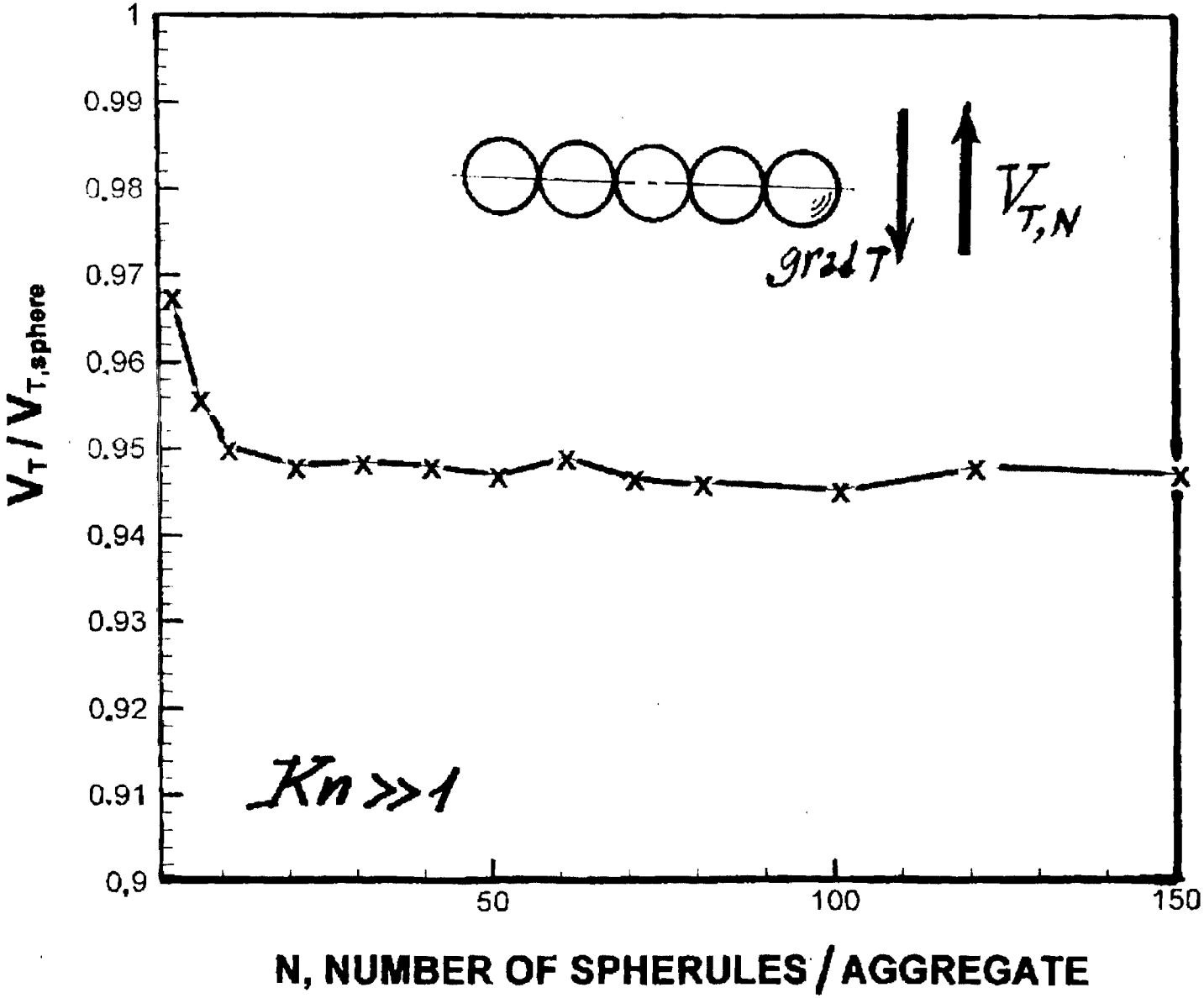
1
0.99
0.98
0.97
0.96
0.95
0.94
0.93
0.92
0.91
0,9
50
100
150
$V_T / V_{T,sphere}$
N, NUMBER OF SPHERULES / AGGREGATE
grad T
$V_{T,N}$
Kn >> 1

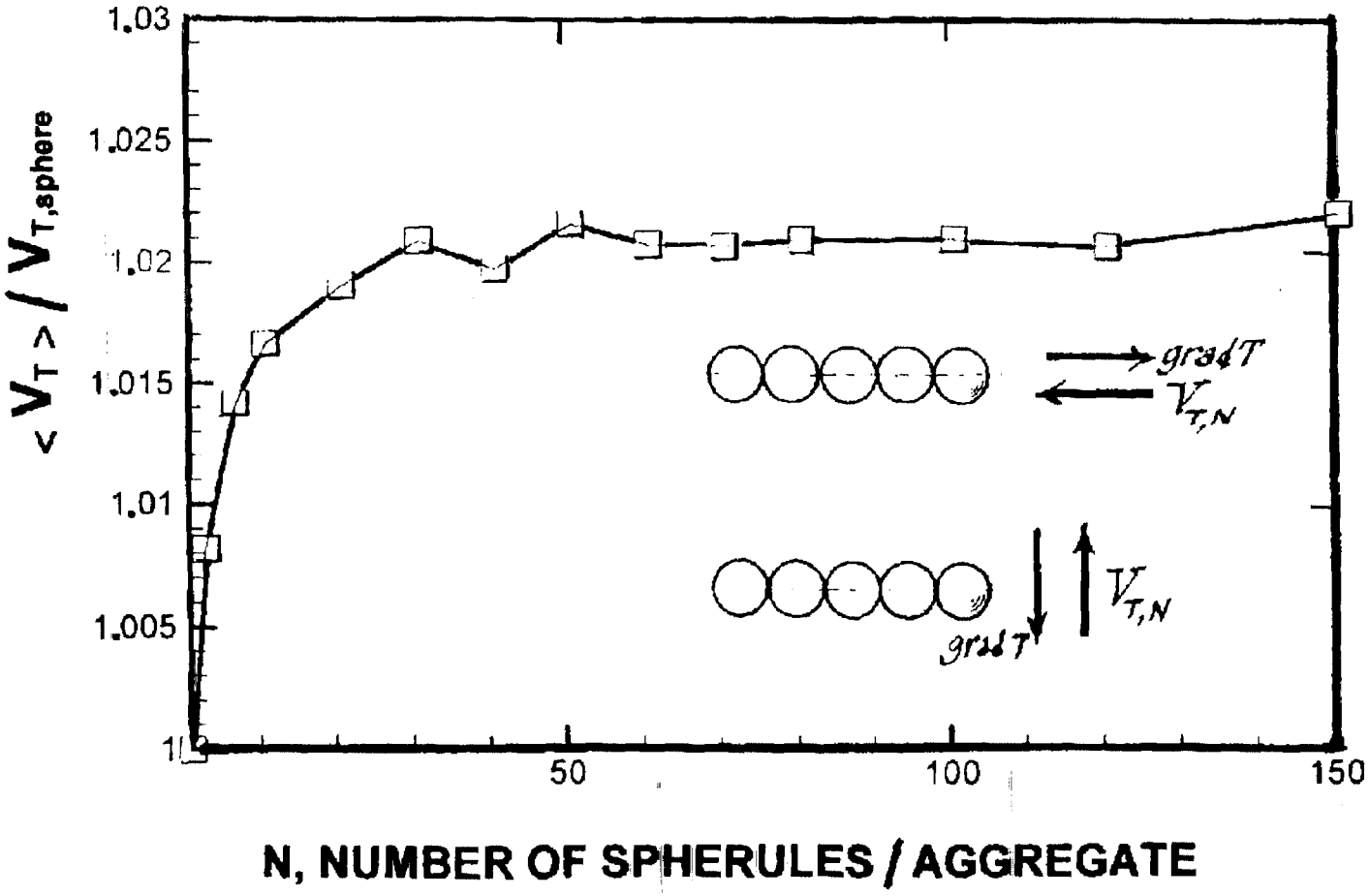
1.03
1.025
1.02
1.015
1.01
1.005
1
50
100
150
< V_T > / V_T,sphere
N, NUMBER OF SPHERULES / AGGREGATE
grad T
V_T,N
grad T
V_T,N

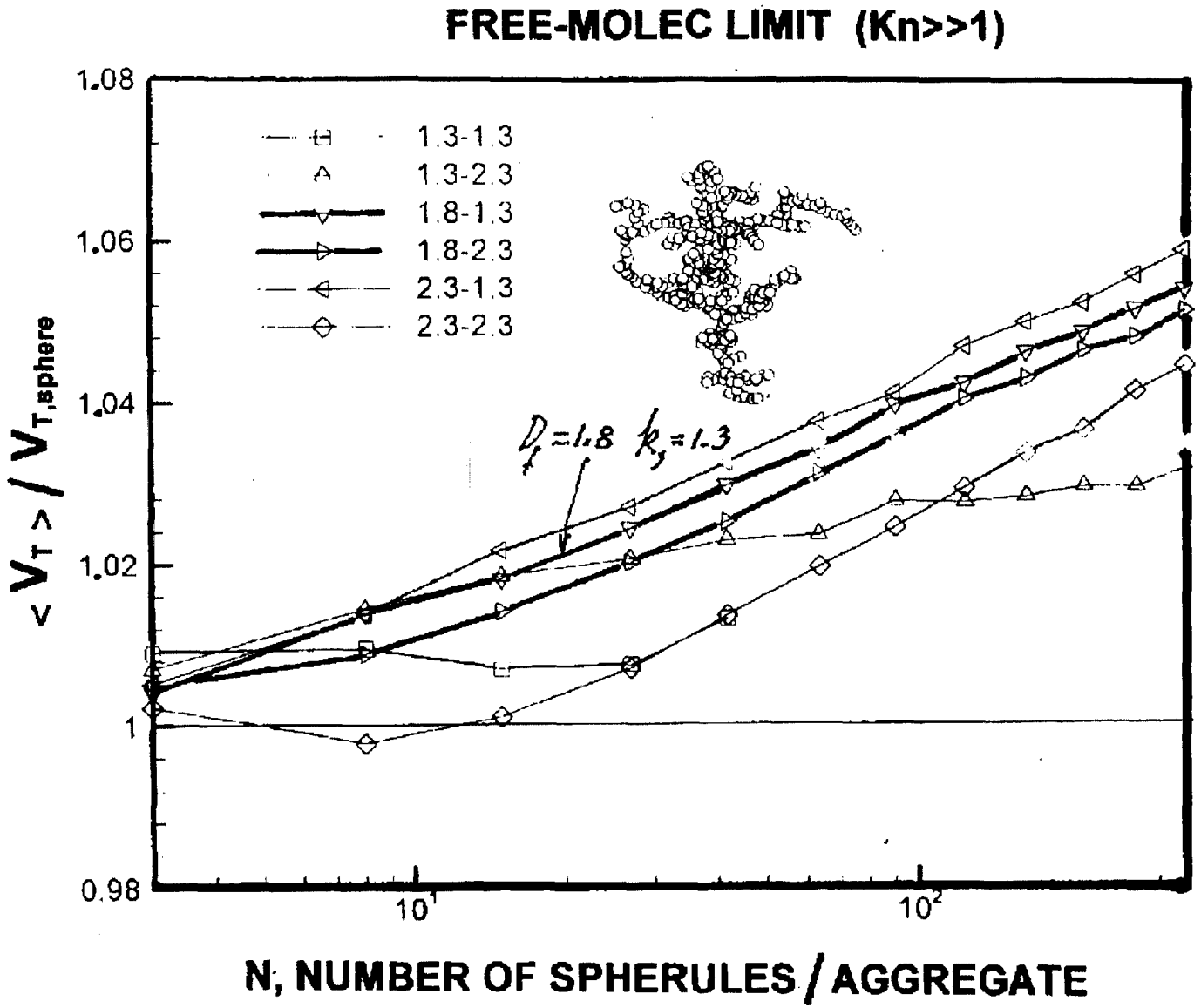
FREE-MOLEC LIMIT (Kn>>1)
1.3-1.3
1.3-2.3
1.8-1.3
1.8-2.3
2.3-1.3
2.3-2.3
$D_f = 1.8$ $k_f = 1.3$
1.08
1.06
1.04
1.02
1
0.98
10^1
10^2
< V_T > / $V_{T,sphere}$
N, NUMBER OF SPHERULES / AGGREGATE

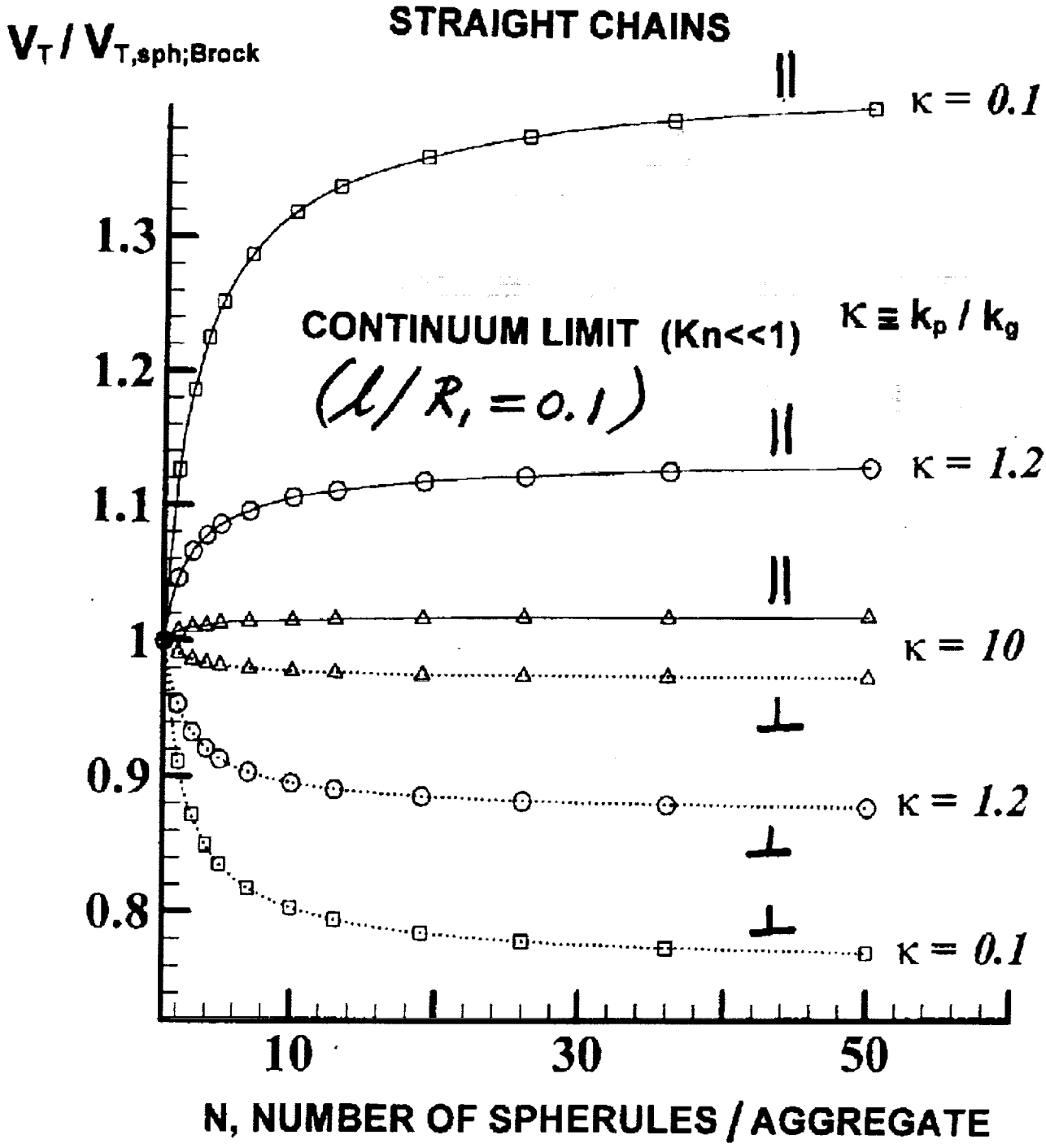
STRAIGHT CHAINS
$V_T / V_{T,sph;Brock}$
κ = 0.1
1.3
CONTINUUM LIMIT (Kn<<1)
κ ≡ k_p / k_g
(l/R, = 0.1)
1.2
κ = 1.2
1.1
1
κ = 10
0.9
κ = 1.2
0.8
κ = 0.1
10
30
50
N, NUMBER OF SPHERULES / AGGREGATE

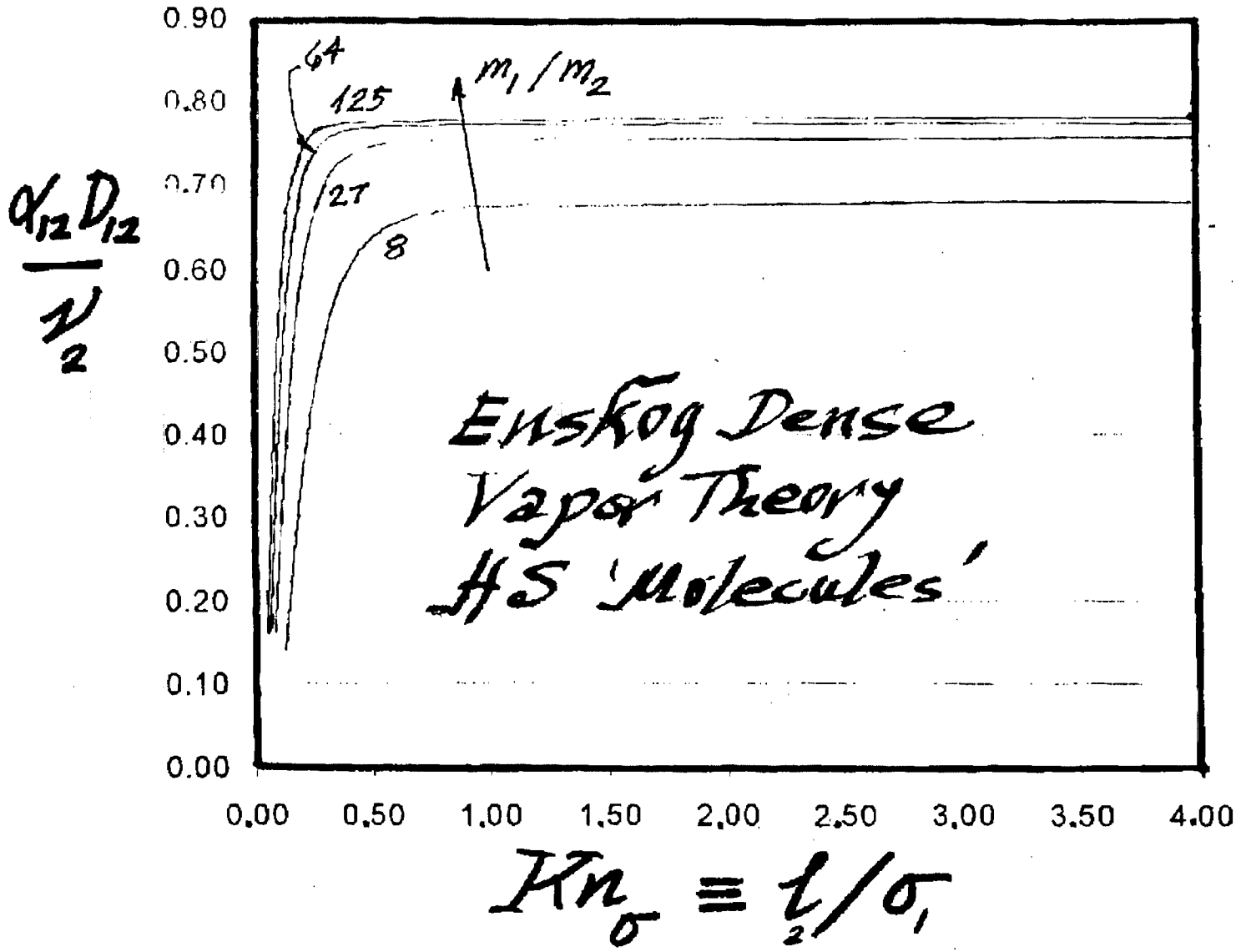
0.90
0.80
0.70
0.60
0.50
0.40
0.30
0.20
0.10
0.00
0.00
0.50
1.00
1.50
2.00
2.50
3.00
3.50
4.00
64
125
27
8
m_1/m_2
Enskog Dense Vapor Theory HS 'Molecules'
$\frac{\alpha_{12} D_{12}}{\nu_2}$
$Kn_\sigma \equiv \ell_2/\sigma_1$

FLUID/SOLID *BOUNDARY CONDITIONS* IN NON-ISOTHERMAL SYSTEMS

PI: Daniel E. ***Rosner***, **Prof. ChE/ME Yale University ChE Dept.**
Collaborators: A.V. Filippov, M. Zurita-Gotor
Monitor: Dr. R. **Balasubramaniam**
NASA Microgravity *Fluid Physics* **Grant NAG # 3-1951**

RELEVANT PUBLICATIONS:

- **Rosner, D.E.(1989), "Side-wall Gas 'Creep' and 'Thermal Stress Convection' In Microgravity Experiments on Film Growth by Vapor Transport ", *Physics Fluids A (Fluid Dynamics)* , 1 (11) 1761-1763 (led to present research program)**

- **Filippov, A.V., Zurita M., and Rosner, D.E.(2000), "Fractal-like Aggregates: Relation Between Geometry and Physical Properties", (*J. Colloid Interface Sci.*; in press)**

- **Rosner, D.E. and Khalil, Y.F. (2000), "Particle Morphology and Knudsen Transition Effects on Thermophoretically Dominated Mass Deposition Rates From 'Coagulation-Aged' Populations", *J. Aerosol Sci.* 31,(3) 273-292**

- **Filippov,A.V.(2000), "Theory of Hydrodynamic Interaction of N Arbitrary Spheres at Low Reynolds Number", (*J. Colloid Interface Sci.*; in press)**

- **Rosner, D.E., Zurita-Gotor, M. and Filippov, A.V.(2000) "Knudsen Number Dependence of the Thermophoretic Diffusivity in the 'Nano-particle'/Dense Vapor Limit" (in preparation,summer '00)**

- **Mackowski, D.W, Papadopoulos, D.H., and Rosner, D.E.(1999) "Comparison of Burnett- and DSMC- Predictions of Pressure Distributions and Normal Stress in One-dimensional, Strongly Non-isothermal Gases", *Physics of Fluids* (AIP) 11(8)2108-2116**

August 11, 2000
Session 4A

Multiphase Flow and Phase Change IV

FLUID DYNAMICS OF BUBBLY LIQUIDS

D. L. Koch, Y. Tsang, R. Zenit
School of Chemical Engineering, Cornell University
Ithaca, NY 14853
A. Sangani
Department of Chemical Engineering, Syracuse University
Syracuse, NY 13244

Experiments have been performed to elucidate the average flow properties of bubbly liquids. The experiments examine a particular class of inertially dominated multiphase flows that are particularly amenable to theoretical analysis. High-Reynolds-number, low-Weber-number bubbles produce a fluid velocity disturbance that may be approximated as a potential flow and extensive theoretical and numerical simulation work has been performed based on this approximation. We studied the behavior of monodisperse suspensions of bubbles with diameter of about 1.4 mm rising in water in vertical and inclined channels. Measurements of the liquid phase velocity fluctuations were obtained with a hot wire anemometer. The shear stress at the wall was measured using a hot film probe flush mounted on the wall. The gas volume fraction, bubble velocity, and bubble velocity fluctuations were measured using a dual impedance probe. Digital image analysis was performed to quantify the small polydispersity of the bubbles as well as the bubble shape.

A rapid decrease in the average bubble velocity in vertical channels with bubble concentration in very dilute suspensions is attributed to the effects of bubble-wall collisions. The more gradual subsequent hindering of bubble motion is in qualitative agreement with the predictions of Spelt and Sangani (1998) for the effects of potential-flow bubble-bubble interactions on the mean velocity. The ratio of the bubble velocity variance to the square of the mean is O(0.1). For these conditions Spelt and Sangani predict that the homogeneous suspension will be unstable and clustering into horizontal rafts will take place. Evidence for bubble clustering is obtained by image analysis of video images. The fluid velocity variance is larger than would be expected for a homogeneous suspension and the fluid velocity frequency spectrum indicates the presence of velocity fluctuations that are slow compared with the time for the passage of an individual bubble. These observations provide further evidence for bubble clustering.

Inclination of the channel at angles of 2 to 10 degrees to gravity, produces a variation in bubble volume fraction across the channel. The resulting buoyancy variation drives a shear flow in the channel and provides a convenient means of observing the effects of weak shear on a bubbly liquid. The tendency of buoyancy driven motion to cause the bubbles to accumulate on the upper wall is balanced by lift forces and by an effective hydrodynamic diffusion of bubbles, leading to a modest bubble volume fraction variation across the gap. The magnitude of the shear flow produced by the bubbles can be interpreted in terms of a balance between buoyancy forces and an effective viscous stress. The effective viscosity is more than 100 times larger than the viscosity of the suspending water. The effective viscosity is large because it arises from Reynolds stresses in the liquid which are much larger than the stress due to fluid viscosity at high Reynolds numbers. The Reynolds stress is further enhanced by the presence of bubble clusters.

Presentation not available at time of printing.

SONOLUMINESCENCE IN SPACE: THE CRITICAL ROLE OF BUOYANCY IN STABILITY AND EMISSION MECHANISMS

R. Glynn Holt (rgholt@bu.edu) and Ronald A. Roy (ronroy@bu.edu), Boston University, Dept. of Aerospace and Mechanical Engineering, 110 Cummington St, Boston, MA 02215

INTRODUCTION AND MOTIVATION

Sonoluminescence is the term used to describe the emission of light from a violently collapsing bubble. Sonoluminescence ("light from sound") is the result of extremely nonlinear pulsations of gas/vapor bubbles in liquids when subject to sufficiently high amplitude acoustic pressures. In a single collapse, a bubble's volume can be compressed more than a thousand-fold in the span of less than a microsecond. Even the simplest consideration of the thermodynamics yields pressures on the order of 10,000 ATM. and temperatures of at least 10,000K. On the face of things, it is not surprising that light should be emitted from such an extreme process. Since 1990 (the year that Gaitan discovered light from a single bubble) there has been a tremendous amount of experimental and theoretical research in stable, single-bubble sonoluminescence (SBSL).

Yet there remain at least four unexplained phenomena associated with SBSL in 1g:

- *the light emission mechanism itself,*
- *the existence of anisotropies in the emitted light,*
- *the disappearance of the bubble at some critical acoustic pressure, and*
- *the appearance of quasiperiodic and chaotic oscillations in the flash timing.*

Gravity, in the context of the buoyant force, is implicated in all four of these.

We are developing microgravity experiments probing the effect of gravity on single bubble sonoluminescence. By determining the stability boundaries experimentally in microgravity, and measuring not only light emission but mechanical bubble response, we will be able to directly test the predictions of existing theories. By exploiting the microgravity environment we will gain new knowledge impossible to obtain in earth-based labs which will enable explanations for the above mysteries. We will also be in a position to make new discoveries about bubbles which emit light.

OBJECTIVES

The objectives of the planned investigation are:

(1) To develop an experimental apparatus to perform controlled experiments aboard parabolic flight aircraft to attempt to quantify the effect of gravity on SBSL. Measurements of the light emission and especially the mechanical oscillations of bubbles in 1g, mg, and 2g will be performed. We will investigate the possibility of μg experimentation.

(2) To model the hydrodynamic effects of acceleration on bubble dynamics and SBSL in realistic acoustic resonators. The primary Bjerknes force, buoyancy, drag, mass diffusion, shape stability and (empirically) light emission will be accounted for in the model.

(3) To measure (as a function of acceleration during parabolic flight) a bubble's position, equilibrium radius, maximum radius, oscillatory radius, and spatially and temporally resolved light emission. This will be done for a range of dissolved gas concentrations in order to compare with predictions of our hydrodynamic model.

(4) To measure (as a function of acceleration during parabolic flight) the precise values of acoustic pressure and equilibrium radius that leads to the extinction of a light-emitting bubble, a

phenomenon which occurs at a well defined critical acoustic pressure in 1g experiments. This will test theories which postulate either a nonlinear levitation instability, or a Rayleigh-Taylor instability mechanism for the bubble disappearance.

(5) To test the prediction that chaotic and quasiperiodic timing of the flashes observed in 1g are due to buoyancy-related effects, which could either be induced shape oscillations or a global levitator instability due to time-varying detuning of the levitation cell resonance resulting from the nonlinear bubble oscillations.

RESULTS

We have completed 1 KC-135 flight campaign in August, 1999 utilizing a cubic test chamber operating at 14 kHz. We attempted to test the prediction of our model [1] that hydrodynamics alone dictate a 5 – 35 % change in SBSL intensity, (depending approximately linearly on the dissolved gas concentration) for the 10^{-4}g to 1.8g swing typical of a K-135 parabolic maneuver. The driving mechanism for this effect is the small change in head pressure experienced by the bubble when the acceleration changes. Figure 1 shows the measured bubble dynamics during a single parabola for the August flights. The main result is that for nearly 0g, the bubble grows and emits more light, while at 2g the bubble shrinks and emits less light. The results are in rough agreement with our model.

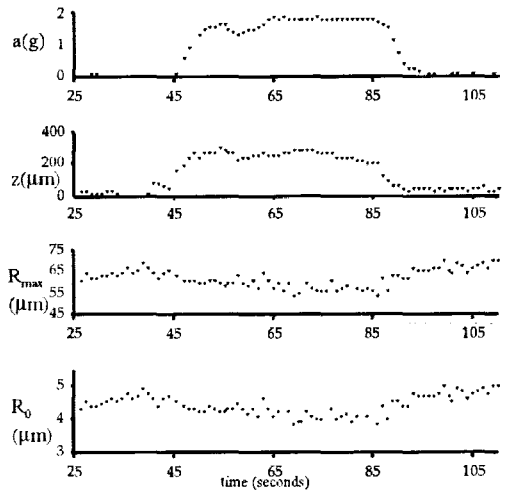

Figure 1. Measured bubble dynamics during KC-135 parabolic maneuver.

MICROGRAVITY RELEVANCE

SBSL bubbles experience a time-varying buoyancy (quantified by the oscillatory volume ratio V_{max}/V_0, see Fig. 2) which reaches maximal excursions precisely where sonoluminescence is observed. This results in a strong nonlinear coupling between volume and translatory motions. Removing the acceleration of gravity from the system will eliminate buoyancy-driven translatory oscillations of the bubble. This would be a decisive test of light emission mechanisms, and will also shed light on the chemical reaction theory of mass flux for volume stability as well as the resonance-controlled shape oscillation instability. Thus, a microgravity environment will change the geography of the parameter space, and the only hope for a clear understanding of the SBSL phenomenon is to perform experiments which locate light emission within the context of the instability boundaries that exist in the parameter space.

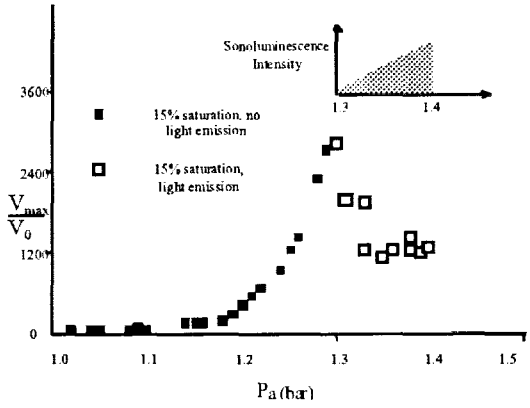

Figure 2. The measured ratio of V_{max} / V_0 during 1 acoustic cycle as a function of acoustic pressure.

REFERENCES

[1] Holt, RG, RA Roy and SC Wyatt, J. Acoust. Soc. Am. 105, No. 2, Pt. 2, p. 960. (Joint EAA/ASA/DAGA meeting, Berlin, 1999)

NASA/CP—2000-210470

Sonoluminescence in Space
Bubble dynamics and SBSL in a variable acceleration environment

Glynn Holt and Ron Roy
Dept. of Aerospace and Mechanical Engineering Boston University

Students:
Sean Wyatt, MS
Charles Thomas, PhD
Gretchen Snoeyenbos, HS
Dominic Rizzo, BS

Special thanks to:
Phil Marston's group at WSU
Tom Matula's group at APL/UW
for sending their KC-135 flight data

Collaborators:
Felipe Gaitan
Joachim Holzfuss

Work supported by NASA

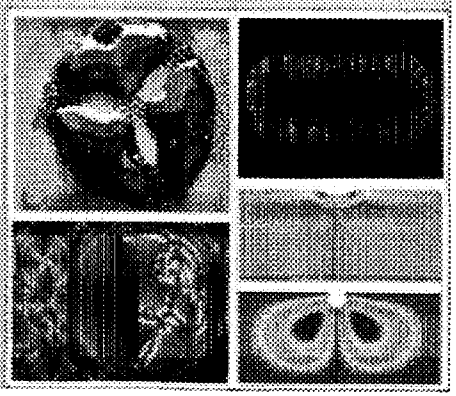

Sonoluminescence

Sonoluminescence (SL, "light from sound") is the result of nonlinear collapses of acoustically forced gaseous bubbles in liquid.

Generic Sonoluminescence Cycle:

- Isothermal Expansion
- Rapid adiabatic collapse
- Chemical Dissociation

Collapse estimates:

R_{min} ~ $R_0/8.8$

$T_{collapse}$ ~ 20,000 Kelvin

$P_{collapse}$ ~ 10,000 atmosphere

t_{pw} ~ 150 picoseconds

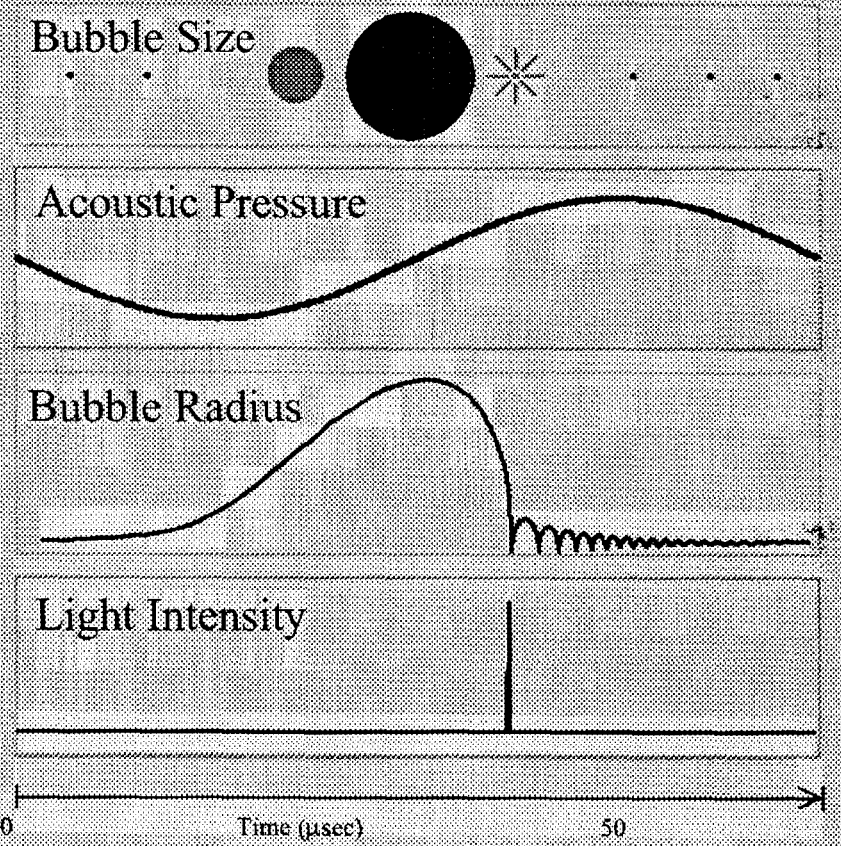

Bubble oscillation cycle

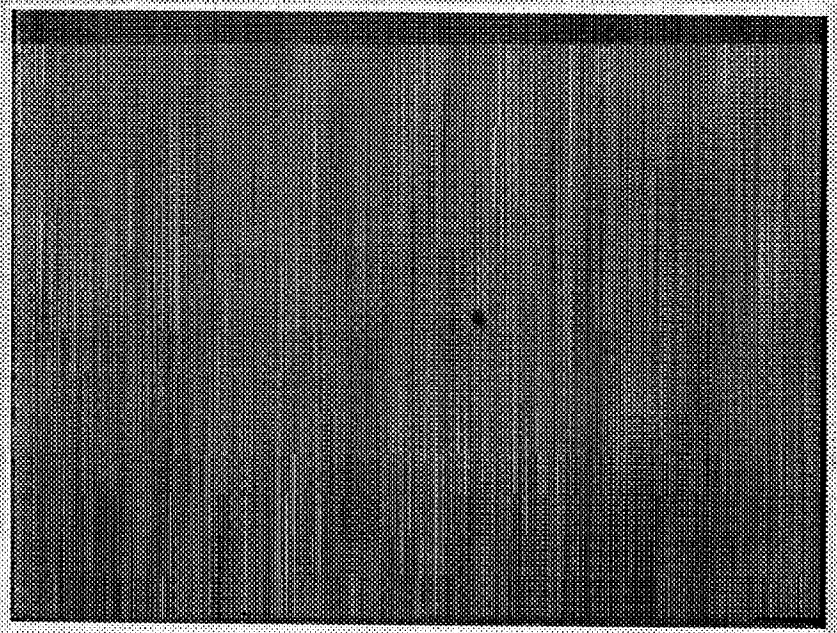

- 14 kHz, 1.3 atm
- $R_0 \sim 10\ \mu m$, $R_{max} \sim 110\ \mu m$
- 20% air/water
- Alias imaging

Why Microgravity?

Single Bubble Sonoluminescence (SBSL) has been intensively investigated both experimentally and theoretically in the past few years. Despite such recent attention, there remain (*at least!*) 4 unexplained phenomena associated with SBSL:

- The light emission mechanism itself,
- The disappearance of the bubble at some critical acoustic pressure
- The appearance of quasiperiodic and chaotic oscillations in flash timing, and
- Spatial anisotropy in the emitted SL light intensity.

Gravity, in the context of *time-varying buoyancy*, is implicated in these unexplained phenomena which have all been observed in 1g experiments

NASA/CP—2000-210470

BOSTON UNIVERSITY

Gravity-induced emission mechanisms

"Fractoluminescence"
(Prosperetti 1996)

- An asymmetric collapse due to translational oscillations, water jet 'cracks' crystalline H_2O . . . light emitted
- Fundamentally true (if not the explanation for SBSL …)
- Verified by hydrodynamic cavitation experiments of 20-30 years ago
- Able to explain many features: anisotropy, spectrum, noble gas effect
- Directly due to gravity, not instability

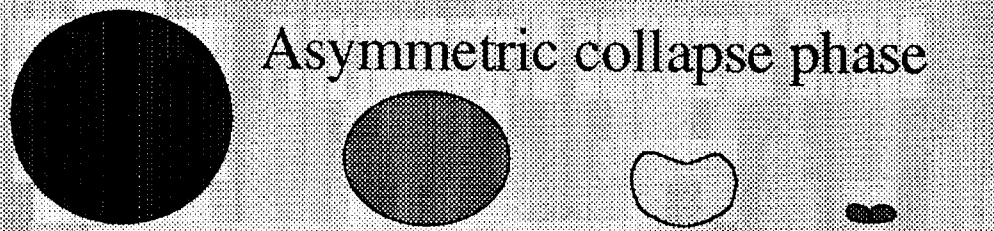

"Plasma Discharge" *(Lepoint et al. 1996)*

- An asymmetric collapse due to Rayleigh-Taylor instability, charge accumulation and dielectric breakdown (Lightning!) inside the bubble
- All oscillating bubbles are Rayleigh-Taylor unstable during some portion of their cycles
- Able to explain many features: anisotropy, spectrum, noble gas effect
- Indirectly due to gravity

Chaotic Light Flashes

The persistence of memory

Period-doubling, chaos, and quasiperiodicity observed in flash interval

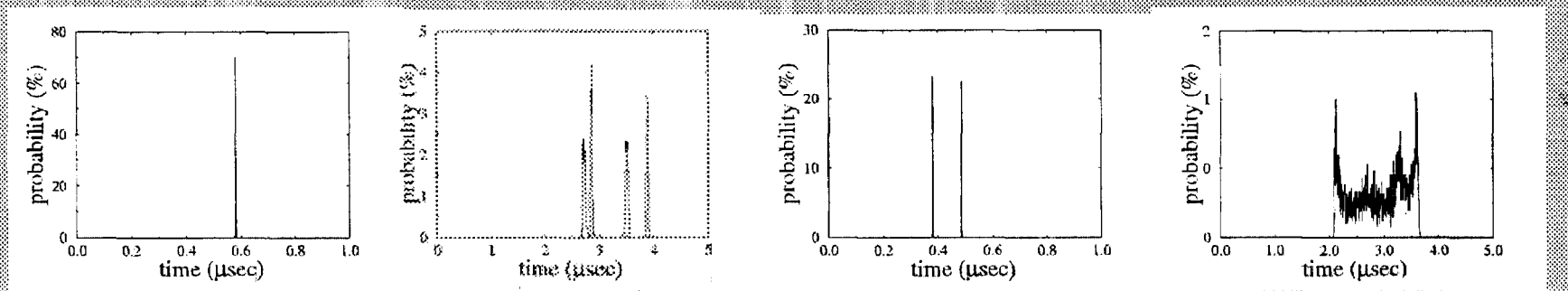

(Holt et al. 1994)

Conjecture 1: Result of levitation detuning instability

gravity exacerbates

Conjecture 2: Coupling of volume and translation oscillations

gravity directly responsible

Conjecture 3: Diffusion oscillations

gravity unrelated

Disappearance of the Bubble

The 'off switch' for sonoluminescence

- *Reported in all experiments*
- *Distinct from parametric shape instability*
- *Occurs at 1.4 bar for air bubble in water at STP*

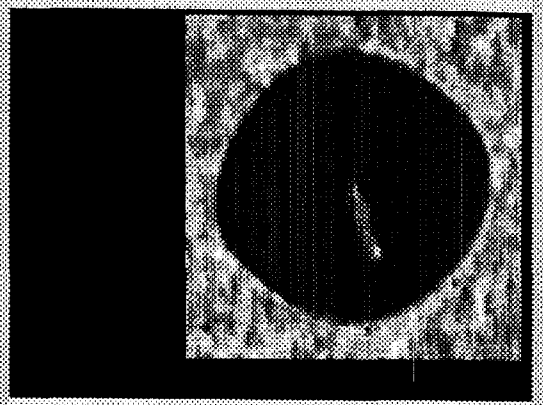

Conjecture 1:

Loss of levitation due to Bjerknes force and gravity: bubble response is self-limiting

Conjecture 2:

Rayleigh-Taylor instability (with necessary perturbation supplied by g-coupled translation) suddenly destroys the bubble

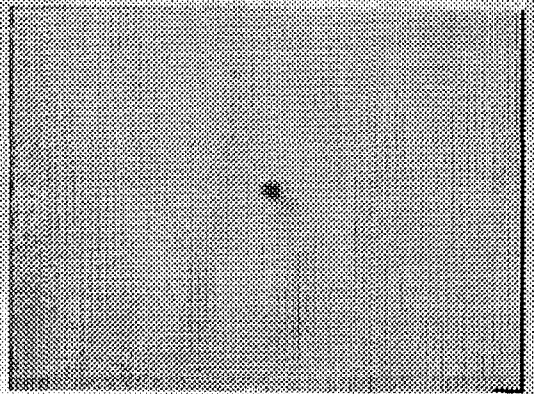

If gravity / buoyancy is removed, perhaps **no** (or **delayed**) disappearance: *stronger forcing and more energetic collapse*

Spatial anisotropy in SL emissions in 1g

2-detector correlation vs angle between detectors:

Isotropic emissions should yield zero

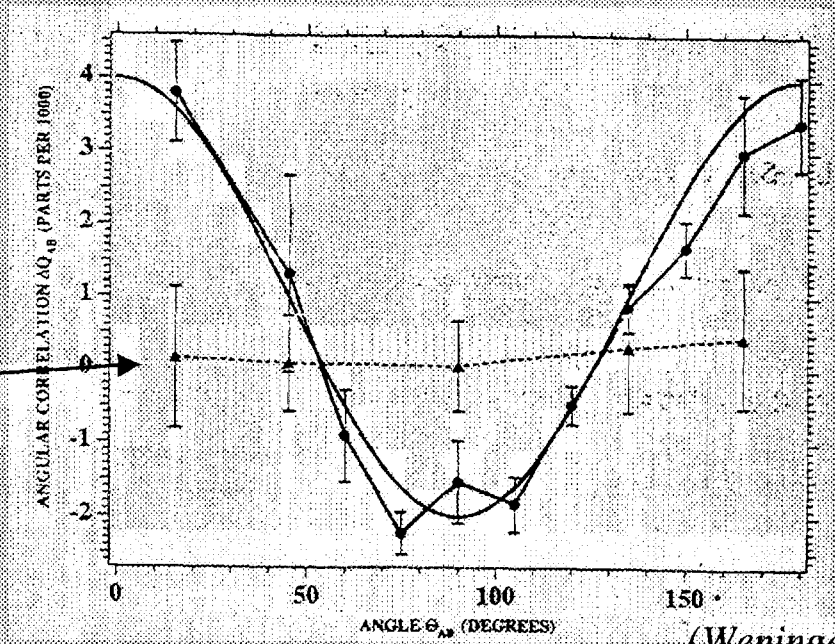

(Weninger et al 1996)

- Evidence of a dipolar component of the emitted light in 1g experiments -- not always, not correlated with QP flash timing
- Gravity implicated (directly or indirectly) in almost every conjectured mechanism for such an anisotropy

Time-Varying Buoyancy

Acoustic Levitation (Bjerknes) force *[Bjerknes 1906]*

$$\mathbf{F}_a = \langle V(t) \cdot \nabla \mathbf{P}_a(r,t) \rangle$$

Where <...> denotes a time-average over one acoustic cycle, $P_a(r,t)$ is the acoustic pressure field, and V(t) is the (nonlinearly) time-varying bubble volume. The force for small (subresonant) bubbles is *towards* the pressure maximum

Buoyant Force (**g** downwards)

$$F_b = \rho g V(t)$$

$F_b / F_a = 1$, defines acoustic levitation *if* oscillations in V(t) are small and sinusoidal

But oscillations of V(t) are large and nonlinear for SL bubbles!!

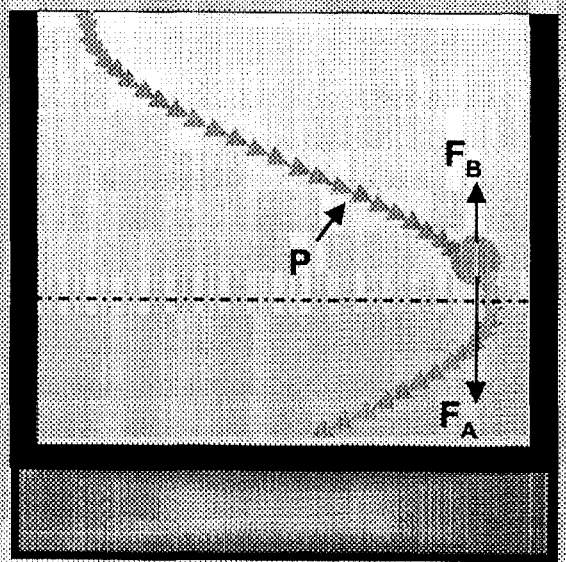

The potential for translations on the slow and fast time scales if g > 0.

Modeling effort

Want to model ONLY bubble dynamics effects of changing acceleration in realistic levitator -- deviations observed in experiment would be ***SL specific***

Dual constraints of SHAPE STABILITY and DIFFUSIVE STABILITY•• require R_0 to respond to any changes due to acceleration *(within the confines of known parameter space)*

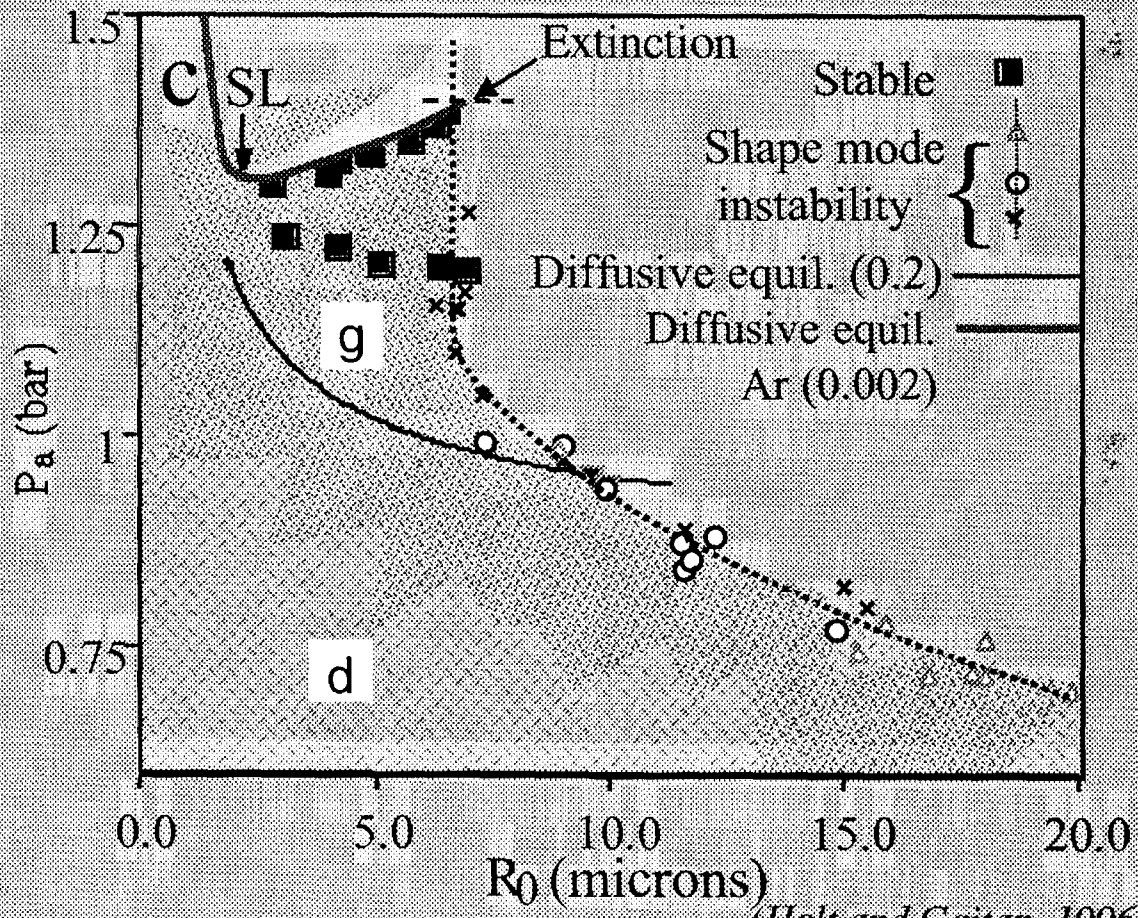

(Holt and Gaitan, 1996)

BOSTON UNIVERSITY

Modeling Acceleration Effects

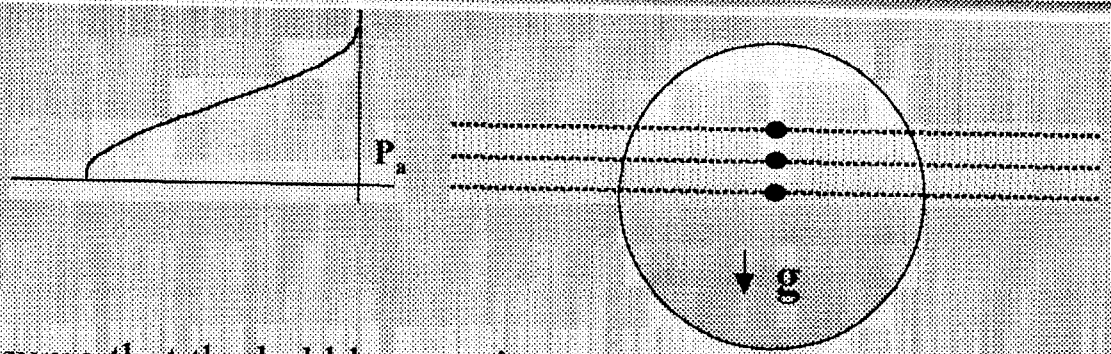

$r = ?, a = 2\ g$
$r \neq 0, a = 1\ g$
$r = 0, a = 0\ g$

Assume that the bubble experiences some total acceleration **a(t)**.

$$F_a' = -\langle V(t) \cdot \nabla P_a(r,t) \rangle - \rho \cdot \mathbf{a} \langle V(t) \rangle$$

1. **a(t)** will cause the levitation position of bubble to change:
   new position $\Rightarrow$ new P_a
   solve RP @ new P_a $\Rightarrow$ new R_o (diffusive stability: Pa Ro)
   solve RP @ new R_o $\Rightarrow$ new R_{max}
   $\Rightarrow$ **change in SL intensity** ΔI_{SL}
2. **a(t)** will cause the ambient pressure at the bubble to change:
   $P_{amb} = P_\infty + \rho \cdot a\ (R_s - r)$
   solve RP @ new P_{amb} $\Rightarrow$ new R_o and R_{max} at new P_a
   $\Rightarrow$ **change in SL intensity** ΔI_{SL}
3. KC-135 profile input as **a(t)**, total ΔI_{SL} calculated

Total ΔI_{SL} compared to KC-135 measurements

Experimental Acceleration Profile

Effect of imposing diffusive equilibrium

For a static bubble, the gas pressure p_g at the surface of the bubble is

$$p_g = P_0 + \frac{2\sigma}{R_o}, P_0 = P_{cabin} + \rho a\left(R_s - r\right)$$

This implies that the dissolved (inert) gas concentration, c_i/c_o in diffusive equilibrium is

$$\frac{c_i}{c_o} = \left(1 + \frac{2\sigma}{R_o P_0}\right) \frac{\left\langle \frac{R}{R_o} \right\rangle}{\left\langle \left(\frac{R}{R_o}\right)^4 \right\rangle}$$

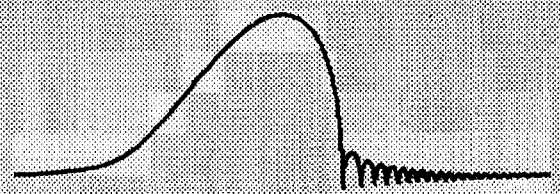

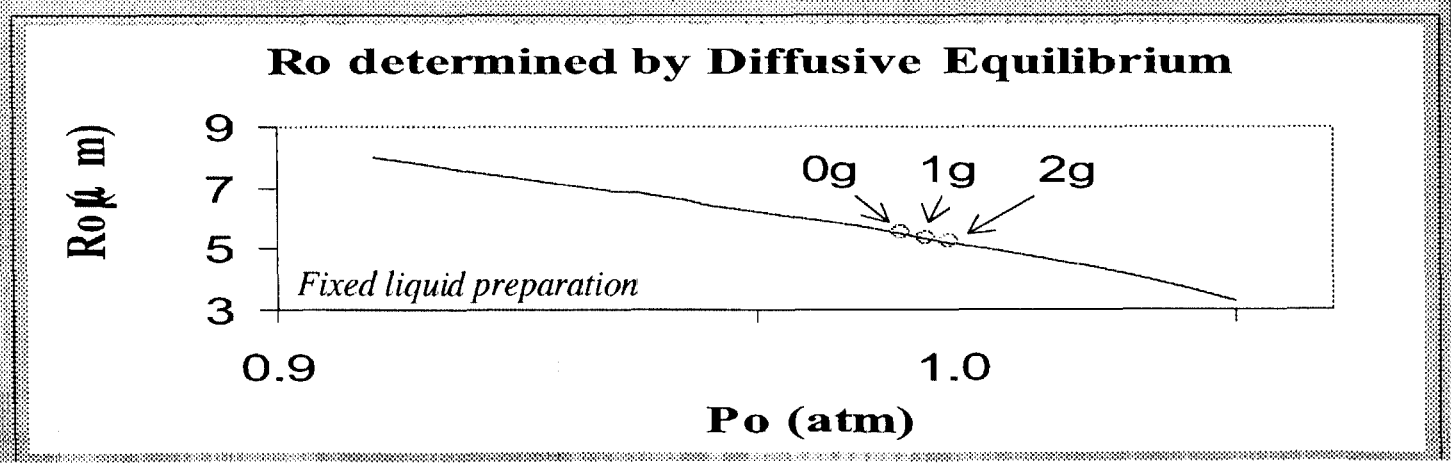

Closure: SL light emission

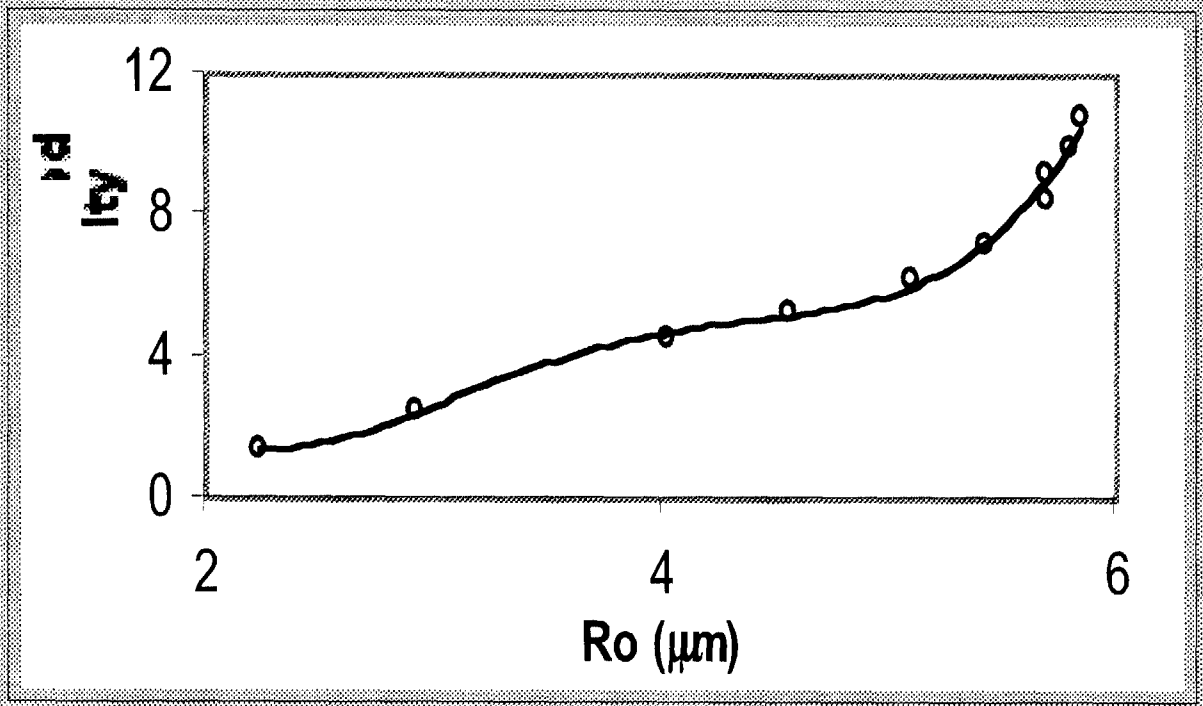

Empirical data from experiments in Ig (Gaitan and Holt, PRE **59**, 99)

Polynomial fit equation

$y = 0.2437x^4 - 3.6307x^3 + 19.487x^2 - 42.902x + 34.426$

23 kHz Test Case

Test Case

- Water filled sphere (radius, R_s=5.8 cm)
- $P_a(r) \propto P_{max}\sin(kr)/kr$ (max at center = 1.445 atm)
- f_o=23 kHz
- DGC = 0.002

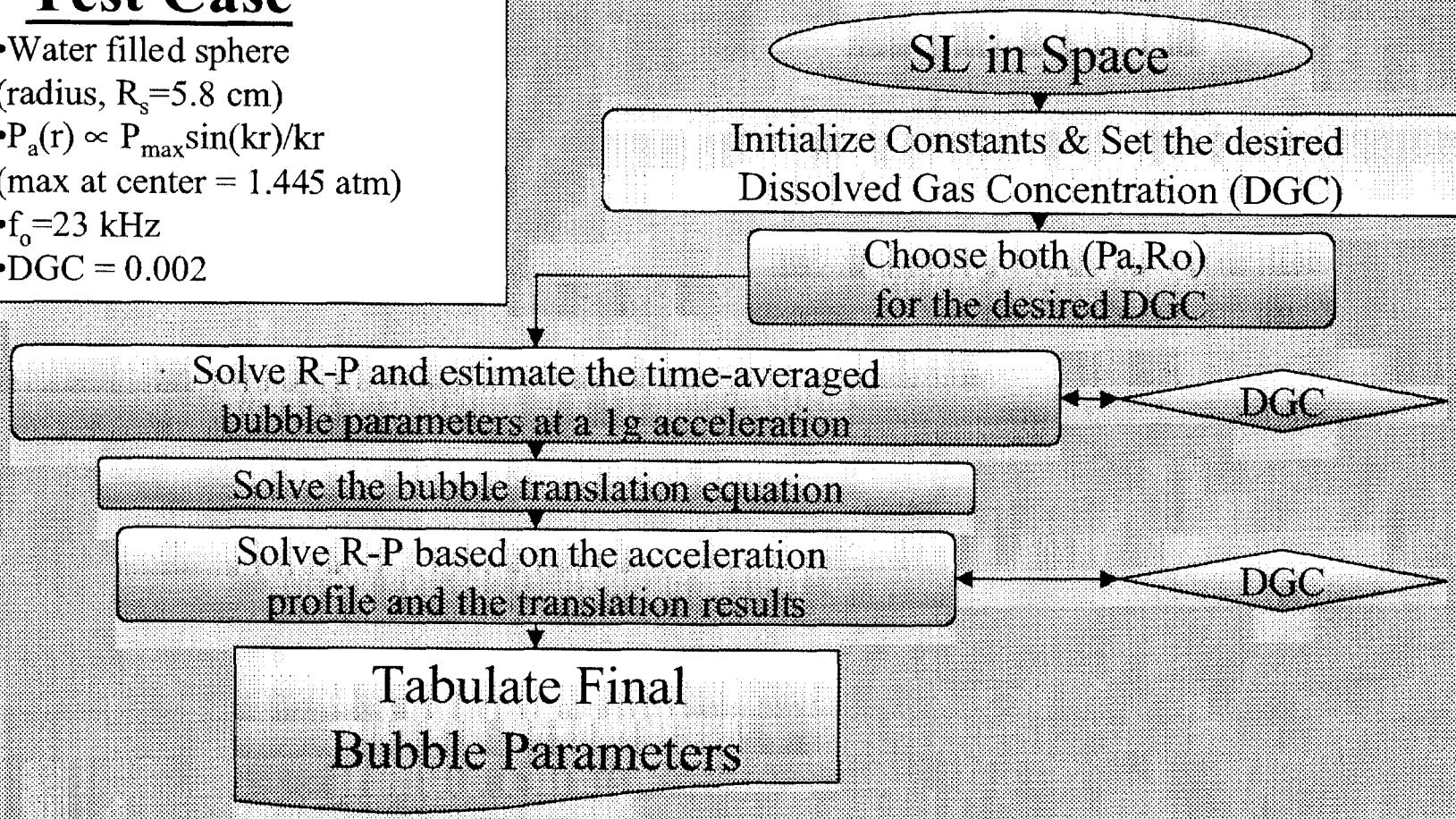

23 kHz Test Case: Numerical results

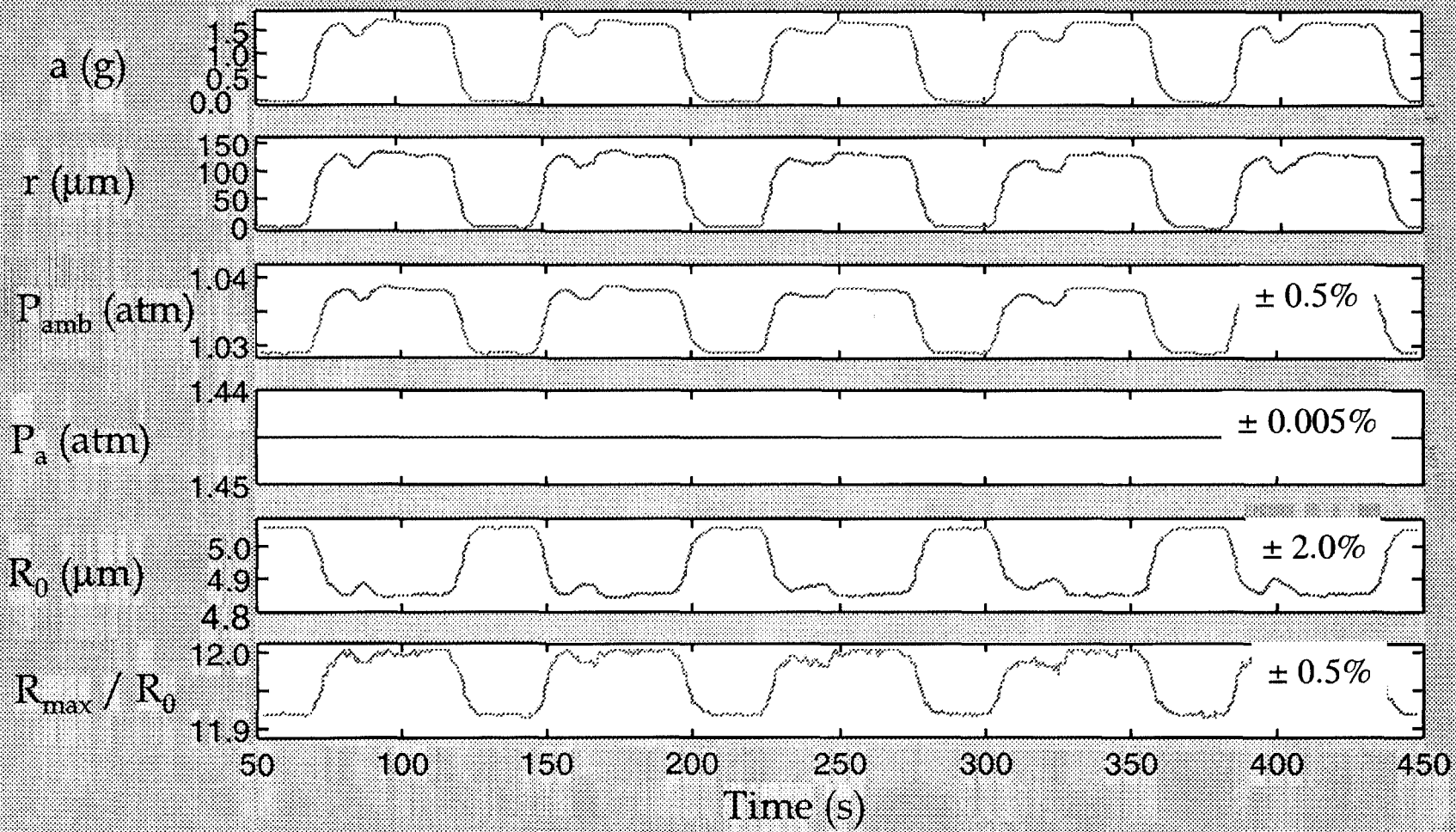

23 kHz Test Case Predicted Intensity Results

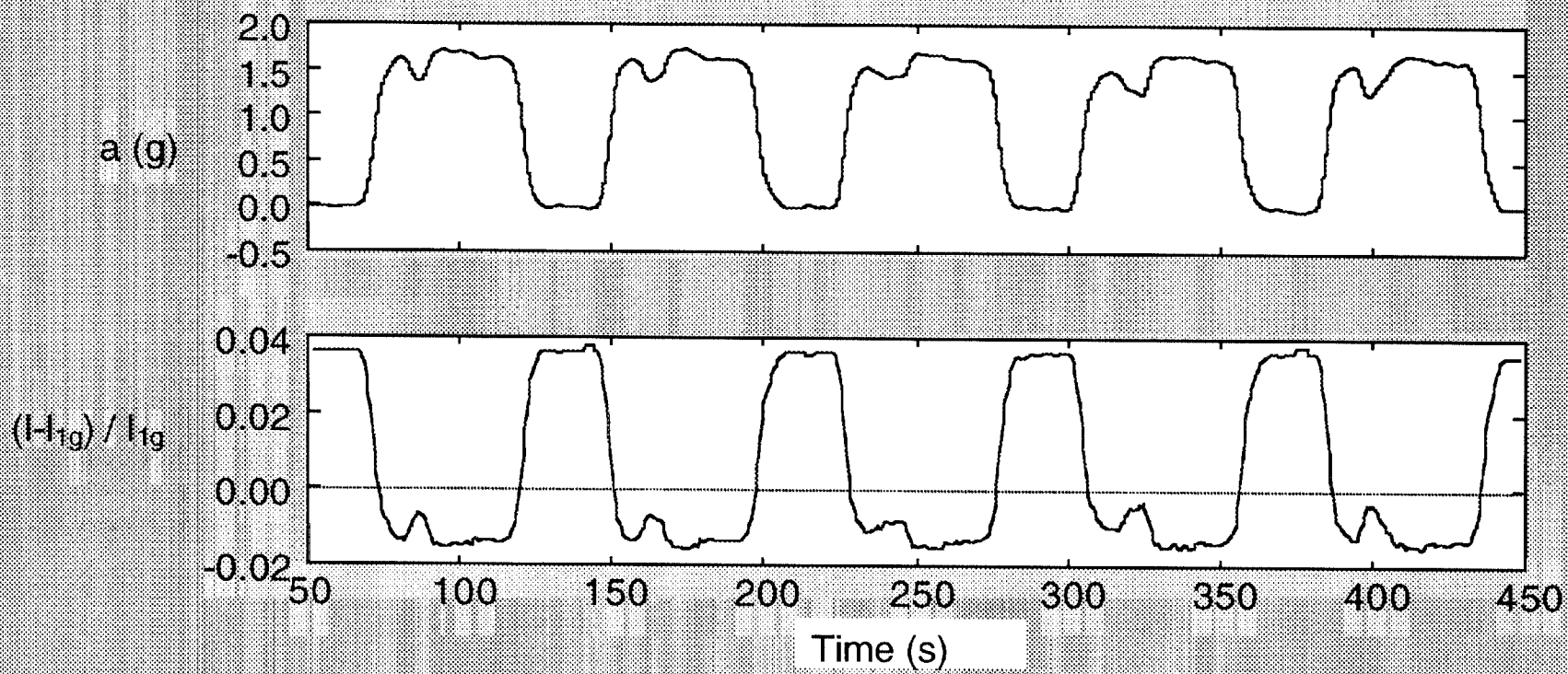

$f_o = 23$ kHz, $P_{max} = 1.445$ atm, DGC = 0.002

Intensity Comparisons
WSU group

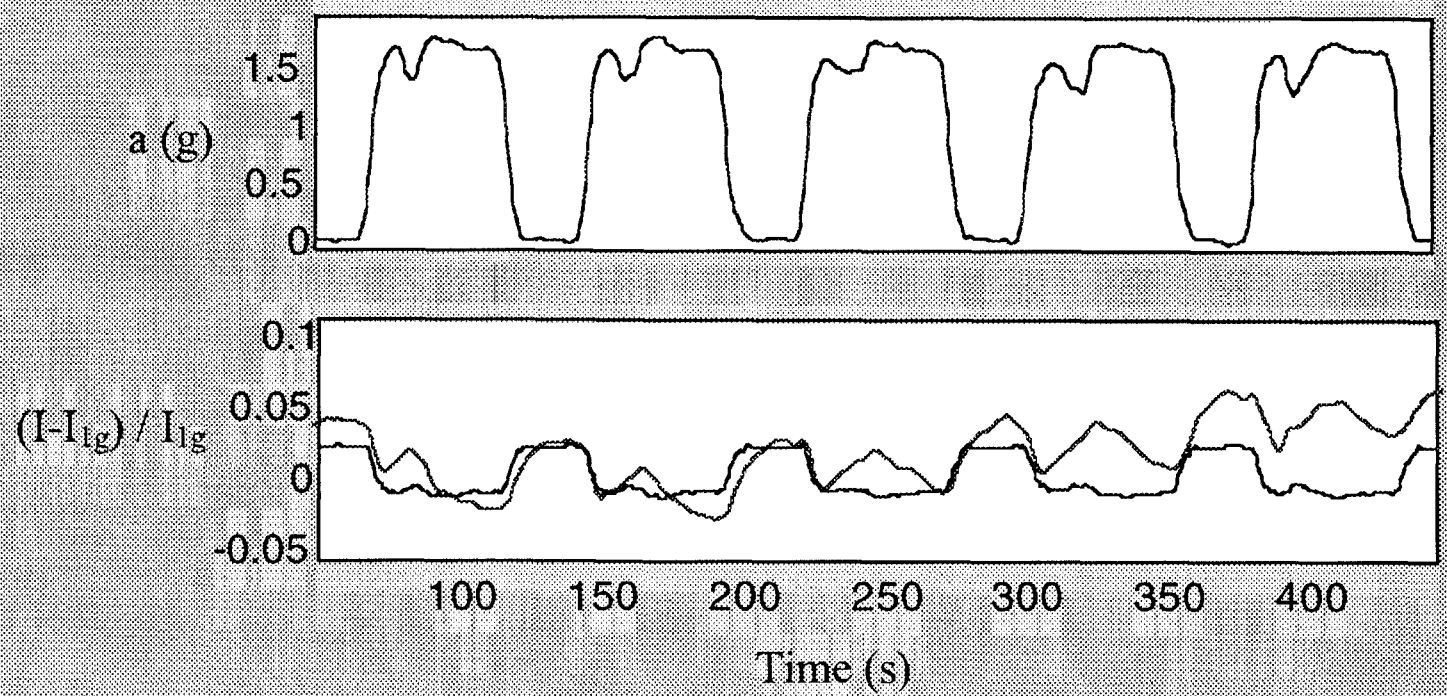

Date: 7/30/98
f_o = 34 kHz
c_i/c_o = 0.0015

——— Numerical
——— Experimental

Intensity Comparisons

APL/UW group

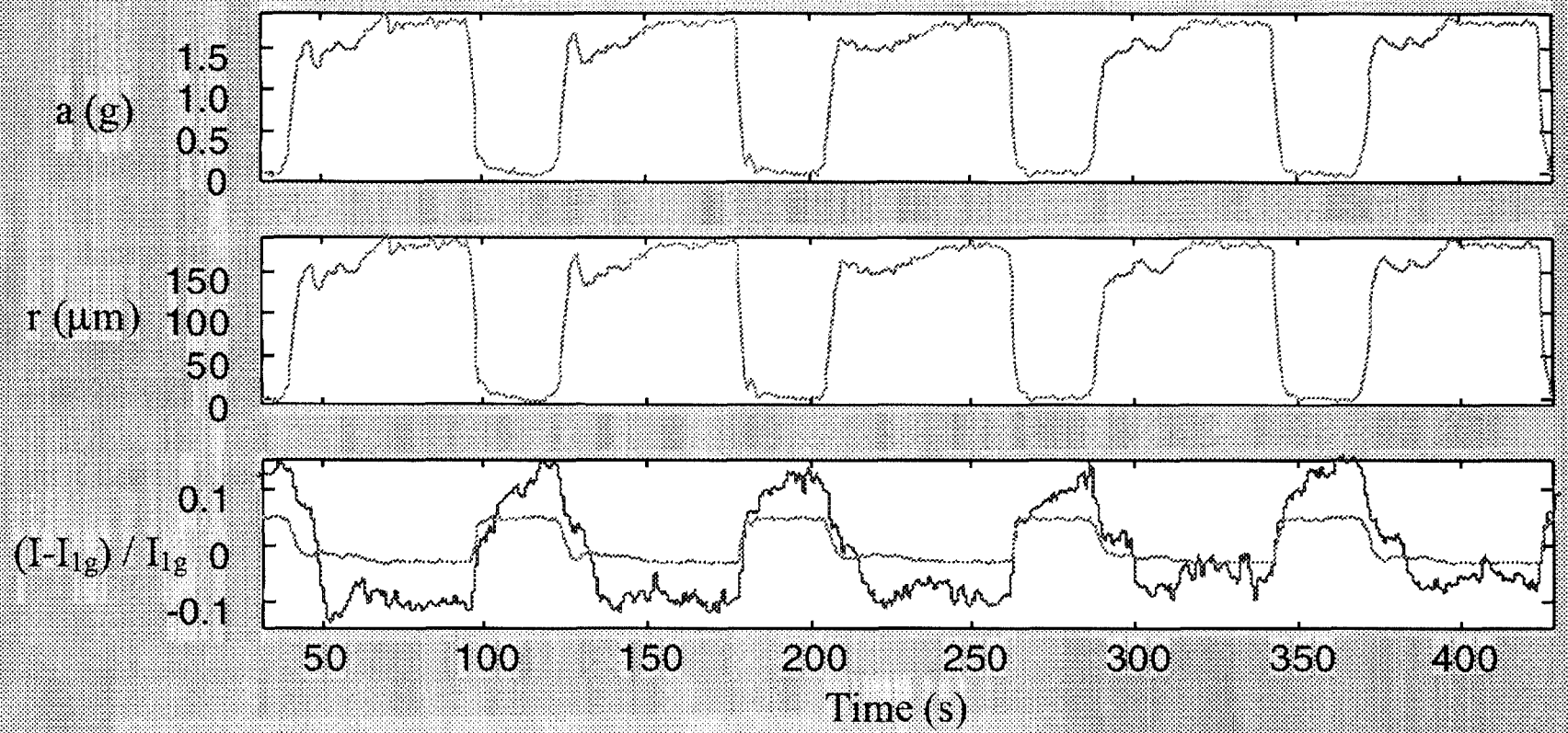

Date: Summer 98

f_o = 30 kHz

c_i/c_o = 0.0016

——— Numerical

——— Experimental

Effect of dissolved gas concentration

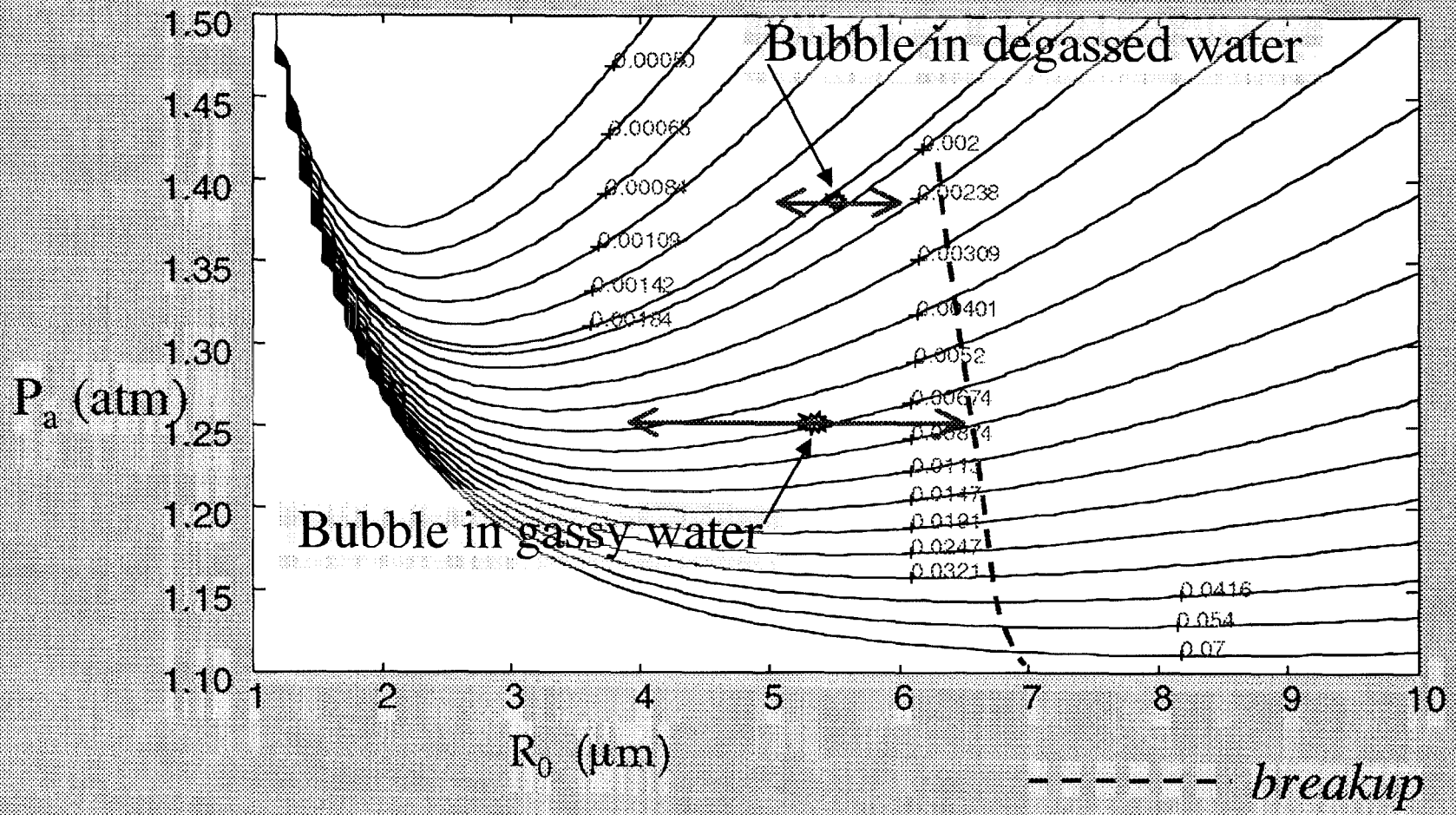

Bubbles in gassy water grow and shrink ***more*** *for the same change in acceleration*

Effect of dissolved gas concentration

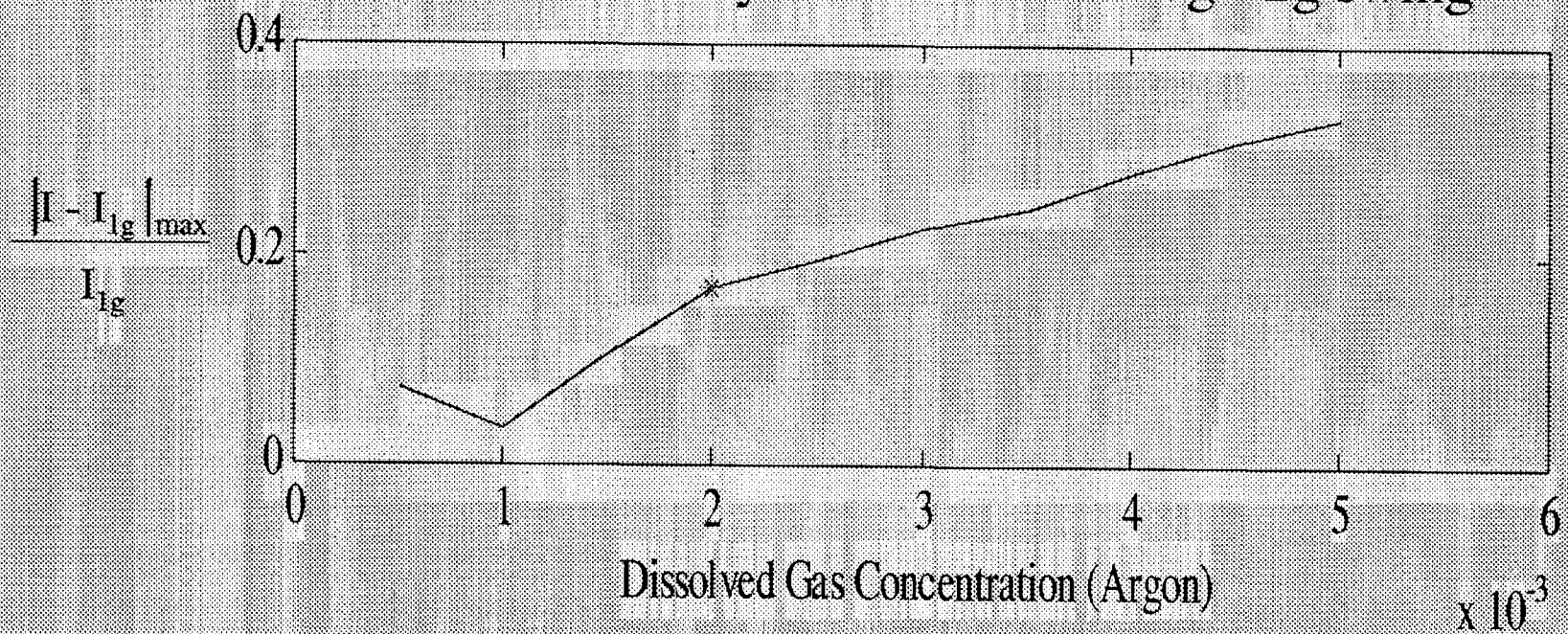

Experimental setup

Diagnostics:

a(t)	in situ accelerometer
P_∞(t)	in situ pressure transducer
P_a (t)	in situ hydrophone
Mie I(t)	PMT, Mie scattering
R_o, R_{max} , Shape, Position	digital imaging
SL Pulse <I>	PMT array

Schematic

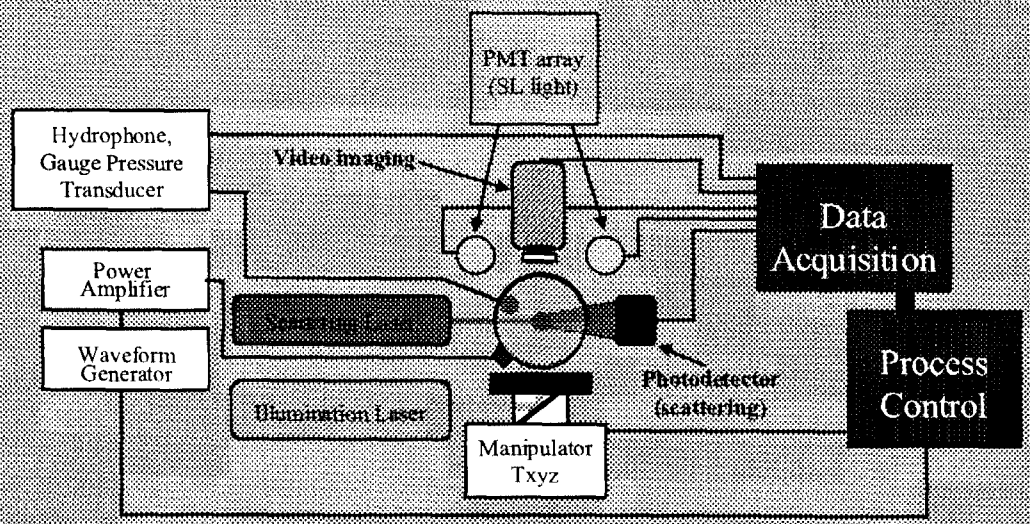

Acoustic levitation

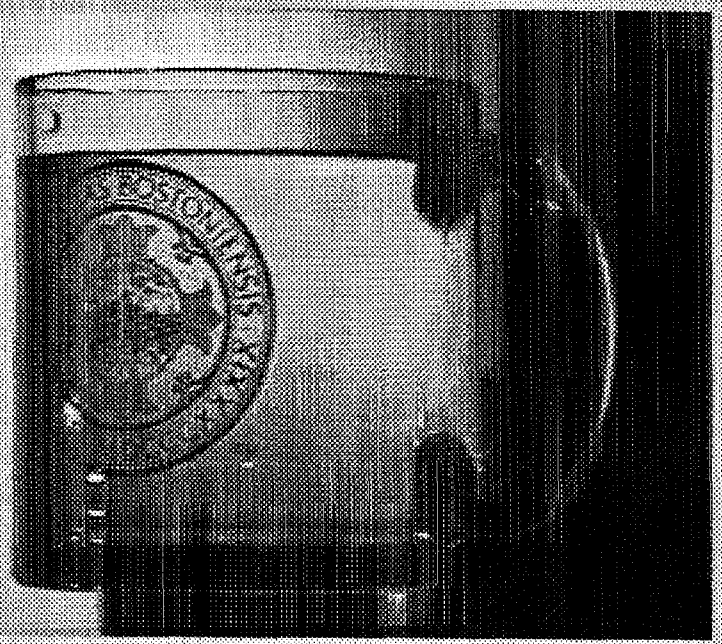

Uncharacterized resonator

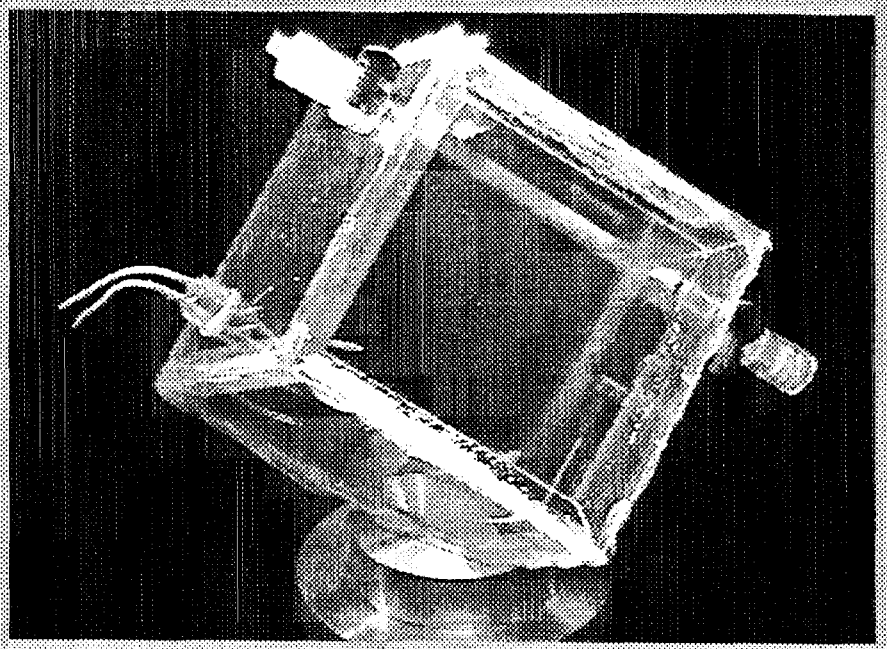

Cubic flight cell

...All you need is an acoustic standing wave in an appropriate resonator

Aug 1999 KC experiment

- Deck-mounted rack
- Simultaneous imaging and SL emission data
- Engineering shakedown
- Science if possible…

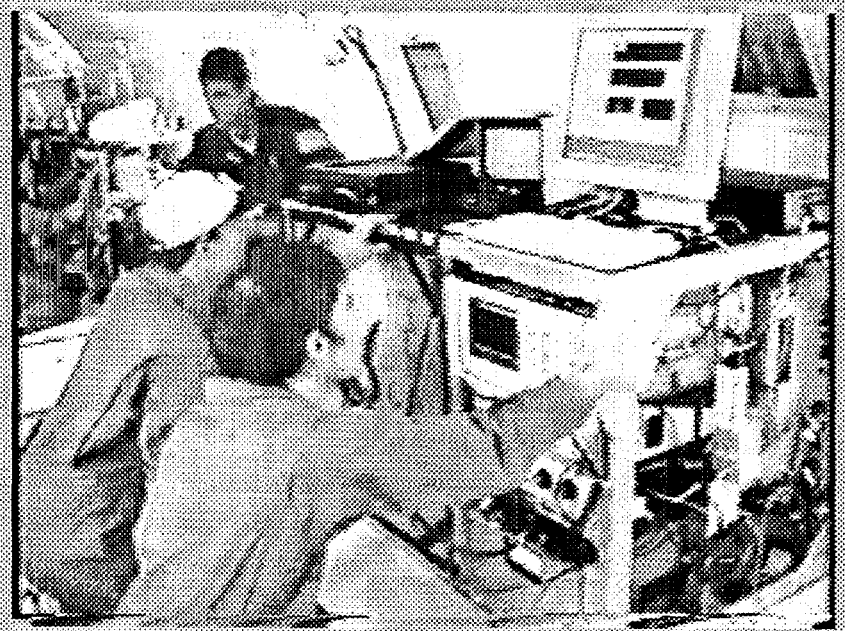

August 25,1999 results: SL emission vs acceleration and cabin pressure

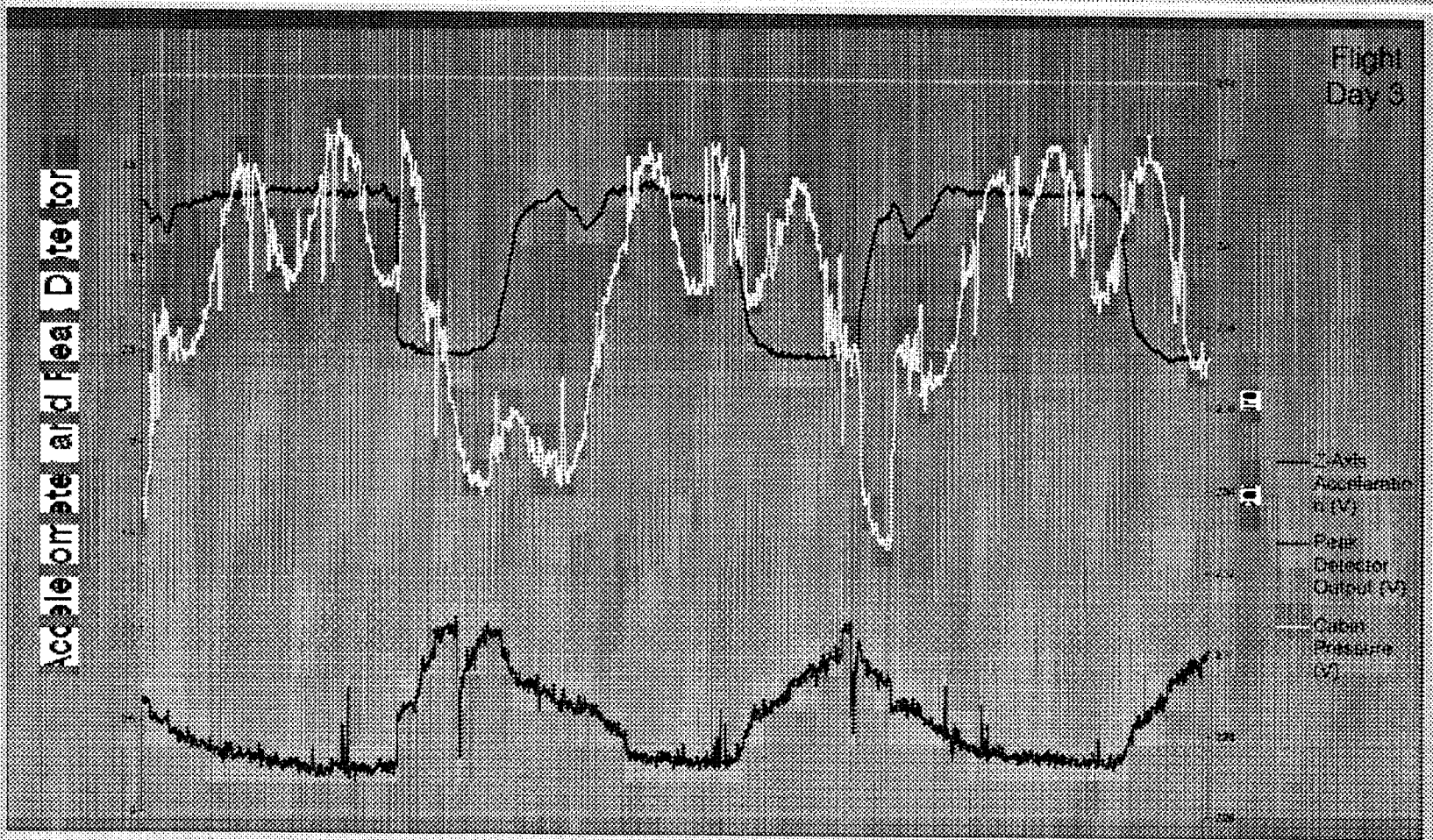

- *Resonator not sealed: bubble responds to cabin pressure fluctuations of ± 25 torr at mean of ~ 600 torr in flight.*

Bubble imaging movie

- 30 fps images of 2g-0g swing
- CW LED illumination
- ~1mm field of view

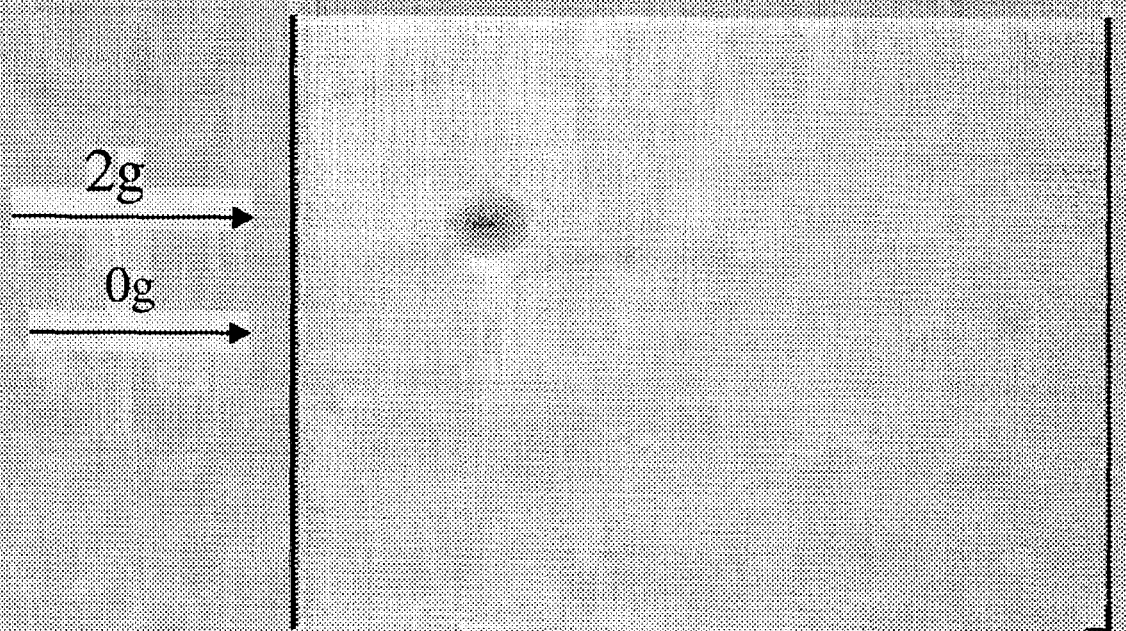

BOSTON UNIVERSITY

August 25, 1999 results: Bubble size and position

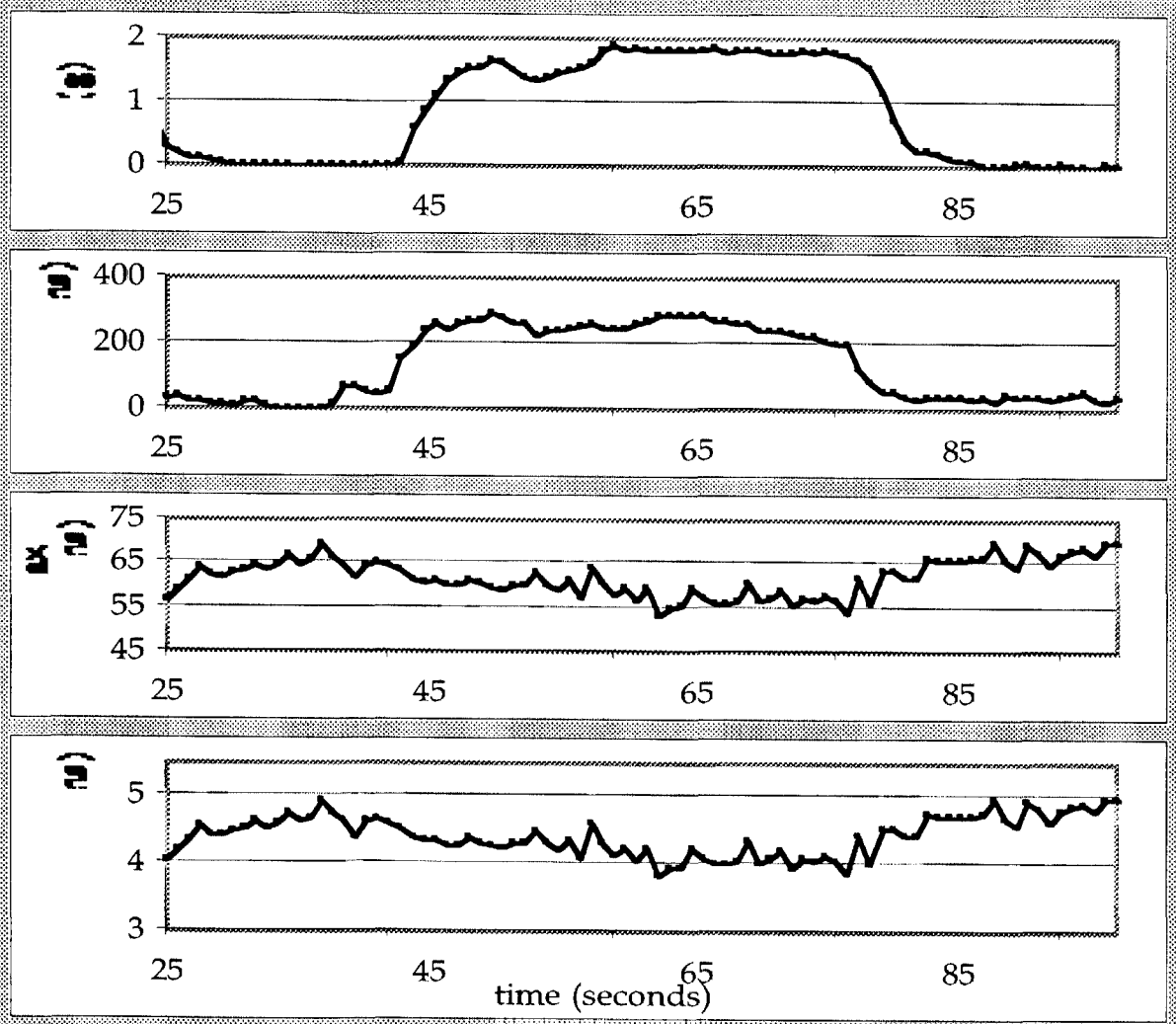

Aug. 1999 results: Extinction threshold

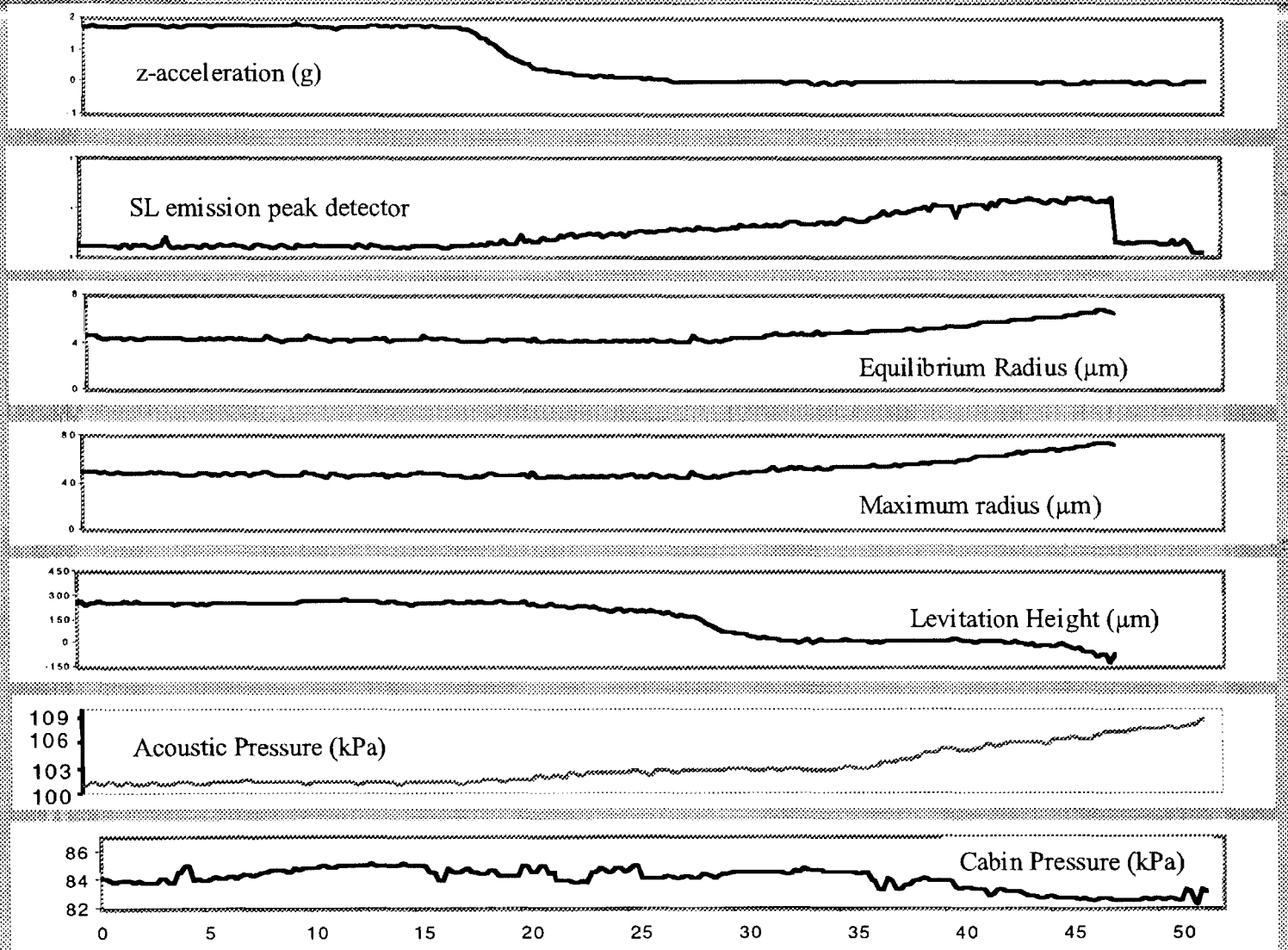

NASA/CP—2000-210470

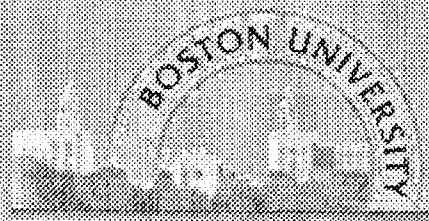

Finally....

Summary

1. Light emission mechanism:

•*Have testable hydrodynamic hypothesis for light emission effects*

•*Trends agree with other groups experiments*

•*Trends agree with our initial experiments*

2. Chaotic SL flash timing

•*Have an initial flight hardware configuration*

3. Extinction

•*Initial experiment inconclusive -- not a dramatic difference from 1g, however*

4. KC experiments limiting....

Future

1. KC experiments:

Rebuild hard/software

sealed cell, more automation

Diagnostics in work

Flash timing

SL emission anisotropies

2. Improve model

Add time-dependent diffusion

Add shape instabilities

?Add Bremstrahlung emission model?

3. Extended microgravity experiments

parameter space stability boundaries are unknown in 0g

ATTENUATION OF GAS TURBULENCE BY A NEARLY STATIONARY DISPERSION OF SOLID PARTICLES

John K. Eaton and Wontae Hwang
Department of Mechanical Engineering
Stanford University
Stanford, CA 94305

ABSTRACT

Turbulent gas flows laden with a dilute distribution of solid particles or liquid droplets are common in industrial and natural environments. Experiments in simple flows such as pipes and channels have shown that fine particles can cause substantial reductions in the turbulence kinetic energy of the gas phase. For example, Kulick et al. [1] found turbulence attenuation in a fully developed channel air flow laden with 70 micron diameter copper particles at mass loading ratios around 50%. Figure 1 shows streamwise turbulence intensity measurements from that experiment, and indicates nearly an order of magnitude reduction in the turbulence kinetic energy at the highest mass loading ratio.

There has been little success in modeling turbulence attenuation in situations where the attenuation is large. For Reynolds averaged models, there is not even agreement on the correct form of the Reynolds-averaged equations. Chen and Wood [2] represent the particle force on the fluid as a continuous force field proportional to the velocity difference between the fluid and particles. They then derive a turbulent kinetic energy transport equation containing a term representing extra dissipation of turbulence by particles. Eaton [3] has shown that this term does not produce results that agree with experiment. Crowe [4] argues that the force the particles exert on the fluid must be averaged over volumes. However, he neglects the fact that such averaging filters some of the turbulence, and must be accounted for by modifications to the other terms in the TKE transport equation. There are parallel efforts to develop appropriate models for large eddy simulations, but these methods have had little success in predicting the strong attenuation observed in some experiments.

It is hard to understand how particles with diameters near the Kolmogorov scale can have such a large effect on the turbulence. We believe that particle wakes play a critical role. At typical particle Reynolds numbers, the wake is much larger than the particle diameter. These wakes can produce distortions of energy containing eddies and thus increase the turbulence dissipation rate. Unfortunately, this effect is difficult to study with numerical simulations which cannot resolve flow structures on the order of the particle diameter.

Our research has two primary goals: First to obtain planar velocity measurements with sufficient resolution to observe distortion of the small and moderate scale turbulence by particles. Second, to conduct experiments in which the mean velocity of the particles relative to the turbulence is zero in order to eliminate the steady flow wake which usually occurs behind particles. It is desired to conduct the experiments in the simplest possible flow, homogeneous, isotropic turbulence. We require a flow system to provide turbulence with zero mean velocity and microgravity to allow the particles to also have zero mean velocity.

The apparatus (Figure 2) uses eight synthetic jet actuators mounted on the corners of a square plexiglass box. Each synthetic jet drives an ejector which discharges through a square-bar turbulence grid. Synthetic jets were chosen because they have zero net mass flow, a requirement for operation in typical micro-gravity facilities. This arrangement was chosen over rotating or moving grids to eliminate moving parts and increase the reliability. Also, the arrangement is spherically symmetric which enhances isotropy and virtually eliminates the mean velocity.

We developed a custom DPIV system to acquire the velocity measurements. The system must be able to resolve the smallest scales of the turbulence and also have high accuracy. It must also be capable of measuring the fluid velocity in the vicinity of particles, where large amounts of light are scattered. These requirements make the optical setup and the seeding particle size distribution critical. Special software has been developed (Paris & Eaton [5]) to separate the particle and tracer images. Optimization of the system for use in the turbulence chamber is still underway. Preliminary turbulence measurements in the chamber indicate that rms velocities above 1 m/s can be achieved with excellent isotropy. An earlier configuration had a small mean velocity of approximately 0.1 m/s. We believe the present setup which is fully spherically symmetric will eliminate even this relatively small mean velocity. We anticipate completing the single phase qualification soon and the acquiring laden flow data with several particle sizes.

REFERENCES

[1] Kulick, J.D., Fessler, J.R., and Eaton, J.K. (1994) "Particle response and turbulence modification in fully developed channel flow," *J. Fluid Mech.*, **277** 109-134.

[2] Chen, P.E. and Wood, C.E. (1985) "A turbulence closure model for dilute gas-particle flows," *Can. J. Chem.* Engr, **63**, 349-360.

[3] Eaton, J.K. (1995) "Turbulence modification by particles in shear flows," *ASME Vol. FED-228*, 273-278.

[4] Crowe, C.T. (2000) "On models for turbulence modulation in fluid-particle flows," *Int. J. Multiphase Flow*, **26** 719-727.

[5] Paris, A.D. and Eaton, J.K. (1999) "Measuring velocity gradients in a particle-laden channel flow," *Proc. 3rd Intl. Workshop on Particle Image Velocimetry*, Santa Barbara.

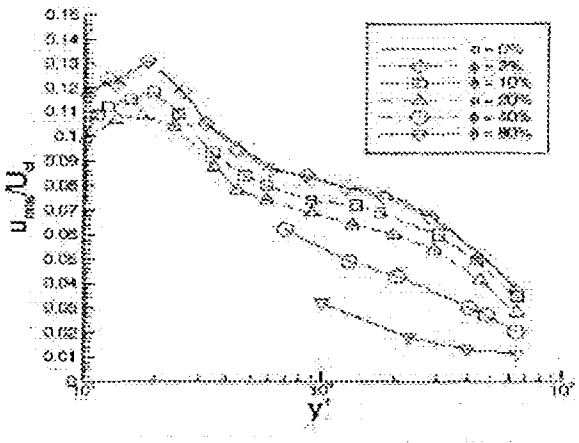

Fig. 1

Fig. 2

NASA/CP—2000-210470

Attenuation of Gas Turbulence by a Nearly Stationary Dispersion of Solid Particles

Principal Investigator: John K. Eaton

Research Assistants: Wontae Hwang, Anthony D. Paris

Sponsor: NASA

Motivation

- Strong attenuation of turbulent kinetic energy observed in gas flows laden with solid particles
- Conditions typical of pulverized coal, sprays, pneumatic conveying

$$\rho_p / \rho_f = O(1000)$$

$$\dot{m}_p / \dot{m}_f = O(0.1-1)$$

$$d_p / \eta_f = O(1)$$

- Attenuation not captured by existing models or simulation techniques

Turbulence Attenuation

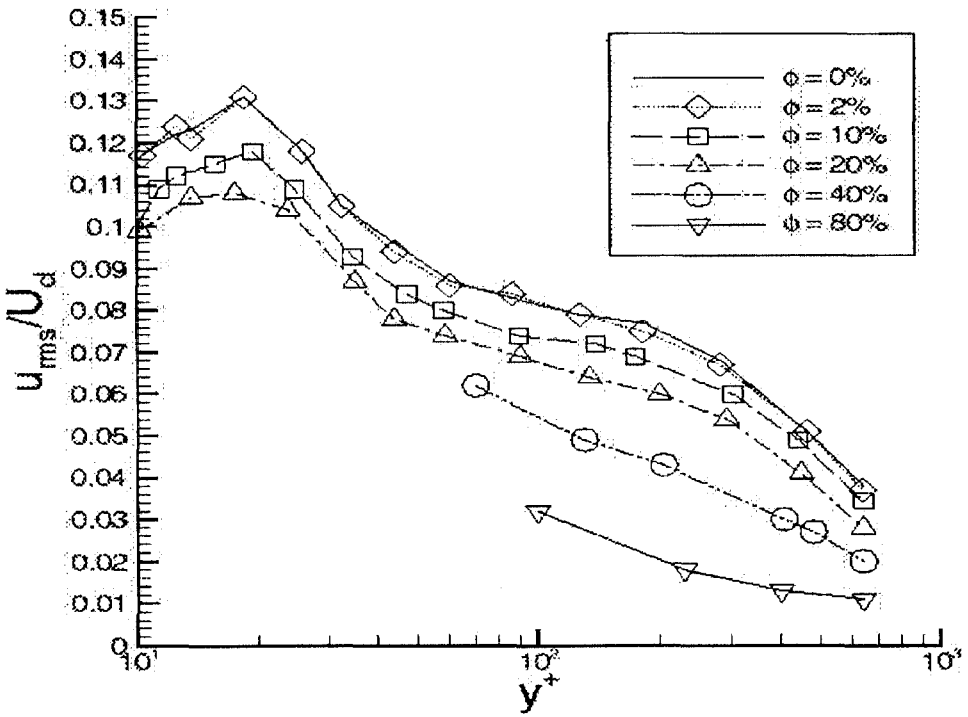

Streamwise turbulence intensity with various loadings of 70 Om copper particles. From Kulick et al. (1994).

Mathematical Description

Transport equation for turbulence kinetic energy in homogeneous flow:

$$\frac{Dk}{Dt} = -\overline{u_i' u_k'} \partial_k U_i - \nu \overline{\partial_k u_i' \partial_k u_i'} - \frac{1}{\rho_f \tau_p} \left[C(\overline{u_i' u_i'} - \overline{u_i' v_i'}) + (\overline{c' u_i' u_i'} - \overline{c' u_i' v_i'}) + (U_i - V_i)\overline{c' u_i'} \right]$$

production from mean gradient

dissipation by viscosity

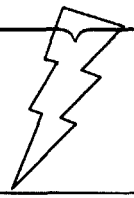

Represents the drag on turbulent eddies by particles. Incorporated in current models, but does not capture full turbulence modification.

Possible Cause

The gravitational potential energy of particles is converted to turbulent velocity fluctuations which distort the turbulent eddies, leading to higher dissipation rate.

NASA/CP—2000-210470

Objectives

- Provide turbulence attenuation data in a simple homogeneous flow
  - no mean flow
  - gravitationally driven mean particle motion
- Required data
  - turbulent kinetic energy
  - dissipation rate
  - spatial spectra
  - particle motion

NASA/CP—2000-210470

Isotropic Turbulence Chamber

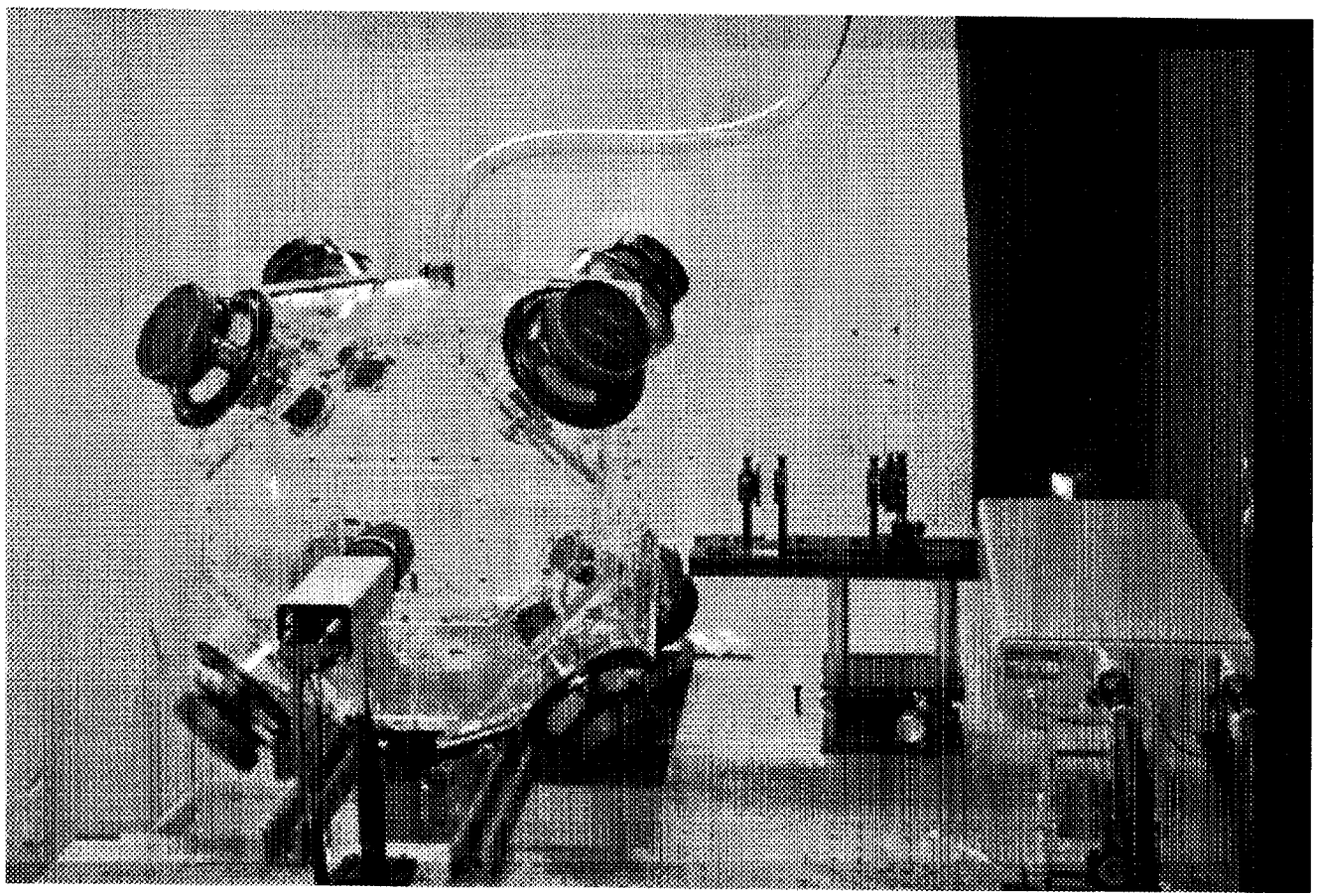

Synthetic Jet Actuator

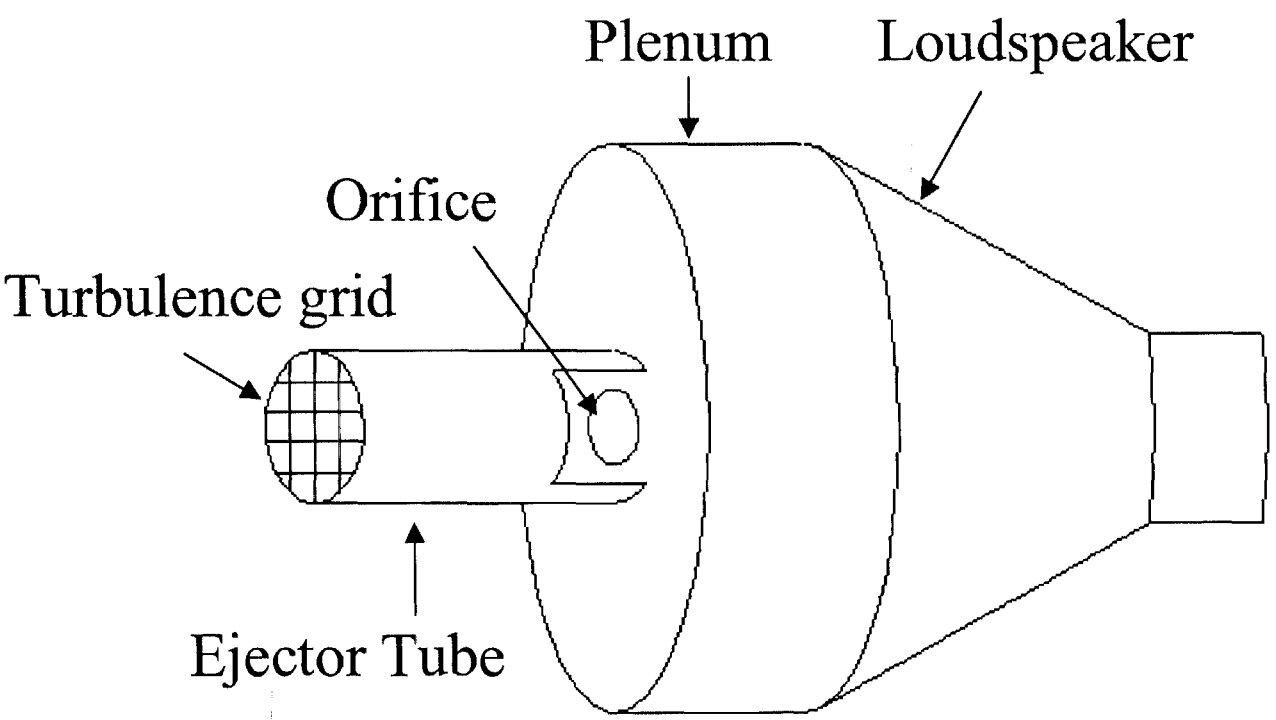

PIV/PTV System

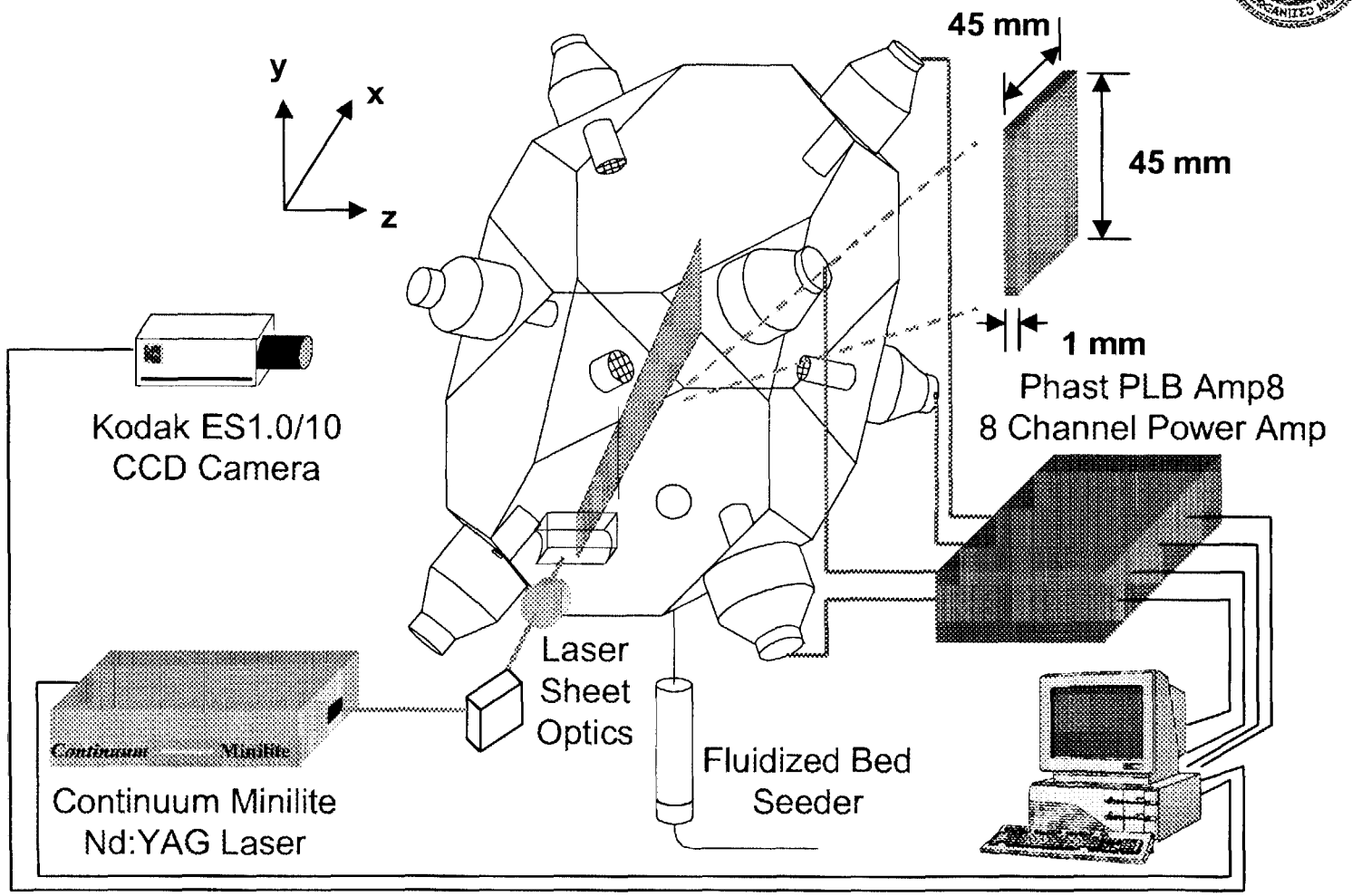

Image of Tracers & Particles

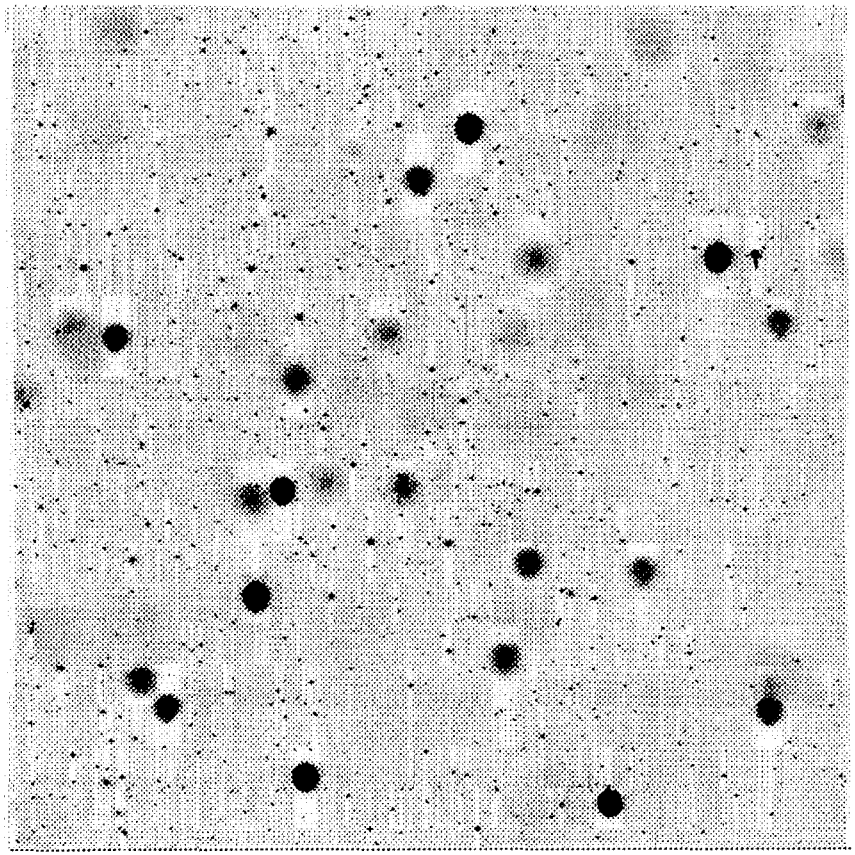

Particles: 150 μm glass
Tracers: 0.3 μm alumina

Separated Images

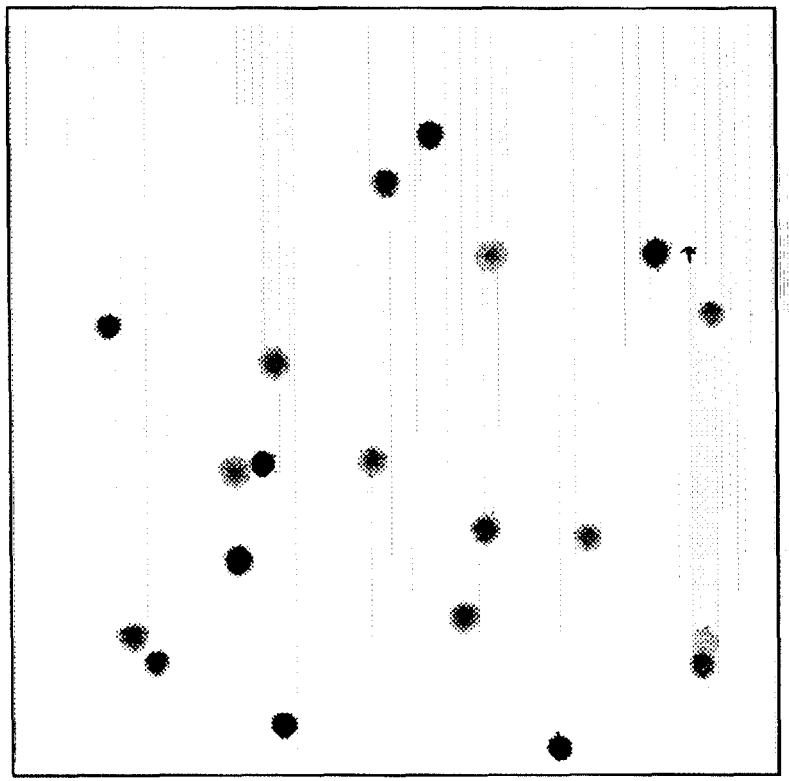

(a) 150 μm glass only

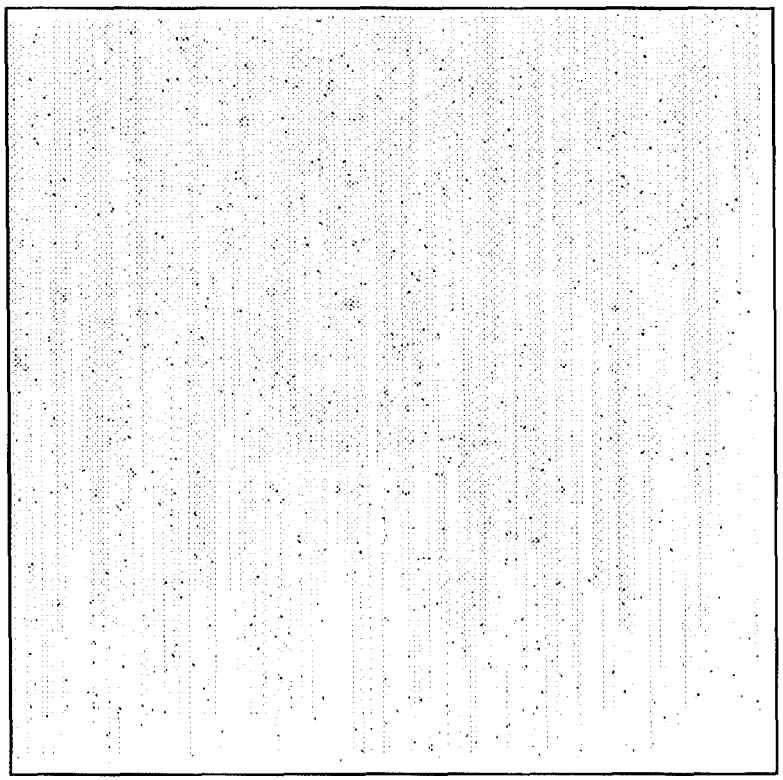

(b) 0.3 μm alumina only

Flow Quantification

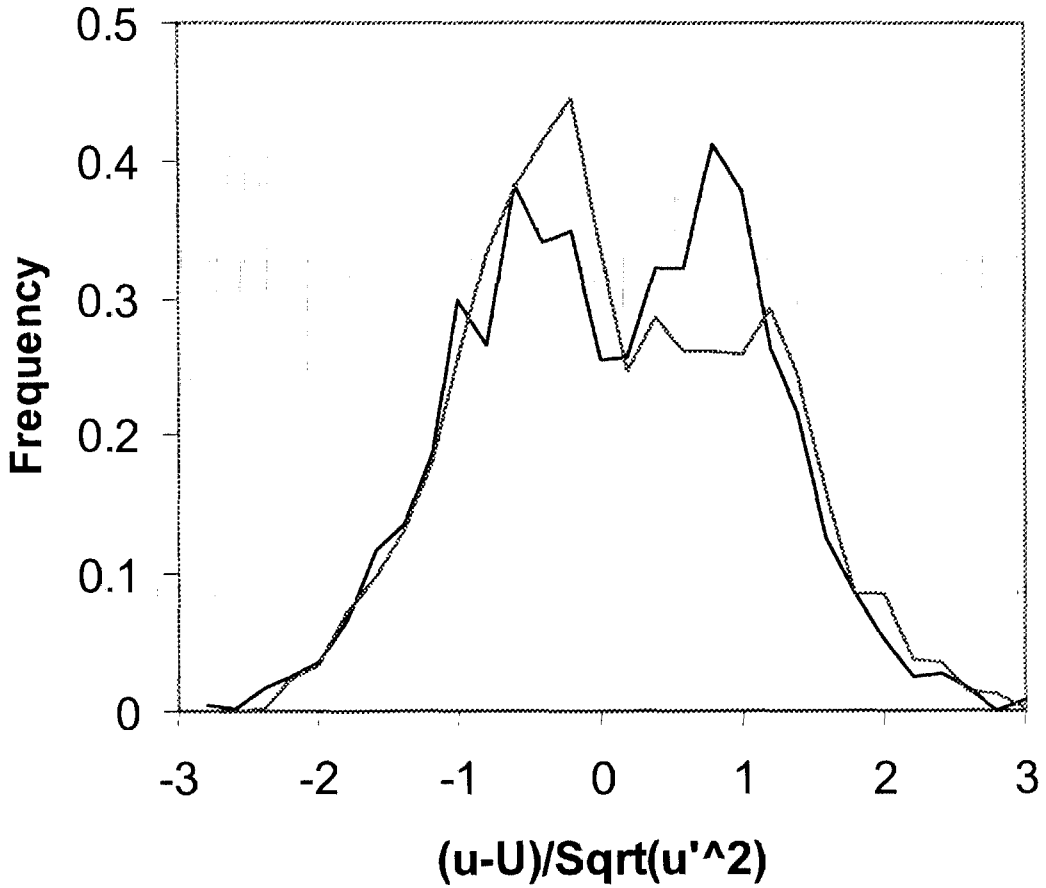

w (out of plane vel.)
u (horizontal vel.)

w mean = 0.184 m/s
w RMS = 1.23 m/s
w skewness = -0.020
w flatness = 2.49

u mean = -0.142 m/s
u RMS = 1.21 m/s
u skewness = 0.183
u flatness = 2.42

Summary

- Turbulence chamber developed
- Qualification nearly complete
- Hybrid 2-phase PIV/PTV system working
- Optimization with light flow tracers needed

Planned Experiments

1. Falling Particles
    a. Forced isotropic turbulence
    b. Decaying isotropic turbulence

2. Zero-G suspended particles
    a. Forced isotropic turbulence
    b. Decaying isotropic turbulence

THERMOCAPILLARY FLOW AND AGGREGATION OF BUBBLES ON A SOLID WALL

Hiroki Kasumi, Yuri E. Solomentsev[1],
Scott A. Guelcher[2], John L. Anderson and Paul J. Sides
Carnegie Mellon University, Department of Chemical Engineering, Pittsburgh, PA 15213,
ps7r@andrew.cmu.edu, [1] Motorola, Austin, TX 78721,
[2] Bayer Corporation, South Charleston, WV 25303

ABSTRACT

During the electrolytic evolution of oxygen bubbles forming on a vertically oriented transparent tin oxide electrode, bubbles were found to be mutually attractive [1, 2]. The mechanism of the aggregation had never been explained satisfactorily until Guelcher *et al.* [3] attributed it to thermocapillary flow. The gradient of surface tension of the liquid at the bubble's surface, which was established because of reaction heat and ohmic heat loss at the electrode wall, drives flow of the liquid adjacent to each bubble; the bubble "pumps" fluid along its surface away from the wall. Fluid flows toward the bubble to conserve mass and entrains nearby bubbles in the flow pattern. The same logic would apply when two bubbles of equal size are adjacent to each other on a warm wall. Each bubble drives thermocapillary flow and hence entrains the other in its flow pattern, which drives the aggregation. Our objective here is to perform experiments where the temperature gradient at the wall is well known and controlled. The theory can be quantitatively tested by studying aggregation of bubble pairs of equal size, and by varying system parameters such as temperature gradient, bubble size and fluid viscosity. The results are then compared with the theory in a quantitatively rigorous manner. We demonstrate that the theory without adjustable parameters is capable of quantitatively modeling the rate of aggregation of two bubbles.

The equations governing the thermocapillary flow around a single stationary bubble on a heated or cooled wall in a semi-infinite domain were solved. Both Reynolds number and Marangoni number were much less than unity. The critical result is that liquid in the vicinity of a warm wall flows toward a stationary collector bubble (Figure 1). Consequently the thermocapillary flow around the stationary bubble entrains another bubble toward itself. The bubbles undergo hindered translation parallel to the wall with velocity **U** while the fluid flow field is described with **u**. Two velocities were equated by using a wall hindrance parameter q:

$$\mathbf{U} = q\mathbf{u} \tag{1}$$

which shows the velocity of bubble is proportional to the entraining velocity. The hindrance parameter q can experimentally be measured independently. q can also be calculated by solving the equations of motion for a bubble translating parallel to a solid wall.

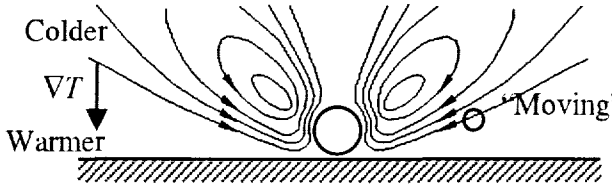

Figure 1 Streamlines of the flow around a bubble near a heated wall.

The experimental cell is cylindrical with an ID of 10 cm and consists of a 1 cm deep main cell filled with silicone oil and flanked by two thermal reservoirs. The upper thermal reservoir was heated and the lower thermal reservoir was cooled so that the bubbles aggregate. Two types of silicone oil (η = 0.02 and 0.50 Pa s) were used. Two equal sized air bubbles were injected into the cell with a syringe. The center-to-center distance of bubbles was observed through a microscope. Bubble radius ranged from 0.40 mm to 0.65 mm and the temperature gradients along with the cell ranged from 1400 to 5000 K/m.

The bubbles aggregated when heat flows from the wall to the fluid. The velocities of bubbles were in the range of 1 – 10 μm/s. The separation r decreased more quickly when the temperature gradient was higher, bubble size was larger, and the oil viscosity was lower. r decreased more rapidly as the bubbles approached each other. Figure 2 is a plot of scaled data by appropriate time scale and bubble radius. Dimensionless time was arbitrarily set to be zero when the dimensionless center-to-center distance between the bubbles was 4. All the bubble trajectories fall onto one line, especially in the range of dimensionless distance from 4 to 3. This means the relative movement of the bubble pair is proportional to the temperature gradient and bubble size and it is inversely proportional to the viscosity of the oil. This result strongly suggests that the thermocapillary flow-based aggregation mechanism is correct.

A value of q can be estimated by fitting the scaled data to Eq. [1]. A best fit value of q was obtained as q = 0.26 with a standard deviation of 0.03. Independent experimental results for q for a 0.5 mm radius bubble, give values of q in the range 0.11 to 0.23. The value of q obtained from solving the equations of motion reveals q has values in the range 0.23-0.30. Since the full scale of possible values of q is zero to one, the maximum deviation of independently determined values of q from the best fit value was 15% of this full scale. Thus reasonable quantitative agreement between theory and experiment has been obtained.

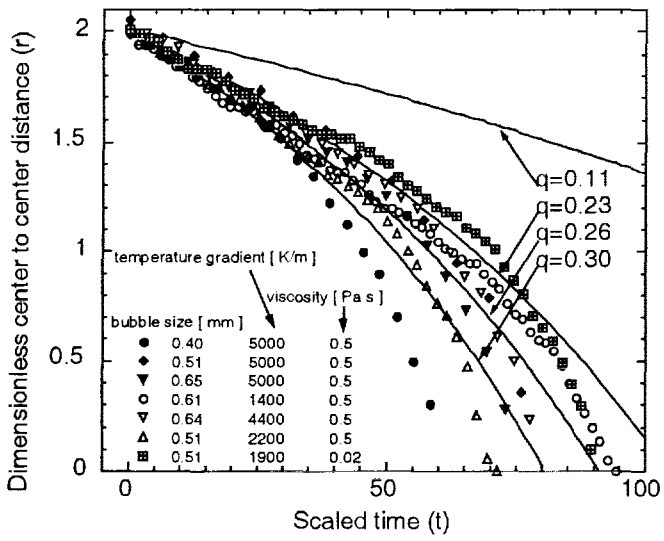

This work was supported by the NASA Microgravity Program, grant NAG3-2159. We acknowledge the use of a macro for the image software written by Professor Darrell Velegol of the Pennsylvania State University.

REFERENCES

[1]. Sides, P. J., Ph.D. Thesis, University of California, Berkeley, California (1981).

[2]. Sides, P. J., and Tobias, C. W., *J. Electrochem. Soc.*, **132**, 583 (1985).

[3]. Guelcher, S. A., Solomentsev, Y. E., Sides, P. J., and Anderson, J. L., *J. Electrochem. Soc.*, **145(6)**, 1848 (1998).

Figure 2 Scaled experimental bubble trajectories trajectory. The ordinate shows the center-to-center distance of the bubbles scaled by the bubble radius, and the abscissa shows the dimensionless time. Solid lines are the bubble trajectory calculated from Eq. 1.

NASA/CP—2000-210470

Thermocapillary Flow and Aggregation of Bubbles on a Solid Wall

Hiroki Kasumi, Yuri E. Solomentsev ,Scott A. Guelcher,
John L. Anderson and Paul J. Sides

Carnegie Mellon University
Department of Chemical Engineering
Pittsburgh, PA 15213

Supported by: NASA
Microgravity Research Program,NAG3-2159

Motivation

Radial specific coalescence, Sides and Tobias (1981)

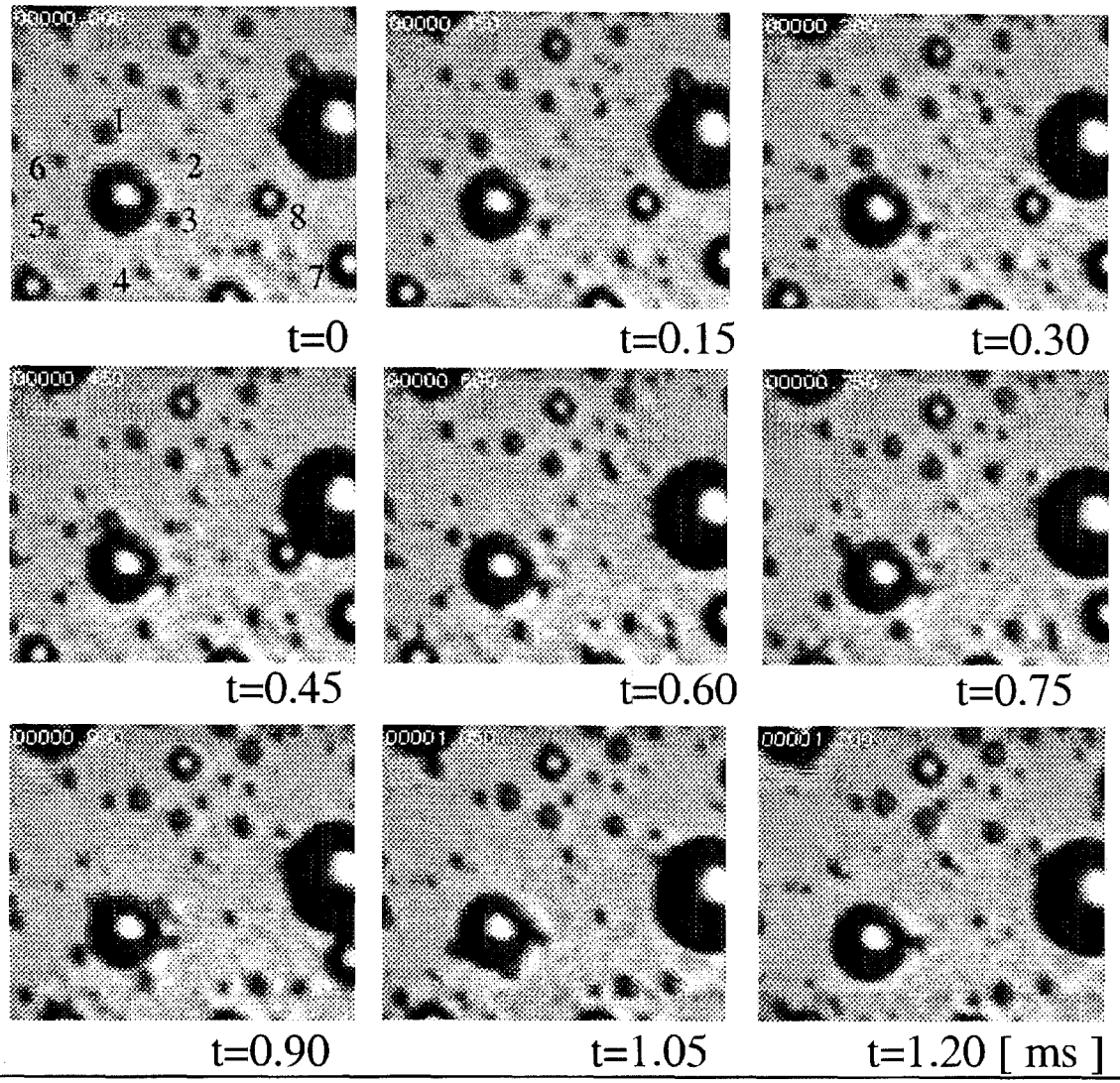

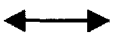

Electrolytic Gas Evolution

Electrolyte - KOH (0.1 M)
Bubbles - oxygen
diameter 5 to 50 μm

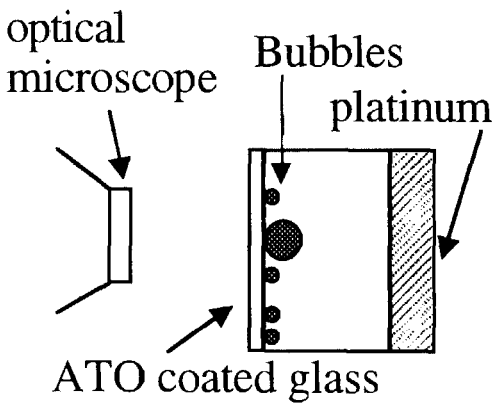

What is the mechanism?

Thermocapillary Flow

The surface tension gradient drives the thermocapillary flow.

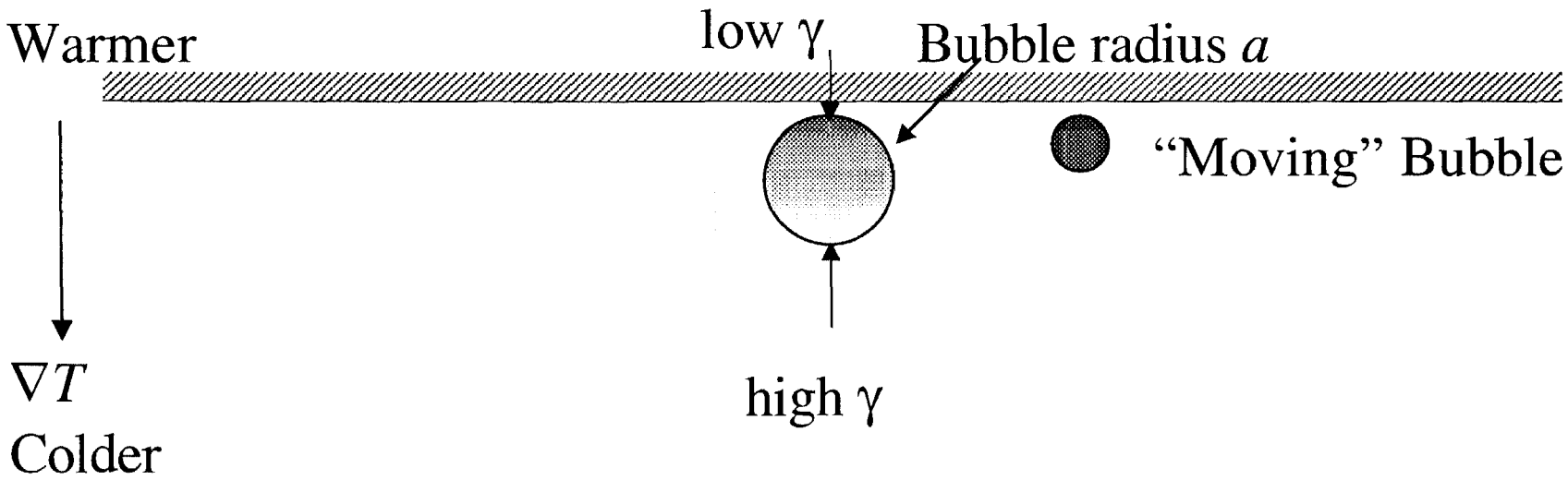

$\gamma\ (T)$: Surface tension

Velocity Scale: $U = \dfrac{-\dfrac{d\gamma}{dT} a \left| \nabla T \right|_\infty}{2\eta}$

(Young, Goldstein and Bloch, 1959)

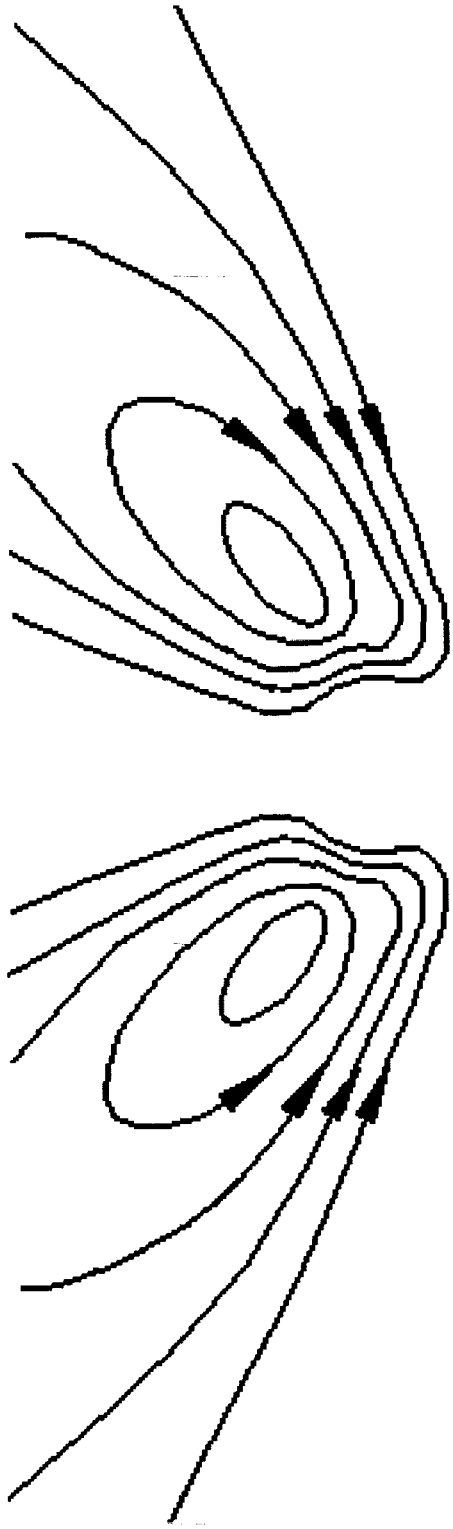

Experiment

Measure center to center distance d as a function of time.

$10 < \Delta T < 80$ K
$Re < 10^{-3}$
$Ma < 10^{-1}$

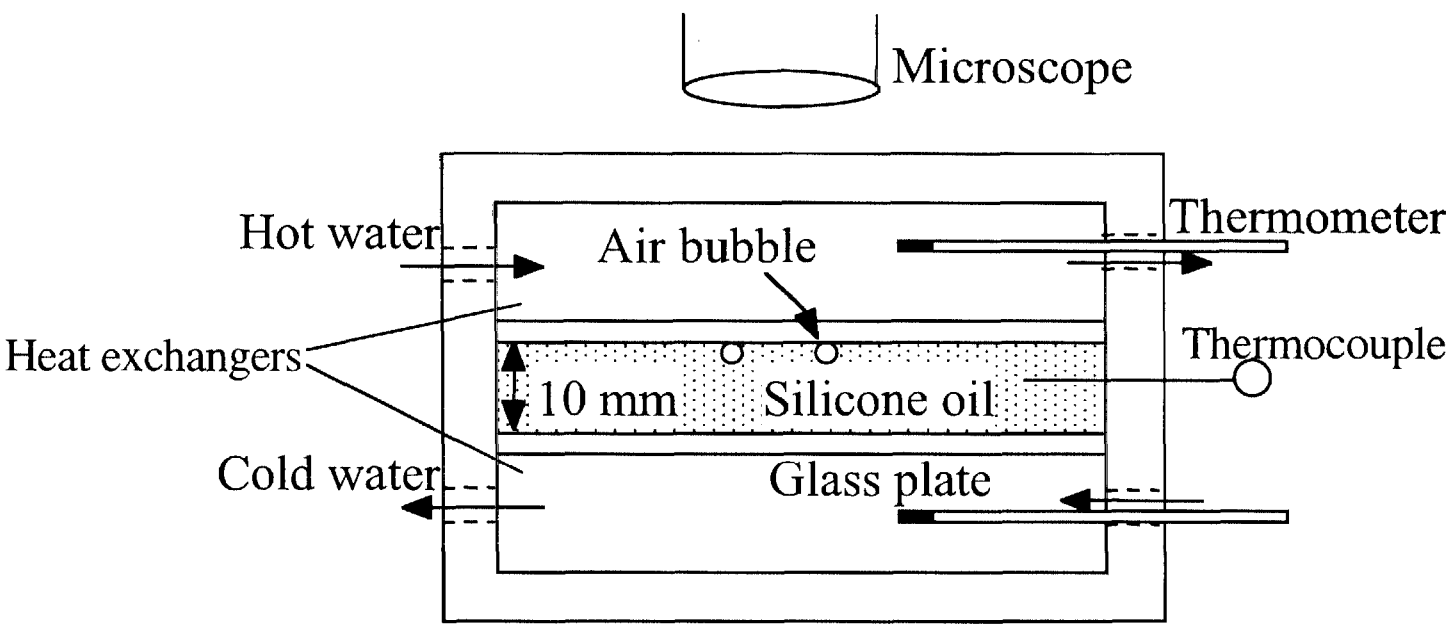

Bubble Aggregation

Bubble radius = 0.42 mm, temperature gradient = 3400 K/m

Viscosity of Silicone oil = 0.02 Pa s

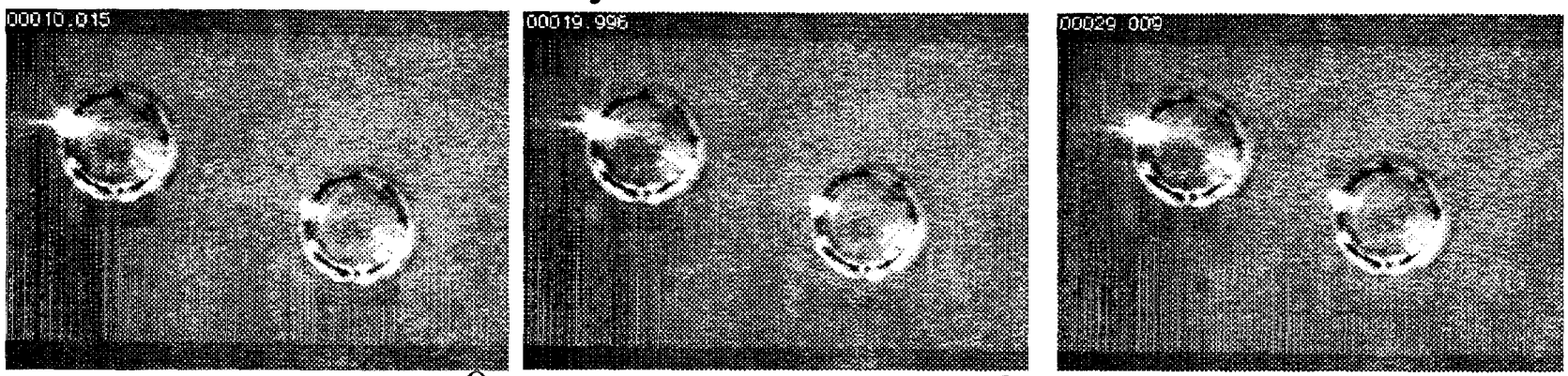

t=0 t=10 t=19

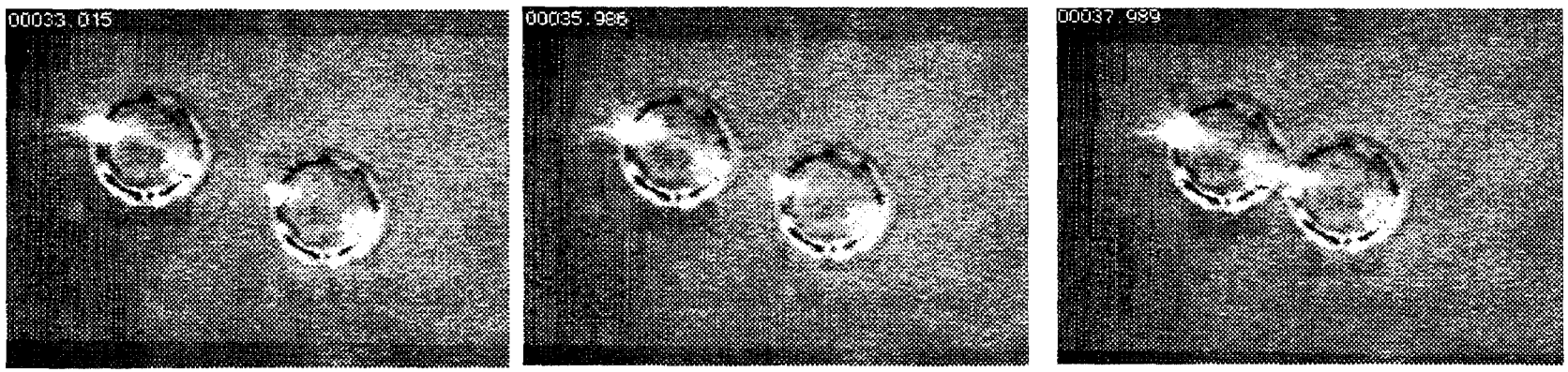

t=23 t=26 t=28 [s]

Bubble Separation

Bubble radius = 0.52 mm, temperature gradient = 2600 K/m

Viscosity of Silicone oil = 0.02 Pa s

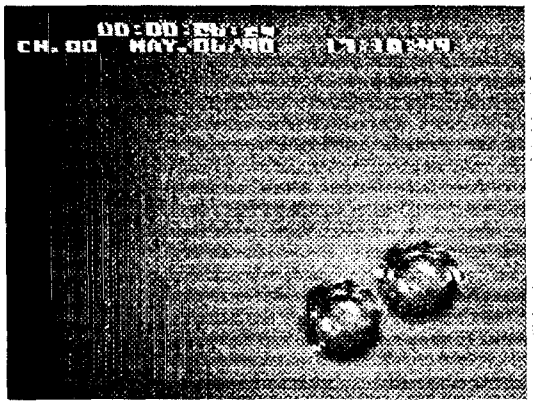

t=0

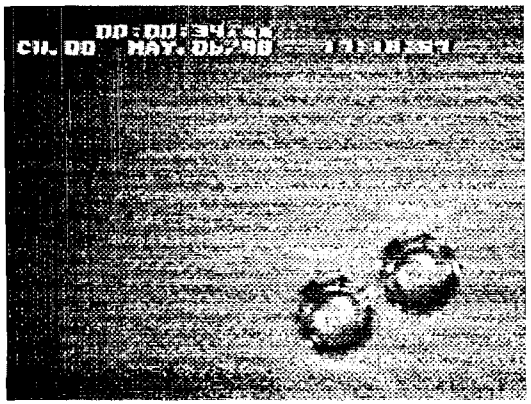

t=8

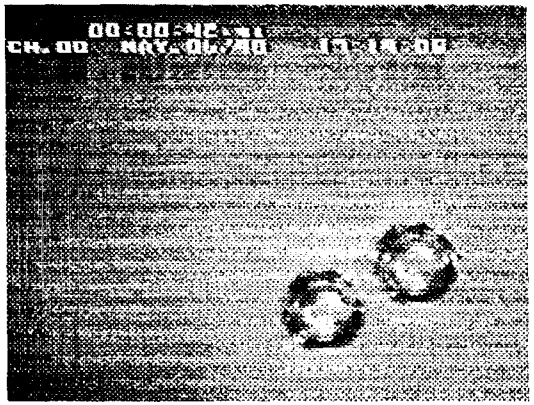

t=16

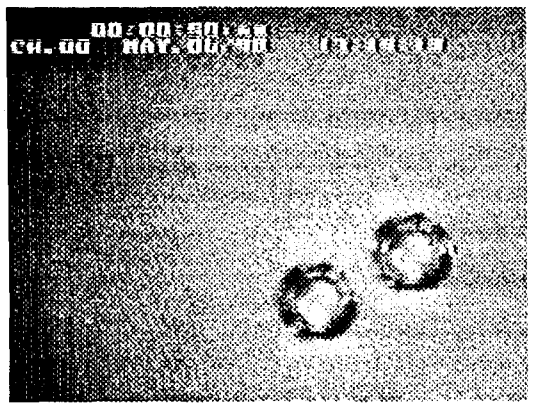

t=24

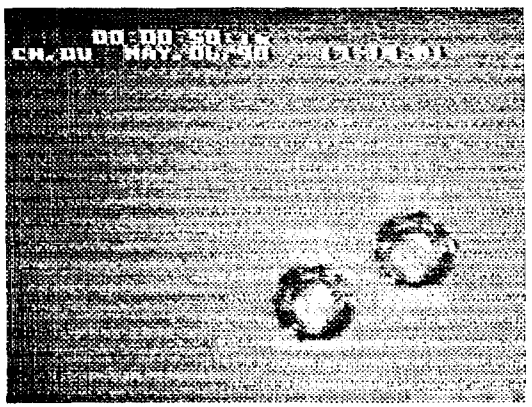

t=32

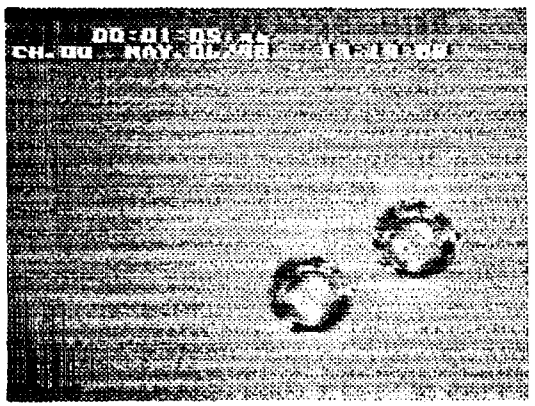

t=40 [s]

Scaling parameters

Velocity Scale *Length scale* *Time scale*

$$U = \frac{-\frac{d\gamma}{dT} a \left| \nabla T \right|_\infty}{2\eta} \qquad a \qquad \tau = \frac{a}{U} = \frac{2\eta}{-\frac{d\gamma}{dT}\left| \nabla T \right|_\infty}$$

(Young, Goldstein and Bloch, 1959)

- Velocity is proportional to
  1. Temperature gradient
  2. Bubble size
  3. Inverse of fluid viscosity
- Check linear scaling of bubble trajectories with these parameters

Effect of Scaling

Unscaled data

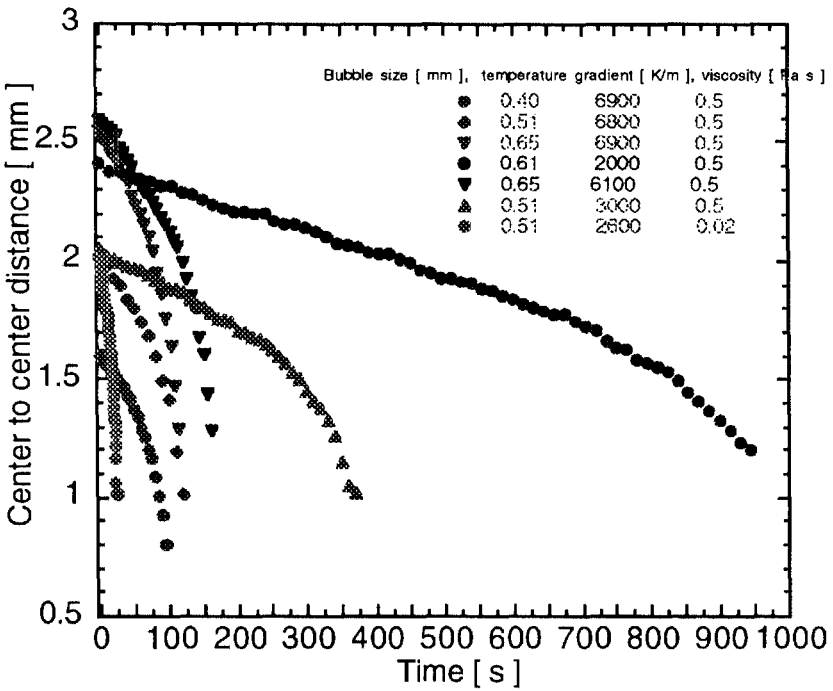

Scaled data

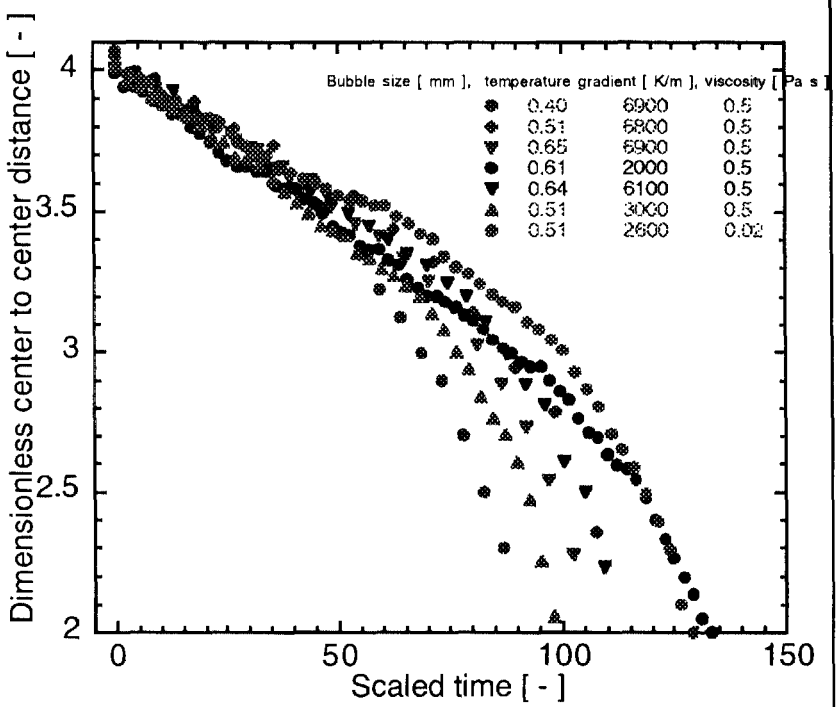

Note: Bubble aggregation scales linearly with temperature gradient, bubble size and the inverse of fluid viscosity

Wall Hindrance Coefficient q

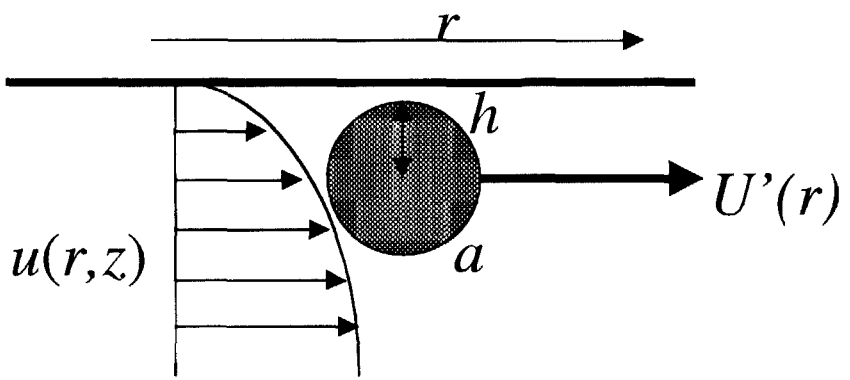

Additional hydrodynamic effect
due to the presence of the wall

$$F_r = -\frac{4\pi a \eta U}{q}$$

q :hindrance parameter

$0 < q < 1$

$$U'(r) = qU(r) \longrightarrow$$

Bubble trajectory

$$\frac{dr}{dt} = 2U'(r)$$

I.C.: $d = 4$ @ $t = 0$

Theoretical calculation of q

$$\nabla \cdot \mathbf{u} = 0$$
$$\nabla^2 \mathbf{u} - \nabla p = 0$$

B.C.

at $z = 0$: $\mathbf{u} = 0$

at $z = \infty$: $\mathbf{u} \rightarrow 0$

$p \rightarrow$ constant

On bubble surface:

$u_n = U\mathbf{i}_r \cdot \mathbf{n}$

$\tau \cdot (\mathbf{I}\text{-}\mathbf{nn}) = 0$

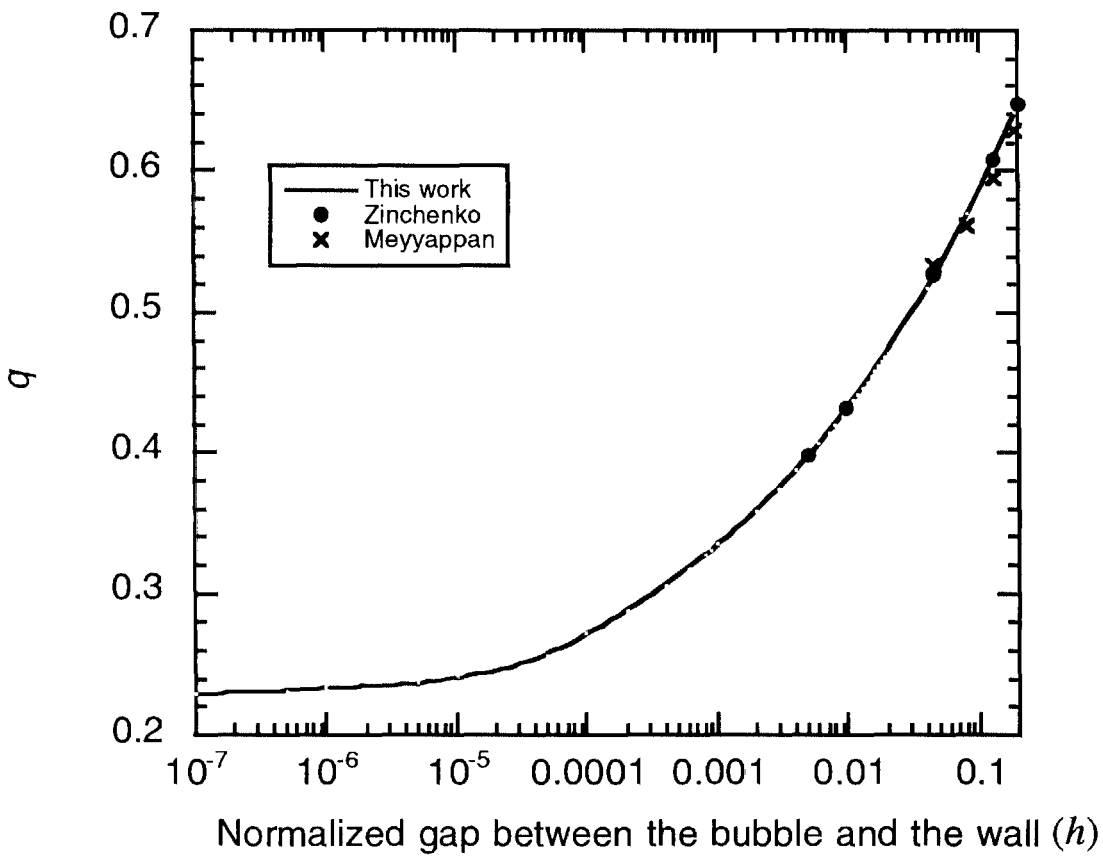

Independent measurement of q

Bubble radius = 0.49 mm, room temperature

Viscosity of Silicone oil = 0.5 Pa s

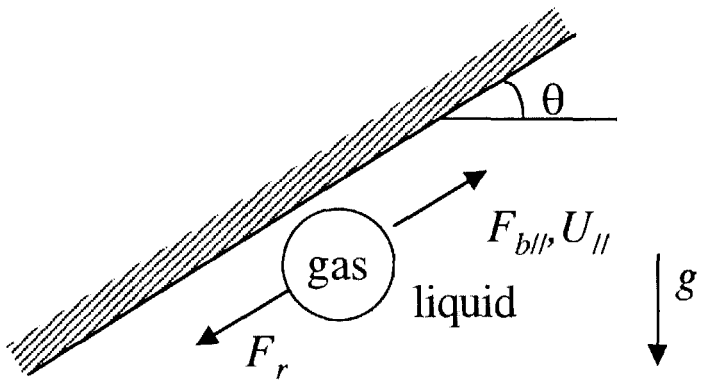

$$F_{b//} = \frac{4}{3}\pi a^3 \Delta\rho g \sin(\theta)$$

$$F_r = \frac{4\pi a \eta U}{q}$$

$$\longrightarrow \quad q = \frac{3\eta U}{\Delta\rho g a^2 \sin(\theta)}$$

Tilted Wall Experiment

Bubble radius = 0.49 mm, room temperature

Viscosity of Silicone oil = 0.5 Pa s

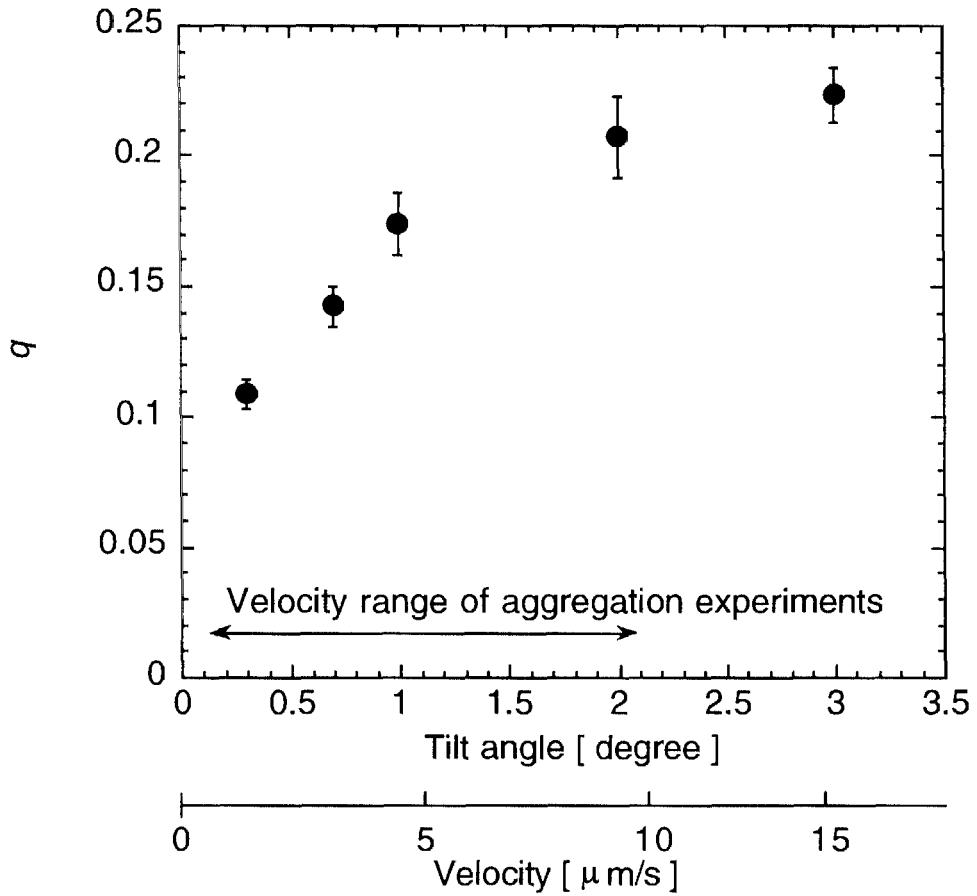

Summary of hindrance parameter *q*

Possible range of q	0 - 1
Theoretical calculation	0.30
Tilted wall experiment	0.11-0.23
Fitting of thermocapillary data	0.26

Quantitative Comparison of Theory and Data

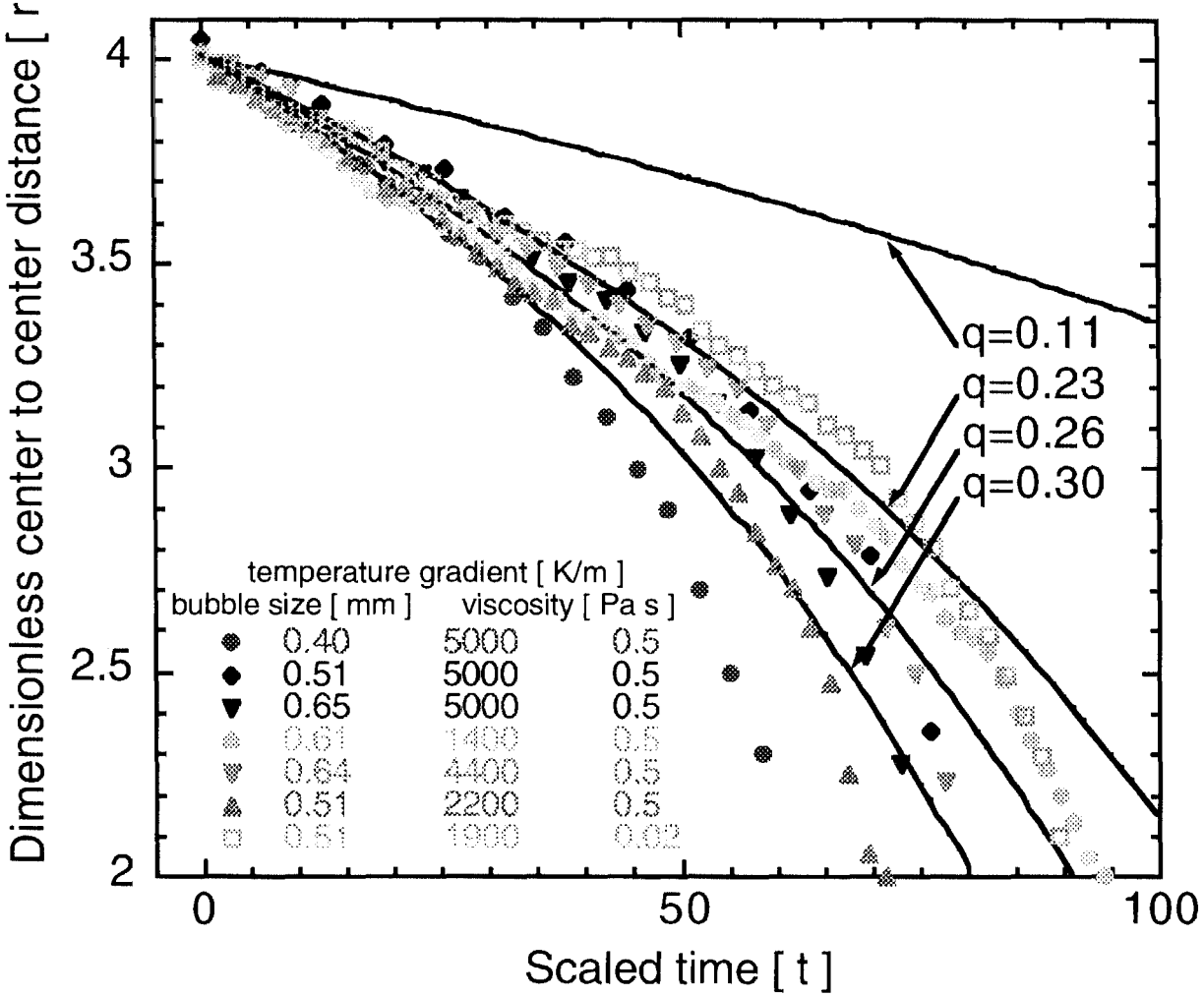

Conclusions

- Bubbles aggregate when there is temperature gradient.
- Bubble aggregation scales linearly with temperature gradient, bubble size and the inverse of fluid viscosity.

Therefore, thermocapillary flow drives bubble aggregation.

- The effect of the hindrance from the wall explains well the behavior of the bubble aggregation trajectory. The hindrance parameter was determined by two methods and fitting to the data.

TRANSITION FROM POOL TO FLOW BOILING - THE EFFECT OF REDUCED GRAVITY

V.K. Dhir

University of California Los Angeles, Department of Mechanical and Aerospace Engineering, Los Angeles, CA 90095, U.S.A , e-mail: vdhir@seas.ucla.edu

ABSTRACT

Application of boiling heat transfer in space can be found in the areas of thermal management, fluid handling and control, and power systems, on-orbit storage and supply systems for cryogenic propellants and life support fluid, and for cooling of electronic packages for power systems associated with various instrumentation and control systems. Recent interest in exploration of Mars and other planets, and the concepts of in-situ resource utilization on Mars highlights the need to understand the effect of gravity on boiling heat transfer at gravity levels varying from $1 \geq g/g_e \geq 10^{-6}$.

The objective of the proposed wok is to develop a mechanistic understanding of nucleate boiling and critical heat flux under low and micro-gravity conditions when the velocity of the imposed flow is small. For pool boiling, the effect of reduced gravity is to stretch both the length scale as well as the time scale for the boiling process. At high flow velocities, the inertia of the liquid determines the time and the length scales and as such the gravitational acceleration plays little role. However, at low velocities and at low gravity levels both liquid inertia and buoyancy are of equal importance. At present, we have little understanding of the interacting roles of gravity and liquid inertia on the nucleate boiling process. Little data that has been reported in the literature does not have much practical value in that it can not serve as a basis for design of heat exchange components to be used in space.

The proposed work consists of both experimental and complete numerical simulations of the low velocity, low-gravity nucleate boiling process. A building block type of approach will be used in that first the detachment process of a single bubble and flow and heat transfer associated with the sliding motion of the bubble over the heater surface after detachment will be studied. Thereafter, the complexity of the experiments with respect to the number of nucleation sites will be increased in steps. Liquid subcooling and flow velocity will be varied parametrically. The experiments are proposed to be conducted at 1 g_e, 10^{-2} g_e and 10^{-5} g_e. The experiments at 10^{-2} g will be conducted in the KC-135, whereas those at 10^{-5} g_e will be performed in the Two Phase Flow Facility of the space station. In the laboratory experiments, particle velocimetry and holographic interferometry will be used to obtain data on velocity and temperature fields associated with a bubble prior to, and after detachment and during sliding motion. Numerical simulations modeling the micro and macro regions of the bubble will be carried out in three dimensions. Scaling the effect of gravity will be a prerequisite of the model. The results of the experiments will be used to validate analytical/numerical models.

NASA/CP—2000-210470

UCLA

TRANSITION FROM POOL TO FLOW BOILING — THE EFFECT OF REDUCED GRAVITY

by

Vijay K. Dhir

University of California, Los Angeles
Mechanical and Aerospace Engineering Department
Los Angeles, CA 90095

Presented at the
FIFTH MICROGRAVITY FLUID PHYSICS AND TRANSPORT PHENOMENA CONFERENCE
August 9-11, 2000, Cleveland, Ohio

UCLA

TRANSITION FROM POOL TO FLOW BOILING - THE EFFECT OF REDUCED GRAVITY

Synopsis

- Experimental and Numerical Study of Low Velocity, Low Gravity Nucleate Boiling Process
- Single and Multiple Bubble Dynamics Subjected to Flow along the Heater and Gravity Normal to or along the Heater
- Experiments are to be Conducted in Laboratory, KC-135, and in the Space Station
- Visual Observations along with Data for Temperature Field and Velocity Field during Bubble Sliding Motion (only at earth normal gravity) will be Taken

NASA/CP—2000-210470

UCLA

EARTH NORMAL GRAVITY EXPERIMENTS

3

FLOW BOILING

Experimental Apparatus: Flow Loop

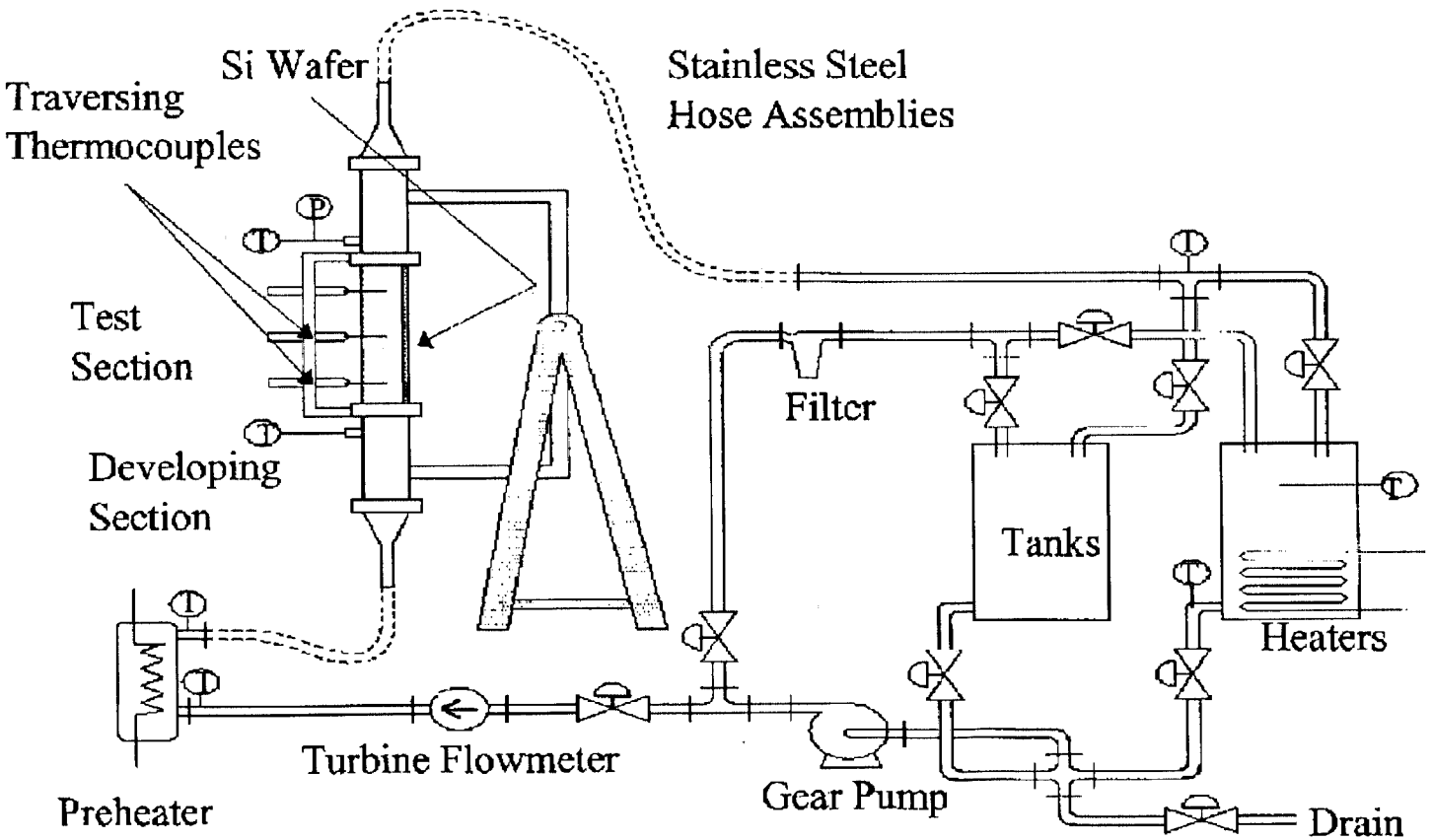

UCLA

FLOW BOILING (Cont'd)

Experimental Apparatus: Test Section

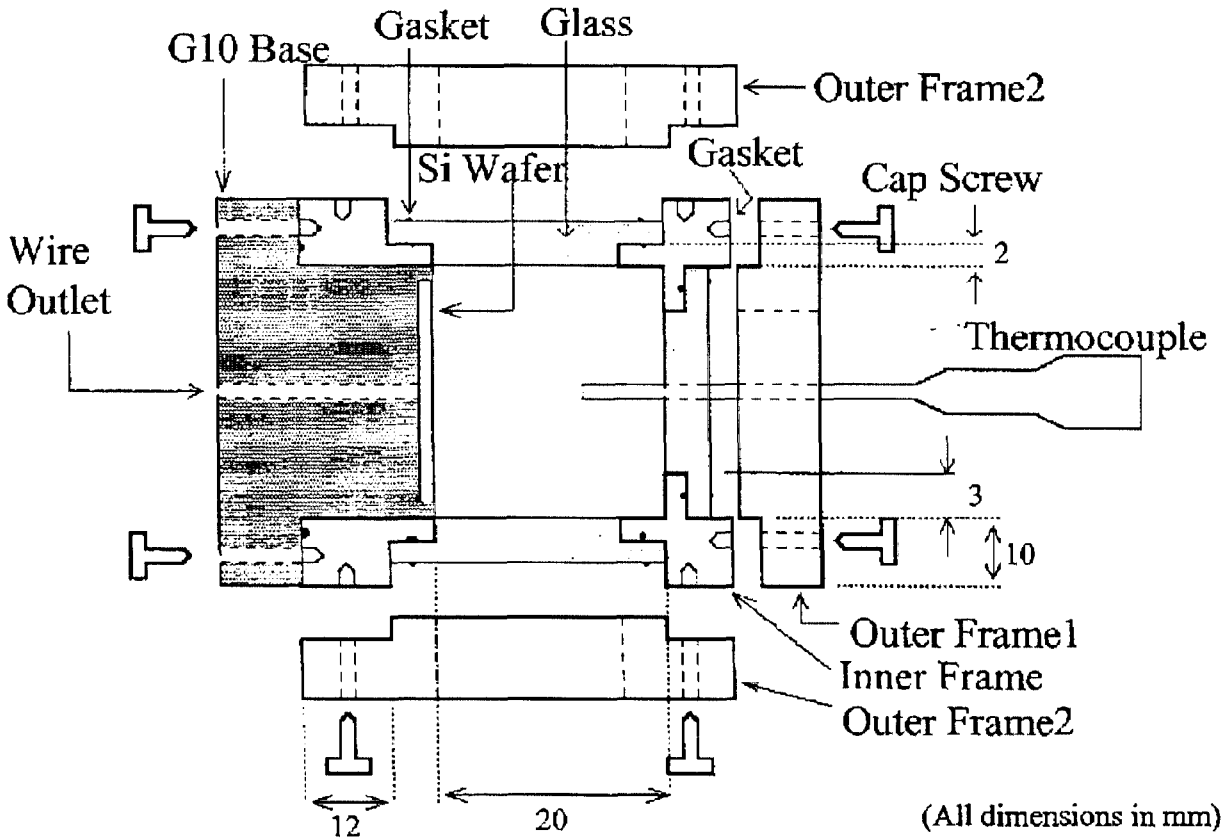

FLOW BOILING (Cont'd)

Experimental Apparatus: Silicon Wafer

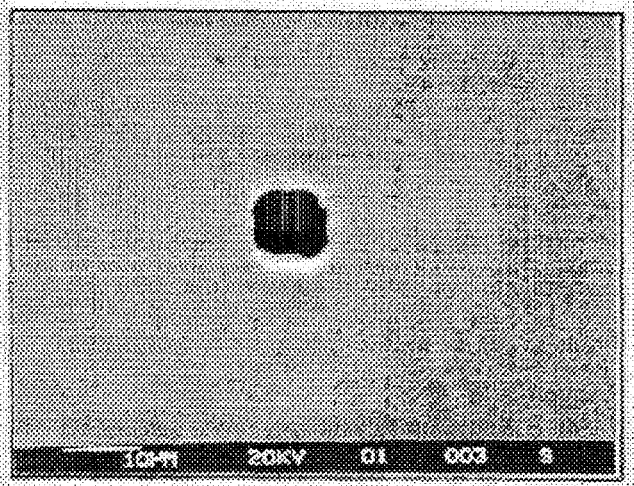

SEM Picture of Cavity on Silicon Wafer

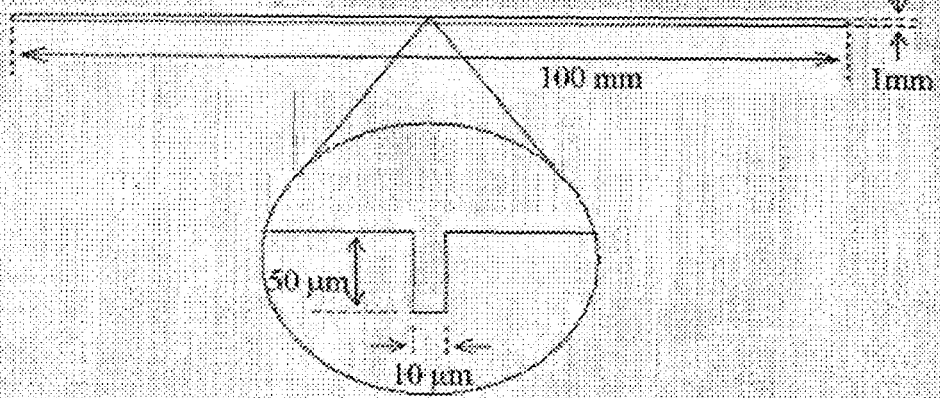

Side View of Silicon Wafer & DRIE Cavity

UCLA

FLOW BOILING (Cont'd)

Experimental Apparatus: Silicon Wafer (Cont'd)

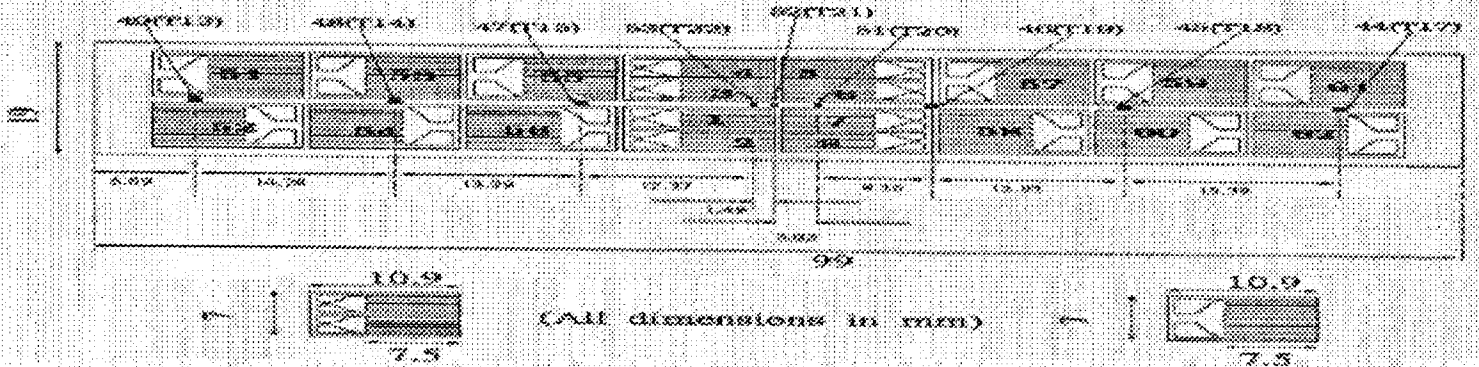

Schematic of Positions of Strain Gage Heaters and Thermocouples at the back of Wafer

Picture of Heaters & Thermocouples at the back of wafer

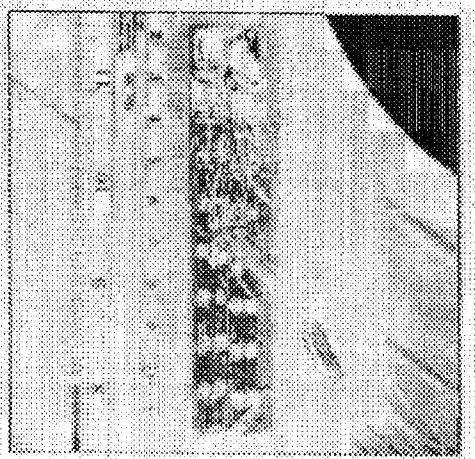

FLOW BOILING (Cont'd)
- Horizontal Flow

Temperature Profiles: $V = 0.135$ m/s , $\Delta T_{sub} = 0.3$ K

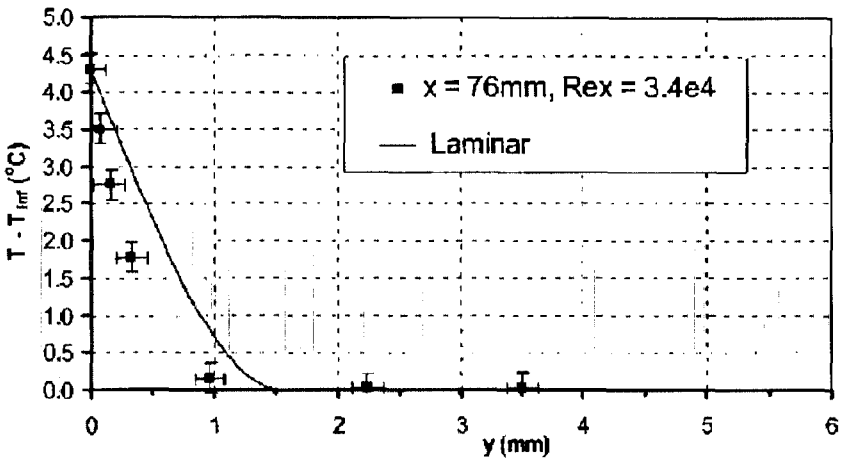

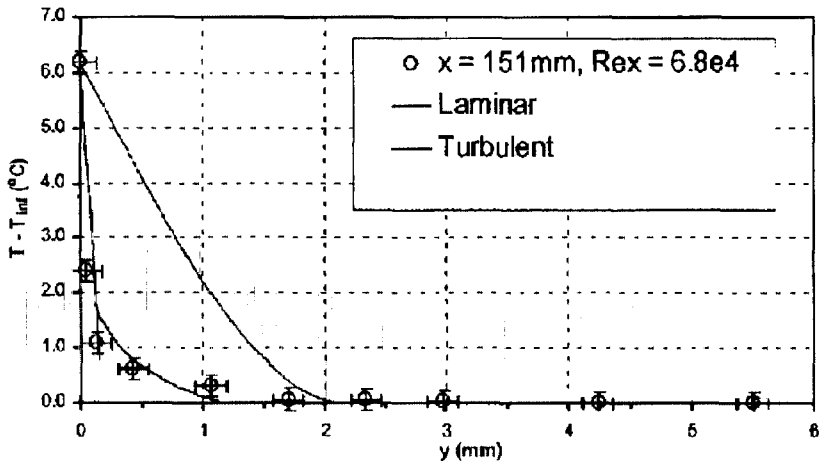

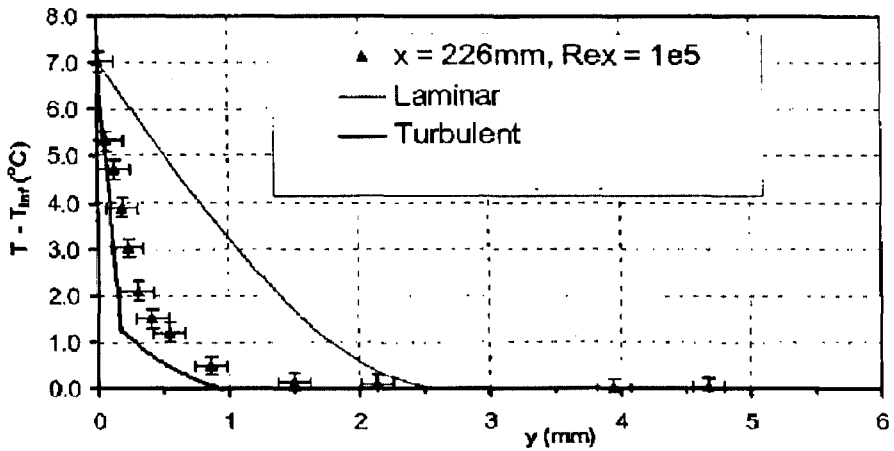

UCLA

FLOW BOILING (Cont'd)
- Horizontal Flow

Results: $V = 0.135$ m/s , $\Delta T_{wall} = 5.9$ K , $\Delta T_{sub} = 0.3$ K

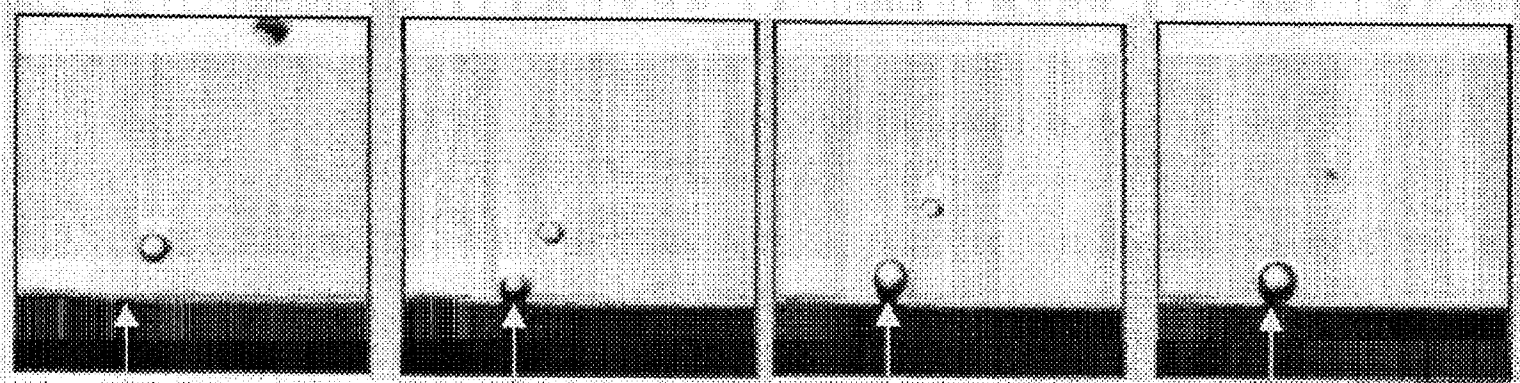

Cavity_____ t = 0 ms t = 2 ms t = 4 ms t = 6 ms

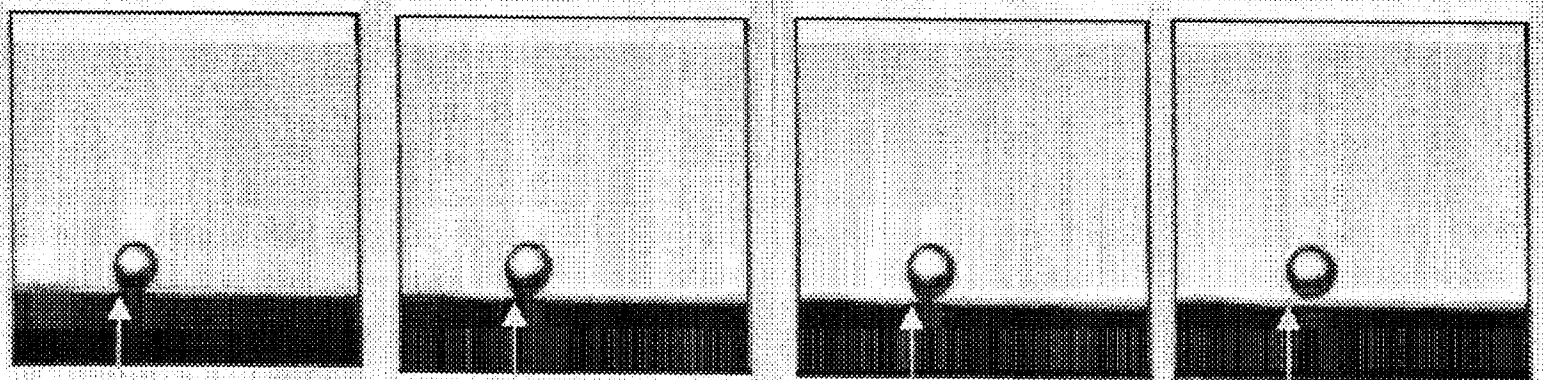

t = 8 ms t = 10 ms t = 12 ms t = 14 ms

UCLA

FLOW BOILING (Cont'd)
- Horizontal Flow

Results: $V = 0.135$ m/s , $\Delta T_{wall} = 5.9$ K , $\Delta T_{sub} = 0.3$ K

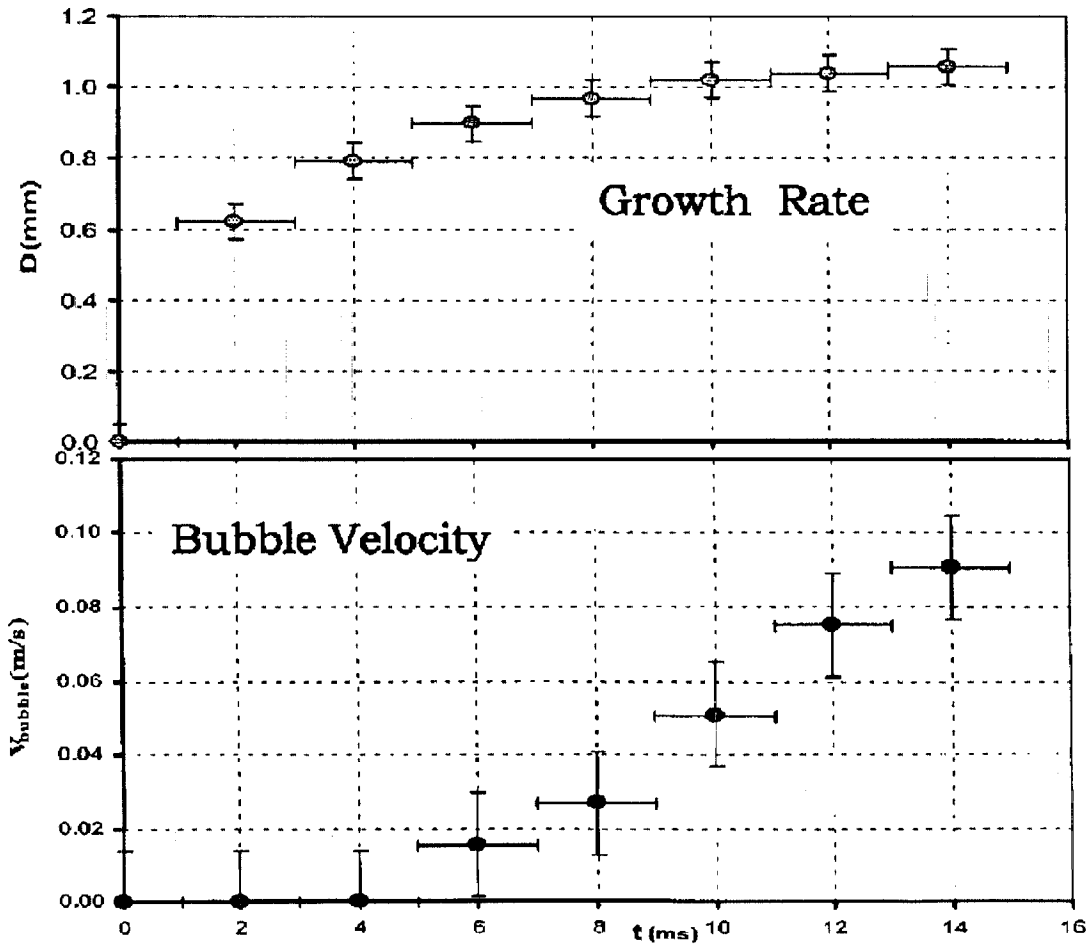

FLOW BOILING (Cont'd)
- Vertical Upflow

Results: $V = 0.149$ m/s , $\Delta T_{wall} = 5.9$ K , $\Delta T_{sub} = 0.2$ K

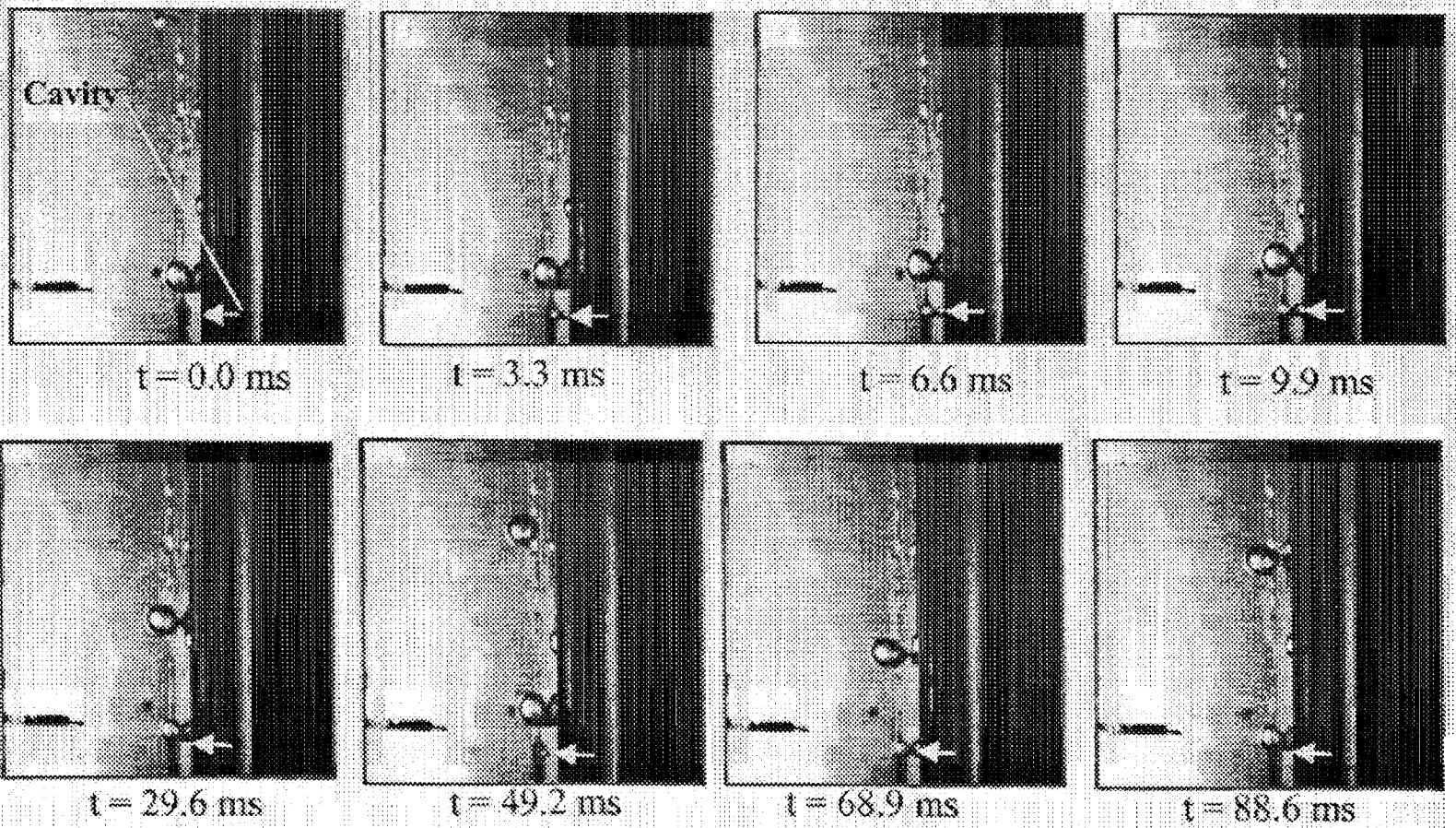

FLOW BOILING (Cont'd)
- Vertical Upflow

Results: $V = 0.149$ m/s , $\Delta T_{wall} = 5.9$ K , $\Delta T_{sub} = 0.2$ K

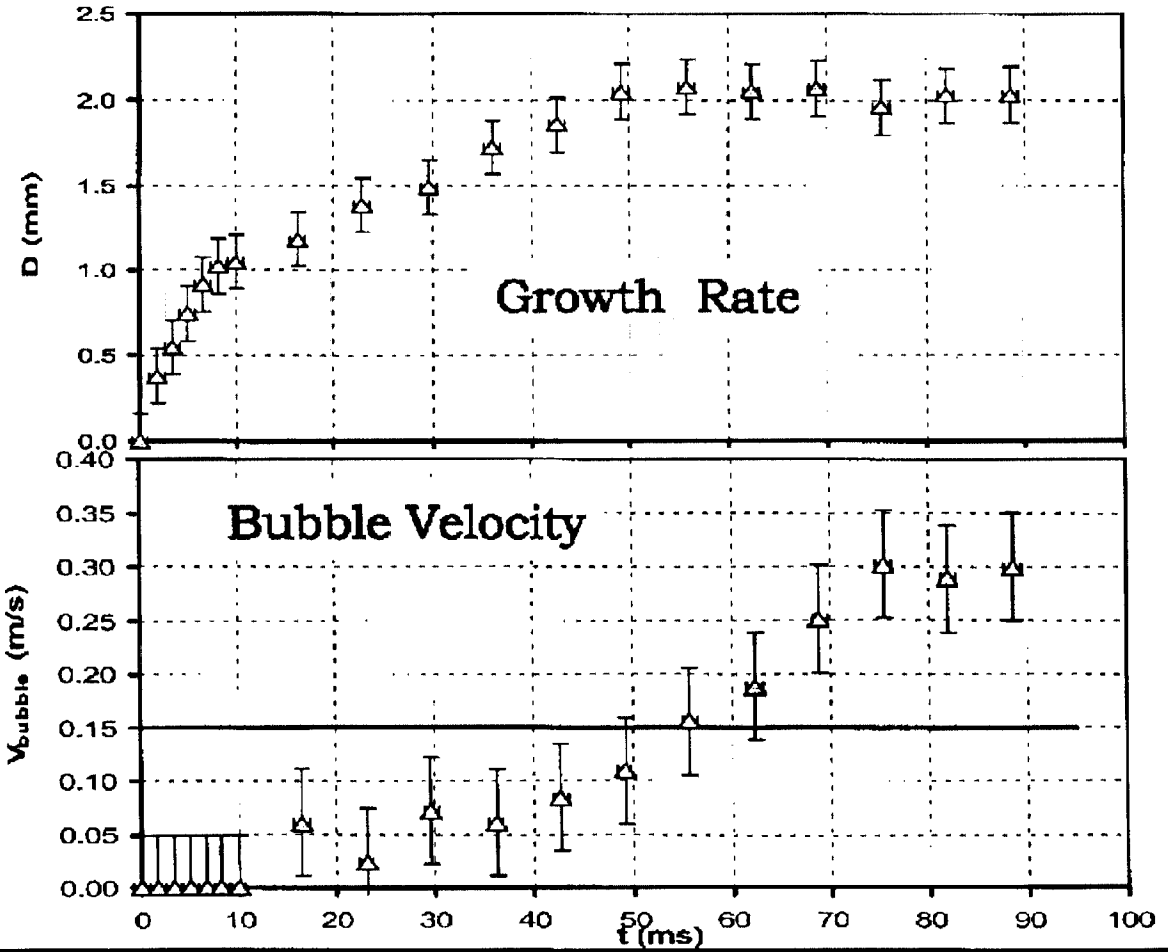

FLOW BOILING (Cont'd)
- Vertical Upflow

Results: $v = 0.25$ m/s, $\Delta T_{wall} = 5.9$ K, $\Delta T_{sub} = 0.3$ K

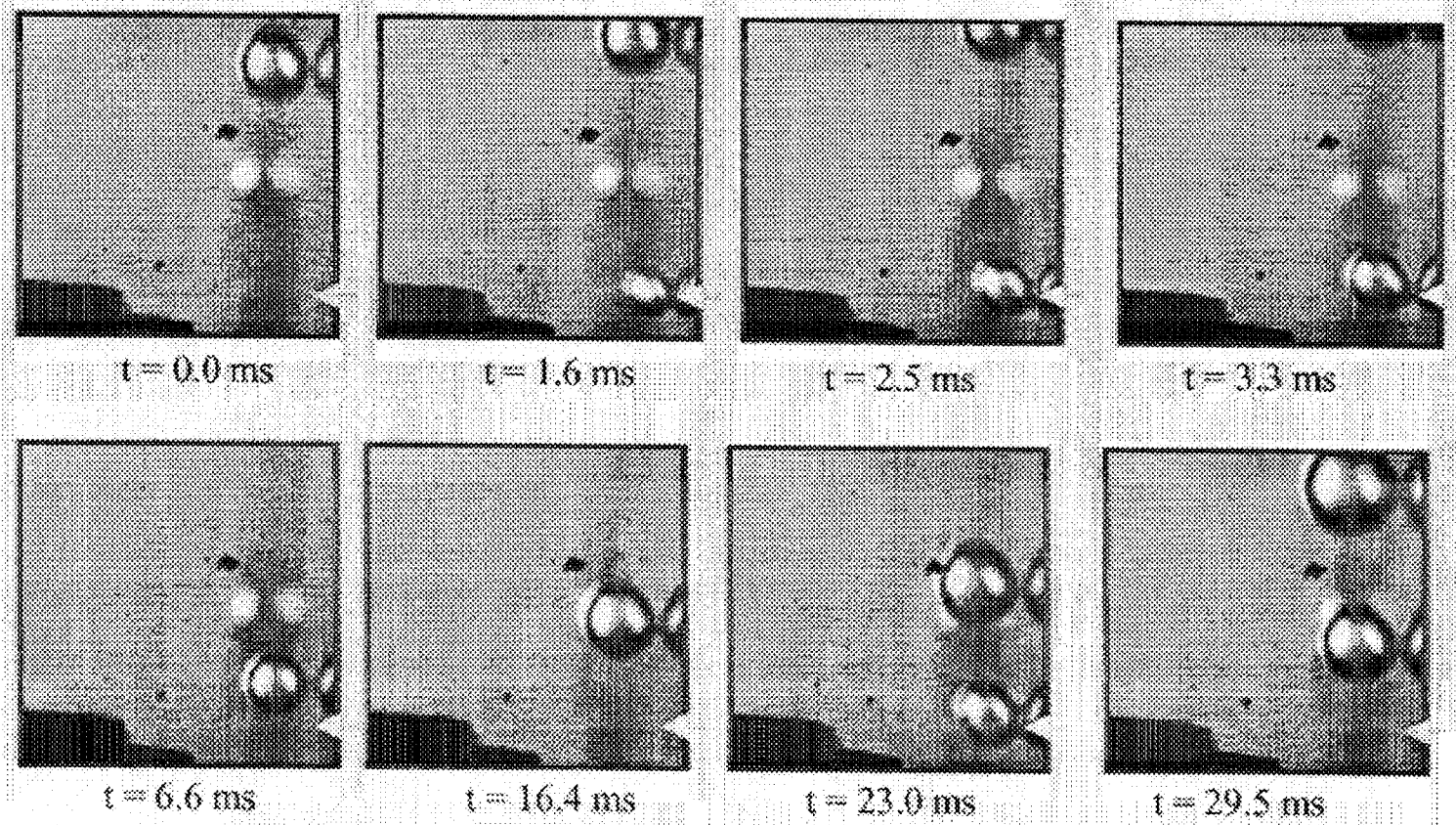

FLOW BOILING (Cont'd)

- Vertical Upflow

Results: $v = 0.25$ m/s , $\Delta T_{wall} = 5.9$ K , $\Delta T_{sub} = 0.3$ K

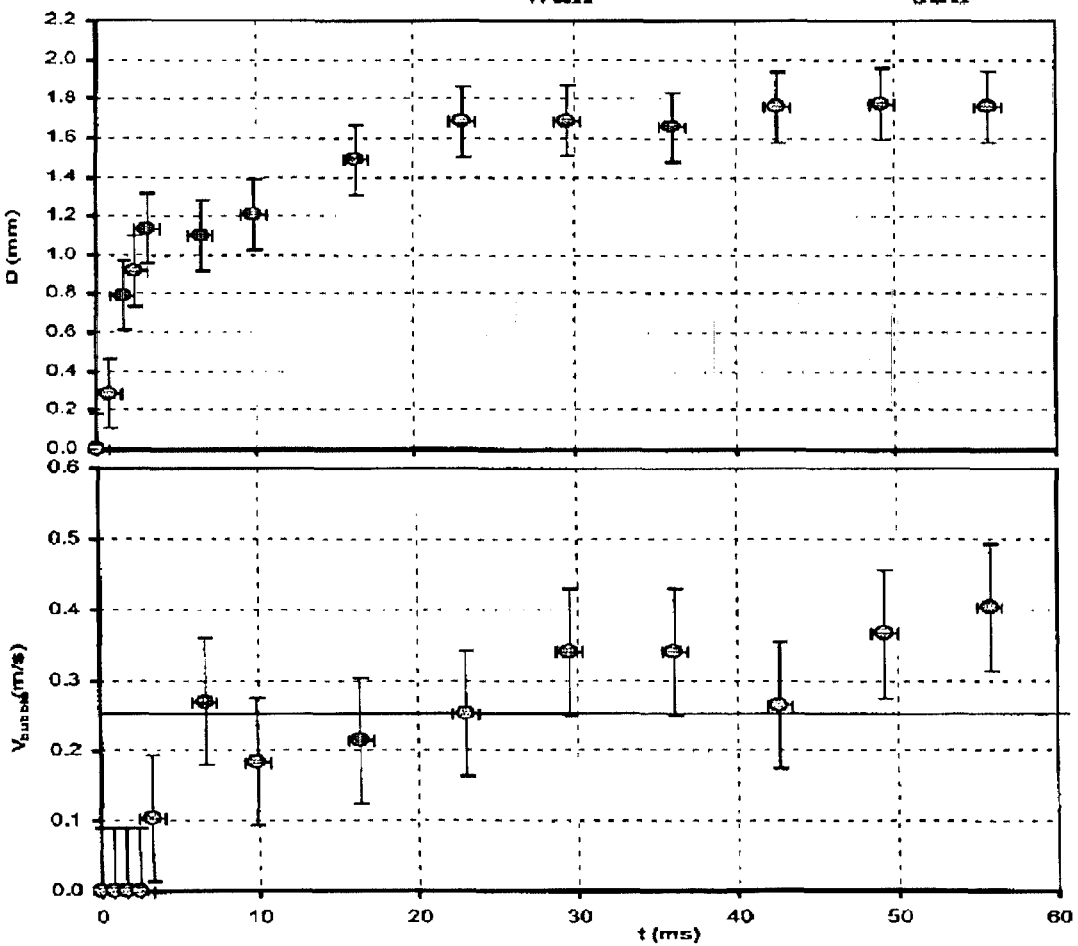

UCLA

FLOW BOILING (Cont'd)
- 135^0 Upflow

Results: $V = 0.145$ m/s , $\Delta T_{wall} = 5.9$ K , $\Delta T_{sub} = 0.3$ K

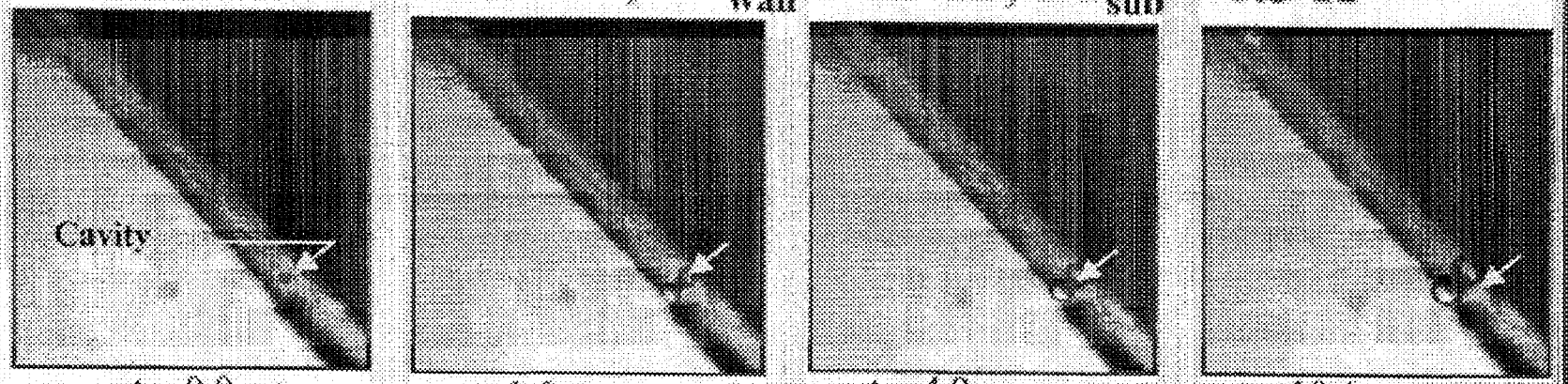

t = 0.0 ms | t = 1.6 ms | t = 4.9 ms | t = 10.6 ms

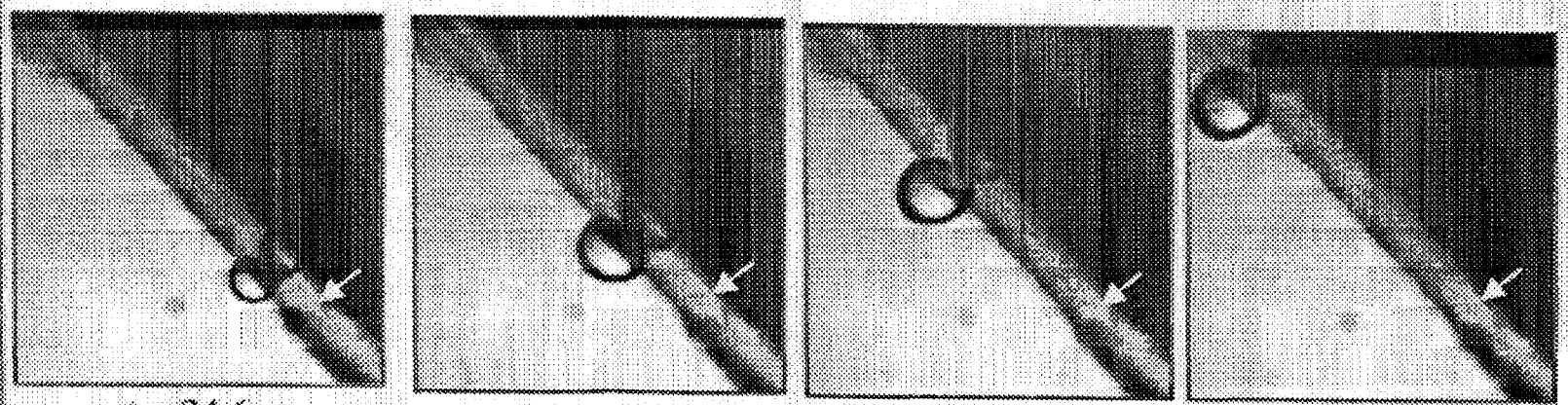

t = 24.6 ms | t = 41.8 ms | t = 59.0 ms | t = 76.2 ms

FLOW BOILING (Cont'd)
- 135^0 Upflow

Results: V = 0.145 m/s , ΔT_{wall} = 5.9 K , ΔT_{sub} = 0.3 K

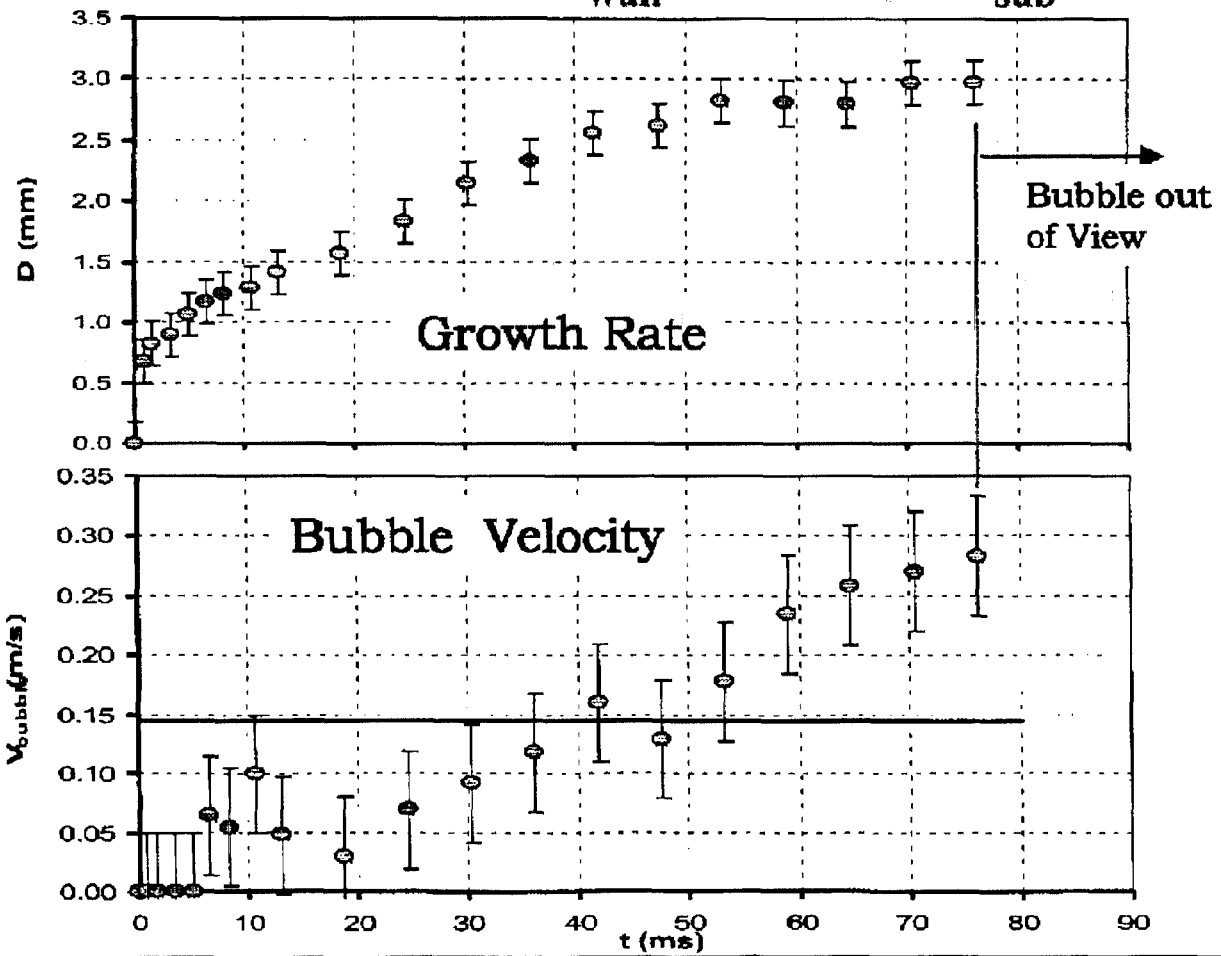

UCLA

FLOW BOILING (Cont'd)

Results: Effect of Orientation & Velocity

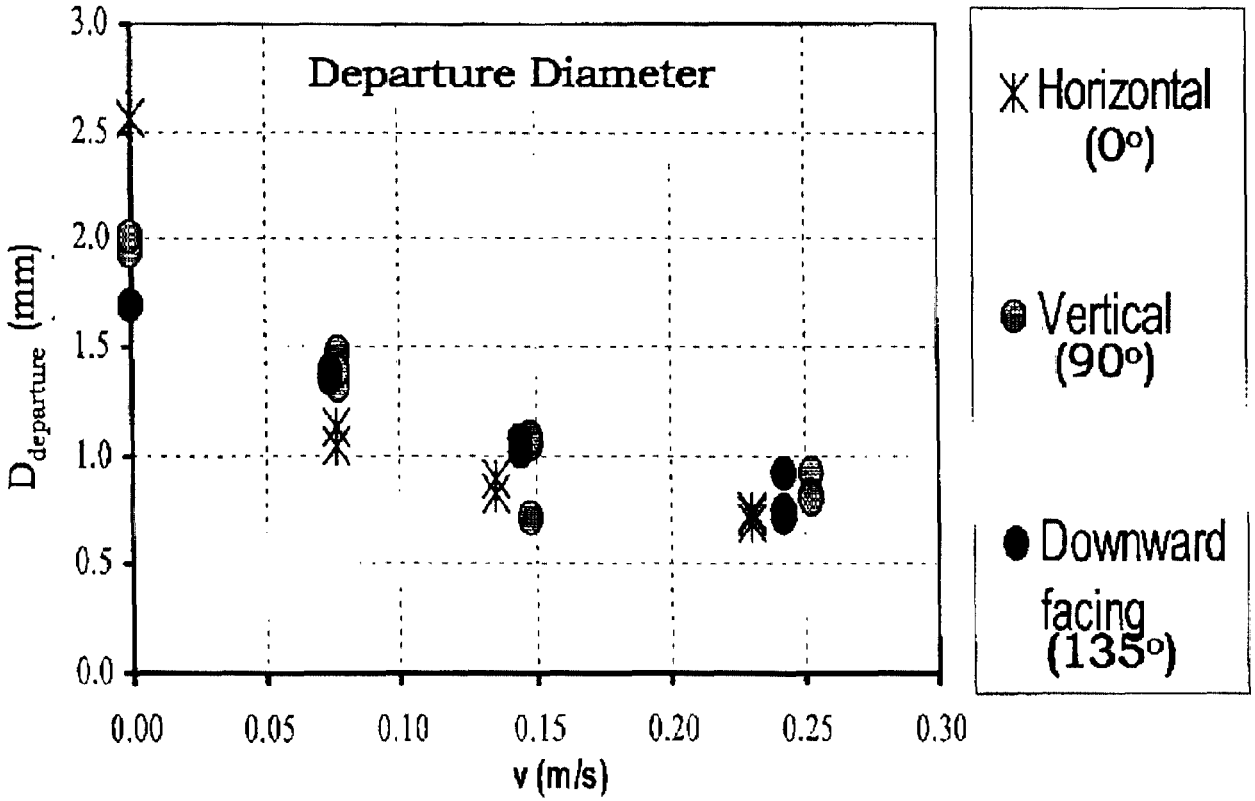

UCLA

FLOW BOILING (Cont'd)

Results: Effect of Orientation & Velocity

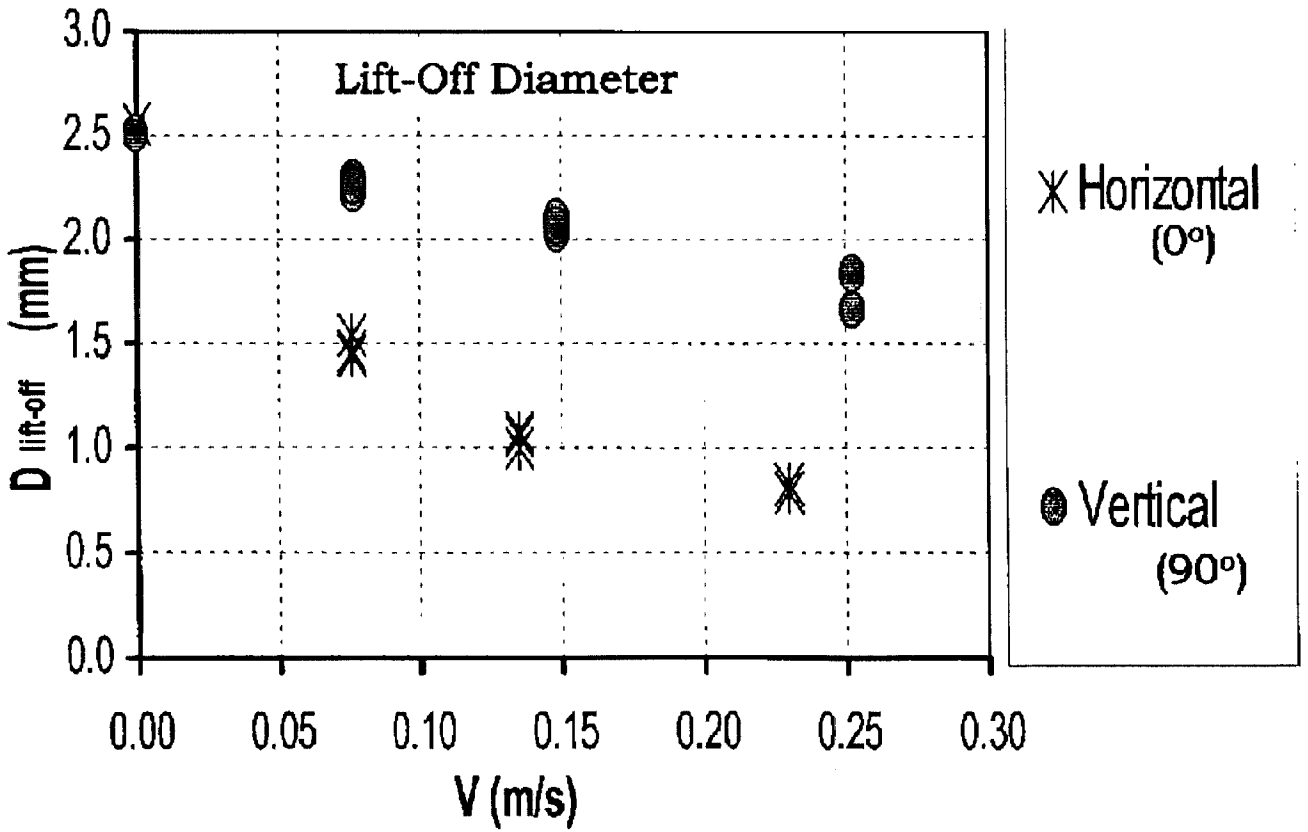

FLOW BOILING (Cont'd)

Results: Effect of Orientation & Velocity

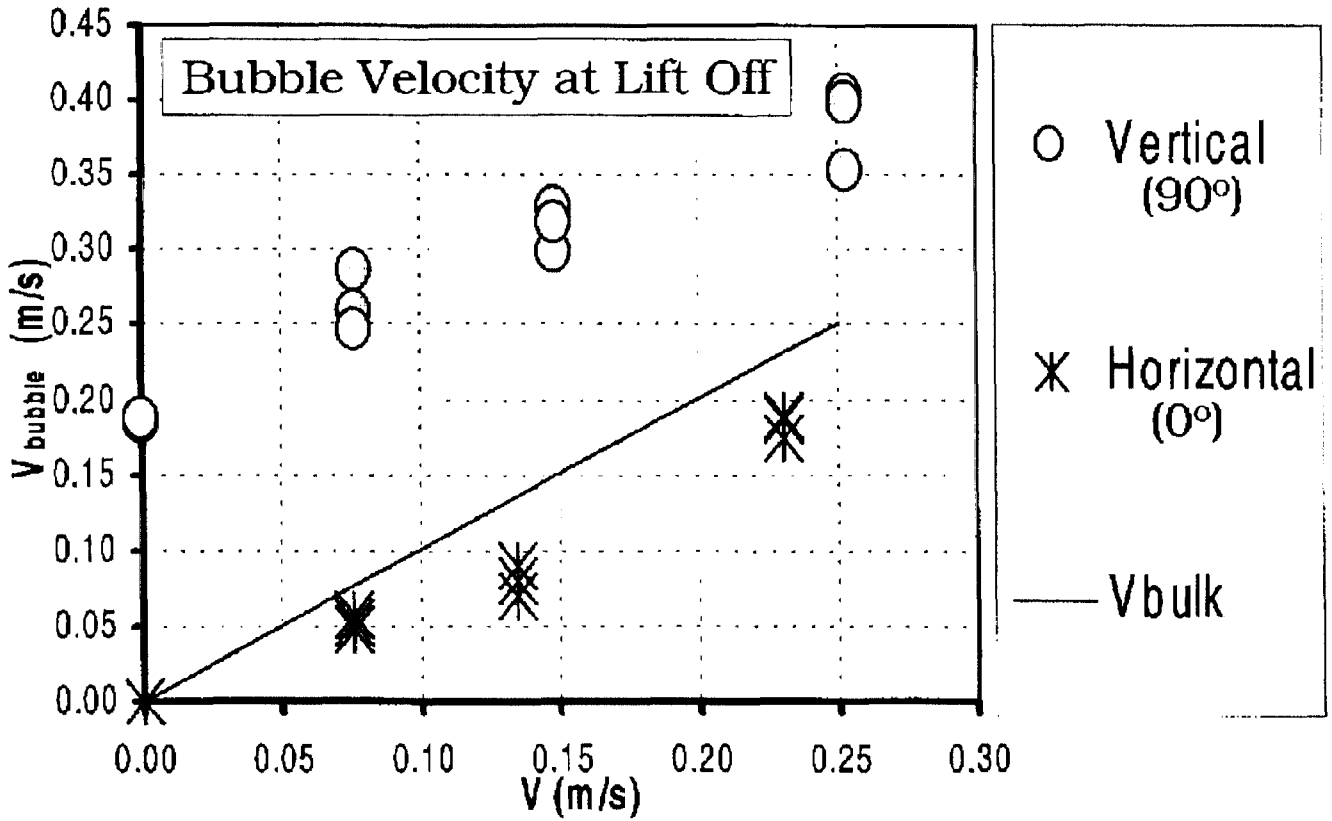

UCLA

FLOW BOILING (Cont'd)

Results: Effect of Orientation & Velocity

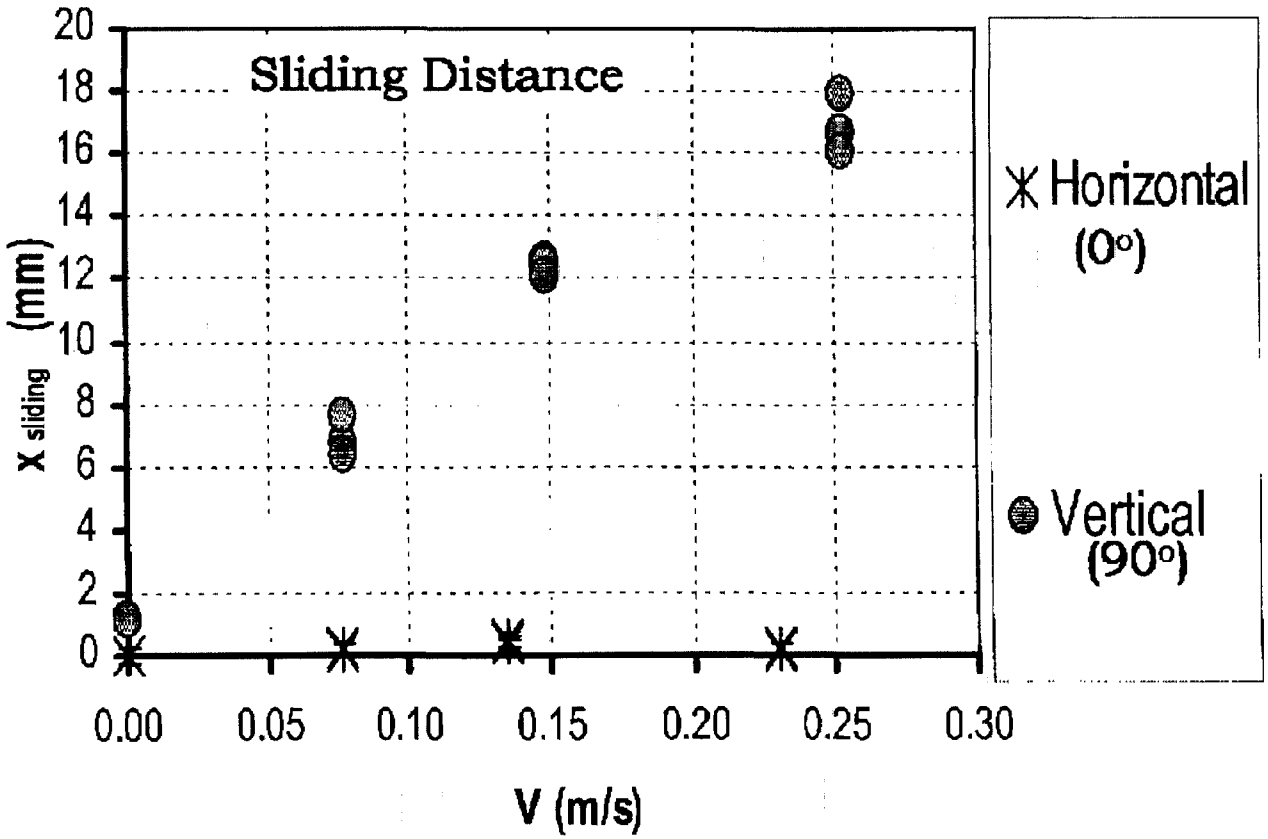

EXPERIMENTAL RESULTS

-- Flow and Heat Transfer Associated with Sliding Bubbles

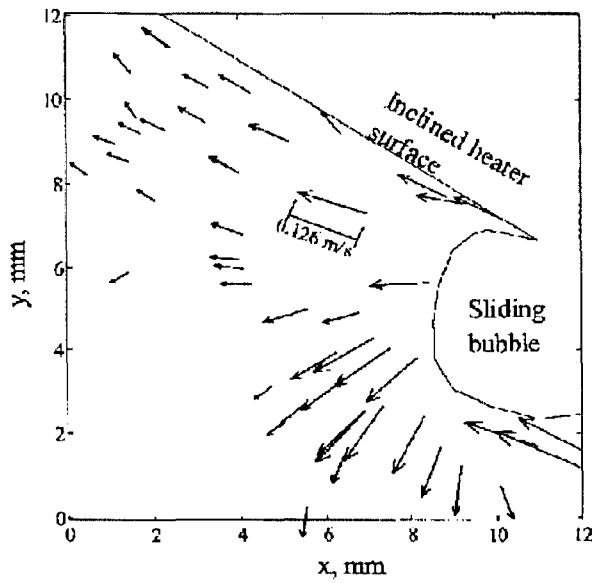

In the front of the sliding bubble

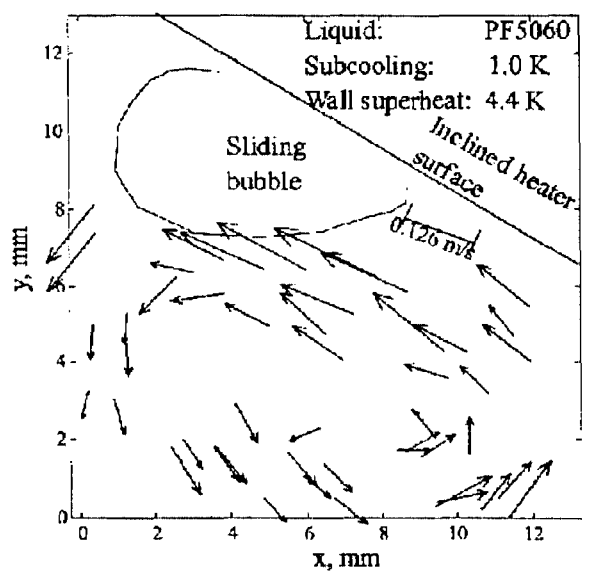

In the rear of the sliding bubble

Velocity Field Associated with a Bubble Sliding along the Surface at 150 ° Inclination Angle Measured Using Particle Velocimetry

EXPERIMENTAL RESULTS (Cont'd)

- Flow and Heat Transfer Associated with Sliding Bubbles

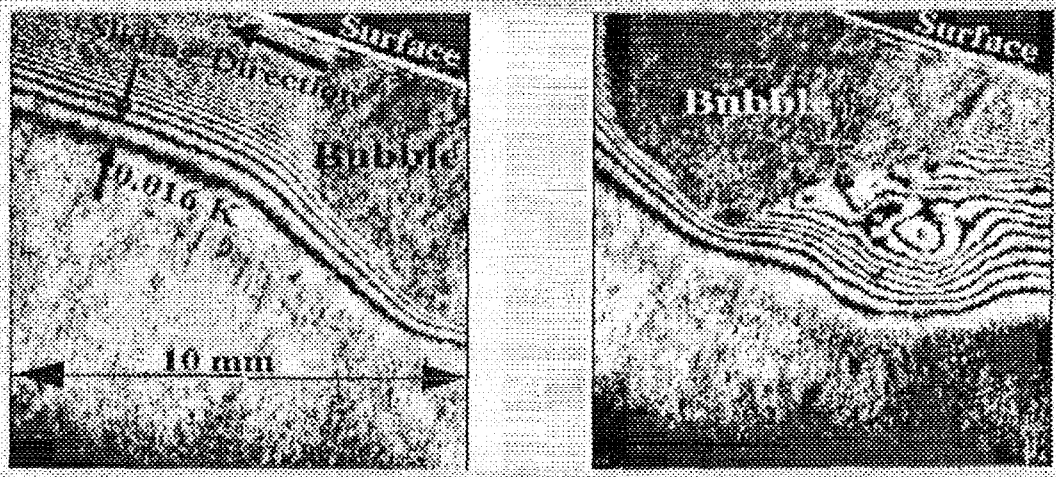

In the front of sliding bubble In the rear of sliding bubble

(PF-5060, $T_w - T_{sat}$ =0.6 °C, ΔT_{sub}=1.1 °C, Inclination Angle: 165 °)

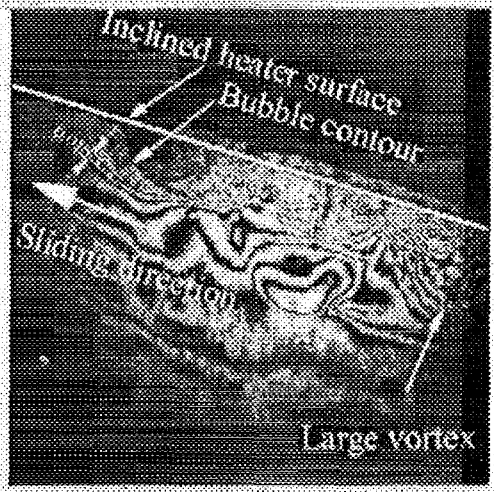

Over larger area behind the bubble on the heater

(Inclination Angle: 165°, $T_w - T_{sat}$ =0.8 °C, ΔT_{sub}=2.5 °C)

Fringe Patterns of the Temperature Field surrounding a Sliding Bubble from the Interferometric Holography

UCLA

NUMERICAL SIMULATIONS

UCLA

NUMERICAL SILMULATIONS

- Saturated flow boiling model and boundary conditions

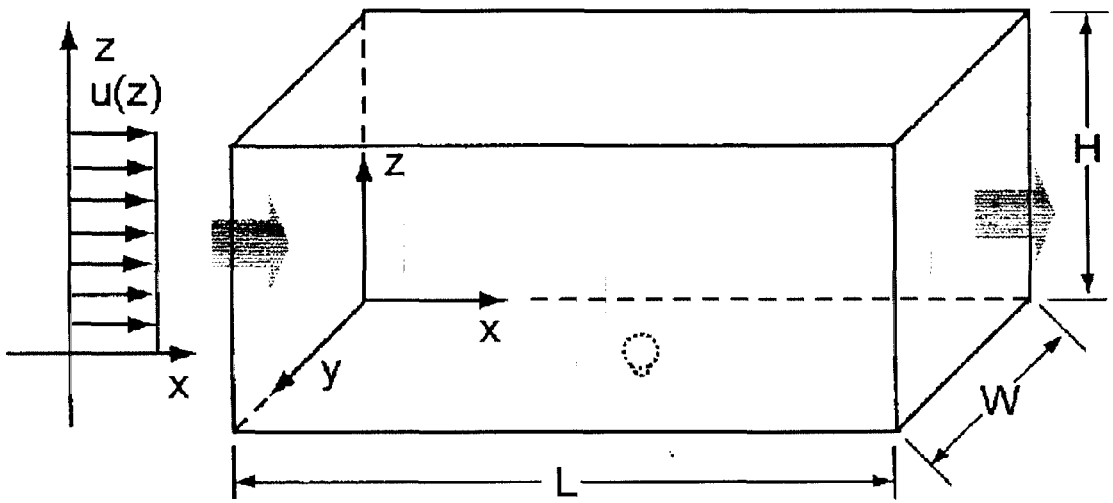

Boundary conditions:

x= 0, uniform flow;

y= 0, slip, insulated boundary;

z= 0, no-slip boundary,T=Con.;

x= L, volume conservation;

y= W, slip, insulated boundary;

z= H, slip, insulated boundary.

UCLA

NUMERICAL SILMULATIONS

- Calculated domain and relative parameters

- **Dimensionless Domain size :** L=2.0, H=1.0, W=0.5
- **Reference parameters:**

  L_0=2.5 [mm], U_0=0.16 [m/s], t_0=16[ms]

- **Unity inlet flow:** u(y,z) = 1.0
- **Wall superheat:** ΔT_{wall}=7.0 K
- **Contact angle:** $\phi = 38^o$
- **Initial bubble position and size:**

  center of x-y plane and D_{ini}=0.197

- **Mesh size and time step:** 129*65*33, $\Delta t=5*10^{-4}$

NUMERICAL SILMULATIONS

- Calculated results

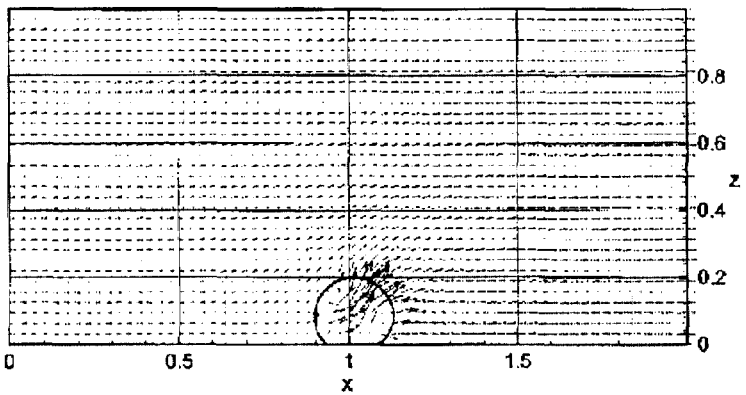

$t=5*10^{-3}$

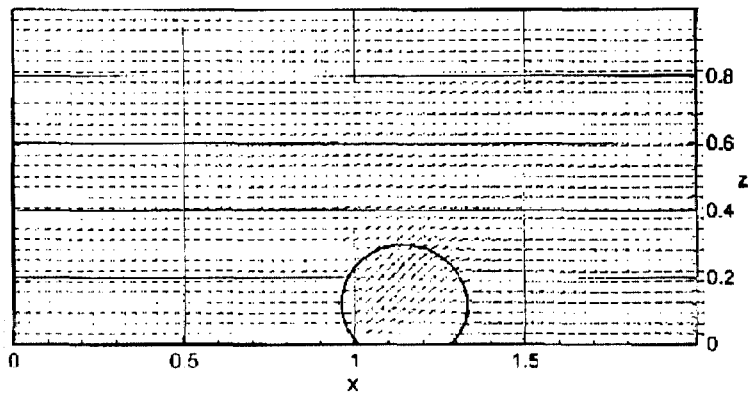

t=0.10

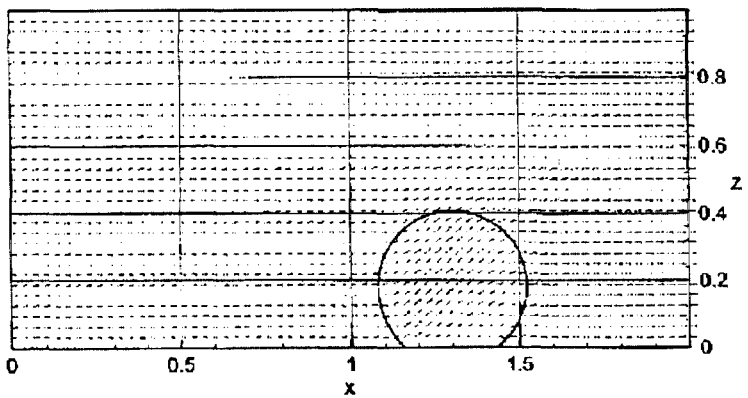

t=0.22

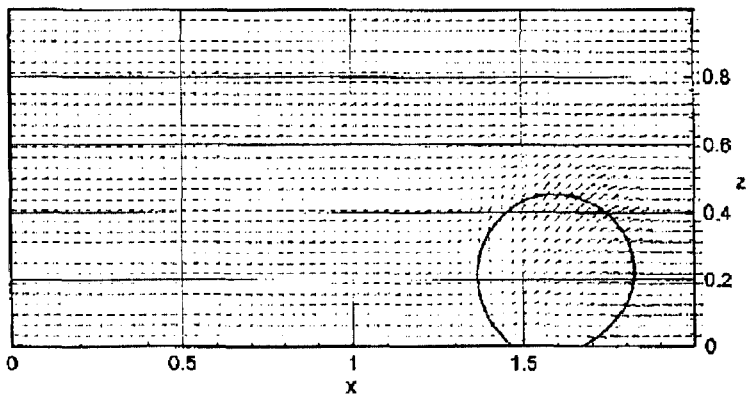

t=0.47

UCLA

NUMERICAL SILMULATIONS

- Calculated results

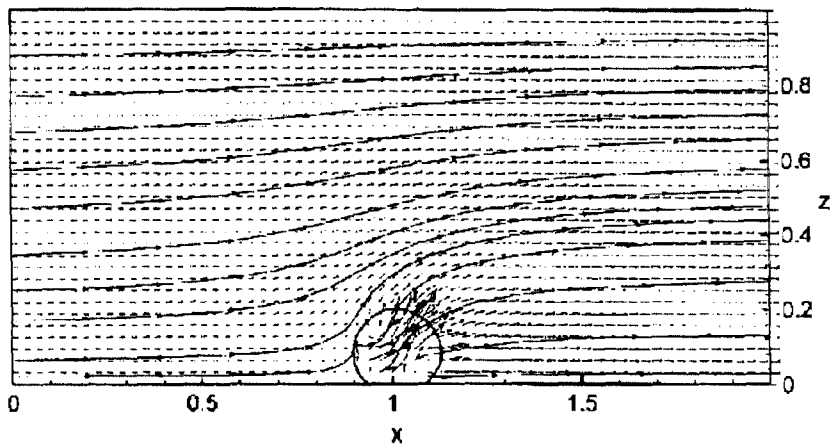

$t=5*10^{-3}$

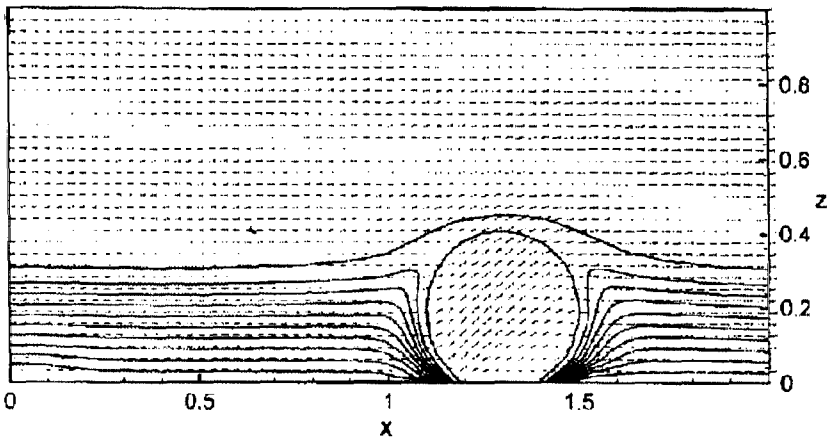

t=0.22

UCLA

CONCLUDING REMARKS

- **Experimental studies of single bubble dynamics under low velocity parallel to the heater have been initiated.**
- **Preliminary results show that lift force resulting from relative velocity between the bubble and the liquid is an important force.**
- **Three dimensional numerical simulations of bubble dynamics and associated heat transfer under forced flow have also been initiated.**
- In Future we plan to extend these experiments to low gravity ~~condition~~ environment

August 11, 2000
Session 4B

Complex Fluids III

INERTIAL EFFECTS IN SUSPENSION DYNAMICS

G. Subramanian and J.F. Brady

Division of Chemistry and Chemical Engineering
California Institute of Technology
Pasadena, CA 91125
e-mail: ganesh@its.caltech.edu, jfbrady@caltech.edu

ABSTRACT

The present work analyses the dynamics of a suspension of heavy particles in shear flow. The magnitude of the particle inertia is given by the Stokes number $St = m\dot{\gamma}/6\pi\eta a$, which is the ratio of the viscous relaxation time of a particle $\tau_p = m/6\pi\eta a$ to the flow time $\dot{\gamma}^{-1}$. Here, m is the mass of the particle, a is its size, η is the viscosity of the suspending fluid and $\dot{\gamma}$ is the shear rate. The ratio of the Stokes number to the Reynolds number, $Re = \rho_f \dot{\gamma} a^2/\eta$, is the density ratio ρ_p/ρ_f. Of interest is to understand the separate roles of particle (St) and fluid (Re) inertia in the dynamics of suspensions. In this study we focus on heavy particles, $\rho_p/\rho_f \gg 1$, for which the Stokes number is finite, but the Reynolds number is sufficiently small for inertial forces in the fluid to be neglected; thus, the fluid motion is governed by the Stokes equations. On the other hand, the probability density governing the statistics of the suspended particles satisfies a Fokker-Planck equation that accounts for both configuration and momentum coordinates, the latter being essential for finite St. The solution of the Fokker-Planck equation is obtained to $O(St)$ via a Chapman-Enskog type-procedure, and the conditional velocity distribution so obtained is used to derive a configuration-space Smoluchowski equation with inertial corrections. The inertial effects are responsible for asymmetry in the relative trajectories of two spheres in shear flow, in contrast to the well known symmetric structure in the absence of inertia. Finite St open trajectories in the plane of shear suffer a downward lateral displacement resulting from the inability of a particle of finite mass to follow the curvature of the zero-Stokes-number pathlines. In addition to the induced asymmetry, the $O(St)$ inertial perturbation dramatically alters the nature of the near-field trajectories. The stable closed orbits (for $St = 0$) in the plane of shear now spiral in, approaching particle-particle contact in the limit. All trajectories starting from an initial offset of $O(St^{1/2})$ or less (which remain open for $St = 0$) also spiral in. The asymmetry of the trajectories leads to a non-Newtonian rheology and diffusive behavior. The latter because a given particle (moving along a finite St open trajectory) suffers a net displacement in the transverse direction after a single interaction. A sequence of such uncorrelated displacements leads to the particle executing a random walk. The inertial diffusivity tensor is anisotropic on account of differing strengths of interaction in the gradient and vorticity directions. Since the entire region (constituting an infinite area) of closed orbits in the plane of shear spirals onto contact for finite St, the latter represents a singular surface for the pair-distribution function. The exact form of the pair-distribution function at contact is still, however, indeterminate in the absence of non-hydrodynamic effects. It should also be noted that finite St non-rectilinear flows do not support a spatially uniform number density owing to the cross-streamline inertial migration of particles.

NASA/CP—2000-210470

Inertial Effects in Suspension Dynamics

G. Subramanian & J.F. Brady

Division of Chemistry and Chemical Engineering
California Institute of Technology
Pasadena, CA

Supported by: NASA

5th μg Fluid Physics Conf.
Cleveland, OH
9-11August 2000

Problem & Motivation

- Understand the effects of inertia on the behavior of concentrated suspensions.
- Inertial effects are important in many natural and industrial suspensions flows, e.g., fluidized beds, drilling fluids, debris flow, etc.
- There is a considerable body of knowledge for small particle suspensions – low Reynolds numbers – and a quantitative understanding/predictive ability is emerging. The advances have come from an intimate interplay among experiment, theory and simulation.
- For suspensions where inertial forces are important much less is known and our predictive ability is severely limited.

Need for microgravity

There are two distinct inertial effects in suspensions:

- **Particle inertial: characterized by the Stokes number**

$$St = \frac{\rho_p U a}{\eta}$$

- **Fluid inertial: characterized by the Reynolds number**

$$Re = \frac{\rho_f U a}{\eta}$$

- **Of course, $St = \rho_p / \rho_f Re$, but we would like to vary independently the effects of particle and fluid inertia. This can only be done in microgravity because of the gravitational settling that occurs when the particle and fluid densities do not match.**

Related work

- Considerable body of work on very dilute dispersions ($\phi << 0.1$) of heavy particles moving through and modifying turbulent flows. No (or very limited) particle-particle interactions.

- Very nice, and ever expanding, body of work on granular flows – essentially infinite *Re* and *St* – that is, there is no fluid.

- Limited experiments on the rheology of inertial suspensions, e.g., Bagnold's (1954) experiments are still the most complete.

- Emerging simulation studies of concentrated inertial suspensions (e.g., D.D. Joseph and coworkers).

- Theory and simulation for finite *St*, zero *Re* suspensions in sedimentation and shear by D.L. Koch and coworkers.

This work

- Analytical theory for zero *Re*, small *St* dilute suspensions in shear flow.
- Dynamic simulation of zero *Re* suspensions in shear flow for arbitrary *St* and ϕ.
- Dynamic simulation for nonzero *Re*, *St*, and ϕ in shear flow.

Analytical theory: $Re = 0$, O(St)

Fokker-Planck Equation: $P_N(\boldsymbol{x}, \boldsymbol{u}, t)$

$$\frac{\partial P_N}{\partial t} + \nabla_x \cdot \dot{\boldsymbol{x}} P_N + \nabla_u \cdot \dot{\boldsymbol{u}} P_N = 0$$

$$\dot{\boldsymbol{x}} = \boldsymbol{u} \quad , \quad \dot{\boldsymbol{u}} = \boldsymbol{m}^{-1} \cdot \left[-\boldsymbol{R}(\boldsymbol{x}) \cdot \boldsymbol{u} + \boldsymbol{F}^O(\boldsymbol{x}) - \boldsymbol{D}(\boldsymbol{x}) \cdot \nabla_u \ln P_N \right]$$

hydrodynamic drag

shear/interparticle force

$$\boldsymbol{F}^O = 6\pi\eta a \dot{\boldsymbol{\Gamma}} \cdot \boldsymbol{x}$$

Brownian motion

$$\boldsymbol{D} = kT\boldsymbol{R} \cdot \boldsymbol{m}^{-1}$$

Integrate out the momentum variables using the method of multiple scales (Chapman-Enskog–type expansion) to derive the configuration-space Smoluchowski equation with inertia.

Method of Multiple Scales

$$\left.\begin{array}{rcl} \tau & \sim & m/6\pi\eta a \\ t & \sim & \dot{\gamma}^{-1} \end{array}\right\} \quad St = \frac{m\dot{\gamma}}{6\pi\eta a} \ll 1$$

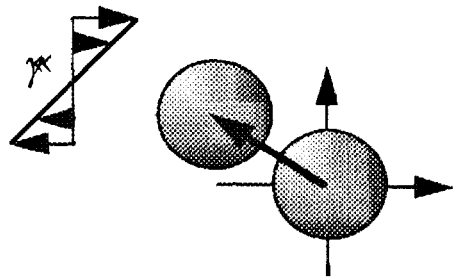

Conditional Probability

$$P(\boldsymbol{x}, \boldsymbol{u}, t, \tau) = g(\boldsymbol{x}, t) P'(\boldsymbol{u}, \tau | \boldsymbol{x}, t)$$

Expand: $$P'(\boldsymbol{u}, \tau | \boldsymbol{x}, t) = P'^{(0)} + St\, P'^{(1)} + \cdots$$

For large τ, $P'^{(0)}$ is a Maxwellian about $(\boldsymbol{u} - \boldsymbol{R}^{-1} \cdot \boldsymbol{F}^{O})$, and $P'^{(1)}$ gives the first inertial correction to the Maxwellian. Integration over the velocity coordinates gives the inertially corrected Smoluchowski equation:

$$\frac{\partial g}{\partial t} + \nabla_x \cdot (\boldsymbol{R}^{-1} \cdot \boldsymbol{F}^{O} g) \;=\; St\, \nabla_x \cdot (\boldsymbol{V} g)$$

Simple Shear Flow: $O(\phi^2)$

The pair-distribution function, $g(x,t)$, determines the suspension structure. In the absence of inertia, the microsturcture has fore-aft symmetry, the suspension is Newtonian (no normal stresses) and there is no shear-induced diffusion. Inertial breaks the symmetry as illustrated below.

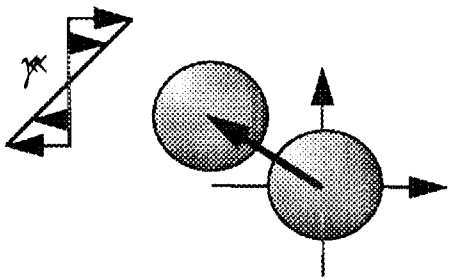

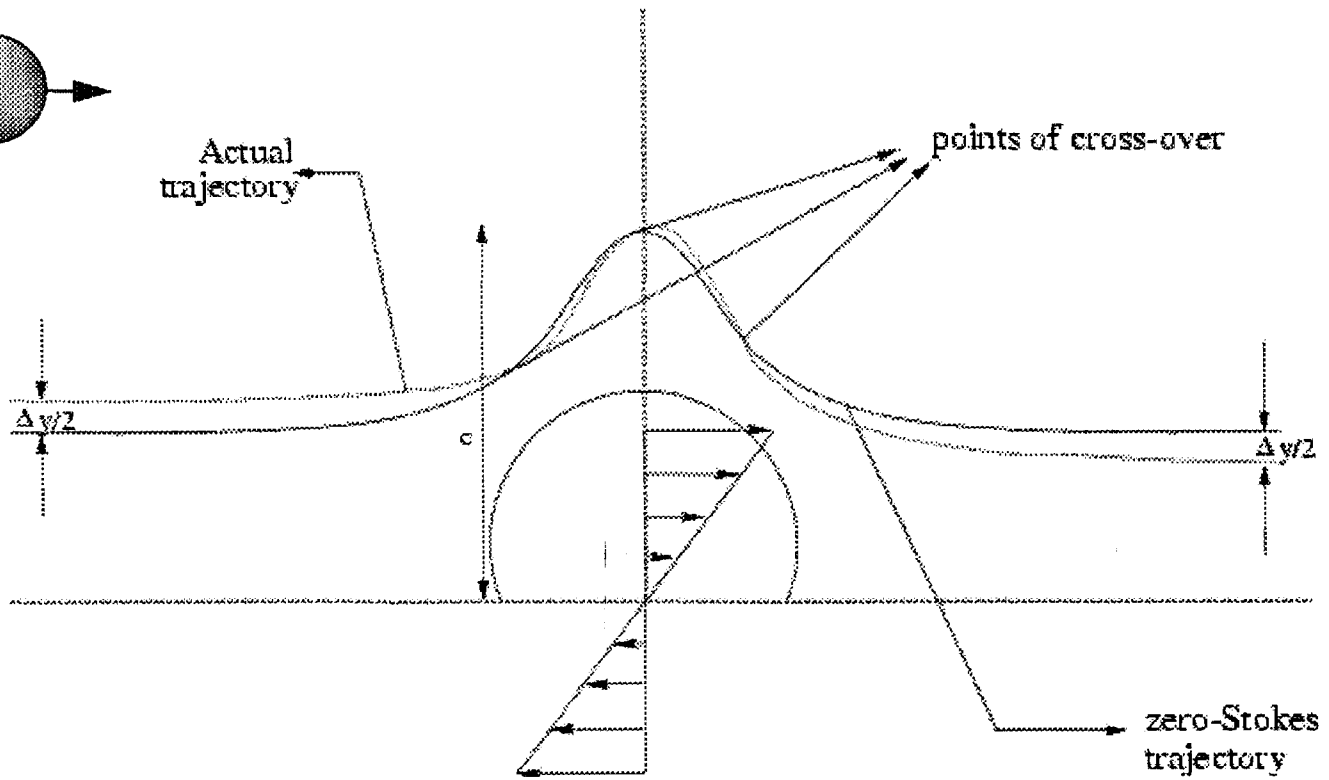

Closed Trajectories

Inertia increases the region of bound trajectories. In the plane, all particles starting off with an offset of O($St^{1/2}$) or less spiral in towards contact with the reference sphere.

Typical bound trajectory

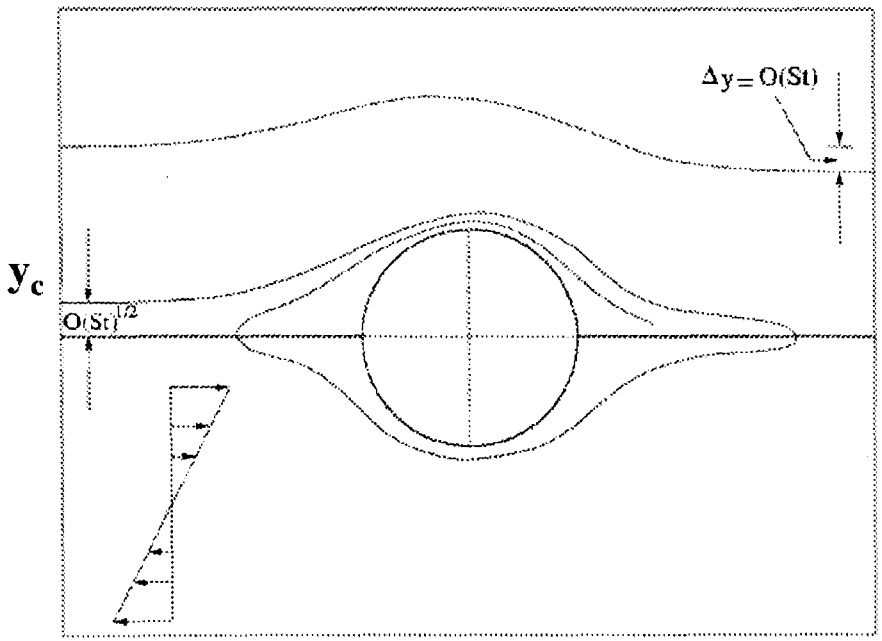

Up stream offset

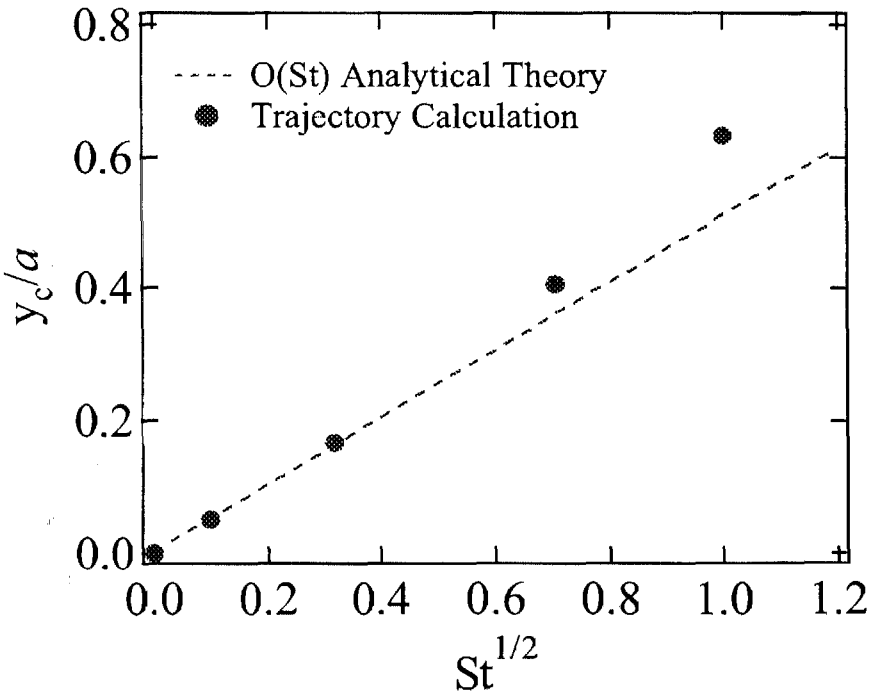

Shear-induced diffusivity: D_{yy}

$$D_{yy} \sim \int \frac{(\Delta y)^2}{\tau}\, d(y_\infty/a) \quad , \quad \tau \sim (\dot\gamma y_\infty/a)^{-1}$$

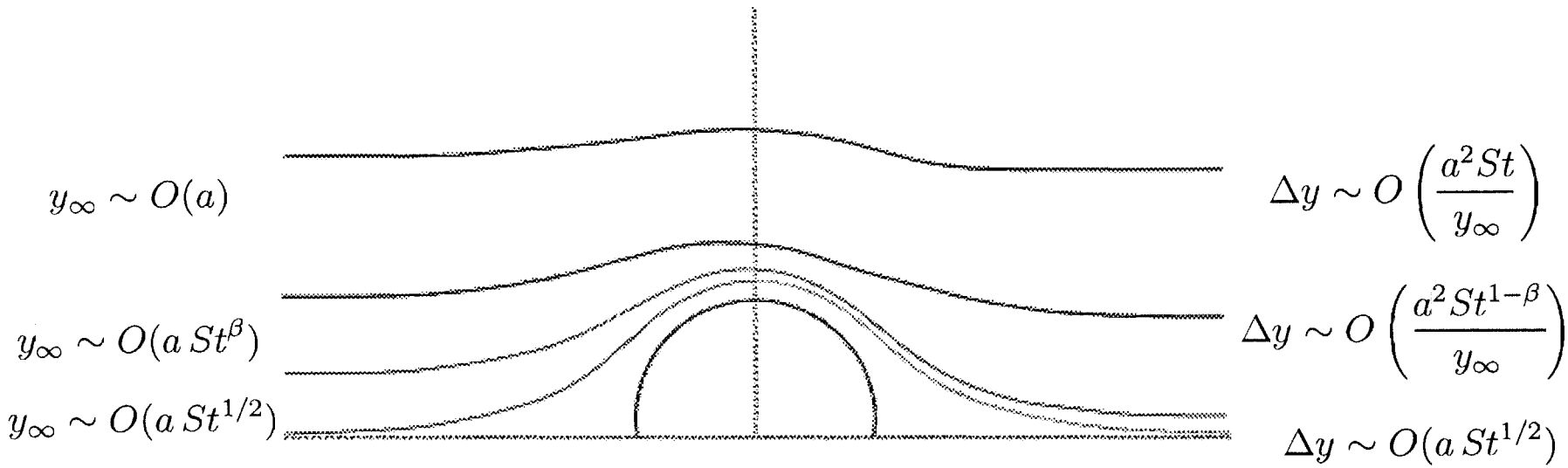

$$y_\infty \sim O(a): \quad D_{yy} \sim O(\dot\gamma a^2 St^2)$$

$$y_\infty \sim O(a\,St^\beta; \beta < 1/2): \quad D_{yy} \sim O(\dot\gamma a^2 St^2 \ln St)$$

$$y_\infty \sim O(a\,St^{1/2}): \quad D_{yy} \sim O(\dot\gamma a^2 St^2)$$

Inertial Dynamics Simulation

Early results on the shear viscosity and first and second normal stress differences as a function of *St*.

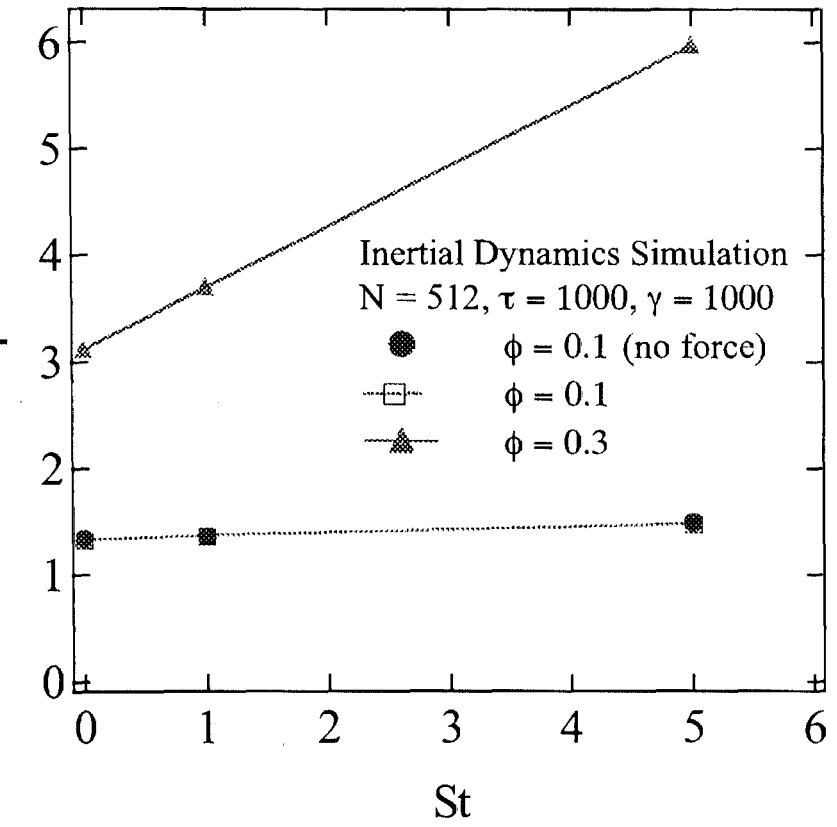

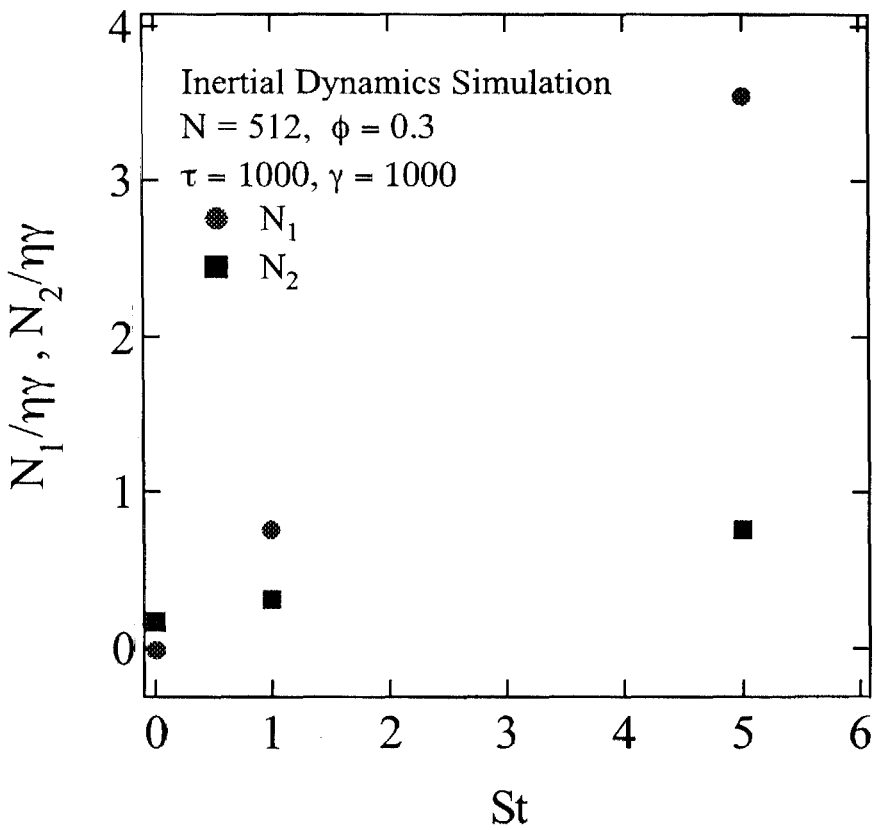

Conclusions

- Derived the O(St) inertially-corrected Smoluchowski equation.
- In simple shear flow the region of closed trajectories is enlarged by particle inertia, and the trapped particles spiral in.
- The shear-induced self diffusivity in the gradient direction is predicted to scale as $St^2 \ln St$ for small St.
- Inertial Dynamics Simulations with an O($N \ln N$) method have been initiated.

PLASMA DUST CRYSTALLIZATION

John A. Goree
Department of Physics and Astronomy
The University of Iowa
john-goree@uiowa.edu, http://dusty.physics.uiowa.edu/~goree

ABSTRACT

A dusty plasma is an ionized gas, containing small particles of solid matter, which are charged and interact through a Coulomb repulsion. Dusty plasmas are like colloidal suspensions, except that the interparticle medium is a plasma rather than a liquid, and therefore the damping rate is reduced as much as a factor of 10^5. The particles are typically 6 μm polymer microspheres, and they acquire a charge of approximately 10^4 e.

The dusty plasma is said to be "strongly-coupled" or a "plasma crystal" when the interparticle potential energy $Q^2 / 4\pi\varepsilon_0 a$ is greater than the particle kinetic energy $k_B T$. Expressing this as the Coulomb coupling parameter, $\Gamma_0 = Q^2 / (4\pi\varepsilon_0 k_B T a)$, where a is the inter-particle spacing, the strong-coupling regime is $\Gamma_0 > 1$. Under these conditions the plasma behaves like a liquid or solid, unlike most plasmas, which are like agas. It is easy to attain a large value $\Gamma_0 > 10^3$ in a dusty plasma, because Q is large, while the gas background cools the particles to a low T. This yields a solid-phase suspension.

The field of dusty plasmas is growing rapidly. Figure 1 shows that the publication rate in major U.S. journals is increasing at an annual rate of approximately 25%. It is also a highly interdisciplinary field, with a mixture of astronomy, applied, and basic science. In astronomy, the rings of Saturn, interstellar clouds, comet tails, and many other objects consist of dust particles mixed with plasma. In industry, semiconductor and solar cell manufacturers have found that contaminating dust particles are synthesized in the chemical plasmas used to etch and deposit thin films of materials on silicon substrates. In basic science, researchers have focussed on strongly-coupled dusty plasmas, including structural studies like those for 2D colloids as well as dynamical studies that exploit the low damping rates of dusty plasmas.

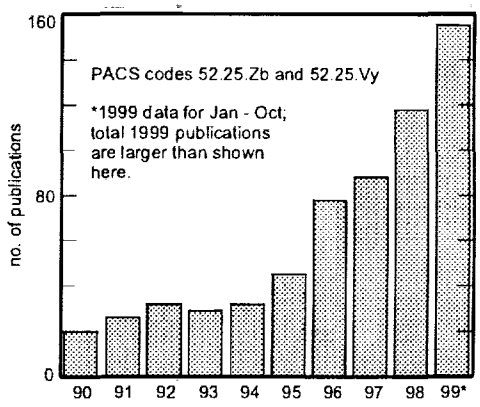

Fig. 1 Dusty plasma publications in APS & AIP journals

In this project, we have been led laboratory studies of 2D strongly-coupled dusty plasmas, and we have collaborated on 3D experiments under microgravity conditions.

The microgravity experiments are PKE (Plasma Kristall Experiment), which has flown on sounding rockets[1] and will be uploaded to the ISS in December 2000 for experiments by the first crew of ISS. The PI for PKE is Prof. Greg Morfill of the Max Planck Institute in Garching Germany. At Iowa, we are also preparing for parabolic flight campaigns.

Under laboratory conditions, the charged particles in a dusty plasma suspension have no buoyancy, and consequently they sediment rapidly to the bottom of the vacuum chamber. This results in a 2D suspension, which provides excellent opportunities to explore 2D physics topics, such as melting and waves in 2D crystals. Performing experiments in 3D, however, requires the elimination of gravity.

In the laboratory, we have made several discoveries.[2] As an example, Figure 2 shows Mach cones, which are V-shaped shock waves produced by a supersonic object. Although Mach cones are familiar in gasdynamics, they were almost unknown in solids until we found them in our plasma crystal. Mach cones are also predicted to occur in the dusty plasmas of Saturn's rings, where they might be observed by spacecraft Cassini.

The future of microgravity experiments with dustyplasmas lies with IMPF, the proposed International Microgravity Plasma Facility.[3] Presently funded by the DLR, IMPF will be a users facility on ISS. We plan for IMPF to become an international facility, drawing on resources from multiple ISS partners. Basic and applied experiments by various scientists worldwide will be rotated on a 6-month cycle.

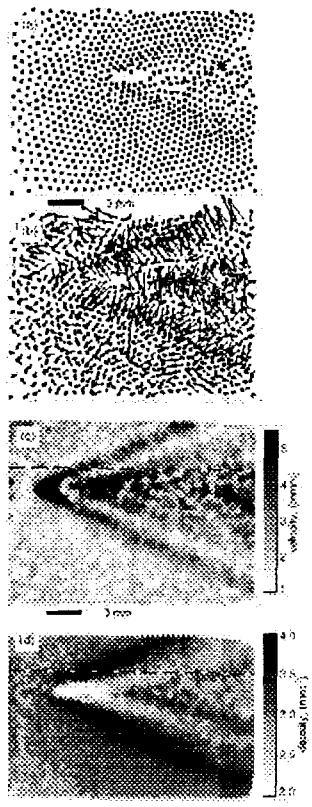

Figure 2. Mach cones in a 2D plasma crystal.
(a) particle positions
(b) particle velocities
(c) particle speed map
(d) particle number density.

---

1 G.E. Morfill, H.M. Thomas, U. Konopka, H. Rothermel, M. Zuzic, A. Ivlev, and J. Goree
Condensed Plasmas under Microgravity
Physical Review Letters Vol. 83, pp. 1598-1601 1999.

2 *Representative publications:*
D. Samsonov, J. Goree, Z.W. Ma, A. Bhattacharjee, H.M. Thomas, and G.E. Morfill
Mach Cones in a Coulomb Lattice and a Dusty Plasma
Physical Review Letters Vol. 83, pp. 3649-3652 1999.
U. Konopka, D. Samsonov, A.V. Ivlev, J. Goree, V. Steinberg, and G.E. Morfill
Rigid and Differential Plasma Crystal Rotation Induced by Magnetic Fields
Physical Review E Vol. 61, pp. 1890-1898 2000.
S. Nunomura, D. Samsonov, and J. Goree
Transverse Waves in a Two-Dimensional Screened Coulomb Crystal
Physical Review Letters Vol. 84, pp. 5141-5144 2000.

3 IMPF's home page is http://www.microgravity.net

NASA/CP—2000-210470

Plasma Dust Crystallization

John Goree

The University of Iowa

Dusty plasma publications in APS & AIP journals

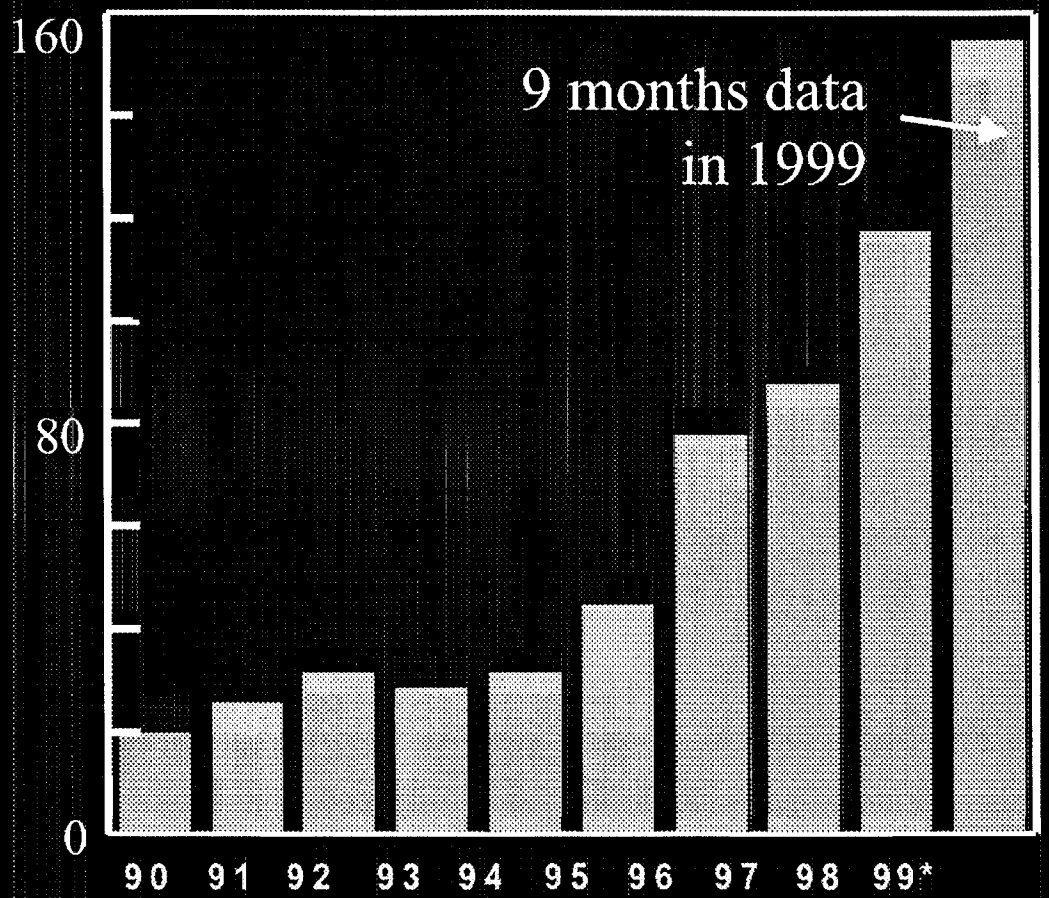

What is a dusty plasma?

- Electrons + ions + neutral gas atoms + small particles of solid matter
- About the particles:
  - typically:
    - 5 nm - 50 microns
    - dielectric material
  - charged by collecting electrons & ions

What is a dusty plasma?

It's also termed: *complex plasma*

analogy with: *complex fluids*

Who cares about dusty plasmas?

Astronomy
- Rings of Saturn
- Interstellar space
- Comet tails

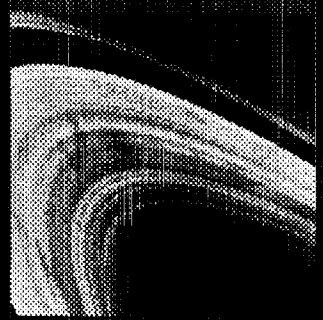

Manufacturing
- Particle contamination (Si wafer processing)
- Nanomaterial synthesis

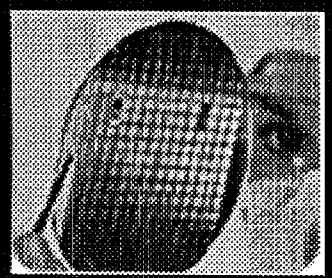

Basic physics
- Coulomb crystals
- Waves
- Much more ...

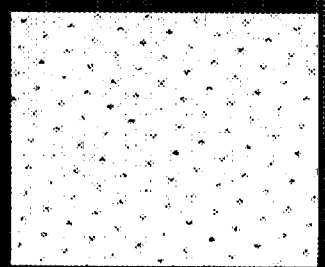

Forces acting on a particle

Coulomb

- trapping potential
- inter-particle

$\propto r^1$

Gravity

$\propto r^3$

- Gas drag
- Ion drag
- Thermophoresis

$\propto r^2$

IOM

Need for microgravity

- Gravity ⇒ sedimentation
- No buoyancy to offset sedimentation

Microgravity enables 3-D physics

ground-based $\Rightarrow$ 2-D experiments

microgravity $\Rightarrow$ 3-D experiments

Particles

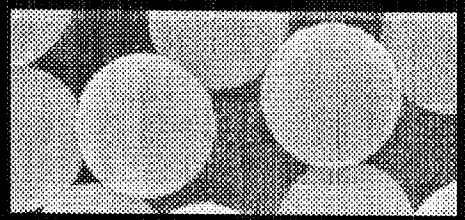

6 μm polymer microspheres

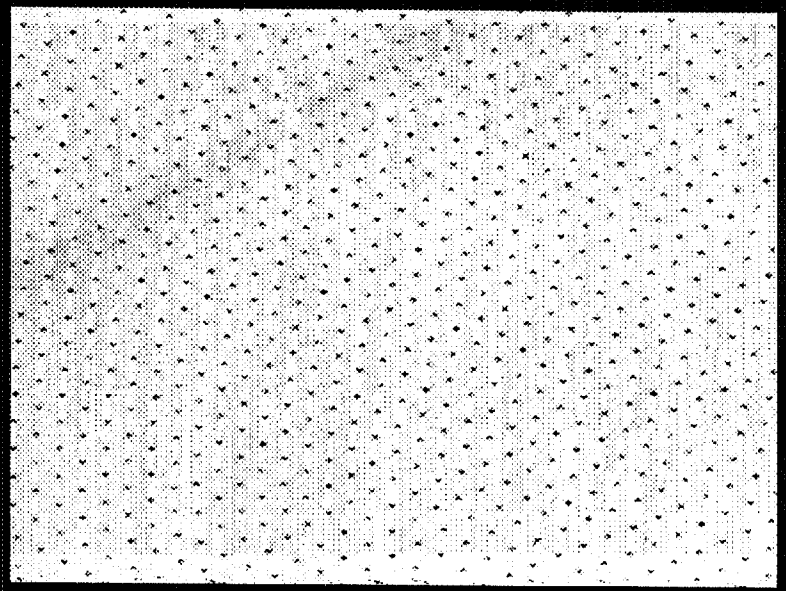

separation $a \approx 0.3$ mm

$Q \approx -8000\ e$

Yukawa interparticle interaction (in a monolayer)

Electrostatic trapping of particles

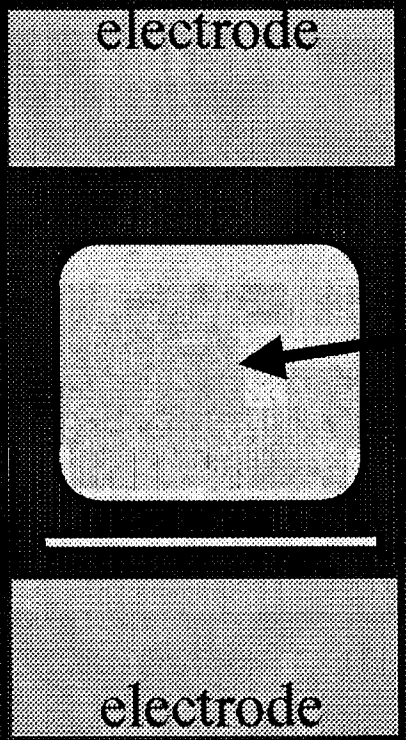

Equipotential contours

Without gravity, particles fill 3-D volume

With gravity, particles sediment to high-field region
⇒ 2-D layer

2-D experiments

ground-based

results

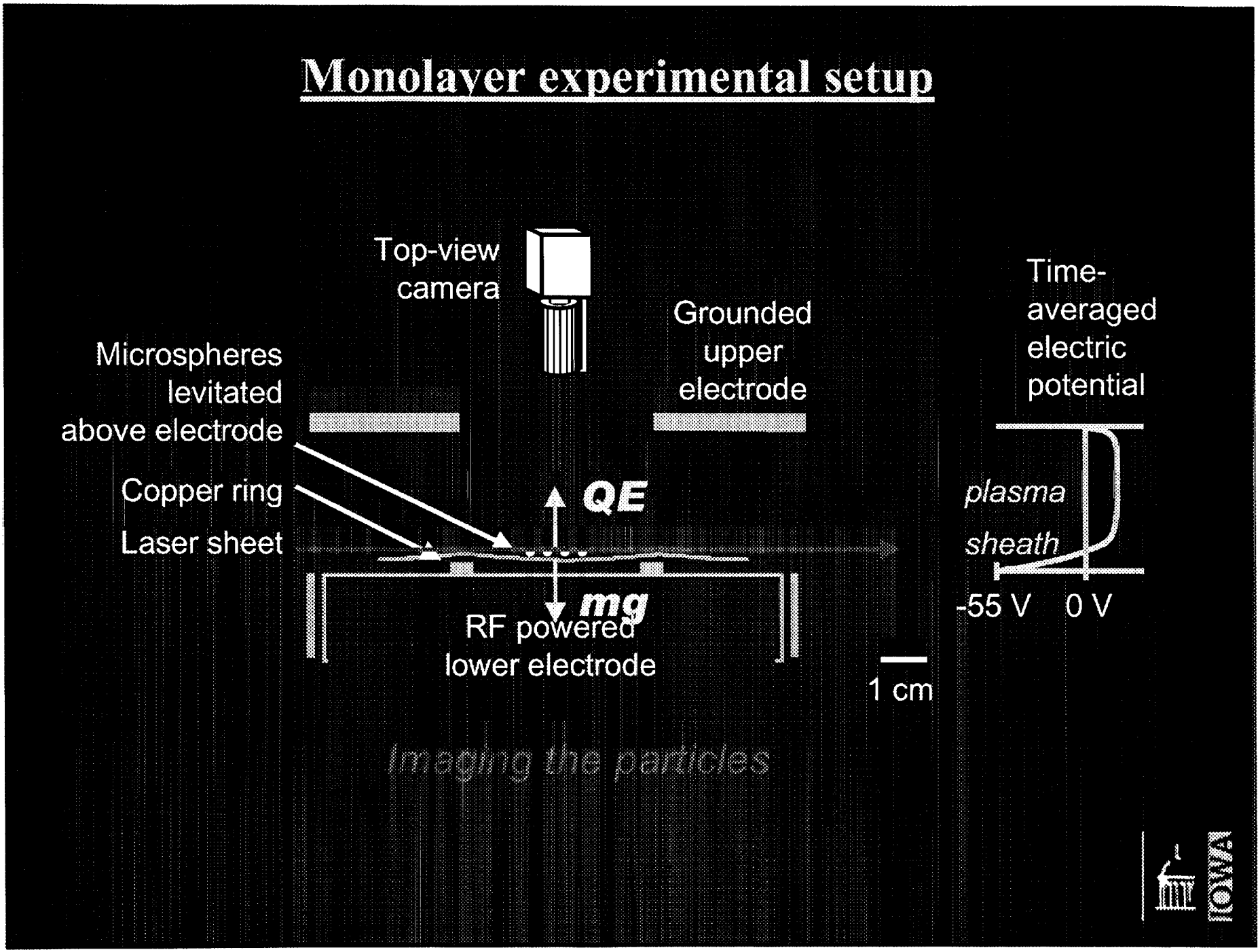
Monolayer experimental setup
Top-view camera
Grounded upper electrode
Time-averaged electric potential
Microspheres levitated above electrode
Copper ring
Laser sheet
QE
mg
plasma
sheath
-55 V
0 V
RF powered lower electrode
1 cm
Imaging the particles

Experiments

- Structure & dynamics
- Easily compared to MD simulations

Laboratory results:

- Coulomb cluster
- monolayer with 19 particles

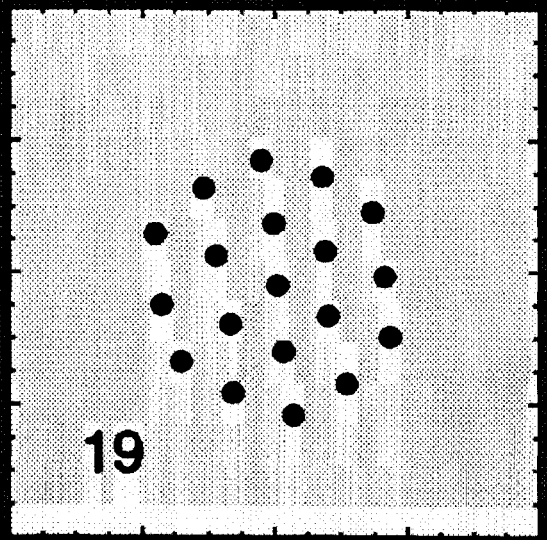

view from top camera

Laboratory results:

monolayer with 948 particles

particles *triangulation*

view from top camera

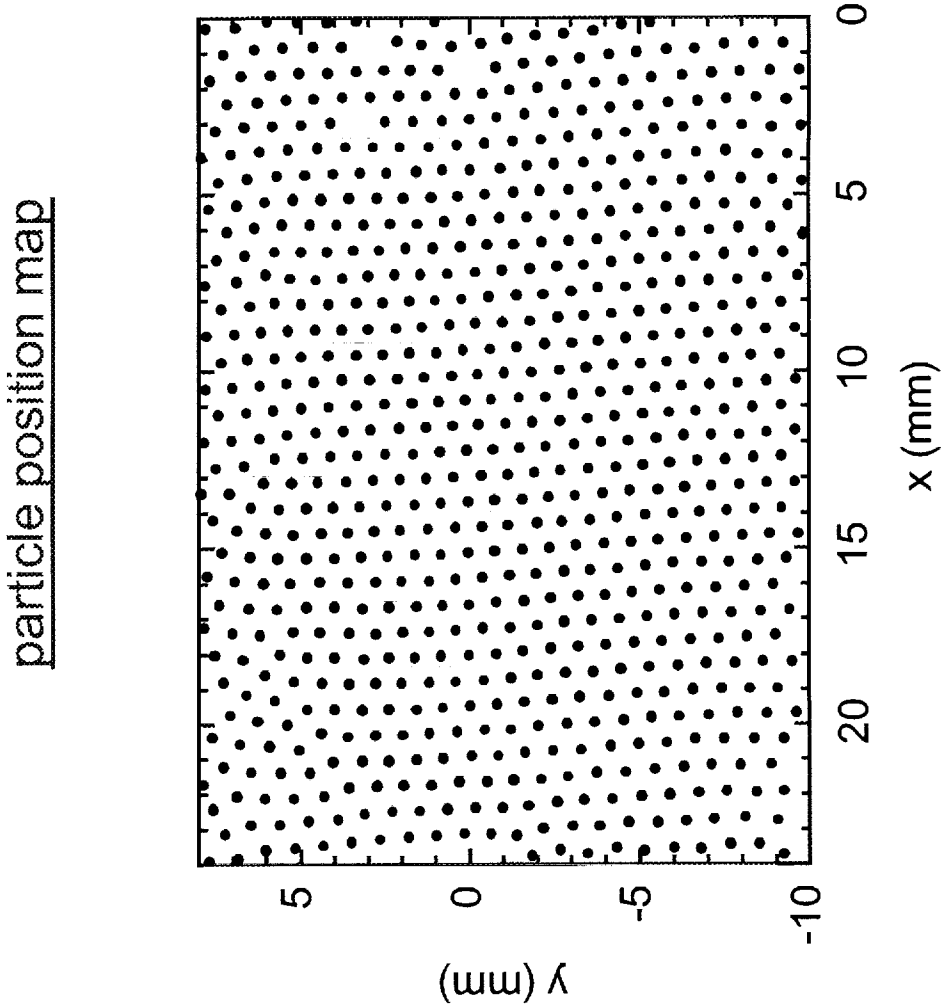
particle position map
y (mm)
5
0
-5
-10
0
5
10
15
20
x (mm)

Pair correlation function

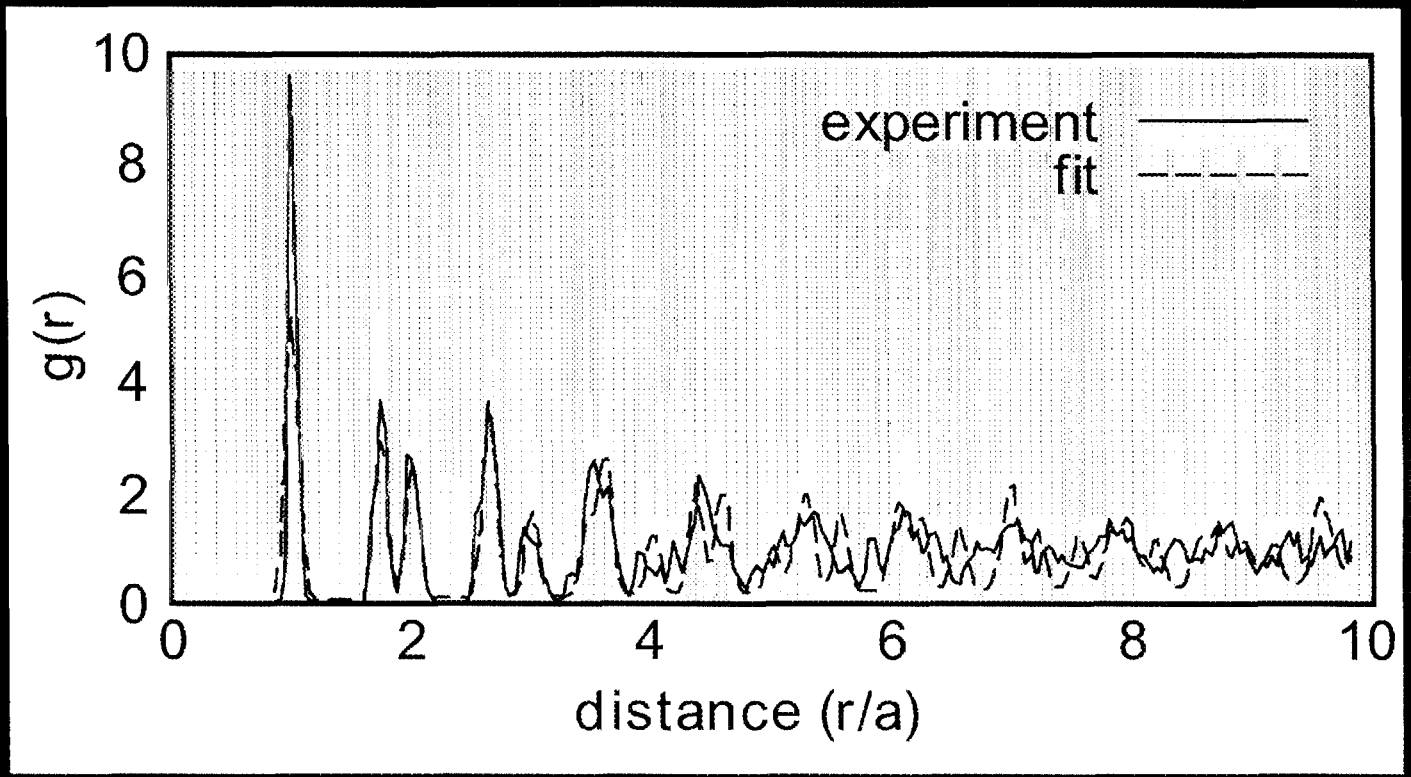

Compressional and shear waves

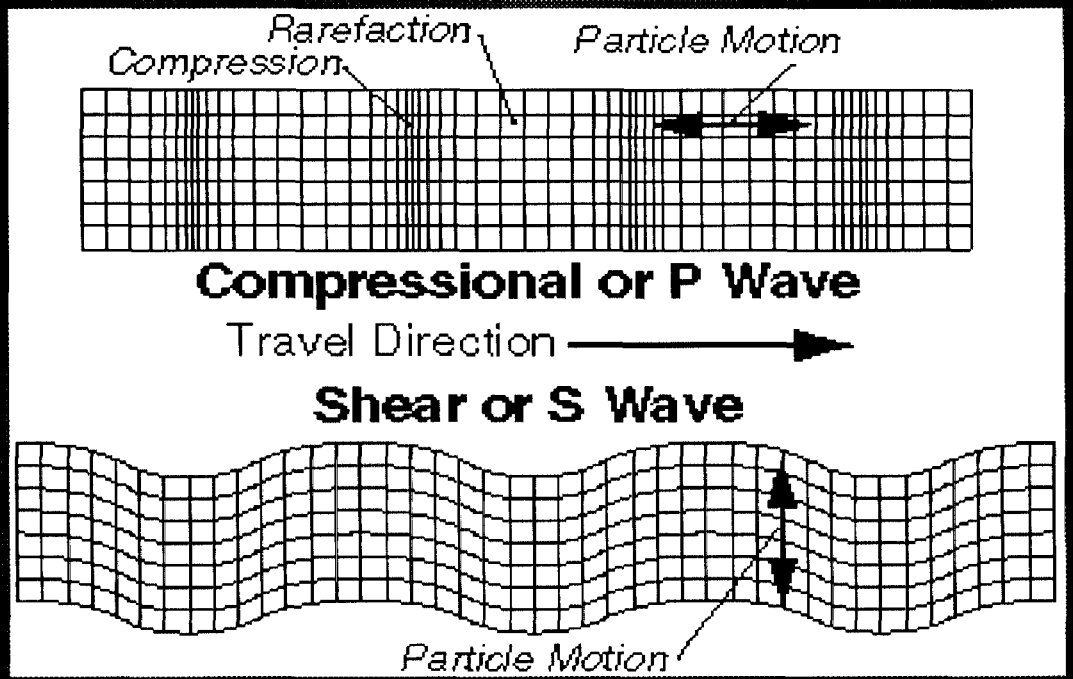

Compressional and shear waves

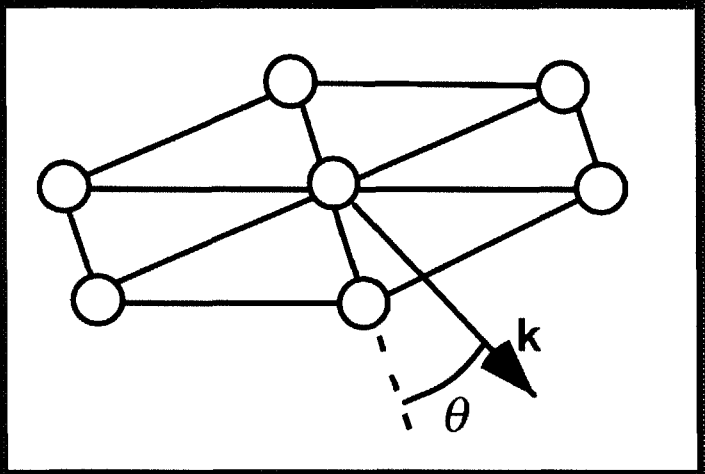

Dispersion relation depends on direction of propagation, θ

Here we present results for $\theta = 0°$.

Dispersion relation (phonon spectrum)

Theory for a triangular lattice, $\theta = 0°$

Wang, Bhattacharjee, Hu (2000)

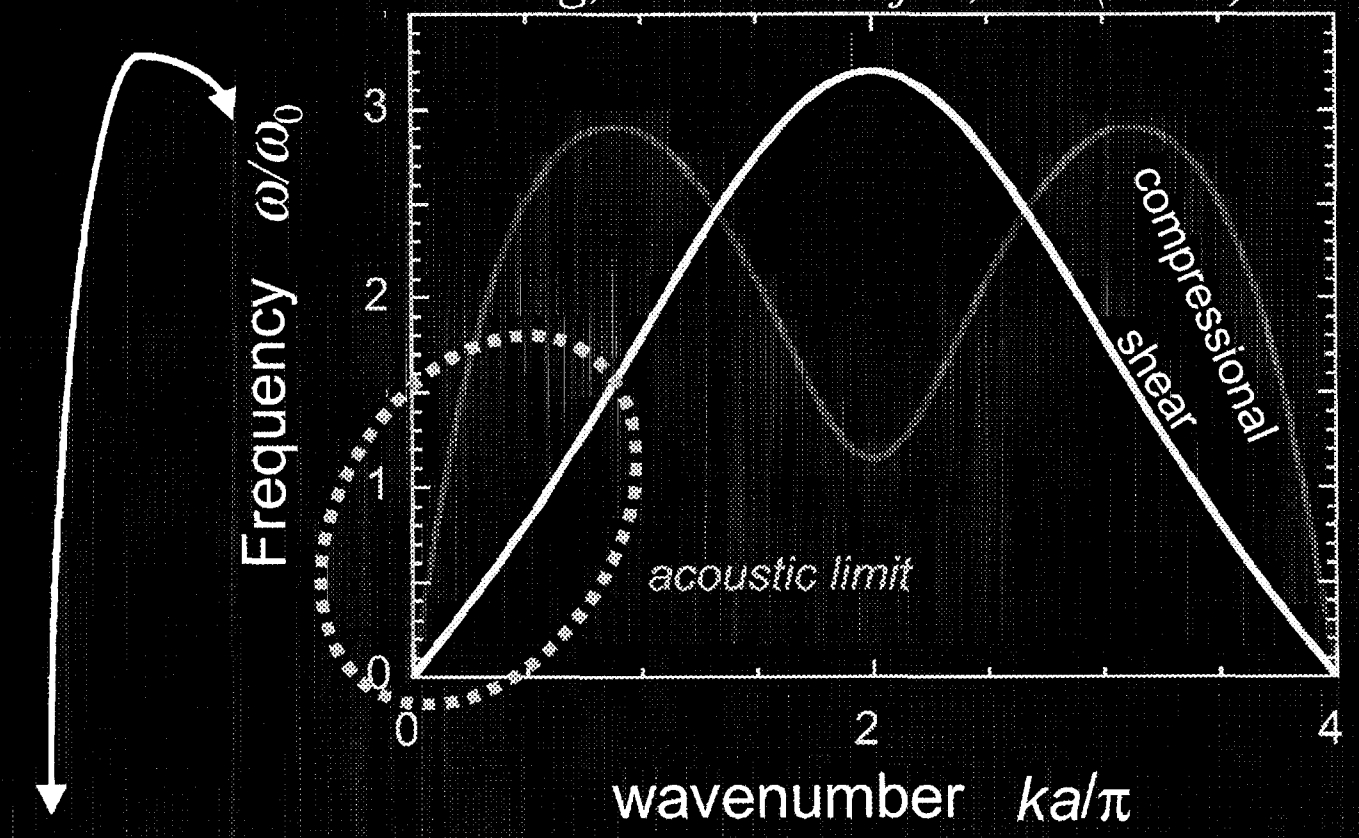

$$\omega_0^2 = Q^2 / 4\pi\varepsilon_0 m a^3$$

Compressional & shear waves

- The *shear* wave is:
  - slow
  - propagates only in a *solid*
- The *compressional* wave is:
  - fast
  - propagates in solids and liquids

IOWA

Here, we show two kinds of experiments with the *transverse wave*

- Pulse propagation
  - pulsed laser, duration = 0.33 s
- Periodic wave
  - modulated laser, sine wave excitation

apparatus

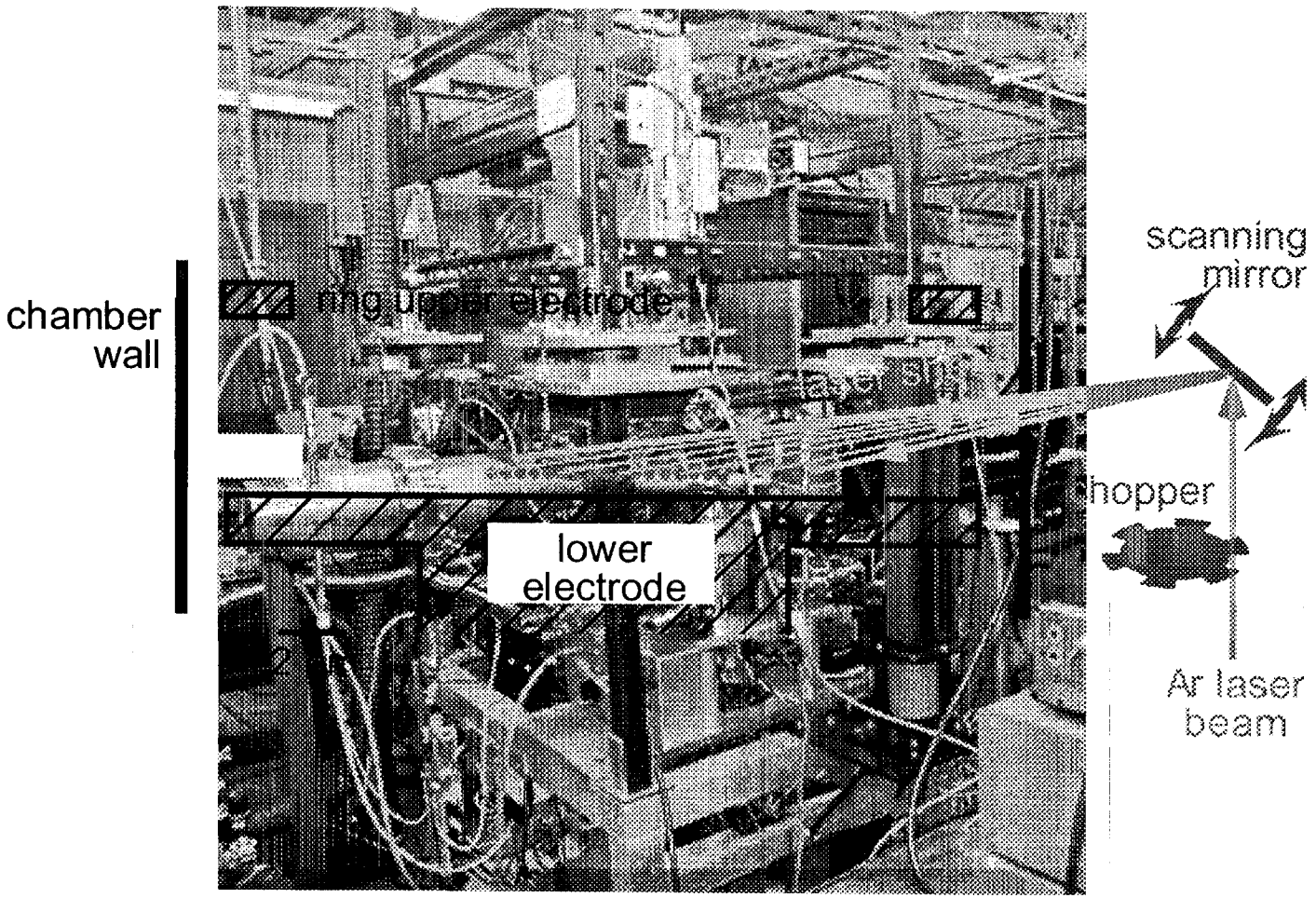
chamber wall
ring upper electrode
scanning mirror
chopper
lower electrode
Ar laser beam

Velocity map for pulse propagation

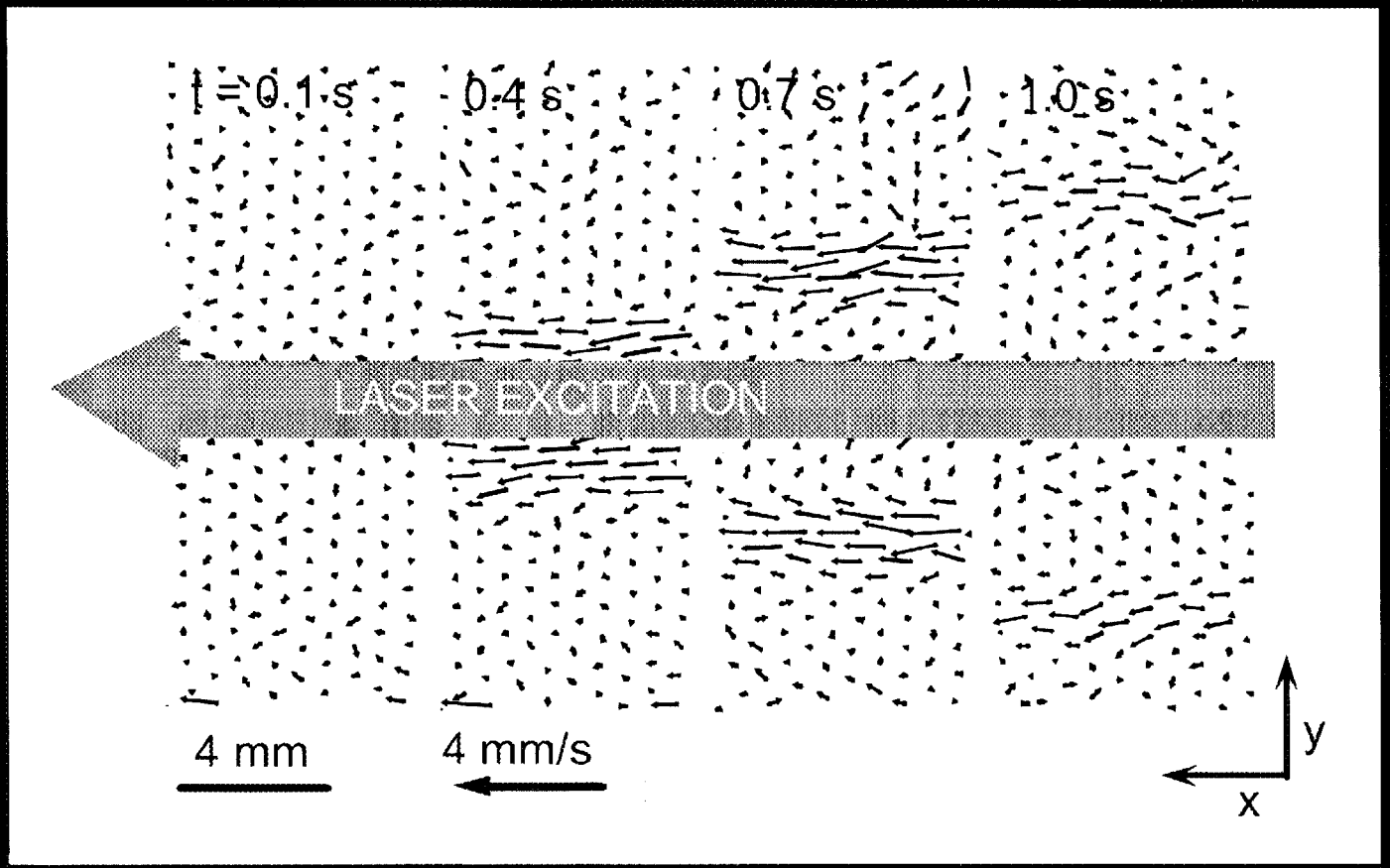

Dispersion relation of a *sinusoidal* transverse shear wave

Dispersion relations

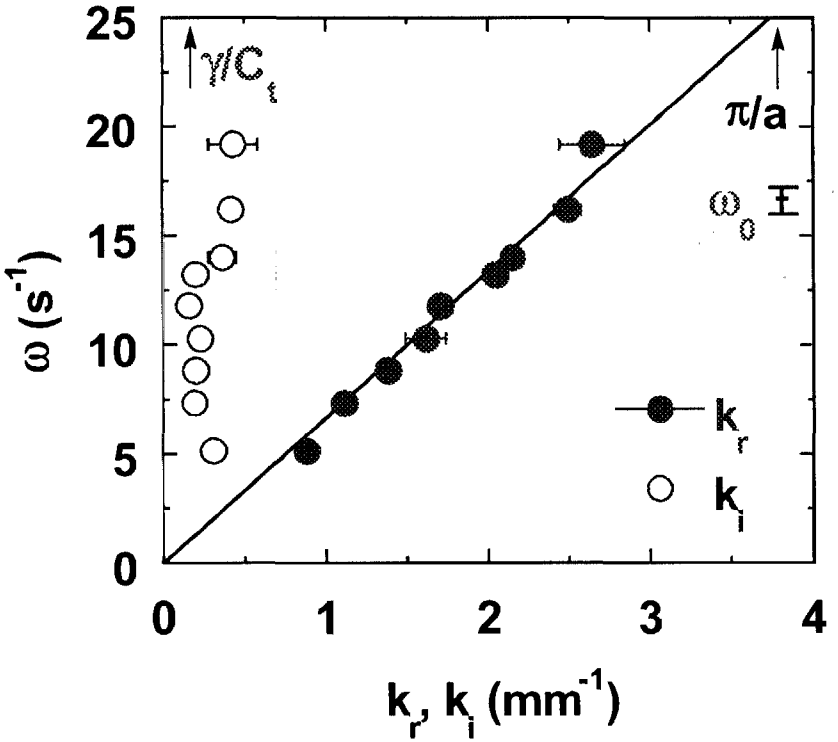

Experiment

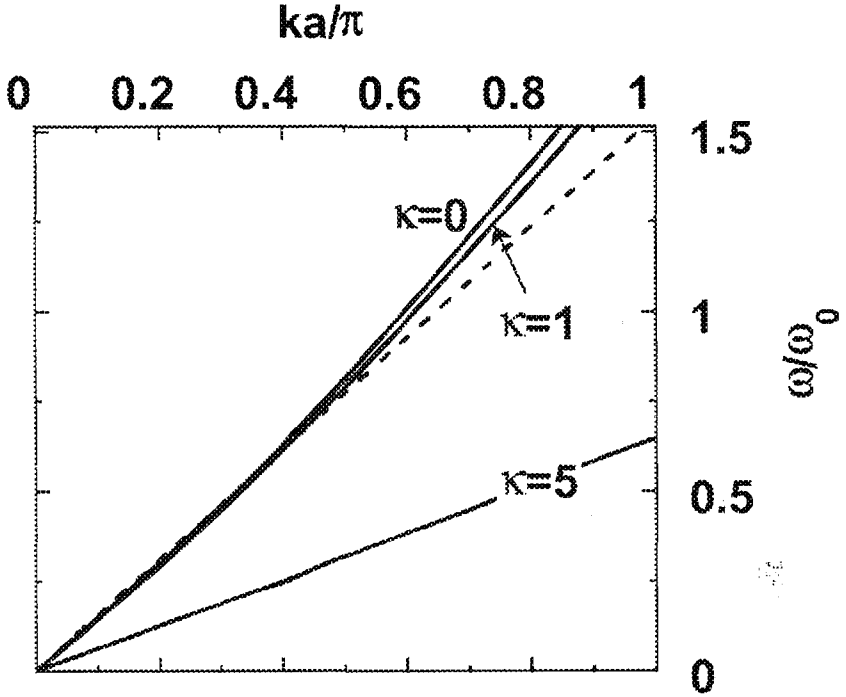

Theory

NASA/CP—2000-210470

17746

Using the dispersion relation to measure Q

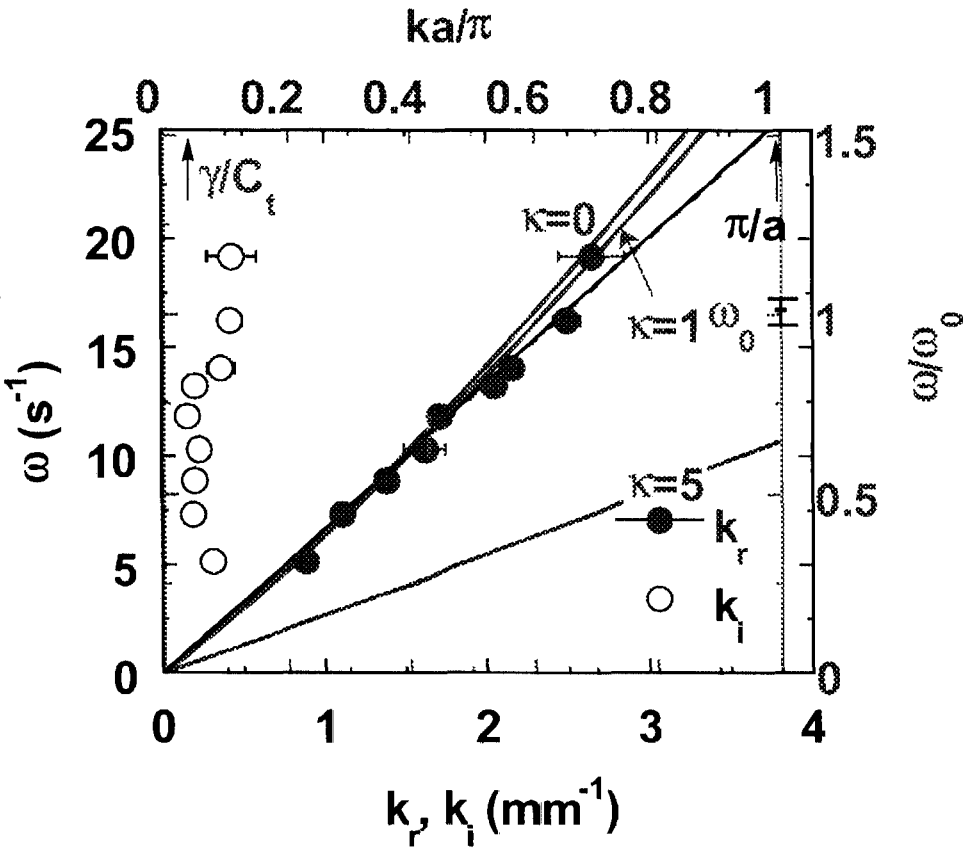

$$\omega_0^2 = Q^2 / 4\pi\varepsilon_0 \, m \, a^3$$

We choose ω_0, and therefore Q, so that experiment and theory have the same wave speed.

Our observation of
transverse waves proves:

*Our plasma crystal was in a **solid** phase.*

Wave Summary

- We excited transverse shear waves
  - 2D plasma crystal
  - using laser manipulation.
- Measured dispersion relation
- Compared to theory $\Longrightarrow$ measurement of Q
- 2-D experiments on ground
- 3-D possible with microgravity

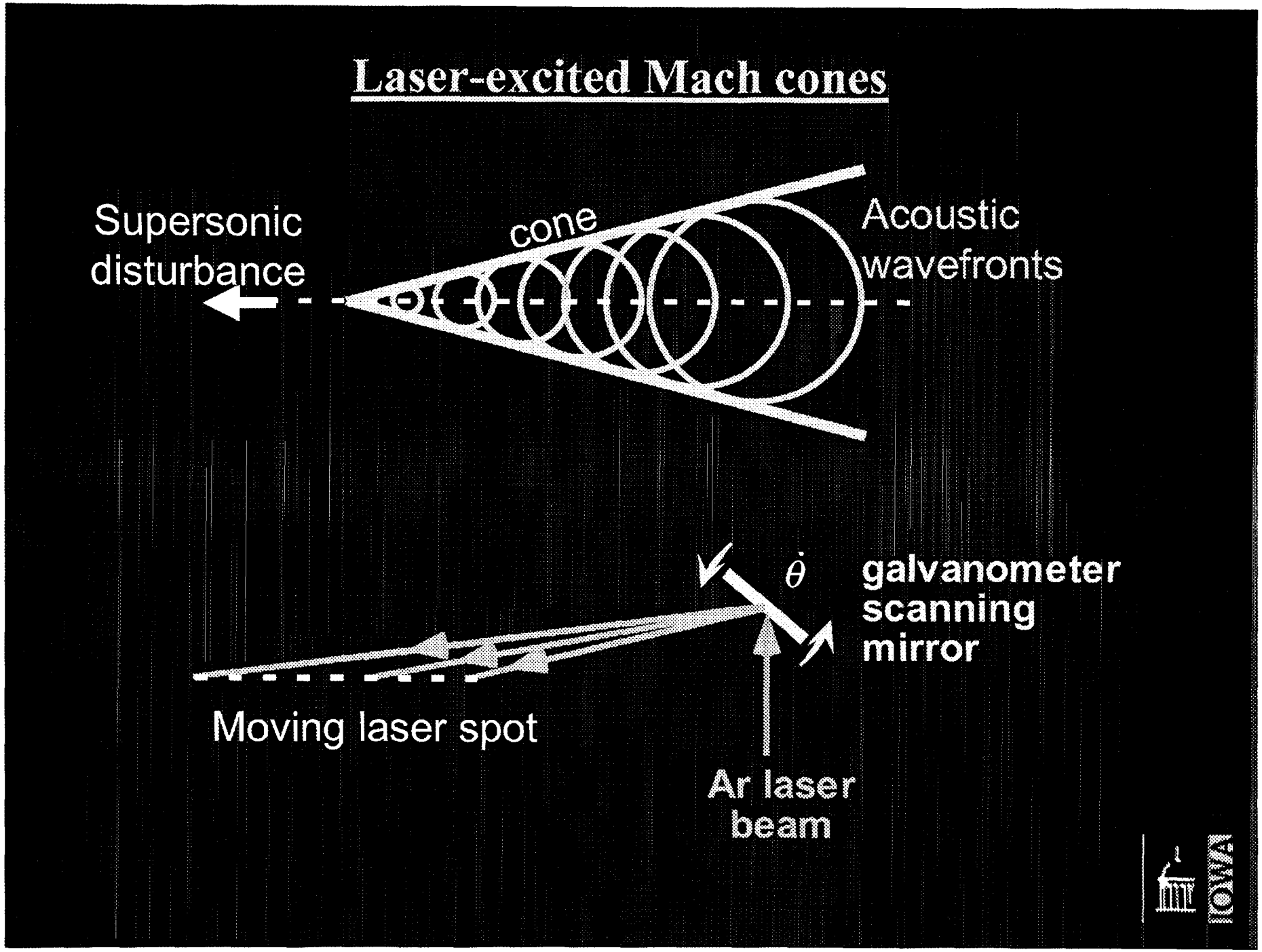
Laser-excited Mach cones
Supersonic disturbance
cone
Acoustic wavefronts
$\dot{\theta}$
galvanometer scanning mirror
Moving laser spot
Ar laser beam
IOWA

Laser-excited Mach cones

map of particle speed

IOWA

Mach Cone Summary

- 2-D Mach cone excitation on ground
- 3-D possible with microgravity

Microgravity

Microgravity experiments

VTMS

PKE - Plasma Kristall Experiment

Germany, Russia, U.S.

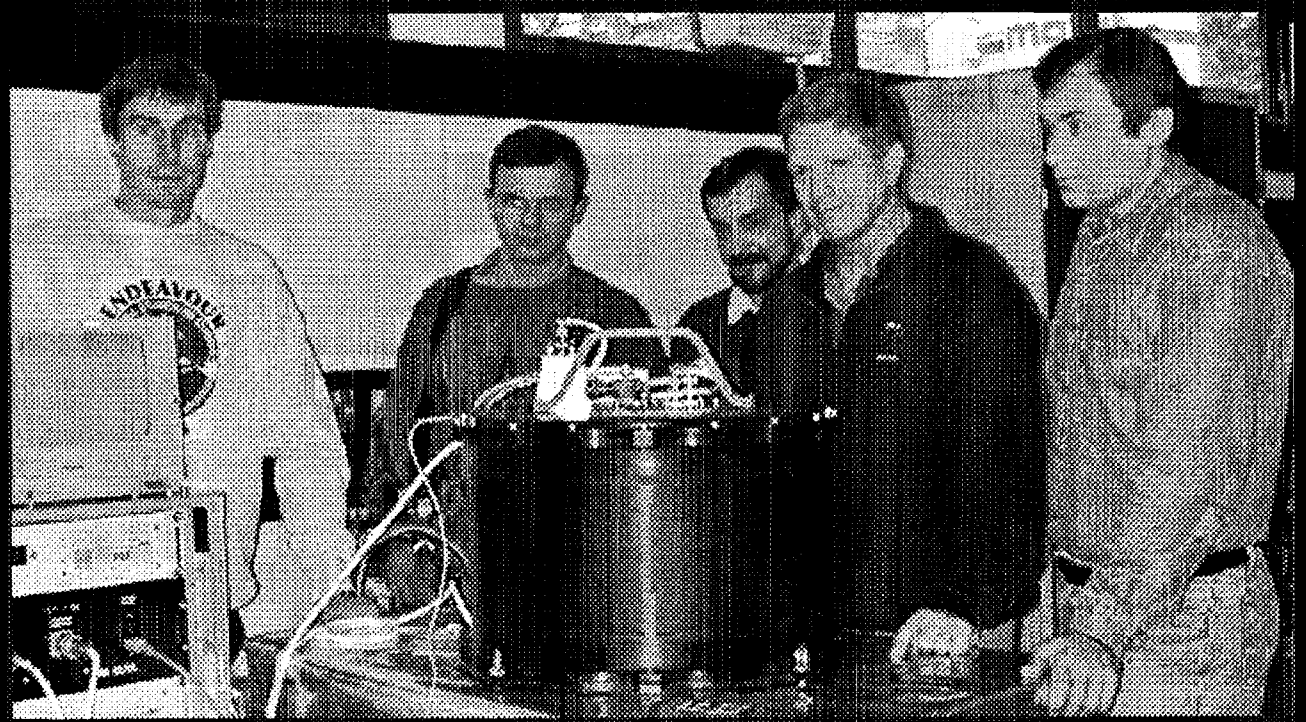

PKE flight hardware with 1st & 3rd ISS crews

IOWA

PKE
MPE
RAS
HEDRC
Plasmakristall
MPE
HEDRC IPST
KAISER-THREDE
DLR
ISS
RKA RKK ENERGIA
KAISER-THREDE
DLR
Российское
Космическое
Агентство
IOWA

PKE chamber

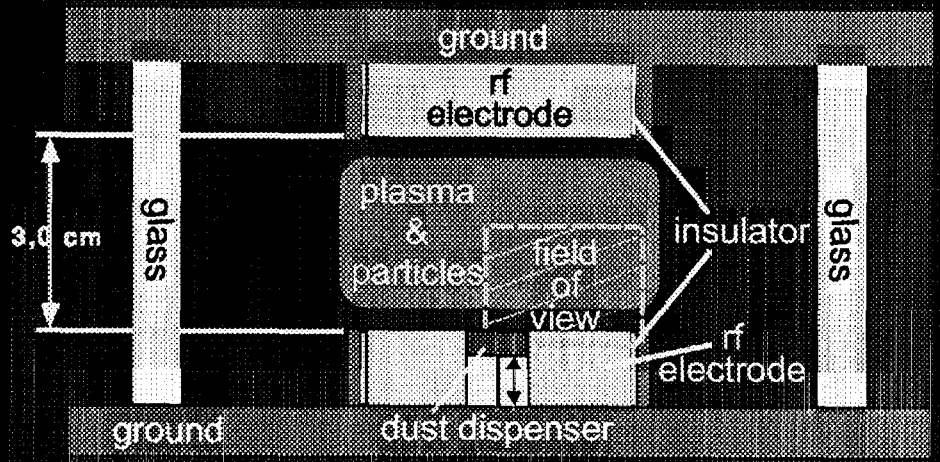

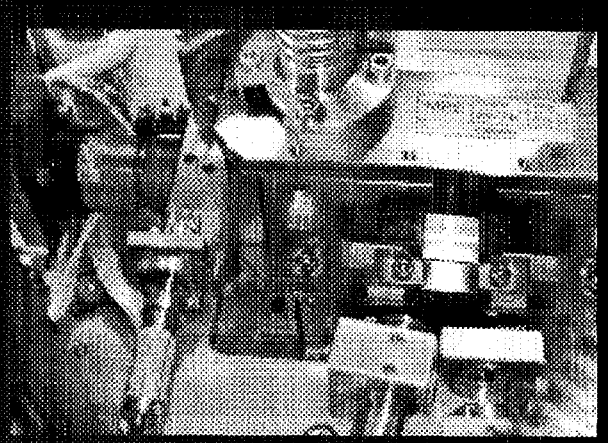

Laser sheets for illuminating particles

Cameras for imaging particles

Predecessor to PKE: Sounding rocket experiments

Morfill et al.,
Phys. Rev. Lett. 1999

Time-elapsed view of 1/4 cross section
(sounding rocket experiment)

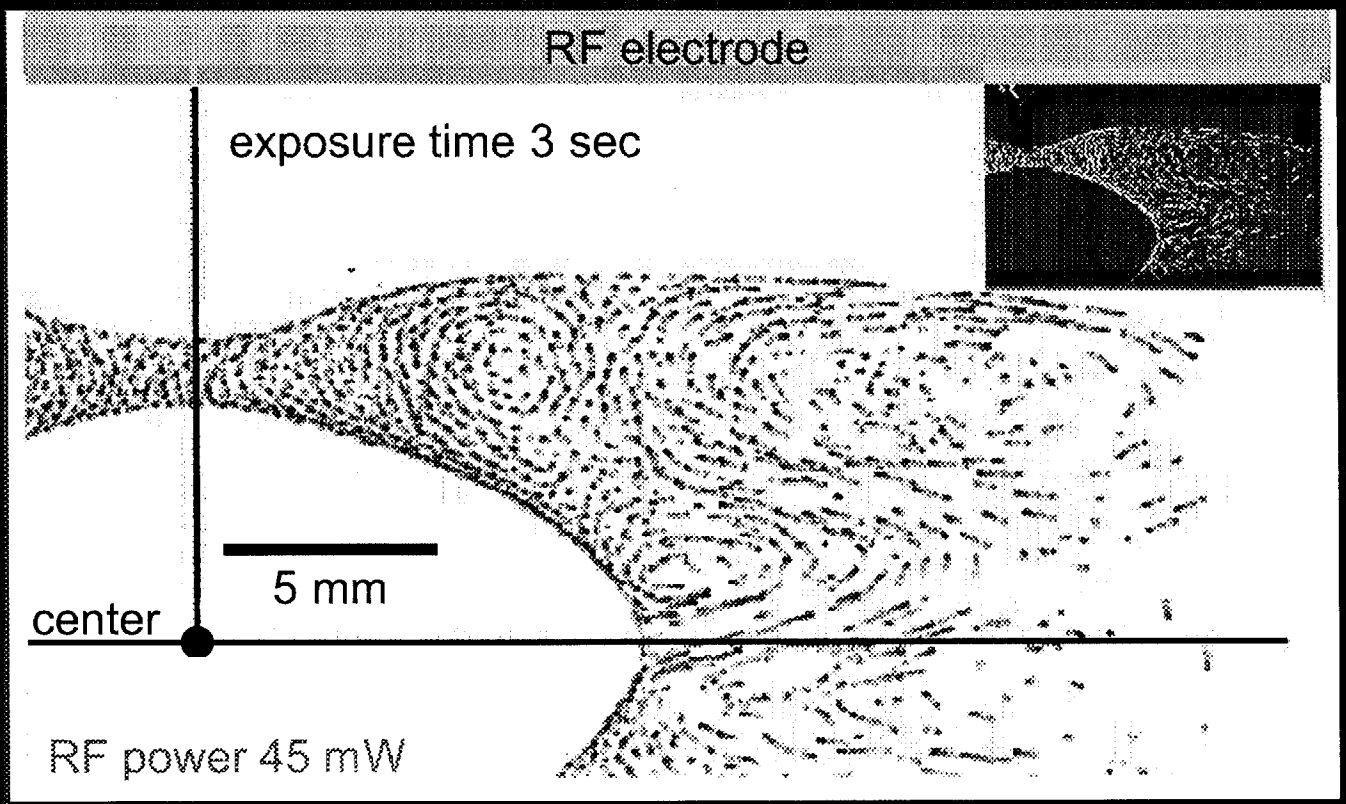

Pair correlation function

(sounding rocket experiment)

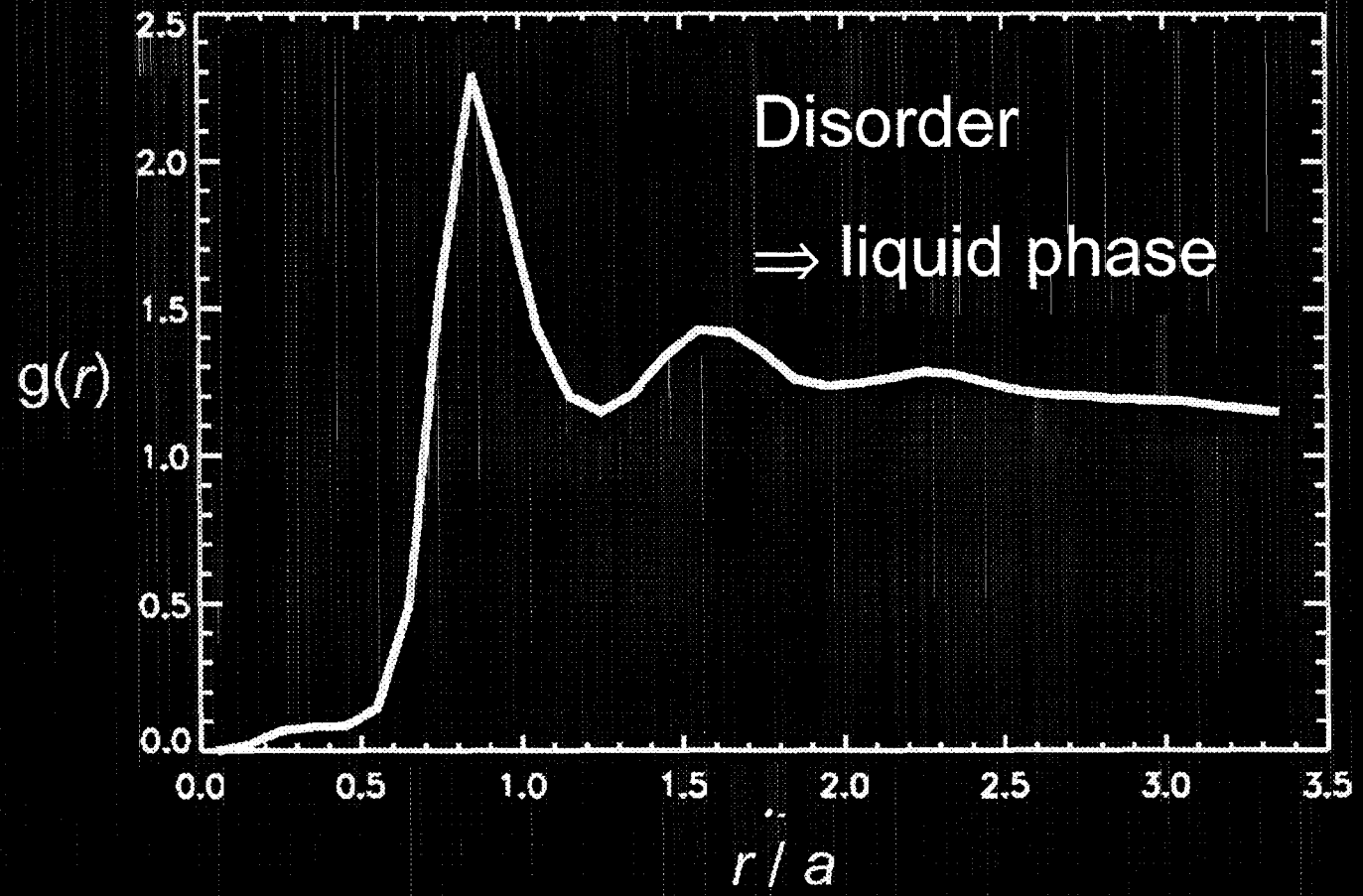

IOMA

PKE Summary

- 3-D particle suspensions
- Sounding rocket experiments (Phys. Rev. Lett. 2000)
- ISS experiments 2001

Overall Summary

- Dusty plasmas - a new field
- 2-D Ground-based experiments: develop ideas & methods for flight experiments
- 3-D Flight experiments

Extra slides

Determining k_r and k_i

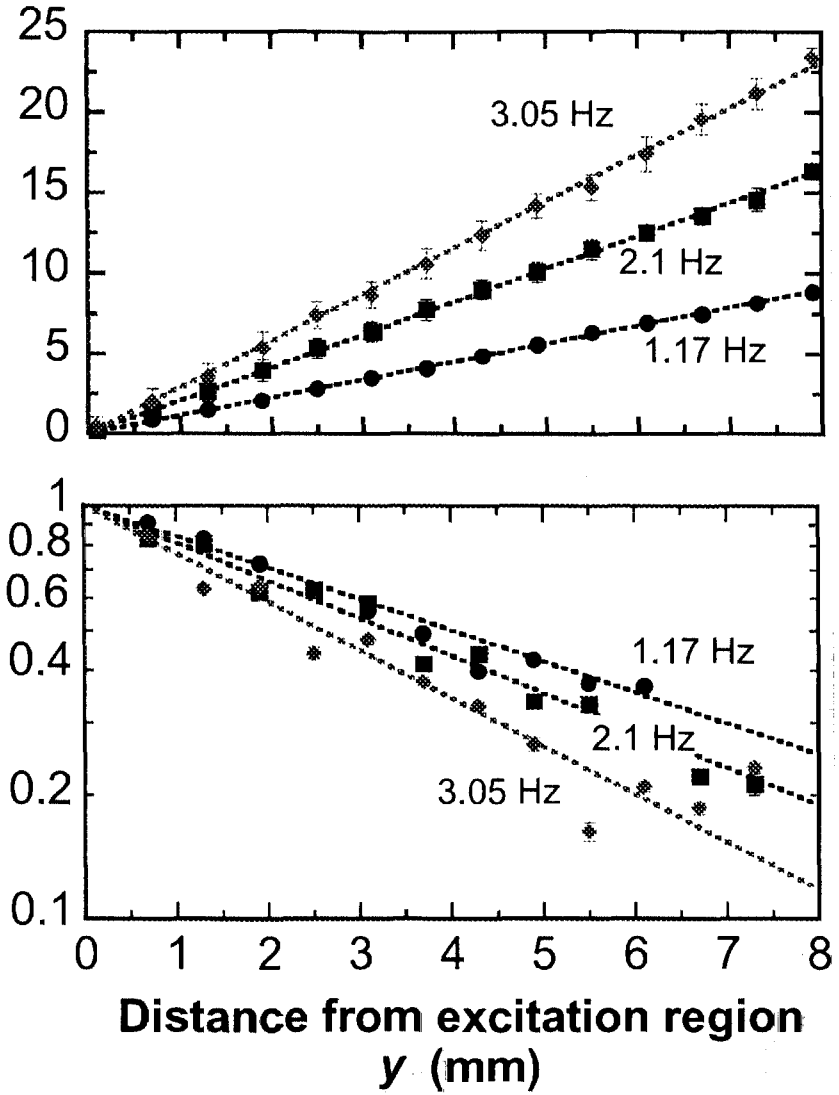

Phase vs. y

slope $\Rightarrow k_r$

Amplitude vs. y

slope $\Rightarrow k_i$

Measuring dispersion relation: k_r & k_i vs. ω

- ω is known (= laser modulation frequency)
- We want to measure k_r and k_i
- Wave propagates in y direction.
- Assume $v_x \propto \cos(k_r y - \omega t) \exp(-k_i y)$
- Calculate every particle's velocity v_x
- Divide image into 30 y bins, so that the x coordinate is ignored
- Average v_x in each bin $\Rightarrow v_x(y, t)$
- Fourier analysis phase & amplitude vs. y
- $\Rightarrow k_r$ and k_i

Velocity profiles for pulse propagation

Group velocity
= 6.1 mm/s

particle velocity
≈ 1 mm/s

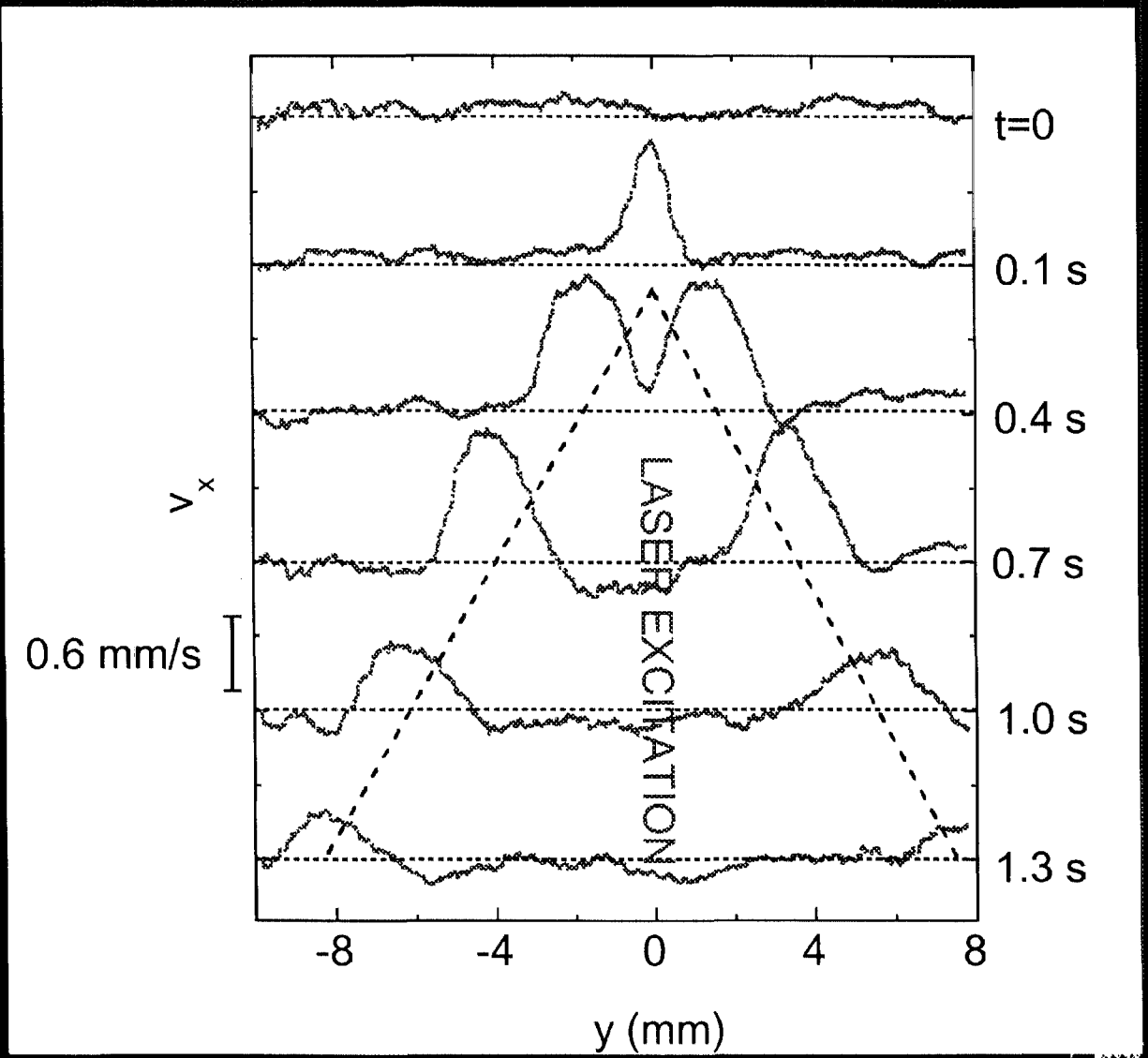

Wave power spectrum excited by modulated of laser

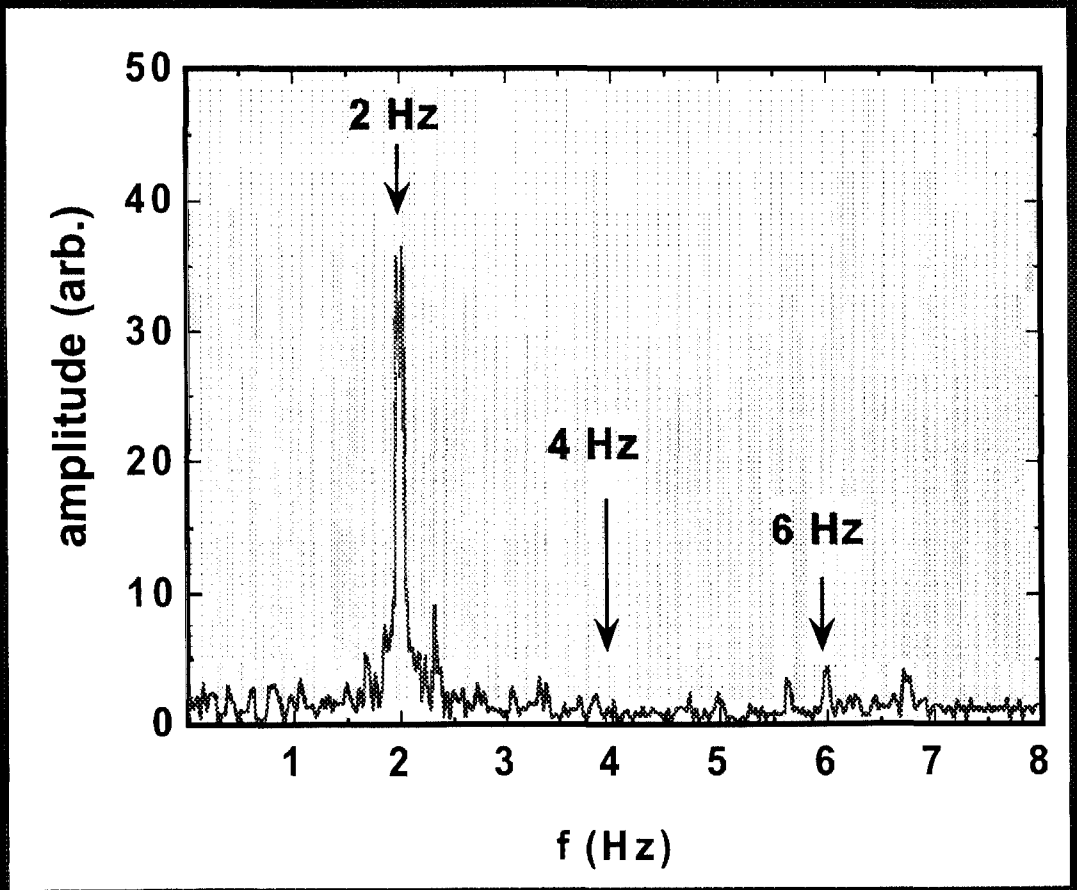

Absence of harmonics shows:

- **sine wave**
- **no nonlinear effects**

CHARACTERIZATION OF ACOUSTO-ELECTRIC CLUSTER AND ARRAY LEVITATION AND ITS APPLICATION TO EVAPORATION

R. Apfel and Y. Zheng
Physical Acoustics Laboratory, Department of Mechanical Engineering, Yale University
New Haven, CT 08520-8286, USA

ABSTRACT

An acousto-electric levitator has been developed to study the behavior of liquid drop and solid particle clusters and arrays. Unlike an ordinary acoustic levitator that uses only a standing acoustic wave to levitate a single drop or particle, this device uses an extra electric static field and the acoustic field simultaneously to generate and levitate charged drops in two-dimensional arrays in air without any contact to a solid surface. This cluster and array generation (CAG) instrument enables us to steadily position drops and arrays to study the behavior of multiple drop and particle systems such as spray and aerosol systems relevant to the energy, environmental, and material sciences.

APPARATUS AND ARRAY FORMATION

Our acousto-electric levitator has a sandwiched ultrasonic horn and a concave reflector, between which there is established a standing acoustic wave (see Fig. 1) [1]. The distance between the horn and the reflector is about the twice the acoustic wavelength so that we can levitate three or more layers of drop arrays. A high DC voltage is applied between the horn and the reflector to form a static electric field. This electric field can charge drops and also provide an extra levitation force. A CCD camera is mounted above or on the side of the levitator to record the motions and changes of the drops.

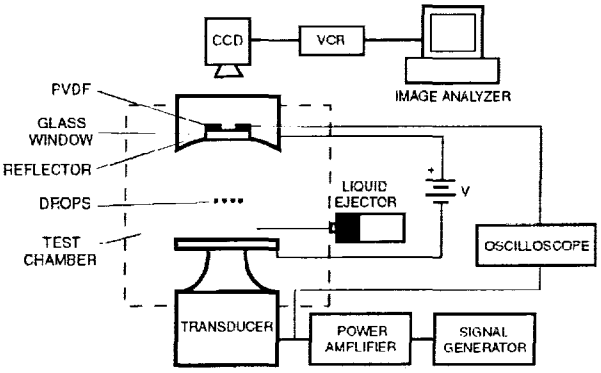

Fig. 1 Apparatus.

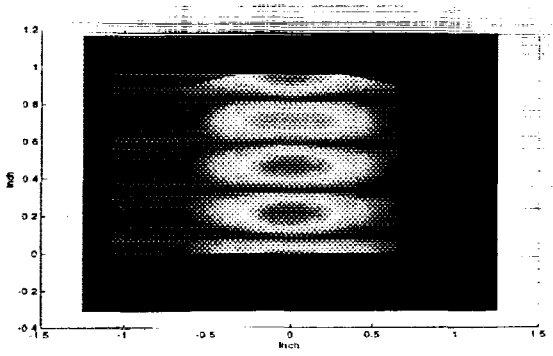

Fig. 2 The driving mode of levitator - one surface moving, one fixed.

If liquid like ethanol is placed on the surface of the ultrasonic horn, it atomizes into very small seed droplets whose diameters are around 25 to 50μm. These seed droplets fly into the levitator and form small 2-D clusters. Some of these flat clusters may contain a very large number of droplets, as many as 240. When the acoustic field increases, the droplets in a cluster will coalesce into a big drop. All of these larger drops form a stable 2-D array at a position near the pressure node. Several layers of these 2-D arrays can be levitated. The size of the drops, the

spacing between drops, and the total number of drops in one array can be controlled by varying the values of the voltage and the acoustic field intensity. Another high frequency acousto-electric levitator is also being developed to form a quasi 3-D drop array, in which the drop spacing and the distance between two layers are almost the same.

FEM NUMERICAL MODELING OF ACOUSTIC FIELD

The vertical levitation forces are the acoustic radiation force plus the electric force. The force that holds the array in the center of the levitator is the lateral acoustic force. In order to analyze the forces on the drop arrays, we employ a finite element method with numerical perfectly matched layers [2] to model the acoustic field in this open-sided acoustic resonator with a concave reflector. The results are shown in Fig. 2 for the driving mode. The forces on drops can be calculated from this acoustic profile.

EVAPORATION STUDIES

This device has been used to study the evaporation of single and multiple component drops. The theory of evaporation of a pure isolated drop follows the d^2 law if a quasi-steady state is assumed, which means that the diameter squared of the drop decreases linearly with time when the evaporation continues [3]. For a multi-component drop, both the equation of energy and continuity should be applied to each species. We also assume fast mixing processes inside the drop and use Raoult's law for the vapor pressures around the drop. Since the temperature, liquid, and gas components change with time during evaporation, we have to solve several coupled differential equations numerically. The materials in the evaporation study are heptane, octane and dodecane, which are the primary components of gasoline fuel. Since it is impossible to charge pure alkanes, an additive called Statis 450 is added to the alkane samples to increase their conductivities. Experiments show that a small amount of Statis 450 does not change the evaporation rates of alkanes. To avoid acoustically induced flows, a minimum acoustic force plus the electric force are used to levitate drops. The minimum acoustic field also reduces the deformation of the drop's shape. Using both fields provides the flexibility for controlling the position of drops. Results of single component drops with minimum acoustic field show that the evaporation is similar to the results of drops suspended by a thin glass fiber; whereas with a strong acoustic field the evaporation rate is somewhat affected. Experimental results for multicomponent drops of octane and dodecane agree reasonably well with theoretical calculations. Experiments on multi-component drop arrays are currently in progress.

REFERENCES

[1] R. E. Apfel, Y. B. Zheng, and Y. R. Tian, "Studies of acousto-electrically levitated drop and particle clusters and arrays," *Journal of the Acoustical Society of America* 105 (5), L1-L6 (1999).

[2] Z. S. Sacks, D. M. Kingsland, R. Lee, and J. F. Lee, "A perfectly matched anisotropic absorber for use as an absorbing boundary condition," *IEEE trans. Antennas Propagat.*, vol. 43, 1460-1463 (1995)

[3] K. Annamalai, and W. Ryan, "Interactive Processes in Gasification and Combustion .1. Liquid-Drop Arrays and Clouds", *Progress in Energy and Combustion Science,* 18 (3), 221-295 (1992).

NASA/CP—2000-210470

1768

Characterization of acousto-electric cluster and array levitation and its application to evaporation

Robert E. Apfel and Yibing Zheng

Physical Acoustics Laboratory
Department of Mechanical Engineering, Yale University
New Haven, Connecticut, USA

(Work supported by NASA Grant NAG3-2147
And NSF CTS-987005)

Cleveland, August, 2000

Outline

- Introduction
- An acousto-electric levitator
- Acoustic field profile in a levitator with an acoustic open resonator (a finite element approach)
- Cluster and array generation
- Evaporation of drops and arrays
- High frequency levitator
- Conclusion and future work

Introduction: acoustic levitation

- An acoustic levitator uses a standing acoustic wave to levitate a drop or particle.
- The acoustic levitation force for a small single incompressible drop in a one-dimensional standing acoustic field is

$$F \propto -_a p \langle \nabla p \rangle_t$$

- In air, this force always points to a pressure node. The drop is suspended a little bit below the pressure node.

An acousto-electric levitator

- An acousto-electric levitator uses both a vertical acoustic standing wave and an electric static field.
- Liquid drops or metal-coated solid particles are charged by the electric field.
- The levitation force is provided by the acoustic radiation force and the electric force, which give us more flexibility to control.
- Drops or particles are separated by Coulombic force and form arrays.

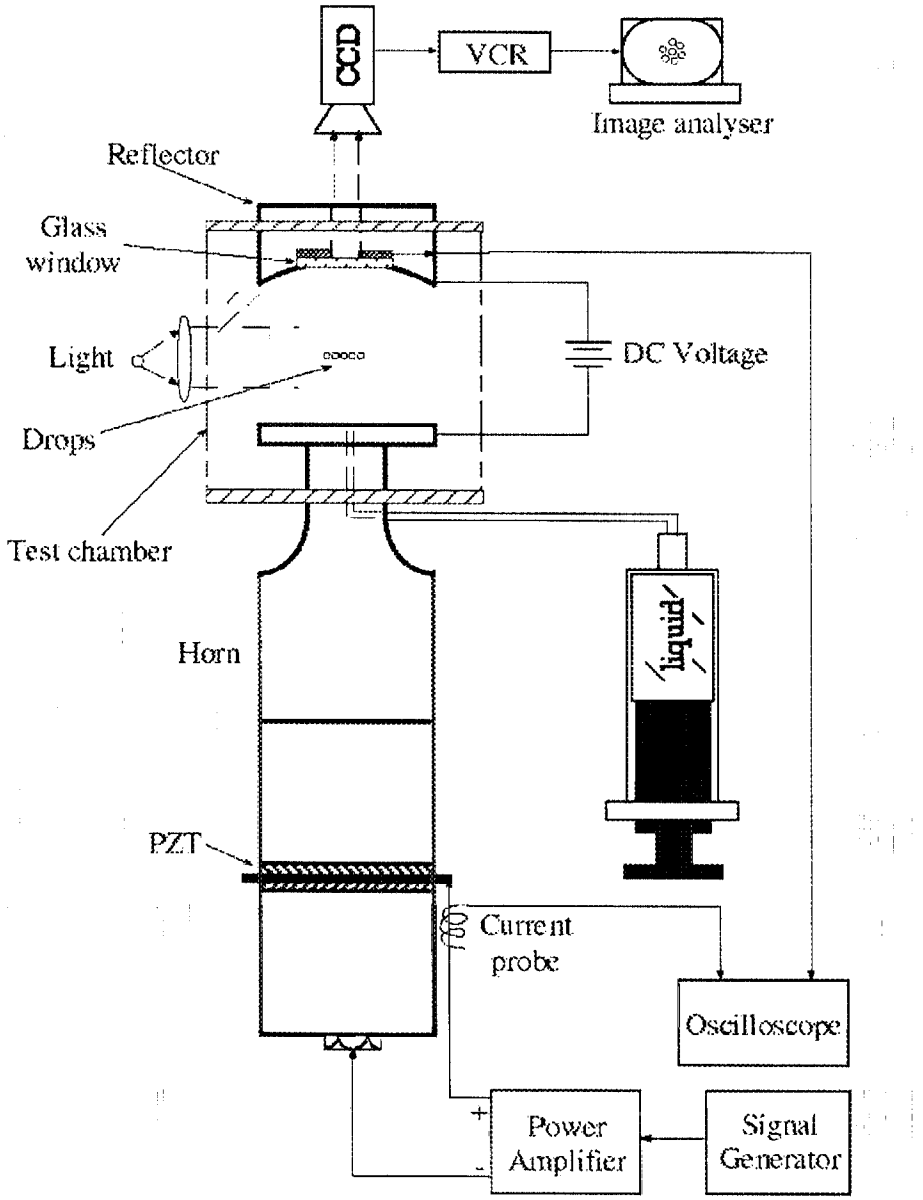
CCD
VCR
Image analyser
Reflector
Glass window
Light
DC Voltage
Drops
Test chamber
Horn
liquid
PZT
Current probe
Oscilloscope
Power Amplifier
Signal Generator
+
-

Experimental apparatus

- Transducer frequency: 28 to 100 kHz
- Acoustic wavelength in air: 1.23 to 0.34 cm
- DC voltage range: 500 to 3000 V

FEM analysis of the acoustic field

- 2-D finite element analysis of an open acoustic resonator with a concave reflector and artificial anisotropic perfectly matched layers (PML)

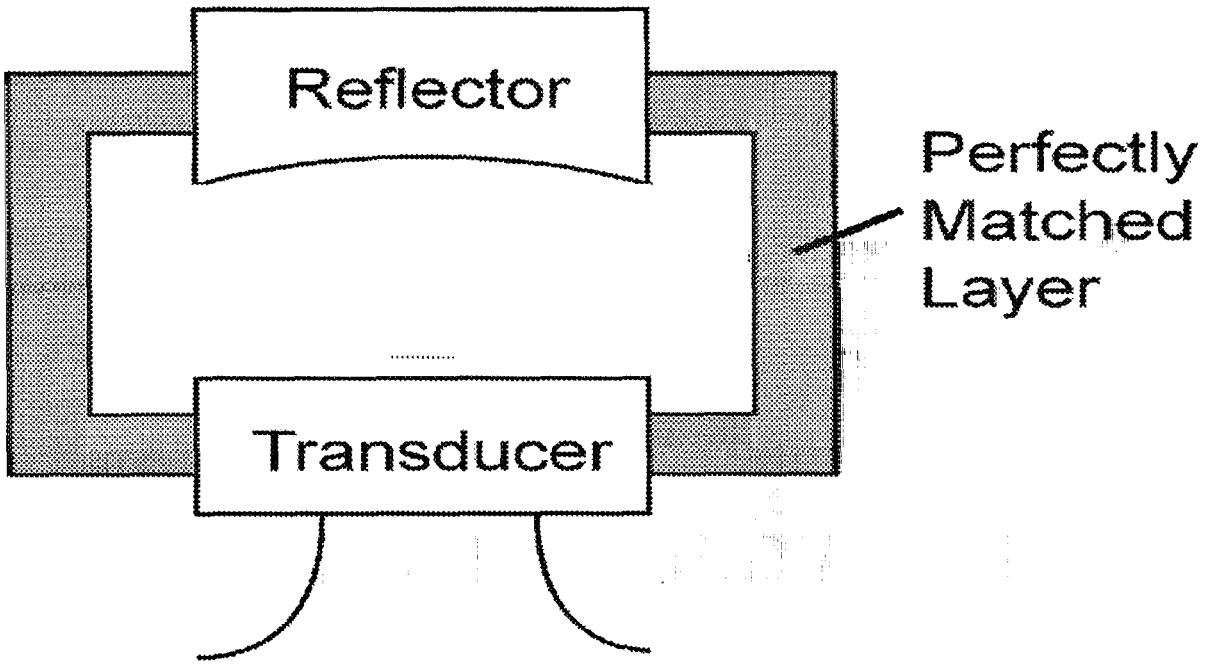

Resonance mode of the acoustic resonator

- The fourth resonance mode of our acousto-electric levitator

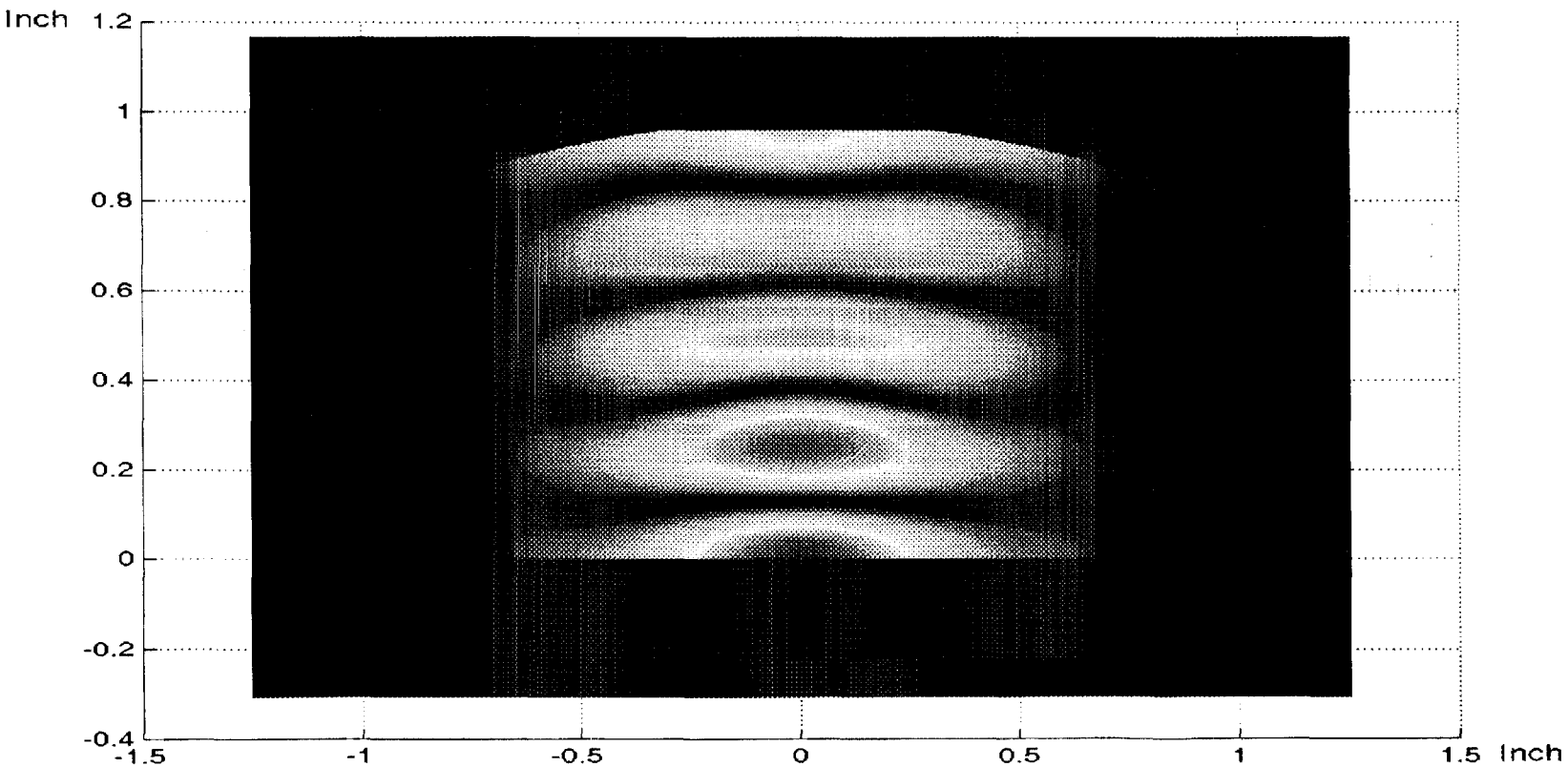

Acoustic field driven by the vibration of the transducer

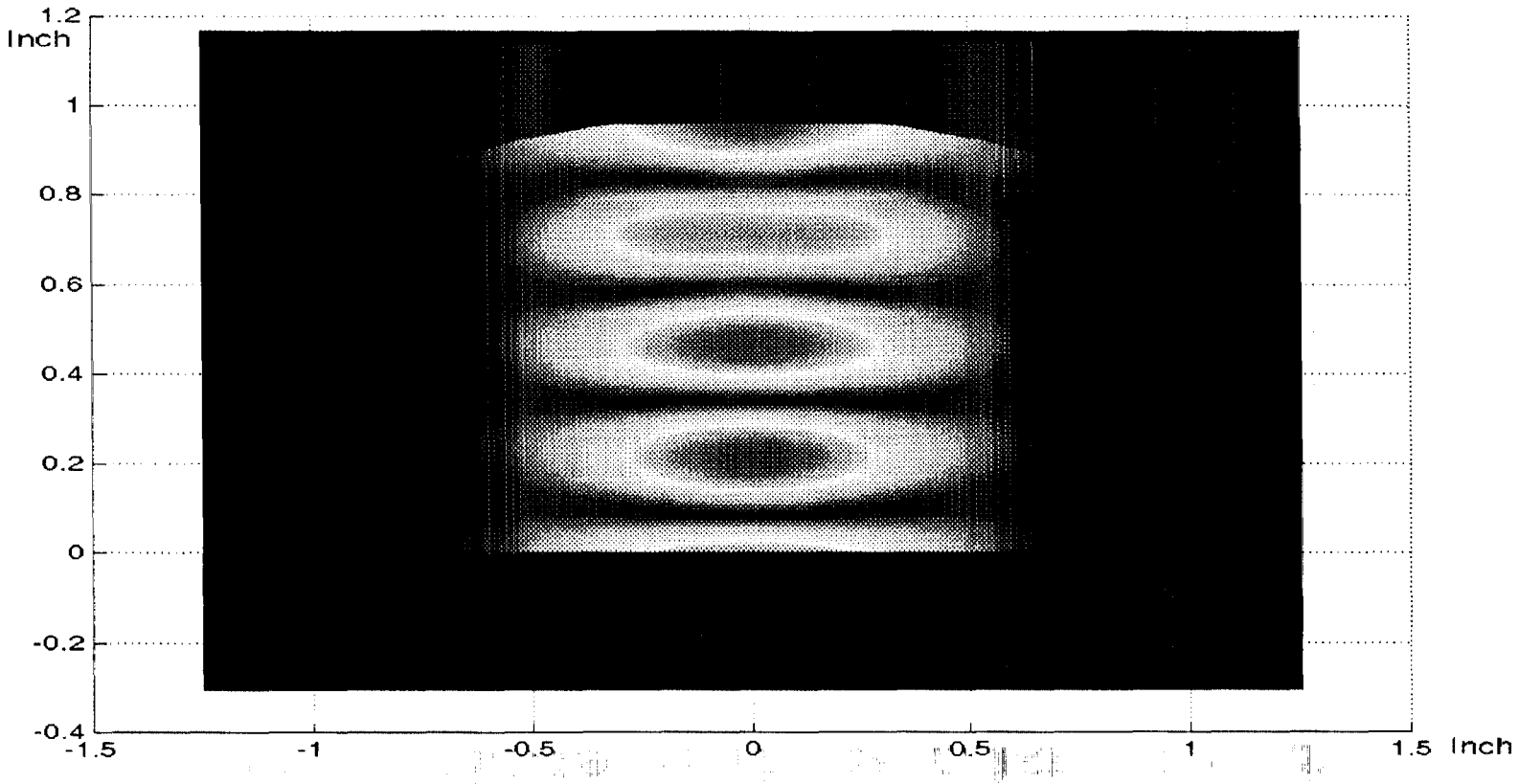

Acoustic field with a levitated 1mm particle

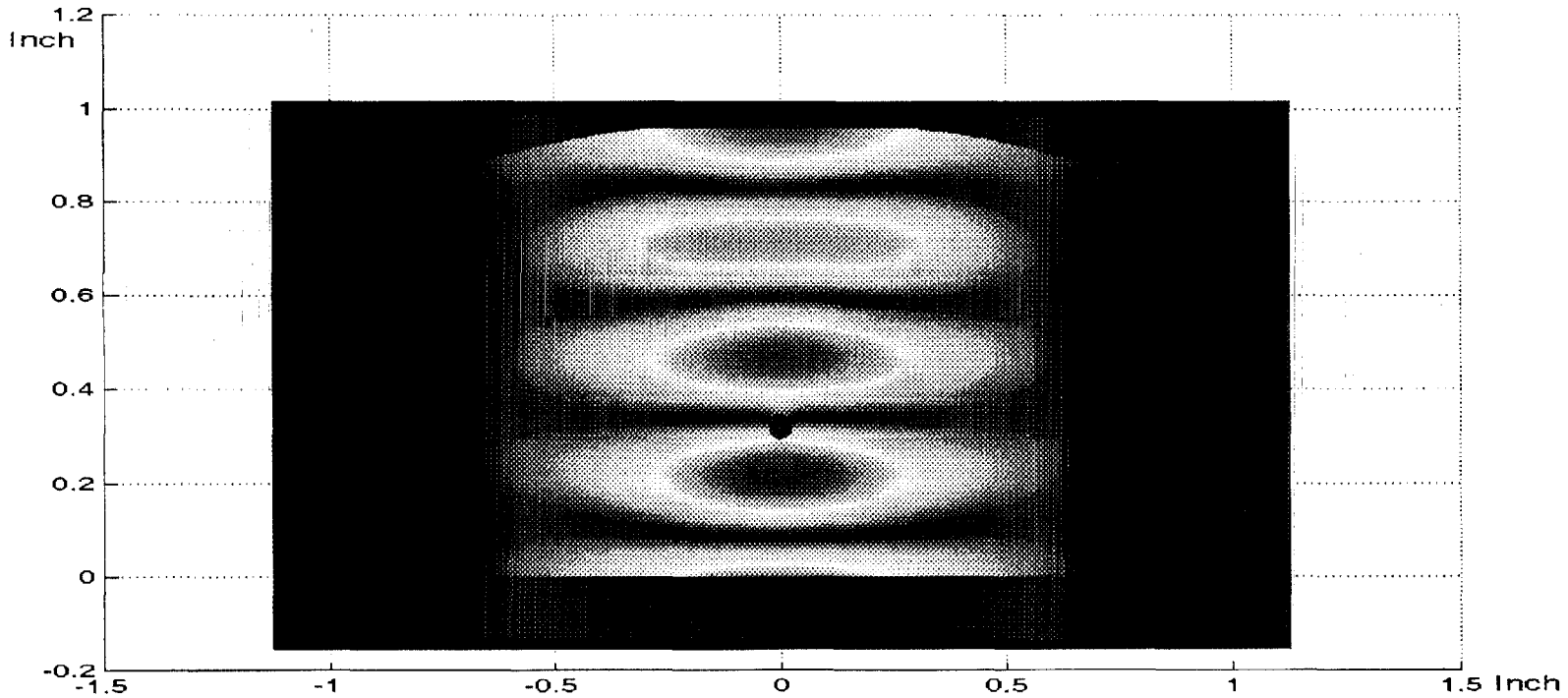

Cluster and array generation

There are two ways to generate drop arrays.

- Liquid atomization
  - Liquid is first placed on the transducer surface and atomized to small charged seed droplets. In a stronger acoustic field, seed droplets form stable big drop arrays.
- Direct drop spray
  - Directly spray charged drops into the levitator. Good for drop evaporation study.

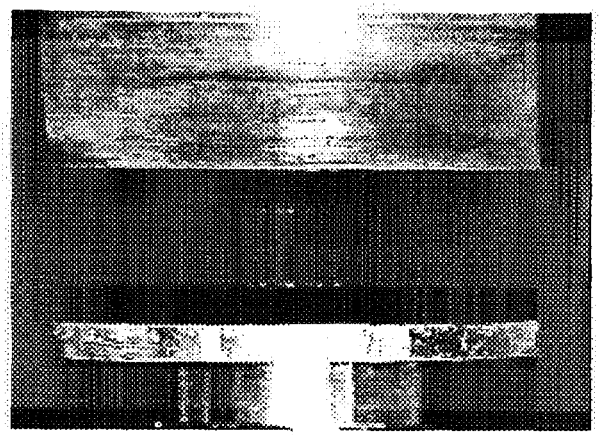

Two planes of collected ethanol drops near the acoustic pressure nodes in the acousto-electric levitator

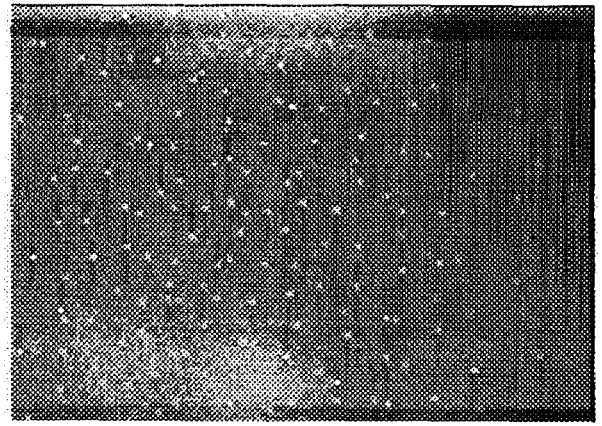

A mist of seed droplets (25-40 μm) rising from the bottom plate of the resonator

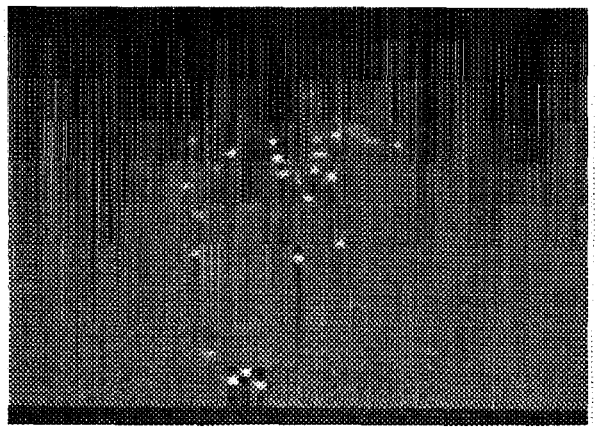

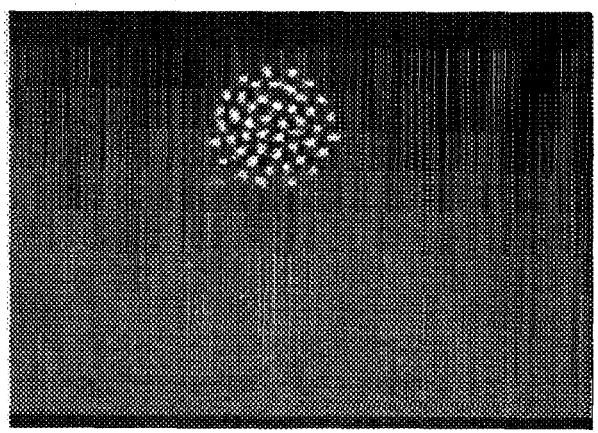

When the acoustic intensity increases a little bit, the seed droplets aggregate together into a two dimensional cluster, as shown in the above two-figure sequence. Because of the small electrical charge on each drop, they do not immediately coalesce.

Drop array generation (video clips)

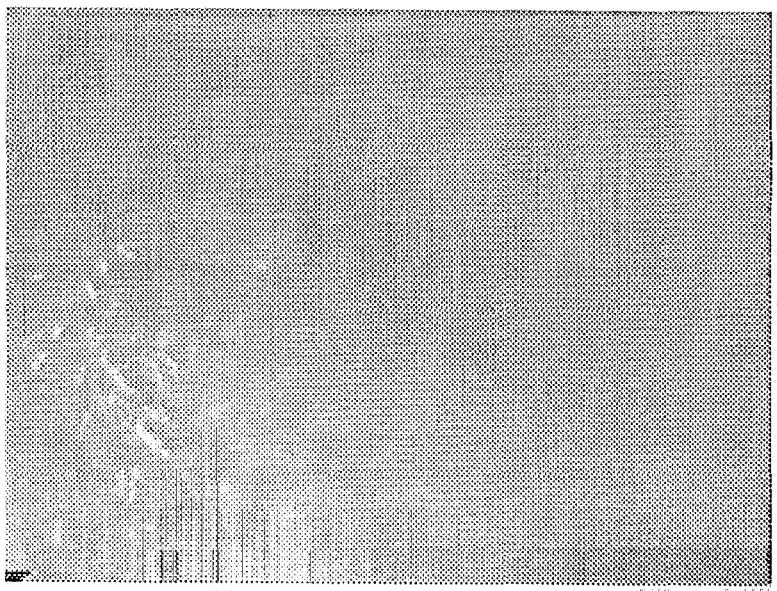

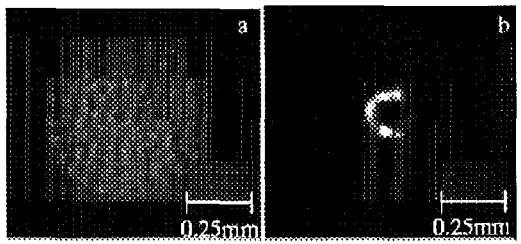

Droplet cluster coalescence. On the left is an 85 drop cluster; on the right is the drop resulting from the coalescence.

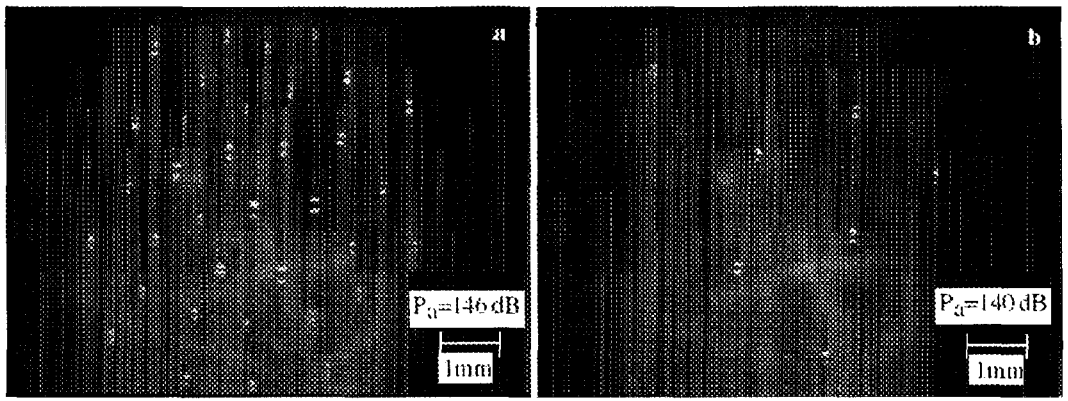

Charged drop array, varying pressure in a constant electric field. Drop size is sensibly constant whereas spacing changes.

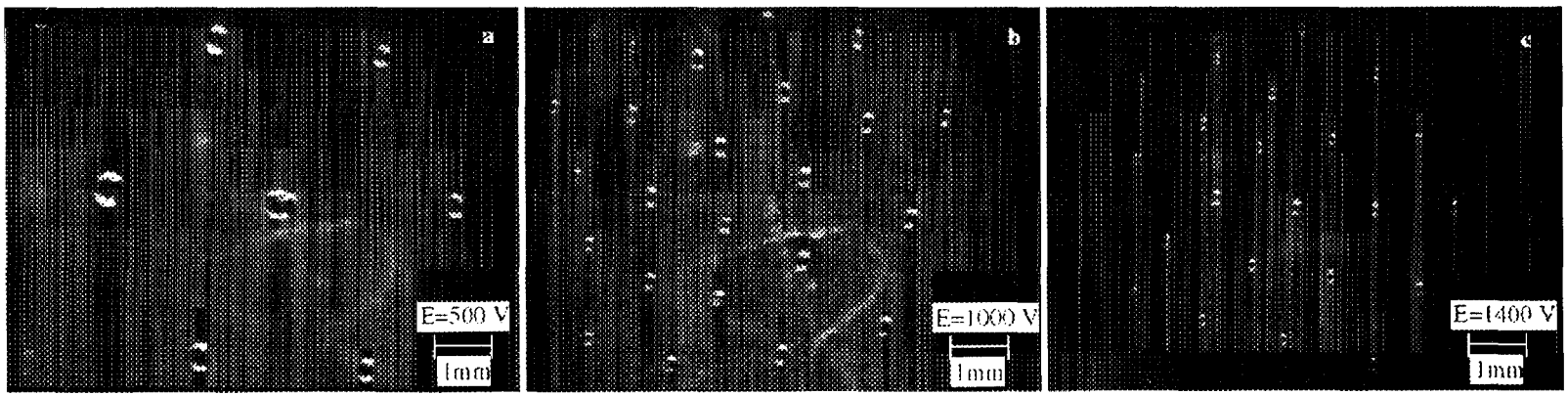

Charged drop array, varying electric field in a constant pressure field.

Application to drop evaporation study

- Materials
  - Heptane, Octane and Dodecane

    Primary components of gasoline fuel

- Additive
  - Stadis 450

    It is added to alkanes to increase the conductivity so that alkanes can be charged. A every small amount of Statis 450 (0.3% by weight) does not affect the evaporation of alkanes.

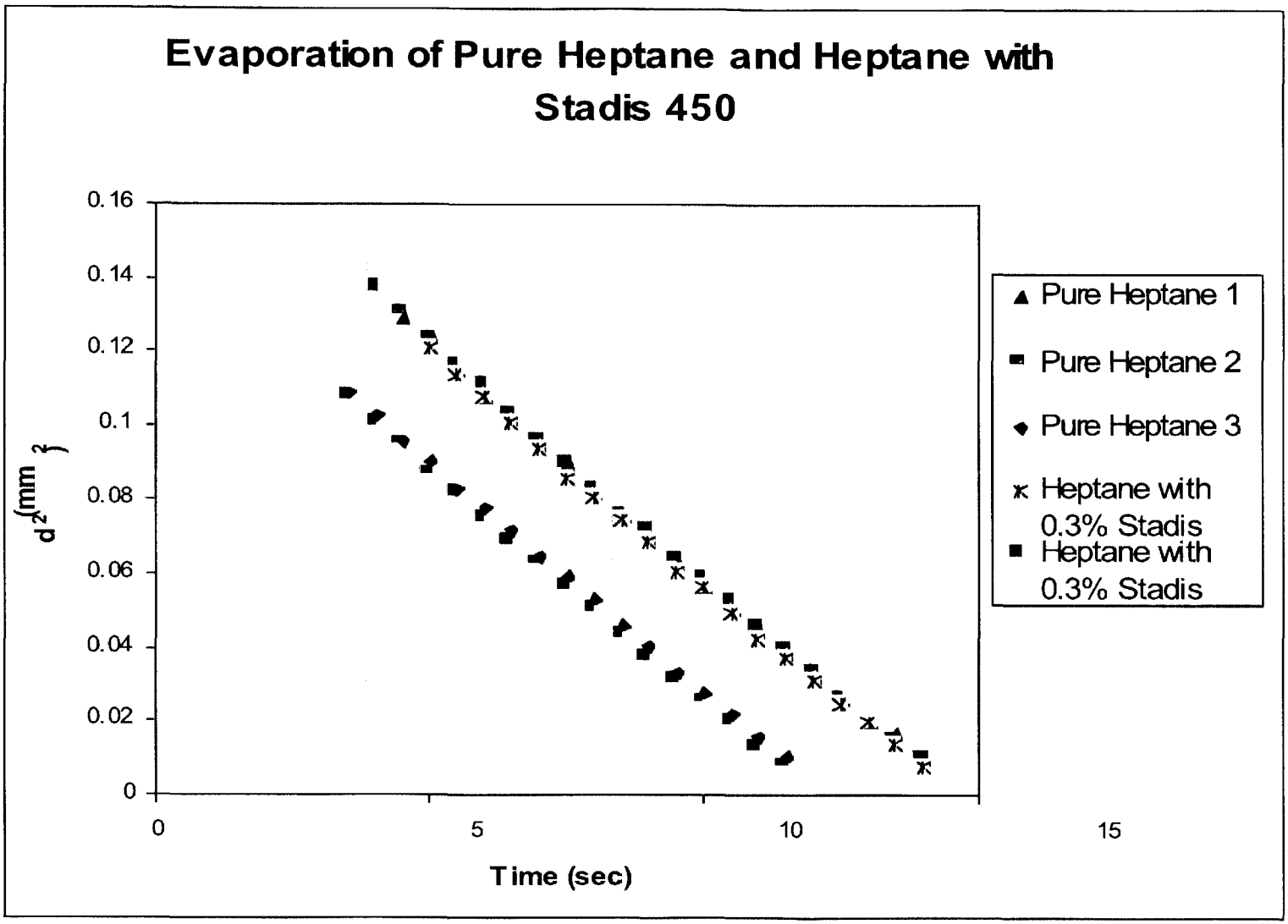
Evaporation of Pure Heptane and Heptane with Stadis 450
0.16
0.14
0.12
0.1
0.08
0.06
0.04
0.02
0
d2 (mm2)
0
5
10
15
Time (sec)
Pure Heptane 1
Pure Heptane 2
Pure Heptane 3
Heptane with 0.3% Stadis
Heptane with 0.3% Stadis

Single component evaporation

- d^2 law

  The mass and energy equations of such an isolated drop are

$$- \quad mY \quad 4\pi\rho Dr^2 \frac{dY}{dt} = m$$

$$- \quad (\quad m\epsilon \; T \quad)Ts \quad 4\pi Kr^2 \frac{dT}{dt} = \quad -mL$$

  where m is the mass gasification rate at the drop surface. With a quasi-steady assumption, its evaporation follows the d^2 law, where d is the drop diameter and κ is the evaporation constant.

$$d^2 = d_0^2 - \kappa t$$

Experiment with minimum acoustic field

Even in the single drop evaporation study, both acoustic and electric levitation forces should be used.

- The acoustic field should be minimum to reduce the flows around the drop such as acoustic streaming, which affects the evaporation rate.
- Using both levitation forces can reduce the deformation of the drops.
- Easy to control the position of the drop when evaporation continues.

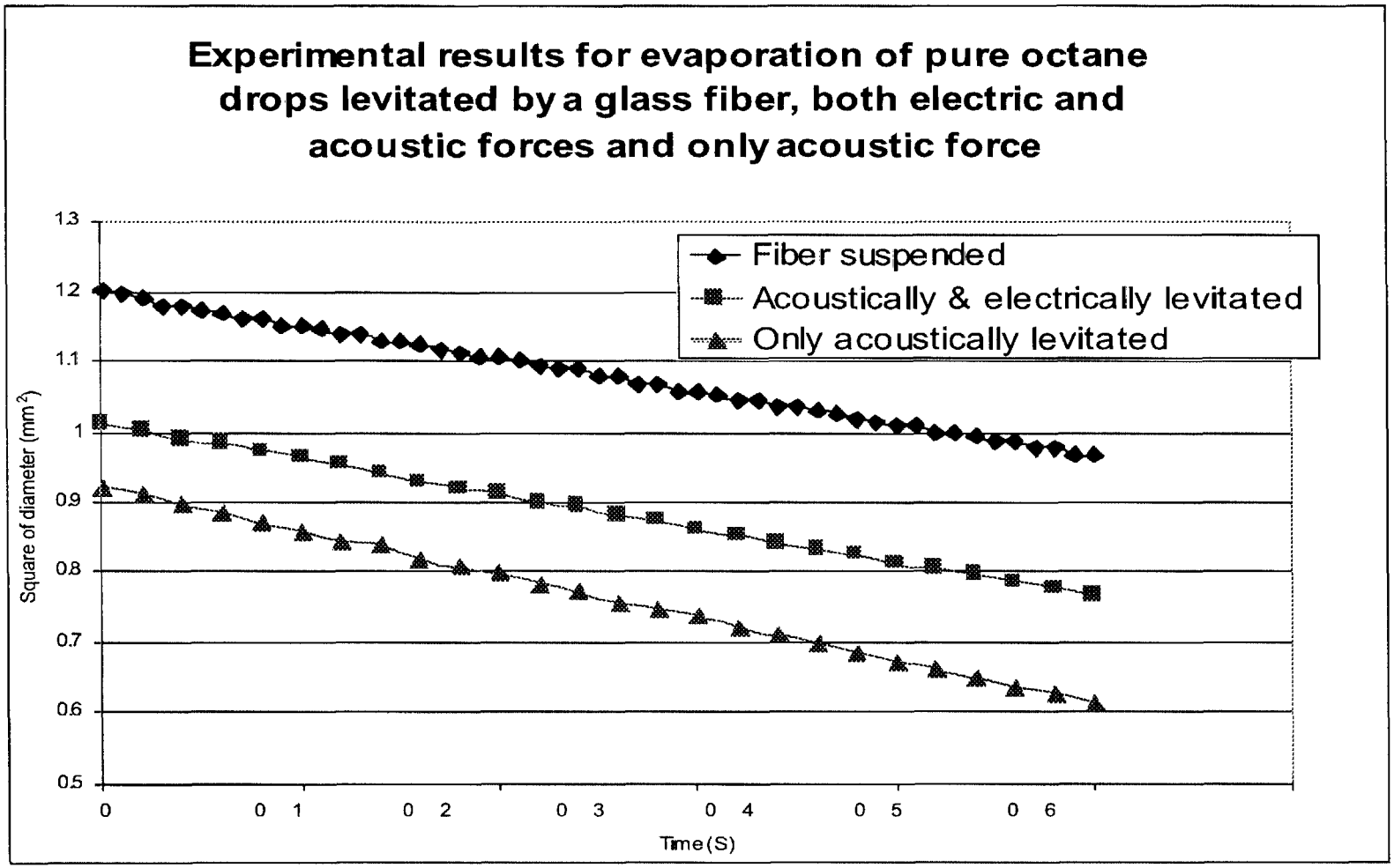

	Fiber Suspended Drop	Acoustically and Electrically Levitated Drop	Only Acoustically Levitated Drop
κ (mm^2/s)	0.0046	0.0048	0.0062

Multi-component drop evaporation

- Evaporation of an isolated multi-component drop can be solved by using the mass conservation law for each species and applying Raoult's law to the gas phase.
- The fast mixing process inside the drop is assumed.
- The drop temperature, liquid and gas phase component fractions all change with time and are updated at each step of calculation.
- Newton-Raphson and Runge-Kutta methods are used to solve coupled differential equations

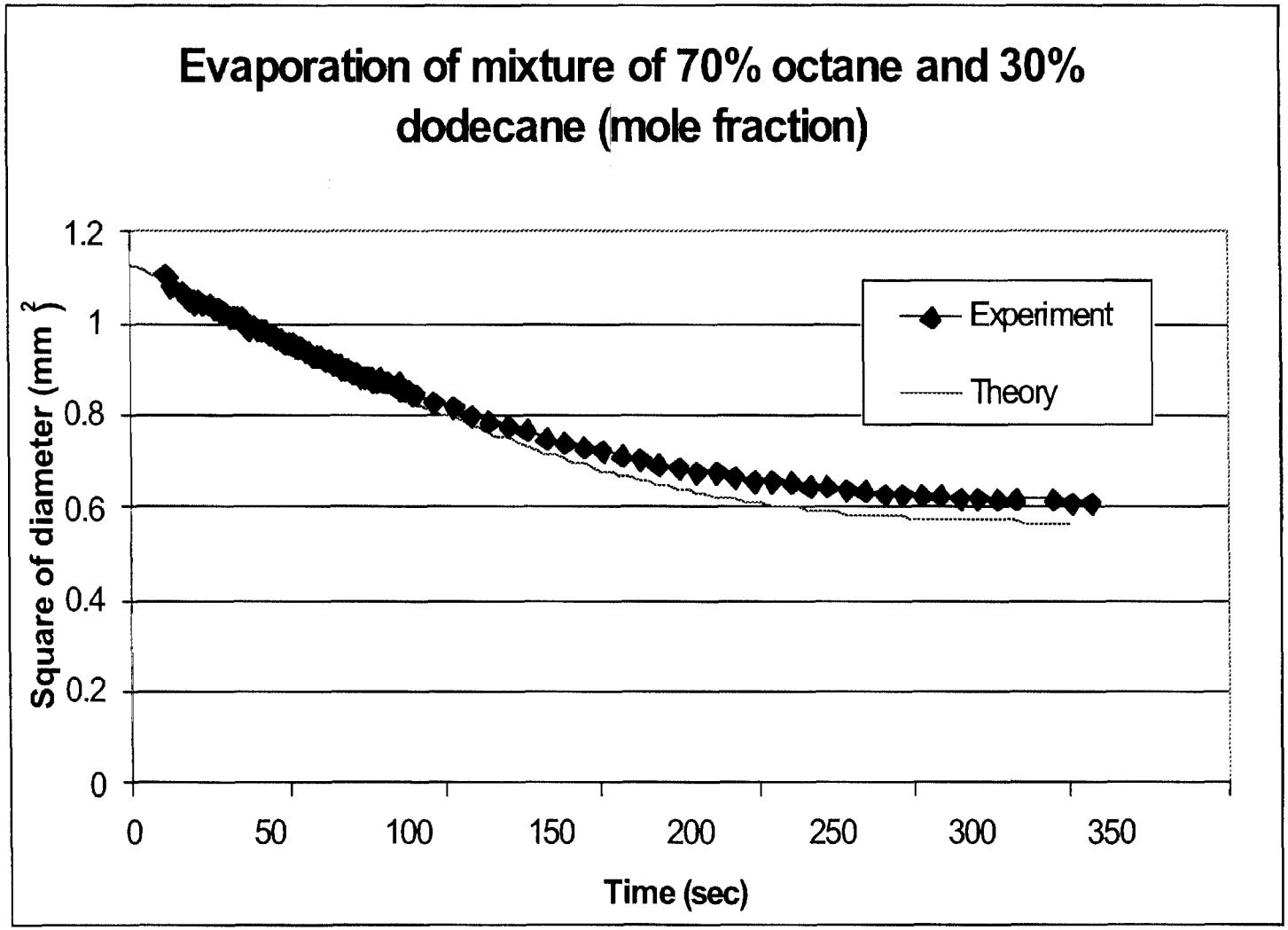
Evaporation of mixture of 70% octane and 30% dodecane (mole fraction)
Square of diameter (mm 2)
1.2
1
0.8
0.6
0.4
0.2
0
0
50
100
150
200
250
300
350
Time (sec)
Experiment
Theory

High frequency levitator for 3-D arrays

- The operation frequency of the acousto-electric levitator has been increased to more than 100kHz.
- The spacing of 2-D drop layers is reduced to 1.7mm.
- Try to form a possible stable 3-D array for combustion study in drop tower or any stable 3-D array in microgravity environment in space.

3-D array

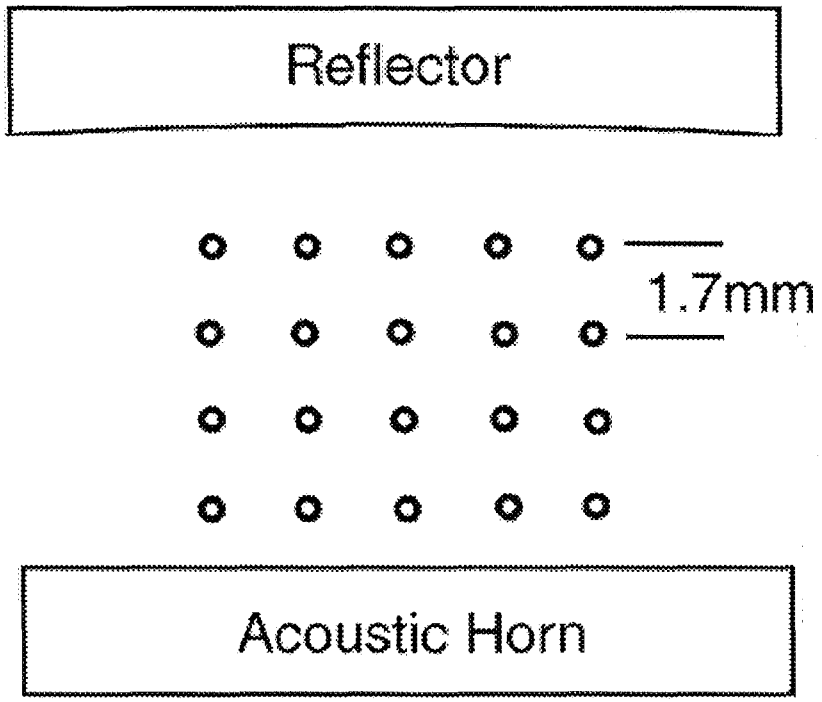

Side view of a 3-D array

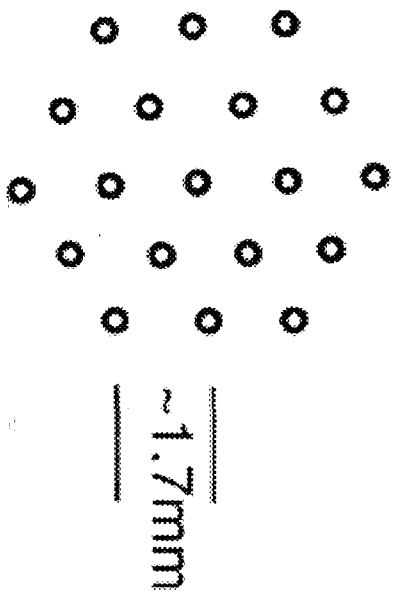

Top view of a 3-D array

Conclusion

- The acousto-electric levitator can generate and stably levitate drop and particle arrays.
- Finite element analysis with anisotropic perfectly matched layers is successfully used to calculate the 2-D acoustic profile of an acoustic levitator in order to study acoustic forces on 2-D drop arrays.
- The data for isolated multi-component drops with minimum acoustic levitation are in reasonable agreement with the theory including both mass and energy transfer.

Future work

- Stable 3-D arrays for studies in drop tower and Space Station.
- Establish a benchmark experiment for both single and multiple component drop array evaporation.

PARTICLE SEGREGATION IN A FLOWING SUSPENSION SUBJECT TO HIGH-GRADIENT STRONG ELECTRIC FIELDS

Andreas Acrivos and Anne Dussaud
The Levich Institute, City College of the City University of New York
140th Street & Convent Avenue, New York, NY 10031

Boris Khusid
New Jersey Institute of Technology, University Heights, Newark, NJ 07102

INTRODUCTION

If a spatially non-uniform electric field is applied to a suspension, in which the particles and the suspending fluid have different dielectric permittivities and/or conductivities, the particles migrate to the regions of high or low electric fields depending on the sign of their polarization. Numerous applications of this phenomenon, called *dielectrophoresis*, include a great variety of processes that involve the control and manipulation of particle motions [1, 2]. In spite of tremendous advantages of electro-technologies little is known either of the mechanisms, or of the important parameters responsible for the electric field driven effects in a flowing suspension under the action of strong fields. Here we present the main results of a study of the motion of individual particles in a suspension subject to high-gradient ac electric fields.

EXPERIMENTS

We fabricated a transparent channel in which a flowing suspension is subjected to a high-gradient strong ac electric field (~ several kV/mm), generated by alternating energized electrodes with grounded ones (Fig. 1). We designed the electrode array such that the electric-field lines and the dielectrophoretic force were along the plane perpendicular to the streamlines of the main flow. This channel is equipped with a laser-sheet particle visualization system which enables us to monitor and record the field-driven particle motions and pattern formations. By adjusting the frequency and the strength of the applied field we were able to eliminate the undesirable secondary effects on the suspension flow through the channel due to electro-convection and thermal convection in the suspending fluid. Experiments were performed on very dilute suspensions of neutrally buoyant hollow ceramic spheres (about 50 μm in diameter) in oils which exhibited negative dielectrophoresis. Since our suspensions could not be treated as a perfectly insulating or perfectly conducting medium, we needed to know the frequency dependence of the real part of the particle polarizability in order to compute the dielectrophoretic force. To calculate the particle polarizability, we measured the concentration dependence of the complex permittivity of the suspension in a spatially uniform low electric field (~ several V/mm) and then employed the Maxwell-Wagner model to evaluate the particle polarizability.

We found that the application of a high-gradient field to a quiescent suspension caused the particles to move away from the electrodes and then to concentrate above the grounded electrodes forming a distinct boundary between the clean fluid and the remaining suspension. This same field, when applied to a flowing suspension, caused the particles to concentrate within thin stripes parallel to the flow above the grounded electrodes and to travel with the suspending fluid within these stripes. Figure 2 shows the particle distribution across the channel for a suspension subjected to an electric field of 2150 Vrms, 10 Hz at a flow rate of 1.6 ml/min.

THEORY

Since a flowing suspension is exposed to an ac field with a frequency greater than the inverse time-scale of hydrodynamic phenomena, we can use the time-average of the electric forces. The theoretical model concerning the particle motions and pattern formations presented includes only two forces acting on the particles, namely, the dielectrophoretic force [1] and the viscous drag, and requires no fitting parameters:

$$3\eta \frac{d\mathbf{r}}{dt} - \mathbf{U}_f(\mathbf{r}) = a^2 \varepsilon_0 \varepsilon_f \, \mathrm{Re}[\beta(\omega)] \; \mathbf{E}^2(\mathbf{r}) \qquad \mathbf{r}|_{t=0} = \mathbf{r}_0 \qquad (1)$$

where β is the complex polarizability of the particle, a is the particle radius, ε_f is the fluid dielectric permittivity, ε_0 is the vacuum permittivity, η is the fluid viscosity, $\mathbf{U}_f(\mathbf{r})$ is the local fluid velocity, and $\mathbf{r}_0$ is the initial position of a particle. To calculate the right-hand side of Eq.(1), we solved Laplace's equation within our channel (Fig. 1).

The computed particle motions and pattern formations were found to be in a good agreement with experimental data (Fig. 3). These results demonstrate that the expression for the dielectrophoretic force which employs the value of the particle polarization measured in low fields can be used for describing the particle motions in strong fields. This approach enables one to model a broad range of electro-hydrodynamic phenomena in suspensions.

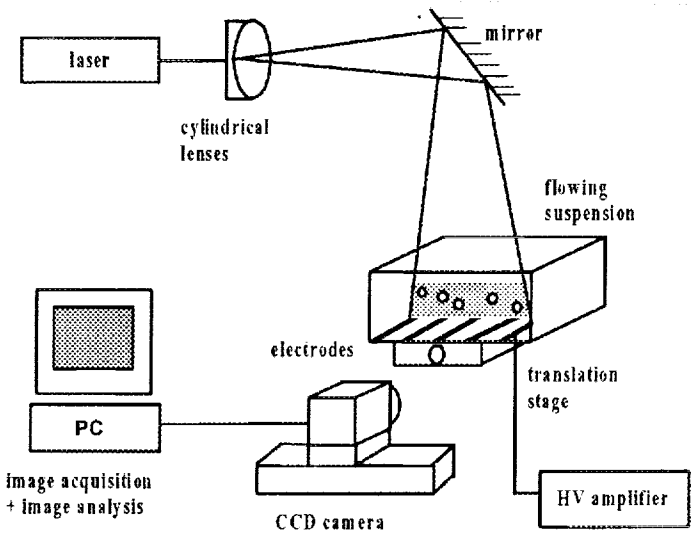

Figure 1. The channel and optical arrangement for image generation, collection, and analysis.

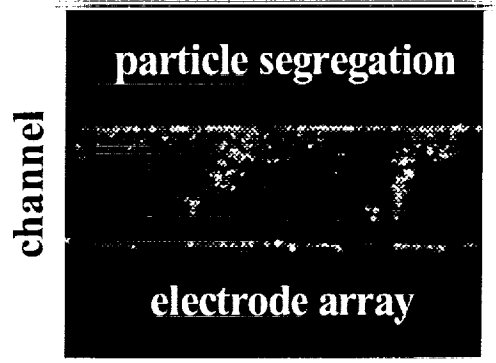

Figure 2. A flowing suspension.

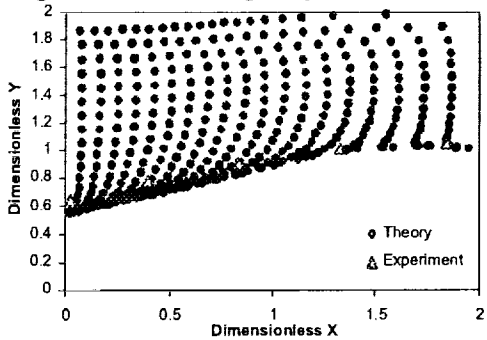

Figure 3. The particle front between the grounded (left) and high-voltage (right) electrodes; 2150 Vrms, 10 Hz, 13.4 ml/min

References

[1] T.B. Jones, *Electromechanics of Particles* (Cambridge University Press, 1995)

[2] B. Khusid and A. Acrivos, *Phys. Rev. E* **52**, 1669 (1995); **54**, 5428 (1996); **60**, 3015 (1999)

Particle Segregation in a Flowing Suspension Subject to High-Gradient Strong Electric Fields

Andreas Acrivos and Anne Dussaud

The Levich Institute
City College of New York
140 St & Convent Ave, New York, NY 10031
Tel: 212-650-8159, Fax: 212-650-6835
E-mail:acrivos@scisun.sci.ccny.cuny.edu

Boris Khusid

New Jersey Institute of Technology
University Heights, Newark, NJ 07102
Tel: 973-596-3316, Fax: 973-642-4282
E-mail: khusid@adm.njit.edu

ELECTRO-MANIPULATION OF PARTICLES

The ponderomotive electric force acting on a particle subject to a gradient electric field is

$$\mathbf{F}_e = Q\mathbf{E} + (\mathbf{P}\cdot\nabla)\mathbf{E}$$

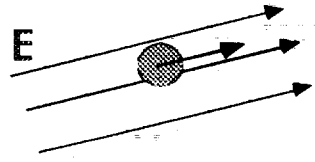

Electrophoresis is the motion of a charged particle in a DC field

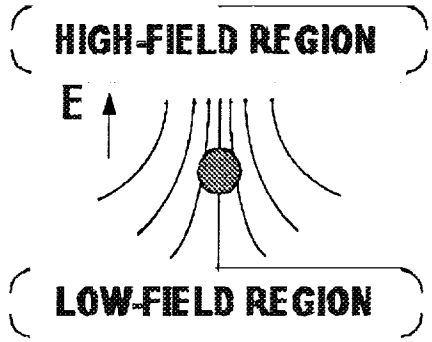

Dielectrophoresis is the motion of a neutral particle in gradient DC and AC fields

The time average dielectrophoretic force in an AC field

$$\langle \mathbf{F} \rangle = 2\pi\varepsilon_c a^3 \mathrm{Re}(\beta(\omega))\nabla E_{rms}^2$$

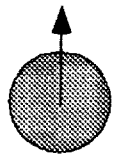

Positive $\mathrm{Re}(\beta)>0$ **dielectrophoresis**

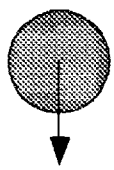

Negative $\mathrm{Re}(\beta)<0$ **dielectrophoresis**

THE MAIN DIFFICULTIES

When the particles and the liquid are not perfectly insulating or perfectly conducting:

1. There is no quantitative verification of the expression for the dielectrophoretic force.

2. There are no constitutive relations for the energy and ponderomotive force in concentrated suspensions.

EXPERIMETAL PROCEDURES

- **Requirements to validate a theory**

  Neutrally buoyant particles → no sedimentation

  Low particle concentration → no interparticle interactions

  AC electric field → no electrophoresis

- **Suspension of monodisperse hollow ceramic spheres in oil (56 cp)**

- **the Maxwell-Wagner expression for the complex permittivity**

$$\frac{\varepsilon_s^* - \varepsilon_c^*}{\varepsilon_s^* + 2\varepsilon_c^*} = \varphi\beta$$

EXPERIMENTAL SET-UP

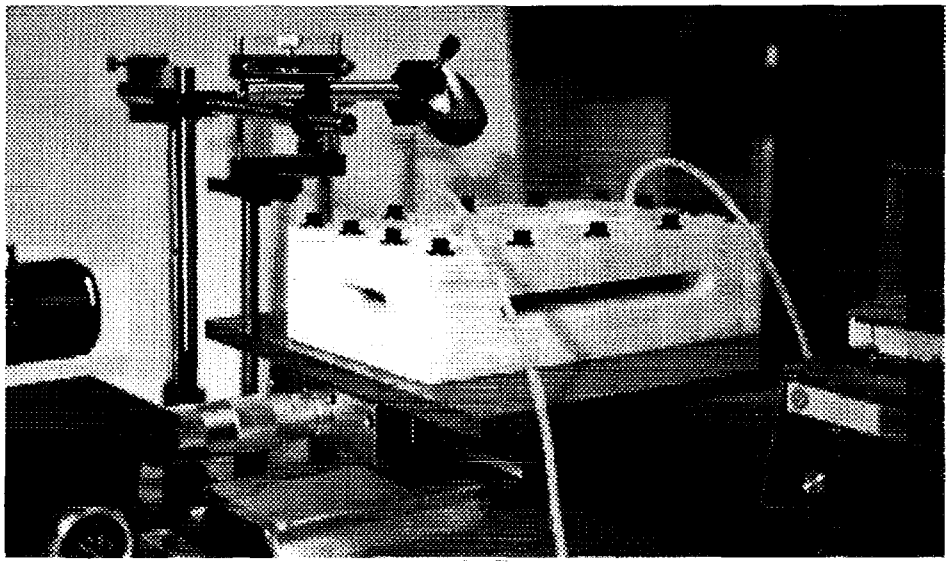

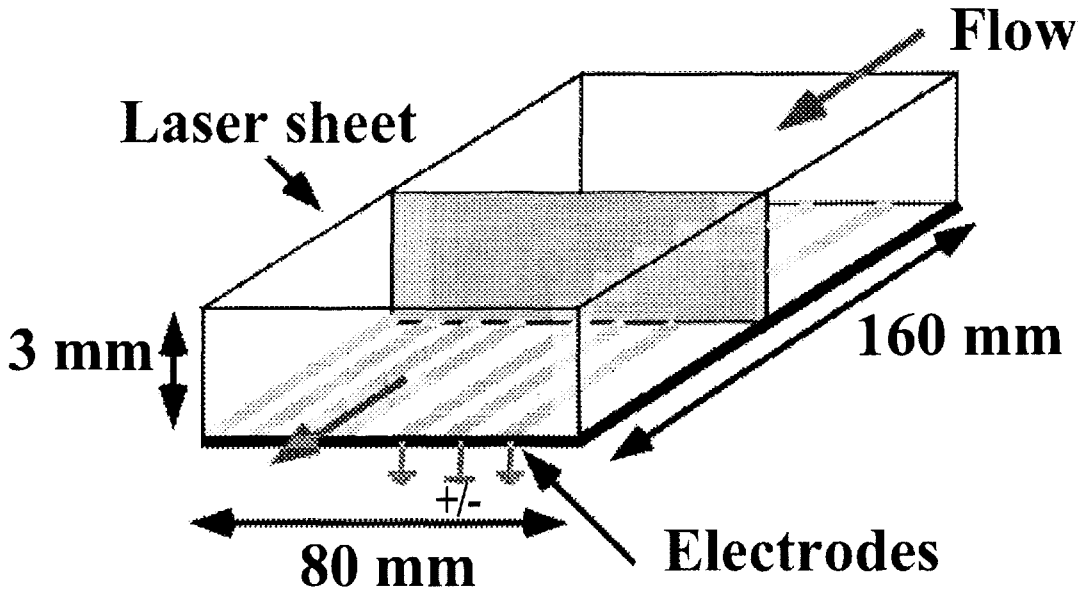

THEORETICAL MODEL

- **The balance of the Stokes drag force and the time averaged dielectrophoretic force**

$$2\pi\varepsilon_c a^3 \mathrm{Re}(\beta)\nabla E_{rms}^2 = 6\pi\eta a\mathbf{u}$$

- **The field-induced particle displacement**

$$\frac{d\mathbf{r}}{dt} = \mathbf{u} \qquad \mathbf{r}|_{t=0} = \mathbf{r}_0$$

- **The characteristic time of dielectrophoresis**

$$\tau = \frac{3d^4\eta}{a^2\varepsilon_c V_{rms}^2 |\mathrm{Re}(\beta)|}$$

COMPUTATION OF THE ELECTRIC FIELD

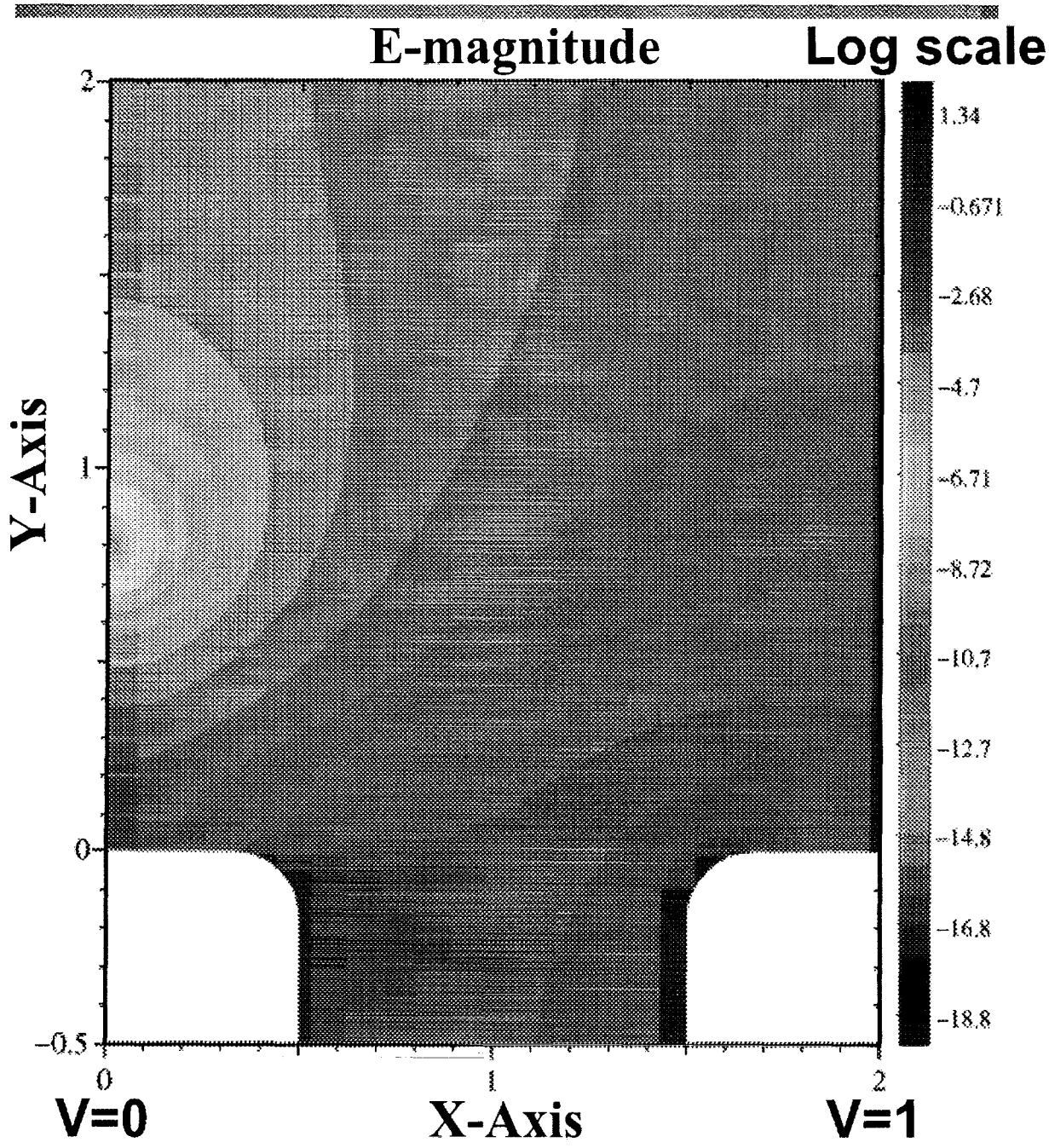

PARTICLE REDISTRIBUTION IN A QUIESCENT SUSPENSION

Vmax=2150 V rms, 10 Hz

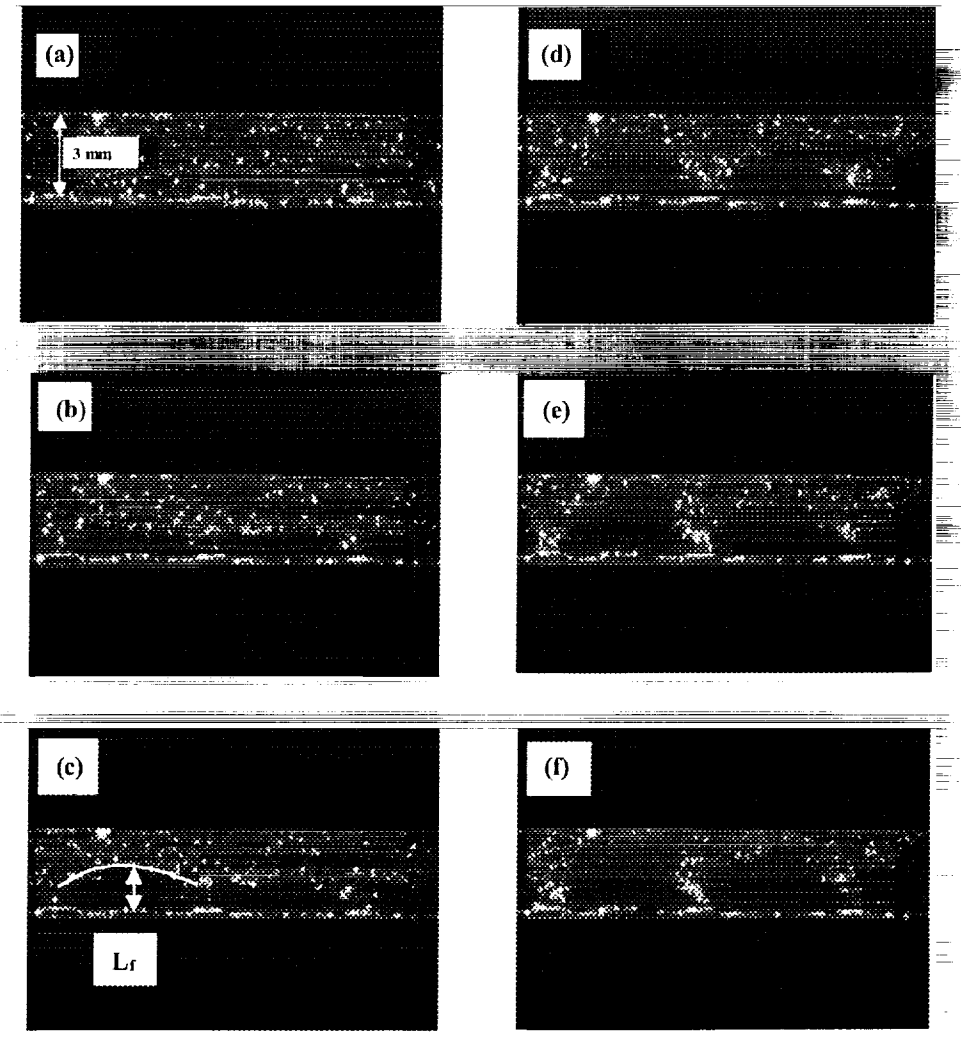

(a) initial, (b) 80 s, (c) 2 min, (d) 5 min, (e) 7 min, (f) 10 min

PARTICLE FRONT IN A QUIESCENT SUSPENSION

Vmax=2150 V rms, 10 Hz

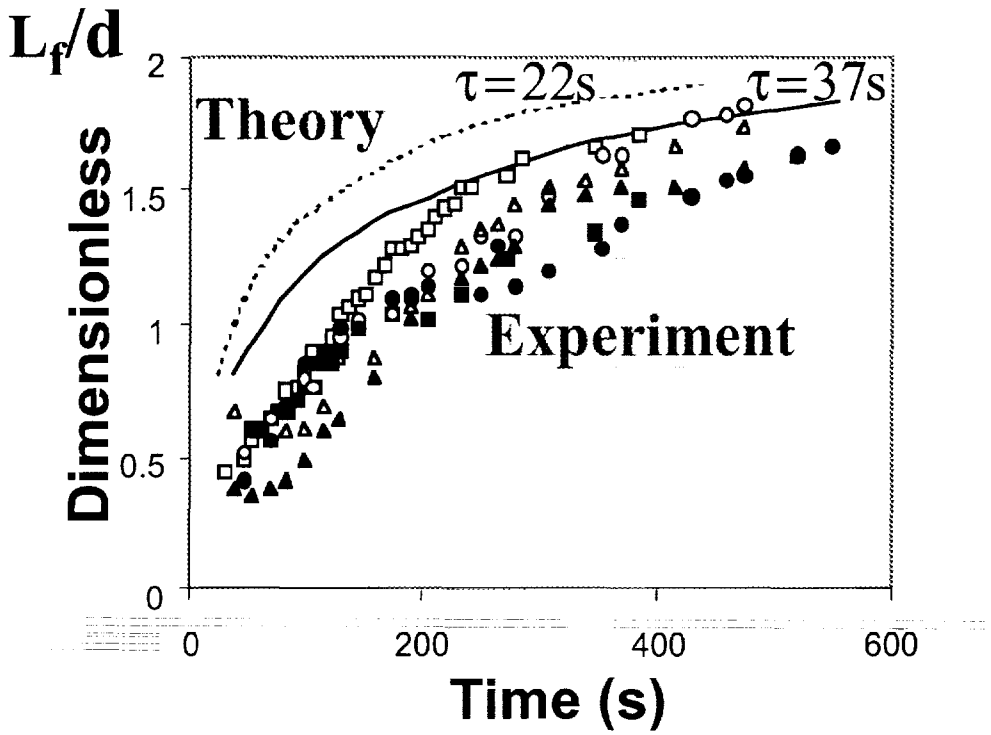

$\tau = 37s$ **for** $\mathrm{Re}(\beta) = -0.048$

$\tau = 22s$ **for** $\mathrm{Re}(\beta) = -0.080$

PARTICLE REDISTRIBUTION IN FLOWING SUSPENSIONS

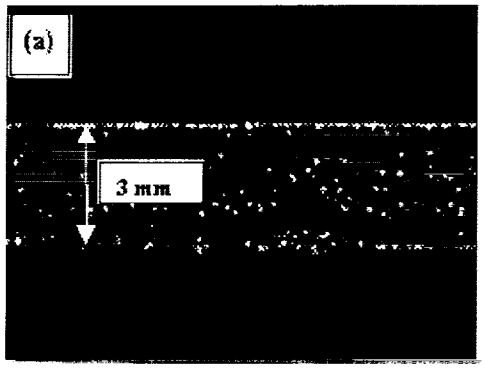

(a) no electric field

Vmax=2150 V rms, 10 Hz

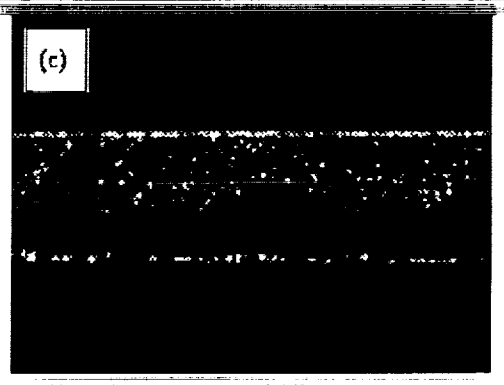

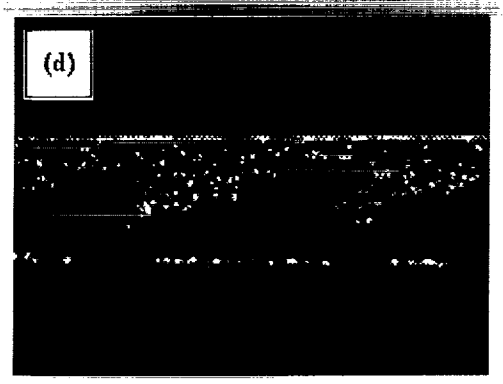

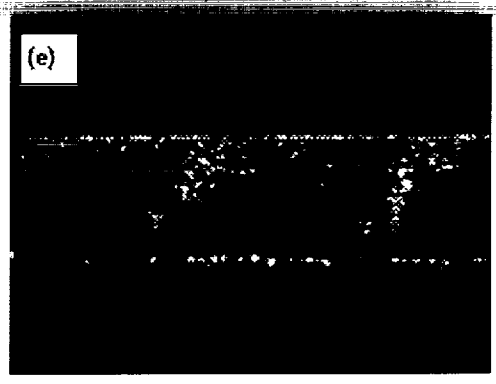

Flow rate: 13.4 (b), 9 (c), 4 (d), 1.6 (e) ml/min

PARTICLE FRONT IN FLOWING SUSPENSIONS

Vmax=2150 V rms, 10 Hz

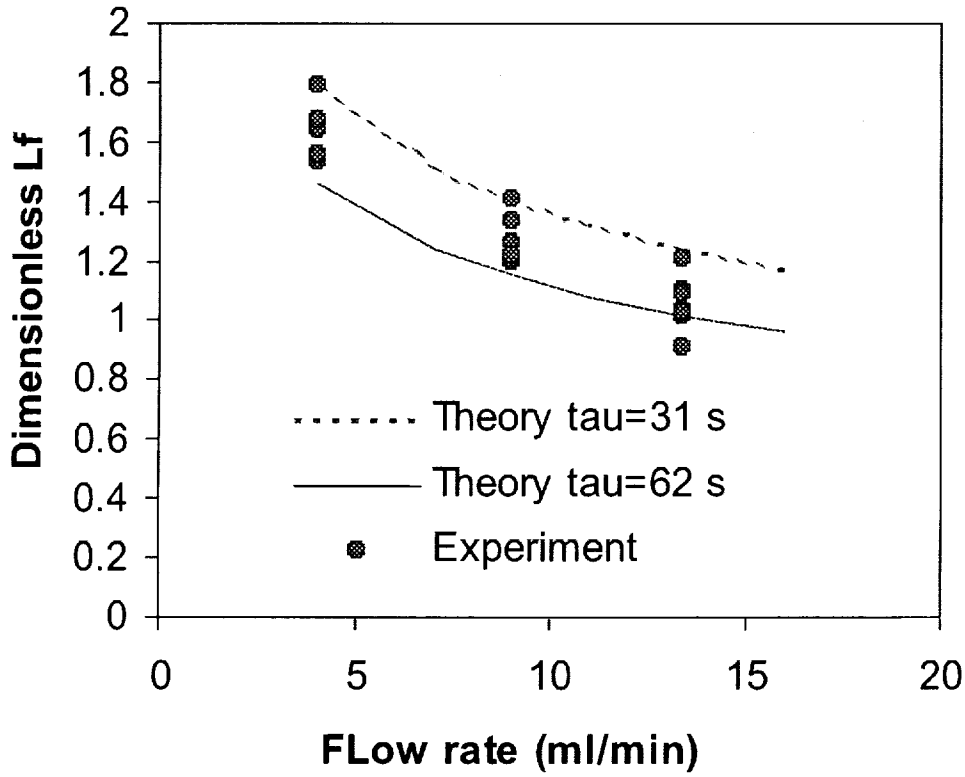

$\tau = 31s$ **for** $\mathrm{Re}(\beta) = -0.074$

$\tau = 62s$ **for** $\mathrm{Re}(\beta) = -0.037$

PARTICLE POSITIONS IN CHANNEL CROSS-SECTION

(a) tau=31 s

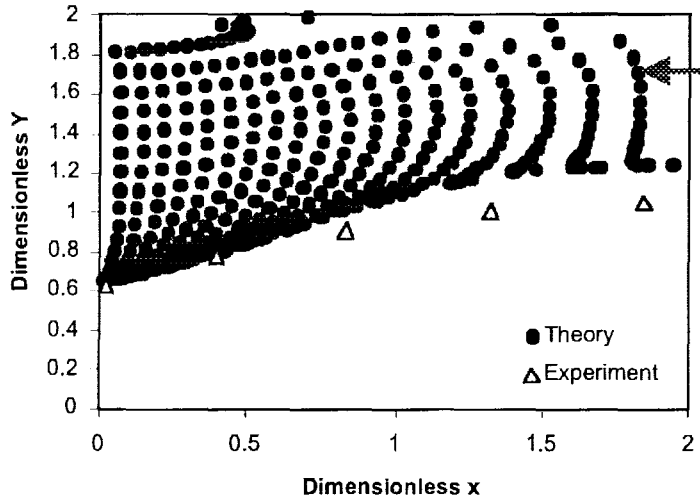

Computed particle positions

$Re(\beta) = -0.074$

(b) tau=62 s

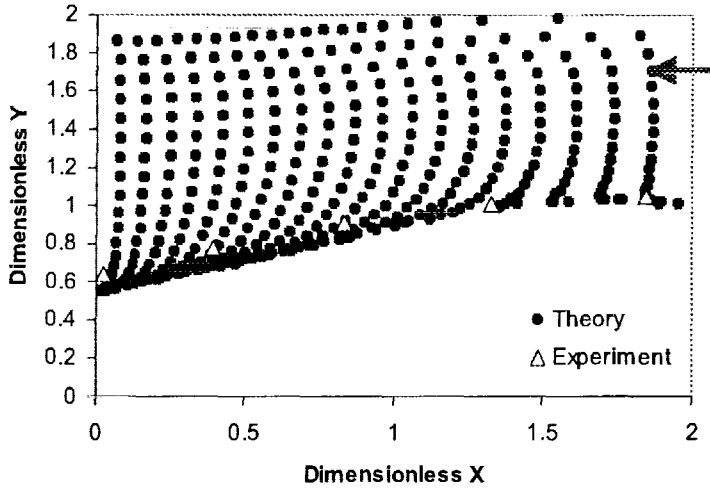

Computed particle positions

$Re(\beta) = -0.037$

Vmax=2150 V rms, 10 Hz; Flow rate: 13.4 ml/min

LIMITATIONS OF GROUND-BASED EXPERIMENTS

Requirements

- **Neutrally buoyant suspensions**

  → **Matching the densities**

- **Transparent suspensions**

  → **Matching the refractive indices**

- **Visualization techniques**

  → **Relatively large particles**

Impossible to vary the particle polarization over a significant range !

APPLICATIONS

ELECTRO-FILTER FOR CLEANIING CONTAMINATED FLUIDS

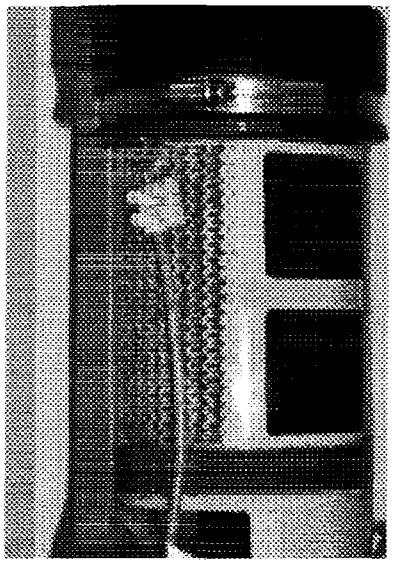

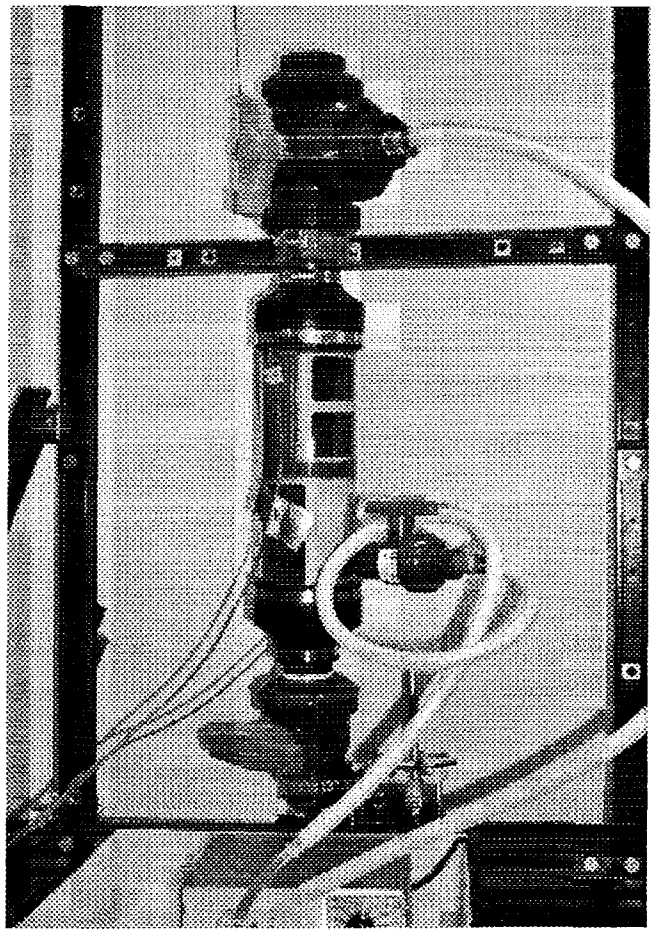

APPLICATIONS

MICRO-FLUIDIC DEVICE

174 chambers on a 4"- silicon wafer

3mm×6mm×3μm , 54 nL

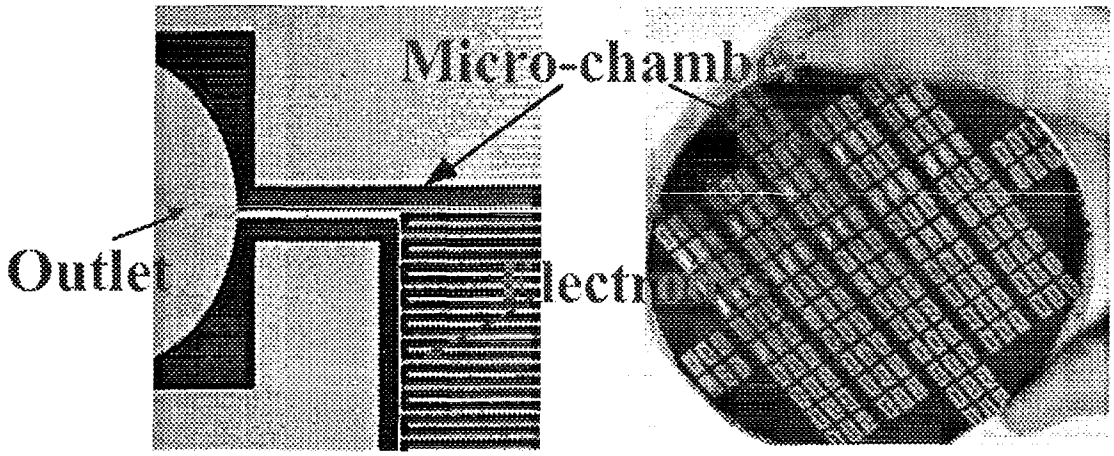

Negative dielectrophoresis of cells

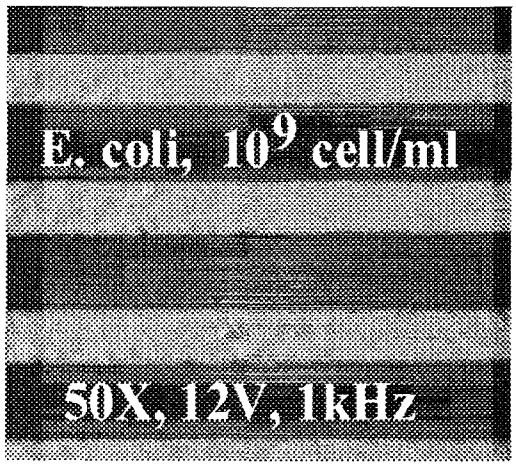

ENGINEERING NOVEL BIOCOLLOID SUSPENSIONS

Daniel A. Hammer[1], Amy L. Hiddessen[1], Steve Rodgers[1], and David Weitz[2]
[1]Department of Chemical Engineering, University of Pennsylvania, Philadelphia, PA 19104 and
[2]Division of Engineering and Applied Science, Harvard University, Cambridge, MA 02138

ABSTRACT

The diverse use of colloidal suspensions in materials such as paints, lubricants, food, pharmaceuticals and optoelectronic devices has fostered extensive development in the fabrication of colloidal particles. These colloidal particles may be assembled into complex materials, such as gels or solids, driven by interactions between the particles. For single component repulsive particles, substantial work has been done to characterize the phase behavior of the colloidal suspensions as a function of volume fraction and temperature. Much of this work focused on the phase behavior of model hard-sphere suspensions where the interparticle interaction is infinitely repulsive at contact and zero otherwise [1]. In this paper, we explore the use of specific lock-and-key biomolecules to assembly of colloidal materials through attractive interactions, holding promise for the assembly of novel structures at low total volume. Ideally, the ability to control both the strength and specificity of the specific interaction should make it possible to control the formation of a large variety of material structures with a diverse array of potential applications.

Bio-adhesion molecules make readily feasible the possibility of making binary colloidal alloys. The use of single-sized particles having identical properties ultimately limits the variety of structures and useful materials that can be made. Although one may vary the properties of the single particle, the range of material structures is always restricted by the single particle size. Bidisperse colloidal suspensions increase the flexibility in the structure and applications of colloidal materials. In a binary suspension, one has control over the material properties of each of the two colloidal species, the ratio of particle sizes, the volume fractions of the two species, and the total volume fraction. These additional parameters greatly increase the range of possible structures that can form. In fact, many more crystalline states can be formed from bidisperse colloidal materials than from monodisperse materials. As a result, considerable attention has been paid to the formation of binary alloys using mixtures of colloidal particles. By placing the lock on one type of bead, and the key on the other, one can direct the ordered assembly of unlike particles through the specificity of the lock-and-key interaction.

In this paper, we have used a relatively weak biological adhesion interaction to assemble two types of colloidal particles. Our laboratory has worked with selectin/carbohydrate interactions for many years; these molecules are found in the immune system and mediate blood cell adhesion to blood vessel walls[2]. While specific, they are weak, with off-rates on the order of several sec^{-1}; thus one can expect that binding would be reversible at low densities. At high densities, the adhesion would be irreversible. Thus, the structure of the colloidal system containing these molecules would be *tunable*, depending on the density of molecules used.

We developed bidisperse biocolloidal suspensions consisting of 0.94 μm (further denoted as "A" particles) and 5.5 μm (further denoted as "B" particles) polystyrene microspheres coated with E-selectin (further denoted as α) and the carbohydrate sialyl-Lewis^x sLe^X (further denoted as β) molecules, respectively. Using this unique system, we have confirmed our hypothesis that binary structures can be formed through attractive, heterotypic, biological interactions.

Moreover, we have shown that a variety of binary structures, from colloidal micelles (a single large particle coated with smaller particles) and binary colloidal clusters (panel A, with a number ratio of $N_A/N_B = 200$), to clusters (panel B, $N_A/N_B = 100$), to elongated chains (panel C, $N_A/N_B = 10$ & panel D, $N_A/N_B = 2$), can be made by decreasing the number fraction of small to large particles. The adhesion is specific, and can be reversed by the addition of a calcium chelator, since selectin interactions depend critically on the calcium concentration[3]. We project that additional manipulation of the number of E-selectin (α) and sLe^X (β) molecules per particle will allow us to use this same system to test our hypothesis that weaker (low affinity) interparticle interactions can lead to the formation of equilibrium (perhaps crystalline) states, rather than kinetically-trapped non-equilibrium structures.

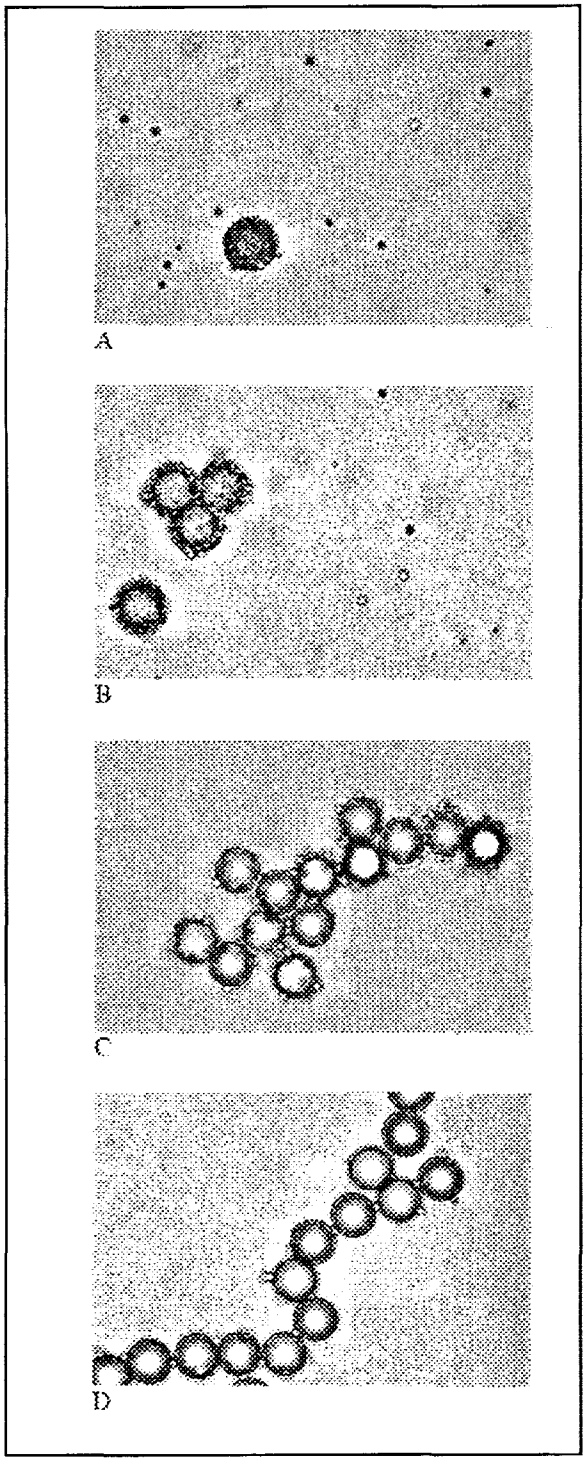

In more recent experiments, we have shown that the aggregation of small and large particle can spontaneously reverse itself at low densities of the of the molecules. We have observed small particles moving by Brownian motion into contact with large particles, docking, and then releasing within seconds to minutes. Thus, it appears we have achieved our original goal of making binary colloidal alloys using reversible bioadhesion, and it remains to be seen if the reversibility will allow us to achieve the self assembly of crystalline materials.

References:

1. Pusey, P. N.; van Megen, W. *Nature* **1986**, *320*, 340.
2. Brunk, D. K.; Hammer, D.A. *Biophysical J.* **1997**, *72*, 2820.
3. Alon, R.; Hammer, D. A.; Springer, T. A. *Nature* **1996**, *374*, 539.

Presentation not available at time of printing.

August 11, 2000
Session 4C

Dynamics and Instabilities II

NON-COALESCENCE IN MICROGRAVITY: SCIENCE AND TECHNOLOGY

G. P. Neitzel
The George W. Woodruff School of Mechanical Engineering
Georgia Institute of Technology
Atlanta, GA 30332-0405

ABSTRACT

The existence of either a *permanent* non-coalescent state between two bodies of the same liquid or a non-wetting state between a liquid and a solid normally wetted by that liquid is something which has come to light only recently. Research by Dell'Aversana *et al.* [1-3] has demonstrated that the physical mechanism responsible for both the non-coalescence and non-wetting phenomena is the existence of lubricating film of gas preventing the subject liquid surfaces or the liquid and solid surfaces from coming into contact with one another. This gas film may be provided via standard lubrication techniques of forcing relative tangential motion between the surfaces in question or driven by thermocapillary effects due to the temperature difference between the bodies (see Figure 1). For cases in which thermocapillarity is the responsible mechanism, we have referred to such systems as *self-lubricating*.

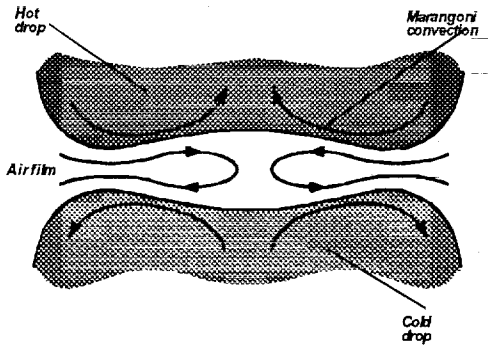

Figure 1. Schematic of the *self-lubricating* mechanism.

It is clear from Figure 1 and from a knowledge of lubrication theory that the film sustaining a non-coalescent or non-wetting state is supporting a load. Further, this load is clearly dependent on the properties of the liquid and the surrounding gas. Our recent work has begun to quantify these dependencies and also to explore ways in which self-lubricating systems might be employed in a technological fashion. Two of the most attractive characteristics of such systems are *i*) the load-carrying capacity just mentioned and *ii*) the fact that the lubricating film provides a virtually frictionless "contact" between the two surfaces in question.

We have found that the loads capable of being carried by self-lubricating systems in terrestrial environments are at least several times the weight of the liquid droplets employed and that this load scales with the radius R of the droplet. While the sizes of these systems are naturally limited in terrestrial environments, establishment of self-lubricated systems of several centimeters in size has already been demonstrated in microgravity[1] and these theoretically possess the capability of supporting quite massive loads. This is one of the potential technological applications weshall examine.

Although we have learned much in the course of our previous research, there are still unanswered scientific questions which must be considered along with the development of self-lubricating systems as a technology. For instance, we have observed[2] for large drops in "contact" with *baths* of the same liquid that, under certain conditions, the flow in the drop becomes unsteady. It is presumed that this unsteadiness is a result of the same hydrodynamic instability responsible for the transition from steady to oscillatory flow in liquid bridges. While we have also observed this for non-wetting situations but not for drop-drop non-coalescence, this has not yet been examined in a systematic way. Its importance from the standpoint of the technological application mentioned above is clear— one would not want flow oscillations transmitted to the load being supported. While a theoretical treatment of this stability problem is feasible, the level of disagreement between theoretical and experimental results for the liquid-bridge problem suggests that such an analysis may not be adequate to guarantee the avoidance of oscillations in practice. Hence, these studies shall be experimental in nature to map out regimes to be avoided in practice.

Also of interest is the response of self-lubricated systems to an external vibratory environment. The existence of "g-jitter" aboard manned microgravity platforms is well-known and the subject of former and current study due to its potential impact on fluid systems [4, 5]. Of interest to the potential technological development of self-lubricated systems is the influence of g-jitter on the mechanical stability of the system (i.e., is there failure of the lubricating film or of the pinned contact line in such cases?) as well as the potential damping characteristics of such oscillations and how effectively or ineffectively these vibrations are transmitted to the suspended package.

One ultimate objective of our research is to develop a set of flight experiments to demonstrate one or more technological applications of self-lubricated systems in microgravity environments. In order to best design these experiments, further scientific questions regarding the behavior of self-lubricating systems need to be addressed and answered. The need for a microgravity environment to pursue questions of technological development of self-lubricated systems is clear. The benefits to be gained from the successful completion of this research are also evident. In addition to increased quantitative knowledge of the behavior of self-lubricated systems, potentially useful technologies will result which could have positive implications for future microgravity experimentation and space exploration.

REFERENCES

[1] P. Dell'Aversana, J.R. Banavar, and J. Koplik, Phys Fluids, 8 (1996), 15-28.
[2] P. Dell'Aversana, V. Tontodonato, and L. Carotenuto, Phys Fluids, 9 (1997), 2475-2485.
[3] P. Dell'Aversana and G.P. Neitzel, Phys. Today, 51 (1998), 38-41.
[4] J.I.D. Alexander, *et al.*, J. Cryst Growth, 178 (1997), 657-661.
[5] R. Monti, R. Savino, and G. Alterio, Acta Astro, 40 (1997), 369-381.

NASA/CP—2000-210470

1816

Georgia Institute of Technology

Non-Coalescence in Microgravity: Science and Technology

G. Paul Neitzel

The George W. Woodruff School of Mechanical Engineering

Georgia Institute of Technology, Atlanta, GA

Pasquale Dell'Aversana

Microgravity Advanced Research and Support Center, Naples, Italy

Motivation

- Permanent non-coalescence and non-wetting have been demonstrated in both terrestrial and microgravity environments.

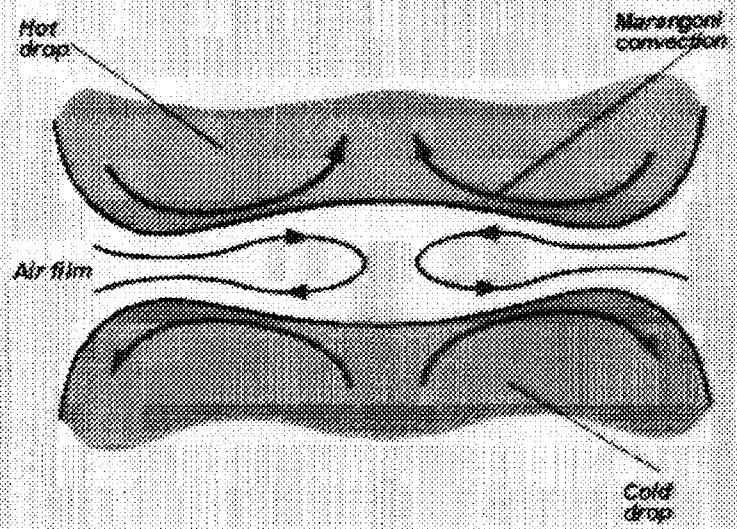

Motivation - Continued

- Non-coalescing systems have been demonstrated to be capable of supporting loads.

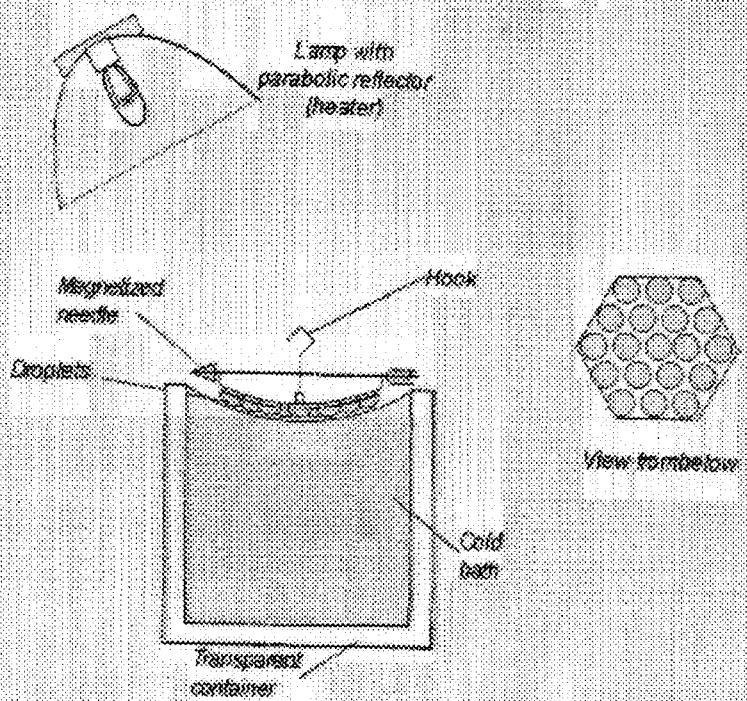

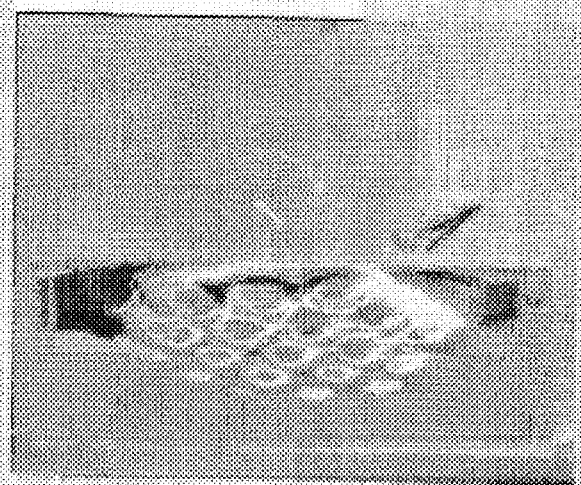

Motivation - Continued

- It may be possible to employ these "self-lubricated" systems to perform useful functions in low-load environments, e.g., microgravity and/or very small scale.
- What are the research issues remaining to be answered to permit this?

Recent results

- Load measurements

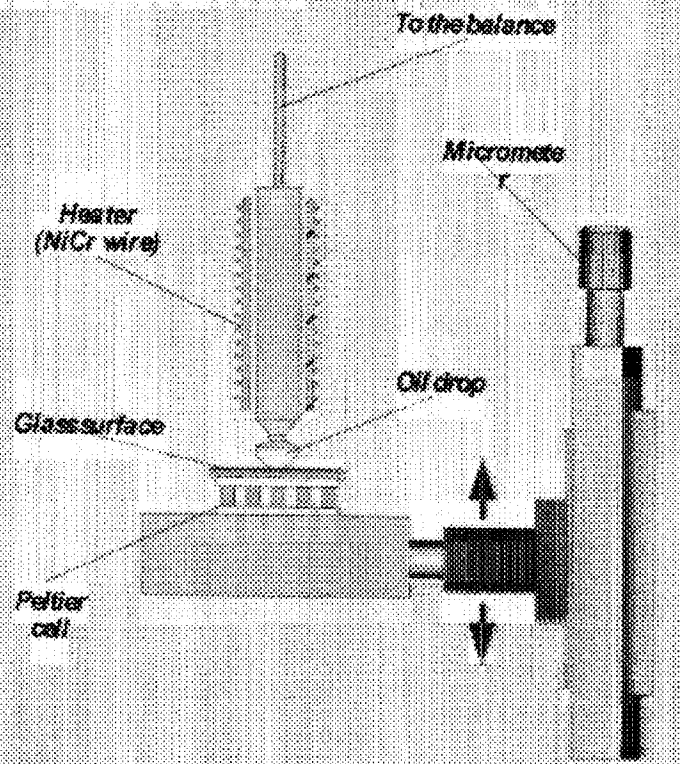

Load Measurements

- Previously reported measurements were in poor agreement with computed loads for *static* deformed droplets due to inaccuracies in measurement of droplet volume.

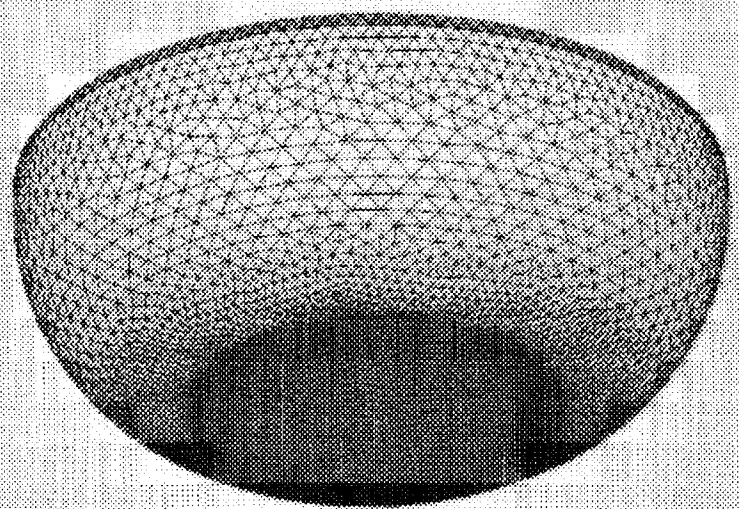

Experimental and Computed Loads

Lubrication Analysis

- Thin drop, thin gas film approximation
- Leading-order solutions:

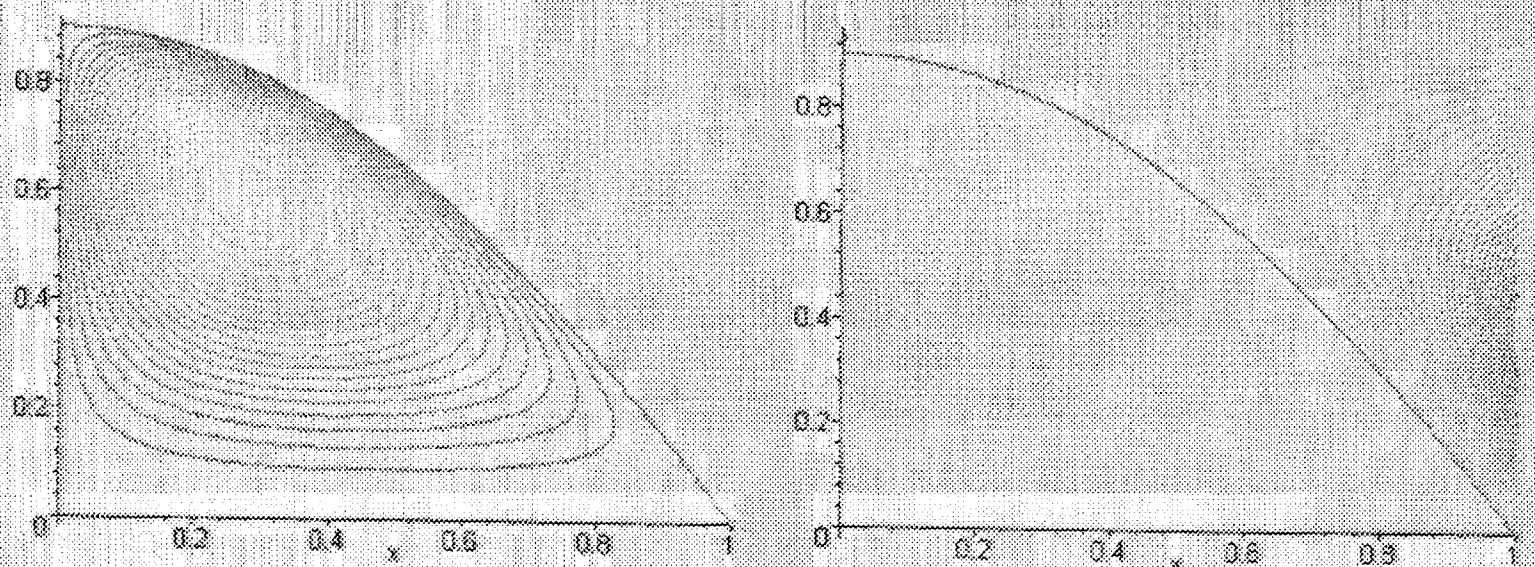

Numerical Simulations

Isothermal Non-Wetting

Isothermal Non-Wetting Fringes

- 100 cS silicone oil droplet

Envisioned Application

- The load-carrying capacity of these systems suggests their use as "frictionless" bearings of vibration isolation mounts in low-load environments

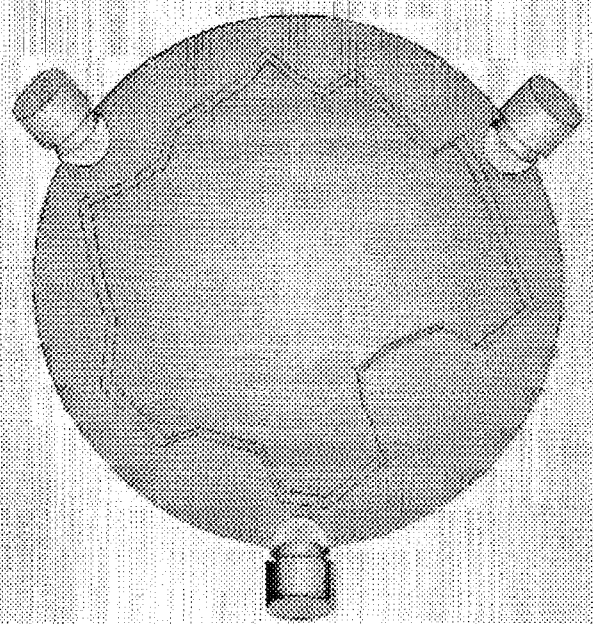

Research Issues

- Stability of droplets under the action of self-lubrication

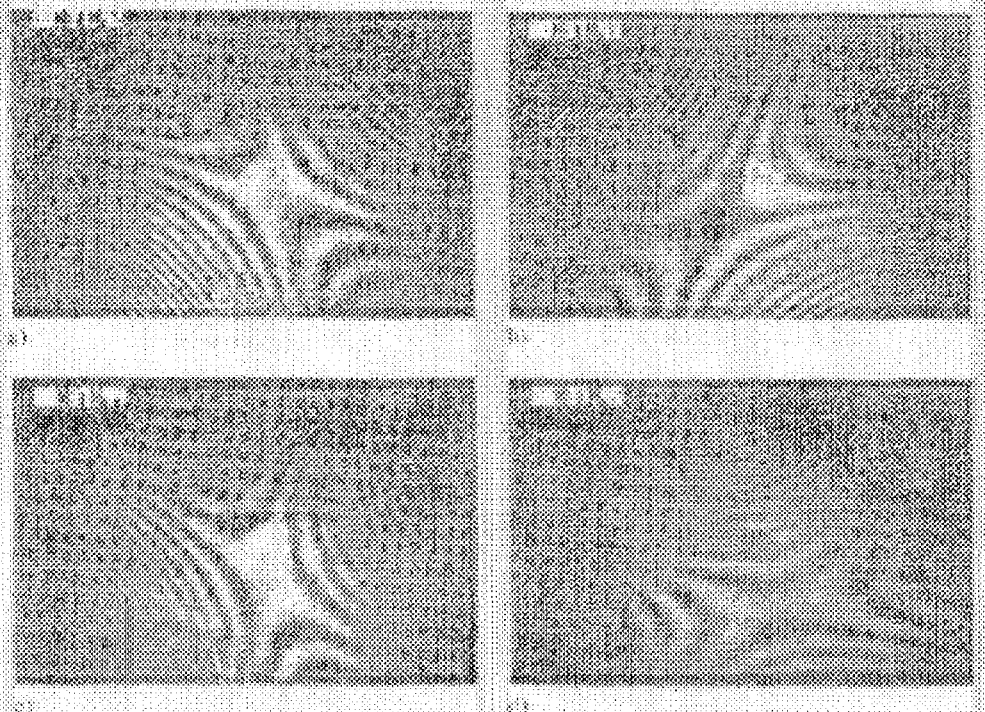

Research Issues - Continued

- Response to oscillations and damping characteristics

Research Issues - Continued

- Counterbalancing evaporation
- Influence of dusty environments
- Effects of static electrical charge
- Does load-carrying capacity scale as predicted?

NASA/CP—2000-210470

Current Collaborators

- *At Georgia Tech*
  - Peter Nagy
  - Andrea Wood
  - Kristina Wines
- *At the MARS Center*
  - Maria Rosaria Vetrano
  - Valentino Tontodonato
- *At National Central University, Taiwan*
  - Jyh-Chen Chen

Critical Velocities in Open Capillary Flow

Uwe Rosendahl, Michael E. Dreyer, Hans J. Rath
Center of Applied Space Technology and Microgravity (ZARM)
University of Bremen, Germany
Email: rosend@zarm.uni-bremen.de

Abstract

A forced liquid flow through an open capillary channel with free liquid surfaces is investigated experimentally under low gravity. Since the free surfaces can only withstand a certain difference between the liquid pressure and the ambient pressure the flow rate in the channel is limited. The maximum flow rate is achieved when the surfaces collapse. The aim of the investigation is to determine the limitation of the flow rate and the corresponding critical flow velocity. The investigations were performed on board the sounding rocket mission TEXUS 37 providing a microgravity environment of $10^{-4}g$ in all axis for 6 minutes.

Introduction

As shown in Fig. 1 the channel consists of two parallel plates and the liquid volume inside forms free surfaces at the sides. The liquid is pumped through the channel with a constant volume flux Q. Due to friction and changes in cross section the liquid pressure decreases in flow direction s depending on the flow rate. To achieve stationary flow conditions the difference to the ambient pressure P_a has to be balanced by the capillary pressure of the free surface. The capillary pressure is proportional to the curvature of the free surface and consequently the curvature decreases in flow direction.

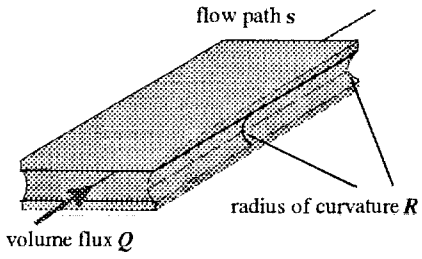

Figure 1: Model of the channel consisting of two parallel plates.

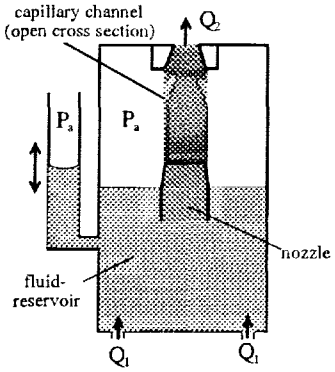

Figure 2: Schematic drawing of the TEXUS experiment module.

Thus the radius of curvature R at the outlet is smaller than the radius at the channel inlet. When Q is increased the radius of curvature at the channel outlet decreases further. The limit approximately is reached, when R equals half the plates distance. The surfaces collapse and stationary flow is no longer possible. Gas ingestion occurs at the outlet.

TEXUS experiment

For determining the maximal volume flux a TEXUS experiment module was developed. The core of the module, shown in Fig. 2, consists of the fluid reservoir, the compensation tube

and the capillary channel (length 47 mm, breadth 25 mm, plates distance 5 mm). Two gear pumps adjustable in 0.05 ml/s steps enable the flow through the channel. The supply pump drives the liquid of volume flux Q_1 through an annular gap at the bottom into the fluid reservoir. Via a nozzle especially designed to achieve best velocity distribution the liquid accelerates into the channel. A second pump withdraws the liquid at the outlet. Differences in volume fluxes are balanced by the compensation tube (i. d. 45 mm). For evaluating the surface contour by digital image processing the channel view is divided into two picture details each observed by a CCD camera. All experiment procedures can be hand controlled via telescience.

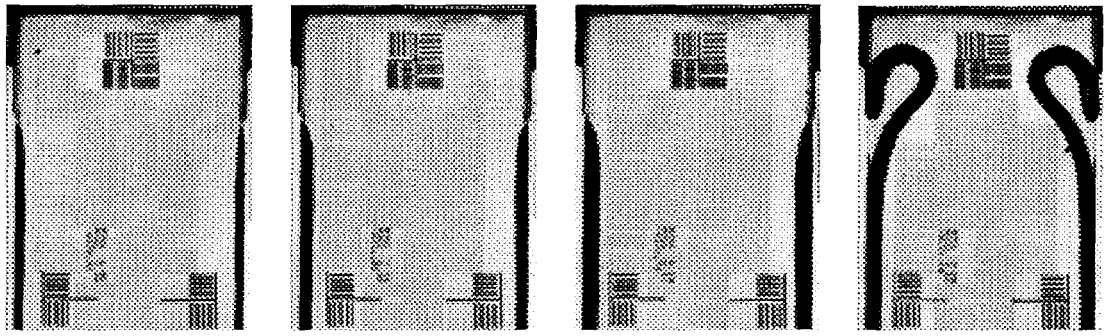

$Q = 6.0$ ml/s $Q = 8.5$ ml/s $Q = 9.1$ ml/s $Q > 9.1$ ml/s

Figure 3: Liquid flow between two parallel plates at different volume flux (upper camera view). The camera view is perpendicular to the top plate referred to the model in Fig. 1. Since the plates are transparent the free surface appears as a dark contour. The flow at $Q > 9.1$ ml/s is no longer stationary.

After the experiment was launched the channel and compensation tube had to be filled at first. The filling procedure worked well without any loss of liquid into the observation chamber. Starting with a stationary flow at low Q the volume flux was increased in large steps (0.5 ml/s) up to the critical value. The first three pictures in Fig. 3 show the increase of the free surfaces's curvature leading to reduction in flow cross section, but stationary flow conditions are still present. The volume flux referring to the last picture is above the critical value and leads to a collapse of the free surface.

Results

For the fine approach the step size was changed to 0.05 ml/s and the critical volume flux was determined as $Q_c = 9.1 \pm 0.1$ ml/s (Silicon Fluid 200 DOW Corning 0.65 cSt at 20 °C). This result as well as the evaluated surface contours not discussed in detail here show good agreement with theoretical predictions available from a 1d model [1] and 3d computations. Further work assuming the critical fluid velocity as a characteristic signal velocity is under preparation.

The funding of the TEXUS 37 flight by the European Space Agency (ESA) and funding of the research project by the German Aerospace Center (DLR) is gratefully acknowledged.

References

[1] Dreyer, M., Rosendahl, U., Rath, H.J., AIAA-98-3165, 1998

Fifth Microgravity Fluid Physics and Transport Phenomena Conference

ZARM

Critical Velocities in Open Capillary Flows

Uwe Rosendahl, Michael Dreyer, Hans J. Rath

- Motivation
- Introduction
- Experiment on Sounding Rocket TEXUS 37
- Results
- Conclusion

esa

Support for the research project by the German Aerospace Center (DLR) and the European Space Agency (ESA) is gratefully acknowledged

DLR

Motivation

ZARM

Open capillary flow

- Arbitrary channel
- Free surface
- Surface tension dominant

Applications:

- Heat pipes
- Surface tension tanks

⇨ Steady state behavior?

⇨ Transient behavior?

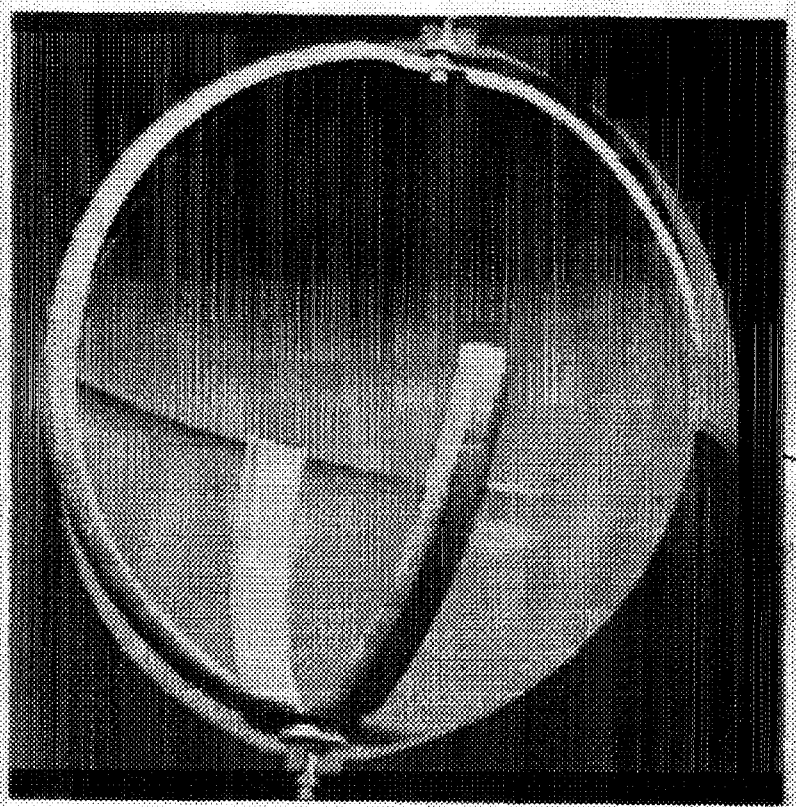

Surface tension tank
(with friendly permission of ASTRIUM, Bremen)

Investigated Model

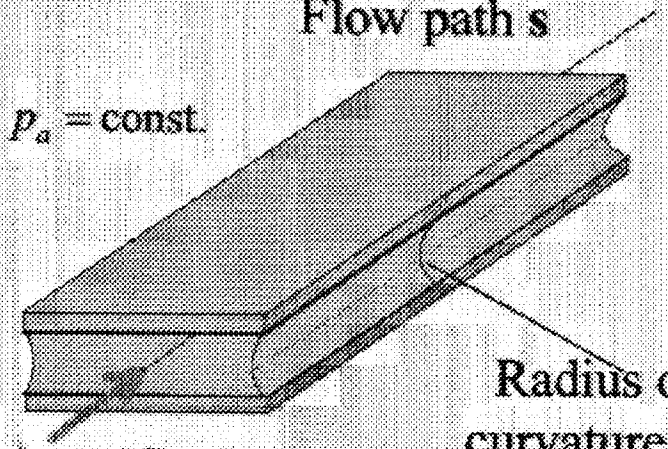

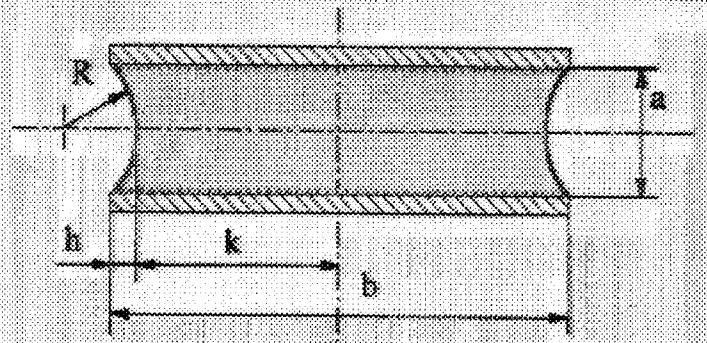

Pressure: $p - p_a = \frac{\sigma}{R}$

Scaling: a, b, $v_s = \sqrt{\frac{2}{\rho}\frac{\sigma}{a}}$

Ohnesorge number: $\mathrm{Oh} = \frac{\mu}{\sqrt{2a\rho\sigma}}$

Aspect ratio: $\Lambda = \frac{a}{b}$

Length: $l_s = \mathrm{Oh}(l/a)$

Eq.: $$\frac{dR}{ds} = \frac{\frac{\mathrm{Oh}}{8}\frac{A^2}{Q}\left\{k_{pr} + k_{pe}e^{-s/s_0}\right\}}{\frac{dA}{dR} - \frac{A^3}{Q^2R^2}}$$

BC: $R(0) = R_0$

➡ h(s), $v^* = f(\Lambda, \mathrm{Oh}, l_s)$

Choked Flows

Choking: Mass flow is limited

Similarities: Compressible gas flow
(Mach number - problem)

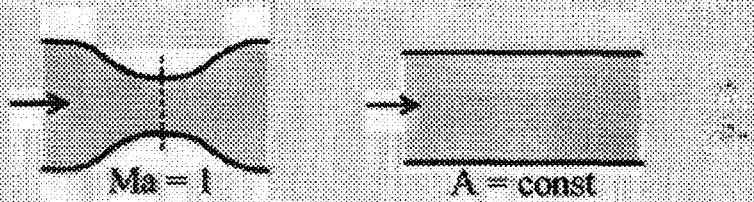

Open channel flow
(Froude number - problem)

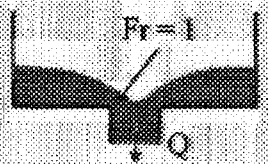

Open capillary flow

$$V = \frac{v}{v_c} \qquad v_c(R) = \sqrt{\frac{A(R)}{\rho}\,\frac{\sigma}{R^2}\,\frac{dR}{dA(R)}}$$

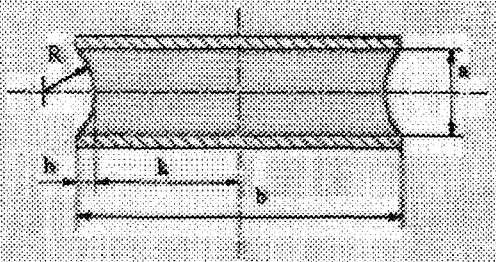

v_c : Wave speed in a channel of variable cross section

Results from Drop Tower

Drop tower Experiments

- Good agreement with 1D theory
- Error theory/experiment < 10%
- Short experimental time (4.74 s)
- Inertia effects

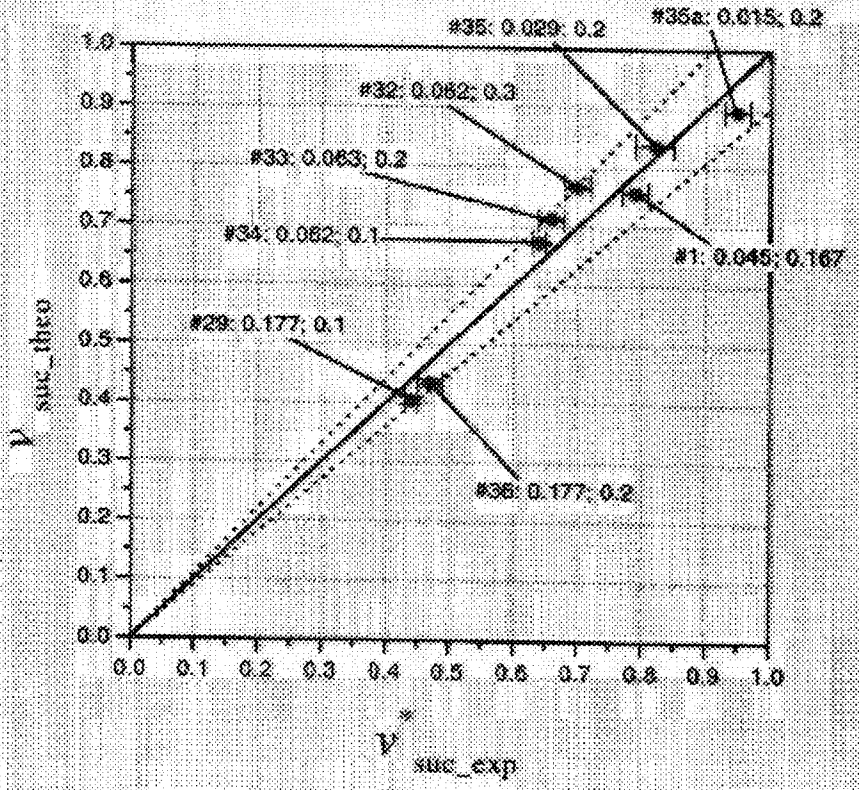

$$v^* = \frac{v}{v_c\sqrt{1-\Lambda}} \qquad v_c = \sqrt{\frac{2\,\sigma}{\rho\,a}}$$

Dreyer, M.E., et al., AIAA 98-3165

Experiment on TEXUS 37

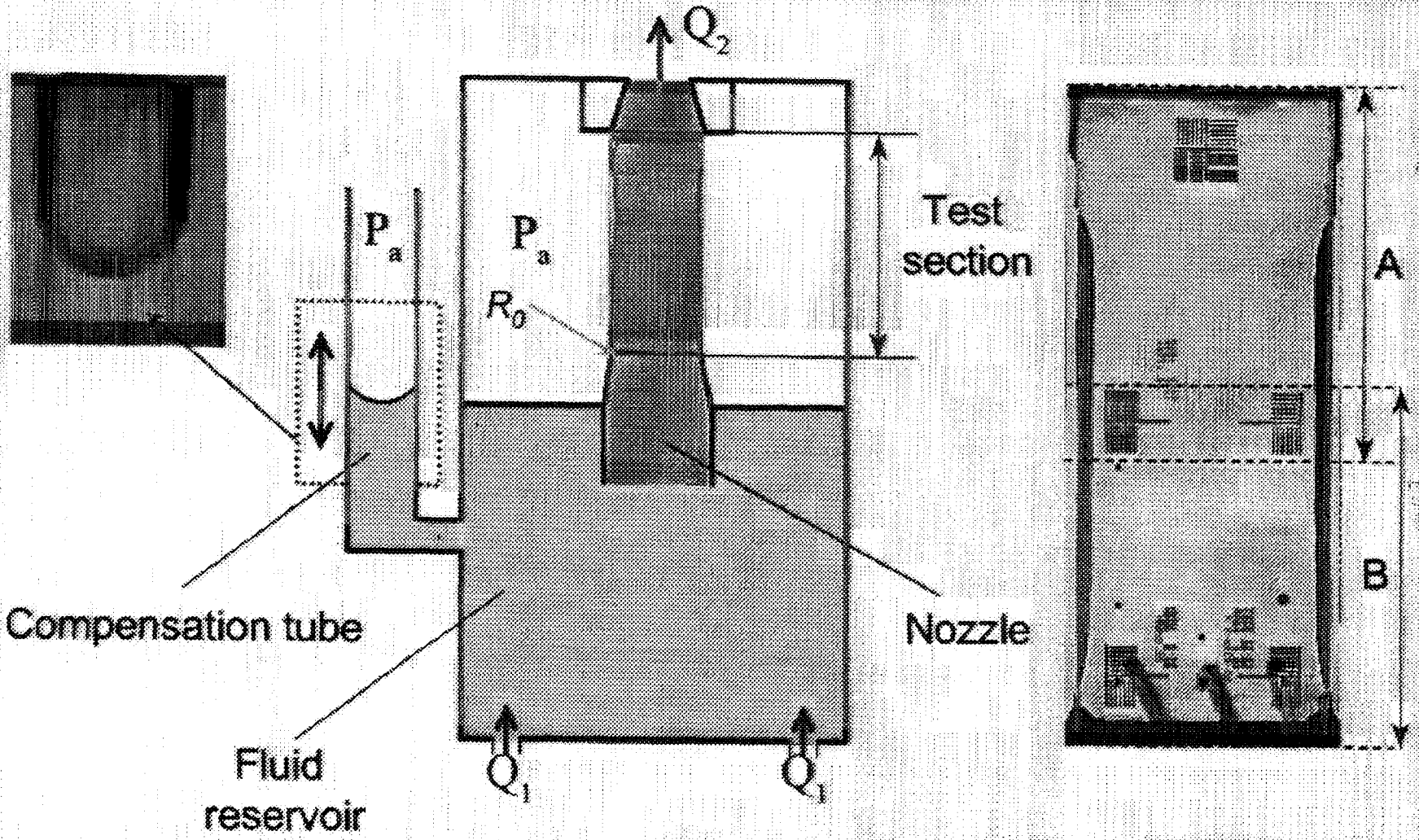

Experiment on TEXUS 37

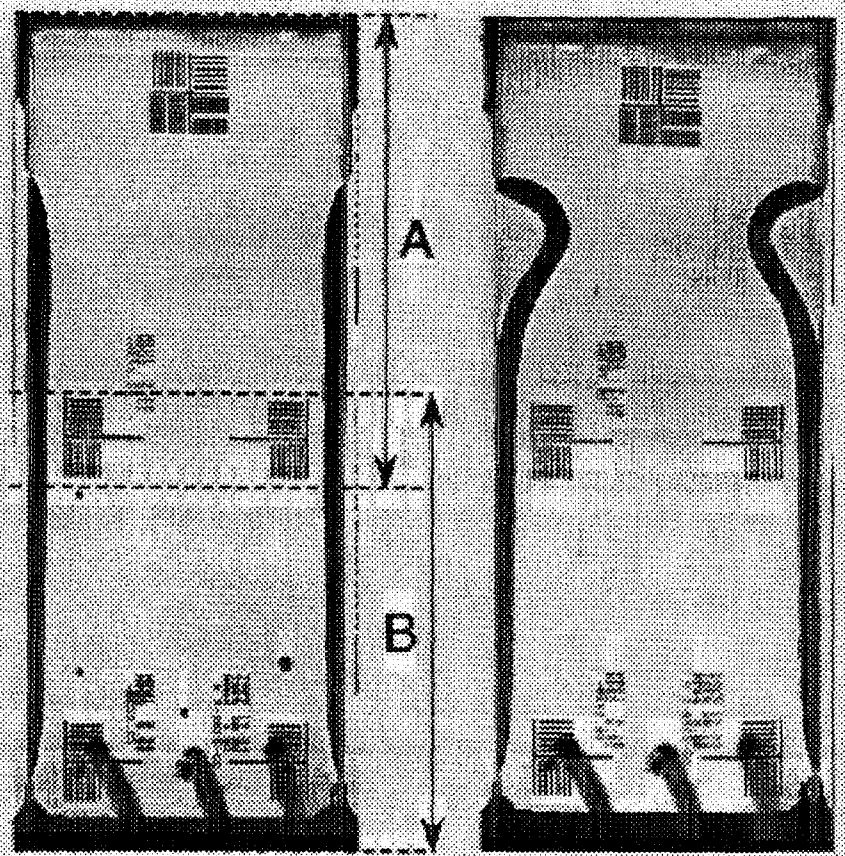

subcritical supercritical

capillary channel flow

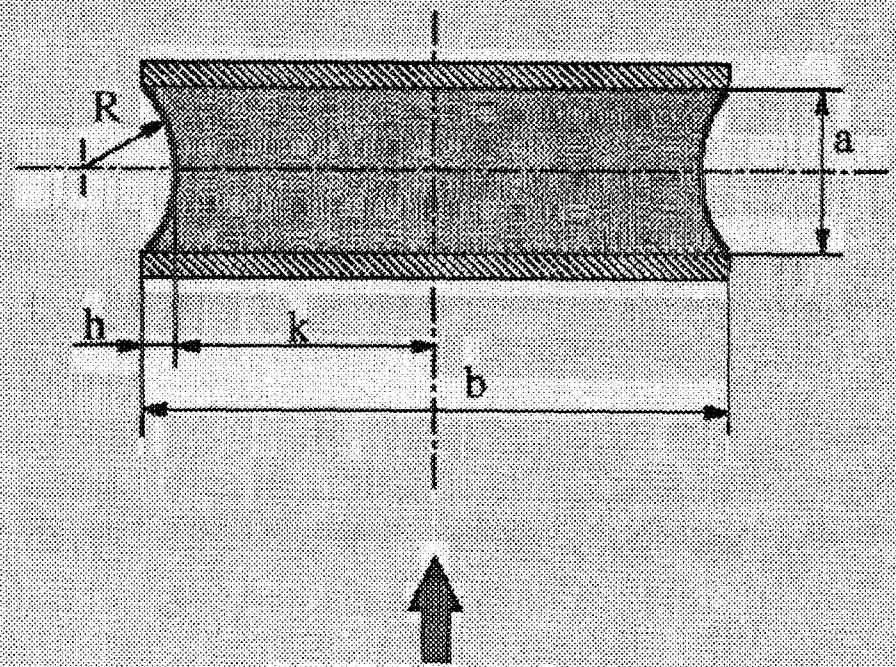

camera view

Subcritical Flow

ZARM

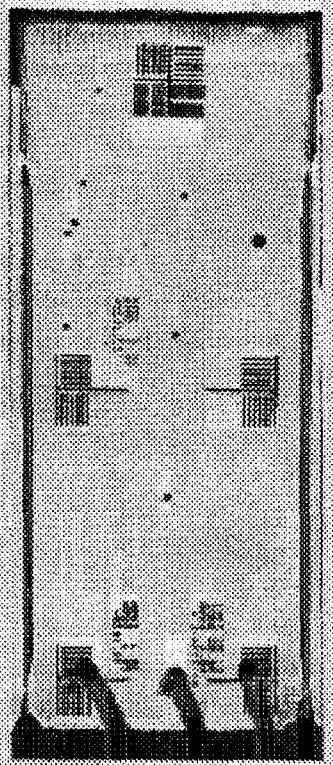

Q = 6 ml/s

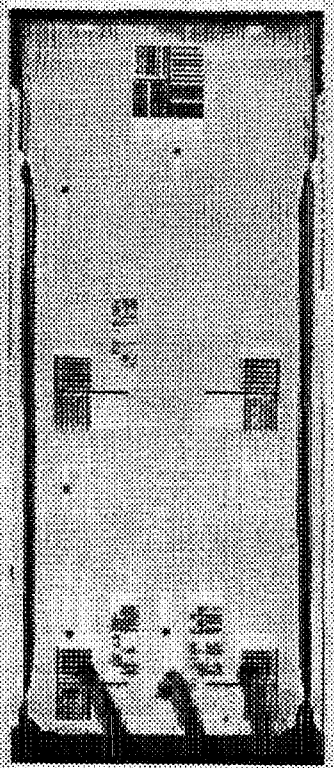

Q = 7 ml/s

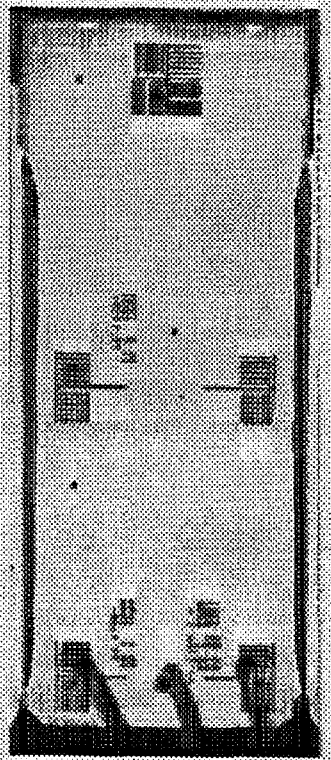

Q = 8 ml/s

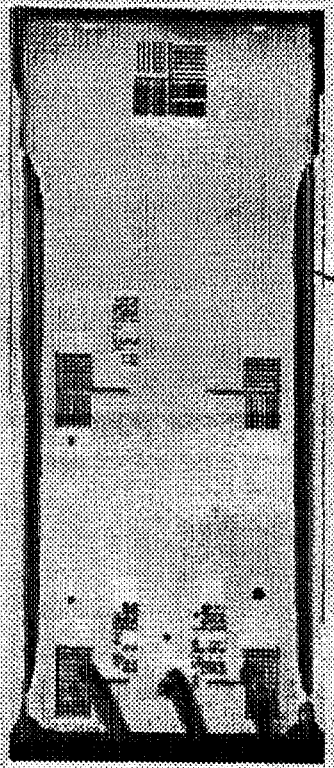

Q = 9.1 ml/s

Supercritical Flow

Results

Determination of Q

Experiment:

$$Q_{\exp}^{\max} = 9.1 \text{ ml/s} \pm 0.1 \text{ ml/s}$$

$$\nu_{\exp}^{*} = 1.02$$

Theory:

$$Q_{\exp}^{\max} = 8.8 \text{ ml/s}$$

$$\nu_{\text{theo}}^{*} = 0.98$$

$$\nu^{*} = \frac{\nu}{\nu_s \sqrt{1-\Lambda}} \qquad \nu_s = \sqrt{\frac{2\,\sigma}{\rho\, a}}$$

Evaluation of Surface

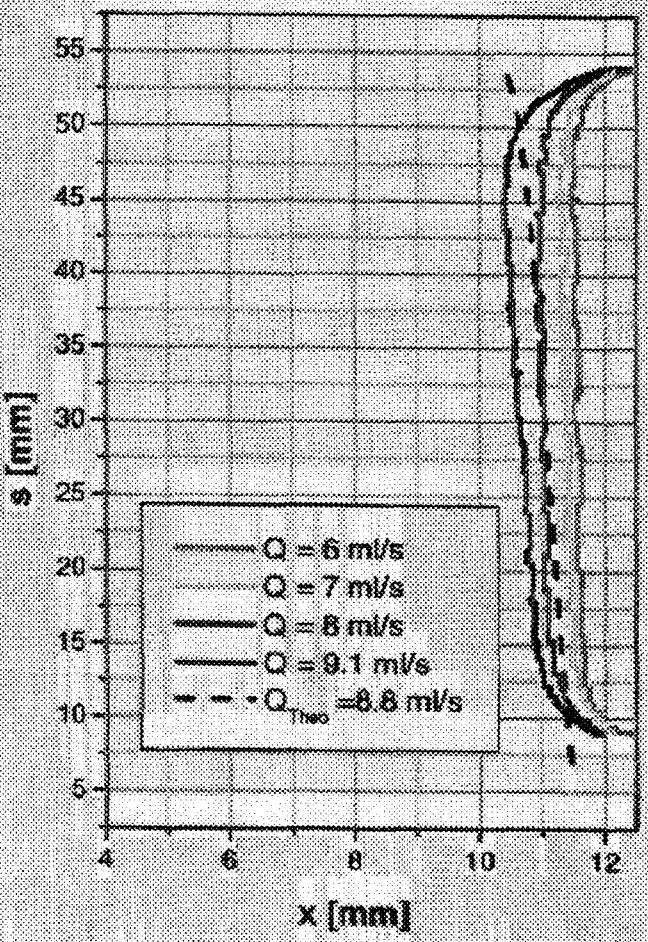

Results

ZARM

Influence of $V = \frac{v}{v_c}$

Liquid velocity:

$v = Q / A_{\min}$

Wave speed:

$v_c = v_c(R_{\min})$

$$v_c(R) = \sqrt{\frac{A}{\rho}\frac{\sigma}{R^2}\frac{dR}{dA}}$$

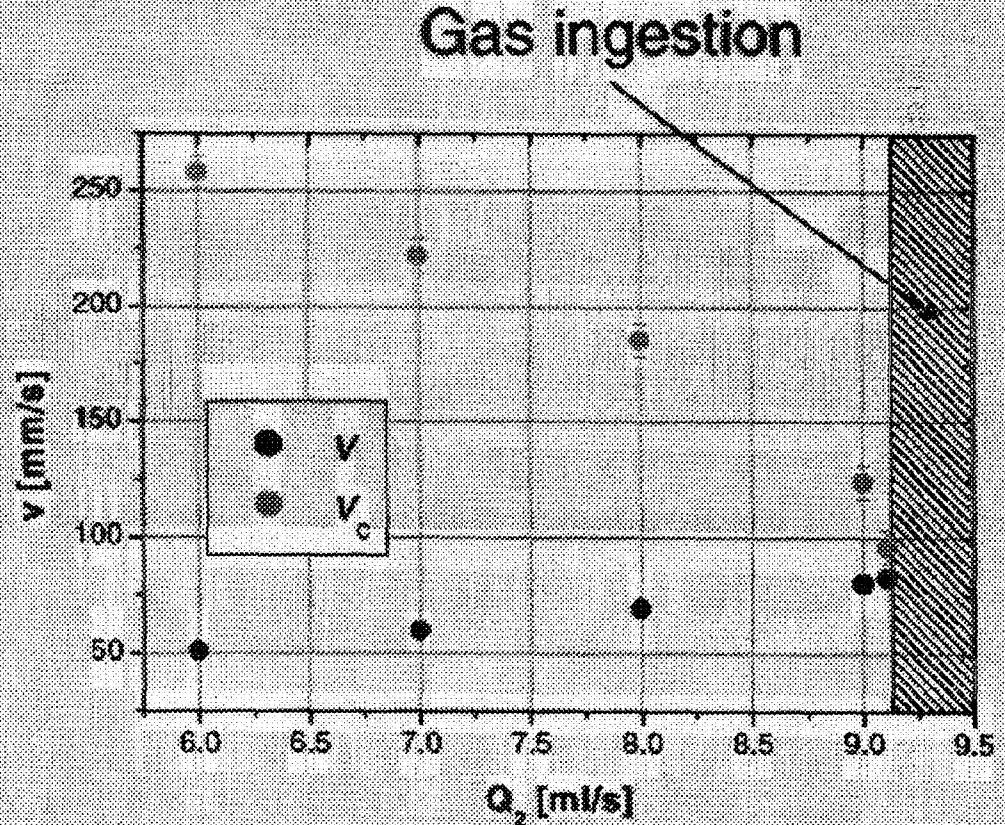

V(9.1 ml/s) = 0.84

Conclusion and Outlook

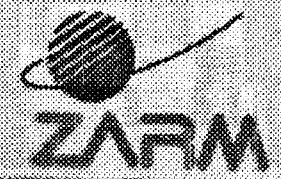

Summary

- Experiment set up to establish capillary liquid flows
- Determination of the limiting volume flux and critical velocity ($Oh = 1.52^{*}10^{-3}$, $\Lambda = 0.2$, l_s=0.014)
- Measured volume flux in good agreement with theoretical prediction
- Flow rate limitation due to choking

Outlook

- Consideration of second radius of curvature
- Further investigations to an expanded parameter field (Λ, Oh, l_s)
- Investigation of different geometries

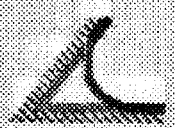

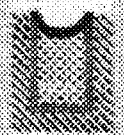

Geophysical Flow Experiments in Rotating Spherical Capacitors

John Hegseth, Department of Physics
University of New Orleans, LA 70148

Thermal convection in spherical geometry includes many important situations in physics, chemistry, and engineering. Spherical geometry is especially important in geophysical flows, a class of flows providing insights into geology, meteorology, and planetary science as well as inspiring such concepts such as deterministic chaos and two-dimensional turbulence. In planetary atmospheres, oceans, mantles, and cores the rapid rotation, the density stratification, and the spherical geometry are considered fundamental features in large-scale geophysical fluid dynamics. The latitude dependent Coriolis force and the strongly non-linear equations of motion in geophysical fluid flows have lead to a dependency on asymptotic mathematical methods and computational methods for theoretical understanding. Much of the data regarding geophysical flows has come from direct planetary observations. These observations are made with little or no control over the many complicated factors influencing the flow. Although no experimental system is perfect, an experiment never misses a nonlinear interaction and may be accessible to a wide range of parameters. At the very least, a well-controlled experiment can provide important information to help validate numerical models.

In our proposed experimental system, a central-force is applied to, incompressible, compressible, and two-phase fluids in spherical geometry. The central force is created using an AC electric field in a spherical capacitor filled with dielectric fluid between the spheres. A fluid may be made compressible or two-phase by controlling a sample fluid's density and ambient temperature. In other words, our system is filled to the critical density and is placed near its liquid-gas critical point by controlling the ambient temperature. Because of the temperature dependence of the dielectric constant and the temperature dependence of the fluid density, a buoyancy force drives a flow when the inner sphere is heated to a higher temperature than the outer sphere. Our previous work was limited in geophysical similarity because our system was not rotated and it is also subjected to the usual gravitation buoyancy force from the earth that breaks the spherical symmetry. Our proposed new system will be rotated in micro-gravity. In this talk I will survey our previous results and discuss our proposed experimental system.

Real time holographic interferometry and shadow-graph visualization are used to study convection in the fluid between two concentric spheres when two distinct buoyancy forces are applied to the fluid. The heated inner sphere has a constant temperature that is greater than the outer sphere's constant temperature by ΔT and an AC voltage difference, ΔV, is applied between the inner and outer spheres. The resulting electric field gradient in this spherical capacitor produces a central polarization force. The temperature dependence of the dielectric constant results in a radial buoyancy force that is especially large near the inner sphere. The normal buoyancy is always present and, within the parameter range explored in our experiment, always results in a large-scale axi-symmetric cell with the axis along the vertical. We have found that this flow becomes unstable to toroidal or spiral rolls that travel vertically upward when ΔT and ΔV are sufficiently high. These rolls start near the center sphere's equator and travel vertically

upward. The onset of this instability depends on both the temperature difference ΔT and the voltage difference ΔV and these two quantities appear to be related, within the parameter range accessible to our experimental system, by a power law. Measurements of the heat transfer show that these traveling rolls increase the heat transfer at onset. Far above onset the heat transfer may actually decrease with increasing ΔT. The traveling roll's frequency increases with increasing ΔT near onset and with increasing ΔV far above onset. These results have been interpreted in terms of the flow structure that includes a thermal boundary layer-like behavior with a width that increases from the bottom pole to an unstable "latitude" near the equator where the rolls appear.

By varying the ambient temperature of the capacitor filled with near-critical fluid, we have observed the effects that an applied voltage has on the fluid during a parabolic flight. Although we had hoped to observe and verify that a spherical density gradient is produced in the fluid, the actual conditions in flight did not allow this to happen. We did, however, see clear evidence of the existence of the influence of this force on the fluid. Below the critical temperature the liquid was clearly attracted by the polarization force while the gas was repelled. Figure 1 shows the this repelling effect on a bubble that is pushed to the outer sphere. As can be seen the electric field attracts the higher density liquid toward the center electrode where the electric flux is higher.

In the 0g to 2g part of a parabolic flight and above the critical temperature, a supercritical fluid forms a vertical density gradient because of its very high compressibility. The resulting horizontal near-critical fluid layer is clearly modified by the electric field, i.e., the higher density fluid is attracted toward the inner sphere. Figure 2 shows that the initially horizontal layer is deformed by attracting higher density fluid toward the inner sphere while the lower density fluid moves away producing the curved layer shown. These experiments clearly suggest that geophysical analogies using near-critical fluids in micro-gravity are possible when this system in heated and rotated.

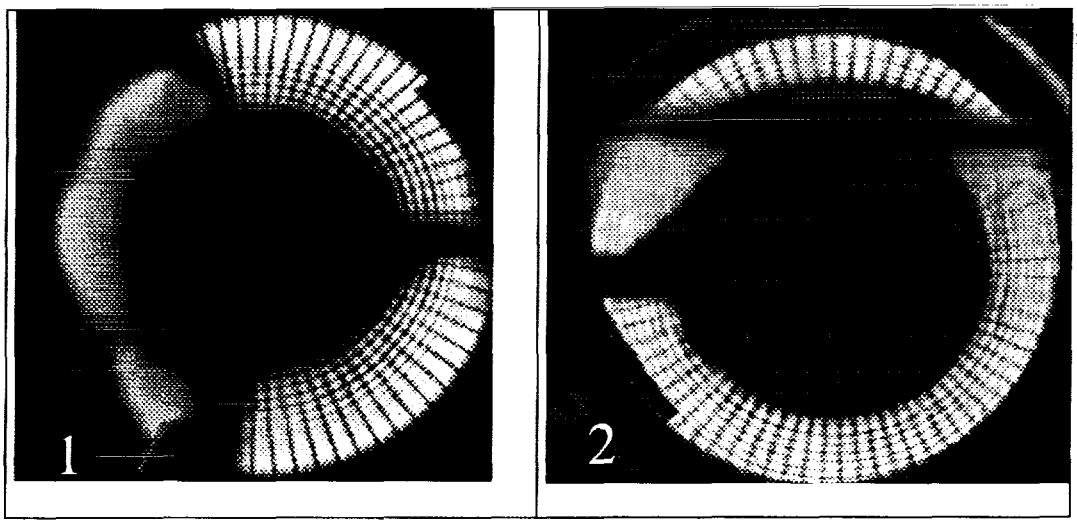

Geophysical Flow Experiments in Rotating Spherical Capacitors

John Hegseth

Department of Physics
University of New Orleans
LA 70148

jhegseth@uno.edu

Introduction

CGFE uses polarization forces create a central force on a fluid in spherical geometry

A molecule in an E field

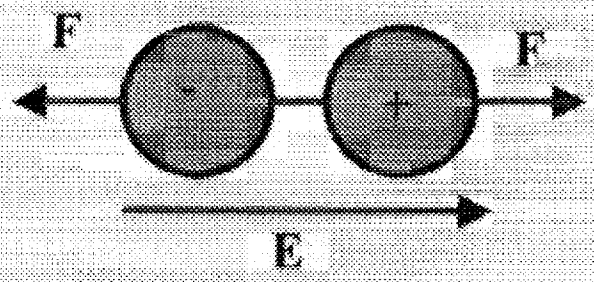

A molecule in an E field gradient

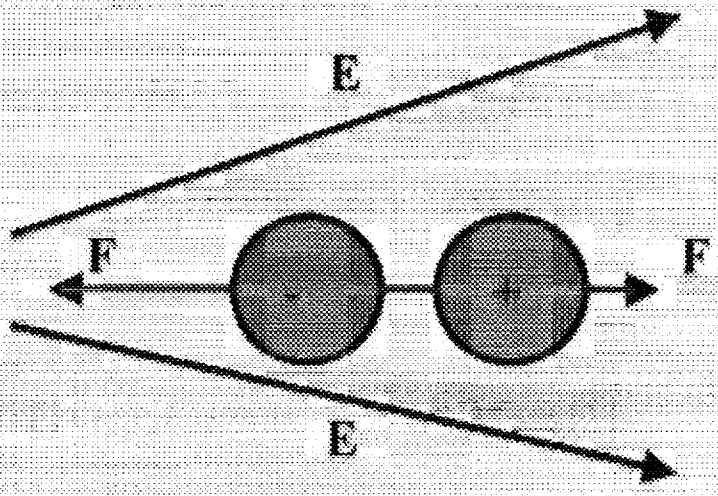

In the continuum approximation

$$\mathbf{F} = q\mathbf{E} - \frac{1}{2}\mathbf{E}^2\nabla\varepsilon + \frac{1}{2}\nabla\left(\mathbf{E}^2\rho\frac{d\varepsilon}{d\rho}\right)$$

In an AC field with

$$\omega \gg \frac{\sigma}{\varepsilon}$$

Then

$$q\mathbf{E} = 0$$

In incompressible fluid, ρ and ε change with T

J.E. Hart, et. al., JFM 132 '86

$$\gamma = \frac{1}{\varepsilon}\frac{\partial\varepsilon}{\partial T} \qquad \alpha = \frac{1}{\rho}\frac{\partial\rho}{\partial T}$$

So that

$$\varepsilon = \varepsilon_a(1-\gamma\Delta T) \qquad \rho = \rho_a(1-\alpha\Delta T)$$

And

$$\mathbf{F} = -\frac{\varepsilon_a\gamma\Delta T}{2\rho_a}\nabla\mathbf{E}^2 + \nabla\left(\mathbf{E}^2\rho\frac{d\varepsilon}{d\rho} + \frac{1}{2}\mathbf{E}^2(\varepsilon_a - \varepsilon)\right)$$

Second term modifies the pressure in the fluid

So the "buoyancy" force/mass is:

$$\mathbf{F}_b = -\frac{\varepsilon_a \gamma \Delta T}{2\rho_a} \nabla \mathbf{E}^2$$

E in the spherical geometry is:

$$E(r) = d(1+\beta)\beta \frac{\Delta V}{r^2}$$

$$d = R_o - R_i,\ \beta = R_i/d$$

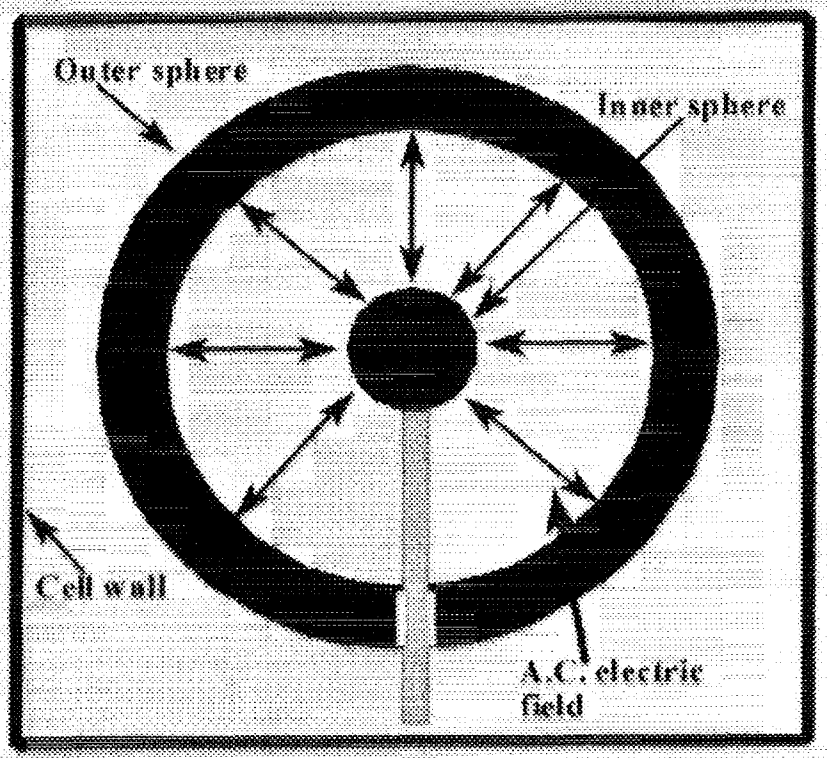

$$\mathbf{F_b} = \gamma \Delta T g_e$$

where

$$g_e = \frac{\varepsilon_a}{2\rho_a} \nabla E^2 = \frac{2\varepsilon_a \Delta V^2 \beta^2 R_o^{\ 5}}{\rho_a (1+\beta)^3 d^3 r^5}$$

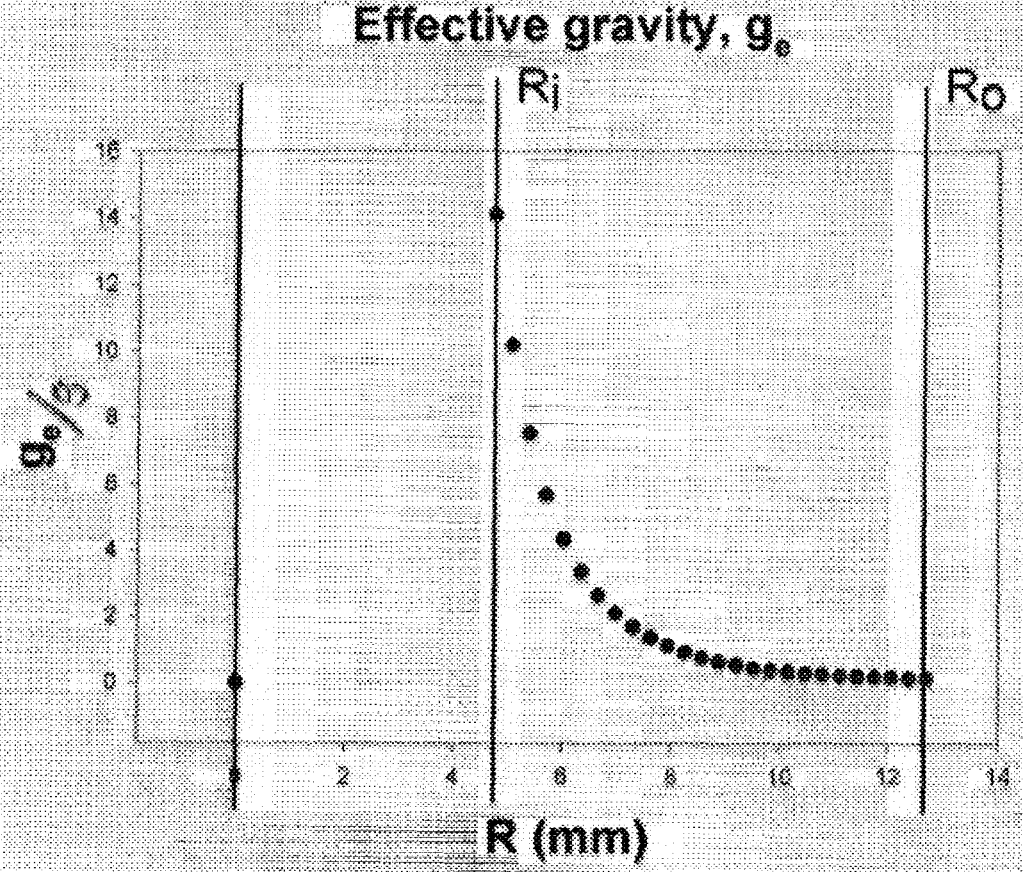

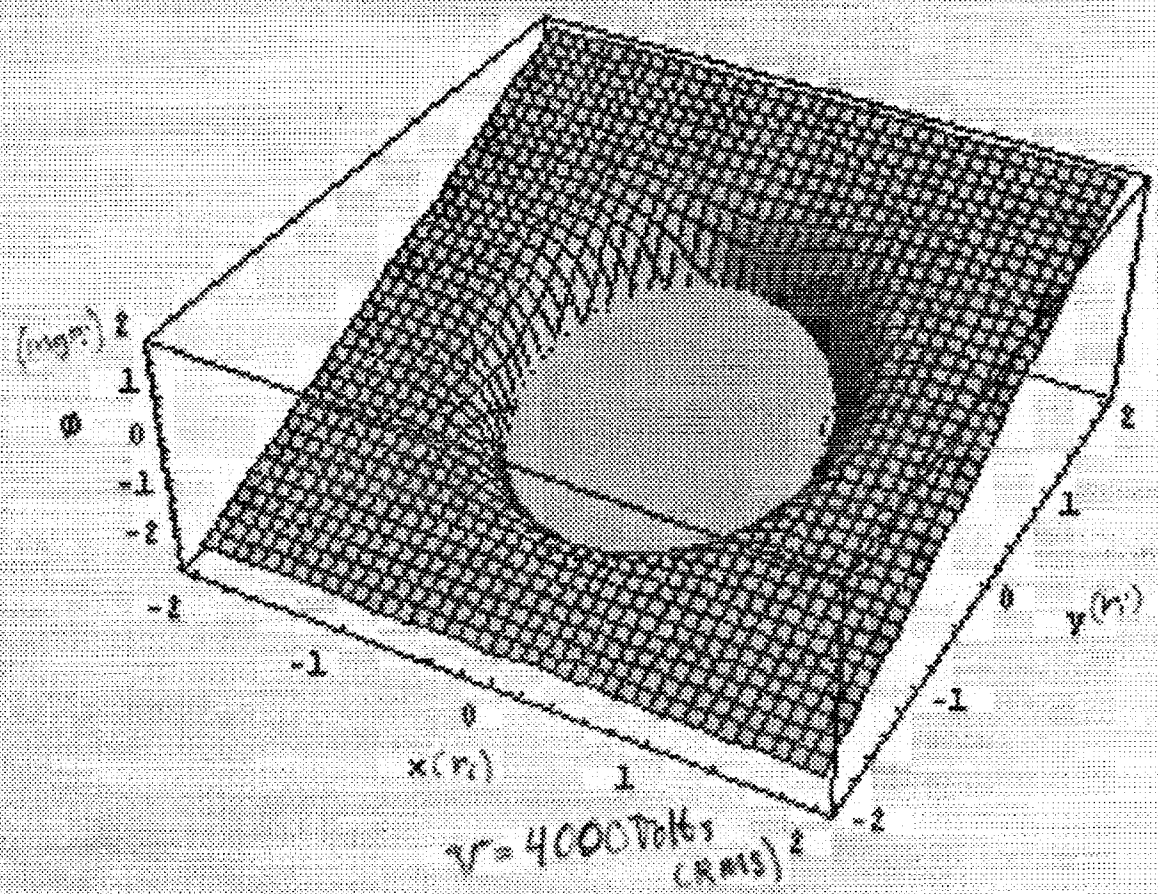
V = 4000 Volts (rms)

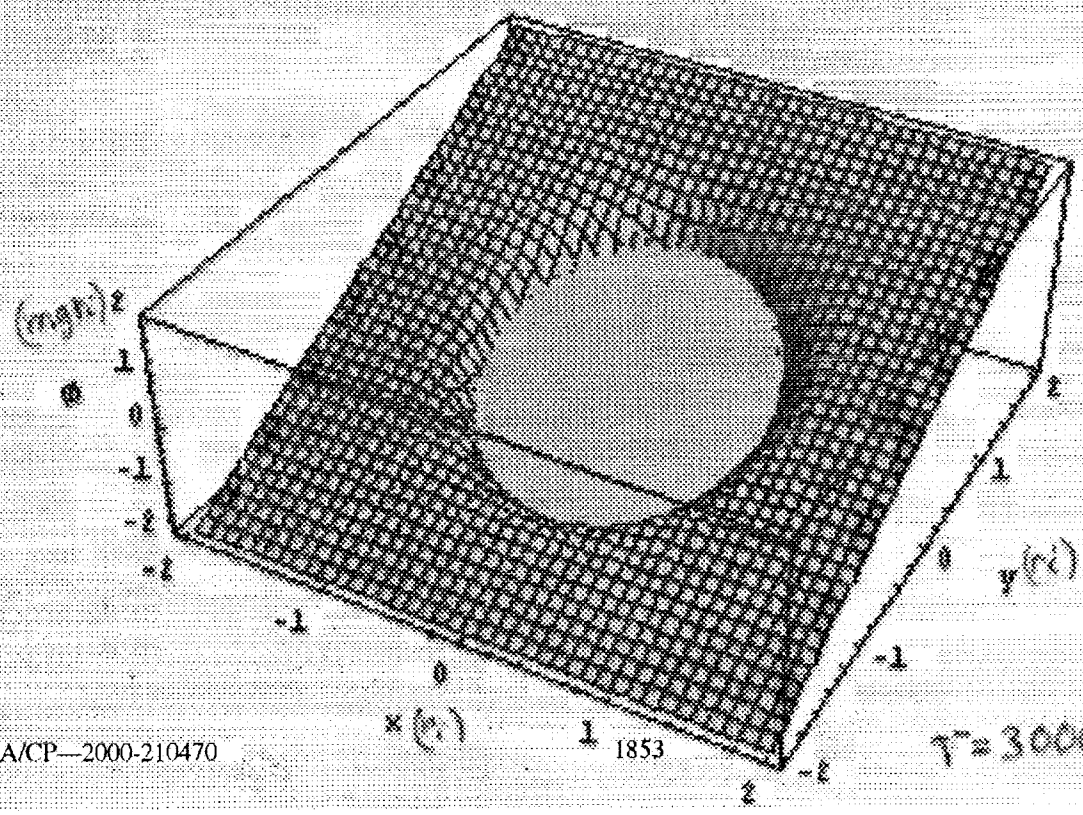
V = 3000 volts (rms)

Transient rolls,
ΔV=4kV, ΔT=2.5°C

Traveling rolls,
ΔV=5kV, ΔT=3.0°C

Traveling rolls

$\Delta V = 4.5kV$, $\Delta T = 3.0°C$

Traveling rolls: $\Delta t \approx 0.5sec$

$\Delta V = 5kV$, $\Delta T = 1.1°C$

EXPERIMENTAL RESULTS IN AN INCOMPRESSIBLE FLUID

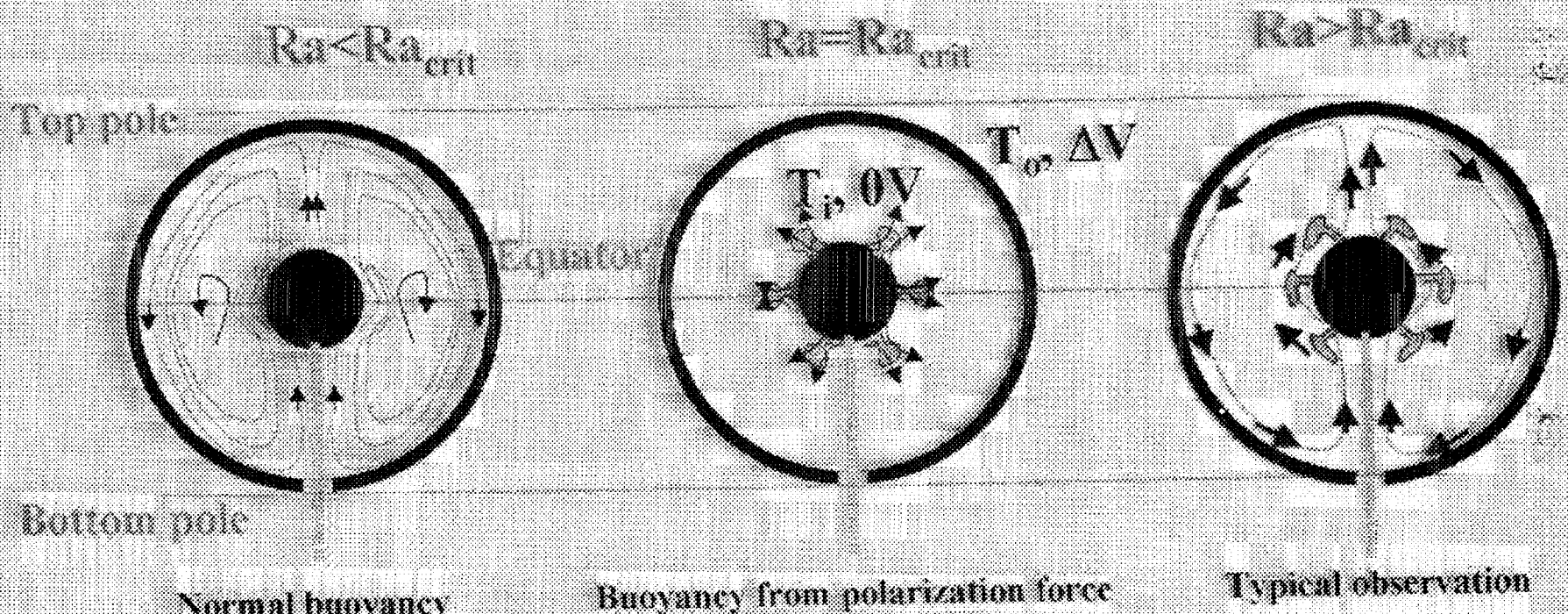

Interaction between gravitational and dielectrical buyoancies forces:
sketch of the observations: thermal plume, first rolls, then successive rolls moving upward

Critical ΔV and ΔT for the onset of rolls

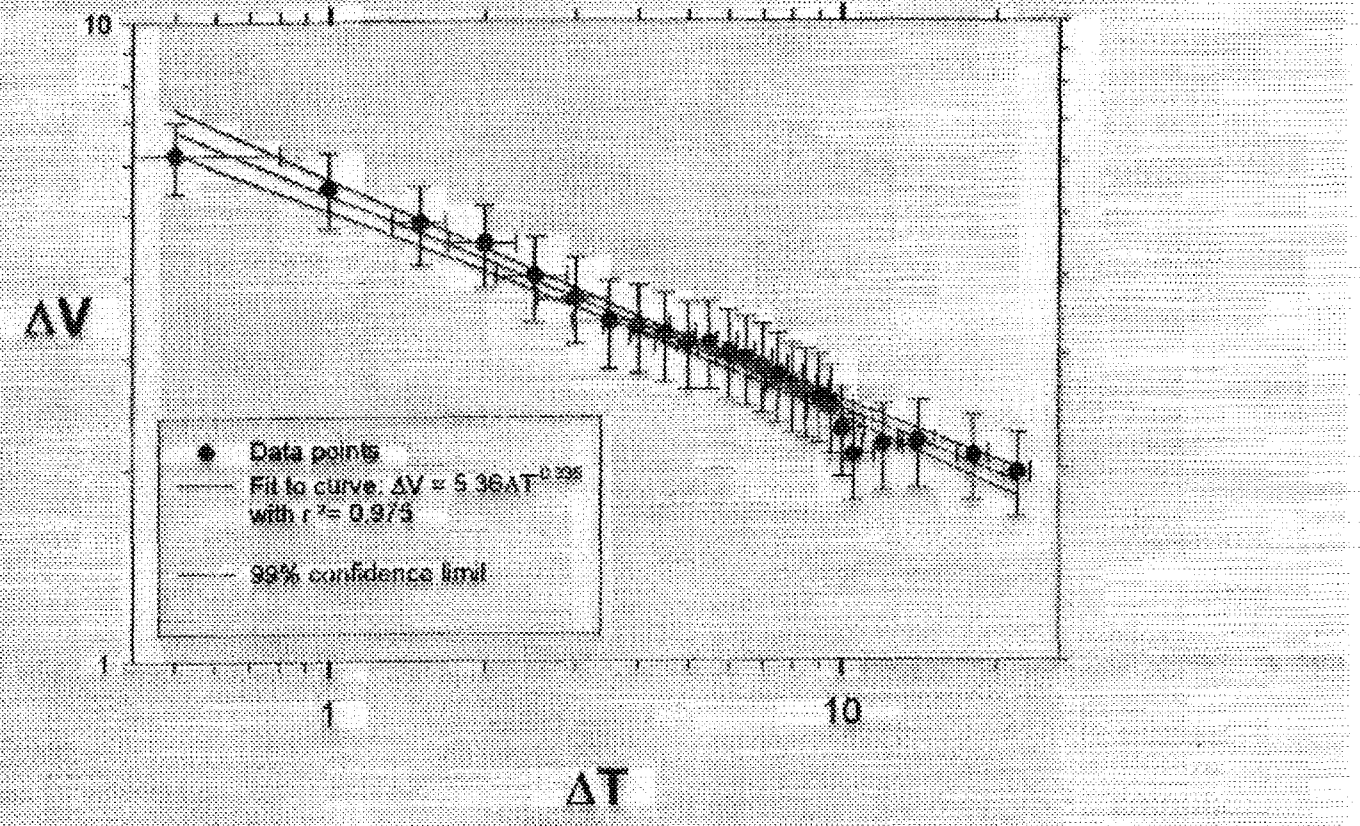

Critical point

At (P_c, T_c, v_c) - liquid and gas differences disappear.

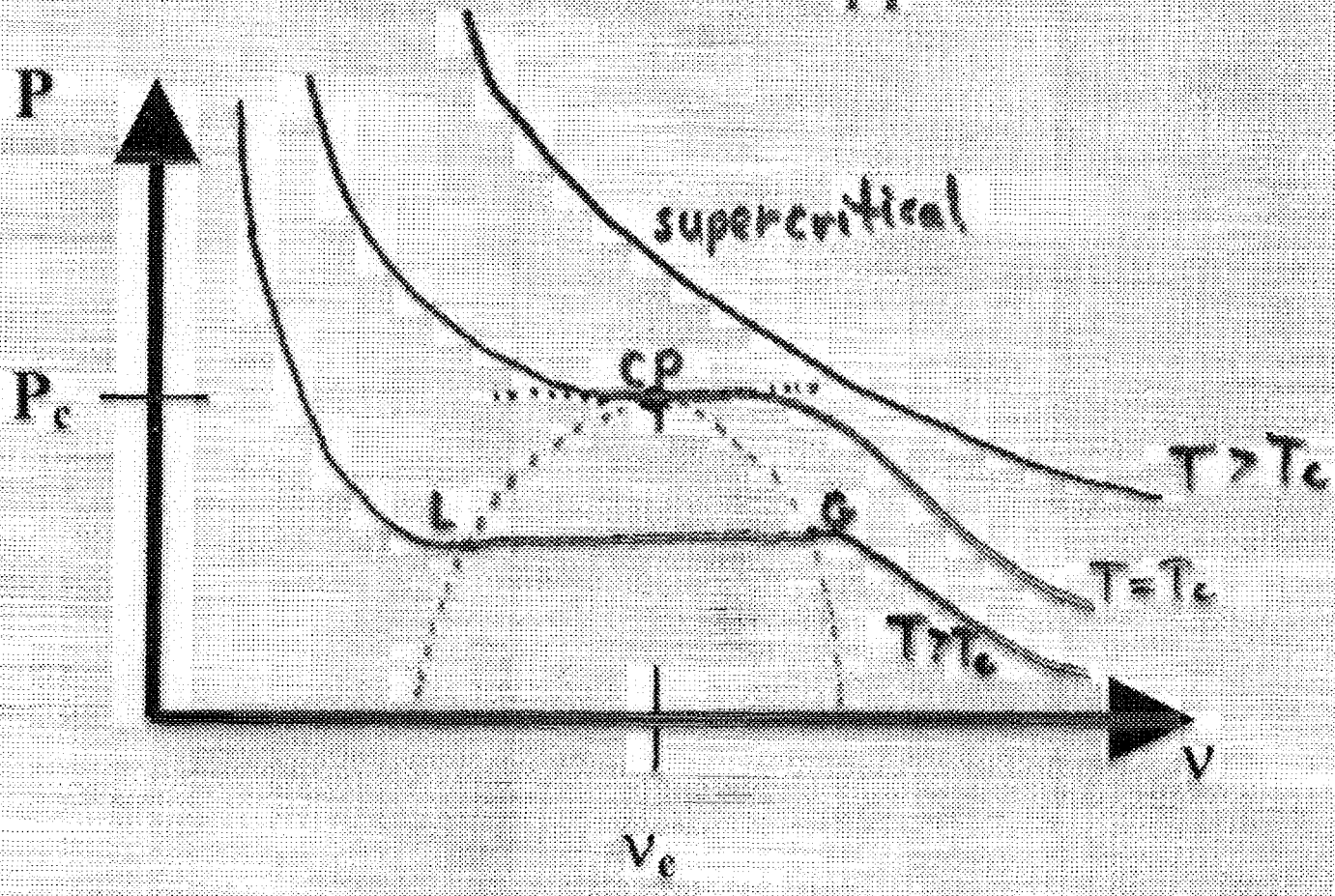

$$\kappa_T = -(1/v)(\partial v/\partial P)_T \rightarrow \infty$$

at (P_c, T_c, v_c).

Compressible Fluid Cell

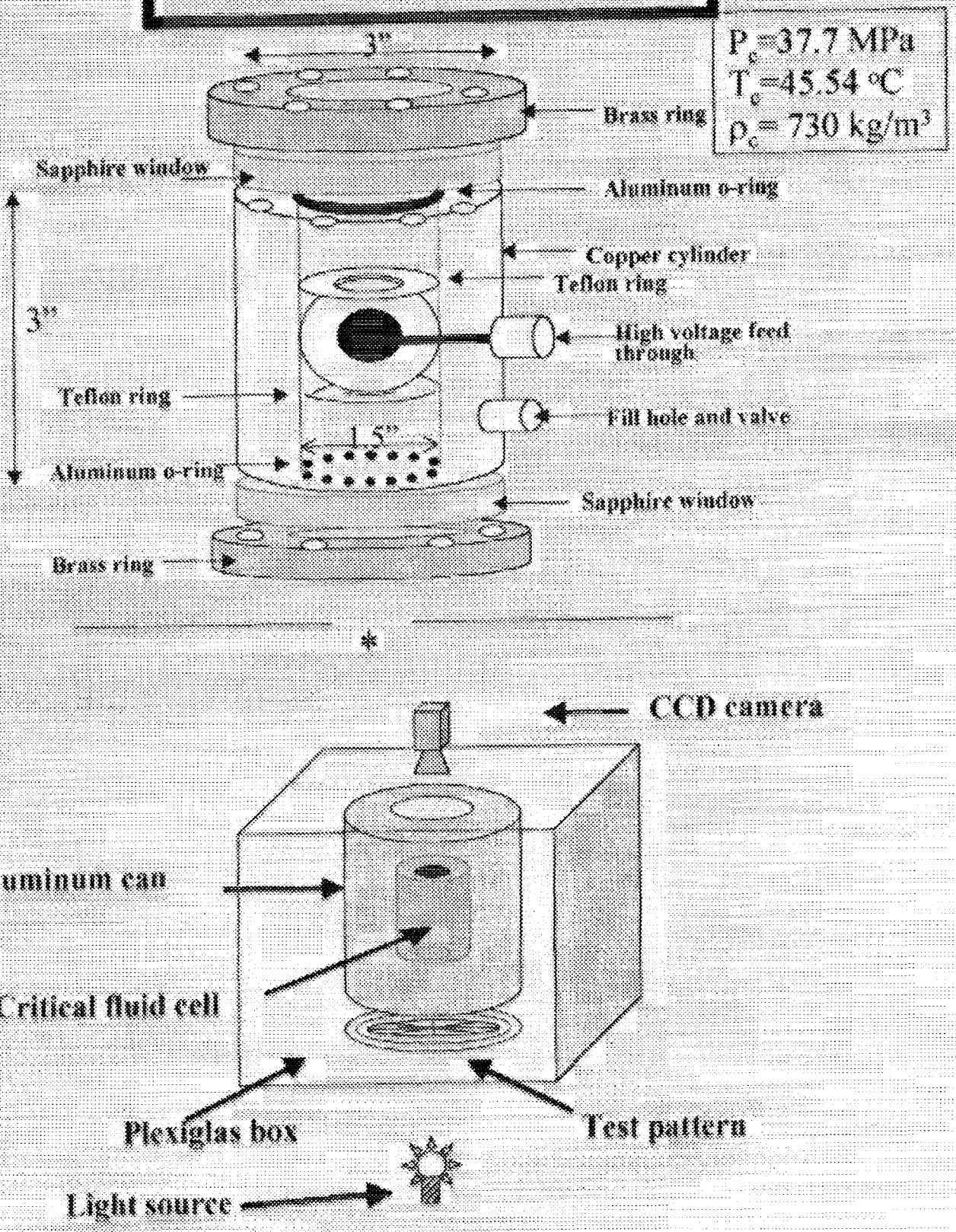

Effective Gravity

Close to T_c, $\dfrac{d\kappa}{d\rho} \approx const.$

Ponderomotive force: $f_e = \rho\left(\dfrac{\varepsilon_0}{2}\dfrac{d\kappa}{d\rho}\nabla\left(E^2\right)\right) = \rho . g_e$

where

$$g_e(r) = \frac{12\varepsilon_0}{\rho_c}\frac{\kappa_e - 1}{\kappa_e + 2}\frac{\Delta V^2 r_o^2 r_i^2}{d^2 r^5}$$

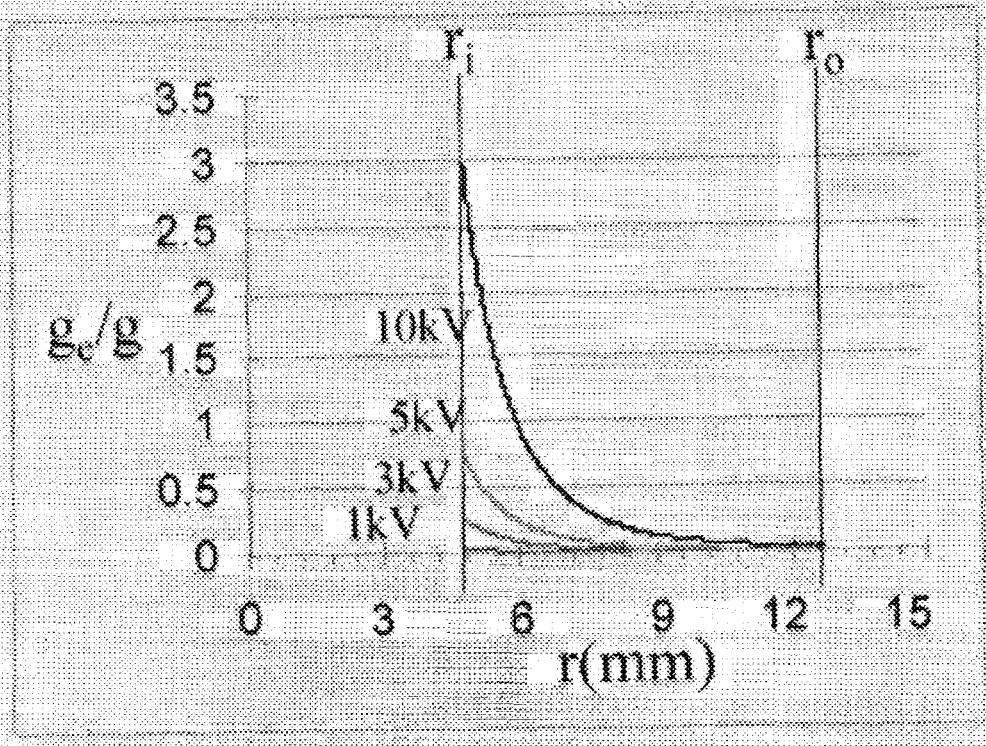

Plot of the variations of g_{eff} inside the capacitor gap for different ΔV values

Radial density gradient

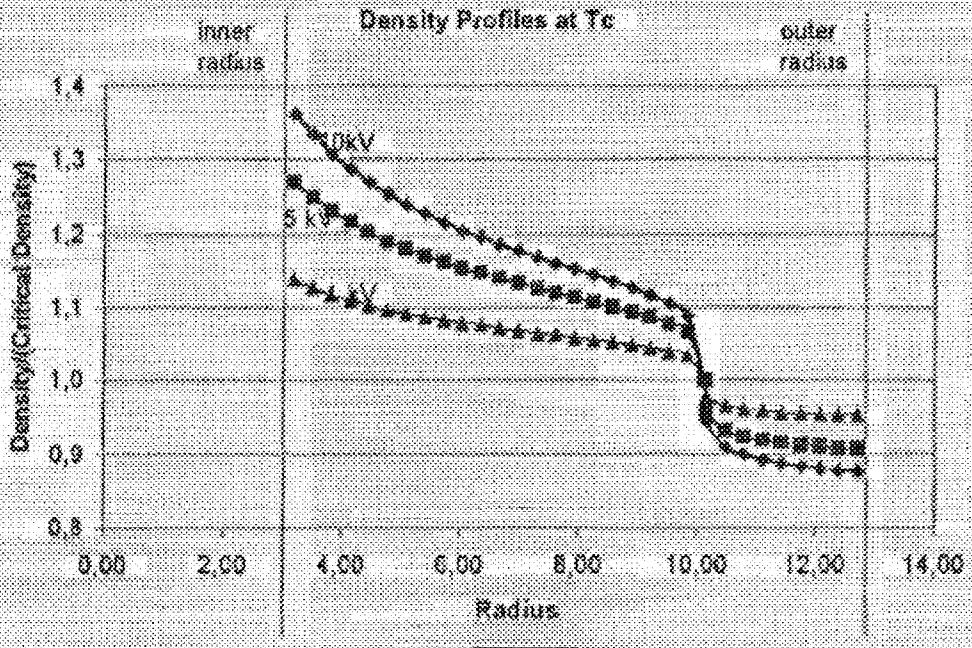

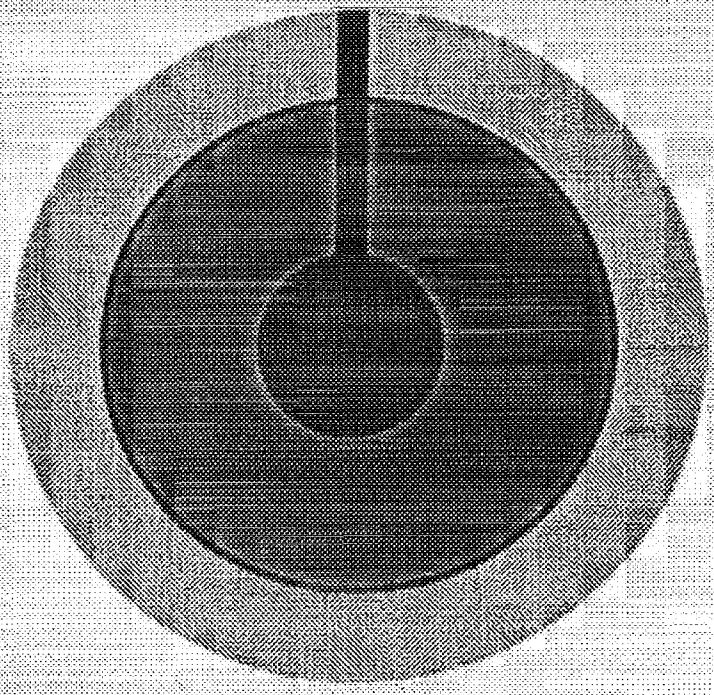

Procedures & Results

PROCEDURES:

- keep the voltage OFF(0V) or ON during a whole parabola
- after 5 to 8 s from the beginning of the parabola, switch ON the voltage or the inverse.
- apply a square wave high voltage oscillation during the parabola.

OBSERVATIONS:

⟹ closer to Tc, longer are the times needed by the fluid to become homogenous

⇨ **In 1g,**

* $T<T_c$: The meniscus is deflected by the high voltage

* $T \approx T_c$: -The large density gradient is deflected by the high voltage
-The critical fluid responds to the high voltage oscillations

⇨ **In 0g,**

* $T<T_c$: The high density fluid is attracted toward the inner sphere the lower density gas bubble is repelled by buoyancy

* $T \geq T_c$: - A deflection of 3pixels was detected near r_i
- Synchronous respond of the density gradient to the oscillating electric field (2s period)

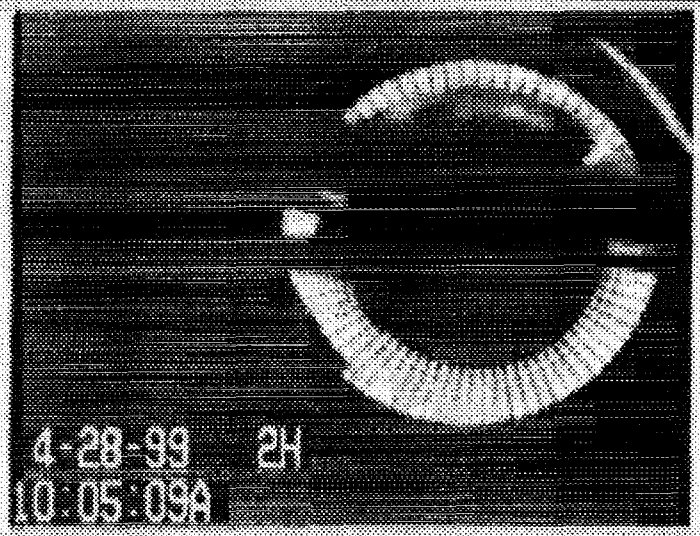

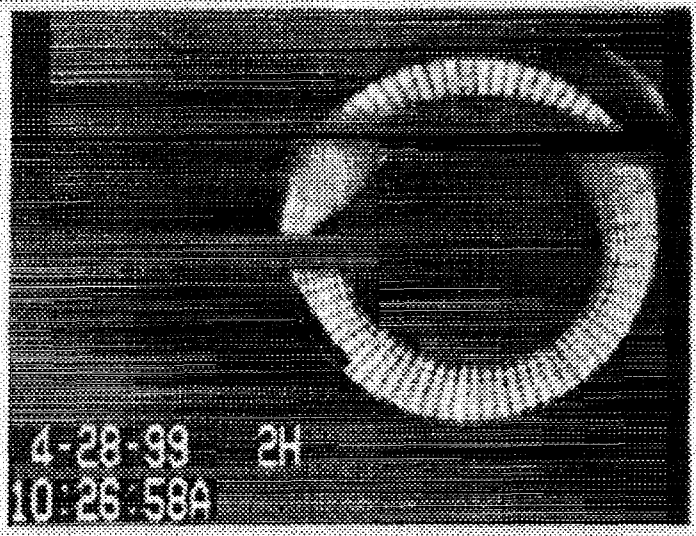

ΔT=1.7 °C and ΔV=3.5 kV

ΔT=0.4 °C and ΔV=4 kV

HORIZONTAL CONFIGURATION

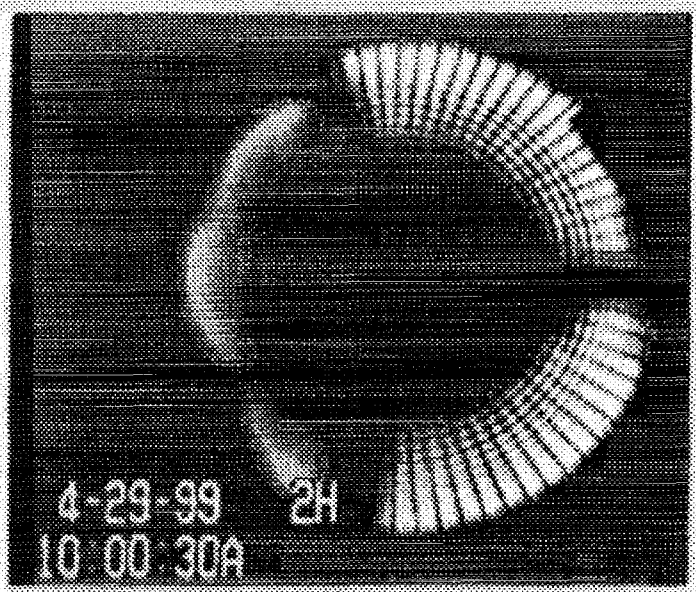

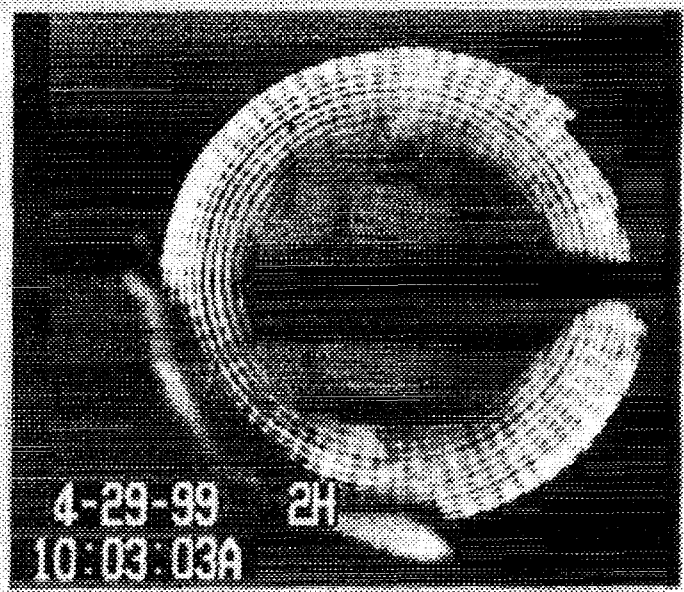

ΔT=4.94 °C and ΔV=0V

ΔT= 4.88 °C and ΔT= 5 kV

VERTICAL CONFIGURATION

Oscillating AC field

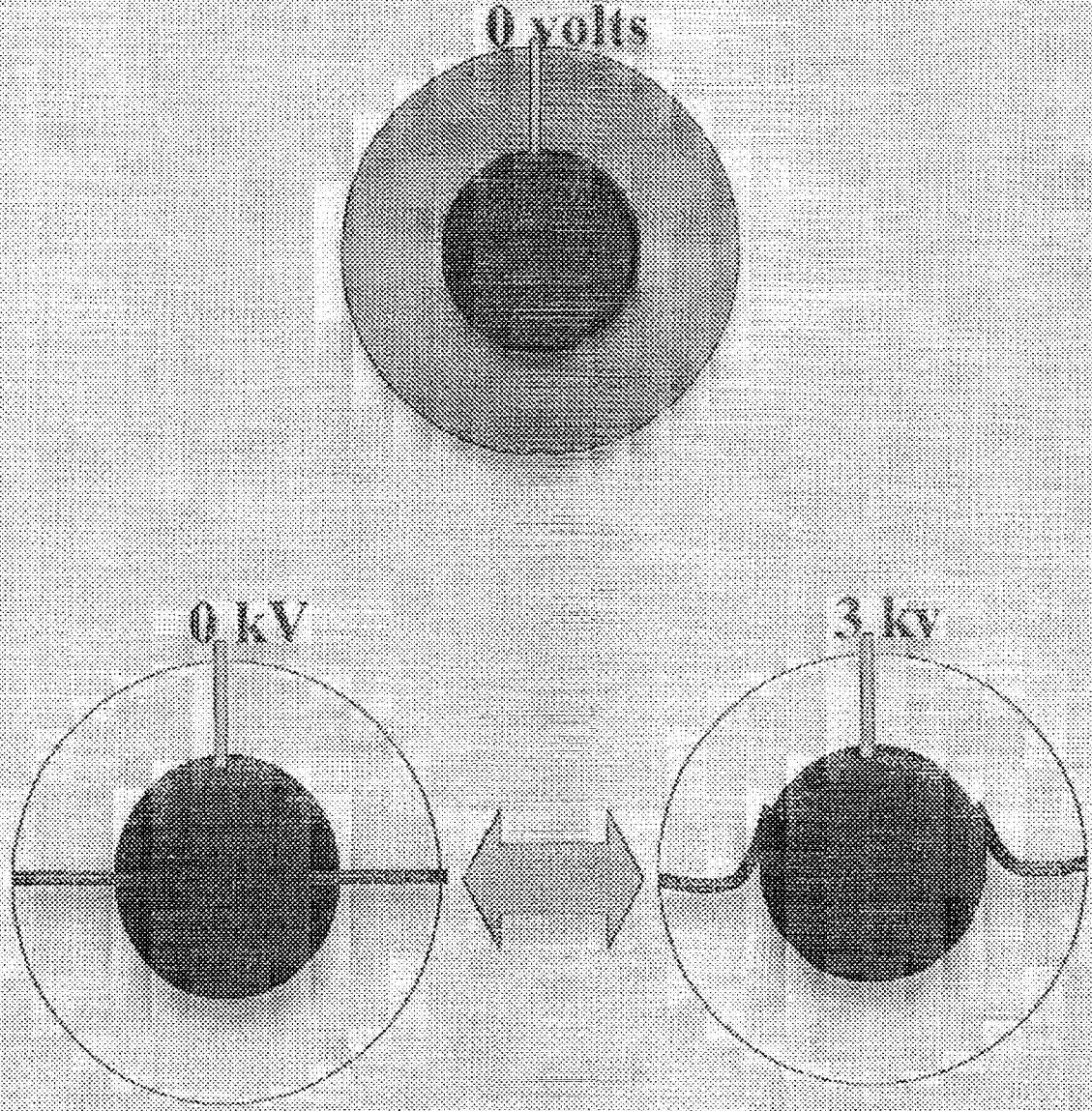

In a stratified fluid a fluid particle oscillates when it is displaced to a different vertical position.

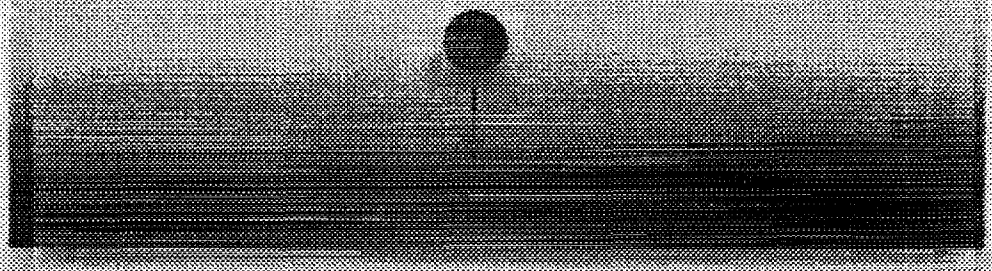

N is the natural frequency for internal wave oscillations.

$$N^2 = -\frac{g}{\rho_a}\frac{d\rho}{dr}.$$

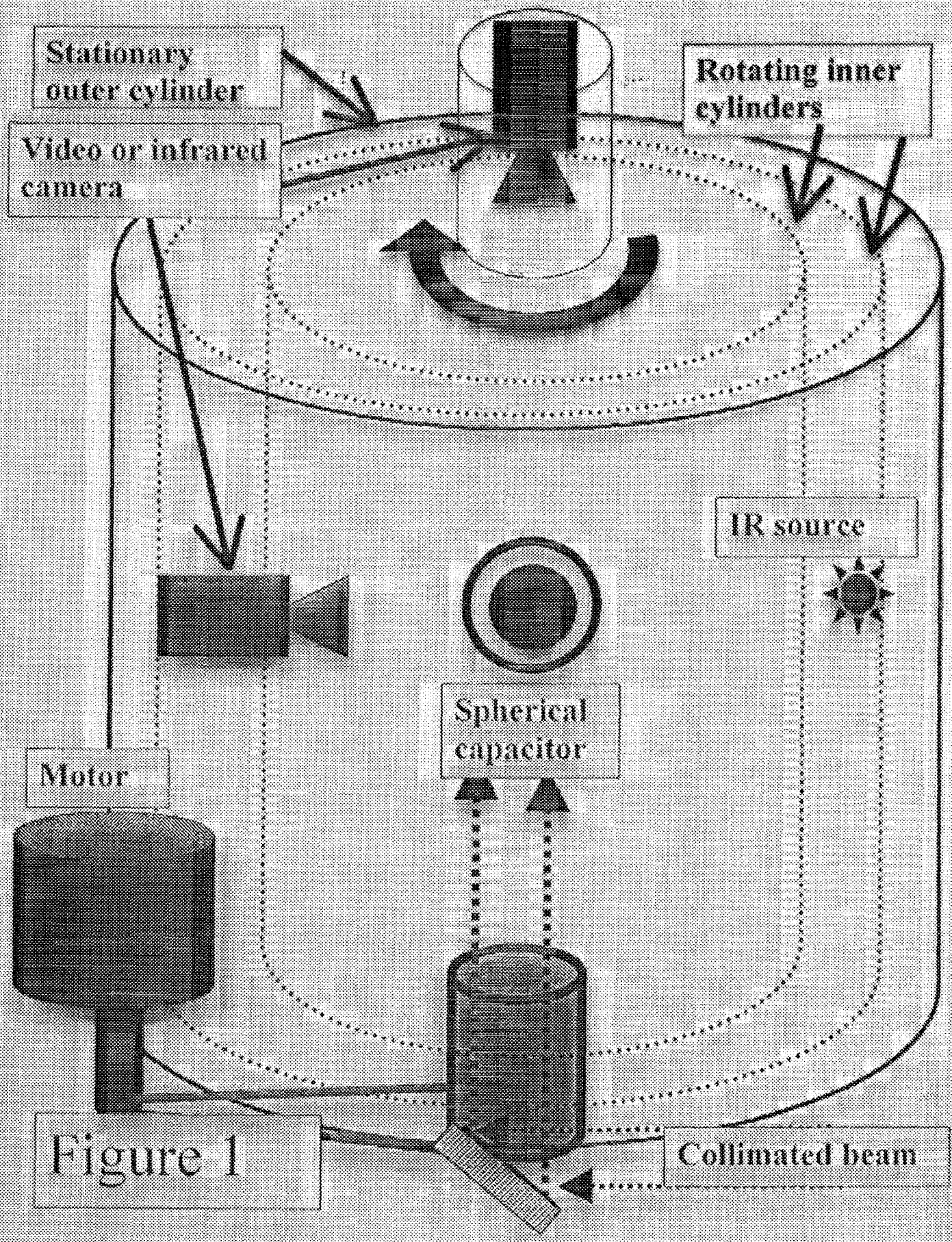
Stationary outer cylinder
Rotating inner cylinders
Video or infrared camera
IR source
Spherical capacitor
Motor
Collimated beam

Figure 1

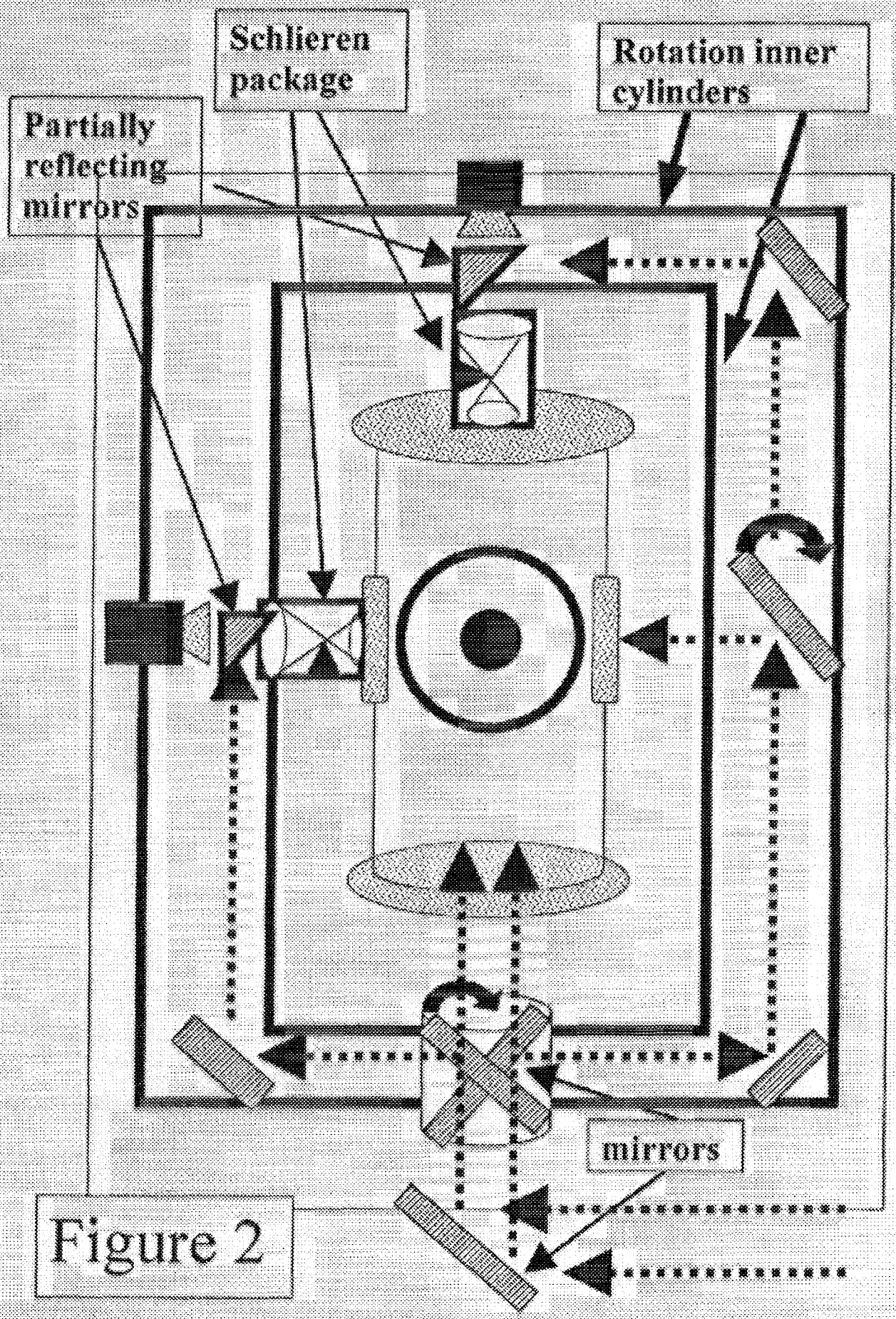
Schlieren package
Rotation inner cylinders
Partially reflecting mirrors
mirrors

Figure 2

Conclusion

- Studied traveling rolls in incompressible fluid in (nearly) spherical geometry in 1-g
- Observed compression by polarization force of near-critical fluid
- Observed repulsion of gas by polarization force of near-critical fluid
- Proposed system to study instability in the rotating frame

THE EVOLUTION OF TENSILE STRESSES IN UNIAXIAL ELONGATIONAL FLOWS OF DILUTE POLYMER SOLUTIONS SUBJECTED TO A KNOWN PRESHEAR HISTORY

Shelley L. Anna[1] and Gareth H. Mckinley[2]
[1]Division of Engineering and Applied Sciences, Harvard University, Cambridge, MA 02138,
[2]Department of Mechanical Engineering, M.I.T. Cambridge, MA 02139

INTRODUCTION

Complicated deformation histories make the extensional behavior observed in many strong flows of polymeric liquids extremely difficult to characterize precisely. The generation of a homogeneous uniaxial deformation flow in a microgravity environment is the goal of the Extensional Rheology Experiment (ERE). In advance of obtaining flight data from this experiment, we attempt to gain insight into the effect of complex deformation histories by imposing a known and controlled preshear history on a liquid bridge prior to imposing a nearly ideal uniaxial elongational flow in a Filament Stretching device. The instrument can apply either steady shear flow perpendicular to the stretching direction, or oscillatory squeeze flow parallel to stretching. We observe that oscillatory, parallel pre-straining accelerates strain hardening in dilute polystyrene-based polymer solutions, while steady, orthogonal preshearing delays strain hardening. These results are qualitatively consistent with the predictions of the finitely extensible nonlinear elastic (FENE) dumbbell model.

Recent experimental and numerical studies of stretching DNA chains by Chu & co-workers [1,2] show that the transient evolution of the polymeric microstructure is very sensitive to the initial configuration of the chains. Larson [3] recently reported results of Brownian dynamics simulations investigating the effect of preshearing on the molecular configuration of the chain. The simulations showed that preshearing reduces the occurrence of folds and kinks in the chain conformations observed during subsequent uniaxial elongation. Simple shear flow perpendicular to the stretching direction yielded a faster approach of the transient tensile stresses to the steady state plateau.

The filament stretching rheometer presents new possibilities for investigating preshearing effects more quantitatively than has previously been possible. We examine the effects of (*i*) steady shear flow perpendicular to the stretching direction, and (*ii*) oscillatory squeeze flow parallel to stretching, on the transient stress growth in a dilute polymer solution.

EXPERIMENTAL CONFIGURATION

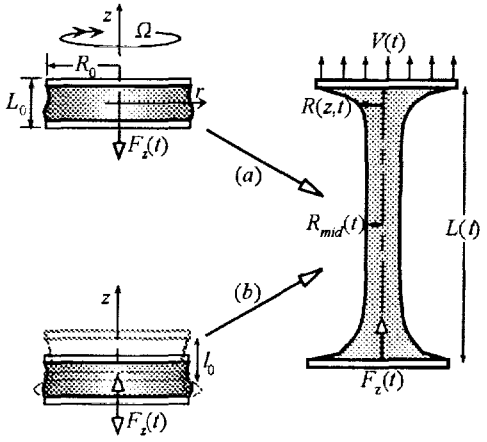

Figure 1. Schematic diagram of filament stretching with prior deformation imposed. Pre-deformation is either (*a*) orthogonal, rotational preshearing, or (*b*) parallel, oscillatory pre-straining.

In a filament stretching device such as that shown in Figure 1, a small cylindrical fluid sample fills the gap between two circular endplates, which are then moved apart using an open-loop control strategy [4] such that the mid-filament diameter decreases exponentially:

$$D_{mid}(t) = D_0 \exp\left(-0.5\dot{\varepsilon}_0 t\right), \quad (1)$$

where D_0 is the plate diameter, and $\dot{\varepsilon}_0$ is the strain rate. The tensile force on the endplate, $F_z(t)$ is monitored along with the diameter and, after applying an appropriate force balance on the fluid column to account for surface tension and gravity [5] the dimensionless extensional viscosity, or Trouton ratio Tr, is computed from the raw quantities:

$$Tr(\varepsilon) \equiv \frac{\overline{\eta}^{+}(\dot{\varepsilon}_0, t)}{\eta_0} = \frac{\left[\tau_{zz} - \tau_{rr}\right]}{\eta_0 \dot{\varepsilon}_0} = \frac{F_p(t)}{\eta_0 \dot{\varepsilon}_0 \pi \left(D_{mid}(t)/2\right)^2}, \quad (2)$$

where $\overline{\eta}^{+}$ is the transient extensional viscosity, and η_0 is the zero-shear-rate viscosity. The Trouton ratio is measured as a function of the deformation in the filament, or the Hencky strain, ε, which is computed from the mid-filament diameter profile, $\varepsilon = -2\ln\left(D_{mid}(t)/D_0\right)$. Finally, the Trouton ratio is measured as a function of the dimensionless stretch rate, or Deborah number, where λ_Z is the Zimm (longest) relaxation time of the fluid determined from linear viscoelastic measurements.

Our filament stretching device has been modified to impose the two types of pre-deformation history mentioned earlier. To achieve oscillatory squeeze flow parallel to the stretching direction, a cyclic motion profile is downloaded to the linear motors that control the endplates. To generate a steady shear flow in which the principal flow direction is orthogonal to the direction of stretching, the upper plate is rotated using a DC motor. The range of rotation rates attainable is approximately $1.5 \le \Omega \le 30$ rad/s.

RESULTS

Filament stretching experiments were carried out using a dilute polystyrene solution at a fixed Deborah number, $De \stackrel{a}{=} 11$, and a range of oscillatory or steady preshear rates. The value of De was chosen to minimize effects of sagging due to gravity on the stretching filament under $1g$, and also to maximize the Hencky strain achievable within the physical limits of the rheometer. At this Deborah number, a final Hencky strain of $\varepsilon_f \stackrel{a}{=} 5.6$ is realized, allowing the transient tensile stresses to approach a steady state value. Transient tensile forces are shown in Figure 2 for the oscillatory pre-straining experiments. The tensile force profiles measured during subsequent stretching show similar qualitative shapes, but the quantitative response of the fluid shows a 'memory' of the pre-oscillation frequency.

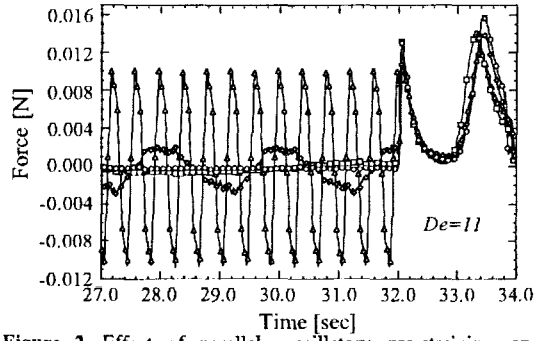

Figure 2. Effect of parallel, oscillatory pre-straining on the transient tensile forces for PS025. (○, $Wi_{ij} = 0$;□, $Wi_{ij} = 2.39$; ◇, $Wi_{ij} = 12.2$; △, $Wi_{ij} = 61.1$)

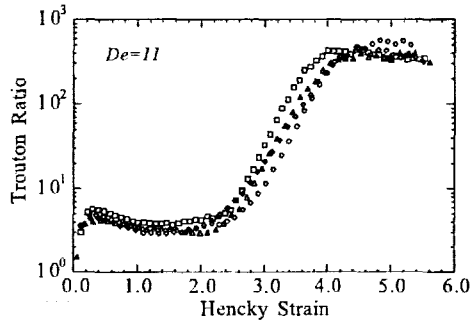

Figure 3. Effect of parallel, oscillatory pre-straining on the transient extensional viscosity of PS025. (○, $Wi_{ij} = 0$; □, $Wi_{ij} = 2.39$; ◇, $Wi_{ij} = 12.2$; △, $Wi_{ij} = 61.1$)

The evolution in the transient Trouton ratios computed from the measured force and radius profiles are shown in Fig. 3. Without preshearing, dilute polymer solutions yield transient Trouton ratios that are nearly independent of Deborah number. The shape of the Trouton ratio curve is dependent on the pre-oscillation frequency. At all frequencies, the rate of stress growth is greater than it is in the no preshear case, and the steady state plateau value is reduced; however, the dependence is not monotonic. Preliminary calculations show that this non-monotonicity is consistent with the predictions of the FENE constitutive equation.

REFERENCES

[1] D.E. Smith and S. Chu, *Science* (1998) 281 1335-1340.

[2] R.G. Larson, H. Hu, D.E. Smith and S. Chu, *J. Rheol.* (1999) 43 (2) 267-304.

[3] R.G. Larson, (2000) preprint for submission to *Rheol Acta.*

[4] S.L. Anna, C. Rogers and G.H. McKinley, *J. Non-Newtonian Fluid Mech.* (1999) 87 307-335.

[5] P. Szabo, *Rheol. Acta* (1997) 36 277-284.

NASA/CP—2000-210470

Extensional Rheometry of Polymer Solutions & The Uniaxial Elongation of Viscoelastic Filaments

Gareth H. McKinley
Fluid Mechanics Laboratory,
Department of Mechanical Engineering, M.I.T.

What Makes a Fluid Sticky ??

Slimy...

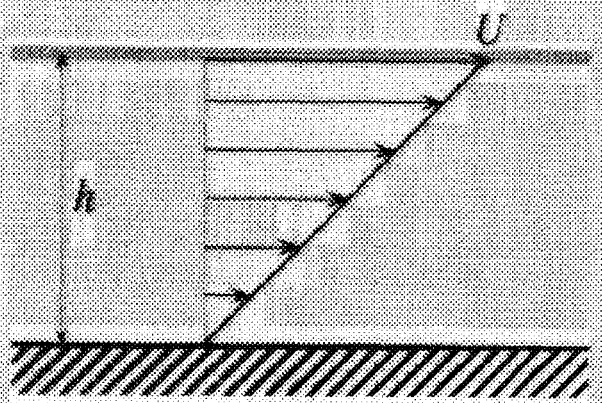

$$\tau_{yx} = \eta(\dot{\gamma})\dot{\gamma}_{yx}$$

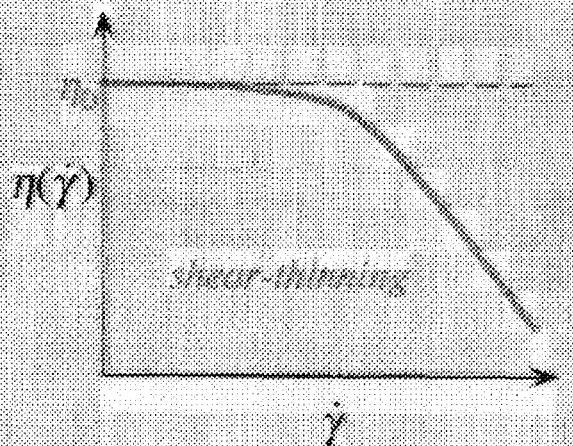

Sticky...

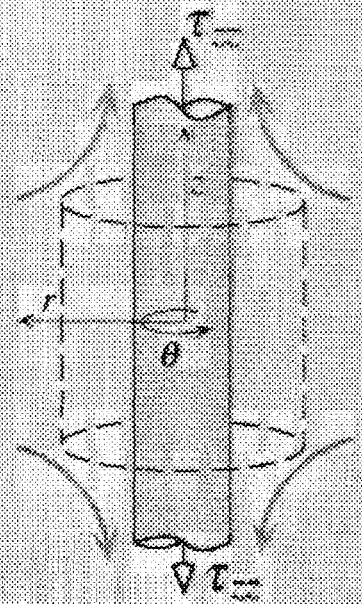

$$\tau_{zz} - \tau_{rr} = \overline{\eta}(\dot{\varepsilon})\dot{\varepsilon}_{zz}$$

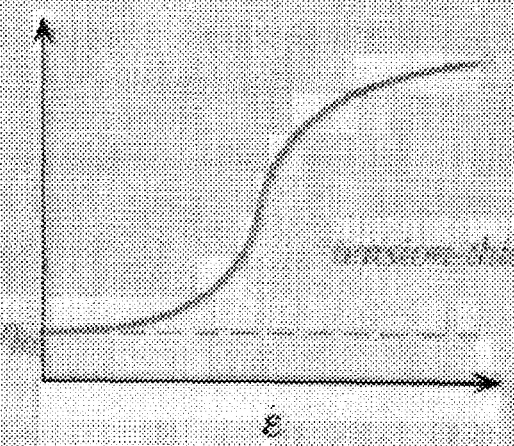

Shear History Extensional Rheology Experiment

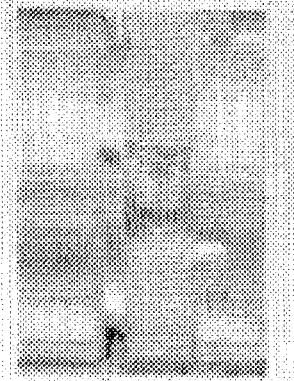

Breadboard demonstration of test fluid deployment and stretching in microgravity

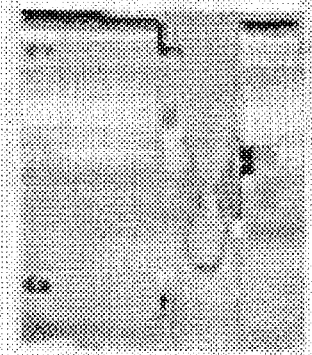

Fluid Deployment

Fluid Sagging in 1g

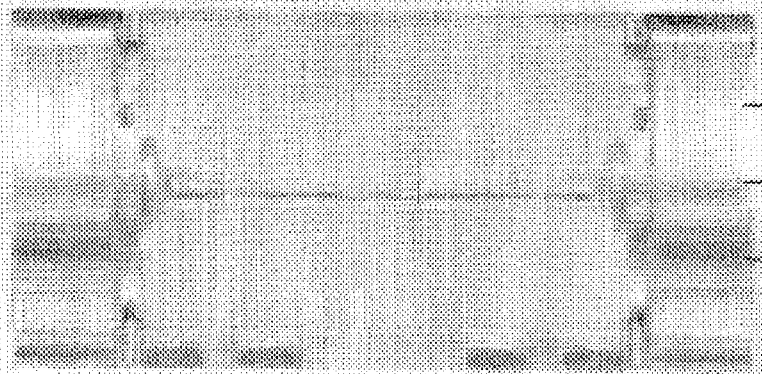

Stretching of a Polymeric Liquid Bridge in Microgravity

NASA/CP—2000-210470

NASA/CP—2000-210470

ACCESSIBLE PARAMETER SPACE FOR A SUCCESSFUL FISER EXPERIMENT

QUESTION: What fluids can be tested in a filament stretching device?

ANSWER: Newtonian, Dilute & Conc. Polymer Solutions, Associating Polymers, Suspensions, ...

CAVEAT: Fluid cannot be stretched too slowly OR too quickly

Sagging $Bo/Ca > 1$

$$De > De^{*}_{sag} = \lambda_2\left(\rho g R_0/\eta_0\right)$$

$\lambda_2 \propto M_w^{3/2}$ $\quad$ $\eta_0 = \eta_s + \eta_p$, $\eta_p \propto M_w^{1/2}$

(becomes large for very elastic fluid)

Endplate Instability

Filament loses axisymmetry; thin fibrils form and grow radially outward

* fractal-like tip splitting and branching

$$\tau > \tau_c(De, G, \beta, Ca) \equiv \eta\dot{\epsilon}$$

(must be computed numerically for FENE models)

$\eta_\infty \propto \eta_p L^2 \propto M_w^{3/2}$

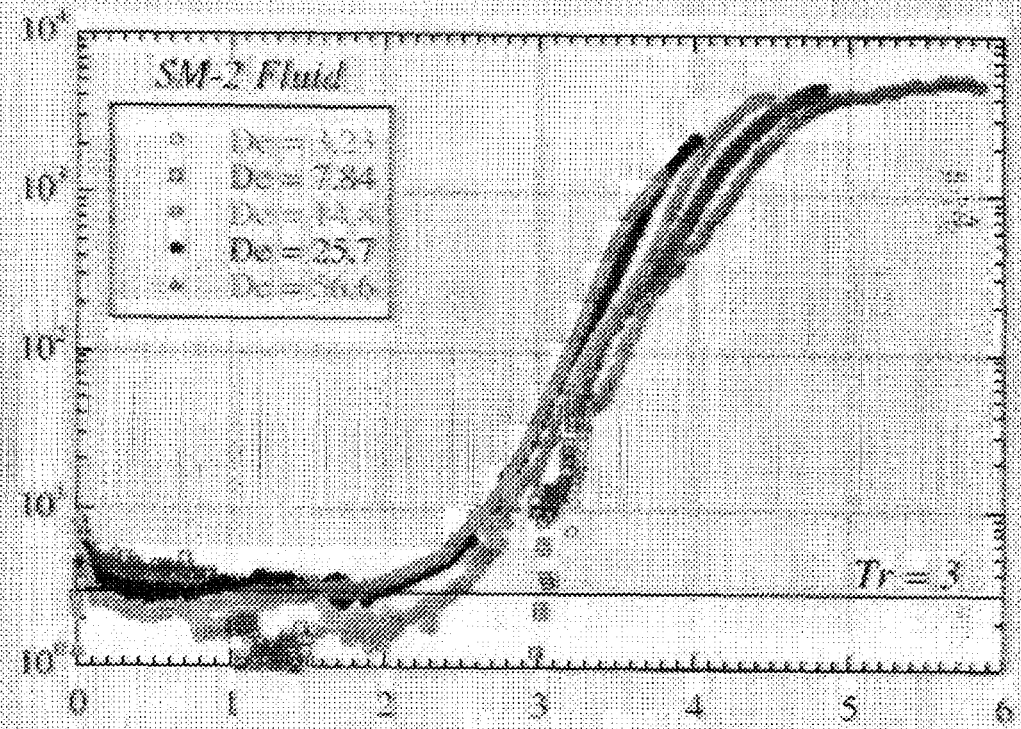

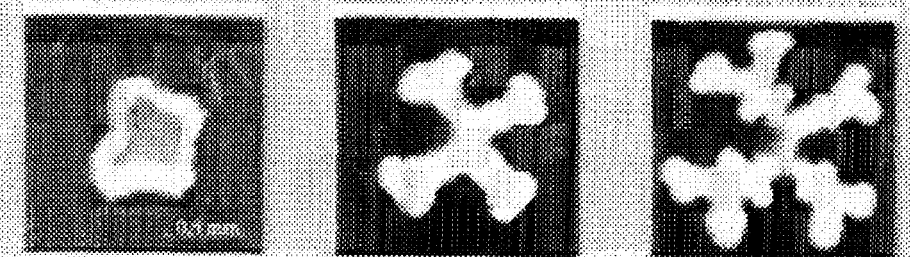

(Spiegelberg & McKinley, *JNNFM* 1996;
Anna, Spiegelberg & McKinley, *Phys. Fluids* 1997)

Combined Preshear/Transient Elongation

- Impose a controlled *Preshear History* on the cylindrical fluid sample before imposing a controlled exponential stretching (type II)

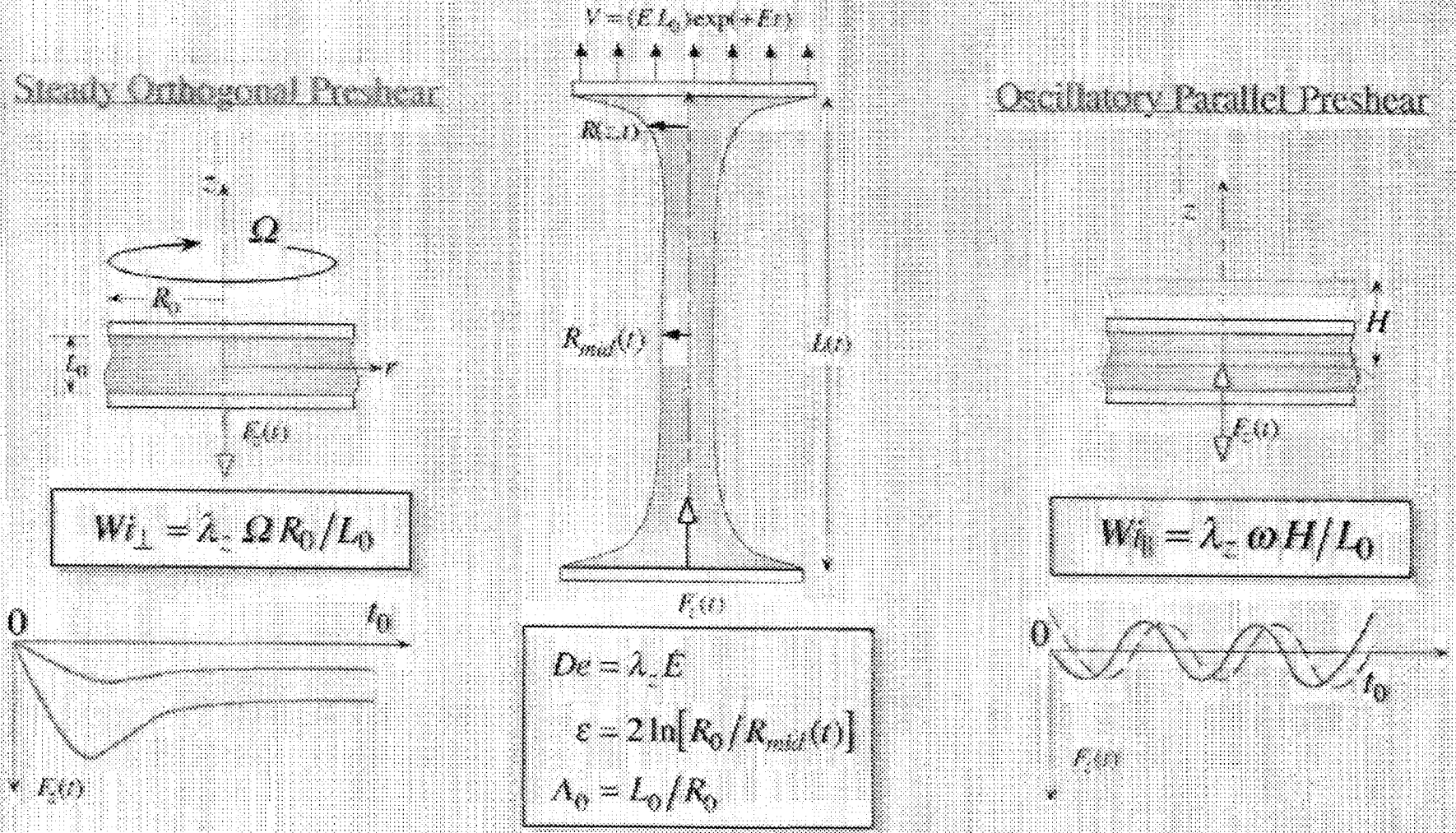

- Parallel plate geometry selected over cone-and-plate to eliminate large additional *uncontrolled* shear arising from reverse squeeze-flow at start of stretch.

Previous Observations of Effect of Shear History

Bulk Rheometry

Shear history effects thought to explain behavior observed in turbulent flows, etc.

- *James, McLean and Saringer* (1987)
- *Vissmann and Bewersdorff* (1990)

Measured apparent $\bar{\eta}$ in inhomogeneous orifice flow as function of preshear in channel or concentric cylinders

Observations: $\bar{\eta}_{app} \uparrow$ and $\dot{\epsilon}_c \downarrow$ as $\dot{\gamma} \uparrow$

CAN WE SIMPLIFY AND CONTROL PRE-SHEAR HISTORY?

Microrheometry

- *Perkins, Smith and Chu* (1997) observed evolution of individual chain conformations in planar elongational flow.

"...differences in [onset of stretching] imply a *sensitive dependence on the polymer's initial conformation*...these variations arise directly from the *multitude of accessible conformations at equilibrium*..."

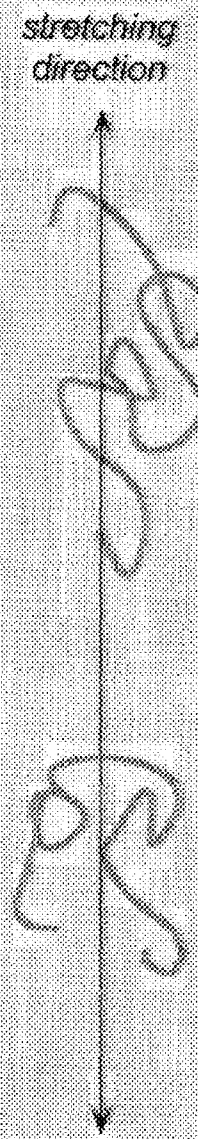

Molecular "Pre-destination"

Larson, Hu, Smith, Chu (1999)

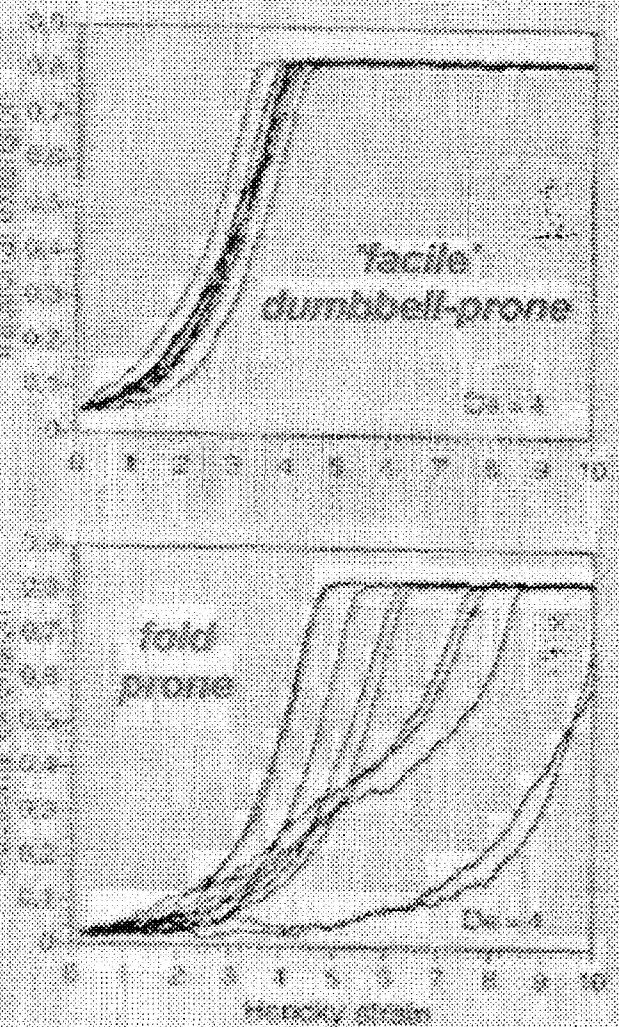

WHAT HAPPENS IF WE CONTROL THE INITIAL CHAIN CONFIGURATION?

Force Balance Analysis of Pre-Sheared Filament

Force balance of Szabo (1997)

$$\frac{F_z(t)}{\pi R_0^2} = (\tau_{zz} - \tau_{rr})_{mid} + \frac{1}{2}(\tau_{rr} - \tau_{\theta\theta})_{mid} + \frac{1}{2}\frac{d}{dz}(r\tau_{rz}) + \frac{1}{2}\frac{\rho V_0^2}{\pi R_0^2}\frac{a}{R_{mid}}\left(1 + R_{mid}^2 R_{mid}^{-2}\right) - \textit{inertial terms}$$

axial stress *hoop stress* *shear stress* *body force* *surface tension*

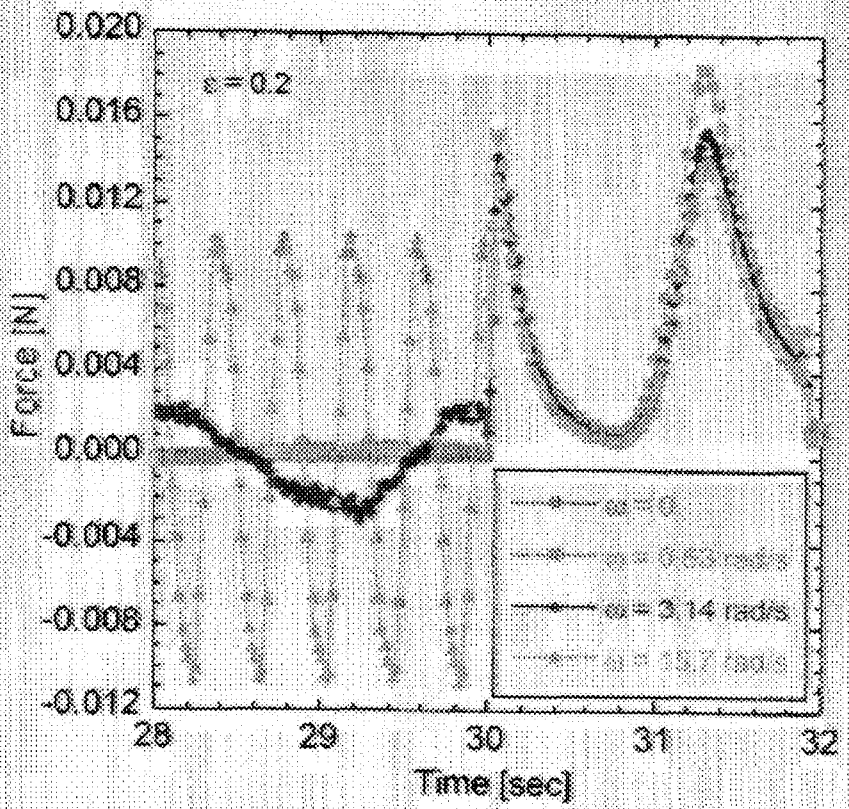

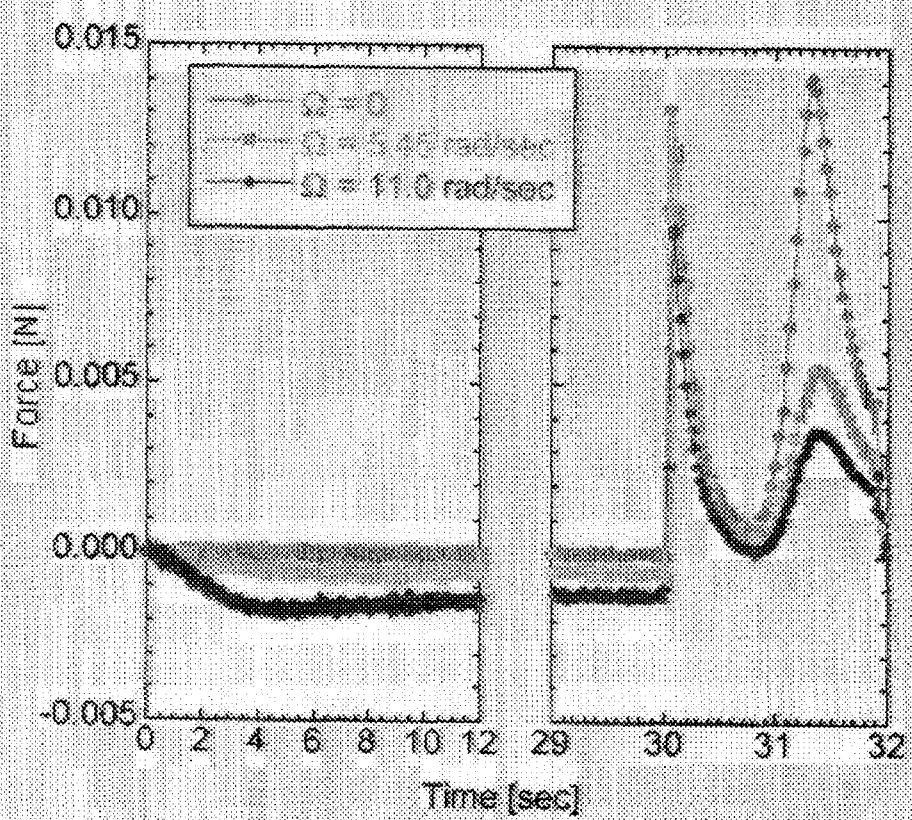

Effect of Steady Torsional Flow on Extensional Rheology

- Steady shear flow pre-aligns molecules *orthogonal to stretch direction*

  ⇒ Larger Hencky strain required to align and unravel chains during stretching

- Strain hardening is *delayed* relative to no preshear case

- Amount of delay monotonically increases with increasing rotation rate

  (until spiral instability occurs)

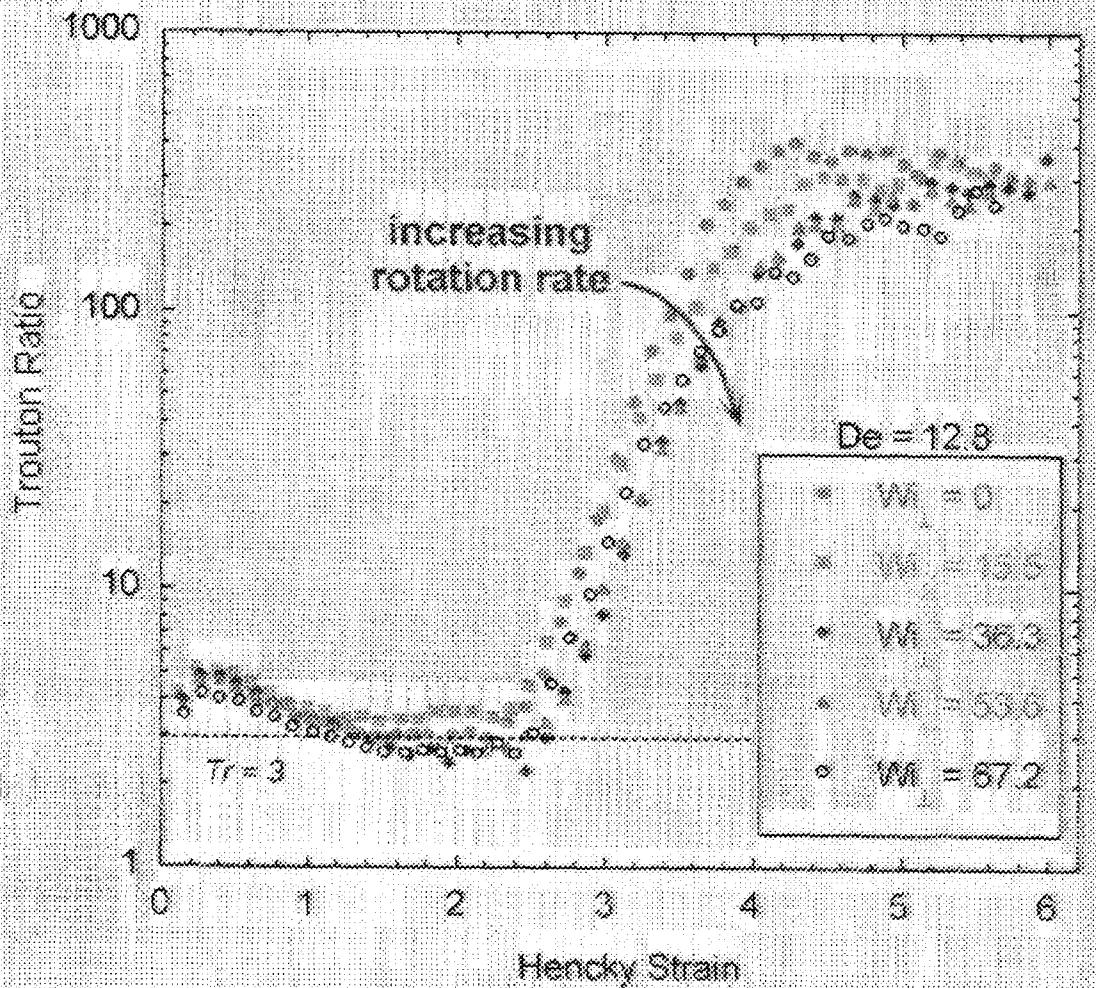

Effect of Oscillatory Squeeze Flow on Extensional Rheology

- Oscillatory squeezing pre-aligns molecules *in stretch direction*
- Strain hardening is accelerated relative to no preshear case
- Lowest frequencies and largest amplitudes lead to largest acceleration

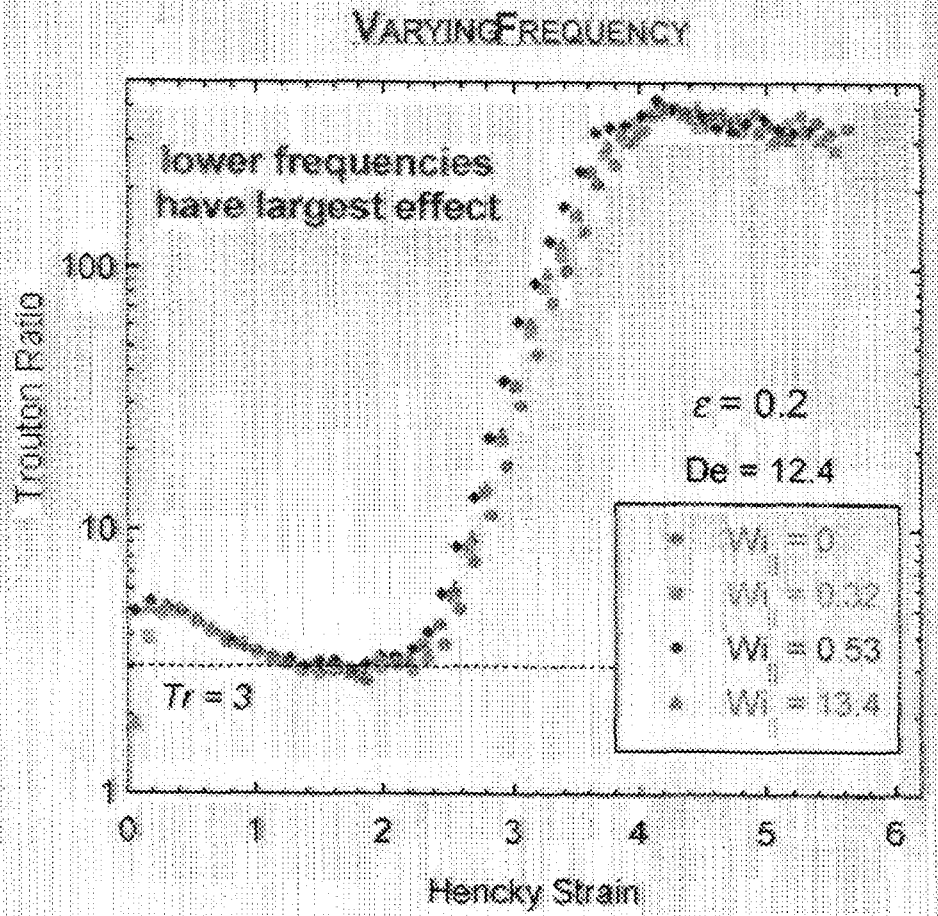

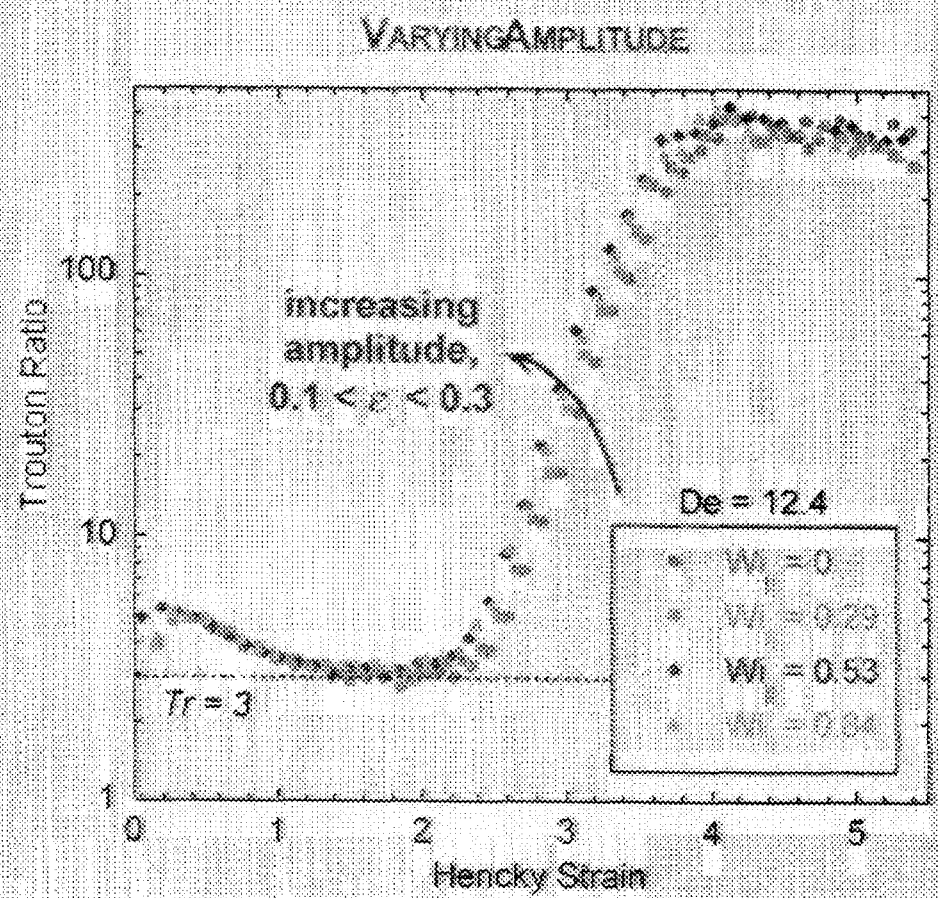

Evaluating Effect of Oscillatory Squeeze Flow Using FENE-P Model

- Model polymer chains as *finitely extensible, nonlinear* springs
- Incorporate oscillatory squeezing using known squeeze flow solution *(lubrication approximation)*
- Excellent agreement of trends with experimental observations

$$\lambda_1 \mathbf{A}_{(1)} = \mathbf{I} - f(\mathrm{tr}\mathbf{A})\mathbf{A}$$

$$f(\mathrm{tr}\mathbf{A}) = 1/(1 - \mathrm{tr}\mathbf{A}/L^2)$$

$$\tau_p = \frac{\eta_p}{\lambda_1}[f(\mathrm{tr}\mathbf{A})\mathbf{A} - \mathbf{I}]$$

$$\tau = \tau_p + \tau_s$$

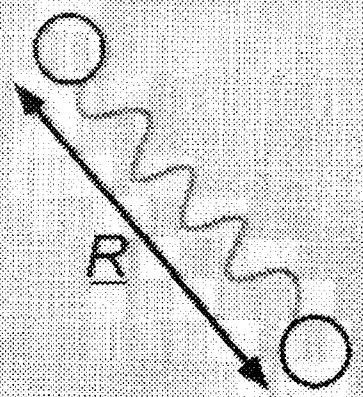

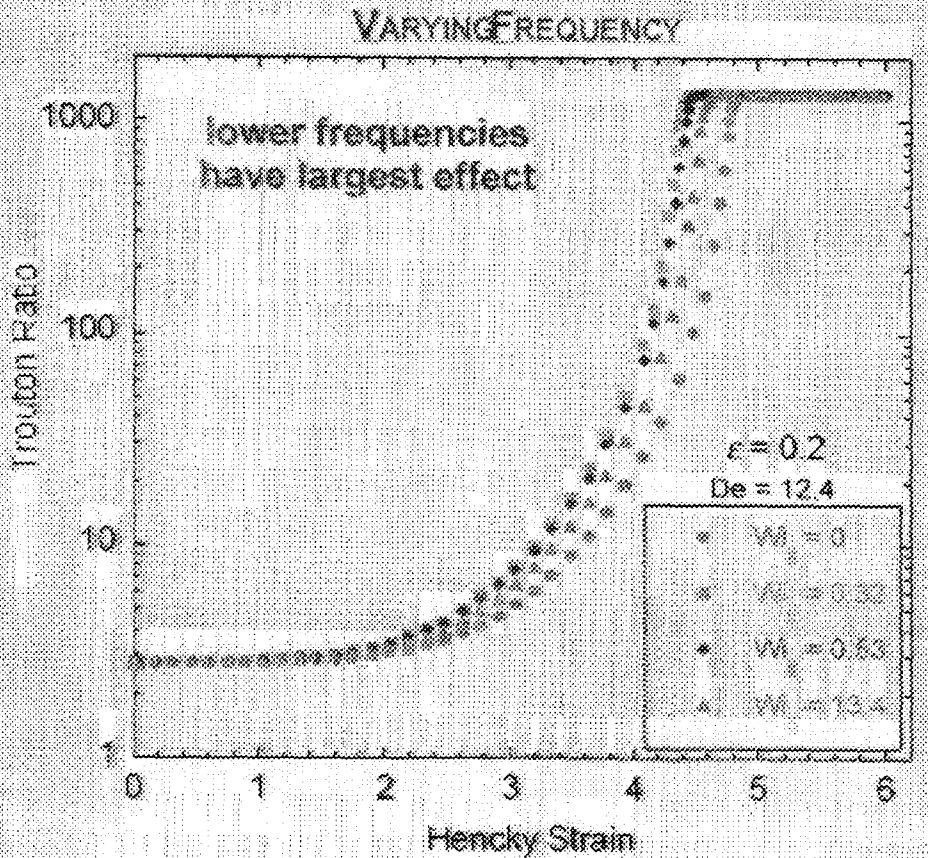

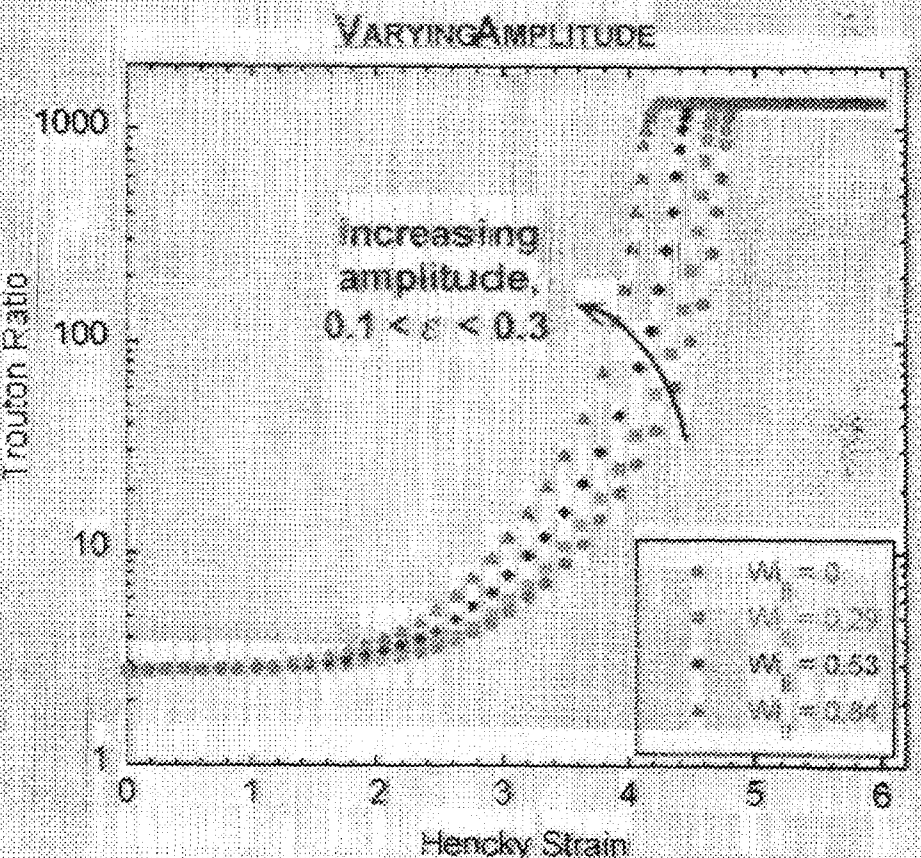

THE MICROFILAMENT RHEOMETER

(Bazilevsky, Entov, Rozhkov; *Euro. Rheology. Conf.* 1990; Entov & Hinch, *JNNFM* 1997)

- A quantitative version of the 'thumb & forefinger' test!
- Allow fluid filament to deform and fail *on its own time scales (elasto-capillary thinning)*

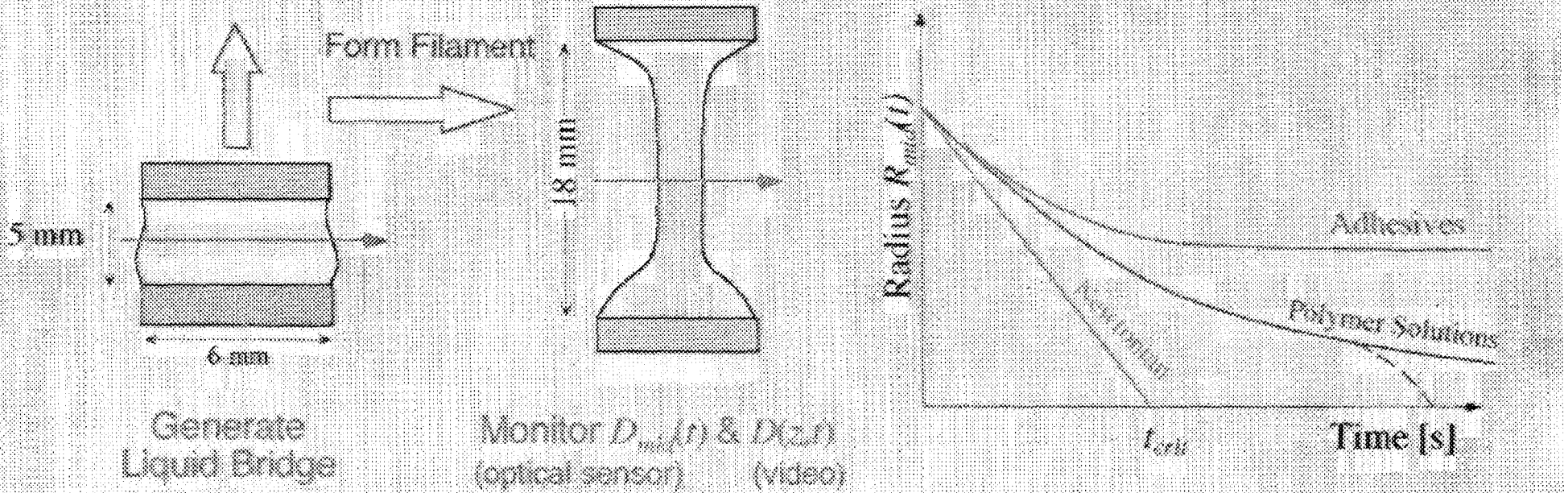

- *Shape of $D_{mid}(t)$ curve* and *time to breakup* can provide rheological information about a fluid's extensional properties at large fluid strains.

• Viscous Newtonian Fluid	$R_{mid}(t)/R_0 \sim (\sigma/\eta_0 R_0)(t_c - t)$
• Viscoelastic fluid (intermediate times)	$R_{mid}(t)/R_0 \sim (GR_0/\sigma)^{1/3} \exp(-t/3\lambda_1)$
• Viscoelastic fluid (long times)	$R_{mid}(t)/R_0 \sim (\sigma/\bar{\eta}R_0)(t_c - t)$

Filament Failure in a MicroFilament Rheometer

Styrene Oligomer

$$Bo = \frac{\rho g R_0^2}{\sigma} = 19$$

$$t^* = (\eta_0 R_0 / \sigma) = 8.5\text{sec}$$

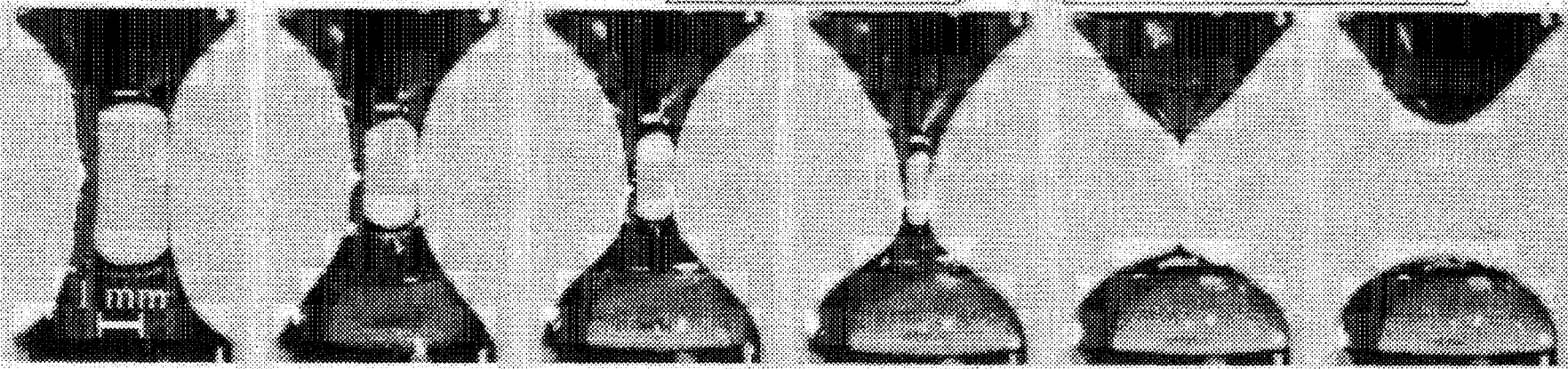

$t = 0$ s $\quad t = 2.1$ s $\quad t = 4.2$ s $\quad t = 6.3$ s $\quad t_{crit} = 8.6$ s $\quad t = 10.5$ s

SM-1 Fluid: 0.05 wt.% 2×10^6 g/mol polystyrene in styrene oligomer

$$t^* = 9.8\text{sec}$$

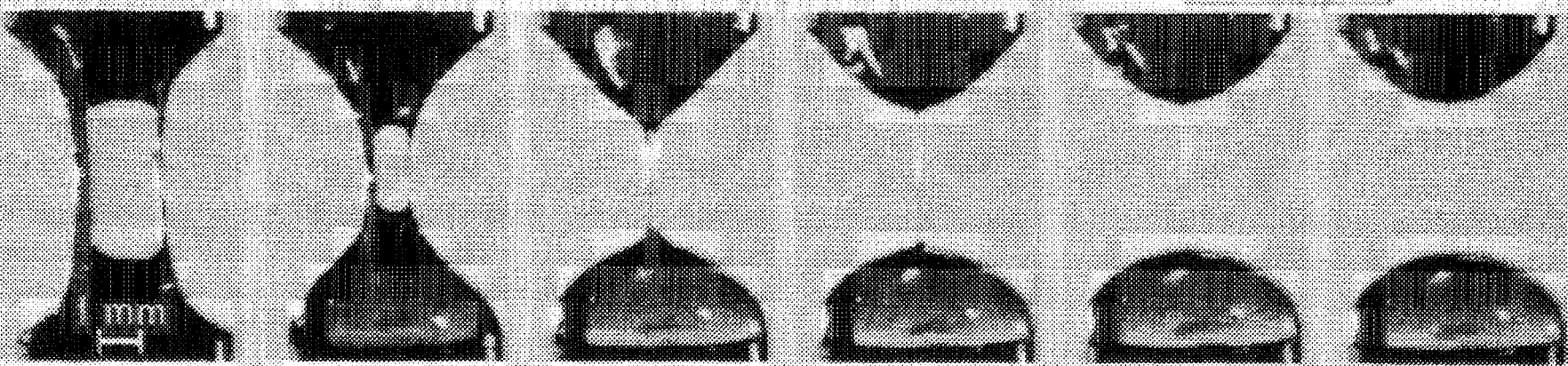

$t = 0$ s $\quad t = 8.5$ s $\quad t = 17.0$ s $\quad t = 25.5$ s $\quad t = 34.0$ s $\quad t_{crit} = 42.5$ s

The Newtonian Fluid

- Plateau (1873); Rayleigh (1892)

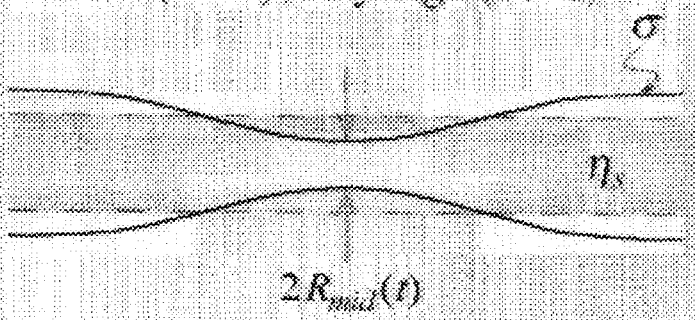

- Capillary velocity: $\frac{\sigma}{\eta_s}$ [m/s]
- Axial Force Balance:

$$3\eta_s\left\{\frac{-2}{R_{mid}(t)}\frac{dR_{mid}(t)}{dt}\right\} \sim \frac{\sigma}{R_{mid}(t)}$$

viscous stress ~ *capillary pressure*

Nonlocality
(similarity solution: Papageorgiou, 1995)

$$R_{mid}(t) = 0.0709\frac{\sigma}{\eta_s}(t_c - t)$$

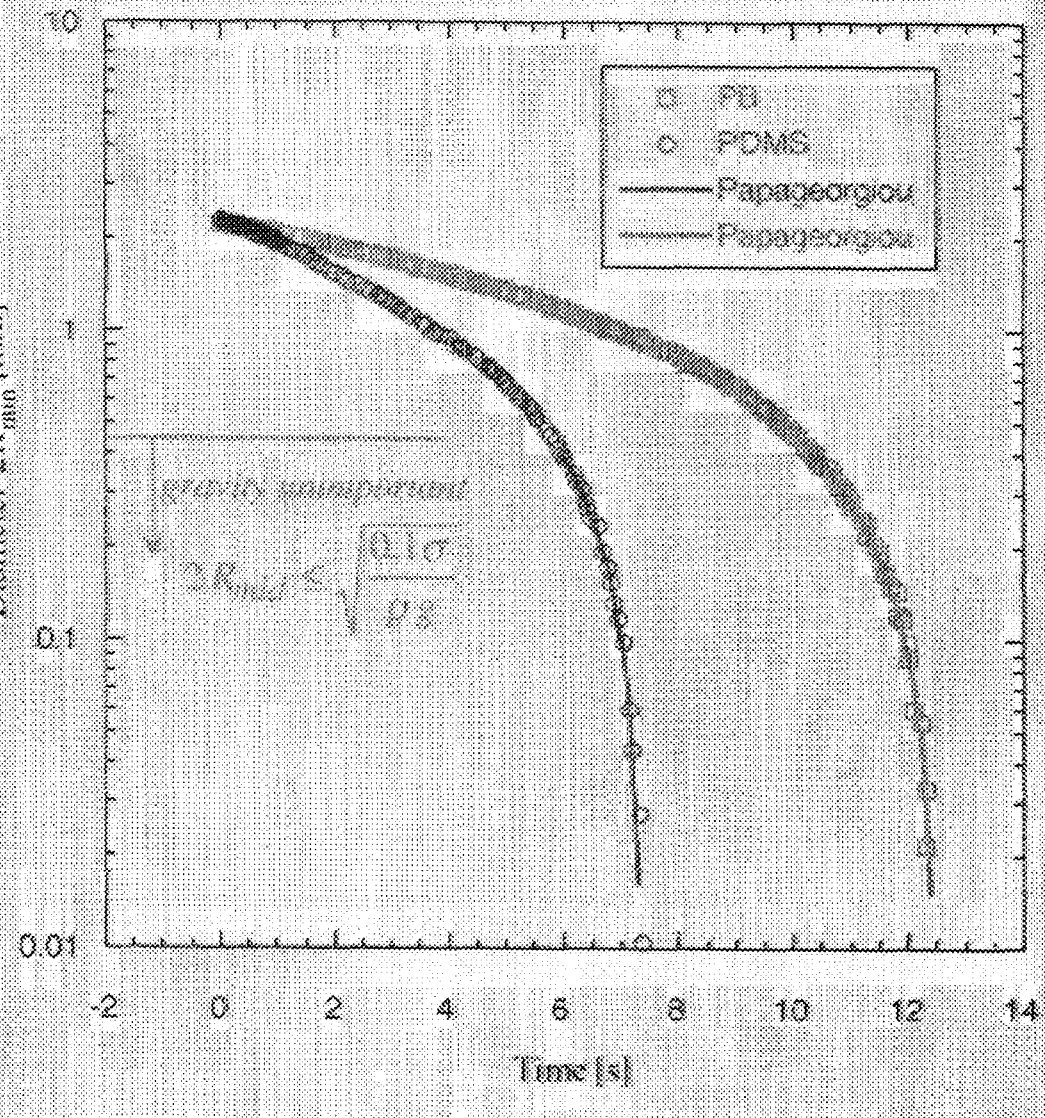

McKinley & Tripathi, *J. o. R.* 2000

The Role of Gravity

- Straightforward to incorporate using Lagrangian formulation of Renardy (1995)

$$3\eta_s\left(-\frac{2}{R}\frac{\partial R}{\partial t}\right)=\frac{f(t)}{\pi R^2}-\frac{\sigma}{R}-\rho g z \longrightarrow \text{Bond Number: } Bo=\frac{\rho g R_0^2}{\sigma}$$

- Gravitational body force affects both the short and long time dynamics
  - *short times*: slumping (bulk motion)
  - *long times*: symmetry-breaking axial flow superimposed on similarity solution

Kolte & Szabo, *J. Rheol* 1999; Fig. 7

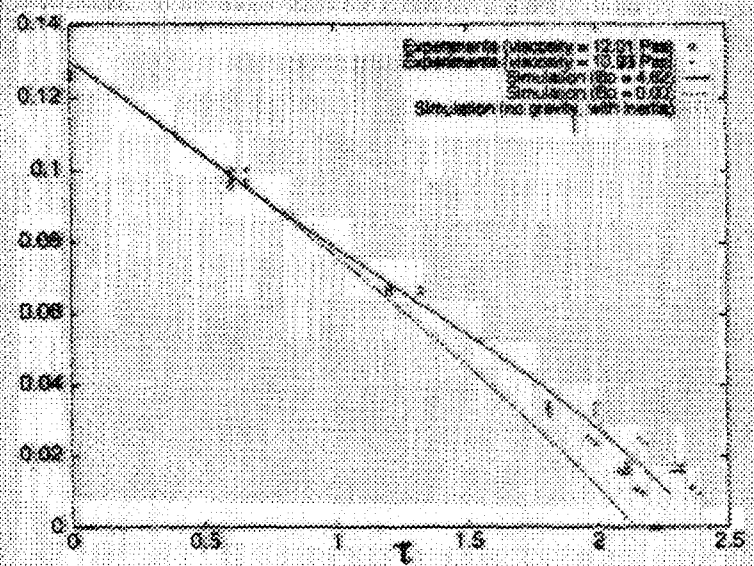

results for two alternative Bond numbers compared with experiments with the liquid . The two sets of data points (◇ and +) represent the experiments described. As the exact erature was not known two different viscosities have been used to nondimensionalize the

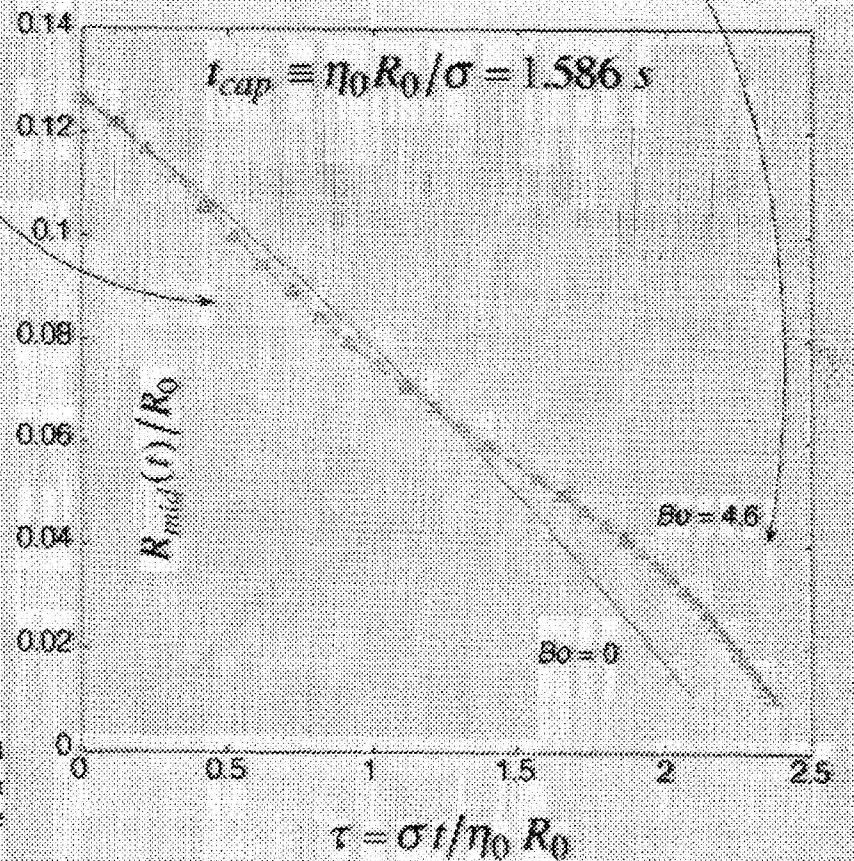

Scaling of Time to Breakup in the Microfilament Rheometer

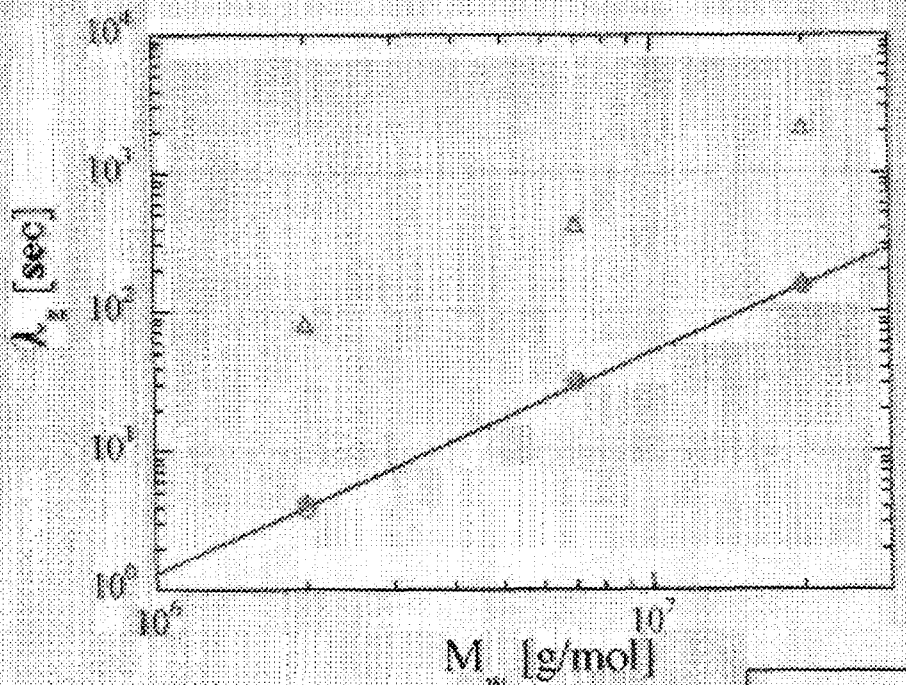

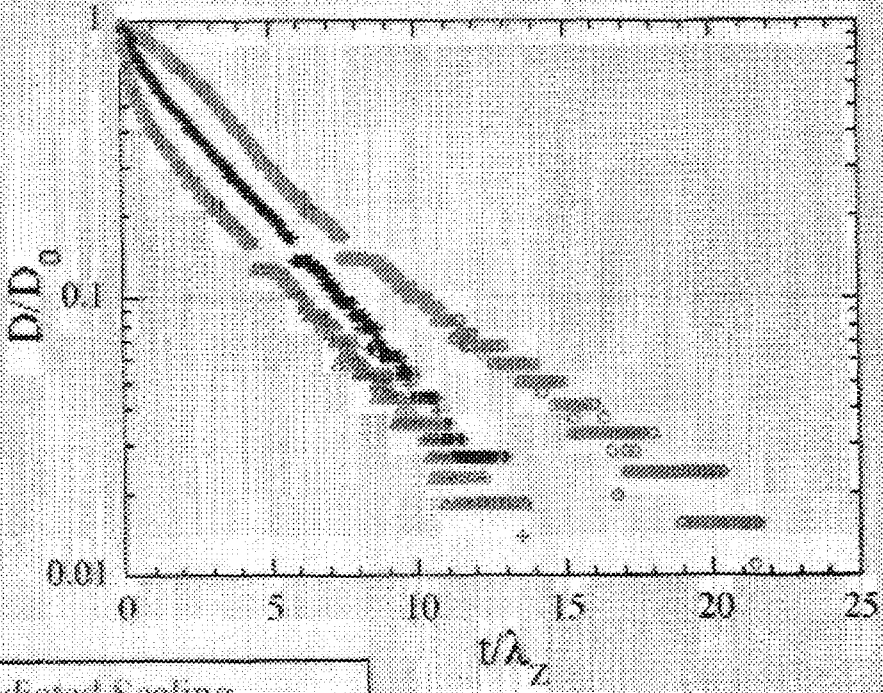

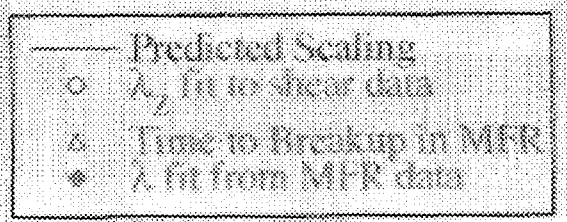

$$S \equiv \frac{t_{break}}{\lambda_{MFR}} = 15.3 \pm 2.4$$

$$\frac{\lambda_{MFR}}{\lambda_Z} = 1.0510 \pm 0.077$$

- For elastic fluids (dilute polymer solutions) λ_{MFR} is an accurate measure of the longest relaxation time in fluid.
- Use apparatus to measure relaxation time of other more complex structured fluids (e.g. associating polymers, micellar systems, adhesives, ...)

Direct Comparison of Filament Stretching and Breakup Experiments

- Utilize the axial force balance on the necking filament:

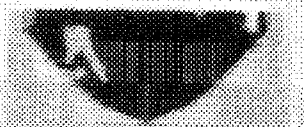

$$\frac{F_z}{\pi R_{mid}(t)^2} = 3\eta_s\dot{\varepsilon} + \left[\tau_{p,zz} - \tau_{p,rr}\right] + \frac{\sigma}{R_{mid}(t)}$$

$$\dot{\varepsilon} = -\frac{2}{R_{mid}(t)}\frac{dR_{mid}(t)}{dt}$$

$$\left[\tau_{zz} - \tau_{rr}\right] \equiv \bar{\eta}_{app}(\varepsilon)\,\dot{\varepsilon}$$

$$F_z \to 2\sigma\pi R_{mid}(t)$$

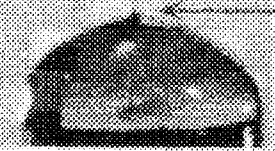

- Rearrange equations to obtain an *"Apparent Extensional Viscosity"*

$$\bar{\eta}_{app}(\varepsilon) = \frac{\sigma}{-2\,dR_{mid}(t)/dt}$$

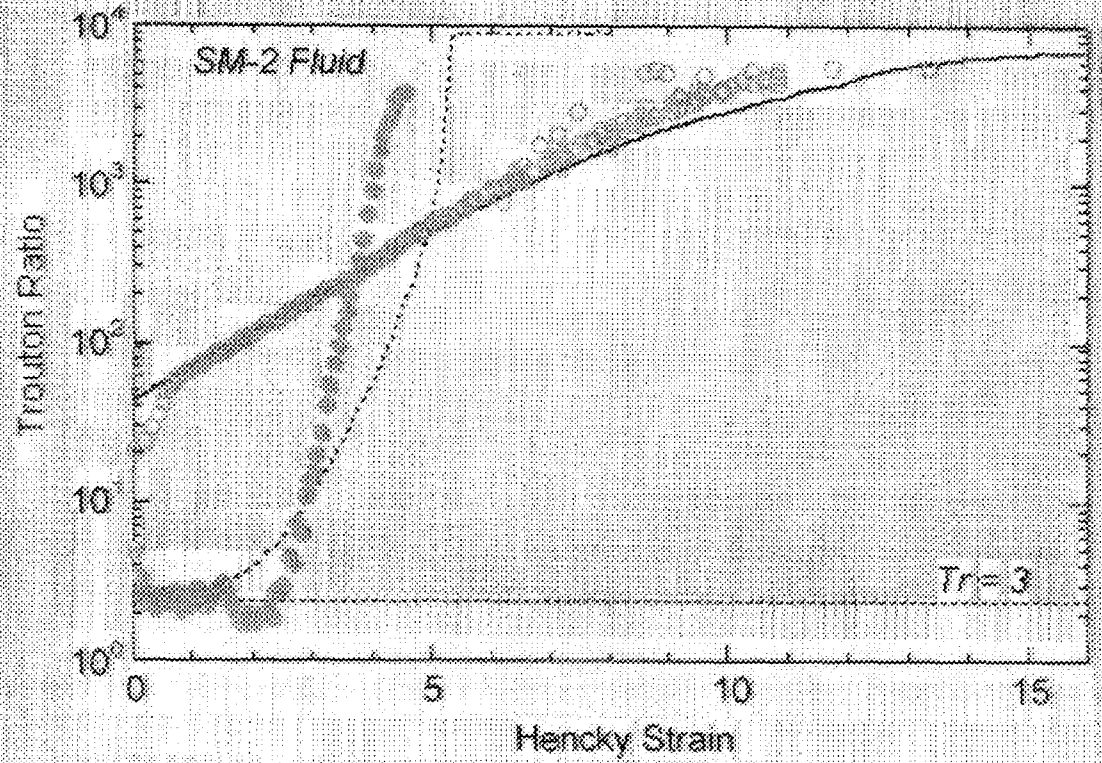

(●) Filament Stretching

$De = 15.2$

Stress Growth ~ $\exp(2\varepsilon)$

(○) Elasto-Capillary thinning

$De \approx 2/3$

Stress Growth ~ $\exp(\varepsilon/2)$

- Asymptotically approach same value at large Hencky strains

Conclusions

- Theory developed for the *visco-elasto-capillary thinning* of Newtonian, power-law and elastic fluids
- Filament stretching and filament breakup experiments probe extensional behavior of fluids in different but mutually complementary ways
  - Filament stretching imposes a time-scale $t_c \sim 1/\dot{\varepsilon}_0$ ⇒ *Limitations due to endplate instabilities and mechanical implementation*
  - Filament breakup allows fluid to select its own time scale for deformation $\dot{\varepsilon}_0 \sim 1/(3\lambda)$ ⇒ *Easy to realize but more complex analysis required*
- Can extract transient extensional viscosity information from both types of experiments
  - ⇒ Filament breakup device provides a test protocol similar to many commercial processes
  - ⇒ Readily incorporate additional effects (heat transfer, mass transfer,...)
- Simple test amenable to QC applications...

ACOUSTIC STUDY OF CRITICAL PHENOMENA IN MICROGRAVITY

M. R. Moldover,[1] K. A. Gillis,[1] and G. A. Zimmerli[2]
[1]*Process Measurements Division, NIST, Gaithersburg MD 20899-8360*
[2]*National Center for Micrgravity Reserch, MS 110-3, Cleveland OH 44135*

We plan an acoustic study of xenon near its liquid-vapor critical point in microgravity. We will use a novel, compact acoustic resonator in microgravity to determine both the speed of sound c and the bulk viscosity ς. In lowest order, the resonance frequencies determine c and the "quality factors" of the resonance modes determine ς. In microgravity, the data for ς will be a factor of 60 closer to the critical temperature T_c than is possible on earth. The microgravity data will provide the most rigorous possible test of the fundamental theory for ς, *i.e.* the theory for the time-correlations of pairs of critical fluctuations. By using both Helmholtz and organ-pipe modes of the same compact resonator, the acoustic data will span a 30:1 frequency ratio at unusually low frequencies: 120 Hz to 4 kHz. Within 6 mK of T_c, where the reduced temperature $t \equiv (T - T_c) / T_c < 2\times10^{-5}$, the critical fluctuations are so slow that the equilibrium condition: (acoustic frequency) x (fluctuation lifetime) << 1 is violated, even at 120 Hz. In this very-near-critical region, c is frequency-dependent and the attenuation of sound is dominated by ς. Further from the critical point, where $t > 2\times10^{-5}$, the low-frequency speed-of-sound data obtained in microgravity will determine the constant-volume heat capacity C_V, perhaps with higher resolution than direct measurements of C_V. If so, the acoustic data will further constrain the theory for the "crossover" of C_V from an asymptotic divergence with the critical exponent (α) to non-critical behavior. The quality-factor data will test the theory of the thermal boundary layer in heretofore inaccessible ranges of frequency and fluid properties.

The planned experiment will exploit hardware that two of PIs (Moldover and Zimmerli) helped develop for the Critical Viscosity of Xenon (CVX) experiment. The CVX flight package consisted of two "Hitchhiker"canisters that can be accommodated by many Shuttle missions. In 1997, the package was flown in the cargo bay of the shuttle Discovery (STS 85). The package successfully measured the shear viscosity of xenon 100 times closer to T_c than ground-based experiments and it produced the first reliable measurements of visco-elasticity near any critical point. With minor modifications, the proposed experiment will use the CVX flight thermostat and hardware for temperature measurement and control.

Two of the PIs (Gillis and Moldover) developed the double Helmholtz resonator (now called the "Greenspan acoustic viscometer") to measure the viscosities of gases accurately. To date, no acoustic viscometer has been operated with a near-critical fluid. Thus, the first task is to design an acoustic viscometer for use with a near-critical sample of xenon. This may require modifying electro-acoustic transducers and developing a surface coating for the viscometer's interior. Extensive tests will be required to verify that the viscometer operatesin accord with the theory for the instrument. Then, the viscometer will be used to make the best possible measurements of c and ς on earth over the full range of accessible frequencies. These measurements will be used to define the microgravity experiment and they will be used to compare ground-based and microgravity data.

NASA/CP—2000-210470

NIST

National Institute of Standards and Technology
Technology Administration, U.S. Department of Commerce

MICHAEL R. MOLDOVER

NIST Fellow
Process Measurements Division

Keith Gillis NIST
Greg Zimmerli NCMR

Acoustic Study of Critical Phenomena in Microgravity

5th Microgravity Fluid Physics, Cleveland Ohio, Aug. 9, 2000

Acoustic Study of Critical Phenomena in Microgravity

What is the Problem?

- bulk viscosity
- liquid-vapor critical points

Proposed experiment

- requirements
  - low frequency, fine temperature resolution
  - fine bulk viscosity resolution
- Greenspan acoustic viscometer (Helmholtz resonator)

We are imitating CVX: a successful measurement of the critical anomaly of the viscosity of xenon in microgravity

CVX hardware

CVX results

Definition of shear viscosity η and "bulk" or " second" viscosity ζ in terms of pressure tensor $\mathbf{P}_{\alpha\beta}$, the stress tensor $\mathbf{S}_{\alpha\beta}$, the unit tensor $\mathbf{U}_{\alpha\beta}$

$$\overline{\overline{\mathbf{P}}} = p\overline{\overline{\mathbf{U}}} - 2\eta\overline{\overline{\mathbf{S}}} - \zeta\left(\frac{\partial}{\partial \boldsymbol{r}}\cdot\boldsymbol{v}\right)\overline{\overline{\mathbf{U}}}$$

$$S_{\alpha\beta} = \frac{1}{2}\left[\frac{\partial v_\beta}{\partial v_\alpha} + \frac{\partial v_\alpha}{\partial v_\beta}\right] - \frac{1}{3}\delta_{\alpha\beta}\left(\frac{\partial}{\partial \boldsymbol{r}}\bullet\boldsymbol{v}\right)$$

Why is bulk viscosity often ignored?

(1) low densities:

$\rho \to 0$; $\eta \to$ constant (Maxwell)

$$\rho \to 0; \quad \zeta \to \eta \times \rho^2 = \eta \times \left(\frac{\text{volume of molecules}}{\text{volume of container}}\right)^2 \to 0$$

(2) high densities

liquid xenon: $\zeta \approx 0.3\,\eta$, but liquids are "incompressible"

When is bulk viscosity important?

(1) low densities:

polyatomic gases and high (f/ρ)

sound absorption

$$\alpha_\lambda = \frac{\pi\omega}{c^2}\left((\gamma - 1)\frac{\lambda}{\rho C_p} + \frac{\eta}{\rho} + \frac{\zeta}{\rho} + (\gamma - 1)\frac{c^2}{\omega}\frac{C_{relax}}{C_p}\frac{\omega\tau}{1 + (\omega\tau)^2} \right)$$

heat cond — viscosity — bulk viscosity — internal modes relaxing

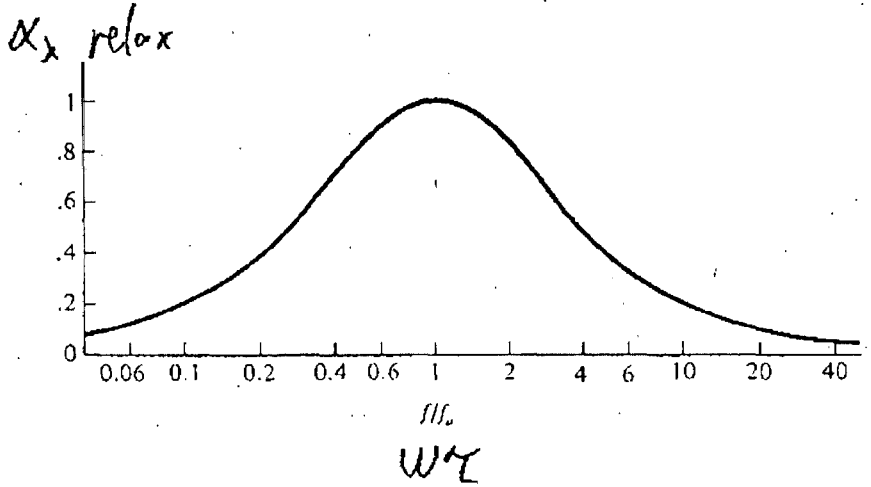

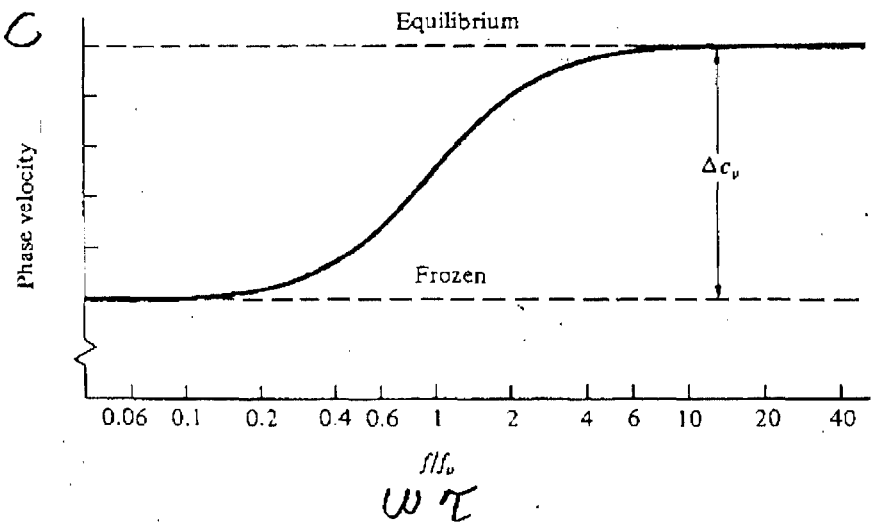

When is bulk viscosity important?

(2) critical point:

monatomics behave like huge polyatomics with a distribution of relaxation times

$$\tau \equiv 6\pi\eta\xi^3/(k_B T_c) = \tau_0 t^{-\nu(3+z_\eta)} \approx \tau_0 t^{-1.93}$$

In a very loose sense, near-critical xenon behaves like a gas composed of polyatomic molecules. The density fluctuations in near-critical fluids are characterized by size ξ, the correlation length, and a relaxation time τ. The relaxation time is defined in terms of ξ and η by [Here, T is the temperature, $t \equiv (T - T_c)/T_c$ is the reduced temperature measured from T_c.] As $t \to 0$, the correlation length and the viscosity diverge as $\xi = \xi_0 t^{-\nu} \approx \xi_0 t^{-0.63}$ and $\eta \approx \eta_0 t^{-0.041}$.

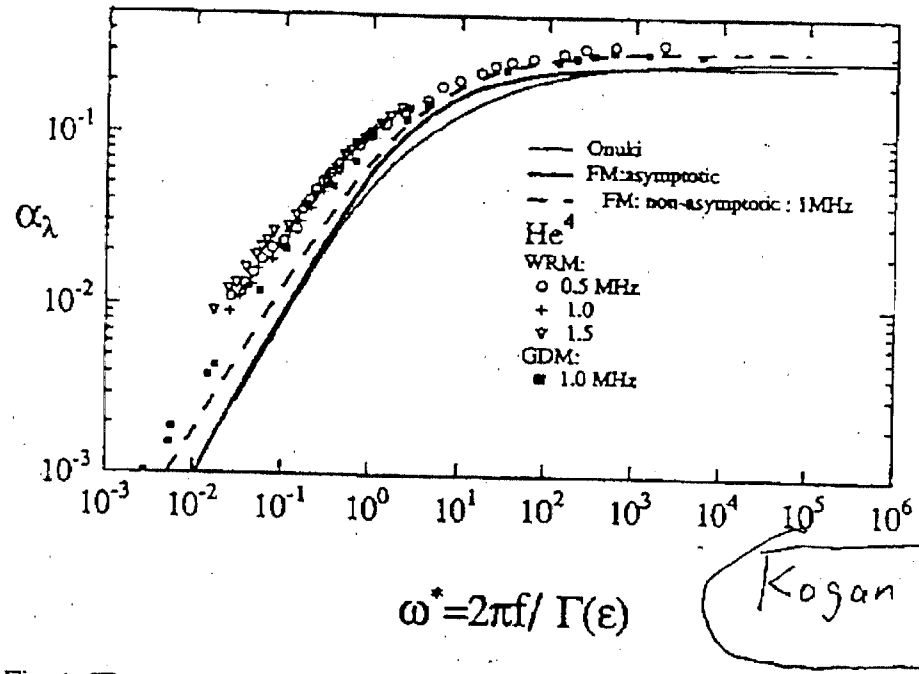

Fig. 4. The comparison of the sound attenuation data versus the reduced frequency ω^* for ^{3}He and ^{4}He from different experiments, Roe *et al.* (RWM), (RM) and Doiron *et al.* (DGM),[9-11] and comparison with theory by Onuki and by Folk and Moser (FM).[3,5] The uncertainty in the ^{3}He dispersion data at all frequencies is $\delta D = \pm 1 \times 10^{-4}$ for $\varepsilon < 0.01$. This reduced temperature corresponds to $\omega^* = 0.07$ and 0.7 for $f = 0.5$ MHz and 5 MHz. (See Table 1 and Appendix B.)

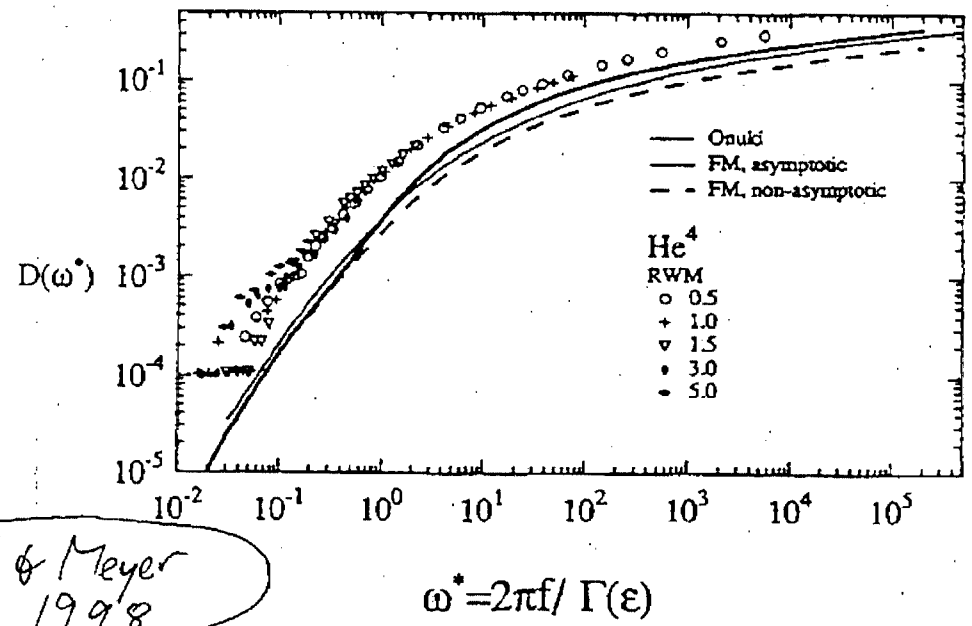

Kogan & Meyer 1998

Fig. 5. The comparison of dispersion data versus the reduced frequency ω^* for ^{4}He and ^{3}He from different experiments, Roe *et al.* (RWM), (RM) and Doiron *et al.* (DGM),[9-11] and comparison with theory by Onuki and by Folk and Moser (FM).[3,5]

The critical point

The critical point is the highest temperature where liquid and vapor can coexist in the same container.

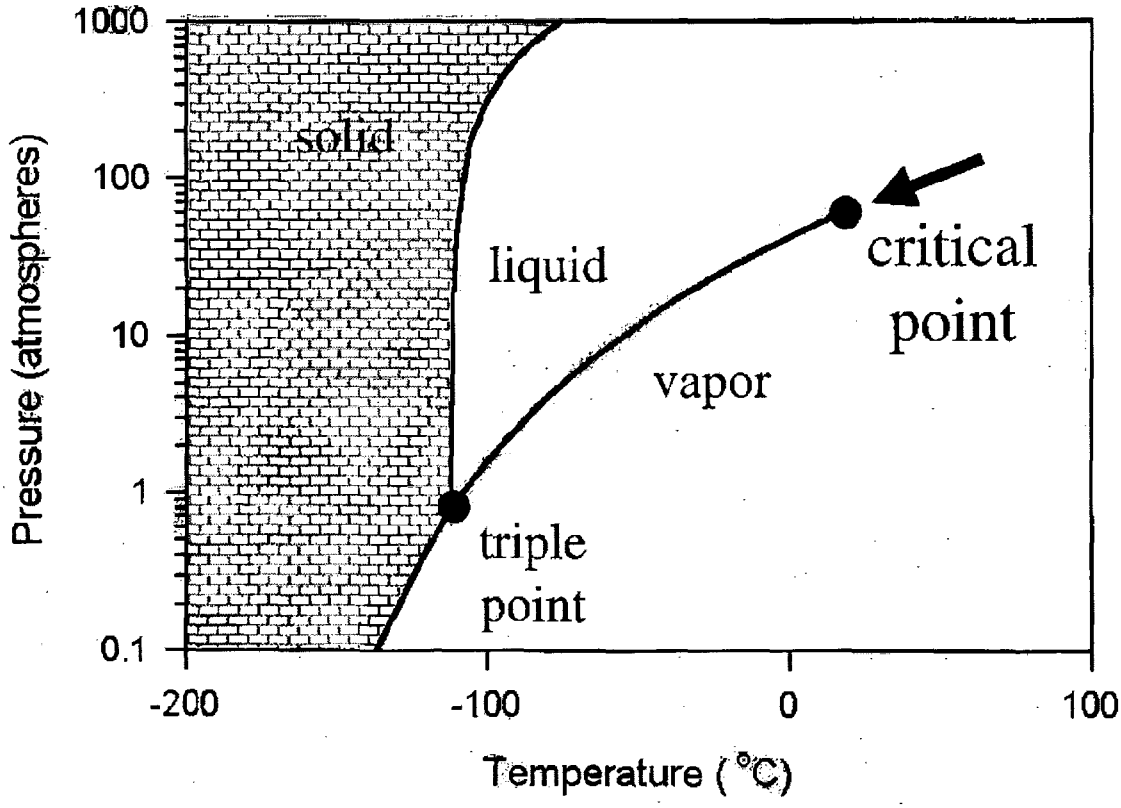

Near the critical point:

- Density fluctuations are greatly amplified, thus affecting the fluid's properties, including viscosity.
- The fluid becomes extremely "soft" and compresses under its own weight in Earth's gravity.
- Heat diffuses extremely slowly.

Density stratification in Earth's gravity

- All fluids compress under their own weight.
- Compressibility diverges near the critical point.

$$\frac{P}{\rho}\left(\frac{\partial \rho}{\partial P}\right)_T = \begin{cases} 1 & \text{air at ambient temperature} \\ 5\times10^3 & \text{xenon at } T_c + 30\ \text{mK} \\ 1.5\times10^6 & \text{xenon at } T_c + 0.3\ \text{mK} \end{cases}$$

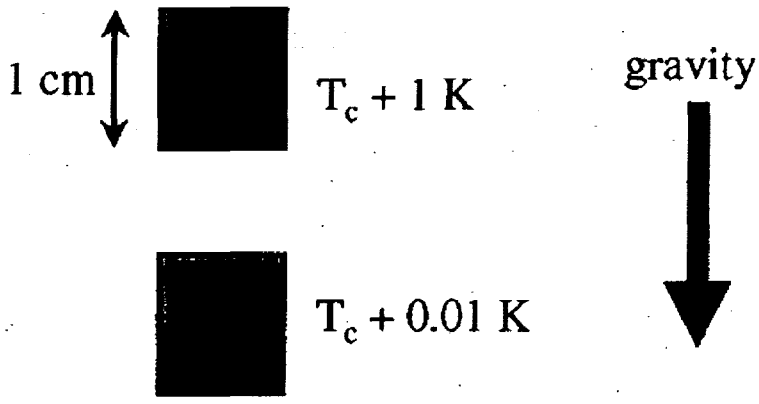

Critical Viscosity of Xenon

Microgravity measurement of viscosity near the liquid-vapor critical point

CVX flew on Space Shuttle flight STS-85 in August 1997.

Microgravity allowed:

- Measurements 100 times closer to the critical point
- First direct observation of the increase of viscosity
- First measurement of viscoelasticity (complex viscosity)

Principal Investigators:
Robert F. Berg and Michael R. Moldover
National Institute of Standards and Technology
Gregory A. Zimmerli
National Center for Micrgravity Research

Project Management & Funding:
NASA Lewis Research Center

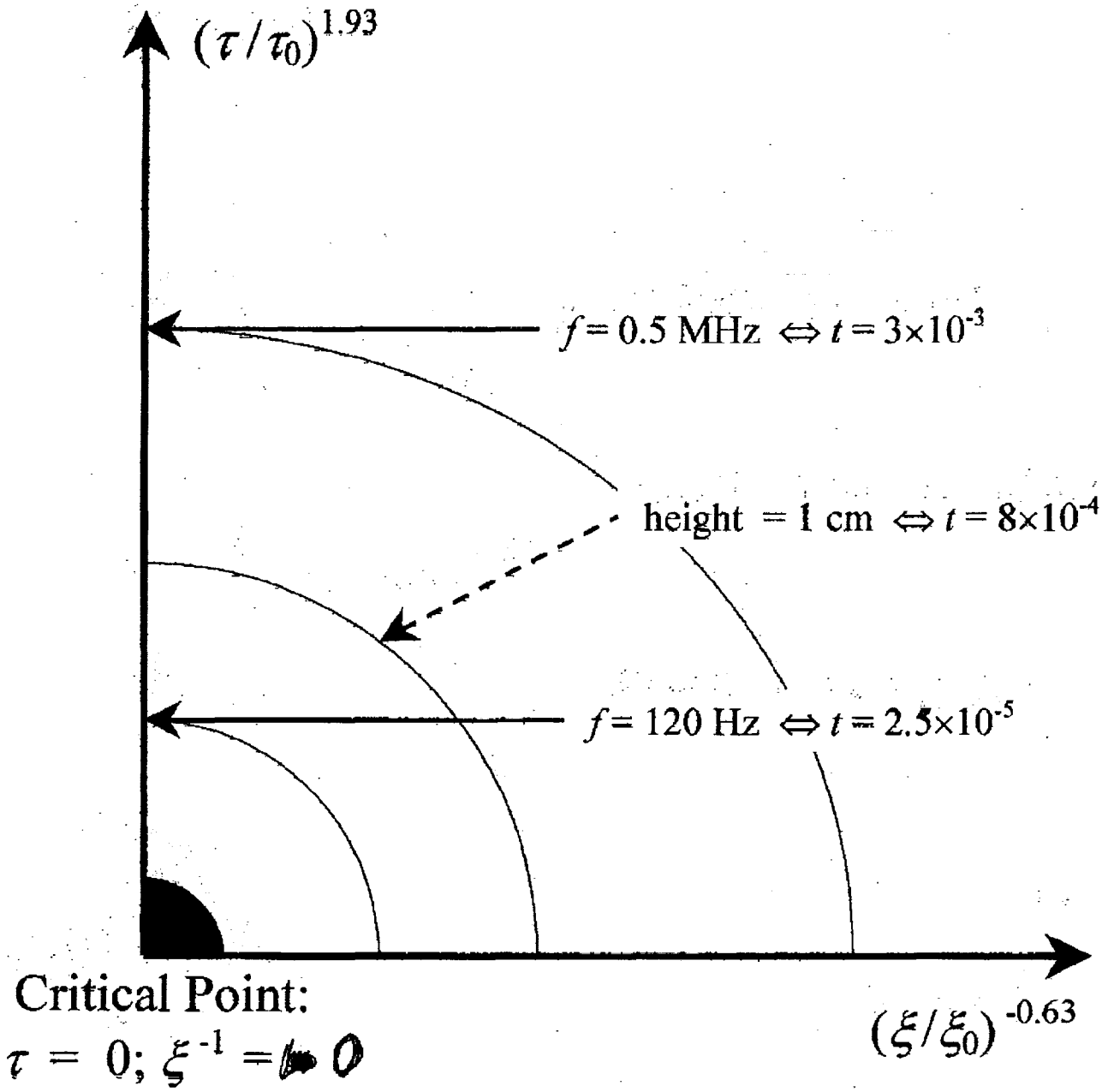
$(\tau/\tau_0)^{1.93}$
$f = 0.5$ MHz $\Leftrightarrow t = 3\times10^{-3}$
height = 1 cm $\Leftrightarrow t = 8\times10^{-4}$
$f = 120$ Hz $\Leftrightarrow t = 2.5\times10^{-5}$
Critical Point:
$\tau = 0; \xi^{-1} = 0$
$(\xi/\xi_0)^{-0.63}$

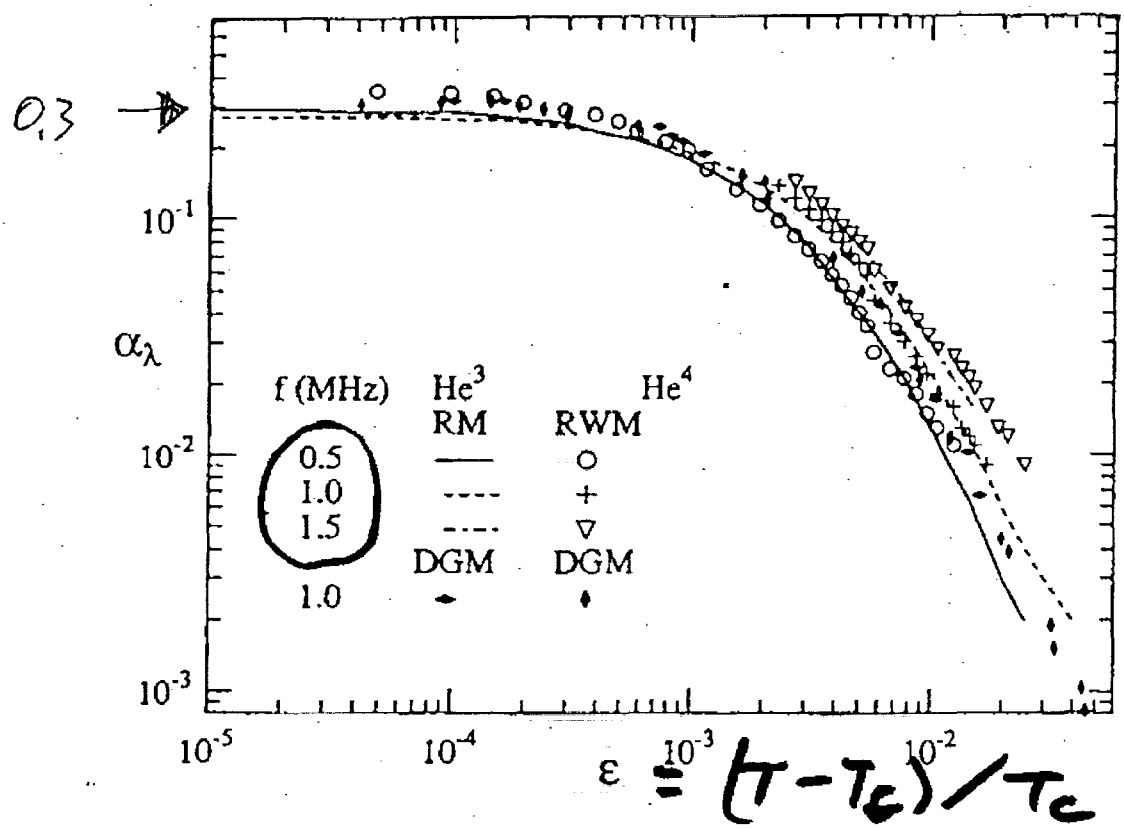

Fig. 2. Comparison of the attenuation data of He^3 and He^4 from different experiments versus ε at frequencies 0.5, 1 and 1.5 MHz (Roe *et al.* (RWM), (RM) and Doiron *et al.* (DGM)[9–11]). The lines represent the ^{3}He data of RM, while the other data are marked by symbols.

Kogan & Meyer 1998

$\alpha_\lambda = 0.3 \Rightarrow$ sound barely propagates.

NASA/CP—2000-210470

Gas motion in a double Helmholtz resonator

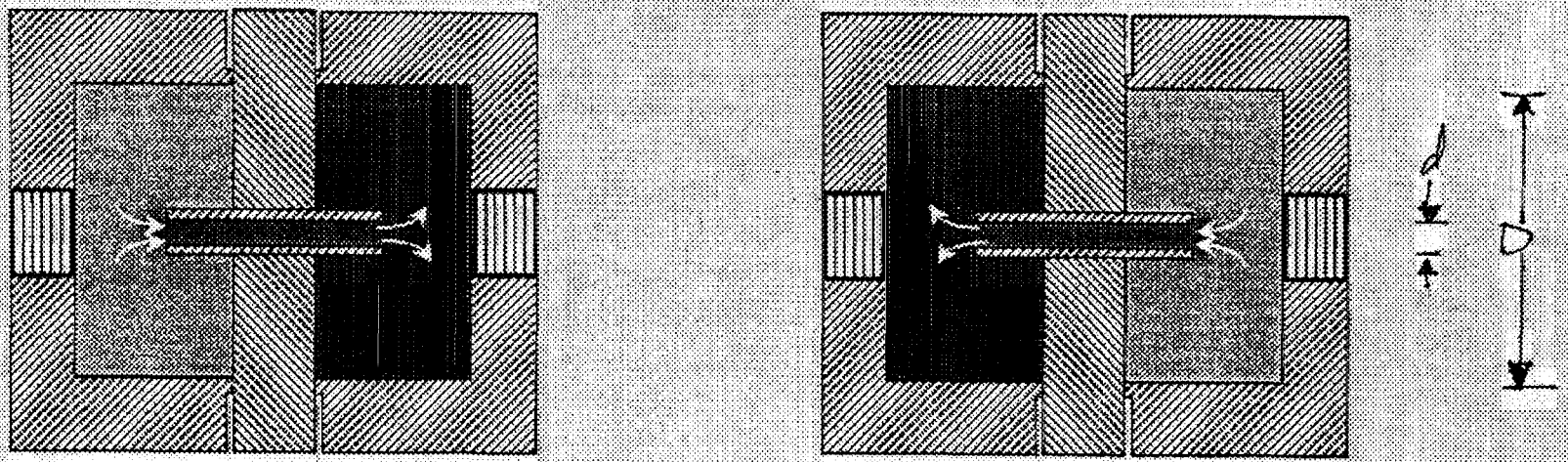

$$\lambda_{sound} \sim L \left(\frac{D}{d}\right)^2 2\pi$$

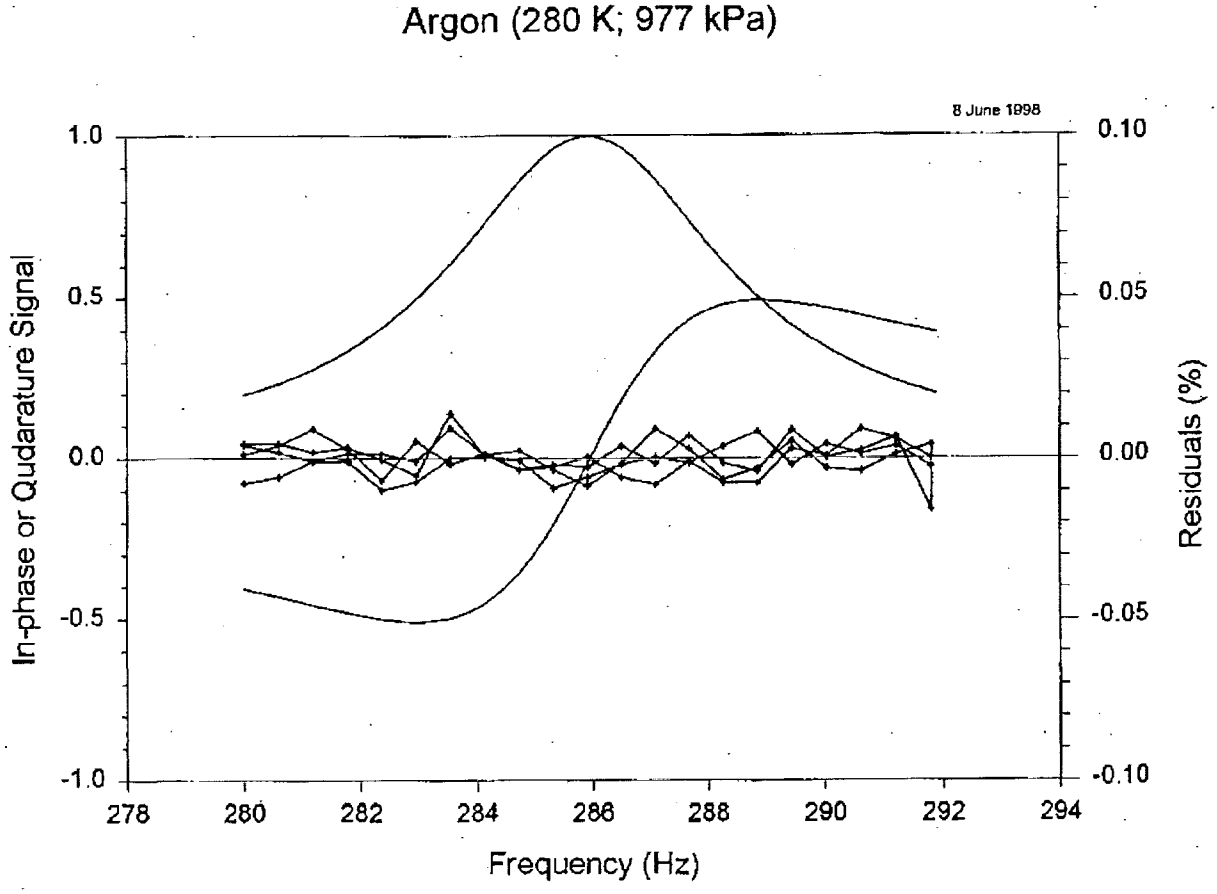
Argon (280 K; 977 kPa)
8 June 1998
In-phase or Qudarature Signal
Residuals (%)
Frequency (Hz)
1.0
0.5
0.0
-0.5
-1.0
0.10
0.05
0.00
-0.05
-0.10
278
280
282
284
286
288
290
292
294

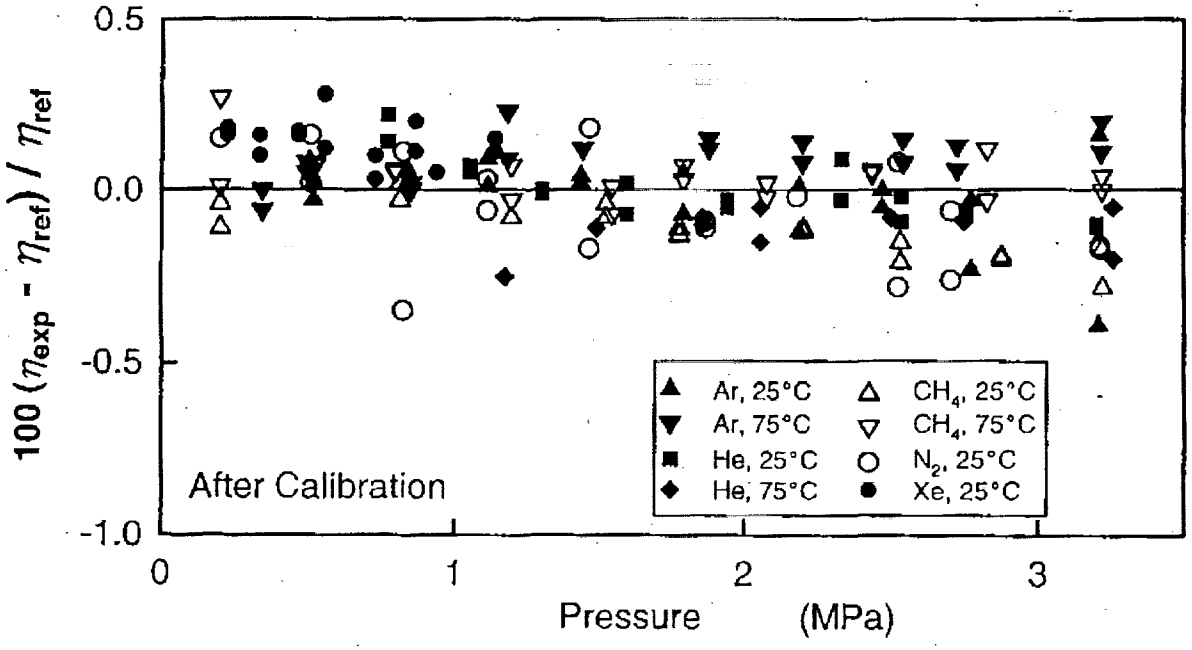
100 (η_exp - η_ref) / η_ref
Pressure (MPa)
After Calibration
Ar, 25°C
Ar, 75°C
He, 25°C
He, 75°C
CH4, 25°C
CH4, 75°C
N2, 25°C
Xe, 25°C
0.5
0.0
-0.5
-1.0
0
1
2
3

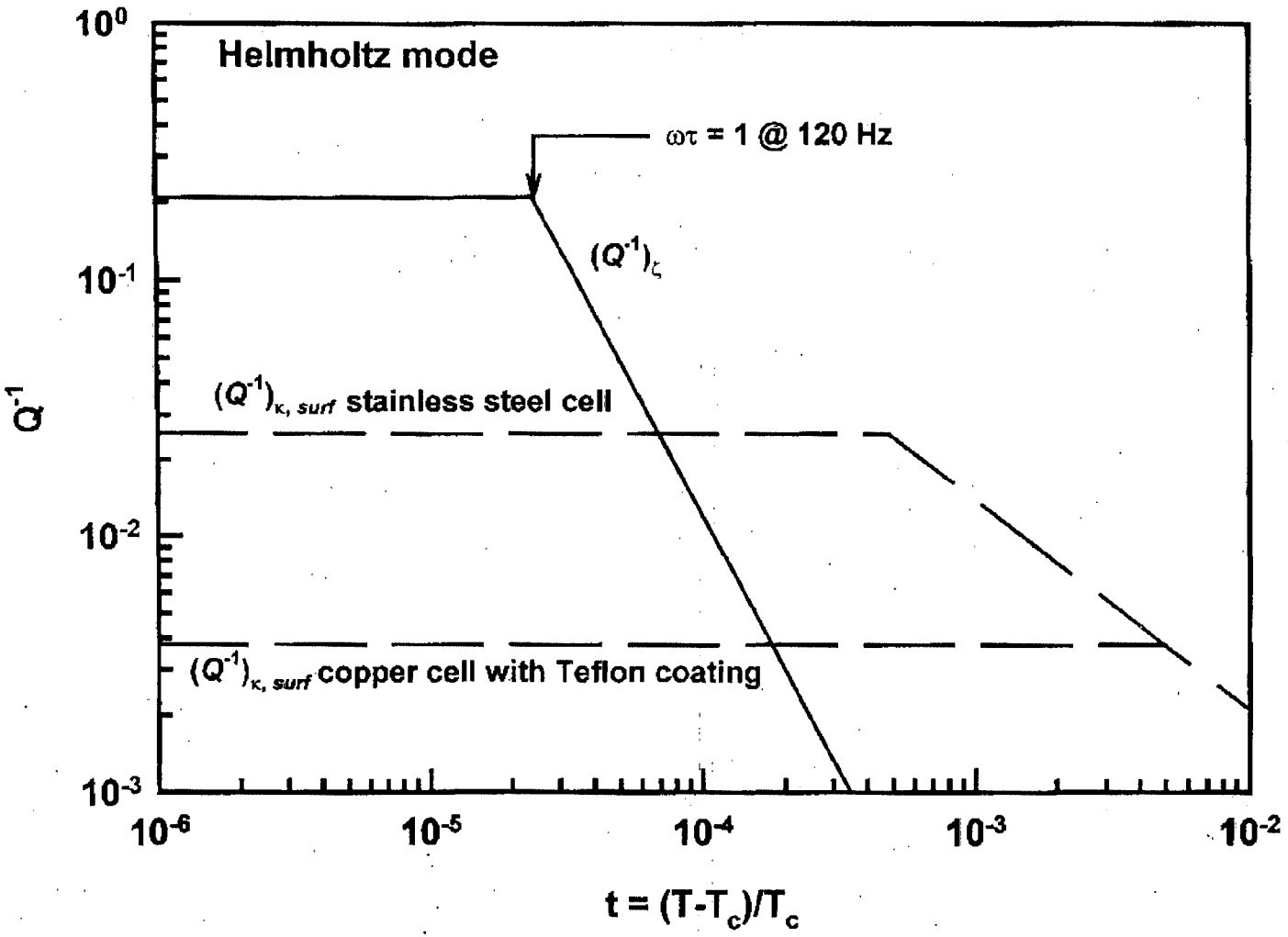
Helmholtz mode
ωτ = 1 @ 120 Hz
$(Q^{-1})_{\zeta}$
$(Q^{-1})_{\kappa,\ surf}$ stainless steel cell
$(Q^{-1})_{\kappa,\ surf}$ copper cell with Teflon coating
Q^{-1}
10^{0}
10^{-1}
10^{-2}
10^{-3}
10^{-6}
10^{-5}
10^{-4}
10^{-3}
10^{-2}
$t = (T-T_c)/T_c$

Comparision of ultrasonic and Helmholtz techniques

method	Ultrasonic	Helmholtz Resonator
frequency range	0.5 MHz - 1.5 MHz	120 Hz - 3800 Hz
$\omega\tau = 1$ @ $t =$	3×10^{-3}	2.4×10^{-5}
resolution in α_λ	~5 %	0.5 % ?
frequency ratio	3 : 1	32 : 1
temperature ratio	1.8	6
min t @ 1 g (1 cm)	8×10^{-4}	8×10^{-4}

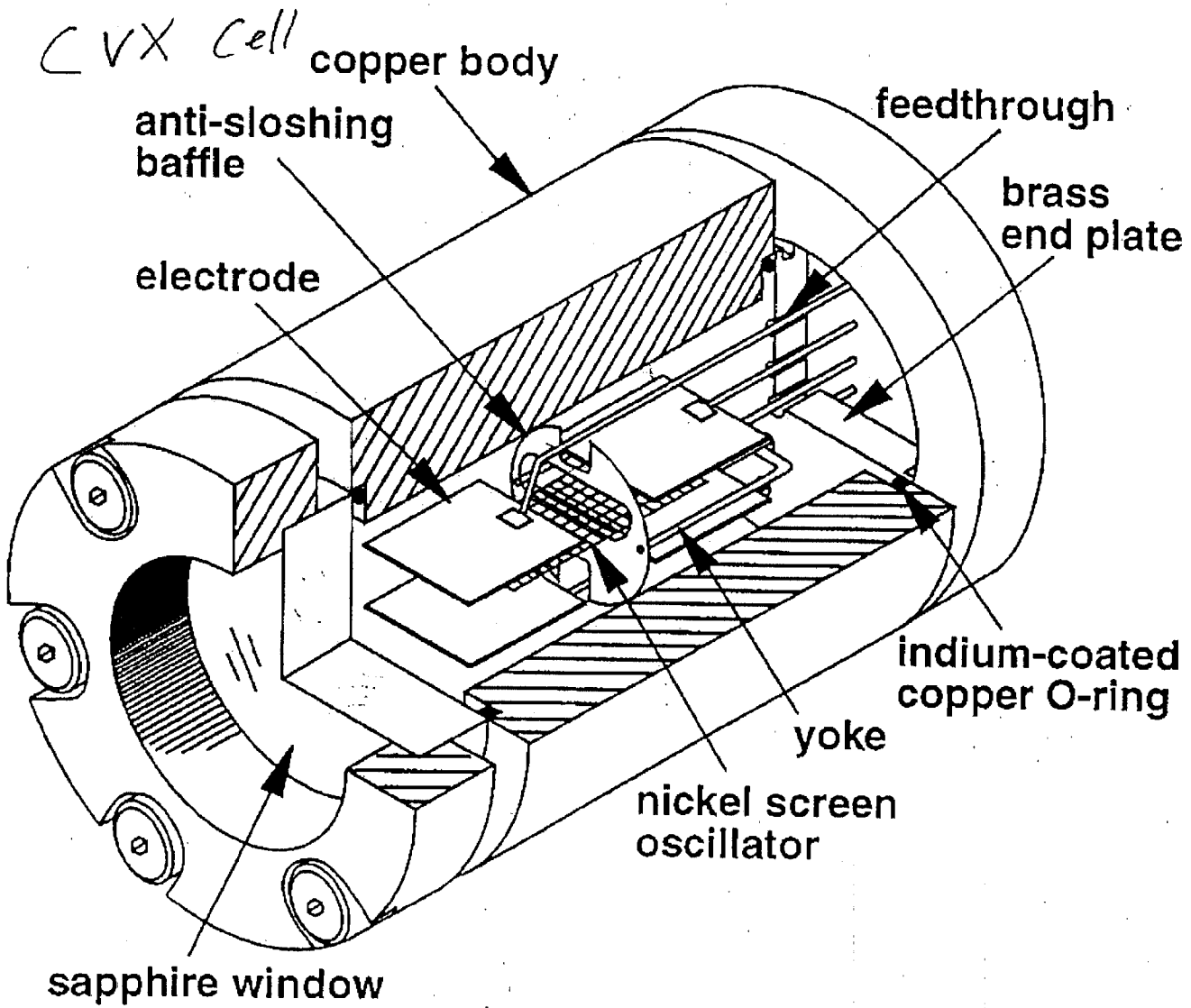

Cylinder, 4 feedthroughs

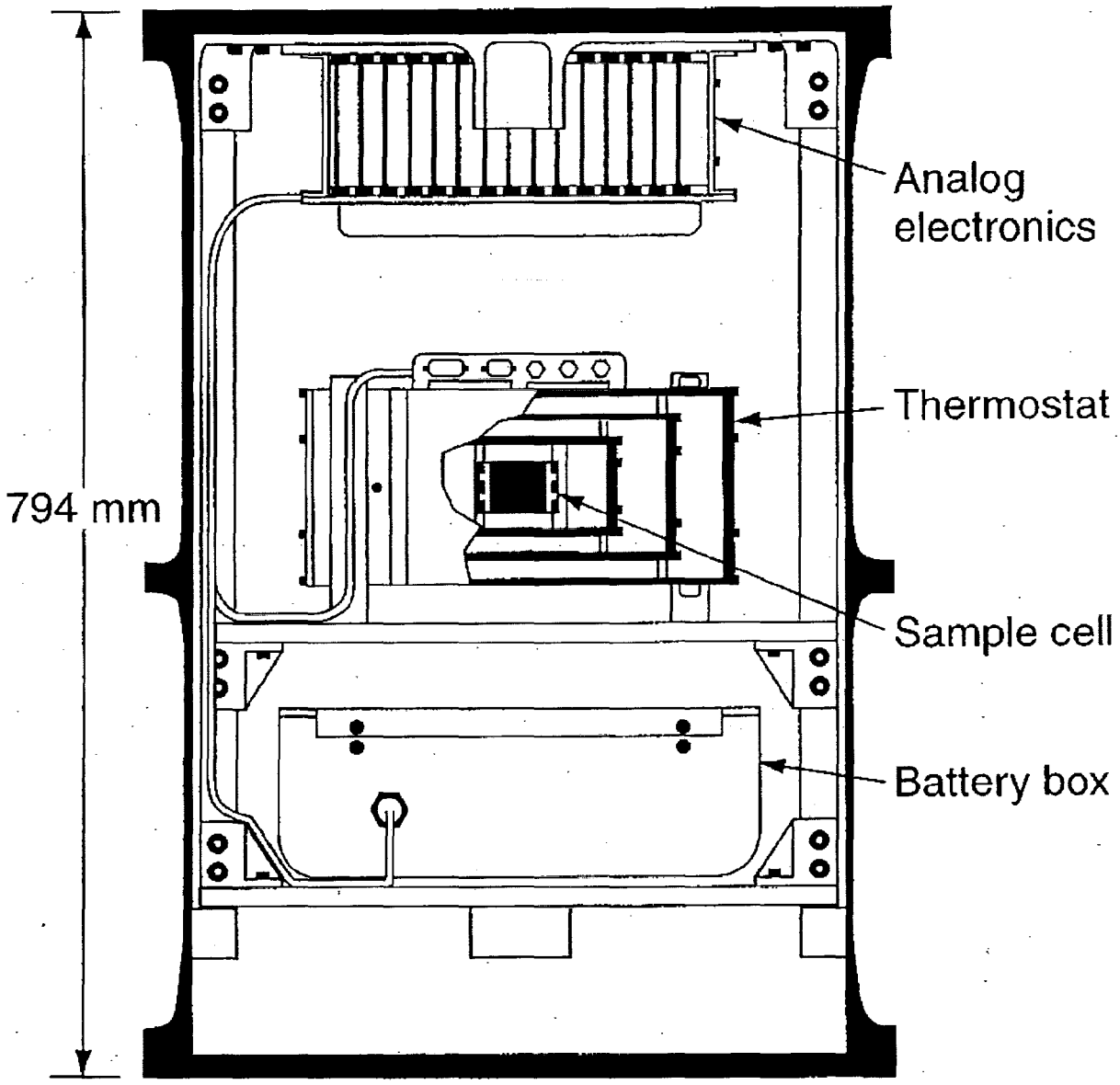
794 mm
Analog electronics
Thermostat
Sample cell
Battery box

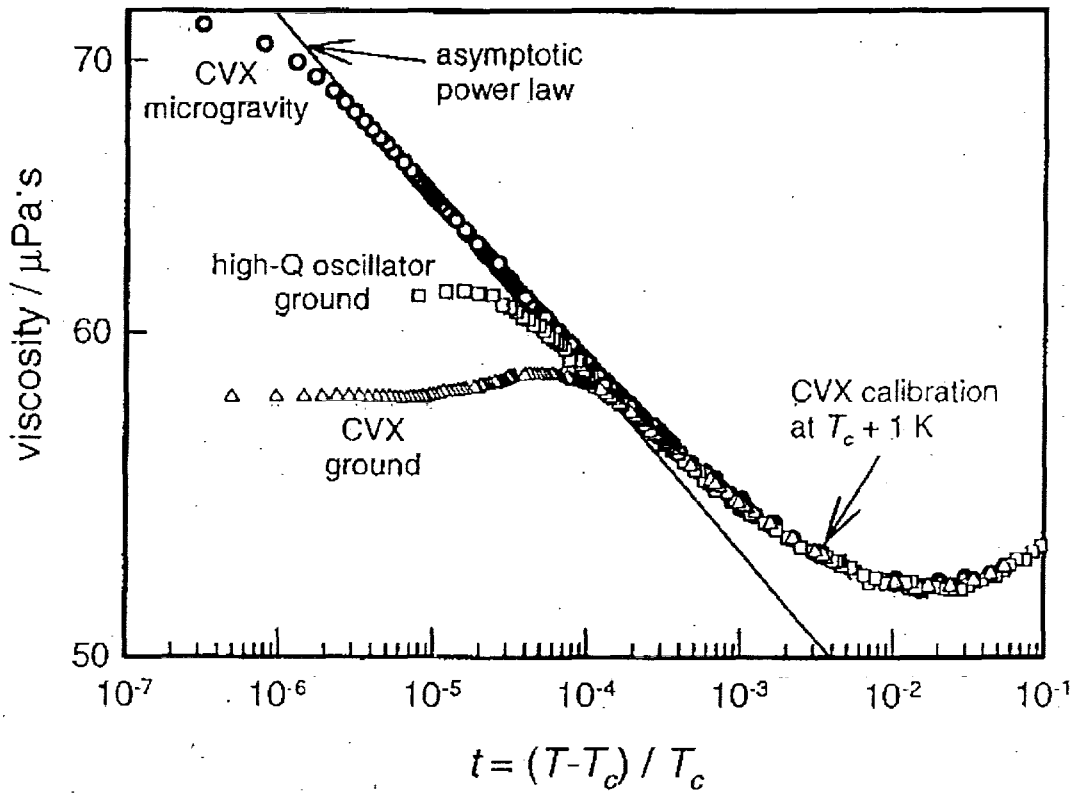

1

Figure 1

1g0g.jnb

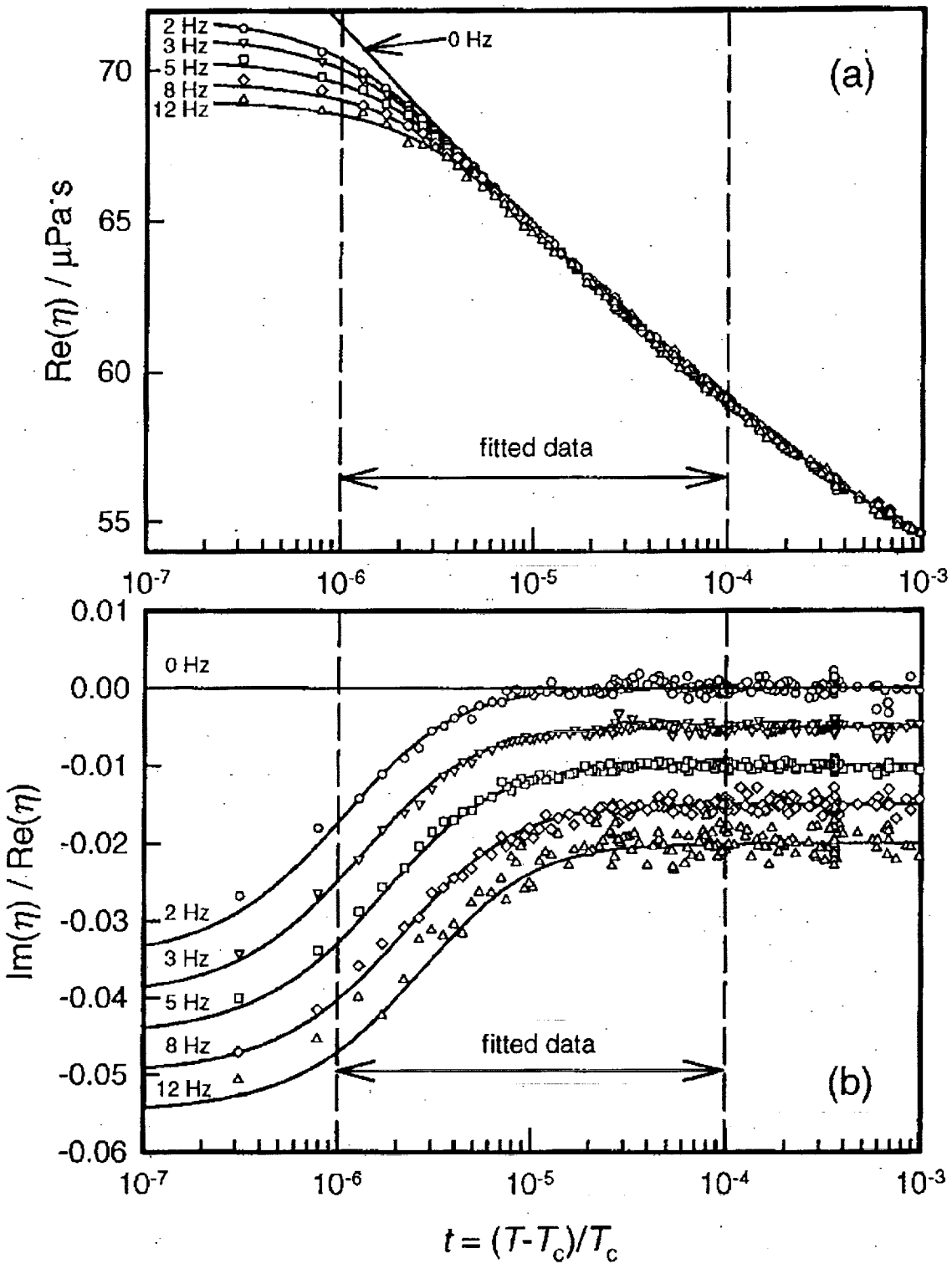

Figure 2

ReIm.jnb

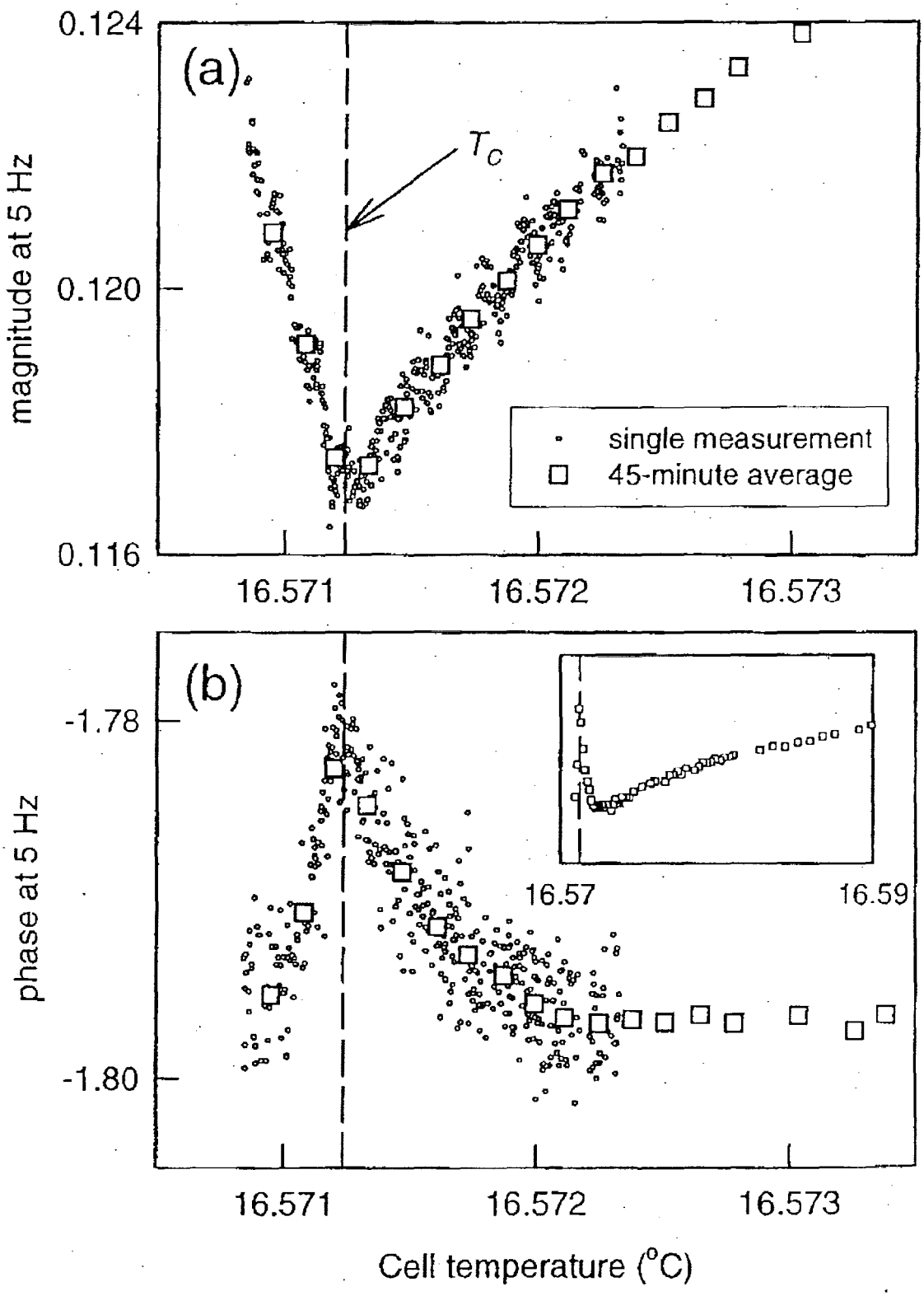
(a)
0.124
0.120
0.116
magnitude at 5 Hz
T_C
single measurement
45-minute average
16.571
16.572
16.573
(b)
-1.78
-1.80
phase at 5 Hz
16.57
16.59
16.571
16.572
16.573
Cell temperature (°C)

August 11, 2000
Guest Speaker

Fluid Physics Research on the International Space Station

Robert Corban
NASA Glenn Research Center

NASA/CP—2000-210470

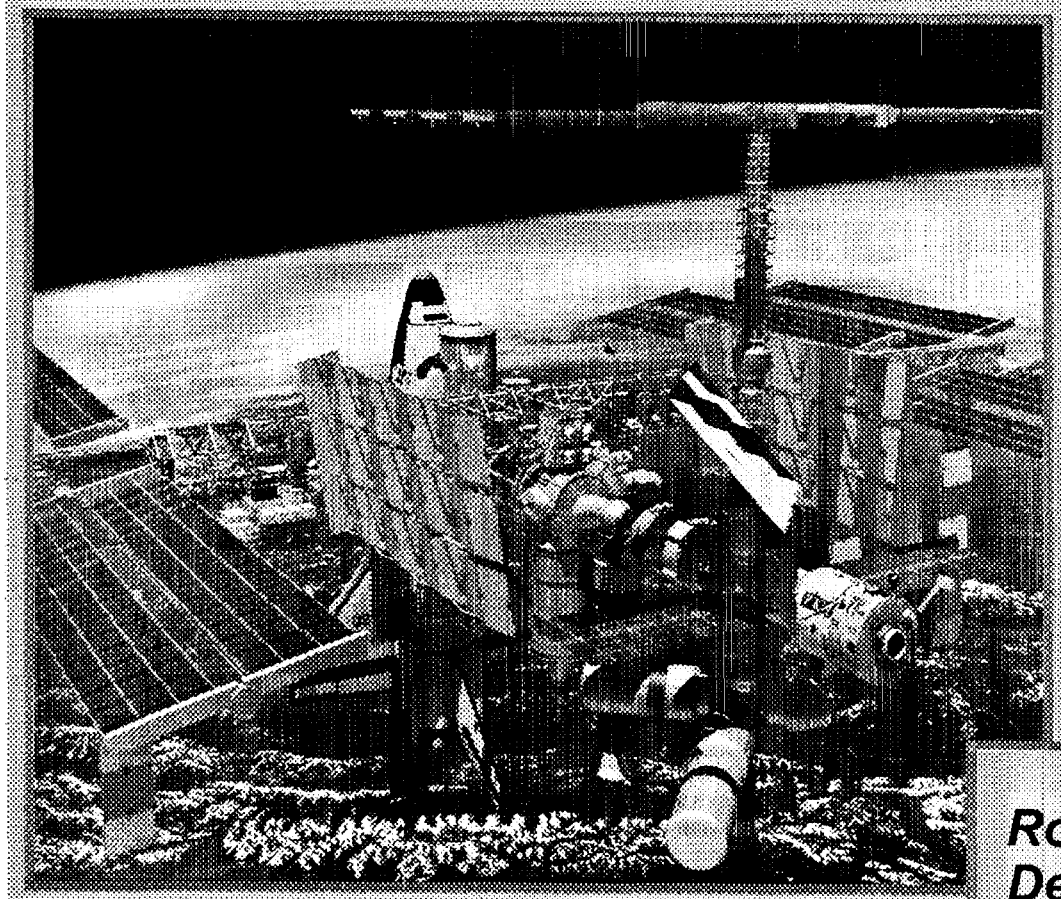

Fluids Physics Research on the International Space Station

Robert Corban
Deputy Project Manager
Fluids & Combustion Facility
August 11, 2000

NASA/CP—2000-210470

1910

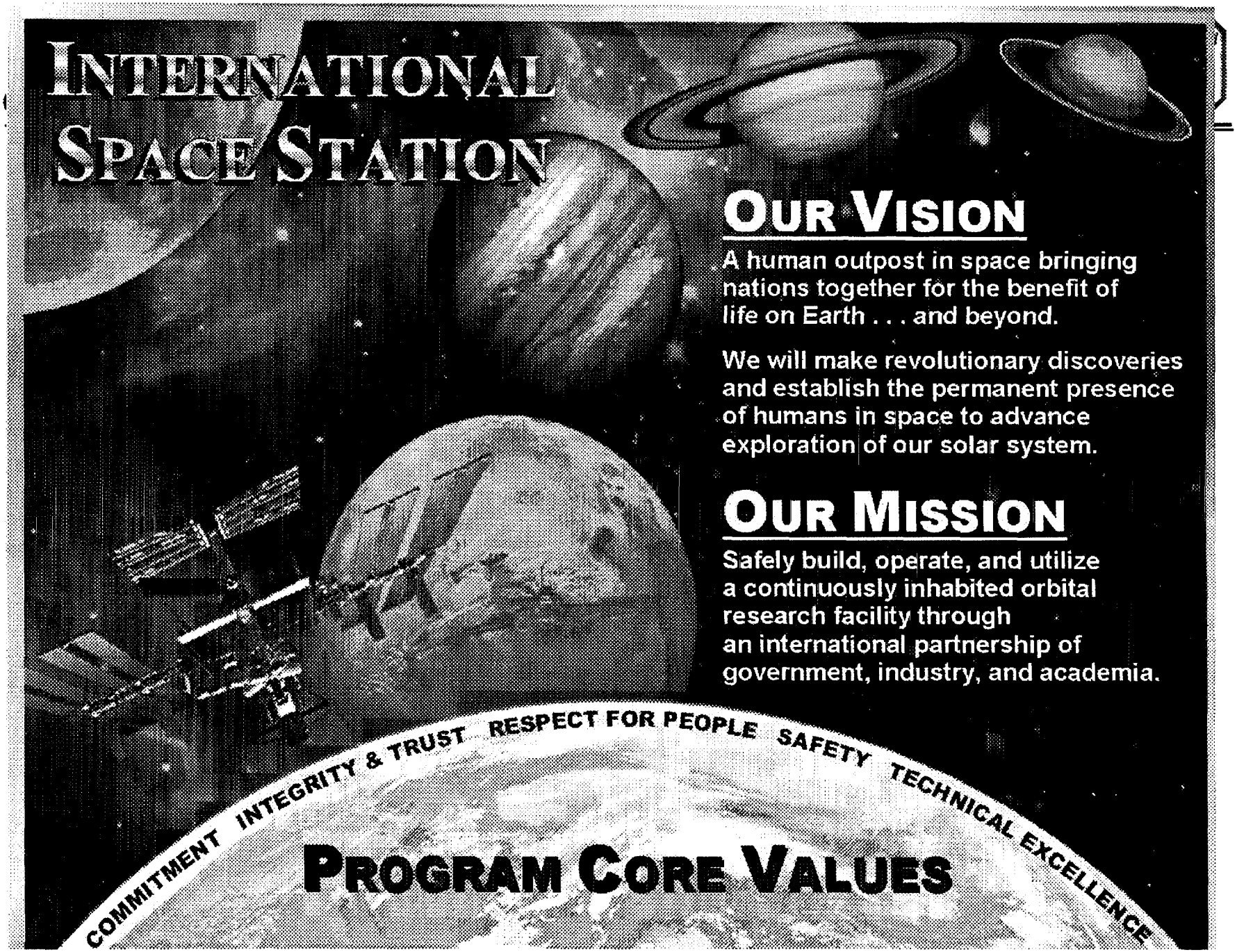

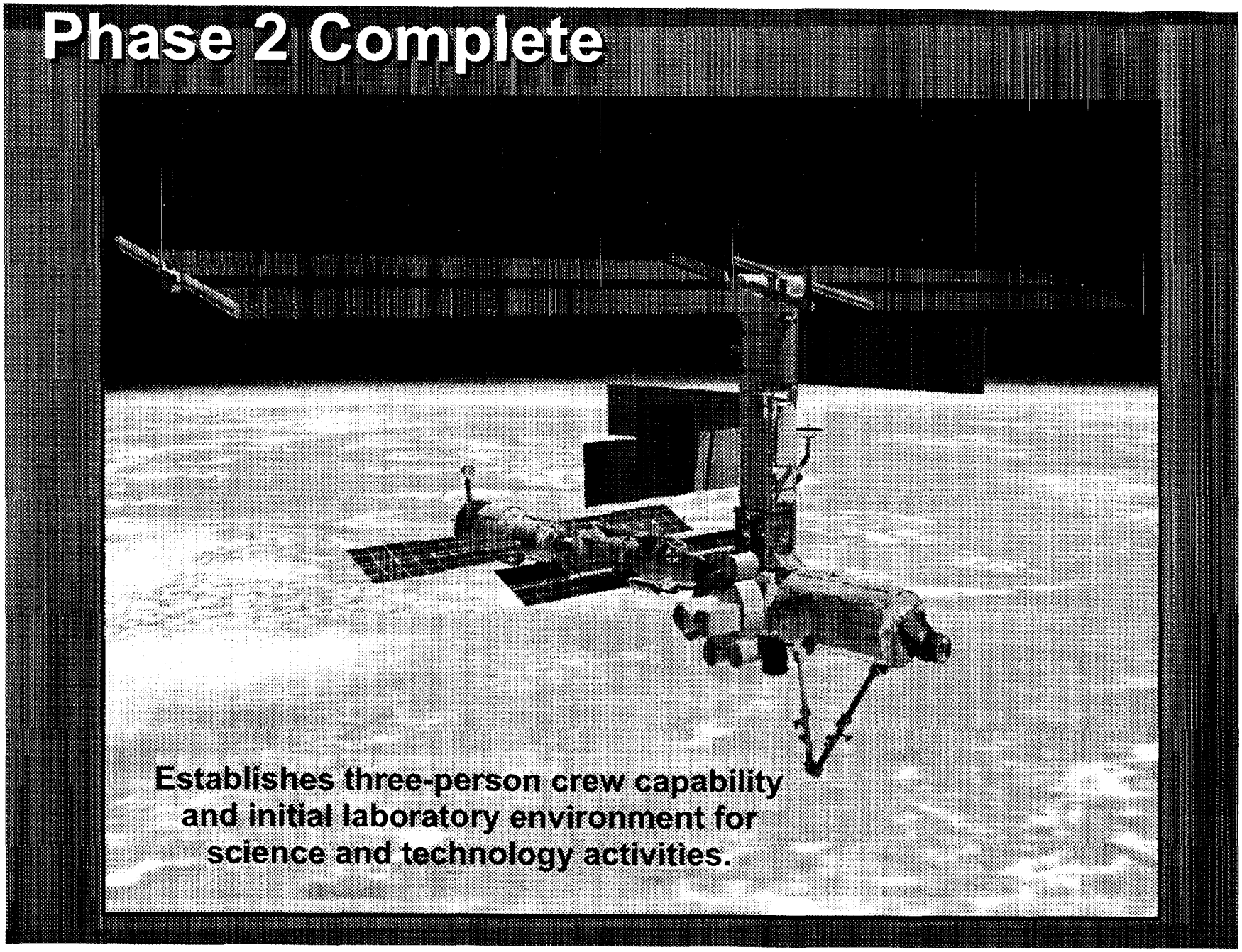
Phase 2 Complete
Establishes three-person crew capability
and initial laboratory environment for
science and technology activities.

GRC Microgravity Science Program

Fluids and Combustion Facility

On-Orbit Assembly Through Phase 2

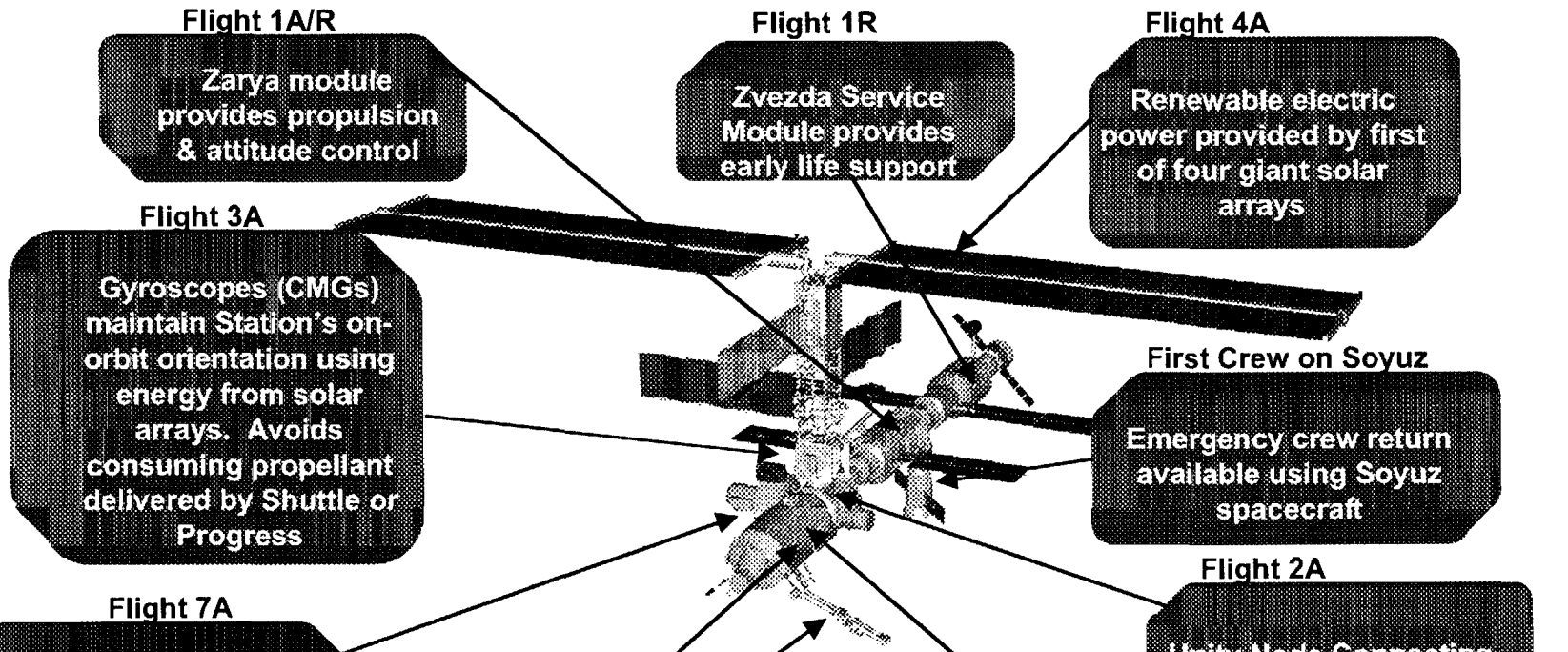

Flight 1A/R
Zarya module provides propulsion & attitude control

Flight 1R
Zvezda Service Module provides early life support

Flight 4A
Renewable electric power provided by first of four giant solar arrays

Flight 3A
Gyroscopes (CMGs) maintain Station's on-orbit orientation using energy from solar arrays. Avoids consuming propellant delivered by Shuttle or Progress

First Crew on Soyuz
Emergency crew return available using Soyuz spacecraft

Flight 2A
Unity Node Connecting Module

Flight 7A
Airlock Enables Spacewalks without Shuttle present

Flight 6A
Robotic arm marks initial Canadian contribution

Lab Outfitting: Flight 5A.1
U.S. Lab "Destiny" sets the stage for research

Lab Launch: Flight 5A
Improved command and control from Mission Control Center Houston (MCC-H) with electronics in U.S. Lab

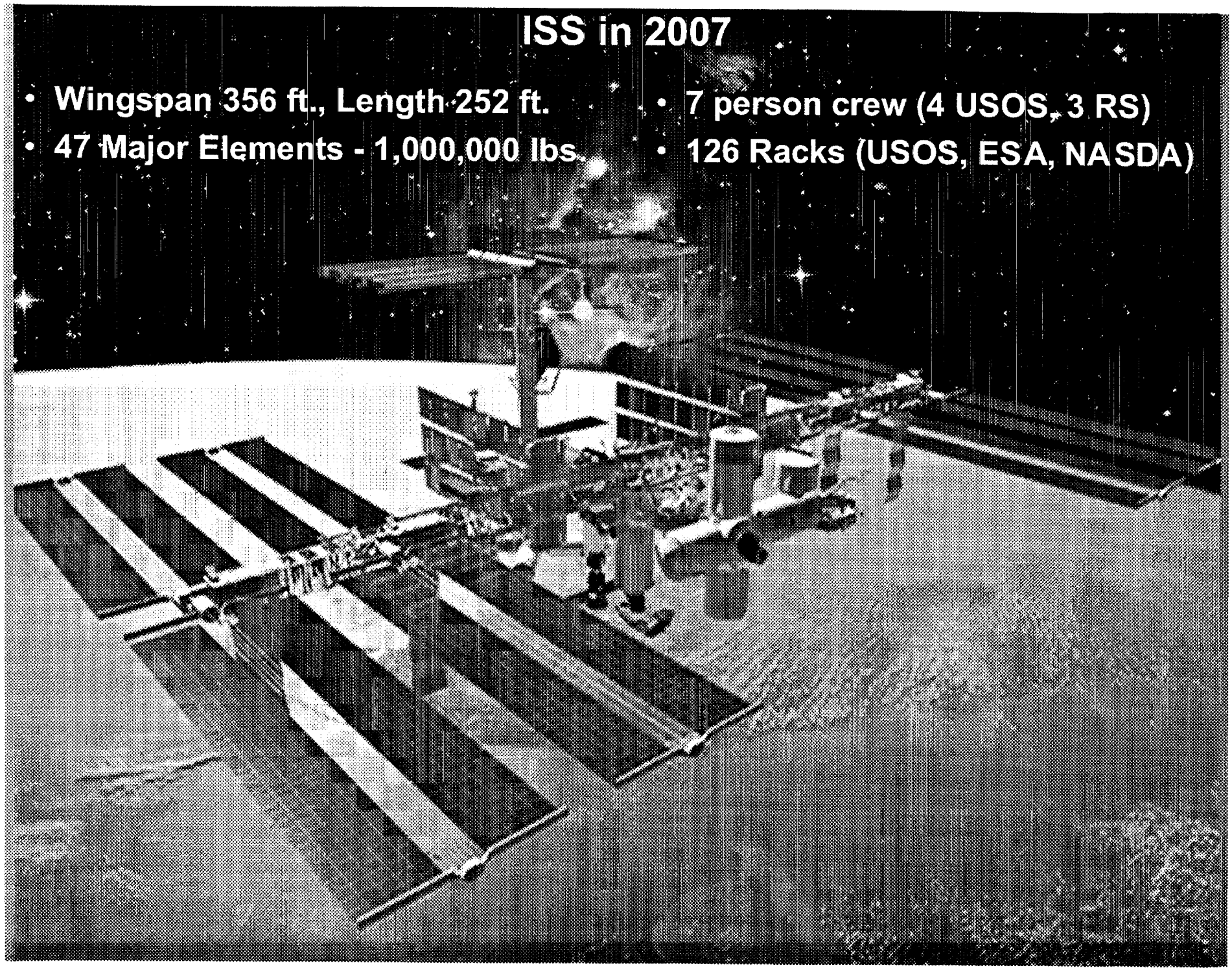
ISS in 2007
• Wingspan 356 ft., Length 252 ft.
• 47 Major Elements - 1,000,000 lbs.
• 7 person crew (4 USOS, 3 RS)
• 126 Racks (USOS, ESA, NASDA)

ISS in 2007

- **2M lines of flight code**
  - 4M lines of ground/test code
- **Integrated logistics program consisting of:**
  - 5 different vehicles visiting ~14 times each year
    - STS (5), Progress (5), Soyuz (2), HTV (1), ATV (1)
  - 4 launch systems in different countries
    - Shuttle, Ariane, Soyuz, HII
  - More than 40,000 items to track on orbit at any given time
  - 2 crew rescue vehicles attached to ISS
    - (CRV/Soyuz)
  - 10 - 20 EVAs per year
    - Russian, U.S.

ISS, The Overall Challenge

- Building and assembling the ISS is a major undertaking with no parallel in the history of space flight
  - Involves 16 countries, 47 major elements, and more than 100 smaller ones
  - Requires 47 space flights just to assemble (38 shuttle and 9 Russian)
  - At assembly complete, ISS will consist of 1 million pounds of hardware orbiting the earth every 90 minutes with 6 laboratories available full time to conduct research for at least 10-15 years
- More than a half million pounds of hardware has been delivered to the Space Station Processing Facility at KSC, where it is undergoing integrated testing and preparation for launch
  - Hardware for 9 of the next 10 flights is currently at KSC with more on the way
  - Testing and preparation of the hardware is complete for some elements and progressing well for the remainder
  - The hardware will be ready to meet the launch schedules for the upcoming missions

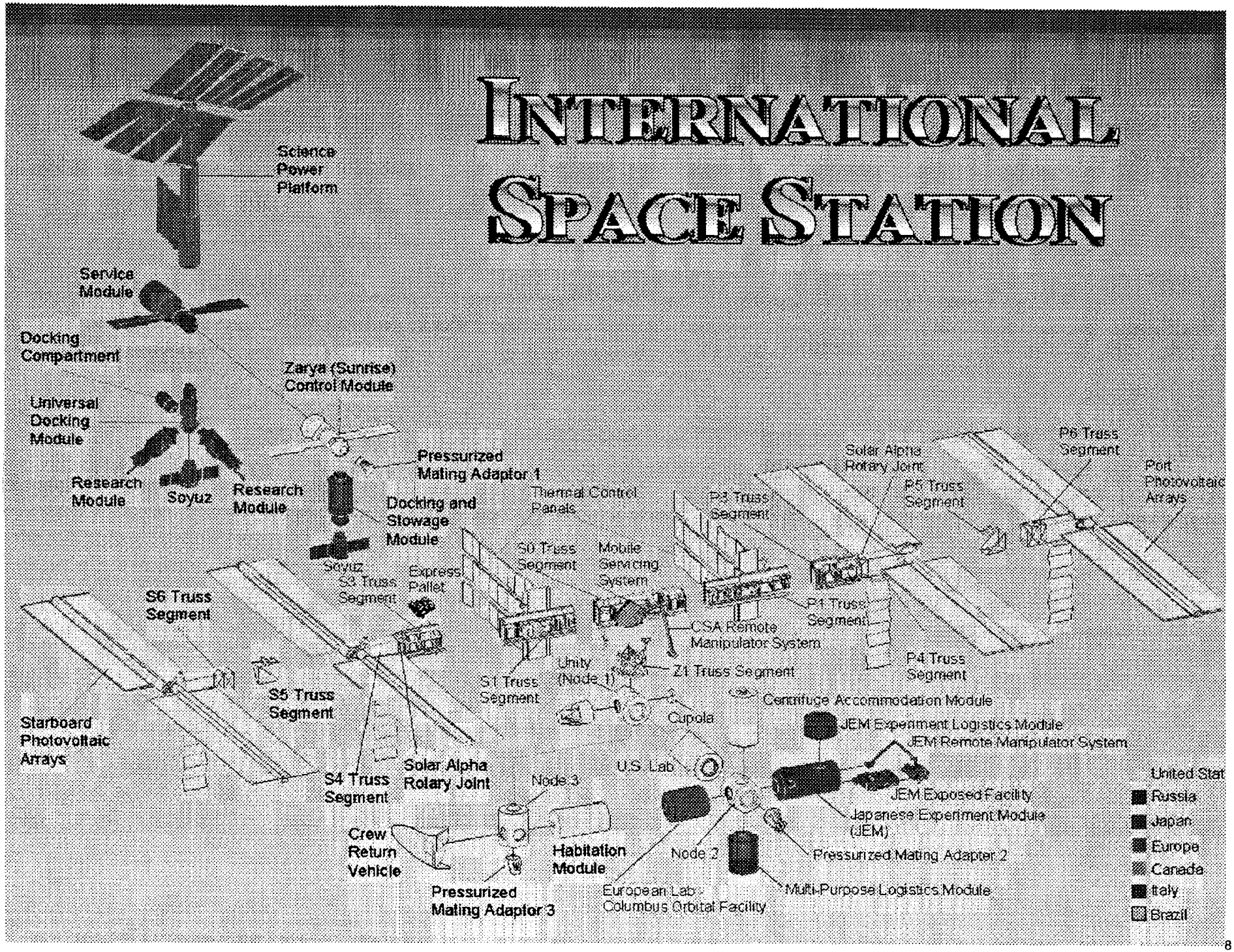
INTERNATIONAL SPACE STATION
Science Power Platform
Service Module
Docking Compartment
Zarya (Sunrise) Control Module
Universal Docking Module
Pressurized Mating Adaptor 1
Research Module
Soyuz
Research Module
Docking and Stowage Module
Thermal Control Panels
P6 Truss Segment
Solar Alpha Rotary Joint
P5 Truss Segment
P3 Truss Segment
Port Photovoltaic Arrays
Soyuz
S3 Truss Segment
Express Pallet
S0 Truss Segment
Mobile Servicing System
S6 Truss Segment
P1 Truss Segment
CSA Remote Manipulator System
Unity (Node 1)
Z1 Truss Segment
P4 Truss Segment
S1 Truss Segment
Centrifuge Accommodation Module
Cupola
JEM Experiment Logistics Module
JEM Remote Manipulator System
S5 Truss Segment
Starboard Photovoltaic Arrays
U.S. Lab
Node 3
Solar Alpha Rotary Joint
S4 Truss Segment
JEM Exposed Facility
Japanese Experiment Module (JEM)
Crew Return Vehicle
Habitation Module
Node 2
Pressurized Mating Adapter 2
Pressurized Mating Adaptor 3
European Lab: Columbus Orbital Facility
Multi-Purpose Logistics Module
United Stat
Russia
Japan
Europe
Canada
Italy
Brazil

NASA/CP—2000-210470

Space Station Research
An Investment in Our Future

- **Improving Industrial Processes**
  - Combustion Science
  - Fluid Physics
  - Materials Science
- **Increasing Fundamental Knowledge**
  - Fundamental Physics
  - Fundamental Biology
  - Earth Science
  - Space Science
- **Looking After Our Health**
  - Biomedical Research
  - Crew Care and Countermeasures
  - Protein Crystal Growth Research
  - Cell and Tissue Science
  - Advanced Medical and Life Support Technologies
- **Enabling Exploration**
  - Engineering Research
  - Scientific Research
- **Researching Tomorrow's Products Today**
  - Commercial Cooperative Research
  - Testbed for New Commercial Processes, Products, and Services

We'll Do Research While We Build

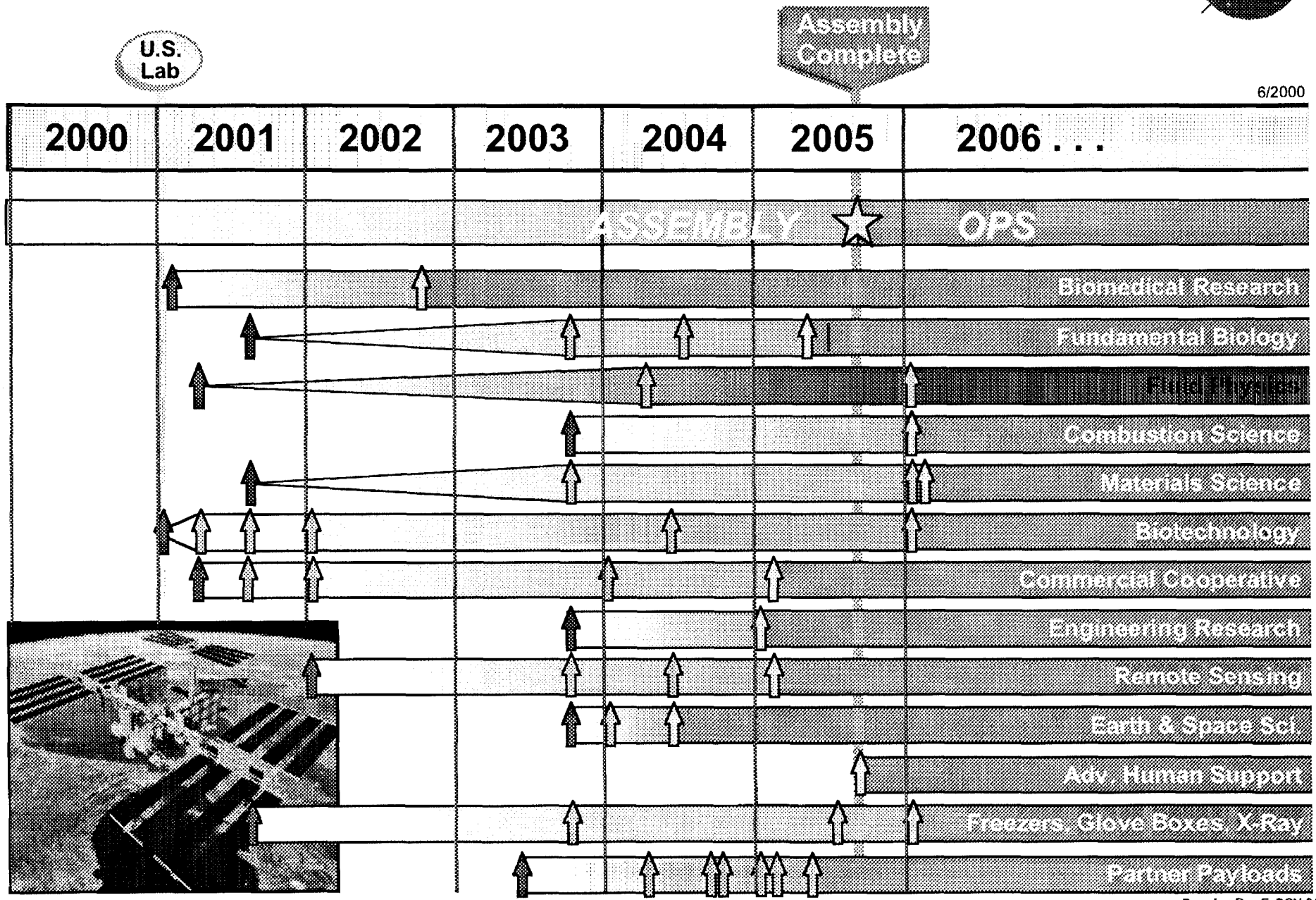

GRC Microgravity Science Program

Fluids and Combustion Facility

Facility for World-Class Research U.S. Laboratory Module Interior

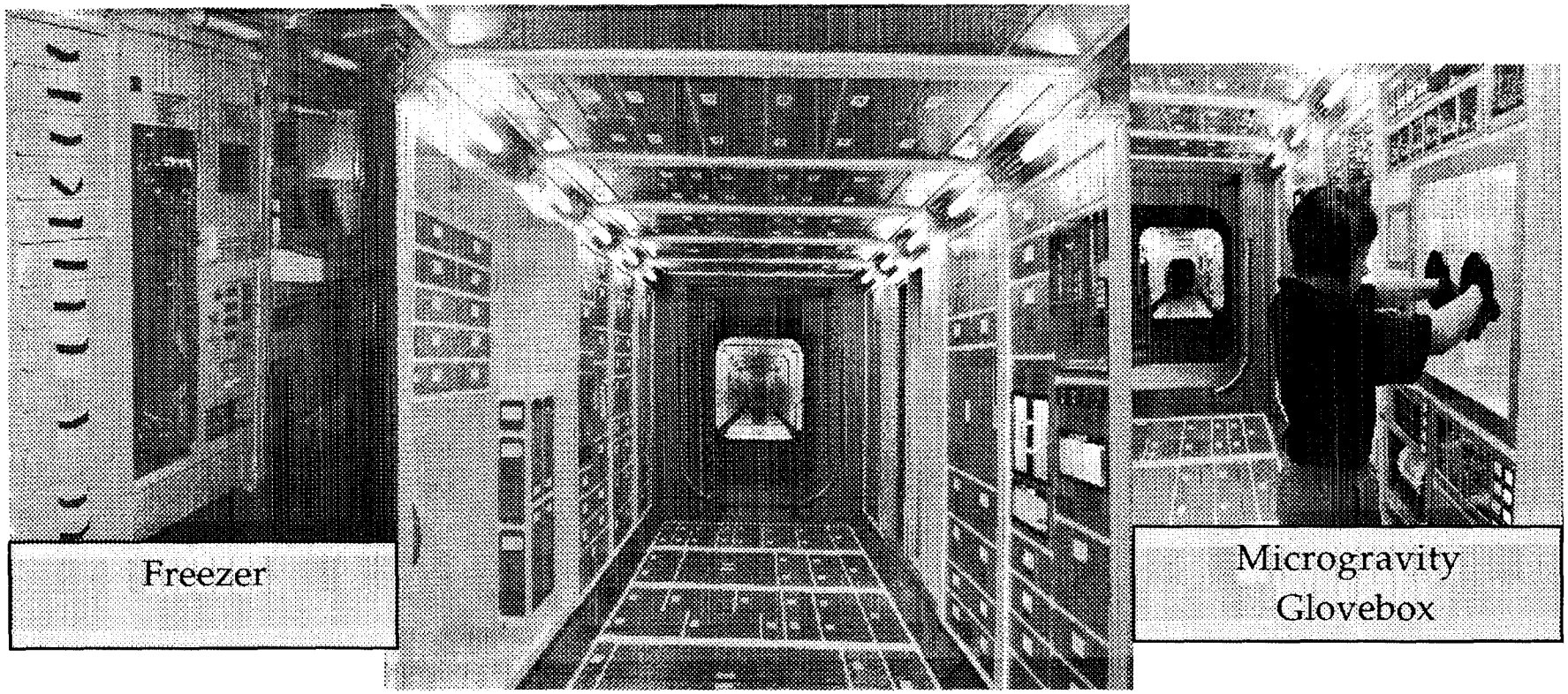

The Space Station is the largest structure ever built in Space

- Pressurized volume will be roughly equivalent to the interior of two 747 jets
- 6 labs with 24 experiment racks (about the size of a refrigerator) and 11 vibration isolation racks for experiments that require quiescent environment

GRC Microgravity Science Program

Fluids and Combustion Facility

Expedite the PRocessing of Experiments to Space Station - EXPRESS

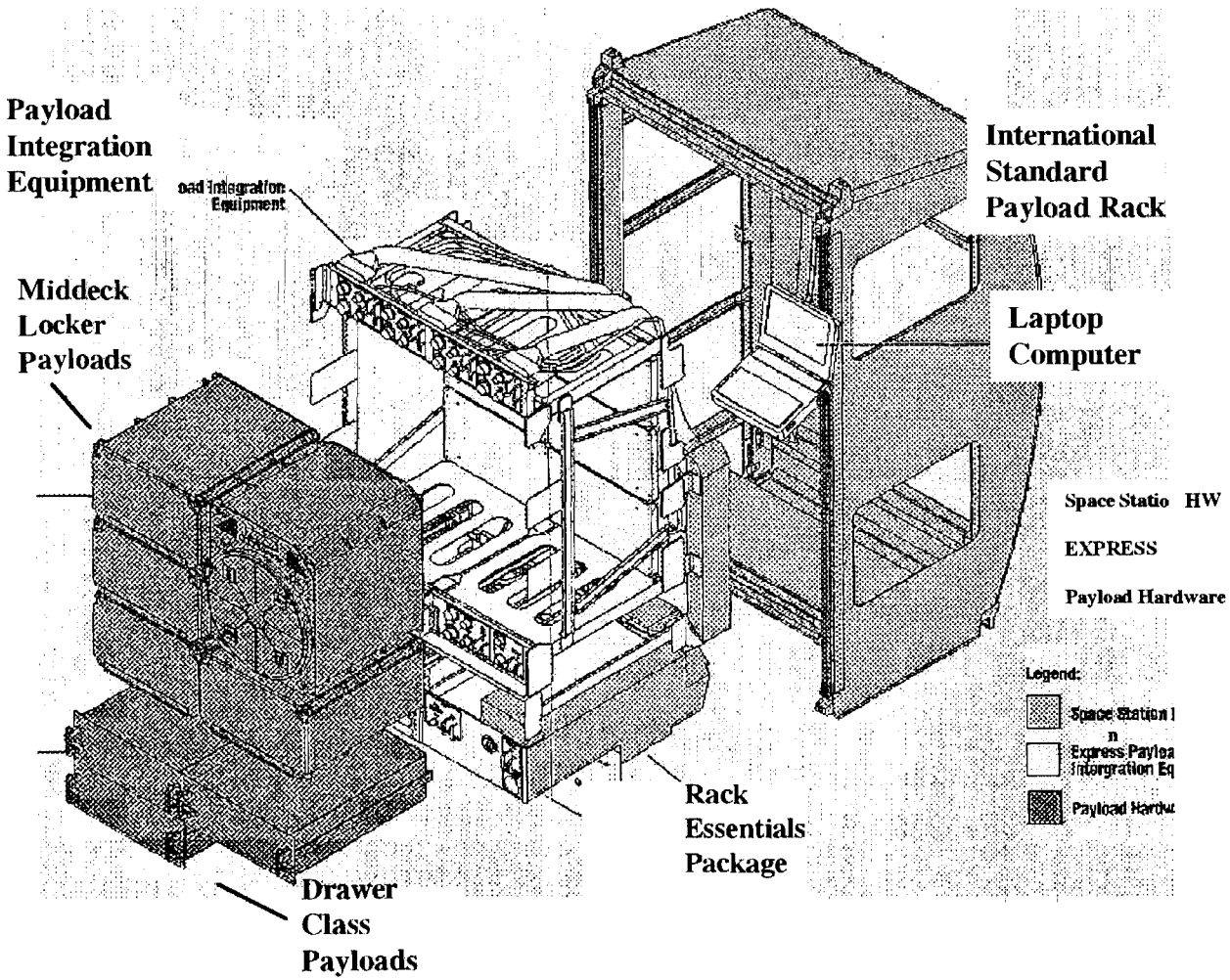

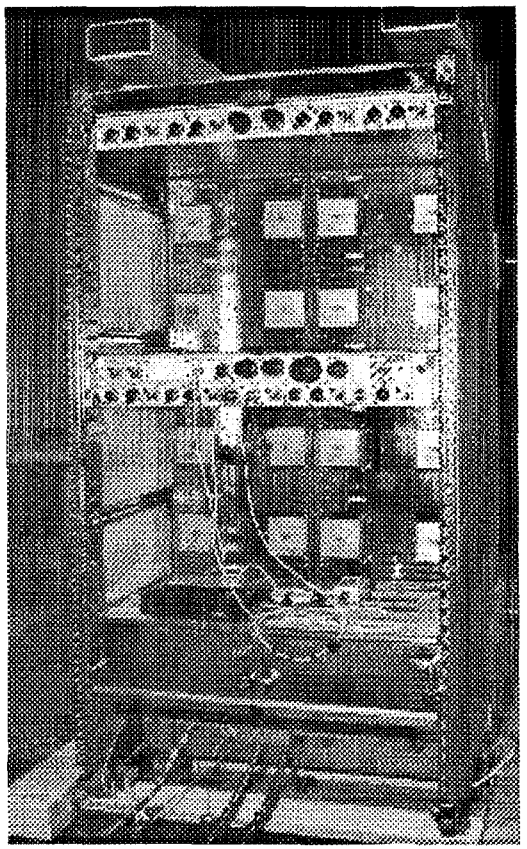

Developed by: MSFC

Launch Date: 2001

GRC Microgravity Science Program

Fluids and Combustion Facility

Microgravity Science Glovebox

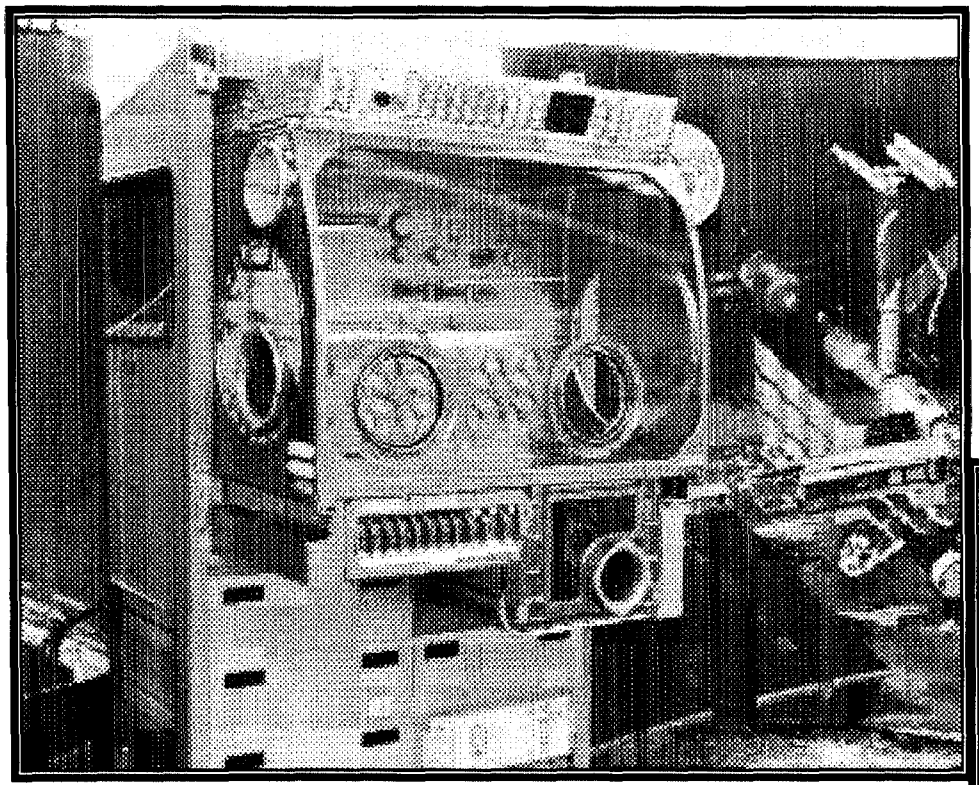

Managed by: MSFC
Developed by: ESA
Launch Date: September 2001

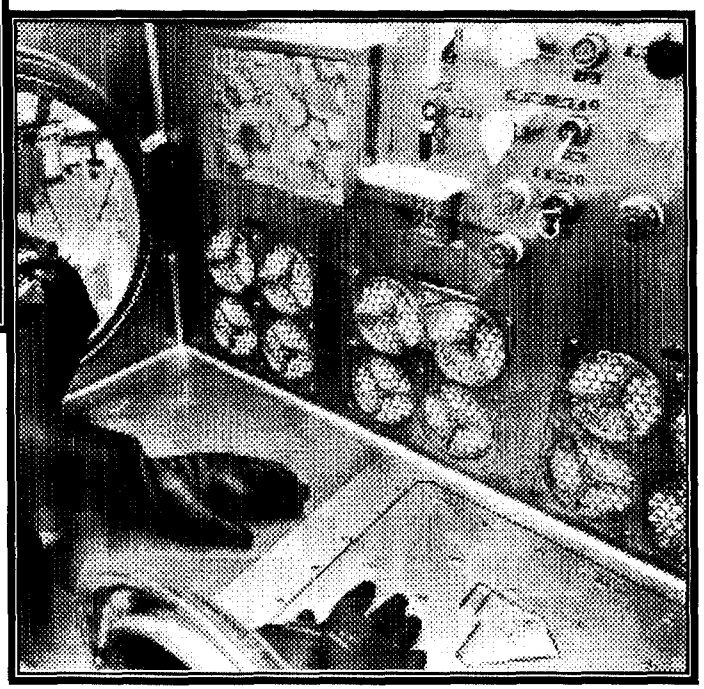

Work Volume: 255 liters
Power Available: 1 KW (for PI usage)
Containment: 2 Levels
Video: 3 Color Cameras
1 B&W Camera
4 Digital Recorders

astrium

Fluid Science Lab

Developed by: ESA

Launch Date: September 2001

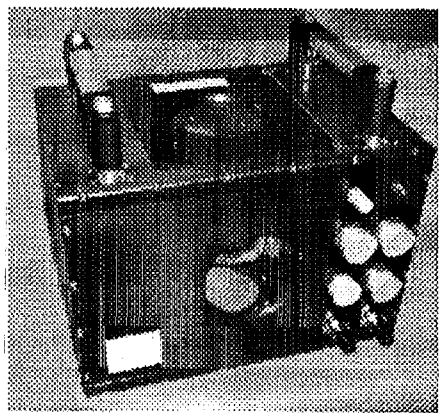

Exp, Container:	40 x 27 x 28 cm
Power Available:	100 -200 W (430 W Max)
Containment:	2 - 3 Levels
Mass (Typical):	20-30 kg (40 kg max)
Central FOV:	80 x 80 mm

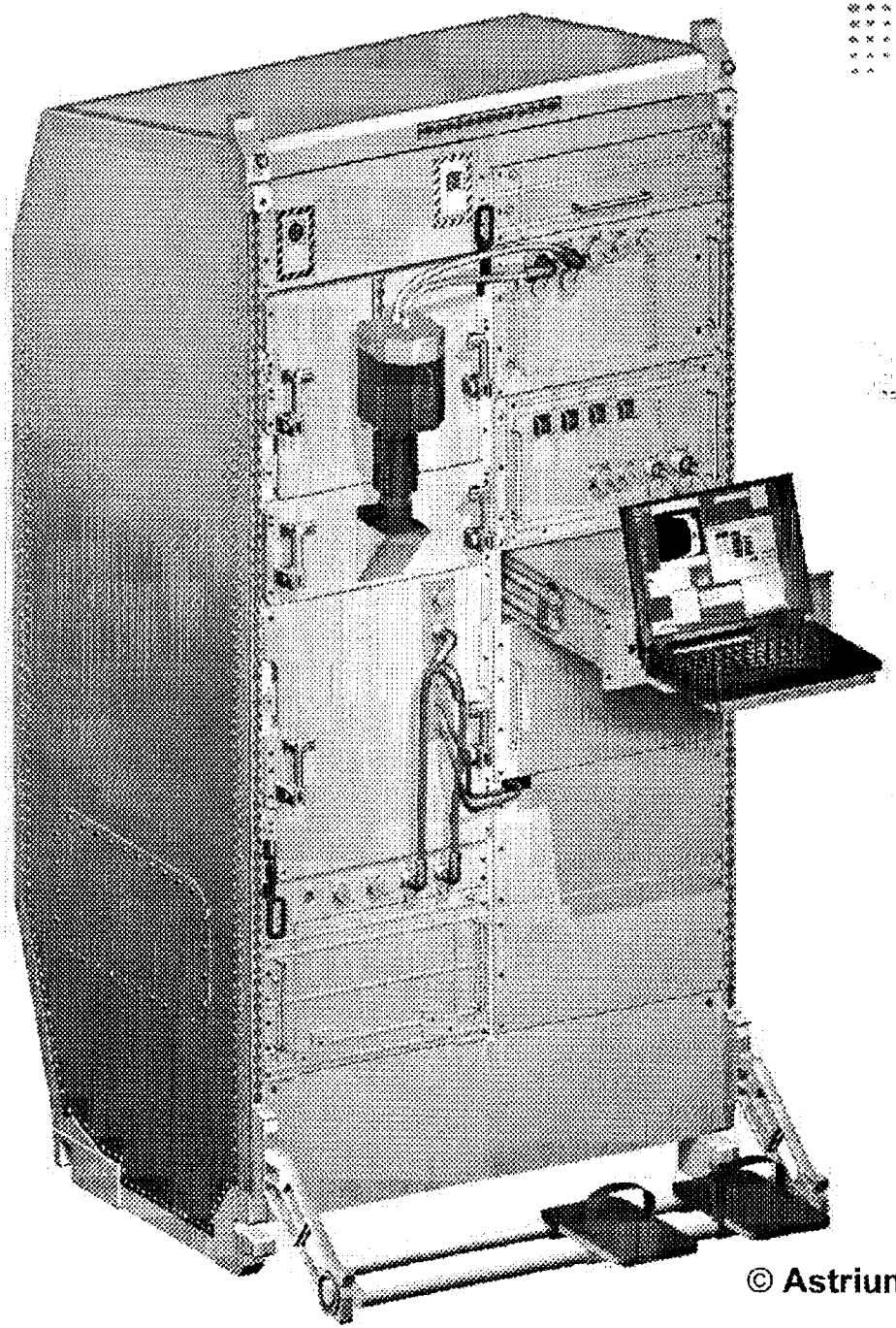

© Astrium

astrium

FSL Optical Diagnostic Methods Science Lab

Diagnostic Elements:

- Variable Background illumination
- Variable Lightsheet (f. Velocimetrie, PIV)
- Schlieren
- Wollaston/Shearing Interferometer (var. Sensitivity)
- Electronic Speckle Pattern Interferometer (ESPI)
- Holographic Interferometer (with TPC)
- Holography
- Standard Recording with dig. CCD (1K_, 30 Hz)
- Frontmounted CCD Cameras (Highspeed, Highres., Film)
- Experimentspec. Diagnostics (Tomograph., LDA, spher. Optics, direct Laserbeam, etc.)
- digital + analog Videointerfaces at Exp. Container

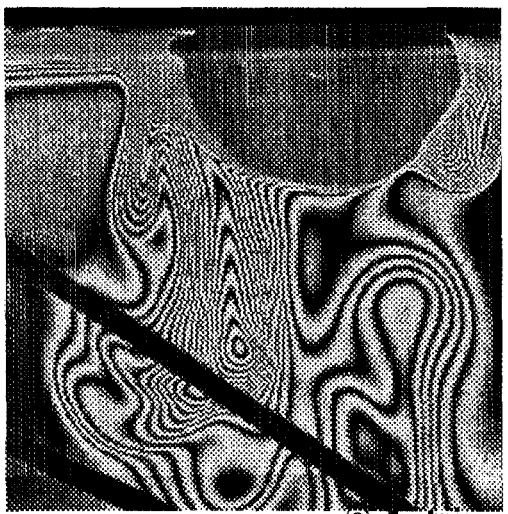

Video Management Unit:

- Simultaneous Management of 3 CCD-Cameras
- Intermed. Recording of Video Data (36 GB HDD, Tape)
- Variable Videodata Compression (JPEG)

© Astrium

GRC Microgravity Science Program

Fluids and Combustion Facility

ISS Fluids and Combustion Facility in US Lab Mockup

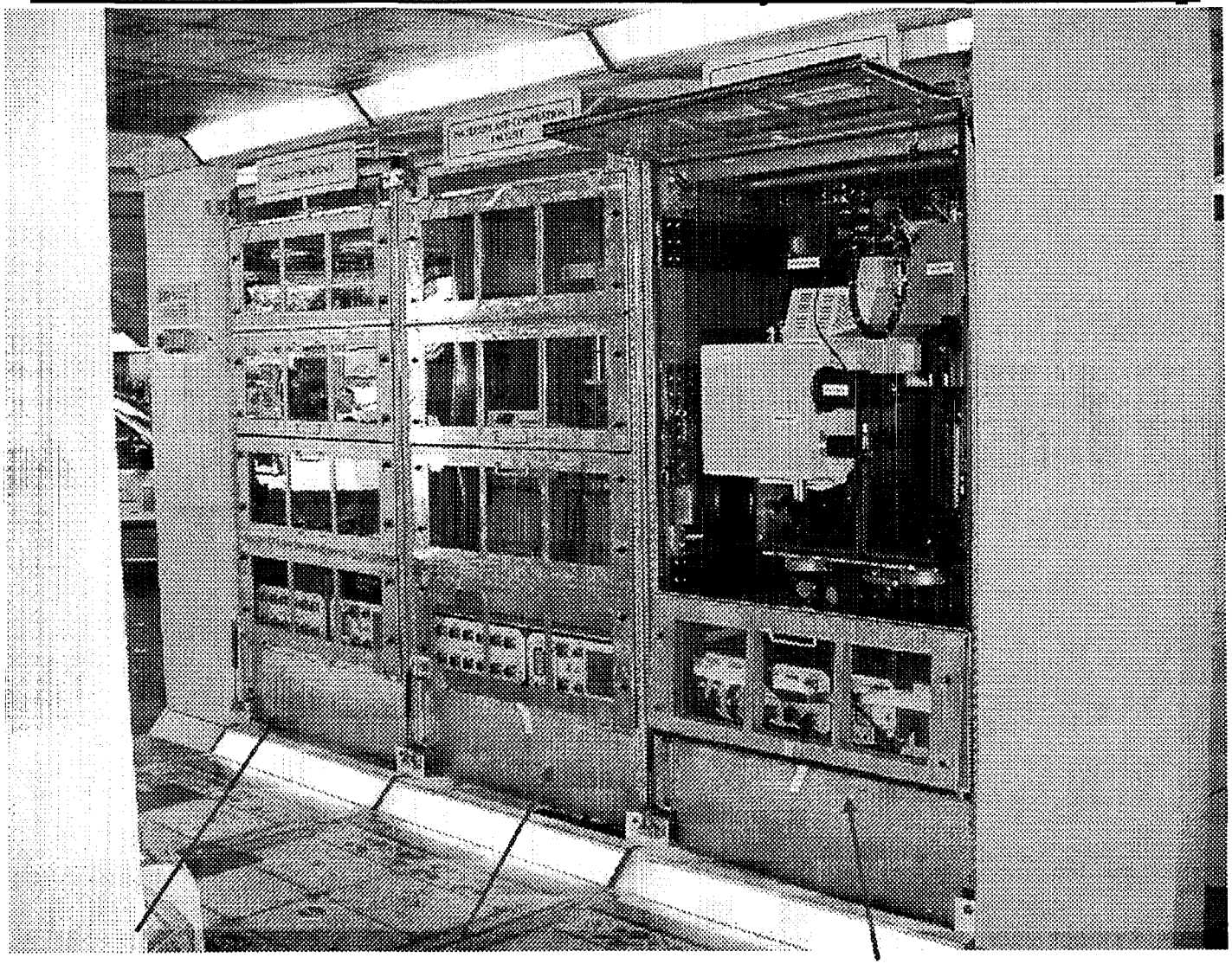

Combustion Integrated Rack (CIR)

Shared Accommodations Rack (SAR)

Fluids Integrated Rack (FIR)

GRC Microgravity Science Program

Fluids and Combustion Facility

FCF Flight Segment

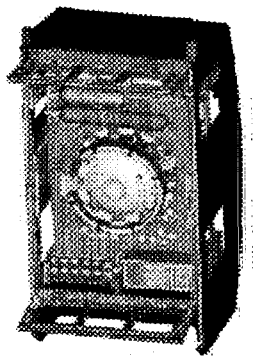

Combustion Integrated Rack (CIR) UF-3

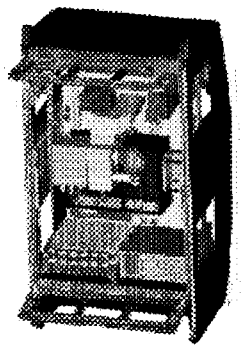

Fluids Integrated Rack (FIR) UF-5

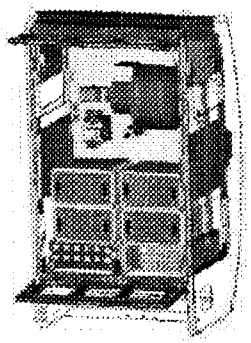

Shared Accommodations Rack (SAR) 2006

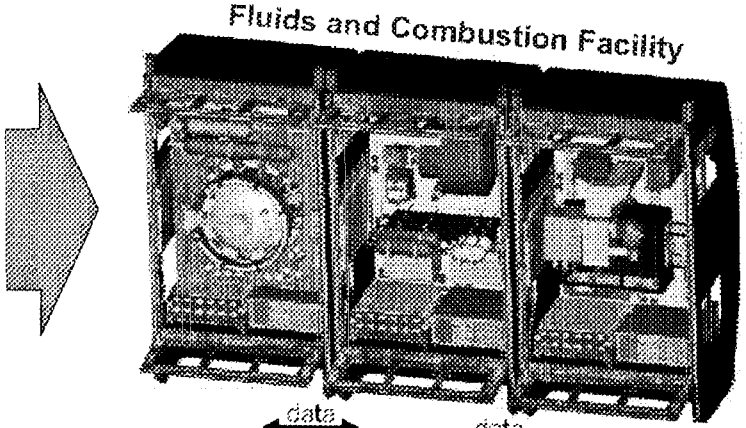

CIR and FIR operate independently until SAR is deployed to ISS.

Assembly of FCF is completed by the addition of the SAR. Fluid Physics and Combustion Science disciplines then share racks and mutually necessary hardware/software.

FCF will accommodate all envisioned experiments at the rate of 10 or more per year for the lifetime of the Space Station.

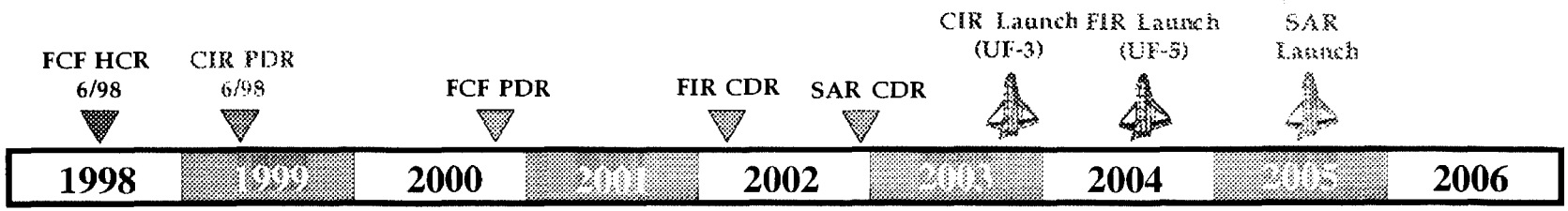

GRC Microgravity Science Program

Fluids and Combustion Facility

Mission: Fluid Physics Research

Interfacial Phenomena

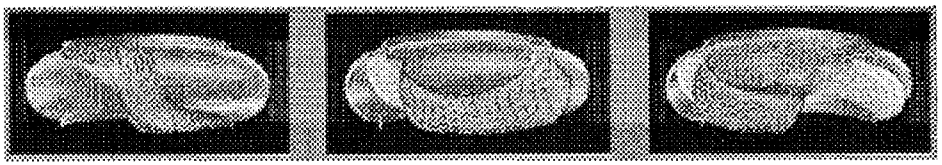

Interfacial configuration experiment (ICE)

Complex Fluids

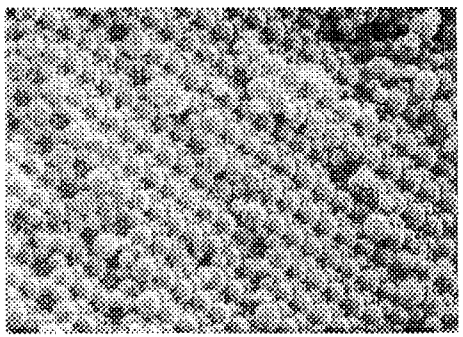

colloidal crystals

16 Basis Experiments

Dynamics & Stability

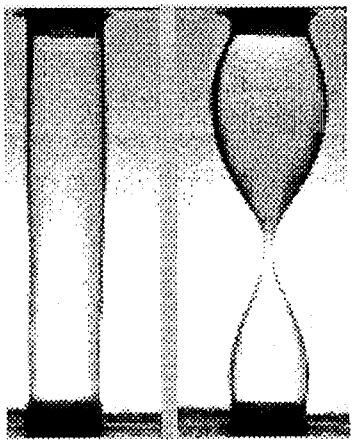

Electrohydrodynamics

Multiphase Flow and Heat Transfer

Normal Gravity

Lunar gravity

Microgravity

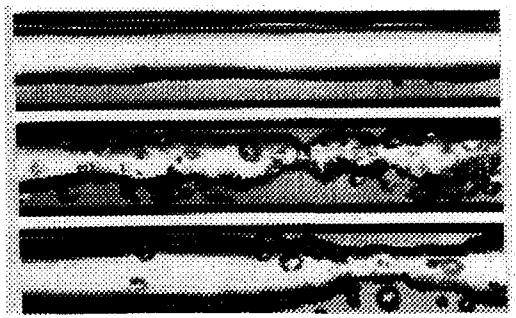

Gas

Liquid

GRC Microgravity Science Program

Fluids and Combustion Facility

Typical ISS Increment - Diverse Fluids Science Complement

Fluids Integrated Rack with LMM

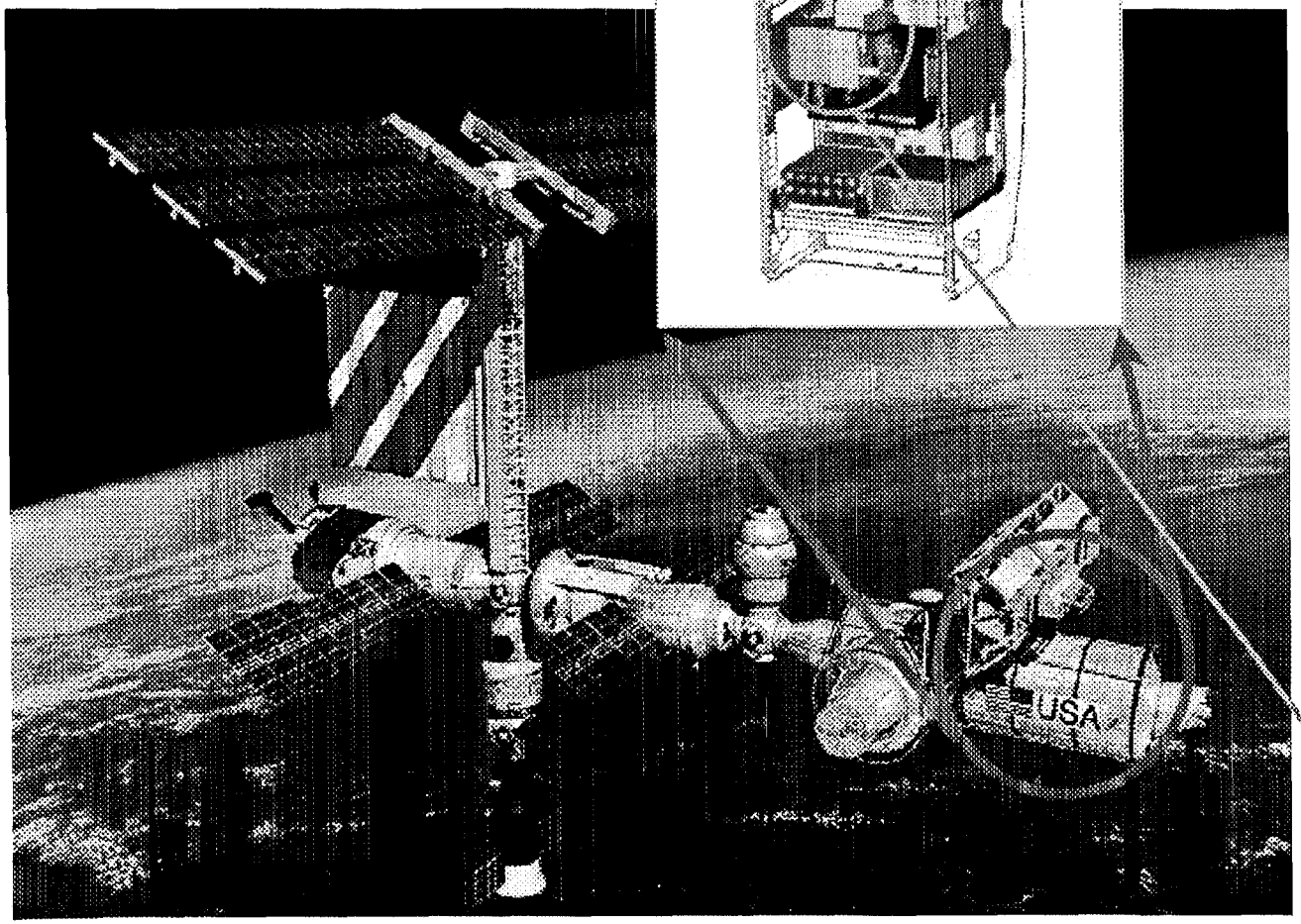

Example Experiment Packages

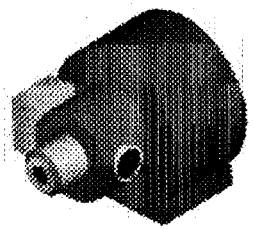

Pool Boiling

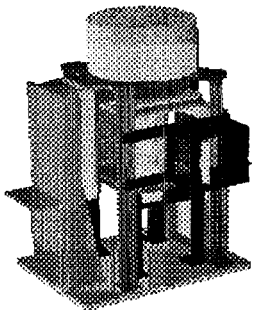

Microscale Hydrodynamics

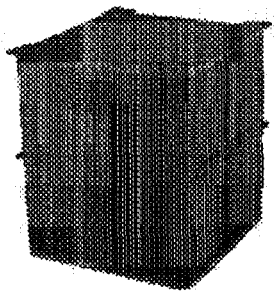

Physics of Colloid In Space

GRC Microgravity Science Program

Fluids and Combustion Facility

FCF Hardware Development Plan

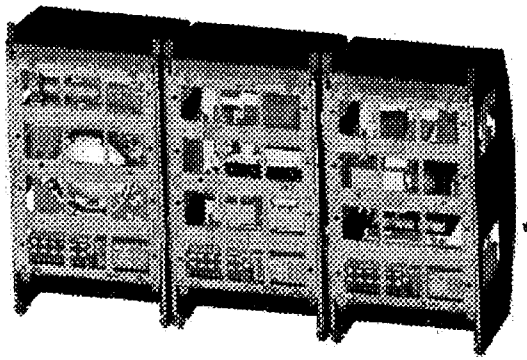

Protoflight Unit

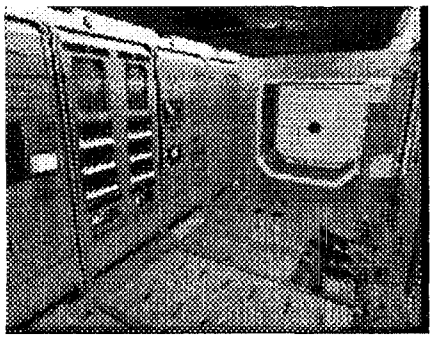

ISS US Laboratory

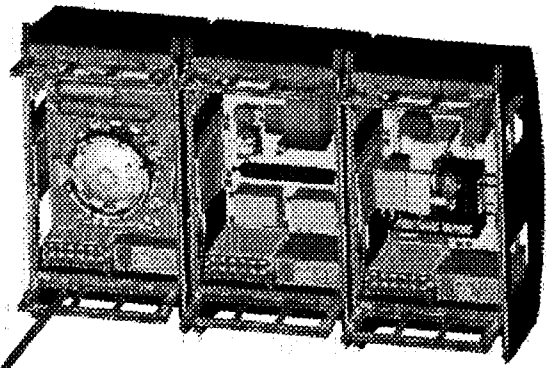

Engineering Development Unit

Remodeled Engineering Unit

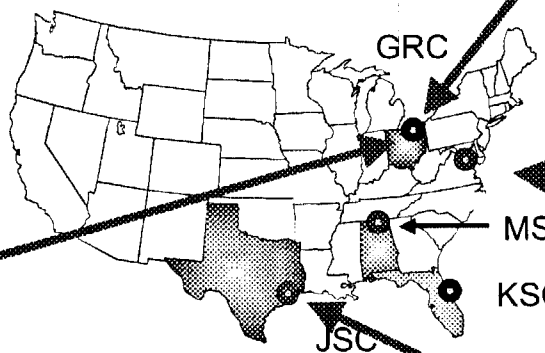

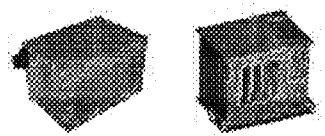

Diagnostic Simulators

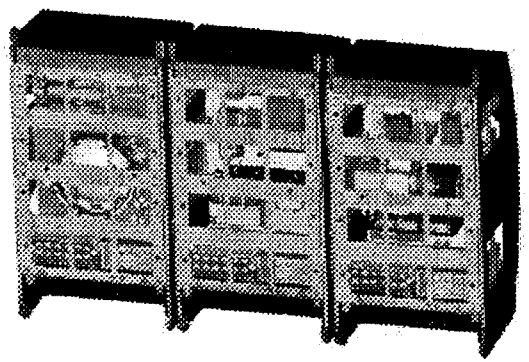

Ground Integration Unit

Identical to Protoflight Unit

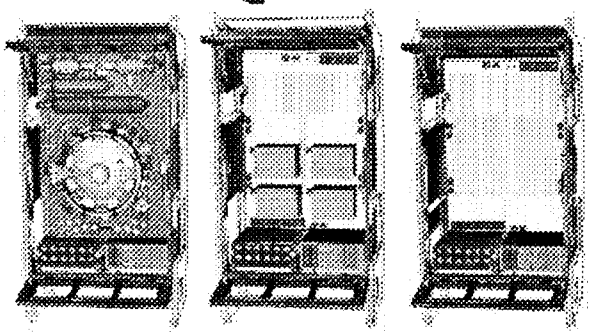

Payload Training Center

(PTC) Trainers

GRC Microgravity Science Program

Fluids and Combustion Facility

Integrated FIR/SAR System

The FCF concept includes the development of support subsystems and laboratory style diagnostics common to the discipline specific researchers and then supplements the laboratory with unique science hardware developed for each Principal Investigator (PI). The PI unique hardware customizes the facility in a unique laboratory configuration to perform a given PIs research effectively.

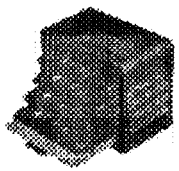

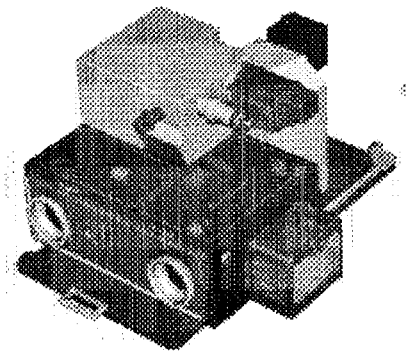

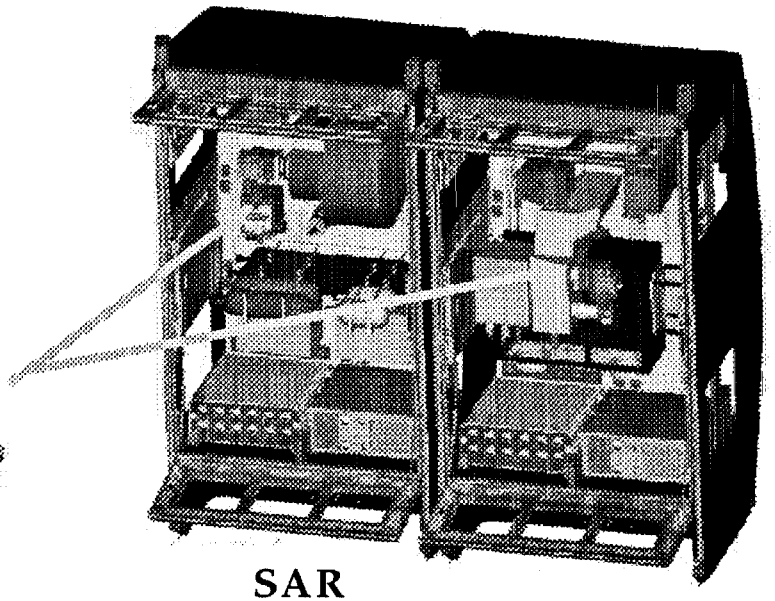

SAR

FIR

PI Specific Samples

- Samples with supporting hardware
- Specific Conditioning
- Specific Diagnostic

Multi-User Apparatus

- Science Infrastructure (hardware/software) items that uniquely meet the needs of the PIs
- Unique Diagnostics
- Specialized Imaging
- Fluid Containment

Fluids Integrated Rack/ Shared Accommodations Rack

- Power Supply
- Avionics/Control
- Common Illumination/Lasers
- Optics Bench
- Imaging Capture
- Environmental Control
- Command and Data Handling
- Active Rack Isolation

FCF Fluids Integrated Rack Overview

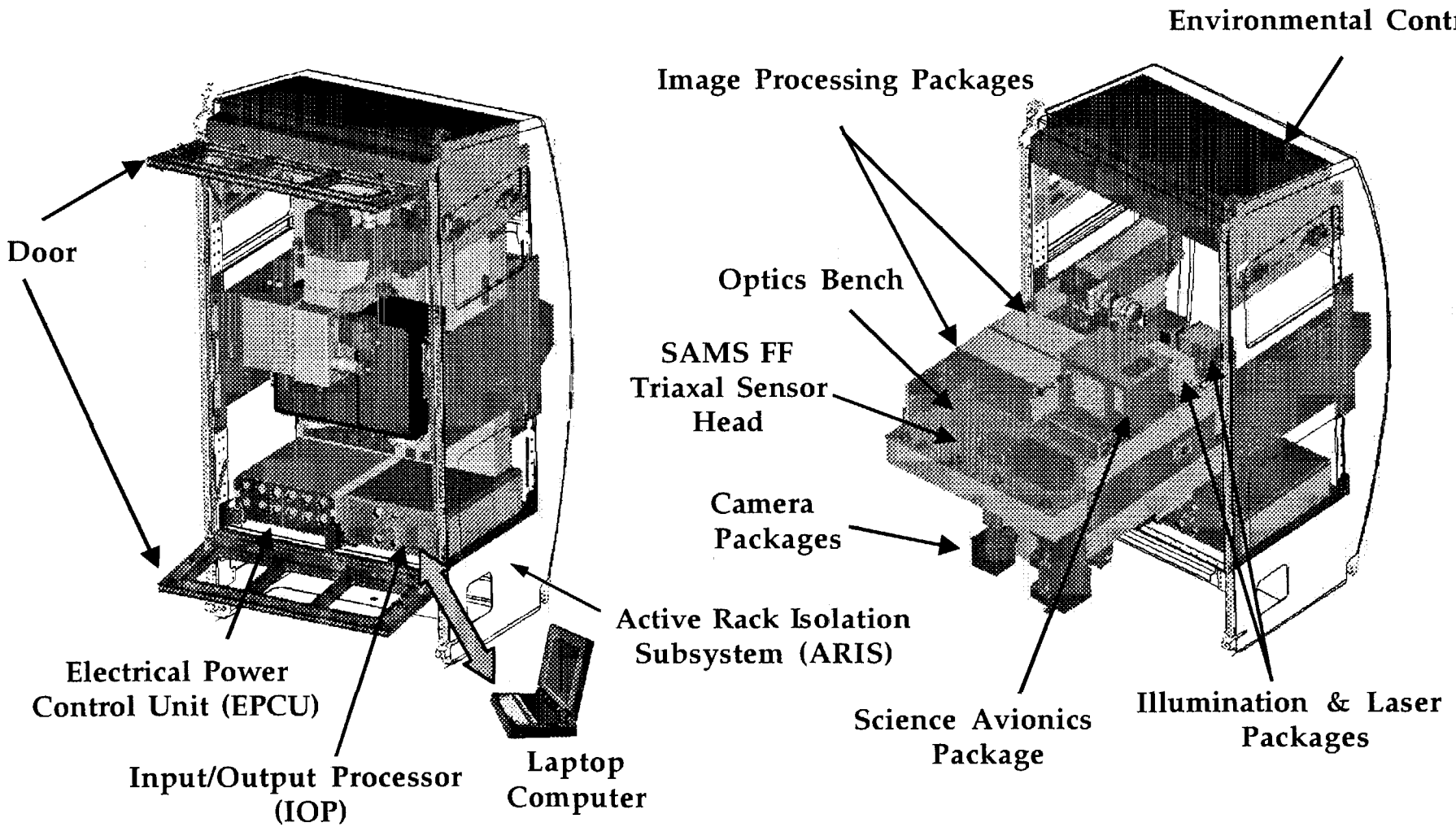

The FIR and SAR Build Upon CIR Subsystems

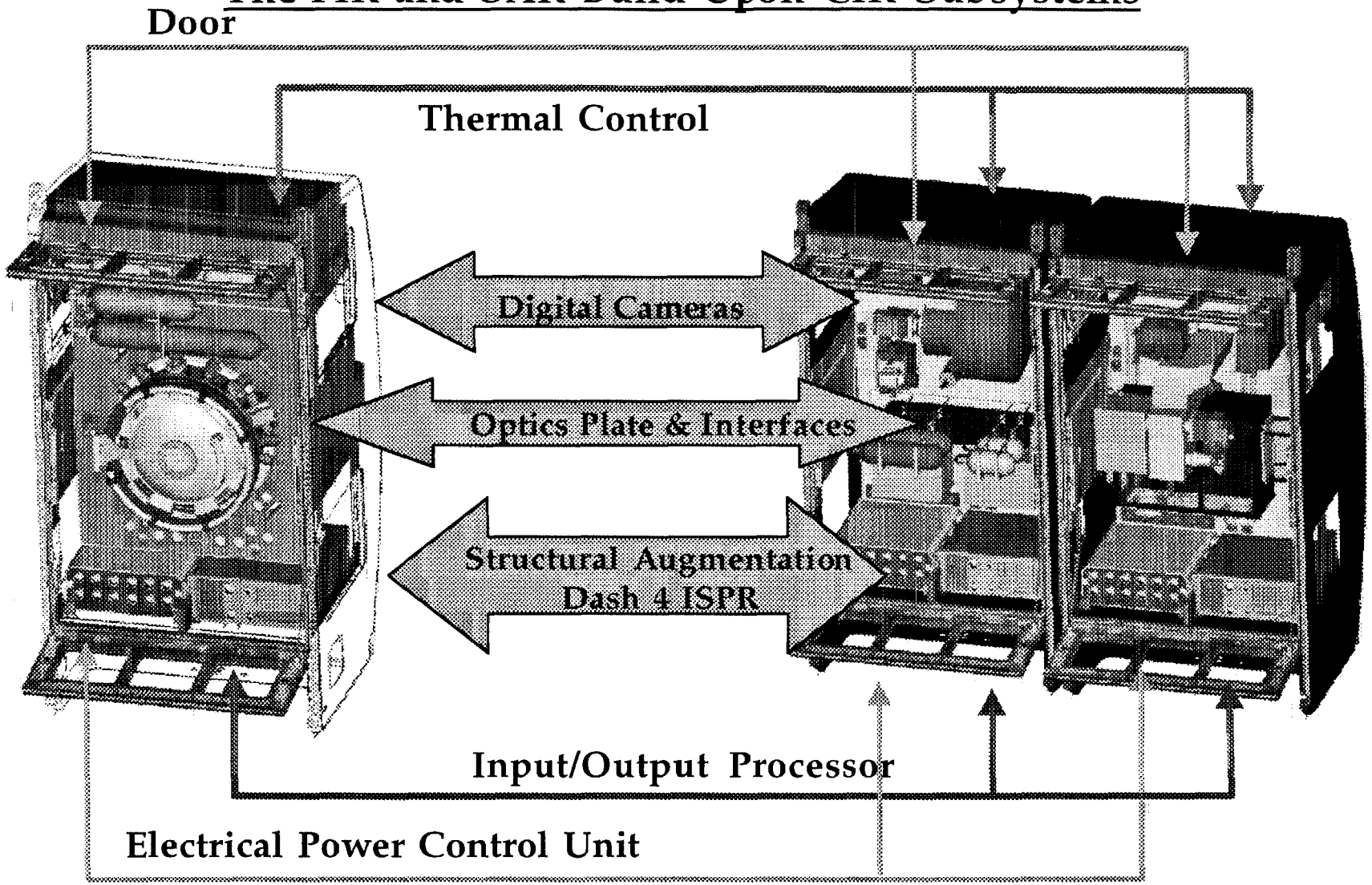

GRC Microgravity Science Program

Fluids and Combustion Facility

Combustion Integrated Rack Overview

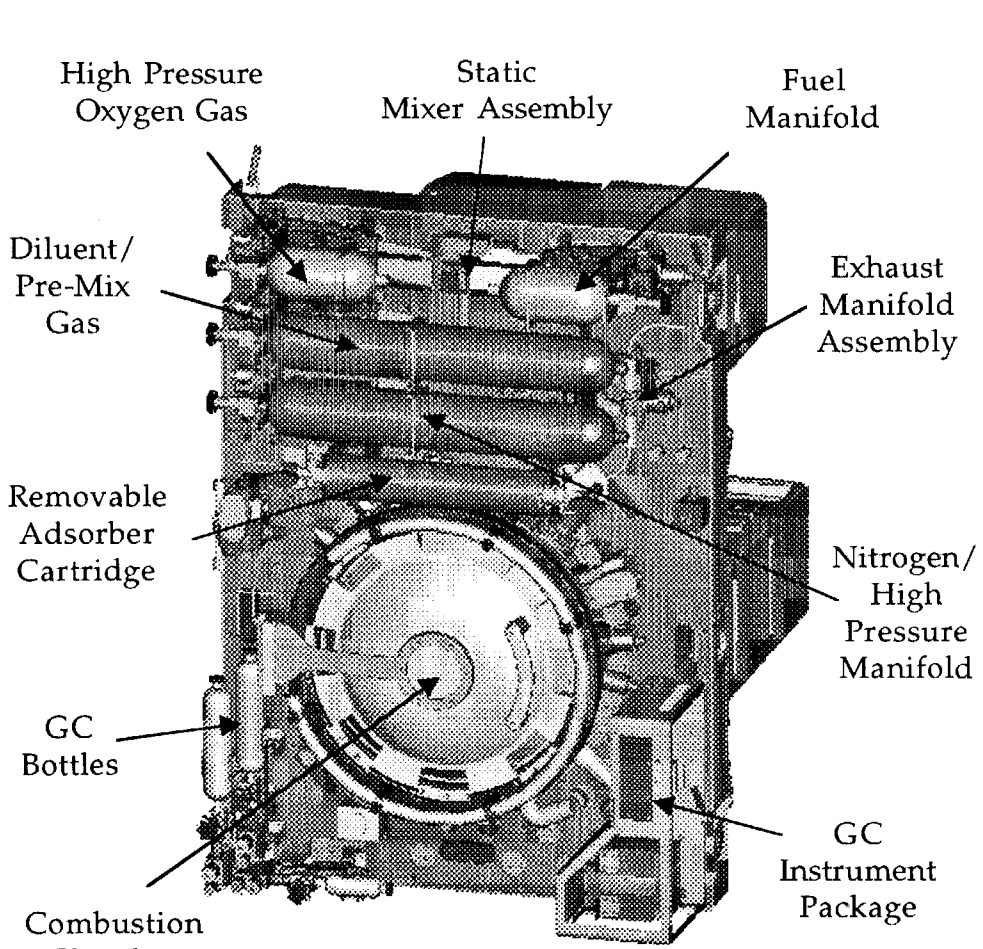

(Front View)

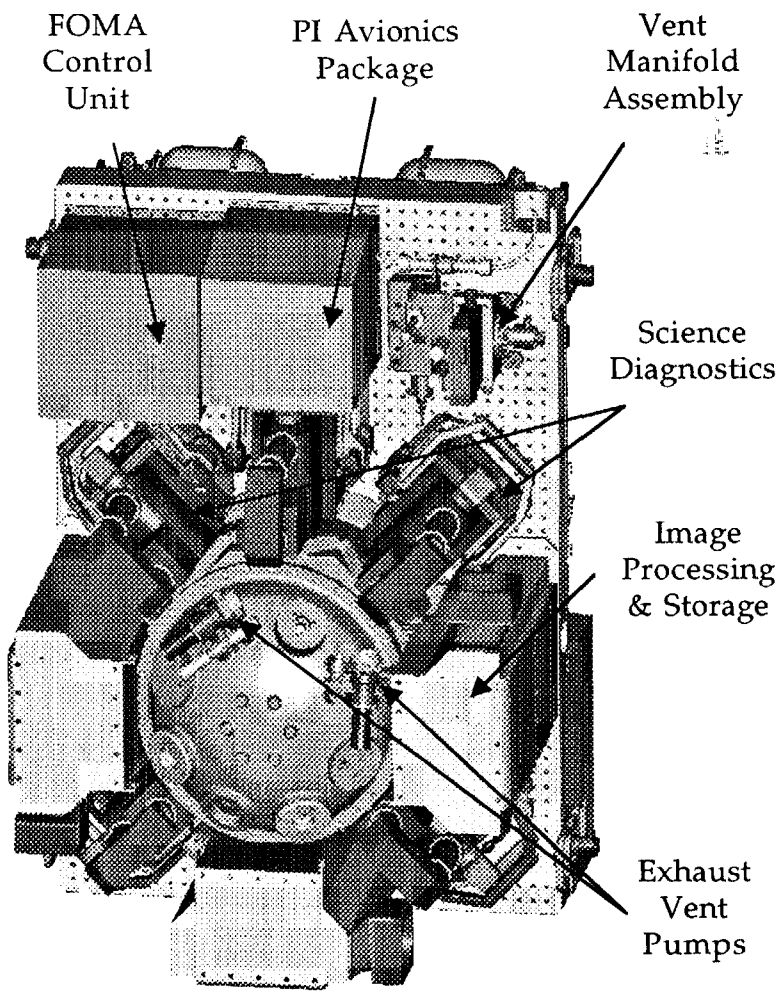

(Rear View)

GRC Microgravity Science Program

Fluids and Combustion Facility

FCF Shared Accommodations Rack Overview

Environmental Control Subsystems
- Water Thermal Control
- Air Thermal Control (Fan/Hx)
- Fire Detection and Suppression
- Gas Interfaces

Power Controller
- Electrical Power Control Unit
- 120 VDC to 28 VDC Conversion
- Configurable by User Loads

Rack Door
- Provides Thermal Containment
- Provides for Fire Detection
- Acoustic Noise Containment

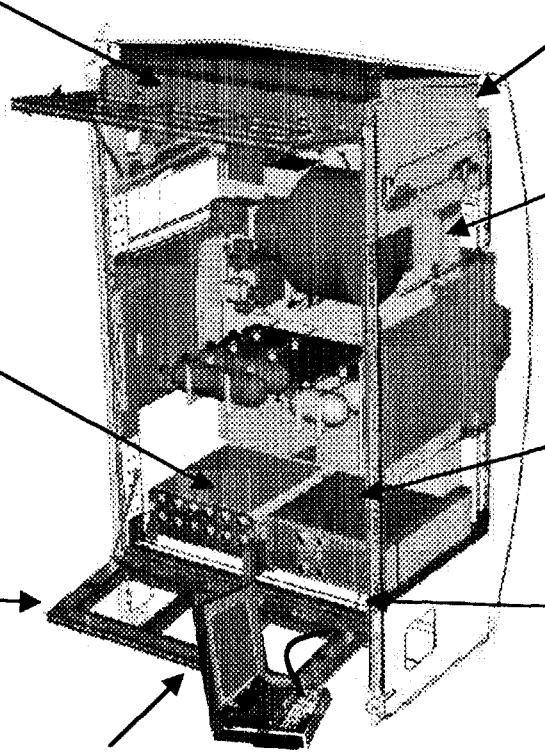

Rack
- ARIS
- 4 Post ISPR Configuration

Utility Plate
- Translates, Folds Out for Access
- Flexible Mounting Configuration
- 16 PU Plate

Input/Output Processor
- 4 PU IOP

Rack-to-Rack Umbilicals
- Fiber
- Configurable From Front of Rack

Facility Laptop Computer
- Station PCS Compatible

Power, Data, Environmental Control and Structural Subsystems in SAR Patterned After Those in FCF Combustion Rack and FCF Fluids Rack.

GRC Microgravity Science Program

Fluids and Combustion Facility

FIR Accommodations

FIR Features:

- Easy access via fold down bench
- Diagnostics easily reconfigured, replaced/interchanged on optics plate
- Accommodates many experiment configurations and disciplines

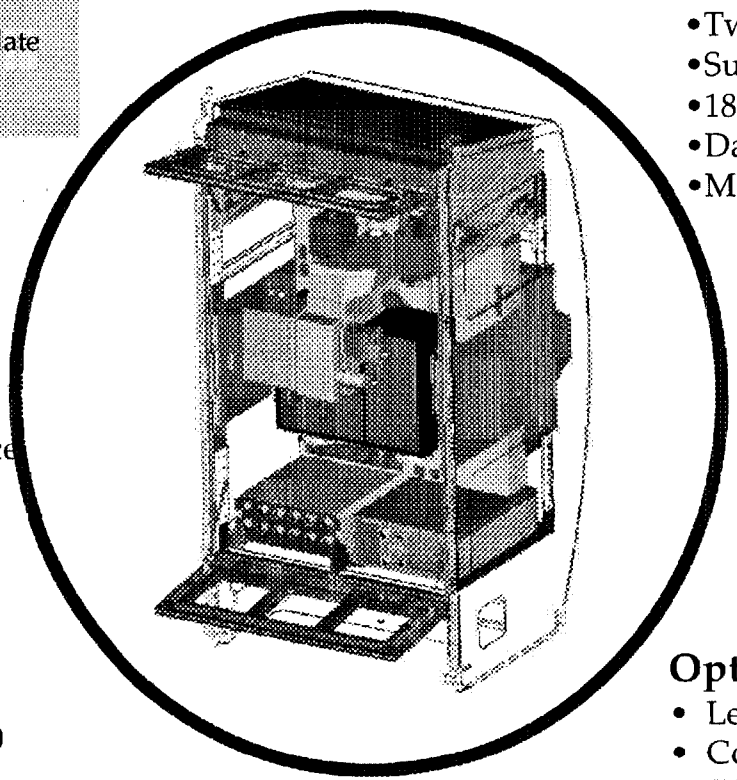

Basic Services

- PI Volume: 460 liters
- Rotating Optics Bench
- Electrical Power
- Remote Operation Capability
- Environmental Control
- ISS Command and Data Interface
- Control/Timing

Illumination & Laser Packages:

- White Light via fiber Weave
- LED Array
- Laser Diodes (680 and 780 mm)
- Nd: YAG

Image Processing & Storage Units

- Two Independent Image Processors
- Support for High Resolution Digital Camer
- 18.2 GB Hard Drives
- Data Compression
- Motion Control for A

Cameras:

- Color Camera
- Hi Resolution
- Ultra High Speed

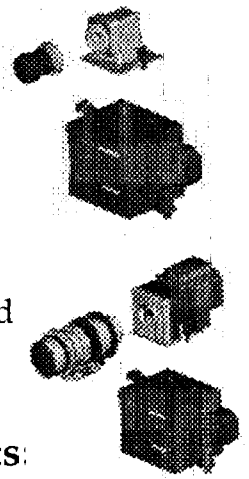

Optical Components:

- Lenses
- Collimators
- Fiber optic cables

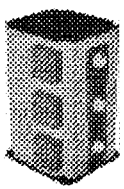

Laser Diodes

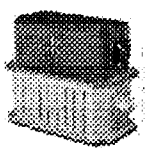

Nd:YAG

LED Array

Lenses

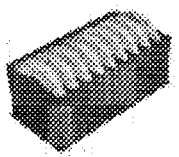

Optical Fibers

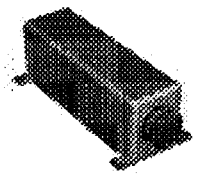

Collimating Optics

GRC Microgravity Science Program

Fluids and Combustion Facility

FCF/FIR Customized for Each New Fluid Physics Experiment

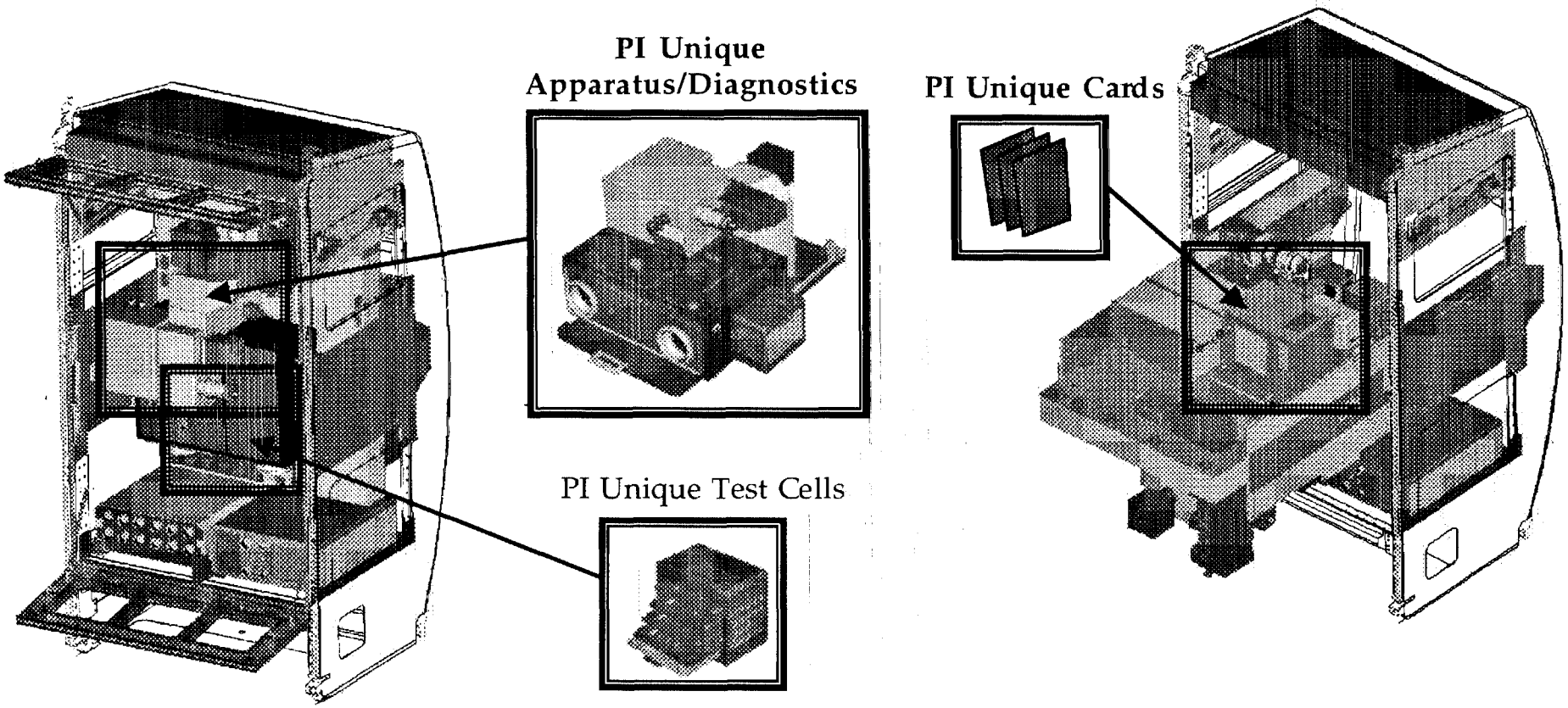

Commonly needed equipment, optimized for fluid physics experimentation, remains on-orbit and reconfigured

PI unique equipment customizes the FIR to do the required science

GRC Microgravity Science Program

Fluids and Combustion Facility

Fluids Rotating Bench Package Overview

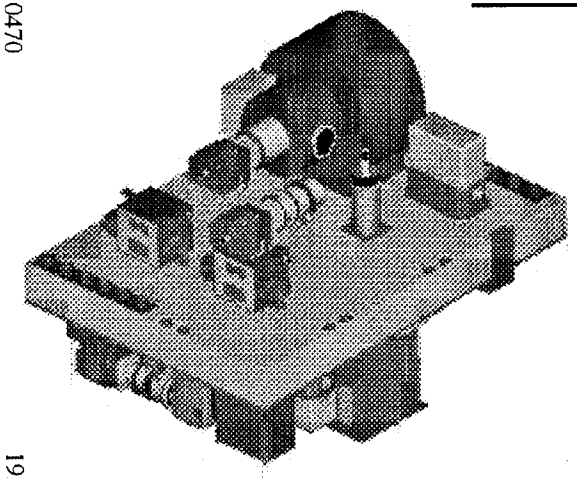

Optics Bench Front

Science

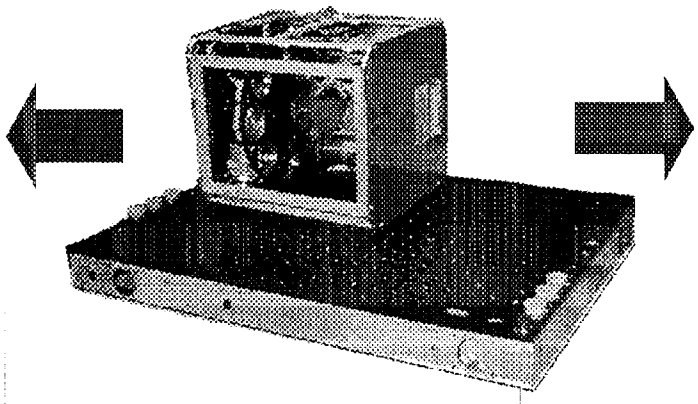

Optics Bench Concept

Fluids Integrated Rack

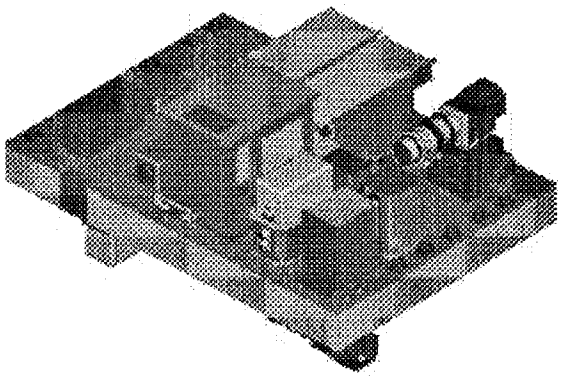

Optics Bench Rear

Science Support

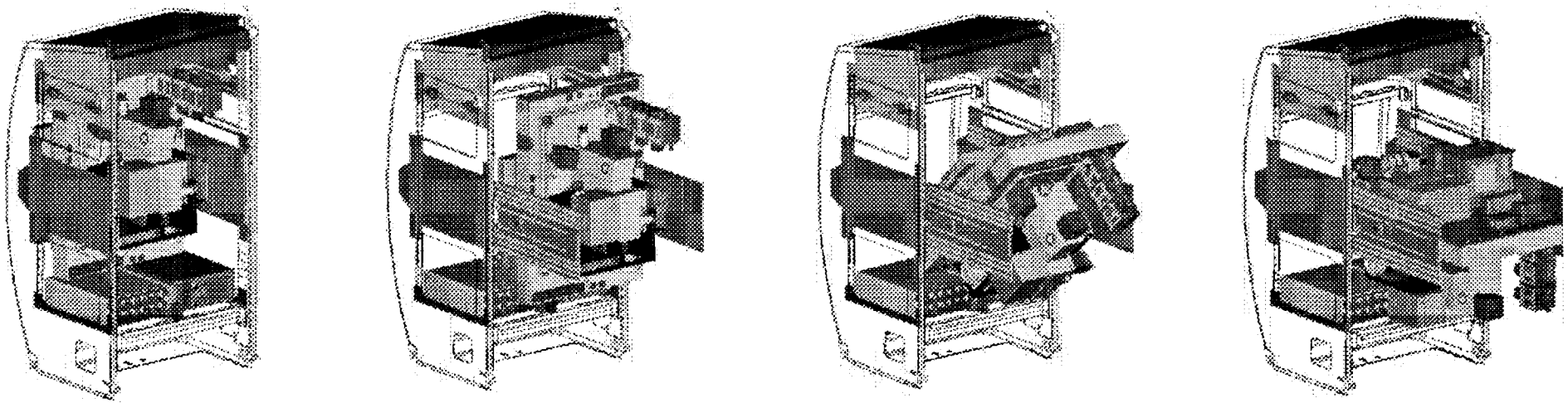

FIR Rotating Bench: Operational to Diagnostic Reconfiguration Orientations

Fluids Rotating Optics Bench Package:

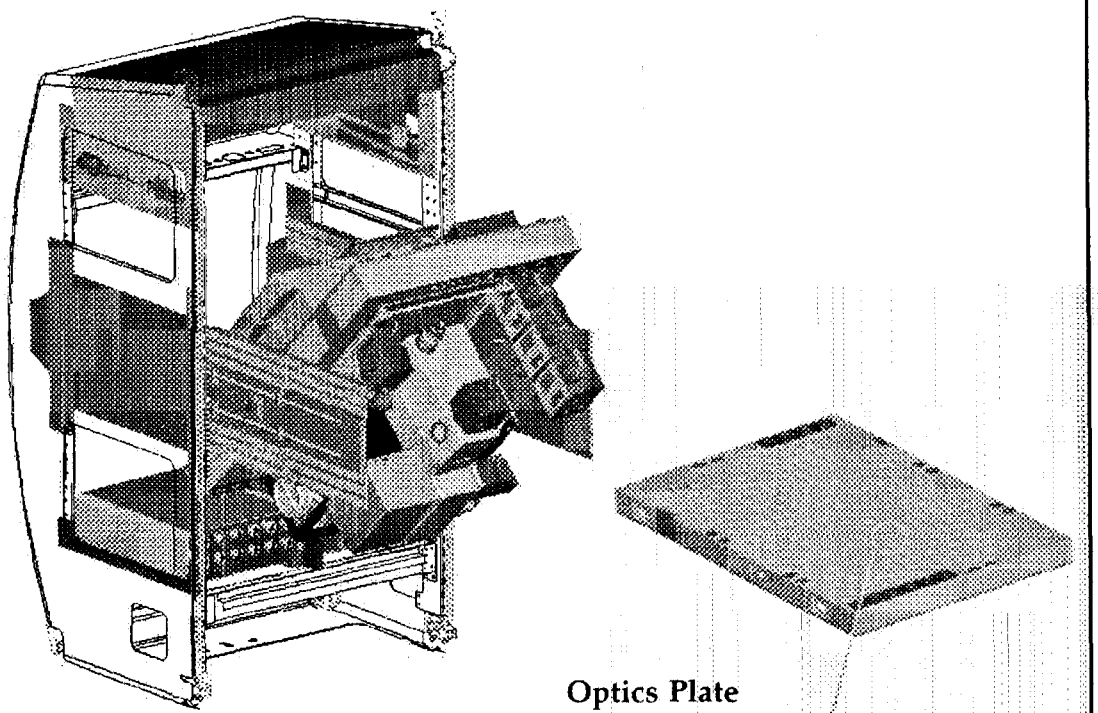

Optics Plate
Rail Design

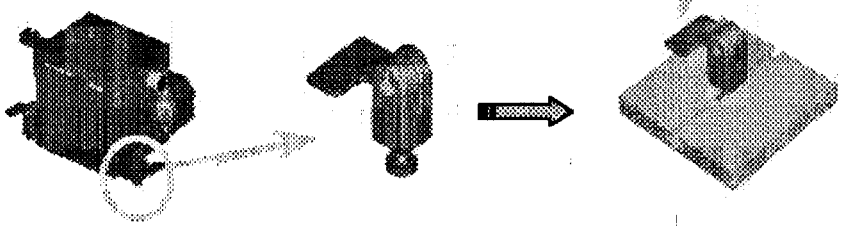

Quick connect assembly attached to baseplate of package

Quick connect assembly mounted in optics plate rails

Platform for PI hardware

- 737mm x 1016mm front bench dimensions
- 460 liters available volume for PI hardware
- Allows for infinite reconfigurability for PI hardware custom set-up

Rotating bench for ease of access to back of bench

Internal Rail Design

- High accuracy positioning, 2mm and 2 degrees point to point
- Flatness <0.5mm
- Quick connect interface for easy crew operations
- Standard Optics Hole mounting also available for PI use

FIR Laser & Illumination Packages

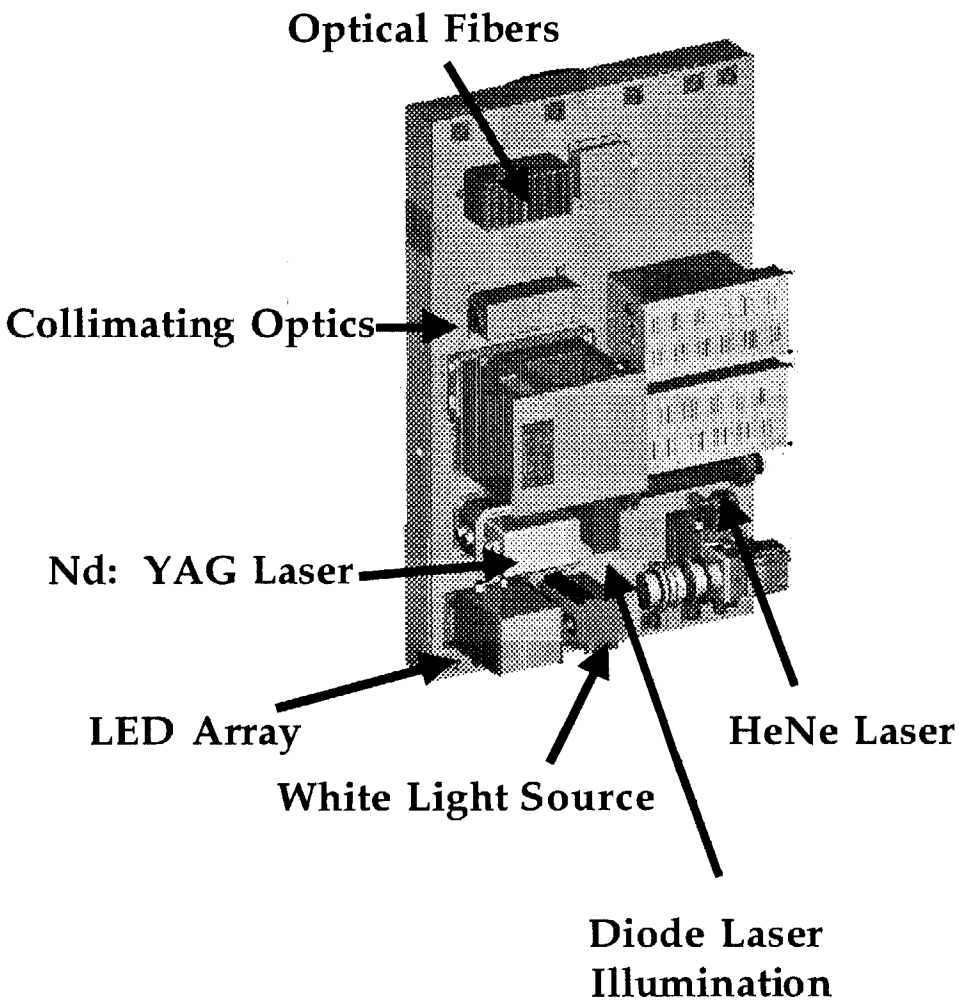

Nd: YAG Laser
- 532nm Wavelength, solid state laser
- > 50mW Power to PI hardware
- Coherence Length ~30m

HeNe Laser
- 633nm Wavelength
- single mode, 1mW Power
- Polarization ratio 500:1

Laser Diodes
- 680 nm, 10mW and 780 nm, 15mW
- Supplemental laser diode drive available for PI hardware

LED Array
- 150mm x 150mm, 640nm illumination strobing capability, variable intensity

Collimating Optics
- 2.5 mm beam, <1.5 milliradians divergence
- 50mm beam, <0.8 milliradians divergence

White Light Source
- 140mm x 140mm fiber weave panel
- Highly uniform intensity

GRC Microgravity Science Program

Fluids and Combustion Facility

FIR Cameras and Lenses

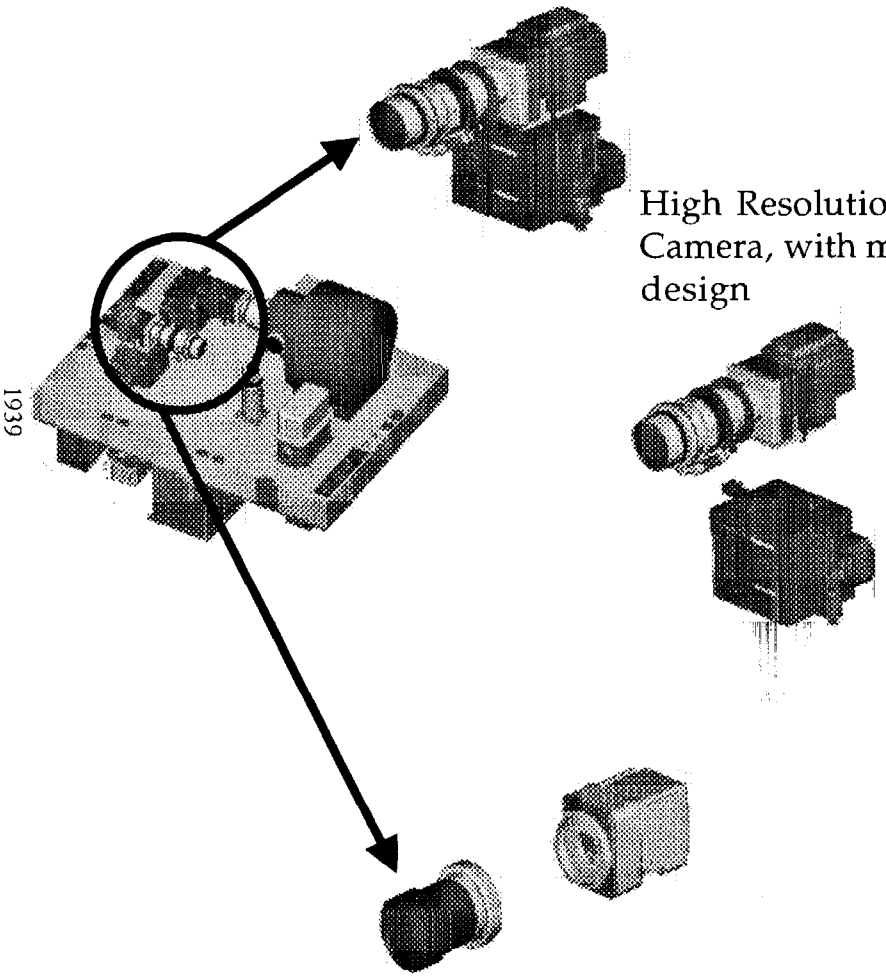

High Resolution Camera, with modular design

Color Camera Body and interchangeable lens

- High Speed Cameras
  - 1024 x 1024 12-bit pixels up to 30 fps
- High Resolution Microscopic Camera
  - 8x magnification for 1 mm x 1mm field, 3 micrometer resolution
- Color Camera
  - 484x768 pixels
  - 3 chip design for individual R,G,B readout
  - C-mount lens for interchangeability
- Ultra- High Speed Camera (Generation II)
  - 1000 fps w/ significant longer duration and higher resolution
  - Enhanced Image Processing & Storage Unit
- Macroscopic Zoom Lens
  - 19mm - 100mm Fields of View (FOV)
- Microscopic Lens
  - 200um x 200um FOV - 18mm x 18mm FOV

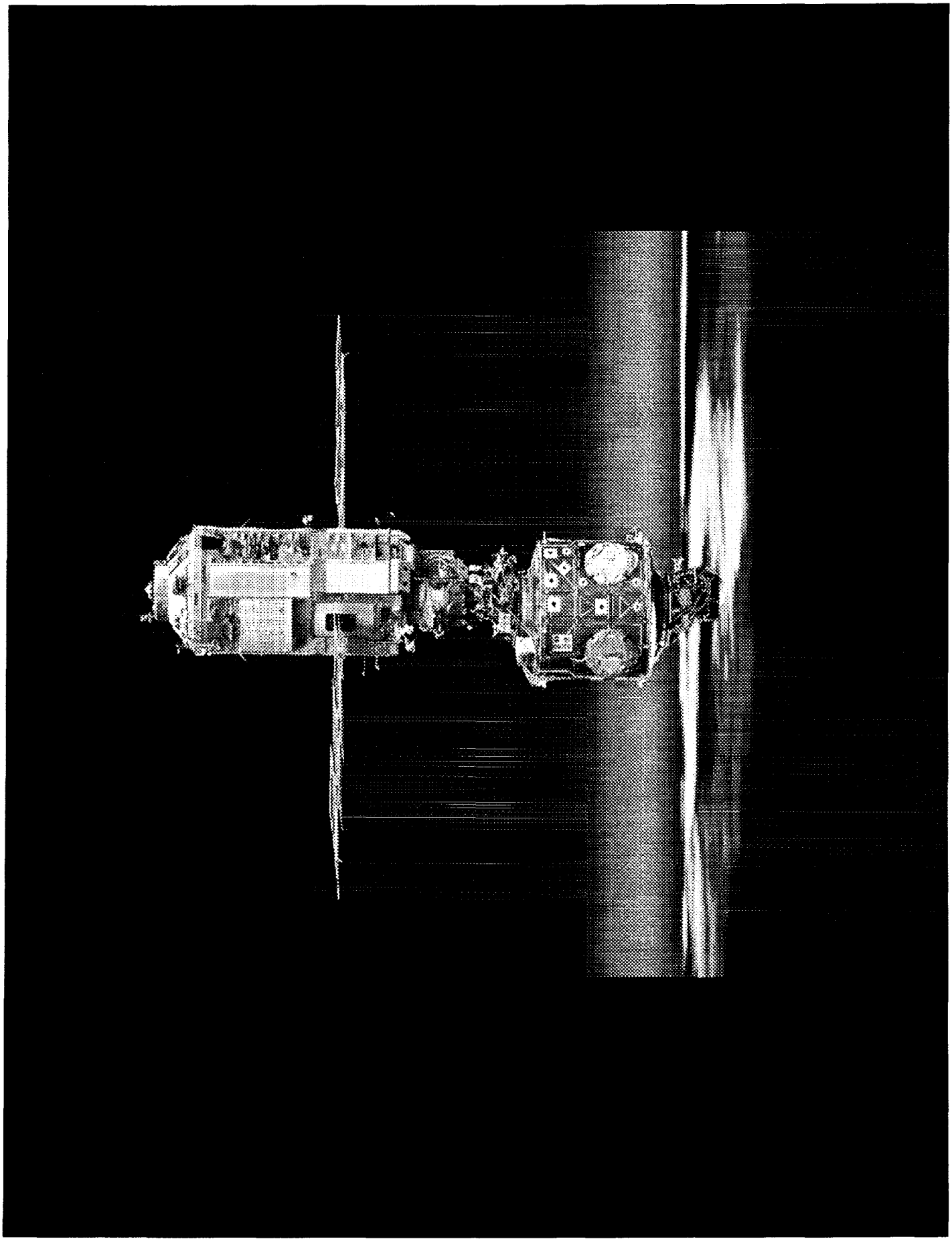

August 11, 2000
Guest Speaker

International Microgravity Plasma Facility (IMPF)

Professor John Goree
University of Iowa

INTERNATIONAL MICROGRAVITY PLASMA FACILITY (IMPF)

John A. Goree
Department of Physics and Astronomy
The University of Iowa
john-goree@uiowa.edu

ABSTRACT

The International Microgravity Plasma Facility (IMPF)[1] is a flexible platform for experiments dealing with the new scientific field of dusty plasmas. It is a facility intended for experimenters worldwide.

A dusty plasma is an ionized gas containing small particles of solid matter, which are charged and interact through a Coulomb repulsion. Dusty plasmas are analogous to colloidal suspensions, except that the interparticle medium is plasma rather than liquid, and therefore there is no buoyancy to prevent sedimentation. The particles are typically 6 μm polymer microspheres, and they acquire a charge of approximately -10^4 *e*. With a volume fraction of 10^{-5}, it is easy to image an entire 3D volume. The damping rate in a plasma is reduced by as much as $\times 10^5$, as compared to a colloid. Because of sedimentation, only experiments with 2D suspensions are practical under laboratory conditions. Microgravity enables a wide class of experiments with 3D suspensions.

The field of dusty plasmas is growing rapidly, with publications increasing at a rate of 25% per year. It is also a highly interdisciplinary field:

- In *basic science*, so-called "plasma crystals" are Coulomb lattices, analogous to colloidal crystals Suspensions can be in a solid, liquid or gas phase. Experiments have included structural as well as dynamicalstudies, such as experiments with shear waves[2] and measurements of the interparticle potential.[3]
- In *industry*, there are opportunities for synthesizing high-value-added materials by suspending particles in plasmas. On the other hand, particles in plasmas can pose a problem, which must be eliminated, in semiconductor manufacturing. Microchip manufacturers have found that dust particle contaminants grow in chemical plasmas used to etch and deposit thin films of materials on silicon substrates.
- In *astronomy*, the rings of Saturn, interstellar clouds, comet tails, and many other objects consist of dust particles immersed in plasma. The Cassini mission to Saturn is the next major opportunity for gathering data on dusty plasmasin space.

---

[1] IMPF has a home page at http://www.microgravity.net
[2] S. Nunomura, D. Samsonov, and J. Goree, Phys. Rev. Lett. 84, 5141(2000).
[3] U. Konopka, G.E. Morfill, and L. Ratke, Phys. Rev. Lett. **84**, 891 (2000).

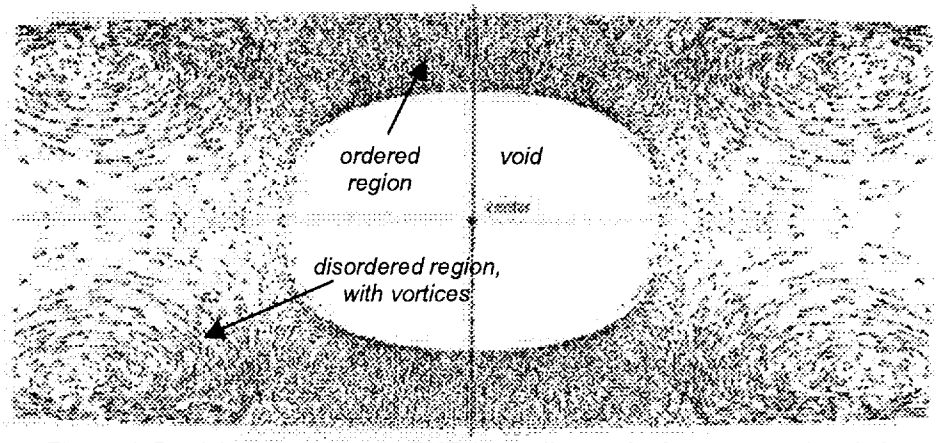

Figure 1. Particle trajectories in PKE (sounding rocket), cross-sectional view.

IMPF's predecessor is PKE (Plasma Kristall Experiment), which is a series of microgravity experiments led by Prof. G. Morfill and funded by the DLR. For its next flight, PKE will be uploaded to the ISS in December 2000 aboard a Progress rocket, and experiments will be performed by the first ISS crew. Russian partners including HEDRC will provide upload and accommodation in the Service Module. Experiments will focus on the structure and dynamics of 3D plasma crystals, and their melting. Earlier sounding rocket flight experiments were successful,[4] but did not allow sufficient time to explore parameter space, or to allow a crystal to anneal throughout the entire suspension.

The future of dusty plasma microgravity experiments lies with IMPF, which can be uploaded in 2004. We plan for IMPF to become internationalized, for use by experimenters anywhere. We propose combining resources from multiple ISS partners, including upload & download, ground-based data archiving, and on-orbit accommodation, telescience and storage. IMPF has developed a governance body consisting of an International Advisory Board with members from 8 countries worldwide.

Configurations for both basic and applied experiments are being developed. The IMPF apparatus can be accommodated in one-half of an Express Rack, with one of the four lockers serving as an interchangeable experimental drawer. This drawer will contain vacuum and optics for imaging and manipulating the particles. It will be exchanged on a six-month cycle of up/downloads. The first configuration will have a parallel-plate radio-frequency plasma, which will allow both basic and applied experiments. The second configuration will have a dc plasma. Ground-based work will develop of "pipeline" of future experiments for the facility.

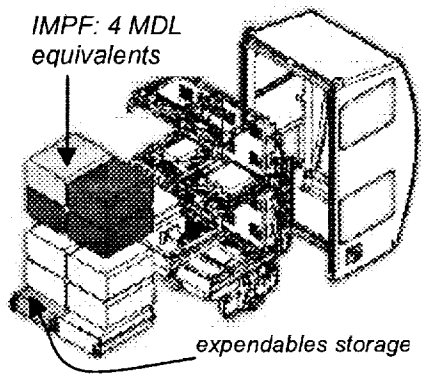

Figure 2: Locker-type accommodation in an Express Rack

[4] G.E. Morfill, H.M. Thomas, U. Konopka, H. Rothermel, M. Zuzic, A. Ivlev, and J. Goree "Condensed Plasmas under Microgravity," *Physical Review Letters* 83, pp. 1598-1601 1999.

NASA/CP—2000-210470

International Microgravity Plasma Facility

IMPF

John Goree *The University of Iowa*

IMPF *International Microgravity Plasma Facility*

IOWA

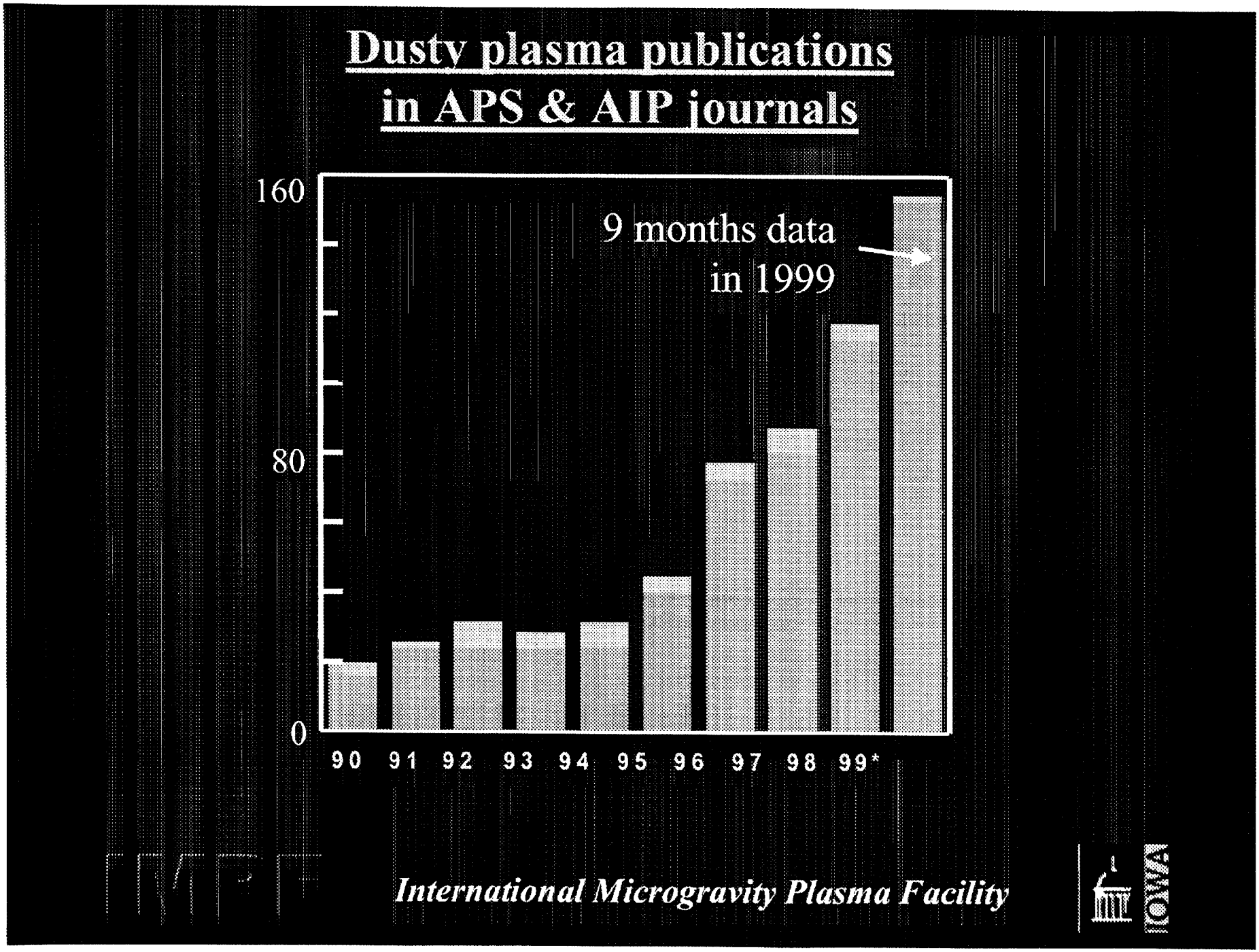
Dusty plasma publications
in APS & AIP journals
160
80
0
9 months data
in 1999
90 91 92 93 94 95 96 97 98 99*
International Microgravity Plasma Facility
IOWA

What is a dusty plasma?

- Electrons + ions + neutral gas atoms + small particles of solid matter
- About the particles:
  - typically:
    - 5 nm - 50 microns
    - dielectric material
  - charged by collecting electrons & ions

International Microgravity Plasma Facility

Who cares about dusty plasmas?

Astronomy
- Rings of Saturn
- Interstellar space
- Comet tails

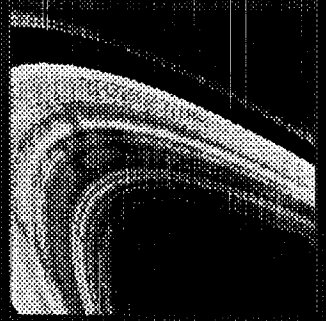

Manufacturing
- Particle contamination (Si wafer processing)
- Nanomaterial synthesis

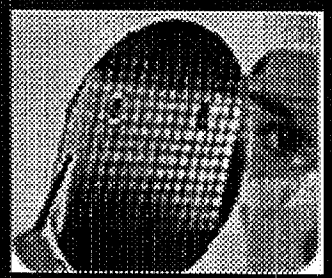

Basic physics
- Coulomb crystals
- Waves
- Much more ...

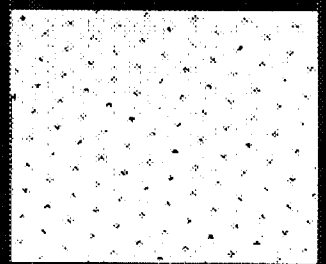

International Microgravity Plasma Facility

IOWA

Forces Acting on a Particle

Coulomb
- trapping potential
- inter-particle

$\propto r^1$

Gravity

$\propto r^3$

- Gas drag
- Ion drag
- Thermophoresis

$\propto r^2$

International Microgravity Plasma Facility

IOWA

Need for microgravity

- Gravity ⇒sedimentation
- No buoyancy to offset sedimentation

International Microgravity Plasma Facility

Particles

- polymer microspheres
- ≈ 6 μm diameter

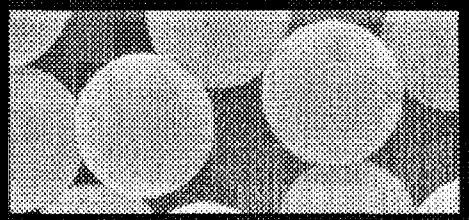

- separation $a \approx$ 0.3 mm
- volume fraction 10^{-6}
- damping rate ≈ 1 sec
- $Q \approx -8000\ e$

International Microgravity Plasma Facility

IOWA

Typical chamber for 3-D experiments

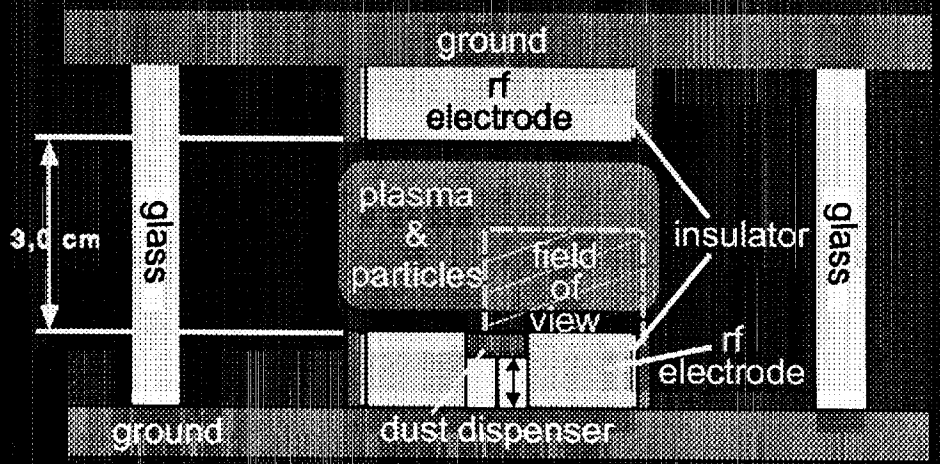

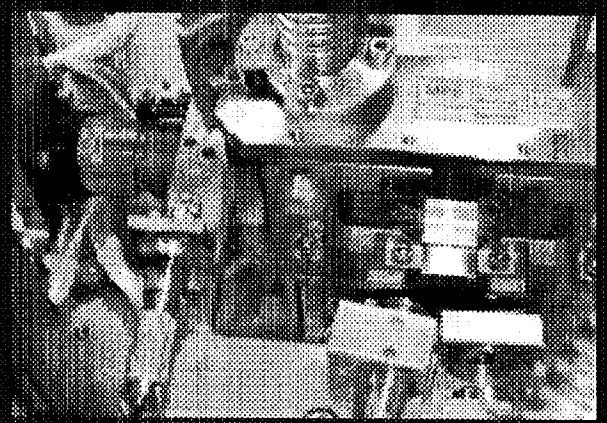

Laser sheets for illuminating particles

Cameras for imaging particles

International Microgravity Plasma Facility

IOWA

Electrostatic trapping of particles

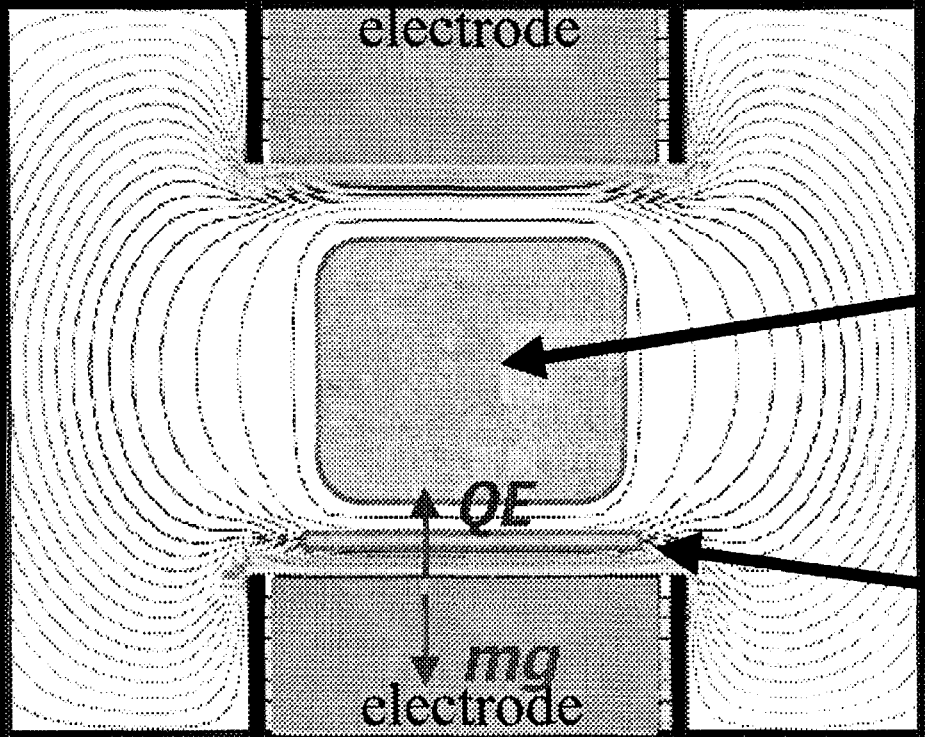

Equipotential contours

Without gravity, particles fill 3-D volume

With gravity, particles sediment to high-field region ⇒2-D layer

International Microgravity Plasma Facility

IOWA

Laboratory results:

- Coulomb cluster
- monolayer
- only 948 particles here

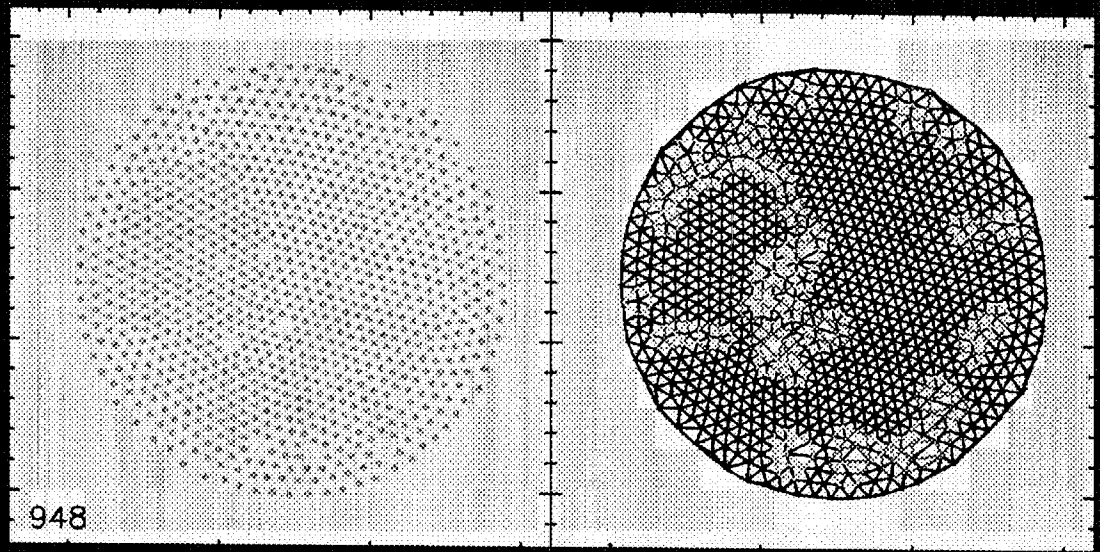

particles *triangulation*

view from top camera

International Microgravity Plasma Facility

IOWA

History of IMPF

1999

- Proposal to ESA by PI Greg Morfill
  result: one of six rated excellent
- International Advisory Board
  formed
- DLR funds feasibility study

2000

- Study done, Phase B started

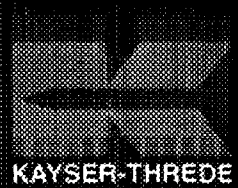

International Microgravity Plasma Facility

Other microgravity experiments

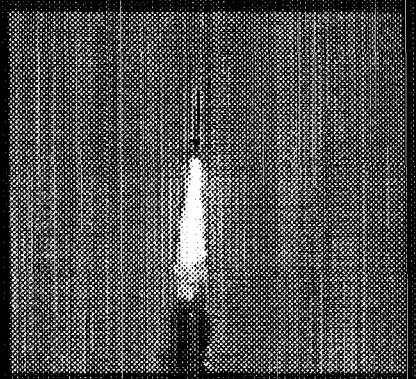

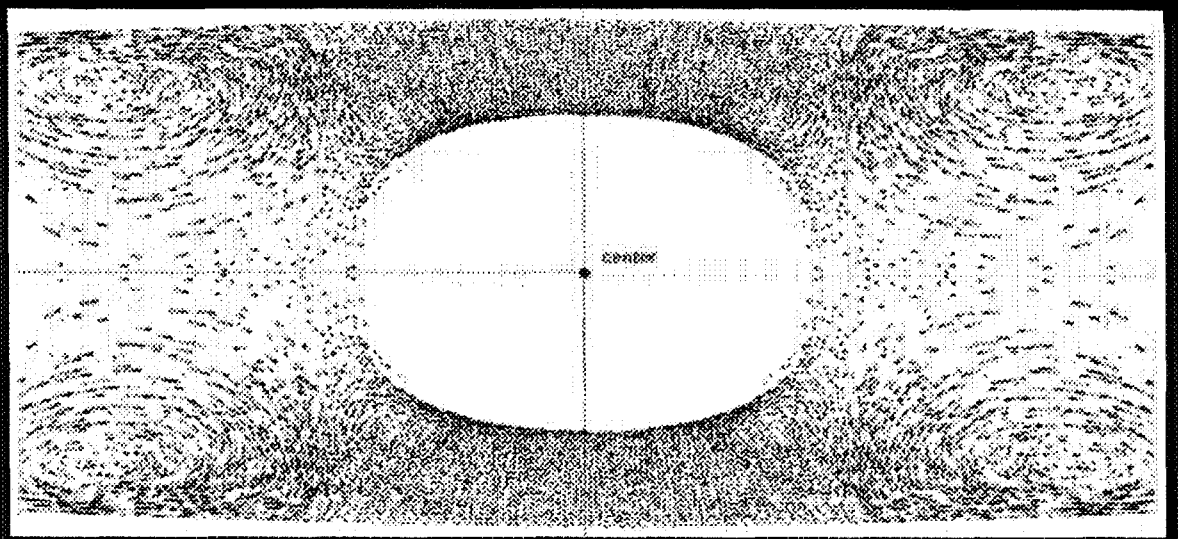

1996-1998 Sounding rockets

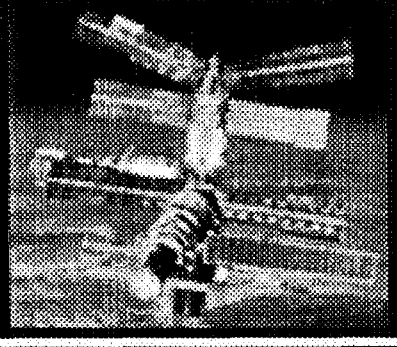

2000 - NRL

International Microgravity Plasma Facility

IOWA

Other microgravity experiments

PKE - Plasma Kristall Experiment *Germany, Russia, U.S.*

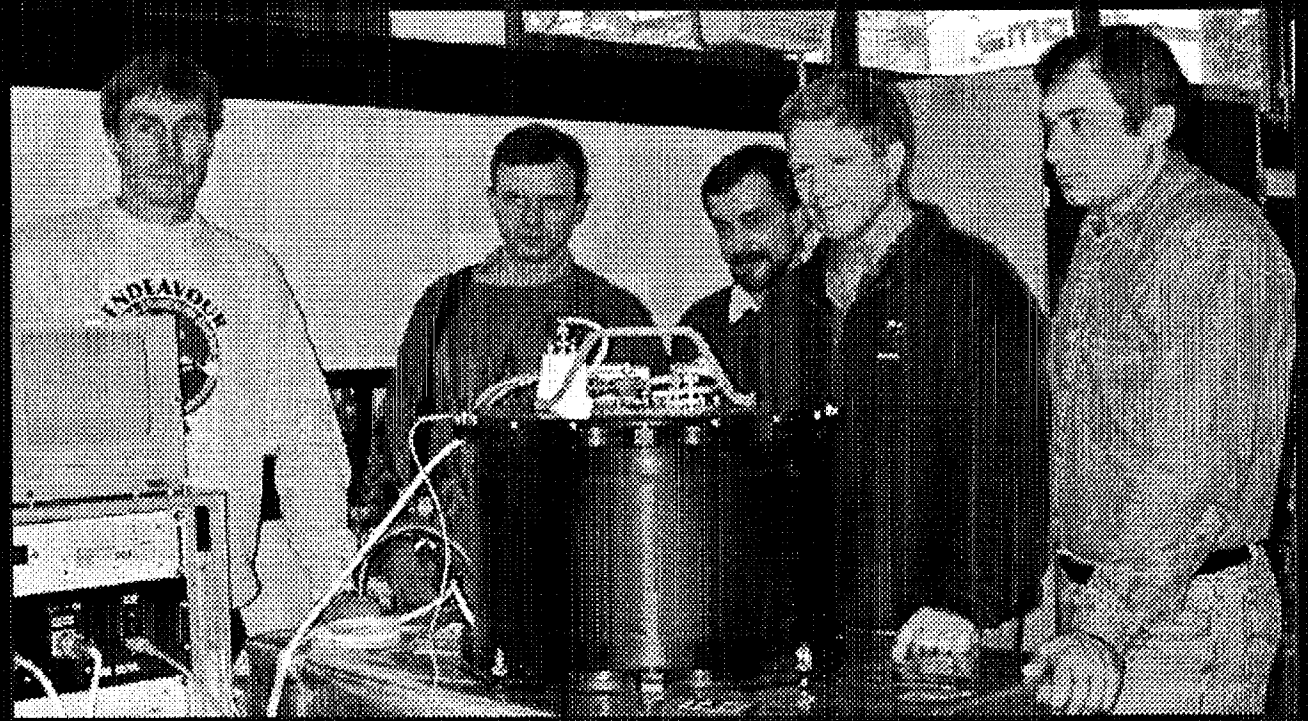

PKE flight hardware with 1st & 3rd ISS crews

International Microgravity Plasma Facility

IOWA

Internationalizing the Project

Why:

- Project exceeds DLR's resources
- Scientific users around the world

Precedents:

- Space Astronomy
- Space Exploration

Requires:

- Bilateral agreements between agencies
- Governance by international scientific body

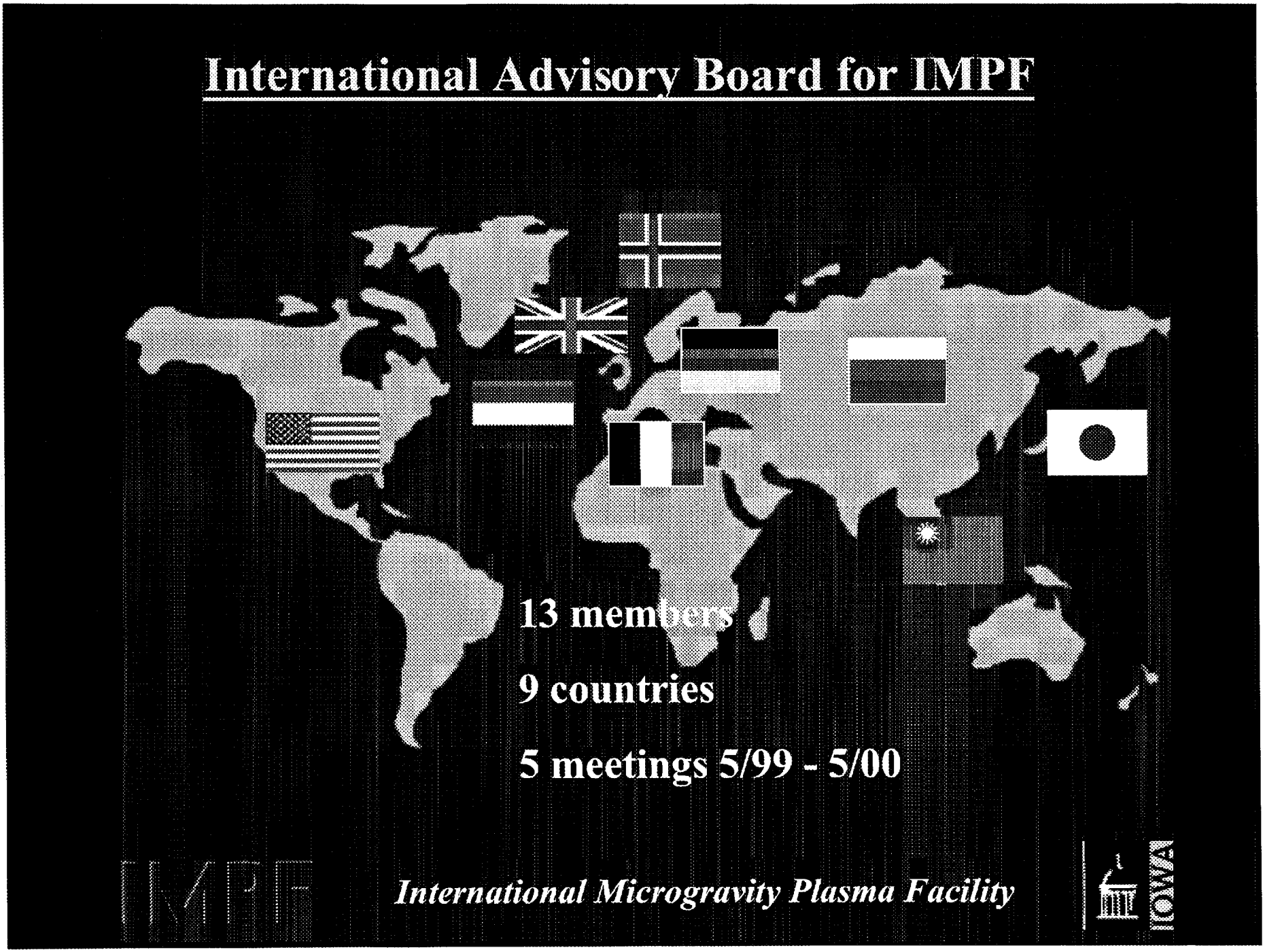
International Advisory Board for IMPF
13 members
9 countries
5 meetings 5/99 - 5/00
IMPF
International Microgravity Plasma Facility
IOWA

Timeline as of April 2000

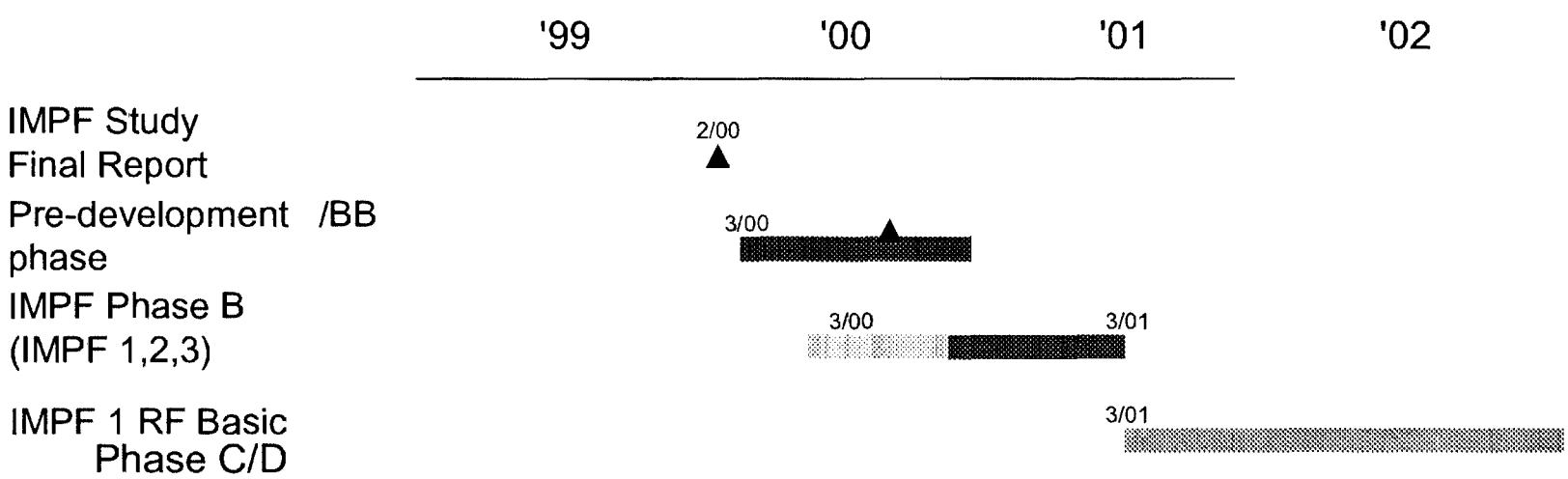

International Microgravity Plasma Facility

IOWA

Modular Construction

- 200 liter volume
- Housed in 4 Mid-Deck Lockers

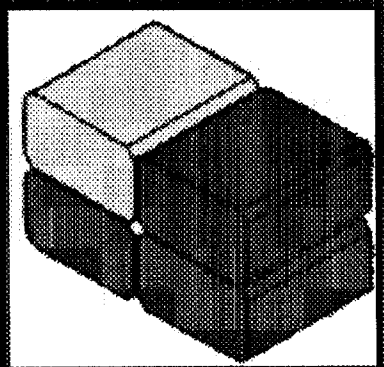

1 Locker = 1 Module

- Gas/Vacuum
- Power Distribution
- Data Processing
- Experimental insert

Exchanged on a 6-month cycle

IMPF

International Microgravity Plasma Facility

IOWA

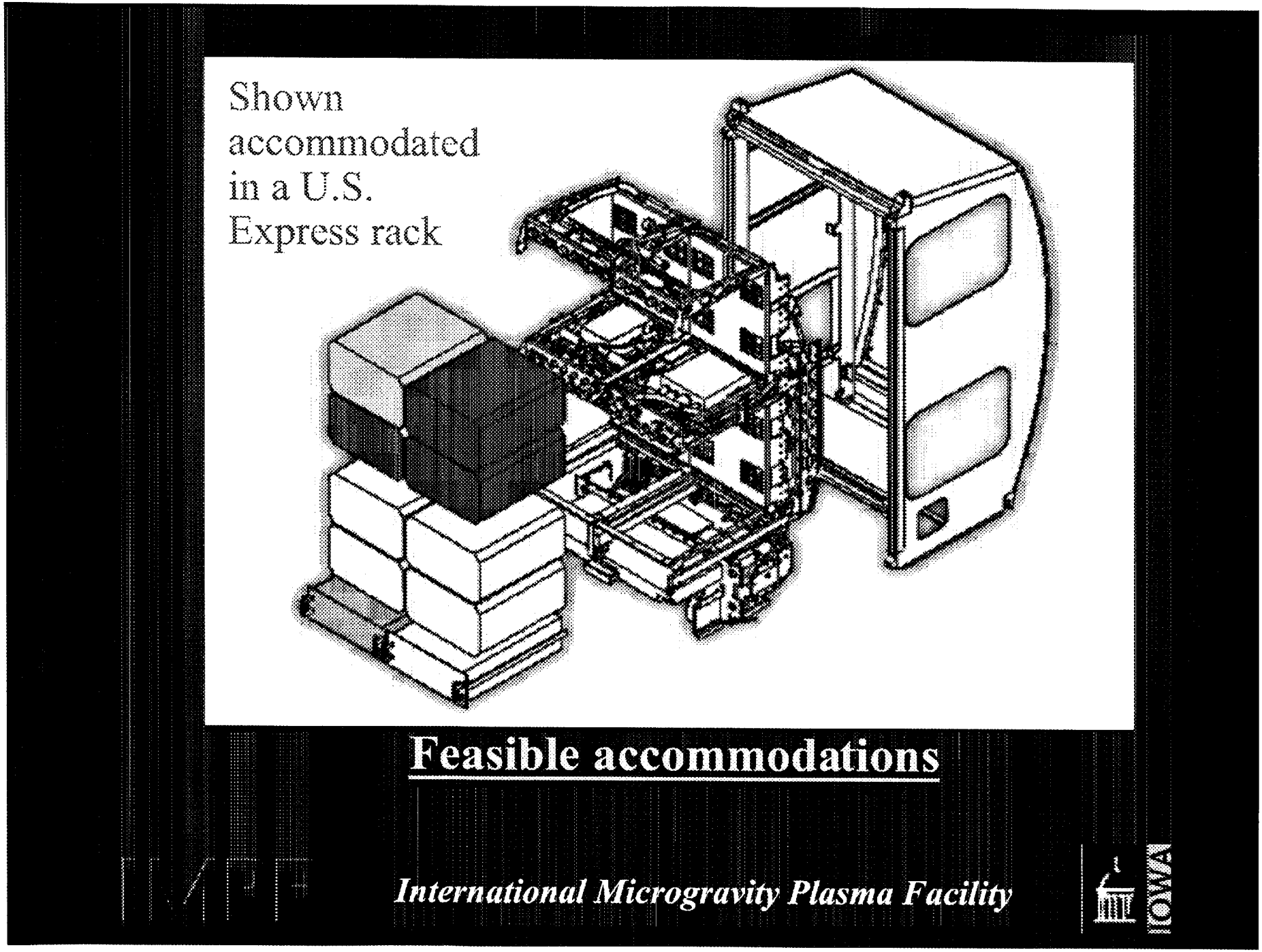
Shown
accommodated
in a U.S.
Express rack
Feasible accommodations
International Microgravity Plasma Facility
IOWA

NASA/CP—2000-210470

First Scientific Insert: RF Plasma

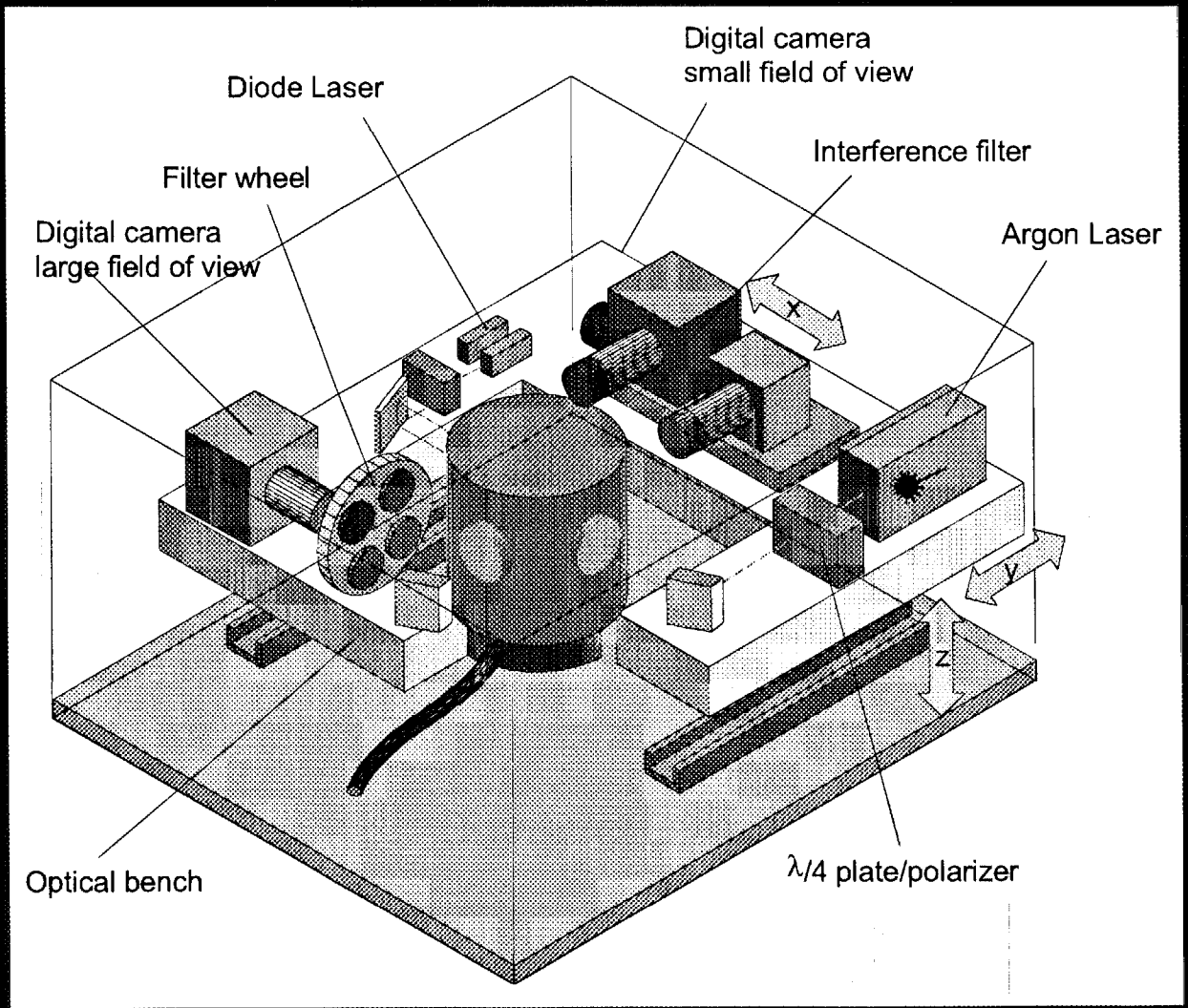

International Microgravity Plasma Facility

IOWA

Manipulating Particles

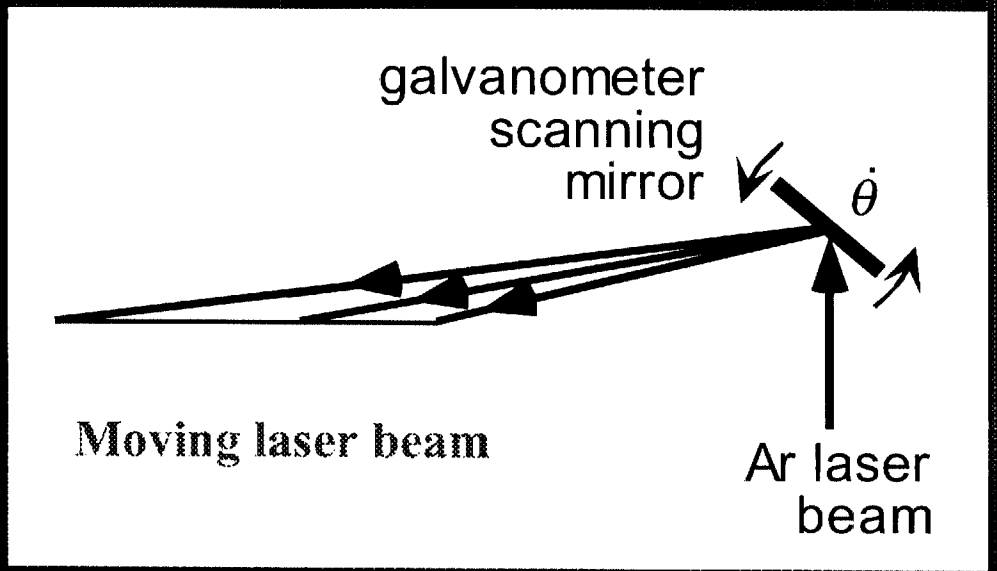

International Microgravity Plasma Facility

Scope of IMPF Science Projects

Applications:

- Particle coating
- Nanoscale mfg.
- Particle growth

International Microgravity Plasma Facility

International AO

- Expected Fall 2000
- A vehicle for proposing to use facilities, including IMPF

Filling the pipeline for 10 years of experiments

Theory

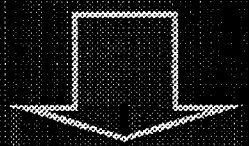

Ground-based
experiments

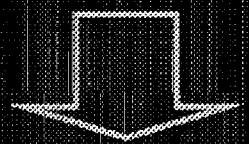

Flight:

IMPF experimental
inserts #3, #4, ...

International Microgravity Plasma Facility

IOWA

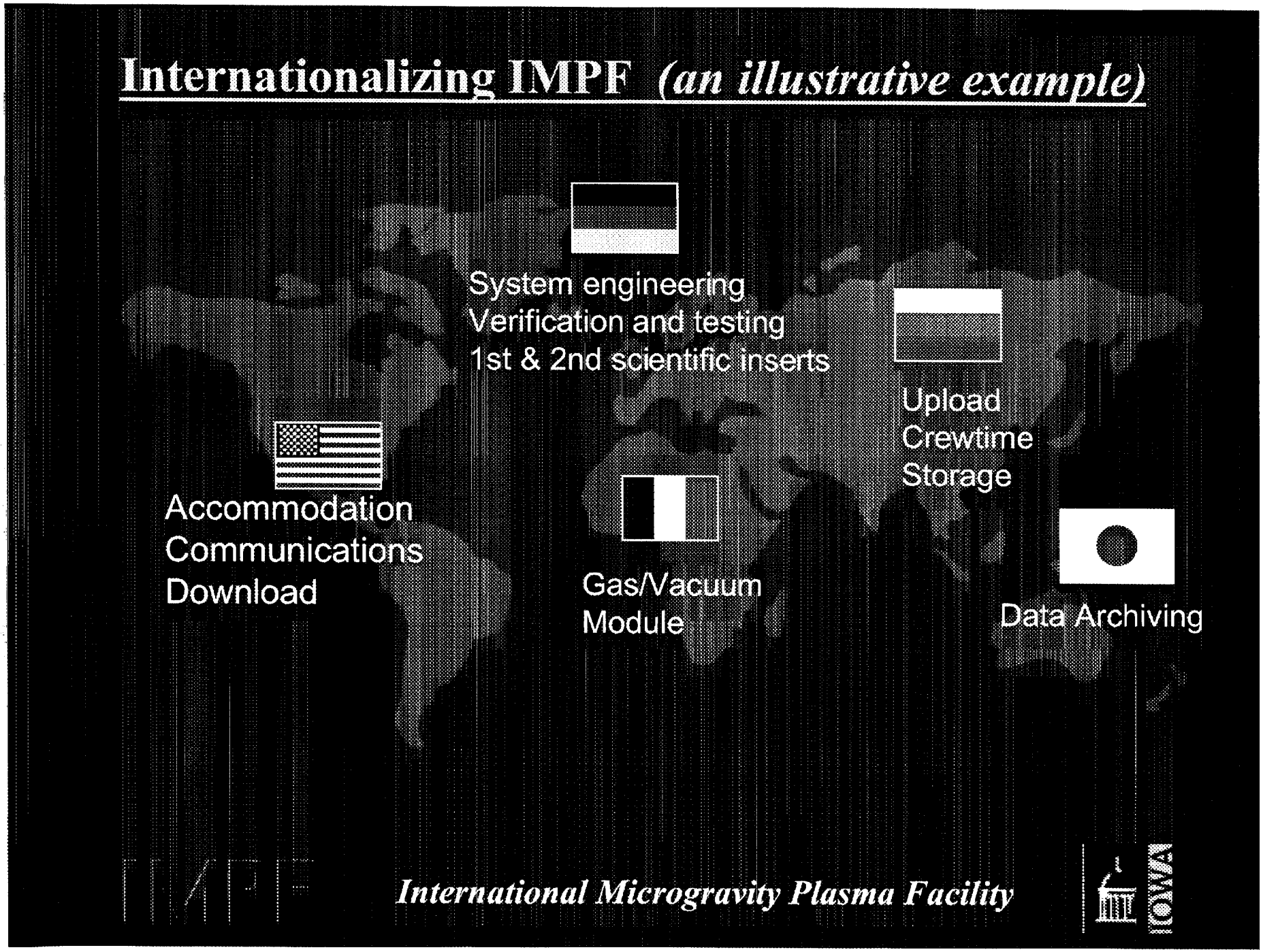
Internationalizing IMPF (an illustrative example)
System engineering
Verification and testing
1st & 2nd scientific inserts
Upload
Crewtime
Storage
Accommodation
Communications
Download
Gas/Vacuum
Module
Data Archiving
International Microgravity Plasma Facility
IOWA

NASA/CP—2000-210470

1968

IMPF

www.microgravity.net

International Microgravity Plasma Facility

IOWA

Extra slides

International Microgravity Plasma Facility

IOWA

module configuration

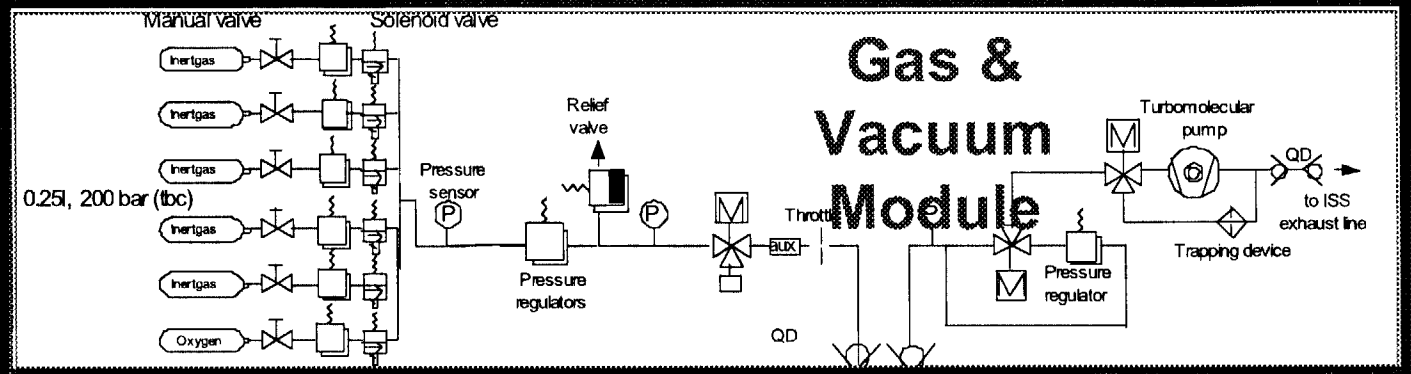

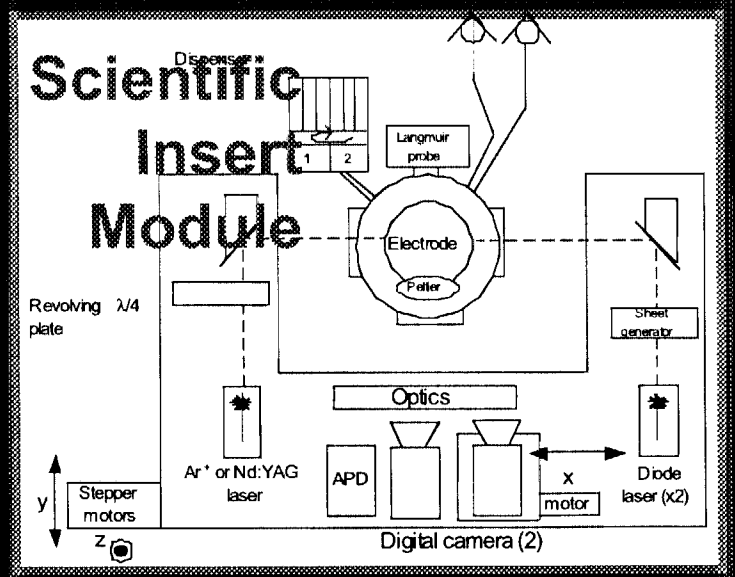

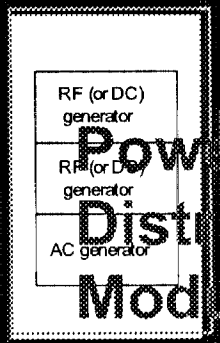

International Microgravity Plasma Facility

IOWA

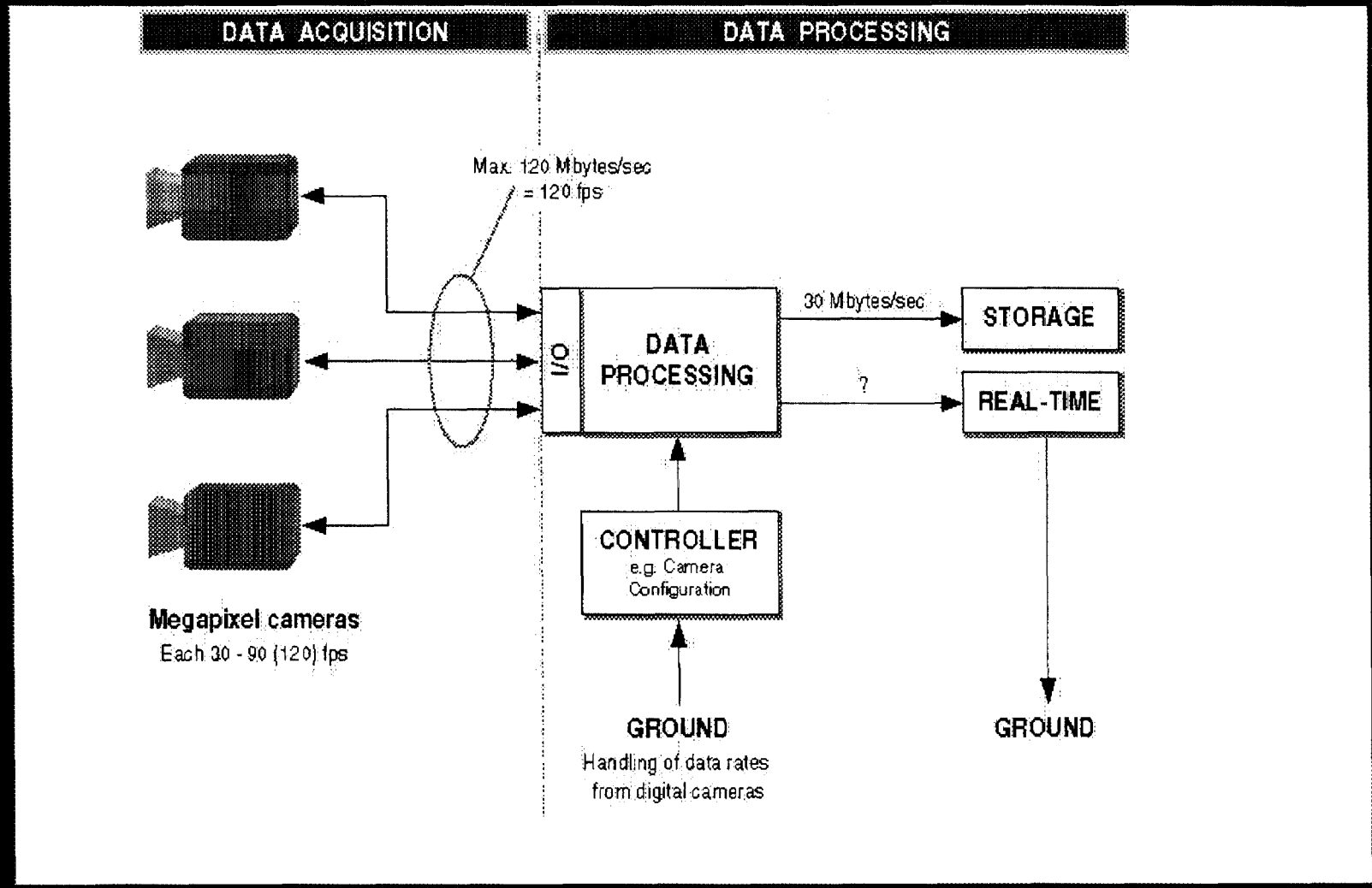
DATA ACQUISITION
DATA PROCESSING
Max. 120 Mbytes/sec
= 120 fps
I/O
DATA PROCESSING
30 Mbytes/sec
STORAGE
?
REAL-TIME
CONTROLLER
e.g. Camera Configuration
Megapixel cameras
Each 30 - 90 (120) fps
GROUND
Handling of data rates from digital cameras
GROUND

Space Commercial Opportunities for Fluid Physics and Transport Phenomena Applications

R. Gavert

NASA Headquarters
Space Utilization and Product Development Division

ABSTRACT

Microgravity research at NASA has been an undertaking that has included both science and commercial approaches since the late 80s and early 90s. The Fluid Physics and Transport Phenomena community has been developed, through NASA's science grants, into a valuable base of expertise in microgravity science. This was achieved through both ground and flight scientific research. Commercial microgravity research has been primarily promoted thorough NASA sponsored Centers for Space Commercialization which develop cost sharing partnerships with industry. As an example, the Center for Advanced Microgravity Materials Processing (CAMMP) at Northeastern University has been working with cost sharing industry partners in developing Zeolites and zeo-type materials as an efficient storage medium for hydrogen fuel. Greater commercial interest is emerging. The U.S. Congress has passed the Commercial Space Act of 1998 to encourage the development of a commercial space industry in the United States. The Act has provisions for the commercialization of the International Space Station (ISS). Increased efforts have been made by NASA to enable industrial ventures on-board the ISS. A Web site has been established at http://commercial.nasa.gov which includes two important special announcements. One is an open request for entrepreneurial offers related to the commercial development and use of the ISS. The second is a price structure and schedule for U.S. resources and accommodations. The purpose of the presentation is to make the Fluid Physics and Transport Phenomena community, which understands the importance of microgravity experimentation, aware of important aspects of ISS commercial development. It is a desire that this awareness will be translated into a recognition of Fluid Physics and Transport Phenomena application opportunities coordinated through the broad contacts of this community with industry.

Author Index

REPORT DOCUMENTATION PAGE

Form Approved
OMB No. 0704-0188

Public reporting burden for this collection of information is estimated to average 1 hour per response, including the time for reviewing instructions, searching existing data sources, gathering and maintaining the data needed, and completing and reviewing the collection of information. Send comments regarding this burden estimate or any other aspect of this collection of information, including suggestions for reducing this burden, to Washington Headquarters Services, Directorate for Information Operations and Reports, 1215 Jefferson Davis Highway, Suite 1204, Arlington, VA 22202-4302, and to the Office of Management and Budget, Paperwork Reduction Project (0704-0188), Washington, DC 20503.

1. AGENCY USE ONLY (*Leave blank*)	2. REPORT DATE	3. REPORT TYPE AND DATES COVERED
	December 2000	Conference Publication

4. TITLE AND SUBTITLE

Proceedings of the Fifth Microgravity Fluid Physics and Transport Phenomena Conference

5. FUNDING NUMBERS

WU–101–43–0B–00

6. AUTHOR(S)

Bhim S. Singh, Editor

7. PERFORMING ORGANIZATION NAME(S) AND ADDRESS(ES)

National Aeronautics and Space Administration
John H. Glenn Research Center at Lewis Field
Cleveland, Ohio 44135–3191

8. PERFORMING ORGANIZATION REPORT NUMBER

E–12466

9. SPONSORING/MONITORING AGENCY NAME(S) AND ADDRESS(ES)

National Aeronautics and Space Administration
Washington, DC 20546–0001

10. SPONSORING/MONITORING AGENCY REPORT NUMBER

NASA CP—2000-210470

11. SUPPLEMENTARY NOTES

Proceedings of a conference sponsored by the NASA Glenn Research Center and held at the Sheraton City Centre, Cleveland, Ohio, August 9–11, 2000. Responsible person, Bhim S. Singh, organization code 6712, 216–433–5396.

12a. DISTRIBUTION/AVAILABILITY STATEMENT

Unclassified - Unlimited
Subject Category: 34 Distribution: Nonstandard

Available electronically at http://gltrs.grc.nasa.gov/GLTRS
This publication is available from the NASA Center for AeroSpace Information, 301–621–0390.

12b. DISTRIBUTION CODE

13. ABSTRACT ***(Maximum 200 words)***

The Fifth Microgravity Fluid Physics and Transport Phenomena Conference provided the scientific community the opportunity to view the current scope of the Microgravity Fluid Physics and Transport Phenomena Program and research opportunities and plans for the near future. Consistent with the conference theme "Microgravity Research an Agency-Wide Asset" the conference focused not only on fundamental research but also on applications of this knowledge towards enabling future space exploration missions. The conference included 14 invited plenary talks, 61 technical paper presentations, 61 poster presentations, exhibits and a forum on emerging research themes focusing on nanotechnology and biofluid mechanics. This web-based proceeding includes the presentation and poster charts provided by the presenters of technical papers and posters that were scanned at the conference site. Abstracts of all the papers and posters are included and linked to the presentations charts. The invited and plenary speakers were not required to provide their charts and are generally not available for scanning and hence not posted. The conference program is also included.

14. SUBJECT TERMS	15. NUMBER OF PAGES
Microgravity; Reduced gravity; Fluid physics; Heat transfer; Multiphase flow; Colloids; Granular media flows; Phase change	2001
	16. PRICE CODE A99

17. SECURITY CLASSIFICATION OF REPORT	18. SECURITY CLASSIFICATION OF THIS PAGE	19. SECURITY CLASSIFICATION OF ABSTRACT	20. LIMITATION OF ABSTRACT
Unclassified	Unclassified	Unclassified	